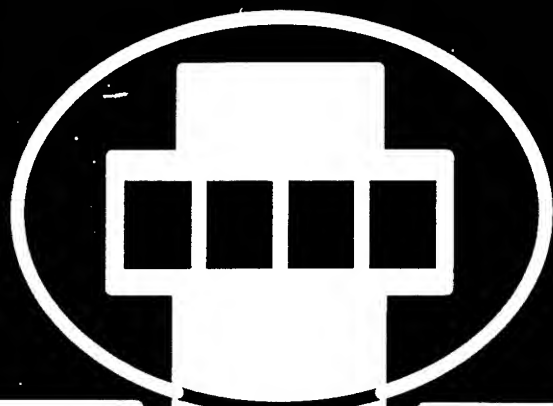
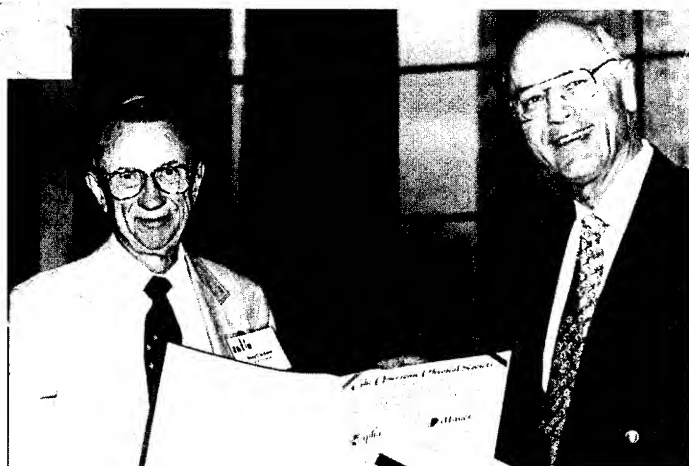


**Proceedings of the 1995
Particle Accelerator Conference
and International Conference
on High-Energy Accelerators**



PROCEEDINGS OF THE 1995
PARTICLE ACCELERATOR CONFERENCE
AND INTERNATIONAL CONFERENCE
ON HIGH-ENERGY ACCELERATORS





The
American
Physical
Society

Proceedings of the 1995 Particle Accelerator Conference

N00014-95-1-0791

Volume 2 of 5

Papers from the sixteenth biennial Particle Accelerator Conference, an international forum on accelerator science and technology held May 1-5, 1995, in Dallas, Texas, organized by Los Alamos National Laboratory (LANL) and Stanford Linear Accelerator Center (SLAC), jointly sponsored by the Institute of Electrical and Electronics Engineers (IEEE) Nuclear and Plasma Sciences Society (NPSS), the American Physical Society (APS) Division of Particles and Beams (DPB), and the International Union of Pure and Applied Physics (IUPAP), and conducted with support from the US Department of Energy, the National Science Foundation, and the Office of Naval Research.

19960705 126

PROCEEDINGS OF THE 1995 PARTICLE ACCELERATOR CONFERENCE

Abstracting is permitted with credit to the source. Libraries are permitted to photocopy beyond the limits of U. S. copyright law for private use of patrons those articles in this volume that carry a code at the bottom of the first page, provided the per-copy fee indicated in the code is paid through the Copyright Clearance Center, 222 Rosewood Drive, Danvers, MA 01923. Instructors are permitted to photocopy isolated articles for noncommercial classroom use without fee. For other copying, reprint, or republication permission, write to the IEEE Copyright Manager, IEEE Operations Center, 445 Hoes Lane, Piscataway, NJ 08855-1331. All rights reserved. Copyright © 1996 by the Institute of Electrical and Electronic Engineers, Inc.

IEEE Catalog Number: 95CH35843 (softbound)
95CB35843 (casebound)

Library of Congress Number: 88-647453

ISBN Softbound: 0-7803-2934-1
ISBN Casebound: 0-7803-2935-X
ISBN Microfiche: 0-7803-2936-8
ISBN CD-ROM: 0-7803-2937-6

Additional copies of this publication are available from

IEEE Operations Center
445 Hoes Lane
P. O. Box 1331
Piscataway, NJ 08855-1331 USA

Phone: 1-800-678-IEEE (1-800-678-4333)
1-908-981-1393
FAX: 1-908-981-9667
Telex: 833-233
e-mail: customer.service@ieee.org

The CD-ROM version is available from

Dan Rusthoy, PAC95 Treasurer
Los Alamos National Laboratory
P. O. Box 1663 - M/S H811
Los Alamos, NM 87545 USA

Phone: 505-667-2796
FAX: 505-667-0919
e-mail: drusthoy@lanl.gov

Volume 1

Plenary and Special Sessions

CEBAF Commissioning and Future Plans (Invited) — Hermann A. Grunder.....	1	MAD01
The Advanced Photon Source (Invited) — John N. Galayda.....	4	MAD02
Commissioning and Performance of the HIMAC Medical Accelerator (Invited) — S. Yamada.....	9	MAD03
Accelerator Field Development at Novosibirsk (History, Status, Prospects) (Invited) — A. Skrinsky.....	14	MAD04
A Personal Perspective of High Energy Accelerators (Invited) — Gustav-Adolf Voss.....	27	FPD01
Photon-Photon Colliders (Invited) — Andrew M. Sessler.....	30	FPD02
Transmutation and Energy Production with High Power Accelerators (Invited) — G.P. Lawrence.....	35	FPD03
The Large Hadron Collider (Invited) — L.R. Evans.....	40	FPD04
Frontiers of Particle Physics (Invited) — L. Okun.....	45	FPD05
R. R. Wilson Prize Lecture: Pretzels (Invited) — R. Littauer.....	manuscript not submitted	MXG01
Experimental Studies of Longitudinal Dynamics of Space-Charge Dominated Electron Beams (Invited) — D.X. Wang.....	48	MXG02
High-Energy High-Luminosity $\mu^+ \mu^-$ Collider Design (Invited) — Robert B. Palmer, Richard Fernow, Juan C. Gallardo, Y.Y. Lee, Yagmur Torun, David Neuffer, David Winn.....	53	MXG03
Cosmic Acceleration Mechanisms (Invited) — J. Arons.....	manuscript not submitted	MXG04

Accelerator Applications

Hadron Particle Therapy (Invited) — Jose R. Alonso.....	58	WPE01
Micromechanics via Synchrotron Radiation (Invited) — H. Guckel.....	63	WPE02
Radionuclide Production for the Biosciences (Invited) — Thomas J. Ruth.....	67	WPE03
X-Ray Lithography - Status and Projected Use (Invited) — W.A. Johnson.....	manuscript not submitted	WPE04
Microelectronic Applications for RF Sources and Accelerators (Invited) — Cha-Mei Tang.....	70	WPE05
A High-Gradient Electron Injector to an X-Ray Lithography Ring (Invited) — D. Yu.....	manuscript not submitted	FAG01
X-Ray Holography (Invited) — I. McNulty.....	manuscript not submitted	FAG02
Medical and Surgical Applications of FELs (Invited) — Benedikt Jean.....	75	FAG03
Medical Uses of Monochromatic X-Rays (Invited) — Frank E. Carroll.....	80	FAG04
Texas Regional Medical Technology Center — R. Sah, T.D. Cain, E.K. Cleveland, K. Saadatmand, M.E. Schulze, R.A. Winje.....	83	FAG05
A Proposed 100-400 MeV Beam Facility at Fermilab — C. Johnstone, C. Ankenbrandt, S. Bjerklie, D. Boehnlein, M. Foley, T. Kroc, J. Lackey, A. Lennox, A. Leveling, E. McCrory, M. Popovic, C. Schmidt, K. Vaziri.....	86	FAG06
Cyclotrons for Isotope Production — B.F. Milton, N.R. Stevenson.....	89	FAG07
European Heavy Ion ICF Driver Development — G. Plass.....	92	FAG08
A 3-Stage Cyclotron Complex for Driving the Energy Amplifier — P. Mandrillon, N. Fietier, C. Rubbia.....	95	FAG09
Accelerator-Based Gamma Neutron Transmutation of Radionuclides as a New Technology for the Nuclear Fuel Cycle — I.P. Ereemeev.....	98	FAG10
A High-Average-Power FEL for Industrial Applications — H.F. Dylla, S. Benson, J. Bisognano, C.L. Bohn, L. Cardman, D. Engwall, J. Fugitt, K. Jordan, D. Kehne, Z. Li, H. Liu, L. Merminga, G.R. Neil, D. Neuffer, M. Shinn, C. Sinclair, M. Wiseman, L.J. Brillson, D.P. Henkel, H. Helvajian, M.J. Kelley.....	102	FAG11
X-Ray Radiation by Relativistic Electrons in Condensed Media on Base of MSU Race-Track Microtron — V.K. Grishin, A.S. Chepurnov, K.A. Gudkov, B.S. Ishkhanov, S.A. Kosterin, E.V. Lasutin, S.V. Blazhevich, N.N. Nasonov.....	105	FAG12
Applications of MeV Proton and Deuteron Linear Accelerators — George H. Gillespie, Gerald E. McMichael.....	107	FAG13
Accelerator Requirements for Fast-Neutron Interrogation of Luggage and Cargo — B.J. Micklich, C.L. Fink, T.J. Yule.....	110	FAG14

Energy Varying Resonant Beam Extraction from the Synchrotron — K. Hiramoto, <i>M. Tadokoro, J.I. Hirota, M. Nishi, K. Noda.....</i>	113	TAB03
Radiotherapy Process Integration Using a Compact Photon Source Together with Fluence Control and Patient Imaging — D. Tronc, F. Dugardin, J.P. Georges, R. Letoumelin, <i>J.L. Pourre.....</i>	116	TAB04
A 1.5 GeV Compact Light Source with Superconducting Bending Magnets — A.A. Garren, <i>D.B. Cline, M.A. Green, D.E. Johnson, J.J. Kolonko, E.M. Leung, D.D. Madura,</i> <i>L.C. Schachinger.....</i>	119	TAB06
Applications of Industrial Electron Accelerators at Samsung Heavy Industries — <i>Bumsoo Han, Keeman Kim, Kihun Joh, Sungmyun Kim, Byungmun Kim, Heunggyu Park,</i> <i>Jongpil Park, Jinsoo Kim, Wongu Kang, Kyungwoo Kang, Yuri Kim, Sangil Lee, Younghee Kim</i>	122	TAB09
Application of Accelerated Electron Beams for Rubber and Polymer Modification — <i>A. Shalnov, B.Yu. Bogdanovich, A. Ignatyev, V. Senyukov.....</i>	125	TAB13
Status on Low Energy (10 MeV Range) X-band Linacs Developed Worldwide — <i>A.V. Michine.....</i>	128	TAB15
Linear Accelerator for Radiation Chemistry Research at Notre Dame — K. Whitham, <i>S. Lyons, R. Miller, D. Nett, P. Treas, A. Zante, R.W. Fessenden, M.D. Thomas, Y. Wang</i>	131	TAB17
IREN Status: New Electron Linac Driven Intense Resonance Neutron Source — A. Krasnykh	134	TAC01
A Cost Estimation Model for High Power FELs — George R. Neil	137	TAC03
Details of the Initial Part of the Tungsten Ion Linac for Particle Track Membranes Production — V. Kushin, T. Kulevoy, N. Nesterov, A. Oreshnikov, S. Plotnikov, D. Seleznev, <i>V. Zubovskiy.....</i>	140	TAC05
A Series of Ion Accelerators for Industry — B.N. Sukhina, N.I. Alinovsky, I.L. Chertok, <i>S.N. Chumakov, N.S. Dikansky, A.D. Goncharov</i>	143	TAC06
A Pulsed Source of Neutron Focus for Fundamental and Applied Research in High-Energy Electron Accelerator Centres — I.P. Ereemeev.....	146	TAC11
Moderator/Collimator for a Proton/Deuteron Linac to Produce a High-Intensity, High-Quality Thermal Neutron Beam for Neutron Radiography — R.C. Singleterry Jr., <i>G.R. Imel, G.E. McMichael</i>	149	TAC12
Experimental Set-up for Multiplication Coefficient Fluctuation Study vs Accelerator Parameter Deviations on the JINR Pulsed Accelerator Driven Neutron Source — <i>V. Belkovets, A. Ivanov, A. Kaminsky, A. Krasnykh, N. Malakhov, L. Menshikov, Yu. Popov,</i> <i>V. Piataev, N. Pilyar, V. Rudenko, L. Somov, A. Sumbaev, V. Tarabrin.....</i>	152	TAC16

Synchrotron Light Sources and Free Electron Lasers

European Synchrotron Radiation Storage Rings (Invited) — H. Zyngier.....	155	TPG01
Development of the JAERI FEL Driven by a Superconducting Accelerator (Invited) — <i>E.J. Minehara, M. Sugimoto, M. Sawamura, R. Nagai, N. Kikuzawa.....</i>	159	TPG02
Status of New Light Sources in Russia (Invited) — G. Kulipanov	manuscript not submitted	TPG03
Free Electron Laser Research in China (Invited) — Jialin Xie.....	162	TPG04
Accelerator Physics Trends at the ESRF — A. Ropert, L. Farvacque, J. Jacob, J.L. Laclare, <i>E. Plouviez, J.L. Revol, K. Scheidt</i>	167	TPG05
Commissioning of the PLS 2 GeV Storage Ring — M. Yoon, J.Y. Huang, J.S. Jang, M. Kwon, <i>T. Lee, S.H. Nam.....</i>	171	TPG06
Femtosecond X-Rays from 90° Thomson Scattering — W. Leemans, R. Schoenlein, A. Chin, <i>E. Glover, R. Govil, P. Volfbeyn, S. Chattopadhyay, K.-J. Kim, C.V. Shank.....</i>	174	TPG07
Design of a Diffraction Limited Light Source (DIFL) — D. Einfeld, J. Schaper, M. Plesko	177	TPG08
Updated Plans for DIAMOND, a New X-ray Light Source for the UK — V.P. Suller, <i>J.A. Clarke, J.B. Fitzgerald, H.L. Owen, M.W. Poole, X. Queral, S.L. Smith.....</i>	180	TPG09
Design Optimization for an X-Ray Free Electron Laser Driven by SLAC Linac — Ming Xie.....	183	TPG10

The FERMI FEL Project at Trieste — <i>D. Bulfone, F. Cargnello, G. D'Auria, F. Daclon, M. Ferianis, M. Giannini, G. Margaritondo, A. Massarotti, A. Rindi, R. Rosei, C. Rubbia, R. Visintini, R.P. Walker, A. Wrulich, D. Zangrando, F. Ciocci, G. Dattoli, A. De Angelis, A. Dipace, A. Doria, G.P. Gallerano, F. Garosi, L. Giannessi, E. Giovenale, L. Mezi, P.L. Ottaviani, A. Renieri, E. Sabia, A. Segreto, A. Torre, M. Castellano, P. Patteri, S. Tazzari, F. Tazzioli, F. Cevenini, A. Cutolo</i>	186	TPG11
Studies on a Free Electron Laser for the TESLA Test Facility — <i>J. Rossbach</i>	189	TPG12
MIT Microwiggler for Free Electron Laser Applications — <i>P. Catravas, R. Stoner, J. Blastos, D. Sisson, I. Mastovsky, G. Bekefi, X.-J. Wang, A. Fisher</i>	192	TPG14
DORIS III as a Dedicated Source for Synchrotron Radiation — <i>H. Neseemann, W. Brefeld, F. Brinker, W. Decking, O. Kaul, B. Sarau</i>	195	FAA02
Beam Lifetime and Beam Brightness in ALS — <i>C. Kim, A. Jackson, A. Warwick</i>	198	FAA03
Asynchronized Energy Ramping at SRRC Storage Ring — <i>Gwo-Huei Luo, L.H. Chang, Y. Cheng, K.T. Hsu, C.C. Kuo, W.C. Lau, Ch. Wang, P.K. Tseng, Y.C. Liu</i>	201	FAA04
Emittance Measurements in the ALS Booster Synchrotron — <i>D. Massoletti, C.H. Kim, A. Jackson</i>	204	FAA05
Compton Scattering in the ALS Booster — <i>D. Robin, C. Kim, A. Sessler</i>	207	FAA06
Beam Stability at SRRC Storage Ring — <i>W.T. Weng, H.P. Chang, J.R. Chen, Y. Cheng, K.T. Hsu, C.C. Kuo, J.C. Lee, K.K. Lin, Y.C. Liu, G.H. Luo, K.L. Tsang</i>	210	FAA07
Commissioning of the Duke Storage Ring — <i>V.N. Litvinenko, Y. Wu, B. Burnham, J.M.J. Madey, F. Carter, C. Dickey, M. Emamian, J. Gustavsson, N. Hower, P. Morcombe, S.H. Park, P. O'Shea, R. Sachtschale, D. Straub, G. Swift, P. Wang, J. Widgren</i>	213	FAA08
Pulsed VUV Synchrotron Radiation Source — <i>S.H. Kim, Y.S. Cho, T.Y. Kim, K.H. Chung</i>	216	FAA10
Merits of a Sub-Harmonic Approach to a Single-Pass, 1.5-Å FEL — <i>W.M. Fawley, H.-D. Nuhn, R. Bonifacio, E.T. Scharlemann</i>	219	FAA12
Operation of the ELETTRA Injection Linac in the FEL Mode — <i>G. D'Auria, C.J. Bocchetta, M. Plesko, C. Rossi, L. Tosi, R.P. Walker, A. Wrulich</i>	222	FAA13
Free Electron Laser - FEL - Study in Institute of Nuclear Physics of MSU — <i>V.K. Grishin, B.S. Ishkhanov, T.A. Novikova, V.I. Shvedunov</i>	225	FAA14
A Chirped-Pulse Regenerative-Amplifier FEL for the Gamma-Gamma Collider — <i>K.C.D. Chan, J.C. Goldstein, D.C. Nguyen, H. Takeda</i>	228	FAA16
Alignment and Magnet Error Tolerances for the LCLS X-Ray FEL — <i>H.-D. Nuhn, E.T. Scharlemann, R. Schlüter</i>	231	FAA17
Electron Transport and Emittance Diagnostics in CIRFEL — <i>J. Krishnaswamy, I.S. Lehrman, R. Hartley, R.H. Austin</i>	234	FAA19
Study on Accelerator Noise Effects on a Far-Infrared FEL Oscillator — <i>Shinian Fu, Yinbao Chen, Zhibin Huang</i>	237	FAA21
Status of the UCLA High-Gain Infrared Free Electron Laser — <i>M. Hogan, C. Pellegrini, J. Rosenzweig, G. Travish, A. Varfolomeev</i>	240	FAA23
Accelerator Design for the High-Power Industrial FEL — <i>D.V. Neuffer, S. Benson, J. Bisognano, D. Douglas, H.F. Dylla, D. Kehne, J. Fugitt, K. Jordan, Z. Li, H.-X. Liu, L. Merminga, G. Neil, M. Shinn, C. Sinclair, M. Wiseman, M. Cornacchia</i>	243	FAA25
Free Electron Laser Amplifier Experiment Based on 3.5 MeV Linear Induction Accelerator — <i>Ding Bainan, Deng Jianjun, Hu Shenzong, Shi Jinsui, Zhu Wenjun, Li Qing, He Yi</i>	246	FAA26
A High Duty Factor Electron Linac for FEL — <i>T.D. Hayward, D.H. Dowell, A.M. Vetter, C. Lancaster, L. Milliman, D. Smith, J. Adamski, C. Parazzoli</i>	248	FAA27
A Kilowatt Class Visible Free Electron Laser Facility — <i>J.L. Adamski, D.H. Dowell, T.D. Hayward, C.G. Parazzoli, A.M. Vetter</i>	251	FAA28
Self-Consistent Analysis of Radiation and Relativistic Electron Beam Dynamics in a Helical Wiggler Using Lienard-Wiechert Fields — <i>M. Tecimer, L.R. Elias</i>	254	FAA29
First Lasings at Visible and IR Range of Linac-Based FELs at the FELI — <i>T. Tomimasu, E. Oshita, S. Okuma, K. Wakita, K. Saeki, A. Zako, T. Suzuki, Y. Miyauchi, A. Koga, S. Nishihara, A. Nagai, E. Tongu, K. Wakisaka, A. Kobayashi, M. Yasumoto</i>	257	FAA30
The Northrop Grumman Compact Infrared FEL (CIRFEL) — <i>I.S. Lehrman, J. Krishnaswamy, R.A. Hartley, R.H. Austin</i>	260	FAA31
A Proposed NSLS X-Ray Ring Upgrade Using B Factory Technology — <i>E.B. Blum</i>	263	FAR01
A Low Emittance Lattice for the NSLS X-Ray Ring — <i>J. Safranek</i>	266	FAR02

Design of a 1.2 GeV Synchrotron Light Source for X-Ray Lithography at Samsung Heavy Industries — Keeman Kim, Bumsoo Han, Kihun Joh, Sungmyun Kim, Byungmun Kim, Heunggyu Park, Jongpil Park, Jinsoo Kim, Wongu Kang, Kyungwoo Kang, Yuri Kim, Sangil Lee, Younghee Kim.....	269	FAR03
ANKA, A Synchrotron Light Source for Microstructure Fabrication and Analysis — H.O. Moser, M. Ballauff, V. Bechtold, H. Bertagnolli, J. Bialy, P. v. Blanckenhagen, C. Bocchetta, W. Bothe, C. Coluzza, A.N. Danilewsky, K.D. Eichhorn, B. Eigenmann, D. Einfeld, L. Friedrich, M. Haller, N. Holtkamp, V. Honecker, K. Hümmer, E. Huttel, J. Jacob, V. Kashikin, J. Kircher, H. Klewe-Nebenius, A. Knöchel, A. Krüssel, G. Kumpe, K.D. Möller, J. Mohr, M. Nagaenko, F.J. Pantenburg, M. Plesko, J. Schaper, K. Schlösser, G. Schulz, S. Schuppler, H. Schweickert, I. Seidel, Y. Severgin, I. Shukeilo, L. Steinbock, R. Steininger, M. Svandrlík, G. Williams, K. Wilson, J. Zegenhagen.....	272	FAR06
An Undulator at PETRA II - A New Synchrotron Radiation Source at DESY — K. Balewski, W. Brefeld, U. Hahn, J. Pflüger, R. Rossmanith.....	275	FAR07
Electron Storage Ring, KSR for Light Source with Synchrotron Radiation — A. Noda, H. Dewa, H. Fujita, M. Ikegami, Y. Iwashita, S. Kakigi, M. Kando, K. Mashiko, H. Okamoto, T. Shirai, M. Inoue	278	FAR08
A Lattice for the Future Project of VUV and Soft X-Ray High Brilliant Light Source — H. Takaki, Y. Kobayashi, K. Matsuda, Y. Kamiya.....	281	FAR09
Millimeter Wave Coherent Synchrotron Radiation in a Compact Electron Storage Ring — J.B. Murphy, E. Blum, R. Heese, J. Keane, S. Krinsky	284	FAR10
Commissioning of the Argonne Positron Accumulator Ring — M. Borland.....	287	FAR11
APS Storage Ring Commissioning and Early Operational Experience — G. Decker.....	290	FAR13
New Specifications for the SOLEIL Project — M.-P. Level, P. Brunelle, A. Nadji, M. Sommer, H. Zyngier, J. Faure, P. Nghiem, J. Payet, A. Tkatchenko.....	293	FAR14
A Combined Magnet Lattice of the Synchrotron Light Source ISI-800 — I. Karnaukhov, S. Kononenko, A. Shcherbakov, V. Nemoshkalenko, V. Molodkin, A. Shpak.....	296	FAR16
Progress of the ISI-800 Project — E. Bulyak, S. Efimov, A. Gevchuk, P. Gladkikh, I. Karnaukhov, S. Kononenko, V. Kozin, V. Markov, N. Mocheshnikov, A. Mytsykov, A. Shcherbakov, Yu. Telegin, A. Zelinsky, V. Molodkin, V. Nemoshkalenko, A. Shpak.....	299	FAR17
Reduction of Open-Loop Low Frequency Beam Motion at the APS — G. Decker, Y.G. Kang, S. Kim, D. Mangra, R. Merl, D. McGhee, S. Sharma.....	303	FAR19
Horizontal-Vertical Coupling Correction at Aladdin — R.A. Bosch, W.S. Trzeciak.....	306	FAR20
One and a Half Years of Experience with the Operation of the Synchrotron Light Source ELETTRA — C.J. Bocchetta, D. Bulfone, F. Daclon, G. D'Auria, A. Fabris, R. Fabris, M. Ferianis, M. Giannini, F. Iazzourene, E. Karantzoulis, A. Massarotti, R. Nagaoka, N. Pangos, R. Richter, C. Rossi, M. Svandrlík, L. Tosi, R. Visintini, R.P. Walker, F. Wei, A. Wrulich	309	FAR21

Low and Intermediate Energy Accelerators

First Generation ISOL Radioactive Ion Beam Facilities (Invited) — D.K. Olsen.....	312	RPG01
Latest Developments in Superconducting Cyclotrons (Invited) — H.W. Schreuder.....	317	RPG02
Synchrotron-Driven Spallation Sources (Invited) — P.J. Bryant.....	322	RPG03
Heavy Ion Cooling Rings (Invited) — J.S. Hangst.....	manuscript not submitted	RPG04
Commissioning the MIT-Bates South Hall Ring — K. Jacobs, R. Averill, S. Bradley, A. Carter, G. Dodson, K. Dow, M. Farkhondeh, E. Ihloff, S. Kowalski, B. McAllister, W. Sapp, C. Sibley, S. Sobczynski, D. Tieger, C. Tschalaer, E. Tsentalovich, W. Turchinets, A. Zolfaghari, T. Zwart	327	RPG05
The AmPS Ring: Actual Performance and Future Plans — G. Luijckx, R. Bakker, H. Boer Rookhuizen, C. de Jager, F. Kroes, J. van der Laan, R. Maas, J. Noomen, Y. Wu.....	330	RPG06
Feasibility Study for Using the FNAL Antiproton Source as a Low Energy Proton-Antiproton Collider — Mike Church, Stephan Maury.....	333	RPG07
CIS, A Low Energy Injector for the IUCF Cooler — D.L. Friesel, S.Y. Lee.....	336	RPG08
The R&D Works on the High Intensity Proton Linear Accelerator for Nuclear Waste Transmutation — N. Ito, M. Mizumoto, K. Hasegawa, H. Oguri, J. Kusano, Y. Okumura, M. Kawai, H. Ino, H. Murata, Y. Touchi	339	RPG09
Development of the RFD Linac Structure — D.A. Swenson, K.R. Crandall, F.W. Guy, J.W. Lenz, A.D. Ringwall, L.S. Walling.....	342	RPG10

Proposed Upgrade of the NSCL — R.C. York, H. Blosser, T. Grimm, D. Johnson, D. Lawton, F. Marti, J. Vincent, X. Wu, A.F. Zeller.....	345	RPG11
ISAC-1: Radioactive Ion Beams Facility at TRIUMF — P.G. Bricault, R. Baartman, J.L. Beveridge, G.S. Clark, J. Doornbos, G. Dutto, T. Hodges, S. Koscielniak, L. Root, P.W. Schmor, H.R. Schneider.....	348	RPG12
First Beam Tests of the INS Split Coaxial RFQ for Radioactive Nuclei — S. Arai, A. Imanishi, K. Niki, M. Okada, Y. Takeda, E. Tojyo, N. Tokuda.....	351	RPG13
Accelerator Complex for a Radioactive Ion Beam Facility at ATLAS — J.A. Nolen.....	354	RPG14
The Lattice Design of Indiana University Cyclotron Facility Cooler Injector Synchrotron — D. Li, X. Kang, D.L. Friesel, S.Y. Lee, J.Y. Liu, A. Pei, A. Riabko, L. Wang.....	357	TAP03
Design Study of AntiProton Accumulation and Deceleration Ring in the KEK PS Complex — S. Machida, M. Yoshii, Y. Mori, N. Tokuda, Y. Ishi.....	360	TAP04
Feasibility Study of a 1-MW Pulsed Spallation Source — Y. Cho, Y.-C. Chae, E. Crosbie, M. Fathizadeh, H. Friedsam, K. Harkay, D. Horan, S. Kim, R. Kustom, E. Lessner, W. McDowell, D. McGhee, F. Mills, H. Moe, R. Nielsen, G. Norek, K.J. Peterson, A. Rauchas, K. Symon, K. Thompson, D. Warner, M. White.....	363	TAP05
ORIC Central Region Calculations — J.D. Bailey, D.T. Dowling, S.N. Lane, S.W. Mosko, D.K. Olsen, B.A. Tatum.....	366	TAP07
An Internal Timing Probe for Use in the MSU K1200 Cyclotron — J.D. Bailey, J. Kuchar, F. Marti, J. Ottarson.....	369	TAP08
Axial Injection and Phase Selection Studies of the MSU K1200 Cyclotron — J.D. Bailey.....	372	TAP09
Study and Redesign of the NSCL K500 Central Region — S.L. Snyder, F. Marti.....	375	TAP10
Heavy Ion Acceleration Strategies in the AGS Accelerator Complex -- 1994 Status Report — L.A. Ahrens, J. Benjamin, M. Blaskiewicz, J.M. Brennan, C.J. Gardner, H.C. Hseuh, Y.Y. Lee, R.K. Reece, T. Roser, A. Soukas, P. Thieberger.....	378	TAP11
Observation of Intensity Dependent Losses in Au(15+) Beams — M. Blaskiewicz, L.A. Ahrens, H.C. Hseuh, T. Roser, Y. Shoji, K. Zeno.....	381	TAP12
High Intensity Proton Operations at the Brookhaven — M. Blaskiewicz, L.A. Ahrens, E.J. Bleser, J.M. Brennan, C.J. Gardner, J.W. Glenn, R.K. Reece, T. Roser, M.J. Syphers, W. VanAsselt, S.Y. Zhang.....	383	TAP13
Fast Extracted Proton Beams at Low Energies in the CPS East Experimental Area — R. Cappi, L. Durieu, J.-Y. Hémerly, M. Martini, J.-P. Riunaud, Ch. Steinbach.....	386	TAP14
Ion-Optics Systems Of Multiply Charged High-Energy Ions For High Emittance Beams — V.O. Naidenov, L.A. Baranova, G.M. Gusinskii, A.V. Matyukov, S.Ya. Yavor.....	389	TAP16

High Energy Hadron Accelerators and Colliders

The Status of the Fermilab Main Injector Project (Invited) — D. Bogert, W. Fowler, S. Holmes, P. Martin, T. Pawlak.....	391	MPG01
Status and Future of the Tevatron (Invited) — V. Bharadwaj.....	396	MPG02
The RHIC Project - Status and Plans (Invited) — M. Harrison.....	401	MPG03
HERA Status and Plans (Invited) — R. Brinkmann.....	406	MPG04
The CERN Heavy Ion Accelerating Facility (Invited) — H.D. Haseroth.....	411	MPG05
UNK Status and Plans (Invited) — G. Gurov.....	416	MPG06
Reduction of Particle Losses in HERA by Generating an Additional Harmonic Tune Modulation — O.S. Brüning, F. Willeke.....	420	MPG07
Acceleration of Lead Ions in the CERN PS Booster and the CERN PS — F. Blas, P. Bossard, R. Cappi, G. Cyvoct, R. Garoby, G. Gelato, H. Haseroth, E. Jensen, D. Manglunki, K. Metzmacher, F. Pedersen, N. Rasmussen, K. Schindl, G.C. Schneider, H. Schönauer, L. Sermeus, M. Thivent, M. van Rooij, F. Völker, E. Wildner.....	423	MPG09
Highly Efficient Deflection of the Divergent Beam by Bent Single Crystal — V.I. Baranov, V.M. Biryukov, A.P. Bugorsky, Yu.A. Chesnokov, V.I. Kotov, M.V. Tarakanov, V.I. Terekhov, S.V. Tsarik, O.L. Fedin, M.A. Gordeeva, M.P. Gur'yev, Yu.P. Platonov, A.I. Smirnov.....	426	MPG10
Potential Accelerator Improvements Required for the Tevatron Upgrade at Fermilab — G. Jackson, G.W. Foster.....	428	MPG11
Beyond the LHC: A Conceptual Approach to a Future High Energy Hadron Collider — M.J. Syphers, M.A. Harrison, S. Peggs.....	431	MPG12

132 nsec Bunch Spacing in the Tevatron Proton-Antiproton Collider — S.D. Holmes, <i>J.A. Holt, J. Johnstone, J. Marriner, M. Martens, D. McGinnis</i>	434	WAP01
Aluminum Beam Tube for the Super Collider: An Option for No-Coating & No-Liner — <i>W. Chou</i>	437	WAP02
Variable Bunch Spacing in Super Collider — W. Chou	440	WAP03
Fermilab Collider Run 1B Statistics — V. Bharadwaj, J. Crawford, R. Mau	443	WAP04
Optimizing the Luminosity in the Tevatron by Independently Moving the Horizontal and Vertical Beta Stars Longitudinally — M.A. Martens, G.P. Goderre	446	WAP05
A Model of the Fermilab Collider for Optimization of Performance — Elliot S. McCrory, <i>Peter W. Lucas</i>	449	WAP06
Coupling in the Tevatron — Norman M. Gelfand	452	WAP07
Calculating Luminosity for a Coupled Tevatron Lattice — J.A. Holt, M.A. Martens, <i>L. Michelotti, G. Goderre</i>	455	WAP08
Remarks Concerning the γ-Production Probability of High Relativistic Dirac-Electrons in the Positron Bunch — Huschang Heydari	458	WAP09
Field Quality Evaluation of the Superconducting Magnets of the Relativistic Heavy Ion Collider — J. Wei, R.C. Gupta, A. Jain, S.G. Peggs, C.G. Trahern, D. Trbojevic, P. Wanderer	461	WAP10
High Intensity Proton Beams in a Multi-cycled SPS — A. Faugier, X. Altuna, R. Bailey, <i>R. Blanchard, T. Bohl, H. Burkhardt, P. Collier, K. Cornelis, N. Garrel, A. Hilaire, M. Jonker,</i> <i>R. Keizer, M. Lamont, T. Linnekar, G. de Rijk, G. Roy, H. Schmickler, J. Wenninger</i>	464	WAP12
The SPS as Accelerator of Pb⁸²⁺ Ions — A. Faugier, X. Altuna, R. Bailey, R. Blanchard, T. Bohl, <i>E. Brouzet, H. Burkhardt, P. Collier, K. Cornelis, G. de Rijk, F. Ferioli, A. Hilaire, M. Lamont,</i> <i>T. Linnekar, M. Jonker, C. Niquille, G. Roy, H. Schmickler</i>	467	WAP13
Experimental Evidence for Multi-pass Extraction with a Bent Crystal — B. Dehning, <i>K. Elsener, G. Fidecaro, M. Gyr, W. Herr, J. Klem, W. Scandale, G. Vuagnin, E. Weisse,</i> <i>S. Weisz, S.P. Møller, E. Uggerhoj, A. Freund, R. Hustache, G. Carboni, M.P. Bussa, F. Tosello</i>	470	WAP14
Storage Ring for Enhanced Antiproton Production at Fermilab — G. Jackson, G.W. Foster	473	WAP16

Circular Electron Accelerators and Colliders

LEP Status and Plans (Invited) — S. Myers	476	WPG01
CESR Status and Plans (Invited) — David L. Rubin	481	WPG02
PEP II Status and Plans (Invited) — John T. Seeman	486	WPG03
KEKB Status and Plans (Invited) — Shin-ichi Kurokawa	491	WPG04
DAΦNE Status and Plans (Invited) — G. Vignola	495	WPG05
Electron-Positron Colliders at Novosibirsk (Invited) — N. Dikansky	500	WPG06
BEPC Status and Plans (Invited) — Shu-Hong Wang	506	WPG07
The First Attainment and Routine Use of Longitudinal Spin Polarization at a High Energy Electron Storage Ring — D.P. Barber	511	WPG08
Experiments with Bunch Trains in LEP — O. Brunner, W. Herr, G. von Holtey, E. Keil, <i>M. Lamont, M. Meddahi, J. Poole, R. Schmidt, A. Verdier, C. Zhang</i>	514	WPG09
Trapped Macroparticles in Electron Storage Rings — F. Zimmermann, J.T. Seeman, <i>M. Zolotarev, W. Stoeffl</i>	517	WPG10
A Compact-High Performance NLC Damping Ring Using High Magnetic Field Bending Magnets — D.B. Cline, A. Garren, M. Green, J. Kolonko, D. Madura	520	WPG11
Application of Precision Magnetic Measurements for Control of the Duke Storage Ring — <i>B. Burnham, V.N. Litvinenko, Y. Wu</i>	524	RAA01
Wiggler Insertion of the PEP-II B-Factory LER — J. Heim, L. Bertolini, J. Dressler, O. Fackler, <i>B. Hobson, M. Kendall, T. O'Connor, W. Stoeffl, T. Swan, A. Zholents, M.S. Zisman</i>	527	RAA03
Status of the High Energy Ring of the PEP II B-Factory — U. Wienands, E. Reuter, <i>J.T. Seeman, W. Davies-White, A. Fisher, J. Fox, L. Genova, J. Gracia, C. Perkins,</i> <i>M. Pietryka, H. Schwarz, T. Taylor, T. Jackson, C. Belser, D. Shimer</i>	530	RAA04
Design of the PEP-II Low-Energy Ring — M.S. Zisman, R.B. Yourd, H. Hsieh	533	RAA05
Injection Envelope Matching in Storage Rings — M.G. Minty, W.L. Spence	536	RAA06
A Mathematical Model for Investigating Chromatic Electron Beam Extraction from a Pulse Stretcher Ring — Yu.N. Grigor'ev, A.Yu. Zelinsky	539	RAA07

The Dynamical Aperture of ISI - 800 — <i>S. Efimov, I. Karnaukhov, S. Kononenko, A. Shcherbakov, A. Tarasenko, A. Zelinsky</i>	542	RAA08
The Influence of Residual Vertical Dispersion on LEP Performance — <i>P. Collier, H. Schmickler</i>	545	RAA10
Operational Procedures to Obtain High Beam-Beam Tune Shifts in LEP Pretzel Operation — <i>R. Bailey, P. Collier, T. Bohl, H. Burkhardt, K. Cornelis, G. De Rijk, A. Faugier, M. Jonker, M. Lamont, G. Roy, H. Schmickler, J. Wenninger</i>	548	RAA11
Synchrotron Phase Space Injection into LEP — <i>P. Collier</i>	551	RAA12
Systematic Studies of the LEP Working Point — <i>P. Collier, H. Schmickler</i>	554	RAA13
Modification of the LEP Electrostatic Separator Systems for Operation with Bunch Trains — <i>B. Balhan, A. Burton, E. Carlier, J.-P. Deluen, J. Dieperink, N. Garrel, B. Goddard, R. Guinand, W. Kalbreier, M. Laffin, M. Lamont, V. Mertens, J. Poole, H. Verhagen</i>	557	RAA15
Low Emittance Lattice for LEP — <i>Y. Alexahin, D. Brandt, K. Cornelis, A. Hofmann, J.P. Koutchouk, M. Meddahi, G. Roy, A. Verdier</i>	560	RAA17
Radiation Damping Partitions and RF-Fields — <i>M. Cornacchia, A. Hofmann</i>	564	RAA18
Experiments on Beam-Beam Depolarization at LEP — <i>R. Assmann, A. Blondel, B. Dehning, A. Drees, P. Grosse-Wiesmann, H. Grote, M. Placidi, R. Schmidt, F. Tecker, J. Wenninger</i>	567	RAA19
Measurements of Impedance Distributions and Instability Thresholds in LEP — <i>D. Brandt, P. Castro, K. Cornelis, A. Hofmann, G. Morpurgo, G.L. Sabbi, J. Wenninger, B. Zotter</i>	570	RAA20
A Preliminary Lattice Design of a Tau-Charm Factory Storage Ring in Beijing — <i>N. Huang, L. Jin, Y. Wu, G. Xu</i>	573	RAA21
Low Energy Ring Lattice of the PEP II Asymmetric B-Factory — <i>Y. Cai, M. Donald, R. Helm, J. Irwin, Y. Nosochkov, D.M. Ritson, Y. Yan, E. Forest, A. Zholents</i>	576	RAA22
Damping Rates of the SRRC Storage Ring — <i>K.T. Hsu, C.C. Kuo, W.K. Lau, W.T. Weng</i>	579	RAA23
Performance of the SRRC Storage Ring and Wiggler Commissioning — <i>C. Kuo, K.T. Hsu, G.H. Luo, W.K. Lau, Ch. Wang, H.P. Chang, L.H. Chang, M.H. Wang, J.C. Lee, C.S. Hsue, W.T. Weng, Y.C. Liu</i>	582	RAA24
Detector Solenoid Compensation in the PEP-II B-Factory — <i>Y. Nosochkov, Y. Cai, J. Irwin, M. Sullivan, E. Forest</i>	585	RAA25
Swamp Plots for Dynamic Aperture studies of PEP-II Lattices — <i>Y.T. Yan, J. Irwin, Y. Cai, T. Chen, D. Ritson</i>	588	RAA26
Lattice Design for the High Energy Ring of the SLAC B-Factory (PEP-II) — <i>M.H.R. Donald, Y. Cai, J. Irwin, Y. Nosochkov, D.M. Ritson, J. Seeman, H.-U. Wienands, Y.T. Yan</i>	591	RAA27
The APS Booster Synchrotron: Commissioning and Operational Experience — <i>S.V. Milton</i>	594	RAA28
A Preliminary Design for a Tau-Charm Factory — <i>J. Norem, E. Crosbie, J. Repond, L. Teng</i>	597	RAA29
A Spin Control System for the South Hall Ring at the Bates Linear Accelerator Center — <i>T. Zwart, P. Ivanov, Yu. Shatunov, R. Averill, K. Jacobs, S. Kowalski, W. Turchinets</i>	600	RAA31
Beam-Based Alignment of Sextupoles with the Modulation Method — <i>M. Kikuchi, K. Egawa, H. Fukuma, M. Tejima</i>	603	RAA33

Linear Colliders and Advanced Accelerator Concepts

The Stanford Linear Collider (Invited) — <i>Paul Emma</i>	606	WAG01
Options and Trade-Offs in Linear Collider Design (Invited) — <i>J. Rossbach</i>	611	WAG02
Test Facilities for Future Linear Colliders — <i>Ronald D. Ruth</i>	616	WAG03
Channel Guided Lasers for Plasma Accelerators (Invited) — <i>H.M. Milchberg, C.G. Durfee III, T.M. Antonsen, P. Mora</i>	621	WAG04
Inverse Cerenkov Accelerator Results (Invited) — <i>W.D. Kimura</i>	626	WAG05
Measurements of Plasma Wake-Fields in the Blow-Out Regime — <i>N. Barov, M. Conde, J.B. Rosenzweig, P. Schoessow, G. Cox, W. Gai, R. Konecny, J. Power, J. Simpson</i>	631	WAG06
Experimental Study of Electron Acceleration by Plasma Beat-Waves with Nd Lasers — <i>F. Amiranoff, F. Moulin, J. Fusellier, J.M. Joly, M. Juillard, M. Bercher, D. Bernard, A. Debraine, J.M. Dieulot, F. Jacquet, P. Matricon, Ph. Miné, B. Montès, R. Morano, P. Poilleux, A. Specka, J. Morillo, J. Ardonneau, B. Cros, G. Matthieussent, C. Stenz, P. Mora</i>	634	WAG07
A Broadband Electron Spectrometer and Electron Detectors for Laser Accelerator Experiments — <i>C.E. Clayton, K.A. Marsh, C. Joshi, C.B. Darrow, A.E. Dangor, A. Modena, Z. Najmudin, V. Malka</i>	637	WAG08

Photon Acceleration from Rest to the Speed of Light — C.H. Lai, T. Katsouleas, R. Liou, W.B. Mori, C. Joshi, P. Muggli, R. Brogle, J. Dawson.....	640	WAG09
A Constant Gradient Planar Accelerating Structure for Linac Use — Y.W. Kang, P.J. Matthews, R.L. Kustom.....	643	WAG10
Pulse to Pulse Stability Issues in the SLC — C. Adolphsen, R. Assmann, F.J. Decker, P. Emma, J. Frisch, L.J. Hendrickson, P. Krejcik, M. Minty, N. Phinney, P. Raimondi, M.C. Ross, T. Slaton, W. Spence, R. Stege, H. Tang, F. Tian, J. Turner, M. Woodley, F. Zimmermann.....	646	WAG11
HOM-Free Linear Accelerating Structure for e+e- Linear Collider at C-Band — T. Shintake, K. Kubo, H. Matsumoto, O. Takeda.....	649	WAG12
SLAC/CERN High Gradient Tests of an X-Band Accelerating Section — J.W. Wang, G.A. Loew, R.J. Loewen, R.D. Ruth, A.E. Vlieks, I. Wilson, W. Wuensch.....	653	WAG13

Linear Colliders

Performance of the 1994/95 SLC Final Focus System — F. Zimmermann, T. Barklow, S. Ecklund, P. Emma, D. McCormick, N. Phinney, P. Raimondi, M. Ross, T. Slaton, F. Tian, J. Turner, M. Woodley, M. Placidi, N. Toge, N. Walker.....	656	RPB01
Direct Measurement of Transverse Wakefields in the SLC Linac — P. Krejcik, R. Assmann, F.-J. Decker, S. Hartman, R. Miller, T. Raubenheimer.....	659	RPB02
Feedback Performance at the Stanford Linear Collider — M.G. Minty, C. Adolphsen, L.J. Hendrickson, R. Sass, T. Slaton, M. Woodley.....	662	RPB03
Vibration Studies of the Stanford Linear Accelerator — J.L. Turner, C. Adolphsen, G.B. Bowden, F.J. Decker, S.C. Hartman, S. Matsumoto, G. Mazaheri, D. McCormick, M. Ross, R. Stege, S. Virotek, M. Woodley.....	665	RPB04
SLAC Modulator Availability and Impact on SLC Operation — A.R. Donaldson, J.R. Ashton.....	668	RPB05
The SLC as a Second Generation Linear Collider — J.E. Spencer.....	671	RPB06
Status of the Design for the TESLA Linear Collider — R. Brinkmann.....	674	RPB07
The TESLA Test Facility (TTF) Linac - A Status Report — H. Weise.....	677	RPB08
The Infrastructure for the TESLA Test Facility (TTF) - A Status Report — S. Wolff.....	680	RPB09
The Status of the S-Band Linear Collider Study — N. Holtkamp.....	683	RPB12
The S-Band Linear Collider Test Facility — N. Holtkamp.....	686	RPB13
Beam Dynamics Studies for the SBLC — M. Drevlak, R. Wanzenberg.....	689	RPB14
S-Band HOM-Damper Calculations and Experiments — M. Dohlus, M. Marx, N. Holtkamp, P. Hülsmann, W.F.O. Müller, M. Kurz, H.-W. Glock, H. Klein.....	692	RPB15
The S-Band 36-Cell Experiment — B. Krietenstein, O. Podebrad, U. v.Rienen, T. Weiland, H.-W. Glock, P. Hülsmann, H. Klein, M. Kurz, C. Peschke, M. Dohlus, N. Holtkamp.....	695	RPB16

Volume 2

Linear Colliders (cont'd)

Parameters for the SLAC Next Linear Collider — T. Raubenheimer, C. Adolphsen, D. Burke, P. Chen, S. Ecklund, J. Irwin, G. Loew, T. Markiewicz, R. Miller, E. Paterson, N. Phinney, M. Ross, R. Ruth, J. Sheppard, H. Tang, K. Thompson, P. Wilson.....	698	RPC01
A Damping Ring Design for the SLAC Next Linear Collider — T.O. Raubenheimer, J. Byrd, J. Corlett, R. Early, M. Furman, A. Jackson, P. Krejcik, K. Kubo, T. Mattison, M. Minty, W. Moshhammer, D. Robin, B. Scott, J. Spencer, K. Thompson, P. Wilson.....	701	RPC02
A Bunch Compressor for the Next Linear Collider — P. Emma, T. Raubenheimer, F. Zimmermann.....	704	RPC03
A Final Focus System for the Next Linear Collider — F. Zimmermann, K. Brown, P. Emma, R. Helm, J. Irwin, P. Tenenbaum, P. Wilson.....	707	RPC06
Optimization of the NLC Final Focus System — F. Zimmermann, R. Helm, J. Irwin.....	710	RPC07
The SLAC NLC Extraction & Diagnostic Line — J. Spencer, J. Irwin, D. Walz, M. Woods.....	713	RPC08

CLIC - A Compact and Efficient High Energy Linear Collider — <i>H. Braun, R. Corsini, J.-P. Delahaye, G. Guignard, C. Johnson, J. Madsen, W. Schnell, L. Thorndahl, I. Wilson, W. Wuensch, B. Zotter</i>	716	RPC09
CLIC Test Facility Developments and Results — <i>R. Bossart, H. Braun, F. Chautard, M. Comunian, J.P. Delahaye, J.C. Godot, I. Kamber, J.H.B. Madsen, L. Rinolfi, S. Schreiber, G. Suberlucq, I. Wilson, W. Wuensch</i>	719	RPC10
Generation of a 30 GHz Train of Bunches Using a Magnetic Switch-Yard — <i>B. Autin, R. Corsini</i>	722	RPC11
A New Family of Isochronous Arcs — <i>G. Guignard, E.T. d'Amico</i>	725	RPC12
Updating of Beam Dynamics in the CLIC Main Linac — <i>G. Guignard</i>	728	RPC13
Improved CLIC Performances Using the Beam Response for Correcting Alignment Errors — <i>C. Fischer</i>	731	RPC14
Experimental Studies of a CERN-CLIC 32.98 GHz High Gradient Accelerating Structure Driven by the MIT Free Electron Laser Amplifier — <i>P. Volfbeyn, I. Mastovsky, G. Bekefi, I. Wilson, W. Wuensch</i>	734	RPC15
Design of a Relativistic Klystron Two-Beam Accelerator Prototype — <i>G. Westenskow, G. Caporaso, Y. Chen, T. Houck, S. Yu, S. Chattopadhyay, E. Henestroza, H. Li, C. Peters, L. Reginato, A. Sessler</i>	737	RPC16
Beam Dynamics Issues in an Extended Relativistic Klystron — <i>G. Giordano, H. Li, N. Goffeney, E. Henestroza, A. Sessler, S. Yu, T. Houck, G. Westenskow</i>	740	RPC17
Engineering Conceptual Design of the Relativistic Klystron Two-Beam Accelerator Based Power Source for 1-TeV Next Linear Collider — <i>L. Reginato, C. Peters, D. Vanecek, S. Yu, F. Deadrick</i>	743	RPC18
Design of Inductively Detuned RF Extraction Cavities for the Relativistic Klystron Two Beam Accelerator — <i>E. Henestroza, S.S. Yu, H. Li</i>	746	RPC19
Beam-Based Optical Tuning of the Final Focus Test Beam — <i>P. Tenenbaum, D. Burke, S. Hartman, R. Helm, J. Irwin, R. Iverson, P. Raimondi, W. Spence, V. Bharadwaj, M. Halling, J. Holt, J. Buon, J. Jeanjean, F. Le Diberder, V. Lepeltier, P. Puzo, K. Oide, T. Shintake, N. Yamamoto</i>	749	RPC20
Fermilab Contributions to the FFTB — <i>V. Bharadwaj, A. Braun, M. Halling, J.A. Holt, D. Still</i>	752	RPC21
HV Injection Phase Orbit Characteristics for Sub-Picosecond Bunch Operation with a High Gradient 17 GHz Linac — <i>J. Haimson, B. Mecklenburg</i>	755	RPC22

New Acceleration Techniques

Electron Acceleration in Relativistic Plasma Waves Generated by a Single Frequency Short-Pulse Laser — <i>C.A. Coverdale, C.B. Darrow, C.D. Decker, W.B. Mori, K.-C. Tzeng, C.E. Clayton, K.A. Marsh, C. Joshi</i>	758	RAB01
Theory and Simulation of Plasma Accelerators — <i>W.B. Mori, K.-C. Tzeng, C.D. Decker, C.E. Clayton, C. Joshi, T. Katsouleas, P. Lai, T.C. Chiou, R. Kinter</i>	761	RAB02
An Injector-prebuncher for a Plasma Electron Accelerator — <i>M. Lampel, C. Pellegrini, R. Zhang, C. Joshi, W.M. Fawley</i>	764	RAB03
Measurements of the Beatwave Dynamics in Time and Space — <i>A. Lal, K. Wharton, D. Gordon, M.J. Everett, C.E. Clayton, C. Joshi</i>	767	RAB04
A Novel Technique for Probing the Transverse Interactions Between an Electron Beam and a Plasma — <i>D. Gordon, A. Lal, C.E. Clayton, M. Everett, C. Joshi</i>	770	RAB05
Studies of Intense Laser Propagation in Channels for Extended Length Plasma Accelerators — <i>T. Katsouleas, T.C. Chiou, W.B. Mori, J.S. Wurtele, G. Shvets</i>	773	RAB08
UV Laser Ionization and Electron Beam Diagnostics for Plasma Lenses — <i>R. Govil, P. Volfbeyn, W. Leemans</i>	776	RAB10
Plasma Wakefield Acceleration Experiments in Overdense Regime Driven by Narrow Bunches — <i>T. Kozawa, T. Ueda, T. Kobayashi, M. Uesaka, K. Miya, A. Ogata, H. Nakanishi, T. Kawakubo, M. Arinaga, K. Nakajima, H. Shibata, N. Yugami, Y. Nishida, D. Whittum, Y. Yoshida</i>	779	RAB13
The Wake-Field Excitation in a Plasma-Dielectric Structure by a Sequence of Short Bunches of Relativistic Electrons — <i>I.N. Onishchenko, V.A. Kiseljov, A.K. Berezin, G.V. Sotnikov, V.V. Uskov, A.F. Linnik, Ya.B. Fainberg</i>	782	RAB15

A Beam Focusing System for a Linac Driven by a Traveling Laser Focus — <i>A.A. Mikhailichenko</i>	784	RAB18
2 x 2 TeV $\mu^+\mu^-$ Collider: Lattice and Accelerator-Detector Interface Study — <i>N.M. Gelfand, N.V. Mokhov</i>	787	RAB19
Muon Cooling and Acceleration Experiment at TRIUMF — <i>S.A. Bogacz, D.B. Cline, P.H. Sandler, D.A. Sanders</i>	790	RAB20
Helical Siberian Snakes — <i>E. Ludmirsky</i>	793	RAB21
Performance of Achromatic Lattice with Combined Function Sextupoles at Duke Storage Ring — <i>V.N. Litvinenko, Y. Wu, B. Burnham, J.M.J. Madey, S.H. Park</i>	796	RAB22

Accelerators and Storage Rings, Misc.

Matreshka High-Intensity Accelerator of Continuous Particle Beams — <i>F.A. Vodopianov</i>	799	TAR02
The Amplitude and Phase Control of the ALS Storage Ring RF System — <i>C.C. Lo, B. Taylor, K. Baptiste</i>	801	TAR03
Integral Dipole Field Calibration of the SRRC Storage Ring Combined Function Bending Magnets — <i>J.C. Lee, Peace Chang, C.S. Hsue</i>	804	TAR04
Improved Mobile 70 MeV Race-Track Microtron Design — <i>V.I. Shvedunov, A.I. Karev, V.N. Melekhin, N.P. Sobenin, W.P. Trower</i>	807	TAR05
The Improvement of Energy Measurement in BTS Transport Line by Using Beam Tracing Method — <i>M.H. Wang, J.C. Lee</i>	810	TAR06
Design Study of PAL-Stretcher Ring — <i>I.S. Ko, G.N. Kim, J. Choi, M.H. Cho, W. Namkung</i>	813	TAR07
Thermomechanical Analysis of a Compact-Design High Heat Load Crotch Absorber — <i>I.C. Sheng, S. Sharma, R. Rotela, J. Howell</i>	816	TAR08
Novosibirsk Tau-Charm Factory Design Study — <i>N. Dikansky, V. Parkhomchuk, A. Skrinsky, V. Yakimenko</i>	819	TAR11
Development of a RAMI Program for LANSCE Upgrade — <i>K.C.D. Chan, A. Browman, R.L. Hutson, R.J. Macek, P.J. Tallerico, C.A. Wilkinson</i>	822	TAR12
Accelerator Waveform Synthesis and Longitudinal Beam Dynamics in a Small Induction Recirculator — <i>T.J. Fessenden, D.P. Grote, W.M. Sharp</i>	825	TAR13
Progress Toward a Prototype Recirculating Induction Accelerator for Heavy-Ion Fusion — <i>A. Friedman, J.J. Barnard, M.D. Cable, D.A. Callahan, F.J. Deadrick, S. Eylon, T.J. Fessenden, D.P. Grote, D.L. Judd, H.C. Kirbie, D.B. Longinotti, S.M. Lund, L.A. Natrass, M.B. Nelson, M.A. Newton, T.C. Sangster, W.M. Sharp, S.S. Yu</i>	828	TAR14
Three Dimensional Simulations of a Small Induction Recirculator Accelerator — <i>D.P. Grote, A. Friedman, I. Haber</i>	831	TAR15
A Dynamic Momentum Compaction Factor Lattice in the FERMILAB DEBUNCHER Ring — <i>D.N. Olivieri, M. Church, J. Morgan</i>	834	TAR16
Mechanical Design of Recirculating Accelerator Experiments for Heavy-Ion Fusion — <i>V. Karpenko, J. Barnard, F. Deadrick, A. Friedman, D. Grote, S. Lund, J. Meredith, L. Natrass, M. Nelson, G. Repose, C. Sangster, W. Sharp, T. Fessenden, D. Longinotti, C. Ward</i>	837	TAR17
The PEP-II Project-Wide Database — <i>A. Chan, S. Calish, G. Crane, I. MacGregor, S. Meyer, J. Wong, A. Weinstein</i>	840	TAR18
Chromaticity Compensation - Booster Sextupoles — <i>S.A. Bogacz, K.-Y. Ng, J.-F. Ostiguy</i>	843	TAR20
Overview of $\mu^+\mu^-$ Collider Options — <i>D.B. Cline</i>	846	TAR21
HIRFL Status and HIRFL-CSR Proposal — <i>Ye Fang, Wang Yifang</i>	850	TAR22

Particle Sources and Injectors

A Review of Polarized Ion Sources (Invited) — <i>P.W. Schmor</i>	853	MPE01
Sources for Production of Radioactive Ion-Beams (Invited) — <i>Helge L. Ravn</i>	858	MPE02
The TRIUMF High-Curent DC Optically -Pumped Polarized H^- Ion Source — <i>A.N. Zelenski, C.D.P. Levy, K. Jayamanna, M. McDonald, P.W. Schmor, W.T.H. van Oers, J. Welz, G.W. Wight, G. Dutto, Y. Mori, T. Sakae</i>	864	MPE03

Lifetime Test on a High-Performance DC Microwave Proton Source — J. Sherman, <i>D. Hodgkins, P. Lara, J.D. Schneider, R. Stevens Jr.</i>	867	MPE04
Performance Enhancement of a Compact Radio Frequency Ion Source by the Injection of Supplemental Electrons — R.F. Welton, G.D. Alton, D. Becher, G.D. Mills, J. Dellwo, <i>S.N. Murray</i>	871	MPE05
A High-Current Position Source — V.V. Gorev	874	MPE06
Polarized Electron Sources (Invited) — J.E. Clendenin	877	MPE08
High Brightness Electron Sources (Invited) — Richard L. Sheffield	882	MPE09
Polarization Studies of Strained GaAs Photocathodes at the SLAC Gun Test Laboratory — <i>P. Sáez, R. Alley, J. Clendenin, J. Frisch, R. Kirby, R. Mair, T. Maruyama, R. Miller,</i> <i>G. Mulhollan, C. Prescott, H. Tang, K. Witte</i>	887	MPE10
Experimental Results of the ATF In-line Injection System — X.J. Wang, T. Srinivasan-Rao, <i>K. Batchelor, M. Babzien, I. Ben-Zvi, R. Malone, I. Pogorelsky, X. Qiu, J. Sheehan, J. Skaritka</i>	890	MPE11
High Power Testing of a 17 GHz Photocathode RF Gun — S.C. Chen, B.G. Danly, J. Gonichon, <i>C.L. Lin, R.J. Temkin, S.R. Trotz, J.S. Wurtele</i>	893	MPE12
Analytical Model for Emittance Compensation in RF Photo-Injectors — L. Serafini, <i>J.B. Rosenzweig</i>	896	MPE13
Emission, Plasma Formation, and Brightness of a PZT Ferroelectric Cathode — <i>S. Sampayan, G. Caporaso, D. Trimble, G. Westenskow</i>	899	MPE14

Radio Frequency Guns and Linac Injectors

Design and Testing of the 2 MV Heavy Ion Injector for the Fusion Energy Research Program — W. Abraham, R. Benjegerdes, L. Reginato, J. Stoker, R. Hipple, C. Peters, J. Pruyn, <i>D. Vanecek, S. Yu</i>	902	WPA01
K⁺ Diode for the LLNL Heavy Ion Recirculator Accelerator Experiment — S. Eylon, <i>E. Henestroza, F. Deadrick</i>	905	WPA02
A Single Bunch RFQ System for Heavy Ions — J. Madlung, A. Firjahn-Andersch, A. Schempp	908	WPA03
The Design of Low Frequency Heavy Ion RFQ Resonators — A. Schempp, H. Vormann, <i>U. Beisel, H. Deitinghoff, O. Engels, D. Li</i>	911	WPA04
A VE-RFQ-Injector for a Cyclotron — A. Schempp, O. Engels, F. Marhauser	914	WPA05
Fermilab Linac Injector, Revisited — M. Popovic, L. Allen, C.W. Schmidt	917	WPA06
New RF Structures for the Fermilab Linac Injector — M. Popovic, A. Moretti, R.J. Nobel	920	WPA07
High-Power RF Operations Studies with the CRITS RFQ — G.O. Bolme, D.R. Keffeler, <i>V.W. Brown, D.C. Clark, D. Hodgkins, P.D. Lara, M.L. Milder, D. Rees, P.J. Schafstall,</i> <i>J.D. Schneider, J.D. Sherman, R.R. Stevens, T. Zaugg</i>	923	WPA08
Beam Dynamics Studies of the Heavy Ion Fusion Accelerator Injector — E. Henestroza, <i>S.S. Yu, S. Eylon, D.P. Grote</i>	926	WPA09
First Tests at Injector for the S-Band Test Facility at DESY — M. Schmitz, W. Herold, <i>N. Holtkamp, W. Kriens, R. Walther</i>	929	WPA12
RF Phasing of the Duke Linac — Ping Wang, Nelson Hower, Patrick G. O'Shea	932	WPA13
Simulations and Measurements of the TTF Phase-1 Injector Gun — T. Garvey, M. Omeich, <i>M. Jablonka, J.M. Joly, H. Long</i>	935	WPA14
Experimental Studies on Cold Cathode Magnetron Gun — A.N. Dovbnya, V.V. Zakutin, <i>V.F. Zhiglo, A.N. Opanasenko, V.P. Romasko, S.A. Cherenshchikov</i>	938	WPA15
Secondary Emission in Cold-Cathode Magnetron Injection Gun — S.A. Cherenshchikov, <i>A.N. Dovbnya, A.N. Opanasenko</i>	939	WPA16
Design of a High Charge CW Photocathode Injector Test Stand at CEBAF — H. Liu, <i>D. Kehne, S. Benson, J. Bisognano, L. Cardman, F. Dylla, D. Engwall, J. Fugitt, K. Jordan,</i> <i>G. Neil, D. Neuffer, C. Sinclair, M. Wiseman, B. Yunn</i>	942	WPA17
CANDELA Photo-Injector Experimental Results With a Dispenser Photocathode — <i>C. Travier, B. Leblond, M. Bernard, J.N. Cayla, P. Thomas, P. Georges</i>	945	WPB01
A Multi-Cell RF Photoinjector Design — Sanghyun Park	948	WPB02
On the Frequency Scalings of RF Guns — Leon C.-L. Lin, J.S. Wurtele, S.C. Chen	951	WPB03
Waveguide Broad-Wall Coupling for RF Guns — Leon C.-L. Lin, S.C. Chen, J.S. Wurtele	954	WPB04

Charge and Wavelength Scaling of RF Photoinjectors: A Design Tool — J. Rosenzweig, E. Colby.....	957	WPB05
A Photocathode RF Gun Design for a mm-Wave Linac-Based FEL — A. Nassiri, T. Berenc, J. Foster, G. Waldschmidt, J. Zhou.....	961	WPB06
The RF Gun Development at SRRC — C.H. Ho, W.K. Lau, J.I. Hwang, S.Y. Hsu, Y.C. Liu.....	964	WPB07
Design and Construction of High Brightness RF Photoinjectors for TESLA — E. Colby, V. Bharadwaj, J.F. Ostiguy, T. Nicol, M. Conde, J. Rosenzweig.....	967	WPB08
Jitter Sensitivity in Photoinjectors — Patrick G. O'Shea.....	970	WPB09
Asymmetric Emittance Beam Generation Using Round Beam RF Guns and Non-linear Optics — G. Fiorentini, C. Pagani, L. Serafini.....	973	WPB10
The Argonne Wakefield Accelerator High Current Photocathode Gun and Drive Linac — P. Schoessow, E. Chojnacki, G. Cox, W. Gai, C. Ho, R. Konecny, J. Power, M. Rosing, J. Simpson, N. Barov, M. Conde.....	976	WPB11
Witness Gun for the Argonne Wakefield Accelerator — J. Power, J. Simpson, E. Chojnacki, R. Konecny.....	979	WPB12
Microwave Measurements of the BNL/SLAC/UCLA 1.6 Cell Photocathode RF Gun — D.T. Palmer, R.H. Miller, H. Winick, X.J. Wang, K. Batchelor, M. Woodle, I. Ben-Zvi.....	982	WPB13
Subpicosecond, Ultra-Bright Electron Injector — Bruce E. Carlsten, Martin L. Milder, John M. Kinross-Wright, Donald W. Feldman, Steven Russell, John G. Plato, Alan Shapiro, Boyd Sherwood, Jan Studebaker, Richard Lovato, David Warren, Carl Timmer, Ronald Cooper, Ronald Sturges, Mel Williams.....	985	WPB15
Energy Spread Compensation in an Electron Linear Accelerator — Yu.D. Tur, A.N. Dovbnya, V.A. Kushnir, V.V. Mitrochenko, D.L. Stepin.....	988	WPB16
On Enhancement of Limited Accelerating Charge — Yu. Tur.....	990	WPB17
Magnetic Pulse Compression Using a Third Harmonic RF Linearizer — D.H. Dowell, T.D. Hayward, A.M. Vetter.....	992	WPB20
A Comparison of L-Band and C-Band RF Guns as Sources for Inline-Injection Systems — Juan C. Gallardo, Harold G. Kirk, Thomas Meyerer.....	995	WPB21
Progress in the Study and Construction of the TESLA Test Facility Injector — R. Chehab, M. Bernard, J.C. Bourdon, T. Garvey, B. Jacquemard, M. Mencick, B. Mouton, M. Omeich, J. Rodier, P. Roudier, J.L. Saury, M. Taurigna-Quere, Y. Thiery, B. Aune, M. Desmons, J. Fusellier, F. Gougnaud, J.F. Gournay, M. Jablonka, J.M. Joly, M. Juillard, Y. Lussignol, A. Mosnier, B. Phung, S. Buhler, T. Junquera.....	998	WPB22

Particle Sources

Hollow Beam Profile in the Extraction System of ECR Ion Source — Y. Batygin, A. Goto, Y. Yano.....	1001	WPC01
Ion Sources for Use in Research and Applied High Voltage Accelerators — S. Nikiforov, V. Golubev, D. Solnyshkov, M. Svinin, G. Voronin.....	1004	WPC03
Direct Fast Beam Chopping of H⁻ Ion Beam in the Surface-Plasma H⁻ Ion Source — K. Shinto, A. Takagi, Z. Igarashi, K. Ikegami, M. Kinsho, S. Machida, M. Yoshii, Y. Mori.....	1007	WPC07
Emittance Measurements of the High Intensity Polarized Ion Source at IUCF — V. Derenchuk, R. Brown, H. Petri, E. Stephenson, M. Wedekind.....	1010	WPC08
Report on EBIS Studies for a RHIC Preinjector — E. Beebe, A. Herscovitch, A. Kponou, K. Prelec, J. Alessi, R. Schmieder.....	1013	WPC09
Development of a Volume H⁻ Ion Source for LAMPF — D.R. Swenson, R.L. York, R.R. Stevens Jr., C. Geisik, W. Ingalls, J.E. Stelzer, D. Fitzgerald.....	1016	WPC10
Generation of High Purity CW Proton Beams from Microwave-Driven Sources — David Spence, Keith R. Lykke.....	1019	WPC11
Computational Studies for an Advanced Design ECR Ion Source — G.D. Alton, J. Dellwo, R.F. Welton, D.N. Smithe.....	1022	WPC12
Pulsed Ion Sources of Duoplasmatron Type with Cold and Hot Cathodes — A. Glazov, V. Krasnopol'sky, R. Meshcheryov, V. Masalov.....	1025	WPC13
Double Pulse Experiment with a Velvet Cathode on the ATA Injector — G. Westenskow, G. Caporaso, Y. Chen, T. Houck, S. Sampayan.....	1027	WPC16

Emittance Measurements for the Illinois/CEBAF Polarized Electron Source — <i>B.M. Dunham, L.S. Cardman, C.K. Sinclair.....</i>	1030	WPC17
The NLC Positron Source — H. Tang, A.V. Kulikov, J.E. Clendenin, S.D. Ecklund, R.A. Miller, A.D. Yermian.....	1033	WPC18
Ferroelectric Cathodes as Electron Beam Sources — D. Flechtner, G.S. Kerslick, J.D. Ivers, J.A. Nation, L. Schächter.....	1036	WPC19
Studies of Linear and Nonlinear Photoelectric Emission for Advanced Accelerator Applications — R. Brogle, P. Muggli, P. Davis, G. Hairapetian, C. Joshi.....	1039	WPC20
A Derivative Standard for Polarimeter Calibration — G. Mulhollan, J. Clendenin, P. Sáez, D. Schultz, H. Tang, A.W. Pang, H. Hopster, K. Trantham, M. Johnston, T. Gay, B. Johnson, M. Magugumela, F.B. Dunning, G.K. Walters, G.F. Hanne.....	1043	WPC21
Analysis of Positron Focusing Section for SPring-8 Linac — A. Mizuno, S. Suzuki, H. Yoshikawa, T. Hori, K. Yanagida, H. Sakaki, T. Taniuchi, H. Kotaki, H. Yokomizo.....	1046	WPC22
R & D Activity on High QE Alkali Photocathodes for RF Guns — P. Michelato, A. Di Bona, C. Pagani, D. Sertore, S. Valeri.....	1049	WPC23
Development of an Accelerator-Ready Photocathode Drive Laser at CEBAF — S. Benson, M. Shinn.....	1052	WPC24

Linear Accelerators

Analytical Formulae for the Loss Factors and Wakefields of a Disk-loaded Accelerating Structure — J. Gao.....	1055	RPA03
Design Parameters for the Damped Detuned Accelerating Structure — K. Ko, K. Bane, R. Gluckstern, H. Hoag, N. Kroll, X.T. Lin, R. Miller, R. Ruth, K. Thompson, J. Wang.....	1058	RPA04
Operation of PLS 2-GeV Linac — W. Namkung, I.S. Ko, M.H. Cho, J.S. Bak, J. Choi, H.S. Lee.....	1061	RPA06
Radiation Measurements at the Advanced Photon Source (APS) Linear Accelerator — H.J. Moe, J.H. Vacca, V.R. Veluri, M. White.....	1064	RPA07
Positron Focusing in the Advanced Photon Source (APS) Linear Accelerator — Y.L. Qian, M. White.....	1067	RPA08
Bunch Length Measurements at the Advanced Photon Source (APS) Linear Accelerator — N.S. Sereno, R. Fuja, C. Gold, A.E. Grelick, A. Nassiri, J.J. Song, M. White.....	1070	RPA10
Performance of the Advanced Photon Source (APS) Linear Accelerator — M. White, N. Arnold, W. Berg, A. Cours, R. Fuja, J. Goral, A. Grelick, K. Ko, Y.L. Qian, T. Russell, N.S. Sereno, W. Wesolowski.....	1073	RPA11
TW Accelerating Structures with Minimal Surface Electric Field — O. Nezhevenko, D. Myakishev, V. Tarnetsky, V. Yakovlev.....	1076	RPA12
A 100 MeV Injector for the Electron Storage Ring at Kyoto University — T. Shirai, M. Kando, M. Ikegami, Y. Iwashita, H. Okamoto, S. Kakigi, H. Dewa, H. Fujita, A. Noda, M. Inoue, K. Mashiko.....	1079	RPA13
Phase Control and Intra-Pulse Phase Compensation of the Advanced Photon Source (APS) Linear Accelerator — A.E. Grelick, N. Arnold, K. Ko, N. Sereno, M. White.....	1082	RPA14
Error Sensitivity Study for Side Coupled Muffin Tin Structures using a Finite Difference Program — Warner Bruns.....	1085	RPA15
Design of Input Couplers and Endcells for Side Coupled Muffin-Tin Structures — Warner Bruns.....	1088	RPA16
Accelerator Archeology - The Resurrection of the Stanford MARKIII Electron Linac at Duke — P.G. O'Shea, F. Carter, C. Dickey, N. Hower, V.N. Litvinenko, R. Sachschtale, G. Swift, P. Wang, Y. Wu, J.M.J. Madey.....	1090	RPA17
Cold Model Test of Bipariodic L-Support Disk-and-Washer Linac Structure — Y. Iwashita, A. Noda, H. Okamoto, T. Shirai, M. Inoue.....	1093	RPA18
Compact Low Energy CW Linac with High Beam Current — A. Alimov, A. Chepurnov, O. Chubarov, D. Ermakov, K. Gudkov, B. Ishkhanov, I. Piskarev, V. Shvedunov, A. Shumakov.....	1096	RPA19
C-Band Linac RF-System for e+e- Linear Collider — T. Shintake, N. Akasaka, K.L.F. Bane, H. Hayano, K. Kubo, H. Matsumoto, S. Matsumoto, K. Oide, K. Yokoya.....	1099	RPA20
Initial Operation of the UCLA Plane Wave Transformer (PWT) Linac — R. Zhang, P. Davis, G. Hairapetian, M. Hogan, C. Joshi, M. Lampel, S. Park, C. Pellegrini, J. Rosenzweig, G. Travish.....	1102	RPA21

The UCLA Compact High Brightness Electron Accelerator — <i>P. Davis, G. Hairapetian, M. Hogan, C. Joshi, M. Lampel, S. Park, C. Pellegrini, J. Rosenzweig, G. Travish, R. Zhang</i>	1105	RPA22
A Semi-Automated System for the Characterization of NLC Accelerating Structures — <i>S.M. Hanna, G.B. Bowden, H.A. Hoag, R. Loewen, A.E. Vlieks, J.W. Wang</i>	1108	RPA23
SLAC Accelerator Operations Report: 1992-1995 — <i>R. Erickson, C.W. Allen, T.K. Inman, W. Linebarger, M. Stanek</i>	1111	RPA24
Beam Current Limitation in Microwave Accelerators — <i>A.V. Mishin, I.S. Shchedrin</i>	1114	RPA25
Installation and Commissioning of the e+/e- Injector for DAΦNE at Frascati — <i>K. Whitham, H. Amankath, J. Edighoffer, K. Fleckner, E. Gower, S. Lyons, D. Nett, D. Palmer, R. Sheppard, S. Sutter, P. Treas, A. Zante, R. Miller, R. Boni, H. Hsieh, F. Sannibale, M. Vescovi, G. Vignola</i>	1116	RPA26
Recent Studies of Linac for Production of Radioactive Beams in the INR — <i>I.N. Birukov, I.V. Gonin, D.V. Gorelov, A.N. Iljinov, V.A. Moiseev, P.N. Ostroumov, A.V. Tiunov</i>	1119	RPR01
RFQ Cold Model Studies — <i>P.G. Bricault, D. Joffe, H.R. Schneider</i>	1122	RPR02
Simulation of the TRIUMF Split-Ring 4-Rod RFQ with MAFIA — <i>P.G. Bricault, H.R. Schneider</i>	1125	RPR03
A Low-charge-state Injector Linac for ATLAS — <i>K.W. Shepard, J.W. Kim</i>	1128	RPR05
Progress of the Heidelberg High Current Injector — <i>C.-M. Kleffner, S. Auch, M. Grieser, D. Habs, V. Kößler, M. Madert, R. Repnow, D. Schwalm, H. Deitinghoff, A. Schempp, E. Jaeschke, R. von Hahn, S. Papureanu</i>	1131	RPR06
The New Concepts in Designing the CW High-current Linacs — <i>B.P. Murin, G.I. Batsikh, V.M. Belugin, B.I. Bondarev, A.A. Vasiljev, A.P. Durkin, Yu.D. Ivanov, V.A. Konovalov, A.P. Fedotov, I.V. Shumakov</i>	1134	RPR07
A Versatile, High-Power Proton Linac for Accelerator Driven Transmutation Technologies — <i>J.H. Billen, S. Nath, J.E. Stovall, H. Takeda, R.L. Wood, L.M. Young</i>	1137	RPR08
A Compact High-Power Proton Linac for Radioisotope Production — <i>H. Takeda, J.H. Billen, S. Nath, J.E. Stovall, R.L. Wood, L.M. Young</i>	1140	RPR09
Potentialities of Electron and Ion Beam Accelerators for Long-Lived Nuclear Waste Transmutation — <i>A. Shalnov, N. Abramenko, B. Bogdanovich, M. Karetnikov, A. Nesterovich, A. Puchkov</i>	1143	RPR10
RFQ Design for High-Intensity Proton Beams — <i>R. Ferdinand, J.-M. Lagniel, P. Mattei</i>	1146	RPR11
Methods for Increasing of Beam Intensity in Undulator Linear Accelerator — <i>E.S. Masunov</i>	1149	RPR12
Linac Integrated Scheme Using RF Energy Storage and Compression — <i>A.V. Smirnov</i>	1152	RPR13
Magnetic Field Influence on RF-Structures Electrodynamics Characteristics and Sparking Limit — <i>A. Shalnov, N. Abramenko, B. Bogdanovich, M. Karetnikov, A. Nesterovich, M. Tubaev</i>	1155	RPR15
Calculations on the Possibility of the Simultaneous Acceleration of Ions with Different Charge States in a RFQ — <i>H. Deitinghoff</i>	1158	RPR18
Phase-Scan Analysis Results for the First Drift Tube Linac Module in the Ground Test Accelerator: Data Reproducibility and Comparison to Simulations — <i>K.F. Johnson, O.R. Sander, G.O. Bolme, S. Bowling, R. Connolly, J.D. Gilpatrick, W.P. Lysenko, J. Power, E.A. Wadlinger, V. Yuan</i>	1161	RPR19
Accelerator Systems Optimizing Code — <i>C.C. Paulson, A.M.M. Todd, M.A. Peacock, M.F. Reusch, D. Bruhwiler, S.L. Mendelsohn, D. Berwald, C. Piaszczyk, T. Meyers, G.H. Gillespie, B.W. Hill, R.A. Jamison</i>	1164	RPR20
Unexpected Matching Insensitivity in DTL of GTA Accelerator — <i>V.W. Yuan, O.R. Sander, R.C. Connolly, J.D. Gilpatrick, K.F. Johnson, W.P. Lysenko, D.P. Rusthoi, M. Smith, R. Weiss</i>	1167	RPR22
Current Losses and Equilibrium in RF Linear Accelerators — <i>Nathan Brown, Martin Reiser</i>	1170	RPR23
MMF Linac Upgrade Possibilities for the Pulsed Neutron Source — <i>S.K. Esin, L.V. Kravchuk, A.I. Kvasha, P.N. Ostroumov, V.L. Serov</i>	1173	RPR24
Moscow Meson Factory DTL RF System Upgrade — <i>S.K. Esin, L.V. Kravchuk, A.I. Kvasha, V.L. Serov</i>	1175	RPR25

Pulsed and High Intensity Beams and Technology

Heavy Ion Fusion 2 MV Injector (Invited) — <i>S. Yu, S. Eylon, E. Henestroza, C. Peters, L. Reginato, D. Vanecek, F. delaRama, R. Hipple, J.D. Stoker, D. Grote, F. Deadrick</i>	1178	TAE01
Linac-Driven Spallation-Neutron Source (Invited) — <i>Andrew J. Jason</i>	1183	TAE02

High Average Power, High Current Pulsed Accelerator Technology (Invited) — <i>Eugene L. Neau</i>	1188	TAE03
Studies of Localized Space-Charge Waves in Space-Charge Dominated Beams (Invited) — <i>J.G. Wang, M. Reiser</i>	1193	TAE04
Design of the Jupiter Accelerator for Large X-ray Yields — J.J. Ramirez	1198	TAE05
Design and Power Flow Studies of a 500-TW Inductive Voltage Adder (IVA) Accelerator — <i>M.G. Mazarakis, J.W. Poukey, J.P. Corley, D.L. Smith, L. Bennett, J.J. Ramirez, P. Pankuch,</i> <i>I. Smith, P. Corcoran, P. Spence</i>	1201	TAE06
COBRA Accelerator for Sandia ICF Diode Research at Cornell University — David L. Smith, <i>Pete Ingwersen, Lawrence F. Bennett, John D. Boyes, David E. Anderson, John B. Greenly,</i> <i>Ravi N. Sudan</i>	1204	TAE07
Beam Injector and Transport Calculations for ITS — Thomas P. Hughes, David C. Moir, <i>Paul W. Allison</i>	1207	TAE08
Status of the AIRIX Induction Accelerator — Ph. Eyharts, Ph. Anthouard, J. Bardy, <i>C. Bonnafond, Ph. Delsart, A. Devin, P. Eyl, J. Labrousche, J. Launspach, J. De Mascureau,</i> <i>E. Merle, A. Roques, P. Le Taillandier, M. Thevenot, D. Villate, L. Voisin</i>	1210	TAE09
Pulse Modulators for Ion Recirculator Cells — T.F. Godlove, L.K. Len, F.M. Mako, <i>W.M. Black, K. Sloth</i>	1213	TAE10
A High Charge State Heavy Ion Beam Source for HIF — S. Eylon, E. Henestroza	1216	TAE11
Design and Operation of a 700kV, 700A Modulator — J.D. Ivers, G.S. Kerslick, J.A. Nation, <i>L. Schächter</i>	1219	TAE12
The 3 MEV, 200 KW High Voltage Electron Accelerator for Industrial Application — <i>N.G. Tolstun, V.S. Kuznetsov, A.S. Ivanov, V.P. Ovchinnikov, M.P. Svinjin</i>	1222	TAE13
Klystron Modulator for Industrial Linac — Yu.D. Tur, V.I. Beloglazov, E.A. Khomyakov, <i>V.P. Krivchikov, V.B. Mufel, V.V. Zakutin</i>	1225	TAE14
Optimization of High-Current Ion Beam Acceleration and Charge Compensation in Two Cusps of Induction Linac — Vyacheslav I. Karas', Nadya G. Belova	1227	WAA01
2,5-Dimensional Numerical Simulation of Propagation of the Finite Sequence of Relativistic Electron Bunches (REB) in Tenuous and Dense Plasmas — V.I. Karas', Ya.B. Fainberg, <i>V.D. Levchenko, Yu.S. Sigov</i>	1230	WAA02
Kinetic Simulation of Fields Excitation and Particle Acceleration by Laser Beat Wave in Non-Homogeneous Plasmas — V.I. Karas', Ya.B. Fainberg, V.D. Levchenko, Yu.S. Sigov	1233	WAA03
An Upgraded Proton Injection Kicker Magnet for the Fermilab MIR — J. Dinkel, R. Reilly	1236	WAA05
Fermilab Main Injector Abort Kicker System — C.C. Jensen, J.A. Dinkel	1239	WAA07
Analysis of the Electrical Noise from the APS Kicker Magnet Power Supplies — <i>J.A. Carwardine, J. Wang</i>	1242	WAA08
Design and Test Results of Kicker Units for the Positron Accumulator Ring at the APS — <i>J. Wang</i>	1245	WAA09
Development of a Modular and Upgradeable Fast Kicker Magnet System for the Duke Storage Ring — R.J. Sachtshale, C. Dickey, P. Morcombe	1248	WAA10
High Current High Accuracy IGBT Pulse Generator — V.V. Nesterov, A.R. Donaldson	1251	WAA11
Analysis and Design Modifications for Upgrade of Storage Ring Bump Pulse System Driving the Injection Bump Magnets at the ALS — G.D. Stover	1254	WAA14
Eddy Currents Induced in a Muon Storage Ring Vacuum Chamber Due to a Fast Kicker — <i>W.Q. Feng, E.B. Forsyth</i>	1257	WAA15
High Pulse Power Modulator for a S-Band Transmitter — J. DeCobert, B. Binns, R. Campbell, <i>A. Hawkins, D. Wang, A. Zolfaghari</i>	1260	WAA16
Modulator for Klystron 5045 — N.S. Dikansky, V. Akimov, B. Estrin, K. Gubin, I. Kazarezov, <i>V. Kokoulin, N. Kot, A. Novokhatsky, Yu. Tokarev, S. Vasserman</i>	1263	WAA17
High Voltage Nanosecond Generators for SIBERIA - 2 — A. Kadnikov, V. Deviatilov, <i>V. Korchuganov, Yu. Matveev, D. Shvedov</i>	1266	WAA18
High Gradient Insulator Technology for the Dielectric Wall Accelerator — S. Sampayan, <i>G. Caporaso, B. Carder, Y. Chen, C. Holmes, E. Lauer, D. Trimble, J. Elizondo, M. Krogh,</i> <i>B. Rosenblum, C. Eichenberger, J. Fockler</i>	1269	WAA19
Status of the First Stage of Linear Induction Accelerator SILUND-21 — A.A. Fateev, <i>G.V. Dolbilov, I.I. Golubev, I.N. Ivanov, V.V. Kosukhin, N.I. Lebedev, V.A. Petrov,</i> <i>V.N. Razuvakin, V.S. Shvetsov, M.V. Yurkov</i>	1272	WAA20

EMIR-M Installation in the Mode of Operation with Plasma Opening Switch — <i>V.P. Kovalev, V.M. Korepanov, B.M. Lavrent'ev, R.N. Munasyrov, B.A. Filatov</i>	1274	WAA21
--	------	-------

Magnet Technology

New Developments in Niobium Titanium Superconductors (Invited) — D.C. Larbalestier, <i>P.J. Lee</i>	1276	TPE01
Superconducting Magnets (Invited) — R. Perin	1282	TPE02
Assembly and Commissioning of the LHC Test String (Invited) — P. Faugeras	1288	TPE03
Construction and Testing of Arc Dipoles and Quadrupoles for the Relativistic Heavy Ion Collider (RHIC) at BNL (Invited) — P. Wanderer, J. Muratore, M. Anerella, G. Ganetis, A. Ghosh, A. Greene, R. Gupta, A. Jain, S. Kahn, E. Kelly, G. Morgan, A. Prodel, M. Rehak, W. Sampson, R. Thomas, P. Thompson, E. Willen	1293	TPE04
Permanent Magnet Design for the Fermilab Main Injector Recycler Ring — G.W. Foster, K. Bertsche, J.-F. Ostiguy, B. Brown, H. Glass, G. Jackson, M. May, D. Orris, Dick Gustafson	1298	TPE05
Recent Advances in Insertion Devices (Invited) — E. Gluskin, E.R. Moog	1301	TPE06
Permanent Magnet Beam Transport (Invited) — R.F. Holsinger	1305	TPE07
Statistical Analyses of the Magnet Data for the Advanced Photon Source Storage Ring Magnets (Invited) — S.H. Kim, D.W. Carnegie, C. Doose, R. Hogrefe, K. Kim, R. Merl	1310	TPE08
The Magnet System for the BESSY II Injector Synchrotron — T. Knuth, D. Krämer, E. Weihreter, I. Chertok, S. Michailov, B. Sukhina	1316	TPE09
Segmented High Quality Undulators — J. Chavanne, P. Elleaume, P. Van Vaerenbergh	1319	TPE10
Design of the PEP-II Low-Energy Ring Arc Magnets — T. Henderson, N. Li, J. Osborn, J. Tanabe, D. Yee, R. Yourd, W. Du, Y. Jiang, Y. Sun	1322	FAP01
Prototype Development of the BESSY II Storage Ring Magnetic Elements — T. Becker, D. Krämer, S. Kuchler, U. Strönisch, V. Korchuganov, N. Kuznetsov, E. Levichev	1325	FAP02
Design, Construction, and Procurement Methodology of Magnets for the 7-GeV Advanced Photon Source — A. Gorski, J. Argyrakis, J. Biggs, E. Black, J. Humbert, J. Jagger, K. Thompson	1328	FAP03
The Main Injector Trim Dipole Magnets — R. Baiod, D.J. Harding, D.E. Johnson, P.S. Martin, S. Mishra	1331	FAP04
The Main Injector Chromaticity Correction Sextupole Magnets: Measurements and Operating Schemes — C.M. Bhat, A. Bogacz, B.C. Brown, D.J. Harding, Si J. Fang, P.S. Martin, H.D. Glass, J. Sim	1334	FAP05
Magnetic Field Measurements of the Initial Fermilab Main Injector Production Quadrupoles — D.J. Harding, R. Baiod, B.C. Brown, J.A. Carson, N.S. Chester, E. Desavouret, J. DiMarco, J.D. Garvey, H.D. Glass, P.J. Hall, P.S. Martin, P.O. Mazur, C.S. Mishra, A. Mokhtarani, J.M. Nogiec, D.F. Orris, J.E. Pachnik, A.D. Russell, S.A. Sharonov, J.W. Sim, J.C. Tompkins, K. Trombly-Freytag, D.G.C. Walbridge, V.A. Yarba	1337	FAP06
Magnetic Field Measurements of the Initial Fermilab Main Injector Production Dipoles — D.J. Harding, R. Baiod, B.C. Brown, J.A. Carson, N.S. Chester, E. Desavouret, J. DiMarco, J.D. Garvey, H.D. Glass, P.J. Hall, P.S. Martin, P.O. Mazur, S. Mishra, A. Mokhtarani, J.M. Nogiec, D.F. Orris, J.E. Pachnik, A.D. Russell, S.A. Sharonov, J.W. Sim, J.C. Tompkins, K. Trombly-Freytag, D.G.C. Walbridge, V.A. Yarba	1340	FAP07
The Fermilab Main Injector Dipole and Quadrupole Cooling Design and Bus Connections — J.A. Satti	1343	FAP08
Design of the Fermilab Main Injector Lambertson — D.E. Johnson, R. Baiod, D.J. Harding, P.S. Martin, M. May	1346	FAP09
Three-Dimensional End Effects in Iron Septum Magnets — J.-F. Ostiguy, D.E. Johnson	1349	FAP10
Design and B-field Measurements of a Lambertson Injection Magnet for the RHIC Machine — N. Tsoupas, E. Rodger, J. Claus, H.W. Foelsche, P. Wanderer	1352	FAP11
The APS Direct-Drive Pulsed Septum Magnets — S. Sheynin, F. Lopez, S.V. Milton	1355	FAP12
Development of the Pulse Magnets for the Booster Synchrotron of SPring-8 — H. Yonehara, H. Suzuki, T. Nagafuchi, M. Kodaira, T. Aoki, N. Tani, S. Hayashi, Y. Ueyama, T. Kaneda, Y. Sasaki, H. Abe, H. Yokomizo	1358	FAP13
Magnetic Design of the LNLS Transport Line — R.H.A. Farias, Liu Lin, G. Tosin	1361	FAP14
Construction and Characterization of Combined Function Quadrupoles — G. Tosin	1364	FAP15

Dipole Magnets for the SLAC 50 GeV A-Line Upgrade — R. Erickson, S. DeBarger, C.M. Spencer, Z. Wolf.....	1366	FAP16
Design and Testing of the Magnetic Quadrupole for the Heavy Ion Fusion Program — R. Benjegerdes, A. Faltens, W. Fawley, C. Peters, L. Reginato, M. Stuart	1369	FAP17
Design and Construction of a Large Aperture, Quadrupole Electromagnet Prototype for ILSE — M. Stuart, A. Faltens, W.M. Fawley, C. Peters, M.C. Vella.....	1372	FAP18
A Permanent Race-Track Microtron End Magnet — A.I. Karev, V.N. Melekhin, V.I. Shvedunov, N.P. Sobenin, W.P. Trower.....	1375	FAP19
Planar Permanent Magnet Multipoles: Measurements and Configurations — T. Cremer, R. Tatchyn.....	1378	FAP20
Temperature Considerations in the Design of a Permanent Magnet Storage Ring — K. Bertsche, J.-F. Ostiguy, W.B. Foster.....	1381	FAP21
3D Numerical Analysis of Magnets and the Effect of Eddy Current on Fast Steering — T. Nagatsuka, T. Koseki, Y. Kamiya, Y. Terada	1384	FAP22
MEB Resistive Magnets Prototypes Manufacturing — G. Batskikh, G. Mamaev, T. Latypov, I. Tenyakov, Y. Tereshkin.....	1387	FAP24

Volume 3

Magnet Technology (cont'd)

Quench Antennas for RHIC Quadrupole Magnets — T. Ogitsu, A. Terashima, K. Tsuchiya, G. Ganetis, J. Muratore, P. Wanderer.....	1390	FAQ02
Superconducting 8 cm Corrector Magnets for the Relativistic Heavy Ion Collider (RHIC) — A. Morgillo, J. Escallier, G. Ganetis, A. Greene, A. Ghosh, A. Jain, E. Kelly, A. Marone, G. Morgan, J. Muratore, W. Sampson, P. Thompson, P.J. Wanderer, E. Willen.....	1393	FAQ03
Superconducting Sextupoles and Trim Quadrupoles for RHIC — P. Thompson, M. Anerella, G. Ganetis, A. Ghosh, A. Greene, R. Gupta, A. Jain, E. Kelly, M. Lindner, G. Morgan, J. Muratore, W. Sampson, P. Wanderer, E. Willen.....	1396	FAQ04
Study of UNK Quench Protection System on the String of 4 UNK Superconducting Magnets — A. Andriishchin, O. Afanasiev, V. Gridasov, A. Erochin, E. Kachtanov, K. Myznikov, V. Sychev, L. Vassiliev, O. Veselov, N. Yarygin.....	1399	FAQ06
Two Alternate High Gradient Quadrupoles; An Upgraded Tevatron IR and a "Pipe" Design — A.D. McInturff, J.M. van Oort, R.M. Scanlan.....	1402	FAQ07
Superconducting Focusing Solenoid for X-band Klystron — T. Ogitsu, T. Higo, H. Mizuno, Y. Imai, T. Inaguchi, T. Minato, T.H. Kim, T. Uemura, S. Yokoyama, Z. Wolf, D. Jensen, P. Radusewicz.....	1405	FAQ08
A High Gradient Superconducting Quadrupole for a Low Charge State Ion Linac — J.W. Kim, K.W. Shepard, J.A. Nolen.....	1408	FAQ09
Status of the High Brilliance Synchrotron Radiation Source BESSY-II — E. Jaeschke, S. Khan, D. Krämer, D. Schirmer	1411	FAQ12
Harmonic Generation FEL Magnets: Measured B-fields Compared to 3D Simulations — W.S. Graves, L. Solomon.....	1414	FAQ13
Measurement of Ramp Rate Sensitivity in Model Dipoles with Ebanol-Coated Cable — C. Haddock, V. Kovachev, D. Capone.....	1417	FAQ14
Combined Element Magnet Production for the Relativistic Heavy Ion Collider (RHIC) at BNL — S. Mulhall, H. Foelsche, G. Ganetis, A. Greene, E. Kelly, S. Plate, E. Willen	1420	FAQ15
Field Quality Control Through the Production Phase of the RHIC Arc Dipoles — R. Gupta, A. Jain, S. Kahn, G. Morgan, P. Thompson, P. Wanderer, E. Willen	1423	FAQ16
The Elliptical Multipole Wiggler Project — E. Gluskin, D. Frachon, P.M. Ivanov, J. Maines, E.A. Medvedko, E. Trakhtenberg, L.R. Turner, I. Vasserman, G.I. Erg, Yu.A. Evtushenko, N.G. Gavrilov, G.N. Kulipanov, A.S. Medvedko, S.P. Petrov, V.M. Popik, N.A. Vinokurov, A. Friedman, S. Krinsky, G. Rakowsky, O. Singh	1426	FAQ17
Results of Magnetic Measurements and Field Integral Compensation for the Elliptical Multipole Wiggler — D. Frachon, P.M. Ivanov, E.A. Medvedko, I. Vasserman, O. Despe, Y.G. Kang	1429	FAQ18

Status of ELETTRA Insertion Devices — R.P. Walker, R. Bracco, A. Codutti, B. Diviacco, D. Millo, D. Zangrando	1432	FAQ19
Expected Radiation Spectra of a 30-m Long Undulator in SPring-8 — M. Takao, Y. Miyahara.....	1435	FAQ20
Analytical Formulation of a Quasi-periodic Undulator — M. Takao, S. Hashimoto, S. Sasaki, Y. Miyahara	1438	FAQ21
High-Field Strong-Focusing Undulator Designs for X-Ray Linac Coherent Light Source (LCLS) Applications — S. Caspi, R. Schlueter, R. Tatchyn.....	1441	FAQ23
Wigglers at the Advanced Light Source — E. Hoyer, J. Akre, D. Humphries, T. Jackson, S. Marks, Y. Minamihara, P. Pipersky, D. Plate, G. Portmann, R. Schlueter.....	1444	FAQ24
Design of End Magnetic Structures for the Advanced Light Source Wigglers — D. Humphries, J. Akre, E. Hoyer, S. Marks, Y. Minamihara, P. Pipersky, D. Plate, R. Schlueter.....	1447	FAQ25
Passive End Pole Compensation Scheme for a 1.8 Tesla Wiggler — L.H. Chang, Ch. Wang, C.H. Chang, T.C. Fan.....	1450	FAQ26
Insertion of Helical Siberian Snakes in RHIC — A. Luccio, F. Pilat	1453	FAQ28
Modeling of WLS Field with Piecewisely Constant Magnets — Zuping Liu, Aihua Zhao.....	1456	FAQ29
A BESSY-1 6 Tesla WLS Effect Compensation Scheme — Zuping Liu, Aihua Zhao.....	1459	FAQ30
16 Tesla Block-Coil Dipole for Future Hadron Colliders — Peter M. McIntyre, Weijun Shen.....	1462	FAQ31
Automated Methods of Field Harmonic Signal Extraction and Processing for the Magnets in Superconducting Supercollider — T.S. Jaffery, J. Butteris, M. Wake	1465	FAQ32

Radio Frequency Technology

Review of the Development of RF Cavities for High Currents (Invited) — J. Kirchgessner.....	1469	F AE01
Performance of Normal Conducting Structures for Linear Colliders (Invited) — Toshiyasu Higo.....	1474	F AE02
High Gradient Superconducting RF Systems (Invited) — J. Graber.....	1478	F AE03
Development and Advances in Conventional High Power RF Systems (Invited) — P.B. Wilson.....	1483	F AE04
The Upgraded RF System for the AGS and High Intensity Proton Beams (Invited) — J.M. Brennan.....	1489	F AE05
Phase-Stable, Microwave FEL Amplifier — Bruce E. Carlsten, Michael V. Fazio, W. Brian Haynes, Lisa M. May, James M. Potter	1494	F AE06
1.2 MW Klystron for Asymmetric Storage Ring B Factory — W.R. Fowkes, G. Caryotakis, E. Doyle, E. Jongewaard, C. Pearson, R. Phillips, J. Sackett, E. Wright, H. Bohlen, G. Huffman, S. Lenci, E. Lien, E. McCune, G. Miram	1497	F AE07
Analysis of Multipacting in Coaxial Lines — E. Somersalo, P. Ylä-Oijala, D. Proch.....	1500	F AE08
An Accelerator Resonantly Coupled with an Energy Storage (ARES) for the KEKB — Y. Yamazaki, K. Akai, N. Akasaka, E. Ezura, T. Kageyama, F. Naito, T. Shintake, Y. Takeuchi.....	1503	F AE09
Non Integer Harmonic Number Acceleration of Lead Ions in the CERN SPS — D. Boussard, T. Bohl, T. Linnekar, U. Wehrle.....	1506	F AE10
Analysis and Results of the Industrial Production of the Superconducting Nb/Cu Cavities for the LEP2 Project — E. Chiaveri, C. Benvenuti, R. Cosso, D. Lacarrere, K.M. Schirm, M. Taufer, W. Weingarten.....	1509	F AE11
Performance Experience with the CEBAF SRF Cavities — C. Reece, J. Benesch, M. Drury, C. Hovater, J. Mammoser, T. Powers, J. Preble.....	1512	F AE12
Beam Test of a Superconducting Cavity for the CESR Luminosity Upgrade — H. Padamsee, P. Barnes, S. Belomestnykh, K. Berkelman, M. Billing, R. Ehrlich, G. Flynn, Z. Greenwald, W. Hartung, T. Hays, S. Henderson, R. Kaplan, J. Kirchgessner, J. Knobloch, D. Moffat, H. Muller, E. Nordberg, S. Peck, M. Pisharody, J. Reilly, J. Rogers, D. Rice, D. Rubin, D. Sagan, J. Sears, M. Tigner, J. Welch.....	1515	F AE13

Radio Frequency Power Sources

Development of Input & Output Structures for High Power X-Band TWT Amplifiers — S. Naqvi, Cz. Golkowski, G.S. Kerslick, J.A. Nation, L. Schächter.....	1518	TAQ01
Characterization of a Klystron as a RF Source for High-Average-Power Accelerators — D. Rees, D. Keffeler, W. Roybal, P.J. Tallerico.....	1521	TAQ02
Choppertron II — T.L. Houck, G.A. Westenskow, J. Haimson, B. Mecklenburg.....	1524	TAQ03

The Resistive-Wall Klystron as a High-Power Microwave Source — Han S. Uhm.....	1527	TAQ04
Operating Conditions of High-Power Relativistic Klystron — Han S. Uhm	1530	TAQ05
Spurious Oscillations in High Power Klystrons — B. Krietenstein, K. Ko, T. Lee, U. Becker, T. Weiland, M. Dohlus.....	1533	TAQ06
In-House Repair of a 30 Megawatt S Band Klystron — R. Sachtschale, P.G. O'Shea, M. Ponds, G. Swift.....	1536	TAQ07
Development of a High Power 1.2 MW CW L-Band Klystron — K. Hirano, Y.L. Wang, T. Emoto, A. Enomoto, I. Sato	1539	TAQ08
Ultrarelativistic Klystron - a Future Super Power UHF Generator — F.A. Vodopianov	1542	TAQ10
A 200 KW Power Amplifier and Solid State Driver for the Fermilab Main Injector — J. Reid, H. Miller	1544	TAQ11
A 476 MHz RF System for the Storage Mode of the AmPS Ring — F. Kroes, P. de Groen, E. Heine, B. Heutenik, A. Kruijer, B. Munneke, R. Pirovano, T. Sluijk, J. Verkooyen.....	1547	TAQ12
Lifetime Experience with Low Temperature Cathodes Equipped in Super Power Klystrons — Rudolf Backmor.....	1550	TAQ13
Microwave System of PLS 2-GeV Linac — H.S. Lee, O.H. Hwang, S.H. Park, C.M. Ryu, W. Namkung	1553	TAQ14
Klystron-Modulator System Performances for PLS 2-GeV Linac — M.H. Cho, J.S. Oh, S.S. Park, W. Namkung.....	1556	TAQ15
Klystron Modulator Operation and Upgrades for the APS Linac — Thomas J. Russell, Alexander Cours	1559	TAQ16
Prospects for Developing Microwave Amplifiers to Drive Multi-TeV Linear Colliders — V.L. Granatstein, G.S. Nusinovich, J. Calame, W. Lawson, A. Singh, H. Guo, M. Reiser.....	1561	TAQ17
Design of 100 MW, Two-Cavity Gyroklystrons for Accelerator Applications — J.P. Calame, W. Lawson, J. Cheng, B. Hogan, M. Castle, V.L. Granatstein, M. Reiser.....	1563	TAQ18
Design of Three-Cavity Coaxial Gyroklystron Circuits for Linear Collider Applications — W. Lawson, G. Saraph, J.P. Calame, J. Cheng, M. Castle, B. Hogan, M. Reiser, V.L. Granatstein, H. Metz	1566	TAQ19
Numerical Simulation of Magnicon Amplifier — V. Yakovlev, O. Danilov, O. Nezhevenko, V. Tarnetsky.....	1569	TAQ21
RF-Power Upgrade Systems with Energy Compression for Electron Linacs — A. Shalnov, B.Yu. Bogdanovich, A. Ignatyev, V. Senyukov.....	1572	TAQ23
RF-Power Upgrade System with Resonant Loading — A. Shalnov, B. Bogdanovich, A. Ignatyev, V. Senyukov.....	1575	TAQ24
High-Power Test of Traveling-Wave-Type RF-Pulse Compressor — S. Yamaguchi, A. Enomoto, I. Sato, Y. Igarashi.....	1578	TAQ25
Active Radiofrequency Pulse Compression Using Switched Resonant Delay Lines — Sami G. Tantawi, Ronald D. Ruth, A.E. Vlieks.....	1581	TAQ26
Design of a Multi-Megawatt X-Band Solid State Microwave Switch — Sami G. Tantawi, Terry G. Lee, Ronald D. Ruth, A.E. Vlieks, Max Zolotarev	1584	TAQ27
Reduced Field TE01 X-Band Traveling Wave Window — W.R. Fowkes, R.S. Callin, S.G. Tantawi, E.L. Wright.....	1587	TAQ28
Design and High-Power Test of a TE11-Mode X-Band RF Window with Taper Transitions — Y. Otake, S. Tokumoto, H. Mizuno.....	1590	TAQ29
Feasibility Study of Optically Coupling RF-Power at mm Waves — B. Littmann, H. Henke.....	1593	TAQ30
A Low-Frequency High-Voltage RF-Barrier Bunching System for High-Intensity Neutron Source Compressor Rings — T.W. Hardek, D. Rees, C. Ziomek.....	1596	TAQ31
Temporal Evolution of Multipactor Discharge — R. Kishek, Y.Y. Lau, R.M. Gilgenbach.....	1599	TAQ32
Stabilizing a Power Amplifier Feeding a High Q Resonant Load — A.K. Mitra, R.L. Poirier, J.J. Lu, R. Hohbach.....	1602	TAQ33
Study of 14 GHz VLEPP Klystron With RF Absorbing Drift Tubes — G.V. Dolbilov, N.I. Azorsky, A.A. Fateev, N.I. Lebedev, V.A. Petrov, V.P. Sarantsev, V.S. Shvetsov, M.V. Yurkov.....	1605	TAQ34
24-MW, 24-μs Pulse RF Power Supply For Linac-Based FELs — E. Ohshita, Y. Morii, S. Abe, S. Okuma, K. Wakita, T. Tomimasu, I. Ito, Y. Miyai, K. Nakata, M. Hakota	1608	TAQ35
Initial Operation of an X-Band Magnicon Amplifier Experiment — S.H. Gold, A.K. Kinkad, A.W. Fliflet, B. Hafizi	1611	TAQ37

Superconducting RF

The Effects of Tuning and Terminating on the Operating Mode of Multi-Cell Coupled Cavity — Zubao Qian.....	1614	TPP01
Response of Superconducting Cavities to High Peak Power — T. Hays, H. Padamsee.....	1617	TPP02
Development of HOM Damper for B-Factor (KEKB) Superconducting Cavities — T. Tajima, K. Asano, T. Furuya, M. Izawa, S. Mitsunobu, T. Takahashi, N. Gamo, S. Iida, Y. Ishi, Y. Kijima, S. Kokura, M. Kudo, K. Sennyu, S. Tachibana, H. Takashina, N. Taniyama.....	1620	TPP03
Microscopic Examination of Defects Located by Thermometry in 1.5 GHz Superconducting Niobium Cavities — J. Knobloch, R. Durand, H. Muller, H. Padamsee.....	1623	TPP04
RF System for the NSLS Coherent Infrared Radiation Source — W. Broome, R. Biscardi, J. Keane, P. Mortazavi, M. Thomas, J.M. Wang.....	1626	TPP06
Development of TESLA-type Cavity at KEK — M. Ono, E. Kako, S. Noguchi, K. Saito, T. Shishido, M. Wake, H. Inoue, T. Fujino, Y. Funahashi, M. Matsuoka, T. Suzuki, T. Higuchi, H. Umezawa.....	1629	TPP07
Study of Luminous Spots Observed on Metallic Surfaces Subjected to High RF Fields — T. Junquera, S. Maïssa, M. Fouaidy, A. Le Goff, B. Bonin, M. Luong, H. Safa, J. Tan.....	1632	TPP09
Test Results for a Heat-Treated 4-Cell 805-MHz Superconducting Cavity — Brian Rusnak, Alan Shapiro.....	1636	TPP10
An Advanced Rotating T-R Mapping & its Diagnoses of TESLA 9-Cell Superconducting Cavity — Q.S. Shu, G. Deppe, W-D. Möller, M. Pekeler, D. Proch, D. Renken, P. Stein, C. Stolzenburg, T. Junquera, A. Caruette, M. Fouaidy.....	1639	TPP11
Improvements to Power Couplers for the LEP2 Superconducting Cavities — J. Tückmantel, C. Benvenuti, D. Bloess, D. Boussard, G. Geschonke, E. Haebel, N. Hilleret, S. Juras, H.P. Kindermann, J. Uythoven, C. Wyss, M. Stirbet.....	1642	TPP12
Arcing Phenomena on CEBAF RF-Windows at Cryogenic Temperatures — Tom Powers, Peter Kneisel, Ray Allen.....	1645	TPP13
Surface Scanning Thermometers for Diagnosing the TESLA SRF Cavities — T. Junquera, A. Caruette, M. Fouaidy, Q.S. Shu.....	1648	TPP14
Microwave Surface Resistance of YBaCuO Superconducting Films Laser-Ablated on Copper Substrates — J. Liu, K. Asano, E. Ezura, M. Fukutomi, S. Inagaki, S. Isagawa, K. Komori, S. Kumagai, H. Nakanishi, M. Tosa, K. Yoshihara.....	1652	TPP16

Room Temperature RF

Transverse Coupling Impedance Measurement Using Image Current — D. Sun, P. Colestock, M. Foley.....	1655	WPP01
Decreasing Transient Beam Loading in RF Cavities of U-70 Accelerator — O.P. Lebedev.....	1658	WPP02
RF System for Bunch Lengthening — R. Biscardi, G. Ramirez.....	1660	WPP03
Electromagnetic Field Vector Components Precise Measurements in Accelerating Structures — M.A. Chernogubovsky, M.F. Vorogushin.....	1663	WPP04
A New Tuning Method for Traveling Wave Structures — T. Khabiboulline, V. Puntus, M. Dohlus, N. Holtkamp, G. Kreps, S. Ivanov, K. Jin.....	1666	WPP05
RF Systems for RHIC — J. Rose, J. Brodowski, R. Connolly, D.P. Deng, S. Kwiatkowski, W. Pirkel, A. Ratti.....	1669	WPP07
A New RF System for Bunch Coalescing in the Fermilab Main Ring — J. Dey, I. Kourbanis, D. Wildman.....	1672	WPP08
Higher Order Modes of the Main Ring Cavity at Fermilab — J. Dey, D. Wildman.....	1675	WPP09
RF Measurements and Control of Higher Order Modes in Accelerating Cavities — V. Veshcherevich, S. Krutikhin, I. Kuptsov, S. Nosyrev, A. Novikov, I. Sedlyarov.....	1678	WPP10
RF System of VEPP-4M Electron-Positron Collider — E. Gorniker, P. Abramsky, V. Arbutov, S. Belomestnykh, A. Bushuyev, M. Fomin, I. Kuptsov, G. Kurkin, S. Nosyrev, V. Petrov, I. Sedlyarov, V. Veshcherevich.....	1681	WPP11
Storage Ring Cavity Higher-Order Mode Dampers for the Advanced Photon Source — Paul Matthews, Yoon Kang, Robert Kustom.....	1684	WPP12

Reduction of Multipactor in RF Ceramic Windows Using a Simple Titanium-Vapor Deposition System — <i>K. Primdahl, R. Kustom, J. Maj</i>	1687	WPP13
Cooling the APS Storage Ring Radio-Frequency Accelerating Cavities Thermal/Stress/Fatigue Analysis and Cavity Cooling Configuration — <i>K. Primdahl, R. Kustom</i>	1690	WPP14
RF Cavities for the Positron Accumulator Ring (PAR) of the Advanced Photon Source (APS) — <i>Y.W. Kang, A. Nassiri, J.F. Bridges, T.L. Smith, J.J. Song</i>	1693	WPP16
The Proposal of Complex Impedance Termination for Versatile HOM Damper Cavity — <i>V.V. Paramonov</i>	1696	WPP17
The Magnetron-Type Varactor for Fast Control in Accelerator RF Systems — <i>M.I. Kuznetsov, V.V. Paramonov, Yu.V. Senichev, I.B. Enchevich, R.L. Poirier</i>	1699	WPP18
The Distortion of the Accelerating Field Distribution in Compensated Structures due to Steady-State Beam Loading — <i>V.G. Andreev, V.V. Paramonov</i>	1702	WPP19
The Indiana University Cooler Injector Synchrotron RF System — <i>A. Pei, M. Ellison, D. Friesel, D. Jenner, X. Kang, S.Y. Lee, D. Li, J. Liu, A. Riabko, L. Wang, K. Hedblom</i>	1705	WPP20
The Indiana University Cooler Injection Synchrotron RF Cavity — <i>A. Pei, M. Ellison, D. Friesel, D. Jenner, X. Kang, S.Y. Lee, D. Li, J. Liu, A. Riabko, L. Wang, K. Hedblom</i>	1708	WPP21
Determination of Resonant Frequency and External Q Values for the Bessy II HOM-Damped Cavity — <i>Frank Schönfeld, Bengt Littmann</i>	1711	WPP22
106 MHz Cavity for Improving Coalescing Efficiency in the Fermilab Main Ring — <i>J. Dey, I. Kourbanis, D. Wildman</i>	1714	WPP23
On the Higher Order Mode Coupler Design for Damped Accelerating Structures — <i>Jie Gao</i>	1717	WPQ01
High Power Window Tests on a 500 MHz Planar Window for the CESR Upgrade — <i>M. Pisharody, P. Barnes, E. Chojnacki, R. Durand, T. Hays, R. Kaplan, J. Kirchgessner, J. Reilly, H. Padamsee, J. Sears</i>	1720	WPQ02
Operational Performances and Future Upgrades for the ELETTRA RF System — <i>A. Fabris, A. Massarotti, C. Pasotti, M. Svandrlik</i>	1723	WPQ04
X-Band High Power Dry Load for NLCTA — <i>K. Ko, H. Hoag, T. Lee, S. Tantawi</i>	1726	WPQ05
Development of a High-Power RF Cavity for the PEP-II B Factory — <i>R.A. Rimmer, M.A. Allen, J. Saba, H. Schwarz, F.C. Belser, D.D. Berger, R.M. Franks</i>	1729	WPQ06
A Design of Input Coupler for RF-Cavity — <i>T. Nagatsuka, T. Koseki, Y. Kamiya, M. Izawa, Y. Terada</i>	1732	WPQ07
Design of the KEKB RF System — <i>K. Akai, E. Ezura, Y. Yamazaki</i>	1735	WPQ08
RF Characteristics of ARES Cold Models — <i>N. Akasaka, K. Akai, T. Kageyama, T. Shintake, Y. Yamazaki</i>	1738	WPQ09
Design of Traveling Wave Windows for the PEP-II RF Coupling Network — <i>N.M. Kroll, C.-K. Ng, J. Judkins, M. Neubauer</i>	1741	WPQ10
Impedance Spectrum for the PEP-II RF Cavity — <i>X.E. Lin, K. Ko, C.-K. Ng</i>	1744	WPQ12
Measurement and Analysis of Higher-Order-Mode (HOM) Damping in B-Factor R-F Cavities — <i>D.A. Goldberg, M. Irwin, R.A. Rimmer</i>	1747	WPQ13
Planar Structures for Electron Acceleration — <i>H. Henke</i>	1750	WPQ14
Precise Fabrication of X-Band Detuned Accelerating Structure for Linear Collider — <i>T. Higo, H. Sakai, Y. Higashi, T. Takatomi, S. Koike</i>	1753	WPQ15
Development of a Beam-Pipe HOM Absorber for the ATF Damping Ring — <i>F. Hinode, S. Sakanaka</i>	1756	WPQ16
Development of a HOM-Damped Cavity for the KEK B-Factor (KEKB) — <i>T. Kageyama, K. Akai, N. Akasaka, E. Ezura, F. Naito, T. Shintake, Y. Takeuchi, Y. Yamazaki, T. Kobayashi</i>	1759	WPQ17
Possible Cavity Construction Techniques for the DIAMOND Storage Ring — <i>D.M. Dykes, D.S.G. Higgins</i>	1762	WPQ18
The Design of the 26.7 MHz RF Cavity for RHIC — <i>J. Rose, J. Brodowski, D.P. Deng, S. Kwiatkowski, W. Pirkel, A. Ratti</i>	1765	WPQ19
A Design Upgrade of the RF Cavity and Its Power Window for High Current Operation of the NSLS X-Ray Storage Ring — <i>P. Mortazavi, M. Thomas</i>	1768	WPQ20
A Ferrite Loaded Untuned Cavity for a Compact Proton Synchrotron — <i>J.I. Hirota, K. Hiramoto, M. Nishi, Y. Iwashita, A. Noda, M. Inoue</i>	1770	WPQ21
On the Theory of Two Coupled Cavities — <i>N.I. Aizatsky</i>	1773	WPQ22

Measurement of Multipacting Currents of Metal Surfaces in RF Fields — D. Proch, <i>D. Einfeld, R. Onken, N. Steinhauser</i>	1776	WPQ24
Optimization of CLIC Transfer Structure (CTS) Design to Meet New Drive Beam Parameters — A. Millich	1779	WPQ25
A High-Power Multiple-Harmonic Acceleration System for Proton- and Heavy-Ion Synchrotrons — P. Ausset, G. Charreau, F.J. Etzkorn, C. Fougeron, H. Meuth, S. Papureanu, <i>A. Schnase</i>	1781	WPQ26
A Bunch Lengthening RF Cavity for Aladdin — K.J. Kleman	1785	WPR01
Design of a High-Power Test Cavity for the ATF Damping Ring — S. Sakanaka, F. Hinode, <i>M. Akemoto, S. Tokumoto, T. Higo, J. Urakawa, T. Miura, Y. Hirata, K. Satoh</i>	1788	WPR02
Design of an RF System for the ATF Damping Ring — S. Sakanaka, F. Hinode, M. Akemoto, <i>H. Hayano, H. Matsumoto, K. Kubo, S. Tokumoto, T. Higo, J. Urakawa</i>	1791	WPR03
Development of a Damped Cavity with SiC Beam-Duct — T. Koseki, M. Izawa, Y. Kamiya	1794	WPR04
HOM Absorber for the KEKB Normal Conducting Cavity — Y. Takeuchi, K. Akai, <i>N. Akasaka, E. Ezura, T. Kageyama, F. Naito, T. Shintake, Y. Yamazaki</i>	1797	WPR05
PEP-II B-Factory Prototype Higher Order Mode Load Design — R. Pendleton, K. Ko, C. Ng, <i>M. Neubauer, H. Schwarz, R. Rimmer</i>	1800	WPR07
High-Power RF Window and Coupler Development for the PEP-II B Factory — M. Neubauer, <i>K. Fant, J. Hodgson, J. Judkins, H. Schwarz, R.A. Rimmer</i>	1803	WPR08
Input Coupler for the KEKB Normal Conducting Cavity — F. Naito, K. Akai, N. Akasaka, <i>E. Ezura, T. Kageyama, T. Shintake, Y. Takeuchi, Y. Yamazaki</i>	1806	WPR09
Minimum Wakefield Achievable by Waveguide Damped Cavity — Xintian E. Lin, <i>Norman M. Kroll</i>	1809	WPR10
PLS RF System Operation During the Commissioning — M. Kwon, I.H. Yu, H.J. Park, <i>D.H. Han, M. Yoon, Y.S. Kim</i>	1812	WPR11
Acoustic Experimental Studies of High Power Modes in Accelerating Structure of Kurchatov SR Source — M. Gangeluk, A. Kadnikov, Yu. Krylov, S. Kuznetsov, V. Moisseev, <i>V. Petrenko, V. Ushkov, Yu. Yupinov</i>	1815	WPR13
Computer Simulations of a Wide-Bandwidth Ferrite-Loaded High-Power Waveguide Termination — J. Johnson, R. Rimmer, J. Corlett	1818	WPR14
Effects of Temperature Variation on the SLC Linac RF System — F.-J. Decker, R. Akre, <i>M. Byrne, Z.D. Farkas, H. Jarvis, K. Jobe, R. Koontz, M. Mitchell, R. Pennacchi, M. Ross,</i> <i>H. Smith</i>	1821	WPR15
Broadband Coax-Waveguide Transitions — T. Rizawa, R. Pendleton	1824	WPR16
Rectangular Microtron Accelerating Structure — N.P. Sobenin, V.N. Kandrunin, <i>V.N. Melekhin, A.I. Karev, V.I. Shvedunov, W.P. Trower</i>	1827	WPR17
Investigation of the Biparabolic Accelerating Structure For The Free Electron Laser Buncher — N.P. Sobenin, S.N. Yarygin, D.V. Kostin, A.A. Zavadtsev	1830	WPR18
Ferromagnetic Cores Made from Amorphous Material for Broad-Band Accelerating System — I. Bolotin, V. Budilin, A. Glazov, V. Krasnopolsky, V. Skuratov	1833	WPR19
A New Structure with Continuous RF Acceleration and Focusing — J.J. Manca, M.C. Fallis, <i>J.P.J. Manca</i>	1835	WPR20
Spark Location in RF Cavities — Q. Kerns, M. Popovic, C. Kerns	1838	WPR21
RF System for the Duke 1 GeV Storage Ring — Ping Wang, Peter Morcombe, Ying Wu, <i>Grigori Kurkin</i>	1841	WPR22

Injection, Extraction and Targetry

Matching Section to the RFQ Using Permanent Magnet Symmetric Lens — M. Kando, <i>M. Ikegami, H. Dewa, H. Fujita, T. Shirai, H. Okamoto, Y. Iwashita, S. Kakigi, A. Noda,</i> <i>M. Inoue</i>	1843	WAQ01
Conceptual Designs of Beam Choppers for RFQ Linacs — Subrata Nath, Ralph R. Stevens Jr, <i>Thomas P. Wangler</i>	1846	WAQ02
The Role of Space Charge in the Performance of the Bunching System for the ATLAS Positive Ion Injector — R.C. Pardo, R. Smith	1849	WAQ03

Experimental Investigations of Plasma Lens Focusing and Plasma Channel Transport of Heavy Ion Beams — A. Tauschwitz, S.S. Yu, S. Eylon, L. Reginato, W. Leemans, J.O. Rasmussen, R.O. Bangerter.....	1852	WAQ04
A Low Energy Ion Beam Transport System with Variable Field Permanent Magnetic Quadrupoles — Y. Mori, A. Takagi, M. Kinsho, T. Baba, K. Shinto.....	1855	WAQ06
A Comparison of Two Injection Line Matching Sections for Compact Cyclotrons — T. Kuo, R. Baartman, L. Root, B. Milton, R. Laxadal, D. Yuan, K. Jayamanna, P. Schmor, G. Dutto, M. Dehnel, K. Erdman	1858	WAQ07
Stripping Injection Into the New Booster Ring at IUCF — K. Hedblom, D.L. Friesel.....	1861	WAQ08
Accurate Tuning of 90° Cells in a FODO Lattice — K. Bertsche, N. Mao	1864	WAQ09
Design Principles for High Current Beam Injection Lines — H. Liu, D. Neuffer.....	1867	WAQ11
Survey and Analysis of Line-Frequency Interference in the CEBAF Accelerator — M.G. Tiefenback, Rui Li	1870	WAQ12
Location and Correction of 60 Hz in the CEBAF Injector — R. Legg, D. Douglas, G.A. Krafft, Q. Saulter.....	1873	WAQ14
PEP-II Injection Transport Construction Status and Commissioning Plans — T. Fieguth, E. Bloom, F. Bulos, T. Donaldson, B. Feerick, G. Godfrey, G. Leyh, D. Nelson, M. Ross, D. Schultz, J. Sheppard, P. Smith, C. Spencer, J. Weinberg.....	1876	WAQ15
Beam Transport Lines at BESSY-II — D. Schirmer, M. v.Hartrott, S. Khan, D. Krämer, E. Weihrer.....	1879	WAQ17
Matching the Emittance of a Linac to the Acceptance of a Racetrack Microtron — R.W. de Leeuw, M.C.J. de Wijs, J.I.M. Botman, G.A. Webers, W.H.C. Theuws, C.J. Timmermans, H.L. Hagedoorn.....	1882	WAQ19
The Extraction Orbit and Extraction Beam Transport Line for a 75 MeV Racetrack Microtron — R.W. de Leeuw, H.R.M. van Greevenbroek, J.I.M. Botman, G.A. Webers, C.J. Timmermans, H.L. Hagedoorn	1885	WAQ20
Electromagnetic, Thermal and Structural Analysis of the Fermilab Antiproton Source Lithium Collection Lens — S. O'Day, K. Anderson	1888	WAQ22
A New Concept in the Design of the LHC Beam Dump — J.M. Zazula, M. Gyr, G.R. Stevenson, E. Weisse.....	1891	WAQ24
Loss Concentration and Evacuation by Mini-Wire-Septa from Circular Machines for Spallation Neutron Sources — H. Schönauer	1894	WAQ25
Status of the Radioactive Ion Beam Injector at the Holifield Radioactive Ion Beam Facility — D.T. Dowling, G.D. Alton, R.L. Auble, M.R. Dinehart, D.L. Haynes, J.W. Johnson, R.C. Juras, Y.S. Kwon, M.J. Meigs, G.D. Mills, S.W. Mosko, D.K. Olsen, B.A. Tatum, C.E. Williams, H. Wollnik.....	1897	WAQ26
A New Fast Rise Time Kicker System For Antiproton Injection Into The Tevatron — B. Hanna, J. Dinkel, C. Jensen, D. Qunell, R. Reilly, D. Tinsley, J. Walton.....	1900	WAR01
Design of the MI40 Beam-Abort Dump — C.M. Bhat, P.S. Martin, A.D. Russell.....	1903	WAR02
Study on the Metallic Coating of the Ceramic Chamber for the ATF Damping Ring Kicker Magnets — N. Terunuma, H. Nakayama, J. Urakawa.....	1906	WAR03
Prospect of the Fast Extraction from KEK-PS for the Long Base Line Neutrino Experiment — H. Sato, Y. Shoji, T. Kawakubo.....	1909	WAR04
Helium Beam Acceleration in the KEK Proton Synchrotron with a Newly Developed Injection System for Positive/Negative Ions — I. Sakai, A. Takagi, Y. Mori, S. Machida, M. Yoshii, T. Toyama, M. Shirakata, Y. Shoji, H. Sato.....	1912	WAR05
Fast and Reliable Kicker Magnets for the SLC Damping Rings — T.S. Mattison, R.L. Cassel, A.R. Donaldson, G. Gross.....	1915	WAR06
Status of the Nuclotron Slow Extraction System — V.I. Chernikov, I.B. Issinsky, O.S. Kozlov, V.A. Mikhailov, S.A. Novikov.....	1918	WAR09
The RHIC Injection Fast Kicker — E.B. Forsyth, G.C. Pappas, J.E. Tuozzolo, W. Zhang	1921	WAR10
The Active Filter Voltage Ripple Correction System of the Brookhaven AGS Main Magnet Power Supply — I. Marneris, R. Bonati, J. Geller, J.N. Sandberg, A. Soukas.....	1924	WAR11
The Injection Kicker System for the Muon G-2 Experiment — G.C. Pappas, E.B. Forsyth, W. Feng	1927	WAR12
The AGS Accelerator Complex with the New Fast Extraction System — M. Tanaka, E.J. Bleser, J.W. Glenn, Y.Y. Lee, A. Soukas	1930	WAR13
DESY III - Dump System with One Fast Kicker — J. Ruemmler.....	1933	WAR14

Utilizing a Pulsed Deflector for Extraction of Pulsed Beams from the TRIUMF Cyclotron — <i>R.E. Laxdal</i>	1936	WAR15
Requirements for a Beam Sweeping System for the Fermilab Antiproton Source Target — <i>F.M. Bieniosek, K. Anderson, K. Fullett</i>	1939	WAR17
Measurement and Reduction of Quadrupole Injection Oscillations in the Fermilab Antiproton Accumulator — <i>F.M. Bieniosek, K. Fullett</i>	1942	WAR18
Results from Experiments of Crystal Extraction of 900 GeV Proton Beams from the Tevatron Collider — <i>G. Jackson, D. Carrigan, D. Chen, C.T. Murphy, A. Bogacz, S. Ramachandran, J. Rhoades, A. McManus, S. Baker</i>	1945	WAR19
High Energy Beam Line Based on Bending Crystal — <i>V.M. Biryukov, Yu.A. Chesnokov, V.N. Greth, A.A. Ivanov, V.I. Kotov, V.S. Selesnev, M.V. Tarakanov, V.I. Terekhov, S.V. Tsarik</i>	1948	WAR20
Observation of the Influence of the Crystal Surface Defects on the Characteristics of the High Energy Particle Beam Deflected With a Bent Monocrystal — <i>V.I. Baranov, V.M. Biryukov, Yu.A. Chesnokov, V.I. Kotov, M.V. Tarakanov, S.V. Tsarik</i>	1949	WAR21
Beam Extraction with Using of Volume Reflection Effect in Crystals — <i>I. Yazynin</i>	1952	WAR22
Use of a Bent Crystal for Beam Extraction in a Slow Extraction Mode — <i>A.A. Asseev, M.Yu. Gorin</i>	1955	WAR23
Computer Simulation of the Tevatron Crystal Extraction Experiment — <i>Valery Biryukov</i>	1958	WAR24

Power Supplies

PEP-II Magnet Power Conversion Systems — <i>L.T. Jackson, A.H. Saab, D.W. Shimer</i>	1961	RPP01
The AGS Main Magnet Power Supply Upgrade — <i>J.N. Sandberg, R. Casella, J. Geller, I. Marneris, A. Soukas, N. Schumburg</i>	1964	RPP02
Performance of the Ramping Power Supplies for the APS Booster Synchrotron — <i>J.A. Carwardine, S.V. Milton, D.G. McGhee</i>	1967	RPP03
A Distributed Dipole Power Supply System for the EUTERPE Electron Ring — <i>A.H. Kemper, Boling Xi, R.W. de Leeuw, W.H.C. Theuws, J.I.M. Botman, C.J. Timmermans, H.L. Hagedoorn, R.G.J. Oude Velthuis</i>	1970	RPP04
A 20 Ampere Shunt Regulator for Controlling Individual Magnets in a Seriesed String — <i>E.J. Martin, N. Dobeck, G.S. Jones, M.K. O'Sullivan</i>	1973	RPP06
A Multi-Channel Corrector Magnet Controller — <i>G.E. Leyh, A.R. Donaldson, L.T. Jackson</i>	1976	RPP07
Advances in Power Supply and Control System for Electrostatic Accelerators — <i>S.N. Chumakov, A.D. Goncharov, A.N. Malygin, V.P. Ostanin, B.N. Sukhina, V.S. Tupikov</i>	1979	RPP08
Mode Analysis of Synchrotron Magnet Strings — <i>M. Kumada</i>	1982	RPP09
Autotransformer Configurations to Enhance Utility Power Quality of High Power AC/DC Rectifier Systems — <i>Sewan Choi, Prasad N. Enjeti, Ira J. Pitel</i>	1985	RPP11
Performance of a 2-Megawatt High Voltage Test Load — <i>D. Horan, R. Kustom, M. Ferguson</i>	1988	RPP12
Early Operating and Reliability Experience with the CEBAF DC Magnet Power Supplies — <i>W. Merz, R. Flood, E.J. Martin, M. O'Sullivan</i>	1991	RPP13

Cryogenics, Vacuum, Alignment and Other Technical Systems

CEBAF Cryogenic System (Invited) — <i>Claus H. Rode</i>	1994	RPE01
The Large Hadron Collider Vacuum System (Invited) — <i>B. Angerth, F. Bertinelli, J.-C. Brunet, R. Calder, F. Caspers, P. Cruikshank, J.-M. Dalin, O. Gröbner, N. Kos, A. Mathewson, A. Poncet, C. Reymermier, F. Ruggiero, T. Scholz, S. Sgobba, E. Wallén</i>	1999	RPE02
Large Medical Gantries (Invited) — <i>J.B. Flanz</i>	2004	RPE03
Alignment Considerations for the Next Linear Collider (Invited) — <i>Robert E. Ruland</i>	2009	RPE04
Reliability of the LEP Vacuum System: Experience and Analysis — <i>P.M. Strubin, J.-P. Bojon</i>	2014	RPE06
On the Electron Beam Lifetime Problem in HERA — <i>D.R.C. Kelly, W. Bialowons, R. Brinkmann, H. Ehrlichmann, J. Kouptsidis</i>	2017	RPE08
Design and Testing of a High Power, Ultra-High Vacuum, Dual-Directional Coupler for the Advanced Photon Source (APS) Linear Accelerator — <i>S.O. Brauer, A.E. Grelick, J. Grimmer, R.D. Otocky, Y.W. Kang, J. Noonan, T. Russell</i>	2020	RPE09
A Pulse Septum Magnet with Low Outgassing Rate — <i>Yuan Ji Pei, W.M. Li, D.M. Jiang, X.Q. Wang</i>	2023	RPE10

Surveying the Monument System at Lawrence Berkeley Laboratory's Advanced Light Source Accelerator — W. Thur, T. Lauritzen	2026	RPE12
Induced Radioactivity of Thick Copper and Lead Targets Irradiated by Protons, ^4He and ^{12}C Nuclei with Energy 3.65 GeV/Nucleon — A.A. Astapov, V.P. Bamblevski	2029	RPE13
The PEP-II High Power Beam Dumping System — A. Kulikov, J. Seeman, M. Zolotarev	2032	RPE14
Cryogenic Thermometry in Superconducting Accelerators — V.I. Datskov, J.A. Demko, J.G. Weisend, M. Hentges	2034	MPP01
Cryogenic Operation and On-line Measurement of RF Losses in the SC Cavities of LEP2 — G. Winkler, Ph. Gayet, D. Güsewell, Ch. Titcomb	2037	MPP02
Pressure Measurement for the UNK-1 Vacuum System — A. Kiver, V. Komarov, K. Mirzoev, V. Terekhov, A. Vasilevsky	2040	MPP03
Total Pressure Measurements in the ELETTRA Storage Ring According to the Performance of the Sputter-Ion Pumps — F. Giacuzzo, J. Miertusova	2042	MPP04
Insertion Device Vacuum Chamber for the ELETTRA Storage Ring — J. Miertusova, N. Pangos	2045	MPP05
Bellows Design for the PEP-II High Energy Ring Arc Chambers — M.E. Nordby, N. Kurita, C.-K. Ng	2048	MPP07
A Zero-Length Bellows for the PEP-II High-Energy Ring — M. Nordby, E.F. Daly, N. Kurita, J. Langton	2051	MPP08
Processing of O.F.E. Copper Beam Chambers for PEP-II High Energy Ring — E. Hoyt, M. Hoyt, R. Kirby, C. Perkins, D. Wright, A. Farvid	2054	MPP09
Stretchforming Vacuum Chambers for the PEP-II B-Factory High Energy Storage Ring — E.F. Daly, D. Bostic, A. Lisin, M. Palrang, C. Perkins, K. Skarpaas	2057	MPP10
Beam Vacuum Chambers for Brookhaven's Muon Storage Ring — H.C. Hseuh, L. Snydstrup, W.S. Jiang, C. Pai, M. Mapes	2060	MPP11
Test Results of Pre-Production Prototype Distributed Ion Pump Design for the PEP-II Asymmetric B-Factory Collider — F.R. Holdener, D. Behne, D. Hathaway, K. Kishiyama, M. Mugge, W. Stoeffl, K. van Bibber, C. Perkins, E.F. Daly, E. Hoyt, M. Hoyt, M. Nordby, J. Seeman, D. Wright	2064	MPP12
Design of the PEP-II Low Energy Ring Vacuum System — D. Hunt, K. Kennedy, T. Stevens	2067	MPP13
The Vacuum Upgrade of the CERN PS and PS Booster — M. van Rooij, J.-P. Bertuzzi, M. Brouet, A. Burlet, C. Burnside, R. Gavaggio, L. Petty, A. Poncet	2069	MPP15
The Vacuum System for Insertion Devices at the Advanced Photon Source — E. Trakhtenberg, E. Gluskin, P. Den Hartog, T. Klippert, G. Wiemerslage, S. Xu	2072	MPP16
Test Results of a Combined Distributed Ion Pump/Non-Evaporable Getter Pump Design Developed as a Proposed Alternative Pumping System for the PEP-II Asymmetric B-Factory Collider — F.R. Holdener, D. Behne, D. Hathaway, K. Kishiyama, M. Mugge, W. Stoeffl, K. van Bibber, C. Perkins, E.F. Daly, E. Hoyt, M. Hoyt, M. Nordby, J. Seeman, D. Wright	2075	MPP20

Volume 4

Cryogenics, Vacuum, Alignment and Other Technical Systems (cont'd)

Ground Motion Measurements in HERA — V. Shiltsev, B. Baklakov, P. Lebedev, C. Montag, J. Rossbach	2078	TAA01
Alignment of Duke Free Electron Laser Storage Ring — M. Emamian, N. Hower, Y. Levashov	2081	TAA02
Beamline Smoothing of the Advanced Photon Source — H. Friedsam, M. Penicka, S. Zhao	2084	TAA03
Improvement of the Alignment System for the KEK 2.5-GeV Electron Linac — Y. Ogawa, A. Enomoto, I. Sato	2087	TAA04
A Mechanical Feedback System for Linear Colliders to Compensate Fast Magnet Motion — C. Montag, J. Rossbach	2090	TAA06
A Microstrip Based Position System for the Alignment of the TTF Cryostat — D. Giove, A. Bosotti, C. Pagani, G. Varisco	2093	TAA07
Beam-Based Magnetic Alignment of the Final Focus Test Beam — P. Tenenbaum, D. Burke, R. Helm, J. Irwin, P. Raimondi, K. Oide, K. Flöttmann	2096	TAA08

Alignment and Survey of the Elements in RHIC — D. Trbojevic, P. Cameron, G.L. Ganetis, M.A. Goldman, R. Gupta, M. Harrison, M.F. Hemmer, F.X. Karl, A. Jain, W. Louie, S. Mulhall, S. Peggs, S. Tepikian, R. Thomas, P. Wanderer.....	2099	TAA09
RF Radiation Measurement for the Advanced Photon Source (APS) Personnel Safety System — J.J. Song, J. Kim, R. Ostocki, J. Zhou	2102	TAA11
Radiation Shielding of the Main Injector — C.M. Bhat, P.S. Martin.....	2105	TAA12
The Safety Interlock System of Synchrotron Radiation Research Center — T.F. Lin, J.P. Wang.....	2108	TAA14
Radiological Protection Policy Aspects Concerning the Preliminary Design and Operation Modus of the Athens RT Microtron Facility — B. Spyropoulos	2111	TAA15
SLAC Synchronous Condenser — C. Corvin.....	2114	TAA16
Printed-Circuit Quadrupole Design — Terry F. Godlove, Santiago Bernal, Martin Reiser.....	2117	TAA17
Microprocessor Controlled Four-Axis Goniometer — A. Bortnyansky, M. Klopenkov, M. Pavlovets, M. Svinin, P. Kovach, J. Dobrovodsky.....	2120	TAA18
Optically Induced Surface Flashover Switching for the Dielectric Wall Accelerator — S. Sampayan, G. Caporaso, B. Carder, M. Norton, D. Trimble, J. Elizondo	2123	TAA20
Measurements of Magnet Vibrations at the Advanced Photon Source — V. Shiltsev	2126	TAA21
The Vacuum System for the PEP II High Energy Ring Straight Sections — U. Wienands, E. Daly, S.A. Heifets, A. Kulikov, N. Kurita, M. Nordby, C. Perkins, E. Reuter, J.T. Seeman, F.C. Belser, J. Berg, F.R. Holdener, J.A. Kerns, M.R. McDaniel, W. Stoeffl.....	2129	TAA22
Compact X-band High Power Load Using Magnetic Stainless Steel — Sami G. Tantawi, A.E. Vlieks.....	2132	TAA27
Progress on Plasma Lens Experiments at the Final Focus Test Beam — P. Kwok, P. Chen, D. Cline, W. Barletta, S. Berridge, W. Bugg, C. Bula, S. Chattopadhyay, W. Craddock, I. Hsu, R. Iverson, T. Katsouleas, P. Lai, W. Leemans, R. Liou, K.T. McDonald, D.D. Meyerhofer, K. Nakajima, H. Nakanishi, C.K. Ng, Y. Nishida, J. Norem, A. Ogata, J. Rosenzweig, M. Ross, A. Sessler, T. Shintake, J. Spencer, J.J. Su, A.W. Weidemann, G. Westenskow, D. Whittum, R. Williams, J. Wurtele.....	2135	TAA28
Measurement of the Electric Field Uniformity in an Electrostatic Separator — Weiran Lou, James J. Welch.....	2138	TAA29
Analysis and Redesign of RF Filter Bar to Relieve Thermal Stresses — E.G. Schmenk, K.W. Kelly, V. Saile, H.P. Bluem	2141	TAA32
Loaded Delay Lines for Future R.F. Pulse Compression Systems — R.M. Jones, P.B. Wilson, N.M. Kroll.....	2144	TAA33

Controls and Computing

Integrating Industrial and Accelerator Control Systems (Invited) — R. Saban	2147	WAE01
Control System for Fermilab's Low Temperature Upgrade (Invited) — B.L. Norris.....	2152	WAE02
Databases for Accelerator Control - An Operations Viewpoint (Invited) — J. Poole.....	2157	WAE03
Taking an Object-Oriented View of Accelerators (Invited) — Hiroshi Nishimura	2162	WAE04
The CEBAF Control System (Invited) — William A. Watson III.....	2167	WAE05
MECAR (Main Ring Excitation Controller and Regulator): A Real Time Learning Regulator For The Fermilab Main Ring Or The Main Injector Synchrotron — R. Flora, K. Martin, A. Moibenko, H. Pfeffer, D. Wolff, P. Prieto, S. Hays.....	2172	WAE07
Framework for a General Purpose, Intelligent Control System for Particle Accelerators — R.T. Westervelt, W.B. Klein, G. Luger.....	2175	WAE08
Automatic Beam Steering in the CERN PS Complex — B. Autin, G.H Hemelsoet, M. Martini, E. Wildner.....	2178	WAE09
Integrated On-Line Accelerator Modeling at CEBAF — B.A. Bowling, H. Shoaee, J. van Zeijts, S. Witherspoon, W. Watson.....	2181	WAE10
A Self-Describing File Protocol for Simulation Integration and Shared Post-Processors — M. Borland.....	2184	WAE11
Analytic Computation of Beam Impedances in Complex Heterogenous Accelerator Geometries — S. Petracca, I.M. Pinto, F. Ruggiero.....	2187	WAE12
Comparison of CONDOR, FCI and MAFIA Calculations for a 150MW S-Band Klystron with Measurements — U. Becker, T. Weiland, M. Dohlus, S. Lütgert, D. Sprehn	2190	WAE13

Controls

The BEPC Control System Upgraded — J. Zhao, X. Geng, Y. Yu, B. Wang, C. Wang, J. Xu, W. Liu, H. Luo, Y. Wang, M. Zhan.....	2193	MPA01
Control System of PLS 2-GeV Linac — I.S. Ko, W. Namkung.....	2196	MPA02
Control System of the Synchrotron Radiation Source SIBERIA-2 — A. Valentinov, A. Kadnikov, Y. Krylov, S. Kuznetsov, Y. Yupinov.....	2199	MPA04
Control System for the Holifield Radioactive Ion Beam Facility — B.A. Tatum, R.C. Juras, M.J. Meigs.....	2202	MPA05
Control System Design for KEKB Accelerators — S.-I. Kurokawa, T. Katoh, T.T. Nakamura, T. Mimashi, N. Yamamoto.....	2205	MPA06
Design of SPring-8 Linac Control System Using Object Oriented Concept — H. Sakaki, H. Yoshikawa, Y. Itoh, A. Kuba, T. Hori, A. Mizuno, H. Yokomizo.....	2208	MPA07
The Slow Control System of the Muon g-2 Experiment — Arnold Stillman.....	2211	MPA09
The Duke Storage Ring Control System — Y. Wu, B. Burnham, V.N. Litvinenko.....	2214	MPA10
EPICS at Duke University — C. Dickey, B. Burnham, F. Carter, R. Fricks, V. Litvinenko, A. Nagchaudhuri, P. Morcombe, R. Pantazis, P. O'Shea, R. Sachschtale, Y. Wu.....	2217	MPA11
The Integration of Two Control Systems — M. Bickley, K. White.....	2220	MPA12
Upgrade of NSLS Timing System — O. Singh, S. Ramamoorthy, J. Sheehan, J. Smith.....	2223	MPA15
Accelerator Timing at Brookhaven National Laboratory — B. Oerter, C.R. Conkling.....	2226	MPA16
The RHIC General Purpose Multiplexed Analog to Digital Converter System — R. Michnoff.....	2229	MPA17
The Datacon Master - Renovation of a Datacon Field Bus Communications System for Accelerator Control — T.M. Kerner, R. Warkentien.....	2232	MPA18
Upgrade of the Controls for the Brookhaven Linac — W.E. Buxton.....	2235	MPA19
Commissioning Software Tools at the Advanced Photon Source — L. Emery.....	2238	MPR01
Rapid Application Development Using the Tcl/Tk Language — Johannes van Zeijts.....	2241	MPR02
Accelerator Operation Management Using Objects — H. Nishimura, C. Timossi, M. Valdez.....	2244	MPR03
Orbit Control at the ALS Based on Sensitivity Matrices — H. Nishimura, L. Schachinger, H. Ohgaki.....	2247	MPR04
Error Handling in the NSLS Control System — Susila Ramamoorthy, Pauline Pearson, John Smith.....	2250	MPR07
History Data Collection, Retriving and Display in the NSLS Control System — Y.N. Tang, J.D. Smith.....	2253	MPR08
Virtual Instrumentation Interface for SRRC Control System — Jenny Chen, C.H. Kuo, Gloria Huang, J.S. Chen, C.J. Wang, K.T. Hsu, G.J. Jan.....	2256	MPR10
User-Friendly Interface for Operator in the Controls of UNK Beam-Transfer Line. — Yu. Karshev, Yu. Fedotov, V. Komarov, I. Lobov.....	2259	MPR11
Macmon: A Monitoring Program for ELETTRA — Emanuel Karantzoulis, Mark Plesko.....	2262	MPR12
Device Control at CEBAF — S. Schaffner, D. Barker, V. Bookwalter, B. Bowling, K. Brown, L. Doolittle, T. Fox, S. Higgins, A. Hofler, G. Lahti, P. Letta, B. Montjar, N. Patavalis, J. Tang, W. Watson, C. West, D. Wetherholt, K. White, S. Witherspoon, M. Wise.....	2265	MPR13
Automated Frequency Tuning of SRF Cavities at CEBAF — M. Chowdhary, L. Doolittle, G. Lahti, S.N. Simrock, R. Terrell.....	2268	MPR14
Operational Monitoring of the CEBAF RF System — J. Karn, B. Dunham, M. Tiefenback.....	2271	MPR15
Operating Experience with the New TRIUMF RF Control System — K. Fong, M. Laverty, S. Fang.....	2273	MPR16
Managing Control Algorithms with an Object-Oriented Database — M. Bickley, W. Watson.....	2276	MPR19
Design of the Commissioning Software for the AGS to RHIC Transfer Line — C.G. Trahern, C. Saltmarsh, T. Satogata, J. Kewisch, S. Sathe, T. D'Ottavio, S. Tepikian, D. Shea.....	2279	MPR20

Computer Codes

A Relational Database for Magnets and Measurement Systems at the Fermilab Magnet Test Facility — J.W. Sim, B.C. Brown, H.D. Glass, D.J. Harding, C.S. Mishra, A.D. Russell, K. Trombly-Freytag, D.G.C. Walbridge.....	2282	MPB05
---	------	-------

Software for a Database-Controlled Measurement System at the Fermilab Magnet Test Facility — J.W. Sim, R. Baiod, B.C. Brown, E. Desavouret, H.D. Glass, P.J. Hall, D.J. Harding, C.S. Mishra, J.M. Nogiec, J.E. Pachnik, A. Russell, K. Trombly-Freytag, D.G.C. Walbridge	2285	MPB06
BBAT: Bunch and Bucket Analysis Tool — D.-P. Deng.....	2288	MPB08
MASTAC - New Code for Solving Three-Dimensional Non-linear Magnetostatic Problems — M. Rojak, E. Shurina, Yu. Soloveichik, A. Grudiev, M. Tiunov, P. Vobly.....	2291	MPB09
The Computer Code BPERM for Wakepotential & Impedance Calculations — T. Barts, W. Chou.....	2294	MPB10
RESOLVE at CEBAF — Byung C. Yunn, Rui Li, Stefan Simrock.....	2297	MPB11
New Graphic User Interface for the Charged Particle Beam Program PARMILA — George H. Gillespie, Barrey W. Hill.....	2300	MPB14
XWAKE 1.1: A New Impedance and Wake Field Software Package — G.W. Saewert, T.G. Jurgens.....	2303	MPB15
The Los Alamos Accelerator Code Group — Frank L. Krawczyk, James H. Billen, Robert D. Ryne, Harunori Takeda, Lloyd M. Young.....	2306	MPB16
Beam Simulation and Radiation Dose Calculation at the Advanced Photon Source with SHOWER, an Interface Program to the EGS4 Code System — L. Emery.....	2309	MPB17
An Interactive Version of the PBGUNS Program for the Simulation of Axisymmetric and 2-D, Electron and Ion Beams and Guns — Jack E. Boers.....	2312	MPB18
Vector Computer Used for Calculation of 3D Magnetostatic Fields — E.P. Zhidkov, M.B. Yuldasheva, I.P. Yudin, O.I. Yuldashev.....	2314	MPB19
Impedance Study for the PEP-II B-factory — S. Heifets, A. Chao, E. Daly, K. Ko, N. Kurita, X. Lin, C. Ng, M. Nordby, C. Perkins, J. Seeman, G. Stupakov, U. Wienands, D. Wright, M. Zolotorev, E. Henestroza, G. Lambertson, J. Corlett, J. Byrd, M. Zisman, T. Weiland, W. Stoeffl, C. Bolser.....	2317	MPC01
Pressure Stability under a Pump Failure — S.A. Heifets, J. Seeman, W. Stoeffl.....	2319	MPC02
Investigation of the Beam Impedance of a Slowly Varying Waveguide — R.M. Jones, S.A. Heifets.....	2321	MPC03
Optimal Transport of Low Energy Particle Beams — Christopher K. Allen, Samar K. Guharay, Martin Reiser.....	2324	MPC04
Simulation of the Space Charge Effect in RHIC — G.F. Dell, S. Peggs.....	2327	MPC05
Magnetic Shielding for the D0 Detector Solenoid Upgrade — J.-F. Ostiguy, R. Yamada.....	2330	MPC07
Trapped Modes in the PEP-II B-Factory Interaction Region — E. Henestroza, S. Heifets, M. Zolotorev.....	2333	MPC08
A Proof of Principle of a Storage Ring with Fifth-Order Achromatic Bending Arcs — Weishi Wan, Martin Berz.....	2336	MPC09
Analytic Electrostatic Solution of an Axisymmetric Accelerator Gap — John K. Boyd.....	2339	MPC13
3D-Finite Difference Analysis of Planar Loop Couplers as Beam Electrodes in Stochastic Cooling Systems — R. Schultheis, H.L. Hartnagel, B. Franzke.....	2342	MPC15
Some Remarks on the Location of Higher Order Modes in Tapered Accelerating Structures with the Use of a Coupled Oscillator Model — G. Romanov, S. Ivanov, M. Dohlus, N. Holtkamp.....	2345	MPC16
The New Possibilities of SuperLANS Code for Evaluation of Axisymmetric Cavities — D.G. Myakishev, V.P. Yakovlev.....	2348	MPC17
Transverse EM Fields in a Detuned X-band Accelerating Structure — S.A. Heifets, S.A. Kheifets, B. Woo.....	2351	MPC18
RF Cavity Computer Design Codes — P.A. McIntosh.....	2353	MPC19
Arbitrary Order Transfer Maps for RF Cavities — Johannes van Zeijts.....	2356	MPC20
The Computation of the Dynamic Inductance of Magnet Systems and Force Distribution in Ferromagnetic Region on the Basis of 3-D Numerical Simulation of Magnetic Field — N. Doinikov, V. Kukhtin, E. Lamzin, B. Mingalev, Yu. Severgin, S. Sytchevsky.....	2359	MPC21
Advanced Electromagnetic Design of Cavities for High Current Accelerators — Frank L. Krawczyk.....	2361	MPC22
Modified PARMILA Code for New Accelerating Structures — H. Takeda, J.E. Stovall.....	2364	MPC23
Tracking Particles with Wake Fields and Space Charge Effects — A.J. Riche.....	2367	MPC24
On the Importance of Fourth Order Effects on Wakefield Calculations for Short Bunches — Zenghai Li, Joseph J. Bisognano.....	2370	MPC25

Coupling Impedances of Muffin-Tin Structures with Closed and Open Sides — M. Filtz	2373	MPC28
Explicit Soft Fringe Maps of a Quadrupole — John Irwin, Chun-xi Wang	2376	MPC31

Instrumentation and Feedback

Bunched Beam Cooling for the Fermilab Tevatron (Invited) — Ralph J. Pasquinelli	2379	RAE01
Fast Digital Dampers for the Fermilab Booster (Invited) — James M. Steimel Jr.	2384	RAE02
Fast Feedback for Linear Colliders (Invited) — L. Hendrickson, C. Adolphsen, S. Allison, T. Gromme, P. Grossberg, T. Himel, K. Krauter, R. MacKenzie, M. Minty, R. Sass, H. Shoaee, M. Woodley	2389	RAE03
Instrumentation in Medical Systems (Invited) — W.T. Chu	2394	RAE04
Laser Diagnostics of a One-Dimensional Ordered Ion Beam — R. Calabrese, V. Guidi, P. Lenisa, U. Tambini, E. Mariotti, L. Moi	2399	RAE05
Determining Electron Beam Parameters from Edge Radiation Measurement Results on Siberia-1 Storage Ring — O.V. Chubar	2402	RAE06
Absolute Energy Measurement in e- e+ Linear Colliders — Blaine E. Norum, Robert Rossmann	2405	RAE07
INR Activity in Development and Production of Bunch Shape Monitors — S.K. Esin, A.V. Feschenko, P.N. Ostroumov	2408	RAE08
Conceptual design of a Charged Particle Beam Energy Spectrometer Utilizing Transition Radiation Grating — X.Z. Qiu, X.J. Wang, K. Batchelor, I. Ben-Zvi	2411	RAE09
An Analysis of the Operational Performance of the Automatic Global Horizontal Beam Position Control System on the SRS at Daresbury — J.B. Fitzgerald, B.G. Martlew, P.D. Quinn, S.L. Smith	2414	RAE10
A Prototype Fast Feedback System for Energy Lock at CEBAF — M. Chowdhary, G.A. Krafft, H. Shoaee, S.N. Simrock, W.A. Watson	2417	RAE11
Operation and Performance of the PEP-II Prototype Longitudinal Damping System at the ALS — D. Teytelman, R. Claus, J. Fox, H. Hindi, J. Hoeflich, I. Linscott, J. Olsen, G. Oxoby, S. Prabhakar, W. Ross, L. Sapozhnikov, A. Drago, M. Serio, J. Byrd, J. Corlett, G. Stover	2420	RAE12
Commissioning of the ALS Transverse Coupled-Bunch Feedback System — W. Barry, J. Byrd, J. Corlett, J. Johnson, G. Lambertson, J. Fox	2423	RAE13
Operation of a Fast Digital Transverse Feedback System in CESR — J.T. Rogers, M.G. Billing, J.A. Dobbins, C.R. Dunnam, D.L. Hartill, T. Holmquist, B.D. McDaniel, T.A. Pelaia, M. Pisharody, J.P. Sikora, C.R. Strohman	2426	RAE14
Measuring and Adjusting the Path Length at CEBAF — G.A. Krafft, M. Crofford, D.R. Douglas, S.L. Harwood, R. Kazimi, R. Legg, W. Oren, K. Tremblay, D. Wang	2429	WXE01
Simulations of the BNL/SLAC/UCLA 1.6 Cell Emittance Compensated Photocathode RF Gun Low Energy Beam Line — D.T. Palmer, R.H. Miller, H. Winick, X.J. Wang, K. Batchelor, M. Woodle, I. Ben-Zvi	2432	WXE03
Small Gap Undulator Experiment on the NSLS X-Ray Ring — P.M. Stefan, S. Krinsky, G. Rakowsky, L. Solomon	2435	WXE04
Measurements of Longitudinal Dynamics in the SLC Damping Rings — R.L. Holtzapple, R.H. Siemann, C. Simopoulos	2438	WXE05
Single Bunch Collective Effects in the ALS — J.M. Byrd, J.N. Corlett, T. Renner	2441	WXE06
Experiments of Nanometer Spot Size Monitor at FFTB Using Laser Interferometry — T. Shintake, K. Oide, N. Yamamoto, A. Hayakawa, Y. Ozaki, D. Burke, R.C. Field, S. Hartman, R. Iverson, P. Tenenbaum, D. Walz	2444	WXE07
Transverse Electron Beam Size Measurements Using the Lloyd's Mirror Scheme of Synchrotron Light Interference — O.V. Chubar	2447	WXE08

Instrumentation

Charge Balancing Fill Rate Monitor — J.L. Rothman, E.B. Blum	2450	MPQ01
Sensitivity and Offset Calibration for the Beam Position Monitors at the Advanced Photon Source — Y. Chung, D. Barr, G. Decker, K. Evans Jr., E. Kahana	2452	MPQ03
An Sampling Detector for the RHIC BPM Electronics — W.A. Ryan, T.J. Shea	2455	MPQ04
RHIC Beam Position Monitor Characterization		

— P.R. Cameron, M.C. Grau, M. Morvillo, T.J. Shea, R.E. Sikora.....	2458	MPQ05
Duke Storage Ring Tune Measurements System using Razor Blade and Photomultiplier —		
V.N. Litvinenko, B. Burnham, N. Hower, P. Morcombe, Y. Wu	2461	MPQ06
The Development of Beam Current Monitors in the APS — X. Wang, F. Lenkszus, E. Rotela.....	2464	MPQ07
Overall Design Concepts for the APS Storage Ring Machine Protection System —		
A. Lumpkin, R. Fuja, A. Votaw, X. Wang, D. Shu, J. Stepp, N. Arnold, G. Nawrocki, G. Decker, Y. Chung	2467	MPQ08
Status of the Synchrotron Radiation Monitors for the APS Facility Rings — A. Lumpkin,		
B. Yang	2470	MPQ09
Initial Diagnostics Commissioning Results for the Advanced Photon Source (APS) —		
A. Lumpkin, D. Patterson, X. Wang, E. Kahana, W. Sellyey, A. Votaw, B. Yang, R. Fuja, W. Berg, M. Borland, L. Emery, G. Decker, S. Milton.....	2473	MPQ10
Initial Tests of the Dual-Sweep Streak Camera System Planned for APS Particle-Beam		
Diagnostics — A. Lumpkin, B. Yang, W. Gai, W. Cieslik.....	2476	MPQ11
A Transverse Tune Monitor for the Fermilab Main Ring — P.J. Chou, B. Fellenz, G. Jackson.....	2479	MPQ13
Recalibration of Position Monitors With Beams — Kotaro Satoh, Masaki Tejima.....	2482	MPQ14
Simulation of PEP-II Beam Position Monitors — C.-K. Ng, T. Weiland, D. Martin, S. Smith,		
N. Kurita.....	2485	MPQ15
Prototype Bunch Killer System At SRRC — G.J. Jan, Jenny Chen, C.H. Kuo, T.F. Lin, K.T. Pan,		
Glory Lin, K.T. Hsu.....	2488	MPQ16
Beam Diagnostics for the Amsterdam Pulse Stretcher AmPS — J.G. Noomen,		
H. Boer-Rookhuizen, N. Dobbe, J. v. Es, E. Heine, F. Kroes, J. Kuijt, J. v.d. Laan, A. Poelman, H. Nieuwenkamp, T. Sluijk.....	2491	MPQ17
Non-Destructive Beam Profile Measuring System Observing Fluorescence Generated by		
Circulating Beam — T. Kawakubo, E. Kadokura, T. Kubo, T. Ishida, H. Yamaguchi	2494	MPQ18
The Closed Orbit Measurement of SRRC Booster During Ramping — T.S. Ueng, K.T. Hsu,		
K.H. Hwu, K.K. Lin	2497	MPQ19
Lattice Function Measurement with TBT BPM Data — Ming-Jen Yang.....	2500	MPQ20
Optimal Placement of Profile Monitors in a Mismatched FODO Lattice — K. Bertsche	2503	MPQ21
SSRL Beam Position Monitor Detection Electronics — J. Sebek, R. Hettel, R. Matheson,		
R. Ortiz, J. Wachter	2506	MPQ22
Single-Turn Beam Position Monitor for the NSLS VUV Electron Storage Ring —		
R.J. Nawrocky, S.L. Kramer.....	2509	MPQ23
Design of the Button Beam Position Monitor for PEP-II — N. Kurita, D. Martin, S. Smith,		
C. Ng, M. Nordby, C. Perkins.....	2512	MPQ25
Study of Fast Electron Beam Profile Monitor System — Ian Hsu, C.I. Yu, C.C. Chu.....	2515	MPQ26
The Average Orbit System Upgrade for the Brookhaven AGS — D.J. Ciardullo, J.M. Brennan	2518	MPQ30
Feasibility Study of an Orbit Feedback System for the KEKB Facility — Y. Funakoshi,		
M. Tejima, H. Ishii	2521	MPQ31
Turn-by-Turn Beam Position Measurement for 1.3 GeV Booster Synchrotron — T.S. Ueng,		
K.T. Hsu, C.S. Fang, Y.M. Chang, K.K. Lin	2524	MPQ32
Beam Position Monitor for the LNL UVX Synchrotron Light Source — F.S. Rafael,		
E.K.C.S. Hayashi	2527	MPQ33
Transition Radiation Electron Beam Diagnostic Study at ATF — X.Z. Qiu, X.J. Wang,		
K. Batchelor, I. Ben-Zvi.....	2530	TPB01
Machine Parameter Measurement of the Amsterdam Pulse Stretcher AmPS — Y.Y. Wu,		
R. Maas	2533	TPB03
Wire Setup Calibration of Beam Position Monitors — D. Wang, B. Binns, M. Kogan,		
A. Zolfaghari	2536	TPB04
Beam profile data analysis for the RHIC Injection Line — Ping Zhou.....	2539	TPB05
Energy Spread of Ion Beams Generated in Multicusp Ion Sources — M. Sarstedt, P. Herz,		
W.B. Kunkel, Y. Lee, K.N. Leung, L. Perkins, D. Pickard, M. Weber, M.D. Williams, E. Hammel.....	2542	TPB07
A 2 MHz 3-Port Analog Isolation and Fanout Module — Edward R. Beadle	2545	TPB08
A General Purpose Fiber Optic Link with Radiation Resistance — Edward R. Beadle	2548	TPB09
DSP Based Data Acquisition for RHIC — T.J. Shea, J. Mead, C.M. Degen.....	2551	TPB12

Ion-Chamber Beam-Loss-Monitor System for the Los Alamos Meson Physics Facility — <i>M. Plum, D. Brown, A. Browman, R. Macek</i>	2554	TPB13
Development of Beam Position Monitors for Heavy Ion Recirculators — <i>F.J. Deadrick,</i> <i>J.J. Barnard, T.J. Fessenden, J.W. Meredith, J. Rintamaki</i>	2557	TPB14
Laser Compton Polarimetry of Proton Beams — <i>A. Stillman</i>	2560	TPB15
Phase and Synchronous Detector Theory as Applied to Beam Position and Intensity Measurements — <i>J.D. Gilpatrick</i>	2563	TPB16
Testing Coaxial Switches of BPM using a High-Resolution RF Detector — <i>Takao Ieiri</i>	2566	TPB17
A Beam Size Monitor Based on Appearance Intensities for Multiple Gas Ionization — <i>T. Katsouleas, J. Yoshii, W.B. Mori, C. Joshi, C. Clayton</i>	2569	TPB18
Beam Profile Measurement in the Presence of Noise — <i>K. Bertsche, J. Palkovic</i>	2572	TPB19
Beam Shaping Using a New Digital Noise Generator — <i>H. Stockhorst, G. Heinrichs,</i> <i>A. Schnase, S. Papureanu, U. Bechstedt, R. Maier, R. Tölle</i>	2574	TPB20
The RHIC Transfer Line Cable Database — <i>E.H. Scholl, T. Satogata</i>	2577	TPB21
Characterization of Beam Position Monitors for Measurement of Second Moment — <i>S.J. Russell, J.D. Gilpatrick, J.F. Power, R.B. Shurter</i>	2580	TPB22
Beam Diagnostic Systems and Their Use in the New IUCF Beam Line — <i>W.P. Jones, M. Ball,</i> <i>J. Collins, T. Ellison, B. Hamilton</i>	2583	TPB24
Tomographic Method of Experimental Research of Particle Distribution in Phase Space — <i>V.V. Kalashnikov, V.I. Moiseev, V.V. Petrenko</i>	2586	TPB25
Design of the Beam Profile Monitor System for the RHIC Injection Line — <i>R.L. Witkover</i>	2589	TPB26
Beam Intensity Observation System at SRRC — <i>C.J. Wang, C.H. Kuo, J.S. Chen, Jenny Chen,</i> <i>K.T. Hsu, G.J. Jan</i>	2592	TPB29
Performance of the Advanced Photon Source (APS) Linac Beam Position Monitors (BPMs) with Logarithmic Amplifier Electronics — <i>R.E. Fuja, M. White</i>	2595	TPC01
Preliminary Calculations on the Determination of APS Particle-Beam Parameters Based on Undulator Radiation — <i>A. Lumpkin, B. Yang, Y. Chung, R. Dejus, G. Voykov, G. Dattoli</i>	2598	TPC03
Coherent Synchrotron Radiation Detector for a Non-Invasive Subpicosecond Bunch Length Monitor — <i>G.A. Krafft, D. Wang, E. Price, E. Feldl, D. Porterfield, P. Wood, T. Crowe</i>	2601	TPC04
A Beam Test of Button-Type Beam Position Monitor for the ATF Damping Ring — <i>F. Hinode, H. Hayano, M. Tejima, N. Terunuma, J. Urakawa</i>	2604	TPC05
Application of a Transverse Phase-Space Measurement Technique for High-Brightness, H- Beams to the GTA H- Beam — <i>K.F. Johnson, R.C. Connolly, R.C. Garcia, D.P. Rusthoi,</i> <i>O.R. Sander, D.P. Sandoval, M.A. Shinas, M. Smith, V.W. Yuan</i>	2607	TPC06
Precision Intercomparison of Beam Current Monitors at CEBAF — <i>R. Kazimi, B. Dunham,</i> <i>G.A. Krafft, R. Legg, C. Liang, C. Sinclair, J. Mammoser</i>	2610	TPC07
Damped Button Electrode for B-Factory BPM System — <i>T. Obina, T. Shintake, Y.H. Chin,</i> <i>N. Akasaka</i>	2613	TPC08
Beam Monitors for the S-Band Test Facility — <i>W. Radloff, M. Wendt</i>	2616	TPC09
Low Energy Regime for Optical Transition Radiation Emission — <i>D. Giove, C. De Martinis,</i> <i>M. Pullia, P. Mangili</i>	2619	TPC10
Recovery of CTF Beam Signals from a Strong Wakefield Background — <i>Yan Yin,</i> <i>Elmar Schulte, Tord Ekelöf</i>	2622	TPC11
A Low-Cost Non-Intercepting Beam Current and Phase Monitor for Heavy Ions — <i>J.M. Bogaty, B.E. Clift</i>	2625	TPC12
Transverse Emittance Systematics Measured for Heavy-Ion Beams at ATLAS — <i>J.A. Nolen,</i> <i>T.A. Barlow, K.A. Beyer, K.A. Woody</i>	2628	TPC13
Beam Position Monitors in the TESLA Test Facility Linac — <i>R. Lorenz</i>	2631	TPC14
Energy Measurement of Relativistic Electrons by Compton Scattering — <i>Ian Hsu, C.-C. Chu,</i> <i>C.-I. Yu, C.-I. Chen, A.-T. Lai, Y.-C. Liu, P.-K. Tseng, G.-Y. Hsiung, R.-C. Hsu, C.-P. Wang, R.-</i> <i>C. Chen</i>	2634	TPC15
Tests of a High Resolution Beam Profile Monitor — <i>J. Norem, J. Dawson, W. Haberichter,</i> <i>R. Lam, L. Reed, X.-F. Yang, J. Spencer</i>	2637	TPC16
Airix Alignment and High Current Beam Diagnostics — <i>D. Villate, Ch. Bonnafond, A. Devin,</i> <i>E. Merle</i>	2640	TPC17
A New Beam Intensity Monitoring System with Wide Dynamic Range for the Holifield Radioactive Ion Beam Facility — <i>M.J. Meigs, D.L. Haynes, C.M. Jones, C.T. LeCroy</i>	2643	TPC18

Diagnostic Beam Pulses for Monitoring the SLC Linac — <i>F.-J. Decker, M. Stanek, H. Smith, F. Tian</i>	2646	TPC20
Observation of Thermal Effects on the LEP Wire Scanners — <i>J. Camas, C. Fischer, J.J. Gras, R. Jung, J. Koopman</i>	2649	TPC21
CEBAF Beam Loss Accounting — <i>R. Ursic, K. Mahoney, C. Hovater, A. Hutton, C. Sinclair</i>	2652	TPC26
Nanometer Resolution BPM Using Damped Slot Resonator — <i>S.C. Hartman, T. Shintake, N. Akasaka</i>	2655	TPC29
An Automatic Tune-Measurement System for the CELSIUS Ring — <i>T. Lofnes</i>	2658	TPC31

Feedback

Software Architecture of the Longitudinal Feedback System for PEP-II, ALS and DAΦNE — <i>R. Claus, J. Fox, I. Linscott, G. Oxoby, W. Ross, L. Sapozhnikov, D. Teytelman, A. Drago, M. Serio</i>	2660	RPQ01
Digital I/Q Demodulator — <i>C. Ziomek, P. Corredoura</i>	2663	RPQ02
RF Feedback Simulation Results for PEP-II — <i>R. Tighe, P. Corredoura</i>	2666	RPQ03
TM0,1,5,0 Mode Cavity for Longitudinal Bunch Feedback Kicker — <i>T. Shintake</i>	2669	RPQ04
Low Level RF System Design for the PEP-II B Factory — <i>P. Corredoura, R. Claus, L. Sapozhnikov, H. Schwarz, R. Tighe, C. Ziomek</i>	2672	RPQ05
Experiment of the RF Feedback using a Parallel Comb Filter — <i>S. Yoshimoto, E. Ezura, K. Akai, T. Takashima</i>	2675	RPQ06
Digital Transverse Beam Dampers for the Brookhaven AGS — <i>G.A. Smith, V. Castillo, T. Roser, W. Van Asselt, R. Witkover, V. Wong</i>	2678	RPQ07
Design of the PEP-II Transverse Coupled-Bunch Feedback System — <i>W. Barry, J. Byrd, J. Corlett, M. Fahmie, J. Johnson, G. Lambertson, M. Nyman, J. Fox, D. Teytelman</i>	2681	RPQ08
Simulations of the PEP-II Transverse Coupled-Bunch Feedback System — <i>J.M. Byrd</i>	2684	RPQ09
Fermilab Booster Low Level RF System Upgrades — <i>Robert C. Webber</i>	2687	RPQ10
Energy Stability in a High Average Power FEL — <i>L. Merminga, J.J. Bisognano</i>	2690	RPQ11
Automated Beam Based Alignment of the ALS Quadrupoles — <i>G. Portmann, D. Robin, L. Schachinger</i>	2693	RPQ13
First Results with a Nonlinear Digital Orbit Feedback System at the NSLS — <i>Eva Bozoki, Aharon Friedman, Susila Ramamoorthy</i>	2696	RPQ14
Local Beam Position Feedback Experiments on the ESRF Storage Ring — <i>Y. Chung, E. Kahana, J. Kirchman, A. Lumpkin, J. Meyer, E. Plouviez, K. Scheidt, E. Taurel, A. Ando, S. Sasaki, A. Taketani</i>	2699	RPQ15
Implementation of the Global and Local Beam Position Feedback Systems for the Advanced Photon Source Storage Ring — <i>Y. Chung, D. Barr, G. Decker, J. Galayda, J. Kirchman, F. Lenkszus, A. Lumpkin, A.J. Votaw</i>	2702	RPQ16
The RHIC Accelerating Cavity Prototype Tuner — <i>A. Ratti, J.M. Brennan, J. Brodowski, E. Onillon, J. Rose</i>	2705	RPQ17
Ramp Tuning of the APS Booster Synchrotron Magnet Power Supplies — <i>S.V. Milton, J.A. Carwardine</i>	2708	RPQ18
Orbit Stability Improvements at the NSLS X-Ray Ring — <i>J. Safranek, O. Singh, L. Solomon</i>	2711	RPQ19
Digital Orbit Feedback Compensation for SPEAR — <i>J. Corbett, R. Hettel, D. Keeley, D. Mostowfi</i>	2714	RPQ21
Digital Orbit Feedback Control for SPEAR — <i>R. Hettel, J. Corbett, D. Keeley, I. Linscott, D. Mostowfi, J. Sebek, C. Wermelskirchen</i>	2717	RPQ22
Beam Position Feedback Systems for the PF Storage Ring — <i>N. Nakamura, K. Haga, T. Honda, T. Kasuga, M. Katoh, Y. Kobayashi, M. Tadano, M. Yokoyama</i>	2720	RPQ23
The New Booster Synchronization Loop — <i>E. Onillon, J.M. Brennan</i>	2723	RPQ25
Recent Progress in the Development of the Bunch Feedback Systems for KEKB — <i>E. Kikutani, T. Kasuga, Y. Minagawa, T. Obina, M. Tobiya</i>	2726	RPQ26
60 Hz Beam Motion Reduction at NSLS UV Storage Ring — <i>Om V. Singh</i>	2729	RPQ27
The CEBAF Fiber Optic Phase Reference System — <i>K. Crawford, S. Simrock, C. Hovater, A. Krycuk</i>	2732	RPQ29
RF System Modeling for the High Average Power FEL at CEBAF — <i>L. Merminga, J. Fugitt, G. Neil, S. Simrock</i>	2735	RPQ30

Beam Positioning and Monitoring in the Racetrack Microtron Eindhoven — W. Theuws,		
<i>R.W. de Leeuw, G.A. Webers, J.I.M. Botman, C.J. Timmermans, H.L. Hagedoorn</i>	2738	RPQ31
Multi-Bunch Systems at DESY — Rolf-Dieter Kohaupt	2741	RPQ32

High Energy Accelerator Beam Dynamics

Results of Final Focus Test Beam (Invited) — V.A. Alexandrof, V. Balakin, A. Mikhailichenko,		
<i>K. Flöttmann, F. Peters, G.-A. Voss, V. Bharadwaj, M. Halling, J.A. Holt, J. Buon, J. Jeanjean,</i>		
<i>F. LeDiberder, V. Lepeltier, P. Puzo, G. Heimlinger, R. Settles, U. Stierlin, N. Akasaka,</i>		
<i>H. Hayano, N. Ishihara, H. Nakayama, K. Oide, T. Shintake, Y. Takeuchi, N. Yamamoto,</i>		
<i>F. Bulos, D. Burke, R. Field, S. Hartman, R. Helm, J. Irwin, R. Iverson, P. Raimondi, S. Rokni,</i>		
<i>G. Roy, W. Spence, P. Tenenbaum, S.R. Wagner, D. Walz, S. Williams</i>	2742	TAG01
Comparison of Measured and Calculated Dynamic Aperture (Invited) — F. Willeke	2747	TAG02
Ion Effects in Future Circular and Linear Accelerators (Invited) — T.O. Raubenheimer	2752	TAG03
Nonlinear Wave Phenomena in Coasting Beams (Invited) — P.L. Colestock, L.K. Spentzouris,		
<i>F. Ostiguy</i>	2757	TAG04
The Cure of Multibunch Instabilities in ELETTRA — M. Svandrlik, C.J. Bocchetta, A. Fabris,		
<i>F. Iazzourene, E. Karantzoulis, R. Nagaoka, C. Pasotti, L. Tosi, R.P. Walker, A. Wrulich</i>	2762	TAG05
Nonlinear Analyses of Storage Ring Lattices Using One-Turn Maps — Y.T. Yan, J. Irwin,		
<i>T. Chen</i>	2765	TAG06
Precise Determination and Comparison of the SPS Dynamic Aperture in Experiment and		
Simulation — W. Fischer, F. Schmidt	2768	TAG07
Coherency of the Long Range Beam-Beam Interaction in CESR — Alexander B. Temnykh,		
<i>James J. Welch</i>	2771	TAG08
Effect of Quadrupole Noise on the Emittance Growth of Protons in HERA — T. Sen,		
<i>O. Brüning, F. Willeke</i>	2774	TAG09
Nonlinear Mode Coupling Analysis in the Tevatron — S. Assadi, C.S. Mishra	2777	TAG10
Lattice Design for KEKB Colliding Rings — H. Koiso, K. Oide	2780	TAG11
Entropy and Emittance Growth — Patrick G. O'Shea	2783	TAG12
Analysis of Optical Stochastic Cooling Including Transverse Effects — K.-J. Kim	2786	TAG13

Volume 5

Linear and Nonlinear Orbit Theory

Reduction of Non Linear Resonance Excitation from Insertion Devices in the ALS —		
<i>D. Robin, G. Krebs, G. Portmann, A. Zholents, W. Decking</i>	2789	FAB01
Sum Betatron Resonances under Linear Coupling of Oscillations — P.N. Chirkov,		
<i>I.I. Petrenko</i>	2792	FAB02
Linear Orbit Parameters for the Exact Equations of Motion — G. Parzen	2795	FAB03
Tune Modulation Due to Synchrotron Oscillations and Chromaticity, and the Dynamic		
Aperture — G. Parzen	2798	FAB04
Normal Mode Tunes for Linear Coupled Motion in Six Dimensional Phase Space —		
<i>G. Parzen</i>	2801	FAB05
Fast Symplectic Mapping and Quasi-invariants for the Large Hadron Collider —		
<i>R.L. Warnock, J.S. Berg, E. Forest</i>	2804	FAB06
Nonlinear Dependence of Synchrotron Radiation on Beam Parameters — G.H. Hoffstätter	2807	FAB07
Effects of Imperfections on the Dynamic Aperture and Closed Orbit of the IPNS Upgrade		
Synchrotron — E. Lessner, Y.-C. Chae, S. Kim	2811	FAB09
Paraxial Expansion of a Static Magnetic Field in a Ring Accelerator — Lee C. Teng	2814	FAB10
Experimental Determination of Linear Optics Including Quadrupole Rotations —		
<i>J. Safranek</i>	2817	FAB11
Perturbation of Beam Energy Due to Steering and Pretzel Orbit — W. Lou, M. Billing,		
<i>D. Rice</i>	2820	FAB12
Lattice Studies for a High-Brightness Light Source — D. Kaltchev, R.V. Servranckx,		
<i>M.K. Craddock, W. Joho</i>	2823	FAB14

Transfer Maps Through Ideal Bends (Again?) — <i>Leo Michelotti</i>	2826	FAB15
Skew Chromaticity in Large Accelerators — <i>S. Peggs, G.F. Dell</i>	2829	FAB20
The Effect and Correction of Coupling Generated by the RHIC Triplet Quadrupoles — <i>F. Pilat, S. Peggs, S. Tepikian, D. Trbojevic, J. Wei</i>	2832	FAB22
The Beam Envelope Equation - Systematic Solution for a FODO Lattice with Space Charge — <i>Edward P. Lee</i>	2835	FAC01
Analytic Second- and Third-Order Achromat Designs — <i>Chunxi Wang, Alex Chao</i>	2838	FAC02
Measurement of Chromatic Effects in LEP — <i>D. Brandt, P. Castro, K. Cornelis, A. Hofmann,</i> <i>G. Morpurgo, G.L. Sabbi, A. Verdier</i>	2841	FAC03
The Lattice of the CERN Large Hadron Collider — <i>W. Scandale, B. Jeanneret, J.-</i> <i>P. Koutchouk, X. Luo, F. Méot, R. Ostojic, T. Risselada, C. Rufer, T. Taylor, T. Trenkler,</i> <i>S. Weisz</i>	2844	FAC04
Sorting Strategies for the LHC Based on Normal Forms — <i>W. Scandale, M. Giovannozzi,</i> <i>R. Grassi, E. Todesco</i>	2847	FAC06
Algorithms to get a Circulating Beam — <i>André Verdier, Frank Richard</i>	2850	FAC07
Non-Linear Chromaticity Correction with Sextupole Families — <i>André Verdier</i>	2853	FAC08
Simulation of Charged Particle Transport in Nonlinear Axisymmetrical Electrostatic Potential — <i>I.P. Yudin, V.V. Andreev</i>	2856	FAC09
Stochastic Effects in Real and Simulated Ion Beams — <i>Jürgen Struckmeier</i>	2860	FAC10
Magnetic Field Correction in Nuclotron — <i>I.B. Issinsky, V.A. Mikhailov, V.A. Shchepunov</i>	2863	FAC12
Effects of the CHESS Wigglers on a Beam with an Angular Offset — <i>James J. Welch</i>	2866	FAC14
Particle Tracking with Generating Functions of Magnetic Fringing Fields — <i>Godehard Wüstefeld</i>	2868	FAC16
Computation of Lattice Maps Using Modular BCH and Similarity Composition Rules — <i>J. Irwin</i>	2871	FAC18
Treatment of Wiggler and Undulator Field Errors in Tracking Codes — <i>W. Decking,</i> <i>O. Kaul, H. Neemann, J. Roßbach</i>	2874	FAC19
Experimental Study of the Duke Storage Ring Dynamic Aperture — <i>Y. Wu, V.N. Litvinenko,</i> <i>B. Burnham, J.M.J. Madey</i>	2877	FAC20

Beam-Beam Interaction and Beam Cooling

A New Model of the e ⁺ e ⁻ Beam-Beam Interaction — <i>K.D. Cromer, B.E. Norum</i>	2880	RAP01
A Study of Beam-Beam Interactions at Finite Crossing Angles for a B-Factory — <i>K. Hirata,</i> <i>K. Ohmi, N. Toge</i>	2883	RAP02
Simulation of Beam-Beam Effects in Tevatron — <i>C.S. Mishra, S. Assadi, R. Talman</i>	2886	RAP03
The Dynamic Beta Effect in CESR — <i>David Sagan</i>	2889	RAP04
Lifetime and Tail Simulations for Beam-Beam Effects in PEP-II B Factory — <i>D.N. Shatilov,</i> <i>A.A. Zholents</i>	2892	RAP05
Gamma Ray Sources Based on Resonant Backscattering of Laser Beams With Relativistic Heavy Ion Beams — <i>E.G. Bessonov, Kwang-Je Kim</i>	2895	RAP06
Observations of the Effects of the Beam-Beam Interaction on the Orbits of Stored Beams in CESR — <i>E. Young</i>	2898	RAP07
Calculations on Depolarization in HERA due to Beam-Beam Effects — <i>M. Böge, T. Limberg</i>	2901	RAP08
A Map for the Thick Beam-Beam Interaction — <i>J. Irwin, T. Chen</i>	2904	RAP09
Transient Beam Loading in the SLC Damping Rings — <i>M.G. Minty, R.H. Siemann</i>	2907	RAP10
Studies of Halo Distributions Under Beam-Beam Interaction — <i>T. Chen, J. Irwin,</i> <i>R.H. Siemann</i>	2910	RAP11
The Effect of Phase Advance Errors Between Interaction Points on Beam Halos — <i>T. Chen,</i> <i>J. Irwin, R.H. Siemann</i>	2913	RAP12
Compensation of the "Pacman" Tune Spread by Tailoring the Beam Current — <i>Miguel A. Furman</i>	2916	RAP14
Disruption Effects on the Beam Size Measurement — <i>P. Raimondi, F.-J. Decker, P. Chen</i>	2919	RAP15
Flat Beam Spot Sizes Measurement in the SLC-Final Focus — <i>P. Raimondi, F.-J. Decker</i>	2922	RAP16
Polarization Correlations in the SLC Final Focus — <i>F.-J. Decker</i>	2925	RAP17
Supercooling of Bunched Beams by Coherent Synchrotron Radiation — <i>M. Bergher</i>	2928	RAP19

Analysis of the Tevatron Collider Beam Spectrum for Bunched Beam Stochastic Cooling — <i>G. Jackson</i>	2931	RAP20
Asymmetric Hopf Bifurcation for Proton Beams with Electron Cooling — <i>X. Kang, M. Ball, B. Brabson, J. Budnick, D.D. Caussyn, P. Colestock, G. East, M. Ellison, B. Hamilton, K. Hedblom, S.Y. Lee, D. Li, J.Y. Liu, K.Y. Ng, A. Pei, A. Riabko, M. Syphers, L. Wang, Y. Wang</i>	2934	RAP21
Space Charge Effects and Intensity Limits of Electron-Cooled Bunched Beams — <i>S. Nagaitsev, T. Ellison, M. Ball, V. Derenchuk, G. East, M. Ellison, B. Hamilton, P. Schwandt</i>	2937	RAP22
Stability Conditions for a Neutralised Electron Cooling Beam — <i>J. Bosser, S. Maury, D. Möhl, F. Varenne, I. Meshkov, E. Syresin, E. Mustafin, P. Zenkevich</i>	2940	RAP23
Neutralisation of the LEAR Electron-Cooling Beam: Experimental Results — <i>J. Bosser, F. Caspers, M. Chanel, R. Ley, R. Maccaferri, S. Maury, G. Molinari, G. Tranquille, F. Varenne, I. Meshkov, V. Polyakov, A. Smirnov, O. Stepashkin, E. Syresin</i>	2943	RAP24
Crystalline Beam Properties as Predicted for the Storage Ring ASTRID and TSR — <i>Jie Wei, Xiao-Ping Li, Andrew Sessler</i>	2946	RAP25

Instabilities and Cures

Impedance Matrix - an Unified Approach to Longitudinal Coupled-Bunch Feedbacks in a Synchrotron — <i>S. Ivanov</i>	2949	TPQ01
The Coupling Impedance of Toroidal Beam Pipe with Circular Cross Section — <i>H. Hahn</i>	2952	TPQ02
Bunch Lengthening Study in BEPC — <i>Z. Guo, Q. Qin, G. Xu, C. Zhang</i>	2955	TPQ03
Practical Criterion of Transverse Coupled-Bunch Head-Tail Stability — <i>S. Ivanov, M. Pozdeev</i>	2958	TPQ04
A Code to Compute the Action-Angle Transformation for a Particle in an Arbitrary Potential Well — <i>J. Scott Berg, Robert L. Warnock</i>	2962	TPQ07
Study of Longitudinal Coupled-Bunch Instabilities in the SRRS Storage Ring — <i>W.K. Lau, M.H. Wang, K.T. Hsu, L.H. Chang, Ch. Wang, C.C. Kuo</i>	2965	TPQ08
Suppression of the Transverse Oscillation in the SRRS Storage Ring by RF Knockout Method — <i>J.C. Lee, M.H. Wang, K.T. Hsu, R.J. Sheu, G. Lin, C.S. Hsue</i>	2968	TPQ09
The Observation of Longitudinal Coupled Bunch Motion on Streak Camera at SRRS — <i>M.H. Wang, K.T. Hsu, W.K. Lau, C.S. Hsue, H.J. Tsai, H.P. Chang, J.C. Lee, C.C. Kuo</i>	2971	TPQ10
Resistive-Wall Instability Experiment in Space-Charge Dominated Electron Beams — <i>H. Suk, J.G. Wang, M. Reiser</i>	2974	TPQ11
Mode-Coupling Instability and Bunch Lengthening in Proton Machines — <i>K.Y. Ng</i>	2977	TPQ12
Longitudinal Wakefield for Synchrotron Radiation — <i>J.B. Murphy, S. Krinsky, R.L. Gluckstern</i>	2980	TPQ14
Review of Beam Instability Studies for the SSC — <i>W. Chou</i>	2983	TPQ15
Collective Effects in the NLC Damping Ring Designs — <i>T. Raubenheimer, K.L.F. Bane, J.S. Berg, J. Byrd, J. Corlett, M. Furman, S. Heifets, K. Kubo, M. Minty, B. Scott, K.A. Thompson, P.B. Wilson, F. Zimmermann</i>	2986	TPQ16
Emittance and Energy Control in the NLC Main Linacs — <i>C. Adolphsen, K.L.F. Bane, K. Kubo, T. Raubenheimer, R.D. Ruth, K.A. Thompson, F. Zimmermann</i>	2989	TPQ17
Digital Signal Processing for the APS Transverse and Longitudinal Damping System — <i>D. Barr, W. Sellyey</i>	2992	TPQ19
Longitudinal Coupling Impedance of a Hole in an Infinite Plane Screen — <i>Yong-Chul Chae</i>	2995	TPQ20
Investigation of Resistive Wall Instability in the 7-GeV APS Storage Ring — <i>Yong-Chul Chae</i>	2998	TPQ21
Longitudinal Instability Analysis for the IPNS Upgrade — <i>K. Harkay, Y. Cho, E. Lessner</i>	3001	TPQ22
Transverse Instability Analysis for the IPNS Upgrade — <i>K. Harkay, Y. Cho</i>	3004	TPQ23
Longitudinal Emittance Measurements in the Fermilab Booster — <i>D.A. Herrup</i>	3007	TPQ25
Analog Dampers in the Fermilab Booster — <i>D.A. Herrup, D. McGinnis, J. Steimel, R. Tomlin</i>	3010	TPQ26
A Study of the Longitudinal Coupled Bunch Instability in the Fermilab Main Ring — <i>K. Junck, J. Marriner, D. McGinnis</i>	3013	TPQ28
Inference of Wake Field Structure by Driving Longitudinal Coupled Bunch Modes in Main Ring — <i>S. Assadi, K. Junck, P. Colestock, J. Marriner</i>	3016	WAB01
Simulation of Transverse Coupled Bunch Instabilities — <i>S. Khan</i>	3019	WAB03
The Transition Jump System for the AGS — <i>W.K. van Asselt, L.A. Ahrens, J.M. Brennan, A. Dunbar, E. Keith-Monnia, J.T. Morris, M.J. Syphers</i>	3022	WAB04

Measurements of Longitudinal Phase Space in the SLC Linac — R.L. Holtzapple, F.-J. Decker, R.K. Jobe, C. Simopoulos	3025	WAB05
Observation of Induced Beam Oscillation from Actively Displaced RF Accelerating Structures — John T. Seeman, Henk Fischer, William Roster	3028	WAB06
Measurement of the Effect of Collimator Generated Wakefields on the Beams in the SLC — K.L.F. Bane, C. Adolphsen, F.-J. Decker, P. Emma, P. Krejcik, F. Zimmermann	3031	WAB07
Beam Trajectory Jitter in the SLC Linac — Chris Adolphsen, Tim Slaton	3034	WAB08
Emittance Growth due to Decoherence and Wakefields — M.G. Minty, A.W. Chao, W.L. Spence	3037	WAB09
A Weak Microwave Instability with Potential Well Distortion and Radial Mode Coupling — Alex Chao, Bo Chen, Katsunobu Oide	3040	WAB10
Wake Field and the Diffraction Model Due to a Flat Beam Moving Past a Conducting Wedge — A.W. Chao, H. Henke	3043	WAB11
Operating Experience with High Beam Currents and Transient Beam Loading in the SLC Damping Rings — M.G. Minty, R. Akre, P. Krejcik, R.H. Siemann	3046	WAB12
Deflecting Forces for the Case of Multi Mode Beam - RF Cavity Interaction in Linear Accelerators — V.G. Kurakin	3049	WAB14
Photoelectron Trapping Mechanism for Transverse Coupled Bunch Mode Growth in CESR — J.T. Rogers	3052	WAB15
Electron Cooler Impedances — A. Burov	3055	WAB16
Wall Impedances for Low and Moderate Energies — A. Burov	3058	WAB17
Impedance Analysis of the PEP-II Vacuum Chamber — C.-K. Ng, T. Weiland	3061	WAB18
Microwave Instabilities in Electron Rings with Negative Momentum Compaction Factor — S.X. Fang, K. Oide, K. Yokoya, B. Chen, J.Q. Wang	3064	WAB20
Microwave Stability at Transition — J.A. Holt, P.L. Colestock	3067	WAC01
Experimental Observations of Nonlinear Coupling of Longitudinal Modes in Unbunched Beams — Linda Klamp Spentzouris, Patrick L. Colestock, Francois Ostiguy	3070	WAC02
Damping Rate Measurements in the SLC Damping Rings — C. Simopoulos, R.L. Holtzapple	3073	WAC04
Transverse Multibunch Instabilities for Non-Rigid Bunches — J. Scott Berg, Ronald D. Ruth	3076	WAC05
Simulations of Transition Crossing in the Main Injector — C.M. Bhat, J.A. MacLachlan	3079	WAC06
Impedance Budget for the KEK B-Factory — Y.H. Chin, K. Satoh	3082	WAC07
Single-Beam Collective Effects in the KEK B-Factory — Y.H. Chin, K. Akai, Y. Funakoshi, K. Oide, K. Satoh	3085	WAC08
Beam Transfer Function and Transverse Impedance Measurements in the Fermilab Main Ring — P.J. Chou, G. Jackson	3088	WAC09
Experimental Studies of Transverse Beam Instabilities at Injection in the Fermilab Main Ring — P.J. Chou, G. Jackson	3091	WAC10
Longitudinal Multibunch Feedback Experiment with Switched Filter Bank — A. Pei, M. Ball, M. Ellison, X. Kang, S.Y. Lee, D. Li, J. Liu, A. Riabko, L. Wang	3094	WAC12
Field Propagation Effects and Related Multibunch Instability in Multicell Capture Cavities — M. Ferrario, A. Mosnier, L. Serafini, F. Tazzioli, J.-M. Tessier	3097	WAC13
Cure of Transverse Instabilities by Chromaticity Modulation — T. Nakamura	3100	WAC14
A Fast Beam-Ion Instability — F. Zimmermann, T.O. Raubenheimer, G. Stupakov	3102	WAC15
Simulations of the Longitudinal Instability in the New SLC Damping Rings — K.L.F. Bane, K. Oide	3105	WAC16
High-Intensity Single Bunch Instability Behavior In The New SLC Damping Ring Vacuum Chamber — K. Bane, J. Bowers, A. Chao, T. Chen, F.J. Decker, R.L. Holtzapple, P. Krejcik, T. Limberg, A. Lisin, B. McKee, M.G. Minty, C.-K. Ng, M. Pietryka, B. Podobedov, A. Rackelmann, C. Rago, T. Raubenheimer, M.C. Ross, R.H. Siemann, C. Simopoulos, W. Spence, J. Spencer, R. Stege, F. Tian, J. Turner, J. Weinberg, D. Whittum, D. Wright, F. Zimmermann	3109	WAC17
Alignment Tolerance of Accelerating Structures and Corrections for Future Linear Colliders — K. Kubo, C. Adolphsen, K.L.F. Bane, T.O. Raubenheimer, K.A. Thompson	3112	WAC18
Refinements to Longitudinal, Single Bunch, Coherent Instability Theory — S.R. Koscielniak	3115	WAC19
Simulations of Sawtooth Instability — R. Baartman, M. D'Yachkov	3119	WAC20
Characterisation of a Localised Broad-Band Impedance Phenomenon on the SRS — S.F. Hill	3122	WAC21
Cavity-Beam Instabilities on the SRS at Daresbury — P.A. McIntosh, D.M. Dykes	3125	WAC22

Bunch Lengthening Thresholds on the Daresbury SRS — J.A. Clarke.....	3128	WAC23
Estimation of Collective Instabilities in RHIC — W.W. MacKay, M. Blaskiewicz, D. Deng, V. Mane, S. Peggs, A. Ratti, J. Rose, T.J. Shea, J. Wei.....	3131	WAC24
RHIC Injection Kicker Impedance — V. Mane, S. Peggs, D. Trbojevic, W. Zhang.....	3134	WAC25
KRAKEN, a Numerical Model of RHIC Impedances — S. Peggs, V. Mane.....	3137	WAC26
Lattice Design of Beijing Light Source — N. Huang, L. Jin, D. Wang, L. Wang, A. Xiao, G. Xu.....	3140	WAC27
A Theoretical Study of the Electron-Proton Instability in a Long Proton Pulse — Tai-Sen F. Wang.....	3143	WAC28
Recent Progress on Beam Stability Study in the PSR — T. Wang, P. Channell, R. Cooper, D. Fitzgerald, T. Hardek, R. Hutson, A. Jason, R. Macek, M. Plum, C. Wilkinson, E. Colton.....	3146	WAC29

Low Energy Accelerator Beam Dynamics

Halos of Intense Proton Beams (Invited) — Robert D. Ryne, Salman Habib, Thomas P. Wangler.....	3149	RAG01
Polarized Proton Beams (Invited) — T. Roser.....	3154	RAG02
Beam Dynamics in Heavy Ion Fusion (Invited) — Peter Seidl.....	3159	RAG03
Crystalline Beams (Invited) — John P. Schiffer.....	3164	RAG04
Injecting a Kapchinskij-Vladimirskij Distribution into a Proton Synchrotron — E. Crosbie, K. Symon.....	3167	RAG05
Halo of a High-Brightness Electron Beam — G. Haouat, N. Pichoff, C. Couillaud, J.P. De Brion, J. Di Crescenzo, S. Joly, A. Loulergue, C. Ruiz, S. Seguin, S. Striby.....	3170	RAG06
Studies on Halo Formation in a Long Magnetic Quadrupole FODO Channel First Experimental Results — P.-Y. Beauvais, D. Bogard, P.-A. Chamouard, R. Ferdinand, G. Haouat, J.-M. Lagniel, J.-L. Lemaire, N. Pichoff, C. Ruiz.....	3173	RAG07
Radial Mode Evolution in Longitudinal Bunched Beam Instability — S.Y. Zhang, W.T. Weng.....	3176	RAG08
Stability of a Breathing K-V Beam — Robert L. Gluckstern, Wen-Hao Cheng.....	3179	RAG09
Hamiltonian Formalism for Space Charge Dominated Beams in a Uniform Focusing Channel — A. Riabko, M. Ellison, X. Kang, S.Y. Lee, J.Y. Liu, D. Li, A. Pei, L. Wang.....	3182	RAG10
Simulation Studies of the LAMPF Proton Linac — R.W. Garnett, E.R. Gray, L.J. Rybarcyk, T.P. Wangler.....	3185	RAG11
Functional Dependence of Wakefunctions for $v < c$ — Zenghai Li, Joseph J. Bisognano.....	3188	RAG12
Betatron Transients Caused by Rapid Changes in the Closed Orbit — James J. Welch.....	3191	RAG13
Phenomenology of Crystalline Beams in Smooth Accelerators — A.F. Hoffmans, D. Maletic, A.G. Ruggiero.....	3194	RAG14
Beam Dynamics in the 1.3 GeV High Intensity ESS Coupled Cavity Linac — M. Pabst, K. Bongardt.....	3197	TPA01
Final Bunch Rotation and Momentum Spread Limitation for the ESS Facility — K. Bongardt, M. Pabst.....	3200	TPA02
Design Criteria for High Intensity H⁻Injector Linacs — K. Bongardt, M. Pabst.....	3203	TPA03
Measurements of Vacuum Chamber Impedance Effects on the Stored Beam at CESR — M. Billing, Z. Greenwald, W. Hartung, W.R. Lou, M. Pisharody, J. Rogers, D. Sagan, J. Sikora.....	3206	TPA04
The Study of Nonlinear Effects Influenced by Space Charge in High Intensity Linac — A.A. Kolomiets, S.G. Yaramishev, P.R. Zenkevich, A.P. Korolev.....	3209	TPA05
Beam Size Versus Intensity for Resonant Extracted Beam at the Brookhaven AGS — K.A. Brown, R. Thern, H. Huang.....	3212	TPA06
Review of Longitudinal Perturbation Formalism — S.Y. Zhang.....	3214	TPA08
Klystron Power Specifications Based on Transient Beam Loading Analysis in Damping Rings — M.G. Minty, R.H. Siemann.....	3217	TPA09
Transverse Combining of Four Beams in MBE-4 — C.M. Celata, W. Chupp, A. Faltens, W.M. Fawley, W. Ghiorso, K.D. Hahn, E. Henestroza, C. Peters, P. Seidl.....	3220	TPA10
Ion Core Parameters in the Bending Magnets of Electron Storage Rings — E. Bulyak.....	3223	TPA12
Ion Driven Effects in the Intence Electron Beam Circulating in Storage Rings — E. Bulyak.....	3226	TPA13
Disk-Loaded Waveguides for Accelerating High Intensity Short Pulse Electron Beams — N.I. Aizatsky.....	3229	TPA14
The Description of High Current Beam Dynamics Using Lie Algebraic Methods — A.I. Borodich, A.A. Khrutchinsky, V.I. Stolyarsky.....	3232	TPA15

Chaos, a Source of Charge Redistribution and Halo Formation in Space-Charge Dominated Beams — Jean-Michel Lagniel, David Libault	3235	TPA17
Transport of a Partially-Neutralized Ion Beam in a Heavy-Ion Fusion Reactor Chamber — Debra A. Callahan, A. Bruce Langdon	3238	TPR01
Emittance Growth from Rotated Quadrupoles in Heavy Ion Accelerators — John J. Barnard	3241	TPR02
Wakefield Effects on the Beam Accelerated in a Photoinjector: Perturbation Due to the Exit Aperture — J.-M. Dolique, W. Salah	3245	TPR04
Influence of the Photoinjector Exit Aperture on the Wakefield Driven by an Intense Electron Beam Pulse: a Theoretical Approach — J.-M. Dolique	3248	TPR05
Invariability of Intense Beam Emittance in Nonlinear Focusing Channel — Y.K. Batygin	3251	TPR06
Beam Transport for Uniform Irradiation: Nonlinear Space Charge and the Effect of Boundary Conditions — D. Bruhwiler, Yuri K. Batygin	3254	TPR07
Transport of Bunched Beams with Space Charge Through a Periodic Lattice — M.F. Reusch, D.L. Bruhwiler	3257	TPR08
Modeling Space Charge in Beams for Heavy-Ion Fusion — W.M. Sharp	3260	TPR09
Impedance of Periodic Irises in a Beam Pipe — Shicheng Jiang, Robert L. Gluckstern, Hiromi Okamoto	3263	TPR11
Frequency Dependence of the Polarizability and Susceptibility of a Circular Hole in a Thick Conducting Wall — Wen-Hao Cheng, Alexei V. Fedotov, Robert L. Gluckstern	3266	TPR12
Spatial-Temporal Hysteresis Effects in an Intense Electron Beam — A.V. Agafonov, A.N. Lebedev, V.S. Voronin	3269	TPR13
General Wave Equation in the Electrostatic Approximation — A.V. Agafonov	3272	TPR14
Space Charge Effects at KEK-Booster Synchrotron — Chihiro Ohmori, Toshikazu Adachi, Tadamichi Kawakubo, Motohiro Kihara, Isao Yamane	3275	TPR16
On the Relaxation of Semi-Gaussian and K-V Beams to Thermal Equilibrium — S.M. Lund, J.J. Barnard, J.M. Miller	3278	TPR18
Transverse-Longitudinal Energy Equilibration in a Long Uniform Beam — I. Haber, D.A. Callahan, A. Friedman, D.P. Grote, A.B. Langdon	3282	TPR19

Beam Dynamics, Misc.

Variants of Optics Schemes and Accelerator Configurations for Athens Microtron: Preliminary Considerations — A.V. Tiunov, V.I. Shvedunov, I.V. Surma, K. Hizanidis, C. Kalfas, C. Trikalinos, J. Tigelis	3285	RAQ01
Study of Beam Decoherence in the Presence of Head-Tail Instability Using a Two-particle Model — G.V. Stupakov, A.W. Chao	3288	RAQ02
Beam Distribution Function after Filamentation — T.O. Raubenheimer, F.-J. Decker, J.T. Seeman	3291	RAQ03
Measurement of the Interaction Between a Beam and a Beam Line Higher-Order Mode Absorber in a Storage Ring — W. Hartung, P. Barnes, S. Belomestnykh, M. Billing, R. Chiang, E. Chojnacki, J. Kirchgessner, D. Moffat, H. Padamsee, M. Pisharody, D. Rubin, M. Tigner	3294	RAQ04
A New Analytical Model for Axi-symmetric Cavities — D. Burrini, C. Pagani, L. Serafini	3297	RAQ05
Impurity Growth in Single Bunch Operation of PF — M. Tobiyama, A. Higuchi, T. Mitsuhashi, T. Kasuga, S. Sakanaka	3300	RAQ06
Coupling Impedance of a Periodic Array of Diaphragms — G.V. Stupakov	3303	RAQ09
Coupling Impedance of a Long Slot and an Array of Slots in a Circular Vacuum Chamber — G.V. Stupakov	3306	RAQ10
Dark Currents for CEBAF Linacs — Byung C. Yunn	3309	RAQ11
Improvements in Bunch Coalescing in the Fermilab Main Ring — J. Dey, I. Kourbanis, D. Wildman	3312	RAQ13
Slow Extraction of Particles Using a Thin Target for Driving for Resonance — Yu. Severgin, W. Belov, A. Makarov, M. Tarovik	3315	RAQ14
Properties of a Transverse Damping System, Calculated by a Simple Matrix Formalism — S. Koscielniak, H.J. Tran	3317	RAQ15
A Concept for Emittance Reduction of DC Radioactive Heavy-Ion Beams — J.A. Nolen, J.C. Dooling	3320	RAQ16

Measurements of the Octupole-Induced Amplitude-Dependent Frequency Shift in SPEAR — P. Tran, C. Pellegrini, J. Yang, M. Cornacchia, J. Corbett.....	3323	RAQ17
Radiation Damping in Focusing-Dominated Systems — Zhirong Huang, Pisin Chen, Ronald D. Ruth.....	3326	RAQ18
Colliding Crystalline Beams — A.F. Haffmans, D. Maletic, A.G. Ruggiero.....	3329	RAQ20
Helical Spin Rotators and Snakes for RHIC — V.I. Ptitsin, Yu.M. Shatunov, S. Peggs.....	3331	RAQ21
Effects of Enhanced Chromatic Nonlinearity during the AGS gt-Jump — J. Wei, J.M. Brennan, L.A. Ahrens, M.M. Blaskiewicz, D.-P. Deng, W.W. MacKay, S. Peggs, T. Satogata, D. Trbojevic, A. Warner, W.K. van Asselt.....	3334	RAQ22
Effect of Parametric Resonances on the Bunched Beam Dilution Mechanism — L. Wang, M. Ball, B. Brabson, J. Budnick, D.D. Caussyn, G. East, M. Ellison, X. Kang, S.Y. Lee, D. Li, J.Y. Liu, K.Y. Ng, A. Pei, A. Riabko, D. Rich, T. Sloan, M. Syphers	3337	RAQ23
Parametric Resonances and Stochastic Layer Induced by A Phase Modulation — J.Y. Liu, M. Ball, B. Brabson, J. Budnick, D.D. Caussyn, P. Colestock, V. Derenchuk, G. East, M. Ellison, D. Friesel, B. Hamilton, W.P. Jones, X. Kang, S.Y. Lee, D. Li, K.Y. Ng, A. Pei, A. Riabko, T. Sloan, M. Syphers, L. Wang	3340	RAQ24
Nonlinear Space Charge Effect of Gaussian Type Bunched Beam in Linac — Yinbao Chen, Shinian Fu, Zhibin Huang, Zhenhai Zhang.....	3343	RAQ25
Emittance Growth Caused by Bunched Beam with Nonuniform Distributions in Both Longitudinal and Transverse Directions in Linac — Zhibin Huang, Yinbao Chen, Shinian Fu.....	3346	RAQ26
The Envelopes of Beam Motion in the Charged Particle Cyclic Accelerator — Yu.P. Virchenko, Yu.N. Grigor'ev.....	3349	RAQ28
A Semi-analytical Approach to the Design of Low Energy Cylindrically Symmetric Transport Lines — Pedro F. Tavares.....	3352	RAQ29
Stability of Trapped Ions in Electron Storage Rings in View of Parametric Resonance — Y. Miyahara.....	3355	RAQ30
Entropy and Emittance of Particle and Photon Beams — K.-J. Kim, R.G. Littlejohn.....	3358	RAQ02
Effect of the Coupling Slots on Beam Dynamics in Accelerator Structure of Moscow CW RTM — V.I. Shvedunov, A.S. Alimov, A.S. Chepurinov, O.V. Chubarov, D.I. Ermakov, A.V. Tiunov, P.L. Tkachev.....	3361	RAR04
The Electron Beam Orbit Sensitivity on the Photon Flux of the Photon Beam Line — Ian Hsu, G.H. Luo, K.L. Tsang, C.C. Chu, C.I. Yu, W.T. Weng, S.C. Chung.....	3364	RAR05
Ground Motion in LEP and LHC — L. Vos.....	3367	RAR07
Cosmic Particle Acceleration at Very High Energies — K.O. Thielheim.....	3370	RAR09
Trapped Modes in the Vacuum Chamber of an Arbitrary Cross Section — Sergey S. Kurennoy, Gennady V. Stupakov	3373	RAR11
A General Approach for Calculating Coupling Impedances of Small Discontinuities — Sergey S. Kurennoy, Robert L. Gluckstern, Gennady V. Stupakov	3376	RAR12
Polarizabilities of an Annular Cut and Coupling Impedances of Button-Type Beam Position Monitors — Sergey S. Kurennoy.....	3379	RAR13
The Effect of Coupling on Luminosity — D. Sagan.....	3382	RAR15
RFQ-DTL Matching Solutions for Different Requirements — D. Raparia	3385	RAR16
Low-Dispersion γ Jump for the Main Injector — K.Y. Ng, A. Bogacz	3388	RAR17
Wakefields and HOMs Studies of a Superconducting Cavity Module with the CESR Beam — S. Belomestnykh, W. Hartung, G. Flynn, J. Kirchgessner, H. Padamsee, M. Pisharody.....	3391	RAR18
Comparison of the Predicted and Measured Loss Factor of the Superconducting Cavity Assembly for the CESR Upgrade — S. Belomestnykh, W. Hartung, J. Kirchgessner, D. Moffat, H. Muller, H. Padamsee, V. Veshcherevich.....	3394	RAR19
Control of Trapped Ion Instabilities in the Fermilab Antiproton Accumulator — Steven J. Werkema	3397	RAR20
Longitudinal Emittance Oscillation in a Superconducting Drift Tube Linac — J.W. Kim, K.W. Shepard	3400	RAR21
Electric Fields, Electron Production, and Electron Motion at the Stripper Foil in the Los Alamos Proton Storage Ring — M. Plum.....	3403	RAR22
Electron Clearing in the Los Alamos Proton Storage Ring — M. Plum, J. Allen, M. Borden, D. Fitzgerald, R. Macek, T.S. Wang.....	3406	RAR23

Advanced Photon Source Insertion Device Field Quality and Multipole Error Specification — <i>Yong-Chul Chae, Glenn Decker</i>	3409	RAR24
Study of Field Ionization in the Charge Exchange Injection for the IPNS Upgrade — <i>Yong-Chul Chae, Yanglai Cho</i>	3412	RAR25
Lattice Considerations for a Tau-Charm Factory — <i>L.C. Teng, E.A. Crosbie</i>	3415	RAR26
Effects of Vertical Aperture on Beam Lifetime at the Advanced Photon Source (APS) Storage Ring — <i>Hana M. Bizek</i>	3418	RAR27
Rebucketing After Transition in RHIC — <i>D.-P. Deng, S. Peggs</i>	3421	RAR29
Closed-Orbit Drifts in HERA in Correlation with Ground Motion — <i>V. Shiltsev, B. Baklakov,</i> <i>P. Lebedev, C. Montag, J. Rossbach</i>	3424	RAR30
Simulation of the Acceleration of Polarized Protons in Circular Accelerators — <i>Yu. Shatunov, V. Yakimenko</i>	3427	RAR31

Parameters of the SLAC Next Linear Collider*

T. Raubenheimer, C. Adolphsen, D. Burke, P. Chen, S. Ecklund, J. Irwin, G. Loew, T. Markiewicz, R. Miller, E. Paterson, N. Phinney, M. Ross, R. Ruth, J. Sheppard, H. Tang, K. Thompson, P. Wilson, Stanford Linear Accelerator Center, Stanford University, Stanford, CA, 94309

Abstract

In this paper, we present the parameters and layout of the Next Linear Collider (NLC). The NLC is the SLAC design of a future linear collider using X-band RF technology in the main linacs. The collider would have an initial center-of-mass energy of 0.5 TeV which would be upgraded to 1 TeV and then 1.5 TeV in two stages. The design luminosity is $> 5 \times 10^{33} \text{ cm}^{-2} \text{ sec}^{-1}$ at 0.5 TeV and $> 10^{34} \text{ cm}^{-2} \text{ sec}^{-1}$ at 1.0 and 1.5 TeV. We will briefly describe the components of the collider and the proposed energy upgrade scenario.

I. INTRODUCTION

A number of groups around the world are creating designs for a future linear collider. The present state of the designs can be found in Ref. [1] and a summary of the present status and the required R&D can be found in Ref. [2]. In this paper, we describe the SLAC Next Linear Collider (NLC). The NLC would have an initial center-of-mass energy of 0.5 TeV and would then be upgraded to 1 TeV and finally 1.5 TeV in the center-of-mass.

The primary parameters for the three stages of the design are listed in Table 1. The parameters of the 500 GeV collider are based upon technology that has been demonstrated or is expected to be demonstrated within the next few years. The upgrade path to 1 TeV involves a very straightforward extrapolation of the RF technology, which could be expected to be ready by the time the collider starts operating at 500 GeV. Specifically, it requires that each of the 50 MW klystrons be replaced with two 72 MW klystrons. It also requires increasing the linac and final focus lengths by roughly 20%. This additional length could be built into the 500 GeV collider allowing the 1 TeV energy upgrade to be made adiabatically by simply replacing and adding klystrons and modulators and replacing spool pieces at the end of the accelerator with accelerating structures.

At this time, there are many possible upgrade paths to 1.5 TeV. The 1.5 TeV design will require further upgrades of the RF system to limit the AC power consumption. Examples are a Two Beam Accelerator concept from LBL and LLNL, grid-switched and cluster klystrons, and binary pulse compressors. In Table 1, we have listed a set of parameters which assumes a binary pulse compression system. To ensure both the possibility of the 1.5 TeV upgrade and to provide operational flexibility, we are designing the primary components of the collider to allow for a substantial variation in parameters such as beam charge, accelerating gradient, *etc.* In the next sections, we will outline the components of the design and briefly summarize the R&D status.

Table 1. Parameters of NLC designs.

CM Energy [TeV]	0.5	1.0	1.5
Luminosity [10^{33}]	7.1	14.5	16.1
Rep. Rate [Hz]	180	120	120
Bunch Charge [10^{10}]	0.7	1.1	1.1
Bunches/RF Pulse	90	75	75
Bunch Sep. [ns]	1.4	1.4	1.4
$\gamma\epsilon_x/\gamma\epsilon_y$ IP [10^{-8} m-rad]	500/5	500/5	500/5
β_x/β_y IP [mm]	10/0.1	25/0.1	37/0.15
σ_x/σ_y IP [nm]	320/3.2	360/2.3	360/2.3
σ_z IP [μm]	100	100	100
Upsilon	0.09	0.27	0.41
Pinch Enhancement	1.3	1.4	1.5
Beamstrahlung δ_B [%]	2.3	7	9
# Photons per e^-/e^+	0.8	1.1	1.1
Loaded Gradient [MV/m]	37	63	63
Active Linac Length [km]	14.2	17.0	25.5
Total Site Length [km]	20.0	25.5	36.2
# of Klystrons	3940	9456	7092
Klyst. Peak Pwr. [MW]	50	72	76
Pulse Comp. Gain	3.6	3.6	6.8
Power/Beam [MW]	4.2	7.9	11.9
AC Power [MW]	103	202	240

II. e^+/e^- SOURCES

The design of the NLC polarized electron source is based upon the Stanford Linear Collider (SLC) polarized source [3]. The SLC source very reliably delivers highly polarized ($>80\%$) beams to a damping ring at 1.2 GeV with approximately 5×10^{10} in a single bunch, a beam emittance of roughly $\gamma\epsilon_{x,y} = 1 \times 10^{-4}$ m-rad, and an energy spread of $\pm 1\%$. In the NLC design, the polarized electrons originate at a strained GaAs cathode DC biased at -120 kV. To create the bunch train, the drive laser is sinusoidally modulated so that it delivers a pulse train of ninety 700 ps pulses (FWHM) with a repetition rate of 714 MHz. The electrons are prebunched in two 714 MHz subharmonic bunchers and then bunched and accelerated in an S-band traveling wave buncher, an S-band capture section, and a 2 GeV S-band linac.

Because the NLC design requires relatively low single bunch charge, the important design issues relate to the long bunch trains. Compensation techniques have been devised to control the transient beam loading and the long-range transverse wakefields, which are important in the S-band sections, are reduced by using scaled versions of the Damped-Detuned Structures discussed in

*Work supported by the Department of Energy, contract DE-AC03-76SF00515

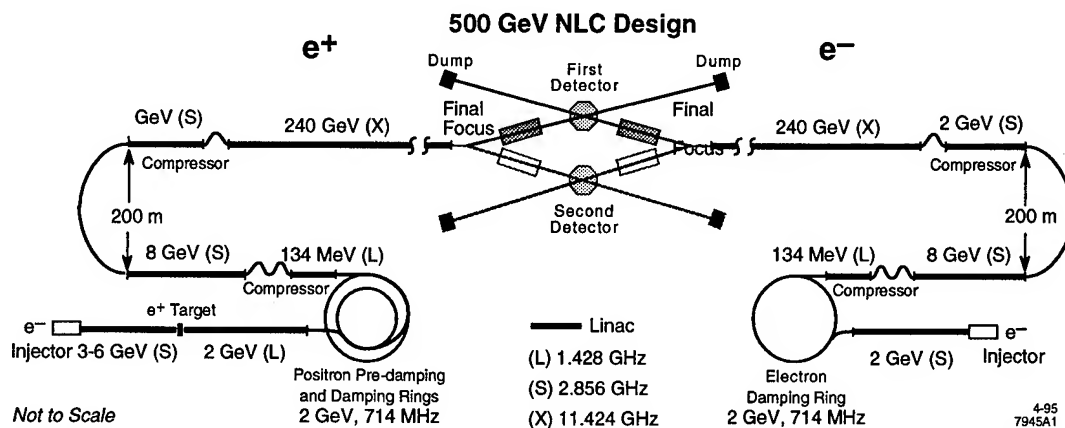


Figure 1. Schematic layout of the SLAC NLC design.

Sect. IV.

The design of the NLC positron source [4] is also based on its SLC counterpart. It is a conventional source which uses an electromagnetic shower generated by colliding a high energy (3~6 GeV) electron beam with a rotating target. Like the SLC design, the target is followed by a flux concentrator and a capture accelerator embedded in a DC solenoid. To reduce the single pulse heating, the beam size at the target is twice that at the SLC target. Because the larger beam size leads to a larger positron emittance and longer bunch length, the NLC design uses L-band (1428 MHz) accelerator structures; the aperture limited emittance is then $\gamma\epsilon_{x,y} = 0.06$ m-rad.

III. DAMPING RINGS AND COMPRESSORS

The damping rings for the NLC [5][6] must produce beams with normalized emittances of $\gamma\epsilon_x = 3 \times 10^{-6}$ m-rad and $\gamma\epsilon_y = 3 \times 10^{-8}$ m-rad. A single damping ring is used to damp the electron beams. It is 220 meters in circumference and damps four trains of 90 bunches simultaneously; the trains are separated by 60 ns, allowing fast kickers to inject and extract individual bunch trains without disturbing the others.

Because the incoming positrons have a much larger emittance, an additional pre-damping ring is used to damp the e^+ beam. The pre-damping ring is half the circumference of the main damping ring and stores two bunch trains at once. It is a relatively simple ring with a large aperture and a large equilibrium emittance. After the pre-damping ring, the positrons are injected into a main damping ring that is identical to the electron damping ring.

The damping ring designs are similar in many ways to the 3rd generation light sources and can benefit from much of the technology that has been developed. Furthermore, the ATF Damping Ring [7], being constructed at KEK, will experimentally verify many of the design concepts.

After the damping rings, the bunch length must be compressed by a factor of 40. This is done in two stages [8]. The first stage, located after the rings at 2 GeV, compresses the rms bunch length from 4 mm to 500 μ m. The first stage also contains a spin rotator system, consisting of four solenoids, that provides full control over the orientation of the beam polarization.

Following the first bunch compression, the beam is acceler-

ated to 10 GeV in an S-band linac and then further compressed to a final bunch length of 100 μ m. This second stage compressor is a telescope in longitudinal phase space, preventing energy errors from the pre-linac from becoming phase errors in the X-band linac.

IV. X-BAND RF

The NLC X-band RF system is based on the SLAC S-band linac RF, but the frequency has been increased to 11.4 GHz to support the higher gradient. The technology to provide the high gradient at high frequency has been under development at SLAC and KEK for the past 8 years. It will be used to provide acceleration at the NLC Test Accelerator (NLCTA) [9] which is presently under construction.

The 500 GeV NLC requires 50 MW 1.25 μ s klystrons [10] as shown in Table 1. For economy and efficiency these are planned to be focussed with a periodic permanent magnet (PPM) lattice. Presently there are two klystrons operating at levels exceeding 50 MW with 1.5 μ s pulses. A third klystron has operated at about 60 MW for short pulses and is presently being conditioned for long pulse operation. These three klystrons will be used in the NLCTA to gain operational experience and the NLC PPM klystron is presently undergoing detailed design.

An RF pulse compression system is needed to compress the klystron RF pulse by a factor of 5 while increasing the power by a factor of 3.6. A prototype SLED-II system is presently operating at SLAC. It has achieved pulse compression gain of 4 to 4.4 and has exceeded 200 MW output power. It is presently being used for accelerator structure tests. The three SLED-II systems for the NLCTA are being fabricated.

The accelerator structures for the NLC must control the long-range transverse wakefield to prevent beam-breakup while accelerating beams with an unloaded gradient of 50~100 MV/m. The wakefield is controlled with a Damped-Detuned Structure (DDS) [11] where the transverse modes are *both* detuned and weakly damped, reducing the Q's to roughly 1000. A test of a detuned structure (no damping) in the ASSET facility [12] verified the rapid fall off of the wakefield roughly 1.4 ns behind the driving bunch; the damping in the DDS structure will further decrease the wake over the long bunch train. This detuned structure has also been tested up to 55 MV/m and will be conditioned up to about

65 MV/m with the prototype SLED-II system. Three additional detuned structures for the NLCTA are being brazed. The DDS structure is presently undergoing detailed mechanical design.

V. X-BAND LINAC

The X-band linacs [13] accelerate the beams from 10 GeV to the final beam energy. Each of the linacs includes roughly 700 quadrupoles placed between the accelerator structures in a FODO lattice. To preserve the low emittance beams, very tight tolerances are required on the alignment and RF control. Beam-based techniques are needed to achieve the alignment tolerances. To this end, dipole mode detectors are used in the structures and BPM's are placed in the quadrupoles. In addition, both the structures and the quadrupoles are supported on separate mechanical movers.

Many of the required beam-based alignment techniques are being verified in the SLC. Further tests will be made using ASSET and the NLCTA. While the alignment concepts are straightforward, experimental verification is necessary to understand the practical limitations and long term stability.

VI. COLLIMATION AND FINAL FOCUS

After the linac and subsequent diagnostics, the beam enters a collimation system [14] which collimates both phases in the horizontal and vertical planes as well as the energy deviation. Although the collimation section is relatively long (1.8 km for the 1 TeV design), it is felt necessary to prevent backgrounds that could overwhelm the detectors.

Following the collimation section, an IP-switch and short arc provide a 10 mrad deflection and direct the beam to one of the two IP's. The design includes two IP's to allow the alternate detector designs and final focus systems that would be required to optimize for $\gamma\text{-}\gamma$ and $\gamma\text{-}e^-$ collisions as well as e^+e^- collisions.

Finally, the beam enters the final focus [15]. At the beginning of the final focus, there are coupling control and beta-matching sections along with phase space diagnostics. The remainder of the final focus optics is similar to the Final Focus Test Beam (FFTB) [16] with the addition of two sextupoles [17] to increase the bandwidth and a crab cavity which is needed due to 10 mrad crossing angle. The system parameters were optimized as described in Ref. [18] and the tolerances are described in Ref. [15]. Based on the SLC and FFTB experience, extensive consideration is being given to the tuning techniques and diagnostics requirements, as well as stability issues. Finally, the beam line from the IP to the dump [19] also contains extensive diagnostics to measure the beam centroid, polarization, and disruption, as well as secondary pairs and beamstrahlung.

VII. DISCUSSION

In this paper, we have given the primary parameters and described the layout of the SLAC NLC. We have also described the upgrade path to 1 TeV, which is being explicitly designed into the collider, and possible upgrade paths to 1.5 TeV. Finally, we are designing the collider to operate over a large range of beam parameters to both ensure the feasibility of the upgrades as well as provide operating flexibility. More detailed descriptions of the subsystems and tolerances can be found in the references.

Much of the design is based on the operating experience with the SLC. In addition, many of the novel components of the collider are being or will be tested in specially designed test facilities. In particular, ASSET and the NLCTA will verify the RF system and accelerating structures, the FFTB is studying the final focus designs, and the KEK ATF will study issues for the damping rings.

References

- [1] *Proc. of the 1995 Workshop on Next Generation Linear Colliders* Tsukuba, Japan, April, 1995.
- [2] International Inter-Laboratory Collaboration for Linear Colliders – Technical Review Committee Report, in preparation.
- [3] R. Alley, et. al., "The Stanford Linear Accelerator Polarized Electron Source," Submitted to Nucl. Instr. Meth. (1995).
- [4] H. Tang, et. al., "The NLC Positron Source," these proceedings.
- [5] T. O. Raubenheimer, et. al., "A Damping Ring Design for the SLAC NLC," these proceedings.
- [6] T. O. Raubenheimer, et. al., "Collective Effects in the NLC Damping Rings," these proceedings.
- [7] J. Urakawa, et. al., *Proc. of the 15th Int. Conf. on High Energy Acc.*, Hamburg, Germany (1992) 124.
- [8] P. Emma, et. al., "A Bunch Compressor Design for the Next Linear Collider," these proceedings.
- [9] R. D. Ruth, et. al., *Proc. of the 1993 Part. Acc. Conf.*, Washington, D.C. (1993) 543.
- [10] G. Caryotakis, et. al., *Proc. of the 4th Euro. Part. Acc. Conf.*, London, England (1994) 1921.
- [11] K. Ko, et. al., "Design Parameters for the Damped Detuned Accelerating Structure," these proceedings.
- [12] C. Adolphsen, et. al., *Phys. Rev. Let.* Vol. 74, No. 13 (1995) 2475.
- [13] C. Adolphsen, et. al. "Emittance and Energy Control in the NLC Main Linacs," these proceedings.
- [14] J. Irwin, et. al., *Proc. of the 1993 Part. Acc. Conf.* Washington, D.C. (1993) 185.
- [15] F. Zimmermann, et. al., "A Final Focus System for the SLAC Next Linear Collider," these proceedings.
- [16] K. Oide, "Results of the Final Focus Test Beam," these proceedings.
- [17] R. Brinkmann, DESY-M-90-14 (1990).
- [18] F. Zimmermann, et. al., "Optimization of the NLC Final Focus System," these proceedings.
- [19] J. Spencer, et. al., "The SLAC NLC Extraction and Diagnostic Line," these proceedings.

A Damping Ring Design for the SLAC Next Linear Collider*

T. O. Raubenheimer, J. Byrd, J. Corlett, R. Early, M. Furman, A. Jackson, P. Krejcik, K. Kubo, T. Mattison, M. Minty, W. Moshhammer, D. Robin, B. Scott, J. Spencer, K. Thompson, P. Wilson
Stanford Linear Accelerator Center, Stanford University, Stanford, CA, 94309
Lawrence Berkeley Laboratory, Berkeley, CA, 94720

Abstract

In this paper, we describe the design of the main damping rings and the positron pre-damping ring for the SLAC Next Linear Collider, a future linear collider with a center-of-mass energy of 0.5 to 1.5 TeV. The rings will operate at an energy of 2 GeV with a maximum repetition rate of 180 Hz. The normalized extracted beam emittances are $\gamma\epsilon_x = 3$ mm-mrad and $\gamma\epsilon_y = 0.03$ mm-mrad. To provide the necessary damping, the rings must damp multiple trains of bunches. Thus, the beam current is large, roughly 1 A. We will present the optical layout, magnet designs, and RF systems, along with the dynamic aperture and required alignment tolerances; collective effects will be discussed in another paper.

I. INTRODUCTION

The primary requirements of the NLC damping rings are summarized in Table 1 for two stages of the NLC design [1]. The rings must produce electron and positron beams with emittances of $\gamma\epsilon_x = 3$ mm-mrad and $\gamma\epsilon_y = 0.03$ mm-mrad at a repetition rate as high as 180 Hz. The beams in the rings consist of trains of as many as 90 bunches, spaced by 1.4 ns, with a maximum single bunch population of 1.5×10^{10} .

Table 1. Damping ring requirements for NLC designs.

	NLC-I (500 GeV)	NLC-III (1.5 TeV)
$\gamma\epsilon_x$	3×10^{-6} m-rad	3×10^{-6} m-rad
$\gamma\epsilon_y$	3×10^{-8} m-rad	3×10^{-8} m-rad
Rep. Rate	180 Hz	120 Hz
Bunch Charge	0.7×10^{10}	1.5×10^{10}
Bunch Sep.	1.4 ns	1.4 ns
Bunches/Train	90	75

The NLC electron injector is based on a polarized photocathode in a DC gun with a subharmonic buncher system. It is designed to produce bunch trains with a normalized emittance of $\gamma\epsilon_{x,y} = 100$ mm-mrad and a momentum spread less than $\pm 1\%$. Thus, the electron vertical emittance must be damped by roughly four orders of magnitude. Since the damping ring must operate uncoupled to produce the flat beams, this specifies the required number of vertical damping times; assuming a vertical equilibrium emittance of 2×10^{-8} m-rad, the beams must be stored for 4.6 vertical damping times.

Thus, the primary design problems in the rings involve attaining both very fast damping and very small equilibrium emittances with a large dynamic aperture since the beam emittances are large at injection. Simple scaling shows that these competing requirements would force one to a large circumference ring which can store and damp many trains of bunches at the same time [2].

The situation is even worse in the case of the positron injector, where to produce the required number of positrons, the captured positron beam emittance is large; in the NLC design [3], the incoming positrons have an emittance that is roughly 600 times the incoming electron emittance and an energy spread of $\pm 2\%$. In this case, it would be extremely difficult to attain the required damping and the necessary dynamic aperture in a single ring. Therefore, we will use a pre-damping ring to damp the incoming positron emittance to the level of the incoming electron emittance; the positrons can then be transferred to the main damping ring which would be identical to the electron damping ring. Assuming a normalized equilibrium emittance of 30 mm-mrad in the pre-damping ring, the positron beams must be damped for 3.2 damping times to attain extracted rms emittances equal to that of the incoming electron beams.

Table 2. Pre-damping ring parameters.

Energy	1.8 ~ 2.2 GeV
Circumference	112 m
Current	1 Amp
ν_x, ν_y, ν_s	10.18, 4.18, 0.015
$\gamma\epsilon_{x,y}$ (fully coupled)	2.5×10^{-5} m-rad
$\sigma_\epsilon, \sigma_z$	0.1%, 7.0 mm
τ_x, τ_y, τ_z	3.0 ms, 4.0 ms, 2.4 ms
V_{RF}, f_{RF}	1.5 MV, 714 MHz

Table 3. Main damping ring parameters.

Energy	1.8 ~ 2.2 GeV
Circumference	223 m
Current	1 Amp
ν_x, ν_y, ν_s	23.81, 8.62, 0.004
$\gamma\epsilon_x, \gamma\epsilon_y$	3×10^{-6} m-rad, 2×10^{-8} m-rad
$\sigma_\epsilon, \sigma_z$	0.09%, 4.1 mm
τ_x, τ_y, τ_z	4.0 ms, 4.6 ms, 2.5 ms
V_{RF}, f_{RF}	1.0 MV, 714 MHz

The principal parameters of the pre- and main damping rings are listed in Tables 2 and 3. The nominal operating energy is 2.0 GeV, although the rings are being designed to operate between 1.8 GeV and 2.2 GeV. This will provide the operational flexibility

*Work supported by the Department of Energy, contracts DE-AC03-76SF00515 (SLAC) and DE-AC03-76SF00098 (LBL).

ity to balance faster damping rates against smaller equilibrium emittances. Both rings will store multiple trains of bunches. The pre-damping ring will store two 90 bunch trains at once while the main damping ring will store four 90 bunch trains. The bunches in a train are separated by 1.4 ns while the trains themselves are separated by 60 ns so that fast kickers can inject and extract individual trains. In this manner, each bunch train is stored for two machine cycles in the pre-damping ring and four machine cycles in the main damping ring. Finally, the maximum average current is roughly 1 A for the NLC-III parameters; note that for NLC-III the bunch trains are only 75 bunches long and the train separation is roughly 80 ns.

The pre-damping ring will operate on the difference coupling resonance. In this case, the equilibrium emittances are $\gamma\epsilon_{x,y} = 30$ mm-mrad and the transverse damping time is $\tau_{x,y} = 3.45$ ms; thus, after two 180 Hz machine cycles, the beams are stored for 3.2 damping times. In the main damping ring, the horizontal equilibrium emittance, including the intrabeam scattering for 1.5×10^{10} , is $\gamma\epsilon_x = 3.1$ mm-mrad while the vertical equilibrium emittance of $\gamma\epsilon_y = 0.02$ mm-mrad is determined by the alignment tolerances. Finally, the vertical damping time is 4.64 ms; this corresponds to roughly 4.8 vertical damping times. In both rings, the damping is slightly greater than that required; this provides a margin for injection transients and mismatches.

In the next sections, we will briefly describe the optical design of the positron pre-damping ring and the main damping rings. Then, we will discuss the injection/extraction and the RF systems. Finally, we will describe the tolerances and dynamic aperture of the rings.

II. OPTICAL DESIGNS

Both rings are designed in a race-track form with two arcs separated by straight sections. The pre-damping ring is roughly 110 meters in circumference while the main damping ring is twice as large.

In the pre-damping ring, each arc consists of 14 FOOF cells plus dispersion matching sections; the FOOF cell is a modified FODO lattice where the defocusing quadrupole is replaced by a combined function bending magnet. Because the ring needs a large dynamic aperture and does not require a small equilibrium emittance, we use a weak focusing lattice. We chose to use the FOOF structure since it constrains the beta functions, allowing us to design a smaller vacuum chamber aperture and thereby less expensive magnets. In the arcs, the vacuum chamber measures 3 cm by 3.2 cm. This provides physical aperture for an injected normalized edge emittance of 0.09 m-rad (50% larger than nominal) plus 2 mm clearance for alignment and steering.

In the main damping ring, each arc consists of 19 TME cells [4] plus dispersion matching sections. The straight sections are roughly 30 meters in length. One side of the ring is devoted to the damping wigglers while the other side contains the injection and extraction components and the RF cavities.

The TME cells consist of a single combined function bending magnet, two focusing quadrupoles and a single defocusing quadrupole. Each cell contains six sextupoles, in three families, to correct the chromaticity. The vacuum chamber is circular with a 25 mm diameter and an ante-chamber to handle the intense synchrotron radiation; the chamber is described further in

Ref. [5]. Preliminary designs have been made of the bending magnets, quadrupoles and sextupoles. The bending magnet has a central field of 15.3 kG with a gradient of 125 kG/m and a half gap of 1.6 cm. The quadrupoles have a maximum gradient of 600 kG/m with an aperture of 1.6 cm while the sextupoles have a maximum gradient $\partial^2 B_y / \partial x^2$ of 30,000 kG/m² with an aperture of 1.7 cm. In all cases, the poles are designed to fit around the ante-chamber.

In addition, the main damping ring requires roughly 25 meters of high field wiggler to attain the desired damping times. The two parameters that are relevant for a damping wiggler are the integral of B_y^2 , which determines the damping, and the quantum excitation, which is set by the field and the period. In the NLC design, we have chosen to consider a relatively short, high field device. If we assume a sinusoidal B_y with a peak of 22 kG (close to the saturation of Vanadium Permanganate), then we need a length of 25.6 meters and a period of 25 cm. Simple scaling laws suggest that such a wiggler could be built as either a permanent magnet hybrid wiggler or an electromagnetic wiggler.

The SSRL Beam-Line 9 wiggler [6], which was recently constructed, nearly meets our requirements. It is a hybrid wiggler with a peak field of 20.5 kG and a 26 cm period. Because the wiggler poles were designed to optimize the total flux, the field is not sinusoidal and the integral of B_y^2 is within 1% of our requirements.

III. INJECTION/EXTRACTION

In both damping rings, injection and extraction are performed using DC septum magnets and pulsed kicker magnets. The design concept is similar to the system developed for the SLC [7]. The kickers are required to inject or extract a single 126 ns bunch train onto or from the closed orbit without disturbing the other stored bunches. Thus the rise and the fall times must be less than the train separation 60 ns. Finally, to reduce RF transients, a new bunch train is injected on the same revolution that a damped bunch train is extracted.

The main damping ring kickers must provide a deflection of 2.5 mrad with a stability of $\Delta\theta/\theta \leq 0.5 \times 10^{-3}$ for the extraction kickers and $\Delta\theta/\theta \leq 3.5 \times 10^{-3}$ for the injection kickers; these tolerances limit the beam jitter due to the kickers to 10% of the beam size. The deflection can be provided using a 1.2 meter kicker with an impedance of 50 Ω and a voltage of 17 kV. Achromatic (double) kicker systems will be used to ease the stability requirements. Here, an identical kicker, powered by the same pulser, is placed in the injection/extraction line and separated from the kicker in the ring by a horizontal $\pm I$ transform. Finally, to reduce the rise and fall times requirements, the injection and extraction kickers in the ring are also separated by a $\pm I$ transform in the horizontal plane; the rising and falling kicker pulses can then be tuned to compensate the deflections to the stored beams.

In the pre-damping ring, because of the large beam emittances, the required deflection is roughly three times larger and the required kicker aperture is roughly 50% larger than in the main damping ring. Fortunately, the stability requirements are relaxed by a factor of two. To maintain conservative magnet and pulser designs, both the injection and the extraction kickers would consist of four 50 cm magnets powered in parallel.

IV. RF SYSTEMS

The RF parameters are summarized in Tables 2 and 3. Both rings will use 714 MHz systems; this is the lowest frequency that is consistent with the 1.4 ns bunch spacing. Because of the long bunch trains, the RF cavities must have HOM damping. At this stage of the design, we have assumed scaled versions of the PEP-II single-mode RF cavities [8]; further discussion can be found in Ref. [5].

In the pre-damping ring, the required RF voltage is determined by the size of the RF bucket. The incoming beam is expected to have a momentum deviation of $\pm 2\%$. This would require an RF voltage of 2.5 MV. Instead, an energy compressor, located at the entrance of the ring, will reduce the incoming energy deviations by a factor of two. Thus, we plan to use an RF voltage of 1.5 MV; this provides an energy bucket of 1.5%.

In the main damping ring, the RF voltage is determined by the energy loss per turn. The synchrotron radiation loss is 635 keV/turn and we have estimated the parasitic losses at 120 keV/turn by scaling from the old PEP ring. This is felt to be a conservative estimate; scaling from the ALS or the PEP-II rings suggest parasitic losses an order of magnitude smaller. In this case, a 1 MV RF voltage would be sufficient. It provides sufficient voltage to prevent the beam loading instability while allowing for a longer bunch length which is desirable.

V. TOLERANCES AND DYNAMIC APERTURE

The tolerances in the pre-damping ring are determined by the requirements on the dynamic aperture while the tolerances in the main damping rings are dominated by the requirements on the vertical equilibrium emittance. In the pre-damping ring, the bare ring (without errors) has a normalized acceptance of $\gamma A \leq 0.45$ m-rad over $\delta p/p = \pm 2\%$; the acceptance is $A_x \equiv \frac{1}{2}(\gamma x^2 + 2\alpha x x' + \beta x'^2)$. With random transverse alignment, rotation, and strength errors of 200 μm , 1 mrad, and 0.1% rms on all elements, the acceptance is reduced to 0.2 m-rad. This is still a factor of two larger than the physical aperture.

In the main damping ring, the primary limitation arises from the vertical dispersion generated by misalignments of the sextupoles and rotation errors of the strong focusing quadrupoles. The alignment tolerances required to attain an equilibrium emittance of 2×10^{-8} m-rad are listed in Table 4. These tolerances assume the use of four skew quadrupoles to corrected the vertical dispersion errors.

Table 4. Alignment tolerances in the main damping ring.

Sextupole (X/Y/ Θ) [$\mu\text{m}/\text{mrad}$]	100/50/1
Arc QFs (X/Y/ Θ) [$\mu\text{m}/\text{mrad}$]	100/100/0.6
Other Quads. (X/Y/ Θ) [$\mu\text{m}/\text{mrad}$]	100/100/1
Bends (X/Y/ Θ) [$\mu\text{m}/\text{mrad}$]	100/100/0.6
BPMs (X/Y/ Θ) [$\mu\text{m}/\text{mrad}$]	100/100/1

The tolerances for the dynamic aperture are looser. Doubling the nominal alignment tolerances listed in Table 4 still yields an aperture in excess of 3σ for an injected beam with ten times the nominal injected emittance and a relative momentum deviation between $\pm 1\%$.

Obviously, both rings have severe alignment tolerances. To attain the required values, we plan to use a beam-based alignment technique where trims on the individual magnets are varied and the resulting orbit deflections are used to infer the magnet centers. Similar techniques are being used successfully at the ALS and LEP storage rings.

VI. DISCUSSION

In this paper, we have presented the design of the SLAC NLC damping rings. Both a large aperture pre-damping ring and a main damping ring are needed to damp the positron beam while a single ring is used for the electron beam. The extracted emittances of the rings are $\gamma\epsilon_x = 3$ mm-mrad and $\gamma\epsilon_y = 0.03$ mm-mrad. We have discussed the optical designs, the RF systems, the injection/extraction kickers, and the alignment tolerances and dynamic aperture. Further discussion of collective effects can be found in Ref. [5].

References

- [1] T. O. Raubenheimer, et. al., "Parameters of the SLAC Next Linear Collider," these proceedings.
- [2] T. O. Raubenheimer, R. D. Ruth, and L. Z. Rivkin, "Damping Ring Designs for TeV Linear Colliders," *Proc. of the DPF Summer Study, Snowmass '88*, Snowmass, CO (1989).
- [3] H. Tang, et. al., "The NLC Positron Source," these proceedings.
- [4] L. C. Teng, "Minimum Emittance Lattice for Synchrotron Radiation Storage Rings," ANL-LS-17 and ANL-LS-17A (1985).
- [5] T. O. Raubenheimer, et. al., "Collective Effects in the SLAC NLC Damping Ring Designs," this conference.
- [6] M. Baltay, private communication (1995).
- [7] T. Mattison, et. al., "Status of the SLC Damping Ring Kicker Systems," *Proc. 1991 Part. Acc. Conf.*, San Francisco, CA (1991).
- [8] Rimmer, R. A., "RF Cavity Development for the PEP-II B-Factory," *Proc. Int. Workshop on B-Factories*, KEK, Tsukuba, Japan (1992).

A BUNCH COMPRESSOR FOR THE NEXT LINEAR COLLIDER *

P. Emma, T. Raubenheimer, F. Zimmermann,
Stanford Linear Accelerator Center, Stanford University, Stanford CA 94025 USA

Abstract

A bunch compressor design for the Next Linear Collider (NLC) is described. The compressor reduces the bunch length by a factor of 40 in two stages. The first stage at 2 GeV consists of an rf section and a wiggler. The second stage at 10 GeV is formed by an arc, an rf section, and a chicane. The final bunch phase is insensitive to initial phase errors and to beam loading in the intermediate S-band pre-linac. Residual longitudinal aberrations of the system are partially compensated. The bunch compressor encompasses a solenoid spin-rotator system at 2 GeV that allows complete control over the spin orientation.

I. INTRODUCTION

The purpose of the NLC bunch compressor is to reduce the bunch length, which is about 4 mm at extraction from the damping rings, to 100 μm , suitable for injection into the main X-band linac. The bunch compressor may have to compensate bunch-to-bunch phase errors due to beam-loading in the damping ring unless the latter is compensated by some other means. This requires a rotation by $\pi/2$ in the longitudinal phase space so that phase errors are converted into energy errors. The compressor also has to compensate for beam-loading effects originating in its various accelerating sections, and it provides a trombone-like arm, reversing the direction of the beam before injection into the main linac. This gives space for abort systems, allows feed-forward from the ring to the linac, and facilitates future upgrades. Furthermore, the bunch compressor includes a spin-rotator system, and provides tuning elements and diagnostics to correct dispersion and coupling. To determine the optimum parameters of the system, three different scenarios are considered, denoted NLC I, NLC II and NLC III, corresponding to different upgrade stages (see Table I). [1]

Table 1. Three different NLC scenarios.

	NLC I	NLC II	NLC III
c.m. energy	500 GeV	1 TeV	1.5 TeV
gradient	36.7 MV/m	61 MV/m	75 MV/m
main linac length	6.9 km	8.3 km	10 km
N/bunch	$0.66 \cdot 10^{10}$	$1.1 \cdot 10^{10}$	$1.5 \cdot 10^{10}$

The proposed bunch compressor comprises two stages and an intermediate S-band pre-linac that accelerates the beam from 2 GeV to 10 GeV [2]. The design is illustrated in Figure 1.

The parameters of the compressor system are chosen such that, first, the energy spread at the end of the X-band linac is smaller than the bandwidth of the final focus system; second, no significant energy tails are generated; and third, both the mean energy and the energy spread at the end of the linac are insensitive to phase and energy errors resulting from beam loading in damping rings and pre-linac, respectively. The phase error at extraction from the damping ring may be as large as 20° S-band (or

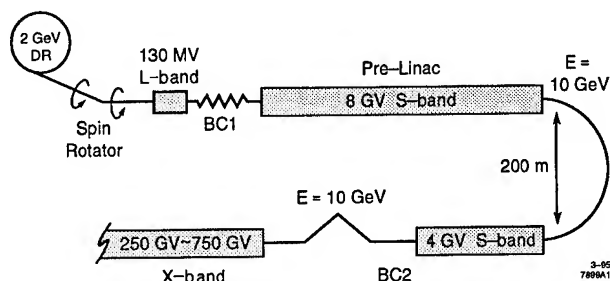


Figure 1. Schematic of the NLC bunch compressor.

6 mm), while at the end of the pre-linac the energy variation over the bunch train due to multi-bunch beam loading is about 0.15% [3]. Tolerance on the phase at the exit of the second compressor is $|\Delta z| < 10 \mu\text{m}$ to limit the relative energy change at the end of the main linac to 0.1%.

The design of the two compressor stages is described in Section II. Section III is devoted to residual longitudinal aberrations and their compensation. Section IV discusses the final beam distribution expected from simulations; Section V discusses the spin rotator system. Tuning elements are described in Section VI.

II. COMPRESSOR STAGES

The first stage (BC1), at 2 GeV, consisting of an rf and a wiggler section, rotates the beam by 90 degrees in the longitudinal phase space, to convert initial phase errors due to beam loading in the damping ring into energy errors, and reduces the bunch length by roughly a factor of 10, from about 4 mm to 500 μm . This compression is realized by an rf section that generates a δ - z correlation, followed by a bending section with energy-dependent path length. In this case the bending section is a wiggler consisting of four 90° cells with quadrupoles at zero dispersion points [2]. For a given rf frequency (here L-band), all other parameters are determined by the incoming beam. If the initial energy spread is $\delta \approx 10^{-3}$ the desired bunch length is obtained with $R_{56} = 0.5 \text{ m}$. Parameters are listed in Table II. In the table, the terms y_a and y_q denote the alignment tolerances for accelerating structures and quadrupoles due to a 1% emittance dilution from single-bunch wakefields or dispersion, respectively, and the superscript c refers to a compensating rf system discussed in the next section.

After BC1, a 500-m long S-band pre-linac accelerates the beam to 10 GeV. The vacuum pressure in the pre-linac has to be better than 10^{-8} torr. This pressure reduces the emittance dilution expected from filamentation and nonlinear coupling due to ions [4] and alleviates the effect of a predicted fast transverse beam-ion instability [5]. After the pre-linac, the second compressor stage (BC2) at 10 GeV performs a 360-degree rotation in phase space, and reduces the bunch length to 100 μm , appropriate for injection into the main X-band linac. A 360- (or 180-

*Work supported by Department of Energy contract DE-AC03-76SF00515

) degree rotation is required to prevent bunch-to-bunch energy errors caused by beam loading in the pre-linac, or phase errors in the damping ring, from translating back into phase errors in the main linac. An arc, a second rf section, and a chicane are the components of BC2. Two parameters may be selected independently, for instance the rf frequency and the R_{56} of the chicane. For the S-band rf chosen, the waveform is more linear and transverse wakefields are less severe than for X-band. The additional length required is a disadvantage of S-band frequency. To reduce the nonlinearities in the longitudinal transformation (T_{566} term in TRANSPORT notation [6]) the R_{56} of the chicane is rather small, namely 36 mm. The necessary rf voltage V_{rf} is then 3.87 GV and the length of the accelerating section is large: 200 m. The arc comprises 60 FODO cells of separated function magnets and does not include distributed sextupoles, the alignment tolerances for which would be severe; its R_{56} can be easily adjusted with the horizontal phase advance. The chicane is constructed from four 10-m bending sections [2]. More parameters are given in Table II. Where two values are listed in the table, the first refers to the arc, the second to the chicane. Note that the horizontal emittance increases by about 2.6% due to synchrotron radiation in wiggler, arc and chicane.

A single-stage compressor does not appear to be a viable alternative to the two-stage design, because the final energy spread of 5% would increase both the effect of nonlinearities in the longitudinal phase space (see next section) and the sensitivity to incoming phase variations. This energy spread would furthermore make transverse emittance preservation a difficult task.

Table 2. Parameters for the two compressor stages.

	1. stage	2. stage
Energy	2 GeV	10 GeV
σ_z	4 mm \rightarrow 500 μ	500 $\mu \rightarrow$ 100 μ
σ_e	0.1% \rightarrow 1.0%	0.25% \rightarrow 2.1%
V_{rf}	136 MV	3.87 GV
f_{rf}	1.4 GHz	2.8 GHz
L_{rf}	9 m	200 m
R_{56}	0.5 m	-0.217 m, 36 mm
' R_{56} ' length	100 m	370 m, 210 m
$\Delta e_{x,SR}/e_x$	1.3%	1.3%, 0.05%
bend hor. aperture	3 cm	10 cm
y_a	40 μ	\sim 8 μ
y_g	17 μ	\sim 8 μ
V_{rf}^c	6.9 MV	276 MV
f_{rf}^c	2.8 GHz	11.4 GHz
L_{rf}^c	0.5 m	8 m
total length	110 m	800 m

III. LONGITUDINAL ABERRATIONS

Second-order dependence on energy of the path-length (i.e., T_{566} transfer-matrix element) in wiggler and chicane introduces an important nonlinear aberration in the longitudinal phase space [7]. This nonlinearity causes a strong sensitivity of the final energy at the end of the main linac to the initial phase. The T_{566} is proportional to the R_{56} : for wiggler and chicane $T_{566}^{w,c} = -\frac{3}{2}R_{56}^{w,c}$ and for the arc $T_{566}^a \approx 1.9 \cdot R_{56}^a$. The T_{566} transfer-matrix element is harmful for two reasons. First, initial phase errors are converted into energy errors by BC1, which in turn, due to the T_{566}^w of the wiggler, cause a phase offset in the pre-linac. The result is an additional energy change that may either add to

or cancel the previous energy error, depending on the sign of the offset. The energy error is further enhanced by BC2 and, due to the T_{566}^c of the chicane, a significant phase error in the main linac is generated. A second effect is that, depending on the sign of the phase error, the T_{566} can either increase or counteract the nonlinearity of the rf over the bunch, giving rise to an asymmetry of bunch length versus phase error, for each compressor stage separately. To reduce these harmful effects, a small value of 36 mm was chosen for the R_{56} of the chicane.

Even then the residual nonlinear effects are still so large that they need to be compensated. In the proposed design this is done by an additional, decelerating rf system in each compressor stage. The required compensating rf voltage is

$$V_{rf}^c = -2 \frac{T_{566}^{w,c} f_{rf}^2 e V^2}{R_{56}^{w,c} f_{rf}^2 E} = 3 \frac{f_{rf}^2 e V_{rf}^2}{f_{rf}^2 E}, \quad (1)$$

where E is the beam energy, e the electron charge, and the superscripts w and c refer to wiggler or chicane. The voltage V_{rf}^c is about 7 MV and 300 MV for an S-band and an X-band compensation in BC1 and BC2, respectively.

The residual longitudinal aberrations are now of third order and higher. An initial phase error or multi-bunch beam loading may cause an energy offset δ of the entire bunch at the entrance to BC2. In addition, the longitudinal wakefields in the pre-linac induce a mainly quadratic correlation between energy and the longitudinal position z of a single particle with respect to the bunch center. Due to the R_{56}^a of the arc, the total energy error translates into a position error at the two rf systems of BC2, which is transformed once more into energy by the rf, and back into longitudinal phase by the T_{566}^c of the chicane. The final phase z_f of a single particle at the exit of BC2 is

$$z_f \approx az - bz^4 - c\delta^2 z^2 - d\delta z^2 - e\delta z^4 + \dots \quad (2)$$

where $a \approx 1/5-1/7$ is the desired linear compression ratio, and the four nonlinear terms on the right-hand side are about the same size (10–20 μ), for typical values $\delta \approx \pm 0.004$ and $z \approx 500 \mu$. These four terms are negligible if either the T_{566}^c or the pre-linac wakefields are absent.

IV. PERFORMANCE

Computer simulations of the longitudinal single-bunch dynamics are performed with the code LITRACK [8], taking into account the nonlinear rf waveform, T_{566} matrix-elements, and single-bunch longitudinal wakefields. A distribution of particles as extracted from the damping ring is tracked through the different compressor subsystems and the main X-band linac. The full-width-half-maximum energy spread for zero-phase error was chosen to be roughly 0.6%. The simulations show that even for NLC III the final average energy and the rms energy spread at the end of the main linac vary by less than 0.1% for initial phase errors up to 20° S-band. Figure 2 illustrates the energy profile at the end of the main linac for no initial phase error. A deformation of the distribution for NLC-III, due to the increased wakefields in the pre-linac, is clearly evident.

V. SPIN ROTATOR

The spin-rotator system located between the damping ring and BC1 (see Fig. 1), is constructed from two solenoid pairs sepa-

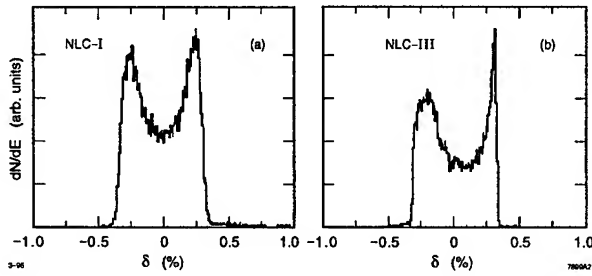


Figure 2. Energy profile at the end of the main linac for NLC I and NLC III (Table I), and no initial phase error.

rated by a 19.83° mini-arc [9]. The two solenoids of each pair are separated by a reflector beamline, whose horizontal and vertical transfer matrices are $+I$ and $-I$, respectively. This cancels the x-y coupling independent of solenoid settings. Each solenoid pair is capable of providing a 90° spin rotation about the longitudinal axis, while the mini-arc rotates the spin by 90° around the vertical axis. In this way arbitrary control over the spin orientation is provided. Relative depolarization in the compressor arc at 10 GeV is less than 1.6%, and total R_{56} of the rotator arc is -40 mm, with no effect on the bunch length after BC1. The chromatic emittance dilution at 0.1% rms energy spread is $\sim 0.5\%$.

VI. TUNING AND DIAGNOSTICS

Extensive simulations of tuning and correction schemes have been performed for the spin rotator and for BC1. So far little work has been done for BC2. Corrections in BC2 are not expected to be difficult.

The large energy spread after BC1 sets tight tolerances on the residual dispersion, e.g., the maximum tolerable dispersion for a 2% emittance dilution is about 175μ behind BC1. Therefore, two orthogonal $-I$ pairs of quadrupoles and skew quadrupoles are placed at large dispersion points in the wiggler section of BC1 for dispersion correction. Two more skew quadrupoles, separated by a phase advance of 90° , are located in the mini-arc section of the spin rotator. These quadrupoles cancel dispersion generated in front of the BC1 rf section. Cross-plane coupling generated in the damping ring or due to imperfections in the rotator system is compensated by a skew correction section (SCS). The SCS follows the spin rotator and contains 4 orthonormal skew quadrupoles (orthogonal and equally scaled) that allow complete decoupling. Four variable quadrupoles match the beam extracted from the damping ring to the rotator optics. To maintain the periodic beta functions in the spin rotator itself for varying solenoid fields, two four-quadrupole beta-matching sections are located in front of and behind the mini-arc. In addition several matching quadrupoles are found between SCS and BC1 and following BC1. The rf in BC1 may be turned off to ease beta matching and decoupling. A correction of second-order dispersion is necessary only if the vertical emittance dilution due to first order dispersion mismatch is larger than a factor of ten. In that case four paired skew sextupoles are added to the wiggler section. Four wire scanners at 45° phase advance intervals are located behind the wiggler and used to adjust the above correctors by minimizing the projected emittance. In addition wire scanners placed at high dispersion points in mini-arc and wig-

gler measure the extracted energy spread and bunch length, respectively. Tuning simulations with the SLC flight simulator [10] for an initial emittance dilution by a factor 200, due to rms quadrupole field errors of 1% and rms dipole roll errors of 0.25° , result in a final emittance dilution of less than 2%. This tuning procedure would require about 16 hours of real machine time.

VII. CONCLUSIONS

A design of a two-stage bunch compressor for the NLC has been described that meets all specifications, as far as single-bunch dynamics is concerned. A single-stage compressor does not appear to be a viable alternative. Multi-bunch effects in the compressor have not yet been studied in detail. Also the optimum bunch shape at the exit of BC2 still needs to be determined. A larger value for the $R_{56}^{a,c}$ matrix elements of arc and chicane is desirable, since it would allow a length reduction of the rf section in BC2. It is not yet known if the increased sensitivity to initial phase errors and to energy-errors in the S-band pre-linac would be tolerable.

References

- [1] T. Raubenheimer et al., "Parameters of the SLAC Next Linear Collider," these proceedings.
- [2] T. Raubenheimer, P. Emma, S. Kheifets, *Proc. of 1993 IEEE PAC*, Washington (1993) 635; T. Raubenheimer, NLC Note 2 (1994).
- [3] R. Miller, private communication (1994).
- [4] T. Raubenheimer, P. Chen, SLAC-PUB-5893 (1992).
- [5] T. O. Raubenheimer and F. Zimmermann, SLAC-PUB-6740 (1995).
- [6] K. Brown, F. Rothacker, D. Carey, C. Iselin, SLAC-91 (1977).
- [7] F. Zimmermann, NLC Note 3 (1994).
- [8] The program LITRACK was written by K. Bane.
- [9] P. Emma, NLC Note 7 (1994).
- [10] M. Woodley, private communication (1994).

A FINAL FOCUS SYSTEM FOR THE NEXT LINEAR COLLIDER *

F. Zimmermann, K. Brown, P. Emma, R. Helm, J. Irwin, P. Tenenbaum, P. Wilson
Stanford Linear Accelerator Center, Stanford University, Stanford, CA 94309 USA

Abstract

The final focus of the Next Linear Collider (NLC) demagnifies electron and positron beams of 250–750 GeV energy down to a transverse size of about $2.5 \times 350 \text{ nm}^2$ at the interaction point (IP). The basic layout, momentum bandwidth, vibration tolerances, wakefield effects, and the tunability of the proposed final focus design are discussed. Also a perspective is given on the crab cavity and on effects of the solenoid field in the interaction region.

I. INTRODUCTION

The purpose of the NLC final focus system is to transport electron and positron beams at 500 GeV from the end of the big bend to the IP, where the demagnified beams are collided. The design spot size at the interaction point (IP) is about 2.5 nm vertically and 250–420 nm horizontally. The normalized emittances before collision are assumed to be as $\gamma\epsilon_x \approx 5 \times 10^{-6} \text{ m}$, $\gamma\epsilon_y \approx 5 \times 10^{-8} \text{ m}$, and the intrabunch rms momentum spread as $\delta \approx 0.3\%$.

The entrance of the final focus system is formed by a skew-correction section (SCS) and a diagnostics section (DS) followed by a beta-matching section (BMS), horizontal and vertical chromatic correction sections (CCX and CCY), and the final transformer (FT). The final focus design is flexible enough to be operated at 500, as well as at 250 GeV. Furthermore, an upgrade to a beam energy of 750 GeV is possible. All data and figures in this report refer to the design for a 500 GeV beam energy, unless noted otherwise.

Table I lists important beam parameters at the interaction point. The luminosity may be doubled by reducing β_x^* to 10 mm. The minimum horizontal beta function at the IP will be determined by the maximum tolerable number of beamstrahlung photons and by the synchrotron radiation in the final doublet ('Oide effect' [8]).

Section II discusses the SCS. Section III presents two options for the DS. Section IV describes the BMS. The CCX, beta-exchanger (BX), CCY and FT are discussed in Section V. Section VI addresses the final doublet, and Section VII discusses the solenoid field and the crab cavity.

II. SKEW CORRECTION SECTION

The large emittance ratio of $\epsilon_x/\epsilon_y \approx 100$ in the NLC makes a dedicated SCS highly desirable. The SCS contains four *orthonormal* skew quadrupoles (i.e., they are orthogonal and equally scaled). Each of the four skew quadrupoles corrects one of the four beam correlations $\langle xy \rangle$, $\langle xy' \rangle$, $\langle x'y \rangle$, and $\langle x'y' \rangle$. The first and second, and also the third and fourth, skew quadrupoles are separated by FODO cells with betatron phase advances of

Table I

Basic interaction-point beam parameters.

c.m. energy	1 TeV	comments
$L [\text{cm}^{-2} \text{s}^{-1}]$	$(2.7 \times 10^{34}) 1.3 \times 10^{34}$	Luminosity
N_b	1.1×10^{10}	Particles per bunch
n_b	90	Number of bunches
f	120 Hz	Bunch trains per s
H_D	1.32	Enhancement factor
σ_x	(220) 420 nm	variable
σ_y	2.5 nm	
β_x^*	(10) 37 mm	variable
β_y^*	100 μm	
ϵ_x	$5 \times 10^{-12} \text{ m}$	$\gamma\epsilon_x = 5 \times 10^{-6} \text{ m}$
ϵ_y	$5 \times 10^{-14} \text{ m}$	$\gamma\epsilon_y = 5 \times 10^{-8} \text{ m}$
$\sigma_{x',y'}$	(22) 12, 22 μrad	IP divergence
σ_z	100 μm	variable
θ_c	20 mrad	Crossing angle
δ_{rms}	3×10^{-3}	Energy spread
l^*	2 m	Free length from IP

$\Delta\phi_{x,y} = \pi/2$ while the phase advances between the second and third are $\Delta\phi_x = \pi$, and $\Delta\phi_y = \pi/2$. The SCS is about 110 m long, and is able to correct a 300% emittance dilution due to linear coupling.

III. DIAGNOSTICS SECTION

The correctors of the SCS are adjusted based on emittance measurements in the DS, which is located immediately downstream. The projected emittances may be measured separately in the horizontal and vertical plane. Alternatively, the DS can be designed such that a four-dimensional measurement determines the two invariant emittances, as well as all four coupling parameters. The first, single-plane scheme would use four wire scanners (with two different wires—horizontal and vertical) separated by a phase advance of $\pi/4$. In this case, the DS is about 70 m long. The linear coupling is removed by minimizing the vertical projected emittance with each skew quadrupole of the SCS in turn. This procedure is invasive, has to be reiterated at least once, and may require several hours to perform. On the other hand, the fully-coupled scheme needs two additional wire scanners, as well as 45° wires on each scanner, and its length is about twice that of the single-plane scheme. This scheme allows a complete coupling measurement and correction within a few minutes, and could possibly be integrated into a feedback loop for automatic continuous decoupling.

IV. BETA-MATCHING SECTION

The BMS is used to adapt the IP beta functions and the waist position to varying incoming beam conditions, and to adjust the phase advance between the collimator region and the IP. The BMS contains six quadrupoles and is 350 m long.

The magnification and waist positions can be verified at a pre-

*Work supported by Department of Energy contract DE-AC03-76SF00515.

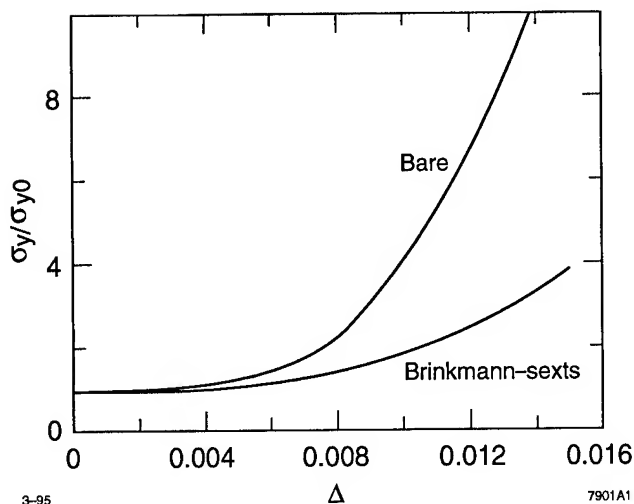


Figure 1. Comparison of relative increase of vertical spot size with and without Brinkmann-sextupoles as a function of the half-width Δ of a uniform momentum distribution, for $\beta_x^* = 37$ mm and $\beta_y^* = 100$ μ m. Synchrotron radiation effects not included.

image of the IP located in the BX, where a sensitive beam size monitor, such as a laser-interferometer [1], will be installed. The energy spread is sufficiently large that, under normal operating conditions, the spot size at the pre-image is dominated by chromatic effects. Therefore, the strength of the main sextupoles in the CCX must be adjusted during tune-up, and only one plane can be measured at a time. The chromatically-corrected beam sizes at the pre-image are $\sigma_x \approx 1.4$ μ and $\sigma_y \approx 100$ nm.

A conventional wire scanner immediately upstream of the CCY, where the spot size is about 100 μ in both planes, serves as a 'divergence' monitor, which is used to determine the actual beta functions at the pre-image.

V. CCX, CCY AND FINAL TRANSFORMER

A. Layout

After the BMS the beam traverses CCX, BX, CCY, and FT. The CCX and the CCY contain sextupole pairs separated by a $-I$ transfer matrix to compensate for the chromaticity of the final doublet. The chromaticity between the two sextupoles of each pair, as well as inside the BX and in the FT, is locally compensated for by means of nine additional sextupoles at locations with nonzero dispersion, similar to those suggested by Brinkmann [2]. The local compensation increases the energy bandwidth by almost a factor of two (see Fig. 1).

The length of the final focus system of about 770 m was optimized by a procedure described in [3]. Orthogonal knobs similar to those suggested by Irwin for the SLC [4] provide control over important terms in the beam-line Hamiltonian. The beam-based alignment of quadrupoles and sextupoles will be performed in the same way as in the SLC [5] or the FFTB [6].

B. Tolerances

B.1 Position Jitter and Ground Motion

The maximum tolerable incoming vertical orbit jitter is about $0.43 \sigma_y$, corresponding to a 2.3% loss of luminosity. An additional contribution to the position jitter at the IP from vibrations of magnets in the final focus (except for the final doublet) should be less than $0.1 \sigma_x$ or $0.2 \sigma_y$, which would be a further 0.5% luminosity reduction each. The tolerable incoherent vibration amplitudes for six magnets are then as small as 3 nm vertically and 25 nm horizontally.

These values are larger than typical ground motion amplitudes at frequencies above a few Hertz [7]. For lower frequency the amplitude of the ground motion increases, but is also better correlated over long distances [7]. At 1 Hz the tolerable ground-wave amplitude is about 5.5 nm. A feedback system will correct residual low-frequency orbit variations.

B.2 Dispersion

In addition to steering, displaced quadrupoles generate dispersion at the IP, both directly by the chromatic kick from the quadrupole and by the orbit-change in the downstream elements. The maximum tolerable dispersion at the IP is 150 nm, corresponding to a 2% blowup of the vertical spot size for an intra-bunch energy spread of $\delta \approx 0.3\%$. Allocating a 2% luminosity loss to the magnets of the final focus, the tolerable vertical displacement is about 13 nm for the first two quadrupoles in the FT, 40 nm for the next upstream quadrupole, and 80 nm for the two quadrupoles in the center of the CCY. These tolerances correspond to an orbit change by about 100 nm at the center of the first doublet magnet, to be compared with a beam size of 40 μ . The horizontal displacement tolerances due to dispersion are 400 nm or larger. The relative field ripple of four CCX quadrupoles must be smaller than 5×10^{-4} , in order not to generate intolerable dispersion at the IP.

One possible way to control orbit and magnet drifts over several minutes with sufficient accuracy, is to integrate high-resolution rf BPMs (which measure nm orbit changes) into the structure of all quadrupoles. The measured orbits will be averaged over a subset for which the incoming orbit jitter is small, in order to detect slow drifts. Corrector magnets will then steer the orbit back to its nominal position.

A maximum tolerable value of 75 μ m for the second order dispersion at the IP translates into an absolute static vertical alignment tolerance, which is about 6 μ for the first two quadrupoles in the FT. A compensation scheme for this aberration will be necessary.

B.3 Skew Coupling and Waist Shift

The vibration tolerance for sextupole magnets is determined by the induced skew coupling and waist shift. A horizontal (vertical) vibration of the two main Y-sextupoles by 160 nm (130 nm) causes a 2% luminosity loss. Skew coupling and waist shift is also generated by a displaced quadrupole in the CCX or CCY, which steers the orbit off-center through the next sextupole. For a few quadrupoles in the CCY, the vertical (horizontal) displacement tolerance due to this effect is 50 (150) nm. In addition, the relative stability of the bending magnets inside the CCY must

be better than 5×10^{-6} or 2×10^{-5} , assuming a magnet string or independently fed magnets, respectively.

Finally, the relative quadrupole field ripple resulting in a 2% luminosity loss due to the induced waist shift is 3×10^{-5} or larger for all quadrupoles, except for the final doublet.

VI. FINAL DOUBLET

A. Steering Jitter Tolerance

The inner magnets (Q_1) of both final doublets are mounted inside a common barrel, which is supported at the magnet center. The tolerance on the relative vertical vibration of these two quadrupoles is 0.5 nm. The second quadrupole on either side (Q_2) has a separate support. For the Q_2 magnets, the maximum tolerable antisymmetric vibration amplitude is 1.4 nm.

B. Synchrotron Radiation

Oide's original formula [8] for the spot-size increase due to synchrotron radiation in the last quadrupole can be generalized to two planes (horizontal and vertical) and two quadrupoles (Q_1 and Q_2). The result is that a significant part of the vertical spot-size increase may be due to the focusing in the horizontal plane within Q_2 . This contribution gets smaller with increasing length of Q_2 . For $\beta_x^* = 25$ mm, the total vertical spot size increase due to synchrotron radiation in the proposed final doublet is about 2%. The Oide effect is enhanced by orbit jitter: a 1σ vertical-orbit change amplifies the increase of the rms spot size by a factor of 4, while the luminosity loss increases only by about a factor of 2 [9].

C. Wakefield

The resistive wakefield kick [10] inside the first magnet of the doublet, Q_1 , is significant. If the magnet is 3 m long and its inner radius 4.5 mm, the jitter amplification, $\Delta y' \beta_y / \Delta y$, varies from 7.5 for a conductivity $\sigma = 10^6 \Omega^{-1} \text{ m}^{-1}$ to 0.75 for $\sigma = 10^{10} \Omega^{-1} \text{ m}^{-1}$. Here $\Delta y'$ is the resistive kick, β_y the vertical beta function, and Δy the beam centroid offset inside Q_1 . The effect of geometric wakefields is small.

VII. CRAB CAVITY AND SOLENOID

The two beams collide with a crossing angle of about 20 mrad. In order to align the bunches during collision, a crab cavity at the entrance to Q_2 provides a displacement with distance at the IP satisfying $\partial x^* / \partial z = \theta_C / 2$, where θ_C is the crossing angle (about 20 mrad for the NLC). A 37.5 cm long X-band cavity requires a maximum voltage of 1.2 MV and an input power close to 250 kW.

The permissible voltage error for a 2% luminosity loss is about 6%. It is important that the phase difference between the two crab cavities is maintained to a very high precision, so that the two beams collide head on. The phase-difference jitter tolerance is 0.2 degree at X-band. If the two cavities are driven by the same klystron, one source of phase jitter is thermal changes of the transmission line. The temperature must be stable to $1/15^\circ \text{ C}$ in 0.2 s (or 20° C per minute). Assuming that the excitation of higher order modes is 10% of the induced fundamental mode, the alignment tolerance of the crab cavity from horizontal steering is 20 μm . The crab cavity phases with respect to beam arrival

times, the crab cavity voltage and the alignment are monitored by feedback systems.

For a peak solenoidal field of 3 T, the maximum field perpendicular to the beam is 300 Gauss. The generator for the solenoid field is of the form $x^* p_y^*$, and is so large that it has to be compensated by one or two skew quadrupoles in front of the CCX (e.g., SCS) or close to the pre-image point. This generator is different from the ordinary $p_x^* p_y^*$ term that generates or corrects most of the skew coupling in the system. The solenoid will vertically steer the two beams in opposite direction by about 35 μ at the IP. The only way to correct this steering without generating an unacceptable dispersion is to displace Q_1 by about 20 μ . The residual dispersion of 9 μ can be corrected by displacing the incoming beam by 5 μ , which is tolerable in view of enhanced synchrotron radiation. Even for a crossing angle of 30 mrad, the spot size increase due to on-axis synchrotron radiation in the solenoid field is less than 1%.

VIII. SUMMARY

A design for an NLC final focus system at 1 TeV c.m. energy has been described. Based on SLC experience, strong emphasis was placed on tunability, redundant diagnostics, insensitivity to orbit-jitter, and upgrade potential. Some of the tolerances, such as those on the vibration of the final-doublet support barrel or on the phase-difference jitter for the two crab cavities, appear tight, but not hopeless.

References

- [1] T. Shintake, KEK-Preprint-94-129, 1994.
- [2] R. Brinkmann, DESY-M-90-14, 1990.
- [3] F. Zimmermann, R. Helm, J. Irwin, these proceedings 1995.
- [4] N.J. Walker, J. Irwin, M. Woodley, Proc. of PAC 93, Washington (1993); F. Zimmermann et al., these proceedings 1995.
- [5] P. Emma, Proc. of 3rd EPAC, Berlin, SLAC-PUB-5787, 1992.
- [6] P. Tenenbaum et al., SLAC-PUB-95-6769, 1995.
- [7] V. Juravlev et al., CERN-SL 93-53, 1993.
- [8] K. Oide, *Phys. Rev. Letters* **61** 15, 1988, 1713.
- [9] K. Hirata, B. Zotter, K. Oide, *Phys. Lett. B* **224**, 1989, 437.
- [10] J. Irwin et al. SLAC-PUB-5165, 1994.

OPTIMIZATION OF THE NLC FINAL FOCUS SYSTEM *

F. Zimmermann, R. Helm, J. Irwin, Stanford Linear Accelerator Center, Stanford University, Stanford, CA 94309 USA

Abstract

An optimization scheme for final focus systems is discussed and applied to the NLC design. The optical functions at the defocusing sextupoles, the sextupole strength, and the length of the system must obey eight conditions that are imposed by the spot size increase due to higher-order aberrations, the effects of synchrotron radiation in the bending magnets, power supply ripple, magnet vibration tolerances, and the estimated orbit stability at the sextupoles. These eight conditions determine the minimum optimum length of the system. The NLC final focus design was shortened to this optimum.

I. INTRODUCTION

In this report, an optimization scheme for final focus systems is proposed. The spot size increase by higher-order aberrations, synchrotron radiation effects, and the tolerances on power supply ripple, mechanical vibrations, and orbit stability depend on the length of the final focus system. This dependence results in scaling laws that are discussed in the next section. To evaluate these for the NLC final focus system, the values of certain length-independent parameters have been extracted from a preliminary, not optimized final-focus design. Based on these values, the optimum choice for dispersion and beta functions at the Y-sextupoles, for the sextupole strength and the length of the bend section are found. We roughly follow the analysis presented in Ref. [1]. However, the final optimization procedure is different.

II. SCALING LAWS

A. A General Telescope

We assume that the final focus system contains a horizontal and a vertical chromatic correction section (CCX and CCY) which are separated by a beta-exchange module (BX). Considering only quadrupole magnets of strength k_i , the Hamiltonian for either one of these three modules may be written

$$H = -\frac{\delta}{2} \sum k_i (x_i + \eta_i \delta)^2 + \frac{\delta}{2} \sum k_i y_i^2. \quad (1)$$

We now transform to the starting point of the module using the sine- and cosine-like trajectories, $x_i = c_i^x x_1 + s_i^x x_1'$, $y_i = c_i^y y_1 + s_i^y y_1'$, to define the chromatic coefficients

$$\begin{aligned} c^{x,y} &\equiv \sum k_i c_i^{x,y} y^2, & c^{x,y'} &\equiv 2 \sum k_i c_i^{x,y} s_i^{x,y}, \\ c^{x,y''} &\equiv \sum k_i s_i^{x,y} y^2, \\ d^x &\equiv \sum k_i \eta_i c_i^x, & d^{x'} &\equiv \sum k_i \eta_i s_i^x, \end{aligned} \quad (2)$$

and get

$$\begin{aligned} H = & -\frac{\delta}{2} \left[c^x x_1^2 + c^{x'} x_1 x_1' + c^{x''} x_1'^2 + \delta d^x x_1 \right. \\ & \left. + \delta d^{x'} x_1' \right] + \frac{\delta}{2} \left[c^y y_1^2 + c^{y'} y_1 y_1' + c^{y''} y_1'^2 \right] \end{aligned} \quad (3)$$

By symmetry, $c^{x'} = d^x = c^{y'} = 0$ for CCX and CCY, and we assume the same for the BX. The β -dependence is then extracted from the coordinates, $x_1 = \sqrt{\beta_1^x} x'$, and $x_1' = \frac{x}{\sqrt{\beta_1^x}}$, $y_1 = \sqrt{\beta_1^y} y'$, $y_1' = \frac{y}{\sqrt{\beta_1^y}}$, where x, x', y, y' are now normalized IP-coordinates, and length-independent chromatic coefficients are introduced, $d^{x'} = \hat{d}^{x'} L$, $c^{x,y} = c_L^{x,y}$, $c^{x',y'} = \hat{c}^{x',y'}$, $c^{x'',y''} = L \hat{c}^{x'',y''}$. The Hamiltonian (3) is then written

$$\begin{aligned} H = & -\frac{\delta}{2} \left[\hat{c}^x \frac{\beta_1^x}{L} x'^2 + \hat{c}^{x''} \frac{L}{\beta_1^x} x'^2 - \hat{c}^y \frac{\beta_1^y}{L} y'^2 \right. \\ & \left. - \hat{c}^{y''} \frac{L}{\beta_1^y} y'^2 + 2\delta L \hat{d}^{x'} \frac{1}{\sqrt{\beta_1^x}} x' \right]. \end{aligned} \quad (4)$$

Finally, the dispersion at the y-sextupoles is converted into a length-independent parameter \bar{r}_{12} via

$$\eta = \theta_B L \bar{r}_{12}, \quad (5)$$

where θ_B is the bend angle of the last bending section at the end of the CCY, and L the total length of the final focus system.

B. The CCX and the BX

We rewrite Eq. (4) for the CCX in the form

$$e^{-H_{CCX}} \approx e^{-\frac{1}{2} F(x', y')} e^{-G(x, y)} e^{-\frac{1}{2} F(x', y')}, \quad (6)$$

where

$$F(x', y') = -\frac{\delta}{2} \xi_x^{CX} x'^2 + \frac{\delta}{2} \xi_y^{CY} y'^2 \quad (7)$$

$$G(x, y) = -\frac{\delta}{2} \left[\hat{c}^{x''} \frac{L}{\beta_F^x} x'^2 - \frac{\delta}{2} \hat{c}^{y''} \frac{L}{\beta_F^y} y'^2 + 2\delta^2 \hat{d}^{x'} \frac{L}{\sqrt{\beta_F^x}} x' \right],$$

and we have introduced the horizontal and vertical chromaticities $\xi_x^{CX} \equiv \hat{c}^x \frac{\beta_F^x}{L}$, $\xi_y^{CY} \equiv \hat{c}^y \frac{\beta_F^y}{L}$. The Hamiltonians of the two X-sextupoles at the beginning and the end of the CCX, denoted by 1 and 2, read

$$H_1 = \tilde{H}(x_F + \eta_F \delta, y_F), \quad (8)$$

$$H_2 = -\tilde{H}(x_F + \eta_F \delta, y_F) + k_F \eta_F \delta (x_F^2 - y_F^2), \quad (9)$$

respectively, where \tilde{H} is the usual sextupole-Hamiltonian

$$\tilde{H}(x, y) \equiv \frac{1}{3!} k_F (x^3 - 3xy^2), \quad (10)$$

the term k_F denotes the integrated sextupole strength and $x_F \equiv \sqrt{\beta_F^x} x'$, and $y_F \equiv \sqrt{\beta_F^y} y'$ are the coordinates at the first X-sextupole. Now the total CCX, including sextupoles, is

$$e^{-H_1} e^{-\frac{1}{2} F(x', y')} e^{-G(x, y)} e^{-\frac{1}{2} F(x', y')} e^{-H_2} = e^{-G_K^{CX}} e^{-H_K^{CX}}, \quad (11)$$

*Work supported by Department of Energy contract DE-AC03-76SF00515.

where

$$G_R^{CCX} \equiv G \left(x + \frac{\partial}{\partial x'} (H_1 + F), y + \frac{\partial}{\partial y'} (H_1 + F) \right) \quad (12)$$

and

$$H_R^{CCX} \equiv F^{CCX} + k_F \eta_F \delta (x_F^2 - y_F^2). \quad (13)$$

In much the same manner the chromaticity can be propagated through the BX to give

$$H_R^{BX} = F^{BX} + F^{CCX} + k_F \eta_F \delta (x_F^2 - y_F^2) \quad (14)$$

and a term C_R^{BX} analogous to C_R^{CCX} . The generators G_R^{CCX} and G_R^{BX} contain fourth- and fifth-order terms, which have to be small.

C. The CCY

The Hamiltonian (14) to be carried through the CCY is of the form

$$H \approx -\frac{\delta}{2} \xi_x^{(3)} x'^2 + \frac{\delta}{2} \xi_y^{(3)} y'^2 + \dots, \quad (15)$$

where

$$\xi_{x,y}^{(3)} \equiv \xi_{x,y}^{CX} + \xi_{x,y}^{BX} + \frac{1}{2} \xi_{x,y}^{CY} - 2k_F \eta_F \beta_F^{x,y} - k_D \eta_D \beta_D^{x,y}, \quad (16)$$

and it interacts with a term analogous to $G(x, y)$ above,

$$G^{CY}(x, y) = -\frac{\delta}{2} \hat{c}_{CY}'' \frac{L}{\beta_D} x^2 - \delta^2 L \hat{c}_{CY}' \frac{1}{\sqrt{\beta_D^x}} x + \dots \quad (17)$$

The largest aberrations generated by the kick in x is a δ^3 -dispersion that could, at least in principle, be canceled downstream, and a δ^3 -chromaticity, from which

$$\beta_D^x \geq \frac{\sqrt{15}}{\Delta_x} \delta^3 \xi_x^{(3)} \frac{2}{\hat{c}_{CY}''} L, \quad (18)$$

where $\Delta_x \approx 1$ denotes the maximum tolerable relative increase of the horizontal spot size. Similarly, the y -kicks generate a third-order vertical chromaticity and a $x'^2 y'^2 \delta$ -term, giving rise to the two conditions

$$\sqrt{15} \delta^3 \hat{c}_{CY}'' \frac{L}{\beta_D} \xi_y^{(3)} \leq \Delta_y, \quad (19)$$

$$\sqrt{3} \delta \hat{c}_{CY}'' k_D^2 L \beta_D^x \beta_D^y \epsilon_x \leq \Delta_y, \quad (20)$$

where $\Delta_y \approx 1/\sqrt{2}$ (see Section F).

D. Synchrotron Radiation and Chromaticity

The beam size increase, due to the additional energy spread δ_{rms} , induced by synchrotron radiation inside and behind the CCY and to the uncompensated doublet chromaticity, $\xi_y^{FD} \approx 2\xi_y^{(3)}$, has to be small:

$$2\delta_{rms} \xi_y^{(3)} < \Delta_E \quad (21)$$

where $\Delta_E \approx 1$ denotes the maximum tolerable relative increase of the vertical spot size due to synchrotron radiation (see later), and the energy spread δ_{rms} is [3]

$$\delta_{rms}^2 \approx 2 \frac{55}{24\sqrt{3}} \frac{1}{2\pi} r_e \lambda_e \gamma^5 \frac{\theta_B^3}{L_B^2}. \quad (22)$$

Here, L_B denotes the length of the last bending section behind the CCY, and the factor 2 accounts for the contributions from bending magnets in the center of the CCY. The length of the central section is more than two times L_B , but in this case about half the doublet chromaticity is compensated by the final sextupole. Combining Eqs. (5), (20) and (21) and using $\alpha \equiv \frac{L}{L_B}$ we find

$$\eta_D \leq \bar{r}_{12} \left(\frac{\Delta_E}{2\xi_y^{(3)}} \right)^{\frac{2}{3}} \left(\frac{L^5 2\pi}{(\frac{55}{24\sqrt{3}}) r_e \lambda_e \gamma^5 \alpha^2} \right)^{\frac{1}{3}}. \quad (23)$$

The overall chromaticity balance reads approximately

$$\eta_D k_D \beta_D^y \approx \xi_y^{(3)} + \frac{b}{2} \hat{c}_{CY}'' \frac{\beta_D^y}{L}, \quad (24)$$

where $b \approx 2$.

E. Long-Sextupole Effect

A long sextupole generates octupole-like aberrations [2], which impose a limit on the tolerable sextupole length. For two sextupoles separated by a $-I$, these aberrations are described by the Hamiltonian

$$H_{ls} = \frac{k_D^2 l_D}{24} (\beta_D^x \beta_D^y x'^4 + 2\beta_D^x \beta_D^y x'^2 y'^2 + \beta_D^y \beta_D^y y'^4), \quad (25)$$

where l_D denotes the sextupole length. From the resulting increase of the vertical spot size, we deduce

$$\frac{k_D^2 l_D}{6} (\sqrt{3} \beta_D^x \beta_D^y \epsilon_x + \sqrt{15} \beta_D^y \epsilon_y) \leq \Delta_y. \quad (26)$$

Decomposing the integrated sextupole strength as $k_D = l_D \tilde{k}_D$, it follows that

$$l_D \leq \left(\frac{6\Delta_y}{\tilde{k}_D^2 (\sqrt{3} \beta_D^x \beta_D^y \epsilon_x + \sqrt{15} \beta_D^y \epsilon_y)} \right)^{\frac{1}{3}} \quad (27)$$

Assuming a pole tip field of 0.5 T at a radius of 5 mm, the maximum value of \tilde{k}_D is about

$$\tilde{k}_{D,max} \approx 24 \text{ m}^{-3} \text{ at 500 GeV beam energy.} \quad (28)$$

F. The Δ -Values

To determine the optimum relative spot-size increases Δ_x , Δ_y , and Δ_E , we take $\Delta \equiv \Delta_E = \Delta_y$. Using $\beta_{x,y}^* \sim 1/\Delta_{x,y}$ (which follows from $\xi_{x,y}^{(3)} \sim 1/\beta_{x,y}^*$, $\beta_D^{x,y} \sim 1/\beta_{x,y}^*$, and Eqs. (18), (19), and (20)), we find

$$\sigma_y^2 \propto \frac{1}{\Delta} (1 + 2\Delta^2) \quad \text{and} \quad \sigma_x^2 \propto \frac{1}{\Delta_x} (1 + \Delta_x^2), \quad (29)$$

from which the smallest spot size is obtained for

$$\Delta_y \approx \Delta_E \approx \frac{1}{\sqrt{2}} \quad \text{and} \quad \Delta_x \approx 1. \quad (30)$$

G. Vibration Tolerance and Power Supply Ripple

Denoting the horizontal vibration amplitude of the Y-sextupoles (this is equivalent to an orbit-change due to a vibrating quadrupole between the sextupole-pair) by Δx , we find

$$k_s \beta_D^y \leq \frac{1}{5 \Delta x}, \quad (31)$$

allowing a maximum spot size increase of 2% due to the induced waist shift. Moreover, if we suppose that the strength of all quadrupoles in the CCY varies by a factor $\Delta k/k$ due to power supply ripple, it follows

$$\beta_D^y \leq \frac{L}{5 \frac{\Delta k}{k} \hat{c}_{CY}^y}. \quad (32)$$

This has to be compared with inequality (19).

III. OPTIMIZATION

The minimum length of a final focus can be derived from the eight conditions (18), (19), (20), (23), (24), (26), (31) and (32). The achievable orbit stability at the second Y-sextupole regarding perturbations internal to the CCY, Δx , determines the maximum value of $k_D \beta_D^y$ via Eq. (31), while Eq. (18) gives a minimum value of β_D^y/L . If these two limits are inserted into Eq. (20), a lower bound on β_D^y/L^2 is obtained. Inequality (23) shows that the smallest value for η_D allows the shortest length L . Ideally, therefore, we would like to choose the smallest value for β_D^y/L on the right-hand side of (24). However, a compromise has to be made in order to keep the sextupole strength k_D at a tolerable level. The semi-arbitrary requirement that the second term on the right-hand side contribute about 15% to the total may be a reasonable choice. Inserting the optimum value of the dispersion η_D , deduced from Eq. (24), into Eq. (23), the minimum length L follows. It still remains to be verified whether the usually looser conditions (19), (26) and (32) are fulfilled.

As an example, from the initial design of an NLC final focus at 1 TeV, we extract $\bar{r}_{12} \approx 0.062$, $b \approx 1.6$, $\hat{c}_{CY}^y \approx -24$, $\hat{c}_{CY}^{y''} \approx -0.67$, $\hat{c}_{CY}^{x''} \approx 0.12$, $\xi_x^{(3)} \approx -2000$ (for $\beta_x^* \approx 25$ mm), $\xi_y^{(3)} \approx 15\,800$, and $\alpha \approx 34$. The rms-energy spread is taken to be $\delta \approx 2 \times 10^{-3}$, the horizontal normalized emittance $\epsilon_{xN} \approx 5$ mm mrad, and the emittance ratio $\epsilon_x/\epsilon_y \approx 100$.

Assuming that at the second sextupole an orbit stability of $\Delta x \approx 230$ nm can be achieved, the optimum final-focus parameters are obtained by the outlined procedure. They are listed in Table I and compared with the initial and the present final focus design. The length of the final focus was shortened by about a factor of two. This was achieved by lowering the value of dispersion and beta functions at the Y-sextupoles, while increasing the sextupole strength k_D . The present design is even somewhat shorter than the estimated optimum. The reason for this is that new sextupoles, similar in spirit to those proposed by Brinkmann [4], have been added throughout the system, which locally correct the chromaticity in each module. For more details on the NLC final focus, see Ref. [5].

IV. SUMMARY

We have derived eight scaling laws that characterize the length-dependent effects in a final focus system, and can be used as a guideline for optimization. The optimum length of the NLC

Table I

Initial and optimized CCY parameters for an NLC final focus system at 1 TeV c.m. energy.

Parameter	1 TeV		
	Initial	Optimum	Present
β_D^y [km]	160	140	120
η_D [mm]	45	24	23
k_D [m ⁻²]	2.8	6.4	7.4
l_D [m]	0.4	0.4	0.4
Δx [nm]	400	230	230
$\Delta k/k$	$8 \cdot 10^{-5}$	$6 \cdot 10^{-5}$	$6 \cdot 10^{-5}$
L_{tot} [m]	1461	917	791

final focus is primarily determined by the achievable level of orbit perturbations internal to the CCY, as measured at the second Y-sextupole, and by the effect of synchrotron radiation in the bending magnets. Assuming an orbit stability of $\Delta x \approx 230$ nm, the initial length of the final focus design for an NLC with 1 TeV c.m. energy was reduced by about a factor of two. The distance from the CCX to the IP is now about 800 m. For a final focus system at a c.m. energy of 1.5 TeV, the optimum length is estimated to be about 1000 m.

References

- [1] J. Irwin, "Final Focus System Optimization," in the Proc. of "Linear Colliders. 3rd International Workshop, LC 91, Protvino, USSR," Vol. 3, V. Balakin et al. (ed.), 1991.
- [2] J. Irwin, "The Application of Lie Algebra Techniques to Beam Transport Design," *SLAC-PUB-5315*, published in *NIM A298*, 460, 1990.
- [3] M. Sands, "The Physics of Electron Storage Rings," *SLAC-121*, 1971.
- [4] R. Brinkmann, "Optimization of a Final Focus System for Large Momentum Bandwidth," *DESY-M-90-14*, 1990.
- [5] F. Zimmermann et al., "A Final Focus System for the Next Linear Collider," these proceedings, 1995.

THE SLAC NLC EXTRACTION & DIAGNOSTIC LINE*

J. Spencer, J. Irwin, D. Walz and M. Woods

Stanford Linear Accelerator Center, Stanford University, Stanford, CA 94309 USA

Abstract

A prototype extraction line for the Next Linear Collider is discussed that has several important functions that include optimizing luminosity, characterizing beam properties at the Interaction Point and transporting beams from the IP to a dump. Beam characterization includes measurements of current, position, profile, energy, polarization and low-order correlations on a bunch-to-bunch basis for feedback and stabilization. Prototype optical and diagnostic layouts are described that provide such functions. We also consider possibilities for e , μ and γ secondary beam lines and dump experiments as well as energy recovery and local reuse of an assumed 10MW in each 500 GeV beam.

I. Introduction

Our overall goal is to optimize the luminosity. While an important objective is to get the beams into their respective dumps with minimal detector backgrounds, it is also important to provide any monitoring and feedback that can optimize the usable collision rate at the IP. To accomplish this, we need to know the detailed composition and characteristics of the outgoing disrupted beams. These beams have a significant number of pairs and more photons than leptons. Based on a 'worst' case prediction for these beams we then describe how we arrive at our 'final' result.

Due to the high power in the outgoing photon beam and the cost of beam dumps we decided that the photons and leptons should share a common dump. This implies an available distance for beam studies of 150 m. Because the SLC was a prototype for the NLC we begin by reviewing the SLC and FFTB experience relative to the NLC design.

II. Comparison with SLC

One advantage for the NLC relative to SLC is a horizontal crossing angle ($\theta_{c,x} \approx 2 \times 10$ mrad) at the IP that allows us to avoid kickers and septa for separating the counterpropagating beams. This enables us to reverse polarities between the ingoing and outgoing quadrupoles for better control of the larger horizontal disruption angles.

Rather than 30 kW in each SLC beam one has to deal with nearly 10 MW in each NLC beam. There is a factor of ten in energy i.e. 500 GeV beams for the NLC, the same RF pulse repetition rate of 120/s and a factor of twenty or so in beam current per RF pulse from accelerating a multibunch train in each pulse. This increased beam power poses certain problems for intercepting detectors and implies significantly higher operating costs. For 10¢/kWh, this represents a potential refund of as much as \$45K/day if energy is restored to the grid or otherwise recycled.

The lower invariant emittances and the factor of ten in energy result in significantly greater disruption effects in the NLC that permit most of the SLC measurements and others that aren't practical there. However, because the disruption angle is dominated by energy, we can measure the energy loss distribution and use precise RF BPMs in the beginning of the line to measure position, angle and timing of individual bunches. This is impractical for SLC e.g. $\Sigma_y = 1 \mu\text{m}$ and $N = 3.5 \cdot 10^{10}$ produces a peak deflection angle that is more than double our worst case.

III. Basic Design Procedures and Constraints

The optics can only be realized in practice after we know the characteristics of the outgoing beam. The procedure was to take the upstream final focus design in the form of TRANSPORT[1] and convert this to DIMAD[2] for predicting the spot characteristics at the IP due to emittance growth from synchrotron radiation in the dipoles and quadrupoles. One assumption here was that the energy loss, especially in the quads, can be neglected. The predicted beam parameters resulting from DIMAD were then used in ABEL91[3] to predict the composition and characteristics of the outgoing beam as well as to produce ray sets for all particle types for analysis and tracking. The ABEL calculations were compared to analytic calculations before being used to simulate the dump line with TRANSPORT (for design) and TURTLE (for tracking)[4].

The available length of the dump line was set by the outgoing photons and the assumed size of the dump:

$$12\sigma_{x'} \times L_D \leq 2R_D$$

where L_D is the distance from the IP to the dump face and R_D is its radius. For a dump window of 20 cm in diameter and outgoing angular spreads of $\sigma_{x',y} = 92,43 \mu\text{rad}$ from ABEL, we have 150 m of space available for beam studies.

The design procedure was complicated by the different species of outgoing particles that had to pass without intercepting *anything* as well as by the comparatively large angular and energy spreads induced by the beam-beam interaction. Besides constraining our design options this forced us to continually constrain the magnet apertures and lengths to insure reasonable magnets. Other constraints were imposed by the measurements and experiments that might be required. For example, electron spin rotation and depolarization constrained the strength and disposition of the dipoles. A related constraint was the need to capture off energy bunches or ones that did not collide and lose energy. The latter includes those resulting from beam-beam deflection scans. Other constraints will be discussed in the relevant sections.

IV. Optics

Once the disrupted electrons have cleared the detector, taken to be ± 5 m along the IP, using essentially a quadrupole doublet,

*Supported under Dept. of Energy contract DE-AC03-76SF00515.

we observe where the disrupted beam crosses the photon beam using third order TURTLE. Because this was nearly 20 m from the IP and it took 10 m to get the full energy beam moving parallel toward the dump, we find the first available space for diagnostics between 11 and 16 meters. RF BPMs [5] are assumed to begin at 5 m where the outgoing beams are still small and C-Band cavities could have apertures comparable to the quads ($\approx \lambda/4$).

The first dipole of a horizontal chicane, used to separate the outgoing photon and electron beams, begins at 16 m. It allows separate experiments, before recombining both beams into a common dump. Figure 1 shows the Twiss functions when the four bends are sized to separate the two beams by 12σ . Their maximum separation is

$$\Delta x = 2\rho_B(1 - \cos\theta_B) + L_1 \tan\theta_B$$

where θ_B is the bend angle for the full energy of any one rectangular dipole of length $L_B = \rho_B \sin\theta_B$ and L_1 is the separation between bends BD1 and BD2. Notice that this is just the dispersion η_x in the center of the chicane. This separation requires a minimum distance of

$$L_{min} = 2\rho_B \sin\theta_B + L_1.$$

The change in the bunch separation, due to the chicane, after this point in the central region is

$$R_{56} = \frac{\delta l_z}{\delta p/p} = 2\rho_B(\tan\theta_B - \theta_B) + L_1 \tan^2\theta_B.$$

This is proportional to the RF phase shift[6]. Thus we have a common beam pipe and sufficient dispersion to measure the energy and spread of the undisrupted beam.

For example, if we want to use the first bend for analyzing low energy particles from the IP or from a laser interaction before this bend, then the first order resolving power for some downstream location L is

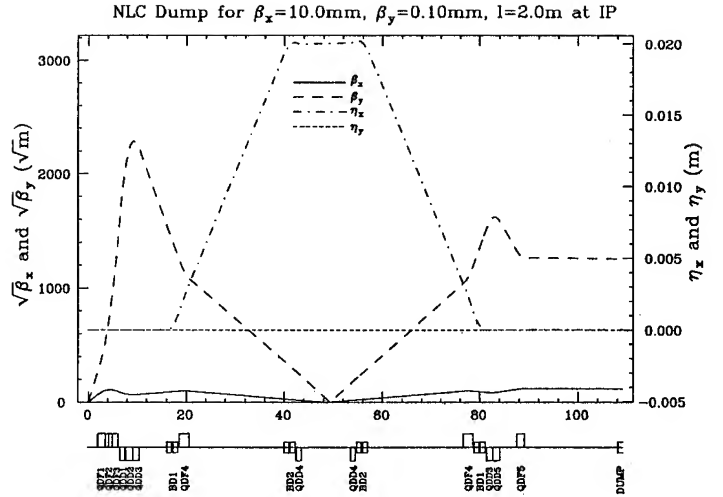
$$R_1(\rho, \theta, L) = \frac{\rho(1 - \cos\theta) + L \cdot \tan\theta}{[x_i \cos\theta + x'_i(\rho \sin\theta + L/\cos\theta)]}.$$

In the middle of the chicane R depends on the optics we impose. $R_{12} \rightarrow 0$ for point-to-point so $R = \Delta x / (10\sigma_x^* = 8000$ for a magnification of 10 i.e. this region of the chicane can resolve a single beam, undisrupted energy spread of $\delta p/p = 0.0125\%$ while the region directly in front of BD2 gives $R \approx 800$ or 0.13% capability.

Notice that there were several factors that constrained the bends e.g. electron spin rotation as well as the energy resolution necessary to resolve low-energy electrons near the Compton edge (required for monitoring beam polarization). Further, dipoles drive many higher order aberrations that act to blow the beam up that require higher multipoles to correct. These were not needed to get the beams into the dump with the 12σ constraint through the line.

V. Instrumentation

The guiding principle in the instrument layout Fig. 2 was to minimize the material in the high power beams. Thus, there is a significant use of lasers to control the production of additional particles. Nevertheless, since beamstrahlung is unavoidable, there are possibilities[7] to use either Compton or beamstrahlung photons that could prove quite useful for monitoring



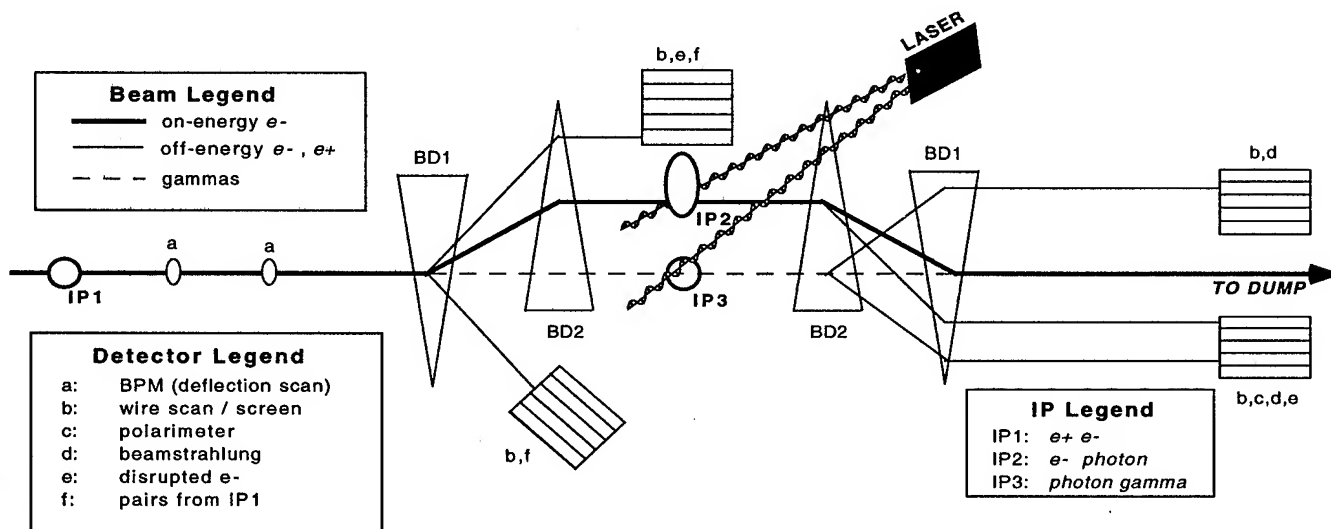


Fig 2: NLC Electron Extraction & Diagnostic Line

the dump or other measurements. While this can be done at other locations, it is done here in the middle of the chicane shown in Fig. 2 because this is where the dispersion is largest and the net rotation from the bends is zero. In our worst case scenario 20% of the beam goes undisrupted i.e. should have its original polarization. Compton scattering can then be used to monitor the polarization at this point by measuring the asymmetry in the scattered electrons as a function of laser polarization[10].

For best results, one needs to measure the electrons near the Compton edge with good resolution. In lowest order:

$$\epsilon_c^{edge} = \frac{\epsilon_{in}}{1+x} = \frac{\epsilon_{in}}{1+0.0153\epsilon_{in}(GeV)\omega_L(eV)} \approx 26 \text{ GeV}.$$

Because these electrons fall on the far tail of the disrupted beam spectrum, the only requirement is the ability to resolve their energy to one-half GeV i.e. a resolving power of only $R=P/\Delta P \geq 50$. Because $R=8000$ for the full energy beam, there is clearly no problem i.e. the laser spot can be any required size up to $\eta\delta \approx 4$ mm. This is also a good place to measure the electron beam profile and disruption characteristics to monitor bunch overlap, synchronization and luminosity.

VI. The Beam Dump

The dump has to dispose of essentially all of the power. Water is the primary absorber in a cylindrical vessel housing a vortex-like flow of water with vortex velocity $\approx 1-1.5$ m/s normal to the beam momentum. The vessel is 1.5 m diameter and has a 5.5-6.5 m long water section, followed by ≈ 1 m of water-cooled solids to attenuate a 500-750 GeV EM cascade shower. The beam enters through a thin window ≈ 1 mm thick and 20cm diameter. Production of ≈ 3 l $H_2/10$ MW beam power from radiolysis[11] can be mitigated with a catalytic H_2/O_2 recombiner that has a closed loop system that contains all radioisotopes.

References

- [1] K.L. Brown et al., TRANSPORT, SLAC Report 91, May 1977.

- [2] R.V.Servranckx, User' Guide to DIMAD, July 1993.
- [3] K. Yokoya, ABEL, A Computer Code for the Beam-Beam Interaction in Linear Colliders, NIM B251(1986)1 and Toshiaki Tauchi et al. Part. Accel. 41(1993)29. We thank Mike Ronan for help in getting the latest version of ABEL (Analysis of Beam-beam Effects in Linear colliders) running on VM system.
- [4] D.C. Carey et al., DECAY TURTLE, SLAC Report 246, March 1982.
- [5] S. Hartman and N. Shintake, private communication.
- [6] For energy recovery we want the dispersion and the angular dispersion to be zero to all orders in δ , x' and y' because of the beam-beam interaction. This implies a high order achromat that was not otherwise required.
- [7] J. Norem, et al., Tests of a High Resolution Beam Profile Monitor, These Proceedings.
- [8] Clive Field, NIM, To Be Published.
- [9] P. Bambade, et al., Observation of Beam-Beam Deflections at the SLC, Phys. Rev. Lett. 62(1989)2949.
- [10] M. Woods, Polarization at SLAC, SLAC-PUB-6694, October 1994.
- [11] D.R. Walz et al., Radiolysis and H Evolution in the A-Beam Dump Radioactive Water System, SLAC-TN-67-29, October 1967.

CLIC - A COMPACT AND EFFICIENT HIGH ENERGY LINEAR COLLIDER

H.Braun, R.Corsini, J-P. Delahaye, G.Guignard, C.Johnson,
J.Madsen, W.Schnell, L.Thorndahl, I.Wilson, W.Wuensch, B.Zotter
CERN, CH-1211, Geneva 23, Switzerland

I. RF SYSTEM

A description of the original CLIC two-beam scheme is given in [1]. The overall layout of the 1 TeV machine is shown in Fig.1. The main linac consists of normal conducting travelling wave accelerating structures operating at a frequency of 30 GHz and a gradient of 80 MV/m. One in ten of these sections have an asymmetric geometry and act as microwave quadrupoles for BNS damping. For multi-bunch operation damped and/or detuned structures would be required. The 30 GHz RF power is supplied by transfer structures which extract energy from a 3 GeV high-intensity electron drive linac running parallel to the main linac in the same tunnel. The transfer structure consists of a 11.5 mm diameter circular beam tube coupled through two diametrically-opposite ≈ 5 mm wide slots to two periodically-loaded rectangular waveguides. Each 50 cm long section produces two simultaneous 11.6 ns long 44.6 MW power pulses which drive two accelerating structures. This output power corresponds to 95% of the energy extracted from the beam. Two full-length (84 cell) constant impedance undamped accelerating section have been tested to an average accelerating gradient of 94 MV/m without any signs of breakdown and the periodically-loaded output waveguides of a full-length transfer structure have withstood 60 MW of 30

GHz RF power without breakdown but the structure itself has not yet been tested with a bunched beam Prototype diamond machined discs with the asymmetric geometry required for microwave quadrupole sections have been successfully produced by industry, and studies of damped structures for multibunch operation are underway. High gradient tests have also been made at SLAC on a 26-cell CERN-built X-band section [2]. Average accelerating gradients of 125 MV/m (a peak surface field of 285 MV/m) were obtained after 10^7 shots at 60 Hz with a pulse length of 150 ns. After conditioning, the dark current was $2 \mu\text{A}$ at 50 MV/m and $150 \mu\text{A}$ at 80 MV/m.

II. DRIVE LINAC

Each of the four drive linac has a starting energy of 3 GeV and a final energy of about 350 MeV. The total drive beam charge of $2.58 \mu\text{C}$ is contained in four trains of 22 bunches per train with 1 cm between bunches and an rms bunch length of 0.6 mm. The first bunch of each train loses very little energy as it passes down the linac whereas the last bunch of the train is strongly decelerated. The limit to this energy extraction process is reached when the energy of the last bunch reaches about 350 MeV and the blown-up beam completely fills the 11.5 mm diameter available aperture [3].

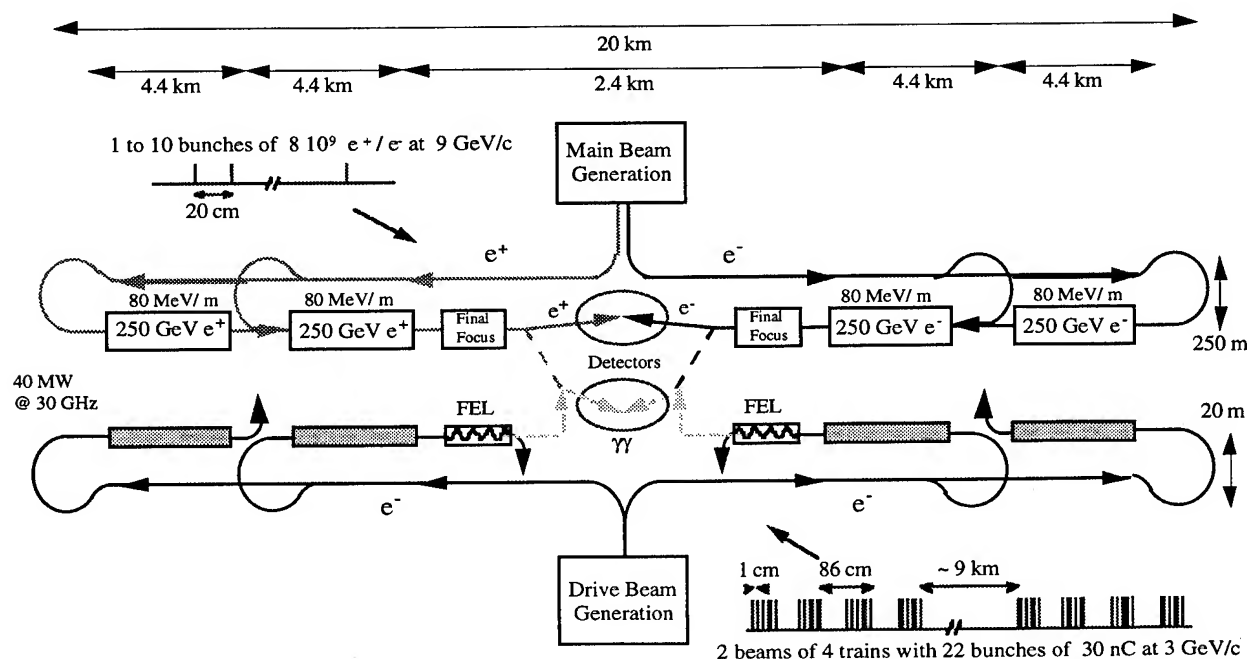


Fig.1 Schematic layout of 1 TeV CLIC machine

Half way down the linac when the mean energy of the trains is still 1.65 GeV an "energy exchange" section of 1.81GV of 700MHz SC cavities and 0.27GV of 1400MHz SC cavities is used to invert the energy distribution along the four trains to allow further energy extraction to take place. At the end of the linac when the beam is dumped the mean energies of the bunch trains are about 770 MeV for the first and about 350 MeV for the others. 72% of the beam energy is converted into RF power.

A 95 MeV drive beam consisting of a train of 24 bunches spaced at 10cm with a charge per bunch of 4.2nC and an rms bunch length of 1.3mm has been used in the CLIC Test Facility (CTF) to generate 76 MW of 30 GHz power from a single high impedance transfer structure and this power has been transmitted to a CLIC accelerating section in a two-beam configuration and has been used to accelerate a low intensity electron beam. The CTF work is reported in detail in [4].

III. DRIVE BEAM GENERATION

The 88 bunches of the drive beam are produced by a battery of 11 S-band photoinjector linacs. Each photoinjector linac consists of a laser-illuminated (262nm) photocathode (Cs_2Te) in an S-band RF gun (100MV/m) followed by an S-band RF booster. The energies of the 11 linacs (around 50 MeV) are slightly different allowing the 11 outputs to be merged in a magnetic spectrometer [5]. The resulting 12ns long bunch train is accelerated to 3 GeV using 3.8 GV of 350 MHz (6MV/m) SC cavities and 0.45 GV of 1400 MHz (10MV/m) SC cavities for RF wave flattening. Short sections (each 220 MV) of SC cavities operating at 333 and 366 MHz compensate the effects of beam loading.

One of these S-band photoinjector linacs has been built in the CLIC Test Facility (CTF) and has produced a maximum single bunch charge of 35nC with an rms bunch length of 2.4mm from the gun-booster at 11 MeV.

An alternative method to generate the 88 bunches of the drive beam directly at 50 MeV using an FEL is also being considered. Experiments to measure the degree of bunching produced by such a system at low energy (2-3MeV) are at present being carried out at the Centre d'Etudes Scientifiques et Techniques d'Aquitaine (CESTA) near Bordeaux. In a later phase it is planned to use this beam to generate power in a CLIC transfer structure.

IV. ISOCHRONOUS RING DRIVE BEAM SCHEME

A more efficient alternative to the "reference" drive beam scheme described above is being studied.

A laser illuminated L-band RF gun supplies 2×20 trains spaced at 1.97km of 17 bunches ($\sigma=6\text{mm}$) spaced at 20cm and of relatively low intensity (17nC) to a 1.5 GHz SC linac which accelerates them singly on the crest of the wave to the top drive beam energy of 2.7 GeV. The trains are then injected

using 1.5 GHz transverse deflectors into each of two 1km circumference isochronous rings to produce 10 trains of 34 bunches spaced at 10cm. After extraction and the introduction of a linear correlated energy spread along the bunch using a 140 MV 3 GHz cavity, the bunch length is reduced by a factor of 10 in a magnetic bunch compressor. Finally bunch trains from each ring are combined by a 3 GHz transverse deflector to create two beams (one for each drive linac) of 5 trains each containing 68 bunches spaced at 5cm distance. Each train is used to supply power for a 100 GeV section of the main linac.

V. MAIN LINAC INJECTOR SYSTEM

A 1.5 GHz SC linac accelerates the e- and e+ beams to 2.15 GeV for injection into the damping rings. The e- beam is supplied by a 200 MeV normal-conducting photoinjector linac. The e+ beam is created from the 2.15 GeV e- beam using a rotating conversion target and a SLC-like flux concentrator for enhanced capture. A second 1.5 GHz SC re-circulating 1.37 GV linac boosts the energy of the e- and e+ beams to 9 GeV. A predamping ring also running at 2.15 GeV is used to match the positron emittance to the acceptance of the main positron damping ring. Simulations of the positron delivery system have shown that a comfortable safety margin in positron yield can be expected. The whole injector scheme is described in detail in [6].

VI. OVERALL MACHINE PARAMETERS

The single-bunch parameters have been re-optimised to obtain an acceptable compromise between luminosity and beam-strahlung effects [7]. The new parameters are given in Table 1 and are based on simulations of the beam behaviour in the main linac and the beam-beam interaction at the collision. A luminosity of $10^{33} \text{ cm}^{-2}\text{s}^{-1}$ is obtained using 100MW of RF power with single-bunches at 500 GeV. At 1 TeV however a multibunch operation (10 bunches) is required to reach a luminosity of $10^{34} \text{ cm}^{-2}\text{s}^{-1}$.

An option to make $\gamma\gamma$ or γe^\pm collisions in a second interaction region is planned [8]. In this case one or more bunches of the CLIC drive beam would be used to produce an intense beam of polarised light in an FEL. This laser light would be transported via mirrors into the interaction region where it would be converted into a polarised γ beam by Compton back-scattering of the photons on the incoming electron beam. The ability to generate the photon beam in this way at a relatively high repetition rate with a drive beam to photon beam efficiency of 3-4% gives CLIC a distinct advantage over other machines which rely on conventional lasers. Detailed studies show that $\gamma\gamma$ luminosities of $4 \times 10^{32} \text{ cm}^{-2}\text{s}^{-1}$ and $2 \times 10^{33} \text{ cm}^{-2}\text{s}^{-1}$ respectively can be obtained for single and ten bunch operation by re-optimising the final focus parameters to take into account the fact that there is no disruption.

		500 GeV	1000 GeV	
RF Frequency	f	30	30	GHz
Accelerating field	E	80	80	MV/m
Number of bunches	n	1-10	1-10	
Distance between bunches	Δ	20	20	cm
Repetition frequency	f_r	2.5-1.2	4.0-1.8	kHz
Total two-linac power	P_{ac}	100	275	MW
Beam power per linac	P_b	0.82- 3.92	2.6- 11.7	MW
Beam power / AC power	η	2-8	2-9	%
Particles per bunch	N	$8 \cdot 10^9$	$8 \cdot 10^9$	
Normalised emittances (horizontal / vertical)	$\gamma \epsilon_{x,y}$	3/0.15	3.9/0.2	10^{-6} rad.m
RMS bunch length	σ_z	200	200	μm
RMS beam dimensions	$\sigma_{x,y}^*$	250/7.5	200/6	nm
Beamstrahlung parameter	Υ	0.08	0.18	
Relative energy loss	δB	0.04	0.08	
Luminosity enhancement	H_D	1.42	1.31	
Luminosity with pinch	L	1.0-4.8 10^{33}	2.2-10 10^{33}	$\text{cm}^{-2}\text{s}^{-1}$

Table 1 CLIC Parameter List

VII. BEAM DYNAMICS AND FINAL FOCUS STUDIES

Beam dynamics studies have focused on minimisation of the emittance blow-up in the main linac. Nominal emittances can be achieved with rms alignment tolerances of about 10 μm on both accelerating structures and beam position monitors using a dispersion-free trajectory correction algorithm with three monitors between quadrupoles. Emittances below the nominal values have been obtained by applying a new correction algorithm which uses differences between trajectories for variable bunch currents and momentum [9]. The tolerance on quadrupole position jitter for a 10 % emittance dilution is estimated to be about 30 nm. A detailed layout of the scaled focusing scheme based on a division of the main linac in sectors with constant betatron function has been implemented. This required the addition of matching between sectors and a separation of the phase advances in the two transverse planes by 10 degrees to minimise coupling [10]. Shaping of the bunch particle distribution by collimation in the compressor has been introduced to minimise the energy spread.

The final focus system will have to be adapted to multi-bunch operation. It is proposed to use either a large enough crossing angle (about 10 mrad) so that the outgoing beam can exit through a separate channel in the quadrupole nearest to the interaction region, or to use a small enough crossing angle (0.25-0.5 mrad) to enable the beam to pass through the same beam hole as the incoming one. In order not to lose too much luminosity, the first option requires "crabbing" of the bunches with transverse RF fields with rather stringent phase

tolerances. The second option will need somewhat larger apertures, and hence longer or stronger (SC) quadrupoles. In both cases, the incoming beam should remain on axis in order to minimise the emittance growth by radiation in the magnetic fields of the quadrupoles.

VIII. ALIGNMENT TEST FACILITY AND BEAM POSITION MONITOR TEST RESULTS

An active alignment test facility has been built in an unused underground tunnel at CERN to study the feasibility of making controlled submicron displacements and to test alignment systems. Accelerating structures are supported by V-blocks on 1.4m long silicon carbide girders. The ends of adjacent girders sit on a common platform which ensures continuity of position between units. The platforms are positioned by three stepping-motor-driven precision jacks (two in the vertical plane for vertical displacement and axial rotation, and one in the horizontal plane). Quadrupoles are positioned and moved independently of the structures by similar motors. In the test facility a stretched-wire running along the axis of the structures and passing through capacitive position transducers where the BPMs would normally be is used to simulate the beam. After deliberate misalignments of 1mm, the system which is programmed for automatic alignment with respect to the transducers, returns to its original position within <1 μm .

A prototype E110 resonant cavity type CLIC beam position monitor has been tested with an antenna in the laboratory, and with a beam in the CTF. Resolutions down to 10 μm have so far been demonstrated in pilot data taking runs in the CTF. The antenna tests however clearly demonstrated a resolution of 5nm.

IX. REFERENCES

- [1] W.Schnell, CERN-LEP-RF / 86-06.
- [2] J.Wang et al. " SLAC/CERN high gradient tests of an X-band accelerating section", this conference.
- [3] A.Riche, "Tracking particles with wakefield and space charge effects", this conference.
- [4] R.Bossart et al., "CTF Developments and Results," this conference.
- [5] B.Autin and R.Corsini, "Generation of a 30 GHz train of bunches using a magnetic switchyard" this conference.
- [6] J.P Delahaye, CERN/PS 94-14 (LP).
- [7] G.Guignard and I.Wilson, "Single-bunch parameters proposed for 500 GeV and 1 TeV CLIC options", CLIC Note 264, Dec.1994.
- [8] R.Corsini and A.Mikhailichenko, "The feasibility of $\gamma\gamma$ or γe^\pm collisions for CLIC", CLIC Note 254, Dec. 1994.
- [9] C.Fischer, " Improved CLIC performances using the beam response for correcting alignment errors" this conference.
- [10] G. Parisi and G. Guignard, "Arrangement in Sectors of CLIC Linac Focusing", CERN SL/94-56 (AP).

CLIC TEST FACILITY DEVELOPMENTS AND RESULTS

R. Bossart, H. Braun, F. Chautard, M. Comunian, J.P. Delahaye, J.C. Godot, I. Kamber, J.H.B. Madsen, L. Rinolfi, S. Schreiber, G. Suberlucq, I. Wilson and W. Wuensch,
CERN, 1211 Geneva 23, Switzerland

INTRODUCTION

The objectives of the CLIC Test Facility (CTF) are to study the generation of short intense electron bunches using a laser driven photocathode in an RF gun, to generate 30 GHz RF power for high gradient tests of prototype CLIC components, and to test beam position monitors. The performance of the CTF has improved dramatically in the course of the past year and highlights are presented here. The layout of the CTF is shown in Fig. 1.

The RF gun now has a Cs_2Te photocathode, enabling the use of the fourth harmonic of the YLF laser system (262 nm). Laser pulse lengths down to 8 ps full-width-half-height (FWHH) and energies of 0.5 mJ have been produced. The CTF operates with a repetition rate of 10 Hz with either single bunches or trains of up to 48 bunches. Trains are produced by splitting the laser pulse. The RF gun consists of a 1 1/2 cell cavity, a photocathode, a focusing solenoid and a 4 cell booster cavity. The beam exits the gun with a momentum of 4.5 MeV/c and is then accelerated up to 92 MeV/c by the S-band travelling wave accelerating section. 30 GHz power is generated when the beam is passed through the - un-powered - prototype CLIC main linac accelerating section [1]. The power is fed to the second prototype main linac accelerating section and the accelerating gradient produced in it is directly measured by reaccelerating the lead bunch of the drive train.

PERFORMANCES

In the 1994 run, the CTF produced 30 GHz powers of up to 76 MW, which corresponds to a peak gradient of 123 MV/m in the 30 GHz decelerating section and an average gradient of 94 MV/m in the 30 GHz accelerating section. Consistency between accelerating fields determined through RF power measurement and reacceleration was confirmed up to 76 MV/m. There has never been any sign of RF breakdown in either accelerating section, any 30 GHz component or waveguide at any power

level achieved so far. In addition, the output periodically loaded waveguide of a prototype transfer structure was tested to 60 MW without RF breakdown. These results show that CLIC can be operated at nominal field levels with little or no conditioning.

The maximum power achieved in the 1994 CTF run was almost a factor 2 higher than that achieved in the 1993 run [2]. This improvement is mainly due to an increased beam energy of 92 MeV which reduces the detrimental effect of long range transverse wakefields in the decelerating section. A second modulator and klystron allowed the generation of the extra 3 GHz power. Further improvement came from raising the number of bunches to 48 which increased the charge passing through the decelerating section. This was made possible by an upgrade of the laser pulse train generator. The train generator upgrade has also given the capability to vary the laser pulse lengths. A longer laser pulse length reduces the effect of space charge in the RF gun and has given a single bunch charge at the gun output to 35 nC. This charge is more than twice the previous CTF record. The electron bunch length at this charge was $\sigma_z = 2.4$ mm and thus further improvement can be expected. The maximum charges achieved in the CTF are summarized in Table 1. The single bunch charge is limited by space charge effects in the gun and short range transverse wakefields in the 3 GHz structure. Multibunch charge at the RF gun exit is limited by the available laser energy. The downstream charge is further limited by long range transverse wakefields and chromatic effects due to beam-loading in the S-band accelerating structure. The highest 30 GHz powers were produced by a 48 bunch train with a total charge of 80 nC transmitted through the 30 GHz decelerating section. For this charge the measured bunch length was $\sigma_z \approx 1$ mm which corresponds to the resolution limit of the streak camera.

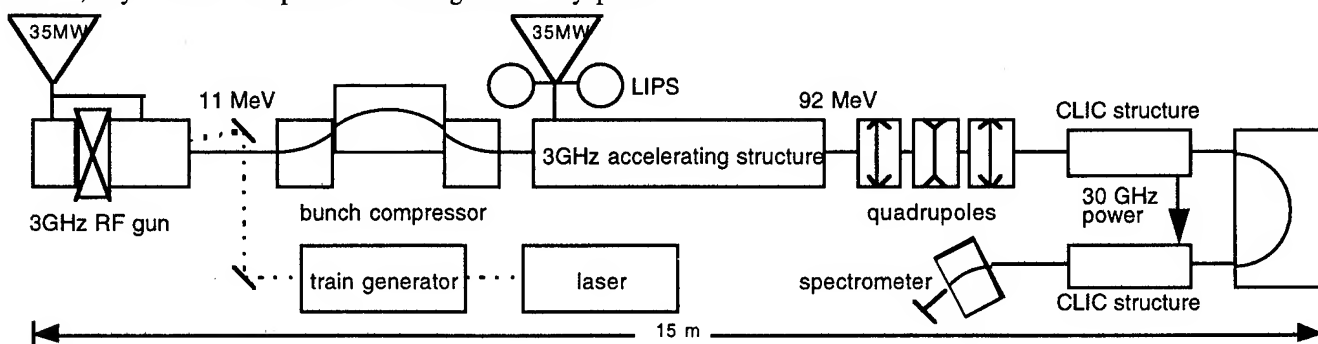


Figure 1: Layout of the CTF planned for 1995

position in beamline	single bunch [nC]	48 bunches [nC]
RF Gun exit	35	450
3GHz structure exit	20	160
30GHz structure exit	7	81

Table 1: Maximum measured charges

EMITTANCE MEASUREMENTS

Emittance measurements were performed with single bunches by varying the strengths of two quadrupoles downstream of the 3 GHz structure and measuring the beam profiles on a transition radiation screen just upstream of the 30 GHz accelerating section. The measurement results together with simulation results from PARMELA are shown in Fig. 2 [3]. The normalized, 1σ , rms emittance is used. For these measurements the laser spot on the photocathode had a radius of 5 mm and a duration of 8 ps FWHH. The phase difference between the zero crossing of the electric field in the gun and the arrival of the laser pulse was 30° . Although the variation of emittance with bunch charge is qualitatively similar for measured and computed values, the measured emittances are systematically higher. This effect is not understood. The large error bars on measured emittances at high charges are caused by unstable beam conditions.

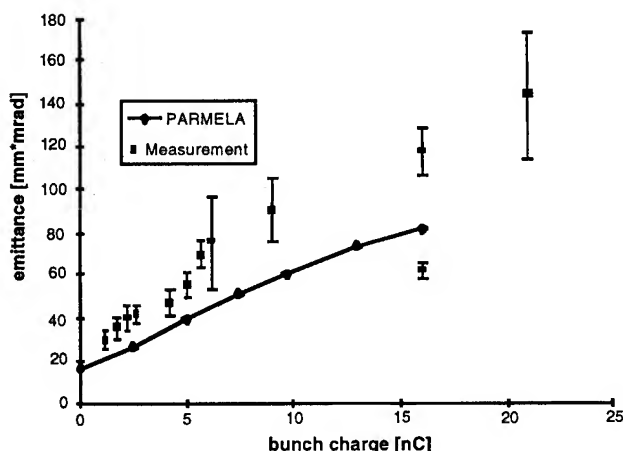


Figure 2: Emittance as a function of bunch charge

RF PULSE COMPRESSION

The 3 GHz accelerating section is powered by a 35 MW klystron with a $4.5\mu\text{s}$ long pulse compressed to $1.2\mu\text{s}$ by two LIPS cavities as shown in Fig. 1. This type of pulse compression requires a phase shift near the end of the klystron output pulse [4]. Using a new programmable 3 GHz low level RF phase shifter, three phase shift schemes were tested.

A: A phase jump of 180° $1.2\mu\text{s}$ before the end of the RF pulse. This has been the standard mode of operation before the programmable phase shifter was available.

B: A phase jump of $+68^\circ$ $1.2\mu\text{s}$ before the end of the RF pulse, followed by a gradual phase shift from $+68^\circ$ to $+180^\circ$ during the remainder of the pulse.

C: A linearly decreasing phase by -30° during the first $3.3\mu\text{s}$, then a jump of $+68^\circ$, followed by a linear phase shift of $+112^\circ$ during $1.2\mu\text{s}$.

Scheme A produced a sharp rise followed by an exponential decay with an overshoot 2.5 times larger than the average pulse power. Scheme B delivered a nearly flat power pulse with an overshoot of only 20% above the average power. Nonetheless scheme B provided 10% less acceleration of the beam than method A. This occurred because scheme B introduces a frequency shift of about 30 kHz at the output of the LIPS cavities. This has been compensated in scheme C by the negative phase ramp at the beginning of the RF pulse. The energy gain of the beam with scheme C is 5% lower than scheme A for constant klystron power. Because the beam energy was not limited by klystron power but rather RF breakdowns in the 3 GHz accelerating section the lower overshoot of scheme C is more important. An energy gain of 87 MeV was achieved with scheme C and only 70 MeV with scheme A.

PHOTOCATHODES

Nine photocathodes have been used in the RF gun during the 1994 CTF run. Four Cs_2Te cathodes were used at 100 MV/m for a total of 159 days. However, three others worked only at a lower field, 70 MV/m, and were used for only a total of 22 days. The typical starting quantum efficiency (QE) was about 5%, measured in a dc gun at 8 MV/m. The QE was found to increase with increasing electric field during measurements with the photocathode in the RF gun, see Fig. 3.

The QE does not show a strictly exponential degradation with time. During a period of 4 to 5 days after installation in the RF gun, a rather fast decay with a $1/e$ lifetime of approximately 6 days is observed, while afterwards the QE decreases more slowly, with the $1/e$ decay time varying between 34 and 67 days for the next two months (the beam duty factor is typically 30%). Measurements with closely spaced laser pulses have demonstrated that the relaxation time of electrons in the photocathode material is less than a few picoseconds. Two new photocathode materials which can be transported in air, unlike Cs_2Te which requires a vacuum transfer system and preparation chamber, were tested. CsI with a thin layer of germanium has a QE of 0.19% at 100 MV/m. A magnesium layer on a copper substrate has a QE of only 0.027% for the same electric field.

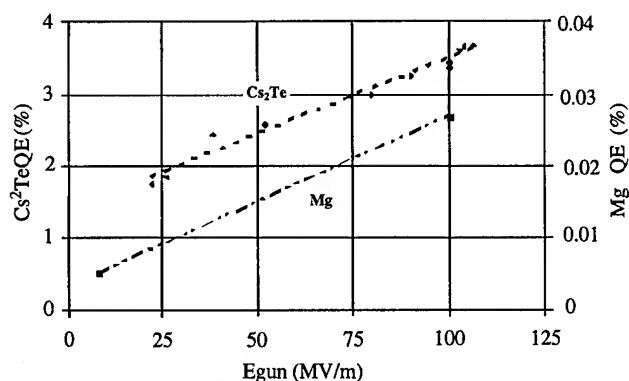


Figure 3: Quantum efficiency versus electric field for Cs₂Te and Mg photocathodes.

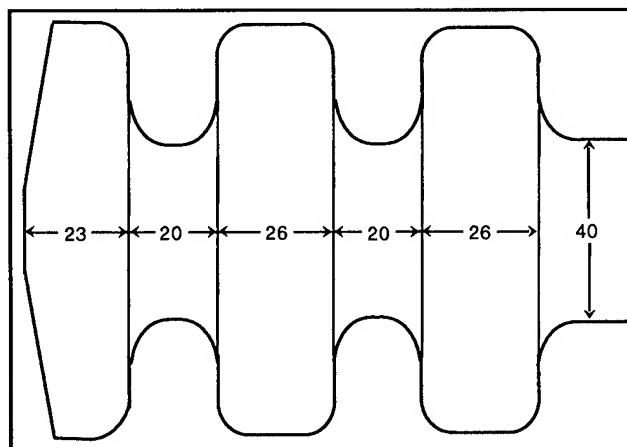


Figure 4: Sketch of the new RF gun (distances in mm)

MODIFICATIONS FOR THE 1995 RUN

In order to reduce the beam-loading and transverse wakefields in the 3 GHz accelerating section, the old spare LIL section used until now will be replaced by a high gradient, 1 m long structure borrowed from LAL [5].

A magnetic chicane bunch compressor between the RF gun assembly and the accelerating structure will be used in the 1995 run. An energy/phase correlation in a bunch (introduced by appropriate phasing of the booster cavity) together with the energy/path length dependence in the chicane compresses the bunch. The chicane consists of two 15 cm long left bending magnets and a 30 cm long right bending magnet [6]. Two quadrupoles upstream of the chicane and four downstream (not shown in Fig. 1) are used to match the beam in the transverse plane.

In order to increase the high charge performance of CTF, a new RF gun is being constructed. A drawing of the RF geometry is shown in Fig. 4, and the main parameters are listed in Table 2. The design goals were to maximize aperture to allow a large beam radius, maximise acceleration in the first cell to keep the effect of space charge small, and to minimize the r/Q to minimize energy spread in bunch trains. These goals are achieved with a large iris aperture, a 10° concave cone around the cathode, and re-optimized cell lengths.

number of cells	3
iris diameter [mm]	40
cone angle	10°
frequency [MHz]	2998.55
output energy [MeV]	6.58
input power [MW]	13.6
max. field on photo cath. [MV/m]	100

Table 2: Parameters of the new RF gun

REFERENCES

- [1] H. Braun, R. Corsini, J.P. Delahaye, G. Guignard, C.D. Johnson, J.H.B. Madsen, L. Thorndahl, I. Wilson, W. Wuensch, B. Zotter, "CLIC - a compact and efficient high energy e^+/e^- Linear Collider," this conference.
- [2] R. Bossart, H. Braun, J.P. Delahaye, K.K. Geissler, J.C. Godot, J.H.B. Madsen, A.J. Riche, L. Rinolfi, S. Schreiber, S. Sladen, G. Suberlucq, I. Wilson, W. Wuensch, "Performances Obtained with the CERN Linear Collider Test Facility," European Part. Acc. Conf., London, 1994, p. 680-682.
- [3] M. Comunian, "Emittance Measurements in CTF," Tesi per il corso di perfezionamento in Fisica, Università di Padova, 1995.
- [4] A. Fiebig and Ch. Schieblich, "A SLED Type Pulse Compressor with Rectangular Pulse Shape," European Part. Acc. Conf., Nice, 1990, p. 937-939.
- [5] G. Biennu and P. Brunet, "Dark Current under Low and High Electric Field," European Part. Acc. Conf., London, 1994, p. 775-777.
- [6] F. Chautard, "Le compresseur de paquets d'électrons pour le banc de test du collisionnaire linéaire du CERN", PhD-thesis in preparation, Paris University VI.

GENERATION OF A 30 GHZ TRAIN OF BUNCHES USING A MAGNETIC SWITCH-YARD

B. Autin, R. Corsini, CERN, CH 1211 Geneva 23, Switzerland

A possible technique of generation of high-frequency drive beam for a linear collider consists in creating electron bunches in a battery of guns and merging them in a magnetic circuit (switch-yard) at the end of which all the bunches are aligned on a common line with the right spacing. Two types of scheme are discussed. The properties of the structure in terms of orbit dispersion, focusing and bunch lengthening due to finite momentum spread and emittance are analyzed.

I. INTRODUCTION

The CLIC project of a $e^+ e^-$ linear collider is based on the two-beam accelerator scheme [1]. The electron and positron beams are accelerated in 30 GHz accelerating structures, the needed rf power being generated by the interaction of a high power relativistic electron beam (the Drive Beam), running parallel to the main linac, with appropriate rf structures resonant at 30 GHz (transfer structures). Each drive beam (one for the positrons, and one for the electrons) has an energy of 3 GeV and is composed of 2.5 μC , 12 ns long electron bursts, at the same ~ 2 kHz repetition rate of the main beam. Each burst is composed of typically four trains of 22 short ($\sigma \sim 1$ mm) bunchlets. The bunch charge is 30 nC, and the bunches are spaced by 1 cm. This spacing corresponds to the 30 GHz frequency of the transfer structures. While it seems feasible to generate and accelerate single 30 nC bunchlets in an S-band photocathode rf gun + booster, with the desired bunch length (possibly by using magnetic pulse compression), the correct spacing between bunchlets cannot be directly achieved. Furthermore, the beam loading limits the number of bunchlets that can be accelerated in such a system during the 12 ns duration of each burst. Therefore, one needs more of these sources to generate the full drive beam, and a method of combining the pulses together at the right spacing. The proposed technique consists of using one array of 11 electron guns for each drive beam [2]. Each gun delivers 2 bunchlets per train, and each operates at a different energy from 25 to 50 MeV. The bunchlets are then merged in a single trajectory using a dipole magnet and undergo further acceleration downstream. This bunch recombination scheme could be tested in future (possibly with only two lines) in the CLIC Test Facility (CTF) [3].

The general shape of a switch-yard is shown in figure 1. The optical structure of the channels is presented for two types of scheme christened C and S. The C-scheme is presently contemplated for the big machine and the S-scheme seems to be more appropriate for the test facility. It has also to be noted that such structures can be of interest all along the drive beam each time the beam has to be bent while satisfying the condition of isochronicity.

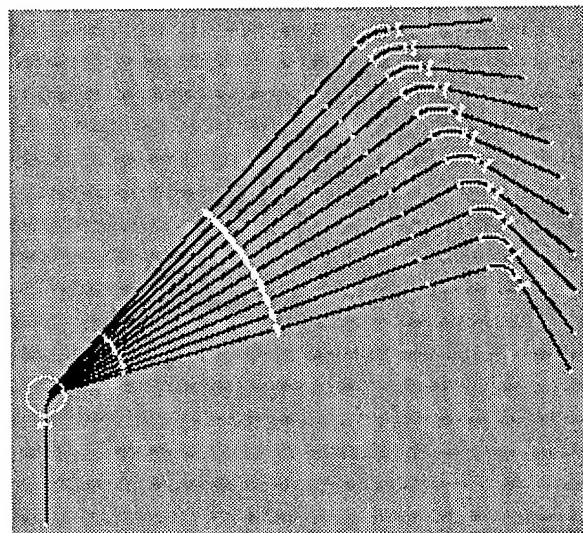


Figure 1. Orbits in a switch-yard

II C- and S-schemes

Two symmetric configurations of switch-yard channels are compared in this paper. The C-scheme is symmetrical with respect to an axis and the deflections of the two bending magnets add up. The S-scheme is symmetrical with respect to a point and the two deflections are of opposite sign so that the input and output trajectories are parallel. Their schematic structure is shown in figure 2. The bending magnets are represented by white circles. The shape is indeed circular for the magnet in which all the bunches are merged before exiting on a common straight section.

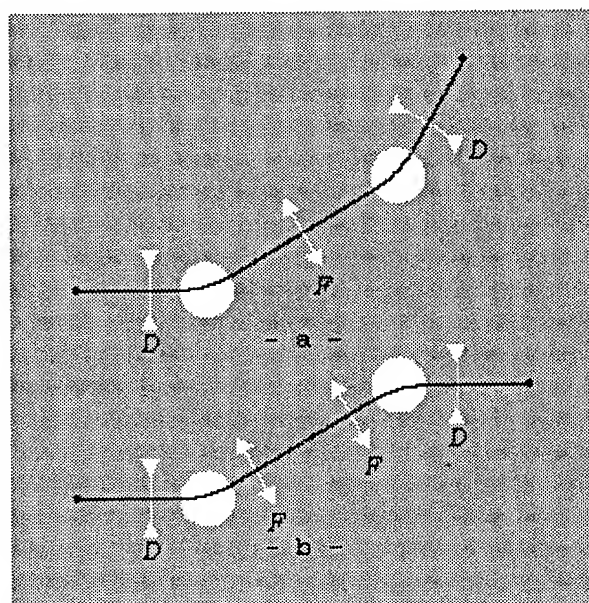


Figure 2. C-channel (a) and S-channel (b).

When few beams have to be combined, a static dipole may advantageously be replaced by a radio frequency dipole. In this configuration, the bunches receive the same deflections but with an alternating sign. The other dipole is actually a sector magnet proper to each channel. The focusing structure is idealized by thin lenses which permit algebraic calculations and an analytical formulation of the properties of the schemes. Detailed analysis using thick lenses is beyond the scope of this study. For reasons which will be discussed in the next chapter, the focusing is performed with singlets in the C-case and doublets in the S-case.

III. Optics of a switch-yard channel

A magnetic switch-yard is easily analyzed when the particles are traced backwards from the straight section where the bunches are merged to the photo-injectors. The bunch motion is traditionally split into the motion of its centre of gravity and the oscillations of the other particles about the centre of gravity.

A. Orbits

The orbits (see figure 1) are the trajectories of the centers of gravity of the bunches. They start with a common straight section and are then discriminated by a spectrometer whose magnetic field is constant and shape is a circle of radius R . The trajectories in the spectrometer are arcs of circles orthogonal to the contour circle; their radius is proportional to the particle momentum. With respect to a reference orbit of momentum p and deflection ϕ , a neighbour orbit of momentum $p + \Delta p$ is radially displaced at a distance l from the end of the spectrometer by the quantity $D \Delta p/p$ where the orbit dispersion D is given by:

$$D = (R + l) \sin \phi$$

This separation is needed for placing focusing elements. In order to keep the whole system compact, the separation is to be small and the space reserved to the quadrupoles is comparable to the spectrometer radius and of the order of 20 cm which is compatible with permanent magnet technology. The second separation to be achieved concerns the photo-injectors at the end of the channel. In a symmetric configuration, it is determined by the distance $2d$ between the two spectrometers. For the C- and S-scheme they are equal to

$$s_C = (R + d) \sin \phi + R(1 + \cos \phi)$$

$$s_S = 2(R + d) \sin \phi$$

The C-scheme is more practical than the S-scheme because of its fan shape but, for a separation of 30 cm at the location of the injectors, the distance between the spectrometers is of the order of 5 m in both cases.

B. Focusing

The switch-yard channel is dispersive in its very principle but it connects two straight sections where both the

orbit dispersion D and its longitudinal derivative D' must be zero. The dispersion increase in the spectrometers is always the same but keeps rising in the C-scheme up to the F-lens where it is bent back towards the second spectrometer whereas, in the S-scheme, it is immediately focused to the center of symmetry. Such orbit dispersion patterns impose the focal length of the F-lens:

$$f_C = \frac{R + d}{2}$$

$$f_S = \frac{(R + l)(d - l)}{R + d}$$

In the S-case, l is the distance from the end of the spectrometer to the F-lens. It turns out that the focusing is much stronger for the S- than for the C-scheme. The variation of the orbit dispersion is shown in figures 3 and 4.

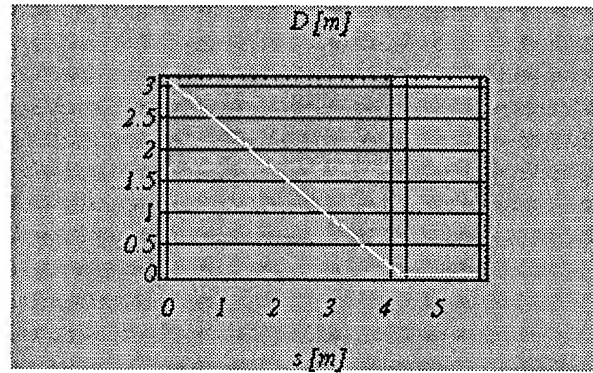


Figure 3. Orbit dispersion in a half C-channel.

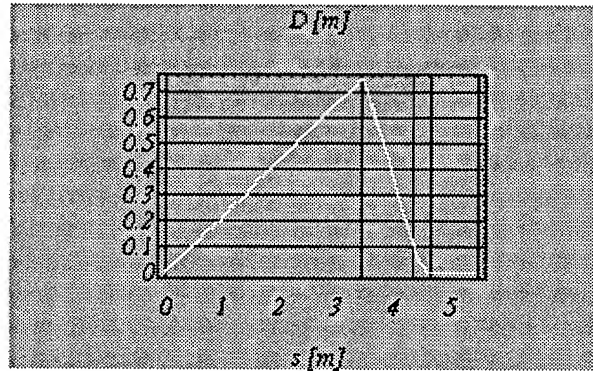


Figure 4. Orbit dispersion in a half S-channel.

The horizontal focusing being fixed, the vertical focusing is provided by D-lenses located in zero dispersion regions, i.e. the input and output straight sections. The structure is made of alternating D- and F-lenses in the C-scheme and of two symmetric doublets in the S-scheme. The conditions

$$\beta_h - \beta_v = 0$$

$$\alpha_h + \alpha_v = 0$$

at the end of the channel are canonical to match a FODO cell directly or via a quarter wave-length transformer [4]. The two unknowns of the problem are the focal length of the D-lens and the distance from the D-lens to the matching point. With the help of a symbolic program, factorizations can be

performed and the physical solutions turn out to be uniquely determined though they are solutions of a fourth degree equation. The β -functions are somewhat arbitrary since the periodic lattice which surrounds the channel is not a priori defined but rather fitted to the switch-yard. The β -functions at the symmetry point which serve as input values to the β -tracking have been chosen so as to minimize the α -function at the end point to facilitate the betatron matching. The variations of the β -functions are shown in figures 5 and 6.

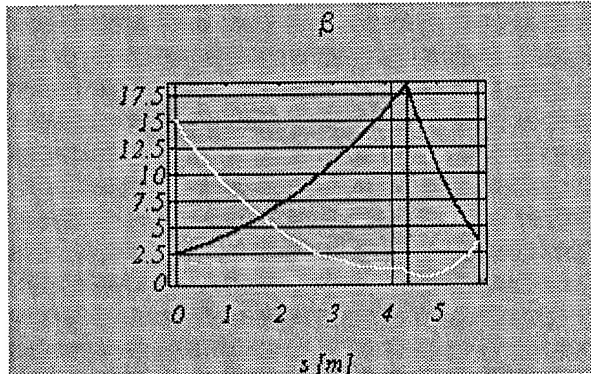


Figure 5: β -functions in a half C-channel.

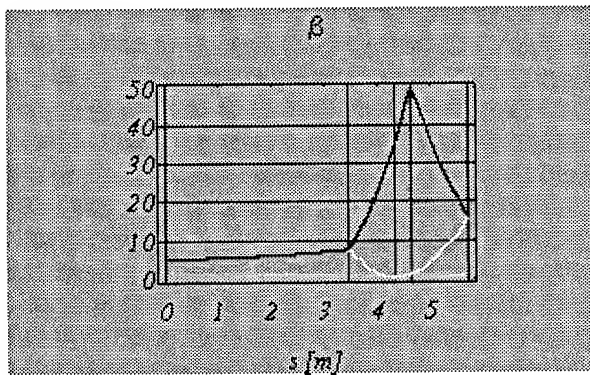


Figure 6: β -functions in a half S-channel.

In each bunch the particles have a finite momentum spread and it is indispensable to superimpose on the quadrupolar component of the lenses a sextupolar component

$$f' = Df$$

where f' is the radial derivative of the quadrupole focal length. This correction can only be performed in the F lenses where the orbit dispersion is non-zero and the chromatic aberrations, yet not fully compensated, remain tolerable.

C. Path length

In the generation of the train of bunches the distance between bunches is determined by the trigger of the injectors and by the path length of the various channels. A bunch lengthening due to the transverse emittance of the beam and to its momentum spread must also be kept under control.

When two particles of same momentum and longitudinal position enter a spectrometer, they leave it at different longitudinal positions distant by

$$dz = (x - Rx') \sin \phi$$

if their radial distance is x and their horizontal angles differ by x' at the input. From this stand point, an S-scheme is self compensated at least to first order. Position and angle are related by the Courant and Snyder invariant and it can be shown that for a given emittance ellipse of area ϵ , the bunch lengthening varies from zero to a maximum value which depends on ϕ , R , ϵ and the β -function at the end of the dipole.

The change in path length is related to the relative momentum error through the path length dispersion D_l ,

$$\Delta z = D_l \frac{\Delta p}{p}$$

whose expression in a dipole is

$$D_l = \rho(\phi - \sin \phi)$$

In contrast to the case of the emittance dependence, the path length always increases in a dipole because the radius of curvature ρ and the deflection ϕ have the same sign. D_l can nevertheless be controlled by shifting the quadrupoles radially. A displacement Δx produces a kick

$$\Delta \phi = \frac{\Delta x}{f}$$

and a change in path length $D \Delta \phi$. The focal distance f of the F-lens has a new expression because the extra kick modifies the orbit dispersion

$$f_C = \frac{(R+d) \sin \phi}{2 \sin \phi + \Delta \phi}$$

$$f_S = \frac{(R+l)(d-l) \sin \phi}{(R+d) \sin \phi + (d-l) \Delta \phi}$$

IV. CONCLUSION

The characteristics of optical structures which can be inserted in zero dispersion regions with a controlled isochronicity have been described in the framework of a linear model which gives the basic parameters in an analytical way. The simulation of higher order and space charge effects is not reported here but has been done and confirms the feasibility of a magnetic switch-yard.

V. REFERENCES

- [1] H. Braun et al., "CLIC - A Compact and Efficient High Energy Linear Collider", This Conference.
- [2] W. Schnell, "The Drive Linac for a Two-Stage Linear Collider", CERN-LEP-RF/88-89 and CLIC Note 85.
- [3] R. Bossart et al., "CLIC Test Facility Developments and Results", This Conference.
- [4] K.L. Brown and R.V. Servranckx, AIP Conference Proceedings, 127, pp 62-138 (1985)

A NEW FAMILY OF ISOCHRONOUS ARCS

G. Guignard and E.T. d'Amico, CERN, 1211 Geneva 23, Switzerland

For the Compact Linear Collider (CLIC), the bunch time structure should be preserved in the injector complex, especially in the recirculation arcs and after the final bunch compression stage up to the main linac injection. At the same time, because the transverse emittances are so tiny, their growth, essentially due to synchrotron radiation, should be kept as low as possible. In other projects, several isochronous arcs have been designed numerically to meet these requirements for a particular arc layout. These designs cannot be easily adapted to different configurations. The purpose of this study is to obtain analytically the main parameters of a new class of isochronous arcs which can be quickly tailored to special applications. Some of these are presented and they emphasize the small transverse emittance growth achievable even at large injection energy while keeping the arc radius in a reasonable range. Because locally the first-order anisochronicity is fully cancelled, higher-order contributions are less important than in other designs.

I. INTRODUCTION

In the Compact Linear Collider (CLIC) many considerations (wake-field effects, high luminosity) require that the bunch time structure should be preserved after the last bunch compression has taken place. This condition in general cannot be fulfilled when the beam passes through a deflecting system because of the difference in length between the individual orbits due to the energy spread and to the different initial conditions. The system is called isochronous when it does not change the bunch time structure. It can be proved [1] that in the linear approximation such a system should be nondispersive and such that:

$$\int_{S_1}^{S_2} \frac{D(s)}{\rho(s)} ds = 0 \quad (1)$$

where $D(s)$ is the horizontal dispersion, $\rho(s)$ the radius of curvature and S_1, S_2 are the positions of the beginning and end of the insertion.

The relation (1) shows that contributions to the integral come only from deflecting magnets and off-centred quadrupoles.

Several schemes of isochronous arcs have been developed [2], [3]. They are based on lattices encompassing several deflecting magnets where the integral (1) is minimized numerically over the whole arc. The purpose of this study was to investigate analytically an isochronous module with the minimum number of deflecting magnets. The juxtaposition of identical modules allows the building up of a whole family of isochronous arcs depending upon some parameters which can be adjusted to meet special design constraints, such as minimization of the emittance growth due to synchrotron radiation.

It can be proved [1] that the minimum number of deflecting magnets in an isochronous module is three. For reasons of simplicity we have chosen a symmetric module about the mid-plane of the central deflecting magnet.

II. ISOCHRONICITY CONDITION

Let us consider an isochronous insertion with three bending magnets (see Fig. 1), where we neglect for the moment the presence of other magnetic elements assumed to be perfectly centred. To simplify the algebra the bending magnets will be treated as sector magnets of the same length but of different curvature radii ρ_1 and ρ_2 , the deflection angles being respectively ϕ_1 and ϕ_2 .

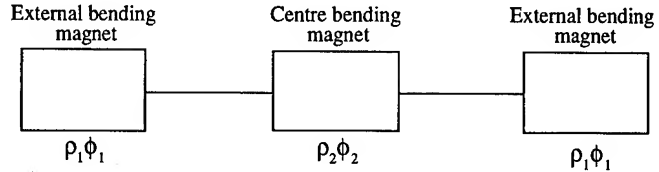


Figure 1: Isochronous insertion: bending magnet configuration.

Assuming that the dispersion and its derivative are zero at the entrance of the first magnet, it is easy to show that the isochronicity and symmetry conditions yield the following expressions for the dispersion and its derivative at the entrance of the centre magnet [4]:

$$\begin{aligned} D_j &= \rho_2 [D_j' \cot(\phi_2/2) + 1] \\ D_j' &= -\frac{\rho_1}{\rho_2} \left(\frac{3}{2} \phi_1 - \sin \phi_1 \right) \end{aligned} \quad (2)$$

III. INSERTION DESIGN

To transport the beam through the insertion described in Fig. 1, we have to add quadrupoles between the bending magnets. The simplest configuration is a FODO, as shown in Fig. 2 where only a half-insertion is drawn.

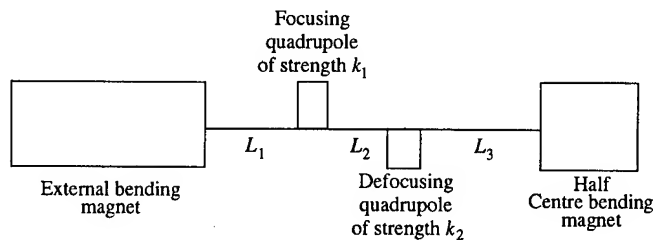


Figure 2: Layout of half isochronous insertion.

The three spaces L_1, L_2, L_3 and the two quadrupole strengths k_1, k_2 have to be chosen in order for the expressions (2) to be satisfied. After some manipulation of the transfer matrices (see Appendix A of reference [4]) the following expressions for the three drift lengths as functions of k_1, k_2 and of the free parameter $\Delta L_3 = L_3 - D_j/D_j'$, may be obtained:

$$\begin{aligned} L_1 &= a \frac{C_2 q_1}{C_1 q_2} (\Delta L_3 + q_2) - l + q_1 \\ L_2 &= q_1 - q_2 + \frac{b}{\Delta L_3 + q_2} \end{aligned}$$

Table 1: Permitted ranges of k_1 , k_2 , ΔL_3

$k_1 \leq \text{Min}\{k_1^{(1)}, k_{\max}\}$	$q_2 < q_1 - d$ and $\Delta L_3 > \text{Max}\{d - D_j/D'_j, -q_2\}$
	$q_2 > q_1 - d$ and $\text{Max}\{d - D_j/D'_j, -q_2\} < \Delta L_3 < \Delta L_3^{(1)}$
$k_1^{(1)} < k_1 \leq \text{Min}\{k_1^{(2)}, k_{\max}\}$	$\sqrt{k_2} > \text{Max}\left\{\frac{\text{acosh}(\text{Max}\{1, C_2^*\})}{l_q}, \sqrt{k_2^{(1)}}\right\}$ and $\text{Max}\{d - D_j/D'_j, \Delta L_3^{(2)}\} < \Delta L_3 < \Delta L_3^{(1)}$
$k_1^{(1)} < k_1 \leq \text{Min}\{k_1^{(2)}, k_1^{(3)}, k_{\max}\}$	$\sqrt{k_2} < \frac{\text{acosh}(C_2^*)}{l_q}$ and $\text{Max}\{d - D_j/D'_j, \Delta L_3^{(2)}\} < \Delta L_3 < \Delta L_3^{(1)}$
$k_1^{(2)} < k_1 < \text{Min}\{k_1^{(3)}, k_{\max}\}$	$\sqrt{k_2} < \text{Min}\left\{\sqrt{k_2^{(1)}}, \frac{\text{acosh}(C_2^*)}{l_q}\right\}$ and $\text{Max}\{d - D_j/D'_j, \Delta L_3^{(2)}\} < \Delta L_3 < \Delta L_3^{(1)}$
$k_1^{(1)} < k_1 < k_{\max}$	$q_2 < q_1 - d$ and $\Delta L_3 > \text{Max}\{d - D_j/D'_j, \Delta L_3^{(2)}\}$
where $k_1^{(1)}, k_1^{(2)}, k_1^{(3)}, k_2^{(1)}$ are the solutions of the following transcendental equations:	
$(l+d)\sqrt{k_1^{(1)}} \tan(L_q \sqrt{k_1^{(1)}}) = 1, \quad \sqrt{k_1^{(1)}} = \frac{\cos(L_q \sqrt{k_1^{(2)}}(l+2d) + \sqrt{[l \cos(L_q \sqrt{k_1^{(1)}})^2 + 4d(l+d)]}}{2 \sin(L_q \sqrt{k_1^{(2)}}d(l+d))}$	
$(l+d)\sqrt{k_1^{(3)}} \sin(L_q \sqrt{k_1^{(3)}}) - \cos(L_q \sqrt{k_1^{(3)}}) = a, \quad \sqrt{k_2^{(1)}} \sinh(l_q \sqrt{k_2^{(1)}}) - \sqrt{k_2^*} \left \cosh(l_q \sqrt{k_2^{(1)}}) - C_2^* \right = 0$	
and $C_2^*, k_2^*, k_{\max}, \Delta L_3^{(1)}, \Delta L_3^{(2)}$ are given by the expressions	
$C_2^* = \frac{aq_1}{C_1(l-q_1+d)}, \quad k_2^* = \frac{1}{[d-q_1(1+\frac{C_2^*}{aC_1})]^2}, \quad k_{\max} = \frac{\pi}{4L_q^2}, \quad \Delta L_3^{(1)} = \frac{b}{d+q_2-q_1} - q_2, \quad \Delta L_3^{(2)} = \frac{q_2 C_1}{a q_1 C_2} (l - q_1 + d) - q_2$	

$$L_3 = D_j/D'_j + \Delta L_3 \quad (3)$$

where

$$\begin{aligned} l &= \rho_1 \tan(\phi_1/2), & a &= -D'_j / \sin(\phi_1), \\ b &= \frac{q_2}{C_2} \left(\frac{q_2}{C_2} + \frac{q_1}{aC_1} \right), & q_i &= \frac{C_i}{S_i \sqrt{k_i}}, \\ C_1 &= \cos(L_q \sqrt{k_1}), & S_1 &= \sin(L_q \sqrt{k_1}), \\ C_2 &= \cosh(L_q \sqrt{k_2}), & S_2 &= \sinh(L_q \sqrt{k_2}) \end{aligned} \quad (4)$$

L_q being the quadrupole length. Table 1 gives a subset of the ranges of k_1 , k_2 , ΔL_3 for which the three drift lengths are larger than a given value d , when

$$\frac{1}{q_1} \leq \frac{1}{l+d} + \frac{1}{L_q/2+d}.$$

This can be shown to be the case for most of the usual hardware configurations. The full set of conditions may be found in Appendix C of [4].

IV. ARC DESIGN

To build up an arc we have to connect as many insertions as are necessary to obtain the desired deflection. To avoid large excursions of the betatron functions, the easiest way is to take advantage of the insertion symmetry and to ensure that the values of the Twiss parameters at both ends of a module composed of an insertion as described above and of a matching section are the same. It is easy to show that this is possible only when the betatron function and its derivative at both ends of such a module are respectively:

$$\beta_0 = \sqrt{1 - m^2}/|m_{21}| \quad \text{and} \quad \beta'_0 = 0 \quad (5)$$

where $m = m_{11} = m_{22}$ and m_{21} are the elements of the transfer matrix for the module. It is very difficult to do without the matching section while satisfying these constraints in both planes. We

have preferred to choose as a matching section half a triplet at both ends of the insertion to obtain a module with $-1 < m < 1$ in both planes. The Twiss parameters at the end of the transfer line injecting in the arc should then be matched to the values given by the expressions (5). In order to reduce to a minimum the contribution of magnetic errors and the sextupole effects we add the condition that the phase advance over a small number of modules should be an integer multiple of π in both planes.

After some manipulations it is possible to show that the growth of the normalized horizontal emittance $\Delta \gamma \epsilon_x$ is in good approximation inversely proportional to the fourth power of the number of modules required to assemble an arc [4]. The diameter of a full-circle arc is of course proportional to the number of modules. Clearly a compromise must be found between these two very important design parameters. To find it we have written a simple interactive program as an Excel spreadsheet which permits one to quickly obtain the main features of a 2π arc according to different choices of the number of required modules, of the ratio between the radii of curvature of the external and central bending magnets, and of the gradients of the two quadrupoles and of the distance ΔL_3 .

V. APPLICATIONS

In each branch of CLIC, two 360-degree arcs are needed to guide the particles in the reverse direction, one at 3 GeV for the drive beam and the other at 9 GeV for the main beam. These arcs should not perturb the bunch length, which is carefully chosen for optimum performance at the final interaction region in the main linac and for power transfer efficiency in the drive linac. Thus they have to be isochronous. A preliminary study of them has been carried at the first order using the tools described in the previous section. The results are summarized in Table 2 and Figs. 3 and 4.

The less stringent constraint on the horizontal emittance

growth for the drive beam allows one to obtain a smaller arc radius than could be expected from the energy scaling alone. Thus larger horizontal emittance growth would be acceptable but difficult to achieve due to limitations in optics matching.

On the contrary for the main beam the fractional horizontal emittance growth ($\sim 7.4\%$) cannot be further relaxed to obtain a smaller arc radius because it would induce a significant loss of luminosity.

VI. DISCUSSION

This report shows the existence of a parametric family of isochronous arcs and analytical procedures to design them. Simple interactive programming tools have been developed to implement these procedures which speed up the search of near optimized isochronous arcs. The first-order anisochronicity is fully eliminated and the low values of the dispersion contribute to the second-order effects as well as to limiting the horizontal emittance growth. On the other hand, this makes the correction of the chromaticity with sextupoles more difficult because they cannot be placed where the dispersion is sufficiently high. This, however, becomes a severe problem when the arc is part of a ring through which the beam passes several times. Further investigations will be aimed at limiting these effects and studying the energy spread acceptance of such arcs. Tracking should provide results on the behaviour of this family of isochronous arcs at higher orders.

Table 2: Parameters of the 360-degree isochronous arcs

Parameter	3 GeV arc	9 GeV arc
Number of insertions	3	48
Length of bending magnet	1.8 m	1 m
Quadrupole length	0.3 m	0.5 m
Gradient of the focusing Quad	55 T/m	60 T/m
Gradient of the defocusing Quad	55 T/m	60 T/m
L_1	1.366 m	2.068 m
L_2	0.227 m	0.925 m
L_3	1.164 m	0.310 m
Overall arc diameter	15 m	214 m
Horizontal phase advance	$\pi/2$	$\pi/2$
Vertical phase advance	$\pi/3$	$\pi/3$
Nominal $\gamma\epsilon_x$ (m-rad)	5×10^{-4}	2.5×10^{-6}
$\Delta\gamma\epsilon_x$ (m-rad)	8.16×10^{-6}	1.84×10^{-7}

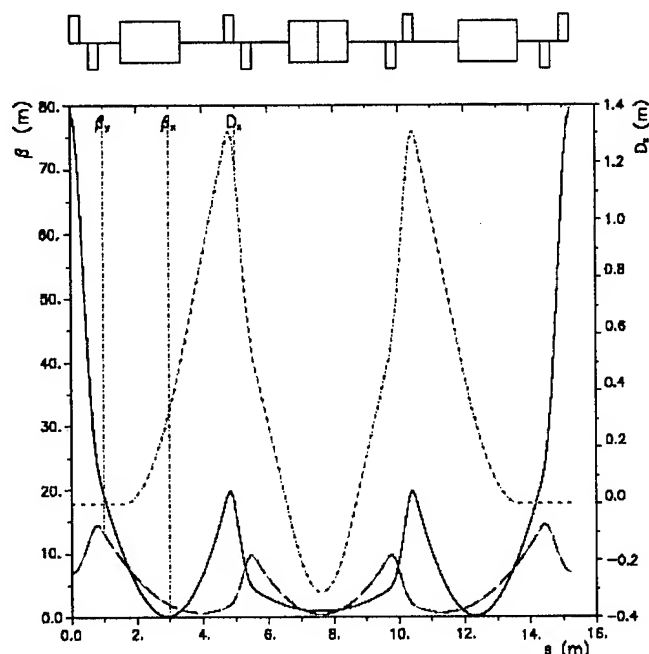


Figure 3: Optics functions of the 3 GeV isochronous module.

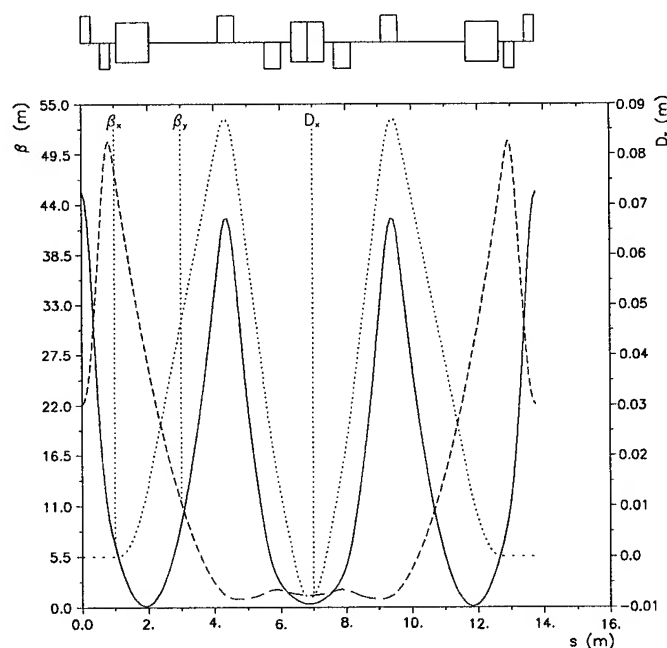


Figure 4: Optics functions of the 9 GeV isochronous module.

VII. REFERENCES

- [1] K.G. Steffen, High Energy Beam Optics, New York: Interscience, 1965.
- [2] G. Guignard, A Lattice with no Transition and Large Dynamic Aperture in Proc. 13th Particle Accelerator Conference, Chicago, 1989.
- [3] CEBAF Design Report, May 1986.
- [4] E.T. d'Amico and G. Guignard, CLIC note (in preparation).

UPDATING OF BEAM DYNAMICS IN THE CLIC MAIN LINAC

G. Guignard, CERN, 1211 Geneva 23, Switzerland

For the Compact Linear Collider (CLIC) study, the beam dynamics has been revisited in order to search for consistent beam parameters that simultaneously satisfy the emittance requirements and the experimental conditions. In the main linac, emphasis was put on the minimization of the energy-spread for limiting losses in the telescope acceptance, on the increase in the ratio between the bunch intensity and the vertical beam-size for improving luminosity, and on the preservation of the very small vertical emittance, in the presence of strong wakefields. Simultaneously, the emittance ratio and beam-size aspect ratio were adjusted in order to keep the average energy loss in the collisions low and boost the fraction of luminosity contained to within two percent of the centre-of-mass energy. The conclusions directly apply to single-bunch mode and can be extended to multibunch mode after adequate adjustments.

I. INTRODUCTION

In a linear collider, the dynamics of the beam that travels in the linac is simultaneously constrained by the focusing conditions and the wakefields that are unavoidably present in the linac, and by the strong forces that disrupt the bunch when it collides with a counter travelling bunch of opposite charge. On the one hand, the three dimensions of the bunch as well as its population must satisfy criteria to ensure beam stability and bunch coherence while minimizing perturbations such as linear coupling and wakefield deflections in order to prevent emittance dilution. On the other hand, the same beam parameters must be carefully selected for optimizing the luminosity, its distribution at collision as a function of the energy of the leptons that interact and emit photons, and the intrinsic energy spread of the beam before collision. In the Compact Linear Collider (CLIC), the wakefields associated with the high frequency (R-band) of the accelerating structures are so strong that in the past our attention was focused mainly on the control of the emittance dilution, the optimization of the collision parameters coming later. However, this proved not to provide satisfactory physics conditions at the interaction point, the average energy loss during collision in particular being too large and unacceptable [1]. This consideration made obvious the necessity to perform a general optimization of the single-bunch parameters that includes all the conditions briefly recalled above. If the luminosity remains below the desirable values the multi-bunch option should be added. The present article deals with the reoptimization of the single-bunch parameters recently carried out for CLIC and reviews the arguments on which it was based.

II. BEAM-BEAM PHENOMENA

The beam-beam phenomena can be described approximately by algebraic formulae which are partly deduced from numerical simulations [2, 3]. Although they are not very reliable in the intermediate use of quasi-flat beams, they offer the advantage of giving good results for either round or flat beams and of providing simple scaling laws. They were therefore used in our search

for optimized beam parameters, though verification by numerical simulations remains essential [4, 5]. The most important formulae are recalled hereafter, starting with the luminosity L and including the disruption effects at collision which pinch the transverse beam sizes and depend on the nominal beam aspect ratio $R = \sigma_x^*/\sigma_y^*$

$$L = \frac{N_b^2 f_{rep}}{4\pi \bar{\sigma}_x^* \bar{\sigma}_y^*}$$

$$\bar{\sigma}_x^* = \frac{\sigma_x^*}{(H_{D_x})^{1/2}} \quad \bar{\sigma}_y^* = \frac{\sigma_y^*}{(H_{D_y})^{f(R)}} \quad (1)$$

with

$$f(R) = \frac{1 + 2R^3}{6R^3}$$

N_b is the number of particles per bunch and f_{rep} the repetition rate. The pinch effect is described by the factors H_D , the behaviour of which are deduced from simulations [3]

$$H_D = 1 + D^{1/4} \left(\frac{D^3}{1 + D^3} \right) \left[\ln(\sqrt{D} + 1) + 2 \ln \frac{0.8}{A} \right] \quad (2)$$

with

$$D_{x,y} = \frac{2r_e N_b \sigma_z}{\gamma \sigma_{x,y}^* (\sigma_x^* + \sigma_y^*)}, \quad A_{x,y} = \frac{\sigma_z}{\beta_{x,y}^*}.$$

A is the ratio of the bunch length σ_z to the β -function at the interaction point and D is the so-called 'disruption parameter'. Starting from Eqs. (1) and (2), the consequent beam-beam phenomena can be characterized by three basic quantities: the beamstrahlung parameter Υ proportional to the fractional energy of the photons emitted in the collision, the average number n_γ of emitted photons per electron, and the relative energy loss δ_B due to beamstrahlung [2].

$$\Upsilon = \frac{5}{6} \frac{r_e^2 \gamma N_b}{\alpha \sigma_z (\bar{\sigma}_x^* + \bar{\sigma}_y^*)} \quad n_\gamma \cong 2.54 \frac{\alpha \sigma_z \Upsilon}{\lambda_e \gamma} \frac{1}{(1 + \Upsilon^{2/3})^{1/2}}$$

$$\delta_B = \left\langle -\frac{\Delta E}{E} \right\rangle \cong 1.24 \frac{\alpha \sigma_z \Upsilon^2}{\lambda_e \gamma} \frac{1}{[1 + (1.5\Upsilon)^{2/3}]^2} \quad (3)$$

where the physics constants r_e , λ_e and α have their usual meaning. When the beam is flat and Υ is small, δ_B can be approximated by

$$\delta_B \sim \frac{N_b^2}{\sigma_z \bar{\sigma}_x^{*2}}, \quad \text{with} \quad L \sim \frac{N_b^2}{\bar{\sigma}_x^* \bar{\sigma}_y^*} \quad (4)$$

and these two relations can then be combined by eliminating $\bar{\sigma}_x^*$ and by using the relation $\sigma_z = \beta_y^*$ (minimizing the hourglass effect):

$$L \sim N_b \sqrt{\frac{\delta_B}{\epsilon_y}}. \quad (5)$$

The previous beam parameters of CLIC suffered from the fact that the aspect ratio R was as low as ~ 11 and, consequently, that the horizontal disruption was high (> 1).

Both transverse beam dimensions were therefore strongly pinched, leading to an average energy loss δ_B larger than 20–25%. Looking at Eq. (4), there are three ways to reduce δ_B :

- Decrease the bunch population, but this involves an unacceptable reduction in the luminosity.
- Increase the bunch length σ_z , which does not change L directly, but may boost wakefield effects and then raise σ_y^* . The complete dependence of δ_B on σ_z , shown in Fig. 1 for the CLIC parameters, indeed indicates that a significant gain on δ_B implies a prohibitive increase of σ_z by a factor of three or four. Moreover, the apparent gain on δ_B for small σ_z is not welcome for physics, since it corresponds to an enlarged spread of the L -distribution.
- Widen the horizontal beam size σ_x^* , with the advantage that, according to Eq. (4), L decreases less rapidly than δ_B . In addition, for constant δ_B , N_b and σ_x^* can be adjusted independently, as can be seen from Eqs. (4) and (5).

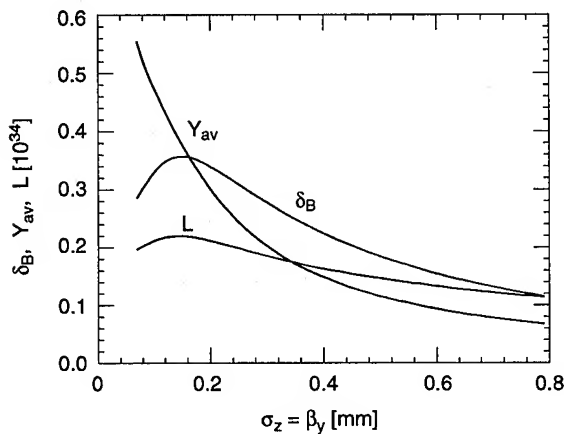


Figure 1. Variation of δ_B , γ and L with σ_z .

These considerations indicate that a reoptimization should start from a given value of δ_B (say 3.5% for 500 GeV c.m. energy) that determines the requirement on the aspect ratio R (≈ 33). The other beam parameters must then be deduced from the dynamics in the linac, independently of the arguments based on beam-beam phenomena. The bunch length can hence be selected in order to minimize the energy spread and the ratio $N_b/\sqrt{\epsilon_y}$ has to be raised as much as possible, taking into account the emittance dilution along the linac due to wakefields, which are in turn proportional to N_b . The next section describes how this was done for CLIC.

III. BEAM DYNAMICS IN THE MAIN LINAC

Previous tracking in the main linac [6] indicated the possibility of obtaining a vertical normalized emittance $\gamma\epsilon_y$ of 2×10^{-7} rad·m at 250 GeV, in the presence of wakefields, for an intensity of $N_b = 6 \times 10^9$ and for an emittance at injection of 0.5×10^{-7} . As mentioned in Section II, the next step consisted in looking for

the maximum of $N_b/\sqrt{\epsilon_y}$ when increasing N_b . Limited investigations, based on simulations with a simple one-to-few trajectory correction [6], produced a curve (Fig. 2) with a maximum at around $N_b = 8 \times 10^9$. Figure 2 shows also the emittance $\gamma\epsilon_y$, which begins to blow up significantly beyond this bunch current. Although this kind of threshold may depend on the kind of correction applied, this new value of 8×10^9 has been adopted for the bunch population. All the trackings have been naturally done with the betatron scaling with energy that is specific to CLIC ($\beta \sim \gamma^{0.35}$), for it gives the right balance between dispersion and wakefield effects.

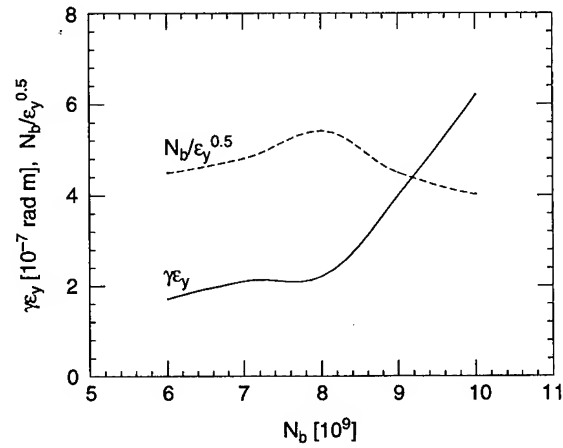


Figure 2. Variation of $N_b/\sqrt{\epsilon_y}$ with bunch population.

Once the intensity is fixed, one can turn to the determination of the bunch length σ_z . Let us recall at this point that there is no need in CLIC for a deliberate energy spread ensuring beam stability, since BNS damping is achieved with microwave quadrupoles [7]. This gives us all the necessary freedom for the selection of a positive RF phase ϕ_{RF} and of the appropriate σ_z , which ensures the best compensation of the longitudinal wakefield variation by the RF wave. In addition, the bunch can be shaped with a sharp edge in the front so as to obtain a quasi-linear increase of W_L that better matches the rise of the RF voltage. Such a shaping can be provided by momentum collimation in the first stage of the bunch compressor [8]; this momentum collimation then transforms into longitudinal cuts when the bunch is rotated by the second stage. The best cuts are determined by tracking through the linac and iterating until the charge distribution with energy, at the extraction, is perfectly symmetrical and does not exceed the acceptance of the final focus ($\sim \pm 5\%$) [9]. Figure 3 shows the distribution obtained with $\phi_{RF} = 12^\circ$ and $\sigma_z = 0.2$ mm. It corresponds to a ‘peak-to-peak’ energy separation of $\sim 6\%$ and to an r.m.s. energy spread of $\sim 2.3\%$. Such a minimization of the energy spread in the linac is a required condition for specific physics experiments.

The next critical parameters are of course the absolute values of the emittances, which depend directly on the control of the wakefields, on the misalignments of the linac components and on the quality of the trajectory correction. Because the aspect ratio must be large, the vertical emittance must be very small, and studies of the CLIC dynamics have shown that final values at 250 GeV of $\gamma\epsilon_y = 2 \times 10^{-7}$ can be considered. Such an emittance

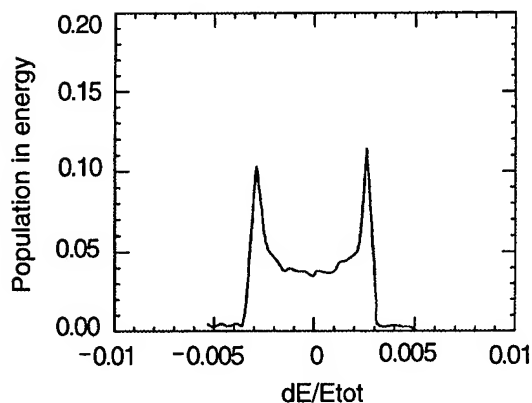


Figure 3. Relative energy distribution at the linac end.

control has been obtained while coping with r.m.s. misalignments of accelerating structures and position monitors of $10\ \mu\text{m}$ [10], using dispersion- and wake-free algorithms. Recent investigations of beam-based corrections [11] indicate that even better performance can be hoped for with the same misalignments and the higher bunch current retained. They are based on trajectory difference measurements made at full intensity and, say, at a tenth of the intensity, changing simultaneously the momentum by a few percent. With such a method and a good optimization of the microwave quadrupoles, one can achieve $\gamma\epsilon_y = 1.5 \times 10^{-7}$ at 250 GeV and $\gamma\epsilon_y = 2 \times 10^{-7}$ at 500 GeV. Then, experience tells us that such a minimization of $\gamma\epsilon_y$ is easier when $\gamma\epsilon_x$ is about 20 times larger (at the end of the linac). This explains the proposed values of $\gamma\epsilon_x = 3 \times 10^{-6}$ at 250 GeV and 3.9×10^{-6} at 500 GeV, which can be reached easily if $\gamma\epsilon_x = 2.5 \times 10^{-6}$ at injection (9 GeV). Now, given the required aspect ratio of 33 at the interaction point (Section II), the β^* ratio has to be equal to ~ 55 . In addition, the hourglass effect is minimum when β_y^* is about 90% of σ_z . These last two conditions dictate the β^* -values, that is $\beta_y^* = 0.18\ \text{mm}$ and $\beta_x^* = 10\ \text{mm}$.

IV. NEWLY PROPOSED PARAMETERS

The updating of the beam dynamics in the CLIC linac, described in Sections II and III, reconcile the requirements for emittance preservation on the one side and for acceptable conditions in the physics experiments on the other side. Table 1 summarizes the parameter values corresponding to the new conditions obtained by the formulae quoted in II. One can emphasize the low values that are now achieved for the horizontal disruption, Υ , n_γ and δ_B . All these values have been cross-checked by programs simulating the collisions [4, 5] and found to agree to within approximately 20%. As an indication, single-bunch luminosities are also given for repetition rates dictated by power consumption considerations [12]. It is interesting to know that CLIC can deliver with one bunch only an already valuable luminosity of 1 or $2 \times 10^{33}\ \text{cm}^{-2}\ \text{s}^{-1}$ for the energies retained. However, it relies on multibunch mode for improving the performance; using 10 bunches with lower repetition rates in order to keep the power constant increases the luminosity by a factor of 5, approximately. The beam dynamics of a train of bunches has still to be studied in detail before final conclusions can be drawn.

Table 1
Newly proposed CLIC parameters

Final energy (GeV) per linac	250	500
Bunch population	8×10^9	
Bunch length (mm)	0.2	
Final normalized emittances ($10^{-7}\ \text{rad}\cdot\text{m}$)	30×1.5	39×2
Final Focus β^* -values (mm)	10×0.18	
Nominal FF beam sizes (nm)	247×7.4	200×6
Pinched FF beam sizes (nm)	232×5.6	194×4.75
Hourglass factor	0.94	
Disruption parameters	0.29×9.7	0.22×7.4
Parameter Υ	0.075	0.179
Number of photons n_γ	1.35	1.53
Energy loss δ_B (%)	3.5	7.5
Luminosity with pinch ($10^{33}\ \text{cm}^{-2}\ \text{s}^{-1}$)	1.0	2.2
Repetition rate (kHz)	2.53	4.0
Luminosity in $> 98\%$ c.m. (%)	63	68

V. ACKNOWLEDGEMENTS

The author is very grateful to P. Chen and V. Telnov, who introduced him the physics of beam-beam phenomena.

VI. REFERENCES

- [1] G. Loew, B. Wiik, Proc. LC93, SLAC-436, 1993.
- [2] K. Yokoya, P. Chen, Lect. Notes in Physics 400, 1990.
- [3] P. Chen, Proc. PAC93, Washington, 1993.
- [4] K. Yokoya, KEK Report 85-9, 1985.
- [5] V. Telnov, private communication.
- [6] G. Guignard, Proc. PAC93, Washington, 1993.
- [7] W. Schnell, I. Wilson, PAC91, San Francisco, 1991.
- [8] G. Guignard, T. d'Amico, Proc. EPAC 94, 1994.
- [9] O. Napoly, CLIC Note 227, CERN, 1994.
- [10] C. Fischer, Proc. EPAC 94, London, 1994.
- [11] C. Fischer, this conference.
- [12] H. Braun et al., this conference.

IMPROVED CLIC PERFORMANCES USING THE BEAM RESPONSE FOR CORRECTING ALIGNMENT ERRORS

C. Fischer, CERN, 1211 Geneva 23, Switzerland

It has been demonstrated that in the Compact Linear Collider (CLIC) alignment errors of the order of 10 microns r.m.s. can be tolerated on the main linac components, in particular on pick-ups. These results imply the application of trajectory-correction processes involving several correctors and beam-position monitors, of the 'dispersion-free' or 'wake-free' types. The disturbing effects to be corrected have so far been simulated by gradient variation of the lattice quadrupole chains. Recently, the idea of a direct evaluation of these effects was suggested. In particular, one can measure the response of the trajectory when the beam intensity is modulated. By incorporating into the above-mentioned algorithms the measured trajectory differences in order to minimize them, better performances are achieved than when these undesirable effects are simulated. The results presented show a gain of a factor of two on the vertical emittance blow-up.

I. INTRODUCTION

The transverse emittance control is an important issue for future linear colliders. Alignment errors affect the position of lattice quadrupoles and of R.F. cavities. Dispersive effects as well as transverse wakefields are then generated, leading to emittance dilution. The relative importance of these effects is related to each collider design. It is possible to use processes involving the minimization of expressions related to the basic trajectory, measured at nominal momentum, as well as expressions related to trajectories taken for different detuned machine conditions. The efficiency of the method is directly related to the assumptions made on pick-up alignment and resolution errors. These processes can be of the dispersion-free (DF) or wake-free (WF) types as initially suggested at SLAC [1]. In the first, the focusing and defocusing quadrupole chains are detuned by the same relative amount, whereas in the second case their setting is modified in opposite directions. The application of these methods to the Compact Linear Collider (CLIC) main linac is discussed in Ref. [2]. One interesting aspect is that quantities involving trajectory differences are invoked in addition to the basic trajectory. The importance of pick-up alignment errors, supposed to be static during the process, is then diminished and it is possible to rely more on pick-up resolution errors, which will remain confined in the sub-micron range. The last results obtained for CLIC are described in Ref. [3]: assuming alignment errors of 10 μm (r.m.s.) on quadrupoles, cavities, and pick-ups, vertical emittance values of around 20×10^{-8} rad-m can be obtained at the end of the linac (3200 m for a final energy of 250 GeV per beam).

Recently, the idea of a direct evaluation of the wakefields has emerged, instead of their simulation by quadrupole detuning. One way is to measure the beam trajectory at various currents and to minimize differences. This concept was used to perform simulations in the case of the NLC, with promising results [4]. It has also been tried for CLIC.

II. WAKEFIELD CORRECTION WITH MEASURED WAKEFIELDS (MW)

With respect to NLC the transverse wakefield strength is stronger by a factor of 18 (it scales as f_{RF}^3) in CLIC. In the case of the NLC the bunch current is increased for a proper evaluation of the wakefield effects [4]. In CLIC the wakefields dominate all the beam dynamics effects at the nominal bunch charge value ($N_p = 6$ to 8×10^9 particles). Therefore, the problem is rather to find conditions where the influence of the wakefields is small enough and which can be used to determine a trajectory followed by a beam not affected by wakefields. Simulations show that this condition is reached when the bunch population is reduced by one order of magnitude from its nominal value (Fig. 1): the trajectory taken at nominal current with wakefields switched off is similar to the trajectory measured with a bunch charge ten times smaller in the presence of wakefields.

The application of a wakefield correction with measured wakefields (MW) not only requires the measurement of differences Δx_j between trajectories taken for different charges N_p and $N_p/10$, but also their prediction ΔX_j [2]. The determination of ΔX_j requires the knowledge of all the transfer matrix coefficients $R_{12}(i, j)$ from a kick θ_i to each pick-up j with $j > i$ (located downstream). This is needed for the nominal machine and for $N_p/10$ (description of the linac without wakefield). However, in order to avoid having to evaluate these coefficients twice, the linac description used in the absence of wakefield is simply the basic optics model. The implementation of the method is then simpler, but this is an approximation compared to the actual case, as some effects, for example energy dispersion within the bunch, are neglected. Then, in our case:

$$\Delta X_j = X_j(\text{nominal}) - X_j(\text{model})$$

with

$$\begin{aligned} X_j(\text{nominal}) &= \sum_{i < j} R_{12}(i, j, \text{nominal}) \theta_i \\ X_j(\text{model}) &= \sum_{i < j} R_{12}(i, j, \text{optics model}) \theta_i \end{aligned}$$

For a kick, supposed to be located at lattice quadrupoles, the 50 subsequent pick-ups are considered (one pick-up being installed every two girders).

The results of this MW process application after 800 m (80 cells) are represented in Fig. 2: alignment errors: 10 μm (r.m.s.) on quadrupoles, pick-ups and cavities.

Starting from a pre-aligned machine (Fig. 2a) the emittance evolution is shown (Fig. 2b) after the application of 19 iterations on 18 quadrupoles (nine cells) each, with an overlap of nine half-cells between consecutive iterations. The process converges straight off (no second pass is needed) and is the most efficient when the maximum number of cells is considered per iteration

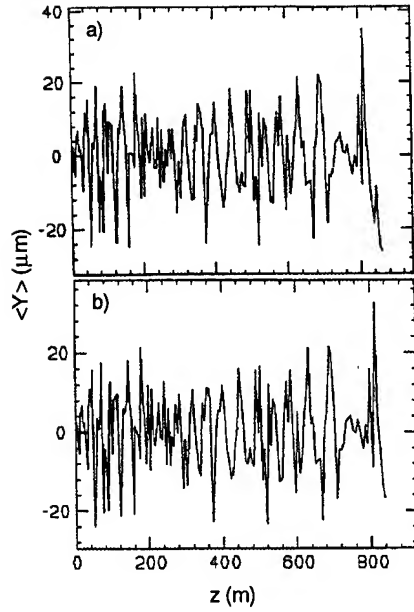


Figure 1. Measured trajectory on the first 800 m: a) $N_p = 6 \times 10^9$, wakefields OFF, b) $N_p = 6 \times 10^8$, wakefields ON.

(the 50 pick-ups considered for a kick are distributed over nine cells). The efficiency is best when weighing 10 to 100 times more the term describing wakefield effects compared to the trajectory term.

However, correction of the dispersion on this wakefield-corrected linac, disturbs the results (Fig. 2c). A solution is to consider simultaneously a term describing the effects of wakefields and a term related to dispersive effects.

III. DISPERSIVE WAKEFIELD ALGORITHM (DW)

In order to at the same time minimize wakefields and dispersion, with the first term related to the trajectory, taken for nominal current N_p and nominal momentum p_0 , two other terms should come in the algorithm: one related to wakefield effects, dealing with trajectory differences at nominal energy between bunch charges N_p and $N_p/10$,

$$\begin{aligned} \Delta x_j &= x_j(N_p, p_0) - x_j(N_p/10, p_0) \\ \Delta X_j &= X_j(N_p, p_0) - X_j(\text{optics model}) \end{aligned} \quad (1)$$

and one extra to correct dispersion, describing the differences between a particle having nominal momentum p_0 and another particle with an energy excursion $\pm\delta = \pm\Delta p/p_0$,

$$\begin{aligned} \Delta x_j^{\pm\delta} &= x_j(N_p/10, p_0 \pm \delta p_0) - x_j(N_p/10, p_0) \\ \Delta X_j^{\pm\delta} &= X_j(N_p/10, p_0 \pm \delta p_0) - X_j(\text{optics model}) \end{aligned} \quad (2)$$

Each term can be properly weighed with respect to the others. The determination of the quantities X_j coming into the third term requires a further description of the linac ($R_{12}(i, j)$ coefficients) for the energy deviations $\pm\delta$. Again, this was taken from the model at the relevant energies. Using this algorithm gives good results (Fig. 3a): the improvement with respect to Fig. 2b can be

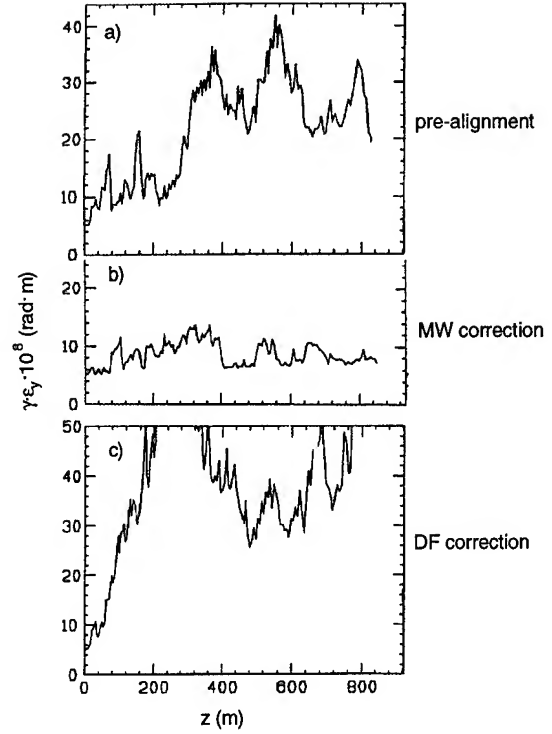


Figure 2. Vertical normalized emittance over 800 m.

appreciated. The terms related to wakefields and dispersion are weighed 100 times more than the term dealing with the trajectory.

The second and third terms can then be combined into a single term which will at once take care of wakefields and dispersion and can be referred to as a Dispersive Wakefield (DW) term. Here, the trajectories with energy excursion $+\delta$ and $-\delta$ and without wakefield, are compared to the nominal trajectory:

$$\begin{aligned} \Delta x_j^{\pm\delta} &= x_j(N_p/10, p_0 \pm \delta p_0) - x_j(N_p, p_0) \\ \Delta X_j^{\pm\delta} &= X_j(N_p/10, p_0 \pm \delta p_0) - X_j(N_p, p_0) \end{aligned} \quad (3)$$

This scheme is more efficient as the number of trajectories to be measured and calculated is decreased.

IV. RESULTS

The application of a DW correction on the same machine gives the results represented in Fig. 3b. Again, a relative weight of 100 is given to the term describing wakefields and dispersion. The efficiency is as good as when the two terms are distinct (Fig. 3b compared to Fig. 3a). Applying this strategy up to the end leads to the results presented in Fig. 3c: an emittance value $\gamma\epsilon_y = 10 \times 10^{-8}$ rad·m is obtained after 51 iterations from the pre-aligned machine. This represents an improvement by a factor of two compared to the results cited in Ref. [3].

The scheme was tested on another machine with the same longitudinal parameters (RF phase 7° , bunch length 0.17 mm, bunch charge 6×10^9 considered between $\pm 3\sigma_z$) but with completely different alignment-error distribution (still of $10 \mu\text{m}$ r.m.s.). Results are presented in Fig. 4 after 2000 m and 43 iterations ($\gamma\epsilon_y = 9 \times 10^{-8}$ rad·m is obtained — Fig. 4a) and at the end of the linac after 90 iterations (Fig. 4b). It was necessary to add a few iterations between 2000 m and 3000 m, placing

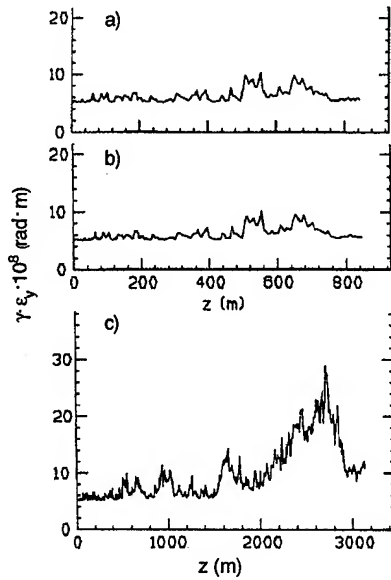


Figure 3. Vertical normalized emittance evolution: a) MW+DF process; b) and c) DW process.

more emphasis on a wakefield term without dispersive component (MW correction), and also on the trajectory term. A value $\gamma\epsilon_y = 10 \times 10^{-8}$ rad·m is observed at the end of the linac.

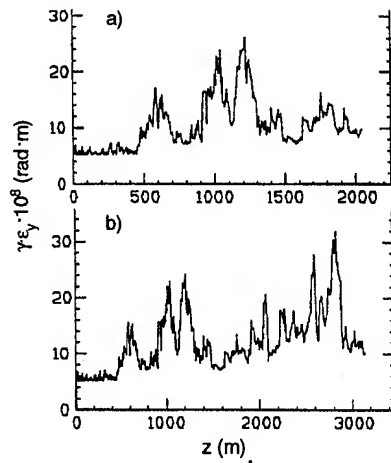


Figure 4. Vertical normalized emittance: a) DW process after 2000 m; b) at the end of the linac.

A third machine was considered (Fig. 5) with the latest longitudinal parameters proposed for CLIC [5]: RF phase 12° , bunch length 0.2 mm, bunch charge 8×10^9 considered between $\sim +1\sigma_z$ and $\sim -2\sigma_z$ (this machine has an energy spread reduced by a factor of two). As in the previous case, the DW process was efficient in the first half of the linac but the correction process had to be resumed from 1500 m with a MW algorithm, and the basic trajectory term stressed near the end. This strategy kept the emittance below 20×10^{-8} rad·m along the linac and led to a final value $\gamma\epsilon_y = 10 \times 10^{-8}$ rad·m after 95 iterations.

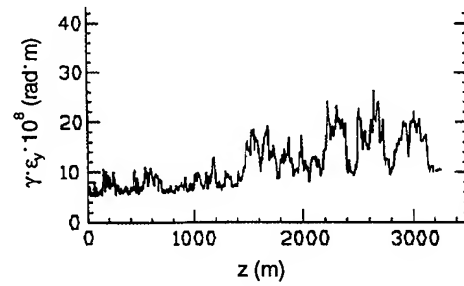


Figure 5. Emittance growth on the third (nominal) machine.

V. DISCUSSION AND CONCLUSION

A method based on the measurement of wakefield effects by modulating the bunch charge has been tried in CLIC and appears more efficient than when these effects are simulated by quadrupole detuning. This is particularly true in the first half of the linac, where, using the largest number of kicks and pick-ups in a given iteration (only limited by the model description), the process converges straight off, hence limiting the number of iterations needed. Wakefields and dispersive effects can then be combined into a single term in the algorithm; the process is thus easier to implement, the number of machine conditions to be described being reduced. The implementation of such a scheme, in particular the way of regularly modulating the bunch charge during its application, remains to be studied.

At higher energies, this DW algorithm appeared less powerful, and adding a simpler MW algorithm or merely a trajectory correction was sometimes beneficial. A possible reason could come from the model used to describe the machine without wakefields. Another possibility is the artificial splitting of the linac into sectors in the model, without their overlapping. The final vertical emittance value is improved by a factor of two, with a process relying on the beam response, keeping alignment tolerance at $10 \mu\text{m}$ (r.m.s.).

VI. REFERENCES

- [1] T. Raubenheimer, R. Ruth, EPAC, Nice, June 1990.
- [2] C. Fischer, Proc. PAC, Washington DC, 1993.
- [3] C. Fischer, Proc. EPAC, London, 1994.
- [4] K. Kubo, T. Raubenheimer, LINAC 1994, Tsukuba.
- [5] G. Guignard, these proceedings.

EXPERIMENTAL STUDIES OF A CERN-CLIC 32.98 GHZ HIGH GRADIENT ACCELERATING STRUCTURE DRIVEN BY THE MIT FREE ELECTRON LASER AMPLIFIER*

P. Volfbeyn, I. Mastovsky, G. Bekefi, MIT

I. Wilson, W. Wuensch, CERN-CLIC

Experimental studies on a CERN-CLIC 32.98 GHz 26-cell High Gradient Accelerating (HGA) section were carried out with input powers from 0.1 MW to 50 MW. MIT's Free Electron Laser (FEL) amplifier driven by a mildly relativistic electron beam (750 kV, 300 A, 30 ns) served as the RF power source for the structure. The maximum power in the transmitted pulse was measured to be 15 MW for an input pulse of ~35 MW. The theoretically calculated shunt impedance of 116 M Ω /m predicts a field gradient of 65 MeV/m inside the HGA. For power levels >3 MW the pulse transmitted through the HGA was observed to be shorter than the input pulse and pulse shortening became more serious with increasing power input. At the highest power levels the output pulse length (about 5 nsec) was about one quarter of the input pulse length. Various tests suggest that these undesirable effects occur in the input coupler to the HGA. Light and X-ray production inside the HGA have been observed. A feasibility study suggests that conditioning is a likely candidate for improving the performance of the HGA.

I. INTRODUCTION

The two-beam accelerator [1] is a promising candidate for achieving the ultra-high electron energies (of the order of or higher than 1 TeV) required in the next generation linear colliders. The HGA is a prototype of a section of the accelerating line of a two-beam accelerator.

For driving the HGA we used the MIT FEL [2,3] It produces 60 MW r.f. power, 18 ns long pulses. A high power magnetron is the input power source for the FEL amplifier. It essentially determines the tunability of the FEL. The operating frequency range of the magnetron is from 30 to 35 GHz. The frequency of the magnetron pulse is stable to within at least 5 MHz. However the frequency shift induced by the FEL interaction could be of some concern. In the FEL used in the tests the frequency shift is measured to be 16 MHz with 5 MHz scatter in the Reversed Field regime [3]. The bandwidth of the HGA is greater than 500 MHz. Thus the MIT's FEL is acceptable for the purposes of the experiments described in this paper. For actual acceleration however, where the phase stability is of much greater importance, a phase stability better by one order of magnitude (less than 1 MHz) would be needed.

The 32.98 GHz disc-loaded constant gradient traveling-wave accelerating structure was built as prototype of an element in the accelerating line of the two-beam

CERN-CLIC accelerator [4,5]. It is a $2\pi/3$ mode, $v_p = c$, constant gradient iris disc-loaded waveguide structure. It consists of 26 cells, each of 3.029 mm in length and 2 coupler cells 3.56 mm long. The total length of the structure is 0.08587 m. The fill time of the structure is 3.42 ns, with a group velocity of 0.083c. The two side-couplers are at right angles to the axis of the structure. They couple the power from a standard WR-28 rectangular waveguide into the desired mode of the structure. The high vacuum of around 10^{-7} Torr is maintained by two 30 liters/sec ion-pumps and two smaller auxiliary ion pumps with pumping speed of 2 liters/sec. The structure was designed to have shunt impedance of 116 M Ω /m. This means that for input power level of 60 MW the maximum accelerating gradients approximately 110 MV/m. The CERN-CLIC structure was designed for accelerating gradients of approximately 80 MV/m.

II. EXPERIMENTAL RESULTS

A. High Power Testing

With use of crystal detectors and variable attenuators attached to the ports of the high vacuum directional couplers it was possible to sample the time profile of a radiation pulse input into the HGA, transmitted through the HGA, and reflected back by the HGA. A scan in the input power level ranging from 0.1 MW to about 35 MW was taken.

At low powers the transmitted pulse resembled the input pulse in shape and the percentage difference in power magnitudes was equal to the 'cold' attenuation as measured with a network analyzer (with very small ~1 mW power levels). As the power levels increased (~3 MW) the transmitted power pulse became shorter than the input power pulse in time duration. The early part of the transmitted power pulse still resembled the input pulse, while the transmitted power was attenuated stronger and stronger the closer it approached the end of the pulse. The transmitted power 'rolled off' at the end of the pulse. At power levels from 20 MW and higher the transmitted power pulse shape became effectively independent of the input pulse shape. The transmitted pulse peak power value was no longer proportional to that of the input pulse. With the increase of the input power, the transmitted power pulse saturated at a level of ~14 MW. The reflected power rose to a maximum of about 6 MW. The plot of the FWHM of the transmitted pulse vs. the average power in the input pulse is

* Work supported by the U.S. Department of Energy,
Division of Nuclear and High Energy Physics

shown in Figure 1. The fraction of the power in the reflected pulse would be expected to grow as the input power level increased, because the amount of the input power transmitted through the HGA was seen to decrease with increasing input power levels. It turned out to be only partly true. Power levels of the reflected pulse agreed with the cold test results when the input power level was small. The reflected power did grow to become comparable to the input power at high input power levels. But this growth did not fully account for the difference in energy between the input and transmitted pulses. A representation of our data is in terms of the energy in the pulse obtained by integrating the measured power over the respective pulse widths. In Figure 1 we present the dependence of the transmitted and the reflected energies on the average power in the input pulse. Note that at high input energies (corresponding to power levels of 20 MW) the transmitted and reflected energies together account for only a half of the input energy. This leads to the conclusion that a substantial fraction of the radiation energy is dissipated inside the HGA.

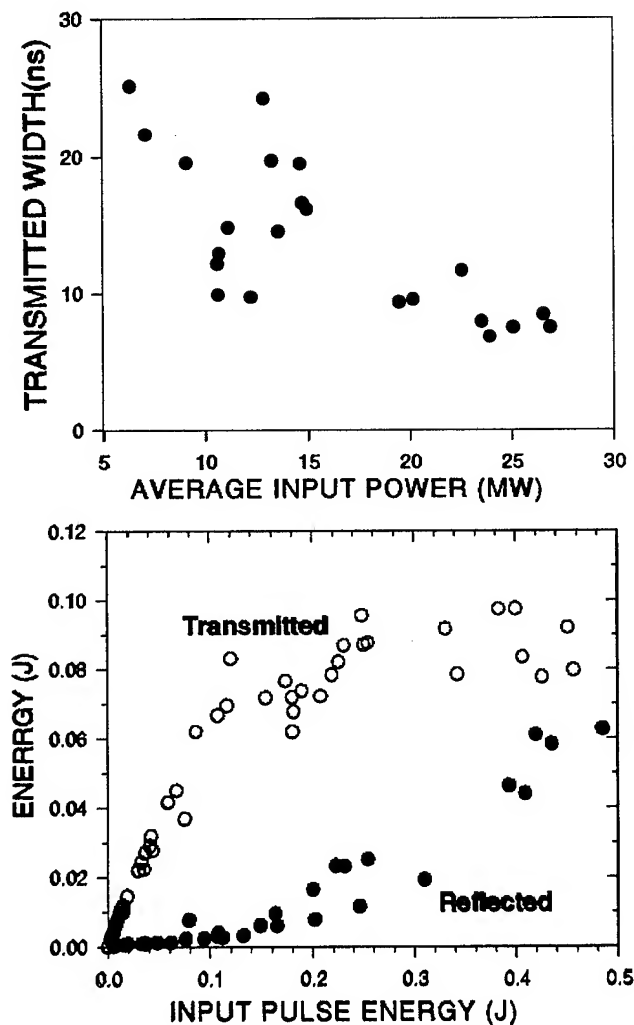


Figure 1: FWHM of the transmitted pulse vs. average input power, upper graph. Transmitted vs. input energy, lower.

B. X- RAY and Visible Light Measurements

Both light and X-ray induced photomultiplier signals were recorded for a range of r.f. input powers (0.1 MW to 30 MW) from the FEL. In Figure 2 we show plots of the maximum photomultiplier voltage from light and X-ray vs. average r.f. input power. Both light and X-ray generation starts around 1 MW of input power and continues to rise exponentially with input power thereafter. To demonstrate this exponential growth we present the photomultiplier voltage plots on a logarithmic scale. The observed growth of both X-ray and visible light intensities begin around 1 MW of input power which correlates well with the energy plots of Figure 1.

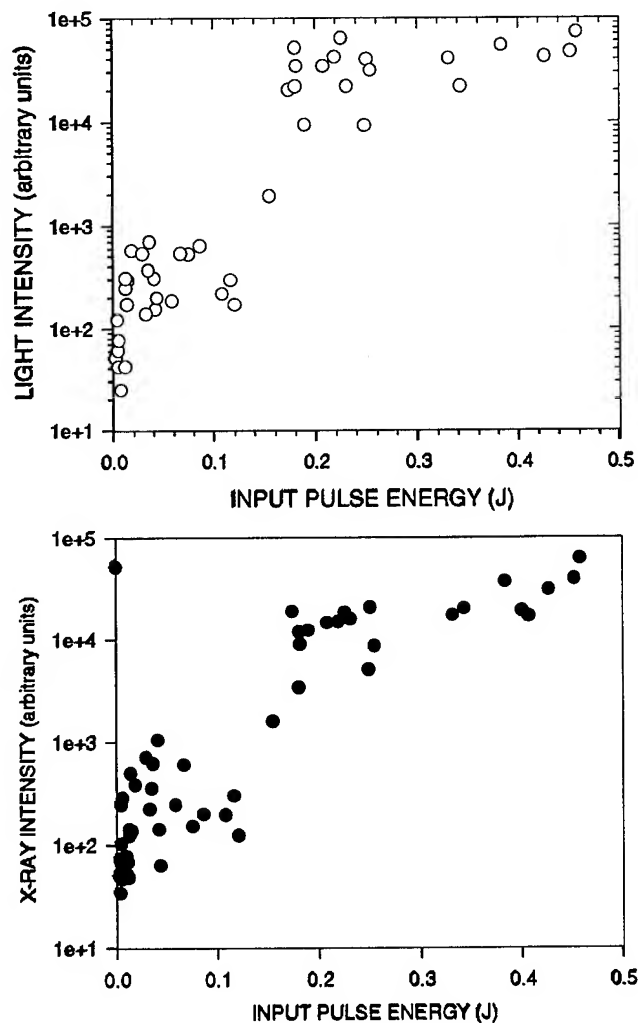


Figure 2: Light and X-ray induced photomultiplier signal vs. input energy, "log" scale.

C. Operating at Different Frequency

To show that there is an undesirable process in the input side coupler to the HGA we detune the FEL off the 0.5 GHz wide transmission band of the HGA to a new frequency $f = 33.682$ GHz. The 33.682 GHz radiation couples to an evanescent mode in the structure. The major portion of the pulse is reflected, with only about 10% of the incident energy is transmitted through the structure at this frequency. Thus the electric field gradients inside the

structure itself are now much smaller than those in the input coupler. If the coupler causes the pulse shortening, the pulse shortening should be seen at the detuned frequency. Indeed, strong pulse-shortening was observed in reflected pulses. For high input energies ~ 0.6 J the reflected energy constitutes only 20% of the input and the transmitted energy accounts for maybe another 2%. A large fraction of the input energy is thus dissipated. The last two subsections have shown that there are strong indications that it is mainly in the input coupler that the pulse shortening takes place.

D. Conditioning, Feasibility Test

In this section we examine if the performance of the HGA improves with the number of shots, so that future conditioning could perhaps eliminate the pulse shortening. The estimated number of shots required for conditioning varies from a hundred thousand to several millions [6]. It did not seem possible to fully condition the HGA using the existing FEL (for it produces only one shot every two-three minutes and is manually operated). It is noted, however, that the rate of improvement was much greater during the first 5,000-10,000 shots. This motivated the following test of the feasibility of conditioning in our HGA.

A power scan was made of the output and input pulses with the input power level ranging from 0.1 to 30 MW. An attempt to condition the structure was made with some 800 shots at power levels gradually increasing from 3-5 MW to around 20 MW were taken. The power scan was then repeated. Figure 3 shows plots of output vs. input energy before and after the conditioning.

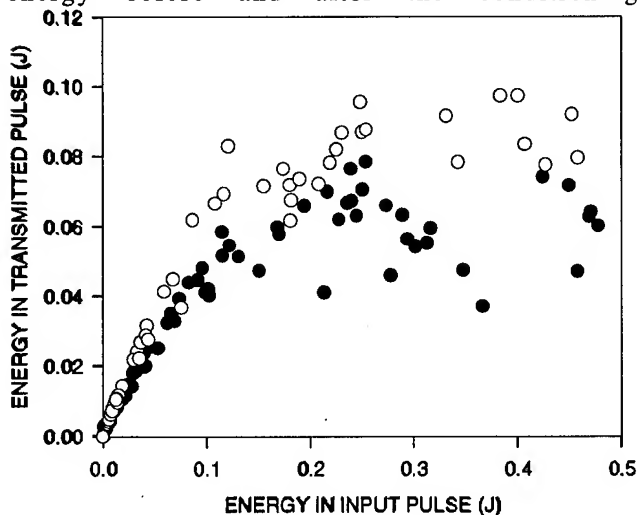


Figure 1: Transmitted vs. input energy. Black dots correspond to the data taken before 800 conditioning shots, hollow dots are after the attempt to condition..

The filled circles represent the data taken before conditioning, the hollow - after. One observes a definite improvement in transmission. There is evidence in favor of possibility of conditioning, provided a high enough power and repetition rate source at 33 GHz is available.

III. CONCLUSIONS

The high power testing of a 33 GHz HGA yielded the maximum accelerating gradient of 65 MeV/m. A pulse-shortening phenomenon was observed for power levels > 3 MW. At the highest power level the output pulse length (about 5 ns) was about one quarter of the input pulse length. Various tests suggest that these undesirable effects occur in the input coupler to the HGA. Light and X-ray production inside the HGA have been observed.

A study of feasibility of conditioning (limited by the low repetition rate of our FEL) suggest that conditioning is a likely candidate for improvement of the HGA power handling performance.

IV. REFERENCES

- [1] D.B. Hopkins, A.M. Sessler, and J.S. Wurtele. The Two-Beam Accelerator. Nucl. Inst. and Meth. in Phys. Res. 228, pp. 15-19, 1984.
- [2] M.E. Conde and G. Bekefi. Experimental Study of a 33 GHz FEL with a Reversed Axial Guide Magnetic Field. Phys. Rev. Lett., 67:3082, 1991.
- [3] P. Volfbeyn, K. Ricci, B. Chen, G. Bekefi. Measurements of the Temporal and Spatial Phase Variations of a Pulsed Free Electron Laser Amplifier. IEEE Trans. on Plasma Science v. 22, no. 5, pp. 659-665, Oct 1994.
- [4] Y. Baconnier et. al. The CERN Linear Collider Test Facility. Presented at the 1992 Linear Accelerator Conf. (Ottawa), CERN PS 92-49[LP].
- [5] R. Bossart et. al. Performances Obtained with the CERN Linear Collider Test Facility. EPAC 94, Proc. v. 1, page 680, 1994.
- [6] D.B. Hopkins and G.T. Conrad. Plans for Testing the 33.3 GHz High Gradient Accelerator. CP-49 Sept. 27, 1989.

DESIGN OF A RELATIVISTIC KLYSTRON TWO-BEAM ACCELERATOR PROTOTYPE*

G. Westenskow, G. Caporaso, Y. Chen, and T. Houck, Lawrence Livermore National Laboratory, Livermore, CA 94550, S. Yu, S. Chattopadhyay, E. Henestroza, H. Li, C. Peters, L. Reginato, and A. Sessler, Lawrence Berkeley Laboratory, Berkeley, CA 94720 USA

We are designing an experiment to study physics, engineering, and costing issues of an extended Relativistic Klystron Two-Beam Accelerator (RK-TBA). The experiment is a prototype for an RK-TBA based microwave power source suitable for driving a 1 TeV linear collider. Major components of the experiment include a 2.5-MV, 1.5-kA electron source, a 11.4-GHz modulator, a bunch compressor, and a 8-m extraction section. The extraction section will be comprised of 4 traveling-wave output structures, each generating about 360 MW of rf power. Induction cells will be used in the extraction section to maintain the average beam energy at 5 MeV. Status of the design is presented.

I. BACKGROUND

Relativistic klystron two-beam accelerator [1] research has reached a point where we are ready to construct and test components that have been specifically designed for linear collider applications. Our planned program will take advantage of recent technical advances in three related areas: the experimental program in relativistic klystrons at LLNL [2], a preliminary design report (PDR) by a joint LBL-LLNL team on the RK-TBA concept as a power source candidate for a large linear collider, and the development of related technologies in heavy ion fusion (HIF).

First, the experimental program at LLNL has provided a firm physics base for the key RK-TBA feasibility issues of rf extraction, reacceleration of a modulated beam, and suppression of transverse instabilities. Power conversion from electron beams to rf at 11.4 GHz has been demonstrated at the hundreds of megawatts level, and the phase and amplitude shown to be stable over a substantial portion of the beam pulse. The relationship between rf stability and energy flatness of the drive beam is well understood. Reacceleration experiments at ATA have successfully demonstrated the transport of a bunched beam through three rf extraction structures and two intervening induction cells. The critical issue of transverse instability was addressed experimentally, higher order mode damping

techniques were demonstrated, and detailed comparisons with simulations were made. Overall, these experiments demonstrate the feasibility of the TBA concept, and add confidence to the predictive power of the computer codes.

Secondly, the RK-TBA PDR [3] investigated an rf power source for the NLC linear collider. This design would provide the rf power requirements for a 1-TeV collider using the NLC accelerating structures. A bottom-up cost estimate shows that providing the rf power for the 1-TeV NLC with technology based on this design could be cost competitive with conventional klystrons using pulse compression. Our estimate of the conversion efficiency of wall plug energy to rf energy is 40%. Theory and simulations show acceptable drive beam stability over the relativistic klystron, and no insurmountable technological issues were uncovered.

Thirdly, the new RK-TBA design borrows heavily from ongoing HIF technology development [4]. Recent advances in that field have direct impact on the technical feasibility of our design. Metglas™ cores, permanent magnet quadrupoles, and low-voltage pulsed power systems are important features of the induction accelerators used in both areas.

II. Proposed Layout of the Experiment

The rf power source described in the PDR consists of 50 units, each about 340 m in length. The cost of building even one unit for developmental studies is prohibitive. Instead, we propose to build a smaller (29 m) prototype unit to validate the required physics and engineering technologies. To be compatible with the rf parameters for the NLC, we need to produce 11.4-GHz rf power that has a 200-ns flat top with good phase and amplitude stability. A schematic of the beamline for the prototype is shown in Fig. 1. The experiment will be housed in the existing shielded vault area of Building 58 at LBL.

a. Injector/Accelerator

The SNOWTRON injector, used in early relativistic klystron experiments [5], will be modified for use as the electron source. The SNOWTRON was a linear induction injector comprised of twelve 150-kV induction cells. It has a triode electrode configuration with a stalk mounted 12.5-cm diameter dispenser cathode. Modifications will include replacing the ferrite induction cores with Metglas™ cores to increase the pulse length, and a new electrode package to minimize emittance. The injector will be operated at about

*The work was performed under the auspices of the U.S. Department of Energy by Lawrence Livermore National Laboratory under contract W-7405-ENG-48 and Lawrence Berkeley Laboratory under contract AC03-76SF00098.

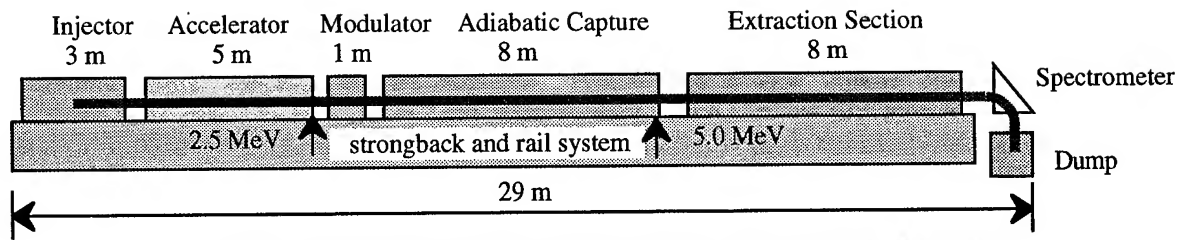


Figure 1. Schematic of the beamline for the RK-TBA Prototype experiment.

1 MV. Approximately 15 Experimental Test Accelerator (ETA) [6] induction cells will be used to accelerate the beam to 2.5 MeV prior to the modulator. The ETA cells will also have their ferrite cores replaced with Metglas™ cores.

The primary design issue remaining to be resolved is the generation of the desired current profile with suitable energy flatness. The goal is to linearly increase the current from 0 to 1.5 kA over the first 100 ns and then maintain a constant 1.5 kA for another 100 ns. The energy profile of the beam exiting the injector can be corrected to a certain extent in the accelerator. However, the energy variation over the entire pulse must be less than 1% as the beam enters the modulator. Other solutions being studied include gated cathodes, ferroelectric cathodes, and photocathodes.

b. Modulator

The Choppertron modulator [7] will be refurbished close to its original design. A schematic of the modulator is shown in Fig. 2. The modulator operates by deflecting the beam in the horizontal plane with a 5.712 GHz TM_{110} cavity. This causes the B_z immersed beam to describe semi-helical trajectories along the $\lambda_g/4$ drift, and to scan in the vertical plane across an on-axis aperture of a water-cooled collimator. Emittance growth can be minimized by matching the B_z field to the energy, diameter, and emittance of the beam. The maximum transverse deflection of the beam at the aperture determines the harmonic content of the modulated beam. To lessen the impact of modulation on overall system efficiency, the 11.4 GHz component will not be optimized. The bunch length will extend over about 240° of longitudinal phase space at the exit of the modulator.

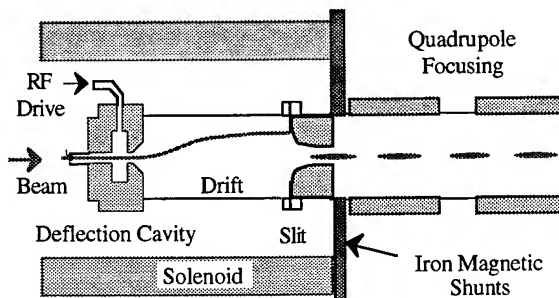


Figure 2. Schematic of the modulator.

c. Adiabatic Capture Section

The Adiabatic Capture Section will be comprised of four 2-m units similar to those in the Extraction Section. The modulated beam will be compressed in longitudinal phase space ($240^\circ \Rightarrow 107^\circ$) and accelerated to 5 MeV. Figure 3 shows simulation results of how the phase space and energy of the beam is changed in this section. Each unit will have six induction cells and one "idler" cavity. The "idler" cavity design is based on the traveling-wave output structure studied in the PDR, but without the extraction ports.

The compact, efficient induction cells described in the PDR are used in both the Adiabatic Capture and Extraction Sections. A drawing of one of these cells is shown in Fig. 4. Features of the cell that contribute to its high efficiency are the small inner diameter of the Metglas™ cores and periodic permanent quadrupole magnets. Each of the five cores in a cell will be pulsed at 20 kV producing 100 kV across the gap. This arrangement permits the use of a low-voltage, thyatron switched, pulsed power system with no high-voltage step-up transformers.

d. Extraction Section

The Extraction Section will consist of four of the 2-m units shown in Fig. 6. About 360 MW will be extracted in each unit using a traveling-wave structure like that shown in Fig. 5. The output structures used for the prototype will vary somewhat from the PDR structures to compensate for differences in rf current between the two designs. Features of the output structures include two coupling ports, relatively large aperture, and a short rf cutoff section. The energy extracted from the beam is restored by the six induction cells in the unit.

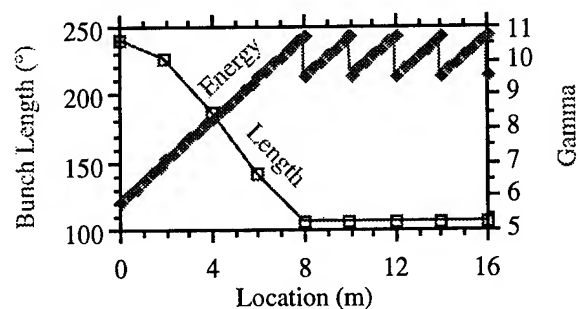


Figure 3. Simulation of Adiabatic Capture and Extraction.

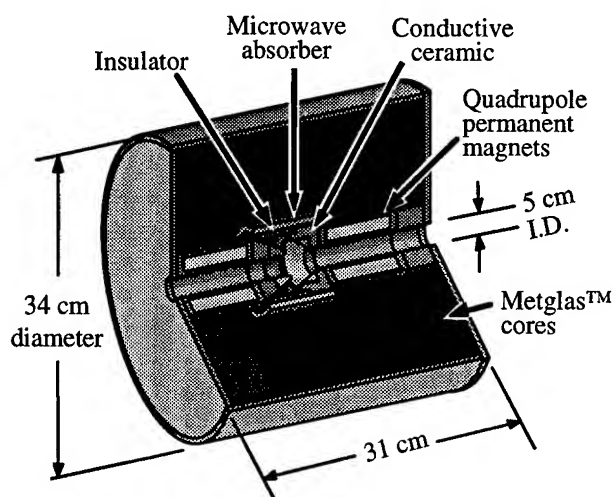


Figure 4. Drawing of the compact induction cell.

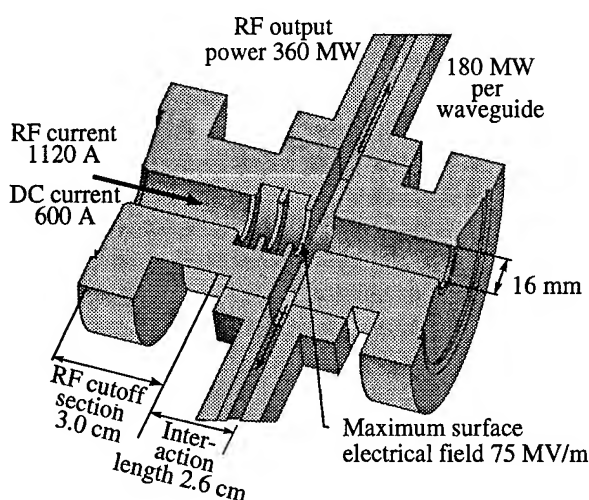


Figure 5. Drawing of traveling-wave output structure.

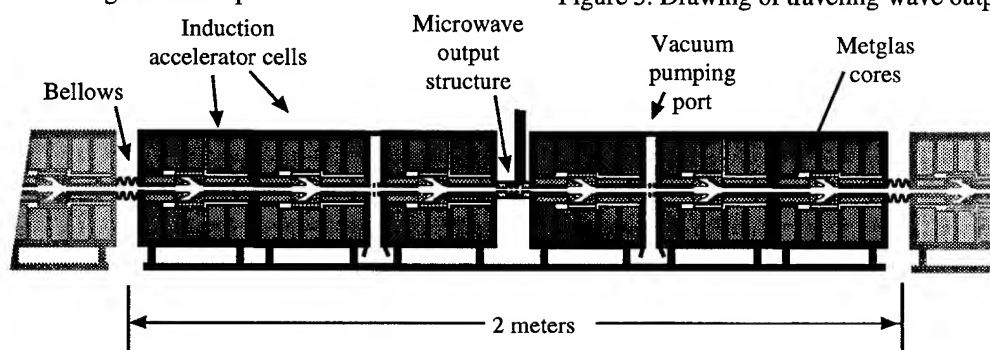


Figure 6. A 2-meter unit of the Extraction Section.

III. PROGRAM OBJECTIVES

The overall objective of the prototype is to validate the PDR findings related to cost, efficiency, and feasibility, and provide a technological base for a practical power source for large linear colliders. Specific objectives are:

1. Validate cost and efficiency projections. Our design is very modular in terms of the machine architecture and the associated pulsed power. The prototype uses several 2-m modules described in the PDR for a full-scale RK-TBA. Our experiments will allow us to verify the pulsed power system efficiency. As the prototype involves substantial R&D, we do not expect construction costs to be representative of a RK-TBA employing mass production techniques. But, we do expect to gain the engineering experience required for accurate cost projections of a full scale system.

2. Demonstrate technological feasibility. Technology of individual components is well known, and the PDR found no pathology, but an actual integrated system needs to be demonstrated. The prototype will constitute the first of these new, long, compact induction accelerators.

3. Progress towards demonstrating beam stability. Key beam dynamic processes will not be fully exhibited in the relatively short prototype. Nevertheless, impedances of the rf and induction cells, and beam response characteristics can be determined. The fundamental concepts of the

"Betatron Node Scheme" [8] for suppressing transverse instabilities and inductively detuned traveling-wave structures for longitudinal stability can be measured. We expect to gain a sufficient experimental base for code validation.

4. Production of high quality rf power at 11.4 GHz. The rf extraction structures described in the PDR are required to generate a peak power of 360 MW with good phase and amplitude stability over 200 ns. The objective of our experiment is to produce this level of quality power from each of the four rf extraction structures in the prototype. The pulse length for the prototype will be set by the performance of the modified SNOWTRON injector, but is expected to be approximately 200 ns.

IV. REFERENCES

- [1] A. Sessler and S. Yu, *Phys. Rev. Lett.* **54**, 889 (1985).
- [2] G. Westenskow and T. Houck, *IEEE Trans. on Plasma Sci.*, **22**, 750 (1994).
- [3] S. Yu, et al., "RK-TBA Based Power Source for a 1 TeV NLC," LBID-2085/UCRL-ID-119906, Feb 1995.
- [4] S. Yu, "Induction Accelerators and Injectors for Heavy Ion Fusion," this conference.
- [5] M.A. Allen, et al., *Phys. Rev. Lett.* **63**, 2472 (1989)
- [6] D. Prono, 1989 PAC IEEE Conf. 89CH2669-0, p. 1441.
- [7] J. Haimson and B. Mecklenburg, 1989 PAC IEEE Conf. 89CH2669-0, p. 243.
- [8] H. Li, et al., "Beam Dynamics Issues in an Extended Relativistic Klystron," this conference.

Beam Dynamics Issues in an Extended Relativistic Klystron*

G. Giordano[†], H. Li, N. Goffeney, E. Henestroza, A. Sessler, S. Yu, Lawrence Berkeley Laboratory, Berkeley, CA 94720, T. Houck and G. Westenskow, Lawrence Livermore National Laboratory, Livermore, CA 94550 USA

Preliminary studies of beam dynamics in a relativistic klystron were done to support a design study for a 1 TeV relativistic klystron two-beam accelerator (RK-TBA), 11.424 GHz microwave power source. This paper updates those studies. An induction accelerator beam is modulated, accelerated to 10 MeV, and injected into the RK with a rf current of about 1.2 kA. The main portion of the RK is the 300-m long extraction section comprised of 150 traveling-wave output structures and 900 induction accelerator cells. A periodic system of permanent quadrupole magnets is used for focusing. One and two dimensional numerical studies of beam modulation, injection into the main RK, transport and longitudinal equilibrium are presented. Transverse beam instability studies including Landau damping and the "Betatron Node Scheme" are presented.

I. BACKGROUND

A preliminary design report (PDR) by a joint LBL-LLNL team investigated an rf power source for the NLC linear collider. [1] This design promises to be competitive both in cost and total efficiency with systems based on conventional klystrons using pulse compression. However, it will be necessary to transport the modulated induction beam through a 300-m relativistic klystron to achieve the high efficiency. Thus, an important part of the PDR studies was simulating the motion of the beam. Two codes developed at LLNL were used for these simulations: RKS2 Code [2] is a 2-1/2 D PIC code with a coupled cavity circuit model used to simulate the interaction of the beam with the operating field, TM_{01} mode, while OMICE [3] is a slice code with a coupled cavity circuit model used to simulate the transverse dynamics of the beam interacting with a dominant dipole mode.

II. LONGITUDINAL DYNAMICS

The longitudinally dynamics that is acceptable for an extended RK can be achieved in the following way:

(1) In the main RK section the rf output cavities are inductively detuned (i.e. the phase velocity, v_{ph} , of the 3-cell traveling-wave structures (TWSs) is made faster than the

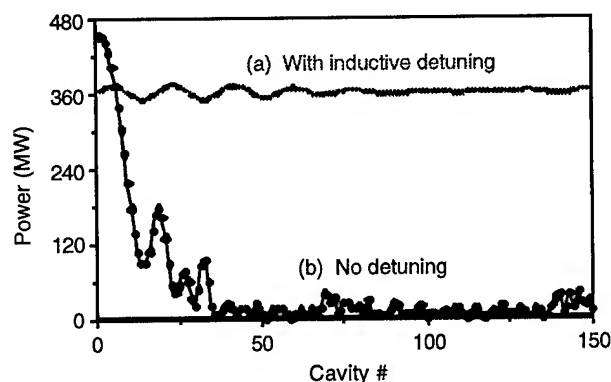


Figure 1. Power extraction from 150-cavities in an extended RK: (a) with inductive detuning ($v_{ph} = 1.33c$); (b) no detuning ($v_{ph} = 1.0c$).

velocity of the particles) to counter the debunching effects caused by space-charge and rf-induced energy spread. In this scheme the particle bunch lags behind the decelerating crest of the wave, with the particles at the bunch tail losing the least energy. Kinematics lead to a 'catching up' mechanism and subsequent synchrotron oscillation in stable rf buckets. The RKS simulations show stable propagation through 150 cavities (Figure 1). For comparison, cavities with no inductive detuning are shown to result in particle debunching after a few cavities.

(2) Before the main RK there is a chopper section and an 'adiabatic capture' section, which serve to modulate an initial DC beam into a train of tight bunches. These have the desired properties for beam transport and power extraction in the main RK. The chopper, based on the original Choppertron [4], should generate cleanly separated microbunches at 11.4 GHz with the length of the bunches equivalent to about 240° in longitudinal phase space. In the 'adiabatic capture' region, the microbunch lengths are further reduced by a number of (highly inductive) idler cavities, to 70° [1] which is the desired bunch length for the main RK. In addition to microbunch sharpening, this section also serves to provide the energy transition from 2.5 to 10 MeV [1] with the beam continuously accelerated by the induction machine between the bunching cavities.

(3) At the end of the RK is an 'afterburner' section which is to increase overall system efficiency by extracting more power out of the still bunched beam that exits the main RK (without reaccelerating it). The spacing and the impedances of the extraction cavities in this section are varied to compensate the continuous decline of the average energy of the beam as well as changes in the rf bucket.

*The work was performed under the auspices of the U.S. Department of Energy by Lawrence Berkeley Laboratory under contract AC03-76SF00098 and Lawrence Livermore National Laboratory under contract W-7405-ENG-48.

[†]Visiting scholar from the University of Milano, Italy.

III. TRANSVERSE DYNAMICS

The primary issue for transverse dynamics is beam breakup (BBU) caused by the excitation of higher order modes in beam line structures. The PDR identified two components as sources of BBU. The first is the 900 induction cells in the RK with a trapped resonant mode near 4 GHz. A highly damped, conventional cell design described in the PDR has a transverse impedance less than 4 k Ω /m. This value is acceptably low, with Landau damping from the predicted energy spread, to avoid BBU.

The output structures are a greater difficulty. The "Betatron Node Scheme," that relies on the RK's strong periodic quadrupole focusing, is used to suppress BBU. The technique is described in the following example: A monoenergetic beam describes a betatron oscillation under the influence of a periodic focusing system. Passing through a series of thin cavities, the transverse position of individual electrons is unchanged. However, the transverse momentum increases by $\Delta p_x = Rx$, where R is an integral operator. The position and momentum from the exit of one cavity to the next is related through the following matrix transformation.

$$\begin{pmatrix} x \\ p_x \end{pmatrix}_n = \begin{bmatrix} 1 & 0 \\ R & 1 \end{bmatrix} \begin{bmatrix} \cos(\theta) & \frac{1}{\omega_\beta} \sin(\theta) \\ -\omega_\beta \sin(\theta) & \cos(\theta) \end{bmatrix} \begin{pmatrix} x \\ p_x \end{pmatrix}_{n-1} \quad (1)$$

The first matrix represents the momentum change, and the second describes the betatron motion. If the phase advance, θ , is 2π between all cavities, the position and momentum at the n^{th} cavity can be related to the initial conditions:

$$\begin{pmatrix} x \\ p_x \end{pmatrix}_n = \begin{bmatrix} 1 & 0 \\ nR & 1 \end{bmatrix} \begin{pmatrix} x \\ p_x \end{pmatrix}_0 \quad (2)$$

Equation (2) indicates that the growth in the transverse momentum, and, therefore, the maximum displacement, increases linearly with the number of cavities. For θ not equal to an integral multiple of π , the growth can be exponential with the number of cavities [5]. While our design has a periodic structure, strong ppm focusing, and a

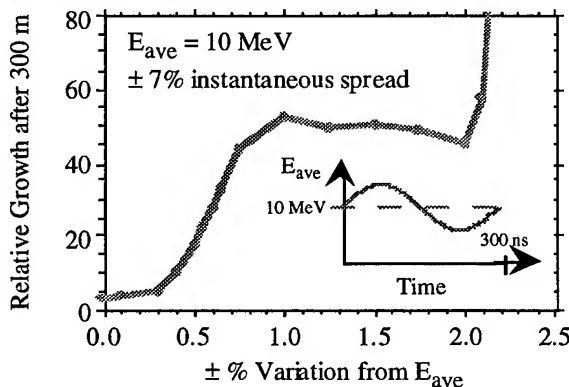


Figure 2. Simulation showing the effect of E_{ave} variation. The insert shows the E_{ave} profile over the pulse.

constant average beam energy, there will be energy spread, variation in average energy, errors in the focusing system, and extended cavities. Numerical studies were performed to determine tolerances for realistic conditions. Using reasonable design parameters [6], errors of $\pm 1.5\%$ in the magnetic focusing and/or average energy are acceptable. In Fig. 2 the result of one of these studies is shown.

IV. RADIAL DEFOCUSING

2D numerical simulations carried out with the RKS2 code have shown that when the phase velocity, v_{ph} , of the operating mode (TM_{01}) in a TWS extraction cavity is different from the speed of light (detuned cavity) the beam experiences a radial kick from the field much larger than the case when v_{ph} is equal to c (non-detuned cavity). The radial kick is significantly larger than what is predicted by the Panofsky-Wenzel (P-W) theorem [7] for a closed cavity. The radial kick, if true and uncompensated, will cause the loss of the beam as it traverses the extended RK, as shown in Figure 3. Preliminary analytical and numerical studies have been performed in order to identify and understand the source(s) of the above discrepancy. Two questions need to be answered: (1) How reliable the simulation results are; and (2) How good the resonant cavity model, which the RKS2 code is based upon is in describing the radial focusing force.

In developing the analytical model, we assumed a single dominant traveling-wave mode (TM_{01}) in a cylindrically symmetric cavity. Then, using the impedance of the mode, it can be shown that the radial force acting on an electron traveling in a cavity is $(e/2\gamma^2)E_r$ for a non-detuned cavity and $e(1-v_{ph}/c)E_r$ for a detuned cavity (where E_r is the radial electric field and γ is the relativistic factor). This indicates immediately that the radial force increases by two order of magnitude when the cavity is detuned as compared to the synchronism case (In our present RK design, $\gamma = 20.6$ and $|1-v_{ph}/c| \approx 0.3$).

The corresponding radial momentum change of the particle can be calculated in a first order approximation by integrating the force over the length of the cavity, assuming that the electron's trajectory in the cavity is not affected by the field. For the case where $v_{ph} \neq c$ the formula is given as the following

$$\Delta p_x = \left(\frac{e\xi}{c} \right) x \cdot \sin \left[\left(1 - \frac{v_{ph}}{c} \right) \frac{\phi}{2} \right] \sin \left[\left(1 - \frac{v_{ph}}{c} \right) \frac{\phi}{2} - \omega t_o \right] \quad (3)$$

where ϕ is the phase advance of the wave field per cell, ξ is the amplitude of the electric field on axis, x is the transverse position of the electron with respect to the axis and ωt_o is the phase of the electron at the entrance of the cavity with respect to the field.

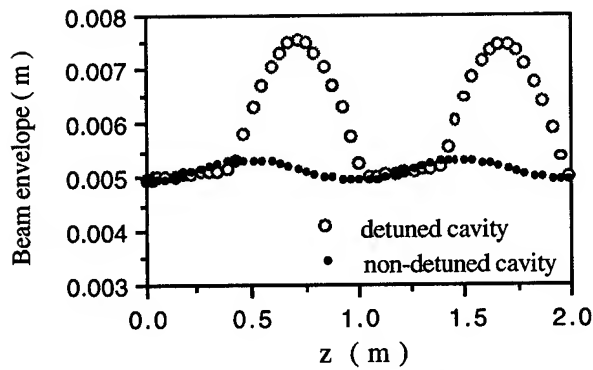


Figure 3 Beam envelopes in a 2-m reacceleration section after inductively detuned and non-detuned cavities.

From eq. (3) we can see that the increase of the radial momentum of the electron due to the wave field has the following features: i) a sinusoidal dependence on the detuning of the cavity (measured by v_{ph} and ϕ); ii) a sinusoidal dependence on the longitudinal position of the electron in the bunch ωt_0 ; iii) a linear increase with the distance of the particle from the axis.

The above observations agree with the numerical results from RKS2 to within 10% (as shown in Figure 4).

The resonant cavity model the RKS2 code based on has been used rather successfully for power balance for TM_{01} and BBU study for a dominant dipole mode. However, the validity of the model for the radial focusing force of the field has never been tested.

V. CONCLUSIONS

We have demonstrated in 1-D numerical studies the modulation and transport of the induction beam through the RK. Approximately 360 MW of rf (11.424 GHz) power was generated in each of 150 output structures. Longitudinal stability was accomplished by detuning the traveling-wave output structures to compensate for space charge effects and energy spread. Transverse stability required damping of higher order modes in resonant structures, Landau damping, and the "Betatron Node Scheme."

2-D numerical studies are required to study issues related to beam emittance, transverse space charge, and radial focusing. Initial 2-D studies show that the beam experiences a large radial momentum change during transit of the detuned output structures, which does not agree with the P-W theorem. Additional analytical and numerical studies tend to suggest that the discrepancy could be caused by the less rigorous treatment in the RKS2 code of the boundary condition that affect the transverse dynamics. So, the effect might not be as serious as the code predict. But,

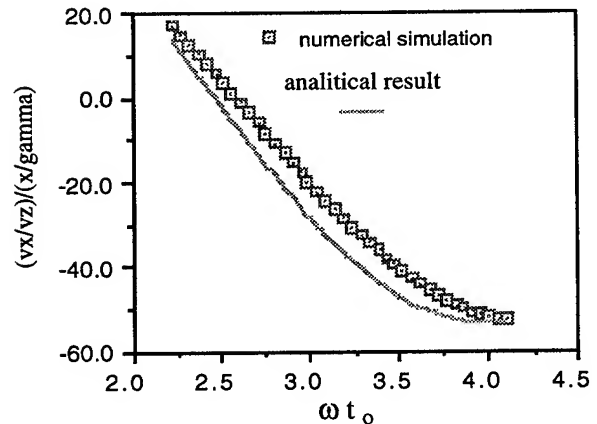


Figure 4. Normalized transverse phase space vs. phase after one inductively detuned cavity ($v_{ph} = 1.33c$), analytical and numerical results.

if it is, there are available several compensating schemes which can be explored:

- 1) Use exterior cavities that are coupled to the detuned TWSs to compensate the radial defocusing;
- 2) Use non-detuned TWSs as extraction cavities with the longitudinal bunching being provided by idler cavities positioned before and after each of the TWS.

VI. REFERENCES

- [1] S. Yu, et al., "RK-TBA Based Power Source for a 1 TeV NLC," LBID-2085/UCRL-ID-119906.(Feb 1995).
- [2] R. Ryne and S. Yu, Proceedings of 1990 LINAC, pp. 177 and 190 (1990).
- [3] T. Houck, et al., Proceedings of 1992 LINAC, p. 495 (1992).
- [4] J. Haimson and B. Mecklenburg, "Design and Construction of a Chopper Driven 11.4GHz Traveling Wave RF Generator," Proceedings of 1989 IEEE-PAC Conf., pp. 243 (1989).
- [5] V. Neil, et al., Part. Acc. 9, 213 (1979).
- [6] E. Henestroza, et al., "Design of Inductively Detuned RF Extraction Cavities for the Relativistic Klystron Two-Beam Accelerator," this conference.
- [7] W. K. H. Panofsky and W. A. Wenzel, Rev. Sci. Instr., 967 (1956).

ENGINEERING CONCEPTUAL DESIGN OF THE RELATIVISTIC KLYSTRON TWO-BEAM ACCELERATOR BASED POWER SOURCE FOR 1-TEV NEXT LINEAR COLLIDER

L. Reginato, C. Peters, D. Vanecek, S. Yu, Lawrence Berkeley Laboratory, Berkeley, CA 94720
F. Deadrick, Lawrence Livermore National Laboratory, Livermore, CA 94550

ABSTRACT

Ultra-high gradient radio frequency linacs require efficient and reliable power sources. The induction linac has proven to be a reliable source of low energy, high current and high brightness electron beams. The low energy beam is bunched, transported through resonant transfer cavities in which it radiates microwave energy that is coupled to an adjacent high energy accelerator. The low energy beam is maintained at a constant energy by periodic induction accelerator cells. This paper describes the engineering aspects of the induction accelerator based relativistic klystron. The physics issues are covered in another paper at this conference.*

INTRODUCTION

During the past decade, several rf power sources using relativistic Klystrons have been tested for driving high gradient accelerators. In order for these power sources to be competitive with the conventional Klystrons, they must be capable of producing equivalent peak power levels, reliably, economically and efficiently. At first glance, it would seem that building low gradient, high current accelerator in order to drive another would be a more complex and costly proposition. Experiments in generating a relativistic electron beams and extracting the energy by passing it through cavities have shown that very high peak RF levels can be efficiently generated. The practicality of such a method is determined in part by the system which generates and drives the relativistic electron beam. The paper addresses the engineering issues associated with building an efficient and reliable electron accelerator where the energy is extracted periodically after re-acceleration. The physics design and the beam dynamics are covered elsewhere at this conference.

INDUCTION ACCELERATOR

The induction accelerator has provided a reliable and efficient way to accelerate high current beams. Currents from hundreds of amperes to many kiloamperes have been accelerated to many tens of MeV's. They are capable of producing beam pulses from tens of nanoseconds to microseconds in duration at kilohertz repetition rates. Fig.

1 shows the equivalent circuit of an induction accelerator cell. I_C is the magnetizing current required to drive the core, I_B is the beam current, and I_N is any compensating network current.

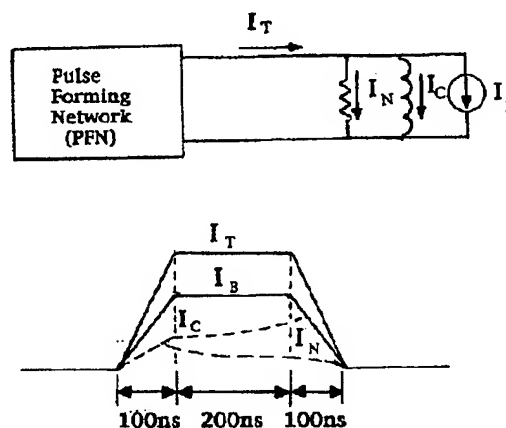


Fig. 1

The efficiency of an induction accelerator can approach 100% if the beam current is much greater than the current required to magnetize the transmission line transformer (or autotransformer) which forms the induction cell. For example, the advanced test accelerator (ATA) induction cell required less than 1 kA of magnetizing current while it accelerated a 10 kA beam for 70 ns.

The efficiency of the TBA accelerator will depend on a number of factors. Beam transport dynamics will determine the size of the beam pipe and the accelerating gradient. The output power requirement will determine the pulse duration, beam current and repetition rate. Once these factors are established, then the induction cell outer diameter and drive will be determined once the optimum magnetic material has been selected. For accelerators with pulse duration less than 100 ns, Ni-Zn ferrites have been used as the magnetic material for the induction cell. For pulse duration in the several hundred nanoseconds to several microseconds, magnetic materials such as Ni-Fe and Metglas¹ have been used. The optimum choice of material for the TBA, which requires a pulse of 300 ns duration, is established by the material's losses and the economics for achieving the desired pulse. From Fig. 2, one can see that the saturation losses for the ferrites are about one fifth the losses of nickel-iron or Metglas. However, the ferrites have a flux

* This work was supported by the Director, Office of Energy Research, Office of Fusion Energy, U.S. Dept. of Energy, under Contract No. DE-AC03-76SF00098.

¹Metglas is a trade name of Allied-Signal

swing which is about one fifth that of the Metglas. This, of course, requires a cross-sectional area of material which is five times larger. As previously discussed, the inner radius and the length of cells (gradient) is fixed by the physics requirements, hence, the only way to increase the area of the core is to increase the outer radius. Since the volume of material increases nearly as the radius squared, smaller, more efficient and lower cost induction cells are obtained

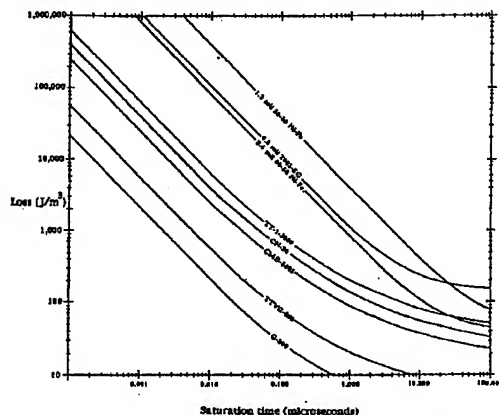


Fig. 2 Losses of ferri and ferro-magnetic materials at different saturation times

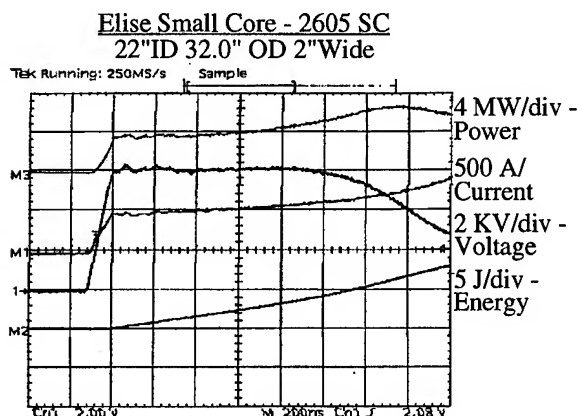


Fig. 3 Voltage, Current, Power and Energy Loss for Metglas 2605SC unannealed

by using the higher delta B materials. Presently, the most cost-effective material for the TBA is the Metglas alloy 2605SC. This ferromagnetic material comes in ribbon form 20 μm thick and is wound into cores with an insulating layer of mylar 2.5 μm thick. Fig. 3 shows the voltage, current, peak power, and joules required to drive a large (1 m OD) core for heavy ion fusion. Fig. 4, shows the B-H characteristics for that core which is unannealed or as cast. Since the rates of magnetization (dB/dt) are higher for the TBA application, the losses will be about $900 \text{ J}/\text{m}^3$. Fig. 5 shows a complete block diagram of the drive system and the cross-section of six induction modules consisting of five cells each generating 20 kV or a total of 100 kV for the high current low energy beam. Three of these modules will generate the required 300 kV/m acceleration gradient. At a repetition rate of 120 Hz, about 3.24 kW will be dissipated in each 100 kV

module. This will require active cooling to the five cells to maintain an acceptable temperature rise.

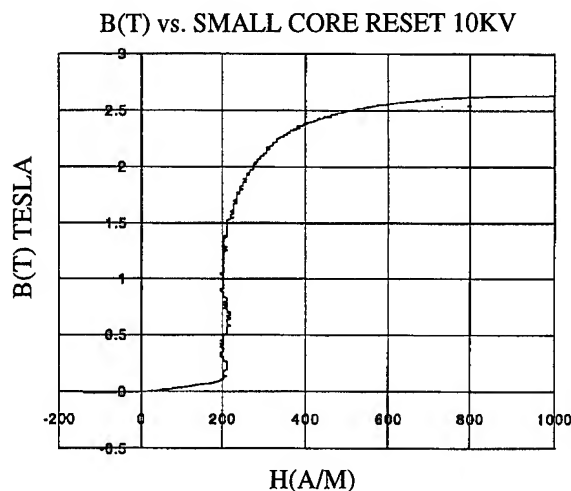


Fig. 4 B-H loop for 2605 SC as cast

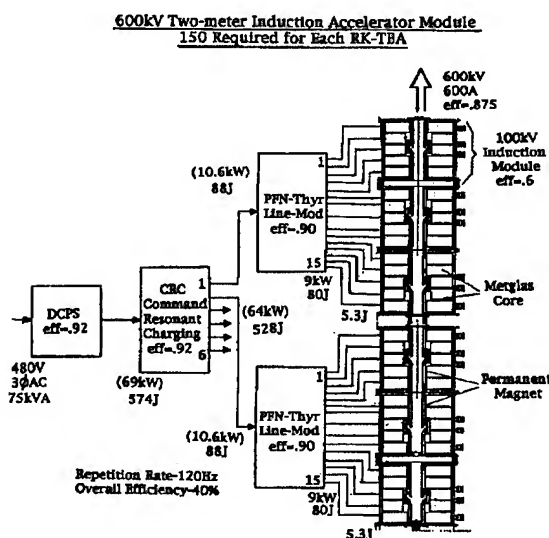


Fig. 5 Two meter section of the low energy induction accelerator with all power conditioning system

POWER CONDITIONING

The most reliable power conditioning system at high repetition rates (kHz) and short pulses is the nonlinear magnetic pulse compression modulator. This system has been used in a number of laser and induction accelerator drivers. Solid state devices are typically used to initiate the pulse compression cycle and a combination of step-up and pulse compression stages can generate practically any voltage and pulse duration with unlimited life.

For application where the repetition rate is not high (120 Hz) and the rate of rise in current is not too demanding, a simple thyatron driven modulator offers acceptable reliability with simpler design and at a lower cost. The modularity of the induction cell offers several options in the voltage and current drive to achieve 100 kV.

In this case, we have chosen to drive each of the five cores with 20 kV inducing a total voltage across the cell of 100 kV. Driving at this voltage level avoids any step-up

dissipates 300 watts and this heat is removed by circulating oil which also acts as a high voltage insulator at the acceleration gap. Further studies are required, but it

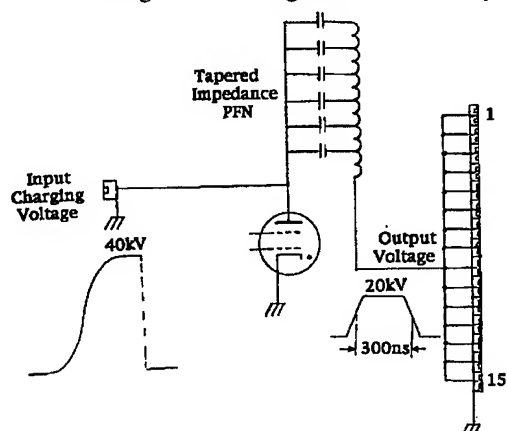


Fig. 6 Simplified schematic of line modulator. The tapered impedance PFN will have the same temporal impedance as the nonlinear magnetic core of the induction cells.

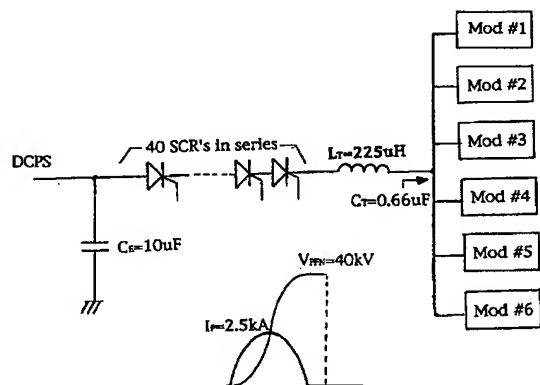


Fig. 7 The command resonant charging (CRC) system charges six modulators and also resets the induction accelerator cores.

transformers and can be generated directly by a thyatron with 40 kV charging voltage on the pulse forming network (PFN). As shown in Fig. 3, the current drive to the cores is somewhat nonlinear, but a constant amplitude pulse can be generated, within bounds, simply by tapering the impedance of the PFN stages. The PFN will consist of many coupled L-C stages each with impedance which temporally matches the impedance of the induction core. This tapered impedance PFN is resonantly charged to twice the output voltage required. From Fig. 7, one can see that the PFN charging current flows through the induction core, thus resetting the core to $-B_r$ ready for the next acceleration cycle.

COOLING OF INDUCTION CORES

Each 100 kV induction module will dissipate about 1500 watts at 120 Hertz. Each magnetic core will be supported by a mandrel with voltage feeds on each side of the core which allow for cooling channels. Each core

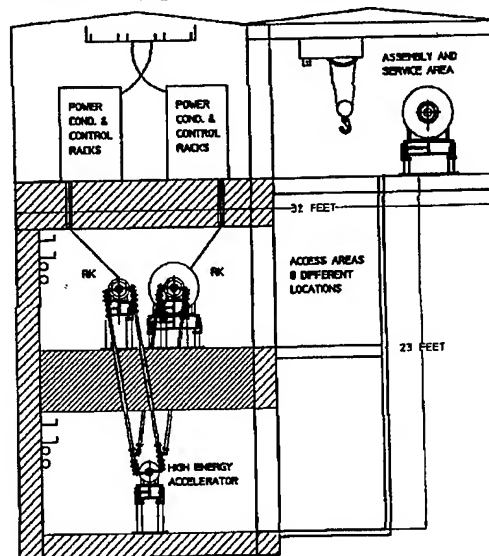


Fig. 8 Elevation view of the RK-TBA accelerator.

may be feasible to use sulfur hexafluoride under pressure to insulate and remove the 1500 watts dissipated in the cores.

CONCLUSION

A simple power conditioning system has been conceptualized for driving induction cells at a relatively high efficiency. The power conditioning system is based on previous experience which incorporates conservative thyatron line modulators without nonlinear magnetic pulse compression or step-up transformers. It is expected that at 120 Hz, the thyatron will offer acceptable reliability which is comparable to the life of a Klystron driven system. This conceptual design will be prototyped over the next several months to confirm our studies.

REFERENCES

- [1] Westenskow, G.A., and Houck, T.L., "Results of the Reacceleration Experiment: Experimental Study of the Relativistic Klystron Two-Beam Accelerator Concept," presented at the 10th International Conference on High Power Particles Beams, San Diego, CA, June 20-24, 1994, to be published in the Proceedings.
- [2] Yu, S., Deadrick, F., Goffeney, N., Henestroza, E., Houck, T., Li, H., Peters, C., Reginato, L., Sessler, A., Vanecek, D., and Westenskow, G., "Relativistic Klystron Two-Beam Accelerator As A Power Source For A 1 TeV Next Linear Collider - Design Report," preliminary draft, LBL, Berkeley, CA, September, 1994.

DESIGN OF INDUCTIVELY DETUNED RF EXTRACTION CAVITIES FOR THE RELATIVISTIC KLYSTRON TWO BEAM ACCELERATOR*

E. Henestroza, S.S. Yu, and H.Li
Lawrence Berkeley Laboratory,
University of California
Berkeley, California 94720

ABSTRACT

An inductively detuned traveling wave cavity for the Relativistic Klystron Two Beam Accelerator expected to extract high RF power at 11.424 GHz for the 1 TeV Center of Mass Next Linear Collider has been designed. Longitudinal beam dynamics studies led to the following requirements on cavity design:

- a) Extraction of 360 MW of RF power with RF component of the current being 1.15 kAmps at 11.424 GHz,
- b) Inductively detuned traveling wave cavity with wave phase velocity equal to $4/3$ the speed of light,
- c) Output cavity with appropriate Q_{ext} and eigenfrequency for proper matching.

Furthermore, transverse beam dynamics require low shunt impedances to avoid the beam break-up instability. We describe the design effort to meet these criteria based on frequency-domain and time-domain computations using 2D- and 3D- electromagnetic codes.

I. INTRODUCTION

An LBL-LLNL team has presented recently a preliminary point design for an 11.424 GHz power source for a 1 TeV Center of Mass Next Linear Collider (NLC) based on the Relativistic-Klystron Two-Beam-Accelerator (RK-TBA) concept [1].

The point design requires that the bunched drive beam delivers 360 MW of rf power with an rf current of 1.15 kA (600 A DC) at 11.424 GHz in each of the 150 rf extraction cavities in a 300-m long RK-TBA unit. To achieve this goal, and to maintain longitudinal beam stability over these long distances, the extraction cavities must be inductively detuned; furthermore, in order for a 3-cell disk loaded cavity structure to behave like a traveling wave structure with no reflected waves, the output ports must be properly matched. To maintain low surface fields to avoid breakdown, we consider traveling-wave structures.

The required cavity parameters have already been discussed elsewhere in this conference [2]; here we will present electromagnetic calculations to determine the structure of the extraction cavities. We have chosen in this design effort one specific path to meet the general requirements. The procedure adopted is by no means unique, and we anticipate further optimizations and more detailed calculations in the future.

II. THE EXTRACTION CAVITY DESIGN

Present designs evolve around traveling-wave-structures with 3 cells of 8-mm inner radius. The rf output is extracted through 2 separate ports in the 3rd cell, with 180 MW each transported through separate waveguides, and fed directly into the two input couplers of the high gradient structure.

The tools we have used to calculate the rf properties of the cavity are URMEL and SUPERFISH for 2-D frequency-domain calculations, ABCI and TBCI for 2-D time-domain calculations, and MAFIA for 3-D frequency- as well as time-domain calculations. The calculations in frequency-domain are obtained for standing-wave solutions. We have followed a procedure described in a paper by Loew et al. [3] to convert these results to traveling-wave properties.

The design procedure is carried out in several steps, starting with the simplest approximations, and adding more realistic features with each successive iteration. At each step we calculate the rf properties of the cavity including frequency, the (R/Q) , and group velocity for the longitudinal mode, and the synchronous frequency and shunt impedance of the dipole mode; we also calculate the field enhancement factor to determine the surface field for assessing breakdown risks. The field enhancement factor calculated by URMEL is defined as the ratio of the maximum amplitude of the electric field in the whole structure to the average electric field along the axis (including the transit time factor) for standing-wave solutions. The enhancement factor that we are

*Work supported by the U.S. Department of Energy under Contract DE-AC03-76SF00098.

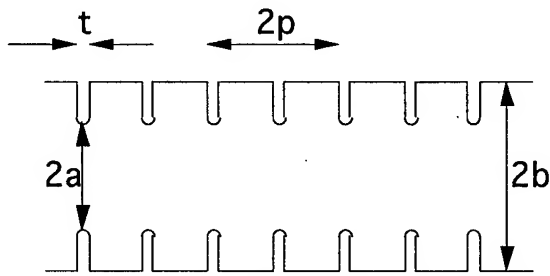


Figure 1: Schematic cross section of the infinitely periodic structure.

interested in is defined for traveling-wave structures without the transit time factor.

III. INFINITELY PERIODIC STRUCTURE

First, we want to determine roughly the geometry of the overall structure. As a starter, we construct a 3-cell disk-loaded traveling-wave structure that is synchronous with the beam ($v_p=c$). The rf structure should give 360 MW with a tightly bunched drive beam with an rf current of 1-1.5 kA. We choose initially a conventional $2\pi/3$ structure with cell length (p) of 8.75 mm. The power extraction formula gives a requirement of $(R/Q)/v_g$. URMEL is exercised for an infinitely periodic structure, varying the inner radius a and outer radius b of a disk-loaded structure, and the set of solutions with $v_p=c$ is obtained, following the procedure of Thompson, et al. [4]. For each value of the aperture radius satisfying $v_p=c$, the cavity parameters R/Q and v_g are determined. Figure 1 shows a schematic cross section of the cells.

The inductively detuned structure is next constructed by a variation of the previous step. What we want is a structure whose resonant frequency remains unchanged, but the wavelength is increased by a factor of 1.33. This will result in a phase velocity of 1.33 c , which is the desired detuning angle to maintain longitudinal beam stability. To achieve this, we choose to fix the cell length at $p=8.75$ mm as before, and reduce the outer radius b for each value of a , until the $2\pi/3$ field configuration becomes a $\pi/2$ configuration at the same frequency of 11.424 GHz. Each wavelength now extends over 4 cells, instead of the 3 cells. The R/Q and v_g for this new configuration are determined with URMEL. The required geometry is determined by ensuring that the corresponding R/Q and v_g provides the right power extraction. The solution is $a=8$ mm, $b=12.5$ mm, $R/Q=13.5 \Omega$ and $v_g=0.28 c$. Slight-refinements from this geometry are obtained by numerically iterating on the power extraction formula to account for the

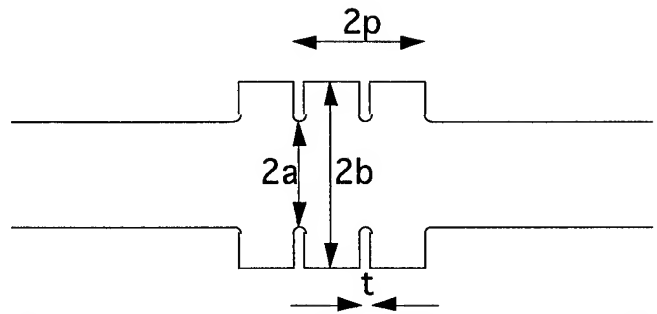


Figure 2: Schematic cross section of the 3-cell cavity with beam pipes.

reduction in power due to inductive detuning. The field enhancement factor is 1.5.

IV. FINITE STRUCTURE (2-D)

The finite cell structure is included by modeling the detuned 3-cell structure with finite beam pipes. The effect of the modified geometry on the field configuration and cavity parameters are then studied. Figure 2. shows a schematic cross section of the 3-cell cavity with beam pipes. As calculated by SUPERFISH a 3 cm beam pipe on each side of the structure will adequately contain the fringe fields. The cavity fields still retain their $\pi/2$ structure. Wakefield calculations using ABCI/TBCI was performed to find the resonant frequencies and impedances of the structure and to compare the results with the frequency-domain calculations to check for consistency. The resonant frequencies as well as the relative impedance behavior agree with those calculated in frequency-domain.

A very important point to note is that the dipole wake is heavily damped. This is due to the strong coupling of the cavity field to the TE_{11} mode in the beam pipe. This results in a very low Q . To translate the wake calculation to the Q of individual cells in a coupled cavity formulation is somewhat subtle, and has not been fully understood yet but initial estimates suggest that the dipole Q for the first and last cavity of our 3-cell structure could be as low as 10.

V. FINITE STRUCTURE (3-D)

Finally, the 3-D aspects of the output ports are studied using MAFIA. Recalling that the matching condition demands that the frequency and Q -value of the last cell be uniquely determined to absorb the reflected waves from the 3-cell structure, MAFIA is exercised by variation of the geometry of the output until the right value of Q and ω for proper matching are

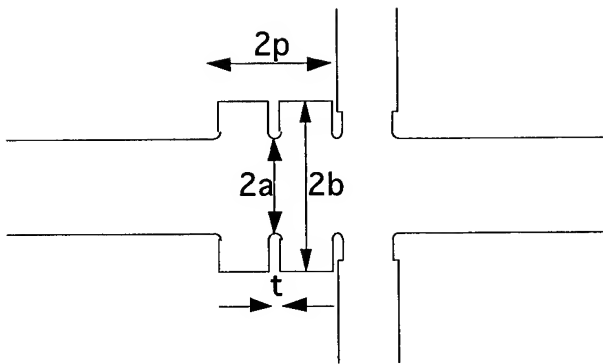


Figure 3: Axial cut of the 3-D cavity with output structures.

obtained. Figure 3 shows an axial cut of the 3-D cavity with output structures.

The output structure consists of two WR90 RWG waveguides attached to the last cell of the cavity. The shorter (0.4" long) side is oriented along the z-axis. The last cell is required to have a $Q_{ext} < 10$ in order to have only a forward traveling wave in the cavity.

The determination of the external Q of the 3-D cavity with output structure is based on the Kroll-Yu method [5]. For a given waveguide iris aperture several calculations (at least four) are performed varying the length of the output waveguide. The phase change along the waveguide, ψ , is defined as $2\pi D/\lambda_g$, where λ_g is the waveguide wavelength and D is the waveguide length. The mode of interest (in our case the $\pi/2$ mode) is identified and the frequency recorded. From the phase change versus frequency relationship the external Q is approximately given by $-(1/2)f(d\psi/df)$. Taking into account the whole structure we calculated $Q_{ext} \approx 80$ for various waveguide iris apertures. The equivalent Q for the 3rd cavity can be shown, using a method developed in Ref. [1], to be less than 10.

The calculation of the Q_{ext} of the last cell for a $\pi/2$ mode configuration is facilitated from the fact that such configuration is obtained naturally by applying neuman and dirichlet boundary conditions at the left and right boundaries of that cell. Using the Kroll-Yu method we calculated a $Q_{ext} \approx 5$ for a waveguide iris aperture of 1.24 cm, a value of Q_{ext} that is within that required to meet the matching condition. Figure 4 shows the phase versus frequency curve.

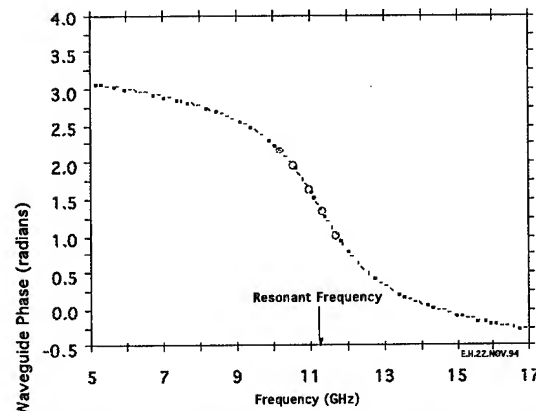


Figure 4: Phase versus frequency curve for last cell.

VI. CONCLUSION

We do not consider the cavity geometries obtained so far to be final in any sense. There are still large degrees of freedom for design modifications, and further refinements will be conducted to reduce transverse focusing fields and to ensure minimal surface fields over the entire 3-D structure. The calculated Q's are close to the values required to satisfy the matching condition. The induction cavity design need to be optimized to make sure that both the longitudinal as well as transverse impedances are adequately small.

VII. REFERENCES

- [1] S.S. Yu, Deadrick, F., Goffeney, N., Henestroza, E., Houck, T., Li, H., Peters, C., Reginato, L. Sessler, A., Vanecek, D., and Westenskow, G., "Relativistic Klystron Two-Beam Accelerator As A Power Source For A 1 TeV Next Linear Collider - Design Report," preliminary draft, LBL, Berkeley, CA, September, 1994.
- [2] H. Li, et al., "Beam Dynamics Issues in an Extended Relativistic Klystron," this conference.
- [3] G.A. Loew,, R.H. Miller, R.A. Early and K. Bane, "Computer calculations of traveling-wave periodic structure properties", IEEE Trans. Nucl. Science, Vol. NS-26, No. 3, June 1979, pp. 3701-3704.
- [4] K.A. Thompson, et al, "Design and simulation of accelerating structures for future linear colliders", SLAC-PUB-6032, Nov. 1993.
- [5] N.M. Kroll, and D.U.L. Yu, "Computer determination of the external Q and resonant frequency of waveguide loaded structures", Particle Accelerators, 1990, Vol. 34, pp. 231-250.

BEAM-BASED OPTICAL TUNING OF THE FINAL FOCUS TEST BEAM*

P. Tenenbaum, D. Burke, S. Hartman, R. Helm, J. Irwin, R. Iverson, P. Raimondi, W. Spence
Stanford Linear Accelerator Center, Stanford University, Stanford, CA 94309 USA

V. Bharadwaj, M. Halling, J. Holt

Fermi National Accelerator Laboratory, Batavia, Illinois, USA

J. Buon, J. Jeanjean, F. Le Diberder, V. Lepeltier, P. Puze**

Laboratoire de l'Accélérateur Linéaire, Orsay, France

K. Oide, T. Shintake, N. Yamamoto

National Laboratory for High Energy Physics, KEK, Tsukuba, Japan

In order to reduce the SLAC 46.6 GeV beam to sub-micron sizes, the Final Focus Test Beam (FFTB) must meet tight tolerances on many aberrations. These aberrations include: mismatch and coupling of the incoming beam; dispersion; chromaticity; lattice errors in the chromatic correction sections; lattice coupling; and residual sextupole content in the quadrupoles. In order to address these aberrations, we have developed a procedure which combines trajectory analysis, use of intermediate wire scanners, and a pair of novel beam size monitors at the IP. This procedure allows the FFTB IP spot to be reduced to sizes under 100 nanometers.

I. INTRODUCTION

In order to achieve luminosity in the range of $10^{34} \text{ cm}^{-2} \text{ sec}^{-1}$, a TeV-scale linear collider will need to reduce the size of electron and positron bunches at collision to sizes on the order of several nanometers. This vertical size mandates a demagnification from the linac to the IP of a factor of 400. Such a severe demagnification places unprecedented tolerances on many optical aberrations of the final focus system, most of which cannot be met *ab initio*, but only as a result of beam-based tuning of the final focus. Any linear collider must have an algorithm and diagnostics which will allow such tuning to converge in a finite time.

The Final Focus Test Beam (FFTB) is a prototype linear collider final focus, designed to reduce the 46.6 GeV SLAC beam to a size of 2 microns by 60 nanometers. The FFTB has the horizontal and vertical demagnifications required by a future linear collider, and thus addresses all the same optical aberrations. We have developed such an algorithm for the FFTB, which allows the spot to be focused to 70 nanometers.

II. THE FINAL FOCUS TEST BEAM

The optics of the FFTB have been discussed in detail elsewhere[1]. The optical layout consists of: a 5-quadrupole beam matching section; a horizontal chromatic correction section (CCSX) with a pair of sextupoles separated by a $-I$ transform; a beta exchanger (BX), which enlarges the vertical beam size and reduces the horizontal; a vertical chromatic

correction section (CCSY); a final telescope (FT), including the final doublet (FD) magnets; and an extraction line.

The primary aberrations which affect the horizontal beam size are: waist and magnification errors; dispersion; chromaticity; and a single normal sextupole aberration, for a total of 5. The vertical beam size is affected by these aberrations, plus an additional two skew sextupole aberrations, and two xy coupling effects, for a total of 9 aberrations.

III. INCOMING BEAM MATCHING

Because of the "stair-step" phase advance properties of a linear collider final focus, the multi-wirescanner technique for measuring incoming beam emittance, Twiss parameters, and coupling[2] is not applicable in the FFTB. Instead, the incoming beam is measured by scanning a quadrupole magnet and measuring the beam size on a downstream wire scanner as a function of the magnet strength. This technique has been described elsewhere[3], and has been used for many years at SLAC. In the FFTB, the first quadrupole magnet is scanned, and a wire scanner in the beam-matching section is used[4]. For this measurement the beam matching quads are set to a special optics which focus both x and y waists on the wire, and the beam is stopped before entering the CCSX.

Because of the sensitivity of the FFTB to xy coupling, the beam measurement scanner contains 7 micron wires set to measure the beam in x, y, and v (one of the diagonals). Two algorithms have been developed to measure the fully-coupled sigma matrix using this wire scanner and quadrupole strength scans. It was determined that the incoming beam coupling is dominated by a single term, which can be eliminated using a skew quadrupole upstream of the first normal FFTB quadrupole. When this is done, the measured vertical projected emittance agrees with the emittance measured at the end of the SLAC linac by the multi-wire system there ($\gamma\epsilon_y = 2 \times 10^{-11} \text{ m.rad}$), and is below the FFTB design value.

The five normal quadrupoles of the beta matching section are then employed to match the incoming Twiss parameters onto the desired IP parameters. This allows us to adjust the IP divergence (and hence the focused size) up or down, depending on requirements of the experimental program. The beam is then allowed to travel to the dump.

The BX section contains horizontal and vertical "intermediate waists," with respective beta functions of 8.3 cm and 2.5 cm (design), separated by 2.85 meters. Special wire scanners[4] with 4 micron wires at angles optimized for

*Work supported by the Department of Energy, contract DE-AC03-76SF00515.

**Current address: European Laboratory for Particle Physics (CERN), Geneva, Switzerland

measuring flat beams are used to verify and tune the beta match (both magnification and waist). The beam size on the horizontal waist wire is 5 microns by 80 microns, and on the vertical waist wire is 200 microns by 710 nanometers.

IV. LOCAL TUNING AND DIAGNOSTICS

Wherever an aberration can be traced to an error in a single magnet, it is preferable to correct the error in that device rather than to apply a global tuning correction. The primary localized aberrations arise from misalignments of quadrupoles and sextupoles, and errors in the strengths or roll angles of quadrupoles. To maximize tunability, all quadrupoles upstream of the IP are powered by separate power supplies, and all quadrupoles and sextupoles are mounted on remote-controlled magnet movers with positioning accuracy of under 1 micron in x and y [5]. All quadrupoles up to the first doublet magnet contain stripline beam position monitors (BPMs) with resolutions of 1 micron[6].

The procedure for quadrupole and sextupole alignment is described elsewhere[7]. The technique uses a shunt technique for the quadrupoles, and scans of the mover positions vs downstream bpm's for the sextupoles. The overall tuning procedure is guaranteed to converge if the RMS misalignments of quadrupoles and sextupoles is below 100 microns in the horizontal and 30 microns in the vertical, and these tolerances are met by the alignment algorithm. The alignment is done with the IP divergence low, and this reduces the beam size in all the limiting apertures of the FFTB. Because the procedure does not rely on beam size diagnostics at any time, the specifics of the beam matrix are not important, and in fact alignment is usually performed before incoming beam reconstruction for this reason.

In order to minimize sextupole aberration, it is necessary to tune the $-I$ transforms of the CCSX and CCSY as thoroughly as possible. This is done by introducing closed orbit oscillations, generated by moving quadrupole magnets on their movers in appropriate linear combinations to probe all phases of oscillation[8]. The technique allows quadrupole strength measurements of 1 part per thousand, and roll measurements of 1 milliradian. These are adequate for guaranteeing convergence of the overall algorithm.

V. IP BEAM SIZE MONITORS

Because the IP beam size is smaller than at any other point in the beam line, it is subject to aberrations which cannot be measured elsewhere. Consequently, once incoming beam and FFTB lattice properties have been tuned to the limits of the upstream measuring devices, it is necessary to use measurements of the IP spot size itself.

Initial tuning of the beam can be accomplished using wire scanners set in the IP region. These scanners use 4 micron carbon wires, and are useful down to a beam size of about 1 micron, although wire damage becomes a likely occurrence at this point[4]. The spot can be measured down to its design size by a pair of novel beam size monitors (BSMs) set 52 cm apart in the IP region.

A. Gas Time of Flight Beam Size Monitor[9]

A Gas Time-of-Flight BSM injects a small amount of Helium gas into the beam as it passes through the device. The beam produces ions, which are then accelerated transversely by the electric field of the beam. The maximum velocity of the ions is proportional to the maximum field. Additionally, the vertical beam is small enough that the ions are trapped by its intense electric field and oscillate with horizontal and vertical amplitudes proportional to the coordinates of their creation point inside the beam. In average, horizontal amplitudes are larger than vertical ones for horizontally flat beams, leading to an anisotropy in the distribution that scales as the beam flatness.

By measuring the velocity and angular distributions of escaped ions (via a ring of multi-channel plates surrounding the IP), the beam size in both planes can be measured. Figure 1 shows a typical distribution, which indicates a beam size of 1.6 microns by 80 nanometers.

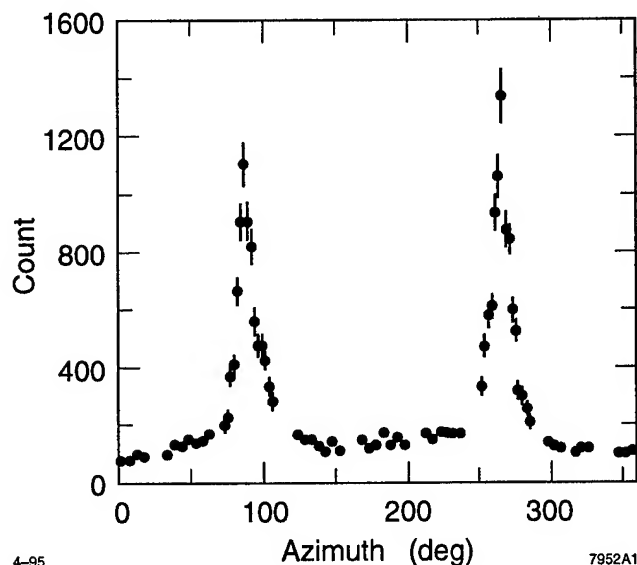


Figure 1. Angular distribution of He^+ ions produced by beam ionization of Helium gas. The distribution is peaked in the horizontal direction (90° and 270°), indicating a flat beam.

B. Laser Interferometer Beam Size Monitor[10]

A laser interferometer BSM splits a Nd:YAG laser pulse and crosses the two beams thus produced at an angle in the path of the electron beam. This produces an interference pattern with a characteristic modulation spacing. When the beam encounters the laser, the laser photons are Compton-scattered forward into a detector. The amplitude of the signal depends upon the relative transverse position of the electron beam and the laser pattern, and also upon the relative size of the electron beam and the modulation spacing. Scanning the electron beam across the interference fringes gives a sinusoidally-varying Compton signal, whose modulation

depth gives the beam size. Figure 2 shows such the results of such a scan, and indicates a beam size of 73 nanometers.

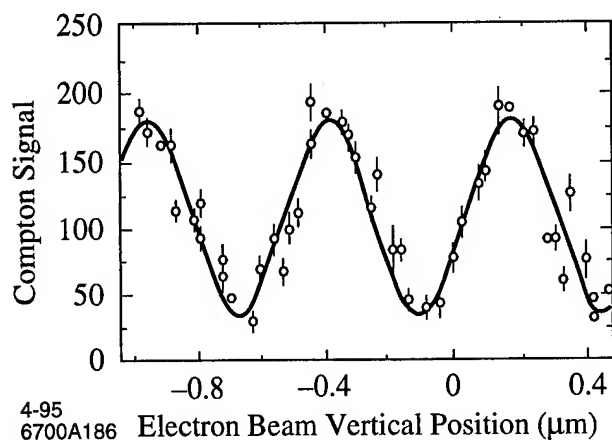


Figure 2. Laser-Compton Beam Size Monitor Compton photon signal vs. beam position, showing the sinusoidal modulation expected. The beam size indicated is 73 nm, with a statistical uncertainty of 4 nm.

VI. GLOBAL TUNING ON IP BEAM SIZE

In order to minimize the IP beam size, it is necessary to prepare linear combinations of tuning elements ("knobs"), which are properly orthogonal. Knobs which cause more than trace alterations in secondary aberrations require additional iterations, and may prohibit tuning altogether.

The knobs of greatest concern are waist, dispersion, and the single coupling term ($x'y$) which arises from any rolled quadrupoles in the FFTB line, including the doublet. Because these knobs are scanned repeatedly, and need to be incremented by small amounts, magnet hysteresis and power supply granularity are significant issues. These issues are addressed by moving the CCS sextupoles, via their movers, in patterns which generate orthogonal waist shifts, dispersion shifts, and coupling at the IP. Because the mover positions are monitored by a sensor system independent of the stepper motors, the positions are not subject to hysteresis, and have the step size needed to change aberrations by the small increments required. In order to minimize the sextupole offsets from their aligned positions, only small changes in these aberrations are implemented via the mover knobs. Large changes are converted to an equivalent magnet knob. The tuning elements for each aberration are as follows:

A. Waist Position

The waist positions are moved by changing the strengths of the final doublet quadrupoles.

B. Dispersions

The IP dispersions are changed by steering the beam off-axis across the final doublet magnets.

C. Coupling ($x'y$)

The "Rolled Quadrupole" coupling term is changed via a skew quadrupole close to the final doublet.

D. Chromaticity

The lattice chromaticity is changed by changing the strengths of the CCSX or CCSY sextupoles. In order to keep this correction orthogonal from the linear aberrations above, the sextupoles must be near their aligned positions, thus the use of magnet knobs for coarse changes.

E. Geometric Sextupole

The geometric sextupole aberrations are changed via two normal and two skew sextupoles in the dispersion free region of the FT. Of the four aberrations these magnets generate, one effects only the horizontal beam size, one effects only the vertical, and two have combined effects. These magnets are scanned in combinations which excite aberrations singly.

VII. RESULTS

The scheme described above has been used repeatedly to tune the beam size of the FFTB, and 70 nanometers has been regularly achieved. Further improvements in the spot size are anticipated as unexpected effects are fully understood.

VIII. ACKNOWLEDGMENTS

The authors would like to thank the SLC Beam Delivery Task Force for pioneering many of the approaches used here, and the SLAC Operations staff for their hours of vigilance.

IX. REFERENCES

- [1] G. Roy, "Analysis of the Optics of the Final Focus Test Beam Using Lie Algebra Based Techniques." SLAC-Report-397 (1992).
- [2] K.D. Jacobs *et al*, "Emittance Measurements at the Bates Linac," Proc. 1989 IEEE Part. Acc. Conf., 1526 (1989).
- [3] M.C. Ross *et al*, "Automated Emittance Measurements at the SLC," Proc. 1987 IEEE Part. Acc. Conf., 725 (1987).
- [4] C. Field, "The Wire Scanner System of the Final Focus Test Beam," SLAC-PUB-6717 (1994).
- [5] G. Bowden *et al*, "Precision Magnet Movers for the Final Focus Test Beam," SLAC-PUB-6132 (1994).
- [6] H. Hayano *et al*, "High Resolution BPM for FFTB," Nucl. Inst. Methods A320:47-52 (1992).
- [7] P. Tenenbaum *et al*, "Beam-Based Magnetic Alignment of the Final Focus Test Beam," these proceedings.
- [8] V. Bharadwaj, "Fermilab Contributions to the FFTB," these proceedings.
- [9] J. Buon *et al*, "The Orsay Spot Size Monitor for the Final Focus Test Beam," Proc. 1992 Int. Conf. on High-Energy Accelerators, 219 (1992).
- [10] T. Shintake *et al*, "Design of Laser-Compton Spot Size Monitor," Proc. 1992 Int. Conf. on High-Energy Accelerators, 215 (1992).

Fermilab Contributions to the FFTB

V. Bharadwaj, A. Braun, M. Halling, J. A. Holt, D. Still
Fermi National Accelerator Laboratory
P. O. Box 500, Batavia, IL 60510, USA

Abstract

The Final Focus Test Beam (FFTB) project at SLAC is a demonstration of the feasibility of making the extremely small spot sizes needed for future e^+e^- linear colliders. Fermilab joined the FFTB collaboration in late 1993. This paper describes the Fermilab contributions to FFTB, emphasizing the work on lattice diagnostics.

I. Introduction

There has been an ongoing involvement by Fermilab in work on high energy e^+e^- linear colliders [1]. In 1993 Fermilab joined the Final Focus Test Beam Collaboration. The FFTB [2] is an experiment to demonstrate the feasibility of making the small beam spot sizes that are required for the success any future linear collider project. The experiment has already yielded impressive results [3] and has shown that the demagnifications needed for the NLC design are feasible. Fermilab joined the collaboration after almost all of the hardware was already installed. However an earlier engineering run indicated the need for an additional $x-y$ halo collimator, which Fermilab built and helped commission in the FFTB beamline. The FFTB beamline requires very careful alignment and the magnet strengths have to be correct [4] for the beam to be focused down to its design value at the final focus. Fermilab was responsible for checking the magnet strengths (i.e. lattice diagnostics) and developed two independent methods for this project. This paper deals mostly with these lattice diagnostic methods.

II. Offline Analysis

One method of measuring the FFTB lattice is to fit beam data from a large number of 3 and 4 bumps. There are 12 precision trim magnets in the beamline that are used to create trajectory bumps. There are not however, enough trims to make bumps over a short region in the lattice. Typical 3-bumps with the correctors include about 10 quads. Almost every quad in the beamline is mounted on a movable stand that can be positioned to about 1 micron accuracy. Trajectory bumps were also made using these quad movers. The advantage of using bumps created by the movers is two-fold; the movers do not suffer from hysteresis, and there are movers on each quad allowing us to make a wide variety of very short bumps. This gives many more combinations of bumps than can be made using the limited number of precision dipole trim elements.

The BPMs have demonstrated accuracy in many cases better than 1 μm for small displacements. For large displacements the non-linear nature of their response limits their accuracy to about

30 microns absolute accuracy. An overall scale factor error of 10%, and channel to channel non-linear errors of a few percent are two other effects that limited the absolute precision of the BPM system at large displacements.

The most precise test that the BPM's can make is to require that a bump be closed so that there is zero deflection downstream. The BPMs used in the FFTB are capable of measuring small changes in the trajectory from one pulse to the next with a precision of 1 μm or better. In order to measure the lattice properties to 0.1% or better accuracy closed 3 and 4 bumps are used to test the lattice. Small imperfections in the lattice appear as small movements of the beam downstream of the bump.

The complication of using closed bumps for the measurement is that each measurement includes the effect of several quads. In order to separate out the trajectory errors from each quad without any correlation with its neighbors we made many overlapping orthogonal closed bumps. We used over 100 different closed bumps to measure the individual strengths of about 30 quads. The large amount of redundancy in the measurements allow the measurement of each quad strength with little ambiguity. The lattice properties were then extracted by the simultaneous fitting of all the experimental data

Each closed bump was tried with 5-10 steps of different strengths. Each of these steps in bump strength was repeated 5-10 times. For each bump the trajectories of between 50 and 100 different linac cycles were taken. A correction is made for each linac beam pulse to correct for the pulse to pulse variation of the SLAC linac.

The lattice properties were measured by fitting the processed BPM measurements for all of the different 3 and 4 bumps simultaneously. Each bump trajectory was compared to a model prediction based on a tracking simulation originating from the SLAC control system online model. The fitting was performed using the MINUIT optimization program, using a χ^2 that based on the measured errors determined by the reproducibility of the measurements. The quantity used for the minimization is the χ^2/dof of all BPMs for all bump measurements.

By far, the most important parameter needed to fit the data is an overall BPM scale factor. In one sub-sample of our data the overall χ^2/dof is reduced from 50 to 25 by including a 13% scale factor change. In addition the beam energy may also be fit to all the data.

Table I shows the strength of each quad in our test region relative to the online model, obtained by fitting each quad separately. In most cases the precision is of order 10^{-3} .

The two most critical sections of the FFTB lattice are the $-I$ transformers in the chromatic correction sections. Each of these sections contains five quads. Table II shows the results of a simultaneous fit to four of the five quads in each of these sections. If the measured errors had been large enough to cause

Table I
Quadrupole strengths in the test region relative to the model.

Name	Value	Error
QN3A	1.0033	0.001239
QN3B	0.99639	0.001677
QN2A	1.0009	0.000602
QN1	1.0006	0.000867
QN2B	1.0007	0.000659
QN3C	1.0021	0.002117
QT1	1.0032	0.002992
QT2A	0.89738	0.045050
QT2B	0.99909	0.002033
QT3	1.0011	0.001594
QT4	1.0027	0.001393
QM3B	1.0022	0.001767
QM1A	0.99437	0.002336
QM2	1.0005	0.001641
QM1B	0.99936	0.003753
QM3C	1.0026	0.002999
QM3D	1.0027	0.002816
QM3D	1.0018	0.006240
QM1C	1.0017	0.004884
QM1C	0.99699	0.001475
QC5	1.0040	0.001516
QC4	0.99958	0.002699
QC3	0.99084	0.006982
QX1	0.97512	0.013512
QC1	0.97981	0.010615
QP1A	0.96081	0.032226

prototype lattice changes and to calculate various lattice parameters (eg. twiss parameters). The bumps generated for the offline analysis were checked with this model. The program can read data files produced by the SLAC control system.

During one of the FFTB commissioning periods, data from a series of correction dipole bumps and quad displacement bumps were taken and compared to the model. A correlation plot data file was made of all of the magnet currents and read into the model. A correlation plot data file was made for each type of bump. The bump strength was varied over a $\pm 1mm$ range with five to ten data samples taken for each bump value. When the data are read into the model program, the user can select whether or not to average the data points or whether or not to subtract the orbit with zero bump value (the reference orbit). The user can also read in the multi-knob file which produced the bump.

Figure 1 shows the comparison between BPM data and the model for a particular four-bump using the horizontal quadrupole movers. The circles are the BPM data and the solid line is the model. The bump is not closed because of lattice errors and a momentum offset of .03% which was input to the model.

The model was very useful for quickly zeroing in on problem areas in the lattice. For example it was very easy to discover that there was crosstalk in the quadrupole movers; for a $400 \mu m$ movement in x there was $\approx 2 - 3 \mu m$ movement in y .

Table II
Results of simultaneous fit to four of the five quads in both of the chromaticity correction sections.

NAME	VALUE	ERROR
QN3B	0.99651	0.0016
QN2A	0.99793	0.0006
QN1	0.99950	0.0009
QN3C	1.00430	0.0021
QM3B	1.0015	0.0007
QM2	1.0005	0.0010
QM1B	0.99756	0.0027
QM3C	1.0012	0.0015

distortion of the spot size at the IP we could have used these measurements as a guide to tune the $-I$ sections to match the perfect $-I$ sections in the model.

In addition to the strengths of the quads, this technique can also be used to measure the alignment and rotation angles of individual quads.

III. Interactive Model

Using the object-oriented beamline class library under development at Fermilab, an interactive model of the FFTB lattice was created to be used as a lattice diagnostic tool, to quickly

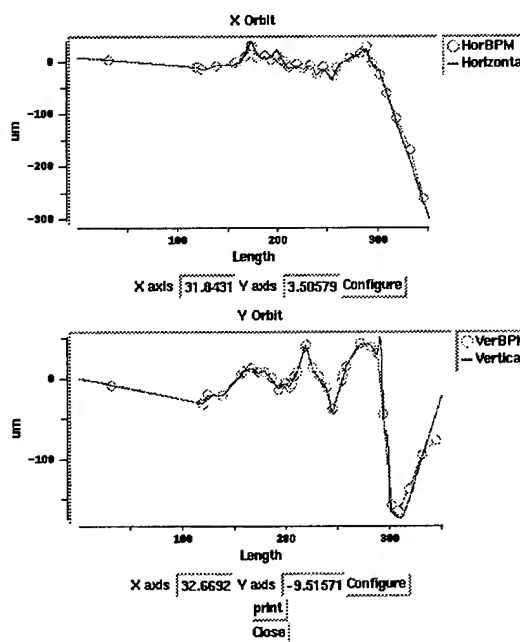


Figure 1. Comparison of model with BPM data.

References

- [1] "The TESLA Test Facility (TTF) Linac - A Status Report", This conference.
- [2] "Final Focus Test Beam Project Design Report", SLAC-376, (1991).
- [3] V. Balakin *et al.*, "Focusing of Submicron Beams for TeV e^+e^- Linear Colliders", *Physical Review Letters*, **74**,2479, (1995).
- [4] P. Tenenbaum *et al.*, "Beam-based Optical Tuning of the Final Focus Test Beam", This conference.

HV INJECTION PHASE ORBIT CHARACTERISTICS FOR SUB-PICOSECOND BUNCH OPERATION WITH A HIGH GRADIENT 17 GHz LINAC*

J. Haimson and B. Mecklenburg, Haimson Research Corporation, Santa Clara, CA 95054 USA

The results of phase orbit computations are presented showing typical cutoff and acceptance characteristics for high voltage electrons injected into a 60 MV/m, 17 GHz traveling wave (TW) disc loaded structure. The RF fringing fields at beam entry to the TW structure and the presence of a standing wave domain at the input cavity have a dominating influence on the capture and bunching process and on the asymptotic bunch location of the accelerated beam. The effects of beam loading and of different injection energies and input RF power levels are investigated; and injection operating parameters with RF chopped and prebunched beams to ensure high resolution, sub-picosecond bunch performance with the 17 GHz linac, are presented.

I. INTRODUCTION

For conventional gradient S-band linacs, it has been shown [1] that (a) the presence of RF fringe fields at the beam entry port of a traveling wave (TW) accelerator, side coupled, input cavity, (b) the existence of a standing wave domain in the immediate entry region of such a cavity, and (c) the influence of space harmonics (especially in the first few cavities), all play critical roles in the initial bunching and capturing process and in the subsequent asymptotic phase location of the accelerated bunch. It can be expected that these field interactions will have an even greater influence on beam performance for structures designed to operate at high gradients and short wavelengths. Neglecting to carefully analyze these critical effects can result in an incorrect choice of the electron gun operating potential, poor bunching and a substantial reduction in the energy gain of a synchronously operated accelerator waveguide section.

The multi-orbit, time domain, TW linac simulation code HRC-ELOR, [1,2] especially developed to analyze the above effects was used to study the initial bunching and subsequent acceleration through five different configuration, nonuniform impedance, 17 GHz TW structures (refer Table I). The structures were designed to have a 200 mA loaded beam energy of 25 MeV with an input RF power of 20 MW [3]. The phase orbit studies were conducted in parallel with the structure design work to ensure convergence of parameters so that the impedance required to ensure correct field conditions for electron capture and bunching also satisfied the group velocity and impedance requirements for the desired quasi-constant gradient conditions. By iteration, it was possible to establish a suitable set of parameters for the initial uniform impedance segment of the structure so that near optimum

injection conditions and asymptotic bunch location could be achieved without having to adopt tapered, reduced phase velocity circuit techniques [1,4]. The phase orbit investigations were directed mainly at studying two different injection energy regimes, namely, 400 to 600 keV and approximately 2 MeV, so that beam injection using either pulsed HV or RF electron guns could be evaluated.

Table I. Comparison of 17 GHz Structure Designs

Design Type	Gradient Type and Total Number of Cavities	Number of Different Cavities in Structure	Iris Diameter 2a (cm)		Attenuation Parameter τ (Np)
			Input	Output	
A	Constant n=90	90	0.5758	0.4130	0.550
B	Quasi-C. n=90	15	0.5842	0.4242	0.540
C	Quasi-C. n=90	15	0.5690	0.4318	0.522
D	Quasi-C. n=90	15	0.5690	0.4318	0.564
D(94) (final)	Quasi-C. n=94	15	0.5690	0.4318	0.590

II. PHASE ORBIT CHARACTERISTICS

Initial phase orbit calculations for the constant gradient (Design A) structure, performed under simplified conditions of zero beam loading, are shown in the Figure 1 plots of injected particle entry phase (ϕ_0) at the input coupler fringe field versus electron energy (V_a) at emergence from the accelerator structure. These initial computations, based on an input coupler peak field of 67 MV/m, and an initial average accelerating field strength (\hat{E}_0) of 52 MV/m, provided important early information on acceptance, asymptotic phase location, etc., and presented guidelines for establishing the final design parameters of the 17 GHz quasi-constant gradient accelerator structure shown listed in Table II [Design D(94)].

The classical injection characteristic of decreasing phase acceptance with reduced injection energy is clearly illustrated in Figure 1, with a 260° acceptance at 2 MeV and approximately 190° at 400 to 600 keV. An unexpected and important finding during this 17 GHz high gradient accelerator investigation was the strong rejection of particles at injection energies of 100 to 200 keV, i.e., at the energy levels commonly used by the majority of existing high power research linacs (operating at lower frequencies and gradients). It can be noted that even at an electron gun voltage of 250 kV, there are no injection phase angles that allow the maximum available energy to be achieved under synchronous operating

*Work performed under the auspices of the U.S. Department of Energy SBIR Grant No. DE-FG03-93ER81487.

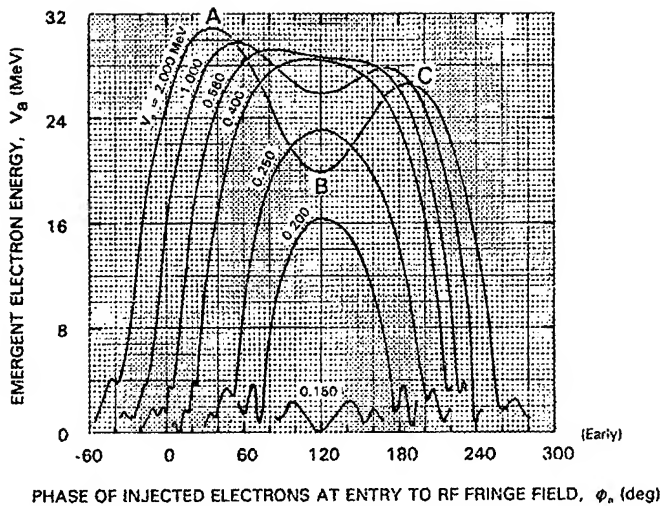


Figure 1: Phase Orbit Plots Showing Cut-off and Acceptance Characteristics of an Unloaded 17.136 GHz, $v_p=c$, Constant Gradient TW Linac Structure (Design A) for a Range of Injection Energies (V_0).

conditions, because the electrons are asymptotically phased well behind the crest of the wave. [Higher injection energies, especially with narrow RF bunches ($\approx \pi/10$), assist considerably in achieving beams of low emittance [4] because of the beam formation advantages and because the use of $v_p < c$ capture structures can be totally avoided.]

The 17.136 GHz structure binding field conditions were chosen to provide near optimum acceptance and asymptotic phase location for injection energies in the 400 to 600 keV range, by ensuring that for a specified given spread of entry phase angles, the emergent energy remained essentially constant and close to the maximum available value. For example, at 400 keV, because of the flat-top characteristic shown in Figure 1, it can be seen that a narrow bunch injected in the vicinity of $\phi_0 = 120^\circ$ will produce an emergent beam having a sharp spectrum and a mean energy that is relatively insensitive to small variations of entry phase. Although it is necessary to also evaluate the emergent bunch phase characteristics before deciding on the best mode of linac operation, as discussed below, the Figure 1 $V_0=2$ MeV curve shows $\partial V_a / \partial \phi_0 \rightarrow 0$ at three locations, A, B and C, where narrow bunch injection will result in sharp spectra operation but at different absolute values of emergent beam energy.

The phase orbit characteristics of the Design D(94) structure, taking into account the effects of space charge, changing bunch geometry, reactive phase distortion and power transfer to the beam and circuit are shown plotted in Figure 2 for an injected bunch width of 20° at two different entry phase intervals and for zero and 200 mA beam loading at a 580 keV injection energy. The curves indicate that for an injection phase interval between 105° and 125° , the bunch advances only 1° due to beam loading and emerges with narrow spectra and a longitudinal phase space of $< 2^\circ$, i.e., a bunch width of less than 1/3 of a picosecond. An indication of the versatility of the linac system is given by the results of phase orbit

Table II. 17 GHz Linac Structure Design D(94) Parameters

Operating Frequency in Vacuo at 22°C	17.136 GHz
Total Voltage Attenuation	0.59 Np
Input Group Velocity	0.0474c
Output Group Velocity	0.0196c
Harmonic Mean Group Velocity	0.0316c
Filling Time	57.8 ns
Shunt Impedance Range	100.3 \rightarrow 124.1 M Ω /m
Output Phase/Frequency Sensitivity	20.8 deg/MHz
Output Phase/Frequency Sensitivity	5.9 deg/ $^\circ$ C
Steady-State Beam Loading Derivative	13.3 MeV/A
Accelerating Gradient at Zero Beam Loading	—
Maximum in Cavity No. 76	$14\sqrt{P_0(\text{MW})}$ MV/m
Maximum Surface Electric Field	$30.5\sqrt{P_0(\text{MW})}$ MV/m

computations using the same injection conditions as in Figure 2 ($\phi_0 = 105$ to 125°) but with the input RF power lowered from 20 to 10 MW. For these conditions, the emergent phase (δ_a) is delayed 28° (from -88° to -116°), the 200 mA loaded beam energy is reduced from 25.7 to 17.1 MeV, and the bunch width is increased by only 20%, to 1.2° . (Increasing the operating frequency by 1080 kHz will re-advance δ_a , causing V_a to be increased by 3% and the bunch width to be reduced by 4%.)

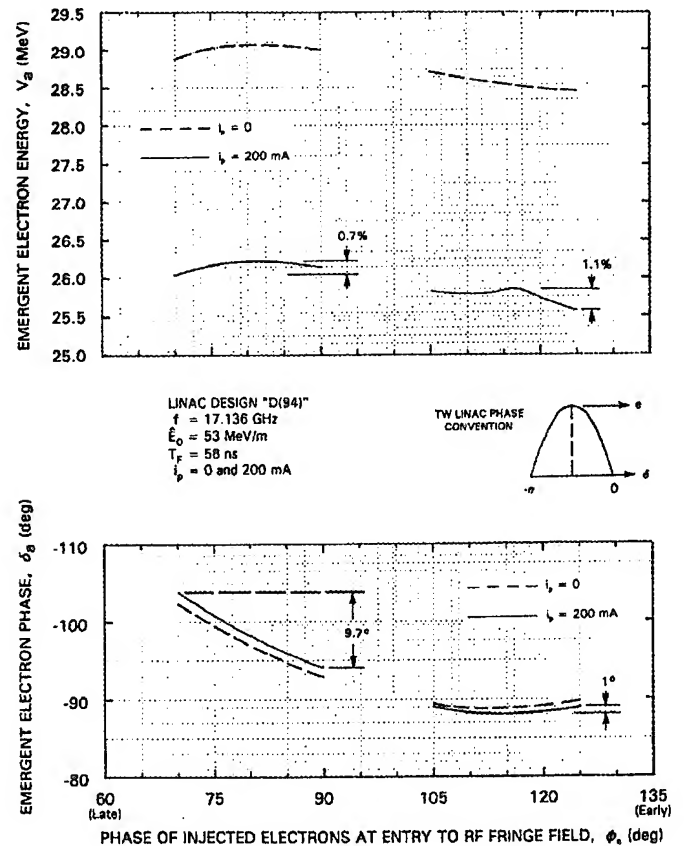


Figure 2: Phase Orbit Characteristics of a 17.136 GHz, $v_p=c$, Quasi-Constant Gradient TW Linac Structure [Design D(94)] for an Injection Energy of $V_0= 580$ keV at $i_p=0$, and at a Steady-State Beam Loading of $i_p=200$ mA, for an Entry Beam Diameter of 2 mm.

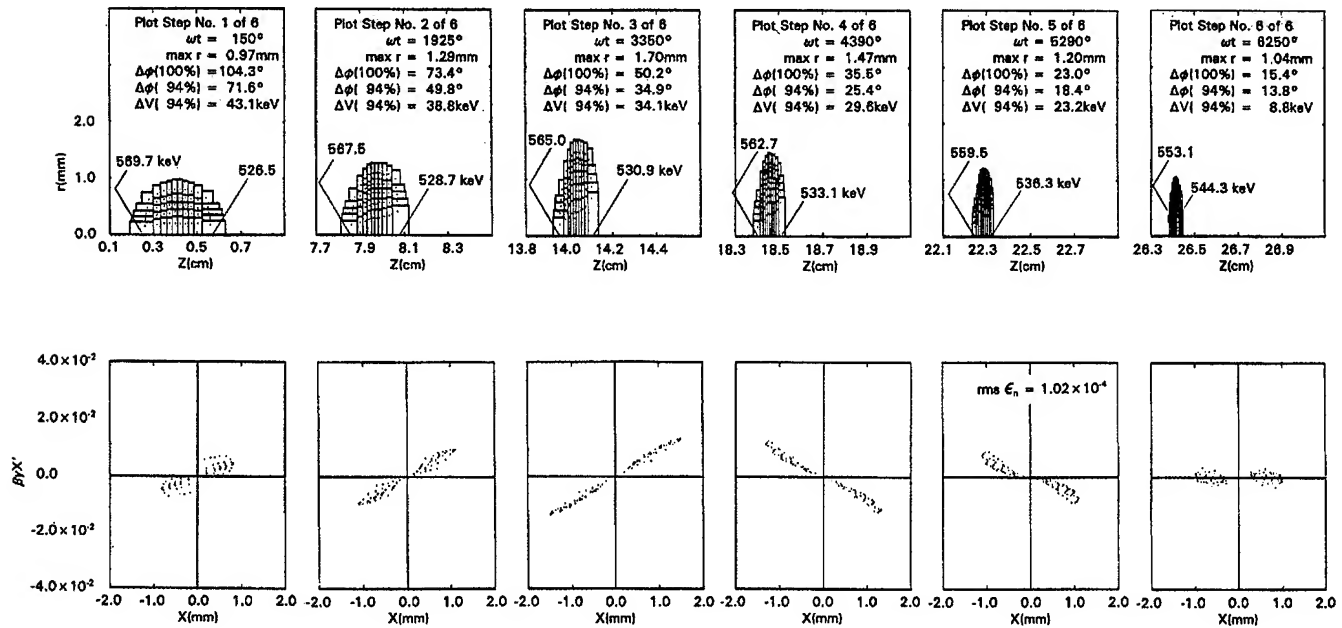


Figure 3: HRC-PRELOR Plots of the 550 kV Chopper-Prebuncher System Showing Progressive Bunch Compression and the Transverse Phase Space during Beam Traversal of the Final Drift Space Prior to Injection into the 17 GHz Accelerator Structure. (Prebuncher Drift = 30 cm, Thin Lens Peak Field = 2400 gauss, $i_p = 320$ mA, Beam Waist at Injection = 2.1 mm.)

III. 17 GHz CHOPPER-PREBUNCHER

A 550 kV electron gun, chopper-prebuncher, three lens injection system has been designed to satisfy the stringent beam specifications at entry to the linac, [$\beta\gamma\epsilon \approx 5\pi$ mm-radians, $\Delta\beta_0 < 0.3\%$ (± 5 keV) and $\Delta\phi_0 < 20^\circ$ (including 5° of phase modulation due to gun voltage variations)]. A biased, RF magnetic field chopping system [2] will be used to produce fully gated bunches at 17.136 GHz so that electrons are injected into the linac only during periods when the RF deflection is passing through a reversal, i.e., when $\partial V_{RF}/\partial\omega t$, p_\perp and $\partial p_\perp/\partial\omega t \rightarrow 0$. A high field prebuncher cavity with a short drift space and final focusing lens has been designed to give 10:1 charge compression, with the initially introduced 50 keV energy spread being reduced to < 10 keV by the beam focusing and bunching space charge forces, prior to injection into the linac. Figure 3 shows a simulation of the space charge influenced energy and charge distributions within the compressing bunch as it diverges from the chopper collimator through the final drift space lens and is re-converged to a waist at entry to the accelerator waveguide. These $i_p = 320$ mA beam bunching computations, based on an initial multi-annular model having a prolate spheroidal geometry with nonuniform longitudinal and radial charge distributions, indicate that $> 90\%$ of the charge will be injected into the linac with an energy spread of 8.8 keV and a longitudinal phase space of less than 15° (in the absence of phase modulation due to gun voltage variations). The linac phase orbit characteristics, based on the Figure 3 injected electron energy and charge distributions, are shown in Table III and confirm the high probability of demonstrating a 20 MeV beam with 160 femtosecond bunches and a bunch current of 100 A.

Table III. Phase Orbit Performance of the Design D(94) 17 GHz Linac Structure Based on the Figure 3 Injected Bunch Characteristics ($i_p = 320$ mA, $P_0 = 20$ MW).

Input Orbits		Exit Orbits		
V_0 (MeV)	ϕ_0 (deg)	V_a (MeV)	δ_a (deg)	$\Delta\delta_a$ (deg)
0.544	121.00	24.270	-91.01	0.93
0.545	118.28	24.219	-91.08	
0.546	115.57	24.172	-91.22	
0.548	113.39	24.137	-91.29	
0.550	109.86	24.106	-91.74	
0.553	107.19	24.092	-91.94	

IV. REFERENCES

- [1] J. Haimson, "Electron Bunching in Traveling Wave Linear Accelerators," *Nucl. Instr. and Meth.*, **39** p. 13, 1966.
- [2] J. Haimson and B. Mecklenburg, "Microwave and Beam Optics Design Features of a Preinjector Linac for a Synchrotron Radiation Source," in *Proc. IEEE PAC 1991*, 91CH3038-7, pp. 3183-3185, 1991.
- [3] J. Haimson, B. Mecklenburg and B.G. Danly, "Initial Performance of a High Gain, High Efficiency 17 GHz Traveling Wave Relativistic Klystron for High Gradient Accelerator Research," in *Pulsed RF Sources for Linear Colliders*, R.C. Fernow, editor, *AIP Conference Proceedings*, AIP Press, 1995.
- [4] J. Haimson, "Low Emittance High Duty Factor Injector Linac," *IEEE Trans. Nucl. Sci.*, **NS-18** No. 3, pp. 592-594, June 1971.

Electron Acceleration in Relativistic Plasma Waves Generated by a Single Frequency Short-Pulse Laser

C.A. Coverdale, C.B. Darrow, C.D. Decker
Lawrence Livermore National Lab, P.O. Box 808, Livermore, CA 94550

W.B. Mori, K.-C. Tzeng, C.E. Clayton, K.A. Marsh, and C. Joshi
Departments of Physics and Electrical Engineering
University of California, Los Angeles 90024

Abstract

Experimental evidence for the acceleration of electrons in a relativistic plasma wave generated by Raman forward scattering (SRS-F) of a single-frequency short pulse laser are presented. A 1.053 μm , 600 fsec, 5 TW laser was focused into a gas jet with a peak intensity of $8 \times 10^{17} \text{ W/cm}^2$. At a plasma density of $2 \times 10^{19} \text{ cm}^{-3}$, 2 MeV electrons were detected and their appearance was correlated with the anti-Stokes laser sideband generated by SRS-F. The results are in good agreement with 2-D PIC simulations. The use of short pulse lasers for making ultra-high gradient accelerators is explored.

I. INTRODUCTION

There have been many recent analyses on the stability of short laser pulses propagating through underdense plasmas.[1]-[5] These analyses have shown that such pulses are susceptible to several instabilities which can generate large plasma-wave wakes. One such instability is stimulated Raman forward scattering (SRS-F). SRS-F is a parametric instability in which an incident electromagnetic wave (ω_o, k_o) decays into an electron plasma wave (ω_p, k_p) and two forward propagating electromagnetic waves at frequency $\omega_o - \omega_p$ (Stokes) and $\omega_o + \omega_p$ (anti-Stokes), where $\omega_p = (4\pi e^2 n_o / m)^{1/2}$. [6] Energetic electrons are generated by the resulting electron plasma wave. The simultaneous observation of the Stokes and anti-Stokes features and energetic electrons is the strongest evidence for the excitation of SRS-F. The few previous experimental observations of the spectral signature of SRS-F [7] and the energetic electrons associated with the Raman forward scatter [8] were obtained using long pulse lasers (≥ 10 psec). The development of short pulse, high intensity laser systems in recent years has provided a new experimental regime in which to study SRS-F. The experiments and supporting particle-in-cell (PIC) simulations described here show both the spectral features and accelerated electrons, clear evidence of forward stimulated Raman scattering in short pulse, high intensity, underdense plasma interactions.

II. EXPERIMENTS

In these experiments, a 1.053 μm , 600 fsec, 5 TW laser was focused with an f/8.2 aspheric lens into a burst of helium exiting a gas jet, generating a plasma approximately 0.8 mm long. [9] The peak laser intensity used was approximately $8 \times 10^{17} \text{ W/cm}^2$ ($v_{osc}/c = 0.8$). The plasma density was varied by varying the backing pressure of the gas jet (200-1000 psi); the plasma density ranged from $1 \times 10^{19} \text{ cm}^{-3}$ to $2.5 \times 10^{19} \text{ cm}^{-3}$. Near forward scattered light (5° - 7° from the laser axis) was collected and spectrally analyzed using a 0.25 m, 150 grooves/mm spectrometer coupled to a liquid nitrogen cooled silicon CCD camera.

The first and second anti-Stokes features were clearly observable in these spectra, as shown in figure 1. The $\Delta\omega$ between the first and second anti-Stokes and between the pump and the first anti-Stokes is the same to within 3%. Poor sensitivity of the CCD for wavelengths greater than 1100 nm precluded observation of the Stokes features. Although not shown here, the density inferred from the frequency shift of the first anti-Stokes feature monotonically increased with the backing pressure of the gas jet, as expected.

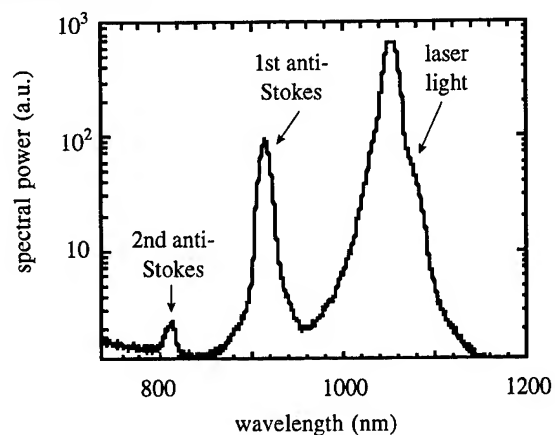


Figure 1: Spectrum of the near-forward scattered light (5° - 7° from the laser axis) showing the pump and two anti-Stokes sidebands.

High energy electrons produced by the forward SRS were measured with a 90° bending magnet electron spectrometer placed eight centimeters past the jet in the direct forward path of the laser. Electrons escaping the plasma in an $f/4$ cone were deflected by the magnet and detected using a 1 mm thick silicon surface barrier detector (SBD). The magnetic field (1.5 kG) was chosen to collect 2.0 ± 0.1 MeV electrons in these experiments. The SBD was shielded to minimize the direct x-ray flux. Additional shielding blocked the line of site between the plasma region and the SBD, ensuring that electrons reaching the SBD were deflected with the magnet. A second SBD was placed 15 cm from the gas jet 135° from the laser propagation direction to monitor x-ray signal. The x-ray contribution to the signal on the electron SBD was measured by reversing the magnet polarity and correlating the x-ray signals measured on the two detectors. The electron-plus-x-ray was then measured on the electron detector with the correct polarity B field while the control detector measured the x-ray contribution. In this manner, the x-ray contribution (typically about 10%) to the electron signal could be subtracted.

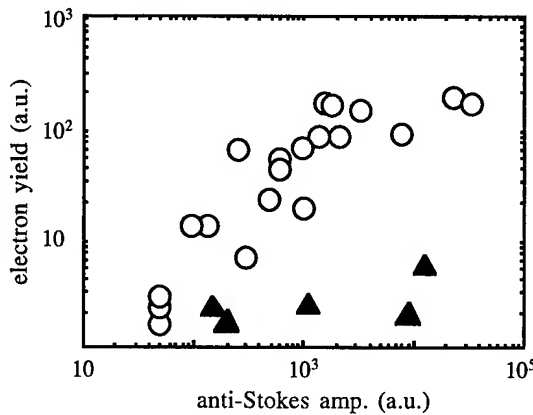


Figure 2: Correlation of the 2.0 MeV electron signal with the amplitude of the first anti-Stokes feature (open circles). The solid triangles represent signal on the electron detector when the magnet polarity was reversed (null tests).

The electron measurements were made at or near 800 psi, the pressure at which the anti-Stokes levels were highest. The electron signal was generally seen to increase with an increase in the anti-Stokes level whereas the x-ray noise level remained more-or-less constant. This correlation is illustrated in figure 2 (open circles). The results of a null experiment are also shown in figure 2 (solid triangles). The null values were obtained by reversing the polarity of the magnet, i.e., deflecting energetic electrons away from the electron SBD.

III. SIMULATIONS

The advent of massively parallel supercomputers has made possible more realistic modeling of short pulse laser-plasma experiments than in the past; i.e., the spatial dimensions (transverse and longitudinal), laser pulsewidth, laser to plasma frequency ratio, and propagation distance in the simulation are the same as in the experiments. We have developed a parallelized fully relativistic, two dimensional electromagnetic PIC code which uses the basic algorithm of ISIS on a cyclic mesh. [5] The computational box is a 8192×256 cartesian grid and the simulations follow 1.2×10^7 particles for 3×10^4 time steps. The main difficulties with quantitatively modeling the experiment are that the noise level in the simulation is typically larger than in the experiment and that the simulations are two dimensional (slab geometry).

In order to model the experimental conditions accurately, an estimate of the effective plasma length is required. This estimate was made by performing a series of simulations which covered a range of laser intensities and plasma densities: (A) $\omega_o/\omega_p=10$, $v_{osc}/c=0.33$, (B) $\omega_o/\omega_p=10$, $v_{osc}/c=0.8$, and (C) $\omega_o/\omega_p=5$, $v_{osc}/c=0.5$. In each simulation, the laser pulse duration was 600 fsec, the plasma was preformed with a uniform density, and the ions were immobile. The evolution of the electron distribution function and the electromagnetic mode spectra were monitored as a function of distance the rising edge of the laser pulse propagated into the plasma.

In figure 3, we show for simulation B the electron distribution function, $f(P_x)$, and the k spectrum of the laser, $E_z(k_x, k_y)$, after the pulse has penetrated 0.48 mm and 0.64 mm into the plasma. We calculate the total energy within each anti-Stokes line and find that after 0.64 mm (0.48 mm), the ratio of anti-Stokes/pump = 0.06 (0.006) and second anti-Stokes/anti-Stokes = 0.04 (in the noise). The experimentally measured ratios at 5° - 7° for the anti-Stokes/pump and the 2nd anti-Stokes/1st anti-Stokes were 0.034 and 0.027 respectively. The second anti-Stokes was not seen on every shot and there was substantial shot-to-shot variation (factor of 2) in the normalized anti-Stokes level. The results from the experiment and the simulations are in reasonable agreement, within the shot-to-shot variation, for a plasma length of 0.64 mm. Importantly this distance is less than the presumed dimension of the gas jet. In addition, the edge of the electron distribution does not exceed 2 MeV until the laser has penetrated 0.48 mm into the plasma (figure 3(a)). It extends to 5 MeV after 0.64 mm of plasma, with a few electrons at 20 MeV (figure 3(b)). We emphasize that in simulation A ($v_{osc}/c=0.33$), no MeV electrons or higher order anti-Stokes sidebands were

observed for laser penetration distances less than 1 mm. Furthermore, the simulations show that if the interaction length is extended to 1.3 mm, the maximum energy of the self-trapped electrons approaches 60 MeV.

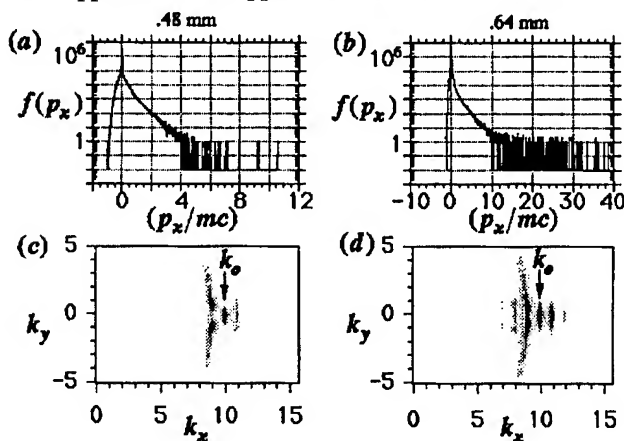


Figure 3: The electron distribution function at (a) 0.48 mm and (b) 0.64 mm and the corresponding electromagnetic k spectrum at (c) 0.48 mm and (d) 0.64 mm for $\omega_0/\omega_p=10$ and $v_{osc}/c=0.8$.

IV. CONCLUSIONS

To summarize, forward stimulated Raman scatter was observed in short pulse, high intensity laser, underdense plasma interaction experiments. Two anti-Stokes features were resolved in the near-forward spectra. Electrons accelerated to 2 MeV were monitored and correlated with the first anti-Stokes feature of the SRS-F. The experimental results are in good agreement with PIC simulations results. The simulations show that if the interaction length could be extended to 1.3 mm, the electrons would be accelerated to energies as high as 60 MeV by gradients of order 100 GeV/m. Therefore a short pulse, single-frequency laser could form the basis of a robust, ultra-high gradient, modest beam quality electron accelerator.

This work is supported by U.S. DOE grant number DE-FG03-92ER40727 (UCLA) and DOE contract number W-7405-ENG-48 (LLNL).

V. REFERENCES

- [1] E. Easery *et al.*, Phys. Rev. Lett., **72**, 2887 (1994); J. Krall *et al.*, Phys. Rev. E **48**, 2157 (1993).
- [2] T. Antonsen and P. Mora, Phys. Rev. Lett. **69**, 2204 (1992); Phys. Flu. B **5**, 1440 (1993).
- [3] N. E. Adreiev *et al.*, JETP Lett. **55**, 571 (1992).
- [4] W. B. Mori *et al.*, Phys. Rev. Lett. **72**, 1482 (1994)
- [5] C. B. Decker, PhD. Dissertation, UCLA-PPG #1526 (1994); C. B. Decker *et al.*, Phys. Rev. E **50**, R3338 (1994).
- [6] D.W. Forslund *et al.*, Phys. Fluids **18**, 1002 (1975) and references therein; K. Estabrook and W.L. Kruer, Phys. Fluids **26**, 1892 (1983).
- [7] R.E. Turner *et al.*, Phys. Rev. Lett. **57**, 1725 (1986); S.H. Batha *et al.*, Phys. Rev. Lett. **66**, (1991).
- [8] C. Joshi *et al.*, Phys. Rev. Lett. **47**, 1285 (1981).
- [9] C. Clayton and M. Everett, submitted to Rev. Sci. Instr.

Theory and Simulation of Plasma Accelerators

W. B. Mori, K-C. Tzeng, C. D. Decker, C. E. Clayton, and C. Joshi
UCLA, Departments of Electrical Engineering and Physics

T. Katsouleas, P. Lai, T. C. Chiou, and R. Kinter
USC, Department of Electrical Engineering

Abstract

We report on some of the recent theoretical and computational results at UCLA and USC on plasma-based accelerator concepts. Topics discussed include beat-wave excitation from short-pulse lasers, self-trapped electron acceleration from self-modulational instabilities and wakefield excitation in preformed channels.

INTRODUCTION

For some time now plasma structures have been considered as the basis for future accelerators. The plasma serves two purposes: (1) the plasma has no breakdown limits because it is already ionized and (2) the plasma supports large longitudinal waves. In these waves the electrons oscillate back and forth at $\omega_p \equiv (4\pi e^2 n/m)^{1/2}$ due to the space charge of the immobile ion background irrespective of the wavelength. Therefore by properly phasing these oscillations it is possible to create a wave with $v_\phi \approx c$, i.e., a relativistic plasma wave. In such a wave electrons can acquire relativistic energies before they dephase from the wave. The accelerating gradient of a relativistic plasma wave is given by $\epsilon \sqrt{n} V/cm$ where n is the plasma density in cm^{-3} and ϵ is the density perturbation of the wave. For a density of $10^{16} cm^{-3}$ gradients of 10 GeV/m are possible in a plasma.

Relativistic plasma waves can be generated by propagating either intense laser beams¹ or intense particle² beams through a plasma. During the past two years there have been several exciting experimental results on laser beam excitation,^{3,4,5} so in this brief report we limit the results to those related to laser-plasma accelerators.

In 1979, Tajima and Dawson¹ published the seminal paper on laser-plasma accelerators. They showed that relativistic plasma wave wake is excited behind a short pulse with a pulse length matched to half a plasma wavelength, $L_p = \pi c/\omega_p$. This is now called the Laser Wakefield Accelerator (LWFA).⁶ In addition, Tajima and Dawson suggested two alternative ways to excite a plasma wave: 1) use two longer pulses with a frequency separation equal to ω_p to resonantly excite a wave or 2) rely on a long pulse to undergo the Raman forward scattering instability.⁷ The first is now called the Plasma Beat Wave Accelerator (PBWA) and the second is related to a scheme named the self-modulated LWFA.⁹ We will present some results related to each scheme.

PBWA

Theory,⁸ simulations⁸ and experiments³ make it poignantly clear that the PBWA will work best for pulse lengths matched to the Rosenbluth and Liu detuning time

and less than an ion period. Laser technology now makes it possible to generate pulses which satisfy these constraints for plasma densities above $10^{16} cm^{-3}$. Based on these considerations, we have investigated the feasibility of a 1 GeV PBWA experiment using existing technology.¹⁰ The proposed parameters are given in Table I. The parameters were modeled

Laser wavelengths	1.05 μm and 1.06 μm
Plasma Density	$10^{17} cm^{-3}$
Plasma Source	Multiphoton Ionization
Laser Pulselength	4 ps
Laser Power	14 TW
Laser Spot Size (2σ)	200 μm
Rayleigh length (Z_R)	3.1 cm
Plasma Homogeneity	$\pm 7\%$
Peak Plasma Wave Amplitude	0.5
Peak Gradient	160 MeV/cm
Final Energy	1 GeV

TABLE 1.

using a combination of simulation codes. In Fig. 1a we plot the peak accelerating wave amplitude as a function of axial position. These amplitudes were obtained by integrating the Rosenbluth and Liu envelope equations for each local position within the focal cone of the laser. Treating each position locally has been verified in PIC simulations⁸ as long as the spot size exceeds a few c/ω_p . In Fig. 1b results from a 2-D PIC simulation which uses a prescribed ponderomotive force are presented. This simulation demonstrates that near the focus the plasma wave is nearly planar. The peak accelerating gradient corresponds to 15 GeV/m. In Figs. 1c and 1d we show the results from test particle simulations using the accelerating field of Fig. 1a. The injected beam is a 1 nC, 4 ps long continuous e-beam at an energy of 10 MeV with a spot size of 20 μm and an emittance of .1 mm-mr. The results show that 10^8 (2% of the injected) electrons are accelerated into microbunches 30 fs long separated by 300 fs. To illustrate the evolution of these short laser pulses as they propagate through a Rayleigh length of plasma, we present results from a 1-D PIC simulation in Fig. 2. We show the accelerating field and the laser envelope after the laser has gone through a Rayleigh length (10 pulse lengths) of plasma. The plasma wave and the envelope look almost identical to their initial profiles. We end this section by noting that experimental design parameters can also be put forth for bunching electron beams at lower energies, e.g., 100 MeV.

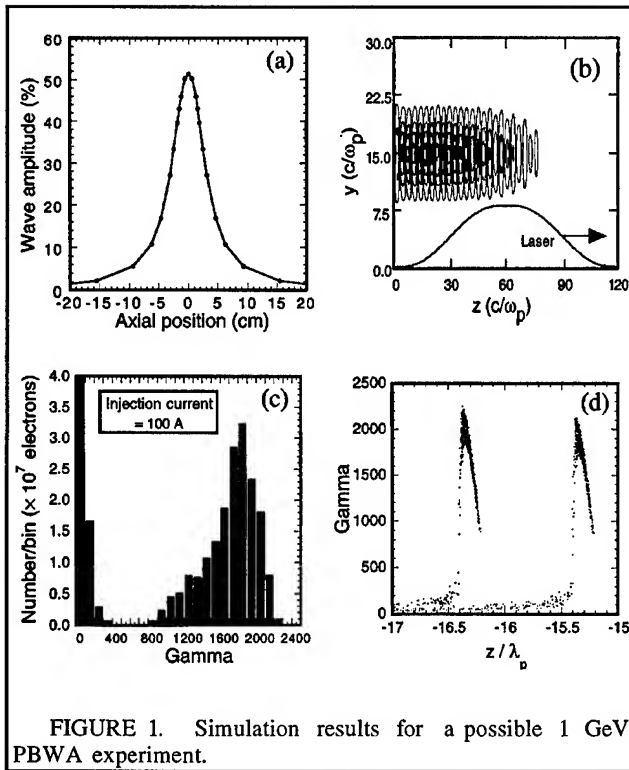


FIGURE 1. Simulation results for a possible 1 GeV PBWA experiment.

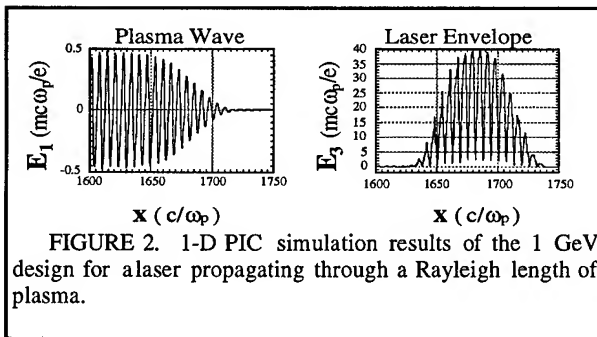


FIGURE 2. 1-D PIC simulation results of the 1 GeV design for a laser propagating through a Rayleigh length of plasma.

SELF-MODULATED LWFA

It has been well known that beat wave excitation is related to a laser-plasma instability called Raman forward scattering (RFS).^{1,7,13} However, RFS was not considered a serious accelerator concept because its growth rate was slow enough that ion motion disrupted the acceleration process. Simulations showed that this and wavebreaking led to inefficient acceleration and low beam quality.

The development of short-pulse lasers has led to new work and ideas for the use of laser instabilities. In 1992, Antonsen and Mora¹⁵ and Sprangle¹⁶ et al. demonstrated by using fluid codes that a short pulse high-intensity laser will self-modulate in a distance of a few Rayleigh lengths and generate large wakes. Recently, Krall et al.⁹ and independently Andreev et al.⁹, investigated the feasibility of using these wakes for an accelerator. Krall et al call this concept the self-modulated LWFA.

We have been investigating the stability of short-pulse lasers using particle-in-cell codes¹² rather than fluid

codes. In addition we have been investigating the theoretical¹³ differences between RFS of short-pulses and the self-modulation instability of Esarey et al.¹² For brevity we only present the simulations results while the theoretical results can be found in the references.¹³ The simulations are done using a parallelized version of ISIS with a moving grid. These improvements make it possible for the first time to simulate the actual spatial and temporal scales of a laser-plasma accelerator experiment using a 2-D fully explicit PIC code.⁴ The experimental parameters are $\lambda = 1 \mu\text{m}$, $I = 10^{18} \text{ W/cm}^2$, $\tau_p = 600 \text{ fs}$, $n \approx 1 \times 10^{19} \text{ cm}^{-3}$ and $W_0 = 18 \mu\text{m}$. These parameters are representative of both the LLNL⁴ and RAL⁵ laser systems. Typical simulations results are shown in Figs. 3 and 4. These results show that under most situations RFS of a short intense laser pulse inevitably leads to self-trapped electrons. In Figs. 3a and 3b the evolution of the laser pulse is shown. It is clear that the laser pulse breaks apart into beamlets spaced at the plasma wave wavelength in distances less than a Rayleigh length. This breakup is dominated by RFS as illustrated by the power spectrum in Fig. 3c which shows multiple stokes and anti-stokes sidebands. This beam breakup results in the plasma wave evolution depicted in Figs. 3d-g. The wave amplitude never reaches the cold wavebreaking value because it self-traps large amount of Raman back and sidescattered generated electrons. The electron distribution function is shown in Fig. 4 for two different propagation distances. Fig. 4a is representative of the LLNL interaction length while Fig. 4b is representative of the RAL interaction length. For the plasma density simulated, $n = 10^{19} \text{ cm}^{-3}$, the maximum electron energy saturates at $\sim 60 \text{ MeV}$. These simulation results are in good quantitative agreement with the LLNL experimental results.⁴ The exact RAL parameters have not yet been simulated. The PIC simulations clearly demonstrate that RFS and other self-modulational type instabilities can lead to self-trapped electrons generating a high current, 10 kA, poor beam quality electron beam. The experimentally inferred accelerating gradients are $\sim 100 \text{ GeV/m}$.

LWFA IN A HOLLOW CHANNEL

In any accelerator the energy gain is given by $q \int d\ell \cdot \vec{E}$. In plasma accelerators the gradient qE can be very large but the interaction length $\int d\ell$ can be limited.

One limitation is the diffraction length of the laser. To overcome this, methods for optical guiding are being actively investigated.¹² One method is to guide a laser pulse in a hollow plasma channel where the density at the channel wall is still much less than the critical density.¹⁴ However, since the channel is completely evacuated, the plasma wave wake will not be excited in the same manner as in the conventional LWFA. We have investigated the wakes created

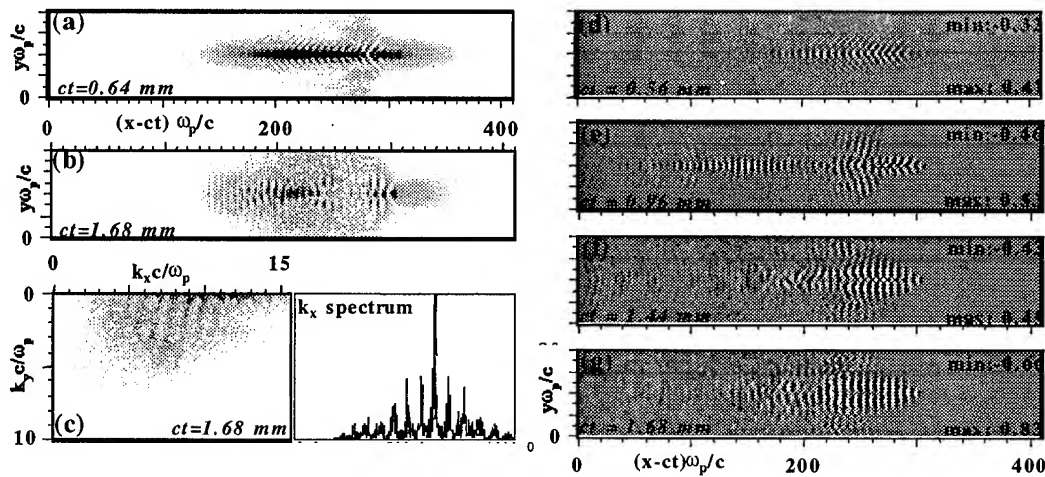


FIGURE 3. Results from a 2-D PIC simulation which models experiments at LLNL and RAL.

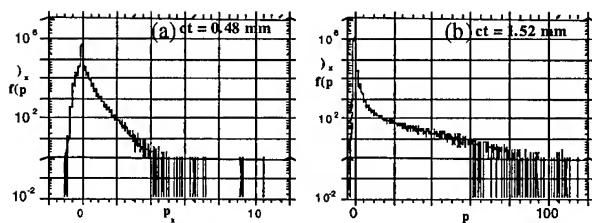


FIGURE 4. Distribution functions of the self-trapped electrons from the 2-D PIC simulation. P is normalized to mc .

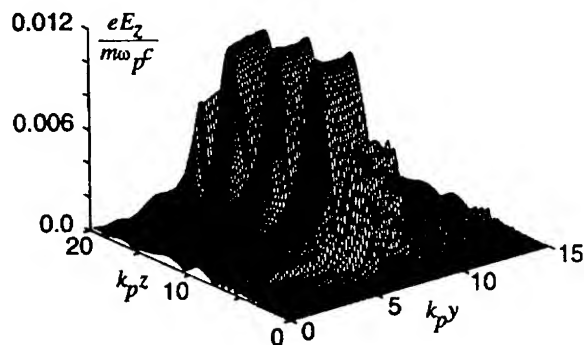


FIGURE 5. The accelerating wake generated by a short-pulse laser propagating in a hollow channel.

by a short-pulse, propagating in such a channel. The wake is supported by surface currents excited at the channel boundaries by the ponderomotive force of the laser. We find for sufficiently narrow channels that the accelerating gradient on axis is only slightly lower than that achieved in the conventional LWFA. Furthermore, the accelerating wake is uniform across the channel and the focusing wake varies linearly across the channel. These wake properties are advantageous for generating high quality beams. This is illustrated in Fig. 3 where the accelerating wake obtained in a PIC simulation is presented. The disadvantages of these scheme, (and other wakefield schemes in a channel), is that the wake is susceptible to

resonance absorption at the channel walls. More details can be found in the references.

CONCLUSIONS

We briefly review some of the recent work done at UCLA and USC on laser-plasma accelerators. This field has been bolstered by several laser-plasma experiments. Based on these results we believe it is possible to demonstrate in a PBWA experiment bunching of injected particles in the energy range of 100 MeV to 1 GeV using existing technology. Furthermore, single frequency excitation of wakes could form the basis of a robust, modest energy, ultra-high gradient but poor beam quality accelerator.

Work supported by U.S. Department of Energy under grant numbers DE-FG2-92ER40727 and DE-FG03-92ER40745.

REFERENCES

1. T. Tajima and J. M. Dawson, Phys. Rev. Lett. **43**, 267 (1979).
2. P. Chen et al., Phys. Rev. Lett. **54**, 693 (1985).
3. M. Everett et al., Nature **368**, 527 (1994); C. E. Clayton et al., Phys. Rev. Lett. **70**, 37 (1993).
4. C. Coverdale et al., accepted in Phys. Rev. Lett.
5. A. E. Dangor et al., submitted to Nature.
6. P. Sprangle et al., Appl. Phys. Lett. **53**, 2146 (1988).
7. D. W. Forslund et al., Phys. Rev. Lett. **54**, 558 (1985) and attached references.
8. C. Joshi et al., Nature **311**, 525 (1984); W.B.Mori IEEE Trans. Plasma Sci. **PS-15**, 88 (1987); W. B. Mori, Ph.D. Dissertation, UCLA.
9. J. Krall et al., Phys. Rev. E **48**, 2157 (1993); N. E. Andreev et al., JETP Lett. **57**, 2200 (1992).
10. C. Joshi et al., Comments on Plasma Physics **16**, 65 (1994).
11. C. Joshi et al., Phys. Rev. Lett. **47**, 1285 (1981).
12. T. Antonsen and P. Mora, Phys. Rev. Lett. **69**, 2204 (1992); P. Sprangle et al., Phys. Rev. Lett. **69**, 2200 (1992); E. Esarey et al., Phys. Rev. Lett. **72**, 2887 (1994).
13. C. D. Decker et al., Phys. Rev. E **51**, R3338 (1994); W. B. Mori et al., Phys. Rev. Lett. **72**, 1482 (1994); C. D. Decker, Ph.D. dissertation, UCLA PPG-1526.
14. T.C. Chiou et al., Phys. Plasmas **2**, 310 (1995).

An Injector-prebuncher for a Plasma Electron Accelerator

M. Lampel, C. Pellegrini, R. Zhang, UCLA, Dept of Physics, C. Joshi, UCLA, Dept of EE, Los Angeles, CA 90095, and W. M. Fawley, LBL, Berkeley, CA 94720

ABSTRACT

Optimum operation of a plasma beat-wave or wakefield accelerator requires an injected beam consisting of a train of electron bunches separated by the plasma wavelength, with each bunch in the train having a length much shorter than the plasma wavelength, and the capability of controlling the relative phase of the electron bunches and plasma wave. The typical plasma wavelength is about 0.1 mm, requiring a bunch length of about 10 to 20 μm , which is difficult to achieve with conventional RF based injectors. In this paper we describe an electron accelerator-buncher system based on a photoinjector and an FEL, which can satisfy the plasma accelerator requirements.

INTRODUCTION

An injector of up to 25 MeV beam energy is proposed to supply the Plasma Beat Wave Accelerator (PBWA) [1] with a high quality ($\epsilon = 0.5 \pi \text{ mm-mrad}$ at full energy) electron beam of sufficient intensity ($\sim 1 \text{ nC}$ per pulse) to allow capture and acceleration by the PBWA of a significant number of electrons to the GeV energy range. The injector will be based on proven technology from the Saturnus laboratory [2], with upgrades of both the BNL RF gun [3], and the Plane Wave Transformer (PWT) accelerator [4]. The system will provide 1 nC average micropulse charge focused to a 100 μm spot diameter at the injection point. A FIR FEL is proposed as an optical pre-buncher. Phase locked pre-bunching of the electron pulse into 10 - 20 μm long bunchlets will allow control of the relative phase of the electron bunchlet and the plasma wave. Such control will aid in minimizing PBWA electron beam final energy spread and emittance. The optical pre-buncher/ final focus system may need to be an achromatic and isochronous system to second or perhaps third order to maintain the bunchlets shape after exiting the optical resonator.

PBWA REQUIREMENTS

A PBWA operates by mixing two lines from a drive laser in a plasma whose parameters are chosen so that the beat between the laser lines matches the plasma frequency. We assume a multi-terawatt 1 μm laser system as the drive laser system for the PBWA. The PBWA requirements dictate the design of the injector so that efficient matching can occur. Table 1 shows the top level parameters upon which

the design is based.

TABLE I

Parameter	Design Value
Emittance (unnormalised, rms.)	$0.5 \pi \text{ mm-mrad}$
Energy spread (rms.)	2%
Injector beam energy	$>2 \text{ MeV}$
Average charge in bunch (bunchlet)	1 nC ($10^8 e^-$)
Bunchlet length	30 - 60 fs
Bunchlet diameter (2σ)	$<200 \mu\text{m}$
Phase Control	
absolute	$\pm 1 \text{ ps}$
relative	$<30 \text{ fs}$

Injection phase control of the bunchlets facilitates optimization of the PBWA for acceleration, reducing the energy spread and emittance of the PBWA accelerated beam. Absolute timing is relaxed because the electron pulse can be much longer than the laser pulse. However relative timing of the plasma beat waves with the electron bunchlets becomes necessary. A nonlinear optics control method of phase locking bunchlet formation to the beat wave produced by the lasers is necessary. Several possibilities exist to achieve this and detailed studies will be done to identify the most likely candidates so that the issue will be resolved before the optical bunching experiment is begun. We note that the options include: 1) Use of a beatwave-plasma interaction to produce 100 μm phase locked radiation to seed an FEL amplifier and; 2) use of nonlinear index of refraction changes in a plasma, due to a plasma beat-wave interaction, to control the optical path length, thus the relative phase, of 100 μm light.

The baseline injector system uses the technology of the Saturnus experiment. The Saturnus hardware represents all the hardware needed for the injector, except for the experiment specific final focus into the PBWA, and phase locking of the electron pulse to the PBWA laser system.

INJECTOR DESCRIPTION

A standard RF power system consisting of a modulator and klystron runs a photo-cathode RF gun (0-5 MeV) and an PWT (pulse wave transformer) accelerator section (5-25 MeV). The electron beam generated in the gun is focused by bucking solenoids so that it has proper size entering the accelerator. X-Y steering magnets correct for any small mechanical misalignments. After exiting the accelerator section the beam travels through a beamline guided and focused by dipole and quadrupole magnets. These magnets match the electron pulse into the FIRFEL for prebunching. A final transport section matches the beam into the PBWA for acceleration by the plasma wave.

The modulator and klystron provide up to 35 MW, approximately 7 MW to the electron gun and the rest available to the PWT. The design of the modulator is taken from the present modulator for the Saturnus experiment, capable of running at 5 pps. The klystron will be a SLAC XK-5 of which UCLA currently has two available for this project.

Fourth harmonic light of the PBWA laser drives the photocathode. The gun itself is the second generation of the successful Brookhaven National Laboratory rf gun. A slight modification of the length of the first cavity, to 0.6λ , results in an increased electron beam brightness (a decrease in beam emittance) over the original "half cavity" design.

The PWT is a high gradient standing wave accelerator. Several engineering and fabrication improvements are proposed for the new injector: A simplification of the internal cooling of the structure; use of all metal sealing surfaces for greater radiation resistance and better vacuum properties; redesign of the "disks" to reduce the maximum surface gradient. This improved PWT has been fabricated and tested with low level RF power and has been installed into the Saturnus beamline. In order to reach 25 MeV two PWT structures will be used.

THE FEL AS AN OPTICAL BUNCHER

The requirements on the pre-buncher are that $\sim 10\ \mu\text{m}$ bunches spaced $100\ \mu\text{m}$ apart are injected into the plasma beat wave accelerator with emittance and energy spread within the acceptance of the PBWA. An FEL naturally bunches electrons onto a fraction of the optical wave being amplified, one wavelength apart. From this it is quite clear why an FEL can be used as the PBWA pre-buncher.

Matching operation of the pre-buncher to produce the beam desired for injection into the PBWA leads to setting the operating point of the FEL in terms of energy, undulator length, and field

strength.

GINGER calculations for a master oscillator-power amplifier (MOPA) FIR FEL configuration have been done to begin examining the performance of a pre-buncher. Table II gives the GINGER parameters of the electron and optical beams studied for the oscillator and the amplifier.

Table II

Electron Beam Parameters Oscillator and Amplifier	
Electron beam energy	21 MeV
Micropulse current	150 A
Micropulse length (fwhm)	12 ps
Micropulse spacing	10 ns
Normalized emittance (edge)	$10\ \pi\ \text{mm-mrad}$
Resonator Parameters, osc.	
Single pass gain	2.4
Power in spontaneous emission after 1 pass	15 W
Saturated power (peak)	180 MW
Resonator length	1.5 m
Round trip time	10 ns
Undulator Parameters Oscillator and Amplifier	
Undulator period	4 cm
Undulator length, osc.	1 m
Undulator length, amp.	0.8 m
On axis magnetic field	1.04 T
path length correction factor $K^2/2$	11.3

The GINGER code test case is based on a parabolic electron bunch in z of total length 16 ps. The undulator is linear with external quadrupoles providing focusing in the wiggle plane.

The oscillator is assumed to have 60% net cavity reflectance, with a net cavity detuning that is 0% of slippage.

Figure 1 displays results from GINGER showing the bunching of the electrons at the end of the amplifier undulator. The first pulse displayed, at a time 1.33 ps into the bunch, demonstrates the excellent bunching possible through the FEL mechanism. The majority of electrons are clearly bunched very sharply in phase over

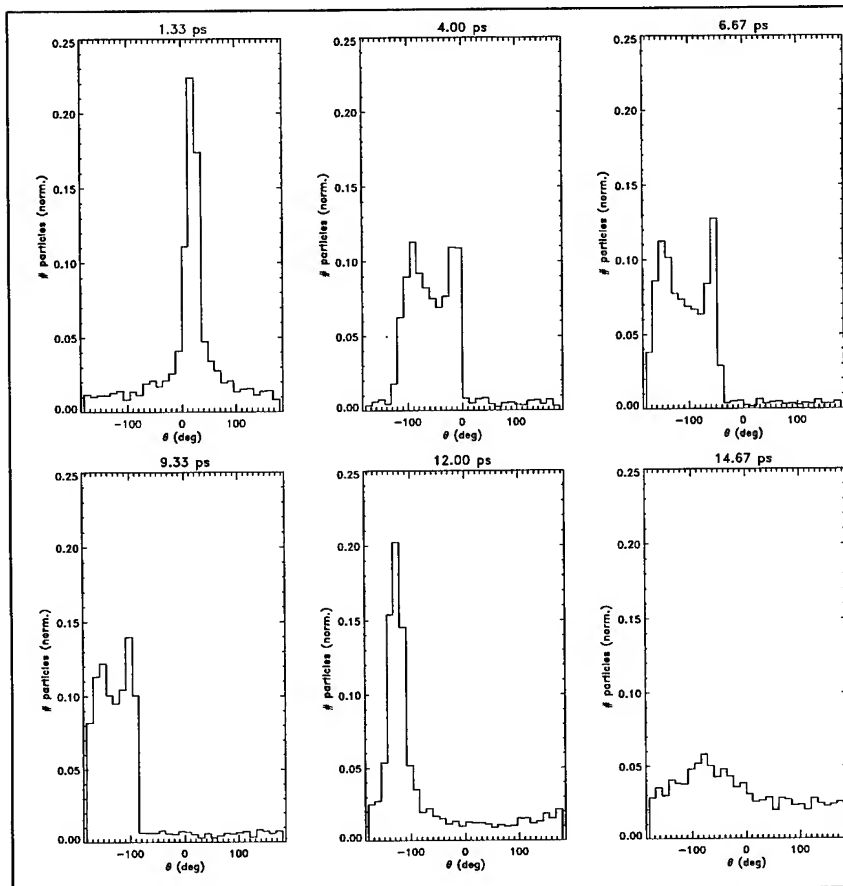


Figure 1:
Electron Beam bunching at six slices in time
at the amplifier undulator exit.

$\sim 60^\circ$, corresponding to less than $20 \mu\text{m}$. The forward part of the electron pulse is well bunched because the optical fields propagate from the rear to the front due to the slippage of the electron beam. The bunching parameter is about 0.7. To increase the number of well bunched slices, we will consider in future calculations two potentially beneficial effects: 1) tapering the undulator, and; 2) use of a waveguide in the amplifier to reduce slippage.

The amplifier needs a source of $100 \mu\text{m}$ light to start it. Two possibilities exist: The FEL oscillator could be built as the source. The MOPA configuration clearly provides a complete solution to the problem of getting $100 \mu\text{m}$ light, but is expensive and does not solve the phasing problem between the bunchlets and the PBWA beatwave. A second possibility would be to use the beatwave to produce a $100 \mu\text{m}$ seed for the FEL amplifier directly. This gives automatic phasing between the bunchlets and the wave. An initial calculation indicates that injecting the two lines from the drive laser into a plasma will produce at least 100 kW of coherent $100 \mu\text{m}$ light in a $f/1$ cone angle. As can be seen from Table II this power is several orders of magnitude greater than the spontaneous emission at the end of the first pass.

REFERENCES

- 1) Measurements of the Beatwave Dynamics in Space and Time, A. Lal, K. Wharton, D. Gordon, C.E. Clayton, M. Everett, C. Joshi, PAC 95, May 1-5, Dallas, TX
- 2) The UCLA Compact High Brightness Accelerator, P. Davis, G. Hairapetian, M. Hogan, C. Joshi, S. Park, C. Pellegrini, J.B. Rosenzweig, G. Travish, R. Zhang
- 3) Multipole Field Measurements in the SLAC/BNL #3 RF Gun, D. Palmer, R. H. Miller, H. Winick, X.J. Wang, K. Batchelor, M. Woodle, I. Ben-Zvi, PAC 95, May 1-5, Dallas, TX
- 4) Initial Operation of the Plane Wave Transformer (PWT) Linac R. Zhang, P. Davis, G. Hairapetian, M. Hogan, C. Joshi, S. Park, C. Pellegrini, J.B. Rosenzweig, G. Travish, PAC 95, May 1-5, Dallas, TX

Measurements of the Beatwave Dynamics in Time and Space*

A. Lal, K. Wharton, D. Gordon, M.J. Everett, C.E. Clayton, C. Joshi
Electrical Engineering Department, University of California, Los Angeles 90024

Abstract

We report on continuing experiments on the Plasma Beat Wave Accelerator, which uses an intense two-frequency CO₂ laser pulse to resonantly drive a large amplitude, relativistically-propagating electron plasma wave suitable for electron acceleration. Previously, energy gains of a factor 15 (from 2 MeV to 30 MeV) have been obtained [1]. Also, collective scattering of a probe laser beam has allowed us to measure $\tilde{n}(\omega, k)$ and $\tilde{n}(\omega_m, t)$ where $m=1,2$ are the fundamental and harmonic of the large amplitude plasma wave. This powerful Thomson scattering technique has now been extended to measure $\tilde{n}(z, t)$, where z is the coordinate along the CO₂ propagation direction. Nonlinear dynamics such as relativistic detuning and ponderomotive effects can complicate the longitudinal amplitude profile and coherence. Experimental results show a plasma wave with a peak amplitude of approximately 35%, with a FWHM of 100 ps, and extending for 1 cm in space. These wave parameters are consistent with the observed energy gains of accelerated electrons.

I. INTRODUCTION

In plasma based accelerator schemes, a relativistically propagating ($\gamma_{ph} \gg 1$) plasma wave is used for accelerating charged particles. Since the accelerating field is directly related to the plasma wave amplitude, it is important to know both the spatial and temporal structure of the wave in order to predict the energy gain or loss of a particle. In the Plasma Beat Wave Accelerator, a relativistic plasma wave (RPW) is resonantly excited by two laser beams in a tunnel ionized plasma such that the frequency difference of the lasers $\Delta\omega = \omega_0 - \omega_1$ is approximately equal to the plasma frequency ω_p . The spatial and temporal structure of the RPW depends on many factors, including the laser pulse shape and profile, the plasma ionization and expansion times, and the transverse ponderomotive forces of the laser and of the plasma wave itself. The features of the plasma wave are diagnosed with frequency and wavenumber resolved Thomson scattering.

II. EXPERIMENTAL SETUP

In the experiment, the plasma wave is generated by the ponderomotive force exerted on the plasma electrons by beating two frequencies in a short (150 ps rise, 300 ps FWHM) CO₂ laser pulse. The laser also creates the plasma by fully ionizing hydrogen gas via tunneling ionization, typically in the first 20-30 psec. The hydrogen gas pressure is adjusted so that the resonant plasma frequency matches the frequency difference of the two laser lines ($\lambda = 10.6 \mu\text{m}$ and $10.3 \mu\text{m}$). The initial density must be set about 10-15% higher than the resonant density ($= 9.4 \times 10^{15} \text{ cm}^{-3}$) to compensate for plasma blowout induced by the laser [2].

The plasma density fluctuations associated with the RPW are measured using collective Thomson scattering by a 2 ns (FWHM), 50 MW, $0.53 \mu\text{m}$ optical probe beam incident on the plasma at an angle of 87° relative to the CO₂ laser axis. Both the frequency and wavenumber of the waves in the plasma can be determined as a function of time by this diagnostic, since the ω and k of the scattered light is shifted by the plasma waves.

The driven RPW has a wavenumber that is determined by the wavenumber difference of the two laser lines at $\Delta k = k_0 - k_1 = 1.83 \times 10^{-2} \mu\text{m}^{-1}$. Due to this small k , a line focus of the probe beam is required to resolve the k spectrum. The experimental setup is shown in Figure 1. The input lenses bring the probe beam to a line focus of length 6 mm and height $100 \mu\text{m}$ at the plasma. The output lenses eliminate the astigmatism in the beam and refocus the unscattered light on a razor blade beam dump. The angular shift of the scattered light, $\Delta k/k_{pr}$, is 1.48 mrad, which corresponds to a shift of 1.05 mm per RPW harmonic at the razor blade. The razor blade blocks the main beam, but allows the scattered light to pass.

After the razor blade beam dump, the optical system has two possible configurations. In the first method, the plane of the razor blade (k space) is imaged onto the entrance slit of an imaging spectrometer, with each harmonic separated vertically by $190 \mu\text{m}$. The spectrometer disperses the harmonics in frequency on the axis perpendicular to the k dispersion. The output of the spectrometer is then sent to a streak camera, which

* Work supported by DOE grant number DE-FG03-92ER40727.

disperses the signal in time to give $\tilde{n}(\omega_m, t)$. If the streak camera is operated on a slow sweep speed, the output is $\tilde{n}(\omega, k)$, a snapshot of the ω - k space [1].

In the second configuration, an additional cylindrical lens is used to re-image the scattered light from the plane of

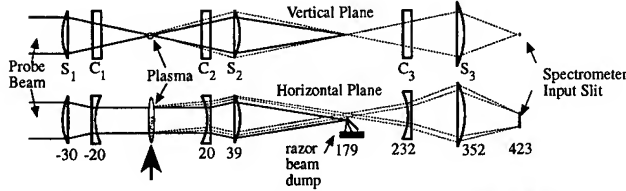


Figure 1: Thomson scattering setup. Numbers below lenses are the position relative to the plasma in centimeters. The letters S and C stand for spherical and cylindrical respectively, and the focal lengths are $S1=S2=30$ cm, $C1=C2=-20$ cm, $S3=50$ cm, and $C3=-50$ cm. The probe goes from left to right, coming to a line focus at the plasma, and then the scattered light is imaged onto a spectrometer followed by a streak camera. Lens C3 has been added for the spatial Thomson scattering

the plasma onto the slit of the spectrometer. The spectrometer then disperses the light in frequency, which gives the amplitude as a function of space and frequency, $\tilde{n}(z, \omega)$. Also, the spectrometer can be used to select a single frequency, and the amplitude of this frequency as a function of time and space, $\tilde{n}(z, t)$, can also be seen.

III. EXPERIMENTAL RESULTS

A. Time Resolved Thomson Scattering

Figure 2 shows a streak of the plasma wave amplitude, with frequency on the vertical axis, and time moving to the right. The scattered light shows a clear signal with a frequency shift of ω_p , and also a signal shifted by $2\omega_p$. The downward shift in frequency of the fundamental and 2nd harmonic of approximately 10% over 100ps is too large to be explained by relativistic frequency detuning, and thus strongly suggests a decrease in plasma density due to blowout of the plasma.

There are two ways to compute the plasma wave amplitude from this experimental data. First, the wave amplitude is directly proportional to the ratio of scattered power in the first harmonic to the power in the incident probe beam. Second, the ratio of power in the 2nd harmonic to the power in the fundamental is also proportional to the amplitude of the fundamental. Both of these methods show a peak wave amplitude of about 35% with a duration of about 100 ps. Simulations show that the

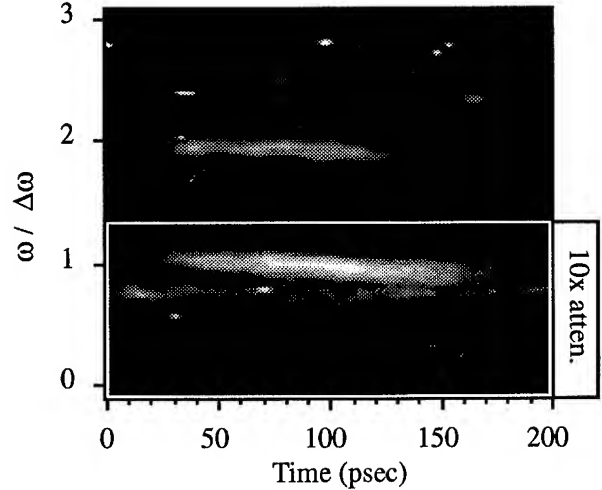


Figure 2 : Time resolved spectrum of Thomson scattered light from the fundamental and 2nd harmonic of the beat wave. Stray light at $0.8 \Delta\omega$ and the beat wave fundamental are attenuated by a factor 10.

peak wave amplitude is limited by ponderomotive blowout of the plasma due to the beat wave itself [3].

B. Space Resolved Thomson Scattering

The experimental data in Figure 2 shows the plasma wave amplitude averaged over the 6 mm length of the probe beam. However, the energy gain of a particle is determined by the $\int E_{ac} \cdot dl$ seen by the particle, where $E_{ac} = \epsilon \sqrt{n_e}$ is the accelerating field, ϵ is the wave amplitude, and n_e is the plasma density. Therefore, it is important to know the wave amplitude along the particle's axis of propagation. A numerical solution of the wave amplitude differential equation shows the FWHM of the wave to extend for approximately 1 cm [4]. To determine this experimentally, the probe beam was expanded to 1.2 cm, and then the scattered light from this line focus was imaged onto the spectrometer. To see the wave amplitude vs. space and frequency, the streak camera was operated at a slow sweep speed (2 ns/mm), so the image had no time resolution. A lineout of the scattered light shifted by a frequency of $\omega = (1 \pm 0.1) \Delta\omega$ is shown in Figure 3(a), and extends for approximately 1 cm.

In order to see the wave amplitude vs. space and time, the streak camera had to be rotated 90° , so space and time would be on opposite axes. Figure 3(b) shows a typical streak, where the spectrometer has been set to only pass light shifted by $\Delta\omega$. This streak shows a plasma wave extending for approximately 8 mm. In addition, a lineout through the center shows a rise time of approximately 60 ps, and a much faster fall time. This is consistent with the

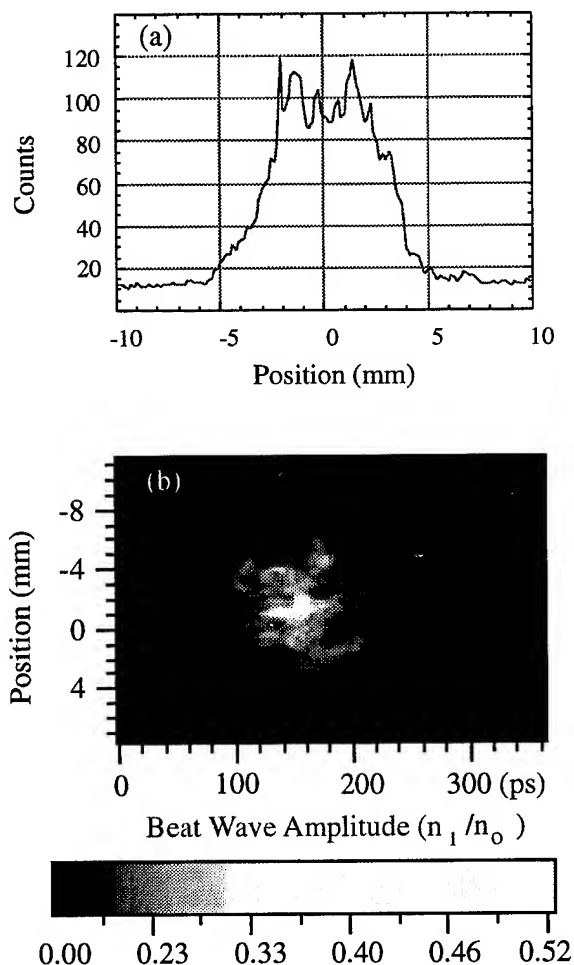


Figure 3 : (a) Line out of the scattered power at a frequency shift of $\Delta\omega$, as a function of space. The wave extends for approximately 8 mm. (b) Streak image of the scattered light shifted by $\Delta\omega$, with space on the vertical axis, and time moving to the right. Near best focus of the CO_2 laser, the beat wave reaches a peak amplitude of 40%.

simulations, which show the wave growing linearly with the laser intensity, and then crashing near the peak due to rapid plasma blowout [3]. Also, the streak shows the wave amplitude to be peaked near the best focus of the CO_2 laser, and to be smaller in the areas where the laser intensity is lower. The spatial resolution of the system is approximately 1 mm. The fine structure in the scattered light may be due to x-ray noise and statistical variations in the number of photoelectrons in the streak camera.

The expected energy gain of a electron in a plasma wave can be estimated by integrating the product of the accelerating field and the length of the wave. For example, a wave with amplitude of 30% for 1 cm at a density of $9.4 \times 10^{15} \text{ cm}^{-3}$ would produce an energy gain of approximately 28 MeV. From the experimental streaks, it is possible to numerically integrate the wave amplitude

along the laser axis, and compare this with the measured experimental electron energies from an electron energy spectrometer.

The calculated maximum energies from the streak data (assuming perfect phasing of the electrons and the plasma wave over its full length) agree well with the energy spectrometer. For example, on shots where the energy spectrometer showed electrons up to 25 MeV, the Thomson scattering showed peak wave amplitudes of up to 40%, with a spatial FWHM of about 8 mm. Similarly, when the Thomson scattering only showed wave amplitudes of 10% (due to shot-to-shot variations in the laser intensity), the highest electron energies seen on the spectrometer were around 5 MeV.

IV. CONCLUSIONS

The relativistic plasma waves generated in the Plasma Beat Wave Accelerator have been extensively studied with collective Thomson scattering. The plasma wave amplitude has been studied as a function of several parameters, including frequency, time, space, and wavenumber. Experimental results show a plasma wave with a peak amplitude of approximately 35%, with a FWHM of 100 ps, and extending for 1 cm in space. These wave parameters are confirmed by the observation of accelerated electrons, in which the energy gains are consistent with the $\int E_{ac} \cdot dl$ of the plasma wave.

V. REFERENCES

- [1] M. Everett et al., "Trapped Electron Acceleration by a Laser-Driven Relativistic Plasma Wave," *Nature* **368**, p. 527 (1994).
- [2] C.E. Clayton et al., "Ultrahigh Gradient Acceleration of Injected Electrons by Laser Excited Relativistic Plasma Waves," *Physical Review Letters* **70**, p. 37 (1993).
- [3] M. Everett, Ph.D. thesis, UCLA, 1994.
- [4] C.E. Clayton et al., "Acceleration and Scattering of Injected Electrons in Plasma Beat Wave Accelerator Experiments," *Physics of Plasmas* **1**, p. 1753 (1994)

A Novel Technique for Probing the Transverse Interactions Between an Electron Beam and a Plasma*

D. Gordon, A. Lal, K. Wharton, C.E. Clayton, M.J. Everett, C. Joshi
UCLA Dept. of Electrical Engineering, Los Angeles 90024

Abstract

In laser-plasma interaction experiments there are a variety of effects which will scatter or deflect a probing electron beam. For example, a longitudinally probing electron beam is defocused by the ponderomotive force of a laser, but in a plasma the laser can set up fields which actually confine the electron beam. In the cases of plasma wave excitation via the beatwave or wakefield mechanisms, the thermalization of the electron distribution function can lead to large scale magnetic fields via the Weibel instability. A novel Cherenkov probe has been built and tested which measures the transverse current distribution of an electron beam with at least 50 ps time resolution. A solenoid lens is used to map angular deflections within the interaction region into x - y space at the location of the Cherenkov probe. This allows the cases mentioned above to be experimentally studied.

I. INTRODUCTION

The transverse current distribution of a relativistic electron beam has been time resolved to 50 ps using a novel Cherenkov probe. This probe consists of a two-dimensional mesh of optical fibers arranged in such a way that a collimated beam striking the probe chuck at a prescribed angle of incidence will inject electrons into each fiber at the Cherenkov angle with respect to that fiber's axis (Fig. 1). In addition, the mesh is square when projected onto a plane orthogonal to the trajectory of the electron beam. With this arrangement, electrons impinging upon any fiber will emit the maximum fraction of their Cherenkov cones within the numerical aperture of the fiber. The ends of the fibers are brought together in a linear array, which is imaged onto the photocathode of a streak camera. Streaking the image gives the current in every fiber as a function of time. With this information, one can obtain

$$k(x,t) = \int j(x,y,t)dy \quad \text{and} \quad k(y,t) = \int j(x,y,t)dx$$

where $j(x,y,t)$ is the unknown distribution of current density in the transverse plane, and k is lineal current density. $j(x,y,t)$ itself can only be deduced if it is assumed to be separable in x and y .

* This work is supported by DOE contract number DE-FG03-92ER40727

II. PROBE DESIGN

The fibers chosen for our probe consist of a 400 μm diameter PMMA core with a 50 μm thick acrylic cladding. The overall length of the fibers is 20 cm. Plastic fibers are advantageous since in glass, electrons of less than 5 MeV would be quickly scattered out of the fiber's numerical aperture. X-ray production is also minimized in plastic. Higher energy electron beams will produce more signal in silica fibers provided UV is transmitted throughout the entire optical system.

The fibers are glued onto a 25×41 mm oval chuck of black acrylic. Machined onto the chuck are a series of nine parallel ridges running the length of the ellipse, making a 31° angle with the major axis. These are 750 μm high, 1 mm wide, and are set 3 mm apart. One set of nine fibers sits atop the ridges while the other nine tunnel through the ridges at -31° to the major axis. A beam striking the chuck at 37° to the major axis and 90° to the minor axis will see a mesh of 2.5 mm squares. Every fiber will make a 45° angle with the beam trajectory.

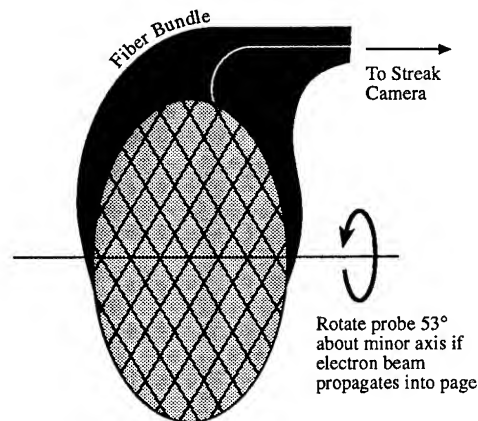


Figure 1: All fibers must make an angle of 45° with the e-beam trajectory. Therefore they must lie on the surface of any 45° cone whose axis is parallel with the e-beam trajectory. Choose two straight lines on the cone which are perpendicular when projected onto the base of the cone. The angle between these lines is the angle between the crossed fibers, and the plane they lie in is the plane of the probe chuck.

III. ELECTRON BEAMLINE

The electron beam in our experiment is generated by a 9 GHz RF linac. The beam energy is 2 MeV, and the emittance of the beam is 6π mm-mRad. The average current is 30 mA and the pulse length is 1.5 ns. The linac has been described in detail elsewhere [1].

In experiments with the Cherenkov probe, the electron beam will be propagated collinearly with a 300 ps, 100 J CO₂ laser pulse. The laser and electrons are simultaneously focused into a static fill of hydrogen gas where a plasma is formed via tunneling ionization. We are interested in measuring angular deflections of the electron beam by the plasma. To use the Cherenkov probe in this situation it is necessary to move the electrons away from the laser somewhere beyond the interaction point.

At the interaction point the electron beam is at a 500 μ m waist. A collimating solenoid lens with a bore diameter of 3.2 cm is placed 20 cm from the waist. This provides a linear mapping between angle and transverse position. A 5x5 cm square dipole is situated 15 cm from the solenoid. This deflects the electron beam by about 10°. Since the focusing of the laser is f/11 this is sufficient to move the electrons off the laser beam. The Cherenkov probe is placed 25 cm from the dipole.

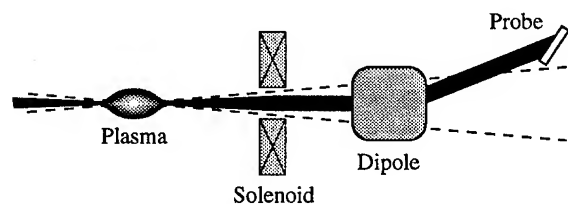


Figure 2: Cartoon of electron optics after the interaction point. The dotted lines represent the laser envelope while the black area represents the electron beam.

The beamline was characterized by inserting a hole pattern in the beam immediately prior to the solenoid. A fluorescer was placed at the position of the Cherenkov probe. It was determined that the spot size at the lens is 6 mm, and the beam is rotated 50° when collimated by the solenoid. This is convenient since the probe axes then line up with the laser polarization. It was also verified that the dipole magnet does not distort the beam, and that the beam is well centered on the lens. The only problem that emerged was that the lens smeared the shadow of the hole pattern radially as if due to chromatic aberration. However, the length of the smearing was less than an interfiber spacing, and is not resolved by the Cherenkov probe.

IV. PROBE PERFORMANCE

The Cherenkov probe has been tested within the setup described above by firing the electron beam but not the laser beam. Figure 3 shows a streak in which we consider only the temporal information. In this streak, the microbunches associated with the RF frequency of the linac are clearly shown. The time resolution of the probe in this case was evidently 50 ps since from previous measurements the microbunches are known to be less than 10 ps long. The time resolution of our setup is affected by the size of the image on the streak camera photocathode, modal dispersion in the fibers, and time of flight differences between electrons hitting different areas of the probe.

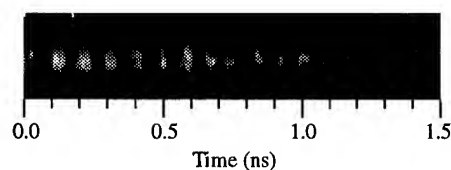


Figure 3: Streak with microbunches. The spatial information is not emphasized here. Note that the apparent chirp in the RF frequency is due to a nonlinearity in the sweep speed of the streak camera.

Figure 4 shows a streak including spatial information. On this shot the electron beam was aligned to the interaction point, collimated by the solenoid, and steered onto the center of the probe. The microbunches were not clearly visible at this sweep speed.

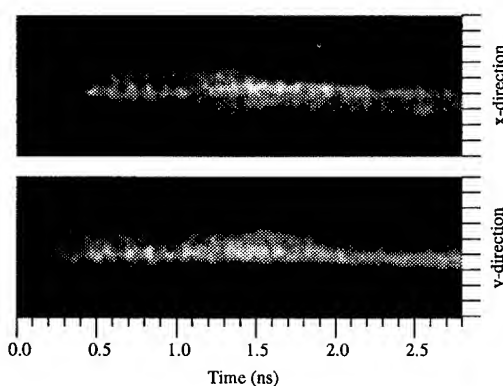


Figure 4: Streak with spatial information. White space has been artificially inserted between the upper and lower halves of the streak for clarity of viewing. The image of the fibers is arranged such that each half of the streak is an intensity plot of current with the horizontal axis time and the vertical axis one of the transverse spatial dimensions. The vertical tick marks are spaced such that the image of one fiber fits between them.

The most outstanding feature of Fig. 4 is that the electron beam is increasingly deflected in the negative x and y directions as time advances. This feature is reproducible on every shot. The reason for this deflection is that the energy of the electron beam droops in time. Thus, the dispersive electron optics both before and after the interaction point will conspire to put the beam at slightly different locations at different points in time. Since we wish to measure only deflections occurring at the interaction point, any dispersion in the electron optics is undesirable. However, since the effects of the dispersion are reproducible and small, they will not seriously affect the interpretation of future results.

Another issue associated with the dispersion in the electron optics is that when a large amplitude plasma wave is driven significant numbers of electrons in the probe beam can be drastically accelerated in the longitudinal direction. We have previously reported measurements demonstrating this effect [2]. Accelerated electrons will create a spatial variation at the Cherenkov probe which is indistinguishable from some particular angular deflection. Again, we would prefer that the spatial dimensions of the probe map only to the angles at which electrons leave the interaction point. On the other hand, accelerated electrons would lead to a specific spatial structure at the Cherenkov probe which could be easily identified, and would correspond to no plausible deflection scenario.

Finally, the sensitivity of the probe at the sweep speed associated with Fig. 4 can be easily determined. The highest number of counts produced on one pixel of the CCD was 200. The peak current of the electron beam is 250 mA. For this streak, the ratio of the area of the electron beam to the area of the section of fiber illuminated by the electron beam was 9.3. This implies that the sensitivity of each fiber is about 7 counts/mA. The background level of our CCD typically fluctuates by one or two counts. However, if we average over all the pixels illuminated by a single fiber during one microbunch we will be able to statistically resolve less than one count. Hence, we expect to be able to resolve 100 μ A of current running through any fiber.

V. CONCLUSIONS

A means of using a streak camera to time resolve the angular deflections of an electron beam by a laser-produced plasma has been developed. In future experiments we will use the new probe to study a number of effects. The laser can be fired into either vacuum or plasma, and can be run in either single or dual frequency mode. When in dual frequency mode, the plasma density can be set to resonate with the beat-frequency of the laser so that a large

amplitude plasma wave is excited. Probing the interaction region some time after this plasma wave breaks up may reveal evidence of the Weibel instability.

VI. REFERENCES

- [1] C.E. Clayton and K.A. Marsh, "A 2 MeV, 100 mA electron accelerator for a small laboratory environment", *Rev. Sci. Instr.* **64**, 728-731 (1993).
- [2] M.J. Everett et al., "Trapped Electron Acceleration by a Laser Driven Relativistic Plasma Wave", *Nature* **368**, 527 (1994).

Studies of Intense Laser Propagation in Channels for Extended Length Plasma Accelerators

T. Katsouleas, T. C. Chiou

Department of Electrical Engineering-Electrophysics,
University of Southern California
Los Angeles, CA 90089-0484

W. B. Mori

University of California, Los Angeles, CA 90024

J. S. Wurtele, G. Shvets

Massachusetts Institute of Technology, Cambridge,
MA 02139

Abstract

Progress on modeling plasma-based accelerator concepts in plasma channels is presented. Such schemes offer the potential for large accelerating gradients, high beam quality and acceleration over many Rayleigh lengths by optically guiding intense laser pulses. Recent results include modeling of non-ideal channels, higher order laser modes, and instabilities. Curiously we find that Raman scatter and laser hosing are to a large extent suppressed in a hollow channel.

I. NON-IDEAL PLASMA CHANNELS AND RESONANT ABSORPTION

Recently we have investigated the propagation of short laser pulses in hollow channels [1,2] ($n_e = n_i = 0$ on axis, $\omega_p = \text{constant} < \omega_{\text{laser}}$ for $r > a$). We showed that pulses shorter than $\lambda_p \sqrt{1 + k_p a}$ (where $k_p = \omega_p/c$ and a is channel radius) effectively excite a large surface wake of frequency $\omega_p/\sqrt{1 + k_p a}$. These wakes were found to be attractive because the accelerating fields were large (of the order 10 GeV/m), transversely uniform and with linear focusing.

In the previous discussion, the plasma was assumed to have a step function radial profile. That is, $n_0(y) = 0$ for $y < a$ and $n_0(y) = n_0$ for $y > a$. In this section we consider the more realistic case when there is a finite scale length for the vacuum plasma boundary. As a first approximation, we consider the plasma density $n_0(y)$ to be zero for $y < a/2$, to ramp linearly from $y = a/2$ to $y = 3a/2$ up to the value n_0 , and $n_0(y) = n_0$ for $y > 3a/2$.

Since the laser frequency (ω_0) is much greater than the plasma frequency (ω_p), there is no resonant absorption of the laser. However, because the wake frequency ω_{ch} is less than ω_p , there exists a resonant absorption layer in the channel wall which will damp the wakefield seriously. A thorough investigation of this phenomenon have been given in Ref.[3]. In Figs. 1 to 3 we show the simulation results. The damping of the axial wakefield after the first cycle implies that the wakefield accelerator scheme can be effective, but only if the beam load is placed on the first accelerating bucket. The transverse slices of E_z vs. y show the absorption of the wake energy at the resonant layer.

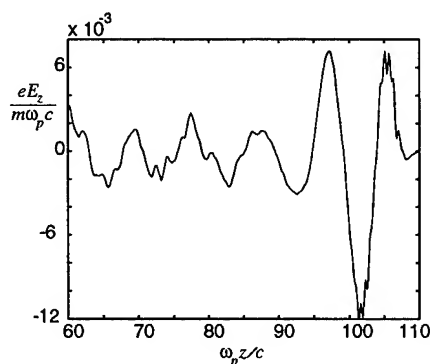


Figure 1. Axial wakefield $eE_z/m\omega_p c$ vs. z

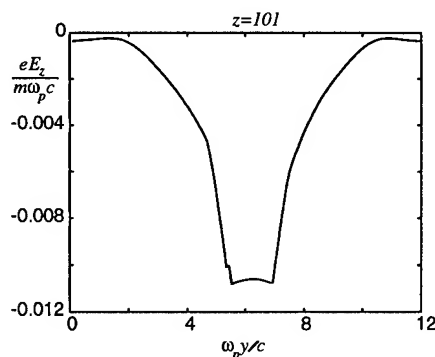


Figure 2. Axial wakefield $eE_z/m\omega_p c$ vs. y at $z = 101c/\omega_p$

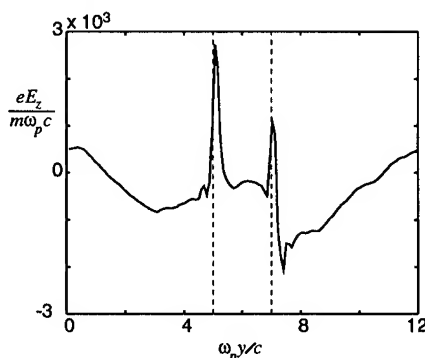


Figure 3. Axial wakefield $eE_z/m\omega_p c$ vs. y at $z = 80c/\omega_p$

II. HIGHER ORDER OPTICAL FIBER MODES FOR RELAXED CHANNEL REQUIREMENTS

In previous work we found that the accelerating field is large only when the channel width is of order c/ω_p (typically $20\mu m$). For wider channels, the surface wake amplitude decreases because the intensity of the fundamental laser mode at the edge becomes very weak compared to the intensity at the center. This is unfortunate because it may be easier to realize wider channels in actual experiments. Fortunately, there is a solution; namely, we can use higher order guided laser modes in a wider channel. These modes have larger intensity at the edge than does the fundamental mode. Figs. 4 and 5 show the transverse profile of the laser in a plasma fiber at $z=0$ and $z=50 c/\omega_p$ from a PIC simulation. The TE_{01} character is apparent. The laser is well guided and excites a wake very similar to what would be excited by the fundamental TE_{00} mode.

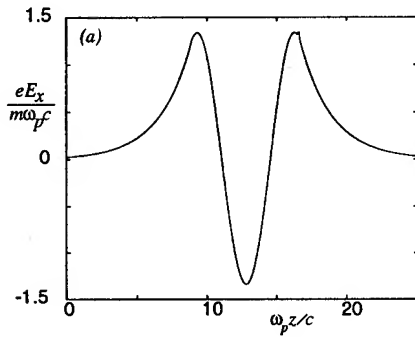


Figure 4. Transverse electric field of the laser showing its TE_{01} character at $z=0$ in PIC simulation (for $k_p a = 4$).

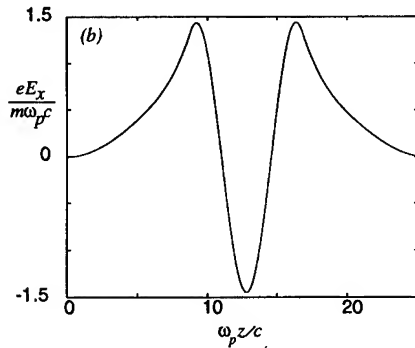


Figure 5. Transverse electric field of the laser showing its TE_{01} mode character at $z=50 c/\omega_p$ in PIC simulation (for $k_p a = 4$).

III. STABILITIES IN CHANNELS

It is well known that the propagation of intense laser pulses in homogeneous plasma is limited to relatively short distances by diffraction, pump depletion and parametric instabilities. Since depressed density channels act as optical fibers to guide the laser, they overcome diffraction. Short pulses excite a large plasma wake as just described that depletes the laser energy over a distance $\lambda_p \omega_0^2 / \omega_p^2 (1 + 1/(V_{osc}/c)^2)$. However, for pulses longer than $\lambda_p = 2\pi c/\omega_p$, three-wave and four-wave Raman forward

[4] and side scatter and laser hosing instabilities [5] limit the intensity that can be stably propagated through the channels. Below we briefly summarize results of analysis and simulation of instabilities in channels.

Analytic solutions for the growth rate of Raman Forward Scatter (RFS) in homogeneous plasma [4] and the hose instability in parabolic channel plasma [5] have been proposed in several articles. We address the same problem in a hollow channel plasma. The derivation will be given in a longer paper. The result is

$$\gamma = \frac{1}{2\sqrt{2}} \left(\frac{V_{osc}}{c} \right) \frac{\omega_p^2}{\omega_0} \sqrt{1 - \left(\frac{4p}{k_p} \right)^2} \quad (1)$$

where p satisfies the following dispersion relation for the laser pulse in hollow channel [2],

$$\begin{aligned} p^2 + h^2 &= k_p^2 \\ p &= h \tan(ha) \end{aligned} \quad (2)$$

We see that the growth rate is less than the homogeneous growth rate by a factor $\sqrt{1 - (4p/k_p)^2}$. It is easy to see that as $k_p a \approx 0$ the growth rate approaches the homogeneous result. In addition, if $k_p < 4p$ or equivalently $k_p a > 0.26$, γ becomes imaginary and even the decaying of the $E_0(\omega_0)$ wave into the body mode ($\omega = \omega_p$) is non-resonant. PIC simulations support the conclusion that Raman instability is suppressed except in very narrow channels ($k_p a < 1$).

Next we examine hosing instability in parabolic channels for various cases of initial laser misalignment. We found through simulations that for a uniform misalignment of the laser centroid defined as $\langle y_c \rangle = \frac{\int y E^2 dy}{\int E^2 dy}$, the RFS of the laser will overwhelm the hose instability, if any, in the parabolic channel. On the other hand, if we seed some wiggle in the laser centroid the laser will execute hosing instability significantly. Fig. 6 shows the initial laser centroid where we have offset sinusoidally by 2 cells. The wiggling wavelength is equal to λ_p . After propagating about 4 Rayleigh lengths, as was shown in Fig. 7, the growth of the laser centroid was evident.

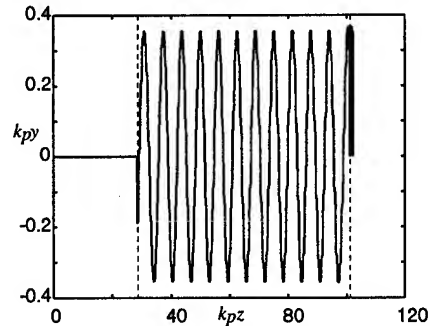


Figure 6. Centroid of the laser pulse in parabolic channel plasma at $z=0$. The dashed lines show the position of the laser pulse

IV. Discussion

We have examined the propagation of intense laser pulse through plasmas of various kinds of density profiles. The RFS

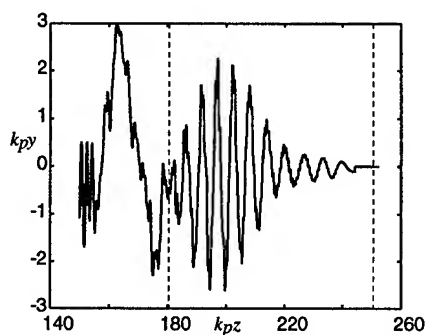


Figure 7. Centroid of the laser pulse in parabolic channel plasma at $z=180 c/\omega_p$. The dashed lines show the position of the laser pulse

instability in both homogeneous and parabolic channel plasmas are observed in PIC simulations (not shown here). The pulse in parabolic channel seems to be more unstable than in homogeneous plasma. This may be partly due to guiding of Raman side scatter by the channel. In hollow channels, we have found a reduced growth rate for RFS if $k_p a < 0.26$. The instability of the pulse is not significantly affected by the thickness of the channel wall. Overdense channels will be the subject of another work. We comment that underdense channels are of interest because they avoid resonant absorption of the laser by the plasma.

Work supported by US Department Of Energy DOE - AC#DE - FG03 -92ER40745.

REFERENCES

1. T. Katsouleas, T. C. Chiou, C. Decker, W. B. Mori, J.S. Wurtele, G. Shvets and J. J. Su . in Advanced Accelerator Concepts, AIP Conf. Proc. 279, J. S. Wurtele, ed., 480 AIP, New York 1992.
2. T. C. Chiou, T. Katsouleas, C. Decker, W. B. Mori, J.S. Wurtele, G. Shvets and J. J. Su, Phys. of Plasmas **2**, 310 (1995).
3. G. Shvets, PhD thesis.
4. W. B. Mori, C. D. Decker, D. E. Hinkel and T. Katsouleas, Phys. Rev. Lett., **72**, 1482 (1994).
5. G. Shvets and J. S. Wurtele, Phys. Rev. Lett., **73**, 3540 (1994).

UV LASER IONIZATION AND ELECTRON BEAM DIAGNOSTICS FOR PLASMA LENSES*

R. Govil, P. Volfbeyn and W. Leemans, Lawrence Berkeley Laboratory, Berkeley CA 94720 USA

A comprehensive study of focusing of relativistic electron beams with overdense and underdense plasma lenses requires careful control of plasma density and scale lengths. Plasma lens experiments are planned at the Beam Test Facility of the LBL Center for Beam Physics, using the 50 MeV electron beam delivered by the linac injector from the Advanced Light Source. Here we present results from an interferometric study of plasmas produced in tri-propylamine vapor with a frequency quadrupled Nd:YAG laser at 266 nm. To study temporal dynamics of plasma lenses we have developed an electron beam diagnostic using optical transition radiation to time resolve beam size and divergence. Electron beam ionization of the plasma has also been investigated.

I. INTRODUCTION

Plasma lenses [1] have been proposed for focusing relativistic electron beams to small spot sizes and for luminosity enhancement in future linear colliders. Plasma lenses can be overdense (plasma density, n_p , much greater than electron beam density, n_b) or underdense ($n_p < 2 n_b$). In overdense lenses the space-charge force of the electron beam is canceled by the plasma and the remaining magnetic force causes the electron beam to self-pinch. The focusing gradient is non-linear, resulting in spherical aberrations. In underdense lenses, the self-forces of the electron beam cancel, allowing the plasma ions to focus the beam. Such linear focusing (proportional to n_p) leads to more desirable beam qualities. The performance of an underdense lens can be improved by tapering the plasma density in a such a way as to maximize the focusing strength at all times [2]. To avoid the Oide limit on spot sizes due to synchrotron radiation by the e-beam, adiabatic lenses have been proposed [3].

Overdense plasma lens focusing has been observed at the Argonne National Laboratory, at KEK and most recently at UCLA[4-6]. Only the UCLA experiment showed clear beam size reduction and the effect of temporal lens dynamics. To this date no experiments have been reported showing focusing of electron beams by plasma lenses operating in the underdense regime, nor has there been a systematic study of return currents, adiabatic lenses, etc.

II. PLASMA LENS EXPERIMENT

The plasma lens experiment at the Beam Test Facility (BTF) is designed to study the properties of plasma lenses in both overdense and underdense regimes. In particular, we will

study important issues such as time response of the lens, lens aberrations and shot-to-shot reproducibility.

The Beam Test Facility provides a 50 MeV electron beam with a charge of 1-2 nC in 15 ps bunches at 1-10 Hz. The unnormalized emittance is 0.32 mm-mrad. The line is equipped with a wide range of diagnostics including integrating current transformers for charge measurement, high bandwidth BPMs, fluorescent screens, and optical transition radiation (OTR) diagnostics [7]. OTR is produced when electrons cross a boundary between materials of different dielectric constants. It can provide information about the electron beam energy (cone opening angle), bunch length, spot size and divergence (beam emittance).

A. Plasma Lens Design

Using the nominal linac parameters, we have previously [8] determined the plasma requirements (density, location and length) and the e-beam requirements (size and charge) required for studying the different regimes. For a more realistic design, here we use experimentally measured electron beam properties. In addition, the following issues have been taken into consideration in designing the experiment.

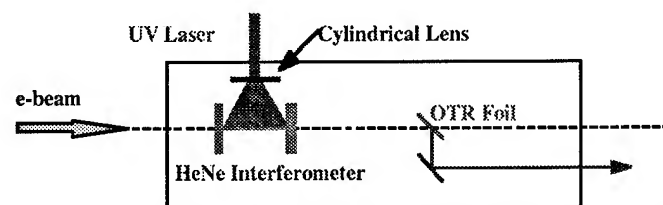


Figure 1. Experiment layout for adiabatic plasma lens. The laser is brought to a line focus at the position of the e-beam. Backward OTR is collected for electron beam diagnostics.

The plasma chamber is separated from the electron beam transport line by a 3 μm beryllium window. For the overdense lens, the laser beam enters the vacuum chamber through an AR coated window and is made to propagate colinearly with the e-beam axis using an ultra-thin UV mirror ($R=90\%$), made from 5 μm nitrocellulose substrate. The substrate and Be-foil increase the e-beam emittance by 15-40%, in good agreement with calculations [9]. For the adiabatic lens (which requires better beam qualities), we avoid this emittance growth by bringing in the ionizing laser at right angles to the e-beam. The laser is brought to a line focus at the position of the electron beam. The plasma length will be adjusted by changing the laser focusing. The longitudinal profile of the plasma will be tapered using intensity or phase masks on the laser beam. Since the required change in density for planned adiabatic lenses is about an order of magnitude and the plasma

* This work was supported by the Director, Office of Energy Research, Office of High Energy and Nuclear Physics, High Energy Physics Division, of the US Dept. Of Energy under Contract No. DE-AC03-76SF00098.

density varies as the square of intensity, the mask needs to provide a factor of 3 gradient in intensity.

Our calculations show that the contribution of beam induced ionization to the plasma density is negligible. Preliminary experimental observations made by propagating the electron beam through a 0.75 m long section filled to 2 Torr tri-propylamine (TPA) confirm this calculation.

Table 1. Typical overdense and underdense plasma lenses.

	Overdense	Adiabatic
Electron Beam		
Emittance [mm-mrad]	.32	.32
Charge [nC]	1.3	1.5
Initial density [10^{13} cm^{-3}]	.33	1.4
Initial size [microns]	139	113
Plasma Parameters		
Length [cm]	8.3	3.3
Density [10^{13} cm^{-3}]	1.0	0.2 - 3.2
Electron Beam at Exit		
Beam size [microns]	76	59
Overall size reduction factor	3.4	2.1

Overdense lenses require 5-15 cm long plasmas with densities ranging from 8×10^{12} - $2 \times 10^{13} \text{ cm}^{-3}$. For example, a 5 cm long plasma placed 8 cm before vacuum focus of the e-beam, reduces the spot size from 187 microns to 63 microns. We find that for high plasma densities return currents play a significant role by canceling the effect of the lens. Sensitivity studies show that overdense lenses do not place very stringent requirements on the electron beam. A bunch charge of about 1.3 nC with emittance ranging from 0.3 to 0.5 mm-mrad is sufficient. Table 1 describes a typical overdense lens design.

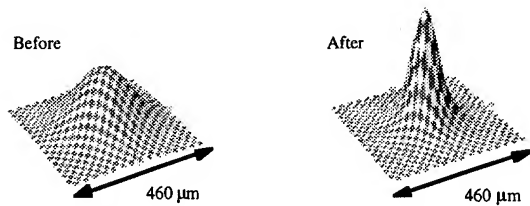


Figure 2a. Effect of plasma lens on transverse profile of electron beam. Here the z axis represents the charge density.

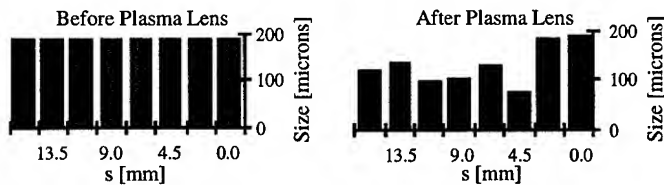


Figure 2b. Successive longitudinal slices of the e-beam experience different focusing strengths due to plasma response. Here s is the distance along the e-beam.

The focusing force in an underdense lens is proportional to the plasma density; since the plasma density has to be lower than the electron beam density, it is essential to achieve high e-beam density for high gradients and fast time response. Description of a typical underdense adiabatic lens is given in

Table 1. We find that (ignoring the temporal response of the plasma) a 15% drop in charge leads to a 5% drop in beam size reduction. A comparison between time-integrated and time-resolved effect of plasma lens focusing is shown in Fig. 2, clearly indicating the temporal modulation of the beam size.

B. Plasma Production

Overdense and underdense plasmas are produced through resonant two-photon ionization of tri-propylamine (TPA) by a frequency quadrupled Nd:YAG laser at 266 nm. The plasmas produced through this method are field free and do not require magnetic confinement. TPA has a high vapor pressure (3.5 Torr) and a large ionization cross-section. Previously, we have measured the ionization cross-section of TPA at 248 nm using an Excimer KrF laser [8]. The plasma density as a function of neutral gas density N_0 [cm^{-3}] and laser intensity I [W/cm^2] is given by [10]

$$n_p = \frac{N_0 \alpha^2 \Delta t}{h\nu} \quad (1)$$

Here Δt the FWHM of laser pulse [s], $h\nu$ the photon energy [J] and α the two-photon ionization coefficient [cm^4/W]. The Nd:YAG provides 5 mm diameter pulses with about 100 mJ of energy at 266 nm in 7 - 9 ns (FWHM). Because the laser pulse length is short compared to the lifetime of the intermediate state, an alternate description of two-photon ionization may be more appropriate [10]:

$$n_p = \frac{N_0 \sigma_1 \sigma_2 I^2 (\Delta t)^2}{2(h\nu)^2} \quad (2)$$

where σ_1 and σ_2 are the cross-sections for photoexcitation of the intermediate level and for photoionization, respectively.

The plasma is diagnosed using 94.3 GHz microwave interferometry described previously [8]. The microwave signal is launched transversely to the plasma column. The line averaged plasma density (no attenuation or refraction included) is proportional to the microwave phase change:

$$\bar{n} = \frac{\int_0^L n(x) dx}{L} = \frac{2\epsilon_0 mc}{e^2} \omega \frac{\Delta\phi}{L} \quad (3)$$

where ω is the microwave frequency and $\Delta\phi$ is the change in phase seen by the microwave signal.

Using the interferometer we have experimentally verified the pressure and intensity scaling laws as predicted by the two-photon ionization model (Fig. 3). Since the plasma sizes (3 - 5 mm diameter) are comparable to the microwave wavelength (3.2 mm), the plasma signal is modified by refraction. In addition, significant absorption of microwaves is observed at higher densities. The microwaves expand as they propagate through the plasma (which acts as a negative lens) and the receiving horn collects a smaller percentage of the transmitted waves, leading to a smaller relative signal. Thus the measured phase accumulation and, hence, the plasma density, is significantly smaller than its true value. Using plexiglass rods (which act as positive lenses and overfocus the microwave beam) of varying diameters (4 - 6 mm), we have

verified that refraction does lead to a significant modification to the collected signal. However, there is a way to bypass this problem. When the phase accumulation reaches 90° , the plasma signal turns around, retracing its steps past zero towards 270° . The signal at these "turning points" provides a measurement of phase, namely, at odd multiples of $\pi/2$, independent of the magnitude of the signal. An analysis of such points (Fig. 3b) reveals that the plasma density is in fact larger than it appears to be with refraction effects.

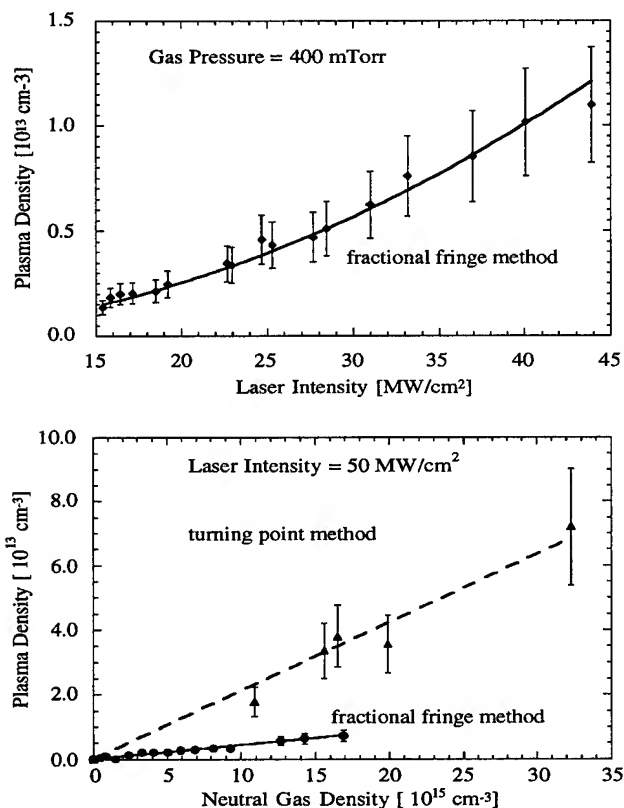


Figure 3. Plasma density scales (a) quadratically with intensity and (b) linearly with neutral gas density. The dashed curve is a measurement of density using the phase "turning point" method (at odd multiples of $\pi/2$) described in Section IIB.

Laser intensity of 50 mJ in about 400 mTorr TPA produces $3 \times 10^{13} \text{ cm}^{-3}$ plasma density, corresponding to 0.25% ionization efficiency. The ionization coefficient (Eq. 1) is found to be about $8.24 \pm 2.4 \times 10^{-29} \text{ cm}^4/\text{W}$ compared to $3 \times 10^{-26} \text{ cm}^4/\text{W}$ for 248 nm ionization reported earlier [8]. The corresponding value of $\sqrt{\sigma_1 \sigma_2}$ (Eq. 2) is $1.2 \pm 0.3 \times 10^{-19}$ compared to 6×10^{-19} reported by Woodworth et al. [10]. The actual plasma density may be higher because the turning point method may not fully account for plasma refraction and absorption. Slab plasmas will be produced through line focusing to resolve these issues. For diagnosing higher density plasmas required for adiabatic and tapered lenses and to achieve better spatial resolution, we are currently building a novel Fabry-Perot based optical interferometer at 633 nm, capable of measuring 10^{14} - 10^{16} cm^{-3} plasma densities with about 50 μm spatial resolution.

C. Electron Beam Diagnostics

To study the temporal dynamics of the plasma lens, it is necessary to time resolve the electron beam properties. Using a streak camera we have measured the electron beam spot size and divergence with 2 ps resolution at a location upstream of the plasma lens experiment. Fig. 4 shows a typical measurement of time-resolved beam divergence.

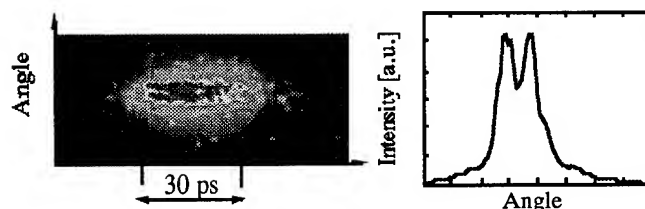


Figure 4. Beam divergence (proportional to ratio of "valley" to peak intensity) measured with 2 ps resolution.

At the plasma lens exit the electron beam properties will be measured using an OTR foil on a retractable arm moving along the direction of propagation of the e-beam (Fig. 1). This will allow us to image the electron beam at various location as it comes to a tight focus. Time resolved images of the electron beam will help determine the temporal response of the plasma.

III. SUMMARY

A status report on the plasma lens experiment at BTF has been given, where a comprehensive study of over and underdense plasma lenses will take place. We have produced plasmas with densities varying from 10^{12} to 10^{14} through resonant two-photon ionization at 266 nm. Measured plasma densities agree with theoretical scaling laws with intensity and neutral gas pressure. Time-dependent e-beam emittance has been measured. Preliminary results show beam induced ionization of the gas fill to be insignificant. Design of intensity masks for producing tapered plasma profiles is in progress.

IV. ACKNOWLEDGMENTS

The authors thank Glen Westenskow, Mike Perry and Bob Stever from LLNL for lending the Excimer and Nd:YAG laser systems and the microwave interferometer, respectively.

V. REFERENCES

- [1] P. Chen, Part. Accel. **20**, 171 (1987).
- [2] T. Katsouleas et al., Proc. 1992 Adv. Accel. Workshop.
- [3] P. Chen et al., Phys. Rev. Lett. **64**, 1231 (1990).
- [4] J.B. Rosenzweig et al., Phys. Fluids **B2**, 1376 (1990).
- [5] H. Nakanishi et al., Phys. Rev. Lett. **66**, 1870 (1991).
- [6] G. Hairapetian et al., Phys. Rev. Lett. **72**, 2403 (1994).
- [7] M. de Loos et al., Proc. 1994 European Part. Accel. Conf.
- [8] W. Leemans et al., Proc. 1994 European Part. Accel. Conf.
- [9] M.B. Reid, J. Appl. Phys. **70**, 7185 (1991).
- [10] J. Woodworth et al., J. Appl. Phys. **57**, 1648 (1985).

Plasma Wakefield Acceleration Experiments in Overdense Regime Driven by Narrow Bunches

T. Kozawa, T. Ueda, T. Kobayashi, M. Uesaka, K. Miya

Nuclear Engineering Research Laboratory, Faculty of Engineering, The University of Tokyo,

2-22 Shirakata-Shirane, Tokai-mura, Naka-gun, Ibaraki 319-11, Japan

A. Ogata, H. Nakanishi, T. Kawakubo, M. Arinaga, K. Nakajima

National Laboratory for High Energy Physics, Tsukuba, Ibaraki 305, Japan

H. Shibata

Research Center for Nuclear Science and Technology, the University of Tokyo,

2-22 Shirakata-Shirane, Tokai-mura, Naka-gun, Ibaraki 319-11, Japan

N. Yugami, Y. Nishida

Department of Electrical and Electronic Engineering, Utsunomiya University,

Ishii-machi, Utsunomiya, Tochigi 321, Japan

D. Whittum

Stanford Linear Accelerator Center, Stanford University, Stanford, California, USA

Y. Yoshida

Institute of Scientific and Industrial Research, Osaka University, Mihogaoka, Ibaraki, Japan

Abstract

Experiments of plasma wakefield acceleration driven by narrow bunches were performed in overdense regime at the University of Tokyo. Changes of energy and beam size of test bunches caused by the driven bunches were observed. Acceleration gradient about 1 MeV/m was observed.

Introduction

Plasma wakefield acceleration is one of the methods which are proposed in order to obtain an acceleration gradient high enough for the next generation of linear colliders[1]. The concept has been first tested experimentally in 1988 at the Argonne National Laboratory[2]. More recently, gradient of 20 MeV/m has been produced by a train of bunches from the 500 MeV linac at KEK[3].

In this experiments, we have investigated dependence of acceleration characteristics on the plasma density in the overdense regime, in which plasma density is higher than the beam density. The drive beams were narrow; in other words, the product of plasma wavenumber and the beam size was less than unity. Changes in size and energy of test bunches caused by drive bunches were studied as a function of plasma density.

Experimental

The wakefield accelerator [4] consists of two linacs, achromatic lines, plasma chamber and energy analyzer, as shown in Fig. 1. Beams from one linac excite wakefields in a plasma, while beams from the other linac witness the wakefields. The time interval between the two beams is controllable with an accuracy of 1 ps. Plasma was produced in a chamber with .15m diameter and .36m length by pulse discharges between four lumps of LaB_6 cathodes and the chamber[5]. The cathodes were heated by a 10V-80A direct current source. The discharge pulse had

a voltage of 80-120V, a current of 10-20A, a duration of 2 ms and a rate of 12.5 Hz equal to the linac beam repetition rate. The multi-dipole field of permanent magnets, 0.7 kG at the inner surface of the air-cooled chamber, was applied to confine the plasma. Argon gas was filled the chamber for the plasma production. The plasma density was controlled by the gas flow controller, the cathode temperature and the discharge voltage. The plasma density and electron temperature were measured by a Langmuir probe. The electron temperature was found to be 2-3eV. We adopted differential pumping in order to isolate the linacs from the test section.

The beam energy was measured by a 45° bending magnet at the end of the plasma chamber and beam sizes and positions were measured by using phosphor screens (Desmarquest AF995R). The energies of the drive beams and test beams were 24.1 MeV and 16.6 MeV, respectively, and the respective charges in each bunch were 300-400 pC and 70-80 pC at the exit of the energy analyzer. Vertical and horizontal beam sizes of the drive bunch were around 1.5 mm.

Experimental results and discussion

Beam images on the phosphor screen at the exit of the energy analyzer were observed as a function of time delay between drive and test bunches. Figure 2 shows time dependence of energy shift, which was derived from the position in horizontal direction, at the plasma density of $7.86 \times 10^{11} \text{ cm}^{-3}$. Figure 3 shows change of beam sizes in horizontal and vertical directions at the plasma density of $7.86 \times 10^{11} \text{ cm}^{-3}$.

The delay dependences obtained experimentally were fit to the equation

$$f(t) = e^{-t/\tau} [a_1 \sin(\omega t + \phi_1) + a_2 \sin(2\omega t + \phi_2)]. \quad (1)$$

The $\sin 2\omega t$ term is phenomenological and was included to im-

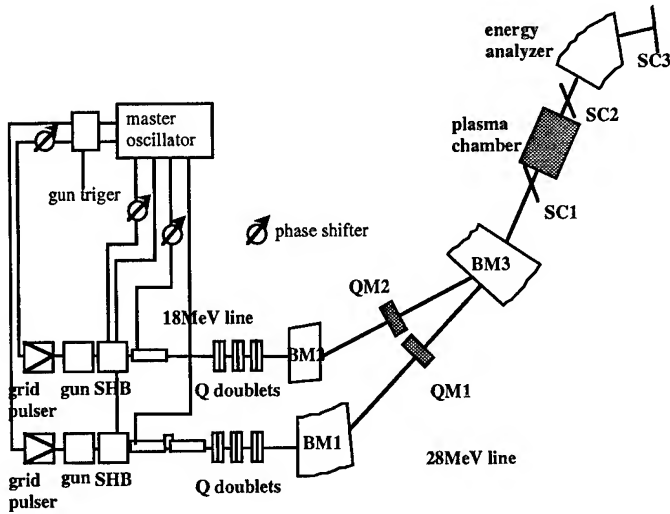


Figure 1. Schematic diagram of the wakefield accelerator and positions of four phosphor screens SC1 to SC3.

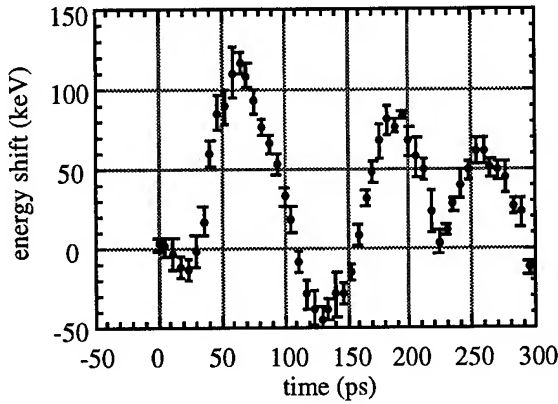


Figure 2. Time dependence of energy change of test bunches at the plasma density of $7.86 \times 10^{11} \text{ cm}^{-3}$.

prove the fit. Plasma frequencies and consequent plasma densities were derived from the ω values.

Measured plasma density distributions along the beam axis were shown in Fig. 4. The acceleration experiments were, however, performed in the density region far higher than those given in Fig. 4. The density distributions were then calculated by a similar method described in ref. [6]. This is possible because the damping characterized by τ in eq. 1 can be attributed to the heterogeneity of the density distribution as following. The plasma density and the resultant plasma frequency at the ends of the plasma column are lower than those at the plasma center. The test bunches suffer from the phase difference of the plasma oscillation, which becomes more severe as the time difference becomes longer. The phase difference tends to offset the positive and negative effects of the wakefield to decrease the amplitude of the oscillation.

In this specific data processing, a trapezoidal distribution was first assumed as $n(z)$. The solid line in Fig. 4 shows the trapezoidal approximation of the distribution and data given by circle were obtained experimentally. The delay time dependence of the wakefield is then calculated by the relation

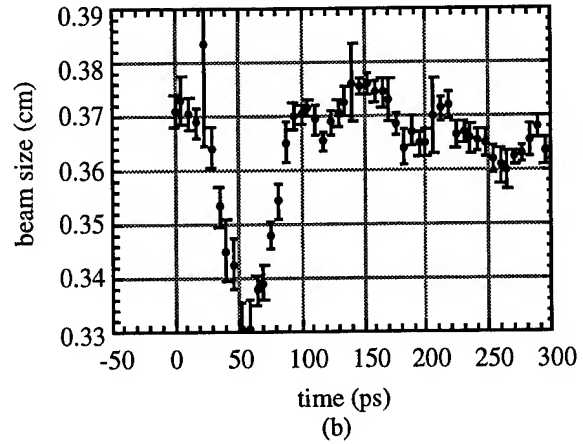
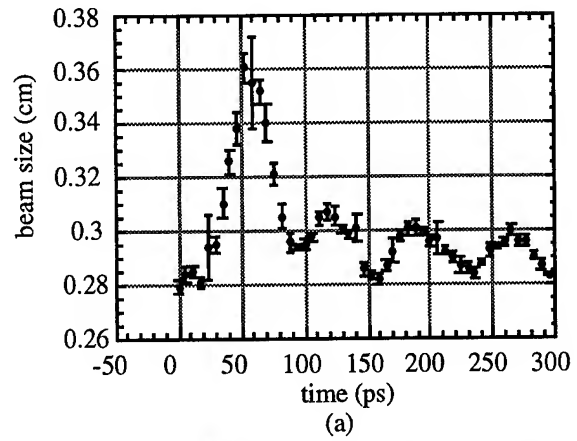


Figure 3. Time dependence of beam sizes of test bunches in (a) horizontal and (b) vertical directions at the plasma density of $7.86 \times 10^{11} \text{ cm}^{-3}$.

$$E(t) \sim \int_0^{L_0/2} -n(z) \cos(\omega_p(z)t) dz, \quad (2)$$

where $\omega_p(z)$ is the plasma frequency, assumed to agree with ω in eq. 1 at the flat top of the trapezoidal distribution. The length of flat top of the trapezoid was adjusted so that its decay characteristics agree with the experimental data and the reduction of the wakefield amplitude was derived.

The acceleration gradient at the center of the distribution thus derived is given in Fig. 5. The solid line in the figure shows the prediction of linear theory,

$$W_z = -\frac{8r_e mc^2 N}{a^2} \exp\left[-\frac{k_p^2 \sigma_z^2}{2}\right] \left[1 - \frac{4}{k_p^2 a^2} + 2K_2(k_p a)\right], \quad (3)$$

where N is the number of electrons in the drive bunch, k_p is the plasma wavenumber, σ_z is the bunch length, 1.2 mm, and a is the beam size, 1.5 mm.

The transverse wakefield caused by a drive bunch is given by

$$W_r(r, \xi) = -\frac{16r_e mc^2 N}{a^2} \left[K_2(k_p a) I_1(k_p r) - \frac{r}{k_p a^2}\right] \times \exp\left(-\frac{k_p^2 \sigma_z^2}{2}\right) \text{sinc}_p \xi. \quad (4)$$

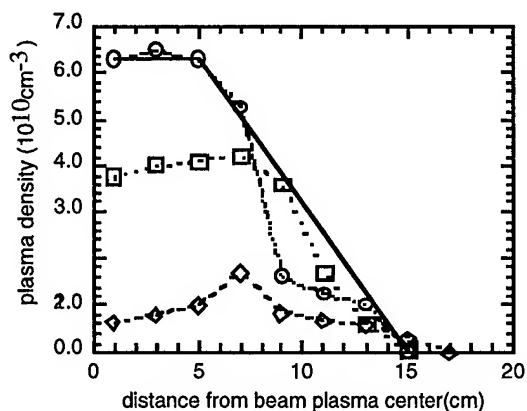


Figure 4. Plasma density distributions along the beam axis. The solid line shows trapezoidal approximation.

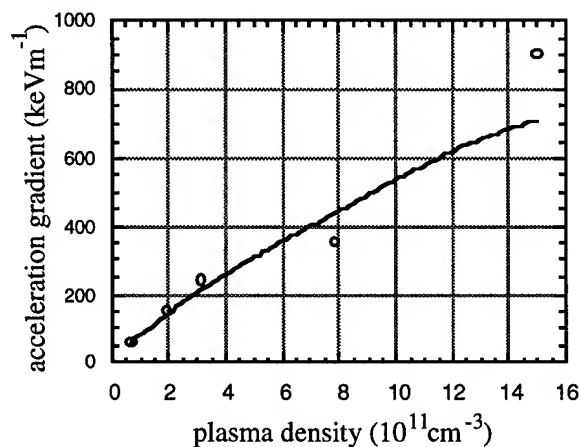


Figure 5. Dependence of acceleration gradient on plasma density. Solid line shows prediction of a linear theory.

Calculated and experimental value of wakefield are shown in Fig. 6. The experimental value is estimated from beam images on SC1, SC2 and SC3, assumed linear field and thin lens. Figure 7 shows the dependence of beam sizes at the maximum focusing phase on the plasma density. The beam sizes were observed at the exit of the energy analyzer. The solid line shows numerical simulation. The experimental value is smaller than the theoretical. The difference between theoretical value and experimental one is due to the displacement of trajectories of the drive bunch and the test bunch.

References

- [1] P. Chen *et al.*, Phys. Rev. Lett. **54**, 693 (1985).
- [2] J. Rosenzweig *et al.*, Phys. Rev. Lett. **61**, 98 (1988).
- [3] A. Ogata, in AIP Conf. Proc. 279; Advanced Accelerator Concepts, Port Jefferson, New York, 1992, edited by J. Wurtele, (American Institute of Physics, New York, 1993) p.420.
- [4] H. Nakanishi *et al.*, Nucl. Instr. Meth. **A328**, 596 (1993).
- [5] H. Nakanishi *et al.*, Phys. Rev. Lett. **66**, 1870 (1990).
- [6] A. Ogata *et al.*, Phys. Scripta, **T52**, 69 (1994).

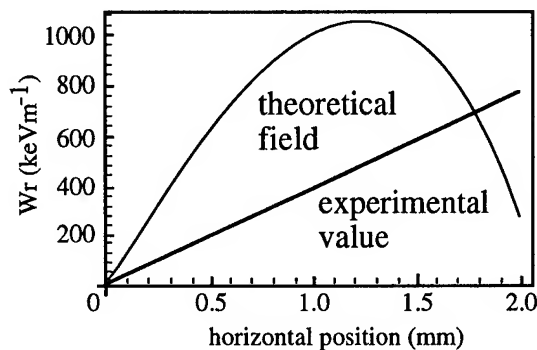


Figure 6. Transverse wakefield at the maximum focusing phase. Plasma density was $1.5 \times 10^{12} \text{ cm}^{-3}$.

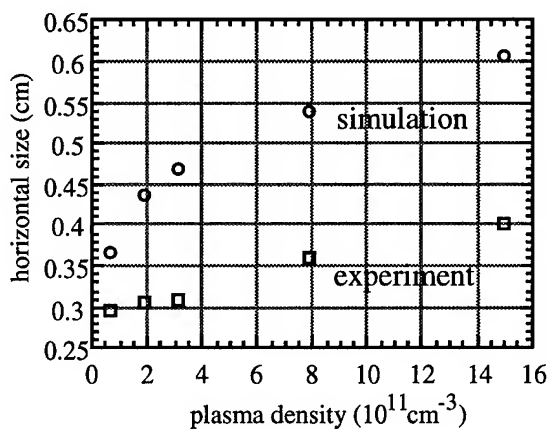


Figure 7. Dependence of beam sizes at the maximum focusing phase on the plasma density.

THE WAKE-FIELD EXCITATION IN PLASMA-DIELECTRIC STRUCTURE BY SEQUENCE OF SHORT BUNCHES OF RELATIVISTIC ELECTRONS*

I.N. Onishchenko,, V.A. Kiseljob, A.K. Berezin, G.V. Sotnikov, V.V. Uskov, A.F. Linnik, Ya.B. Fainberg
National Science Center, "Kharkov Institute of Physics and Technology," Kharkov 310108, Ukraine

I. INTRODUCTION

To the excitation of wakefields in dielectric structure some theoretical works are devoted. The project of slow wave structure based on this concept is proposed with the acceleration rate up to 100 MeV/m [4]. On Argonne Lab the efforts are undertaken to investigate experimentally wake-field excitation in dielectric by a single high density bunch of charge 100 nC and of energy 150 MeV [5].

In present work we aim for two goals. Firstly, instead of a single notsimply realized dense bunch, the wake-field is proposed to excite by a sequence of bunches of the same total charge but with a smaller density, obtained in the resonance linear accelerator. Secondly, plasma filling of the beam transit channel in dielectric permits to avoid the excited field sagging at channel axis that arises significantly the excitation efficiency.

The electrodynamics of dielectric and hybrid plasma-dielectric structures, the simulations of processes of wake-field excitation by the sequence of bunches of relativistic electrons are represented in the work.

The experiments are carried out on wake-field excitation in dielectric Teflon tube by long train of bunches. The installation with plasma filling of transit channel in dielectric with plasma of density up 10^{13} cm^{-3} have been prepared, and preliminary experiments are performed.

II.

The longitudinal component of electric field E_z excited by sequence of N bunches in the form of infinitely thin disks of radius R_b moving in the drift tube of the plasma dielectric structure is given by the expression

$$E_z = \frac{4eN}{R_1} \sum_{i=1}^N \sum_n \frac{\psi_n}{E_n} \frac{J_0(k_{\perp n} R_b)}{k_{\perp n} J_0(k_{\perp n} R_1)} \times \\ \times \Theta(t - z/v_0 - iT_0) \times \\ \times \cos[\omega_n(t - z/v_0) - iT_0],$$

where

$$\psi_n(r) = \begin{cases} J_0(k_{\perp n} r)/J_0(k_{\perp n} R_1), & r \leq R_1, \\ F_0(k_{\perp n} r), & R_1 \leq r \leq R_2 \end{cases} \\ E_n = 1 + \frac{J_1^2(k_{\perp n} R_1)}{J_0^2(k_{\perp n} R_1)} + \frac{R_2^2}{R_1^2} [F_0'^2(k_{\perp n} R_2) - F_0'^2(k_{\perp n} a) - 1],$$

*This work was supported in part by International Science Foundation, Grant N U27000.

$$k_{\perp n}^2 = -\frac{\omega_n^2}{v_0^2 \gamma^2} \epsilon_{3n},$$

$$\epsilon_{3n}^2 = -\frac{\omega_n^2}{v_0^2} (\beta^2 \epsilon - 1),$$

$$F_0(\alpha r) = \frac{J_0(\alpha r) Y_0(\alpha R_2) - Y_0(\alpha r) J_0(\alpha R_2)}{J_0(\alpha R_1) Y_0(\alpha R_2) - Y_0(\alpha R_1) J_0(\alpha R_2)},$$

$$F_0^1 = \frac{\partial F_0}{\partial(\alpha r)}; \epsilon_{3n} = 1 - \omega_p^2/\omega_n^2,$$

The function $\Theta(x)$ is equal 1 if $x > 0$ and 0 if $x < 0$; v_0 is beam velocity, R_1 , R_2 are inner and outer radius of dielectric tube, ϵ is dielectric permeability, J_0 , J_1 are the zero and first order Bessel functions, Y_0 are the zero-order Weber functions, T_0 is the bunch-to-bunch time, N is the number of particles of bunch. The frequencies ω_n , excited by an electron bunch, are found from the dispersion equation

$$\frac{\epsilon_{3n}}{k_{\perp n}} \frac{J_1(k_{\perp n} R_1)}{J_0(k_{\perp n} R_1)} + \frac{\epsilon}{\epsilon_{3n}} F_0(\epsilon_n a) = 0. \quad (1)$$

The dielectric structure was calculated so that for the parameters of the experiment ($\epsilon = 2.6$; $\gamma = 5$), the frequency ω_0 should provide the synchronism between the fundamental mode of the excited field (wake-field) and the bunch-repetition frequency ω_M of modulated beam bunches

$$\omega_0(R_1, R_2, \epsilon, \gamma) = \omega_M. \quad (2)$$

In the vacuum case ($\omega_p = 0$), the crossing of the beam and fundamental modes for the calculated transverse dimensions $R_1 = 1.1 \text{ cm}$, $R_2 = 3.5 \text{ cm}$ determines the frequency ω_0 satisfying condition (2). At moderate plasma density ($\omega_p \leq \omega_0$), the plasma waves are not excited directly ($v_b > v_{ph}$). However, the field topography of main electromagnetic mode becomes volumetric, because $\epsilon_{3n} < 0$, that enhances the efficiency of the wave excitation by the bunch. Note that in the calculation of the slowing plasma-filled structure, one should take into account the resonance frequency shift ω_0 due to plasma filling.

At high plasma densities ($\omega_p > \omega_0$), the wake-field is mainly excited as a plasma wave, and in this case the wake-field in the dielectric can arise due to the parametric coupling between electromagnetic and plasma waves (space periodicity, plasma density modulation, etc.).

III.

Experiments have been run to investigate wave excitation in the plasma-dielectric structure by a sequence of relativistic electron bunches. The electron beam was produced by a linear accelerator and had the following parameters: energy – 2 MeV, individual bunch length 60 ps, number of bunches 300 to 600, bunch

diameter 1 cm, number of electrons per bunch $2 \cdot 10^9$, beam modulation frequency $f_0 = 2825$ MHz. The energy spectrum of beam electrons could be varied within 8% to 50%. Parameters of the dielectric structure (DS) were: inner radius $R_1 = 1.1$ cm, outer radius $R_2 = 3.5$ cm, length $l = 70$ cm, $\epsilon = 2.6$. The DS could be filled with plasma by the use of coaxial plasma gun, through the hollow electrode of which the beam passed to the DS. The plasma density could vary between 10^{10} cm^{-3} to 10^{13} cm^{-3} . For comparison, experiments were carried out with both DS and thin glass tube, whose inner diameter coincides with that of the DS.

Beam current measurements at the output of the system have shown that in the glass tube case the whole accelerator output current ($I_b = 1.4$) passed through the tube, whereas only 60-70% of the beam current passed through the vacuum dielectric structure. For a wide energy spectrum ($\Delta W/W = 50\%$), the beam passage through the structure was about 80 to 90%.

Energy spectrum measurements by a magnetic analyzer at the output from DS have shown that for a narrow spectrum ($\Delta W/W = 8\%$) the spectral peak shifts by 500 KeV, i.e., 25% of the beam energy are lost. At the same time, there are some electrons (about 10%) which have energy higher than their initial one. For a small number of bunches ($N=300$) the shift of the spectral peak decreased down to 100-200 KeV. With a broad spectrum ($\Delta W/W = 50\%$) there were practically no energy losses observed. The measurements of "instantaneous" spectra have shown that the greatest energy losses were in the middle of the beam current pulse ($t = 2 \mu\text{s}$), while the losses were at the head of the beam pulse.

The probes arranged at the output of the structure have indicated the presence of intense microwave radiation at the wavelength $\lambda = 10 \text{ cm}$ with both E_z and E_θ field components. The spectrum width of radiation ($\Delta f = 10 - 12$ MHz) is not much greater than the spectrum width of the driving generator of the accelerator ($\Delta f_0 = 8$ MHz). The microwave radiation amplitude as a fraction of the number of bunches that have passed through the structure (beam current pulse length) has shown that the field grows by nearly a linear law up to 3000 bunches. Then the saturation sets. The same conclusion follows from the comparison between the oscillogram of the radiation signal and the beam pulse oscillogram.

When the beam with a broad electron energy distribution function passed through the DS, microwave signal amplitude decreased nearly by order of magnitude. With filling the above-mentioned DS with plasma we have observed the decrease in the radiation amplitude at the DS output and the improvement in the beam passage. This is apparently due to the detuning of synchronism (2) with plasma filling, which results in the offset upwards of the dispersion curve corresponding to the fundamental mode. Experiments with fields excitation in the plasma-dielectric system, taking into account this offset, will be continued.

IV. CONCLUSIONS

Based on the results obtained we can draw the following conclusions:

1. As the sequence of relativistic electron bunches passes through a dielectric structure, the energy losses up to 25%

of the initial value are experimentally observed. The energy is mainly consumed to excite wakefields whose intensity is 10 KeV/cm on the average. In these fields the bunch electrons acquire the transverse velocity and this results in a significant beam interception (up to 40%).

2. The presence of probe-detected microwave radiation at the DS output, as well as the dependence of microwave radiation amplitude on the number of bunches passed through structure, give evidence for the summation of wake-fields of the first 3000 bunches.
3. The use of a beam with a broad electron energy function essentially diminishes the effects observed. This suggests the conclusion that for the excitation of high-intensity wakefield, it is necessary to use bunches with a minimal energy spread.
4. Plasma filling essentially changes electrodynamic characteristics of the DS. Therefore, in the calculations of DS dispersion, one should take into account the synchronous frequency displacement caused by plasma.

References

- [1] W. Gai, P. Schoesow, B. Cole, *et al.*, Phys. Rev. Lett., 1988, **61**, 2756.
- [2] A.K. Berezin, Ya. Fainberg, N.M. Zemlyanskij, *et al.*, Proc. 8th Intern. Conf. High-Power Particle Beams. Novosibirsk, 1990, **1**, 250.
- [3] K.A. Barsukov, A.D. Kanareykin, A.I. Kustov, "Longitudinal Bunch Dynamics in the DWA." Proc. of HEACC '92.
- [4] R. Keinigs, M.E. Jones, W. Gai, "The dielectric wakefield accelerator." ANL-HEP-RR-88-27; LA-UR-88-1822.
- [5] J.B. Rosenzweig, "Nonlinear plasma and beam physics." FERMILAB-Conf.-90-40. 1990.

A BEAM FOCUSING SYSTEM FOR A LINAC DRIVEN BY A TRAVELING LASER FOCUS

A.A. MIKHAILICHENKO, BudkerINP, 630090, Novosibirsk, Russia¹

Described is a focusing system for charged particles in a laser driven linac, with an accelerating structure that is open on one side. The structure is illuminated from the open side by a focused laser spot, which is traveling along the structure in correlation with the position of the particles. This method allows for the reduction of the power required for generation of the necessary accelerating gradient, and reduction of the time of illumination of each point in the structure. This makes a laser driven linac a realistic system. The focusing system is a combination of FODO structure arranged with quadrupole lenses of appropriate dimensions and RF focusing. The Final Focusing system is arranged with the help of a bifrequency RF focusing system supplied by laser radiation of fundamental and doubled frequency.

Introduction

The method proposed is described in [1]. The basis is that the focused laser spot is moved in the longitudinal direction by a special sweeping device, so that the focal point follows the particle in its motion along the accelerating structure.

Because the sweep of the laser focus is limited to a distance of about 2-3 cm, the accelerating device looks like a sequence of 2 cm long accelerating structures with the focusing elements between them. For an appropriate accelerating structure, the pass holes have a dimensions that is a fraction of a wavelength of the laser radiation.

In this report the focusing required to keep the beam inside the transverse dimensions like a fraction of a micrometer is explored. This is connected with the smallest emittance available.

For realization of high luminosity the envelope function in the interaction region must be of the order of the bunch length, which is about $0.1-1\lambda$, where λ is the wavelength of the laser radiation. This requires the final focusing lenses have extremely short focal lengths and placed close to the interaction region.

The method

The scheme that realizes the method proposed is represented on Fig. 1. Here the source of coherent radiation 1, provides a ray 2 with necessary direction of polarization. A half wavelength plates are used for preparing it. Further there is installed an electro-optical crystal 3 with triangle metallization 4, what makes the deflecting prism [2] (a sweeping device). Focusing lens 5, serve for focusing the laser beam in longitudinal direction. Further, the laser beam 6 goes through a cylindrical lens 7 which focuses the laser beam on the surface of the structure 8 in transverse direction into a spot 9 with a transverse size of a few wavelengths of the laser light. In this particular moment, the accelerated particles are placed here. The beam is moving along the trajectory 10 and is focusing by quadrupole lenses 11, 12.

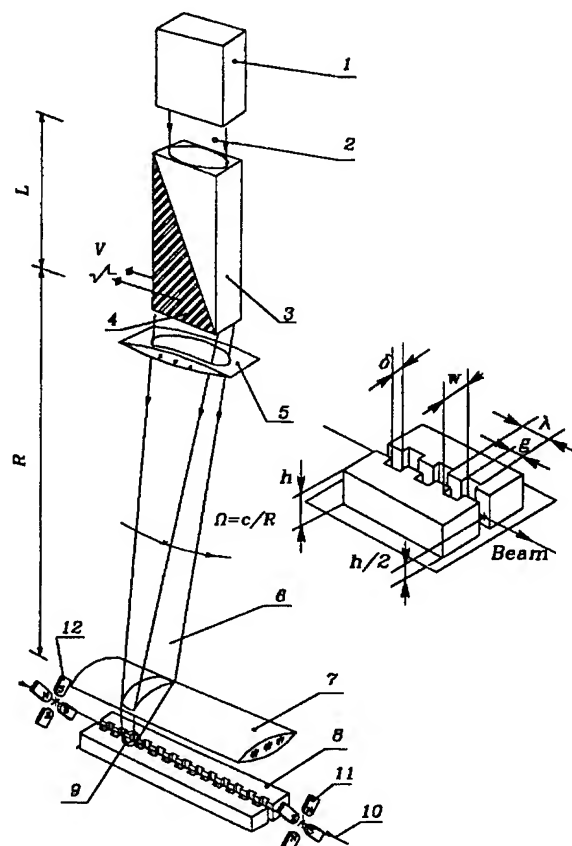


Fig.1. The Accelerating Device. The accelerating structure is represented also.

The operating voltage initially deflects the laser beam to the beginning of the accelerating module (left side on Fig.1). Starting of this moment of time and synchronized with the motion of the particles accelerated, the sweeping device 3 is supplied by the changing voltage on the metallization 4. This voltage changes the direction of the laser beam 6, so that the focal point 9 follows the beam.

The device 1 can be treated as a device for splitting the light from a unique source with optical techniques. This yields a simple way for the phase synchronization for few modules. Synchronization between the particle's motion and the focal spot motion must be made in such a manner that the particles does not on average, come out of the laser spot. The typical power required to supply one structure of 2 cm long is ≤ 10 milliJoules in this method. For radiation with $\lambda \approx 1 \mu m$ this provides ≥ 30 GeV/m.

After the passage of one module, the particle goes to the second module and so on.

¹ Present Address: Cornell University, Newman LNS, Ithaca, NY, 14850. e-mail: mikhail@lns62.cornell.edu

The size of the laser focus in the region of the second short focusing cylindrical lens 7 defined by the diffraction angle $\cong \lambda/a$ where a is the aperture of the sweeping device. So it has the order $l_i \approx \lambda \cdot R/a$, where R is the distance between the sweeping device (lens 5 on Fig. 1) and the lens 7.

Utilization the shot focusing cylindrical length 7 reduces the transverse size of the spot to the few wavelengths due to that circumstance that it is installed close to the accelerating structure and the ratio $r/a \approx 1$, where r is the distance between the second lens 7 and the structure 8.

The maximal aperture of the deflecting system in longitudinal direction, can be made equal to the sum of the accelerating structure and focusing elements' lengths. If we accept for the practical reason this figure as $a \cong 3 \text{ cm}$, $R \approx 3 \text{ m}$, then ratio $R/a \approx 100$. So the diffraction length of the spot in longitudinal direction can be of the order $l_f \cong 100\lambda$. This value gives the maximal possible value for Q -factor of one cell of accelerating structure.

The deflection angle may be increased by the optical elements, but the number of resolved spots M is invariant. $M \cong \Delta n \cdot (L/\lambda)$, where $\Delta n = \Delta n(V)$ is a change of refraction index by the voltage $V(t)$, applied to metallization, L is the length of deflecting device along the light direction. In KDP (potassium dihydrogen phosphate) crystal $\Delta n \cong 10^{-4}$, in KTN (potassium tantalate niobat) crystal $\Delta n \cong 7 \cdot 10^{-3}$ is possible [2,3]. Basically, M value gives the number for the lowering the laser power and, also, the number for reducing the duty of the structure heating. For segmented crystal with $L \cong 30 \text{ cm}$, one can expect $M \cong 30 + 700$.

Each part of the grating structure is illuminated by duration, which is defined by the longitudinal size l_i . For example, if we consider $l_i \cong 100\lambda$, $\lambda = 1 \mu\text{m}$, then $l_i/c \cong 3 \cdot 10^{-13} \text{ sec}$. For $\lambda = 10 \mu\text{m}$ this value is ten times more.

The dimensions

The number of the particles required for the method [1] is four orders of magnitude lower, than for the linear collider projects with the same level of luminosity.

A lot of damping rings were considered for linear collider schemes. The typical emittances referred to 3 GeV are $\varepsilon_x \approx 5 \cdot 10^{-8} \text{ cm} \cdot \text{rad}$ - radial and $\varepsilon_y \approx 5 \cdot 10^{-10} \text{ cm} \cdot \text{rad}$ - vertical. The energy spread about $\sigma_e \cong 10^{-3}$ and the bunch length $\sigma_z \cong 5 \text{ mm}$. The length of the beam after one stage compression is of the order 500 μm and the number of the particles is about $N \approx 10^{10}$. The second stage compresses the beam typically to 100 μm at 10 GeV. So if we need only $N \approx 10^8$ we can loose four orders of magnitude in intensity by *scrapping* the extra particles ejected from appropriate damping ring, thereby coming to the necessary figures in the emittance $10^{-10} \text{ cm} \cdot \text{rad}$ at 3 GeV. For pre-bunching the FEL mechanism can be used here.

There are proposals for an accelerating structure what could be scaled to the wavelength, corresponding to laser radiation [4,5,6]. We will consider the requirements for the

structure described in [5] (See Fig.1). The channels for the passing of the beam have a size $\delta \leq 0.2\lambda$.

Transverse electron focusing

The beam size must be kept small enough to pass through the channels. A short wavelength of betatron oscillations helps against the resistive wall instability [7] and wakefield influence reduce. The longitudinal and transverse wakes *normalized for one cell* are $W_l \cong -7kV/pC$ and $W_t \cong 2.2 \cdot 10^2 V/pC/\mu\text{m}$ correspondingly for the accelerating structure with $\lambda \cong 10 \mu\text{m}$, $\delta = 2 \mu\text{m}$, $w = 7 \mu\text{m}$ (see Fig.1) and the bunch with the longitudinal length $\sigma_l \cong 1 \mu\text{m}$ [8].

The focusing system includes the quadrupole lenses of appropriate dimensions and a RF focusing of different nature. The lenses are displayed at the distance, which defined by the emittance of the accelerating beam between the grating and by technical reasons. In case of the traveling laser focus supply, this is the maximal possible sweeping distance for the unit. If we consider the focusing system such as FODO structure, with the lenses having the length $2l$ with the distance between them L , the period of FODO structure will be equal to $2(L+l)$. For the betatron tune shift we have an expression $\cos\mu \cong 1 - (L+2l)^2/2F^2$, where F is the lens focal distance. So $F \cong (L+2l)/\sqrt{2(1-\cos\mu)} = (Hp)/(2Gl)$, where G is the lens gradient, (Hp) is the magnet rigidity of the particle. From the last expression it yields

$$G/(Hp) = k = \sqrt{2(1-\cos\mu)} / (2l(L+2l)),$$

where k is the focusing parameter of the lens, $k [1/\text{m}^2] = 3 \cdot G [kGs/\text{cm}]/p [\text{GeV}/c]$. The modulation M of the β -function between the lenses looks like [9]

$$M^2 = \frac{\beta_{\max}}{\beta_{\min}} = \frac{1 + \tanh\phi \cdot \left(\tan\phi + \frac{L}{l}\phi \right)}{1 - \tanh\phi \cdot \left(\tanh\phi + \frac{L}{l}\phi \right)}$$

$\phi = l\sqrt{k}$ - is the phase shift in the half of the lens. If we estimate $L = 2 \text{ cm}$, $l = 0.2 \text{ cm}$, $\mu = \pi/6$, then $k = 0.5/(2l(L+2l)) = 0.5 \cdot 10^5/(2 \cdot 2 \cdot 2.4) \cong 5 \cdot 10^3 1/\text{m}^2$, $\phi^2 = l^2 \cdot k = 2 \cdot 10^{-2}$, and $M^2 \cong 1.5$. For maximal value of the envelope function we have [9]

$$\beta_{\max} \cong M \frac{1}{|k| \cdot l} \sqrt{\frac{2+L/l}{2/3+L/l}} = \frac{2M \cdot (L+2l)}{\sqrt{2(1-\cos\mu)}} \sqrt{\frac{2+L/l}{2/3+L/l}}$$

which for previous values of L and l gives $\beta_{\max} \cong 15 \text{ cm}$ and $\beta_{\min} \cong 10 \text{ cm}$. If the beam has the emittance $\varepsilon \cong 10^{-10} \text{ cm} \cdot \text{rad}$, then the transverse beam size $\sigma_{\perp \max}$ will be of the order $\sigma_{\perp \max} \cong \sqrt{\varepsilon \beta_{\max}} \cong 3.9 \cdot 10^{-5} \text{ cm}$, or $0.4 \mu\text{m}$.

Thus, the focusing with the quadrupole lenses at initial stage of acceleration is acceptable *only* for the wavelength of the laser light about 10 μm , what defines the transverse dimensions of the structure.

With such dimensions, the radius of aperture b of the quads can be also made small enough, providing high gradient G with small value of the pole field H , $G = H/b$. If we estimate $H \approx 15$ kGs, $b = 0.01$ mm (20 μ m in dia of aperture), then $G = 1.5 \cdot 10^4$ kGs/cm. From the other side, for obtaining the value k [$1/m^2$] for the particles with momentum p [GeV/c], the gradient required is $G \approx 0.3pk$. For the particles with $p = 10$ GeV/c, this yields for $k \approx 5 \cdot 10^3 \cdot 1/m^2$, $G = 1.5 \cdot 10^4$ kGs/cm. At higher energy the actual emittance becomes adiabatically lower and the envelope function value can be increased.

Let us estimate the RF focusing [10,11] what occurs if the particle is going out of the RF crest in a phase φ . If $x, y \approx 0$ (the transverse coordinates, calculated from the beam axes) the effective factors of the lens can be evaluated as

$$k_x = -\frac{1}{pc} \frac{\partial \langle F_x \rangle}{\partial x} \approx -\frac{e\lambda E_m}{2mc^2 \gamma w^2} \sin \varphi,$$

$$k_y = -\frac{1}{pc} \frac{\partial \langle F_y \rangle}{\partial y} \approx -\frac{e\lambda E_m}{2mc^2 \gamma w h} \sin \varphi.$$

Substitute here $\lambda = 10 \mu$ m, $\gamma = 2 \cdot 10^4$ (10 GeV), $w \approx 5 \mu$ m, $E_m \approx 10^{11}$ V/m, we obtain $k_x \approx 2 \cdot 10^5 \sin \varphi$ [m^{-2}]. There is a proposal to use this force for alternating phase focusing (APF), when the phase of the beam with respect to the RF crest is periodically changed, $\varphi = \pm \varphi_0$ [11]. In our case this can be made by arranging periodical delay of the accelerating light arriving to the grating, for example, by modulation of the thickness of the lens 7.

The possible scheme also is that the RF focusing by the slots of the structure is going in horizontal direction and vertical focusing made by quadrupoles. This can reduce the betatron wavelength, in principle, two times.

The final focus

If we suppose, that the beta function value in the interaction region β^* is of the order of the bunch length σ_z , i.e. $\sigma_z \approx \beta^* \approx 0.5 \mu$ m, then the variation of the envelope function from the interaction point at the distance $s = 1$ cm will be $\beta = \beta^* + s^2/\beta^* \approx 1/0.5 \cdot 10^{-4} \approx 2 \cdot 10^4$ cm. With such an envelope function $\sigma_{\perp max}$ will be of the order $\sigma_{\perp max} \approx \sqrt{\epsilon \beta} \approx 1.4 \cdot 10^{-4}$ cm, or 1.5 micrometers for the transverse emittance value $\epsilon \approx 10^{-12}$ cm rad.

The mostly natural way to arrange the final focus lens is the RF focusing, discussed above. A laser radiation of general and multiple frequency can be used here.

The laser radiation, phased with the main driving one can excite the single groove directly from the side. The quadrupole parameter for the particle what is going out of the RF crest is described above. Substitute here $\lambda = 10 \mu$ m, $\gamma = 2 \cdot 10^6$ ($pc = 1$ TeV), $w \approx 5 \mu$ m, $E_m \approx 10^{11}$ V/m, we obtain $k_x \approx 4 \cdot 10^4 \cdot \sin \varphi$ [m^{-2}]. For $\varphi = \pi/2$ this expression has a maximum and variation of the focusing strength has a quadratic dependence with the deviation ψ from the angle $\varphi = \pi/2$, $k_x \approx \cos \psi$. For the longitudinal length of the groove about $g \approx 5 \mu$ m, the focal distance will be

$$F \approx 1/kg \approx 1/4 \cdot 10^4 \cdot 5 \cdot 10^{-6} = 5 \text{ [Meters/cell]}.$$

Equivalent gradient of the quadrupole lens is $G \approx 0.3pk \approx 1.2 \cdot 10^7$ kGs/cm. Of course there is no possibility to arrange a magnetic quadrupole with such a gradient. So the lens with ≈ 500 cells will have the focal length $F \approx 1$ cm. So, this multicell lens will have the total length of 0.5 cm.

For flattening the longitudinal dependence of the gradient (elimination the quadratic term in $k_x \approx \cos \psi$ as a function of ψ), one can use the *second and higher harmonics* of the laser radiation, excited an additional groove, placed on the beam trajectory close to the first groove. For phasing, the highest harmonics can be generated by the multiplying the frequency in nonlinear crystal. As initial, the splitted radiation from the general source can be used both for driving the first harmonic groove and, after doubling, the second groove. For arranging a doublet of the focusing lenses, one can use the phase shift between the RF crest and the beam $\varphi = -\pi/2$. Such a tiny lens, not sensitive for the magnetic field can be easily installed inside the detector.

Conclusion

Due to emittances available, the first stage of the laser driven linac at the energy about 10 GeV will require a 10 μ m wavelength if the only FODO structure with the quadrupole lenses is used.

The necessity to obtain the beta function in the interaction region of the order of 1 μ m requires very strong focusing lenses. The RF focusing system looks attractive for this purpose.

The general conclusion is that the necessary focusing can be arranged for the system described.

References

- [1] A.A. Mikhailichenko, "Excitation of the Grating by Moving Focus of the Laser Beam", EPAC 94, London, to be published. Author's certificate USSR N 1609423, Priority 1989, BI 1994.
- [2] F.S. Chen et. al., Journ. Applied Physics, Vol.37, N1, 388(1966).
- [3] V.J. Fowler, J. Schlafer, Applied Optics, Vol.5, N10, 1657(1966)
- [4] R.B. Palmer, Particle Accelerators, vol. 11, p.81, 1980.
- [5] R.C. Fernow, J. Claus, AIP Conf. Proceedings 279, 1992, p. 212.
- [6] H. Henke, "mm Wave Linac and Wiggler structure", EPAC 94, London, 1994, to be published.
- [7] A.A. Mikhailichenko, V.V. Parkhomchuk, "Resistive wall instability of a single bunch in Linear Collider", Preprint BINP 91-55, Novosibirsk, 1991.
- [8] A. Milich, A private communication.
- [9] K. Steffen, "High Energy Beam Optics", Intersc. Pub. 1965.
- [10] W. Schnell, "Microwave quadrupoles for linear colliders", CLIC Note 34, 1987.
- [11] F.E. Mills, A. Nassiri, "Alternating phase focusing in mm-wave linear accelerators", Argonne National Laboratory, internal report ANL/APS/MMW-9, 1994.

2 × 2 TEV $\mu^+\mu^-$ COLLIDER: LATTICE AND ACCELERATOR-DETECTOR INTERFACE STUDY*

N. M. Gelfand and N. V. Mokhov

Fermi National Accelerator Laboratory, P.O. Box 500, Batavia, IL 60510 USA

Abstract

The design for a high-luminosity $\mu^+\mu^-$ superconducting storage ring is presented based on first-pass calculations. Special attention is paid to two low- β interaction regions (IR) whose optics are literally interlaced with the collider detectors. Various sources of backgrounds in IR are explored via realistic Monte Carlo simulations. An improved design of the collider lattice in the neighborhood of the interaction points (IP) is determined by the need to reduce significantly background levels in the detectors.

I. INTRODUCTION

An increasing interest to a high-energy high-luminosity $\mu^+\mu^-$ collider project [1], [2] is based on the high physics potential of such a machine [3] beyond what can be accomplished at e^+e^- and pp (LHC) colliders. Even though there are some problems to be examined, especially on a technical side, no obvious show stopper has yet been found [4]. The collider complex will consist of a few essential parts: a high-intensity rapid-cycling 10 to 30 GeV proton synchrotron, muon production and muon cooling sections, a cascade of re-circulating linacs, and a 2-TeV storage ring providing collisions in two low- β regions with a luminosity $\approx 10^{34} \text{ cm}^{-2} \text{ s}^{-1}$. This paper deals with a prototype design for the final stage, 2 × 2 TeV collider. This is, to our knowledge the first complete lattice of the 2 × 2 TeV collider with a β^* of 3mm [5]. Muon decay and beam loss induced backgrounds in the collider detectors have the potential of killing the whole concept unless there is significant suppression via special shielding in the vicinity of the detector [6]. Here we continue collider/detector interface study to mitigate further this problem.

II. LATTICE DESIGN

This is a geometric design, that is the beam energy does not enter into the properties of the elements of the design. At the muon beam energy of 2 TeV, and with superconducting dipoles of $\approx 8\text{T}$ the circumference of the ring is $\approx 6\text{km}$, which corresponds to ≈ 1000 turns for the $\approx 25\text{ms}$ beam lifetime. This model design has been constrained as follows [5]:

- it uses magnets which are reasonable extrapolation from existing superconducting magnets;
- the β^* at the interaction point be 3mm in both planes;
- the dispersion, η at the interaction point be zero;
- the lattice has two low- β IRs and two long high- β utility straight sections;
- the lattice functions at the end of the insertions, low- β and high- β , be matched with the lattice functions in the arcs.

Lattice design calculations are done with the MAD and TEVLAT codes [7]. The design of a dispersion killer is most inexpensively done if the phase advance of the standard cell is either 60° or 90° . We have chosen a 60° phase advance for the standard cell. The other parameter for the standard cell is β_{max} . In principle this is arbitrary but in order to match the low- β insertion into the arcs we found it better use a relatively low β_{max} of 75m. With a more elaborate IR it would be possible to use a larger value. The advantage of a larger value might be to increase the packing fraction, the percentage of the ring filled with dipoles, and hence reduce the cost, and the length. With $\beta_{\text{max}}=75\text{m}$ the packing fraction in the standard cell is 91%.

The design of the utility straights is straight forward using the idea of matching quads due to Tom Collins. The β at the middle of the straight is 200m but can be adjusted within reasonable limits. Within the utility straight the maximum β is $\approx 300\text{m}$. The dispersion across the utility straight is matched by having dispersion killers at each end of the straight. This, of course, lengthens the ring, and if a zero dispersion straight is not needed then perhaps a different design could be developed. The designed the low- β IR matches to the arcs. The parameters of the quadrupoles are shown in Table 1 for $(B\rho)=6671.28139$ at 2 TeV.

Table 1 : Quadrupole parameters in the arc FODO cells, utility straight sections, low- β triplets, and IR/FODO matching sections. $F=(G/(B\rho))^{1/2}(\text{m}^{-1})$.

Sector	Name	Length(m)	F	G(T/m)
FODO	QF1	1.257	0.1929	248.2569
Utility	QFC1	4.200	0.1306	113.7638
	QF2	4.200	0.1235	101.8044
	QF3	4.200	0.1462	142.5645
Low- β	QFT1	3.467	0.1982	262.0556
	QFT2	7.548	0.1982	262.0556
	QFT3	3.762	0.1982	262.0556
Matching	QFM1	2.769	0.0794	42.0365
	QFM2	2.859	0.0932	57.9832
	QFM3	5.166	0.1823	221.7979
	QF1X	0.066	0.1929	248.2569

The tunes for this lattice depend on the number of FODO cells in the arcs and can be adjusted with correction quadrupoles. The natural chromaticity, that is the chromaticity with no sextupole correctors, is very large with $\zeta_x \approx \zeta_y \approx -3500$, that comes from the low- β insertions. One can correct this chromaticity with correctors in the arcs in which case one needs very strong sextupoles $B''/(B\rho) \approx 4$, to be compared with the values, $B''/(B\rho) \approx 4 \times 10^{-2}$, typically used in the Tevatron to correct and control the chromaticity. Sextupoles in the insertions cannot be used to correct the chromaticity because of the zero dispersion in the insertions.

*Work supported by the U. S. Department of Energy under the contract No. DE-AC02-76CHO3000

III. APERTURES AND IMPERFECTIONS

The current lattice design has no non-linear elements or imperfections. The stable region will have a non-zero value for the non-integer part of the tune. With a chromaticity of ≈ 3500 this yields a full width for the *momentum aperture* of $\approx 1/3500$ or $\approx 2.8 \times 10^{-4}$. This has been confirmed with a modeling code. With the chromaticity correcting sextupoles third integer values of the tune become unstable as well as integer values. In addition the chromaticity is now non-linear. Model calculations indicate that the momentum aperture is reduced by perhaps a factor of 2.

For the linear lattice the *dynamic aperture* is given by the value of β in the physical aperture. At the maximum value of β in the lattice, which occurs in the inner triplet, of $\approx 2 \times 10^5$ m (200km) and a radius for the physical aperture of 80mm as in [2], [4], [6], the maximum normalized emittance is $\approx 600\pi$ mm mr. Using in addition the results of shower simulations ([6] and the following section) and a realization of the problems with large, very high field magnets, we have found that 45mm radius aperture in the triplet (± 110 m from the IP) and 25mm radius aperture in the rest of the ring is an optimal choice. The size of the dynamic aperture has been confirmed by tracking calculations. The dynamic aperture is not restricted by the values of the chromaticity sextupoles.

An ideal lattice is described here, i. e. a lattice whose components have precisely the strengths given by the lattice design code. Further calculations based on a model with magnet errors are obviously needed. One point is interesting however. The $\mu^+\mu^-$ collider is the only collider where one can track for the full life time of the beam (≈ 1000 turns) using a reasonable amount of computer time.

Imperfections in the magnets in the low- β quadrupoles will result in a mismatch in the lattice functions and will generate a " β wave". One can get an idea of the magnitude of the problem by looking at the lattice functions for a off-momentum particle.

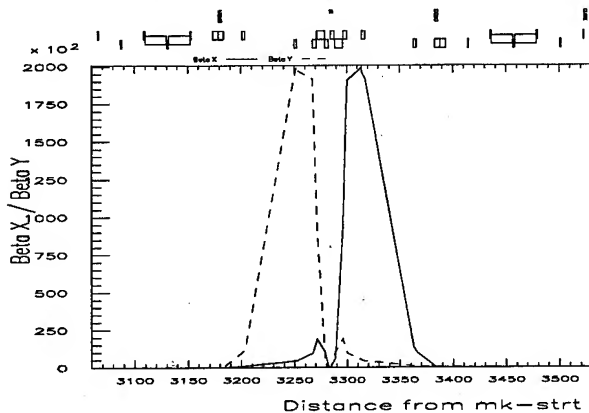


Figure 1. Beta functions in the interaction region

Figure 1 shows the lattice functions in the low- β region for particle of nominal momentum. The maximum value of β is ≈ 200 km. For a $\Delta p/p$ of 10^{-5} (this value of $\Delta p/p$ is equivalent to changing the strengths of all the quadrupoles in the ring by 5×10^{-6}) the maximum value of β is somewhat smaller ($\approx 17.5 \times 10^4$ m) and β^* is increased to 3.5mm. In the arcs is a strong " β wave" appears, which does not cause a loss of dy-

namic aperture. The effect of the momentum offset in the utility straights is negligible. One infers from this that if we want the lattice to match then we will need to control the strengths of the low- β quads to $\approx 10^{-6}$.

IV. BACKGROUNDS

Shower simulations are done with the MARS code [8]. The calculations include forced muon decays, the tracking of electrons with emission of the synchrotron photons along the track, the simulation of electromagnetic showers in the accelerator and detector components induced by electrons and synchrotron photons hitting the beam pipe, and simulation of muon interactions in the lattice and detector including electromagnetic showers originating from those interactions. The 3-D geometry and magnetic fields in the triplet and in the model detector are used. Figure 2 shows the γ and e^+e^- spectra in the lattice elements closest to the IP. Note the very high energy of decay electrons ≈ 1 TeV and photons ≈ 1 GeV, and enormous number of those photons.

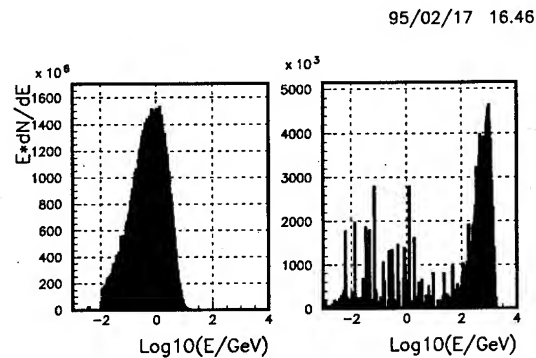


Figure 2. Photon (left) and electron/positron (right) energy spectra in the inner triplet accelerator components

Due to the energetic showers, a source term for backgrounds in the central detectors is extended over hundred meters from the IP. As was found in [6] the most efficient way to suppress background levels is a collimation as close to the detector as possible. Especially helpful is a very small tapered aperture tungsten nozzle sitting in the 0.15–1.2m region from the IP with the low- β quadrupole starting at 1.2m inside the detector. Figure 3 shows charged particle fluxes in the central tracker per crossing of two 10^{12} muon beams. Fluxes are dropping rapidly with distance from the beam axis, but at the flux maximum these are unacceptably high.

One sees that with the tungsten nozzle the fluxes are significantly reduced. With additional collimators in the triplet the overall effect can be as high as a factor of 500, with maximum hit rate of order of $200\text{--}400\text{ cm}^{-2}$. Further reduction is possible with a suppression of synchrotron photon production by keeping the high field dipoles as far from the IP as possible. Results for the lattice [6] with a dipole field in the triplet turned off are shown in Fig. 3. Backgrounds in the part of the tracker toward the ring center are thousands times lower. On the outside the reduction is about a factor of 2 to 5. This approach is incorporated into the proposed lattice where the nearest dipole starts at 130m from the IP. Figure 4 shows a contribution to energy deposition in the central tracker ($6 \leq r \leq 100$ cm) from muon decays along the IR. The

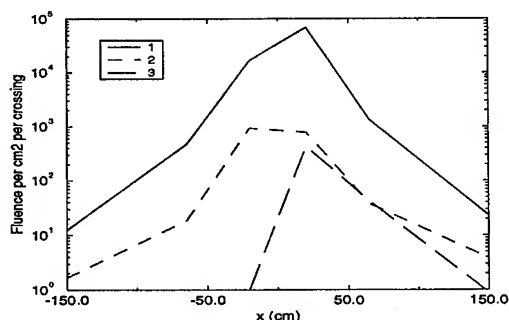


Figure 3. Distribution of e^+e^- flux in the central tracker horizontal plane. 1 – no collimation, 2 – with tungsten nozzle, 3 – dipole field turned off in the triplet

existence of long drifts in the proposed lattice, gives possibilities for a collimation and spoiling in a vicinity of the detector.

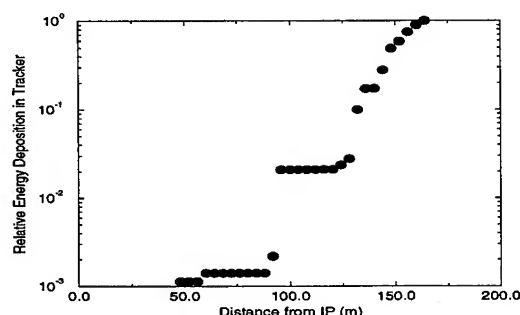


Figure 4. Cumulative energy deposition in the central tracker as a function of shower origin coordinate

The detector muon system can be protected from low-energy large-angle particles created along the lattice with a shielding wall at ≈ 20 m. Its efficiency for the reduction of showers and neutrons can be as high as required. As for the muon component other measures are needed such as a beam scraper system well upstream of the IR.

V. HEAT LOAD TO SC MAGNETS

Due to muon decays ≈ 30 Joules of energy are deposited in every meter of the ring. With the 10 to 30 Hz repetition rate this results in a heat load which significantly exceeds the levels tolerated in existing superconducting (SC) magnets. Our calculations show that in addition the peak energy deposition in the coils exceeds the quench limit. The problem is especially serious in the β_{peak} region. The way to mitigate this would be to intercept most of the shower energy at the nitrogen temperature level by inserting a liner between the beam pipe and the SC coils. We found that a copper liner does a good job. With the coil apertures defined above, the liner occupies the region between 10 and 25mm in the arcs, and 30 and 45mm in the triplet. Further optimizations are certainly required.

VI. CONCLUSIONS

A prototype lattice for a $\mu^+\mu^-$ collider has been constructed. The dynamic aperture is determined. The momentum aperture

is found first by the chromaticity of the lattice, and if the chromaticity is corrected by sextupoles, by the third order resonance. The practical physical aperture with a 15-mm copper liner is determined compatible with beam dynamics, detector performance and heat load in the SC magnets. The effect of the IR scheme on particle fluxes in the collider detector has been studied.

References

- [1] E. A. Perevedentsev, and A. N. Skrinsky, in *Proc. 12th Int. Conf. on High Energy Accelerators*, F. T. Cole, and R. Donaldson, eds., p. 485 (1983); A. N. Skrinsky, and V. V. Parkhomchuk, *Sov. J. of Nucl. Physics*, **12**, p. 3 (1981).
- [2] D. V. Neuffer, and R. B. Palmer, "A High-Energy High-Luminosity $\mu^+\mu^-$ Collider", *BNL-61267, CAP-109-Muon-94C*, June 1994.
- [3] V. Barger et al., "Physics Goals of a $\mu^+\mu^-$ Collider", *BNL-61593, CAP-118-Muon-94C*, March 1995.
- [4] R. B. Palmer et al., "Beam Dynamics Problems in a Muon Collider", *BNL-61580, CAP-120-Muon-95J*, March 1995.
- [5] N. M. Gelfand, "A Prototype Lattice Design for a $\mu^+\mu^-$ Collider", *Fermilab TM-1933*, April 1995.
- [6] G. W. Foster, and N. V. Mokhov, "Backgrounds and Detector Performance at a 2×2 TeV $\mu^+\mu^-$ Collider", *FERMILAB-Conf-95/037*, March 1995.
- [7] N. M. Gelfand, and A. D. Russell, "TEVLAT", Fermilab (1990); H. Grote, and F. C. Iselin, "The MAD Program User's Reference Manual", Version 8.1, *CERN/SL/90-13 (AP)* (1990).
- [8] N. V. Mokhov, "The MARS Code System User's Guide, Version 13(95)", *Fermilab FN-628*, April 1995.

MUON COOLING AND ACCELERATION EXPERIMENT AT TRIUMF

S.A. Bogacz, D.B. Cline, P.H. Sandler and D.A. Sanders, Department of Physics and Astronomy,
University of California Los Angeles, Los Angeles, CA 90024-1547

Abstract

Here, we propose to develop an effective method for cooling and accelerating muons by channeling them in a crystal structure. Leading schemes for future high energy $\mu^+ \mu^-$ colliders [1, 2] rely on fast cooling and high gradient acceleration of short-lived muons. This experiment aims to prove that both processes can be integrated and achieved in the ultra-strong focusing environment of a solid state system. Practical demonstration of transverse cooling in a continuous focusing channel and verification of theoretically predicted cooling efficiencies are the first steps towards meeting the challenges of $\mu^+ \mu^-$ colliders [2]. Furthermore, experimental demonstration of high-acceleration gradients around GeV per meter promised by the high fields in a crystal channel would make $\mu^+ \mu^-$ colliders a real possibility.

I. THEORETICAL OVERVIEW

A. Cooling

Recent results on the radiation reaction of charged particles in a continuous focusing channel [3], indicate an efficient method to damp the transverse emittance of a muon beam. This could be done without diluting the longitudinal phase-space significantly. There is an excitation-free transverse ground state to which a channeling particle will always decay, by emission of an X-ray photon. In addition, the continuous focusing environment in a crystal channel eliminates any quantum excitations from random photon emission, by constraining the photon recoil selection rules. A relativistic muon entering the crystal with a pitch angle of θ_p that is within the critical channeling angle of a few mrad, will satisfy the "undulator" regime requirements given by the following inequality

$$\gamma\theta_p \ll 1. \quad (1)$$

In this case, the particle will lose a negligible amount of the total energy while damping to the transverse ground state. Muons of the same energy but different θ_p will all end up in the same transverse ground state, limited by the uncertainty principle. Theoretically predicted ground state emittance is given by the following expression

$$\gamma\epsilon_{\min} = \frac{\lambda_\mu}{2}, \quad (2)$$

where λ_μ is the Compton wavelength of a muon. Following the solution of Klein-Gordon equation [3], photons emitted in a "dipole regime", given by Eq.(1), obey the following selection rule

$$\Delta n = n_i - n_f = 1, \quad (3)$$

linking energies of the initial, E_i , and the final, E_f , state of a radiating particle according to the following formula

$$E_f \approx E_i \left[1 - \frac{1}{2}(\gamma\theta_p)^2 \right], \quad (4)$$

which yields a small longitudinal energy spread.

This combination of both the transverse and the longitudinal phase-space features makes a radiation damping mechanism a very interesting candidate for transverse muon cooling in an ultra strong focusing environment inside a crystal.

For μ^+ s channeling in a Silicon crystal the characteristic transverse damping time, τ , is given by the following formula

$$\frac{1}{\tau} = 2r_\mu \frac{e\phi_1}{3m_\mu c}, \quad (5)$$

where r_μ is the classical radius of a muon and $e\phi_1 = 6 \times 10^{11}$ GeV/m² is the focusing strength for Silicon crystal [4].

Although the characteristic damping time, $\tau \approx 10^{-6}$ sec, for a spontaneous channeling radiation damping is rather long one can enhance the lattice reaction [9] by using the crystal lattice as a micro-undulator (external strain modulation of the inter atomic spacing in the crystal lattice, e.g. an acoustic wave of wavelength ℓ). If the acoustic wavelength, ℓ , matches the Doppler shifted betatron oscillations of the beam, $\gamma\lambda_\beta$, according to the following matching condition

$$\gamma\lambda_\beta = \sqrt{2} \ell, \quad \lambda_\beta = 2\pi \sqrt{\frac{m_\mu c^2}{e\phi_1}}, \quad (6)$$

a stimulated enhancement of the channeling radiation will occur – similar effect to the FEL amplification. In fact, if one could generate a standing acoustic wave of sizable amplitude in a crystal, then the relaxation time would shorten the damping time by more than three orders of magnitude.

B. Acceleration

According to previous calculations [4, 6], one can achieve acceleration gradients of GeV/m in the high fields found in a crystal channel. The first paper [4] explores the idea of inverse FEL coupling to a high-power optical driver. A strain modulated Silicon crystal acts as a microundulator for a channeled muon beam. This crystal is then placed in an optical cavity – between two axicon mirrors powered by a GWatt laser at visible frequencies.

A beam of relativistic particles while channeling through the crystal follows a well defined trajectory. For planar channeling of charged particles in [110] crystallographic direction the center of the channeling axis is modulated by the

acoustic wave periodicity to produce an undulator effect: i.e., the particles are periodically accelerated perpendicular to their flight path as they traverse the channel. The micro-undulator wavelength, ℓ , (for a typical acoustic modulation) falls in the range 1000–5000 Å, far shorter than those of any macroscopic undulator. Furthermore, the electrostatic crystal-fields involve the line averaged nuclear field and can be two or more orders of magnitude larger than the equivalent fields of macroscopic magnetic undulators. Both of these factors hold the promise of greatly enhanced coupling between the beam and the accelerating electromagnetic wave.

The key to collective acceleration via inverse FEL mechanism is a spontaneous bunching of initially uniform beam channeling through a periodic crystal structure and interacting with the electromagnetic wave. Appropriate phase matching results in energy flow from the wave to the particle beam. This particular kind of particle density fluctuation has the form of a propagating density wave of the same frequency, ω , as the emitted electromagnetic wave. The phase velocity of the moving bunch matches the velocity of particles in the beam. This energy-momentum conservation condition translates into the following acoustic – optical wavelength constraint

$$\lambda = \left(1 + \frac{1}{\beta}\right) \ell, \quad \beta = 1, \quad (7)$$

which in our numerical example fixes the accelerating optical wavelength at $\lambda = 1000$ nm.

The nominal acceleration efficiency in units of MeV/m will, obviously, depend on the energy density of the actual optical cavity. The recent advances in high power laser technology based upon diode laser pumped solid state lasers [5] promise a power of a few MWatts, optically focused to provide energy densities of $E^{\max} = 10^{10}$ V/m, where E^{\max} is the electric field amplitude of the standing cavity mode. The final accelerating efficiency [4] is equivalent to an accelerating gradient of 2 GeV/m.

One can also test the inverse Cerenkov acceleration mechanism [6], since the index of refraction for Silicon is very large, $n = 1.5$. Matching the phase velocity of the optical mode to the muon velocity requires relatively large crossing angle (between the beam and the laser pulse). This enhances the longitudinal projection of the radial component of the electric field, which in turn yields high accelerating gradient.

II. EXPERIMENTAL OVERVIEW

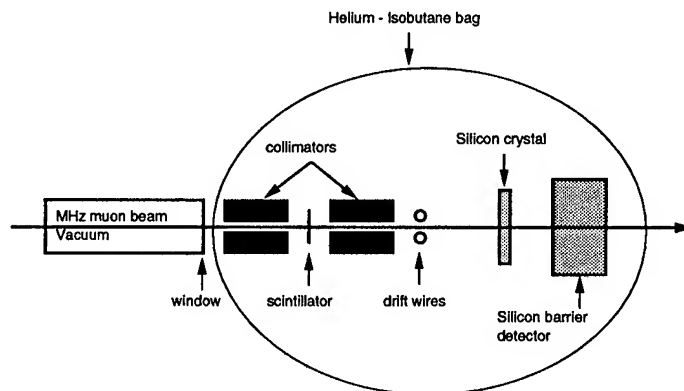
The experiment will be done in three stages. The first step, called the transmission experiment, will show channeling of muons in a 4-mm thick Silicon crystal wafer. The second step will measure the cooling of channeled muons. Finally, the third step will incorporate acceleration.

A. Phase I - Transmission

TRIUMF's M13 beamline is the best choice for effective channeling through a 4-mm sample of Silicon crystal. It provides surface muons at high intensity – about 1.2×10^6 per

second [7]. They carry momentum of 35 MeV/c with a longitudinal spread of about 4% FWHM. As a TRANSPORT simulation shows, for optimum tuning of the final focus quadrupole doublet in M13 one could achieve a spot size of 2 cm x 2 cm with horizontal and vertical divergences of 10 mrad and 65 mrad respectively. The critical planar channeling angle in a Silicon crystal is about 12 mrad for 35 MeV/c positive muons, if one extrapolates critical angle measurements from proton channeling [8]. In this case, a sizable fraction of the incident muons will channel into the crystal.

We intend to carry out a measurements of the critical angle for channeling muons and the ionization energy loss for channeled versus unchanneled muons. We will use the 35 MeV/c momentum surface muons provided by the M13 beamline at TRIUMF, which was selected based on our assessment of the quality of the muon beam. At this energy, the stopping power of amorphous Silicon is high, about 3 mm. In this case, only channeled muons will survive the crystal. Unchanneled particles are subject to typical energy loss mechanisms of ionization and bremsstrahlung. Whereas, the energy loss of channeled particles is severely reduced [8]. A schematic of the proposed setup for the transmission experiment is illustrated schematically below.



As a multiple scattering estimate shows a muon beam going through 75 microns of mylar gains 20 mrad divergence, which is comparable with the incident beam divergence coming from M13 beamline (12 mrad critical angle for planar channeling in Silicon). The beam will incident from the left. After it passes through a window the beam is collimated with a lead brick with 1 mm hole, followed by a thin scintillator and another lead brick with a hole. A pair of drift wires are placed just outside the second collimator exit. A 3 mm Silicon crystal wafer is mounted on a goniometer table (appropriate orientation in two planes). The muons then enter the crystal at some incident angle, θ with respect to the axis of the crystal. The crystal's orientation is controlled remotely by a goniometer (just downstream of the crystal). It is important to align the crystal with the beam. A rough

alignment will be performed with X-rays. Then we will use the tracking information and a goniometer to maximize the number of channeled muons exiting the crystal.

Entire set up will be enclosed in a Helium bag. The multiple scattering angle of 0.3 mrad per cm of Helium characterizes the level of beam divergence increase due to the background medium. Silicon barrier detector will be placed immediately after the Silicon wafer to measure energy spectrum of the channeled muons. The exiting muon energy and flux will be measured with a surface-barrier detector. Such detectors are capable of about 20 keV energy resolution at 35 MeV/c. The data will indicate the yield as a function of θ , allowing extraction of the critical angle within which muons are effectively channeled. Furthermore, we can measure the energy spread of the exiting beam. This will indicate the degree of energy straggling we should expect when compared to the incident energy distribution provided by the beamline.

B. Phase II - Cooling

This phase of the experiment will test the cooling mechanisms summarized in the theory section above. The beam momentum will be about 250 MeV/c as provided by forward decay muons [7] in M11. In this case, both channeled and unchanneled muons will penetrate the 4-cm crystal and the cooling process can be compared for the two. In addition, a higher energy beam, tests cooling at the energies considered for realistic collider schemes. The first step of Phase II is to measure initial and final emittances of an unmodified crystal. A schematic of our proposed experimental setup is similar to the one described previously. We will track each muon individually using five sets of drift chambers. This way we can identify channeled and unchanneled particles on an event-by-event basis. We can also obtain the exact initial and final emittances for channeled and unchanneled muons separately. It is also possible to separate channeled and unchanneled muons by plotting their energy loss. The trigger will be provided by scintillation counters upstream, combined with a veto counter that rejects muons which do not intersect the crystal. A time-of-flight counter will be placed in a downstream position, to be used in concert with the 1 picosecond timing pulse provided by the M11 beamline. This will aid in particle identification since some positrons and pions will likely contaminate the beam. To enhance the cooling, we will generate a strain modulation of the planar channels. An acoustic wave of 1 GHz is excited via a piezoelectric transducer. We will also detect predicted channeling radiation by surrounding the crystal with CsI scintillation detectors, which are sensitive to X-rays. The M11 beamline is presently a source of high energy pions [7]. Straightforward modification of the beamline will provide a collimated beam of forward-decay muons at high intensity – about 10^6 per second at 250 MeV/c. The longitudinal momentum spread is about 2% FWHM. Assuming optimum tuning of the final focus quadrupole doublet in M11, we can achieve a spot size of 3 cm \times 2 cm with horizontal and vertical divergences of 10 mrad and 16 mrad respectively. The critical angle for planar channeling of μ^+ at 250 MeV/c in Silicon is about 7 mrad,

extrapolating from proton channeling data. A sizable fraction of the muons should channel through a few centimeters of the crystal.

C. Phase III - Acceleration

Two schemes high gradient acceleration will be tested. Initially, an unmodified crystal will be used to demonstrate inverse Cerenkov [7] and inverse FEL [4] acceleration of muons. The optical setup is analogous to the Inverse Cerenkov Accelerator Experiment at Brookhaven. It provides a pulse of radially polarized light, which couples energy to the muon beam channeling through a crystal via the inverse FEL mechanism. Here a strain modulation in the crystal imposed by an acoustic wave plays the role of an ultra-short wave undulator. Optical energy will be transferred to the muon beam with an efficiency of GeV per meter. A 4-cm Silicon crystal would provide a 40 MeV energy burst. Using a bending magnet in between drift chambers, we will measure the final energy of muons channeling through the crystal. The initial energy of each muons is provided by a spectrometer in the beamline.

References

- [1] D.V. Neuffer, Nuclear Instruments and Methods in Physics Research A **350** (1994) 27-35.
- [2] D.B. Cline, Nuclear Instruments and Methods in Physics Research A, **350** (1994) 24-26.
- [3] Z. Huang, P. Chen, R.D. Ruth, Phys. Rev. Lett. **74**, 10, 1759 (1995).
- [4] S.A. Bogacz, Particle Accelerators, **42**(3-4), 181 (1993).
- [5] S. Basu and R.L. Byer, Optic Letters, **13**, 458 (1988).
- [6] L.C. Steinhauer and W.D. Kimura, Journal of Applied Physics, **68**, 10, (1990).
- [7] G.M. Marshall, Z. Phys. C **56** (1992) S226-S231.
- [8] V.A. Bazylev and N.K. Zhevago, Sov. Phys. Usp. **33** (12) 1021 (1990).
- [9] S.A. Bogacz and J.B. Ketterson, Journal of Applied Physics, **60** (1), 177, (1986).

HELICAL SIBERIAN SNAKES

E.Ludmirsky, Institute for High Energy Physics, Protvino, Moscow Region, Russia

Abstract

The helical dipole is a new type of magnet element for charged particle accelerators. Helical dipoles are long dipoles twisted into a helix; one can be constructed with laminations, each lamination is rotated by some small angle with respect to the previous lamination. Siberian snakes using helical dipoles would have several advantages: the closed orbit excursions within the snake would be smaller; there would be fewer magnets required; and potentially the snake could be shorted so it would require less space in the ring. Fabrication techniques are explained. Construction problems and their solutions are reviewed.

I. INTRODUCTION

Polarized proton beams, when accelerated in a circular ring, encounter various resonances in the motion of their spin, and that will ultimately lead to depolarization. Since there are generally many depolarizing resonances in a strong-focusing synchrotron, a polarized beam can not be accelerated without using several correction methods to suppress the depolarizing resonances. There are several methods to reduce the depolarizing effect of the resonance field harmonics, but the Siberian snake technique was demonstrated to be most effective in maintaining beam polarization. A snake is a configuration of magnets that, in the orbit frame, rotates the spin by 180° about an axis which lies in the horizontal plane. This proposal has been made by Y.S.Derbenev and A.N.Kondratenko^[1].

In low energy machines excursions inside a standard Siberian snake design become excessively big. For this reason it is necessary to find compact helical dipole magnets designs that minimize both excursions and length. A snake with very small orbit excursions is the helical snake proposed by E.D.Courant, Ya.S.Derbenev and A.N.Kondratenko^[2,3]. One of the most compact snakes is a helical snake. This minimizes the orbit displacements.

Equations for the helical field and the conditions for π spin flip and orbit restoration schemes, see^[3,4].

The trajectory in the helical magnet is determined by the equations

$$x'' = -\frac{1}{\rho} \sin ks,$$

$$y'' = \frac{1}{\rho} \cos ks.$$

General solution for the particle motion inside a helix contains spiral trajectory plus straight line solution with parameters depending on initial conditions of incoming beam.

By means of matching initial conditions at the helix with the pure spiral solution one can reduce orbit excursion inside the helix up to the value of $r = 1/\rho k^2$.

Table I

Major parameters of I and II type helical dipole magnets

Type of magnet	I	II
Maximum field [T]	1.7	1.7
Aperture [mm]	200	120
Power dissipation/magnet [kW]	1200	450
Total weight [kg]	57000	26000

II. HELICAL DIPOLE MAGNETS

We have designed two helical dipole magnets for use as Siberian snake in the accelerators Fig.1. Helical dipoles are long dipoles twisted into a helix; one can be constructed with laminations, each lamination is rotated by some small angle with respect to the previous lamination. Such a magnets design ensures a uniform field ($\sim 10^{-3}$) up to 1.7 T.

A plane and a helicoid are only complete surfaces of zero middle curvature. A helicoid is obtained as a result of two straight line motions: i.e. in one dimension with a constant speed and rotatory with constant angular velocity in the orthogonal to the translation vector plane. These mentioned mathematical qualities of the helicoid permit to work out the construction and manufacturing technology for the vacuum chamber, coils and magnet core of a helical dipole magnet.

The main parameters of the laminated helical dipoles are summarized in Table 1 for conditions corresponding to the nominal accelerator operating energy of $\sim 8-10$ GeV.

The most possible field error in the magnet gap is caused by the accuracy of pole profile. The field variation along the orbit may be produced by the fluctuation of the permeability and coercive force of the core materials. In high-field magnets, one important property of the iron is lost: the field-shaping property. As the relative permeability approaches unity, the iron surface is no longer equipotential. Field-shaping is now entirely due to magnet coil configuration, and correcting coils, is required.

Modern steels used in direct current magnets have an impurity content ($N_2 + S + P + Al + Mo$) of less than 0.1%, ($Cr + Cu + Mn + Ni + Si$) of less than 0.7%. Carbon, which is the most dangerous impurity, is limited to 0.1%. Pure iron is costly and too soft to be machined and handled for magnet cores.

From our experience, the conclusion is that using laser cutting techniques to cut laminations may be a good method to built laminated magnet. The laser cutting technique is advertised to have a very high machining accuracy of 0.05 mm tolerance over a 1000 mm length.

The coil consists of the several section with square cross-section. In order to wind the rectangular wire helically, it is required to twist the wire continuously. The coil, located in gap, are designed of water-cooled cooper, insulated with epoxy resin and fiberglass and vacuum potted in an alumina-based epoxy.

Standard technique for insulating magnet coil is to use epoxy resin, reinforced with fiberglass. Standard resin systems, such as Novolac, or Bisphenyl-A, with NMA hardener, can be expected to tolerate 10^9 rad. By using a kapton layer between the coil and the core, one achieves a further ground insulation and also provides a slip plane to allow the coil to move in the core upon thermal expansion of either component.

The size requirements of the beam chambers are determined by the helix with radius $r = 1/\rho k^2$, beam emittances and energy spreads.

The vacuum chamber can be made from any metal, but, as it is usual in accelerative technique stainless steel is the most preferable material. The technology of manufacturing the chamber includes several stages.

The vacuum chambers of the helical dipole magnet is made from unrolling helicoids. These helicoids have as their return rib a spiral of a constant pitch on the circular cylinder. Four such elements which are preliminarily moulded as helicoids, are welded all over the return ribs. So the vacuum chamber of the helical dipole magnet is obtained.

The vacuum chambers experience atmospherical pressure all over its external surface. To reduce the vacuum chamber deformation we can install the hardness ribs on it. But it is not efficient because the necessary dipole aperture increases. It is more expedient to apply helicoids as chamber elements, moulded in the cross direction as a sloping arch.

We have constructed a model of a helical dipole which could be used in a Siberian snake for the accelerators. Our purpose was to show the feasibility of constructing a helical dipole. The model was run in a low duty factor test; the low duty factor avoided the overheating during DC operation at 1.6 T of a $\sim 10\%$ mechanical scale model for which the current density is $\sqrt{10}$ larger than in a full scale model.

The model of the helical dipole magnet which we made, shown in Fig.2 has a four-turn coil with a copper conductor and copper water pipes brazed to its upper and lower ends. The current flow in the coils is in series whereas the coolant flow is in parallel.

The magnetic field properties of helical dipole magnet model were measured and found to be close to the design. The helical dipole magnet model was pulsed about 10^4 times in the IHEP laboratory without any incident.

III. CONCLUSION

The second variant of helical dipole has considerable advantages in use for accelerators.

In application to each specific accelerator project the helical dipole used needs careful consideration of beam dynamics both theoretically and by computer modeling.

The $\sim 10\%$ model fabrication, operation and demonstrated reliability has advanced the technology of helical dipole magnets. Helical dipole magnets are now ready for applications in accelerator physics such as use in a ring at IHEP, PS (CERN) or Fermilab.

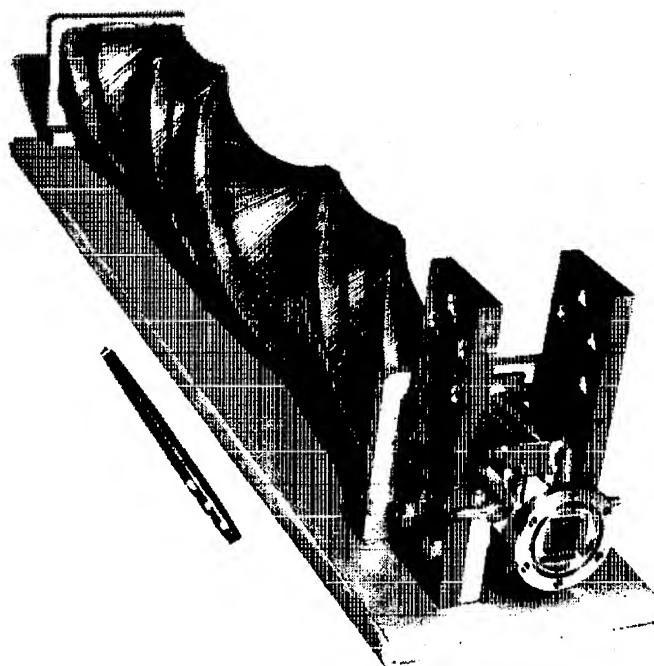


Figure 2. Helical dipole magnet.

References

- [1] Ya.S.Derbenev and A.N.Kondratenko, Proceedings of 10-th International Conference on High Energy Accelerators, Protvino, USSR, 1977.
- [2] Ya.S.Derbenev and A.N.Kondratenko, Proc. Int. Conf. on High Energy Physics with Polarized Beams and Polarized Targets, Argonne, III, (1978), p. 292ff.
- [3] E.D.Courant, EHF Internal Report 86-07 and 87-09 (Mainz, F.R.G., and 1987) (unpublished), and E.D.Courant, Proc. 8-th Int. Symposium on High Energy Spin Physics, Minneapolis, MN, (1988), p. 1085f.
- [4] U.Wienands, Helical Siberian Snakes Using Dipole Magnets. TRI-PP-90-65, Sept. 1990.

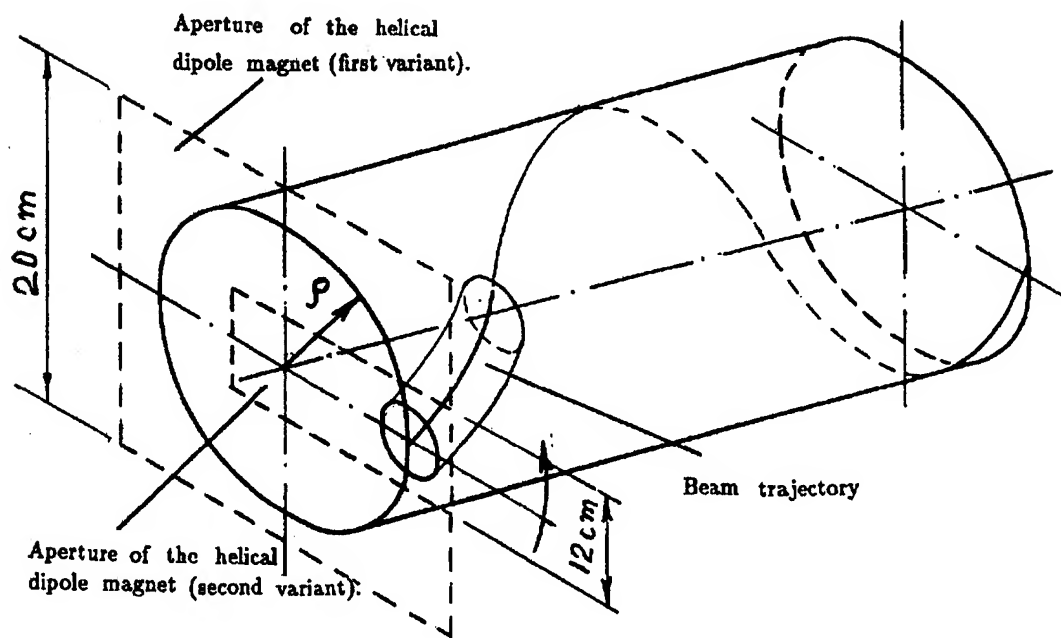


Figure 1. The magnet apertures. The aperture makes a (complete) revolution.

PERFORMANCE OF ACHROMATIC LATTICE WITH COMBINED FUNCTION SEXTUPOLES AT DUKE STORAGE RING*

V. N. Litvinenko, Y. Wu, B. Burnham, J. M. J. Madey, and S. H. Park
Duke University, Free Electron Laser Laboratory, Durham, NC 27708-0319 USA

Abstract

The 1 GeV Duke Storage Ring was very successfully commissioned with performance exceeding initial specifications [1]. In this paper we present design and performance data of its unique achromatic lattice with combined function magnets in the ring arcs.

I. INTRODUCTION

The third generation 1 GeV Duke storage ring is designed to drive UV and soft X-ray FELs as well as to produce high brightness synchrotron radiation from the bending magnets and insertion devices. The ring itself is a strong focusing race-track with two 34 meter long straight sections. The south straight section lattice is designed to optimize FEL operation with 7 to 28 m long FELs. The north straight section is used for injection and installation of the RF system and synchrotron radiation insertion devices. There are plans for installation of a variety of FELs and undulators in the straight sections. It was essential to develop a lattice which can be adjusted for variable configurations in straight section without reduction of the ring performance and its dynamic aperture.

Two typical practical examples demonstrate flexibility of the lattice:

1. Present design of the south straight section includes eight quadrupoles and is optimized for 8 m long OK-4 FEL. This system can accommodate also 26 m FEL wiggler without losing performance;
2. The lattice for location of the 4 m NIST undulator in the North straight section was designed after completion of the Duke ring design. There was no problem to incorporate this device into the ring by modifying the last 7 m of the North straight section without any loss of the ring performance.

To satisfy these and other vaguely defined, but complicated, requirement we chose to use modified second order achromatic lattice for the ring arcs. All sextupoles required for chromaticity compensation are located in the arcs. The arc lattice design eliminates second order geometrical aberrations caused by sextupole moments. In this case, the ring dynamic aperture does not depend on the straight section lattice as soon as the β -functions are matched.

The new design of the Duke storage ring lattice was initiated in February of 1991 and was completed in October in the same year [2,3].

The modified second-order achromatic lattice for the ring arcs [2] solved the fundamental dynamic aperture problems

encountered with the original Stanford design [4]. The new design provides a dynamic aperture exceeding the mechanical aperture [3].

The ring design was driven to a large extent by the necessity to use most of the hardware already acquired for the ring prior to 1991. A number of unusual concepts were used to incorporate existing hardware into the new design. The most unusual idea was the use of asymmetric excitation of quadrupole coils for generation of both quadrupole and sextupole moments [3,5]. Precision magnetic measurements [6] have confirmed the excellent quality of these combined function magnets. This idea eliminates individual sextupole magnets from a tightly packed arc lattice and creates arc symmetry for all magnetic moments.

All dipoles on the Duke storage ring are fed by one 560 kW PEI power supply, while all quadrupoles have individual power supplies. This feature provides flexibility for the lattice design.

The layout of the Duke storage ring can be found elsewhere in this proceedings [1].

Table I. Parameters of Duke Storage Ring

Operating energy [GeV]	0.20 - 1.1
Ring circumference [m]	107.46
Arc and straight section length [m]	19.52; 34.21
Number of dipoles and quadrupoles	40; 64
Betatron tunes, Q_x and Q_y	9.111, 4.180
Orbit compaction factor, α	0.0086
Natural chromaticities, C_x and C_y	-10.0, -9.78
Acceptances [mm mrad], A_x and A_y	56.0, 16.0
Energy acceptance, $\Delta E/E$, of ring	$\geq \pm 5.0\%$
Maximum arc β -functions [m], x and y	2.5, 5
Maximum η -function [m]	0.245

II. THE ARC LATTICE

The Duke storage ring arc comprises 20 dipole magnets and 21 quadrupoles divided into eight regular FODO cells and two end-of-arc matching cells.

Combined functions magnets.

The Duke arcs are packed very tightly - there are only 18 cm between the dipoles and quadrupoles. The original Stanford design [4] of the ring called for the use of "dimples and noses" as dipole endpieces to create main sextupole

* Work supported by ONR grant #N00014-94-1-0818 and AFOSR grant #F49620-93-1-0590

moments and individual sextupoles squeezed into 18 cm gaps with 2 cm gap between poles of different magnets. It was discovered that this design suffered from severe asymmetric saturation causing intolerable orbit shifts and field non-linearity.

We replaced the dimples and noses with a smooth symmetric endcaps to achieve a high quality of the magnetic field up to 20.5 kGs [6]. We also decided to remove the individual sextupoles which also caused saturation.

We now use asymmetric excitation of the arc quadrupoles by shunting part of the current from the inner (towards the center of the ring) coils. Thus, each arc quadrupole has an individual power supply which provides current I_1 (see sketch below) and individual shunt regulator which by-pass part of current $\Delta I = I_1 - I_2$ from inside coils.

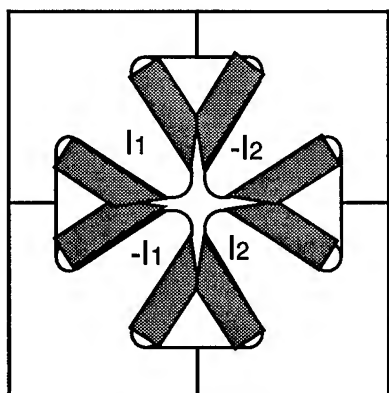


Fig.1. Asymmetric excitation of the arc quadrupole.

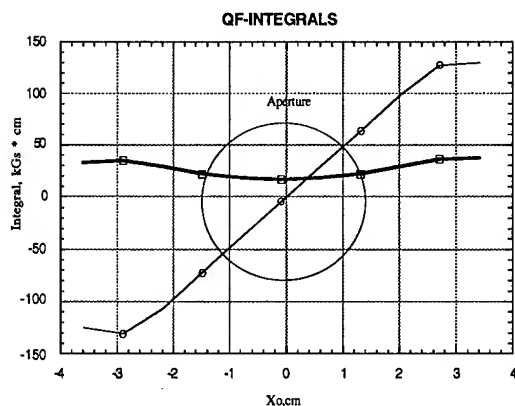


Fig.2. Symmetric and asymmetric part of the combined quadrupole function field.

The Duke ring arc quadrupoles have an inside radius of 2 cm and can operate with gradients up to 4 kGs/cm. There is no pole tip saturation even at maximum current - light saturation occurs in the neck of the yoke.

This condition provides good separation of the odd and even multipoles. Computer simulations and magnetic measurements demonstrated the excellent quality of these combined dipole-quadrupole-sextupole fields. We saw only a weak dodecapole term in the field expansion.

Typical values for the Duke ring combine function quadrupoles with 18-20% asymmetry of excitation are:

Gradient	3500 kGs/cm
Sextupole	350 Gs/cm ²
Magnetic center shift	2.25 mm.

Fig 2. show measured dependence of symmetric and asymmetric part of combined function quadrupole at 1 GeV.

It is obvious that asymmetric excitation shifts magnetic center of the quadrupole. To make shift of magnetic centers the same in both focusing and defocusing quadrupoles, we installed small shims creating defocusing sextupole moment at the center of the dipoles (see [6,7] for details). This combination provides compensation of natural chromaticity and enough flexibility to build second order achromatic lattice.

Modified Second Order Achromat.

The regular FODO cell is 1.76 m long and is comprised of two 0.33 m dipole-sextupoles (BS), one 0.20m focusing quadrupole-sextupole (QFS), and one 0.14 m defocusing quadrupole-sextupole (QDS) (all in effective length). The cell has bilateral symmetry of all magnetic multipoles with respect to the quadrupoles centers. Half-cell is sketched on Fig.3

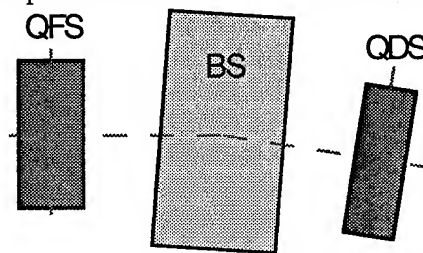


Fig.3 Half of regular arc FODO cell.

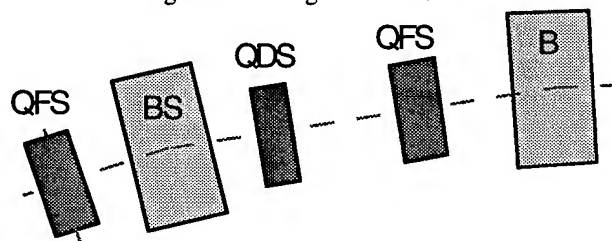


Fig.4 End-of-arc matching cell.

We chose $\Delta Q_x = 3/10$; $\Delta Q_y = 1/10$ tunes advances per cell. This lattice will provide for natural compensation of geometrical aberrations (caused by sextupole moments in the arcs) in the case of ten identical cells. Requirements for low emittance and zero dispersion (η -function) in straight sections do not allow the use of a regular 10-cell second order achromat. We modified end-of-arc cells to match η to zero at the end of the arc and to have β -functions which are easy to match from straight sections.

The 2.02 m matching cell (measured from the center of QDS) is longer than the regular FODO cell - see Fig. 4.

Because of zero dispersion in the straight sections, the natural chromaticity must be compensated in the arcs. We used combined function magnets with sextupole moments excited in both quadrupoles and dipole magnets. We do not

use sextupoles in the end-of-arc dipoles where the η -function is close to zero.

We slightly modify the sextupole strength in the end-of-the-arc cells to compensate the second order geometrical aberrations in the horizontal plane [1]:

$$\int_{Arc} S(s) \beta_x^{3/2}(s) e^{i\psi_x(s)} ds = 0;$$

$$\int_{Arc} S(s) \beta_x^{3/2}(s) e^{i3\psi_x(s)} ds = 0;$$

where $S(s)$ is sextupole moment, β_x is horizontal betatron function, and ψ_x is the betatron phase. We also minimize coupling nonlinear geometrical aberrations. These conditions provide for a transverse dynamic aperture exceeding the physical aperture, and an extremely high energy acceptance (more than $\pm 5\%$) on the ring [3].

III. CONCLUSIONS

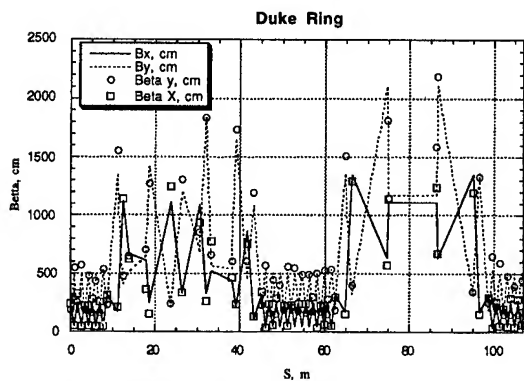


Fig.5 Measured and design values of β -functions.

Operation of the Duke storage ring lattice has not shown any indication of dynamic aperture limitation. Betatron tunes differ very little from design values: $\Delta Q_x = 0.06$; $\Delta Q_y = -0.04$ in all 0.23 - 1.1 GeV energy range. Measurements confirm the theoretical chromaticity compensation within 3% accuracy.

The preliminary measurements of β -functions are shown on Fig.5. There are indications, that the errors in Fig.5 are caused by a coil failure in one of the quadrupoles. We are investigating this possibility.

The orbit distortions without any correction are small: less than ± 5 mm horizontal and less ± 4 mm vertical. Direct measurements of the ring acceptance confirm the predicted dynamic aperture of the ring. The width of coupling resonance is small $\Delta Q = 0.007$ and is consistent with value of orbit distortions.

We measured the electron beam emittances at 1 GeV using visible optics and CCD digitizer (shown below). The measured horizontal emittance is $(17 \pm 2) \cdot 10^{-9}$ m*rad in perfect agreement with 18 nm*rad theoretical value. The resolution of the vertical size measurements was limited by diffraction. Thus, we can only state that vertical emittance is less than $1 \cdot 10^{-9}$ m*rad.

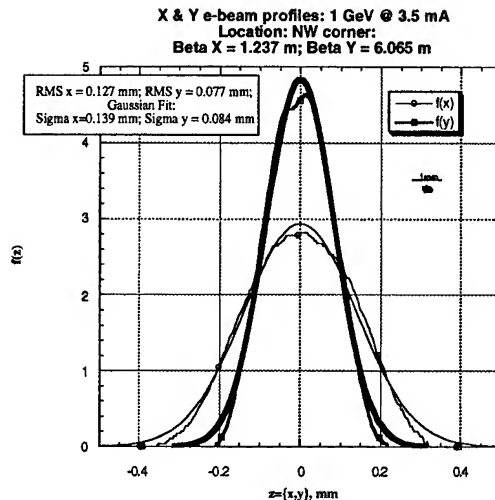


Fig.5 Measured e-beam profiles.

We did not observe any very strong resonances in the wide tune range of $Q_x = \{9.1-9.3\}$, $Q_y = \{4.05-4.3\}$. We used eight straight section quadrupoles for tune adjustments using the flexibility built into the lattice. Direct measurements of the transfer matrix confirm the absence of second order terms in the full arc transport map as predicted by theory [3]. It is remarkable because the half-of-the-arc map has second order terms which create a factor two asymmetry at full aperture.

We found the energy acceptance is $\pm 6\%$ and is limited by the vacuum chamber aperture in the focusing quadrupoles.

The overall performance of the achromatic lattice with combined function magnets is exceptionally good.

IV. REFERENCES

- [1] V.N.Litvinenko et al., "Commissioning of the Duke Storage Ring, These Proceedings.
- [2] V.Litvinenko, Y.Wu, "New Lattice for the Duke Storage Ring", Duke FEL Lab. Report, October 1991
- [3] Y.Wu, V.N.Litvinenko, J.M.J.Madey, in Proceedings of the 1993 Particle Accelerator Conference, Washington D.C., p. 218
- [4] L.Emergy et al., IEEE CH 2387-9, 1496 (1987)
- [5] V.Litvinenko, DFELL Report, March 1991;
- [6] B.Burnham, N.Hower, V.Litvinenko, J.Madey, Y.Wu, Proceedings of the 1993 Particle Accelerator Conference, Washington D.C., p. 2889
- [7] B.Burnham, V.Litvinenko, Y.Wu, "Application of Precision Magnetic Measurements for Control of the Duke Storage Ring", These Proceedings.
- [8] Y.Wu, V.N.Litvinenko, B.Burnham, "Experimental Study of the Duke Storage Ring Dynamic Aperture", These Proceedings.

MATRESHKA — HIGH INTENSITY ACCELERATOR OF CONTINUOUS PARTICLE BEAMS

F.A. Vodopianov

Moscow Radiotechnical Institute of Russian Academy of Sciences, Russia

The schematic MATRESHKA arrangement is illustrated in Figure 1. The electron gun 1, vacuum pump, optical control and measuring systems are mounted with a feeding source in cylindrical metallic shield Seg (only a loading condenser C1 is shown). Around Seg the MATRESHKA's shields S25-S1 are mounted with high voltage sources (C25-C1) connected to these screens. Parts of the accelerating tube including the radial insulators 2, vacuum tubes 3, and focusing magnets 4, are mounted to them also. Screens are kept in a position needed by means of supporting insulators. The front doors 5 permit the operator to work with parts of the accelerating tube (without high voltage!).

Elements 6 (grouping device), 7 (UHF resonators), 8 (vacuum tube) and 9 (focusing winding) are parts of the UHF generator which is describing [1]. Parts 10, 11, and 12 are the MATRESHKA body. The bending magnet 10 analyses the MATRESHKA bunch and direct accelerated particles to corresponding lamelles of energy analyser 11. Lamelles 12 by means of the conductors 13 are connected to the screens S23-S1 and therefore have the corresponding potentials. Electrons caught by them without energy losses are directed in condensers C25-C1. This energy recuperation system makes MATRESHKA a very efficient source of relativistic electron beams for the UHF generator.

The MATRESHKA accelerator was developed for the UHF power excitation of many resonator systems [1] with moderate, for example 5 MW, level for each of them. If the number of resonators are 100, the complete power is 500 MW and with the efficiency 50%, MATRESHKA's beam power must be about 1000 MW. Electron beam can have such power with particle energy 5 MeV and current 200 A. If particles of the beam will have energy, for example, 10 MeV effects of the remainder radioactivity are dangerous. If higher currents are used, then losses of the particles will be higher.

Returning now to a MATRESHKA arrangement, we shall choose a number of the screens and voltage between them. If voltage is 200 kV, then number of the screens are 25, and distance between screens is 600 mm (for operator passage and power sources installation), and horizontal dimension will be 15 m. On the other side 200 mm gap will be sufficient, and the whole width will be about 22 m. Then the vertical dimension will be 12 m.

It is clear that creation of such a colossal installation can be realised only for an outstanding UHF generating system with continuous power gigawatt level. Our times is exactly time to solve like problem—the problem of gigawatt proton beams generation for nuclear transmutation and for nuclear energy stimulation [2,3]. The UHF feeding of the linear proton accelerators with power of the proton beam of gigawatt level is the problem of our days.

But with such power level the MATRESHKA efficiency must

be near to 100%. Only with energy recuperator is it possible to have such a situation [4]. On our schematic representation, the recuperator 11 is fulfilled in ordinary form of energy analyser, but the beam power is used in a nonordinary manner: It is involved in accelerating tube elements. It is to be short to say that this recuperation system was not proved experimentally and therefore it is needed to fulfill a corresponding work. On our schema the return conductors 13, connected to screens in parallel to power sources C1-C25, are shown in coaxial form (they are placed in vacuum for electrical securing). In our early publication [5], and in experiments, we considered a cascaded rectifier system, but now we prefer more efficient electrical alternators driven from outside by means of ceramics rollers. If the electrical alternator is combined with the transformer and rectifier, then parallel connection of such sources with the recuperator conductors is no problem. Magnet 10 can be fulfilled with rotation to prevent a smelting the recuperator lamelles.

In conclusion, the shield system, accelerating tube and return conductors 13 must be done individually in cylindrical form with the ledges on their screens parts. After involving the tube in screen system and turning coupling of system is achieved. After this operation it can be possible to remove a montage bars.

References

- [1] F.A. Vodopianov, "Ultrarelativistic Klystron—A Future Super Power UHF Generator", EPAC-95.
- [2] R. Jemeson, EPAC-92, report THY02A.
- [3] M. Mizumote, EPAC-90, p. 346, R. Bock, EPAC-88, V. 1, P. 249.
- [4] G.D. Kosmal, Proc. IEEE, V. 70, N 11, 1982, P. 93.
- [5] F.A. Vodopianov, Sc-Techn. Reports of Moscow Radiotechnical Institute, USSR Academy of Science, 1990, p. 105.

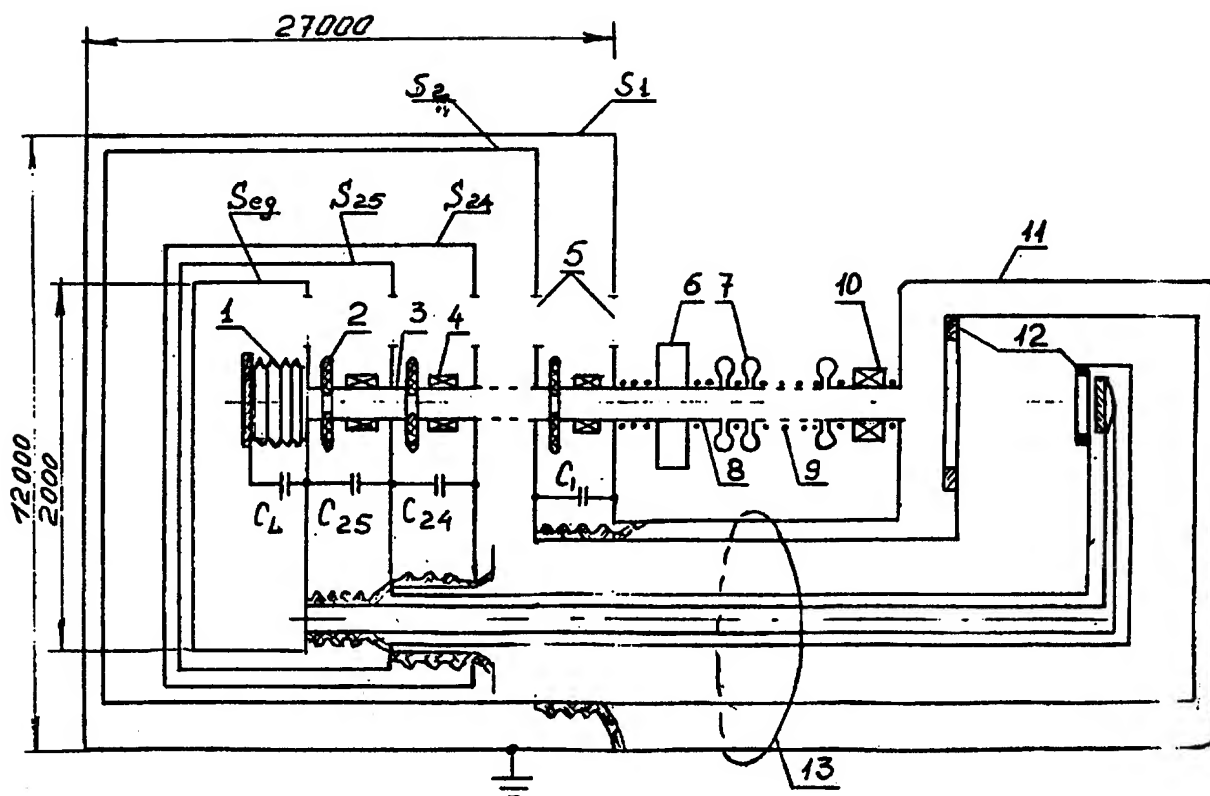


Figure 1. Schematic representation of MATRESHKA

The Amplitude and Phase Control of the ALS Storage Ring RF System

C.C.Lo, B. Taylor and K. Baptiste

Lawrence Berkeley Laboratory

University of California, Berkeley, CA 94720

Abstract

A 500MHz, 300KW Klystron power amplifier provides RF power to the ALS Storage Ring. In order to accommodate the amplitude and phase changes during beam stacking and decay, which demand continuously varying power levels from the Klystron, four loops are used to keep the system operating properly, with two of those loops dedicated to keeping the two cavity tuners on tune. Description of the control loops and their performance data will be given. Using the modulation anode of the Klystron in the amplitude loop will be discussed.

Introduction

Figure 1 shows a simplified block diagram of the ALS SR (Storage Ring) RF system. The RF power is provided by one single 300KW Klystron. The output power is split into two equal parts to drive two similar cavities with a Hybrid or a Magic Tee. In the 1.5 GeV operation the dissipation of each cavity is 35KW with a coupling factor of 1.5. The cavity power dissipation should remain constant through the entire range of operating beam current of 0mA to 400mA. As the beam is demanding more power from the RF through the cavities the amplitude loop will adjust the drive of the RF system providing more power for the beam and keeping the cavities' voltage constant.

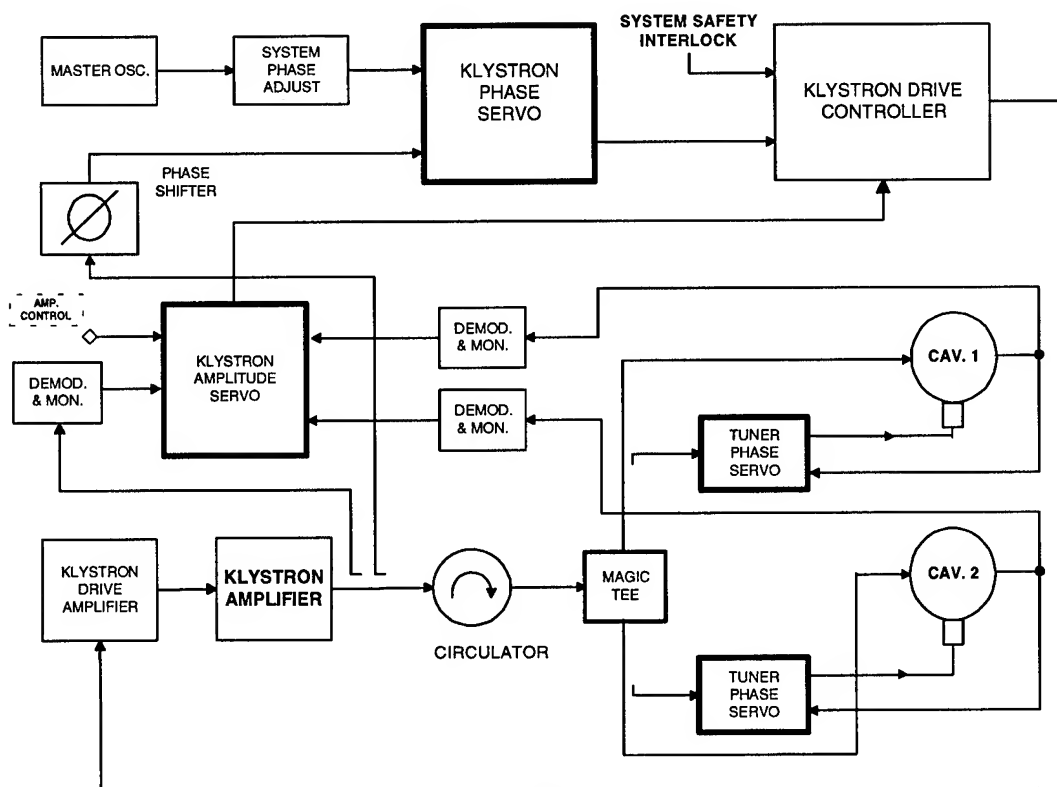


FIG.1 SIMPLIFIED BLOCK DIAGRAM OF THE AMPLITUDE AND PHASE LOOPS OF THE ALS SR RF SYSTEM

Since the RF signal must go through a phase shifter, a couple of amplifiers, an electronic attenuator and finally the Klystron, the phase of the RF signal will vary with the output power level. The phase variation may have some effect during beam stacking; therefore a phase loop has been implemented to keep the phase constant through the range of operating power. In order to keep the two cavities on tune during operation, each cavity tuner phase servo loop utilizes a stepping motor moving a metallic plunger in and out of the cavity to keep it on tune. The Tuner Phase Servo system has been described in detail in Ref. 1.

The master oscillator signal goes through the Klystron Phase Servo and then the Drive Controller. The Drive Controller contains an electronic attenuator and a fast RF switch. The electronic attenuator serves as the amplitude control element, the fast RF switch will shut off the RF power upon receiving an interrupt signal from the personnel and equipment safety interlock systems. The output of this Drive Controller provides input to the Klystron driver amplifier which in turn drives the Klystron amplifier. A circulator is used to protect the Klystron from power reflected from the rest of the system. The Magic Tee splits the power into two equal parts to drive the two cavities. Signals from the cavities' pick up probes are used by the Tuner Phase Servos and the Amplitude Servo to keep the cavities on tune as well as keeping the cavity voltage constant respectively.

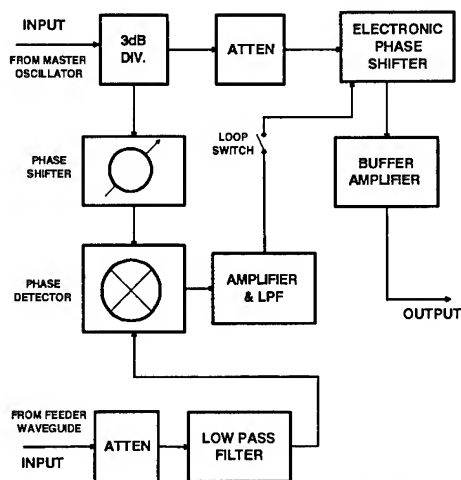


FIG.2 SIMPLIFIED BLOCK DIAGRAM OF THE PHASE SERVO

The Phase Loop

Figure 2 is a block diagram of the Phase Servo. The master oscillator signal is split into two parts. One part goes to the electronic phase shifter and the output amplifier, the other part goes through a mechanical phase shifter to a double balance mixer as the Local reference signal. A directional coupler in the feeder waveguide picks up portion of the RF signal and feeds it back to the RF port of the mixer. The IF output of the mixer is filtered and amplified and fed back to the Electronic Phase Shifter to compensate for the phase change in the signal path. During testing without beam, the amount of phase variation of the system without feedback is more than 30 degrees between an operating power level of 30KW and 80KW. By closing the loop the phase variation is reduced to less than 0.25 degree. At the present time 80KW is the operating power for the two cavities without beam. With a beam current of 400mA at 1.5GeV the total RF power required is about 115KW. With the phase loop open between 80KW and 115KW the phase variation is less than 10 degrees. With the loop closed the phase variation is reduced to less than 0.25 degree. For normal operation the power is brought up to 80KW and the phase error is adjusted to zero, the phase loop is closed at this point. Any phase variation from this point on will be compensated by the electronics phase shifter according to the phase error voltage from the phase detector. The electronics phase shifter has a range of 300 degrees.

The Amplitude Loop

Figure 3 shows a simplified block diagram of the Amplitude Servo. During operation the DC amplitude control signal normally comes from the control system. A preset value is used to provide 80KW of power to the two cavities for 1.5GeV - 1.9GeV operation. An adjustable input amplitude limiter is used to limit the input amplitude control to ensure that the set point would not exceed 80KW. This amplitude control signal is used as the reference voltage for both the feeder feedback loop and the cavity feedback loop. At the power level of 80KW, equal weights of cavity one and cavity two signals are summed together and adjusted

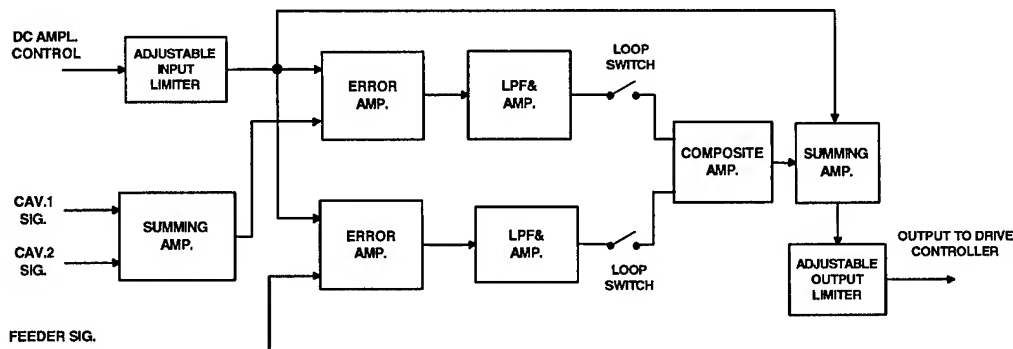


FIG.3 SIMPLIFIED BLOCK DIAGRAM OF THE AMPLITUDE SERVO

to the same level as the reference signal. The same procedure is carried out for the feeder channel. The error amplifiers on both channels produce correction signals which are filtered and amplified. The two loops can be opened or closed by the two loop switches. The two correction signals are then summed and monitored by the output amplitude limiter before it is used to control the Klystron drive. The output amplitude limiter is used mainly to limit the maximum power output of the Klystron in case of any mishap occurring in the signal path that may demand an exceedingly high power output from the system. The feeder loop is mainly used to reduce ripple in the power supply; more than 35dB of reduction of ripple has been achieved. The cavity loops are essential for counteracting beam loading effects. During beam accumulation more and more power is supplied to the beam to compensate for the losses due to bending magnets and insertion devices, the amplitude loop detects any drop in cavity voltage and increase the drive power to the Klystron to make up for the losses. The cavity loop has successfully kept the cavity voltage constant through the entire range of beam current of 0 mA to 400 mA at 1.5 GeV operation. We expect the same in the 1.9GeV operation.

Conclusion

The Tuner Phase loops, the amplitude loops have been operating successfully since ALS began operation. The amplitude feedback loop is using an electronic attenuator in the Klystron Drive Controller to control the power output of

the Klystron. The modulation anode in the Klystron was originally planned to be used as the amplitude control element, however due to problems in the factory supplied control system, design changes have to be made before the modulation anode can be used for that purpose. The present system works well as long as the Klystron beam current demand does not exceed the maximum allowed collector dissipation of 300KW. The Klystron Phase loop has been operating only for a short time, its performance will be reported in due time.

Acknowledgment

The work was supported by the Director, Office of Energy Research, Office of Basic Energy Sciences, Materials Sciences Division, of the U.S. Department of Energy under Contract No. DE-AC03-76SF00098 with Lawrence Berkeley Laboratory.

References

1. C.C.Lo & B. Taylor, "The Phase Servo Tuner Control System of The ALS 500MHz Cavity", Proceedings of the 1993 IEEE PAC, Vol. 2, pp. 1142-1144, LBL-33190.
2. A. Massarotti, "The Low Level System for the ELETTRA RF System", Proceedings of the 1993 IEEE PAC, Vol. 2, pp. 1145-1147.

Integral Dipole Field Calibration of the SRRC Storage Ring Combined Function Bending Magnets

J. C. Lee, Peace Chang and C. S. Hsue*
Synchrotron Radiation Research Center

Abstract

Due to the presence of fringe field on both magnet edges, the real trajectory traced out by the beam will deviate from expectation. The integral dipole strength seen by the beam will then have a discrepancy to design value. The beam tracing method is employed to correct fringe field effect and to calibrate integral dipole strength of the bending magnets by tuning magnet current. Final correction factor was achieved in the condition of simulated results meet to design requirements. During machine commissioning, the measured betatron tunes were found different from modeling and a correction factor was applied to correct this tune differences. This factor is in well agreement with that predicted by the beam tracing method.

I: Introduction

The bending magnet for the SRRC storage ring is a C-type magnet. It is an assembly from lamination iron plates with its pole face tilted to combine dipole field and quadrupole field. Though the magnetic field has been well measured, the measurement is based on ideal trajectory, curve in bending region and straight for the other section. For the presence of fringe field at magnet edges the real trajectory of the beam would deviate from ideal one. The magnetic field seen by the beam will have a little difference due to this trajectory discrepancy. It implies a fine calibration is necessary if the difference has significant effect. In this report, beam tracing method is employed to check this difference by taking the eighth mass produced bending magnet as an ensemble. A tracing program is written to simulate the real trajectory of the electron in real magnetic field and the dipole field is calibrated based on this simulated trajectory. Since simulated trajectory dependent on the field the beam encountered, there are several way to get the correction by changing field distribution such as shifting, rotating the magnet^[1] or changing its power current. However it is very difficult to take into account shifting (rotating) factor in installation. Correction on power current is selected for field adjusting tool.

In this paper, results from tracing prediction are compared with that obtained from commissioning. Algorithm for the beam tracing method is described in section II. Error estimation of the tracing program and the tracing prediction are also given in section II. Commissioning results for this topics can be found in section III. The consistency of these two approaches are quit good.

II: Tracing program and tracing prediction

The beam tracing program simulates the median plane trajec-

tory of the electron and obtains related parameters from the measured magnetic field. Cartesian coordinate system (X,Z) is used for tracing study with X the horizontal and Z the longitudinal coordinate respectively. Origin of the coordinate system is chosen at the magnet center. The motion of the electron in the median plane obeys^[2]

$$\frac{X''}{(1 + X'^2)^{3/2}} = -\frac{B}{B_0\rho} \quad (1)$$

in which X is the horizontal position of tracing point, $B_0\rho$ is the ring rigidity and B the vertical magnetic field of tracing point, which is interpolated from measured field by three or four-point bivariate method^[3]. Since no significant difference between these two field interpolated method, less than 2×10^{-7} , three-point bivariate method is used. The differentiation in equation (1) is w.r.t. the longitudinal. Interpolation from one point to the next point is calculated from equation (1) by Runge-Kutta method. Since rigidity includes the information of beam energy, the program can simulate the trajectory for fixed energy of electron in the known field distribution or, on the contrary, to get the information of beam energy and simulated trajectory in the fixed field distribution. The former situation is applied in this report while the latter can be applied to measure the beam energy^[4].

A testing tracing was first performed to check the accuracy of the tracing program by ideal isomagnet field distribution with design field value and effective length. Error bar of the traced parameters in this testing tracing are all within 0.007%, which is quite enough for the study, and position error for testing tracing point is also within the alignment tolerance. Accuracy of the tracing program would be increased a little bit in real field tracing for it has continuous field distribution instead of hard edge one.

In tracing simulation, the following strategies were considered: a) integral dipole strength (bending angle) within design requirement, b) symmetry simulated trajectory w.r.t. magnet center, c) position error for tracing points outside effective bending within alignment tolerance. Strategy a) ensures the electron beam will be bent to a circle within a tolerable error. Strategies b) and c) push simulated trajectory meeting to ideal trajectory except that in effective bending section. These considerations are very important for the beam diagnostics.

Since field measurement extended far away from the magnet, the magnetic field outside the measured area is assumed to zero for the field is neglectable small at this large distance. The tracing step is the same as that used in testing tracing, 5mm for far away region and 0.2mm for points close to the magnet. Under above conditions, design energy of electron were traced in the ensemble field distribution, which is measured at the median plane of the eighth mass produced bending magnet powered at nominal current. Table 1 lists this uncorrected tracing results.

Table I

Comparison of the raw data tracing results with the ideal values, in which Bl integral strength, l_{eff} effective length, θ bending angle, B_c center field, subindex s indicates tracing starting point, t the magnet entrance point, e the magnet exit point, and d the tracing ending point.

	Ideal Value	tracing Results	Error
Bl (T*m)	1.513666	1.521917	0.54 %
l_{eff} (m)	1.22	1.222098	—
θ (deg)	20	20.10779	0.54 %
B_c (T)	1.24071	1.245336	—
x_s/z_s (mm)	-912.198/-106.928	-912.198/-106.928	—
x_t/z_t (mm)	-606.998/-53.113	-606.998/-53.418	—
x_e/z_e (mm)	607.002/-53.114	607.002/-54.872	—
x_d/z_d (mm)	911.002/-106.660	911.002/-108.789	—

From the data shown in table 1 it is clear that design energy of electron is overbent by about 0.5% as magnet is powered at nominal current. The 0.5% overbent has been taken into account the effect from trajectory as well as the contribution of fringe field. It is straightforward to scale down the magnetic field by this amount approximately and design energy of electron is traced again in this scaled down field. After some efforts the final correction factor for the magnetic field is 0.575% instead of 0.5%. This small discrepancy is coming from the magnetic field seen by design energy of electron is slightly changed due to different trajectory followed. Table 2 lists these corrected tracing results.

Table II

Comparison of the corrected tracing results with the ideal values.

	Ideal Value	Tracing Results	Error
Bl (T*m)	1.513666	1.513827	0.01 %
l_{eff} (m)	1.22	1.223162	—
θ (deg)	20	20.00821	0.04 %
B_c (T)	1.24071	1.237635	—
x_s/z_s (mm)	-912.198/-106.928	-912.198/-106.928	—
x_t/z_t (mm)	-606.998/-53.113	-606.998/-53.417	—
x_e/z_e (mm)	607.002/-53.114	607.002/-53.583	—
x_d/z_d (mm)	911.002/-106.660	911.002/-106.958	—

Correction on the magnetic field is achieved by tuning its power current. The necessity of 0.575% reduction on the magnetic field also reveals nominal current is too large for design energy of electron. From the good field uniformity and the linear relation between the field and its power current within this small range, final correction factor on the current is also predicted by 0.575%.

The tracing results listed in table 2 are in good agreement with the design except magnet center field and effective length. These discrepancies are coming from simulated trajectory deviated from ideal. As we known the main function of the bending magnet is to bend design energy of electron with the desired angle. Hence bending angle and integrated dipole strength are the most important parameters to be considered. The error of integrated dipole strength (bending angle) is within 4×10^{-4} , which is well within the specification of 1×10^{-3} . From above simu-

lated results it is clear that integral dipole strength has been well calibrated from reducing the nominal current by 0.575%.

III: Experience in the storage ring commissioning

In storage ring commissioning, the measured tunes are found not consistent with modeling. The tune difference makes the application program, which is based on modeling, don't work well. With the study and correction of the tune differences, a model closing to real machine is gotten. The tunes of machine are then measured under different lattices and compared with that predicted by modeling, as shown in table 3.

Table III

Tune Differences between measurement and modeling before correction.

Lattice	measured ν_x/ν_y	modeling ν_x/ν_y	$\Delta\nu_x/\Delta\nu_y$
A	7.353/4.080	7.4448/4.1133	0.0918/0.0333
B	7.232/4.080	7.3220/4.1151	0.0900/0.0351
C	7.236/4.080	7.3210/4.1120	0.0850/0.0320
D	7.206/4.092	7.2927/4.1272	0.0867/0.0352
F	7.210/4.087	7.2949/4.1186	0.0849/0.0316
G	7.227/4.091	7.3147/4.1228	0.0877/0.0318
H	7.221/4.086	7.3078/4.1169	0.0868/0.0309
I	7.235/4.082	7.3245/4.1121	0.0895/0.0301

The contribution of individual quadrupole in tunes are also investigated by the formula

$$\delta\nu = \frac{1}{4\pi} \int k_1 \beta ds \simeq \frac{\bar{\beta}}{4\pi} \frac{1}{f} \quad (2)$$

with $\bar{\beta}$ is averaged β function and $\frac{1}{f} = k_1 l$ the inverse of focus length, and results of one super-period in the 6-fold symmetry lattice are shown in table 4.

Table IV

Estimated $\delta\nu_x/\delta\nu_y$ in one super period with k_1 strength (T/m), l length (m), and β_x/β_y beta functions (m).

Name	k_1	l	$\bar{\beta}_x$	$\bar{\beta}_y$	$\delta\nu_x$	$\delta\nu_y$
Q_1	-1.50815	0.35	12.3	5.9	-0.51189	+0.24783
Q_2	2.87048	0.35	18.8	4.6	+1.50304	-0.36777
Q_3	-1.15592	0.24	6.2	9.9	-0.13687	+0.21857
DM_1	-0.37	1.22	1.2	10.81	-0.04311	+0.38831
Q_4	2.73087	0.35	6.3	2.5	+0.47318	-0.19015
DM_2	-0.37	1.22	1.82	5.71	-0.06538	+0.20511
Q_4	2.73087	0.35	6.3	2.5	+0.47318	-0.19015
DM_1	-0.37	1.22	1.2	10.81	-0.04311	+0.38831
Q_3	-1.15592	0.24	6.2	9.9	-0.13687	+0.21857
Q_2	2.87048	0.35	18.8	4.6	+1.50304	-0.36777
Q_1	-1.50815	0.35	12.3	5.9	-0.51189	+0.24783

If we add up all of the contribution of quadrupole elements in tunes in table 4, ratio for the summation of horizontal tune to the vertical is around 3.1434, which is very close to the difference tune ratio for individual element in table 3. This fact indicates the

discrepancy in tunes between real machine and modeling could come from one source, by which all of the quadrupole strength in the ring can be scaled up or down. The beam energy, which is used as a normalization factor in modeling program, is suspected to produce this scaling factor. If the beam energy increased by a factor of 0.5% then the tune difference between measurement and modeling is reduced to reasonable level, as shown in table 5.

Table V
Tune differences between measurement and modeling with correction factor 0.995.

Lattice	measured ν_x/ν_y	modeling ν_x/ν_y	$\Delta\nu_x/\Delta\nu_y$
0715-00	7.230/4.082	7.2449/4.0793	0.0149/-0.0027
0715-01	7.208/4.092	7.2220/4.0913	0.0120/-0.0007
0715-02	7.244/4.079	7.2619/4.0750	0.0179/-0.0040
0715-03	7.226/4.088	7.2410/4.0864	0.0150/-0.0016
0715-04	7.235/4.080	7.2514/4.0770	0.0164/-0.0030
0715-05	7.261/4.081	7.2778/4.0787	0.0168/-0.0023
0715-06	7.251/4.086	7.2666/4.0850	0.0156/-0.0010
0715-07	7.276/4.078	7.2946/4.0743	0.0186/-0.0037
0715-08	7.258/4.088	7.2736/4.0857	0.0156/-0.0023
0715-09	7.267/4.080	7.2841/4.0762	0.0171/-0.0038
0715-10	7.203/4.083	7.2127/4.0798	0.0097/-0.0032
0715-11	7.193/4.088	7.2012/4.0858	0.0082/-0.0022
0715-12	7.218/4.079	7.2301/4.0756	0.0121/-0.0034
0715-13	7.200/4.089	7.2086/4.0868	0.0086/-0.0022
0715-14	7.208/4.080	7.2191/4.0774	0.0011/-0.0026
0715-15	7.174/4.083	7.1807/4.0803	0.0067/-0.0027
0715-16	7.295/4.080	7.3106/4.0781	0.0156/-0.0019

This indicates the integral dipole strength is too strong for design energy of electron and need to be reduced. After some efforts, final scaling factor is 0.99448. That means the correction factor in dipole field and its powered current is 0.552%, which is in good agreement with that predicts by the tracing simulation.

IV: Conclusion

The beam tracing method is a good tool to calibrate the magnetic dipole field w.r.t. its powered current as well as for the study of beam energy and its possible tracing trajectory in the known field distribution. In above study design energy of electron is used to calibrate the magnetic field and its powered current by beam tracing method. Design energy of electron is found to be overbent by the dipole at its nominal current setting. The excessive factor for integral dipole strength is around 0.5%. As dipole current is reduced by 0.575%, a good results was found with a symmetry trajectory w.r.t. magnet center and position error outside the magnet within alignment tolerance. Integral dipole strength and bending angle are also well within the specification after this reduction. From storage ring commissioning a tune discrepancy between real machine and model prediction was found. This discrepancy finally is indicated to be coming from magnetic dipole field is too strong. As the magnet powered current is reduced by 0.552% the discrepancy in tunes is canceled. This fact shows the good consistency of these two approaches, tracing prediction and the commissioning verification.

In this paper the linear relation between dipole field and its powered current is assumed. Within a small range of variation

this linear assumption is a very good approximation. While as the deviation is too much the linear assumption is not hold again and the tracing study need to be performed at this deviated field distribution to give precise prediction.

Since SRRC bending magnet is a combined function one, correction on the dipole field will slightly change the combined quadrupole field. While the correction algorithm for bending magnet is to correct the dipole field first. Due to the good tunability of the chosen lattice, error of the combined quadrupole field in bending magnet is easier to be overcome by triplet quadrupoles outside the achromate.

Acknowledgement

The authors would like to thank the magnet measurement group for providing the field data.

Reference

- [1] J. C. Lee, C. C. Kuo and C. S. Hsue, Beam Tracing of the SRRC First Prototype Bending magnet, SRRC/BD/IM/89-14.
- [2] K. Steffen, Basic Course on Accelerator Optics, CERN 85-19, 1985.
- [3] M. Abramowitz and I. A. Stegn, Handbook of Mathematical from U.S. Dept. of Commerce, NBS 55, 1964.
- [4] M. H. Wang and J. C. Lee, The Algorithm of Energy Measurement in BTS Transport Line, these proceedings.

Improved Mobile 70 MeV Race-Track Microtron Design

V.I. Shvedunov, Institute of Nuclear Physics, Moscow State University, 119899, Moscow, Russia

A.I. Karev, Physical Institute, Russian Academy of Science

V.N. Melekhin, Institute for Physical Problems, Russian Academy of Science

N.P. Sobenin, Moscow Engineering Physics Institute

W.P. Trower, Physics\Virginia Tech, Blacksburg VA 24061 USA

To increase the reliability, simplify the tuning, and boost the efficiency of our 70 MeV mobile Race-Track Microtron design we use a narrow rectangular asymmetric accelerating structure, rare-earth permanent end magnets, wiggler-like vertical focusing lenses on the return paths, and a beam buncher preceding the linac. We present here beam dynamics simulation results and construction details.

I. INTRODUCTION

Our original 70 MeV mobile Race Track Microtron design [1] was based on proven principles but included new features which decreased the RTM weight and size while increasing its efficiency: Beam reflection in the end magnet fringe field on the first orbit to bypass the linac followed by acceleration in the reverse direction; End magnets with main and reverse field coils optimized to reduce size and weight; Tuning of the reverse field amplitude and position; Vertical focusing by the end magnet fringe fields and internal field gradients; Horizontal focusing by an on-linac-axis quadrupole singlet; and A linac optimized for efficient low-energy beam capture and high-energy beam acceleration.

Our design, as well as those of most pulsed RTMs, had inherent problems: Precisely retro-reflecting the beam on the linac axis combined with accurate fringe field focusing; Increasing parasitic losses when the dispersed reflected beam enters linac; Achieving stable phase oscillations by adjusting both end magnet positions; Synchronous phase drift decreasing the phase stability region and increasing the number of orbits, owing to the end magnet field gradient; Decreasing the RTM efficiency and increasing the environmental radiation by beam losses (10-20 % with a specially optimized linac depending on the injected beam transverse emittance).

To solve these problems we introduce a narrow asymmetric rectangular accelerating structure [2] which, together with short-tail fringe field Rare Earth Permanent Magnet end magnets [3], allows the beam to clear the linac after the first acceleration. The beam dispersion after the first end magnet passage is compensated for by the second end magnet. The position of only one magnet need be adjusted to achieve stable phase oscillations. Our REPM end magnets, smaller than conventional electromagnets with coils, require no power supply or cooling.

We vertically focus the beam with REPM wiggler-like lenses installed on the return paths instead by end magnet field gradient. These lenses negligibly influence the horizontal motion, no synchronous phase drifts are induced, and the phase stability region is easily maximized.

Table I
RTM parameters.

Injection energy	55 keV
Energy gain per turn	5.26 MeV
Number of turns	14
Output energy	10 - 74 MeV
Output current at 70 MeV	45 mA
Increase in orbit circumference per turn	1 λ
Operating frequency	2,450 MHz
Klystron power pulsed/average	5 MW/5 (15) kW
End magnet field induction	0.9 T
RTM dimensions	2 x 0.6 x 0.6 m ³

We have placed a beam buncher at the accelerating structure entrance to increase the beam capture and decrease the beam losses. The principle RTM parameters are given in Table I and the RTM block-diagram is shown in Fig. 1.

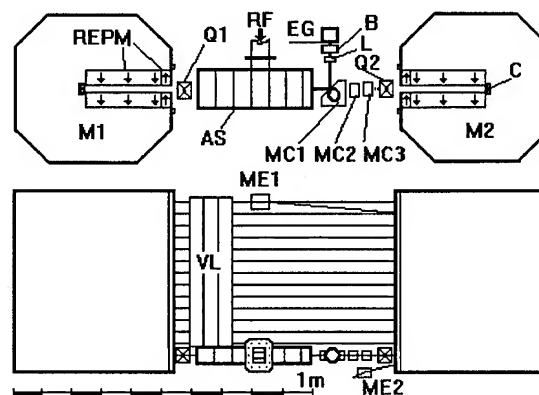


Fig. 1. RTM schematic: M1 & M2 REPM end magnets, correcting Coils, Accelerating Structure, Electron Gun, Buncher, Quadrupole singlets, MC1-3 chicane magnets,

solenoid Lens, Vertical Lenses, and ME1 and ME2 extraction magnets.

II. END MAGNET AND ACCELERATING STRUCTURE FOCUSING

After first acceleration and end magnet passage, an orbit's displacement from the linac axis, depends on the orbital circumference increase per turn, v , the injection energy, the energy gain per turn, and the end magnet fringe field configuration. Injecting at several tens of keV and making $v = 1$ by changing the reverse field amplitude and position at the end magnet entrance, this displacement can be adjusted from zero (i.e., retro-reflection on-the-linac axis) to a value exceeding the orbit diameter in a fringe fieldless ideal end magnet. To realize the maximum orbit diameter without strong fringe field defocusing the reverse field maximum must be in as close proximity as possible to the main magnet yoke (i.e., a short-tail fringe field similar to that of ref. 4). For magnets with main and reverse coils this distance usually exceeds the reverse pole gap so that magnetic flux will not penetrate the main yoke.

The end magnet fringe field tail is shorter in our REPM end magnet [3] than in our original electromagnet with coils, as seen in Fig. 2. The REPM end magnet fringe field is focusing in the first orbit which is $\sim 0.33 \lambda$ from the linac axis. The fringe field, whose focusing energy dependence [5] is shown in Fig. 3, is slightly defocusing for higher energies with a ~ 60 m focal length on the last orbit.

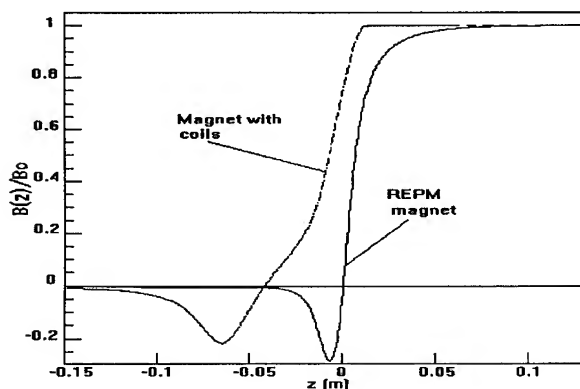


Fig. 2. End magnet fringe fields.

Our original axially symmetrical accelerating structure with optimized effective shunt impedance and operating in a E_{01} -like mode has a $\sim 0.375 \lambda$ radius. Thus, even neglecting wall thickness, the first orbit beam would hit the accelerating structure. This radius can be decreased by capacitive loading the accelerating cells with long drift tubes, but the effective shunt impedance for adequate structure radius will at least be halved from the quality factor decrease.

We break the axial symmetry of the accelerating structure to reduce its dimensions in the orbit plane. Guided by our

experience with rectangular classical microtron cavities [6] and with collider accelerating structures lacking axial symmetry [7], we use a standing wave on-axis coupled rectangular accelerating structure with circular beam holes [2]. Our calculations [8] and experiments [2] show that in the orbit plane our linac with half-width $\sim 0.27 \lambda$ and vertical-to-horizontal dimension ratio of 2:1 has a shunt impedance 10-20% higher ($\sim 90 \text{ M}\Omega/\text{m}$ for $\lambda = 0.1224 \text{ m}$) than our previous optimized axially symmetric structure.

For relativistic particles the radial electric and azimuthal magnetic field forces nearly cancel in axially symmetric structures. In an axially asymmetric structure there is a strong energy dependent quadrupole effect, focusing vertically while defocusing horizontally, as seen in Fig. 3, where the linac (one $\beta = 0.67$ cell and six $\beta = 1.0$ cells) has an on-axis voltage ratio of $U_1/U_{2-7} = 0.96$. Theoretical calculations [6] support our computer simulated results [5,8]. RTM optics compensate in the first few orbits for this strong focusing/defocusing whose strength varies directly with the accelerating structure vertical-to-horizontal dimension ratio. Our linac focusing will be further improved by using non-circular beam holes.

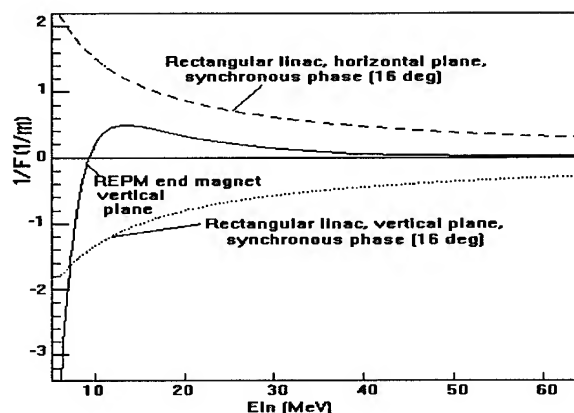


Fig. 3. REPM end magnet fringe field and rectangular linac focusing.

III. RTM OPTICS AND BEAM CAPTURE

To compensate for the horizontal linac defocusing we install a REPM quadrupole singlet, Q1, at the linac exit. The 55 keV beam injected into the linac is not focused with the energy dependence of Fig. 3 ($1/F_x = 3.1 \text{ m}^{-1}$, $1/F_y = 0.97 \text{ m}^{-1}$ for synchronous particles) so we add a second REPM quadrupole singlet, Q2, at the end magnet M2 exit. For strong vertical focusing we use REPM wiggler-like lenses [9] at the beginning of each orbit return path. These lenses consist of three equal-length parallel-edged dipole magnets with the center dipole field doubled and reversed. The vertical focal length is $F_v = -d/4 \tan(\alpha)^2$, where α is side magnet bending angle, and d is its length chosen to be 5 cm.

The horizontal focal length is nearly infinite. The optimal bending angle range is 4° - 7° and the maximum central magnet field at the last orbit is ~ 0.87 T. The optimal quadrupole field gradient for both lenses is ~ 1.75 T/m for effective length 5 cm.

Figure 4 shows that vertical and horizontal particle trajectories, displaced from the linac axis on entrance, oscillate with decreasing amplitude. In the vertical there are nonlinear effects (different vertical oscillation periods for different initial displacements) owing to end magnet fringe field.

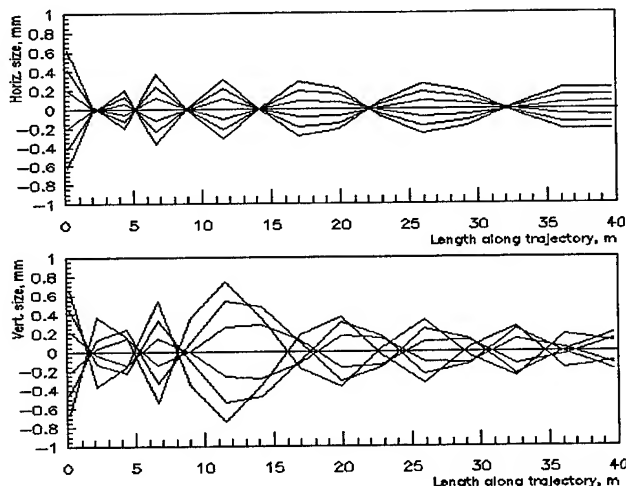


Fig. 4. Vertical and horizontal particle trajectories with displacement from the linac-axis at entrance.

To increase RTM capture efficiency and decrease parasitic beam losses we install a buncher resonator between the electron gun and the linac with buncher-linac distance of 15 cm and the buncher electric field amplitude of $\sim 2.2\%$ of that of the first accelerating cell. For a continuous zero transverse emittance beam there is a three-fold increase in the longitudinal capture efficiency. Otherwise the capture efficiency depends on the transverse beam emittance, its match to the RTM acceptance, and the linac injection phase. About 34% of an electron gun beam with radius \times divergence of $2 \text{ mm} \times 10 \text{ mrad}$ (i.e., a $80 \text{ mm} \times \text{mrad}$ transverse phase space) reaches the RTM output, twice that of our original design [1]. Thus only a ~ 140 mA current need be injected into the RTM to realize a 45 mA beam at exit.

Bending magnet MC1 has little influence on the longitudinal beam dynamics for the energy modulated 55 keV beam since the decreased path length for lower energy electrons is partially compensated for by their reduced velocity. However, for dispersion introduced by MC1 increases beam losses, so we inject the beam on the linac axis using a zero dispersion alpha magnet [10]. Magnets MC2 and MC3 compensate for the effect of the alpha magnet on higher orbit beams. To match the electron gun beam to the RTM acceptance we install a solenoid lens after the buncher.

IV. CONCLUSIONS

Our re-designed mobile 70 MeV pulsed race-track microtron has two essential new features -- a rectangular linac and rare-earth permanent magnets throughout --which improve its performance and efficiency.

REFERENCES

- [1]. N.P. Sobenin, A.I. Karev, V.N. Melekhin, V.I. Shvedunov, and W.P. Trower, in *Proc. 1994 European Particle Accelerator Conf.*, V. Suller and Ch. Petit-Jean-Gernaz, editors (World Scientific, Singapore, 1994) p.512.
- [2]. N.P. Sobenin, V.N. Kandurin, A.I. Karev, V.N. Melekhin, V.I. Shvedunov and W.P. Trower, Rectangular Microtron Accelerating Structure, in these Proceedings.
- [3]. A.I. Karev, V.N. Melekhin, V.I. Shvedunov, N.P. Sobenin, and W.P. Trower, A Permanent Race-Track Microtron End Magnet, in these Proceedings.
- [4]. H. Babic and M. Sedlacek, *Nucl. Instr. and Meth.* vol. 56, p.170, 1967.
- [5]. V.G. Gevorkyan, A.B. Savitsky, M.A. Sotnikov, and V.I. Shvedunov, VINITI, No. 183-B89 (1989) 54p. (in Russian).
- [6]. S.P. Kapitza and V.N. Melekhin, *The Microtron* (Harwood, London, 1978).
- [7]. B.V. Zverev and N.P. Sobenin, *Accelerator Structures and Resonators* (Energoatomizdat, Moscow, 1993) (in Russian).
- [8]. R. Klatt, F. Krawczyk, W.R. Novender, C. Palm, T. Weiland, B. Steffen, T. Barts, M.J. Browman, R. Cooper, C.T. Mottershead, G. Rodenz, and S.G. Wipf, in *Proc. 1986 Linear Accelerator Conf.*, SLAC-303 p.276 1986. A version this MAFIA code, obtained by V.S. in 1989 from T. Weiland, and installed at 586/90 was used in these calculations.
- [9]. L.M. Young, *IEEE Trans. Nucl. Sci.* NS-20, p.81 1973.
- [10]. H.A. Enge, *Rev. Sci. Instr.* vol. 34, p.385 1963.

The Improvement of Energy Measurement in BTS Transport Line by Using Beam Tracing Method

M. H. Wang and J. C. Lee
Synchrotron Radiation Research Center

Hsinchu Science-Based Industrial Park, Hsinchu, Taiwan, R.O.C.

Abstract

A method which measures the e^- beam energy in the booster to storage ring transport line is introduced. One of the bending magnet in the BTS transport line is chosen as the reference dipole for the energy measurement. The beam tracing method which takes into account of the fringe field effect is employed to calibrate the I-B curve of the reference dipole to enhance the accuracy of the energy measurement. The desired trajectory of the e^- beam is traced for different energy by adjusting the reference dipole current. The current correction factor with and without this calibration is -0.33 % for 1.3 GeV e^- beam for SRRC. The possible error sources of this measurement are also discussed and estimated.

I: General Description

One simple method to measure the beam energy in transport line is to use one dipole magnet as the reference dipole. By proper adjusting the strength of reference dipole the beam will go through the center of the BPM at down stream. The relationship of beam energy and the dipole strength is:

$$B\rho = C \times E \quad (1)$$

where B the magnetic field in Tesla, ρ the bending radius in meter, E the beam energy in GeV and C is a constant. For electron the constant is 3.335646. The beam goes through the center of the BPM implies that we have the designed ρ . Thus the energy is proportional to dipole field strength. The beam has to be steered such that it can launch at the designed entrance point of the reference dipole. So before the reference dipole there needs at least two correctors in the bending plane to adjust the position and the angle of the beam. It also needs two monitors to observe the result. According to the above consideration, the DM2 in transport line of SRRC was chosen as the reference dipole. The schematic layout of BTS transport line related to this measurement is shown in figure 1. The septum and horizontal corrector HC1 before DM2 is used to adjust the entrance point of the beam. BPM1 and screen monitor SCN2 are employed to help steering the beam to enter DM2 with right position and right angle. After the beam entering DM2, the strength of DM2 is adjusted to steer the beam go through the desired trajectory. The BPM2 after DM2 was used to monitor the beam to make sure the desired trajectory was achieved. Of course all the other magnets between BPM1 and BPM2 were off during the measurement.

As one can see the reference dipole is the key point in this measurement. The accuracy of the energy measurement depends on how "standard" the B field is. Thus the calibration of the DM2 has to be done to enhance the accuracy of the measurement.

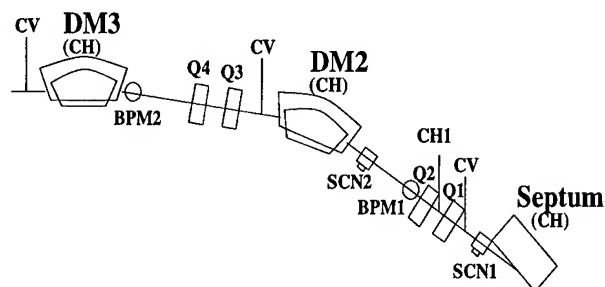


Figure. 1. The schematic layout of the BTS transport line to DM3.

II: The Calibration of reference dipole

The integrated B-I curve of the reference dipole has been provided by the Magnet Measurement Group^[1] of SRRC. The assumed reference trajectory in the field measurement is an ideal trajectory. Based on this assumed reference, multipole field expansion and corresponding integrated strength is obtained. But in the real case the field and its distribution of the magnet are not ideal. It has fringe field and the trajectory of the tracing particle will deviate from the design. The beam starts to bend earlier when it encounters the fringe field. If the field is stronger than the design, bigger bending angle results. On the contrary, smaller field will give smaller bending angle. In both cases an unsymmetry tracing trajectory is obtained. Therefore the current need to be tuned to reach a symmetry trajectory as close to the design as possible.

The beam tracing program is employed to simulate the trajectory of the particle in the real magnetic field. From the discrepancy between tracing result and the design, the correction factor for the integrated B-I curve can be obtained and a symmetry trajectory will be constructed. The same method has also been applied to the ring combined function bending magnet of SRRC^[2]. In the simulations of this case the coordinate is chosen to be the Cartesian coordinate with the origin at the magnet center. The tracing starts from the point of (-0.622m, -0.03909m), which is on the ideal trajectory and is the starting point of the magnetic field mapping. The tracing is ended at the intersection point of the ideal trajectory and the line of $x=0.622m$. The initial tracing angle is the design angle of 5 degree and the tracing step is chosen to be 1mm in Z-axis which is the direction of beam motion. The field at the mapping edge is few ten gauss. Hence the field outside the mapping area is set to zero.

The point by point measurement of magnetic field at the current settings of 341A, 390A and 438A were measured and provided by the Magnet Measurement Group^[1]. From the integrated B-I curve these three settings are interpreted as the trac-

ing particles with the energy of 1.1651Gev, 1.3323Gev and 1.4782Gev respectively when particles trace in the same bending radius of DM2. Hence ideally particles with these three different current settings and energies will follow the same design trajectory. These three energy of beams were then traced in the corresponding measured field and the results are given in table 1. It is found that the bending angle and the integrated strength are 0.48% higher for 1.1651 Gev, 0.33% higher for 1.3323 Gev and 2.18% higher for 1.4782 Gev respectively. It is also found that the discrepancy between the tracing trajectories and the design is also larger than alignment tolerance. The integrated B-I curve approximate linear from 300A to 430A and begins to saturate above 430A. The fringe field will effect more serious on the field in saturation region. Since 1.4782 Gev beams are traced in the field powered at saturation region (438A) the field distribution will different from the linear one. This is why the current correction factor for the 438A case are about 2% higher than the unsaturated one which is only 0.3-0.5%.

In order to reduce the exceeded field and to correct the trajectory discrepancy the field is scaled down by a proper factor to make up for these two imperfections. The three energy of beams were traced again in the corresponding scaled down field and the results are also listed in table 1. Here the relationship of field and power current is assumed linear. Hence the scaled down factor for the field can be also applied to the current. From table 1 it is found that the errors of the bending angle and integrated strength are corrected to the order of 10^{-6} except that for the 1.4782Gev particles. A symmetrical trajectory is also obtained with the position discrepancy between the starting point and the end point less than the alignment tolerance. Since the BPM2 is 6 m down stream from the reference dipole, the angle error is also an important parameter to be checked. From table 1 the angle error is less than 1.7×10^{-6} rad at exit point of DM2, which will propagate about 0.01mm position offset to the down stream BPM2. That means a very good symmetrical trajectory is obtained after the corrections. Hence our attempt of trying to get a symmetrical trajectory with the position error at starting points and ending points less than the alignment tolerance is achieved. Thus particles will not deviate from the design trajectory before and after passing the reference dipole magnet. Furthermore the position discrepancy within measured field region between this obtained symmetrical trajectory and the design is also checked. It is found the maximum discrepancy in X-axis is about 0.5mm. It is much small than the good field width of ± 30 mm for the separated function dipole of DM2. Hence no obvious effects can be seen for this discrepancy.

The tracing result of 1.4782 Gev after field correction is bad. It is found the bending angle error is of the order of 10^{-5} and the integrated strength error is large up to 14%. This is because that the dipole current for this energy is in saturation such that the tracing trajectory deviates much from the ideal and can't be taken as a reference.

The design field of DM2 is powered at current 381A for 1.3 Gev. The measured data at 381A were not provided. But since current 381A locates in the linear region of the integrated B-I curve and is very close to 390A. Hence the measured field at 390A is scaled down to simulate the design field of 381A case. The tracing result at 381A shows the same behavior as the cur-

rent at 341A and 390A, 0.3-0.5% exceeded field and an unsymmetrical trajectory. Following the same correction steps both imperfections are corrected to the acceptable levels, also shown in table 1.

III: Error Estimation

A few possible error sources are investigated for this measurement. The accuracy of the tracing program is checked first. By comparing the tracing result of the hard edge field with the design, the accuracy of the program can be obtained. The tracing step within the field distribution is 1 mm while in the neighborhood of the edge is 0.02mm to improve the tracing accuracy. By comparing with the design trajectory, it is found that the maximum position error, occurred at the exit point, is about 10^{-3} mm, the angle error is within 2×10^{-4} mrad and error of the integrated strength is 2×10^{-6} . The position error at the down stream monitor BPM2 due to the errors at the exit point of DM2 is 2 μ m, which is well within the accuracy of the BPM. Hence error produced by the program is neglectable.

The second error source which will effect the accuracy of the measurement is the magnetic field error. From equation (1) we see that the errors are mainly divided into tow parts:

$$\frac{\Delta E}{E} = \frac{\Delta \rho}{\rho} + \frac{\Delta B}{B} \quad (2)$$

This classification is convenient for the theoretic analysis. In the measurement the bending radius is kept to the design value. Hence $\frac{\Delta \rho}{\rho}$ can be set to zero and all the energy measurement error can be interpreted as the field error independently. This simplification is reasonable since the only observable effect of the errors is the displacement at the BPM. The error from magnetic field is reduced by the calibration method provided in section II. The error left for the field is the dynamic field stability, which is believed to be below 10^{-3} .

Another important error source in this energy measurement is the position and angle deviation. The position errors are mainly due to the misalignment of BPM and its reading accuracy. In the beginning of commissioning the misalignment of the BPM was estimated to be 0.5 mm relative to the dipole magnet and the accuracy of the BPM reading is within 0.5 mm. As mention at section I BPM1 and SCN2 will be used to help the adjusting of position and angle of the beam into the DM2. The errors occur at BPM1 and SCN2 will cause the beam launching at the entrance point of DM2 with ± 1 mm position and ± 0.4 mrad angle errors. Accommodating with these entrance errors the beam is steered to the design trajectory within the monitor reading accuracy of BPM2 at the 6 m long down stream after DM2. Taking the field distribution of 390A after beam tracing calibration as an example, the possible tuning range for the magnetic field strength caused by these errors is simulated by the same tracing method and its result is from -0.36% to 0.37%. If we take 0.5 mm misalignment of BPM2 into consideration, the possible tuning range will be up to $\pm 0.42\%$.

The total error is obtained by taking root mean square of all the above errors, the dynamic field stability of 0.1 %, errors due to position and angle discrepancy of 0.42 % and for safety the miscellaneous error of 0.5 % for the unknown. While the 0.42

% error is enlarged to 0.5 % for the possible error of field distribution used in the simulation. Hence the possible error for this energy measurement algorithm is about 0.72%.

IV: Discussion and Conclusion

The algorithm of the energy measurement presented in this report is easy to achieve. It is based on the original design of the BTS transport line and no extra equipments are needed. The integrated B-I curve is an important information for this measurement and needs to be calibrated. By using the method of beam tracing a calibrated integrated B-I curve is obtained.

It is found that the current needs to be scaled down by an amount of about 0.3% for the linear region near the designed energy 1.3 GeV. It is also found that the current can not be tuned to the saturation region for the SRRC.

The accuracy of the measurement is significantly effected by dynamic field(current) stability, the reading accuracy of BPM, alignment error, launching error and other unknown errors. By appropriate treatment the effect due to reading accuracy of BPM, alignment error and launching error can be factored out by the beam tracing method. By taking the root mean square of all the contribution of error sources, the possible error of this energy measurement algorithm is about 0.72 %, of which 0.5% unknown error has been assumed. There are also the unexpected errors when doing the experiment. However the accuracy is expected to be below 1% in the real experiment. From the above simulations it is also found that the alignment error and the BPM reading accuracy are important factors for the error estimation. If these two error sources are reduced the launching error will become smaller also. Hence the measurement accuracy can be better when the alignment error and the BPM accuracy are improved.

Acknowledgement

The authors would like to thank the magnet measurement group of SRRC for providing the magnetic field measurement data.

Reference

- [1] C.S.Hwang, F.Y.Lin, T.C.Fan, S.Yen, P.K. Tseng, SRRC/MM/IM/92-01
- [2] J. C. Lee, Peace Chang and C. S. Hsue, "Integral Dipole Field Calibration of the SRRC Storage Ring Combined Function Bending Magnets", these proceedings.

Table 1. The tracing results of DM2

	Energy (GeV)	I (amp)	bending angle (degree)	$\int B_0 ds$ (T.m)	current correction factor	ending point		
						x_{end} (mm)	y_{end} (mm)	exit angle (degree)
design	1.3	381.062	10	0.756832	———	622	-36.91	-5
ideal tracing	1.3	———	10.00001	0.756831	———	622	-36.91	-5.00001
initial tracing	1.1651	341.22	10.048	0.681564	———	622	-37.35	-5.048
	1.3	381.062	10.034	0.759384	———	622	-37.19	-5.034
	1.3323	390.51	10.033	0.778212	———	622	-37.18	-5.033
	1.4872	438.62	10.218	0.884681	———	622	-38.00	-5.218
tracing after adjustment	1.1651	339.58	9.9999	0.678297	-0.48 %	622	-36.82	-4.9999
	1.3	379.80	10.00006	0.756838	-0.33 %	622	-36.82	-5.00006
	1.3323	389.21	10.00001	0.775633	-0.33 %	622	-36.82	-5.00001
	1.4872	429.27	10.00045	0.865866	-2.13 %	622	-35.65	-5.00045

DESIGN STUDY OF PAL-STRETCHER RING*

I. S. Ko, G. N. Kim, J. Choi, M. H. Cho, and W. Namkung
Pohang Accelerator Laboratory, POSTECH
Pohang 790-784, Korea

We completed the commissioning of the PLS 2-GeV electron linac, which is a full energy injector for the storage ring of the Pohang Light Source, in June 1994. The prime mission for providing beams to the storage ring requires a few minutes for each injection, and a few times per day when the PLS is under the normal operation. Hence, we can utilize high energy electron beams to the electron scattering experiments. In order to produce high current and high duty factor beams, the design of a pulse stretcher ring is underway. This paper presents the result of the design study as well as the experimental plan.

I. INTRODUCTION

During the last few decades, the electron has been a preferable probe for the study on a short distance structure of nucleons. Since the electron does not have internal structures, the interactions with the nucleons is considered as a single-step character. It also gives a quantitative analysis on the electron-nucleon interaction since the electromagnetic interaction of the electron is explicitly calculable in terms of quantum electro-dynamics. Thus, the electron-nucleon scattering experiments can be unambiguously interpreted in terms of the structure of the nucleon to be proved. Such experiments performed in the 1960's showed that the nucleon form factors fell rapidly with increasing momentum transfer. These suggest a composite picture of the nucleon. It is now well known that nucleons are made of quarks, and that the force between quarks is generated by the exchange of a particle called the gluon. This fundamental force is described by the theory of color interaction known as quantum chromodynamics (QCD). However, it is far from easy to calculate hadronic and nuclear properties in terms of this theory. In order to have a better understanding on such matters, one continues experiments on the structure of nuclei and nucleons over decades. Such experiments demand higher energy and intensity of electron beams along with more sophisticated detectors.

The electron linac, which is generally used for electron scattering and photonuclear reaction experiments, provides a beam of a relatively high average current ranging up to several hundreds of μA . However, the linac usually gives a poor duty factor ranging up to at most a few percent. Such characteristics provide no difficulties for experiments such as inclusive electron-nucleon scattering experiments, in which only a scattered electron is detected. But, coincident experiments, in which emitted particles are detected in coincident with the scattered electron, are difficult to be performed because of bad accidental coincident rate (which is inversely proportional to the duty factor). Electron beams with high-current and nearly 100%-duty-factor are essential for such experiments. A linac-stretcher combination of a conventional

electron linac and a pulse stretcher ring is one of the most promising solutions.

The Pohang Accelerator Laboratory (PAL) has recently completed the 2-GeV synchrotron radiation source named the Pohang Light Source (PLS). The PLS will serve as a low-emittance light source for various research such as basic science, applied science, and industrial and medical applications [1]. There is a 2-GeV linear accelerator as a full energy injector to the PLS. The prime mission for providing electron beams to the storage ring requires a few minutes for each injection and a few times per day when the PLS is under the normal operation. Hence, we can utilize the high energy electron beams of various energies for nuclear physics and other branches of basic and applied sciences. There are also increasing demands on the nuclear physics experiments using the PLS linac by many nuclear physicists in Korea [2]. The low duty-factor of present electron linac makes electron scattering experiments difficult. Such motivations encourage us strongly to design a pulse stretcher at the Pohang Accelerator Laboratory.

The future expansion of the PLS 2-GeV linac has been fully exploited during the site planning period in 1990. So the site of the stretcher ring and the extension of the beam transport line to the stretcher have been well considered as shown in Fig. 1 with other expansion plans. There is even a branch tunnel of about 5-m long at the end of the linac tunnel in order to minimize the PLS operation from the construction of the stretcher ring if such a plan approved.

II. STRETCHER DESIGN

There are several pulse stretcher rings under operations, and also several proposals to build them [3]. In the PAL stretcher ring, we fix the energy to 2-GeV since our injector linac provides 2-GeV beams. We also fix the repetition rate to 120 Hz because all modulators are designed to operate at maximum 120 Hz. Otherwise, increasing the repetition rate will require significant modifications to the modulators and high-power RF loads.

Usually, the stretcher ring requires a fast radiation-damping time to have a smaller energy spread for extracted beams. To have fast damping time, we need a higher magnetic field in the bending magnets. This gives a smaller circumference ring which is less costly. If the repetition rate is high, there is not enough time for the radiation damping. This restriction demands a smaller energy spread for the injection beam from the linac, which is also difficult to achieve. Instead, if we reduce the repetition rate low enough, then we have to keep a larger stored beam current in the stretcher before the beam is fully extracted. Otherwise, the extraction current will be reduced. Maintaining a large current in the stretcher ring may raise various beam instabilities or simply impossible due to the RF bucket limit. For 100% duty factor, it may give a poor energy spread for the first part of the extracted beam unless the injected beam has an excellent energy spread.

* Work supported by Pohang Iron & Steel Co., and Ministry of Science and Technology, Korea

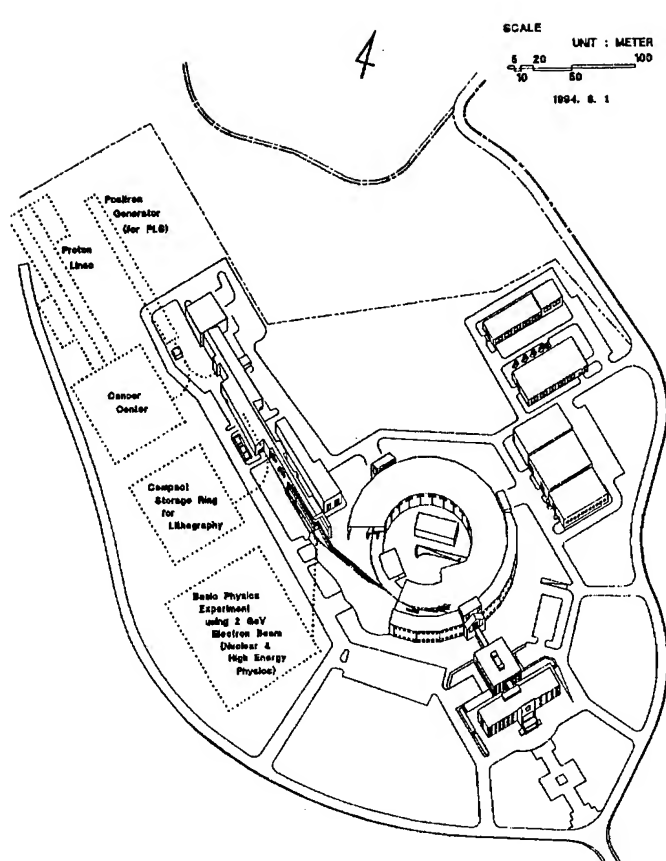


Fig. 1: Site Layout of Pohang Accelerator Laboratory

Such demands are sometimes self-conflicted, so we have chosen important parameters of the PAL stretcher ring listed in Table 1. The lattice of the PAL stretcher ring is shown in Fig. 2, and its beta functions are shown in Fig. 3.

There will be two beam exits; one for coincident experiments and the other for photon tagging experiments. The beam extraction will be made by slow excitations using sextupoles.

III. LINAC UPGRADE

In order to provide such electron beams, we need to improve the present PLS 2-GeV linac quite significantly. First of all, we have to deliver the number of electrons at least 100 (even 1,000) times more. We have to face significant beam loading effects and/or beam breakups. There must be several ways to compensate the energy spread such as a chicane or frequency-shifted energy spread compressions [4]. Furthermore, it may require to install wigglers in the stretcher ring for faster radiation damping. At present, we use 10 pulse compressors to accelerate the electron beam more effectively to 2-GeV. Such pulse compressors can not provide 4 μ s flat-top pulses to accelerate the electron beam uniformly. There is a 15-m long space at the end of the linac to extend the 2-GeV linac if a higher energy beam is required. At present, this space is a part of the beam transport line to the storage ring. When we install one more klystron and 4 accelerating columns in this space, we can get the 2-GeV beams without using

pulse compressors. Regardless of the PAL stretcher project, this upgrade plan will be carried out in 1996-1997 period to provide the 2-GeV beams for more secure operation of the Pohang Light Source.

It is also required to reduce the beam loss during the acceleration in order to improve injection/extraction efficiency in the stretcher ring and also to avoid extremely high radiation level.

Table 1: Major parameters for PAL stretcher ring.

Beam Energy	2-GeV
Circumference	241.5 m
Lattice Type	FODO
Symmetry	2 (racetrack type)
Bending Magnet	
Number	64 sets
Bending Angle	5.625°
Magnetic Field	0.7 T
Length	1.0 m
Curvature	10.19 m
RF Frequency	2,856 MHz
Harmonic Number	2,300
Repetition Rate	60/120 Hz
Revolution Time	0.81 μ s
Extraction Current	100 μ A
Injection Current	3.25 μ s x 400 mA
Duty Factor	0.78
Injection	multi-turn
Energy Spread (injection)	< 0.1 %
Energy Spread (extraction)	+/- 0.02 %

IV. ACKNOWLEDGMENTS

We are grateful to thank to Professor J. C. Kim of Seoul National University for his valuable efforts in leading the study group on the nuclear physics issues possible at the Pohang Accelerator Laboratory.

V. REFERENCES

- [1]. Design Report of Pohang Light Source (revised ed.), Pohang Accelerator Laboratory, 1992.
- [2]. J. C. Kim and W. Namkung (ed.), "Proceedings of Workshop on Nuclear and High Energy Physics Experiments using Pohang Accelerator," PLS/LN-94-02, Pohang, April 9, 1994.
- [3]. D. Husmann, "Review of CW Electron Machines," Proc. of Fourth European Particle Accelerator Conference, London, U.K., June 1994, pp 62-66, and references in there.
- [4]. F. Hinode, et. al. (ed.), "Accelerator Test Facility: Design and Study Report," KEK (Japan), 1995.

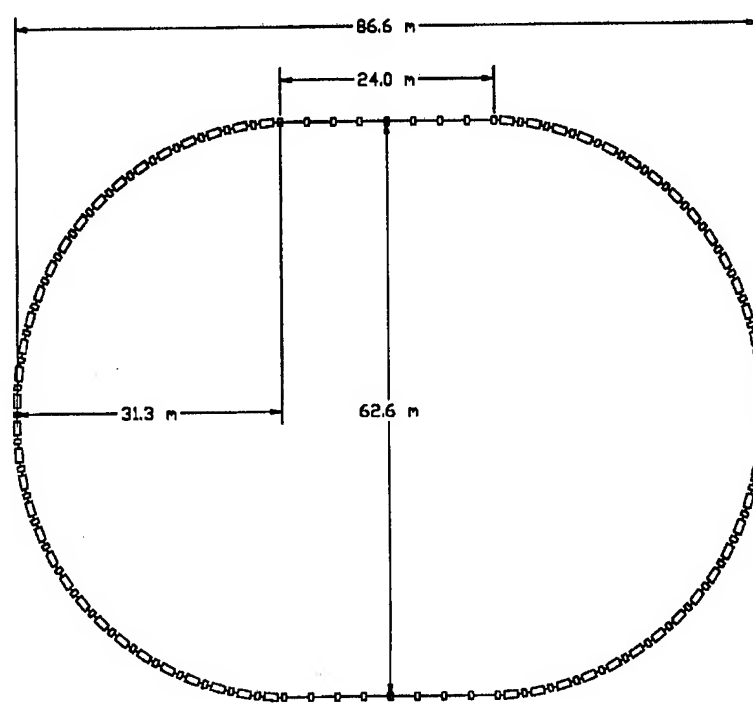


Fig. 2: Lattice of PAL stretcher.

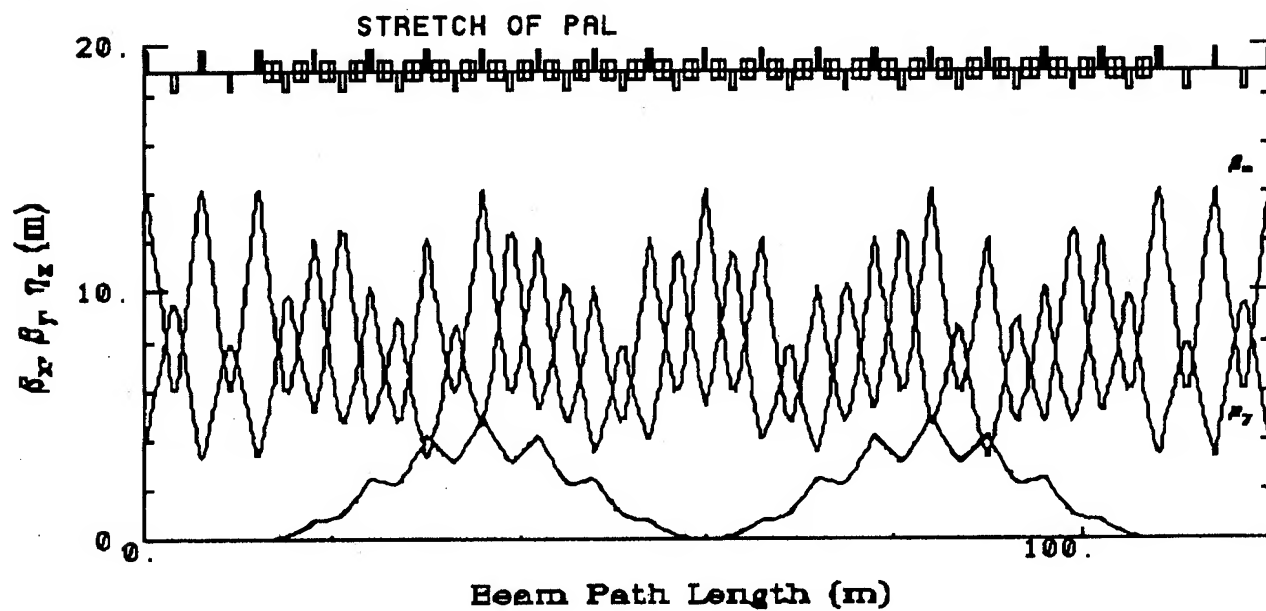


Fig. 3: Beta functions of the PAL stretcher ring.

Thermomechanical Analysis of a Compact-Design High Heat Load Crotch Absorber*

I. C. Sheng, S. Sharma, R. Rotela and J. Howell

Advanced Photon Source, Argonne National Laboratory

9700 South Cass Avenue, Argonne, Illinois 60439

Abstract

The Advanced Photon Source (APS) is a third-generation synchrotron facility built to generate extremely powerful x-rays. x-ray absorbers in the APS dipole vacuum chambers, known as crotch absorbers, are subjected to a very high power density of 750 Watt/mm² at 300 mA of beam current. In the compact design of the APS crotch absorbers, this high heat load is handled by a combination of optimized geometry, fins for power dispersion and cooling efficiency, and a material with high fatigue strength (Glidcop). The basic design and the results of detailed thermomechanical finite element analysis are presented in this paper.

I. INTRODUCTION

Each of the bending magnets of the APS storage ring emits a horizontal x-ray fan of 78.5 mrad with a power density of 750 Watt/mm² at 300 mA. Only 1.8 mrad of this fan is extracted to the beamline. The remaining fan is intercepted by a string of water-cooled absorbers in order to protect the vacuum components. A crotch absorber located at the downstream end of the dipole vacuum chamber intercepts most of these x-rays. With a source distance of approximately 1.8 m, the vertical x-ray beam size at the crotch absorber is 0.2 mm at normal incidence. This results in a vertically-integrated linear power density of 145 w/mm, which is too high for the conventional water-cooled copper absorbers. One approach to deal with this extreme power density is to use a beryllium diffuser brazed to the copper absorber [1]. The beryllium diffuses the x-ray power by absorbing softer x-rays through its thickness, thus spreading the heat load over a larger volume. The earlier APS crotch absorber designs [2,3] were based on this concept. In addition, Glidcop [4] was used for the absorber body instead of OFHC copper, because Glidcop has high fatigue strength at elevated temperatures. However, these designs were found to be difficult to implement in production because of unreliable braze joints between beryllium and Glidcop. In the present design, which has been used successfully for the fabrication of all crotch absorbers, the use of beryllium as a diffuser has been eliminated.

II. BASIC DESIGN

The present crotch absorber (see Figure 1) has two distinct features: a central nose region, and two side wings. Each of the side wings, as well as the nose, intercepts approximately 4 kilowatts of beam power. The side wings are inclined to the incident beam by approximately 20 degrees. This reduces the linear power density and the resulting temperature rise in the

wings by 66 percent. The absorber's nose is inclined vertically by 11 degrees, which spreads the beam power vertically. However, since the initial beam size at normal incidence is very small (0.2 mm vertically), the advantage of vertical inclination is not significant. At 300 mA, the temperature rise in the nose region would be 350 °C which is unacceptable for Glidcop under thermal cycles.

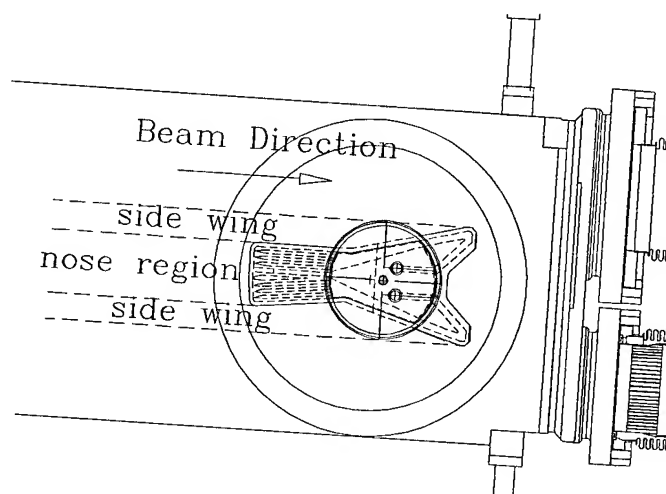


Figure 1. Plane View of the Crotch Absorber

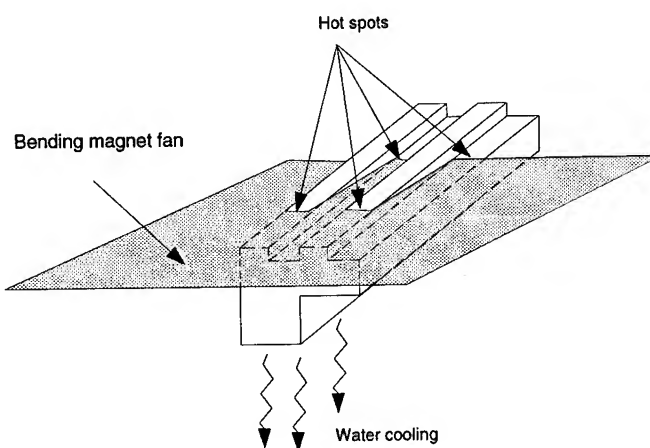


Figure 2. Bending Magnet Fan Intercepted by the External Fins

A new approach is used to spread the beam power more effectively in the nose region. In this approach, illustrated in Figure 2, vertical fins are machined on the Glidcop surface, which split the beam footprint into two parts. The first part is intercepted by the fins, whereas the second part is intercepted by the grooves between the fins. At the 11-degree angle of in-

*Work supported by U.S. DOE Office of Basic Energy Sciences under Contract No. W-31-109-ENG-38.

cidence, the separation between the two beam intercepts is 8 mm. Since the water channels are only about 5 mm away from the surface, this separation reduces the surface temperature rise considerably (see below). The beam power can be distributed even more effectively by using V-shaped fins. However, for the present beam power, the V-shaped fins are not needed and are not used in order to reduce the machining cost.

Internal fins are also used inside the water channels of the absorber to enhance the heat transfer. The water channels and the internal fins are made by EDM (electric discharge machining) to meet an important design criterion of avoiding water-to-vacuum joints. The Glidcop body is brazed to an OFHC copper plug, which directs the water flow, and a stainless steel cylinder, by which the absorber is attached to a Conflat flange. All brazing is done in a vacuum furnace with 50-50 gold-copper alloy. Further details on the absorber design, fabrication, and brazing are given in [5].

III. TEMPERATURE RISE

Finite element models were constructed to determine the temperature rise and stresses in the crotch absorber. Only the results for the nose region, where the temperature rise and stresses are highest, are presented here. For the thermal analysis only a representative strip of the absorber--consisting of two external fins, one water channel, and one internal fin--was modeled. A film coefficient of $1.5 \text{ Watt}/(\text{cm}^2 \text{ } ^\circ\text{C})$ was used based on a 7.5 gallon/minute (GPM) water flow in the cooling channels.

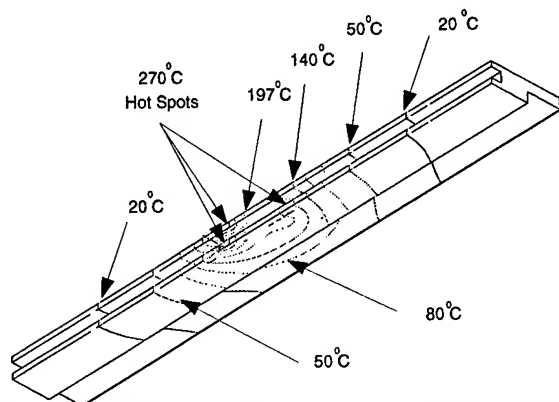


Figure 3. Temperature Rise Contour in the Nose Region

The temperature contours are shown in Figure 3. In the two spots where the beam is intercepted, the temperature rises by 270°C . The isotherms in the figure show spreading of the beam power due to the external fins. At the cooling channels, the maximum temperature rise is approximately 135°C , and the heat flux is $2 \text{ Watt}/\text{mm}^2$, both of which are well below the critical boiling conditions. If no external and internal fins are used, then the maximum temperature rises at the fins and the cooling channels are 350 and 145°C , respectively.

IV. STRESS

The fins in the absorber body also help in reducing the pressure stresses from the cooling water at 150 psi. Moreover, the pressure stresses, in contrast to the thermal stresses, are compressive on the water channel side, and tensile on the incident beam side. The combined effective (von Mises) stress is therefore reduced when both the thermal and pressure loads are considered.

Due to symmetry, only one-half of the nose section was modeled. Figure 4 shows the von Mises stress contours in this 3-D model. As expected, the two spots where the beam is intercepted experience the highest stress with a magnitude of about 20 ksi. In comparison, the yield strength and tensile strength of Glidcop are 55 ksi and 65 ksi, respectively [6].

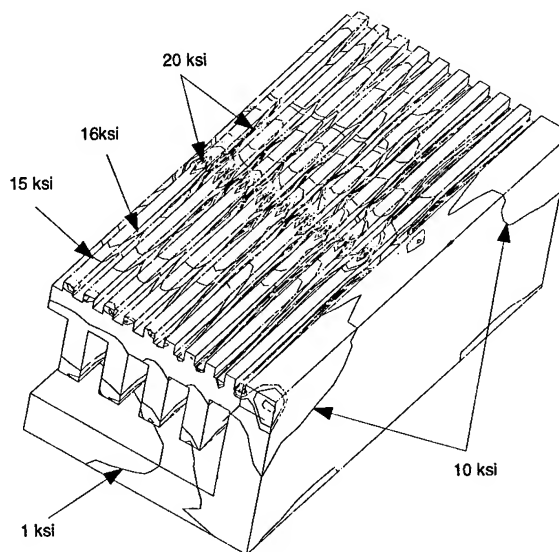


Figure 4. Stress Contour in the Nose Region

V. CONCLUSIONS

The basic design features of the APS crotch absorber have been described, and analysis results have been presented to show the effect of external and internal fins in reducing the temperature rise and stresses in the absorber. The compact design, which does not use beryllium as an x-ray diffuser, has been shown to safely handle 300 mA of beam current.

VI. ACKNOWLEDGMENTS

The authors would like to thank Ms. Catherine Eyberger for editing this paper.

VII. REFERENCES

- [1] D. M. Mills, D. H. Bilderback, and B. W. Bateman, "Thermal Design of Synchrotron Radiation Exit Port at CESR," *IEEE Transactions on Nuclear Science*, NS-26, 3854-3856, June 1979.
- [2] I. C. Sheng and J. Howell, "Thermal Analysis of the Crotch

Absorber in APS," *Proc. of SPIE--The International Society for Optical Engineering, High Heat Flux Engineering*, Ali M. Khounsary, Editor, **1739**, 200-213, 1992.

- [3] I. C. Sheng, S. Sharma, E. Rotela and J. Howell, "A Conceptual Design and Thermal Analysis of High Heat Load Crotch Absorber," *Proc. of the 1993 Particle Accelerator Conference*, **2**, 1497-1499, 1993.
- [4] "Glidcop Grade AL-15 Dispersion Strengthened Copper," Technical Data, SCM Metal Products, Inc., 1988.
- [5] S. Sharma, E. Rotela, I. C. Sheng and J. Howell, unpublished paper.
- [6] J. B. Conway, R. H. Stentz and H. T. Berling, "High Temperature, Low-Cycle Fatigue of Advanced Copper-Base Alloys for Rocket Nozzles; Part II -NASA1.1, Glidcop, and Sputtered Copper Alloys," NASA-Lewis Research Center, N-75-11076, 1974.

Novosibirsk Tau-Charm Factory Design Study

N. Dikansky, V. Parkhomchuk, A. Skrinsky, V. Yakimenko,
Budker Institute of Nuclear Physics, Novosibirsk, 630090, Russia

Abstract

A method of colliding beams is developed to study the fundamental properties of matter in two directions. The first direction is aimed at achieving higher energies allowing the discovery of new particles and fields. The goal of the second one is the study of more delicate fundamental properties of quarks and fields by increasing luminosity in crudely studied energy ranges. The study of CP violation is the most famous example. To study the CP violation in the region of B-quarks, the project of a B-factory as an asymmetrical electron-positron collider with a beam energy of 7/4 GeV and luminosity up to $10^{34} \text{ cm}^{-2} \text{ s}^{-1}$ was developed at BINP. During the development of this project, it became clear that the Institute's economical situation, which grew worse in the period of 1990-1993, did not allow us to carry out this project in a reasonable time. Besides, Japan (KEK) and USA (SLAC) began to build the B-factories. Therefore, it is hardly probable to obtain any new results on the third B-factory. On the other hand, a beam energy region of 0.7-2.5 GeV, which still is very interesting, is not studied completely. The interest in this field of research is due to a great body of information obtained on a LEAR facility which is utilized to study proton-antiproton annihilation approximately in this energy region. Studying the cross-section of production of observed resonances in electron-positron annihilation noticeably increases the value and reliability of their interpretation. In 1993, as a result of discussions, the International Program Committee on High-Energy Physics of the Ministry of Science recommended to reorientate the Novosibirsk project VEPP-5 into a Tau-Charm-factory with high luminosity [1].

I. Parameters of Colliding Beams and Interaction Region

The beam parameters for the Tau-Charm-factory should satisfy the requirements for obtaining a maximum high luminosity of $1.010^{34} \text{ cm}^{-2} \text{ s}^{-1}$. In addition to the maximum luminosity regime, it is planned to obtain the beam parameters required for the so-called monochromatization of colliding beams and polarized colliding ones. To work in these regimes, the beam emittance control systems are needed. Thus, to obtain the monochromatic colliding beams, it is necessary that the main contribution to the vertical size be made by energy spread at the interaction point and the vertical betatron size be substantially less. To control and preserve polarization, rather long solenoids with a longitudinal magnetic field are required. It is undoubtedly impossible to provide simultaneously all these regimes; so, regime-to-regime transition will be made by replacing magnetic elements in straight sections. In this case, the contribution of half-rings into emittances should be as small as possible. The maximum luminosity of the facility with round beams is determined by the expression

$$L_{\max} = \frac{c N_{\max} \gamma \xi_{\max}}{r_e D_{\min} \sigma_l}, \quad (1)$$

where N_{\max} is the maximum number of particles in a bunch; D_{\min} is the interbunch distance, ξ_{\max} is the parameters of beam interaction; r_e is the classical electron radius; $\gamma = E/mc^2$, and σ_l is the bunch length (sigma). Assuming that a RF system is used at a 700 MHz frequency and the interbunch distance is multiple to the RF wave length, we can present the beam parameters for the maximum luminosity in Table.1.

In the energy monochromatization regime, the value of a vertical energy dispersion is chosen according to the energy spread. In this case, the value of monochromatization is determined by the ratio of the vertical betatron size and the vertical energy one.

It is necessary to completely reconstruct the experimental straight section to obtain the ultra monochromatic colliding beams $\sigma_M \approx 6 \text{ keV}$. The strong quadrupoles and weak dipoles should be used for beam separation and control of the vertical dispersion function at the interaction point. The length of such section is estimated to be more than 30 m. The beam parameters in this case are presented in table:

Number of particles in bunch	1.510^{11}
Interbunch distance (m)	16.28
Beta-function at IP (cm) β_x/β_y	20 / 2
The value of ξ_{\max}/ξ_D	0.05 / 0.01
Beam emittance ϵ_x/ϵ_y (cm)	$10^{-5} / 10^{-9}$
Beam current (A)	0.4
Energy resolution σ_M (keV)	6
Luminosity ($\text{cm}^{-2} \text{ s}^{-1}$)	5.010^{31}

The Tau-Charm-factory is located in a tunnel with a $3 \times 3 \text{ m}^2$ cross-section, whose floor and ceiling are 163 and 166 m above

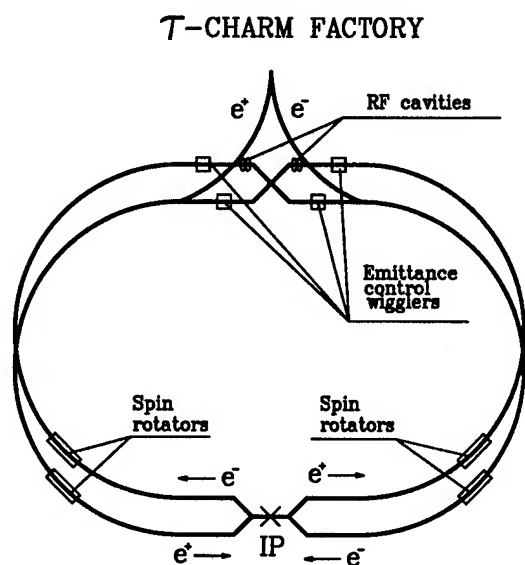


Figure. 1. Schematic layout

Energy (Gev)	2.1
Circumference (m)	773.036
Ring radius (m)	89.63
Interbunch distance (m)	8.14
Straight section length (m)	100
Beam radius at IP (μ m)	33
Number of rings	2
Number of bunches per beam	95
Number of particle per bunch	2×10^{11}
b-function at IP (cm)	1
Beams emittance ($\epsilon_x = \epsilon_y$) (cm/rad)	10^{-5}
RMS bunch length (cm)	0.8
Compaction factor	$0.001 \div 0.0017$
Betatron tune ν_x	29.077
Betatron tune ν_y	31.077
Vertical damping time (s)	0.11
RF voltage (kV)	1000
RF frequency (MHz)	700
Energy loss per turn (keV)	100
Energy spread	5×10^{-4}
Harmonic Number	1805
Tune shift parameter $\xi_x = \xi_y$	0.1
Design Luminosity ($cm^{-2}s^{-1}$)	10^{34}

Table.1

the sea level, respectively. The underground room consists of two half-rings, 89.58 m in radius, and straight section 100 m long, which connects the half-rings. In this case, the length of an ideal orbit is 773.036 m, corresponding to 1805 lengths of the RF wave. With such a geometry, each 19th separatrices contains a particle bunch; in all, the ring has 95 bunches. To install the injection equipment and magnetic systems of emittance control, the technical gap is increased up to $3 \times 5m^2$. The gap should be widened to the side of injection channels so that to have 1.5 m to the inner wall and 3.5 m to the external one. The nearest-to-the-surface point of the tunnel is at a 10 m depth; the nearest-within-reach point is the bottom of a technological line, which is 168.6 m above the sea level, corresponding to a ground thickness of 2.6 m above the ceiling of the Tau-Charm-factory tunnel. At present, the tunnel, 200 m long, beginning from the injection complex to a shaft, where the injection channel of the Tau-Charm-factory begins, has been built. In the nearest future, we shall begin to build the channels distributing the electron and positron bunches into an injection gap. The factory is built by the firm "Gornyak" at a pace depending mainly on the financial possibilities. Keeping the pace, we shall need about 5 years to build the underground part.

II. Element of Magnetic System Periodicity

The Tau-Charm-factory magnetic system consists of two storage rings located over each other and intercrossing at the interaction point. To provide collisions of longitudinally polarized beams, spin rotators are supposed to be installed in the half-rings. As an example of the specific magnetic system, we present a simple system which consists of a dipole magnet, 1.5 m long, with a field of 1024 G and quadrupole lenses, each has a 0.4 m length, whose parameters are given in detail in table :

	Length (cm)	Field (kG)	Gradient (kG/cm)
Quad	40		1.0631
Gap	30		
Dipole	150	1.042	
Gap	30		
Quad	40		-1.0631
Gap	30		
Dipole	150	1.042	
Gap	30		

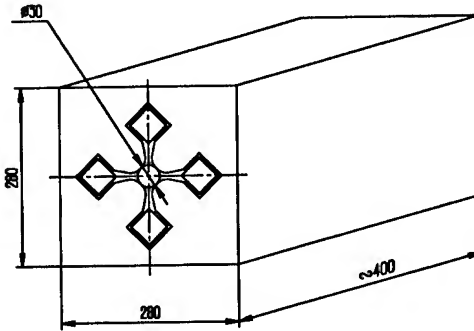
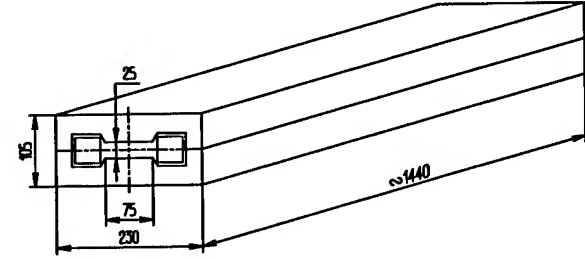


Figure. 2. Magnet elements of periodicity cell

III. Emittance Control Section

To control emittance, it is necessary to use special magnetic system sections where the magnetic field can be changed. A well-known element used for this purpose is the wiggler-magnet which allows us to noticeably increase the energy loss for radiation. As a rule, the ψ -function is small in the wiggler-magnet. As a result, introducing strong decay, the magnet does not give a considerable increase in the emittance. Let us consider a special magnet design which gives a strong dispersion and the introducing of which will significantly increase the emittance. The equation for the ψ -function has the form

$$\frac{d^2\psi}{ds^2} + G\psi = K \quad (2)$$

In a smoothed approximation, in the case where the phase is assumed to be constant along the magnetic gap and the dipole magnetic field to be modulated by the resonance frequency, the amplitude of the ψ -function beats increases linearly. To obtain the necessary emittance under these conditions, the length of such a section should be several tens meters. At the point where ψ is maximum, the wiggler-magnet controlling the emittance value in the given direction is placed. For two rings, the electron and positron ones, we need four sections with wiggler-magnets to independently tune the beam emittances.

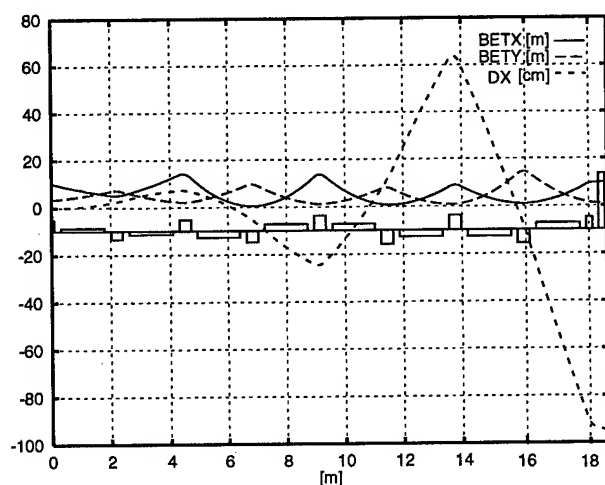


Figure. 3. Insertion of the ψ -function control

IV. Interaction Region

The most interesting possibility of obtaining the maximum luminosity is the setting up of the interaction point with a small β -function using a strong longitudinal field (9.6 T and 2.18 m long). Possessing symmetrical focusing in both directions, such a system satisfies the idea of operation with round beams and can allow us to obtain the parameters for a space charge $\xi \geq 0.1$. The main problem in setting up the interaction point is a necessity of electrostatic beam separation. The total length of separation plates with a field of 100 kV/cm is 2 m. They are located at the point where the β -function value is high, presenting the difficulties in providing the coherent beam stability. A steady obtaining of a powerful electrical field under the conditions of synchrotron irradiation of the separation plates is also a rather serious problem. It is planned to carry out experiments on VEPP-2M for producing on extremely high field strength under the synchrotron light.

V. Conclusion

The construction of the Tau-Charm-factory under the existing economic conditions in Russia is not a simple problem. However, the successful completion of this project will allow us to enter the third millenium with an interesting machine which the world scientific community needs to acquire fundamental knowledge.

References

- [1] Dikansky N.S., et al. *Status of the VEPP-5 Complex*, Proc. of EPAC94, London, 1994, p.482

DEVELOPMENT OF A RAMI PROGRAM FOR LANSCE UPGRADE*

K. C. D. Chan, A. Browman, R. L. Hutson, R. J. Macek, P. J. Tallerico, and C. A. Wilkinson
Los Alamos National Laboratory, Los Alamos, NM 87545

ABSTRACT

Improvement of beam availability is a prime objective of the present LANSCE (Los Alamos Neutron Scattering Center) Upgrade. A RAMI (reliability, availability, maintainability, and inspectability) program is being developed to identify the most cost-effective improvements to achieve the availability goal. The beam-delivery system is divided into subsystems appropriate for the modeling of availability. The availability of each subsystem is determined from operation data and assessment of individual component designs. These availability data are incorporated in an availability model to predict the benefit of improvement projects to achieve cost-benefit prioritization. Examination of the data also identifies a comprehensive list of factors affecting availability. A good understanding of these factors using root-cause analysis is essential for availability improvement. In this paper, we will describe the RAMI program and the development of the availability model.

I. INTRODUCTION

Presently, the Los Alamos Meson Physics Facility (LAMPF) is undergoing an availability upgrade [1] so that the accelerator can become a reliable driver for the Los Alamos Neutron Scattering Center (LANSCE). The availability goal is to operate LANSCE at 100 μ A with better than 85% availability over an operation period of eight months per year. Because the typical duration of neutron-scattering experiments is 2-3 days, it is important to keep the downtimes longer than 8 hours to less than 10% and those longer than 24 hours to less than 1%. A RAMI (reliability, availability, maintainability, and inspectability) program is being developed to analyze the cost effectiveness of the upgrade. It can be used to plan, monitor, predict, and improve the availability of the LANSCE beam-delivery system.

The RAMI Program is also being used to plan the maintenance and upgrade of LAMPF in the next five years. The purpose is to systematically replace obsolete and unreliable equipment from the LAMPF beam-delivery system so that the Facility can extend its lifetime for another 20 years.

RAMI studies have been carried out previously at LAMPF. In the late 70's, a RAMI program was instituted to bring the availability from 65% to 80% [2]. The system tracked the failures of equipment and the repair cost. The program was later terminated. A review of the recent RAMI studies at LAMPF have been given by Macek in Ref. 3. In 1994, a pilot project, Development of a Reliability, Availability, Maintainability, and Inspectability Model for High-Power Accelerators, was carried out. This project concentrated on a few major subsystems of the LANSCE

beam-delivery system as test examples of the RAMI model [4]. The work described in this paper is the continuation of the recent RAMI studies.

II. RAMI PROGRAM

The RAMI Program has three parts: availability model, root-cause analysis, and maintenance plan. The beam-delivery system is divided into subsystems which are collections of individual components. The availability model uses a database that contains the availability data of all the components to predict the overall availability of the beam-delivery system and the subsystems. The commonly used assumptions for models can be found in Ref. [3] and [5]. Predictions should reproduce the observed overall system availability and should be able to predict the gain in overall availability and cost effectiveness of improvements. The availability model will also be used to identify the low-availability subsystems so that a root-cause analysis can be done on the subsystems. The root-cause analysis is an indepth analysis of specific failures which contribute to understanding of failures and suggest improvements. Analysis of the frequency of failure, repair times, and the consequences will aid in the development of an effective maintenance plan.

II. AVAILABILITY MODEL

The database used by the availability model is assembled by first listing all the components in the LANSCE beam-delivery system. Examples of components are power supplies, klystrons, and beam-position monitors. Components with similar location and purpose along the beam-delivery system are grouped into subsystems. They are grouped with enough components to have sufficient availability statistics. Examples of subsystems are injector, PSR (Proton Storage Ring), and Neutron Production Target. Components are also assigned function designators according to their functions. Examples of function designators are magnet, water, and vacuum. Both subsystem and function designators are used in sorting database information to conform with the functions of maintenance groups and with subsystems based on a single design concept. For example, one can easily find the availability of the water system in PSR by selecting all the components that have subsystem designator of PSR and function designator of water and summing their availabilities.

After listing all the components, availability data of these components were collected. These availability data are in the form of MTF (mean time to failures) and MTR (mean time to repairs). They are based on failure rates, manufacturer's data, and estimates by experts. At this point, the assembly of the database is complete and predictions of availability of subsystem can be made in conjunction with assumptions made in the availability model.

The present availability-model database for the LANSCE beam-delivery system has a total of 385 component types

* This work is supported by Los Alamos National Laboratory Institutional Supporting Research, under the auspices of the United States Department of Energy

separated into nine subsystems. Similar components are counted as one component type. These components are separated into nine subsystems. Subsystem names are given in Table 1. There are 14 function designators (Table 2).

Table 1: List of subsystems in the LANSCE beam-delivery system

Injector	Sector A	Sector B-H
Switchyard	Area A	Line D
PSR	Target	WNR

Table 2: List of functions in the LANSCE beam-delivery system

Aperture	Beamline	Control/data
Diagnostic	Facility	Magnet
RF	Safety	Source
Structure	Timing	Vacuum
Water	Misc.	

The availability model can be benchmarked by comparing its availability prediction with observed availability for subsystems. The observed availabilities of subsystems are provided through operation logs where operators record the times and causes of component failures and repairs. In the present format, the availability-model subsystem and function designators have been chosen to correlate with the operators log for ease of comparison. Figure 1 shows the observed distribution of time-between-failures for subsystems injector and Sector A during the operation in 1994. These data were used to derive the availability, MTF, and MTR for the subsystems.

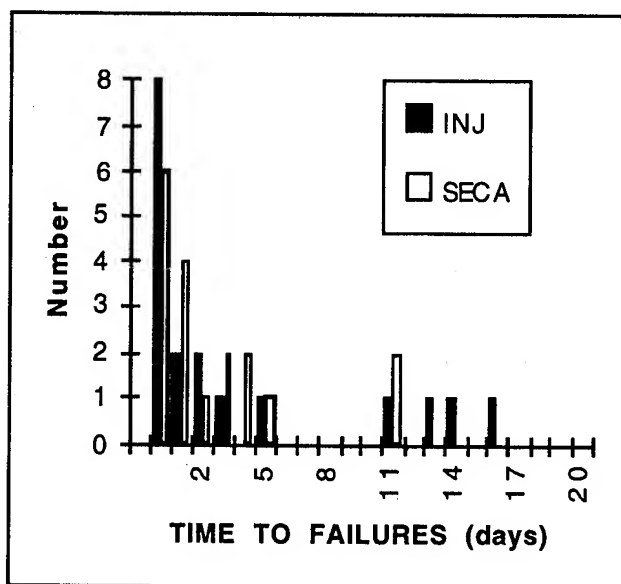


Figure 1: Distribution of time-to-failure for the LAMPF injector and Sector A of the linac

The PSR Pulsed Power System has been studied before using an availability model and is described here as an example [6]. The complete system was divided into four subsystems: switchyard kicker magnets (LDKIs), PSR injection linekicker magnet (RIKI), the 2.8 MHz RF beam buncher (SRHM), and

the electromagnetic extraction kickers (SRFK). Table 3 shows the part of the database used for RIKI. The availabilities predicted using the database for the subsystems and complete system were compared to observed availabilities from operators logs (Table 4). Results showed that the prediction of the availability model is within 2% of the observed availability.

III. ROOT-CAUSE ANALYSIS

The availability model and the observed data can identify the low-availability subsystem. A root-cause analysis is needed to identify the failure modes so that improvements can be made. These improvements include a better design, preventive maintenance, and monitoring programs. Assuming these improvements, new MTF and MTR data can be generated and used in the availability model to predict the improved availability. Examples of Root-Cause Analysis can be found in Ref. [3].

IV. MAINTENANCE PLAN

Maintainability and inspectability will be addressed with maintenance plan. Regular monitoring and maintenance are needed to reduce failure and downtime. In an older facility like LAMPF, a sustained replacement program is also needed for equipment that is reaching the end of its useful lifetime. Because of budgetary constraints, the replacement program is not in place yet. A conscious effort has been made, instead, to keep an inventory of spare parts of long-downtime components. A record of these spare parts will be incorporated in the availability-model database. The availability-model database will be examined to identify components whose failures are eminent or whose failures have high consequences. In the future, component maintainability, monitoring, and inspectability will also be incorporated in the designs of components.

V. SUMMARY

RAMI analysis is currently being applied to the LANSCE beam-delivery systems. Previous studies and use of this analysis at LAMPF have shown that it can be a useful tool for determining the best assignment of budget and resources to provide maximum beam availability. The current work has established a RAMI model of the entire LANSCE beam-delivery system, based on individual components and their availability histories. The model will be used to predict the impact on availability of the LANSCE beam-delivery upgrades currently in progress and can be used to determine the effect of any future improvements. Components or systems with the probability for high consequence failure can be identified by the model database and root-cause analysis can be applied to the failure modes. Steps can then be taken to avoid or minimize beam downtime due to failures of these components and systems. The model database will also be used to develop a maintenance plan which will provide adequate spares, timely replacement, and preventative maintenance for all beam line components. The end result of this effort should be improved, cost-effective beam availability for LANSCE users over both near and long terms.

VII. REFERENCES

[1] R. J. Macek, Performance Improvements of the Los Alamos Neutron Science Facility, Los Alamos Work-for-Others Proposal, R-1339-94-2 (Revised), July 11, 1994.

[2] R. A. Jameson, R. S. Mills, M. D. Johnston, "Management Information for LAMPF", LA-5707-MS Informal Report, UC-28, LASL, August 1974.

[3] Report of the Committee on a TA-53 Upgrade, Chapter 5, Arch Thiessen (Chairman), Los Alamos National Laboratory Report.

[4] C. Wilkinson, Development of a Reliability, Availability, Maintainability, and Inspectability Model for High Power Accelerators, Los Alamos National Laboratory LDRD Report, in preparation.

[5] E. E. Lewis, Introduction to Reliability Engineering, published by John Wiley & Sons, 1987.

[6] R. Hutson, Preliminary Availability Analysis of PSR/LANSCE Pulsed Power Systems (For Five-Year Period, 1988-1992, Cycles 51-62), Los Alamos National Laboratory, AOT-2 Technical Notes, Sept. 30, 1994.

Table 3: Availability-Model Database for RIKI

Subsystem	Component	Function	MTF (days)	MTR (h)	Spares	Avail.
PSR	Magnet:					
PSR	Magnet current connections	magnet	20000	6	Parts	0.999988
PSR	Coils	magnet	10800	340	1	0.998690
PSR	Charging system:					
PSR	PS, Sorenson DCR 600-8T	magnet	3600	4	1	0.999954
PSR	PS, Christie 1C015-600EBBX4S	magnet	3600	8	some parts	0.999907
PSR	Modulator:					
PSR	Resonate Charge SCR	magnet	3600	8	3	0.999907
PSR	Zener Diode Assembly	magnet	1000	5	3	0.999792
PSR	Charge Recover SCR	magnet	3600	8	3	0.999907
PSR	Freewheel SCR	magnet	3600	8	3	0.999907
PSR	Transfer Chassis	magnet	1800	16	0	0.999630
PSR	Controls and Interlocks:					
PSR	RIKI01 Run Permit	safety	3600	1	Parts	0.999988
PSR	NIM Crate	safety	1800	8	Parts	0.999815
PSR	Short Nim Crate	safety	1800	8	Parts	0.999815
PSR	Computer Interface:					
PSR	CAMAC	control/data	7300	4	?	0.999977
					Sub. Avail	0.997280

Table 4: Comparison of observed availability and availability predicted with availability model. All availabilities are in percentages.

	LDKI	RIKI	SRHM	SRFK	Total
Observed	99.1	98.8	96.5	97.8	92.4
Predicted	97.7	99.7	98.6	98.4	94.6

ACCELERATOR WAVEFORM SYNTHESIS AND LONGITUDINAL BEAM DYNAMICS IN A SMALL INDUCTION RECIRCULATOR*

T.J. Fessenden, Lawrence Berkeley Laboratory
D.P. Grote and W.M. Sharp, Lawrence Livermore National Laboratory

SUMMARY

A recirculating induction accelerator requires accelerating waveforms that produce current amplification and provide bunch length control throughout the acceleration process. Current amplification occurs because of both an increase in the beam velocity and a shortening of the length of the beam bunch. The pulsed acceleration and control waveforms seen by the beam change as the pulse duration shortens. For one acceleration cycle of the small recirculator, each accelerating gap is driven by a burst of 15 pulses. As the beam gains velocity, the time interval between pulses shortens from approximately 20 to 10 μsec . A zero-dimensional design code REC is used to develop the accelerator waveforms. An envelope/fluid code CIRCE and a 3-D particle code WARP3d are used to confirm the REC design and study the effects of errors. We find that acceleration errors can lead to space-charge waves launched at the bunch ends that strongly affect or even destroy the current pulse shape. The relation between the rate of longitudinal compression and the velocity of space charge waves is studied.

INTRODUCTION

To serve as a heavy-ion accelerator/driver, a recirculator must operate at much larger currents than common in existing circular accelerators. In order to minimize collective particle effects, all acceleration must occur very rapidly--within a very few turns (≈ 100). As in a linac, longitudinal bunch control must be supplied by the accelerating waveforms and current amplification during acceleration must be maintained. Much of the basic accelerator physics and beam manipulations of an induction recirculator can be examined in a "proof-of-principal" experiment. The companion paper of Friedman et al [1] at this conference describes a small experiment that is being assembled at the Lawrence Livermore National Laboratory to demonstrate many of the fundamental principles of this type of accelerator. This paper describes the development of the acceleration waveforms for this experiment along with physics studies of beam behavior under different acceleration scenarios.

The small recirculator design contains 20 full lattice periods each 72 cm long that form a ring approximately 4 m in diameter. Transverse focusing is provided by permanent magnet quadrupoles, and bending is supplied by electric dipoles. The reference design accelerates 2 mA of K^+ from an energy of 80 kV to 320 kV and a final current of 8 mA. Acceleration occurs over 15 laps in a time period

of approximately 230 μs . Current amplification results from both a doubling of the pulse speed and a halving of the bunch length during acceleration. Of the 40 half lattice period in the ring, four will be used for beam insertion and extraction and 36 will have gaps for applying the accelerating and longitudinal control waveforms (ears).

COMPUTER CODES

We have employed three different codes for developing the reference accelerating and control waveforms for the experiment. The first, REC, is a zero dimensional synthesis code that is useful for obtaining initial estimates of beam parameters and timing during acceleration. The REC code uses the acceleration procedure developed by C. Kim and L. Smith [2] to generate the proper waveforms to produce self-similar current amplification over the accelerator cycle. Transversely, the code assumes that the beam is completely dominated by space charge and always matched to the transport lattice. The effects of space charge on the longitudinal beam dynamics are ignored. The code also calculates the electric dipole waveforms to keep the beam on axis and estimates the beam size at head, center, and tail during acceleration using the method developed by Lee *et al.* [3]. The waveforms and timing data from REC are used as input to the CIRCE and WARP codes.

CIRCE [4] is a fast-running macroscopic beam-dynamics code that uses a truncated moment or "envelope" description of transverse dynamics, with equations for the radii and the centroid co-ordinates of the elliptical beam. Equations for longitudinal dynamics are obtained by treating the beam as a Lagrangian fluid. Proper terms are included to account for the effects of image forces, beam emittance, and space charge in the limit of paraxial motion, and the beam is focused and accelerated by a user-specified lattice of electric or magnetic dipoles and quadrupoles.

For these calculations the waveforms and timing data from REC are used to start the code and the longitudinal and transverse behavior of the beam in the recirculator is examined. In this paper, a particularly simple model of the beam space charge was used, in which the axial electric field averaged over the beam cross-section is proportional to the spatial derivative of the line-charge density multiplied by a logarithmic "geometry" factor.

WARP3d [5] is a three-dimensional particle-in-cell code simulation code that includes a framework for specifying a lattice of accelerating elements. The lattice elements can be modeled as finite-length, hard-edged elements where "residence corrections" are done to ensure that the correct impulses are given, or, for electric elements, can be modeled self-consistently by inclusion of the conductor geometry in the calculation of the fields. A

* Work performed under auspices of U.S. DoE by LLNL and LBL under contract W-7405-ENG-48 and DE-AC03-76SF00098.

warped coordinate system is used to model accelerator bends. The finite-length accelerating gaps can be time dependent. For these simulations, the hard edged quadrupole model was used and the electric dipole bending plates were included self-consistently.

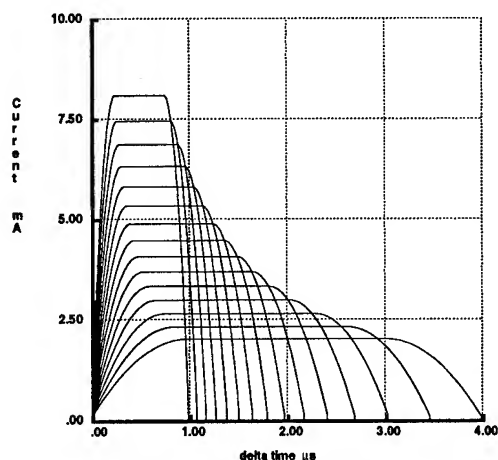


Fig 1. Self-Similar current waveforms at gap 5.

RECIRCULATOR WAVEFORM DESIGN

Figure 1 shows the anticipated self-similar current waveforms at gap 5 for each of the 15 turns of the beam generated by the REC code for the parameters of the small recirculator. Figure 2 shows the accelerating waveforms at gap 5 that are required to produce the current waveforms shown in Fig. 1. The length control waveforms (ears) are not shown. The first waveform applied to the first 8 gaps is essentially triangular. These accelerate the bunch tail more than the head and establish the proper velocity ramp for current amplification. The remaining 280 ideal waveforms (excluding ears) required when the beam is present in each gap are essentially rectangular.

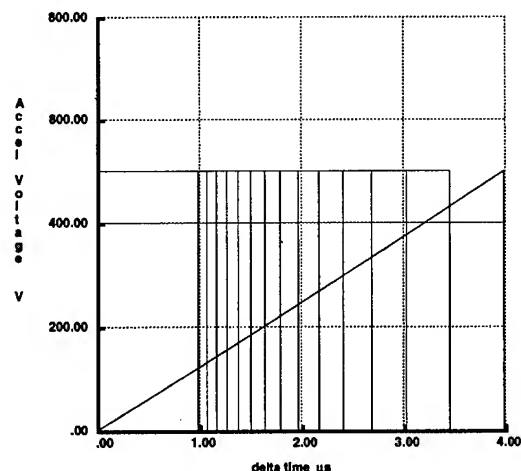


Fig 2. Ideal accelerator waveforms at gap 5 for self-similar current amplification

The waveforms that control the beam longitudinally are presented in Fig 3. These were calculated with CIRCE and are very close to those needed to confine the beam against its longitudinal space charge and axial temperature.

Time is measured from beam center so that both the front and back "ears" can be seen.

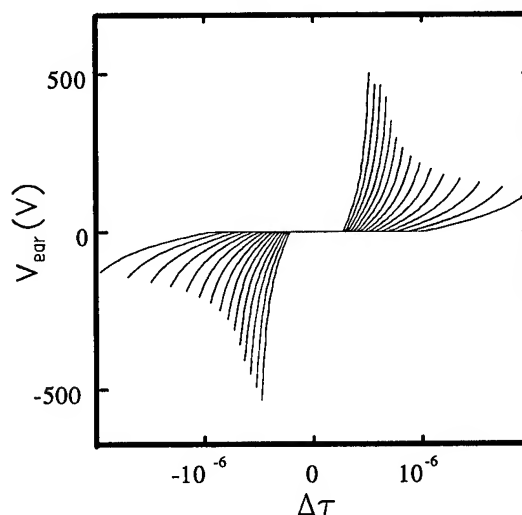


Fig. 3 Waveforms from CIRCE needed to provide longitudinal beam control for this design.

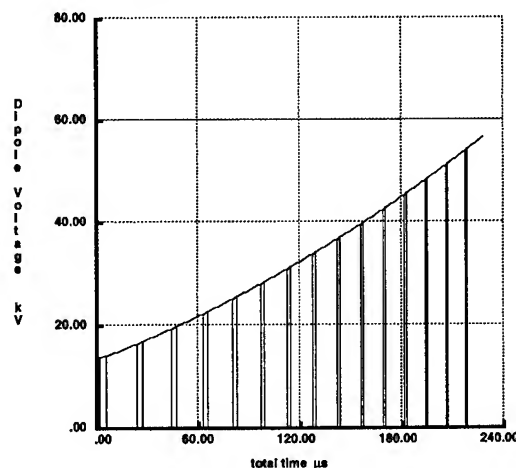


Fig. 4 Dipole bending voltages at gap 5 for the reference acceleration schedule

The voltage versus time that must be applied to each of the 40 bending dipoles of the recirculator for the acceleration schedule presented in this paper are shown in Fig. 4. The curve was calculated from the instantaneous energy of the beam center as it passes each bending dipole. This algorithm is only strictly correct for acceleration schedules that preserve the bunch length during acceleration. For the bunch-shortening schedule of this paper this simplification produces an error of $\leq 0.2\%$. As a consequence all 40 bending quadrupoles may be powered from the same supply and no fine tweaking requiring 40 separate supplies is believed necessary. Also shown is the timing of the beam for the 15 passes of the beam past gap 5. The accelerator pulses must be carefully synchronized to the beam at each of the 36 active gaps. As the beam gains energy, the ideal accelerator pulse duration shortens as shown in Figs. 1, 2, and 3 and the interval between pulses decreases.

LONGITUDINAL DYNAMICS

The CIRCE and WARP3d codes are used to study effects produced by errors in acceleration schedules. Fig. 5 presents an example in which compression was attempted by only applying the "ear" control waveforms of Fig. 3. That is, the initial triangular waveforms suggested by the REC code were not used. Strong space charge waves are generated at the ends of the beams that propagate toward beam center and double when they collide at the center. As the waves separate longitudinal beam heating is observed and the code crashes before the beam completes 15 laps.

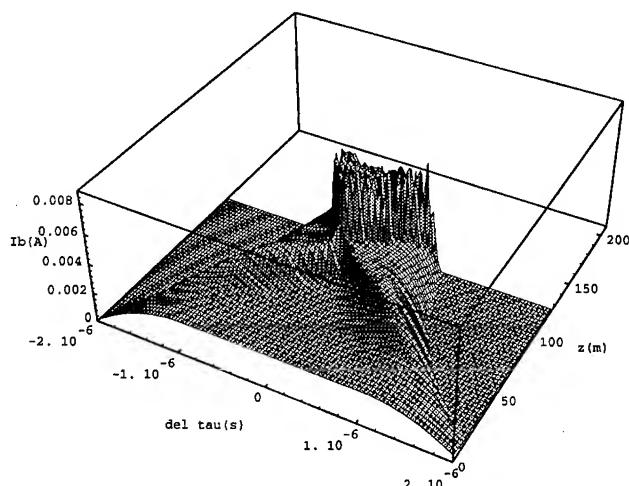


Fig. 5 Beam compression using only axial control waveforms (ears). The beam current is shown in the beam frame versus time and acceleration distance.

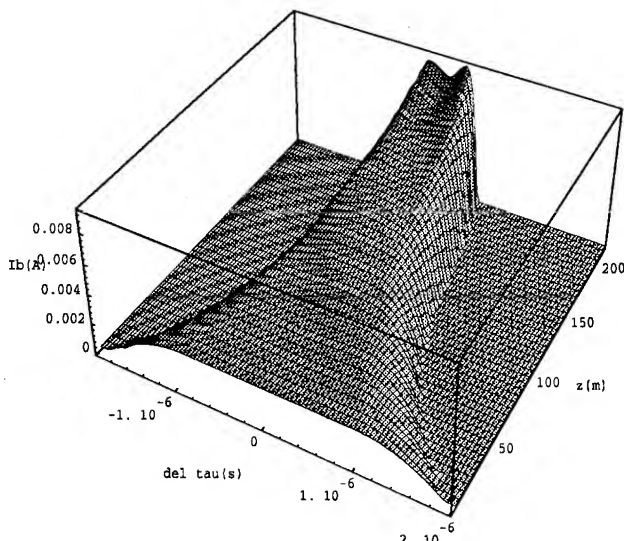


Fig. 6 CIRCE calculations of Beam compression using the compression schedule provided by REC.

A CIRCE calculation that incorporated all the waveforms and timing suggested by the REC code is shown in Fig. 6. This compression reasonably reproduces the self-similar current amplification of the REC code

except over the last 50 meters of acceleration. WARP3d calculations using the REC waveforms and timing and the CIRCE "ears" of Fig. 3 is shown in Fig. 7. Much of the noise apparent in Fig. 7 is numerical.

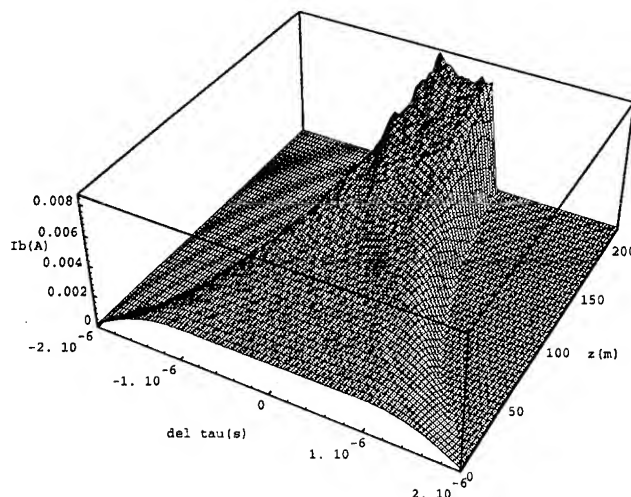


Fig. 7 WARP3d calculations of the same compression schedule as in Fig. 6.

CONCLUSIONS

The Kim-Smith self-similar current amplification procedure as embodied in the REC code provides an initial prescription and timing data for developing the acceleration waveforms needed for the small induction recirculator. Such a procedure is necessary for maintaining control of the current waveform over acceleration distances that are long compared with the length of the bunch. Moreover, bunch length compression must be effected by waveforms that act over the entire bunch length.

Results from the WARP3d and CIRCE codes are in good qualitative agreement. However, the algorithm used by the CIRCE code for generating the waveform control waveforms ("ears") used in these simulations was not quite adequate. As a consequence, neither code was able to preserve the self-similar current waveforms over the entire acceleration cycle. Further improvements in treating the effects of space charge at the bunch ends have been made and are reported in Ref. [6].

REFERENCES

- [1] A. Friedman *et al.*, These proceedings.
- [2] C.H. Kim and L. Smith, Part. Accel. **85**, 101-103 (1986).
- [3] E.P. Lee, T.J. Fessenden, and L.J. Laslett, IEEE Trans. Nuc. Sci. **32**, 2589 (1985).
- [4] W. M. Sharp, J. J. Barnard, D. P. Grote, S. M. Lund, and S. S. Yu, AIP Press, **297**, R. D. Ryne, ed., pp. 540-548 (1994).
- [5] A. Friedman, D. P. Grote, and I. Haber, Phys. Fluids B, **4**, p. 2203 (1992).
- [6] W. M. Sharp, These proceedings.

PROGRESS TOWARD A PROTOTYPE RECIRCULATING INDUCTION ACCELERATOR FOR HEAVY-ION FUSION*

A. Friedman, J. J. Barnard, M. D. Cable, D. A. Callahan, F. J. Deadrick, S. Eylon,[‡]
T. J. Fessenden,[†] D. P. Grote, D. L. Judd,[†] H. C. Kirbie, D. B. Longinotti,[§] S. M. Lund,
L. A. Nattrass, M. B. Nelson, M. A. Newton, T. C. Sangster, W. M. Sharp, and S. S. Yu[†]

Lawrence Livermore National Laboratory, L-440, Livermore CA 94550 USA

[†]*Lawrence Berkeley Laboratory; [‡]Titan Beta; [§]EG&G*

The U.S. Inertial Fusion Energy (IFE) Program is developing induction accelerator technology toward the goal of electric power production using Heavy-Ion beam-driven inertial Fusion (HIF). The recirculating induction accelerator promises driver cost reduction by repeatedly passing the beam through the same set of accelerating and focusing elements.[1] We present plans for and progress toward a small (4.5-m diameter) prototype recirculator,[2] which will accelerate K^+ ions through 15 laps, from 80 to 320 keV and from 2 to 8 mA. Beam confinement is effected via permanent-magnet quadrupoles; bending is via electric dipoles. Scaling laws, and extensive particle and fluid simulations of the space-charge dominated beam behavior, have been used to arrive at the design. An injector and matching section are operational. Initial experiments are investigating intense-beam transport in a linear magnetic channel; near-term plans include studies of transport around a bend. Later experiments will study insertion/extraction and acceleration with centroid control.

I. RECIRCULATOR CONCEPT

A recirculating induction accelerator potentially offers cost reduction relative to a "conventional" ion induction linac. The overall accelerator length is reduced (by a factor of ~ 2 -3, to about 3.6 km in the "C-design" recirculator of Ref. [1] and possibly shorter), and the accelerating cores are smaller because acceleration can be slower. Research on recirculator drivers has centered on four-beam multi-ring designs, with each ring augmenting the beam's energy by an order of magnitude over 50 to 100 laps. In contrast with most HIF induction linac concepts,[3] the recirculator designs considered to date do not employ beam merging. Hybrid designs (with a recirculator at the low-energy end) are also possible and may prove attractive.

The beam-dynamics issues which must be resolved before a recirculating driver can be built include centroid control, longitudinal control, avoidance of phase-space dilution in bends, and insertion/extraction of the beam into/out of the rings. As described below, these can be addressed at reduced scale in a small prototype recirculator. The waveform generators in a driver must supply variable accelerating pulses at repetition frequencies ~ 50 kHz, and accurate time-varying dipole fields with good energy recovery. These requirements are challenging, but advances in solid-state power electronics should make it possible to meet them through a technology development program.

*This work was performed under the auspices of the U.S. Department of Energy by LLNL and LBL under contracts W-7405-ENG-48 and DE-AC03-76SF00098.

Present technology has achieved 200 kHz bursts at 5 kV and 800 A with pulse widths of 0.5-2 ms, but with a non-variable format.[4] Because of its long (~ 200 km) beam path length and the fact that the beam repeatedly visits each section of the beam line, a recirculator driver will require a vacuum of $\sim 10^{-10}$ to 10^{-11} torr.

II. DESIGN OF SMALL RECIRCULATOR

LLNL, in collaboration with LBL, Titan-Beta, and EG&G, is currently developing a small prototype ion recirculator. This "small recirculator" is intended to explore, in a scaled manner, the beam-dynamics issues in a recirculating driver for inertial fusion energy. The small recirculator will be assembled and operated as a series of experiments over several years' time. Fig. 1. illustrates the overall physics design of the final small recirculator, and lists some of the elements which must all work together, both in it and in a full-scale fusion driver.

The small recirculator will have a circumference of 14.4 meters, a 3.5 cm aperture radius (pipe radius) for the beam focusing and bending elements, and a half-lattice period of 36 cm. The beam will be transversely focused with alternating-gradient permanent magnet quadrupoles with a field of ~ 0.294 T at the pipe wall, and will be bent

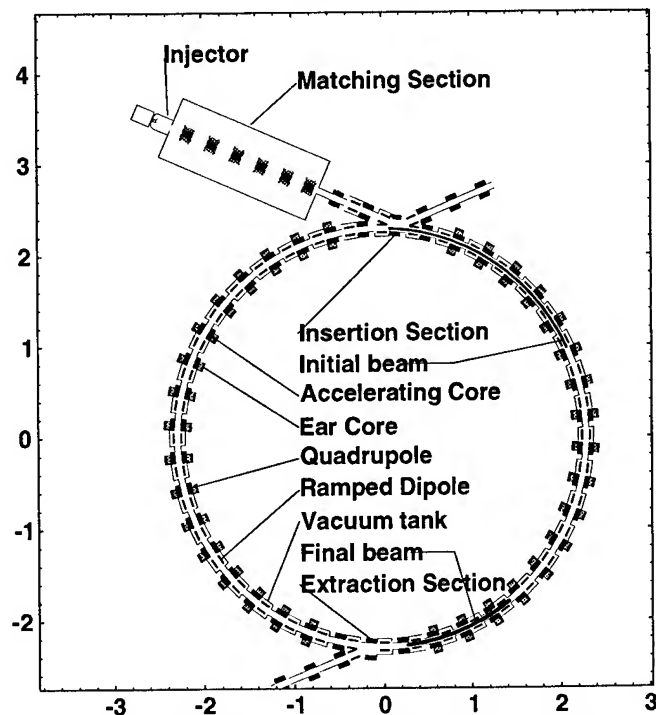


Fig. 1. Overview of final configuration (scales in meters).

with electric dipole deflector plates. These quadrupoles and dipoles will each physically occupy about 30% of the axial lattice length, and the full recirculator ring will consist of 40 half-lattice periods, including two using special large-aperture quadrupole magnets through which the beam will be inserted and/or extracted. The beam ion is K^+ (mass 39 AMU), and the beam will be accelerated from an initial particle kinetic energy of 80 keV to 320 keV over 15 laps by 34 induction cores. The initial current of the beam will be 2 mA, corresponding to a line-charge density of $0.0036 \mu\text{C/m}$ and characteristic beam radius of 1.1 cm, and the initial pulse duration will be 4 μsec . Also, the initial phase advance per lattice period will be $\sigma_0 = 78^\circ$, depressed to $\sigma = 16^\circ$ by space charge. After 15 laps of acceleration, the beam current will have increased to 8 mA, with a corresponding line-charge density of $0.00721 \mu\text{C/m}$, an average beam radius of 1.3 cm, and a final pulse duration of 1 μsec . Also, the phase advances will decrease to $\sigma_0 = 45^\circ$ and $\sigma = 12^\circ$.

Because the heavy-ion beam in the small recirculator is nonrelativistic and accelerating, the variable-format waveforms required to accelerate and bend the beam will require repetition rates ranging from approximately 40 to 90 kHz at the initial and final beam energies.[5] The voltage pulses for the electric dipoles must be correctly ramped in concert with the changing beam energy. Detailed "ear" pulses and lap-to-lap variation of the pulse duration and shape must be added to the accelerating waveforms to maintain or decrease the beam length. In order to switch the beam into or out of the ring, it is necessary to apply dipole fields that vary in time. Transverse confinement of the beam must be carried out during the insertion or extraction process. The design we are developing uses a permanent-magnet quadrupole with an expanded aperture.

III. EXPERIMENT PLANS

Linear experiments now getting underway will measure space-charge-dominated beam quality after transport through a permanent-magnet quadrupole lattice, will characterize the beam prior to injection into the recirculator, provide a test-bed for diagnostic development and afford a preliminary assessment of the role of electrons in magnetic beam transport (see Fig. 2).

The next experiments will study beam transport around

a $\sim 90^\circ$ bend (without acceleration, at first). Emittance growth can result from the non-uniform distribution of beam space-charge resulting from the action of centrifugal forces. As revealed in particle simulations using WARP3d [6] and interpreted theoretically [7], it occurs at changes in the accelerator's curvature where the distribution of beam particles relaxes toward a new equilibrium. Also, the electric dipoles introduce field aberrations. Detailed 3-D simulations show that proper shaping of the dipole plates should render the beam distortion minimal. In the small recirculator, a measurable amount of emittance growth is expected to take place over the fifteen laps, mostly occurring in the first two laps.[8]

Later experiments will study insertion and extraction, acceleration (at first in a partial ring to facilitate measurement of the beam using intercepting diagnostics), beam steering, bunch compression, and full integrated operation of the recirculator.[2] Preservation of a small emittance will again be the central beam physics issue to be addressed.

The principal non-intercepting diagnostic is a segmented capacitive pickup located inside the quadrupoles.[9] Until the ring is complete it will be possible to employ intercepting diagnostics. As currently planned, the ring will incorporate two extraction sections 180° apart, and the extracted beam can be diagnosed with detailed intercepting diagnostics twice each lap. As with earlier linac experiments at LBL, excellent shot-to-shot repeatability is anticipated and, so far, observed.

The long beam residence in the machine, up to (and possibly exceeding) 300 full lattice periods, will provide a unique opportunity to observe and characterize the longitudinal propagation of space-charge waves along the beam. Such waves will be launched (deliberately or otherwise) by mismatching the applied ear fields. The small recirculator will afford the longest beam path length of any near-term facility, and so will be able to explore issues such as slow thermalization which are important to both recirculating and linear drivers.

IV. STATUS AND INITIAL RESULTS

The injector diode[10], matching section, and straight experiment have been fabricated and are now operating; the layout is depicted schematically in Fig. 2. Fifteen

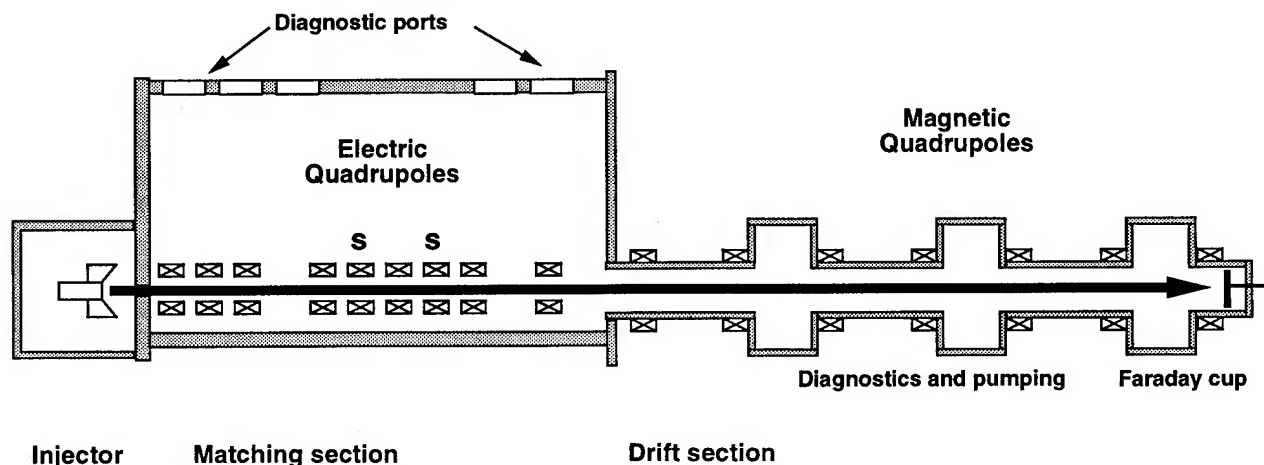


Fig. 2. Linear configuration (overall length 4.568 m from source plate to final Faraday cup).

permanent-magnet quadrupoles have been procured; seven will be used in the straight experiment (a shorter line will serve as the link from matching section to ring). The mechanical design of the "half-lattice period" is nearly complete.[11]

The electrostatic-quadrupole matching section gives the circular beam from the diode an elliptical cross-section, suitable for alternating-gradient transport in the transfer line and the recirculator. A section of the SBTE apparatus from LBL was adapted by EG&G to serve this function. The voltages applied to the various quadrupole elements in order to obtain a matched beam were derived using an envelope calculation and range from ± 1.8 to ± 4.0 kV. The fifth and seventh elements are intended for minor beam steering rather than for focusing. Insertable Faraday cups are located after the third and ninth elements.

Time-resolved measurements of beam properties have been obtained at various locations throughout the matching and magnetic transport sections. The current has been measured using Faraday cups at positions .67 and 1.9 m downstream of the diode source in the matching section, as well as at a position 3.16 m downstream in the magnetic transport section. An energy analyzer developed at LBL (consisting of curved electrostatic plates, across which various potential differences are placed) was located 1.75 m downstream of the source. A two-slit scanner was placed at positions .2 and 1.6 m downstream of the source, providing measurements of emittance, beam radius and beam centroid location.

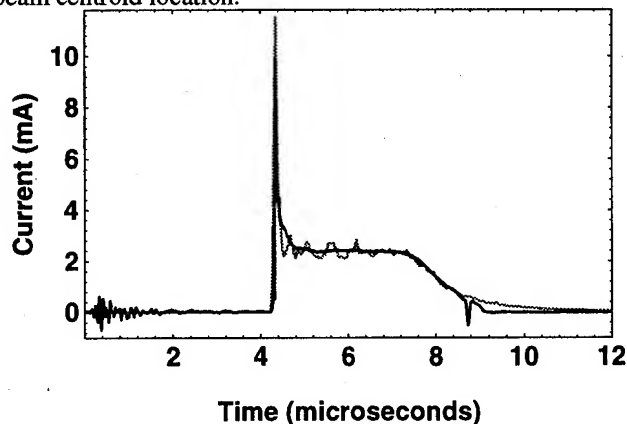


Fig. 3. Experimental (black) and simulated (gray) current.

Figure 3 shows an example of the current vs. time at the second Faraday cup location. Also plotted are results from the 1-D Code HINJ[12] showing close agreement between simulation and experiment. The plot shows a large current spike at the head of the pulse. The spike arises because the rise time of the diode voltage (about 1 μ s) is longer than the ideal rise time of 0.48 μ s.[13] With the slower rise time, particles emitted at the beginning of the pulse have significantly lower energy than particles emitted subsequently and so particle overtaking occurs. A modification of the pulser circuitry to halve the rise time is planned. The code results are slightly noisier than the experiment; this results from a numerical deconvolution of the voltage waveform (to account for time lags in the voltage monitor), which introduced noise into the voltage waveform used by the code. Shown in Fig. 4 is a

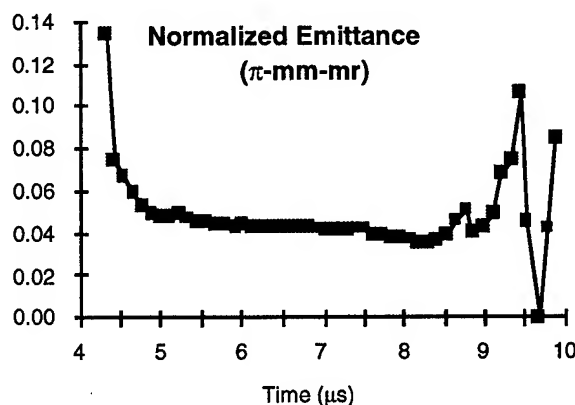


Fig. 4. Normalized emittance at end of matching section

measurement of the horizontal normalized edge emittance (4σ rms) at the end of the matching section. The high initial value appears to be due to the instantaneously high line-charge density.

REFERENCES

- [1] J. J. Barnard, F. Deadrick, A. Friedman, D. P. Grote, L. V. Griffith, H. C. Kirbie, V. K. Neil, M. A. Newton, A. C. Paul, W. M. Sharp, H. D. Shay, R. O. Bangerter, A. Faltens, C. G. Fong, D. L. Judd, E. P. Lee, L. L. Reginato, S. S. Yu, and T. F. Godlove, "Recirculating Induction Accelerators as Drivers for Heavy-Ion Fusion," *Phys. Fluids B: Plasma Physics* **5**, 2698 (1993).
- [2] A. Friedman, R. O. Bangerter, and W. B. Herrmannsfeldt, "Progress in Heavy-Ion Drivers for Inertial Fusion," *Proc. IAEA Tech. Comm. Mtg. on Drivers for Inertial Confinement Fusion*, Paris, Nov. 14-18, 1994.
- [3] R. O. Bangerter, "The Induction Approach to Heavy-Ion Inertial Fusion: Accelerator and Target Considerations," *Il Nuovo Cimento* **106 A**, N. 11, 1445-1457 (1994).
- [4] H. C. Kirbie, W. R. Cravey, S. A. Hawkins, M. A. Newton and C. W. Ollis, "A FET-Switched Induction Accelerator Cell," *Proc. Ninth Int. Pulsed Power Conf.*, IEEE Cat. No. 93CH3350-6 p. 415 (1993)
- [5] T. J. Fessenden *et al.*, *these Proceedings*.
- [6] A. Friedman, D. P. Grote, and I. Haber, "Three-Dimensional Particle Simulation of Heavy-Ion Fusion Beams," *Phys. Fluids B: Plasma Physics* **4**, 2203 (1992)
- [7] J. J. Barnard, H. D. Shay, S. S. Yu, A. Friedman, and D. P. Grote, "Emittance Growth in Heavy Ion Recirculators," *Proc. 1992 Linear Accel. Conf.*, Ottawa, Ontario, Canada, AECL-10728, 229(1992).
- [8] D. P. Grote *et al.*, *these Proceedings*.
- [9] F. J. Deadrick *et al.*, *these Proceedings*.
- [10] S. Eylon *et al.*, *these Proceedings*.
- [11] V. Karpenko *et al.*, *these Proceedings*.
- [12] J. J. Barnard, G. C. Caporaso, S. S. Yu, "1-D Simulations of Heavy-Ion Injectors," *Proc. 1993 Particle Accel. Conf.*, Washington, DC., May 1993, **1**, 712.
- [13] M. Lampel and M. Tiefenback, "An Applied Voltage to Eliminate Current Transients in a One-Dimensional Diode," *App. Phys. Lett.* **43**, 57 (1983).

THREE DIMENSIONAL SIMULATIONS OF A SMALL INDUCTION RECIRCULATOR ACCELERATOR*

D. P. Grote and A. Friedman, Lawrence Livermore National Laboratory, Livermore, CA 94550 USA,
and I. Haber, Naval Research Laboratory, Washington, DC 20375-5346 USA

Abstract

A recirculating induction accelerator has potential cost advantages for a heavy-ion fusion driver. In order to explore the physics and technological issues, a small prototype recirculator is being built[1]. The three dimensional particle-in-cell code, WARP3d[2], is being used in the design and analysis of the experiments. WARP3d is used to examine the behavior of the beam in the electric dipoles and in the non-linear fields associated with the accelerator lattice elements. The dipoles have focusing and fringe fields which can adversely affect the beam quality. Both single particle and full beam dynamics are examined in the dipoles using realistic geometries. Dipole plate designs which minimize the adverse effects are described. The non-linear fields associated with the permanent magnetic quadrupoles have been included in the simulations. They were found to have little effect on the quality of the beam.

I. WARP3d

The realization of heavy ion driven inertial fusion requires a detailed quantitative understanding of the behavior of high-current ion beams. The three-dimensional particle-in-cell simulation code WARP3d is used to study the transport and acceleration of space-charge dominated ion beams in present-day and near-term experiments, and in fusion drivers. WARP3d includes a number of novel techniques and capabilities that both enhance its performance and make it applicable to a wide range of problems. The techniques include a method for sub-grid scale resolution of conducting boundary locations in the solution of Poisson's equation, a warped coordinate system to model accelerator bends, and "residence corrections" to ensure that particles receive the correct impulse from sharp-edged finite-length external fields whose edges are intercepted at different times during a time step. The capabilities include the ability to model the time-dependent accelerator gap fields used for axial beam confinement and compression, application of field multipole components as a function of axial location (or along with the residence correction for hard-edged elements) and multi-species beams. WARP3d is built on top of the Basis[3] system which allows interactive (run time) control of the code and access to its internal database.

II. Induction Recirculator

A small scale recirculating induction accelerator is being built to study beam dynamics in a recirculating accelerator and to examine various engineering design issues. The accelerator was designed to have beam dimensionless parameters relevant to those of a driver. With a circumference of 14.4 m, there are 40 half

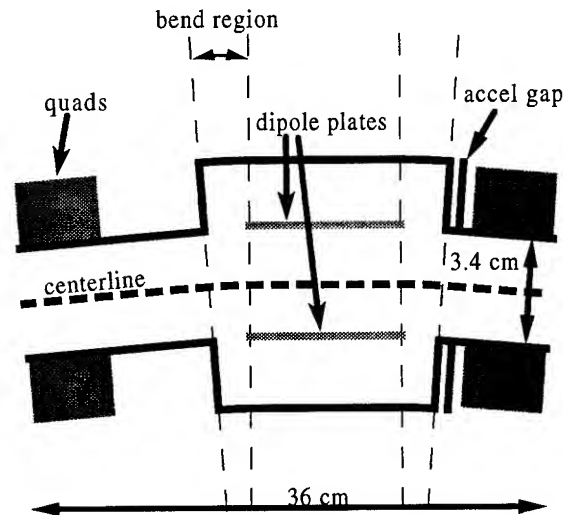


Figure 1. The top view of the geometry of the recirculator half lattice period as used in WARP3d.

lattice periods, each with a permanent magnetic quadrupole, an electric dipole, and an induction acceleration gap. A beam of singly charged potassium ions will be accelerated from 80 to 320 keV over 15 laps, at a current increasing from .2 to .8 Amps. With a low emittance, the beam behavior is space-charge dominated. As designed, the phase advance is initially depressed from 72° to 16° .

III. Electric Dipoles

To make the construction of the recirculator easier and less costly, electric dipole plates were chosen to bend the beam. The length of the plate is constrained by the amount of space available for focusing and bending the beam. The maximum length that would fit is roughly one and a half times the plate separation. Also, the ends of the plates are near the structure supporting the quadrupole magnets. With the height of the plates limited similarly, the plates are nearly square. As a result of the constraints, there are significant nonlinear fields produced by the dipole plates.

Analysis of the dipoles' effect on the behavior of the beam calls for self-consistent simulations which include both the fields produced by the plates and the self-fields of the beams. WARP3d was used to carry out the simulations. Figure 1 shows the layout of the half lattice periods as used in the simulations.

The dominant nonlinear component of the field from the dipole plates is the sextupole component, $\phi \propto r^3 \cos(3\theta)$. With flat plates, the sextupole rapidly alters the beam shape. After one quarter of a lap the transverse profile of the beam becomes markedly triangular. The addition of ridges on the top and bot-

*Work performed under auspices of U.S. DoE by LLNL and NRL under contracts W-7405-ENG-48 and DE-AI02-93ER40799, DE-AI02-94ER54232.

tom of the plates can alter the sextupole component. The ridges that are typically added to dipole plates have a height that is 10% of the plate separation and minimize the sextupole induced by finite plate height[4]. However, in this case, because the axial fringe fields also introduce a significant sextupole, minimizing the sextupole due to finite plate height only is not satisfactory. The ridges have to be made larger, driving the sign of the sextupole in the center of the plates negative so that the average of the sextupole over the lattice period is minimized. The height of the resultant ridges is roughly 30% of the plate separation.

The transverse variation of the potential across the beam in the dipole gives rise to a focusing effect in the plane of the bend. The outer edge of the beam slows down in the dipole and is bent more, whereas the inner edge of the beam speeds up and is bent less. The result is a focusing of the beam. There is also a focusing (or defocusing) in the plane out of the bend from the vertical fringe fields. The combination results in different phase advances in the two planes. Shifting the plates radially, i.e. in the plane of the bend, changes focusing in both transverse directions; an outward shift lowers the in-plane focusing and raises the out-of-plane focusing. The plates can be shifted so that the phase advance is the same in both planes.

The change in potential along the beam centroid in the dipole changes the speed of the beam in the dipole, changing the overall timing of the beam. If the resulting timing change is not included in the timing of the axially confining fields, significant line charge waves will be launched from the ends of the beam. The change in the timing can be controlled by adjusting the radial location of the dipole plates, which changes the location of the potential in the beam relative to ground. There is a radial plate position which minimizes the timing change, avoiding the necessity of having to include the change in the accelerator timing.

Unfortunately, the plate location giving matched phase advances and the plate location giving zero timing change do not coincide. Further plate shaping is therefore needed. With the plates located to minimize the timing change, the in-plane focusing is larger than the out-of-plane focusing. The plates can be curved out of the plane of the bend to increase the vertical focusing.

The plate shape has been tuned to minimize the effects described above. The gridded representation of the plate developed is shown in figure 2. The undepressed phase advances in both planes are near 79° with a phase advance with quadrupoles only of 72° . With a beam energy of 80 kV, the outer plate is held at 6889 V and the inner plate is held at -6262 V. The design was arrived at by iteratively adjusting the curvature and ridges until the in-plane and out-of-plane focusing matched, and then adjusting the radial location of the plates and the voltages on the plate to bring the timing change to zero.

IV. Simulation Results

WARP3d is being used to simulate the beam in the recirculator for 15 laps. Typically, the beam, which is about 3.5 half-lattice periods or $2 \mu s$ long, is made up of 100,000 simulation particles. The field grid has dimensions 32×16 in the transverse plane and 128 cells axially, covering four half lattice periods. The symmetry is taken advantage of and only the top half of the accelerator is simulated, allowing the use of half the number of grid cells

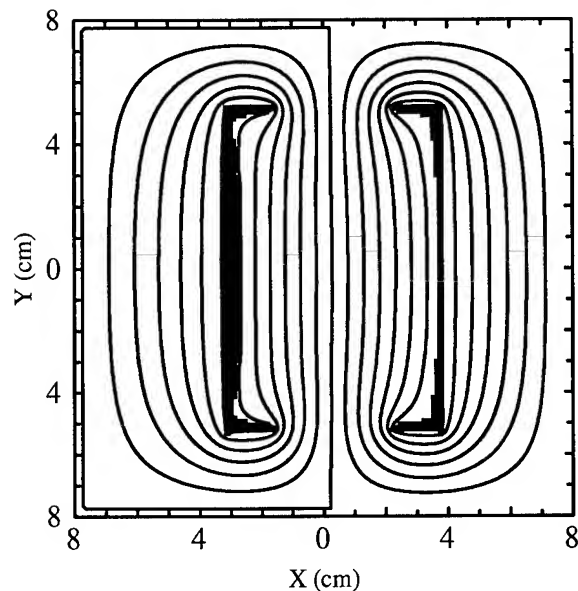


Figure 2. The optimized design of the dipole plate, minimizing emittance growth. The beam goes into the page and will be bent to the left. The lines are contours of constant potential.

in the vertical direction. The quadrupoles are modelled as hard edged, with no nonlinear components.

The dipole plates are modelled fully self-consistently except for image fields effects. The field from the dipole plates is calculated with Laplace's equation including the detailed shape of the plates and the surrounding conductors with SOR. During the simulation, the pre-calculated field of the dipole is overlaid on top of the beam self-fields. The self-fields are calculated with a 3-D FFT, which is faster than SOR, in a rectangular box with the images on the sides. The transverse dimensions of the box are the same as the plate separation. This only approximates the true images on the dipole plates and quadrupole pipe, but the images are small and the difference is negligible.

The accelerating schedule and axially confining fields give a beam with constant physical length. The accelerating field is ramped up linearly in time when the beam is in the first lap. After that, the field is held constant. The axially confining fields, which are not varied throughout the simulation, are continuously applied to the beam ends.

In the simulations, there is an initial increase in emittance on the order of 50% as the beam matches itself from a straight path to a curved path. This growth is due to a separation of the particles with differing axial velocities in the bends producing nonlinearities in the space charge[1]. The nonlinearities thermalize producing an increase in emittance. The amount of growth agrees with theoretical analysis[5].

The simulations showed that the behavior of the beam is sensitive to the design of the dipole plates. Flat plates with no ridges very rapidly produce a triangular shaped beam. Shifting the plates by 2 mm radially without including the resulting timing change in the timing of the axially confining fields produces line charge waves on the order of 10%. When the in-plane and out-of-plane focusing are not matched, the beam becomes ellip-

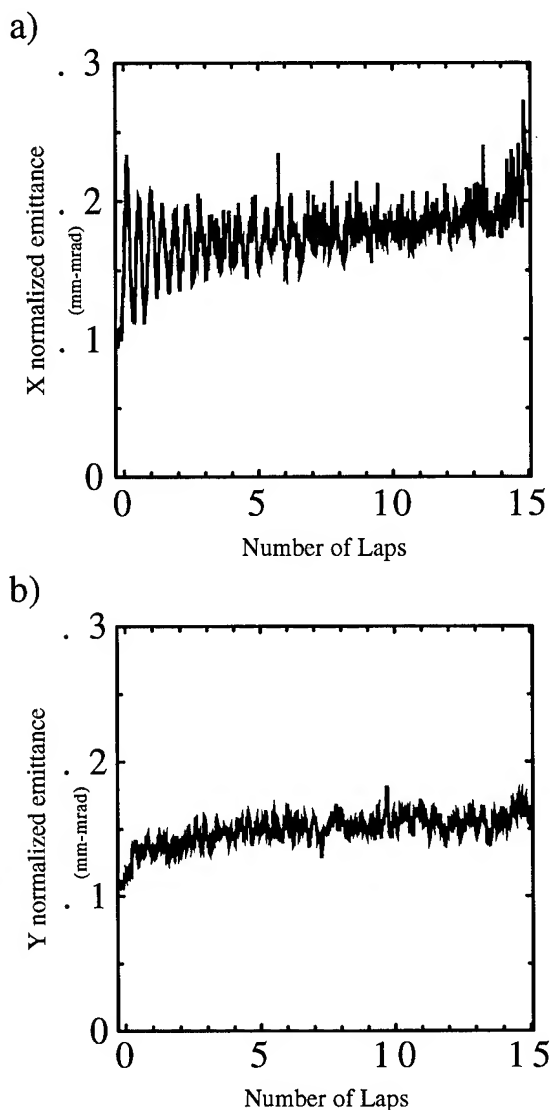


Figure 3. Time histories of the mid-pulse normalized emittance a) in the plane of the bend and b) out of the plane of the bend with the optimized design of the dipole plates. There is little growth after the initial increase which is due to the beam matching to the bends.

tical and the emittance grows more rapidly in the direction with the larger size.

Use of the tuned plate shape described in the previous section corrects the problems. In a simulation over the 15 laps, there was little growth in the emittance after the initial growth from matching to the bends. Figure 3 shows the time history of the x and y normalized emittances at the beam mid-pulse. The line charge waves were negligible.

In the experiment, pulse compression will be done to increase the line charge, and the transverse size of the beam will correspondingly grow. The simulations do not yet include pulse compression. Two cases were therefore simulated, one with the size of the simulated beam set to the size of the beam as it enters the recirculator, and the other with it set to the larger size of the beam after it exits the recirculator and after pulse compression.

Figure 3 shows the results of the former case. The latter case has the same result, little emittance growth after the initial increase.

V. Nonlinear Fields of the Quadrupole Magnets

Estimates were made of the nonlinear fields associated with the permanent magnetic quadrupole design[6]. These fields were included in multi-lap simulations and did not increase the growth of the emittance. These simulations did not include the nonlinear fields which would result from misalignments in the magnet.

VI. Conclusions

A simulated beam was successfully accelerated in a model of the planned small induction recirculator for 15 laps with minimal growth in transverse normalized emittance. There was little further emittance increase after the initial unavoidable increase due to matching to the bends. Critical to the success was the design of the electric dipole plates. They were designed to minimize the effects resulting from the plates' separation being comparable to their length and from the plates being close to the surrounding conductors. The design also has the in-plane and out-of-plane focusing from the dipoles the same.

References

- [1] A. Friedman et. al., these Proceedings.
- [2] A. Friedman, D. P. Grote, and I. Haber, "Three-dimensional particle simulation of heavy-ion fusion beams," *Phys. Fluids B* 4, 2203 (1992).
- [3] P. F. Dubois et. al., "The Basis System," LLNL Document M-225 (1988).
- [4] Andris Faltens, *Private communication* (1994)
- [5] J. J. Barnard, H. D. Shay, S. S. Yu, A. Friedman, D. P. Grote, "Emittance Growth in Heavy Ion Recirculators," 1992 Linear Accelerator Conference Proceedings, AECL 10728, p. 229 (1992).
- [6] Steve Lund, *Private communication* (1994)

A Dynamic Momentum Compaction Factor Lattice in the FERMILAB DEBUNCHER Ring

D.N. Olivieri, M. Church, and J. Morgan
Fermi National Accelerator Laboratory*
P.O. Box 500
Batavia, IL 60510

I. Introduction

The primary purpose of the Fermilab Debuncher ring is twofold; to accept approximately $7\mu\text{A}$ /pulse of 8.9 GeV antiprotons (\bar{p}) downstream from the production target and to subsequently reduce the momentum spread, from $\Delta p/p \sim 4\%$ to $\sim .2\%$, and transverse emittance, from $\epsilon \sim 20\pi$ mm-mrad to $\sim 5\pi$ mm-mrad, for improved transfer and stacking performance in the Antiproton Accumulator ring. To accomplish this objective, rf- cavities are used to rotate and adiabatically debunch the beam on the time scale of ~ 40 msec, after which stochastic cooling systems, both transverse and longitudinal, are used to reduce the transverse emittance and longitudinal momentum spread throughout the remainder of the $\sim 2.4\text{sec}$ \bar{p} production cycle.

In the initial and present design of the Debuncher ring, the momentum compaction factor (α), or equivalently the slip factor, $\eta = \alpha - 1/\gamma^2$, was chosen to have a value which is a compromise between the two competing functions of the ring - that of accepting and debunching a large number of \bar{p} s/pulse and subsequently employing stochastic cooling feedback systems to pre-cool before injection into the Accumulator. The goal of this experiment is to reconcile this compromise by changing η between two desired values during each \bar{p} production cycle.

II. On Magnetic Optics Modifications to the FNAL Debuncher

The momentum compaction factor is the difference in the perimeter between the orbits of particles with differing momentum from that of the ideal design particle. Thus,

$$\frac{\Delta C}{C} = \alpha \frac{\Delta p}{p}$$

$$\alpha = \frac{1}{C} \oint \frac{D(s)}{\rho(s)} ds$$

These relations suggest the following simple fact, that in order to modify α of an existing lattice, it is sufficient to change the dispersion function.

The Debuncher ring has a circumference of 505 m and is composed of a sixfold symmetric separated function optical lattice[1]. The basic arrangement of the ring consists of three long dispersion free straight sections together with arc sections consisting of 57 regular FODO achromats in total. Transition from the arcs to the straights is accomplished with a missing magnet scheme to produce a strictly zero horizontal dispersion in

the straight sections for the purpose of locating rf- cavities and stochastic cooling devices. As a result of the dispersion killer chosen, each regular FODO cell has a phase advance of $\pi/3$. The ring operates on the positive side of transition with large dispersion in the arcs, thus limiting the momentum acceptance upon injection. The dispersion function in the arcs reaches a maximum value of 2.4 m and the maximum transverse beta functions are approximately 14 m with tunes typically operated at 9.79 horizontal, and 9.77 vertical.

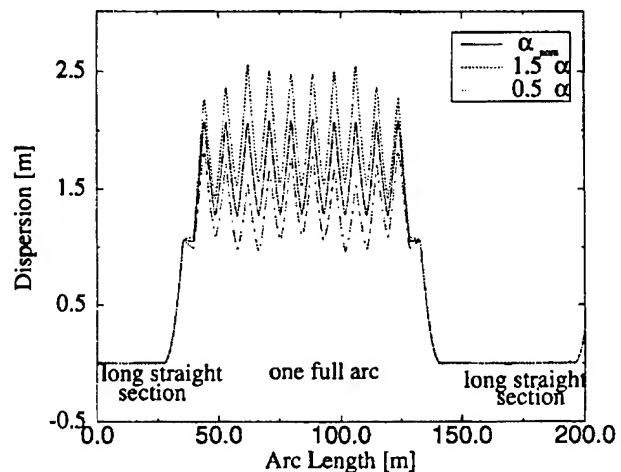


Figure 1. Comparison of the dispersion function for different design cases to that of the nominal case with α (nominal)

To accomplish the task of uniformly changing the dispersion function in the arc sections, while maintaining a large number of practical constraints, interleaved localized dispersion waves were created by perturbing the strengths of judiciously chosen quadrupole pairs separated by π in nominal betatron phase advance. Amongst some of the constraints were the requirements that: (i) perturbations to any quadrupole should not exceed $\approx \pm 20$ Amps due to the present power supply limitations, (ii) the tunes shifts in either plane may not exceed $\Delta\nu_{x,y} \sim \pm .005$ to avoid resonance crossing, (iii) the dispersion function remain strictly zero in the straight sections due to the location of stochastic cooling devices and rf- cavities, and (iv) the β functions not exceed 10% of their nominal values (except at the locations of the stochastic cooling pickup and kickers, for which one desires a large amplitude for increasing the sensitivity factor). Together with these constraints is the very important constraint that the phase difference between the pickup and kicker either remain the same or move closer to optimal for the correct phasing of the stochastic cooling system.

*Operated by the Universities Research Association, Inc. for the U. S. Department of Energy

A comparison of the dispersion functions in one sector for the nominal lattice and that for the lattice with a value of α 1.5 times larger is given in Figure 1. The lattice design for both large and small α maintain six-fold symmetry. Furthermore, the lattice designs for each case are symmetric in the required δI of each quadrupole from the nominal design lattice, i.e. it is merely a change of sign of each δI in the change from $.05\alpha \rightarrow 1.5\alpha$.

A. Sensitivity to the Resonance Lines

A change in dispersion function in the arcs is accompanied with relatively large tune shifts, which must be removed through adjustments of the quadrupole fields in the zero dispersion straight sections. Thus it is required to understand the features of the resonance structure in the vicinity of the operating point. In particular, if the tunes are not properly corrected while differentially changing the lattice at each step with non-linear ramps, relatively large tune excursions can occur during the ramping process for which beam loss may result due to resonance crossing. An experimental investigation was undertaken to map out the amplitude and widths of the resonances throughout a relatively large area of tune space (± 1 units in both planes) sufficient for the purposes of this project. The major resonance lines together with their relative width and strength are given in Table 1. Avoiding these resonances during the ramping process puts heavy restrictions on allowable tune excursions.

Resonance.	% Beam Reduction	Width in tune units
2/3	~ 100	$\pm .006$
3/4	~ 60	$\pm .003$
4th order sum	~ 45	$\pm .002$

III. On Improvements to the Stochastic Cooling of Particle Beams

With each revolution, the Schottky signal from a given group of particles is sampled, and that signal is applied (with a large gain) back upon the same sample of particles downstream from the pickup. If there is a large spread in revolution frequencies due to a large dispersion, then particles from adjacent samples will mix during subsequent turns through the ring. In the limit of complete mixing of particles between different samples, the cooling system would be most effective since it acts upon a statistically independent set of particles upon each revolution. This mixing of particles between adjacent samples is related to the optics of the storage ring through the momentum compaction factor, or equivalently the slip factor ($\alpha = 1/\gamma_t^2$, $\eta = \alpha - 1/\gamma^2$).

A quantity which is useful in quantifying the particle sampling of the cooling system is the mixing factor, M . The mixing factor is the number of turns it takes to mix a sample of particles. Presently, the numerical value of M in the Debuncher ring is approximately 12 at the end of the cooling cycle. An expression for the mixing factor assuming a gaussian distribution function ψ representing the density of particles, momentum spread σ_p/p , and bandwidth W is

$$M = \frac{\psi_0}{2W|\eta|\sqrt{\pi}\sigma_p/p}$$

Increasing the machine η results in a decrease in M , which increases the cooling rate. M appears naturally in the theory of stochastic cooling [2][3][4].

Estimates for an increased transverse stochastic cooling rate, due to the larger α , can be obtained through an integration of the first moment integral of the Fokker Plank equation which describes the time evolution of the transverse density function.

$$\frac{d\epsilon}{dt} = \frac{\psi_0}{N} \sum_l \Re[g_l(\omega_l)T(\omega_l)] - \frac{\pi N}{\Omega} |g_l(\omega_l)T(\omega_l)|^2 [M(\omega_l) + U(\omega_l)]$$

g_l is the gain factor, T_l is the signal suppression, M_l is the mixing factor, U_l is the noise to signal ratio, $\Omega = 2\pi f_0$ is the revolution frequency, and the sum is over the Schottky bands in the cooling bandwidth.

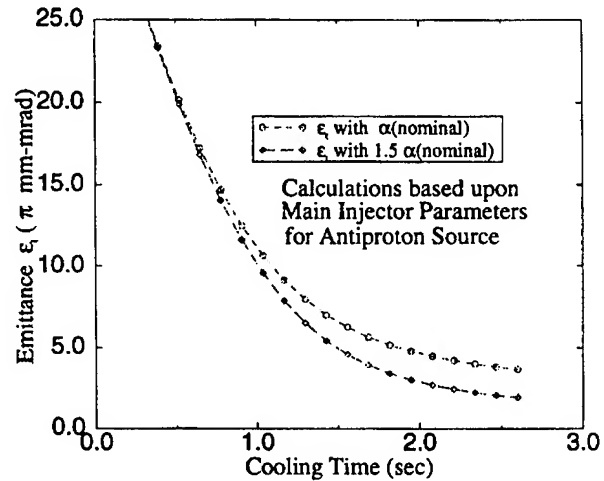


Figure 2. Comparison of the transverse emittance ϵ_t as a function of time for the cases with and without a dynamic momentum compaction factor.

Using model fits to experimental data of the cooling system under the present conditions, Figure 2 compares two cases of emittance cooling with and without the application of a dynamic momentum compaction factor. The theoretical predictions are based upon future design upgrade parameters necessary for Main Injector operation. The model predicts an improvement to the transverse cooling rate of $\sim 15\%$. An improvement to the Debuncher to Accumulator (D/A) transfer efficiency is expected to be nearly commensurate on the basis of Figure 3, in which the increases in the D/A efficiency has been correlated to a smaller beam size prior to transfer. In that figure, quantities are plotted as a function of the amount of time that beam is allowed to remain in the Debuncher, or equivalently the production cycle time. Beyond the improvements in D/A transfer efficiency, there is also sufficient evidence suggesting the Accumulator \bar{p} stacking rate is a strong function of the beam size upon injection.

IV. On a Larger Momentum Acceptance and Better Longitudinal Phase Space Rotation

A reduction of the momentum compaction factor from the nominal design value is expected to have two effects. First, a smaller value of η will allow for a larger momentum acceptance upon injection of antiprotons into the Debuncher. The second effect is to increase the rf-bucket.

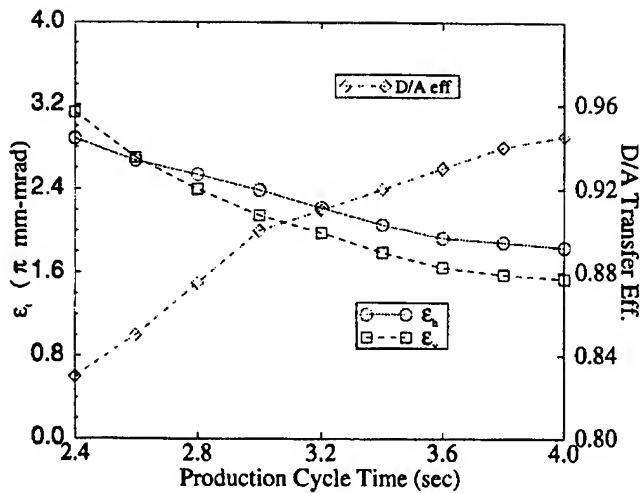


Figure 3. Debuncher to Accumulator (D/A) transfer efficiency as a function of the duration of the Production cycle. Also plotted are the transverse emittance in the Debuncher illustrating the correlation of improved D/A efficiency with decreased beam size.

With regard to the first effect, Figure 4 is a comparison between the beam size for the nominal lattice (α_{nom}) design and that for a design with a $.48 \times \alpha_{nom}$ with an emittance of 20π mm-mrad and $\Delta p/p = 4\%$. Given the reduction in beam size for the small α lattice, a 25% increase in momentum acceptance of antiprotons upon injection is possible.

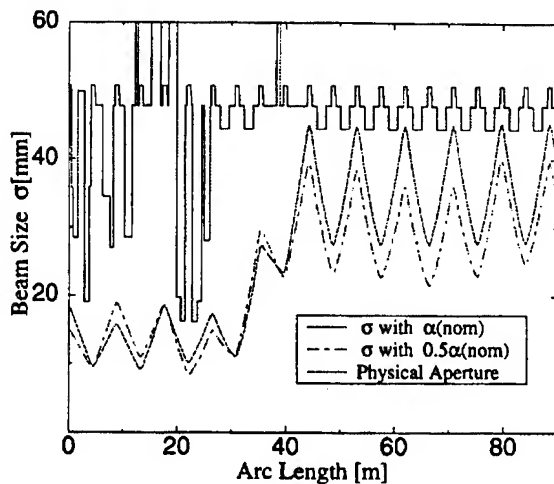


Figure 4. Comparison of the beam size σ between the present Debuncher lattice design having α and that with 0.5α . $\epsilon_t = 20\pi$ mm-mrad and $\Delta p/p = 4\%$

The narrow time structure of the antiprotons inherited by the proton beam after targeting from the Main Ring is exchanged for a narrow energy spread through longitudinal rf- bunch rotation through 1/4 of a synchrotron period in the Debuncher ring.

The longitudinal dynamics can be described by the differential equation

$$\frac{d^2\phi}{dt^2} + \frac{eVh\eta\omega_o^2 \cos \phi_s}{2\pi E_o \beta^2 \gamma} b(\phi - \phi_s) = 0$$

where the synchronous frequency is given by

$$\Omega_s^2 = \frac{eVh\eta\omega_o^2 \cos \phi_s}{2\pi E_o \beta^2 \gamma}$$

For the Debuncher $V = 5\text{MV}$, $f_o = 0.590035\text{MHz}$, and $h = 90$. From these equations, it can be shown that the phase space area of the oscillatory orbits is inversely proportional to $\sqrt{\eta}$. A larger phase space area is beneficial for the rf bunch rotation process to avoid filamentation, which lead to lower debunching efficiencies.

V. Conclusions

Commissioning of the project described in this paper is underway. At the present time, we are implementing only the case for $\alpha \rightarrow 1.5\alpha$. The largest gains of this project, in general, both through an 15% increase in the cooling rate and a large increase ($\sim 25 - 30\%$) in momentum acceptance, are expected to come to fruition in the Main Injector era.

References

- [1] Tevatron 1 Design Report, September 1984
- [2] D. Möhl, G. Petrucci, L. Thorndahl, S. van der Meer, *Physics and Techniques of Stochastic Cooling*, Physics Reports **58**, (1980), 73-119
- [3] J. Bisognano, C. Leemann *Stochastic Cooling*, in Physics of High Energy Accelerators, R.A. Carrigan editor, AIP Conf. Proc. **87**, 583 (1982)
- [4] M. Church, J.P. Marriner *The Antiproton Sources: Design and Operation*, Ann. Rev. Nucl. Part. Sci. 1993, 43:253-95

MECHANICAL DESIGN OF RECIRCULATING ACCELERATOR EXPERIMENTS FOR HEAVY-ION FUSION

V. Karpenko, J. Barnard, F. Deadrick, A. Friedman, D. Grote, S. Lund, J. Meredith, L. Natrass,
M. Nelson, M. Newton, G. Repose, C. Sangster, and W. Sharp
Lawrence Livermore National Laboratory, P.O. Box 808, L-481, Livermore, CA 94550

T. Fessenden
Lawrence Berkeley Laboratory

D. Longinotti and C. Ward
EG&G

I. INTRODUCTION

Recirculating induction accelerators have been studied as a potential low-cost driver for inertial fusion energy. At LLNL, we are developing a small (4.5-m diameter), scaled, experimental machine which will demonstrate many of the engineering solutions of a full scale driver[1]. The small recirculator will accelerate singly ionized potassium ions from 80 to 320 keV and 2 to 8 mA, using electric dipoles for bending and permanent magnet quadrupoles for focusing in a compact periodic lattice. While very compact, and low cost, this design allows the investigation of most of the critical physics issues associated with space-charge-dominated beams in future IFE power plant drivers. Additionally, a straight magnetic-transport experiment is being carried out to test diagnostics and magnetic transport in preparation for the recirculator.

II. DESCRIPTION OF THE RECIRCULATOR

This small recirculator will have an aperture of 68 mm for the focusing element, and a half-lattice period of 360 mm. The full recirculator will consist of 40 half-lattice periods. Figure 1 illustrates a 90° section of the ring. The electric dipoles and quadrupoles and associated stand-off distances occupy the majority of the axial space of the half-lattice period, thereby, dictating its mechanical design (see Fig. 2). The present experimental plans call for accelerating the K^+ ions through 15 laps. To minimize beam losses during the 15

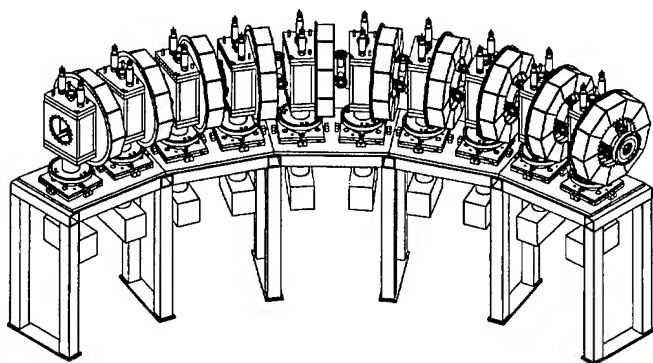
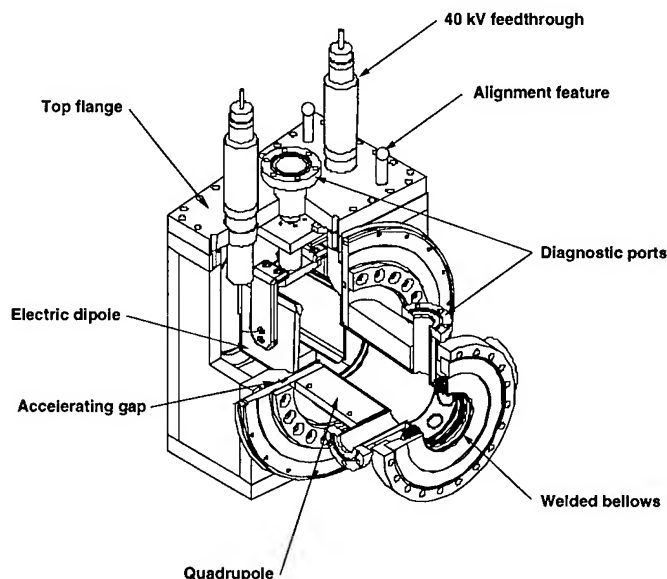


Figure 1. A 90° segment of the recirculator.



40-00-0695-1169 p001

Figure 2. A quarter section view of the half-lattice period illustrating its major features.

laps, a vacuum of better than 10^{-8} torr is required. Each half-lattice period is individually assembled, aligned, and installed on the ring using a coordinate measuring machine and multiple optical surveying transits to meet the demanding 250 μ m positioning tolerance of the dipoles and quadrupoles. The half-lattice periods are mounted on kinematic mounts to facilitate removal for operational reasons without the need for realignment.

III. MECHANICAL DESIGN

The recirculator half lattice period is constructed from two non-magnetic stainless steel subassemblies each of which house the electric dipole and permanent magnet quadrupoles. Space constraints of the electric dipole, quadrupole, induction core, and the ring geometry required dipole vacuum housing to have a trapezoidal shape (see Fig. 3). Investigation into manufacturing techniques revealed that the most cost effective method is to machine six individual plates and

IV. VACUUM DESIGN

The vacuum design requirement for the recirculator of an operating pressure of less than 10^{-8} torr requires the use of metal seals and ultra high vacuum design features. The design of the half lattice period utilizes a number of metal seal designs. Where applicable, conventional copper-sealed knife edge and metal o-ring seals are used. All components will be cleaned and handled following standard UHV practices. Each half lattice period will have a 60 l/s ion pump.

The sealing of the two trapezoid flanges to the dipole body required a unique application of existing metal seal technology. After reviewing a number of metal seal designs for ease of fabrication, reliability, and cost, a version of the knife edge joint was selected. This seal design was adapted by MDC specifically for rectangular flanges. Its application to the trapezoidal shape of the dipole body was natural adaptation. The unique feature of this design is the orientation of the knife edge. Unlike the conventional design, the tapered face of the knife edge points to the interior of the flange. This design feature allows the sealing surface to be machined on a conventional milling machine with a specially ground tool. An additional feature of this process is that the machine marks are essentially circumferential, similar to lathe machining, therefore additional polishing is not required.

The accelerating gap in the half-lattice period consists of a 127 μ m sheet of Kapton sandwiched between two stainless flanges. A single metal o-ring provides the vacuum seal.

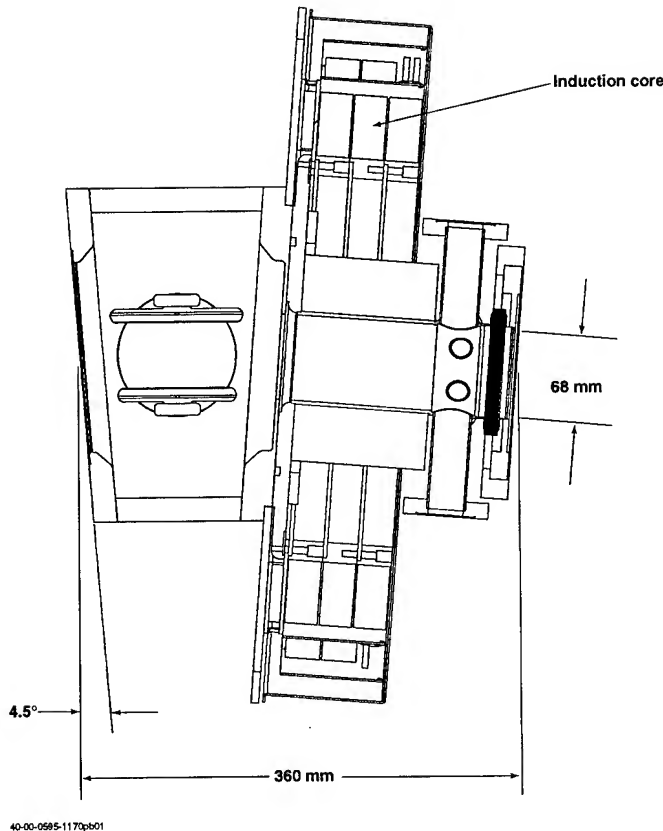


Figure 3. A half section view of the half-lattice period illustrating the integration of the compact design.

assemble them by either welding or vacuum brazing. The dipole is mounted on the trapezoidal top flange. Each of the dipoles is supported by a vacuum-compatible, machinable ceramic. This ceramic mount is in turn mounted to a commercially available optic mount which allows precision roll and pitch adjustments of the plates. The optical mount is mounted to allow two additional translations of the dipole assembly. Two 40 kV feedthroughs and a 32 mm diagnostic port are provided on the dipoles mounting flange. The quadrupole subassembly consists of a precision tube, three 32 mm diagnostic ports, flanges, and a welded bellows. The key design feature is the precision machining of the outside diameter of the tube to locate the quadrupole magnet. The quadrupole magnet is clamped to this surface during assembly. This feature establishes the datum for aligning each half-lattice period to the plane of the ring. The half-lattice period is joined with an insulated, bolted assembly capable of holding off 2 kV. Each of the subassemblies requires heat treating to remove residual magnetism resulting from the welding procedures.

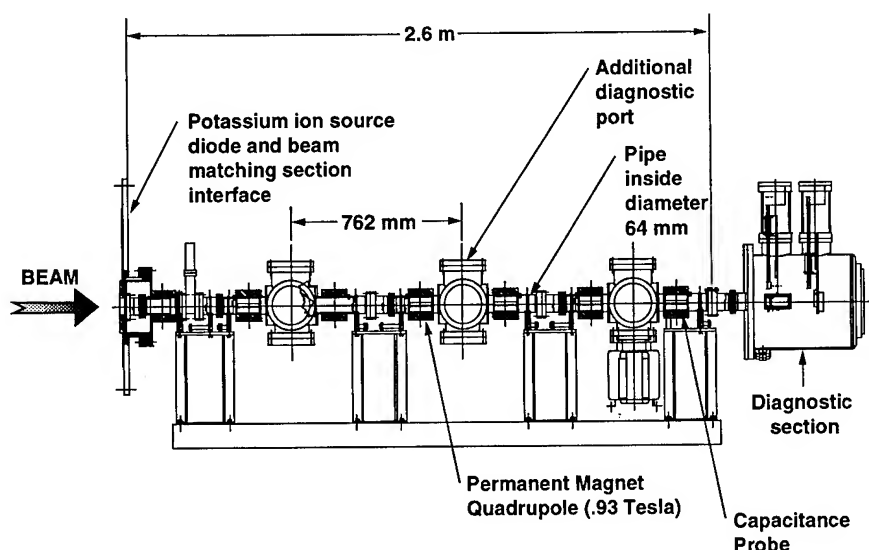
The vacuum connection on the lower trapezoidal flange also serves as the mounting structure for the half-lattice period. A large circular flange at the interface between the ion pump and the bottom spool piece provides the structure for the kinematic mount.

V. ALIGNMENT PROCESS PROCEDURE

The alignment for the recirculator was derived from techniques used for the precision alignment of SLAC and other similar accelerators. The alignment method consists of using multiple optical surveying transits referenced against at least two benchmarks to absolutely position the individual half-lattice periods into the recirculator beam path diameter. The method reduces the chance of propagating errors during assembly and provides the capability for repeatable realignment after performing regular maintenance, upgrades, or disassembly.

The alignment method is comprised of four processes. The first process is the alignment of the beam tube assembly that includes the aligning of the electric dipole and the magnet using a coordinate measuring machine. The second process is alignment of the recirculator platform relative to a benchmark using precision, optical transits, and triangulation. The third process is the mounting and connecting of the beam tube assembly to the recirculator platform, and the final process is the alignment of the beam tubes relative to the plane of the ring.

A critical dimension for the recirculator is the relationship of the dipole center line with the quadrupole axis for each half-lattice. This dimension will be adjusted and measured before installation using a coordinate measuring machine that will project the quadrupole axis by sweeping



40-00-0595-1171 pb01

Figure 4. Linear configuration of the Magnetic Transport Experiment.

out the inner and outer diameter of the beam tube. The next step is to sweep the surface of the electric dipoles and project its center line. The dipole adjustment stage will be used to manipulate the dipole centerline relative to the quadrupole axis. A final check will be made to define the locations of the beam tube, dipole, and the tooling balls mounted on the half-lattice structure. These tooling balls will act as reference targets for the optical alignment during assembly of the recirculator.

VI. MAGNETIC TRANSPORT EXPERIMENT

As a precursor to the development and deployment of the recirculator, it is necessary to study the magnetic transport of intense ion beams. The Magnetic Transport Experiment (MTE) is primarily intended to provide an experimental apparatus to assess the role of electrons in magnetic beam transport. It will also provide a test-bed for the development of intercepting and non-intercepting beam diagnostics and permit characterization of the potassium ion beam before injection into the ring. The MTE consists of three spools, each supporting two recirculator-design magnetic quadrupoles (see Fig. 4). Each spool provides a 35 mm radius beam-tube and access ports to allow insertion of beam diagnostics, and vacuum pumping ports. An entry spool consisting of a beam tube, a single magnetic quadrupole, and a gate valve provides connection to the potassium ion source and matching section. The MTE terminates in a diagnostics module designed to house a Faraday cup detector and a developmental optical diagnostic consisting of a scintillator and imaging system. The MTE is approximately 2.5-m in length, excluding the terminal diagnostics box.

Spool diagnostics for each stage include LBL-designed slit scanners for measuring beam emittance and an LLNL-developed four-lobe capacitive probe. Access ports are designed to permit insertion of the capacitive probe without disassembly of the spool, which permits modifications to be

made with minimal impact. Vacuum pumping is achieved by a 60 liter/second ion pump on each spool, with appropriate provisions for attachment of roughing pumps as required. Vacuum requirements are less stringent than the recirculator since multiple passes of the beam will not occur. Pressures in the range of 1×10^{-6} torr are adequate for this experiment. Pressure will be measured by monitoring ion pump current. The gate valve at the entry stage allows the MTE to be brought up to air separately from the source and matching section, which saves pump-down time and reduces the likelihood of contaminating these stages.

Alignment of the MTE is accomplished by using optical bore-sighting with precision cross-hair targets inserted in the beam tube. Initial alignment will establish the beam line by referencing back to the source diode. Later stages will be added using the established line and referencing back to the source only if problems occur. Alignment tolerances for the beam-line quadrupoles are 250 μ m.

The MTE, which is scheduled to be operational in May 1995, will offer a convenient apparatus with which to explore fundamental physics issues associated with recirculating ion accelerators as well as to develop the unique diagnostics required for multiple lap operation. In addition, it is proving to be a valuable exercise for resolving fabrication, assembly, alignment, and operational issues prior to ring deployment.

VI. ACKNOWLEDGMENTS

This work was performed under the auspices of the U.S. Department of Energy by the Lawrence Livermore National Laboratory under Contract No. W-7405-ENG-48.

VII. REFERENCES

- [1] A. Friedman *et. al.*, *these Proceedings*.

THE PEP-II PROJECT-WIDE DATABASE

A. Chan, S. Calish, G. Crane, I. MacGregor, S. Meyer, J. Wong, Stanford Linear Accelerator Center, Stanford University, Stanford, CA 94309 USA

A. Weinstein, Lawrence Livermore National Laboratory, Livermore, CA 94550, U.S.A.

The PEP-II Project Database is a tool for monitoring the technical and documentation aspects of this accelerator construction. It holds the PEP-II design specifications, fabrication and installation data in one integrated system. Key pieces of the database include the machine parameter list, magnet and vacuum fabrication data, CAD drawings, publications and documentation, survey and alignment data, and property control (see Fig. 1). The database can be extended to contain information required for the operations phase of the accelerator and detector. Features such as viewing CAD drawing graphics from the database will be implemented in the future. This central Oracle database on a UNIX server is built using Oracle*Case tools. Users at the three collaborating laboratories (SLAC, LBL, LLNL) can access the data remotely, using various desktop computer platforms and graphical interfaces.

I. GOALS

The PEP-II Project Management during the R&D phase in 1992 had conceived of using a central database as a tool for the three collaborating labs to:

1. track and ensure quality assurance during construction of the project
2. track down problems faster when they develop
3. facilitate the construction process.

Corresponding systems for the BABAR detector were included in this vision. These functions required an integrated technical and administrative database. Data that existed then was on multiple, disparate desktop computer systems or on paper, which made data less reliable and harder to share amongst users. Project Management decided to support the design and implementation of a central database based on Oracle. Oracle was chosen because it is a modern, relational database; it runs on the client/server

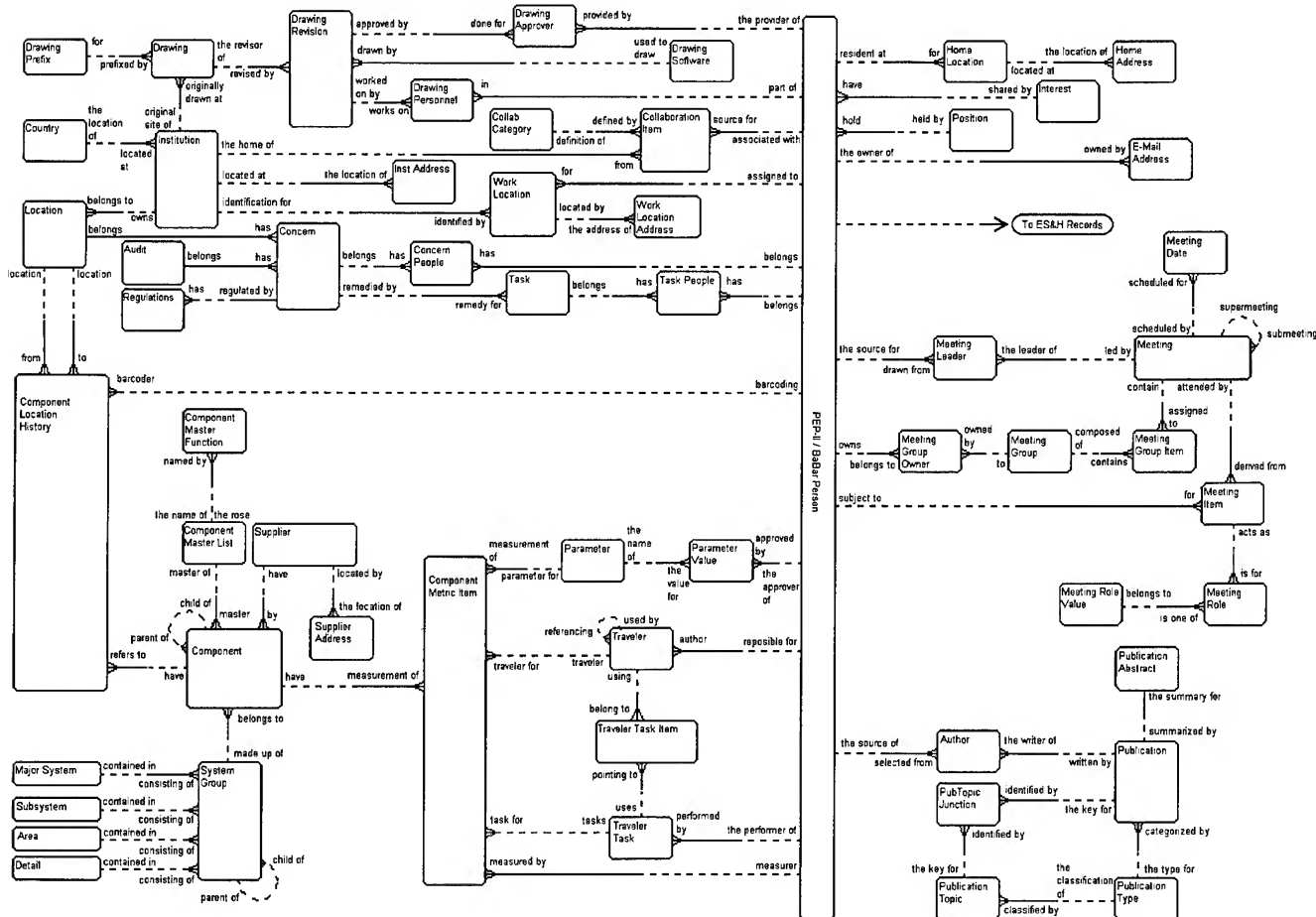


Fig. 1. PEP-II Project-Wide Database Entities and Relationships Diagram generated by Oracle*CASE.

*This work was supported by the U.S. Department of Energy, under contract numbers DE-AC03-76SF00515 and W-7405-Eng-48.

architecture PEP-II is using (clients being Macintosh and IBM-PC, server being UNIX RS6000), it is already site-licensed at SLAC and, in addition, is widely used at other DOE labs.

In July 1992, several Project Managers and programmers visited CERN to learn from their 10-year experience working with Oracle databases. The trip was most useful and we brought away the following key points:

1. have a vision of the overall database from the beginning so hooks are left for further expansion (otherwise data from different systems might not converge later or might be in the wrong format)
2. use Computer Aided System Engineering (CASE) for a structured database analysis, and for faster development and modifications since the database, screens, and reports are one integrated package within CASE rather than loose pieces of code
3. management commitment is crucial
4. involve users in the design from the beginning.

II. IMPLEMENTING KEY PIECES

To deal with the contradiction between the large scope of an enterprise-wide database and the pressing immediate needs of a construction project, we focused on getting key pieces of the skeleton database running right away. Other pieces were tied to management and production needs, as they arose.

Key pieces (see Fig. 2) were:

1. Personnel (most systems in the database have relationships with this entity); this includes a platform-independent e-mail distribution system
2. Drawings (mainly, but not exclusively, CAD)
3. Components

The Components system was the heart of the technical part of the database, and we revised this design many times. In Fig. 1, the Entities and Relationships Diagram shows that for a component to exist in the database it must be entered in the Component Master List entity. The component can have many parameters and their corresponding design values. It can also have a drawing number and a revision

number. Each instance of the component is entered into the Component entity. The component instance is produced according to the order of procedures from a traveler which has a traveler number and revision number. A traveler is a set of fabrication instructions and measurements to manufacture that component instance. In the traveler, the fabrication instructions and measurements are identified by task numbers. The measurement values are stored in the Component Metric Item entity. The Component Location History entity records the history of physical locations of the component instance, with the final designation being its destination in the PEP-II tunnel.

For example, a Component Master List entry of PEP-II High Energy Ring (HER) dipole magnet will have design parameters like Bdl measured at 650 A. An instance of a component is the HER dipole magnet with serial number 148 (see Fig. 3). It is refurbished according to instructions on traveler number 1, revision number 4. In this traveler, the measurement for Bdl at 650 A is task number 1000032. The Bdl at 650 A (relative to the reference magnet) for magnet serial number 148 is 0.99167.

We have tested this Components design with PEP-II magnet and vacuum systems, and the BABAR calorimeter crystals system. Through these normalized tables relating to the Components system, we are able to retrieve fabrication and measurement data by many criteria. The users can query against views that we have built which join these normalized, but fragmented, tables together. Data can also be dumped from the database by the Clear Access program into many other software packages preferred by the users, like Microsoft Excel (see Fig. 4).

Important data that are under change control, like changes in parameter values, are journaled by the database. Historical data for the refurbished PEP components are also stored in the Components system.

III. USER INTERFACE ISSUES

A Graphical User Interface (GUI) that is intuitive and easy to use is key to the PEP-II Project Database being widely adopted by the Project Management and the general user community. In fact, while the database means solid design of entity relationships and table definitions to the programmers, to the users the screens and reports interface is the database. Therefore, we have tried to quickly give key pieces of the database to the users so that they can test the interface and the data. CASE has been an important part in shortening this development cycle. Although using CASE requires a greater investment in startup time (more efforts at design and populating common tables), it is easier later to add modules to the enterprise-wide database and respond to user modifications.

Since a construction project like PEP-II has a tight schedule, generally we do not have the luxury of having sufficient analysis time with the engineers and physicists to gather their requirements. We had to rely on very short

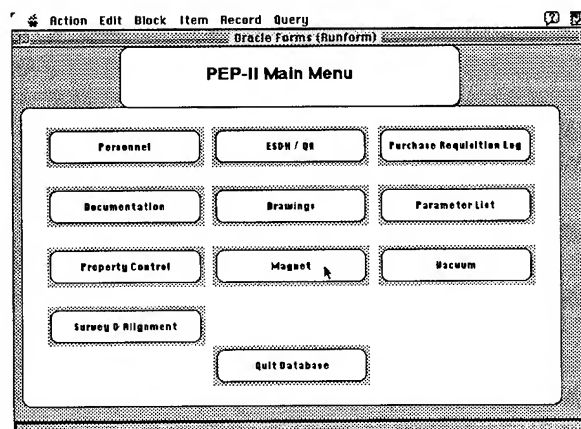


Fig. 2. Main Menu from Oracle Forms4.

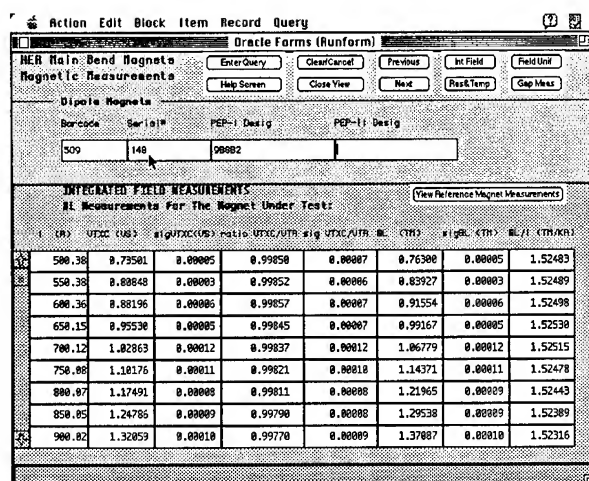


Fig. 3. Bdl measurements for HER Dipole Magnet serial number 148 from Oracle Forms4

meetings for analysis, followed by developing the screens and reports based on what we hope was close to 80% correct in the relationships and functions. Time and again, the users told us that they themselves have only a vague idea of what they want. They need to play with the interface in order to know what an enterprise database will do, and to be able to give us feedback to correct the initial design. So in our situation, the textbook case of heavy up front investment to get as close as possible to 100% correct analysis is not practical, unlike the situation for mission-critical databases like accelerator controls or banking.

The World Wide Web (WWW) interface to the Project Database that we built in recent months has been very popular. Besides being easy to use and easy to access, WWW can retrieve and join data from Oracle to legacy databases such as SPIRES (see Fig. 5). We see WWW as the preferred interface for systems in our database that have been well tested and have stabilized.

The users at present capture data in a myriad of ways—in Oracle Forms4 screens, in spreadsheets, flat files, non-relational databases, barcode readers—and will continue to

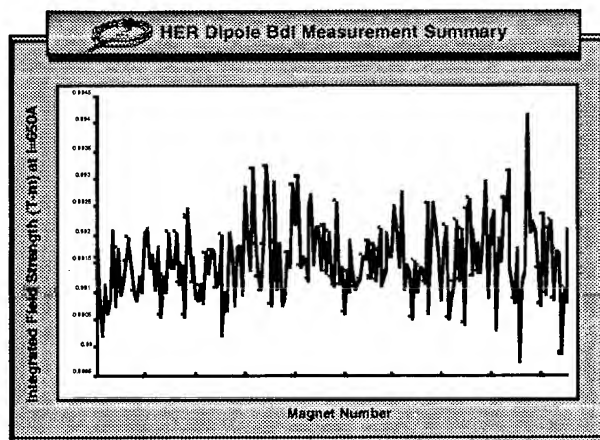


Fig. 4. Graph of Bdl measurements at 650 A for all HER Dipole Magnets from data retrieved by Clear Access and charted in Microsoft Excel.

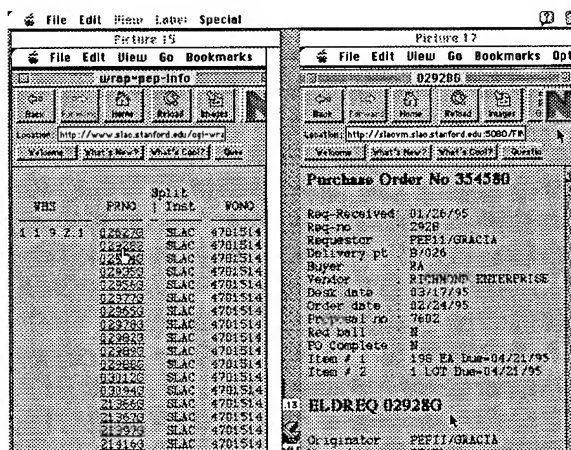


Fig. 5. World Wide Web interface to PEP-II Purchase Requisitions joining Oracle and legacy SPIRES data

do so. Often we work with them to record the data in this intermediate format until our Oracle tools catch up with the analysis and development so that we can reverse-engineer these sub-systems into the Project Database. The use of barcodes and barcode readers in facilitating data capture in PEP-II (from barcoding components to assigning barcodes to buildings) is spreading. In retrieving records from the database, similarly, a variety of interfaces are used and supported. An example of graphing data through Clear Access/Excel is shown in Fig. 4. Other tools used have been WWW, Oracle Forms4 and Oracle Reports.

VII. SUMMARY

During the last three years with a small team averaging two and a half full time employees per year, we have developed nine modules in the PEP-II Project Database. This short development time would not have been possible without the reliance on Oracle*CASE tools. The database is used by many of the ~300 PEP-II (and ~450 BABAR) collaborators from multiple computer platforms and sites. It is a useful tool to facilitate management and coordination of the three labs. It is also helping to maintain quality assurance during the construction of PEP-II. This integration of administrative and technical data is an innovative use within the accelerator community of a central project-wide database.

VIII. ACKNOWLEDGMENTS

We are grateful for the support and vision that Jonathan Dorfan, David Hitlin and Michael Zisman gave us in 1992 which launched this exciting enterprise-wide effort. We also thank the present PEP-II Project Management for their continued support, the Data Administrators of the different systems for helping with the design and for maintaining the integrity of their thousands of records, and our colleagues at CERN from whom we learned much.

CHROMATICITY COMPENSATION – BOOSTER SEXTUPOLES

S.A. Bogacz, Department of Physics and Astronomy, University of California Los Angeles, Los Angeles, CA 90024-1547
K-Y. Ng and J-F. Ostiguy, Fermi National Accelerator Laboratory P.O. Box 500, Batavia, IL 60510

Abstract

Current Booster lattice is studied in the context of full chromaticity compensation in the presence of the sextupole fields generated by the combined function magnets. The sextupole excitation at various energies, found from chromaticity measurements and Booster lattice analysis, was compared with magnetostatic multipole calculations. Both results agree very well and they are consistent with the original design specifications. Two families of correcting sextupole magnets are employed to compensate the sextupole excitations and to adjust the chromaticity (in both planes) to a desired value, which is set by head-tail stability consideration. Analysis of the required correcting sextupole strengths is carried out along the momentum ramp with the measured sextupole excitations of the combined function magnets. The results of our calculation give quantitative insight into the requisite performance of the sextupole magnets. It calls for much stronger sextupole strengths – at the level which can no longer be supported by the present correcting sextupole magnet design.

I. INTRODUCTION – BOOSTER LATTICE

The Booster lattice is made up of 24 identical FDOODFO cells: horizontally focusing magnet – short drift space – horizontally focusing magnet – horizontally defocusing magnet – long drift space – horizontally defocusing magnet, provides room for the RF cavities within the standard cells. Since the lattice half-cell is not symmetric, the beam size is different in each magnet and, consequently, the focusing strengths of F and D combined function magnets are different. The magnets are assembled in 48 modules. Apart from the F and D magnets, each module consists of a choke, a capacitor bank, an ion pump, a set of correction magnets and a beam position monitor. Two trim correction magnet packages are placed in each period. Each package contains a horizontal dipole, a vertical dipole, a quadrupole and a skew quadrupole. There are also two families of correcting sextupoles, but they are not considered a part of the correction packages. All Booster corrections elements are air core magnets.

The nominal betatron frequencies in the horizontal and vertical planes are $\nu_h = 6.7$ and $\nu_v = 6.8$, respectively. Therefore, there are no second or third order structure resonances adjacent to the working diamond. The lattice tunes are set by the quadrupole strengths of the combined function magnets (focusing and defocusing).

As we will show in this study, more sextupole field is needed to compensate the net chromaticity to the desired level set by head-tail instability present in the Booster. This calls for either stronger sextupole magnets, or for larger number of correcting sextupoles. Both options are explored here.

Possible performance improvement of the present air core sextupole magnet (enhanced sextupole strength) can be achieved by surrounding a sextupole magnet with an iron shell (to decrease the reluctance of the exterior magnetic path). The maximum enhancement level is estimated using magnetostatic calculation assuming an infinitely thick shell. The second option – putting additional sextupole correctors at various new locations, which have recently opened was also examined. Both options of stronger sextupole compensation were studied from the point of their impact on the dynamic aperture. No significant second order distortions effects were found, which supports our claim that one can safely add more sextupole field.

II. BOOSTER CHROMATICITY

The integrated sextupole strength, g , of an individual sextupole magnet of length L , in Tesla/m is introduced as follows

$$\Delta x' = - \left(\frac{1}{B_0 \rho} \int_0^L \frac{1}{2} B''(l) dl \right) x^2 = - \frac{1}{B_0 \rho} g x^2, \quad (1)$$

where x, x' are generic coordinates of a transverse phase-space. Here $B_0 \rho$ is the magnetic rigidity and B'' is the second derivative of the vertical magnetic field with respect to x .

Apart from two families of correcting sextupoles, there are also additional sextupole fields contributed by the 96 combined function magnets (F and D). The sextupole contribution from a combined function magnet is due primarily to pole geometry and remanent magnetization. Detailed numerical modeling of the multipole content of the F and D magnet geometries is presented in the next section.

For the purpose of our model, the sextupole content of each F and D magnet can be accounted for in the Booster lattice by inserting identical zero-length sextupoles at five equally spaced locations along each magnet. Significant variation of the horizontal and vertical beta functions along the F or D magnet calls for distributed sextupole contribution, rather than a lumped sextupole inserted at the middle of the magnet.

The goal of the two families of sextupoles (h and v) is to compensate the natural chromaticity, χ^0 , in the presence of the F and D magnet sextupole excitations, S_F and S_D , to some desired value, χ . Assuming that the net chromaticity (in both planes) depends linearly on four independent sextupole sources (S_h, S_v, S_F, S_D) one can quite generally write down chromaticity in terms of eight sensitivity coefficients. Using matrix multiplication this relationship assumes the following compact form

$$\underline{\chi} = \underline{\chi}^0 + \mathbf{M} \begin{pmatrix} S_h \\ S_v \end{pmatrix} + \mathbf{D} \begin{pmatrix} S_F \\ S_D \end{pmatrix} . \quad (2)$$

Here, the underlined symbols denote 2-dim column vectors (their components correspond to the horizontal and vertical planes). The bold face characters, \mathbf{M} and \mathbf{D} , represent two-by-two matrices – one can easily identify the eight sensitivity coefficients with the elements of the two matrices. One can notice in passing, that both \mathbf{M} and \mathbf{D} depend exclusively on the lattice properties. A generic sensitivity coefficient can be expressed in terms of the Twiss functions according to the following relationship

$$M_{\mu\nu} = \frac{1}{2\pi} \sum_{i(v)} \beta_i^\mu D_i^\nu . \quad (3)$$

Here, the summation $i(v)$ goes over locations of all sextupoles of a given family (v), where β_i^μ and D_i^ν are values of the beta function and dispersion at those locations (μ indicates either horizontal or vertical Twiss functions).

Solving Eq.(3) with respect to the correcting sextupole strengths \underline{g} (in Tesla/m) yields the following formula

$$\underline{g} = (B_0\rho) \mathbf{M}^{-1} \left[\underline{\chi} - \underline{\chi}^0 - \mathbf{D} \begin{pmatrix} S_F \\ S_D \end{pmatrix} \right] . \quad (4)$$

The above expression will be used to analyze the required sextupole strength as a function of changing momentum along the Booster ramp. The sensitivity coefficients for all four families of sextupoles, \mathbf{M} and \mathbf{D} , are simulated for the Booster lattice using MAD tracking code [1]

To complete the sextupole strength analysis, outlined by Eq.(4), one has to gain some insight into the sextupole excitations of the combined function magnets (F and D) and their variation with the B-field. This will be discussed in detail in the next section via magnetostatic simulation for both geometries of the F and D magnets.

Another independent way of obtaining information about the sextupole excitation of the combined function magnets comes from the beam measurement. Using available chromaticity measurement [2] with both families of correcting sextupoles (h and v) turned off, one can calculate the sextupole excitations of the F and D magnets at various energies along the ramp. This information could be recovered by solving Eq.(2) with respect to S_F and S_D . The corresponding expression is given below:

$$\begin{pmatrix} S_F \\ S_D \end{pmatrix} = \mathbf{D}^{-1} \left[\underline{\chi} - \underline{\chi}^0 - \frac{1}{B_0\rho} \mathbf{M} \underline{g} \right] \quad (5)$$

III. SEXTUPOLE CONTENT

The bending guide field in the Booster synchrotron is provided by 96 combined function magnets, each

approximately 3 m long. The magnetic field varies from approximately 500 Gauss at injection up to 7000 Gauss at extraction. The magnets are powered in a resonant circuit by a 15 Hz sinusoidal waveform resulting in a field of the form [3]

$$B(t) = B_{\min} + \frac{1}{2} (B_{\max} - B_{\min}) [1 - \cos(\omega t)] . \quad (6)$$

Calculations were performed using a standard finite element code (PE2D). The results confirmed the design dipole and focusing strength. Furthermore, higher multipole values (up to the 24-pole) were also calculated for both F and D magnets. The multipoles are normalized values at 1 inch. For the D magnet, the calculated dipole field was 6.65239×10^2 Gauss with an excitation of 1518 Ampere-turn and 6.18884×10^3 Gauss for an excitation of 14145 Ampere-turn. For the F magnet, 8.31474×10^2 Gauss for 1384 Ampere-turn and 7.68313×10^3 Gauss for 12900 Ampere-turn.

The Booster magnets are operated well below saturation and not surprisingly, the calculations show that there is no significant dependence of the field harmonics on the excitation current. The magnitudes of the dipole and quadrupole components of the field are in excellent agreement with the design values. As explained before, the sextupole component of the bending magnet magnetic field can be extracted from a beam-based chromaticity measurement. The beam-based (measured) [2] values of b_2 in $[m^{-2}]$ are listed as: 2.0×10^{-5} for the F magnet and -6.9×10^{-5} for the D magnet. One can see that the calculated sextupole components at 8 GeV are in good agreement with the values inferred from chromaticity measurements. The distinctive characteristic of the remanent magnetization contribution is that it tends to be relatively independent from the excitation. Therefore, when normalized with respect to the main field, the relative contributions from the remanent magnetization to the magnetic field are expected to gradually be reduced to zero as the excitation current is increased from its minimum to its maximum value.

IV. POTENTIAL IMPROVEMENTS TO AIR CORE SEXTUPOLES

It has been suggested to increase the strength of the existing air-core chromaticity correction sextupole magnets by introducing an external iron shell. The field enhancement effect due to an iron shell can be estimated by using the following result: for a filament of current located at (ρ, ϕ) inside a circular hole of radius R carved into a medium of relative permeability μ the complex coefficients $C_n e^{i\alpha_n}$ – the multipole expansion of the field are given below [4]

$$\frac{C_n e^{i\alpha_n}}{R^{n-1}} = -\frac{\mu_0}{2\pi} \int \frac{dI}{\rho^n} \left[1 + \frac{\mu - 1}{\mu + 1} \frac{\rho^{2n}}{R^{2n}} \right] e^{in\phi} . \quad (7)$$

For a pure sextupole current layer of inner radius a and outer radius b , with a uniform current density given by

$$J_3(\rho, \phi) = J_3 \cos 3\phi \quad (8)$$

one can easily carry out the integration in the right hand side of Eq.(7), which reduces to the following simple expression

$$\frac{C_3}{R^2} = -\frac{\mu_0 J_3}{2} \left[\frac{b-a}{ab} + \frac{\mu-1}{\mu+1} \frac{b^5-a^5}{5R^6} \right]. \quad (9)$$

Under ideal conditions, i.e. $\mu = \infty$ (μ is about 100 for iron) and $a = b = R$, the sextupole field could be doubled. More realistically, let $a \approx b < R$ and $t = b - a \ll R$. The above expression becomes

$$\frac{C_3}{R^2} = -\frac{\mu_0 J_3 t}{2a^2} \left[1 + \frac{\mu-1}{\mu+1} \frac{a^6}{R^6} \right]. \quad (10)$$

It is probably unrealistic to expect an enhancement factor larger than 1.5 in a real device. We note that because the exterior field decays faster as the pole number increases, field enhancement with an iron shell is less effective for a sextupole than for a dipole magnet.

V. HEAD-TAIL INSTABILITY LIMITS

Following Sacherer's argument [5] the inverse growth-time as a function of chromaticity was evaluated for different slow head-tail modes ($l = 0, 1, 2, 3$). The $l = 0$ mode appears to be unstable above transition for small negative chromaticities and might lead to significant enhancement of coherent betatron motion. The obvious cure to stabilize the dipole mode [6] is to maintain appropriate sign (positive) of the net chromaticity. Otherwise, this potentially offending mode can be effectively suppressed by the active damper system. This efficient cure for the $l = 0$ mode obviously does not work in case of the higher modes, since its feedback system picks up only the transverse position of a bunch centroid, which remains zero due to the symmetry of the higher modes. Another possible cure especially effective for the $l \geq 1$ modes would involve the Landau damping, e. g. through the octupole-induced betatron tune spread. Increasing betatron amplitude of initially unstable mode causes increase of the tune spread, which will eventually self-stabilize development of this mode. Therefore, presented head-tail stability analysis suggests adjusting the net chromaticity at -7 ($+7$) units below (above) transition energy.

VI. CONCLUSIONS – SEXTUPOLE STRENGTH

Our analysis of the required correcting sextupole strengths, carried out along the momentum ramp with the measured and simulated sextupole excitations of the combined function magnets, concludes that maintaining the net chromaticity at the level set by head-tail instability limits requires much stronger sextupoles. The required sextupole strength is at the level, which can no longer be supported by the present correcting sextupole magnet design. One has to consider either a new iron core sextupole magnet design, or the upgraded air core magnets placed at all accessible high beta locations – the ‘enhanced’ sextupole layout, which is proposed in this paper. Quantitative assessment of the effect

of the stronger compensating sextupoles on the dynamic aperture, carried out in terms of the distortion functions shows that the requisite sextupole configuration would not significantly enhance the third order resonance stop-band – the dynamic aperture remains at acceptable level.

References

- [1] H. Grote and C. Iselin, *The MAD program users reference guide*, CERN/SL/90-13 (AP), (1990).
- [2] Y. Chao, FERMILAB, EXP-151, (1987).
- [3] J. Lackey, Private Communication.
- [4] E. Willen, P. Dahl and J. Herreza, BNL, AIP Conference Proceedings, (1987).
- [5] F. Sacherer, Proc. 9-th Int. Conf. on High Energy Accelerators, p. 347, Stanford (1974).
- [6] S. A. Bogacz, FERMILAB FN-498, (1988).

OVERVIEW OF $\mu^+\mu^-$ COLLIDER OPTIONS

D. B. Cline, Center for Advanced Accelerators, Physics Department, University of California Los Angeles, Los Angeles, CA 90095-1547 USA

Two dedicated workshops have been held in California on $\mu^+\mu^-$ colliders: Napa in 1992 and Sausalito in 1994. As a result of this and a new round of simulations, as well as μ^\pm cooling experimental plans, it is possible to consider the feasibility of constructing a $\mu^+\mu^-$ collider. However, the energy range and required luminosity must be specified by the particle physics goals before proceeding. Also, the unique features of the physics potential vs LHC must be shown. We will describe the status of this field and the key problems that must be solved before a definite proposal can be made.

I. INTRODUCTION

At Port Jefferson Advanced Accelerator Workshop in the Summer of 1992, a group investigating new concepts of colliders studied anew the possibility of a $\mu^+\mu^-$ collider since e^+e^- colliders will be very difficult, in the several TeV range[1]. A small group also discussed the possibility of a $\mu^+\mu^-$ collider[2]. A special workshop was then held in Napa, California, in the fall of 1992, for this study. There are new accelerator possibilities for the development of such a machine, possibly at an existing or soon to exist storage ring[3]. For the purpose of the discussion here, a $\mu^+\mu^-$ collider is schematically shown in Figure 1. In this brief note we study one of the most interesting goals of a $\mu^+\mu^-$ collider: the discovery of a Higgs Boson in the mass range beyond that to be covered by LEP I & II (~ 80 -90 GeV) and the natural range of the Super Colliders $\geq 2M_Z$ [4,5,6]. In this mass range, as far as we know, the dominant decay mode of the h^0 will be

$$h^0 \rightarrow b\bar{b} \quad (1)$$

whereas the Higgs will be produced by the direct channel

$$\mu^+\mu^- \rightarrow h^0 \quad (2)$$

which has a cross section enhanced by the ratio

$$\left[\frac{M_\mu}{M_e} \right]^2 \sim (200)^2 = 4 \times 10^4 \quad (3)$$

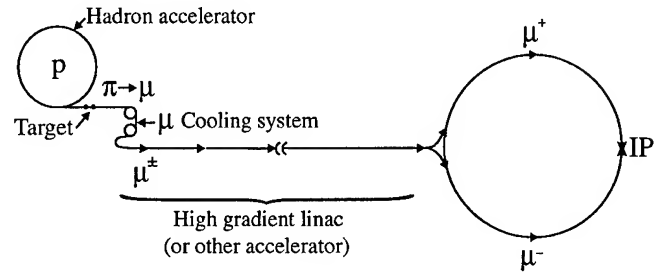


Figure 1: Schematic of a possible $\mu^+\mu^-$ collider scheme - few hundred GeV to few TeV.

much larger than the corresponding direct product at an e^+e^- collider. However, the narrow width of the Higgs partially reduces this enhancement. Recent results suggest that the low mass Higgs is preferred[5](Figure 2a).

In the low mass region the Higgs is also expected to be a fairly narrow resonance and thus the signal should stand out clearly from the background from[3]

$$\begin{aligned} \mu^+\mu^- &\rightarrow \gamma \rightarrow b\bar{b} \\ &\rightarrow Z_{tail} \rightarrow b\bar{b} \end{aligned} \quad (4)$$

If the resolution requirements can be met, the machine luminosity of $\sim 10^{32} \text{cm}^{-2} \text{sec}^{-1}$ could be adequate to facilitate the discovery of the Higgs in the mass range of 100-180 GeV.

Finally, another possibility is to use the polarization of the $\mu^+\mu^-$ particles orientated so that only scalar interactions are possible. However, there would be a trade-off with luminosity and thus a strategy would have to be devised to maximize the possibility of success in the energy sweep through the resonance (see Figure 2b for other physics issues)

II. RESULTS FROM THE NAPA AND SAUSALITO $\mu^+\mu^-$ COLLIDER WORKSHOP

At the Napa meeting (1992) a small group of excellent accelerator physicists struggled with the major concepts of a $\mu^+\mu^-$ collider; some results are published in NIM, Oct. 1994[3]. At the Sausalito (1994) meeting a larger group of accelerator, particle and detector physicists were involved. The proceedings will be published by AIP press in 1995.

The major issue confronting this collider development is the possible luminosity that is achievable. Two collider

energies were considered: 200x200GeV and 2x2TeV. The major particle physics goals are the detection of the Higgs Boson(s) in the s channel for the low energy collider and

Table 1: Parameter list for 400GeV $\mu^+\mu^-$ collider, Sausalito, 1994, 200x200GeV working group report.

Parameter	Symbol	Value
Collision energy	$E_c m$	400GeV
Energy/Beam	E_μ	200GeV
Luminosity	$L = \frac{f_n n_s n_b N_\mu^2}{4\pi \sigma^2}$	$1 \times 10^{31} \text{cm}^{-2} \text{sec}^{-1}$
Source Parameters		
Proton Energy	E_p	30GeV
Protons/Pulse	$N - p$	$2 \times 3 \times 10^{13}$
Pulse Rate	$f - o$	10Hz
μ (prod./accept.)	μ/p	0.03
μ survival	N_μ/N_{source}	0.33
Collider Parameters		
Number of μ /bunch	$N_{\mu\pm}$	3×10^{11}
Number of bunches	n_B	1
Storage turns	$2n_s$	1500 (B=5T)
Normalized emittance	ϵ_N	10^{-4} m-rad
μ -beam emittance	$\epsilon_t = \epsilon_N / \gamma$	5×10^{-8} m-rad
Interaction focus	β_0	1cm
Beam size at interaction	$\sigma = (\epsilon_t \beta_0)^{1/2}$	2. μ m

WW scattering as well as supersymmetric particle discovery[3].

The workshop goal was to see if a luminosity of 10^{32} to $10^{34} \text{cm}^{-2} \text{sec}^{-1}$ for the two colliders might be achievable and useable by a detector. There were five working groups on the topics of (1) Physics, (2) 200x200GeV Collider, (3) 2x2TeV Collider, (4) Detector Design and Backgrounds, and (5) μ Cooling and production methods.

Table 1 gives the parameters and luminosity for the low energy collider. Table 2 gives the somewhat more optimistic parameter list for a 2x2TeV collider from the work of Neuffer and Palmer[7]!

The $\mu^+\mu^-$ collider has a powerful physics reach, especially if the μ^\pm polarization can be maintained. One interesting possibility is the observation of the supersymmetric Higgs Boson(s) in the direct channel (see the

report by V. Barger et al., from Sausalito meeting). The detector backgrounds will be considerable due to high energy μ decays upstream of the detector.

Table 2: Parameter list for 4TeV $\mu^+\mu^-$ Colliders (Neuffer and Palmer)[7].

Parameter	Symbol	Value
Collision energy	$E_c m$	2TeV
Energy per beam	E_μ	200GeV
Luminosity	$L = f_n n_s n_b N_\mu^2 / 4\pi \sigma^2$	$10^{34} \text{cm}^{-2} \text{sec}^{-1}$
Source Parameters		
Proton energy	E_p	30GeV
Protons/pulse	N_p	$2 \times 3 \times 10^{13}$
Pulse rate	f_0	10Hz
μ (prod./accept.)	μ/p	15
μ survival	N_μ/N_{source}	25
Collider Parameters		
Number of μ /bunch	$N_{\mu\pm}$	10^{12}
Number of bunches	n_B	1
Storage turns	$2n_s$	500
Normalized emittance	ϵ_N	3×10^{-5} m-rad
μ -beam emittance	$\epsilon_t = \epsilon_N / \gamma$	1.5×10^{-9} m-rad
Interaction focus	β_0	0.3cm
Beam size at interaction	$\sigma = (\epsilon_t \beta_0)^{1/2}$	2.1 μ m

In the summary of working group 4 it was concluded that these backgrounds might be manageable. One key to achieving a high luminosity collider is the collection of the μ^\pm from π^\pm decays over nearly the full phase space over which they are produced. This is far from trivial and leads to conclusions from groups 2 and 3 that the present uncertainty in luminosity is of order $10^{2\pm 1}$ (at most 4 orders of magnitude, but perhaps, realistically, 2 orders of magnitude, which, unfortunately, spans the range from being uninteresting to being very interesting). Hopefully, before the next meeting this uncertainty can be reduced. Perhaps the most interesting aspect of a $\mu^+\mu^-$ collider is the need to cool the μ^\pm beams over a very large dynamics range. Three experimental programs were discussed and are being initiated to study μ cooling: at BNL, FNAL, and a UCLA group is proposing to study cooling and acceleration in crystals at TRIUMF[8]. One major conclusion of the meeting is that $\mu^+\mu^-$ colliders are complimentary to both pp (LHC)[6] and e^+e^- (NLC) colliders, especially for the Higgs Sector and for the study of supersymmetric particles.

III. THE POSSIBLE LUMINOSITY OF A $\mu^+\mu^-$ COLLIDER

The luminosity is given by

$$L = M \frac{N_{\mu^+} N_{\mu^-} f}{4\pi \epsilon_N \beta^* \gamma} \quad (5)$$

The N_{μ^\pm} depend directly on the μ^\pm production and capture rate (μ/p), f is related to the magnetic field of the collider, ϵ_N the final μ invariant emittance from the final stage of cooling, and β^* will depend on the bunch length (and the longitudinal cooling of the μ^\pm beams), as well as the collider lattice.

We can rewrite the luminosity as

$$L \propto \frac{(\mu/p)^2 B_{\text{collider}} \gamma}{\epsilon_N (\text{final } \beta^*)} \quad (6)$$

In order to increase L we must increase (μ/p) and B and decrease ϵ_N and β^* . At the Napa meeting the best judgment of the group was that $(\mu/p) \sim 10^{-3}$ and $\epsilon_N \sim 1 \times 10^{-5} \pi \text{m-rad}$, $\beta^* \sim 1 \text{cm}$. For the case of $\gamma = 200$, $L = 2 \times 10^{30} \text{cm}^{-2} \text{sec}^{-1}$. If, on the other hand, we use the optimistic values of $(\mu/p) = 0.2$ [7], $\beta^* = 1/3 \text{cm}$, and $\epsilon_N = 3 \times 10^{-5} \text{m-rad}$, we find

$$L = [2 \times (4 \times 10^4) \times 3] L_0 = 4.8 \times 10^{35} \text{cm}^{-2} \text{sec}^{-1} \quad (7)$$

a very large luminosity, never before achieved by any collider! Clearly this must be far too optimistic. It is clear that the (μ/p) ratio is the key parameter of the machine. Table 1 and 2 give some parameters of low energy and high energy colliders.

IV. MUON COOLING EXPERIMENT AT TRIUMF

This phase, the first phase of the experiment TRIUMF, will test the cooling mechanisms summarized in the proposal to TRIUMF. The beam momentum will be about 250 MeV/c unchanneled muons will penetrate the 4cm crystal and the cooling process can be compared for the two. In addition, a higher energy beam tests cooling at the energies considered for realistic collider schemes. The first step of Phase II is to measure initial and final emittances of an unmodified crystal.

To enhance the cooling, we will generate a strain modulation of the planar channels. An acoustic wave of

1GHz is excited via a piezoelectric transducer. We will also detect predicted channeling radiation by surrounding the crystal with CsI scintillation detectors, which are sensitive to X-rays. Recent ideas on crystals and beams are very interesting.[9,10]

The M11 beamline is presently a source of high energy pions[11,12]. Straightforward modification of the beamline will provide a collimated beam of forward-decay muons at high intensity – about 10^6 per second at 250 MeV/c. The longitudinal momentum spread is about 2% FWHM. Assuming optimum tuning of the final focus quadrupole doublet in M11, we can achieve a spot size of 3x2cm with horizontal and vertical divergences of 10m-rad and 16m-rad respectively. The critical angle for planar channeling of μ^+ at 250 MeV/c in silicon is about 7m-rad, extrapolating from proton channeling data. A sizable fraction of the muons should channel through a few centimeters of the crystal.

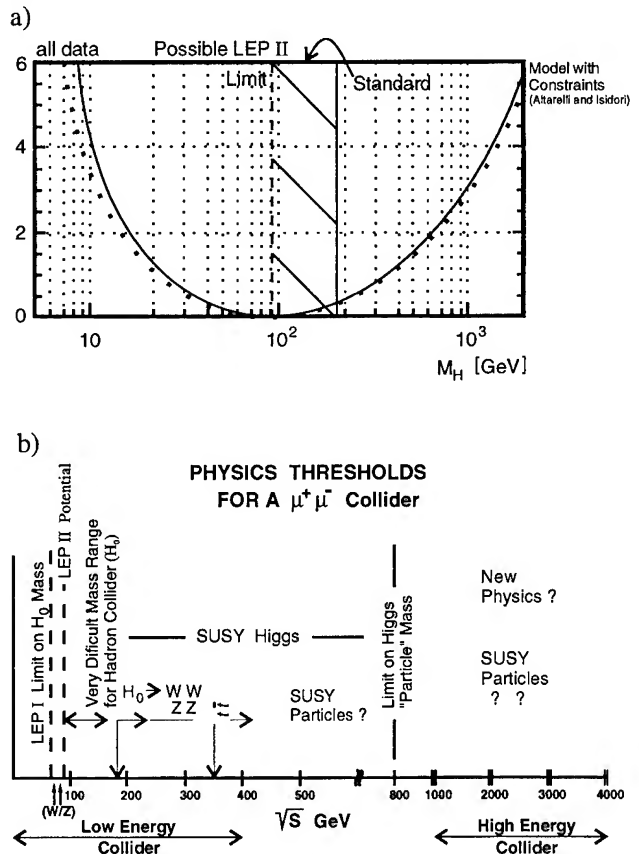


Figure 2 a) Upper and lower bounds on m_{ϕ_0} as a function of m_t , coming from the requirement of a perturbative theory[4]. b) Physics threshold for a $\mu\mu$ collider.

V. HOW TO GET A $\mu^+\mu^-$ COLLIDER STARTED

There are many problems and also possibilities to start a $\mu^+\mu^-$ collider in the USA. For example, if crystal cooling could be used a collider of the type shown in Figure 3 might

be constructed[13]. We list the major issues in the development of a collider in Table 3. In the past the only example of such an innovative machine is the $p\bar{p}$ collider initiated by Cline, McIntyre and Rubbia in 1976[14]. In Table 3 we attempt to make a comparison between these two projects! In my opinion the key problem is comparison with the NLC and LHC.

I wish to thank W. Barletta, D. Neuffer, A. Sessler, R. Palmer, F. Mills, and the other participants of the Napa and Sausalito workshops for many interesting discussions. Thanks also to A. Bogacz and P. Sandler for help with this paper.

Table 3:

For a $\mu^+\mu^-$ Collider Development	Example in Past $p\bar{p}$ Collider (1976-1987)[14] (Cline, McIntyre, Rubbia proposal)
1) <u>Strong Physics Motivation</u> Higgs, SUSY, etc. etc. (Higgs mass unknown - but it may be at low mass)	W/Z Discovery (M_W , Z known)
2) <u>Parameters Study</u> Are they realistic? How can we make a convincing argument	FNAL/CERN Studies (1976-1981)
3) <u>Beam Manipulation and Cooling</u> Rapid Acceleration Possibility? (μ lifetime constraint)	AA Ring and Beams (p production yield)
4) <u>Demonstration of μ^\pm Cooling</u> (Experiments) (New Ideas)	p/\bar{p} Cooling ICE Ring Novosibirsk, FNAL (1976-1981)
5) <u>Detector Concepts and Feasibility Study</u>	UA1/UA2 CDF/D0 Designs 1977-1987

V. REFERENCES

[1] M. Tigner, presented at the 3rd Int. Workshop on Adv. Accel. Concepts, Port Jefferson, NY (1992); other paper to be published in AIP, (1992), ed. J. Wurtle.

[2] Early references for $\mu\mu$ colliders: E.A. Perevedentsev and A. Skrinsky, Proc. 12th Int. Conf. on H.E. Accel., eds. R.T. Cole and R. Donaldson, (1983), p. 481; D. Neuffer, Part. Accel. 14 (1984) 75; D. Neuffer in Adv. Accel. Concepts, AIP Conf. Proc. 156 (1987) 201.

[3] D. Cline, NIM, A350, 24 (1994) and 4 following papers constitute a mini-conf. proc. of the Napa meeting.

[4] See for primary references to the theoretical estimates here, S. Dawson, J.F. Gunion, H.E. Haber and G.L. Kane, The Physics of the Higgs Bosons: Higgs Hunter's Guide (Addison Wesley, Menlo Park, 1989).

[5] Most recently limits on Higgs mas were reported in a talk by D. Schaile at the WW meeting at UCLA, Feb. 1995.

[6] For example, the Compact Muon Solenoid Detector at the LHC, CERN reports and proposal.

[7] Presentation of D. Neuffer and R. Palmer at the Sausalito workshop (to be published in the proc. of the conf.).

[8] Proposal to TRIUMF for μ Cooling Experiment, A. Bogacz, et al., unpublished.

[9] Z. Hong, P. Chen and R.D. Ruth, Radiation Reaction in a Continuous Focusing Channel, SLAC prep. SLAC-PUB-6574, July 1994.

[10] S. Basu and R.L. Byer, Optic Letts., 13, 458 (1988).

[11] Z.A. Bazylev and N.K. Zhevago, Sov. Phys. Usp., 33, 1021 (1990).

[12] C.J. Oram, J.B. Warren, G.M. Marshall and J. Dornobos, J. Nucl. Instr. & Meth. in Phys. Res., A179, 95 (1981).

[13] D. B. Cline, A Crystal μ Cooler for a $\mu^+\mu^-$ Collider, in Proc. of the 1994 Adv. Accel. Workshop, Lake Geneva, 1994.

[14] C. Rubbia, P. McIntyre and D. Cline, Proc. of 1976 Aachen Neutr. Conf., p. 683 (eds. H. Faissner, H. Reithler and P. Zerwas) (Viewag Braunschweig, 1977).

New Scheme for a $\mu^+\mu^-$ Collider

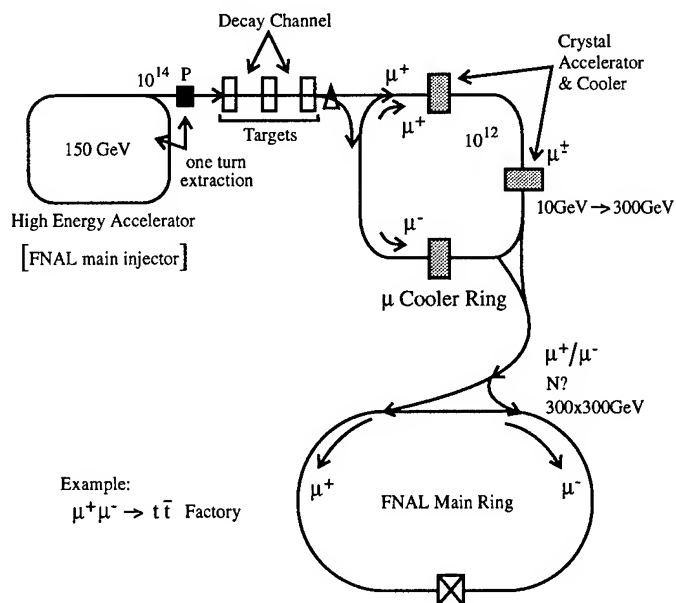


Figure 3: A scheme for a $\mu^+\mu^-$ collider using crystal cooling.

HIRFL STATUS AND HIRFL--CSR PROPOSAL

Ye Feng Wang Yifang

Institute of Modern Physics, 253 Nanchang Rd., Lanzhou 730000, P.R.China

Since the Heavy Ion Research Facility at Lanzhou (HIRFL) was put into operation in 1989, 19 kinds of ion have been extracted for the experiments and a lot of improvements was finished. In order to provide high quality stable and unstable nuclear beams for many experiments, the HIRFL Cooler--Storage Ring Proposal has been submitted to Chinese Academy of Sciences. The HIRFL status and the main performance, lattice as well as the main technical problems of Cooler-Storage Ring (CSR) are described in this paper.

I. HIRFL STATUS

A. Operation

After the first beam was extracted from the main accelerator SSC (k=450) on Dec.12,1988, HIRFL has been operated successfully except 1991 when the injector SFC (k=69) was shut down to upgrade and install ECR source as well as its beam line. Layout of HIRFL is shown in Fig.1 and the accelerated ions are listed in Table 1.

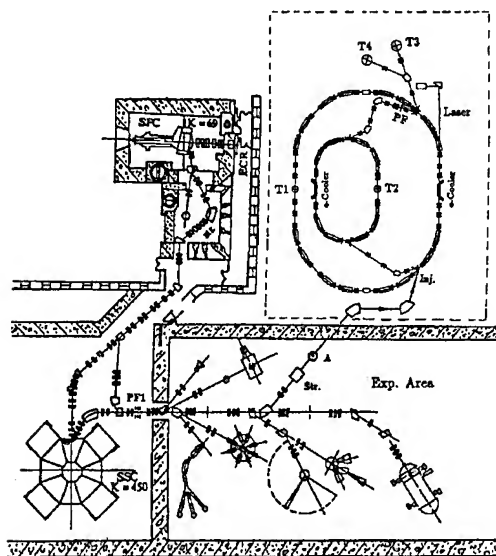


Fig.1 Layout of HIRFL

The layout of CSR is shown in the block of dotted line. T1--Internal target for atomic physics and RIB physics; T2--Internal target for the studies of exotic nuclei and atomic physics; T3--External target for cancer therapy research; T4--External target for researches on the properties of nuclear matter under extreme conditions.

Table 1 Accelerated beams and operated parameters of HIRFL

SFC					
ION	Z	RF(MHz)	h	E(MeV/u)	I(μ A)
^{12}C	4	6.26	1	4.5	5
^{16}O	5	6.26	1	4.5	3
^{12}C	4	7.53	1	6.6	3
^{40}Ar	8	13.54	3	2.4	2
^{20}Ne	4	13.54	3	2.4	2
^{18}O	6	6.26	1	4.5	2
^{14}N	5	6.26	1	4.5	3
^{16}O	6	8.54	1	8.5	2
^{12}C	5	8.23	1	7.9	2
^{12}C	4	8.02	1	7.5	2
^{84}Kr	13	10.98	3	1.5	0.25
SSC					
^{12}C	6	9.39	2	50	0.4
^{16}O	8	9.39	2	50	0.05
^{12}C	6	11.29	2	75	0.05
^{40}Ar	15	13.54	4	25	0.05
^{20}Ne	8	13.54	4	25	0.04
^{18}O	8	9.39	2	50	0.04
^{14}N	7	9.39	2	50	0.05
^{16}O	8	12.80	2	100	0.01

B. Improvements

1. ECR ion source and its beam line installation

In order to increase the ion species and improve the beam qualities, a Caprice ECR source purchased from CENG Lab, and the beam line from ECR to SFC had been installed in 1991. To meet the need for ions of heavier element, some

possible modifications had been tried. As a result, a considerable increase in beam current with a factor of 1.5 to 2 is gotten for Ne and Ar respectively^[1]. Meanwhile a new 10GHz ECR ion source has been developed in our laboratory and its performance is satisfactory.

2. Upgrading the SFC

To meet the requirement of the external injection system a lot of improvements had been done. The central region of SFC was redesigned. Following the general design principles and the equations of motion a slanted electrostatic inflector had been designed and fabricated^[2]. The central trajectories had been studied carefully and in detail. Because the new coils took the place of the original one which had been used for about 30 years and the external injection system was adopted, the magnet field must be mapped again. At same time the Dee and dummy Dee was rebuilt. The electrostatic deflector was replaced by new one. Two HIRFL-800 cryopumps took the place of two oil diffusion pumps. And the microcomputer--CAMAC system is used to control SFC and the beam line.

3. Bypass beam line construction

The bypass beam line from former beam line to the post one was constructed to deliver the beam extracted from SFC directly to the experimental terminals in 1993.

4. Improvement of phase stabilization system

There are 6 sets of RF amplifier with different frequency range and power in RF system. The No. 0 cabinet was added as the reference phase to improve the phase stability of RF system. Using the vector resultant principle a new 360° phase shifter adjusted by microprocessor with phase resolution of better than $\pm 0.1^\circ$ has been developed and took the place of the mechanical phase shifter.

5. Development of HIRFL--800 cryopump

Owing to larger consumption of liquid nitrogen, the Balzers cryopump of RKP 800 with a combined pumping speed of about 20000l/s was replaced by the HIRFL 800 cryopump without using liquid nitrogen. Its pumping speed has been tested at a standard test dome to be 25000 and 27000l/s for nitrogen and hydrogen respectively.

II. HIRFL--CSR PROPOSAL

A. General Description

HIRFL-CSR, a heavy ion Cooler-Storage Ring, is a new accelerator plant. It could provide stable and unstable nuclear beams with high quality for experimental researches. The CSR consists of a main ring (CSRm) with a circumference of 141.051m and an experimental ring (CSRe) with a circumference of 70.525m. It will accelerate the particles up to 900MeV/u for light heavy ions ($Z/A=1/2$) and 600MeV/u for heavier ions ($Z/A=1/2.6$) by using the existing two cyclotrons SFC ($k=69$) and SSC ($k=450$) as injectors respectively. The heavy ions from the injectors will be accumulated, cooled and accelerated in the main ring, and then extracted to produce radioactive ion beams (RIB) or high charge state heavy ions. After that the secondary beams can be injected into the experimental ring for internal target experiments. Those beams stored in the experimental ring can also be decelerated to low energy (≈ 10 MeV/u) for physical experiments, or reinjected into the main ring for acceleration to high energies (500--900MeV/u) for the internal or external target experiments.

The expected mean luminosity of internal target experiment in CSRe will be of 10^{21-24} for short lifetime RIB (0.1-100 ms) and of 10^{24-28} for long lifetime RIB (0.1-5 s).

B. Main Parameters and Lattice of CSR

The main parameters of CSR are tabulated in Table 2. Fig.2 and Fig.3 show the distributions of β -functions and dispersions for CSRm and CSRe respectively.

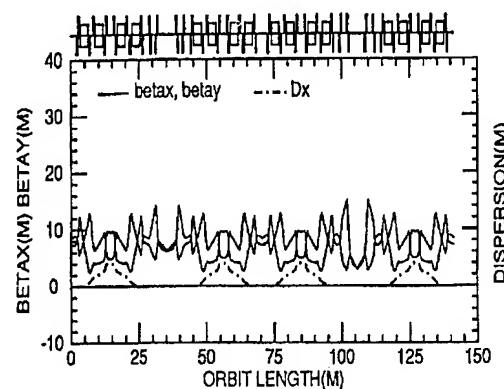
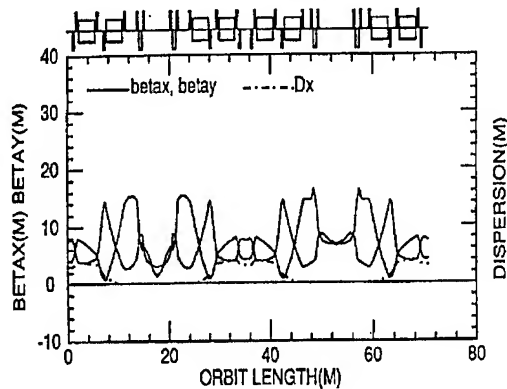


Fig.2 β -functions and dispersions of CSRm

Table 2 Main Parameters of CSR

Ring	CSRm	CSRe
Circumference (m)	141.051	70.525
Average radius (m)	22.449	11.2244
$B\rho_{\max}/B\rho_{\min}$ (T.m)	10.584/0.64	6.4/0.91
Acceptance		
ε_1 (mm.mrad)	50	25
$\Delta p/p$ (%)	1.0	1.0
Lattice		
χ_{tr}	4.44	2.35
Q_h/Q_v	4.24/3.23	2.73/2.35
Max. β_h/β_v (m)	14.94/14.11	16.34/14.32
Max. D_x (m)	3.971	3.944
Electron cooling		
E_{\max} (keV)	165	165
I_{\max} (A)	4.8	4.8
cathode diameter (mm)	50	50
β_{hc}/β_{vc} (m)	6.0/6.0	6.2/6.2
cooling section length (m)	3	3
RF-system		
harmonic number	1	1
f_{\max}/f_{\min} (MHz)	2.0/0.2	3.05/0.62
voltages (n×kV)	2×8	2×12
Vacuum (Torr)	1×10^{-10}	1×10^{-10}

Fig.3 β -functions and dispersions of CSRe

C. Lifetime of Stored Ion beams^[3]

At the injection energies the main factors defining the survival of ion beams are related to the three processes. 1. Single and multiple Coulomb scattering on residual gas molecules. 2. Charge exchange (i.e., electron capture and electron stripping) with residual gas molecules. 3. Radioactive electron capture (REC) in the e-cooler.

The theoretically calculated partial lifetimes demonstrate that the REC process in the electron cooler restricts the lifetimes of light heavy ions (C-Kr) injected into CSRm, the

electron capture mechanism dominates the lifetimes of heavier ions (Xe-U), and the beam loss caused by Coulomb scattering is negligible. However, under the vacuum conditions of CSRm, lifetimes of the typical heavy ions at the injection energies are longer than the needed time for RF stacking (~5s) and electron cooling (~1s). This allows to obtain high intensity accumulated ion beams.

Besides the above three processes, the charge exchange with target atoms and Coulomb scattering on target atoms have to be taken into account when determining lifetimes for thin internal target experiments. In this case electron capture on target atoms dominates the circulating beam lifetimes. Anyhow, the calculation results predict that the CSRe internal target thickness of 10^{15} atoms/cm² is reasonable.

D. Electron Cooling Time

The electron cooling time has been computed by using the more accurate cooling theory^[4]. The results show that for the combination method of multiturn injection and RF stacking at the injection energies, beam emittance of the order of 0.1 mm.mrad is achieved in a typical cooling time of less than 1.0s, while the longitudinal momentum spread at the top of stack is damped from 2.5×10^{-4} to 2.0×10^{-5} in a time of 1.0ms, which is much shorter than RF stacking period (~20ms), while for the multiple single-turn injection the emittance and momentum spread are decreased by 2 orders in a cooling time of less than 60ms and 120ms respectively.

Hence this fast cooling makes it possible to increase the accumulated ion beam intensity to a limitation of space charge effect rather than the phase space of machine.

III. REFERENCES

- [1] B.W.Wei, Z.W.Liu et al., "Study of the magnetic field of CAPRICE type ECR ion source", Proc. of 13th Intern. Conf. on Cyclo. and their Appli., Vancouver, 1992
- [2] J.B.Belmont, "Axial injection and central region of the AVF cyclotron", Lecture Notes of 1986 RCNP KIKUCHI Summer School on Accelerator Tech., 1986.
- [3] H.Habs et al., Nucl. Instrum. Methods Phys. Res. B43(1989)398.
- [4] I.N.Meshkov, Phys. Part. Nucl. 25(6)(1994)631.

A REVIEW OF POLARIZED ION SOURCES

P.W. SCHMOR, TRIUMF, 4004 Wesbrook Mall, Vancouver, B.C., V6T 2A3, CANADA

The two main types of polarized ion sources in use on accelerators today are the Atomic Beam Polarized Ion Source (ABIS) source and the Optically Pumped Polarized Ion Source (OPPIS). Both types can provide beams of nuclearly polarized light ions which are either positively or negatively charged. Heavy ion polarized ion sources for accelerators are being developed.

I. INTRODUCTION

There have been significant advancements in the capabilities of polarized ion sources in the four years following the last review given to the Particle Accelerator Conference in 1991[1]. Polarized nuclei are an important nuclear physics probe and present day experiments require that the polarized ion source provide beams with high polarization, high beam current, exceptional beam quality and long term reliability. Although polarized ion sources have been in use for nearly 40 years, the development of enhanced ion source capabilities continues to be driven by the fact that the physics is fruitful and exciting.

New facilities will become available shortly in Japan, the Netherlands, Germany, China and South Africa. In addition, polarized ion sources are being upgraded with major modifications at a number of existing facilities. The possibility of accelerating polarized protons is being seriously examined for facilities such as RHIC[2] and FNAL[3]. Each of these accelerators has its own particular requirements and for optimal performance requires a unique polarized ion source. A number of recent review papers provide an excellent overview of polarized ion source design, development and operation[1,4,5,6].

Present day experiments are often precision experiments measuring rare processes and require intense, stable beams within a small emittance. For example, the measurement of the parity violation amplitude in pp scattering at TRIUMF requires a modest polarized current of only $0.5 \mu\text{A}$ at 230 MeV but with a challenging spin-flip coherent current modulation (i.e., current intensity modulation correlated with spin flip) less than 1 part in 10^5 at a spin flip rate of approximately 100 Hz. In order to ensure that the experimental specifications are met for stability it is necessary for the source to produce at least $15 \mu\text{A}$. Another experiment, at TRIUMF, examining pion production in np scattering used cyclotron slits to reduce, substantially, the cyclotron accep-

tance and even though the experiment required only $0.5 \mu\text{A}$ at 475 MeV, it was necessary for the ion source to provide more than $8 \mu\text{A}$ of polarized H. This deliberate reduction in emittance to achieve the differing experimental requirements is realized by making the phase space cuts on different parts of the emittance and at different places in the acceleration process. The ion source must be capable of filling, efficiently, an acceptance which is larger than that required for one particular experiment. Many of the sources being built today are flexible and include the possibility to tailor the performance to meet an experiment.

There are a number of factors which must be taken into account in deciding the best polarized source for a particular accelerator. The experimental program defines parameters such as current, polarization, spatial polarization uniformity, stability requirements, spin-flip criteria and polarized species. The accelerator defines the allowed beam emittance, the overall source size and the required ion charge state. The administration is concerned with the cost, reliability and risk. The risk is often minimized by purchasing an ion source from a commercial company, if possible, in order to minimize the research and development required to meet the experimental requirements. With regard to statistical accuracy in an experiment, a commonly used figure of merit to compare the performance of the various polarized ion sources is given by P^2I , where P is the nuclear polarization and I is the current at the target.

Polarized ions are generally produced in an ion source comprised of four stages. The first step is to produce an intense high quality atomic beam. Next this atomic beam is electronically polarized in a magnetic field by selecting the hyperfine states of one of the Zeeman levels. Occasionally as in the optically pumped proton polarized sources, these two steps may overlap. Next nuclear polarization is achieved by inducing transitions, from the occupied hyperfine states (of an undesired nuclear spin direction), to the unoccupied hyperfine states (of correct nuclear spin). Finally the remaining beam which is now nuclearly polarized is ionized in the presence of a magnetic field to preserve the polarization. The strength of this magnetic field (and therefore the effective transverse emittance) depends on the particular hyperfine states being ionized [7,8]. Table 1 lists the 'advertised' performance characteristics for a number of polarized ion sources selected for their unique capabilities.

Table 1 Performance characteristics for selected polarized ion sources

LAB.	TYPE	BEAM	DUTY CYCLE	IONIZER	EMITTANCE (π mm mrad)	POL'N (%)	CURRENT (μ A)
INR	ABIS	H ⁺	0.0005	plasma	2.0	0.80	6000
ETHZ	ABIS	H ⁺	dc	ExB	1.2	0.85	400
INR	OPPIS	H ⁺	0.0001	Na vapor	0.8	0.65	4000
ETHZ	ABIS	H	dc	Na vapor			16
BNL	ABIS	H	0.0003	Cs beam	0.35	0.80	60
INR	ABIS	H	0.0003	plasma	0.23	0.70	500
TRIUMF	OPPIS	H	dc	Na vapor	0.8	0.85	150
TRIUMF	OPPIS	H	dc	Na vapor	2.0		1600
KEK	OPPIS	D ⁺	0.0014	Rb vapor		0.70	
KEK	OPPIS	D ⁺	0.0014	Rb vapor	2.0		380

II ATOMIC BEAM ION SOURCES

In an atomic beam ion source (ABIS), hydrogen (or deuterium) atoms are generated, initially, in a dissociator by a radio-frequency discharge and then formed into a low-velocity (thermal) atomic-beam with the aid of a cooled nozzle and a system of skimmers. Tapered magnets (quadrupole, sextupole) are used to separate (Stern-Gerlach effect) and focus one set of hyperfine states (with the electron spin aligned to the magnetic field) from the other set of hyperfine states (with the electron spin aligned in the opposite direction). Transitions between hyperfine states are induced by applying appropriate radio-frequency fields. These transitions are chosen to transform the separated atomic states which now have a similar electron spin direction (electron polarization) to hyperfine states of similar nuclear polarization. Frequently a second set of separation magnets is used to select a single hyperfine state. The beam of atoms in the selected state(s) are then ionized for ion acceleration or used as polarized atoms in experimental targets.

There are a number of approaches being used to ionize the nuclearly-polarized atomic beam. To produce positively charged ions, an electron impact ionizer is frequently used. This is achieved either by producing an intense electron beam with a hot filament in a solenoid magnet or by using the electrons generated in an electron-cyclotron-resonance (ECR) heated plasma. Space charge forces within the intense electron beam give rise to an energy spread in the polarized ions which limit the amount of polarized beam which can be matched into an accelerator. The ECR ionizer avoids the space charge problems of the intense electron beam by using the electrons in a quasi neutral plasma and the resulting polarized beam is considerably brighter (more current within a

given emittance). However, experience has shown that the polarization is slightly degraded (~5%) by the ECR ionizer[9]. The PSI source, for example, produces about 150 μ A of dc positive beam with about 79% polarization within a normalized emittance of less than 1.2π mm-mrad. The ETHZ group has reported positive currents as high as 400 μ A using an ExB ionizer within a normalized emittance of 1.2π mm mrad[10]. To produce negatively charged ions, the positively charged ions are accelerated to about 5 keV prior to being directed through an alkali vapor target where about 7% of the positive ions are converted to negative ions by double charge exchange. The achieved intensity was 16 μ A at ETHZ. An alternate approach to producing the negative ion beam has been to use charge exchange directly between the slow moving polarized, neutral atomic beam and a counter-flowing, coaxial, neutral beam of cesium atoms at 40 keV. This approach provides a highly polarized beam (60 μ A of 0.80 polarization) of excellent emittance (~0.35 π mm-mrad normalized by $\beta\gamma$)[11]. At the INR in Moscow, very high currents (~6 mA) have been achieved (albeit with 100 μ s long pulses at a 1 Hz repetition rate within a normalized emittance of 2π mm-mrad) by making use of the larger charge exchange cross-sections of $^2\text{H}^+$ (compared to electrons) in a plasma to ionize directly the polarized atoms[12]. A similar arrangement at INR with the exception that the source was modified to make use of charge exchange with ^2H (instead of $^2\text{H}^+$) has recently yielded a peak current of 500 μ A of negatively charged hydrogen ions in a 200 μ s pulse[13]. A polarization of approximately 70% within a normalized emittance of approximately 2.3π mm mrad is reported by the INR group.

The neutral beam intensity at the ionizer entrance (and consequently the source current) should improve as the beam velocity (temperature) is reduced. The predicted gains in

polarized currents which should result by cooling the nozzle were not obtained, initially. The source must be treated as a whole and when the atomic beam velocity is changed, the magnet systems must be re-matched to this new velocity distribution. As the result of improved (reliable) computer tracking programs and the use of high field permanent magnets, it has been possible to realize a gain of 2 in the polarized atomic beam flux at Madison and at Heidelberg[14]. It appears, from results obtained at BNL that additional increases by further lowering the beam velocity will not provide further significant increases in atomic beam flux since intrabeam scattering prevents the atomic flux from substantially exceeding the 10^{17} atoms/cm²/sec already achieved by the best sources[11]. Intrabeam scattering becomes a more severe problem as the temperature (beam velocity) is reduced.

Atomic beam polarized ion sources have been used for over 35 years and are being used successfully in many laboratories including; BNL, Bonn, Dubna, ETHZ, IUCF, INR, Julich, PSI, Saclay, TUNL, University of Washington and the University of Wisconsin. New sources are planned or being commissioned at IUCF, KVI, NAC (South Africa), RIKEN and Uppsala. Similar technology is used/planned for polarized gas targets at Dubna, Heidelberg, Madison, Novosibirsk, UNK and CERN.

In general, a higher peak current is obtained from sources with a small duty cycle. The INR plasma ionizer is very efficient, ionizing nearly all of the atomic beam. The difference in current between dc and pulsed ion sources is not due to the physics per se but rather a consequence of technology limitations and the larger current could, in principle, be achieved by steady state sources given the correct technology and financial resources. Negative beams tend to be at least an order of magnitude smaller than positive beams for a given ion source. Each source has been designed to be compatible with a particular accelerator or particular type of experiment and consequently does not have the same hardware nor the same emittance.

III OPTICALLY PUMPED SOURCES

A review of the status of optically pumped polarized ion sources in 1993 has been given by Mori[15]. The optically pumped polarized ion source (OPPIS) is based on a proposal by Anderson[16]. Lasers are used to achieve electronic spin alignment in an alkali vapor. Initially, as proposed by Anderson, sodium was pumped with dye lasers tuned to the D1 transition at 596 nm, but more recently titanium sapphire lasers are being used to pump rubidium (or potassium) vapor at 795 (770) nm. Protons are directed at an energy of about 2 to 5 keV through the polarized vapor where by charge exchange they can pick up a spin aligned electron. The charge

exchange process must take place in a large magnetic field (~ 2.5 T) in order to preserve the spin alignment. After removing any charged particles by means of transverse electric fields, the beam emerging from the alkali vapor is a neutral atomic hydrogen beam (at energy 2 to 6 keV) with two hyperfine states (of similar electronic spin) predominately occupied. This fast neutral beam has a number of advantages compared to the thermal ABIS beam. A Sona type transition is then used, as in the Lamb-shift source to transform the electron alignment to a nuclear alignment prior to ionization. The nuclearly polarized atomic beam is ionized in either an alkali to form negative ions or in helium to form positive ions. Because of the higher velocity atomic beam in an OPPIS compared to an ABIS, alkali ionizers can operate at a sufficient thickness to realize an equilibrium fraction of negative ions, by double charge exchange, without a substantial emittance increase due to scattering.

Optically pumped polarized ion sources, based on charge exchange, have been developed at INR[17], LAMPF [18], KEK[19] and TRIUMF[20]. The performance of the OPPIS source is improving rapidly. It has been only 12 years since the first OPPIS at KEK[21]. The performance figures of an OPPIS depend on the emittance and duty cycle of the ion beam. The current can be increased by opening apertures until the ion source emittance matches the accelerator acceptance. The efficiency for ionization to protons is about a factor of ten larger than the efficiency for ionization to H with the result that negative currents from the source are about a factor of ten less than positive currents. Both the current and the polarization also depend on the thickness of alkali vapor that can be polarized. The alkali thickness that can be polarized, in turn, depends on the power available from the lasers. Peak power from lasers can be substantially increased through pulsing. Thus for an accelerator (or for a particular experiment) requiring a pulsed polarized beam it is possible, under some conditions, to provide higher peak currents by matching the laser repetition rate to that of the accelerator (or experiment). For a given laser power, higher currents at lower polarization result from an increase in alkali thickness. With the TRIUMF source operating in a dc mode the measured nuclear polarization (by low energy polarimeter) is about 0.85 @ 150 μ A of H⁺ (at the source) within a normalized emittance of 0.8π mm mrad and after some optimization a polarized H⁺ current of 1.6 mA within a normalized emittance of 2.0π mm mrad was achieved[22]. At LAMPF, 0.77 polarization was measured at 2 μ A, 0.64 @ 38 μ A and dropped to 0.56 @ 50 μ A. It is worth noting that the usual figure of merit, P^2I , increases with increasing current (over the above range) even though the polarization is decreasing.

The OPPIS, based on charge exchange, has limitations on the output brightness (current/emittance²) as a result of the

magnetic field required to preserve (decouple **L** & **S**) the electron polarization during charge transfer as well as due to the magnetic field of the ionizer which is needed to preserve the nuclear spin orientation. The charged alkali atoms are radially confined by the magnetic field and contribute to the space charge on the proton beam. It seems feasible, certainly for low duty cycle operation, to achieve much higher currents from an OPPIS. Using the neutral beam technology, initially developed for fusion research, it is proposed to develop an OPPIS which is conservatively estimated to yield a highly polarized 10 mA of H⁺ within a normalized emittance of 1.5 π mm mrad[22,23].

It has been proposed to avoid the space-charge problem by using spin exchange with a neutral hydrogen beam instead of charge exchange with a proton beam. The cross section for spin exchange is nearly an order of magnitude (for hydrogen atoms in the few keV energy range) smaller than for charge exchange. Consequently it is necessary to optically pump thicker targets. The availability of high power pulsed alexandrite lasers and titanium sapphire has made the technique feasible. Initial experiments at INR and TRIUMF have demonstrated a polarization of 0.5[24]. The cross section for spin exchange increases as the energy of the atomic hydrogen beam is decreased. Commercial cw titanium sapphire lasers should already be capable of polarizing a sufficiently thick rubidium vapor target for atomic hydrogen beams at thermal energies. The currents for spin exchange ion sources are estimated to be considerably larger than for charge exchange sources.

Another approach, described by Poelker[25] and Jones [26], is a combination of atomic beam techniques and spin exchange. The source uses a dissociator to produce hydrogen/deuterium atoms which are allowed to diffuse at thermal energies through a potassium vapor polarized by optical pumping. The electron spin orientation is transferred to the atoms by spin exchange collisions. A beam is formed from the atoms leaving the potassium spin exchange cell. The nuclear polarization of the hydrogen/deuterium atomic beam is then achieved by a combination of rf induced transitions and separation magnets in a scheme identical to that used in atomic beam polarized ion sources. The Argonne group have reported[23] intensities of $1.7 \cdot 10^{18}$ atoms/s for hydrogen which is almost an order of magnitude higher than that for conventional atomic beam ion sources. Atomic polarization exceeds 0.8 at intensities less than $2.0 \cdot 10^{17}$ and decreases as the intensity is increased. With the addition of high magnetic fields surrounding the optical pumped cell, nuclear polarizations of over 0.5 are achieved even at intensities of $1.6 \cdot 10^{18}$ atoms/s.

The KEK group has reported a novel extension of the OPPIS technique to demonstrate vector polarized deuterium. To achieve this result, they also polarized the ionizer alkali

by optical pumping and were able because of the Pauli exclusion principle to select either one of the two spins by controlling independently the electron spin alignment of the two alkali cells[27]. The KEK group has obtained a nuclear-spin vector polarized negative deuterium ion beam with a polarization of 0.7. This group has also recently demonstrated 380 μ A of negative deuterium after some optimization[28].

IV HEAVY ION SOURCES

An ion source for polarized beams of ^6Li , ^7Li and ^{23}Na was developed and used at Heidelberg[29,30]. An electron polarized beam was achieved by passing an unpolarized atomic beam through a Stern-Gerlach separation magnet (quadrupole). Subsequently, three sets of rf transitions were used to populate appropriate hyperfine states and provide various different vector and tensor nuclear polarizations. Positive ionization was achieved through surface ionization. These positive ions were converted to negative ions in a cesium vapor. With the use of lasers it is possible to pump alkali hyperfine states directly. This technique has yielded currents in the range of 2 to 6 μ A and polarizations of about 80% for beams of ^7Li and ^{23}Na . Heavy ion polarized ion sources for cyclotrons are under development at the Institute for Nuclear Research in Kiev and at RCNP in Osaka[31,32]. The INR source is designed to provide polarized alkalis and is similar to the Heidelberg design. The RCNP source is of the OPPIS design and will be used initially to produce beams of polarized ^3He .

IV LOW ENERGY POLARIMETERS

In order to optimize a polarized ion source, efficiently, it is essential to have a dedicated on-line low energy polarimeter near the ion source. There is, in general, too much competition for accelerator time to allow adequate scheduling of the accelerator and its polarimeters for ion source optimization. Moreover, experience at TRIUMF has shown that the overhead, in terms of time and manpower, in preparing the cyclotron and high energy polarimeters is a significant fraction of the optimization process. At TRIUMF two different low energy polarimeters have been extremely useful. The most frequently used polarimeter, a Lyman- α polarimeter, yields the polarization of protons in the energy range of 1 to 10 keV[33]. This polarimeter measures the Lyman- α emission of photons by selective quenching of polarized hydrogen atoms excited to the 2S metastable states. Count rates are of the order of 0.5 MHz. This type of polarimeter was developed at INR and is also being used at KEK and TUNL. The TUNL polarimeter uses a rf spin filter and is being used to determine both proton and deuteron polarization[34]. TRIUMF also uses a nuclear polarimeter based on the

${}^6\text{Li}(p, {}^3\text{He})\alpha$ reaction[35]. The analyzing power for detecting ${}^3\text{He}$ at 130° is approximately 0.21 at 300 keV. For deuterons the ${}^3\text{H}({}^2\text{H}, n){}^4\text{He}$ reaction has been used for energies around 100 keV.

V CONCLUSION

Today's polarized ion sources are frequently optimized to meet the needs of a particular accelerator or experiment and as such the emittance, polarization and/or resulting current may be different if the same source were optimized for a different accelerator. However, there are several general guidelines. First, for accelerators requiring polarized beams of negative hydrogen, the best choice is an OPPIS. Second, for accelerators requiring polarized beams of positively charged hydrogen, the best choice is not obvious. Third, for accelerators requiring vector polarized beams of negatively charged deuterium the best choice is an OPPIS. Fourth, for accelerators requiring beams of tensor polarized beams of deuterium the best choice, at present, is an ABIS. Much of the recent work on polarized internal targets overlaps and complements the work being done with sources. In summary, polarized ion source development remains a very active research endeavor and large improvements in source performance are still being realized.

VI REFERENCES

- [1] Clegg, T. B., 1991, *Conference Record of the 1991 IEEE Particle Accelerator Conference*, Vol. 4, 2083.
- [2] Lee, S. Y., 1990, *Particles and Fields Series 42, AIP-Conference Proceedings No 223*, 30.
- [3] *Report on Acceleration of Polarized Protons to 120 and 150 GEV in the Fermilab Main Injector*, SPIN collaboration, Michigan, Indiana, Fermilab, N. Carolina/TUNL, Protvino, Dubna, Moscow, KEK, March 1992.
- [4] Schiemenz, P., 1992, *Proc. of the 5th Int. Conf. on Ion Sources*, Rev. Sci. Instrum. **63** (4), 2519.
- [5] Schmelzbach, P. A., 1994, *Proc. of the 5th Int. Conf. on Ion Sources*, Rev. Sci. Instrum. **65** (4), 1379.
- [6] *Polarized Ion Sources and Polarized Gas Targets*, Eds, L. W. Anderson & W. Haerberli, AIP Conference Proceedings **293**, 1993.
- [7] Law, W. M., *et al.*, 1988, Nucl. Instrum. Methods **A263**, 537.
- [8] Ohlsen, G. G. *et al.*, 1969, Nucl. Instrum. Methods **73**, 45.
- [9] Schmelzbach, P. A., 1990, KEK Report **90-15**, 329.
- [10] Greubler, W., 1990, KEK Report **90-15**, 56.
- [11] Alessi, J. G. *et al.*, 1990, KEK Report **90-15**, 93.
- [12] Belov, A. S. *et al.*, 1990, KEK Report **90-15**, 69.
- [13] Belov, A. S., *Private Communication*.
- [14] Haerberli, W., *Proc. of 10th Int. Symp. on High Energy Spin Physics*, 1992, Nagoya, Japan, Frontiers of High Energy Spin Physics, Universal Academy Press, Inc., 335.
- [15] Mori, Y., 1993, Reference [6], 151
- [16] Anderson, L. W., 1979, Nucl. Instrum. Methods **167**, 363.
- [17] Zelenskii, A. N. *et al.*, 1990, KEK Report **90-15**, 154.
- [18] York, R. L. *et al.*, 1990, KEK Report **90-15**, 170.
- [19] Mori, Y., 1988, *AIP Conference Proceedings No. 187, Particles and Fields Series 37, Vol. 2*, 1200.
- [20] Levy, C. D. P. *et al.*, 1992, Rev. Sci. Instrum. **63**, 2625.
- [21] Mori, Y. *et al.*, 1984, *Workshop on Polarized Proton Ion Sources, AIP Conference Proceedings No 117*, 123.
- [22] Zelenski, A. N., *et al.*, *These Proceedings*.
- [23] Zelenski, A. N. *et al.*, 1993, *Proc. of the 1993 Particle Accelerator Conference*, Vol. 4, 2991.
- [24] Zelenski, A. N., *et al.*, 1994, *Proc. of the Fourth European Particle Accelerator Conf.*, Vol. 1, 205
- [25] Poerlker, M., *et al.*, 1993, Reference [6], 125.
- [26] Jones, C. E., *et al.*, 1993, Reference [6], 131.
- [27] Kinsho, M., *et al.*, 1994, "A Dual-Optically-Pumped Polarized Negative Deuterium Ion Source", to be published in proceedings of *8th Symp. on Polarization Phenomena in Nuclear Physics*, September, 1994, Bloomington, Indiana.
- [28] Kinsho, M., *Private Communication*.
- [29] Steffans E., *et al.*, 1975, Nucl. Instrum. Methods **124**, 601.
- [30] Krämer, D., *et al.*, 1984, Nucl. Instrum. Methods **220**, 123.
- [31] Zaika, N. I., 1992, "Spin Dynamics and Polarized Ion Sources on Isochronous Cyclotron U-240", to be published in the *Proceedings of the XIII International Conference on Cyclotrons and Their Applications*, Cyclotrons '92, Vancouver, July 1992.
- [32] Tanaka, M., *et al.*, 1990, KEK Report **90-15**, 288.
- [33] Zelenskii, A. N. *et al.*, 1986, Nucl. Instrum. Methods **A245**, 223.
- [34] Lemieux, S. K., *et al.*, *Proc. of 10th Int. Symp. on High Energy Spin Physics*, 1992, Nagoya, Japan, Frontiers of High Energy Spin Physics, Universal Academy Press, Inc., 351.
- [35] Buchmann, L., 1991, Nucl. Instrum. Methods **A301**, 383.

Sources for Production of Radioactive Ion-Beams

Helge L. Ravn, CERN-ISOLDE, Geneva 23, Switzerland

The possibility to accelerate unstable nuclei is presently considered to be one of the major opportunities of nuclear physics. Around the world a rising number of laboratories are engaged in the operation, construction or planning of accelerators dedicated to production of Radioactive Ion Beams (RIB) with energies above the coulomb barrier. This report reviews the special ion-source technique which is used to produce such secondary beams suitable for injection into an accelerating structure. A short introduction is given to the already well developed ion source and target technique in which on-line nuclear reactions are used continuously to produce and refine the unstable source feed material and convert it into a low energy singly charged DC beam. Emphasis is then given to a discussion of the techniques applied to fulfil the particular new requirements set to the radioactive ion sources in order efficiently match modern accelerators.

I. INTRODUCTION

Facilities that make use of Isotope Separators On-Line (ISOL) in which high intensity primary beams are used to produce low energy secondary beams of nuclei far from stability have now been operational for some decades. Systematic developments in that field now provide a large diversity of techniques for production of beams of unstable nuclei which now serve as a solid basis for further developments [1]. The many new projects and facilities dedicated to production of Radioactive Ion Beams (RIB) [2] with energies above the coulomb barrier which now emerge all make use of the on-line mass separator and its target and ion-source technology as injector or as starting point for new specific developments.

The interplay between the four involved issues: nuclear reactions, target, ion-source A and Z separation and post-acceleration has shown that the target and ion-source are the most crucial links of the chain and are so intimately linked that they usually are discussed together. The techniques used here distinguishes themselves in a number of ways from current accelerator ion-sources which are usually optimised for high current of stable species. This report starts with a brief introduction to the basic principles and particularities of the target and ion-sources for on-line mass separators followed by selected examples which illustrates the diversity of techniques used and the directions for future developments. Most of my examples are taken from the field I am familiar with where high energy protons are

used as primary beam which allows to use thick targets and presently are giving the highest secondary beam intensities. A recent discussion of thin target catcher systems mainly used with ISOLs at heavy ion accelerators is found in ref. [3]. A more extensive overview of recent developments in the field may be found in the proceedings of the last EMIS conference [4.5].

II. THE PRINCIPLES OF ISOL ION-SOURCES

The essential point in developing ion sources for radioactive species is that the ion-source feed material has continuously to be produced and transferred from an adjacent nuclear target. Many different nuclear reactions may be used for production and with few exceptions they are very complex with many exit channels leading to a variety of short-lived and rare nuclei. Efficiency and speed are therefore the essential parameters. The processes which are needed to produce pure beams of radioactive nuclei are strongly dependent on the physical and chemical properties of the individual element and have to be developed specifically for each element or group of elements. Today the development of such systems has reached a stage that allows the production of low-energy beams of the radioactive isotopes of most elements in the periodic system. The principles of the individual systems vary only little with the chosen primary particles [1] used to produce the radioactivity. However, the variety and intensities of beams that may be obtained strongly depend on the primary beam as discussed in ref. [6].

A. Release and transfer of products to the ion source

The general problem is one of mass transfer, i.e. typically to separate the 10^{-1} to 10^{12} produced nuclei (per second) from the 10^{23} target atoms and to transfer them to the ion source. The different steps of this process and the losses from various effects are illustrated in Figure 1.

The separation of the products from the bulk of the target can be done by merely heating a target material with a low vapour pressure to a sufficiently high temperature so that the more volatile nuclei of interest, which are stopped in the target, are released by diffusion and desorption processes. In this way the flow of material can be kept sufficiently low to allow the ion source to perform optimally. A number of such materials have been found and their release properties studied [5].

The chemical affinity of the desired species to the walls of the target container, the transfer tube, and the ion source chamber determine the decay losses caused by the length of time the atoms are adsorbed. This phenomena may make apparently efficient ion sources useless for radioactive ions.

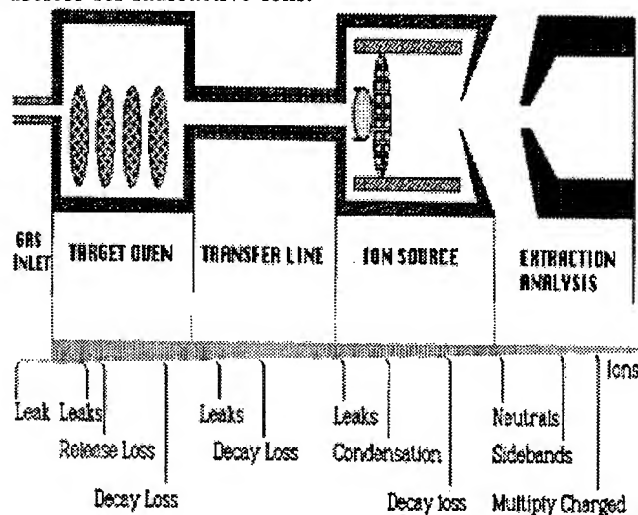


Figure 1: Layout of the ISOLDE concept of an ion-source connected via a short transfer line to a thick target. Also shown are the various mechanisms responsible for losses in the transfer of the reaction products from the target into the ion beam.

B. Overall efficiency

The obtainable beam intensities I are determined by Eq.(1)

$$I = \sigma \cdot \Phi \cdot N \cdot \epsilon_1 \cdot \epsilon_2 \cdot \epsilon_3 \quad (1)$$

where σ is the formation cross section, Φ is the primary-beam intensity, N the target thicknesses, ϵ_1 the release and transfer efficiency of the product from the target to the ion-source, ϵ_2 the ionisation efficiency and ϵ_3 the transfer efficiency determined by the radioactive decay losses during the transfer process. In favourable cases the release from the target and the transfer into the ion source ϵ_1 occurs with an efficiency of 90–100% and the ionisation efficiency ϵ_2 reaches 10–100%.

C. Time scale and structure

The time taken by the processes discussed in the previous sections resulting in the efficiency ϵ_3 caused by decay of the radioactive products can be theoretically described in terms of diffusion and desorption processes. A detailed discussion is found in Refs. [1] and [9]. So far the fastest systems developed are based on solids in the form of foils, wires, and powders, kept at high temperature. The crucial parameter is a function $p(t)$ which can be measured for the entire system but is often determined by the slowest step in the process. A simple description of this function is the

delay half-time i.e. the time it takes for one half of the produced atoms to leave the target. For a powder target characterised by an average grain radius R and a product diffusion constant D , in the case where the delay is governed by the diffusion in the target grains, the delay time distribution which is the probability $p(t)$ per unit time that an atom produced at time zero crosses the grain boundary at time t is:

$$p(t) = \frac{6D}{R^2} \sum_{n=1}^{\infty} \exp\left[\frac{-n^2\pi^2Dt}{R^2}\right] \quad (2)$$

Expressions of a similar type describe $p(t)$ if the delay is governed by diffusion in target materials of other shapes, diffusion in the pores of the target material, or diffusion to and in the source. With reasonable assumptions for D and R , good fits to the experimentally observed release data can be obtained. For a product with mean lifetime T_m much shorter than the average delay time, the delay transfer efficiency is given by

$$\epsilon_3 = \frac{3\sqrt{DT_m}}{R} \quad (3)$$

D. Charge state and emittance

A new requirement to the ISOL sources is production of high charge states ions and several groups are now developing ECR and EBIS technique for fast ionisation of radioactive species. The emittance of most the ISOL sources are around 25π mm mr or a few eV which may be further improved by cooling in traps as discussed below.

III. ION SOURCES

A. Surface ionisation sources.

The concept of surface ionisation has proven to be particularly successful for production of singly charged positive and negative radioactive ion-beams due to its simplicity, high efficiency and selectivity. As shown by the Langmuir equation ionisation efficiencies for positive ions of 50–100% may be obtained for elements with ionisation potential <5 eV and of negative ions for elements with electron affinity > 2 eV. For further details see ref. [8]. A typical example of this type of ion source developed at ISOLDE [9] for selective production of the halogens is seen in Figure 2. Here the vapour flow of mixed nuclear reaction products are allowed to impinge onto an LaB_6 surface. Due to its low work function ($\phi=2.6$ eV) elements with high electron affinity like the halogens will be ionised with high selectivity. In fact ionisation efficiencies of 10–50% for the elements Cl Br I and At were obtained. Contrary to its positive

counterparts the negative ionising surface presents some drawbacks. The low work function materials are like the LaB_6 all chemical compounds which are prone to poisoning and decomposition at the high temperatures needed in order to obtain short delays. For this reason the LaB_6 source can only be operated at 1000°C for extended periods. This temperature is too low in order rapidly to desorb and efficiently ionise the number of other elements with interesting high electron affinities. In principle the problem can be solved by replacing the LaB_6 pellet by a flow of Ca vapours [10] which allows to rise the temperature while maintaining a low work function of the tubular ionising surface by constantly recovering it with a low work function layer. New developments in which high ionisation efficiencies of Cl^- and Na^- ions have been obtained from a tubular W-ionise kept at 2000°C and covered by Ba vapour have recently been reported [11].

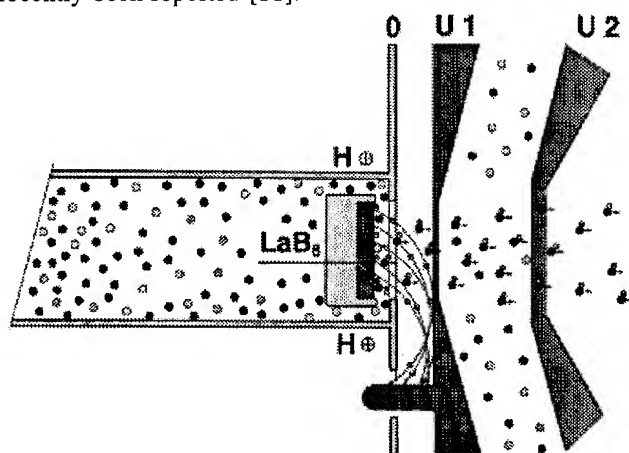


Figure 2: Surface ionisation source for production of negative ions. H magnetic field, U1 electron suppression electrode U2 extraction electrode.

B. High power density target for high energy protons

At ISOLDE $0.6\text{--}1\text{ GeV}$ protons with a maximum current of $4\text{ }\mu\text{A}$ has been used successfully in conjunction with thick targets of up to 100 g/cm^2 . A Radioactive Ion Source Test (RIST) [10] aiming at the development of a target and ion source to produce higher intensity RIBs is presently being carried out at RAL where at the ISIS spallation neutron source 0.8 GeV proton currents of up to 200 mA are available. The RIST target will use the concept of the ISOLDE Tantalum foil target for simplicity equipped with a W-surface ioniser which will allow a test of the production of neutron rich Li, Na, K and proton rich Rare earth elements. This target material which operates at 2400°C will be heated by the proton beam only and the crucial point is one of cooling since the ISIS proton

beam will dissipate up to 30 KW of power in the target. Off line heating tests show that for a proton beam of up to $100\text{ }\mu\text{A}$ the cooling of such a target may still be achieved by means of simple radiation cooling provided the foil lay out is changed such that good thermal contact between the foils and the outer tube is obtained. This is achieved as shown in Figure 3 by welding discs and spacers together to form a cylindrical target with a tapered hole through the centre which assures a uniform beam power dissipation along the length of the target, helping temperature uniformity. At the same time the delay time is shortened due to the lower pumping impedance as compared to the usual ISOLDE targets which employs Ta powder or foil rolls.

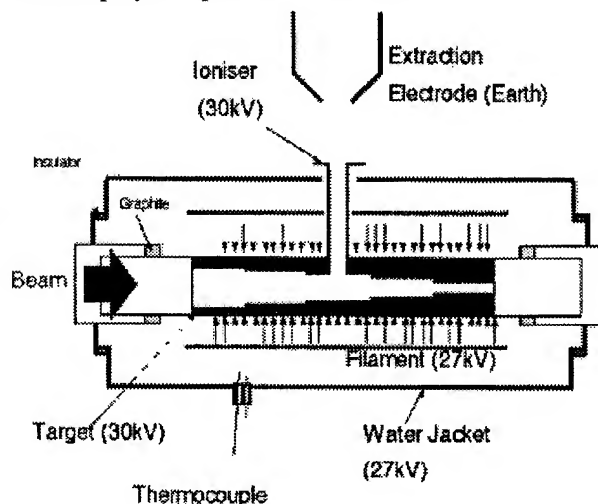


Figure 3. Details of the RIST Ta-disk target with a tubular W-surface ioniser. Electron beam heating is used to outgas the target or to keep it at operating temperature also at lower beam currents.

C. Hot cathode discharge ion sources

Although the special version of the surface ion-source the thermoionising cavities allows quite efficient ionisation of elements with ionisation potentials up to $\sim 7\text{ eV}$ [13] electron impact ionisation in various types of plasma discharge ion sources are generally used for ionisation of elements with ionisation potentials $>6\text{ eV}$. Due to the distribution of electron and ion energies in the plasma these ion sources have low chemical selectivity and ionises quite efficiently all elements that can be kept predominantly in the gas phase.

The main type of such sources especially developed for ISOL applications is the FEBIAD-source [14] of which the ISOLDE version [15] is shown in Figure 4. The advantage of this source is that it avoids the arc threshold pressure and associated instabilities by extracting the primary electrons by means of a grid. This allows the source to ionise many elements heavier than

Ne with efficiencies of 20-70% and widely independent of pressure.

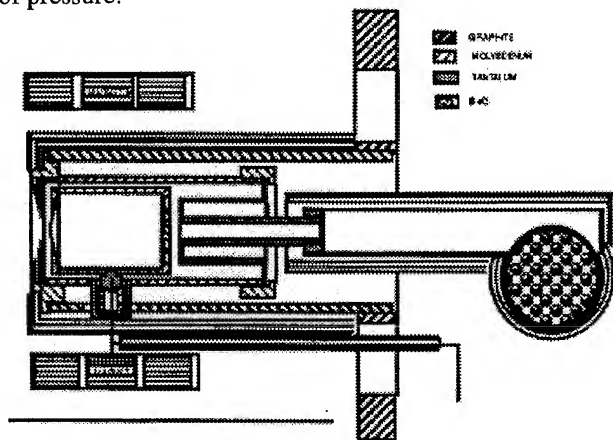


Figure 4: FEBIAD target and ion source unit with ohmic loss heated cathode and body which allows to operate at 1800-2000 °C.

D. Electron-Cyclotron Resonance (ECR) ion sources

One would think that the ECR ion source is the obvious accelerator source also for high-charge-state radioactive ions. In fact it has already been introduced at ISOL because of its very high efficiency for production of singly charged ions of the light gaseous elements [16, 17, 18, 19]. In particular the absence of the hot cathode avoids the very high losses due to adsorption of the elements C, N and O on hot metallic surfaces. For ionisation of less volatile metallic elements the cold enclosure may cause unacceptable delays despite its attractive efficiency of around 1% for a given high charge state metallic ion. Presently this source type receives much attention in order to solve this problem as well as its quite high emittance. The

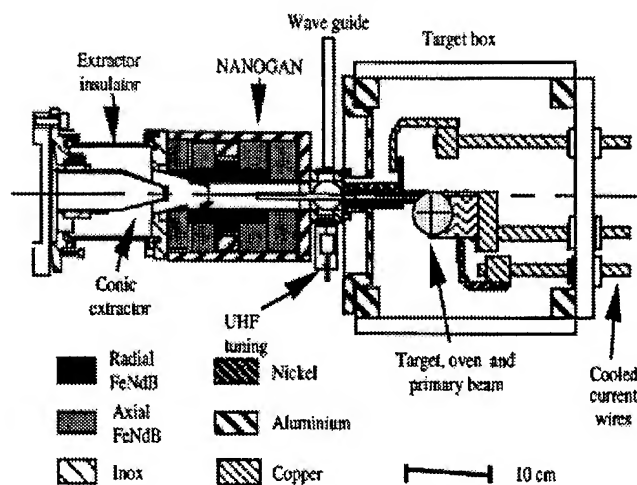


Figure 5: ECR ion source with permanent magnets combined with a porous carbon target at high temperature.

present status is illustrated in Figure 5 which shows the NANOGAN ECR-source coupled to a GANIL target for which on-line efficiencies of $^{18}\text{Ne}^{5+}$ have been measured to be 20% [20, 21].

E. Resonant laser ionisation sources

The most selective ion source principle is based on resonance excitation of atoms. Laser ion-sources where 2 to 3 beams of intense laser light which is at least resonant in one step followed by transitions which lead into auto-ionising- or Rydberg states have been used both at ISOL [22] and for trace analysis [23] to ionise a number of metallic elements with efficiencies of 20-30%. Presently only low duty cycle pulsed lasers (10kHz) are used to saturate the transitions. In order to overcome the losses the photo ions are stored between laser pulses in the potential trough of a gas cell [24] or a hot cavity [25] as shown in Figure 6. The consequently bunched ion-beam structure may be useful for post acceleration. By combining this principle with laser ablation more freedom in the timing of the bunching may be obtained [26].

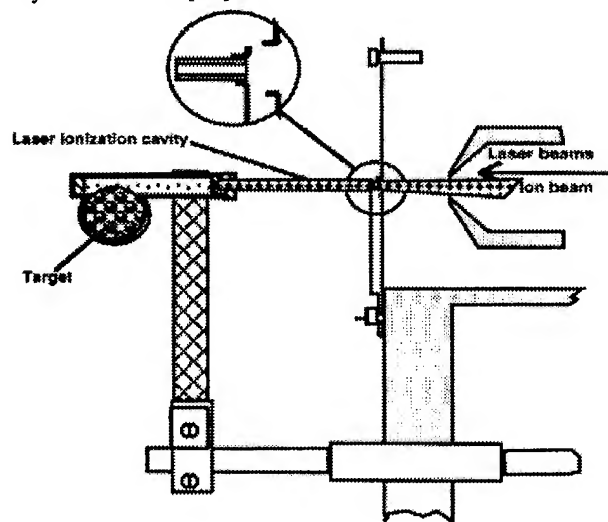


Figure 6: Layout of the ISOLDE laser ion source

F. Penning trap and EBIS as charge breeder

An alternative solution to obtain the needed high charge states directly, is to divide the mass transfer process into the following separate steps: release and singly charge ionisation, transfer of the singly charged ions away from the hostile target region to a first magnetic analysis stage, bunch and cool the singly charged ions in an electromagnetic trap [27] and transfer them to an Electron Beam Ion Source (EBIS) acting as a charge breeder before final acceleration. Such a novel and highly efficient acceleration scheme has recently been proposed by the ISOLDE collaboration [28, 29].

The singly charged radioactive ions presently being delivered by the ISOLDE on-line mass separators are continuously injected into a large Penning trap where they are stopped by collisions with the atoms of a buffer gas accumulated and finally extracted in pulses. That this scheme allows to accumulate and eject 10^7 - 10^8 ions/bunch with an efficiency that approaches 100% and an emittance $< 10 \pi$ mm mrad has recently been demonstrated [30, 31].

Due to the low emittance the bunches from the Penning trap can now without losses be transferred to the EBIS structure [32] as shown in Figure 7. Here the ions are captured in the radial potential well of an intense electron beam where they undergo stepwise electron impact ionisation until the desired charge state is reached. The advantages of this scheme are the more narrow charge state distribution compared to the ECR sources and its independence of the chemical properties of the elements. The total efficiency of external ion injection into the CRYISIS of the Manne Siegbahn Laboratory and the subsequent ejection was measured to be 14.5% and independent of ion confinement times up to 200 ms [33]. Similar measurements performed at DIONE at Saclay [34] showed total efficiencies for N^{1+} and Ar^{1+} of 59% and 52% respectively and after a confinement time of 40 ms an efficiency of 30% for N^{7+} and 9.4% for Ar^{14+} .

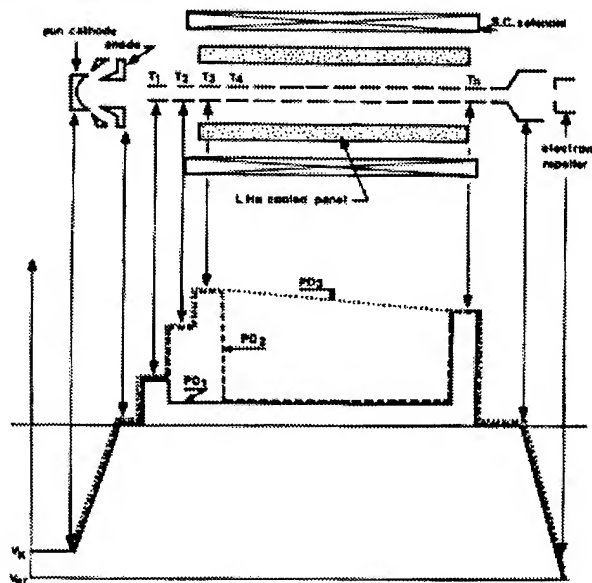


Figure 7: Layout of a typical EBIS ion source

IV. CONCLUSION

Space did not allow to make a complete review of the field of ion-sources for RIB accelerators. Instead references were given to the field of ISOL ion-sources which forms the basis for the new developments. By means of a few examples it is demonstrated that the

field is rapidly developing. In particular recent development of elegant ion handling techniques by means Penning traps, EBIS, ECR- and Laser ion sources holds much promise for new and exciting physics with RIB in the coming years.

VI. REFERENCES

- [1] H. L. Ravn and B. W. Allardyce, in *Treatise on Heavy Ion Science*, Ed. D. A. Bromley (Plenum, New York, 1989), Vol. 8, p. 363.
- [2] D. K. Olsen, *Proceedings of this conference*.
- [3] P. Van Duppen, et. al., *Rev. Sci. Instrum.* 63(1992)2381.
- [4] *Nucl. Instrum. and Meth.* B70(1992)1.
- [5] H. L. Ravn, *ibid* B70(1992)107.
- [6] H. L. Ravn et. al., *ibid* B88(1994)441.
- [7] H. L. Ravn, *Phys. Rep.* 54(1979)201.
- [8] R. Kirchner, *Nucl. Instrum. and Meth.* 186(1981)275.
- [9] B. Vosicki et. al., *ibid* 186(1981)307.
- [10] R. Mueller et. al., *ibid* 127(1975).
- [11] T. Kozłowski, *Private communication*.
- [12] J. R. J. Bennett, et. al., *RAL Report RAL-94-095*, p. 11.
- [13] R. Kirchner, *Nucl. Instrum. and Meth.* A292(1990)203.
- [14] R. Kirchner et. al., *ibid* 133(1976)187 and B70(1992)56.
- [15] S. Sundell et. al., *ibid* B70(1992)160.
- [16] V. Bechtold et. al., *Proc. 7th. Workshop on ECR ion-sources*, Jülich, 1986 p. 248.
- [17] P. Decroock et. al., *Nucl. Instrum. and Meth.* B58(1992)252.
- [18] L. Buchmann et. al., *ibid* B63(1992)521.
- [19] G. Gimmond et. al., *ibid* B70(1992)118.
- [20] P. Sortais, et. al., *XIth Workshop on ECRIS*, Groningen 5-7/5/93, KVI Report 996 p. 97
- [21] P. Sortais, *7th. Int. Conf. on Physics of Highly Charged Ions*, 19-23/9/94, Wien, *Nucl. Instrum. and Meth. B* To be published.
- [22] G.D.E. Alkhazov, et. al., *Nucl. Instrum. Meth.* A280(1989)141.
- [23] F. Ames et. al., *Appl. Phys.* B51(1990)200.
- [24] L. Vermeeren et. al., *Phys. Rev. Lett.* 73(1994)1935.
- [25] V. I. Mishin, et. al., *Nucl. Instrum. Meth.* B73(1993)550.
- [26] H. L. Ravn, *ibid* B70(1992)107.
- [27] R. B. Moore et. al., *J. Mod. Opt.* 39(1992)361.
- [28] H. Haas et. al. *Proc. Int. Conf. On Radioactive Nuclear beams Berkeley, CA 1989*, Eds. W. D. Meyers,

T. M. Nitchke and E. B. Norman World Scientific
Singapore 1990, p 59

[29] Proposal To The ISOLDE Committee: ISC/P68,
CERN/ISC 94-25, 14.11.1994.

[30] G. Bollen, Proc. Nobel Symposium 91,
Lysekiel, Sweden, 1994, Physica Scripta , To be
published

[31] J. Stein, diploma thesis University of Mainz
and G. Bollen Private communication.

[32] E. D. Donets, Rev. Sci. Instrum. 61(1990)225.

[33] E. Beebe, et. al., Nucl. Instrum. and Meth.
B93(1994)378.

[34] J. Faure, et. al., ibid 219(1984)449.

THE TRIUMF HIGH-CURRENT DC OPTICALLY-PUMPED POLARIZED H⁻ ION SOURCE

A.N. Zelenski

Institute for Nuclear Research, Russian Academy of Sciences, 117312 Moscow, Russia

C.D.P. Levy, K. Jayamanna, M. McDonald, P.W. Schmor,

W.T.H. van Oers, J. Welz, G.W. Wight and G. Dutto

TRIUMF, 4004 Wesbrook Mall, Vancouver, B.C., Canada V6T2A3

Y. Mori

KEK, Oho 1-1, Tsukuba-shi, Ibaraki-ken 305, Japan

T. Sakae

Kyushu University, Fukuoka 812, Japan

ABSTRACT

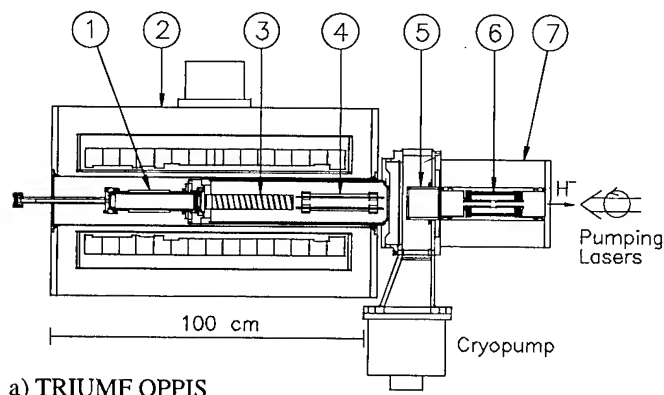
The TRIUMF optically-pumped polarized H⁻ ion source (OPPIS) produces in excess of 150 μ A DC of H⁻ ion current at 85% polarization within a normalized emittance of 0.8 π mm mrad. A 20 μ A beam was accelerated to 500 MeV through the small acceptance of the injection line and the cyclotron. A feasibility study of higher current production for application to multi-GeV accelerators has been performed. A polarized H⁻ ion current of 1.6 mA within a normalized emittance of 2.0 π mm mrad was obtained after upgrading the ECR primary proton source. The source performance now well exceeds the original design parameters and clearly confirms the potential of the OPPIS technique for other accelerators.

I. INTRODUCTION

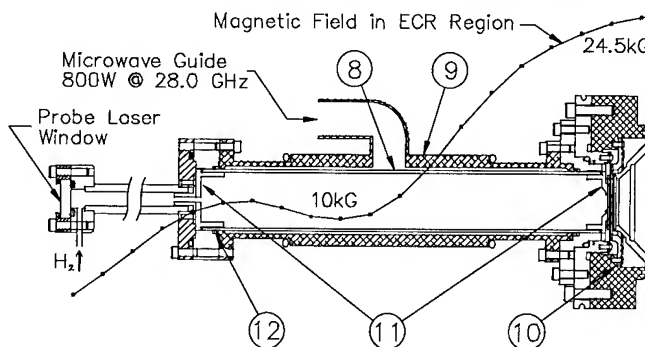
Early OPPIS development immediately demonstrated high current in pulsed mode [1,2]. Polarization was initially limited to 65-70% at the KEK, INR and LAMPF OPPIS's. At TRIUMF, the use of a higher magnetic field, Ti:sapphire lasers for optical pumping of Rb vapour and optimization of all source parameters resulted in 85% H⁻ nuclear polarization, as measured in a beam injection line polarimeter [3]. Depolarization during acceleration due to weak imperfection resonances was recently studied and

minimized by tuning the cyclotron harmonic coils so as to reduce betatron oscillations. As a result, a proton polarization of 82% was measured at 200 MeV, 79% at 350 MeV and 76% at the full 500 MeV beam energy. At present the TRIUMF OPPIS delivers polarized beam to a number of experiments for 30-40% of the cyclotron running time. The most demanding of these is study of parity violation in proton-proton scattering at 220 MeV [4]. Although the latter requires only 0.5 μ A at the target, to satisfy requirements for beam quality - especially modulation of beam current, energy and emittance correlated with spin reversal - we must sacrifice most of the beam intensity by using a low Rb vapour thickness, a narrow stripping extraction foil and no buncher. Therefore, increasing the current is a high priority.

After PAC93, where a high current pulsed OPPIS for high energy accelerators was proposed [5], TRIUMF and INR Moscow joined the SPIN Collaboration, which is working on a proposal for polarization experiments at the FNAL Tevatron-Collider [6]. A pulsed polarized H⁻ current of 1.2 mA is required to operate the Tevatron-Collider with equal luminosity, whether the beam is polarized or not. Demonstration of such current production was considered a major milestone in development of polarization facilities. We are approaching this goal in three ways. First, by upgrading the TRIUMF DC OPPIS, the results of which are presented in this paper. A second approach is based on the INR-type scheme which uses an external atomic hydrogen



a) TRIUMF OPPIS



b) ECR PROTON SOURCE

Fig. 1. 1) ECR Proton Source, 2) Superconducting Solenoid, 3) Optically-Pumped Rb Cell, 4) Deflection Plates, 5) Sona Transition Region, 6) Ionizer Cell, 7) Ionizer Solenoid, 8) Quartz Tube, 9) ECR Cavity, 10) Three Grid Extraction System, 11) Boron-Nitride End Cups, 12) Indium Seals.

injector instead of an ECR primary proton source [5]. The third option, the use of spin-exchange polarization, has been studied experimentally at the INR [7] and TRIUMF OPPIS's [3]. Results are promising for future OPPIS's in the 10-20 mA range.

II. THE ECR PROTON SOURCE UPGRADE

The OPPIS current is essentially determined by the electron-cyclotron-resonance primary proton source (ECRIS), since the optimal neutralization efficiency in the optically-pumped Rb vapour is 50-70%, the sodium ionizer efficiency is constant (9% at 2-5 keV beam energy) and the emittance specification determines the ionizer diameter. The OPPIS ECR source operation is quite different from conventional ECR ion sources developed for multiply charged heavy ion production. Obtaining a high polarization requires a high 25 kG magnetic field in the optically pumped cell and ion extraction region. The highest frequency (28 GHz) microwave generator in use for an ECRIS is operating at the TRIUMF OPPIS. Despite that, the resonant field is only 10 kG and the mirror ratio of 2.5 is too large compared with other sources. Also the OPPIS ECRIS should be optimized for proton production, and therefore the electron temperature in the plasma should be of order 100 eV compared with several keV in a conventional ECR ion source.

The TRIUMF OPPIS and ECRIS are presented in Fig. 1a, b. The microwave power up to 800 W which is required for saturating the proton current yield is produced by a CW extended interaction oscillator (VARIAN VKQ2435F3). The power is introduced transversely into the plasma cavity. The plasma volume is confined within a quartz tube and boron-nitride end cups. The latter prevents coating of the quartz by sputtered metal and extends the quartz liner lifetime. The tube also serves as the microwave input window. It is sealed at the ends by indium O-rings and is cooled by flowing nitrogen gas around it. A high sensitivity of the polarized current to the magnetic field shape and superconducting solenoid alignment was observed. The solenoid has three independent coils which allow control of the magnetic field shape. No multipole magnetic field is used because no substantial improvement was observed with a sextupole magnet in earlier tests. The magnetic field optimized for polarized current production is presented in Fig. 1b. It is characterized by a very short and shallow ECR zone. Apparently we have a combined action of ECR and non-resonant microwave electron heating. In the latter case the microwave power is absorbed at magnetic fields above resonance. Non-resonant microwave heating is more efficient at higher gas pressures and results in low electron and ion temperatures, exactly what is required for high extracted current density and low emittance.

An ion extraction system (IES) should take advantage of the low plasma temperature. To get high current at the low beam energy required for polarization by charge-exchange collisions, a multi-hole IES is used. The IES consists of three 1mm thick planar molybdenum electrodes spaced 1.2mm apart, having 0.95mm diameter apertures in a hexagonally close-packed configuration with a 1.15mm distance between centers. Precise manufacturing and alignment of multihole electrodes is required. The three electrodes are now drilled together (by a spark-erosion technique). Slight differences in hole sizes and positions don't

degrade system performance, since each set of three holes is perfectly aligned. Equally important is that the cost of manufacturing is much lower now, so experiments with a large number of holes are possible.

As a result of the above improvement the polarized H^- ion current became rather reproducible and systematic studies of the current dependence on the proton beam energy, the IES gap width and the microwave power were made. The polarized H^- ion current dependence on the Rb vapour thickness for different sets of extraction grids is presented in Fig. 2.

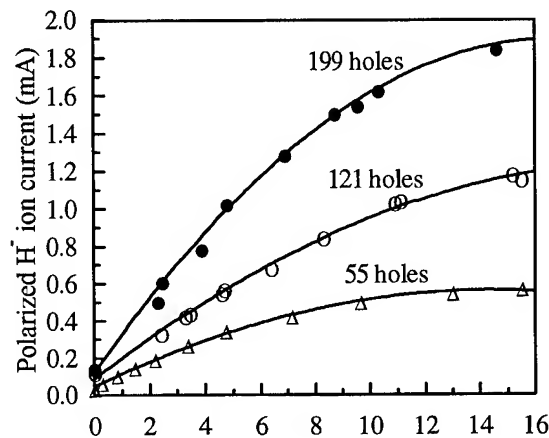


Fig. 2. Rb vapour thickness (10^{13} atoms/cm 2)

The currents are quite accurately proportional to the number of IES holes. The maximum polarized current per hole is about 8 μ A at a Rb vapour thickness of 10^{14} at/cm 2 , where 85% H^- nuclear polarization could be obtained. The diameter of the 199 hole IES is only 17.5 mm and, apparently, a larger diameter IES could produce higher current. The higher gas flow should be handled with a proper vacuum system. The possibility of gas flow pulsing could be also considered. DC operation imposes severe requirements on the IES. The electrode heating and sputtering reduces the grid lifetime. To balance cost and performance for the DC source we used grids with relatively thick walls between holes. For example, the wall thickness is 1.2mm for the 121 hole IES. The lifetime of such a grid is about 1500 hours in DC mode. In pulsed operation, the grid transparency could be increased, and hence larger currents could be obtained for the same beam size.

III. POLARIZATION MEASUREMENTS

The H^- nuclear polarization was measured at 300 keV in a polarimeter based on the ${}^6\text{Li}(p, {}^3\text{He}){}^4\text{He}$ reaction. This polarimeter was calibrated by comparison with the reference 200 MeV polarimeter. In all experiments spin reversal at 40 s $^{-1}$ and a synchronous detection technique for noise reduction were used. Proton polarization measurement accuracy was $\pm 1.5\%$ with a 5 minute integration time. For Rb thickness and polarization measurements the well developed technique of Faraday rotation was used. The results of polarization measurements for a 61 hole IES - a 9mm diameter primary proton beam - are presented in Fig. 3. With two Ti:sapphire lasers, laser power density of 14 W/cm 2 was available for optical pumping of the 9 mm diameter

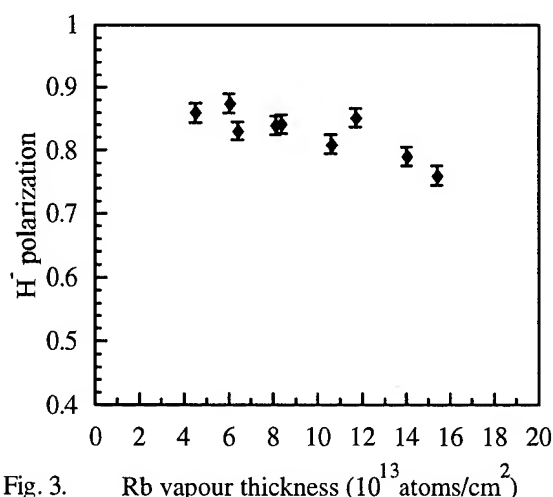


Fig. 3. Rb vapour thickness (10^{13} atoms/cm 2)

Rb vapour column overlapping the proton beam. For the 199 hole IES the beam cross-sectional area is 2.5 cm 2 and a laser power of about 50 W is required to get 80-85% H polarization. This power can be easily produced by a pulsed laser. KEK has loaned a pulsed Ti:sapphire laser for experiments at TRIUMF. The laser was tested for long pulse duration, and 120 μ s was obtained with power above 1 kW. The polarization measurements were done with a relatively large 20 mm diameter ionizer aperture. The Sona region is very close to the ionizer, so the ionizer diameter determines the beam diameter in the transition region and hence possible polarization losses. The observed polarization is consistent with our best results for a 31 hole IES and 12 mm diameter ionizer, so we conclude that Sona depolarization is negligible with the larger beam diameter.

IV. PULSED OPPIS WITH THE BINP ATOMIC HYDROGEN INJECTOR

The results of the high current test with the TRIUMF OPPIS are important for estimates of the current expected from the INR-type pulsed OPPIS with BINP (Novosibirsk) atomic H injector [5]. The full ECRIS proton current was as high as 170 mA for a 199 hole IES and the corresponding emission current density was 120 mA/cm 2 . The use of the atomic injector, having similar current density but much smaller beam divergence, should increase polarized current to at least 5 mA. Experiments at BINP are now in progress to study the limits on the OPPIS pulsed polarized current.

V. CONCLUSIONS

An accelerated polarized beam current of 20 μ A was observed at the TRIUMF cyclotron. The polarization of the injected beam was 85%. Extracted beam polarizations of 82% at 200 MeV and 76% at 500 MeV were obtained. Following high current development, highly polarized 150 μ A was obtained within a normalized emittance of 0.8 pi mm mrad, making feasible 50 μ A accelerated polarized current for experiments at TRIUMF. We note that 10 times higher polarized proton current (i.e. 1.5 mA DC) can be obtained using a gaseous helium ionizer instead of sodium vapour.

Higher current production was studied for the proposed polarization facilities at the FNAL Tevatron-Collider. A polarized H $^-$ current of 1.64 mA DC within a normalized emittance of 2.0 pi mm mrad was obtained at an optically pumped Rb vapour thickness of 10^{14} atoms/cm 2 . H $^-$ nuclear polarization of 85% was measured for a 61 hole IES with 14 W/cm 2 laser power at a Rb vapour thickness of 10^{14} atoms/cm 2 and a 20 mm diameter sodium ionizer cell. Modified for pulsed operation, the TRIUMF OPPIS should produce at least 2 mA polarized H $^-$ ion current, so the 1.2-1.5 mA desired for the FNAL project could be comfortably met with the existing very reliable ECR source technique. The use of the BINP atomic hydrogen injector should boost pulsed polarized H $^-$ current to at least 5 mA.

VI. ACKNOWLEDGEMENTS

We would like to thank R. Laxdal and R. Baartman for help in carrying out polarization and current measurements of accelerated beam and A.D. Krisch for his encouragement and support of high-current OPPIS development. T. Sakae was supported by the international fund of Kyushu University. The work was partially funded by a SPIN collaboration grant.

VII. REFERENCES

1. A.N. Zelenski *et al.*, "Laser Source of Polarized Protons and H $^-$ Ions", in Proc. 6th Int. Symp. on Polarization Phenomena in Nuclear Physics., Osaka 1985, J. Phys. Soc. Japan. 55, 1064 (1986).
2. Y. Mori *et al.*, "Recent Progress on the Optically-Pumped Polarized H $^-$ Ion Source at KEK", AIP Conf. Proc. No.158, 605 (1986).
3. A.N. Zelenski *et al.*, "Spin-Exchange Polarization Study at the TRIUMF OPPIS", Proc. of SPIN'94 Conf., Bloomington, Indiana, Sept. 1994.
4. J. Birchall *et al.*, "Parity Violation in p-p Scattering", Nucl. Phys. A553, 823 (1993).
5. A.N. Zelenski *et al.*, "Proposal for a Pulsed Optically-Pumped Polarized H $^-$ Ion Source for High Energy Accelerators", Proc. 1993 IEEE PAC, 2991 (1994).
6. 1994 SPIN Progress Report, Univ. of Michigan, spokesman A.D. Krisch.
7. A.N. Zelenski and S.A. Kokhanovski, "A Study of Spin-Exchange Polarization Transfer in H-Rb Collisions", Madison 1993, AIP Conf. Proc. 293, 164 (1994).

LIFETIME TEST ON A HIGH-PERFORMANCE DC MICROWAVE PROTON SOURCE*

J. Sherman, D. Hodgkins, P. Lara, J. D. Schneider, and R. Stevens, Jr.
Los Alamos National Laboratory, Los Alamos, NM 87545 USA

Powerful CW proton linear accelerators (100 mA at 0.5 - 1 GeV) are being proposed for spallation neutron source applications. These production accelerators require high availability and reliability. A microwave proton source, which has already demonstrated several key beam requirements, was operated for one week (170 hours) in a dc mode to test the reliability and lifetime of its plasma generator. The source was operated with 570 W of microwave (2.45 GHz) discharge power and with a 47-kV extraction voltage. This choice of operating parameters gave a proton current density of 250-mA/cm^2 at 83% proton fraction, which is sufficient for a conservative dc injector design. The beam current was 60 - 65 mA over most of the week, and was sufficiently focused for RFQ injection. Total beam availability, defined as 47-keV beam-on time divided by elapsed time, was 96.2%. Spark downs in the high voltage column and a gas flow control problem caused all the downtime; no plasma generator failures were observed.

I. INTRODUCTION

Several new applications for high-power proton linacs are being proposed [1] for spallation neutron sources with nuclear processing applications such as transmutation of nuclear waste and the production of tritium. Proton injector requirements for these linacs have been summarized [2], and, for radio frequency quadrupole (RFQ) injection, parameters are typically 110-mA proton-beam current at 75 keV. At these beam parameters the ion source reliability and longevity become difficult. One MW accelerators at Villigen, Switzerland and Los Alamos, New Mexico use a dc filament-driven volume source [3] and a pulsed duoplasmatron [4] to deliver the required proton currents. The basic technology accelerator (BTA) in Japan [5] is using a filament-driven volume source.

A microwave proton source [6] has been chosen for the dc ion source at Los Alamos for the high-intensity linac injector. Its higher-power efficiency and lower H_2 gas consumption [2] suggest it may be a more reliable, longer-lived proton source. Long lifetime electron-cyclotron resonance (ECR) oxygen ion sources similar to this microwave proton source have been reported [7]. This paper reports on a 170 hour continuous run in which the microwave source produced 60 - 65 mA hydrogen-ion current at 47 keV without a plasma-chamber fault.

II. EXPERIMENT

This experiment was performed on the 50-keV injector brought from Chalk River Laboratories (CRL) to Los Alamos. The microwave proton source power supplies

operate at ground potential except for the gas-flow controller which is powered through a small isolation transformer. Figure 1 shows the ion-source and accelerating-column installation at Los Alamos [8]. As configured, this injector cannot meet the energy and current requirements of the proposed CW linacs; an advanced injector to meet these requirements has been designed [2], and is now undergoing tests at Los Alamos.

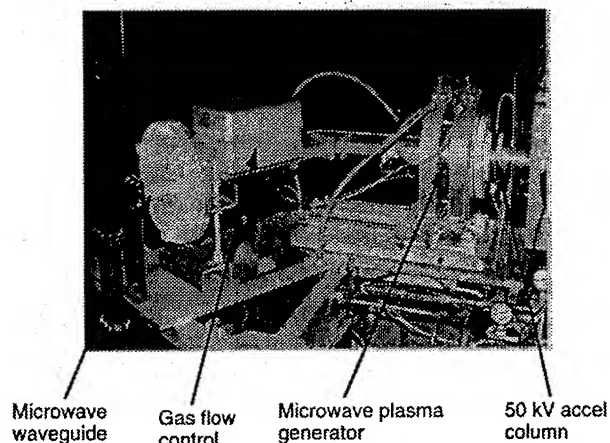


Figure 1. Installation of the 50-keV injector at Los Alamos. Locations for the 2.45-GHz microwave waveguide, the gas-flow controller, the microwave plasma generator, and the 50-keV accel column are shown in the picture. The isolation transformer is located immediately under the gas-flow controller.

The 47-keV extraction voltage was chosen to provide a well-focused beam with $> 200\text{-mA/cm}^2$ proton current density. The advanced injector would attain the required 110-mA proton current through a 4.2-mm radius emission aperture at 200 mA/cm^2 current density. The present experiment was operated with $> 60\text{-mA}$ hydrogen-ion current extracted through a $r_e = 2.5\text{-mm}$ radius emission aperture. The 83% proton beam fraction measured at the conclusion of the seven-day run is shown in Fig. 2. The proton current density $j_p = (60\text{ mA})(0.83)/(\pi r_e^2) = 250\text{ mA/cm}^2$ thus exceeds the advanced injector design requirement by 25%. The ion source was run with 570 W forward power with 1 - 10 W reflected power at the 2.45 GHz operating frequency. The H_2 gas flow was 2.7 sccm, which implies 13% efficiency for conversion of H_2 gas into proton beam current. The 47-keV hydrogen-ion beam was dumped on a watercooled copper beam stop. Taking the copper sputtering coefficient $S = 3.7 \times 10^{-3}$ atoms/ion and a 1 cm beam radius, a beam dump lifetime of 274 days was

* Work supported by the United States DOE, contract W-7405-ENG-36.

calculated. No beam dump problems were encountered over this seven day run.

During preparation for the seven-day longevity test, a problem with the O-ring seal at the microwave window was encountered. The vacuum interface between the WR284 waveguide and plasma chamber is formed by a 2-mm thick piece of aluminum nitride (AlN) which compresses an O-ring seated in the back wall of the plasma chamber. During earlier

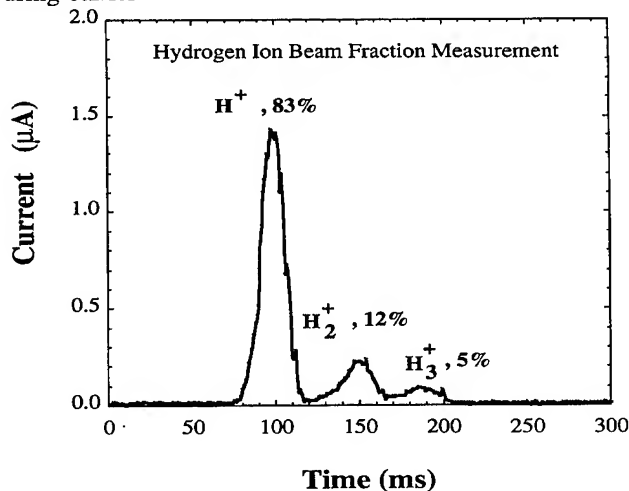


Figure 2. Hydrogen-ion beam fractions measured at the conclusion of the seven day run. The beam-fraction diagnostic uses a massively cooled 0.15-mm slit, a ramped magnetic dipole field, and a collector cup which samples the separated hydrogen-ion currents.

discharge operation, this O-ring failed unpredictably. The problem was solved by installing a 0.025-mm metal sheet at the AlN window-O-ring interface, where it does not interfere with the microwave transmission into the plasma chamber. This failure mode was apparently unique to our operation, as others [9] working with this proton source have not encountered this problem.

III. RESULTS

A. Ion Source Availability and Longevity Test

Figure 3 shows the beam availability as a function of the elapsed time. Beam availability is defined as the 47-keV beam on time divided by elapsed clock time. During the first 24 hours of operation significant downtime was encountered because of gas-flow instabilities brought about by rising temperature in the confined high-voltage (HV) area (see Fig. 1). This problem was overcome by installing fans on the HV enclosure to circulate the stagnant air. From 24:00 hours onward, the beam availability increased continuously to 96.2% at the end of the seven-day period. Most of this 4% downtime was spent recovering from HV sparks in the HV column. The average recovery time from a beam-off event was 83 seconds, which is dominated by the resetting of the HV power supply to the extraction potential. The longest uninterrupted run time was five hours. After completion of the seven day run, the ion source was inspected for wear or imminent component failure. No obvious signs of wear were found, and it is unknown how long the source would have run

before failing. The ion source longevity is now demonstrated to be greater than 170 hours.

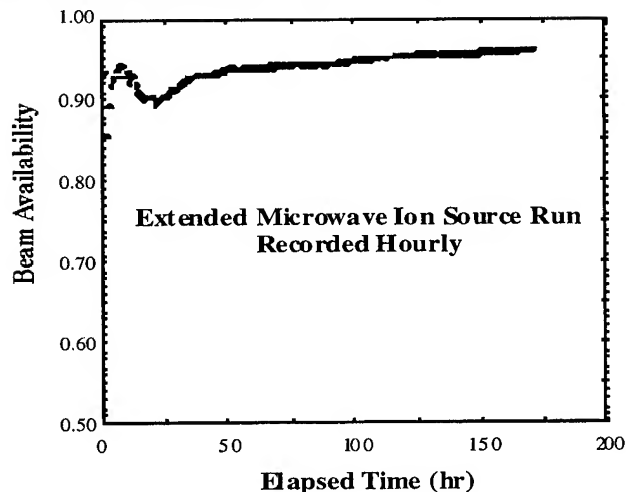


Figure 3. Beam availability vs. elapsed time curve. Beam availability is defined as the 47 keV beam-on time divided by the elapsed clock time.

B. Beam Emittance Measurement

Previous proton emittance measurements have been made with the microwave ion source only [6] and ion source plus single-solenoid low energy beam transport (LEBT) [10] for 50 keV, 60 - 70-mA beams. The ion source-only results give rms normalized emittances in the 0.10 - 0.12 (π mm-mrad) range while the ion source plus LEBT measurements yield 0.20 (π mm-mrad). The LEBT measurements relied on a Gaussian extrapolation procedure to eliminate the H_2^+ and H_3^+ components, which is a reasonable approach because the hydrogen ion beam was dominated by the 75% proton fraction.

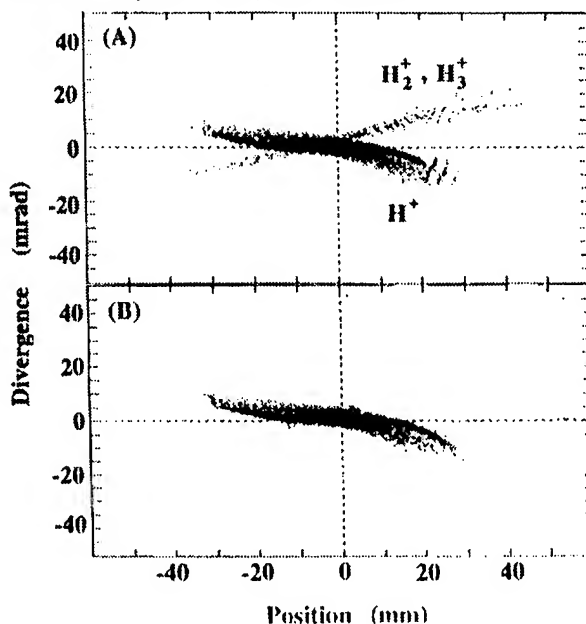


Figure 4. (A) Hydrogen-ion beam distribution after transport through a single-solenoid LEBT. (B) The same distribution as (A) but with the H_2^+ and H_3^+ species removed.

Table 1. Requirements and status of demonstrated injector parameters for 100-mA CW linac program.

Injector Parameter:	Requirement:	Observed:
Beam Availability (%)	>98	96.2
Minimum ion source lifetime (hours)	>160	>170
Beam energy (keV)	75	47
Beam current, protons (mA)	110	50
Proton beam current density (mA/cm ²)	200	250
Beam emittance (π mm-mrad), rms normalized @ 110 mA, 75 keV. RFQ injection.	0.20	0.20 @ 50 keV, 56 mA, through a single-solenoid LEBT.

The LEBT emittance data in ref. [10] have now been reanalyzed by removing the H_2^+ and H_3^+ contributions to the measured phase-space distribution. An original distribution is shown in Fig. 4(A) where the main proton distribution plus the H_2^+ and H_3^+ components are separated by the magnetic field of the focusing solenoid. The distribution in Fig. 4(B) shows the same datafile with the H_2^+ and H_3^+ components removed. Analysis of the Fig. 4(B) distribution in terms of beam fraction vs. total emittance [11] gave 0.20 (π mm-mrad) proton beam emittance for 100% beam fraction, which agrees with results presented in ref. [10].

IV. SUMMARY

LANL proposals for 100-mA CW linacs have a RFQ [1] as the first rf acceleration stage, and the RFQ sets injector parameters. The injector parameters and requirements are summarized in columns 1 and 2 of Table 1. A consistent set of observed microwave ion source/injector parameters is shown in column 3. The present ion source results exceed the ion source lifetime and beam current density requirements, and is close to meeting the beam availability requirement. During a 170 hour run, 47-keV beam was available for 96.2% of the elapsed time. Most of the beam off time came from HV column sparkdown recovery, and it is anticipated that the > 98% specification can be achieved with an optimized column design and high-voltage power supply. No plasma generator failures were observed over the 170 hours.

Greater than 50-mA proton current was maintained over the 170 hours. This parameter needs to be doubled for the CW linac applications. The observed 250-mA/cm² proton current density exceeds the advanced injector design requirement [2] by 25%. An increase in proton current, at a constant discharge power, is likely from the work at Argonne National Lab and Los Alamos [12] where proton beam fractions > 90% have been measured from the microwave source. The beam energy needs to be increased 60% from 47 to 75 keV.

Proton beam emittance of 0.20 (π mm-mrad) rms normalized, has been inferred from hydrogen ion beam emittance measurements through a single-solenoid LEBT [10]. The inferred 0.20 (π mm-mrad) emittance has been confirmed here by analysis of a datafile with the H_2^+ and H_3^+ species removed. Maintaining the required proton beam emittance at the RFQ injection point while increasing the proton current and energy may be the most severe remaining technical injector challenge. The advanced 75-keV injector design, based on the microwave proton source, for 110-mA proton current at 75 keV is now

under development at Los Alamos to address these questions.

V. ACKNOWLEDGEMENTS

We thank Chalk River Laboratories, Ontario, Canada, for transferring the microwave proton source technology and 50-keV injector to Los Alamos. With this help, LANL has been able to make good progress towards demonstrating a proton injector for the 100-mA CW linac programs.

VI. REFERENCES

- [1] George P. Lawrence, "New Applications for High-Power Proton Linacs," Proc. of the 1990 Linear Accelerator Conference, Los Alamos National Lab report no. LA-12004-C, 553 (1990).
- [2] R. R. Stevens, Jr., J. D. Sherman, and J. D. Schneider, "Injector Design for High-Current CW Proton Linacs," Proc. of the 1993 Particle Accelerator Conference, IEEE Catalog Number 93CH 3279-7, 3166, (1993).
- [3] M. Olivo, E. Mariani, and J. Sherman, "The PSI 870 keV High Intensity Cockcroft-Walton Preinjector," Rev. of Scientific Instrum. **63**, 2714 (1992).
- [4] C. Robert Emigh, Earl A. Meyer, Donald W. Mueller, and Ralph R. Stevens, Jr., "LASL Experience with a Duoplasmatron Feeding a 750 kV Exact Pierce Column", Proc. of the Symposium on Ion Sources and Formation of Ion Beams, Brookhaven National Laboratory report BNL 50310, 113, (1971).
- [5] H. Oguri, "A High-Brightness Hydrogen Ion Source for the BTA at JAERI," Proc. of the 17th International Linac Conf., Tsukuba, Japan, 381 (1994).
- [6] Terence Taylor and Jozef Mouris, "An Advanced High-Current Low-Emittance dc Microwave Proton Source," Nuclear Instrum. and Methods in Physics Research A **336**, 1(1993).
- [7] Y. Torii, M. Shimada, I. Watanabe, J. Hipple, C. Hayden, and G. Dionne, "A High-Current Density and Long Lifetime ECR Source for Oxygen Implanters", Rev. Sci. Instrum. **61**, 253 (January, 1990).
- [8] J. David Schneider, Jerry Bolme, Vaughn Brown, Martin Milder, George Neuschaefer, Daniel Rees, Patrick Schafstall, Joseph Sherman, Ralph R. Stevens, Jr., Thomas Zaugg, G. E. McMichael, Javid Sheikh, and Terence Taylor, "Installation of a CW Radiofrequency Quadrupole Accelerator at LANL", Proc. of the 17th International Linac Conf., Tsukuba, Japan, 149 (1994).

[9] Terence Taylor, Chalk River Laboratories, and David Spence, Argonne National Lab, private communication.

[10] Ralph R. Stevens, Jr., Patrick Schafstall, J. David Schneider, Joseph Sherman, Thomas Zaugg, and Terence Taylor, "DC Proton Beam Measurements in a Single-Solenoid Low-Energy Beam Transport System", Proc. of the 17th International Linac Conf., Tsukuba, Japan, 549 (1994).

[11] Paul Allison, Joseph D. Sherman, and H. Vernon Smith, Jr., "Comparison of Measured Emittance of an H Ion Beam with a Simple Theory", Los Alamos Technical Report LA-8808-MS, (June, 1981).

[12] David Spence and Charles L. Fink, "Production of High Proton Fractions from ECR Sources by Plasma Modification", Proc. of the 17th International Linac Conf., Tsukuba, Japan, 396 (1994), and David Spence and Kieth Lykke, these conference proceedings, paper WPC11.

Performance enhancement of a compact radio frequency ion source by the injection of supplemental electrons

R.F. Welton, G.D. Alton, D. Becher, G.D. Mills, J. Dellwo and S.N. Murray
Oak Ridge National Laboratory*, P.O. Box 2008, Oak Ridge, Tennessee 37831

A versatile, high brightness, volume type, RF source, capable of producing positive ion beams with intensities as high as 1 mA from gaseous feed materials and microamperes of negative ion beams has been characterized. The source can also be operated as a plasma sputter negative ion source to generate up to 1 mA of a selected species. The performance of the source in the positive and negative volume modes of operation can be greatly enhanced by addition of a removable, water cooled filament assembly in place of the negative sputter probe. For example, the material utilization efficiencies of gaseous feed species can be more than doubled, total current intensities increased up to 40%, N₂ molecular dissociation fractions increased by 20% and minimum operating pressures reduced by a factor of four when operated in the volume mode. These added electrons also favorably effect, as a consequence of lower pressures, the emittance apparently through a reduction of scattering in the beam through the transport system. A brief description of the source and performance data for the positive volume mode of operation will be presented.

I. INTRODUCTION

The design features of the source are described in reference 1. Plasma sputter negative ion sources of this type have been utilized by several groups for a number of applications including accelerator based atomic and nuclear physics, material processing and isotope separation (see e.g. the references contained in ref. 1). In addition to the sputter mode of operation, both positive and negative ions can be extracted directly from the RF plasma when operated in the volume mode. The capability to operate in

any of these three modes greatly extends the number and variety of ionic species that can be generated by the source. Because of this versatility the source can be used for numerous applications [1]. Source reliability, multimode operation, high gas load tolerance, long lifetime, low emittance and high efficiency for dissociative ionization of molecules into positive and negative singly charged atomic ions also make the radio frequency ion source a candidate for Radioactive Ion Beam (RIB) generation. However, issues concerning the ionization efficiencies when operated in the positive mode have not yet been resolved for these applications.

The effect of injecting electrons into a high frequency discharge ion source has been explored extensively for microwave ECR sources [2-9] and to a lesser degree in radio frequency ion sources [10]. Lynies has shown [2] that the performance of microwave ECR sources could be enhanced through the addition of injected electrons either from a gun or by a coating of SiO₂ on the metallic plasma chamber. Others employ a plasma cathode or biased disk technique to augment the electron density in the main stage of the source [8,9]. Abdelaziz et al [10] have explored the improvement to beam brightness of a magnetized radial extraction RF ion source, finding nearly an order of magnitude improvement in electron density, an increase in extracted beam current and a decrease in emittance resulting in a significant increase in ion beam brightness. In this work, we characterize the performance of a compact RF source for operation in the volume mode for the generation of positive ions. Total analyzed current yields, ionization efficiency, molecular dissociation and emittance have been measured with the filament on and off.

* Managed by Martin Marietta Energy systems, Inc., under contract No. DE-AC05-84OR21400 with the U.S. Department of Energy.

"The submitted manuscript has been authored by a contractor of the U.S. Government under contract No. DE-AC05-84OR21400. Accordingly, the U.S. Government retains a nonexclusive, royalty-free license to publish or reproduce the published form of this contribution, or allow others to do so, for U.S. Government purposes."

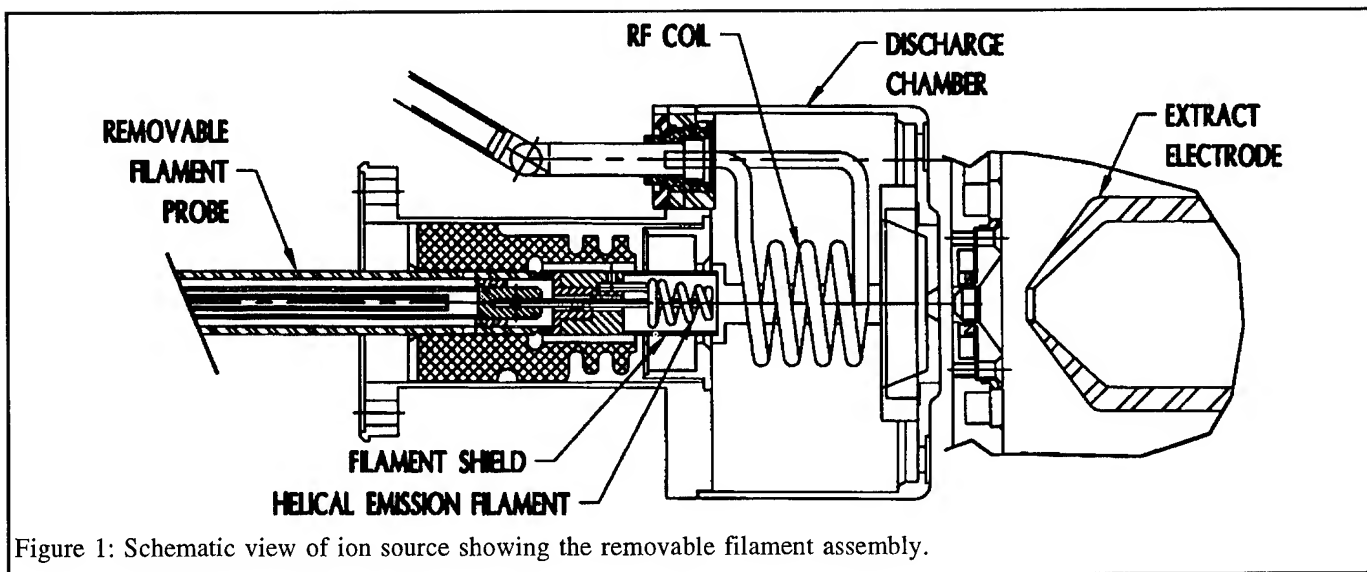


Figure 1: Schematic view of ion source showing the removable filament assembly.

II. THE ION SOURCE AND FILAMENT PROBE ASSEMBLY

Fig. 1 shows a cross sectional view of the RF source with the removable filament assembly in place. Radio frequency power is coupled into the plasma through a copper coil shown in the figure, matching is achieved by a network controlled remotely and located adjacent to the RF feedthrough. Power is generated in a 0-1kW, 13.56 MHz supply. Atomic and molecular gas mixtures can be fed into the source from a system of variable and calibrated leaks through an opening directed through the RF coil windings. A converging helical tantalum element of thickness 1.5 mm is raised to emission temperature by a current of ~70 A flowing through a water cooled copper central conductor and out through a copper shield. High temperature components are isolated from the copper by a tantalum cylinder which forms a shield about the filament to prevent direct bombardment of the copper RF coil. The entire assembly can be biased with respect to the plasma.

III. EXPERIMENTAL RESULTS

Total extracted argon current, nitrogen dissociation fractions and trace flow (9×10^{-5} sccm) Xe efficiencies were measured with the filament on and off as a function of operating pressure, RF power and extraction voltage. Optimal conditions of filament operation were 70A heating

current, -10V bias and an emission current of 1.5A. Variation of ion current, dissociation fraction and Xe efficiency with RF power is shown in fig. 2. In each case, the source was maintained at the lowest pressure that allowed reliable operation. Use of the filament resulted in a lowering of the normalized emittance from 2.4 to 2.12π mm mrad (MeV) $^{1/2}$ for the 90% contour of the beam. In addition, the minimum pressure for stable plasma operation was reduced on the average by a factor of four.

IV. CONCLUSION

This work quantifies the performance enhancement that can be expected with the addition of a relatively simple filament structure to an inductively coupled RF ion source operating at modest powers. Measurements were geared to both accelerator (injector) ion source applications where intensity is desired and ISOL (radioactive beam) applications where ionization efficiency of trace material and molecular dissociation is most important. Under optimal conditions, the ionization efficiency of a trace flow of Xe was found to increase from 8% to 16%. The electrons appear to benefit the source plasma in three important respects: (1) the minimum operating pressure is lowered four fold (to 4×10^{-4} Torr in the source), (2) the emittance is improved and (3) the electron density is increased which subsequently lowers the plasma potential, as observed in ref. 2 and 7.

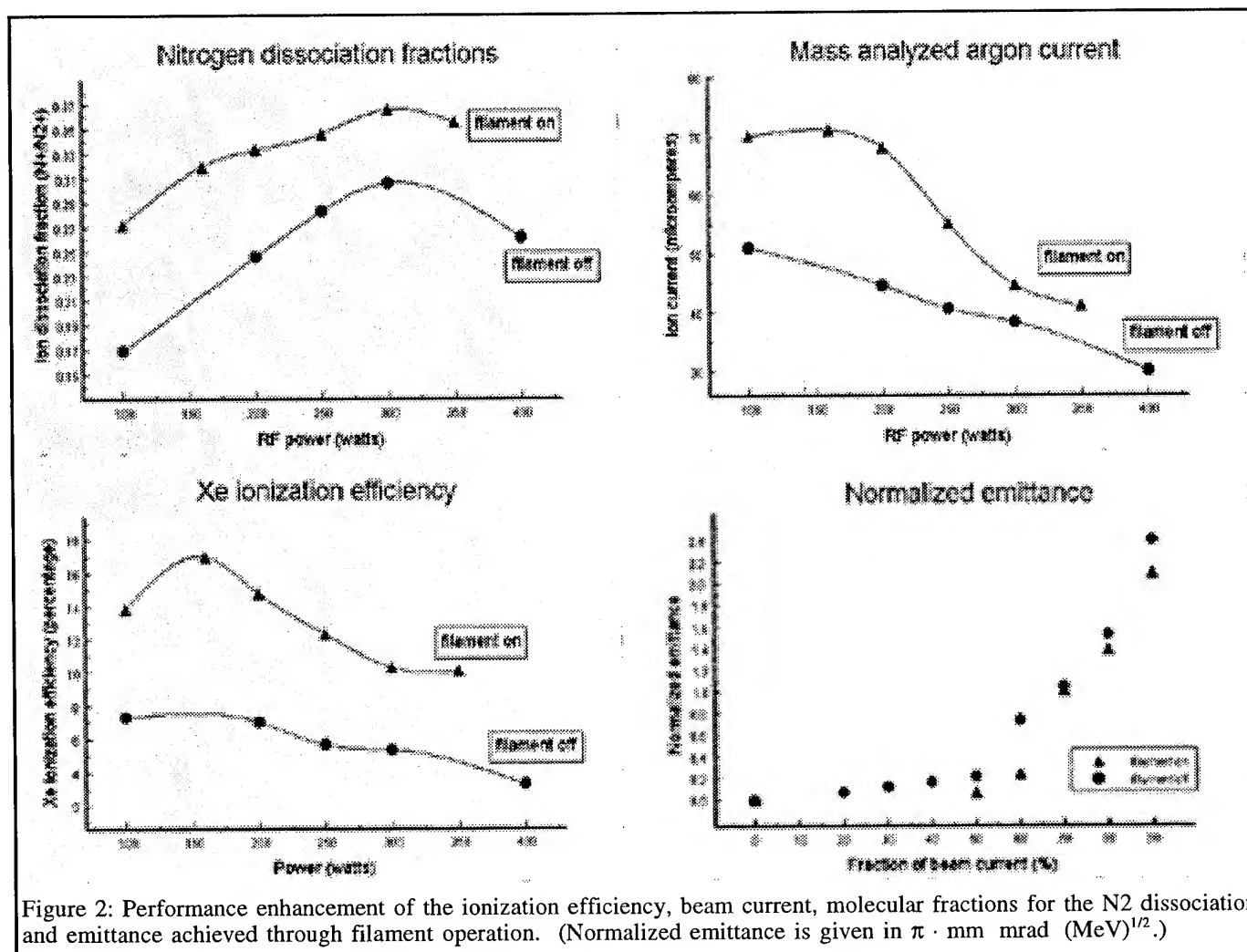


Figure 2: Performance enhancement of the ionization efficiency, beam current, molecular fractions for the N₂ dissociation and emittance achieved through filament operation. (Normalized emittance is given in $\pi \cdot \text{mm} \cdot \text{mrad} (\text{MeV})^{1/2}$.)

V. REFERENCES

1. G.D. Alton, G.D. Mills and J. Dellwo, Rev. Sci. Instrum. 65, 2006 (1994)
2. Z.Q. Xie, C.M. Lynies, R.S. Lam and A. Lungdren, Rev. Sci. Instrum. 62, 775 (1991)
3. T. Nakagawa, T. Kageyama, M. Kase, A. Goto and Y. Yano, Jpn. J. Appl. Phys. 32, L1335 (1993)
4. G. Melin et al. Proc. of the Tenth Int. Workshop on ECR Ion Sources, Knoxville, TN, Nov. 1-2, (1991) p.1
5. T. Nakagawa, T. Kageyama, Jpn. J. Appl. Phys. 30, L1588 (1992)
6. S. Gammino, J. Sijbring and A.G. Drentje, Rev. Sci. Instrum. 63, 287. G. Mouchaty, R.C. Rogers, P. Smelser and D.P. May: Proc. 13th Int. Conf. Cyclotrons and their Applications, Vancouver (1992) p.369
7. T. Nakagawa, T. Kageyama, M. Kase, A. Goto and Y. Yano Jpn. J. Appl. Phys 31 (1992) L1129
8. Y. Matsubara, H. Tahara, S. Nogawa and J. Ishikawa: Rev. Sci. Instrum. 61 (1990) 541
9. M.E. Abdelaziz, M.M. Abdelbaki and S.G. Zakhary, Rev. Sci. Instrum. 63, 2749 (1992)

A HIGH-CURRENT POSITRON SOURCE

V.V.Gorev RRC "Kurchatov Institute" and Institute of Physical Ballistics

The positron sources now in use have an intensity of about 10^6 - 10^8 e⁺/s or a positron current of about 10^{-13} - 10^{-11} A [1]. This is less than the current of electron and ion beams used in science and technology by 10-20 orders of magnitude. A high-current, quasistationary positron source can be created on the basis of a $^{64}_{29}\text{Cu}$ isotope produced in irradiation natural copper by thermal neutrons in a nuclear reactor [2,3]. If the irradiation is performed in the central cell of the highest-flux channel of an SM-3 reactor for several days, the $^{64}_{29}\text{Cu}$ specific activity will be as high as 130-190 Ci/g at neutron flux density of about $A \approx 1.5 \cdot 10^{15} \text{ cm}^{-2} \text{ s}^{-1}$. In such a case the starting material (a rod made from copper of natural isotopic composition) must have a diameter $d \leq 1 \text{ cm}$ and a length $L \leq 30 \text{ cm}$. The standard TUE targets must be inserted in the cells. Thus, the total mass of copper Cu^{64} that can be produced in a single irradiation run amounts to about 200g. Its total activity will be 20-30 kCi, corresponding to a positron current of 10^{-3} - 10^{-4} A. Indeed, only 0.1% of positrons can escape from the cylinder specimen; the remaining positrons are used in the bulk. To increase the yield of positrons the specimen withdrawn from the reactor must be transformed to foils, for example, by a magnetron sputtering technique in a "hot" chamber. If the foil thickness is $20 \mu\text{m}$, the yield of positrons will be as high as $100\% \cdot \exp(-17.8 \cdot 9 \cdot 0.66^{-1.14}) \approx 60\%$ of the theoretically possible value. The area of the foil will be 2 m^2 .

Can the quasistationary positron current exceeding 10^{-3} - 10^{-4} A be reached on the basis of the present state of the art? To do this the following scheme should be realized: a quasistationary isotope source → a means based on plasma mirror traps (for example, of the open-trap type) for accumulating and retaining positrons → a means for fast extracting positrons from the trap. If the positron source provides a positron current of 10^{-3} - 10^{-4} A, while the plasma trap is capable of efficiently trapping and retaining positrons for 10-100s [4] and then being opened in 10^{-3} - 10^{-4} s, the positron current pulse will be as high as 1 to 1000 A. Thus, the solution of the high-current positron source problems lies at the junction of several engineering branches including production of highly active isotopes, plasma traps and acceleration engineering (e⁺-sources).

Let us consider two schemes of sources.

1. A POSITRON SOURCE BASED ON FOCUSING THE DECAY PRODUCTS FROM AN EXTENDED β^{\pm} -ACTIVE ISOTOPE IN A MAGNETIC AND AN ELECTRIC FIELDS.

The simplest solution for the problem of focusing the positrons emitted by the foil consists in using a convergent magnetic field. An electric field applied towards the neck of the mirror will evidently improve such a system [4-5]. In this case

the value of the transit angle becomes dependent on the positron energy

$$\sin^2 \theta < \frac{(E + e\Delta\phi)^2 - m^2 c^4}{R_m (E^2 - m^2 c^4)},$$

where E is the total energy of positron; R_m is the mirror ratio; $\Delta\phi$ is an accelerating potential difference. At the energies

$$e\Delta\phi / E_F > \left(R_m - \left(mc^2 / E_F \right)^2 \cdot (R_m - 1) \right)^{1/2} - 1,$$

all the positrons will travel through the mirror regardless of the angle of inclination of their trajectory. Here E_F is the maximum energy in the radiation spectrum (Fermi energy).

The quasistatic focusing system was analyzed for the maximum feasible parameters: an accelerating potential, $e\Delta\phi$, of up to 10 MeV, a maximum magnetic field, B_{max} , of up to 100 kG and a length of 5-10 m. Therefore, the results obtained demonstrate the ultimate in the static focusing that can be attained by this way.

Figure 1 shows the current delivered to the target as a function of the potential difference ($E_F = 1.17 \text{ MeV}$, $R_m = 100$, $B_{\text{max}} = 100 \text{ kG}$). The current delivered to the target and its density as a function of the mirror ratio at $e\Delta\phi = 10 \text{ MeV}$ and $B_{\text{max}} = 100 \text{ kG}$ are shown in Figs. 2 and 3.

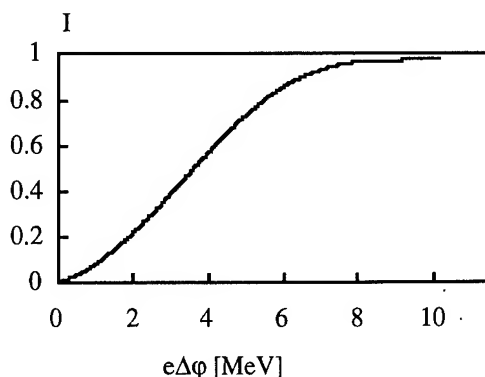


Fig.1

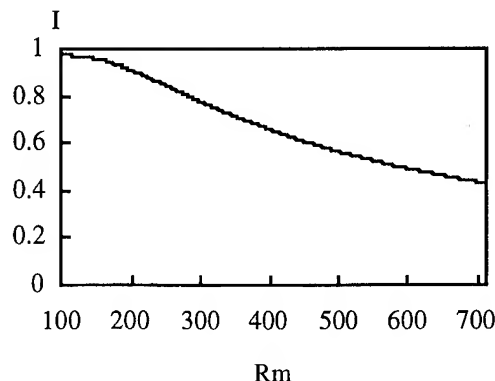


Fig.2

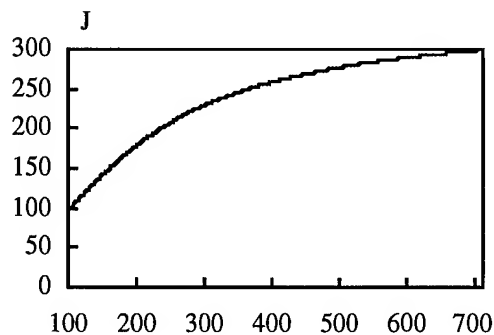


Fig.3.

Rm

The theoretical calculations and the numerical simulations showed that for a $^{64}_{29}\text{Cu}$ foil the beam can be focused onto an area of 24-25 times less than the initial radius by losing up to 50% of the initial current. Despite the high mirror ratio (≈ 600) the drift theory is still applicable to this case (to an accuracy of 10%) and the beam formation process can be easily described theoretically.

For a foil area of 2m^2 , a positron current of $10^{-3}-10^{-4}\text{A}$ and $m \approx 200\text{g}$ the focusing spot has a radius of about 2.8cm and $J \sim 3 \cdot 10^{-5}-10^{-6}\text{A/cm}^2$.

A small source made of foil ($m \approx 0.36\text{g}$, $A \approx 10^{15}$, foil radius $\approx 2.5\text{cm}$, foil thickness $d=20\mu\text{m}$) allows a current of $10^{12}\text{e}^+/\text{s}$ to be focused onto an area of radius $R_f \sim 0.1\text{cm}$.

The strong longitudinal and, first of all, transverse heating of the positron flux ($T_{\perp} \approx e\phi_{\text{max}}$) can be assigned to the shortcomings of the scheme. If we attempt to use the beam focused in such a way as a source of annihilation γ -quanta and direct it on to a plane target, the positrons penetrating the substance will thermalize to form a hemisphere of about 1cm diameter in the volume of the target. It is this hemisphere that will be a volume source of annihilation γ -quanta. On the other hand, severe difficulties appear in transporting the focused beam. Finally, because of the considerable geometric dimensions of the foil a strong constant electric and magnetic fields should be created in a large volume. True, the foil could be convoluted to form a cylinder [8], however, in so doing no great gain could be obtained.

2. A HIGH-INTENSITY "TRANSPARENT" POSITRON SOURCE * ("SHASHLYK") [6-7]

To extract positrons from a massive β^+ -active specimen it can be made as a system of β -transparent elements (for example, foils $d \sim 10-20\mu\text{m}$ in thickness) with sufficiently small cross-sectional dimensions so that outgoing beam could be easily focused (see Fig.4).

If we assume that all the foils are similar and that the same potential differences $e\Delta\phi_{i,i+1}$ sufficient to compensate for the angular scattering applied between the foils, then at a fixed total potential difference there exists

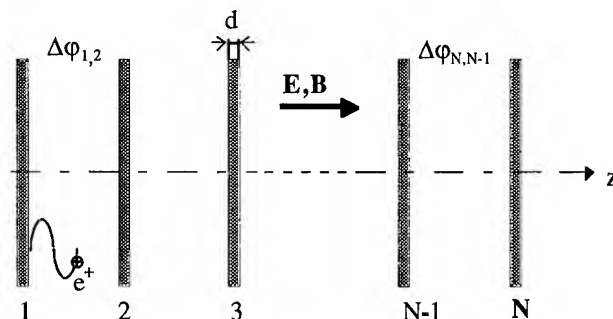


Fig.4.

an optimal number of foils for which the current at the exit is maximum.

Figure 5 shows the optimal output current normalized to the half activity of a $20\mu\text{m}$ -thick foil in the absence of self-absorption as a function of the thickness of the individual foil. The numerals denote the optimal number of foils for the given voltage and the given thickness. The curves differ in the value of applied voltage:

- $e\phi_2 = 500\text{keV}$, —▲— $e\phi_2 = 1\text{MeV}$,
- ▼— $e\phi_2 = 5\text{MeV}$, —□— $e\phi_2 = 10\text{MeV}$.

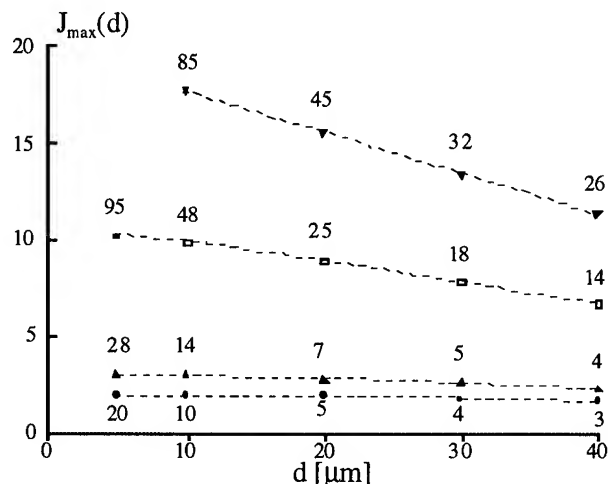


Fig.5

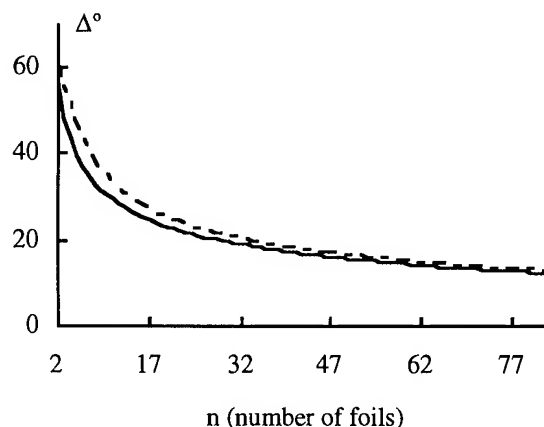


Fig.6

* Shashlyk is a culinary term standing for the pieces of mutton roasted on a spit

The angular width of the distribution of the partial current as a function of the number of foils through which the beam has passed is plotted in Fig. 6. The parameters of the system are: $e\phi_x = 20\text{MeV}$, $d=20\mu\text{m}$, $N=83$. The solid and dotted curves correspond to the numerical and analytical calculations, respectively.

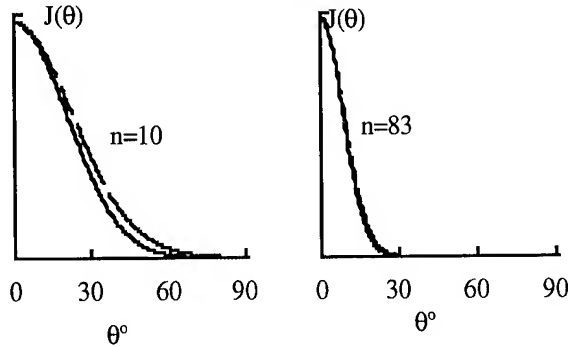


Fig.7

Figure 7 shows the angular distribution of the partial current. Different plots correspond to the different numbers of the foils n through which the beam has passed.

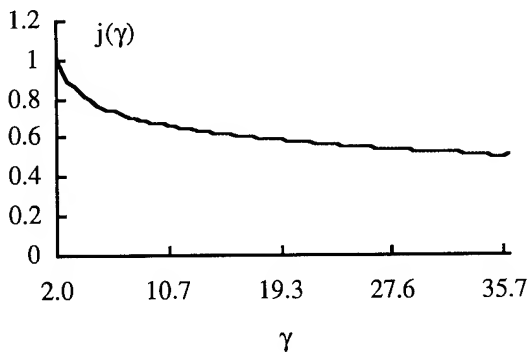


Fig.8

Figure 8 shows the energy distribution function of the total current $j(\gamma)$. Here γ is total energy of positrons normalized on mc^2 . The steep drop of $j(\gamma)$ at great γ corresponds to a weak absorption of high-energy particles by the foils.

We offer the concrete example basing on the numerical calculations in the framework of a source model described in Section 2. Let the energy of an accelerator be 20MeV . Choose the isotope ^{64}Cu . Let the area of each foil be 10cm^2 and its thickness - $20\mu\text{m}$. Then the optimal number of the foils ~ 80 . If the irradiation occurs in the highest-flux channel of an SM-3 reactor (the flux is about $10^{15} \text{ n}/(\text{cm}^2\text{s})$), each of such foils emits about $5 \times 10^{11} \text{ e}^+/\text{s}$ on one side. The total positron current at the exit will be $\sim 2 \times 10^{13}$, that is, $\sim 50\%$ of the half activity of all the foils (with allowance for the self-absorption). The majority of the positrons having passed through the last foil are concentrated within an angle 20° . The energy distribution at the exit from the source is in the form of a "plateau" with a dispersion of 20MeV .

REFERENCES

1. Schultz P.J. Lynn K.G. // *Rev. Modern Phys.* 1988. V.60. N.3. P.701.
2. V.V.Gorev Certificate of Auto ship No. 1723677 USSR. Claimed January 21th 1991.
3. L.D.Hullet,JR, and C.C.Eberle. A High Intensity Slow Positron Facility for the Advanced Neutron Source. "Abstracts for the Thirteen International Conference on the Application of Accelerators in Research and Industry". Denton, Texas USA. November 1994.
4. V.V.Gorev, K.O.Kachalov, K.S.Serebrennikov // *Plasma Physics Reports*. 1994. V.20. N.3. P.271.
5. V.V.Gorev, K.O.Kachlov, K.S.Serebrennikon, and S.D.Stolbetsov. Formation of positron beam from an extended β^\pm -radioactive source in a magnetic and an electric static fields. Preprint IAE -5721/14, Moscow, 1994 (in Russia).
6. V.V.Gorev. A High Current Transparent Positron Source. "Abstracts for the Thirteen International Conference on the Application of Accelerators in Research and Industry". Denton, Texas USA. November 1994.
7. V.V.Gorev, K.O.Kachlov, and K.S.Serebrennikon. Two schemes of a high-current positron source based on β^\pm -active isotopes. Preprint IAE -5859/14, Moscow, 1995 (in English).
8. H.Markowitz "The NEAR concept", *Transactions of American Nuclear Soc.* V.60. 1989. p.209-210.

POLARIZED ELECTRON SOURCES*

J. E. Clendenin, Stanford Linear Accelerator Center, Stanford University, Stanford, CA 94309 USA

Polarized electron sources for high energy accelerators took a significant step forward with the introduction of a new laser-driven photocathode source for the SLC in 1992. With an electron beam polarization of $>80\%$ and with $\sim 99\%$ uptime during continuous operation, this source is a key factor in the success of the current SLC high-energy physics program. The SLC source performance is used to illustrate both the capabilities and the limitations of solid-state sources. The beam requirements for future colliders are similar to that of the SLC with the addition in most cases of multiple-bunch operation. A design for the next generation accelerator source that can improve the operational characteristics and at least minimize some of the inherent limitations of present sources is presented. Finally, the possibilities for producing highly polarized electron beams for high-duty-factor accelerators are discussed.

I. INTRODUCTION

Polarized electrons have long been used in the study of atomic and condensed matter physics[1]. With the development of high-energy electron accelerators, the possibility to study nuclei, quarks, and gauge bosons using polarized electrons presented itself. The first polarized electron source to be used for a modern accelerator was an atomic-beam source in which a state-selected beam of atomic Li was photoionized by intense light from a pulsed lamp[2]. This source, which began operating at SLAC in 1974, produced the desired 1.6- μ sec pulse at 180 pps with high polarization P_e , on the order of 85%, but the maximum current in the pulse was typically ≤ 0.25 mA, well below the accelerating capability of the linac. Although this intensity was roughly matched to what the target for the high-energy electron beam could accommodate, the electron spin direction could be reversed only slowly by reversing a large magnetic field, which introduced many unwanted effects, and most importantly, the source, even after several years of intermittent operation was very difficult to operate and relatively unreliable. The operational efficiency of the atomic-beam source at SLAC over a several year period was $\sim 50\%$ at best. A similar atomic-beam source using Cs but based on the Fano effect was developed during this same period for the Bonn synchrotron.

Although there were several other types of sources under development in the 1970s, the real breakthrough came following the suggestion in 1974[3] that GaAs, a III-V

semiconductor with interesting properties, might prove to be a good polarized electron source. Photoemission from GaAs treated to have a negative electron affinity (NEA) surface was known to be an efficient process, the quantum yields ranging well above 10%. Photoluminescence studies had also demonstrated that if the incident light were circularly polarized and monoenergetic with a wavelength corresponding to the near band-gap energy, the electrons promoted to the conduction band in the solid would be polarized at or just below 50%. Following the initial suggestion, it was quickly shown that there is no significant depolarization when extracting the electrons from the solid. Although the expected polarization from unstrained GaAs is lower than for the atomic-beam sources, the intensity promised to be limited only by the energy of the light source, the polarization direction should be reversible optically, and the operational characteristics of a solid-state source promised a high degree of reliability.

At SLAC, a GaAs source was quickly built and successfully operated in 1978 for a high-energy physics experiment[4]. For this experiment, 1.6- μ sec pulses with currents up to 15 mA were accelerated at 180 pps. P_e measured at high energy was $\sim 37\%$. With two photocathode guns available during the experiment, the operational efficiency during each session was $\sim 75\%$, a significant improvement over that for the atomic-beam source.

At Bonn, the Fano source was soon dropped in favor of a GaAs source, and other laboratories, such as MIT/Bates and Mainz, also installed GaAs-type sources for their electron accelerators. These latter two accelerators in particular saw extensive polarized beam operation in the late 1980s, while there was a long hiatus of polarized beams at SLAC from 1981 until three years ago.

With the commissioning of a new GaAs source for the SLC in 1992, a new era of highly reliable polarized-beam accelerator operations began. The polarization of this source has increased to the level of 80-86%. The source and its performance will be described below. The operational aspects of the SLC source are extremely well-matched to the SLC capabilities. For the most part, this performance should be repeatable for the NLC/JLC. The reservations implied here concerning suitability for operation of future colliders will also be discussed below.

A major limitation of GaAs sources has proven to be operation at high polarization for a high-duty-factor accelerator. The possibilities for overcoming this limitation are also discussed.

* Work supported by Department of Energy contract DE-AC03-76SF00515.

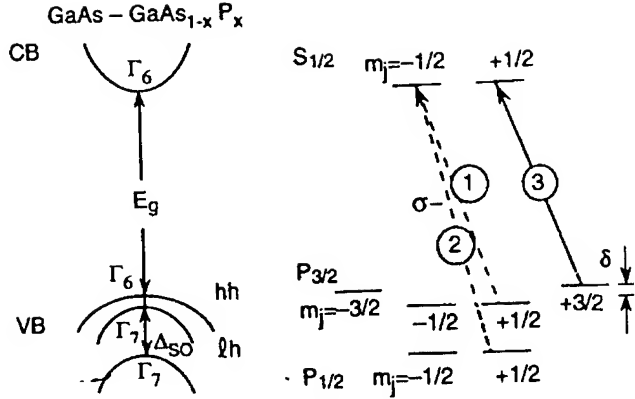


Figure 1. Energy level diagram and transition probabilities at the Γ point for a strained-lattice GaAs cathode.

II. PRODUCTION OF POLARIZED ELECTRONS FOR HIGH PEAK-CURRENT ACCELERATORS

A. GaAs sources

The process by which highly polarized electrons are produced in strained-lattice GaAs is illustrated in Figure 1. At the left of the figure are shown the energy bands at the Γ point. For direct band gap semiconductors such as GaAs, the valence band (VB) maximum and conduction band (CB) minimum are aligned in momentum space at the Γ point, allowing optical transitions between energy bands that follow the angular momentum selection rules for optical transitions in atoms. The transitions for illumination with left circularly polarized light (σ^-) are shown on the right of Figure 1 for photon energies between the band gap (E_g) and $E_g + \Delta_{so}$, where Δ_{so} is the energy separation of the spin-orbit split-off band. The relative transition rates are in circles. A small energy difference, δ , can be introduced into the $P_{3/2}$ substates by applying a strain in the growth direction of the crystal. The $m_j = \pm 3/2$ substates will be higher in energy than the $m_j = \pm 1/2$ if the strain is tensile. With sufficient strain, if the energy of the excitation photons is further adjusted to be between E_g and $E_g + \delta$, only the transition shown by the solid line is allowed, and consequently the polarization can in principle be 100%. The most successful technique developed so far for producing the desired strain is to grow a thin layer of GaAs on a sublayer material that has a slightly smaller lattice constant[5]. The high-polarization cathodes now used at SLAC consist of a 100-nm layer of GaAs, p-doped to $5 \times 10^{18} \text{ cm}^{-3}$, grown by MOCVD on a sublayer of GaAsP[6]. The wavelength dependence of the polarization and QE of a high-QE SLAC cathode is shown in Figure 2. The wavelength dependence of the QE is primarily related to the rapid drop in optical absorption as the band gap is approached. There is a small QE dependence of the polarization peak as illustrated

in Figure 3. Since the higher polarizations are correlated with very low QE, when the surface most likely has a positive electron affinity (PEA), the presumption is that the CB electrons originating away from the surface undergo some depolarization, either as they lose energy while thermalizing, or while they diffuse to the surface. For low QE, the PEA condition allows only electrons promoted near the surface (so called "hot electrons") to be emitted to vacuum.

The electrons that are excited into the conduction band can be extracted efficiently by creating an NEA surface. First the p-doping of the crystal lowers the energy bands at the surface by as much as half the band gap. This is a significant effect for large-band-gap semiconductors. Coating an atomically clean surface with a layer of Cs and an oxide (at SLAC, NF_3 is used) at the level of a monolayer or so will then lower the work function below the CB level in the bulk of the crystal. The clean surface is achieved by heating the crystal to 600°C for ~ 1 hour. The heat-cleaning plus application of Cs and oxide is said to "activate" the surface. The diffusion length for minority carriers in the CB of GaAs is on the order of $1 \mu\text{m}$ at room temperature, while the optical absorption depth near band gap is slightly larger. Thus when even a modest negative bias is applied to the crystal, a very high percentage of the CB electrons are emitted to vacuum.

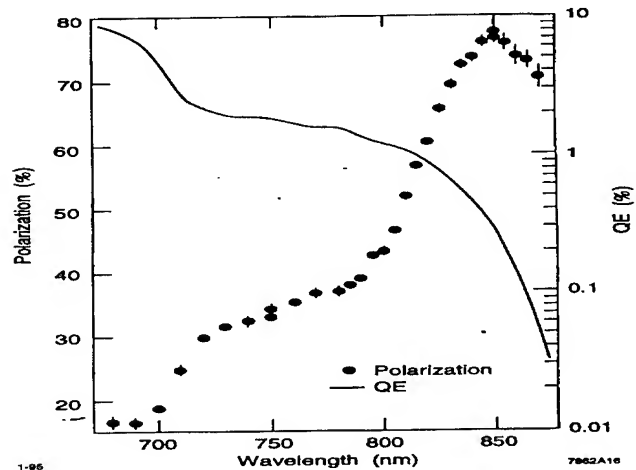


Figure 2. P_e and QE for a SLAC 100-nm strained-lattice cathode as a function of the excitation wavelength, measured at room temperature. See [10].

Since the QE scales roughly as the crystal thickness normalized to the diffusion length, the QE is considerably reduced in the thin cathodes. Nonetheless, with one important limitation to be discussed next, it has been found that the charge that can be extracted scales simply with the laser pulse energy up to the space-charge limit of the gun. The band gap for the strained-lattice cathodes is about 850 nm. The tunable, Q-switched, cavity-dumped, Ti:sapphire laser system for the SLC produces pulse energies up to and

exceeding several hundred microjoules. Since the SLC requires about 10^{11} e⁻ per micropulse at the source, this implies sufficient photons for a QE as low as 0.01%, whereas the typical operating QE is ~0.1%. These high laser energies are for single pulses and at rather low repetition rates. The repetition rate is presently limited by the lasers available for pumping the Ti:sapphire[7].

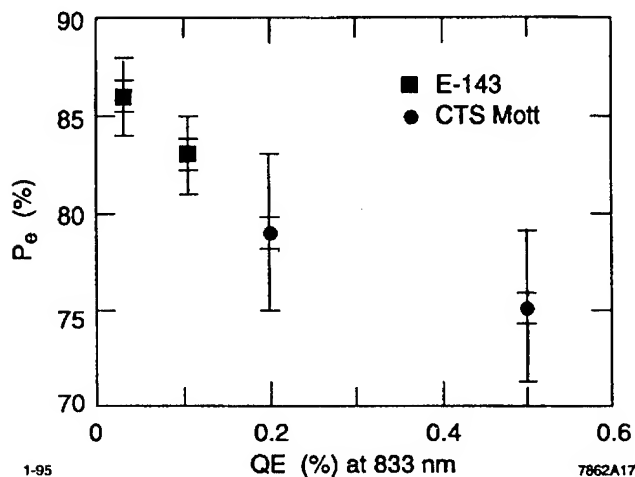


Figure 3. Polarization at the polarized electron source as a function of QE. See [10].

B. Cathode emission limitation

The exception to the scaling rule occurs when one attempts to extract a large amount of charge in a short interval (high peak current). Negative charge tends to build up at the surface during extraction due to the presence of surface states. At a certain point the discharge process for this buildup falls behind, and a surface barrier begins to grow until equilibrium is again established[8]. The surface barrier may arise quite rapidly, perhaps on the picosecond level, while the discharge can be much slower, on the nanosecond level and perhaps even containing microsecond-level components. The cathode charge limit scales roughly as the QE. For the SLAC cathodes, the charge limit for a QE of 0.1% at the polarization peak is about 5×10^{10} e⁻ cm⁻² in a 2-ns pulse. The discharge time is about 100 ns. Since separate Ti:sapphire lasers are used to produce the two SLC microbunches, the second laser is tuned to a much higher photon energy (since the second electron bunch need not be polarized), for which the QE and charge limit are both high. Thus the second bunch can be matched in intensity to the first.

A principal factor affecting the discharge rate is the dopant density. If the density is increased to $\sim 2 \times 10^{19}$ cm⁻³, the discharge time decreases to about 10 ns. However, higher densities seem to result in lower polarization. The solution to the emission limitation problem may be to increase the

dopant density at the surface while (possibly) lowering it in the bulk. Since high-temperature heat cleaning removes the surface layer (and also results in diffusion of the dopant material from the surface into the bulk), a cathode preparation technique that avoids high temperatures is essential for this solution.

Although the motivation here for suggesting a differentially doped cathode is to reduce the emission-limiting effect of the surface-charge buildup, obvious benefits in addition are higher QE at all emission levels (due to increased band bending at the surface) and possibly higher polarization (if the dopant density in the bulk is reduced). Differentially-doped, strained-lattice GaAs cathodes of the SLAC type should produce a stable polarization of at least 85-90% polarization at all QE levels[9].

C. The SLAC polarized electron source

Because of the high operating cost of accelerators, it is extremely important that the source operate reliably. The present polarized electron source[10] for the SLAC linac has operated for the past 3 years (2.4 years of equivalent full-time operation) with >95% efficiency overall, where operating efficiency is defined as the percentage of time the source is operating or able to operate upon demand with nominal beam during all scheduled accelerator operating time. The principle factors contributing to the reliability of the SLAC source are:

- 1) Careful design of the gun to provide a base pressure of $\sim 10^{-12}$ Torr exclusive of H₂;
- 2) Differential pumping between the gun and the downstream vacuum system;
- 3) A 38° bend, 1-m downstream of the gun, which isolates the cathode from reflected or reverse accelerated electrons;
- 4) Careful design of the electron optics to reduce beam interception in the first meter to <0.1%, and in the first 3 meters to <1%;
- 5) Incorporation of diagnostics to measure the beam interception to the level of 0.1%;
- 6) Providing the required field gradient at the crystal (1.8 MV/m) while keeping the maximum gradient along the cathode electrode ≤ 7 MV/m;
- 7) Processing of the high voltage (120 kV) for the cathode bias to reduce dark current to <50 nA DC as read by a nanoammeter floating on the high voltage terminal of the gun;
- 8) Backup guns;
- 9) A means to install and remove activated GaAs crystals without breaking the gun vacuum (load lock); and
- 10) A reliable tunable laser with a stable laser beam transport system.

The source uses a conventionally designed gun in which the cathode electrode is supported by a large ceramic insulator that also provides a major portion of the vacuum wall. The laser beam enters, and the emitted electrons exit, through a hole in the anode. The load-lock system for inserting the activated GaAs crystal into the gun after the vacuum bake of the gun chamber and after the high-voltage processing is essential for a gun that is to be operated at high voltage, otherwise the processing irreversibly destroys the QE of the cathode. In addition, the QE that can be achieved when the GaAs is not in the gun during the vacuum bake of the chamber is typically higher by a factor of ~ 2 and is more reproducible. Although SLAC now has 4 interchangeable photocathode guns, the guns have only been changed between accelerator operating cycles.

Table 1. Operating characteristics of SLAC polarized electron source for 1994-5 SLC run.

SLC operating time	~ 230 days
Beam structure at source	Two 2-ns pulses, 60 ns apart, at 120 pps, 7×10^{10} e ⁻ /pulse
Source operating efficiency	$> 99\%$
Cathode	100-nm strained-layer GaAs
Cathode bias (gradient)	120 kV (1.8 MV/m)
Active area of GaAs	1.5 cm^2
Typical QE	0.1% at polarization peak
QE lifetime (1/e)	1200 \rightarrow 300 hours
Number of cesiations	~ 50
Time between cesiations	4 days typical
Polarization, P_e	$\sim 80\%$ at 845 nm
Excitation wavelength	845 nm at 0°C

Typical operating characteristics of the SLAC source for the 1994-5 operating cycle of the SLC are illustrated in Table 1. The only task necessary to perform on the gun during the entire 10 months of continuous operation (if the time provided for other accelerator operations is included) was to periodically apply a small amount of Cs to the cathode, a computer controlled process (initiated by the accelerator operator) that took ~ 20 minutes. The required charge of 7×10^{10} e⁻ per microbunch was only slightly below the peak charge ($8\text{--}9 \times 10^{10}$ e⁻) following a full application of Cs to the cathode. To maximize the polarization (see Figure 3), only enough Cs was applied to give 3-5 days of operating time between cesiations[11]. Once the run began, there were no more cathode activations and no more NF₃ was applied.

III. POLARIZED SOURCE DESIGN FOR THE NEXT GENERATION OF LINEAR COLLIDERS

The SLC source already meets most of the requirements for NLC/JLC. The principle remaining tasks are to develop

the proper light source, and also to eliminate or avoid the effect of the charge limit.

A. Laser requirements

If we assume the beam requirement is a train of 100 micropulses spaced by 1.4 ns, each with a charge at the interaction point of 1×10^{10} e⁻, then the total charge required at the source is about 1.5×10^{12} e⁻ per macropulse if generated by an optical pulse train. With present technology, one should be able to generate such a train with the required macropulse stability of 0.5% rms[12]. The present SLAC approach is to use a resonant Pockels cell driven at 714 Mhz to chop (50% duty cycle) a long laser pulse. The required laser energy (5 kW for 140 ns) can be produced using a Q-switched laser with a sufficiently long optical cavity.

B. Charge limitation effect

While the selection of a laser for the NLC source can be considered a technical problem whose solution is foreseen, the charge limitation is an inherent property of the semiconductor crystals presently in use at SLAC. A new design for the cathode structure which eliminates or avoids the charge limit must not sacrifice polarization. A high QE must also be maintained.

The emission limitation is not a problem if the total charge to be extracted within the discharge time is considerably less than the charge limit. The active area of a SLAC cathode has been increased to 3 cm^2 , resulting in a charge limit for a 0.1% cathode (medium doped) of $\sim 1.5 \times 10^{11}$ e⁻ in 2 ns. This limit increases beyond the space-charge limit of the gun (about 2×10^{11} e⁻ in 2 ns) if the dopant density is increased to $2 \times 10^{19} \text{ cm}^{-3}$. For the NLC source, the total charge to be extracted in 10 ns is $\sim 1 \times 10^{11}$ e⁻, which at most is half the charge limit. Nonetheless, the charge limits for medium- and high-dopant densities need to be measured using laser pulses in the range of 10 to 100 ns.

C. Gun design

Although the SLAC gun has performed exceptionally well, the requirement that the load-lock mechanism float at the high voltage of the cathode bias is awkward at best, resulting in unnecessary complications when using load lock. A more compact gun design that places the high voltage insulators inside the grounded gun vacuum structure (the "inverted-geometry" design) is shown in Figure 4. A gun of this design has been built at SLAC[13] with an electrode design similar to that of the accelerator gun. The load-lock mechanism can be removed during gun operation if desired, but if left attached would be at ground potential. This gun design is a very promising candidate for a next-generation GaAs source.

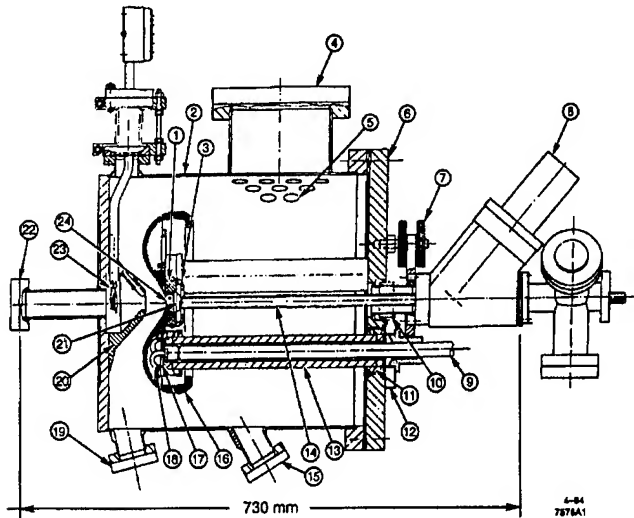


Figure 4. Cross section of the SLAC inverted-geometry gun. The electrons exit from the cathode (16) to the left through the anode (20). One of the 3 high voltage insulators is shown at (13). The cathode insertion tube (withdrawn when producing electrons) is shown at (14). For the remainder of the components, see [13].

IV. HIGH POLARIZATION ELECTRONS FOR HIGH DUTY FACTOR ACCELERATOR

The duty factor (DF) of the SLAC linac ranges from 2×10^{-4} for long pulse operation to 5×10^{-7} for SLC. For the SLC design performance, the source is required to generate a peak current I_p of ~ 10 A (an average current I_A of $I_p \times DF = 4.8$ μ A). For linac operations with 1.6 μ sec beam pulses, the source has produced an I_p of 30 mA (thus an I_A of ~ 6 msec).

The pulse width for lasers cannot be extended much beyond the tens of microseconds, and certainly not for high repetition rates. As the pulse width is increased, the maximum possible power also decreases. Thus, photocathode sources for high-duty-factor accelerators use cw lasers. Tunable cw lasers are at present limited to a few watts of output power. A QE of $\sim 2\%$ is routinely achieved with sources employing thick, unstrained GaAs, making possible cw currents > 10 mA. However, the *highest* QE achieved with the SLAC high-polarization cathodes has been about 0.2%, with 0.1% being typical. This implies a maximum cw current of ~ 1 mA. (It should be noted that long lifetimes of the cathode QE may be difficult to achieve for such high average currents.)

Several possibilities exist for producing higher cw currents using high-polarization cathodes. A GaAs-AlGaAs superlattice design has been shown to give $\sim 70\%$ polarization at ~ 750 nm and, using a load lock, a QE of over 2% [14].

A second possibility is a distributed Bragg reflector (DBR) strained-lattice cathode [15]. In principle this cathode can enhance the optical absorption efficiency by nearly an order of magnitude.

The QE of the simple strained-lattice cathodes can presumably be increased substantially by applying a high-dopant density to the surface, as was done for the superlattice mentioned above, and as was discussed earlier in this paper. If successful, such a cathode might still benefit from the addition of a DBR.

The author would like to thank his colleagues at SLAC, particularly J. Frisch, R. Miller, G. Mulhollan, H. Tang, and K. Witte, for many useful discussions which have been important for this paper.

V. REFERENCES

- [1] J. Kessler, *Polarized Electrons*, 2nd. ed. (Berlin: Springer-Verlag, 1985) 299 pp.
- [2] M.J. Alguard et al., *Nucl. Instrum. and Meth.* 163 (1979) 29.
- [3] E.L. Garwin et al., *Helv. Phys. Acta* 47 (1974) 393; G. Lampel and C. Weisleuch, *Solid State Commun.* 16 (1975) 877.
- [4] Prescott et al., *Phys. Lett.* 77B (1978) 347.
- [5] The superlattice structure is a competing technique.
- [6] T. Maruyama et al., *Phys. Rev.* B46 (1992) 4261; see also T. Nakanishi et al., *Phys. Lett.* A158 (1991) 345.
- [7] A pulse train of only a few micropulses per macropulse can be produced using multiple lasers as is done for the 2 micropulses produced for the SLC.
- [8] A. Herrera-Gómez and W.E. Spicer, *Proc. SPIE* 2022 (1993) 51.
- [9] Having a constant polarization has a real benefit to the high-energy experimenters since it would eliminate one variable in the polarization at high energy. Fixed-target experiments using Møller polarimeters to monitor the polarization are especially dependent on a stable polarization.
- [10] R. Alley et al., "The Stanford linear accelerator polarized electron source," SLAC-PUB-6489 (1994), submitted to *Nucl. Instrum. and Meth.*
- [11] Consistently under-cesiating results in a gradual decrease in the lifetimes. Adding excess Cs reverses this trend.
- [12] The intensity stability of the SLC Ti:sapphire laser is $\sim 1\%$ rms.
- [13] M. Breidenbach et al., *Nucl. Instrum. and Meth.* A350 (1994) 1.
- [14] Y. Kurihara et al., *Jpn. J. Appl. Phys.* 34 (1995) 355.
- [15] T. Saka et al., *Jpn. J. Appl. Phys.* 32 (1993) 1837.

High Brightness Electron Sources

Richard L. Sheffield, Los Alamos National Laboratory *

ABSTRACT

High energy physics accelerators and free electron lasers put increased demands on the electron beam sources. This paper describes the present research on attaining intense bright electron beams using photoinjectors. Recent results from the experimental programs will be given. The performance advantages and difficulties presently faced by researchers will be discussed, and the following topics will be covered. Progress has been made in photocathode materials, both in lifetime and quantum efficiency. Cesium telluride has demonstrated significantly longer lifetimes than cesium antimonide at 10^{-8} torr. However, the laser system is more difficult because cesium telluride requires quadrupled YLF instead of the doubled YLF required for cesium antimonide. The difficulty in using photoinjectors is primarily the drive laser, in particular the amplitude stability. Finally, emittance measurements of photoinjector systems can be complicated by the non-thermal nature of the electron beam. An example of the difficulty in measuring beam emittance is given.

I. INTRODUCTION

The following two sections of this paper cover the basic photoinjector types and their operational characteristics. The subsequent section covers the measurement of emittance using the quadrupole scan technique. Although the quad scan is a commonly used technique for measuring emittance, in a photoinjector-based system this technique can lead to erroneous emittance measurements.

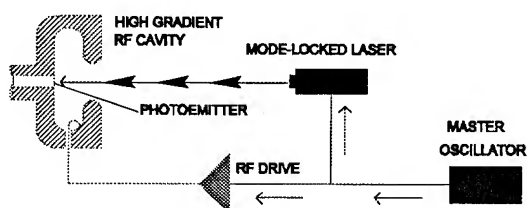


Figure 1 Basic components of a photoinjector are a laser, a photocathode, an rf source, and an rf cavity.

Photoinjectors [1], conceptually shown in Figure 1, have several unique characteristics. A high gradient rf cavity is used to supply the accelerating field. The high-gradient not only reduces space charge effects, but the gradient also enables laminar flow from the cathode through the accelerator to the beamline. Since the electron beam does not undergo transverse or axial mixing, a large fraction of the

emittance growth due to space charge can be corrected by a technique called emittance compensation [2]. The high gradient also allows the extraction of high charge for closely spaced pulses resulting in a high average current [3].

Since the electron source is a photocathode illuminated with a laser, the machine designer has complete control over the spatial and temporal characteristics of the electron emission process. The gun can directly produce very short electron pulses limited only by the gun gradient and charge in the pulse. For instance, 1 nC from a cathode with a surface gradient of 30 MV/m will have a 6 ps pulse length.

II. BASIC PHOTOINJECTOR TYPES

The motivation for the first photoinjector experiment, shown in Figure 2, was the need for an electron source that has an rms emittance of less than 40π mm-mrad and the capability of generating greater than 1 A average current. From the first use of a photoinjector in 1985 [1], many different systems have been designed to meet the needs of very different applications. The applications include high-average-current electron beams, high-brightness source for free-electron lasers and colliders, high pulse charges for wakefield accelerators, high-duty factor picosecond high-energy x-ray pulses, and picosecond soft x-rays by Compton scattering. The advantage of this source for Compton scattering is that the drive laser for the photocathode can be used as the scattering laser. Using the drive laser provides sub-picosecond synchronization of the electron pulse and the laser pulse.

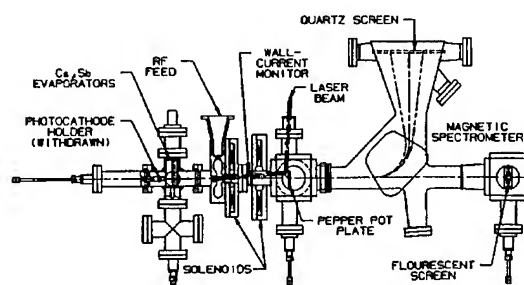


Figure 2 The first photoinjector experiment demonstrated an emittance of less than 30π mm-mrad at 10 nC, a maximum 27 nC per 53 ps long micropulse, and 2.9 A average current for a 6 μ s long macropulse. The current density was estimated to be 600 A/cm² from a Cs₃Sb cathode.

* Work supported by Los Alamos National Laboratory Directed Research and Development under the auspices of the United States Department of Energy.

Research is still proceeding on high-average current machines at Boeing [4], and at Bruyeres-le-Chatel [5]. The first demonstration of a high-average current using a

photoinjector was on the Boeing accelerator. This 25% duty factor machine has demonstrated an average current of 32 mA at 5 MeV, giving a average beam power of 160 kW. The macropulse average current was 0.13 A. The beam emittance was 5 to 10 π mm-mrad for 1 to 7 nC pulse charge. An example of the machine located at Bruyeres-le-Chatel is shown in Figure 3.

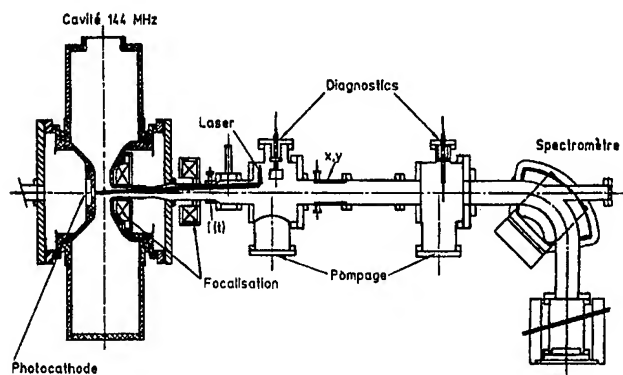


Figure 3 Photoinjector at LEL-HF Bruyeres-le-Chatel. RF cell produces a 2.0 MeV beam at 5 nC with a pulse length of 20 to 50 ps. They have measured 4 π mm-mrad at 1 nC.

Many designs are based on the work done at Brookhaven National Laboratory at 2856 Mhz [6]. A schematic of one of their 1-1/2 cell guns is shown in Figure 4.

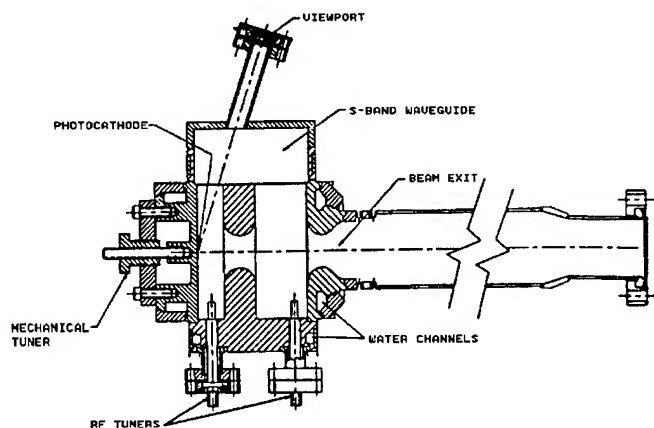


Figure 4 Brookhaven's 2856 MHz photoinjector operates at 3 MeV and has produced 4 π mm-mrad at 1 nC with a cathode field of 70 MV/m. The gun has generated 4.5 MeV beams.

The Brookhaven type of gun is being used for advanced accelerator studies, free-electron lasers, and linear collider injectors. One of the advantages of operating near 3 GHz is the higher cathode surface electric fields that can be obtained relative to operating at lower frequencies.

A new photoinjector operating at 17 GHz has been constructed at the Massachusetts Institute of Technology. This gun has 1-1/2 cells with peak surface fields of 250 MV/m and a peak cathode surface field of 200 MV/m. The rf source is a gyro-amplifier developed at MIT [7].

III. PHOTOINJECTOR OPERATIONAL CHARACTERISTICS

This section covers the operational characteristics of photoinjectors. This section covers three topics: photocathodes, photocathode lasers, and photoinjector performance.

A. Photocathodes

Photocathodes can be divided into two classes based on quantum efficiency (QE): low QE and high QE.

Low QE cathodes are characterized by having reduced vacuum requirements and are relatively easy to produce. These cathodes fall into two groups, metals and thermionic emitters.

Many different metals have been considered for photoinjector cathodes. Copper and magnesium [8] are the most common choices. Other metals that have been considered are: Al, Au, stainless steel, Sm, Y, W, Zn, Au, Mo, Ta, Pd, Zr, Ba, Na, Ca [9],[10]. Measurements of quantum efficiency vary considerably among individual researchers. This variation can in part be attributed to differences in samples, preparation techniques, and contamination before and during measurements. Also the UCLA group has reported non-uniform emission occurring after use in a photoinjector [11]. Overall, the measured quantum efficiency of metals varies from less than 10^{-8} to 3×10^{-3} near a wavelength of 250 nm.

The thermionic emitters, LaB₆ [12] and BaO, have also been used as cathodes, both heated and unheated. Again, the measured quantum efficiencies are dependent on many factors and varies among laboratories. Quantum efficiencies of greater than 10^{-4} have been measured. The temporal response in the picosecond regime for these cathodes has not been measured.

Another metal cathode being used in the ATF at the Kharkov Institute is pressed BaNi. They quote a QE of 1.7×10^{-3} [13].

High QE photocathodes, in general, require a good vacuum and have a more sophisticated fabrication procedure. These types of cathodes can be subdivided into three categories: multialkali, crystal-like, and GaAs.

The Cs₃Sb multialkali cathode was the first cathode used in a photoinjector. Since then a large number of other multialkali cathodes have been used, such as CsK₂Sb, AgO:Cs, CsNaKSb, K₃Sb, and NaK₂Sb.

Multialkali cathodes have a significant advantage over metal cathodes. These cathodes have QE's over 2% at 532

nm, making the drive laser requirements less stringent. Unfortunately, since they are used with lower energy photons, they tend to be very susceptible to contamination and require 10^{-10} torr vacuum systems. Because of contamination issues, these cathodes have limited lifetimes.

The crystal-like cathodes, Cs_2Te , CsI , K_2Te all require laser wavelengths of at least 250 nm for quantum efficiencies over 2%. Their advantage is that they can survive in 10^{-8} vacuum systems [9],[14]. Also these cathodes can be rejuvenated by heated to 150 C and reused.

Finally, GaAs has been used for many years as a polarized electron source. KEK plans to use this cathode in a specially cleaned photoinjector that exhibits almost no change in impurities and background pressure with and without rf power [15].

There is a wide variety of photocathodes to choose from based on the system requirements. The photocathode, though difficult, is no longer a major impediment to using this technology.

B. Photoinjector Lasers

The key to the stability and reliability of a photoinjector is the drive laser. The advantage of using a laser is that the cathode can be illuminated with any temporal and spatial profile required to optimize the gun performance. Lasers have excellent temporal stability, with almost all of the present systems in use having less than picosecond temporal jitter. Also, if only single pulses are required, a laser can generate very large energy per pulse (LLNL NOVA laser can generate nearly 1 kJ in less than 10 ns).

The remaining difficulty in the laser systems is the macropulse to macropulse amplitude stability. Achieving less than 10% amplitude stability is very difficult with present systems. The technology exists to achieve less than 1% stability, but not the resources.

Lasers can generate high peak energy in short pulses easier than long (many microseconds) pulses. It follows that for long pulse trains a minimum QE of 0.5% is required.

One other issue that can be critical to stable operation is pointing stability. Since the laser defines the spatial profile of the emission, the laser must be stably pointed at the cathode. For example, the large solenoid around the gun region of the Advanced Free-Electron Laser [16] acts to amplify small transverse spatial variations of the cathode position. This amplification occurs because of the long distance from the large solenoid to the first focusing element (2.5 m lever arm). Even though the cathode diameter is 8 mm, a shift of 100 microns in the centroid will image to a 25 micron shift in the middle of the wiggler.

C. Performance Characteristics

Photoinjectors routinely generate greater than 500 A/cm². For most systems this current density is limited only by the field gradient on the cathode or the laser intensity.

Most photoinjectors generate between 1 and 10 nC per micropulse. Argonne National Lab has generated greater than 50 nC per micropulse.

Electron pulse lengths are limited by space charge effects in the first few centimeters in front of the cathode. Typically, less than 10 ps pulses are generated for 1 nC of charge in a micropulse (in the AFEL 6 ps for 1 nC)

The measured electron beam's rms emittance varies, depending on the machine design, between 1 and 5 π mm-mrad for 1 nC in a micropulse. Some newer designs give less than 1 π mm-mrad for 1 nC [17].

IV. EMITTANCE MEASUREMENTS ON A PHOTOINJECTOR

Emittance measurements in a photoinjector are complicated by one of the photoinjector's advantages. Because of the rapid acceleration and lack of other beamline components in the gun region, the longitudinal phase space of the beam does not thermalize. As a result of the non-thermalization, different longitudinal parts of the beam propagate with their own trajectories. This complicates the analysis of the beam's phase space ellipse. Commonly used techniques for measuring emittance, such as pepperpot technique or quadrupole scans, can lead to erroneous emittance and phase-space ellipse measurements.

In the first photoinjector experiment, a pepperpot was used to measure the emittance [18]. Because of the longitudinal variations in phase-space, the emittance was underestimated by a factor of four. In this section, I will describe difficulties in using a quadrupole scan technique to determine the beam's emittance.

For a thin lens, the rms unnormalized emittance, ϵ_{un} can be calculated by fitting the beam spot size x_s to the coefficients of $1/f$ in the following

$$x_s^2 = x_{min}^2 \left[1 + \{ L^2 \epsilon_{un} (1 - f_w / f) / (x_{min}^2 f_w) \}^2 \right],$$

where ϵ_{un} is the unnormalized rms emittance, L is the spacing between the quadrupole and the image screen, f is the focal length of the quadrupole, f_w is the focal length that gives the minimum spot size x_{min} [19]. The focal length of a quadrupole is $\beta \gamma m_e c / (leB)$, where β , γ are the relativistic factors, m_e is the mass of an electron, c is the speed of light, l is the quadrupole length, e is the electron charge, and B is the quadrupole field gradient.

For a thick lens, the spot size x_s can be fit using the Twiss parameters 20 with the following formula,

$$x_s^2 = \epsilon_{un} \left[m_{12}^2 \gamma_q - 2m_{11}m_{12}\alpha_q + m_{11}^2 \beta_q \right],$$

where γ_q , β_q and α_q are the Twiss parameters of the beam at the quadrupole. The coefficients of the Twiss parameters are from the Twiss parameter transfer matrix for a thick lens,

$$m_{11} = \cos(\theta) - d\theta \sin(\theta) / L$$

$$m_{12} = d \cos(\theta) + L \sin(\theta) / \theta$$

$$\theta = L \sqrt{eB / (\beta \gamma mc)}$$

where d is the quadrupole's axial length and L is the spacing from the end of the quadrupole to the image screen. Using the identity $\beta_q \gamma_q - \alpha_q^2 = 1$, then the rms unnormalized emittance can be calculated from the coefficients of the fit.

The experimental data and the fit using the Twiss parameters are shown in Figure 5. The thin lens fitting procedure was also used on the experimental data and the results were within 10%. The rms emittance as calculated from the fit for either the data spot sizes or for the PARMELA spot sizes is 2.3π mm-mrad. The PARMELA simulation gives an integrated rms emittance of 5π mm-mrad.

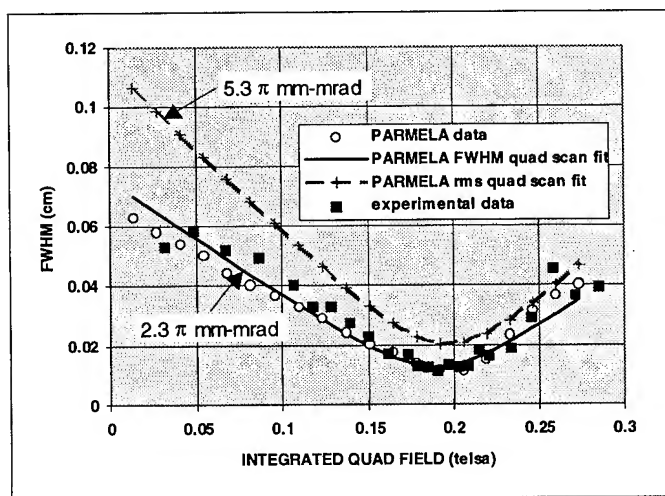


Figure 5 The data and PARMELA simulation are for a quadrupole scan with the FWHM taken at a screen 30 cm downstream from the quadrupole. The electron pulse is 1.9 nC at 17.2 MeV. The beam is produced by a Cs₂Te cathode illuminated by a 8 ps laser pulse. The laser's spatial profile is a 6 mm FWHM gaussian clipped with a circle of 5.2 mm diameter. The FWHM of each slice at the screen is plotted as a function of the quadrupole gradient.

The discrepancy in emittance is due to the manner in which the data is analyzed. Measuring the full distribution of an image on a screen is susceptible to many errors. In particular, the correction of data due to baseline shifts and the non-linear response of cameras, especially at low intensity, is very difficult. Unfortunately, the rms emittance numbers are very sensitive to the tails of the distribution. So instead, many researchers measure an unambiguous parameter of the spot-size, the full-width half-maximum. As can be seen in Figure 5, the agreement between the FWHM's from the experimental measurement and the FWHM's from

PARMELA is very good. However, because of the longitudinal dynamics of different slices, the FWHM measurement cannot be used to directly compute the beam's emittance. In Figure 5, the dashed curve shows the FWHM as calculated from the rms spot sizes from PARMELA. Now the quadrupole scan fit gives an emittance close to the calculated emittance.

The variation of FWHMs at the screen of the individual slices with changing quadrupole strength is shown in Figure 6. The reason for the discrepancy in emittance is readily apparent. The ends of the micropulse are focused differently than the middle of the pulse. The FWHM spot size measurement is thus complicated by the different longitudinal portions of the pulse contributing to the FWHM in differing amounts as the quadrupole is varied.

The minimum spot size is dependent on the cathode temperature and any residual magnetic field on the cathode. Thus far, the cathode temperature of Cs₂Te has not been measured. The cathode initial emittance can be inferred by adding a minimum spot size to the PARMELA spot sizes (square root of sum of squares). From the experimental data, this gives an initial emittance of 2.8π mm-mrad, corresponding to a transverse energy of 1.2 eV. The partition of this energy between residual magnetic field at the surface of the cathode and cathode temperature cannot be determined.

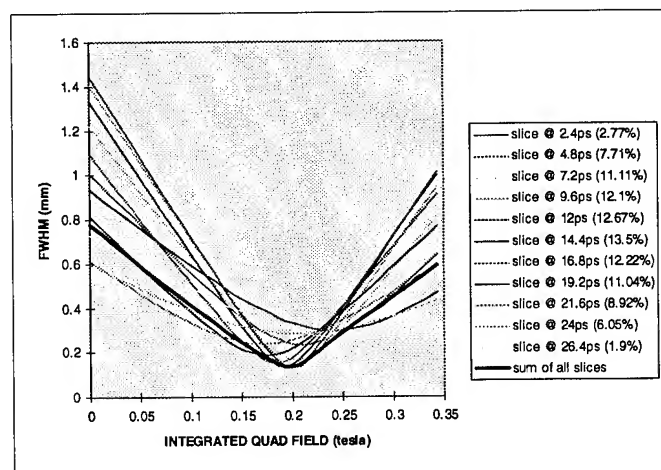


Figure 6 The TAPE2 PARMELA output was processed by dividing the longitudinal length of the pulse into 11 equal segments. The FWHM of each slice at the screen is then plotted as a function of the quadrupole gradient. The fraction of charge in each slice is shown in the legend. The thick black line is the summation of all the individual FWHM's. To make sure the slicing was done properly, the summation is compared with the normal output of PARMELA (an integration over all slices).

Finally, the large solenoid around the cathode region is the main steering and focusing element in the system. This

results in the beam's phase space ellipse being very sensitive to the magnitude of the solenoid's field. In the case shown above, the measured value of the large solenoid's field was within 1% (the experimental error was 5%) of the value predicted by PARMELA. Changes in magnetic field as small as 1% are easily observable in simulation and have a significant effect on the beam's Twiss parameters.

V. SUMMARY

Photoinjector technology has had significant developments in the decade since its inception. Designs now span a large range in frequencies and electron pulse requirements. The photocathode source, though difficult, is not a major impediment to implementing a photoinjector-based system. However, the amplitude stability of the drive laser for the photocathode is an issue.

The measurement of the phase space of the pulse produced from a photoinjector is not straightforward. An exact comparison with simulation is required for a thorough understanding of the phase space of the pulse. For a good simulation, an accurate measurement of magnetic fields, photocathode laser profile, accelerating fields, and phasing of the laser and rf is required. With accurate measurements, good agreement between experiment and simulation can be obtained.

A large solenoid around the cathode region is sometimes used to reduce the emittance of the beam by the technique of emittance compensation. In these types of photoinjectors, the transport of the beam downstream is very sensitive to the location of the electron emission, collinearity of the magnetic field with the beam trajectory, and the magnitude of the magnetic field.

The author is indebted to many individuals for information on their projects. In particular, I wish to thank Chris Travier, Steve Kong, John Adamski, Shien-Chi Chen, Harold Kirk, Claudio Pelligrini, and Jim Simpson.

- [1] J. S. Fraser, R. L. Sheffield, and E. R. Gray, "High-Brightness Photoemitter Development for Electron Accelerator Injectors," *Laser Acceleration of Particles AIP Conf. Proc.*, no. 130, pp. 598, 1985; J. S. Fraser, R. L. Sheffield, and E. R. Gray, "A New High-Brightness Electron Injector for Free Electron Lasers," *Nucl. Inst. And Methods*, vol. 250, pp. 71-76, 1986.
- [2] B. E. Carlsten, *Nucl. Inst. And Methods*, vol. A285, pp. 313-319, 1988.
- [3] J. S. Fraser and R. L. Sheffield, *IEEE J. Quant. Elec.*, vol. QE-23, pp. 1489-1496, 1987.
- [4] D. H. Dowell, K. J. Davis, K. D. Fridell, E. L. Tyson, C. A. Lancaster, L. Milliman, R. E. Rodenburg, T. Aas, M. Bemes, S. Z. Bethel, P. E. Johnson, K. Murphy, C. Whelen, G. E. Busch, and K. K. Remelius, "First Operation of a Photocathode Radio Frequency Gun Injector at High Duty Factor," *Appl. Phys. Lett.*, vol. 63, no. 15, pp. 2035-2037, (1993).
- [5] S. Joly et al., "Progress Report on the BRC Photoinjector," *Proc. 1990 European Part. Accel. Conf.*, Nice June 12-16, pp. 140-142, 1990.
- [6] K. Batchelor, et al. "Performance of the Brookhaven Photocathode RF Gun," *Nucl. Inst. and Methods*, vol. 318, pp. 372-376, 1992.
- [7] S. C. Chen, J. Gonichon, L. C-L. Lin, R. J. Temkin, S. Trotz, B. G. Danly, and J. S. Wurtele, "High Gradient Acceleration in a 17 Ghz Photocathode RF Gun," *Proc. 1993 Par. Accel. Conf.*, vol. 4, pp. 2575-2577, 1993.
- [8] J. Fischer, T. Srinivasan-Rao, and T. Tsang, "Mg Photocathode Performance Overview," *Sources '94, Schwerin, Germany, Sept. 29 - Oct.4*, pp.287-289, 1993.
- [9] G. Suberlucq, "Photocathodes for the CERN CLIC Test Facility," *Sources '94, Schwerin, Germany, Sept. 29 - Oct.4*, pp.557-561, 1993; C. Travier, "High-Brightness Photocathode Electron Sources," *6th Workshop on Advanced Accel. Concepts, Lake Geneva, WI, June 12-18*, 1994.
- [10] Private communication from M. E. Conde, UCLA/ANL.
- [11] Private communication from C. Pellgrini, UCLA.
- [12] D. J. Bamford, M. H. Bakshi, and K. A. G. Deacon, "The Search for Rugged, Efficient Photocathode Materials," *Nucl. Inst. And Methods*, vol. A318, pp. 377-380, 1992.
- [13] Y. Tur, "A Photoinjector Test Accelerator Complex: Current Status and Future Prospects," *Sources '94, Schwerin, Germany, Sept. 29 - Oct.4*, pp.572-576, 1993.
- [14] S. H. Kong, J. Kinross-Wright, D. C. Nguyen, and R. L. Sheffield, "Cesium Telluride Photocathodes," *J. Appl. Phys.*, vol. 77, no. 11, pp 1-8, 1995.
- [15] M. Yoshioka, "High Gradient Study on UHV Copper Cavity at S-Band," *Sources '94, Schwerin, Germany, Sept. 29 - Oct.4*, pp.624-629, 1993.
- [16] R. L. Sheffield, R. H. Austin, K. D. C. Chan, S. M. Gierman, J. M. Kinross-Wright, S. H. Kong, D. C. Nguyen, S. J. Russell, and C. A. Timmer, "Operation of the High Brightness LINAC for the Advanced Free-Electron Laser Initiative at Los Alamos," *Proc. 1993 Par. Accel. Conf.*, vol. 4, pp. 2970-2972, 1993.
- [17] H. Kirk, "A Comparison of L-Band and C-Band RF guns as Sources for Inline-Injection Systems," *Sources '94, Schwerin, Germany, Sept. 29 - Oct.4*, pp.392-398, 1993.
- [18] J. S. Fraser, R. L. Sheffield, E. R. Gray, and P. M. Giles, R. W. Springer, and V. A. Loebs, "Photocathodes in Accelerator Applications," *1987 IEEE Part. Accel. Conf, March 16-19, Washington, D. C.*, pp. 1705-1709, 1987; R. L. Sheffield, "Photocathode RF Guns," *AIP Conf. Proc.*, vol. 2, no. 184, pp. 1500-1531, 1989.
- [19] B. E. Carlsten, J. C. Goldstein, P. G. O'Shea, and E. J. Pitcher, "Measuring Emittance of Nonthermalized Electron Beams," *Nucl. Inst. And Methods*, vol. A331, pp. 791-796, 1993.
- [20] S. Humphries, Jr., "Charged Particle Beams," *John Wiley and Sons, Inc.*, pp. 143, 1990.

Polarization studies of strained GaAs photocathodes at the SLAC Gun Test Laboratory*

P. Sáez, R. Alley, J. Clendenin, J. Frisch, R. Kirby, R. Mair, T. Maruyama, R. Miller, G. Mulhollan, C. Prescott, H. Tang and K. Witte

Stanford Linear Accelerator Center
Stanford University, Stanford, CA 94309

ABSTRACT

The SLAC Gun Test Laboratory apparatus, the first two meters of which is a replica of the SLAC injector, is used to study the production of intense, highly-polarized electron beams required for the Stanford Linear Collider and future linear colliders. The facility has been upgraded with a Mott polarimeter in order to characterize the electron polarization from photocathodes operating in a DC gun. In particular, SLAC utilizes *p*-type, biaxially-strained GaAs photocathodes which have produced longitudinal electron polarizations greater than 80% while yielding pulses of 5 A/cm² at an operating voltage of 120 kV. Among the experiments performed include studying the influences of the active layer thickness, temperature, quantum efficiency and cesiation on the polarization. The results might help to develop strained photocathodes with higher polarization.

I. INTRODUCTION

The Stanford Linear Accelerator Center (SLAC) conducts experiments in high-energy physics to study the structure of elementary particles. Recent experiments have required high-intensity, high-polarization electron beams. Advances in III-V semiconductors have led to photocathodes which produce beams with polarization in excess of 80%.

The Gun Test Laboratory was created to study guns and photocathodes for the SLAC injector and the Next Linear Collider project. Of particular interest in this work has been to investigate the polarization dependence on cathode thickness, temperature, quantum efficiency (QE) and cesiation. The results of these experiments have shed light on understanding semiconductor properties which will aid us to develop better photocathodes for future experiments.

II. APPARATUS

A schematic of the Gun Test Laboratory apparatus is shown in Fig. 1. The injector section includes an ultra-high-vacuum, high-voltage electrostatic gun, a load-lock chamber for cathode transfer and activation (not shown in Fig.1), a beamline with magnetic components for electron beam transport, and several instruments for steering and characterizing the beam [1]. The gun consists of a pair of

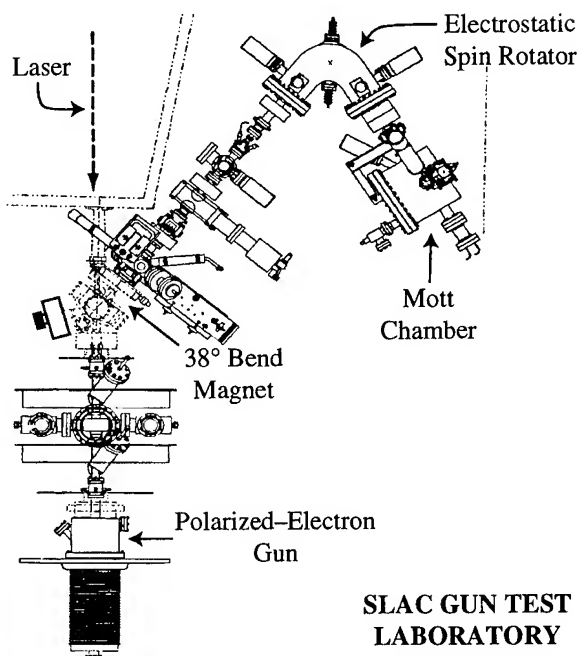


FIG. 1. Schematic of the Gun Test Laboratory apparatus.

cylindrical Pierce electrodes with a 20 mm diameter photocathode. The cathode is normally biased at -120 kV. After transport beyond the bend, the beam is injected into the recently commissioned Mott beamline [2]. This section includes an electrostatic spin rotator and a Mott scattering chamber with two CaF₂(Eu) scintillator detectors located 120° with respect to the incident beam axis. The Mott-scattering target is 700 Å gold on 1.3 μm carbon backing.

The light for electron photoemission is provided by two independent Ti:Sapphire cavities which are pumped by a pulsed Nd:YAG laser [1]. The cavities are not designed for rapid tuning of the wavelength, thus limiting each experiment to at most two wavelengths. Each pulse is 2 ns FWHM. A Pockels cell is used to produce >99% circularly-polarized light, reversible from pulse to pulse.

The polarimeter calibration was performed with a 'standard' photocathode whose polarization has been measured by highly accurate instruments [2,3]. The absolute uncertainty of the polarization measurements is ~5%, expected to become ~3%. The cathodes studied include a 100 nm active-layer (110) GaAs (C1), 100 nm strained-active-layer (100) GaAs (C2) and a bulk (100) GaAs (C3). The biaxial-compressive stress in C2 is obtained by growing GaAs on GaAs_{0.72}P_{0.28} which has a lattice constant

* Work supported by Department of Energy contract DE-AC03-76SF00515.

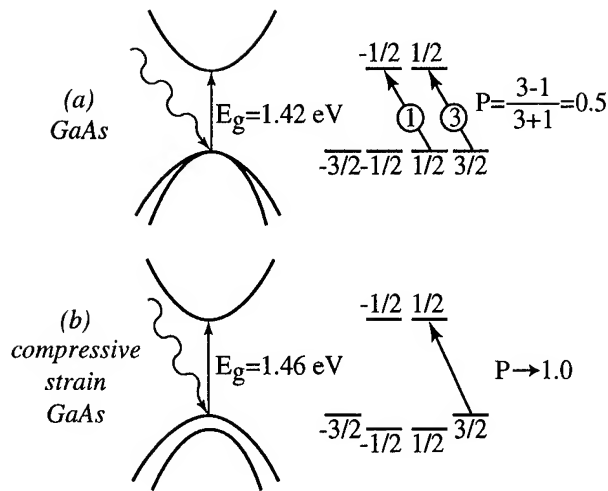


FIG. 2. Energy-band diagrams of the electromagnetic transitions at the Γ point for (a) GaAs and (b) strained GaAs. The polarization corresponds to excitation of valence band states by left-circularly-polarized illumination. The circled numbers indicate the relative transition strengths.

approximately 1% smaller than bulk GaAs [4]. C1 and C2 are doped to $5 \times 10^{18} \text{ cm}^{-3}$ while C3 is doped to $2 \times 10^{19} \text{ cm}^{-3}$. The electromagnetic transitions that lead to electron beam polarization are shown in Fig. 2.

III. RESULTS

Several conduction band spin-relaxation effects take place in the bulk of a semiconductor [5,6]. Electron depolarization as a function of material thickness has been observed previously and has prompted the use of thin samples [7]. Thus the higher room-temperature polarization of C1 ($P=44\%$) over C3 ($P=29\%$) is brought about by reduced travel time of electrons in the semiconductor.

Large improvements in polarization from bulk materials brought by lower temperatures [8] led us to investigate the possibility of existence of this effect in C1 and C2. Figure 3 shows a plot of C2's polarization as a function of temperature. The small improvement in P indicates that spin relaxation mechanisms, which typically have strong temperature dependencies [6], do not play a major role in the depolarization of electrons from thin materials.

To see how temperature affects the spin orientation of electrons in thin samples, consider the electron polarization in the conduction band at the time of recombination

$$P = \frac{P_0}{1 + \frac{\tau}{\tau_s}} \quad (1)$$

where P_0 is the initial electron polarization, τ is its lifetime in the conduction band and τ_s is the spin-relaxation time. Strictly speaking, Eqn. (1) applies to the ideal photoluminescence experiment; however, it can be used to *approximate* the spin orientation of a photoemitted electron. (A complete model for

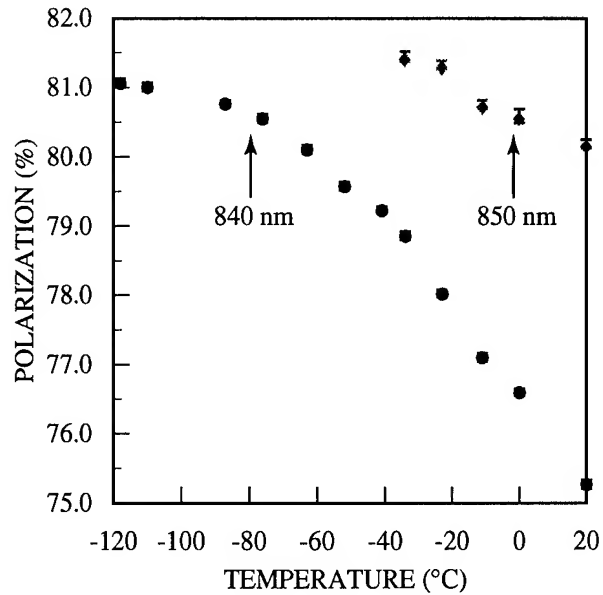


FIG. 3. Electron polarization versus temperature for 100 nm strained GaAs (p -doped to $5 \times 10^{18} \text{ cm}^{-3}$). Two wavelengths were used to track the increase in bandgap with lower temperatures. Peak polarization at low temperatures increases by $\sim 1\%$ from its room-temperature value.

the polarization of a photoemitted electron would include light absorption, diffusion to the surface, and emission from the band-bending/surface region.) The travel time of a thermalized electron in 100 nm in the absence of collisions is about $2.5 \times 10^{-13} \text{ s}$ ($\langle v \rangle \approx 4 \times 10^7 \text{ cm/s}$ at room temperature [9]). Such time is already much smaller than the spin-relaxation time $\tau_s \approx 2 \times 10^{-11} \text{ s}$ [6]. Substitution into Eqn. (1) of a considerably longer spin-relaxation time due to lower temperatures increases the electron polarization by only 2%.

After cesiating a photocathode beyond its photoemission peak, the QE and polarization will have dropped as shown in Fig. 4. This excess cesium might contribute to depolarization [11]. As the cesium state on the surface of the photocathode changes with time, the QE and polarization improves. However, when the surface conditions worsen, the QE drops but the polarization keeps improving. This polarization dependence on QE, with lower QEs yielding higher polarizations, has been seen before [1,8]. This effect is larger on strained samples like C2 ($\Delta P/P \sim 5\%$) than on unstrained samples like C1 ($\Delta P/P \sim 1\%$). As the QE decreases, the rise of the work function helps to filter out those electrons that have lost energy due to scattering during their trip (or trips, in the case of reflected electrons) to the surface. These electrons might have lower polarization than ballistic electrons.

The stronger dependence of polarization on QE in strained samples is due to their broad-band configuration. The lack of well-defined, split- $P_{3/2}$ states is caused by partial strain relaxation [10]. The combination of various stages of strain relaxation results in electrons higher in the broad conduction band having higher polarizations than those at the very bottom of the band [2]. As the surface degrades with time, the rising work function prevents low conduction band

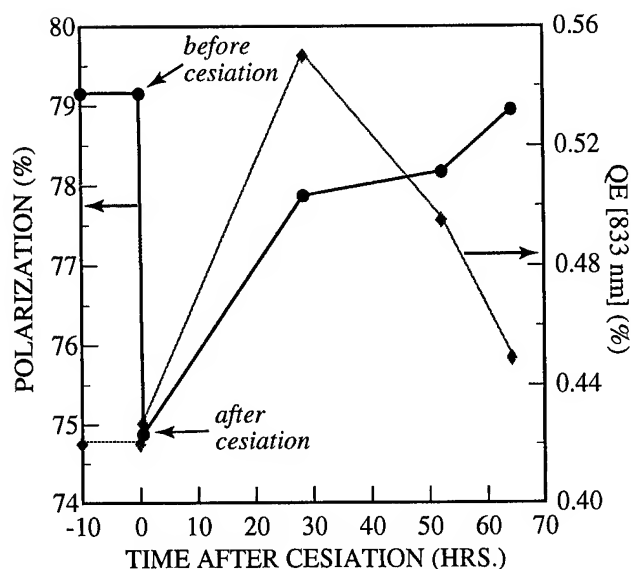


FIG. 4. Polarization and QE after cesiation for strained GaAs. The large drop in P is due to the new cesium on the surface. Also shown is the rise of P as the QE decreases.

electrons from escaping. Such an effect is shown in Fig. 5.

IV. DISCUSSION

The lower polarization in thin (110) GaAs ($P=44\%$ instead of $P=50\%$) and its weak dependence on temperature might indicate that the source of depolarization is not in the bulk but in the surface/band-bending region instead. A polarization dependence on crystal orientation has been observed before [12]. The crystal orientation and surface composition determine the density of surface states and the amount of band-bending [13]. In cases with large band-bending, the electron can be reflected at the surface due to its interaction with the L-valley in the conduction band [9,14]. (The L-valley is shown as the upper dotted line in Fig. 5.) During the repeated attempts at escape in the band-bending region, the electron can recombine with surface states or the valence band, lose energy through scattering and become unable to escape, and suffer spin relaxation. In addition, large electron kinetic energies in the band-bending region are thought to increase the probability of spin relaxation [15].

A (111B) surface (arsenic terminated), on the other hand, has much less band-bending (0.1 eV at the surface and 50 Å wide) which leads to lower probability of electron reflection and lower scattering in the band-bending region. Hence the probability of escape is higher and less depolarization is expected. Fortunately, the valence band splitting of (111) strained samples is similar to that of (100) samples [16]. A strained (111B) GaAs sample could be the next step towards higher polarization and higher QE photocathodes.

V. CONCLUSION

Experiments in the upgraded Gun Test Laboratory have illustrated the behavior of photocathodes under various

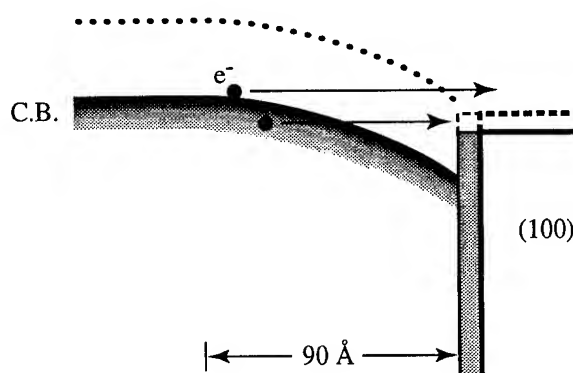


FIG. 5. Surface band diagram showing the filtering of low-conduction-band electrons by a rising work function. The (100) GaAs band-bending is 0.3 eV at the surface and 90 Å wide for p -type doping of $5 \times 10^{18} \text{ cm}^{-3}$. The upper dotted line represents the upper-conduction-band L-valley which is responsible for reflections at the surface.

conditions. A thin active region minimizes the travel time of electrons in the conduction band and thus reduces the effect of depolarization mechanisms. It was shown that low temperatures do not greatly improve the polarization in thin photocathodes. The 10% lower polarization than theoretically expected in thin, unstrained (110) GaAs could indicate that depolarization mechanisms occur instead in the band-bending/surface region. Strained (111B) GaAs seems like a promising material for higher polarization and QE because of its small band-bending region.

REFERENCES

- [1] R. Alley *et al.*, SLAC-PUB-95-6489; submitted to Nucl. Instr. and Meth. (1995).
- [2] P. Sáez, Ph.D. dissertation, Stanford University, Stanford, CA, in progress.
- [3] G. Mulhollan *et al.*, these proceedings.
- [4] T. Maruyama *et al.*, Phys. Rev. B **46**, 4261 (1992).
- [5] G. Fishman and G. Lampel, Phys. Rev. B **16**, 820 (1977).
- [6] G. Pikus and A. Titkov, in *Optical Orientation*, edited by F. Meier and B. Zakharchenya, (North-Holland, Amsterdam, 1984), Ch. 3.
- [7] T. Maruyama *et al.*, Appl. Phys. Lett. **55**, 1686 (1989).
- [8] D. Pierce *et al.*, Rev. Sci. Instr. **51**, 478 (1980).
- [9] M. Clark, J. Phys. D: Appl. Phys. **9**, 2139 (1976).
- [10] H. Aoyagi *et al.*, Phys. Lett. A **167**, 415 (1992).
- [11] F. Meier, D. Pescia and M. Baumberger, Phys. Rev. Lett. **49**, 747 (1982).
- [12] S. Alvarado *et al.*, Z. Phys. B - Condensed Matter **44**, 259 (1981).
- [13] L. James *et al.*, J. Appl. Phys. **42**, 4976 (1971).
- [14] M. Burt and J. Inkson, J. Phys. D: Appl. Phys. **10**, 721 (1977).
- [15] H. Riechert, H.-J. Drouhin and C. Hermann, Phys. Rev. B **38**, 4136 (1988).
- [16] F. Pollak and M. Cardona, Phys. Rev. **172**, 816 (1968).

Experimental Results of the ATF In-line Injection System

X.J. Wang, T. Srinivasan-Rao, K. Batchelor, M. Babzien, I. Ben-Zvi, R. Malone

I. Pogorelsky, X. Qui, J. Sheehan and J. Skaritka

Brookhaven National Laboratory, Upton, NY 11973 USA

The initial experimental results of the Brookhaven accelerator test facility (ATF) in-line injector is presented. The ATF in-line injector employed a full copper RF gun with a pair of solenoid magnets for emittance compensation. The maximum acceleration field of the RF gun was measured to be 130 MV/m. The electron yield from the copper cathode was maximized using p- polarized laser and the Schottky effect. The quantum efficiency under optimum conditions was measured to be 0.04%. The measured electron bunch length was less than 11 ps, which agreed with the laser pulse length measurement using a streak camera. The normalized rms. emittance for 0.25 nC charge is 0.9 ± 0.1 mm-mrad, which is almost four times smaller than the emittance predicted by the space-charge effect for a non-emittance compensation photocathode RF gun. The normalized rms emittance for 0.6 nC charge was measured range from 1 to 3 mm-mrad. This measurement was first experimental demonstration of emittance compensation in a high-gradient, S-band photocathode RF gun.

I. INTRODUCTION

A new photocathode RF gun injector based on the emittance compensation technique [1] was installed at the Brookhaven accelerator test facility (ATF).

The ATF is a facility dedicated for FEL and laser acceleration research [2], consisting of a laser driven RF gun injector [3], 70 MeV linac and experimental beam lines.

We will present experimental results of photoemission and electron beam emittance measurement for the emittance compensation RF gun. Comparison of experimental results with simple analytical predictions show that the measured emittance smaller than the uncompensated emittance. This indicates that the emittance compensation actually works.

II. THE ATF IN-LINE INJECTOR

The design of the injector [4] optimized the distance between the RF gun and the linac. The small emittance produced by the emittance compensation was frozen through the acceleration in the linac. The cell photocathode RF gun was followed by a solenoid magnet. A second solenoid magnet was placed behind the RF gun to buck the first solenoid magnet. Following the solenoid magnet is a six-way cross for vacuum pumping port, and a 45 degree aluminum mirror mounted on an actuator for monitoring the laser beam profile and optical transition radiation (OTR). There were beam profile and charge measurement devices located before and after the ATF two sections linac. A group of quadrupole magnets positioned subsequently can be used for emittance

*This work was performed under the auspices of US DOE under Contract No. DE-AC02-76CH00016.

measurement or beam matching for the experimental lines. There are two beam profile monitors with five meter separation after the linac. A pop-up beam profile monitor and momentum slit were installed after the dipole magnet for energy spread measurement and energy selection.

The ATF diode-pumped Nd:YAG oscillator can generate 81.6 MHz pulses with 14 ps FWHM pulse length and 100 mW power. The IR was frequency quadrupled to UV (266 nm) on the laser table. The UV laser pulse was transported to the RF gun hutch via 20 meter long evacuated pipe. The optics in the gun hutch was designed to compensate for the ellipticity of the emitting area caused by the oblique incidence.

III. RF GUN CHARACTERIZATION AND ELECTRON EMISSION MEASUREMENTS

It took about a week of conditioning for the RF gun to reach the designed acceleration field 100 MV/m. A four inch mirror was mounted on a precision optical rotation stage outside the window of the six-way cross for angular distribution measurement of optical transition radiation (OTR). A PMT was used to detect angular distribution of OTR while a CCD camera was used to measure the beam profile from OTR. Fig.2 plotted OTR experimental data and theoretical fittings for two different RF power levels. The data showed that the highest electron beam energy is about 6 MeV, which corresponds to the peak acceleration field 130 MV/m. The peak surface field in the RF gun cavity is about 20 % higher than the acceleration field.

The effect of the coupling slot between the waveguide and RF

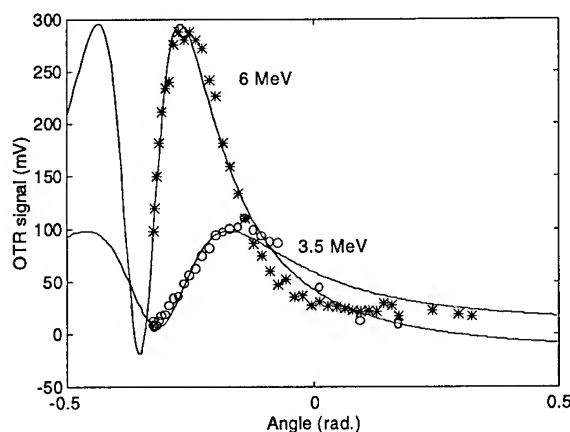


Figure 1 Angular distribution of OTR.

gun cavity was investigated experimentally. The main effect of the coupling slot is introduction of TM_{110} mode besides the acceleration mode TM_{010} mode in the RF gun cavity. The combining effect of those two modes is that the electric center of the cavity shifted toward the coupling slot. The field

emission current (dark current) profile was used to determine the electric center of the cavity because its strong dependence on the field strength. We aligned the laser spot on the RF gun cathode to the RF gun cavity mechanical center within 50 μm . It was found that the laser spot has to be shifted toward the coupling slot by about 1 mm in order to overlap the photoelectron beam and dark current.

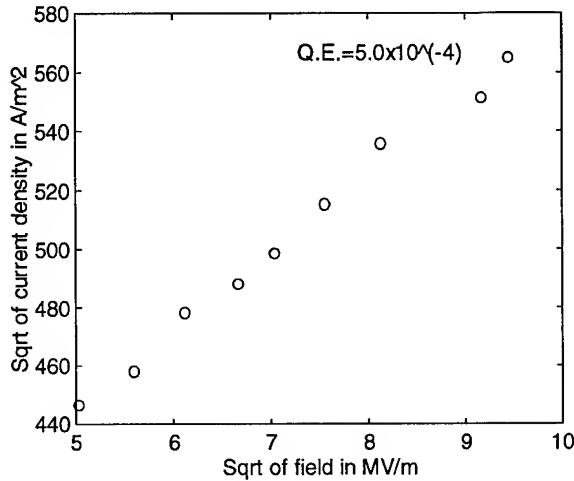


Figure 2 The Schottky effect measurement.

Photoemission from a cathode in an RF gun is influenced by the relative energy difference between the photon energy and the work function of the cathode, modification of this work function by the strong electrical fields present in the cavity, absorption coefficient of the cathode for the irradiating photon beam, and other material dependent properties such as the density of states, and surface dependent properties such as the enhancement due to surface irregularities. The current density for a field assisted single photon process can be written in a general form as,

$$j = AI(1 - R_i)(h\nu - \phi + \alpha\sqrt{\beta E})^2 \quad (1)$$

A is a material dependent constant, I is the intensity of the photon beam, R_i is polarization dependent reflectivity, $h\nu$ is the photon energy, ϕ is the work function of the cathode, α is $(e/4\pi\epsilon_0)^{1/2}$ in MKS units, β is the field enhancement on the surface and E is the applied electric field. The term $\alpha\sqrt{\beta E}$ expresses the lowering of the work function due to the Schottky effect. The Schottky effect measurement for optimized polarization was shown in Fig.2.

IV. ELECTRON BEAM MEASUREMENT

There are many factors that affect the performance of an emittance compensation RF gun injector. Extensive studies were carried out to simulate emittance compensation injector and to produce a procedure to achieve the emittance compensation experimentally. We compared the electron beam profile from RF gun to the exit linac in two cases. The first

case considered is that, optimized conditions for emittance compensation are assumed, good transmission through six meter linac was achieved, and a small good beam profile can be observed on the collimator right after the linac. Using computer program TRANSPORT, if no emittance compensation assumed, either poor transmission or large beam profile at the exit linac would be observed for any setting of the solenoid current. The reason for that is when emittance compensation realized, electron beam follows laminar flow trajectory while in the other case that electron beam will follow a cross over trajectory in the linac.

Generally speaking, to measure the beam emittance is to determined the three parameters in the beam matrix. We have used two profile monitors emittance measurement method for its simplicity and short time for data acquisition. In this method, the electron beam was focused to produce a beam waist at one of the beam profile monitors. The first measurement was with 50 MeV electron beam, table 1 lists the normalized 100% emittance and quadrupole currents for focusing the beam at two beam profile monitor separately.

Table 1: Initial emittance and corresponding quadrupole current.

	Focus at near BPM	Focus at far BPM
Emittance(mm-mrad)	22	15
Focusing quadrupole current (I)	6.65	4.5

The large emittance was determined to be the result of some emittance growth mechanisms. There are many mechanism could cause emittance growth, such space-charge effect, wake field effect, nonlinear magnetic field and chromatic effect. Since measurement was done at high energy (higher than 10 MeV), space charge effect is negligible. Also wake field effect can be ignored since the measurement was using relative low charge (0.25 nC). The ratio of the emittance being equal to the ratio of the quadrupole magnet currents suggested chromatic effect. Emittance growth for a single quadrupole magnet from chromatic effect can be estimated by[5],

$$\Delta\epsilon = \frac{\sigma^2}{f} \frac{\Delta p}{p} \quad (2)$$

where σ is the beam size at the quadrupole, f is the focal length of the quadrupole, and $\Delta p/p$ is the relative energy spread of the electron beam. Since the focal length of the quadrupole magnet is inverse proportional to its current. We concluded from Eq.(2) that the large emittance measured was caused by the emittance growth due to the chromatic effect.

To reduce chromatic effect, we first steered the laser so the photoelectron beam and dark current overlap on each other, this will reduce the energy spread and beam steering from dipole mode. Since the chromatic effect causes geometric emittance growth, we lowered the linac power to reduce the electron

beam energy to 37 MeV. The injector design called for 2.0 mm laser diameter with 1 nC charge. Due to a defect in the double crystal, the largest laser spot that we could produce at the time with good mode quality was about 1 mm. We scaled the charge down to about 0.25 nC by reducing the laser energy. The peak acceleration field at the gun was set to about 80 MV/m.

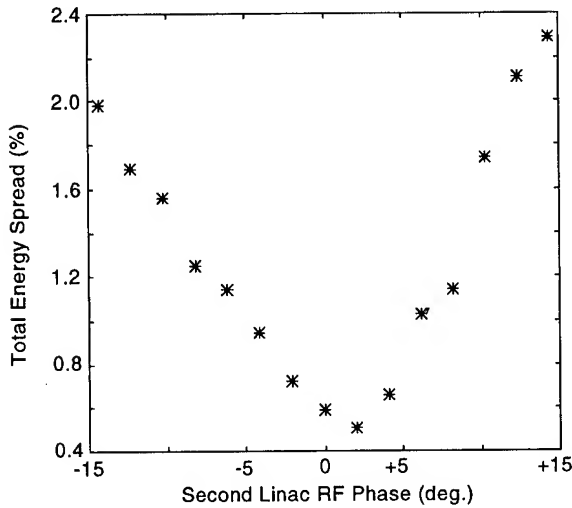


Figure 3 Energy spread vs. linac RF phase.

We then transported the electron to the momentum slit. The horizontal beam size observed on the momentum slit is given by,

$$x = \sqrt{\beta\epsilon} + D \frac{\Delta p}{p} \quad (3)$$

where β is the beta function at momentum slit, ϵ is the horizontal emittance, $D = 5.4$ mm/% is the dispersion at the slit. We adjusted beam optics so that the beam size due to the energy spread was dominant over the emittance term. The RF gun phase and linac phase were optimized to minimize the energy spread. The energy spread of the electron beam bunch was measured by changing the RF phase of the second linac section. The electron beam energy was about 17 MeV at the entrance of the second linac section, space charge effect was negligible. The energy spread as the function of the second linac RF phase was plotted in Fig.3. The minimum full width energy spread (100 % of the beam) is 0.5%, which corresponds to the full width electron beam bunch length less than 11 ps. The laser pulse was measure to 9 ps FWHM using a single shot streak camera.

We then observed electron beam on the collimator right after the linac, we adjusted solenoid magnet until we had 100 % electron beam transmission and the smallest beam profile. We also modified beam optics so the electron beam will be smaller at the quadrupole magnets. The normalized 100 % emittance measured is 4.7 mm-mrad, which corresponding 0.9 mm-mrad

normalized rms emittance. Upton repeated the measurements the spread of the measured emittance is about ± 10 %.

When increased the charge of electron to 0.6 nC, a beam halo was observed. Therefore instead of measuring total emittance, we measured the emittance of the core beam (FWHM). The measured normalize rms emittance range from 0.5 mm-mrad to 1.5 mm-mrad. Realizing that we may under estimated the emittance [6], we believed that the real emittance is between 1 to 3 mm-mrad.

The emittance due to space-charge contribution in a non-compensation photocathode RF gun can be estimated using following simple analytical formulas[7],

$$\epsilon_c = \frac{c^2}{8\sqrt{2\pi}\alpha f} \frac{Q}{I_A} \frac{1}{(3\sigma_x + 5\sigma_z)} \quad (4)$$

where $\alpha = eE_0 / 2mc^2k$, I_A is Alfven current equal to 17000 A. For $Q = 0.25$ nC, the space charge emittance would be 3.4 without emittance compensation. Similarly, the space charge emittance for 0.6 nC would be 8.2 mm-mrad. Comparing our experimental results with the predictions from Eq.(4), we concluded that we have experimentally demonstrated emittance compensation in a S-band, high-gradient photocathode RF gun.

V. ACKNOWLEDGMENT

Authors thank many useful conversations with Drs R. Hess, J. Gallardo, H. Kirk, D.T. Palmer, R. Palmer and G.Rakowsky. The technical support from C. Biscardi, W. Cahill, M. Montemagno, R. Harrington and J. Schill is gratefully acknowledged.

VI. References

1. B.E. Carlsten, Nucl. Instr. and Meth. in Phys. Res. A 285 (1989) 313.
2. I. Ben-Zvi, AIP Conf. Proc., vol. 279, 560 - 619 (1993).
3. X.J. Wang et al, Proc. of 1993 Part. Accel. Conf., 3000 - 3002 (1993)
4. J.C. Gallardo et al, Proc. of 1993 Part. Accel. Conf., 3615 - 3617 (1993).
5. X.J. Wang et al, Proc. of 1989 Part. Accel. Conf., 307 - 309 (1989).
6. B.E. Carlsten et al, Nucl. Instr. and Meth. in Phys. Res. A 331 (1993) 791 - 796.
7. K.J. Kim, Nucl. Instr. and Meth. in Phys. Res. A 275 (1989) 201.

High Power Testing of a 17 GHz Photocathode RF Gun *

S.C. Chen, B.G. Danly, J. Gonichon, C.L. Lin, R.J. Temkin, S.R. Trotz, J.S. Wurtele,
Plasma Fusion Center
Massachusetts Institute of Technology
Cambridge, Massachusetts 02139

Abstract

We report experimental high power test results on a high gradient 17 GHz RF photocathode gun. The $1\frac{1}{2}$ cell, π -mode, copper cavity was tested with 5-10 MW, 100 ns, 17.145 GHz pulses from a 24 MW Haimson Research Corp. klystron. A maximum surface electric field of 250 MeV/m was achieved corresponding to an on-axis gradient of 150 MeV/m. The gradient was verified by a preliminary electron beam energy measurement. Conditioning with $\sim 10^5$ shots resulted in a low field emission current, less than 6 mA. Future research will concentrate on measurements of the quality of electron beams produced by ps laser photoemission.

I. Introduction

To meet the stringent requirements set by future applications such as high-energy linear colliders and next generation free electron lasers, efforts have been made recently to create novel electron beam sources[1]. Operation at high frequency allows for high accelerating gradient without breakdown, a compact system, and high brightness. While existing RF guns operate from 144 MHz to 3 GHz, MIT is constructing and testing a 17.136 GHz photocathode RF gun[2].

When operating with a photoemission, cathode The expected beam parameters of the MIT 17 GHz RF gun are, : output energy 2 MeV, normalized emittance 0.47π mm-mrad, energy spread 0.18%, bunch charge 0.1 nC, and bunch length 0.47 ps. The experimental setup and status are described.

II. Experimental Layout

A. RF Source and Gun

Figure 1 shows the RF Gun cavity. Next to the cavity is the mandrel from which a previous version was electroformed. Later versions were constructed from machined OFHC pieces which were clamped together. Future versions will be brazed. The $1\frac{1}{2}$ cell cavity length is about 1.3125 cm. Figure 2 is a schematic of the experiment. The RF power source is a 17 GHz relativistic klystron developed by Haimson Research Corporation[3] and presently installed on the MIT High Voltage Modulator. The modulator voltage pulse is 560 kV, 95 A, and 1 μ s. The klystron has a peak output power level of 26 MW corresponding to a saturated gain of 67 dB and an efficiency of 51%. Following the klystron are a dual-directional coupler, a twist, a bend, an RF window, and a second dual-directional coupler. The two couplers are used to monitor the forward and reflected power exiting from the klystron and entering the cavity. A fast Faraday cup is placed just at the exit of the RF gun cavity in order to

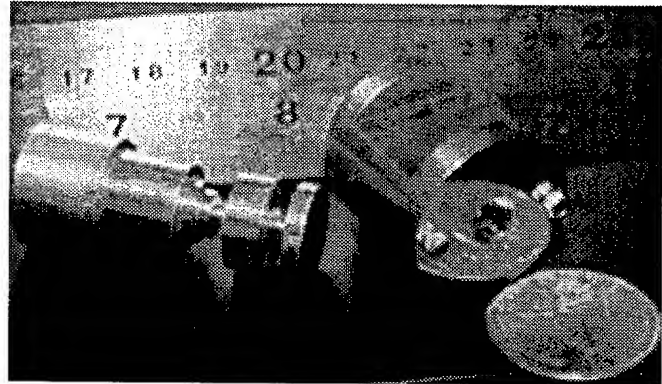


Figure 1. RF Gun Cavity and Mandrel

measure the accelerated current. Lastly, the inside of the cavity can be observed optically with a prism built into the Faraday cup and a viewport in the vacuum vessel which holds the RF gun. The vessel is evacuated by a 220 l/s ion pump. A vacuum of 3×10^{-9} Torr was achieved inside the RF gun chamber after a few weeks of pumping. This viewport permitted the detection of arcing and breakdowns which occurred inside the RF gun cavity. The breakdowns were characterized by flashes of light visible to the naked eye with the help of a remote television camera looking into the viewport. These flashes were coincident with shots in which a large spike of Faraday cup voltage was observed. The rectangular TE₁₀ mode is coupled to the cavity through two rectangular apertures, one on each cell of the cavity, to excite the π -mode resonance. An intensive study of this waveguide sidewall coupling scheme has been conducted both theoretically and experimentally[4]. The values of Q_0 , Q_1 , and β are 1790, 808, and 1.22. The results of these tests and preliminary high-power gyro-amplifier operation were reported in [5].

B. Laser

An Argon-Ion pumped Ti:Sapphire laser produces a regeneratively modelocked CW train of 10^{-8} J pulses at 780 nm which enter a pulsed Ti:Sapphire laser amplifier. The amplifier is pumped by a 1 J frequency doubled Nd:YAG laser. One pulse is captured and amplified to 2 mJ. Pulse-to-pulse laser power fluctuation in the infrared is approximately $\pm 10\%$. To date, the amplified IR pulse has been frequency doubled using a KDP crystal with an efficiency of 50%. The pulse still must be frequency summed to generate UV using a BBO crystal. For typical quantum efficiencies of 10^{-5} in copper, the expected electron bunch charge is 0.4 nC. The design parameters of the laser system are summarized in Table I.

*Supported by the Department of Energy under grant DE-FG02-91-ER40648

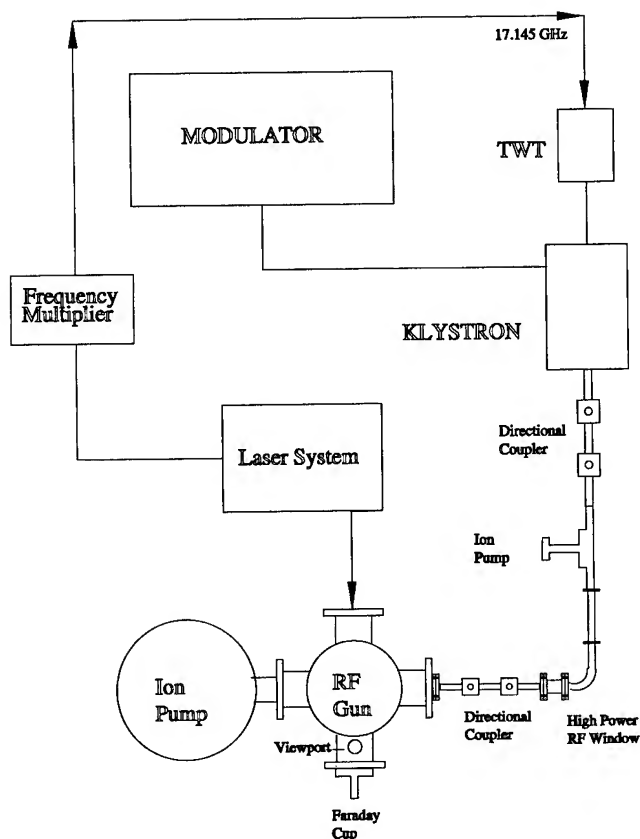


Figure 2. Schematic of the experiment

C. Timing

Simulations have shown that the beam quality is strongly dependent on the RF phase of photoemission[6]. The phase jitter is required to be less than 1 ps in our experiment. The highly stable Ti:Sapphire laser system serves as the system clock in the timing chain. The modelock frequency of 84 MHz is defined by the round-trip time of the laser cavity. The laser oscillator cavity mirrors are mounted on an Invar tube to minimize length variations. The 84 MHz signal is multiplied up by a solid state frequency multiplier ($\times 204$) into 17 GHz to drive the RF amplifier chain (see Fig. 2).

III. Results

A. Accelerating Gradients and Maximum Surface Field

For the results presented in this section, the RF gun was powered by the klystron but the laser system was not operational. Figure 3 is the record of a typical shot showing filling of the RF gun cavity and buildup of a strong electric field. The horizontal axis is time. Two of the traces are the forward and reflected power as measured by the 60 dB directional couplers just before the RF gun. The third trace, that of the electric field, is calculated from the forward and reflected power using the energy balance equation. The incident power is 7.5 MW . After the electric field builds up, the Faraday cup signal increases, remains nonzero for tens of nanoseconds, and then decays. This signal can be interpreted as partial breakdown or field emission. In addition, there

Table I
Parameters of the laser system

Wavelength	220-280 nm
Repetition rate	Single pulse and 0-10 Hz (adjustable)
Final output energy (per pulse)	0-200 μJ (adjustable)
Energy output fluctuation	$\leq \pm 10\%$
Pulse Length	$< 2\text{ ps}$
Phase Jitter	$< 1\text{ ps}$
Timing Jitter	$< 3\text{ ns}$
Polarization	$> 99\%$
Beam Divergence	0.5 to 1 mrad
Beam Pointing Error	$< 10\text{ }\mu\text{rad}$
Mode-Lock Frequency	84 MHz

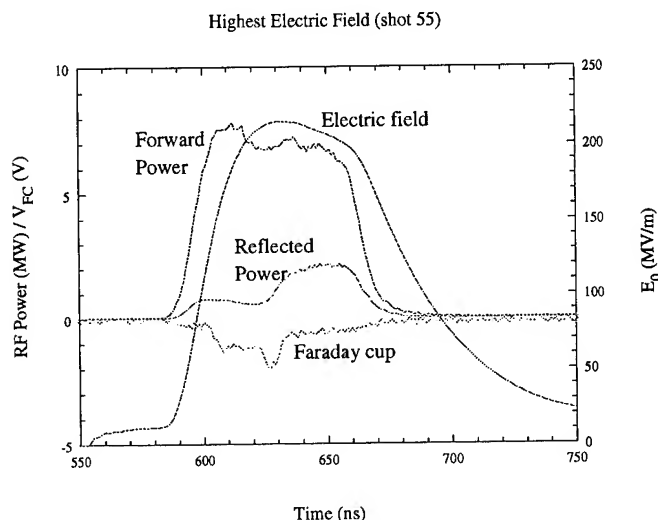


Figure 3. Shot Number 55

is an increase in the reflected power coincident with a jump in the Faraday cup voltage. This pattern suggests a momentary true RF breakdown. However, the electric field still builds up to 210 MV/m on-axis corresponding to 250 MV/m on the cathode surface. This field gradient is the highest observed in the experiment to date.

B. Field Emission Level

Figure 4 illustrates the history of the conditioning of the RF gun cavity. As time progressed, the maximum sustainable electric field increased and stabilized. Similarly, the amount of field emission decreased with time.

C. RF Breakdown Observations

Figure 5 shows a typical shot in which RF breakdown occurred. The traces are as described in the previous shot. After an initial period corresponding to the filling time of the cavity, one observes that the cavity became mismatched and totally reflecting. This breakdown is correlated with a large spike on the Faraday cup, a pressure rise, and a visible flash inside the RF gun cavity. These four events are clearly signs of RF breakdown. This type of shot occurred frequently when the incident power exceeded 7 to 8

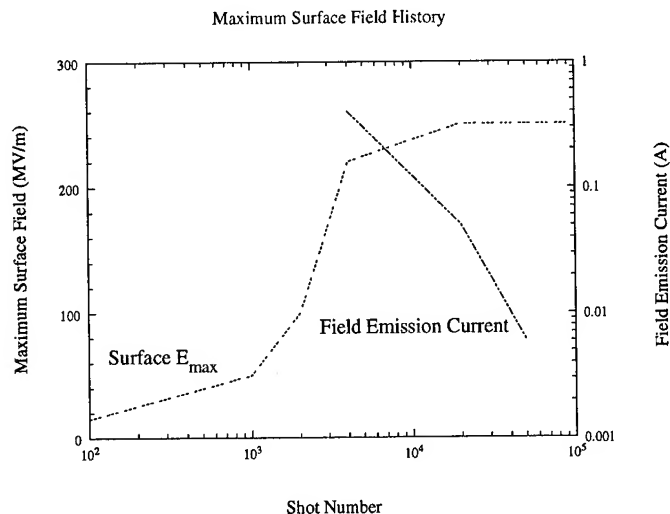


Figure 4. Max Field History
Typical Breakdown Shot

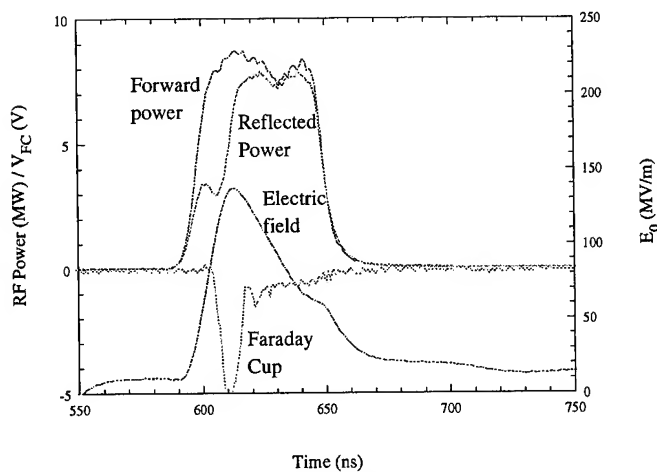


Figure 5. Shot Number 70

ergy gain corresponds to an average electric field between 110 MeV/m and 171 MeV/m . This measurement is consistent with the 150 MeV/m average field gradient deduced from the RF power balance calculation described above. Future experiments will employ a magnetic spectrometer for more precise determination of the electron energy spectrum.

IV. Conclusion and Future Work

A 17 GHz photocathode RF gun experiment is being performed at MIT. High power tests have been conducted at 5-10 MW power levels with 100 ns pulses. A maximum surface electric field of 250 MV/m was achieved. This peak value corresponds to an average on-axis gradient of 150 MeV/m . The gradient was verified by a preliminary electron beam energy measurement. Higher gradients are expected in future experiments utilizing a brazed cavity. To date, more than 90,000 pulses have been accumulated in the RF conditioning process.

Future plans for the 17 GHz RF gun experiment include the use of a brazed cavity design, integration of the laser to generate high quality electron beams, and improved beam diagnostics.

MW . However, the % of RF breakdown shots decreased from 90 to 10 % during the conditioning process.

D. Preliminary Beam Energy Measurements

The current experimental setup of the Faraday cup yields the total charge emitted during a shot and the coarse time profile of the current emission. In order to gain some information about the kinetic energy of the emitted electrons, the following diagnostic was used. The ability of electrons to pass through sheets of various metals depends on the type of metal, the thickness of the sheet, and the energy of the electrons. Thus, aluminum and titanium foils of varying thicknesses were placed between the exit of the RF gun and the Faraday cup. The metal sheets act as filters allowing only electrons with an energy greater than some level to pass. Then, the integrated Faraday cup signal becomes an indication of the number of electrons to exit the gun with energy greater than this level. The thicknesses and materials of the metal sheets were chosen to stop 99% of electrons with energies below 220, 650, 1450, and 2250 KeV . Faraday cup signals were observed when the 1450 KeV sheet was in place. This result brackets the maximum electron kinetic energy between 1.45 and 2.25 MeV . Using the cavity length of 1.3125 cm , the en-

ANALYTICAL MODEL FOR EMITTANCE COMPENSATION IN RF PHOTO-INJECTORS

L.Serafini, INFN-Milan, Via Celoria 16, 20133, Milan, Italy
J.B.Rosenzweig, Department of Physics, UCLA, Los Angeles, CA 90024

In this paper we present a new model to represent analytically the transverse beam dynamics in RF photo-injectors. It consists basically of an enhanced Kim's model [1], with incorporation of RF ponderomotive focusing effects, external magnetic focusing and a perturbative treatment of space charge along the beam envelope. Applying the resulting formulas it is possible to predict with high accuracy the transverse beam envelope behaviour in a multi-cell RF gun, as well as the operating conditions to achieve space charge emittance compensation according to Carlsten's scheme [2]. The agreement with sophisticated numerical simulations is really quite satisfactory, as well as the match with experimental measurements of the predicted operating range for emittance compensation.

I. BEAM ENVELOPE IN MULTI-CELL RF GUNS

The basic model adopted for calculating the beam envelope consists actually of an indefinitely long RF gun, supporting a $TM_{010-\pi}$ standing resonant mode (frequency ν) with accelerating field $E_z = E_0 \cos(kz) \sin(\omega t + \phi_0)$ (E_0 is the peak field at the cathode, located at $z=0$, $k=\omega/c$, $\omega=2\pi\nu$). The field is expanded linearly off-axis to find the transverse E_r and B_ϕ components [1]. An external solenoid is assumed to be folded around the first $2+1/2$ cells of the RF gun cavity, producing a constant magnetic field $B_z = B_0$ from $z=0$ up to $z_C=(5/4)\lambda$.

Under the approximation $\alpha > 1/2$, where $\alpha = eE_0/(2mc^2k)$ is the dimensionless field intensity, it has been extensively shown elsewhere [3] that the beam envelope conditions σ_2 and σ_2' at the second iris location $z_2=(3/4)\lambda$ can be written, for a gaussian charge density distribution in the bunch, as

$$\begin{aligned} \sigma_2 &= \sigma_{cat} (1 + \Delta_{SC} - \Delta_B) \\ \sigma_{orb}' &= \frac{\gamma'}{\gamma_2} \sigma_{cat} \left[\Delta p^{RF} + \mu_{SC} - 2\Delta_B (1 + \Delta p^{RF} - \Delta_B) \right] \\ \sigma_2' &= \sigma_{orb}' - \frac{\gamma'}{2\gamma_2} \sigma_2 \end{aligned} \quad (1)$$

where σ_{cat} is the laser spot size at the cathode, Δp^{RF} is the RF defocusing kick

$$\Delta p^{RF} = 2 - \frac{\text{Log}(\gamma_1)}{\gamma_1 - 1} - \frac{\text{Log}(\gamma_2)}{8} \left[2 - \frac{\text{Log}(\gamma_1 \sqrt[3]{\gamma_2})}{2(\gamma_2 - 1)} \right],$$

Δ_B is the magnetic focusing term $\Delta_B = (1/2)[k_s \text{Log}(\gamma_2/\gamma_B)]^2$ ($k_s = cB_0/E_0$) and Δ_{SC} is the space charge defocusing kick $\Delta_{SC} = (1 + \mu_{SC})[1 - \text{Log}(\gamma_2)/(\gamma_2 - 1)]$, calculated *à la Kim*. The space charge dependence on bunch and field parameters is specified by $\mu_{SC} = Z_0 I \zeta / (8\gamma' E_0 I_a \sigma_{cat}^2)$, where $Z_0 = 377$ ohm, I is the bunch peak current, $I_a = \text{Alfven current}$, $\gamma' = \alpha k$ is the dimensionless energy gain per unit length and ζ specifies the dependence on the bunch aspect ratio $A = \sigma_r / \sigma_z$,

$\zeta = 1 / (2.45 + 1.82A^{1.25} - 0.55A^{1.5})$. The beam energies γ_1 and γ_2 (in rest mass units) at the first and second iris are given by $\gamma_1 = 1 + \alpha\pi/2$ and $\gamma_2 = 1 + 3\alpha\pi/2$ ($\gamma_B = 1 + \alpha\pi/4$).

After the second iris the beam envelope can be easily tracked, as far as the space charge can be assumed negligible beyond this point, by applying the RF focusing transport matrix for relativistic beams [4] with initial conditions σ_2 and σ_{orb}' given by eqs.1 (σ_2' gives the *secular* orbit divergence and will be used later as initial condition for the envelope equation). The matrix gives at any position the beam spot σ of the average *secular* orbit and the beam divergence σ' of the actual orbit.

The agreement between analytically predicted envelopes and numerical simulation results are shown in Fig.1 for two $10+1/2$ cell guns at typical frequencies and peak fields.

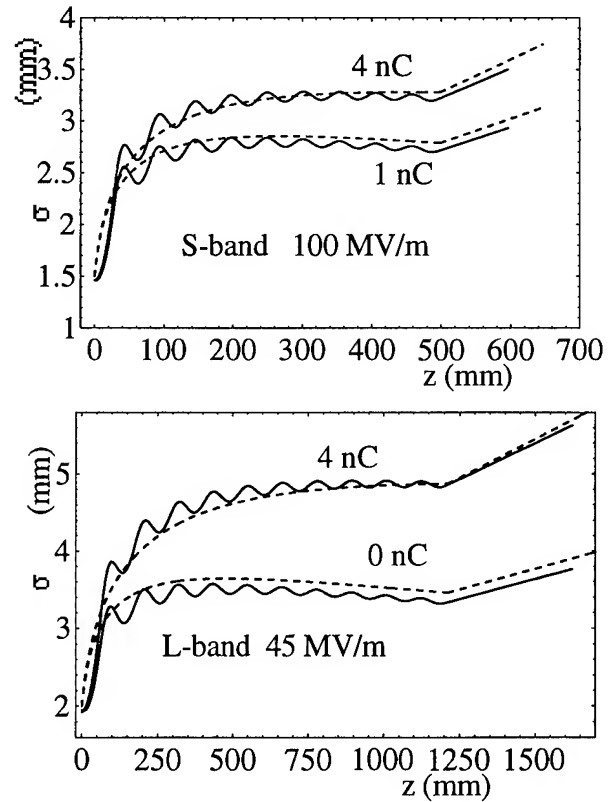


Figure 1: Beam envelopes through two different $10+1/2$ cell RF guns ($\nu=2.856$ GHz upper diagram, $\nu=1.3$ GHz lower diagram). Dashed lines give the secular orbits analytically predicted, while solid lines are numerical simulation results.

In the upper diagram the bunch aspect ratio is $A=1.25$ with $\sigma_{cat}=1.5$ mm, corresponding to a peak current $I=100$ A at 1 nC and 400 A at 4 nC ($z_2=79$ mm, $\gamma_2=8.7$, $\alpha=1.64$); in the lower diagram $A=0.83$ with $\sigma_{cat}=1.74$ mm, $\gamma_2=8.6$, $\alpha=1.62$). The simulations were performed with the codes ATRAP [5] for the S-band gun and ITACA [6] for the L-

band one. In this way the beam envelope can be predicted just on the basis of six main free parameters: three of them characterize the external fields, namely E_0 , v , B_0 , while the bunch characteristics, determining the collective field, are specified by σ_{cat} , A , and I .

Eqs.1 are derived under the basic assumption of self-similar expansion of the charge density distribution, which stays gaussian in the (r,z) space under the effect of all the external as well as the collective forces acting on the bunch particle. The average bunch phase $\langle\varphi\rangle$ is assumed to be $\langle\varphi\rangle=\pi/2$, corresponding to maximum acceleration in the gun.

In case the magnetic focusing is not applied ($B_0=0$, as for Fig.1), the beam envelope behaviour is such that the space charge effects can be considered negligible after the second iris. In presence of an external magnetic focusing we need a different treatment of the beam dynamics. The envelope equation for a relativistic beam [7] seems the best approach:

$$\sigma'' + \sigma' \left(\frac{\gamma'}{\gamma} \right) + K_r \cdot \sigma - 2 \frac{(I/I_a)}{\sigma \cdot \gamma^3} - \frac{\epsilon_n^2}{\sigma^3 \gamma^2} = 0 \quad (2)$$

where $\sigma' = d\sigma/dz$, ϵ_n is the rms normalized emittance and K_r is the RF focusing gradient [4] $K_r = (k_s^2 + 1/8)(\gamma'/\gamma)^2$, which incorporates the contribution (k_s) from the magnetic field. This equation actually holds for an un-bunched beam: since the bunch aspect ratio in its rest frame, given by A/γ , can be considered small enough beyond the second iris, where typically $\gamma > 5$, we assume eq.2 can be taken as a good approximation. Moreover, since we are interested in studying the conditions which give rise to space charge emittance compensation, the hypothesis of beam laminarity will be set up, implying that the emittance term in eq.2 is negligible. This is equivalent to assume that the beam envelope will not go through any crossover from the cathode up to the gun exit.

Under these assumptions, we can apply a Cauchy transformation to eq.2, setting $y = \text{Log}(\gamma/\gamma_2)$ (recalling that $\gamma = 1 + \alpha k \cdot z = 1 + \gamma' z$) and obtaining

$$\frac{d^2 \sigma}{dy^2} + \Omega^2 \sigma = \frac{S}{\sigma} e^{-y} \quad (3)$$

with $\sigma = \sigma(y)$ and $S = 2I / (I_a \gamma'^2 \gamma_2)$. We solve eq.3 following two different techniques, according to two different domains: the first one is defined by $z_2 < z < z_c$ ($0 < y < y_c$) and it is characterized by the focusing from the magnetic field, so that $\Omega^2 = 1/8 + k_s^2$. The 2nd one is defined by $z > z_c$ ($y_c = \text{Log}((1+5\pi\alpha/2)/\gamma_2)$, $z_c = 5\lambda/4$), hence $\Omega^2 = 1/8$. In the first domain the beam size σ is varying slightly with respect to σ_2 , allowing to assume $\sigma = \sigma_2$ in the non linear term on the r.h.s. of eq.2. The general solution σ_I of the linearized equation becomes

$$\sigma_I = \sigma_2 \frac{\cos \Omega y}{\sqrt{S}} + \sigma_2 \frac{\sin \Omega y}{\Omega \sqrt{S}} + \frac{\left[e^{-y} - \cos \Omega y + \frac{\sin \Omega y}{\Omega} \right]}{\sigma_2 (1 + \Omega^2) / \sqrt{S}} \quad (4)$$

where $\dot{\sigma} = d\sigma/dy$ and $\dot{\sigma}_2 = \sigma'_2 \gamma_2 / \gamma'$.

Setting $\sigma_c = \sigma_I (y=y_c)$ and $\dot{\sigma}_c = \dot{\sigma}_I (y=y_c)$, we can solve perturbatively eq.3 in the second domain, assuming that the non linear term on the r.h.s. may be represented by a particular solution of the form 4). The perturbative solution σ_{II} becomes

$$\sigma_{II} = \left\{ \left[\sigma_c - \frac{S e^{-y_c}}{\sigma_c \Psi} \right] \cos \left(\frac{y - y_c}{\sqrt{8}} \right) + \frac{S e^{-y + (y_c - y)} \sigma'_c / \sigma_c}{\sigma_c \Psi} + \left[\sigma'_c - \frac{S e^{-y_c} (1 + \sigma'_c / \sigma_c)}{\sigma_c \Psi} \right] \sin \left(\frac{y - y_c}{\sqrt{8}} \right) \right\} / \sqrt{S} \quad (5)$$

where $\Psi = 1/8 + (1 + \dot{\sigma}_c / \sigma_c)^2$. Eq.5 produces envelopes as those shown in Fig.2, for the same bunch and field parameters of Fig.1 (lower diagram, L-band gun), at various values for B_0 . One should note that an angular kick $\Delta\sigma' = +\gamma'/2\gamma$ [4] must be added to the secular envelope at the gun exit in order to transform it back into the actual envelope.

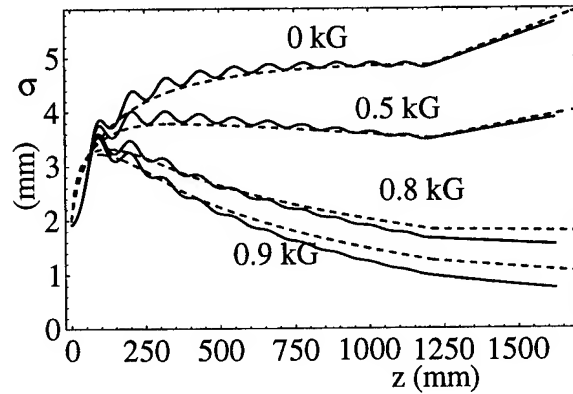


Figure 2: Beam envelopes through a 10+1/2 cell L-band RF gun ($E_0=45$ MV/m, $I=200$ A, $Q=4$ nC).

II. UNIVERSAL SCALING

Due to the excellent agreement between the analytical treatment and the numerical data, we believe that is possible to extract from the envelope expressions, eqs.4,5 and 1, useful informations on beam quality and RF gun performances. First of all, let us normalize the envelope eq. 3, which, in Cauchy space (σ, y) , reads, for $y > y_c$, $\ddot{\sigma} + \sigma/8 = S e^{-y}/\sigma$, in order to reduce all the parameters to dimensionless quantities.

By defining the dimensionless quantity $\tau \equiv \sigma / \sqrt{S}$, the envelope eq. in the Cauchy dimensionless space (τ, y) reads

$$\frac{d^2 \tau}{dy^2} + \frac{\tau}{8} = \frac{e^{-y}}{\tau} \quad (6)$$

which is a universal scaled equation, independent on any external parameter. It is interesting to note that the function τ can be expressed as $\tau = \gamma' \cdot \lambda_p \sqrt{\gamma_2 / \gamma}$: under this form it is clearly shown that τ scales like the ratio between the plasma wavelength $\lambda_p = 2\pi c / \omega_p$ and the energy gain length $L_g = 1/\gamma'$. Moreover, a particular exact solution of equation 6) can be found to be $\tau^* = \sqrt{8/3} e^{-y/2}$: this solution is characterized by

a constant ratio between the two fundamental scale lengths, L_g and λ_p , i.e. $\lambda_p/L_g = \sqrt{8/3}$. The corresponding beam size σ^* comes out to scale like $1/\sqrt{\gamma}$, namely $\sigma^* = \sqrt{8S\gamma_2/(3\gamma)}$, but, more relevant, τ^* is the only solution displaying a constant phase space angle δ , which is independent on initial conditions σ_c and $\dot{\sigma}_c$ in all of the three spaces (Cauchy dimensionless, Cauchy, real). In fact, $\delta^* = \dot{\tau}^* / \tau = \dot{\sigma}^* / \sigma = \gamma\sigma^* / (\sigma\gamma') = -1/2$, so that in both Cauchy spaces the phase space angle is a universal constant. The most relevant consequence is that δ , on this particular envelope σ^* , which will be called the *invariant envelope*, does not depend on the beam current (whose dependence is embedded in the expressions for σ_c and $\dot{\sigma}_c$): this is exactly the basic condition to get a vanishing linear correlated emittance. In fact, it is well known that the emittance growth from linear space charge effects is due basically to the spread in phase space distribution of different bunch slices, which get different kicks from the space charge field: these may be thought to be represented by different current amplitudes in the envelope eq.2.

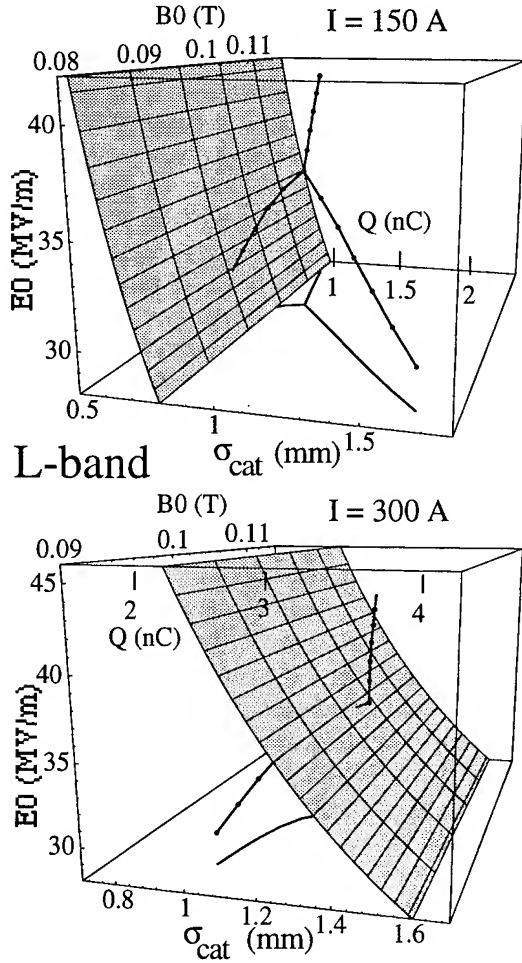


Figure 3: Solutions of eq.7 at $\nu=1.3$ GHz, $A=1$, $I=150$ (upper diagram) and $I=300$ A (lower diagram), represented by the solid-dotted lines in 3-D sub-space (E_0 , B_0 , σ_{cat}). Since the bunch aspect ratio is kept constant, the displayed bunch charges are given by $Q=\sqrt{2\pi} I \sigma_{cat} / A$.

III. RF GUN OPERATING CONDITIONS FOR EMITTANCE COMPENSATION

In order to find the operating points, as functions of the six free parameters, we must solve the equation:

$$[\sigma_c - \sqrt{8S\gamma_2/(3\gamma_c)}]^2 + [\dot{\sigma}_c + (1/2)\sqrt{8S\gamma_2/(3\gamma_c)}]^2 = 0 \quad (7)$$

whose solutions, in the 6-D space (ν , I , A , E_0 , B_0 , σ_{cat}), assure that σ_c and $\dot{\sigma}_c$ match the initial conditions of the invariant envelope. In this way the beam is transported from the cathode up to the gun exit with no space charge correlation, hence the emittance compensation is achieved.

In order to simplify the search for the solutions, we fix three parameters, namely ν , I and the aspect ratio A . The roots found in the 3-D sub-space (E_0 , B_0 , σ_{cat}) are plotted in Fig.3 for a L-band gun at $I=150$ A and $I=300$ A. The projections on the plane (B_0 , σ_{cat}) are also plotted in the figure (solid lines), while the shaded surfaces set the limit of maximum charge extractable from the cathode (only points on the right of the surface are allowed).

Selecting one possible solution from Fig.3, namely $\nu=1.3$ GHz, $A=1$, $I=150$ A, $E_0=35$ MV/m, $B_0=1.02$ kG and $\sigma_{cat}=0.84$ mm (so that $Q=1$ nC), we plot the corresponding envelope in Fig.4, for the nominal 150 A current and for lower and higher currents, 110,130,170,190 A, respectively: it is worthwhile to note that envelopes corresponding to currents different from the nominal one spread out in the first cells (see enclosed box), where the focusing action of the solenoid is dominant, but converge down into a common *invariant envelope* along the second domain ($z_c > 330$ mm) of eq.6.

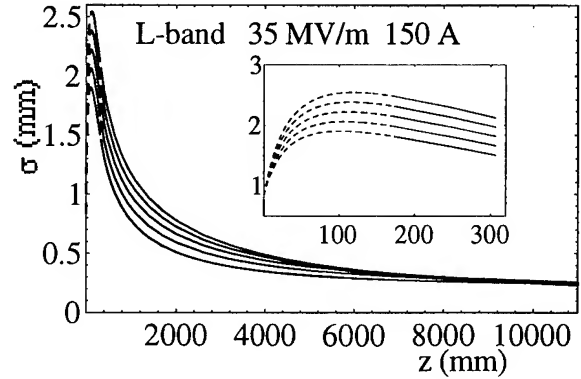


Figure 4: Envelopes corresponding to one of the solutions shown in Fig.3, for various currents around the nominal one.

IV. REFERENCES

- [1] K.J. Kim, NIM A275 (1989), p.201
- [2] B.E. Carlsten, IEEE Catalog no. 89CH2669-0
- [3] L. Serafini, *Analytical Approach to Transverse Dynamics in Multi-Cell RF Guns*, Proc. of VI AIP Workshop on Advanced Accelerator Concepts, Lake Geneva (WI), June 1994.
- [4] J.B.Rosenzweig, L.Serafini, Phys. Rev. E-49 (1994) 1599
- [5] J.M. Dolique and J.C. Coacolo, NIM A340 (1994), p.231
- [6] L.Serafini and C.Pagani, Proc. 1st EPAC, Rome, June 1988, Ed. World Scientific, p.866
- [7] J.D.Lawson, *The Physics of Charged Particle Beams*, 2nd ed. (Oxford Univ. Press, New York, 1988)

EMISSION, PLASMA FORMATION, AND BRIGHTNESS OF A PZT FERROELECTRIC CATHODE*

S. Sampayan, G. Caporaso, D. Trimble, and G. Westenskow,
Lawrence Livermore National Laboratory, Livermore, CA 94551 USA

We have measured a current emission density of 36 A-cm^{-2} over an 11.4-cm^2 -area Lead-Titanate-Zirconate (PZT) ferroelectric cathode with a pulsed anode-cathode (A-K) potential of 50 kV. We have also observed currents above those predicted by classical Child-Langmuir formula for a wide variety of cases. Since a plasma within the A-K gap could also lead to increase current emission we are attempting to measure the properties of the plasma near the cathode surface at emission time. In other measurements, we have observed strong gap currents in the absence of an A-K potential. Further, we continue to make brightness measurements of the emitted beam and observe spatially non-uniform emission and large shot-to-shot variation. Measurements show individual beamlets with a brightness as high $10^{11} \text{ A m}^{-2} \text{ rad}^{-2}$.

I. INTRODUCTION

Pulsed ferroelectric electron emission was observed as early as 1964 [1]. New materials have shown extremely high peak current densities ($>100 \text{ A-cm}^{-2}$) and high brightness ($10^{11} \text{ A-m}^{-2}\text{-rad}^{-2}$) [2,3]. Further, these emitters can be operated at non-UHV pressures, do not require elevated operating temperatures or a pulsed laser system, making them a potentially very attractive alternative to conventional cathode technology.

Pulsed electron emission from a ferroelectric results during a rapidly switched internal polarization change. The exact emission mechanism has not yet been unambiguously identified but is believed to result from the expulsion of charge stimulated by the large, uncompensated, bound charge generated during the induced polarization change [2,4,5].

Ferroelectric emission has many unique properties which we have previously reviewed [5]. They are as follows: (1) emission is energetic and has been measured to be from 0.5-100 KeV depending on switching method and material type, (2) emitted current densities are above those determined by the Child-Langmuir formula, (3) strong

emission can occur from a switched material without an applied A-K potential, (4) the quality of the emitted beam can be high: comparable to photoemitters, and (5) emission can take place over a wide pressure range from below 10^{-7} to above 10^{-3} T .

II. APPARATUS

We have reported on our apparatus in a previous paper [6]. Briefly, the apparatus consists of an A-K diode gap, an anode mask and fast phosphor for brightness measurements. The brightness diagnostic was replaceable with a screen mesh and view port for recording gated images of the cathode. The entire vacuum system and housing was fabricated from stainless steel; ceramics were used as insulators. Turbo-molecular pumps were used throughout. Base pressures in the 10^{-7} T range were easily achieved and maintained.

Additional diagnostics included a nude ion gauge and biased Faraday Cup. The nude ion gauge, for detection of neutral bursts, was electrically shielded from the main A-K gap and placed normal to the axis of the test stand. The Faraday cup, for detecting ion or electron current and inferring plasma density, was also placed normal to the diode axis and eventually circumferentially around the entire A-K gap.

Pre-poled and lapped PZT ferroelectric disks were placed behind and in contact with a conductive grid connected to the cathode. This conductive grid was either a square mesh composed of $25 \mu\text{m}$ diameter tungsten wires spaced approximately $750 \mu\text{m}$ on centers or an evaporated gold grid consisting of either $90 \mu\text{m}$ wide conductors, $300 \mu\text{m}$ on centers, or $50 \mu\text{m}$ conductors $760 \mu\text{m}$ on centers. A rear planar electrode received a pulsed high voltage which defined the switching electric field.

Sample orientation was such that the bound positive charge (negative screening charge) was positioned toward the A-K gap. Sample dimensions were typically 1 mm thick and with a 5.1 cm diameter. All but the 3.8 cm diameter central area of the sample was apertured. The grid-emitter assembly was recessed into the cathode shroud approximately 0.23 cm; the distance from the emitter surface to the anode was varied from approximately 0.6 to 2 cm.

* The work was performed under the auspices of the U.S. Department of Energy by Lawrence Livermore National Laboratory under contract W-7405-ENG-48.

Brightness measurements were performed with an anode mask consisting of nine 50 μm holes; 5 equally spaced vertically and the remaining spaced equally horizontally. A fast phosphor, ZnO(Ga), was used to image the pattern after a 24.5 cm drift distance. Charging was eliminated with a conductive film placed over the phosphor substrate. An image-intensified, gated camera allowed observation of the phosphor image. Gate width used was typically 40 ns.

To observe the luminosity on the surface of the ferroelectric cathode, the anode mask was replaced with a screen mesh and the phosphor coated window was replaced with a transparent viewport. Fast gated, on axis images of the cathode surface could then be captured during the induced polarization change and subsequent emission.

II. EXPERIMENTAL RESULTS AND DISCUSSION

We observed stronger emission from cathodes prepared with a fine wire grid placed in close contact with the surface than with thin evaporated conductors. Emission from the ferroelectric was generally achieved with a negative 1 to 1.5 kV switching pulse. A-K potential was varied from zero to approximately 60 kV. Typical voltage and current waveforms are shown in Fig. 1. Peak currents of approximately 36 $\text{A}\cdot\text{cm}^{-2}$ over the 11.4 cm^2 surface area were achieved during these measurements.

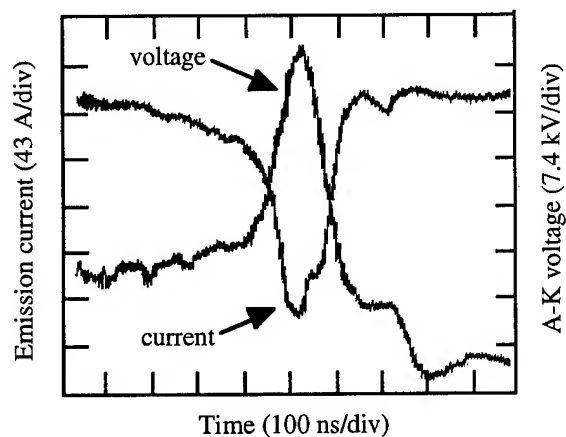


Figure 1. Typical current and A-K voltage pulse.

As was generally observed at lower A-K potentials, the measured current density, J , was unipolar, consistent with electron flow, and above the Child-Langmuir limit, J_{CL} , for electrons with zero initial kinetic energy (Fig. 2). In this data, the A-K potential was varied from 5 kV to 50 kV, peak; the emitted current varied from 9.5 A to 411 A, peak. The data indicated that the emitted current exceeded J_{CL} at lower A-K potentials. The largest ratio of J/J_{CL} occurred at low potentials, on average, with much decreased ratios at

increased potentials. As we previously described, the increased currents at low A-K potentials is believed to result from the electrons being emitted from the surface with significant kinetic energy [6].

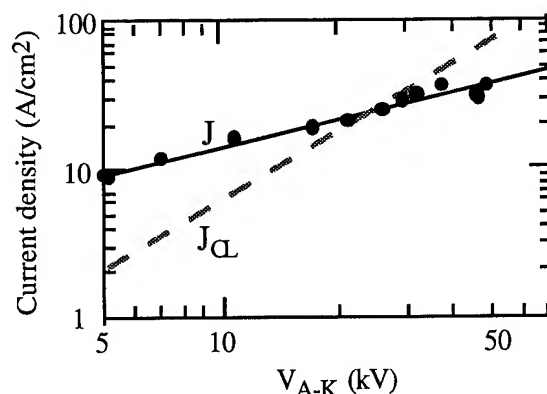


Figure 2. V-I characteristics for a 0.6-cm A-K gap.

With our present switching mode, e.g., maintaining the electric field on the ferroelectric until emission occurs, we have also observed on some samples strong emission (of order 0.4 $\text{A}\cdot\text{cm}^{-2}$ and greater) in the absence of an applied A-K potential (Fig. 3). Under the assumption that this electron emission is distributed uniformly over the cathode surface, a kinetic energy of over 3 KeV was implied from this data.

During application of the switching pulse we characteristically observed visible light from the emitter surface. With a gated camera, we correlated this luminosity to the application of the high voltage pulse used to induce a polarization change. In this measurement, strong luminosity is present on the emitter surface from the initiation of the switching current pulse until cessation; strong correlation to the emitted current pulse, however, was not observed. By contrast, we generally observed

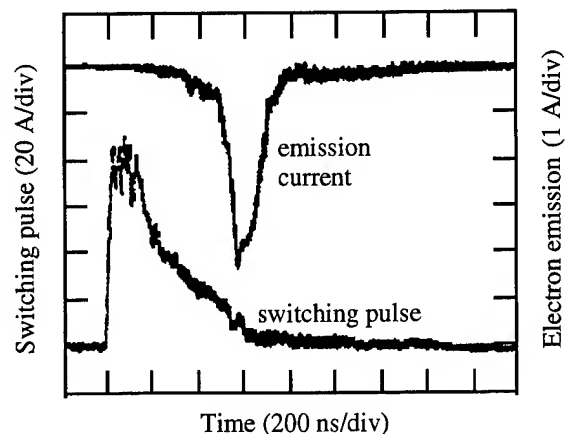


Figure 3. Emission without an applied A-K potential.

strong luminosity from samples that had been strongly poled. Strong electron emission, however, did not always accompany this luminosity with or without an applied A-K pulse.

In these experiments, we have also sought to determine the existence of an expanding cathode plasma. From the data presented in Fig. 2, the existence of this plasma should manifest itself as a change in the gap permeance. From the Child-Langmuir equation, the slope of a plot of the square-root of the inverse of the diode permeance (or the equivalent diode gap) as a function of time would be directly proportional to the plasma velocity [7]. In this data (Fig. 4), we observe no such slope indicating the existence of a stagnated plasma [8] or a plasma so tenuous that the emission in the diode gap was not affected.

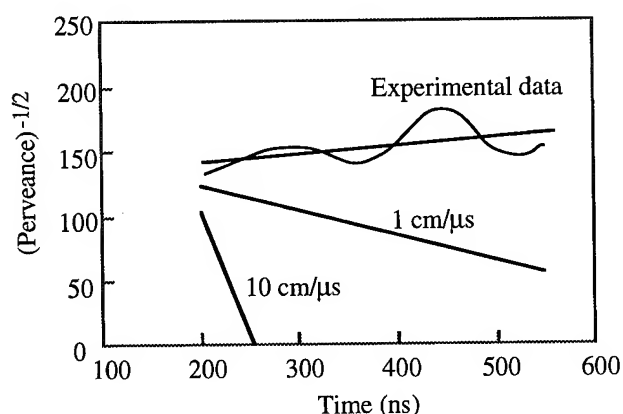


Figure 4. Effective gap during emission pulse.

In an additional attempt to determine the existence of a cathode plasma during emission without an A-K potential, a biased Faraday Cup collector transverse to the emitter axis was implemented. With a detection threshold of 0.25 mA-cm^{-2} , no ion current was observed. Further, significant neutral bursts, as could be detected by the ion-gauge, were also not observed. From the observed emission current of 0.4 A-cm^{-2} and the necessary cathode plasma density for such emission to take place, this detection threshold should have been more than adequate to detect the existence of ions from such a plasma.

Brightness measurements were accomplished with the multi-aperture mask previously described. In general, we observed distortion of the mask pattern on the phosphor and variation shot-to-shot.

In our particular geometry, the phosphor subtends an area of about 1 mm^2 on the cathode surface. On a given shot, we sometimes observed faint multiple images of a single anode mask hole projected onto the phosphor. This observation strongly suggested that non-uniform, multiple emission sites, within areas of order 1 mm^2 , exist on the cathode surface and appear to be consistent with other ferroelectric emission processes described [9]. From typical

data, we observed a divergence of 6.4 mrad at a current density of 18 A-cm^{-2} and energy of 33 KeV . From this data we set a lower bound on the brightness of the individual beamlets as $10^{11} \text{ A-m}^{-2} \text{ rad}^{-2}$.

IV. SUMMARY

We observed emitted current densities greater than those that would be predicted by the Child-Langmuir formula which assumes that electrons are emitted with zero initial energy. The existence of an interelectrode plasma, perhaps responsible for this result, was not evident in our measurements to date. Emission in the absence of an applied A-K potential was also observed. Observed surface luminosity did not correlate to electron emission nor did the luminosity always indicate the presence of emission. Measurement of the expansion of the individual beamlets yield a brightness of order $10^{11} \text{ A-m}^{-2} \text{ rad}^{-2}$. We continue to optimize the grid structure of the emitter and will attempt to stabilize the emission processes with reset and fine grain structure ferroelectric materials.

V. REFERENCES

- [1] L. Belayev, G. Bendrikova, *Fiz. Tverdogo*, 6 (1964) 645.
- [2] H. Gundel, H. Riege, J. Handerek, and K. Zioutas, CERN Report No. CERN/PS/88-66 (AR), 1988.
- [3] G. Kirkman, B. Jiang, and N. Reinhardt, presented at the IEEE International Electron Devices Meeting, San Francisco, California, 1992 (IEEE, New York).
- [4] G. Rozenman and I. Rez, *J. Appl. Phys.*, 73 (1993) 1904.
- [5] S. Sampayan, G. Caporaso, W. Orvis, and T. Wieskamp, submitted to *J. Vac. Sci. and Technology* and as UCRL-JC-120507.
- [6] S. Sampayan, G. Caporaso, C. Holmes, E. Lauer, D. Prosnitz, D. Trimble, and G. Westenskow, *Nucl. Instr. and Methods*, A340 (1994) 90.
- [7] R. Parker, R. Anderson, and C. Duncan, *J. Appl. Phys.*, 45 (1974) 2463.
- [8] R. Shefer, L. Friedland, R. Klinkowstein, *Phys. Fluids*, 31 (1988) 930.
- [9] B. Rosenblum, P. Braunlich, and J. Carrio, *Appl. Phys. Lett.*, 25 (1974) 17.

DESIGN AND TESTING OF THE 2 MV HEAVY ION INJECTOR FOR THE FUSION ENERGY RESEARCH PROGRAM

W. Abraham, R. Benjegerdes, L. Reginato, J. Stoker, R. Hipple, C. Peters, J. Pruyn, D. Vanecek, S. Yu, Lawrence Berkeley Laboratory, Berkeley, CA 94720

ABSTRACT

The Fusion Energy Research Group at the Lawrence Berkeley Laboratory has constructed and tested a pulsed 2 MV injector that produces a driver size beam of potassium ions. This paper will describe the engineering aspects of this development which were generated in a closely coupled effort with the physics staff. The details of the ion source and beam transport physics are covered in another paper at this conference. This paper will discuss the design details of the pulse generator, the ion source, the extractor, the diode column, and the electrostatic quadrupole column. Included will be the test results and operating experience of the complete injector.

INTRODUCTION

The new 2 MV, 800 mA K^+ injector for heavy ion fusion has been operational since January 1994. The injector utilizes electrostatic quadrupoles (ESQ) to simultaneously focus and accelerate the ion beam. Experiments in ion sources and beam emittance have been carried out during the past year. This paper will describe the engineering design and tests of the 2 MV Marx generator, the beam extraction and the acceleration ESQ column. The overall cross-section of the injector is shown on Fig 2. The pressure vessel is 25' long and has an inside diameter of 64". The left side houses the 38 stage Marx generator and is connected to the diode and ESQ column by the high voltage dome which houses the ion source.

ION SOURCE ELECTRONICS

The high voltage dome houses the hydraulically driven 400 Hz, 10 kVA alternator which powers all the source electronics including the telemetry system. Fig. 1 is a simplified block diagram of the source electronics. The source is an indirectly heated alumino-silicate coated on porous tungsten requiring 2500 watts. The source is biased at -80 kV and the extractor electrode is at dome potential inhibiting ion emission from the hot surface. Ion extraction is obtained by pulsing the source from a -80 kV to +80 kV with the step-up transformer driven by a tunable pulse forming network (PFN). The extractor waveform can be adjusted temporally in amplitude by $\pm 5\%$ simply by changing the coupled inductance of the PFN. The source filament transformer not only supplies the heater power, but is also a high voltage isolation transformer allowing the source to be biased at -80 kV.

Trigger, timing, and diagnostics information is transmitted to and from the high voltage dome by fiber optics links.

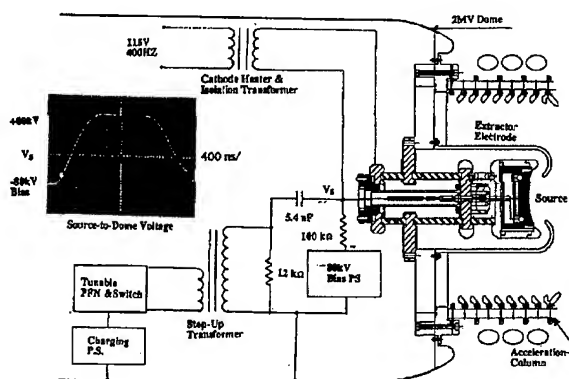


Fig. 1

THE MARX GENERATOR

In order to maintain a low spread in particle energy, an acceleration voltage variation or flat-top of less than 1% is required. The ion transit time through the length of the acceleration column is about 2 μs , hence the flat-top in voltage requirement for 4 μs was chosen to insure good overlap. Many of the standard pulse forming networks were considered to produce a 4 μs pulse with less than 1% variation in amplitude. They were modeled on the computer and all contained a large number of elements (L's and C's). Since this injector was an upgrade of an existing one, space for the Marx Stages was limited by the old geometry. The networks which synthesized the desired pulse were difficult to fit on the existing space. In the circuit simplification process it was discovered that a simple two-harmonics network could produce a flat-top of better than 0.5% when properly matched into the stray capacitance of the dome and the resistive column voltage divider. A multistage low level Marx generator was constructed using this network and it was found to agree closely with the computer modeling efforts. This network was very simple and fit very nicely in the existing space. Fig. 3(a) shows the schematic of the network, Fig. 3(b) is the actual physical layout of one stage, Fig. 3(c) is the 2.2 MV output pulse. The output pulse is generated by 38 identical stages; the first four stages from ground are triggered and the remainder are self-triggered by the previous overvoltage. The 10-90% risetime is less than 1 μs and the flat-top is 4 μs . The output voltage can actually be made to have a slight increasing ramp by underloading or a decreasing ramp by overloading with the liquid resistor which is externally adjustable.

MECHANICAL SYSTEMS

The 2 MV Injector column is 2.4 meters long and contains a diode section and four ESQ sections. The overall arrangement is shown in figure 4. Each of these

* This work was supported by the Director, Office of Energy Research, Office of Fusion Energy, U.S. Dept. of Energy, under Contract No. DE-AC03-76SF00098.

sections consist of a series of ceramic rings, 71 cm. outside diameter, brazed together with thin niobium

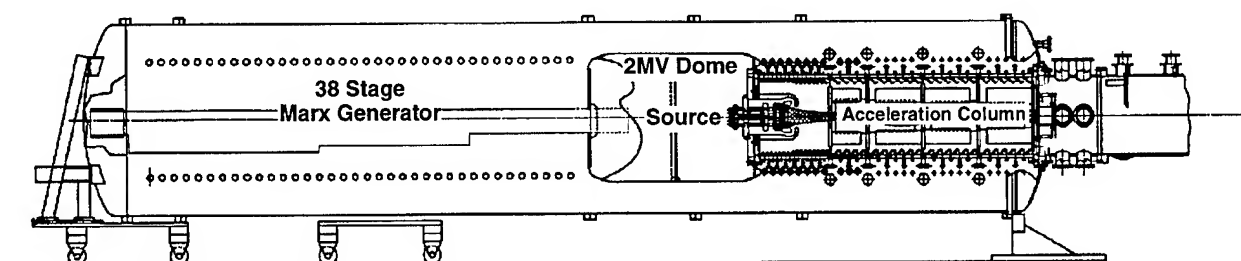


Fig. 2 Overall cross-section of the 2 MV Injector

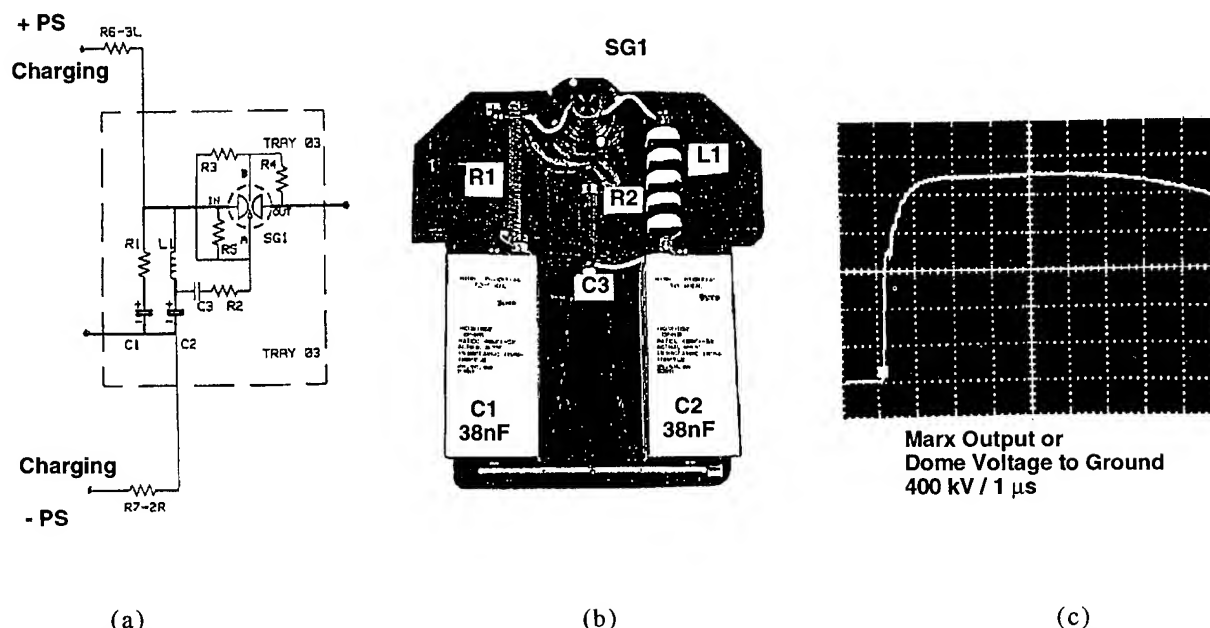


Fig. 3 (a) Schematic of charging tray (one of 38). (b) Layout of charging tray (c) Output waveform of Marx generator

flanges between each ring. The ESQ electrodes are mounted on plates captured between the ends of the brazed ceramic sections. Stainless steel x-ray shields are attached to the inside edge of each niobium ring. These also hide the triple points formed at the niobium to ceramic joints. A water resistor is electrically attached to the outside edge of each niobium ring. Semi-rigid polyethylene tubing is used in a helical configuration.

Each surface of the ceramic rings was ground very flat and lapped to remove microcracks. The brazing process required heating slowly to 843° C, soaking, and then cooling at a precise rate. Carbon fixtures were used to hold and align each stack during the braze cycle. Each braze cycle took about 24 hours. After brazing each stack was cleaned and excess braze material was removed by etching and grinding.

Larger diameter niobium flanges were used at the ends of each brazed section to provide a means of bolting the sections together. This detail is shown in figure 5. The strength of these joints was a major concern. After careful analysis, consultation with the ceramic manufacturer, and review of available test data, 17,000 cm-Kg was selected as a design limit for the bending

moment at the joints between sections. As a result, careful procedures had to be developed in order not to exceed this limit during any phase of assembly and installation.

The installed column weighs 2800 Kg. and is supported by 2 fiberglass tension struts on each side attached to a heavy collar between the diode and the first ESQ. This arrangement is shown in figure 4. This arrangement provides the required vertical support force of 2300 Kg. necessary at the 1.8 meter point on the column. Also, the rods load the column in 9200 Kg. compression since they are oriented primarily horizontally. This load turns out to be very useful as it keeps the tensile stress at the end flanges of the brazed sections below the level equivalent to the 17,000 cm-Kg. design limit. In other words, if the column was simply supported by a vertical support at the 1.8 meter point, without the compressive force created by the struts, the brazed joints would crack and come apart.

It was necessary to split the collar vertically in order to enable assembly. Collar geometry was designed in such a way that under load, the collar deforms into the

flat condition. This keeps the deformation of the first ESQ plate axisymmetric which keeps electrode

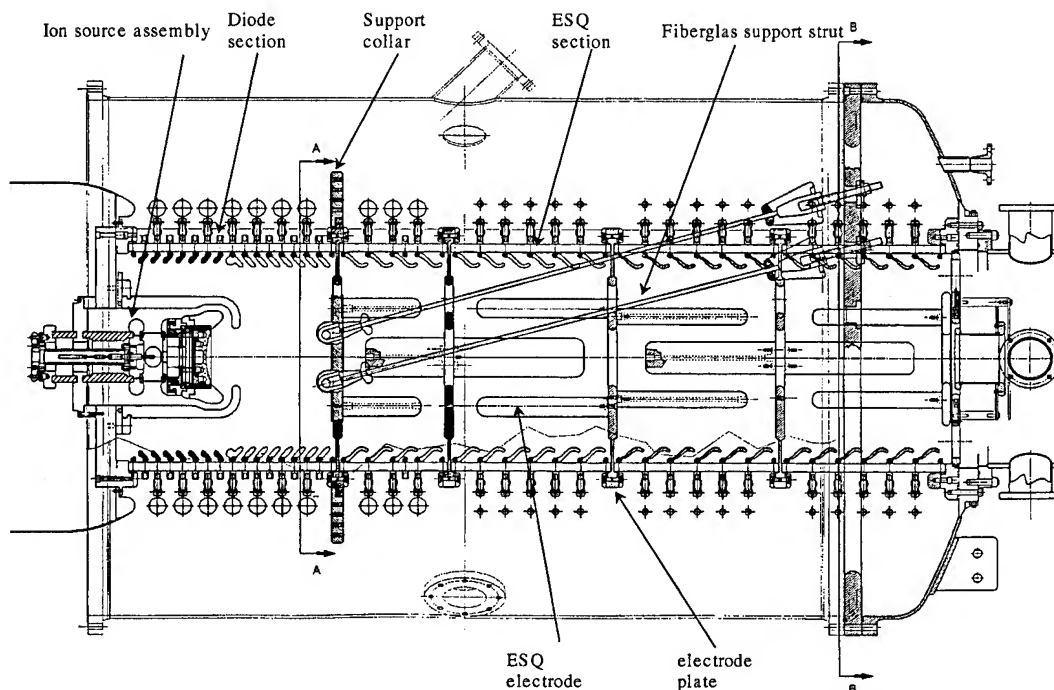


Figure 4. 2 MV Injector column showing fiberglass support struts. Column length is 2.4 meters, and insulator diameter is 71 cm.

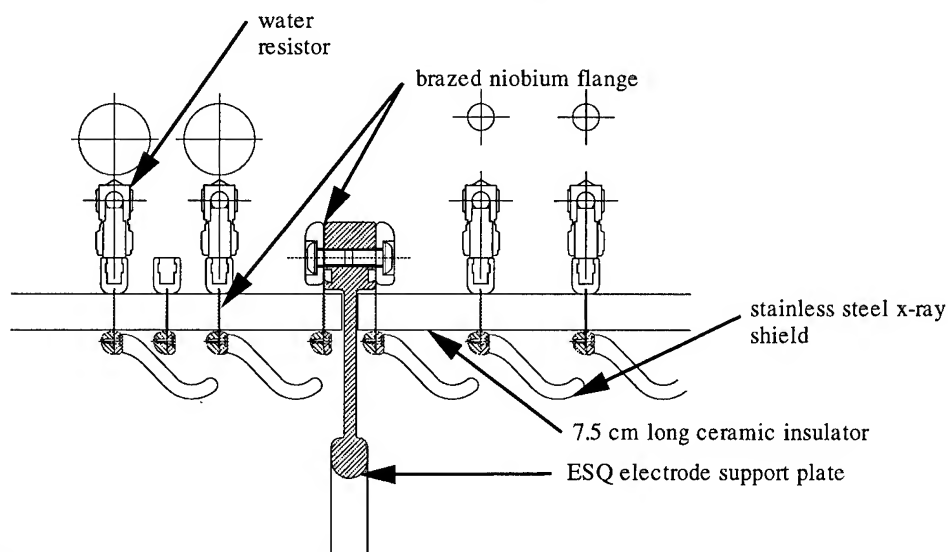


Fig. 5 2 MV Injector column detail. Thin niobium flanges at ends of brazen ceramic section attach to ESQ plate.

misalignment minimal and prevents damage to the ceramic end surfaces.

The ESQ electrodes are mounted on plates captured between the ends of the brazen ceramic sections. The outside diameter of these plates were supported by precise fixtures on a granite table to align all the electrodes in the column during assembly. Measurement of the electrode positions after assembly showed the RMS position error for the electrodes to be 0.3 mm.

CONCLUSION

The 2 MV injector has been operational for over one year. Initial operation was limited to below 1.5 MV due to capacitors which did not meet full specifications. Those capacitors were all replaced with new ones which meet specifications at no cost to LBL. The diode and the electric quadrupole column have operated very reliably with little conditioning required for operation at 2 MV.

Experiments in ion sources, beam transport, beam matching and emittance will continue over the next year.

K⁺ DIODE FOR THE LLNL HEAVY ION RECIRCULATOR ACCELERATOR EXPERIMENT*

S. Eylon, Titan Beta, 6780 Sierra Court, Dublin, CA 94568
E. Henestroza, LBL and F. Deadrick, LLNL

ABSTRACT

An 80keV K⁺ diode source that will deliver up to 9mA of beam current has been developed for the LLNL Small Recirculator experiment [1]. The diode consists of a hot plate alumino-silicate (Zeolite) source, a graphite Pierce electrode, and an exit extraction electrode. The K⁺ source emitting surface is planar, and one inch in diameter. A fine (70 line/inch) high transparency (90%) mesh is placed in the exit beam extraction electrode. The exit mesh reduces the sensitivity of the diode optics to possible variations in the diode gap and exit aperture shape, without a growth in the beam emittance. Numerical EGUN simulations were used for the diode physics design. The simulations showed that the diode can deliver a uniform 9mA K⁺ beam with a normalized emittance of about 0.05 mm-mr, resulting mainly from the source temperature at 1000°C. The beam at the diode exit is aperture to a diameter of 11mm to meet the recirculator experiment requirements of a 2mA beam with 0.01 mm-mr normalized emittance. The 80kV source acceleration potential is provided by a thyatron switched, 4μs long 8-section PFN which drives a 1:10 step-up pulse transformer. We shall report on the source performance including measurements of the beam total current, current density profile, phase space profile, angular divergence, and transverse emittance.

I. THE INJECTOR SYSTEM

A. Introduction and Requirements

A small-scale recirculator experiment is being built at the Lawrence Livermore National Laboratory to study the feasibility of recirculating induction accelerators for future heavy ion fusion applications. The injector system for this scale model experiment is required to deliver a K⁺ ion beam with a normalized emittance of less than 0.1 mm-mr at an energy of 80 KeV. The injector is to provide a 4μs wide beam pulse at a current of 2mA, operating at a pulse repetition rate of 10 Hz.

B. Injector Design

The injector system shown in Fig 1 consists of an hot plate contact ionization source which emits a K⁺ ion beam into a diode configuration. The source is mounted on a

Pierce shaped graphite plate anode connected to a 80kV pulser. The beam, focused along the diode passes through a fine mesh into the injector electrostatic quadrupole (ESQ) matching section.

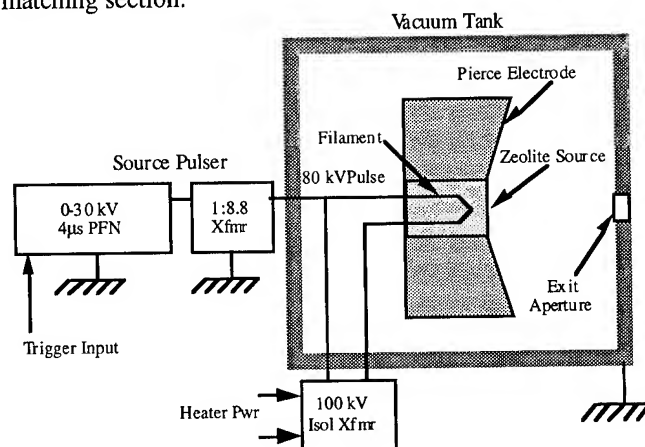


Fig. 1. Block diagram of K⁺ ion injector system.

Beam parameters needed for characterizing and matching the injector can be monitored at the source and the injector exits. Time resolved total beam current is measured using Faraday cups [2], beam envelope, phase space (transverse rms emittance) and current density profiles can be measured using slit-slit cup scanners [2] and beam longitudinal energy using an electrostatic coaxial bend energy analyzer [2].

C. Source Design

The source uses a standard 1" diameter flat Spectra-Mat source cup. The cup has a porous tungsten surface which is coated with a layer of alumino silicate. To emit ions (above emission limit) the source coated surface is heated to about 980°C. The source heater power (about 150W) is delivered through a high voltage isolation transformer to allow connection of the source emitting surface to an 80kV pulse anode voltage. The source intrinsic normalized emittance ϵ_n of 0.02 mm-mr (due to source surface temperature) is given by

$$\epsilon_n = 2a \left(\frac{kT_f}{m_i c^2} \right)^{1/2}$$

where $m_i=40$ is the ion mass, $a=6\text{mm}$ is the beam radius, $c=3e8\text{m/s}$, and $T_f=1273^\circ\text{K}$ is the source surface temperature. The diode geometry was designed using

EGUN code calculations [3]. Fig 2 shows the resulted diode geometry and the ion beam trajectories in the diode.

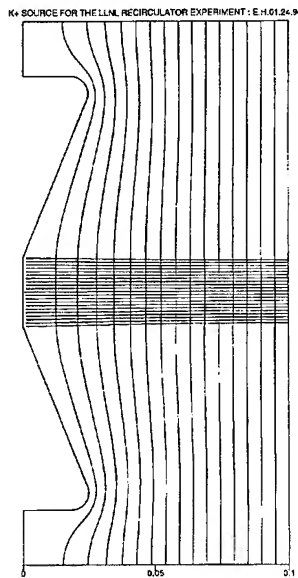


Fig. 2 EGUN evaluation of source ion trajectories.

The diode current is limited to 2mA using a 1cm diameter aperture in the diode exit plate (ground potential). To improve the diode beam optics a fine mesh is placed on the diode exit aperture. The mesh parameters (70 line/inch, transparency of 90%) were determined in early experiments [4] showing no degradation in the beam emittance when passing through the mesh.

D. Source Pulser

The source is pulsed on with a +80 kV - 4 μ s electrical pulse. The 4 μ s pulse is generated from a triggered pulse forming network (PFN) connected to a 1:8.8 high voltage step-up transformer. Fig. 3 shows the pulser circuit, and Fig 4 shows the pulse waveform. The pulser is capable of continuous operation at a repetition rate of 10 Hz.

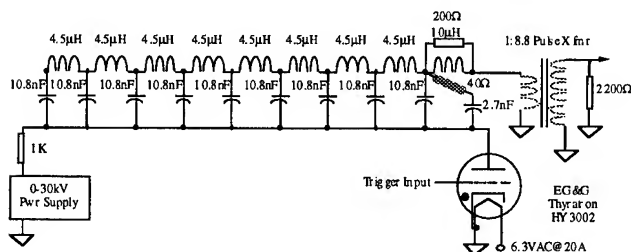


Fig. 3 Schematic diagram of injector pulser PFN.

Approximately 150 watts of filament power is required to heat the ion source to operating. Since the ion source is pulsed to +80kV, the filament circuit must be electrically isolated from ground potential, and a 200kV isolation

transformer is used for this purpose. Both the isolation transformer and the 1:8.8 step-up transformer are located in a tank containing Dyala oil for electrical insulation.

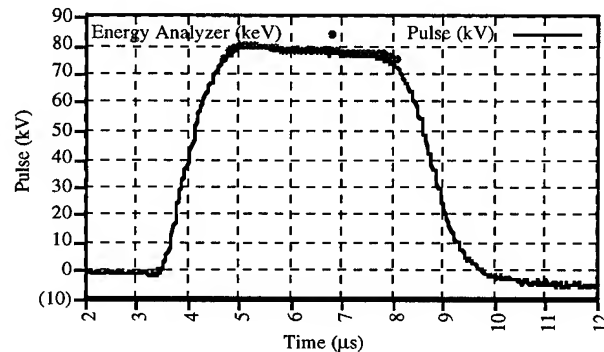


Fig 4. Ion source pulser waveform and measured beam energy.

II. INJECTOR SOURCE AND BEAM CHARACTERIZATION RESULTS

The source surface temperature was measured using a hot wire pyrometer. Fig 5 presents the source temperature T_f dependence on heater power W_h , showing that a P_h of 200W is needed to obtain a working T_f of 970°C.

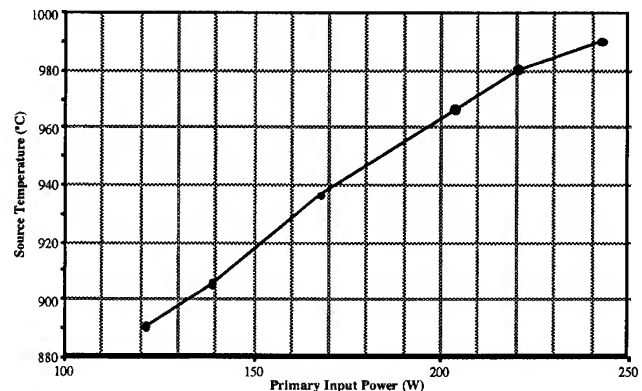


Fig. 5. Source temperature vs input power.

Beam parameters were measured at the diode exit and injector matching section exit were measured and compared with the physics design calculation. Fig. 6 shows the beam total current wave form measured using a Faraday cup at the injector exit. One can see a fast rise about 0.1 μ s in the measured current wave form compared with 1 μ s in the diode pulser voltage wave form. The slow rise in the diode voltage generates slow ions in the beam head leading to a time compressed rise in the beam current. This observation is consistent with beam transient simulations along the injector using the HINJ [5] code.

Improving (shortening) the diode pulser rise time will improve the shape of the beam head.

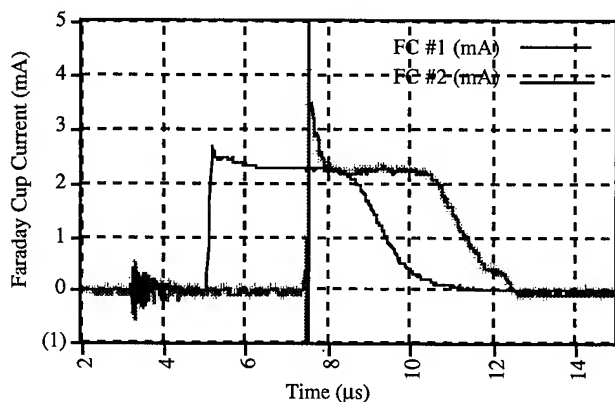


Fig 6. Ion beam current measured at the diode exit and at the end of the beam matching section.

Fig. 4 also shows the measured beam longitudinal mean energy wave form, using an electrostatic 90 deg. bend at the matching section output. The measured beam energy was found to be consistent with the measured diode pulser wave form Fig 4. The beam transverse dynamics i.e. the beam transverse phase space density profile in x, x' (horizontal direction) and y, y' (vertical direction) were measured using the slit slit-cup beam scanners. Beam phase space measurements at the source exit, Fig 7, showed a beam radius (circular symmetry) of 6mm consistent with the diode exit aperture diameter of 12mm and a divergence of 3mr. This measurement together with Faraday cup beam current measurements at the diode exit were found to be in agreement with the diode design EGUN simulations. The measured 80kV beam unnormalized rms transverse emittance was 4 mm-mr leading to a normalized emittance of 0.03 mm-mr, consistent with the above calculated beam normalized emittance of 0.02 mm-mr (beam radius of 6mm) due to the source surface temperature.

These measurement results (at the diode exit) were used as the beam input parameters to the MATCH code beam matching calculation. Following the MATCH code calculations, the quadrupoles voltages were set for matching conditions. The matched beam phase space profile in the vertical direction at the matching section exit was measured. The measurement was repeated with the quadrupoles voltage polarities switched to allow the measurement of the beam phase space in the horizontal direction. The measured beam parameters were consistent with the MATCH code calculation. The MATCH code being a 2D code does not incorporate the curved shape of the quadrupole ends. To improve the calculation accuracy one can use available 3D beam simulation or an effective

quadrupole length that can be obtained either experimentally or by using 3D simulations.

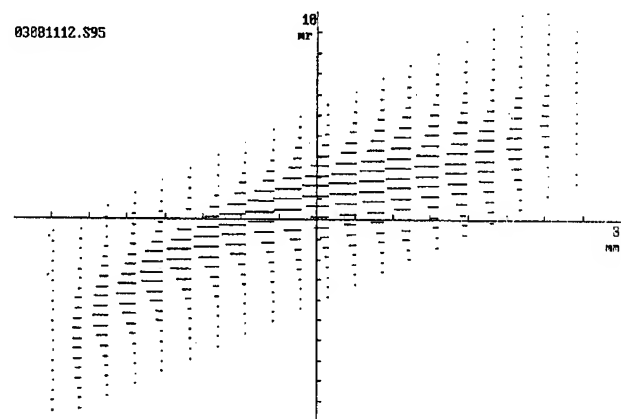


Fig 7 Unnormalized emittance scan of beam at diode exit.

III CONCLUSIONS

The performance of the injector has met our requirements in terms of beam current, emittance and energy level. Further work on the pulser to improve the risetime and voltage flat-top will be needed for operation with the recirculator.

The authors would like to offer their sincere thanks and appreciation to Chuck Ward, John Meridith and Chuck Cadwalder of EG&G-AVO, and to Geoff Mant for their mechanical design and support of this injector development. We would also like to thank Dave Pendleton and Jim Sullivan for their work on the development of the injector pulser.

IV. REFERENCES

- [1] A. Friedman, et. al., "Progress Toward a Prototype Recirculating Induction Accelerator for Heavy Ion Fusion", 1995 Particle Accelerator Conf., Dallas, TX.
- [2] S. Eylon, "The Diagnostics System for the Multiple Heavy Ion Beams Induction Linac Experiment, MBE-4", Proc. of the Accelerator Instrumentation Third Annual Workshop, Newport News, VA, 1991.
- [3] E. Henestroza, "K⁺ Source for the LLNL Recirculator Experiment", HIFAR Note 405, LBL, January 1994.
- [4] S. Eylon, "K⁺ Ion Source for the AccSys Technology Final Focus Scaled Experiment (FFSE)", HIFAR Note 340, LBL, May 1992.
- [5] J. J. Barnard, C. Caporaso, S. S. Yu, "1-D Simulations of Heavy Ion Injectors", Proc. of the 1993 Particle Accelerator Conference, Washington, DC, May 1993.

*Work performed under the auspices of U.S. DoE by LLNL under contract W-7405-ENG-48.

A SINGLE BUNCH RFQ SYSTEM FOR HEAVY IONS*

J. Madlung, A. Firjahn-Andersch, A. Schempp
Institut für Angewandte Physik, Johann Wolfgang Goethe-Universität
D-60054 Frankfurt/Main, Germany

Abstract

A novel scheme for the generation of single, isolated bunches has been developed. The design of the multi-gap deflector geometry and the results of particle simulations will be discussed. A planned experimental setup for a single bunch RFQ system and a combination of a two-beam RFQ with such a deflector for beam funneling is presented.

I. INTRODUCTION

The deflection of single beam bunches is needed in several accelerator applications, e. g. for time-of-flight experiments in atomic and nuclear physics where bunched ion beams with pulse pauses of up to several μsec are necessary. Another field of interest for a defined microstructure is the injection into booster synchrotrons for e. g. spallation sources. Also the funneling of ion beams needs a deflection system, which bends the two beams to one common axis [1].

To deflect single beam bunches one has to apply transversal electric fields e. g. with a plate capacitor. The electric fields can be produced by pulsed static deflectors with short rise time ($\tau < 1/2 f$, f = accelerator frequency) [2], where the deflection angle is proportional to the applied electric field and the deflector length l or by an rf-deflector which can be driven by resonant structures. So it is possible to reach higher voltages than in static deflectors, because the voltages of amplifiers with short rise times are limited to approximately 1 kV. In the rf-case the deflector length must be proportional to the particle velocity and the deflection angle depends on the rf-phase ϕ at the entry of the deflector. For the optimal lengths and phase the rf-amplitude is the static voltage times $\pi/2$ for the same deflection angle. The electric field is not homogenous, so that boundary effects have to be taken into account. In this paper a new concept, based on a resonator driven multi-gap deflector, will be discussed.

II. THE DEFLECTOR GEOMETRY

The electrode geometry of the multi-gap deflector consists of some capacitors with equal length but different distances. In this geometry the particles will see the deflecting field in one direction several times but the deflection in the opposite direction is always less. The length of the capacitors have to be proportional to the particle velocity and to the inverse of

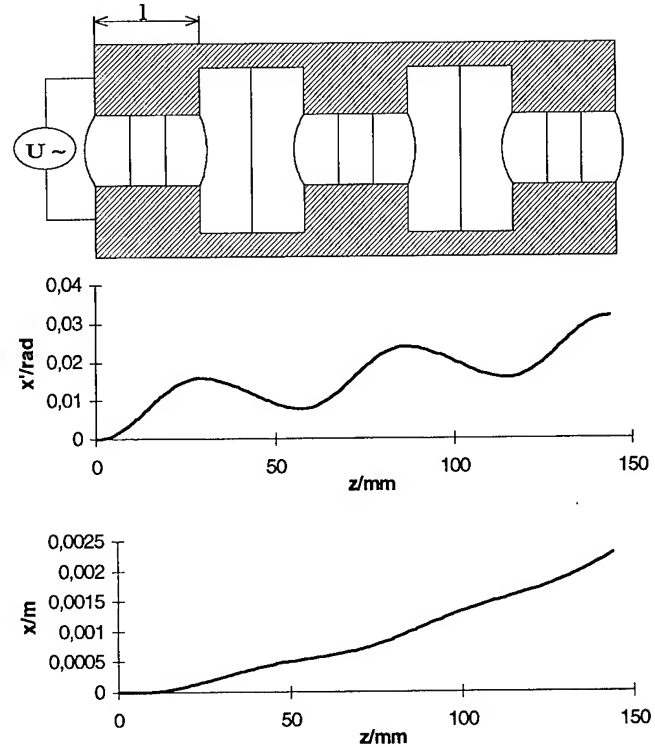


Fig. 1: Scheme of the multi-gap deflector electrode geometry and the behavior of the deflection angle x' and the deflection x .

the frequency of the deflection system. In Figure 1 the scheme of the multi-gap deflector electrode geometry and the behaviour of the particles along the deflector are shown.

The single cells can be treated like isolated rf-deflectors. If the electric field is taken as a constant field with the cell length l , the deflection angle $x'(z)$ and the deflection $x(z)$ in one cell can be written as:

$$x'(z) = \frac{a}{k} (\cos(\phi) - \cos(k \cdot z - \phi)) + x'(0)$$

$$x(z) = \frac{a}{k} (\cos(\phi) \cdot z - \frac{1}{k} \sin(k \cdot z - \phi) + \frac{1}{k} \sin(-\phi)) + x'(0) \cdot z + x(0)$$

$$\text{where } a = \frac{\xi \cdot e \cdot U}{A \cdot m_0 \cdot d \cdot v^2} \text{ and } k = \frac{\omega}{v}$$

with ξ/A = relative charge to mass ratio; e = electron charge, m_0 = mass unit; U = gap voltage; d = gap width; v = particle velocity, $\omega = 2 \pi f$ with f = frequency; $x'(0)$, $x(0)$ = angle and displacement at cell entry.

* supported by the BMFT

The advantages of the multi-gap deflector are lower electric fields than in single gaps and so a smaller influence of boundary effects. Another possibility is to add focusing elements in the cells with greater aperture [3].

III. APPLICATIONS

A. Single Bunch Deflection System

For the chopping of bunched ion beams a combination of one single gap deflector and a multi-gap deflector, running on an asynchronous frequency compared to the bunch repetition rate, could be used. The multi-gap deflector has to prepare the different angles between the succeeding bunches and the single gap deflector has to form the longer time structure. Here the length of one deflection cell should be $\beta\lambda/2$ ($\beta = v/c$; c = speed of light) to get a maximal deflection angle $x(l)$ which for $\varphi = 0$ then can be written as

$$x'(l) = 2 \frac{a}{k}$$

Figure 2 shows a scheme of a single bunch deflection system for He^+ , an ion energy of 50 keV/u and a repetition rate less than 5.4 MHz. The static deflector is designed to inject 10 bunches of the RFQ beam into the rf deflector with a variable distance between the packages. Only one bunch passes the multi gap deflector. The time structure is shown in figure 3.

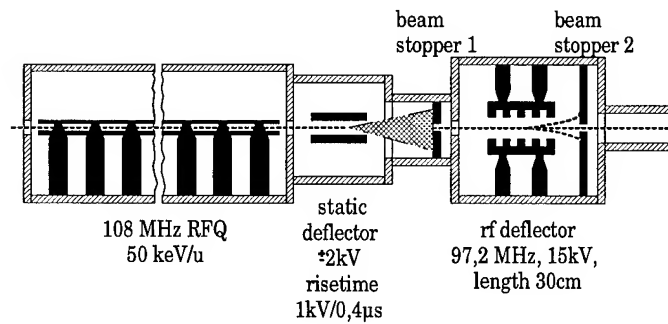


Fig. 2: Scheme of the single bunch deflection system for He^+ at 50 keV/u and a repetition rate < 5.4 MHz.

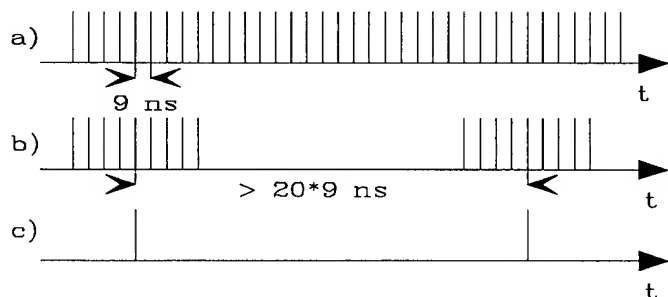


Fig. 3: Time structure of the single bunch system.
a) RFQ output, b) behind beam stopper 1,
c) multi-gap deflector output.

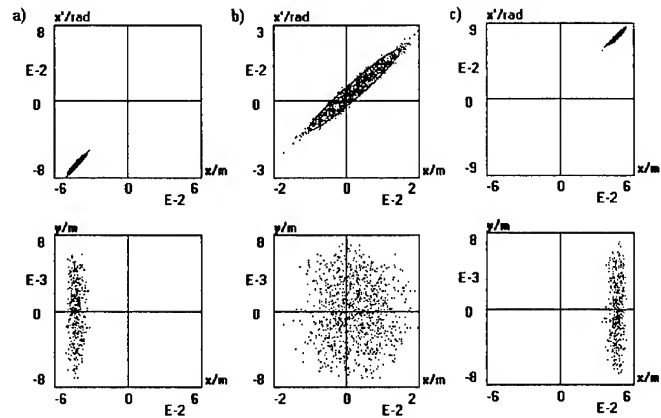


Fig. 4: Output of the multiparticle calculations for the single bunch deflection system for three succeeding bunches
a) and c) go to the beam stopper, b) to experiment.

a) and c) go to the beam stopper, b) to experiment.

In Figure 4 the output of multiparticle simulations for three succeeding bunches is shown. Behind the multi-gap deflector the bunches are separated more than 1 mm, so only one bunch can pass the aperture of the second beam stopper.

B. Funneling

The multi-gap deflection structure could also be used for beam funneling. Here the frequency of the deflector has to be the same like the accelerator frequency so that the bunches from different beam axes will see opposite field directions, caused by the phase shift of 180° between each bunch. If the two incoming beams are parallel the cell length of the deflector has to be $\beta\lambda$ to get only a displacement, because then for $\varphi = 0$ the deflection angle $x' = 0$ and the deflection x is maximal. Our favoured scenario for beam funneling is a two-beam RFQ with convergent beam axes and a multi-gap funneling element with a cell length of $\beta\lambda/2$, placed before the beam crossing. Figure 5 shows a layout of a planned funneling experiment for He^+ with two ion sources, a two-beam RFQ and a multi-gap deflector [4,5].

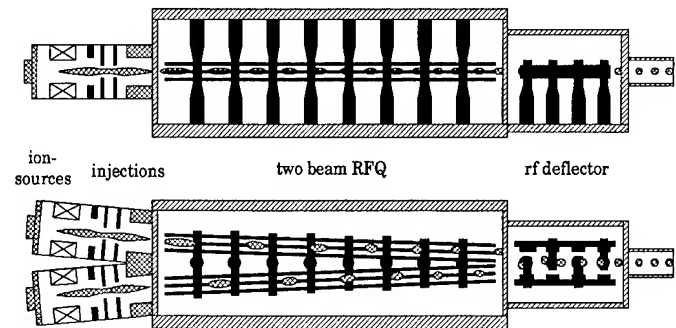


Fig. 5: Scheme of the planned experimental setup for funneling.

The two-beam RFQ structure is under development and a prototype with parallel beam axes passed the high power test.

First multiparticle calculations for the deflector design have been done. In table 1 the main parameters of the planned experiment with He^+ which is a scaled version for Bi^+ as it would be required in a first funneling stage of a heavy ion fusion driver are shown. In figure 6a the input distribution for the particle simulation and in figure 6b the output is plotted.

two-beam RFQ	He^+	Bi^+
f_0 [MHz]	54	27
Voltage [kV]	3.5	180
R_p -value [k Ω m]	100	250
Q_0 -value	2000	3000
T_{in} [keV]	4	230
T_{out} [MeV]	0.2	12.54
Length [m]	2	16
angle between beam axes [mrad]	75	75
rf deflector		
f_0 [MHz]	54	27
Voltage [kV]	5.2	200
Length [cm]	43	100

Table 1: Main parameters of the planned experiment with He^+ and design parameters of Bi^+ .

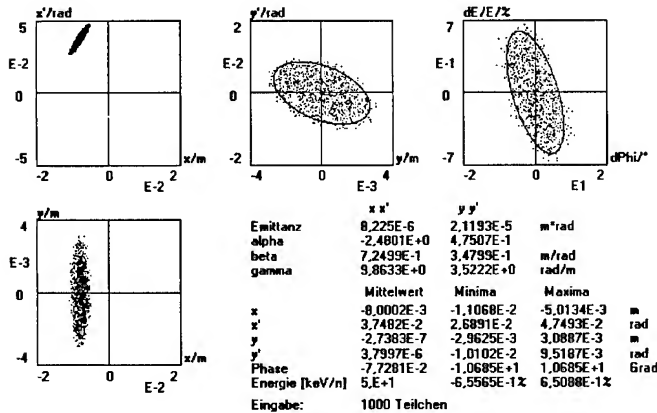


Fig. 6a: Input distribution for the funneling simulation.

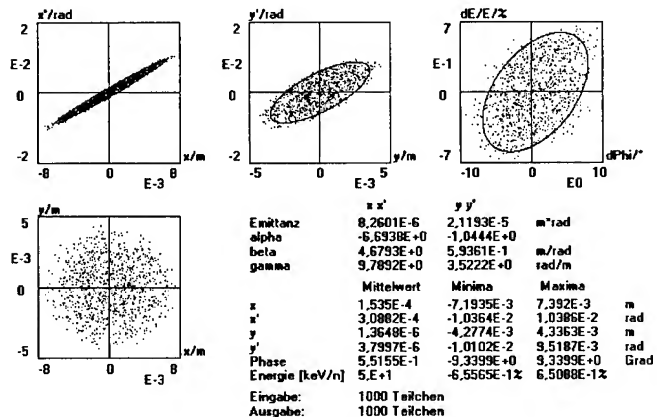


Fig. 6b: Output distribution of the simulation of the funneling section.

For an input distribution with displacement and angle in the opposite direction and a phase shift of 180° the results are the same. The bunch is bend 37.5 mrad to the common axis. These results show, that such a system can be used for funneling.

IV. OUTLOOK

The presented designs show, that the novel approach with the multi-gap deflector can be applied for the generation of single, isolated bunches and beam funneling. Further work and detailed multiparticle calculations for optimization have to be done. To take real field geometries in account, MAFIA and OPERA simulations have been done. Also the boundary effects, space charge forces and resonator structures have to be studied. A two-beam RFQ with convergent beam axis is under development, the RFQ electrode design is in progress.

V. REFERENCES

- [1] W. Barth, A. Schempp, "Funneling study with a low energy proton beam", P. 3076, IEEE PAC Conf. (1991)
- [2] J. M. Brennan, L. Ahrens, J. Alessi, J. Brodowski, J. Kats, "A fast chopper for programmed population of the longitudinal phase space of the AGS booster", P. 1154, IEEE PAC Conf. (1989)
- [3] A. Schempp, Habilitationsschrift, Universität Frankfurt am Main (1990)
- [4] A. Firjahn-Andersch, A. Schempp, C. Staschok, W. Barth, "Funneling of ion beams", P. 28, GSI-Report-94-10 (1994)
- [5] A. Firjahn-Andersch, A. Schempp, C. Staschok, J. Madlung, "A two-beam RFQ for funneling of ion beams at low energies", GSI, Annual-Report 1994, to be published

THE DESIGN OF LOW FREQUENCY HEAVY ION RFQ RESONATORS *

A. Schempp, H. Vormann, U. Beisel, H. Deitinghoff, O. Engels, D. Li⁺

Johann Wolfgang Goethe Universität,
Frankfurt am Main, Germany

⁺on leave from Department of Technical Physics, Peking University, Beijing, China

Abstract

The development of the 4-Rod-RFQ as injector for low charged heavy ions has demonstrated that structures with spiral shaped and straight stems can be made highly efficient, very stable and compact. The design of the RFQ structures and results of impedance optimizations and the effects of monopole and dipole mode generation will be discussed.

I. INTRODUCTION

Because of improvements in ion source technology a new layout of the GSI High Current Injector can use higher charged ions: U^{4+} instead of U^{2+} , as used for the "old" High Current Injector design. The old HCI was planned as a 27 MHz-RFQ for U^{2+} as injector for the Wideroe and a stripper for producing U^{10+} with a necessary current of 25 mA. In the new concept a beam current of only 10 mA U^{4+} is required, because a stripper is not needed any more, the beam will be injected directly into a new IH-Linac.

II. RF-CALCULATIONS

The specific parameters of the rf-properties of the different RFQ resonators have been checked by model measurements and calculations with the program MAFIA. Special considerations has been given to dipole effects, distribution of losses along the structure, and the influence of electrode-capacitance on the rf-parameters.

A. Capacitance of electrodes

The capacitance of the electrodes has a strong influence on the resonance frequency of the resonator. A resonator loaded with a big capacitance usually is less efficient, the Rp-value (shuntimpedance) is smaller. Although the vane-shaped geometry has 20 % more capacitance than the circular cylindric one, the impedance is nearly equal, the greater surface produces less losses. Table 1 shows a comparison of resonators with vane- respectively rod-shaped electrodes. The numeric calculations of characteristic resonator-data was done with the programs MAFIA and OPERA. It is a question of manufacture and cooling, which shape of electrodes will be chosen. So mechanical parameters and costs may determine the choice.

	Vanes	Rods
Frequency / MHz	30.50	32.24
Quality-Factor	12700	11500
Shunt-imp./kΩm	277.3	258.5

Table 1: RF-Parameters for different electrode-shapes.

B. Dipole effects

Dipole contributions in the electrode fields correspond to differences in the potential of the electrodes, e.g. the beam axis is not on zero potential. They can be a reason for beam losses, depending on their strength and beam emittances. Dipole-components of the electrode-voltage can be reduced by shaping the stems with an angle α as shown in fig. 1, which has been used in all operating four-rod RFQs [1]. With an inclination of about 45 degrees the dipole effect can be minimized to $(U-U_{AV})/U_{AV} = 0.4\%$ (see table 2), A dipole of 2 % or less is insignificant [2], it is below the experimental tuning tolerances of RFQs.

Dipole / %	α / Degrees
1.41	0
1.17	10.2
1.04	19.9
0.89	28.5
0.76	35.9
0.60	43.9
0.45	50.3

Table 2: Dipole-effects versus shape of stems.

The dipole-effects can be reduced by longer stems too, at a lower frequency. Table 3 shows the decrease of dipoles as function of the length of the stems (rectangular cross-section).

Length of Stems / mm	Dipole / %
600	1.27
622	1.22
644	1.18
666	1.14
688	1.10
710	1.06

Table 3: Dipole-effects versus length of stems.

* supported by the BMFT

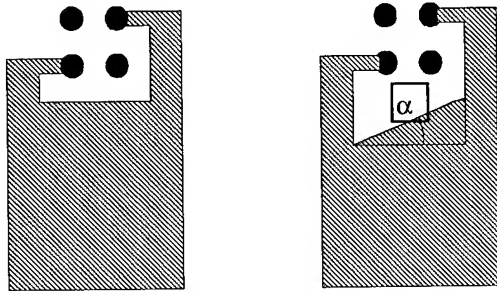


Fig. 1: Shape of four rod RFQ stems.

C. Alternative structures

Alternative structures are the spiral loaded RFQ, which has been successfully tested (27 MHz) and reached full beam current recently at GSI [3]. There, this structure was felt to be not stable enough, so that the structure with the linear straight stems discussed above was favoured at first.

Another structure was proposed, which can be characterized as an Interdigital-H-shaped resonator loaded with Four-Rod electrodes and supports [4]. To study this resonator, a model scaled to about 100 MHz has been built.

This model showed dipole effects of 8 %, what scales to 2 % at a frequency of 36 MHz. No distinctly advantage compared to the stems-type RFQ can be seen, whereas other technical difficulties may appear.

MAFIA-calculations may show different results for dipoles because of different paths of integration. Integration paths, shown in fig. 2, give voltage values, which are in good agreement with experiments. Direct integration on the beam axis typically has too small values, smaller than the errors of the MAFIA code.

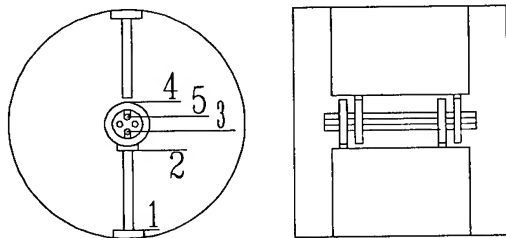


Fig. 2: Interdigital-H-structure.

III. COOLING CONSIDERATIONS

Due to the maximum duty factor of about 3 % the rf-power distribution has been checked. Less than 20 % of the losses appear on the electrodes. Nevertheless this is critical, because of the mechanical precision required. In a stem-RFQ with distances of 400 mm the electrodes will have to be cooled with water like at the HLI-RFQ, which operates at

25 % duty factor [5]. For omitting the cooling, the stems must be arranged with smaller distances, e. g. 250 mm.

Experiments with the 27 MHz Spiral loaded RFQ have shown that water cooled electrodes are not necessary anyhow, because the conduction of heat by the electrode carriers is sufficient [3].

For a higher frequency (e. g. 200 MHz at ESS- or ATW-projects) the average power is higher (5 % duty factor up to c. w., 5 - 100 kW/m). A high duty factor prototype with a frequency of 200 MHz is being built at IAP Frankfurt for experiments on cooling and stability.

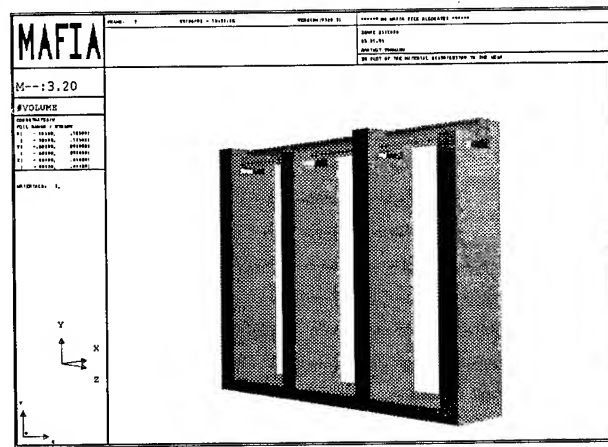


Fig. 3: MAFIA-Plot of the stems-prototype.

A. Distribution of losses

Measurements with four-rod RFQs have been confirmed by MAFIA-calculations: The RFQ losses are distributed as follows: 17 % on the electrodes, 9 % on the blocks where the electrodes are fixed to the stems (electrode carriers), 58 % on the stems, 7 % on the base plate and only 9 % on the walls of the cavity, which is one of the big advantages for high power operation.

IV. BEAM DYNAMICS

The low input energy of 2.2 keV/N allows a relatively short RFQ with a sufficient number of cells to achieve a convenient beam formation for good beam quality. The RFQ has to be designed for a short bunch width and a small energy spread at the output and a minimum transverse emittance growth.

In figs. 4 and 5 the results of beam dynamics calculations are shown. The calculations have been done with the program PARMTEQ for an input beam with transverse waterbag distribution and no initial energy spread. In fig. 4 the emittances behind the RFQ are shown for a normalized input emittance of 0.3π mm mrad. The transmission is 90%, the emittance growth only 5.5%.

RFQ FOR U4, F=36.1MHZ, U=125KV
NCELL=356, NPOINT=1810, NTOTAL=2000, Iin=15 mA

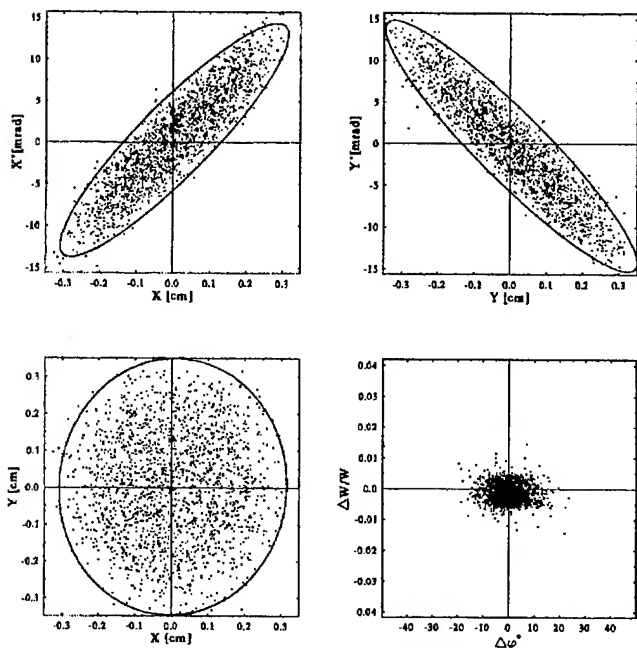


Fig. 4: RFQ output emittances, with space charge (15 mA).

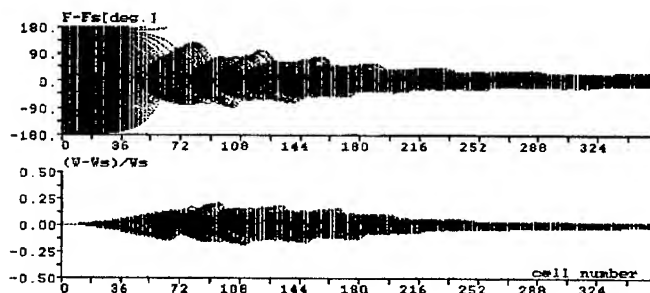


Fig. 5: Beam transmission along the RFQ.

A. RF-Power Requirements

An expected R_p -value of 500 $k\Omega m$ enables the operator of an RFQ with a length of 9 meter ($\approx 55 k\Omega$) to reach an electrode voltage of 125 kV with an rf-power of 280 kW.

Table 4 shows a comparison of different RFQ-resonators. The stems have rectangular cross-section with different width and length, except number 5 which has stems with a circular cross-section of 120 mm, and the IH-structure with 15 mm distance of the supports of the electrodes, according to the GSI design. [4]

The low power model has a simple geometry: The stems with a cross-section of 200 mm \times 10 mm have a distance of 400 mm and a height of 400 mm. The electrodes are optional cylindric with a radius of 5 mm or vane-like with a shape of 10 mm \times 20 mm, each 1240 mm long, the aperture is 10 mm. The resonator was only screwed, so bad contacts reduce the shuntimpedance. Table 5 shows the comparison between calculation and measurements.

Stems	Frequency / MHz	Quality-Factor	Shunt-impedance
400 x 400	30.7	10400	770
250 x 600	36.9	13000	790
250 x 700	34.6	12900	830
250 x rad 60	33.5	11500	840
IH-Structure	37.1	8000	360

Table 4: Properties of different RFQ-resonators.

	Measurement	MAFIA
Frequency / MHz	34.3	32.2
Quality-Factor	2900	10500
Shuntimp. / $k\Omega m$	270	770

Table 5: Comparison of calculated and measured properties.

V. CONCLUSIONS

Four-rod type RFQs for low frequencies have high efficiency, good mechanical stability, good operational characteristics and suffer no dipole mode problems, which has been shown in calculations, prototypes and operating structures. Spiral shaped and straight stems supports give compact resonators. GSI will go on working with the IH-driven four-rod RFQ, for which prototyping on a number of design issues is the next stage.

VI. REFERENCES

- [1] A. Schempp et al, "A Light Ion Four-Rod RFQ Injector", Proc. IEEE PAC 1987, p. 267,
- [2] J. Klabunde et al, "Beam Dynamics Simulation in a Four-Rod RFQ", Proc. Linac 1994, p. 710,
- [3] U. Bessler et al, "Status of the beam experiments with the 27 MHz-Spiral-RFQ at GSI", to be published,
- [4] U. Ratzinger, GSI Note, HSP 27 104.STR, 1994,
- [5] J. Klabunde et al., "Upgrade of the HLI RFQ Accelerator", Proc. Linac 1994, p. 704..

A VE-RFQ-INJECTOR FOR A CYCLOTRON*

A. Schempp, O. Engels, F. Marhauser
Institut für Angewandte Physik, 60054 Frankfurt, Germany
H. Homeyer, W. Pelzer
Hahn-Meitner-Institut, 14109 Berlin, Germany

Abstract

Based on the development of the variable energy 4-rod-RFQ a new injector for the ISL heavy ion cyclotron at the HMI Berlin (the former VICKSI machine) is under construction. The ECR source together with two VE-RFQs will replace the 8UD-Tandem injector to meet the demands of solid state physics users. The design of the new RFQ injector and the status of the project will be discussed.

I. INTRODUCTION

The ISL [1] is an isochronous cyclotron with four separated sectors. It has an external injection of beams with variable energy from either a CN-Van-de-Graaff or an 8UD-Tandem. Figure 1 shows the layout of the accelerator complex.

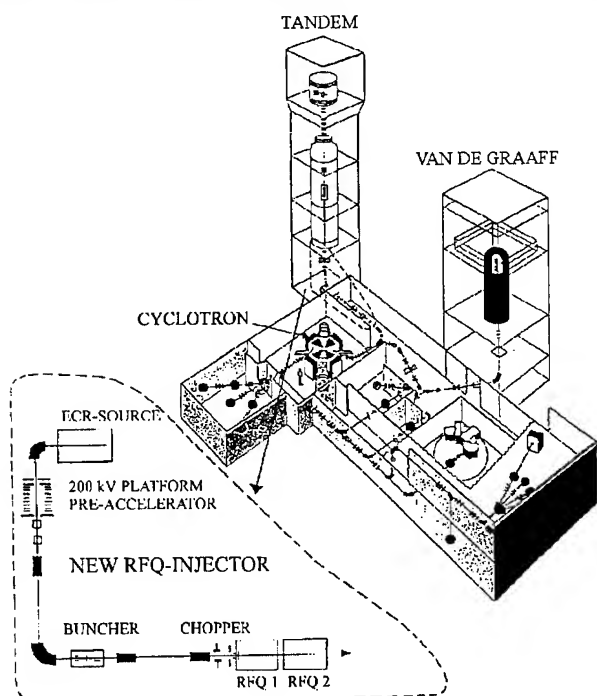


Fig. 1 Scheme of the heavy ion accelerator complex with the planned changes in the encircled area

The scientific program at the ISL has been changed from nuclear physics to solid state physics [2]. To get higher intensities in the energy range between 2 to 6 MeV/u, the tandem injector will be replaced by a combination of an ECR

ion source on a 200 kV platform and a VE-RFQ, to meet demands from solid state physics users. The combination will accelerate the ions to energies between 0.09 and 0.36 MeV/u to cover the range of final energies out of the cyclotron between 1.5 and 6 MeV/u.

II. THE VE-RFQ-STRUCTURE

In a Radio Frequency Quadrupole (RFQ) structure [3,4] acceleration is achieved by a geometrical modulation of quadrupole electrodes leading to axial components of the field.

The fixed velocity profile is typical for RFQs. It can only be changed by varying the cell length L or the frequency f . The second possibility of changing the Wideröe [5] resonance condition: $L = \beta_p \lambda_0 / 2 = v_p / 2f$, is the way which has been used for RFQs with variable energy (VE-RFQ) [6]. For this reason it's possible to change the output energy using the same electrode system by varying the resonance frequency of the cavity: $v_p \sim f$, $T \sim v_p^2$.

To change the frequency of the 4-Rod-RFQ, a type of RFQ resonator developed in Frankfurt [7], the resonator can be tuned capacitively or inductively. Figure 2 shows the latter way of tuning by a movable tuningplate, which varies the effective length of the stems.

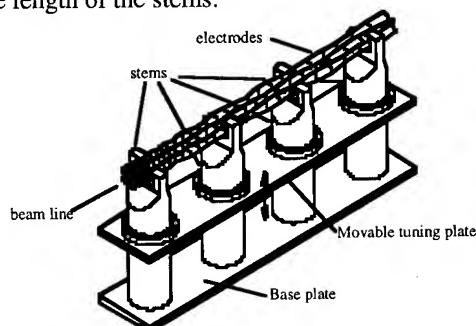


Fig. 2 Scheme of the VE-RFQ

In Frankfurt the VE-RFQ was developed at first for the application as a cluster postaccelerator at the 0.5 MV Cockcroft-Walton facility at the IPNL in Lyon (France) [8,9]. It is designed for $E_n = 10$ keV/u and an output energy between $E_{out} = 50$ keV/u and $E_{out} = 100$ keV/u for $m = 50u$.

Based on the positive experiences of this project, a first combination of an ECR ion source with an VE-RFQ has been built for the IKF Frankfurt. The VE-RFQ structure is designed for a minimum specific charge of $q/A = 0.15$, an output ion energy of $E_{out} = 100$ -200 keV/u, a maximum electrode voltage of 70 kV and has a structure length of 1.5 m.

* supported by the BMFT

III. RFQ AS CYCLOTRON-INJECTOR

A first proposal to use an RFQ to improve the axial injection system of a compact cyclotron was made by Hamm [10]. To inject in a Separated Sector Cyclotron, the RFQ has to provide a bunched beam at a well defined injection energy given by the inner radius of the SSC. The operating frequency of the RFQ must be synchronised with the cyclotron frequency, which for RFQs normally means a fixed output energy per nucleon, which would match to fixed energy cyclotrons. To keep the energy variability of the cyclotron it's necessary to have an injector which has also a variable energy and frequency. VE-RFQs have a fixed ratio of output to input energy given by the length of the first and last modulation cell. This is similar to the energy gain factor of a SS-Cyclotron which makes them well suited as injectors [11]. To cover the energy range of 1.5-6 MeV/u the injection energy E_{in} of the ISL must be between $E_{in}=90$ keV/u and $E_{in}=360$ keV/u, at cyclotron frequencies of 10 to 20 MHz.

The new injector consisting of an ECR-source and a VE-RFQ has to fit into the existing tandem beam line. To stretch the energy range the RFQ will be split into two RFQ stages. Each stage with a length of 1.5 m consists of a ten stem 4-Rod-RFQ-structure. With a rf-power of 20 kW per stage an electrode voltage of 50 kV is possible. In the first mode of operation both RFQs accelerate, the output energy of the cyclotron is between $E_{out}=3$ MeV/u and $E_{out}=6$ MeV/u with a harmonic number of 5 for the cyclotron. There are two possibilities for the low energy beam mode, where the RFQ₂ works as a transport channel. RFQ₁ accelerates while the frequency of RFQ₂ is detuned. The second possibility is that RFQ₂ has the same frequency as RFQ₁, but is detuned in phase. In this mode the energy range of the cyclotron is between $E_{out}=1.5$ MeV/u and $E_{out}=3$ MeV/u. The cyclotron works on the harmonic number 7. In both modes the RFQs are tuned to the eighth harmonic of the cyclotron frequency. A overview of the ECR-RFQ-Cyclotron complex is shown in figure 3, characteristic data are given in table 1.

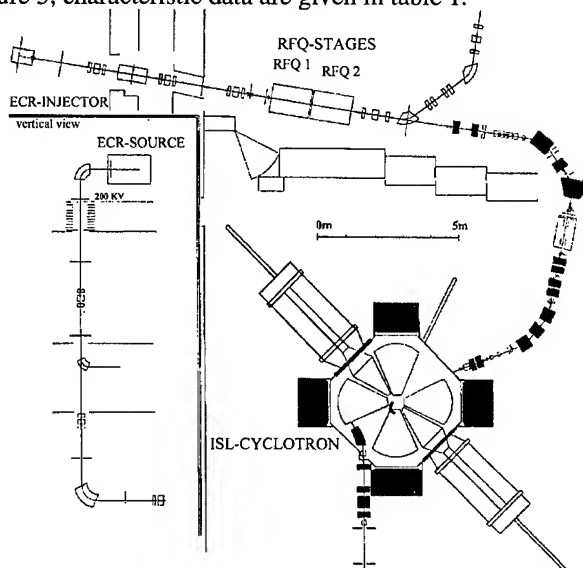


Fig. 3 Overview of the cyclotron with the new injector

RFQ:	
min./max. E_{in}	15.16/29.72 [keV/u]
min./max. E_{out} RFQ 1	90.98/178.35 [keV/u]
min./max. E_{out} RFQ 2	178.35/355.09 [keV/u]
Energy gain factor RFQ 1	6
Energy gain factor RFQ 2	1.96
charge-to-mass-ratio	1/8-1/4
Frequency	85-120 [MHz]
Electrode voltage (max.)	50 [kV]
Length/diameter	3/0.5 [m]
Cyclotron:	
K-factor	134 [MeV]
Injection radius	0.43 [m]
Extraction radius	1.8 [m]
Rf-frequency	10 to 20 [MHz]
max. dee-voltage	140 [kV] (peak)
energy gain factor	16.8-18.6
Harmonic number H	2 to 7

Table 1: Main accelerator parameters

The RFQ-output emittance depends largely on the input conditions. For matched input beams with $\Delta E/E < 1.5\%$, normalised emittance $\epsilon_n < 0.5 \pi$ mm mrad and a bunch length $\Delta t < 1$ ns a transmission of 100 % is expected. To reach this beam quality it's necessary to have a buncher-chopper system between the ECR and the RFQs [12].

The ECR-source is mounted on the 200 kV platform, formerly used for the tandem. The vertical beam is bent 90° , passes through the buncher-chopper-system and will be injected into the RFQs. The final matching into RFQ₁ will be done by a triplet lens. The beam from RFQ₂ is transported into the injection beamline of the cyclotron, to which a rebuncher has been added to make a proper time focus for the cyclotron.

IV. BEAM DYNAMICS

The beam dynamic calculations were made with the code PARMTEQ. Figure 4 shows results for the first mode of operation, both RFQs accelerate, at a frequency of 120 MHz, with rms-emittances.

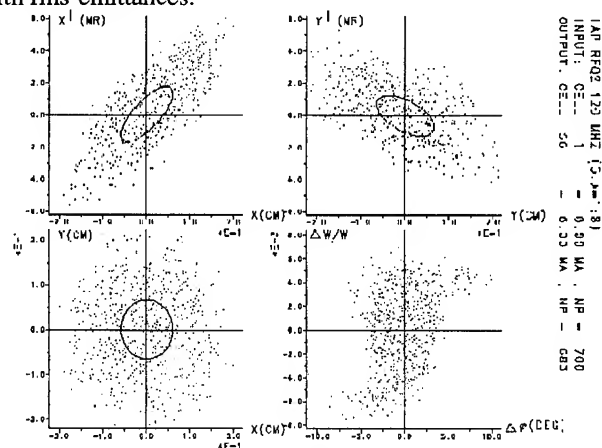


Fig. 4 Output beam, both RFQs accelerate

In the low energy beam mode the two possibilities of transportation through RFQ₂ were investigated. With RFQ₂ detuned in frequency, there is no stable phase relation between RFQ₁ and RFQ₂. Therefore all the minimum and maximum energies shown in figure 5a are possible. Figure 5b shows the region (arrow) with a proper phase for the possibility with RFQ₂ detuned in phase. The figures show E_{out} as a function of the input phase of RFQ₂. The output beam with $\Delta\phi=65^\circ$ is shown in figure 6.

V. STATUS AND SCHEDULE

At present the RFQ-design is being optimised, especially the low energy beam mode. The mechanical design of the RFQ-tank is done, the details of structure support stems and electrode cooling are fixed (see figure 7).

The RFQ-system is being manufactured by NTG [13]. First tests are scheduled for December 1995.

VI. REFERENCES

- [1] H. Homeyer, W. Pelzer, Vorschlag zur Realisierung eines Ionenstrahl-labors im HMI (ISL-Berlin), HMI-Berlin, 1992
- [2] H. Homeyer, K. Ziegler, NIM B64 (1992) 937-942
- [3] I.M. Kapchinskiy and V. Teplyakov, Prib. Tekh. Eksp 119, No.2 (1970) 17
- [4] K.R. Crandall, R.H. Stokes, T.P. Wangler, Linac 79, BNL 51134 (1979) 205
- [5] R. Wideröe, Archiv f. Elektrotechnik 21 (1928) 387
- [6] A. Schempp, NIM B40/41 (1989) 937
- [7] A. Schempp, M. Ferch, H. Klein, PAC 87, IEEE 87CH2387-9 (1987) 267
- [8] A. Schempp et al., EPAC 90 (1990) 40
- [9] M.J. Gaillard et al., Z.Phys. D26, (1993) 347
- [10] R.W. Hamm et al., Proc. 9th. Cyclotron Conf. Caen, France (1981) 359
- [11] A. Schempp, Habilitationsschrift, Universität Frankfurt am Main (1990)
- [12] W. Pelzer, K. Ziegler, Atomenergie Kerntechnik Vol. 46-3 (1985) 147
- [13] Neue Technologien, D-63571 Gelnhausen

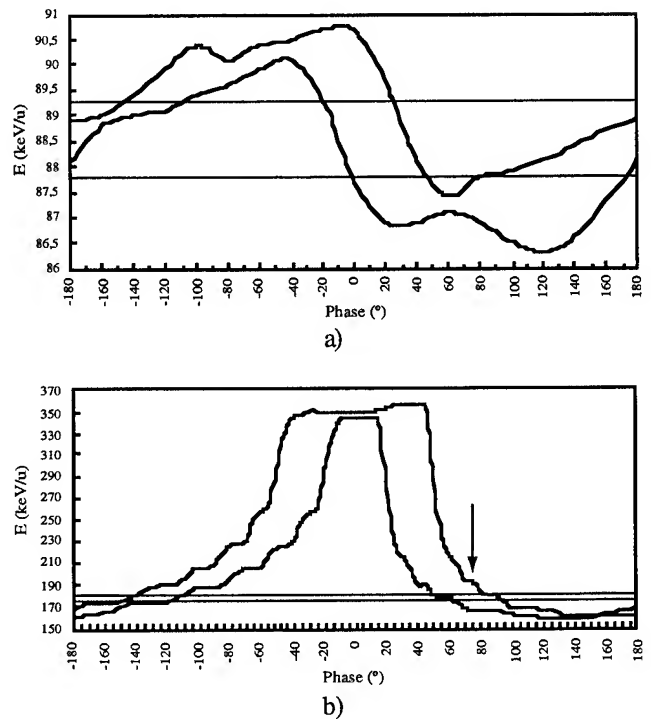


Fig. 5 E_{out} -Phase, a) $F_{\text{RFQ1}}=85$ MHz, $F_{\text{RFQ2}}=120$ MHz, b) $F_{\text{RFQ1}}=F_{\text{RFQ2}}=120$ MHz

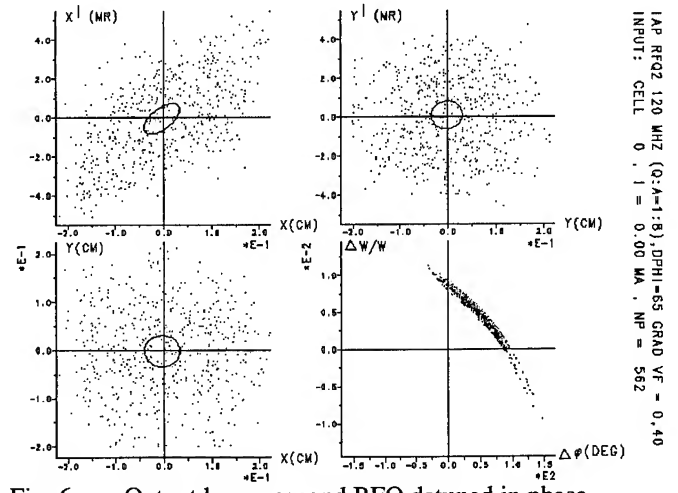


Fig. 6 Output beam, second RFQ detuned in phase

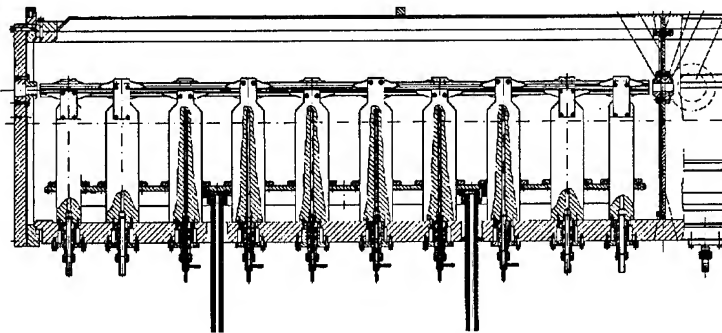
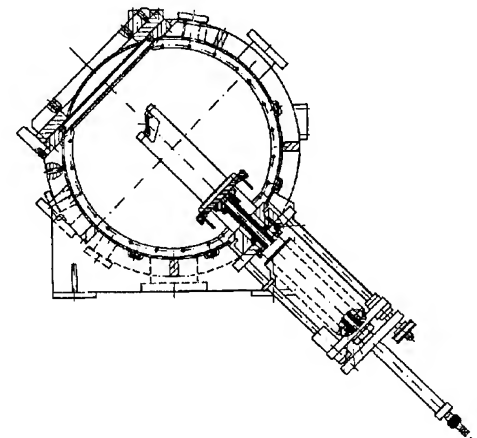


Fig.7 View of the first RFQ stage



FERMILAB LINAC INJECTOR, REVISITED

M. Popović, L. Allen and C. W. Schmidt
Fermi National Accelerator Laboratory*
P.O. Box 500, Batavia, Illinois 60510

Abstract

The Fermilab linac has been operating at 200 MeV since 1971 and was upgraded to 400 MeV in 1993 with a peak current of ~ 35 mA. The injector consists of a Haefely Cockcroft-Walton, H^- source, an high gradient accelerating column (750 kV), 4 and 10 meter long transfer lines and a single gap 201.24 MHz cavity. The performance of the injector has been very gratifying although some tuning must be done approximately daily. The purpose of this report is to present representative experimental data and numerical simulations that are used as a guide for improvements to the Fermilab Linac. Today, the Fermilab Linac delivers a 400 MeV H^- beam with a peak current over 45 mA.

I. INTRODUCTION

The Fermilab Linac Upgrade increased the energy of the H^- linac from 201 to 401.5 MeV[1]. This was achieved by replacing the last four 201.24 MHz drift-tube linac cavities with seven 804.96 MHz side-coupled cavity modules. The energy increase has improved the brightness of the beam in the Booster and the rest of the Fermilab accelerator complex. In the past few months a further increase in the peak beam current has lead to a further increase in the beam brightness and hence an increase in luminosity for collisions. The increase in the H^- peak current to 45 mA or higher at the end of the linac is a result of work done on the injector area. The ion source work is described in the next section. Section 3 presents modeling results of the transport line using TRACE3D and section 4 presents experimental data and PARMILA modeling of the buncher cavity effects on the beam from Tank 2. Figure 1 shows the injector area, transfer line from the source to the buncher cavity and Tank 1.

II. ION SOURCE

For twenty years Fermilab has been using a H^- magnetron source. Until last May the source typically provided a beam current of 50-55 mA with a lifetime of four to six months. This source has a slit aperture of 1 by 10 mm^2 and is at a potential of -750 kV. The ions are extracted from the source at 18 to 20 kV. To compensate for the large asymmetry in the two planes and obtain a nearly circular beam, a 90° bending magnet with a radius of 8 cm and an index $n=1$ is used after the extractor. Following the bending magnet beam enters the accelerating column and is accelerated to 750 keV. For the source to work in an acceptable regime, with a lifetime of several months, there are about ten parameters that must be adjusted carefully[2]. An extensive search of that parameter space has been done which resulted in:

*Operated by the Universities Research Association under contract with the U. S. Department of Energy

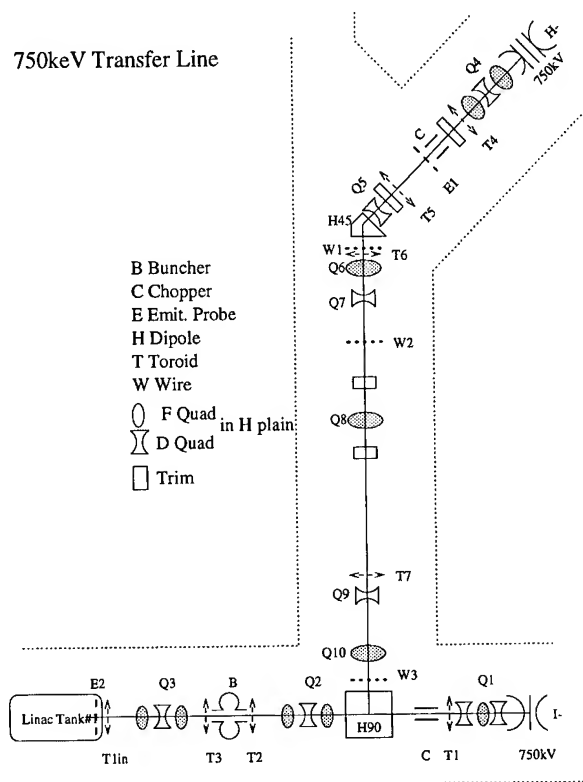


Figure 1. H^- Source and 750 keV transfer line.

1. an increase of the extraction voltage,
 2. an increase of the cathode temperature,
 3. a decrease of the hydrogen gas usage, and
 4. adjustment of the hydrogen gas timing,
- to give more then 65 mA peak current with a lifetime longer than four months. Figure 2 displays the output current as a function of the pulsed hydrogen valve on and off times. It shows that the output current depends strongly on timing and hydrogen usage.

Figure 3 shows the beam current (h4tor) following the H^- source and 750 kV accelerating column. The lower curve is the beam current at the end of the linac (d7tor). From May to August 1994 the second source and accelerating column was in use. Since the beam is transported through the straight line this produces a gap in h4tor of figure 1. From the ratio of the two curves in figure 3 it is clear that the extracted current from the source and that the overall efficiency of the linac as a whole has increased.

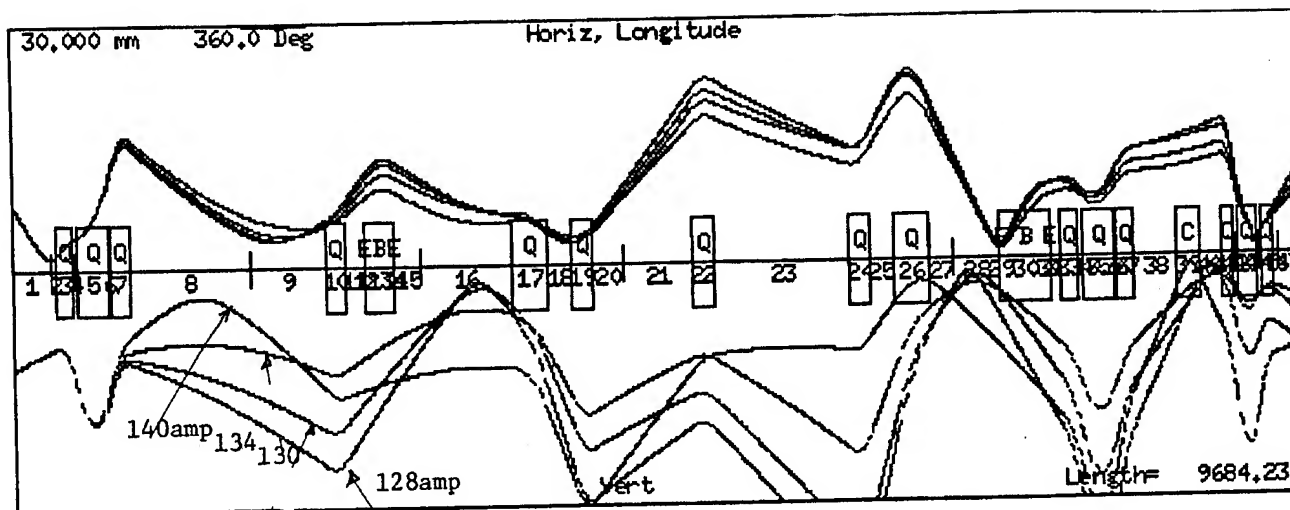


Figure 4. Search for the optimal setting of the first H^- quad.

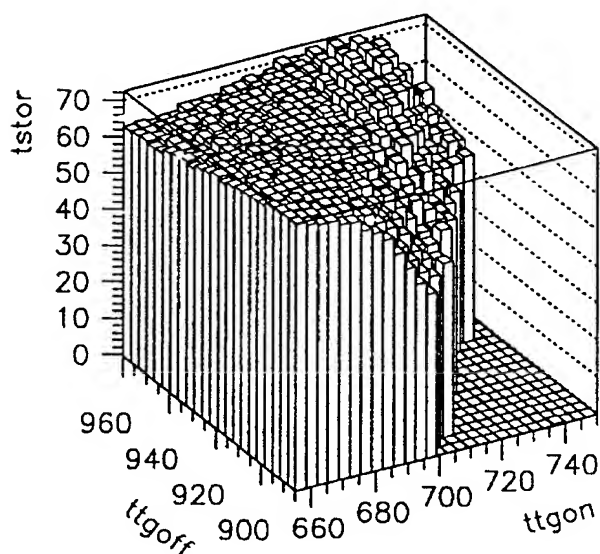


Figure 2. The horizontal axes are the gas valve times in μ sec. The vertical axis is beam current in mA.

III. 750 keV TRANSPORT

The H^- transport line between the source and Tank 1 is about 10 meters long with limited diagnostic. The main diagnostic tools are six current transformers and four emittance probes. Two emittance probes (horizontal and vertical) are located after the first quadrupole triplet near the exit of the 750 kV column. The other two are just before the entrance of linac Tank 1. Each probe consists of a single slit, a drift space and a 20-segment target oriented with the segments parallel to the slit. Table 1 lists emittance values at these two locations for 50 and 65 mA beam currents.

Emittance measurements were used to reconstruct the beam ellipse orientation in phase space. These were used as beam input parameters for TRACE3D simulation of the 750 keV transport line. Figure 4 shows a search for the optimal current value for one of the quadrupoles. Simulations are interfaced with the control system so that currents in the magnets and quadrupoles are directly read by the program. There is good agreement between

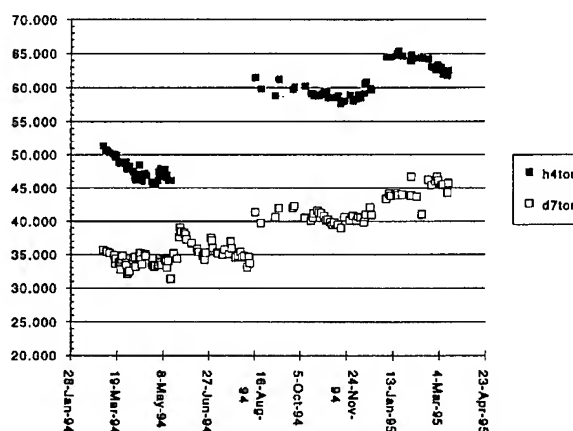


Figure 3. Upper points are current in mA at 750 keV. Lower boxes are beam current in mA out of the Linac, 400 MeV.

Table I
Normalized emittances at the beginning and end of the 750 keV transport line. Units are π mmrad.

Peak Current	50 mA	65 mA	
Emittance Probe H1	1.6	1.8	90 %
Emittance Probe V1	1.8	2.6	90 %
Emittance Probe H2		2.6	90 %
Emittance Probe V2		2.1	90 %

simulation and transfer efficiency along the line. This result is obtained for input parameters of the ellipses taken from measurements of the input beam. Measured ellipse orientations at the end of the line are not in full agreement with simulation possibly due to beam neutralization. According to the simulation the transfer line is "almost" achromatic. Operating with a completely achromatic condition as predicted by TRACE3D causes a degradation in the transmission efficiency.

IV. BUNCHER

The low energy buncher cavity is located about 95 cm upstream of linac Tank 1. Experiments have been done changing the phase and rf amplitude in the bunching cavity and in the Tank 1. Figure 5 shows the best experimental as well as simulation data using PARMILA code[3]. Comparison of the beam entering the buncher with the beam at the end of Tank 5 shows a capture efficiency of about 75% of the 750 keV DC beam.

References

- [1] E. McCrory, "The Commissioning and Initial Operation of the Fermilab 400 MeV Linac", Proceedings of the 1994 Linac Conf., pp. 36-40.
- [2] C. W. Schmidt, "Review of Negative Hydrogen Ion Sources", Proceedings of the 1990 Linac Conf., pp. 259-263.
- [3] M. Popovic, "Longitudinal Beam Dynamics of the 10 MeV Fermilab Linac", Bulletin of APS, Vol 40, No. 2, 1995, pp. 953.

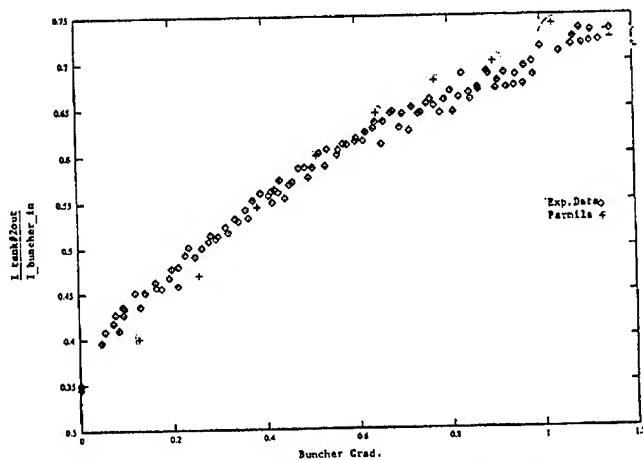


Figure 5. Linac capture versus buncher field.

NEW RF STRUCTURES FOR THE FERMILAB LINAC INJECTOR

M. Popović, A. Moretti and R.J. Noble
Fermi National Accelerator Laboratory*
Batavia, Illinois 60510, USA

Abstract

The critical parameters which may limit the luminosity of the Fermilab Tevatron Collider are the beam intensity and emittance growth at each stage in the acceleration chain. It is commonly believed that the major emittance growth occurs at the low energy acceleration stage. In this paper we examine recent advances in RFQ, DTL and superconducting linac technology that should permit a significant increase in the beam brightness of the Fermilab Linac.

I. INTRODUCTION

The Fermilab Linac Upgrade increased the energy of the H^- linac from 201 to 401.5 MeV[1]. This was achieved by replacing the last four 201.24 MHz drift-tube linac cavities with seven 804.96 MHz side-coupled cavity modules. The energy increase has improved the beam brightness in the Booster and the rest of the Fermilab accelerator complex. In the last couple months we have increased the linac's peak current from 35 mA to 45 mA which has lead to a further increase in the beam brightness and an increase in collider luminosity. The recent measurements of the emittances along the linac are summarized in Table 1. We quote normalized emittances for 90% of the beam.

Energy(in MeV)	.75	.75	10	116	400
Emitt. Horizontal	1.6	2.6	3	4	6
Emitt. Vertical	1.8	2.6	3	3	5

Emittance measurements are in units $\pi \text{ mm mrad}$

The increase in the H^- peak current to values above 45 mA at the end of the linac is a result of work done in the linac's low-energy injector area. Currently measured emittances with 45 mA output current do not show any noticeable increase as the result of the beam current increase. It is believed that the beam coming from the ion source at 18 keV has emittances in both planes of about $1 \pi \text{ mm mrad}$. Some old records show that the emittances at 10 MeV were measured at between 2.5 and 3.5 $\pi \text{ mm mrad}$. Due to the need for continuous collider operation, we have not been able to measure emittance at this position since the completion of the 400 MeV upgrade. All this information leads us to believe that there is room for improvement at each stage in the linac chain. In the next section we will analyze the RFQ as a possible accelerating structure from the source at 35 keV to 10 MeV. This would replace the existing DTL Tank 1. Section 3 will describe our work on asymmetric drift-tube structures to improve beam focusing, and Section 4 discusses our new high-gradient, superconducting cavity program.

II. RADIO-FREQUENCY QUADRUPOLE

A redesign of the low energy section of the linac was considered earlier by C. Schmidt et al[2]. In that paper, the H^- source was assumed to have a circular aperture, the RFQ had a final energy of 2 MeV and a new, post-coupled Alvarez tank was proposed to accelerate beam to 10 MeV. We have considered four possible examples of RFQ's to accelerate a 50 mA H^- beam to 0.75, 2, 5 or 10 MeV. We are assuming that the beam's input energy will be 35 keV and that the beam comes from a slit aperture with a 90° magnetic bend and a field index $n = 1/2$. Our main concern is space charge degradation of the emittance. To reduce this effect, we allow the beam to remain wide at the early stage of transport and minimize undulations during acceleration. We estimate that after the 90° bend, we will have a round beam of radius 0.5 cm. This beam will be matched to the RFQ entrance using a short quad triplet. In this study we have limited ourselves to the frequency 201 MHz, a final energy less than 10.2 MeV, a peak surface field of 1.9 Kilpatrick and peak powers less than 4 MW. As an extreme case, we have analyzed L. Young's long coupled cavity RFQ linac[3]. In all our designs we found that the minimal bore radius was 0.3 cm for a 50 mA beam.

III. ASYMMETRICAL DRIFT-TUBE LINAC

The asymmetrical drift-tube linac has elliptical inner and outer surfaces on the drift-tubes to achieve both acceleration and focusing (Figure 1).

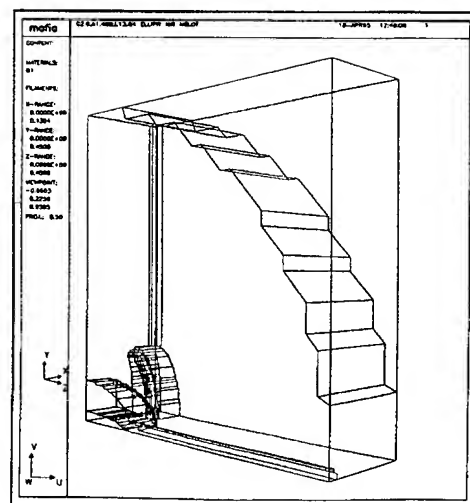


Figure 1. Asymmetric DTL, Mafia calculation.

This type of DTL is useful for low-energy beams (protons below 10 MeV). The major axis of a drift-tube is rotated ninety

*Operated by the Universities Research Association under contract with the U. S. Department of Energy

degrees with respect to the major radius of adjacent drift tubes. This produces a focusing and defocusing set of transverse fields in the horizontal and vertical planes similar to the field pattern in an RFQ. This structure at 200 MHz has been studied using the MAFIA 3-D electromagnetic code to determine the field strengths and shunt impedance (ZT^2). The shunt impedance of the structure has been found to be nearly ten times higher than for an RFQ in the same energy range. The structure has relatively higher accelerating fields but lower focusing fields than a comparable RFQ.

Thin lens calculations have indicated that the fields are strong enough to contain a space charge dominated beam for all energies below 10 MeV with a minor bore radius of 1.4 cm. The fields are strong enough to allow a 200 MHz linac to be designed in the form of short tanks of five gaps followed by an external quadrupole magnet. These quadrupoles allow independent control for beam transport and tuning in the asymmetric DTL. A filling factor of 90% will not significantly reduce ZT^2 which ranges from 8.4 M Ω /m at 750 keV to 37.4 M Ω /m at 10 MeV.

To further increase the beam intensity in the 8 GeV Booster synchrotron at injection for high energy physics and antiproton production as well as to provide an intense proton source for a future muon collider, a 2 GeV H^- linac is being studied. The linac would be capable of accelerating up to 10^{14} protons per pulse at 60 Hz. Two designs are being investigated (Figures 2 and 3), both of which use superconducting 805 MHz cavities for the final acceleration stage. Peak beam currents of 80 mA in 200 μ sec pulses are envisioned. Multi-cell superconducting cavities at 805 MHz have recently supported CW accelerating fields up to 17 MV/m with cavity conditioning limited only by available RF peak power.[4] Higher gradients are certainly possible making a short, high-energy proton linac feasible.

The 2 GeV linac may take one of two forms depending on the low energy arrangement adopted. The first option is to build a complete new linac (Figure 2), consisting of a 400 MHz RFQ, a normal conducting 400 MHz DTL (part of which may be asymmetrical), a normal conducting 800 MHz coupled-cavity linac (CCL) and a high-gradient, 800 MHz superconducting linac (SCL). The RF plus structure costs are estimated at \$9M for the RFQ plus DTL, \$16M for the CCL and \$29M for the SCL. The SCL costs assume a cavity plus cryostat cost of \$200K/meter and an RF cost of \$100K/MWatt of peak power. The total linac length would be about 180 meters. Adding ancillary systems, beamlines, utilities and civil construction results in a total cost of about \$70M for a complete 2 GeV linac.

An alternate approach would be to use the existing Fermilab 400 MeV Linac, upgrade its RF systems and add a superconducting linac to the existing enclosure. The arrangement however is somewhat novel, and is called the "hairpin linac" (Figure 3). The normal conducting, 200 MHz DTL and 800 MHz side-coupled linac would be physically reversed in the linac enclosure as would be the RF systems in the upstairs gallery. A 200 MHz RFQ would be added as a new injector. The 400 MeV beam emerging from this linac is then turned 180 degrees with low-field magnets in the vacated Cockcroft-Walton Pre-acc pits and injected into a new superconducting linac, anti-parallel to the 400 MeV linac, for acceleration to 2 GeV. The cost of this option is about \$45M due to savings incurred by using much of

the existing 400 MeV linac.

An 805 MHz superconducting cavity R&D program was started at Fermilab in early 1994. The goals are to increase accelerating gradients beyond previously achieved values and to fabricate and test a 4-cell superconducting cavity with 400 MeV linac beam in late 1997. A high power processing (HPP) facility is being constructed using the 12 MW RF system and shield cave at the A0 lab, leftover from the Linac Upgrade Project. A horizontal cryostat is being fabricated using a former vertical dewar on loan from Los Alamos National Lab as the outer vacuum vessel (Figure 4). Two input power couplers have been built and the cryostat is about 25% complete. In early 1996 single-cell niobium cavities previously tested at Los Alamos will be conditioned. Fabrication of a 4-cell cavity and a special beamline cryostat will begin in mid-1996.

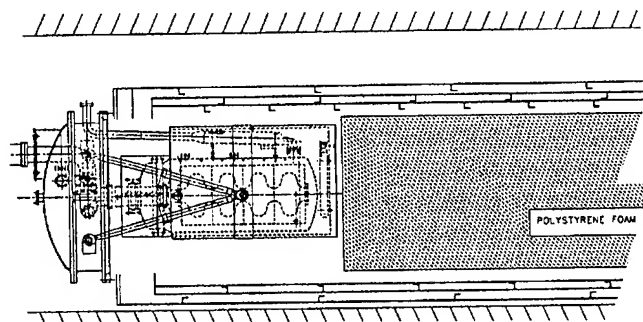


Figure 2. Cryostat, and 4-cell superconducting cavity.

IV. SUPERCONDUCTING LINAC

References

- [1] E. McCrory, "The Commissioning and Initial Operation of the Fermilab 400 MeV Linac", Proceedings of the 1994 Linac Conf., pp 36- 40.
- [2] C. W. Schmidt et al, "Redesign of the Low Energy Section of the Fermilab Linac to Improve Beam Brightness", Proceedings of the 1988 Linac Conf., pp. 188-189.
- [3] L. Young, "An 8-Meter-Long Coupled Cavity RFQ Linac", Proceedings of the 1994 Linac Conf., pp 178 - 180.
- [4] B. Rusnak, LANL, private communication.

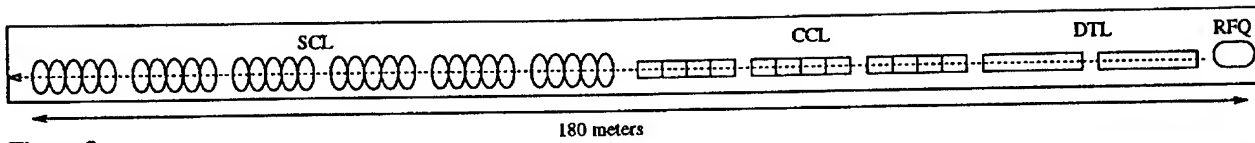


Figure 2.

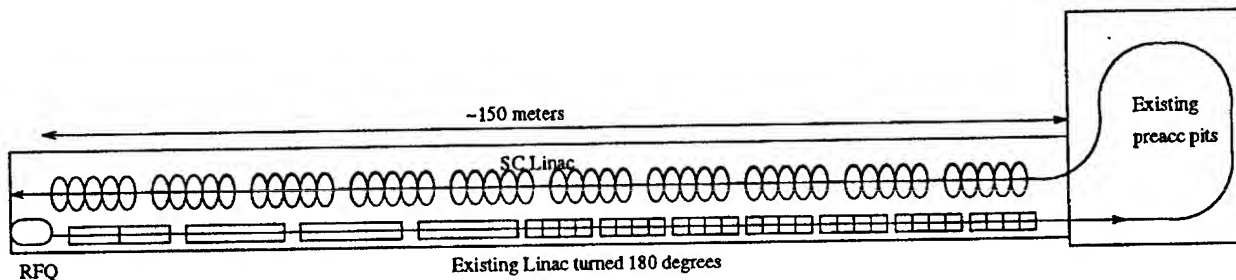


Figure 3.

HIGH-POWER RF OPERATIONS STUDIES WITH THE CRITS RFQ*

G.O. Bolme, D.R. Keffeler, V.W. Brown, D.C. Clark, D. Hodgkins, P.D. Lara, M.L. Milder,
D. Rees, P.J. Schafstall, J. D. Schneider, J.D. Sherman, R.R. Stevens, T. Zaugg
Los Alamos National Laboratory, Los Alamos, NM 87545 USA

J.Y. Sheikh, A.D. Davidson, and B.H. Smith
Chalk River Laboratories, Chalk River, Ontario K0J1J0 Canada

High-current, cw linear accelerators have been proposed as spallation neutron source drivers for applications to tritium production, transmutation of nuclear waste, and safe nuclear power generation. Key features of these accelerators are high current (100 mA) low emittance-growth beam propagation, cw or high duty-factor operation, high efficiency, and minimal maintenance downtime. A 267.1 MHz, cw RFQ and klystron based RF system were obtained from CRL[1] and installed at LANL to support these next generation accelerator studies. The reconditioning of the RFQ accelerator section to its design power of 150 kW at 100% duty factor is being accomplished with studies focusing on the details of high-power RF structure operation, personnel and equipment safety systems integration, and RF controls integration.

I. INTRODUCTION

The Chalk River Injector Test Stand (CRITS) RFQ was the 267.1 MHz, cw proton accelerator section from the Chalk River Laboratories (CRL) RFQ1 program, a program to develop 100% duty factor, high-current proton accelerators. This accelerator section is the second version of the RFQ operated at CRL and provides a 1.25 MeV output beam. The RFQ is powered by a 250 kW, klystron-based amplifier system which was also commissioned at CRL[1]. The accelerator section and support equipment were obtained under contract from the Chalk River Laboratories and installed at Los Alamos National Laboratory (LANL) with the purpose of supporting studies applicable to the operation of high-power, cw accelerators.

II. INSTALLATION

The RFQ was shipped from CRL with a minimal amount of disassembly. Components such as the driveline, slug tuner assembly, and vacuum pumps were removed in order to reduce shipping size and preclude damage to

protruding apparatus. Because of the robust design of this RFQ, it was decided to reassemble the RFQ and measure the RF parameters rather than proceed through further mechanical examination for shipping damage. The RFQ resonant frequency, driveline coupling (β), and Q were measured and compared to similar measurements originally made at CRL[2].

	<u>CRL</u>	<u>LANL</u>
f_0 (MHz)	267.1	267.15
β	1.15	1.18
Q_u	7325	7150

The close agreement of the RFQ parameters and the further integrity of the vacuum and water coolant systems provided the assurance that high-power RF operations could be commenced with minimal risk.

III. CONDITIONING

The RFQ was operated at its design field level at CRL with a measured peak input power of 150 kW. Although the RFQ had been previously conditioned to the design field level and had sustained cw operation, the reconditioning at LANL was done in a conservative manner in case unobserved shipping damage had occurred.

The RF directional couplers and RFQ monitor loops were calibrated for power measurement by three redundant systems -- a power meter, peak-to-peak RF signal measurements, and crystal detectors. Spark and light emissions from the RFQ were monitored remotely by video, and vacuum and temperature readouts were available for observation.

Initial reconditioning was done using pulsed power. The RF system was pulsed at a 60 Hz rate with the pulse length advanced throughout the conditioning process. The initial pulse length (167 μ sec) resulted in a 1% duty factor, and the RFQ was conditioned up to a measured peak power of 150 kW. This process was repeated at increased duty factors up to 50%.

At 100% duty factor, it was determined that sparks inside the vacuum region of the RFQ system developed

*Work supported by the United States DOE, contract W-7405-ENG-36.

into arcs which were sustained by the available cw power. These sustained arcs sputtered the copper in the driveline resulting in damage to the vacuum window. It was learned at CRL that providing a momentary power interruption quenched the arc and protected the system from damage. An RF blanking module was developed which interrupted power upon the detection of high VSWR (reflected power) and provided a ramped turn-on after system recovery. The key features of this module were the detection of the high VSWR, a response feature providing a brief RF OFF period, and a ramped restoration of RF power to minimize repeat sparks. Through the use of this module, power could be restored to the RFQ within 50 μ sec, a desirable feature for future high-intensity accelerators. Because this module protected against system damage, its design featured a no-deadtime requirement allowing it to protect against repetitive sparks. During the integration of this module at CRL, it was determined that the optimal configuration provided blanking to the RF drive setpoint rather than attenuation of the RF power between the low-level RF amplifier and the intermediate drive amplifier[1]. Recent modifications integrated the setpoint control within the module. The setpoint response to a spark is shown in Figure 1 and the resulting RF response is shown in Figure 2.

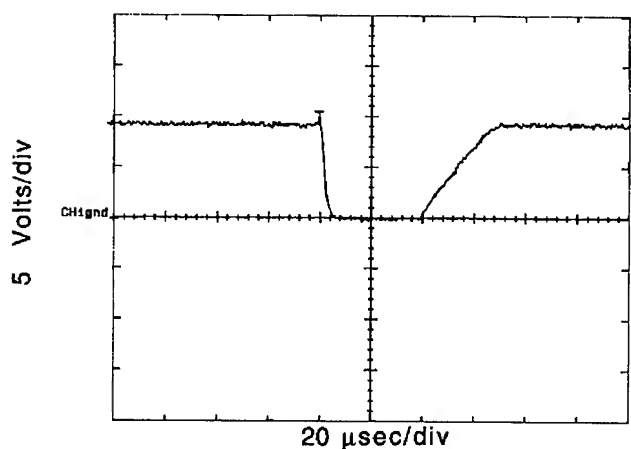


Figure 1. RF power drive setpoint response to an RFQ spark.

With the protection of the blanking module, cw conditioning was completed to a measured power of 150 kW.

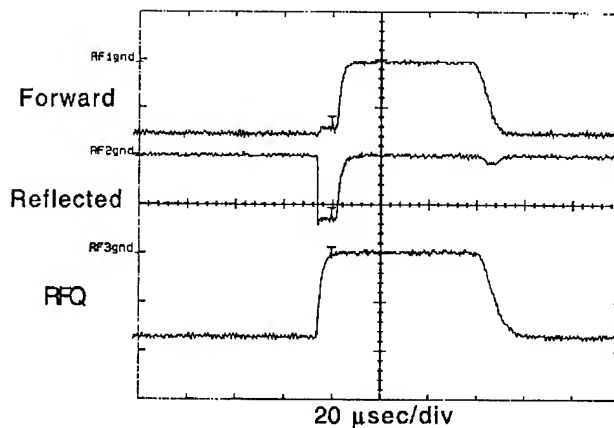


Figure 2. 267.1 MHz video envelope signals (negative signals) resulting from an RFQ spark.

IV. FIELD MEASUREMENT

The RFQ peak intervane gap voltage was measured at several powers using the x-ray endpoint technique[3]. Figure 3 displays the peak gap voltage as a function of measured RFQ power and a fit to the data.

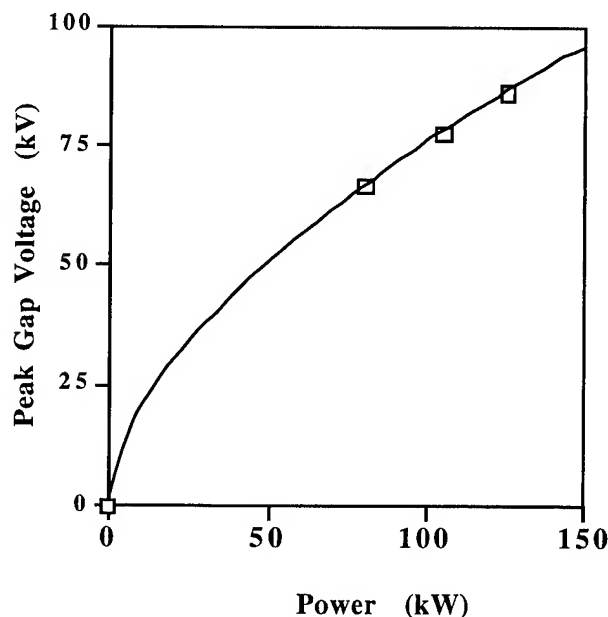


Figure 3. Peak intervane gap voltage as a function of measured RF power.

The measurements indicate that the design intervane peak gap voltage of 77.4 kV is reached at a measured power of 105.0 kW. This power level is far less than predicted by simulations and previous CRL measurements. The discrepancy between the required power as predicted and measured at CRL and that measured at LANL is

probably due to inaccuracies in the latest power calibrations and errors in this preliminary x-ray measurement. These measurements will be repeated and the results rechecked.

V. SUMMARY

The CRITS RFQ has been conditioned to the design field levels and has demonstrated the capacity to operate for an extended period without failure. The RFQ is now operational and ready to commence operations with a proton beam.

VI. ACKNOWLEDGMENTS

We would like to thank and express our appreciation to the many named and unnamed personnel at Chalk River Laboratories who designed, fabricated, assembled, and commissioned this accelerator section under the RFQ1 program. Their work has provided us with outstanding equipment to continue the study of cw accelerators and has also provided a strong technical base supporting our future projects.

VI. REFERENCES

- [1] J.Y. Sheikh, A.D. Davidson, G.E. McMichael, L.W. Shankland and B.H. Smith, "Operation of a High-Power CW Klystron with the RFQ1 Facility", Proc. 1993 Particle Accel. Conf., IEEE 93CH3279-7, p. 1175.
- [2] J.Y. Sheikh, Private Communication.
- [3] G.O. Bolme, G.P. Boicourt, K.F. Johnson, R.A. Lohsen, O.R. Sander, and L.S. Walling, "Measurement of RF Accelerator Cavity Field Levels at High Power from X-ray Emissions" in Proceedings of the 1990 Linear Accelerator Conference, LA-12004-C,219 (1990).

BEAM DYNAMICS STUDIES OF THE HEAVY ION FUSION ACCELERATOR INJECTOR*

E. Henestroza, S.S. Yu, and S. Eylon
Lawrence Berkeley Laboratory,
University of California
Berkeley, California 94720

D.P. Grote
Lawrence Livermore National Laboratory,
University of California
Livermore, California 94550

ABSTRACT

A driver-scale injector for the Heavy Ion Fusion Accelerator project has been built at LBL. This machine has exceeded the design goals of high voltage (> 2 MV), high current (> 0.8 A of K^+) and low normalized emittance ($< 1 \pi$ mm-mr). The injector consists of a 750 keV diode pre-injector followed by an electrostatic quadrupole accelerator (ESQ) which provides strong (alternating gradient) focusing for the space-charge dominated beam and simultaneously accelerates the ions to 2 MeV. The fully 3-D PIC code WARP together with EGUN and POISSON were used to design the machine and analyze measurements of voltage, current and phase space distributions. A comparison between beam dynamics characteristics as measured for the injector and corresponding computer calculations will be presented.

I. INTRODUCTION

The Fusion Energy Research Program at Lawrence Berkeley Laboratory has built a driver-scale injector for heavy ion fusion research. The principal design criterion was that the beam delivered should be at the same line charge density as expected in a full-scale heavy-ion driver. The injector will provide 0.8 Amperes of 2 MeV K^+ ions, equivalent to a line charge density of $0.25 \mu\text{C/m}$; it is further specified that the beams must have a low normalized emittance ($\approx 1 \pi$ mm-mr), repetition rate of 1 Hz and pulse length of $1 \mu\text{s}$.

On the basis of reliability, driver scalability, and beam specifications an ESQ design was selected for the injector. The ESQ accelerator consists of a diode followed by a sequence of quadrupoles arranged to focus and accelerate the beam at the same time. The

ESQ concept was first proposed by Abramyan and Gaponov [1]. The ESQ is generally a long machine with correspondingly low gradients. The secondary electrons are swept out by the large transverse fields, which reduces significantly the breakdown risks. In addition, the sources in an ESQ are generally smaller, so their intrinsic emittance is reduced. The ESQ is also attractive from the standpoint of driver scaling; it has the potential advantage of operating at energies much higher than 2 MeV, since the critical issues in an ESQ tend to center in the transition from the pre-injector to the first accelerating quadrupoles.

The key issue for this design is the control of beam aberration produced by the energy effect — in a strong electrostatic quadrupole field, ions at beam edge will have energies very different from those on the axis. The "inter-digital" structure of the electrostatic quadrupoles could enhance the aberrations. The resulting kinematic distortions lead to S-shaped phase spaces, which, if not corrected, will lead eventually to emittance growth. These beam aberrations can be minimized by increasing the injection energy and/or strengthening the beam focusing. It may also be possible to compensate for the energy effect by proper shaping of the quadrupoles electrodes to include octupole corrections.

A schematic of the one-beam injector is shown in Fig. 1. The components of the injector are a large hot alumino-silicate source, a diode column in which the beam is extracted and accelerated, and electrostatic quadrupoles that accelerate the beam to 2 MeV.

II. THE PRE-INJECTOR

For a $0.8 \text{ A } K^+$ beam to be accelerated to 2 MeV, numerical calculations showed large normalized emittance growth ($\approx 2 \pi$ mm-mr) for the case of a 500 keV beam injected into a representative ESQ. A smaller normalized emittance growth ($\approx 0.6 \pi$ mm-mr) was obtained for the case of a 1 MeV injected beam. The ini-

*Work supported by the U.S. Department of Energy under Contract DE-AC03-76SF00098.

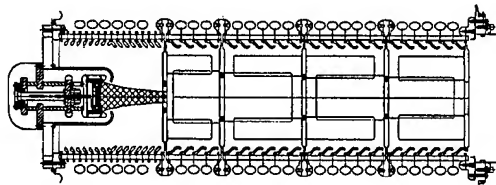


Figure 1: Schematic of the ESQ injector showing the diode column and the electrostatic quadrupoles.

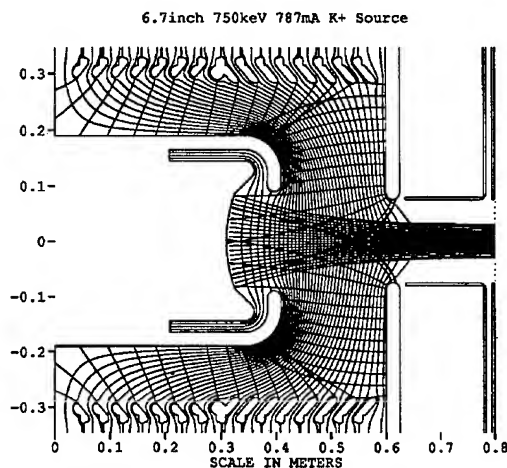


Figure 2: EGUN output showing the geometry of the axisymmetric injector diode, ion and electron trajectories, and field equipotential surfaces.

tial normalized emittance in both cases was 0.4π mm-mr. To check the physics of the energy effect of the ESQ a scaled experiment was designed to accommodate the parameters of the source, as well as the voltage limitations, of the Single Beam Transport Experiment (SBTE) apparatus. Phase space distortions predicted by simulations have been observed in the 570 keV scaled experiment leading to a factor of 8 growth in the beam normalized emittance. A growth of less than a factor of 2 in the beam emittance observed in the 1 MeV scaled experiment agrees with the expected decrease in emittance growth by an increase in injection energy. Therefore a major effort was launched to design a high energy diode that would deliver a high current (0.8 A) and low normalized emittance ($\approx 1 \pi$ mm-mr) K^+ beam. A diode designed to hold up to 1 MV, with minimal breakdown risks, consists of a hot alumino-silicate source with a large curved emitting surface surrounded

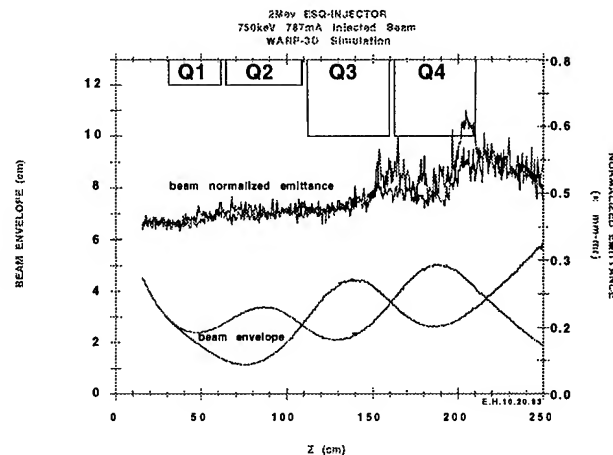


Figure 3: WARP3D simulation of the beam in the ESQ.

by a thick "extraction electrode." An extraction pulser switches the source from -80 kV to +80 kV relative to the extraction electrode during beam turn-on. The geometry of the diode, beam envelope and field equipotential surfaces as calculated by the EGUN [2] code are shown in Fig. 2. A cross-check of the design was obtained by running an π z particle-in-cell calculation using the GYMNOS code [3].

III. THE INJECTOR

The design of the ESQ Injector was based on the three-dimensional PIC (particle-in-cell) codes WARP3D [4] and ARGUS [5] running in a steady state mode. A full 3-D PIC simulation code was required to incorporate the beam space-charge-field as well as the self-consistent fields from the accelerating quadrupoles, including their "inter-digital" structure. The parameters of this design represent optimal choices to have a proper balance between breakdown risks and emittance growth. Fig. 3 shows the beam envelope and normalized emittance along the ESQ column as calculated by WARP3D, showing a small emittance degradation.

The construction of the 2 MeV Injector has been completed. The actual operation of the injector has exceeded the design parameters.

IV. NUMERICAL SIMULATIONS

Measurements of the transverse phase space distribution has shown excellent agreement with WARP3D calculations. Fig. 4 shows a comparison of measured and calculated phase space distribution in the horizontal plane.

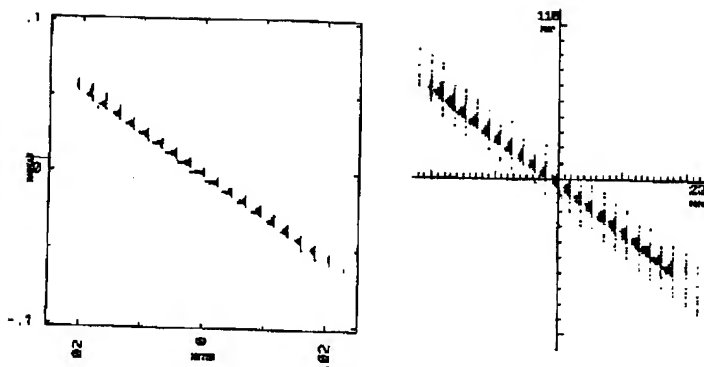


Figure 4: Horizontal phase space at the end of the injector as calculated and as measured.

The transient longitudinal dynamics of the beam in the ESQ was simulated by running GYMNOS and WARP3D in a time dependent mode.

During beam turn-on the voltage at the source is biased from a negative potential, enough to reverse the electric field on the emitting surface and avoid emission, to a positive potential to start extracting the beam; it stays constant for about 1 μ s, and is reversed to turn-off the emission. Since the Marx voltage applied on the accelerating quadrupoles and the main pre-injector gap is a long, constant pulse (several μ s), the transient behavior is dominated by the extraction pulser voltage time profile. The extraction pulser voltage profile has, in general, a 0.5 μ s rise time, a 1 μ s flat top and a 0.5 μ s falloff. The pulser rise used in the simulations followed the Lampel-Tiefenback functional dependence on time which eliminates current transients in a one-dimensional diode [6].

The results of both simulations codes showed a significant spike in current and energy at the head of the beam. A similar spike appeared in the experimental results. Fig. 5 shows the current profile at the end of the ESQ as calculated by WARP3D. The current waveform from the experiment shows a similar profile. The extraction voltage pulser shapes used in the simulations does not exactly match the experimental pulser shape.

The height of the initial spike is dependent on the rise time of the pulser. Simulations of the pre-injector with varying rise time showed that the minimal spike height was obtained with a 500 ns rise time. In an ideal, one-dimensional injector, with a rise time equal to the transit time, the Lampel-Tiefenback relation would result in no spike being formed.

Another feature seen in the simulations is the shortening of the current rise time with respect to the

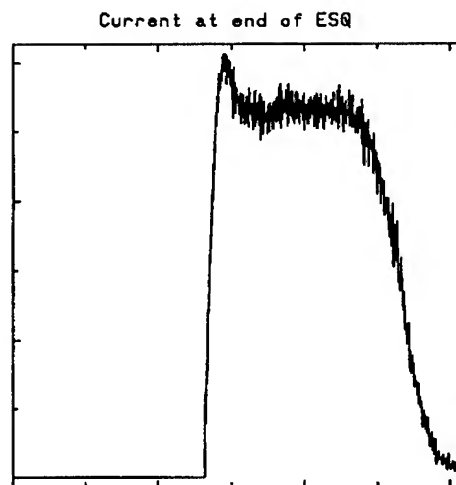


Figure 5: Current waveform at the end of the ESQ as calculated by WARP3D.

pulser rise time. With the pulser rise time of 500 ns, the current rise time produced is 200 ns; significantly shorter. This is in agreement with the experiment which showed the same behavior. After the initial rise and spike, a stable flat top was maintained for a time comparable to the flat top of the pulser voltage. The tail of the current waveform showed a long falloff as expected.

V. CONCLUSION

The 2 MeV ESQ Injector was designed using three-dimensional particle-in-cell calculations. Measurements of the beam parameters at the end of the injector have shown excellent agreement with computer simulations.

VI. REFERENCES

- [1] E.A. Abramyan and V.A. Gaponov, *Atomnaya Energiya* **20**, 385(1966).
- [2] W.B. Herrmannsfeldt, "EGUN- An electron optics and gun design program," *SLAC-Report-331*, 1988.
- [3] D.W. Hewett and D.J. Larsen, "The Best of GYMnos: a user's guide", *UCRL-ID-110499*, May 1992.
- [4] A. Friedman, D. Grote, and I. Haber, "Three-dimensional particle simulation of heavy-ion fusion beams," *Phys. Fluids* **B4**, 2203(1992).
- [5] C.L. Chang, et al., "Three-Dimensional Modeling of Accelerators", *LA-11857-C*, 1990.
- [6] M. Lampel, and M. Tiefenback, "Elimination of current transients in a one-dimensional heavy-ion diode", *LBL-14416*, 1983.

FIRST TESTS AT INJECTOR FOR THE S-BAND TEST FACILITY AT DESY

M. Schmitz, W. Herold, N. Holtkamp, W. Kriens, R. Walther*

Deutsches Elektronen Synchrotron (DESY), Notkestraße 85, 22603 Hamburg, GERMANY

* Student from Fachhochschule Ostfriesland, Constantia Platz 4, 26721 Emden, GERMANY

The s-Band Test Facility currently under construction at DESY requires $2\mu\text{s}$ long macropulses with 8ns, 16ns or 24ns interbunch spacing at an average current of 300mA in each case and a maximum repetition frequency of 50Hz. The injector design is based on a conventional scheme using a pulsed thermionic gun, two subharmonic bunchers (125MHz and 500MHz) and two travelling wave bunchers ($\beta=0.6$ and $\beta=0.95$). Together with a high power gunpulsor and adequate triggering, the gun is expected to generate a $2\mu\text{s}$ long train of pulses with less than 2.5ns FWHM-pulsewidth and a peak current of up to 6A. The first 50cm of the injector beamline equipped with a wall current monitor, a button type position monitor and a faraday-cup at the end were built up in order to commission the gun and its pulser. First results of the gun and pulser operation are presented here and compared with calculated performance.

I. INTRODUCTION

The s-Band Test Facility at DESY will be constructed in order to study the feasibility of a large s-Band Linear Collider project. The Test Facility consists of an injector followed by 4 ($\beta=1$, 17MV/m) accelerating structures of 6m length each, intersected by quadrupole triplets. Before being dumped the beam passes through a spectrometer arm and other diagnostics to analyze the beam quality.

Based on a 50Hz repetition rate the testlinac requires $2\mu\text{s}$ long bunchtrains with the possibility of switching between 3 different modes of time structure, while keeping the average current within the bunchtrain constant at 300mA, i.e.:

1. 250 bunches with 8ns bunch to bunch spacing and $2.4\text{nC/bunch} \Leftrightarrow 1.5 \cdot 10^{10} \text{ e}^-/\text{bunch}$
2. 125 bunches with 16ns bunch to bunch spacing and

$$4.8\text{nC/bunch} \Leftrightarrow 3.0 \cdot 10^{10} \text{ e}^-/\text{bunch}$$

3. 83 bunches with 24ns bunch to bunch spacing and $7.2\text{nC/bunch} \Leftrightarrow 4.5 \cdot 10^{10} \text{ e}^-/\text{bunch}$

The injector which should deliver these bunchtrains was designed on a conventional scheme [1], where the pulses are generated at the thermionic gun and compressed by means of two subharmonic (125MHz and 500MHz) and two travelling wave bunchers ($\beta=0.6$, 6.7MV/m and $\beta=0.95$, 14MV/m). To avoid deflecting systems such as choppers, the gun uses a gridded cathode in order to produce the desired bunchtrain right at the beginning. The generation of short electron pulses (FWHM-pulselength $\leq 2.5\text{ns}$) with high bunchcharge of up to 12nC (60% safety margin included) in combination with 3 modes of multibunch operation is quite a challenging task for the gunpulsor, especially in terms of amplitude and time jitter stability.

Since the generation of the pulsetrain at the gun is one essential part of the injector, only the very first part of the injector beamline was built up in order to be independent of commissioning all the other components of the injector at the same time. This setup, as shown in figure 1, is instrumented with a wall-current monitor (CM1) at $z=31.6\text{cm}$, a button-type position monitor (BPM1) at $z=36.4\text{cm}$ and a faraday cup at the end of the beamline, i.e. 46.1cm downstream of the gun anode which is at $z=0$. The whole system has an aperture of 34mm in diameter, except the hole in the anode of the gun which has a diameter of 20mm. Pumping is done directly at the gun via a short pumping port by means of a 400l/s getterpump.

For transverse focussing two solenoids AF2 (5.6cm long, 320 turns) and AF3 (8.7cm long, 500 turns) are centered around $z=12.2\text{cm}$ and $z=24.3\text{cm}$ respectively. With the same inner radius of 4.5cm and an outer radius of 6.4cm

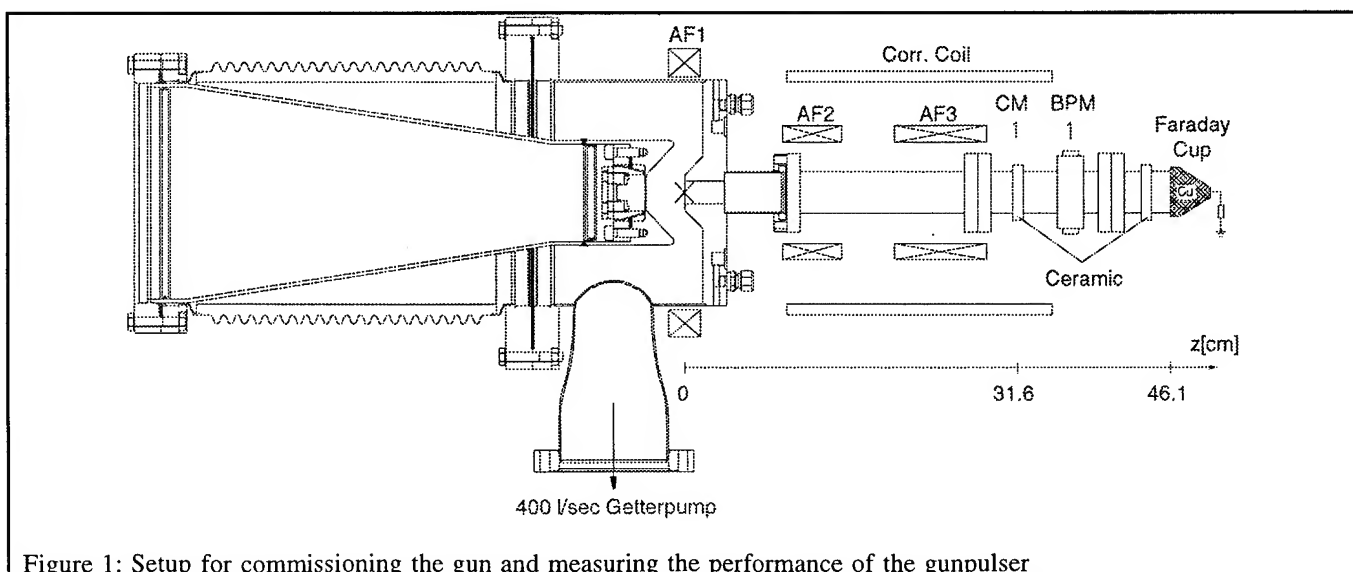


Figure 1: Setup for commissioning the gun and measuring the performance of the gunpulsor

the magnetic fieldstrength in the center of each solenoid reaches 35 Gauss/A for AF2 and 45 Gauss/A for AF3. A third solenoid AF1 centered at $z=0$ is used for compensation purposes to keep the cathode free from magnetic field. With a length of 2.3cm, 100 windings, an inner radius of 10.4cm and an outer radius of 12.5cm, AF1 produces roughly 5 Gauss/A in its center.

In the first phase of commissioning the gun was operated by a testpulsar, which supplies the cathode with single pulses of $3\mu\text{s}$ length and variable amplitude at 50Hz repetition rate. Results of this operation mode, in which the current capability of the gun and the beam transport to the faraday cup were investigated, are described in section III. During this operation the gun was conditioned and the vacuum improved. Thus the setup was well prepared, when the shortpuls gunpulser was delivered by HERMOSA Electronics. Its performance in combination with the gun during the first week of operation is presented in section IV. Before dealing with the experimental results the following section reviews the design of the gun.

II. GUN DESIGN

For clean capture by the first subharmonic buncher (125MHz) the FWHM-length of the gunpulse should be in the order of 90° of 125MHz, i.e. 2ns. The maximum charge which is required in that pulse is given for the 24ns inter-bunch spacing operation by 7.2nC. Including a 60% safety margin the gun has to deliver about 12nC in a pulse of about 2ns length. Thus the gun has to be designed for a current capability of approximately 6A.

In order to relax the requirements on the SHB amplitudes and to simplify the process of bunching the gunvoltage of 90kV has been chosen as low as possible. On the other hand PARMELA simulations show that this value is high enough to keep space charge effects (bunchlengthening and energy modulation) in the 75cm long drift between gun and first SHB still acceptable.

Based on the EIMAC Y796 cathode-grid assembly the gun geometry as it can be seen in figure 1 was modelled with the EGUN code. With a 34mm anode cathode gap this gun has a calculated perveance of $0.22\mu\text{A}/\text{V}^{1.5}$, i.e. at 90kV it delivers the desired 6A of space charge limited current. Due to EIMAC fabrication tolerances the exact position of the cathode relative to the cathode-electrode has an accuracy of $\pm 0.4\text{mm}$. EGUN simulations show that this affects the perveance in the order of $\pm 10\%$, since the electrical fieldstrength at the surface of the cathode is quite sensitive on its position.

At 90kV a maximum electrical fieldstrength of 81kV/cm appears at the surface of the anode "nose". The normalized and absolut emittances at the gun exit are $\epsilon_{n,100\%}=9.3\pi\text{mm}\cdot\text{mrad}$ and $\epsilon_{abs,100\%}=15.0\pi\text{mm}\cdot\text{mrad}$ respectively.

The gun is operated at air and a 240mm long ceramic with an inner diameter of 200mm insulates anode from cathode potential. The cathode itself is carried by a conical metallic tube, that runs through the ceramic and is flanged on to the high voltage end of the isolator. At the same time this tube serves as a coaxial housing for the gunpulser, which uses a three stage triode tube circuit. Short current

pathes and coaxial setup provides a low impedance arrangement, which bring up the short pulses to the cathode.

Pulsing the cathode by a resonant amplifier is not applicable. On the one hand each of the 3 time structures would require an extra amplifier (125MHz, 62.5MHz and 41.6MHz) and on the other hand the bias voltage in order to produce only 2ns long pulses would exceed the EIMAC specification, especially in the 24ns (41.6MHz) case. A linear broadband amplifier with a bandwidth in the order of 1GHz could be used. Since it has to deliver 6A at a forward voltage (net drive) of about 150V, the output peak power has to be at least 1kW. In this combination of bandwidth and power, such an amplifier is not available right off from the shelf. That's why the nonlinear pulser based on triode tube technology is used.

III. GUN-OPERATION WITH TESTPULSER

In order to get experienced with the new hard- and software setup, the gun was driven by a testpulsar. It delivers single pulses of $1-3\mu\text{s}$ length and variable amplitude to the cathode. The gunbias was fixed to 60V. Driven by this testpulsar the maximum current which was measured at the faraday cup saturated at about 5.2A at 90kV independant of increasing the gunheater (7.5V) or the netdrive (175V). The vacuum was about $2\cdot 10^{-8}\text{Torr}$ at this time. This perveance limit of $0.19\mu\text{A}/\text{V}^{1.5}$ corresponds to 87% of the EGUN predicted value.

The current settings of AF2(5A) and AF3(4A) for maximum transmission agreed well with PARMELA predictions. The impact of AF1 on the transmission is negligible in a wide range of $\pm 3\text{A}$, but it should deteriorate the emittance which could not be measured so far.

By means of this operation the vacuum quality improved automatically. With high voltage and gunheater on but beam off the vacuum is now at a level of $3\cdot 10^{-9}\text{Torr}$. During beam operation the average current and transmission losses determine the rise of the vacuum pressure.

IV. PERFORMANCE OF GUNPULSER

For the production of multibunchtrains with the time structure mentioned in section I a special gunpulser was used. It consists of 3 triode tube stages (2*EIMAC 8755 and 1*EIMAC 8940), with the last one acting as a perveance limited current source, which can be varied by setting its anode voltage (0-3kV) in order to determine the current that drives the guncathode. At a 20Ω dummy load the maximum current at the output of the pulser was measured to be 8.8A. Since the gunpulser input with an impedance of $\approx 50\Omega$ requires 2ns wide pulses of about 60V peak, a very broadband high gain system is needed to produce the pulse-trains at the pulserinput.

Produced by a tektronix stimulus triggergenerator the desired triggerchains are brought up into the high voltage deck of the gun with a 3GHz bandwidth laser driven optical transmission system. The 500mV output of the receiver is fed into an 1GHz bandwidth A-type amplifier made by Amplifier Research to produce 60V level pulsetrains, which it did very clean even for the 8ns spacing.

At first we checked the single pulse performance of the gunpulsar by feeding it with a 60V pulse from an avalanche pulser. This pulse had a FWHM-length of 2.1ns, a FW of 3.5ns and a risetime of 1.2ns. The corresponding beampulse measured at CM1 showed a length of FWHM=2.4ns resp. FW=3.5ns, a risetime of 0.9ns and a peakcurrent of 2.3A.

The faraday cup, which has a slower response due to capacitive effects showed a peakcurrent of 1.7A and a FWHM of 3.3ns. Nevertheless the product of both values, which is a rough estimate on the pulsecharge, gives the same result of 5.6nC for both measurements. During this test the gun ran at 60kV (heater 7.5V, bias 60V, vacuum $6 \cdot 10^{-9}$ Torr) and the 8940 anode voltage in the gunpulsar was set to 800V.

By the time the 1GHz bandwidth amplifier was delivered, the avalanche pulser was replaced by this device. Triggered with single pulses the beamresults, as can be seen in figure 2 were similar to the tests with the avalanche pulser, except that without changing the peakcurrent even shorter bunches down to FWHM=2ns could be produced by decreasing the low level trigger pulsewidth down to 1.25ns

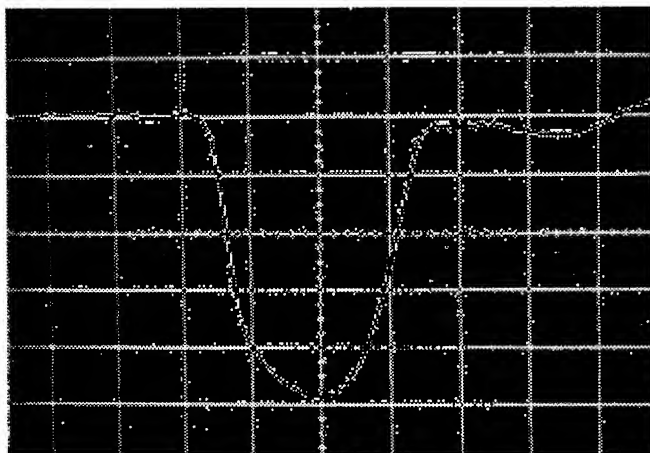


Figure 2: The first of 250 bunches with 8ns spacing measured at CM1, (1ns/div, FWHM=2.35ns, risetime=0.8ns)

instead of 1.5ns. At the first time operating with multibunches a strong amplitude droop of the beampulses along the train occurred. Caused by saturation of the interstage transformer cores in the gunpulsar this was cured by some inductances to reset the core bias between two micropulses.

After that the multibunch performance of the gunpulsar was quite impressive. In all the 3 time modes (see section I) the pulseshape of each micropulse in the train has the same characteristics as the single pulse, i.e. a FWHM-length ≤ 2.5 ns and FW ≤ 3.5 ns as specified. Concerning the amplitude stability one has to distinguish between the 3 modes. For the 24ns spacing only the first pulse is about 10% less in amplitude, while all the rest of the train is flat within 4% as it was guaranteed. At the 16ns mode we observed a resonance effect, which causes to start with a 20% higher amplitude decreasing within the first 5 pulses down to the level of all following bunches. In addition this resonance creates parasitic pulses ≈ 7 ns after each main pulse. They can be suppressed by reducing the 8940 plate voltage. When the origin of this oscillation is understood it can be

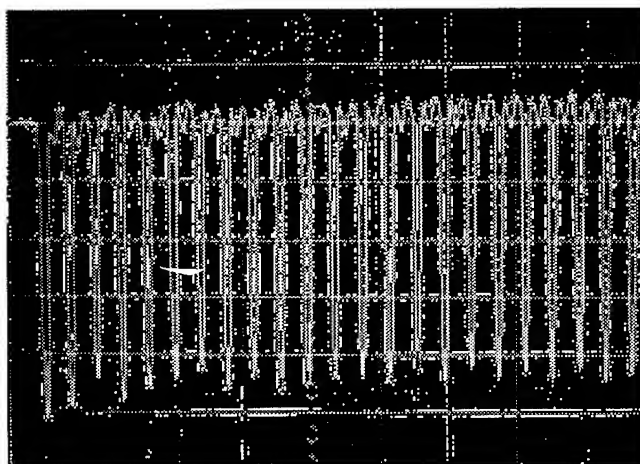


Figure 3: The 1. to 23rd of 250 bunches with 8ns spacing measured at CM1, (20ns/div)

eliminated or shifted to a frequency where it does not interfere with our time modes. Although it was not guaranteed even the 8ns mode showed good performance. Some kind of a sawtooth amplitude modulation of $\leq 15\%$ happens for the first 10 pulses, before coming to an equilibrium as can be seen in figure 3. In addition a continuous slow amplitude droop over the 2 μ s train of about 10% in total was observed. One reason might be that the 3x0.5nF HV-capacitors, which are located directly around the ceramic of the gun are not coupled low inductive enough to keep up the gunvoltage over the bunchtrain.

The maximum bunchcurrent was about 3.2A at 80kV. Since this is not the perveance limit of the gun (see section III) it has to be investigated in more detail what is limiting this value. The pulse jitter observed on a 8GSa/s scope in a 100ps/div scale was less than 50ps which still includes the trigger jitter as well.

V. SUMMARY

The 90kV thermionic gun for the s-Band Test Facility at DESY was commissioned. With μ s long single pulses 87% of the EGUN predicted perveance was measured. For the production of multibunchtrains a high gain high bandwidth system was built up for pulsing the gun. In a short beamline behind the gun the beamquality was measured. Bunchtrains of up to 250 bunches with 8ns, 16ns or 24ns bunch to bunch spacing, a non perveance limited peak current of up to 3.2A and an amplitude stability within less than 5% except from the first few pulses were produced. The micropulses had a FWHM-length of typically 2.3ns and a subnanosecond risetime.

VI. REFERENCES

- [1] The Injector for the s-Band Test Linac at DESY, M. Schmitz, A.D. Yeremian, Proceedings of the 1994 International Linac Conference, p71-73, Tsukuba, Japan

RF Phasing of the Duke Linac*

Ping Wang, Nelson Hower, Patrick G. O'Shea

Duke University Free Electron Laser Laboratory
Box 90319, Duke University, Durham, NC 27708-0319

Abstract

The injector of Duke storage ring is a 295 MeV S-band linear accelerator (linac) which consists of 3 klystrons and 11 accelerator sections. The phase adjustment between klystrons is achieved by means of 2 commercial coaxial phase shifters in the klystron drive line. The phase between accelerator sections is balanced on the low power level after the waveguide installation. A mechanical high power waveguide phase changer has been developed and installed for each accelerator section. During the high power operation, the waveguide phase can be changed remotely by driving gearmotor to deform the waveguide cross section. The test results and high power performance are reported.

I. INTRODUCTION

A 295 MeV S-band linac has been in operation at Duke University since October 1994 (see [1]). It serves the Duke 1 GeV storage ring as an injector. The linac consists of three ITT 30 MW klystrons, eleven 10-foot long accelerator sections and a RF gun cavity. The RF frequency is 2856.76

MHz. The first klystron feeds the gun cavity and first 3 sections. The other two klystrons each feed four sections. The RF phase adjustment between 3 klystrons is achieved by means of 2 motorized coaxial phase shifters in the klystron drive lines. Only one high power waveguide phase shifter is employed in the gun cavity feed line. The electrical phase length of each waveguide branch was measured and adjusted at low RF level using a double balance mixer. A mechanical high power waveguide phase changer has been developed and installed for each accelerator section. During the operation, the phase between the bunched beam and the RF wave in each individual section can be corrected remotely in the control room. The test results and high power performance are reported. Overall this paper provides a very simple and economical method of RF phasing for short or medium size linac injectors.

II. WAVEGUIDE NETWORK

Aluminum waveguide WR284 pressurized with 26 PSIG of Sulfur Hexafluoride (SF₆) are used throughout the

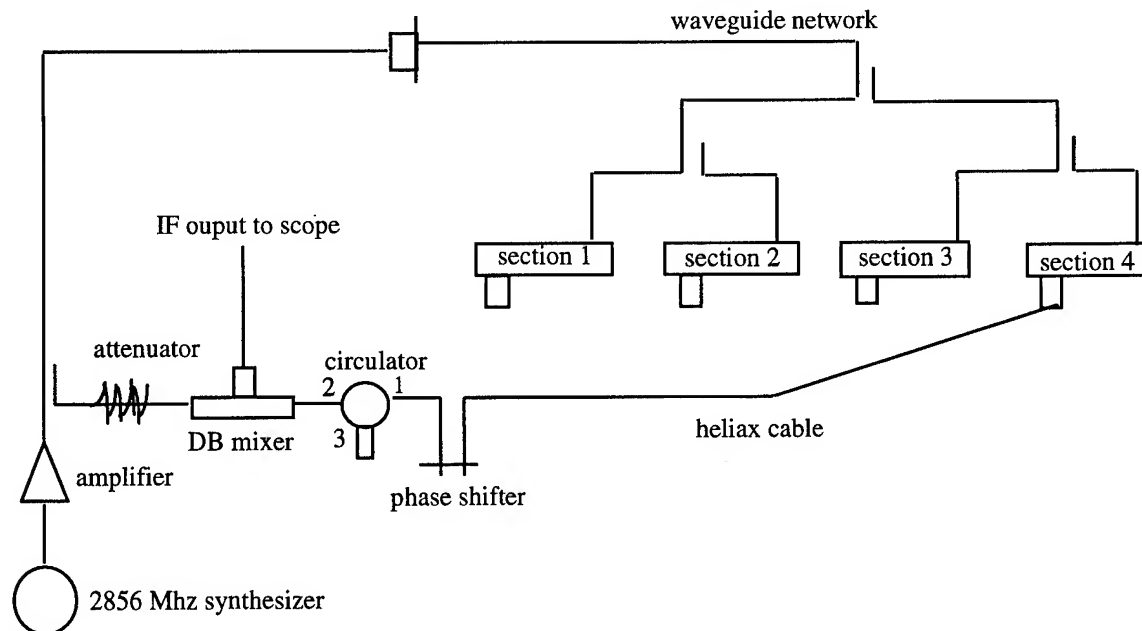


Figure 1. Block diagram of low level RF phase measurement

* Work supported by U.S. Air Force Office of Scientific Research Grant F49620-93-1-0590 and U.S. Army Space & Strategic Defense Command Contract DASG60-89-C-0028.

whole system. They are carefully designed to have equal electrical phase length among the waveguide network branches. To reduce the phase differentials caused by waveguide temperature or pressure (see [2]), considerable care was also taken to obtain a symmetrical waveguide network design.

The branches from first 3-dB power divider to each section have an about equal physical waveguide length (around 20 feet). This results in a close to equal power dissipation in the accelerator sections and waveguide lines. The installation of our high power waveguide phase changer has eliminated the regulation requirements on waveguide temperature and pressure; therefore, no cooling water for waveguide was required. The pressurized SF₆ circulates through a dryer in the waveguide system and is not pressure regulated either. The aluminum waveguide flange CPR284F and gaskets (Parker 5906-284-1) are used throughout the waveguide system. Most of the waveguide components were made in house. Some pieces were made locally to size at the time of installation.

III. RF PHASE ADJUSTMENT

After the installation of waveguides and accelerator sections, the RF phase adjustment was performed. Figure 1 is a block diagram of RF phase measurement set-up. A frequency stable signal generator gives a CW signal at the operation frequency of 2856.76 MHz. The waveguides were pressurized at 26 PSIG and the accelerator sections were cooled at 30.2 degree centigrade which are the normal operation conditions. Four aluminum waveguide spools have been machined to connect the Skarpaas flanges at section's output to the commercial waveguide flanges CPR284F which are used on the waveguide to coaxial adapters. Helix coaxial cable and semi-rigid coaxial cable are used for the purpose of phase stability.

The phase measurement was made by a double balance mixer (mini-circuit ZEM-4300MH) as a nulling detector. A 20-foot long Helix coaxial cable is connected to one of the four sections at each time. The RF signal output from each section is compared with the same reference signal at the mixer. First of all, take a rough phase scanning for all of the four sections; then choose one section whose phase error lays in the middle of others as the standard one; adjust the coaxial phase shifter in the RF line to get a zero output from the intermediate frequency (IF) port of the mixer; then switch the 20-foot cable to the next section; use a C-clamp to indent the waveguide wall to get the same nulling output of IF port. Bowing in of the narrow wall of waveguide decreases its phase length and bowing in of the broad wall increases its phase length. The waveguide deformation has to be permanent. With 26 PSIG pressure, a hand-operated C-clamp can easily obtain the desired phase adjustments. After the four branches reaching their phase balance, we leave them for overnight and recheck their phase next day. The

typical phase difference between branches is around 10 degrees and the maximum one is 35 degrees.

It was found that measurement is reproducible within ± 1.5 degrees which is caused mainly by reconnecting the 20-foot Helix cable. Since the zero crossing point of the mixer's IF output is used for phase detecting, the RF signal's amplitude is not a critical issue any more. We set the RF level for the best phase resolution which is 3 mV per degree of phase differential. The four commercial waveguide to coaxial adapters have a phase difference within ± 1 degree. Assuming the sections are among ± 2.5 degrees of their design length, the overall accuracy of this method is better than ± 5 degrees.

IV. WAVEGUIDE PHASE CHANGER

The remotely operable phase changer assembly consists of a flanged 30-inch long piece of aluminum WR284 waveguide suitably equipped with a mechanism for compressing together or pulling apart the broad sides of the waveguide over approximately 80% of its length (see Fig. 2). An aluminum strip .25x.30x24 inch with 14 tapped holes was welded along the centers of each of the broad sides of the waveguide section. To this was fastened with screws a 0.37x2.0x24 inch steel bar which acts as a stiffening rib to distribute a centrally applied compression or tension force along the length. The force is generated by a DC gearmotor driving a shaft with right and left-hand screw threads machined onto its ends. Pivoted nuts riding on these threads move some hinged levers in or out, thereby causing a large deforming force to be applied to the centers of the stiffening ribs. The waveguide walls each move in or out by up to approximately ± 2 mm (which takes the aluminum in the waveguide well beyond its elastic stress limit), and the phase of the RF wave propagating in the deformed waveguide is changed by about 30 degrees from the fully compressed to fully expanded states (see [3]).

The readback of phase information is provided by an LVDT displacement transducer mounted on one of the two stiffening ribs and activated by a rigid arm which is mounted on the opposite rib. The LVDT signal is thus a direct measure of changes in the wall-to-wall dimension in the center of the broad walls of the waveguide. As measured using a slotted line attached to one end of this waveguide section, the phase shift is a very linear and reproducible over many cycles function of the LVDT signal.

V. SYSTEM PERFORMANCE

The described system has been in operation for six months and has functioned very well. Two energy spectrometers are employed for monitoring the phase relationships between RF traveling wave and electron beam. The low energy spectrometer is located after first accelerator

section and the high energy spectrometer is at the end of linac. Phasing is performed manually in the control room. The phasing criteria are to maximize the beam energy and minimize the energy spectrum width.

The availability of phase adjusting for each individual

accelerator section has proven valuable. After installation it was found that the beam line length between first and second accelerator sections was mistakenly manufactured 1.074 inch shorter than the designed 69-wavelengths. We shortened the waveguide length to that section correspondingly and performed a phase measurement similar to the low power

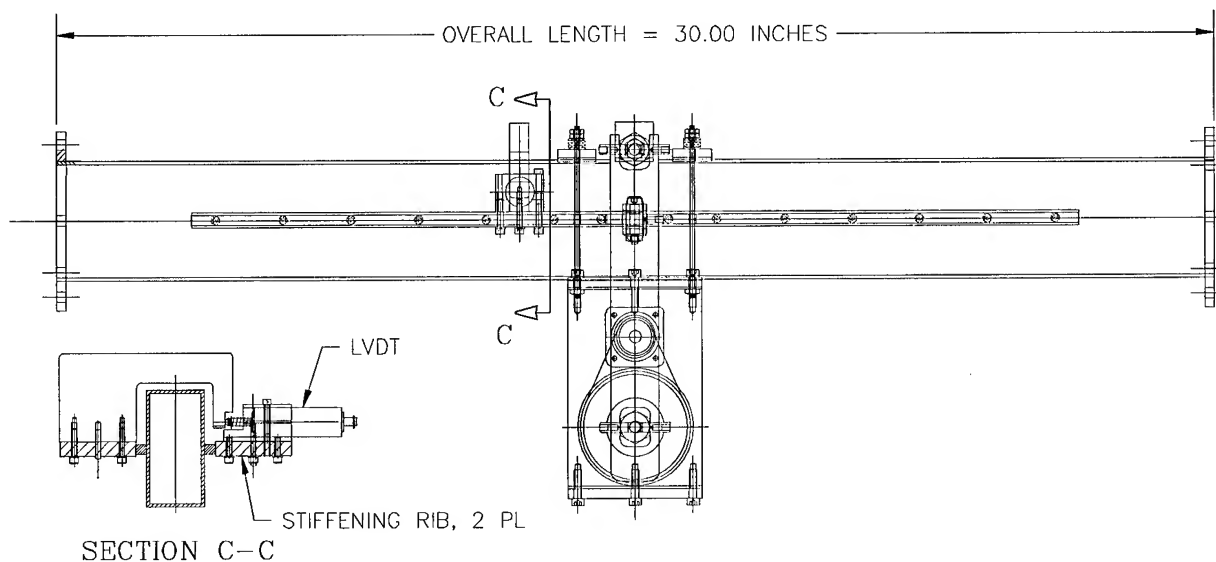


Figure 2: Waveguide Phase Changer

one but operated at a high power level. The phase measurement accuracy performed at high power level is around ± 10 degrees. The fine phase adjustment for these two sections was made by their waveguide phase changers.

Each waveguide phase changer has a phase adjusting range of ± 15 degrees. But the actual phase range is not limited by it. If one of the phase changes reaches its limits, it is possible to indent the waveguide wall adjacent to it to bring the phase to its middle. The waveguide phase changer can be used like a phase indicator during the high power operation which gives the phase direction needed for the phase adjustment.

The current phasing system accuracy is limited by our high energy spectrometer which has a sensitivity of 0.2%. The further improvement is to have a more sensitive spectrometer or using the beam induced signal as phase measurement.

VI. ACKNOWLEDGMENTS

The authors wish to thank M. Emamian and S. Goetz for their mechanical designs on waveguide network, C. Dickey and J. Meyer for their work on the electronic controls, and J. Faircloth, J. Detweiler and P. Cable who did

the waveguide fabrication and installation; their contributions are much appreciated.

References

- [1] P. O'Shea, et al., Accelerator Archeology-The Resurrection of the Stanford MKIII Electron Linac at Duke, these proceedings.
- [2] R. B. Neal, The Stanford Two-mile Accelerator P.345 (1968).
- [3] L. Young, Microwave J. 9. 45 (1966).

Simulations and Measurements of the TTF phase-1 Injector Gun

T. Garvey and M. Omeich

Laboratoire de l'Accélérateur Linéaire, IN2P3 - CNRS, Orsay, France.

M. Jablonka, J.M. Joly and H. Long
CEA, DSM/DAPNIA, Saclay, France.

Abstract

The TTF phase-1 injector will use a conventional thermionic triode gun as its electron source. The temporal structure of the injector will be obtained by the application of fast (< 1 ns) pulses to the gun cathode. As it is necessary to operate the injector at a fixed average macropulse current of 8 mA, while having the ability to vary the repetition frequency of the micropulses, the gun has to function at peak currents varying from 100 mA to 400 mA. We report on both measurements and simulations (using EGUN) of the current-voltage characteristics of the TTF gun. In addition we report on measurements of the emittance of the gun over a limited range of current and voltage. The emittance is seen to be dependent upon the operating perveance and is smallest for perveances closest to the space-charge limited value.

1. INTRODUCTION

The TTF phase-1 injector must provide the TTF linac with an average macropulse current of 8 mA. In addition it is foreseen that this current should be provided using a time structure (micropulse frequency) that can be varied. The highest frequency at which the injector can operate is 216.7 MHz, corresponding to the frequency of the sub-harmonic buncher (SHB) used on the injector [1]. However it is desirable that the injector provide 8 mA average current at sub-multiples of the above frequency, notably 72.2 MHz. In order to achieve variable frequency operation of the injector we propose to modulate the gun current by the application of fast pulses to the cathode delivered via a wide-band amplifier. An average current of 8 mA for pulses at 216.7 MHz / 72.2 MHz implies a bunch population of 2.3×10^8 e⁻ / 6.9×10^8 e⁻. Test measurements on the wide-band amplifier indicate that the gun output pulses will be quasi-triangular in form. As the base width of the pulses should be of the order of 0.64 ns, in order to ensure sufficient compression in the SHB, the figures above imply the need for peak gun currents of 115 mA / 345 mA.

In addition to the above beam current requirements the electron source for the TTF injector must deliver a beam of 250 keV energy. Although a suitable gun was commercially available we have preferred the solution, inspired from the S-DALINAC at the TH-Darmstadt [2,3] of using a triode gun providing 30 kV with the additional energy of the beam being furnished by an electrostatic accelerating column capable of sustaining 300 kV in air.

2. DESCRIPTION OF THE GUN

The triode gun is a modification of the gun, built by Hermosa Electronics, for use on the ALS linac at Saclay [4].

It has a classical "Pierce-like" geometry and employs an Eimac Y-845 cathode (emitting surface area = 0.5 cm^2 , cathode-grid spacing = $140 \text{ }\mu\text{m}$). In its original form the gun had an anode-cathode (A-K) gap distance of 97 mm and provided a nominal current of 100 mA at 40 kV. In order to have some margin for safety we should like to be able to operate the gun at 400 mA with 30 kV A-K voltage, consequently the gun has to be modified to increase its perveance, $K (= I/V^{3/2})$ to $0.077 \text{ }\mu\text{Pervs}$. A schematic of the modified gun is shown in fig. 1.

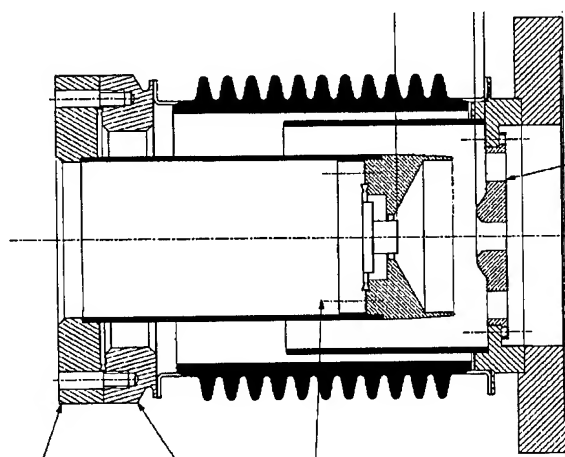


Figure 1. Schematic of TTF Gun. The distance from the cathode plane to the anode nose is 37.5 mm

3. GUN CHARACTERISTICS

The space-charge limited (SCL) current for a planar diode is given by the Child-Langmuir law,

$$I = \frac{4\epsilon_0}{9} \sqrt{\frac{2e}{m_e}} V^{1.5} \frac{A}{d^2}$$

or,

$$I = k V^{1.5} \frac{A}{d^2}$$

where A is the cathode area, d is the A-K distance, V is the A-K voltage, $k = 2.33 \times 10^{-6} \text{ A/V}^{3/2}$ and the other symbols have their usual meaning. Approximating our gun geometry as a planar diode one would expect therefore that we should reduce the A-K gap to 39 mm. Following quick exploratory runs with the E-GUN code [5] we have settled on a gap of 37.5 mm. We have reduced the A-K spacing by welding the focus electrode onto a long cylindrical stalk which is, in turn, welded to the original cathode flange (fig. 1).

3.1 EGUN Simulations

For the geometry corresponding to figure 1, EGUN runs predict that the SCL current will be 402 mA at 30 kV operating voltage. As well as reducing the A-K gap distance we have also performed simulations and measurements for the case where the length of the "nose" of the focus electrode is halved, from 14 mm to 7 mm. This modification was considered due to concern about electrical breakdown between the tip of the nose and the anode for the reduced gap distance. EGUN runs for this case show an additional increase of 25% in the perveance, i.e. $K = 0.1 \mu\text{Pervs}$. However the outputs also show some increase in the divergence of the extracted beam, an effect which turned out to be much greater for the measured case (see below). For this reason, and following high voltage tests which showed that breakdown did not occur with the original focus electrode for A-K voltages up to 60 kV, we intend to work with the original focus electrode dimensions.

Examination of the EGUN output file shows that the current density at the the outer radius is only 5% higher than that on axis. However the phase-space at the edge of the beam suffers from a certain degree of aberration which is less severe for higher currents. A re-design of the focus electrode might allow some reduction of the effects of aberration.

3.2 Perveance Measurements

The measured characteristics of the gun are shown in figure 2 for various A-K voltages. One can see that the measured SCL current is 406 mA, in excellent agreement with the EGUN prediction of 402 mA (note that the planar diode approximation predicts 430 mA). Measurements for the reduced focus electrode nose length resulted in exactly the same 25% increase in perveance seen in the simulations.

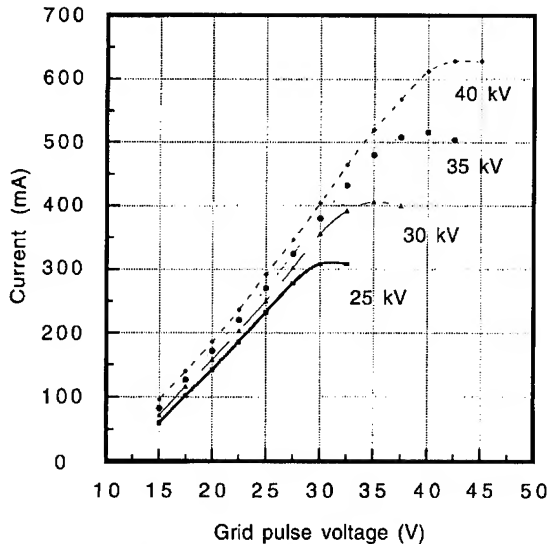


Figure 2. Measured characteristics of the modified gun for varying A-K voltages.

4. THE GUN EMITTANCE

To be consistent with the definition used in EGUN we take the normalised emittance, $\epsilon_n = 4\gamma\beta\epsilon_{rms}$, where

$$\epsilon_{rms} = (\langle x^2 \rangle \langle x'^2 \rangle - \langle xx' \rangle^2)^{1/2},$$

x and x' are the positions and slopes of the particles with respect to the beam axis and γ and β are the usual relativistic factors. The brackets imply the weighted averages of the quantities within them. The emittance specification for the injector is set by the requirement to maintain a small rms spot size (2 mm rms radius) in the linac for non-accelerated beams. This results in the need for a normalised emittance of the order of 20 mm-mrad. Higher charge electron injectors normally have emittances which are dominated by the beam dynamics in pre-bunching and bunching cavities. However, for our low charge case (37 pC/microbunch), PARMELA simulations indicate that emittance growth from the source (250 keV) to the end of the injector (10 MeV) is less than a factor of 2, hence the beam emittance is dominated by the value provided by the gun.

The intrinsic emittance of a non-relativistic thermionic gun is given by the expression,

$$\epsilon_n = 2R \sqrt{\frac{kT}{m_e c^2}}$$

where R is the cathode radius and T is the cathode temperature. For our case, with $R = 4$ mm and $T = 0.1$ eV we would expect an emittance of 3.7 mm-mrad. However this value is well known to be optimistic as field non-uniformities around the grid wires will increase the angular spread of the electrons as they pass through the grid [6] (this effect would be minimised for the case where the grid is biased at a potential difference, w.r.t. the cathode, which just corresponds to the same potential difference which would exist in the absence of the grid [7]). Increases in emittance by factors of four to seven have been reported for guns employing triode configurations over identical geometries using simply a diode [8].

4.1 Emittance Measurements

The emittance of the beam has been measured using a previously reported technique which takes into account the effects of the space-charge of the beam [9]. Since then, the process has been computerised with Labview. Beam profiles are digitally recorded, and 2σ radii are calculated. The range of current measurements was restricted to 200 mA due to the damage threshold of the current detector. Although the gun will be operated in a very short pulse mode (< 1 ns) the emittance measurements to date have been made using relatively long pulses of 3 μs as the fast pulser for the cathode was not available at the time of the measurement. The measured emittances, as a function of beam current and anode voltage, are shown in figure 4. One can see that, in general, for a given beam current the emittance increases with increasing voltage and that, for a given voltage, the emittance appears to decrease with increasing current. Of the ten data points one (50 mA, 35 kV) is not consistent with this remark however this point is sufficiently close to the point at 50 mA, 30 kV that the measurement error could easily account for this exception. These observations are consistent with the fact that the gun optic is optimised for one single value of perveance, i.e. the space-charge limited value. For this perveance the

external focus force provided by the gun geometry balances the self space-charge field of the beam. The further one reduces the beam current below the SCL value, for any given A-K voltage, the further this balance is reduced, resulting in increased emittance [10]. Care should be exercised in using this argument to explain the measured values as the situation is further complicated by the fact that different grid voltages are used to extract a particular current for a given A-K voltage. Therefore the contribution from the 'grid effect' mentioned above is not always the same.

As the EGUN runs are performed for the case of a diode, i.e. the simulations do not include the effect of the grid, one cannot expect to obtain good agreement between the calculated values and the measured ones [11]. The calculated emittance is found to be an increasing function of current but never exceeds the intrinsic value, consequently it is always inferior to the measured values. This same grid effect is responsible for the large measured beam divergences in comparison to the calculated values.

The smaller emittance values shown in figure 3 for smaller gun voltages might imply that it is best to operate the gun at the lowest voltage which will produce the required current. However, we wish to minimise growth of the transverse beam size in the electrostatic column (approximately 90 cm long) and therefore it may be advantageous to have the beam exit the anode aperture at higher voltages. Now that tests of the 40 kV gun are complete we will determine the optimum operating conditions for the gun-column assembly during forthcoming tests at SEA (Saclay).

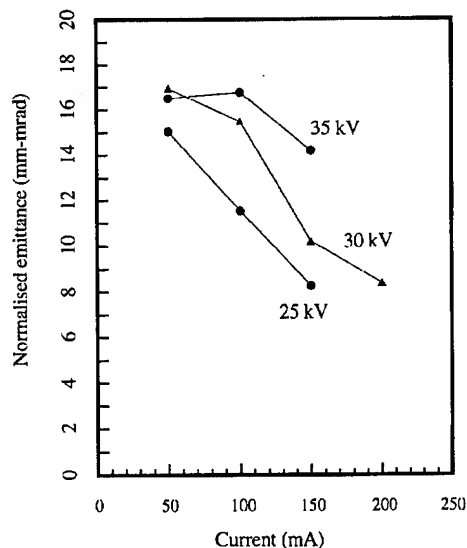


Figure 3. Measured emittance as a function of gun voltage and current.

5. ACKNOWLEDGEMENTS

We are indebted to Bernard Jaquemard and the staff of the SECAP group at LAL for mechanical engineering work on the gun and to J.C. Bourdon and B. Aune for many

discussions on the gun. One of us (T.G.) is grateful to Bernard Mouton for computer support.

REFERENCES

- [1] M. Bernard et. al., "The TESLA Test Facility Linac Injector", The proceedings of the 4th European Particle Accelerator Conference (London) 1994.
- [2] K. Alrutz-Ziemssen et. al., "Status of the Darmstadt Near Infra-Red Free Electron Laser", Proceedings of EPAC 90, Nice, France, 1990, pp 562-564.
- [3] The tube is available from High Voltage Engineering Europa, (Holland).
- [4] B. Aune et. al., "Improvement of the Electron Injection for the ALS Electron Linac", Proc. of the Linear Accelerator Conference, California, USA, SLAC report 303, 1986.
- [5] W.B. Herrmansfeldt, "EGUN - An Electron Optics and Gun Design Program", SLAC report 331, 1988.
- [6] R.H. Helm and R. Miller, "Particle Dynamics", in Linear Accelerators, edited by Septier and Lapostolle, p 124.
- [7] Ron Koontz, private communication.
- [8] B. Strongin and A. Salop, "Emittance determination of electron guns by analysis of beam profile measurements", Proceedings of the 1990 Linac Conference (Albuquerque), pp 758-760, Los Alamos report LA-12004-C, 1990.
- [9] B. Aune et. al., "A Device for Gun Emittance Measurement", IEEE Trans. Nucl. Sci., Vol NS-32, pp1896-1898, 1985.
- [10] R. Chaput, "Canon SLL de CLIO", Internal Report of the LURE Laboratory, Orsay, Linac/CLIO/8087, 1987
- [11] M. Castellano et. al. "Commissioning and performance of a low emittance, long pulse electron gun for the superconducting linac LISA", Nuclear Instruments and Methods, Vol A 332, pp 354-362, 1993.

EXPERIMENTAL STUDIES ON COLD CATHODE MAGNETRON GUN

A.N.Dovbnya, V.V.Zakutin, V.F.Zhiglo, A.N.Opanasenko, V.P.Romasko, S.A.Cherenshchikov
National Science Center, Institute of Physics & Technology, Kharkiv, 310108 Ukraine.

Abstract

Experimental data on obtaining electron beam by the magnetron gun with a cold cathode are presented. Two possible emission mechanism such as electron secondary emission and explosive emission as well as methods of identifying it are discussed. Data on measuring amplitude and form of the beam current pulses and the beam diameter with variation of the electrical and magnetic fields are given. The final aim of these researches is production of the stable pulse beam with the currents nearly 100 amperes and the long life time of the gun. The research is carried out to create the magnetron injection gun for the high power cluster klystron for the Next Linear Colliders.

I. EXPERIMENT

This paper presents the experimental results of electron beam generation in a cold-cathode magnetron gun, operating in secondary-emission mode [1].

The research was performed on an experimental facility which contained a negative HV-pulse source, the pulse of the amplitude $U \leq 40$ kV and width 0.5-2.0 μ s being fed on to a finger-like copper cathode, while the anode, made from a stainless steel tubing 35 mm in diameter, 250 mm long, was grounded via resistor. The gun was placed in a pulsed magnetic field of the strength $H \leq 0.5$ T. The beam current was measured using the resistor connected to an electron collector.

The above-device was used to measure the relationship of beam current amplitude vs. magnetic field strength H (Fig. 1) which has a threshold nature of beam current rise and disruption.

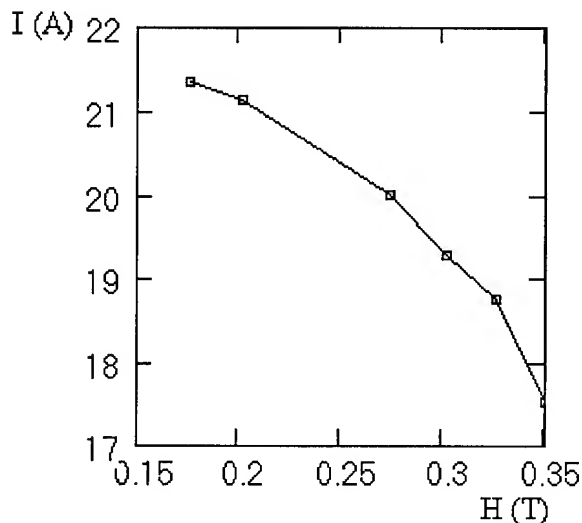


Fig. 1. $U \approx 40$ kV

Particle energy measurements were made using the technique of absorption of the particle energy in aluminium foil 10 μ m thick. During the measurements the absorption coefficient was ≈ 0.1 corresponding to electron energy about 32 keV, the voltage pulse amplitude being 39 kV and magnetic field 0.2 T. The peculiarity of these measurements had to do with a decreasing longitudinal electron pulse caused by spiral-line electron motion in the magnetic field.

The beam dimensions were measured by producing its imprint on photo-film, photo-paper and thin metallic foil in two cases: 1) for cathode diameter 5 mm and 2) for cathode diameter 8 mm. The beam had annular transverse cross-section. In the first case, the beam outer diameter (OD) was 9.5 mm and its inner diameter (ID) 5.5 mm ($U=40$ kV, $H=0.3$), in the second one, its OD was 15 mm and ID - 9 mm ($U=40$ kV, $H=0.25$ T).

Upon increasing the voltage pulse duration, it was observed that current grew in the beam current pulse which exceeded the secondary emission current pulse amplitude by a factor of 1.5-2.0 and had a serrated top. Concurrently, the chamber pressure grew from $3.0 \cdot 10^{-5}$ Torr to $1.0 \cdot 10^{-3}$ Torr. From our view-point this is associated with gas desorption from electrode surfaces under the impact of bombarding electrons, and, as a consequence, with development of breakdown in the anode-cathode gap [2]. In order to preclude this undesirable phenomenon one has condition and heat the electrodes in vacuum.

In all our results demonstrate the feasibility on construction of a powerful cold-cathode electron gun with long pulse duration.

REFERENCES

- [1] S.A.Cherenshchikov "The multipactor emission of electron in the cold - cathode - magnetron gun". Abstract to reports of 13-Th conference at charge particle accelerators. JINR, Dubna (13-15 October, 1992), p.143.
- [2] L.V.Tarasova, V.G.Kalinin "Excitation of Electric Breakdown in high vacuum using a heat pulse". Zhurnal Tehnicheskoi Fysiky, 36, 2148-2153, 1966.

SECONDARY EMISSION IN COLD-CATHODE MAGNETRON INJECTION GUN

S.A.Cherenshchikov, A.N.Dovbnya, A.N.Opanasenko,
National Science Center, Institute of Physics & Technology, Kharkiv, 310108 Ukraine.

Abstract

The experiments of secondary emission in the magnetron injection gun and using of such a gun in electron linear accelerator are described. Up to now it was attained 65 amperes of beam current in short-pulse regime of the gun and 3 milliseconds of pulse duration in the low current regime. Characteristics of the gun operating in the secondary emission regime and the methods of calculating it are added. Main advantages of this regime may be long life time of the gun and high stability of beam current at employing purely-metal cathodes. Prospects of using the gun in the secondary emission regime in linac technology (mainly in high power RF-sources) are discussed.

I. EXPERIMENT AND RESULTS

The magnetron injection gun is a well known device. The experiments with the cold-cathode devices of such a type are known too [1]. We describe some new experiments with the cold-cathode magnetron injection gun that are made in our institute [2-6].

The representation of the gun are shown in Fig. 1.

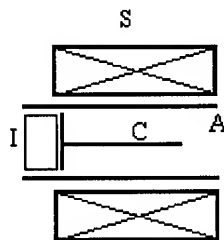


Figure 1: Schematic representation of the cold-cathode magnetron injection gun. S is the solenoid, A and C are the anode and cathode accordingly, I is the insulator.

It was established that if between the anode and cathode a short pulse of voltage (several tens nanoseconds duration and several tens kilovolt amplitude) is applied, then the gun will generate the short pulse of an electron beam. If the magnetic field is less than its value at which return of the electrons to the cathode is impossible then the beam current will be absent. We had supposed that the cause of the beam current generating was the secondary electron emission. Later the investigation confirmed this idea. For example, long-pulse regime (3000 μ s) had been obtained [5]. Such a regime is impossible at plasma explosion phenomenon at the cathode. In Tab. 1 it is shown the regimes of the gun operation and the parameters of the beam. Further on we will call the gun

operating in the regime secondary emission a secondary-emission magnetron-injection gun (SEMIG).

In process of the investigations [6] it was observed the possibility of controlling (switching) SEMIG. At the very small but quick variation of the gun voltage the deep pulse modulation of the beam with the modulation frequency about 200 MHz and the pulse duration 1 ns was noted. The pulse current reached 12 A at 60 kV voltage. More smooth variation of the gun voltage did not cause the beam modulation and the current behaved in accordance with the C-V law (see Fig. 2).

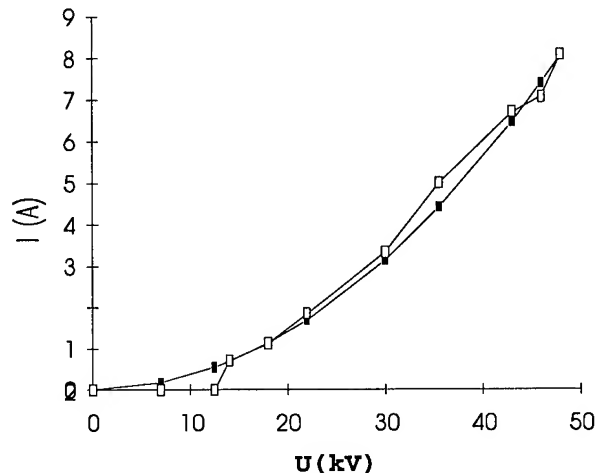


Figure 2: Current-Voltage (C-V) performances of SEMIG at 0.135 T magnetic induction. The transparent squares are the experimental points, and the shaded squares are corresponded to the approximation using the quadratic parabola [3].

The full control effect is reached by possibility to drive the energy of back electron bombardment and then the control of the secondary emission is acquired, too.

SEMIG was also tested as the injector for the resonance linac of S-band (3 GHz) [4]. The gun was located near RF-buncher so that RF-field could influence the gun work. In the case of the RF-field absence, it was obtained and accelerated the short electron pulses with 20 ns duration and 0.5 A current at 20 A current from the gun. Presence of RF-power in the buncher allowed to generate the more lengthy beam pulse up to 1 μ s with 20 mA accelerated current at 1 A current from the gun. Such regime was observed in narrow interval of the magnetic fields corresponding the frequency of electron cyclotron resonance. It should be noted that the low acceptance of particles in acceleration was because of the insufficient voltage on the gun.

Table 1. SEMIG's experimental regimes of operation.

Cathode material	Gun voltage kV	Beam current A	Current density A/cm ²	Beam diameter mm	Pulse duration μs	Repetition rate Hz	Magnetic induction T	Pub. year, [ref.]
Copper	68	12	20	9	0.01	single	0.19	1991 [2]
Copper	48	8	10	8	1.3	single	0.14	1992 [3]
Copper		20, (1.0)			0.02, (1.0)	50, (50)		1993 [4]
Stainless-steel	10÷150	0.005÷65			0.4÷3000	3÷50	...÷0.29	1994 [5]

II. METHOD OF CALCULATION

On the base of the scale method of modeling for magnetron gun with cylindrical electrodes [7], it was derived the following relationships of beam current I and beam diameter D_b depend of diameters of cathode D_c , anode D_a , magnetic field B and gun voltage U :

$$I = C_1 \frac{U^2}{B D_c \ln^2(D_a / D_c)}, \quad (1)$$

$$D_b = D_c + C_2 \frac{U}{B^2 D_c \ln(D_a / D_c)} \quad (2)$$

C_1, C_2 are constants extracted from experimental data and depending on emission properties of cathode materials used.

As shown in Fig. 2, the experimental current-voltage characteristic corresponds to the formula (1) quite accurately. The preliminary estimates showed that the beam current dependence on the magnetic field corresponds to the formula (1) qualitatively. That way, it is possible to calculate the gun parameters at not very distinctive values of the magnetic field. It should be marked, with increasing of the magnetic field the measured beam current was more then calculated by (1).

III. ADVANTAGE OF SEMIG

After applying of full voltage to SEMIG the speed excitation of secondary-emission current allows to produce a very short beam pulse directly from the gun. Apart from that, out estimates indicated that secondary emission from pure metal may provide higher current densities then those in thermionic or photo-emissions at the same energy inputs. This observation gives hope for production of high current densities that are otherwise precluded by cathode destruction from evaporation or pulsed heating [8]. To date, secondary-emission current density more than 50 A/cm² already produced [9]. Associated with this fact is the principal advantage of secondary-emission metallic cathodes, i.e. their long life times, exceeding in our appraisal 100,000 hours. The underlying physical reason for this is the impossibility of principle of occurrence of electron-stimulated cathode material desorption, and, accordingly, its destruction in case of

the metallic connection loading at bombarding electron energies sufficient for secondary-emission to occur [10].

IV. OUTLOOK ON APPLICATION OF SEMIG IN HIGH POWER RF-SOURCES

In review on secondary electron emission sources [11] it was shown the SEMIG had the best beam parameters of current density and total current among secondary emission guns. In the review the secondary emission gun was consider as an alternative of the thermionic magnetron-injection gun [12] in the high power RF-source project, the Immersed Field Cluster Klystron [13]. As shown in the report [7] the application of SEMIG may be solution of the problem of increasing of a cathode life time.

As shown above, the main advantage of the SEMIG in comparison with a traditional thermionic magnetron-injection gun is a possibility to obtain high current density as well as a very long life time (above 100,000 hours) of a secondary emission metallic cathode, simultaneously. Apart from that, insensibility of a purely metallic cathode (platinum) to poisoning and to atmospheric air allows to create an accelerator and RF-source with common vacuum system, that cuts off the problem of an exit window.

Magnetron gun is already employed in klystrons and gyrotrons. Such devices with the proposed SEMIG can have the all above advantages.

Observed current modulation may be the base for creation of high power electron tubes with high efficiency. In relatively low frequency band it may be a prototype of injectrons and klystrodes and for shorter waves it may be a klystron or gyrotron. Injectrons using SEMIG may be the base for creation of highly efficient high voltage pulse modulators with high repetition frequency.

REFERENCES

- [1] M.Friedmun and M.Ury, "Microsecond duration intense relativistic electron beams". The Rev. Sci.. Instrum., vol. 43, No. 11, 1972, p.1659-1661.
- [2] V.S.Balagura, B.G.Safronov, S.A.Cherenshchikov. "Short-pulses electron guns with no heating cathodes for linacs". Abstract to reports of 12-Th. all-Union seminar of charge

particle linear accelerators. (Kharkov, 28-30 of May 1991) Kharkov, p.40, 1991. The article with the same title: Vopr. At. Nauki i Tekh. Ser. Yadernofiz. Issled (Teor. Exp.) (Kharkov) 14(25), p.48-51, 1991.

[3] S.A.Cherenishchikov. "The multipactor emission of electrons in the cold-cathode-magnetron gun". Abstract to reports of 13-Th. conference of charge particle accelerators. JINR, Dubna (13-15 October, 1992) p.143. (The full text of the report will be published in the proceeding of that conference.)

[4] G.M. Ivanov, S.A.Cherenishchikov " The magnetron gun with no heating cathode as an electron source for a resonance electron liner accelerator". Abstract to reports at 13-Th. Kharkov seminar of charge particle linear accelerators. (Kharkov, 25-28 of May 1993) Kharkov, p.27, 1993.

[5] S.A.Cherenishchikov, G.M.Ivanov, B.G.Safronov "Secondary-emission crossed-field discharge as an electron source with a cold cathode". Abstract to reports of EPAC, (London, 27 June to 1 July 1994).

[6] B.G.Safronov S.A.Cherenishchikov "Possibility of full manipulation with high speed in a cold-cathode magnetron gun". Abstract to reports at 13-Th. Kharkov seminar of charge particle linear accelerators. (Kharkov, 25-28 of May 1993) Kharkov, p.27, 1993.

[7] S.A.Cherenishchikov, A.N.Opanasenko, A.N.Dovbdya, V.V. Zakutin, "Secondary emission magnetron injection gun as high current durable electron source". Proceeding of the Workshop on Pulsed RF Sources for Linear Colliders. (RF-94), Montauk, US, October 2-7, 1994.

[8] V.F.Kovalenko, Thermally-physical processes and electrically-vacuum devices: Moscow: "Sov. radio", 1975.

[9] I. M. Vigdorchik, V. D. Naumenko, V. P. Timofeev, "The secondary-emission-cold-cathode magnetrons of the millimeter wavelength". Reports Academy of Sciences, Ukrainian SSR, Ser.A, 1 7, p. 634-637, August, 1975.

[10] V.N.Avgeev, Yu.A.Kuznecov, B.V.Yakshinskiy, "Electron stimulated desorption of atoms of cesium from oxidized wolframite.". Solid State Physics , vol. 24, No. 24, 1982, p. 349-355.

[11] S.A.Cherenishchikov, A.N.Opanasenko, A.N.Dovbdya, V.V. Zakutin, "Review of secondary electron emission sources". Work supported by of the US Department of Energy, contract WC-716344 (BNL).

[12] H.Wang, R.Palmer, J.Gallardo, "The magnetron-injection-gun design for the cluster klystron". International Workshop on Pulsed RF Power for Linear Colliders (RF-93), Dubna, Russia, July 5-9,1993.

[13] R.B.Palmer, W.B.Herrmannsfeld K.R.Eppley "An immersed field cluster klystron", Particle Accelerators vol. 30 No. 1-4 1990 p. 197-209.

DESIGN OF A HIGH CHARGE CW PHOTOCATHODE INJECTOR TEST STAND AT CEBAF

H. Liu, D. Kehne, S. Benson, J. Bisognano, L. Cardman, F. Dylla, D. Engwall, J. Fugitt, K. Jordan, G. Neil, D. Neuffer, C. Sinclair, M. Wiseman and B. Yunn

CEBAF, 12000 Jefferson Avenue, Newport News, VA 23606, USA

A 10 MeV high-charge CW electron injector test stand has been designed for the CEBAF UV FEL driver accelerator. It consists of a 500 kV DC photocathode gun, a 1500 MHz room-temperature buncher, a modified CEBAF cryounit (quarter cryomodule) with an SRF accelerating gradient of ~ 10 MV/m, two solenoids in the 500 kV region and an achromatic, non-isochronous injection transport line delivering 10 MeV beam to the driver accelerator. Experimental work is in progress toward establishing design system performance.

I. INTRODUCTION

Based on a 500 kV DC laser gun [1] and the 1500 MHz SRF technologies established at CEBAF, a 10 MeV CW high charge electron injector has been designed and is being built for a recirculating, 200 MeV SRF accelerator [2] which will drive kW-level industrial UV/IR FELs [3]. The design approach we have adopted is shown schematically in Fig. 1. It is composed of a DC laser gun, a 1500 MHz room-temperature buncher, two solenoids, a cryounit containing two CEBAF SRF cavities, and an injection line consisting of a "zoom" lens (4 quads) and a 3-magnet achromatic, non-isochronous bending system. The injection line design is discussed elsewhere [4].

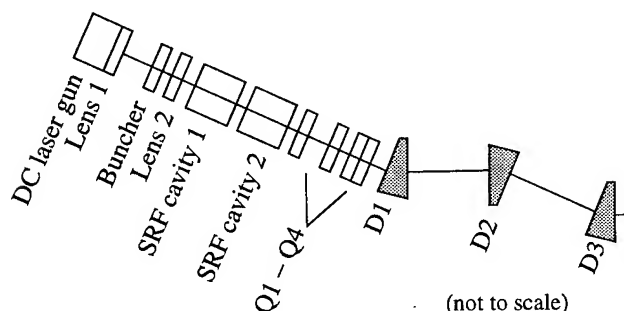


Fig. 1 Block diagram of the CEBAF FEL injector.

The design goal is to achieve the smallest practical transverse and longitudinal beam emittances at the end of the injector with a 135 pC charge/bunch. Electrons originate from a GaAs photocathode illuminated by a train of 60 ps (4σ) laser pulses. The design was carried out through extensive space-charge-dominated beam dynamics calculations consistently from the cathode to the entrance of the accelerator using a point-by-point space charge algorithm [5]. The modeling results show that this injector should be an excellent high-brightness source for an FEL, and that the requirements listed in Table 1 may be met. The details of the system components and performance modeling will be presented in the following sections.

tions.

Table 1 Requirements on the CEBAF FEL injector

Beam parameters	Requirements
Momentum (p)	10 MeV/c
Charge/bunch (Q)	135 pC
Repetition rate (f_p)	37.43 MHz
Average current (I)	5 mA
Tran. norm. emittance (ϵ_{nrms})	8π mm mrad
Longitudinal emittance ($\epsilon_{\phi rms}$)	20π keV-deg
Bunch length (σ_l)	1.5 ps
Matching conditions ($\beta_x/\beta_y, \alpha_x/\alpha_y$)	30/30 m, 0/0

II. HARDWARE COMPONENTS

The performance of the 500 kV photoemission gun is the most technically challenging aspect of this injector. The gun design is based on experience from photoemission gun studies at SLAC [6] and the University of Illinois [7]. The gun electrode structure permits the electric field at the photocathode to be varied between 6 MV/m and 10 MV/m at a constant gun voltage of 500 kV, and can be high voltage processed to approximately 600 kV with the available equipment. The gun is being assembled in the Test Lab where the original CEBAF injector was successfully developed.

Operation of the gun will involve activating a GaAs negative electron affinity (NEA) photocathode in the gun structure proper. This activation requires the application of cesium to the cathode. If this cesium application creates difficulties in maintaining the cathode field strength, we will either fabricate the cathode outside the gun structure, and transfer it to its operating position through a load lock system, or improve the high-field performance of the cathode electrode by appropriate surface treatment.

Ions formed in the immediate vicinity of the photocathode are accelerated back to the cathode, and can cause loss of quantum efficiency through either sputtering or damage to the cathode material. This problem is reduced by minimizing the vacuum pressure in the vicinity of the cathode. The vacuum in the cathode area will be established by non-evaporable getters located in the immediate vicinity of the cathode.

The photocathode will be illuminated by a commercially available CW mode-locked Nd:YLF laser [8]. The fundamental laser light is frequency-doubled to 527 nm in an LBO crystal. The laser provides over 5 W at 527 nm in a mode-locked pulse train at 74.85 MHz. The repetition rate will be halved electro-optically to provide a 37.425 MHz pulse train to the photoemission gun. The 2.5 W of useful laser light will support the required 5 mA average current

for cathodes with quantum efficiencies greater than 1%, assuming losses of no more than 50% in the optical chopping and transport systems. Typical GaAs photoemission cathode quantum efficiencies are an order of magnitude greater than this at 527 nm wavelength, providing a reasonable operating margin.

The two identical solenoids are being fabricated. The design was carried out using POISSON/PARMELA. The spherical aberration from these lenses is negligible. The first solenoid has been placed close to the anode to control the divergent beam out of the gun. It is water-cooled to prevent heat conduction to the gun. Each lens may be operated a factor of 2 stronger than the nominal design requirement.

The 1500 MHz buncher and its associated RF power and control system are under development. The single cell buncher cavity is similar to the fourth cell of the CEBAF capture section, but has a larger inner-bore diameter for the larger beam at this location [9].

The two cryounit cavities must provide ~ 10 MV/m at Q_0 of 5×10^9 , both values twice the original CEBAF cavity specification. The cavities are modified to handle the HOM (high order mode) heating, and the increased RF power needed to accelerate the high average current beam. In the injector, each of the four HOM load absorbs 7.5 W of power, sixty times that of CEBAF. This power is dissipated in the 50 K thermal shield rather than the 2 K helium bath. RF shielding is added to the stainless steel bellows and gate valves in the cryounit to minimize beam impedance and heating effects. Since the RF power needed in the injector is fourteen times that of CEBAF, the CEBAF style polyethylene warm RF vacuum window is replaced with a ceramic window.

III. PERFORMANCE MODELING

Numerical calculations were needed for: (1) the design of some system components like the solenoids and the injection line magnets; (2) the determination of the optimal element-to-element distances in the system; and (3) the prediction of the system performance. An appropriate space charge algorithm was required for all these tasks.

PARMELA was the skeleton code we used for overall beam dynamics calculations with space charge included consistently from the cathode to the end of the injector. The electric and magnetic field data were provided by other auxiliary codes. The fields in the gun and in the solenoids were calculated using POISSON, which ensured that the field aberrations were included. Mafia was used for calculating the 3-D electromagnetic fields in the SRF cavities [10]. The skew quad effect and steering effect were thus included. The injection line was designed using DIMAD and PARMELA from a large number of iterations between zero-charge and full-charge runs.

A point-by-point space charge algorithm [5] has been used in designing this injector. It is time-consuming but does not assume cylindrical symmetry for the beam. However, for this algorithm, it is crucial to choose properly the particle size factor. This concept simply comes from the fact that when two macroparticles overlap, the charge carried with the source particle must be reduced to account for the shielding effect. A too small particle size factor may result in significant noise in numerically calculating the

space charge fields of a beam [11]. This numerical noise may cause artificial emittance growth, and must be eliminated to obtain a more reliable system layout and a more accurate prediction of the system performance. To size the macroparticles properly, the algorithm was bench-marked against ISIS [12] and MASK [13]. The details of benchmarking will be published elsewhere [14].

The simulated performance of this injector is given in Table 2. As is seen, both transverse and longitudinal emittances are within the requirements by a factor of nearly 2. The simulated rms bunch length of 0.5 ps is within the requirement by a factor of 3. This 0.5 ps is the space-charge-limited minimum bunch length with perfect axial matching [15, 16]. One can trade bunch length for energy spread within at least a factor of 2 by adjusting the degree of axial matching into the bending system, while keeping both the transverse and longitudinal emittances approximately constant.

Table 2 Simulated injector performance

Beam parameters	Sim.	Req.	Units
Momentum	10	10	MeV/c
Charge/bunch	135	135	pC
Tran. norm. rms emit.	4.4	8	π mm mrad
Longitudinal rms emit.	11	20	π keV-deg
Bunch length (rms)	0.5	1.5	ps

The simulated performance in Table 2 was obtained with 8000 macroparticles, and with space charge included through the entire system from the cathode to the end of the injector. The following initial beam parameters were used: gun voltage $V_0 = 500$ kV, DC field gradient at the cathode $E_0 = 10$ MV/m, laser spot size $d_0 = 2$ mm (diameter, $4\sigma_r$) at the cathode, laser pulse length $\Delta t = 90$ ps ($6\sigma_r$); the thermal energy distribution of the electrons emitted at the cathode was assumed to be Gaussian with a mean kinetic energy of $T_e = 0.3$ eV and an rms energy spread of $\sigma_e = 0.1$ eV. System sensitivity studies and alternative operating point studies were conducted as well; see [17] for the details.

IV. EMITTANCE GROWTH

Emittance growth is one of the major concerns with this design. To obtain the best emittance performance for this injector with all the other requirements satisfied, a prescription of minimizing the number of crossovers (very small beam waists) along the system has been adopted. It is obvious that wherever a crossover occurs, more thermal energy will be introduced in the beam due to Coulomb interactions, and beam emittance will increase. The beam phase space distributions may bifurcate after a crossover [13, 18], causing additional emittance growth. With our prescription, the emittance growth from the gun anode to the end of the injector has been minimized to 2π mm mrad for the transverse normalized rms emittance and 4π keV-deg for the longitudinal rms emittance.

In Fig. 2, we show the evolution of various beam properties along the system from the gun anode to the

entrance of the accelerator. The simulations started from the cathode with the initial beam parameters described in the previous section, and continued through the gun, the buncher, the cryounit and the injection beam line to the entrance of the accelerator. With those parameters, the initial transverse normalized rms thermal emittance at the cathode is 0.5π mm mrad. Over the 9-cm distance from the cathode to the gun anode, the emittance increases from 0.5 to 2.3π mm mrad, as shown in Fig. 2, with the beam being accelerated to 500 kV. The beam is strongly divergent before being focussed by the first solenoid located 24 cm from the cathode. In this region, a crossover or electrons trajectory crossing occurs.

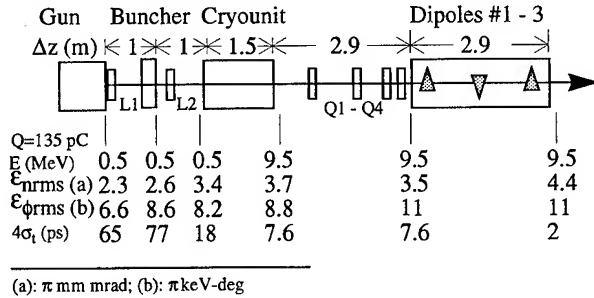


Fig. 2 Beam property evolution along the system

The beam is collimated between the two solenoids. To match the beam into the cryounit, suitable beam conditions must be set up prior to the cryounit. This requires appropriate beam dimensions and correlations in both transverse and longitudinal phase spaces. On the other hand, to avoid emittance growth due to various nonlinear RF field effects, the beam must be three-dimensionally compressed into a small size prior to the cryounit. In this region, the repulsive space charge fields significantly counteract the compression under the external forces from the second solenoid and the buncher. The second crossover occurs between the buncher and the cryounit. As a result, the emittance increases from 2.6 to 3.7π mm mrad with the beam being accelerated to ~ 10 MeV at the exit of the cryounit. As the beam moves through the 3-magnet bending system, the emittance further increases to 4.4π mm mrad at the end of the injector due to space-charge-induced momentum variations [4, 19].

V. A PARAMETRIC COMPARISON

We complete this paper with a parametric comparison of our design with two other DC laser guns in Table 3. The symbols in the first column represent the gun voltage, DC field at the cathode, charge/bunch, diameter of the cathode, diameter of the laser spot on the cathode, rms laser pulse length, repetition rate, and average current. The CEBAF design is characterized by high voltage, short laser pulse length, moderate charge/bunch, and high average current. The SLAC design [20] is characterized by extremely high charge, low voltage, and very long laser pulse length. The design from Ref. [21] is characterized by low average current, moderate pulse length, moderate charge/bunch and low gun voltage.

Table 3 Parametric comparison for DC laser guns

	CEBAF	SLAC	Ref. [21]	Units
V_0	400-500	120	30 - 60	kV
E_0	6 - 10	1.8	15	MV/m
Q	0.07 - 0.2	16	0.02 - 0.6	nC
d_{cath}	25	14	unknown	mm
d_{emit}	2 - 6	14	2	mm
σ_t	15	500	38	ps
f_{rep}	37 MHz	120 Hz	10 Hz	-
\bar{I}	5 mA	4 μ A	0.2 - 6 nA*	-

* The design average DC current is 5 A in Ref. [21].

We plan to complete the gun performance characterization by the end of this year. This will provide the foundation for us to develop the full injector and also reveal interesting space charge beam physics in our particular parameter regime.

We should note that this design may have other applications besides an FEL driver. One possibility worth studying is use as a source for polarized electrons for a linear collider, though the design would have to be scaled to higher charge.

We wish to thank B. Carlsten and T. Raubenheimer for discussions. This work was supported by the Virginia Center for Innovative Technology and DOE Contract # DE-AC05-84ER40150.

VI. REFERENCES

- [1] C. Sinclair, Nucl. Instr. Meth. A **318** (1992) 410.
- [2] D. Neuffer et al., these proceedings.
- [3] F. Dylla et al., these proceedings.
- [4] H. Liu and D. Neuffer, these proceedings.
- [5] K. McDonald, IEEE Trans. Electron Device **ED-35** (1988) 2052.
- [6] C. Sinclair, in *Advanced Accelerator Concepts*, AIP Conf. Proc. No. 156 (Amer. Inst. of Phys., 1987).
- [7] L. Cardman and D. Engwall, private communication.
- [8] S. Benson et al., these proceedings.
- [9] B. Yunn, CEBAF TN# 94-021.
- [10] Z. Li, private communication.
- [11] H. Liu, in *Computational Accelerator Physics*, AIP Conf. Proc. No. 297 (1994).
- [12] M. Jones and B. Carlsten, Proc. 1987 IEEE Part. Acce. Conf., IEEE Catalog No. 87CH2387-9 (1987) 139.
- [13] H. Hanerfeld et al., SLAC-PUB-4916 (1989).
- [14] H. Liu, to be published.
- [15] T. Raubenheimer, Workshop on 4th generation light sources, SSRL, 1993, p.263.
- [16] H. Liu, CEBAF TN # 95-004, 1995.
- [17] FEL Conceptual Design Report, CEBAF, 1995.
- [18] H. Liu et al., Nucl. Instr. Meth. A **358** (1995) 475.
- [19] B. Carlsten and T. Raubenheimer, Phys. Rev. E, **51** (1995) 1453.
- [20] H. Tang et al., Proc. 1993 PAC, p. 3036.
- [21] A. Aleksandrov et al., Phys. Rev. E, **51** (1995) 1449.

CANDELA PHOTO-INJECTOR EXPERIMENTAL RESULTS WITH A DISPENSER PHOTOCATHODE*

C. Travier, B. Leblond, M. Bernard, J.N. Cayla, P. Thomas
Laboratoire de l'Accélérateur Linéaire, IN2P3-CNRS et Université de Paris-Sud
Bât. 200, F-91405 Orsay

P. Georges
Institut d'Optique Théorique et Appliquée, Université de Paris-Sud, Bât. 501, F-91405 Orsay

Abstract

The CANDELA photo-injector is a two cell S-band photo-injector. The dispenser photocathode is illuminated by a 500 fs pulse from a frequency-tripled Ti:sapphire laser. In this paper we report charge measurements showing that the dispenser photocathode has a quantum efficiency as high as 10^{-3} . This efficiency decreases with a lifetime of 12 hours, but can be recovered by heating the cathode during 5 minutes.

I. INTRODUCTION

The CANDELA photo-injector is an RF gun made of two decoupled 3 GHz cells [1], [2], [3], [4]. The laser system used to illuminate the photocathode is a Ti:sapphire laser designed by the "Institut d'Optique Théorique et Appliquée" at Orsay [5]. CANDELA was first operated at the end of 1993 [6], with a copper photocathode. A maximum charge of 0.11 nC was extracted corresponding to an effective quantum efficiency of 5×10^{-6} . For laser fluences larger than 1 GW/cm^2 , very high charge can be produced (up to 35 nC), but in this case the pulse length is increased to 50 ns [7]. Since this "intense emission" process limits the maximum charge that can be obtained in the normal photoemission regime, we replaced the copper photocathode by a dispenser cathode that has a quantum efficiency more than 100 times better [8]. This paper presents the first results obtained with this cathode.

II. CATHODE CONDITIONING

The dispenser cathode (S-type) is normally used as a thermionic cathode in klystrons and electron guns for linear accelerators. The cathode we are using has a non-standard diameter of 9.2 mm, and was fabricated for us by THOMSON TTE (Velizy), according to their standard fabrication procedure. The cathode consists of a porous tungsten matrix impregnated with barium calcium aluminate (4 BaO , 1 CaO , $1 \text{ Al}_2\text{O}_3$). This W matrix is heated via a filament. A thin molybdenum jacket is used to diminish heat losses (see figure 1).

The details of the cathode mounting in the gun cavity have already been reported [3]. The RF contact is made via a tungsten spring. In order to keep the required cathode heating power at a reasonable level, the part of the cavity in contact with the spring,

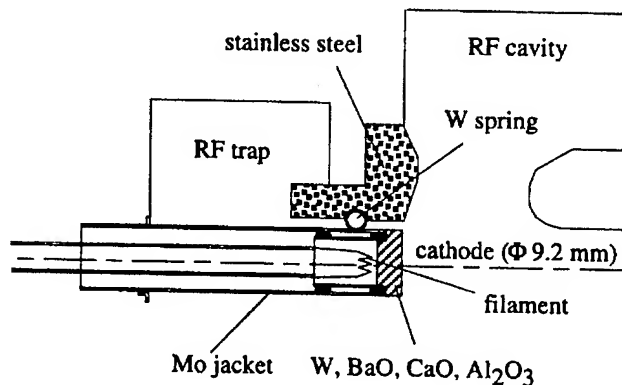


Figure 1. Schematic of the cavity with dispenser cathode

is made of stainless steel which has a low thermal conductivity (see fig. 1).

The cathode first needs to be conditioned to 1200°C , in order to break the alumina and oxides molecules, so that free atoms of Ba and Ca can diffuse to the surface. During this conditioning, one has to maintain a vacuum pressure not higher than 10^{-6} mbar. But since the outgassing is quite significant during this procedure, it can not be done inside the gun due to the limited pumping speed. However, since it was shown before that this cathode could sustain exposure to air without losses in photoemissive properties [8], the conditioning is made in a specific vacuum chamber, with a pumping speed of 400 l/s. After conditioning, which lasts for about 5 hours, the cathode is installed in the gun. This latter operation takes around one hour.

After the cathode installation, the gun is baked out at 150°C for three days. Then, the cathode should be slightly reconditioned. This is done by heating it to 1100°C for 5 minutes. This corresponds to a heating power of 56 W. These two operations should be done each time the gun and cathode have to be exposed to air.

III. LASER AND BEAMLIN

The laser is a Ti:sapphire laser described in reference [5]. It produces one single pulse (at 12.5 Hz), with an adjustable duration from 150 fs to 15 ps, and a maximum energy of $200 \mu\text{J}$ at 260 nm.

The laser synchronization and modelocking starter systems have been improved since the description given in reference [5]. Originally, the starting of the modelocking and the synchroniza-

*Work supported by IN2P3 and ULTIMATECH under contract number 90N89/0018

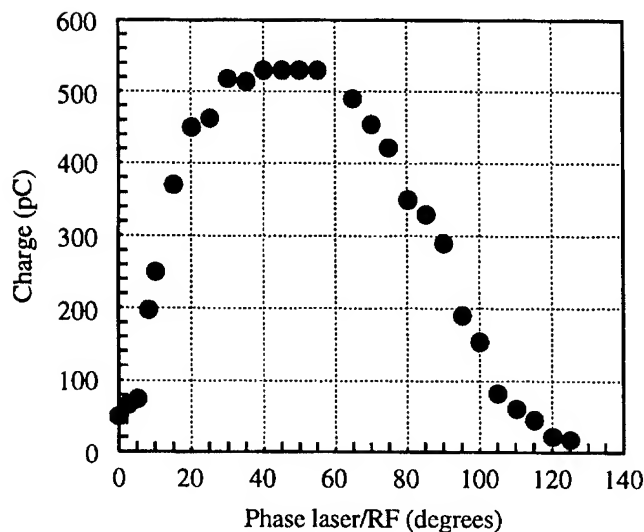


Figure 2. Charge vs. laser/RF phase

tion of the laser frequency with the RF master oscillator were made via a single piezo-electric transducer on which one of the mirrors of the laser oscillator cavity was mounted. These operating conditions were not very comfortable, since very often we lost the modelocking operation while trying to lock the laser to the RF frequency. To improve this situation, we decoupled the two functions. The modelocking starter is now made with a pair of oscillating Brewster plates [9]. The synchronization is still achieved via a piezo-electric transducer and the slow thermal drifts are compensated by a translation stage driven by a DC motor. This new system proved very efficient and reliable.

The beamline including the beam diagnostics devices is described in reference [7]. At the time of measurements presented here, the first wall current monitor located right at the gun exit was not available. The charge measurements reported in the next sections were made with the coaxial Faraday cup situated about 1 m downstream of the gun, and an integrator. They were obtained in the following conditions:

- the laser pulse length is set to the sub-picosecond regime
- the laser illuminates the cathode with a 54.5 degrees angle with respect to normal incidence
- only the first cell of the gun is powered with 1.06 MW, which corresponds to a peak on axis field of 68 MV/m and a cathode field of 50 MV/m
- the relative phase between laser and RF is chosen to optimize the extracted charge. The typical dependence of the charge with this phase is shown on figure 2.

IV. QUANTUM EFFICIENCY AND LIFETIME

Figure 3 shows the measured charge as a function of the laser energy on cathode. The slope of these curves gives the effective quantum efficiency (QE) including the potential losses in the beam transport. Two different curves corresponding to two different situations are shown. The lower efficiency curve is obtained with the photocathode at room temperature after several hours spent in the gun at a residual static vacuum pressure better than 10^{-10} mbar (a few 10^{-9} with RF on). In these conditions

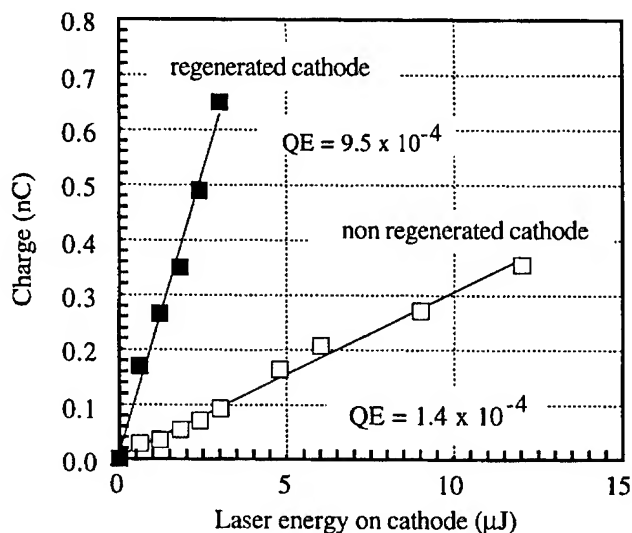


Figure 3. Quantum efficiency of dispenser cathode

the efficiency is just slightly above 10^{-4} . In order to improve the efficiency by almost one order of magnitude, it is necessary to regenerate the cathode prior to operation. This is done by heating it to around 700°C , during five minutes (this corresponds to 25 W of heating power). After letting the cathode cool down during 15 minutes, it is ready to operate. In these conditions, the QE almost reaches 10^{-3} , which is better than any pure metallic cathode¹. Due to the pollution caused by the residual gas, the QE then drops with time. If the lifetime is defined as usual as the time necessary to decrease the QE by a factor $1/e$, the cathode operated at cavity temperature (31°C), has a lifetime of only two hours. However, the lifetime is improved drastically by slightly heating the cathode during operation. The temperature should of course stays below the thermoemission threshold. In our case we use 6 W of heating power. Under these conditions, the lifetime is increased to more than 12 hours. At any time one can recover the original QE by regenerating the cathode according to the procedure described above.

V. SATURATION

The charge that can be extracted from the photocathode is limited by space charge effects. When the charge increases, the self field of the bunch can balance the accelerating field, so that no more charge can be extracted. Since the laser transverse profile is not uniform, but closer to Gaussian, the charge reaches the limit in the center of the cathode first. As explained by Hartman et al. [10], the charge can still be increased till the limit is reached also on the edge. See figure 4 for the results corresponding to the dispenser cathode with and without regeneration.

During these experiments, we did not have any camera to monitor the laser transverse profile. However, by fitting the experimental data of figure 4 with the theoretical model of the saturation effect as described in reference [10], it is possible to infer the spot size. Figure 4 shows the result of this fit assuming a laser profile with a gaussian distribution truncated at $\pm 3\sigma$.

¹ Magnesium for example has an efficiency of 5×10^{-4} [11]

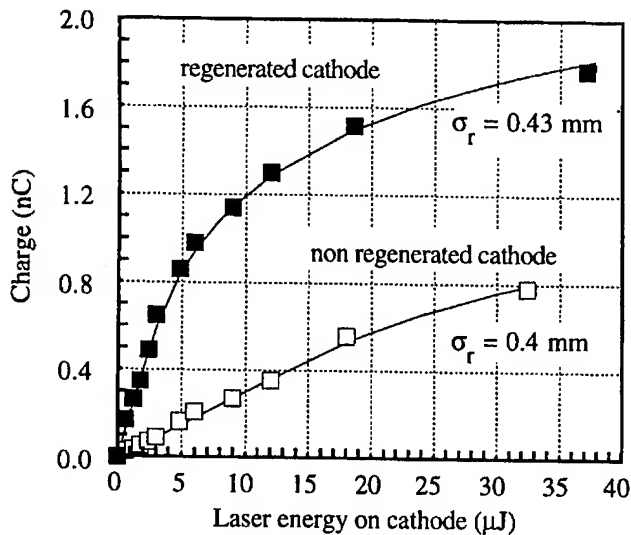


Figure 4. Charge saturation

VI. FUTURE PROSPECTS

In the near future, the other parameters of the beam will be measured, especially the pulse length and emittance. The pulse length will be measured by observing, with a streak camera (resolution < 2 ps), the Cerenkov light produced by a 300 μm thick sapphire. The emittance will be measured both with the three gradient method and with the "pepper-pot" method.

VII. CONCLUSION

This paper has described the first use of a dispenser photocathode in a S-band RF gun. It is shown that this type of cathode when properly conditioned and operated, has a quantum efficiency of 0.1 %, which is better than that of pure metallic cathodes. The lifetime of this cathode is larger than 12 hours, and the original quantum efficiency can be recovered in 20 minutes, by heating. A total charge of 1.8 nC was measured, only limited by saturation effects due to the relatively small spot size.

VIII. ACKNOWLEDGEMENTS

The design and construction of the CANDELA photo-injector has involved several people, who should be duly acknowledged. We also thank J.P. Chamberret (ENSTA/LOA) for the loan of the oscillating Brewster plate system. Finally, a special thanks for T. Garvey who carefully read this manuscript.

References

- [1] C. Travier, J. Gao, Proc. European Particle Accelerator Conference, Nice, June 12-16, 1990, pp. 706-708.
- [2] C. Travier, J. Gao, H. Liu, Proc. Linear Accelerator Conference, Albuquerque, September 10-14, 1990, pp. 602-604.
- [3] J. Gao et al., Proc. European Particle Accelerator Conference, Berlin, March 24-28, 1992, pp. 1020-1022.
- [4] C. Travier et al., Nucl. Instr. & Meth. B89 (1994), pp. 27-32.
- [5] P. Georges et al., Proc. Particle Accelerator Conference, Washington, May 17-20, 1993, pp. 3053-3054.

- [6] C. Travier et al., Proc. European Particle Accelerator Conference, London, June 27 - July 1, 1994, pp. 1462-1464.
- [7] C. Travier et al., Proc. Linear Accelerator Conference, Tsukuba, August 21-26, 1994.
- [8] B. Leblond, Nucl. Instr. & Meth. A317 (1992), pp. 365-372.
- [9] Mira 900 data sheet, Coherent Inc.
- [10] S.C. Hartman et al., NIM A340 (1994), pp. 219-230.
- [11] X.J. Wang et al., NIM A356 (1995), pp. 159-166.

A Multi-Cell RF Photoinjector Design*

Sanghyun Park

Department of Physics, University of California
Los Angeles, California 90024-1547

Abstract

A research and development effort has been underway to realize a high-brightness, low-emittance rf photoinjector to produce 1 to 3 nC bunch of photoelectrons at an energy of up to 20 MeV with a normalized rms emittance of 10π mm-mrad or less. It consists of a half cell at the photocathode and seven full cells, operating in 2856 MHz, π -mode, standing wave. Numerical calculations with POISSON/SUPERFISH and PARMELA codes indicate that the design goal can be achieved within realistic constraints on mechanical device tolerances and rf source availability. The latest among the series of numerical models is somewhat similar to the SLAC type accelerator in geometric dimensions, although the device characteristics are vastly different.

I. INTRODUCTION

In order to raise the gain of a free-electron-laser oscillator/amplifier, or to increase the luminosity in high-energy particle colliders, it is compelling to produce a low-emittance, high-brightness electron beam. Since the emittance is approximately an invariant in a drift space, it must be kept low during acceleration, especially when the electrons are non-relativistic. The BNL type $1\frac{1}{2}$ -cell gun has a dipole mode caused by the side coupling of rf to the cells which gives rise to emittance growth. The BNL/SLAC/UCLA rf gun [1] is believed to improve the situation by eliminating the asymmetry at the first cell and through higher gradient at the cathode. The energy at the exit, however, is still too low to drive even an infrared FEL so that one needs to append a linac, standing or travelling wave, to boost the energy at the cost of structural complexity and added expense. The AFEL [2] of LANL is a compact system without an additional booster linac, and it is a complicated structure. Even fabricating a copy of it will be quite involved. Therefore it is desirable to design a simple system that meets the performance requirements. The design reported here contends to be such a device.

II. BOUNDARY CONDITIONS

Unlike an accelerator with open boundaries both at the entrance and the exit, an injector has a longitudinally asymmetric boundary condition. The field balance among the cells can be achieved by adding a half cell at the end [3]. This turns out to be quite artificial; when an opening of adequate size is made for particle exit, the broken symmetry forces the rf power to accumulate near the cathode [4] and it decays out as one moves away from it. Similar field unbalance can be seen at the photoinjector of the APEX [5] system. The recipe to avoid this problem is as follows. A number of full cells are connected in series and a half

Overall length	42.0 cm
Full cell length	5.250 cm
Cell diameter	8.2220 cm
Last cell diameter	8.2006 cm
Iris diameter	2.400 cm
Iris radius of curvature	0.3200 cm
Disk thickness	0.6400 cm

Table I
Geometric dimensions of the $7\frac{1}{2}$ -cell injector

cell is added at either end, as mentioned above. Adjust the inner radius of all cells by the same amount for a correct resonance frequency and mode separation. Take one full cell out. This has an individual resonance frequency f_r , different from that of the assembly. Prepare a full cell with an identical aperture to others on one side, but with a long drift, which serves as an rf choke as well as a beam exit, on the other. Tune the frequency of this cell to f_r using the inner diameter as a control knob. Then add to the rest of the assembly. A fine tuning of the last cell must be done to maintain the overall resonance frequency and field balance.

III. SUPERFISH RESULTS

The geometric parameters obtained through the procedures described above are shown in Table I, and the distribution of the accelerating field along the axis is shown in Fig 1. With the dimensions shown above as input, the SUPERFISH code [6] produced the field distribution inside the cavity that can be approximately represented by

$$E_z(z) = E_0 \sin(kz)$$

where the axial field $E_0=97$ MV/m at $r = 0$ for the input power of 24 MW, $k = 2\pi f_0/c$ is the wavenumber for the frequency $f_0=2.856$ GHz. The electrical characteristics of the design is summarized in Table II.

IV. CONSIDERATIONS AT HIGH POWER

The disk thickness is comparable to those in the SLAC travelling wave structure, and much thinner than either BNL [7] or Grumman/BNL gun [8] disks. The latter, a $3\frac{1}{2}$ cell injector, has water channels to remove the dissipated heat from the disks at high duty cycle. The present design has the surface power dissipation of about 3 kW/cm^2 around the iris, and twice as much at the rest of the disk. This rate goes up to 15 kW/cm^2 at the wall with the input power of 24 MW. With a duty cycle low enough, say 10 pulses per second, cooling and tuning by temperature control will be less of a problem. If the maximum surface field is too high at the operating rf power level, it may be the source of dark

*Work supported by the U. S. Department of Energy, under Grant DE-FG03-92ER-40493

Resonance freq.	2856 MHz
Separation to next mode	1.3 MHz
Cavity Q , unloaded	17,200
Transit time factor	0.737
Effective shunt impedance	45.3 M Ω /m
Input rf power	24 MW
Accel. field at cathode	97 MV/m
Max. surface field	134 MV/m

Table II

Summary of SUPERFISH results for the device, with the driving input rf power of 24 MW

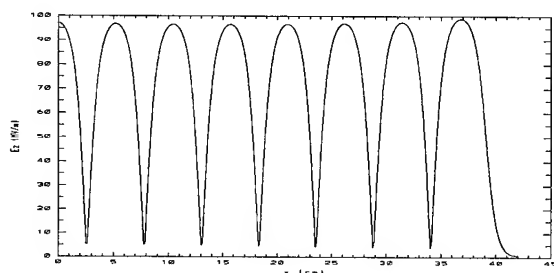


Figure 1. Magnitude of the accelerating field in MV/m for $z=0$ to 45cm. The full scale is 100MV/m, and the last cell ends at 39cm.

current, or it may cause a breakdown. From the SUPERFISH result, it is about 130 MV/m, not too high to be a cause for concern. Another factor of practical importance is the available length of the high-power rf pulse. The fill time is, in the case of a standing-wave structure, $\tau_{fill} = Q_L/\omega$ where Q_L is the loaded Q . If the rf power is critically coupled, Q_L is one half times the unloaded Q , leading to a fill time of about $0.5 \mu s$ at $\omega/2\pi=2.856$ GHz.

V. PARTICLE DYNAMICS

With a photoelectron bunch of a few nanoCoulombs over the bunch length of a few picoseconds, the space-charge forces become dominant in the emittance growth. For a photoinjector, a compensation is done by applying a solenoidal focusing field over the first few cells. In this case the axial field is nulled out at the cathode by a bucking coil. Although this method was shown to be effective, it is not a part of the injector. It can be added on for the optimization of the beam characteristics. The phase of the rf when the photoelectrons are emitted is an important parameter. Again, it can be experimentally chosen for either highest particle energy or the lowest energy spread. Without regard to these points, the PARMELA code was used for the purpose of demonstration. For an electron bunch of 3 nC, 2 mm radius, and 3.5 ps length, 2000 particles were followed throughout the 40 cm long injector followed by the drift space of 60 centimeters. At about $z=55$ cm, the particle losses begin to occur and continues to the end, where about 80% of the charge is left. The initiation of the particle loss is accompanied by a slight increase in the transverse rms beam size and a sharp decrease in normalized emittance in x and y . At the injector exit, the emittance is about 35 mm-mrad. It increases a few percent over a 10 cm distance. For almost lin-

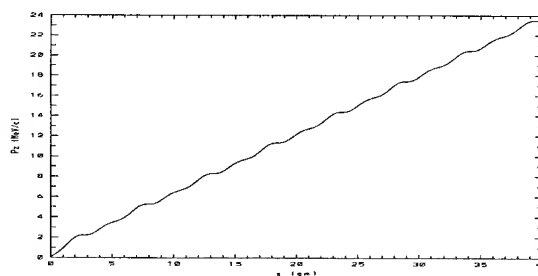


Figure 2. Electron momentum in MeV/c. At $z=40$ cm, $P_z=23.5$ MeV/c

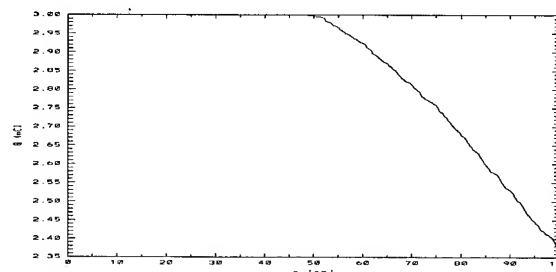


Figure 3. Charge in nC of the photoelectron bunch for $z=0$ to 100 cm. At $z=100$ cm, about 80% of the original charge of 3nC is retained.

ear increase in beam size by a small fraction and about same rate of particle loss, the emittance is lowered by more than factor of five. This seems to indicate that the largest contribution in emittance is from those uncorrelated in phase space. Nevertheless, the rest of the bunch propagates along the drift space with most of the charge still retained. The energy spread is on the order of a few percent in the acceleration period. At the exit, it is about 0.3%, and at the end of the simulation, it is lowered to 0.12%. The final momentum of the beam was 23.5 MeV/c. During the drift the bunch length was shortened to the final value of 2 ps whereas it was a steady 3.6 ps during the acceleration phase. The plots of these parameters are shown in Figs 2 through 7.

VI. COUPLING AND OTHER ASPECTS

In principle, the rf power may be introduced into the cavity in many ways. The BNL gun employs magnetic coupling to suppress a zero-mode by driving both cells, whereas the new design calls for the full-cell drive to minimize the dipole-mode effect. The same rationale may be applied for the 7-1/2 cell structure,

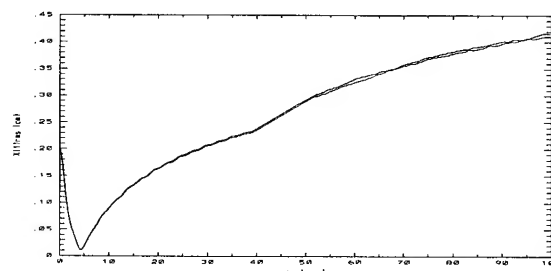


Figure 4. Transverse sizes of the bunch x_{rms} and y_{rms} in cm. At $z=1$ m, they are about 0.4 cm.

References

- [1] D. T. Palmer et al., These proceedings
- [2] R. L. Sheffield et al., *NIM*, **A318**,182 (1992)
- [3] S. Park and C. Pellegrini, Proc. 1993 Part. Accel. Conf., p. 570
- [4] S. Park et al., Proc. 1994 Linac Conf., p. 280
- [5] P. G. O'Shea et al., Proc. 1991 Part. Accel. Conf., p. 2754
- [6] K. Halbach and R. F. Holsinger, *Particle Accelerators* **7**, 213 (1976)
- [7] K. T. McDonald, IEEE Trans. Electron Dev. **ED-35**,2052 (1988)
- [8] I. S. Lehrman et al., Proc. 1992 Linac Conf., p. 280
- [9] Z. Li et al., Proc. 1993 Part. Accel. Conf., p. 179
- [10] L. C. Maier and J. C. Slater, *Journal of Applied Physics*, Vol.23, Num1 69 - 77, Jan 1952

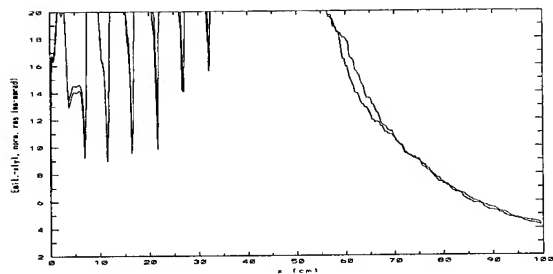


Figure 5. The normalized rms emittances in x and y. At $z=1\text{m}$, they are about 4 mm-mrad.

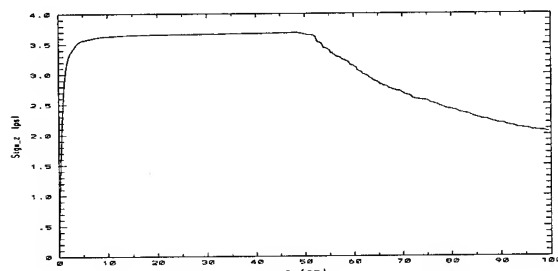


Figure 6. The bunch length in picoseconds. At $z=1\text{m}$, it is about 2 ps.

feeding the power through the last cell. In fact, a study was reported on driving a five-cell superconducting cavity [9] from the downstream end of the structure. Whether electric coupling is better than magnetic coupling has to be resolved during the cold test.

VII. CONCLUSION

Based on the wave studies and particle simulations, an aluminum model has been made. Aside from the measurements of the field structure through a bead pull method [10], there are a series of low-power tests possible. This series includes scattering parameter measurements in the steady state, and transient-coupling studies with pulsed low power at about 1 watt. Higher-order-mode outcoupling needs to be investigated if more than one microbunch is desired in every macropulse. While progress is still being made in the search for reliable photocathode materials with high quantum efficiency, it is equally important to explore an injector that is simple to manufacture, and which has high shunt impedance with lower content of unwanted modes.

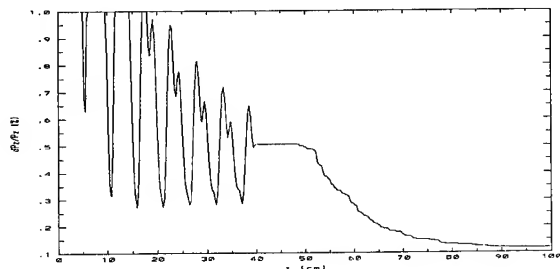


Figure 7. The energy spread in %. At $z=1\text{m}$, it is 0.12%.

ON THE FREQUENCY SCALINGS OF RF GUNS *

Leon C.-L. Lin, J. S. Wurtele, and S. C. Chen
Plasma Fusion Center
Massachusetts Institute of Technology

Abstract

A frequency scaling law for RF guns is derived from the normalized Vlasov-Maxwell equations. It shows that higher frequency RF guns can generate higher brightness beams under the assumption that the accelerating gradient and all beam and structure parameters are scaled with the RF frequency. Numerical simulation results using MAGIC confirm the scaling law. The scaling of wakefield is discussed. A discussion of the range of applicability of the law is presented.

written as

$$\hat{n} \times \mathbf{E} = 0, \quad (2)$$

where \hat{n} is normal to the surface. The total fields \mathbf{E} and \mathbf{B} can be split into two parts

$$\mathbf{E} = \mathbf{E}^{rf} + \mathbf{E}^{sc}, \quad (3)$$

$$\mathbf{B} = \mathbf{B}^{rf} + \mathbf{B}^{sc}, \quad (4)$$

where \mathbf{E}^{rf} and \mathbf{B}^{rf} are the fields in the absence of the beam and \mathbf{E}^{sc} and \mathbf{B}^{sc} are the fields due to the electron beam. Since the RF fields \mathbf{E}^{rf} and \mathbf{B}^{rf} already satisfy Maxwell equations and the boundary condition, \mathbf{E}^{sc} and \mathbf{B}^{sc} satisfy

$$\nabla \times \mathbf{E}^{sc} = -\frac{1}{c} \frac{\partial}{\partial t} \mathbf{B}^{sc} \quad (5)$$

$$\nabla \times \mathbf{B}^{sc} = \frac{1}{c} \frac{\partial}{\partial t} \mathbf{E}^{sc} + \frac{4\pi e}{c} \int v f(\mathbf{x}, \mathbf{p}, t) d^3 \mathbf{p} \quad (6)$$

$$\nabla \cdot \mathbf{E}^{sc} = 4\pi e \int f(\mathbf{x}, \mathbf{p}, t) d^3 \mathbf{p} \quad (7)$$

$$\nabla \cdot \mathbf{B}^{sc} = 0, \quad (8)$$

together with the boundary condition $\hat{n} \times \mathbf{E}^{sc} = 0$.

The total number of electrons in the cavity, $N(t)$, can be found from the distribution function $f(\mathbf{x}, \mathbf{p}, t)$:

$$N(t) = \int f(\mathbf{x}, \mathbf{p}, t) d^3 \mathbf{x} d^3 \mathbf{p}. \quad (9)$$

It is convenient to define $\tau = \omega t$, $\xi = \frac{\omega \mathbf{x}}{c}$, and $\beta = \frac{v}{c}$. The RF fields are now

$$\mathbf{E}^{rf} = E_0 e(\xi, \tau), \quad (10)$$

$$\mathbf{B}^{rf} = E_0 b(\xi, \tau), \quad (11)$$

where e is a dimensionless field profile and b is determined from Faraday's law

$$b(\xi, \tau) = - \int_{\tau}^{\tau} \nabla_{\xi} \times e(\xi, \tau') d\tau'. \quad (12)$$

The normalized electron distribution

$$\tilde{f}(\xi, \beta, \gamma, \tau) = \frac{1}{N(t)} \left(\frac{mc^2}{\omega} \right)^3 f(\mathbf{x}, \mathbf{p}, t), \quad (13)$$

is defined so that

$$\int \tilde{f}(\xi, \beta, \gamma, \tau) d^3 \xi d^3(\beta, \gamma) = 1. \quad (14)$$

I. INTRODUCTION

The brightness achieved by conventional DC guns followed by RF bunchers may not meet the stringent requirements of future high-energy linear colliders and free electron lasers. This has motivated research on high brightness photocathode RF guns [1]. The frequencies of operational systems range from 500MHz to 3GHz, and a 17GHz gun [2] is to be tested shortly. In this paper we examine the frequency scaling of RF guns. Our analysis is based on the Vlasov-Maxwell equations. By defining coordinates normalized with the RF frequency, all the frequency dependencies are absorbed into two parameters: α^{rf} , which characterizes the accelerating gradient, and α^{sc} , which characterizes the space-charge force. The resultant dimensionless Vlasov-Maxwell equations have the same solution for any frequency as long as α^{rf} , α^{sc} and the functional form of the initial distribution in phase space are fixed. This gives a frequency scaling which shows that higher brightness bunches can be generated at higher frequencies, albeit with less total charge. Our conclusions are confirmed by numerical simulation. Practical limits on high frequency operation are discussed.

II. NORMALIZED VLASOV-MAXWELL EQUATIONS

Consider a RF gun operated at frequency ω . Since collisions are insignificant for the parameters of the RF gun, the electron distribution function, $f(\mathbf{x}, \mathbf{p}, t)$, evolves according to the Vlasov equation:

$$\left\{ \frac{\partial}{\partial t} + \mathbf{v} \cdot \frac{\partial}{\partial \mathbf{x}} + e \left(\mathbf{E} + \frac{\mathbf{v} \times \mathbf{B}}{c} \right) \cdot \frac{\partial}{\partial \mathbf{p}} \right\} f(\mathbf{x}, \mathbf{p}, t) = 0. \quad (1)$$

The fields \mathbf{E} and \mathbf{B} are determined self-consistently from Maxwell equations and an appropriate boundary condition. The boundary condition on a perfectly conducting wall, namely that the transverse electric field must vanish on the surface S , can be

*Supported by the Department of Energy under Grant DE-FG02-91-ER40648.

With the definitions

$$\alpha^{rf} \equiv \frac{eE_0}{mc\omega}, \quad (15)$$

$$\alpha^{sc} \equiv \frac{4\pi\omega r_e}{c} N(\tau), \quad (16)$$

$$e^{sc} \equiv \frac{E^{sc}}{E_0}, \quad (17)$$

$$b^{sc} \equiv \frac{B^{sc}}{E_0}, \quad (18)$$

where $r_e = e^2/mc^2$ is the classical electron radius, we obtain the normalized Vlasov equation

$$\left\{ \frac{\partial}{\partial \tau} + \beta \cdot \nabla_{\xi} + \alpha^{rf} [(e + e^{sc})\beta \times (b + b^{sc})] \cdot \nabla_{\beta\gamma} \right\} \tilde{f}(\xi, \beta\gamma, \tau) = 0. \quad (19)$$

In Eq. (19), the normalized space-charge fields e^{sc} and b^{sc} satisfy the normalized Maxwell equations

$$\nabla_{\xi} \times e^{sc} = -\frac{\partial}{\partial \tau} b^{sc}, \quad (20)$$

$$\nabla_{\xi} \times b^{sc} = \frac{\partial}{\partial \tau} e^{sc} + \frac{\alpha^{sc}}{\alpha^{rf}} \int \beta \tilde{f}(\xi, \beta\gamma, \tau) d^3(\beta\gamma), \quad (21)$$

$$\nabla_{\xi} \cdot e^{sc} = \frac{\alpha^{sc}}{\alpha^{rf}} \int \tilde{f}(\xi, \beta\gamma, \tau) d^3(\beta\gamma), \quad (22)$$

$$\nabla_{\xi} \cdot b^{sc} = 0, \quad (23)$$

with the boundary condition $\hat{n} \times e^{sc} = 0$. Note that Eq. (19)–(23) are dimensionless and all frequency dependencies have been absorbed in the normalized field strengths α^{rf} and α^{sc} .

The performance of an RF gun can be easily scaled in frequency. As long as α^{rf} , α^{sc} , and the initial particle distribution in the normalized phase space are fixed, the particle distribution in the normalized phase space is independent of the frequency. In other words, if the accelerating gradient is proportional to the frequency (so that α^{rf} is fixed, see Eq.(15)), the total bunch charge is inversely proportional to the frequency (so that α^{sc} is fixed, see Eq.(16)), and (for a photocathode gun) the laser temporal and spatial profiles scale with wavelength (which fixes the initial particle distribution in normalized phase space), then the current, beam divergence, mean energy, and energy spread will be invariant, the beam radius, bunch length, and emittance will be inversely proportional to the frequency, and therefore the electron beam brightness and laser power density will be proportional to the frequency square. These scalings are summarized in Table 1.

III. SCALINGS OF WAKEFIELDS

Some wakefield effects have been included in our formulation when we impose the perfectly conducting boundary condition. The effects of finite conductivity will be dealt with later in this paper. Our frequency scalings hold not only for RF guns, but also for general accelerating structures. However, they seem to differ from traditional wakefield scalings.

Traditional wakefield theory [5] assumes an axisymmetric disk-loaded structure and uses a cylindrical coordinate (r, ϕ, z) to treat the problem. Assume a is the radius of the disk opening,

parameter	scaling
cavity dimensions	ω^{-1}
accelerating gradient	ω^1
peak current	ω^0
bunch charge	ω^{-1}
bunch energy	ω^0
bunch energy spread	ω^0
bunch emittance	ω^{-1}
bunch radius	ω^{-1}
bunch length	ω^{-1}
bunch divergence	ω^0
bunch brightness	ω^2
laser peak power	ω^0

Table I
Frequency scaling of a photocathode RF guns.

r_q is the transverse displacement of the particle, E_{0n} is the field strength of the n - the traveling wave mode at the disk opening, and ω_n , m , and w_n are the frequency, azimuthal wavenumber, and the field energy per unit length of that mode, respectively. Then the longitudinal and transverse wakefields can be written as [7]

$$w_{||n}(\rho, \phi, \tilde{\tau}_n) = -2qk_n\rho_q^m \rho^m \cos m\phi \cos \tilde{\tau}_n, \quad (24)$$

$$w_{\perp n}(\rho, \phi, \tilde{\tau}_n) = \hat{r} 2m \frac{k_n c}{\omega_n a} \rho_q^{m-1} \rho^m \cos m\phi \cos \tilde{\tau}_n \quad (25)$$

$$- \hat{\phi} 2m \frac{k_n c}{\omega_n a} \rho_q^{m-1} \rho^m \sin m\phi \sin \tilde{\tau}_n,$$

where $k_n = E_{0n}^2/(4w_n)$ is the loss parameter, and $\rho = r/a$, $\rho_q = r_q/a$, and $\tilde{\tau}_n = \omega_n(t - z/c)$ are the normalized variables. Wilson [5] assumes that the transverse displacement r_q is fixed regardless of the operating frequency ω_n . This regards the transverse displacement as limited by practical constraints such as the machining tolerance and the alignment. However, if the transverse displacement is scaled as ω_n and thus ρ and ρ_q are fixed, the scalings will be

$$w_{||n} \sim \omega_n^2 \quad \text{for any } m, \quad (26)$$

$$w_{\perp n} \sim \omega_n^2 \quad \text{for any } m. \quad (27)$$

These are scalings of wakefields induced by a single particle. For a bunch of particles, the total wakefield is obtained by integrating the wakefields induced by all particle. Assuming the functional form of the particle distribution in the normalized coordinate $(\rho_q, \phi, \tilde{\tau}_n)$ is fixed regardless of ω_n yet the magnitude is scaled as ω_n^{-1} (so that the total charge scales as ω_n^{-1}), then the total wavefield will scale as

$$w_n^{tot} \sim \omega_n^1 \quad \text{for any } m, \quad (28)$$

with ρ , $\tilde{\tau}_n$, and ϕ being fixed. Therefore, the total wakefield scales in the same way as the RF field and the space-charge field.

RF frequency (GHz)	2.856	17.136
Peak field on cathode (MV/m)	41.7	250
RF phase for laser pulse	12°	12°
Exit beam energy (MeV)	2.1	2.1
Energy spread (%)	0.22	0.22
Laser spot radius (mm)	2.9	0.49
Laser pulse length (ps)	9.6	1.6
Charge in bunch (nC)	0.6	0.1
Beam emittance (π mm-mrad)	6.6	1.1
Beam bunch length (mm)	0.96	0.16
Beam radius (mm)	4.0	0.67
Beam divergence (mrad)	19	19
Peak current (A)	180	180
Beam brightness ($A/\pi^2 m^2$)	4.1×10^{12}	1.5×10^{14}

Table II

MAGIC simulation results for BNL's 2.856GHz photocathode RF gun and a scaled gun at 17.136GHz.

References

- [1] For a review, see C. Travier, "RF guns, bright injectors for FEL," *Nuclear Instruments and Method in Physical Research*, A304, pp. 285, 1991.
- [2] S. C. Chen *et al.* "High Gradient Acceleration in a 17GHz Photocathode RF Gun," these proceedings.
- [3] K. T. McDonald, "Design of the Laser-Driven RF electron Gun for the BNL Accelerator Test Facility," *IEEE Trans. Electron Devices*, Vol. 35, No. 11, pp. 2052, Nov., 1988.
- [4] Bruce Goplen *et al.*, *MAGIC USER'S MANUEL*, Mission Research Corporation Technical Report MRC/WDC-R-282, 1991.
- [5] For example, see Perry B. Wilson, "High Energy Electron Linacs: Applications to Storage Ring RF Systems and Linear Colliders," SLAC-PUB-2884 (Rev.), Nov., 1991
- [6] Leon C.-L. Lin, S. C. Chen, and J. S. Wurtele, "Waveguide Side-Wall Coupling for RF Guns," to be published in *Proc. European Particle Accelerator Conf.*, 1994.
- [7] C.-L. Lin, "Theoretical and Experimental Studies of a 17 GHz photocathode RF Gun," Ph.D. Thesis, Massachusetts Institute of Technology, 1995.

It confirms that our frequency scalings are correct even when the wakefields are included, as long as the beam size and total charge are scaled down with frequency.

Nonetheless, the field profile of the n - the traveling wave mode will change slightly when we scale the operating frequency, since the skin-depth does not scale linearly with frequency. One way to study the skin-depth effect on RF gun beam dynamics is to use numerical simulation. As will be shown in next section, the skin-depth effect in RF guns is negligible in the regime of practical interest, since the scaling law still holds when the skin-depth effect is taken into account.

IV. NUMERICAL RESULTS AND DISCUSSION

Numerical simulations with the particle-in-cell code MAGIC confirm the frequency scaling. The performance of the BNL photocathode RF gun [3] operated at 2.856GHz was compared with that of a scaled BNL design at 17.136GHz ($\times 6$ higher frequency). The results are summarized in Table 2.

The practical assumptions made herein are (1) that very high gradients can be (more readily) achieved at higher frequencies, (2) that the bunch length and beam size can be scaled inversely with frequency, (3) that the laser peak power remains below the damage threshold to the cathode, and (4) that that changes to coupling geometry do not affect the field profile in the cavity. This implies that sufficiently powerful RF sources are available at the higher frequency, and that short laser pulses can be mode locked to RF with the same degree of relative error in temporal and spatial jitters. Since the skin depth does not scale linearly with frequency, coupling from the RF source to the cavity cannot be linearly scaled.

In summary, while high frequency systems may be difficult to realize technically, they may prove to be compact sources of high brightness bunches.

WAVEGUIDE BROAD-WALL COUPLING FOR RF GUNS *

Leon C.-L. Lin, S. C. Chen, and J. S. Wurtele
Massachusetts Institute of Technology
Cambridge, MA 02139

Abstract

A theoretical analysis of the waveguide broad-wall coupling of RF gun structures is presented. The analysis of this three dimensional problem yields an equivalent circuit whose elements are either directly calculated from the frequency and geometry of the gun, or are inferred from the two dimensional numerical solver URMEL. Good agreement between experiment and theory is seen in cold tests of our 17GHz $1\frac{1}{2}$ - cell RF gun.

I. INTRODUCTION

Photocathode RF guns are a promising source of high brightness electron beams for free electron lasers and future linear colliders. Among existing RF gun systems, the $1\frac{1}{2}$ - cell RF cavity design with a waveguide broad-wall coupling scheme, as shown in Fig. 1, is most widely used [1], [2], [3]. Most experiments have been conducted at an RF frequency of 2.856GHz. However, until now there has been no solid theoretical understanding of this coupling. Such understanding is important if guns are to be scaled to the high RF frequencies under consideration for future linear colliders and compact high gradient accelerators.

We present a theoretical study of the waveguide broad-wall coupling for the $1\frac{1}{2}$ - cell RF gun cavity, and a detailed comparison with experimental measurements. Our method consists of the following: (1) The problem is initially simplified by ignoring the iris, exit hole, and ohmic loss. (2) Each coupling aperture is represented by a three-dimensional dipole vector. (3) The two dipole vectors are solved for self-consistently using the small aperture approximation and appropriate Green's functions. (4) The dipole radiation is used to calculate the reflection and transmission coefficients. From these coefficient an impedance and equivalent circuit are derived. (5) The iris, exit hole, and ohmic loss are included by introducing additional circuit elements. Details are presented in [6].

II. CONSTRUCTION OF THE EQUIVALENT CIRCUIT

Consider the waveguide broad-wall coupling problem shown in Fig. 1. The RF energy is coupled into the cavity through two apertures which are assumed to be small compared to the wavelength of the incident RF field. Let $i = 1, 2$ refer to these two apertures. The effects of a small aperture can be represented [4] by a dipole vector which consists of three components: an electrical component normal to the broad-wall, and two tangential magnetic components. The dipole vector \mathbf{d}_i at each aperture is related to a field vector \mathbf{F}_i , whose components are the normal electric and two tangential magnetic field components. From the quasi-static solution of the wave equation it can be shown

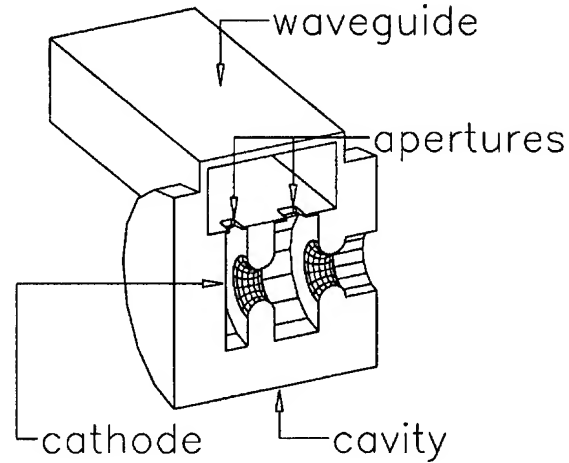


Figure 1. A cross section view of a $1\frac{1}{2}$ - cell RF cavity coupled to a rectangular waveguide via two apertures in the broad-wall.

that

$$\begin{bmatrix} d_1 \\ d_2 \end{bmatrix} = \begin{bmatrix} \bar{\alpha}_1 & \bar{O} \\ \bar{O} & \bar{\alpha}_2 \end{bmatrix} \begin{bmatrix} F_1 \\ F_2 \end{bmatrix}, \quad (1)$$

or simply $\mathbf{d} = \bar{\alpha} \cdot \mathbf{F}$. Here, $\bar{\alpha}_i$ is the aperture's polarizability tensor, readily given in terms of geometry [5]. To obtain a self-consistent, and thus a physically meaningful solution, one needs to include both the incident and the radiated fields. The total field at the aperture should thus be of the form $\mathbf{F} = \mathbf{F}^{inc} + \mathbf{F}^g + \mathbf{F}^c$, where \mathbf{F}^{inc} denotes the incident field, and \mathbf{F}^g (\mathbf{F}^c) denotes the total field radiated by \mathbf{d} on the waveguide side (cavity side) of the aperture.

Since this is a linear system, there exist reaction tensors $\bar{\chi}^g$ and $\bar{\chi}^c$ such that $\mathbf{F}^{g,c} = \bar{\chi}^{g,c} \cdot \mathbf{d}$. Thus the dipole vector \mathbf{d} can be written in terms of the incident field \mathbf{F}^{inc} as

$$\mathbf{d} = [\bar{\delta} - \bar{\alpha} \cdot (\bar{\chi}^g + \bar{\chi}^c)]^{-1} \cdot \bar{\alpha} \cdot \mathbf{F}^{inc}, \quad (2)$$

where $\bar{\delta}$ is the identity tensor. The coupling problem is thus determined by \mathbf{d} , which depends on the reaction tensors for the waveguide and the cavity. These tensors are readily obtained from the Green's functions of the waveguide and pillbox cavities [6].

A two-port network, characterized by a two-by-two scattering matrix \bar{S} , gives physical insight into the coupling. The matrix \bar{S} is related to its impedance matrix by

$$\bar{Z} = Z_0(\bar{\delta} - \bar{S})^{-1} \cdot (\bar{\delta} + \bar{S}), \quad (3)$$

where Z_0 is the waveguide characteristic impedance. From the Green's function for waveguide, we calculate the radiated

*This research is supported by DOE under grant DE-FG02-91-ER40648.

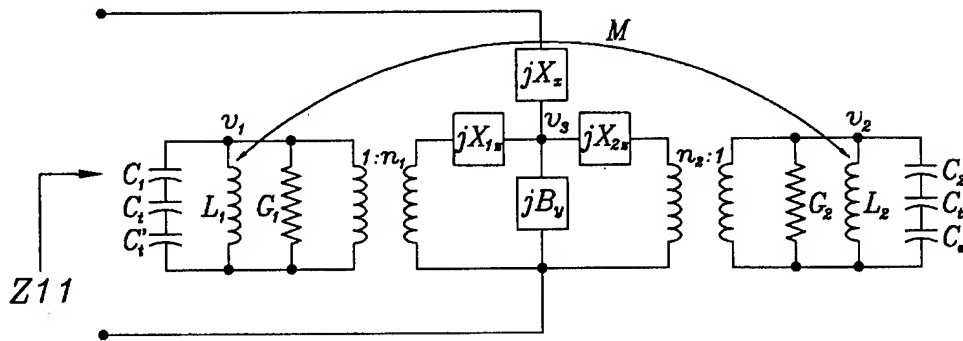


Figure 2. An equivalent network for the complete wave-guide broad-wall coupled $1\frac{1}{2}$ -cell cavity system.

fields and then obtain the reflection coefficient S_{11} and the transmission coefficient S_{21}

$$S_{11} = \frac{j\beta}{2} \mathbf{f}^+ \cdot [\bar{\delta} - \bar{\alpha} \cdot (\bar{\chi}^g + \bar{\chi}^c)]^{-1} \cdot \bar{\alpha} \cdot \mathbf{f}^+, \quad (4)$$

$$S_{21} = 1 + \frac{j\beta}{2} \mathbf{f}^- \cdot [\bar{\delta} - \bar{\alpha} \cdot (\bar{\chi}^g + \bar{\chi}^c)]^{-1} \cdot \bar{\alpha} \cdot \mathbf{f}^+, \quad (5)$$

where $\beta = \sqrt{(\omega/c)^2 - k_c^2}$ (k_c is the cutoff wavenumber) and the elements \mathbf{f}^\pm are given in [6]. In practice, the waveguide is shorted at a quarter-wave distance from the apertures. This maximizes the incident fields on the apertures. In this case, port two is open and the two-port network becomes a one-port network with an impedance Z_{11} . Inserting Eqs. (4) and (5) into Eq. (3) yields an expression for the impedance Z_{11} . The result is the compact expression:

$$Z_{11} = jX_x + 1/jB_y + 1/Y_{1z} + 1/Y_{2z} \quad (6)$$

where $Y_{iz} = jX_{iz} + n_i^2/(j\omega C_i + 1/j\omega L_i)$. Each element is rigorously given in terms of frequency and geometry [6].

The iris can be represented by a mutual inductor M and a capacitor C_t , the exit hole can be represented by a capacitor C_e , and ohmic loss can be represented by conductances G_1 and G_2 . Their numerical values can be obtained from the numerical solver URMEL [6]. This yields the equivalent network shown in Fig. 2. In this equivalent network, we have introduced an additional capacitor C_t' to represent the tuner used to change the frequency of the first cell in our experimental apparatus.

In Figure 2, L_1 - C_1 (L_2 - C_2) represent the oscillation of the first (second) cell, M represents the coupling due to the iris, C_t represents the tuning due to the iris, C_e represents the tuning due to the exit hole in the second cell, C_t' represents the tuning due to the tuner in the first cell, G_1 and G_2 models ohmic losses in two cells, the two transformers $n_1 : 1$ and $n_2 : 1$ represent the impedance transforming features of the waveguide-cavity junction, and jX_x , jB_y , jX_{1z} , and jX_{2z} represent the waveguide-cavity coupling.

III. COUPLED OSCILLATORS MODEL

In our gun, the coupling is primarily through the z component of the dipole. This implies jX_x and jB_y are negligible. Near resonance we obtain, from the equivalent circuit, two driven

coupled oscillators equations:

$$\begin{bmatrix} j(\omega - \omega'_1 - j\tau_1) & -\kappa \\ -\kappa & j(\omega - \omega'_2 - j\tau_2) \end{bmatrix} \begin{bmatrix} u_1 \\ u_2 \end{bmatrix} = \begin{bmatrix} q_1 \\ q_2 \end{bmatrix}.$$

Here, u_i is the normalized accelerating field amplitude, ω'_i the resonant frequency, τ_i the loss factor (which is related to the cavity Q factor), q_i the driving force, and κ the coupling coefficient.

The eigenvalues and eigenvectors of the coupled oscillators are

$$\omega'_\pm = \frac{\Omega_1 + \Omega_2}{2} \pm \sqrt{\left(\frac{\Omega_1 - \Omega_2}{2}\right)^2 - \kappa^2},$$

$$\bar{U} = \begin{bmatrix} \mathbf{u}_+ & \mathbf{u}_- \end{bmatrix} = \begin{bmatrix} \cos \theta & -\sin \theta \\ \sin \theta & \cos \theta \end{bmatrix},$$

where $\Omega_i = \omega'_i + j\tau_i$ and

$$\theta = \tan^{-1} \frac{j(\omega'_+ - \Omega_1)}{\kappa}. \quad (7)$$

The eigenmodes \mathbf{u}_+ and \mathbf{u}_- are the π -mode and the 0-mode for the waveguide broad-wall coupled $1\frac{1}{2}$ -cell RF cavity, respectively. The angle θ is the mode mixing angle. We can represent the response \mathbf{u} as a linear combination of \mathbf{u}_+ and \mathbf{u}_- :

$$\mathbf{u} = \left[\frac{c_+}{j(\omega - \omega'_+)} \mathbf{u}_+ + \frac{c_-}{j(\omega - \omega'_-)} \mathbf{u}_- \right] \quad (8)$$

where

$$c_+ = q_1 \cos \theta + q_2 \sin \theta \quad (9)$$

$$c_- = -q_1 \sin \theta + q_2 \cos \theta. \quad (10)$$

Note that c_+ and c_- represent the magnitude of the π -mode and the 0-mode, respectively. If c_+ is much greater than c_- , then the π -mode has been selectively excited.

IV. COMPARISON BETWEEN EXPERIMENT AND THEORY

Now we present the comparison between the theory and the experiment for a 17 GHz gun [3]. In Fig. 3, theoretical and measured values of the reflection coefficient S_{11} of a waveguide broad-wall coupled RF gun are plotted as a function of frequency for an initially untuned gun. Without tuning the system

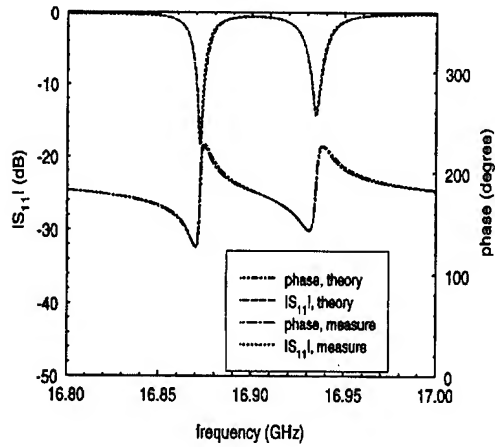


Figure 3. S_{11} of the waveguide broad-wall coupled $1\frac{1}{2}$ - cell cavity as a function of frequency when the cavity is untuned.

is in the weak coupling region; in our case the first cell has the lower resonant frequency. The two apertures are commensurate in size and consequently $q_1 \sim q_2$. Therefore, one observes two distinct resonances with comparable magnitude.

As we tune the first cell, the resonant frequency of the first cell (ω'_1) becomes larger and thus closer to that of the second cell (ω'_2). Therefore, the coupling becomes stronger. Finally, two resonances become undistinguishable when the difference in frequency is greater than the bandwidth, as shown in Fig. 4. In these figures, the theoretical predictions agree very well with measurement.

V. CONCLUSION

We have constructed an equivalent network representation for the waveguide broad-wall coupled $1\frac{1}{2}$ - cell RF cavity. The coupling between the rectangular waveguide and the cylindrical $1\frac{1}{2}$ - cell cavity (without the iris, the exit hole, and ohmic losses) has been studied using the small aperture approximation and rigorously represented by an equivalent network, in which all circuit elements are derived from first principles. The iris, the exit hole, and ohmic loss have been modeled by introducing appropriate circuit elements obtained from the numerical field solver URMEL. The resultant equivalent circuit has been analyzed and well approximated by two driven coupled oscillators. We have shown that with proper tuning the waveguide broad-wall coupling scheme can selectively excite a linear combination of π - and 0- modes so as to optimize the RF gun performance. Experimental measurements are in excellent agreement with the theory.

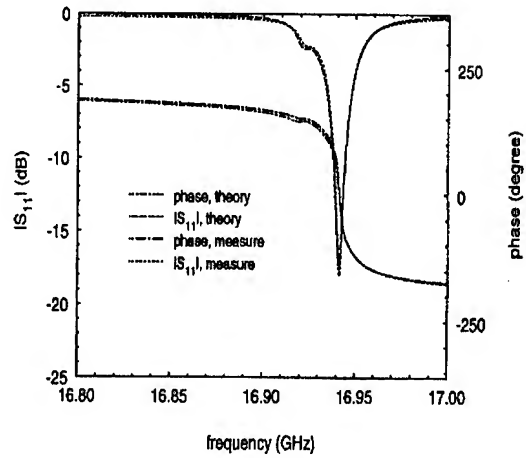


Figure 4. S_{11} of the waveguide broad-wall coupled $1\frac{1}{2}$ - cell cavity as a function of frequency when the cavity is properly tuned.

References

- [1] K. Batchlor *et al.*, "Design and Modelling of a 5MeV Radio Frequency Electron Gun", BNL-41766, 1988.
- [2] F. Aghamir *et al.*, "SATURNUS: The UCLA High Gain Infrared FEL Project," UCLA-CAA0068-9/90, 1990.
- [3] S. C. Chen *et al.*, "High Gradient Acceleration in a 17GHz Photocathode RF Gun," *AIP Conference Proc.* 279, pp. 694-705, 1993.
- [4] H. A. Bethe, "Theory of Diffraction by Small Holes," *Phys. Rev.*, vol. 66, pp. 163-182, 1944.
- [5] R. E. Collin, *Field Theory of Guided Waves*, New York: IEEE Press, pp. 499-511, 1991.
- [6] L. C.-L. Lin, "Theoretical and Experimental Studies of a 17 Ghz Photocathode RF Gun," Ph.D. Thesis, Massachusetts Institute of Technology.

CHARGE AND WAVELENGTH SCALING OF RF PHOTOINJECTORS: A DESIGN TOOL*

J. Rosenzweig and E. Colby

UCLA Department of Physics and Astronomy, Los Angeles, CA 90024, USA

The optimum design of an emittance compensated rf photoinjector is very complicated and time-consuming, relying heavily on multi-particle simulations without good analytical models as a guide. Emittance compensated designs which have been developed, however, can be used to generate other designs with no additional effort if the original design is scaled correctly. This paper examines the scaling of rf photoinjector design with respect to charge and wavelength, and presents emittance and brightness scaling laws for these variables. Parametric simulation studies are presented to illustrate these scaling laws. A practical design for the TESLA FEL rf photo-injector is developed using these scaling techniques.

I. INTRODUCTION

The optimization of an rf photoinjector[1-6] design is typically an iterative and somewhat haphazard process. This is because, while some scaling laws concerning photoinjector performance have been derived from first order integration of the transverse force equations [2], an optimized photoinjector will necessarily use emittance compensation [3], which is a dynamical process with only a qualitative theoretical understanding. A full design requires a search of the relevant parameter space, which includes the rf amplitudes of the gun and linac, the focusing lens position and strength, the gun-to-linac separation, the cathode cell length, and the beam charge, spot size and pulse length. Because this is such an involved process, including detailed rf and magnet design calculations and multiparticle simulations, any analytical understanding of the optimization process would be a useful and time-saving tool. While a full analytical theory of the beam dynamics in an rf photoinjector remains a difficult result [7], this work presents a new method, that of scaling an existing rf optimized photoinjector design with respect to charge and wavelength variation to design entire families of optimized photoinjectors.

II. DYNAMICS EQUATIONS

The longitudinal and transverse dynamics of the electrons in an rf photoinjector can be described by some relatively straightforward equations. Since the longitudinal motion is dominated by the applied rf fields, and the collective effects due to the electrons are perturbations on the motion of a single electron, for this discussion it is sufficient to examine the single particle dynamics. The rf acceleration

field in a pure π -mode standing wave accelerator gives energy gain equation [2]

$$\frac{d\gamma}{dz} = \frac{eE_0}{2m_e c^2} [\sin(\phi) + \sin(\phi + 2k_z z)], \quad (1)$$

where $k_z = \omega/c$ is the rf wave number, and E_0 is the peak acceleration field. The evolution of phase angle $\phi = k_z z - \omega t + \phi_0$ (relative to the forward wave) is

$$\frac{d\phi}{dz} = k_z (1 - \beta^{-1}) = k_z \left[1 - \frac{\gamma}{\sqrt{\gamma^2 - 1}} \right]. \quad (2)$$

By recasting the equations using the dimensionless independent variable $\tilde{z} \equiv k_z z$,

$$\frac{d\gamma}{d\tilde{z}} = \alpha [\sin(\phi) + \sin(\phi + 2\tilde{z})] \quad (3)$$

$$\text{and } \frac{d\phi}{d\tilde{z}} = \left[1 - \frac{\gamma}{\sqrt{\gamma^2 - 1}} \right], \quad (4)$$

where $\alpha \equiv eE_0/2k_z m_e c^2$ is the single parameter[2] which describes the longitudinal motion. This immediately gives the result that the scaling of an rf design with wavelength implies that α must be kept constant as the wavelength is varied.

The transverse dynamics of an optimized rf photoinjector are a bit more intricate to describe, because the collective forces due to space-charge are non-negligible throughout the device. In fact, the uncorrelated thermal motion of the beam particles is nearly ignorable in optimized rf photoinjectors because of the dominance of space charge and externally applied forces. This situation allows a key simplification in modeling the collective transverse dynamics, that the motion can be assumed to be nearly laminar and an ordering of particles in the spatial coordinates is preserved in this case.

Given this situation, assuming the configuration space distribution functions of the beam at the cathode are the scaled correctly, the scaling of the transverse motion of the electron distribution can be deduced by examining the scaling of the rms transverse envelope equations. For this work, we write the envelope equation describing the evolution of a cylindrically symmetric beam, ignoring thermal emittance effects [7],

$$\sigma_x'' + \sigma_x' \left(\frac{(\beta\gamma)'}{\beta\gamma} \right) + K_x \sigma_x = \frac{2I}{I_0 (\beta\gamma)^3 \sigma_x} f\left(\frac{\sigma_x}{\beta\gamma\sigma_i}\right), \quad (5)$$

* Work supported by U.S. DOE grants DE-FG03-90ER40796 and DE-FG03-92ER40693, and Sloan Foundation grant BR-3225.

where an analogous equation exists for σ_y . In Eq. 5 the prime indicates the derivative with respect to z , the focusing strength (which is the square of a betatron wave number) $K_x \equiv k_\beta^2 = -F_{\text{ext}}/\beta^2 \gamma m_e c^2 x$ for all linear static externally applied forces, I is the peak current, and $I_0 \approx 17$ kA.

III. CHARGE SCALING

Often, one designs an rf photoinjector with a particular application in mind, specifying the charge Q , bunch length σ_z , and total (including nonthermal sources) emittance ϵ , only to find another significantly different application arising later. An rf photoinjector design can be scaled quite straightforwardly by scaling the defocusing forces of the bunch appropriately. This can be seen by writing $I = Qc/g\sigma_z$, where g is a distribution function dependent form factor, and using the defocusing space charge term in Eq. 5 to define the rms defocusing (imaginary) wave number as

$$\kappa_{sc}^2 = \frac{2I}{I_0(\beta\gamma)^3 \sigma_r^2} f\left(\frac{\sigma_x}{\beta\gamma\sigma_z}\right) = \left[\frac{2c}{I_0\beta^2\gamma^3} \right] \left[\frac{Q}{g\sigma_z\sigma_x^2} \right] f\left(\frac{\sigma_x}{\beta\gamma\sigma_z}\right) \quad (6)$$

The first bracketed factor in Eq. 6 is a bunch independent constant, the second is, up to a distribution shape dependent constant, the peak beam density, and the last factor is dependent only on the bunch aspect ratio. Therefore one can scale a design keeping all of the applied focusing forces the same by preserving the defocusing space charge wave number, which implies that peak the beam density, aspect ratio and distribution shape must be kept constant. Quantitatively we can write this as a simple scaling law,

$$\sigma_i \propto Q^{1/3}, \quad (7)$$

all bunch dimensions scale as the cube-root of the total charge.

To check on how well this scaling works in actual practice, a series of simulations were performed using the code PARMELA, which includes all applied fields and an electrostatic approximation to the self-consistent space charge fields. A test injector composed of a high gradient 1-1/2 cell S-band (2856 MHz) photoinjector gun with BNL-style cavity profiles [4], followed by a focusing solenoid, and a drift long enough to allow the compensation minimum to be clearly discerned was chosen for the scaling studies.

The results of these studies are discussed in detail in Ref. 8, and are summarized here. The evolution of the beam profiles for various charge beams is essentially of the same form. In addition, the evolution of the rms normalized emittance displays qualitatively similar behavior. It is then reasonable to ask how the emittance quantitatively scales following this prescription for Q

scaling. This is not a trivial task, as there are a number of contributions to the normalized rms emittance, defined by

$$\epsilon_x = (m_e c)^{-1} \sqrt{\langle x^2 \rangle \langle p_x^2 \rangle - \langle x p_x \rangle^2}. \quad (8)$$

To begin, we examine the dependence of the space-charge derived emittance. All of the force integrals needed to find the rms transverse momentum scale (including the nonlinear components of the force, but not including the cathode effects) as the beam size, and the space-charge derived emittance scales as

$$\epsilon_x^{sc} \propto \sigma_x^2 \propto Q^{2/3} \quad (9)$$

This is the same dependence that Kim[2] has deduced for the uncompensated space charge emittance.

Another source of rms emittance is the differential focusing (as a function of longitudinal position) due to the linear transverse rf forces. This effect has been analyzed to lowest order by Kim[2], who found

$$\epsilon_x^{rf} \approx \left(\frac{eE_0}{\sqrt{8}m_e c^2} \right) (k_z \sigma_z)^2 \sigma_x^2 \propto Q^{4/3}. \quad (10)$$

The emittance again scales as the square of the transverse beam size, and additionally scales as the length of the beam squared.

A final contribution to the total rms emittance arises because of the beam's energy spread. Since this quantity increases as the square of the beam length, the possible emittance growth due to chromatic aberrations in the focusing system will increase with bunch charge. This effect scales as

$$\epsilon_x^{ch} \propto \left(\frac{\Delta p}{p} \right) \left(\frac{\sigma_x^2}{f} \right) \propto (k_z \sigma_z)^2 \sigma_x^2 \propto Q^{4/3}. \quad (11)$$

The chromatic effects have the same scaling as linear rf emittance contribution.

Simulation results of all of the Q scaled designs is shown in Fig. 1. The asymptotic predictions of the emittance growth, that it should be space-charge dominated at low charge ($\epsilon_x \propto Q^{2/3}$) and rf/chromatic dominated ($\epsilon_x \propto Q^{4/3}$) at high charge are shown, as is a simple fit to a curve which is the sum of squares of these two asymptotic effects ($\epsilon_x = \sqrt{(aQ^{2/3})^2 + (bQ^{4/3})^2}$). Note that for a large range of charges, the dependence of emittance on charge is in the transition between the two limits, and is approximately linear.

IV. WAVELENGTH SCALING

Another situation which can arise is that one laboratory develops a sophisticated rf photoinjector design at a certain rf wavelength, and a different laboratory wishes to take advantage of this work in adapting the design to another, more convenient wavelength. This naturally brings up the question of wavelength (λ) scaling of photoinjector design.

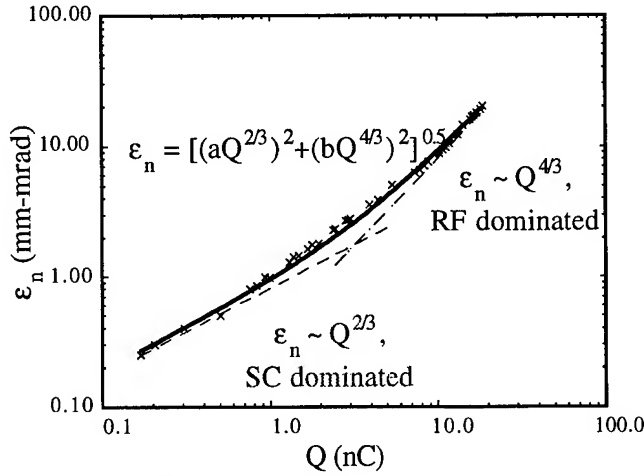


Figure 1. PARMELA simulation of emittance compensated BNL-style gun, emittance dependence of charge scaling.

This discussion proceeds immediately from Eqs. 3 and 4, which dictate the scaling of the electric field, as mentioned before. To preserve the longitudinal motion in a design - the injection phasing, compression of longitudinal phase spread, the energies at the exit of the rf structures, etc. - one must simply follow the scaling $E_0 \propto \lambda^{-1}$. This implies that the structure length is simply proportional to the rf wavelength. Further, preservation of the relative energy spread requires that the beam's injected phase spread be constant, $\sigma_z \propto \lambda$.

For preservation of the transverse dynamics, one must scale all of the transverse wave numbers inversely with the rf wavelength, since all distances must scale with wavelength. For solenoidal focusing, this implies $B \propto \lambda^{-1}$. It can be shown that the transverse rf effects naturally scale correctly with wavelength if the field is inversely proportional to the wavelength [8]. For space charge, we recall that the aspect ratio of the beam must remain constant when scaling, and thus we have $\sigma_{x,y} \propto \lambda$. To scale the space charge defocusing wave number correctly, we deduce from Eq. 6 that $Q \propto \lambda$.

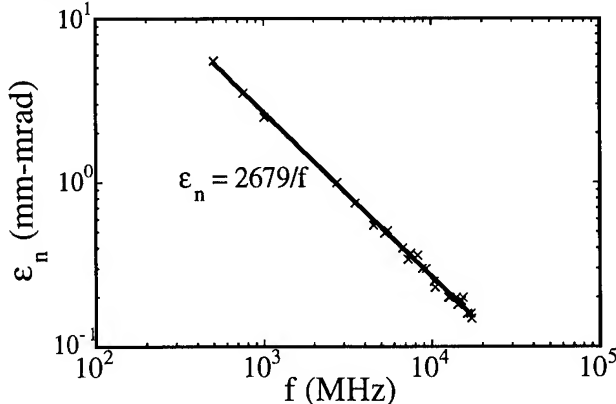


Figure 2. PARMELA simulation of emittance compensated BNL-style gun, emittance dependence of wavelength scaling.

These scaling rules have also been tested with PARMELA simulations, as described in Ref. 8. The evolution of the beam size along the beamline, with all lengths normalized to the rf wavelength, are invariant in these simulations. In addition, the emittance evolution in displayed identical scaling behavior. To see why this is so, we note that for λ scaling, the rms momentum integrals are proportional to the defocusing strength ($\sim \lambda^{-2}$), the beam size ($\sim \lambda$) the total rest frame integration time ($\sim \lambda$). Multiplied by the rms beam size ($\sim \lambda$), we find that $\epsilon_x^{sc} \propto \lambda$. The rf contribution to the emittance scales with wavelength, using Eq. 10, as $\epsilon_x^{rf} \propto E_0(k_z \sigma_z) \sigma_x' \propto \lambda$. Finally, the contribution to the emittance from chromatic aberrations scales, using Eq. 11, as

$\epsilon_x^{ca} \propto (\Delta p/p)(\sigma_x'/f) \propto f^{-1}(k_z \sigma_z) \sigma_x' \propto \lambda$. These results, which lead to the conclusion that the emittance is yet another "length" simply proportional to λ , is easily shown to be valid by the numerical simulations, as seen in Fig. 2.

V. SCALING: A DESIGN EXAMPLE

A short wavelength FEL has been proposed for The TESLA Test Facility (TTF) [9]. While a 1.3GHz BNL-style photoinjector has been designed for the TTF [10], its focusing scheme has been optimized to produce high charge (8.3 nC) bunches. When charge scaling is applied to reduce the charge to the FEL design-driven 1 nC, one does not obtain an emittance below 2 mm-mrad. On the other hand, if one scales the BNL 1 nC design (with its focusing scheme) first to 1.3 GHz (so the charge is 2.2 nC) and then scales the charge back down to 1 nC, the BNL focusing scheme produces much better emittances, well below the 1 mm-mrad demanded by the FEL after acceleration in a booster linac. This excellent example of the use of scaling in design is shown in Fig. 3.

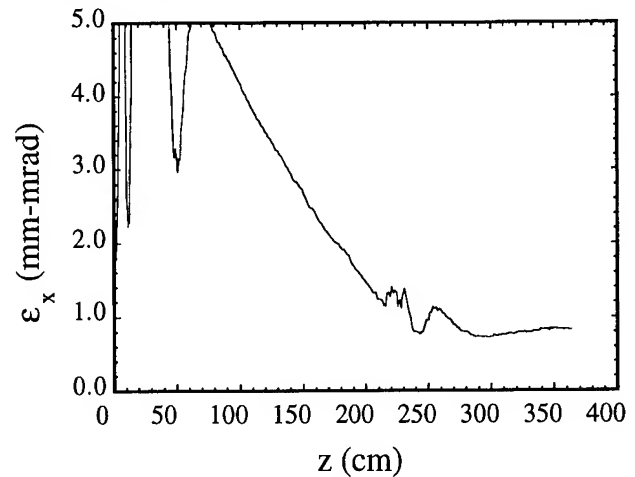


Figure 3. BNL-style design scaled to $f=1.3$ GHz, and 1 nC. A TESLA cavity (15 MV/m) booster linac at $z=240$ cm aids and preserves emittance compensation. In the gun $E_0=45$ MV/m.

VI. REFERENCES

- [1] J. Fraser, *et al.*, *IEEE Trans.Nuc.Sc.* **NS-32**,1791 (1985)
- [2] K.J.Kim, *Nucl. Instr. Methods A* **275**, 201 (1988).
- [3] B.E. Carlsten, *Nucl. Instr. and Meth. A* 285 (1989) 313.
- [4] J.C. Gallardo and H. Kirk, *Proc. Particle 1993 Accel. Conf.* 3615 (IEEE, 1993)
- [5] R. Sheffield, *et al.*, *NIM A* **341**, 371 (1994)
- [6] L. Serafini, *Nucl. Instr. Methods A* **340**, 40 (1994).
- [7] L. Serafini and J. Rosenzweig, these proceedings.
- [8] J. Rosenzweig and E. Colby, to be published in *Proc. of the 1994 Advanced Accelerator Workshop (AIP, 1995)*.
- [9] J. Rossbach, these proceedings.
- [10] E. Colby *et al.*, these proceedings.

A Photocathode RF Gun Design for a mm-Wave Linac-Based FEL*

A. Nassiri, T. Berenc†, J. Foster†, G. Waldschmidt†, and J. Zhou

Advanced Photon Source, Argonne National Laboratory
9700 South Cass Avenue, Argonne, Illinois 60439 USA

Abstract

In recent years, advances in the rf gun technology have made it possible to produce small beam emittances suitable for short period microundulators which take advantage of the low emittance beam to reduce the wavelength of free-electron lasers (FELs). At the Advanced Photon Source, we are studying the design of a compact 50-MeV superconducting mm-wave linac-based FEL for the production of short wavelengths (~300 nm) to carry out FEL demonstration experiments. The electron source considered for the linac is a 30-GHz, 3 1/2-cell π -mode photocathode rf gun. For cold model rf measurements a 15-GHz prototype structure was fabricated. Here we report on the design, numerical modeling and the initial cold-model rf measurement results on the 15-GHz prototype structure.

I. INTRODUCTION

Short wavelength FELs impose stringent requirements on the quality of the electron beams. The key factor in obtaining a single-pass UV or x-ray FEL is the generation of small emittance electron beams with ultra-high brightness. In the past decade, a tremendous amount of R&D has taken place to improve the performance of rf gun design [1,2]. With the emergence of new photocathode materials with good quantum efficiencies and improvements in laser technology to produce ultra-short pulses, it is now possible to produce small emittance electron beams suitable for short wavelength FEL applications. The linac structure being considered is a 60-GHz constant gradient superconducting structure fabricated by using a precision microfabrication process known LIGA (Lithographie, Galvanoformung, Abformung).

The limitations on the emittance and beam brightness of an electron gun are mainly due to nonlinear electromagnetic forces, space charge forces, and the maximum current density that can be obtained from the cathode. Alkali semiconductors photocathode such as Cs₃Sb can produce peak current density of 600 A/cm². These cathodes may be operated at pulse lengths ranging from a few picoseconds to microseconds at high pulse repetition rates. However, excellent vacuum (~10⁻⁹ Torr) must be maintained. Field emission array (FEA) cathodes could produce current density in excess of 100 A/cm². However, at the present time, their limited lifetime due to various breakdown modes does not make them attractive for accelerator applications.

II. RF GUN DESIGN

The rf gun considered for this project is a 30-GHz 3 1/2-cell structure. However, for ease of the initial fabrication and assembly, a prototype 15-GHz structure was designed and built as a first test structure. Although there are many technical difficulties associated with high-frequency rf gun structures, a 30-GHz photocathode rf gun allows us to reach very high gradient in excess of 500 MV/m. This drastically reduce the effects of space-charge forces and allows high-brightness beams. For a cylindrically symmetrical structure, the transverse magnetic field (TM modes) can be uniquely determined by the axial electric field, E_z [3]:

$$E_z(z, r) = E_z(z, 0) - \frac{r^2}{4} h''(z) + O((pr)^4), \quad (1)$$

$$E_r(z, r) = -\frac{r}{2} \frac{d}{dz} E_z(z, 0) - \frac{r^3}{16} h'''(z) + O((pr)^5), \quad (2)$$

$$B_\phi(z, r) = \frac{pr}{2c} E_z(z, 0) - \frac{pr^3}{16c} h''(z) + O((pr)^5), \quad (3)$$

where $h(z)$ satisfies

$$h(z) = \left(\frac{d^2}{dz^2} + p^2 \right) E_z(z, 0). \quad (4)$$

For ideal cavity shape it is required to make both $h(z)$ and $h'(z)$ zero. In this case, the cavity's radius is given by [4]

$$r = \sqrt{\left(a^2 - \left(\frac{4d}{\pi} \right)^2 \log \left(\sin \frac{\pi z}{2d} \right) \right)} \quad (5)$$

As z goes to zero, it requires that r approaches infinity. In a real situation one can optimize the cells' geometry and the shape of the cavity around the exit in a way which is close to the ideal shape. The effects of nonlinear rf forces and self-fields of the electrons on the emittance growth of the electron beam has been described in detail by K.-J. Kim [5]. Emittance growth due to nonlinear rf forces can be controlled by ensuring that nonlinear transverse components of the rf fields are minimized. This can be achieved by placing a thick disk between cells and adjusting the diameter of the apertures so as to minimize nonlinear transverse components. The effects of nonlinear space charge forces are reduced since the initial electron distribution from the cathode are launched in a high gradient electric field and the space charge beam blowup scales as the inverse of the peak electric field gradient. For simulations, a laser pulse of 2 ps is chosen. MAFIA [6] numerical codes were used to model the 3 1/2-cell rf gun including particle-in-cell simulations. The main parameters of the prototype photocathode rf gun are listed in Table 1. The gun's cell radius and aperture diameter were optimized to provide the correct longitudinal

* Work supported by the U.S. Department of Energy, Office of Basic Energy Sciences, under Contract No. W-31-109-ENG-38.

† Senior Research Students at Argonne.

Table 1: 15-GHz Prototype Gun RF Parameters

Parameter	Value
Frequency	15 GHz
Peak accelerating gradient	200 MV/m
Exit beam energy	4 MeV
Charge per bunch	1 nC
Cathode radius	0.5 mm
Emittance	2 mm-mrad
Shunt impedance	254 M Ω /meter
Q	7000

accelerating field for the desired π -mode. For particle-in-cell simulations, a Gaussian bunch of 2-ps length (FWHM) and a total number of particles of 6×10^9 (total charge/bunch = 1 nC) is assumed to be ejected from the copper cathode surface of radius 0.5 mm. The initial velocity of the bunch is assumed to be $v = 0.01 c$ with a peak rf accelerating gradient of 200 MV/m. Figure 1 shows the longitudinal field pattern for the accelerated bunched beam. Figure 2 is a plot of the particles' energy (γ -distribution) along the z-axis.

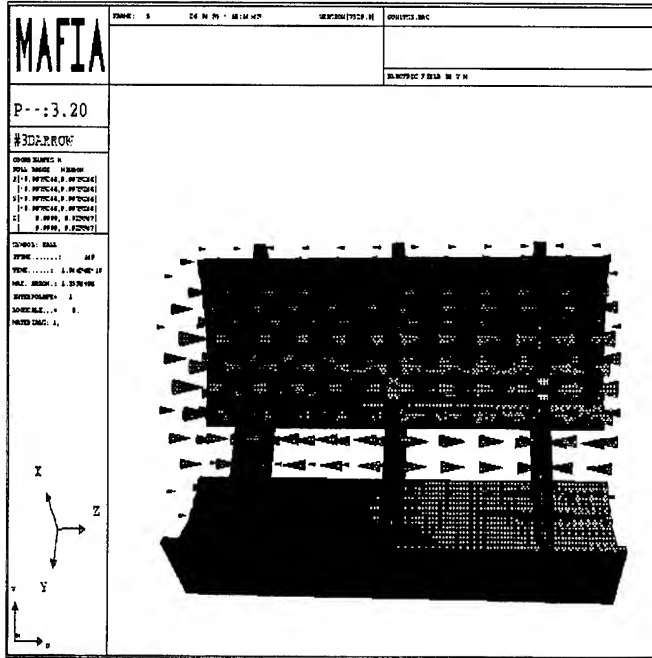


Figure 1: Longitudinal field for the accelerated beam

III. PROTOTYPE GUN RF MEASUREMENTS

The field perturbation method was employed to determine the axial field distributions of the excited modes in the 15-GHz prototype rf gun structure. The perturbation is achieved by using small cylindrical aluminum beads deposited on nylon lines and optical fibers with a diameter of $\sim 100 \mu\text{m}$. A stepping

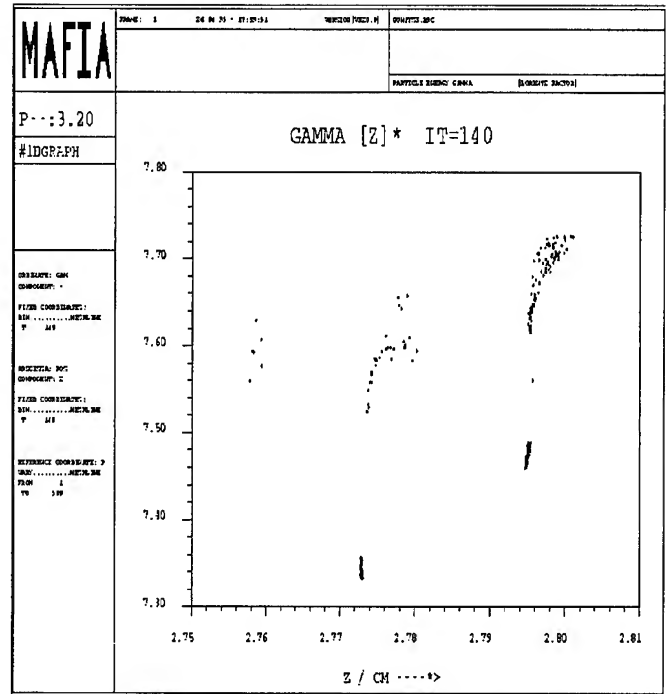


Figure 2: Particle beam energy distribution

motor with a $0.1\text{-}\mu\text{m}$ minimum step size was used to pull the bead through the structure. For a bead having a dimension that is small compared to the structure wavelength, the perturbation relation is given by [7]

$$\frac{\Delta f}{f_0} \approx \frac{3\Delta V}{4U} \left[\epsilon_0 \left(F_1 |E_{\parallel}|^2 + F_2 |E_{\perp}|^2 \right) - \frac{\mu_0}{2} \left(F_3 |H_{\parallel}|^2 + F_4 |H_{\perp}|^2 \right) \right] \quad (6)$$

where E_{\parallel} (E_{\perp}) and H_{\parallel} (H_{\perp}) are the electric and magnetic fields parallel (perpendicular) to the perturbing object axis and F_n ($n=1,2,3,4$) are the perturbational form factors. For a metallic sphere, these form factors are all equal to 1 [7].

The measurement setup (Figure 3) consists of two shorting plates located at the entrance and the exit of the structure to

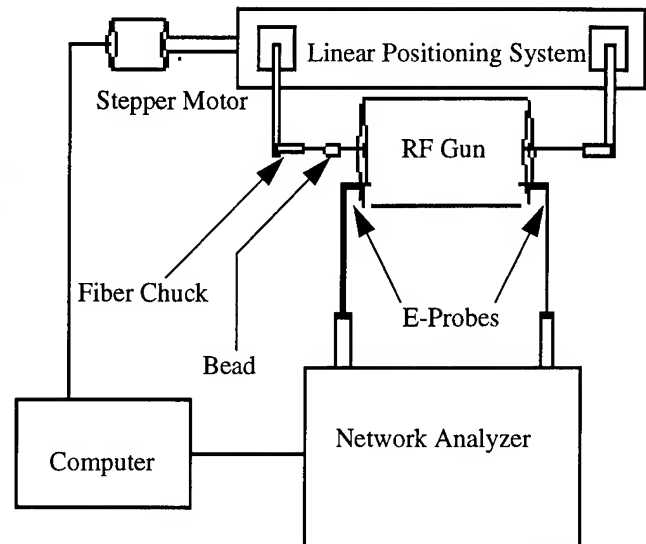


Figure 3: Bead pull field measurement setup

generate a standing wave field pattern. An on-axis hole was drilled in each plate to provide an opening for the bead's travel path. To excite the longitudinal electric field, a field probe of 1.194-mm outer diameter was fabricated. An identical probe was used as a pickup. Two fiber chuck holders held the ends of the fiber line while the bead was pulled through the structure. The bead was advanced through the structure in small increments ($\sim 94 \mu\text{m}/\text{step}$) through computer control of the stepper motor. At each bead position, the phase of the transmission coefficient, S_{12} , was measured using an HP 8510 network analyzer with an automatic data acquisition system. Figure 4 is the frequency spectrum of the excited modes in the structure and Figure 5 is a plot of perturbation measurement results of the π -mode.

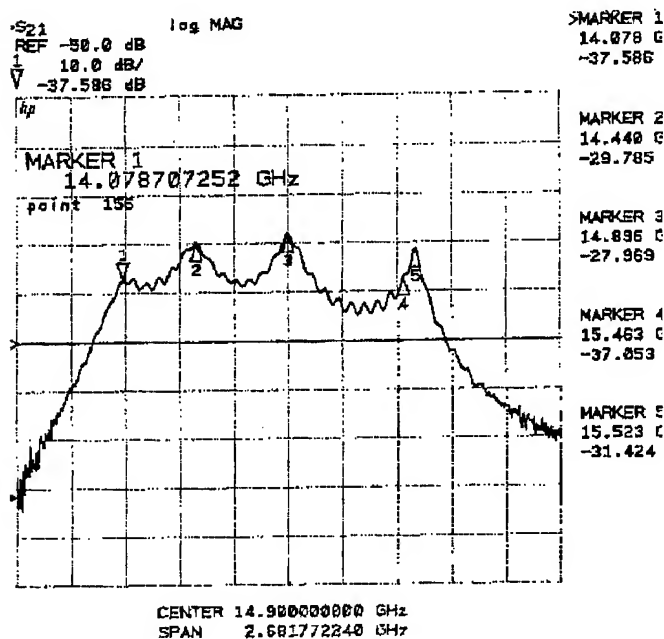


Figure 4: Frequency spectrum of the excited modes

IV. SUMMARY AND DISCUSSION

A 30-GHz photocathode rf gun is being considered as a low emittance electron source for a short-wavelength 50-MeV single pass linac-driven FEL. To understand the rf properties of the high-frequency rf gun, a 15-GHz 3 1/2-cell copper structure was fabricated and bench tested. Numerical modeling results using MAFIA give a resonant frequency of 15 GHz for the desired π -mode accelerating field with a shunt impedance of $254 \text{ M}\Omega/\text{m}$ ($Q=7000$). Beadpull measurements of the rf gun resulted in 15.5 GHz for the π -mode with a shunt impedance of $3.4 \text{ M}\Omega/\text{m}$ ($Q = 312$). The huge discrepancy between the calculated and measured shunt impedance are mainly due to mechanical imperfections of the cavity during fabrication. This structure was fabricated in many separate pieces with relaxed tolerances and was assembled in a "Lego-Block" manner (i.e., it was fitted inside a copper block with a set of bolts and nuts to hold it together at both ends). This resulted in poor rf contacts

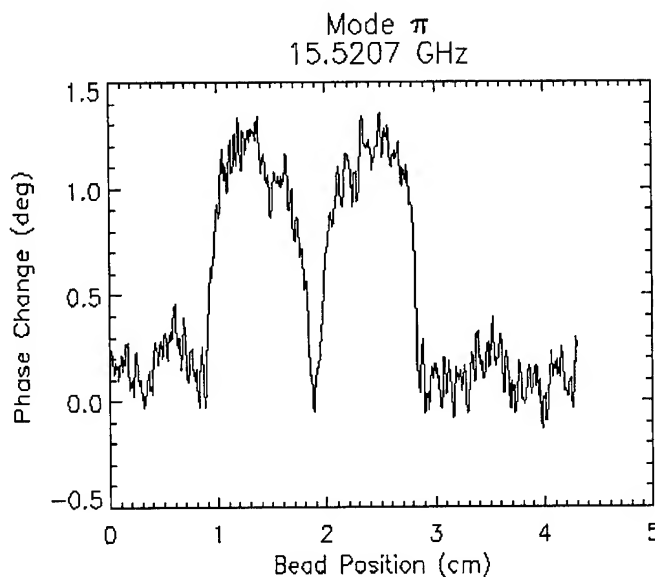


Figure 5: Perturbation measurement result for π -mode

between pieces (cells) which severely affected the rf measurements. Improvements on the structural fabrication and measurement methods are planned.

V. REFERENCES

- [1] R.L. Sheffield, E.R. Gray and J.S. Fraser, "The Los Alamos Photoinjector Program," NIM A272, 222-226 (1988).
- [2] P. O'Shea, "High Brightness Photo-Cathode Guns for Single Pass X-Ray FELs," 16th International FEL Conference, Stanford, CA, August 21-26, 1994.
- [3] J. Gao, "Theoretical Investigation in the Optimization Design of Microwave Electron Gun," Proc. 12th Free Electron Laser Conference, 1990.
- [4] K. McDonald, "Design of the Laser-Driven RF Electron Gun for BNL Accelerator Test Facility," IEEE Trans. Electron Devices, 35 No. 11, 2052-2059 (1988).
- [5] K.-J. Kim, Nucl. Instr. and Meth. A 250 396 (1986).
- [6] R. Klatt, et. al., "MAFIA, A Three-Dimensional Electromagnetic CAD System," Proc. of the 1986 Linear Accelerator Conference, SLAC-303, 276-278 (1986).
- [7] L. C. Maier and J. C. Slater, "Field Strength Measurements in Resonant Cavities," Journ. Appl. Physics, 23, 68-77 (1952).

THE RF GUN DEVELOPMENT AT SRRC

C. H. Ho, W. K. Lau, J. I. Hwang, S. Y. Hsu, Y. C. Liu
Synchrotron Radiation Research Center
Hsinchu 30077, Taiwan

The rf gun technology is of increasing interest due to its promising ability of producing high-brightness electron beams. Therefore it is a very attractive injector for any accelerator system demanding high current or low emittance beams, such as free electron lasers, linear colliders and other advanced accelerator applications. It is desirable to develop this technology at SRRC for future applications. The prototype cavities were fabricated and the low power level rf measurements were performed. The preliminary results are presented.

I. INTRODUCTION

Since the invention of the rf gun around mid eighties [1,2], it has attracted more than thirty research projects worldwide [3]. The promise of the photocathode rf gun to offer a high-brightness electron source has made many applications possible.

We plan to develop this technology at the Synchrotron Radiation Research Center (SRRC). Since the S-band rf gun system of the type developed by the Brookhaven National Laboratory (BNL) [4] has been widely used in many places, and the linac frequency of the SRRC booster synchrotron is also around 3 GHz, we decided to investigate this system as a start. The first step was to scale the frequency from 2856 MHz of the BNL gun up to around 3 GHz of our linac frequency by using the URMEL code. For the purpose of a quick start, we sent the very primitive design for the fabrication of a prototype copper cavity without further optimization yet. We would like to gain more experiences for tuning this one and a half cell structure through the cold tests first. On the other hand, we also fabricated an L-band (1.3 GHz) rf gun prototype cavity of the same type used in the AWA project [5]. We made low level rf power measurements for both gun cavities using the HP8510C network analyzer.

Recently, we are also involved in the collaboration for the X-band (8568 MHz) photoinjector project [6]. A prototype copper cavity will be manufactured very soon.

II. EXPERIMENTAL SETUP

The main experiment to be performed is to measure the electric

field distribution along the center axis of the cavity in the longitudinal direction. This is accomplished by the frequency perturbation method, usually called the bead-pull measurement. The whole setup for the bead-pull measurement of the S-band gun cavity is shown in Fig. 1. A copper bead with 3.98 mm diameter was used as the perturbation object. A fishing string passing a 1 mm diameter hole in the center of the cathode plug, the copper bead and the end cover plate of the cavity was laid on the V-shaped grooves of the pulleys. One of the pulley was connected to a driving motor. A supporting stand was made to accommodate the gun cavity for the bead-pull measurement. The central frame which is detachable from the supporting stand is used to hold all parts of the cavity and waveguide tightly together. For different gun cavities, we only need to replace the central frame.

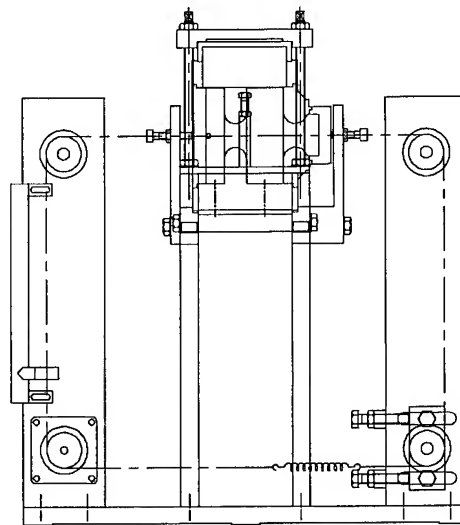


Figure 1. Assembly drawing for bead-pull measurement

We have not installed the tuner on each cell yet. At present we only used the cathode plug for tuning purpose. The cathode plug is made as big as 6 cm in diameter to avoid the high field area for the rf choke joint surrounding the cathode. We hope this will reduce the arcing around the choke joint under high power

operation. The cathode surface will be flush with the cavity inner surface and be held still in full power operation. The tuning of field balance will be achieved through the tuner on each cell. The resonant frequency of the structure will be controlled by the cooling temperature. The S-band waveguide is shorted on one end and the other end is connected to the network analyzer through the WR284 waveguide to coax adapter. We used a sliding brass block of 3 cm thick to find the best coupling position for the shorting plate.

In order to build the cooling channel inside the cavity instead of just braze it on the outer surface, we modified the outer shape of the AWA drive gun cavity to be rectangular for easier machining. Figure 2 shows the outlook of the cooling channel.

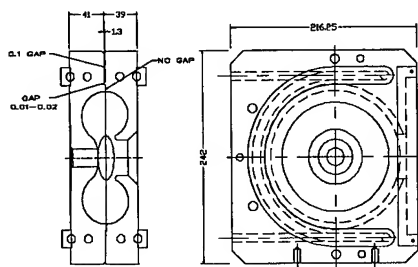


Figure 2. The cooling channel for the AWA drive gun cavity.

III. PRELIMINARY RESULTS

Before the bead-pull measurement, we first adjusted the sliding block to search the maximum rf power coupling position for the shorting plate. The S-band cavity resonant frequency was around 2922 MHz. It was found a shorting plate located at a distance of 11.5 cm from the center of the coupling hole gives the best coupling. This distance is very close to $3/4$ guide wavelength which is 11.78 cm.

A complete turn of the cathode for the S-band cavity is made to be 1 mm. Therefore we are able to measure the frequencies of π -mode and 0-mode as a function of the cathode position. The results are shown in Fig. 3. We did notice the same phenomenon as observed in BNL and UCLA. The frequencies of both π -mode and 0-mode approach each other when the cathode surface get closer to be flush with the cavity inner surface and then turn into one another when the cathode is away from the inner surface of the cavity.

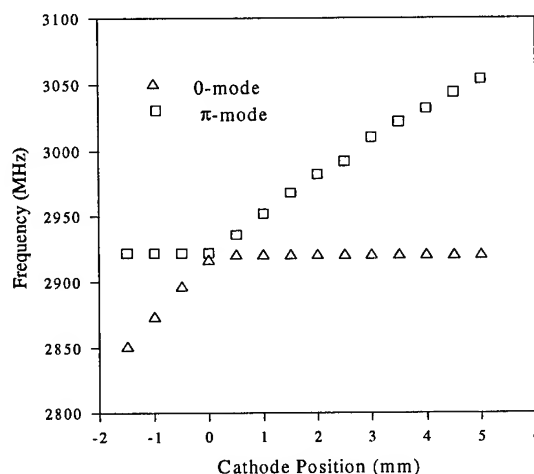


Figure 3: Frequencies vs. cathode position

The tuning for the field balance on both cells of the cavity is very sensitive to the cathode position. The field balance position is around where both π -mode and 0-mode frequencies approach each other. Figure 4 shows a bead-pull measurement result where the ratio of the maximum field amplitude in the first cell to second full cell is around 0.87. The cathode surface is at 0.13 mm outward from the cavity inner surface for this case.

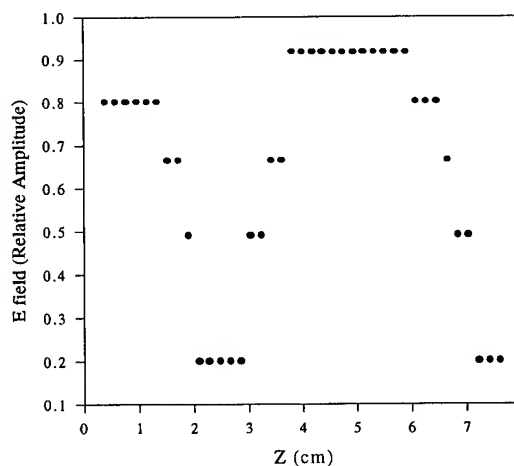


Figure 4: E-field distribution along the axis

We also performed the bead-pull measurement for the AWA drive gun cavity. We compared the measurement results with the URMEL prediction [7] by normalizing both field amplitudes to be the same around the cathode surface. Figure 5 shows the consistency between URMEL calculation and the measurement.

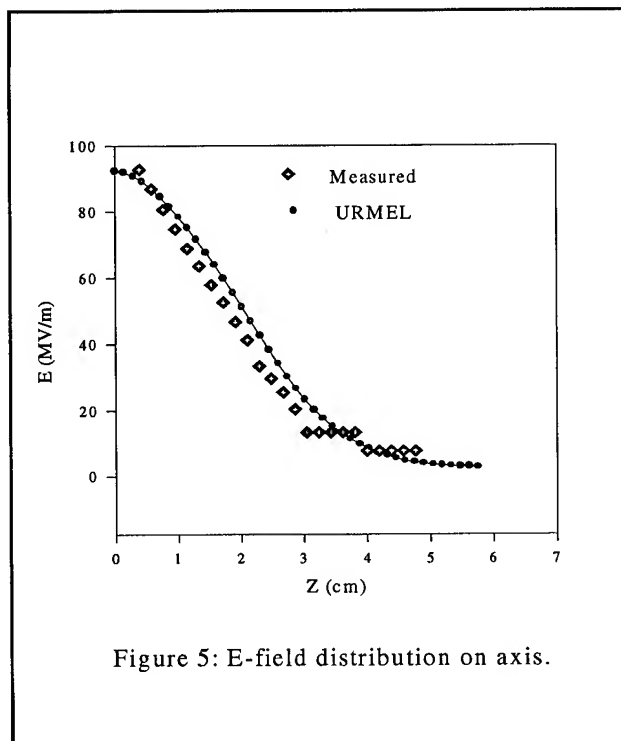


Figure 5: E-field distribution on axis.

The quality factor for the 1.3 GHz AWA gun cavity was measured to be around 12827 which is very close to what they measured before [7].

IV. SUMMARY

We performed some cold tests for both 3 GHz and 1.3 GHz rf gun cavity. The preliminary results show good agreements with URMEL prediction and previous works performed at other places. But it's only a beginning of a more complete investigation. After that we will begin to send the cavity for a vacuum furnace brazing. Also as mentioned before, the X-band prototype cavity will be fabricated in the near future.

V. ACKNOWLEDGMENTS

One of the authors (C. H. Ho) would like to thank Prof. C. Pellegrini of UCLA for providing useful information for the fabrication of the S-band cavity. He is also indebted to all helpful communications with R. Zhang, R. Konecny, and C. Travier. This work is supported in part by the National Science Council (Taiwan) under contract No. NSC-84-2112-M-213-002.

VI. REFERENCES

- [1] G.A. Westenskow and J.M.J. Madey, "Microwave Electron Gun", Laser and Particle Beams (1984), Vol. 2, Part 2, p. 223.
- [2] J.S. Fraser, R.L. Scheffield, E.R. Gray, and G.W. Rodenz, "High-Brightness Photoemitter Injector for Electron Accelerators", in Proc. 1985 IEEE Particle Accelerator Conf. (Vancouver, BC), p. 1791.
- [3] C. Travier, "RF Guns: A Review", RFG Note SERA/90-219/RFG, Laboratoire De L'Accelérateur Lineaire, August 1990.
- [4] K. Batchelor, J. Sheehan and M. Woodle, "Design and Modelling of a 5 MeV Radio Frequency Electron Gun", BNL-41766, August 22, 1988.
- [5] P. Schoessow, et al., "The Argonne Wakefield Accelerator High Current Photocathode Gun and Drive Linac", in this conference.
- [6] F.V. Hartemann, et al., "2.142 GHz Repetition Rate High Brightness X-Band Photoinjector", in this conference.
- [7] C.H. Ho, "A High Current, Short Pulse Electron Source for Wakefield Accelerators", Ph.D Dissertation (UCLA), 1992.

Design and Construction of High Brightness RF Photoinjectors for TESLA

E. Colby, V. Bharadwaj, J.F. Ostiguy, T. Nicol

Fermi National Accelerator Laboratory*, P.O. Box 500, Batavia, IL 60510

M. Conde, J. Rosenzweig

UCLA Dept. of Physics, 405 Hilgard Ave., Los Angeles, CA 90024

Abstract

The design, construction and testing of a high brightness high bunch charge RF photoinjector matching the requirements of the TESLA Test Facility is discussed. Engineering design work, the results of cold test measurements, and the planned experimental program are presented. Conceptual design work leading to an advanced high-brightness asymmetric emittance RF photoinjector for application to TESLA500 is also briefly discussed.

I. INTRODUCTION

The TESLA Test Facility (TTF), as proposed, is a 500 MeV superconducting linac designed to study technological issues involved in constructing and operating TESLA500, a 0.5 TeV superconducting linear accelerator. Studies of higher order mode power deposition at cryogenic temperatures will require a train of bunches with the same frequency spectrum as will be present at TESLA500. The combination of relatively high bunch charge (8 nC), short pulse length (1 mm), moderate transverse emittances ($< 20 \pi$ mm-mr) and long pulse train (800 pulses with 1μ s spacing) make the design challenging. In addition, the potential for operating the gun over a large range of bunch charges (0.5 nC to 10 nC), a range of accelerating gradients (35 MV/m to 50 MV/m) and with different focussing fields required a flexible focussing assembly. Asymmetric transverse emittances of 1π mm-mr vertically and 20π mm-mr horizontally are required for TESLA500, and are potentially achievable directly from an RF photoinjector, eliminating the need for an electron damping ring. Given that the long pulse trains demand large damping rings, elimination of the electron damping ring would represent a significant cost savings.

II. DEVELOPMENT

A. Symmetric Emittance Photoinjector for TTF

An injector producing the required bunch properties and pulse train structure was designed with the space and RF power constraints of the TTF in mind. A Brookhaven-style[2] 1 1/2 cell π -mode structure was modified to operate at 1.3 GHz with substantially increased (factor of 5) intercell coupling to reduce field balance tuning sensitivity. A single-cell iris coupler drives the full cell only, leaving clear sufficient space to mount a focussing solenoid over the half cell, shown in figure 1. An additional focussing solenoid follows immediately after the gun to provide a continuously variable magnetic center of the focussing lens, a flexibility that will allow wide ranging examination of space

charge emittance compensation[3] over a wide range of bunch charges.

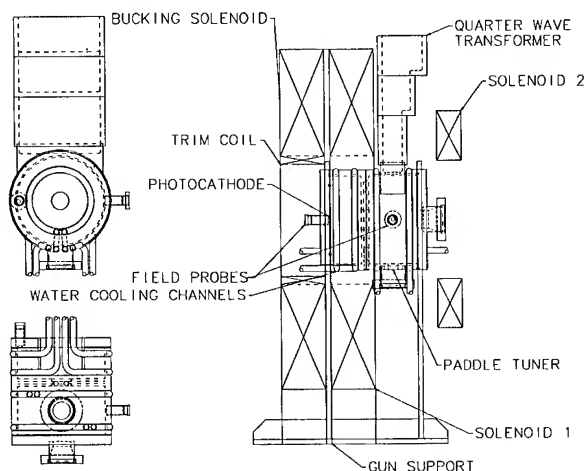


Figure 1. Symmetric emittance photoinjector

The gun is followed by a drift to allow the space charge induced correlated emittance growth to reverse before entering a moderate gradient (15 MV/m) linac. At the TTF, the linac will be a 9-cell superconducting structure, and thus studies of dark current deposition were carried out, and have shown that strategic placement of several collimators ahead of the linac, together with the strong overfocussing that naturally occurs from the emittance compensating solenoid, are enough to reduce the dark current reaching the linac by two orders of magnitude. Initial testing of the injector at the Argonne Wakefield Accelerator (AWA) Facility will be carried out with a retrofitted copper 9-cell TESLA structure to reproduce the spatial field profiles of the actual structure.

The linac is rephased to impart a negative α_ϕ sufficient to permit pulse compression by a factor of two in a dispersive chicane. A positive time dispersion in the chicane is chosen to cause the space charge forces to oppose the compression, stabilizing against charge fluctuations. The compression chicane is composed of four identical C-frame dipoles with moderate field strength (0.9 kG) and a suitably formed vacuum chamber with collimation slits placed in the maximum dispersion region to permit momentum collimation of the beam.

Numerical simulation of all components of the injector was carried out using a version of the beam dynamics code PARMELA modified to accept externally generated field maps for RF cavity and static magnetic focussing fields. RF field profiles for the gun and linac cavities were derived from Superfish runs, and static field profiles for the solenoid focussing assembly were derived from Poisson runs. Table I below outlines the

*Operated by the University Research Association, Inc., under contract with the U.S. Department of Energy

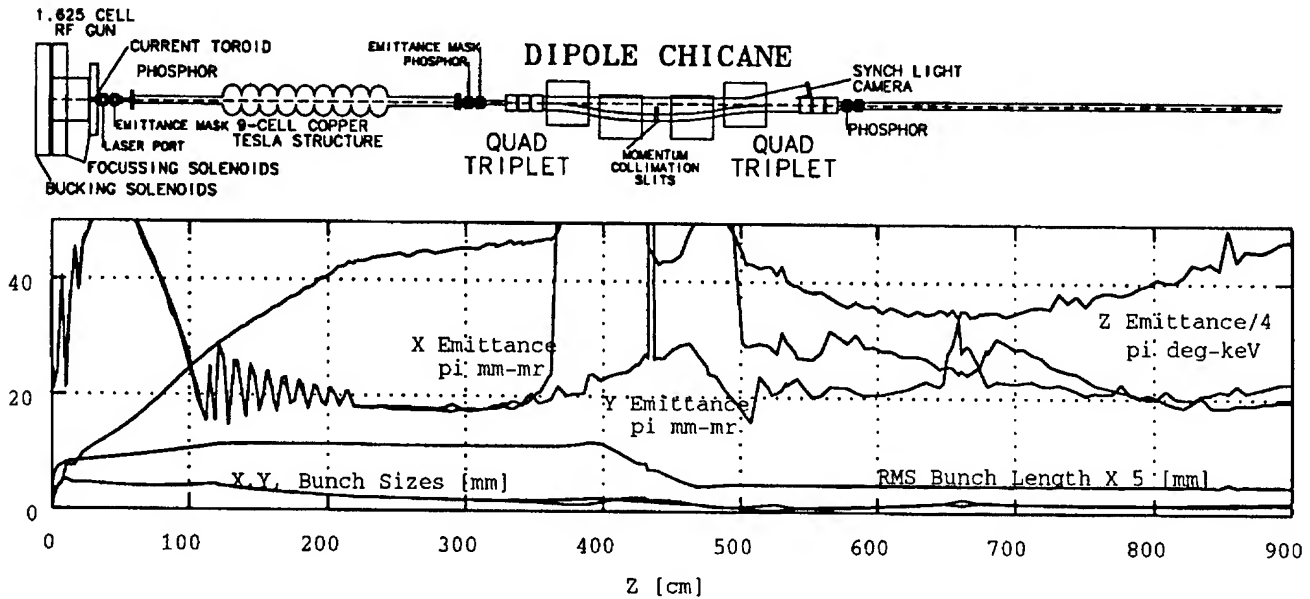


Figure 2. Symmetric RF Photoinjector Test Layout (top), Emittance and Beam Size Evolution the Injector (bottom)

predicted performance of the TTF injector prototype from simulations. Transverse emittances are listed as full-width-at-half-maximum emittances, as would be measured using a slit emittance mask and phosphor screen, while longitudinal emittance is listed as 100% RMS. All emittances are normalized. Figure 2 shows the proposed beamline layout for the prototype tests at Argonne, together with emittance and beam size evolution. The longitudinal emittance has been scaled by a factor of 0.25 and the bunch length has been scaled by a factor of 5 to permit display on the same axis as the other quantities.

Parameter	Value
Bunch Charge	8 nC = $5 \times 10^{10} e^-$
Laser pulse length FWHM	7.4 ps
Launch Phase (w.r.t. $E_z = 0$)	50°
Beam radius at cathode	6.53 mm
Peak field on cathode	35 MV/m
Post-Gun Energy	3.8 MeV
Average Linac Gradient	15 MV/m
Post-Linac Energy	18.5 MeV
Horizontal Emittance	19.3π mm-mr
Vertical Emittance	19.7π mm-mr
Longitudinal Emittance	189 deg-keV
Momentum Spread	1.15 %
Bunch Length	0.74 mm
Peak Current	1.28 kA

Table I
Predicted performance of the symmetric injector

Thermal analysis of the injector structure under the 1% duty cycle of TTF has been carried out. The peak power dissipation of 4.5 MW (corresponding to a peak cathode field of 50 MV/m)

during the > 1 ms RF pulse has been found to cause less than 6 kHz detuning of the cavity, or less than a twentieth of the cavity's 3 dB bandwidth, a frequency change that can be compensated for by a low bandwidth feedforward system. Structural stress analysis using ANSYS shows that the peak stress intensity does not exceed 40 MPa, safely below the yield strength of OFHC copper, 76 MPa. In anticipation of possible microphonic detuning of the cavity from turbulent water flow in the cooling channels, a channel of geometry similar to the proposed cooling channels for the high duty cycle gun have been included in the prototype. Deformation measurements show the deformation due to 110 psi pressurization is $1.7 \mu\text{m}$. Pressure fluctuations due to turbulence are generally less than $\Delta P/P_0 \propto 10^{-2}$ for non-erosive flow rates, and thus the amplitude of wall vibrations will be completely negligible.

Cold testing of the gun structure has been carried out on a composite copper/brass model. The coupling has been measured at 0.21 %, in reasonable agreement with the Superfish-calculated value of 0.19 %. Tuning characteristics of the cathode (which is mounted on a micrometer) and a separate paddle-style tuner in the full cell have been examined, and also found in reasonable agreement with simulation. Field profiles derived from resonant frequency perturbation methods closely correspond to expectations from Superfish calculations, as shown in figure 3 below. Measurements of the dipole shift in the full cell induced by the input coupler show less than 1.1 mm ($1/200$ of an RF wavelength) deviation from the geometric center of the structure, as is shown in figure 3 below. Data for the longitudinal field profile were taken at monotonically increasing longitudinal coordinate, while transverse data were taken in random order, illustrating more clearly the contribution to the resonant frequency shift from thermal effects during the measurement.

Preliminary calculations[4] have shown that the beam density is high enough to generate significant coherent synchrotron radiation in the compression chicane at wavelengths comparable

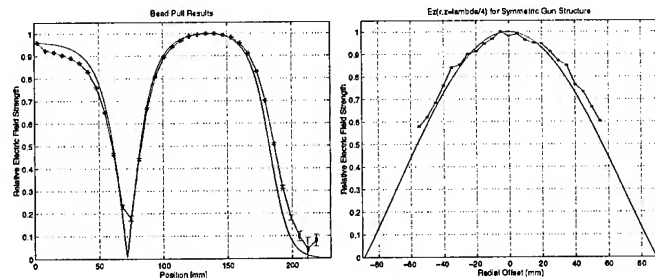


Figure 3. Measured and calculated longitudinal and transverse field profiles for the symmetric gun structure

to the bunch length (1 mm). Further simulation work is underway at this time, including modification to PARMELA to include retardation and radiation effects in the space charge calculation. The vacuum chamber in the dipole chicane will be fitted with a tangent optical viewport in the final dipole (where beam density and radiation intensity are maximum) to allow observation of the emitted IR synchrotron radiation.

Commissioning of the symmetric emittance photoinjector is scheduled to take place mid-summer, with preliminary high power RF testing of the linac structure occurring earlier. Full testing of the injector including pulse compression is expected by year's end. In addition to a full characterization of the gun, emittance compensation studies will be carried out using the double solenoid to examine the effects of lens location and strength on emittance compensation. A unique time-resolved emittance measurement using a streak camera to streak the light from a Čerenkov gas cell placed to intercept the beamlets generated from a slit emittance mask will be attempted, to provide the first experimental verification of the physical mechanism of emittance compensation.

B. Asymmetric Emittance Photoinjector for TESLA500

Emittance compensation for the flat beam photoinjector requires the use of quadrupoles to focus the beam in both planes, as solenoidal focussing would couple the transverse phase planes and results in severe degradation of the small vertical emittance. A quadrupole doublet, positioned around the gun itself, provides the initial focussing kick for compensation. A subsequent triplet at the exit of the gun allows for matching the beam into the subsequent linac section for further acceleration. Initial studies have demonstrated compensation for the vertical emittance, while the planned approach of using substantial guard charge at the horizontal extrema of the bunch to minimize the nonlinear space charge emittance growth of the core, followed by collimation of the nonlinearly heated portions of the bunch at the horizontal edges after further acceleration has reduced the space charge forces.

After considering a number of geometries, an RF structure suitable for accelerating a flat beam with minimal energy spread and minimal coupling of the transverse phase planes a structure composed of shorted sections of ridged waveguide was chosen[5]. Field profiles from Hewlett Packard's High Frequency Structure Simulator in figure 4 below show that a very large flat-field region is available for accelerating large aspect ratio beams.

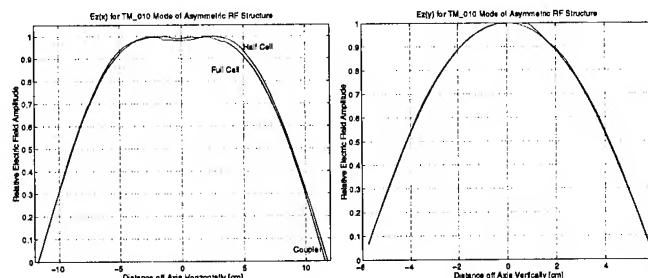


Figure 4. Transverse field profiles of the TM_{010} mode

Testing of the asymmetric gun structure will proceed with fabrication of a cold test model to examine field balance and field flatness issues. Powered testing of the injector at the AWA reusing the injector beamline and diagnostics developed for the symmetric TTF gun prototype is tentatively planned in the coming year.

III. CONCLUSION

Design of an input coupler for the normal conducting 9-cell TESLA structure and subsequent testing at operating RF power levels will complement the gun construction activities, leading to first beam dynamics studies of the gun by mid summer. The linac and compression chicane will be commissioned in early fall, with design of the full-power TTF gun structure following shortly thereafter. A continued attack on the beam dynamics issues, and construction of a cold test model of the RF structure will form the main asymmetric injector effort.

References

- [1] J. Rosenzweig, *et al*, *Proc. of 1993 Part. Accel. Conf.*, 3021-3 (IEEE, 1993).
- [2] I. Lehrman, *et al*, *NIM A318*, 247-53, (1992).
- [3] B. Carlsten, *NIM A285*, 313-9 (1989).
- [4] P. Gürtler, TESLA FEL Meeting, Feb 10, 1995.
- [5] R. Miller, in the *Proc. of Wrkshp. on Appl. High Brightness High Current Electron Sources*, UCLA, Jan 5-6, (1995).

Jitter Sensitivity in Photoinjectors*

Patrick G. O'Shea,
Free-Electron Laser Laboratory, Department of Physics, Box 90319,
Duke University, Durham NC 27708 USA

Photoinjectors are becoming the electron source of choice for high brightness, high current applications such as very-short wavelength free-electron lasers and electron linear colliders. In both of these applications the electron beam will be bunched to a multi-kiloampère current from its initial value of a few hundred ampères. The performance of such aggressive bunchers is very sensitive to the correlations in the longitudinal phase space. One of the major performance-determining factors is the timing of the injection of the electrons in the gun relative to the rf field. Of particular concern is the jitter of the drive-laser timing and amplitude. We develop a model of the system and use it to study the implications for photoinjector design*.

INTRODUCTION

In the past decade the invention and refinement of the rf photocathode gun has resulted in a dramatic improvement in electron beam brightness over that delivered by conventional injectors [1]. As rf photocathode guns evolve from being laboratory curiosities they are being considered as electron sources for such challenging applications as linear colliders and single-pass x-ray free-electron laser amplifiers.

Previously, the primary beam characteristics of interest have been charge, current, emittance and brightness. Recently, Travier [2] has reported the results of a survey of the photoinjector community where the primary concern of the experimenters has been drive-laser stability. A number of proposed machines, including electron linear colliders and single pass X-ray free-electron lasers, require that the beam be bunched by a factor of ten or more. Consider the Linac Coherent Light Source (LCLS) [3], a proposed single pass X-ray FEL at SLAC, as an example system.

The final specifications of the LCLS are still in flux, however the following design guidelines provide a basis for discussion in this paper. The rf photocathode gun will generate a beam with 3-10 MeV, 1 nC in a 2 ps rms bunch and a normalized rms emittance of 1π mm-mrad and an rms energy spread of 0.2%. The beam will be accelerated to 7 GeV and compressed by a factor of ten to reach a peak current of 2.5 kA. The compression will occur in two stages: a factor of two at 100 MeV and a further factor of five at 2 GeV. The gain length of the FEL is very sensitive to both the emittance and the peak current of the beam [3]. The transverse emittance

required is approximately a factor of two better than has been demonstrated in an rf photocathode gun to date. The bunching is very sensitive to the longitudinal phase space of the bunch and hence to timing and amplitude jitter in the rf gun [4]. The stability required is somewhat better than has been demonstrated in operational photoinjectors.

As indicated above the bunching schemes necessary for the LCLS require precise control of the phase-energy correlations in longitudinal phase space. Phase jitter of the drive laser relative to the gun rf fields impacts both the phase-energy correlation at the gun and the evolution of the correlations in the linac. Current jitter in the gun alters the wakefield induced phase space distortions. Because of phase buffering in the gun, the phase jitter of the beam in the linac is not necessarily equal to that of the drive-laser relative to the rf phase.

JITTER SENSITIVITY

To evaluate the sensitivity of the bunching to drive-laser phase jitter we use a simple model in which we assume that the correlated energy spread is much greater than the uncorrelated energy spread and $\gamma \gg 1$, where γ is the electron energy divided by its rest energy. Then we may write the bunching ratio (B) i.e. the ratio of the bunch length after (σ_2) and before bunching (σ_1) as:

$$B = \frac{\sigma_2}{\sigma_1} \approx \left| 1 - \frac{2\pi f R_{56}}{c\gamma} \frac{\partial \gamma}{\partial \phi_B} \right| \approx \left| 1 - \frac{2\pi f R_{56}}{c} \cot \phi_B \right| \quad (1)$$

where f is the rf frequency, c is the velocity of light, ϕ_B is the asymptotic phase in the linac before the buncher of the bunch centroid relative to zero rf phase, $R_{56} = \frac{\Delta \ell}{\Delta p/p}$ is the bunching

parameter of the buncher. The sensitivity of B to injection phase of the drive-laser (ϕ_0) is:

$$\frac{\partial B}{\partial \phi_0} = \frac{\partial B}{\partial \phi_B} \frac{\partial \phi_B}{\partial \phi_0} = \pm \frac{2\pi f R_{56}}{c \sin^2 \phi_B} \frac{\partial \phi_B}{\partial \phi_0} \quad (2)$$

where the positive sign corresponds to under compression and the negative to over compression in the buncher. In general in a multi-section linac $\phi_B \neq \phi_G$, the asymptotic phase at the end of the gun. For $\gamma \gg 1$ at the end of the gun we can write $\frac{\partial \phi_B}{\partial \phi_0} \approx \frac{\partial \phi_G}{\partial \phi_0}$ in Eq. 2.

Our concern is with the sensitivity of ϕ_G to variation in ϕ_0 . Travier [5] has shown (using a combination of Kim's theory [6] and simulation) that the asymptotic phase (ϕ_G) of the

* Work supported by ONR under contract N00014-91-c-0226

central particle in the bunch at the end of the gun, for $\gamma \gg 1$, is given in terms of its injection phase (ϕ_0) at the cathode as:

$$\phi_G = \phi_0 + \frac{1}{2\alpha \sin(\phi_0 + \frac{\pi}{6\sqrt{\alpha}})} + \frac{\pi}{15\alpha} \quad (3)$$

where $\alpha = eE_0/4\pi fmc$ with e the electronic charge, m its mass, E_0 is the peak accelerating electric field. Differentiation of Eq. (1) with respect to ϕ_0 gives:

$$\frac{\partial \phi_B}{\partial \phi_0} = \frac{\partial \phi_G}{\partial \phi_0} = 1 - \frac{\cot(\phi_0 + \frac{\pi}{6\sqrt{\alpha}})}{2\alpha \sin(\phi_0 + \frac{\pi}{6\sqrt{\alpha}})} \quad (4)$$

In Fig. 1 and subsequent figures we compare two common photoinjector cases:

- a) $f = 2856$ MHz and $E_0 = 100$ MV/m, i.e. $\alpha = 1.63$.
- b) $f = 1300$ MHz and $E_0 = 25$ MV/m, i.e. $\alpha = 0.89$.

We see that there can be significant buffering of the phase jitter for small ϕ_0 . Therefore sensitivity of the bunching ratio to phase jitter can be significantly reduced by running at small ϕ_0 .

The asymptotic phase (and hence the bunching ratio) is also sensitive to the accelerating gradient in the gun E_0 . Fig. 2 shows a plot of $\frac{\partial \phi_G}{\partial E_0}$ versus injection phase. The sensitivity to

fluctuations in E_0 is small but may not be negligible. Fluctuations in gun current will result in changes in E_0 to an extent dependent on the beam loading and cavity Q of the gun. In contrast to the phase sensitivity, gradient sensitivity is minimized for larger ϕ_0 . If we ignore current fluctuations it should be possible to stabilize the accelerating gradient to approximately 0.1%.

The fractional change in the mean energy of the beam at the exit of the gun is given approximately by:

$$\frac{1}{\gamma_G} \frac{\partial \gamma_G}{\partial \phi_0} = \frac{\partial \phi_G}{\partial \phi_0} \cot(\phi_G) \quad (5)$$

For an FEL driven by such a beam the FEL wavelength jitter will be given by $\frac{1}{\lambda} \frac{\partial \lambda}{\partial \phi_0} = 2 \frac{\partial \phi_G}{\partial \phi_0} \cot(\phi_G)$. Eqn. (5) is plotted

in Fig. 3 for the two cases of interest. Note that the energy shift becomes negative when $\phi_G > \pi/2$. It is evident that the energy of the beam is most sensitive to phase fluctuations for $\phi_0 \in [20, 30]^\circ$.

The requirement to minimize the transverse emittance generally requires that $\phi_G \approx \pi/2$. [6] This results in the requirement that $\phi_0 \approx 30^\circ$ for the 1300 MHz gun and up to 60° for the 2856 MHz gun, however, this may differ from one design to another depending on whether emittance compensation is used on the relative importance of space-charge and rf induced emittance growth. [6, 7]. It is evident from Eq. (2) that sensitivity to jitter may be reduced by having two bunchers one of which over compresses and one of which

under compresses so as to cause the jitters to cancel. Simulations [4] with twin bunchers indicate that the tolerance for phase jitter is $\pm 0.45^\circ$ (± 0.5 ps) and the gun current jitter tolerance is $\pm 2.2\%$. The choice of injection phase will depend on compromise between bunching stability (governed by achievable drive-laser stability) and transverse emittance considerations.

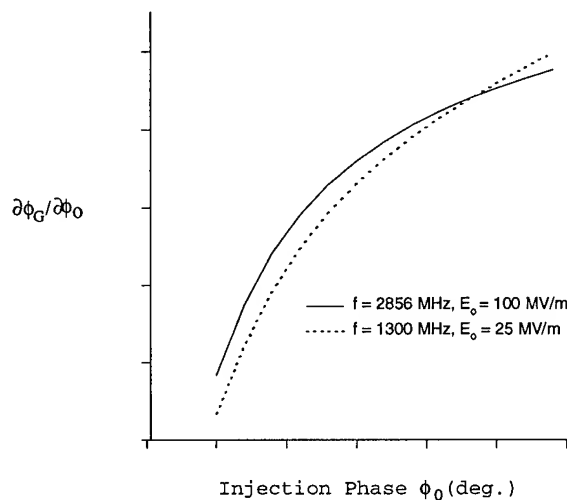


Fig 1. Asymptotic phase jitter sensitivity versus injection phase

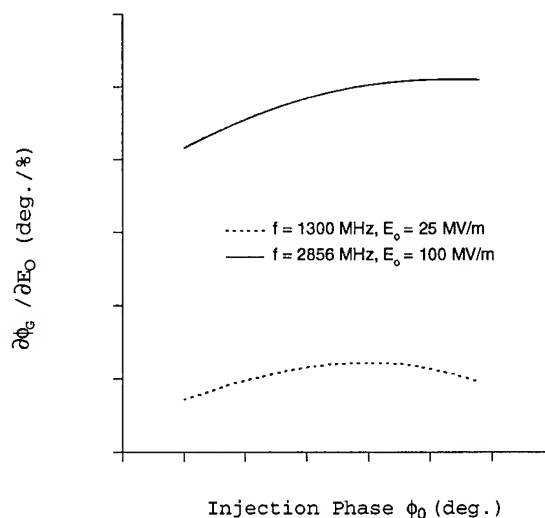


Fig 2 Sensitivity of asymptotic phase to accelerating gradient jitter versus injection phase

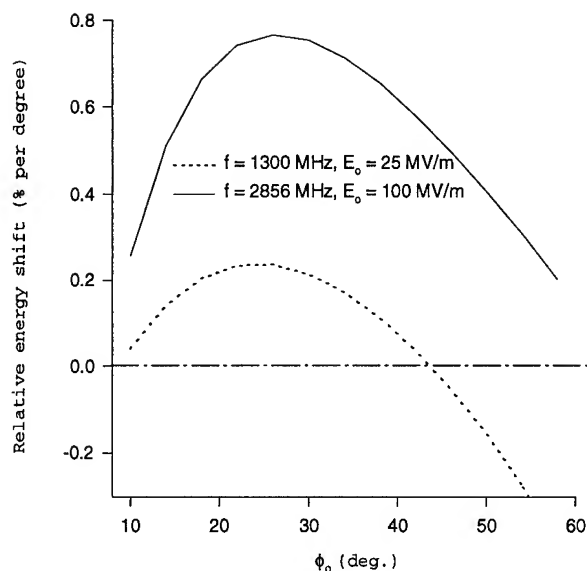


Fig. 3. Fractional energy shift per degree phase change at asymptotic phase for $\gamma \gg 1$, versus injection phase.

DRIVE LASER STABILITY

There are currently two types of mode-locked lasers in common use: fourth harmonic Nd:YAG or Nd:YLF [2,8]. Recently 3rd harmonic Ti:SAF is being studied for producing very short (sub-picosecond) pulse lengths [9]. When operated under ideal conditions, the phase and amplitude jitter of mode-locked lasers can be very small i.e. < 1 ps and 1% peak to peak respectively. The long-term performance of drive lasers has been degraded by some or all of the following conditions: poor temperature control, a non clean-room environment, cavitation in cooling water, and flash-lamp and harmonic crystal aging.

The most extensively studied drive-laser has been that of the second-harmonic Nd:YLF laser at the APEX facility in Los Alamos. The published data for pulse-to-pulse energy stability has been reported to be between 1%-5% peak to peak [10]. Phase jitter with respect to the rf has been reported to the order of 5 ps peak-to-peak over short time scales (seconds) with 10 ps per hour long term drifts [10,11].

Unpublished data [24] from APEX show that phase jitters of 2 ps peak to peak (0.5 to 1 ps rms) and long term drifts of 2 ps were achieved using a phase mixing technique to measure the phase of the drive-laser output relative to the rf in conjunction with active feed forward control.

Spatial jitter of the drive laser spot must also be considered. Centroid jitter of the drive-laser spot will result in dipole wakefield modes being excited while mode shape jitter will result in higher-order wakefield modes. Analysis of

centroid jitter indicates that a factor of two emittance growth is possible in a 1-nC bunch with a 0.5 mm transverse displacement of 1-mm drive-laser spot in the first six metres of an S-band linac [12]. Simulations for the LCLS indicate that over longer distances emittance growth of 50% is possible with transverse beam displacement of as little as 10 μm [13]. The centroid stability of a 2nd harmonic Nd:YLF drive-laser spot striking the cathode at close to normal incidence has been demonstrated to be approximately 50 μm rms over a few minutes in the APEX photoinjector [11].

The published data show that drive-laser performance will need some improvement for applications such as the LCLS. It should be emphasized that most drive-lasers in operation to date have been one of a kind prototype lasers. The introduction of commercially-produced integrated laser systems along with the use of diode pumped Nd:YLF oscillators and amplifiers offers the possibility of significantly enhanced performance. Preliminary results [14] with such systems indicate sub-picosecond phase stability and less than 50 μm transverse centroid jitter.

CONCLUSION

It is evident that jitter considerations should be taken into account in designing photoinjector systems. For fixed α higher rf frequencies are less desirable. We have not addressed the sensitivity of the transverse emittance. This is of particular importance in cases where compensation for space-charge induced emittance growth is used. [15]

REFERENCES

1. C. Travier, Particle Accelerators 36, (1991) 33.
2. C. Travier, LAL SERA publication 94-388, to appear in the Proceedings of the Advanced Accelerator Workshop, Lake Geneva, Wisconsin, June 1994.
3. H. Winick et al., Nucl. Instr. and Meth A347 (1994) 199.
4. K.L. Bane, T.O. Raubenheimer and J.T. Seeman, in Proc. 1993 Particle Accelerator Conference, Washington DC (1993) 596.
5. C. Travier, Nucl. Instr. and Meth A341 (1994) 26
6. K.J. Kim, Nucl. Instr. and Meth A275 (1989) 201.
7. B.E. Carlsten et. al. J. Quantum Electronics, 27 (1991) 2580.
8. J.W. Early et. al. Nucl. Instr. and Meth A18 (1992) 381.
9. P. Georges et al. in Proc. 1993 Particle Accelerator Conference, Washington DC (1993) 3053
10. A.H. Lumpkin and J. W. Early, Nucl. Instr. and Meth A18 (1992) 389.
11. J.W. Early, personal communication
12. J.C. Gallardo and H. Kirk, to be published.
13. T.O. Raubenheimer, Proceedings of the 1994 International FEL Conference, Stanford, August (1994)
14. I.S. Lehrman, personal communication.
15. B.E. Carlsten, Particle Accel., 49, (1995) 27.

ASYMMETRIC EMITTANCE BEAM GENERATION USING ROUND BEAM RF GUNS AND NON-LINEAR OPTICS

G. Fiorentini, C. Pagani, L. Serafini, INFN - Milano
LASA, Via Fratelli Cervi, 201, 20090 Segrate (MI), Italy

ABSTRACT

Future generation electron-positron linear colliders need asymmetric flat beams in order to properly control the beam-beam interaction at the final focus. Room temperature collider designs ask for normalized rms transverse emittances which look not attainable by RF Photo-Injectors, whilst the requirements of the TESLA superconducting collider ($\epsilon_{nx} = 20$ mm mrad, $\epsilon_{ny} = 1$ mm mrad) are at the edge of the present RF gun status of the art, except for the asymmetric emittance requirements. In this paper we explore the efficiency of conventional round-beam RF guns in conjunction with non-linear optical devices, namely sextupole triplets, as converters of round beams into flat beams, in order to match the TESLA specifications. Basically the beam emittance, at the exit of the gun, must be dominated by non-linear effects (spherical aberrations). A quadrupole doublet and a sextupole triplet, placed downstream the beam transport line, provide respectively a geometric astigmatism and an asymmetric emittance correction in the vertical and in the horizontal phase-spaces. The possibilities to produce asymmetric beams using this technique are presented here. In Section 1 we introduce the subject, premises and general performances of the device. In Section 2 we give results of some analytical scaling laws. In Section 3 we show some preliminary simulations of ray-tracing throughout the structure.

I. INTRODUCTION

The present study arises from the following considerations:

- 1 - a consolidated knowledge of state of the art RF-guns to generate high quality round beams ($\epsilon_{nr} = 2-4$ mm mrad).
- 2 - a great interest in finding "slim" structures to convert round beams into asymmetric beams, which may offer an alternative to the damping rings.
- 3 - there exists no linear transformation that allows to increase the emittance aspect ratio $\epsilon_{nx}/\epsilon_{ny}$: belonging to the class of symplectic matrixes[1], any of them conserves the squared sum $\epsilon_{nx}^2 + \epsilon_{ny}^2$, and the product $\epsilon_{nx} \cdot \epsilon_{ny}$.

Starting from these assumptions, we found that non-linear optical components could produce asymmetric emittances if the original beam emittance (equal in both planes) is dominated by spherical aberrations. In Fig. 1 we present a layout of the non linear optical system (the *flat beam converter*) which accomplishes this task.

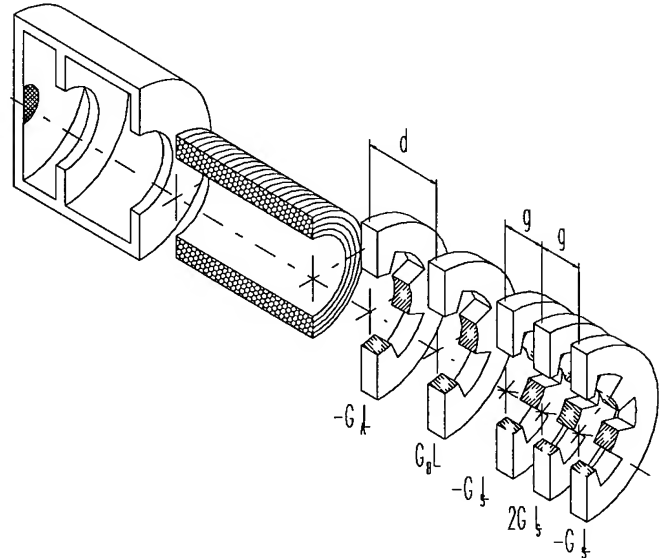


Fig. 1: Layout of the flat beam converter.

The input phase space can be described by:

$$\begin{aligned} p_{r0}(r_0) &= c_1 \cdot r_0 + c_3 \cdot r_0^3 \\ p_{x0} &= c_1 x_0 + c_3 (x_0^2 + y_0^2) x_0 \quad 0 < r_0 < R_0, c_3 > 0 \\ p_{y0} &= c_1 y_0 + c_3 (x_0^2 + y_0^2) y_0 \end{aligned} \quad 1.1$$

It has been shown[2] that disk-like bunches (geometric aspect ratio $R/L \gg 1$), generated by high gradient RF guns (100 MV/m), present the desired phase-space profile: in laminar flow regime, the linear correlation gives negligible emittance $\left(\epsilon_{nr} = \left(\langle r^2 \rangle \cdot \langle p_r^2 \rangle - \langle r \cdot p_r \rangle^2 \right)^{1/2} \right)$,

while the third order correlation becomes dominant. Moreover, depending on the radial charge density profile at the cathode, from pure uniform to pure gaussian, spherical aberrations assume positive, null or negative values. For pure uniform distributions the emittance of the generated beam shows a positive spherical aberration, $\epsilon_{nr0} = c_3 R_0^4 / \sqrt{72}$, ($\epsilon_{nr0} = 2\epsilon_{nx0}$).

The beam generated by the RF gun is then driven through a solenoid, a quadrupole doublet and a sextupole triplet. The quadrupole lens is set to provide the beam with a proper astigmatism ratio, $y_{\max} / x_{\max} = t$, and cancel (double waist) both horizontal and vertical linear correlation. The sextupole lens[3] applies a non linear radial focusing kick $\Delta p_r = -\alpha \cdot r^3$, which depends on the integrated gradient of the sextupoles $G_s L$, the drift distance between the sextupoles

g , and the longitudinal momentum of the particles p_z , through the coefficient

$$\alpha = -4 \cdot \frac{g}{p_z} \left(\frac{q}{m_0 c} \cdot G_s L \right)^2 \cdot r^3$$

The sextupole triplet has been properly matched to correct at best the third order correlation in the horizontal phase-space. Due to the astigmatism, in the vertical phase-space, emittance correction cannot be optimized at the same time. This is the origin of the asymmetry.

In this scheme the solenoid has a secondary role, it reduces the transverse divergence of the electrons at the entrance of the quadrupole lens: actually, the higher is the particle radial momentum, p_{r-in} , the stronger has to be the quadrupole focusing powers (to have a double waist. Transverse momentum corrections consistently influence the particles motion, changing their longitudinal momentum, $p_z = \sqrt{\gamma^2 - 1 - p_r^2}$. At first order, $\Delta p_{z-out} \approx p_{r-in}^2 / p_{z-in}$; the solenoid is then inserted to lower p_{r-in} and damp undesired non-linear effects.

II. ANALYTICAL RESULTS.

In this section we study the dynamics of the particles, through the quadrupole doublet and the sextupole lens. We want to write some scaling laws to describe the output beam characteristics, emittance aspect ratio and beam brilliance. To describe the efficiency of the device: we follow the track of a particle beam, starting with an emittance dominated by spherical aberrations, in a laminar flow regime. The results show that the efficiency of the device depends slightly on the input characteristic of the initial beam (charge, energy, divergence, strength of the spherical aberration...), the dominant parameter being only the beam astigmatism ratio t , introduced by the quadrupole doublet.

Let $Q_{y,x}$ be the matrixes of the quadrupole doublet,

$$Q_{y,x} = \begin{pmatrix} 1 & 0 \\ \mp 1/f_{A,B} & 1 \end{pmatrix} \begin{pmatrix} 1 & d \\ p_z & 1 \end{pmatrix} \begin{pmatrix} 1 & 0 \\ \pm 1/f_B & 1 \end{pmatrix}; \quad (2.1)$$

where $1/f_{A,B} = q/mc \cdot G_{A,B} L / p_z$ (the focusing powers of the quadrupoles) and d (the drift distance), represent the free parameters ($G_{A,B} L$ are the integrated gradients). Since we assume a *laminar flow* (the divergence depends only on the radial position in the bunch) we may apply a *point to point* computation instead of matrix transport. The double waist condition, $Q_x \begin{pmatrix} x \\ C \cdot x \end{pmatrix} = \begin{pmatrix} m \cdot x \\ 0 \end{pmatrix}$, $Q_y \begin{pmatrix} y \\ C \cdot y \end{pmatrix} = \begin{pmatrix} n \cdot y \\ 0 \end{pmatrix}$, allows

to reduce the free parameters to one, and to express, $Q_{y,x}, 1/f_{A,B}$, and the resulting magnitude factors m and n , as functions of d :

$$\frac{1}{f_A(d)} = \sqrt{1 + \frac{p_z}{d} C} \quad m(d) = \left(1 + \frac{d}{f_A(d) p_z} \right) + \frac{dC}{p_z},$$

$$\frac{1}{f_B(d)} = \frac{p_z / g}{\sqrt{1 + \frac{p_z}{d}}} \quad n(d) = \left(1 - \frac{d}{f_B(d) p_z} \right) + \frac{d}{p_z} \quad (2.2a-d)$$

In this matrix computation we have disregarded the existence of the third order term in the momentum expression, thus finding the best quadrupole settings to cancel the linear correlation. Now we insert expressions for A and B into matrixes $Q_{y,x}$ and apply a point to point transport, using the third order expression (1.1) for the input phase-space (Fig. 2). Having done so, the beam distribution at the exit of the quadrupoles is described by the equations (Fig. 3):

$$p_{x1} = \frac{c_3}{m^4} (x_1^2 + y_1^2) \cdot x_1 + \frac{c_3}{m^4} \left(\frac{m^2}{n^2} - 1 \right) y_1^2 \cdot x_1$$

$$p_{y1} = \frac{c_3}{n^4} (x_1^2 + y_1^2) \cdot y_1 + \frac{S}{n^4} \left(\frac{n^2}{m^2} - 1 \right) x_1^2 \cdot y_1 \quad (2.3a,b)$$

The particles are uniformly distributed over an ellipse of semi-axes $x_{1max} = m \cdot r_0$ and $y_{1max} = n \cdot r_0$. Eqs (2.3) do not return two pure spherical aberrations. We can look at them as the combination of a pure cubic term, respectively of coefficient c_3 / m^4 and c_3 / n^4 , and a residual part, given by

$$\frac{c_3}{m^4} \left(\frac{m^2}{n^2} - 1 \right) y_1^2 \cdot x_1 \quad \text{and} \quad \frac{c_3}{n^4} \left(\frac{n^2}{m^2} - 1 \right) x_1^2 \cdot y_1,$$

that is not removable with sextupoles. It is clear now that the efficiency of the flat beam converter has to deal with these terms. Referring to the astigmatism ratio, $t = n/m$, we see that:

- the closer is t to unity, the weaker are residuals: no asymmetry has been generated, but we can completely cancel the emittance;

- the farther is t to unity, the larger are the residuals: there is big asymmetry but we have bad chance to correct any of the two phase-spaces for their consistent residuals.

Here below we report the scaling law for the emittance variations, $\epsilon x = \epsilon_{nx} / \epsilon_{nx0}$ and $\epsilon y = \epsilon_{ny} / \epsilon_{ny0}$, the aspect ratio $\epsilon_{ny} / \epsilon_{nx}$, and the emittance cross product $(\epsilon_{ny} \epsilon_{nx}) / (\epsilon_{ny0} \epsilon_{nx0})$ (in units of the initial values), obtained correcting the spherical aberration in the horizontal motion, by means of a sextupole triplet of strength $\alpha = c_3 / m^4$:

$$R = \frac{\epsilon_{ny}}{\epsilon_{nx}} = \frac{\sqrt{5}}{5} \cdot \left(\sqrt{8 + 12 \cdot t^2 + 9 \cdot t^4} \right) \quad (2.6)$$

$$\epsilon x = \frac{\sqrt{10}}{4} |1 - t^2|, \quad \epsilon y = \frac{\sqrt{2}}{4} |1 - t^2| \sqrt{8 + 12 \cdot t^2 + 9 \cdot t^4} \quad (2.7a,b)$$

$$P = \epsilon x \cdot \epsilon y = \frac{\sqrt{5}}{8} (1 - t^2)^2 \cdot \sqrt{8 + 12 \cdot t^2 + 9 \cdot t^4} \quad (2.8)$$

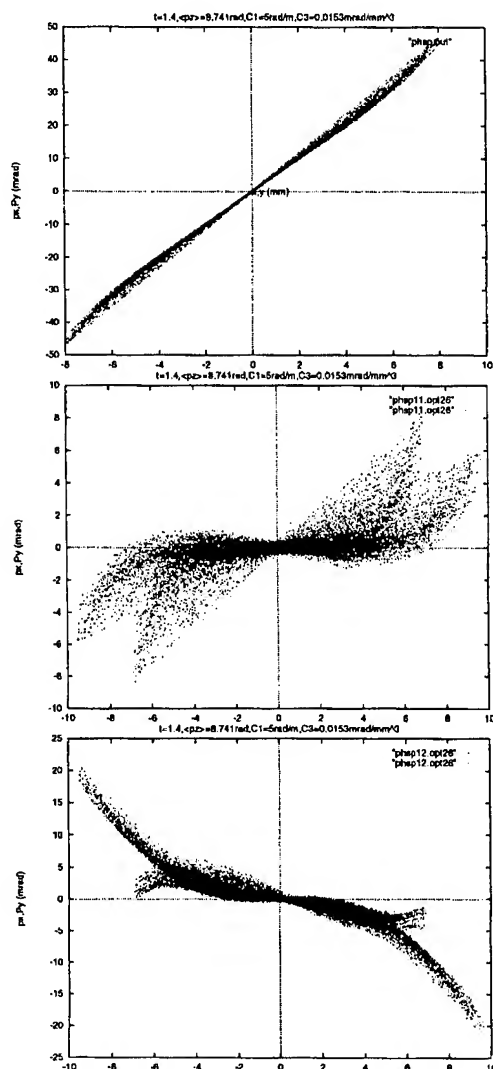


Fig. 2: Phase-space of a spherically aberrated round beam
 Fig.3: Beam phase-space after the quadrupoles (since $t=1.4>1$, the larger dimension is y , the smaller is x).
 Fig.4: Phase-space after the sextupoles (spherical aberration has been corrected).

As brilliance scales like $(\epsilon_{ny}\epsilon_{nx})^{-1}$, the product P is an index of the beam degrade. We remind that t is the astigmatism ratio m/n between the vertical and the horizontal orientation. Hence, choosing to damp the horizontal emittance, for $t<1$ the lower emittance is assigned to the larger dimension, while for $t>1$ the lower emittance is assigned to the smaller one.

III.COMPARISON BETWEEN SIMULATIONS AND ANALYTICAL SCALING LAWS

We briefly present in the following the results of simulations for a flat beam converter. The beam has been generated with the code ITACA, from a 1+1/2 cell injector, assuming a cathode field of 100 MV/m and a geometrical aspect ratio of 10. The beam dynamics through the flat beam

converter has been simulated with a ray-tracing code, based on the thin lens approximation.

A comparison between simulations (dotted line) and analytical expressions (solid line) is shown in Figs. 5 and 6, where the emittance aspect ratio $R(t)$ and the emittance product $P(t)$ are plotted as a function of the astigmatism ratio t . When the astigmatism is null ($t=1$) the solid curves do not agree with the results from the scaling laws, because the latter assume zero thermal emittances; in effect the thermal emittance generated by ITACA prevents the product $P(t)$ from dropping to zero and forces the aspect ratio to be one. Fig. 5 and 6 also show that high values of aspect ratios cannot be reached without degrading the beam brightness: the optimal work-point for applications is close to $t=1$, but strictly different than 1. For $1<t<2$ we may reach aspect ratios much larger than 1 without degrading the beam too much: in particular for $t=1.30$ and $R=3.2$ we fit the condition of conservation of beam brightness, $\epsilon_{xyN}=1$.

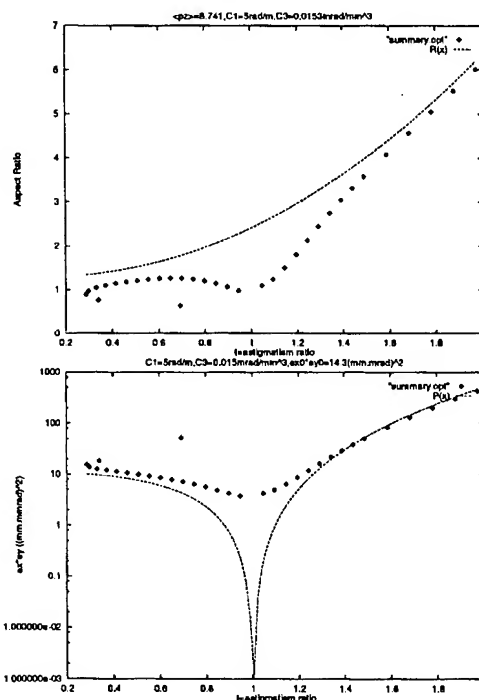


Fig. 5 and 6: aspect ratio and emittance product comparison (see text for further details).

REFERENCES

- [1] J.Dragt, F.Neri, G.Rangarajan, Phys Rev A 45 (1992), 2572;
- [2] L.Serafini, Nucl. Instrum. and Methods A340 (1994), 40;
- [3] J.C.Gallardo, R. Palmer, Nucl. Instrum. and Methods A304 (1991), 345; "Preliminary Study of Gun Emittance Correction" J.C. Gallardo, R. Palmer - BNL-43862 internal report.

THE ARGONNE WAKEFIELD ACCELERATOR HIGH CURRENT PHOTOCATHODE GUN AND DRIVE LINAC *

P.Schoessow, E.Chojnacki, G.Cox, W.Gai, C.Ho, R.Konecny, J.Power, M.Rosing, J.Simpson
Argonne National Laboratory, 9700 S.Cass Ave., Argonne IL 60439
N.Barov, M.Conde

UCLA Dept. of Physics, 405 Hilgard Ave., Los Angeles, CA 90024

Abstract

The Argonne Wakefield Accelerator (AWA) is a new facility for advanced accelerator research. A major component of the AWA is its drive linac, consisting of a unique high current short pulse L-Band photocathode based gun and special standing wave preaccelerator designed to produce 100 nC, 30 ps electron bunches at 20 MeV. Commissioning on the drive linac is now underway. We report on our initial operating experience with this novel machine, including bunch length and emittance measurements.

I. INTRODUCTION

The generation of high accelerating gradients (>100 MeV/m) in wakefield structures requires a short pulse, high intensity electron drive beam. The main technological challenge of the AWA program is the development of a photoinjector capable of fulfilling these requirements. In the past year we have made considerable progress towards attaining the design goals of the AWA, and in this paper we report on the commissioning of the AWA photoinjector and drive linac. The main emphasis so far has been measurement of beam current and testing various photocathode materials. A general overview of the AWA program may be found in [1] and references therein.

II. PHOTOINJECTOR AND LINAC STATUS

The gun and drive linac are shown in fig. 1. The laser photocathode source was designed to deliver 100 nC bunches at 2 MeV to the drive linac. Some of the novel features incorporated into the gun to attain high intensities include a large (2 cm diameter) photocathode, a large accelerating field at the photocathode, the use of a curved laser wavefront, and nonlinear focussing solenoids matched to the angle-energy correlation computed for the 100 nC bunch.

Fine tuning of the gun cavity frequency was originally effected by moving the photocathode plug. To attain the desired frequency required the plug to extend past the cavity surface, causing serious arcing. This difficulty was overcome by simply installing a tuning slug on the outer radius of the gun. The cathode can then be inserted flush with the cavity surface.

The gun cavity is presently capable of operating at 80% of design field (75 MV/m on photocathode). This does not significantly impact the performance of the source.

The laser operates at a wavelength of 248 nm and can produce 3 ps pulses of energy in excess of 5 mJ. In order to monitor the position of the laser spot on the photocathode during

machine operation, a mirror can be inserted which transports laser light reflected from the photocathode to a CCD camera. The laser injection mirror can be adjusted remotely to maintain proper alignment of the laser spot. For initial operations the laser pulse shaping system was not installed; all results so far have been obtained with a flat laser wavefront.

The linac tanks have performed without serious difficulties. The rf supply is currently operating at a lower power which limits the final beam energy to 15 MeV.

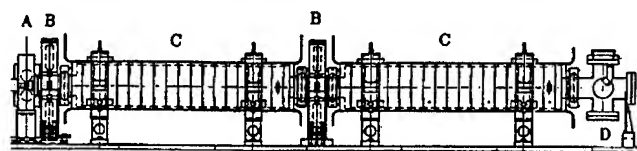


Figure. 1. Drive linac. A: High current photocathode gun, B: Focussing solenoids (bucking solenoid not shown), C: Linac cavities, D: Laser port

III. DIAGNOSTICS

A temporary diagnostic beamline is installed downstream of the linac. Insertable luminescent screens are used for beam position monitoring and beam profile measurements. Graphite/lead beam dumps are instrumented as Faraday cups for beam intensity measurements.

Transverse emittance is measured using a "pepper pot" emittance plate. A quartz Cherenkov radiator is used in conjunction with a streak camera for measurements of bunch length.

IV. INITIAL RESULTS

We tested a number of different photocathode materials. Quantum efficiencies are measured at very low laser intensities so that space charge effects are negligible.

For simplicity copper was chosen for the initial measurements. We observed a quantum efficiency of 4×10^{-5} . At an intensity of 30 nC/pulse we obtained a bunch length of 27 ps FWHM, and rms emittance 17π mm mr.

The quantum efficiency for magnesium is known to be large [4], and as a result was our primary choice as a photocathode material. Using a cathode consisting of a layer of Mg mechanically deposited on a Cu substrate we observed beam intensities of > 110 nC/bunch due to explosive emission [3] of electrons from the cathode surface when the laser intensity exceeded ~ 10 mJ/cm². This effect results from a discharge on the cathode surface initiated by the laser but continuing beyond the duration of the laser pulse.

*Work supported by U.S. Department of Energy, Division of High Energy Physics, Contract W-31-109-ENG-38.

Streak camera measurements of the time structure show the beam consists of a train of bunchlets separated by one rf period (fig. 2). The length of the macropulse was measured to be < 25 ns. The total charge/macropulse is rather stable ($\sim 10\%$ pulse to pulse).

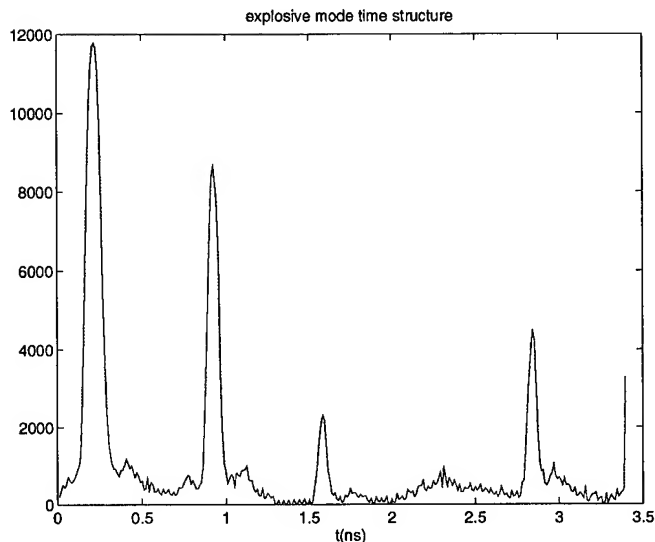


Figure 2. Streak camera measurement of the time structure of the beam produced by explosive emission from a Mg photocathode. The bunch spacing corresponds to one rf period.

Using a solid Mg photocathode and maintaining a sufficiently large laser spot on the cathode so that the explosive emission threshold was not exceeded, we were able to study the beam produced by prompt photoemission. Up to about 40 nC/pulse the scaling of transmitted beam intensity (fig. 3) is linear with laser energy, giving a quantum efficiency of 1.3×10^{-4} . At higher laser intensities the beam charge begins to roll off to a maximum of 56 nC at 4 mJ. This is expected based on PARMELA simulations of the beam dynamics in the accelerator [2]. The shape of the fields in the focussing solenoids was optimized for the divergence angle- energy correlations computed for the beam produced by a curved laser wavefront. We do not expect to transport more than 60 nC using a flat laser wavefront.

At the highest intensities observed, the spot size at the drive linac exit is 9 mm (rms). The intensity distribution is shown in figure 4. The rms width is $\simeq 6\%$, consistent with the level of shot to shot laser energy fluctuations. We have not yet measured the energy and bunch length for the highest current beams obtained, due to reconfiguration of the diagnostic beamline for the initial plasma wakefield experiments.

A number of other candidate photocathode materials were evaluated. Yttrium was found to have a low quantum efficiency $\simeq 1 \times 10^{-5}$. The relatively low work function (2.9 eV) of Calcium made it appear a good candidate photocathode material. We observed a quantum efficiency however of only $\simeq 4 \times 10^{-5}$.

The quantum efficiency found for Y and Mg is somewhat lower than other measurements [4]. The reason for this is not yet

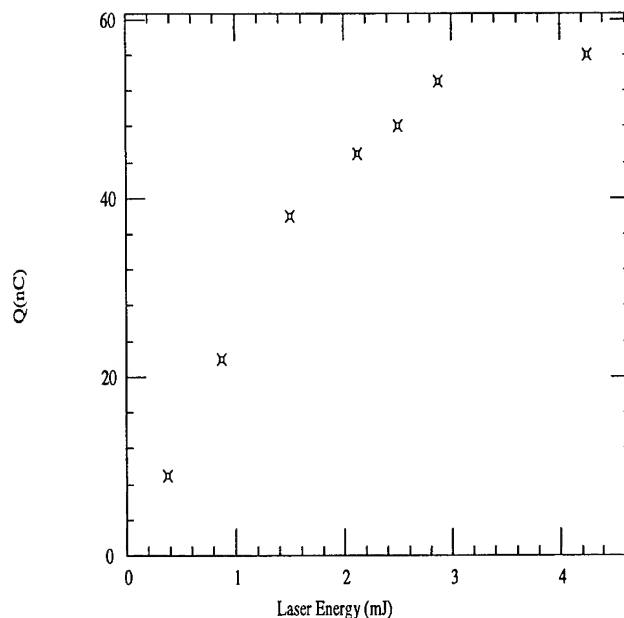


Figure 3. Measured beam intensity as a function of laser energy. (Magnesium photocathode).

understood. Nevertheless, the observed quantum efficiency for Mg is sufficient to produce 100 nC from the drive gun as well as supply the requirements of the witness gun and thus meet the goals of the AWA program.

V. FIRST EXPERIMENTS

Experiments planned for the AWA include studies of dielectric wakefield structures and plasma wakefield acceleration. Some initial plasma measurements have been performed.

A second rf gun designed to produce witness pulses for wakefield measurements is being fabricated and is described in [6]. In the meantime, a second method for generating witness pulses at small delays has been developed using the drive linac alone and has been used for the plasma experiment [5]. Using two concentric mirrors, the center of the laser pulse is delayed with respect to the outer portion. After striking the photocathode, two bunches are produced. Drive- witness bunch separations of 30- 60 ps are obtained by this technique. Intensities delivered to the plasma source are 11 nC for the drive bunch and 3 nC for the witness.

VI. CONCLUSIONS

The AWA program has demonstrated operation of a unique, high current photoinjector. The design goals of the machine are within reach. In the near term, the laser pulse shaping system will be installed, which should permit the design intensity of 100 nC/pulse to be attained.

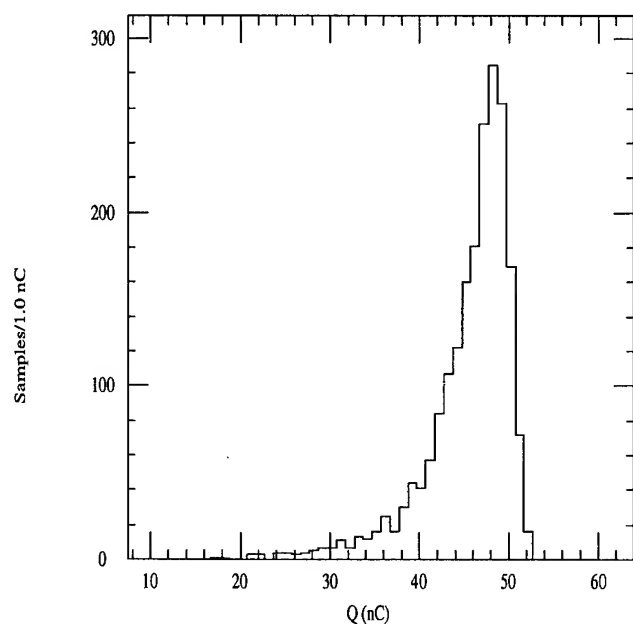


Figure. 4. Charge/pulse distribution measured over several minutes of high current running. The low tail is primarily due to laser mistriggers.

References

- [1] P.Schoessow et al., Proceedings of the 1993 IEEE Particle Accelerator Conference, pp. 2596-2598
- [2] C.H.Ho, PhD Thesis, UCLA 1992
- [3] X.J. Wang, PhD Thesis, UCLA 1992
- [4] T. Srinivasan-Rao et al., J. Appl. Phys **69** (5), 1991 p. 3291,
X.J. Wang et al., Submitted to J. Appl. Phys.
- [5] N.Barov et al., These Proceedings
- [6] J. Power and J. Simpson, These Proceedings

WITNESS GUN FOR THE ARGONNE WAKEFIELD ACCELERATOR

J Power, J Simpson, E Chojnacki, R Konecny
Argonne National Laboratory, Argonne, IL, 60439

I. INTRODUCTION

The witness gun [1] for the Argonne Wakefield Accelerator (AWA) is a six-cell, copper, iris loaded, rf photocathode operating at 1.3 GHz in a $\pi/2$ standing wave mode. An intense drive beam (up to 100 nC @ 20 psec FWHM) will be used in the AWA project [2] to excite (i.e. drive) wakefields in at least two separate test devices: a dielectric loaded cylindrical waveguide and a plasma cell. In both cases a low charge, low emittance witness beam (0.1 nC charge, 1 π mm-mrad 90% physical emittance) is required to probe (i.e. witness) the wakefields left behind by the drive beam [3]. This paper will primarily discuss the recent progress in the construction of the witness gun, while also briefly summarizing the central design issues of the gun. A brief status report on the dielectric witness gun option is also included. We conclude with a short statement on our near term future plans.

II. MARK IV TYPE WITNESS GUN

The conventional copper rf photocathode gun that we have selected to build is actually a scaled down version of the s-band Mark IV accelerator that was used at SLAC, as described in reference [1]. Since the Mark IV Accelerator was a linac, some adjustments were made to turn it into a photocathode using the rf design code URMEL. The witness gun (fig 1) has a photocathode (dark square) in the first 1/2 cell, a coupling iris in the fourth full cell and a beam exit hole in the last half cell.

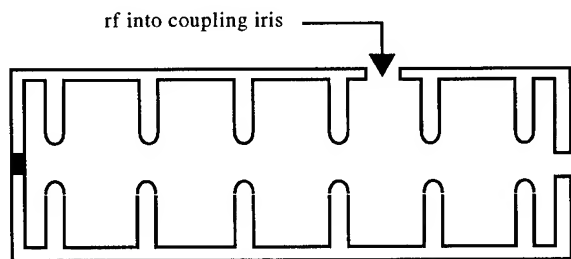


Figure 1 The Mark IV Witness Gun with Coupling Iris and photocathode (dark square) shown.

In order to probe the test devices properly, the witness beam must have a kinetic energy of four to five MeV, a physical emittance of 1 π mm-mrad, an energy spread of less than 1% and a bunch length of about 5 psec. Extensive simulations with PARMELA have shown the Mark IV type gun to be capable of achieving the design parameters. Using a 1.5 mm spot size and a phase launch of 65 degrees we obtain the following results

Energy	90% Emittance	Energy Spread	Bunch Length
4.53 MeV	0.76 π mm-mrad	0.5% FW	5.6 psec

A. Construction, Tuning and Matching

When constructing a resonant structure, such as an rf photocathode, one attempts to use an electromagnetic mode solver, like URMEL, to obtain the cavity dimensions. However, the dimensions given by such a code can only serve as an approximation to the parameters shown in figure 2. Therefore, some dimensions must be left undercut so that the resonant frequency of the gun can be fine tuned by making small machine cuts. The problem of matching or coupling rf to the gun appears to be intractable by any means except tedious iterations of cutting and measuring. In any case, the authors of this paper are unaware of either analytic or computer techniques capable of ameliorating this problem.

While radius b is used to set the resonant frequency of the gun, the other dimensions (fig 2) are arrived at in the following manner. The cell length d is chosen by setting the phase shift ($\Delta\phi$) equal to the desired value ($\pi/2$ in the case of the witness gun) and then satisfying the relationship

$$\left(\frac{2\pi}{\Delta\phi}\right)d = \frac{v_{phase}}{f}$$

Once d is fixed, the remaining parameters a and t (fig 2) are chosen as a compromise between optimizing for mechanical strength, high shunt impedance and strong cell-to-cell coupling. Thin iris walls (small t) and large iris radii (large a) give strong cell-to-cell coupling which is desirable, but these values also give low shunt impedance which is undesirable. For an excellent discussion of the problem of tradeoffs and the discussion pertaining to the Mark IV accelerator upon which this gun is based, see reference [4].

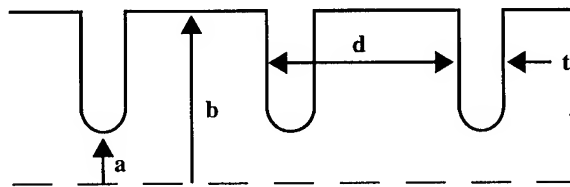


Figure 2: The relevant iris loaded cavity dimensions for the code URMEL. (Iris radius a, cavity radius b, cell length d, iris thickness t.)

A.1 Tuning the gun to 1300 MHz

All the cavity dimensions were machined (fig. 2) according to the URMEL values except b , the cavity's inner radius. Since the iris loaded gun acts like six coupled pill box cavities operating in the TM_{010} mode, we see that the resonant frequency is determined primarily by the pill box's radius, b . Based on this we chose b as our knob for tuning the cavity.

Although the rf will eventually be coupled to the gun through an iris (fig 1) in the coupler cell (CC) we first stacked together seven similar cells (two half cells and five full cells) in order to bring the tune near to 1300 MHz. The code URMEL predicted that the $\pi/2$ mode would be found at 1300 MHz for $2b = 7.153$ inches. This prediction turned out to be in excellent agreement with the actual result, it's accuracy was within 0.02% ($\Delta f = 0.2$ MHz). Of course, the consistency of the prediction with the measurement depends on both URMEL's accuracy and the machining accuracy of the local machine shop. The radius, b , was initially cut to 96% of the target radius ($b_{\text{URMEL}} = 7.153$ inch) and consequently, the initial resonant frequency ended up 50 MHz high ($f = 1350$ MHz). The procedure was then to make a sequence of small cuts of the radius b and measurements of the resonant frequency of the $\pi/2$ mode as we approached 1300 MHz slowly. The general agreement of the measurements with URMEL as the gun was tuned was excellent. (fig 3).

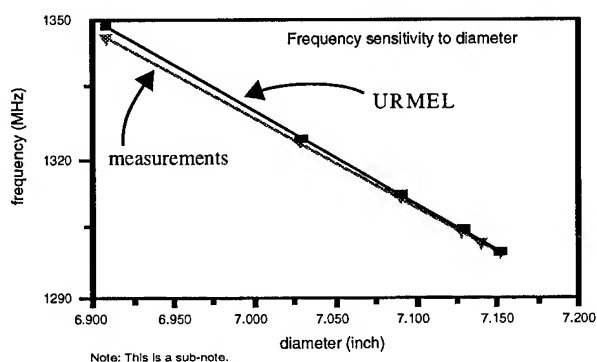


Figure 3: The resonant frequency of the witness gun as a function of the diameter, $2b$.

Although the data in figure (3) looks linear ($\Delta f / \Delta(2b) \approx 200 \text{ kHz/mil}$) this isn't quite true. The frequency sensitivity, $\Delta f / \Delta b$, varies significantly enough so that it must be taken into account while tuning the gun. The reader should also take caution to realize that this is a very narrow frequency band and just about anything will look linear over such a small interval.

A.2 Matching rf to the gun

The other major issue in the gun's construction is coupling power to the gun or impedance matching. During the initial tuning phase, coupling was achieved with a pin probe on axis. This was sufficient to bring the resonant frequency near the target frequency of 1300 MHz. At this stage, however, we obviously needed to place the actual CC into the gun stack (fig 1). At this point we were operating somewhat blindly (i.e.

without a numerical code) since URMEL cannot model the effect of the coupling iris on the resonant frequency.

Unfortunately, when the cells were stacked together, the Q of the cavity was very low. It was discovered that a significant amount of rf was leaking out through faces where the cells joined. Even with tight clamping of the stack, the measured Q remained around 2000, compared with URMEL's prediction of 13,800. Since S11 measurements are extremely sensitive to these leakage fields we decided to braze two half stacks together. We brazed together the 3 1/2 cell stack on the upstream side of the CC and the 1 1/2 cell stack on the downstream side of the CC (fig. 1).

The brazing of the half stacks had the desired effect and raised the Q to 8000. Although still significantly below the final expected value, this was enough of an improvement to proceed with matching and tuning. Since the effect of the coupling iris is to lower the frequency of the gun, the diameter of the CC was left lower than the diameter of the other five cells.

When the CC was placed into the stack with the two brazed sections, the frequency of the entire stack measured about 4 MHz high. We then began an iterative process of opening the iris and cutting the radius, b , of the CC while carefully measuring the resonant frequency and reflection coefficient S11. Unlike the initial tuning of the stack with 6 similar cells, this stack's frequency and coupling had a highly nonlinear dependence on the diameter and the coupling slot dimensions. Far from 1300 MHz, the cavity's tune was not very sensitive ($\Delta f / \Delta 2b = 8 \text{ kHz/mil}$) to changes of the radius b . But when the cavity was back to within 0.5 MHz of 1300 MHz, the resonant frequency became extremely sensitive ($\Delta f / \Delta 2b = 90 \text{ kHz/mil}$) to changes in b .

Since there were still two unbrazed joints in the stack, there continued to be problems in obtaining reliable measurements of S11. The reflection coefficient lied in the band between -5dB and -15dB at a slot length and width of 2 and 1/2 inches respectively. Since it would have been very easy to over couple the cavity by opening the slot further, we decided to send the gun out for it's final braze. The final adjustment of the iris will be done after the complete cavity is brazed together.

B Pre-Braze Results

The first task was to identify the seven TM_{010} like modes of the six cell cavity. When the stack was put together with all similar cells instead of the CC, all seven modes were easily identified. However, when the CC was in the stack, we only observed six modes (fig 4). It is likely that the $5\pi/6$ and the π modes have become degenerate, since all modes are live in the CC and therefore should be driven. The ultimate resolution of this will come when the cavity arrives back at ANL so we can do a bead pull to identify the modes. Summary of the modes

mode	0	$\pi/6$	$\pi/3$	$\pi/2$	$2\pi/3$???
freq	1284.3	1286.9	1293.0	1299.3	1207.0	1313.9

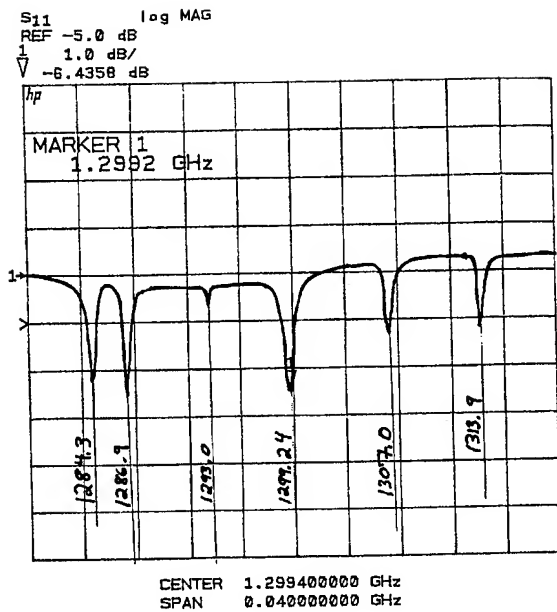


Figure 4: Six of the Seven TM_{010} like modes of the witness gun

Although the gun hadn't been completely brazed together at the time of this writing, a bead pull was performed on the $\pi/2$ mode (fig 5). The experiment (performed on HP 8510 Network Analyzer) clearly identifies the mode as $\pi/2$. The CC is located approximately between 200 and 250 mm in figure 5, which explains the odd shape in that region. The last "hump" in the plot doesn't come up to full field balance due in part to the leaky rf joint of the CC. The last hump will probably not come all the way up to full field balance even after brazing since that is the side on which the beam exit hole resides. The fields that exist after the dashed line of figure 5 are the fields that attenuate in the beam exit hole.

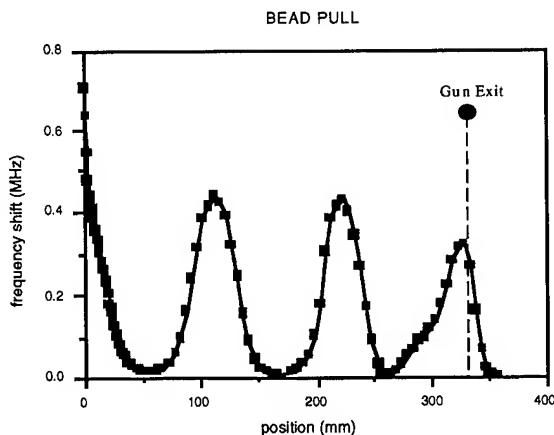


Figure 5: Bead pull showing the $\pi/2$ mode in the witness gun

III. DIELECTRIC GUN

The dielectric gun [1] option for the witness beam has been put on the back burner for the time being. Since Phase I of the AWA project needed a reliable witness beam quickly, it was decided that the development of the dielectric gun would be to great of an undertaking. Briefly, the dielectric photocathode gun consists of a dielectric tube (1 cm ID x 5.44 cm OD x 32.57 cm length) inserted into a copper jacket. The central advantage of this gun is that the rf fields of the gun are almost completely linear and may produce a lower emittance beam. The authors of this paper still consider this a worthwhile endeavor.

IV. FUTURE PLANS

As of this writing, all components of the witness gun are being brazed together. The first order of business upon arrival of the gun will be to complete the tuning and matching of the gun. After some cold test on the gun we plan to mount the gun in place and begin conditioning. We plan to see the first laser pulse strike the photocathode in June. This event will mark the beginning of an exciting era of research to take place at the AWA.

V. REFERENCES

- [1] J. Power et. al., "Witness Gun for the Argonne Wakefield Accelerator", Proc. 1992 Particle Accelerator Conference.
- [2] P. Schoessow et. al., "The Argonne Wakefield Accelerator: Overview and Status" (same as reference [1])
- [3] W. Gai, et. al., "Experimental Demonstration of Wake-Field Effects in Dielectric Structures" Phys. Re. Lett., **61**, 2756 (1988)
- [4] The Stanford Two-Mile Accelerator, (Chpt. 6)

MICROWAVE MEASUREMENTS OF THE BNL/SLAC/UCLA 1.6 CELL PHOTOCATHODE RF GUN*

D. T. PALMER, R. H. MILLER AND H. WINICK

Stanford Linear Accelerator Center

Stanford University, Stanford CA 94309

X.J. WANG, K. BATCHELOR, M. WOODLE AND I. BEN-ZVI

Brookhaven National Laboratory Accelerator Test Facility

Upton, NY 11973

Abstract

The longitudinal accelerating field E_z has been measured as a function of azimuthal angle in the full cell of the cold test model for the 1.6 cell BNL/SLAC/UCLA #3 S-band RF Gun using a needle rotation / frequency perturbation technique [1]. These measurements were conducted before and after symmetrizing the full cell with a vacuum pump out port and an adjustable short. Two different waveguide to full cell coupling schemes were studied. The dipole mode of the full cell is an order of magnitude less severe before symmetrization for the θ -coupling scheme. The multi-pole contribution to the longitudinal field asymmetry are calculated using standard Fourier series techniques. The Panofsky-Wenzel theorem [2] is used in estimating the transverse emittance due to the multipole components of E_z .

I. INTRODUCTION

To produce high brightness low emittance electron beams necessary for X-ray FEL application such as the LCLS [3] we have developed a 1.6 cell emittance compensated S-band photocathode RF Gun that is designed to minimize emittance growth due to the dipole component of E_z . To accomplish this we have eliminated the side coupling into the half cell that is used in the original BNL RF gun design [4], which is designed to suppress the zero-mode. The coupling between the two cells was improved by an increase in the beam iris, which also increased the mode separation between the zero and π -modes. The coupling between the waveguide and full cell was studied using two different coupling schemes. The full cell was symmetrized to minimize emittance growth due to the TM_{110} mode. The half cell length has been increased to provide more RF focusing. Resistive temperature control was elected over water cooling to facilitate design and minimize construction costs.

II. FIELD BALANCE VERSUS MODE SEPARATION

The full cell to half cell coupling is vital since side coupling was not used in this gun design. We further improved the technique of using mode separation for field balance tuning [5]. To measure the field balance versus mode separation it is necessary to measure E_z on axis for the π -mode, f_π and f_0 for different full and half cell frequencies. For large difference in the full and

half cell frequencies the f_π and f_0 are essentially the independent cell frequencies, but when the cell frequencies are close to each other the coupling, which is frequency independent, separates the cell frequencies into the f_π and f_0 [6]. Field balance versus mode separation data is presented in figure 1. This data was taken using a .472 cm diameter dielectric sphere and a self excited loop instead of a network analyzer which increased the accuracy of the frequency measurement down to 100 Hz.

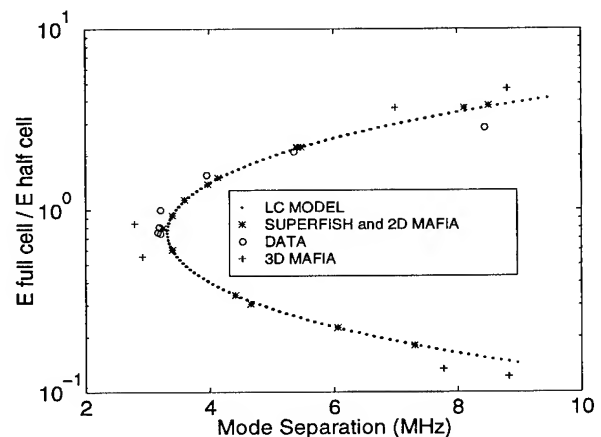


Figure 1. Field Balance versus Mode Separation

The predictions of our equivalent circuit model, 2-D field solvers such as SUPERFISH [7] and the 3-D field solver MAFIA [8] are also shown in figure 1.

III. WAVEGUIDE TO FULL CELL COUPLING

We have investigated two different types of waveguide to full cell coupling schemes. The θ -coupling scheme was produced using a .375" diameter cutting flute running $\pm .2268''$ center to center in the x direction, the thickness of the coupling iris is .0917". The z -coupling scheme was produced by cutting out a .913" x .650" rectangle with the long dimension in the z -direction, the thickness of the coupling iris was .108". In the final gun design we have elected to use the θ -coupling scheme since its dipole field, before symmetrization, is an order of magnitude less than the z -coupling scheme. We have measured the dipole field offset by a transverse disk pull in the waveguide plane and the multi-pole field components of the full cell by a needle rotation technique before and after symmetrizing the full cell for both schemes.

*Work supported by the Department of Energy, contracts DE-AC03-76SF00515 and DE-AC02-76CH00016

IV. TRANSVERSE DISK PULLS

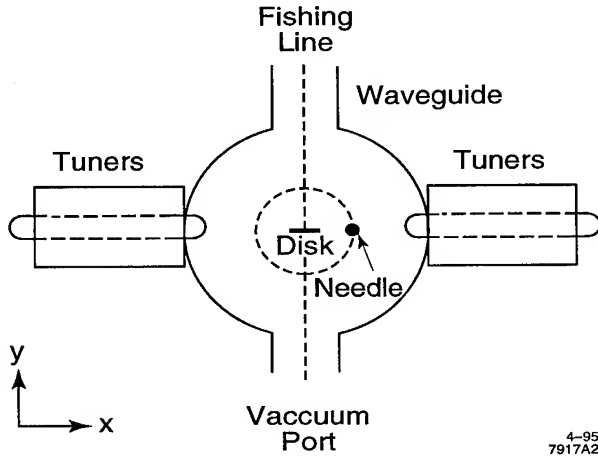


Figure 2. Experimental Setups for Full Cell Disk Pull and Transverse View of Full Cell Needle Rotation

Figure 2 shows the experimental setup for our transverse disk pull, using a 6.35 mm diameter 0.30 mm thick Cu disk, used to measure $E_z(x_0, y)$. The dipole offset is directly measured by this technique assuming that E_z can be modeled near the beam pipe axis by $E_z(x_0, y) = A + B(y - C)^2$. Experimental disk pull data is shown in figure 3 for the θ -coupling scheme. The θ -coupled dipole data along with waveguide to full cell coupling as a function of short position is shown in figure 4.

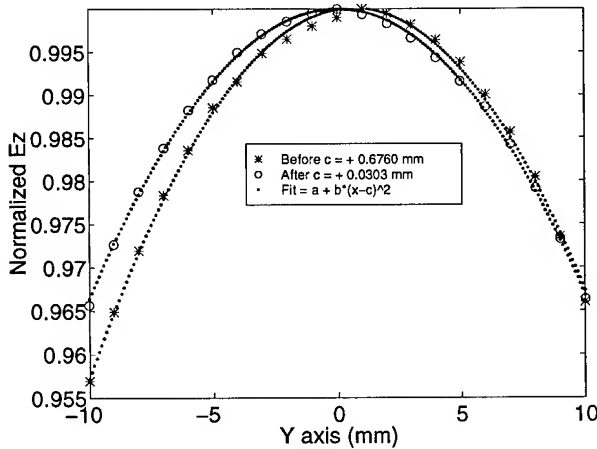


Figure 3. θ -coupled Disk Pull Data Before and After Symmetrization

V. MULTI-POLE MODES

In previous measurements of the dipole field in an RF cavity, needles were pulled longitudinally offset from the beam axis [9] or were pulled transversely [10] to the beam axis. In our needle rotation technique a 1.27 cm long .635 mm diameter needle is parallel to the beam axis and was rotated in the θ direction such that a cylinder was swept out, and thereby only perturbing the E_z . The experimental setup used for the needle rotation can be seen in figure 2 and figure 5. Accurate positioning of the needle was accomplished by using a compound arrangement of translation and rotation stages. The translation stage allowed the positioning of the needle in the r direction with respect to the beam

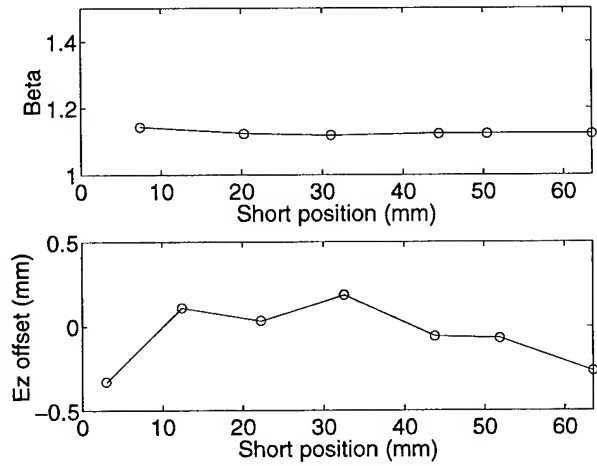


Figure 4. θ -coupled Full Cell to Waveguide Coupling β and Dipole Offset versus Short Position

pipe center. The rotation stage allowed the positioning of the needle in the θ direction with respect to a fiducial mark that we defined as the x -axis. It should be noted that the disk pull data is a subset of the needle rotation data. The full cell field, E_z , can be expressed as an infinite sum of modes represented by

$$E_z = \sum_{m=0}^{\infty} \sum_{n=1}^{\infty} \sum_{l=0}^{\infty} A_{mnl} T M_{mnl} \quad (1)$$

By measuring $E_z(r_1, \theta)$ as shown in figure 6 we can calculate the Fourier series coefficient A_{mnl} of the infinite series, whose absolute values are shown in figure 7. These coefficients are then used in the calculation of the emittance growth due to these multipole fields. Note that there is a large and changing (before and after) x -axis dipole field component, because the tuners were impossible to position precisely and in general were not symmetrical. Symmetrically feeding RF into the full cell would remove the phase asymmetry that exists in the cavity due to an asymmetric Poynting vector.

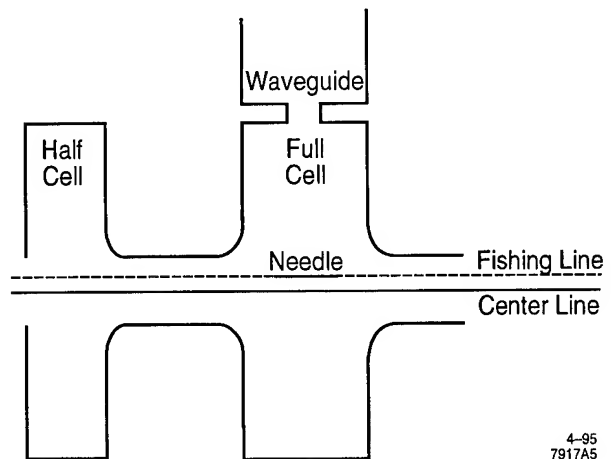


Figure 5. Needle Rotation Experimental Setup

VI. EMITTANCE GROWTH ESTIMATION

The change in the transverse normalized emittance is given by,

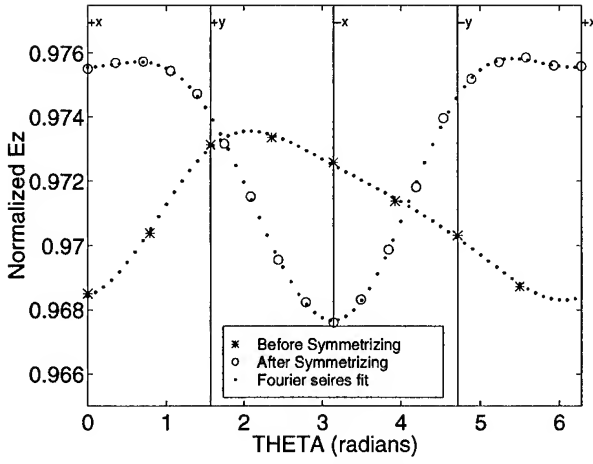


Figure 6. $E_z(r_1, \theta)$ Before and After Symmetrization for the θ -Coupling Scheme Using a Needle Rotation Technique

L	.05 m	λ	10.5 cm
σ_y	2.00 mm	σ_z	3 psec
E_o	100 $\frac{MV}{m}$	r_1	10.00 mm
$m = 1$	Dipole	$m = 2$	Quadpole
$\frac{E_1}{E_o}$	0.000094	$\frac{E_2}{E_o}$	0.000084

Table I
Electron bunch and RF gun cavity parameters

$$\Delta\epsilon_y = \sigma_y \frac{\Delta p_y}{mc} \quad (2)$$

Using the Panofsky-Wenzel Theorem to find the change in momentum, which is in phase quadrature with $\frac{\partial E_z}{\partial y}$ we find that

$$\frac{\Delta p_y}{mc} = \frac{e}{mc^2} \frac{\lambda}{2\pi} \int_0^L \frac{\partial E_z}{\partial y} dz \quad (3)$$

Therefore the change in the transverse emittance is

$$\Delta\epsilon_y = \frac{e}{mc^2} \frac{\sigma_z}{2\pi} \sigma_y \lambda \int_0^L \frac{\partial E_z}{\partial y} dz \quad (4)$$

For the TM_{110} and TM_{210} type modes, $\frac{\partial E_z}{\partial y}$ is given by

$$E_z \approx E_m \frac{r^m}{r_1^m} \sin(m\theta + \phi_m) \Rightarrow \frac{\partial E_z}{\partial y} = m \frac{E_m}{E_o} \frac{r^{m-1}}{r_1^m} E_o \quad (5)$$

Therefore the change in the transverse emittance is

$$\Delta\epsilon_y \approx \frac{e}{mc^2} \frac{\sigma_z}{2\pi} \sigma_y \lambda n \frac{E_m}{E_o} \frac{r^{m-1}}{r_1^m} \int_0^L E_o dz \quad (6)$$

Inserting the appropriate parameters from table I of the electron bunch and the symmetrized RF gun that we are modeling. Where r_1 is the radius at which E_z was measure at using the needle rotation technique and σ_y is the beam size in the middle of the full cell.

Assuming that $\frac{\partial E_z}{\partial y}$ can be approximated by a cosine like function of z we find that the emittance growth in the symmetrized case is given by

$$\Delta\epsilon_y \approx \begin{cases} 0.1 \pi \text{ mm mrad} & \text{Dipole mode} \\ 0.05 \pi \text{ mm mrad} & \text{Quadrapole mode} \end{cases} \quad (7)$$

VII. CONCLUSIONS

The dipole field components caused by the asymmetric RF coupling before and after symmetrizing the full cell were investigated. Data on the waveguide to full cell coupling and dipole offset versus short position was also taken. A needle rotation technique was used to measure the Fourier coefficient of the multipole field components of the full cell accelerating field. The dipole coefficient was seen to decrease by an order of magnitude after the full cell was symmetrized, with the proper positioning of the adjustable short that is located in the vacuum pumping port.

References

- [1] L. C. Maier and J. C. Slater, *Journal of Applied Physics*, Vol.23, Num1 69 - 77, Jan 1952
- [2] W. K. H. Panofsky and W. A. Wenzel, *Rev. Sci. Instrum.*, 27,967 (1956)
- [3] H. Winick et al *NIM*, A347, (1994), 199-205
- [4] K. Batchelor et al, *Proc. of 1990 EPAC* 541 - 543
- [5] X.J. Wang et al, *Proc. of 1993 PAC*, 3000 - 3002
- [6] I. Wilson and H. Henke, CERN 89-09
- [7] K. Halbach and R. F. Holsinger, *Particle Accelerators* 7, 213 (1976)
- [8] T. Weiland et al. *DESY Report*, M-86-07 1986
- [9] A. M. Vetter and R. P. Friedman, 1988 Linac Conf. Proc., CEBAF-Report-89-001, 58-60, June 1989
- [10] Greg Loew private communication

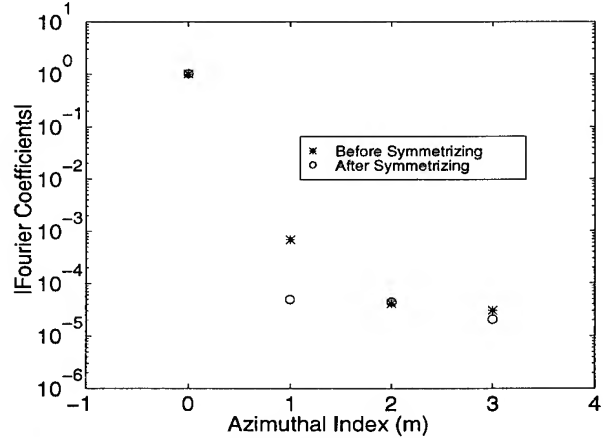


Figure 7. θ -coupled Fourier Coefficients Before and After Symmetrization

SUBPICOSECOND, ULTRA-BRIGHT ELECTRON INJECTOR*

Bruce E. Carlsten, Martin L. Milder, John M. Kinross-Wright, Donald W. Feldman, Steven Russell,
John G. Plato, Alan Shapiro, Boyd Sherwood, Jan Studebaker, Richard Lovato, David Warren,
Carl Timmer, Ronald Cooper**, Ronald Sturges**, and Mel Williams**
Los Alamos National Laboratory
Los Alamos, NM 87545 USA

We have designed and are building a subpicosecond electron injector. The injector is based on an 8 MeV photoinjector, used previously at Los Alamos in the APEX experiment. The nominal design includes magnetically compressing a 20 ps long, 3 nC bunch to a FWHM bunch length of 2/3 ps (peak current in excess of 3 kA) using a four dipole chicane buncher. The geometrical averaged transverse normalized transverse emittance after compression is about 15π mm mrad.

I. INTRODUCTION

The prospect of advanced accelerator applications such as linear colliders [1,2] and short-wavelength free-electron lasers [3,4] has motivated research into developing shorter and shorter electron bunches with high brightness. The current state-of-the art bunch compression is from 10 ps to 0.6 ps at 37 MeV with 0.15 nC, with a transverse normalized emittance of about 25π mm mrad [5]. Also of note is the compression reported using an alpha-magnet and rf gun [6], which has reported bunch lengths as low as 0.1 ps, but with charges on the order of 0.05 nC. These combinations of charge, bunch length, and emittance are not sufficient to meet the requirements for the advanced accelerator applications.

In order to further extend compression technology, we have designed and are currently commissioning an 8-MeV linac which has a predicted compression capability down to 0.7 ps for charges up to 3 nC, with a final transverse normalized emittance of about 15π mm mrad. This machine, the Subpicosecond, High-brightness Accelerator Facility, is the first linac designed specifically for performing compression experiments, and includes diagnostic features required for picosecond-type bunches.

This linac will be used for measuring noninertial emittance-growth mechanisms, which may exist in magnetic compression systems [7]. This will require development of a new emittance measurement technique using beam-position monitors [8]. In addition, this linac will be used to drive an extreme ultraviolet (EUV) source, using the anomalous energy loss of a short electron bunch in a plasma due to the induced wakefield [9,10]. This type of source is considered as an option for next-generation lithography.

In this paper we will first discuss the physics motivation for this experiment, including the noninertial emittance growth mechanisms and the EUV radiation mechanism. In the following section we will describe the design of the linac,

and in particular the four-dipole chicane compressor. Next we will provide simulation results describing the linac's predicted performance. In the final section we will discuss the status of the machine and future plans.

II. PHYSICS MOTIVATION

If an electron beam is not accelerating, it is easy to show that both the transverse and longitudinal space-charge forces scale inversely with the square of the relativistic mass factor. Because of this fact, designs for advanced accelerators which include bunch compression have the bunch compression occurring when the beam is at a relatively high energy (often greater than a GeV). However, it has been recently shown that this scaling for the space-charge forces does not hold for beams being bent in a dipole field [7]. Direct calculation of the longitudinal field from a moderate length line of charge that is bending yields

$$E_{\theta} = E_s (1/\gamma^2 - \beta^2 x/R) \quad (1)$$

where E_s would be the electric field in the direction of the bunch's motion if the motion was straight, x is the transverse displacement from the line (in the bend plane) and R is the bend radius. Integrating over a uniform transverse bunch density, this field leads to an rms normalized emittance growth of

$$\Delta \epsilon_n \approx \frac{1}{2} \alpha^2 \frac{I}{I_A} \ln\left(\frac{b}{a}\right) \frac{a^2}{\delta} \quad (2)$$

where α is the bend angle, I is the peak bunch current, I_A is about 17 kA, a is the beam radius, b is the beam pipe radius, and δ is the bunch length. This expression can be in turn integrated through a bunch compressor, resulting in this prediction for the emittance growth:

$$\Delta \epsilon_n \approx \frac{1}{2} \alpha^2 \frac{I_o}{I_A} \ln\left(\frac{b}{a}\right) \frac{a^2}{\delta} \left(\ln\left(\frac{I_o}{I_p}\right) + \frac{I_p}{I_o} - 1 \right), \quad (3)$$

where I_o is the uncompressed peak current and I_p is the compressed peak current. This emittance growth can be quite large - for example it is about 200π mm mrad for a 1-nC, 1-mm-radius bunch compressed to 1 ps in a 1-radian bend. If the bunch length is sufficiently short, however, this emittance growth will not occur because of causality. This emittance growth mechanism can impact advanced accelerator designs significantly, and an experimental study of this effect needs to be made.

* Work supported by the Los Alamos Laboratory Directed Research and Development program and by a Los Alamos CRADA with Grumman, CRADA number LA93C10102, under the auspices of the US Department of Energy.

** EG&G, Los Alamos, NM 87544

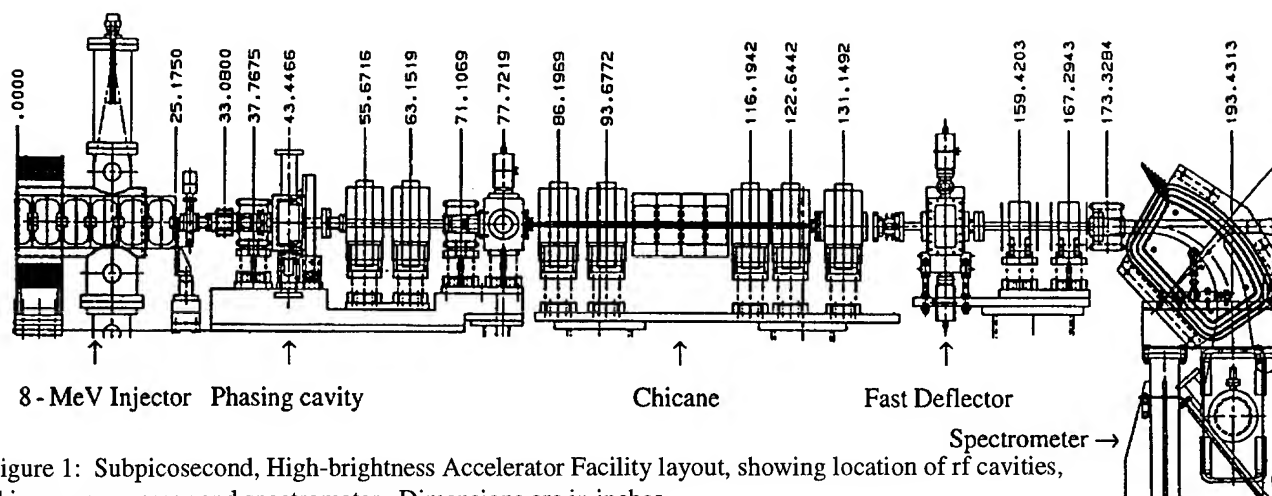


Figure 1: Subpicosecond, High-brightness Accelerator Facility layout, showing location of rf cavities, chicane compressor and spectrometer. Dimensions are in inches.

The EUV source is based on a wakefield generation in a plasma by a picosecond electron bunch. The plasma is generated by classical collisional ionization as a series of electron bunches pass through a gas target. If the electron density exceeds a critical value of about $1.6(10^{15})/\tau^2 \text{ cm}^{-3}$, where τ is the bunch FWHM in picoseconds, the wakefield in the plasma generates a large collective plasma wave. Detailed particle-in-cell simulations of the interaction indicate that an 8-MeV, 0.65 ps electron bunch will be fully decelerated after only 3 mm [10]. This plasma wave heats the background plasma electrons to about 30 eV, which then de-excite by line radiation. By optimizing the gas density, efficient (>0.1%) conversion of electron beam power to radiated power near 13 nm is possible [10].

III. LINAC DESIGN

The Subpicosecond, High-brightness Accelerator Facility, shown in Figure 1, is based on an 8-MeV photoinjector tank previously used at Los Alamos as the first acceleration tank of the 40-MeV APEX machine [11,12]. This injector will produce a low emittance ($\sim 5 \pi \text{ mm mrad}$), 10-20 ps electron bunch with a peak current of 200-300 A. The main components of the new linac are: (1) the APEX 8-MeV injector, (2) a 1-MeV phasing cavity which can modify the initial beam energy-phase correlation, (3) a four-dipole chicane for bunching, (4) a "fast-deflector" cavity which transversely spreads out the beam for time-resolved diagnostics [13], and (5) a spectrometer. All rf structures operate at 1.3 GHz.

The chicane (dipoles and beam-box) are shown in Figure 2. The first and last dipole deflect the beam upwards (in the figure) and the middle two dipoles deflect the beam downwards. As a result the beam trajectory is curved. Particles with higher energy are bent less and have a shorter path length within the dipoles while particles with lower energy are bent more and have a longer path length [14]. By adjusting the phasing cavity so the particles at the front of the bunch have a lower energy than the particles at the end of the bunch, the bunch can be compressed. The beam box is wide at the center of the chicane where the dispersion is greatest. Thus the dipoles can be gradually turned on from zero field to the condition of maximum compression, with full beam

transmission for all cases. The dipoles are H-magnets to minimize the fringe fields. The k_1 value for the fringe fields between the central magnets is 0.045, the k_1 value for the fringe fields between the dipoles of opposite polarity is 0.12, and the k_1 value for the end fringe fields is 0.22.

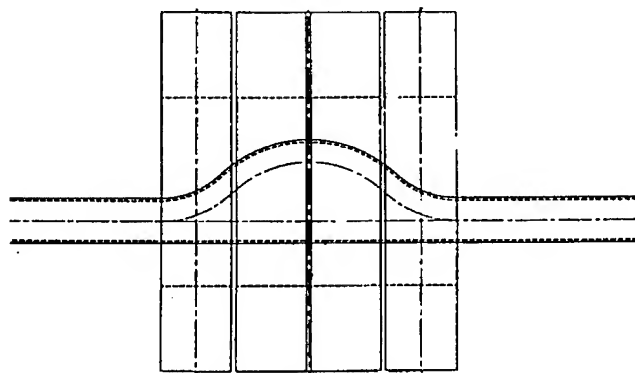


Figure 2: Top view of chicane design showing dipoles and curved beam box. The beam box maintains at least a 3:1 ratio of horizontal width to vertical width throughout.

The fast deflector, developed for the Los Alamos free-electron laser program, has a TM₁₁₀ mode operating at the same frequency as the injector and phasing cavity. The magnetic field is vertical as the bunch passes through it. If the phase of the cavity is adjusted so the field is zero when the center of the bunch is at the center of the cavity, the bunch center will not be transversely deflected. However, the front of the bunch will be deflected sideways, and the rear of the bunch will be deflected in the opposite direction. The bunch will be spread out horizontally in time, in a manner similar to the light in a streak camera. Subsequently, the spectrometer will deflect the beam vertically; the image of the beam on the screen in the spectrometer will show the phase of the particles transversely and the energy of the particles in the direction of the beam line. Thus the combination of the fast deflector and the spectrometer will provide a direct measurement of the beam's longitudinal phase space. With the distances shown in Figure 1, we predict a displacement of

1 cm on the spectrometer screen per ps, or a time resolution of at least 0.25 ps.

IV. PREDICTED PERFORMANCE

We have used the particle-pushing code PARMELA [15] to predict the performance of the Subpicosecond, High-brightness Accelerator Facility. It should be noted that PARMELA does not include the energy-independent space-charge forces described in section II, but does include all other known emittance growth mechanisms.

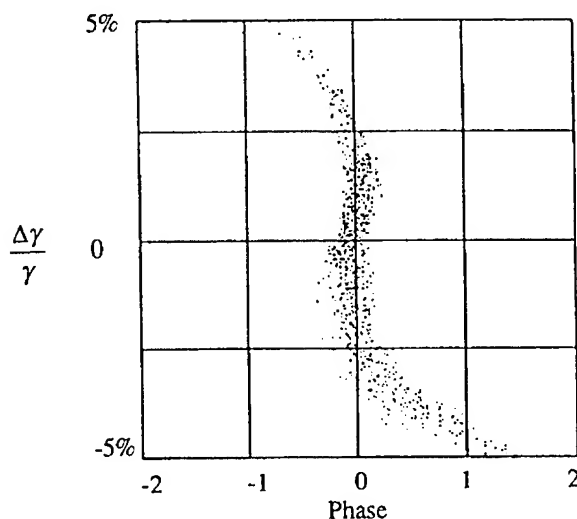


Figure 3: Longitudinal phase space of the bunch after chicane. Horizontal units are in degrees of phase at 1.3 GHz.

In Figure 3 we see the longitudinal phase space of the bunch just after the chicane. The optimum bunching occurs for a maximum bend of 39 degrees within the chicane, with an energy spread of about $\pm 2.5\%$, and leads to a bunch length FWHM of 0.65 ps. Unfortunately, at this low beam energy, the bunch length grows quickly. Simulations indicate that the bunch length roughly doubles (to about 1.2 ps) after only 75 cm and is about 2 ps after 100 cm.

V. CURRENT STATUS AND FUTURE PLANS

The machine has been constructed and is being commissioned. Compression studies have begun in anticipation of the EUV generation experiment.

Particle-in-cell calculations of the energy loss mechanism in the plasma for the EUV experiment show that accelerating gradients are produced by the plasma wave on the order of 5 GV/m. Future plans include passing a witness bunch through this plasma to fully diagnose the fields present and to demonstrate this acceleration mechanism at these gradients. The generation of a witness bunch with an arbitrary timing separation between it and the main bunch is simplified by the fact that the machine uses a photoinjector. The dense plasma will also pinch the electron beam to a small equilibrium radius. Calculations show that the equilibrium radius is about 10 μm . It should be noted that many advanced accelerator concepts operate at high frequency, and which need a picosecond-type injector. For example, at 17 GHz, 1 ps is

about 6 degrees of phase. Thus, we are also proposing to use this machine as an injector for a 100 MeV linac using the inverse axial-free-electron laser acceleration mechanism [16], operating at 17 GHz.

VI. REFERENCES

- [1] R. H. Sieman, "Overview of linear collider designs," *Proc. 1993 Part. Accel. Conf.*, Washington, D. C., May, IEEE catalog number 93CH3279-7, 532 (1993).
- [2] T. O. Raubenheimer, R. Emma, and S. Kheifets, "Chicane and wiggler based bunch compressors for future linear colliders," *Proc. 1993 Part. Accel. Conf.*, Washington, D. C., May, IEEE catalog number 93CH3279-7, 635 (1993).
- [3] K. L. Bane, T. O. Raubenheimer, and J. T. Seeman, "Electron transport of a linac coherent light source (LCLS) using the SLAC linac," *Proc. 1993 Part. Accel. Conf.*, Washington, D. C., May, IEEE catalog number 93CH3279-7, 596 (1993).
- [4] I. Ben-Zvi, J. Corbett, E. Johnson, K. J. Kim, R. Sheffield, *Proc. Workshop on Fourth Generation Light Sources*, Stanford, CA, SSRL 92/02, 68 (1992).
- [5] M. Uesaka, K. Tauchi, T. Kozawa, T. Kobayashi, U. Ueda, and K. Miya, "Generation of a subpicosecond relativistic electron single bunch at the S-band linear accelerator," *Phys. Rev. E*, **50**, 3068 (1994).
- [6] P. Kung, H. Lihn, and H. Wiedemann, "Generation and measurement of 50-fs (rms) electron pulses," *Phys. Rev. Lett.*, **73**, 967 (1994).
- [7] B. E. Carlsten and T. O. Raubenheimer, "Emittance growth of bunched beams in bends," *Phys. Rev. E*, **51**, 1453 (1995).
- [8] S. Russell, D. Gilpatrick, J. Power, and B. Shurter, "Characterization of beam position monitors for measurement of second moment," these proceedings.
- [9] R. Keinigs, M. E. Jones, and J. J. Su, "Simulations of the Wisconsin-Argonne plasma wakefield experiment," *IEEE Trans. Plasma Sci.*, **PS-15**, 199 (1987).
- [10] R. D. Fulton, J. Abdallah, J. C. Goldstein, M. E. Jones, D. P. Kilcrease, J. M. Kinross-Wright, S. H. Kong, and D. C. Nguyen, "A debris free, electron beam driven, lithography source at 130 Å," submitted to OSA Topical Meeting on EUV Lithography, Monterey, CA, Sept. 1994.
- [11] B. E. Carlsten, L. M. Young, M. E. Jones, L. E. Thode, A. H. Lumpkin, D. W. Feldman, R. B. Feldman, B. Blind, M. J. Browman, and P. G. O'Shea, "Design and analysis of experimental performance of the Los Alamos HIBAF facility accelerator using the INEX computer model," *IEEE Journ. Quant. Elec.*, **QE-27**, 2580 (1991).
- [12] P. G. O'Shea, S. C. Bender, B. E. Carlsten, J. W. Early, D. W. Feldman, R. B. Feldman, W. J. D. Johnson, A. H. Lumpkin, R. L. Sheffield, R. W. Springer, W. E. Stein, and L. M. Young, "Performance of the photoinjector accelerator for the Los Alamos free-electron laser," *Proc. 1991 IEEE Part. Accel. Conf.*, San Francisco, CA, May, 1991, IEEE Cat. No. 91CH3038-7, 2754 (1992).
- [13] R. L. Sheffield, W. E. Stein, R. W. Warren, J. S. Fraser, and A. H. Lumpkin, "Electron-beam diagnostics and results for the Los Alamos free-electron laser," *IEEE Journ. Quant. Elec.*, **QE-21**, 2580 (1985).
- [14] B. E. Carlsten, B. D. McVey, E. M. Svaton, G. R. Magelssen, and L. M. Young, "Magnetic bunchers for the generation of high peak current, low emittance electron pulses at medium energy," *Proc. 1990 Linear Acc. Conf.*, Los Alamos National Laboratory report LA-12004-C, 641 (1991).
- [15] L. M. Young, private communication.
- [16] B. E. Carlsten, W. B. Haynes, and R. L. Sheffield, "Particle acceleration by the inverse axial-free-electron laser interaction," submitted to *Part. Accel.*

ENERGY SPREAD COMPENSATION IN AN ELECTRON LINEAR ACCELERATOR

Yu. D. Tur, A. N. Dovbnya, V. A. Kushnir, V. V. Mitrochenko, D. L. Stepin, National Science Center - Kharkov Institute of Physics & Technology, 310108Kharkov, UKRAINE

Abstract

Results are presented of experimental studies on beam parameters at the exit from an rf-injector and a single-section accelerator. It is demonstrated that owing to an assigned amplitude and electromagnetic field phase relationship in the rf-gun during the pulse, one can get in a position to optimize bunches inflight phases into the accelerating section during which compensation is observable of the beam energy spread induced by current loading of accelerating section.

1. INTRODUCTION

One of the well known techniques of an intense beam energy spread compensation, the spread being accounted for by current loading of accelerating structure, is the one of bunch inflight optimization into the accelerating field [1]. Simply put, this technique is such that, owing to an assigned variation of the current pulsehead bunch inflight, in other words, owing to variation of the accelerating field amplitude, governing the bunch behavior, from the initially assigned value up to very maximum, the pulsehead bunch energy increment becomes equal to the bunch energy increment during the steady-state acceleration mode of a loaded section. Below we will show that these conditions can be materialized in single-section accelerator that have rf-gun-based injectors and a magnetic compressor [2].

2. DESCRIPTION OF THE DESIGN

The electron beam whose phase-energy characteristics are shown in Fig.1 is formed in the rf-gun, then energy-separated (hatched region in Fig.1), while bunches passing through the magnetic compressor (α -magnet) and compressed along the longitudinal coordinate. It should be noted that on account of beam cavity loading the field amplitude temporal characteristic inside the cavity (oscillogram b, Fig.2). As shown from some auxiliary research [3], a substantial contribution is made by electron back-bombardment under rf-field and cathode heating.

As a result, due to field amplitude-phase variations inside the cavity, the integrated bunch phase width during the entire pulse exceed 17° FWHM. Fig.3 shows results of particle phase distribution measurements in a pulse-averaged bunch. The technique is based on the analysis of the amplitude of current passing through the slot collimator during the beam circular sweep in the cavity while transverse-type oscillations of the fundamental frequency field are present [4].

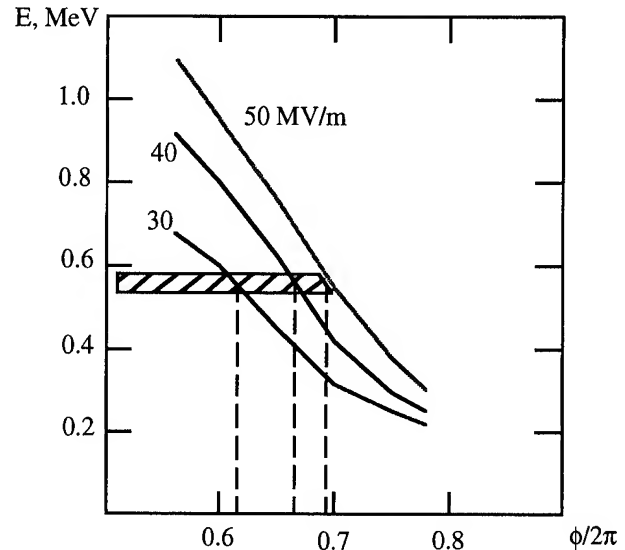


Figure 1. Particle phase-energy distribution per bunch at different rf-gun field strengths.

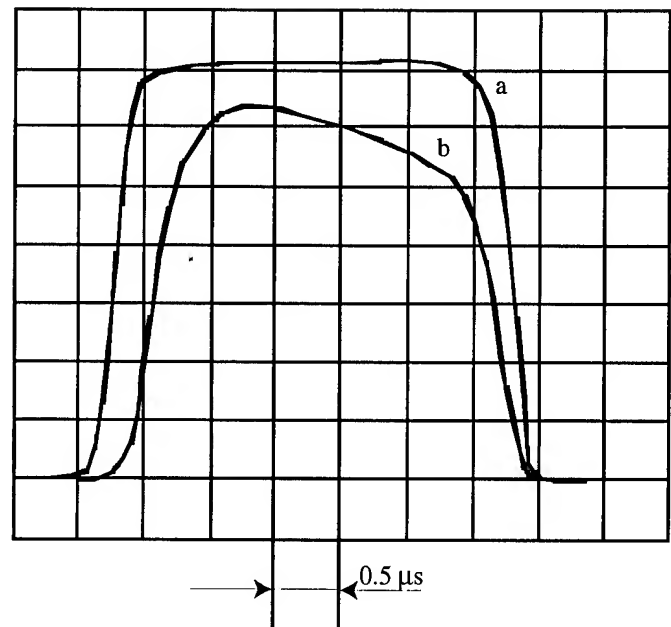


Figure 2. Oscillograms: a) rf-gun input rf-signal; b) rf-gun cavity field.

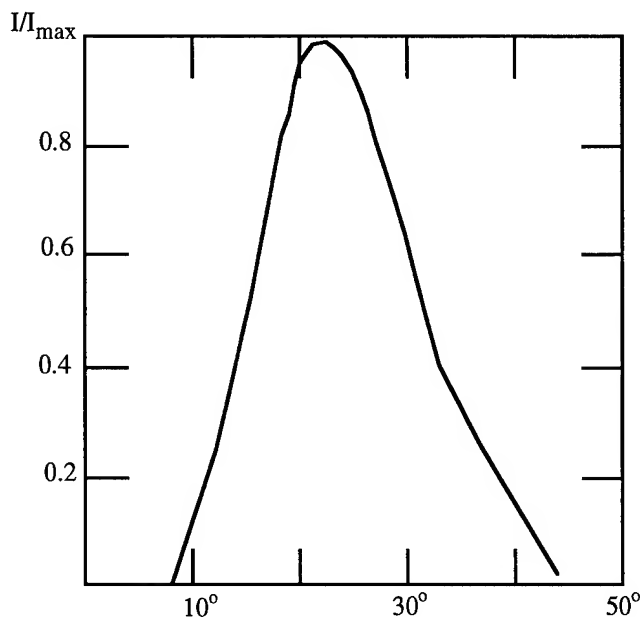


Figure 3. Pulse averaged particle phase distribution in bunches leaving the magnetic compressor.

Using the electrostatic deflector for selecting the current pulse in the downward field region of the cavity (oscillogram b, Fig.2) and by accelerating these 25-ns pulses at invariable field amplitude-phase characteristics of the accelerating section, we succeeded in determining the regularity of bunch inflight phase distribution such that bunch energy increment varied during 0.4 μ s macropulse from 56 MeV to 59 MeV (Fig.4). This done, the current (0.1A) energy spectrum measurement spread for 90% particles does not exceed 2% which corresponds to the resolution limit of the spectrometer used. For this structure this value is 13%, the filling time being 1 μ s, loading characteristic 80 MeV/A during the routine acceleration mode (some inflight phase for all bunches in the 1 μ s pulse at 0.1 A current). In this manner, the conclusion can be made that there is observation of the energy spread compensation effect which occurs due to the bunch inflight phases optimization during current pulse.

3. CONCLUSION

Finally, a few words must be said about some possible techniques of monitoring the flow phase characteristic variations at the rf-gun exit. Evidently, for this purpose one could use various rf-devices, allowing to change rf-gun amplitude-phase and temporal characteristics. Yet, from our standpoint, of more practical interest shall be the technique of cavity load manipulations by using the back-bombardment electrons effect.

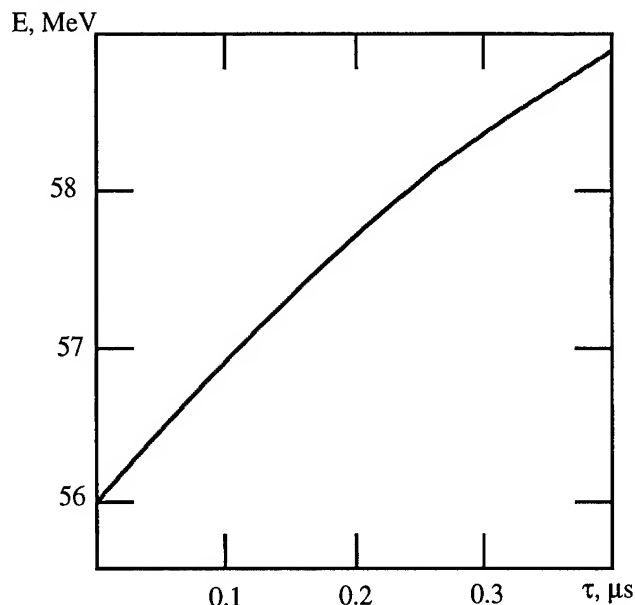


Figure 4. Relationship of energy increment of 25 ns select pulses vs. their temporal position inside the macropulse.

As shown in paper [5], application of a transverse magnetic field provides for the effective back-particles characteristic variations, i. e. cathode heat loads, and, accordingly, for those of emission currents and amplitude-temporal and phase characteristics of the cavity field. We have plans for more detailed study on this problem.

REFERENCES

1. A.N. Lebedev, A.V. Shal'nov. Fundamentals of Accelerator Physics and Technology, Moscow, Ehrgoatomizdat, 1991
2. A.N. Dovbnya, V.A. Kushnir, D.L. Stepin et al. Experimental studies on beam parameters of a compact 60-MeV electron linac. Voprosy Atomnoi Nauki i Tehniki{VANT}, 1991, 3/21/p.3
3. N.V. Demidov, V.S. Demin, A.N. Dovbnya et al. RF-gun with Ba-Ni oxide cathode, VANT, 1992, 4/25/, p.10
4. E.S. Zlunitsyn, A.I. Zykov, V.A. Kushnir et al. Electron beam phase analysis device on circular sweep resonator. VANT, Kharkov, 1986, 2/28/, p.34
5. C.B.McKee and John M.J. Madey. Optimization of a Thermionic Microwave Electron Gun. Nuclear Instrument and Methods in Physics Research, A 304 (1991), p.386

ON ENHANCEMENT OF LIMITED ACCELERATING CHARGE

Yu. Tur, National Science Center - Kharkov Institute of Physics & Technology,
310108 Kharkov, UKRAINE

Abstract

Results are presented of theoretical analysis of electron flow interactions with the accelerating field of superposed multiple parts of the first and second harmonics. It is shown that at certain phases and amplitudes relationships the limited charge value can be increased in bunches of considerable phase lengths owing to the preservation of identical accelerating conditions and decreasing of the losses to radiation by the beam.

One of the fundamentals problem of the physics of accelerators is the one of increasing the accelerated charge limit at restrained levels of rf-power input and rf emittance growth suppression. Underlying this proposal are the effects of the non-linear relationship of bunch-radiated field amplitude vs. its phase length and, also, the feasibility of providing the identical acceleration conditions for all particles in a lengthy bunch and emittance preservation in the "table-type" rf-field, realized by way of inclusion in the acceleration mode of multiple frequency harmonic superposition. It must be noted that the acceleration technique, providing for excitation in each of the accelerating space of rf-fields at multiply frequencies with the resulting envelope shape being close to rectangular, is well known and employed, for instance, in proton synchrotron for widening the region of phase stability and lowering the space charge effect (see, for instance [1]). Below is given the evaluation of this technique to the problems of increasing the accelerating charge limit.

Considered is a cavity of arbitrary transverse cross section with a length of the interaction region d and two resonances at frequencies ω and 2ω . Let's consider excitation of this cavity in the approximation assigned current from an external oscillator by the current with density

$$\vec{j} = \vec{j}_{11} \cos(\omega\tau) + \vec{j}_{12} \sin(\omega\tau) + \vec{j}_{21} \cos(2\omega\tau) + \vec{j}_{22} \sin(2\omega\tau) \quad (1)$$

as well as by a beam with pulsed current I , bunches of which of the length 2τ moving with the velocity v , are taken to be rectangular, then expanding into the Fourier series we have for the beam current density

$$\begin{aligned} j_{xn} &= j_{yn} = 0 \\ j_{zn} &= j_0 f(x, y) \left[\frac{\sin \omega\tau}{\omega\tau} \cos \omega \left(t - \frac{z}{v} \right) + \frac{\sin 2\omega\tau}{2\omega\tau} \cos 2\omega \left(t - \frac{z}{v} \right) \right] \end{aligned} \quad (2)$$

Expanding the vector-potential of the excited field into the cavity eigen-modes

$$\vec{A} = \sum_i q_i(t) \vec{A}(\vec{r}),$$

the set of equations for cavity field will be written down as follows:

$$\ddot{q}_1 + 2\beta_1 \dot{q}_1 + \omega^2 q_1 = 4\pi \cdot c \frac{\int (\vec{j}_{12} + \vec{j}_{1n}) \vec{A}_1 d\vec{v}}{\int \vec{A}_1^2 d\vec{v}}. \quad (3)$$

$$\ddot{q}_2 + 2\beta_2 \dot{q}_2 + 4\omega^2 q_2 = 4\pi \cdot c \frac{\int (\vec{j}_{22} + \vec{j}_{2n}) \vec{A}_2 d\vec{v}}{\int \vec{A}_2^2 d\vec{v}}$$

Considering for the sake simplicity that E is independent of z and doing the integration, we will obtain:

$$q_1 = \frac{D_1 I_0 \frac{\sin \omega\tau}{\omega\tau} - I_1}{2\beta_1 \omega_1} \sin \omega_1 t; \quad q_2 = \frac{D_2 I_0 \frac{\sin 2\omega\tau}{2\omega\tau} + I_2}{2\beta_2 \omega_2} \sin \omega_2 t \quad (4)$$

where

$$I_1 = -4\pi c \frac{\int \vec{j}_{11} \vec{A}_1 d\vec{v}}{\int \vec{A}_1^2 d\vec{v}}; \quad I_2 = 4\pi c \frac{\int \vec{j}_{12} \vec{A}_2 d\vec{v}}{\int \vec{A}_2^2 d\vec{v}} \quad (4a)$$

$$D_1 = 4\pi c \frac{2 \frac{v}{\omega} \sin \frac{\omega d}{2v} \int f(x, y) \vec{A}_{z1} dx dy}{\int \vec{A}_1^2 d\vec{v}} \quad (4b)$$

$$D_2 = 4\pi c \frac{\frac{v}{\omega} \sin \frac{\omega d}{v} \int f(x, y) \vec{A}_{z2} dx dy}{\int \vec{A}_2^2 d\vec{v}}$$

At which, the harmonic phases are chosen such that $I_1 > 0$ and $I_2 > 0$, while

$$\int \vec{j}_{11} \vec{A}_1 d\vec{v} = \int \vec{j}_{22} \vec{A}_2 d\vec{v} = 0$$

Hence the expression for the resulting cavity field in the steady-state regime:

$$\bar{E} = \frac{I_1 - D_1 j_0 \frac{\sin \omega \tau}{\omega \tau}}{2\beta_1 c} \bar{A}_1(\bar{r}) \cos \omega t - \frac{I_2 + D_2 j_0 \frac{\sin 2\omega_0 \tau}{2\omega_0 \tau}}{2\beta_2 c} \bar{A}_2(\bar{r}) \cos(2\omega t) \quad (5)$$

We'll find the increment of particle energy:

$$\Delta W = e \int_{-d/2}^{d/2} E(t = t_0 + z/v) dz \quad (6)$$

here t is the particle time-of-flight through the center of cavity.

Substituting (5) and integrating (6), we will obtain:

$$\Delta W = \Delta W_{\bar{A}_1} \cos \omega t_0 - \Delta W_{\bar{A}_2} \cos 2\omega t_0 - c_1 j_0 \frac{\sin \omega \tau}{\omega \tau} \cos \omega t_0 - c_2 j_0 \frac{\sin 2\omega \tau}{2\omega \tau} \cos 2\omega t_0 \quad (7)$$

where

$$\Delta W_{\bar{A}_1} = \frac{evI_1}{\beta_1 \omega \cdot c} A_{1z}(x_0, y_0) \sin\left(\omega \frac{d}{2v}\right) \quad (7a)$$

$$\Delta W_{\bar{A}_2} = \frac{evI_2}{2\beta_2 \omega \cdot c} A_{2z}(x_0, y_0) \sin\left(\omega \frac{d}{v}\right)$$

$$c_1 = \frac{evD_1}{\beta_1 \omega \cdot c} A_{1z}(x_0, y_0) \sin\left(\omega \frac{d}{2v}\right) \quad (7b)$$

$$c_2 = \frac{evD_2}{2\beta_2 \omega \cdot c} A_{2z}(x_0, y_0) \sin\left(\omega \frac{d}{v}\right)$$

x_0, y_0 are the beam transverse coordinates.

Let's compare the obtained result with the single-harmonic interaction case with small phase space of the bunch ($\omega\tau \rightarrow 0$)

$$\frac{\Delta W_{\text{max}}}{\Delta W_1^{\text{max}}} = \frac{\Delta W_{\bar{A}_1} - \Delta W_{\bar{A}_2} - c_1 j_0 \frac{\sin \omega \tau}{\omega \tau} - c_2 j_0 \frac{\sin 2\omega \tau}{2\omega \tau}}{\Delta W_{\bar{A}_1} - c_1 j_0} \quad (8)$$

and at ($\omega\tau > 1$)

$$\frac{\Delta W_{\text{max}}}{\Delta W_1^{\text{max}}} = \frac{\Delta W_{\bar{A}_1} - \Delta W_{\bar{A}_2}}{\Delta W_{\bar{A}_1} - c_1 j_0} \quad (9)$$

As an example, let's consider beam acceleration in the cavity excited by the first and second harmonic at power input ratio 10:1 with angle of flight at the fundamental frequency $\frac{\omega \cdot d}{2v} = \pi/2$. In this case, the identical conditions for accelerating all particles become feasible to fulfill for bunches with the phase space up to 30°, and, as it is easy to deduce from the above relationships, the losses to radiation by the beam can be decreased as compared to the single-frequency case, by $\approx \frac{\omega \tau}{\sin \omega \tau}$, i.e. the limit of accelerated charge is thus raised.

REFERENCES

- [1] L.Z. Barabash, P.I. Lebedev et al. Enhancement of particle capture in proton synchrotron by adding the second harmonic to the accelerating field-Proc. All-Union Seminar on Charge Particle Accelerators, Moscow, 1968, vol.2, 123-127.

Magnetic Pulse Compression Using a Third Harmonic RF Linearizer*

D.H. Dowell, T. D. Hayward and A.M. Vetter
Boeing Defense & Space Group
Seattle, Washington

Abstract

A scheme for compressing 4 nC, 55 ps long bunches to 7 ps at 18 MeV uses, in addition to a magnetic chicane, a third harmonic RF section serving the dual functions of (1) removing the nonlinear distortion placed on the bunch by the upstream linac and (2) impressing on the bunch the linear energy slew required for compression in the chicane. The performance improvement expected from using the linearizer is estimated using an heuristic model based on bunching experiments[1].

Introduction

Electron beam applications, such as free electron lasers, require electron beams with both low emittance and high peak current. While the RF photocathode injector has demonstrated excellent beam quality, the emittance has been observed to grow as the micropulse charge (and hence the peak current) at the photocathode is increased. For the injector discussed in this paper the rms emittance increases at the rate of 1.1π mm mrad per nanocoulomb of charge[2]. This emittance growth can be controlled by beginning with a long, but high charge micropulse with a low peak current in the injector, and then, when the beam is relativistic, compressing it in a non-isochronous bend.

In this scheme the compression factor, the ratio of the before and after pulse lengths, is limited by the non-linearities introduced by RF and space charge forces. The space charge effects are already reduced by limiting the peak current at the cathode and are included by using the results of a longitudinal emittance experiment. The accelerating RF waveform introduces a curvature to the longitudinal phase space. This paper discusses the use of a third harmonic accelerator section to both linearize the phase space to increase the compress factor, and to impress the required energy slew for compression in a three dipole chicane.

Description of the Experiment

The layout of the Boeing 18 MeV photoinjector accelerator is shown in Figure 1 [3]. The accelerator consists of a 433 MHz, two cavity injector using a K_2CsSb photocathode driven by a frequency doubled Nd-YLF mode-locked laser[4]. The energy after the injector cavities is 2 MeV. This is followed by four 433 MHz accelerator sections which accelerate the beam to 18 MeV. Besides quadrupoles and electron beam diagnostics, the beamline consists of the third harmonic linearizer (a 1300 MHz accelerator section), a three dipole chicane buncher and an electron beam dump.

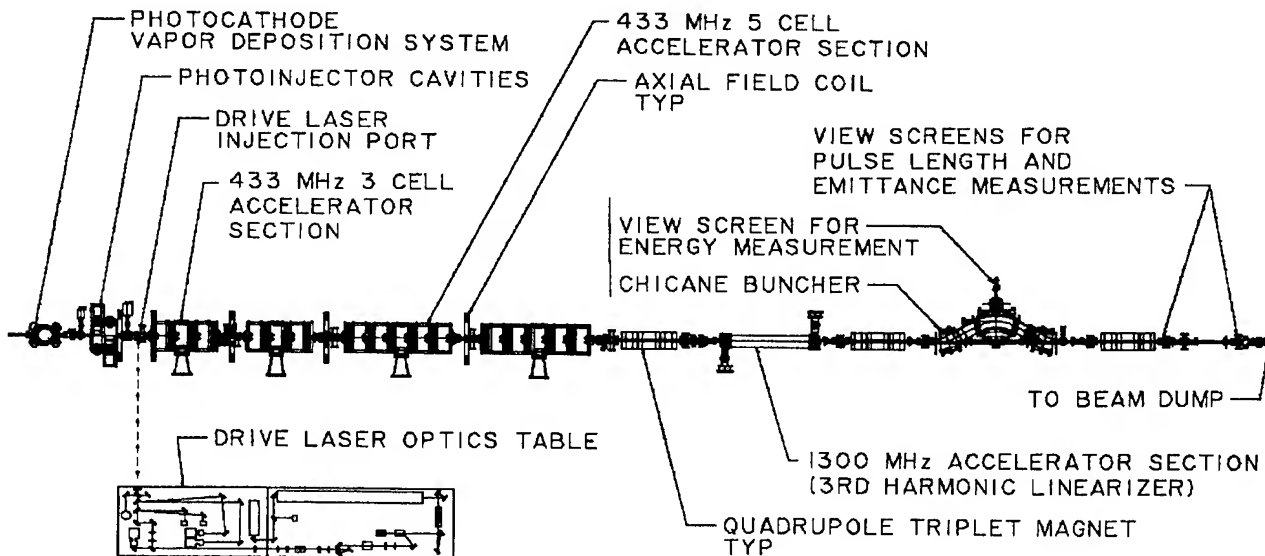


Figure 1. Accelerator configuration showing the injector cavities, 433 MHz accelerator sections, the 1300 MHz third harmonic linearizer and the three dipole chicane buncher.

*Work supported by USASSDC under contract DASG60-90-C-0106.

The object of this experiment is to determine the pulse compression factors both without and with the linearizer in operation. This is done by measuring the pulse length after the chicane with a streak camera, and the energy spread at the view screen in middle dipole of the chicane, first using the 433 MHz sections and then the linearizer to produce the energy slew.

Calculation of Beam Compression

The compression factor is calculated by beginning at the exit of the injector cavities and using the following relations to transform the beam's longitudinal phase space through the accelerator sections and the chicane. Since the phase space is distorted by non-linear effects it is necessary to perform a ray tracing calculation[1].

In terms of the initial paraxial longitudinal coordinates ΔE_0 and Δt_0 , the accelerator transformation is

$$\Delta E_1 = E_{433} [\cos(\omega_{433} \Delta t_0 + \phi_{433}) - \cos \phi_{433}] + \Delta E_0$$

$$\Delta t_1 = \Delta t_0$$

Here E_{433} is the peak energy gain in the 433 MHz accelerator sections and ϕ_{433} is the micropulse synchronous phase relative to the accelerating peak of the 433 MHz waveform. Similar relations transform the beam through the 1300 MHz linearizer, so that at the entrance to the bunching chicane the transformation is

$$\Delta E_2 = E_{1300} [\cos(\omega_{1300} \Delta t_1 + \phi_{1300}) - \cos \phi_{1300}] + \Delta E_1$$

$$= E_{1300} [\cos(3\omega_{433} \Delta t_0 + \phi_{1300}) - \cos \phi_{1300}]$$

$$+ E_{433} [\cos(\omega_{433} \Delta t_0 + \phi_{433}) - \cos \phi_{433}] + \Delta E_0$$

$$\Delta t_2 = \Delta t_1 = \Delta t_0$$

The 1300 MHz RF voltage is adjusted so that its second derivative exactly cancels that of the 433 MHz waveform; i.e., so that

$$\left. \frac{d^2 \Delta E_2}{d \Delta t_2^2} \right|_{\Delta t_2=0} = 0.$$

This condition is obtained when

$$E_{1300} \cos \phi_{1300} = - \frac{E_{433} \cos \phi_{433}}{9},$$

or when the third harmonic section removes 1/9 of the beam energy, or 2 MeV. Generally, $\phi_{433} = 0$, and ϕ_{1300} is chosen to provide the temporal ramp required for bunching in the chicane, where the transformation is

$$\Delta E_3 = \Delta E_2$$

$$\Delta t_3 = \delta \Delta E_2 + \Delta t_2,$$

δ being the longitudinal non-isochronicity of the chicane (for our chicane, $\delta = 50$ ps/MeV). For the tightest possible bunching, we would require an end-to-end energy slew of 1.1 MeV over the 55 ps duration of the bunch in order to collapse the bunch completely. This requires

$$E_{1300} \sin \phi_{1300} = 2.45 \text{ MeV}.$$

Given that

$$E_{1300} \cos \phi_{1300} = 2 \text{ MeV},$$

we have

$$E_{1300} \approx 3.2 \text{ MeV}, \quad \phi_{1300} \approx 50^\circ.$$

The calculation begins at the exit of the injector cavity and the initial phase space is obtained from the experiment performed at the ELSA FEL facility at Bruyeres-le-Chatel, France[1,5]. In this experiment the uncorrelated energy spread of the injector beam was observed to increase from 14 KeV to 22 KeV as the peak current density at the photocathode was increased from 200 A/cm² to 400 A/cm² with negligible pulse length elongation. For our case of 4 nC and 55 ps, the peak current density is 237 A/cm². Therefore the uncorrelated energy spread after the injector is estimated to be 15 KeV.

The longitudinal phase space beginning at the injector cavity exit and its transformations to the entrance and exit of the chicane are shown in Figure 2. The curvature distortion due to the 433 MHz waveform is most evident at the chicane exit where the phase space has been rotated to bunch the beam. Figure 3 shows the compressed phase space with the third harmonic linearizer in use. The s-shape is due

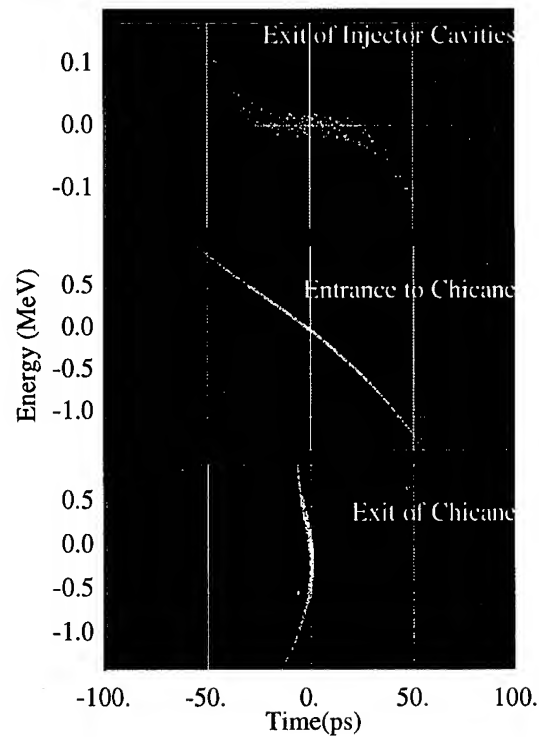


Figure 2. Evolution of the longitudinal phase space during compression without the linearizer.

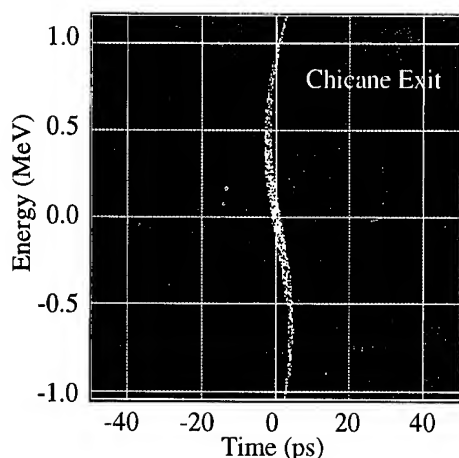


Figure 3. Longitudinal phase space after the chicane when the beam is linearized and compressed.

to space charge distortion in the injector and is the result of the data analysis in Reference 1.

The projections of the compressed phase spaces onto the time-axis are given in Figures 2 and 3 are shown in Figure 4. While the non-linearized beam has a smaller FWHM,

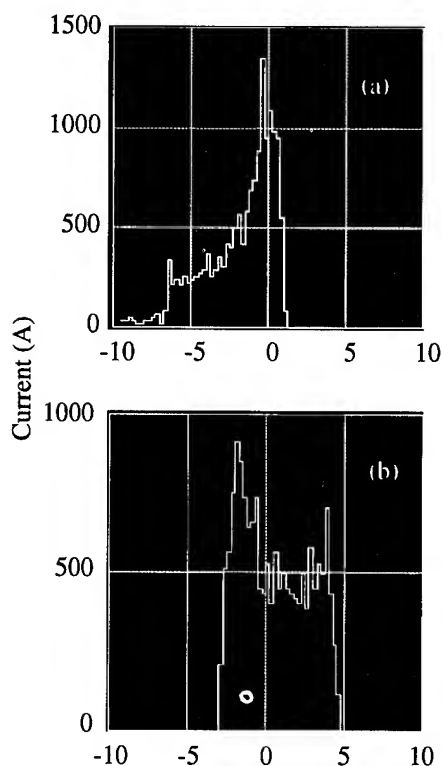


Figure 4. Comparison of the compressed electron beam pulse shapes without (a) and with (b) the phase space linearized.

it has a long tail reducing the number of well bunched electrons by approximately half. In contrast, the linearizer produces a square pulse shape of nearly constant peak current.

Conclusions

Using a third harmonic RF linearizer before a three dipole chicane buncher generates a nearly flat-topped 4 nC electron beam pulse 7 ps wide with a peak current 500 A. This square pulse shape makes efficient use of the electrons and leads to improved performance of devices such as free electron lasers[6].

References

1. S. Joly et al., "Brightness Measurements of the ELSA Electron Beam", Contribution to the 1994 Linear Accelerator Conference, Tsukuba, Japan.
2. D.H. Dowell et al., "First Operation of a High Duty Factor Photoinjector", Proc. of the 1993 Particle Accelerator Conference, Washington D.C., 2967 (1993).
3. T.D. Hayward et al., "A High Duty Factor Linac for FEL", submitted to this conference.
4. D.H. Dowell, S.Z. Bethel and K.D. Friddell, "Results from the Average Power Laser Experiment Photocathode Injector Test", Nuclear Instruments and Methods, in press.
5. D.H. Dowell and S. Joly, private communication.
6. J. Adamski et al., "A Kilowatt Class Visible Free Electron Laser Facility", submitted to this conference.

A COMPARISON OF L-BAND AND C-BAND RF GUNS AS SOURCES FOR INLINE-INJECTION SYSTEMS

Juan C. Gallardo and Harold G. Kirk

Physics Department, Bldg. 901-A
Brookhaven National Laboratory
Upton, New York 11973-5000

and

Thomas Meyerer

Fachhochschule Ostfriesland
Constantiaplatz 4
D-2970 Emden, Germany

Abstract

We consider the beam dynamics associated with installing a BNL type $1\frac{1}{2}$ cell L-band or C-band rf gun before two TESLA L-band cryomodules. This system will deliver a 25 MeV electron beam with peak currents on the order of 100 A suitable for further magnetic compression. We evaluate the injection systems utilizing the electron beam dynamic code PARMELA from the point of view of minimizing the transverse invariant emittance.

INTRODUCTION

High-brightness beams are of great interest to the accelerator physics community because of the promise they hold to access new regimes of physics. These regimes include high-luminosity colliders, high-gain free-electron lasers, and high-brightness photon beams which have applications in both the physical and life sciences. Rf guns remain the focus of efforts to produce such high-brightness beams. L-band (1300 MHz) rf guns built at Los Alamos National Laboratory¹ and S-band (2856 MHz) rf guns built at Brookhaven National Laboratory² have demonstrated experimentally the value of this approach.

The dynamics of electron beams produced by rf guns has been the subject of much attention, especially the beam dynamics pertaining to the production and subsequent dilution of beam emittance in both transverse and longitudinal phase space. The two most significant contributors to emittance dilution in the production of electron beams are the rf dynamics (important for long bunches relative to the period of the rf cycle) within the rf gun and space-charge effects (important for short bunches with high charge content) associated with self fields within the electron bunch. In this paper we will model beams which fall into the later category.

It has been shown that the emittance dilution associated with space-charge effects within an electron bunch can be compensated and reversed by the simple technique of focusing the beam with a solenoidal lens and allowing the beam to drift³. If one takes the additional step of accelerating the beam at an appropriate point, it is possible to lock in the reduced emittance of the compensated beam near the minimum value. Further, it has been demonstrated that this technique can be extended beyond

the L-band regime to an S-band system⁴ which in general has higher accelerating gradients within the rf gun.

In this paper we continue to explore this emittance compensation technique by applying it to an rf gun-focusing solenoid-superconducting linac system (see Fig. 1). We examine two possible rf guns: a $1\frac{1}{2}$ cell BNL type 1300 MHz rf gun and a 5200 MHz rf gun. Table 1 gives design parameters for the two rf guns. For the linac section we model two TESLA 9-cell cryomodules which, when run at accelerating gradients of 10 MV/m, are capable of boosting the beam energy by 20 MeV. An important advantage to using superconducting linac sections, aside from the high duty factor, is that the larger apertures of the accelerating structures greatly reduce possible emittance growth due to wake field effects acting on the beam. This has been shown to be potentially harmful to the electron beam when an S-band traveling wave linac is used during the acceleration stage⁵.

Table 1. Parameters of the modeled rf guns

RF frequency [MHz]	1300	5200
RF Peak Power [MW]	4.8	7.7
Field on cathode [MV/m]	50	180
Radius of aperture [cm]	2.2	.55
Radius of nose [cm]	2.2	.55
First cell length [cm]	5.765	1.45
Second cell length [cm]	13.53	2.90
Gun Exit Energy, MeV	4.8	4.6

BEAM DYNAMICS

A bright beam at the exit of an rf gun does not assure an equivalent beam at the final focus. The transport of the beam in conjunction with space-charge forces must be an integral part of the study. It has been pointed out in the previous section, that the interplay of space-charge forces with solenoidal focusing forces can lead to a reduction of the transverse emittance inside the linac. Details of the dynamics of this emittance compensation have already been given in references 4 and 5.

Our studies have been carried out by modeling the injection system with the $2\frac{1}{2}$ -d simulation code PARMELA⁶. The optimization procedure incorporates the four principle elements of the system: an rf-photocathode gun, a solenoid pair, drift sec-

tions, and the linac sections.

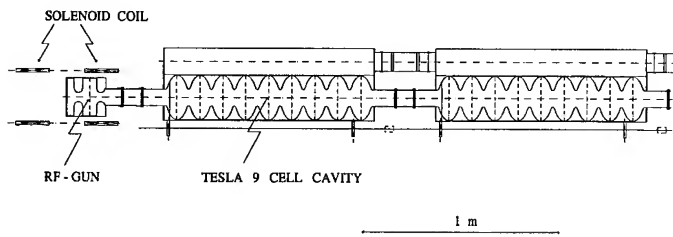


Figure 1. Schematic showing a general layout of an rf gun—focusing solenoid—superconducting linac system.

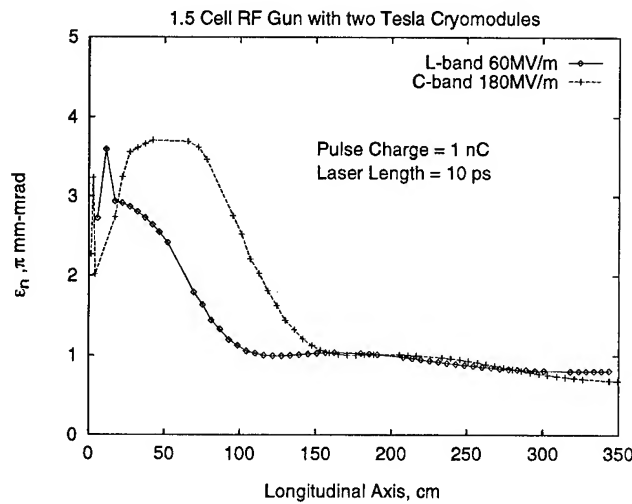


Figure 2. Invariant transverse emittance ϵ_n vs. the distance of the electron bunch from the cathode for the cases of an L-band (1300 MHz) rf gun and a C-band (5200 MHz) rf gun.

The parameter space for this system is complex. We have chosen to keep some variables fixed while we vary others. We vary the radius and bunch length of the initial electron beam as well as the time of launch relative to the rf phase. The bunch charge is fixed at 1 nC, the length of the solenoid is fixed at 15 cm, and the average accelerating gradient of the linac sections is set at 10 MV/m. The distance from the cathode to the linac entrance is varied as is the position of the focusing solenoid relative to the cathode. In general, it is found that the solenoid needs to be closer to the cathode when the accelerating gradient within the rf gun is low. A uniform beam distribution is used as it offers significant advantages over Gaussian distributions in terms of minimizing the final beam emittance. Parameters ranges used in this analysis are shown in table 2.

Table 2. Parameters used in the PARMELA simulations for axially symmetric $1\frac{1}{2}$ -cell guns in a π -mode configuration with a solenoid pair.

Field on cathode [MV/m]	40 to 300
Initial phase [degree]	20 to 70
Laser spot size ^a [cm]	0.05 to 0.4
Laser pulse width ^a [ps]	5 to 20
Charge [nC]	1
Solenoidal field B_0 [kG]	1.5-5.0
Solenoid length [cm]	15.0

^aUniform profile

We show in Fig. 2 solutions for delivering a 1 nC beam through the linac. The L-band rf gun result assumes a peak axial electric field of 50 MV/m. It is of particular interest that the emittance compensation technique continues to work for the C-band rf gun operating with peak axial electric fields at 180 MV/m.

We explore this effect further by obtaining the minimum transverse emittances achievable when operating the rf gun with different accelerating gradients. The results of this analysis are shown in Fig. 3. Both rf guns exhibit a strong upturn of emittance at lower accelerating gradients showing that it is advantageous to apply high accelerating gradients at the electron source. These high gradients reduce the development of emittance growth but do not seriously detract from the ability to compensate for the emittance growth that does occur.

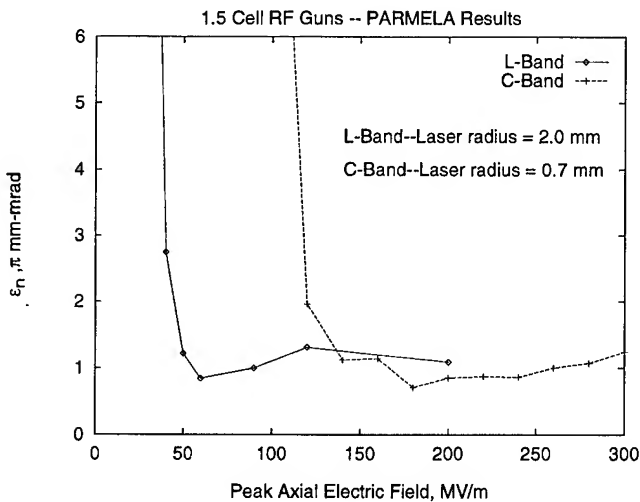


Figure 3. Invariant transverse emittance ϵ_n vs. the cathode peak electric field for the cases of an L-band (1300 MHz) and a C-band (5200 MHz) rf gun

CONCLUSIONS

We have verified that the emittance growth resulting from space-charge induced phase-space dilution can be compensated when an L-band rf gun is incorporated into an inline-injection system. In addition, we have shown that this compensation works as well or better when higher accelerating gradients are introduced into the rf gun. Unfortunately, the application of high gradients in an L-band gun is limited by Kilpatrick scaling⁷ to axial accelerating fields on the order of 60 MV/m. However,

we have shown that it is still possible to achieve good emittance compensation at higher frequencies where higher accelerating gradients are attainable.

ACKNOWLEDGMENTS

This research was supported by the U.S. Department of Energy under Contract No. DE-ACO2-76-CH00016.

REFERENCES

1. J.S. Fraser et al, *Photocathodes in Accelerator Applications*, Proceedings of the 1987 IEEE Particle Accelerator Conference, Washington D.C., E. Lindstrom and L.S. Taylor eds. (1987) p. 1705.
2. K. Batchelor, H. Kirk, J. Sheehan, M. Woodle, K. McDonald, *Development of a High-brightness Electron Gun for the Accelerator Test Facility at Brookhaven National Laboratory*, Proceedings of the 1988 European Particle Accelerator Conference, Rome, Italy, (1988).
3. B. Carlsten, *New photoelectric injector design for the Los Alamos National Laboratory XUV Fel accelerator*, Nucl. Instr. and Meth. **A285** (1989) 313.
4. J. Gallardo and H. Kirk, *An injection scheme for the Brookhaven ATF utilizing space-charge emittance growth compensation*, Proceedings of the 1993 Particle Accelerator Conference (1993) 3615.
5. J. Gallardo and H. Kirk, *Optimization of the Brookhaven ATF Inline-injection System Utilizing PARMELA*, Submitted to the Proceedings of the 6th Workshop on Advanced Accelerator Concepts, Lake Geneva, Wisconsin, July 12-18, 1994.
6. L. Young, private communication.
7. W.D. Kilpatrick, *Criterion for Sparking Designed to Include both RF and DC*, Review of Scientific Instruments, **28**, p. 824, 1957.

Progress in the Study and Construction of the TESLA Test Facility Injector

R. Chehab, M. Bernard, J.C. Bourdon, T. Garvey, B. Jacquemard, M. Mencick, B. Mouton, M. Omeich, J. Rodier, P. Roudier, J.L. Saury, M. Taurigna-Quere and Y. Thiery.
Laboratoire de l'Accélérateur Linéaire, IN2P3 - CNRS, Orsay, France.

B. Aune, M. Desmons, J. Fusellier, F. Gougnaud, J.F. Gournay, M. Jablonka, J.M. Joly, M. Juillard, Y. Lussignol, A. Mosnier and B. Phung.
CEA, DSM/DAPNIA, Saclay, France.

S. Buhler and T. Junquera
Institut de Physique Nucléaire, IN2P3-CNRS, Orsay, France.

Abstract

A 500 MeV, 1.3 GHz superconducting linear accelerator is being studied and built to serve as a test facility for the TESLA linear collider project. The phase 1 injector, having an energy of 8 - 14 MeV and an intensity of 8 mA with a high duty cycle (800 microseconds, 10 Hz repetition rate), consists of a 250 keV electron gun, a 216.7 MHz sub-harmonic buncher and a superconducting capture cavity at the main linac frequency. The main characteristics (intensity, position, emittance, bunch length, energy spread) are to be measured using different techniques. A particular effort will be made on the use of optical transition radiation (OTR) for the determination of the transverse beam emittance as well as the bunch length. The injector, involving the participation of three French laboratories (LAL, CEA/DAPNIA, IPN), will be tested partly in France (Orsay-Saclay) and then completely at DESY (Hamburg).

1. INJECTOR DESCRIPTION

The TTF linac injector can be conveniently divided into 5 sections; (i) a 250 kV electron source and its associated power supply, (ii) a 250 keV electron transport line, (iii) a superconducting RF "capture cavity" to bunch and accelerate the incoming beam to energies of 8 to 14 MeV, (iv) a beam analysis station to measure the properties of the accelerated beam, and (v) a high energy transport line to match the beam to the TTF linac.

As the TTF injector has already been described elsewhere [1,2,3] we will give only a brief description of each of these sections before describing in more detail the diagnostics which will be used on the injector. Table 1 shows the main specifications for the injector. A brief description of the TTF linac can be found in reference 4.

Table 1
Specification of the TTF Injector

Beam energy	> 8 MeV
Average current	8 mA
Pulse length	800 μ s
Bunch length (rms)	1 mm
Energy spread (rms)	< 1%
RMS emittance	10 mm-mrad
Repetition rate	10 Hz

1.1 The Electron Source and Power Supply

The injector employs a 250 keV electron source in which the electrons are first accelerated to a nominal 30 keV in a conventional thermionic triode gun before receiving the additional energy by acceleration in a 90 cm long electrostatic column. Further details of the 30 kV gun can be found in a companion paper [5]. The electrostatic column is a commercial tube employing a series of metallic field-grading electrodes interspersed by glass insulators glued to the electrodes. The gun and the column are fed by individual power supplies, 40 kV for the former and 300 kV for the latter. To obtain a stable voltage during the 800 μ s macropulse the column is powered via a 33 nF capacitor. Measurements of the long term voltage stability show the variations in the power supply are inferior to 1×10^{-4} . The entire power supply equipment, which was constructed by Sefelec, has been tested to full voltage. The column-gun arrangement is pumped via a 200 l/s pump at the out of the column. The vacuum conductance of the column limits the pumping speed at the gun to 35 l/s. Following baking of the gun (80°C) and the column (60°C - limit recommended by manufacturer) the base pressure in the column is 4×10^{-9} mbar. Modulation of the gun is obtained by applying a train of -100 V, 1 ns pulses to the cathode from a wide-band amplifier. The input pulse to the amplifier can be varied in repetition rate from 217 MHz down to 1 MHz. The amplifier (Nucleudes, France) and its associated electronics has been tested into a dummy load and performs according to specification.

1.2 The 250 keV Transport Line

Along with the diagnostics (described below) the main elements of the 250 keV line consist of 4 shielded solenoidal focus lenses, and a 216.7 MHz sub-harmonic pre-bunching cavity. The lenses, required to transversely confine the beam during transport to the capture cavity, each provide an integrated strength of 8×10^{-5} T²m over an active length of 9.4 cm and with a peak field of 350 Gauss. One of the four lenses is constructed as a 'double lens', i.e. two lenses with their magnetic fields in opposing directions. This means that there is no net rotation for the beam on passing through the lens and thus it can be conveniently used for beam emittance measurements. Each lens (purchased from Sigmaphi) incorporates a pair of horizontal and vertical steering elements in which the conductors are drawn onto printed circuit boards mounted inside the solenoids. The sub-harmonic bunching (SHB) cavity is a single re-entrant cell fabricated in stainless steel. To reduce the cavity RF losses the internal surface has

received a thin (40 μm) deposition of copper. The cavity is powered by a 2 kW RF amplifier capable of delivering 5 ms pulses at 10 Hz. The amplifier (RFTS, Bordeaux), which was specified to have phase stability of 0.5° and an amplitude stability of 0.5% during a 1 ms pulse has been fully tested and shown to meet its specifications. The cavity has been conditioned with full RF power and bench measurements have confirmed the computed shunt impedance and unloaded Q of the cavity ($R_s = 3 \text{ M}\Omega$, $Q_0 = 22000$). With the exception of the SHB all elements on the 250 keV beam line have been mounted on a common girder and the girder has been installed at the output of the high voltage column. At the time of writing tests of the 250 keV beam are planned to commence at the beginning of May 1995.

1.3 The Capture Cavity

After the SHB further bunch compression is performed by a superconducting (SC) cavity. The SC cavity is a standard niobium, 9 cell, TESLA cavity, fabricated by CERCA S.A. (France). After hydroforming the half cells, heat treatment in a vacuum furnace was performed at Saclay (1300°C for 1000 minutes) which improves the residual resistivity ratio (RRR) of the niobium to an estimated value of 360. Following this treatment, complete electron welding of the cells, coupler ports and helium tank connecting flanges was accomplished. The chemical polishing treatment of the cavity internal surface (105 μm) was followed by High Pressure Water Rinsing (100 bar) at DESY.

The cavity was tested at DESY in a vertical cryostat equipped with a special coupler and waveguide transition for RF conditioning using High Peak Power (HPP) processing. Initial HPP in LHe at 4K was applied to the cavity with 1 MW peak power RF pulses at a repetition rate of 2 Hz and progressively increasing pulse lengths (50 μs , 100 μs , 200 μs). During this first experiment the accelerating field reached 21 MV/m with a $Q_{\text{ext}} = 10^6$. After cooling the helium bath to 1.8 K further HPP conditioning was applied culminating in a maximum accelerating field of 23 MV/m with a 300 μs RF pulse. Measurement of the Q vs E_{acc} at 1.8 K in cw mode shows a very good low field Q_0 (1.4×10^{10}) and absence of electron emission, however the accelerating field was limited to 14.5 MV/m by a quench. In conclusion the fabrication methods and the treatments were validated giving very good results for this cavity so allowing its mounting into the capture cryostat. Simulation studies of the injector show a large tolerance for the acceptable accelerating field (8 - 15 MV/m) in order to achieve the required electron beam specifications at the entrance to the first cryomodule.

The cold tuning system is now ready to be mounted in the cavity. It was assembled on a TESLA cavity and tested at room temperature giving a frequency tuning range of ± 470 kHz. A complete mechanical test, including the stepping motor, was performed in a LN₂ bath.

The main parts of the capture cryostat are now fabricated and the assembly has started. A special interface cold box is under construction in order to perform a complete test of the cavity with its coupler at the nominal operating conditions, both with cryogenic and RF power.

The capture cavity klystron has been successfully tested to 300 kW peak power with RF pulses of 2 ms (10 Hz repetition rate). The modulator exhibits a plateau stability of 0.1%

during the pulse. The phase and amplitude control loops are now constructed and the design concepts were successfully tested in the MACSE facility at Saclay with the nominal pulsed condition of the TTF linac.

1.4 The Beam Analysis Line

In order to verify the beam parameters after acceleration in the capture cavity, and to allow regulation of the RF phases, a beam analysis line is installed down stream of the capture cavity. The high energy beam is deviated by a dipole magnet having a bend radius of 700 mm and a bend angle of 60° . Vertical edge focusing is provided by introducing a wedge angle of 18.24° at the exit and entrance faces. The resulting horizontal focal plane is 1242 mm downstream of the exit face, and consequently energy spread measurements will be made in this plane as described below. The maximum allowable field in the magnet is 0.1T, permitting electrons of energies up to 20 MeV to be measured.

1.5 The High Energy Transport Line

The principal elements of the high energy transport line, again with the exception of the diagnostics described below, consist of a pair of quadrupole triplets which will be used to transport the beam emerging from the capture cavity to the first cryomodule of the TTF linac. Again, the triplets incorporate steering elements to properly centre the beam at the input to the first cryomodule. At a later stage we plan to install a magnetic chicane on this line to permit experiments with off-axis beams in the linac. X-ray diodes, situated close to beam collimators, will indicate the presence of beam losses when tuning the injector. While tuning, the beam will be stopped in a cooled Faraday cup capable of handling the 1 kW average beam power.

2. BEAM DIAGNOSTICS

In order to measure and check the beam characteristics appropriate instrumentation is installed along the linac. On the 250 keV beam line, up to the first cryomodule, numerous monitors are provided due to the necessity to verify and, if possible, improve the initial beam characteristics. Non destructive monitors are used for beam intensity, position and RF phase but all profile monitors are destructive.

2.1 Intensity and Position Measurements

The beam pulse at the gun exit will be checked with a capacitive pick-up made from an alumina ring with a copper deposition on its inner and outer surfaces. The capacitance is 120 pF. Current monitors using toroids, placed before and after the capture cavity permit beam intensity monitoring and allow beam losses to be detected to provide a "trip" signal to turn off the gun.

Beam position monitors (BPM's) of the "button electrode" type have been constructed to monitor the beam position throughout the injector. An additional electrode on one BPM allows a measurement of the RF phase of the beam with respect to the master oscillator phase. The beam centroid is evaluated using the signals delivered by four electrodes. These signals are first filtered and then RF multiplexed before being treated in a single analogue electronic channel so as to avoid discrepancies due to different gains, bandwidths or zero offsets

between four different channels. Results concerning the beam position are represented on a graphic page using written indications (position in mm) or bargraphs. Acquisition and timing procedures are monitored through a VME card. Time shuttering inside the macropulse is foreseen. This will allow a sharper analysis of the beam position.

2.2 Beam Profile Measurements

The 6-D emittance is obtainable through transverse and longitudinal profile measurements. Developments in optical methods and of the associated software tools make them preferable for this task [6]. Nevertheless, more classical methods using, for example, secondary electron emission are also considered.

Transverse Beam Profiles

Secondary electron emission with SEM-grids and optical transition radiation with aluminium foils and luminescent screens are used. Retractable aluminium oxide screens with a thin, transparent, deposition of indium oxide are used before and after the capture cavity to get approximate information on the beam dimensions. Quantitative information on the beam profile is obtained by an SEM-grid placed between the SHB and the capture cavity. The low beam energy (250 keV) implies short stopping ranges and high energy deposition in the grid material. Therefore titanium strips of only 12 μm thickness were chosen. To permit high enough resolution and measurement range, an SEM-grid with 32 strips of 300 μm width and 400 μm separation has been constructed. Integrators with LF356 op-amps are connected to the strips. An adjustable gain amplifier is added in each channel. Digitisation is ensured via a MAX255 circuit. Each of these modules has 8 sample-and-holds with a multiplexer, an 8 bit ADC and an 8 bit x 8 channel memory. Data treatment is done with standard VME. Beam profiles are displayed on a monitor and the corresponding widths (FWHM, RMS...) sent to a data base. Due to space-charge effects at this energy an appropriate procedure is necessary for the emittance calculation. It uses the integration of the Kapchinsky-Vladimirsky envelope equation,

$$R'' + K(z)R - 2I_A(\beta\gamma)^3 R - \epsilon^2/R^3 = 0$$

This equation is integrated successively for n different settings of a magnetic focusing lens placed before the SEM-grid. The calculated radii are then compared to the measured ones and a least squares fit method gives the value of the emittance, radius and divergence of the beam upstream of the magnet. The Twiss coefficients are then derived and the ellipse constructed and displayed [7]. A 100 ns gating system allows emittance analysis inside the macropulse.

An SEM-grid made of 40 tungsten wires (20 micron diameter, 2 mm separation) placed in the horizontal focal plane of the bending magnet of the injector analysis line will provide energy spread measurements with a dispersion of 16 mm/%. Profiles and associated widths are processed as described above. After acceleration in the capture cavity, the transverse beam profile will be measured using OTR. N profiles, corresponding to N different settings of the quadrupole triplet

upstream will permit the emittance to be calculated using the "method of three gradients" and a least square fitting routine. An intensified CCD camera permits time resolved emittance measurements in the macropulse with a minimum time window of 100 ns. The beam divergence at the OTR location will be obtained by collecting part of the optical image after a beam splitter. This will be done by placing the CCD camera in the focal plane of the lens. A digitising card (IPP/ELTEC) working on a VME standard will allow digital conversion, on 8 bits, of 4 cameras at video standard CCIR or EIA. An interlaced mode, however, is not allowed here. Image storage will be done in a 1 Megabyte memory zone. External synchronisation for the acquisition is used. Gain and offset at the entrance of the ADC is programmable. A video output is used to obtain the beam spot. A C-library is connected to this card. The use of numerical filters, mathematical transforms and histogram construction is available by this means. Moreover, this library supports the hardware functions. It works under OS9 and some modifications have made it usable under LynxOS and VXWorks.

Longitudinal Beam Profile

A second beam splitter will take part of the optical light to a streak camera (ARP-RGM-SC1) having a resolution of 3 ps. Bunch lengths will thus be determined.

3. SUMMARY

A brief description of the status of the TTF injector has been given. The electron source and the 250 keV beam line are essentially complete and beam tests will begin soon. A capture cavity with the desired RF performance has been produced and its cryostat is under fabrication. The klystron has been tested to full power. The magnets for the high energy beam line have been specified and are on order from industry.

4. REFERENCES

- [1] J.C. Bourdon et al., "An Injector for the TESLA Test facility Linac", Proceedings of the 6th RF Superconductivity Conference (CEBAF, Virginia), pp 1188-1191, 1993.
- [2] M. Bernard et. al., "The TESLA Test Facility Linac Injector", Proceedings of the 4th European Particle Accelerator Conference (London), pp 692-694, 1994.
- [3] T. Garvey, "Electron Source Activities at LAL", Proceedings of the International Workshop on e^+e^- Sources and Pre-Accelerators for Linear Colliders, (Schwerin), 1994, pp 302-308.
- [4] H. Weise, "The TESLA Test Facility - A Description of the Superconducting 500 MeV Linac", Proceedings of the 4th European Particle Accelerator Conference (London), pp 689-691, 1994.
- [5] T. Garvey et. al., "Simulations and Measurements of the TTF Phase 1 Injector Gun", these Proceedings.
- [6] R. Chehab et. al., "Beam Emittance Determination Using Optical Transition Radiation" Proceedings of the 3rd European Particle Accelerator Conference (Berlin), pp 1139-1141, 1992.
- [7] B. Aune et. al., "A Device for Gun Emittance Measurement", IEEE Trans. Nucl. Sci., Vol NS-32, pp1896-1898, 1985.

HOLLOW BEAM PROFILE IN THE EXTRACTION SYSTEM OF ECR ION SOURCE

Y. Batygin, A. Goto and Y. Yano

The Institute of Physical and Chemical Research (RIKEN), Wako-shi, Saitama 351-01, Japan

Abstract

Nonlinear optics effect of the beam extracted from ECR ion source is studied. Hollow beam formation due to aberrations of einzel lens is examined both numerically and analytically. Description of beam intensity redistribution due to nonlinear focusing field is given. The analytical relationship between the initial and the final beam distribution in the extraction region is derived.

I. INTRODUCTION

Beam quality of a heavy ion accelerator complex is mostly defined by the extraction region of ion source where a space charge and a nonlinear external focusing field are essential. The extraction region of the 18 GHz ECR ion source which is under construction to upgrade RIKEN Accelerator Research Facility consists of an extraction electrode under the voltage of $U_{ext}=10\text{kV}$ followed by a three-electrode Einzel lens (see fig.1). After passing the lens, the beam has to be focused into a spot with a diameter of 10 mm to be matched with the following transport system. The purpose of this study is to examine nonlinear beam optics effects which can influence the beam profile and emittance shape of the extracted beam.

II. BEAM EMITTANCE

In ECR ion source particles are born in strong longitudinal magnetic field B fulfilling the ECR resonance condition $2\omega_L = \omega_{RF}$ where $\omega_L = qB_z/2m$ is Larmor's frequency and ω_{RF} is a microwave frequency. The effective phase space area occupied by the ensemble of particles is defined by the value of root-mean-square (RMS) normalized beam emittance

$$\epsilon = \frac{4}{m_0 c} \sqrt{\langle x^2 \rangle \langle P_x^2 \rangle - \langle x P_x \rangle^2}, \quad (1)$$

where x is a transversal Cartesian coordinate and P_x is a canonical conjugate momentum of particle. For particles in ion source one can put $\langle x P_x \rangle = 0$. Canonical momentum of a particle P_x in longitudinal magnetic field is a combination of mechanical momentum p_x and qA_x where q is a particle charge and A_x is a x -component of vector potential of magnetic field:

$$P_x = p_x - qA_x = p_x - q \frac{B_z y}{2}. \quad (2)$$

Calculation of RMS value of canonical momentum gives:

$$\langle P_x^2 \rangle = \langle p_x^2 \rangle - q B_z \langle p_x y \rangle + \frac{q^2 B_z^2}{4} \langle y^2 \rangle. \quad (3)$$

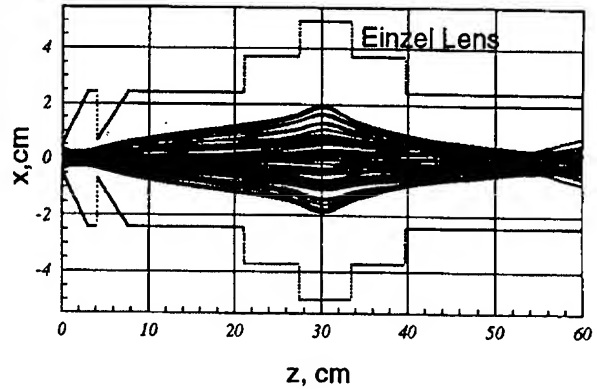


Fig. 1: Particle trajectories in the extraction region of the 18 GHz ECR ion source.

The first integral in eq. (3) describes the thermal spread of mechanical momentum of particles in plasma. The values of mechanical momentum are defined by temperature of ions T_i therefore one can put $\langle p_x^2 \rangle = \langle p_{th}^2 \rangle = m_0 k T_i$ where $k = 8.617 \times 10^{-5} \text{ eV} \cdot \text{K}^{-1}$ is Boltzmann's constant. The middle integral equals zero due to symmetric property of distribution function f and thermal momentum p_x with respect to coordinate y . The last integral is proportional to the RMS value of transverse coordinate $\langle y^2 \rangle$. For most of the beam distributions $\langle y^2 \rangle = R^2/4$ where R is a beam radius comprising around 90% of particles. Finally the value of $\langle P_x^2 \rangle$ is defined as follows:

$$\langle P_x^2 \rangle = \langle p_{th}^2 \rangle + \frac{(q B_z R)^2}{4}. \quad (4)$$

Combining the obtained value of $\langle P_x^2 \rangle$ with equation (1) the value of normalized beam emittance ϵ is given by:

$$\epsilon = 2 R \sqrt{\frac{k T_i}{m_0 c^2} + \left[\frac{\omega_L R}{2 c} \right]^2}. \quad (5)$$

The formula (5) is usually used for estimation of emittance of the beam with ambient magnetic field on the cathode [1].

For the considered case of the 18 GHz ECR ion source the resonant value of magnetic field is $B=0.637 \text{ T}$. The normalized beam emittance of an Ar^{+5} beam with the temperature $kT_i = 3\text{eV}$ is:

$$\epsilon = 2 \times 5 \times 10^{-3} \times \sqrt{0.8 \times 10^{-10} + 10^{-9}} = 3.3 \times 10^{-7} \pi \text{ m rad}. \quad (6)$$

The beam emittance is mostly defined by the value of magnetic field.

III. NUMERICAL STUDY OF BEAM OPTICS

Numerical calculation of beam extraction was performed with the computer program BEAMPATH [2]. Ion trajectories start from a concave plasma emitting surface within the beam convergence angle θ defined by an aspect ratio R/d of extraction region and a ratio of beam perveance $P = I/U_{ext}^{3/2}$ to Child-Langmuir perveance $P_0 = (4\pi/9)\epsilon_0(R^2/d^2)(2q/m)^{1/2}$ of one dimensional diode [3]:

$$\theta = -0.625 \frac{R}{d} \left(\frac{P}{P_0} - 1 \right). \quad (7)$$

For the expected value of beam current $I=100\mu A$ of Ar^{+5} the flow of particles is not space charge dominated and therefore initial convergence of the beam $\theta = -0.075$ is mostly defined by the focusing properties of extraction region.

Particle trajectories obey the equations of motion derived from a single particle Hamiltonian:

$$H = \frac{1}{2m} [p_r^2 + \left(\frac{P_\theta}{r} - qA_\theta \right)^2 + p_z^2] + q(U_f + U_c), \quad (8)$$

where p_r , P_θ and p_z are components of momentum of the particle, U_f is a potential of the focusing field, U_c is a space charge potential of the beam and $A_\theta = B_z r/2$ is a vector potential of the magnetic field. From computer simulation of the beam extraction problem in the ECR ion source it follows that the beam can obtain hollow structure at the point of crossover (see fig. 2). The same phenomenon is observed in high perveance electron guns [4] and under focusing of an electron beam by short solenoid lenses with large aberrations [5]. For more details, let us consider the following analytical model.

IV. HOLLOW BEAM FORMATION

For particles born in the magnetic field of ECR ion source, the value of azimuth component of canonical momentum is:

$$P_\theta = qB_z \frac{r^2}{2}. \quad (9)$$

If the thermal spread of particle momentum is negligible the value of normalized beam emittance is connected with the maximum value of canonical momentum:

$$\epsilon = \frac{1}{m c} R \frac{P_{\theta \max}}{R} = \frac{\omega_L R^2}{c} \quad (10)$$

After extraction from ECR source particles pass through the focusing lens and then move in a drift space. Electric field of the lens provides focusing which consists of a linear term and higher order terms. We restrict our consideration to the first nonlinear term of electric field G_3 . The transverse equation of motion of a particle in this region is given by

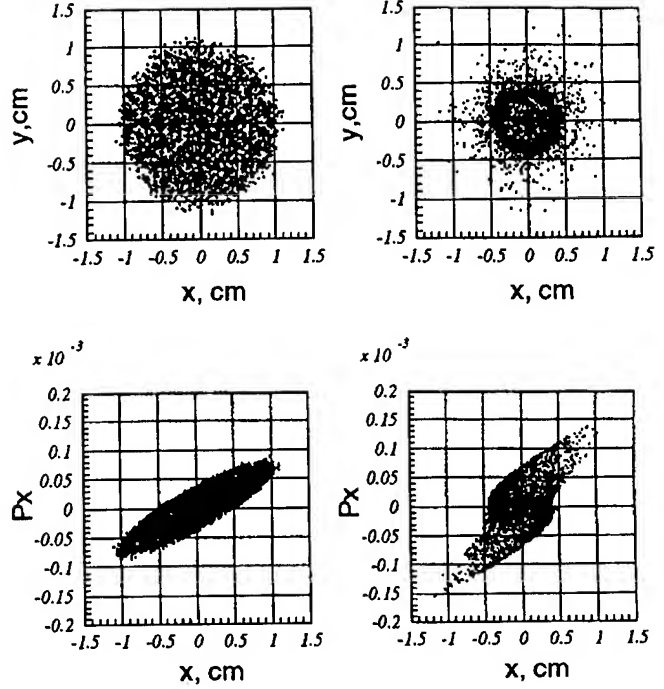


Fig. 2: Cross section of the beam (top) and phase space projections of particles (bottom) at $z=16$ cm (left column) and at $z=60$ cm (right column).

$$\frac{d^2 r}{dt^2} = \frac{P_\theta^2}{m^2 r^3} - \frac{q}{m} [G(z) r + G_3(z) r^3 + \dots]. \quad (11)$$

We assume the thin lens approximation which means that the length of the lens is small in comparison to the focal length. Therefore the radius of particle r_0 is not changed during the time of passing through the lens t_1 . Equation (8) can be integrated to obtain the relationship between the initial and the final radii of particle in the drift region:

$$r^2 = r_0^2 \{ [1 - f(r_0) \tau]^2 + \tau^2 \}, \quad (12)$$

where $\tau = \omega_L t$ is a dimensionless time of particle drift and the following notations are used:

$$f(r_0) = (1 - \delta) r_0^2 \tau_1; \quad \delta = \frac{G_3}{G - \frac{m}{q} \omega_L^2};$$

$$\tau_1 = \left(\frac{q}{m} G - 1 \right) t_1 \omega_L. \quad (13)$$

To find the beam density redistribution let us take into account that the number of particles dN inside a thin ring $(r, r+dr)$ is constant during the drift of the beam, hence the particle density $\rho(r) = dN/(2\pi r dr)$ at any z is connected with the initial density $\rho(r_0)$ by the equation $\rho(r) dr^2 = \rho(r_0) dr_0^2$ or:

$$\rho(r) = \rho(r_0) \frac{1}{\tau^2 + 2 r_0^2 \tau \tau_1 \delta (\tau f - 1) + (\tau f - 1)^2} \quad (14)$$

From this relationship it follows that changing of the beam profile is observed when a nonlinear term of the focusing field is not zero ($\delta \neq 0$). The linear focusing lens ($\delta = 0$) conserves the beam profile and changes only sizes of the beam. Introducing the nonlinear component of focusing field results in beam intensity redistribution according to the above formula and finally in hollow beam formation (see fig.3).

The hollow beam profile formation can be understood from the fact that spherical aberration of an electrostatic lens increases focusing of particles in comparison with the ideal linear focusing [6]. As a sequence the peripheral particles in the drift region move faster to the axis than the inner beam particles. It results in a most populated boundary of the compressed beam than the core of the beam at the point of crossover.

Hollow beam formation is accompanied by emittance growth of the beam due to nonlinearity of a focusing lens. In the considered case the effective root-mean-square emittance is increased by 1.3 times (see fig. 2). For keeping the quality of the beam obtained from an ion source the nonlinearity of the focusing lenses have to be minimized.

V. CONCLUSIONS

Nonlinear beam effect associated with hollow beam profile formation in the extraction region of ECR ion source was examined via numerical particle tracking and analytical treatment. Simple formula has been derived to control the significance of aberrations with respect to linear focusing and value of longitudinal magnetic field in ECR source. Calculations done are important in the problem of matching of the beam with accelerating structures.

VI. REFERENCES

- [1]. I.Ben-Zvi, Proceedings of the PAC95, Washington D.C., (1993), 2962.
- [2]. Y.Batygin, Proceedings of the EPAC92, Berlin, (1992), 822.
- [3]. J.Kim, J.Whealton and G.Schiling: J. Appl. Phys. 49 (2) (1978), 517.
- [4]. M.Reiser, "Theory and Design of Charged Particle Beams", Wiley, New York, 1994.
- [5]. P.Loschialpo et.al., J. Appl. Phys., 57, (1985), 10.
- [6]. J.D.Lawson, "The Physics of Charged Particle Beams", Clarendon Press, Oxford, 1977.

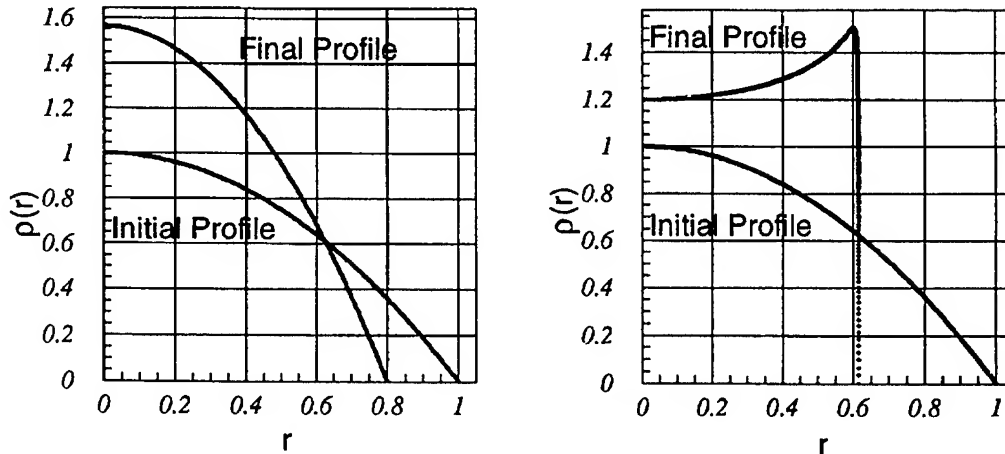


Fig. 3: Beam profile conservation in linear focusing field (left) and hollow beam formation in nonlinear field (right), calculated by formula (11).

ION SOURCES FOR USE IN RESEARCH AND APPLIED HIGH VOLTAGE ACCELERATORS

S. Nikiforov, V. Golubev, D. Solnyshkov, M. Svinin, G. Voronin,
Efremov Research Institute of Electrophysical Apparatus, P.O. Box 42, St. Petersburg, 189631, Russia

Brief description of design and performance of some ion sources, developed at the Efremov Institute for use in different types of accelerators, is given. They are several modifications of duoplasmatron ion source including H-version; RF-, Penning, Freeman and ECR ion sources for positive ion and cesium sputter source for negative ion production. Extracted current range spans 10^{-4} - 10^{+2} mA.

I. INTRODUCTION

Ion sources (IS) of different types have been developed at the Efremov Research Institute and many of them are in operation during long time in Van de Graaf accelerators, tandems, in linear accelerators' injectors, neutron generators, ion separator installations, ion implantation setups, etc. Hereafter we will outline some of the sources recently improved or developed.

II. DUOPLASMATRON

There are many modifications of duoplasmatron IS have been developed at the Efremov Institute during more than 30 years [1-3]. The basic construction of the source is being used in recent years is shown in Fig.1. One of its design feature is using the silver- or copper-soldered metal-ceramic

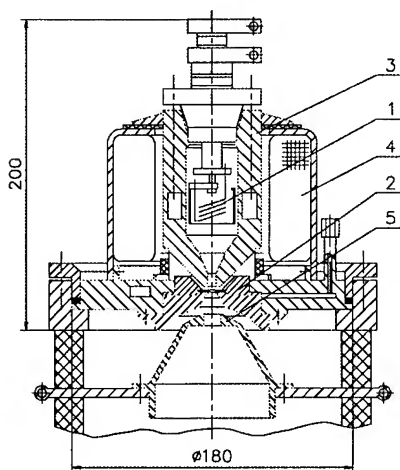


Fig. 1 Duoplasmatron Ion Source
1 - cathode, 2 - anode, 3 - intermediate electrode, 4 - magnet coil, 5 - extracting electrode.

The life time of such cathodes in hydrogen plasma is more than 1000 hours. The different models of the duoplasmatron are designed to generate H^+ , N^+ , He^+ , Ar^+ and another ion species beam

with current in 1 - 100 mA range in cw and 100 - 1200 mA in pulse mode of operation.

The similar source with 1.2 - 1.5 mm displaced emissive hole provides the H_1 beam current up to 120 μA . It can be used also for high brightness H^+ beam generation with current up to 100 μA and 60% proton component.

The duoplasmatron with hollow tubular discharge developed yields H_1 beam current up to 1 mA in cw and up to 20 mA in pulse mode without cesium adding [2].

III. RF ION SOURCE

Some of the Van de Graaf accelerators manufactured at

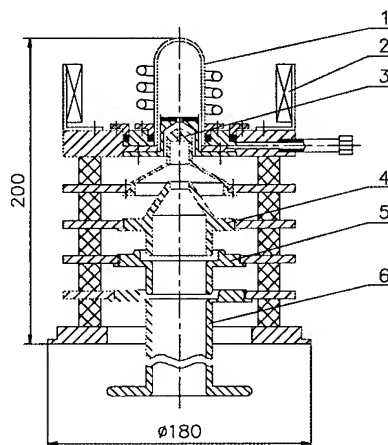


Fig. 2 RF Ion Source.

1 - discharge tube, 2 - permanent magnets (BaFe), 3 - extracting electrode (Al), 4 - accelerating electrode, 5 - focusing electrode, 6 - interface electrode.

the Efremov Institute are under operation during many years in different scientific centers. The model of RF source developed in particular for upgrading in such machines is shown in Fig. 1. The quartz tube is used as the discharge chamber. The plasma potential is defined by the holders of anode quartz shield. The source flange is completed with changeable insert that allow to use the quartz tubes 30 ± 2 mm in diameter. The four-electrodes initial beam forming system is applied to correlate the beam angular characteristics with the accelerating structure. The newly developed thermo-resistant glue is used for stainless steel electrodes to ceramic insulators vacuum sealing connections. The beam current up to 100 μA for such ion species like H^+ , N^+ , He^+ , Ar^+ is provided at gas flow rate not more than 10 cm^3 /hour at atmospheric pressure.

IV. PENNING ION SOURCE

The Cold Cathode Penning IS with axial extraction to be used in Van de Graaf accelerators have been developed too [4]. It is intended first of all to produce inactive gaseous ion

beams. As to hydrogen ions, the H^+ component content in extracted beam is less than 15% when discharge current is in the milliamps range. The general view of the source attached to initial beam forming system is shown in Fig. 2. The discharge system consists of two magnetic steel flanges with cathode and anticathode mounted in, stainless steel anode and ceramic rings connected together through Al vacuum seals. The magnetic field of about 0.12 T is produced by permanent magnets.

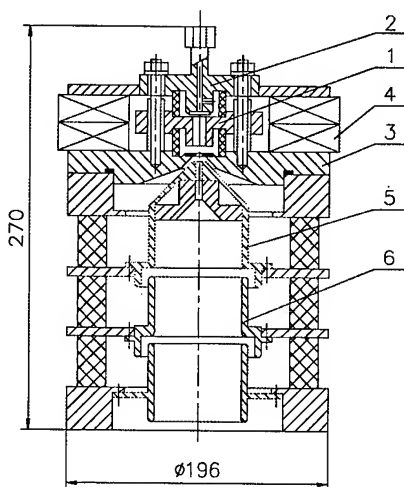


Fig. 3 Penning Ion Source

1 - anode, 2 - top flange with LaB_6 cathode, 3 - bottom flange with LaB_6 anticathode, 4 - permanent magnets, 5 - extracting electrode, 6 - focusing electrode. To decrease discharge voltage and thus to increase source life time we employ LaB_6 as a cathode and anticathode material. The source provides the beam current of 70 μA for inactive gaseous ions at the 10 mA discharge current. The gas flow rate is not more than 12 cm^3 /hour at atmospheric pressure when the $\varnothing 4$ mm x 28 mm channel in extracting electrode is applied.

V. CESIUM SPUTTER ION SOURCE

A broad spectrum of negative ions can be obtained from the cesium sputter ion source shown in Fig. 4.

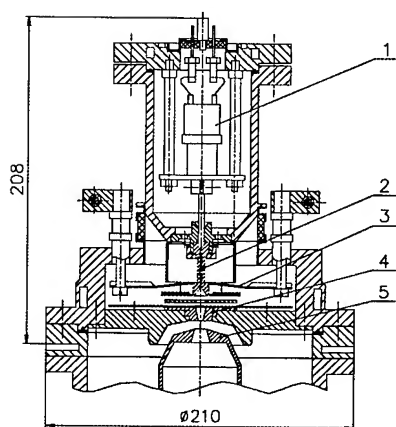


Fig. 4 Negative Sputter Ion Source
1 - Cesium container with heater, 2 - ionizer, 3 - ionizer heater, 4 - sputter cone insert, 5 - extracting electrode.

The cesium vapor is led to ionizer from the furnace, filled with Cs_2Cr_4 pills. The tube ionizer efficiency is about 70% for 0.5 - 2.0 mA Cs^+ current.

It is intended for using in tandem accelerators [5]. The negative ions are produced as the result of secondary ion-ion emission when the cone target is bombarded by 1 - 3 keV Cs^+ ions. The Mo or Re tube ionizer with outlet focusing cone is used for Cs^+ ions production.

The cesium vapor is led to

ionizer from the furnace, filled with Cs_2Cr_4 pills. The tube ionizer efficiency is about 70% for 0.5 - 2.0 mA Cs^+ current.

The extracted beam current is in the range of 0.1 - 50 μA for various negative ions. The version with several cone sputtering targets placed on the disk and changed under vacuum without ion source disconnection have been designed too.

VI. FREEMAN ION SOURCE

The variant of Freeman type positive heavy ion source

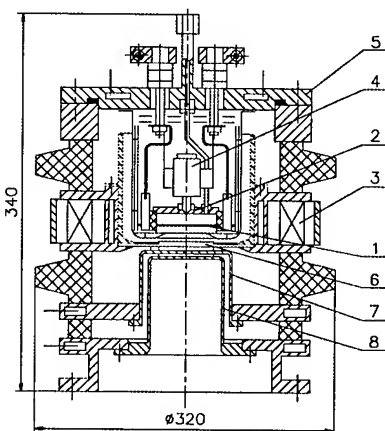


Fig. 5 Freeman Ion Source

1 - cathode, 2 - anode, 3 - permanent magnet, 4 - furnace, 5 - top flange, 6-8 - accel/decel electrodes.

has been designed for use in ion implanters and ion separators (Fig. 5). The directly heated tungsten cathode is displaced relative to discharge chamber axis to extracting sleet for increasing plasma density in extraction region. The magnetic field is about 0.015 T in value along the discharge chamber is produced by permanent magnets. The ion source is supplied by internal and external furnaces

to provide the evaporation of solid and liquid feed materials. Ions are extracted through 50 x 2 mm sleet in anode. One of the source feature is the design of the three electrodes accel/decel system employing of special thermoresistant glue to provide metal-ceramic vacuum sealing.

VII. ECR ION SOURCE

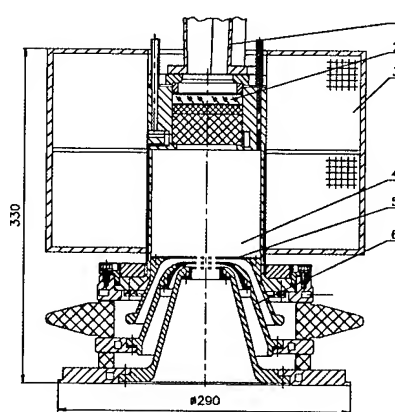


Fig. 6 ECR Ion Source

1 - rectangular waveguide, 2 - triple-layer window, 3 - magnet coils, 4 - discharge chamber, 5 - diaphragm, 6 - accel/decel electrodes.

Research into microwave source has been performed at the Efremov Institute for several years [6]. One of the ECR-source version, designed for application to intense neutron generators and oxygen ion implanters, is shown in Fig. 6.

We employ a 600 W, 2.45 GHz magnetron as a microwave power

Table 1. Ion Sources performances

No	Ion Source (IS)	Ion Species	Beam Current, ma	Power Consump., kW	Lifetime, hr.	Notes
1	Radio Frequency IS	H^+_1, D^+_1	0.07	0.2	300	f=80 MHz.
		He^+, N^+_1, O^+_1, Ar^+	0.03	0.2	100	
2	Penning IS /cold cathode/	H^+_1, D^+_1	0.01	0.015	700	Cathode material - LaB ₆
		He^+, Ar^+	0.05	0.015	300	
3	Duoplasmatron	H^+_1, D^+_1	5 - 100	0.7 - 1.2	300	
		He^+, N^+_1, Ar^+	1 - 30	0.7 - 1.2	150	
		H^-_1, D^-_1	1.0/20*	0.7	200	hollow tubular discharge, *-cw/pulse
		H^-_1, D^-_1, He^+, Ar^+	0,07	0.5	500	Displaced emission hole
4	Negative Sputter IS	O^-	0.008	0.25	80	Negative ions of most elements in the Periodic table are obtainable
		Al^-_2	0.003	0.25	120	
		Cu^-	0.03	0.25	120	
5	Magnetron IS /Freeman type/	B^+, P^+, As^+, Sb^+	1 - 10	1.5 - 2.2	40 - 80	Gas, liquid and solid feed material are possible to use
		Ti^+	5	2.0	40	
6	ECR IS	H^+_1, D^+_1	10-100	2.5	500	f=2.45 GHz, one or multiple aperture extracting system is used
		N^+_1, O^+_1	5-50	2.5	300	
		Ti^+	1 - 5	2.5	50	

generator. The microwave circuitry includes a three-stub tuner and a block of directional couplers. A circulator with dummy load can be added optionally. The TE₁₁ oscillation mode is employed to provide more uniform radial distribution of the plasma density. The microwave power is input into the discharge chamber through a quartz window. A disk of silicon nitride (Si₃N₄) is added to protect the window from accelerated electrons. Finally, an intermediate alumina (Al₂O₃) disk is placed to reduce the reflection of microwave power. A longitudinal magnetic field is induced by two structurally united solenoid coils. The optimal magnitude of the magnetic field and its axial distribution are provided by way of separate current control in the coils and their movement along the source axis. A movable diaphragm, dictating the active length of the discharge chamber is placed in front of the emission electrode. An ion beam is extracted through one, four or seven holes 3 - 6 mm in diameter, depending on a particular application. Such a version is realized in the high voltage accelerator for powerful neutron generator and provides production of accelerated ion beams ($^1H^+_1$ and D^+_1) with current at the Ti-T target up to 60 mA. The atomic ions' content in the extracted beam is about 70% [7].

The ion sources performances are tabulated in Table 1.

REFERENCES

- [1] M. Abroyan et al, "Duoplasmatron Parameters for Optimum Positive or Negative Ion Yield", Particle Accelerators, No. 2 (1971), pp. 133-138.
- [2] V. Golubev et al, "The Source of Negative Ions", Proceed. of the Proton Linear Accel. Conference, October 10 - 13, 1972, Los Alamos, LA-5115, pp. 356-357.
- [3] G. Voronin et al, "Research and Applied Neutron Generators", Proceed. of the EPAC90, June 12 - 16, 1990, Nice, v. 2, pp. 1827-1830.
- [4] M. Pavlovic et al, "An Ion Beam Injector for Electrostatic Accelerator", J. of Electrical Engineering, v. 45 (1994), pp. 214-220.
- [5] V. Golubev et al, "Design Features and Operational Parameters of Charge-Exchange Heavy Ion Accelerator UKP-2-1", Proceed. of the EPAC90, June 12 - 16, 1990, Nice, v. 2, pp. 1852-1854.
- [6] S. Nikiforov et al, "Development of an ECR Ion Source for Accelerators and Plasma Processing Applications", Proceed. of the EPAC94, June 27 - July 1, 1994, London, v. 2, pp. 1427-1429.
- [7] G. Voronin et al, "Development of the Intense Neutron Generator SNEG-13", Proceed. of the EPAC94, June 27 - July 1, 1994, London, v. 3, pp. 2678-2680.

DIRECT FAST BEAM CHOPPING OF H⁻ ION BEAM IN THE SURFACE-PLASMA H⁻ ION SOURCE

K. Shinto

The Graduate University for Advanced Studies

1-1 Oho, Tsukuba-shi, Ibaraki, 305 JAPAN

A. Takagi, Z. Igarashi, K. Ikegami, M. Kinsho, S. Machida, M. Yoshii

National Laboratory for High Energy Physics (KEK)

1-1 Oho, Tsukuba-shi, Ibaraki, 305 JAPAN

Y. Mori

Institute for Nuclear Study, University of Tokyo (INS)

3-2-1 Midori-cho, Tanashi-shi, Tokyo, 118 Japan

Abstract

A fast beam chopping directly in a surface-plasma H⁻ ion source was proposed and a preliminary test has been examined. The converter bias voltage is modulated and the extracted H⁻ beam is observed. The direct fast chopped H⁻ beam extracted from the ion source responds to the modulated converter bias voltage as expected. The extracted beam using this method has been accelerated by the 40 MeV linac.

I. Introduction

Recently, the increase of the beam intensity is more desired at 12 GeV proton synchrotron in KEK(KEK-PS)[1]. One of the difficulties to increase the beam intensity is the beam loss at the beam injection from the linac to the booster synchrotron. In order to eliminate the beam loss at the beam injection, the fast chopped beam synchronized with the rf frequency of the booster synchrotron is required.

Although the fast beam choppers such as electrostatic deflection devices have been developed and successfully achieved, the serious problems have arisen in actual operation. Because of the destruction of the space charge neutralization, the beam loss and the emittance growth become severe. In the case of the negative ion beam, the neutralizing particles are the positive ions and those mobility is too small to take more than several hundred nsec to sweep out the beam line. The frequency of the fast chopper is several MHz adjusted to the injection rf frequency of the booster synchrotron. Hence, the tune of the transport line would be affected by the chopped pulse length of the beam.

It would be ideal that the fast beam chopping can be achieved the H⁻ formation in the ion source. Some new methods are attempted to make the fast chopped beam in the ion source. For example, there are two methods to make the fast chopped beam by applying the pulsed high voltage at the collar electrode in the PIG type H⁻ ion source[2] and at the plasma electrode in the volume-production-type H⁻ ion source[3].

In this paper, a new method of the fast beam chopping for the surface-plasma H⁻ ion source at KEK and the preliminary results from the direct fast H⁻ beam chopping are presented.

II. Experimental Apparatus

At KEK-PS, a surface-plasma H⁻ ion source has been used for the formation of H⁻ ion beam. In this ion source, an electrode called *converter* is put into the ion source chamber to produce the H⁻ ions. The converter is shielded from the plasma by the ion sheath. By applying the negative bias voltage to the converter in the ion source, the H⁻ ions are produced by the interaction between the positive ions in the plasma and the converter surface. However the ion sheath is broken by applying the rf voltage beyond the ion-plasma frequency. The ion-plasma frequency, ω_i , is given by,

$$\omega_i = \sqrt{\frac{Z^2 e^2 n_i}{\epsilon_0 m_i}}, \quad (1)$$

where n_i is the ion density in the plasma. In this ion source, the ion density seems to be about $1 \times 10^{12} \text{ (cm}^{-3}\text{)}$. The ion-plasma frequency is estimated about 200 MHz. The frequency of modulated voltage for the direct fast beam chopping is about 2 MHz which is a negligible value from the ion-plasma frequency. Therefore, in principle it is possible to produce the direct fast beam chopping in the surface-plasma H⁻ ion source.

Schematic drawing of a surface-plasma H⁻ ion source used in this experiment is shown in figure 1. There are permanent magnets surrounding to a plasma chamber to confine the plasma by the cusp magnetic field. The hydrogen plasma is produced by the electron emission from a couple of LaB₆ filaments. To produce much more H⁻ ions, the work function of the converter must be lowered. By introducing the Cs vapor into the ion source, the thin layer (half-monolayer) of Cs atoms is formed on the converter surface and then the work function of the converter can be lowered. The fast chopped H⁻ beam is produced by changing the H⁻ formation efficiency following the frequently changed bias voltage of the converter.

A circuit diagram of the rf modulated power supply for the converter is shown in figure 2. In this circuit, the modulation frequency can be changed from 100 kHz to 10 MHz. The rf power amplifier can be operated up to 300 W maximum output.

The rf pulse is supplied through a coupling circuit to overlap the dc bias voltage of the converter. The flatness of the rf pulse height depends on a coupling capacitance in the coupling circuit. The dc component of the rf pulse is decreased transiently,

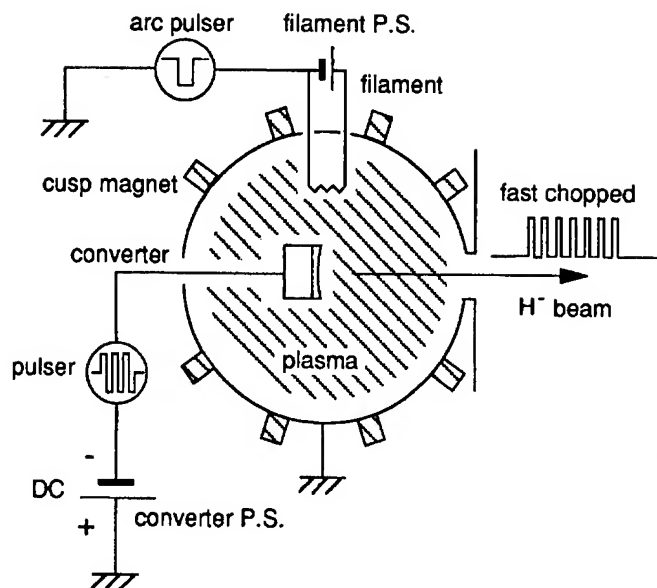


Figure 1. The schematic drawing of the surface-plasma H^- ion source.

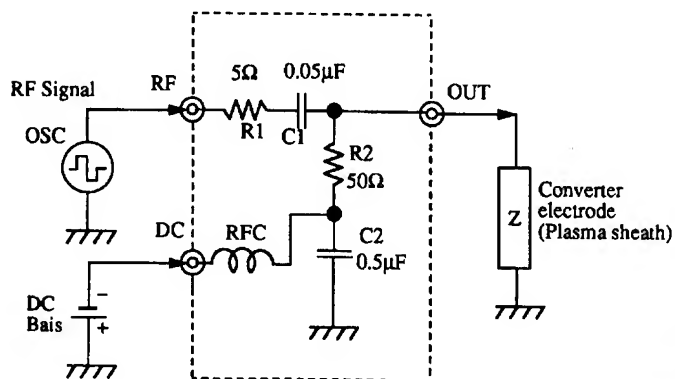
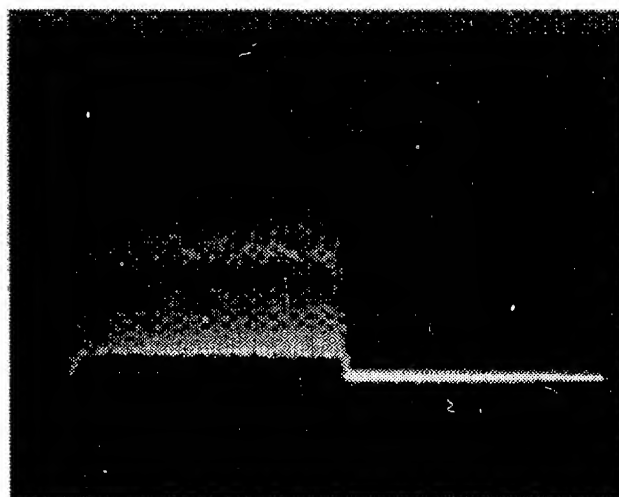


Figure 2. The circuit diagram of the rf frequency modulated power supply for the converter.

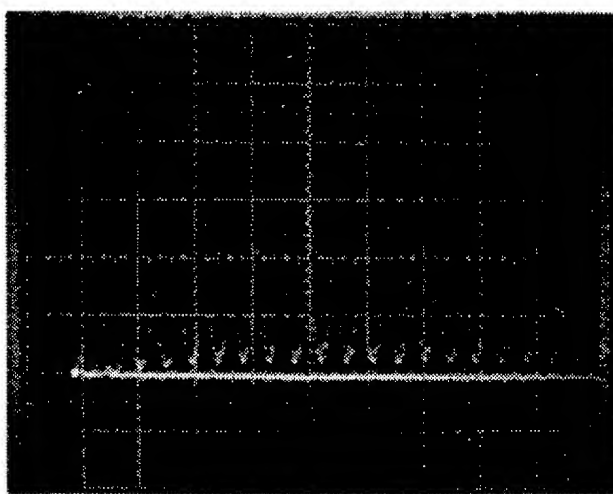
because the value of a coupling capacitance for the rf modulation of the converter bias voltage is insufficient, and then a new coupling circuit whose coupling capacitance is larger than the present one is under prepared. The large amplitude of the rf modulating voltage is required to overcome the negative potential of the floating electrode in the rf plasma.[4] To solve this problem, a new pulsed power supply which can operate with high voltage ($500 V_{p-p}$) and fast rise time (10 nsec) for the direct fast H^- beam chopping is under construction.

III. Extraction of rf Modulated H^- Beam

The H^- ion source is operated in pulse mode ($200 \mu\text{sec} \times 20 \text{ Hz}$) and the fast chopped H^- beam produced from the ion source is accelerated up to 30 keV at the test stand. The chopped H^- beam current is measured by the Faraday cup after passing the magnetic mass separator. It is found that the fast chopped H^- beam current is in good response to the modulated converter voltage for the wide range (from 100 kHz to 10 MHz).



(a)



(b)

Figure 3. An example of the waveform of the fast chopped H^- beam measured by the Faraday cup at 40 MeV beam line. (a):vertical axis:2 mA/div., horizontal axis:10 $\mu\text{sec/div.}$ (b):vertical axis:2 mA/div., horizontal axis:1 $\mu\text{sec/div.}$ About 94% of the maximum H^- beam current is suppressed by the converter bias modulation.

IV. 40 MeV Beam Acceleration of Direct Fast Chopped H^- Beam

The fast chopped H^- beam current is measured by a bunch monitor at the 40 MeV beam transport line between the linac and the booster synchrotron. An example of the waveform of the fast chopped H^- beam measured by the Faraday cup at 40 MeV beam line is shown in figure 3. In this figure, about 94% of the maximum H^- beam current is suppressed by the converter bias modulation.

An example of the waveform of the fast chopped H^- beam synchronizing the rf frequency of the booster synchrotron is shown in figure 4. The rectangle fast pulse (2.2 MHz, 220 nsec width, 300 V_{p-p}) is applied to produce the chopped H^- beam.

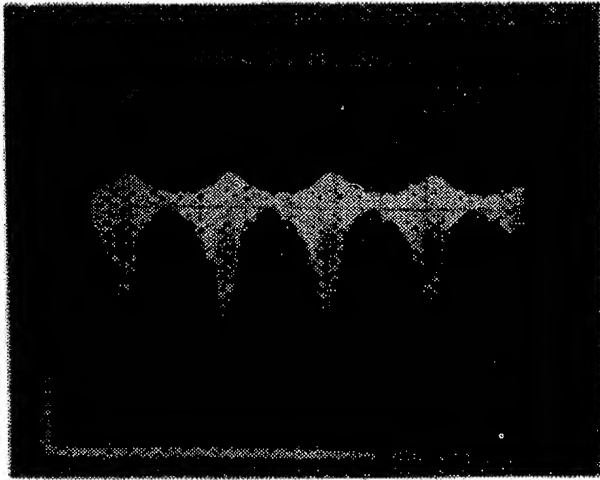


Figure 4. An example waveform of the fast chopped H^- beam synchronized with the rf frequency of the booster synchrotron. This beam is measured by a bunch monitor at the 40 MeV beam transport line between the linac and the booster synchrotron.

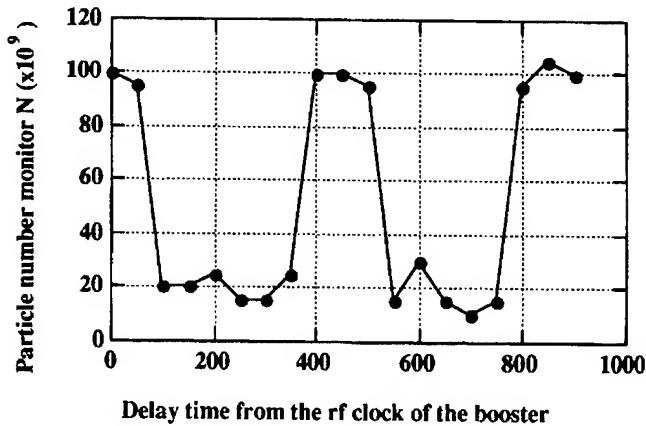


Figure 5. The capture efficiency of the booster synchrotron as a function of the delay time of the direct fast H^- beam chopping

However the waveform of the H^- beam has not the ideal shape of the waveform which is applied to the converter. There might be a reason why the nonlinearity of the H^- formation efficiency as a function of the converter bias voltage.

The capture efficiency of the booster synchrotron as a function of the delayed time of the direct fast chopped H^- beam is shown in figure 5. From this figure, the correlation between the capturing efficiency and the delayed time from the rf clock is observed obviously. To eliminate the beam loss at the injection, the fine adjustment of the delayed timing to the rf bucket in the booster synchrotron is very important.

V. Summary and future plan

The production of the direct fast chopped H^- beam in a surface-plasma H^- ion source is realized by the high frequency voltage modulation of the converter voltage. The extracted chopped H^- beam is in good response to that of the modulation

of the converter bias voltage, and the 40 MeV beam acceleration of the direct fast chopped H^- beam for a surface-plasma H^- ion source has been examined successfully.

In near future, the comparison of the capture efficiency at the booster injection with the bunch to bucket method using the direct fast chopped H^- beam and the adiabatic capture method using the continuous beam will be investigated.

References

- [1] Y. Mori, Proc. of the 17th Int'l Linac Conference, Tsukuba, Japan 1994, pp.671-675.
- [2] R. L. York, D. Tupa, D. R. Swenson and R. Damjanovich, Proc. of 1993 IEEE Particle Accelerator Conference, Washington, pp.3175-3177.
- [3] H. V. Smith Jr., P. Allison, J. D. Schneider and J. E. Stelzer, Proc. of the 17th Int'l Linac Conference, Tsukuba, Japan 1994, pp.393-395.
- [4] M. Konuma, "Film Deposition by Plasma Techniques", Springer-Verlag, 1995.

EMITTANCE MEASUREMENTS OF THE HIGH INTENSITY POLARIZED ION SOURCE AT IUCF

V. Derenchuk, R. Brown, H. Petri, E. Stephenson, M. Wedekind
Indiana University Cyclotron Facility, Bloomington, IN 47408

Abstract

The IUCF high intensity polarized ion source (HIPIOS) is now being routinely used to deliver beam to experiments. Recent efforts have been focussed on measuring beam properties in order to improve beam transmission through the cyclotrons and maximize P^2I , the product of the polarization and current delivered to the user. The results of measurements using a pepperpot beam emittance apparatus is presented relative to several source parameters.

I. INTRODUCTION

The IUCF high intensity polarized ion source (HIPIOS) has been used to deliver beam to users for over a year. Neutron time of flight and polarimetry measurements with the recently completed Indiana Neutron Polarimeter (INPOL) facility require polarized proton beam intensities of up to 500 nA at 200 MeV, with a microscopic time structure of ≈ 400 ps and a period of ≈ 340 ns. Both INPOL and internal polarized target experiments in the Cooler ring requiring high circulating beam intensities have recently benefitted from the use of HIPIOS. Development of HIPIOS and the 600 keV beam transport line have been described elsewhere[1,2], but to summarize the latest operating parameters, HIPIOS is currently able to deliver 170 μ A DC of mass analyzed \bar{H}^+ , $p_z \geq .76$, with an emittance of 0.5 π -mm-mrad normalized, for 80% of the beam to the entrance of the 600 kV electrostatic accelerator column. While recent operating experience has been promising, HIPIOS beam characteristics continue to be studied in order to improve transmission through the cyclotrons and the P^2I delivered to the user.

II. TRANSMISSION AND POLARIZATION

Emittance matching to the 600 keV accelerator column is critical because of the tight focus and high divergence required at the first accelerating segment. If these conditions are not met, the column will introduce aberrations that will lead to emittance growth. Measurements in the 600 keV beam line (described elsewhere in these proceedings[3]) indicate that the normalized beam emittance decreases with terminal potential. At 400 keV, the emittance for 75% of the beam is less than 1/2 that at 600 keV. Transmission through the

length of the beam line is improved at these lower energies.

The source has delivered $p_z \geq .75$ in both states with close to the highest ion beam intensity, but it appears that the beam, polarization may vary through its cross-section. It was concluded that a knowledge of how the beam emittance varied as a function of source parameters would help in understanding this phenomena.

III. IONIZER OPERATION

The ECR ionizer for this polarized source is unique in several ways. The beam is extracted from the source at an energy of 15 keV by biasing the plasma using the first electrode of the extraction system. This poses the primary problem of beam extracted toward the grounded atomic beam section of the source. We have experienced damage to the surfaces of and melting of insulators in the transition units immediately upstream of the ionizer. Beam extraction in this direction would also cause sparking, general instability of the plasma and a large energy spread. The solution has been to carefully isolate the plasma from ground potential by using quartz glass liners and a glass ECR buffer gas feed tube.

The ECR operates at 4.0 GHz, with a resulting higher average ionizer field strength than is used with the standard 2.45 GHz generator. The axial magnetic field strength in the valley of HIPIOS is greater than 1.30 kG at 4.0 GHz.

The buffer gas used in the ECR, for operation with atomic hydrogen beam, is D_2 gas. To avoid hydrogen gas loading of the cryo-pumps, they are regenerated during dissociator maintenance periods. Operation and beam intensity using N_2 gas is degraded due to a higher sputtering rate of the gridded extraction system and a decrease in plasma stability. A beam intensity increase of about 30% was observed when using D_2 buffer gas. This effect was predicted by A.Belov[4] as a result of his experience with the deuterium plasma charge exchange ionizer.

The accel-accel extraction system is a gridded design with a high transparency for atomic hydrogen that passes through the ECR without being ionized. There are two well aligned grids with a transmission of 95% followed by a tube lens. The beam emittance has been measured as a function of the voltage difference between the two gridded elements for several ECR parameters.

IV. EMITTANCE MEASURING APPARATUS

Emittance measurements in the beam transport line between the ion source and accelerator column are made using a pepperpot apparatus. A 0.05 mm foil with a matrix of 0.5 mm holes on a 3 mm center is placed 137 mm upstream of a wire scanner. The beamlets that pass through the foil are easily seen on a wire scanner trace (Figure 1).

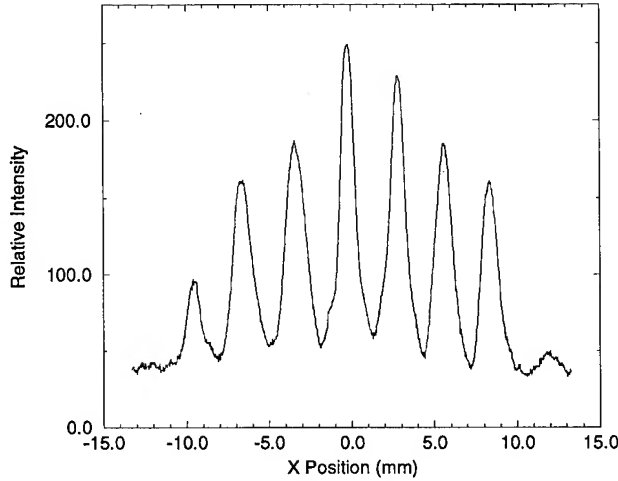


Figure 1: The horizontal part of a wire scanner oscillogram for an approximately parallel beam with few aberrations. The beam has passed through a foil with a 3 mm matrix of 0.5 mm holes.

Scans were stored on a HP digital scope and downloaded to a PC. Each peak was ascribed to one row or column of holes in the foil. An RMS analysis of the data points was made to give a rough estimate of a phase space ellipse that would best contain the beam. The Courant-Snyder parameters α , β and γ were calculated and used to evaluate the fraction of beam that fell within the boundary of a phase space ellipse of fixed size according to the following boundary condition;

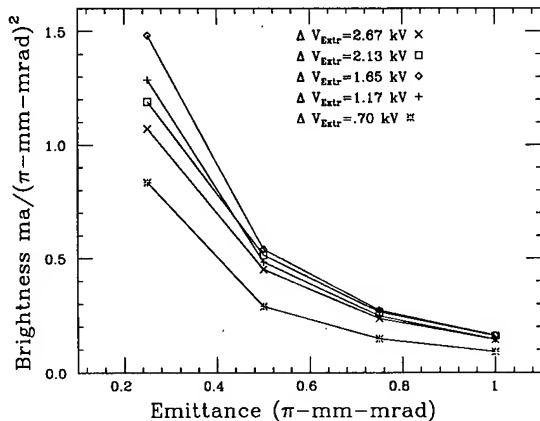


Figure 2: Brightness versus emittance for several values of the voltage difference between the two extraction grids.

$$\gamma(x - x_0)^2 + 2\alpha(x - x_0)(x' - x'_0) + \beta(x' - x'_0)^2 \leq \epsilon_x$$

where x and x' are position and divergence, x_0 and x'_0 are the ellipse centroid and ϵ_x is the unnormalized emittance.

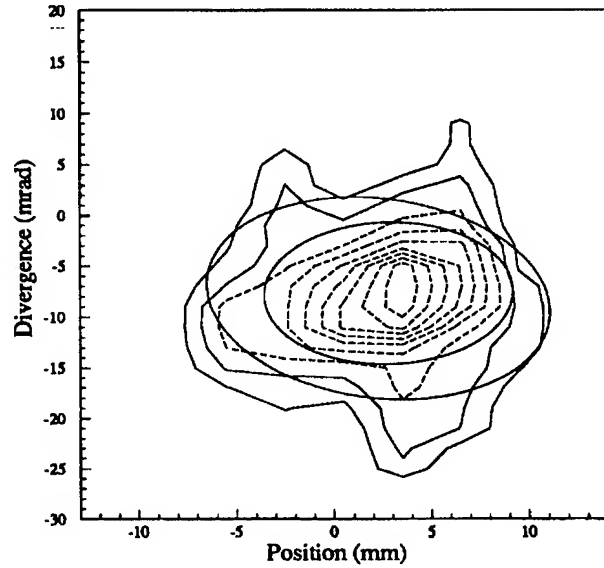


Figure 3: Emittance contour of a 170 μA beam. An ellipse of 0.5 and 0.25 π-mm-mrad contain 80% and 55% of the total beam. The ellipses are superimposed on the real data.

Brightness was calculated for various values of the elliptical phase space area (Figure 2) using the total beam current on a stop downstream from the apparatus. All values of the phase space and the brightness are normalized to $\beta\gamma$.

In Figure 3, emittance contours of a 170 μA beam with good transmission are compared against a 0.5 π-mm-mrad and a 0.25 π-mm-mrad phase space ellipse calculated as described above.

IV. EMITTANCE MEASUREMENTS

The emittance as a function of several source parameters has been measured using the pepperpot emittance apparatus. The voltage between the two extraction grids, ΔV_{Ext} , was varied for different extraction energies, buffer gas pressures, and ECR RF power levels. The data for 4 different ECR pressures, adjusted by regulating the amount of D₂ buffer gas, and for 4 different values of the ECR power levels are plotted against ΔV_{Ext} in Figures 4 and 5 respectively. The optimum operating condition for the buffer gas variable is clearly indicated in the sharp peak in brightness at $\Delta V_{Ext} = 1.7$ kV at a pressure of 5.3×10^{-7} T. Higher and lower pressures require a larger voltage difference to extract highest brightness beam. A similar but less obvious effect is seen for the ECR power level. During operation, it is clearly important to maintain the pressure at the optimum value. The normalized

brightness for 80% of an optimized 170 μA beam is $0.54 (\pi\text{-mm-mrad})^2$.

Tuning of the beam is very sensitive to this voltage difference. Best transmission through the accelerator column occurs in a very narrow range of ΔV_{Ext} . One explanation of the variation in the peak brightness with respect to the ΔV_{Ext} could be that the shape of the ECR plasma surface near the grids is affected by the electric field strength. Variation in the pressure of the buffer gas and the ECR power level also affect the plasma density which would subsequently change the shape of the plasma surface near the grids due to space charge effects. Aberrations in the shape of the electric field between the grids cannot totally account for this behaviour.

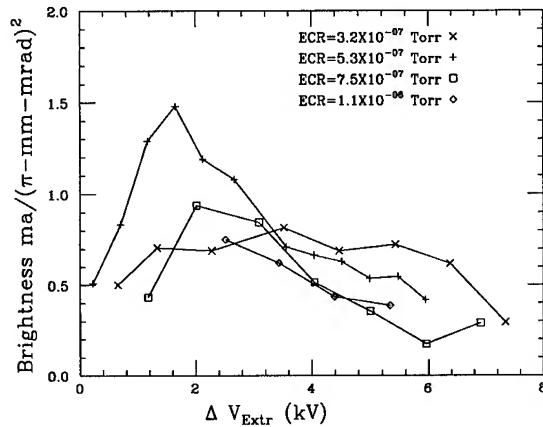


Figure 4: Plot of the beam brightness in a $0.25 \pi\text{-mm-mrad}$ ellipse as a function of ΔV_{Ext} for different pressures. The peak in the brightness varies with pressure.

Beam brightness is also related to the atomic beam density. Transmission of proton beam ionized from a deuterium hydrogen gas mixture leaked into the ECR is significantly less than beam produced from the atomic beam with a deuterium buffer gas. Emittance of the leaked gas beam will be measured and compared against the total emittance of the polarized beam to determine what contribution an unpolarized background gas will have on the final beam polarization. This is currently under study.

V. CONCLUSIONS

Beam emittance from a two gridded extraction system in the IUCF high intensity polarized ion source has been measured for several different parameters. The optimum voltage difference between the two extraction grids for best beam transmission and brightness varies with the ECR pressure and power. This could be explained by the change in the plasma density in the ECR.

The optimum tune results in a beam current of 170 μA at the entrance to the 600 keV accelerator column. The emittance of 80% of this beam is $0.50 \pi\text{-mm-mrad}$ has a brightness of $0.54 (\pi\text{-mm-mrad})^2$. This beam was measured to have a polarization of $p_z=0.75$ in both states.

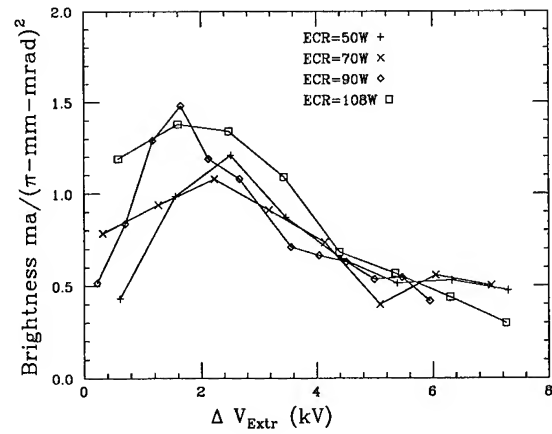


Figure 5: Plot of the beam brightness in a $0.25 \pi\text{-mm-mrad}$ ellipse as a function of ΔV_{Ext} for different ECR RF power levels. As in Figure 4, the peak varies with power.

VI. ACKNOWLEDGEMENTS

The authors express their appreciation to Alexander Belov, Tom Clegg, and the entire technical staff at IUCF. Special thanks to Karin Hedblom who taught us how to analyze the data. The HIPIOS project is supported by NSF Grant PHY-891440.

VII. REFERENCES

- [1] V.Derenchuk, A.Belov, R.Brown, J.Collins, J.Sowinski, E.Stephenson and M.Wedekind, "IUCF High Intensity Polarized Ion Source Operation," in *Proceedings of the 8th International Symposium on Polarization Phenomena in Nuclear Physics*, 1994, to be published.
- [2] V.Derenchuk, M.Wedekind, R.Brown, T.Ellison, D.Friesel, J.Hicks, D.Jenner, A.Pei, H.Petri, P.Schwandt, J.Sowinski, "Performance and Status of the IUCF High Intensity Polarized Ion Source," in *Proceedings from the 13th International Conference on Cyclotrons and Their Applications*, Vancouver, Canada, 1992, pp. 330-333.
- [3] M.Ball, J.Collins, T.Ellison, B.Hamilton, and W.P.Jones, "Beam Diagnostic Systems and Their Use in the New IUCF Beam Line," *This conference*.
- [4] A.Belov, Private communication.

REPORT ON EBIS STUDIES FOR A RHIC PREINJECTOR *

E. Beebe, A. Herscovitch, A. Kponou, K. Prelec, J. Alessi Brookhaven National Laboratory
R. Schmieder, Sandia National Laboratory

Abstract

At Brookhaven, an Electron Beam Ion Source (EBIS) is now operational. This source is being used as a test bed to answer questions relevant to the eventual design of an EBIS-based heavy ion injector for RHIC. Such a source can easily produce ions such as Au^{43+} , but the challenge lies in reaching intensities of interest for RHIC (3×10^9 particles/pulse). The source studies are planned to address issues such as scaling of the electron beam to 10 A, possible onset (and control) of instabilities, ion injection, and parametric studies of output emittance.

I. INTRODUCTION

The Relativistic Heavy Ion Collider (RHIC) at Brookhaven National Laboratory is scheduled to be commissioned in 1999. The Tandem Van de Graaff accelerator presently supplies ions for the fixed target heavy ion program at the Alternating Gradient Synchrotron (AGS), and will initially serve as the preinjector for RHIC as well. We are now considering an alternative approach, where high charge state heavy ions would be produced in a source, accelerated in an RFQ followed by a short linac, and then injected into the AGS Booster. In principle such a preinjector should be simpler than a Tandem, more flexible in that it will offer a full spectrum of ion species, and allow for future increases in RHIC luminosity. Unfortunately, a high charge state heavy ion source that would satisfy the RHIC requirements still does not exist, but may be developed by scaling up of a device now available. The rest of the preinjector, an RFQ and linac, is a technology already adopted by industry.

From the point of view of the RFQ and linac, it is preferable to get from the source ions in charge states as high as possible, to make the preinjector more compact and efficient. We have considered several possible approaches to develop such an ion source, and have concluded that scaling-up of an Electron Beam Ion Source (EBIS) should be the most straightforward. EBISs deliver highly charged ions of virtually any species which are injected into the ion trap either as neutral gas or as low-charged ions. An EBIS operates best as a pulsed device, and can be well matched to a synchrotron with respect to pulse length. (Since the total charge per pulse is essentially independent of the extracted pulse width, short pulses can be extracted for efficient single-turn injection into a synchrotron). The evolution of charge states depends on the electron beam energy E and the product of the electron beam density and the ion confinement time, so that the charge state is easily optimized by variation of these parameters. While existing EBIS yields are lower than that required for RHIC by at least an order of magnitude, this can at least in part be attributed to the fact that before the advent of large colliders there was little need for high intensities of high charge state heavy ions.

*work performed under the auspices of the U. S. Dept. of Energy.

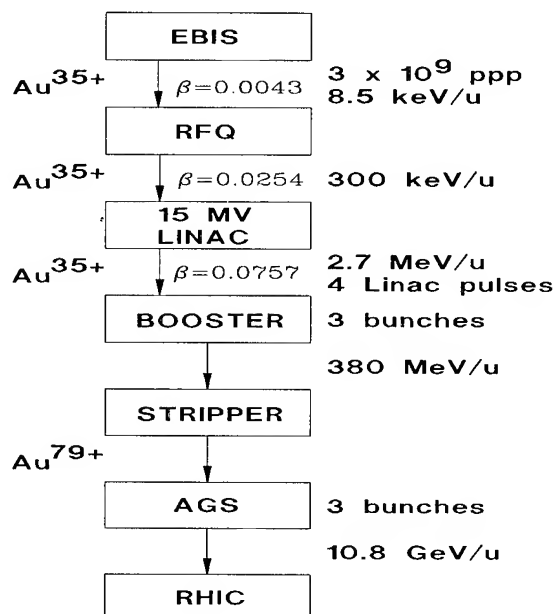


Figure 1. Stages for the EBIS-based injector for RHIC

Electron beam current	10 A
Electron beam voltage	20 kV
Length	1.5 m
Trap capacity	1.1×10^{12} charges
Yield, positive charges	5.25×10^{11}
Yield, Au^{35+} , design value	3×10^9 ions/pulse
Yield, Pb^{53+} , design value	2×10^9 ions/pulse

Table I
Parameters for an EBIS meeting RHIC requirements.

II. EBIS INJECTOR TO MEET RHIC REQUIREMENTS

The proposed acceleration stages for the EBIS-based injector are shown in Fig. 1. Starting with an estimate of $3 \times 10^9 \text{ Au}^{35+}$ ions per pulse of source output necessary to yield 1×10^9 ions per bunch in the 57 RHIC bunches, Prelec et. al.[1] have worked out the main operating parameters of the source, based on the experience of existing EBISs. These parameters are summarized in Table I. The 10 A electron beam current is much higher than existing EBISs produce (0.5 A). However, the requirement on the ion charge state is modest, thus allowing a relaxation of other parameters which have made EBISs technically difficult.

Although it would be convenient for us to design both systems for the 201.25 MHz frequency of the present 200 MeV Linac for H^- ions at BNL, we have made our preliminary designs of the RFQ and linac using 80 and 160 MHz, respectively

[2]. The focusing strength of an RFQ is related to its phase advance/focusing period, the optimum value of which is approximately 60 degrees. For the range of q/m we are dealing with, the frequency at which optimum phase advance occurs is approximately 80 MHz. On the other hand, a high frequency is necessary for the linac if the cavities are to have reasonable dimensions comparable to, say, the cavities in the ATLAS Positive-Ion Injector Linac at Argonne [3], since the starting β is 0.0254 (see Fig. 1), compared with 0.009 in the ATLAS.

We were very mindful of the successful experience of the ATLAS project at Argonne National Laboratory [4] with constructing and operating an independently phased superconducting resonant cavity linac. For now, we have chosen this approach for further study. The key features of this type of linac are: one gets maximum use of the available voltage from all the cavities for essentially any mass ion, and every cavity can be operated at its full potential. These provide the highest energy beam for injection into the synchrotron which is always important for overcoming losses due to stripping and space charge.

III. BNL EBIS R&D PROGRAM

Many of the issues which need to be addressed prior to the design of an EBIS for the new AGS Booster injector require an operating Test EBIS. Fortunately, we have obtained on a long term loan the Sandia National Laboratory "SuperEBIS" [5], and put it into operation in our ion source laboratory. So far, we have operated this source with electron beam currents up to 110 mA and have extracted helium-like argon ions (Ar^{16+}). Over the next two years our plans for this Test EBIS are the following:

a) Increase the electron beam current in steps up to 1 A, exceeding the current of any operating device of this type. With a 1 mm dia. LaB_6 cathode in the electron gun, we have obtained an electron beam current of 110 mA. A 2 mm dia. cathode, which we are now testing, should allow operation at currents up to 500 mA. We may then test a 3 mm dia., which should raise the current to the 1 A level. If our experiments on an electron gun test stand show that other cathode types are promising, they too may be tried on the Test EBIS.

b) External ion injection will be studied in order to provide the variety of ions (especially metallic) required for RHIC. There are several candidates for the primary ion source and they will be tested first on a separate stand to determine the yield and charge state distribution. We presently have a pulsed MEVVA [6] source of metallic ions (up to uranium) and several steady state sources using zeolite cathodes (Na, Cs, Tl) but other types may be investigated as well.

c) Possible sources of instabilities will be investigated to see whether they might develop in an EBIS as the electron beam current is increased above the levels presently achieved in similar devices.

d) Simultaneously with an increase of the electron beam current, we shall do parametric studies of the yield and charge state distributions to verify EBIS scaling laws.

e) Fast extraction of ions will be studied because the single turn injection of ions into the Booster would greatly simplify the process and lead to a high capture efficiency. In order to achieve this, ions must be extracted in a pulse of less than 10 microsecond duration. There are several methods for a fast extrac-

tion (ramping the axial electric field in the trap, pulsing schemes for trap electrodes) and we have to develop and select the one which gives the best combination of extraction efficiency and beam emittance.

f) Cooling of ions in the trap will be studied and applied to improve the performance of the test EBIS.

g) Measurements of the output beam emittance will be performed in order to characterize beam parameters and design the matching section to the next element, the RFQ. Parametric studies will be made of the emittance of the extracted beam vs. ion extraction method, magnetic field strength, ion confinement time, ion charge state, ion beam intensity, etc.

IV. PROGRAM STATUS

Initial operation of the source has been made using continuous (d.c.) electron beams of 5-110 mA and current densities of 100-400 A/cm². The 1 mm diameter LaB_6 cathode is immersed on axis in the solenoidal field of an unshielded superconducting solenoid to a level of 400-800 Gauss. The beam is then compressed by the increasing axial field which is currently operated at about 1.2 Tesla. Modifications are underway to increase the electron gun apertures to accommodate a 2 mm LaB_6 cathode which should allow the propagation of electron beams on the order of 500 mA.

Axial "drift tube" electrodes are used to control the ion production processes. The potentials to these electrodes are supplied by custom built HV power supplies with a dynamic range of 1 kV and risetimes on the order of 10 microsec. A d.c. bias can be imposed which allows the application of potentials of up to 5 kV to the trap region with respect to laboratory ground.

In EBIS sources the working species is typically introduced by radial injection of neutral gas into a special drift tube, or by injection of low charge state ions from an external source along the EBIS axis. At BNL we have been working on both methods. The gas injection method allows immediate verification of the EBIS performance. Ion injection is somewhat more difficult to implement but is expected to provide better performance for our long term goal of producing milliampere currents of moderate charged metallic ions.

Neutral gas injection is the most commonly used method for introducing the species to be ionized in an EBIS. Low charged ions formed in the gas injection region are allowed to reach the main trap region during a specified injection period according to the value of potential applied to an intervening electrode. Transfer of ions using this method is called "electronic injection" following the early description of this process by Donets [7]. In Figure 2, a time of flight spectrum for neutral gas injection of argon is given. Present are contaminant peaks of H^+ , He^{2+} and He^+ due to a helium leaks and residual hydrogen background. Argon charge states from Ar^{11+} through Ar^{16+} are observed after a injection period of 50 ms and confinement period of 300 ms. The total charge extracted in this case was 925 pC during an extraction pulse of duration 75 μs FWHM, corresponding to a beam neutralization of 77%.

Tests are currently being made using a sodium impregnated zeolite ion source for external ion injection. Typically, extraction from the auxiliary source is made at 5 kV and the beam is retarded to 1-3 kV, i.e., the potential of the EBIS trap region

electrodes. Na^+ beams of about 5 microamps are obtained at a Faraday cup just outside the EBIS electron collector. We have observed injected ions propagating through the EBIS to a point just in front of the electron gun cathode but we have not yet observed an extracted high charge state sodium ion spectrum. Nevertheless, ion injection into EBIS has been well demonstrated at Saclay [8] and Stockholm [9]. Improvements to the control system which will allow greater control of the ion optics, beam energies, and timing are expected to facilitate the ion injection procedure.

The development of a control system has been an important part of our program. A simple EBIS controller has been constructed around commercially available PC timing boards which can be used to specify events at the microsecond level. A timeline is generated which multiplexes preset analog reference potentials to control the EBIS trap electrode high voltage. In addition, pulses are generated to control the external ion source, ion optics, and diagnostics such as the time-of-flight spectrometer. The duration of a complete EBIS cycle is on the order of 100 ms with several distinct subperiods such as injection, confinement, and extraction. Eventually, the control system will facilitate setting and monitoring all potentials and intervals through a graphic oriented PC interface.

An ion source test stand has been constructed for developing the auxiliary ion sources and EBIS diagnostics. The impregnated zeolite and micro MEVVA ion sources have been configured to be interchangeable modular units. They have been adapted to include a deceleration stage which provides high extraction energies for increased beam current, while accommodating the rather low injection energies necessary for ion trapping in the EBIS. Compact, harp-type beam profile monitors have been constructed at BNL and tested at the Stockholm EBIS. They are 95% transparent and are especially useful for adjusting the focus and positions of the injected and extracted ion beams when external ion injection is used to load the EBIS. A compact emittance head suitable for measuring the EBIS extracted beam has been constructed and is currently under test using a Na^+ beam from the zeolite source in the auxiliary test stand.

V. ACKNOWLEDGEMENTS

We would like to thank D. Boeje, L. DeSanto, B. Erickson, W. Hensel, R. Lockey, D. McCafferty, D. Raparia, and W. Tramm for their help on this project. We thank the RPI Plasma Dynamics Group for providing us with the zeolite guns.

References

- [1] K. Prelec, J. Alessi, and A. Hershcovitch, "EBIS Option for the Relativistic Heavy Ion Collider - RHIC", Proceedings of the 1994 European Particle Accelerator Conference, London, 1435.
- [2] A. Kponou, J. Alessi, E. Beebe, J. M. Brennan, A. Hershcovitch, K. Prelec, D. Raparia, "An Evis-Based Heavy Ion Injector for the AGS", Proceeding of the 1994 Linac Conference, Tsukuba, Japan, 716.
- [3] K. Shepard, A Superconducting Heavy Ion Injector Linac, IEEE Trans. Nucl. Sci., NS-32, (5) 3574 (1985).

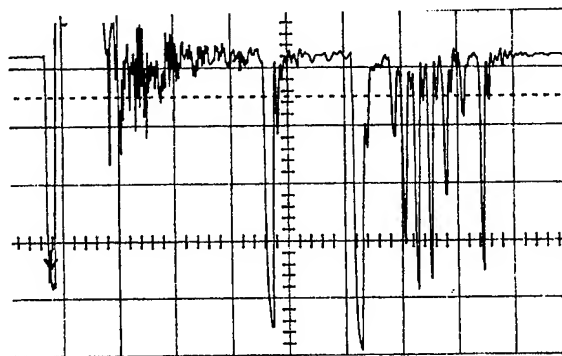


Figure 2. Argon TOF spectrum from the EBIS. Charge states 11+ through 16+ are observed.

- [4] R.C. Pardo et al., Operational Status of the Uranium Beam Upgrade of the ATLAS Accelerator, Proc. of the 1993 IEEE/American Physical Society Particle Accelerator Conference, 1694 (1993).
- [5] R. W. Schmieder, *et al.*, Rev. Sci. Instrum. 61, (1990), 259.
- [6] I. G. Brown in "The Physics and Technology of Ion Sources", edited by I. G. Brown, (Wiley, New York 1989), chap. 16.
- [7] E.D. Donets in "The Physics and Technology of Ion Sources", edited by I.G.Brown, (Wiley, New York 1989), chap. 12.
- [8] J. Faure, B. Feinberg, A. Courtois and R. Gobin, Nucl. Instr. and Meth. 219 (1984) 449.
- [9] E. Beebe, L. Liljeby, A. Pikin, E.D. Donets, D. Habs, K. Janko, O. Tengblad and P. Van Duppen, Nucl. Instr. and Meth. B 93 (1994) 378-381.

DEVELOPMENT OF A VOLUME H⁻ ION SOURCE FOR LAMPF

D.R. Swenson, R.L. York, R.R. Stevens, Jr., C. Geisik, W. Ingalls, J. E. Stelzer and D. Fitzgerald
Los Alamos National Laboratory, Los Alamos, NM 87545

We have continued the development of a toroidal-filter volume H⁻ ion source with the goal of providing a better ion source for the proton storage ring at the Los Alamos Neutron Scattering Center (LANSCE). A prototype source has produced H⁻ beam currents of 6.3 mA from a 3-mm-diameter emission aperture (89 mA/cm²) and 18 mA from a 10-mm-diameter emission aperture (23 mA/cm²). These results were achieved when cesium was added to the discharge. The cesium increased the H⁻ current by a factor of 2-3 while the extracted electron current was strongly suppressed. The magnetic filter can be configured so that the electron to H⁻ ratio is 2:1 and is weakly dependent on operating parameters, with only a moderate loss of H⁻ current. Tests indicate there is essentially no explicit dependence of extracted beam current on duty factor up to 10% duty-factor. Emittance data were taken for various operating conditions in a mass-analyzed beam line and a comparison is made to the surface conversion H⁻ ion source now in operation for the storage ring.

I. INTRODUCTION

High-intensity proton compression rings, such as that now in operation at the Los Alamos Meson Physics Facility (LAMPF), are being considered as drivers for the next generation pulsed spallation neutron sources. Substantial increases in beam intensity can now be considered if the necessary high-brightness ion source can be developed. The requirements for the LAMPF ring entail operation with moderate peak beam currents but high duty factor in order to obtain the desired average currents. Although there are several candidate ion sources that meet many of the requirements needed in the application, none has yet demonstrated the simultaneous combination of intensity, emittance, duty factor, reliability, and availability, that are required in this application.

After a preliminary evaluation of available ion sources was made, work was initiated to evaluate the BNL toroidal-filter volume source and the LBL dipole-filter volume source. A high duty factor version of the BNL source was then built and tested

on the LAMPF injector [1]. The present work reports on the further testing of this source.

II. EXPERIMENTAL SETUP

The toroidal-filter ion source was mounted on an ion source test stand which operates up to 80 kV with 12 % duty factor and provides all necessary beam diagnostics on a mass-analyzed beam line. The ion source is described and diagrammed in reference [1]. Ion beams were accelerated with a four electrode accelerating column which permits independent variation of the extraction voltage on the first gap and the total beam energy. Thus, the extracted beams can be perveanced matched at a given energy over a range of operating conditions of the ion source. The electron current was inferred by subtracting the measured mass-analyzed H⁻ beam current from the drain current of the high voltage power supply. No significant contamination of higher mass ions (mostly O⁻) was observed in the mass-analyzed beams. Emittance

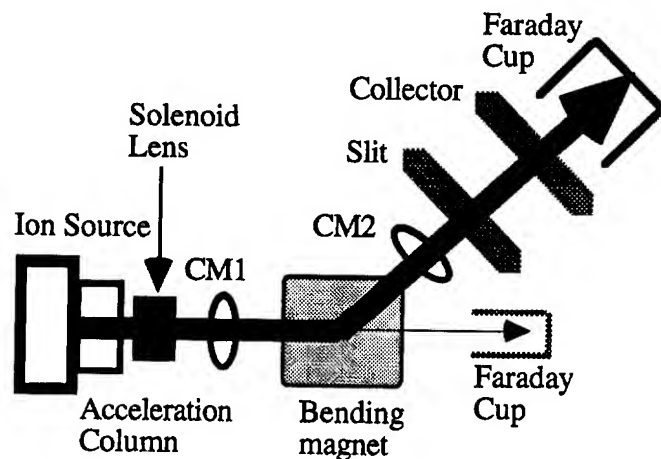


Figure 1: Layout of LAMPF's high-duty-factor ion source test stand.

measurements were carried out with a conventional slit and collector scanner. Beam currents were measured both with beam current toroids (CM) and with a suppressed Faraday cup. In the mass analyzed line, the two methods of measuring the H⁻ current agreed with each other within a few percent. The operating vacuum in the test stand depended on

the gas flow from the ion source but was typically in the 10^{-6} to low 10^{-5} range. For the higher gas pressures, some stripping loss ($\approx 10\%$) was observed, and somewhat higher mass-analyzed currents could have been obtained if more pumping were used in the beam line. Our reported H^- currents have not been corrected for stripping losses.

Most of the results were obtained for 30 Hz, 500 μs beams to limit power loading on the emittance scanners, but some data were taken up to 12% duty factor. A single solenoid lens was used to provide the focusing of the beams and a 45° bending magnet was employed for the mass analysis. A diagram of the test stand is shown in Fig. 1.

The previous tests on the toroidal filter source prototype, were performed in the LAMPF injector using the low-gradient accelerating column employed with LAMPF's surface-conversion production ion source. For our tests, it was anticipated that higher current densities would be produced, and hence a higher gradient accelerating column was designed and built. The plasma electrode was fitted with an insert so that the extraction gap could be varied. The gap was set at 1.7 cm so the space-charge limited current at 16 kV was 30.0 mA which was more than adequate for the present operation where a maximum of 18 mA was obtained.

III. EXPERIMENTAL RESULTS

The dependence of the beam current density on the discharge (arc) current for the two emission apertures studied is shown in Fig. 2. The hydrogen flow was adjusted to give the optimum extracted beam current. We see that the dependence is linear with arc current up to the maximum value (160 A) that was run. The arc voltage was run above 150 volts where there is only a weak dependence of beam current on arc voltage. We note that for this source, there is an explicit dependence of extracted current density j on aperture radius R consistent with a $jR = \text{constant}$ scaling law. Thus, extracted beam current will scale linearly with aperture radius. Similar behavior has been observed in other volume ion sources. This conclusion is also consistent with the previously reported j value of 40 mA/cm² with a 7-mm-diameter aperture [1]. The dependence of the electron/ H^- ratio is shown in Fig. 3. This ratio varies from 6:1 to 1:1 depending on the emission aperture size and the filter field strength.

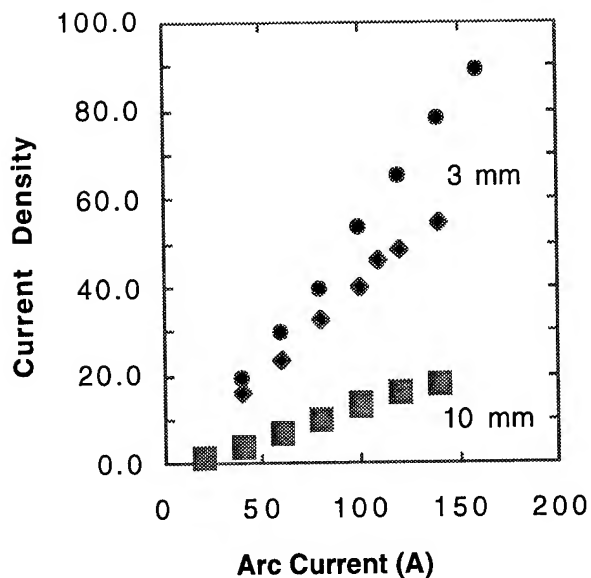


Figure 2: The current density (mA/cm²) as a function of arc current for a 10-mm emission aperture and a strong filter field, and for a 3-mm aperture (\bullet weak filter field, \blacklozenge intermediate filter field).

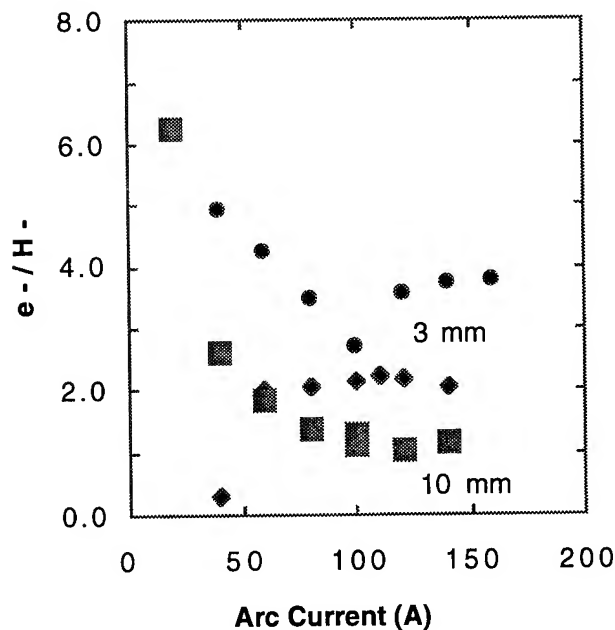


Figure 3: The ratio of electron current to H^- current as a function of arc current for a 10-mm emission aperture and a strong filter field, and for a 3-mm aperture (\bullet weak filter field, \blacklozenge intermediate filter field)..

The original BNL design for the toroidal filter employed a magnet configuration in which a conical, transverse magnetic field was set up between the filter magnet and the inner-most ring of cusp-field magnets in the front of the source. If the filter magnet polarity is reversed, a cusped-field filter, similar to that on the present LAMPF surface conversion source is formed. It was found that the best operation (highest current density and least electron/ H^- ratio) for the high duty factor source we built, occurred for the cusp-field filter. All results presented here are for this case. It was possible to vary the strength of the filter field by using combinations of magnets of various strengths and sizes. As the filter field increased, both the H^- current and the extracted electrons decreased as well as the electron/ H^- ratio. For a moderate filter strength of 170 μ Weber (the product of the peak magnetic field and the area of the filter magnet), an electron/ H^- ratio of 2:1 can be obtained with only a moderate decrease in the maximum current of H^- ions.

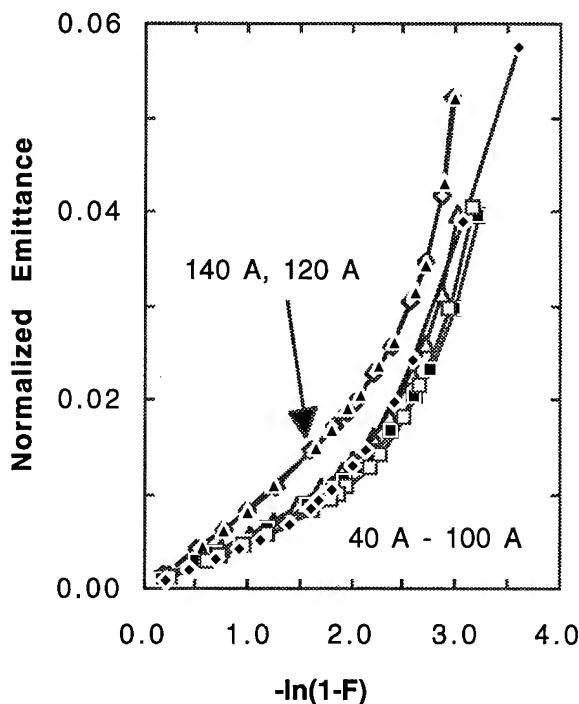


Figure 4: Normalized emittance (π cm mrad) as a function of $-\ln(1-F)$ for arc currents from 40 A to 140 A. These data correspond to the 3-mm-aperture weak-filter data of figures 2 and 3.

Emittance measurements were taken with both emission apertures and for wide range of ion source parameters. For the 3-mm-diameter aperture, the

observed normalized emittance at a given beam fraction F is plotted against $-\ln(1-F)$ for various arc currents. Figure 4 shows such a plot for a weak filter field. An rms emittance can be obtained from the slope of these plots at low beam fraction and was typically 0.007 π cm-mrad with only a weak dependence on arc current, except for the highest arc currents. For the 10-mm-diameter emission aperture, the larger beam sizes resulted in emittance growth in the third order aberrations in the solenoid lens. The rms emittances, however, scaled as the aperture size and 0.02 π cm-mrad was typical. Large bore solenoid lenses will be needed for the 10 mm-diameter case to limit this emittance growth.

IV. CONCLUSIONS

The toroidal filter volume H^- ion source compares favorably with LAMPF's surface conversion source. Higher beam currents can be achieved with comparable emittances. The cesiated operation is much simpler and more reliable; a much smaller amount of cesium is needed; a precise constant flow of cesium is not required; the source can run for days after being cesiated once; the source recovers quickly from interruptions to the arc current. These qualities and the absence of the converter's water-to-vacuum seals, should make the volume source more reliable. The source lifetime also appears to be good. The prototype source has accumulated approximately 400 hours service in intermittent operation using the original 1.5-mm-diameter tungsten filament cathodes.

Future development will focus on refinement of the extraction and transport optics to reduce the aberrations that are apparent in Fig. 4. We will also continue our investigation of the RF-heated dipole filter volume source developed at Lawrence Berkeley Laboratory.

V. ACKNOWLEDGMENTS

We thank J. Alessi for helpful discussions. We acknowledge the contributions of D. Tupa, R. Damjanovich, J. Wieting, H. Williams, W. Potter, and J.D. Paul.

VI. REFERENCES

- [1] R.L. York, et al., Conference Record of the 1993 IEEE Particle Accelerator Conference, 3175

GENERATION OF HIGH PURITY CW PROTON BEAMS FROM MICROWAVE DRIVEN SOURCES *

David Spence[†] and Keith R. Lykke*, Technology Development[†] and Materials Science/Chemistry* Divisions, Argonne National Laboratory, Argonne, IL 60439 USA

We describe a technique we have developed to significantly increase the proton fraction extracted from high pressure (mTorr) electron cyclotron resonance (ECR) sources of the type developed by Chalk River Laboratories (CRL)[1]. Specifically, this proton enhancement is achieved by the addition of environmentally benign additives (H_2O being the most effective) to the plasma, in molecular concentrations of the order of 1%. Typically, operating under non-resonant source conditions, this technique will enhance the proton fraction from about 75% to greater than 95% for a power input of 700W at 2.45 GHz. Similar results are achieved for deuteron beams. We believe this technique is capable of similar results in arc-discharge (bucket) sources, Penning sources and any other gas discharge sources, under suitable conditions.

I. INTRODUCTION

High current cw proton sources of high reliability are a current requirement for several proposed accelerator applications, including spallation neutron sources and accelerator production of tritium. A desirable property of such sources is that the proton fraction of the extracted beam be as high as possible so as to avoid the need for selection of the desired ion, i.e., to enable direct injection into an accelerating structure. A number of sources have been described in the literature that yield proton fractions of the order of 80% of the extracted beam, the other unwanted beam components being H_2^+ and H_3^+ . These advanced sources include the arc-driven multi-cusp generator developed for the Basic Technology Accelerator (BTA) at JAERI [2] and the high pressure ECR source developed at CRL. Although the CRL source has generated a beam with a proton fraction under resonant conditions of 90%, most experiments reported by the CRL group [3] have been performed when operating off-resonance where proton fractions of 75 - 80% were obtained. Normal operation for this source is off resonance because of problems in maintaining long term plasma stability when operating on resonance, an observation also noted by ourselves using an identical source purchased from CRL. Similarly, the CRL ECR source supplied to Los Alamos National Laboratory (LANL)[4] generally produces beams with a proton fraction of about 80%. While beams with a proton fraction of 80% have been shown by the CRL group to be suitable for direct injection

into a room-temperature radio frequency quadrupole (RFQ) [5], they would certainly not be suitable for injection into a superconducting structure because of the possible unacceptable thermal loading caused by the deleterious H_2^+ and H_3^+ ion species. Unless beam purity of the order of 99% or so can be achieved, direct injection into a superconducting structure does not appear likely, thus requiring magnetic separation before injection. Magnetic separation inevitably leads to emittance growth and loss of beam brightness, a situation that is also undesirable for high current cw superconducting accelerators. An additional benefit of very high purity proton beams has been pointed out by Sherman, [5] i.e., the higher the proton fraction, the less is the effective mass of the beam. Hence, for a given beam current density, the electric field can be reduced, thus reducing voltage breakdown and yielding a more reliable injector.

II. BACKGROUND

It has long been known that the addition of minor constituents to microwave generated plasmas can greatly modify the species composition of the plasma, and, specifically, increase atomic neutral fractions with respect to molecular species [6]. This technique has sometimes been used by those in atomic and molecular physics to produce high purity atomic hydrogen beams [6]. Because the molecular fraction of the additive required is generally so small (<1%), it seems unlikely that its catalytic action is a gas phase property and more likely that it results from some surface action, though for a long time controversy existed on this point. Systematic studies [6] of atomic hydrogen fractions from microwave driven plasmas, however, strongly indicate that any catalytic action of the additive results from (largely unknown) surface phenomena by preventing atomic recombination on the surface. This is analogous to the prevention of recombination by fused-alumina ion source liners. Neutral atomic hydrogen sources with close to 100% purity have been made using this technique, leading us to recognize that this may be a viable technique for the production of high purity ion beams.

* Work supported by the United States Department of Energy via ANL Science and Technology, Laboratory Directed Research and Development funds.

III. EXPERIMENTAL SETUP

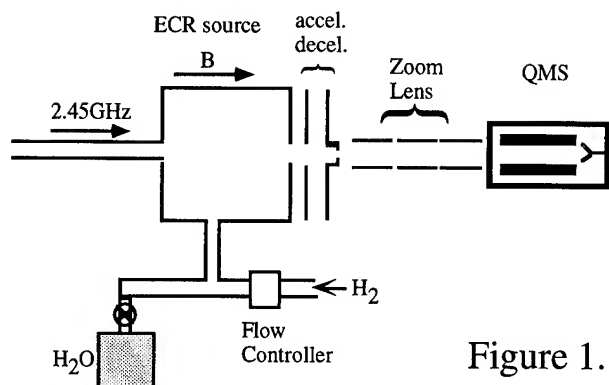


Figure 1.

A schematic of our experimental setup and beam diagnostic is shown in Fig. 1. The major components of our apparatus include an ECR source purchased from CRL which is powered by a 2.45 GHz microwave generator rated at 2.0 kW. The microwave generator is coupled to the source via a circulator and a four-stub autotuner. The ion source is attached to a large, flexibly designed, high-vacuum, oil-free diagnostic chamber that is pumped by three cryopumps and a turbo pump giving a base pressure of 1.0×10^{-8} Torr without baking. When operating the ion source at a hydrogen-feed flow rate of 1 sccm, the base pressure in the diagnostic chamber rises to about 6×10^{-6} Torr as measured on an (uncorrected) ion gauge. The catalytic additive (generally H_2O) is introduced to the plasma downstream of the hydrogen flow control unit via a leak valve as shown in figure 1. The molecular fraction H_2O/H_2 is estimated from the ion gauge measurements taking into account the very different gauge constants for these two gases. This fraction is generally of the order of 1% or less and the ion gauge measurements are consistent with the fraction of O^+ we see in the extracted beam as described below.

In the present experiment, 5 to 15 mA of beam current is extracted from the source at a few hundred volts by an accel-decel arrangement, with the main beam being collected and monitored on the decel electrode. A small hole in the decel electrode allows a portion of the beam to be imaged at the entrance plane of a quadrupole mass spectrometer (QMS) by means of a three element zoom lens whose design is based on focal properties tabulated by Harting and Read [7]. The zoom lens gradually decelerates the beam which emerges from the decel electrode to the 10-20 eV required by the QMS for quantitative analysis. The beam trajectories for the zoom lens were calculated using SIMION [8]. With the typical operating voltages shown in Fig. 1, 50% of the sampled beam lies in a circle of only 0.25 mm dia. at the entrance plane of the QMS, and the

resulting rays within this circle easily meet the parallelity requirements for quantitative mass spectrometry[9].

IV. RESULTS

All of the measurements reported here are conducted with the ECR source operating slightly off resonance, as chosen by the magnitude of the magnetic confining field. Similar results were obtained with the source magnetic field operating either 10% above or below the resonant field. Though operation off-resonance usually produces a smaller fraction of protons, such is not the case in the present experiment with H_2O as an additive.

Figure 2 shows the mass analysis of a beam extracted from the source with 1 sccm H_2 flow and 700 W microwave power to the source. Under these conditions, the proton fraction of the total beam (consisting of $H^+ + H_2^+ + H_3^+$) is about 0.75, consistent with the measurements of Taylor [1] under similar non-resonant conditions.

Figure 2.

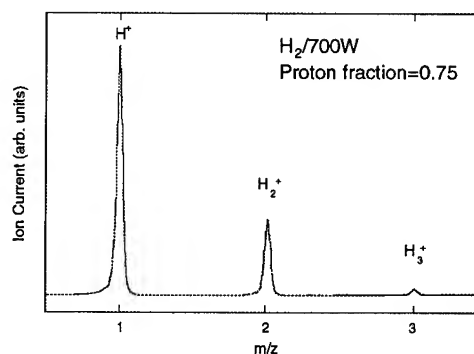


Figure 3 shows a beam composition obtained under the same conditions as figure 2, but with ~ 1% H_2O added to the source. In this case the proton fraction is slightly higher than 0.95. Notable in figure 3 is the absence of H_3^+ . This is expected since H_3^+ is produced via the reaction $H_2^+ + H_2 \rightarrow H_3^+ + H$ and is thus quadratic with respect to the H_2 partial pressure in the source. Reduction of the H_2^+ peak by a factor of about 5 by the addition of 1% H_2O thus reduces the H_3^+ intensity by a factor of 25. The increase in concentration of hydrogen atoms in the source by the addition of H_2O is dramatically visual to the eye, the plasma changing color from pale bluish-pink to a dramatic deep violet characteristic of Balmer (H_α and H_β) radiation. The addition of H_2O to the source appears to have the added benefit of significantly stabilizing the plasma and producing a less noisy beam.

Figure 3.

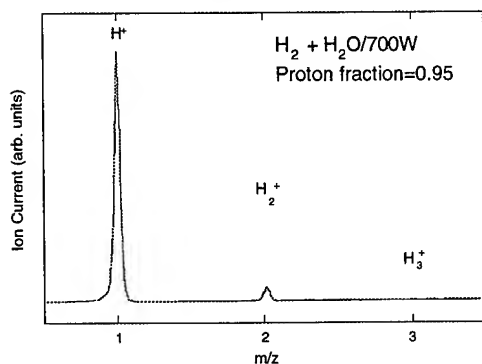
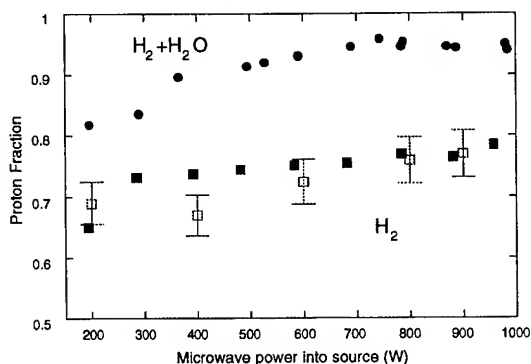


Figure 4 shows the proton fraction obtained as a function of microwave power to the source for 1 sccm H_2 flow rate, both with (solid circles) and without (solid squares) H_2O additive and operating under non-resonant conditions. Alternate data points in figure 4 were taken under conditions of increasing and decreasing power so as to illustrate the absence of any long term drift. Figure 4 also shows the reproducibility of Taylor's earlier results [1] (open squares) under similar non-resonant conditions.

Figure 4.



Under the conditions of figure 4, measurements of other impurities introduced into the beam by admitting H_2O to the source show these to be O^+ (0.4%) and OH^+ and H_2O^+ (each at the level of a few parts per thousand). Finally, we have obtained a similar improvement in deuteron (D^+) enhancement by use of either H_2O or D_2O , each being equally effective but producing extraneous peaks (H^+ , HD^+ and HD_2^+) in the case of $H_2O + D_2$, as expected.

V. SUMMARY AND FUTURE

We have demonstrated significant enhancement in the proton and deuteron fractions of beams extracted from high pressure ECR sources by the addition of about 1% of

H_2O or D_2O to the source under non-resonant conditions. An additional benefit seems to be a more stable operation of the source. We believe this technique may be applied to any type of gas discharge proton source, provided that the source may be made to operate thermally cool. Further, we believe that with minor modifications the source may realistically yield proton fractions of 98 to 99%, the remaining part consisting primarily of O^+ , OH^+ , and H_2O^+ resulting from the H_2O .

Finally, a preliminary analysis of collaborative experiments by ANL and LANL[10] performed on the CRITS injector located at LANL, indicate higher proton fractions and lower proton beam emittances at 40-45keV beam energies using this technique.

VI. ACKNOWLEDGMENTS

We thank C. L. Fink for performing trajectory calculations in the early phase of this work, and C. Batson for capable construction and maintenance of our apparatus.

VII. REFERENCES

- [1] T. Taylor and J. F. Mouris. "An Advanced High-Current Low-Emittance DC Microwave Proton Source". Nucl. Instr. And Meth. **A366**. (1993) 1.
- [2] Y. Okomura, R. Inove, H. Oguri and H. Tanaka. "Development of a High Brightness Ion Source for the Proton Linear Accelerator (BTA) at JAERI". 1992 Linac Conference, Ottawa, AECL-10728. Vol 2. P. 645.
- [3] G. M. Arbique, T. Taylor, A. D. Davidson and J. S. C. Wills "High current Direct Injection to CW RFQ Using an ECR Proton Source" 1992 Linac Conference, Ottawa, AECL-10728 Vol. 2. P. 52.
- [4] J. Sherman, D. Hodgkins, P. Lara, J. D. Schneider and R. Stevens, Jr. "Lifetime Test on a High-Performance DC Microwave Proton Source". Paper MPE04. These Proceedings.
- [5] J. Sherman - personal communication.
- [6] D. Spence and O. J. Steingraber "Factors Determining Dissociation Fractions in Atomic Beams Generated by Straight-Through Microwave Discharge Sources". Rev. Sci. Instrum. **59**, (1988) 2464.
- [7] E. Harting and F. H. Read "Electrostatic Lenses" Elsevier (1976).
- [8] D. A. Dahl and J. E. Delmore. "The SIMION PC/PS2 Users Manual Version 4.0" EGG-CS-7233. 1988.
- [9] P. H. Dawson (Ed) "Quadrupole Mass Spectrometry and Its Applications" Elsevier (1976).
- [10] D. Spence, J. D. Schneider, J. Sherman, R. Stevens, Jr. and D. Hodgkins, to be published.

COMPUTATIONAL STUDIES FOR AN ADVANCED DESIGN ECR ION SOURCE

G. D. Alton, J. Dellwo, and R.F. Welton

Oak Ridge National Laboratory, * P. O. Box 2008, Oak Ridge, TN 37831-6368 USA

D. N. Smithe

Mission Research Corporation, 8560 Cinder Bed Road, Suite 700, Newington, VA 22122 USA

An innovative technique for increasing ion source intensity is described which, in principle, could lead to significant advances in ECR ion source technology for multiply charged ion beam formation. The advanced concept design uses a minimum-B magnetic mirror geometry which consists of a multi-cusp, magnetic field, to assist in confining the plasma radially, a flat central field for tuning to the ECR resonant condition, and specially tailored mirror fields in the end zones to confine the plasma in the axial direction. The magnetic field is designed to achieve an axially symmetric plasma "volume" with constant mod-B, which extends over the length of the central field region. This design, which strongly contrasts with the ECR "surfaces" characteristic of conventional ECR ion sources, results in dramatic increases in the absorption of RF power, thereby increasing the electron temperature and "hot" electron population within the ionization volume of the source.

I. INTRODUCTION

Ion sources based on the Electron Cyclotron Resonance (ECR) principle have played indispensable roles in the advancement of our knowledge of atomic and nuclear physics and in many areas of applied science and technology. For accelerator-based research applications, the final energy of an ion beam is directly proportional to the charge on the ion during acceleration and, therefore, a premium is placed on ion sources which are capable of generating very high charge state ion beams. Heavy-ion cyclotrons, linear accelerators, synchrotrons, and new generation heavy ion colliders now under construction, such as the relativistic heavy-ion collider (RHIC) at the Brookhaven National Laboratory and the large hadron collider (LHC) which has been proposed for construction at CERN, would benefit immensely from the advent of advanced ECR ion sources with charge states and intensities superior to sources presently available. The source that we describe offers this distinct possibility with many applications in atomic physics and applied research, as well.

II. PRINCIPLES OF ECR ION SOURCES

The energy source for plasma generation and maintenance in the ECR ion source is electron cyclotron resonance (ECR) heating of the plasma electrons. The energy (electron temperature) and energy distribution (temperature distribution) are two of the fundamental properties which govern the performance of the ion source in terms of degree of ionization and multiple ionization capabilities of the source. In ECR ion sources, electrons can only be excited whenever the magnetic field meets the ECR resonant condition:

$$\omega_{\text{ECR}} = Be/m = \omega_{\text{rf}} \quad (1)$$

where ω_{ECR} is the electron-cyclotron resonant frequency, ω_{rf} is the resonant frequency of the microwave power source, B is the magnetic field which meets the resonance requirement, and e is the electron charge and m the mass of the electron. The physical region over which the ECR condition is met is referred to as the ECR zone. Electrons passing through the ECR zone, which are coincidentally in phase with the RF electric field, are accelerated by the transfer of electromagnetic energy to the electron perpendicular to the direction of the magnetic field; electrons arriving out of phase with the electric field undergo deceleration. On subsequent passes through the ECR zone, the electrons gain a net energy and are said to be stochastically heated. At low collision frequencies (low ambient pressures), some of the electrons can be excited to energies sufficiently high to remove tightly bound electrons and thereby produce multiply ionized atoms.

III. CONVENTIONAL ECR ION SOURCE DESIGNS

The "volume" ECR ion source is contrasted with that of the more conventional "surface" ECR ion sources in Fig. 1. Improvements in ECR performance can, in principle, be realized by redesigning the magnetic field configuration so that the ECR zone is a "volume" rather than a "surface," as is the case in conventional ECR ion sources. In traditional ECR sources, the electrons gain energy in the fairly thin ECR zones in or near the mirror field regions. The ECR zones in conventional sources are usually annular, ellipsoidal surfaces

*Managed by Martin Marietta Energy Systems, Inc., under contract No. DE-AC05-84OR21400 with the U.S. Department of Energy.

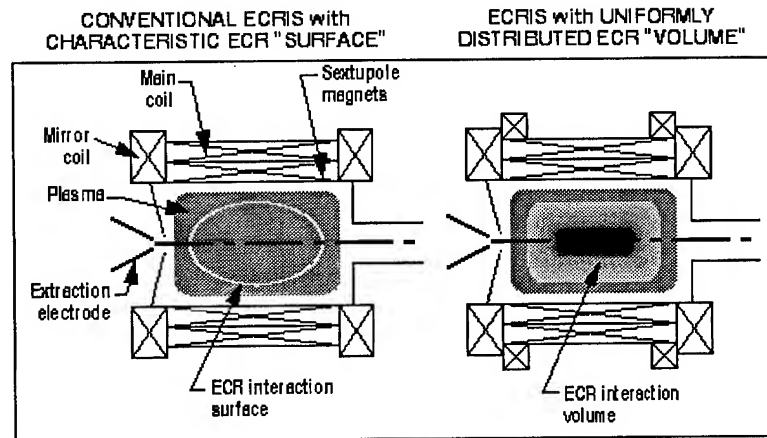


Fig. 1 Schematic drawings of a conventional ECRIS with characteristic ECR "surface" and an ECRIS with a large, uniformly distributed ECR "volume."

and, in general, lie off of the axis where ions are extracted; the microwave power can only be coupled to the plasma in these zones, which occupy a small percentage of the ionization chamber volume, leaving the remainder of the plasma chamber as "unheated" zones. In addition, the thin ECR zone in the mirror field is a relatively small fraction of the device volume, hence the absorptivity of the plasma is governed not by the size of the plasma, but by the size of the ECR region. The new ECR ion source, described below and in a previous publication,¹ overcomes this limitation. For detailed descriptions of sources which reflect the present state of conventional ECR ion source technology, reference is made to the proceedings of recent workshops on this source type (see, e.g., Refs. 2-4).

IV. DESIGN FEATURES OF THE NEW ECR ION SOURCE

We have used magnet design codes, plasma dispersion solvers, and particle-in-cell (PIC) simulation codes to simulate the relative adsorption characteristics in a conventional ECR source and in the new ECR ion source concept described in this report. The codes were also used to design the magnetic field geometry and to track particle motion in the magnetic field. The advanced concept design uses a minimum-B magnetic mirror geometry, which consists of a multi-cusp magnetic field to assist in confining the plasma radially, a flat central field for tuning to the ECR resonant condition, and specially tailored mirror fields in the end zones to confine the plasma in the axial direction.

The advanced ECR ion source considered in this document allows for heating of a large fraction of the total volume of the ECR ion source. The ECR volume can be varied by increasing the number of poles used for radial confinement. In all cases for $N \geq 4$, the ECR zone in the central region of the proposed ECR ion source concept is continuous and on-axis. The magnetic field is designed to

achieve an axially symmetric plasma volume with constant mod-B, which extends over the length of the central field region.

V. ELECTRON HEATING CHARACTERISTICS

In order to achieve a flat field profile in the radial direction, it is necessary to use a high-order multi-cusp magnetic field. The effect of increasing the field multiplicity on the physical size of the respective ECR zones for $N=6$ and $N=22$ multipole fields is illustrated in Fig. 2 which displays, respectively, magnetic field versus radial position (lower portion), and the velocity of the electrons which are resonantly excited as a function of radial position (upper portion). In Fig. 2, the transition from heated to nonheated regions of the plasma at the ECR condition is very apparent. Electron heating studies show that the ECR microwave power can be coupled more efficiently in the new ECR ion source than in conventional ECR ion sources. For the same time duration, microwave adsorption is increased by more than a factor of seven over conventional ECR sources.

VI. DISCUSSION

The ECR ion source described in this paper has a much larger volume of resonant plasma resulting in greater absorptivity of the microwave power with higher electron temperatures. By varying the multiplicity of the radial-cusp magnetic field, the size of the ECR "volume" can be varied. The more uniform distribution of the ECR power and the greater proportion of hot electrons, as a consequence, implies a greater degree of ionization of the plasma and higher charge states of multiply charged ions within the plasma volume.

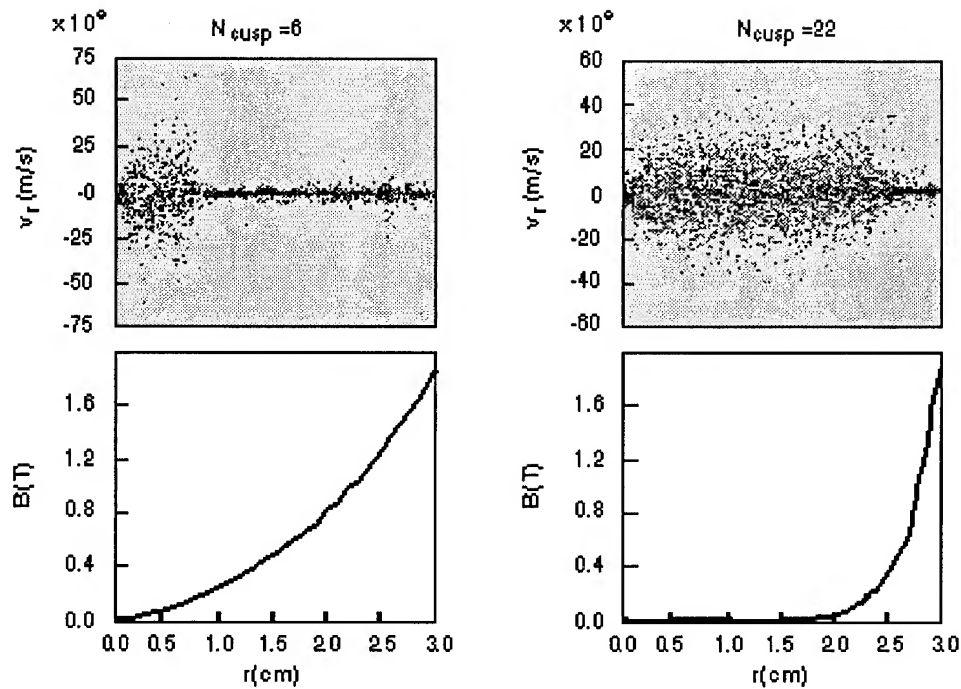


Fig. 2 Illustration of the effect of varying the number of cusps N on the volume of central (flat) magnetic field plasma that can be tuned to the ECR condition for $N=6$ and $N=22$ cusps. The transition from heated to nonheated regions of the plasma is very apparent from the plots of the radial velocities of the electrons in the respective plasma confinement geometries; the lower order azimuthal field results in a much smaller field volume of resonant plasma.

VII. REFERENCES

1. G. D. Alton and D. N. Smithe, Rev. Sci. Instrum. **65**, 775 (1994).
2. Proc. Int. Conf. on ECR Ion Sources and their Applications, ed. by J. Parker (NSCL Michigan State University Publisher, East Lansing, MI) (1987), MSU-CP 47, 151.
3. Proc. of the Tenth Int. Workshop on ECR Ion Sources (Knoxville, TN, Nov. 1-2, 1990), ed. by F. W. Meyer and M. I. Kirkpatrick, CONF-9011136 (1991).
4. Proc. of the Eleventh Int. Workshop on ECR Ion Sources (Gronigen, The Netherlands, May 6-7, 1993), ed. by A. G. Drentje, KVI-Report 996 (1993).

VIII. ACKNOWLEDGMENTS

The authors express their gratitude to Ms. Jeanette McBride for typing the manuscript.

PULSED ION SOURCES OF DUOPLASMATRON TYPE WITH COLD AND HOT CATHODES

A. Glazov, V. Krasnopolsky, R. Meshcherov, V. Masalov, MRTI RAN

A description of H^+ ion sources construction and results of examination of their operating characteristics are presented. The beam energy is between 20 and 120 keV. The ion source with a hot cathode having a continuous bleeding of a working gas (the pressure in the discharge chamber is 0.02 Torr) operates at a pulse repetition frequency up to 25 Hz and a rectangular pulse length between 30 and 250 mcs. At the output of the source a ion beam 10 mm in diameter is formed. The amplitude of current pulse is up to 60 mA. The ion energy is 60 keV at a maximum pulse repetition frequency and a maximum pulse length. The source admits operating with a medium power consumption of 300 W during the discharge. The source is also used in a continuous regime at a lower beam current. The source with a cold cathode uses pulse gas bleeding in order to decrease gas consumption at a

pressure (0.2...1) Torr in the discharge chamber. The main discharge current reaches the value between 100 and 170 A at a pulse length from 30 to 40 mcs. The maximum output current equals from 0.8 up to 0.9 A at an extracting voltage of 90 kV.

I. HOT - CATHODE ION SOURCE

The source with a hot cathode of the type described in [1,2] is intended for use in installations with a small relative pulse duration. Therefore it uses the continuous submission of working gas (hydrogen) with the help of adjustable bleeding and the compulsory water cooling. For higher reliability in design the isolators made of ceramics and refractory metals are applied. The schematic diagram of the discharge chamber of the ion source and the accelerating gap is shown in Fig.1.

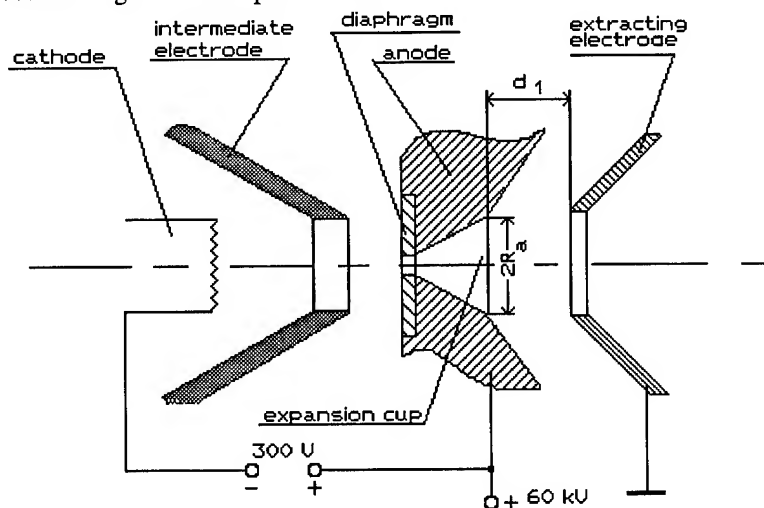


Figure 1. Schematic diagram of the discharge chamber of the ion source with hot cathode.

The working gas from the side of the hot cathode is supplied into the discharge chamber where the pressure of 0.02 Torr is supported as it is necessary for the charge existence. The pressure difference between the discharge chamber and the container with a pumping-out post ($P=1.5 \cdot 10^{-5}$ Torr) is reached by using a small hole (1 mm) in the diaphragm. Within the gap between the intermediate anode and the main one the contracted magnetic field is created with the help of a magnetic coil. The design admits the disassembly into the main units: replacement of the hot-cathode, the diaphragm and the expansion cup. The ion source was tested in the frequency mode as well as in DC mode. At first the allowable level of the source

power at which its long-term operation is possible was determined in the continuous regime. It was found that at a constant power in the discharge up to 200 W (200 V, 1A) and the power supplied to the hot cathode and the magnetic coil of 200 W and 20 W respectively, the flow rate of cooling water of 1 litre/minute is enough. The constant voltage adjustable over the range (20...60) kV was applied to the accelerating gap of 13 mm wide. The frequency regime was provided by pulsed power supply of the discharge gap with rectangular pulses 250 mcs in length and 300 V in amplitude. The pulse frequency as adjusted and reached 25 Hz, at the same time the pulse amplitude of the discharge current did not exceed 12 A. The steady pulse

height of the beam current of 65 mA at the length of 250 mcs is achieved at the accelerating voltage of 60 kV, the average power of the discharge of 12 W and the aperture in the expansion cup of 9 mm. The beam size at the distance of 200 mm from the source was not over 43 mm with no focusing elements. The experiments carried out with the help of collimating diaphragms and partitioned Faraday cup have allowed to evaluate the top level of the normalized emittance to be $\varepsilon=0,12 \pi \cdot \text{cm} \cdot \text{mrad}$. The source design allowed to carry out experiments in DC mode. The discharge start was executed with the help of a single

voltage pulse as well as with a smooth change of a constant voltage on the intermediate electrode. At an extracting voltage up to 40 kV the current of H^+ , N^+ ions was within the mA-range. The experiments conducted permit to make the conclusion about the opportunity to use the presented source at high frequencies of current pulse repetition, therefore at a higher average current.

II. COLD-CATHODE ION SOURCE

The duoplasmatron with a cold cathode of the type described in [3] is schematically shown in Fig.2.

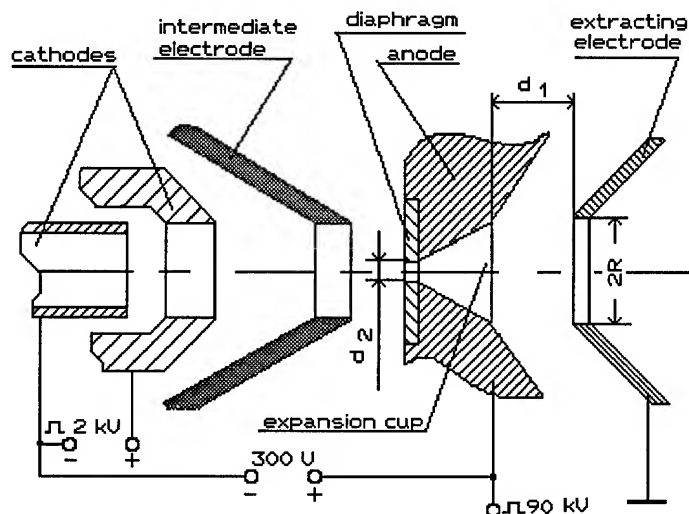


Figure 2. Schematic diagram of ion source with cold cathode.

It uses pulsed gas bleeding which is executed with the help of an electromagnetic valve. The construction of the valve permits to set up the regime of its operation during the experiment without the disassembly of the source. The opportunity of the pressure adjustment in the discharge chamber of the source within the interval (0.2...1.0) Torr is provided. The source can operate in a single pulse regime as well as in a frequency one as the system of water cooling is used. In comparison with the source considered above the hot cathode is replaced with a discharge cell using a cold hollow cathode made from molybdenum. The first discharge cell with a hollow cathode (the cathode cell) is supplied with a voltage pulse up to 2 kV and 10 mcs long. The plasma which appears during the start plays the part of emitter for the next discharge cell (the main) which is supplied with a voltage pulse up to 300 V and 100 mcs long. The anode of the main cell has the emission aperture with the diameter from 1,3 mm to 2,6 mm which was changed during the experiments. The discharge in the main cell occurs in the magnetic field which was changed up to 0,25 T during the experiment. The extracting voltage was of the pulsed type 90 kV in amplitude and 30 mcs in length. The conducted investigations have allowed to determine the following optimum operating mode of the source: the current of the main discharge can vary from 140 to 150 A; the delay time between the turn-on of the valve and the discharge equals

(4...5) ms. The optimum gap size between the intermediate electrode and the anode insert is equal to 5 mm. At the source output the stable pulse amplitude of the current of H^+ beam was not less than 0.65 A at an extracting voltage of 90 kV; $d_1=25$ mm, $2R=20$ mm (see Fig.2). The diameter of the anode aperture is equal to 2,3 mm. The control of the total current amplitude of H^+ beam was executed by the adjustment of the magnetic field as well as the value of the discharge current. The considered ion sources were tested in pilot operation and have confirmed their reliability and convenience in use.

III. REFERENCES

1. M.Ardenne "Tabellen der Elektronenphysik, Ionenphysik und Übermikroskopie" Bd 1,2 Berlin, 1956.
2. I. V. Orfanov, V. A. Teplyakov "50 kV Ion Tube" PTE (Pribery i Tekhka Experimenta) **2**, 150 (1960).
3. V. V. Nizhegorodtsev, Plasma Ion Source, Author Certificate USSR No. 439232, published in Bulletin Izobreteney **27**, 175 (1975).

DOUBLE PULSE EXPERIMENT WITH A VELVET CATHODE ON THE ATA INJECTOR*

G. Westenskow, G. Caporaso, Y. Chen, T. Houck, and S. Sampayan,
Lawrence Livermore National Laboratory, P.O. Box 808, Livermore, CA 94551 USA

Double pulse transport experiments were conducted on the front end of the ATA accelerator to obtain data on the capability of a velvet cloth cathode to produce two successive pulses. Pulses of approximately 3 kA were extracted from the cathode with interpulse spacings varying from 150 ns to 2.8 μ s using an anode-cathode voltage of about 1 MV. Analysis of the current and voltage waveform data from the injector indicate that the effects of cathode plasma on the second pulse of a two-pulse burst is minimal.

I. BACKGROUND

The ATA injector has typically used velvet cathodes [1] to obtain its 10 kA operation at 2.5 MV. Although the precise mechanism by which these cathodes operate is uncertain, it is believed that there is field emission from the tips of velvet fibers that extend into the gap. The emitted current is believed to lead to the creation of a plasma layer at the cathode surface. Velvet cathodes have been used occasionally at ATA for short bursts at repetition rates up to 1 kHz. Velvet sources were employed for a short time on another high repetition rate injector. Above a 50 Hz rate the emission current would die out, but recover as the repetition rate was lowered. This suggested that the source of the plasma from which the electrons were extracted might be adsorbed gasses on the fiber's surface which were totally depleted above a certain repetition rate. The rate of deposition of gas onto a clean surface is proportional to the pressure, and there is an equilibrium thickness of adsorbed gasses on a surface for a given ambient pressure.

These inferences suggest that there might be a suitably large amount of adsorbed gasses on the velvet surface to permit multiple-pulse operation.

II. INJECTOR CONFIGURATION

A schematic of the injector used in the Double Pulse Experiments is presented in Fig. 1. The ATA injector is composed of two sections, each with five 250-kV induction cells in series, that in normal operation provides a nominal 2.5-MV, 70-ns FWHM pulse across the anode-cathode

(A-K) gap. During the experiments a 5.25-inch diameter velvet cathode was used as the electron source. The separation between the anode and the cathode was about 14 cm during most of the experiment. At an anode-cathode voltage, V_{ak} , of about 2.5 MV (normal operation) approximately 8 kA of current is drawn from the cathode. At $V_{ak} \approx 1.0$ MV, as used in the double pulse experiments, approximately 2.5 kA of current is drawn from the cathode. The average emission current density to provide 2.5 kA of current from a 5.25 inch cathode is 18 A/cm².

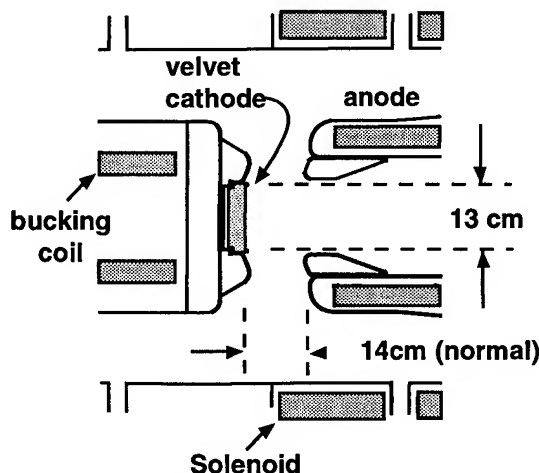


Figure 1. Electrode configuration used for double pulse experiment.

III. DOUBLE PULSE OPERATION

For these experiments the triggering arrangement of the ATA injector was modified so that the even and odd cells of the injector could be fired independently. Extra lengths of cable were added to the high voltage trigger of the odd cells so their firing could be delayed in fixed increments. Since for each pulse only half the cells were involved, the anode-cathode voltage was about half of its normal value. The electrode package was not modified for the reduce voltage operation. We expect that the beam brightness would decrease for the lower voltage operation. When the A-K gap was shortened by about 3 cm in the latter part of the experiment, there was a further decrease in the beam brightness.

Figure 2 shows data for a 2.2 μ s time separation between the first and second shot. It also shows a source of error involved with trying to determine changes between

* The work was performed under the auspices of the U.S. Department of Energy by Lawrence Livermore National Laboratory under contract W-7405-ENG-48.

the two pulses. If the two pulses are captured on the same oscilloscope, the amplitude resolution is not good. If the data is captured on two oscilloscopes, care must be taken to ensure the calibrations are identical to permit detection of small differences between the two traces. The voltage of the second pulse could be adjusted independently of the first pulse.

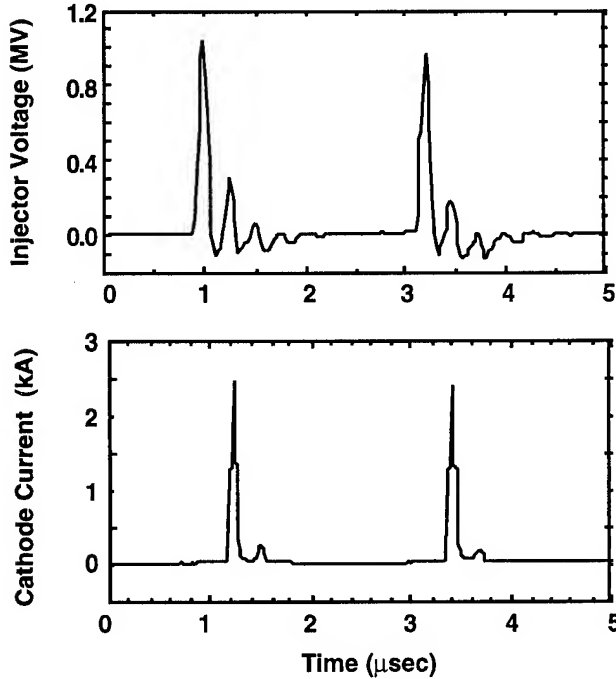


Figure 2. Example of waveforms for a double pulse. There is a small time shift between the two graphs. Current is only emitted on the positive part of voltage pulse.

A. Effective gap closure

The emission current density, J_0 , that will be drawn across an infinite diode with separation d_0 , and voltage V_0 is given for the steady-state non-relativistic case by:

$$J_0 = \chi \frac{V_0^{3/2}}{(d_0)^2}$$

where $\chi = \frac{4 \epsilon_0}{9} \left(\frac{2e}{m} \right)^{1/2}$. For our experiments we define an effective gap, d_g , such that:

$$J_c = \chi \frac{V_{ak}^{3/2}}{(d_g)^2}$$

where J_c is the average cathode current density. During the experiments d_g was about 12 cm. We were looking at gap closure, or a change in d_g , of about 1% d_g between the first and second pulse. Figure 3 shows a collection of data on this change in the effective gap between the first and second pulse. As plasma drifts into the gap from the cathode surface after the first shot, the value of d_g will

decrease. If the active emission area of the cathode increases between the two pulses, d_g will also be reduced.

B. Reduced AK gap experiments

The first group of experiments was performed with $d_g = 12$ cm. For these setting $J_c \approx 18$ A/cm². We wished to know if the plasma closure problem would be more severe at higher J_c , so in the latter experiments we shorten d_g to about 10 cm. This gap spacing increased J_c to about 27 A/cm². The change in the effects of the surface plasma on the second pulse between $d_g = 12$ cm and $d_g = 10$ cm was smaller than our ability to resolve. In the later experiments we were able to transport 3.2 kA through a 12-m transport section, and focus the beam to a small radius on the beam dump.

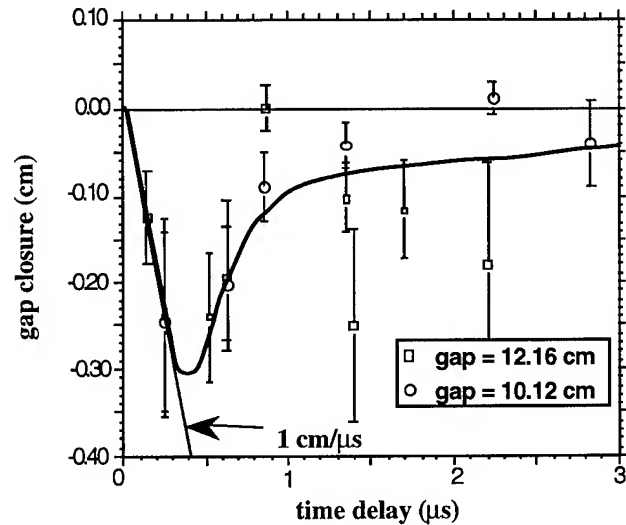


Figure 3. Changes of d_g between the first and second pulse as function of time delay.

For a long pulse we would expect [1,2] the gap to close at rate of 1-3 cm/μs. The first pulse is about 70 ns long. The gap does seem to close at about 1 cm/μs rate for the first few hundred nanoseconds. After about 400 ns the effect of the cathode surface plasma on the second pulse is weakened implying that the plasma is tenuous. There is considerable scatter in data after this time. However, the effect on the second pulse is small, and somewhat masked by calibration problems. Following a pulse there is considerable "ringing" on the cell voltage from the mismatched impedance at the lower voltage operation (as shown in Fig. 2). Thus it is difficult to obtain flat waveshapes on the second pulse at short delay times.

C. Emittance variation

Although the injector may have the same perveance for the two pulses, it is important that the beam quality of the second pulse is not degraded. Analysis of the current

and voltage waveform data from the injector indicate that there is no large emittance change between the two pulses for the core of the beam. For the first set of experiments there was a 1-m-long 2-cm-diameter collimator immersed in a magnetic field in the beamline after the injector. This section is normally used to select the inner core of the beam's phase space for downstream experiments, and is called the emittance selector. In the first set of experiments it selected about 10% of the beam, which was then transported through a 8-m transport section to the beam dump (current at dump is shown in Fig. 4). Small energy variations can explain the differences between the two sets shown in Fig. 4. The vertical and horizontal position were also shown to have similar waveshapes for the first and second pulse. From this we believe that the core beam emittance is about the same for the two pulses.

Latter experiments in which most of the current (with no emittance collimator in the system about 3.2 kA of current was transported to the dump) also indicate that the change in emittance between the first and second pulse is small. However, in these experiments the magnetic field was not zeroed on the cathode. The injector electrodes would need to be rebuilt for a good determination of the emittance variation between the first and second pulses.

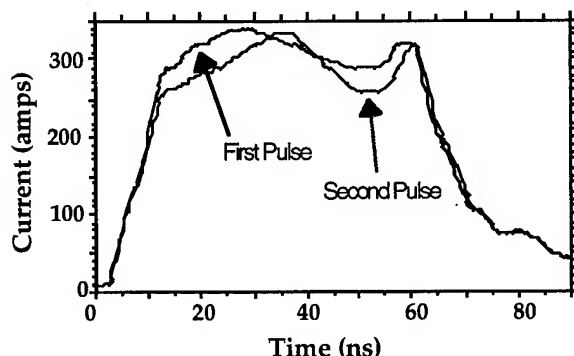


Figure 4. Beam current after collimator and a 8-m transport section. Each pulse is an average of six pulses.

IV. PLASMA DENSITIES

The data shown in Fig. 3 suggests that the plasma becomes too tenuous to support emission from its boundary at about 400-500 ns after the first pulse. Initially, the inferred plasma velocity is approximately 1 cm/ μ s with a density sufficiently high that some point on its boundary can act as an effective emitting surface. As the plasma expands into the A-K gap its density drops until it can no longer sustain emission from its surface and the effective emitting surface retreats towards the physical surface of the

velvet. We may roughly estimate this critical density by calculating the electron density required to provide the average current density J_c . We may estimate the electron energy at a distance d from the velvet by using the non-relativistic expression for the Child-Langmuir solution:

$$V = V_{ak} \left(\frac{\Delta}{d_g} \right)^{4/3}$$

where d_g is the effective A-K gap distance and V_{ak} is the anode-cathode potential. From Fig. 3, after the plasma had propagated about 0.3 cm into the gap the cathode emission density started to drop. Using d_g as 12 cm and Δ as 0.3 cm for a 1 MV anode potential yields an energy of 7.3 KeV. A current density of 18 A/cm² then requires an electron density $n \approx 2 \times 10^{10}$ cm⁻³. If the ion density is equal to or greater than this value then the effective emitting surface is located at distance Δ from the cathode surface. However, if the plasma density is less than this value then the effective emitting surface shifts back towards the cathode.

V. CONCLUSIONS

The experiments clearly show that a velvet cathode is capable of producing two pulses at 20-30 A/cm² at interpulse spacings from 150 ns to 3 μ s. For a long pulse machine we would expect that the anode-cathode gap would continue to close at order of 1 cm/ μ s. However, for a short pulse injector the plasma effects from the first pulse decrease after about 400 ns. Analysis of the current and voltage waveform data from the injector indicates that the effects of cathode plasma on the second pulse of a two pulse burst is minimal.

VI. ACKNOWLEDGEMENTS

We would like to thank Steve Petz, Dave Trimble, and Al Myers for technical assistance with the experiments. L. Multhaupt and R. Scarpetti helped provide support for the experiment.

VII. REFERENCES

- [1] R. J. Adler, et al, "Improved electron emission by use of a cloth fiber cathode," Rev. Sci. Instrum., 56(5), May 1985.
- [2] R. Parker, et al., "Plasma Induced Field Emission and the Characteristics of High Current Relativistic Electron Flow," Appl. Phys., 45, 2463 (1974).

Emittance Measurements for the Illinois/CEBAF Polarized Electron Source*

B. M. Dunham[†], L. S. Cardman[†]

Nuclear Physics Laboratory and Department of Physics
University of Illinois at Urbana-Champaign, Champaign, IL 61820,
and

C.K. Sinclair

Continuous Electron Beam Accelerator Facility
12000 Jefferson Avenue, Newport News, VA 23606

Abstract

The transverse thermal properties of the electrons photo-emitted from GaAs determine the intrinsic beam emittance, an important quantity in applications such as polarized electron sources and high-brightness sources. In this paper, emittance measurements using the Illinois/CEBAF polarized electron source are described. The emittance was measured as a function of both the laser beam spot size and laser wavelength at low currents. The data was used to infer the transverse thermal energy of the electrons photoemitted from GaAs for wavelengths between 514 and 840 nm. Near the bandgap the transverse energy is ~ 34 meV, a factor of 3 lower than that of the beam from a typical thermionic electron gun.

I. Introduction

Semiconductor photoemission electron sources are widely used for the production of polarized electrons. They are also attractive for non-polarized source applications such as free electron lasers [Si92] and linear colliders which require high brightness electron injectors that can deliver a wide range of currents with demanding time structures and a low emittance. As the intrinsic beam emittance is determined by the effective temperature of the electrons emitted from the photocathode, it is then important to know this temperature for the semiconductor in use under the operating conditions of the injector. The effective temperature of GaAs (the semiconductor most used for polarized electron production) has been measured at low acceleration voltages by other groups using several different methods with results around 0.1 eV, close to the value obtained from a typical thermionic gun.

In this paper, we report measurements of the emittance of the electron beam emitted from GaAs for various excitation wavelengths and laser beam diameters at 100 kV in order to study the thermal properties of GaAs photocathodes.

II. Emittance Measurements

A. Theory

Consider the motion of a particle through a beamline consisting of drift spaces and non-dispersive focusing magnets. In the x-plane (similar equations hold for the y-plane), the position vector at the end of the beamline is given by the product of the initial

position vector and a transfer matrix, $X_{final} = R X_{initial}$. Note that the motion in the x and y-planes must be decoupled to be able to use a separate 2×2 matrix representation for x and y, otherwise a more complete representation must be used.

A beam is made up of a collection of particles which is described by the ellipse, $X^T \sigma^{-1} X = 1$, where σ is the usual 2×2 beam matrix. The beam matrix is propagated through the beamline by $\sigma_f = R \sigma_i R^T$. Expanding the beam matrix at the end of a set of magnets and drifts in terms of the initial beam matrix then gives

$$\sigma_{11,f} = R_{11}^2 \sigma_{11,i} + 2R_{11}R_{12} \sigma_{12,i} + R_{12}^2 \sigma_{22,i}. \quad (1)$$

Since the beam radius is given by $\sqrt{\sigma_{11}}$, equation 1 shows that a measurement of the beam size at the exit of the beamline for three different magnet settings is sufficient to determine σ at the entrance to the beamline if the transfer matrix, R , is known [Ro87]. The emittance is then the area of the beam ellipse, or $\pi \sqrt{\det \sigma}$.

The most commonly used definition of emittance is that of the rms emittance, defined as

$$\epsilon_{rms} = 4 \sqrt{\langle x^2 \rangle \langle x'^2 \rangle - \langle x x' \rangle^2}. \quad (2)$$

As an example of an application of rms emittance, consider the calculation of the emittance of an electron gun at low currents [La77]. Assuming that the electrons are emitted uniformly and isotropically from a cathode of radius R in the presence of an accelerating electric field, and if the cathode operates at a temperature T , then the distribution function for x' is Maxwellian and $\langle x'^2 \rangle$ can be calculated to be $kT/mc^2 \beta^2 \gamma^2$. The mean square value of x is simply $\langle x^2 \rangle = R^2/4$. Using equation 2 and the fact that $\langle x x' \rangle = 0$ for this initial beam distribution, the emittance of an electron gun operating at a temperature T is:

$$\epsilon_{rms} = 2R \sqrt{\frac{kT}{m\gamma^2 \beta^2 c^2}}. \quad (3)$$

This equation was used to infer T from measurements of ϵ_{rms} for different initial beam radii.

B. Beamline Setup

The measurements were carried out using the University of Illinois/CEBAF polarized electron source. It consists of a 100 keV GaAs photocathode electron gun, a spin rotation system and a Mott polarimeter (see [En93] and [Du93] for details). Ideally, one would measure the emittance at the exit of the gun to eliminate problems of disturbing the phase volume during beam transport. However, this was not feasible due to other experiments in

*supported by NSF grant PHY 89-21146 and by CEBAF under grant SURA 88-C8531LD

[†]presently at CEBAF

progress, so the emittance was measured after the beam traversed a spin rotation system and polarimeter.

The actual beamline for the emittance measurements consisted of a pair of solenoid lenses followed by a drift space of 1 m to a wire scanner. The two solenoids are identical and powered with current flowing in the opposite sense to insure that they introduce no x-y coupling so that the formalism in section II-A can be used.

C. Laser Setup for the Emittance Measurements

To cover the desired range of wavelengths, three lasers were used: a helium-neon laser (633 nm), an argon-ion laser (514 nm), and a argon-pumped titanium sapphire laser (700-900 nm). To eliminate problems that could arise from poor laser beam pointing stability and a difference in beam profiles between lasers, the laser beam was focused onto a circular aperture which was then imaged to a uniform, circular spot on the photocathode. An achromatic lens with a focal length of 1 m was placed on an x-y positioning stage 2 m from the cathode. The set of apertures was mounted on an adjustable stage another 2 m upstream from the lens along the laser beam path. Each laser in turn was then roughly collimated using a small telescope to produce a 5 mm diameter beam and steered onto the aperture of choice. All of the optical elements were then adjusted until an image of the aperture was centered on the photocathode. Periodically, the image was diverted by a movable mirror so it could be viewed on a CCD camera; the spot was uniform to within $\sim 10\%$ across the beam (see figure 1). To change beam diameters, a different aperture

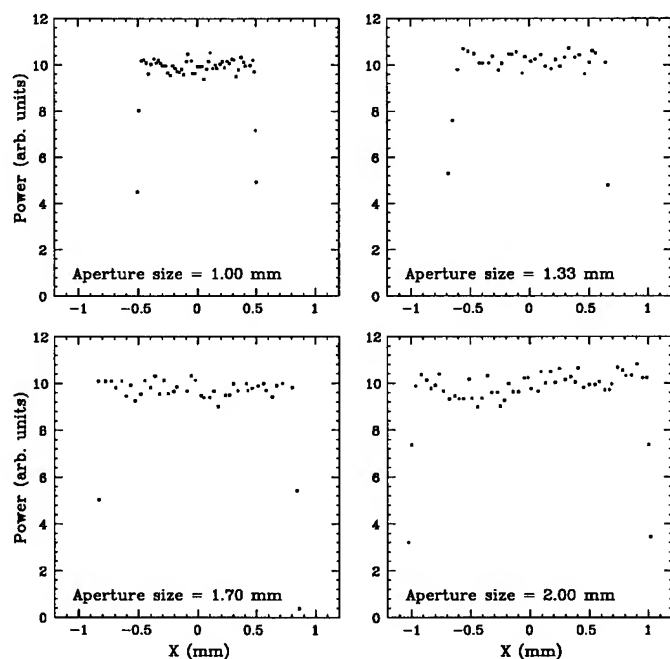


Figure 1. Profiles of the laser beam spot as viewed on a CCD camera. The plots are cuts through the center of the laser beam image for each of the four apertures.

was centered on the laser beam while observing the image on the CCD camera. This setup allowed the laser spot size and location to be reproduced accurately independent of the laser wavelength. It also improved the pointing stability since the collimated laser beam spot was substantially larger than the aperture.

D. Determination of Beam Width

The electron beam profile was measured using a standard wire scanner driven by a stepper motor. The wires were 50 μm gold-plated tungsten and the signals on the x and y wires were read out using an I-V preamplifier with variable gain and an accurate digital voltmeter (all measurements were with a DC beam). The rms beam radius was calculated directly using $\langle x^2 \rangle = \sum (x_i - x_{\text{avg}})^2$, as the beam profile was not, in general, gaussian. Background subtraction was performed by fitting a line to the region of data outside of the beam area.

III. Results and Discussion

The electron beam emittance was measured for wavelengths of 514, 633, 710, and 840 nm for spatially uniform laser beam spots with diameters of 1.00, 1.33, 1.70, and 2.00 mm. The GaAs photocathode that was used had quantum efficiencies of between 1 and 2% at 633 nm after heat cleaning and activation with cesium and nitrogen tri-fluoride. All measurements were made at currents between 5 and 10 μA and a beam voltage of 100 keV so that space charge effects were not important. This was verified by measuring the emittance as a function of current for the smallest spot size.

Figure 2 shows a plot of the rms-emittance data as a function of the laser beam diameter for four laser wavelengths. The straight lines are fits to the data; the transverse thermal electron energy, E_T , is obtained from the fitted slope by inverting equation 3: $E_T = (\text{slope})^2 mc^2 \beta^2 \gamma^2$. The error bars for the emittance values

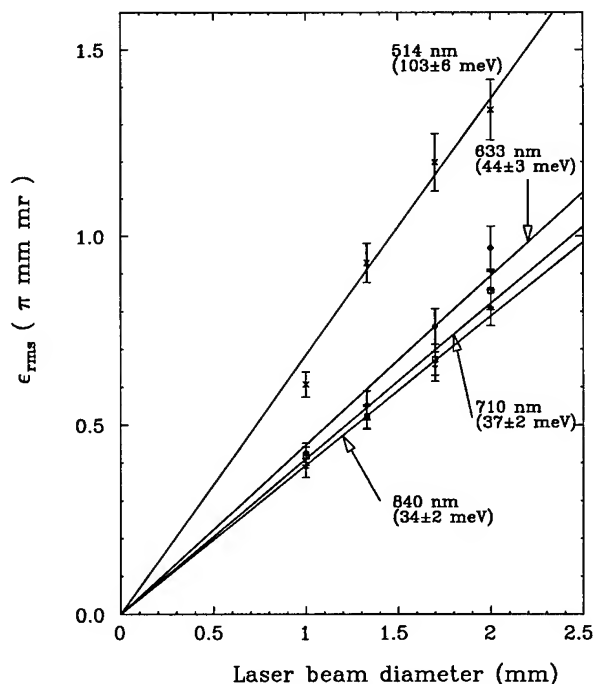


Figure 2. The rms-emittance as a function of laser beam diameter for several laser wavelengths. The inferred thermal energies are shown in parenthesis.

are mainly instrumental in nature and were determined to be $\sim 6\%$ [Du93].

A number of researchers have measured the transverse thermal energy of electrons emitted from GaAs photocathodes using a variety of methods different than the method used here. Most of the experiments made measurements either with only one excitation wavelength or with a white light source, and all made the measurements at low electron energies, typically under a thousand volts.

For example, Feigerle *et al* [Fe84] were interested in GaAs photocathodes as a intense source of monochromatic electrons. They measured the electron distribution curves (EDC's) for electrons emitted from a GaAs cathode (driven by a 810 nm laser diode) with a spherical deflection electron kinetic energy analyzer. The measured widths (FWHM) of the EDC's were 97 meV at 300K and 31 meV at 77K.

In a study of the photoemission from activated GaAs, Drouhin [Dr85] measured very high resolution EDC's using a cylindrical deflection energy analyzer. They measured an E_T of ~ 40 meV at 800 nm and reported a doubling of the effective energy at wavelengths lower than 633 nm. They suggest that the increase in width of the EDC's with increasing photon energy is due to two effects. First, electrons excited by higher energy photons have more energy to lose as they become thermalized into the conduction band minimum so that their complete thermalization would require a longer time. Second, because of the decreased absorption depth of the higher energy photons, the electrons are excited closer to the surface of the crystal and thus spend less time in the crystal before emission. The combination of the two effects means that electrons excited by higher energy photons are more likely to leave the crystal before completely thermalizing than lower energy photons. They also discuss the effects on the shape and width of the EDC's due to the amount of negative electron affinity and the doping level. For example, as the cathode quality degrades over time, the electron affinity rises nearer to the vacuum level and decreases the width of the EDC's, thus reducing the effective energy of the emitted electrons.

Bradley [Bra77] derived the effective transverse energy of electrons photoemitted from GaAs (using a white light source) from limiting resolution measurements. As their interest was in the resolution of imaging tubes, the method involved measuring the smallest resolvable spacing of a standard bar pattern projected onto the cathode. They determined the effective electron energy to be 108 meV over an electric field range of 1–4 MeV/m (our source operates at 1 MeV/m at the cathode) using voltages of several thousand volts. They also studied models of electron emission from rough surfaces to explain the high values of the E_T (compared to room temperature). If the surface is rough, small areas will have local surface normals different from the average normal of the crystal. If the local normal is much different than the average normal, the projection of the local normal onto the surface will contribute to a larger effective transverse electron energy than might be measured for a perfectly smooth crystal surface.

In conclusion, the effective transverse thermal energy of the electrons emitted from a GaAs photocathode was measured as a function of wavelength by a new method. The measurements were carried out at a beam energy of interest for accelerator applications, 100 keV; this energy is much larger than the voltage used in earlier experiments. The value of E_T inferred from

the measured rms emittance increased with decreasing photon wavelength from 34 meV at 840 nm to 103 meV at 514 nm. The measured results were generally lower than those of other researchers, where possible differences could be due to the beam energy, surface preparation techniques, surface quality, surface roughness, and heat treatment cycles. E_T also increased with increasing photon energy, as expected. The most interesting conclusion that can be drawn is that the effective transverse electron energy was measured at an energy of interest for accelerator applications, and was found (for wavelengths less than 633 nm) to be a factor of three lower than a thermionic gun operating at 1160K.

References

- [Bra77] D.J. Bradley, M.B. Allenson, and B.R. Holeman, J. Phys. D: Appl. Phys. **10**, 111 (1977).
- [Dr85] H.-J. Drouhin, C. Hermann, and G. Lampel, Phys. Rev. B **31**, 3859 (1985).
- [Du93] B.M. Dunham, Ph.D. Thesis, Department of Physics, University of Illinois, Urbana-Champaign, 1993.
- [En93] D.A. Engwall, B.M. Dunham, L.S. Cardman, D.P. Heddle, and C.K. Sinclair, Nucl. Instr. and Meth., **A324**, 409 (1993).
- [Fe84] C.S. Feigerle, D.T. Pierce, A. Seiler, and R.J. Celotta, Appl. Phys. Lett. **44**, 866 (1984).
- [La77] J.D. Lawson, *The Physics of Charged Particle Beams*, Oxford University Press, (1977).
- [Ro87] M.C. Ross, N. Phinney, G. Quickfall, H. Shoaee, and J.C. Sheppard, SLAC Report No. 4278 (1987).
- [Si92] C.K. Sinclair, Nucl. Instr. and Meth. **A318**, 410 (1992).

The NLC Positron Source*

H. Tang, A. V. Kulikov, J. E. Clendenin, S. D. Ecklund, R. A. Miller, and A. D. Yeremian
Stanford Linear Accelerator Center, Stanford University, Stanford, CA 94309 USA

A baseline design for the NLC positron source based on the existing SLC positron system is described. The proposed NLC source consists of a dedicated S-band electron accelerator, a conventional positron production and capture system utilizing a high-Z target and an adiabatic matching device, and an L-band positron linac. The invariant transverse acceptance of the capture system is 0.06 m-rad, ensuring an adequate positron beam intensity for the NLC.

I. INTRODUCTION

The Next Linear Collider (NLC) proposed by SLAC [1] uses a pulsed multi-bunch positron beam with an intensity requirement that is over an order of magnitude greater than the SLC design limit of 7×10^{10} positrons per beam pulse. This presents the primary challenge in designing the NLC positron source since a simple scale up of the SLC positron source would not be feasible due to the excessively high beam energy that the target would have to withstand. Thus, a significant improvement in the positron capture efficiency is essential in realizing the NLC source [2]. In this paper we present a baseline design that is reasonably conservative and uses only existing technologies. We use the SLC positron source [3] as the basis for our design, as its design principles have been well tested in many years of SLC operation, and make necessary changes to accommodate the significantly higher beam intensity requirement for the NLC. Table 1 lists the important parameters for the NLC positron source, along with the SLC positron source parameters for comparison.

As in the SLC, the conventional technique of producing positrons by bombardment of a conversion target with high energy electrons will be used. The proposed NLC positron source consists of three systems: an electron accelerator complete with a thermionic gun, an RF bunching system and a linac, a positron production target and a capture system, and a positron linac. In what follows the designs for these systems that meet the NLC-II specifications will be discussed.

II. ELECTRON ACCELERATOR

A thermionic gun and an RF bunching system incorporating two subharmonic bunchers and a S-band buncher similar to those on the SLC injector are used to generate an electron beam with the desired NLC time

structure. Then, the electron beam is accelerated in an S-band (2856 MHz) linac with damped-detuned structures [4] to an appropriate energy (3.11 GeV for NLC-I or 6.22 GeV for NLC-II) for positron production. Beam loading compensation in the accelerator will be accomplished using pairs of structures operated at 1 MHz above and below the main RF frequency, i.e., the so-called Δf approach.

Table 1. NLC and SLC Positron Source Parameters

Parameters	SLC 94	NLC-II
Electron Drive Beam		
Electron Energy (GeV)	30.00	6.22
No. of bunches per pulse	1	75
Bunch Intensity	3.5×10^{10}	1.5×10^{10}
Pulse Intensity	3.5×10^{10}	113×10^{10}
Beam Pulse Energy (J)	168	1120
Repetition Rate (Hz)	120	120
Beam Power (kW)	20.2	134
Beam σ on target (mm)	0.8	1.6
Pulse Energy Density ρ (GeV/mm ²)	5.22×10^{11}	8.70×10^{11}
Positron Collection		
Wall Emittance (m-rad)	0.01	0.06
Energy Cut (MeV)	20	20
Longitudinal Cut (psec)	15	60
Yield (No. of e^+ s per e^-)	2.4	2.1
Bunch Intensity	8.4×10^{10}	3.2×10^{10}
Pulse Intensity	8.4×10^{10}	236×10^{10}

III. POSITRON PRODUCTION AND CAPTURE

A. Positron Production Target

Since each electron beam pulse deposits a large amount of energy in the target, the target must be moving with respect to the beam position to avoid successive beam pulses hitting the same spot on the target which would damage the target. For the NLC positron source, we propose a rotating target design. While this design minimizes possible intensity modulation of the captured positron beam due to target motion, sealing of the target chamber needs special consideration.

For a moving target, target failure may still occur if the energy density of the drive beam is so high such that excessive thermal stress is created due to instantaneous, localized beam heating from the impact of a single beam

* Work supported by Department of Energy contract DE-AC03-76SF00515.

pulse. By virtue of its good thermal and mechanical properties and its high Z characteristic, $W_{75}Re_{25}$ is chosen to be the target material. Laboratory tests at SLAC [5] established an upper limit on the pulse energy density of the impinging electron beam at

$$\rho_{\max} = N_- E_- / (\pi \sigma^2) = 2 \times 10^{12} \text{ GeV/mm}^2,$$

where N_- is the number of electrons per pulse, E_- the energy of the incident electrons, and σ the rms radius of the electron beam at the target. Thus, we choose the electron beam size at the target to be 1.6 mm, sufficient to keep the energy density comfortably at $8.70 \times 10^{11} \text{ GeV/mm}^2$.

Considerations of the drive beam power and target cooling lead to a ring-shaped target design with an outer and inner diameter of 20 cm and 19 cm, respectively. A rotating frequency of 2 Hz should be adequate to allow for sufficient separation between successive pulse impacts on the target. Cooling tubes will be located in a silver casting in close contact with the inner target ring surface to maximize the rate of heat conduction from the target to the cooling tube walls. Cooling water flowing at a rate of 1.3 - 2.0 l/s will keep the steady-state temperature of the target at a safe level so as not to degrade the material properties.

One of the key engineering issues is to vacuum seal the rotating target shaft which must pass from atmosphere into the target vacuum chamber where the vacuum is on the order of 1×10^{-7} Torr. Our proposal is to use a combination of radiation resistant conductance-limiting seals and several stages of differential vacuum pumping along the length of the drive shaft. These seals rely on tight clearance ($< 10 \mu\text{m}$) between the shaft and seal surfaces and long path length ($\gg 1 \text{ cm}$) to limit vacuum conductance through them. A conceptual design of the NLC positron target system shown in Fig. 1 calls for three stages of differential pumping employing oil-free scroll and turbo pumps, while two ion pumps maintain the vacuum in the target chamber. The drive shaft is supported by two sets of bearings, one inside the target vacuum chamber and the other in atmosphere. Cooling water is coupled to tubings embedded in the shaft via a mating unit surrounding the shaft employing radiation-resistant seals.

B. Positron Capture

The positrons emerging from the converter target have small spatial and temporal but large angular and energy distributions. Therefore, the use of a large bandwidth phase-space matching device, such as a pulsed flux concentrator similar to the one used on the SLC positron source [3], is essential to allow for efficient positron capture into the accelerator section embedded in a long solenoid magnet. In this design, the maximum field requirement from the flux concentrator is 5.8 T along its axis. The minimum radius of its internal cone needs to be

increased to 4.5 mm from 3.5 mm for the SLC version to accommodate the slightly larger radial extent of the emerging positron beam as a result of the increased drive beam size. As for the SLC, the DC solenoid that surrounds the capture accelerator is required to produce a 0.5 T field.

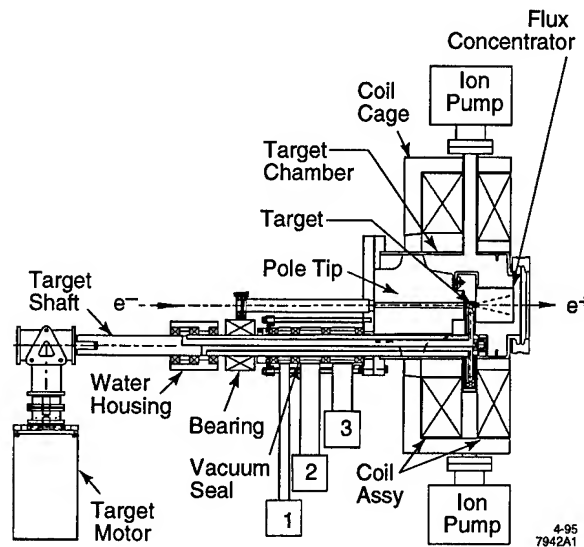


Figure 1: A conceptual design of the NLC target system with three stages of differential pumping.

In order to maximize the transverse as well as the longitudinal phase space acceptances, we propose to use an L-band (1428 MHz) capture accelerator as opposed to the S-band design for the SLC positron source. This L-band design allows the accelerator structures to have a 20 mm radius aperture. Embedded in the 0.5 T uniform longitudinal field, the capture accelerator has an invariant transverse acceptance of $0.06 \text{ m} \cdot \text{rad}$, with a headroom of 2 mm to allow for possible steering and alignment errors. The total length of the L-band capture accelerator surrounded by the DC solenoid is 12 m, and the loaded accelerating gradient is 20 MV/m.

C. Positron Yield Calculation

The positron yield from the target has been calculated using the EGS program [6] for 6.22 GeV electrons impacting a $W_{75}Re_{25}$ target of thicknesses ranging from 4 to 6 radiation lengths ($1 \text{ RL} \cong 3.43 \text{ mm}$). By considering both the yield and the amount of beam energy deposited in the target, the optimal target thickness is found to be about 4 RL. At this thickness, the target yield defined as the number of positrons produced per incident electron is 12.5, and about 14% of the electron beam energy is deposited in the target.

The particle rays obtained from the EGS simulation have been traced through the flux concentrator and the capture accelerator up to the nominal 250 MeV end point

using the ETRANS program [7] – a ray tracing program developed at SLAC that integrates particle trajectories through static magnetic and RF fields while ignoring the effect of space charge and wake fields. By varying the RF phase of the accelerating field, the best positron yield at the end of the capture accelerator is found to be 2.1 within an energy window of 20 MeV and a longitudinal window of 60 psec. Thus, with 1.5×10^{10} electron/bunch in the drive beam, the captured positron beam would have a bunch intensity of 3.2×10^{10} , which is nearly three times the required intensity of 1.1×10^{10} at the interaction point for NLC-II. We feel that such a safety margin should be adequate to offset any unaccounted for beam loss in the capture section due to space charge and wake field effects and additional beam losses in downstream accelerator components.

D. Maintenance and Reliability Considerations

Due to the high radiation activity in the areas around the target in particular and the low energy electron beam dump as well, access to these radiation-hot areas during a physics run must wait until the radiation activity drops to an acceptable level. As such cooling periods can be up to a month long, any maintenance work in these areas means a long down time for the accelerator. A logical approach to increase the efficiency of the positron source is to build two identical positron production and capture systems adequately shielded from each other such that access to one system is permitted while the other is running. A schematic layout of the NLC positron source with two side-by-side positron vaults is shown in Fig. 2. Calculations

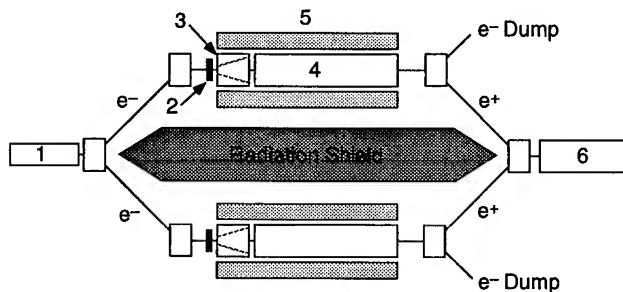


Figure 2: Schematic layout of the NLC positron source with two side-by-side positron production and capture systems: 1 – electron accelerator, 2 – positron target, 3 – flux concentrator, 4 – L-band capture accelerator, 5 – tapered-field solenoid and uniform-field solenoid, 6 – 1.8 GeV positron linac.

show that a 6-m thick concrete wall is sufficient to shield one vault from the other. The input electron beam can be directed to either system via bending magnets that are isochronous and linearly achromatic. Likewise, the 250

MeV positron beam after the capture accelerator from either system is directed into a common 1.8 GeV L-band linac. The first bending magnet following the capture accelerator also serves to separate the captured electrons, which are co-produced along with the positrons from the electromagnetic shower cascade in the target, from the positron beam. The two-vault design should greatly improve the serviceability of the positron source and, therefore, boosts its operation efficiency.

IV. POSITRON LINAC

The optics for the 1.8 GeV L-band positron linac is a strong focusing FODO lattice consisting of large aperture quadrupole magnets. The phase advance of the lattice is chosen to be $60^\circ/\text{cell}$, while the beta function is chosen to scale as $E^{0.5}$ along the linac. Coupled with a Gaussian detuning of 10% total fractional frequency spread in the accelerating structures, there should be negligible wake-field induced multi-bunch beam blow-up. As in the S-band electron drive linac, the Δf approach will be used for beam loading compensation.

V. ACKNOWLEDGMENTS

We thank P. Emma, G. Gross, W. Nelson, K. Thompson, J. Turner, T. Umemoto, and V. Vylet for their important contribution to the design of the NLC positron source.

VI. REFERENCES

- [1] T. Raubenheimer, et al., "Parameters of the SLAC Next Linear Collider", these proceedings.
- [2] For early works on the NLC positron source, see S. Ecklund, "NLC positron source - A first look", SLC Positron Source Group internal memorandum, 3/22/90; H. Braun, et al, "A possible design for the NLC e^+ source", Proc. of EPAC92, vol. 1, p. 530, 1992.
- [3] See, for example, J.E. Clendenin, "High-yield positron systems for linear colliders", Proc. of the 1989 Part. Acc. Conf., Chicago, IL, 1989, p. 1042.
- [4] K. Ko, et al, "Design parameters for the damped detuned accelerating structure", these proceedings.
- [5] S. Ecklund, "Positron target material tests", SLAC-CN-128, 1981.
- [6] W. Nelson, H. Hirayama, and D. Rogers, "The EGS4 Code System", SLAC-Report-265, 1985.
- [7] H.L. Lynch, "ETTRANS", SLAC memorandum, 1989.

FERROELECTRIC CATHODES AS ELECTRON BEAM SOURCES *

D. Flechtner, G. S. Kerslick, J. D. Ivers, J. A. Nation and L. Schächter, Laboratory of Plasma Studies & School of Electrical Engineering, Cornell University, Ithaca, NY 14853, USA

Abstract

In the past decade a number of research groups have studied electron emission from ferroelectric ceramics. These materials have saturation polarization P_s , of up to $100\mu\text{C}/\text{cm}^2$. The emission occurs when the polarization state of the ferroelectric is changed rapidly by an applied electric field, and a fraction of the surface screening charge is released. We report experimental results obtained using Lead-Zirconate-Titanate (PZT) ceramic as the electron source in a planar diode geometry. Experimental measurements of time-dependent variations in the emission are presented and results from a theoretical model are compared to these measurements. We also present new data on the scaling of the emission current density for anode voltages of up to 50kV . The new data will be used in the design of an electron gun using a ferroelectric cathode.

I. INTRODUCTION

In the recent years a substantial effort [1]-[6] has been dedicated to the generation of dense electron beams from ferroelectric ceramic cathodes. Current densities of at least $70\text{A}/\text{cm}^2$ can be achieved for average diode electric fields as low as $60\text{kV}/\text{m}$. In addition, measurements show good beam quality and stable operation at high repetition rate. Electron emission from ferroelectric ceramics is based on the release of screening charge from the surface of the ceramic when its internal polarization field is switched. In previously published work the ferroelectric was switched at the same time as the voltage was applied to the anode. However, one can anticipate that the potential well in the diode gap is not dependent only on the switching voltage but also on the dynamic characteristics of the ceramic. In the following sections we examine the effects of delaying the anode voltage pulse relative to that applied to the ferroelectric. We also report scaling of the gap current with the anode voltage at voltages ($\leq 50\text{kV}$), up to 100 times that used in our previous experiments ($\sim 400\text{V}$).

II. EXPERIMENTAL DATA

The experimental setup [5] is shown schematically in fig. 1. A 1mm thick, 2.5cm diameter ferroelectric disk is coated with a thin uniform silver layer on the back and a gridded silver layer on its front surface; in both cases the thickness is $\sim 1\mu\text{m}$. The silver strips are $200\mu\text{m}$ wide and are separated by a similar distance.

The gridded electrode is grounded and its effective emission area is approximately $A \approx 0.8\text{cm}^2$. For these experiments we used Lead-Zirconate-Titanate as the ferroelectric sample. This sample is mounted as a load on a 10Ω transmission line which generates a 150ns , $1 - 3\text{kV}$ pulse. A positive or negative pulse is applied to the back electrode of the ferroelectric and the grid

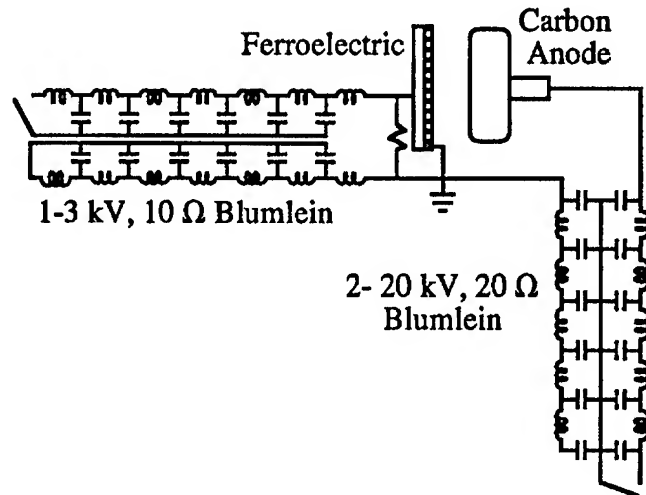


Figure 1. Ferroelectric experimental setup.

is grounded. A planar carbon anode is located at a distance of $g \approx 3 - 5\text{cm}$ from the grid. In the time variation experiments the anode is pulsed to $\sim 14\text{kV}$, by a charged transmission line with a characteristic impedance of $Z_{TL} = 20\Omega$. The applied pulse length is about 300ns . The delay between the switching of the ferroelectric and the application of the anode pulse is varied between $0 \leq \tau \leq 2.5\mu\text{s}$.

Figure 2 illustrates the anode voltage and current for two different delays: 165ns and $1.2\mu\text{s}$. The average currents range from somewhat less than 12A in the first case to 50A for the larger delay. The latter represents an increase by a factor of more than 4 over that obtained with 165ns delay. For longer delays the current decreases.

Figure 3 shows the anode current for various delays at an anode voltage of $\sim 14\text{kV}$. The behavior is similar if either positive or negative voltage is applied to the back of the ferroelectric. Results displaying a similar time dependence have been obtained at an anode voltage of $\sim 35\text{kV}$.

We have also extended our previous scaling results for the gap current as a function of the anode voltage. The Blumlein pulser mentioned above is used to feed the primary of a 4:1 step up transformer and the secondary output is applied to the diode. The source impedance is now $\sim 320\Omega$. Figure 4 shows the results of this investigation. The V-I characteristics are still approximately linear although there is now evidence of current saturation in at least the 3cm gap data. The resistances of the gap for the 3cm and 5cm spacings are about 300Ω and 1000Ω respectively. The data reported were obtained with $\sim 150\text{ns}$ delay between the ferroelectric pulse and the anode voltage. The current waveforms are quite flat and repeatable especially, as expected, when the gap resistance is comparable to the source impedance.

*Work supported by US DOE and the US/Israeli Bi-National Science Foundation.

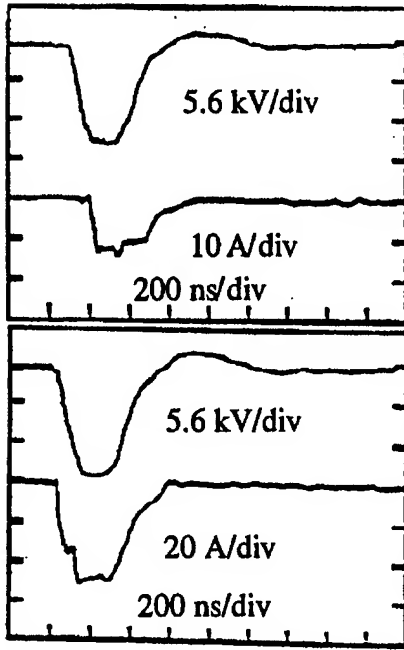


Figure 2. Anode voltage and gap currents for two delays [Upper: 165ns, Lower: 1.2μs].

III. DISCUSSION OF RESULTS

The current measured in various experiments exceeds [5] the space-charge (Child-Langmuir) limit for electrons with zero (or low) energy electrons emitted from the cathode. Measurements show that the emission energy of the electrons is less than 60eV in our experiments. Since the space charge limit is based on energy conservation in the system, the excess of current requires an external energy source other than that applied to the anode. This is provided by a fraction of the energy initially stored in the ferroelectric [6]. On pulsing the ferroelectric some electrons are forced into the diode gap. For zero voltage applied to the gap and assuming zero diode current we obtain a deep potential well in the diode and the electrons oscillate in the well. The well depth may be estimated and is found to be much larger than the maximum energy measured for the electrons emitted from the cathode. In other words, the electron kinetic energy on emission ($\leq 60\text{eV}$) cannot account for the excess current. Assuming that the applied anode voltage V_{AN} is small enough such that it has a negligible effect on the initial charge distribution, the gap becomes resistive and has a resistance of

$$R_{gap} \equiv \frac{V_{AN}}{I_{AN}} = \eta_0 \frac{1}{36} \frac{g^2}{A} \gamma_0^2 \sqrt{\frac{\gamma_0 + 1}{\gamma_0 - 1}}; \quad (1)$$

where $\gamma_0 = 1 + (eQ_{gap}g)/(36\epsilon_0 mc^2)$ is the average energy of the electrons in the potential well and $\eta_0 \approx 377\Omega$ is the vacuum characteristic impedance. The linear $I - V$ characteristic predicted for the diode is consistent with the experimental results reported previously [5]. For example, given a 4mm gap and 2.5cm cathode diameter with $1\mu\text{C}$ of charge released into the gap, the diode resistance is 10Ω . For the present data, where the applied voltages are about 100 times greater than those used in the earlier work, the above relationship continues to give agreement with the measured gap resistance to within thirty-five per-

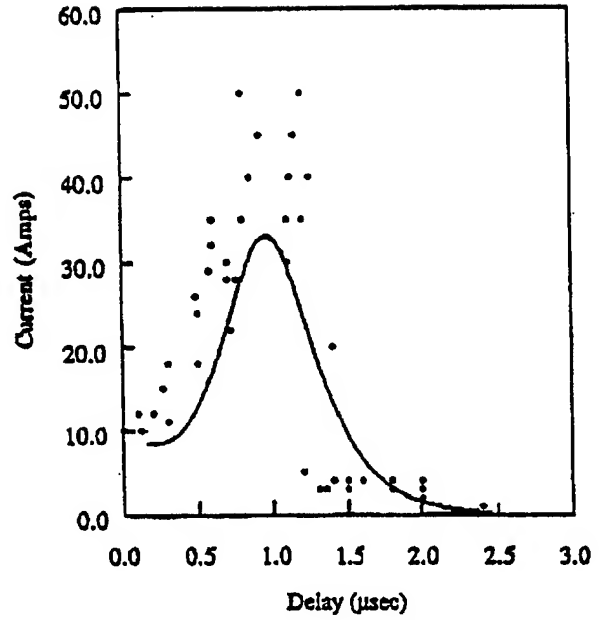


Figure 3. Gap current as a function of delay at 14kV, 5cm.

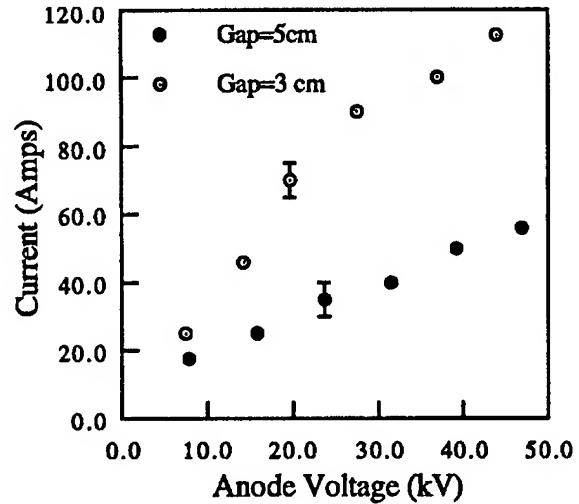


Figure 4. Current as function of anode voltage for 3 and 5cm gaps.

cent. It should be noted that the applied voltages are now sufficiently large that one would expect them to modify the charge distribution significantly. However it appears that the model's assumption of a charge distribution with zero applied voltage is still relevant.

The dynamics of the polarization field are described by a Weiss model (as in ferromagnetics) and hence the surface charge $Q(t)$ may be represented by

$$\frac{dQ}{dt} + 2\Omega Q \cosh\left(\frac{CV_{FE} + Q}{CV_1}\right) = 2\Omega Q_0 \sinh\left(\frac{CV_{FE} + Q}{CV_1}\right); \quad (2)$$

where V_{FE} is the voltage on the ferroelectric, $V_1 = k_B T d/p$, $C = \epsilon_0 \epsilon_r A/d$ and $Q_0 = P_1 A$. The dipole moment of an individual dipole in the material is denoted by p , k_B is Boltzmann

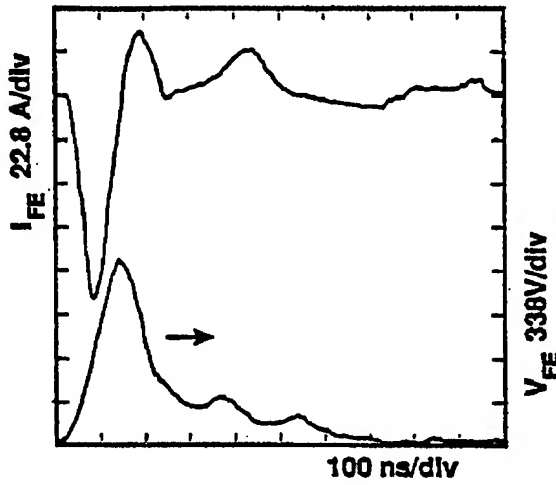


Figure 5. Current and voltage pulses applied to switch the ferroelectric

constant, ϵ_r and P_1 are characteristic of the material. The equilibrium surface charge, is denoted by $Q^{(eq)}$ and it is a solution of

$$Q^{(eq)} = Q_0 \tanh \left(\frac{Q^{(eq)}}{CV_1} \right) \quad (3)$$

The free charge due to the applied voltage is denoted by Q_{app} and is given by $C_0 V_{FE}$ where $C_0 = \epsilon_0 A/d$. The total change in the charge, δQ , of the capacitor is $\delta Q \equiv Q + Q_{app} - Q^{(eq)}$; a fraction of this charge is released into the gap. This fraction is assumed to be unity in the data displayed in fig. 3.

These equations were used to simulate the performance of the ferroelectric with the delayed anode pulse and the result is overlaid in fig. 3. The model is in good accordance with the experimental data. The timing of the peak and "cut-off" current were predicted theoretically and confirmed experimentally. The same simulations indicate that the delay difference between the peak current and cut-off depends primarily on the properties of the ceramic. No clear dependence on other time-parameters was observed.

The peak emission occurs exactly at the point where the voltage on the ferroelectric drops to zero. This can be understood in terms of total number of charges released into the gap since this process continues as long as the applied voltage is non-zero. Once the voltage drops to zero, electrons from the gap return to the ferroelectric. Consequently, less electrons are present in the diode gap and its resistance increases causing a decrease in the anode current. Figure 5 shows the ferroelectric switching voltage. Note that it drops to zero after $\sim 900ns$ which corresponds with the occurrence of the peaks in the theoretical and experimental data of fig. 3.

In conclusion, it was shown that the anode current increases when extending the delay time between the ferroelectric and the anode pulses. This increase continues for the entire duration of the ferroelectric voltage pulse. Once this voltage drops to zero, electrons from the gap return to the ferroelectric and the current decreases. In addition, it was shown that the emission is not dependent on the applied voltage and the same scaling laws which were developed for the low voltage ($V_{AN} < 600V$) hold for the

higher voltage regime ($\leq 50kV$) as indicated throughout this set of experiments.

References

- [1] H. Riege, *Nucl. Instrum. Methods in Phys. Res. A*, **340**, 80 (1994).
- [2] S. E. Sampayan, G. J. Caporaso, C. L. Holmes, E. J. Lauer, D. Prosnitz, D. O. Trimble & G. A. Westenskow, *Nucl. Instrum. Methods in Phys. Res. A*, **340**, 90 (1994).
- [3] G. A. Mesyatz, *Tech. Phys. Lett.*, **20**, 8 (1994).
- [4] T. C. Cavazos, W. L. Wilbanks, C. B. Fleddermann and D. A. Shiffler, *Appl. Phys. Lett.*, **65**, 2612 (1994).
- [5] J. D. Ivers, L. Schächter, J. A. Nation, G. S. Kerslick and R. Advani, *J. Appl. Phys.*, **73**, 2667 (1993).
- [6] L. Schächter, J. D. Ivers, J. A. Nation and G. S. Kerslick. *J. Appl. Phys.*, **73**, 8097 (1993).

Studies of Linear and Nonlinear Photoelectric Emission for Advanced Accelerator Applications

R. Brogle, P. Muggli, P. Davis, G. Hairapetian, and C. Joshi

Department of Electrical Engineering, University of California, Los Angeles, CA 90024

Abstract

Various electron emission properties of accelerator photocathodes were studied using short pulse lasers. The quantum efficiencies (QE's) of copper and magnesium were compared before and after above-damage threshold laser cleaning. Changes in the emission properties of copper photocathodes used in the UCLA RF photoinjector gun were observed by mapping the QE's of the cathode surfaces. The electron yield of thin copper films resulting from back-side illumination was measured. Multiphoton (nonlinear) emission was studied as a means of creating ultrashort electron bunches, and an RF gun Parmela simulation investigated the broadening of such pulses as they propagate down the beam line.

I. COPPER AND MAGNESIUM QUANTUM EFFICIENCY MEASUREMENTS

In a radio-frequency (RF) photoinjector gun, short pulse electron beams are created using a laser pulse incident on a photocathode placed in a high RF field accelerating structure. The laser is synchronized with the RF cycle to achieve maximum acceleration and minimum energy spread of the electron bunch. For high peak currents, a photocathode material should be chosen which has a high quantum efficiency at the laser wavelength. It must also be robust to withstand the high RF fields and high incident laser intensity, and should have a smooth, nonreactive surface for uniform emission over long periods of operation.

Copper and magnesium are two materials commonly used in these devices.^{1,2} The work function of copper is 4.6 eV and thus ultra-violet (UV) laser pulses are required to achieve linear photoemission. In the UCLA RF gun¹ these pulses are created by frequency quadrupling an amplified Nd:YAG laser pulse to obtain 266 nm (4.7 eV photon energy) radiation. Magnesium has a 3.7 eV work function and therefore may exhibit a higher electron yield than copper. However, Mg is more reactive than Cu and subject to greater surface contamination which can hinder photoemission.

A DC field test gun was devised to measure the QE's of copper and magnesium photocathodes. Laser pulses of 266 nm wavelength, 50 ps pulsewidth, and 3 mm spot size were sent through a hollow anode onto the cathode sample at normal incidence. The anode was biased at +5 kV and located 3 mm from the cathode, resulting in an electric field of 1.6 MeV/m. In the actual RF gun the electric field is 100 MeV/m, which enhances the electron emission via the Schottky lowering of the

potential barrier. No such enhancement was observed in the DC gun. Thus the QE of a photocathode in the RF gun is typically an order of magnitude greater than that of the same cathode measured in the DC gun. The anode-cathode system of the DC gun was enclosed in a vacuum system at a pressure of 10^{-6} torr. The energy of each laser pulse was measured on line by a photodiode placed behind a UV mirror in the laser line. The emitted charge was measured by a charge preamplifier placed across a 1 M Ω load resistor.

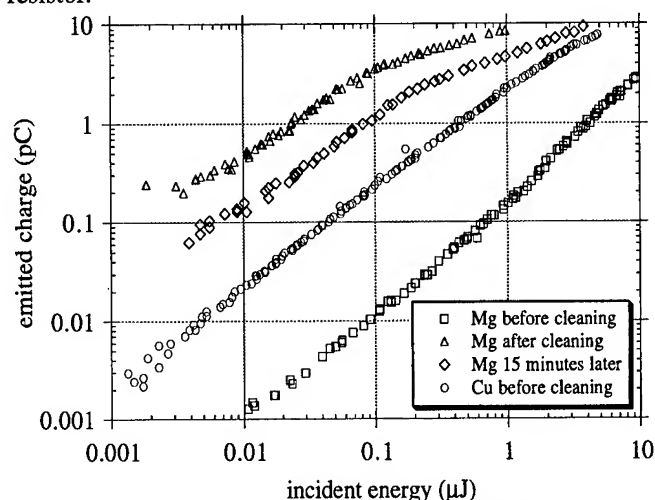


Fig. 1. Electron yields of Cu and Mg.

The cathodes were 1" diameter OFHC copper and 95% Mg-Zn-Al alloy samples hand polished to 1 μ m. The QE of each sample was determined by varying the incident laser energy and measuring the corresponding emitted charge. For the single-photon (linear) photoelectric effect, the emitted charge should be directly proportional to the incident laser energy. The constant of proportionality of this relationship is the electron yield.

The results of the Cu and Mg measurements are shown in Fig. 1. The curves show the linear relationship between charge and laser energy at moderate charge levels -- at high charge levels the curves bend due to space charge saturation. Initially, the electron yield of copper was 2.2 pC/ μ J (QE = 1.0×10^{-5} electrons per photon) while the magnesium yield was only 0.15 pC/ μ J. We then performed above-damage threshold laser cleaning on the magnesium sample, and observed the electron yield increase to 33 pC/ μ J (a factor of 220 -- 15 times greater than Cu). However, within minutes the yield decayed to 10 pC/ μ J where it remained steady. Even in a vacuum of 10^{-6} the magnesium surface can quickly become contaminated and lose quantum efficiency. Similar cleaning on copper

showed a modest (factor of two) increase in QE but no such emission degradation over time. Although this technique enhances electron yield, the resulting damaged area may produce non-uniform emission which could impair the emittance of the accelerator beam.

II. CHANGES IN RF GUN PHOTOCATHODE EMISSION CHARACTERISTICS

In an RF photoinjector gun, the cathode is exposed to many adverse physical conditions: extreme RF fields, high voltage arcing during conditioning, impurities in the vacuum, and repetitive incident UV laser shots. These factors may induce physical changes on the surface of the photocathode which modify its photoemission characteristics. Such changes were observed for copper cathodes in the UCLA RF gun.³

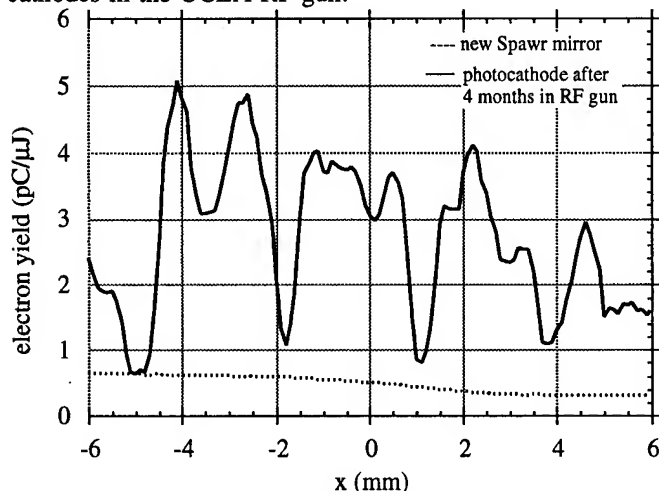


Fig. 2. Spawr polished RF photocathode.

In an attempt to understand the nature of these emission changes, the DC gun was used to create quantum efficiency maps of the cathode surfaces. This was done by focusing the input 266 nm laser pulse to a spotsize of approximately 100 μm , and then moving the cathode with the x,y feedthrough to illuminate different points on the surface.

The first cathode tested was originally polished by Spawr Industries to $\lambda/20$ for 10 μm light. It had been used in the RF gun for 4 months of operation, then removed after its quantum efficiency and emittance characteristics degraded. A QE surface map of this cathode after removal is shown in Fig. 2. Variations greater than a factor of five in the QE are observed across the surface. Such variations are not present on a newly polished Spawr copper mirror, shown for comparison.

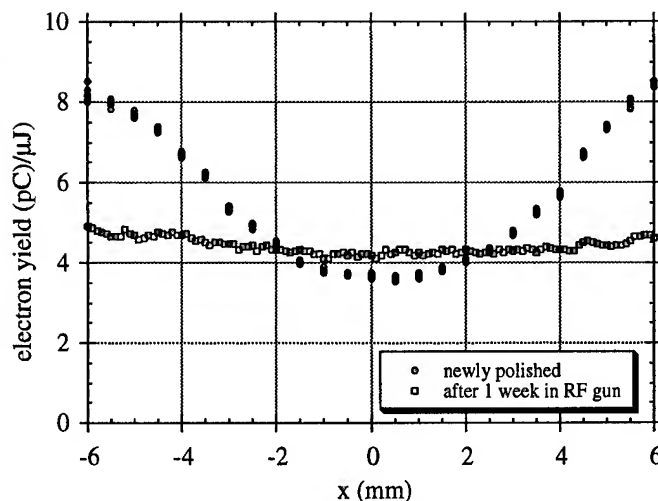


Fig. 3. Hand polished photocathode.

The second cathode was polished by hand to a 1 μm finish. It was installed in the RF gun for one week before its quantum efficiency and emittance characteristics began to deteriorate. Fig. 3 shows the QE maps of this cathode before and after the RF gun installation. Note that originally the electron yield was two times larger toward the edges of the cathode than at the center. This feature was not present for the new Spawr-polished mirror (Fig. 2), and thus seems to be a characteristic of the polishing method. After one week in the RF gun the QE map had changed, becoming fairly constant across the surface. No large scale variations were observed as on the previous cathode.

III. BACK ILLUMINATION OF THIN Cu FILMS

Synchronization of an electron bunch with a laser pulse is important in experiments such as the plasma beat wave accelerator. Using laser-induced photoemission to generate such electron bunches is an effective means of achieving this synchronization. However, if a photoinjector gun is part of an X-band or higher frequency linac, it may be difficult or impossible to illuminate the front surface of a photocathode with a laser pulse. If such a device is driven by a DC gun, it may be possible to circumvent this problem by employing a thin film photocathode that is illuminated from the back side of the film to produce electron emission from the front side. Although this technique will result in some loss of quantum efficiency, it may be useful in systems which do not require a high total charge.

To investigate this possibility, we measured the UV (266 nm) light transmission and electron emission properties of five different thicknesses of copper films. The measurements were done in the back illumination configuration of the DC gun. The films were deposited on 1" diameter fused silica windows and ranged from 270 \AA to 1490 \AA in thickness. The laser pulses propagated through the transparent substrate onto the back side of the copper film. The resulting photoelectrons were then collected on

the opposite (front) side by the hollow anode. A calibrated photodiode was placed after the hollow anode to measure the energy of the light transmitted through the film.

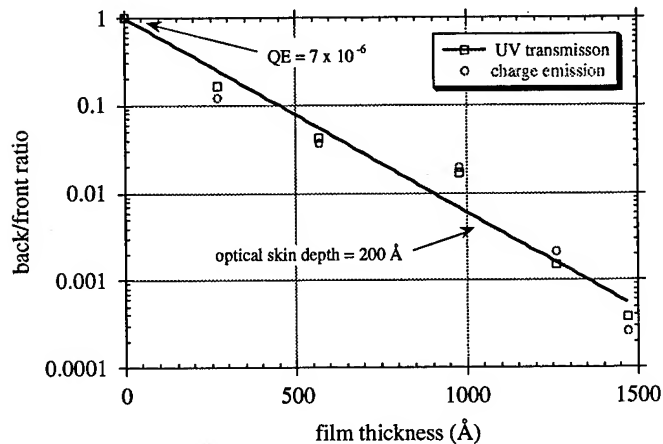


Fig. 4. Back Illumination of copper thin films.

The results are shown in Fig. 4. The exponential fit to the laser transmission data indicates an optical skin depth of 200 Å for 266 nm radiation. Note that the ratio of electrons emitted via back illumination versus front illumination is equal to the fraction of UV light transmitted through that film thickness. This shows that the number of electrons emitted from the front surface during back illumination is proportional to number of photons transmitted through the film to that surface. Thus the mean free path of the photoelectrons in the metal must be short compared to the optical skin depth — only the electrons which absorb a photon very close to the front surface can be emitted.

Using back illumination on the 270 Å sample reduces the electron yield by a factor of eight due to the laser transmission losses through the film. A 266 nm laser system would then require 50 μJ of incident energy to produce 10 pC of charge. For a laser pulsewidth of 1 ps, the peak current would be 10 A. Thus reasonable currents can still be obtained with modest incident laser energies and pulsewidths, and even higher efficiencies could be achieved by using thinner photocathode films.

IV. MULTIPHOTON PHOTOEMISSION

For high laser intensities, photoemission of electrons can occur even for incident photon energies less than the metal work function. This can occur by an electron consecutively absorbing more than one photon in order to gain enough energy to overcome the surface potential barrier. The instantaneous electron current density emitted in such a process is given by the relation $J = a_n I^n$, where I is the laser intensity, n is the minimum number of photons required to overcome the metal work function, and a_n is a constant depending on the material and the photon energy. For a given laser pulsewidth and spotsize, this can be rewritten in terms of the emitted charge Q and the incident energy E as $Q = b_n E^n$.

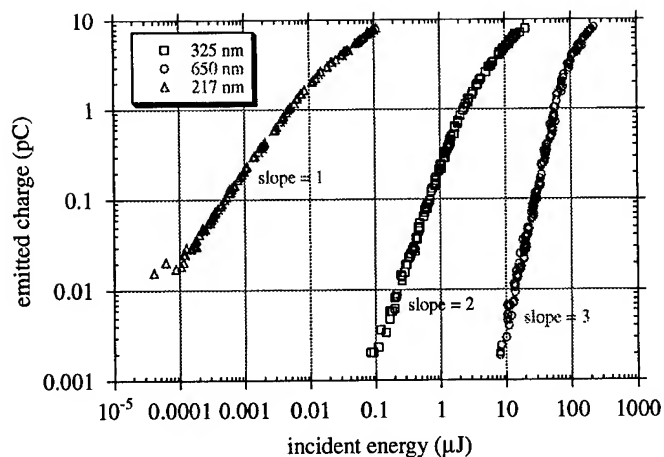


Fig. 5. Multiphoton emission from copper.

Multiphoton emission was investigated using the DC gun front illumination setup. An ultrafast dye laser and dye amplifier system were used to create incident laser pulses of 650 nm wavelength, 500 fs pulsewidth, and 3 mm spotsize. Second and third harmonic generation crystals could be placed in the laser line to generate 325 nm and 217 nm pulses. The photon energies for the 650, 325, and 217 nm wavelengths are 1.9 eV, 3.8 eV, and 5.7 eV respectively. These wavelengths produce 3-2-, and 1-photon photoemission processes in copper. The experimental charge vs. energy traces for these processes are shown in Fig. 5. The slopes of the lines on the log vs. log scale reflect the linear, square, and cubic dependence of the emitted charge on the laser energy for the three wavelengths. Multicolor, multiphoton emission has also been observed.⁴

V. ELECTRON TRANSPORT IN THE RF GUN

Multiphoton emission could be utilized in an RF gun to produce electron bunches that are narrower than the incident laser pulse. The I^n dependence of the photoemission current density implies that a gaussian laser pulse will produce a gaussian electron bunch that is narrower in time by a factor of \sqrt{n} . If a 500 fs FWHM laser pulse at 1.0 μm wavelength ($E = 1.2$ eV per photon) is used to induce photoemission on a copper cathode, the resulting 4-photon emission process will produce an electron bunch that is initially 250 fs in length. A Parmela simulation which modelled the UCLA RF gun was run to investigate the temporal broadening of 250 fs, 30 pC electron bunches of different spot sizes during transport through the gun (Fig. 6). The large spot size bunches were broadened by the fringe fields of the RF and solenoid, while the small spot size bunches were subject to a lesser broadening due to space charge (a factor of 2 for a 1 mm radius spot size). This space charge broadening could be reduced by using a laser pulse train to produce many charge bunches, each containing a fraction of the total charge necessary for the experiment. This method is currently being investigated.

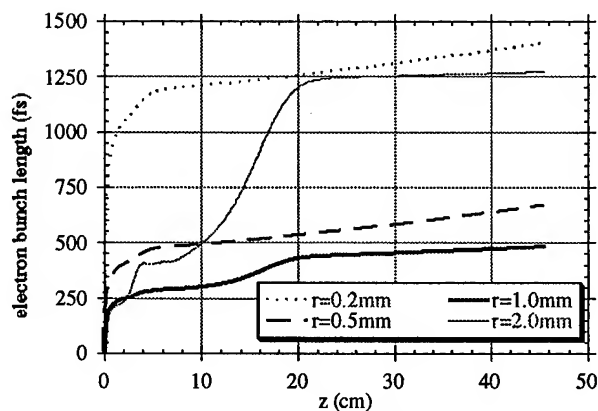


Fig.6. Electron bunch lengthening in the RF gun and transport line. The RF cells end at 8 cm and the focusing solenoid ends at 45 cm.

This work is supported by DOE grant numbers DE-FG03-92ER40727 and DE-FG03-91ER12114. P.M. is supported by 'Fonds national suisse de la recherche scientifique' grant number 8220-040122.

- ¹ S. C. Hartman *et al.*, Nucl Inst Meth A **340** (1994).
- ² T. Srinivasan-Rao *et al.*, J. Appl. Phys **77** 1275 (1995).
- ³ P. Davis *et al.*, paper RPA22, this conference.
- ⁴ P. Muggli *et al.*, J. Opt. Soc. Am. B12(4) April, 1995.

A Derivative Standard for Polarimeter Calibration*

G. Mulhollan, J. Clendenin, P. Sáez, D. Schultz and H. Tang
Stanford Linear Accelerator Center
Stanford, CA 94309

A. W. Pang and H. Hopster
University of California
Irvine, CA 92717

K. Trantham, M. Johnston and T. Gay
University of Nebraska
Lincoln, NE 68588

B. Johnson, M. Magugumela, F. B. Dunning and G. K. Walters
Rice University
P. O. Box 1892
Houston, TX 77251

G. F. Hanne
University of Münster
Münster, D-4400 Münster, Federal Republic of Germany

ABSTRACT

A long-standing problem in polarized electron physics is the lack of a traceable standard for calibrating electron spin polarimeters. While several polarimeters are absolutely calibrated to better than 2%, the typical instrument has an inherent accuracy no better than 10%. This variability among polarimeters makes it difficult to compare advances in polarized electron sources between laboratories. We have undertaken an effort to establish 100 nm thick molecular beam epitaxy grown GaAs(110) as a material which may be used as a derivative standard for calibrating systems possessing a solid state polarized electron source. The near-bandgap spin polarization of photoelectrons emitted from this material has been characterized for a variety of conditions and several laboratories which possess well calibrated polarimeters have measured the photoelectron polarization of cathodes cut from a common wafer. Despite instrumentation differences, the spread in the measurements is sufficiently small that this material may be used as a derivative calibration standard.

I. INTRODUCTION

At present there is no electron spin polarization standard of the same sort as exists for many quantities, e.g., calibrated He leaks. While it can be stated that any one electron has a spin polarization of 100% along some unknown axis, this is not a very useful definition and is in fact incorrect as polarization is only definable for an ensemble. In itself, this lack of a standard would not present a problem provided it were possible and practical to independently calibrate individual polarimeters

to a high degree of accuracy. While several polarimeters exist which are absolutely calibrated to 2%, this is not usually the case. Such inconstancy among polarimeters can make polarization measurements impossible to compare between different laboratories. In laboratories which perform complex transport of polarized electron beams in accelerating structures, undiscovered systematic errors in diagnostic polarimeters along the electron trajectory, particularly if of varying types, can contribute to erroneous conclusions on the quality of spin transport. Furthermore, as progress in high current solid state polarized electron sources pushes the polarization boundary toward the 100% upper limit, it is needful to establish the exact polarization, as this determines, among other things, the viability of pursuing polarization increasing schemes.

II. CHOICE OF MATERIAL

The choice for a standard usable in electron polarimeter calibration is obvious upon a careful examination of the requirements. For such a standard to be useful, it must either operate in existing polarized electron sources or be readily adaptable to them. It must be fairly independent of operating conditions and not drift (much) with time. It should be readily available in its final form, or should be easily made with minor perturbations in manufacturing resulting in no quantitative difference in performance. And ideally, it would be free or very cheap[1].

The ideal standard would be one whose properties could be predicted from first principles, e.g., a naturally occurring source of polarized electrons. One example of this type of source is ^{60}Co . However, such β -decay sources are weak and a usable signal level can only be attained by an increase in source

density past a point where depolarization mechanisms begin to alter the emitted electron spin polarization from the anticipated value[2]. This leaves only the possibility of creating a derivative standard, i.e., one whose properties may not currently be completely accurately predicted from first principles but which meets the rest of the criteria for a standard.

As the preponderance of polarized electron sources utilize photoemission from semiconductors such as GaAs and GaAsP, a derivative standard based on one of these materials is a logical choice. In order to maximize polarization without compromising performance, a layered structure with an active layer of 100 nm was adopted[3]. A diagram of the source material appears in Figure 1. The $\text{Al}_{0.3}\text{Ga}_{0.7}\text{As}$ layer, which has a lattice constant sufficiently close to that of bulk GaAs for unstrained growth, acts to impose an energy barrier to emission

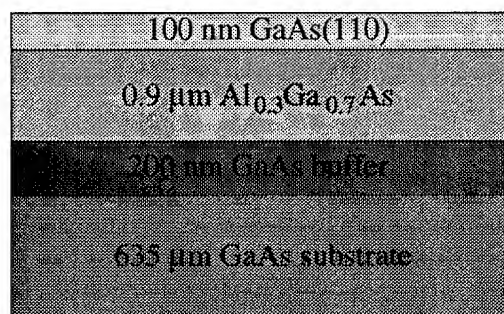


Figure 1: Schematic of standard cathode material

from the underlying GaAs, hence photoemission using light with energy less than 1.85 eV results in photoelectrons from only the top 100 nm of material. The Be dopant concentration was set at $5 \times 10^{18}/\text{cm}^3$ so as to enable creation of a high quality negative electron affinity surface while minimizing depolarizing effects [4].

III. MATERIAL QUALIFICATION

Prior to distribution, material from the 3" diameter wafers [5] was extensively tested in the Cathode Test Laboratory (CTL) at SLAC[6]. Characterization included uniformity of response across the wafer and performance of the material under a variety of conditions. Typical polarization and quantum efficiency (QE) performance data appear in Figure 2. Polarization data are to be viewed for relative values only. QE data from bulk GaAs is shown for comparison. In the region of interest, around 850 nm, the difference in QE between the two is only a factor of two. This is especially important for those measurements taking place in polarimeters with low efficiencies.

The wafer map of the samples tested in the various laboratories appears in Figure 3. Six of the samples labeled "PEGGY" were measured in the CTL at SLAC. The regularity of response in the polarization at a given wavelength and QE, which is a reflection of both cathode uniformity and systematic drifts in the CTL was within 2% relative.

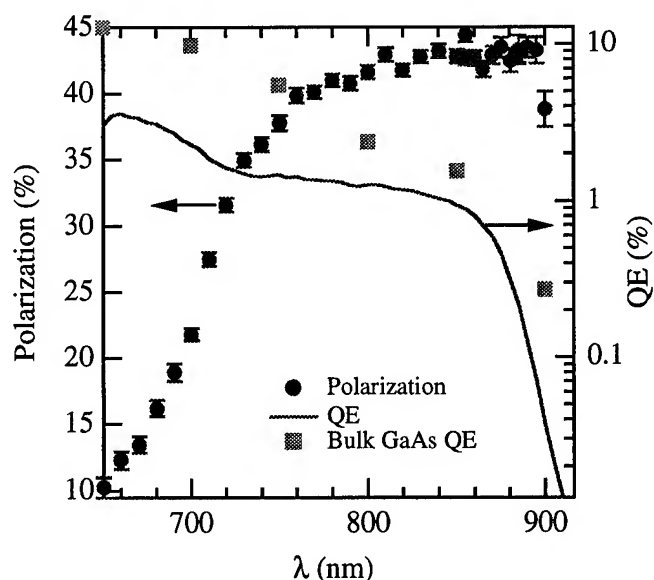


Figure 2: Polarization and QE of standard material. Bulk GaAs QE is shown for comparison. Note that in the region of highest polarization the QE of the bulk GaAs is only a factor of two greater than that of the standard material.

As conditions within source chambers differ from laboratory to laboratory, it was necessary to quantify the change in polarization as a function of QE. One such set of data appears in Figure 4. As can be readily seen, the increase in polarization upon QE decay is rather small. From these observations, we chose a measurement wavelength (841 nm) that would yield a high QE, a maximum in the polarization and little change in polarization as the QE decays.

It was also necessary to determine the effects of different techniques for introducing the cathodes into vacuum, e.g., loadlock versus baking the cathode within the source chamber. Sample treatment differences were tested by baking one of the "PEGGY" samples in the loadlock of the CTL test system. No differences not accounted for by a slightly different QE from the unbaked samples introduced through the loadlock were seen in the polarization.

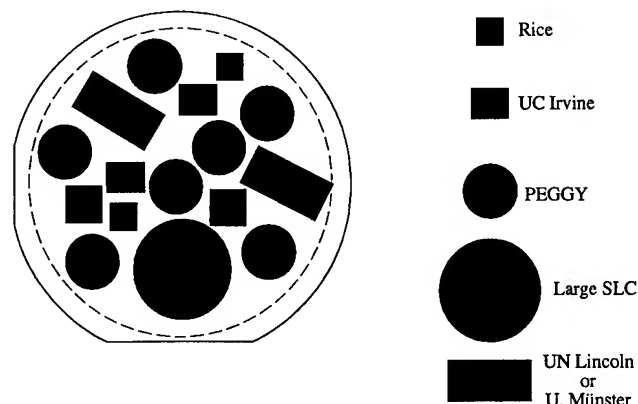


Figure 3: The location of the samples tested in the CTL and samples for measurement in highly accurate polarimeters.

The various processes responsible for QE decay were tested in their effects on the polarization. One sample (shown in Figure 4) was permitted to decay naturally for nearly one month. Another had its QE dropped by the admission of NF_3 . A third had its QE decay rate accelerated by allowing the emitted electrons to impact the chamber walls, bringing about electron stimulated desorption of common background gasses. In all of these tests, no difference was seen in the polarization dependence on the QE at 841 nm between samples with QE decays accelerated by the different techniques.

While some change in the polarization at 841 nm is evident as the QE decays, it is sufficiently small that it does not appear clearly above the statistical scatter in the data. The cumulative data allow us to assign a preliminary polarization value of $43.4 \pm 0.86\%$ for QE ranging from 1.2 – 0.009% . In other words, the polarization is constant to within a relative value of 2%, the degree of stability we required from our standard.

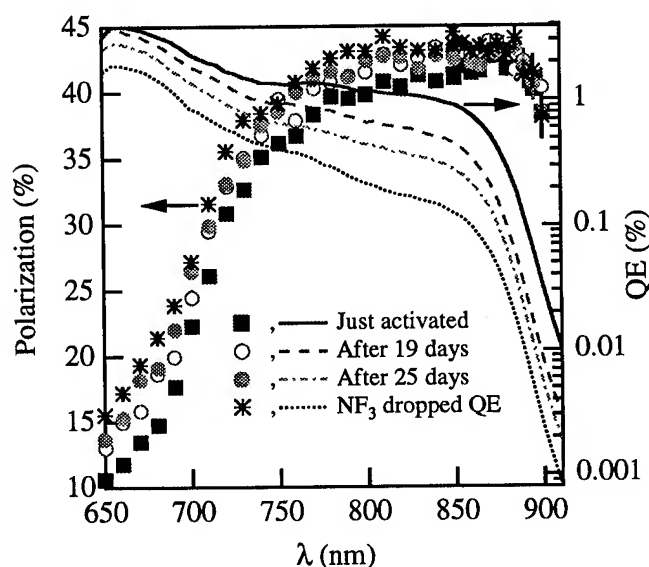


Figure 4: Polarization and QE of standard material as QE decays. The last data set was acquired by dosing the sample with NF_3 . The source lifetime (e-fold time) was 26 days.

IV. POLARIMETER BESTIARY

The polarimeters used in this work fall into two categories, Mott[2] and optical[7]. The Mott polarimeter operates by measurement of a back-scattering asymmetry in the electrons impacting a high atomic mass film. Mott polarimeters may be self calibrated, but great accuracy can be achieved only with much difficulty[8]. Two of the participating institutions utilize Mott polarimeters calibrated through novel techniques. At UC, Irvine, a pseudo-double scattering technique is used to achieve an accuracy within $\pm 2\%$ in a 120 keV Mott polarimeter[9]. Rice University, on the other hand, pioneered the use of surface Penning ionization coupled with an accurate He metastable polarization measurement to calibrate a 20 keV retarding field Mott polarimeter to an accuracy within 3%[10]. Optical

polarimeters, which operate on the principle of measurement of the polarization of de-excitation light from noble gas atoms after electron collision at near-threshold energies, are essentially self calibrating.

V. PRELIMINARY RESULTS AND OUTLOOK

At the time of this writing, measurements have been undertaken at three of the four institutions participating in measurements utilizing highly accurate polarimeters. The measurements at UC, Irvine, which are completed, yielded $P = 42.69 \pm 0.92\%$ at a QE of 0.38% and $P = 44.66 \pm 0.94\%$ at a QE of 0.08%. Measurements at Rice using an 807 nm laser yielded $P = 40.0 \pm 2.5\%$ at a QE $\approx 0.1\%$. The photocathodes at Rice and UC, Irvine were activated with O_2 instead of NF_3 , indicating that the photoelectron polarization is not sensitive to the activation process. Data from UN, Lincoln are still too preliminary to be cited and measurements at the University of Münster have not yet taken place. These initial results show good promise that we may quote a final number for the polarization with an error $\leq 5\%$ relative.

VI. REFERENCES

*Work supported by Department of Energy contract DE-AC03-76SF00515 and the Physics Division of the NSF.

- [1] Samples of the calibration material discussed below may be obtained by contacting the author.
- [2] For a discussion of alternate sources, see T. J. Gay and F. B. Dunning, *Rev. Sci. Instrum.* **63**, 1635 (1992).
- [3] T. Maruyama, et al., *Appl. Phys. Lett.* **55**, 1686 (1989).
- [4] Y. Kurihara, et al., *NIM A313*, 393 (1992).
- [5] Quantum Epitaxial Designs, Bethlehem, PA.
- [6] G. A. Mulhollan, *Proceedings of the Workshop on Photocathodes for Polarized Electron Sources for Accelerators*, Stanford, CA, **SLAC Report 432 Rev**, 211 (1993).
- [7] M. Uhrig, et al., *Rev. Sci. Instrum.* **60**, 872 (1989) and T. Gay, *J. Phys. B* **16**, L553 (1983).
- [8] T. Gay et al., *Rev. Sci. Instrum.* **63**, 114 (1992) and A. Gellrich et al., *Rev. Sci. Instrum.* **61**, 3399 (1990).
- [9] H. Hopster and D. L. Abraham, *Rev. Sci. Instrum.* **59**, 49 (1988).
- [10] D. Oro, et al., *Rev. Sci. Instrum.* **63**, 3519 (1992).

ANALYSIS OF POSITRON FOCUSING SECTION FOR SPring-8 LINAC

A. Mizuno, S. Suzuki, H. Yoshikawa, T. Hori, K. Yanagida, H. Sakaki, T. Taniuchi, H. Kotaki and H. Yokomizo, JAERI-RIKEN SPring-8 Project Team, Kamigori, Ako-gun, Hyogo 678-12, Japan

Abstract

In the SPring-8, positron beams will be used and generated in the linac. In this paper, simulations and experiments of a test apparatus for the convertor are described. Results of simulations are qualitatively coincident with that of experiments, and from simulation results, an electron/positron conversion efficiency of 0.5% is obtained at the end of the convertor, with a feasible design of the convertor system. A future plan of superconducting magnet system for the convertor is also mentioned.

I. INTRODUCTION

We are planning to use positrons to avoid ion-trapping and make a beam-lifetime longer in the SPring-8 Storage Ring. The positrons will be generated in the SPring-8 Linac at 250MeV section, and accelerated up to 900MeV at the end of the Linac. For reducing an injection time to the Storage Ring, we have to achieve high conversion efficiency as possible.

In order to design an electron/positron convertor (target and focusing system) for the Linac, we constructed a test apparatus mounted with the JAERI Linac at Tokai Establishment, JAERI, and obtained energy spectrums of the generated positrons with various parameters of focusing system. Also, we developed a simulation code of tracking particles in the positron focusing section. Results of simulation and experiments are mentioned, and our design of the converter are discussed.

II. TEST APPARATUS AND SIMULATION CODES

The test apparatus at Tokai Establishment is shown in Figure1, which consists of a removable tungsten target (insert or pull out), a focusing section (a pulse solenoidal coil, a DC1 solenoidal coil, a DC2 solenoidal coil, an accelerator structure, and a quadrupole magnet), and a measurement section (an energy analyzing magnet and a Faraday-cup). Electrons bombard to the target with an energy of about 90MeV. Generated positrons are focused and accelerated up to ~35MeV in the focusing section.

The simulation consists of two codes. One is EGS4 and another is our original tracking code. EGS4[1] is a Montecarlo code. It calculates positron production at the surface of the tungsten target. Given parameters are injected electron position, injection angle to the target (we assume that all electrons bombard to the target perpendicularly), and electron energy on the entrance of the target. Output parameters of this code are position, extracted angle from the target, and energy of positrons which are provided to the tracking code as initial conditions.

The tracking code is used fourth-ordered Lunge-Kutta method and tracking positrons from the target to the end of the

focusing section. we assume that there are uniform electric field in the accelerator structure section, and calculated magnetic fields are given in the coil sections.

In the test apparatus, variable parameters are magnetic field of focusing section and rf power to the accelerator structure which are important information as design parameters. And these can be also variable in the tracking codes. So we can compare the experiment results with the simulation's one.

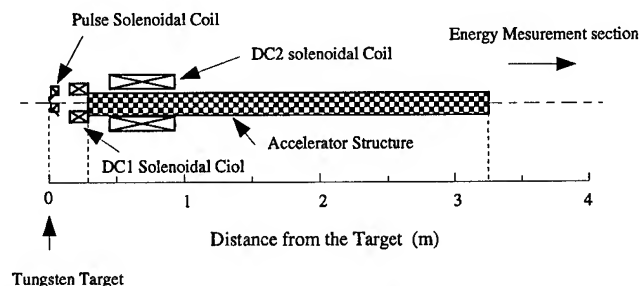


Figure. 1. Outline of the test apparatus

III. RESULTS OF EXPERIMENT AND SIMULATION

Figure2 shows representative data of simulation and experiment. These are energy distributions of positrons at the final point of the focusing section. In Figure2, variable parameter is current of the pulse solenoidal coil. Parameters of the DC1 and the DC2 coils and rf power for the accelerator structure are constant. Magnetic field distribution is shown in Figure3, which corresponds to the case of bottom graph in Figure2. TABLE.1 shows experiment and simulation parameters of Figure2.

From the Figure2, figure of distribution in simulation data is qualitatively coincident with that in experiment data. Furthermore, when the other parameters are varied, DC1 or DC2 coils, they are also in agreement qualitatively. Other data can be referred in ref.[2].

In the Figure2, a lower side peak in the energy distribution shifts to right hand side as pulse solenoidal current increases. From this, pulse solenoidal coil has selectivity of positron energy. Other coils don't have such contribution[2]. This is important issue for designing the focusing section.

A conversion efficiency of produced positrons at the end of the focusing section against injected electrons is obtained of 0.077% in Figure2 simulation data, where produced positrons energy is 0~50MeV on the surface of the target. Within the limited energy, the peak \pm 1MeV, the efficiency is 0.018%.

In the experiment data, energy resolution at the peak is about \pm 1MeV, and an efficiency of positron current at the peak

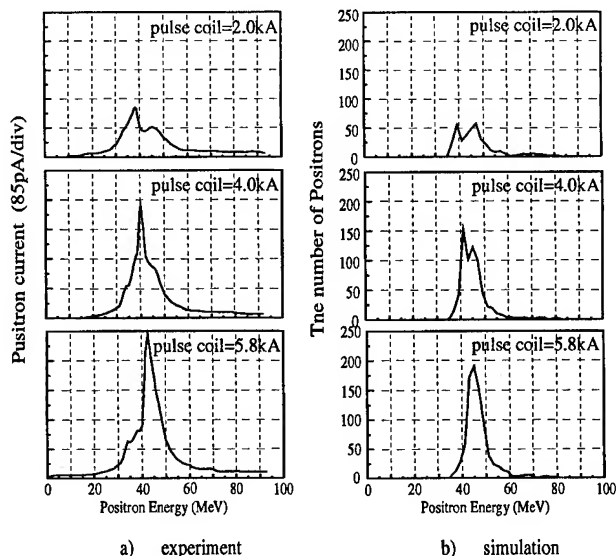


Figure. 2. Energy distribution of Produced positron

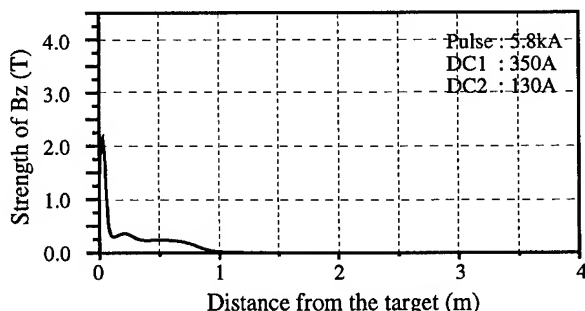


Figure. 3. Magnetic field distribution of the test apparatus

TABLE.1 parameters of experiment and simulatoin

	EXPRIMENT	SIMULATION
Target	Tungsten	Tungsten
Target radius	10.0mm	10.0mm
Target thickness	6.0mm	6.0mm
Injected electron	(current)	(number of histries)
	150nA(average)	1,026,000
Injected electron energy	90MeV	90MeV
Repetition rate	5pps	--
Pulse width of electron current	1&Lsec	--
Energy gain of positrons	33.1MeV	33.1MeV
Radius of injected beam	--	1mm

against injected electron current is 0.01%, which is comparable with simulation data of 0.018%. So experiment efficiency is 55% of simulation data. Reason of this is not cleared to us enough, but all other data show around this rate.[3]

IV. THE CONVERTOR OF THE FOCUSING SECTION FOR THE SPring-8 LINAC

The positron focusing section is now under construction. It's outline is shown in Figure4. Capable magnetic field will be update in Figure5. Produced positrons can be accelerated up to about 50MeV. In this field distribution, positrons with energy of 20MeV at the surface of the target rotate half times in the section of the pulse solenoidal coil, and will be selected by the pulse solenoidal coil. Some topics for designing this section are mentioned below. From simulation data of tilting pulse solenoidal coil, the efficiency was appeared to decrease a lot. When the pulse solenoidal coil tilt 50mrad, the efficiency will become to half of non tilting case[4]. So the pulse solenoidal coil has adjustable mechanism for tilting. The efficiency increase were observed in the simulation when magnetic field distribution of DC2 solenoidal coils is not uniform[4], so 3 power supplies will be prepared independently to

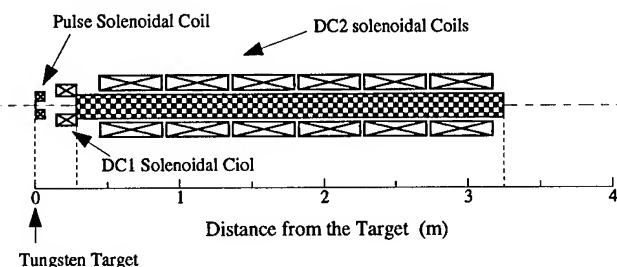


Figure. 4. Outline of the focusing section for the SPring-8 Linac

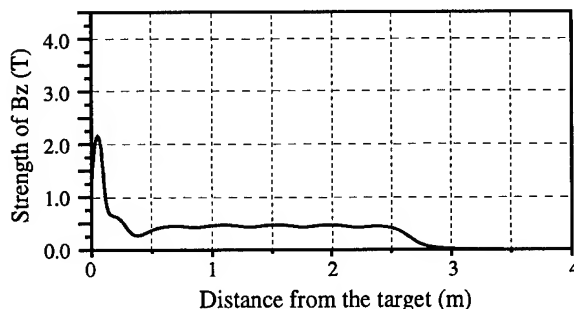


Figure. 5. Capable magnetic field distribution of the SPring-8 Linac

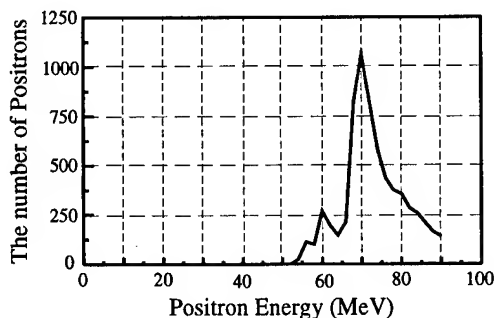


Figure. 6. Energy distribution of the SPring-8 convertor

drive 6 DC2 solenoidal coils. So we can arrange various magnetic field distribution and strength within Figure.4. Figure.6 shows a simulation data with a feasible design of convertor. In this case, produced positrons are accelerated to 40MeV. (Its efficiency is better than that of 50MeV case.) The magnetic field strength in the DC2 solenoidal coil section is increase step by step along beam line. The efficiency of Figure.6 is 0.5% within the limited energy, the peak±5MeV. The actual conversion efficiency will be predicted of around 0.3% from previous rate and Figure.6.

V. PLAN FOR SUPER-CONDUCTING MAGNET

Further studies of super-conducting magnets are mentioned below. In this system, maintenance-free refrigerated super-conducting magnet is used instead of liquid helium type.[5] Figure7 shows capable magnetic field distribution with new type superconducting magnet system. In this system, a DC coil is available instead of the pulse solenoidal coil. But keeping superconductivity against incident power to the coils, which are provided by neutrons, electrons, positrons or photons, is severe problem. Figure8 shows EGS4 simulation data of distribution of the incident power to the wall of the coils with full power injection to the target. (except for contribution of neutrons) In the SPring-8 Linac, full injection power is estimated to be 7.2kW. Parameters of full power injection are seen in TABLE.2. In this case, an inside diameter of the DC coil will be made larger compared with normal pulse solenoidal coil, and a lead will be inserted between the target and the coil. But the incident power to the pulse solenoidal coil part of 16W is about one order lager than the level of keeping super-conductivity. So this system can not to be acceptable this time, it is one of a theme in the future.

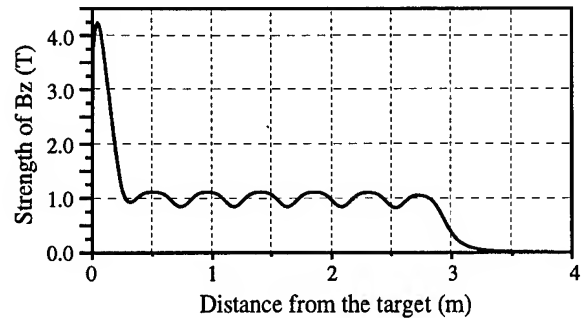


Figure. 7. Magnetic field distribution for the future plan

TABLE.2 Parameters of full power injection to the target

Injection electron energy	300MeV
Injection beam pulse width	40nsec
Injection beam pulse current	10A
Pulse repetition rate	60pps
Injection power	7.2kW

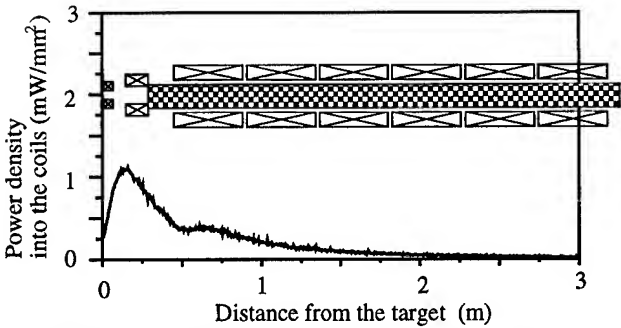


Figure. 8. Incident heat power to the solenoidal coils

VI. CONCLUSION

Simulations and experiments of the electron/positron convertor for the SPring-8 linac was compared. In these data, simulations were qualitatively coincident with experiments, but conversion efficiency of experiment data was obtained to be about 55% of simulation's one. We obtained the conversion efficiency of 0.5% for the actual SPring-8 convertor by simulation. With consideration of above ratio, the actual conversion efficiency will be predicted of around 0.3%.

Reference

[1]Walter R.Nelson, Hideo Hirayama, and David W. O. Rogers, SLAC Report-265, (1985)
 [2]A. Mizuno, et al., Proc. of the 9th Symp. on Accelerator Science and Technology, 122 (1993)
 [3]A. Mizuno, et al., JAERI-Research 94-021 (1994)
 [4]A. Mizuno, et al., JAERI-M 93-030 (1993)
 [5]T. Minato, et al., MITUBISHI DENKI GIHO, Vol.68,No.9, 51 (1994)

R & D ACTIVITY ON HIGH QE ALKALI PHOTOCATHODES FOR RF GUNS

P. Michelato⁺, A. Di Bona[#], C. Pagani⁺, D. Sertore⁺, S. Valeri[#].

⁺INFN Milano - LASA, Via F.lli Cervi 201, 20090 Segrate (Milano), Italy.

[#]Dipartimento di Fisica and INFN, Via Campi 213/A, 41100 Modena, Italy.

ABSTRACT

R&D on high quantum efficiency (QE) alkali photocathode is in progress at Milano in the context of the ARES-TTF (Tesla Test Facility) program. High QE multialkali antimonide and cesium telluride cathodes have been produced in an advanced preparation system. Photoemitter's preparation procedures have been set-up, in collaboration with the SESAMO lab. of the University of Modena, using Auger Electron Spectroscopy (AES): AES technique was used, in conjunction with sputter erosion, to obtain the in-depth profile of the photoemissive film. In this way photocathode preparation parameters (substratum cleaning procedure and temperature, alkali metal deposition rate, etc.) have been optimised. The spectral response of the photocathodes and the QE spatial distribution over the cathode surface has been measured using different light sources ($254 \text{ nm} < \lambda < 670 \text{ nm}$) and an optical scanning system. The photocathode poisoning effect and the changes in the photoemissive response due to the reaction with different gases have been investigated exposing the photoemitters, in a controlled way, to methane, carbon monoxide, carbon dioxide and oxygen. The good results so far obtained brought in Milano the responsibility of the production of cesium telluride photocathodes for the TTF Injector II. A preparation system for this application will be operative at Argonne within the end of 1995.

INTRODUCTION

Alkali based photoemissive materials have been widely used in television camera tubes, photomultipliers and image intensifier devices. Moreover, in the last years a big effort has been devoted to their operation as electron sources inside RF guns, in order to obtain high intensity, high current density electron pulses. A more detailed discussion about the characteristics of photoemitters to be used in an high current injector have been extensively discussed elsewhere [1-4]. Usually the choice of the photoemissive material together with its preparation procedure has been optimised empirically. The Milano and Modena group R&D activity on photocathodes is mainly devoted to overcome this philosophy, applying surface analysis technique (AES, XPS) to go over the alchemy of photocathode preparation and operation. At Milano an advanced UHV preparation system [5] is operative (base pressure is $1 \cdot 10^{-11}$ mbar) to produce photoemissive materials without contamination while, at Modena, a simplified preparation chamber [6], connected to a multitechnique analysis system (AES and depth profile

AES), gives the opportunity to analyse "in situ" prepared photoemitters.

Our activity started with the investigation of alkali antimonide photocathodes: this choice had been induced by the high quantum efficiency (QE) that characterize these materials in visible light range. The result obtained so far for cesium antimonide (Cs_3Sb) are discussed in reference [1]. The R&D activity is now devoted to investigate more robust and stable photoemitters: in this paper we will discuss the results so far obtained on K_2CsSb and the preliminary data obtained on Cs_2Te photoemissive materials.

EXPERIMENTAL

A reproducible recipe for the preparation of stable cesium potassium antimonide photoemissive films with high QE (on a AISI 304 SS substratum) has been worked out with the support of the AES and depth profile AES techniques.

A typical preparation procedure of a K_2CsSb layer starts with the preparation of a Cs_3Sb layer as described in ref. 5 e 6. The AES investigation has shown that, using this procedure, we obtain a photoemissive layer with a chemical composition similar to that of Cs_3Sb Fig. 2A.

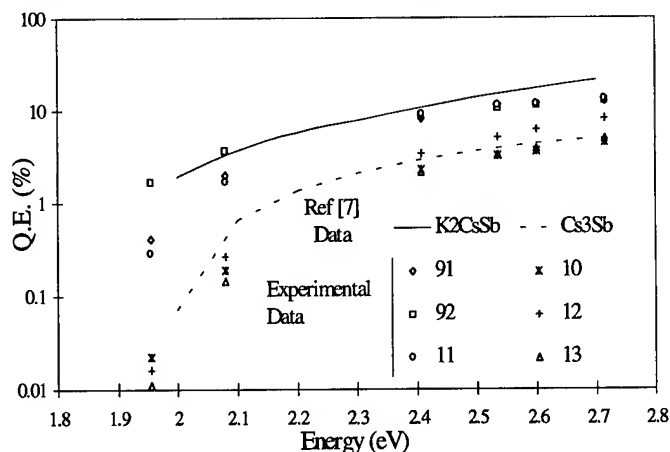


Fig. 1 - Comparison of the spectral response of different kind of cathodes prepared in our lab (K_2CsSb and Cs_3Sb) with the data reported by Sommer [7]. See text for more details.

This composition has been also confirmed by the comparison of the spectral response of this photoemitter with the K_2CsSb produced following the "recipe" here described and also comparing the data we found in literature [7]. This comparison is shown in fig.1. After the cesium deposition, the cathode temperature is raised from 120°C to 230°C in a few tens of minutes, maintained at this temperature for about

60 minutes and then is lowered at 120 °C. At the end of this procedure photoemission is nearly completely destroyed and the QE is lower than 10^{-3} % (@ 543 nm). An AES depth profile performed at this step of the preparation procedure shows that the layer contains not only antimony but also both alkali metals (see Fig. 2B).

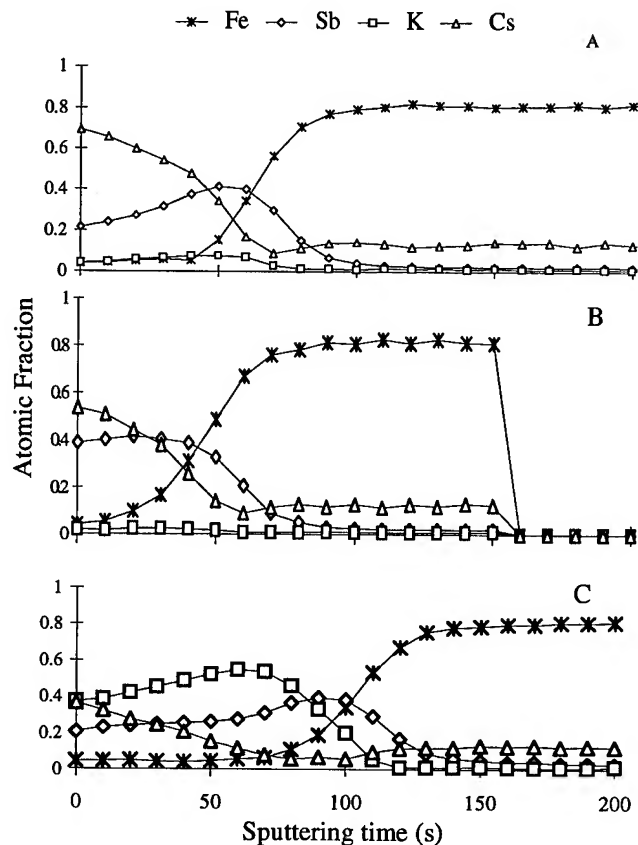


Fig. 2 - AES depth profiles after each step of the K₂CsSb cathode growth: 2A Cs₃Sb layer; 2B at the end of the 230 °C heating procedure; 2C on the definitive K₂CsSb layer.

The next step of the K₂CsSb preparation consists of potassium evaporation: as soon as we heat the K source the photocurrent presents a very rapid increase. The behaviour of the photocurrent during the potassium evaporation is shown in Fig. 3.

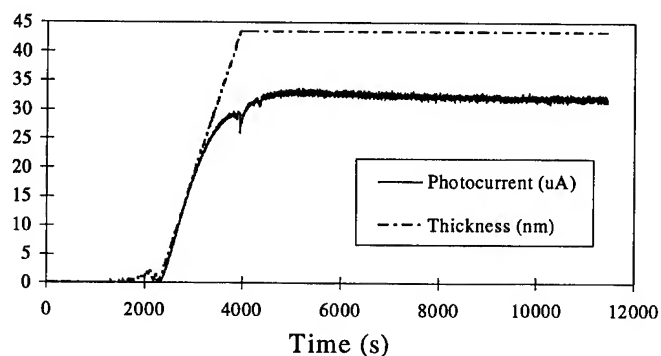


Fig 3 - K₂CsSb cathode photocurrent (@ 543 nm) and K thickness during the last step of the preparation procedure.

An AES depth profile analysis performed on the final layer shows that the chemical composition, at an estimated depth of about 5 nm, is close to the K₂CsSb one (see fig. 2C).

Unfortunately, in front of high QE characteristics, K₂CsSb photoemissive films presents an high reactivity with different gases and these are probably the main phenomena that affect the operation of such a material in a gun. We could investigate the poisoning effect using the Milano preparation system that operates with a base pressure lower than $1.5 \cdot 10^{-11}$ mbar, and is endowed with an accurate gas injection system. K₂CsSb films present a very high reactivity with oxygen and carbon dioxide, while they are rather insensible to methane, carbon monoxide and hydrogen exposition [6].

We have measured also the K₂CsSb spectral response during the poisoning with oxygen: data are shown in Fig. 4.

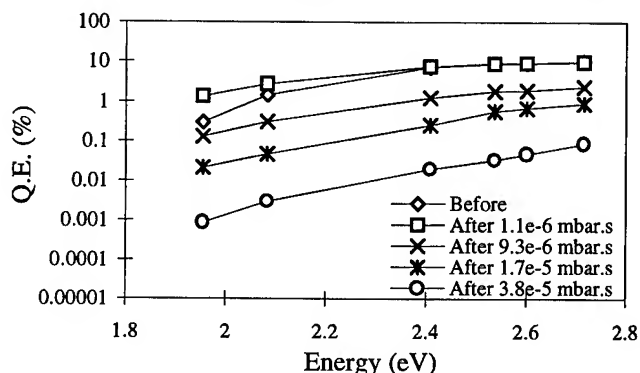


Fig4 - QE variation in K₂CsSb during the poisoning with oxygen.

The enhancement in the cathode response with respect to red light, reported by Sommer [7], is clearly visible after the first exposition. Unfortunately in the following steps the QE rapidly decreases. These measurements confirm the high reactivity of these materials (e.g. 10 ML of oxygen destroy completely the K₂CsSb photoemissive properties) and therefore forces the operation of these photocathode in extremely UHV conditions. The operation of Cs₃Sb and K₂CsSb photoemitters in RF guns is so limited to a few tens of minutes or, at best, to a few hours [8]. This drawback has to be overcome to ensure a reasonably long gun operation.

The strategy followed is to produce more robust and less poisonable photocathodes with a consequent longer lifetime. Following the experience of other laboratories such as LANL [9] and CERN [10], we are now beginning a systematic investigation of the properties of Cs₂Te, using the same procedure we applied in the alkali antimonide photoemitter R&D. Cesium telluride promises to be, at this time, the more probable candidate as the photocathode material for the future guns.

The preparation procedure of a Cs₂Te cathode follows a "recipe" similar to that used at CERN [10] and at LANL. [9] Tellurium is evaporated using a NiCr dispenser, similar to that used for alkali metals (SAES Getters) and antimony, filled with 99.999 % tellurium powder. After filling the tellurium is melted, under helium atmosphere, inside the

dispenser in order to avoid any leakage of the Te powder.

A typical preparation procedure can be described schematically by three mayor steps.

- Molybdenum substratum conditioning. A molybdenum sample is cleaned using the standard procedure used for UHV components: degreasing in a ultrasonic cleaners by successive immersion in MEK and alkaline soap, rinsing in pure water, drying in high purity ethyl alcohol and baking, under UHV, up to 180 °C for some hours.

- Tellurium deposition: a layer of about 5 nm is deposited on the Mo substratum, at a deposition rate of about 1 nm/min.

- Cesium deposition: by heating the proper dispenser cesium is evaporated (dep. rate is about 1 nm/min, substratum is maintained at room temperature) and the alkali metal deposition is continued until a maximum in the photocurrent is reached.

A Cs₂Te cathode preparation procedure is illustrated in Fig.5 where the typical behaviour of the photocurrent (@ 254 nm, 10.4 μW) together with the thickness of the tellurium and cesium films are shown.

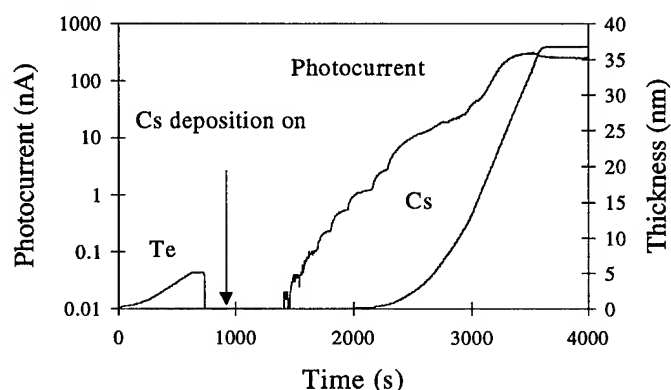


Fig. 5 - Cs₂Te cathode photocurrent together with Te and Cs thickness during the cathode preparation.

Typical QE value of Cs₂Te cathode that we have prepared are reported in the Tab. 1. The UV source is a 100 W high pressure mercury lamp (Oriel 6281) and the power measurement detector is a Coherent LMP2-UV.

Table 1. Cs₂Te QE at different wavelength

λ [nm]	power [μW]	QE [%]
254	10.4	14
334	83.7	0.4

A preliminary AES depth profile of a Cs₂Te cathode prepared on a molybdenum sample shows a sharp interface between the substrate and the photoemissive layer. This result is in opposition with the data obtained, by the same kind of analysis, from a cesium telluride layer grew on a copper substrate. In this case infact there is a great diffusion of the photocathode elements inside the substrate itself. The different behaviour of the substrates, showed by the AES,

could explain the dissimilar QE values of the same photoemissive layer grown on copper or on molybdenum [9,10].

We have evaluated also the poisonability of cesium telluride exposing it to different amount of various gases.

Fig. 6 shows a comparison of the behaviour of the QE of K₂CsSb and Cs₂Te photocathodes as a function of the exposition to oxygen: it is clearly visible the higher robustness of Cs₂Te photoemitter.

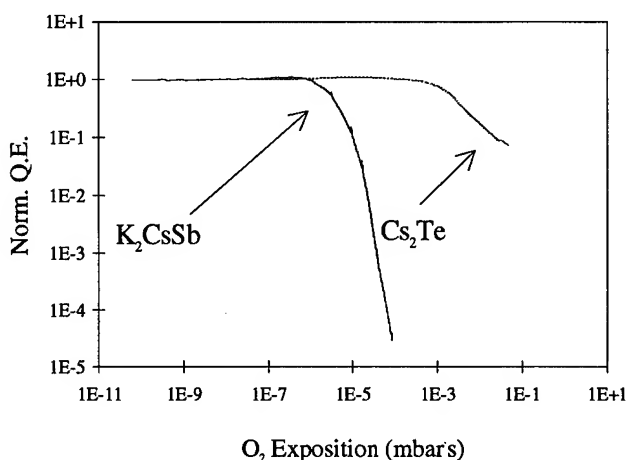


Fig. 6 - Behaviour of QE of K₂CsSb and Cs₂Te photocathodes as a function of the exposition to oxygen.

REFERENCES

- [1] P. Michelato et al, NIM A340 (1994), pag. 176.
- [2] P. E. Oettinger et al., NIM A272 (1988), pag. 264.
- [3] D.W. Feldman, Photocathodes and Photo-Injectors at Los Alamos, Proc. LAL/RT 94-04, pag. 131.
- [4] R. Bossart et al., Performances obtained with the CERN Linear Collider Test Facility (CTF), Proc. EPAC 94, World Scientific, pag. 680.
- [5] P. Michelato et al., Multialkali Thin Photocathodes for High Brightness guns, Proc. EPAC 94, World Scientific, pag. 1456.
- [6] S. Valeri et al., Spectroscopic investigation of in situ prepared multialkali-based photocathodes, Proc. EPAC 94, World Scientific, pag. 1459.
- [7] A. H. Sommer, Photoemissive Materials, J. Wiley & Sons, 1968.
- [8] F. Sabary, Nouveaux developements concernant la fabrication de photocathodes pour le photo-injecteur d'ELSA, Proc. LAL/RT 94-04, pag. 93.
- [9] S. H. Kong et al., Cesium Telluride Photocathodes, to be published on Journal of Applied Physics
- [10] E. Chevallay et al., Photocathodes tested in the dc gun of the CERN photoemission laboratory, NIM A340 (1994), pag. 146.

DEVELOPMENT OF AN ACCELERATOR-READY PHOTOCATHODE DRIVE LASER AT CEBAF

S. Benson and M. Shinn, Continuous Electron Beam Accelerator Facility, Newport News, Virginia
23606 USA

Many injector designs for free-electron lasers and linear colliders use photocathode sources in lieu of a thermionic cathode. These designs require mode-locked lasers with very tight phase and amplitude jitter specifications to achieve the electron beam quality needed for these applications. We have characterized the long term stability of a mode-locked laser for use in the injector test stand at CEBAF. The sources of drift and instabilities were studied and characterized. Initial results indicate that the most important source of drift is a change in the effective cavity length. A possible design for automatically optimizing the length is presented.

I. INTRODUCTION

Many proposed high-brightness sources for driving linear colliders and free-electron lasers plan to use a photocathode injector [1]. At CEBAF we will use a modelocked laser with a dc gun [2] to provide a bright source for a free-electron laser (FEL) driver accelerator [3].

In contrast to general research laboratory use, an accelerator-based laser must generally run unattended for long periods, with remote control and monitoring. The phase and amplitude stability should be comparable to rf sources and the laser phase must be locked to the accelerator master oscillator. The laser output must be remotely controllable to match accelerator conditions and photocathode quantum efficiency. To date no modelocked laser has exhibited performance which would meet these requirements.

Though Q-switched lasers have proven sufficiently stable to operate as part of an accelerator injector for the SLC polarized source [4], a modelocked laser is inherently less stable than a Q-switched laser. It is possible to use feedback techniques to stabilize the laser against amplitude and phase oscillations [5] but passive systems are always preferred due to their reliability.

To drive the CEBAF injector test stand we have purchased a frequency doubled Antares™ modelocked Nd:YLF laser from Coherent, Inc. Though our stability specifications for the laser were quite stringent, the laser has met them. Standard diagnostics were used to monitor the laser. A photodiode with a 65 psec risetime was used to monitor the time structure of the infrared light leaking from the cavity high reflector. Both slow and fast power meters were used to monitor the second harmonic generated (SHG) power and laser power fluctuations. A pickoff plate directed 3% of the laser light to an autocorrelator which monitored the pulsewidth of the second harmonic.

II. DIFFICULTIES IN USING MODELOCKED LASERS

A. Sensitivity of laser parameters to cavity length

Since the performance of a modelocked laser is quite sensitive to the cavity length, the Antares™ laser cavity was designed to have a particularly stable length. All components are mounted on a 5 cm diameter Invar rod to reduce temperature effects. To augment the stability, Coherent has used a Mefford Thermal Compensator [6]. Using this compensator it is possible to cancel out all linear temperature dependence in the cavity round trip time. Note that, even if the Invar rod had no temperature coefficient, the laser would still have some temperature dependence in the round trip time due to changes in the refractive index of air with temperature and to changes in the size of the elements mounted on the Invar bar.

To indicate how critical the cavity length is we show in figure 1 the dependence of the SHG power and the full width at half maximum pulsewidth as a function of cavity length. A typical pulsewidth curve is shown. The shape of the power curve drifts considerably over time. The error bars on the power curve indicate the changes in the power dependence from measurement to measurement. Further work is necessary to characterize the source of this drift. The laser does not modelock stably outside of the range of cavity lengths shown. Note the very narrow maximum in the power and narrow minimum in the laser pulse length. The infrared laser power is not very sensitive to the cavity length and so variation in the SHG power is mainly due to the change in the pulsewidth.

B. Sensitivity to other variables

We looked at the dependence of the laser on other parameters as well. The feedback for the laser head closed loop cooling system has a gain of 9 so the coolant temperature is dependent on the primary loop water temperature. We measured the sensitivity of the power to the primary water temperature and found that the power varied 0.5% for a 1 °C primary water temperature change. The water temperature must therefore remain constant to $\pm 1^\circ\text{C}$.

The refractive index of air changes with barometric pressure and relative humidity [7]. This will not be compensated by the Mefford compensator. The sensitivities are 0.36 parts per million (ppm) per mm-Hg and 0.01 ppm per % change in relative humidity. The dependence on humidity in an air conditioned environment should be negligible. A 10 mm-Hg change in barometric pressure, resulting in an effective cavity length change of 7 μm , is possible when a weather front passes through. From figure 1, it is obvious

that this would cause a major change in the laser performance.

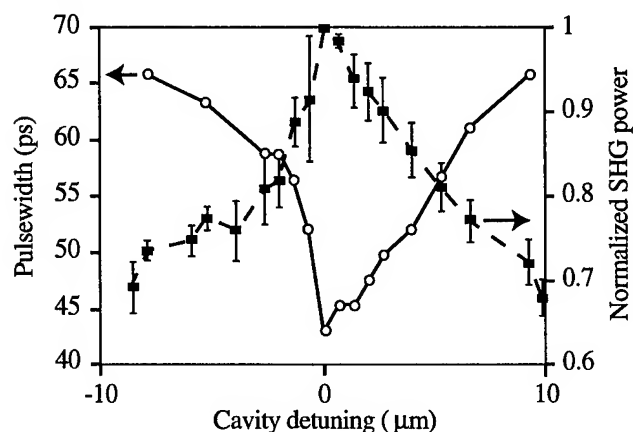


Figure 1: Power and FWHM pulse width vs. laser cavity length. The pulse width is a typical curve. The normalized power curve varies over time. The variation is indicated by the error bars.

III. NOISE RESULTS

Solid-state, lamp-pumped, modelocked lasers inevitably have phase and amplitude noise caused by the water cooling channels that must have turbulent flow to remove the heat from the lamps. Broadband turbulence-induced vibrations can cause phase noise either by vibration in the mirrors causing changes in the cavity length [8] or by acoustically induced changes in the refractive index of the laser rod.

The noise in the laser as a function of cavity length is shown in figure 2. Phase noise was measured on only one side of the cavity length detuning curve. In general it is found that the phase noise levels are highest near the peak in the power curve. Despite this the rms timing jitter in the frequency range of 10 Hz to 5 kHz is on the order of 1 ps. There is an intermittent laser instability which creates higher levels of timing jitter at cavity lengths slightly shorter than the optimum.

The phase noise spectrum is shown in figure 3 for operation at maximum SHG power. There is a general 1/f falloff for the broadband noise between 100 Hz and 100 kHz and broad features at 250 Hz, 500 Hz, and 1000 Hz. These features could be due either to acoustic resonances in the laser head or to noise from the master oscillator which is amplified by poles in the laser gain response. No sharp features were seen in the spectrum of the local oscillator.

Although not a minimum, the 1% peak to peak noise at maximum power meets our specification for the laser. Also shown in figure 2 is the noise monitor output from the laser. This monitors the amplitude noise of the fundamental. It is small and constant over most of the peak in the cavity detuning curve. Note that amplitude noise is not as

serious as phase noise since it can be removed with an acousto-optic attenuator in a feedback loop.

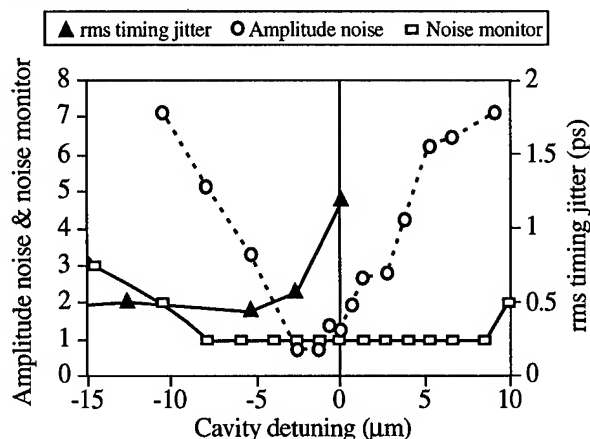


Figure 2: Noise in the drive laser vs. cavity length. The maximum phase noise is at the peak of the power vs. cavity length curve.

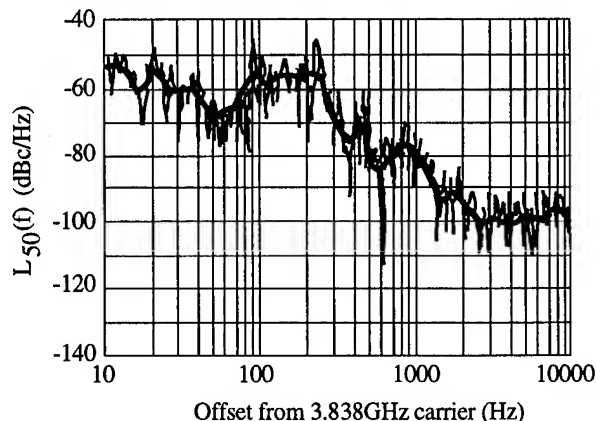


Figure 3. Typical phase noise spectrum measured at the 100th harmonic of the modelocked frequency.

Although the spectrum in figure 3 is typical, we occasionally noticed that the phase noise increased dramatically at high frequencies. Peaks at 8 kHz and harmonics appeared. The fundamental noise level rose when this spectrum was present. The laser persisted in this state for up to several hours. We do not know the cause of this condition but intend to study it to determine which parameters, if any, are out of their typical range when the noisy spectrum appears.

IV. STABILITY WITH TIME FOR ANTARES LASER

As figure 1 shows, very small changes in the effective cavity length can cause large changes in the SHG power and pulsewidth. We carried out several endurance runs during which the second harmonic power, fundamental power, second harmonic pulsewidth, phase noise, fundamental power noise, and temperatures of the coolant

water and the ambient temperature were recorded. We discuss here the results of one of these runs.

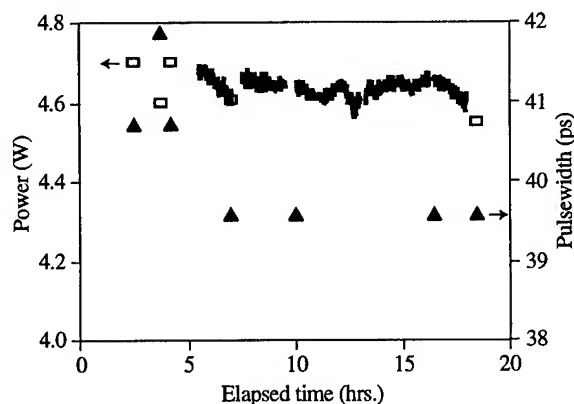


Figure 4 Power and pulse width vs. time during a long laser run. Note offset vertical axis.

After an initial warm up time of about six hours, the ambient temperatures stabilized at values of 29.4 °C in the laser head and 27.1°C outside the laser head. The temperature remained constant to better than $\pm 1^\circ\text{C}$ over the rest of the endurance run. During the warm up period, the fundamental noise and the SHG pulsewidth also varied. After this period the laser was quite stable for a period of 12 hours. The power and pulsewidth vs. time over this endurance run are summarized in figure 4. This performance is adequate for accelerator operations.

V. CONCLUSIONS

Although the performance shown in figure 4 is quite adequate for acceleration operation, other endurance runs had occasional periods of drift and instability. Furthermore, the occasional periods of large phase noise would be quite unacceptable for accelerator operations.

In general, the only adjustment which must be made over any 24 hour period is to the cavity length. One might think that a feedback loop should be able to hold the cavity at the optimum length. One parameter which may be ideal for this purpose, due to its linear dependence on cavity length, is the timing offset between the laser pulses and the master oscillator, shown in figure 5. We plan to study the possibility of using this signal in a simple feedback loop to maintain the laser at the peak in the curve. Note that the timing for optimum power may be dependent on other parameters as well. It is necessary to characterize the laser using the timing as a diagnostic while other parameters are varied so find out how useful this parameter is as a control variable.

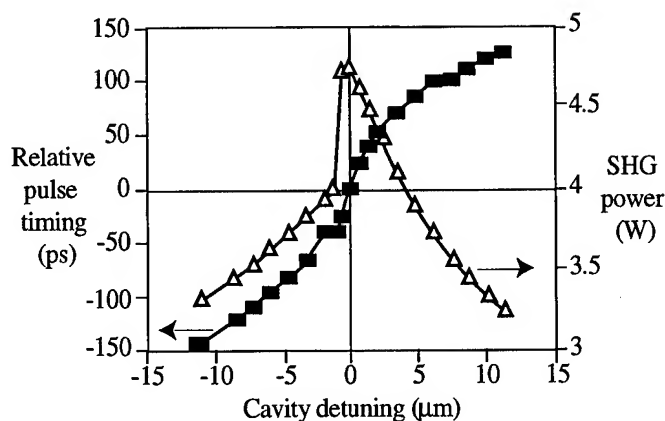


Figure 5. Power and relative phase of the light pulses with respect to the modelocked drive.

ACKNOWLEDGEMENTS

We would like to acknowledge the helpful efforts of Dave Engwall and Gary Slack. This work was supported by the Virginia Center for Innovative Technology and DOE Contract # DE-AC05-84ER40150.

REFERENCES

1. C. Travier, Nucl. Inst. and Meth. **A304** (1991) 285 has references to 21 proposed or operating photocathode rf guns.
2. P. Liger et al. *1992 Linear Accelerator Conference Proceedings* (AECL-10728) 85.
3. H. Liu et al., "Design of a High Charge CW Photocathode Injector Test Stand at CEBAF", these proceedings.
4. J. E. Clendenin et al., *1993 IEEE PAC proc.* (1993) 2973.
5. M. J. W. Rodwell, D. M. Bloom, and K. J. Weingarten, *IEEE J. Quant. Elec.* **25** (1989) 817.
6. For more information on the Mefferd Compensator, contact Coherent Laser Group, P.O. Box 54980, Santa Clara CA 95056 USA
7. F. Jones, "The Refractivity of Air," *J. Res. Natl. Bur. Stand.* **86**, (1981) 81.
8. S. B. Darack, D. R. Dykaar and G. T. Harvey, *Opt. Lett.*, **61** (1991) 1677.

ANALYTICAL FORMULAE FOR THE LOSS FACTORS AND WAKEFIELDS OF A DISK-LOADED ACCELERATING STRUCTURE

J. Gao

Laboratoire de L'Accélérateur Linéaire, IN2P3-CNRS
et Université de Paris-Sud, Centre d'Orsay,
F-91405 Orsay cedex, France

Abstract

In this paper we will give analytical formulae to calculate all synchronous modes' loss factors of a disk-loaded accelerating structure. From these analytical formulae one can easily find out the contribution of each synchronous mode to the total wakefields. The relations between the loss factors (wakefields) and structure geometrical dimensions have been well established. The validity of these formulae has been confirmed by using ABCI code. These analytical expressions of loss factors can be used also for a single pill-box cavity.

I. INTRODUCTION

Wakefields in a disk-loaded accelerating structure play a dominant role in future linear colliders. The wakefields can be calculated either in time domain by directly solving Maxwell equations, or in frequency domain by summing up synchronous modes. Usually, computer codes TBCI [1] and ABCI [2] are used in time domain, KN7C [3] and TRANSVRS [4] are used in frequency domain. In this paper, however, we give analytical expressions for the loss factors of all synchronous modes which can be used to find the delta function wakefields. These analytical expressions reveal the dependence of the loss factors on the geometric structure parameters.

II. LOSS FACTORS OF A DISK-LOADED STRUCTURE

A disk-loaded structure as shown in Fig. 1 can be constructed by connecting two pill-box cavities by a piece of cylindrical tube of radius a and of length d .

Due to the coupling through the aperture between cavities, passbands will form corresponding to each pill-box resonant mode. In the following we will keep using three subscripts mnl to specify the passbands without cutting the result from its origin. We assume that the synchronous frequency $\omega(\theta_{mnl})$ is not very different from the closed pill-box resonant frequency ω_{mnl} , and we will use ω_{mnl} to replace the synchronous frequency of the TM_{mnl} passband. In ref. 5, G. Dôme has made the same assumption to attack the same problem.

The definition of the loss factor of a synchronous mode is expressed as [6]

$$k = \frac{E_{s,z}(r=a)^2}{4dU/dz} \quad (1)$$

where $E_{s,z}(r=a)$ is the synchronous decelerating electric field along the axis of $r=a$, and dU/dz is the energy stored per me-

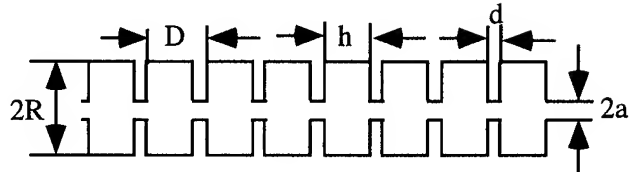


Figure 1. Disk-loaded accelerating structure

ter. For the TM_{mnl} passband by using the same method as in ref. 7, one has $E_{s,z}^{mnl}(r=a) = E_{z,mnl}(r=a)\eta(\theta_{mnl})$ and $dU/dz = U_{mnl}/D$, where $E_{z,mnl}(r=a)$ is the longitudinal electric field of the TM_{mnl} mode in the closed pill-box cavity, and U_{mnl} is the corresponding stored energy. When $m=0$, $\eta(\theta_{mn0})$ is found to be [7]

$$\eta(\theta_{mn0}) = \frac{2 \sin(\theta_{mn0} h/2D)}{\theta_{mn0}} \quad (2)$$

where

$$\theta_{mn0} = D \left(\frac{u_{mn}}{R} \right) \quad (3)$$

Where u_{mn} is the n th root of the m th order Bessel function. However, if $l \neq 0$ the electric field variation inside the cavity should be taken into account. Since

$$\cos(l\pi z/h) \cos(\theta_{mnl} z/D) =$$

$$\frac{1}{2} \cos((l\pi/h + \theta_{mnl}/D)z) + \frac{1}{2} \cos((\theta_{mnl}/D - l\pi/h)z)$$

it is obvious that the effect of $l \neq 0$ is just splitting one synchronous mode into two and it is found by analogy that η_{mnl} can be expressed as

$$\eta(\theta_{mnl}) = \frac{\sin(\theta_{mnl} h/2D + l\pi/2)}{\theta_{mnl} + lD\pi/h} + \frac{\sin(\theta_{mnl} h/2D - l\pi/2)}{\theta_{mnl} - lD\pi/h} \quad (4)$$

where

$$\theta_{mnl} = D \left(\left(\frac{u_{mn}}{R} \right)^2 + \left(\frac{l\pi}{h} \right)^2 \right)^{1/2} \quad (5)$$

We get then the general expression of the loss factor k_{mnl} corresponding to the TM_{mnl} passband

$$k_{mnl} = \frac{E_{s,z}^{mnl}(r=a)^2 D}{4U_{mnl}}$$

$$= \frac{\delta \xi h u_{mn}^2 J_m^2 \left(\frac{u_{mn}}{R} a \right) (S(x_1) + S(x_2))^2}{\left(\left(\frac{u_{mn}}{R} \right)^2 + \left(\frac{l\pi}{h} \right)^2 \right) 2\epsilon_0 D \pi R^4 J_{m+1}^2(u_{mn})} \quad (6)$$

where

$$\delta = \begin{cases} 1, l \neq 0 \\ 1/2, l = 0 \end{cases} \quad (7)$$

$$\xi = \begin{cases} 1, m \neq 0 \\ 1/2, m = 0 \end{cases} \quad (8)$$

$$S(x) = \frac{\sin(x)}{x} \quad (9)$$

and

$$x_1 = \frac{h}{2} \left(\left(\left(\frac{u_{mn}}{R} \right)^2 + \left(\frac{l\pi}{h} \right)^2 \right)^{1/2} - \frac{l\pi}{h} \right) \quad (10)$$

$$x_2 = \frac{h}{2} \left(\left(\left(\frac{u_{mn}}{R} \right)^2 + \left(\frac{l\pi}{h} \right)^2 \right)^{1/2} + \frac{l\pi}{h} \right) \quad (11)$$

It should be pointed out that eq. 6 is the analytical expression of the loss factors of a single pill-box cavity by setting simply $D=h$.

By taking all the modes into account, one can find the delta wakefield functions of a point charge traversing a disk-loaded structure by using the following formulae

$$W_z(\tau) = \sum_{m=0}^{\infty} \sum_{n=1}^{\infty} \sum_{l=0}^{\infty} W_{z,mnl}(\tau) \quad (12)$$

$$W_r(\tau) = \sum_{m=0}^{\infty} \sum_{n=1}^{\infty} \sum_{l=0}^{\infty} W_{r,mnl}(\tau) \quad (13)$$

$$W_\phi(\tau) = \sum_{m=0}^{\infty} \sum_{n=1}^{\infty} \sum_{l=0}^{\infty} W_{\phi,mnl}(\tau) \quad (14)$$

where [6]

$$W_{z,mnl}(\tau) = 2k_{mnl} \left(\frac{rr_q}{a^2} \right)^m \cos(m\phi) \cos(\omega_{mnl}\tau) \quad (15)$$

$$W_{r,mnl}(\tau) = \frac{2mck_{mnl}}{\omega_{mnl}r} \left(\frac{rr_q}{a^2} \right)^m \cos(m\phi) \sin(\omega_{mnl}\tau) \quad (16)$$

$$W_{\phi,mnl}(\tau) = -\frac{2mck_{mnl}}{\omega_{mnl}r} \left(\frac{rr_q}{a^2} \right)^m \cos(m\phi) \sin(\omega_{mnl}\tau) \quad (17)$$

where $\tau = s/c$, s is the distance between the exciting charge and a test charge, r_q is the transverse coordinate of the exciting charge and c is the velocity of light in vacuum. For a Gaussian bunch of charge q and bunch length σ_t one can calculate the integrated wakefield started from delta wakefield functions

$$W_{G,z}(\tau) = \int_{-\infty}^{\tau} W_z(\tau-t) I(t) dt \quad (18)$$

$$W_{G,r}(\tau) = \int_{-\infty}^{\tau} W_r(\tau-t) I(t) dt \quad (19)$$

$$W_{G,\phi}(\tau) = \int_{-\infty}^{\tau} W_\phi(\tau-t) I(t) dt \quad (20)$$

where

$$I(t) = \frac{q}{(2\pi)^{1/2} \sigma_t} \exp\left(-\frac{t^2}{2\sigma_t^2}\right) \quad (21)$$

For the m th mode the total loss factor of a Gaussian bunch will be

$$K_m(\sigma_t) = \sum_{n=1}^{\infty} \sum_{l=0}^{\infty} k_{mnl} \exp(-\omega_{mnl}^2 \sigma_t^2) \quad (22)$$

To evaluate the single bunch energy loss ΔU_t to all the monopole modes, one defines the beam loading enhancement factor as [6]

$$B(\sigma_t) = \frac{K_0(\sigma_t)}{k_{010} \exp(-\omega_{010}^2 \sigma_t^2)} \quad (23)$$

and

$$\Delta U_t = B(\sigma_t) \Delta U_0 \quad (24)$$

where ΔU_0 is the energy lost to the fundamental mode.

III. COMPARISON WITH NUMERICAL RESULTS

In this section a special rf structure will be used to make the comparison between the calculation results from the analytical formulae and those from the ABCI code. The exciting bunch is assumed to have a Gaussian distribution and the loss factors shown in the figures are $k(\sigma_t)$. In the following analytical calculations one has chosen $n = 50$ and $l = 30$ if otherwise stated. It should be declared that the width of the bars in the following pictures has no physical meanings.

We consider a disk-loaded structure as shown in Fig. 1 having the dimension: $D=3.5\text{cm}$, $h=2.92\text{cm}$, $a=1\text{cm}$ and 25cm . The exciting bunch which traverses the structure parallel to the structure axis with an offset of $r = a$ has an rms bunch length σ_z ($\sigma_z = \sigma_t c$). The analytical results of the monopole modes ($m=0$) are shown in Fig. 2 where $\sigma_z = 2.5\text{mm}$. Using the same structure and keeping the same exciting bunch parameters, we use ABCI to get the corresponding results shown in Fig. 3 where three cavities have been used. To verify the HOM mode loss factors estimated by the formulae we will compare the beam loading enhancement factor $B(\sigma_z)$ with those calculated by ABCI. Taking the SLAC type structure parameters: $D=3.5\text{cm}$, $h=2.92\text{cm}$, $a=1\text{cm}$ and 4.02cm . the beam loading enhancement factor $B(\sigma_z)$ has been calculated, compared and shown in Fig. 4 where the fitting curve is $B(\sigma_z) = 4.66\sigma_z^{-0.678}$ which agrees quite well with the diffraction model [8] which implies that the the total loss factor for a short bunch varies as $\sigma_z^{-1/2}$. For the analytical curve shown in Fig. 4, we have taken $n = 200$, and $l = 100$ which ensure the convergency of eq. 22 for the minimum σ_z used.

The agreement between the analytical and the numerical results are obvious. The comparisons for the dipole modes have been done also, however, they are not shown in this paper due to the limited paper length.

IV. ACKNOWLEDGEMENTS

The author thanks J. Le Duff, Y.H. Chin (KEK) and H. Braun (CERN) for the beneficial communication.

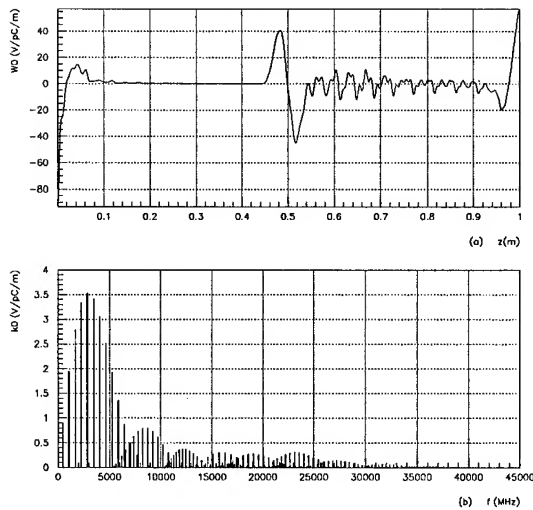


Figure 2. (a) Monopole wakefield and (b) monopole mode loss factors. For both figures $\sigma_z = 2.5$ mm. The dimension of the structure: $D=3.5$ cm, $h=2.92$ cm, $a=1$ cm and $R=25$ cm. (Formulae)

References

- [1] T. Weiland, DESY 82-015, 1982.
- [2] Y.H. Chin, "User's guide for ABCI version 8.8", LBL-35258.
- [3] E. Keil, "Diffraction radiation of charged rings moving in a corrugated cylindrical pipe", *Nucl. Instr. and Meth.*, **A100** (1972) 419.
- [4] K. Bane and B. Zotter, Proc. of the 11th International Conference of High Energy Accelerators, Geneva (1980) p. 581.
- [5] G. Dôme, "Wake potentials of a relativistic point charge crossing a beam-pipe gap: an analytical approximation", *IEEE Trans. on Nucl. Science*, **NS-32** (1985) 2531.
- [6] P.B. Wilson, "Introduction to wake potentials", SLAC-PUB-4547 (1989).
- [7] J. Gao, "Analytical approach and the scaling laws in the design of disk-loaded accelerating structures", *Particle Accelerators*, **43** (1994) 235.
- [8] K. Bane and M. Sands, "Wakefields of very short bunches in an accelerating cavity", SLAC-PUB-4441 (1987).

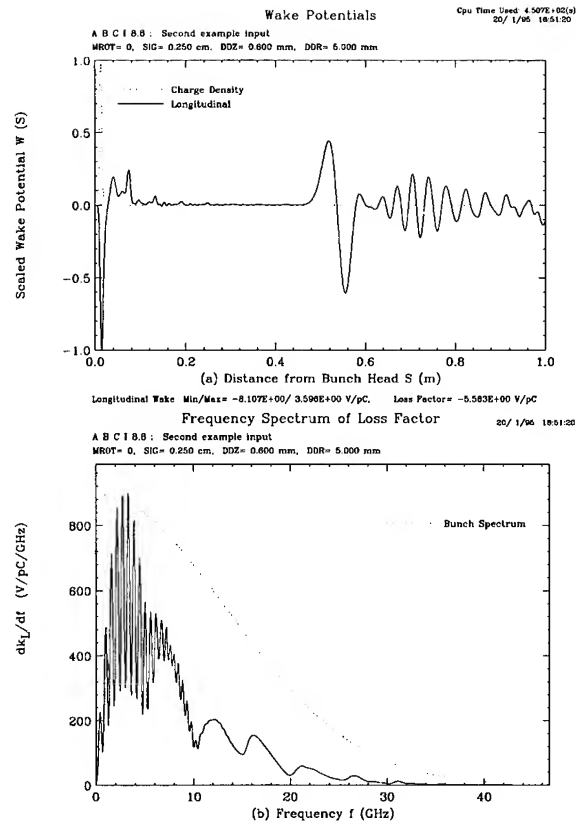


Figure 3. (a) Monopole wakefield and (b) Monopole mode frequency spectrum of loss factors. For both figures $\sigma_z = 2.5$ mm. The dimension of the structure: $D=3.5$ cm, $h=2.92$ cm, $a=1$ cm and $R=25$ cm. (ABCI)

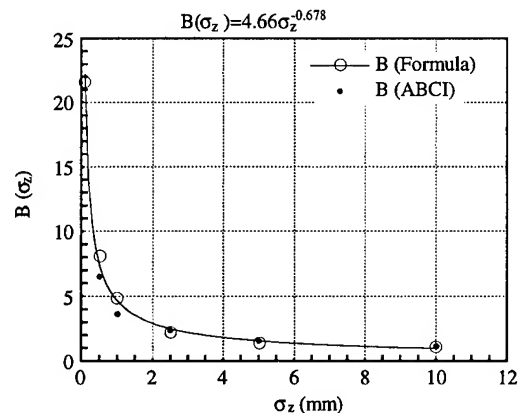


Figure 4. The comparison of the enhancement factors $B(\sigma_z)$ calculated by the analytical formula and ABCI code for a SLAC type structure. The dimension of this structure: $D=3.5$ cm, $h=2.92$ cm, $a=1$ cm and $R=4.02$ cm.

DESIGN PARAMETERS FOR THE DAMPED DETUNED ACCELERATING STRUCTURE*

K.Ko, K.Bane, R.Gluckstern, H.Hoag, N.Kroll, X.T.Lin, R.Miller, R.Ruth, K.Thompson, J.Wang
Stanford Linear Accelerator Center, Stanford University, Stanford, CA 94309 USA,
University of California, San Diego,
University of Maryland, College Park, MD 20740

Abstract

The advanced accelerating cavities for the NLCTA (and anticipated for NLC) will incorporate damping as well as detuning. The damping is provided by a set of four waveguides (which also serve as pumping manifolds) that run parallel to the structure, with strong iris coupling to each cavity cell and terminated at each end by absorbers. The previously reported [1][2] equivalent circuit analysis has been refined and the dependence upon design parameters explored. We find that adequate damping can be provided by a single waveguide mode, leading to designs which are more compact than those initially considered. The design parameters and their rationale will be presented.

I. Introduction

The accelerating cavities for the NLC Test Accelerator (NLCTA) will incorporate damping as well as detuning (the DDS structure) [1][2]. The detuning suppresses the transverse wakefield experienced by closely trailing bunches, and the damping suppresses that experienced by the more remote bunches. The damping is provided by a set of four waveguides (which also serve as pumping manifolds) that run parallel to the structure, with strong iris coupling to each cavity cell and terminated at each end by absorbers. Absorption along the length of the manifold may also be provided. In the following we first review the underlying rationale of the manifold damping scheme and describe improvements in the analyses which have taken place since our last report [2]. This is followed by a description of our proposed design, its conceptual basis, and our current plans for its implementation.

II. The manifold damping scheme

In the detuned structure cell dimensions are varied along the length of the accelerator cavity in a gaussian manner so that the frequencies of the lower dipole mode of the individual cells vary over a range of approximately fifteen percent, and the frequencies of the resultant coupled modes (i.e., cavity modes; when not qualified, "mode" will be taken to mean "cavity mode") vary over a range of approximately 25%. As shown in [3], these modes are localized standing waves with cell to cell amplitude variation which may be viewed as an effective wavelength which varies smoothly and extensively along the length of the mode. Their structure can be interpreted in the following manner. Each cell, if it were part of a periodic structure, would have associated with it a phase advance per cell (and hence a phase velocity) as a

function of frequency. These quantities continue to have a significance in a localized sense when the cells are assembled to form a detuned structure. Thus we speak of a local phase advance ("per cell" is understood) and a local phase velocity. Modes terminate within the structure where the local phase advance is either zero or π , and approximately half the modes are entirely confined within the structure with phase advance π at one end and zero at the other. A particular mode is excited by a velocity of light charge only if the range of local phase velocities associated with it includes that velocity. Similarly the mode couples strongly to a manifold mode only if the range also includes the phase velocity of the manifold mode. This implies that the coupling of a mode to a manifold mode is localized within the mode in the vicinity of the cell where the velocity match occurs.

Our theoretical analysis of these structures has so far been based on the single band equivalent circuit model discussed in [2]. There we derived the following equation for the damped cavity modes:

$$\left(\frac{1}{f_m^2} - \frac{1}{f^2}\right)a_m + \frac{k_{m+\frac{1}{2}}}{2}a_{m+1} + \frac{k_{m-\frac{1}{2}}}{2}a_{m-1} \\ = j\phi \frac{k}{k_g} \frac{Z_0}{Z} \sum_n \hat{k}_m \hat{k}_n \exp(-j\phi|n-m|)a_n \quad (1)$$

The LHS of Eq. (1) corresponds to the cell characteristics and the cell to cell coupling. Here a_m is the excitation of cell m , f_m its resonant frequency, f the coupled mode frequency, and the $k_{m\pm\frac{1}{2}}$'s represent the coupling between adjacent cells. The RHS of Eq. (1) represents the coupling of the cells to one another via the manifold mode and their coupling to the matched loads which are assumed to terminate the manifold mode at each end. A summation over manifold modes (not shown explicitly to simplify the notation) is to be understood. Here \hat{k}_m represents the coupling of the m th cell to the manifold mode, Z its wave impedance, k_g its propagation constant, and $\phi = k_g P$ where P is the period. As discussed in [2], Eq. (1) is a linear eigenvalue equation in $1/f^2$ (with symmetric coefficients) when the RHS is neglected, and standard matrix diagonalization techniques can be used. The associated eigenvectors (column vectors in the a_m) may be used in conjunction with the RHS to evaluate, by means of standard perturbation theory formulas, both the real and imaginary parts of the frequency shift due to the manifold coupling.

Because the matrix elements of the RHS are complex and involve the frequency in a complicated way, standard diagonalization techniques cannot be used to solve the full equation. Our procedure for determining the complex mode frequencies has been based upon the fact that the determinant of the coefficients of the a_m must vanish in order to have a non-trivial solution.

*Work supported by the Department of Energy, contracts DE-AC03-76SF00515.

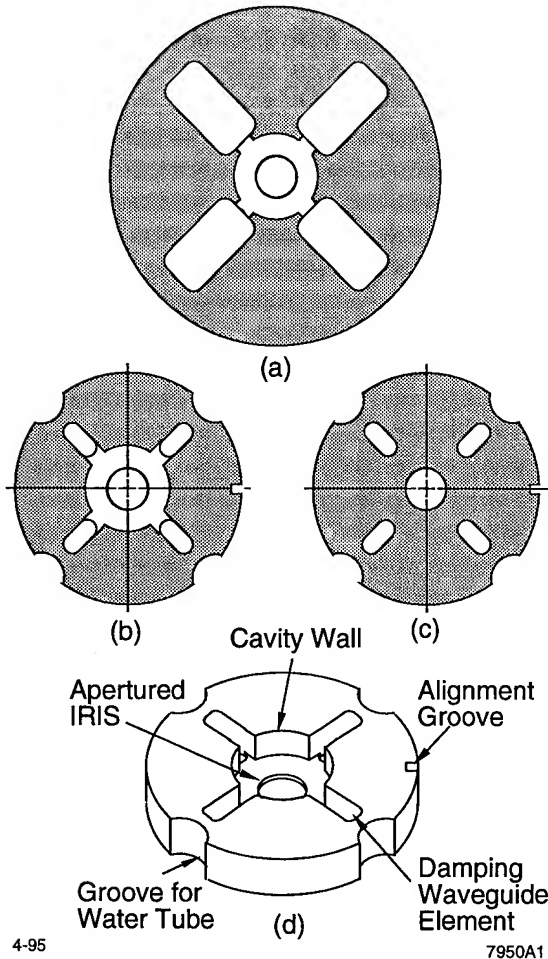


Figure 1. (a) Cell-center cross section of multimode manifold, (b) cell-center cross section of single-mode manifold, (c) iris-centered cross section of single-mode manifold, (d) 3D view of single-mode manifold.

The mode frequencies for the undamped problem provide useful starting frequencies for an iterative procedure to find the roots of the determinant including damping. This approach has proved to be stable only when the change due to the RHS is sufficiently small. Alternating the iterative procedure with successive small increases in the coupling strength has, however, enabled us to overcome this limitation.

Once the frequencies have been determined it is straightforward to determine the mode vectors by means of Cramer's rule. We note that these vectors are also complex and while linearly independent, are no longer orthogonal. We have examined the space time behavior of a typical trapped mode making use of computer graphics. The previously localized portion still dominates the picture, but there is a small tail which extends over the entire length of the structure and represents the response of the cells to the field in the manifold. It has the character of an outgoing wave on both sides of the localization region with uniform wavelength (reflecting the fact that the manifold in this simulation was uniform). On the other hand, the ends of the localization region exhibit an ingoing wave character corresponding to the propagation of energy from the outer regions of the mode to the

region where the mode couples well to the manifold. These wave propagation features can only occur for complex mode vectors.

The Bane-Gluckstern[3] procedure for relating these vectors to the wakefield requires some modification. The details can not be given here but we arrive at an analogue of their Eq. (2.48) which for us takes the form:

$$\tilde{V}(s) \approx 2q_e x_e N L \sum_p [K_p \sin(2\pi f_p s/c + \phi_p) \cdot \exp(-\pi f_p s/Q_p) \quad (s > 0) \quad (2)$$

As compared to Bane and Gluckstern, our equation includes small manifold-induced corrections to the parameters, the small phase shifts ϕ_p , and of course the damping terms. We have omitted a branch cut integral which corrects the behavior as s goes to zero, becomes the dominant term for values of s much larger than those of interest, but is believed to be negligible at s values of interest.

We have compared the "exact" wakefield envelope function obtained using the iterative procedure with that obtained from perturbation theory, for a DDS with a single manifold mode having a 12 GHz cutoff frequency and as large a coupling parameter as we are likely to use. The difference between the iterative and perturbative solutions is very small, and the coupling is strong enough to produce very satisfactory damping (see Ref. [2]). The Q values are about 1000. The shunt impedance degradation due to the manifolds is less than 3% over the first 2/3 of the cells and rises to a maximum of about 5% at the end of the structure.

III. The damped detuned structure design

The manifold geometry discussed in references [1] and [2] is shown in midcell cross section in Fig. 2a. It has five propagating modes within the lower dipole band, the upper four of which contribute significantly to the damping. Because each of the manifold modes has its own dispersion characteristic, each of them couples to a particular cavity mode at a different cell. This is a desirable feature for strong coupling because distributing the damping along a cavity mode reduces the chance that its pattern will distort so that it decouples itself. As discussed above, however, the needed coupling is not strong enough to produce significant distortion even in the single mode case. Thus while calculations showed that the multimode manifold yielded very satisfactory damping with little shunt impedance degradation, it was decided to proceed with a single mode manifold design.

Cross sections of a typical element of the new structure taken at the center of a cell and at the center of the coupling iris are shown in Figs. 2b and 2c, and a 3D view is shown in Fig. 2d. The new structure is seen to be both simpler and more compact than the multi manifold mode structure. MAFIA calculations show that the propagating manifold mode has a strong TE_{10} character. It has significant coupling only with the TE component of the dipole modes. We recall that the dipole modes are hybrid TE-TM modes, and that for the lower dipole mode the TE character is dominant at low phase advance, while the TM character dominates at large phase advance[4]. It is therefore necessary that the phase velocity match between the dipole mode and the manifold mode occur at low phase advance. We satisfy this requirement by adiabatically tapering the properties of the manifold so that

the effective cutoff frequency of the manifold mode increases as one proceeds down the structure. Hence at any specified frequency the phase velocity of the manifold mode increases as one proceeds along the structure. Thus for the new structure the concept of local phase velocity applies both to the cavity mode and the manifold mode, and the coupling between the two occurs where these match.

We note that the manifold structure shown in Figs. 2b and 2c bears little resemblance to a waveguide, since 5/6 of one of the narrow walls is removed for coupling to the accelerator cells. If, however one examines the mode spectrum and mode patterns in a zero phase advance MAFIA calculation, one observes a mode with a strong TE_{10} character well localized in the manifold, and we take its frequency as the manifold cutoff frequency. Furthermore the dependence of frequency on phase advance is, for small phase advance, quite similar to that of a waveguide with the cutoff frequency as defined above. The behavior in the vicinity of an avoided crossing is also very similar to the case of simple waveguide coupling and we have used the same methodology to determine the coupling strength to the manifold.

The general features of our initial design proposal, based upon the approach described above, are as follows: The thickness and beam hole dimensions of the coupling irises are taken to be the same as for the detuned structure already built and tested. The outer diameter of the cell slots (L_1) varies from 2 to 1.5 inches, and their width is constant at 0.1968 inches. The slots in the coupling iris coincide with those of the smaller adjacent cell along width and outer circumference, while the inner diameter (L_2) varies from 1.2 to .71 inches. Over the last third of the structure L_2 is less than the outer diameter of the associated cells. The cutoff frequency increases with decreasing ($L_1 - L_2$) and also with decreasing L_1 . Over the entire structure it ranges from 12.1 to 14.0 GHz. The avoided crossing occurs at phase advance varying from 25 degrees to 82 degrees. As this phase advance increases, the cell to manifold coupling decreases. The decrease in L_2 has the opposite effect and was introduced to maintain the coupling strength. This remedy has the undesirable effect of decreasing the shunt impedance of the accelerating mode, so that it must be applied with circumspection. We note that there are a few modes for which the manifold is cutoff, and a substantial number for which it is cutoff at one end. The latter are presumably damped in an irregular manner due to the reflection from the cutoff end. None of the modes so affected intersect the light line so that their loss factor and their effect on the wakefield envelope function are expected to be small.

Once the manifold dimensions are fixed one must face the delicate task of determining the outer cell diameters (2b) so as to obtain an accurately tuned accelerating mode. This dimension has been accurately determined using a two dimensional finite element program[5] for the detuned structure without manifolds. The dimensions obtained in this way are sufficiently accurate to permit construction with accurately machined parts without requiring subsequent hand tuning. The three dimensional structure with the manifolds is a more difficult computational challenge. We have used a MAFIA based method which aims at computing the difference in the cell diameter with and without slots. This difference, which ranges from approximately 20 to 30 mils, is then used to correct the previously determined accurate cell di-

ameter. A fine triangular mesh which accurately traces circles of constant radius r has been used. The computed radii are believed to be correct to within 0.1 mils, and the frequencies are expected to lie within 3 MHz of the design value (11.424 GHz). This would be close enough to allow hand tuning. As a check on our numerical methods and our evaluation of coupling parameters six samples each of cells number 10, 70, 106, 156, and 196 are being fabricated for cold testing.

Our estimate of the wakefield damping which the new structure will exhibit is based solely upon the rather crude modeling of [2]. It does not take account of the departure of the manifold from a simple waveguide, and the effect of the tapering on the modes which require damping has been inferred from the adiabatic principle without any explicit calculation. We have planned a theoretical program which deals with both of these deficiencies. Also we recognize that the specification that the manifolds be terminated by matched loads in their propagation range may be difficult to realize in practice. Some theoretical effort will be devoted to the design of load structures, and the possibility of distributed loading along the manifold with lossy materials will be explored.

References

- [1] N.Kroll, et.al., 17th Int'l Linear Accel. Conf., Tsukuba, Japan, 21-26 August 1994.
- [2] N.Kroll, et.al., 6th Workshop on Advanced Accelerator Concepts, Lake Geneva, WI, 12-18 June 1994; SLAC-PUB-6660.
- [3] K.L.F. Bane and R.L. Gluckstern, Part. Accel. **42**, 123 (1993); SLAC-PUB-5783.
- [4] J.W. Wang and G.A. Loew, 1990 Linear Accel. Conference, Albuquerque, NM, 10-14 Sept. 1990; SLAC-PUB-5321.
- [5] J.W. Wang and E.M. Nelson, 1993 Part. Accel. Conf., Washington, DC, 17-20 May 1993; SLAC-PUB-6142.

OPERATION OF PLS 2-GeV LINAC*

W. Namkung, I. S. Ko, M. H. Cho, J. S. Bak, J. Choi, and H. S. Lee
Pohang Accelerator Laboratory, POSTECH
Pohang 790-784, Korea

The PLS 2-GeV electron linac at the Pohang Accelerator Laboratory (PAL) has been constructed as a full energy injector to the storage ring of the Pohang Light Source (PLS) project. The 150-m long linac uses 11 klystrons of 80-MW maximum output power driven by 200-MW modulators. There are 42 constant gradient acceleration sections and 6 quadrupole triplets. By December 10, 1993, we completed the linac installation with the beam analyzing station and the beam transport line to the beam dump of 30-m long. We completed the machine commissioning by June 30, 1994. Since September 1, 1994, it provides 2-GeV beams to the PLS storage ring for its commissioning, which is also completed by December 24, 1994 with 300-mA stored current. In this paper, we present the operational experience of the PLS 2-GeV linac.

I. INTRODUCTION

The Pohang Accelerator Laboratory (PAL) has recently completed the 2-GeV synchrotron radiation source named the Pohang Light Source (PLS). The PLS will serve as a low-emittance light source for various research such as basic science, applied science, and industrial and medical applications. There is a 2-GeV linear accelerator as a full energy injector to the storage ring. This linac is consisted of eleven klystrons and modulators, and ten SLAC-type pulse compressors on the ground floor and 42 accelerating columns, six quadrupole triplets, and various components in the tunnel which is placed 6-m below the ground level.

Installation work started on July 1, 1992 has been completed by December 10, 1993. This includes the first section of the beam transport line (BTL) to the beam dumps and the beam analyzing station #3 (BAS3) in order to measure the beam energy and the other physical parameters.

The commissioning started on January 7, 1994. On March 9, 1994, we achieved the 1.5-GeV beam without using SLEDs. Exactly two month later, the 2-GeV beam was obtained, and it was declared that the 2-GeV linac commissioning was successfully completed [1].

During the summer maintenance period, the remaining BTL work was completed. From September 1, 1994, the beam injection to the storage ring (SR) was started. On the first day, the beam arrived in front of the Lambertson septum magnet in the storage ring. During the commissioning period for the storage ring, the linac provides about 600 mA of beams continuously. At present, we are operating the 2-GeV linac 24 hours a day from Monday morning to Friday morning with two shift teams per day.

II. GENERAL DESCRIPTION

The nominal beam energy of the PLS linac is 2-GeV with the operating frequency of 2,856 MHz. There are 42 SLAC-type accelerating columns and 11 klystrons including those for the preinjector. Total length of the linac is 150-m long with an extra length of 15 m before the switching magnet. Therefore, the required accelerating gradient of the main linac is at least 15.8 MV/m. When we consider one or two klystrons as standby, it requires an accelerating gradient of 17.8 and 19.8 MV/m, respectively. In order to achieve this accelerating gradient, we adopted high-power klystrons of 80-MW and SLED-type pulse compressors. In addition, we required the RF pulse length at least 4 μ s for a higher energy gain factor from SLED cavities. Major parameters for the PLS linac are summarized in Table 1.

Table 1: Major parameters of PLS 2-GeV Linac

Beam Energy	2 GeV
Accelerating Gradient	15.5 MV/m (min.)
Energy Spread	+/- 0.3% or less
Machine Length	150 m
RF Frequency	2,856 MHz
Repetition Rate	60 Hz (max.)
E-gun	> 2 A / 1, 2, or 40 ns
Emittance (theory)	75 π nm-rad at 2-GeV
Klystron Output Power	80 MW max.
No. of Klystrons	11 (=1+10)
No. of Pulse Compressors	10
No. of Accelerating Columns	42 (=2+40)
No. of Quadrupole Triplets	6
No. of Support/Girder	22
Beam Exit	100 MeV, 1 GeV, 2 GeV

The linac building has three levels; the tunnel in 6-m below the ground floor for accelerating columns and other components, the ground floor for the klystron gallery, and upper floor for utilities including air-conditioning and air handling units. The air temperature and the humidity of the klystron gallery are maintained within the range of 23 - 25°C and 55% or less throughout the year, respectively. During the machine operation, there is no air exchange in the tunnel to avoid any contamination due to ozone or radioactive dust in the klystron gallery. There is 3-m thick concrete shielding between the tunnel ceiling and the klystron gallery. There are three beam switch yards at 100-MeV, 1-GeV, and 2-GeV locations for the beam extraction to other facilities. Currently, two locations at 100-MeV and 2-GeV are operational.

* Work supported by Pohang Iron & Steel Co. and Ministry of Science and Technology, Korea.

SR Current & Maximum Injection Efficiency

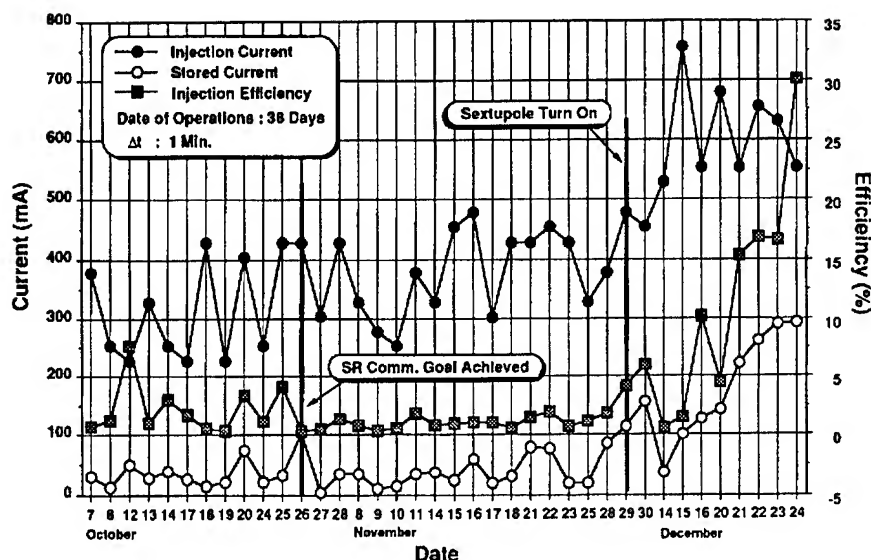


Fig. 1: Beam current and the injection efficiency during the period of October - December, 1994.

Main and auxiliary cooling stations are also annexed in the linac building. Both stations supply cooling water of temperature controlled at $45 \pm 0.2^\circ\text{C}$ and non-controlled at $32 \pm 1^\circ\text{C}$. The auxiliary station had been used for the preinjector initially and is now serving the test laboratory. The linac substation contains various transformers of total 8-MVA with three different groundings.

III. NORMAL OPERATION

A. First Period: August 1994

After successful commissioning of the linac completed by the end of June, 1994, we had an annual preventive maintenance period. We had intensive maintenance work for the main cooling system. We also improved the preinjector cooling and vacuum systems which had been constructed for training our staff in 1992. We removed all the vacuum manifold system and installed distributed pumping system the same as regular sections. Other two module had experienced vacuum vents for visual inspections. On the other hand, we opened the beam tunnel so that the staff could complete the remaining installation work for the BTL to the storage ring. When we resumed the RF conditioning, it had taken about two weeks to recover the stable operation condition. One notes that it was a special case, because the vacuum system of the preinjector was replaced completely. Through the machine operation on August 17 and 18, we were able to obtain beams of 2.23 GeV with a total RF power of 600 MW. The accelerating efficiency with a given RF power is improved due mainly to the fine adjustment of the RF phase by the computer control. During this period, the linac was operated with self-generated trigger signals of 30 Hz.

B. Second Period: September to December, 1995

Just before the commissioning of the storage ring started, we

changed the triggers for the e-gun, the modulators, and other microwave related equipment from self-generated signals to signals synchronized with the RF system of the storage ring. Since the SR injection system is operated at 10 Hz, we reduce the e-gun trigger to the same repetition rate. However, we keep the modulator operation at 30 Hz in order to have stable operations. Currently, the e-gun and the driving RF source such as the solid state amplifier are operated at 10 Hz while all modulators are operated at 30 Hz.

Before the beam injection to the storage ring, the BTL commissioning took place on September 1, 1994. We sent the 2-GeV beam successfully to the SR injection point within 2 hours. From the following day, we supplied 1.4-GeV beams to the storage ring for the storage ring commissioning. The reason to reduce the beam energy to 1.4 GeV was that the injection kicker could provide a full aperture kick at that energy. For 2-GeV beam injection, the storage ring uses correctors imbedded at nearby bending magnets to obtain an extra-kick. The first circulation of the beam at the storage ring was made on September 8, 1994, and the beam was stored for the first time on September 13, 1994. The history of linac operations are summarized in Fig. 1 during October - December period. It shows clearly that the beam current from the linac increased as we achieved experiences for the linac operation. The stored beam and the injection efficiency were also increased drastically. The beam energy was changed from 1.4 GeV to 2 GeV on October 24, 1994. During the brief shutdown period in the beginning of November for the storage ring maintenance, we operated the linac to achieve maximum possible beam energy which was 2.34 GeV on November 7, 1994. It is still the best energy we have obtained. There was another brief shutdown due to the completion ceremony which held on December 7, 1994. The commissioning was resumed from December 11, and we achieved the maximum stored beam current of 300 mA on December 24, 1994. On the same day, we declared the completion of the SR commissioning.

C: Third Period: January to April, 1995

The first three months of 1995 was allocated to replace various diagnostic instruments installed temporarily. And the intensive work for the vacuum cleaning and survey/alignments in the storage ring were also performed. During this period, we replaced the e-gun pulser system which could provide 2 ns pulse only. The new pulser system can provide 1, 2, or 40 ns pulsed beams. About 40 % of the electron beams generated from the e-gun is delivered to the storage ring. In February and March, we trained all the linac division members as machine operators.

Normal operation for the linac started from April 1, 1995. At present, we operate the linac 24 hours a day from Monday morning to Friday morning. A team of two-member serves a operation shift and there are two shift teams per day.

Up to now, we have no significant failures in the linac operations. The operation hours for eleven klystrons are over 120,000 hours as shown in Fig. 2. As of the end of April 1995, the cumulative beam operation time for the linac is about 1,100 hours.

V. FUTURE PLAN AND SUMMARY

The PLS project is the first attempt in Korea for constructing a major accelerator facility. In addition, the 2-GeV injector linac is the third largest electron linac in the world. The prime mission for providing beams to the storage ring requires a few minutes for each injection, and ultimately, it will happen once or twice in a day. Therefore, we planned to use electron beams of various energies to promote other branches of basic and applied sciences.

First, we propose to add a "pulse stretcher" ring for nuclear physics experiments in the other side of the storage ring where there is enough space already prepared [2]. Secondly, there is a plan to build a compact storage ring for commercial use by Samsung Heavy Industries [3]. The PAL will help to design an injector linac and a compact ring, and our experiences will be great

help for them to construct the compact ring.

The PLS 2-GeV linac has been successfully commissioned in June 1994 as scheduled, and its performance exceeds the design values. We have demonstrated that it is a viable option as a full energy injector to the storage rings up to this energy in the construction cost. Through the PLS project, we have established a technology base for particle accelerators and trained young scientists and engineers in Korea. We are mostly benefited from exchanges of personnel and information with other established laboratories through institutional collaborations. We expect to use our experiences for advanced accelerator R&D programs and for new projects.

VI. ACKNOWLEDGMENTS

The authors thank technical staff of the PAL Linac Division for their hard work, and to POSCO and MOST for their commitment and endorsement to the PLS project. Most of all, we would like to dedicated this achievement to late Dr. Hogil Kim, who envisioned the PLS Linac and had been waiting for the completion and normal operations with great eagerness.

VII. REFERENCE

- [1]. W. Namkung, "PLS 2-GeV Linac," Proc. of 1994 International Linac Conference, Tsukuba, Japan, August 1994, pp14-18.
- [2]. I. Ko et. al., "Conceptual Design of PAL Stretcher Ring," these proceedings.
- [3]. K. Kim et. al., "The Design of a 1.2 GeV Synchrotron Light Source for X-ray Lithography at Samsung Heavy Industries," these proceedings.

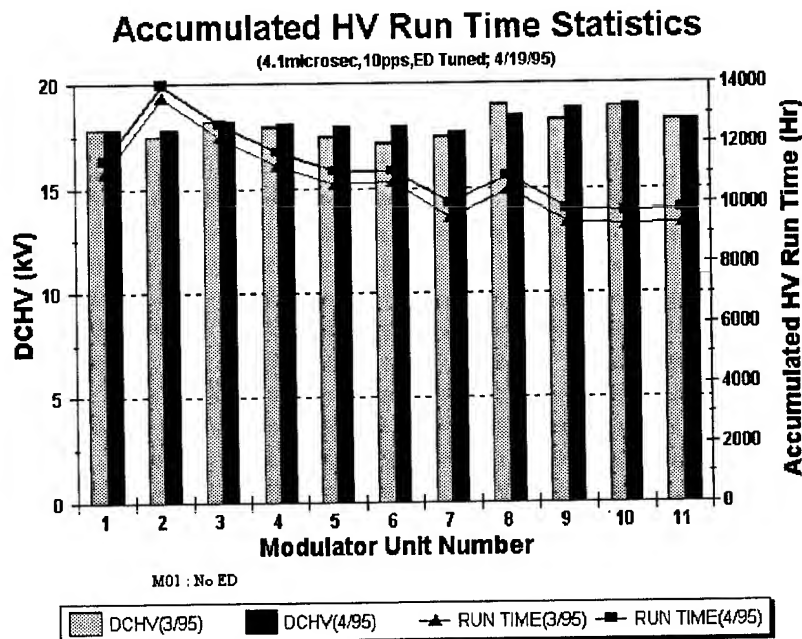


Fig. 2: Cumulative operation times for eleven klystrons.

RADIATION MEASUREMENTS AT THE ADVANCED PHOTON SOURCE (APS) LINEAR ACCELERATOR*

H. J. Moe, J. H. Vacca, V. R. Veluri, and M. White, Argonne National Laboratory, 9700 South Cass Avenue, Argonne, IL 60439 USA

Abstract

The injector and source of particles for the Advanced Photon Source is a 2856-MHz, S-band, electron-positron linear accelerator (linac) [1]. It produces electrons with energies up to 650 MeV or positrons with energies up to 450 MeV. Radiation measurements were made during normal electron and positron operation, as well as during several beam loss scenarios. Neutron and gamma measurements made outside the shielding walls during normal operation are within DOE guidelines. Measured radiation fields are compared to predicted levels for different conditions.

I. INTRODUCTION

The design goal of the APS electron linac is to accelerate 1.7 A of electrons in 30-nsec-long pulses to an energy of at least 200 MeV at a rate of 48 pps. The electrons are then focused to a 3-mm-diameter spot on the tungsten target that serves as a positron converter. To date, 1.4 A of electrons have been accelerated to 225 MeV at a 30-Hz rate, and focused to a ≈ 5 -mm-diameter spot on the target.

The linac is housed inside a concrete-shielded enclosure that protects personnel in nearby areas, including the adjacent klystron gallery, from radiation during linac operation. The linac shielded enclosure is constructed of concrete that is 2 m thick along the entire length between the linac and the klystron gallery. The shield is modified in the vicinity of the positron target, where 0.4-m-thick steel plates are embedded within 1.6-m-thick concrete to further reduce photon radiation levels in the klystron gallery. Calculated unshielded x-ray dose rates inside the linac tunnel 1 m downstream of the positron target are as high as 7×10^9 mrem/hr [2,3]. Unshielded neutron dose rates are on the order of 10^6 mrem/hr.

Measurements of radiation from the target were made in normally occupied areas of the klystron gallery using gamma and neutron instruments. The measured data are compared to computations of the estimated radiation leakage at the nominal and the maximum (safety envelope) operating power. The rationale for defining the safety envelope in terms of beam power is that within the APS linac's energy range, production yields of secondary radiation including positrons, neutrons, and gamma rays are proportional to the beam power. Measurements during some types of beam missteering incidents were performed at low power. In addition, the radiation leakage fields at shield-wall penetrations for waveguide, cable tray, and pipe passages were measured. Additional shielding was added where necessary.

II. MEASUREMENTS

A Victoreen 450P ion chamber survey meter [4] was used for the gamma measurements. The pulse response of this meter was checked by measurements made at the Argonne National Laboratory (ANL) 21-MeV electron linac. Neutron measurements were made with an Andersson-Braun type moderator and a BF₃ tube, supplied by Nuclear Research Corporation [5]. The response of this instrument to pulsed fields was also checked at the ANL linac. Although this device begins to show saturation at 1 μ rem/pulse, it is adequate for these 30-Hz measurements.

Measurements were made every 1 m along the entire length of the klystron gallery, along a line offset 6 m from the beamline, as shown in Figure 1. This line represents the closest distance to the beamline in normally occupied regions of the gallery. In order to separate radiation caused by the target from possible contributions from the klystron waveguides and optical arc-detector ports, the measurements were made in two steps. First, radiation fields were measured with both the beam and the rf on, under conditions that resulted in 225 W of beam power on the target. The beam was then stopped by turning off the electron gun, but the rf power was left on. The radiation measurements were then repeated. The difference between the two sets of measurements represents the contribution from the target, and is shown in Figure 2.

Because of the low levels of leakage radiation from the target, the data are somewhat sensitive to x-ray interference from the klystron waveguides. The small negative values in the difference plot in Figure 2 are the result of such interference. The dose rates shown in Figure 2 are photon radiation dose rates, since neutron levels are still below the 10 μ rem/hr detection limit of the instrument. Additional lead shielding is being installed to mitigate localized x-ray radiation from the klystron waveguides.

Measurements of radiation fields during missteerings to simulate accident conditions have not yet produced any readings that can be compared with predicted values for the postulated maximum credible incident (MCI).

Measurements inside the penetrations have shown photon levels in the few mrem/hr range and neutron levels in the tenths of mrem/hr range, except for the penetration nearest the target. The higher radiation levels measured at that penetration have been mitigated by the addition of lead and polyethylene shielding.

* Work supported by the U. S. Department of Energy, Office of Basic Sciences under the Contract W-31-109-ENG-38.

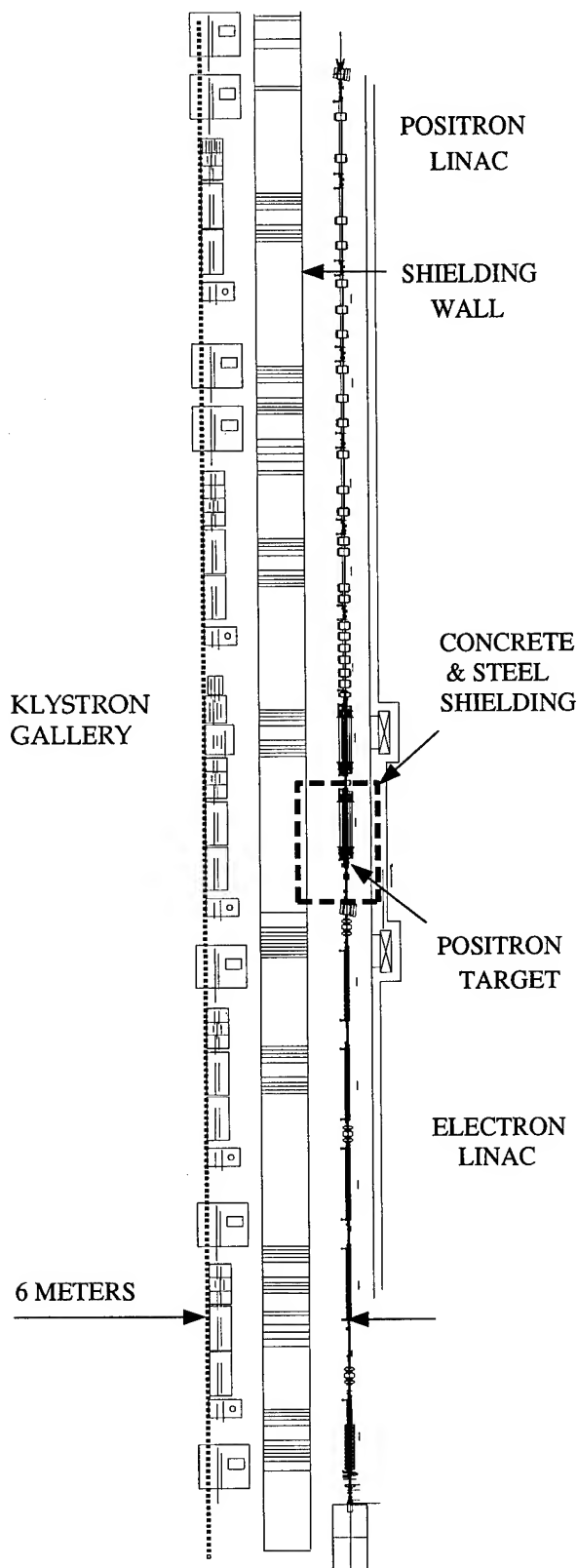


Figure 1: Radiation measurements were made in the klystron gallery along a line offset 6 m from the beamline.

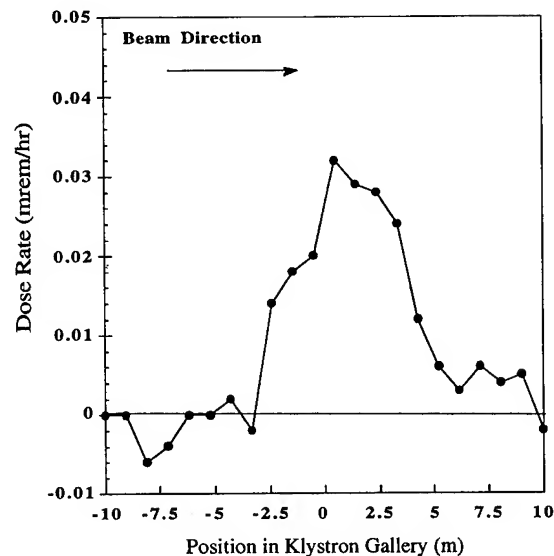


Figure 2: Measured radiation field in the klystron gallery as a result of 225 W of beam power on the target. The difference between the "Beam On" field and the "Beam Off" field is plotted.

III. CALCULATION

The predicted total leakage radiation levels from the target [6] for nominal 480-W operation and operation at the safety envelope (1000 W) are shown in Figure 3.

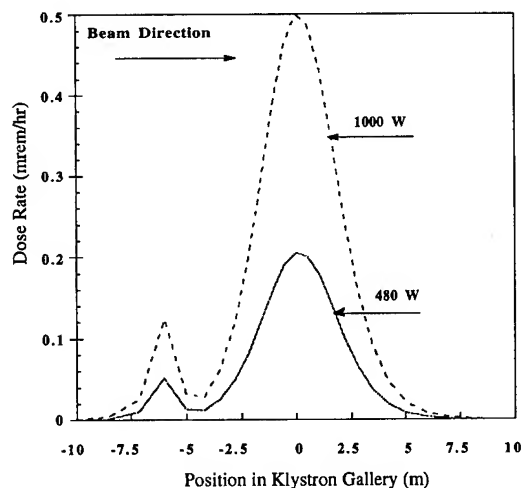


Figure 3: Predicted radiation fields in the klystron gallery at locations comparable to those in Figure 2. The lower curve is at the nominal operating power of 480 W, and the upper curve is at the safety envelope power level of 1 kW.

The maximum predicted dose rate values are 0.21 mrem/hr and 0.5 mrem/hr, respectively. Calculations for the bremsstrahlung dose distribution with angle are based upon the semi-empirical formula of Swanson [7]. The neutron yield and neutron angular distributions are based on the calculations of Gabriel and Alsmiller [8]. Neutron fluence-to-dose conversion constants were obtained from ICRP Publication 51 [9]. Self-shielding provided by the accelerating structures and magnets was not taken into account in these calculations. The peak dose rate occurs at a point adjacent to the target. The small structure in the calculated curve reflects the change in total shielding ability between that portion of the linac shield wall that is constructed only of concrete and the portion with additional steel embedded in the concrete.

IV. RESULTS

Comparing the predicted peak total dose rate of 0.21 mrem/hr for 480-W operation from Figure 3 to the measured peak total dose rate of 0.033 mrem/hr from Figure 2 and normalizing to the same operating power as in Figure 3, indicates a ratio of $\frac{0.21}{0.033 \times 480/225} \sim 3$. Using the peak

value at the safety envelope, the ratio would become $\frac{0.5}{0.033 \times 1000/225} = 3.4$. This result indicates that the DOE

design criterion for new facilities that requires dose rates outside of shielded areas to be less than 0.25 mrem/hr would be met, even at the safety envelope, with no additional mitigation. That the detailed structure predicted by the calculation was not measured can be attributed to masking effects by interference from the x-ray radiation from the klystron waveguides.

V. CONCLUSION

The results obtained in this study indicate that the linac shielding is adequate for operation up to the safety envelope and is in compliance with DOE guidelines. Beam power has been limited thus far by equipment conditioning, and measurements will be made at higher power levels as soon as possible. At the higher levels, the neutron radiation may make a contribution. Beam missteering tests at higher power might possibly also give dose rate data that can be extrapolated to the MCI conditions. At the low dose rates seen in these measurements, great care must be taken to exclude extraneous radiation fields in order to obtain representative results.

VI. REFERENCES

- [1] M. White, et al., "Performance of the Advanced Photon Source (APS) Linear Accelerator," these proceedings.
- [2] H. J. Moe, unpublished document.
- [3] Advanced Photon Source Linac Safety Assessment Document, APS Document Nr. 1.1.10-00017, July, 1993 and Advanced Photon Source Injector Safety Assessment Document. APS-3.2.2.1.0, January 1994.

- [4] Victoreen, Inc., 10101 Woodland Ave., Cleveland. OH.
- [5] NRC Industries, 125 Titus Ave., Warrington, PA.
- [6] H. J. Moe, unpublished document.
- [7] W. P. Swanson, et al., Aladdin Upgrade Design Study: Shielding.
- [8] T. A. Gabriel and R. G. Alsmiller, Jr., "Photoneutron and Photopion Production from High-Energy (50 to 400 MeV) Electrons in Thick Copper Targets," ORNL-4443, 1969.
- [9] "Data for Use in Protection Against External Radiation," ICRP Publication 51, Pergamon Press, Oxford, England, (1987).

POSITRON FOCUSING IN THE ADVANCED PHOTON SOURCE (APS) LINEAR ACCELERATOR*

Y. L. Qian and M. White, Argonne National Laboratory, Argonne, IL, 60439 USA

Abstract

Positrons are created by a bremsstrahlung shower process, and are therefore produced with broad divergence and a large energy spread. The e^+/e^- conversion ratio is on the order of 1/200, so the positron focusing system is critical to ensure good positron capture and transport efficiency. The positron focusing system is described, and functions of the different magnetic elements are discussed. Some improvements to the focusing system are suggested, although the linac's design positron intensity of 8 mA has already been achieved [1].

I. INTRODUCTION

Positrons are used in the APS storage ring in order to avoid ion trapping. Electrons are accelerated to 200 MeV in the electron linac, and focused to a 3-mm to 5-mm-diameter spot on a 2-radiation-length-thick tungsten target. The energy spectrum of positrons emerging from the target is shown in Figure 1. The pair-produced positrons (and electrons) are then accelerated to 450 MeV by the remainder of the linac. Positrons are produced with divergent angles, a broad energy spectrum, and with a much larger emittance than that of the initial electron beam; thus the positron linac focusing system is different from the electron linac focusing system. A short pulsed solenoid serves as first part of the focusing system for the low energy positron beam, followed by 6 m of DC solenoids. Quadrupole magnets focus the positrons as they gain energy and contain them through the remainder of the linac.

II. SOLENOID FOCUSING

A 5-cm-long pulsed solenoidal coil is the first focusing element in the positron linac. The coil has an inner diameter of 25 mm and operates at its design peak current of 5000 A. It is fabricated from a single piece of water-cooled copper tubing that is wound around the inside and the outside of a cylindrical piece of ceramic. There are a total of 16 turns. The tube rests in grooves machined into the inside and outside of the ceramic. The ceramic support is located between the two coil layers to provide mechanical stability. A prototype made with machinable ceramic was used in the first tests, but the ceramic did not withstand the high radiation fields and was replaced with 99.5% pure ceramic [2]. The layout of the pulsed coil and target is shown in Figure 2.

The pulsed solenoid coil serves as a quarter-wave transformer (QWT) for the beam's phase space. It rotates the initial transverse phase space from a small radius and a large slope to a phase space with a larger radius and a smaller slope.

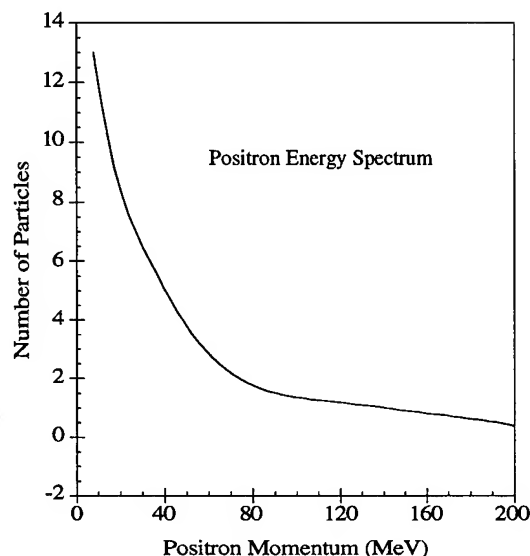


Figure 1: Momentum spectrum of positrons from the target.

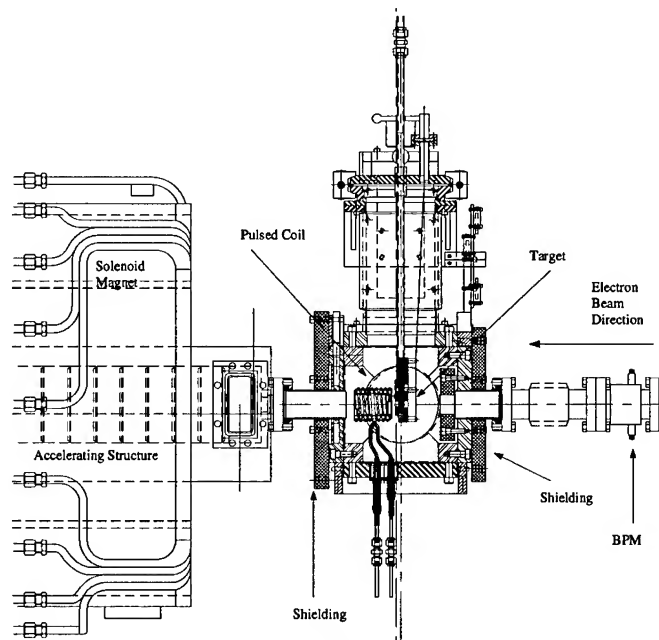


Figure 2: Layout of the pulsed coil and positron target.

The DC solenoidal field is generated by two 2.5-m-long solenoid magnets with a 0.2-m-long solenoid coil between them for matching. The long solenoids have 784 turns in four

* Work supported by the U. S. Department of Energy, Office of Basic Sciences under the Contract W-31-109-ENG-38.

layers with integrated steering and correction coils. The maximum axial field of the long solenoids at 1000 A is 0.36 T.

The acceptance, A , is determined by the field in the long solenoids and the aperture of the accelerating structure:

$$A = \frac{\pi}{2} e B_2 r_2^2, \quad (1)$$

where e is the charge of the particle, B_2 is the longitudinal DC field in the solenoid, and r_2 is the radius of the aperture. The minimum radius of the accelerating structures is 9 mm; therefore the acceptance is about $A = 0.3 \pi \text{ MeV/c cm}$. The maximum transverse momentum, P_r , that can be captured from the target is determined by

$$P_r = \frac{A}{r_1}, \quad (2)$$

where r_1 is the beam-spot radius on the target. With a 1.5-mm-radius beam spot on target, a maximum P_r of 2 MeV/c is accepted into the accelerating structure. Equation (2) shows that a small spot size on the target is an advantage since more particles with higher P_r are accepted.

The matching condition for the two solenoids is:

$$B_1 = \frac{r_2}{r_1} B_2. \quad (3)$$

The optimized length of the QWT pulsed solenoid coil [3] is given by

$$L = \frac{\pi r_2^2}{A} P_z. \quad (4)$$

P_z is 8 MeV, so a 5-cm-long pulsed solenoid coil was used. The longitudinal momentum acceptance of the QWT is

$$\frac{\Delta P}{P} \approx C \frac{B_2}{B_1}, \quad (5)$$

where C is a geometric constant on the order of one. Positrons with longitudinal momentum $8 \pm 1.6 \text{ MeV/c}$ are captured and accelerated. Path lengths of the particles in the QWT depend on P_r . Differences in momenta lead to bunch lengthening that eventually limits the acceptance. Ideally B_1 is constant and the phase difference between a particle of zero transverse momentum and transverse momentum P_r is given by [4]

$$\Delta\phi = \frac{360^\circ}{\lambda_{rf}} L \left(\sqrt{\left(\frac{P_r}{P_z} \right)^2 + 1} - 1 \right). \quad (6)$$

In our case $\lambda_{rf} = 10.5 \text{ cm}$, $L = 5 \text{ cm}$, $P_r = 2 \text{ MeV/c}$, $P_z = 8 \text{ MeV/c}$, and the phase difference is $\Delta\phi = 5.5^\circ$.

The emittance at the exit of a long solenoid is reduced, and that is an advantage in beam transport. The accepted beam emittance at the surface of the target is $1.5 \times 240 \pi \text{ mm mrad}$. The pulsed solenoid changes the emittance at the entry of the long solenoid region to $9 \times 40 \pi \text{ mm mrad}$. Subsequent acceleration increases the beam energy and reduces its

emittance. The longitudinal momentum is $\approx 100 \text{ MeV/c}$ after the 7-m-long solenoid region, and the emittance is reduced to $9 \times 4 \pi \text{ mm mrad}$.

Solenoids are used to focus the low energy positrons in both transverse planes simultaneously, but they do not really reduce the radial beam size. Perturbations or instabilities can lead to beam losses in a long solenoid region, because the transverse beam size is the same as the accelerating structure aperture. The actual beam size just downstream of the DC solenoids is almost the size of the aperture when observed on a fluorescent screen. The transverse beam size downstream of the target must be decreased as early as possible to reduce beam loss, and that is done by quadrupole magnets. Many other positron sources use quadrupoles from a beam energy of about 50 MeV, [5-7] and we feel that a shorter solenoid region could improve the e^+ yield here as well. KEK experienced an increase in their e^+/e^- ratio with a shorter solenoid in their positron linac [7].

Both positrons and electrons are captured and are accelerated in the positron linac, as this linac is not equipped with a chicane that removes the electrons at low energy. Optimizing the positron beam is complicated by the presence of both positive and negative particles. The beam position monitors are not able to distinguish the sign of the charge and cannot be used independently to steer the positrons. However, six fluorescent screens in the positron linac are successfully used in combination with the BPM information.

III. QUADRUPOLE FOCUSING

Quadrupoles that focus the beam and reduce its radial size are the next part of the positron focusing system. The radial beam size should be reduced as soon as practical after the beam exits the solenoidal field. The best way to accomplish that would have been with a small-aperture quadrupole doublet in the 0.5-m-long drift space downstream of the solenoids. The 38-mm-diameter vacuum pipe in the drift spaces is larger than the accelerating structure aperture, and a doublet in that location would reduce the beam size to the extent that the downstream quadrupoles would not cause further beam loss. Without this doublet, the transverse beam size is defocused in one plane by the quadrupoles and easily becomes larger than the aperture of the accelerating structure.

Twenty-three 152-mm-diameter, 300-mm-long large-aperture quadrupole magnets are installed over the accelerating structures in the positron linac. A single large-aperture quadrupole that is only 150 mm long is intended to match the solenoidal field to the quadrupole field before the transverse beam size has been reduced much. This focusing/defocusing action probably leads to some beam loss in our case, since the first quadrupole occurs where the beam size is still large. The large quadrupole aperture does offer flexibility in magnet placement and allows us to use most of our drift spaces for diagnostics, such as fluorescent screens, current monitors, and BPMs. The required distance between the quadrupoles is determined in the thin lens approximation by [5]

$$L = \frac{\pi r_z^2}{A} P_z. \quad (7)$$

More quadrupoles are required at the low energy end than at high energy, so the quadrupole spacing on the first accelerating structure after the solenoids is short. Large-aperture quadrupoles on the first two accelerating structures after the solenoids still provide a reasonable solution for focusing the beam without the use of short accelerating structures.

The positron linac beam envelope was calculated for the existing focusing system using TRANSPORT [8] and is shown in Figure 3. The beam loss at the first accelerating structure after the solenoid could be eliminated by adding a doublet of small-aperture quadrupoles in the drift space after the solenoid. This drift space is only 500 mm long, so magnets with an effective length of 0.1 m and a gradient of 1.0 T/m, similar to those in the electron linac, would be used and could be installed without major disruption.

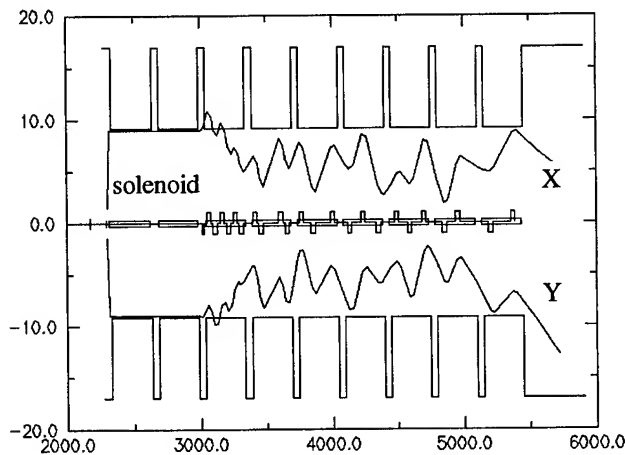


Figure 3: Calculated positron envelope with the existing focusing system.

The calculated positron linac beam envelope with a possible modified focusing scheme is shown in Figure 4. The additional doublet reduces beam losses caused by the downstream quadrupole magnets and significantly reduces beam profile expansion in the first drift space after the solenoid. The 38-mm-diameter vacuum pipe in the drift space allows the quadrupoles to function without causing losses, and it reduces the transverse beam size at the entrance to the next accelerating structure, so that downstream quadrupoles do not cause further beam losses.

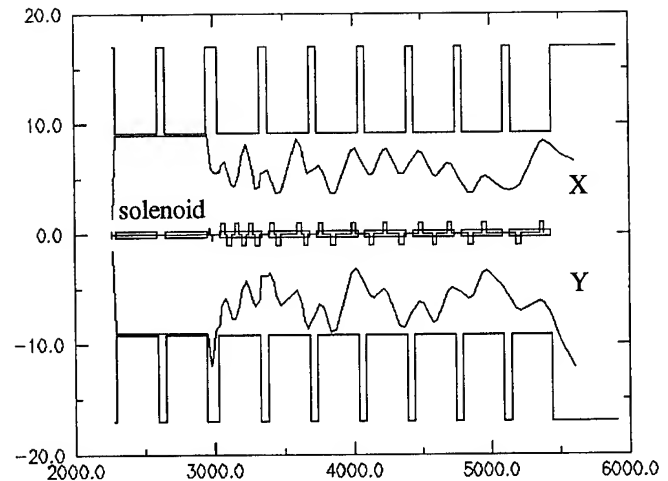


Figure 4: Calculated positron envelope with a possible modified focusing system.

IV. CONCLUSION

The APS linac positron focusing system is adequate to provide the design positron current; however, a few simple modifications might be done that could significantly improve the performance and make the positron linac much easier to optimize.

V. REFERENCES

- [1] M. White, et al., "Performance of the Advanced Photon Source Linear Accelerator," these proceedings.
- [2] Coors Ceramic, Inc.
- [3] G. Stange, *IEEE Trans. Nucl. Sci.* **NS-26** 4146 (1979).
- [4] L. Rinolfi, "The Positron Production at LIL," ESRF Workshop, Grenoble (1992).
- [5] The Stanford Two Mile Accelerator, Chap. 16, Benjamin, New York (1968).
- [6] S. Humphries, Jr., Charged Particle Beams, (John Wiley and Sons, Inc., New York, 1990), p. 402.
- [7] A. Enomoto et al., "Focusing System of the KEK Positron Generator," *Nucl. Inst. and Methods*, **A281** 1-9 (1989).
- [8] TRANSPORT Code, SLAC-91 Rev. 2.

Bunch Length Measurements at the Advanced Photon Source (APS) Linear Accelerator *

N. S. Sereno, R. Fuja, C. Gold, A. E. Grelick, A. Nassiri, J. J. Song, M. White
Advanced Photon Source, Argonne National Laboratory
9700 South Cass Avenue, Argonne, Illinois 60439 USA

Abstract

Measurements of the APS linac micro-bunch length are performed by backphasing a single 2856-MHz, S-band linac waveguide and using a downstream spectrometer to observe the beam. By measuring the beam width in the dispersive plane as a function of rf power into the linac waveguide, the bunch length can be determined absolutely provided the beam energy and dispersion at the spectrometer are known. The bunch length determined in this fashion is used to calibrate a fifth-harmonic bunch length cavity which is used for real-time bunch length monitoring.

I. INTRODUCTION

Bunch length measurements of the APS linac electron beam are required in order to evaluate the performance of the low energy bunching process of the beam emitted by the thermionic gun. Bunching of the 100-keV beam is performed by a standing wave cavity and drift (the prebuncher) followed by a 5-cell traveling wave cavity (the buncher) where each cavity operates at a frequency of 2856 MHz. After the buncher, the beam is accelerated from an energy of 1.4 MeV to 50 MeV by the first 3-m, 86-cell accelerating waveguide operating at 2856 MHz. Four downstream accelerating waveguides further accelerate the beam to 220 MeV at the positron target. After the target, nine accelerating waveguides are used to accelerate the positrons to 450 MeV.

The electron beam consists of 30-ns macropulses repeated at a 2-Hz rate. Each 30-ns macropulse consists of 86 micro-bunches after the bunching process is completed (essentially after the beam passes the buncher). The micro-bunch length of the APS linac electron beam (from now on referred to as the bunch length) has been measured by backphasing a single accelerating waveguide and observing the beam after a downstream spectrometer. The accelerating waveguide is phased so that the centroid of each micro-bunch passes through it when the electric field is zero (zero crossing). Energy spread is induced in the micro-bunch because at zero crossing, depending on the slope of the rf waveform, particles obtain more or less energy depending on their location within the micro-bunch. The induced energy spread is linearly related to the bunch length for bunches that are short compared to the rf period (350 ps at 2856 MHz).

A standing wave cavity operating at the fifth harmonic of the bunching frequency (14.28 GHz) is used for real time monitoring of the bunch length in the linac [1]. The peak output power of the cavity depends on the bunch length. The fifth harmonic frequency was chosen to maximize the output power for small (~ 5 ps rms) micro-bunches consistent with mechanical and

electrical constraints. Calibration of the cavity is accomplished by first measuring the bunch length by the backphasing technique and using the result to determine the effective cavity shunt impedance.

II. THEORY

The basic apparatus for the bunch length measurement consists of an accelerating waveguide through which a relativistic bunched electron beam passes on zero crossing. The beam is subsequently observed downstream of the accelerating waveguide at a spectrometer consisting of a dipole magnet, a drift, and a screen. The transverse position of a given beam particle in the dispersive plane on the screen is given by

$$x = x_\beta + \eta \frac{\delta p + (E_g/c) \sin \phi}{p}, \quad (1)$$

where x_β is the usual betatron oscillation of the particle, η is the dispersion at the viewscreen in meters, δp is the intrinsic momentum offset of the particle, p is the central momentum of the beam, E_g is the maximum energy gain in MeV of a particle that traverses the accelerating waveguide on crest, and ϕ is the phase of the particle in radians relative to the particle that goes through the accelerating waveguide on zero crossing. Equation (1) shows that the transverse position of the particle is linearly related to the phase offset from zero crossing for $\phi \ll 1$ radian.

For a given particle distribution for each micro-bunch, Eq. (1) can be used to write the rms beam size in terms of parameters of the backphased waveguide and spectrometer. The rms size is defined by

$$\sigma^2 \equiv \langle (x - \langle x \rangle)^2 \rangle, \quad (2)$$

where $\langle \rangle$ denotes integration of the particle coordinates over the particle distribution. Inserting Eq. (1) into Eq. (2) results in

$$\begin{aligned} \sigma^2 = & \sigma_{(x_\beta + D \frac{\delta p}{p})}^2 + \{ \langle x_\beta \sin \phi \rangle - \langle x_\beta \rangle \langle \sin \phi \rangle + \\ & \frac{\eta}{p} \{ \langle \delta p \sin \phi \rangle - \langle \delta p \rangle \langle \sin \phi \rangle \} \frac{2\eta}{pc} E_g + \\ & \frac{\eta^2 \sigma_{\sin \phi}^2 E_g^2}{(pc)^2} \end{aligned} \quad (3)$$

$$\sigma_{\sin \phi}^2 \equiv \langle (\sin \phi - \langle \sin \phi \rangle)^2 \rangle. \quad (4)$$

In Eq. (3), the first term is due to the natural emittance and energy spread of the beam. The second term results from correlations between the particle betatron oscillation, phase relative to zero crossing and natural momentum spread. The third term contains the rms bunch length when

$$\sigma_{\sin \phi} \simeq \sigma_\phi, \quad (5)$$

*Work supported by U.S. Department of Energy, Office of Basic Energy Sciences, under Contract No. W-31-109-ENG-38

which is an excellent approximation for short bunches where $\sin\phi \simeq \phi$. Typical rms bunch lengths for the APS linac are $\sim 5^\circ$ and therefore meet the approximation given by Eq. 5 (for comparison $1^\circ = 1.03$ ps for 2856 MHz).

III. MEASUREMENT RESULTS

Equation (3) indicates that the rms bunch length can be obtained by fitting a quadratic curve to a measurement of σ^2 vs E_g . The form the fitting function therefore takes is

$$\sigma^2 = a_0 + a_1 E_g + a_2 E_g^2, \quad (6)$$

where the above terms are readily identified with those of Eq. (3). The second-order term yields the micro-bunch length provided the central momentum (energy) and dispersion at the viewscreen are known. It is desirable to go to a large waveguide energy gain so that the quadratic term dominates the other two. The relative error in the quadratic term will therefore be minimized.

Figure 1 shows the data taken using a single accelerating waveguide driven by a single klystron. The beam energy at the entrance to the accelerating waveguide was 220 MeV. The data were taken at a beam current of 150 mA average current per macropulse (52 pC per micro-bunch) due to the fact that camera and viewscreen saturation effects limit resolution at higher beam currents. The micro-bunch length backphase measurement was performed using the beam resulting from a "standard" setup for the buncher and prebuncher. The resulting beam spot distribution on the spectrometer viewscreen was symmetric and easily analyzed. The beam image analysis software computes σ directly from the measured beam intensity distribution according to Eq. (2). No assumptions about the exact microbunch structure need be made. At each accelerating waveguide energy gain, the rms size was taken to be the average of the rms size of five beam snapshots taken. The error bars are taken to be the standard error for the mean [2]. This averaged out shot-to-shot fluctuations of the rms size due to rf and other noise sources. The quadratic fit to the data is shown as the solid line. The fit is acceptable with most data points lying within a distance of twice their error bar of the fit. Table I summarizes the measurement parameters, the results of the fit, and gives the inferred bunch length. The dominant errors contributing to the bunch length error are the error in the second term a_2 and the dispersion. The last entry in Table I is an estimate of the FWTM (full width at 10% of the maximum height of the distribution) bunch length. The FWTM bunch length was estimated by comparing the ratio of the FWTM beam size to σ for each data point and taking the average of this ratio for all the data points. The average ratio was found to be 4.53 (for comparison, the ratio of the FWTM size and the rms size σ for a Gaussian distribution is 4.3).

IV. FIFTH HARMONIC CAVITY CALIBRATION

The measurement procedure just described, though automated using the SDDS tools [3], is time consuming. A bunch monitor previously described [1] is used for real-time (shot-to-shot) bunch length monitoring. The peak cavity output power for a given beam current is given by

$$P = \frac{RI_0^2}{2} e^{-m^2 \sigma_\phi^2}, \quad (7)$$

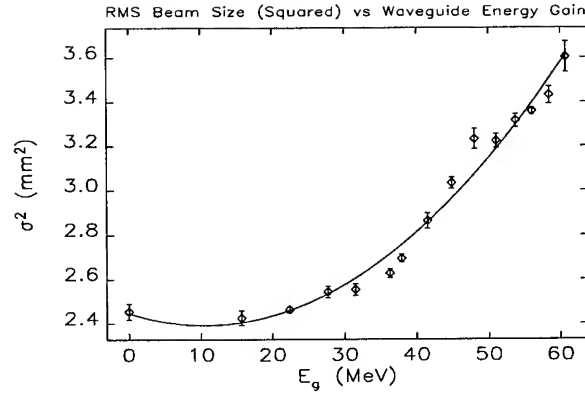


Figure 1. Bunch length measurement data consisting of σ^2 vs E_g . The solid line shows the best fit quadratic curve to the data.

Table I
Bunch length measurement parameters.

Parameter	Value
p	334.8 ± 3.3 MeV
η	194 ± 5 mm
a_0	$2.45 \pm .05$ mm ²
a_1	$(-1.0 \pm .3) \times 10^{-2}$ mm ² /MeV
a_2	$(4.9 \pm .5) \times 10^{-5}$ (mm/MeV) ²
σ_ϕ	$(2.2 \pm .1)^\circ$
FWTM $_\phi$	$(9.9 \pm .6)^\circ$

where I_0 is the average beam current and the notation for the effective shunt impedance R from reference [1] is kept. The power given by Eq. (7) is seen to depend on the bunch form factor $e^{-m^2 \sigma_\phi^2}$. This form factor arises specifically because a Gaussian shape for the microbunch was assumed. For short bunches, the precise functional form of the form factor matters little because the second order Taylor expansion to second order for different form factors is identical for frequencies that are small relative to the rolloff frequency given by the inverse temporal bunch length. The factor multiplying the rms bunch length m , is the harmonic number of the bunched beam signal. Since the fundamental cavity mode operates at the fifth harmonic of the bunching frequency $m = 5$ for the cavity considered here.

The reason for going to as large a harmonic number as possible is to increase measurement sensitivity to short bunches. Equation (7) is now used to estimate the smallest bunch length measurable for a cavity (or any detector) operating at some harmonic of the bunching frequency. Assuming that 0.1-dB power changes are the minimum detectable in the presence of typical noise sources, the minimum rms bunch length is given by

$$\sigma_\phi^{\min} = \frac{1}{10 \sqrt{\log(e)}} \frac{1}{m}, \quad (8)$$

which for our cavity turns out to be 1.74° (7.48° FWTM assuming a Gaussian distribution). Inspection of Table I reveals that the bunch length determined in the backphase measurement is nearly at the theoretical lower limit defined by Eq. (8).

Calibration of the cavity consists of determining the effective shunt impedance in Eq. (7). The peak cavity output power was measured using a calibrated fast diode. Corrected for cable losses, the peak cavity output power was measured to be 45.9 mW for a beam current of 150 mA. Using the measured bunch length listed in Table I and Eq. (7), the shunt impedance turns out to be 4.2Ω . The calculated shunt impedance from SUPERFISH is 33Ω . The order of magnitude difference stems from two primary effects. The first is that for a 30-ns pulse, the cavity is not completely filled, and second, the loaded and unloaded Q results in a mismatch which reduces the peak output power [4]. Both these effects increase the shunt impedance by a factor of two to three.

Further studies are being conducted by varying the beam current to get a more precise value for the shunt impedance and to evaluate the measurement uncertainties involved. A measurement uncertainty of 10 % for the shunt impedance should be adequate and achievable. One way of determining the shunt impedance would be to produce a bunch length smaller than the minimum detectable as given by Eq. (8) and measure the peak power as a function of beam current squared. The slope of this curve from Eq. (7) is simply $R/2$. Bunch lengths greater than that given by Eq. (8) would manifest themselves as a reduction in the slope given by the form factor in Eq. (7). Of course, this measurement of R assumes that the bunch length does not vary appreciably as the beam current is varied. This is a good assumption at the very low beam currents used here, where space charge is negligible. Extension of this idea would require a separate bunch length measurement using the backphase technique at each beam current.

V. CONCLUSION

The bunch length has been measured by backphasing a single accelerating waveguide and observing the beam at a downstream spectrometer. Improvements to the measurement include going to higher values of E_g by using four backphased waveguides driven by a single klystron and SLED [5]. Compared to a single accelerating waveguide, four accelerating waveguides would allow four times the energy spread to be induced in the beam for a given bunch length. Another approach would be to increase the dispersion of the spectrometer which would require hardware modification.

The fifth-harmonic cavity calibration was done at a single beam current and bunch length. Additional measurements will be made at multiple beam currents and bunch lengths to check the calibration over a broad range of beam parameters. The measured cavity shunt impedance agrees with the calculation when the effects of cavity filling during the beam macropulse and mismatch are taken into account.

VI. ACKNOWLEDGEMENTS

The authors would like to thank all those at the APS involved in linac commissioning for their efforts. The first author would

like to thank G. Krafft and B. Bowling at CEBAF for their comments and suggestions regarding this measurement.

References

- [1] A. Nassiri and A. Grelick, "A Fifth Harmonic RF Bunch Monitor for the ANL-APS Electron Linac," *Proceedings of the 1993 Particle Accelerator Conference*, Washington DC, 2412 (1993).
- [2] P. R. Bevington, *Data Reduction and Error Analysis for the Physical Sciences*, McGraw-Hill Book Co. 70 (1969).
- [3] M. Borland, "A Self-Describing File Protocol for Simulation Integration, and Shared Post-Processing," these proceedings.
- [4] D. A. Goldberg and G. R. Lambertson, *AIP Conference Proceedings*, **249**, 560 (1992).
- [5] Z. D. Farkas, H. A. Hogg, G. A. Loew, and P. B. Wilson, "SLED: A Method of Doubling SLAC's Energy," SLAC-PUB-1453, June 1974.

PERFORMANCE OF THE ADVANCED PHOTON SOURCE (APS) LINEAR ACCELERATOR*

M. White, N. Arnold, W. Berg, A. Cours, R. Fuja, J. Goral, A. Grelick, K. Ko, Y. L. Qian, T. Russell, N.S. Sereno, and W. Wesolowski, Argonne National Laboratory, Argonne, IL 60439 USA

Abstract

A 2856-MHz S-band, electron-positron linear accelerator (linac) is the injector and source of particles for the APS [1]. The linac is operated 24 hours per day, with 405-MeV electrons to support commissioning of the other APS accelerators, and with positrons or electrons to support linac studies. It produces electrons with energies up to 655 MeV or positrons with energies up to the design energy of 450 MeV.

I. INTRODUCTION

The design goal of the APS electron linac is to accelerate 30-nsec-long pulses containing 50 nC of electrons to an energy of 200 MeV. The beam is focused to a 3-mm diameter spot on a 7-mm-thick water-cooled tungsten target that serves as a positron converter. Pair produced positrons and electrons are refocused by a 1.5-T pulsed coil, and are directed into the positron linac where they are captured and accelerated to 450 MeV \pm 1%. The design positron current is 8 mA. To date, 1.45 A of electrons were accelerated to 225 MeV at 30 Hz in the electron linac, and were focused to a \leq 5-mm diameter spot on the target. The linac was able to accelerate 9 mA of positrons to 285 MeV within one week of the beginning of positron studies, and has since achieved a positron energy of 450 MeV with an energy spread less than \pm 1.6%. Measured radiation levels near the linac are within DOE guidelines [2].

II. EQUIPMENT DESCRIPTION

Particles are accelerated in the linac by 14 SLAC-type accelerating structures, five in the electron linac and nine in the positron linac. The upstream accelerating structure in each part of the linac is directly powered by a 35-MW klystron, while the remaining 12 structures are powered in groups of four by a klystron and a SLED cavity assembly, as shown in Figure 1. Power to the klystrons is provided by 100-MW line-type modulators. Recent upgrades to the modulators led to improved performance and reliability, and are described elsewhere [3].

The individual timing of each of the five pulse modulators is optimized to gain maximum energy from the available rf power in each sector, and the timing of each of the three SLEDs is also individually optimized for maximum energy gain. The electron or positron beam is bent into the appropriate diagnostic line, and data on timing versus energy, interpreted from the beam position on a fluorescent screen, are taken and analyzed using sdds tools [4]. Timing is reoptimized after modulator upgrades and SLED retuning, and Figure 2 is an example of such a timing curve. Figure 3 is the diagnostic line at which the data were taken.

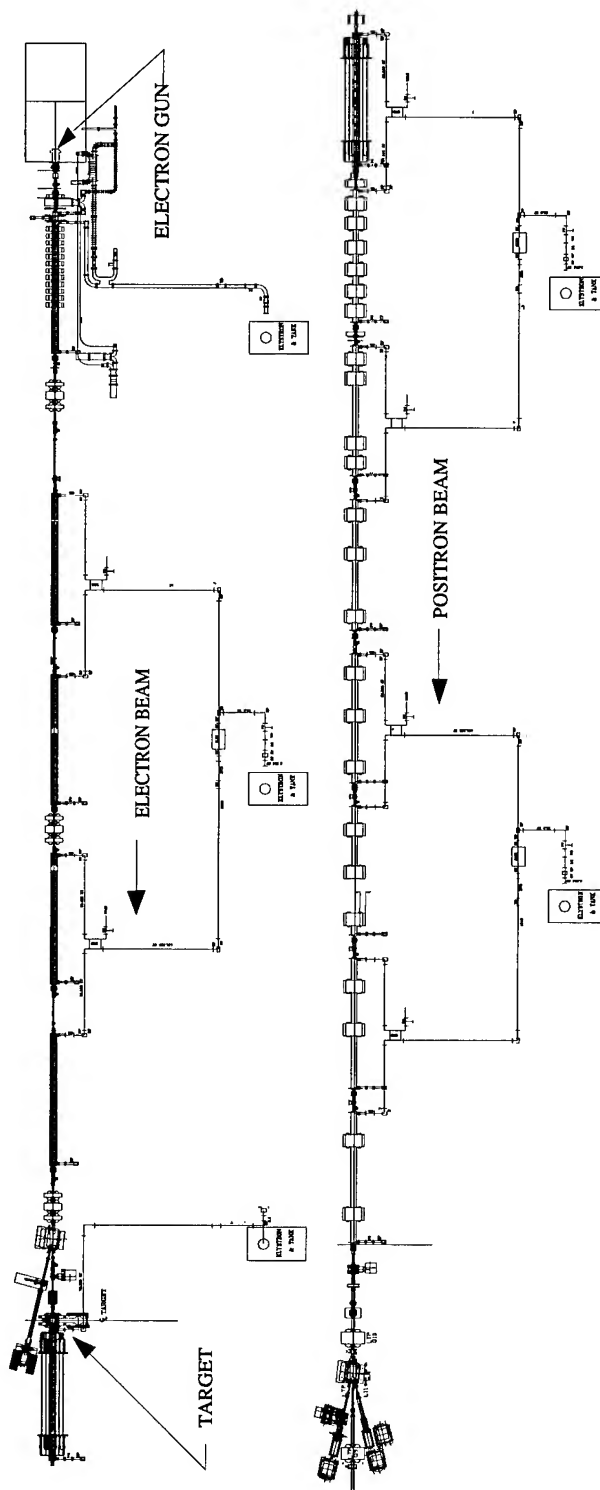
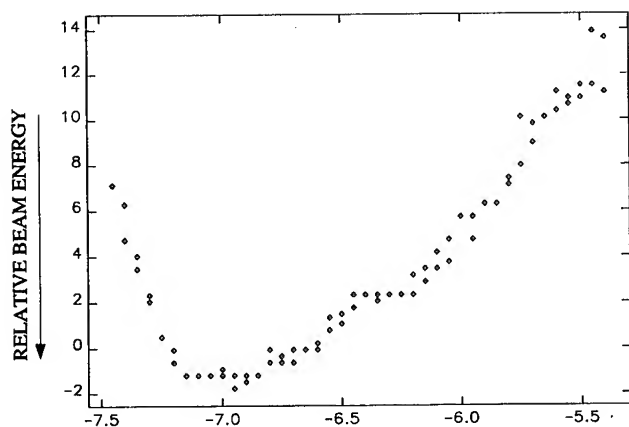


Figure 1: Overview of the electron and positron linacs.

* Work supported by the U. S. Department of Energy, Office of Basic Sciences under the Contract W-31-109-ENG-38.



L4 MODULATOR TRIGGER TIME (μsec)

Figure 2: Modulator (and SLED) timing optimizations are performed for each sector to optimize use of the modulator pulse and thus achieve maximum energy gain. These modulator timing data were collected using sdds tools [2].

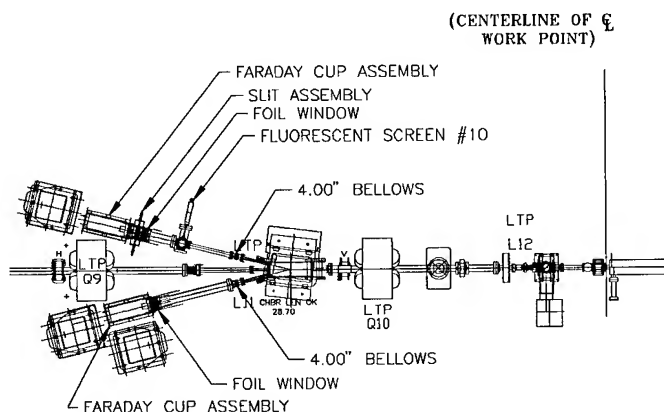


Figure 3: Positron linac diagnostic lines allow energy, energy spread, and phase optimization to be performed for electrons or positrons. Other beam parameters are also measured using information from equipment in this line.

A new beam position monitor (BPM) will be installed at the exit of the dipole magnet shown in Figure 3, and will allow continued development and eventual routine use of automated rf phase optimization programs.

The low-level rf system has functioned well for more than a year and is described elsewhere in these proceedings, along with the existing automatic rf phase control system that maintains constant phase (to within $\pm 2^\circ$) between the five klystrons [5].

Linac beam diagnostics include wall current monitors, BPMs [6], fluorescent screens [7], and loss monitors. The existing BPMs are unable to distinguish between positive and negative signals, so positron optimization must be done using BPMs in conjunction with other information. A new type of BPM currently under development will be able to make the distinction, and will facilitate positron tuning if successful [8]. Average current monitors are installed for the purpose of shutting down the linac in the unlikely event that the average electron current in either the electron linac or the positron linac

becomes excessive. The quantity of each type of diagnostic in each section of the linac is listed in Table 1. The beam's microbunch length has been measured by backphasing, and also by using a 5th-harmonic rf cavity. Descriptions of the technique and the first results are found in [9].

Table 1: Linac Diagnostics.

Type	# in e- linac	# in e+ linac
average current mon.	2	2
wall current mon.	3	1
BPM	5	5
fluorescent screen	3	5
loss monitor	5	9
5th harmonic cavity	1	0

The linac is controlled by the Experimental Physics and Industrial Control System (EPICS) [10]. The system is extremely flexible and when combined with the sdds toolkit, provides a powerful environment for monitoring and control of the linac and its various systems. Figure 4 is an example of an EPICS control screen for the linac.

III. PERFORMANCE

Table 2 lists a summary of the linac's performance to date.

Table 2: Linac Performance Summary.

	Design Goal	Achieved
Electron Linac		
Energy on Target	200 MeV	235 MeV
Pulse Length	30 ns	30 ns
Target Spot Size	$\phi \leq 3$ mm	$\phi \leq 5$ mm
Power on Target	480 W	225 W
Current on Target	1.7 A	1.45 A
Repetition Rate	48 pps at a 60-Hz rate	30 Hz
Maximum Energy	650 MeV	655 MeV
Energy Spread	± 8 %	$\leq \pm 8$ %
Emittance	≤ 1.2 mm mrad	≤ 1.2 mm mrad
Positron Linac		
Output Energy	450 MeV	458 MeV
Output Current	8 mA	9 mA
Energy Spread	± 1 %	$\leq \pm 1.6$ %

IV. SUMMARY

The APS linac has been operational for about a year, and has met most of its design goals. Considerable time was spent conditioning the high power rf equipment, however conditioning is now excellent for most purposes. The design goal for positron current at the design energy has not yet been

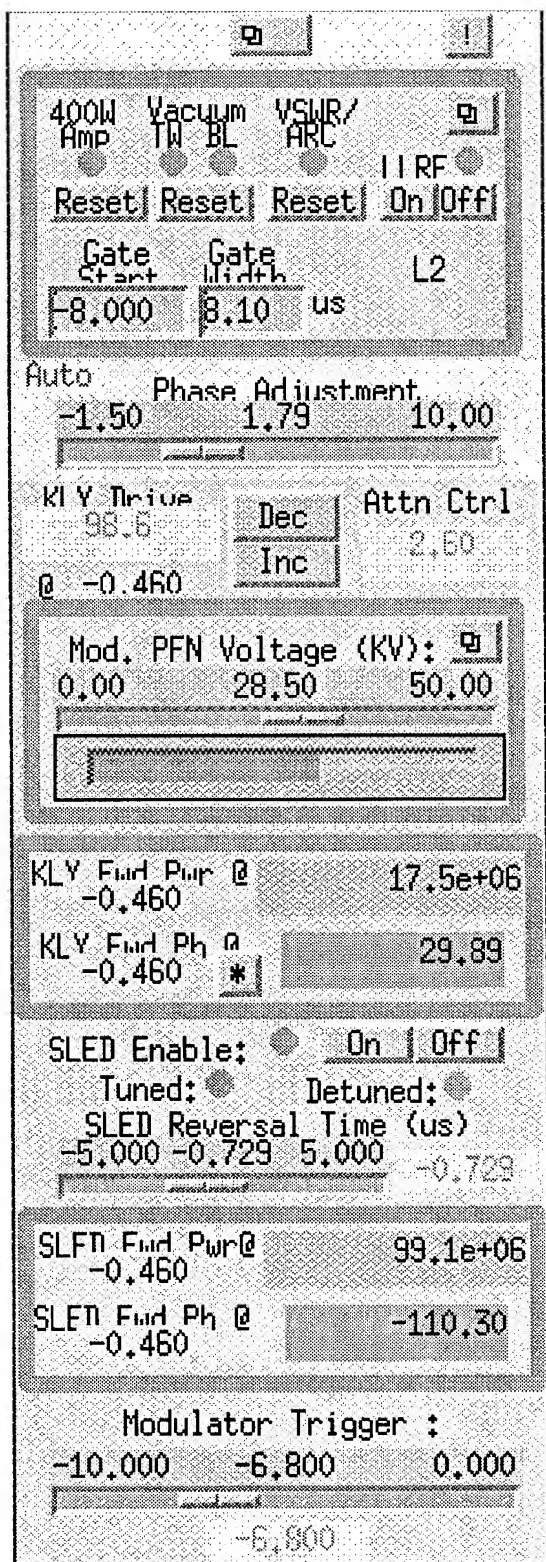


Figure 4: An example of a portion (20%) of the linac rf overview control screen. Rf power, timing, and phase information can be read out and modified from this screen. A limited set of faults can be reset directly, and a variety of "engineering screens" are accessible from pull down menus on this screen.

met. By the time rf conditioning permitted 450-MeV positron runs, the gun cathode performance had degraded significantly. The cathode is scheduled for replacement, and the design positron current at 450 MeV will most likely be achieved during the first shift with the new cathode. The positron focusing system as well as some possible improvements to it are discussed in [11].

The linac operates 24 hours per day to produce 405-MeV electrons for the purpose of commissioning the other APS accelerators. Positrons are used in linac and low energy transport line studies but, will soon be injected into the positron accumulator ring.

Acknowledgments

We gratefully acknowledge the efforts of M. Douell, C. Gold, D. Jefferson, M. Lagessie, D. Meyer, T. Jonasson, S. Pasky, L. Peterson, and D. Yuen during construction and initial operation of the linac, and of D. Fallin for all of the drawings. We also appreciate the advice and experience of G. Mavrogenes.

VI. REFERENCES

- [1] 7-GeV Advanced Photon Source Conceptual Design Report, ANL-87-15, April 1987.
- [2] H. J. Moe, et al., "Radiation Measurements at the Advanced Photon Source (APS) Linear Accelerator," these proceedings.
- [3] T. Russell and A. Cours, "Klystron Modulator Operation and Upgrades for the APS Linac," these proceedings.
- [4] M. Borland, "A Self-Describing File Protocol for Simulation Integration and Shared Postprocessors," these proceedings.
- [5] A. Grelick, et al., "Phase Control and Intra-Pulse Phase Compensation of the Advanced Photon Source (APS) Linear Accelerator," these proceedings.
- [6] R. E. Fuja and M. White, "Performance of the Advanced Photon Source (APS) Linac Beam Position Monitors (BPMs) with Logarithmic Amplifier Electronics," these proceedings.
- [7] W. Berg and K. Ko, "Status of the Fluorescent Screens and Image Processing for the APS Linac Beam Instrumentation Workshop Proc., Santa Fe, NM, Oct. 1993.
- [8] W. Sellyey, private communication.
- [9] N. Sereno, et al., "Bunch Length Measurements at the Advanced Photon Source (APS) Linear Accelerator," these proceedings.
- [10] L. Dalesio, et al., "The experimental physics and industrial control system architecture: Past, present and future," *Nucl. Instrum. and Methods A* **352**, 179 (1994).
- [11] Y. L. Qian and M. White, "Positron Focusing in the Advanced Photon Source (APS) Linear Accelerator," these proceedings.

TW ACCELERATING STRUCTURES WITH MINIMAL SURFACE ELECTRIC FIELD

O. Nezhevenko, D. Myakishev, V. Tarnetsky, V. Yakovlev,
Budker Institute of Nuclear Physics, Novosibirsk, Russia

I. INTRODUCTION

In relation to the development of linear colliders requirement appeared in the accelerating structures with high accelerating rate, that can't exceed the value defined by electric break-down. It has been known that electrical strength depends on maximal electric field on the structure surface E_m , which can be connected with accelerating rate E through the overvoltage factor K_m by the equation $K_m = E_m/E$.

As a result of numerical simulation of the different accelerating structures operating in stored energy mode [1] it has been found that K_m depends on the accelerating structure type (TW, SW) and disk edge shape and can be decreased through the change to elliptical disk edge shape. The criterion of ellipticity is its eccentricity $\varepsilon = t/(2h)$ (Fig.1). Note, that parabolic disk edges [2] has similar shape, but in this case overvoltage at points of conjugation between the disk and paraboloid may occur.

In this report we more extensively consider the possibility of the minimal overvoltage factor obtaining in $2\pi/3$ TW structure, that was chosen as an operating in the main colliders projects [3], [4].

II. GENERAL

We carried out the numeric simulation of $2\pi/3$ TW structure (Fig.2). The simulation was made for the various values of aperture $2a/\lambda$, disk thickness t/λ and eccentricity ε . In order for the structure geometric parameters to be in the limits of developing structures, we chose the following ranges of parameters: $t/\lambda = 0.056 \div 0.11$, $2a/\lambda = 0.19 \div 0.457$, enclosing by this means parameters of SLAC [5], NLC [3] and JLC [4].

The numeric simulation was carried out with the computer code SUPERLANS [6], that allows to calculate the traveling waves in axisymmetrical periodical structures with acceptable accuracy.

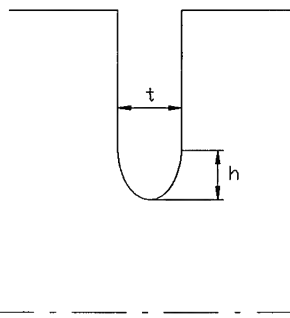


Figure 1. The disk edge geometry.

III. RESULTS

In the Fig.3 the calculated dependences of overvoltage factor K_m from eccentricity ε at various values of structure geometric parameters $2a/\lambda$ and t/λ are shown. Each figure contains curves for three aperture magnitudes at the fixed disk thickness. For convenience the same dependences are shown in the Fig.4, but in this case the curves are grouped together so that the single picture contains dependences for three disk thickness values at the fixed aperture.

As is clear from Fig.1, $\varepsilon = 1$ corresponds to the round edge geometry and $\varepsilon < 1$ – to the more “sharp” one.

For each pair of parameters (a,t) there is an optimal value of ε , at which K_m (i.e. E_m) is minimal, and later eccentricity decreasing leads to the increasing of overvoltage factor. As this takes place the major E_m decreasing (up to 30–40 %) is made possible for the “conventional” structures with rather small apertures (for the group velocity $v_g \simeq 0.01c$). At the largest apertures that are used, for example, in NLC project structure (where $v_g \simeq 0.1c$), E_m decreasing doesn't exceed 5–10 %.

It is reasonable that disk thickness increasing allows some more decreasing of E_m .

In deciding on a structure geometric parameters (a,t) it should be realized that they make a great influence on the shunt impedance Z value. As an illustration in the Fig.5,6 dependences of shunt impedance from a and t are shown. This curves correspond to the operating frequency 11.4 GHz (as in [3], [4] projects) and round disk edge shape. As our calculations show, the eccentricity doesn't make the appreciable influence on Z and v_g .

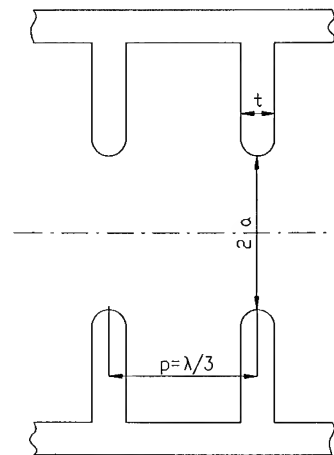


Figure 2. Schematic cross section of $2\pi/3$ TW structure.

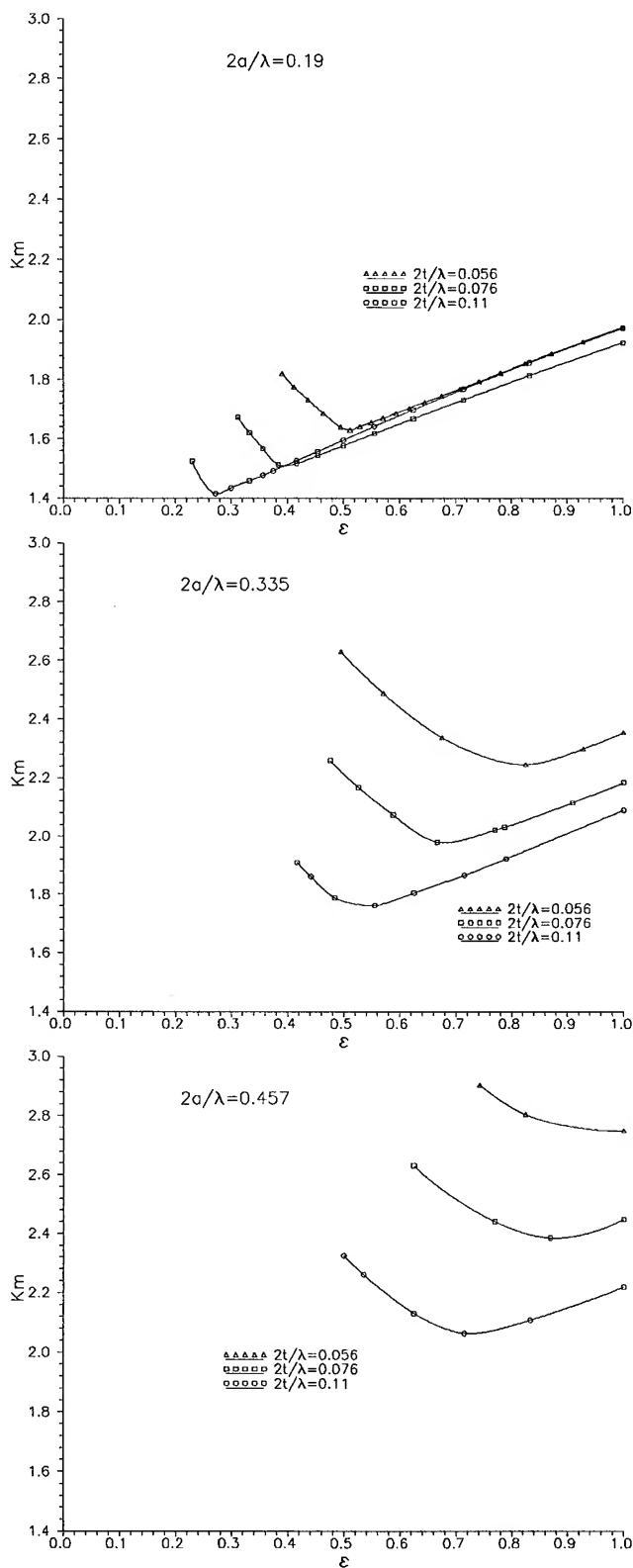


Figure 3. Overvoltage factor against eccentricity for various t/λ at fixed apertures.

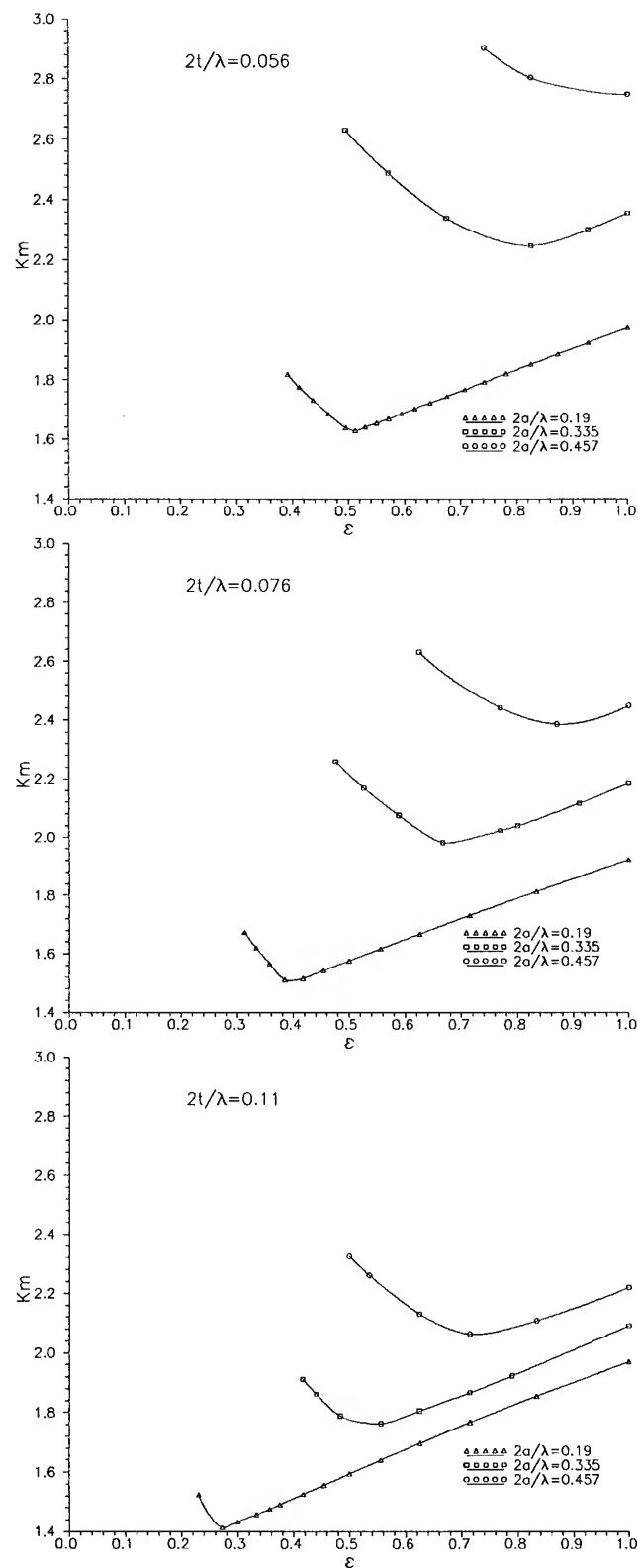


Figure 4. Overvoltage factor against eccentricity for various $2a/\lambda$ at fixed thickness.

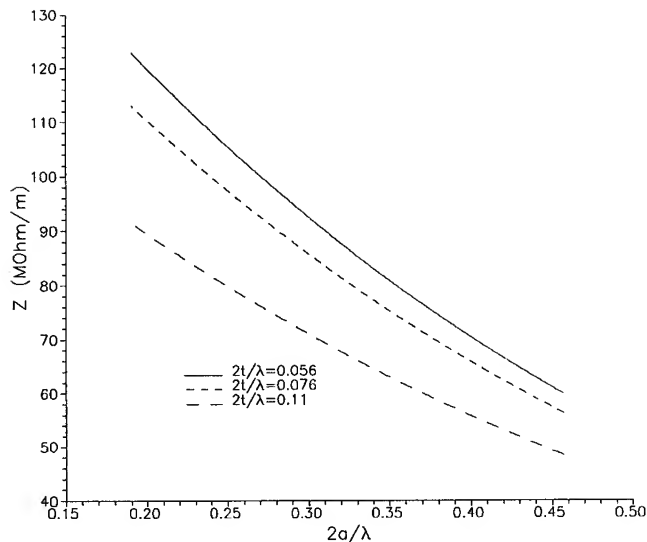


Figure 5. Shunt impedance against aperture for various thickness.

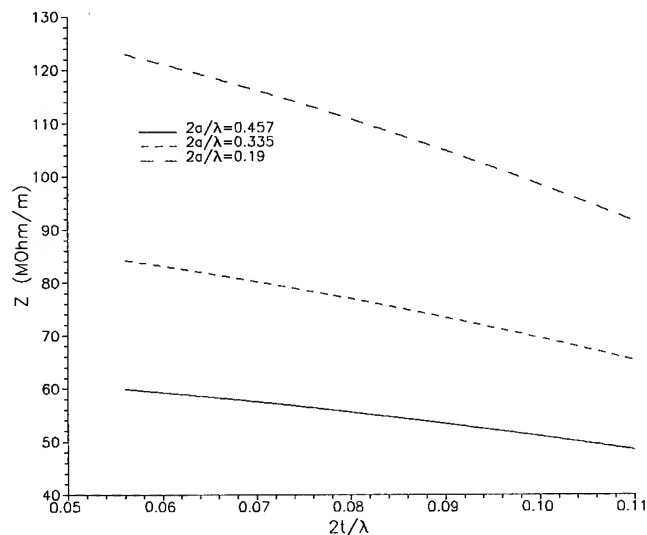


Figure 6. Shunt impedance against thickness for various apertures.

IV. CONCLUSION

Our research displayed that in TW accelerating structures the maximal surface electric field decreasing (i.e. increasing of the structure electrical strength) can be obtained through the choosing of optimal disk edge shape. For "conventional structures" with rather small apertures the E_m decreasing can be as great as 30–40 % practically at the same value of shunt impedance. For structures with enlarged apertures (NLC-type) this effect is more weaker and comprises 5–10 %.

References

- [1] M.M. Karliner at al. "To the Problem on Comparison of Accelerating Structures", – Preprint INP 86-146, Novosibirsk, 1986.
- [2] V.E.Balakin and A.N.Skrinsky "VLEPP – Status Report", in Proc. XIII Inter. Conf. on High Energy Acc., 1987, vol. 1,

pp. 101–108.

- [3] K.A. Tompson at al. "Design and Simulation of Accelerating Structures for Future Linear Colliders", in Particle Accelerators, 1994, vol. 47, pp. 65–109.
- [4] K. Takata "JLC R&D Status", in Proc. ECFA Workshop On e^+e^- Linear Colliders (LC 92), 1992, vol. 1, pp. 209–225.
- [5] The Stanford Two-Mile Accelerator / Gen. Ed. R.B. Neal – W.A. Benjamin, Inc., 1968, New York, Amsterdam.
- [6] D.G. Myakishev and V.P. Yakovlev "An Interactive Code SUPERLANS for Evaluation of RF-cavities and Accelerating Structures", in IEEE Particle Accelerator Conf. Rec., 1991, vol. 5, pp. 3002–3004.

A 100 MeV INJECTOR FOR THE ELECTRON STORAGE RING AT KYOTO UNIVERSITY

T.Shirai, M.Kando, M.Ikegami, Y.Iwashita, H.Okamoto, S.Kakigi,
H.Dewa, H.Fujita, A.Noda, and M.Inoue

Nuclear Science Research Facility, Institute for Chemical Research, Kyoto University
Gokasho, Uji-city, Kyoto 611, Japan

K.Mashiko

Nihon Kensetsu Kogyo Co Ltd., 5-13-11 Shinbashi, Minato-ku, Tokyo 105, Japan

An electron linear accelerator has been constructed at Kyoto University, which is an injector for the 300 MeV storage ring. The output beam energy from the injector is 100 MeV and the designed beam current is 100 mA at the pulse width of 1 μ sec. The component test is under going. The electron beam of 300 mA is extracted from the electron gun and the peak RF power of 20 MW is successfully fed to the accelerating structures at the pulse width of 2 μ sec.

I. INTRODUCTION

An electron storage ring has been developed at the Institute for Chemical Research, Kyoto University. The storage ring (Kaken Storage Ring, KSR) has a race track shape and the maximum energy is 300 MeV. It will be used as the synchrotron radiation source from the dipole magnet and the insertion device [1]. It will be also used for the research of the free electron laser. The electron beam is injected to the KSR by a 100 MeV linear accelerator [2]. The layout of the electron linac and the KSR is shown in Fig. 1.

Table 1 shows the beam parameters and the main specification of the injector. The output beam parameters are determined by the injection requirements of the KSR. The maximum repetition is limited by the capability of the power supply and the radiation shield. The repetition is 0.5 Hz at the

Table 1 Output beam parameters and the main specification of the injector.

Output Electron Beam	
Energy	100 MeV
Beam Current	100 mA
Pulse Width	1 μ sec
Maximum Repetition	20 Hz
Electron Gun (Pierce type)	
Cathode Assembly	Y-796 (Eimac)
Extraction Voltage	-100 kV DC
Grid Voltage (typ.)	100 V
Accelerating Structure	
Mode	$2/3\pi$, Constant Gradient
Number of Cell	85
Bore Radius	11.74 - 13.4 mm
Length	3 m
Operating Frequency	2857 MHz
Shunt Impedance	53 MW/m
Maximum Electric Field	15 MV/m at 20 MW input
Klystron (ITT-8568)	
Cathode Voltage	250 kV, 250 A
Output RF Power	21 MW
Gain	53 dB

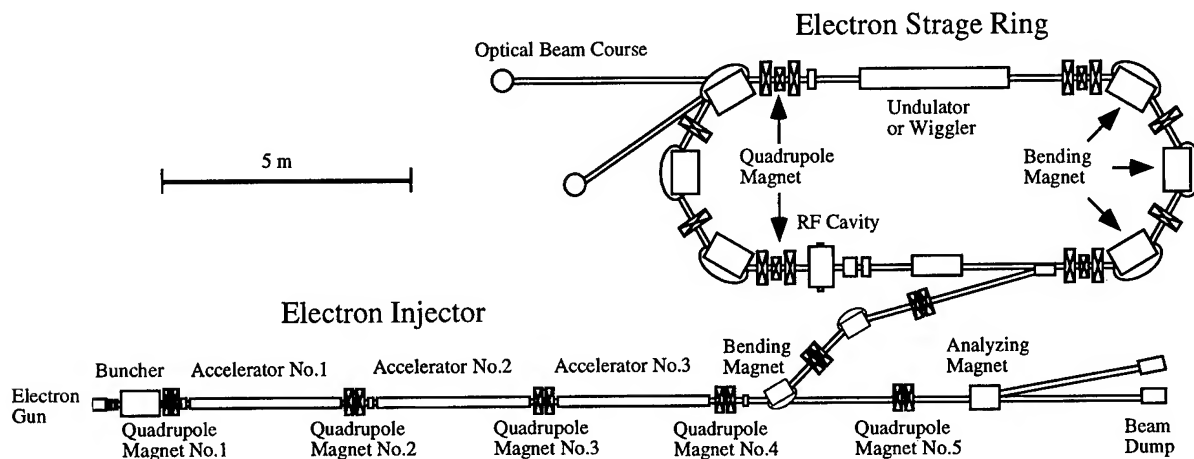


Figure 1. Layout of the electron linac and the KSR.

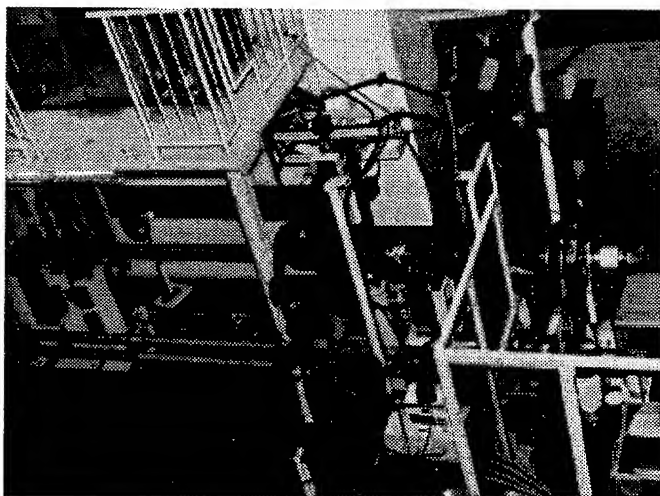


Photo 1 View of the front part of the accelerator. The electron gun, the buncher, and the first accelerating structure from the right to left.

KSR injection and the higher repetition is used for the beam tuning and for some physical and chemical experiments with the electron beam of the linac.

II. ACCELERATOR

The view of the front part of the accelerator (the electron gun, the buncher, and the first accelerating structure) is shown in photo 1.

2-1 Electron Gun

The electron gun has the Pierce electrode and the cathode assembly is the Y-796 (Eimac). The maximum extraction voltage

is -100 kV DC. The pulse width of the grid pulser is variable from 10 nsec to 1 μ sec. The beam current of 300 mA has been achieved at the pulse width of 1 μ sec.

2-2 Pre-buncher and Buncher

The pre-buncher is a single reentrant cavity. It is designed to bunch the beam within the phase spread of 60 degree. The buncher is a disc-loaded and 3 step constant gradient structure. It has 21 cells and the total length is 777 mm. The designed phase spread is within 3 degree at the beam current of 100 mA when the input power is 12 MW.

2-3 Accelerating structure

The main characteristics of the accelerating structure are listed in Table 1. The maximum electric field is 45 MV per an accelerating structure without beam loading at the input power of 20 MW.

The doublet of the quadrupole magnets is used as a focusing element between the accelerating structures. The calculated beam radius is kept within 6 mm along the beam axis. It is assumed that the normalized emittance is 100 π mm-mrad. The steering coils are placed at the entrance of the first and the third accelerating structures.

III. RF SYSTEM

3-1 Low Level System

The block diagram of the RF system is shown in Fig. 2. The master RF oscillator is a synthesized signal generator (HP-8664A). The booster klystron (TH-2436, Thomson) has a gain of 40 dB and the output power is 10 kW. The pulse width is 3.5 μ sec. The output power is divided by the 4-way RF divider and supplied to the four main klystrons. RF attenuators and phase shifters are inserted between them.

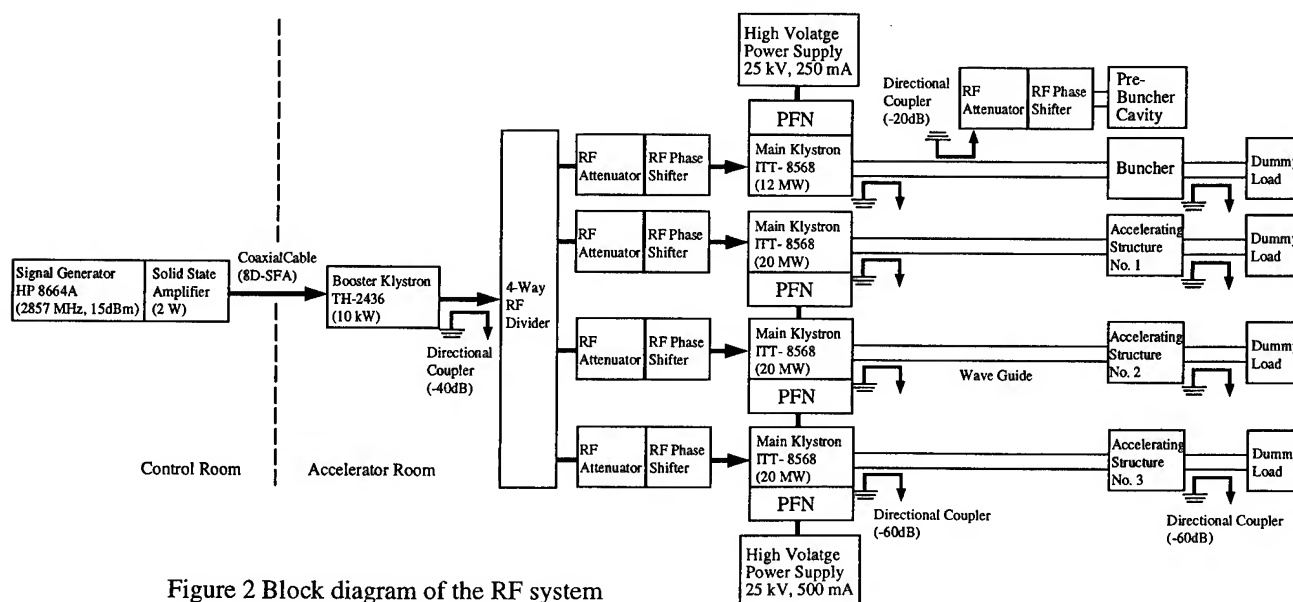


Figure 2 Block diagram of the RF system

3-2 Klystron and Modulator

The main klystron is ITT-8568. The maximum output power is 21 MW. Figure 3 shows the input RF power of the first and third accelerating structures. The peak RF power is 20 MW and the RF frequency is 2857 MHz. The repetition is 3.5 Hz. The RF pulses are picked up by the directional couplers and detected by the RF diodes.

The modulator is composed of the high voltage power supply, the pulse forming network (PFN) and the pulse transformer. The stabilized power supply for the modulator is adopted to keep the electron beam energy constant. The maximum voltage is 25 kV and the current is 500 mA. It can feed the power to the three PFNs for the accelerators at the repetition of 20 Hz. The voltage stability is less than 10^{-3} .

The pulse voltage generated by the PFN is 22.5 kV and the

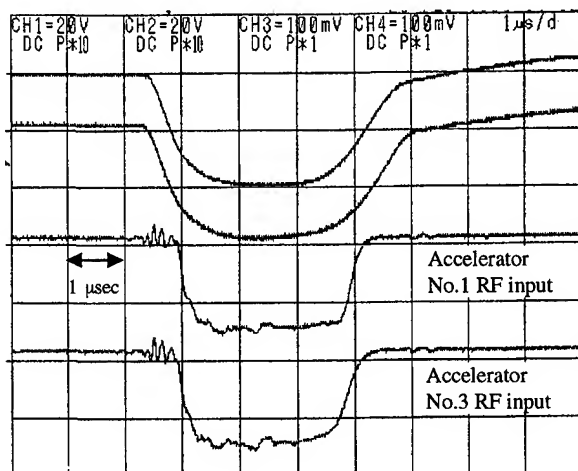


Figure 3 Input RF pulse to the first and third accelerating structures. The peak power is 20 MW and the repetition is 3.5 Hz.

peak current is 3000 A. The pulse width is 2 μ sec. The output voltage is stepped up 12 times by the pulse transformer and supplied to the klystron.

IV. BEAM MONITOR

The current monitor is installed between the accelerating structures. The monitor is the ferrite core with the coil of 30 turns. The current sensitivity is 1 mV/mA.

The beam profile monitors will be installed at the close to the current monitors. The material of the beam screen is an alumina ceramic in which a little chromium oxide is homogeneously doped (Desmarquest, AF995R). The beam profile monitor is also used for the emittance measurements combined with the upstream quadrupole magnets

V. CONTROL SYSTEM

The block diagram of the device control system is shown in Fig. 4. The controller units have the GP-IB interface and connected by the optical fiber each other. The fiber cable isolates each devices and reduces the noise. The master controller is a personal computer IBM-PC/AT with ISA GP-IB card (AT-GPIB, National Instrument). The control software works on the Microsoft Windows system. A user can operate by the mouse or a touch panel.

VI. SUMMARY

The construction of the 100 MeV electron injector had been finished and the tests of the main components such as the klystrons and the electron gun were carried out. We succeeded to feed the 20 MW into the accelerating structure at the low repetition. The conditioning work is now in progress. The beam acceleration test of 100 MeV is scheduled in summer 1995.

VII. ACKNOWLEDGMENTS

The authors thank to Dr. Kobayashi and Dr. Shoji at JAERI for their help and advises about the electron linac.

VIII. REFERENCES

- [1] A.Noda, et al., "Electron Storage Ring, KSR for Light Source with Synchrotron Radiation", contribution to this conference.
- [2] K.Takekoshi, et al., "Design, Construction and Operation of JAERI-Linac", JAERI-Report 1238, 1975

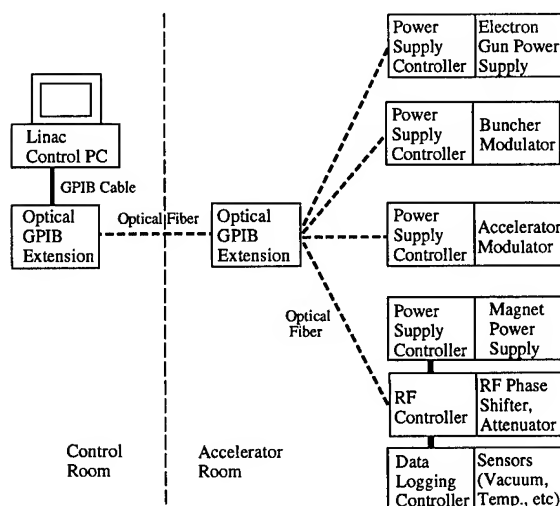


Figure 4 Block diagram of the control system.

PHASE CONTROL AND INTRA-PULSE PHASE COMPENSATION OF THE ADVANCED PHOTON SOURCE (APS) LINEAR ACCELERATOR*

A. E. Grelick, N. Arnold, K. Ko, N. Sereno, and M. White,
Argonne National Laboratory, 9700 South Cass Avenue,
Argonne, Illinois 60439

Abstract

Rf power for the APS linear accelerator is provided by five klystrons, each of which feeds one linac "sector," containing accelerating structures and SLED cavities. A VXI-based subsystem measures the phase of each sector of the linac with respect to a thermally stabilized reference line. The resulting information is used to control a linearized varactor phase shifter. Error correction is done by software, using operator-controllable parameters. A second phase shifter provides an intra-pulse correction to the phase of the klystron drive pulse. When the intra-pulse correction is applied, the resulting phase is flat to within 0.5° after $2.5 \mu\text{sec}$. A second correction, made after the PSK trigger to the SLED and during the filling of the accelerating structures, resulted in an energy gain of 5 MeV from a single sector.

I. INTRODUCTION

The rf schematic for the APS linac is shown in Figure 1. Linac sectors are comprised of a klystron and associated accelerating structures.

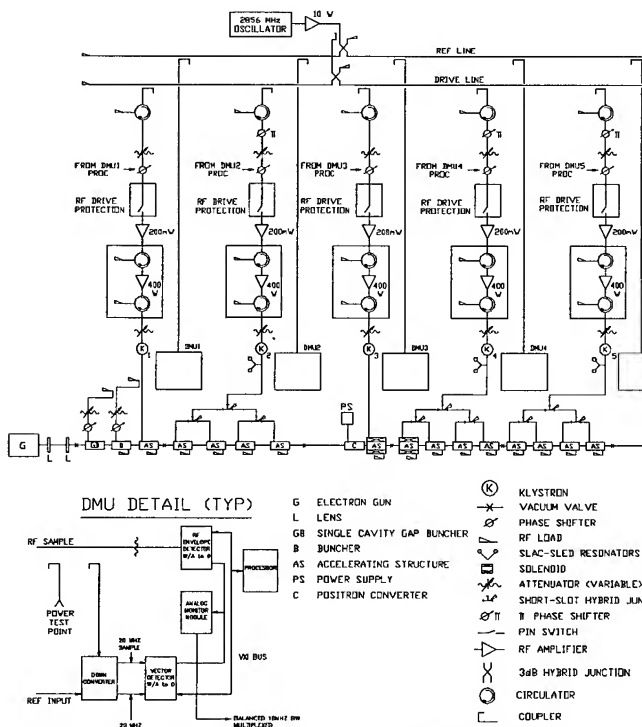


Figure 1: Schematic Diagram of the rf system.

*Work supported by U.S. DOE Office of Basic Energy Sciences under Contract No. W-31-109-ENG-38.

The low-level rf system is principally housed in two separate cabinets for each sector: a VXI-based measuring system and a klystron drive system using a pulsed solid-state amplifier together with NIM modules and rfi-tight chassis.

II. SYSTEM DESCRIPTION

The entire system is driven from an ovenized, synthesized source and a 10-Watt GaAs FET amplifier. Both the drive and reference lines are driven from the amplifier output and are built into a single assembly which is temperature stabilized using water from one of the systems feeding the accelerating structures.

The VXI-based measuring system is based on Los Alamos National Laboratory (LANL) designed modules [1] with upgrades accomplished collaboratively by LANL and ANL. A common digital interface exists on all modules, while three types of on-board signal conditioning allow measurements of rf amplitude, rf phase, and beam position. Each channel digitizes a single measurement during each linac pulse, and the exact time of the sample can be adjusted by the operator. The modules for a sector are located in two C-size VXI mainframes, housed in a single 19-inch rack. MXI modules in slot zero of each of the two mainframes provide links between them.

The following VXI modules are used for rf data collection and conversion:

Envelope Detector Modules (EDMs) provide eight channels of diode-detected signals. Linearized values for each possible raw output value from the analog-to-digital converter, interpolated from calibration of 88 points per channel, are stored in an EEPROM.

A Down Converter Module (DNM) driving a Vector Detector Module (VDM) produces two channels of I and Q data. The VDM operates at 20 MHz and utilizes ovenized I and Q demodulators. Phase is calculated by software.

Analog-to-digital conversion in the EDM and VDM modules is done by a Dattel SHM-49 hybrid track/hold amplifier and an AD574 monolithic analog-to-digital converter, yielding a 10-MHz bandwidth.

A different trigger timing system than the one used at LANL is used for most measurements in the APS linac and improves resolution and jitter by more than an order of magnitude. The upgraded LANL modules allow any of the VXI backplane triggers to be directly selected, or the LANL default triggering system can still be used. A VXI trigger module, designed at ANL, contains a set of eight-bit programmable delay lines which can be used to select sample time in increments of 5

nanoseconds. A separate delay line controls each of the two ECL triggers and eight TTL triggers on the VXI backplane.

Rf samples are available at the input (both forward and reflected) and output of each accelerating structure. Envelope detector channels have been provided for almost all of these signals. Multiplexed phase measurements are available for the forward power samples.

Key elements of the klystron drive chain before the pulsed amplifier are a bi-phase (PSK) modulator which is used to key the SLED [2] cavity assemblies in sectors L2, L4, and L5; a dual linearized phase shifter; a PIN diode switch controlled by a VSWR protection NIM module; and a preamplifier. The pulsed solid-state amplifier has a minimum power output of 400 watts and is followed by a motor-driven attenuator. After minimum attenuation and cable losses, drive power of at least 225 watts is available at the klystron input.

III. PHASE CONTROL

Phase is measured at the input to each sector (at the output of the klystron and SLED) with a single sample each pulse. Software computes a phase between -180° and $+180^\circ$, with a resolution of 0.01° , from measured I and Q data. The smaller in magnitude of I and Q is always used as the numerator in the computation to avoid losing precision near the sine wave maxima. Line stretcher type phase shifters are included at the reference inputs of each sector's phase measuring modules. These phase shifters are set so that the phase reading of each sector can be set to approximately $+90^\circ$ at maximum energy conditions for electrons. Therefore the readings for both electrons and positrons (roughly -90°) will not usually be near the point of discontinuous readings located at ± 180 degrees. It is also desirable that at this point phase is calculated as:

$$\cos^{-1} \left(\frac{I}{(I^2 + Q^2)^{1/2}} \right)$$

with I being near zero since the I channel has a lower noise level than the Q channel.

An Allen-Bradley remote interface link from the VXI-based processor is used to implement phase control. Phase corrections are generally made when the measured phase error exceeds 2° from a preset value chosen after the beam is optimized for energy, energy spread, and spot size and shape. Figure 2 is an example of the on-line window for phase control while operating with target in (i.e. with positrons).

IV. INTRAPULSE PHASE ERRORS AND SOLUTIONS

Pulsed solid-state amplifiers are subject to several sources of phase error. One of the largest and most easily correctable is the variation in junction temperature over the pulse. Since the variation is exponential it can be corrected with an exponential predistorting phase shift. The correction technique used is the one already used on SLC [3] with two minor differences. Instead of combining the correction signal with the main phase control signal in an extremely linear phase shifter, a separate

(but within a common package), commercially available linearized varactor phase shifter is used. Additionally, the range of possible correction time constants was increased from 5 μsec maximum to 9 μsec maximum. The need for longer time constants seems appropriate with the use of newer, larger junction transistors. With the correction optimized, the phase of the klystron drive pulse, after the initial 2.5 μsec , is flat to within $<0.5^\circ$. Noise on the I and Q outputs of the Vector Detector is the principal limiting factor. The klystron drive pulse is timed so that the initial 2.5 μsec has an insignificant effect on the accelerated beam. In the SLEDed sectors, the drive pulse starts before the modulator trigger. In the other sectors, the drive pulse begins at least 3.3 μsec before the electron gun trigger.

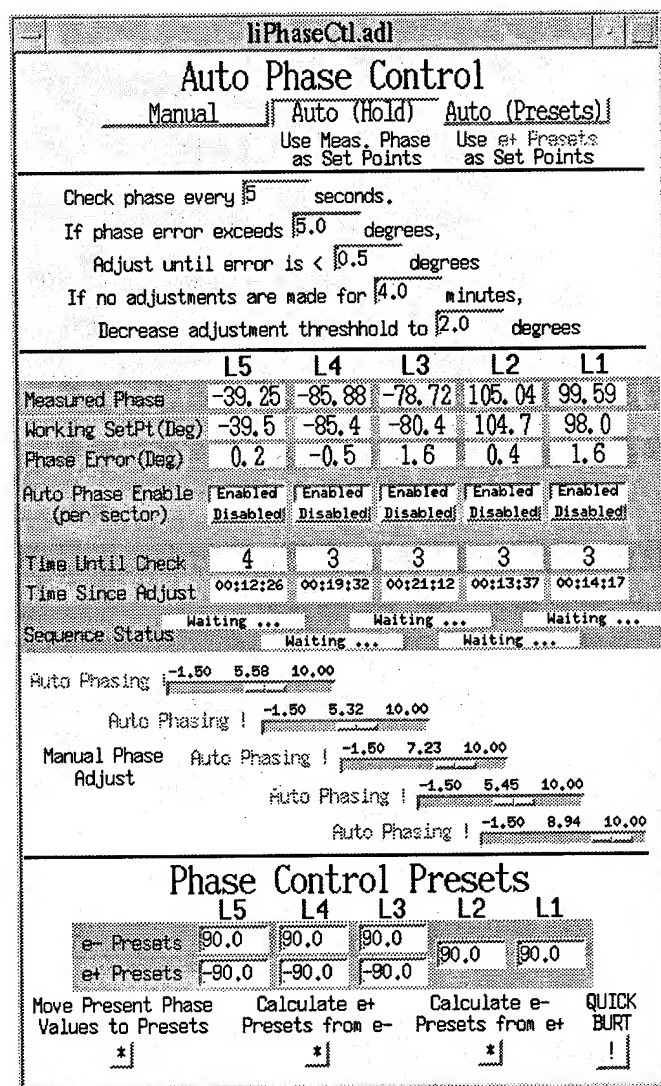


Figure 2: Autophase control screen during a positron run.

During commissioning, it was observed that less than ideal shape of the modulator pulse was limiting maximum available linac energy and that phase shifts over the pulse due to klystron phase pushing was a significant part of the limitation. In the pursuit of additional ways to increase maximum available linac energy, an experiment was performed on linac sector L2 (the best operating SLEDed sector at the time).

An additional correcting signal was summed with the driver amplifier correction signal described above, during the part of the pulse after the PSK trigger, which corresponds to the accelerating structure fill time. A rectangular pulse of variable amplitude and polarity with width extending past the end of the modulator pulse was applied as part of the summed signal to the phase shifter. The limited response of the phase shifter integrated the leading edge of the pulse, giving the effect of adding a ramp phase shift component of variable slope which could be either positive or negative. The resulting slope was varied while watching a fluorescent screen following a calibrated analyzing magnet, giving an immediate readback of changes in beam energy. An energy increase of 5 MeV was observed.

No decision has been reached on whether to implement such a correction. The results show an apparent possible 10-MeV increase in positron energy by applying the additional correction in sectors L4 and L5. However, the magnitude of any possible increase in beam energy can be expected to tend towards zero as the ongoing activity to improve the modulators produces a pulse which more closely resembles the ideal [4].

V. CONCLUSION

This system has operated successfully for more than a year and has achieved repeatability to within its $\pm 2^\circ$ window which has been verified by its regular correlation with linac energy. It has also achieved a good and still improving level of reliability on-line. Basic performance has been at a level that has readily supported commissioning and operation while further refinements are still being pursued. More details of the linac's performance are given in [5].

VI. ACKNOWLEDGMENTS

We would like to sincerely acknowledge the efforts of Messrs. D. Jefferson and J. Hawkins, whose efforts in support of the linac low-level systems were instrumental to the successful results.

VII. REFERENCES

- [1] S. P. Jachim, et al, "The Los Alamos VIXI-Based Modular RF Control System," *Proceedings of the 1993 Particle Accelerator Conference*, Washington, DC., May 1993, pp 1154-1156, 1993.
- [2] Z. D. Farkas, H.A. Hogg, G.A. Loew, and P.B. Wilson, "SLED: A Method of Doubling SLAC's Energy," SLAC-PUB-1453, June 1974.
- [3] J. G. Judkins, J. E. Clendenin and H. D. Schwarz, "A Solid State High Power Amplifier for Driving the SLC Injector Klystron," *IEEE Transactions on Nuclear Science*, NS32, No. 5, pp. 2909-2911, Oct. 1985.
- [4] T. J. Russell and A. Cours, "Klystron Modulator Operation and Upgrades for the APS Linac," these proceedings.
- [5] M. White, et al., "Performance of the Advanced Photon Source (APS) Linear Accelerator," these proceedings.

ERROR SENSITIVITY STUDY FOR SIDE COUPLED MUFFIN TIN STRUCTURES USING A FINITE DIFFERENCE PROGRAM

Warner Bruns, TU Berlin, EN-2, Einsteinufer 17, 10587 Berlin

Abstract

The sensitivity of three previously proposed side coupled standing wave muffin-tin structures are estimated using a finite difference program. The muffin tins consist of rectangular cavities only. Such geometries can be discretized by a program like MAFIA without errors. But as soon as small errors in the cavity dimensions are present, MAFIA is not able to discretize them with sufficient accuracy. Therefore a finite difference program adjusted to the problem has been written that discretizes the cavity volume exactly for all cavities where the position of two of the six cavitywalls is perturbed. This program was used to calculate the shunt impedance of a big number of structures with random errors in the cavity dimensions.

I. INTRODUCTION

A class of linear accelerators has been previously proposed, which should operate at 120 GHz and could be manufactured cheaply by silicon etching or LIGA due to their rectangular geometries [2],[3]. The typical structure dimensions are 1 mm. Because the structures are so tiny, it seems almost impossible to tune them after manufacturing. Therefore it is necessary to evaluate the effects of errors in the geometry.

In a previously published paper [4], the error sensitivity of the geometries was already estimated using a lumped circuit approach. As will be seen from the present paper, the lumped circuit approach was valid. The present paper deals with calculating directly the fields in the perturbed structures and reports the averages of the calculated shunt impedances.

II. THE PROBLEM OF CALCULATING THE FIELDS IN A PERTURBED STRUCTURE

The standard linac structure operates in $2\pi/3$ -mode. The left part of Fig. 1 shows the accelerating field in a quarter of a $2\pi/3$ muffin tin. Perturbing the position of the lower wall of the 2.nd and 3.rd cavity by a fractional amount of ± 1 percent respectively changes the field pattern to that of the right of Fig. 1. Calculating the field in this geometry with MAFIA [1] is possible, but the closeness of three meshlines at the lower boundary gives rise to numerical problems.

As will be seen later, a perturbation of 1% is not tolerable. As the perturbations become smaller, the distance of the meshlines decreases also and the structures become untractable with MAFIA.

III. HOW TO SOLVE THE PROBLEM

In this special problem, where only the lower planes $y = y_n$ of the cavities are perturbed, calculation of the fields is possible with finite differences. The trick is, not to extend the mesh

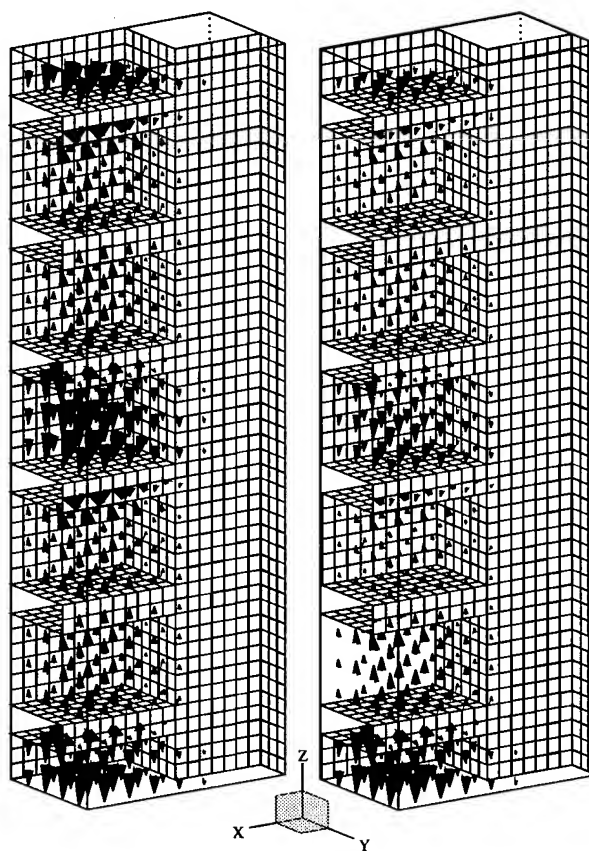


Figure 1. Left: Accelerating field in the ideal structure, Right: Field in the perturbed structure

planes $y = y_n$ over the whole volume, but to define local meshplanes in the parts of the volume that are only partly coupled.

In figure 2 two cells of a perturbed muffin tin are shown. It can be seen, that local within every cavity the grid can be made as in a single cavity, since the fields inside the tins are decoupled from each other.

This idea has been implemented as a computer code called GdfidL [5]. It handles the non regular grid as a 6 times linked list, where every cell has indices to its six neighbours. With this grid definition, it is not necessary to discretize inside the metallic parts of a structure. This has the effect, that for the structures considered here, the number of unknowns to be handled shrinks to about 60% of the number necessary for a regular grid.

The figure 3 show the positions of grid planes $z = z_n$ and $y = y_n$ in the cases of a regular and a non regular grid. For clarity, these grids discretize cavities with errors of 5 percent, because smaller errors are almost invisible.

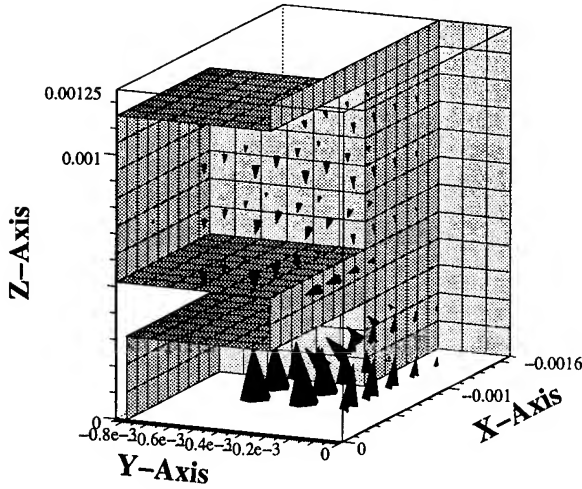


Figure 2. $2\pi/3$ mode in a perturbed muffin tin. The y-extension of the second cavity is perturbed by 5%.

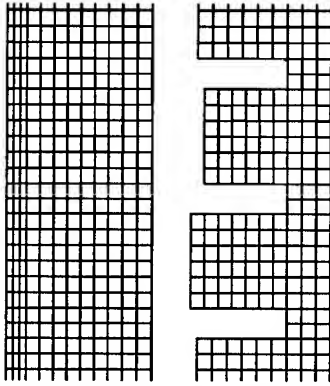


Figure 3. Left: Regular grid, Right: irregular grid, represented as a linked list

IV. ESTIMATION OF THE SENSITIVITIES

To estimate the sensitivity of the muffin tins, the shunt impedance r/Q was calculated for a number of structures with random errors in the cavities. The average of these r/Q 's is a measure of the sensitivity.

GdfidL can discretize arbitrarily small perturbations of the positions of the lower or higher walls of the cavities, but cannot discretize small perturbations in the x-extension of the cavities. Therefore only the positions of the lower cavity walls are perturbed.

GdfidL calculates fast and in small memory, but cannot calculate a side coupled muffin tin in full length on the computer I used. Therefore only 20 mm long sections of the muffin tins were calculated. These sections contain 24 cavities in the case of the single periodic $2\pi/3$ structure and 48 cavities in the case of the side coupled structures.

The figures 4 and 5 present the averages and standard deviations of the shunt impedances, scaled with shunt impedances of the ideal structures. The ordinates are the standard deviations of the relative errors in the y-extension of the cavities. Every marker in the curves is the average of 20 shunt impedances of structures with the same standard deviation of errors. The wall of every single cavity was randomly perturbed, but the perturbations were limited to 2 times the standard deviation.

The exact geometries that are analyzed here are described in [2] and [3].

V. CONCLUSION

It seems that in any case 0.5% errors in the positions of the lower wall are tolerable for 90% of the optimum. The lumped circuit approach [4] predicted 0.2% frequency errors would be ok for the $2\pi/3$ structure, 0.1% for geometry 2 and geometry 3.

The lumped circuit dealt with frequency errors, this paper deals with geometric errors. But since all the muffin tins have approximately the same extension in y- as in x-direction, the frequency of a single cell depends in the same way on the y-extension as on the x-extension. The frequency of a single cell of a muffin tin is approximately given by $(\frac{\omega}{c})^2 \approx (\frac{\pi}{w})^2 + (\frac{\pi}{w+\Delta y})^2$. Therefore a relative error $\Delta y/w$ in the y-extension only, as it was analyzed here, has the effect of a relative frequency error of $\delta f/f_0 \approx -\frac{\delta y/w}{2}$.

This means: when the lumped circuit allows a frequency error of 0.2%, this is equivalent to a geometric error in the y-extension of $2 \times 0.2\%$. The lumped circuit approach was valid.

VI. ACKNOWLEDGEMENT

I thank the APS project at Argonne National Laboratory for supporting this work.

References

- [1] R. Klatt, F. Krawczyk, W. R. Novender, C. Palm, B. Steffen, T. Weiland, T. Barts, M. F. Browman, R. Cooper, C. T. Mottershead, G. Rodenz and S. G. Wipf, Proc. of the 1986 Linear Acc. Conf., Stanford internal report-303, Sept. 1986.
- [2] H. Henke, Y.W. Kang and R. Kustom, "A mm-wave RF structure for relativistic electron acceleration", APS Note MMW-1, 1992
- [3] H. Henke and W. Bruns, "A Broad-Band Side Coupled mm-wave RF structure for relativistic electron acceleration", Proc. 1993 IEEE Particle Accelerators Conference, Washington DC
- [4] W. Bruns, "Error Sensitivity of a Double Side Coupled Muffin tin", Proc. Fourth European Particle Accelerator Conference, London 1994
- [5] W. Bruns, "GdfidL: A Finite Difference Program for Arbitrarily Small Perturbations in Rectangular Geometries", to be presented at the COMPUMAG 95, Berlin

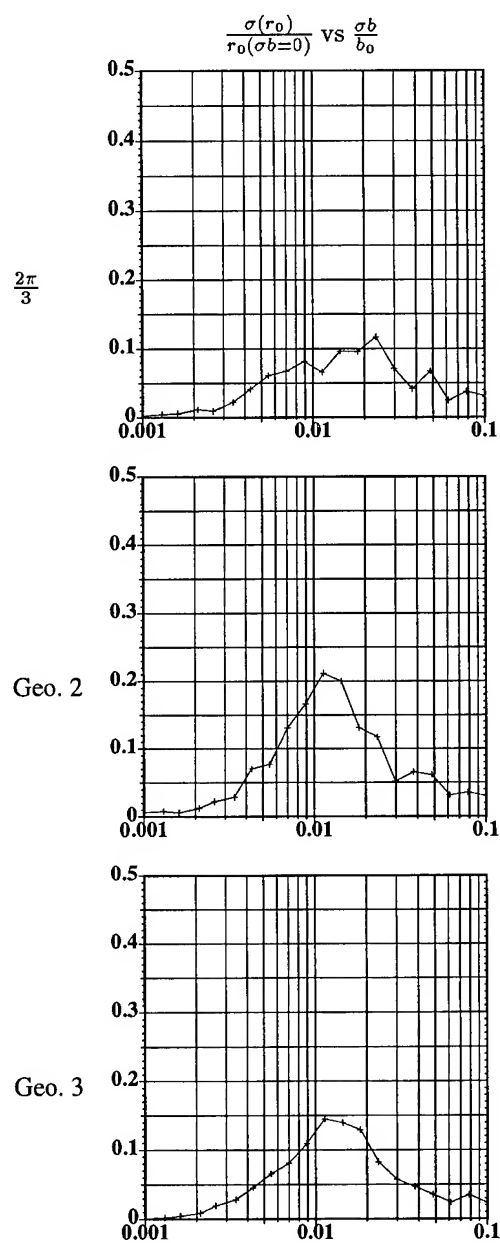
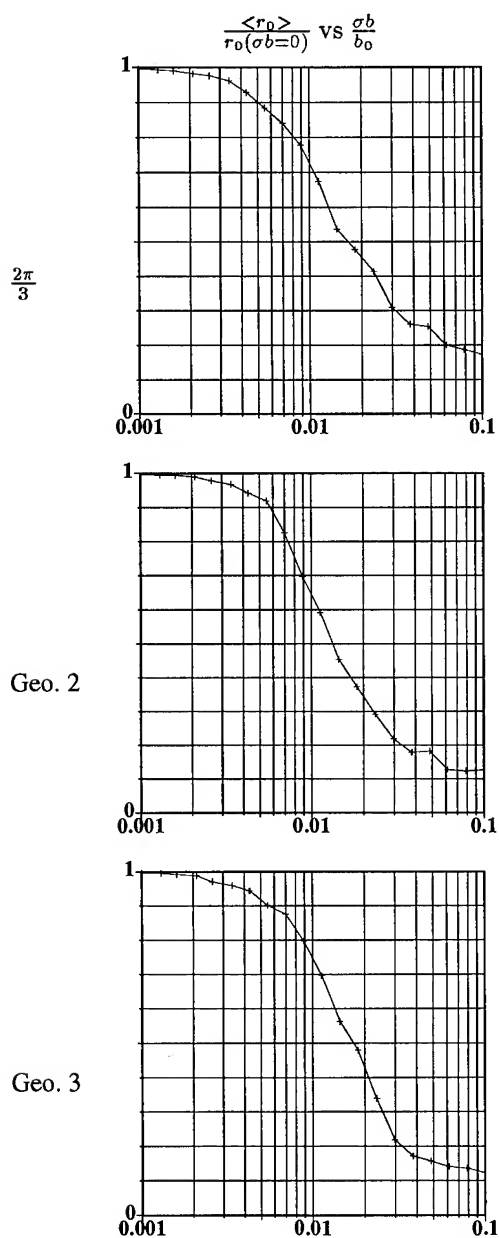


Figure 4. Mean ($\langle r_0 \rangle$) of the shunt impedances as a function of the standard deviation of the errors ($\frac{\sigma b}{b_0}$).

Figure 5. Standard deviation ($\sigma(r_0)$) of the shunt impedances as a function of the standard deviation of the errors ($\frac{\sigma b}{b_0}$).

DESIGN OF INPUT COUPLERS AND ENDCELLS FOR SIDE COUPLED MUFFIN-TIN STRUCTURES

Warner Bruns, TU Berlin, EN-2, Einsteinufer 17, 10587 Berlin

Abstract

The input couplers and endcells for a previously proposed standing wave muffin-tin structure are designed. Thereby the problem is not only to match the coupler but also to choose the endcells in a way that the coupling cells are not excited. The input coupler has to match the external Q of the structure to the unloaded Q in order to get zero reflection. The endcells are designed to reflect the forward travelling wave in such a way, that only the accelerator cells are excited and not the coupling cells. The calculation of the endcell behaviour as well as the calculation of the external Q 's are deduced from the knowledge of resonant fields only. The external Q 's are calculated with the Kroll-Yu method.

I. INTRODUCTION

In a previously published paper [1] side coupled muffin tins were proposed. The structures should operate in a confluent π -mode and therefore as standing wave structures. It follows that they only have input couplers and no output couplers. The structures have to be terminated with proper endcells to reflect the forward travelling wave with the right phase, so that the linear combination of forward and backward travelling wave gives the accelerating standing wave pattern in the main cells.

The input couplers are responsible for achieving a matched load for the power source. For travelling wave structures, an input coupler can be designed by minimizing the reflection of a structure consisting of input coupler - short section of accelerator - output coupler, where the output coupler has the same geometry as the input coupler. The reflection of such a structure can be calculated e.g. with FDTD, assuming a lossless structure.

This does not work for standing wave structures, since they do not have output couplers. Therefore the reflection calculated with e.g. FDTD would ever be one (in magnitude) due to the assumption of no losses. It is quite easy to implement losses in a FDTD-Code, but it is not really necessary for the task of finding an input coupler for a standing wave structure.

It is known, that the reflection from a lossy cavity coupled with a waveguide is zero, if the external Q -value due to the coupler matches the internal Q -value due to losses (wall losses and beam loading).

The Q -value due to the wall losses can be calculated by the power loss method, the beam loading can be neglected since we can assume, that more than 90% of the power will be dissipated in the walls.

How to determine the external Q ? Already Slater [2] stated, that the external Q of a cavity could be calculated (or measured) by moving a totally reflecting plane in the feeding waveguide and observing the frequency shift of the resonance. Kroll and Yu [3] deduced clever formulas from this principle to calculate the external Q from only 3 frequency/position pairs.

Since these formulas require the knowledge of resonant fields only, this approach fits nicely with eigenvalue solvers like GdfidL [4].

II. DESIGN OF THE ENDCELLS

The endcells have to reflect the forward travelling wave in the right way to produce a standing wave pattern in the accelerating cells. Since this field is a standing wave, it can be calculated as an eigenvalue problem.

The optimal endcells produce no field in the side cavities and flat field in the main cavities. Since such a field has the highest shunt impedance, the optimal endcell configuration can be found by maximizing the shunt impedance as a function of the endcell parameters. It was found, that 3 parameters are sufficient for achieving a flat field.

An iterative approach was used: maximize the shunt impedance with respect to the first parameter (gap of the last main cell) the other two parameters held fixed, then maximize with respect to the second (width of the narrow coupling cell), the other parameters held fixed, then maximize with respect to the third. Repeat this procedure three times. It was found that the gap of last main cell should be a factor of 1.1 longer, the width of the last wide coupling cell has to be increased by a factor of 1.2, and the width of the last narrow coupling cell should be decreased by a factor of 0.67.

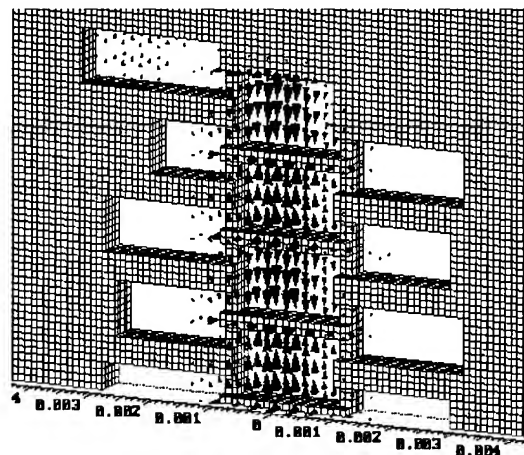


Figure 1. Field near the optimized endcells.

III. DESIGN OF THE INPUT COUPLER

I use a flower paddle coupler. This coupler has two advantages: The used mode in the feeding waveguide is the TE_{01} mode. This mode has a small attenuation that even decreases with growing frequency. The other advantage is, the coupler has to be mechanically attached to only one side of the planar structure.

The internal Q of the structure is about 2700. The external Q gets calculated with the Kroll-Yu method. To have short computation times I do not calculate the fields in the total structure, but only a quarter of a section near the coupler. The external Q of the total structure can be determined by scaling.

The external Q is proportional to the stored energy in the structure and inverse proportional to the power flow through the coupler. For a linac, the stored energy is proportional to the length, the power flow is not. Therefore for a given coupler the external Q grows linearly with the structure length.

Actually I calculated with a quarter of the coupler and $(3+1/2)$ half cells of total 56 cells. My stored energy is only $\frac{(3+1/2)^{1/2}}{56}$ of the total energy, the power flow through the coupler is $\frac{1}{4}$ of the total power flow. This means, my calculated Q values are a factor of $\frac{56}{(3+1/2)^{1/2}} \cdot \frac{1}{4} = 8$ lower than if I had modelled the total structure. With an internal Q of 2700, I have to adjust the external Q to $2700/8 = 340$.

Fig. 2 shows the field in the model structure. Fig. 4 shows calculated values for the external Q of my model section. It can be seen, that by varying the x-position of the coupler, a wide range of external Q's can be achieved. Fig. 3 shows the field in a structure with half a coupler. The ending position of the groove is chosen to produce a zero of the field at the center of the coupler.

IV. ACKNOWLEDGEMENT

I would like to thank the APS project at Argonne National Laboratory for supporting this work.

References

- [1] H. Henke and W. Bruns, "A Broad-Band Side Coupled mm-wave RF structure for relativistic electron acceleration", Proc. 1993 IEEE Particle Accelerators Conference, Washington DC
- [2] J. C. Slater, Microwave Electronics (Van Nostrand, New York, 1950)
- [3] N. Kroll and D. Yu, "Computer Determination of the External Q and Resonant Frequency of Waveguide Loaded Cavities", Particle Accelerators, 1990, Vol. 34, pp. 231-250
- [4] W. Bruns, "GdfidL: A Finite Difference Program for Arbitrarily Small Perturbations in Rectangular Geometries", to be presented at the COMPUMAG 95, Berlin

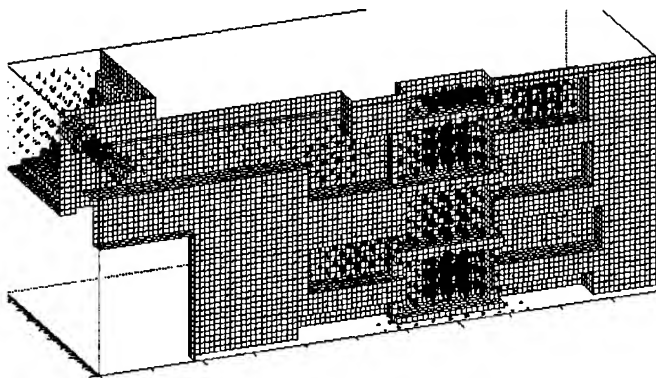


Figure 2. Model which Q values were computed for. This is a quarter of the coupler and $\frac{(3+1/2)^{1/2}}{56}$ of the accelerator. The coupler is at $x = 7.1$ mm.

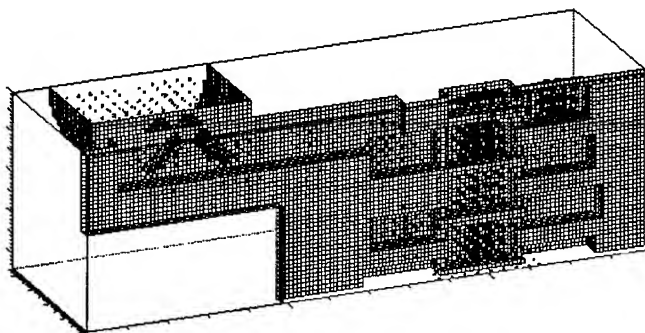


Figure 3. Same structure as above but with a half coupler. Obviously the field is the same in the linac section, but the coupling is twice as high.

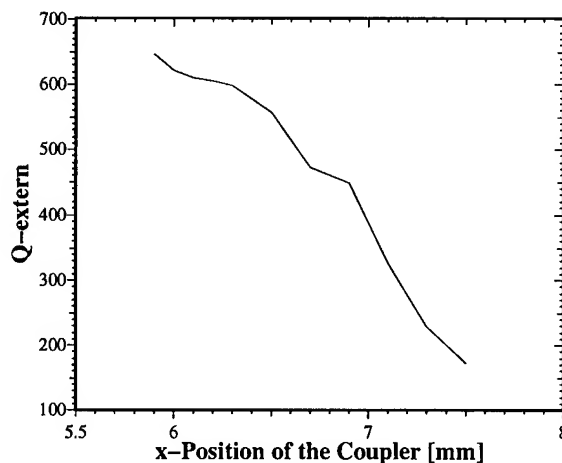


Figure 4. Computed external Q's as a function of the x-Position of the coupler.

ACCELERATOR ARCHEOLOGY - THE RESURRECTION OF THE STANFORD MARKIII ELECTRON LINAC AT DUKE*

P. G. O'Shea, F. Carter, C. Dickey, N. Hower, V.N. Litvinenko, R. Sachtschale, G. Swift, P. Wang, Y. Wu and J.M.J. Madey,
Free-Electron Laser Laboratory, Box 90319, Duke University, Durham NC 27708 USA

In the early 1960s, the Mark III accelerator at the Stanford High Energy Physics Laboratory was used as the prototype test-bed for the SLAC Two-Mile accelerator. In the mid 1980s the accelerator was dismantled and a large part of it was transported to the Duke University Free-Electron Laser Laboratory to form the basis of the injector for the 1-GeV Duke Storage Ring. The plan was to use the original accelerator sections and some rf equipment with new magnetic optics, vacuum system, gun and a modern control system. The first 295-MeV portion of the linac is now operational at Duke. The linac currently consists of eleven sections from the old linac with a single-cell rf gun. Our guiding principal has been one of economy and simplicity. We have not attempted to restore the accelerator to its original form, but have added modern components where necessary. We discuss some of the more interesting features of the linac, and how we have given new life to this venerable machine here at Duke.*

INTRODUCTION

The Mark III electron linear accelerator underwent many incarnations at the Stanford High Energy Physics Laboratory following its initial construction beginning in 1949. A description of the history up to the mid 1960s is given in reference [1]. During 1963 and 1964 the Mark III was reconfigured to its final form using new constant-gradient accelerator sections that had been developed for the SLAC Two-Mile Accelerator. By March 1964 the accelerator had 32 SLAC sections and beams of up to 1.2 GeV were being produced. The nuclear physics program on the Mark III continued until 1970. After that time the accelerator was operated occasionally as a calibration source for various nuclear detectors. The accelerator was dismantled in November 1985 under the supervision of its last operator Don Lee. One of the accelerator sections became the core of what has become known as the Mark III Free-Electron Laser, originally at Stanford, now at Duke. In 1989, 26 of the accelerator sections were shipped to the Duke University Free-Electron Laser Laboratory. During 1993-94 eleven of the sections plus an rf thermionic gun were configured into the initial 295-MeV phase of the injection linac for the Duke Storage Ring.

In its Duke incarnation, the Mark III linac retains only the accelerator sections and rf loads of the Stanford machine. Much of the original equipment at Stanford was not suitable for use in a modern machine. Examples of such equipment included 1960s vintage oil diffusion pumps and early versions of the SLAC klystrons (12 MW peak power!).

When the accelerator was dismantled it was found that many of the sections had been contaminated by back-streaming pump oil. The rf-drive cells of many of the sections could best be described as appearing to be coated with an amber/black colored varnish that had a finely crazed surface. We vacuum-baked the sections to 400°C for 5-10 days and then cleaned the rf input irises and cavity noses. The remaining coating was confined to the outer walls of the cells.

Structure type	SLAC traveling wave
RF frequency (MHz)	2856.76
Number of sections	11 + gun
Section temperature (°C)	30.2
Gun	Thermionic RF with α-magnet
Klystron type	ITT 2960
Number of Klystrons	3
Number of sections per klystron	4
Peak rf power per klystron (MW)	34
RF Macropulse length (μs)	2
Achieved energy (MeV)	295
Nominal injection energy (MeV)	283
Macropulse current (mA)	40
E-beam macropulse length (ns FWHM)	50-1000
Energy spread (macropulse) (%)	0.2
Energy jitter (%)	<0.1%
Macropulse rep. rate (Hz)	2

Table 1 Characteristics and measured performance of the Duke Injection Linac

By the end of its life at Stanford, because of various component failures, the Mark III could only reach 275 MeV. At Stanford there had been one 12-MW klystron per section. At Duke the plan was to use one 30 MW klystron for four sections. Even though the planned power per section at Duke (for most of the sections) was less than that at Stanford, there was some concern that the sections would be difficult to

* Work supported by ONR under contract N00014-91-c-0226

condition to full power. These fears proved to be largely unfounded. All of the sections, except for one, conditioned in a matter of days. The one recalcitrant section took approximately 3 months to reach full power. The first linac section at Duke has been operated at 15 MW input power.

At Duke the linac is housed in a 150-m long tunnel. In its present phase the linac is 47 m long. First beam reached the end-station of the Duke Linac on October 21, 1994. The design energy of 250 MeV was reached on November 1, with first injection into the storage ring on November 2. The linac beam energy reached 295 MeV with 20 mA of beam loading by April 1995. The nominal conditions for ring injection have been 283 MeV at 40 mA. Our plans are to add a further 22 sections (14 Mark III vintage plus 8 new) to the linac to reach a final energy of 1.2 GeV.

RF SYSTEM

The present accelerator is powered by three ITT 2960 S-band klystrons. The accelerator sections are grouped into clusters, with each cluster powered by a single klystron. The first cluster consists of the gun and three accelerator sections with the remaining two clusters consisting of four sections each. The power is split approximately as follows: gun 2 MW; first section 14 MW, all others 7 MW. The nominal energy increment per section is given by $\Delta E \text{ (MeV)} \approx 10\sqrt{P}$, where P is the section input power in MW. The maximum observed beam energy of 295 MeV (with 0.02 A of beam loading) is very close to the predicted value for the available rf power. This indicates that, in spite of their age, the accelerator sections are performing a originally specified at Stanford over thirty years ago.

The waveguide is aluminum WR-284 pressurized to 26.2 PSIG with SF₆. This was chosen because of the reduced expense compared with evacuated waveguide. We have had no significant problems with waveguide arcing. The rf power is split using 4-port 3-dB hybrid couplers. We could only afford one high-power phase shifter, which we use to shift the phase between the gun and the first section. To phase the sections within a cluster we constructed simple remotely actuated mechanical "waveguide phase adjusters" i.e. push-pullers that squeeze or expand the waveguides as necessary to adjust the phase⁷. These allow $\pm 15^\circ$ phase adjustment range for each accelerator section. Initially the phase was set with the help of low-power phase measurements. Once the linac was operational we adjusted the phase shifters for maximum energy. This setting was done only once and resulted in an energy increase of about 1.4% over the low-power settings. We monitor the rf power using simple magnetic loops at the output of each accelerator section just before the rf loads.

The rf drive is provided by a Sperry SAS-61 2-kW klystron. When distribution losses were taken into account, the

SAS klystron was unable to provide the 300-W drive necessary for each klystron. We adopted a novel approach to rf distribution. We used the SAS to drive one of the ITT klystrons then we split off a few kW of the high-power output to provide the drive for the other klystrons. This system works very well in practice. The rf output of the klystron has been flattened by appropriate tuning of the modulator pulse forming networks.

Two of the ITT klystrons have had an unusual history. Even though they had never been operated since leaving the manufacturing plant, they both developed leaks while in storage at Duke. It is likely that the interiors of both tubes were at atmospheric pressure for about one year. Lacking the funds to pay for refurbishment of the tubes, we chose to repair the klystrons in house⁸. The first step involved diagnosing the source of the vacuum leaks. One tube was found to have a leaking rf output window, the other a failed joint in the line leading from the klystron body to the vacuum pump. The tube with the leaking window provided the greatest challenge. Replacing the window was beyond our capabilities. We chose to add a second window by adapting an accelerator-section input window to provide a second window for the klystron, with an evacuated section in between the windows. As a precautionary measure, we added a 20-l/s ion pump to the tube in addition to the existing 2-l/s pump. Once the tube was sealed, pumped and leak-checked, the next step was to attempt to recondition the barium dispenser cathode.

The first prerequisite was to bake the tube to 450 °C. This was done over a period of nine days. The ultimate pressure was less than 1×10^{-9} torr. The cathode heater power was then turned on very slowly, reaching a maximum power of 400 W after twenty-two days. Preliminary emission tests at 500 V indicated a very good cathode perveance of 1.8 μPervs .

We then moved the tube to our 2- μs , 300-kV test modulator. The HV conditioning went very quickly 0 to 270 kV in twenty minutes. We found the peveance to be 1.9 μP at 250 kV. We determined a saturated gain of 52.2 dB at 280 kV and 33 MW output power in a 2- μs pulse at 10 Hz. The performance of the tube met or exceeded the manufacturers specifications in all respects. The tube has been in almost daily use at full power and a 1-Hz repetition rate since October 1994. We have had no problems with the additional rf window on the tube.

The second leaking tube was also repaired and now operates on a daily basis along with its companion.

For future upgrades to the linac we plan to modify some old SLAC klystrons manufactured by RCA. Many of the tubes that we have in-house are capable of producing no more than 20 MW in their present condition. We believe that if we replace the existing oxide cathodes on these tubes with new dispenser cathodes, we will be able to achieve performance specifications similar to that of the ITT tubes.

ELECTRON GUN

The electron gun used on our linac is the same single-cell thermionic rf gun that was previously used on the MKIII FEL at Stanford and later at Duke^{2,3}. For injection into the storage ring a short multi-nanosecond pulse is required⁴. This pulse is generated by chopping the electron beam with a pulsed electrostatic kicker at an energy of 1 MeV just after the gun. We can generate electron macro-bunches with an FWHM of 50 ns and 40 mA current.

The storage ring operates at an rf frequency of 178 MHz and a bucket spacing of 5.5 ns. The present system delivers approximately 0.2 nC per ring bucket and fills approximately 10-15 buckets per fill. Ideal operation requires a single-bunch injection of 1-2 nC of charge with a pulse width of less than 5 ns. The timing uncertainty should be less than 1 ns. It would appear that a photocathode system using an inexpensive pulsed nitrogen laser (337 nm) might be a considered for producing such pulses. The present cathode is LaB₆ whose quantum efficiency has been measured to be 2.5×10^{-4} at 337 nm⁵.

Nitrogen lasers are commercially available for under \$ 7000 that can produce 100-500 μ J of 337-nm light in 1-5 ns long pulses with sub-ns timing jitter⁵. Under ideal circumstances such lasers could produce between 17 and 85 nC per pulse (2-14 linac buckets) at the cathode. The transmission efficiency should be approximately 20% to the ring. (Half the charge generated will be accelerated and up to 40% of that will make it through the gun alpha-magnet.) The huge overhead in optical energy available makes this an attractive option. The peak optical power density on the cathode would be no more than 0.5 MW/cm², so surface damage would not be a problem. The system cost would be < 7 k\$ not including transport optics and diagnostics. We are considering this as an upgrade to our system.

OTHER SYSTEMS

The control and diagnostic systems are lean and effective. A description of the control system is given in a companion paper⁹.

The electron beam diagnostic system is very simple. Current is monitored using six beam current toroids and one fast stripline wall-current monitor. Beam position and match are monitored using six chromium-doped aluminum-oxide insertable screens viewed by inexpensive vidicon cameras. Energy is monitored with two nine-degree magnetic spectrometers, one after the first accelerator section (35 MeV) and one at the end of the linac. Pulse temporal structure is monitored by two methods. One uses a photomultiplier tube that looks at the synchrotron radiation from the electron beam

as it bends in the high energy spectrometer. The other method uses a fast stripline wall-current monitor at the high-energy end of the machine.

The magnetic lattice consists of quadrupole pairs between each accelerator cluster. Each quadrupole has integral two-axis steering. Each accelerator section is covered with μ -metal sheet to block stray magnetic fields.

In contrast to the original vacuum system, with its welded flanges, we installed the latest in HV conflat hardware with copper gaskets. All pumping is done with 20-l/s ion pumps, one per accelerator section.

CONCLUSION

As is evident from the description above the guiding principal in our design and construction philosophy has been one of strict economy. Wherever possible we have procured equipment from government surplus. We estimate that our total expenditure on external procurements for the construction of the linac so far is under 1M\$. This has resulted in a reliable system that has exceeded specifications, and given new life to a venerable accelerator.

ACKNOWLEDGMENTS

We would like to acknowledge the assistance of the electrical, mechanical, and administrative staff at the Duke FEL, without whose unstinting devotion and hard work, none of this would have been possible. Also we would like to thank our sponsors, particularly Dr. Howard Schlossberg, AFOSR, who persevered with this project through difficult times.

REFERENCES

1. R.B. Neal, editor, "The Stanford Two-Mile Accelerator", W.A. Benjamin, New York (1968)
2. G.A. Westernskow and J.M.J. Madey, Laser and Particle Beams, Vol. 2, part 2, 223 (1984)
3. S.V. Benson et al., Nucl. Instr. Meth. A296, 110 (1990)
4. V.N. Litvinenko et al., Commissioning of the Duke Storage Ring", these proceedings.
5. D.J. Banford, M. H. Bakshi, D.A.G. Deacon, Nucl. Instr. Meth., A318, 377 (1992)
6. Oriel Corporation, Stratford, CT, USA
7. P. Wang, N. Hower, P.G. O'Shea, "RF Phasing on the Duke Linac", these proceedings.
8. R. Sachtshale, P.G. O'Shea, M. Ponds, G. Swift, "In-house repair of a 30-MW S-band Klystron", these proceedings.
9. C. Dickey et al. "EPICS at Duke University", these proceedings.

COLD MODEL TEST OF BIPERIODIC L-SUPPORT DISK-AND-WASHER LINAC STRUCTURE

Y. Iwashita, A. Noda, H. Okamoto, T. Shirai, and M. Inoue,
Accelerator Laboratory, Nuclear Science Research Facility, Institute for Chemical Research,
Kyoto University, Gokanoshō, Uji, Kyoto 611, JAPAN

Cold model test of a biperiodic L-support Disk-and-Washer linac structure is performed. Each washer is supported by two L-shaped supports 180° apart azimuthally. The structure is a variant of the biperiodic 4-T support DAW[1]. Because the coupling-mode frequency is pushed up by the supports, it should be compensated to coincide with the accelerating frequency. The biperiodic supports also break the uniformity of the field distribution on the axis. The compensation methods against these perturbations are described.

I. INTRODUCTION

An electron linac[2] has been installed at the Accelerator Laboratory, Institute for Chemical Research, Kyoto University. It is mainly intended as the injector for the electron storage ring KSR [3,4], which is being assembled. The disc-loaded wave-guides are installed as the accelerator tubes, which are operated at 2857MHz. Because of the limited space in the building, only three of 3-m accelerator tubes can be installed. The available RF power from a klystron is up to 20 MW for each tube, and then the output electron energy is expected to be about 100 MeV at the peak current of 100 mA. In order to have a shorter damping time in the storage ring, however, the higher injection energy is desirable. A new accelerating tube with a higher shunt impedance is thus required to achieve the higher accelerating gradient with the same input RF power.

A cold model made of Aluminum is fabricated to study the possibility of a DAW structure with biperiodic washer supports. The results of the cold model test are described.

II. BIPERIODIC L-SUPPORT DAW

The DAW structure has outstanding features in high stability, good vacuum properties, high shunt impedance, and ease of fabrication[5]. It was found that the mode overlapping problem can be overcome by the biperiodic support configuration with the careful choice of the tank diameter (See Fig. 1). There is variety of options for DAW linac structure with such washer support. For example, in the configuration with a large tank-diameter, the operating frequency drops between two split TM₁₁(-like) mode passbands, and the shunt impedance is higher. When the tank diameter is small, both passbands are above the operating frequency, and the mode density is smaller. The basic configuration described here is the extension of the PIGMI[6] geometries, except for the thicker washers and the reduced tank diameter by 20%. This geometry has fewer undesirable modes and a shorter filling time compared with the large diameter 4-T support DAW. The washer thickness is increased for the cooling water channels inside the washers. Because the L-support configuration has only two supports on a washer, there are only one inlet and one outlet for the cooling water. This may simplify the fabrication problem compared with the 4-T support geometry, which has two inlets and two outlets on the washer[7]. A typical design specification based on SUPERFISH calculation is listed in Table 1.

III. TUNING METHOD

The positions of the washer supports are determined so that their effect on the accelerating mode is minimized. Then, the coupling mode frequency is inevitably disturbed by the existence of the supports, and its frequency is pushed up. Ideally, f_c should be coincide with the accelerating-mode frequency, then some compensation procedure is needed. Besides this effect, the biperiodicity of the supports breaks the uniformity of the electric field distribution on the axis. Because the supports reduce the electric field around them, the coupling coefficients between the cells are not uniform, yielding the biperiodic modulation on the field. In order to improve the coefficient unbalance, the disk radii R_{dn} and R_{ds} (see Fig. 2) are changed biperiodically; namely, the disks with the washer supports have a larger radius than that without supports, which enlarges the disk-washer opening. Thus, the coupling coefficients are enhanced biperiodically, and the coupling frequency is corrected by adjusting the average of R_{dn} and R_{ds} . Finally the accelerating frequency will be tuned by modifying the washer radius R_w .

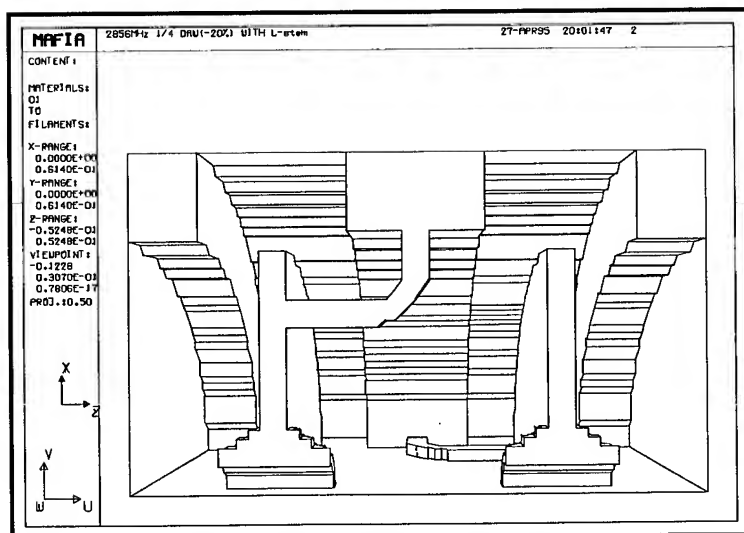


Fig.1 DAW with Biperiodic support

IV. MEASUREMENTS

The measurements are performed with a six-washer geometry. The coupling mode frequency is measured in the geometry with the half washer endplates, which has three disks with supports and three disks without support (See Fig. 3-a). Although the simple biperiodicity of the total system is broken, this geometry will give the correct coupling frequency [1]. There is another option of the support direction; namely, the quad-periodic geometry where the support direction changes alternatively (See Fig. 3-b). Although we measure both configurations, the biperiodic one is of concern. Considering the fact that R_t indicated in Fig. 2 also affects the field distribution, three sets of the supports with different lengths (different R_t) are prepared. Photos 1 and 2 show the typical parts for the model cavity, and the close view of the disk-support-washer assembly.

Figure 4 shows the geometry for the accelerating-mode measurement. The configuration of the measurement system for the field distribution on the axis is shown in Fig. 5. The resonant frequency is tracked by the Phase Locked Loop. The feedback voltage to the DC-FM input of Synthesized Signal Generator is recorded as the frequency shift due to the bead-pull-perturbation.

R_c/λ	0.585	-
β	1.0	-
Frequency	2.856	GHz
$L=\beta\lambda/4$	26.24	mm
R_c (cavity radius)	61.40	mm
R_d (disk radius)	49.6	mm
T_d (half disk thickness)	12.53	mm
R_w (washer radius)	42.	mm
T_w (half washer thickness)	2.5	mm
θ (nose angle)	30	degree
R_n (nose radius)	1.2	mm
R_b (bore radius)	5.13	mm
G (gap)	14.84	mm
R_t (supporting point)	32.3	mm
R_r (support curvature)	9.	mm

Table 1 DAW cavity dimensions

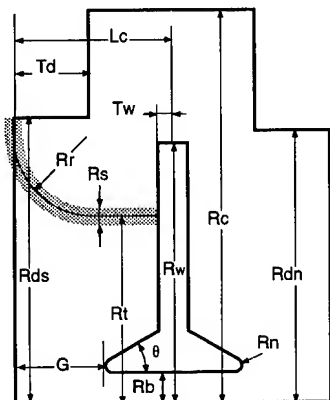


Fig. 2 Notations for DAW dimensions

V. RESULTS

Figure 6 shows the frequencies of the coupling mode and the accelerating mode as a function of R_{dn} . R_{ds} is 46mm in this case. The coupling mode frequency increases with the R_{dn} , while the accelerating mode frequency does not change

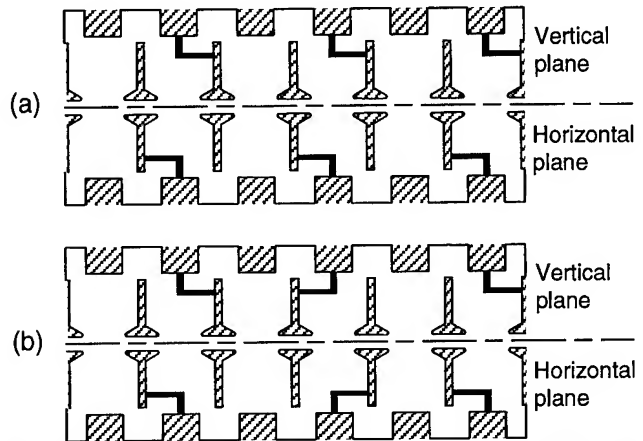


Fig. 3 Geometry for the measurement of the coupling mode frequency. (a) biperiodic (b) quad-periodic.

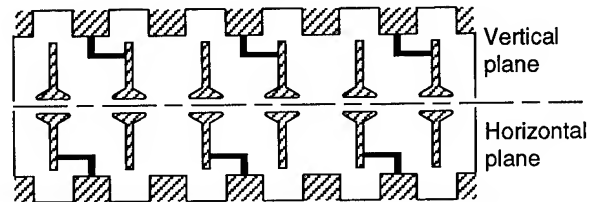


Fig. 4 Geometry for the accelerating mode

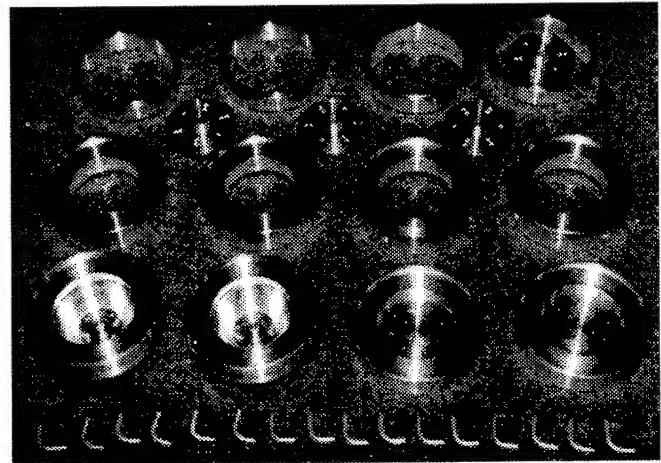


Photo 1 The typical parts for the DAW cold model

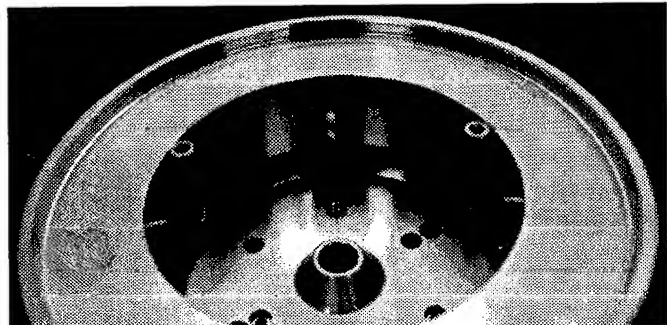


Photo 2 Close view of the disk-support-washer assembly

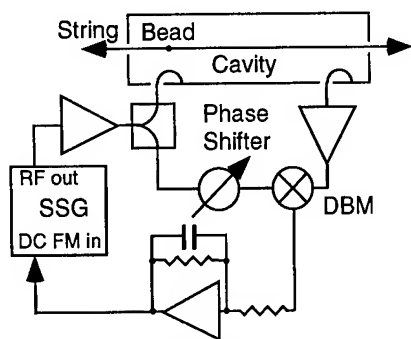


Fig. 5 Phase Locked Loop for the Bead Perturbation Method

much. The typical result of the field distribution measurements is shown in Fig. 7. The values of field strength are taken at the center of the cell where the strength has dip, then the values are averaged among the cells with supports or those without support. Figure 8 shows the uniformity of the field distribution on the axis as a function of R_{dn} , which is the ratio of electric field strength in the cell-with-supports to that-without-support.

It is confirmed that the uniformity can be controlled by adjusting the difference between R_{ds} and R_{dn} . The coupling mode frequency could be controlled by modifying the average of R_{ds} and R_{dn} . The dimensions of R_{dn} , R_{ds} , and R_w may be good parameters to meet the three requirements; 1) f_a and 2) f_c should match to the operating frequency, 3) the field distribution should be as uniform as possible. The research for the tuning process is going on.

VI. ACKNOWLEDGMENT

The authors thank Mr. Tonguu for his help in the measurement. The present work is supported by Grant-in Aid for Scientific Research from Ministry of Education Science and Culture of Japan.

VII. REFERENCES

- [1] Y.Iwashita, "Disk-and-washer structure with bi-periodic support", Nucl. Inst. and Meth. in Phys. Res. A348 (1994) 15-33
- [2] T.Shirai, et al., "A 100 MeV Injector for the Electron Storage Ring at Kyoto University", these proceedings.
- [3] A.Noda, et al., "Design of an Electron Storage Ring for Synchrotron Radiation", Proc. of the 4th European Particle Accelerator Conference, in print.
- [4] A.Noda, et al., "Electron Storage Ring, KSR for Light Source with Synchrotron Radiation", these proceedings.
- [5] R.K.Cooper, et al. "Radio-Frequency Structure Development for the Los Alamos/NBS Racetrack Microtron", Los Alamos National Laboratory document LAUR-83-95 (Jan. 1983)
- [6] L.D.Hansbrough, Compiler, "PIGMI: A Design Report for a Pion Generator for Medical Irradiation", LANL report LA-8880(1980).
- [7] Y.Iwashita, "Bi-periodic L-Support DAW For Electron Acceleration", Bull. Inst. Chem. Res., Kyoto University, Vol. 73 No.1 1995, in print.

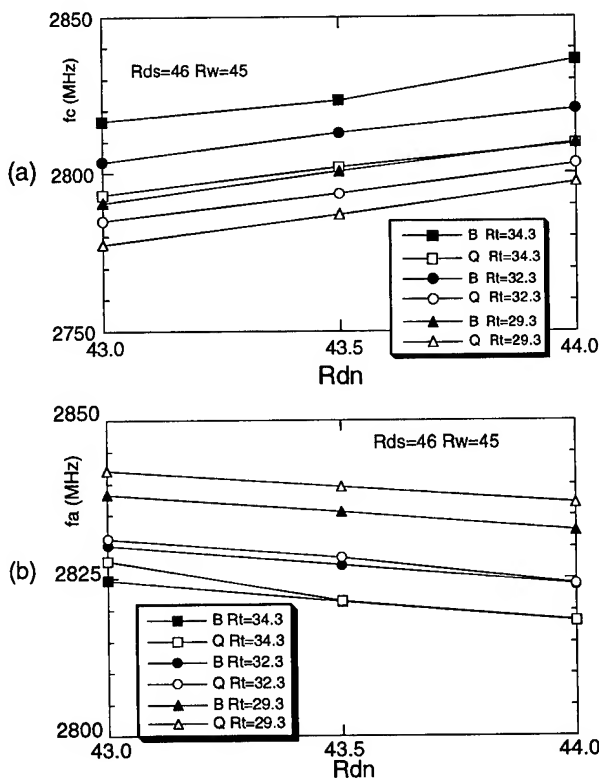


Fig. 6 (a) Coupling mode frequency as a function of R_{dn} .
(b) Accelerating mode frequency as a function of R_{dn} .

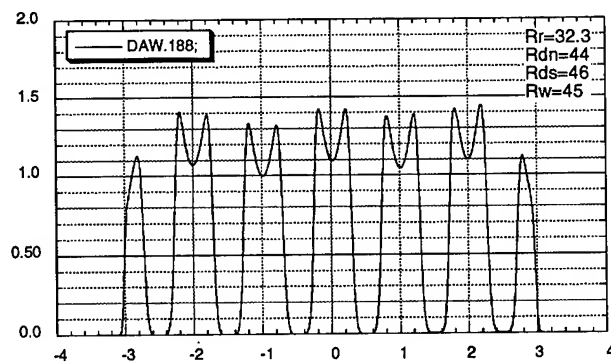


Fig. 7 The typical result of field distribution measurements

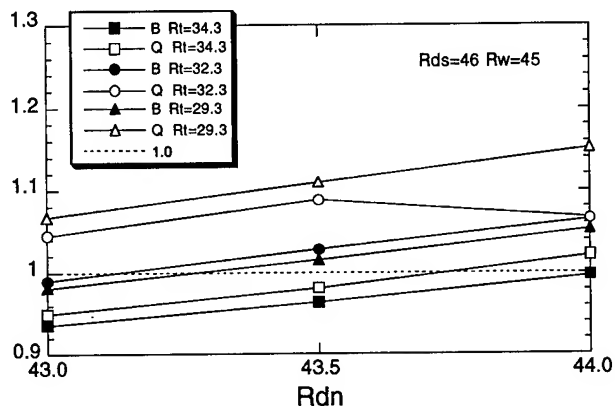


Fig. 8 Field uniformity as a function of R_{dn}

COMPACT LOW ENERGY CW LINAC WITH HIGH BEAM CURRENT

A.Alimov, A.Chepurnov, O.Chubarov, D.Ermakov, K.Gudkov, B.Ishkhanov, I.Piskarev, V.Shvedunov, A.Shumakov, Institute of Nuclear Physics, Moscow State University, 119899, Moscow, Russia.

I. INTRODUCTION

Up till now the main sources of electrons with high average power at low energies were DC accelerators and pulsed linear accelerators. Development of new technologies requires an increase of electron beam energies up to 10 MeV and beam powers up to hundreds kW. For these aims a CW mode of operation is more preferable. However, development of powerful CW linacs faces a number of problems.

1. Because of relatively low values of accelerating fields in a CW mode and a high average power of an electron beam, effective capturing of the particles into acceleration and further acceleration without losses present a serious problem.

2. Powerful accelerators require RF klystrons with high average power and, as a rule, can be designed only as multi-section accelerators, each section being supplied by a separate klystron.

3. Characteristics of the accelerator structures are to be optimised to reach maximum characteristics of CW linacs.

The present paper deals with the experimental investigation of electron capturing, design of a simple RF power system for multi-section accelerator, and beam acceleration at the prototype accelerator with two accelerator sections.

II. ACCELERATOR DESCRIPTION. ACCELERATOR STRUCTURE PARAMETERS

The block-diagram of a prototype two-section accelerator is shown in Fig.1. A DC electron beam of the gun (E-gun) [1] with the energy from 70 to 100 keV, current from 0 to 16 mA, and normalised transverse emittance 5 mm*mrad enters the buncher cavity (B). As a buncher we use a cylindrical copper cavity with TM_{010} mode at a frequency of 2450 MHz. The

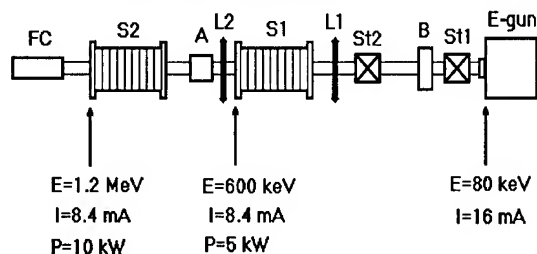


Fig.1. Block-diagram of the accelerator.

buncher has a probe for power supply and a probe for field control. Fine frequency tuning of the buncher is made by a

tuning plunger in the range of 2450 ± 2 MHz. Loaded quality factor of the cavity $Q_1 = 3500$ with a coupling constant 1.0.

The calculated value of intrinsic quality factor $Q_0 = 9000$, shunt impedance $R = 1.4 \text{ M}\Omega$. After the buncher the beam enters the first accelerator section with graded- β (S_1), which accelerates the beam up to 600 keV. The output beam of the first section passes through a cooled aperture (A) with a diameter of 10 mm, which serves as a low-energy filter, and enters the second accelerator section (S_2) with tapered- β which accelerates the beam up to the energy of 1.2 MeV. Beam power and current at the accelerator output are measured by the Faraday cup (FC). To focus the beam solenoidal lenses L_1 and L_2 are used. Beam alignment is carried out by steerers St_1 and St_2 .

The accelerator was constructed with two accelerator sections first designed for the injector linac of Moscow CW RTM [2,3]. Both sections are made on the basis of on-axis coupled accelerator structure with effective shunt impedance $78 \text{ M}\Omega/\text{m}$ (for $\beta = 1$) and operation frequency 2450 MHz. The first section consists of 9 accelerating cells with β from 0.582 (1st cell) to 0.869 (9th cell). The second section consists of 7 accelerating cells - first three cells have $\beta = 0.945$, next three cells have $\beta = 0.975$. Both sections have circumferential cooling only [3]. Loaded quality factors for both sections are $Q_1 = 7000$, and the coupling constant with a feeding waveguide is 1.2 (overcoupling).

III. RF POWER SUPPLY SYSTEM

One of the problems of CW operation of accelerator structures is a shift of a resonant frequency resulting from thermal deformations of the structure during start-up. This frequency shift depends on a level of RF power losses and on cooling efficiency. For our accelerator structure with circumferential cooling the frequency shift can exceed a bandwidth of a resonant curve at a moderate level of RF losses (20 kW/m at RF frequency 2450 MHz) [3]. Dependence of the structure resonant frequency on the dissipated RF power results in an asymmetry of a resonant curve which can be interpreted as a non-linear resonance.

Under these conditions the most simple and reliable method of operation of a single-section accelerator is a self-excited mode in a positive feedback loop between klystron and accelerator section. In this mode of operation the system oscillates at a section's resonant frequency and a klystron's frequency follows it automatically.

A transition from one accelerator section to two accelerator sections complicates the structure of a RF system. The complication arises from the necessity to phase the sections and from a presence of different frequency shifts of the sections. As a result the second section can not operate in a self-excited mode, and should be driven by a reference signal of the first section.

The block-diagram of the accelerator RF system is shown in Fig. 2. 22 kW CW klystrons (K_1 and K_2) at the frequency 2450 MHz [3] are used to drive the accelerator sections. The klystrons are isolated from the sections by T-circulators (C_1 and C_2). The first section (S_1) operates in a self-excited mode and forms a reference signal for the second section (S_2) and the buncher (B). The signal of the first section which is taken from the RF probe passes through the electrically driven coaxial phase-shifter (ϕ_2) and p-i-n attenuator (A_1) and enters the klystron. Phase conditions of self-excitation are chosen by the phase-shifter. The feedback p-i-n attenuator regulates the output power of the klystron and, consequently, the amplitude of the accelerating field. Reflected power level is controlled by a diode D_1 , the accelerating field

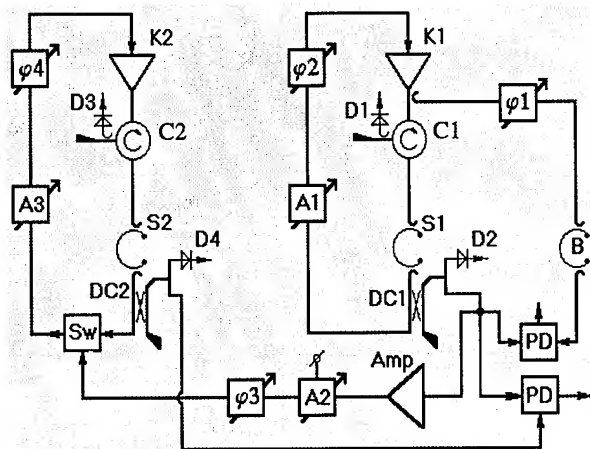


Fig. 2. Block-diagram of the accelerator RF system.

amplitude, by a diode D_2 . D_2 -signal is used by the system of amplitude stabilisation, which controls a p-i-n attenuator (A_1) current stabilising the amplitude of the accelerating field in the first section at the level of 10^{-3} . Such a stabilisation is very essential for our system with high beam loading. A part of the klystron's power (~ 60 W) is used to drive the buncher. The signal is taken from a probe, located in the output waveguide of the klystron. A part of the output section's signal from the directional coupler (DC_1) is used for monitoring phase differences between the first and the second sections, the first section and the buncher, for frequency measurements, and as a reference signal for driving the second accelerator section. Start-up of the second section (S_2) is carried out in a

self-excited mode [3]. A positive feedback loop of S_2 contains the p-i-n attenuator (A_3) and the phase-shifter (ϕ_4). The positive feedback loop is being closed with a help of the RF switch (Sw) which has two input connectors and one output connector. The attenuator and phase-shifter adjust the phase and amplitude of self-excited oscillations, providing the RF power to reach the operating level. When the section's resonant frequency coincides with that of the first section, the klystron's (K_2) drive is switched from the feedback loop to the reference signal of the first section. Phase and amplitude of the reference signal are adjusted by the 4-W RF amplifier (Amp), p-i-n attenuator (A_2), and phase-shifter (ϕ_3). Reflected power level is controlled by a diode D_3 , the accelerating field amplitude, by a diode D_4 . D_4 -signal is also used for amplitude stabilisation at the level of 10^{-3} . A part of the output section's signal from the directional coupler (DC_2) is used for monitoring the phase difference between the first and the second sections and for frequency measurements.

The sources of frequency instability, such as cooling water temperature and flow, change practically in the same way for both sections and do not destructively influence the system operation.

IV. BEAM ACCELERATION EXPERIMENTS

Beam acceleration experiments were carried out in three stages. At the first stage the buncher was switched off and we chose the phase difference between sections 1 and 2 to obtain maximum current and maximum beam power at the Faraday cup. Dependence of the beam current on the phase difference between the accelerator sections is shown in Fig. 3.

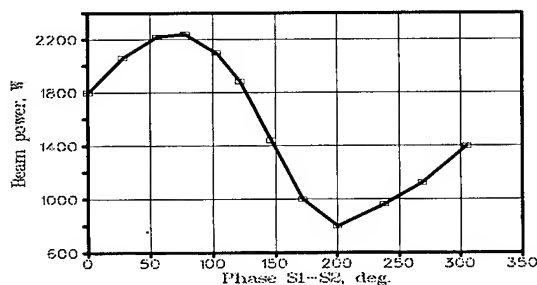


Fig. 3 Dependence of the beam power on the phase difference between the sections.

The measurements were made at gun voltage $U = 80$ kV, cathode current $I_{\text{cath}} = 6.5$ mA. Maximum output parameters of the accelerator obtained without the buncher were as follows: beam energy 1.2 MeV, beam current 5.5 mA (cathode current 16 mA), beam power 6.6 kW.

At the second stage we switched on the buncher and chose the buncher phase (relative to the phase of section 1) and the buncher amplitude (in these measurements section 2

was switched off). Dependence of the output beam current on the buncher phase is shown in Fig.4.

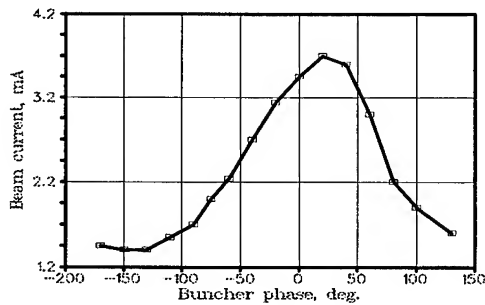


Fig. 4. Dependence of the output beam current on the buncher phase.

The dependence has the expected sinus form and makes it possible to choose the optimal phase of the buncher. It was measured at gun voltage $U = 80$ kV, cathode current $I_{\text{cath}} = 7.0$ mA, section power $P_{S1} = 10$ kW, and buncher power $P_B = 60$ W. The output beam energy was 600 keV. Fig.5 shows the dependence of the output beam current after the first section on the power, dissipated in the buncher. The measurements were made at the optimal value of buncher phase. The buncher power was regulated from 0 to 66 W. This dependence was measured at gun voltage $U = 80$ kV, cathode current $I_{\text{cath}} = 6.8$ mA; beam energy after the first section was 600 keV. With our experimental layout (Fig.1) the electrons which were not captured into acceleration by the first section can not reach the Faraday cup because the focusing length of the lens L_2 for low energy electrons is several centimetres, and these electrons cannot pass through the aperture. Hence, the capture efficiency

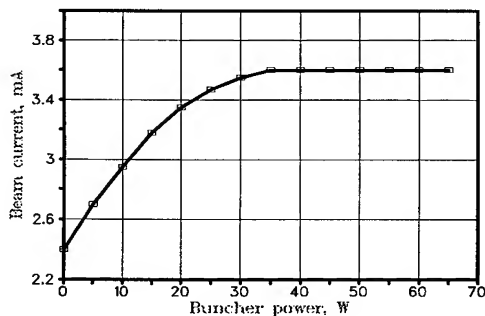


Fig. 5 Dependence of the output beam current on the buncher power.

can be estimated as a relation of the current at the Faraday cup to the cathode current of the gun. Beam energy was estimated using a relation of the measured beam power to the measured beam current. From Fig.5 the capture efficiency is equal to 35% when the buncher is switched off, and increases up to 53% at the optimal level of buncher power 40 - 66 W.

At the third stage we carried out beam acceleration experiments with two accelerator sections and the buncher for optimal values of RF phases and RF amplitudes. The

maximum value of beam current was limited by the parameters of the gun power supply and amounted to 16 mA. Dependence of the beam power on the cathode current up to 16 mA was linear. This means that space charge effects have no essential influence at these currents. With the cathode current of 16 mA, capture efficiency of 53%, the output beam current was equal to 8.4 mA at beam energy of 1.2 MeV. This corresponds to beam power of 10 kW. The value of beam power, measured by the Faraday cup, was also 10 kW. The accelerator operated under these conditions for several hours without additional tuning of its parameters.

V. SUMMARY

The prototype two-section CW linear accelerator with a simple RF power supply system was constructed. The electron beam with the energy of 1.2 MeV and beam power of 10 kW was obtained.

CW linear accelerator of this type, to our opinion, has the following advantages and perspectives:

1. The accelerator is rather compact. The weight of the two-section accelerator with radiation shielding is ~ 2000 kg (without electron gun and klystrons power supply). The length of the accelerator itself (without the gun and the buncher) is ~ 1 m, so, the power gradient is ~ 10 kW/m and the energy gradient 1.2 MeV/m. As it was mentioned above, the beam current in our experiments was limited by the gun power supply. A reserve of klystrons power (maximum power 22 kW) makes it possible to accelerate beam currents of 20 mA with the same energy gradient 1.2 MeV/m. Preliminary PARMELA calculations with space charge show that this current can be accelerated without compensating the space charge influence. Accounting for the 53% capture efficiency a beam current of 20 mA corresponds to a reasonable value of a cathode current ~ 40 mA. In this case the power gradient increases up to ~ 24 kW/m with the same energy gradient of 1.2 MeV/m.

2. Beam energy and beam power can be increased by adding accelerator sections with $\beta=1$. RF power supply system for each new accelerator section will be quite similar to the RF system of the second section of the described accelerator.

V. REFERENCES

- [1] B.S. Ishkhanov et al. "100 keV Electron Gun for Moscow CW RTM", *Pribori i Technika Experimenta*, 3 (1987), pp. 24-26 (in Russian).
- [2] A.S.Alimov et al. "Beam Acceleration Experiments in the Capture Section of CW Race-Track Microtron". INP MSU-89-61\128 (1989), 28 pp.
- [3] A.S.Alimov et al. "Operational Experience with Room Temperature Continuous Wave Accelerator Structures", *Nucl.Instr. and Meth. A328* (1993) pp. 385-397.

C-BAND LINAC RF-SYSTEM FOR e^+e^- LINEAR COLLIDER

T. Shintake, N. Akasaka, ¹K.L.F.Bane, H. Hayano, ¹K. Kubo*,
H. Matsumoto, S. Matsumoto, K. Oide, and K. Yokoya

National Laboratory for High Energy Physics, 1-1 Oho, Tsukuba-shi, Ibaraki, 305 Japan

¹SLAC: Stanford Linear Accelerator Center, Stanford University, Stanford CA, 94309 USA

A C-band (5712 MHz) rf system for a 500 GeV to 1 TeV e^+e^- linear collider is proposed. An accelerating gradient of 30 MV/m (including beam loading) is generated by 50 MW C-band klystrons in combination with an rf-compression system. The klystron and its power supply can be fabricated by conventional technology. The straightness tolerance for the accelerating structures is 30 μm , which is also achievable with conventional fabrication processes. No critical new technology is required in a C-band system. Therefore a reliable system can be constructed at low cost with the minimum of R/D studies.

I. INTRODUCTION

The choice of rf frequency for the main linac is one of the most critical issues for e^+e^- linear colliders. R/D work has been done at several frequencies ranging from L- to X-band, and even beyond to 30 GHz[1,2]. The principal theories required to design the linear collider have been well established, and the first order designs of these systems have been almost completed.

However, several important practical problems concerning the main linac have not yet been satisfactorily solved: how to fabricate the accelerating structure with the tight tolerances required at the high frequencies; how to develop high-power klystrons with reasonable power-efficiency, life-time and focusing system; how to provide high voltage for klystron with reasonable efficiency; and most important at all: how to reduce the construction cost. These difficulties are intimately related to the detailed design of the hardware, which mostly depends on the choice of the rf frequency.

In 1992, we proposed a C-band system as the best solution for reaching 500 GeV center of mass (c.m.) energy, one that does not require critical technology[1]. In this paper, some advantages of the C-band system and details of the current design will be described.

II. ADVANTAGES OF C-BAND SYSTEM

From the point of view of structure efficiency, a higher frequency is desirable, since the shunt impedance scales with the frequency as

$$r \propto \omega^{1/2} \quad (1)$$

This is the main reason for choosing a higher frequency than the traditional S-band frequency. For example at X-band, the shunt impedance becomes twice as high as at S-band, which means we can get the same accelerating gradient with half of the input rf power. However, when a beam is accelerated, the

effective accelerating gradient is lowered due to beam loading. This effect is more severe in a higher shunt impedance structure, and thus the net accelerating gradient does not simply increase as eq. (1). To make use of the benefits of the high shunt impedance at higher frequency, we need to increase the peak input power per unit length proportional to eq. (1). Unfortunately, the peak power available from a klystron tends to go down at higher frequencies. For this reason, extensive long-term R/D programs are under way trying to realize very high power klystrons at the higher frequency bands.

Another difficulty at the higher frequency bands is the very strong single- and multi-bunch wakefield effects. Recent studies have almost solved the multibunch problem by means of damped and/or detuned structures. In our case, we plan on using the choke mode cavity structure[3] running at C-band. This structure strongly damps the higher modes, so that the multibunch instability should be no problem. However, still there is the single-bunch wakefield effect to consider, one that can cause single-bunch emittance dilution in the main linac. The alignment tolerance of the accelerating structure due to this effect scales, assuming the gradient and lattice fixed, as;

$$\Delta y_{\text{structure}} \propto \left(\frac{dW_T}{ds} \right)^{-1} \propto a^4 \propto \omega^{-4} \quad (2)$$

where a is the beam hole radius and W_T is the single bunch transverse wake function. Equation (2) shows that the tolerance decreases dramatically as the frequency increases. In the case of X-band, the alignment tolerance of the structure becomes 256 times tighter than the S-band case.

As a compromise between the above considerations, we consider C-band to be the best choice of frequency. The shunt impedance can be as high as 55 $\text{M}\Omega/\text{m}$ (including 25 % degradation due to the damping structure) while the straightness tolerance is 30 μm , which is achievable using conventional brazing techniques[5].

If we look at the practical details of the rf system, we will find that, additionally, C-band has a big advantage in the power supply (modulator) that is needed for the klystron. The filling time of rf field into the disk-loaded structure is given by

$$t_f = \frac{2Q}{\omega} \tau \propto \omega^{-3/2} \quad (3)$$

where Q is quality factor, and τ is the attenuation constant of the structure, which is usually chosen close to 0.5. We see that the filling time becomes shorter at higher frequencies. Typically, it is 900 nsec at S-band, 300 nsec at C-band and 100 nsec at X-band. Assuming a compression ratio of 5 in the pulse compressor, and including a beam pulse length, the pulse length at the klystron output becomes 9 μsec at S-band, 3 μsec at C-band and 800 nsec at X-band. A pulse length 800 nsec at X-band is rather short, requiring the development of a

* Visiting from KEK

special modulator which provides a high voltage (HV) pulse with a fast rise and fall time. On the other hand, in the case of S-band, to get a HV pulse of 9 μ sec length from a conventional modulator, a long pulse forming network(PFN) line and a large volume transformer are required. The pulse length of 3 μ sec in C-band is quite suitable to the conventional klystron modulators of a simple single-line PFN. Among the R/D programs, the major goal for the klystron modulator is quite simple: reduce its cost. For the C-band power supply, since it is not necessary to develop special technology, we can construct a reliable system at lower cost.

III. SYSTEM DESCRIPTION

The machine parameters of the C-band system are summarized in Table-1. In the 500 GeV c.m. energy case, we accelerate 72 bunches in one pulse, and operate the machine at 150 Hz to get a luminosity of 1×10^{34} /cm²/s.

Fig. 1 shows the schematic diagram of the rf system. The output power of the klystron is enhanced by a factor of 3.5 by the SLED-II type compressor; this is fed into two structures to get a net accelerating gradient of 29.3 MV/m. We need 7.8 km of active length to reach a beam energy of 250 GeV.

A. Klystron Modulator (Pulse Module)

The HV pulse modulator generates a 310 kV and 2.4 μ sec flat top pulse. Since this level of voltage and pulse length are normal in conventional modulators, no special R/D is required for the modulator. We assume a power efficiency of 80 %, which is a reasonable estimate considering existing klystron modulators.

B. Klystron

The C-band klystron is a 50 MW klystron. We assume a power efficiency of 45 %, which seems reasonable if we scale from existing S-band klystrons such as the SLAC 5045-tube: 50 MW peak output and 45 % power efficiency, or the Toshiba E3712 tube: 80 MW peak and 46% power efficiency[6].

It is well known that the energy capability of microwave tubes is lower for higher frequencies because the beam pipe diameter is smaller. In the case of pulsed klystrons, the output energy per pulse roughly scales as,

$$P \cdot t \propto \omega^{-2} \quad (4)$$

The Toshiba E3712 tube can produce : 80 MW x 4 μ sec = 320 Joules/pulse at S-band frequency. It scales down to 80 Joules at C-band. Our design is close to this value. Therefore no critical difficulty will be encountered in development of this class of klystron at a C-band frequency.

C. Pulse Compressor

The pulse compressor is a SLED-II type compressor. In order to reduce its physical length, we use a disk-loaded circular waveguide, whose group velocity is 0.056 of speed of the light. Since extra power will be dissipated on the disks, the attenuation becomes higher than in a simple waveguide delay-line.

Table-1. Machine Parameter of C-band Linear Collider

----- Basic Parameters -----			
Center of Mass Energy	GeV	500	1000
Number of particle per bunch	10^{10}	1.11	1.5
Number of bunches per pulse		72	72
Bunch spacing	nsec	2.8	2.8
Repetition frequency	Hz	150	50
R.m.s. bunch length	μ m	120	120
Normalized emittance at damping ring (x/y)	μ m.rad	3/0.03	3/0.03
----- Parameters Related to Main Linac RF -----			
Injection Energy	GeV	20	20
Nominal accelerating gradient	MV/m	40.0	57.6
Net accelerating gradient	MV/m	29.3	43.2
Active length of main linac per beam	km	7.8	11.1
Total average power into cavities for two linacs	MW	54.0	52.5
Wall-plug power for two linacs	MW	225	220
Assumed efficiency from AC to RF	%	24	24
----- Parameters Related to FFS and IP -----			
R.m.s. beam size at IP (x/y)	nm	260/3.0	372/2.2
Crossing angle	mrad	6.0	6.0
Disruption parameter	Dx/Dy	0.20/17.5	0.067/11.3
Number of beamstrahlung photons		1.5	1.4
Energy loss by beamstrahlung	%	5.3	8.0
Geometrical luminosity reduction factor		0.54	0.64
Pinch enhancement factor		1.6	1.5
Luminosity	10^{33} /cm ² /sec	9.1	6.3

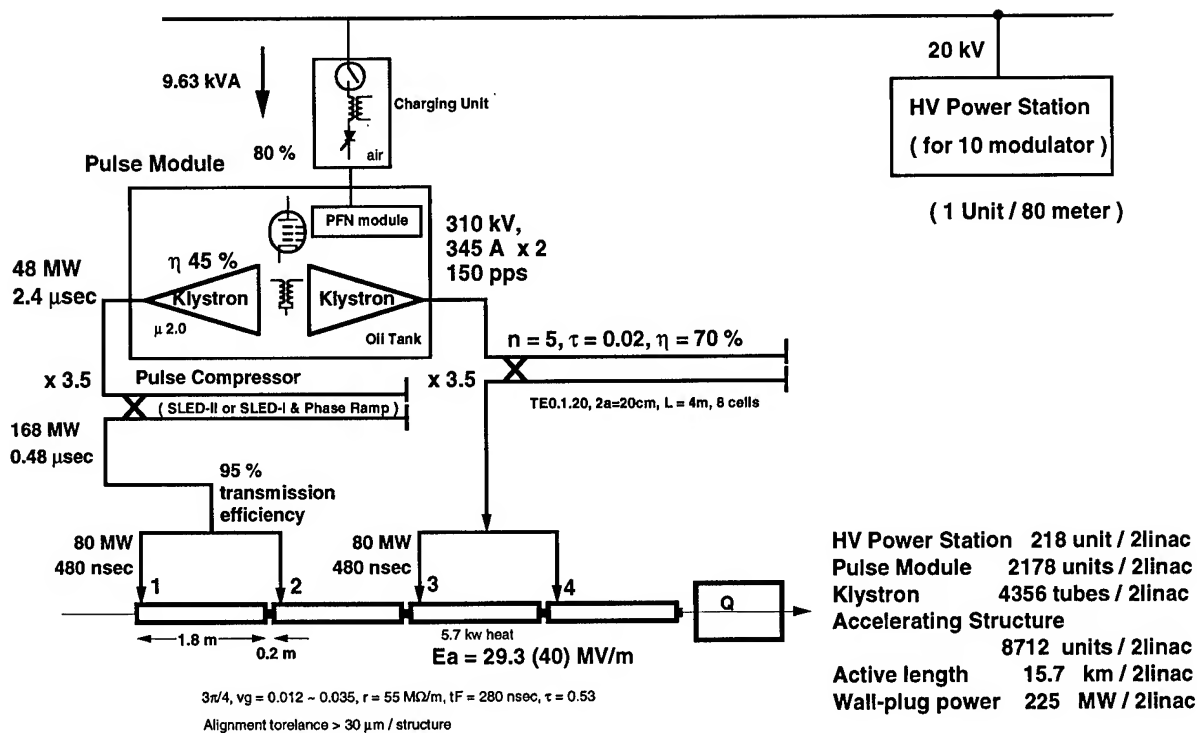


Fig. 1 C-band rf system for e^+e^- linear collider of 500 GeV c.m. energy

According to an analytical estimate, the TE_{0,1,20} mode inside a cylindrical cavity of diameter 20 cm and cell length 50 cm, has a Q-value of 2.7×10^5 . The attenuation parameter of this delay line becomes $\tau = 0.02$. This compressor will provide a power gain of 3.5 and a power efficiency of 70%. In order to reduce its construction cost, the cavity will be made of steel with copper plating.

D. Waveguide

We do not need to use a special low-loss waveguide, which is sometimes required in the higher frequency bands. We use standard rectangular waveguide (EIA WR-187), whose loss factor is as low as 0.03 dB/meter.

E. Accelerating Structure

In order to avoid emittance dilution due to the multibunch wakefields, we use the HOM-free choke mode cavity structure[3]. Such a structure has been tested at high accelerating gradient at S-band[4]. Detailed discussion of the C-band version of this cavity is given in ref. [5]. The outside diameter of this structure at C-band is 140 mm, which is a suitable size for precise machining on a lathe and also for brazing. This is another reason to choose C-band.

IV. EXTENDIBILITY TO 1 TeV C.M. ENERGY

We can extend the system to reach a c.m. energy of 1 TeV by replacing the klystrons by 100 MW klystrons and extending the active length to 11.1 km/beam. By lowering the machine repetition frequency to 50 Hz, we can limit the wall

plug power to 220 MW. Increasing the number of particles per bunch by a factor of 1.4 will allow us to obtain a luminosity of $0.6 \times 10^{34} / \text{cm}^2/\text{s}$.

ACKNOWLEDGMENTS

The author would like to thank Prof. Gregory A. Loew for useful discussions on the accelerating structure and the pulse compressor. The author would like to thank Prof. Hiroataka Sugawara, Prof. Yoshitaka Kimura and Prof. Koji Takata for their encouragement's on this work.

REFERENCES

- [1] JLC Group, "JLC-I", KEK Report 92 - 16, December 1992, A/H/M
- [2] Proceedings of the Fifth International Workshop on Next-Generation Linear Colliders, October 13-21, 1993, SLAC-436
- [3] T. Shintake, "The Choke Mode Cavity", Jpn. J. Appl. Phys. Vol. 31 (1992) pp. L1567-L1570, Part 2, No. 11A. 1 Nov. 1992
- [4] T. Shintake, "High Power Test of HOM-Free Choke Mode Damped Accelerating Structure", Proc. 17th Int. Linac Conf.(LINAC94), Tsukuba, Japan, August 21-26, 1994, p. 293, KEK Preprint 94-82, Sep. 1994 A
- [5] T. Shintake, et. al., "HOM-Free Linear Accelerating Structure for e^+e^- Linear Colliders", contributed to this conference.
- [6] H. Yonezawa, "E3712 Klystron Specification", Toshiba Co. Japan

INITIAL OPERATION OF THE UCLA PLANE WAVE TRANSFORMER (PWT) LINAC

R. Zhang, P. Davis, G. Hairapetian, M. Hogan, C. Joshi, M. Lampel,
S. Park, C. Pellegrini, J. Rosenzweig and G. Travish

Departments of Physics and Electrical Engineering, University of California, Los Angeles, CA 90024

Abstract

We report on the initial operation of a novel compact rf linac — the plane wave transformer (PWT). The PWT is a 42 cm long, 8 cell standing-wave structure, operated at S-band, in a π -mode. We present the properties of this linac at rf power levels from 4 MW to 8 MW and beam energy from 7 MeV to 10 MeV, measured initially using both dark current and photo-electrons. Some technical issues associated with the operation are discussed. Future improvements of the PWT, using a modified design, are also studied.

I. INTRODUCTION

The UCLA rf linac system is designed to provide a high brightness electron beam for physical experiments, such as free electron lasers, plasma focusing and plasma acceleration [1]. It uses a laser-illuminated photocathode rf gun as an injector. The rf linac accelerates the electrons to an energy ranging from 10 to 20 MeV with a high beam quality. To this end, a compact, high gradient and high brightness rf linac structure is needed to achieve our goals. Therefore, the plane wave transformer (PWT) [2] linac, which promises high impedance, high efficiency, low cost, is used in our system.

Since it was first proposed in 1960s [3], the PWT linac structure, named in 1980s [2], had not been under much studies. The PWT is a standing-wave linac, excited in the π -mode. It consists of a cylinder cavity, loaded with disks. The disks are separated from the cylindrical tank and supported by several metal stems parallel to the axis. This structure has features such as operation at TM_{02n} mode (where n is the number of disks), the simplicity in fabrication, and the strong coupling between cells. The PWT structure supports both a longitudinal acceleration field and a TEM-like plane wave between the tank and the disk array. The plane-wave provides the coupling between the individual cells. In this sense, this structure transforms a plane-wave into a longitudinal acceleration electric field. This unique feature makes the PWT structure have advantages of high shunt impedance and low fabrication tolerance. It also has the potentials of compactness, high brightness, high efficiency and low cost. These properties will make the PWT linac a very promising candidate to be widely used in experimental labs and industry communities.

Since the PWT operates on a high order TM_{02} mode, it raises concern on its mode structures and frequency separation of the operation mode from other different modes. It is probable that other undesired modes would be excited by either the rf coupler or the electron beam. Besides, for operation in the π -mode, a linac structure is

sensitive to defects in the manufacture and beam loading. Therefore, the actual application of this structure, if any, to particle accelerators will demonstrate its feasibility to become a promising candidate in the rf linac family.

We started the rf high power conditioning of the PWT late last year. The preliminary results are very encouraging. In this paper, we describe the mechanical design of the linac. We report the properties of the PWT at rf power level from 4 to 8 MW. We present the measured beam parameters. We also discuss the future improvement of this structure.

II. MECHANICAL DESIGN OF THE PWT

The UCLA PWT linac prototype is shown schematically in Fig.1. It consists of eight cells with half-cell termination in both ends. It has a total length about forty two centimeters. The dimensions of the linac are listed in Table 1. The whole structure is removable for the convenience for study.

Geometry dimensions (mm)		Electrical parameters	
total length	420	frequency	2856 MHz
tank inside diameter	136	unloaded Q-value	14000
disk diameter	81	shunt impedance	53M Ω /m
drift tube length	178	transit factor	0.77
disk iris diameter	16	field ratio	2.5

Table 1. Geometry and Electrical Parameters of the PWT

The tank was manufactured from stainless steel with copper plating inside. The disks were made from OFHC copper. The disk-washers are soldered with four water tubes which provide cooling to the linac to stabilize the resonance frequency. The four water tubes pass through one end flange with the joints being vacuum sealed by viton gaskets. There are four small ports at each end of the tank, as shown in Figure 1. In an earlier design, the central array was supported by four connecting bars at both ends [4]. The

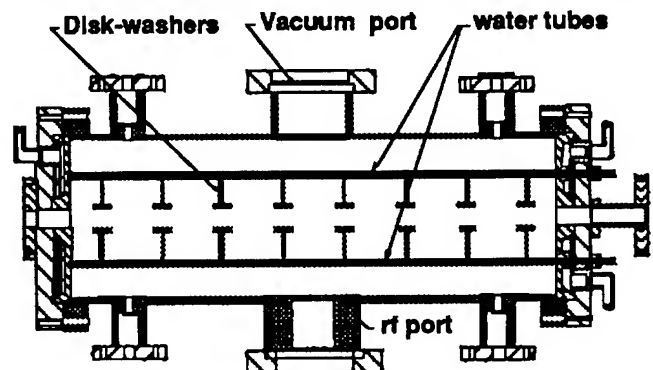


Figure 1: the cross section schematic of the PWT linac

four ports were used to house these connecting bars. Although the previous design simplified vacuum seal, the water cooling could not be provided to the disks, because of the existence of the joints between the central array and the connecting bars. Under the current design, all of these ports are idle, except one of them is used for housing an rf monitor. The cooling water temperature is controlled by a constant temperature bath. No water cooling is provided to the outside tank because its low rf power loss and its insensitive to affecting the resonance frequency.

To minimize the rf power loss and perturbation of the accelerating field, the water tubes, which also serve to connect the disks, are located at places where the field is at minimum. The tuning of the PWT was accomplished by slightly changing the dimensions of the end cells. The tuning from cell to cell is not necessary because of the strong coupling between cells. The fine tuning of the linac resonance frequency is achieved by adjusting the temperature of the cooling water.

III. ELECTRIC PROPERTIES

The linac shares a 25 MW XK-5 klystron with the rf gun. The rf power is distributed to the linac and the rf gun by using a direction coupler at a ratio of 2:1. The RF power was coupled into the linac by cutting an iris in the wall of a central accelerating cell. A high power phase-shifter is installed in the linac branch to adjust the injection phase of the electron beam into the linac. There is no rf isolator connected to the linac at current set-up.

The electrical parameters of the linac are listed in Table 1. Fig. 2 shows the high power rf signals: the forward pulse, the reverse pulse, and the pick-up signal from the rf monitor in the linac. The flat-top duration of the rf power pulse of the system is about 2 μ s. The fill time of the linac is about 0.8 μ s. Therefore, the pick-up signal does not have a flat top. The estimation of the Q-value from the monitor signal is consistent with the cold test.

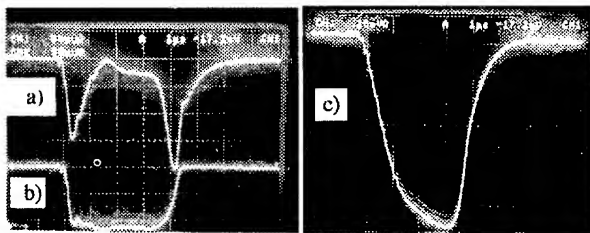


Figure 2: The rf waveforms from the PWT linac: a) reverse power; b) forward power; c) the PWT monitor signal (horizontal scale: 1 μ s / div.).

The highest rf power fed into the linac we recorded is above 8 MW. However, the PWT linac did not sustain this power level for very long time. The possible causes are: a) excessive arcing occurred during conditioning, resulting in damage to the linac surface; b) vacuum problems due to faulty pumps. Besides, the PWT could not be baked to high temperature because viton gaskets are used at the water tube joints with one end-flange.

IV. MEASUREMENT RESULTS

The details of the UCLA rf linac beam line is described in [5]. Two doublets are placed at down stream of the linac, followed by a dipole magnet, which is used to measure the beam energy and the energy spread. Several phosphor screens are used to monitor beam profiles along the beam line. The emittance is measured by using both slits and quads-scanning. Beam charge is measured by an ICT and Faraday-cups.

Most of the measurements of beam parameters were carried out at low charge [5]. At a beam charge of less than 0.1 nC, we obtained a well focused beam by just using the solenoid at the gun exit alone. Fig. 3(a) shows a beam image at the screen after the dipole magnet. Fig. 3(b) and (c) show the beam profiles at horizontal and vertical planes separately. The rms spot size is about 0.5 mm for horizontal plane and 0.4 mm for vertical one (FWHM). The corresponding laser beam rms spot size for this electron beam is about 2 mm.

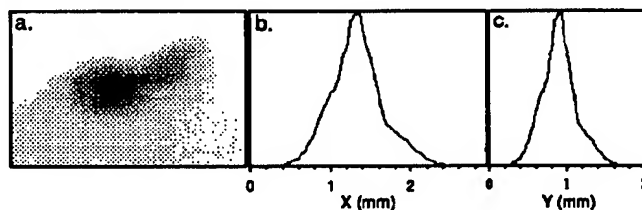


Figure 3: The beam image at the screen after the dipole: a. beam spot image on the screen; b. horizontal beam profile; c. vertical beam profile.

The beam energy is proportional to the square root of input power. Fig. 4 shows the measured electron beam energy variation with the input rf power to the linac. In comparison, the calculated results from measured PWT parameters of cold test are also shown in the figure. For the measurements, the beam energy exit from the rf gun is about 3.2 MeV. The measured energy agrees with the calculated results very well.

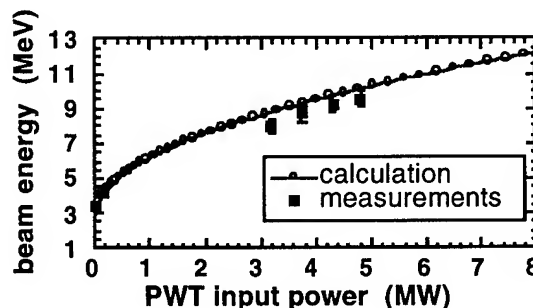


Figure 4: The beam energy variation with input power. At rf power 8 MW to the PWT, we measured a dark current energy of 12.2 MeV.

The beam energy spread is measured by measuring the bunch length after the beam passing a dipole magnet. The

better than 0.1%. Since energy spread is very sensitive to the injection phase, phase-scan of energy spread variation is a good estimation of the beam bunch length. Although the adjustment of the phase shifter changes the rf power into the linac, the effect of the rf power on the beam energy spread is negligible. The measured results by scan of the phase are shown in Fig. 5. To estimate the bunch length, we used PARMELA [6] to simulate the beam dynamics. The solid line in Fig. 5 is the simulation results by assuming a beam bunch length of 2.5 ps (1σ). This indicates that the beam bunch length is around 5 ps (FWHM), which agrees well with the measurement of the laser bunch length [5].

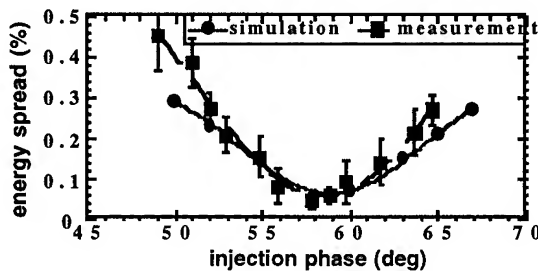


Figure 5: The energy spread variation with injection phase (beam energy around 9.5 MeV, beam charge less than 10 pC, PARMELA simulation assuming bunch length (1σ)=2.5 ps)

We measured the emittance by using the quads-scan technique. One measurement of quads-scan is shown in Fig. 6. The beam energy from the gun is 3 MeV with a charge of less than 10 pC. The beam energy for this measurement is 9.6 MeV. By using thin-lens approximation of the quads, the normalized rms beam emittance is about 5 mm-mrad.

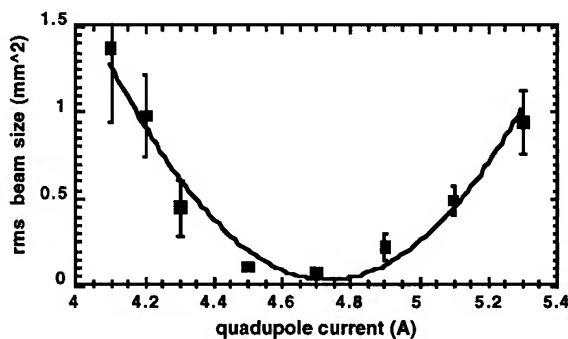


Figure 6: The quadrupole scan of rms horizontal beam size for emittance measurement (charge=5pC; energy =8 MeV).

V. FUTURE IMPROVEMENT

Although the high rf power operation demonstrates that the PWT can be used as an rf linac with many promising features, it is also evident that several improvements need to be done to make it a very robust structure. In order to achieve a high acceleration gradient, the ratio between the

surface field to the on axis acceleration field has to be reduced. Otherwise, the acceleration gradient the rf linac may support will be limited by the high dark current, and even by possible break down. The ratio for the current prototype is over 2.5. Therefore, the surface peak field will, for an energy gain of 10 MeV, be higher than 130 MV/m, which is at the high end of an S-band structure. Another issue associated with high gradient operation is the vacuum pressure. To obtain a low vacuum pressure, the high temperature bake of the linac is essential. Therefore the viton gaskets at the water tube joints can not be used for vacuum seal.

To improve the performance of the PWT linac, a slightly modified structure, PWT3, has been studied and built. In the new design, flat disks are used to replace the loaded disks, reducing the ratio of maximum surface field to on-axis field from above 2.5 to about 1.2. Because the flat disks are much thicker than the loaded disks, water channels can be formed inside disks. Therefore, all the joints between different components can be brazed together. The shunt impedance of the modified structure is about the same as that of the loaded-disk one. The modified structure will be under high power test soon.

VI. CONCLUSIONS

Initial operation of the PWT at high rf power has demonstrated that this structure can be used in a compact, high brightness linac. Because of its advantages, like compactness, high efficiency, low cost, the PWT is also a good candidate for medical and industrial applications. The modified structure, PWT3, has been installed and will be tested in the near future.

VI. ACKNOWLEDGMENTS

The authors wish to thank R. Cooper, R. Miller, S. Schriber and D. Swenson for useful discussions. We are specially grateful for the help received from J. Weaver, B. Roome, H. Lockart, A. Casillas and K. Luck for the fabrication of the structure. We appreciate the help from S. Hanna and A. Menegate in the microwave measurements at SLAC. The help of M. Goertmiller, D. Gooden, C. Hall, R. Hedrick and A. Murokh for the rf conditioning is greatly appreciated. This work is supported by the US DOE Grants DE-FG03-92ER-40493 and DE-FG03-92ER-40727.

VI. REFERENCES

- [1] S. Hartman *et al.*, Proc. of the 1991 Particle Accel. Conf., San Francisco, CA, 2967 (1991).
- [2] D. A. Swenson, European Particle Accel. Conf. 2, 1418, Rome, Italy, ed. S.Tazzari (1988).
- [3] V. G. Andreev *et al.*, Proc. Int'l. Conf. on High Energy Accelerator, Frascati, Italy (1965); V. G. Andreev, Soviet Physics --- Technical Physics 13, 1070 (1969).
- [4] R. Zhang, S. Hartman and C. Pellegrini, Proc. of the 1993 Particle Accel. Conf., Washington, DC (1993).
- [5] P. Davis *et al.*, these proceedings.
- [6] L. M. Young, private communications, LANL (1995).

The UCLA Compact High Brightness Electron Accelerator

P. Davis, G. Hairapetian, M. Hogan, C. Joshi, M. Lampel, S. Park,
C. Pellegrini, J. Rosenzweig, G. Travish and R. Zhang

Departments of Physics and Electrical Engineering, University of California, Los Angeles 90024

Abstract

We report the characteristics and performance of the UCLA S-band compact electron accelerator, consisting of a high brightness, 8 cm long, photo-injector with a copper cathode, followed by a 42 cm long plane wave transformer accelerating structure, delivering a beam energy of 10 MeV. The photo-electrons are produced by a 266 nm laser pulse of less than 4 ps in duration. Over time the laser induced electron emission decreases and the emission from the cathode surface becomes structured. Measurements of the quantum efficiency for Cu before and after this degradation are presented along with images of the non uniform electron emission.

I. INTRODUCTION

The UCLA S-band compact electron accelerator [1] is designed to produce a high brightness beam for experiments in beam-plasma interactions [2] and the generation of coherent radiation [3]. The 4.5 MeV photoinjector is a copy of the original BNL photoinjector with removable photocathode [4], while the main accelerating section is a previously untested structure called a plane wave transformer (PWT) [5]. Because this accelerator is to be used for conducting experiments in a small university laboratory, emphasis in the accelerator design was placed on compactness, reliability and ease of operation. It was with these goals in mind that copper was chosen as the photocathode material.

Neither initial operation of the UCLA photoinjector in 1993 [1] nor the Brookhaven photoinjector [6] indicated any problems with the use of copper photocathodes. It was presumed that copper would be a robust material for which neither special handling nor special vacuum requirements would be necessary. However, our most recent results which were obtained under rf fields of up to 100 MV/m and in vacuum of $< 3 \times 10^{-7}$ Torr, indicate that the copper cathode surface can be poisoned. The electron emission was not only reduced but also became highly structured. This structure results from non uniform emission from the cathode surface

which causes beam degradation and limits the beam brightness.

II. EXPERIMENTAL SETUP

The accelerator layout is depicted in Fig. 1. The Cu photocathode is placed at the endwall of the 1/2 cell in a 1 1/2 cell rf gun. A pair of solenoids is used to transport the beam to the various beam diagnostics and PWT linac while maintaining a zero magnetic field at the cathode surface.

For single photon photo-emission, the photon energy must exceed the work function of Cu (4.65 eV)[7]. The photoinjector drive laser produces < 4 ps laser pulses at 266 nm (4.66 eV) with up to 300 μ J/pulse. This is accomplished using chirped pulse amplification and compression of a mode-locked YAG laser and frequency upconverting using two KD*P doubling crystals. The laser is injected at 3° from normal incidence to the cathode by a mirror which is mounted in vacuum slightly off of the beam axis.

The electron charge is measured with two independent diagnostics, a Faraday cup and an integrating current transformer (ICT). Both these diagnostics agree with each other to within 10%. However, because the Faraday cup collects significant amounts of dark current (> 5 nC), the ICT is used to measure the photo-induced charge per pulse with less than 10% dark current background. A dipole spectrometer is employed to measure the beam energy from both the photoinjector and the PWT linac, while phosphor screens enable verification of the beam position and facilitate the measurement of the beam profile. To fully characterize the beam quality, a venetian blind pepperpot can be inserted for measuring the beam emittance.

Two different Cu cathodes were tested. The first was a commercially polished cathode purchased from Spawr Industries. It was polished to $\lambda/4$ at $.6 \mu$ m flatness and 40/20 scratch and dig. The second cathode was hand polished at UCLA down to 0.3μ m diamond grit size.

III. EXPERIMENTAL RESULTS

A. Commercially polished cathode.

The Spawr cathode was installed in late August, 1994 and rf conditioning continued for 3 months while the PWT was commissioned. Rf breakdown was observed throughout the conditioning process during which the rf power was increased in steps until the occurrence of rf breakdown events reached a prescribed limit of less than three consecutive rf breakdowns and less than a 1% occurrence of breakdown events over a 15 minute interval. When the frequency of breakdown events fell below this limit the rf power was increased until the number of breakdown events once again approached this level. Using

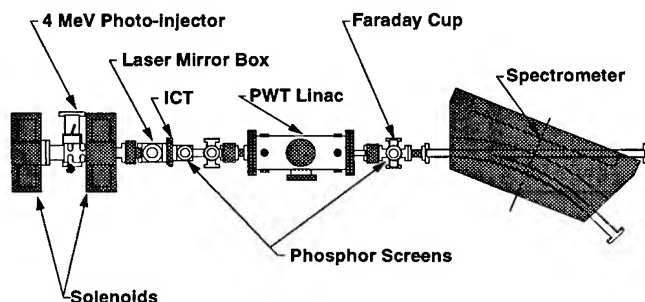


FIG. 1 Schematic diagram of the UCLA accelerator.

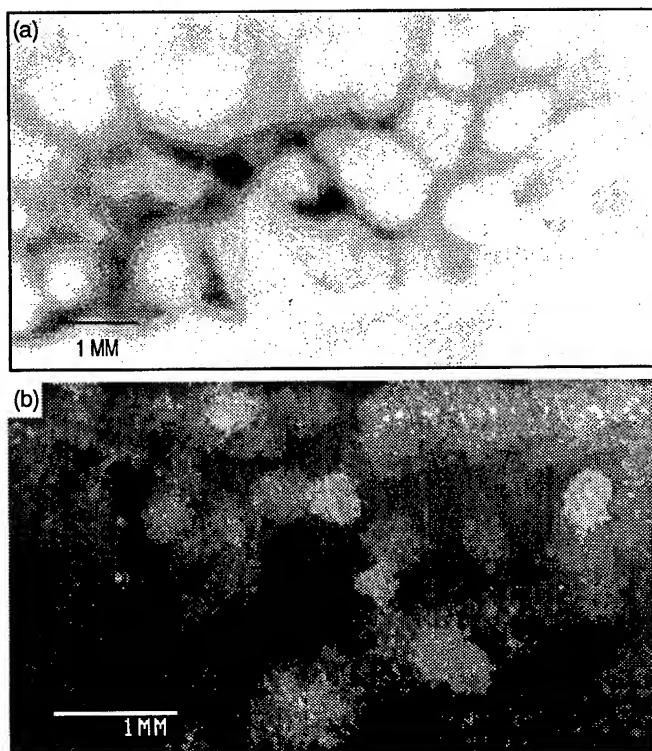


FIG. 3. Spawr Cathode images. (a) Electron beam emission from the cathode surface. (b) SEM micrograph of cathode surface after running in the rf gun.

this guideline the rf power was slowly increased until an input power of 5 MW achieved.

In early December the rf power was raised up to 7 MW and the first quantum efficiency (QE) measurements were made. These resulted in QE up to 1×10^{-4} which is greater than the typical value for Cu in low electric fields ($QE = 1 \cdot 10^{-5}$ [8]). The QE was measured as a function of rf power (Fig. 2) and showed an increase in QE with increasing rf power in agreement with Schottky reduction of the work function from large electric fields present at the cathode surface ($> 50 \text{ MV/m}$).

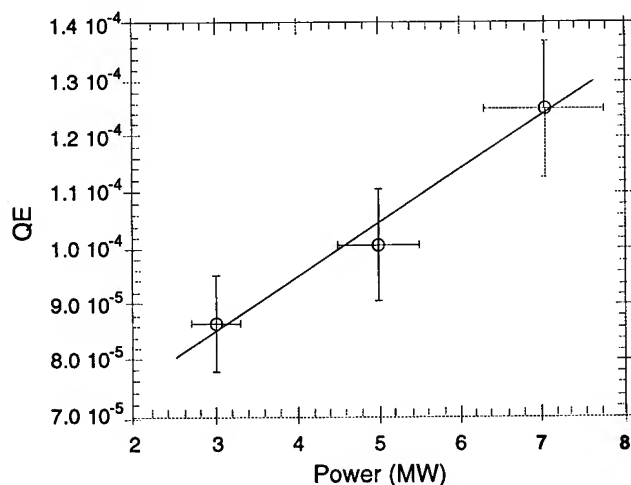


FIG. 2. QE dependence on input rf power to photoinjector.

During the month of December the rf gun and PWT linac were run consistently and measurements of the full beam energy and energy spread were made as a function of rf phase between the photoinjector and the PWT linac. The highest beam energy observed was 10.5 MeV with 3.5 MeV electrons produced at the rf gun, indicating an energy gain of 7 MeV from the PWT linac. As expected, the phase setting which yielded the highest energy also produced the lowest energy spread which was measured to be $\approx 0.3\%$. The energy spread as a function of injection phase was fit to PARMELA simulations with electron bunch length as the fit parameter from which a bunch length of ≈ 5 ps was inferred. The details of these measurements are presented in [5]. Finally, the QE was remeasured in late December and resulted in values within 10% of those measured earlier that month.

In mid January, we noticed that the electron beam had developed severe structure and the solenoid currents were set to image the electron emission from the cathode surface. An image of this emission is depicted in Fig 3(a). Due to this beam structure, the emittance measurement using a venetian blind type of pepper pot could not be performed, so a quad scan was used to measure the emittance of a low charge beam (< 10 pC) at 10 MeV. The measured normalized emittance was 6π mm-mrad. After this change in cathode emission, the QE was again remeasured and we found that it had dropped by a factor of 3.

We discovered that by keeping the gun under vacuum without rf power for a few days, the QE would recover to a level of 2.6×10^{-5} (still below the levels recorded in December). This level could be maintained for many hours as long as the rf power level was maintained below 6 MW. However, once the rf power was increased to 7 MW the QE deteriorated quickly. In just 7 hours the QE dropped from $2 \cdot 10^{-5}$ to 1×10^{-5} , a factor of 2. This test was done with the gun vacuum isolated from the rest of the beamline which is typically maintained at slightly higher pressures (1×10^{-6}). A residual gas analyzer was used to measure the primary contaminants of the vacuum system which were H_2O , H_2 , N_2 , O_2 , Ar and CO_2 in order of decreasing partial pressure.

In an attempt to increase the QE, the cathode surface was damaged using the focused UV laser beam. The laser was focused to a $200 \mu\text{m}$ spot and an array of 5 by 5 damaged spots was created at the cathode center. It was expected that further reduction of the work function could be achieved through the Schottky effect with enhanced electric fields at the surface due to the microporotusions created by the laser damage. In the initial operation of the rf photoinjector in 1993, QE of 1×10^{-4} were routinely measured from a damaged Cu photocathode and no QE degradation was ever observed [1]. However, on the Spawr cathode, the damaged areas did not produce any change in the QE and the recovery and degradation of the QE continued as described above.

This cathode was then removed from the gun and the surface was imaged using a SEM. Fig. 3(b) depicts surface structure which covers the cathode surface except in the laser damaged area. This structure may be the cause of the

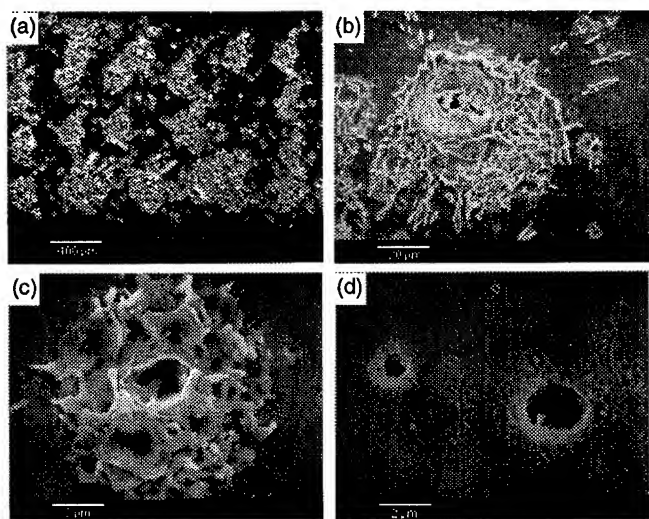


FIG. 4 SEM micrographs of damage on the Spawr cathode. (a) laser damaged region (b) laser produced crater (c) multiple rf breakdown produced crater (d) single rf breakdown crater

nonuniform emission shown in Fig 3(a). The light colored areas show a fractal growth pattern at the edges. This seems typical of a contamination growth on the cathode surface from residual gasses which is facilitated by the field emitted electrons.

Electron micrographs of different types of surface damage produced by laser damage and rf breakdown are shown in Fig. 4. The laser damage typically produces larger scale structures formed from molten copper while the rf damage shows a smaller more symmetric structure.

B. Hand polished cathode.

Following the removal of the commercially polished cathode, a second Cu cathode, was prepared at UCLA. It was machined from OFHC Cu using "Marvel's Mystery Oil" as lubricant. The cathode surface was then polished starting with wet 600 grit sand paper and working down to .3 μm diamond grit. The polishing was done by hand until no surface feature was larger than 1 μm . The cathode was stored in methanol until installation in the rf gun. This cathode was also tested in a dc gun prior to installation in the rf gun and a QE of 1×10^{-5} was measured [8].

During the cathode installation, the rf gun was back filled with nitrogen and maintained at the operating temperature of

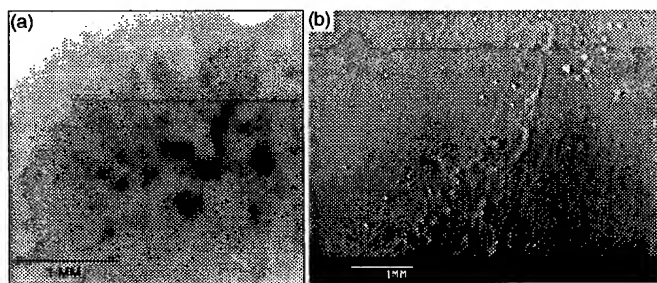


FIG. 5. Hand polished copper cathode. (a) Electron beam emission from the cathode surface. (b) SEM micrograph of cathode surface after running in the rf gun.

55° C. Once vacuum of better than 1×10^{-7} was achieved, the rf conditioning was started. Within a few hours rf power levels of 5 MW were achieved with practically no signs of rf breakdown.

The QE was immediately measured to be 3.3×10^{-5} at an rf power level of only 4 MW. Based on the previous measurements made in December, this would imply a QE of 5×10^{-5} at 7 MW. Furthermore, the beam showed no indication of beam structure.

Two days later, following less than 8 more hours of conditioning which was characterized by minor breakdown in the gun, rf power levels of 6 MW were attained. The QE was again measured and resulted in a reduction from the previous value of more than a factor of 2 to 1.5×10^{-5} . When this beam was imaged, once again beam structure became evident although not as severe as before. (see Fig 5(a)) Because the beam structure was less pronounced, the beam emittance could be measured and resulted in normalized emittances between 5 and 12 π mm-mrad with a beam charge of only 250 pC. Even this beam, however, was not cleanly focused on the slits and therefore the emittance values are most likely a lower bound to the whole beam emittance.

Following the beam quality measurements, this cathode was removed from the rf gun and immediately taken to the dc gun test stand for QE measurements. The QE measurements did not indicate any change in QE, again measuring 1×10^{-5} and also did not show any indication of structure on the cathode surface. When electron micrographs of this cathode were made, almost no structure was seen on the surface (see Fig. 5(b))

IV. CONCLUSIONS

The electron emission from a copper photocathode in a rf photoinjector appears to degrade in time, however, more careful and detailed study is necessary to understand the interaction of the copper surface with both the large rf fields and the UV laser pulses present in rf photoinjectors.

V. ACKNOWLEDGMENTS

The authors acknowledge Richard Lysee for his assistance in making SEM micrographs. This work is supported by US DOE Grant DE-FG03-92ER-40493 and DOE Grant DE-FG03-92ER40727.

VI. REFERENCES

- [1] S.C. Hartman *et al.*, Nuc. Instr. and Meth. A 340 (1994) 219-230.
- [2] G. Hairapetian *et al.*, Phys. Rev. Lett. **72**, 2403 (1994)
- [3] M. Hogan *et al.*, Paper FAA23, these Proceedings.
- [4] K. Batchelor *et al.*, European Particle Accelerator Conf., Rome, Italy, June 7-12, 1988.
- [5] R. Zhang *et al.*, Paper RPA21, these Proceedings.
- [6] X.J. Wang, private communication
- [7] Handbook of Chemistry and Physics p. E-78
- [8] R. Brogle *et al.*, Paper WPC20, these Proceedings

A SEMI-AUTOMATED SYSTEM FOR THE CHARACTERIZATION OF NLC ACCELERATING STRUCTURES*

S.M. Hanna, G.B. Bowden, H.A. Hoag, R. Loewen, A.E. Vlieks, J.W. Wang
Stanford Linear Accelerator Center, Stanford University, Stanford, CA 94309, USA

A system for characterizing the phase shift per cell of a long X-band accelerator structure is described. The fields within the structure are perturbed by a small cylindrical metal bead pulled along the axis. A computer controls the bead position and processes the data from a network analyzer connected to the accelerator section. Measurements made on prototype accelerator sections are described, and they are shown to be in good agreement with theory.

1. INTRODUCTION

Linear accelerators require precise phase relationship to be maintained between the driving rf field and the bunched beam throughout the interaction length [1]. Structures for the Next Linear Collider (NLC) will probably be machined and assembled to such tight mechanical tolerances that no provision for cell tuning is needed. However, prototype structures being developed for the NLC Test Accelerator (NLCTA) will need to be tuned, and will have provision for tuning built into each cell. The X-band structures are long, and employ a large number of cells (204). Tuning has traditionally been checked by the so-called nodal-shift method [2], in which a shorting plunger rests on the irises and is moved from cell to cell along the horizontal structure. Concerns over high-field breakdown and dark current generation in the operating accelerator prohibit the use of this method, which could damage the finely machined copper surfaces.

In Section II of this paper, we describe a semi-automated measurement system being built for testing and tuning NLCTA accelerator sections. The results of traveling wave (TW) perturbation measurements on two prototype sections are reported in Section III. Finally, in Section IV, the measured data are compared to predictions calculated from our analytical model.

II. ACCELERATING STRUCTURE CHARACTERIZATION SYSTEM

The system being developed utilizes a bead field-perturbation technique to evaluate the tuning of X-band accelerators. A small metallic cylindrical bead is attached to a thin nylon string running along the axis of the vertically-mounted accelerator section, as shown in Fig. 1. The position of the bead is determined by a

stepper motor-driven lead screw and carriage attached to the external return loop of the nylon string. This method allows TW perturbation measurements to be made without contacting the clean inner surfaces of the section. The bead can be replaced by a light metal cylinder if it is necessary to make nodal-shift measurements.

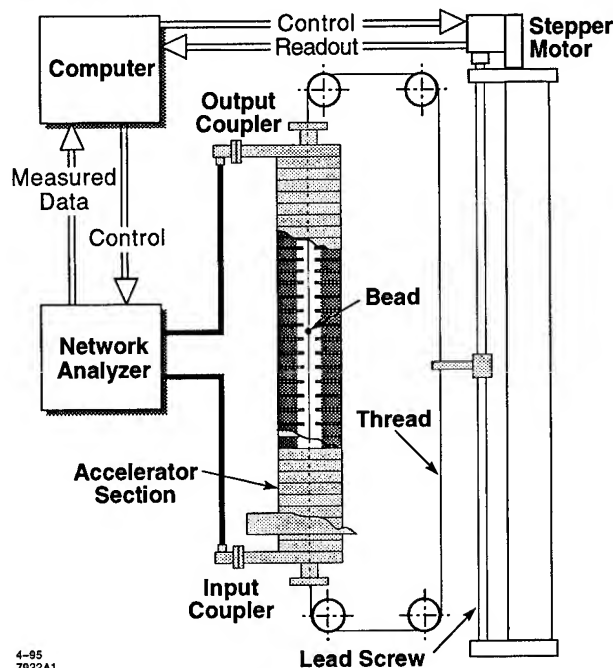


Figure 1. Schematic diagram for the semi-automated test setup.

A rotary encoder is shaft-coupled to the stepper motor. A computer interfaces with both, reading back position data from the encoder and stepping the motor as required by the measurement program. The computer also collects and processes the complex reflection coefficient data from a microwave network analyzer connected to the accelerator section.

III. TW PERTURBATION MEASUREMENT

The system described above will be used to characterize the NLCTA sections as they are built during the next two years. The measurements are based on bead perturbation under traveling wave conditions [3,4].

Preliminary tests to develop this system have been made on two X-band accelerator sections which were built during the early phases of the NLCTA program. Both are constant impedance sections, one 26 cm long (30 cells) and one 75 cm long (86 cells), and have been

* Work supported by Department of Energy contract DE-AC03-76SF00515.

previously tested at high power [5]. The cylindrical bead used was 0.508 mm in diameter and 0.483 mm high. The monofilament nylon string was 0.145 mm in diameter. A network analyzer connected to one port of the accelerator measured the reflection coefficient.

Figure 2 shows the variation in the reflection coefficient as the bead is pulled along the accelerator axis through three consecutive cells. The measured S_{11} is plotted in the complex plane with axial position as parameter. The three-fold symmetry for the $2\pi/3$ mode is clearly manifested. Points on the curve where the bead crosses the center and the iris of one cell are marked. The phase advance from cell-to-cell, which can easily be deduced from the reflection data, is shown in Fig. 3. These results were confirmed by nodal-shift measurements on the same sections [6]. Our measurement technique is capable of detecting small deviations from the required phase shift for any cell in the accelerator structure. This is demonstrated in Fig. 4 for the 26-cm section.

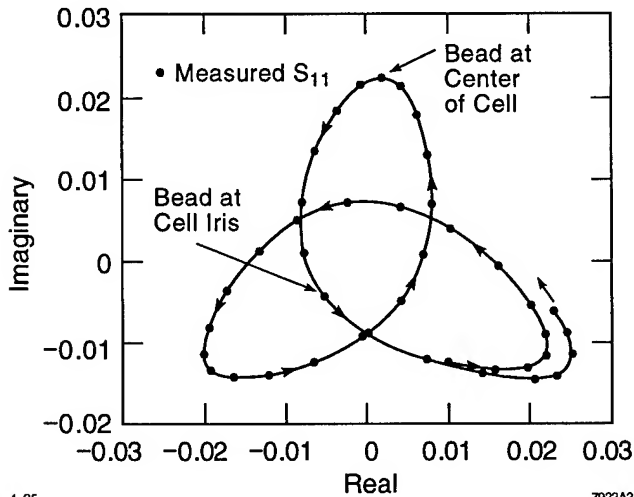


Figure 2. Reflection from the perturbed 75 cm accelerator structure.

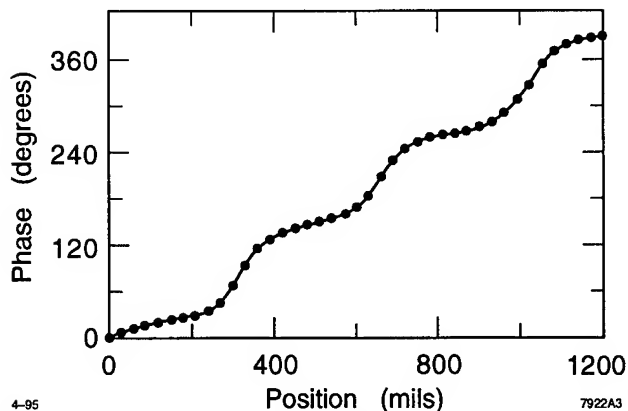


Figure 3. Phase advance as a function of bead position in the structure for the 75 cm structure.

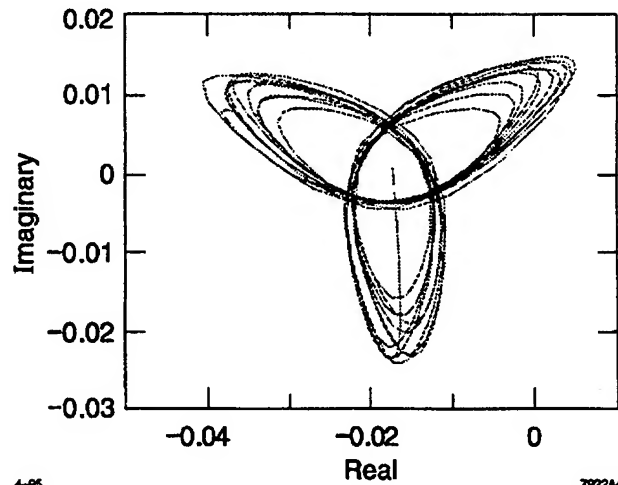


Figure 4. Reflection from the perturbed 26 cm accelerator structure.

IV. COMPARISON WITH ANALYTICAL MODELS

The traces shown in Figs. 2 and 4 are geometrical figures known as hypotrochoids. This response can be predicted from a transmission line model [7], and also from a purely field approach [8]. In the transmission line model, the perturbation introduced by a lossless bead is treated as a reactive discontinuity. Starting with the space harmonics of the longitudinal electric field, E_z , the magnitude and phase of the reflection coefficient at the input port of the accelerator can be obtained as the bead is pulled across the structure. The field model starts with the space harmonics of the longitudinal electric field and derives the magnitude and phase of the reflection coefficient at the input port of the accelerator. Figure 5 shows both the theoretical predictions and the measured values of S_{11} for the 75 cm structure.

V. CONCLUSIONS

Preliminary results from bead perturbation measurements made under travelling wave conditions show good agreement with both nodal-shift measurements and theoretical predictions. This method can therefore be used to characterize the cell-by-cell phase shift pattern through an accelerating structure. Deviations from the desired pattern can then be corrected by tuning the appropriate cells. The corrections can then be verified by performing successive bead pulls until the required phase advance is reached.

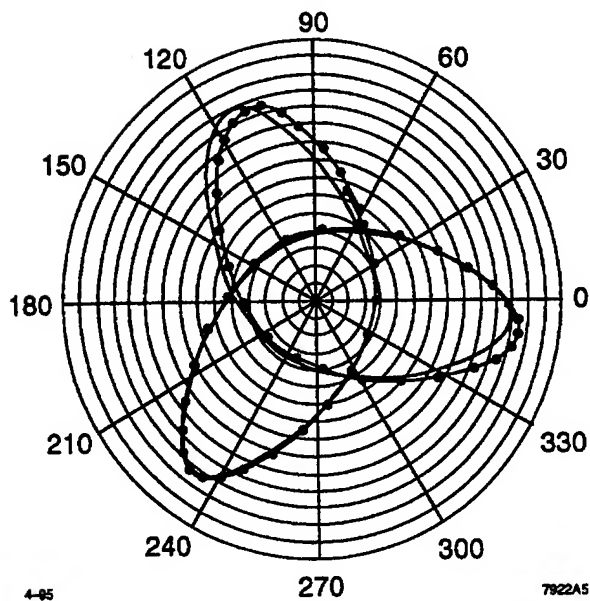


Figure 5. Comparison between calculated and measured S_{11} for the 75 cm accelerator structure.

REFERENCES

- [1] R.D. Ruth, "The Next Linear Colider," in *Frontier of Particle Beams: Intensity Limitations*, eds. M. Dienes, M. Month, and S. Turner, New York: Springer-Verlag, 1992, pp. 562-591.
- [2] E.L. Ginzton, *Microwave Measurements*, New York: McGraw-Hill, 1957.
- [3] R.P. Lagerstrom, "Interaction Impedance Measurements by Perturbation of Traveling Waves," Electronics Research Lab., Stanford University, Stanford, CA, Report 7. 1957.
- [4] K.B. Mallory and R.H. Miller, "On Nonresonant Perturbation Measurements," *IEEE Trans. Microwave Theory and Tech.*, MTT-14, 1966, pp. 99-100.
- [5] J.W. Wang et al., "High Gradient Tests of SLAC Linear Collider Accelerator Structures," SLAC-PUB-6617, 1994.
- [6] S.M. Hanna and R. Loewen, "Comparison between Traveling Wave Perturbation Measurement and Nodal-Shift Techniques for Characterizing Accelerator Structures," to be published.
- [7] S.M. Hanna, "Analytical Model for Traveling Wave Perturbation Measurements for X-band Accelerators," to be published.
- [8] C.W. Steele, "Nonresonant Perturbation Theory," *IEEE Trans. Microwave Theory and Tech.*, MTT-14, 2, 1966, pp. 70-74.

SLAC ACCELERATOR OPERATIONS REPORT: 1992-1995*

R. Erickson, C.W. Allen, T.K. Inman, W. Linebarger, M. Stanek, Stanford Linear Accelerator Center,
Stanford University, Stanford, CA 94309 USA

Operational statistics for the linear accelerator programs at SLAC are presented, including run-time records for the SLC, FFTB, and fixed target programs. Also included are summaries of reliability and maintenance-related statistics and a discussion of the analysis tools used to study error messages generated by the control system.

I. PROGRAM CHRONOLOGY

The SLAC linear accelerator programs are summarized in Table 1 for the period of January 1992 through March 1995. SLC machine development is defined to include extended periods of pre-run system turn-on, new system commissioning, and experiments to characterize and improve the performance of various accelerator systems. SLD logging refers to periods of SLC operation dedicated to producing Z particles in the SLD detector, with the detector on and recording data. Fixed target runs to ESA are periods when polarized electrons were delivered to fixed-target experiments in the End Station A experimental hall. Scheduled off times in this table are relatively long periods typically needed for major installations and upgrades. Time periods when the accelerator was off for holidays are not listed. The FFTB runs are periods of low intensity, low repetition rate (typically 30 Hz) operation in which damped electrons were delivered to the Final Focus Test Beam facility. The FFTB is a beam transport system that extends through the beam switchyard and is used for focusing the electron beam to sub-micron sizes for the study of future linear collider technology and for esoteric physics experiments requiring extraordinarily high charge density.

II. TIME ACCOUNTING

Time accounting records are kept by the accelerator systems operators, who record the number of hours devoted to each of the categories in the first column of Table 2 at the end of each eight hour shift. The experimental runs summarized in this table include only the time periods dedicated to logging data in the indicated detector and exclude extended pre-run turn on and commissioning time. The run periods begin when the accelerator and the

detector are ready to begin production data collection and continue until the detector is scheduled to shut down.

Time period	Program
2 Jan 92 - 1 May 92	SLC machine development.
1 May 92 - 18 Aug 92	SLD logging - First polarized electrons in SLC.
18 Aug 92 - 3 Oct 92	SLC machine development.
4 Oct 92 - 7 Nov 92	Scheduled off - prepare for fixed target program.
8 Nov 92 - 23 Dec 92	Fixed target ESA run - E142.
2 Jan 93 - 26 Feb 93	SLC machine development.
26 Feb 93 - 14 Aug 93	SLD logging.
15 Aug 93 - 1 Sep 93	SLC machine development.
1 Sep 93 - 1 Nov 93	Scheduled off - prepare for fixed target program. Damping ring vacuum chamber upgrade. SLC final focus upgrade.
1 Nov 93 - 23 Dec 93	Fixed target ESA run - E143.
4 Jan 94 - 6 Feb 94	Fixed target ESA run - E143.
7 Feb 94 - 19 Jun 94	SLC machine development - commission new damping rings and final foci. ~15 days of FFTB (Apr, May).
20 Jun 94 - 31 Aug 94	SLD logging.
1 Sep 94 - 19 Sep 94	FFTB run.
20 Sep 94 - 3 Oct 94	SLC machine development.
3 Oct 94 - 23 Dec 94	SLD logging.
3 Jan 95 - 6 Jan 95	FFTB run.
6 Jan 95 - 3 Mar 95	SLD logging.
3 Mar 95 - 18 Mar 95	SLC machine development.
18 Mar 95 - 31 Mar 95	FFTB run.

Table 1. SLAC program chronology 1992-1995.

The "experiment logging" category is defined as the time that a suitable beam (or colliding beams) was available to the scheduled experiment, and the detector equipment was active and recording data. Machine development in Table 2 includes only brief (<1 day) interruptions to data logging, usually dedicated to measuring accelerator system parameters and implementing improvements. The extended periods of scheduled machine development work listed in Table 1 are not included here. Alternate programs are brief tests or

* Work supported by Department of Energy contract DE-AC03-76SF00515.

experiments scheduled on short notice when the primary program can not be carried out as planned. This typically happens when some accelerator subsystem critical to the primary program is undergoing repairs while other accelerator systems, such as the injector system and the electron damping systems, are operating normally. Tuning is defined as any time when no specific hardware or software systems are known to be malfunctioning, yet the beam properties do not meet the requirements of the scheduled program. Typically this is the time spent by operators and accelerator physicists measuring and correcting beam parameters. Unscheduled down time is logged when a system or component has failed, rendering the beam unusable for either the main experiment or an alternate program. Scheduled off represents brief (<1 day) planned interruptions to the primary experimental program, typically for maintenance and minor upgrades or adjustments to existing systems. The extended scheduled off periods shown in Table 1 are not included here, nor are holiday periods.

	SLD 92	SLD 93	SLD 94/5	ESA 92	ESA 93/4	FFTB 94/5
Exp't Logging	51%	63%	56%	66%	69%	69%
Machine Develop.	9%	6%	4%	1%	0%	7%
Alternate Program	1%	1%	4%	0%	4%	1%
Tuning	19%	11%	10%	16%	12%	8%
Unsched. Down	18%	17%	23%	13%	8%	11%
Sched. Off	2%	2%	3%	4%	7%	4%
Total Hours	2616	4079	5065	1088	1439	1560
Total Z (x 1000)	10	55.7	100	-	-	-
Ave. Lum (Z/hr)	7.5	21.7	35.3	-	-	-
Approx. Polarization	21%	65%	79%	40%	85%	-

Table 2. SLAC primary linac program run time accounting 1992-1995.

The percentage of time spent tuning decreased steadily during the period of this study for both SLC and fixed target programs, as diagnostic instruments were improved and new feedback systems were commissioned. This

improvement occurred despite progressively more demanding requirements on beam quality. The decrease in experiment logging efficiency in 1994/95 compared to 1993 and the corresponding increase in unscheduled downtime were due mainly to the long repair and recovery times associated with five independent vacuum failures in the electron damping ring and the loss of two damping ring klystrons.

The bottom part of Table 2 summarizes the total hours corresponding to each experimental run, along with the approximate number of Z particles detected, the average luminosity, and the approximate beam polarization where applicable.

III. RELIABILITY AND MAINTENANCE STATISTICS

Hardware availability, defined here in terms of time when the accelerator hardware is not broken, is a measure of the overall reliability of the accelerator systems needed to carry out the accelerator program. The hardware availability, mean time to failure, and mean time to repair are listed in Table 3 for each of the major accelerator programs in the last three years. These quantities are defined as follows:

Availability = $1 - (\text{Downtime} / \text{Scheduled Operating Hours})$.

Mean Time To Failure (MTTF) = $\text{Sched hrs} / \# \text{ of Failures}$.

Mean Time To Repair (MTTR) = $\text{Downtime} / \# \text{ of Failures}$.

Hardware failures as defined in this section are those failures that noticeably interrupt or impede a scheduled running program and do not require testing or inspections to locate. As these data indicate, the hardware availability is consistently better during ESA and FFTB operation than during SLC operation. This is mainly because the ESA and FFTB programs require only electrons (no positrons) and thus require fewer active devices. These programs are also more tolerant of imperfect beams than is the SLC program.

	Availability	MTTF	MTTR
SLC 1992	81.8 %	8.3	1.5
SLC 1993	82.8 %	7.7	1.3
SLC 1994	80.7 %	8.5	1.6
ESA 1992	87.0 %	12.4	1.6
ESA 1993/4	93.3 %	12.7	0.9
FFTB 1994	90.3 %	12.4	1.2

Table 3. SLAC hardware reliability summary.

IV. CONTROL SYSTEM MESSAGE ANALYSIS

The SLAC accelerator complex consists of thousands of active devices, such as power supplies and mechanical transducers of various kinds, each of which must operate within prescribed tolerances in order to achieve the desired beam characteristics. The acceptable tolerances for many of these devices are stringent compared to the standards normally achieved in large scale industrial applications of commercially available equipment. As a result, parameter variations induced by mechanical vibrations, deviations in ambient temperature or electrical supply voltage, or other effects, occur frequently and often have detrimental effects on the quality of the beams. Constant monitoring and analyses of these effects are essential to identifying and rectifying problems of this kind.

Accelerator systems that drift in and out of prescribed tolerances typically do not interrupt machine operations, but may severely degrade the quality of the beams. Because of the adverse impact on overall efficiency of these kind of problems, a set of software tools and analysis procedures have been developed to address these issues.

The linac and beam delivery systems are monitored and controlled through a VAX-based computer control system. The control system includes a feature called the Summary Information Process (SIP), which checks a selected list of measured device parameters against prescribed database tolerances approximately every 15 seconds. Currently 4894 devices are monitored by this process whenever the SLC is operating. Whenever the status of any of these devices changes to an out-of-tolerance condition, a warning "error message" is generated by SIP. These error messages are presented to the control room operators on scrolling displays and are automatically recorded for later analyses.

By ranking the frequency of messages for each individual device, recurring problems can be identified. Devices with frequent intermittent failures and devices operating too close to their tolerance are easily identified by the large number of messages they generate. Daily and monthly reports are produced that list the highest counting devices in descending order. The data are sorted by major accelerator systems (injector, damping rings, etc.) and by type of device (analog and digital signals, temperatures, magnets and power supplies, stepping motor devices, damping ring RF devices, vacuum devices, etc.). These summaries do not include linac RF systems, which are processed and analyzed separately. The reports are distributed to designated managers responsible for each of the major subsystems.

Table 4 lists the monthly SIP error counts during SLC operations in recent years. The error frequency starts out high at the beginning of each running period as old equipment is reactivated and new or upgraded equipment is commissioned. The monthly count then decreases progressively over the duration of each period of continuous operation as the machine stabilizes and problems are identified and repaired.

	1992	1993	1994	1995
Jan				36
Feb	80	58		21
Mar	46	47		
Apr	69	42		
May	79	43		
Jun	40	40		
Jul	43	37	38	
Aug	43	44	33	
Sep			31	
Oct			30	
Nov			26	
Dec			19	
Avg	57	44	30	28

Table 4. SIP error counts (x 1000) for 1992-1995.

A subset of the SIP error data for the period of November 1994 through January 1995 is presented in Table 5. The 50 worst devices (the specific devices that generated the largest numbers of SIP errors) are grouped by type of device and the corresponding percentages of all the SIP errors for the time period are shown. These 50 devices accumulated 32577 SIP errors or 40.3% of all SIP errors during this time period.

13 Feedback loop devices	10.1 %
10 Stepper motor devices	8.9 %
4 Analog sensors (temps, vacuum, etc.)	4.3 %
2 Damping Ring RF devices	3.5 %
4 Large DC power supplies	3.5 %
5 Vert. steering corrector magnets	3.3 %
3 Gun laser system	1.7 %
3 Horiz. steering corrector magnets	1.5 %
2 Quadrupole trim power supplies	1.4 %
3 Quadrupole power supplies	0.9 %
1 Kicker magnet	0.9 %

Table 5. Summary of the fifty devices that generated the most SIP errors as explained in the text.

BEAM CURRENT LIMITATION IN MICROWAVE ACCELERATORS

A.V.Mishin, Schonberg Research Corporation
I.S. Shchedrin, Moscow Engineering Physics Institute

Abstract

A simplified approach is used to estimate current limit in microwave electron linear accelerators based on the achieved electron concentration and space charge values. A number of examples, presented in the report shows that the proposed technique is applicable for preliminary calculations.

1. Introduction

It is well known that beam efficiency in X-band linear accelerators is rather low compared to S and L-band units. Usually, one wants to reach as high as possible beam energy value for a given amount of power from power source. Power from commonly used magnetrons does not exceed value of 2 MW. Current during pulse in X-band accelerators is usually below 50 mA, for some units value about 100 mA was observed. Besides, measured efficiency is usually lower than calculated value.

2. Power Consumption

If we assume, that power P_i injected into accelerator structure is partially lost in the walls (P_d) and the other part is stored in accelerated beam (P_b).

$$P_i = P_b + P_d, \quad (1)$$

Beam efficiency value Be could be shown as

$$Be = 1 - P_d/P_i. \quad (2)$$

Let us think that P_d is power value required to build the fields to achieve certain energy value W_0 at no beam loading. This value of P_d is constant for a given structure. Now, if one increases power injected into the structure and try to maintain energy value at W_0 while increasing beam loading, efficiency would tend to reach 100% value:

At the extreme, if $P_d/P_i = 0$, $Be = 1$.

Indeed, this is a crude model of power balance.

3. Electron density of a bunch

In practice, beam value is limited by a number of factors. To simplify our further calculations, we will assume that bunch has a cylindrical shape with radius R_b and length L_b .

Bunch volume is

$$V_b = 3.14 \times R_b^2 \times L_b. \quad (3)$$

Charge stored in a bunch is

$$Q_b = I/F = V_b \times N \times e, \quad (4)$$

where I -beam current;
 F -frequency,
 N -number of electrons per unit volume;
 e -charge of electron.

Therefore,

$$I = 3.14 \times V_b \times L_b \times N \times e \times c/W_l, \quad (5)$$

where W_l -wavelength.

Statistical limit value of N is 10^9 1/cm³. For reference, this means that electrons in a bunch are at $4000 \times R_e$ from each other (R_e -classical radius of electron).

Equation (5) lets us estimate limit current in accelerators at various wavelengths and aperture radius.

For maximum beam radius is about 50% or accelerators aperture and bunch length of $0.25 W_l$

$$I [A] = (a/W_l)^2 \cdot W_l^2 [cm]. \quad (6)$$

Surprisingly, these simple calculations led us to some quite realistic numbers.

Table 1. Limit current at various apertures in X band.

2a,mm	:	4	:	8	:	12	:	16
I, mA	:	40	:	160	:	360	:	640

Table 2. Limit current at various wave lengths for $a/Wl=0.1$

Band	X	S	L
Wl, cm	3	10	20
I, A	0.1	1	4

Practical values are somewhat lower, as in practice $Lb < 0.25Wl$ and beam radius is less than it was assumed.

Table 3. Experimentally measured current values in various X-band linacs.

Aperture, mm: Experiment : Estimated			
MINAC-6	: 4.7	: 50	: 75
U-34	: 5	: 27	: 75
U-35	: 10(aver)	: 100	: 250

Conclusions

Some statistical data are used to explain low efficiency in X-band accelerators compared to S and L band. Numbers show, that approach to X-band accelerator design is usually done to get maximum energy for a given power value and sacrifices, therefore, with efficiency.

INSTALLATION AND COMMISSIONING OF THE E+/E- INJECTOR FOR DAΦNE AT FRASCATI

K. Whitham, H. Amankath, J. Edighoffer, K. Fleckner, E. Gower, S. Lyons, D. Nett, D. Palmer,
R. Sheppard, S. Sutter, P. Treas, A. Zante
Titan Beta, Dublin, CA 94568

R. Miller
SLAC

R. Boni, H. Hsieh, F. Sannibale, M. Vescovi, G. Vignola
Istituto Nazionale di Fisica Nucleare

I. INTRODUCTION

The electron-positron injector^{1, 2} for the DAΦNE project at INFN-LFN is being installed and will begin commissioning this summer at Frascati. This is a S-band rf linac system utilizing four 45 MW SLEDed⁴ klystrons and 15, 3 m traveling-wave accelerating sections. It is designed to deliver a 250 MeV, 4 ampere electron beam to the positron converter, followed by an accelerator that captures and accelerates the resulting positrons to the ring injection voltage of 510 MeV. All major subsystems are in place. This system is undergoing final installation, alignment and subsystem testing. Also, system integration is beginning. Beam testing and positron generation will begin this summer. Commissioning and final acceptance are expected to be complete by the end of the year.

II. SYSTEM DESCRIPTION

Figure 1 shows one of the four RF units, consisting of a pulsed modulator, klystron and SLED cavities.

The Linac System consists of (see Table 1):

1. A high current linac designed to produce 250 MeV, 4 ampere beam with a 1 mm radius spot at the position converter. This section includes the electron gun and high current linac, which are useable in both positron and electron ring filling modes.

Table 1: DAΦNE Linac Design Parameters

General

RF Frequency	2856 MHz
Klystron Power	45 MW each
No. of Klystrons	4
No. of SLED Cavities	4
No. of Accelerator Sections	15 + Bun & Prebun
Beam Repetition Rate	50 Hz
Beam Pulse Width (FWHM)	10 ns

High Current Electron Linac

No. of Accelerating Sections	5 + Bun & Prebun
Gun Current	10 Amps
Nominal Gun Voltage	120 KV
Current at Positron Converter	>4.0 Amps
Energy at Positron Converter	250 MeV
Emittance at Pos Conv (geo RMS)	<= 1 mm mrad
Energy Spread (FWHM)	± 5%
Focused Beam Spot (FWHM)	~2 mm

Positron Converter

Type	SLAC SLC
Target	Tungsten
Target Thickness	6, 7, 8 mm (selectable)
Tapered Flux Compressor	4.3 T pulsed
Tapered Solenoid	1.2 T
Solenoidal Field over Capture Section	.5 T
Electron Separation	Chicane Magnet

Positron Linac

No. of Accelerating Sections	10
Final Energy	>510 MeV
Useful Output Positron Current	>36 mA
Emittance at 510 MeV (geometric RMS)	<= 5 mm mrad
Energy Spread (FWHM)	± 1%

High Energy Electron Linac Mode

Final Beam Energy	>510 MeV
Useful Output Current	> 150 ma
Emittance at 510 MeV (geometric RMS)	<= 1 mm mrad
Energy Spread (FWHM)	± 0.5%

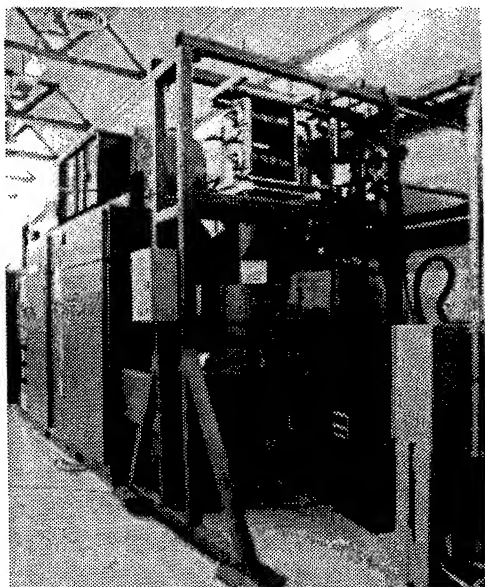


Figure 1: Modulator, Klystron and SLED Cavities

2. An electron to positron converter based on the SLAC SLC positron converter design.

Figure 2 shows the "High Current" portion of the accelerator.



Figure 2: High Current Linac

3. A low current accelerator designed to produce up to 550 MeV, unloaded, for accelerating either positrons or electrons at low current to match the 510 MeV ring energy. There is a chicane magnet after the first two accelerating sections to remove the electrons from the beam.

Figure 3 shows the final focusing triple, positron converter, the solenoid magnets over the capture section and the rest of the "Low Current" portion of the accelerator.

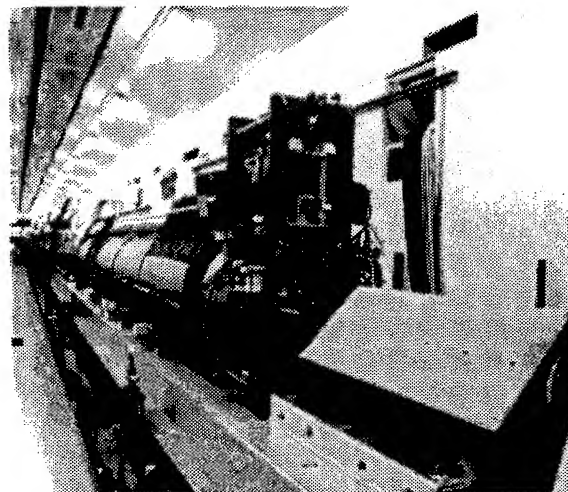


Figure 3: Triple Position Converter and Low Current Linac

4. A control and data acquisition system giving remote control and beam data acquisition and analysis to the main control room operators. The control system runs on an Apple Macintosh under Labview interfaced through CAMAC to the hardware. The data acquisition system similarly runs on an Apple Macintosh under Labview interfaced to two Tektronix TDS644 digital oscilloscopes used as remote transit digitizers. This is an inexpensive but powerful control and data acquisition system.

Figure 4 shows the entire accelerator from the output end.

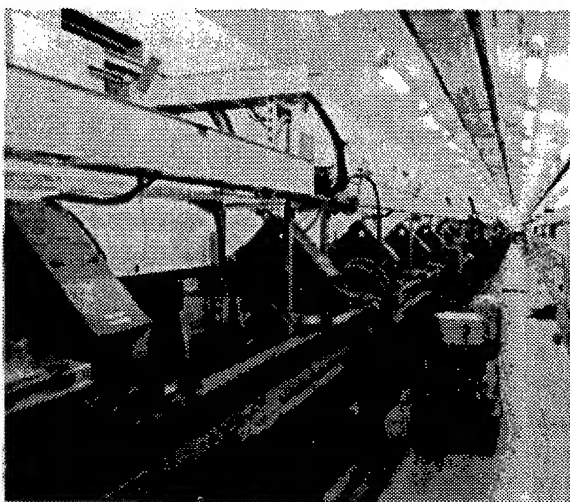


Figure 4: Entire Injector From Output End

III. INSTALLATION STATUS

All subassemblies are in place, wired and plumbed. All the klystrons have been installed and being tested with the modulators. The evacuated rf waveguide is complete on the first two rf subsystems. Installation of the remaining rf waveguide and beamline vacuum components is nearing completion. Alignment of the rf accelerator sections is complete. Alignment of all the magnets is also nearing completion.

IV. COMMISSIONING START

The first two rf subsystems, including the first 7 sections, are about to be rf conditioned. Beam testing is expected to begin within a couple of months.

Verification/repetition of factory testing of the "High Current" portion of the accelerator will be done first¹. The factory test achieved 4 amps at the positron converter position focused to a .94 x 1.56 mm FWHM spot. The energy was measured at 240 MeV, a bit less than the design value of 250 MeV, but within acceptable limits. No attempt was made at the factory to produce positrons because of radiation problems.

Positron production will begin about a month later. Optimizing positron yield and transport with the required beam parameters is expected to take the most time. Final acceptance testing and availability to inject into the damping ring is expected by the end of the year.

V. REFERENCES

- [1] H. Anamkath, J. Edighoffer, S. Lyons, R. Miller, D. Nett, P. Treas, K. Whitham, T. Zante, Titan Beta, R. Miller, SLAC, R. Boni, H. Hsieh, F. Sannibale, M. Vascovi, G. Vignola, INFN-LNF, "Design and Factory Test of the e⁺/e⁻ Frascati Linear Accelerator for DAΦNE", 1994 Linear Accelerator Conf. Proc., Japan, August 1994
and
K. Whitham, et. al., "Design and Factory Test of the e⁺/e⁻ Frascati Linear Accelerator for DAΦNE", EPAC, London, UK, June 1994.
- [2] K. Whitham, H. Anamkath, S. Lyons, J. Manca, et. al., "Design of the e⁻/e⁺ Frascati Linear Accelerator For DAΦNE", 1992 Linear Accelerator Conference Proc., Ottawa, Ontario, Canada, August 24-28, 1992.
- [3] G. Vignola INFN-LNF, "DAΦNE. The Frascati - Factory", PAC '93 Conference Ib4, May 17-20, 1993.
- [4] Z. D. Farkas, H. A. Hogg, G. A. Loew and Pj. B. Wilson, "SLED: A Method of Doubling SLAC's Energy", Ixtgh Int'l Conf. On High Energy Accelerators, SLAC, May 2-7, 1974.

RECENT STUDIES OF LINAC FOR PRODUCTION OF RADIOACTIVE BEAMS IN THE INR*

I.N.Birukov, I.V.Gonin, D.V.Gorelov, A.N.Iljinov, V.A.Moiseev, P.N.Ostroumov
Institute for Nuclear Research, 117312 Moscow, Russia
A.V.Tiunov, Moscow State University, Moscow, Russia

I. INTRODUCTION*

Accelerators for the production of radioactive ion beams have been proposed by many laboratories. A wide range of researches in nuclear physics can be carried out with a 6-10 MeV/n radioactive beam. For the ion source to produce high intensity beams, the initial charge-to-mass ratio must be as low as possible, 1/60, for instance; but the cost of a linac for these beams becomes high. Recently at TRIUMF a 1.5 MeV/n linear accelerator accepting ions with $q/A=1/30$ has been proposed [1]. Possessing the feature of variable energy, this linac can provide for various experiments in astrophysics. A similar project is under consideration at INR. Below we describe the optimized design of the linac for the energy range 2 keV/n to 1.76 MeV/n, calculation of the rf power consumption in the accelerating structures by MAFIA code and end-to-end beam dynamics simulation in the realistic rf field distribution.

II. ACCELERATOR STRUCTURE

The linac comprises five parts: 1) prebuncher; 2) RFQ; 3) prestripper linac (PSL); 4) matching and stripping section (MSS) at beam energy 357 keV/n and 5) poststripper linac (PSL). The linac layout is shown in fig. 1.

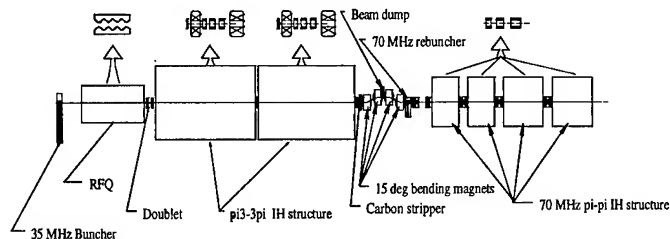


Fig. 1 Linear accelerator layout.

The linear accelerator is characterized with the following properties:

- The 98.6% capture of the 2 keV/n cw ion beam with $q/A=1/30$ and acceleration up to the energy 1.76 MeV/n;
- Extremely low rf power consumption which allows to operate in cw mode for the all ion species with $q/A=1/30$ and mass number up to 240. According to simulation by MAFIA code, the required rf power is ~140 kWt for the whole linac;

* The research described in this publication was made possible in part by Grant N61000 from the International Science Foundation.

- The accelerator includes a spectrometer magnet to separate and dump the parasitic ions formed downstream of the stripper which makes the linac radiation free;

- Despite the very low q/A and frequency (35 MHz) the RFQ is short enough (3.9 m) to have just one tank; the RFQ has been designed to provide longitudinal matching to the following accelerating structure without an additional rebuncher;

- There is an essential rf power saving due to the use of IH type accelerating structure beginning from the very low beam energy (60 keV/n);

- The stripping energy 357 keV/n allows to keep all possible ion species on high intensity level; the linac can be upgraded to higher energies by the addition of further accelerating structures;

- Smooth energy variation in the range 0.2-1.76 MeV/n. In the range 0.2-0.5 MeV/n the rms energy spread is $(\Delta W/W)_{rms} < 0.5\%$, for the higher energies $(\Delta W/W)_{rms} < 0.2\%$; as a rule, the energy spread on the base is $\pm 3 \cdot (\Delta W/W)_{rms}$.

- Due to the negligible transverse emittance growth on the stripper (30%-50% for the most of ion species) the aperture diameter is equal to 2 cm throughout the linac accelerating structures. The transverse normalized acceptance for the whole linac is 0.8π -mm-mrad which is 3 times larger than expected 2 keV/n beam emittance.

The main parameters of the linac are listed in the table 1.

Table 1

Tank	RFQ	IH-1	IH-1	IH-3	IH-4	IH-5	IH-6
q/A	1/30	1/30	1/30	1/9	1/9	1/9	1/9
f , MHz	35	35	35	70	70	70	70
ϕ_s , deg		-25	-25	-25	-25	-25	-25
W_{out} , MeV/n	0.06	0.199	0.357	0.582	0.90	1.297	1.755
L , m	3.89	4.55	4.34	1.02	1.28	1.56	1.92
D , m	1.0	1.8	1.8	1.0	1.0	1.0	1.0
R_{eff} , MOm/m	500 ¹	278	196	310	245	202	164
P , kWt	31.5	8.3	16.6	8.0	15.8	24.7	32.8

¹) The characteristic resistance [kOm-m].

A. RFQ

The geometry generation of the RFQ has been done following ref. [2]. However the shaper has been replaced by a klystron buncher and an external prebuncher has been added one meter upstream the RFQ. During the beam dynamics study the Yamada's design procedure has been slightly modified in order to minimize longitudinal emittance. The

RFQ resonator is followed by the IH structure and between the RFQ and IH tank there is 53 cm space for two matching quadrupoles. To provide longitudinal matching, a bunch rotator containing 10 cells of unmodulated electrodes and four cells of modulated electrodes with $\phi_s = -90^\circ$ has been inserted into RFQ. The RFQ output energy has been chosen from the analysis of the efficiency of RFQ and IH structures [3]. The variation of the main RFQ parameters with respect to the cell number are shown in fig. 2. The evolution of the beam image in longitudinal phase

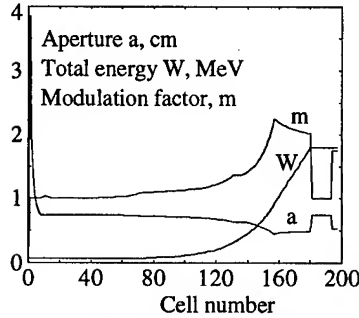


Fig. 2. RFQ parameters VS cell number

space is shown in fig. 3. The bunch rotator forms a converging beam in longitudinal phase space that allows to have a long drift space between RFQ and IH structure. The beam phase portrait at the entrance of the IH structure is shown in fig. 3b.

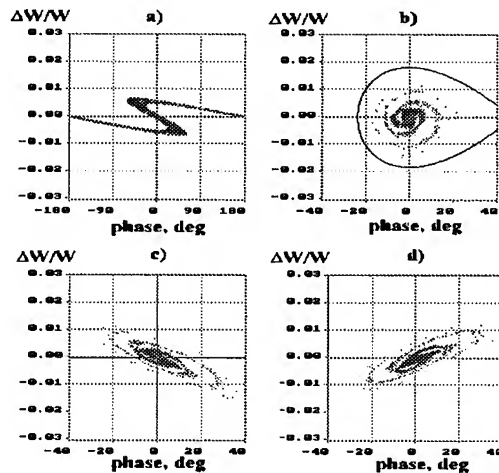


Fig. 3. Beam image evolution in longitudinal phase space
a) RFQ entrance, b) Output of the cell #180 - the end of acceleration, c) Output of the cell #193 - the end of longitudinal drift, d) Output of the RFQ, after bunch rotator.

B. Prestripper Linac

As a prestripper linac in the energy range 60 keV/n to 360 keV/n the IH structure with FODO focusing has been proposed. The use of the FODO focusing structure simplifies the transverse matching between RFQ and IH structure. Having just one quadrupole lens inside the drift tubes per four accelerating gaps, the modified IH structure consumes very low rf power. The superperiod of the accelerating structure consists of 3 accelerating cells with 3π phase advance of the rf field and a long drift tube containing the quadrupole lens and a gap with additional 3π phase advance. A superperiod of the structure is shown in fig. 4 as it is used for the MAFIA

simulation. The total power consumption and effective shunt impedance have been found from the simulation of several superperiods of the whole tank.

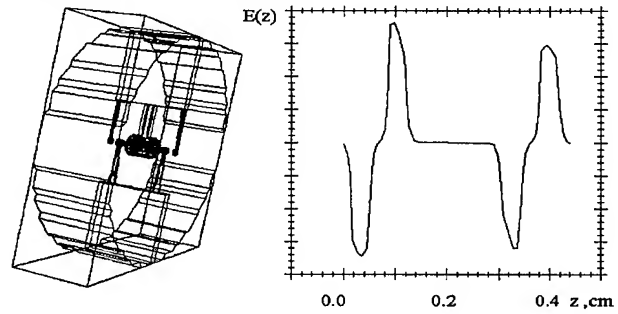


Fig. 4. Superperiod of the $\pi 3-3\pi$ IH structure and accelerating field distribution $E_z(z)$.

Tuning the accelerating field along the IH structure and the mechanical design of the tank can both be simplified if the gap voltage is accepted to be constant along the tank (except the end cells). To keep high accelerating gradients two IH tanks with the total length ~ 9 m have been chosen. The gap voltages are 120 kV and 215 kV in the first and second tank accordingly. For the design of the focusing structure a standard procedure based on the analysis of the transport matrices of the focusing period has been used. The strengths of the focusing gradients satisfy the transverse effective emittance preservation condition $\sigma_T > 0.7\sigma_L$. Where σ_T and σ_L are phase advances of the particle motion per focusing period on transverse and longitudinal phase plane accordingly.

C. Matching/Stripping Section

The matching and stripping section consists of: a carbon stripper, four 15° rectangular bending magnets; 70 MHz rebuncher, one quadrupole triplet and two single lenses, beam dumps for the parasitic ion species.

The carbon stripper is installed at the output of the PSL (fig. 1). Due to the relatively high stripping energy all radioactive ion species with mass number up to 240 will be kept. The transverse rms emittance growth due to stripper is $\sim 30\%-50\%$ for the most of ion species. The additional rms energy spread contributed by the stripper is $\sim 0.1\%-0.2\%$ which slightly increases longitudinal emittance. Four bending magnets allow to separate all radioactive ions with non-equilibrium charge state. The beam dumps installed at the high dispersion points safely absorb parasitic radioactive ions and provide radiation free linac.

D. Poststripper Linac

The $\pi-\pi$ IH type accelerating structure for the POSL has been considered most suitable. Operating at fields well below breakdown, the POSL accepts all ion species produced

downstream of the stripper with q/A as low as $1/9$. The use of lower accelerating gradients promotes lower rf power consumption as well as lower energy spread of the accelerated beam. Main specification to the POSL is the possibility of the smooth energy variation in the range $0.2-1.76$ MeV/n. Therefore the POSL comprises several tanks powered separately. In order to provide maximal shunt resistance, focusing elements are not included inside the tanks. The criteria to choose the tank length are following: short enough to provide transverse beam dynamics stability as well as smooth energy variation keeping energy spread small, long enough in order to avoid a low shunt resistance.

From studies with the MAFIA code as well as beam dynamics code, a 15 gap IH accelerating tanks have been selected. The beam focusing is provided by triplets installed between the tanks. The lengths of the triplet quadrupoles are 9.2 and 16 cm which have been optimized in order to have lowest focusing gradients. The bore radius for all quadrupoles is 1.5 cm and the focusing gradients are in the range $4.1-5.6$ kGs/cm for the lowest value of q/A .

The diameter of all four IH tanks of the POSL are equal to one meter. In order to tune to the resonant frequency and desired voltage distribution along the tank, the magnetic flux inducer size, ridge-to-ridge distance as well as cell parameters will be fitted.

II. BEAM DYNAMICS SIMULATION

For the design and simulation of the RFQ the beam dynamics code DESRFQ has been developed which runs on an IBM PC computer. In addition to standard procedures associated with design and simulation procedure in the RFQ, DESRFQ allows to animate the beam images on the phase planes during the simulation; which is very helpful for the beam parameters optimization. The particle coordinates output from the RFQ are accepted by LANA code [4] in order to simulate the beam dynamics in the PSL, MSS (including a stripper) and POSL. The LANA code produces drift tube geometry using two dimensional realistic electric field distribution $E_z(r,z)$, $E_r(r,z)$ along the tank axis.

The beam envelope taken for all particles accepted by the RFQ (98.65%) along the IH linac is shown in fig. 5. The normalized acceptance of the whole linac is 0.8π mm-mrad which is safe enough in order to avoid any particle losses.

A. Beam energy variation

The beam energy variation can be produced by changing phase (ϕ) or/and amplitude (E) of the rf field in the IH tanks. The energy adjustment procedure does not increase transverse emittance and produces the intermediate beam energies without any degradation of the energy spread. As it follows from beam dynamics simulation, there is an optimal path in the plane (E , ϕ) in order to obtain minimal energy spread during the procedure of the energy variation. The families of curves obtained by the variation of rf field level in the range

$(0.4-1.0) \cdot E_0$ as well as rf phase in the range $(0, -200^\circ)$ in each four tanks are shown in fig. 6. The envelope curve shows minimal energy spread which can be obtained for the certain beam energy selecting rf phase and amplitude on the tank being adjusted. To transport a beam with intermediate energy to the accelerator end the focusing triplets must be retuned.

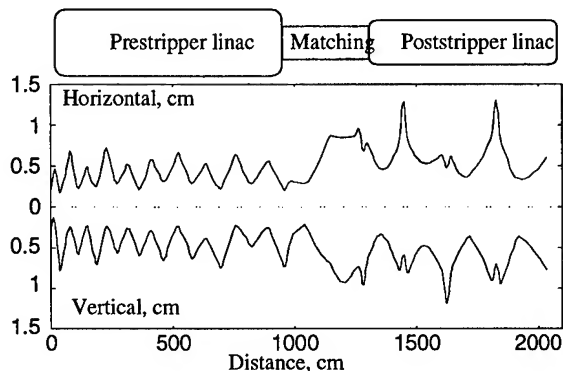


Fig. 5. Beam envelope (100% particles) along the IH linac.

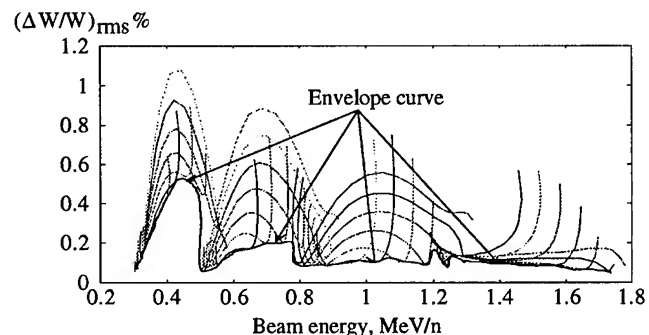


Fig. 6. Beam energy spread as a function of the beam energy obtained by the phase variation in the tanks of the poststripper linac. The parameter is the rf field level in the range (40-100)% of the nominal level.

III. ACKNOWLEDGMENT

One of authors is grateful to TRIUMF team working on the ISAC-1 project for fruitful discussions.

IV. REFERENCES

- [1] P.G.Bricault et al. ISAC-1: Radioactive Ion Beam Facility in TRIUMF, RPG12, this proceedings.
- [2] S.Yamada. Buncher Section Optimization of Heavy Ion RFQ Linacs. Proc. of the 1981 Linac Conf. Santa-Fe, 1981.
- [3] P.N.Ostroumov. Choice of Transition Energy Between RFQ and IH Structure in Radioactive Beam Linac. Preprint INR, 1995.
- [4] D.V.Gorelov and P.N.Ostroumov. The LANA Computer Code for the Beam Dynamics Simulation in Multi-Cavity Linacs. INR internal report, 1993-1994.

RFQ COLD MODEL STUDIES

P. G. Bricault, D. Joffe and H. R. Schneider, TRIUMF, 4004 Wesbrook Mall, Vancouver, B. C., Canada, V6T 2A3

A post accelerator, primarily to provide beams of interest to nuclear astrophysics users, is included in the upgrading and expansion of the radioactive beam facility at TRIUMF. Singly charged ion beams, with $A \leq 30$, delivered from the on line mass separator with an energy of 2 keV/u, will be accelerated in a stage linac consisting of an RFQ and a post-stripper drift-tube. As a consequence of the low charge-to-mass ratio of the ions, a low operating frequency for the RFQ is required to achieve adequate transverse focusing. CW operation is specified to preserve beam intensity. Because of its relatively high specific shunt impedance, mechanical stability, and the absence of vane voltage asymmetries in the end regions, the split-ring 4-rod RFQ structure has been chosen. Several cold models have been built to study three different types of split-ring RFQ structures. Specific shunt impedance and longitudinal field have been measured. A comparison of these measurements for various split-ring structures is presented.

I. INTRODUCTION

A radioactive beam facility based on the ISOL method with a post accelerator was proposed at TRIUMF in 1985 [1]. Two years ago a new study of the post accelerator was started. The specifications dictated primarily by the nuclear astrophysics interests, required a maximum energy of 1.5 MeV/u for ion beams with $A \leq 30$.

The acceleration of ions with small charge to mass ratio requires a low frequency RFQ. At low frequency the size of the conventional 4-vane RFQ tank becomes very large. To reduce the size of the cavity diameter for frequencies less than 200 MHz, the 4-vane structures are replaced by a form of 4-rod structure in which the quadrupole electrodes (rods) are part of a resonant circuit consisting of a combination of lumped and distributed inductances and capacitances. Two basic type of 4-rod structure have been reported in the literature, viz. the stem supported 0-mode 4-rod structure [5,7], and the split-coaxial structure[2,3,4]. A unit cell of the later may be viewed as two end-to-end $\lambda/4$ coaxial lines with orthogonal rod pairs interleaved to form the quadrupole electrode geometry. The distributed inter-electrode capacitance and rod inductance determine the structure resonant frequency. In a unit cell of a stem supported structure on the other hand, the two stems for the two rod pairs form the inductance that resonates with the inter-electrode capacitance.

Since the unstable ion beams are produced continuously in the ISOL target-ion source, operation of the RFQ in cw mode is desirable to preserve beam intensity. To avoid high power dissipation concomitant potential structure distortion, an efficient, i.e., high shunt impedance, RFQ structure is then required. With the exception of a 33 MHz RFQ at the University of Kyoto[6], no other low frequency RFQ operating in cw mode has been reported. To address our

needs therefore, a development program was undertaken at TRIUMF.

II. MODEL DESIGN

According to the beam dynamics the ISAC-1's RFQ will be 8.2 m long, and assuming a power dissipation of 15 kW per meter, the value of the shunt impedance should be larger than 300 k Ω •m. Since the RFQ is very long it will be suitable to select among candidates RFQ one that can be built into several modules. The alignment of the rods in each individual module can be done much easily before insertion of the structure into the tank. In order to do so it is easier if the longitudinal current on the rods presents nulls located at the same position on all the four rods. The current passing through the contact will be negligible. This is the case for the split-coaxial RFQ, the nulls are located at the point where the vanes (or rods) are suspended. In the "0-mode RFQ structure" the surface current is largely confine in the "U" shaped support structures, and are theoretically zero on the rods at the symmetry points between support structures. To optimize the shunt impedance of the later, the supports are equally spaced and then the nulls are not any longer located at the same longitudinal position along the RFQ. This was observed by measuring a voltage unbalance between each rod and the end-plate. We have observed that the voltage asymmetry depends on the separation between the rod's supports.

After many attempts we found that the split-ring RFQ has a very small voltage asymmetry in the end region. In this structure the separation between the stems is much smaller than in the conventional two-stem RFQ structure. Furthermore, the split-ring 4-rod RFQ structure has been chosen, because of its relatively high specific shunt impedance and mechanical stability. The models were made from copper, and a modular assembly technique was used in order to take advantage of the same electrodes, tank and the main ring. Table 1 gives the basic dimensions of the 4-rod split-ring RFQ. The top quarters of the rings were removable, and there were three sets of rod's supports that could be attached to the structure to examine the effects of the different configurations. These three split-ring shapes are labeled RFQ_1, RFQ_2 and RFQ_3. Figure 1 shows the three types of RFQ and fig 2 shows the detail of the rod's attachment in the central region.

Table 1- Dimensions of the 4 rod split-ring RFQ cold models.

R (cm)	8.811
r (cm)	0.952
z (cm)	2.54
S (cm)	2.54
D _{rod} (mm)	4.763
R ₀ (mm)	2.381
Shape	Rectangular
Diameter (cm)	27.5

Table 2 summarizes the results for those three types of split-ring 4-rod RFQ. The number of modules, the total RFQ's length, frequency, Q value and shunt resistance.

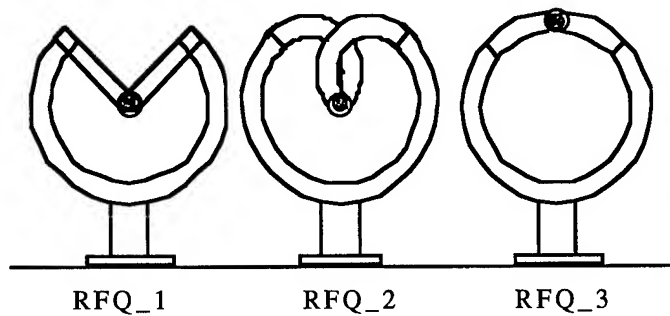


Fig. 1 - Schematic drawing of the 4-rod split-ring RFQ.

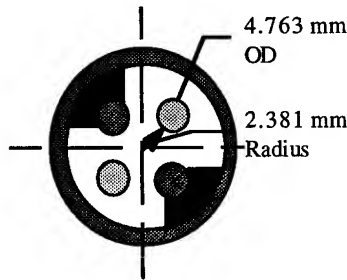


Fig. 2 - Central region of the split-ring 4-rod RFQ.

Table 2 summarize the results obtained for the cold models.

Table 2 - Results of the measurements on the split-ring 4-rod RFQ cold models

Type	# module	L mm	f MHz	Q	R_s k Ω •m
RFQ_1	1	191	77.860	3140	49.6
RFQ_1	5	953	78.244	3040	50.3
RFQ_2	1	191	68.738	3390	56.3
RFQ_2	5	953	67.639	2930	56.4
RFQ_3	1	185	75.150	3372	49.4
RFQ_3	3	572	71.587	3232	69.4

The poor Q-value can be explained by the use of a modular assembly technique chosen to spare machining.

III. ELECTRIC FIELD MEASUREMENTS

A Voltage and phase measurement

The voltage and the phase on each individual rod were measured using a Hewlett Packard vector voltmeter with a Hewlett Packard network analyzer as the rf source.

The split-ring 4-rod RFQ has the advantage that the separation between the rod supports is very small. For this reason the voltages on each pair of rods are nearly equal. We also verify that this RFQ has a pure quadrupole mode. Table 4 shows the results of the cold model measurements of the RFQ structure.

Table 4 - Phase and voltage measurement

Ring radius (mm)		88.11			
Ring width (mm)		25.			
Tip radius (mm)		2.38			
Bore radius (mm)		2.38			
Number of modules		3			
Separation between modules		19.05			
RFQ length (mm)		571.5			
Probe #	$\Delta\Phi$ (Deg.)	ΔV (Volts)	Probe #	$\Delta\Phi$ (Deg.)	ΔV (Volts)
1A	110.6	6.56	1B	110.4	6.97
2A	-69.2	7.08	2B	-69.2	6.52
3A	110.6	6.51	3B	110.5	6.53
4A	-69.3	7.07	4B	-69.2	6.59

$\Delta\Phi$ is the phase difference between the reference signal and the probes. The phase on probes 1-3 and 2-4 should be the same. ΔV is the voltage difference between the vane and the end plate located at ground potential. Here we can see the voltage asymmetry between electrodes 1 - 3 and 2 - 4 is very small. For the split-ring type RFQ the phases on electrodes 1-3 and 2-4 are very close. Also, the phases and the voltages are the same at each end of the rod.

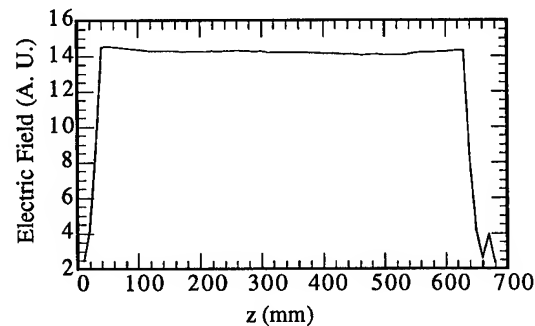


Fig. 3 - Field distribution along the RFQ.

B Electric field distribution

The electric field distribution along the RFQ was measured using the bead-pull technique. The bead was placed between the RFQ electrodes and pulled along the RFQ axis by a computer controlled stepping motor. The frequency shift was measured at each step from which the field strengths were calculated. Figure 3 shows the electric field obtained with the three modules connected to each other.

IV. MODULE LENGTH

Using the cold model RFQ_3 the module length was varied from 10 cm to 20 cm in order to find the optimum value for the specific shunt impedance, $R_s = V_p^2 / (2P/l)$, where V_p is the peak voltage difference between two electrodes and P/l the power loss per unit of length. Figure 4 shows the scaled shunt impedance as a function of the separation between two adjacent split-rings. The solid line is a plot of the calculated shunt impedance using the expression for the q value and the shunt impedance,

$$R_S = \frac{L}{R_{Total} C_T'}$$

where,

$$R_{Total} = \frac{1}{\sigma \delta} \left(\frac{l_{in}}{2r+z} + \frac{L_{Mod}}{12\pi D_{Rod}} \right) \text{ and}$$

$$C_T' = C_T + C_0/L_{Mod}$$

where, C_T is the capacitance per unit length and C_0 the residual capacitance of one module. z is the ring width, $2r$ is the radial width of the ring, l_{in} is the length of the inner surface of the ring and D_{Rod} is the rod diameter. The inductance is expressed using a formula for the self inductance of a ring with rectangular cross section,

$$L = N 4\pi R \left[\frac{1}{2} \left\{ 1 + \frac{1}{6} \left(\frac{r}{R} \right)^2 \right\} \ln 8 / \left(\frac{r}{R} \right)^2 - 0.03 + 0.04 \left(\frac{r}{R} \right)^2 \right]$$

where, r/R is the ratio of the minor to major radius, and N is a normalization factor deduced from a fit of the measured inductances of various split-ring models. For RFQ_3 model N is equal to 0.61.

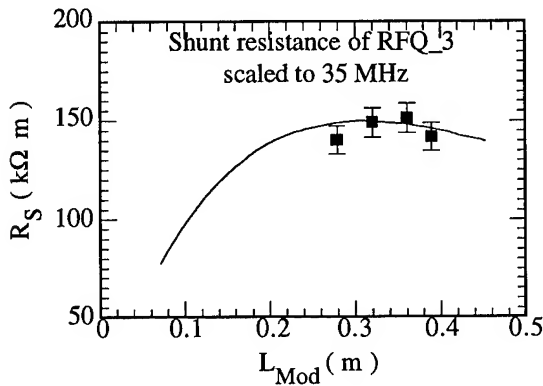


Fig. 4 - Scaled shunt impedance to 35 MHz as a function of the separation between two split-rings.

The shunt impedance shows a broad peak centered around 35 cm. Simulations using MAFIA give a similar value [8].

VI. NEW SPLIT-RING RFQ COLD MODEL

A new cold model split-ring 4-rod RFQ based on the results of the MAFIA simulation, was built, see Fig. 5. The dimensions were optimized for the best shunt resistance. Table 5 gives the dimensions of the structure and also the shunt resistance, phases and voltages between the end plate and the rods.

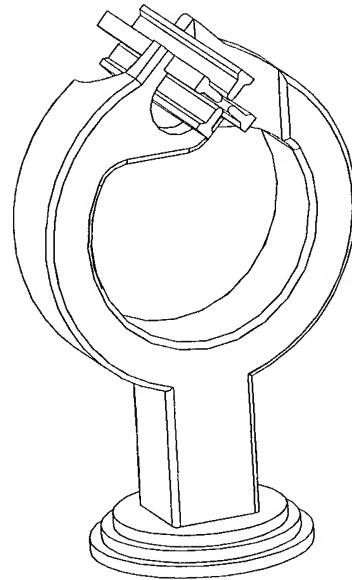


Fig. 5- Scaled cold model of the new split-ring 4-rod RFQ.

Table 6 - Phase and voltage measurement of the split-ring 4-rod RFQ.

Ring radius (mm)		150
Ring width (mm)		70
Tip radius (mm)		3.5
Bore radius (mm)		3.5
Number of module		1
Separation between module (mm)		175
RFQ length (mm)		175
Frequency (MHz)		64.9475
Shunt Resistance(35MHz) (kΩ•m)		282.
Probe no	$\Delta\Phi$ (Deg.)	ΔV (Volts)
1	71.0	11.9
2	-109.4	13.3
3	70.9	12.2
4	-107.7	13.1

Reference

- [1] G. E. McMicheal, B. G. Chidley and R. M. Hutcheon, AECL 8960/TRI-DN-85-3.
- [2] R. W. Müller, "Layout of a High Intensity Linac for Very Heavy Ions with RFQ focusing", GSI-REP-79-7.
- [3] S. Arai et al. IEEE 1991 Particle Accelerator Conf.
- [4] R. W. Müller, U. Kopf, J. Bolle, S. Arai, P. Spädtke, Proceeding of the 1984 International Conference on Linear Accelerator, p. 77.
- [5] A. Schempp et al. Nucl. Instr. & Meth. B10/11 (1985) p. 831.
- [6] H. Fujisawa et al. Bulletin of Institute for Chemical Research, Kyoto University, vol. 70, no 1, 1992.
- [7] A. Schempp et al. Nucl. Instr. & Meth. A278 (1989) p. 766.
- [8] P. G. Bricault, D. Joffe and H. R. Schneider, "Simulation of the TRIUMF split-ring 4-rod RFQ with MAFIA", this conference.

SIMULATION OF THE TRIUMF SPLIT-RING 4-ROD RFQ WITH MAFIA

P. G. Bricault and H. R. Schneider, TRIUMF, 4004 Wesbrook Mall, Vancouver, B. C., Canada, V6T 2A3

To complete the analysis of the 4-rod split-ring RFQ started with cold model studies, computer simulations have also been made using the MAFIA code. Computations of voltage and magnetic field distributions were done for both a three and a ten module RFQ for a range of structure dimensions such as, minor to major radius ratio r/R , ring width, tank diameter, and spacing between adjacent rings. Shunt impedance and power densities derived from these computations were then used to optimize the dimensions of a three module split-ring RFQ now under construction.

I INTRODUCTION

A radioactive ion beam facility is part of the long range plan at TRIUMF. A proposal to install an ISOL (isotope-separator-on-line) and post-accelerator RIB facility at TRIUMF was first made in 1985[1]. Although the full project was not funded at that time, an on-line target/ion source and mass separator test facility were installed on one of the TRIUMF proton beam lines, and has been used since 1987 for both target development, and to provide low energy radioactive beams for experimenters. This project was revisited some years ago and a new proposal is being developed. The radioactive nuclei will be produced by the interaction of an intense and energetic proton beam on a thick target. After ionization and mass analysis the beam will be sent to a post-accelerator.

This post-accelerator is mainly dedicated to the nuclear astrophysics and applied physics program. The main characteristics are the following; 1) cw operation and good transmission are required to preserve beam intensity, 2) must be able to accelerate singly charge ions with mass $A \leq 30$ and 3) the energy must be continuously variable from 0.2 to 1.5 MeV/u.

In our design of the post-accelerator the front end is an RFQ. It has the merit that it can accelerate very low velocity ions with a good efficiency, $\geq 90\%$. The main issue requiring development for the post-accelerator is the front end RFQ since there is no known RFQ operating at low frequency and 100% duty cycle for such a low charge to mass ratio, ($q/A \geq 1/30$). It is important to select from candidate RFQ structures, one that has a high specific shunt resistance, so that the overall RF power requirement is minimized. After building several cold models to study different types of RFQ structure [2], the split-ring 4 rod RFQ structure has been chosen, because of its relatively high specific shunt impedance, mechanical stability, and absence of vane voltage asymmetries in the end regions.

The electromagnetic code MAFIA [3] was used to simulate both three and ten module versions of several split-ring 4 rod RFQ configurations and to assist in optimizing the dimensions of the selected configuration. This obviates construction of a large number of cold models during the optimization process.

II STRUCTURE OPTIMIZATION

The common way to determine the RFQ's RF power requirement is to measure the transverse shunt resistance of the structure. We define the specific shunt resistance of an RFQ by the following expression,

$$R_s = \frac{V_p^2}{2P/l},$$

where V_p is the inter electrode peak voltage, P the power loss and l the RFQ length. Many parameters affect the specific shunt resistance; the most important are the ratio r/R , the ring width, the tank diameter and the spacing between adjacent split-rings. Fig. 1 shows a schematic drawing of the split-ring 4-rod RFQ used in our simulation.

A. R_s vs the ring width, z

Two simulations for ring widths of 10 cm and 15 cm gave computed shunt resistances of 503 $k\Omega \cdot m$ and 560 $k\Omega \cdot m$ respectively. Since wider ring would be impractical from a mechanical point of view the 15 cm width was chosen for all subsequent calculations.

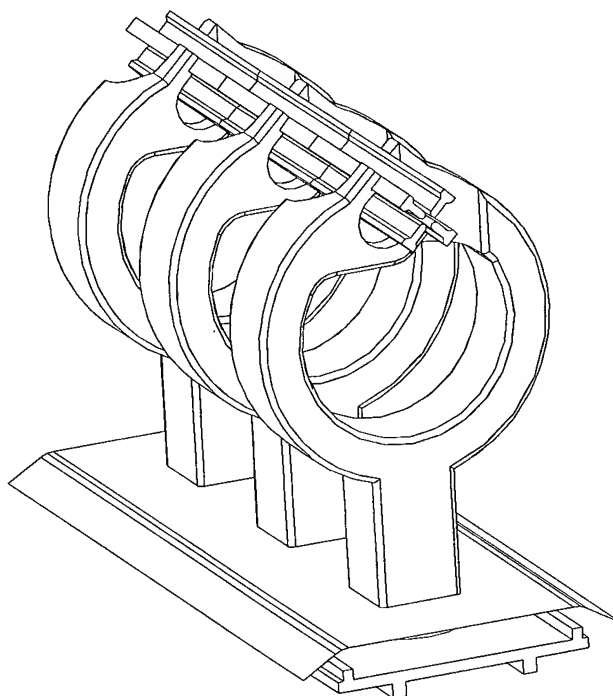


Fig. 1 - Schematic drawing of the split-ring 4-rod RFQ composed of three modules.

B. Variation of R_s with the ratio r/R

Figure 2 shows the computed shunt resistance of a 35 MHz split-ring structure with a module length of 40 cm, as a

function of the ratio r/R , where r is the radial half thickness and R is the mean ring radius. A value for r/R between 0.15 and 0.25 seems to be a good design choice. It should be noted that the inductance of the ring is proportional to R and decreases with increasing r/R , so choosing a larger value for this ratio also implies increasing R if a fixed design frequency is to be maintained.

Shunt Resistance of the Split Ring 4 rod RFQ
as a function of the ratio r/R

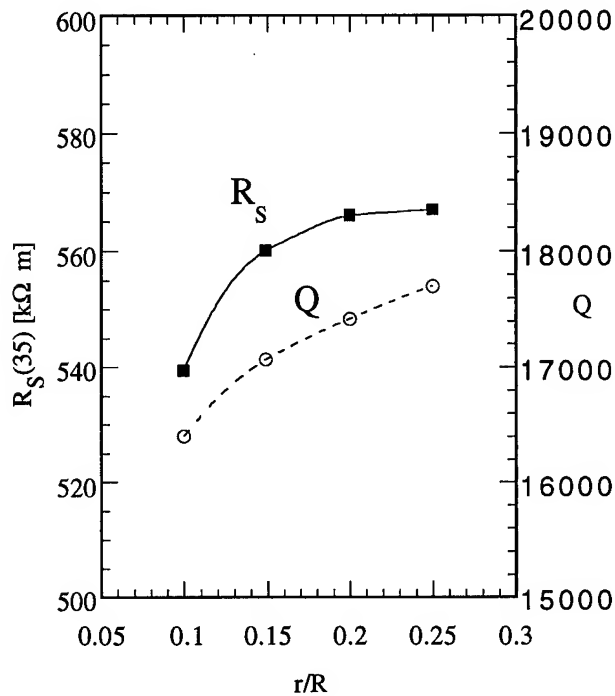


Fig. 2 - The computed shunt resistance and Q value of the split-ring 4-rod RFQ as a function of the ratio r/R for L_{MOD} and z equal 40 and 15 cm, respectively.

C. R_s vs Tank Diameter, D

Each split ring module acts as a half wave transmission line resonator, inductively loaded at the center, having current nulls at rod ends and a voltage null at the ring support stem. If a sufficiently large enclosing tank is chosen so capacitance between the module and the tank wall is small, tank wall currents and power dissipation are then correspondingly small. In Fig. 3 the calculated shunt impedance and Q are plotted as a function of tank diameter for a 35 MHz resonant frequency and a module length of 40 cm. It appears from this that a tank diameter 1 meter or more in diameter is desirable. With this size the tank has little influence on the resonant frequency and serves then only as the necessary vacuum enclosure.

Variation of the Shunt Resistance
as a function of the tank diameter

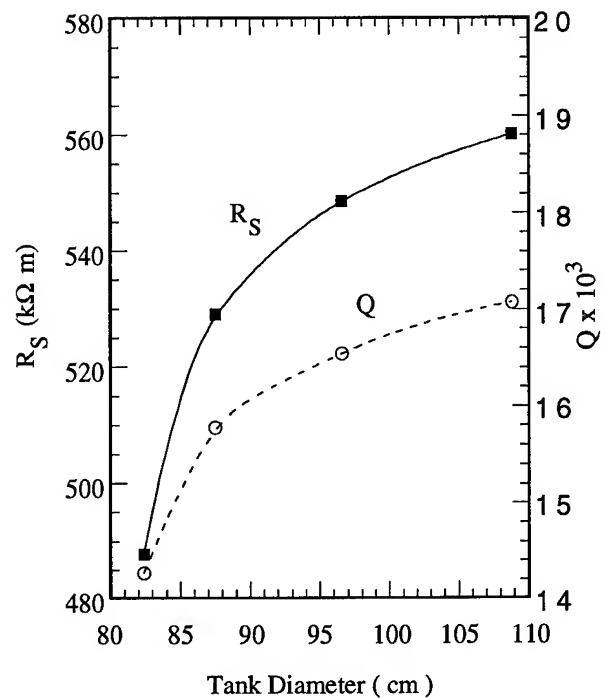


Fig. 3 - Shunt resistance and Q value of the split-ring 4-rod RFQ as a function of the tank diameter.

D. R_s vs module spacing

The spacing between adjacent rings is one of the most important parameters in the design of a split-ring RFQ. Intuitively we expect an optimum value for the spacing since if it is large, the capacitive loading per module is large because of the increased rod length. On the other hand a very small spacing means significant capacitance between the rings. In either case the increase in capacitive load ultimately leads to reduced shunt impedance, so an optimum module length that maximizes shunt impedance is expected.

Initial calculations were done for a three module simulation. Capacitive end effects were however apparent. To circumvent these the space between the rod and the endplate was increased from 5cm to 10 cm and a longer, 10 module structure was simulated. Shunt impedances were calculated for module lengths between 25 cm and 50 cm. Since the resonant frequency changed with module length, all results were scaled to 35 MHz before plotting in Fig. 4. A broad peak centered at a module length of 33 cm is evident for both the 3 module and 10 module simulations. This is in good agreement with the cold model measurements which indicated an optimum length of 35 cm [2].

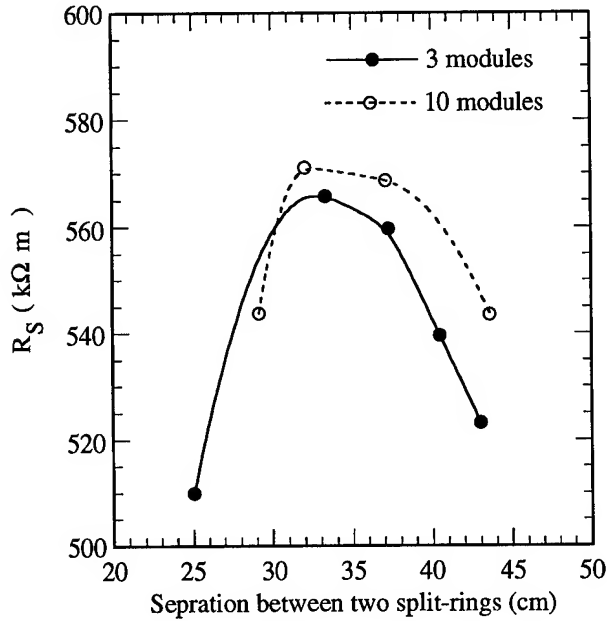


Fig. 4 - Shunt resistance of the split-ring 4-rod RFQ as a function of the separation between two split-rings. The full line and the dashed line represent the simulation of 3 and 10 modules, respectively.

III CONCLUDING REMARKS

Several MAFIA simulation runs have been done in order to complete the analysis of the 4 rod split-ring RFQ started with the cold model studies. The shunt resistance of the split-ring 4-rod RFQ was optimized for different values of the following parameter; ratio of the minor to major radius, r/R , ring width, z , tank diameter, D , and spacing between two adjacent rings.

MAFIA simulations and split-ring 4-rod RFQ's cold model studies are in agreement. Both predict an optimum separation between two adjacent split-ring around 35 cm.

From these simulation, we are confident that an effective shunt impedance of at least 300 kΩ·m is achievable and as a consequence, that the power dissipation per unit length will be easily manageable. Combining the results of these studies with beam dynamics RFQ design calculations allow us to make the basic parameter selection as given in Table 1, for a prototype 3 modules RFQ.

Table 1 -Basic parameters of the RFQ prototype

RF frequency (MHz)	35
Bore radius R_0 (mm)	8.6
Vane tip radius (mm)	7.0
Radial ring thickness $2r$ (mm)	80.
Ring radius R (mm)	220
Tank diameter D (mm)	1200
Ring thickness z (mm)	150
L_{Mod} (mm)	400
Peak inter-electrode voltage V_p (kV)	85
Number of modules	3
RFQ length (mm)	1200
MAFIA estimations	
Unloaded Q	15495
Specific Shunt Impedance (kΩ·m)	506
RF power (kW)	8.3

References

- [1] G. E. McMicheal, B. G. Chidley and R. M. Hutcheon, AECL 8960/TRI-DN-85-3.
- [2] P. G. Bricault, D. Joffe and H. R. Schneider, "RFQ Cold model Studies", this conference.
- [3] MAFIA, the general purpose electromagnetic code produced by THD-DESY-KFA collaboration, T. Weiland, 6100 Darmstadt, Germany.

A LOW-CHARGE-STATE INJECTOR LINAC FOR ATLAS

K. W. Shepard and J. W. Kim, Argonne National Laboratory, Argonne, IL 60439 USA

The design of a low-charge-state linac which is capable of accelerating, for example, $^{132}\text{Sn}^{1+}$ for injection into the existing heavy-ion linac ATLAS is discussed. The injector linac is intended for radioactive beam applications, and will accelerate a low-charge-state beam to energies of 500 keV/nucleon, at which point the ions can be stripped to charge states sufficiently high to be injected into ATLAS. A primary design goal has been to extend the very good longitudinal beam quality typical of ATLAS to low charge state beams. The proposed injector linac consists of several elements. First is a gridded-gap four-harmonic buncher and a short (normally-conducting) 12 MHz RFQ structure, both operating on a 350 kV open-air variable-voltage platform. Then comes an array of 24 MHz and 48 MHz superconducting interdigital accelerating structures interspersed with superconducting quadrupole transverse focusing elements. Numerical ray-tracing studies indicate that a transverse acceptance greater than 0.25π mm-mrad can be obtained while simultaneously limiting longitudinal emittance growth to a very few keV-nsec.

I. INTRODUCTION

This paper discusses the front-end of the secondary-linac portion of a proposed ISOL-type radioactive beam facility, an overview of which is presented elsewhere at this conference [1]. The proposed facility would use the existing ATLAS superconducting heavy-ion linac as an accelerator for radioactive beams. In its present form, ATLAS can accelerate any ion with a sufficiently high ($q/A > 0.1$) charge state [2]. For efficient production of most radioactive beams, much lower charge states must be accelerated, at least for the first few MV of the linac. Adapting ATLAS to radioactive beams, therefore, requires development of a low-charge-state injector linac capable of maintaining the good features of ATLAS, particularly excellent beam quality, large transverse acceptance, and flexibility in configuration.

The size of the injector is determined initially by the mass range and type of ion source, and subsequently by the type, number, and location of charge-strippers. Choice of the type, number, and location of strippers involves a complex balance of factors which determine the beam intensity, beam quality, and size and cost of the required linac for the various possible radioactive nuclei. The options chosen here are discussed in reference [1] and also below.

An important technical challenge is to design a linac for low-charge-state ions which can provide simultaneously both large transverse acceptance and also low longitudinal emittance growth (i.e. good time and energy resolution). Large transverse acceptance facilitates high transmission and ease of tuning which will be particularly important when dealing with very low current radioactive beams.

Large transverse acceptance will also enable good matching to a variety of ion sources. The ability of the linac to maintain small longitudinal emittance (ϵ_l of a few tens of π keV-nsec), even for beams of large transverse emittance, will be critical in enabling experiments to use time-of-flight techniques while simultaneously providing good energy resolution and adequate beam intensity.

II. LINAC CONFIGURATION

The low-charge-state injector linac requires strong transverse focusing at low velocities. For the charge states considered here ($q/A = 1/66$) the 8T solenoid lenses used in the present ATLAS heavy-ion linac are inadequate. Substantially stronger focusing is obtained with either magnetic or electric quadrupole lenses. We are developing a superconducting magnetic quadrupole element which is discussed elsewhere at this conference [3]. This quadrupole, operating at 350 T/m over a 3 cm diam. bore, provides sufficient transverse focusing to base a linac on the same high performance 48 MHz superconducting drift-tube structures that were previously developed for the ATLAS positive ion injector linac [4].

Figure 1 shows a possible configuration for the injector linac: it consists of three distinct sections. The first is a two-meter long, normally conducting, 12 MHz RFQ accelerator section, operating on a 350 kV variable voltage platform. The second section is a short (1.5 m) drift-tube linac, for which we propose to use 24 MHz superconducting drift-tube structures. The third section constitutes 90% of the injector linac and is an array of 40 superconducting 48 MHz interdigital cavities.

Note that the beam is stripped from a $1+$ to a $2+$ charge state at the exit of the RFQ section. By using a non-equilibrium, thin gas stripper at this point, it should be

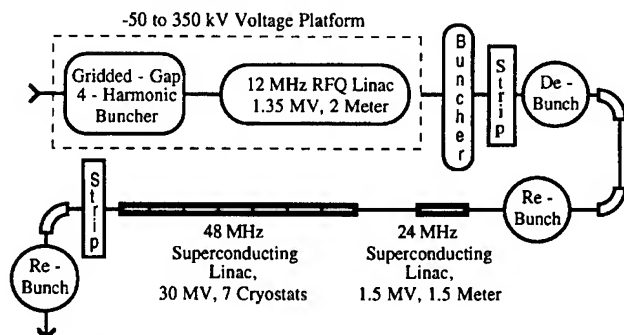


Figure 1: Elements of the low-charge-state injector linac. 1^+ ions at 100 kV are accelerated to energies of 500 keV/nucleon or more, then stripped for injection into the existing ATLAS accelerator. Ions with mass > 70 require an additional stripping immediately following the RFQ section

possible to strip as much as 50% of the beam into a 2+ charge state [1]. Stripping this early in the acceleration process reduces the size of injector linac required while keeping a large fraction of the incoming beam.

A. The Entrance RFQ Section

At an entrance energy of a few hundred keV and charge state 1+, an electric quadrupole provides the strongest transverse focusing. This favors the choice of an RFQ type accelerating structure at the beginning of the linac. For the present application, however, it is highly desirable to maintain a substantially smaller longitudinal emittance than is typical for RFQ implementations. Several features of the design presented here ensure this result.

A separate, gridded-gap bunching system can maintain the longitudinal emittance at a smaller value than is practicable using adiabatic bunching within the RFQ structure itself [5]. Also, by removing the bunching function, the length of the RFQ is reduced and the efficiency enhanced. Placing both the buncher and the RFQ on a variable voltage platform allows operation with a constant velocity profile for a wide range of ion masses. The 12 MHz gridded-gap, four-harmonic bunching system which is presently in use on the ATLAS accelerator would be suitable for this application: this system can bunch up to 70% of a dc beam into 1 nsec bunches. The efficiency could be further improved by development of a finer grid structure.

The RFQ should operate at as low a frequency as is practicable both to minimize longitudinal emittance growth and also to maximize the transverse acceptance. The split-coaxial RFQ geometry is appropriate for this frequency range; RFQ structures have already been developed at nearly the frequency and field required here. The MAXILAC linac developed at GSI operates at 13 MHz and provides both design concepts that can be adapted to the present application, and also a demonstration of the required performance [6]. We propose an RFQ structure with electromagnetic parameters close to those of the MAXILAC, but with a substantially different vane design. In particular, the vanes should be continuous, e.g. milled from one piece of metal. Also, sufficient water cooling should be included to provide good thermal stability during cw operation.

We have numerically modelled an RFQ structure with the following parameters:

Operating frequency	12.125 MHz
Maximum vane voltage	100 kV
Maximum Electric field	12.8 MV/m (1.2 Kp)
Minimum Aperture	8.00 mm
Modulation factor	1.5
Entrance Velocity	0.0024 c
Exit Velocity	0.0047 c
Number of cells	44
Length	198.2 cm
Synchronous phase	- 30 degrees

The RFQ is designed for a minimum charge to mass ratio of 1/132: ions of higher charge state are accommodated by simply scaling both the platform voltage and the RFQ voltage to match. The peak electric field was determined numerically using the RELAX 3D code for a realistic vane geometry. It should be noted that while it seems feasible to obtain a cw vane voltage of 100 kV (based on the present performance of MAXILAC), the beam quality would remain acceptable for a vane voltage below 50 kV

Numerical ray-tracing in three dimensions has been performed for the above design, using a two-term potential approximation. Shown in Figure 2 are some results for a beam of 0.25π mm-mrad transverse emittance (the maximum specified for a benchmark facility by the North American Steering Committee for an Isospin Laboratory) [7].

B. Superconducting Linac Using a Magnetic Quadrupole Lens

We have evaluated the performance of linac sections based on superconducting interdigital (drift-tube) cavities and a 350 T/m, 3 cm diameter bore quadrupole magnet described elsewhere at this conference [4]. The magnet is employed in the form of a triplet lens with an overall length of approximately 26 cm. The linac lattice in all cases consists of a triplet following each superconducting four-gap accelerating structure. Numerical ray-tracing was performed using a cylindrically symmetric approximation to

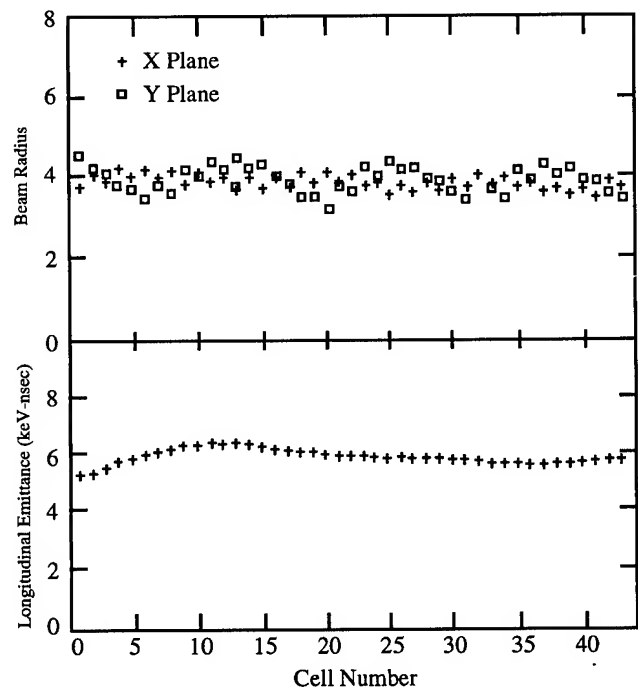


Figure 2: Transverse beam size and longitudinal emittance for a $q/A = 1/132$ beam with 0.25π mm-mrad transverse emittance accelerated through a 2 meter long, 44 cell RFQ operating at 12.125 MHz.

the electric fields in the superconducting drift-tube structures, and quadrupole fields in the magnets.

We consider first a 48 MHz linac section, consisting of forty interdigital cavities and forty triplets. This linac can accelerate any beam with $q/A \geq 1/132$ over the velocity range $.008 \leq \beta \leq .033$. Figure 3 shows the results of numerical ray tracing for a $^{132}\text{Sn}^{2+}$ beam of transverse emittance $\epsilon_T = 0.25 \pi$ mm-mrad [8]. The longitudinal emittance growth through the linac is negligible. In fact, the transverse acceptance of this section is greater than 0.6π mm-mrad, and even for such a large beam the longitudinal emittance growth is small.

Any of several linac structures could be used for accelerating a 2+ charge state beam over the velocity range $.004 < \beta < .008$ following the stripper at the exit of the RFQ to the entrance of the 48 MHz superconducting linac. A possibility considered here is a five resonator array of 25 MHz superconducting drift-tube structures.

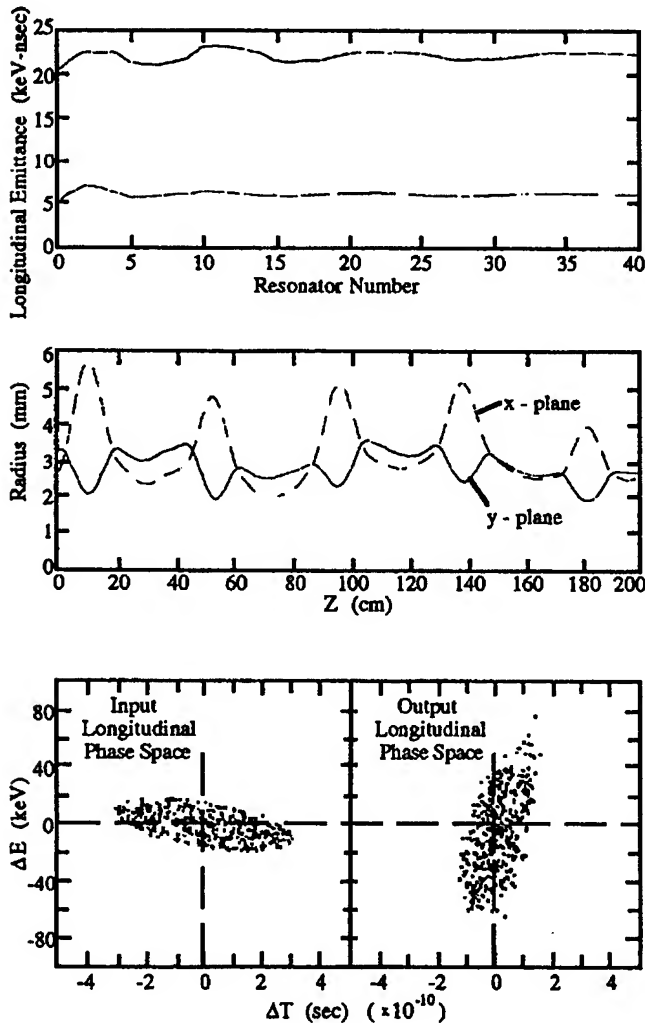


Figure 3: Transverse beam size (for the first 4 cells) and longitudinal emittance for a $q/A = 1/66$ beam traced numerically through a 40 cell superconducting drift-tube linac using magnetic quadrupole focusing. The normalized transverse emittance is 0.25π mm-mrad.

Adequate mechanical stability can be obtained using a folded coaxial line structure (recently implemented as a 25 MHz normally conducting accelerating structure) [9]. The folded line needs have no element longer than $1/8$ wave, and provides mechanical stability comparable to existing 48 MHz drift-tube structures while reducing the frequency a factor of two. Preliminary numerical ray-tracing has been performed for an array of five such 24 MHz cavities, using the above described 350 T/m quadrupole triplet for transverse focusing. For a $^{132}\text{Sn}^{2+}$ beam of transverse emittance $\epsilon_T = 0.25 \pi$ mm-mrad, an acceptably small longitudinal emittance growth of 3 keV-nsec was calculated for a beam with an input emittance of 5 keV-nsec.

III. CONCLUSIONS AND ACKNOWLEDGMENTS

A low -charge-state injector linac has been designed capable of accelerating beams of $q/A \geq 1/132$. The linac exhibits a transverse acceptance greater than 0.25π mm-mrad with a longitudinal emittance growth of no more than a few keV-nsec. The injector would adapt the ATLAS accelerator to the very low charge state ion beams required for radioactive beam applications, while maintaining the present beam quality. Formed of an array of independently-phased superconducting drift-tube structures, the linac would permit the same flexibility in configuration that has characterized the ATLAS accelerator.

The authors would like to thank Jerry Nolen and Alvin Schempp for several helpful conversations and Michael Bruns for performing the RELAX 3D calculations.

IV. REFERENCES

- [1] J. A. Nolen, in the proceedings of this conference.
- [2] R. C. Pardo et al., in the Proc. 1992 Linear Accel. Conf., August 24-28, Ottawa, Ontario, AECL-10728, p70 (1992).
- [3] J. W. Kim, K. W. Shepard, and J. A. Nolen, in the proceedings of this conference.
- [4] K. W. Shepard, in the Proceedings of the 1987 IEEE Particle Accelerator Conference, Washington, D.C., March 16-19, 1987, p1812 (1987).
- [5] John Staples, in the Proc. of the Workshop on Post-Accelerator Issues at the Isospin Laboratory, Berkeley, CA, October 22-29, 1993, edited by S. Chattopadhyay and J. M. Nitschke, P101 (1994).
- [6] R. W. Muller, GSI Report GSI-90-25-ISSN 0171-4546, (1990).
- [7] J. A. Nolen, in the Proc. of the Workshop on Post-Accelerator Issues at the Isospin Laboratory, Berkeley, CA, October 22-29, 1993, edited by S. Chattopadhyay and J. M. Nitschke, p150 (1994).
- [8] J. W. Kim and K. W. Shepard, in the proceedings of this conference.
- [9] K. Yoshida, et al., in the Proceedings of the 1994 International Linac Conference, August 21-26, 1994 Tsukuba, Japan, p771, (1995).

Progress of the Heidelberg High Current Injector

C.-M. Kleffner, S. Auch, M. Grieser, D. Habs, V. Kößler,
M. Madert, R. Repnow, D. Schwalm
Max-Planck-Institut für Kernphysik, Heidelberg, Germany
H. Deitinghoff, A. Schempp
University of Frankfurt, Frankfurt, Germany
E. Jaeschke, R. von Hahn
BESSY, Berlin, Germany
and S. Papureanu
KFA Jülich, Germany

Abstract

The accelerator facilities at the Max-Planck-Institut für Kernphysik in Heidelberg will be upgraded by a new high current injector which is under development. The first phase will consist of a high current ion source (CHORDIS) for singly charged ions, two 4-ROD-RFQ-resonators and eight 7-gap-resonators. The ion source has already delivered the design current of several mA Li^+ . New 'vane-like' electrodes with good cooling properties and good mechanical stability allow the operation of the RFQ-resonators at high power level and duty cycle. The eight 7-gap-resonators were constructed and tested. The final energy of the injector ($E = 1.8 \text{ MeV/u}$) is matched to the existing post-accelerator. By adding an ECR- or an EBIS- source, the new injector-post accelerator system will be able to deliver beams up to uranium with energies above the Coulomb barrier. The progress of the project will be described.

I. Introduction

Laser cooling experiments at the Heidelberg heavy ion storage ring TSR with ultra cold beams [1] of $^9\text{Be}^+$ and $^7\text{Li}^+$ are limited by the low currents delivered from the tandem accelerator. A new injector will increase the beam currents for these two ion species by three orders of magnitude. The high current injector will consist in its first phase of a commercial CHORDIS ion source[2], two RFQs [3] and eight 7-gap resonators [4].

Also experiments with highly charged ions are frequently limited by low beam currents due to losses from stripping. Therefore an ECR- or EBIS-source can be added in a second phase to increase the currents for highly charged heavy ions. In figure 1, the schematic layout of the new injector is shown. The accelerator will be placed parallel to the tandem and the $^7\text{Li}^+$ - or $^9\text{Be}^+$ -beams will be injected directly into the postaccelerator acting as a transfer line. For the second phase, stripping will be used behind the last seven-gap resonator and the proper charge state will be selected by an achromatic separator consisting of four 60° -magnets. The new injector also operates at 108.48 MHz like the existing post accelerator. The ion velocity of $\beta = v/c = 6\%$ after the high current injector is well adapted to the post accelerator and final energies higher than 5 MeV/u can be reached for all ion species in a pulsed mode of operation with up to 25% duty cycle.

II. The Ion Source

For the production of high currents of Li^+ and Be^+ with low duty factor (5 Hz, 500 μs) the commercial ion source CHORDIS [2] is used. The construction of the ion source section consisting of the source on a platform, a 60° magnet for isotope selection and a quadrupole triplet to match the beam to the RFQ section has been finished. The CHORDIS ion source has been in operation on its test-bench for several hundred hours. Table I shows a list of all ion species produced so far and the intensities of the analyzed currents in CW mode. Also the extraction voltage U_{ex} is given. For Be^+ and Li^+ the ion source is used in the sputter version.

Table I
List of ion species and current intensities produced so far
with the CHORDIS-source in CW mode

ion type	regime	$U_{ex}[\text{kV}]$	$I [\text{mA}]$
^4He	gas	17.5	2.5
^7Li	sputter	17.5	2.0
^9Be	sputter	30.0	0.21
^{40}Ar	gas	17.5	2.5
		30.0	9.0
^{48}Ti	sputter	30.0	0.37
^{53}Cr	sputter	30.0	0.17
^{56}Fe	sputter	30.0	0.46

As far as Li^+ is concerned, the design value of 2 mA was achieved with stable operating conditions. Higher currents were reached and could be stably produced by using an additional cooling equipment of the sputter cathodes. For the Be^+ -source an alloy with a Beryllium contents of only 2% was used. The intensity of 0.2 mA is satisfactory for all tests. Higher currents can then be achieved with cathodes made from pure Beryllium. Improvements were made with respect to diagnostic methods for source operation and particle beam optimization. The pulsed mode operation has been established for the gas version, however, some improvements are still necessary in the sputter mode. The emittance of the CHORDIS of $35 \pi \text{ mm mrad}$ has been measured to be within specifications.

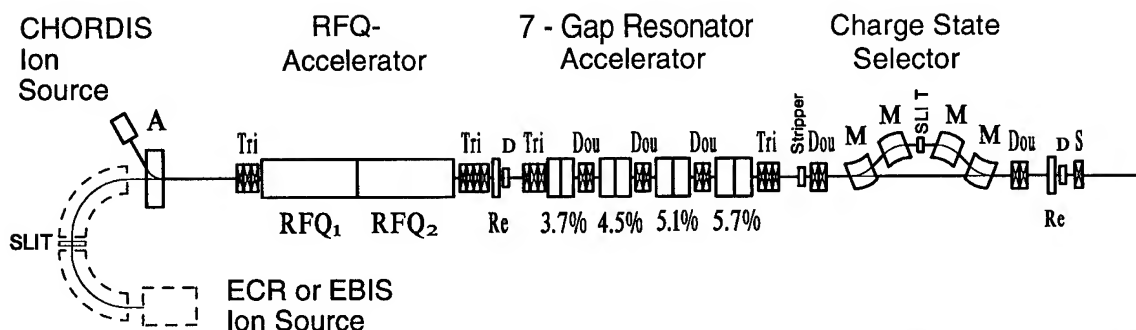


Figure. 1. Schematic layout of the new high current injector. A, M, S, Dou, Tri: magn. dipoles and lenses, Re: rebuncher, D: beam diagnostic. The ion source for highly charged ions (ECR or EBIS) and the charge state selector are planned for the second construction phase. The ion source will then be located one floor below.

III. The RFQ-Resonators

The second section of the high current injector consists of two 4-rod-RFQ resonators [3] operating at a charge to mass ratio $Q/A \geq 1/9$ as required for Be^+ . The two resonators operate at 80 kW rf power with 25% duty cycle. Sufficient cooling of the 3 m long electrodes is as important as the mechanical stability, because more than 35% of the rf power has to be dissipated at the electrodes. However, the maximum diameter of the rods is limited by the capacity between the electrodes to preserve a high shunt impedance. A custom made hollow profile from a copper-tin-alloy combines easy machining in the local workshops and high mechanical stability of the electrodes.

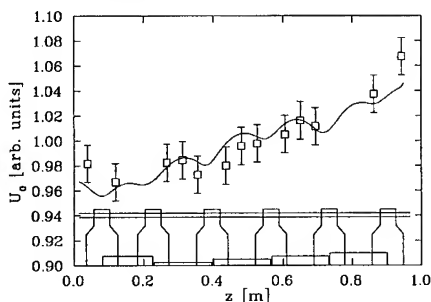


Figure. 2. Inter-electrode voltage distribution. line: MAFIA-calculation

3-D calculations with MAFIA [6] and measurements have been made for the newly designed electrodes with a shortened prototype resonator of 1 m length. Figure 2 shows the measurements and the calculations of the flatness of the voltage between the electrodes.

Power tests were done with the RFQ-prototype at a power level of 15 kW in CW mode. This is more than a factor of 2 higher than the design value for the 3 m long RFQ-resonators. The resonator was operated several weeks without any problems with respect to mechanical stability or sparking between the electrodes. Moreover, by injecting a light ion beam of suitable velocity, bunching and accelerating tests were performed with the prototype resonator, detecting the accelerated bunches with a fast Faraday-cup behind the resonator. Figure 3 shows the measured time structure at a rf-

power level of 10 kW.

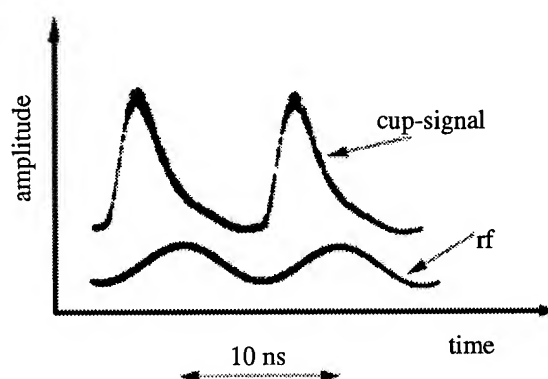


Figure. 3. Cup signal of H_2^+ bunches, accelerated in the RFQ-prototype

The measured peak amplitudes of the bunches at different electrode voltages of the RFQ-prototype were compared with calculations with the program PARMTEQ [7] (Figure 4) to estimate the shunt impedance of the structure. The shunt impedance of $R_s = 115 \text{ k}\Omega\text{m}$ was found in good agreement with the low-level measurements.

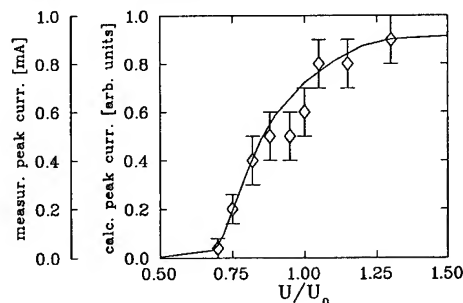


Figure. 4. Measured and calculated (line) peak currents of the accelerated H_2^+ beam in the RFQ-prototype. U_0 : design electrode voltage

After the successful tests with the prototype resonator, the 3 m long electrodes for the first RFQ-resonators were installed in the vacuum tank and aligned (Figure 5). Low level measurements and power tests are in preparation.

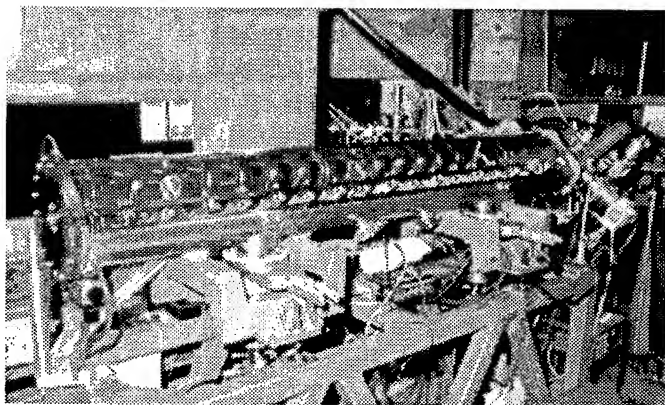


Figure 5. View into the vacuum chamber of the first RFQ-resonator

IV. The Seven-Gap Resonators

With increasing ion velocity, RFQ acceleration becomes less efficient and other accelerating structures such as the seven-gap resonator, developed at the MPI für Kernphysik [4] are more economical. To simplify the construction, the resonators are designed as four pairs of identical resonators for synchronous velocities of $\beta_s = 3.7, 4.5, 5.1$ and 5.7% . Based on measurements for the high velocity prototype of a seven-gap resonator [4], an effective accelerating voltage of 1.4 MV is expected for a low β -resonator, which operate at 80 kW rf power with 25% duty cycle. Scaled down models for the four different resonators have been used to optimize field distributions and shunt impedances. Based on these measurements, all eight seven-gap resonators have been fabricated so far [5]. In figure 6, a seven-gap resonator with a flange removed is shown. Segments on both sides of the inner resonance structure allow to adjust the required eigenfrequency to 108.48 MHz. The tuning plate, below the resonance structure, is clearly visible. The rf power is coupled into the resonator near one of the three legs which connect the resonance structure to the tank.

Table II

Measured resonator voltages with the beam test

β_s [%]	U_0 [MV] (N=80kW)	β_s [%]	U_0 [MV] (N=80kW)
3.7 I	1.73	5.1 I	1.69
3.7 II	1.67	5.1 II	1.62
4.5 I	1.79	5.7 I	1.61
4.5 II	1.73	5.7 II	1.66

All 7-gap resonators have been calibrated with a particle beam with synchronous velocity. From the energy distributions of the beam behind the resonator, the accelerating voltages could be derived (Table II) and were found in agreement with the bead perturbation measurements.

All 7-gap resonators are finished and have successfully undergone high power-rf tests up to 100 kW at a duty cycle of 25%. Neither mechanical vibrations due to ponderomotive forces nor multipactoring problems have been observed.

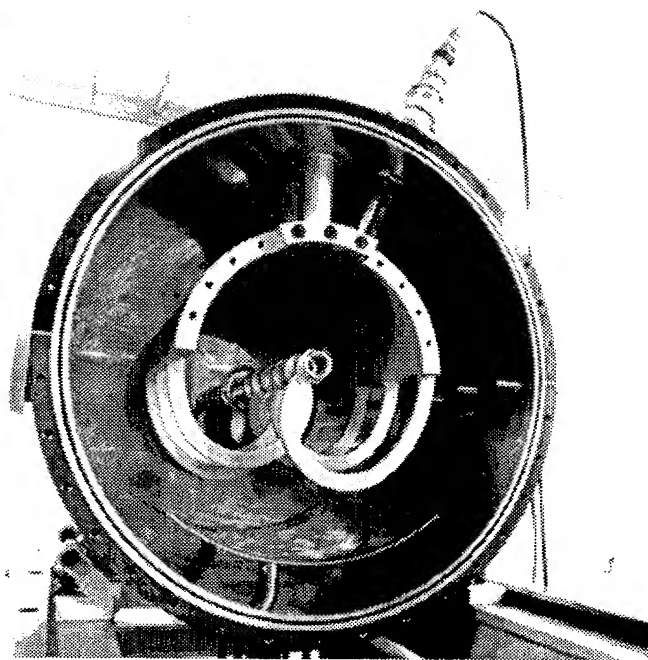


Figure 6. The 7-gap power resonator ($\beta=3.7\%$)

V. Outlook

The shielding vault of the MP-Tandem-Accelerator was constructed from concrete blocks and was completely rebuilt yielding nearly 2 meters of additional space aside the MP for the new injector, thus allow us to assemble the new rf-resonators in their final location on the optical axis of the present postaccelerator. The first beams from the high current injector in its first phase are expected to be available in early 1996.

VI. Acknowledgement

We would like to thank the MPI technicians for their valuable work which made the development of the high current injector possible.

References

- [1] R. W. Hasse, I. Hofmann and D. Liesen, Proc. Workshop on Crystalline Ion Beams, Wertheim, FRG, Oct 4-7, 1988, GSI-89-10, Darmstadt, 1989
- [2] R. Keller, B. R. Nielsen and B. Torp, Nucl. Inst. and Meth. B37/38(1989), p. 74
- [3] C.-M. Kleffner, PhD thesis, Heidelberg, 1994
- [4] M. Grieser, PhD thesis, Heidelberg, 1986
- [5] R. von Hahn, M. Grieser, D. Habs, E. Jaeschke, C.M. Kleffner, J. Liebmann, S. Papureanu, R. Repnow, D. Schwalm and M. Stampfer, Nucl. Inst. and Meth. A328(1993), pp. 270-274
- [6] T. Weiland, On the numerical solution of Maxwell's Equations and Applications in the field of accelerator physics, IEEE PAC 1984, vol. 15, pp. 245-292, 1984
- [7] K.R. Crandall, R.S. Mills, and T.P. Wangler, BNL 51143, p. 20, 1980

THE NEW CONCEPTS IN DESIGNING THE CW HIGH-CURRENT LINACS

B.P.Murin, G.I.Batskikh, V.M.Belugin, B.I.Bondarev, A.A.Vasiljev,
A.P.Durkin, Yu.D.Ivanov, V.A.Konovalov, A.P.Fedotov, I.V.Shumakov

Moscow Radiotechnical Institute of the Russian Academy of Sciences
113519, Moscow, Warshavskoye shosse, 132

The concepts in designing of the two types of high-current proton (deuteron) linacs having the electronuclear purpose with the output energy about 1 GeV and currents 200-300 mA (the first type) and 10 mA (the second type) are developed. The major problems arising in both cases is ensuring high reliability and efficiency of linacs. For the first type the high reliability is mainly connected with solving of the problem of minimizing the particles losses down to the level of 10^{-5} and of building the reliable superhigh-power RF power supply system. For the second type the problem of increasing the efficiency is of major importance. In the report the ways to solving of these problems by means of using the superconducting solenoidal focusing together with the optimized RF power supply systems (for the first linac type) and the superconducting accelerating cavities (for the second type) are shown.

I. INTRODUCTION

Design concepts of linear accelerators with the 1 GeV energy, 250 mA and 10 mA currents are considered.

In the first case (250 mA current) the general problems are provision of high reliability and efficiency, as well as radiation purity. In the present state of the technique reliability and efficiency are dictated by solving the problems of superhigh RF power supply system design and essentially lossless beam (10^{-5}) transport along the length of accelerator [1]. The solving of these problems provide radiation purity as well [2]. As discussed in MRTI papers [1,3] the number of RF power supply channels may not exceed one hundred for high reliability provision. This limitation demands design of RF amplifiers with output power up to 4...5 MW. For this purpose devices named "regotron" have been designed in MRTI [4,8]. With efficiency of about 70% the problem of high efficiency of the linac possess a solution. For the solving of the problem of lossless beam transport the focusing along main linac part based on superconducting solenoids was proposed. This version is considered in Part 2.

In the second case (10 mA current) the problem of high efficiency is brought to the fore. Estimations carried out in MRTI bring out that linac version with superconducting accelerating cavities is preferable. The concept of such linac is considered in Part 3.

II. LINEAR ACCELERATOR WITH SUPERCONDUCTING SOLENOIDS

The considered concept of the linac with 250 mA current is the further outgrowth of the MRTI quests [1-8] for linac for transmutation of long-living radioactive wastes of nuclear reactors. Novelty of this concept is associated with the use of superconducting solenoid focusing in the main accelerating part. It provides a possibility to reduce beam losses to the level of 10^{-5} .

Beam transport along the length of accelerator with minimal losses should be closely studied. The most limiting regions are: initial part of acceleration - IPA (up to 3 MeV); matching between focusing channels with different types and structures; high energy part of accelerator (HBL) with high number of focusing elements and accelerating structure.

Single-channel scheme (HILBILAC-DTL-HBL) is used in the linac as before. High acceptance of HILBILAC [5-7] and high current limit (700 mA on a frequency of 350 MHz) make possible to form beam at the IPA output with good transverse characteristics.

Use of focusing by superconducting solenoids at DTL and HBL alleviates the other problems: a) single-type focusing makes possible good matching between different linac part: (HILBILAC-DTL section and DTL-HBL section); b) changing quadruple lenses to solenoids decreases channel sensitivity to random perturbations approximately by a factor of 10 (computer simulation); c) use SSF at HBL section makes possible use of "long" cavities (10-13 m in length) based on D&W structure without subdivision on sections. Abandonment of sectionalized HBL cavities structure and coupling bridges between sections make possible essential decrease accelerating field sensitivity to geometrical errors of cavity. Requirements for evenness of "long" cavity excitation thought 7 power input from regotron reduce as well [5].

Development of such type linac indicates that DTL section realization is not improbable but there are a diversity of difficulties. The main problems are associated with high inductive coupling between solenoids, with strong ponderomotive forces and with scattering fields. Calculated characteristics of the linac are listed below:

Parameter	HILBILAC	DTL	HBL
Injection energy, MeV	0.15	3	100
Output energy, MeV	3	100	1000
Frequency, MHz	350	350	1050
Length, m	9	100	900
Beam current, mA	250	250	250
Cavity type	opposed vibrator	DTL	D&W
Number of cavities	2	7* (32**)	65*
Power transferred to beam, MW	0.7	24	255
Focusing type	SSF	SSF	SSF
Synchronous phase, grad	90-40	30	30
Channel acceptance, π cm \cdot mrad	2.5	3	7.5
Aperture diameter (R_a), mm	10	10-20	20
R_b/R_a	0.5	0.5	0.5

* regotron excitation, ** klystron excitation

III. CW SUPERCONDUCTING PROTON LINEAR ACCELERATOR

Superconducting linear accelerator (SLA) of protons offers a number of advantages over "warm" accelerator. SLA makes possible to provide CW mode of operation with the currents up to tens mamps, reduce accelerator length at a sacrifice in accelerating rate, decrease RF power consumption and increase total efficiency of accelerator.

The following idea is the base of accelerator design. RFQ accelerator is used in IPA. The first accelerator part with output energy of 50 MeV is based on moderately short four-gap superconducting cavities with drift tubes exited on E₀₁₀-wave. The need for placement permanent magnet lenses between cavities demand cavities division into short parts. At the second accelerator part (HBL) elliptical-shape cavities with niobium plating are used. The number of cells in the cavity changes from 5 to 9 along the accelerator. Operational frequency was chosen moderately high for overall dimensions reduction. Odd ratio of first and second accelerator parts frequencies makes possible, when the occasion requires, simultaneous acceleration of H⁺ and H⁻ ions. General parameters are listed below:

Parameter	Initial part	First part	Second part
Accelerating structure	RFQ	short cavities with drift tubes	9-cells cavities
Input energy, MeV	0.06	3	50*
Output energy, MeV	3	50*	1000
Frequency, MHz	425	425	1275
Focusing type		FODO (PMQ)	FODO (PMQ)

Focusing period, m	0.007-0.056	0.3-1.0	1.0-3.0
Aperture diameter, mm	5-6	15-20	30-40
Inter-electrode voltage, kV	90		
Magnetic field gradient, kG/cm		7-8	1-2
Acceleration rate, MeV/m	1	2-5	5
Accelerator length, m	3.5	20	380
Power for beam acceleration, kW	30	470	9500
Overall losses, removed by helium, W	50	500	4100
Number of cavities	1	29	304
Beam emittance, cm mrad		0.1	0.1

*-the possibility of energy increase up to 100 MeV if under consideration.

Design of RF power supply system of SLA is connected with the decision of a number of specific problems.

With the accelerating rate of about 5 MeV/m beam will take off power about 50 kW. At the same time RF power losses in the cavity is several watts. The following requirements are imposed on RF supply channels: provision of high stability of RF field in the cavities under significant changing of load impedance and output power of generator; possibility of continuous adjustment of field amplitude in the cavities under aging and beam load changing; stable, without unwanted oscillations, operation under high-Q multi-mode load; fast switching-off of cavities excitation when beam is lost.

The ways of these requirements realization may be determine from estimated calculation of two limiting operational mode of "generator-feeder-cavity" assembly: a) under acceleration of the beam with 10 mA nominal current; b) in the absence of acceleration.

It is presumed that for decoupling of generator from cavity circulator with forward a_f and back a_b attenuation is inserted into feeder. Feeder attenuation is a_{feed} .

On retention of nominal amplitude of accelerating field in cavity for both cases, output power of RF generator is estimated at:

$$P_{g1} = P_b \cdot 10^{(a_{feed} + a_f)/10} \quad \text{for } I_b = 10 \text{ mA},$$

$$P_{g2} = 0.25 \cdot P_b \quad \text{for } I_b = 0$$

Standing wave factor K_{sw} in feeder at the generator output as a function of back attenuation in circulator (for $a_{feed} = 0.4 \text{ db}$, $a_f = 0.4 \text{ db}$) is shown below:

a_b, db	10	15	20
K_{sw}	1.76	1.37	1.19

By this means generator has to permit power varying from nominal value (with allowance made for direct losses in feeder and circulator it is estimated at 60 kW) to 15 kW. With zero current maximal voltage in feeder at the section between cavity and circulator is the same as for $I_b = 10 \text{ mA}$ and voltage in feeder at the section between circulator and generator is smaller by a factor of 2. In the case of klystron use a_b should be greater or equal 15 db. For decreasing the number of RF supply channels the scheme with excitation of 2 or 4 cavities from one powerful generator is considered as possible one.

For discussed accelerator the total power of losses by helium (cavities and power inputs) is estimated at 4000 W. According to radiation purity criteria [2] for 400 m length accelerator the additional beam losses power is 400 W. It is 10% of 4000 W. It is reasonable to set that heat flow from environment to criostat is 10% of heat release in cavities and power inputs. As this take place, total heat power abstraction is about 4800 W. The design of crio-unit consisting of several cavities placed in criostat was chosen in accordance with these requirements.

VI. ACKNOWLEDGMENTS

Authors express their gratitude to LANL (specifically to Dr.R.A.Jameson) for support of the work and fruitful discussions.

V. REFERENCES

[1] G.Batskikh et al. Linear Accelerator for Burner-Reactor. 1990 Linear Accelerator Conference, Albuquerque, New Mexico, p.581.

[2] A.P.Fedotov, B.P.Murin, Towards a Radiation-Free Linac of Meson or Neutron Generator Type. Proceedings of the 1976 Proton Linear Accelerator Conference, Chalk-River, Canada, 1976.

[3] V.G.Andreev et al. Basic Principles of Burner-Reactor Linac Design. Specialist Meeting on Accelerator-Driven Transmutation Technology for Radwaste and Other Applications, 24-28 June, 1991, Stockholm, Sweden, LA-12205-C, SKN Report No.54.

[4] B.P.Murin et al. Superhigh-Power RF Regotron-Type Generator For Linear Accelerator with High Mean Current, Ibid.

[5] G.I.Batskikh et al. Development of Advanced Technological System for Accelerator-Driven Transmutation Technologies and Applications, July 25-29, 1994, Las Vegas, Nevada, USA.

[6] B.P.Murin, V.M.Pirozhenko, O.V.Plink. High-Current Low-Energy RF Ion Accelerator. Proceedings of the 1990 Linear Accelerator Conference, Albuquerque, New Mexico, p.707.

[7] B.P.Murin. The Prospects For High-Power Ion Linear Accelerator Construction For Energy Function. Preprint 9210, Moscow Radiotechnical Institute, 1992.

[8] Design of High-Current, High-Energy Linac with Focusing by Superconducting Solenoids (Conceptual Design), Contract 9138K0014-9G between LANL and MRTI, The First Report, Moscow 1994.

A VERSATILE, HIGH-POWER PROTON LINAC FOR ACCELERATOR DRIVEN TRANSMUTATION TECHNOLOGIES*

J. H. Billen, S. Nath, J. E. Stovall, H. Takeda, R. L. Wood, and L. M. Young
Los Alamos National Laboratory, Los Alamos, NM 87545 USA

We are applying the new coupled-cavity drift-tube linac (CCDTL) to a conceptual design of a high-current, CW accelerator for transmutation applications. A 350-MHz RFQ followed by 700-MHz structures accelerates a 100-mA proton beam to 1 GeV. Several advantages stem from four key features: 1) a uniform focusing lattice from the start of the CCDTL at about 7 MeV to the end of the linac, 2) external location and separate mechanical support of the electromagnetic quadrupole magnets, 3) very flexible modular physics design and mechanical implementation, and 4) compact, high-frequency structures. These features help to reduce beam loss and, hence, also reduce potential radioactivation of the structure. They result in easy alignment, fast serviceability, and high beam availability. Beam funneling, if necessary, is possible at any energy after the RFQ.

Table 1. Design Summary

RFQ Parameters	
Frequency	350 MHz
Injection/Final Energy	0.075/6.8 MeV
Output Current	100 mA
Peak Surface Electric Field	<1.8 Kilpatrick
Total Length	8.1 m
Total RF Power	1.82 MW

CCDTL and CCL Parameters	
Frequency	700 MHz
Injection/Final Energy	6.8/1000 MeV
Average Structure Gradient	1.5 MV/m
Energy Gain (real estate average)	1.0 MeV/m
Quadrupole Focusing Lattice	FODO
Transverse Focusing Period	$8\beta\lambda$
Total Length	1 km
Radial Aperture	0.6 to 2.5 cm
Peak Surface Electric Field	<1.5 Kilpatrick
Shunt Impedance (real estate average)	25 $\text{M}\Omega/\text{m}$
Structure Power	40 MW
Beam Power (unfunneled/funneled)	100/200 MW
Number of RF Modules	27
Klystrons/Module (unfunneled/funneled)	7/10

The RFQ/CCDTL/CCL Design

Our design uses room-temperature copper accelerating structures. The accelerator consists of a 350-MHz, 7-MeV radio-frequency quadrupole (RFQ)¹ followed by a 700-MHz CCDTL² and coupled-cavity linac (CCL). We do not discuss details of the RFQ design in this paper. For information about

the RFQ see Ref. 1 and a paper³ on the low-power modeling of the structure. We have not yet completed the design process, but we have done enough calculations and low-power model measurements of the rf cavities to demonstrate their feasibility. Table 1 lists many of the design parameters. The design has several mechanical, rf, and beam-dynamics advantages and includes the following features:

- No transitions in the transverse focusing lattice after the RFQ, with a constant period of $8\beta\lambda$ at 700 MHz,
- Quadrupole magnets mounted and aligned independently from the rf structures,
- Furnace-brazed rf modules that eliminate almost all mechanical rf and vacuum joints typically found in DTLs,
- RF modules of up to 300 cavities driven by multiple, redundant klystrons for high reliability and beam availability,
- High ratio of active structure length to total length,
- No separate matching section between RFQ and CCDTL,
- No bridge couplers, unless diagnostics need more room,
- No beam-line flanges in the magnet spaces except at the ends of rf modules,
- Four cavity types (RFQ, two-drift-tube CCDTL, one-drift-tube CCDTL and CCL),
- Two coupling-cavity orientations in the CCDTL and CCL.

RF Structure and Focusing Lattice

Figure 1 shows a short section of the lowest-energy CCDTL structure that starts at 7 MeV. A transverse focusing period consists of pairs of individual two-drift-tube CCDTL accelerating cavities separated by a drift space of length $3\beta\lambda/2$ between cavities. Electromagnetic quadrupole (EMQ) singlets and diagnostic elements occupy this drift space. The magnets are as far downstream as possible in the $3\beta\lambda/2$ space to maximize room for diagnostic elements, isolation valves, or other items. The overall length of a two-drift-tube CCDTL accelerating cavity is $5\beta\lambda/2$. A focusing period includes two cavities and two $3\beta\lambda/2$ drift spaces. Thus, a FODO lattice has a period of $8\beta\lambda$ at 700 MHz.

Shunt impedance considerations dictate the energy for changing the rf structure. At about 16 MeV, we change to pairs of one-drift-tube CCDTL cavities as shown in Fig. 2. In this section, the drift space between pairs of cavities is $\beta\lambda$ in length. The focusing period length is also $8\beta\lambda$ (at 700 MHz) and the lattice remains FODO. At about 100 MeV, the two CCDTL cavities are replaced with groups of seven CCL cavities with a drift space of length $\beta\lambda/2$ as shown in Fig. 3. Most of these drift spaces contain only a quadrupole magnet. Some spaces will also include diagnostic elements requiring

*Work supported by the US Department of Energy.

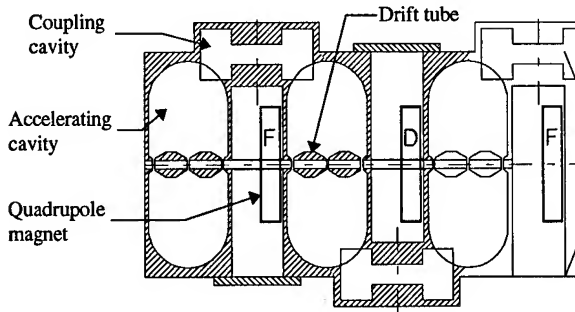


Figure 1. The low-energy section of the accelerator consists of two-drift-tube CCDTL cavities of length $5\beta\lambda/2$ spaced $3\beta\lambda/2$ apart. Sideways-mounted coupling cavities maintain the proper phase between cavities.

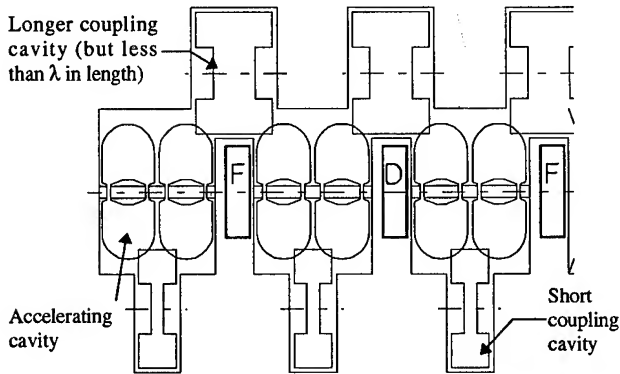


Figure 2. The intermediate-energy section of the accelerator consists of pairs of one-drift-tube CCDTL cavities, each of length $3\beta\lambda/2$. The space between pairs of cavities is $\beta\lambda$.

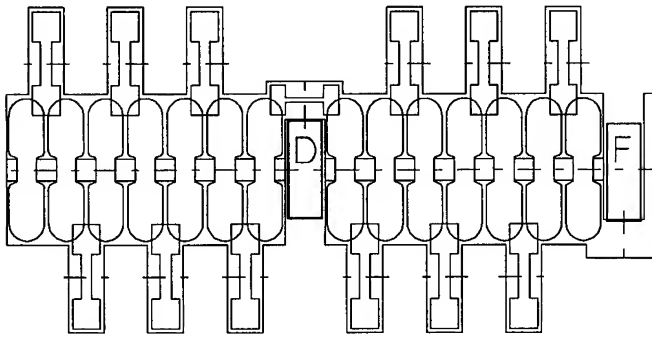


Figure 3. The high-energy section consists of seven CCL cavities, each of length $\beta\lambda/2$. The space between groups of cavities is $\beta\lambda/2$.

more room than available in length $\beta\lambda/2$, especially in the low-energy part of the CCL. Omitting one CCL cell doubles the available space, if needed. The lattice period of $8\beta\lambda$ continues all the way to 1 GeV.

Bore Radius and Focusing Magnets

The bore radius increases gradually between 7 and 100 MeV. Beam dynamics simulations show that an initial CCDTL bore radius of 0.6 cm is sufficient to capture the RFQ output beam. The RFQ beam edge is very sharp, essentially

free of any halo. The pole-tip inner radius of the quadrupole magnets at 7 MeV is 0.8 cm. The magnets fit over the copper bore tube, which is part of the brazed structure. The pole-tip fields are below 12 kG. Magnets with $GI > 3$ T fill only half the $3\beta\lambda/2$ space between cavities at 7 MeV. As the beam gains energy, two effects ease fitting magnets into the available space: the space gets longer as β , and the required GI product decreases as $1/\beta$. By using longer magnets, we can allow the bore radius to increase. A large radius is desirable from the point of view of reducing potential radioactivation of the structure, but it also spoils the shunt impedance. This is especially true at low β where drift tubes shield the beam from decelerating fields. Too large a bore in this part of the linac can dramatically reduce the transit-time factor. Thus, every few MeV we step the radius by 0.25 cm, eventually reaching the maximum radius of 2.5 cm at about 100 MeV. The bore radius remains at 2.5 cm to the end of the linac.

At each step in bore radius, the structure efficiency decreases, but then it recovers as the cell lengths increase in a section of fixed bore radius. Each EMQ design spans a pair of adjacent sections with different bore radii. For example, we use a common magnet with inner radius 1.75 cm in the sections with 1.25-cm and 1.50-cm radial aperture.

Beam-Dynamics Simulations

We are evaluating the beam-dynamics performance of the new design using a modified PARMILA code⁴ that generates cell geometries for graded- β DTL, CCDTL, and CCL structures. Figure 4 shows beam profile plots in the CCDTL from 7 to 20 MeV. This simulation used 1000

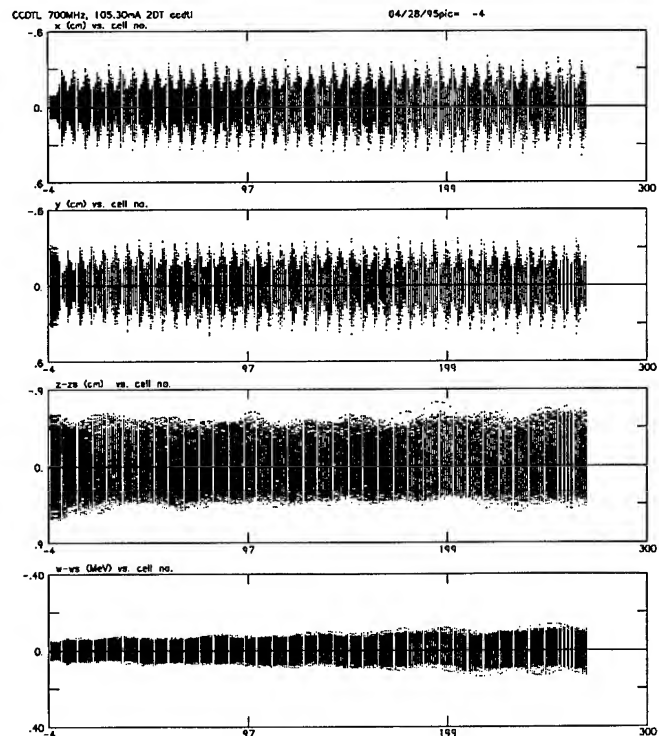


Figure 4. Beam-profile plots from a simulation of 1000 particles through the first 20 MeV of the CCDTL. From top to bottom the plots show the X, Y, Z, and energy profiles.

macro-particles. The input beam had the Twiss parameters and emittance values of the RFQ output beam. There is no separate matching section between the RFQ and CCDTL. Instead, we use the first three cavities of the CCDTL and the first few quadrupole magnets to match the beam to the new structure. Both the phase and the accelerating field vary gradually as the beam energy increases from 6.8 to 12 MeV. The synchronous phase ramps from -60° to -30° , and the average accelerating gradient ramps from 0.62 MV/m to 1.5 MV/m. Results show that within statistical error, there is no growth in either transverse or longitudinal emittance.

Redundant Klystrons, RF Module Lengths, and Funneling Options

The rf modules each contain up to 300 total cavities, including the coupling cells. With 300 or fewer cavities and 5 to 6% coupling between cavities, the mode density near the $\pi/2$ operating mode remains low enough for easy tuning of the structures. A module is driven by multiple klystrons such that the machine can operate at the design field level with one fewer than the full compliment of klystrons. Conservatively estimating the "real-estate" effective shunt impedance at 25 M Ω /m, the structure power is 40 kW/m. For an average energy gain of 1.0 MeV/m, the total power is 140 kW/m for a 100-mA unfunneled system. A typical module uses seven 1-MW klystrons driving about 37 m of structure. The first few rf modules use fewer klystrons because a seven-klystron unit would contain more than 300 cavities. In the unfunneled system, some rf irises are blanked off. A 200-mA funneled system has ten 1-MW klystrons driving the same 37-m-long structure. When a klystron fails, a waveguide switch at the appropriate distance from the now unused drive iris prevents loss of rf power from the accelerator into the unused drive line. The machine can continue to operate while the klystron is repaired or replaced. We have experimentally verified the waveguide-switch technique in a low-power cavity. We are also planning for a high-power test.

The modular design gives flexibility in the choice of energy for funneling, if needed. A single rf module contains several brazed sections joined by flanges. The size of the brazing furnace limits sections to about 2 m in length. An opportunity to break the system for a funnel exists at each flanged section, or roughly every 1 to 2 MeV. Since the field gradient ramps at the low-energy end of the linac, 2 meters corresponds to less than 2.0 MeV at first. The optimum energy for funneling appears to be near 20 MeV. Each leg of CCDTL between 7 and 20 MeV would require only three klystrons, including redundancy.

Space for Diagnostics

We provide space for diagnostics in two ways. First, the magnets are as far downstream as possible in the space between accelerating cavities. In some parts of the linac, this by itself provides enough space for diagnostic elements. Second, we can provide additional space, if necessary, by

eliminating a cavity at the end of a module. The missing cavity has no effect on the transverse focusing lattice. To mitigate the effect on the longitudinal dynamics, we adjust the coupling between cells before and after the missing cavity for a higher end-cell fields to maintain a constant average field gradient. These adjustments eliminate discontinuities in the average "real-estate" longitudinal focusing strength.

Coupling-Cavity Orientation

The accelerator has two coupling-cavity orientations because some sections use half-integral lengths of $\beta\lambda$ between cavities instead of the more traditional $n\beta\lambda$ spacing, where n is an integer. Figures 1 through 3 show both schemes. This flexibility offers two important advantages. First, it allows changes in the rf cavity type (needed for efficiency) without changing the focusing period. Second, it allows a large ratio of active to total accelerator length. We are testing a sideways mounted coupling cavity on a half-scale, 1400-MHz CCDTL low-power model.

Conclusion

We have outlined a new design for a high-current CW proton linac that has significant mechanical, rf, and beam-dynamics advantages over more conventional designs. The new design has no transitions in the focusing lattice after the 7-MeV RFQ. Magnets are not susceptible to drift-tube vibrations because they mount outside the rf structure where they remain accessible and serviceable. Furnace-brazed accelerator modules eliminate the rf and vacuum joints needed in a DTL providing higher reliability for a CW machine. Multiple-klystron rf modules increase reliability and availability. Work continues to refine the design.

References

- ¹D. Schrage, L. Young, J. Browman, J. Merson, and A. Naranjo, "Conceptual Design of a 7-MeV RFQ Linac for the Accelerator Production of Tritium," Los Alamos National Laboratory report LA-UR-93-1790 (May, 1993).
- ²J. H. Billen, F. L. Krawczyk, R. L. Wood, and L. M. Young, "A New RF Structure for Intermediate-Velocity Particles," Proceedings of the 1994 International Linac Conference, Vol. 1, p. 341 (August 21-26, 1994).
- ³L. M. Young, "An 8-Meter-Long Coupled Cavity RFQ Linac," Proceedings of the 1994 International Linac Conference, Vol. 1, p. 341 (August 21-26, 1994).
- ⁴H. Takeda and J. E. Stovall, "Modified PARMILA Code for New Accelerating Structures," this conference.

A COMPACT HIGH-POWER PROTON LINAC FOR RADIOISOTOPE PRODUCTION*

H. Takeda, J. H. Billen, S. Nath, J. E. Stovall, R. L. Wood, and L. M. Young
Los Alamos National Laboratory, MS H817, Los Alamos, NM 87545, USA

Conventional designs for proton linacs use a radio-frequency quadrupole (RFQ), followed by a drift-tube linac (DTL). For higher final beam energies, a coupled cavity linac (CCL) follows the DTL. A new structure, the coupled-cavity drift-tube linac¹ (CCDTL) combines features of an Alvarez DTL and the CCL. Operating in a $\pi/2$ structure mode, the CCDTL replaces the DTL and part of the CCL for particle velocities in the range $0.1 \leq \beta \leq 0.5$. We present a design concept for a compact linac using only an RFQ and a CCDTL. This machine delivers a few mA of average beam current at a nominal energy of 70 MeV and is well suited for radioisotope production.

Accelerator System Design

A compact linear accelerator is a competitive source of beam power for the commercial production of radioisotopes. The linac we describe provides a beam of up to 2 mA of protons at energies of 30, 50, and 70 MeV. Linear accelerator designers try to minimize construction costs by optimizing the relative costs of the accelerating structure and the installed rf power. To first order, structure cost is proportional to length and the rf cost is proportional to the square of the accelerating gradient E_0 . For a given structure power,

to the rf structure. The designer can choose from a broader range of rf power sources. We have based our design on klystron tubes operating at 433 and 1300 MHz. Both of these tubes are available in models that deliver very high peak and average powers. Only one tube at each frequency is required, so cost minimization involves making the best use of the tubes' power capabilities in the linac design.

Figure 1 shows a layout of the accelerating structures. The 433-MHz RFQ accelerates the beam to 10 MeV. The 1300 MHz CCDTL comprises the bulk of the linac and accelerates the beam to a final energy of 70 MeV. The 1300-MHz frequency is the third harmonic of the RFQ frequency. Each structure is powered by a single klystron rf source.

CCDTL

The length of the CCDTL, which depends upon the choice for E_0 , is limited by 1) the total amount of peak power available, 2) the average beam power required, 3) the peak surface electric field, and 4) the maximum local power density on the drift tubes. Figure 2 shows the two types of cavities used in the CCDTL. At the low-energy end, cavities have two drift tubes making three accelerating gaps. Gaps within a cavity are separated by $\beta\lambda$, where β is the relativistic

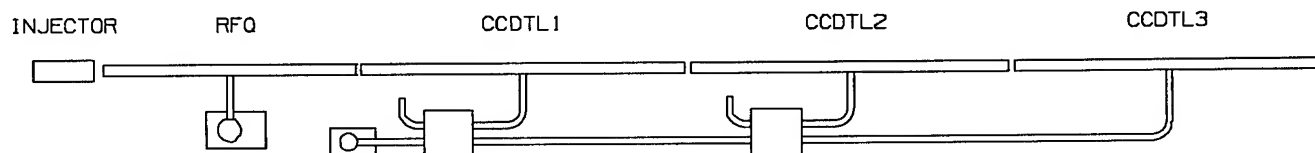


Figure 1. Schematic diagram of the radioisotope production accelerator.

accelerator length is inversely proportional to E_0 . The rf costs are further constrained because rf power is available in quantized units of single klystron tubes. Usually, the minimum total cost occurs where the power cost equals the structure cost.

A CCDTL can operate at higher frequencies than a conventional DTL because the focusing magnets are external

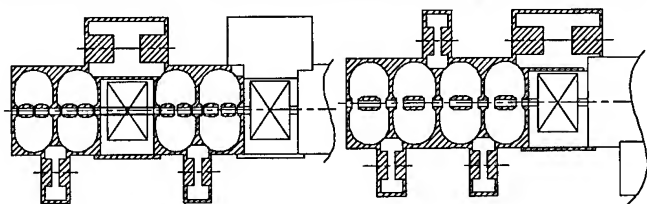


Figure 2. CCDTL structures with two drift tubes per cavity on the left and one drift tube per cavity on the right.

proton velocity, and λ is the free-space wavelength of the resonant mode. Successive gaps between cavities are separated by $\beta\lambda/2$. The other cavity type has one drift tube per cell. Figure 3 shows the effective shunt impedance ZT^2 calculated by the 2-D code SUPERFISH² versus β . Based upon this data, we switch from two-drift-tube cavities to one-drift-tube cavities at $\beta = 0.28$, which corresponds to 40 MeV.

To estimate the linac length and power requirements, we correct these values of ZT^2 for the effect of the coupling slots. Each percent of coupling reduces ZT^2 by about 3%. Figure 4 relates the active structure length to the peak rf power required to excite the cavities. Points for a given length correspond to the same value of E_0 . The lower curve is the structure power requirement without beam. The two upper curves include the power needed to accelerate 42-mA or 84-mA peak beam currents. For a beam duty factor of 2.4%, the corresponding average beam currents are 1 mA and 2 mA.

*Work supported by US Department of Energy

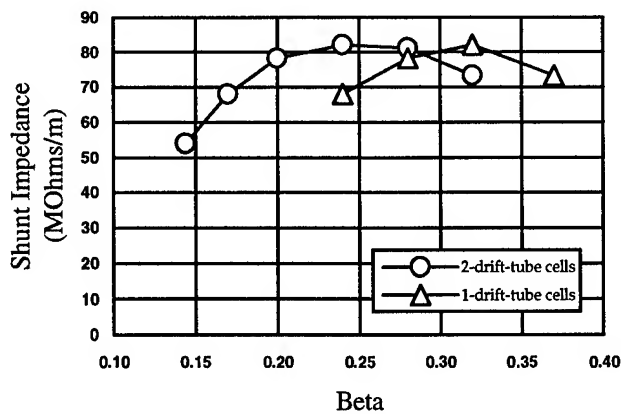


Figure 3. SUPERFISH shunt impedance versus particle velocity β for two types of 1300-MHz CCTDL cavities.

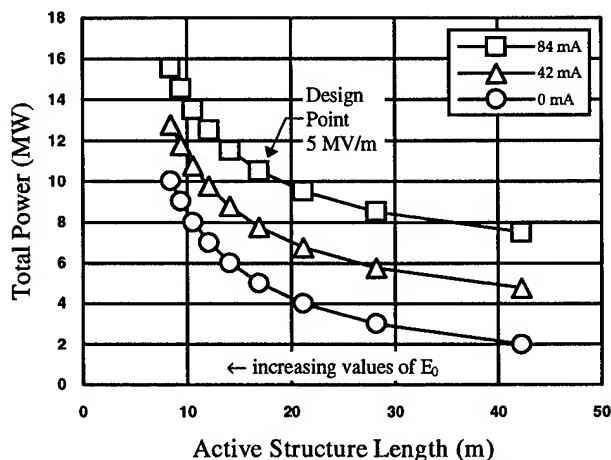


Figure 4. Peak power versus active structure length for nine values of E_0 between 2 and 10 MV/m.

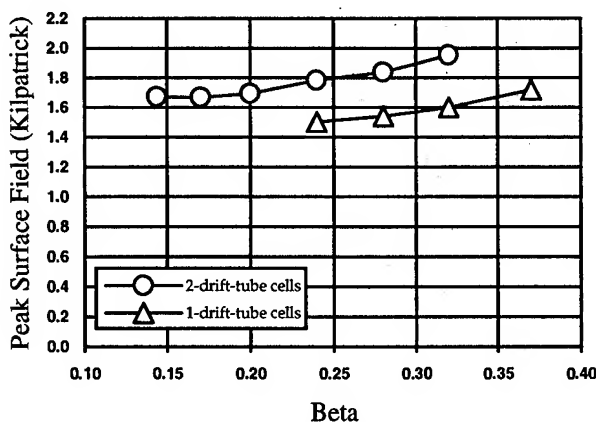


Fig. 5. Peak surface electric field expressed in terms of the Kilpatrick criterion versus β for CCTDL cells operating at $E_0 = 5$ MV/m.

The total power figures for these curves include a 15% control margin. A 10 MW klystron would support a family of interesting linac designs. For example, a 12-m-long linac operating at 7 MV/m could deliver 1 mA at full energy. Another one operating at 4 MV/m would be 21 m long and could deliver 2 mA. Longer linacs can provide even higher beam currents.

For higher values of E_0 , we approach other limits. Figure 5 shows the peak surface electric field in the CCTDL versus β for $E_0 = 5$ MV/m. The ordinate is relative to the Kilpatrick field E_K , which is 32.1 MV/m at 1300 MHz. Kilpatrick made his measurements³ when clean surfaces and good vacuum were difficult to achieve. Experience has shown that we can exceed the Kilpatrick's criterion by an amount often called the "bravery factor." We typically design for peak fields up to $1.8 E_K$. We expect little or no sparking below this value. In a 2-drift-tube CCTDL, the peak field increases with β , reaching $1.8 E_K$ on the drift-tube nose at $\beta = 0.25$ (31 MeV).

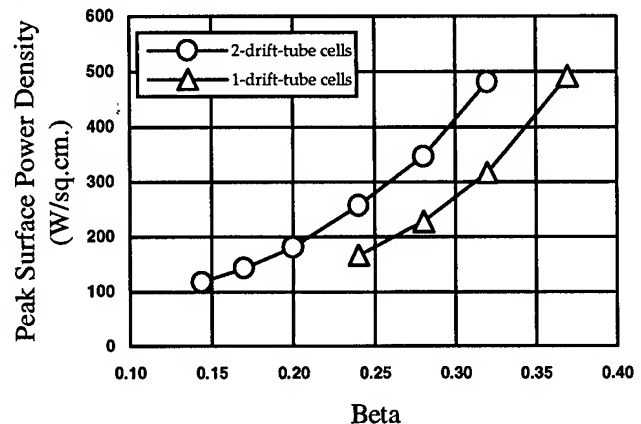


Fig. 6. Peak surface power density versus β for CCTDL cells operating at $E_0 = 5$ MV/m and 100% duty.

Figure 6 shows that as the cells get longer with increasing β , the peak power dissipation increases. The hottest spot is at the longitudinal midpoint of the drift tubes. Power densities increase in proportion to E_0^2 . The plot is for 100% duty factor (i.e. cw), so for a duty factor of 2.5%, the maximum power density is about 12.5 W/cm^2 on the longest drift tube. At this power level all of the drift tubes are simple to build, easily cooled, and inexpensive.

Table 1. Linac Design Parameters.

Linac Parameter	RFQ	CCTDL		
		1	2	3
Injection energy (MeV)	0.075	10	30	50
Final energy (MeV)	10	30	50	70
Length (m)	6.7	9.1	7.1	7.0
RF frequency (MHz)	433	1300	1300	1300
No. of accelerating cavities	--	50	56	45
No. of quadruples	--	25	14	11
Transmission (%)	85	100	100	100
Accel. Gradient (MV/m)	2.75*	5*	5	5
Peak Cu Power (MW)	2.4	1.43	1.44	1.5
Peak beam power (MW)	0.8	1.6	1.6	1.6

* Corresponds to the exit of the RFQ and the entrance of the CCTDL; the field ramps up to 5 MV/m in the CCTDL.

Based upon these cavity properties we have chosen to operate the CCTDL at $E_0 = 5$ MV/m. Table 1 summarizes the properties of the 70-MeV linac. It is 23 m long and contains 151 accelerating cavities. Including the nominally unexcited

coupling cells, the accelerator has a total of 299 resonant cavities in the three tanks. A total of 50 electromagnetic quadrupole (EMQ) lenses provide the transverse focusing. These magnets mount outside the rf cavities and the vacuum system. The FODO lattice has a period of $16\beta\lambda$ at 1300 MHz. The EMQs are 6 cm long and they can achieve a field gradient of 50 T/m. With no adjustment of the focusing strength, they provide excellent confinement of the beam for peak currents of 82 mA over a wide range of energies. At full energy this linac can deliver 2 mA of average beam. At reduced energies, even higher currents are available without raising the peak current by simply increasing the pulse repetition frequency. This scheme takes advantage of the full average power available from the klystron.

Most commercial isotopes are presently made at energies of 30, 50, and 70 MeV. The three separate sections of CCDTL provide a simple and reliable way of producing beams at these energies without multiple rf-power tubes. The same tube drives each tank separately through power splitters connected to a common waveguide. Three independent tanks have fewer cavities per rf module than one long tank, resulting in no appreciable field droop or power-flow phase shift within the rf structures. The machine produces different beam energies by selectively turning off rf power to the downstream accelerating tanks. By building tuning devices into some of the coupling cells we can achieve even finer energy variability.⁴

RFQ

The RFQ operates at the third subharmonic of the CCDTL. There are two commercial klystrons that offer high powers at 433 MHz. Table 2 shows that the RFQ peak-power requirements match the specifications of the TH2120 and the TH2118. The average power and pulse length are best matched by the TH2118.

The RFQ consists of four coupled resonant sections, each one 1.7 m long. The rf power couples into the high energy section through a waveguide iris. In the high-energy part of the RFQ, we specially tailor the vane-tip modulation to reduce the phase width of the exit beam. The CCDTL can directly capture this RFQ output beam and does not require a separate matching section. The first four cells of the CCDTL do little acceleration. Instead, these cells mainly bunch the beam to ensure capture of 100% of the beam into the rf "bucket." Following this capture section is a quasi-adiabatic ramp in both the synchronous phase and the field amplitude. The first few quadrupole lenses in the CCDTL match the beam from the RFQ in the transverse plane.

RF Power and Duty Factor

Table 2 shows that for $E_0 = 5$ MV/m the CCDTL is well matched to the TH2104U klystron. The design takes advantage of both the peak and average power available from this tube without exceeding safe limits for either cavity fields or power densities. To match the power requirement for 2-

mA operation to the tube we have assumed only a 9% rf control margin at full energy. We believe further cavity optimization will reduce the power requirements enough to allow a full 15% control margin within the 10 MW available.

Table 2. RF Systems Parameters.

Parameter	RFQ	TH 2120	TH 2118	CCDTL	TH 2140U
Frequency (MHz)	433	433	433	1300	1300
Total rf power (MW)	3.2	--	--	9.17	--
Control margin (%)	15	--	--	9	--
Peak power, MW	3.7	4.0	6.0	10	10
RF pulse length* (μ s)	208	10^4	220	208	250
Duty factor(%)	2.5	8	3.3	2.5	2.5
Average rf power (kW)	93	500	200	240	250
Klystron efficiency (%)	--	55	58	--	45
Total ac power (kW)	--	185	176		593

*assumes 8 μ sec cavity filling time

Both sections of the linac run with a pulse-repetition frequency of 120 Hz synchronized with the line. The beam pulse is 200 μ s long for a beam duty factor of 2.4%. The cavity filling time adds another 8 μ s. This scheme takes advantage of the entire power capacity of the CCDTL klystron. We estimate that a total ac power of 800 kW is needed to produce 140 kW of beam power. An equal amount of cooling capacity would be required.

Conclusion

We have outlined a new design for a compact proton linear accelerator suitable for radioisotope production. A single 433-MHz klystron rf source powers the RFQ, and a single 1300-MHz klystron powers all three tanks of the CCDTL. The accelerator can provide beam currents up to 2 mA average at essentially any energy between 20 and 70 MeV.

References

- ¹ J. H. Billen, F. L. Krawczyk, R. L. Wood, and L. M. Young, "A New RF Structure for Intermediate-Velocity Particles," Proceedings of the 1994 International Linac Conference, Vol. 1, p. 341 (August 21-26, 1994).
- ² K. Halbach and R. F. Holsinger, "SUPERFISH -- A Computer Program for Evaluation of RF Cavities with Cylindrical Symmetry," Particle Accelerators 7 (4), p. 213-222 (1976).
- ³ W. D. Kilpatrick, "Criterion for Vacuum Sparking Designed to Include Both rf and dc," Nuclear Instruments and Methods 28, p. 824 (1957).
- ⁴ L. M. Young, "A Method of Changing the Final Energy in a CCL or CCDTL," Los Alamos National Laboratory internal memorandum AOT-1:94-159 (August 18, 1994).

POTENTIALITIES of ELECTRON and ION BEAM ACCELERATORS for LONG-LIVED NUCLEAR WASTE TRANSMUTATION

A. Shalnov, N. Abramenko, B. Bogdanovich, M. Karetnikov, A. Nesterovich, A. Puchkov

Moscow state engineering-physics institute, MEPhI, Moscow, 115409, Russia

Transmutation of nuclear materials can be carried out by thermal neutron capture reactions, by spallation type reactions or via photonuclear reactions caused by high-energy γ -rays generated in the electron linacs. These reactions can complete each other. At the present work two different schemes of proton-electron accelerators utilizing successive or simultaneous acceleration of protons and electrons are proposed. In a case of simultaneous acceleration both the efficiency of acceleration increases and the power loss for the beam focusing decreases. The experimental results on the acceleration and focusing of the mixed electron-proton beams are also presented.

The problem of energy guaranteeing will be one of the most actual tasks in the near future. In parallel with the exhaustion of natural resources it is obvious that modern fuel cycles are very bad for the Nature. But at the same time one predicts that rational solution of the both ecological and fuel problems is practicable in general via utilizing nuclear energy [1]. However it is impossible without carrying out the following tasks:

- generation of artificial nuclear fuel since the resources of natural nuclear fuel are not sufficient;
- improving the safety of nuclear plants up to the level eliminating the possibilities of Phenix or Chernobyl type accidents;
- utilizing the rational methods of the nuclear wastes recovery since the modern methods of wastes burying in the special bunkers or in rocks are not reliable and can lead to the accidents under active geological processes or by acts of diversion.

The nuclear power-engineering at the present time has a grate potential for partial solution of above mentioned problems. This is the transmutation of many nuclides in the neutron flux of the reactor; production of nuclear fuel in breeders; the adoption of the nuclear reactors with a feedback loop around reactivity and so on. But the ideal fuel cycle can not be maintained in reactor-type nuclear plants only in consequence of the following circumstances:

- It is impossible to transmutate Cs^{137} and Sr^{90} which define the residual activity of the nuclear waste in general;
- The most perspective fuel cycles U^{238} - Pu^{239} and Th^{232} - U^{233} are characterized by the very low yield of delayed neutrons and it is impossible to supply nuclear safety of these cycles by standard methods;
- Stabilization of reactivity is maintained by replacing of regulation rods and something can possibly seize.

The problem of the "ideal" fuel cycle can be solved by using the external neutron source and by going to the conception of the subcritical blanket of the reactor. Under $K_{\text{eff}} \sim 0.9 \div 0.99$ the chain reaction does not take place but the

reactor can work as the neutron multiplier with a amplification $1/(1-K)$ by the neutron flux and $\xi W_f/W_{\text{ng}}$ by the energy, where ξ is a fraction of neutrons which share in a fission, W_f is the energy released by one act of the fission, W_{ng} is the cost of the neutron in the units of the energy.

The neutron source can be based on the particle accelerator with a heavy metal target. The specialists of JAERI estimated that the 1.5 GeV 25 mA proton beam could incinerate Np^{237} , Am^{241} , Am^{243} , Am^{244} [2]. The energy released by fission promotes to use higher actinides as the fuel in subcritical blanket. The long-lived isotopes Tc^{99} and I^{129} can be also incinerated into stable or short lived isotopes. But transmutation of Cs^{137} and Sr^{90} needs much higher neutron fluxes and consequently much higher beam power. For reaching equal rates of transmutation and decoy one need the neutron flux of $7.6 \cdot 10^{16} \text{ c}^{-1} \text{ cm}^{-2}$ for Sr^{90} and by an order of magnitude smaller for Sc^{137} . The primary activity of Cs^{137} and Sr^{90} are approximately equal but Sr is 37 times more radiotoxic and the final radiotoxication is determined by Sr. On the other hand the effective way of Sr and Cs incineration may be their irradiation within the giant resonance of (γ, n) reaction. The radiological problems of the task is discussed in [3-5] and according to it the mean beam current should be about several A at the 100 MeV energy. Thus the system based on combined electron-proton beam irradiation makes available to incinerate all types of nuclear wastes.

The possible scheme for realization of this idea is given in fig.1 and the typical parameters of the accelerator are presented in table.

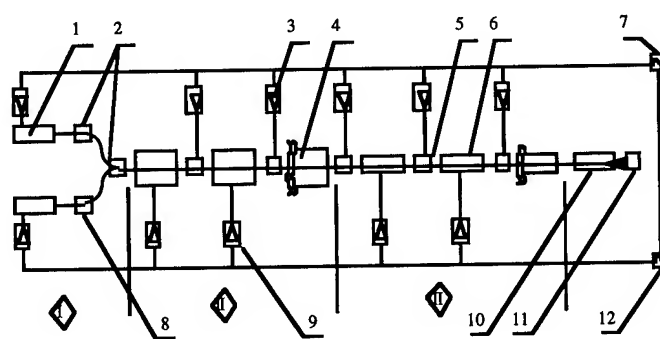


Fig.1 The scheme of the electron-ion beam accelerator for transmutation.

In general the accelerating system consists of the low-energy section (I) in which the separate acceleration of electron in the accelerating structure 1 and protons in the structure 8 as well as the following converging two beams in one mixed beam in the magnet system 2 is carrying out; the middle-energy section (II) and the high-energy section (III). The middle-energy section contains the series of the proton

Accelerator section number	Accelerating structure type	Frequency, MHz	Section output energy, MeV	Energy gain, MeV/m	Focusing
I	RFQ	153,7	3+4	1+2	-
	Iris loaded waveguide	2766	~15	5+7	Solenoid
II	Alvarez structure	461	70+80	~4	Electron beam space charge
	Coupled cavities	2766	30+40	1,5+2	Solenoids in drift tubes
III	π -mode side coupled cavities	922	~800	~10	Electron beam space charge
	Coupled cavities	2766	150	1,5+2	Permanent magnets in drift tubes

accelerating structures 4 with the characteristic length of 1 m, and electron accelerating structures between them with the length of about 10+15 cm. The RF frequency in the proton accelerating structures should be chosen much less and devisable with the respect to the electron accelerating one for reasons of the particle dynamic [6]. If one chooses the "electron" frequency equal to 2766 MHz the "proton" frequency is 18 times larger at the I section, 6 times larger at the II section, 3 times larger at the III one. The schemes of the section II and III are similar to I one. The basic differences center around the type and the parameters of the structures. It is appropriate to use RFQ at the I section, the drift tube structure at the II section and the π -mode side coupled cavities structure at the III section [7]. The other designation in fig.1 are the following: 3- "electron" frequency power amplifiers; 6- proton accelerating structure at the III section; 7- master oscillator on the "electron" frequency; 9-"proton" frequency power amplifiers; 10- output unit of the mixed beam shaping; 11-target; 12- master oscillator on the "proton" frequency. The coupling of 7 and 12 units represents the phasing between "electron" and "proton" RF fields in the presence of the concrete frequency instability.

Proton focusing at the sections II and III is provided by space charge forces of the electron beam, meanwhile the electron beam is focused by the periodic magnetic field created by solenoids and permanent magnets disposed in the drift tubes. This field simultaneously permits to increase RF electrical field breakdown limit since the lines of magnetic force are perpendicular to the lines of electrical force. It prevents acceleration of secondary and field-emission electrons in the accelerating gap. The calculated trajectories of electrons moving from one drift tube are shown in fig.2.

The calculation was carried out for the geometry of the linear accelerator I-101 (Russia) [9]. It is obvious that specific energy liberation, gas and vapour release (and other factors responsible to the electrical breakdown) are much less under magnetic insulation. As the field-emission electrons are not accelerated by the electrical field the likelihood of the electrical breakdown as well as the X-ray

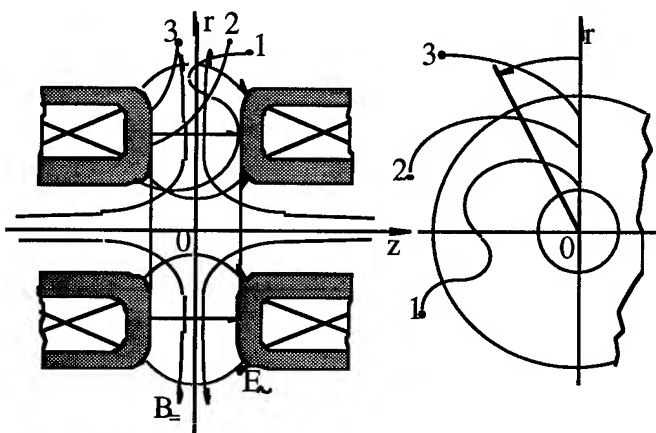


Fig.2. The electron trajectories.

intensity is minimized. Moreover the efficiency of harnessing RF power increases that is important in the high power accelerator. The electron beam current can be as much as several A, proton beam current is about several hundred mA. The total length of the accelerating system is 100+150 m.

At the section III one can recommend permanent ring magnets disposed between accelerating gaps. These magnets can have radial magnetization (fig.3a) or axial magnetization (fig.3b) in the case of the long gaps.

The amplitude of magnetic field is 0.1 T, the electron beam diameter is 4+6 mm, the aperture diameter is 10+15 mm. The authors pursued the experiments to study acceleration and transportation of the electron-proton beam at the system in the form of the series of the single-gap accelerators with the ring magnets placed in the drift tubes and also with solenoids. It was determined that radial component of the magnetic field in the area of the axial electric field promotes in successful accelerating cavity feeding. But it requires high vacuum and the absence of ECR conditions. The coefficient K (number of pulses without RF discharge divided by total number of pulses) vs magnetic field amplitude is shown in fig.4. The frequency was 149 MHz, pulse duration was 0.1 ms, the accelerating gap was 8 mm. It was also recognized that delay (5+10 μ s) of ion beam

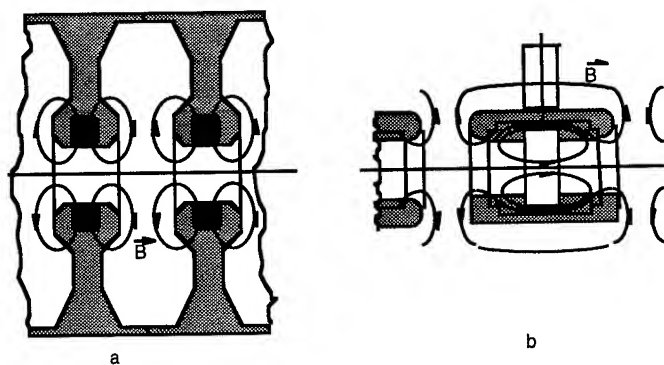


Fig.3. Permanent ring magnets layout in a drift tube: (a)-radial magnetization, (b)- axial magnetization.

pulse respecting RF pulse aided to the coefficient K increase. Furthermore the X-ray emission due to the electron beam bombardment also affected on the stable operation of the device. It was noted that magnetic insulation as well as delay let suppress this phenomena. This can be explained by lower loss of beam and lower secondary particles emission.

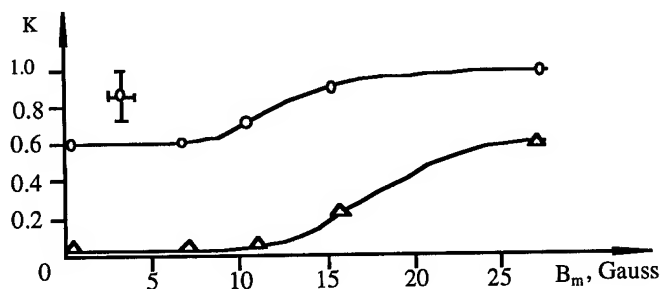


Fig.4. The coefficient K (number of pulses without breakdown divided by total number of pulses) vs magnetic field amplitude: o - with delay of the ion beam pulse; Δ - without delay.

As concerned the mixed beam forming system in the accelerator output (sign 11 on fig.1) the main problem is expected to be tied with the uniformity of the mixed beam intensity within necessary area at the target, in particular with the scanning beam as a whole. This problem can be solved using combined electric and magnetic fields acting to the opposite sides for electrons and ions [9].

Thus, the conducted analysis and the experimental results show the outlook of considered version. The final assessment of this version can be obtained by performing test experiments on electron- proton beam acceleration at the section contains 1 unit for proton and 1 unit for electron acceleration, the total length of the section is about 1m. The proton accelerator focused by electron beam [10] can be used as the injector.

REFERENCES

- [1] Charminat F. et.al. An Energy Amplifier for Cleaner and Inexhaustible Nuclear Energy Production Driven by a Particle Beam Accelerator. CERN/AT/93-47(ET), CERN, Geneva, 1993, p.66.
- [2] Kabo Y. et.al. Accelerator Molten Salt Target for Transmutation of long Lived Nuclides. Proc. of the Specialist Meeting on Accelerator-Based Transmutation, 1992, p.133-143.
- [3] Takashi H. The Role of Accelerators in the Nuclear Cycle. INIS-mf-12714, p.77-91.
- [4] Backih G.I. et.al. Uskoriteli Electronov dlia iadernoi transmutacii produktov delenia. MRTI/9006 (Russia), 1990.
- [5] Matsumoto T. Calculation of Gamma Ray Incineration of Cs137 & Sr90. NIM, Vol.A268 (1988), p.234-243.
- [6] Belousov V. Nesterovich A. Lineinie uskoriteli i fizika puchkov zariagennih chastic. Moscow, 1991, p.12-26.
- [7] Lineinie uskoriteli ionov. Editor B.P.Murin. Moscow, 1978.
- [8] Karetnikov M., Nesterovich A., Shalnov A. Magnitnaia izoliacia fokusiruiuschimi poliami v lineiniah uskoriteliah. MIPhI/044-90 (Russia), 1990.
- [9] Bogdanovich B., Nesterovich A., Shalnov A. //EPAC-90. Proc. of the 2-nd European particle accelerator conference. Nice, June 12-16, 1990, Vol.1, Editions Frontieres, p.626-627.
- [10] Bogdanovich B., Gavrilov N., Shalnov A. Uskoriteli s nakopleniem i generaciei vysokochastotnoi energiei. Moscow, 1994.

RFQ design for High-Intensity Proton Beams

R. FERDINAND, J-M. LAGNIEL and P. MATTEI

Commissariat à l'Energie Atomique - Direction des Sciences de la Matière - GECA
C.E.N. Saclay - LNS, 91191 Gif-sur-Yvette Cedex, FRANCE

Abstract

A CW RFQ, designed to accelerate 100mA proton beams from 100keV to 4MeV, is being studied by the GECA in Saclay. A preliminary design leading to a beam transmission larger than 97% is presented. A logical approach, based on both the choice of transverse and longitudinal phase advances at the end of the gentle buncher and an adiabatic variation of the RFQ parameters in this region is described.

I. INTRODUCTION

For the new generation of high-power accelerators, high-intensity continuous proton beams are required. In this paper, the study of a Radio Frequency Quadrupole linac (RFQ) able to accelerate a 100 mA proton beam with a high transmission is presented. The input and output energy are respectively 100 keV and 4 MeV and the operating frequency is set at 352 MHz.

In the following sections, the choice of the RFQ parameters is explained and the beam dynamics described. Error studies for our « reference design » are also presented.

II. BEAM DYNAMICS

The input beam energy is settled to 100 keV by the pre-injector of the ECR source SILHI being build at the "Laboratoire National Saturne" (LNS). The choice of 4MeV for the RFQ output energy results from both considerations :

- extend the output energy to a high level in order to obtain first DTL cells long enough to allow a FODO focalisation law,
- limit the total RF power below 1.3 MW in order to use only one power klystron to feed the RFQ.

For the beam dynamics study, the input transverse emittance (total, normalized) is $1.5 \pi \cdot \text{mm} \cdot \text{mrad}$ ($0.25 \pi \cdot \text{mm} \cdot \text{mrad}$ for the RMS normalized emittance). This value is actually pessimistic, the total emittance expected at the pre-injector output is about $1.0 \pi \cdot \text{mm} \cdot \text{mrad}$ or less. In addition, as usual for CW RFQ, the maximum peak surface field is kept below $1.8 E_k$.

The dynamics has been calculated using these parameters in order to reach the higher transmission. Calculations were done using both the well known PARMTEQ family codes from the Los Alamos National Laboratory [1] and codes from the LNS [2]. All calculations began at the end of the Gentle Buncher (GB). Indeed, at this point the particles are bunched but weakly accelerated, so it is the area where the space-charge effect is the most important. Using CURLI and RFQUICK, the first design step gives a good starting point. Nevertheless, the PARMTEQ code results show that most of the losses are located at the end of the GB section. Such a

local loss of particles in a CW accelerator involves a local heating of the structure, sparking and pulverization of matter; they must then be avoided. This has been done by tuning the adiabaticity of the acceleration parameter in this region (figure 1). The LNS codes have permitted to choose the phase advances (then the r_0 , a and m parameters) at the end of the GB and to smooth the acceleration parameter as shown in figure 1.

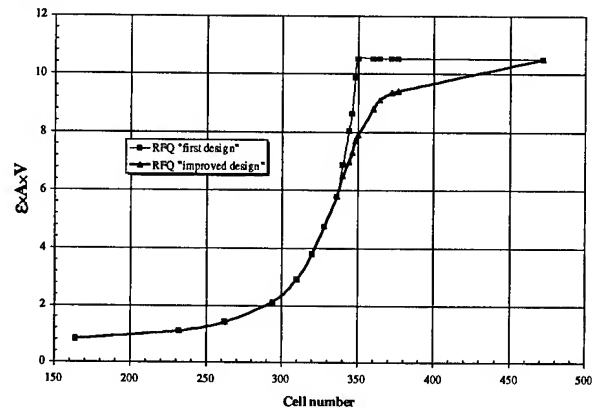


Figure 1 : Modification of the acceleration parameter to avoid localized losses.

The results of this operation are :

- the losses are no longer localized,
- the transmission increases from 94% to 97.4% without the multipole effect (PARMTEQ) and to 97.1% with multipoles (PARMULT),
- for the expected total emittance of $1.0 \pi \cdot \text{mm} \cdot \text{mrad}$ the transmission increases up to 98.3%.

Particle	H^+
Operating Frequency	352 MHz
Duty factor	100%
Input/Output Energy	0.1 / 4.0 MeV
Input/Output Current	100.0 / 97.1 mA
Transmission	97.1%
Trans. Emitt. (RMS, Norm.)	$0.25 \pi \cdot \text{mm} \cdot \text{mrad}$
Peak Surface Field	$1.8 E_k$
Intervane Voltage	90.2 kV
Total Length	6.45 m

Table 1 : Beam and accelerator specification.

The RFQ parameters are listed in table 1. It can be added that $r_0 = 3.75 \text{ mm}$ is kept constant all along the structure and that $p/r_0 = 1.0$. This is not the best choice to reduce the peak surface field but in this case, the multipolar effects are weak. Some of the most important parameters are shown in figure 2 as a function of the cell number.

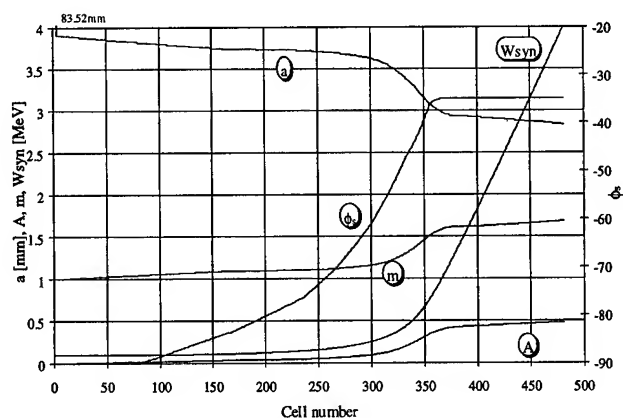


Figure 2 : RFQ parameters versus cell number.

The next figure gives PARMULT simulation results for the two cases previously described. Black points are lost particles. Figure 3-A clearly shows that most of them are located around cell 352 at an energy of about 808 keV (the end of the GB).

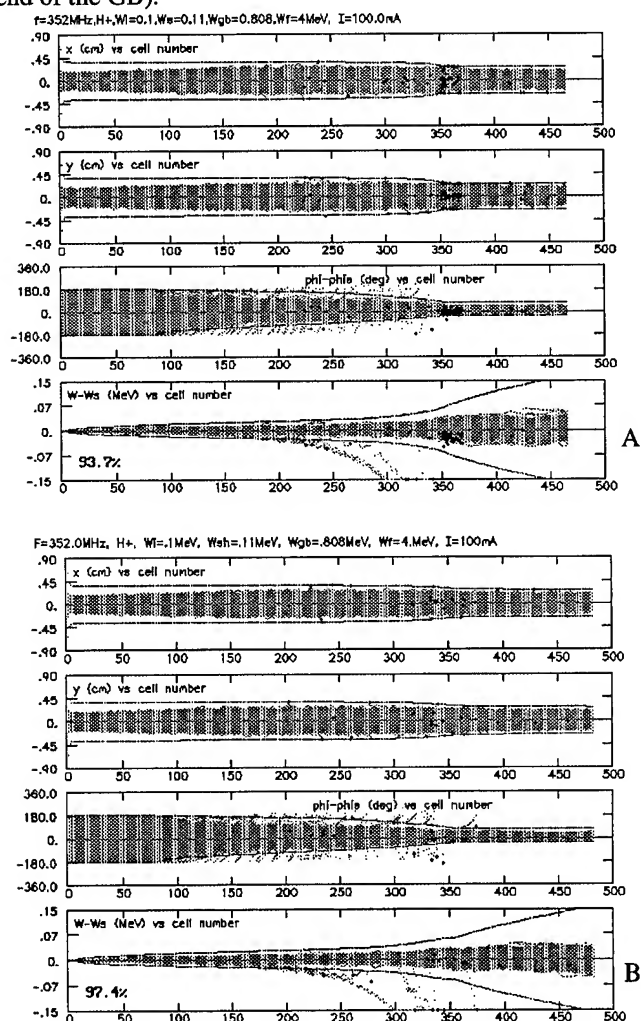


Figure 3 : PARMULT simulation with (A) and without (B) modification of the acceleration parameter.

Next figure shows the improvement obtained on the energy deposited by the beam on the vanes.

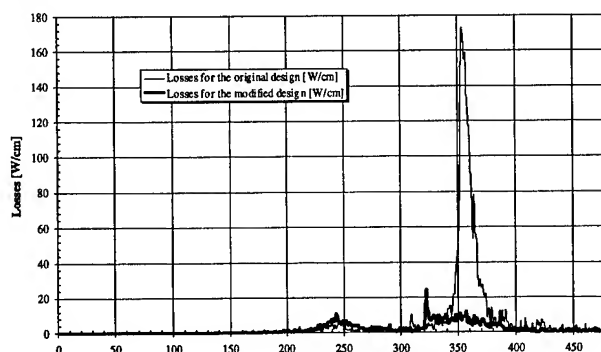


Figure 4 : Losses versus cell number with and without improvement of the dynamics.

III. ERROR STUDIES

All the simulations were carried out using PARMULT with high order multipoles. In order to reach a good accuracy, all the calculations were done with at least 20000 particles. We first studied beam's imperfections at the RFQ entrance : mismatching, displacement in position and angle, energy dispersion and detuning. We have also studied the effects of tilt errors on the vane voltage and some cumulated defaults. Figure 5 shows the evolution of the transmission versus the type of default.

PARMULT permits to modify the Twiss parameter α , β , γ , and ϵ of the beam. The limit of 95% of transmission appears in figure 5-A and 5-B to be at $\pm 15\%$ of x mismatch (β), $\sim \pm 20\%$ of x' mismatch (γ). In the case of beam displacement (figure 5-C) the limit appears to be at $\pm 11\%$ ($\pm 0.5\text{mm}$). Some work is done in order to reduce this sensibility to beam misalignments. The limit in beam angle (steering) do not seems to be so critical as it reaches $\pm 18\text{mrad}$ (figure 5-D). Some studies on energy dispersion show that the RFQ admit $\Delta W/W$ up to 4.5%! The detuning of energy could reach $\pm 2\%$. Studies of transmission versus vane voltage show that the limit of transmission is reached when the vane voltage is reduce by 3%. Another important parameter is the tilt witch could appear on the vane voltage (figure 5-E). The transmission is a little better for a tilt of -7%. For that tilt, the vane voltage is higher at the beginning of the RFQ, where the beam is at low energy and the space-charge effects high. Nevertheless such a tilt increases the peak field and sparking can occur. Furthermore, a negative tilt (more than -10%) involves an important pick of longitudinal losses at the end of the acceleration.

The last study describes cumulated errors which are given in the legend of figure 6. This figure shows the losses in the longitudinal plane. No localized losses appear, and the level remains low. A major point is that expected transmission is 88.5% if all individual errors are cumulated. Despite, the simulation gives 85.8%. The main concern is the effect of accumulated defaults rather than effects of sole defaults. All the beam parameters have to be carefully adjusted.

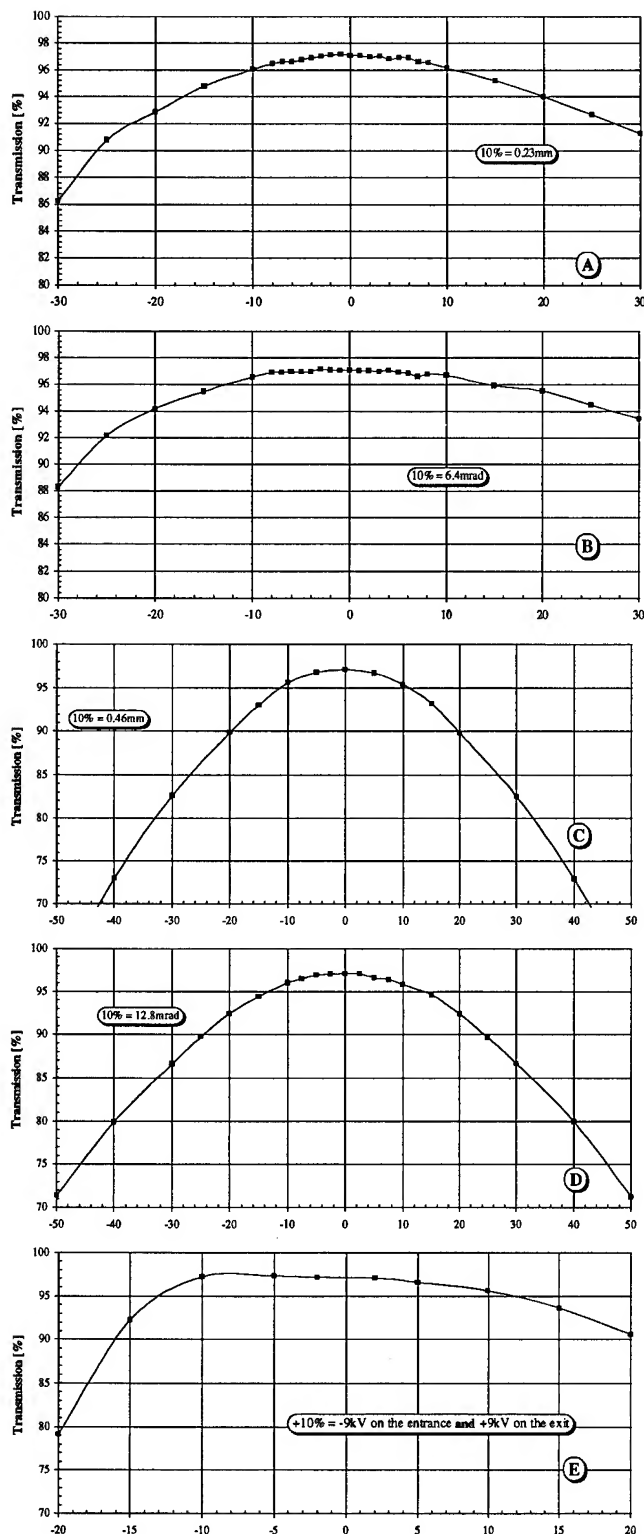


Figure 5 : Transmission versus errors (all in per cent of the original parameter).

- A and B for the sensitivity to the twiss parameters (respectively β and γ)
- C versus input beam displacement
- D versus beam steering errors into the RFQ (beam angle)
- E for a tilt of the vane voltage.

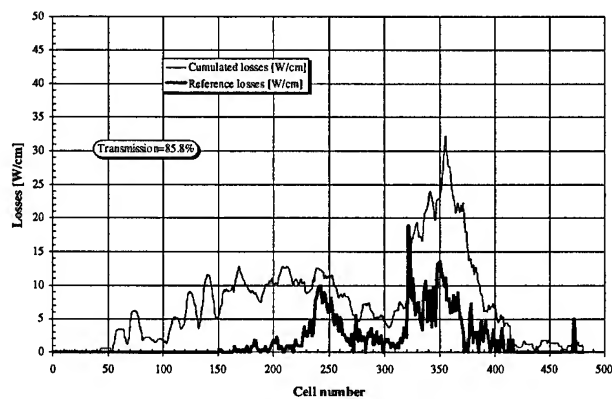


Figure 6 : Losses versus cell number. The reference curve is obtained without any errors. The thin line is obtained with x mismatch = 10%, y' mismatch = 15%, x and y displacements = 10%, x' and y' displacements = 10%, and tilt error = +5%.

IV. CONCLUSION

For the new generation of high-power accelerators, a reliable CW RFQ with a high output energy is required. The life time of such an accelerator will be greatly improved if damages done by beam losses can be avoided. The goals for the beam dynamics are then :

- a transmission as high as possible,
- no pick of losses which could locally damage the vanes,
- an easy ajustement of the beam to the RFQ input.

In the « reference design » presented here, almost all these challenges are completed. The transmission is larger than 97%. Only the sensitivity to beam misalignment must be improved. An optimisation of the adaptation section is expected to fulfill such requirement.

V. ACKNOWLEDGEMENT

The authors would like to thank J. Daussy and S. Joly for their encouragement and support. They are indebted to T.P. Wangler, J.E Stoval and S. Nath for their help concerning the LANL codes. Many thanks also to A. Shempp and M. Mizumoto for their helpful discussions.

VI. REFERENCE

- [1] K.R. Crandall, R.H. Stokes and T.P. Wangler, « RF Quadrupole beam dynamics design studies », LINAC79 Conf. Proc., p. 205.

See also

K.R. Crandall and T.P. Wangler, Linear Accelerator and Beam Optics Codes, AIP Conf. Proc. 177, 22 (1988).

- [2] J-M. Lagniel, « Tools for the design of high-current linacs », LINAC94 Conf. Proc.

METHODS FOR INCREASING OF BEAM INTENSITY IN UNDULATOR LINEAR ACCELERATOR*

E.S.Masunov, Moscow Engineering Physics Institute, Moscow, 115409 Russia.

The paper describes theoretical problems of ion focusing and acceleration in the high-intensity undulator linear accelerator (UNDULAC), where the accelerating force is produced by a combination of a radiofrequency field and undulator field. Both electrostatic and magnetostatic undulators are studied. The main factor limiting the beam intensity in the ion accelerator is space-charge forces. Three methods for increasing of the ion beam intensity in UNDULAC are discussed: (i) enlarging of the beam cross-section; (ii) acceleration of several beams in one RF structure; (iii) compensation of the space charge by acceleration of ions with different signs of the charge in the same bunch.

I. INTRODUCTION

Intensive particle beams with energy of 1-3 MeV are used in neutron generators and for external injection of neutrals in nuclear fusion reactors of TOKAMAK type. For these purposes, beams with high average current and very small emittance growth are required. For energy $W > 1$ MeV linear RF accelerator instead of the accelerator of Cockroft Walton Cascade type must be applied.

Now, two principles of focusing and acceleration of low energy ions in resonant linear accelerators are well-known: 1) radio-frequency quadrupoles focusing (RFQ) and 2) alternating phase focusing (APF).

In UNDULAC there are no drift tubes. As a result, it is possible to use the methods for increasing of beam intensity, which can not be realized in RFQ and APF structures.

II. PARTICLE MOTION EQUATIONS

The motion equation of particle may be written, using Lagrange function

$$\frac{d}{dt} \mathbf{P} = e \nabla (\mathbf{v} \cdot \mathbf{A} - \Phi). \quad (1)$$

Where $\mathbf{P} = \mathbf{p} + e\mathbf{A}$ is the canonical momentum of the particle, $\mathbf{A} = \mathbf{A}_v + \mathbf{A}_0$ the overall vector potential of the RF-field \mathbf{A}_v and the periodical magnetostatic field \mathbf{A}_0 , $\Phi = \Phi_v + \Phi_0$ the overall electrostatic potential of the external field Φ_v and periodical electrostatic field of the undulator Φ_0 .

First of all, let us discuss the motion equation for a

particle in the magnetostatic undulator (UNDULAC-M) in the case when $\Phi = 0$ and RF field harmonics are unsynchronized with the beam. The trajectories of the particles can be represented as a combination of fast oscillations $\tilde{\mathbf{r}}$ and slow variation \mathbf{R}_c . The kinetic momentum of particle is represented by the sum of slowly varying and fast oscillating components $\mathbf{p} = \mathbf{p}_c + \tilde{\mathbf{p}}$. By averaging over fast oscillations, from (1) we obtain the equation, that describes the slow evolution \mathbf{R}_c

$$\frac{d^2}{dt^2} \mathbf{R}_c = -\frac{e^2}{2m} \nabla \langle (\mathbf{A}_v + \mathbf{A}_0)^2 \rangle. \quad (2)$$

Taking into account only the main space harmonic of the magnetostatic undulator and TEM- or TE- wave in the waveguide structure, the equation (2) can be rewritten in the form

$$\frac{d^2}{dt^2} \mathbf{R}_c = -\frac{\lambda}{8\pi} \nabla U_b. \quad (3)$$

Where the potential function

$$U_b = \mathbf{b}_v^2 + \mathbf{b}_0^2 - 2\mathbf{b}_v \cdot \mathbf{b}_0 \sin \psi. \quad (4)$$

Here $\mathbf{b}_{v,0} = e\mathbf{B}_{v,0}\lambda_{v,0}/(2\pi mc)$ the dimensionless amplitudes of the transverse components of the wave magnetic field \mathbf{B}_v and undulator field \mathbf{B}_0 ; $\mathbf{B}_{v,0} = \text{rot} \mathbf{A}_{v,0}$; $\psi = \omega \int_0^z dz_1/v_s - \tau + \psi_0$

- the particle phase in the combined wave field; ω - the frequency of RF field, $\tau = \omega t$, ψ_0 - the initial phase; $v_s = \lambda_0/\lambda_v$ - the normalized velocity of the synchronized particle, λ_v - the RF-field wavelength, λ_0 - the undulator period.

The same equation can be obtained for the electrostatic undulator (UNDULAC-E) when $\mathbf{A}_0 = 0$

$$\frac{d^2}{dt^2} \mathbf{R}_c = -\frac{\lambda}{8\pi} \nabla U_e, \quad (3a)$$

where the potential function

$$U_e = \mathbf{e}_v^2 + \mathbf{e}_0^2 - 2\mathbf{e}_v \cdot \mathbf{e}_0 \sin \psi. \quad (4a)$$

Here $\mathbf{e}_{v,0} = e\mathbf{E}_{v,0}\lambda_{v,0}/(2\pi mc^2)$ - the dimensionless amplitudes of the basic RF-field harmonic \mathbf{E}_v and the first electrostatic field harmonic \mathbf{E}_0 .

* The research described in this publication was made possible in part by Grants # MFQ 300 from the International Science Foundation and Russian Government.

The acceleration gradient is proportional to the amplitudes of the RF and the undulator fields

$$\frac{\Delta W}{\Delta z} \sim \left\{ \begin{matrix} \mathbf{b}_v \cdot \mathbf{b}_0 \\ \mathbf{e}_v \cdot \mathbf{e}_0 \end{matrix} \right\} \cos \psi. \quad (5)$$

The energy increase ΔW on the length λ_0 is maximum, when $\mathbf{B}_v^\perp \parallel \mathbf{B}_0^\perp$ or $\mathbf{E}_v \parallel \mathbf{E}_0$. Therefore the choice of the magnetic (electrostatic) undulator type and its orientation depends on the RF-structure type [1].

Efficient capture and bunching of the beam can be obtained by the adiabatic growth of the values of $\mathbf{b}_{v,0}$ and $\mathbf{e}_{v,0}$ along the longitudinal axis and the corresponding increase of the undulator period λ_0 to maintain the beam synchronism with the combined wave field.

The choice of the functions \mathbf{b}_v , \mathbf{e}_v and \mathbf{b}_0 , \mathbf{e}_0 is not arbitrary because simultaneously with acceleration it is necessary to keep up the transverse focusing of the beam. In absence of the undulator, the transverse RF field can both focus and defocus the beam. The undulator without RF field can focus the beam. The combined field of the wave and the undulator accelerates particles in the longitudinal direction but defocusses them in the transverse direction. The total effect can be found only from the analysis of (4) and (4a). Equilibrium trajectories may exist for all particles of the beam, if two conditions are valid

$$\nabla_\perp \left\{ \begin{matrix} \mathbf{b}_v^2 + \mathbf{b}_0^2 \\ \mathbf{e}_v^2 + \mathbf{e}_0^2 \end{matrix} \right\} = 0, \quad \nabla_\perp \left\{ \begin{matrix} \mathbf{b}_v \cdot \mathbf{b}_0 \\ \mathbf{e}_v \cdot \mathbf{e}_0 \end{matrix} \right\} = 0. \quad (6)$$

The motion around an equilibrium trajectory is stable if the potential function $U_{b,e}$ has an absolute minimum. These conditions obtained have to be tested considering coupling resonances. It is important to study non-linear oscillations of the beam particles for specification of the transverse focusing conditions.

In a simple case the potential function $U_{b,e}$ has been found without considering higher harmonics of the RF field and undulator field. It is important to avoid beam flaking when the beam interacts with the higher harmonics. Limitations imposed on the values of these harmonics specify the shape of the undulator poles, as well as the geometry of the electrodes that form the RF field.

III. THE RIBBON BEAM IN THE UNDULATOR

The current in the UNDULAC may be increased for the large cross-section beam. In the UNDULAC there is no drift tubes and the ribbon or hollow beams can be accelerated. Study of ribbon ion beam interaction with the RF-field in the plane electrostatic undulator was carried out in the papers [2-3]. Here the electrostatic undulator is combined with the RF system forming the transverse electric field. The required field distribution is provided by a system of transverse electrodes mounted in the resonator and dc-isolated between

each other. The periodic undulator field is provided by electrostatic potential, which is supplied across the adjacent pairs of electrodes. Simultaneously, RF potentials are delivered to the electrodes. So the same electrodes are used to generate both fields.

This accelerator (UNDULAC-E) is suitable for demonstration of capabilities of this new method. The condition for providing efficient capture, bunching and acceleration of ions were found in [2]. The influence of coupling resonances on the choice of the field amplitudes was analyzed. An effect of higher harmonics of the space field on the beam dynamics was investigated. Some methods of formation of the required fields configuration were described in [4]. Computer codes for description of the ribbon ion beam dynamics in real fields were developed and the respective calculations were performed. The simulation results were in good agreement with theoretical estimations. Design of the RF-accelerating structure that showed a possibility to create the UNDULAC-E with a plane electrostatic undulator was proposed and studied experimentally [3].

The electrostatic version of UNDULAC is preferable at small values of the injection energy ($W = 30$ KeV for the proton beam). In the case of high injection energy ($W > 100$ KeV for the proton beam) we can substitute the magnetostatic undulator for the electrostatic one. For UNDULAC-M, it is impossible to obtain the large cross-section area of the beam because of technical problems connected with formation of strong magnetic fields in large volumes occupied by the beam. However, there is an opportunity to accelerate more than one beam in the magnetic channel.

IV. SEVERAL BEAMS IN THE UNDULATOR

It is easy to accelerate the several beams in one RF structure of UNDULAC because there are no drift tubes. For UNDULAC-E, two (or N) ribbon beam could be accelerated if three (or N+1) rows of electrodes are used. For UNDULAC-M, there is too an opportunity to accelerate more than one beam in the magnetic channel. The task is to choose a special symmetry of the transverse radio-frequency and periodical magnetostatic fields. The RF system must be a small transverse size to be located inside the undulator. Therefore, it is preferable to use a shielded multielectrode line where transverse electromagnetic (TEM) waves travel. The geometrical size of RF structure and the magnetic undulator must be found to maintain several equilibrium trajectories simultaneously. If the axis of the magnetic undulator coincides with that of RF system and the beam is injected along it, equations (6) are validated automatically. If the later condition is not valid, an equilibrium trajectory exists only if the field amplitudes and their transverse gradients are connected by the relations

$$B_0 = \frac{\lambda_v}{\lambda_0} B_v, \quad \nabla_\perp B_0 = -\frac{\lambda_v}{\lambda_0} \nabla_\perp B_v. \quad (6a)$$

This result may be used at a high value of the aperture of the accelerating channel because it allows to inject particles beyond the axis and to place the beam closer to the poles of the undulators, in order to increase the acceleration gradient.

The simple example of UNDULAC-M with shielded-pair electrodes was considered in the paper [6]. In the paper [6] it was shown that for an axially symmetric undulator and two electrodes of line the potential function (4) has two absolute minima. So, the focusing conditions are valid for two beams. The choice of optimum parameters for bunching and acceleration of two ion beams might be satisfied similarly to the case of one beam.

Acceleration of more than two beams is possible if more than two longitudinal electrodes are used. For N electrodes in the axially symmetric undulator it is possible to accelerate N beams, while in the plane magnetic undulator $N-1$ beams.

V. THE SPACE CHARGE COMPENSATION

Study of the possibility of simultaneous acceleration of both positive and negative ions with the identical charge-to-mass ratio in linear accelerators is great interest. The current limit of the ion beam can be substantially increased by using the space-charge compensation of positively H^+ (D^+) and negatively H^- (D^-) charged ions being accelerated simultaneously.

Let us consider the motion of positive and negative ions for a definite charge-to-mass ratio in UNDULAC. All the harmonics of RF field and the undulator field in the UNDULAC are asynchronous to the beam. After averaging over fast oscillations one can derive an expression for the effective potential function (4), (4a) that describes the averaged particle motion (3), (3a). The potential function $U_{b,e}$ depends on the particle charge squared, i.e. averaged motions of positive and negative charged ions are identical. It is important to note that both the main and high space harmonics have similar averaged influence on motion of the positive and negative ions. These ions will be within the same separatrix.

The averaged transverse trajectories $R_{+,-}$ of positively and negatively charged ions and their focusing conditions coincide. Nevertheless, fast transverse oscillations $\tilde{r}_{+,-}$ of these ions occur in anti-phase ($\tilde{r}_+ = -\tilde{r}_-$).

Usually, amplitudes of fast oscillations are comparable with the mean beam size. For the space-charge compensation it is important that the transverse separation of the oppositely charged beams will not be large. If such the beams with the equal current $|I_+| = |I_-|$ and the same initial emittances and velocities are injected into the accelerating channel, it is necessary at least that the difference between the mass center positions of the two beams is less than by $2\tilde{r}$.

The result of mutual space-charge compensation depends primarily on behaviour of mass centers of the beams. Coherent transverse stability of a two-component ion beam

was studied using the dispersion equation. The analysis of dispersion equation for this case showed that dipole resonances for two-component beam are not observed in presence of external focusing.

Computer simulation of a two-component ion beam, consisting of H^+ and H^- was carried out by a macroparticle method in the paper [7]. The space-charge field was calculated from the 3D Poisson equation. The results of the numerical simulation of intense H^+ and H^- beam dynamics confirm the analytical estimations.

VI. CONCLUSION

Theoretical and experimental studies of the UNDULAC showed a possibility to create a new type of ion linear accelerator. In this accelerator there is no need in drift tubes. As a result, it is possible not only to enlarge the beam cross-section, but also to accelerate several beams in one channel and to use the space charge compensation. Many examples of realization of the RF and the undulator fields can be suggested for increasing of the beam intensity. Such ion accelerators can be used for the neutron generators and the nuclear fusion reactor.

VII. REFERENCES

- [1] E.S. Masunov, "Particle dynamics in a linear undulator accelerator", *Zh.Tekn.Fiz*, vol.60, #9, pp.152-157, 1990 (in Russian).
- [2] E.S. Masunov, A.P. Novikov, "Application of electrostatic undulators for acceleration of intense ion beams", *Conf. Record of the 1991 Particle Accelerator Conference, San Francisco, California, May 1991, V.5*, pp.3177-3179.
- [3] E.S. Masunov, N.V. Leonov et al., "A project of ion linear undulator accelerator with transverse RF-field", in the *Third European Particle Accelerator Conference Proceedings, Berlin, March 1992, V. 1*, pp. 572-574.
- [4] E.S. Masunov, and A.P. Novikov, "Calculation of electrostatic and RF fields in UNDULAC-E with plane electrostatic undulator" *Proc. of the Fourth European Particle Accelerator Conference, London, June 1994, V.2*, pp.1280-1282.
- [5] E.S. Masunov, "Acceleration and Transverse Focusing of Ion Beams in Lineondutron." *Proc. of the 1993 Particle Accelerator Conference, Washington, D.C., May 1993, V.3*, pp.1681-1682.
- [6] E.S. Masunov, "Acceleration of Two Ion Beams in Undulator Linear Accelerator" *Proc. of the Fourth European Particle Accelerator Conference, London, June 1994, V.1*, pp.820-822.
- [7] E.S. Masunov, A.P. Novikov, "Space-Charge Compensation Effects under Acceleration of Oppositely Charged Ion Bunches in UNDULAC-E", *Proc. of the Fourth European Particle Accelerator Conference, London, June 1994, V.2*, pp.1171-1173.

LINAC INTEGRATED SCHEME USING RF ENERGY STORAGE AND COMPRESSION

A.V. Smirnov, Russian Research Center "Kurchatov Institute", Moscow, 123182, Russia

Proposed earlier the conception of a compact rf-linac without an external rf-energy source is analysed here numerically. Under certain conditions an unbunched low voltage electron beam can be accelerated during a short ns pulse by using of rf-energy stored in an external cavity for a relatively long time of self-excited oscillation induced by the same beam in the same special accelerating/oscillating linac structure. Non-steady acceleration is considered in terms of optimal time delays, energy gain and spectra.

I. INTRODUCTION

In the previous paper [1] we showed the feasibility of a low energy linac combining rf-generation and acceleration processes at the same injected beam energy. It is based on use of rf-compression technique developed for high energy linear colliders. Since the RF energy commutation may be one or two orders faster than the electric high voltage energy commutation (conventional modulator), combining the structure proposed and RF energy compression system can give high levels of the average beam power (10-100kW). The linac facility would have considerably reduced weight and sizes as compared to similar industrial linacs. The power supply required is in 40-120 kV range dc source, and an estimated overall wall plug efficiency is about a one percent.

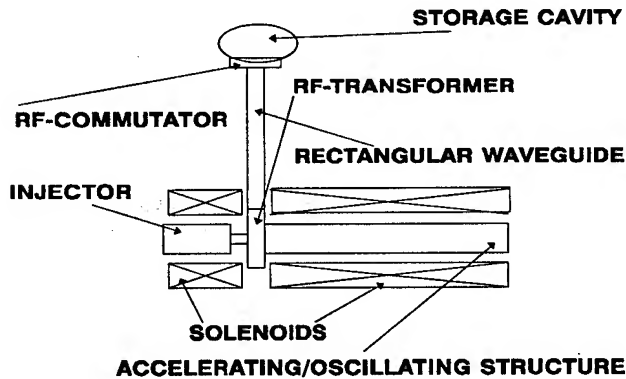


Figure 1. The integrated linac scheme for the case of the acceleration by the forward wave. The rf commutator contains an auxiliary modulator (it is not shown) to control the external Q_e of the storage cavity.

II. PRELIMINARY ASSUMPTIONS AND INPUT CONDITIONS

We are considering here only one of two integrated linac schemes [1]. It utilizes acceleration by the forward wave and oscillation of the backward wave. The schematic layout is shown in the Figure 1.

Concerning the processes of rf generation and compression discussed earlier [1-3], here we consider only more accurately the efficiency of energy transfer from the structure to cavity and back. It is advantageous to use a periodic regime when the cavity is not empty before energy storage. Apart from [4], we assume external rf energy source does not exist during the time interval for energy transfer from the cavity to the accelerating structure. For this case the storage efficiency can be calculated by imposing periodicity condition:

$$\eta_{st} = \frac{2\chi_g}{\mu(1+\chi_g)} \left[1 - \frac{1-e^{-\delta}}{1-e^{-(\mu+\delta)}} e^{-\mu} \right]^2, \quad (1)$$

where $\delta = \pi f_0(1+\chi_u)/Q_0$, $\mu = \pi t_f f_0(1+\chi_g)/Q_0$, t_g is the time duration of the RF power storage in the external cavity, f_0 is the operating frequency, t_f is the section filling time, χ_g is the coupling factor during the rf-energy generation and storage, and χ_u is the coupling factor during the time interval t_u , during that the stored energy is coupled out of the storage cavity with factor Q_0 . The maximum value of η_{st} approaches 1 instead of 0.815 and at the limit of $\chi_u \rightarrow \infty$ we obtain usual expression. It can be seen from (1), that the optimum value of μ is 0.9 (when $\delta=1.26$) instead of usual 1.262.

For a constant impedance structure and a storage cavity with two RF-ports the efficiency η_0 of energy transfer from the cavity to structure is calculated by P.B. Wilson [5]. For our case the corresponding efficiency is:

$$\eta_0 = 2\delta \frac{\chi_\mu}{1+\chi_\mu} \left(\frac{e^{-\delta} - e^{-\alpha L_3}}{\delta - \alpha L_3} \right)^2, \quad (2)$$

where α is the attenuation constant. For a constant gradient structure one can obtain:

$$\eta_0 = 2\delta \frac{\chi_u}{1+\chi_u} \frac{1-e^{-2\tau}}{2\tau} \left(\frac{1-e^{-\delta}}{\delta} \right)^2. \quad (3)$$

Here τ is the attenuation parameter, and to maximise η_0 we should provide $\delta \approx 1.26$.

Time-dependent calculations were undertaken to confirm and specify the analytical estimations (see the first column of the Table 2 in ref.[1]). The RF energy, entering into the section from the storage cavity, and the total charge of the input pulse train were 1.34 J and 83 nC respectively. A constant impedance subsection L_3 was assumed.

The modified code [6] used takes into account non-steady beam loading, accelerating wave propagation in the tapered section and longitudinal space charge effect. As an example we used the optimised DLWG section parameters presented in Fig. 2.

Accurate optimisation of these parameters depends on the current pulse and RF power pulse shapes as well as time delay t_d between them. To simulate real pulse shapes we have used non-ideal profiles for the incident RF pulse (see Fig. 3) and the input current pulse (see Fig. 4, curve 1).

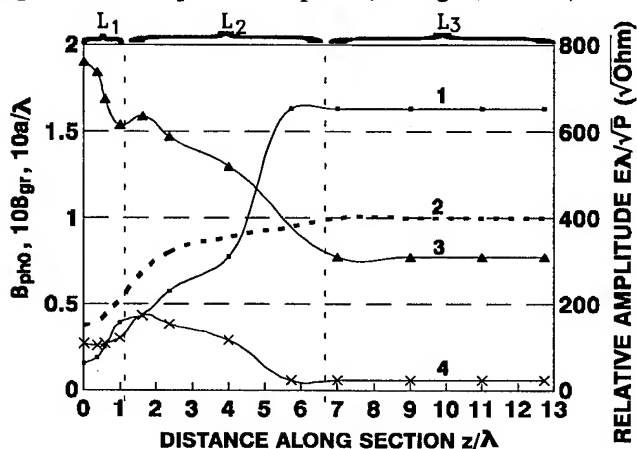


Figure 2. The parameters of the optimised DLWG tapered structure plotted along the section: relative accelerating field amplitude (curve 1), relative phase velocity for the fundamental harmonic β_{ph0} (curve 2), iris relative radius a/λ (curve 3) and relative group velocity (4)

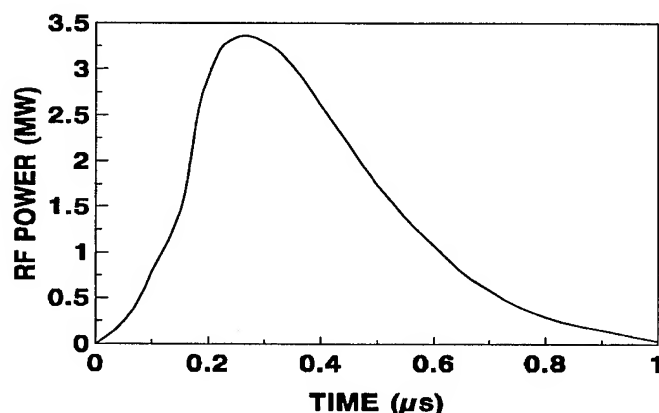


Figure 3. Input RF power pulse profile used in simulations. RF energy is equal to 1.34 J.

III. SIMULATION RESULTS

Under the conditions given above we have found geometrical and RF parameters for the linac section (see Fig. 2) that provide close to the maximum accelerated beam energy (see Fig. 4) and capture coefficient at optimal time delay $t_d \approx 0.6 \mu s$. Note, that the undesirable phase shifting cells were avoided at this optimisation.

It is seen from Fig. 5, that the beam capture is equal to its maximum at $t_d \approx 0.48 \mu s$ and the full width of the energy spectrum at half maximum (FWHM) is equal to the local minimum value with both time delays. Energy spectra calculated for the total accelerated pulse train at these values of time delay are presented in Figs. 6a,b.

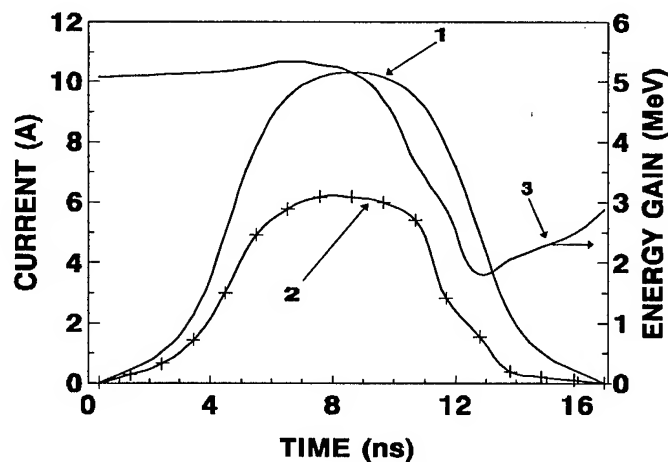


Figure 4. Input current pulse profile (curve 1) used in simulations. Injected pulse charge is equal to 83 nC. Output current pulse profile (curve 2) and energy gain versus time (curve 3) are calculated for the time delay $t_d = 0.58 \mu s$ and RF energy 1.34 J. Accelerated pulse charge is equal to 47 nC.

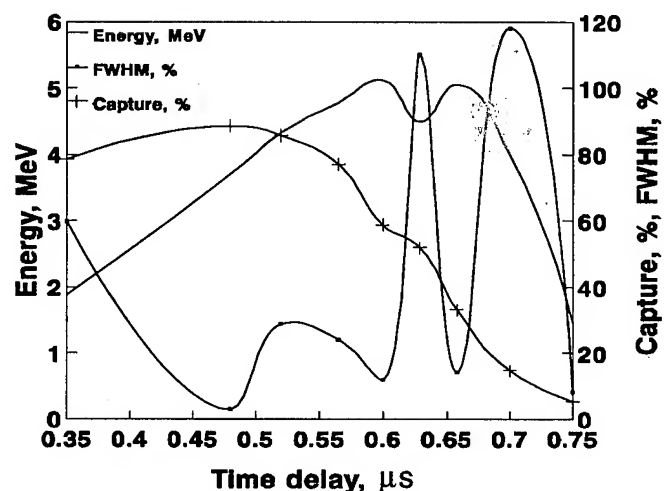


Figure 5. Beam capture coefficient, energy gain and energy spectrum FWHM for the accelerated pulse train as a function of the time delay between the injected current pulse and the RF pulse.

A non-steady beam loading effect is demonstrated in Fig. 4 (curves 2,3) for close to optimal parameters of the section and time delay. We see, that the energy averaged over the bunch is a non-monotonous function of the bunch number. It is caused by a combined effect of the sharp form of the incident RF-pulse and non-ideal injected current profile.

It was found in simulations [6], that the total energy spread is narrower for asymmetric input pulse current profile having long leading edge and short trailing edge if the section filling time and pulse length are comparable.

The simulations presented above imply pulsed injection from ns electron gun. However, it would be interesting to consider the case of continuous beam injection. Calculation results for the input dc $I=9$ A beam are presented in Fig. 7.

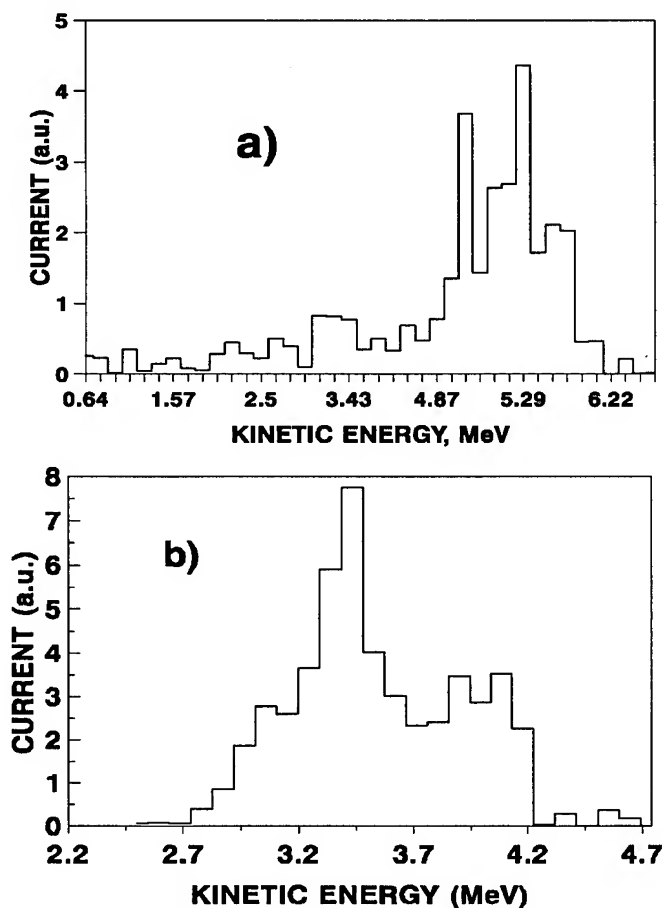


Figure 6. Energy spectra for the accelerated pulse train for two different time delays: $t_d = 0.6 \mu s$ (a) and $t_d = 0.5 \mu s$ (b).

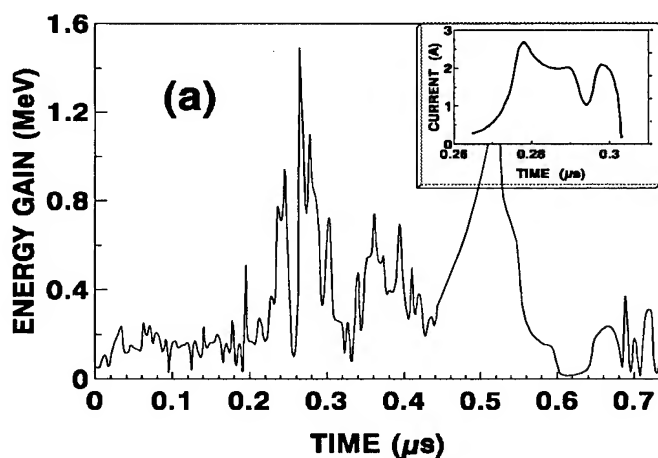


Figure 7.a. Electron beam energy gain and current versus time for RF energy 1.34 J. The inset shows the accelerated current pulse shape corresponding to the maximum energy. RF power pulse shape and duration are the same that depicted in Fig. 3.

The reason of low energy gain (see Fig. 7,a) is a competition between the processes of trapping into acceleration - on the one hand and oscillation (radiation) of the -1 and

fundamental space harmonics - on the other. In accordance with the simulation results Fig. 7,b it is necessary to treble the peak RF power (and, consequently, RF energy stored) to achieve the same peak energy gain.

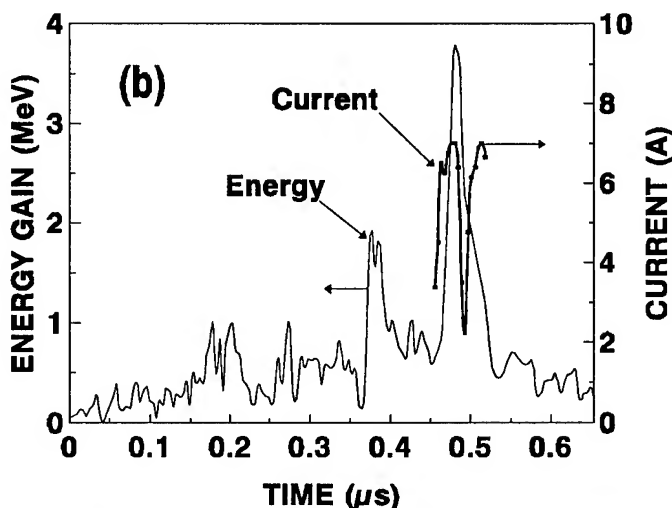


Figure 7.b. Electron beam energy gain and current versus time for RF energy 4 J. RF power pulse shape and duration are the same that depicted in Fig. 3.

IV. SUMMARY

The most effective performance requires the electron gun turning off during the structure filling in by rf-energy and optimization of the time delay between rf-switching and electron gun turning on. In this case analytical estimations are in agreement with simulation results.

V. REFERENCES

- [1] A.V. Smirnov, V.N. Smirnov. A Conceptual Design of a One-Section Linac Using RF-Energy Compression. Proc of the 4-th European Particle Accelerator Conf. EPAC-94, p. 774
- [2] A.V. Smirnov, V.N. Smirnov, Beam Self-Excited Oscillation in Linac Buncher Section. Nucl. Instrum. and Meth. A349 (1994) 614
- [3] A.V. Smirnov, V.N. Smirnov, K.E. Sokolov. An Operative Measurement of RF Parameters for Slow-Wave Systems, Proc. EPAC-94, V. 3, p. 1995.
- [4] Z.D. Farkas. RF Energy Compressor. IEEE MTT-S Int. Microwave Symposium Digest. New York, (1980) p.84-86
- [5] D.L. Bix, Z.D. Farkas, P.B. Wilson. A Look at Energy Compression as an Assist for High Power RF Production. AIP Conf. Proc. 153, Vol.2, New York, 1987.
- [6] A.V. Smirnov. Numerical Investigation of Non Steady Dynamics Effects of Intense Beam in Linac Transition Regime. Proc. of the 11-th All-Union Conf. on Charged Particles Accelerators. Proc. of the 11-th All-Union Conf. on Charged Particles Accelerators, (Dubna, JINR, USSR, 1989), Vol.1, 488

MAGNETIC FIELD INFLUENCE ON RF-STRUCTURES ELECTRODYNAMICS CHARACTERISTICS And SPARKING LIMIT.

A.Shalnov, N.Abramenko, B.Bogdanovich, M.Karetnikov, A.Nesterovich, M.Tubaev

Moscow state engineering-physics institute, MEPhI, Moscow, 115409, Russia

In linear accelerators the focusing magnetic field influence on phase and power spectra of beam, as a rule, is not taken into account, and the recommendations at the focusing system parameters choice are reduced to definition the magnetic field longitudinal components necessary for focusing [1]. However, use of such valuations at designing of focusing systems is frequently insufficient, as far as a number of work, containing experimental results, indicating the essential dependence of the accelerator RF-structure electrodynamics characteristics (EDC) on value and distribution form of the focusing magnetic field along accelerator axis is well known [2,3].

The conducted analysis has given the basis to consider, that this phenomena nature is connected with power absorption in resonant volumes by the RF-discharge in a residual gas. Therefore for definition of the magnetic field influence on accelerating structures EDC a prototyping technique was offered [4]. The given technique consists of researched processes modelling on a separate element of a periodic accelerating system and subsequent generalisation of results received at prototyping for more difficult accelerating structures cases with the elementary ratio help, determining the RF-discharge average parameters.

In this report the theoretical and experimental results of the high-vacuum RF-discharge plasma influence to accelerating structures EDC research are performed, as well as experimental research results of the single gap cylindrical cavity magnetic insulation (MI).

The characteristics measurement of the RF-discharge, arising in S-band cylindrical cavity, was performed at the experimental stand, created on basis single-gap cavity, excited at the lowest mode of electrical prick [4]. The magnitudes received during set-up of self frequency f_0 and quality Q_0 were equals $(2797,5 \pm 0,1)$ MHz and $(9,8 \pm 0,5) \cdot 10^3$, accordingly. The magnetic field in the cavity was created by special focusing solenoids of two types [4]. By work in a continuous mode the solenoids feed was executed from the current stabilised source. In a pulsing mode the power supply system start was executed from the previous pulse through the delay line.

During experimental work quality and frequency shift dependencies on the current in the focusing solenoids I and on power level entered the cavity for various solenoids inclusions (fig.1) were received. As it is visible from the figure, the increase only entered power in three times (in magnetic field absence) results in reduction cavity loaded quality Q_1 to $10 \div 12\%$ and frequency shift Δf_0 occurrence. Availability a magnetic field results in the further reduction Q_1 (up to $20 \div 22\%$) and increase Δf_0 (on 150 kHz). The heaviest change Q_1 and Δf_0 takes place in a range of currents I , appropriate the magnetic field induction value, at which resonant conditions

realisation in equations, of describing behaviour the RF-discharge in parallel and normal electrical magnetic field at frequency 3 GHz [5] is possible. It testifies to essential magnetic field influence for a cylindrical cavity EDC.

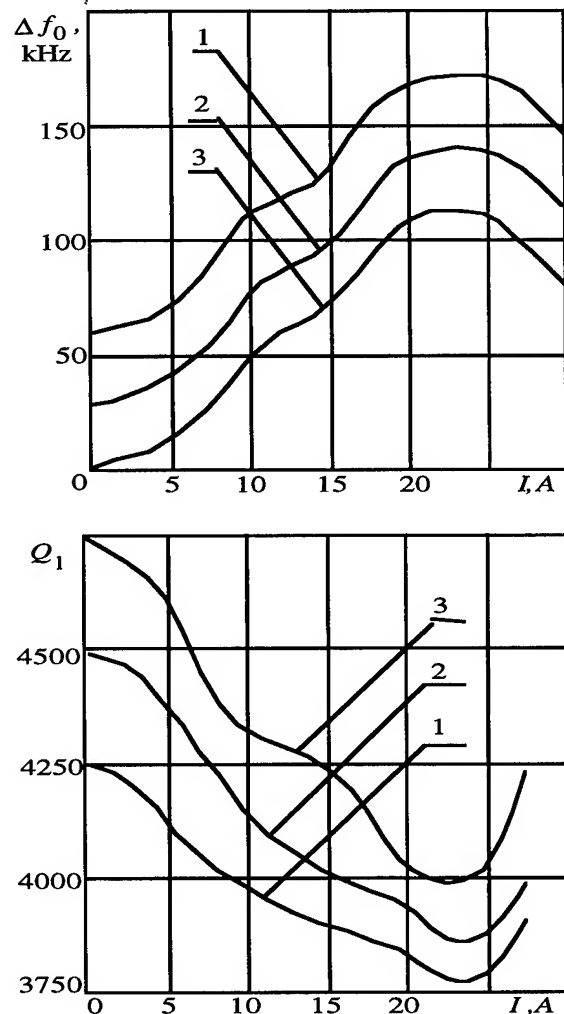


Fig. 1. The dependencies Δf_0 and Q_1 on the current I for various source power (1. $P_{in}=60$ kW, 2. $P_{in}=40$ kW, 3. $P_{in}=20$ kW).

Conducted researches have shown also, that the working pressure increase in accelerating structure results in decreasing of magnetic field influence on the RF-discharge development conditions. It is explained by that collisions number, tested of the RF-discharge plasma electrons during their movement, at low pressure it is not enough and their elimination from volume, engaged by a plasma, occurs preliminary at the

expense of them diffusion to walls with subsequent recombination.

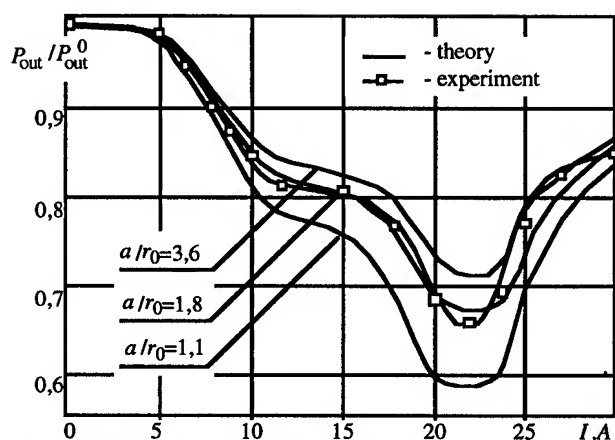


Fig. 2. Dependence of the P_{out}/P_{out}^0 ratio on the current I at the buncher output.

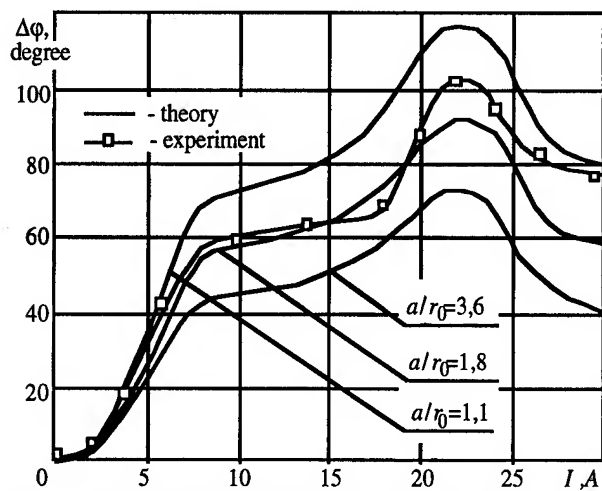


Fig. 3. Phase shift dependence on the current I at the buncher output.

The experimental research of the magnetic field influence for accelerating structure EDC as cylindrical iris loaded waveguide (IW) was conducted on installation, formed on linac buncher base [4]. Buncher represents IW with variable phase speed and frequency $f_0 = 2800$ MHz. As a result dependencies of the output buncher power P_{out}/P_{out}^0 for various current magnitudes in the focusing solenoids I (fig.2) were received. Here P_{out} - RF-power at a buncher output at a zero current in focusing solenoids. Theoretical curves were received by technique described above. Experimental data were obtained on model cavity, similar to cells of given IW. The account was conducted for various values of the output buncher power P_{out}^0 and the RF-discharge radius in waveguide a/r_0 , where a - aperture radius in waveguide iris. The similar experimental and theoretical dependencies were received for a phase shift in the buncher accelerated structure, stipulated by the RF-discharge plasma availability in it (fig.3).

Conducted researches of reflected power dependence on the value I in buncher proved a hypothesis about the RF-discharge arising in IW power absorption, as far as the maximum reflected power magnitude at change of a current in focusing solenoids did not exceed 5% from the output power level, and the qualitative character of received dependencies was close to submitted in fig.2,3 curves. Transients study, arising at RF-discharge formation in IW has shown, that the time, during which RF-discharge will be formed in waveguide, does not exceed $0.3+0.4$ μ s. Hence, the experimental results submitted in fig.2,3 are received in conditions completely created plasma.

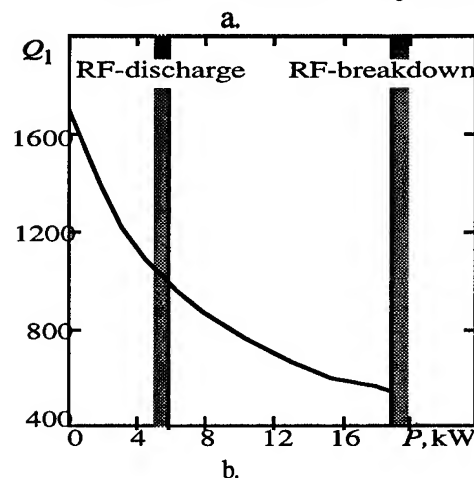
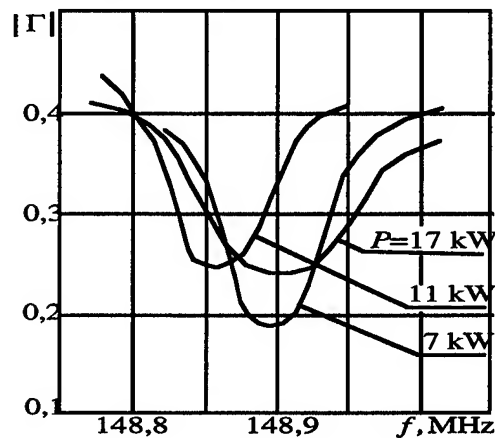


Fig. 4. Frequency and quality Q_1 dependencies for various source power magnitudes.

To research RF-discharge influence on L-band accelerating structures EDC a series of experiments was conducted on the double-gap cavity with drift tube, installed on quarter wave vibrator. Experimental dependencies of reflection coefficient Γ on frequency for various magnitudes of RF-powers are shown in fig.4,a. The given dependencies feature is various resonance curve size that shows a cavity loaded quality value decrease with an arriving in a cavity power increase (fig.4,b).

The following part of experimental researches was devoted the electrons MI issuing in the artificial created autoemission centres area. As measurement object the described above S-band cylindrical capacity was chosen. The determination of

the magnetic field amplitude, created in the cavity by special two types solenoids, and optimum time of RF-pulse delay concerning the modulator pulse was executed with the help of a calibrated induction gauge [4].

The first series of experiments on RF-fields limiting amplitude dependence research from magnetic field induction in the cavity was conducted with solenoids, working in continuous mode. At achievement of power level, as it is visible from fig.5, order $0,3 \cdot P_0$ (where P_0 - the RF-power limiting value at magnetic field absence) was observed RF-pulse breakage. Thus, the pulse envelope form in input waveguide and pressure in a system did not change. The average current density in the winding j_s varied within the limits of 10^6 A/m². The received RF-discharge area top border dependence on the magnetic field induction permits to assume, that the pulse breakage occurrence gear is connected to RF-fluctuations excitation at the electron cyclotron resonance (ECR) frequency. At achievement of some RF-power limiting significance the pulseform in the capacity was strongly deformed, and the pressure in a system was increased at the order. The reduction of the RF-power maximum value entered without capacity breakdown was observed as at counter, as at agree solenoids inclusion in accordance with the power supply current increase (fig.5). As ECR arises under condition of $f = \gamma B/mc$, where γ - the relativistic factor, for exit from the resonance band the magnetic induction B increasing is required.

As far as the limiting current value in focusing solenoids by work in a continuous mode was limited their essential heating and made 10 A, the second series of experiments was conducted with solenoids, working in pulse regime. We shall note also, that after the cavity training the maximum power level P_0 was increased up to 100 kW at a duration pulse 2,5 μ s and the repetition frequency 1 Hz. During measurement the RF-power limiting value reduction P_{br} was marked at the average current density in the solenoids up to 10^8 A/m². However, for higher current density the value P_{br} was sharply increased up to a level $(1,7+2,0) \cdot P_0$ (fig.5), that it is possible to interpret as transition from a regime of power absorption by the RF-discharge to the regime of MI (continuous line in fig. 5). At agree solenoids inclusion or connection only one solenoids took place essential (in 3+4 times) reduction of P_{br} in comparison with P_0 in all significance j_s changes range (a dashed line in fig.5).

The cavity internal surface research after a series of experiments has shown, that cylindrical surface heaviest degradation was subjected. It can be explained by electrons bombardment, driven along magnetic field force lines, normal to a cylindrical surface. The similar character and arrangement of emitted from the cathode electrons flow bombardment traces was marked in [6].

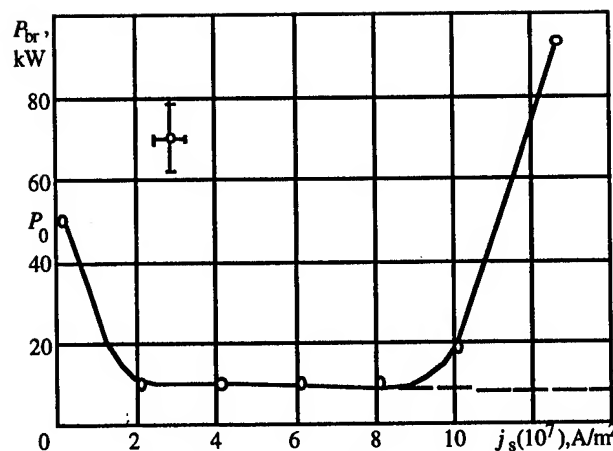


Fig. 5. The dependence P_{br} on the current density.

Thus, the conducted researches have shown, that conventional theoretical account models use in the assumption of ideal vacuum at devices designing with the RF-discharge is not always reasonable from the reliability point of view. The experimental results comparison with calculating has confirmed serviceability by the developed authors technique of the modelling processes, occurring in accelerating structures filled by RF-discharge plasma [4]. The conducted researches, besides have confirmed a opportunity of essential accelerating structures with MI sharking limit increase, in particular, cylindrical cavity. At the expense of focusing solenoids counter inclusion the magnetic field in such structures has cusp configuration, and at this fields sufficient intensity effective MI of emission electrons occur. However, for positive effect reception from MI use it is necessary to exclude the power absorption conditions by the RF-discharge in a residual gas, in particular, to leave a occurrence ECR band.

REFERENCES

- [1] Vlasov A. Teoriya lineinyh uskoritely. M.: Atomizdat, 1965.
- [2] Seleznev V., Sushinin U. // Uskoritely. M.: Atomizdat, 1976, V.15, P.20+24.
- [3] Solomahin V., Sushinin U. // Uskoritely. M.: Atomizdat, 1981, V.20, P.65+69.
- [4] Bogdanovich B., Nesterovich A., Tubaev M. Vliyanie plazmy VCh-razryada na elektrodinamicheskie karakteristiki uskoryayushih struktur i byhodnye parametry puchka. M.: Pre-print / MIPhI, 1993.
- [5] Mac-Donald A. SVCh probai v gasoh. M.:Mir, 1969.
- [6] Karetnikov M., Nesterovich A., Shalnov A. Magnitnaya isolyazhiya fokusiruyuschimy polyamy v lineinyh uskoritelyah ionov. M.: Pre-print / MIPhI, 1990.

CALCULATIONS ON THE POSSIBILITY OF THE SIMULTANEOUS ACCELERATION OF IONS WITH DIFFERENT CHARGE STATES IN A RFQ*

H. Deitinghoff, Institut für Angewandte Physik der J. W. Goethe-Universität, Robert-Maier-Str. 2-4, D-60054 Frankfurt am Main, FRG

Direct injection into a RFQ without mass or charge separation is discussed especially in those cases, where a larger number of accelerated ions or higher beam currents are required. Assuming an electrostatic ion-source extraction system and an Ein-zellens e. g. for focusing the beam into the RFQ, all charge states are offered but with different input energies corresponding to their charge to mass ratio. Particle dynamics calculations show, that ions with higher charge states than the design value are accelerated to the final energy with good beam quality whereas ions with lower charge states are only partly accelerated, partly drifting or are lost. Results of calculations three different cases will be presented and discussed for different ion species.

I. INTRODUCTION

A Radio Frequency Quadrupole (RFQ) accelerator [1,2] is mainly used for the capture, focusing and preacceleration of light as well as heavy ion beams directly behind the ion source the ion energies ranging from some 10 keV at the input up to MeV at the RFQ output. It covers the critical region of very low ion velocities, where the necessary focusing especially in the case of high currents can only be provided with great difficulties in conventional structures. A RFQ is a linear accelerator structure with four quadrupole electrodes, in which an axial field is created by the geometrical modulation of these electrodes. The electrical quadrupole focusing is independent of the ion velocity, which leads to a wide range of masses and energies being stably transported. But for an accelerator the design for a fixed velocity profile is typical, leading to fixed input and output energies per nucleon. Once the electrodes are machined, this profile is fixed and can be changed only by an exchange of the structure or by changing the resonant frequency, the latter is used in VE-RFQ accelerators [3].

In a fixed velocity profile structure all ions can be accelerated with identical particle dynamics for which the product of the charge-to-mass Z/A times the electrode voltage V can be kept constant. Limitations on the highest applicable electrode voltage V_{\max} are imposed by Kilpatrick's criterion for sparking. If V_{\max} is fixed, the particle dynamics layout is made for the lowest charge-to-mass ratio (highest voltage required), for all higher values of Z/A the voltage is reduced correspondingly. For stable acceleration of the ions the particle velocity and phase velocity of the accelerating field component must be always adapted to each other, for a synchronous particle with a phase φ ,

relatively to the rf field the energy gain per cell is proportional to $Z/A \cdot V \cdot \cos \varphi$, with φ between 0° and -90° .

When Z/A is now changed for a fixed electrode voltage, the energy gain changes correspondingly. This can be compensated by shifting the particles to another synchronous phase but is limited by the range of φ for stable particle motion. Higher values of Z/A are preferred, for lower ones the energy gain soon becomes too small and the fall out of the fixed velocity profile for acceleration. In the following results of calculations for different cases are presented and discussed.

II. BEAM DYNAMICS CALCULATIONS

a) Singly charged heavy ions

In Heavy Ion Inertial Fusion (HIIF) projects high currents of single charged very heavy ions are considered for acceleration in a driver linac for a pellet ignition facility [4]. The linac starts with a set of ion sources, RFQs and RF linacs, the beams are successively funneled and finally accelerated in a common main linac [5]. To overcome space charge limitations in the driver, Koshkarev [6] proposed to use ions with many isotopes for simultaneous acceleration in the main linac, but being separately accelerated in the beginning. Using negative and positive ions the final merging of the beams would lead to neutralization of the final beam in the target chamber. The first concept deals with a separate acceleration of each isotope and charge state in an RFQ, which demands for a separation line between source and RFQ. Therefore calculations have been performed for the case, that all different masses are injected into the same RFQ. One ion proposed is Te (A : 130,128,126, 125,124,123,122,120), which is similar in A/Z to an existing data set for an heavy ion prototype RFQ for U^{2+} [7,8] which accelerates ions from 2.2 to 17.6 keV/u. This data set - not optimized for Te - was used for the calculations. Using mass 130 as design value, all lighter isotopes have an higher input energy per nucleon than the design value and a higher charge-to-mass ratio too. Due to this the lighter masses change the synchronous phase and the energy spread increases in comparison to the design mass. This is illustrated in Fig. 1, where the output emittances for mass 130 and mass 122 are plotted, if separately accelerated at the design voltage for mass 130. The transverse emittance growth increases from 20% for 130 to 50% for 120, the longitudinal rms emittance by a factor of 6. For mass 122 the transmission is still 81%

* Work supported by BMFT, contract 06OF359

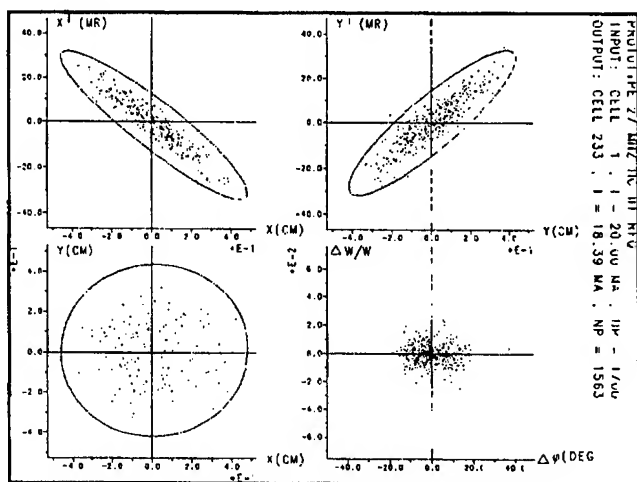


Fig. 1a) Output emittances for design mass 130

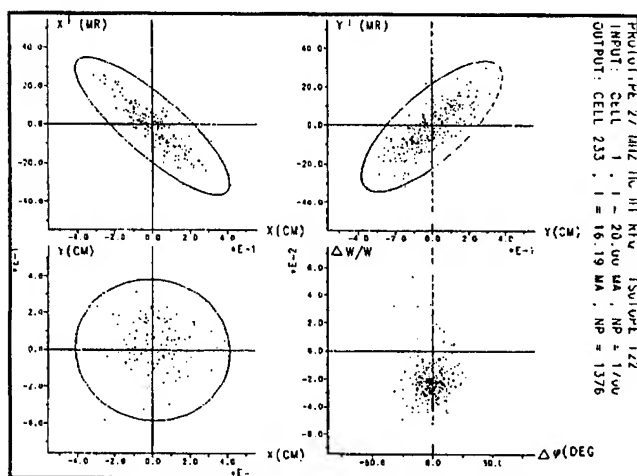


Fig. 1 b) Output emittances for isotope 122, calculated with the voltages for mass 130

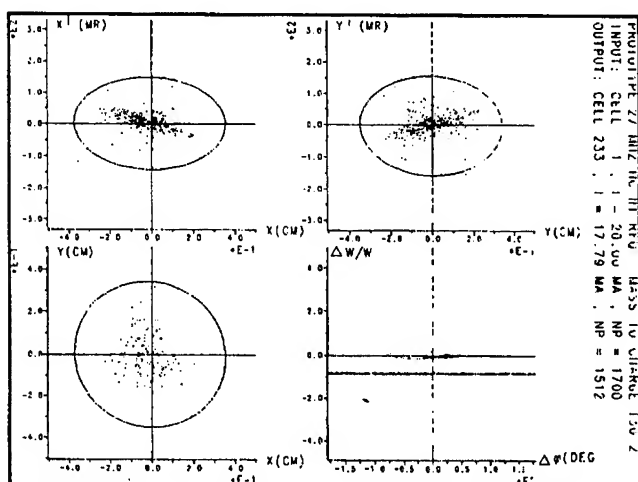


Fig. 2: Output emittances for charge state 2, mass 130 calculated for the voltages for charge state 1

compared to 92% for the design mass. When the three main isotopes 130, 128 and 126 are taken - calculations could be made only for equal parts of them, which is not quite correct - the total transverse emittance growth is 30%, the longitudinal emittance is 3 times larger than for mass 130 alone. The overall transmission is rather high with 88%. It still must be checked, if the large emittances can be tolerated for the following linac structures of the chain, especially funneling may not work in this case properly.

If the ion source also generates ions with charge state 2, which are directly injected, the output emittances will be spoiled. The ions with $A/Z = 65$ have a too high input energy per nucleon and are drifting through the RFQ, well focused and with good transmission. Fig. 2 shows the output emittances, the longitudinal emittances showing a high energy and phase spread. Drifting of ions through a RFQ is well known from measurements and can be reproduced in calculations too with good accuracy [9,10].

b) Highly charged heavy ions

The new high charge state injector of GSI [11] now in routine operation is an example, where highly charged heavy ions are extracted from an ion source, e.g. an ECR source and accelerated by an RFQ to an energy as high as 300 keV/u. The ion source generates a charge spectrum ranging over several charge states. Normally by a separation line one charge state is singled out and injected. For very high charge states it could be desirable to accelerate several charge states simultaneously to increase the number of particles. Here again the RFQ is designed for a fixed charge to mass ratio, ions with higher or lower charge states than the design value must be treated separately. For a higher charge state the results of beam dynamics calculations are identical with those for the lower mass isotopes in chapter a): The input energy again is higher and the ions change to another synchronous phase to compensate the higher energy gain. The output longitudinal output emittances are shifted in phase and show a higher energy spread than for the design ion, but stable acceleration takes place with high transmission. For lower charge states the input energy is too low and the energy gain too, which leads to losses from particles out of the bunches. Finally the particles are widely spread in energy and phase. This behaviour is demonstrated in figs. 3-5. In fig. 3 output emittances and distributions are shown for the design charge 28 and mass 238, in fig. 4 for charge 29 and in fig. 5 for charge 27. For all cases the same transverse input emittances were assumed.

c) Light ions

RFQs are also proposed for the use in high-energy current ion implantation for singly charged N or O ions [12]. The mass-to-charge ratio of 7 or 8 resp. is nearly the same as for the high charge state implanters. When looking to the results we can immediately see, that in an implanter RFQ for Oxygen N^+ ions can be captured and accelerated to the same final energy per nucleon. In an implanter designed for

Nitrogen O^+ ions can be captured too but are only drifting to the end. This is also true for any impurity ions which can have a rather large spectrum of charge-to-mass ratios.

III. REFERENCES

- [1] I.M.Kapchinsky, V.Teplyakov, Prib.Tek.Eksp. 119, No.2 (1970),17
- [2] K.R.Crandall, R.H.Stokes, T.P.Wangler, LINAC79, BNL 51134 (1979), 205
- [3] A. Schempp, NIM B 40/41 (1989), 937
- [4] C. Rubbia, Il nuovo cimento 106A,11 (1993),1
- [5] HIBALL II KFK-Report 3840 (1985)

- [6] D.G. Koshkarev, Il nuovo cimento 106A,11 (1993) 1567
- [7] A. Kipper et al., ibidem, 1525
- [8] H. Deitinghoff et al., ibidem, 1503
- [9] J. Dehen, Thesis, University of Frankfurt (1994)
- [10] J. Staples et al., Conf. on High Energy Accelerators, Batavia 1983
- [11] N. Angert et. al., EPAC90, Ed. Frontieres, (1990) 550
- [12] R. Thomae et. al., Ion Implantation Technology-92, Elsevier (1993), 389

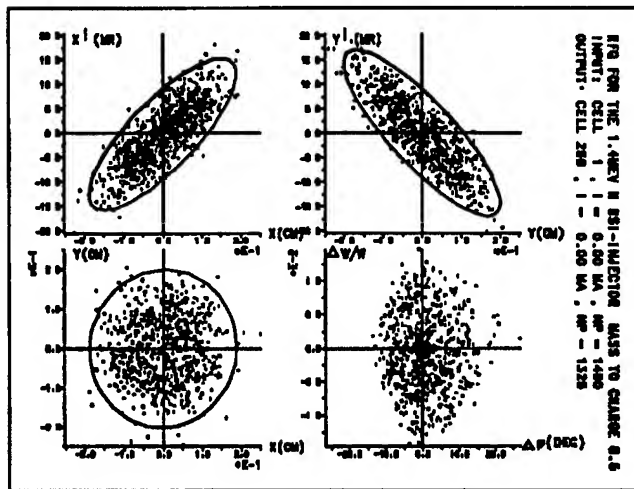


Fig. 3 a) Output emittances for design value of $Z/A = 8.5$

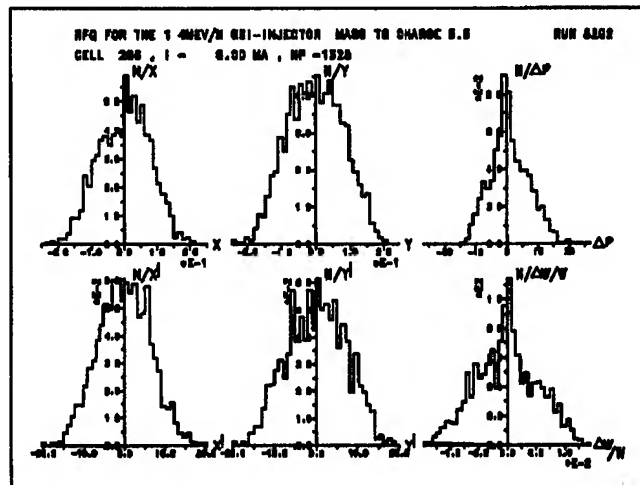


Fig.3 b) Output distributions for $Z/A = 8.5$

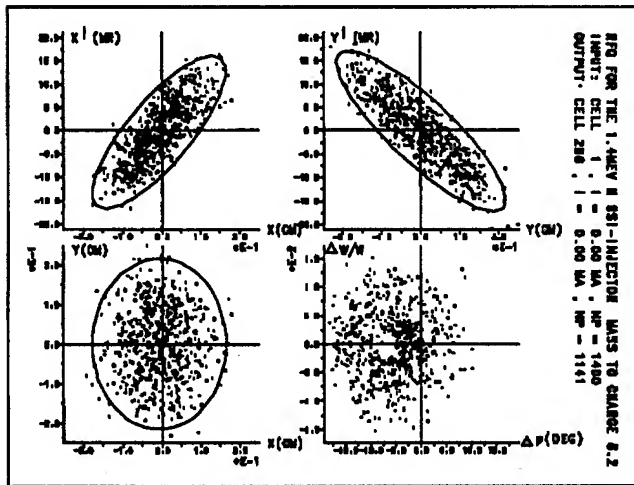


Fig. 4 Charge state 29, mass 238

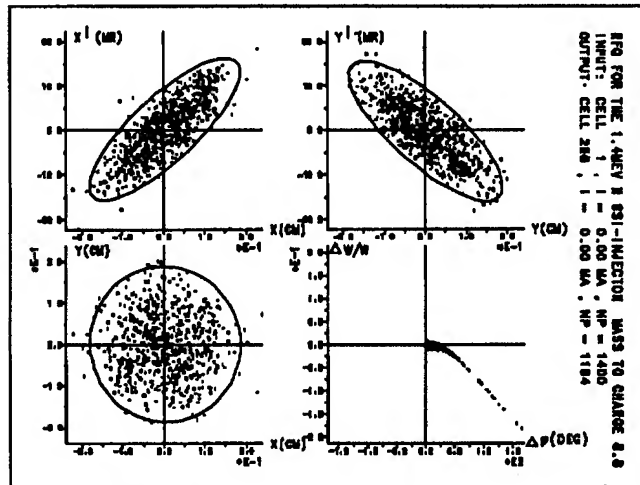


Fig. 5 Charge state 27, mass 238

PHASE-SCAN ANALYSIS RESULTS FOR THE FIRST DRIFT TUBE LINAC MODULE IN THE GROUND TEST ACCELERATOR: DATA REPRODUCIBILITY AND COMPARISON TO SIMULATIONS*

K. F. Johnson, O.R. Sander, G.O. Bolme, S. Bowling, R. Connolly,[†] J.D. Gilpatrick, W.P. Lysenko, J. Power, E.A. Wadlinger, and V. Yuan, Los Alamos National Laboratory, Los Alamos, NM 87545 USA

The Ground Test Accelerator (GTA) had the objective of producing a high-brightness, high-current H^- beam. The major accelerator components were a 35 keV injector, a Radio Frequency Quadrupole, an intertank matching section, and a drift tube linac (DTL), consisting of 10 modules. This paper discusses the phase-scan technique which was used to experimentally determine the rf operating parameters for the commissioning and routine operation of the first DTL module.

I. INTRODUCTION

The objective of phase-scans is to experimentally find, with beam, the rf operating parameters for an accelerator cavity (e.g. drift tube linac (DTL) modules or buncher cavities). The operating parameters to be determined are the relative rf cavity (or input beam) phase and the rf gap voltage (or cavity power) in the cavity. The rf phase and gap voltage can be obtained from measurements of the output beam longitudinal centroids (i.e. energy and phase) and their comparison to theoretical expectations (i.e. simulations)[1,2,3]. Because phase-scan measurements are intended to be made routinely in the turn on of an accelerator (e.g. GTA), it was important to establish the reproducibility of such measurements. The experimental results and comparisons to simulations are presented here.

II. MEASUREMENT

The phase-scan technique was utilized in the two commissioning beam periods of the first GTA DTL module (DTL-1). A microstrip beam probe system was used to measure the beam's longitudinal centroids [4,5] as a function of the DTL-1 gap voltage and cavity phase. The output beam phase was acquired by measuring the signal phase difference between a rf cavity-field probe signal and the signal from a microstrip probe downstream of the cavity. The beam energy was obtained by measuring the phase difference between the signals of two microstrip probes located downstream of the cavity and separated by a

known distance. The phase difference was converted to a time-of-flight (TOF) from which the beam energy was calculated. A comparison of the measured beam phase and energy dependence on the gap voltage and cavity phase to the expected theoretical dependence provides the signature for the determining the cavity's operating set points.

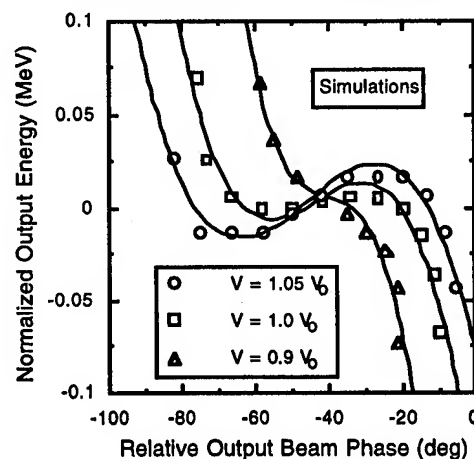


Figure 1: Single-particle simulations of the normalized output beam energy as a function of the relative output beam phase for three DTL-1 gap voltages (V_0 is the design gap voltage). The curves are meant to guide the eye.

II. SIMULATIONS

Single-particle simulations using PARMILA provide the shape signature for determining the gap voltage (cavity power) set point. In this procedure, it is assumed that beam centroids are unaffected by space-charge and that the longitudinal centroid behavior can be predicted by single-particle simulations. Both assumptions are reasonable if the particles in the bunch experience forces that depend on the magnitude of their displacement from the synchronous particle. Figure 1 shows such single-particle simulations for three rf fields corresponding to 1.05, 1.00, and 0.90 times the design gap voltage V_0 . The vertical axis is the normalized output beam energy (actual minus the design energy) and the horizontal axis is the relative input beam phase. The plotted points for each rf field correspond to a different input cavity phase. For a given cavity field, the input phase set point occurs at the zero normalized energy. As the cavity field increases the simulations exhibit a

*Work supported and funded by the US Department of Defense, Army Strategic Defense Command, under the auspices of the US Department of Energy.

[†]Industrial partner, Grumman Corporate Research Center

counterclockwise rotation. All simulations assume the DTL-1 design input energy of 2.50 MeV.

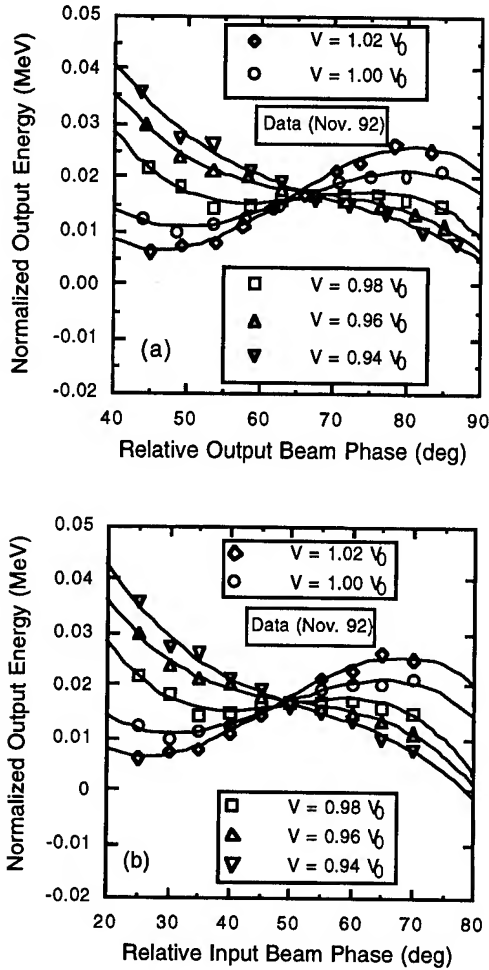


Figure 2: Measured normalized output beam energy as a function of the (a) output and (b) input beam phase. Data are from Nov. 1992 and were obtained for five DTL gap voltages (V_0 is the design gap voltage). The curves are meant to guide the eye.

IV. EXPERIMENTAL RESULTS

Figure 2 shows the measured phase-scan data from the Nov. 1992 commissioning beam period. The data were obtained using an automated phase-scan code which, for a fixed cavity field, systematically varied the rf input phase in uniform steps of 5 degrees, starting from an initial phase of -120 degrees. Scans were made for five rf amplitudes corresponding to gap voltages that were 0.94, 0.96, 0.98, 1.00, and 1.02 times V_0 . Figure 2a (2b) shows the normalized output energy dependence on the relative output (input) beam phase. The solid curves are meant to guide the eye. The data and simulations show the same

counterclockwise rotation as the DTL gap voltage increases.

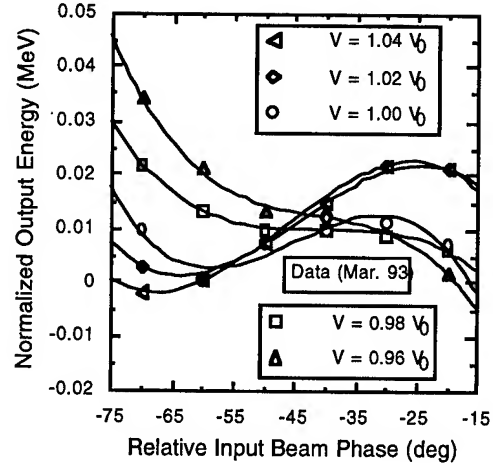


Figure 3: Measured normalized output beam energy as a function of the relative input beam phase. Data are from Mar. 1993 and were obtained for five DTL-1 gap voltages (V_0 is the design gap voltage). The curves are meant to guide the eye.

The measured phase-scan data from the Mar. 1993 commissioning beam period are shown in Figure 3. Because the automated phase scan code was unavailable, phase-scans were made manually (i.e. the rf input phase was varied manually and the output energy was recorded). In this mode the output phase was not determined. To reduce measurement time, the input phase was varied in 10 deg steps rather than the 5 deg used in Nov. 1992. These data show the counterclockwise rotation for decreasing DTL gap voltage as did the simulations and earlier data.

To compare the Nov. 1992 and Mar. 1993 data sets to each other and to simulations, the slopes of the central linear portions of the phase-scans were determined. This was done using the input or output beam phase as the independent variable in the phase-scans plots. The slopes were used to specify the orientation of each scan in the output energy and phase plane. By comparing the change in slopes with respect to changes in gap voltage, the phase-scan counterclockwise rotation was quantified and comparisons were made between data sets and simulations.

The choice of points to be included in the linear region is somewhat arbitrary. In this case the choice was guided by considerations of the Mar. 1993 data and to the sensitivity of the slopes on the input phase range $\Delta\phi_{in}$ or output phase range $\Delta\phi_{out}$. This led [6] to an interval of $\Delta\phi_{in} = 30$ deg or $\Delta\phi_{out} \approx 25$ deg being chosen. Since the output beam phase was not determined for the Mar. 1993 beam period, a full comparison of all data and simulations was only possible for phase-scans using the input beam phase as

the independent variable (see Figs. 2b and 3). The results are shown in Fig. 4 where the consistency between data and the agreement to simulations is good. A similar comparison between the Nov. 1992 data and simulations using phase-scans with $\Delta\phi_{\text{out}} \approx 25$ deg was equally good.

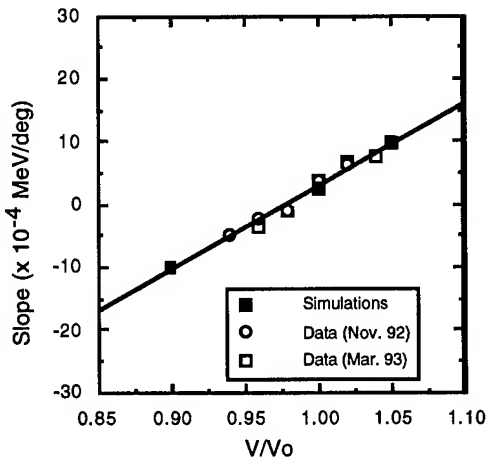


Figure 4: Comparison of the slopes of the linear regions of the DTL-1 phase-scans for all data and simulations. A consistent comparison of data sets resulted in a choice of $\Delta\phi_{\text{in}} = 30$ deg. The line is a linear fit to the simulations.

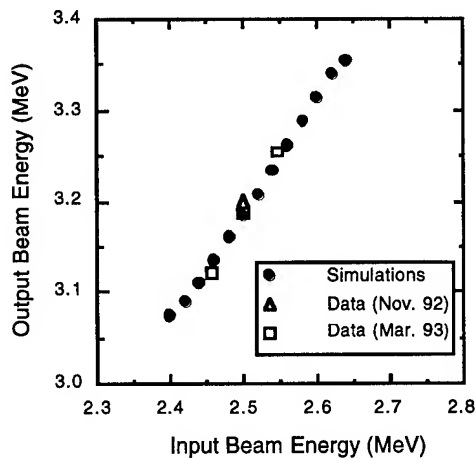


Figure 5: The DTL-1 output beam energy as a function of the input beam energy (data and simulations). There was only one point from the Nov. 92 data set because the input energy was not varied. The DTL was set at its design field (i.e. $V/V_0 = 1$).

In the above discussion, the DTL-1 input energy was fixed at its design value of 2.50 MeV. In the Mar. 1993 beam period a complementary set of measurements were made where the input beam phase was held fixed (at its experimentally determined set point of ≈ -45 deg) and the input energy was varied. This was accomplished by

changing the phase of a downstream buncher cavity in the Intertank Matching Section (IMS) [7]. Only limited energy variations were allowed by this technique (i.e. 2.50 ± 0.046 MeV). The dependence of the measured DTL output energy on input energy and a comparison to simulations is given in Figure 5. The agreement between measurement and expectations is good.

Determination of the of the operating DTL gap voltage was obtained by a comparison of the measured shapes in Figs. 2 and 3 to the expected shapes in Fig. 1. With this criteria the experimental $V/V_0 = 1$ setting agreed with simulations to within 1%. This was independently verified by measuring the energy spectrum of the x-rays generated within the DTL cavity in the absence of beam [8,9].

V. SUMMARY

The phase-scan measurements from the two DTL-1 commissioning beam periods were very reproducible. This was independent of the mode in which the phase-scans were made (automated or manual). The data were in good agreement with single-particle simulations.

VI. REFERENCES

- [1] C.M. Fortgang, et al., 1988 Linear Accel. Conf., Williamsburg, VA (October 1988), Continuous Electron Beam Accelerator Facility CEBAF-Report-89-001 (June 1989), p. 167
- [2] K.F. Johnson, et al., Proc. 1991 IEEE Particle Accel. Conf., San Francisco, CA (May 1991), p. 301
- [3] J.D. Gilpatrick, et al., 1988 Linear Accel. Conf., Williamsburg, VA (October 1988), Continuous Electron Beam Accelerator Facility CEBAF-Report-89-001 (June 1989), p. 134
- [4] J.D. Gilpatrick, et al., Proc. 1991 IEEE Particle Accel. Conf., San Francisco, CA (May 1991), p. 1136
- [5] J.D. Gilpatrick, et al., Beam Instrumentation Workshop, Santa Fe, NM (Oct. 1993), AIP Conference Proceedings 319 (1994), p. 154
- [6] K.F. Johnson, Los Alamos National Laboratory internal document: AOT-10 Technical Note: 94-04 (1994)
- [7] K. F. Johnson, et al., Proc. of the 1992 Linear Accel. Conf., Ottawa, Canada, AECL Research report AECL-10728 (December 1992), p. 61
- [8] G.O. Bolme, et al., Proc. of the 1990 Linear Accel. Conf., Los Alamos National Laboratory report LA-12004-C (March 1991), p. 219
- [9] K. F. Johnson, et al., Proc. 1993 IEEE Particle Accel. Conf., Washington, DC. (May 1993), p. 1669

ACCELERATOR SYSTEMS OPTIMIZING CODE[†]

C. C. Paulson, A. M. M. Todd, M. A. Peacock, M. F. Reusch, D. Bruhwiler,
S. L. Mendelsohn, D. Berwald, C. Piaszczyk, and T. Meyers;
Northrop Grumman Advanced Technology and Development Center,
4 Independence Way, Princeton, New Jersey 08540-6620, USA.

G. H. Gillespie, and B. W. Hill; G.H. Gillespie Associates, Inc. PO Box 2961, Del Mar Ca. 92014

R. A. Jameson; Los Alamos National Laboratory; PO Box 1663, Los Alamos, N.M. 87545

Abstract. Many accelerator applications need a flexible, rapid, and accurate systems analysis tool capable of performing beamline and subsystem plant optimizations. This paper describes a systems code that has been developed to model ion accelerator systems and perform design evaluation and system level trade studies. The code uses a series of FORTRAN modules incorporated into a graphical user interface (GUI) that constructs the accelerator in a window on a computer screen. The studies provide overall systems level performance and subsystem requirements within the context of a fully integrated device. The code allows for system optimization based on global system parameters, individual element parameters, cost, footprint, or other design constraints. The code has been applied to possible Accelerator Production of Tritium (APT) and Fusion Materials Irradiation Facility (FMIF) design concepts. Algorithms used, flow charts showing the code logic, and examples of code applications will be given.

I. INTRODUCTION

System complexity, coupled with the large capital and operating costs of the Accelerator Driven Transmutation Technology (ADTT) accelerator facilities, makes optimization with respect to life cycle, reliability and maintainability, and capital cost essential. This paper describes a systems code the authors have been developing to model ion accelerator systems for design evaluation and for system level trade studies. The code uses a series of FORTRAN modules incorporated into a graphical user interface (GUI) to provide for the "construction" of the accelerator in a window on the computer screen. Three sets of input information, global parameters, element parameters, and user preferences are utilized by the code. Relevant accelerator, beam transport models, and engineering models from earlier systems codes and other work have been adapted and developed within this framework. Separate accelerator and engineering routines are provided for each accelerator element. Each accelerating module has been provided with the capability of generating complete tank and cell designs based on a set of pre-selected geometrical and / or engineering parameters. In addition to tracking the beam and generating / evaluating the physics design, the code provides a complete set of engineering parameters and preliminary costing for the construction of the accelerator. The paper presents the algorithms used and the

results obtained for the Los Alamos APT design.

Due to its elegance and ease of use, the Accelerator Systems Model (ASM)¹ initially developed by G. H. Gillespie Associates (GHGA) was chosen to provide the framework for the code. Section 2 discusses the overall structure of the ASM code, and briefly describes a few Grumman component models presently available within the framework. Section 3 illustrates the application of these models to the Los Alamos APT design. Finally, in section 4, we present our conclusions and future plans.

II. ACCELERATOR MODEL SUMMARY

The goals set for the code were: to provide a comprehensive tool for design and analysis of accelerator systems; to treat the engineering requirements of accelerator design on a basis comparable to the beam physics; to develop a basis for the bridging of different levels of accelerator modeling (CAD, analytic, envelope, particles); to reduce the time required for component / system trade studies; shorten training time for new engineers and scientists; and be accessible to non-specialists. The code has capitalized extensively on existing software. Prior ASM focus has been on accelerator and beam transport physics models, and the GUI I/O (Input/Output) structure. Simultaneously, a Grumman systems code, ABSOC² (Accelerator Based Systems Optimization Code), had evolved to feature fairly complex engineering models of the beamline systems with less emphasis on beamline physics models. The first step was therefore to incorporate the best of the ABSOC engineering and certain useful physics models within ASM. Thereafter, we began the development of those new models required to complete the beamline systems evaluation. A modular approach has been used for the code with each major component described by a group of FORTRAN subroutines. The subroutines are called iteratively, based on the sequence of components set up by the user on, and controlled by, the GUI side of the code. A common I/O structure is maintained for the modules allowing complete interchangeability. Critical physics and engineering parameters are assigned to vectors which are tracked and

[†] This work is supported by the Northrop Grumman Corp., Los Alamos National Laboratory (DOE contract W-7405-Eng-36), and G.H. Gillespie Associates (LANL contract 9119K0014-9Q).

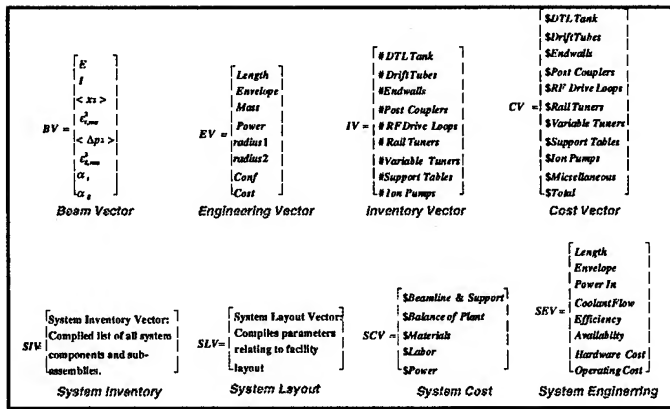


Figure 1: ASM Vectors

updated from element to element. Figure 1 shows a sampling of these vectors. Within each element, the beam is represented by two vectors, the Beam Vector {BV} and the Engineering Vector {EV} which represent the state of the beam and accelerator at that point. Each module generates a BV and an EV as its primary output. In the Beam Vector: E is the beam energy; I, the current; $\langle x^2 \rangle$, the rms transverse size; $\langle \Delta p^2 \rangle$, the square of the momentum dispersion; and α and ϵ , the Twiss alpha and beam emittance. In the Engineering Vector: L is the device length; V, the device volume; M, the device mass; P, the device power; x and y, the device maximum horizontal and vertical dimension; Conf, a confidence factor for the device as modeled; and Cost, an estimate for the device cost. Internally within the accelerator component models, the design is based on a cell by cell determination of the device. The cell and tank parameters thus calculated are read to off-line arrays for archival purposes and for use in the engineering portions of the model. Secondary vectors which count and cost elements within the device are calculated from the arrays.

In addition to the individual element parameters, there are ten user global parameters available in ASM. These are: Charge; Mass, Final Energy, Final Current goal; Fundamental Frequency; duty factor; operating time; temperature regime; Magnetic Quadrupole material; and Structural material. These parameters are available in the parameter window associated with the accelerator building. The first seven are numerical inputs and the final three have a finite set of choices. The code provides flexibility in the design of each of the elements by allowing different definitions. One such example is the provision for a beam $\{\sigma_{Lo}, \sigma_{To}\}$ or a field description $\{E_{acc}, BPT \text{ or } B_{grad}\}$ of each of the accelerator components. The phase advances of the beam definition may be input in the device parameter window or derived from the previous element with a Matching Section element. Similarly, the lattice structure of each device {DTL, BC-DTL, CC-DTL, CCL, and SCL} may be input or derived from the phase advance per unit length of the previous element. When derived within the matching section element, the lattice

structure is obtained by: using the maximum pole tip field allowed and calculating the minimum length magnet that will fit within the size constraints of the following element to determine the minimum intertank spacing; and requesting the maximum number of accelerating cells while maintaining beam stability. Tanking within each device, may be specified as specific energy values, or calculated by requiring equal beam energy gains, power dissipation, cell number, or tank lengths. Inter tanks spacings may be derived from the matching section, specified lengths, or specified multiples of the local cell length.

In both the DTL and BCDTL routines, the beam is characterized by the synchronous particle and the cell lengths are calculated from the local beta. These calculations are relatively straightforward. CCL tanks are characterized by the parameters of the particle at the beam center in the tank center (cell lengths calculated from the tank average beta). Magnetic and cell lattice values for the BCDTL and CCL may be entered as input parameters or derived beam matching requirements.

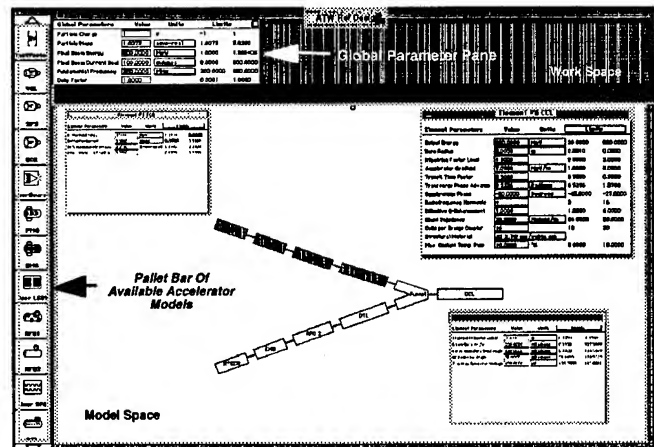


Figure 2: Graphical User Interface

The GUI for the ATW reference design is shown in Figure 2. The window is divided into two sections, a work space in which the global parameters are entered and a model space in which the accelerator is built. The accelerator elements are obtained by dragging them from the pallet bar on the left. Element parameters may be entered into individual windows for each of the elements. Three element parameter windows are shown superimposed upon the model space. These windows are opened by pointing and double clicking on the element. The accelerator is designed in the GUI model space. The element parameters along with the analysis, lattice, and tanking methods are entered using the element windows. The program is then started through a pull down menu. The code initializes all parameter arrays and steps through the modeling and optimizing of each element. Calculated parameters for each cell of each accelerating cavity are stored in arrays such as: DTLValues(Itank, Icell,

Array). Itank refers to the DTL tank number. Icell refers to the cell number within the tank. Array refers to the value being saved. The current APT configuration calls for 342 tanks and thus could impose severe memory problems if maintained internally. To control the sizes of these arrays, we presently store the results in binary files each time the maximum for any array index is reached. The code architecture is shown in figure 3.

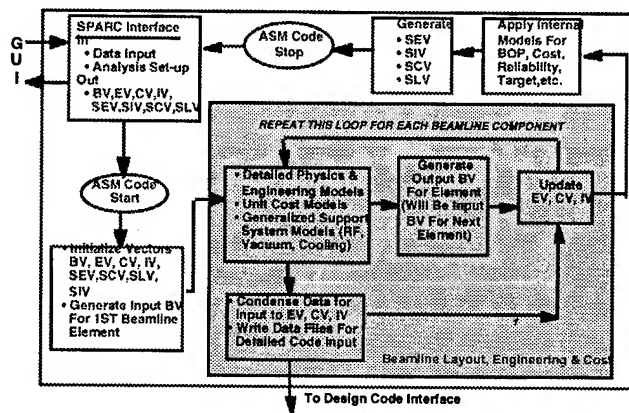


Figure 3. Beamline Code Analysis Flow

in addition to generating the beamline design, the code evaluates it based on physics and engineering desires. This evaluation has been included on both the beam and engineering vector level and on the device level. Automatic iteration has been included for the beam and engineering parameters and trade studies based on these elements are presently underway. On the device level, the code determines the availability of required components for each design. One example of this is for RF power sources. An extensive data base of tube characteristics has been provided in the code to determine the most efficient manner to provide power to each accelerating tank. Figure 4 illustrates the engineering modeling objectives of the code.

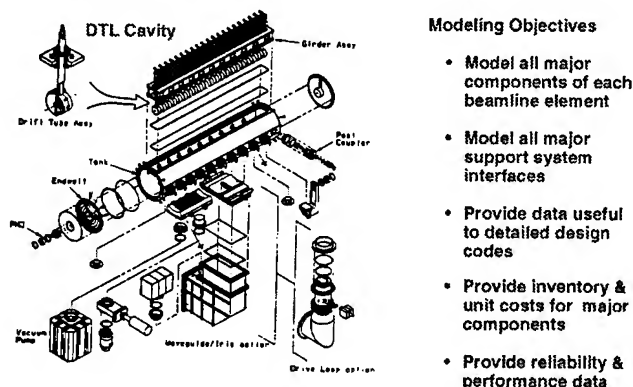
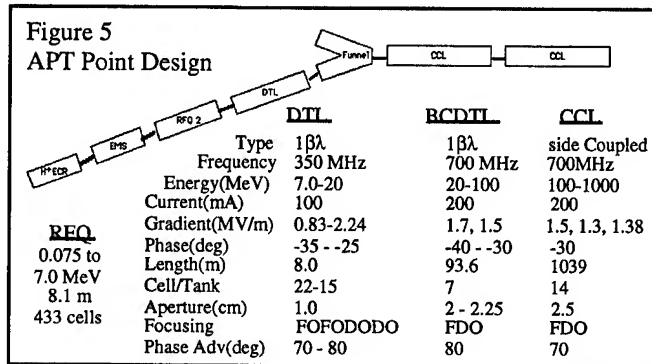


Figure 4. Beamline Modeling Objectives

3. APT DESIGN

Many of these models are already yielding good agreement with the baseline APT design (Figure 5). For instance, using the equal length option set at 250 cm and using

a ramp of 500 cm for phase and electric fields, the code yielded a DTL consisting of 3 tanks of 23, 20, and 16 cells. This is within 1 cell of the actual design. The DTL total length was 8.1 m long ($\approx 1\%$ longer than the design; had a total power dissipation of 2.3 MW ($\approx 6\%$ low) and an output phase advance of 72.7° . These results are in excellent agreement with the published results. The differences are easily attributable to the ramp length and cylinder size. The present BCDTL module yields an estimate for the length within 2% and the total code yields an estimate for the entire system within 1.5%



4. CONCLUSIONS

The immediate goal is to provide a code capable of realistic trade off studies. To completely provide this, we still need to add some transport models. Additionally, we need to totally integrate the models for systems engineering, reliability and maintainability; improve the internal engineering, physics and costing models and complete the interfaces with the external existing facility optimization model and the new target / blanket model. New component models, such as for the HILBILAC accelerator, will be added in the future.

Although not complete, the code does provide a useful and powerful tool for the design and evaluation of future beamlines. Physics and engineering models for most components of interest have been implemented and benchmarked against the existing concepts and the code is presently being used to provide trade studies for the IFMIF project. Continued collaboration with GHGA and Los Alamos based on this work is planned

6. REFERENCES

- [1] G. H. Gillespie et al.; "A New Approach to Modeling Linear Accelerator Systems"; to appear in the Proceedings of the 1994 International Conference on Accelerator Driven Transmutation Technology and Applications, Las Vegas, Nevada; July 1994
- [2] M. A. Peacock et al.; "Overview and Performance of an NPB Accelerator Modeling Code"; Fourth Neutral Particle Beam Technical Symposium; ANL, Chicago, Ill.

UNEXPECTED MATCHING INSENSITIVITY IN DTL OF GTA ACCELERATOR*

V. W. Yuan, O. R. Sander, R. C. Connolly[†], J. D. Gilpatrick, K. F. Johnson, W.P. Lysenko, D. P. Rusthoi, M. Smith, R. Weiss[†], Los Alamos National Laboratory, Los Alamos, NM 87545 USA

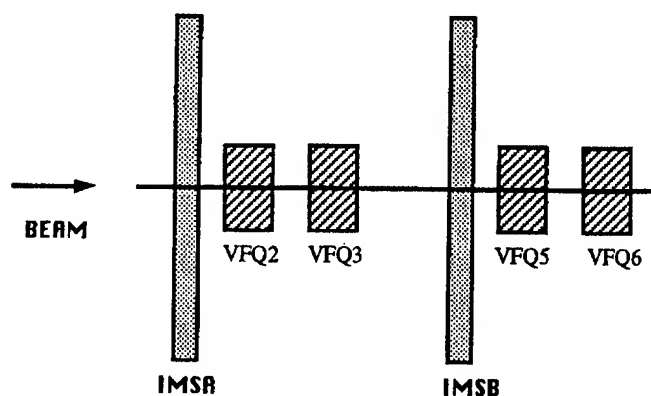


Figure 1. Schematic diagram of IMS

Abstract

The Intertank Matching Section (IMS) of the Ground Test Accelerator (GTA) contains four variable-field quadrupoles (VFQs) and is designed to match beam exiting the Radio-Frequency Quadrupole to the first tank of the Drift-tube LINAC (DTL-1). By varying the VFQ field strengths to create a range of beam mismatches at the entrance to DTL-1, one can test the sensitivity of the DTL-1 output beam to variations in the DTL-1 input beam. Experimental studies made during commissioning of the GTA indicate an unexpected result: the beam exiting DTL-1 shows little variation for a range of mismatches produced at the entrance. Results of the experiment and simulation studies are presented.

I. INTRODUCTION

The Ground Test Accelerator [1] at Los Alamos is a linac that was designed to produce an accelerated H^- beam of high intensity. Initial commissioning tests on the first Drift-Tube Linac section (DTL-1) of the accelerator produced a beam with an energy of 3.2 MeV. The configuration of the accelerator preceding DTL-1 included a source followed by: an injector, a low-energy beam transport section (LEBT), a Radio-Frequency Quadrupole (RFQ), and an Intertank Matching Section (IMS). The IMS (see fig. 1) included 4 Variable-Field Quadrupoles (VFQs) and 2 longitudinal bunchers (IMSA and IMSB) for the purpose of matching the beam exiting the RFQ to the entrance of DTL-1.

An experiment (DTL-1 Experiment) was conducted to produce a wide variety of beam configurations at the entrance to DTL-1. The purpose was to see how the transmission and Courant-Snyder parameters of the transmitted beam would be affected by changes in mismatch at the entrance to DTL-1. The

Table I
Courant-Snyder (C-S) parameters for input beam at simulation starting point. β_x and β_y are in units of mm/mr. β_z is in deg-keV.

α_x	β_x	α_y	β_y	α_z	β_z
-5.4196	.66466	.24527	.06301	.08726	.86140

beam was changed at the DTL-1 entrance by using different tunes of the VFQs contained in the IMS. The experiment showed surprisingly small changes in the beam exiting DTL-1 in spite of what were believed to be large changes in the mismatch of the beam entering DTL-1.

These observed changes at the DTL-1 output were much smaller than are predicted by the beam transport codes TRACE3D [2] and PARMILA [3]. A possible explanation was that the mismatch of the beam at the DTL-1 entrance was not changing by the amount originally believed. An experiment (IMS experiment), therefore, was conducted with DTL-1 replaced by a diagnostics station located just downstream of the IMS, in order to study characteristics of the beam exiting the IMS.

II. INPUT BEAM AND MATCHED BEAM

Simulation work calculated Courant-Snyder parameters for comparison with measured values. We began all simulations at a starting point located immediately upstream of the IMS. In the case of GTA, the IMS was positioned adjacent to the RFQ, and there was not room to place a diagnostic station between them to give a direct measurement of beam characteristics at this starting point. Our best estimate of the beam characteristics at the RFQ exit, therefore, came from emittance-scan measurements taken in the IMS experiment that replaced the DTL-1 tank with a beam-diagnostics station (ES5) located downstream of the IMS across a drift space. TRACE3D code was applied to these measurements to back-trace the beam across the drift space to the desired simulation starting point. The Courant-Snyder parameters for the starting-point input beam are presented in Table I.

The characteristics for the beam matched to the DTL-1 at its entrance were determined [4] by using TRACE3D to match to the 7th focusing period of the DTL-1. This beam was then back-transported using TRACE3D to determine its Courant-Snyder parameters at the DTL-1 entrance. Those Courant-Snyder parameters are presented in Table II.

III. EXPERIMENT DTL-1 TUNES

A particular configuration of field settings for the VFQs of the IMS constitutes what is called a "tune" of the IMS. In the DTL-1 Experiment, the IMS was set to a variety of tunes that, in

*Work supported and funded by the US Department of Defense, Army Strategic Defense Command, under the auspices of the US Department of Energy.

[†]Industrial partner, Grumman Corporation.

Table II

Courant-Snyder parameters of matched beam at input to DTL-1. β_x and β_y are in units of mm/mr. β_z is in deg-keV.

α_x	β_x	α_y	β_y	α_z	β_z
-2.3258	.2015	1.2949	.0862	-0.1892	.2665

Table III

Variable-field quadrupole field strengths (GL) and x mismatch factors (see ref. [5]) at the DTL-1 entrance for the tunes used in the DTL-1 Experiment. Field strengths are given in Tesla.

Tune	VFQ2 (T)	VFQ3 (T)	VFQ5 (T)	VFQ6 (T)	mmf_x
R1	5.583	4.884	6.288	6.136	.19
R2	4.830	5.635	5.667	6.174	1.00
R3	3.864	5.635	5.635	4.830	1.20
R4	3.542	5.635	5.474	4.693	1.44
R5	4.347	5.635	4.959	5.831	1.83
R6	6.054	2.898	3.474	2.840	2.99
R12	5.583	4.884	6.288	6.136	0.39
OLD	4.954	4.674	5.644	5.892	0.91

simulations, were predicted to give a matched beam as well as a wide range of mismatch factors ($mmfs$) [5]. Field values for these tunes are given in Table III. For all tunes except OLD, the longitudinal bunchers IMSA and IMSB operated at power levels of 1.58 and 6.75 kW respectively. In the OLD tune, buncher powers were 4.34 kW and 16.70 kW.

Simulation-determined mismatches at the entrance to the DTL-1 were calculated by using TRACE3D to transport the input beam of Table I from the exit of the RFQ through the IMS. The intended range of simulation-determined mismatch factors (relative to matched beam) was from $mmf_x = .2$ to $mmf_x = 3.0$ in x . However, in the actual experiment the mismatch of $mmf = 3.0$ (tune R6) could not be run because it resulted in fast protects that shut off the beam.

IV. MISMATCH AT THE DTL-1 ENTRANCE

For each tune of DTL-1 Experiment, Table III also presents the calculated mismatch value (relative to matched beam) of beam entering the DTL-1. These values were derived by using TRACE3D to propagate the input beam of Table I through the IMS. We modeled the SMQs in the IMS with soft-edged fringe fields. We know from TOSCA field calculations [6] that the soft-edged model corresponds closer to what physically exists, and steering-model studies [7] indicate that the soft-edged model provides better agreement between simulation and measurements. At the DTL-1 entrance, the range of mismatch values occurring during the DTL-1 Experiment is computed to be in the range of $mmf = .19$ to $mmf = 1.83$.

V. MEASURED VS. SIMULATION

For the DTL-1 Experiment, we have compared output-beam $mmfs$ from experimental measurements with those calculated

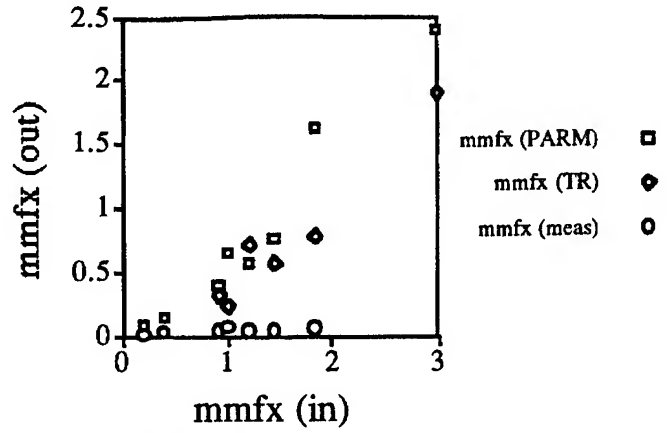


Figure 2. Dependence of mismatch at DTL-1 exit on mismatch at DTL-1 entrance.

from simulation. This comparison was performed at the DTL-1 exit. All mismatch factors were calculated relative to matched beam parameters. Comparisons were made for all the different IMS tunes which were used in the DTL-1 Experiment.

All experimentally-determined mismatch factors are based on Courant-Snyder parameters measured at the ES6 location. Experimentally-determined $mmfs$ cited at the DTL-1 exit were calculated by back-tracing ES6-measured parameters over a drift space to the DTL-1-exit location. Simulation-determined mismatch factors were calculated using TRACE3D to transport beam from the RFQ exit to the DTL-1 entrance, and then TRACE3D and PARMILA were used independently to transport the beam through DTL-1 to the DTL-1-exit.

The predicted mismatches for tunes R1-R5, R12, and "OLD tune" are presented in figure 2. The spread in simulation-determined mismatches at the DTL-1 exit does not differ greatly from the spread at the DTL-1 entrance. The smallest mismatches occur for R1, the tune that is predicted to provide matched beam. The largest mismatches occur for tune R5, and are approximately 10 times larger than those for matched beam. The average mismatch for non-matched tunes is $mmf_x = 1.19$.

Figure 2 shows that both the predicted mismatch values calculated by TRACE3D and those calculated by PARMILA show a similar dependence on input mismatch values. In contrast, the actual DTL-1 measured values shown in figure 2 are insensitive to input mismatch. For tunes other than the matched tune, the measured mismatches are at least a factor of 10 smaller than the predicted values. Taken at face value, the data indicates that the DTL-1 produces an output beam with constant Courant-Snyder parameters regardless of the mismatch of the beam input to the DTL-1.

The lack of change in output beams might be thought to indicate a problem with the system controlling the VFQ settings. For instance, if some failure caused VFQ fields to not be varied, then the input beam to the DTL-1 would not have changed. Archived data show that the magnet encoder values were changing for the various tune changes. The way the magnet control system operates also strongly suggests that the magnet fields must have varied as requested or else warning messages would have been detected. In addition, when we attempted to run at

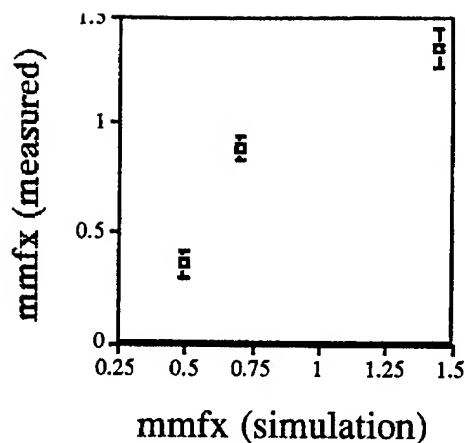


Figure 3. Dependence of IMS experiment mismatches

the R6 tune which is predicted to give a mismatch of 3.0 at the DTL-1 entrance, we were unable to run because of fast protects. So in that particular case it seems obvious that the VFQ's fields were being changed and that the change was such that the resultant beam was scraping enough to set off the fast protects.

VI. IMS EXPERIMENT

If the VFQs were being properly varied in the DTL-1 Experiment, then what can explain the constancy of the beam at the DTL-1 output? One possibility is that the different IMS tunes do not produce the wide range of mismatches, at the entrance to the DTL-1, that are predicted by simulation. Unfortunately, when the DTL-1 was in place, space limitations prohibited the slit and collector diagnostic at the IMS exit from being installed, thus eliminating our ability to directly measure beam characteristics at the DTL-1 entrance.

To study whether parameters at the DTL-1 entrance were changing for different IMS tunes, we performed the IMS Experiment. During this experiment, DTL-1 was replaced by a diagnostics station, and transverse-emittance scans were made at the ES5 location 369.1 cm downstream of the IMS endwall. The location point for the DTL-1 entrance in the DTL-1 Experiment had been 35.0 cm downstream of the IMS endwall. In the IMS Experiment, these two locations were separated by drift space only. Figure 3 presents a comparison of simulation-based and measured Courant-Snyder parameters for the IMS Experiment at the ES5 location. Uncertainties are given for the measured values based on the actual spread of repeated measurements.

Measured mismatch values presented in figure 3 track simulation-determined values for all 3 tunes tested. Since the maximum mismatch at the DTL-1 entrance is only on the order of $mmf = 1.0$, one might ask whether this more limited variation could have resulted in the highly similar beams observed in the DTL-1 Experiment. To answer this question, simulation codes were used to transport the α s and β s of figure 3 through the DTL-1 to ES6. The mismatches based on the extrapolation of IMS-experiment data are larger than those observed in the DTL-1 Experiment.

VII. CONCLUSIONS

Matching studies in the DTL-1 experiment were designed to test the effect of mismatches at the entrance to the DTL-1 on beams exiting the DTL-1. When the experiment was performed, the observed results gave an unexpected result: that the beam exiting the DTL-1 showed little variation for the different mismatches produced at the entrance. Simulations show that the variation in input beams should have produced a larger variation in output beams than was observed. A possible explanation is that the DTL affects the beam in some way so as to produce the same output beam independent of input beam.

References

- [1] O. R. Sander et. al., *Commissioning the GTA Accelerator*, Proc. 1992 Linear Accel. Conf., Chalk River Laboratories Report, AECL-10728 (1992) p.535.
- [2] K. R. Crandall and D. P. Rusthoi, *TRACE 3-D Documentation*, Los Alamos National Laboratory internal report LA-UR-90-4146 (1990).
- [3] G. Boicourt, *PARMILA- an overview*, Los Alamos National Laboratory internal report LA-UR-88-1544 (1990).
- [4] D. Rusthoi, *Experiment 2A: IMS VFQ settings for a matched beam into the DTL-1*, Los Alamos National Laboratory internal document: AT-3 Technical Note:92-512 (1993).
- [5] J. Guyard and M. Weiss, *Use of Beam Emittance Measurements in Matching Problems*, Proc. 1976 Linear Accel. Conf., Atomic Energy of Canada, AECL-5677 (1976), p.254.
- [6] D. Barlow, *TOSCA 3D measurements of GTA IMS VFQ Effective length*, Los Alamos National Laboratory internal document: AT-3 Technical Note:92-490 (1992).
- [7] V. Yuan, *Steering coefficients for IMS steering quadrupoles*, Los Alamos National Laboratory internal document: AOT-10 Technical note: 94-05 (1994).

Current Losses and Equilibrium in rf Linear Accelerators

Nathan Brown and Martin Reiser

Institute for Plasma Research

University of Maryland, College Park, MD 20742

ABSTRACT

In the conventional design of rf linear accelerators the charged particle bunches are not in thermal equilibrium. With high currents, space charge couples the transverse and longitudinal self forces, leading to emittance growth and halo formation as the beam relaxes toward an equipartitioned state. Particle losses to the walls can occur as a result of halo formation and also through the natural tail on the equilibrium distribution. Particle losses due to either a halo or a tail can cause radioactivity in the conducting channel, inhibiting routine maintenance. The properties of the beam are described in a new design for rf linacs in which the beam is kept in thermal equilibrium, and the current loss rate is found for the tail on the thermal equilibrium distribution.

I. INTRODUCTION

Many advanced applications of rf linear accelerators, such as injector linacs for high-energy physics colliders, spallation neutron sources, transmutation of radioactive nuclear waste, heavy ion inertial fusion and free electron lasers, require high beam currents in which space charge forces play a dominant role in the particle motion. In the conventional design of such linacs the bunched beams are not in thermal equilibrium [1]. Space charge couples the longitudinal and transverse forces, driving the beam toward an equilibrium state, causing emittance growth and halo formation [2-4]. Halos are of particular concern in linacs with high average power, in which particle losses as low as 1 nA/m have been predicted to result in nuclear activation, preventing routine maintenance [5]. Simulations using on the order of 10^5 particles are of little use in predicting such a small halo or tail, which corresponds to fractional particle losses of around 10^{-8} per meter. Halos have been observed in existing high-current linacs like LAMPF [6] and in experiments at the University of Maryland [7]. The beam parameters are described here for a linear accelerator in which the beam is kept in thermal equilibrium, minimizing emittance growth and halo formation. When space charge dominates, each bunch has a uniform density profile with a sharp boundary. When emittance is significant, the thermal equilibrium distribution has a tail which can result in current losses. Equations are derived and results are presented for the current losses from the thermal equilibrium distribution, in which the beam is axially centered in a cylindrical conducting pipe. This represents a best-case scenario, since deviations from equilibrium due to mismatch and misalignments add to the particle losses through emittance growth and halo formation. The particle losses from a beam which is kept in thermal equilibrium, however, will always be less than in the conventional linac design, in which equipartitioning adds to the emittance growth and halo formation.

II. AN RF LINAC WITH A BEAM IN THERMAL EQUILIBRIUM

The transverse and longitudinal evolution of a bunched beam is described by the coupled envelope equations [1, 8]. An equipartitioned beam has equal transverse and longitudinal temperatures, $T_{\perp} = T_{\parallel}$. This is equivalent to $\epsilon_{nx} \gamma z_m = \epsilon_{nz} r_m$, in which $\epsilon_{nx} = 5^{1/2} r_m (\gamma k_B T_{\perp} / mc^2)^{1/2}$ and $\epsilon_{nz} = 5^{1/2} z_m (\gamma^3 k_B T_{\parallel} / mc^2)^{1/2}$ are the transverse and longitudinal normalized emittances, r_m is the peak radius and z_m is the half-length, both of the equivalent uniform ellipsoid. The stationary coupled envelope equations with the equipartitioning condition are [8]

$$k_{x0}^2 r_m^4 = \frac{3N r_c \epsilon_{nx}}{2\beta^2 \gamma^2 \epsilon_{nz}} \left(1 - \frac{\epsilon_{nx}}{3\epsilon_{nz}} \right) r_m + \frac{\epsilon_{nx}^2}{\beta^2 \gamma^2}, \quad (1)$$

and

$$k_{z0}^2 z_m^4 = \frac{N r_c \epsilon_{nz}}{\beta^2 \gamma^5 \epsilon_{nx}} z_m + \frac{\epsilon_{nz}^2}{\beta^2 \gamma^6}, \quad (2)$$

where k_{x0} and k_{z0} are the transverse and longitudinal focusing wave numbers, N is the number of particles in the bunch, $r_c = q^2 / (4\pi \epsilon_0 mc^2)$ is the classical particle radius and β and γ are the relativistic velocity and energy factors. It is assumed that the bunch aspect ratio in the beam frame, $\gamma z_m / r_m$, satisfies $0.7 < \gamma z_m / r_m < 4$. Equations (1) and (2) are both of the same form as a fourth order polynomial for which a simple approximate solution was found [9]. Using this solution, the stationary bunch radius and half-length are [8]

$$r_m \approx \left[\frac{3N r_c \epsilon_{nx}}{2\beta^2 \gamma^2 \epsilon_{nz} k_{z0}^2} \left(1 - \frac{\epsilon_{nx}}{3\epsilon_{nz}} \right) + \left(\frac{\epsilon_{nx}}{\beta \gamma k_{x0}} \right)^{3/2} \right]^{1/3} \quad (3)$$

and

$$z_m = \left[\frac{N r_c \epsilon_{nz}}{\beta^2 \gamma^5 \epsilon_{nx} k_{x0}^2} + \left(\frac{\epsilon_{nz}}{\beta^2 \gamma^3 k_{z0}} \right)^{3/2} \right]^{1/3}. \quad (4)$$

With the equipartitioning condition substituted into the coupled envelope equations, the ratio between the transverse and longitudinal focusing wave constants becomes [8]

$$\frac{k_{x0}}{k_{z0}} = \left[\frac{3 \Gamma \epsilon_{nz} / \epsilon_{nx} - \Gamma + 2 \epsilon_{nz}^2 / \epsilon_{nx}^2}{2(\Gamma + 1)} \right]^{1/2}, \quad (5)$$

where $\Gamma = Nr_m/\epsilon_{nx}^2$ is the intensity parameter. This relation between k_{x0}/k_{z0} and $\epsilon_{nz}/\epsilon_{nx}$ is plotted in Figure 1 for several values of the intensity parameter. The traditional method of allowing k_{x0}/k_{z0} to increase in proportion to $\beta^{1/2}\gamma^{3/2}$ increases the temperature anisotropy and the aspect ratio ($\gamma z_m/r_m$) during acceleration and is responsible for the equipartitioning effect and the associated emittance growth in conventional high-current linacs [1, 8]. An example of a linac which uses these results has been given elsewhere [8].

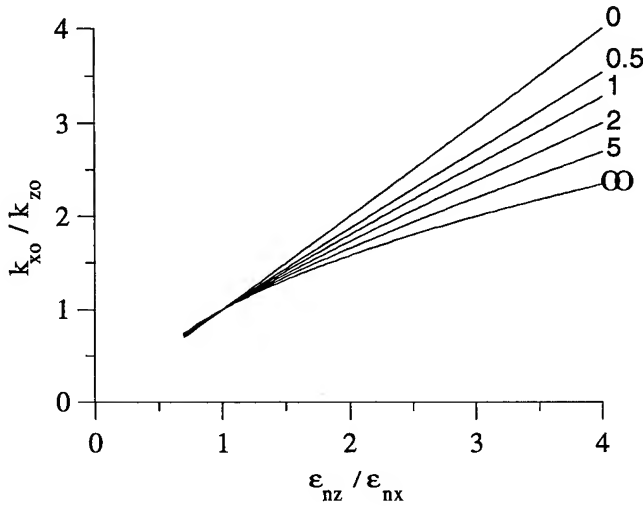


Figure 1: The ratio of the focusing wave numbers as a function of the ratio of the emittances from Equation (5) for several values of the intensity parameter ($\Gamma = 0, 0.5, 1, 2, 5$ and ∞).

III. PARTICLE LOSSES

The fractional particle loss per unit length for bunched and continuous (unbunched) beams in equilibrium can be found by considering the flux across a cylindrical boundary due to thermal motion in the thermal equilibrium distribution. With a Maxwellian velocity distribution with temperature T , the flux of all particles across a cylindrical boundary with radius b is [10]

$$\Phi = \frac{\bar{n}(b)}{(2\pi)^{1/2}} \left(\frac{k_B T}{m} \right)^{1/2}. \quad (6)$$

For bunched beams, $\bar{n}(b) = \int n(b, z) dz / \Delta z$ is the density at the pipe averaged over each bunch in the longitudinal direction, where Δz is the distance between bunches. For unbunched beams, $\bar{n}(b) = n(b)$ is the density at the pipe, which is constant along z .

The number of particles lost per unit length per unit time along the channel is found by multiplying the flux by the circumference ($2\pi b$). Multiplying the result by the particle charge q gives the current lost per unit length, so the fractional loss per unit length along the channel is

$$f = \frac{q(2\pi)^{1/2} b \bar{n}(b)}{I_{ave}} \left(\frac{k_B T}{m} \right)^{1/2}, \quad (7)$$

where I_{ave} is the average beam current ($I_{ave} = I$, the continuous current, for unbunched beams).

Equation (7) can be written in terms of the normalized transverse emittance and rms radius for bunched and unbunched beams. For unbunched beams the normalized transverse emittance is $\epsilon_{nx} = 2^{1/2} a (\gamma k_B T / mc^2)^{1/2}$ and the current is $I = q n_0 \pi a^2 v_0$, where n_0 is the density of the equivalent uniform beam, and $a = 2^{1/2} r$ is the radius of the equivalent uniform beam. The fractional particle loss per unit length along the channel for continuous (unbunched) beams is then

$$f = \left(\frac{1}{4\pi^{1/2} \beta \gamma} \right) \left(\frac{n(b)}{n_0} \right) \left(\frac{b}{r} \right) \left(\frac{\epsilon_{nx}}{r^2} \right). \quad (8)$$

For bunched beams the average current is $I_{ave} = q N v_0 / \Delta z$, where N is the total number of particles in each bunch. The resulting fractional loss per unit length is [10]

$$f = \left(\frac{6}{25\pi^{1/2} \beta \gamma} \right) \left(\frac{\bar{n}(b)}{n_0} \right) \left(\frac{b}{r} \right) \left(\frac{\epsilon_{nx}}{r^2} \right). \quad (9)$$

where \bar{n}_0 is the density on the axis of the equivalent uniform ellipsoid, averaged over the longitudinal direction. The terms containing the densities in Equations (8) and (9) are rapidly decreasing functions of b/r , so that increasing the beam radius or decreasing the pipe radius causes an increase in the particle losses, despite the appearance of b/r and ϵ_{nx}/r^2 as multiplying factors.

Since a continuous beam does not have any image fields from the conducting pipe, the effect of the pipe is only to truncate the thermal distribution. The density as a function of radius required for Equation (8) can be found from previous results [11] for any pipe radius. For bunched beams, thermal equilibria have been found numerically [10, 12] for aspect ratios of 1, 5 and 20; pipe radii of 2, 3 and 5 times r_m ; and transverse space charge tune depressions (k_x/k_{x0}) of 0.2, 0.3, 0.4, 0.5, 0.65, 0.8 and 0.95. The transverse space charge tune depression is calculated from the envelope equations as [8]

$$\frac{k_x}{k_{x0}} = \left(1 - \frac{3Nr_c(1-r_m/3\gamma z_m)}{2\beta^2\gamma^3 r_m^2 z_m k_{x0}^2} \right)^{1/2}. \quad (10)$$

The extent of the thermal tail in the radial direction was found to be independent of the pipe radius with constant k_x/k_{x0} , for all aspect ratios and pipe radii which were tested, just as in the case of unbunched beams.

The extent of the tail was found to have a much greater dependence on temperature than on bunch length. The results were also found, for all aspect ratios tested, to be similar to those for unbunched beams. Figures 2 and 3 show the average

radial density profiles with density on a logarithmic scale (with log base 10), which emphasizes the differences between the tails of the distributions. The solid lines are for unbunched beams, obtained by the same method as in Reference 11. The dashed lines are for spherical bunches ($\gamma z_m/r_m = 1$) in Figure 2 and for profiles with aspect ratio $\gamma z_m/r_m = 20$ in Figure 3. The profile numbers from 1 through 8 correspond to transverse space charge tune depressions of, respectively, 0.95, 0.8, 0.65, 0.5, 0.4, 0.3, 0.2 and 0.0. Radii are in units of the rms radius, which is $2^{-1/2}$ a for unbunched beams and $(5/2)^{-1/2} r_m$ for bunched beams. An example which uses these results has been given elsewhere [10].

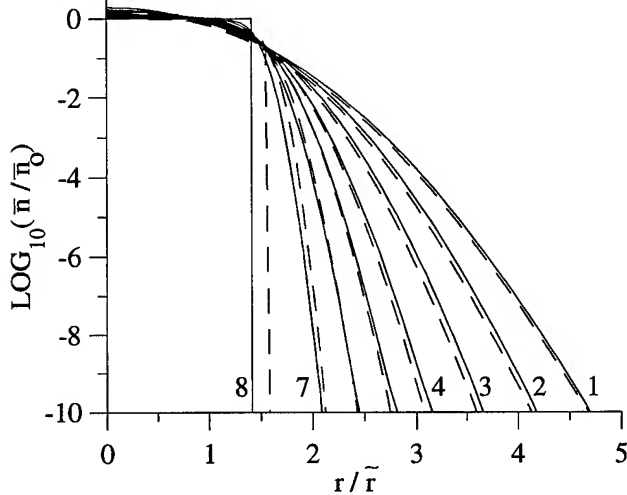


Figure 2: Average radial density profiles on a logarithmic scale, for unbunched beams (solid lines), and bunched beams with an aspect ratio of $\gamma z_m/r_m = 1$ (dashed lines).

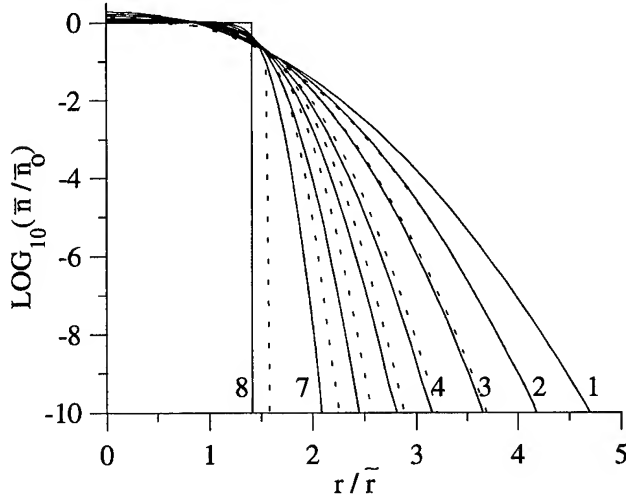


Figure 3: Average radial density profiles on a logarithmic scale, for unbunched beams (solid lines), and bunched beams with an aspect ratio of $\gamma z_m/r_m = 20$ (dashed lines).

CONCLUSION

The properties of the beam in a proposed rf linear accelerator have been described, in which the ratio of the transverse and longitudinal focusing wave numbers is adjusted to keep the beam in thermal equilibrium in order to minimize emittance growth and halo formation. When space charge dominates over emittance, the bunch has a uniform density profile with a sharp boundary. When emittance is significant, the thermal equilibrium density profile has a natural tail. Equations have been derived and results presented graphically for the fractional current loss due to this tail in the thermal equilibrium distribution. In practice there will always be deviations from the equilibrium state due to mismatch and misalignments, but the resulting emittance growth will always be less than in the conventional design in which equipartitioning adds to the emittance increase and halo formation.

REFERENCES

- [1] M. Reiser, *Theory and Design of Charged Particle Beams* (John Wiley & Sons, New York, 1994), Appendix 4 and Section 5.4.11.
- [2] R. A. Jameson, *IEEE Trans. Nucl. Sci.* **NS-28**, 2408 (1981).
- [3] I. Hofmann, *IEEE Trans. Nucl. Sci.* **NS-28**, 2399 (1981).
- [4] R. A. Jameson, in *Advanced Accelerator Concepts*, edited by J. S. Wurtele, AIP Conf. Proc. 279 (AIP, New York, 1993).
- [5] J. M. Lagniel, *Nucl. Inst. Meth. Phys. Res.* **A345**, 46 (1994).
- [6] R. A. Jameson (private communication).
- [7] D. Kehne, M. Reiser and H. Rudd, in *Proceedings of the 1993 Particle Accelerator Conference 93-CH3279-7*, p65; see also Reference 1, Section 6.2.2 and M. Reiser, *J. Appl. Phys.* **70**, 1919 (1991).
- [8] M. Reiser and N. Brown, *Phys. Rev. Lett.* **74**, 7, 1111 (1995).
- [9] N. Brown and M. Reiser, *Part. Accel.* **43**, 231 (1994).
- [10] N. Brown and M. Reiser, *Phys. Plasmas* **2**, 3, 965 (1995).
- [11] M. Reiser and N. Brown, *Phys. Rev. Lett.* **71**, 18, 2911 (1993).
- [12] N. Brown, PhD Dissertation, University of Maryland, College Park, 1995.

ACKNOWLEDGMENT

This research is supported by the U. S. Department of Energy.

MMF LINAC UPGRADE POSSIBILITIES FOR THE PULSED NEUTRON SOURCE

SK Esin, LV Kravchuk, AI Kvasha, PN Ostroumov, VL Serov
Institute for Nuclear Research, Moscow 117312, Russia

1 Introduction

Pulsed Neutron Source based on the proton accelerator is a very promising device for investigations in a fields of nuclear physics and condensed matter. Several installations have been built in USA (LANSCE, IPNS), in England (ISIS), in Japan (KENS). Pulsed Neutron Source IN-06 [1] based on the Moscow Meson Factory (MMF) Linac is under construction now. Next generation of Neutron Sources (ESS, JHF etc.) [2,3] are in R&D study.

The first stage of Neutron Source IN-06 is planned to be put into operation in 1996. The watercooled neutron target of silicious uranium will be exposed to the 500 MeV proton beam. The IN-06 design parameters (thermal neutron peak flow of $5 \cdot 10^{15} n/cm^2 \cdot s$, 35 mks pulse, 50 Hz repetition rate, average flow of $8 \cdot 10^{12} n/cm^2 \cdot s$) may be achieved after storage-compressor ring (PSR) comissioning in 1998.

We studied the possibilities of IN-06 upgrade by means of MMF Linac modernization using existing building areas, shielding and net power consumption. Our analyses have shown that peak flow of $10^{17} n/cm^2 \cdot s$ and average flow of $10^{14} n/cm^2 \cdot s$ could be achieved with the pulse length of 30 mks and repetition rate 25 Hz using PSR and neutron multiplication in target. All necessary linac innovations are not overstep the limits of the contemporary state of art. To get the above mentioned parameters we need to increase the energy of the linac up to 700 MeV and beam pulse length up to 300 mks with the repetition rate 25 Hz. Thus neutron multiplication target will be exposed to 10^{14} proton per pulse which corresponds to 10 MWt power dissipation in target [4].

2 Linac innovations

MMF Linac was designed with following parameters: maximum energy of protons and H^- ions 600 MeV; average beam current 500 mA; pulse current 50 mA; beam pulse length 100 mks; repetition rate 100 Hz. Recently the proton energy of 423 MeV was achieved which is determined

with the number of klystrons on hand which are used for DAW Linac RF power supply. By the end of 1995 6 more klystrons will be manufactured that provide the beam energy of 500 MeV. Regular linac operation take place with the average current of 50 mA (demonstrated 65 mA). Total beam losses are not exceed design value (0, 1 ÷ 0, 2)% [5]. Beam pulse length of 70 mks and repetition rate 50 Hz are determined with experimental requirements as well as with power consumption expenditures.

The following linac systems must be upgraded to get 700 MeV proton energy and 300 mks beam pulse length:

Accelerating system. RF pulse length increase up to 300 mks leads to the thermal heat growth in DTL as well as in DAW (disk and washer) cavities. It seems that necessary heat transfer could be provided with the water flow increase as well as with water temperature lowering in the secondary loop. Additional expenditure of electric power could be compensated due to elimination existing heaters and reduction of the water pumps number in the modernized cavity resonant frequency control system.

Energy upgrade from 600 MeV to 700 MeV could be fulfilled due to addition of one more 4-section DAW module onto the existing girder at the end of accelerating tunnel. This module has to provide the accelerating gradient of 7 MeV/m. Our experience shows that it is fully guaranted in DAW accelerating structure.

DTL Linac RF Power Supply. To meet 300 mks beam pulse we need to increase the modulator pulse length from 360 mks to 500 mks. It requires to increase the number of cells in delay line, to modify the pulsed transformer in the GMI-44A anode circuit, to increase the pulse length of the submodulator. Similar modifications have to be done in modulator of the powerful driver amplifier to increase its pulse length from 420 mks to 550 mks.

DAW Linac RF Power Supply. There are 28 991 MHz 4,75 MWt power supply channels (one for each 4-section DAW cavity) in the DAW Linac. For 300 mks 50 mA beam pulse operation we need to modify the klystron driver amplifier together with its modulator as well as the output

powerfull klystron itself. The number of cells in delay line of the driver amplifier modulator must be increased twice. The pulsed transformer must be redesigned to eliminate the iron saturation due to longer pulse.

To provide 300 mks operation with the same net power consumption and equipment sizes unchanged we have three options:

- powerfull klystron modulator is reconstructed using the same elements of the delay line. The KIU-40 old klystron maybe utilized.
- powerfull klystron modulator is modified for operation with low voltage (50 kV) high efficient 42 beam klystron "Atlant", which was developed recently by the scientific and technical firm "Thorium".
- completely new delay line has to be developed and constructed.

After some modelling and testing one of those three options has to be choosen taking into account its reliability. The RF channel for the last high accelerating gradient cavity differs from those regular ones significantly. It must be developed separately and needs additional net power.

Injection system. Existing injectors on the base of accelerating tube and 750 kV pulsed transformer have to be substituted with RFQ section designed to provide 50 mA in the pulse length of 300 mks with 25 Hz repetition rate. 198,2 MHz RFQ injector must be placed close to the first DTL cavity.

Conclusion

The fulfilment of the above mentioned steps of the MMF Linac upgrade together with proton storage-compressor ring comissioning and neutron multiplication target insted of silicious uranium one installation make the Pulsed Neutron Source based on the MMF Linac beam highly competitive.

Acknowledgment

The author are grateful to Prof. Yu. Stavissky and Dr. M. Grachev for their collaboration and helpful discussions.

References

- [1] Yu. M. Bulkin, S. F. Sidorkin, Yu. Ya. Stavisski et al. Proc. of Neutron Scattering in 90th Conf., Julich, 1985
- [2] Proc. of ICANS XI, KEK, Tsukuba, Oct. 1990, pp. 5, 32, 61, 87
- [3] Proc. of ICANS XII, RAL, Abington, UK, May 1993, P-7, P-13, P-21, P-26, T-53
- [4] M. I. Grachev, L. V. Kravchuk, Yu. Ya. Stavissky. Moscow Meson Factory Pulsed Neutron Source. Possibilities of development. Proc. of PANS-II Conference, Dubna, Russia, 1994.
- [5] S. K. Esin, L. V. Kravchuk, V. A. Matveev et al. Commissioning and operating of the Moscow Meson Factory Linac. Proc. of the LINAC Conference, Tsukuba, Japan, 1994.

MOSCOW MESON FACTORY DTL RF SYSTEM UPGRADE

S.K. Esin, L.V. Kravchuk, A.I. Kvasha, V.L. Serov
Institute for Nuclear Research of the RAS, 117312, Moscow, Russia

I. INTRODUCTION

The Drift Tube Linac RF Power Supply is a critical system in the Moscow Meson Factory (MMF) complex operation. Recent activity in its modernization is under discussion in this paper. DTL RF system consists of 5 identical channels plus reserve one. Every channel includes the four-stage 198.2 MHz amplifier, two anode modulators (one of them for the first two amplifier stages on the valves GS-31B and the other for the two output stages on the valves GI-51A and GI-54A), coaxial system, phase and amplitude automatic control systems (Fig.1).

The RF system was designed nearly twenty years ago in the Radiotechnical Institute of the USSR Academy of Sciences and fully discussed in a broad list of publications. The most detailed description of RF equipment was presented in [1-6].

The main reasons, which have caused the need of RF system modernization are the following ones:

- a low reliability of the valves GMI-44A and GI-54A in the modulator and RF amplifier output stages;
- a self-excitation of the output stages of the RF amplifier;
- a long RF power turn-on transient.

The results of the RF system efficiency improvement are described below.

II. THE RESERVE RF POWER SUPPLY SYSTEM

The DTL RF Power Supply System comprises one reserve channel. In accordance with initial design the entire equipment of the reserve channel may be connected to any of five DTL tanks instead of the failed channel. For that purpose five p-i-n switches have been used, which provide fast connection of the reserve channel instead of the failed one. In a course of this procedure the tank begins to operate with reserve modulators, RF amplifiers and amplitude and phase circuits. It was inconvenient because of the need to calibrate and readjust the amplitude and phase control system circuits of the reserve channel.

Recently the only powerful elements (HV-rectifier, modulators and RF amplifiers) of the reserve channel are connected to the cavities using the double phase-regulator with the switch [5]. It is reasonable since the powerful elements are the causes of failure in most cases. The failure of the amplitude and phase control system elements happens rather rarely, so the amplitude and phase control system elements native to the given tank are never replaced (Fig.1). Now the time to put the reserve channel into operation instead of the failed one does not exceed 25-30 minutes.

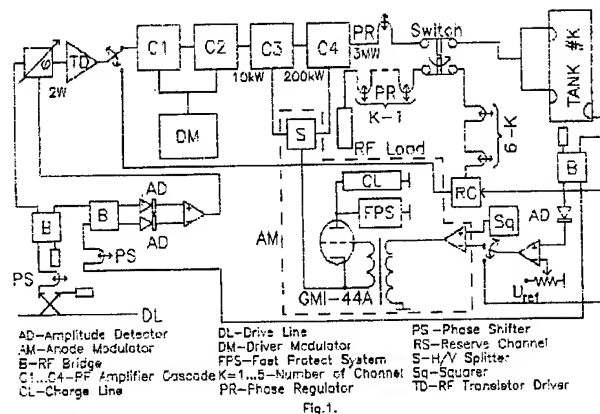


Figure 1. The Reserve Channel Block Diagram

III. INCREASING THE RELIABILITY OF THE RF AMPLIFIER AND MODULATOR OUTPUT STAGES

In the last years some R&D works were initiated in NPO "Toriy" (Moscow) and AO "Svetlana" (S. Petersburg) to develop new more reliable powerful valves for the last stages of the AM modulator and RF amplifier using modern materials and technologies. In the last year powerful water-cooled triodes "Takt-1" were installed in the modulators AM of the channels N2, 3 and 6. Use in them the high efficient electron optic with tape-like electron flows and deep cooling grids allows to apply the high anode voltage and operate large anode current. In addition to that VA characteristic of the valve is near to that of pentode with the low anode voltage drop. The main parameters of the valve "Takt-1" are presented in the Table 1.

The new pulsed powerful RF triode "Katran" (AO "Svetlana") with pyrolytic graphite grid is tested now as well. To investigate the new valve operating on any of the five DTL tanks it was installed in the output stage of the reserve channel. Results of the "Katran" tests have shown that it has the higher then GI-54A breakdown voltage and more reliable cathode heater; new valve has not experienced selfexcitation when the grid driving power is off, which was typical short-coming for a GI-54A. That advantage of "Katran" opens a possibility to control RF power in DTL tank changing the level of the grid driving. The main parameters of the valve "Katran" are presented in Table 2.

IV. IMPROVEMENT OF CHANNEL OPERATION

After beginning a routine work of all RF system channels it was found that there are a lot of cases of a selfexcitation at the low frequencies (a few MHz) in output stages of RF amplifiers, which could switch off one or a few channels due to interfer-

Table I
The Parameters of the "Takt-1" valve.

N	Parameter	Unit of a measur.	Quant.
1.	Anode pulse current when grid-driving pulse is 5 kV and anode voltage - 10 kV	A	750
2.	Maximum anode dissipated power	kWt	300
3.	Maximum anode voltage	kV	100
4.	Grid/anode currents ratio		0.05
5.	D.C. grid bias	V	-50
6.	Filament power	kWt	2.8
7.	Filament A.C. voltage	V	28
8.	Weight	kG	45
9.	Sizes: height	mm	625
	diameter	mm	300

Table II
The Parameters of the "Katran" valve.

N	Parameter	Unit of a measur.	Quant.
1.	Operation frequency	MHz	200
2.	RF pulse power at anode voltage 40 kV	MWt	4
3.	Power gain		10
4.	Maximum anode dissipated power	kWt	140
5.	Filament power	kWt	16
6.	Filament A.C. voltage	V	16
7.	Duty factor		0.05
8.	Weight	kg	45
9.	Sizes: height	mm	460
	diameter	mm	625

After fulfilling of the above mentioned measures the RF system began to work much better. So, if during the first beam production shifts in 1989 the mean time between two breakdowns was about 1h and the maximum time - 3h, then in 1994 those figures have reached 9h and 45h correspondingly. A few channels simultaneous breakdowns have been practically excluded, though previously they happened in 90% of all breakdown cases.

V. IMPROVEMENT OF THE RF POWER TURN-ON TRANSIENT

As it was said above it is difficult to cease entirely accidental switching off of the channels and hence there is a need to take measures to decrease a RF power turn-on transient in a tank. Its duration is determined with noticeable drift tube thermal changes due to RF power dissipation and it takes a time to decrease the temperature of cooling water to keep the cavity resonant frequency. In detail the problem was discussed in [7] where the temperature gradients between copper and cooling water are presented. They are changed from $1C^{\circ}$ (in the tank N 1) to $8C^{\circ}$ (in the tank N 5). Since the relation between a resonant frequency and drift-tube temperature is determined as a linear dependency with the coefficient $K = 1.5 \div 2 kHz/C^{\circ}$ and drift-tube thermal time constant does not exceed 30 sec then the tank will be detuned entirely through $20 \div 30sec$ after the channel is switched off. A slow resonant frequency control system can not help because the only pure delay in a control loop achieves $20 \div 25sec$. To decrease a RF power turn-on transient the special program was developed which fulfills the following operations:

- analyses a cause of the accidental switching off of the channel;
- creates the program control command to switch on the failed channel if the accidental turning off was connected with interferences on timer or p-n-p-n switch in the modulator fast protection circuits;
- keeps the same cooling water temperature for a time approximately equal to three drift-tube thermal constants.

The program allows to decrease a turn-on transient from $5 \div 15$ min to $1 \div 1.5min$.

VI. CONCLUSION

Above mentioned investigations and debugging of the RF system equipment have increased its efficiency noticeably. We are going to continue the works directed on increasing the reliability of the RF system on account of an installation of the new valves "Takt-1" and "Katran" in every channel, optimization of the RF amplifier output stage tuning and decreasing of the interference on the timer and p-n-p-n switch in the modulator AM fast protection circuits.

ence on timer or p-n-p-n switch in the modulator fast protection circuits. The main cause of the selfexcitation was a coupling between two output stages due to common anode power supply circuit. Since the power gain in the last two stages achieves 30 dB the danger of a selfexcitation is very real one.

After the channel is turned off due to self-excitation it takes a long time to restore the nominal level of power in the tank - from 5 minutes for tank N 1 up to 15 minutes for tank N 5. That is why a much effort was spent to investigate the reasons of a selfexcitation and to find the ways to prevent it and its consequences. The following measures have been taken:

- check up and restoration all of welded seams in the two output stage of the RF amplifier;
- change in the modulator AM timing circuits;
- installation of "electronic gate" network in the timing circuit all of modulators aiming to lock the input in a pause between the timer pulses;
- inserting of the LR dumping cells S (Fig.1) which provide decrease of coupling between anodes of GI-51A and GI-54I.

References

- [1] B.I.Polyakov, et al., RF supply system structure and parameters of the Meson Factory Linac. Proc. of the RTI of the AS of the USSR, Moscow, N. 28, 1977, p.26, (in Russian).
- [2] A.V.Mischenko, et al., RF generator circuit and structure for the amplifying channel of the first part of the Meson Factory Linac, *ibid.*
- [3] A.V.Mischenko, et al., The first results of high power generator for the first part of the Meson Factory Linac, *ibid.*
- [4] Yu.S.Tcherkashin et al., Pulse modulators test results for the supply system of the first part of the Meson Factory Linac, *ibid.*
- [5] N.I.Uksusov, B.I.Polyakov, B.V.Romanov, "Coaxial feeder system of the Meson Factory Linac", *ibid.*
- [6] B.P.Murin /Ed. Lineynie uskoritely ionov, Moscow, Atomisdat, 1978, (in Russian).
- [7] A.I.Kvasha, A.S.Kovalischin, A.S. Fokin, G.I. Yamshikov, The main characteristics of the process of the RF power turn-on in resonators of the MMF, Proc. of the XIII Russian Particle Accelerator Conference, Dubna, v.2, p. 222, 1993. (in Russian).

HEAVY ION FUSION 2 MV INJECTOR*

S. Yu, S. Eylon, E. Henestroza, C. Peters, L. Reginato, D. Vanecek, F. delaRama, R. Hipple, J.D. Stoker, Lawrence Berkeley Laboratory, Berkeley, CA 94720

D. Grote, F. Deadrick, Lawrence Livermore National Laboratory, Livermore, CA 94550

ABSTRACT

A heavy-ion-fusion driver-scale injector has been constructed and operated at Lawrence Berkeley Laboratory. The injector has produced 2.3 MV and 950 mA of K^+ , 15% above original design goals in energy and current. Normalized edge emittance of less than 1π mm-mr was measured over a broad range of parameters. The head-to-tail energy flatness is less than $\pm 0.2\%$ over the $1 \mu s$ pulse.*

has been proposed to study all the key beam dynamics issues in a driver-scale accelerator, and the first half of this machine, the electrostatic focusing section has been approved as the 'Elise' project. As a prerequisite to the ILSE/Elise project, a driver-scale, one-beam heavy ion injector has been constructed and operated at Lawrence Berkeley Laboratory

The new injector has as its design goals, the particle energy of 2 MV, line charge density of $0.25 \mu C/m$ (800 mA of K^+) and a normalized edge emittance of less than 1π mm-mr. These design parameters are the same as in a full-

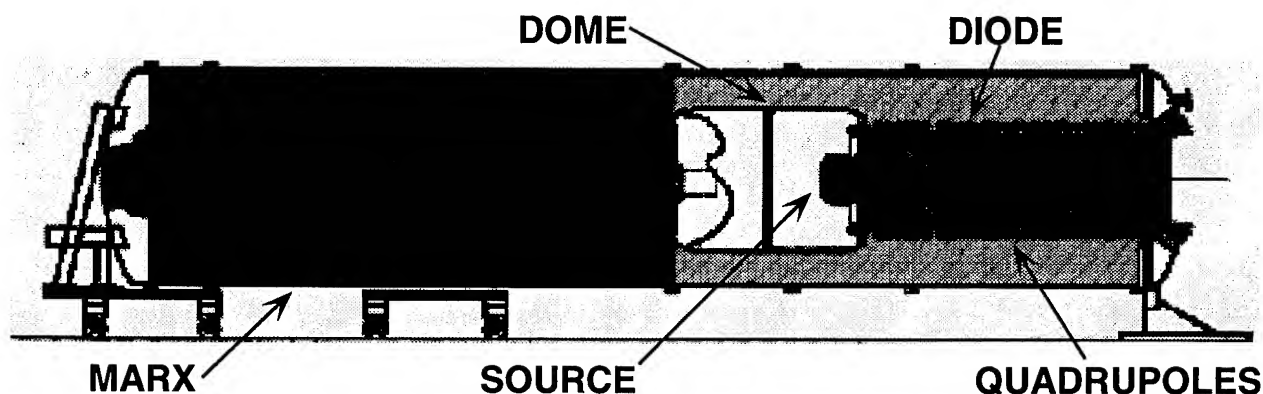


Fig.1

INTRODUCTION

The accelerator required for Heavy Ion Fusion[1] must deliver several megajoules of heavy ions with particle energy of a few GeV, onto a target of 2 to 3 mm radius in 10-15 nanoseconds. The linear induction accelerator approach to the fusion driver consists of multiple beams, each confined to a quadrupole focusing channel, which is electrostatic at the low energies, and magnetic at the high energies, and sharing a common induction acceleration core. A variant of the induction linac approach, which recirculates the heavy ions through quadrupole focusing channels and induction cores in a circular configuration is also being studied as a potentially low cost driver option.[2] The ILSE (Induction Linac Systems Experiments) project

scale driver. The low emittance is essential for final focusing onto a small target. The line density corresponds to the optimal transportable charge in a full-scale electrostatic quadrupole channel, and the high injector energy has significant cost advantages in a fusion-driver. The ultimate injector for a fusion accelerator is conceptually a replicate of this one-beam injector to many beams, with an extended pulse length of many microseconds, instead of the one to two microseconds (budget-determined) in the ILSE/Elise injector. While the particle energy and particle current has been achieved separately in previously built injectors, the unique combination of energy, current, and emittance requirements pose a new technical challenge for the Elise injector. Furthermore, the required beam parameters must stay constant over the entire microsecond long pulse, and the machine must run reliably.

The new injector is based on an electrostatic quadrupole (ESQ) configuration.[4,5] The ion beam, after extraction from an axisymmetric diode, is injected into a set

*This work was supported by the Director, Office of Energy Research, Office of Fusion Energy, U.S. Dept. of Energy, under Contract No. DE-AC03-76SF00098.

of electrostatic quadrupoles arranged to provide simultaneous acceleration and strong focusing. The ESQ configuration was chosen over the more conventional electrostatic aperture column primarily because of high voltage breakdown considerations. The accelerating gradient of an ESQ can be made quite low, and the strong transverse fields sweep out secondary electrons which may initiate breakdown processes. However, the ESQ configuration has an inherent beam aberration mechanism, which must be carefully controlled to minimize emittance degradation. The key design issues center around the control of high voltage breakdown and deleterious phase-space distortions.

HIGH VOLTAGE ENGINEERING

A schematic of the full injector is shown in Figure 1. The Elise injector column consists of a diode followed by four electrostatic quadrupole sections. The ceramic column has an inner diameter of 26" and a total length of about 100". The diode section is brazed from 16 1-1/2" alumina rings separated by thin Niobium plates. The quadrupole sections are composed of 3" rings. The segmented structure prevents continuous plasma avalanching along the ceramic walls, and reduces insulator breakdown risks. The inner surface of the insulator column is further protected with 1 cm thick stainless steel and copper shields carefully shaped to block beam-generated secondary electrons and X-rays. Detailed computer designs were performed to minimize surface field stress to less than 60 kV/cm at all points on the metal surfaces and to very low fields at the "triple points" (interface between insulator, metal, and vacuum). Quadrupole electrodes were also computer-designed to minimize field stress without enhancing higher order multipoles which could distort the phase-space of the beam. The ceramic column is contained in a pressure vessel under 80 psig of SF₆. The outside of the insulator column is further protected with guard rings and metal-oxide-varistors. Water resistors around the column provide graded voltages to the diode and each of the four quadrupoles. The full-size quads were tested to hold voltage of up to 700 kV without beam. The design quad voltages for the full injector were set at less than 400 kV. The diode was tested to up to 1 MV with beam, and the design diode voltage is less than 700 kV.

The source is a 6.7" diameter curved hot aluminosilicate source emitting K⁺ ions. These sources have been shown to produce beams with temperature-limited emittances, and have long life-time and high reliability[6]. The source assembly is coupled to an extraction pulser

which is at -80 kV relative to the high voltage dome at all times except during beam extraction when the pulser is switched to +80 kV in about 500 ns. This extraction pulser configuration allows ion extraction without the need for grids which tend to be unreliable and beam-quality degrading.

The injector is powered by a 2 MV Marx[7] which consists of 38 trays, with parallel LC and RC circuits arranged to produce a 4 μs flat-top (to accommodate the entire ion beam plus transit time across the injector column). The 6 kΩ system is sufficiently stiff to render beam loading transient effects negligible.

BEAM DYNAMICS

A low energy ion beam in a strong electrostatic focusing channel experiences a third-order aberration which we call the "energy effect." The cause of this effect is that ions at a given axial location within the quadrupole channel can have variable energies, depending on their relative proximity to the negative and/or positive electrodes. Variations in beam energy lead in turn to a spread in betatron motion, which results in a kinematic aberration of the beam. The mechanism could be understood if we start with the equation of motion in a focusing channel:

$$\frac{d^2x}{dz^2} = \frac{1}{v_z^2} \left(\frac{eE_{\perp}}{m} \right)$$

Noting that v_z^2 is proportional to the potential in a quadrupolar field

$$\frac{1}{2}mv_z^2 = e\Phi = e(\Phi_0 + \Phi_q r^2 \cos 2\Theta)$$

where Φ_0 is the potential on axis and corresponds to the energy of an on-axis particle, and Φ_q is the quadrupole component. Assuming that $\Phi_q \ll \Phi_0$, we obtain at once, to leading order

$$\frac{d^2x}{dz^2} = -k\beta^2 x \left(1 - \frac{\Phi_q}{\Phi_0} r^2 \cos 2\Theta \right)$$

It is evident that the resulting aberration is third order in the field. It is also clear that the magnitude of the aberration is proportional to the ratio of the quadrupole field to the beam energy, and the effect is most serious when the beam energy is low and quadrupole field is strong.

The beam dynamics of the ESQ is further complicated by the facts that the interdigital geometry of the electrode

package is fundamentally 3-dimensional, and the beam is space-charge dominated. Detailed theoretical predictions require 3-D PIC simulations. Substantial code developments were invested to make WARP3D our "design tool." [8] Realizing that the beam dynamics is sufficiently complicated, a 1/4 scale experiment was designed and conducted using an existing 100 kV K^+ beam at the Single-Beam Transport Experiment facility at LBL, and detailed phase-space measurements were performed over a broad range of parameters. The agreement with WARP3D predictions was excellent.

WARP3D was used to determine the voltages of the diode and the quads that would yield minimal emittance growth. The final quad and diode voltages were determined on the basis of beam dynamics simulations and high voltage breakdown considerations.

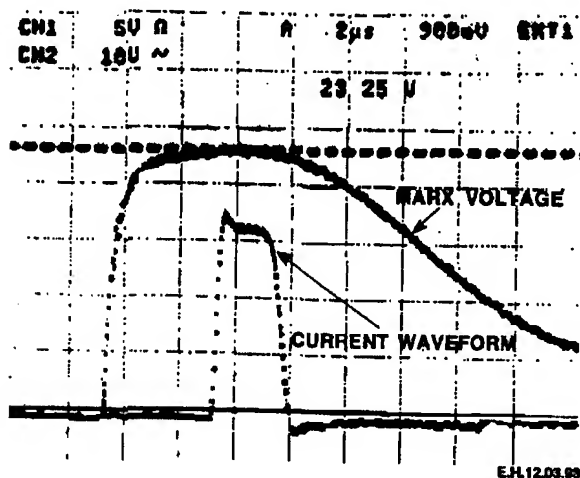


Fig.2

INJECTOR PERFORMANCE

Engineering design and construction of the ESQ injector commenced in November 1992, and the project was completed in October 1993. On the first day of operation, a K^+ beam in excess of the design parameters of 2 MV and 800 mA was produced. (See Figure 2.) The measurement of current was made with a Faraday cup and a ragowski located at the exit of the injector. The current was measured for a range of Marx voltage and pulser voltages, and the agreement with code predictions was excellent. (See Figure 3.)

The highest energy and current achieved thus far is 2.3 MV and 950 mA of K^+ , or 15% above design goals, and we have not yet attempted to push the injector to its limit of performance.

The emittance was measured with a double-slit scanner in both the horizontal and vertical directions. Over a broad range of parameters, the measured normalized edge

emittance was less than 1π mm-mr. (See Figure 4.) As the current is increased (at fixed MARX voltage), phase-space distortions are enhanced, as predicted by theory and simulations. Simulations have successfully predicted details of measured phase-space, subject to an observed sensitivity of code results to the beam extraction conditions near the source, which is not fully understood.

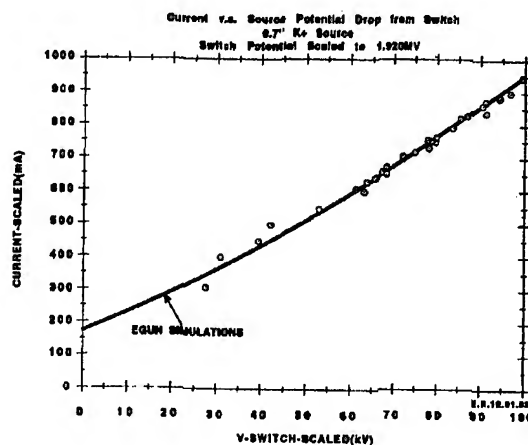


Fig.3

The measured emittance, beam radius, divergence, and beam centroid displacement are reasonably constant over the entire pulse from our measurements. (See Figure 5.)

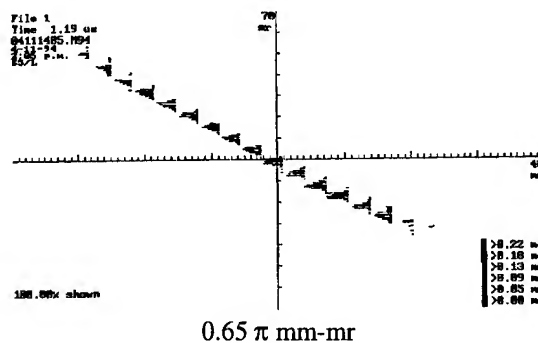


Fig. 4

To provide a high precision measurement of the beam energy from head-to-tail, we have constructed a new energy spectrometer by placing a gas stripper in front of a previously constructed electrostatic spectrometer with a maximum energy measuring capability of less than 1 MV. (See Figure 6.) The gas stripper changes the incoming singly ionized potassium ions to multiply ionized species, and the dynamic range for the K^{+n} is increased up to $n=5$, (See Figure 7.) We have measured ions to $n=5$, allowing this same device to measure ions of the full Elise 5 MeV beams.

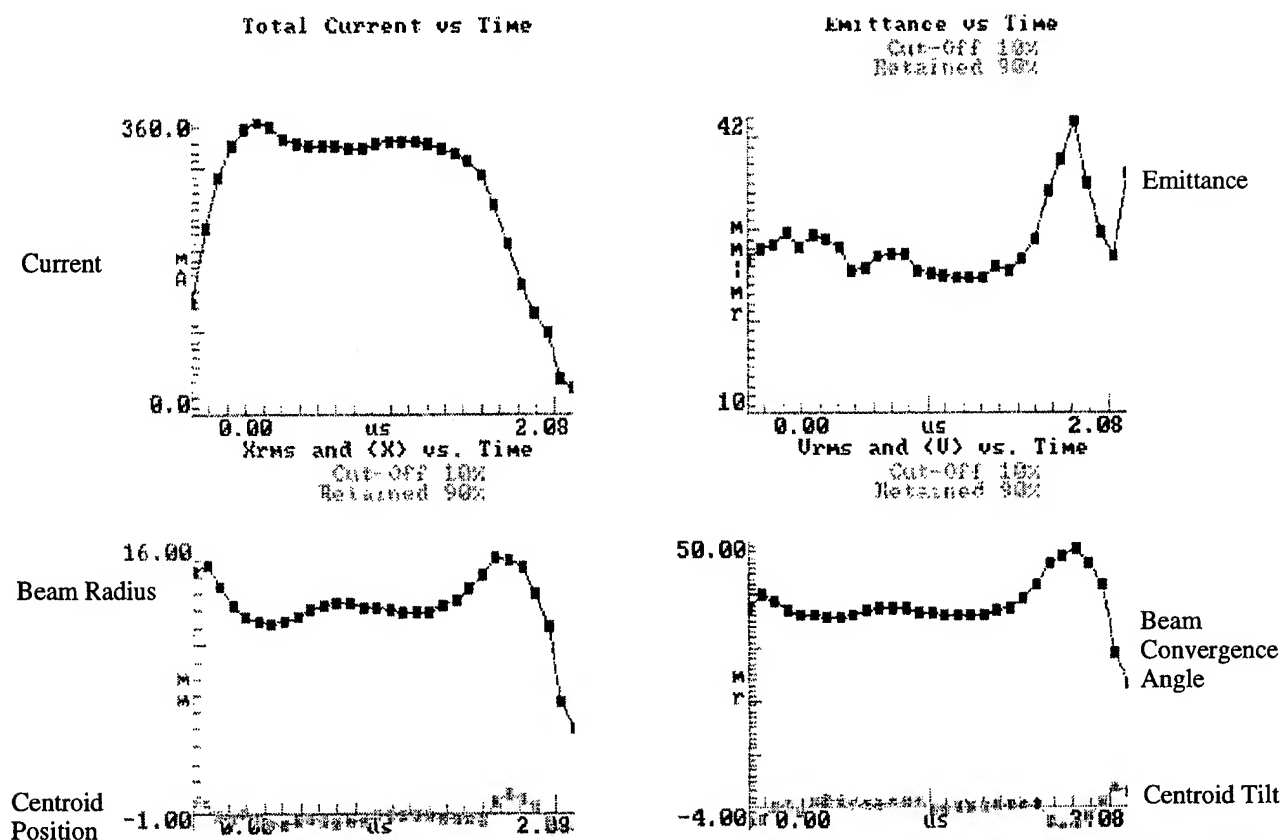


Fig.5

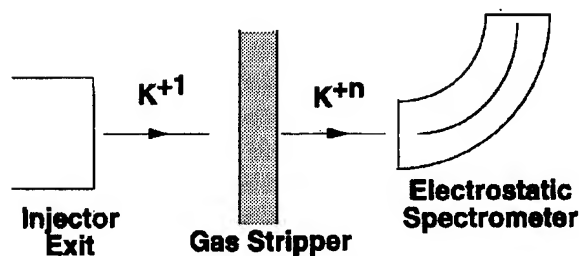


Fig. 6

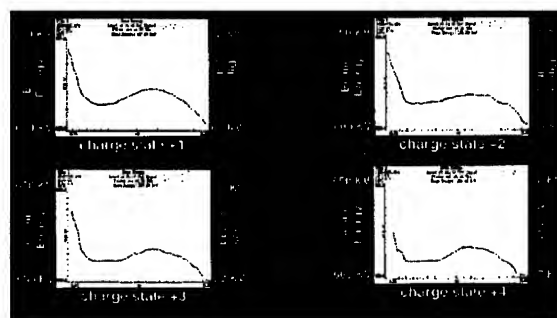


Fig.7

With this sensitive energy measuring device, we were able to "fine-tune" the extraction pulser to the point where the exiting beam is flat to less than $\pm 0.2\%$ over 1 μ s. (Figure 8) The variations of beam emittance and envelope over the pulse for the "flat" beam is expected to be further reduced from our first double-slit scanner measurements.

Detailed comparisons of the transient features observed in the experiments with WARP3D are ongoing. The goal is to deliver the entire pulse through a 3-m long matching section presently under construction, into the 2.3 cm radius Elise focusing channel.

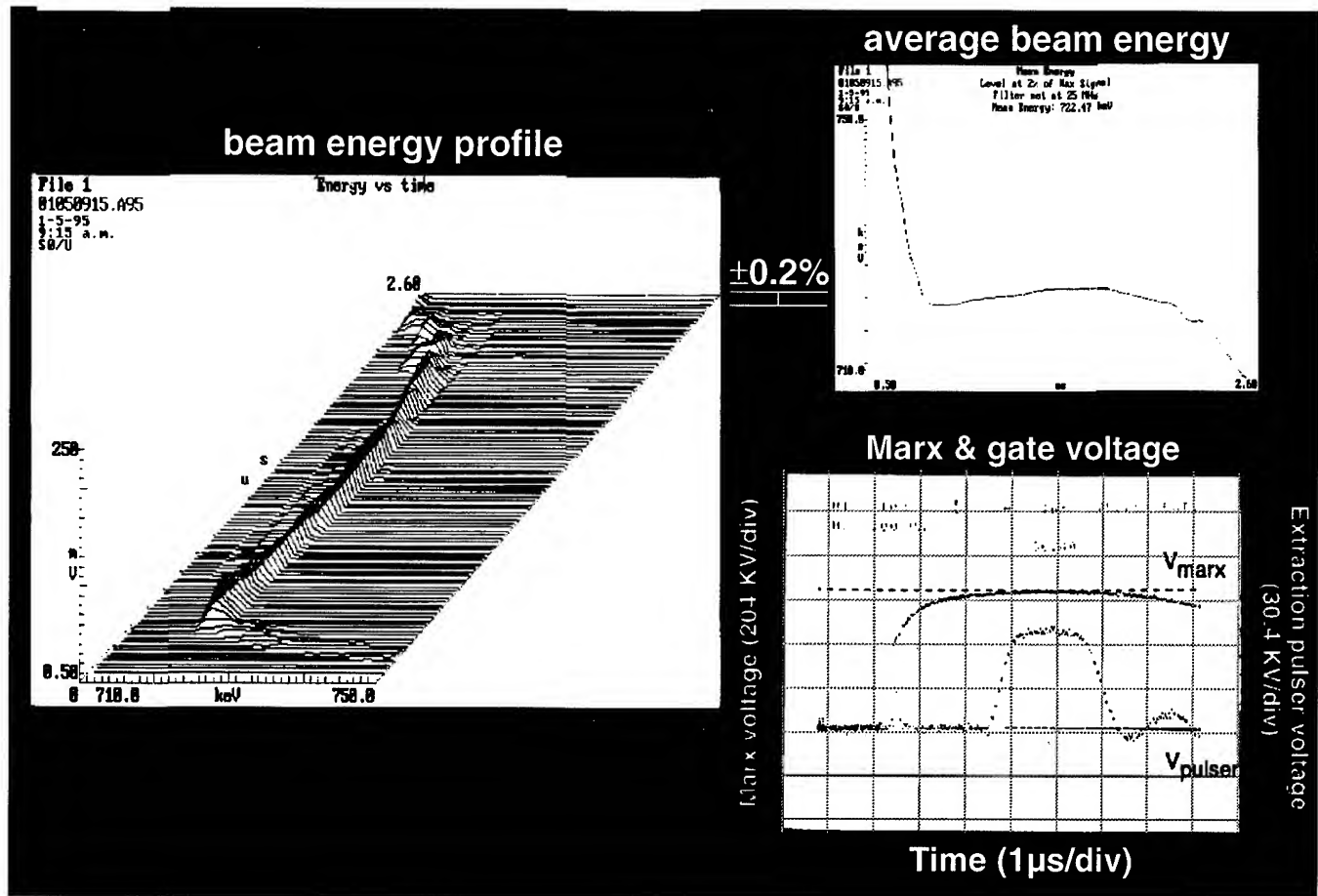


Fig. 8

REFERENCES

- [1] Hogan, W.J., Bangerter, R. and Kulcinski, G.L., "Energy from Inertial Fusion," *Physics Today* **42**, 9 (1992), pp. 42-50.
- [2] Barnard, J.J., et.al., "Study of Recirculating Induction Accelerators as Drivers for Heavy Ion Fusion," UCRL-LR-108095, Sept. 1991.
- [3] "Induction Linac Systems Experiments: Conceptual Engineering Design Study," LBL PUB-5219, March, 1989.
- [4] Abramyan, E.A., and Gapanov, V.A., *Atomnaya Energiya* **20**, 385 (1966).
- [5] Anderson, O.A., et.al., *Proceedings of the 1989 Particle Accelerator Conference, Chicago, March (1989)*.
- [6] Eylon, S., et.al., "Proceedings of the 1993 Particle Accelerator Conference, p. 3199 (1993).
- [7] Abraham, W., et.al., "Design and Testing of the 2 MV Heavy Ion Injector for the Fusion Energy Research Program," *Proceedings of this conference*.
- [8] Henestroza, E., et.al., "Beam Dynamics of the Heavy Ion Fusion Accelerator Injector," *Proceedings of this conference*.

LINAC-DRIVEN SPALLATION-NEUTRON SOURCE*

Andrew J. Jason, Los Alamos National Laboratory, Los Alamos, NM 87545

Abstract

Strong interest has arisen in accelerator-driven spallation-neutron sources that surpass existing facilities (such as ISIS at Rutherford or LANSCE at Los Alamos) by more than an order of magnitude in beam power delivered to the spallation target. The approach chosen by Los Alamos (as well as the European Spallation Source) provides the full beam energy by acceleration in a linac as opposed to primary acceleration in a synchrotron or other circular device. Two modes of neutron production are visualized for the source. A short-pulse mode produces 1 MW of beam power (at 60 pps) in pulses, of length less than 1 ms, by compression of the linac macropulse through multi-turn injection in an accumulator ring. A long-pulse mode produces a similar beam power with 1-ms-long pulses directly applied to a target. This latter mode rivals the performance of existing reactor facilities to very low neutron energies. Combination with the short-pulse mode addresses virtually all applications.

I. INTRODUCTION

Several high-intensity spallation-neutron sources exist throughout the world. These sources are in general driven by very short ($< 1 \mu\text{s}$) and intense proton pulses. The ISIS facility [1] at Rutherford Appleton Laboratory operationally delivers an average 160 kW of beam power to a spallation target at an energy of 800 MeV. The rate of pulse arrival is 50 Hz with each pulse containing 2.5×10^{13} particles. The LANSCE facility at Los Alamos [2] provides 60 kW at 20 Hz and 800 MeV with 2.9×10^{13} particles per pulse. Two other pulsed sources produce lower beam powers; IPNS at Argonne National Laboratory and KENS at KEK Japan produce 7-kW and 2-kW average beam power, respectively.

Both the ISIS and LANSCE facilities utilize a ring to compress a nominally 1-ms linac pulse to less than a microsecond. LANSCE injects into the ring at full energy, using an rf cavity to maintain bunching, while ISIS injects at 70 MeV with subsequent acceleration by rf cavities in the synchrotron ring. The two facilities have similar problems in providing an intense beam (some 15-mA peak current from the source) via a linac for rapid ring filling. However, the LANSCE higher injection energy results in qualitatively different problems and ring behavior [3]. In more recent studies even higher-power beams are proposed for injection into a ring and high-power sources directly driven by a linac are considered. A brief description of such studies and the major problems encountered form the discussion of this paper.

*Work Supported by Los Alamos National Laboratory Directed Research and Development, under the auspices of the United States Department of Energy.

II. THE BASIS FOR RECENT STUDIES

Interest in neutron sources of higher intensity has recently surfaced. In the fall of 1992 a Department of Energy panel noted that the U. S. critically needed new neutron-research facilities. It recommended that the Advanced Neutron Source (ANS), a 330-MW reactor then under study at Oak Ridge, be constructed and a study be undertaken for a 1-MW spallation source producing a short pulse (an SPSS) of less than 1 microsecond. The two types of sources would be complementary and would span the range of desired applications. In general, an SPSS produces higher-energy neutrons and is superior for high-momentum-transfer applications, while a reactor is most useful at low-momentum transfer. There is, however, considerable overlap in the applications at intermediate neutron energies and momentum transfers.

A site-independent study for the SPSS was proposed by the panel, but has not yet occurred. However, Los Alamos, Brookhaven, and Argonne National Laboratories each undertook an informal study considering the feasibility of a 1- to 5-MW SPSS facility at their respective institutions. The Brookhaven and Argonne studies proposed a synchrotron-driven source, while Los Alamos primarily considered an accumulator ring, i. e., a ring injected by a linac at the full spallation energy of 800 MeV, called LANSCE II. In particular, the design attempts to utilize the LAMPF linac and other existing institutional infrastructure.

On a similar time frame, the European Community had begun informal studies of a 5-MW SPSS, known as the European Spallation Source (ESS). The effort has developed into a formal study with respective responsibilities for the linac, ring, and target at the University of Frankfurt, Rutherford Appleton Laboratory, and KFA Jülich. Like LANSCE II, an accumulator ring scheme (at 1.3 GeV and with two rings) has become the primary focus. Other studies, such as the AUSTRON synchrotron have since emerged. These pulsed sources complement the 57-MW ILL reactor at Grenoble, France. It is worth noting that a dc cyclotron-driven 1-MW spallation source has been constructed at PSI in Switzerland.

Recently, it has become evident that the ANS reactor will not soon be constructed. Hence, recent work at Los Alamos has explored the possibility of a long-pulse spallation source (LPSS) that can provide a similar complementarity to a short-pulse source as does a reactor. In this mode, very intense linac pulses, under a millisecond in length, are impinged on a spallation target that has optimized geometry and material content to exploit the pulse time structure. While a precise equivalence between an LPSS and a reactor is difficult to state and depends on the application, an approximate figure for the neutron-source brightness has been determined [4]. This

result places a 1-MW spallation source in equivalence to a 15-MW reactor in average neutron brightness at the respective moderator output surfaces. The general utilization of this pulsed beam requires time-of-flight techniques using mechanical choppers to energy select neutron energies. From the kinetics of the energy-selection process, a further equivalence can be derived [5] that increases the effective power of the LPSS by the inverse duty factor. Hence for a 60-Hz 1-ms pulsed structure, the effective reactor power of a 1-MW LPSS is 250 MW. The validity of this figure varies widely with application.

III. A LINAC-DRIVEN SPSS

Figure 1 shows a schematic overview of the SPSS study results. A principal feature is the retention of the side-coupled-cavity portion of the LAMPF linac (SCL), which constitutes nearly 90% of the present facility and has a proven present capability of 1-MW operation at 800 MeV and at a 120-Hz repetition rate; hence most of the existing LAMPF infrastructure is plausibly retained. The Cockroft-Walton-housed source and 201.25-MHz drift-tube linac (DTL) are replaced by a 402.5-MHz radio-frequency quadrupole (RFQ) and DTL that accelerate 30-mA peak current of H^- ions to 20 MeV. Subsequent acceleration to 100 MeV by an 805-MHz DTL allows injection into the 805-MHz SCL. The change in frequency at 20 MeV permits the future addition of a funnel for possible upgrades in current.

The 1.2-ms macropulse is then injected into a 169-m circumference accumulator ring, using charge-changing injection at a foil, to produce a 560-ns burst of 1.3×10^{14} protons at the two spallation targets via a transport line that

contains switching elements to supply separate pulse trains at 40 and 20 Hz to the two targets.

A review of the design was held by a panel of external experts and an extensive feasibility study document has been prepared as well as previous publication [6]. We concentrate here on the major issues that have been raised by the study and review the evolution from LAMPF and PSR operating experience to the present design.

A. Linac front end

The injector consists of an H^- -ion source that must operate reliably at a duty factor of 8.6% and provide an adequate emittance ($\sim 0.02 \pi$ cm mrad rms normalized) at a nominal 40-mA peak current. While several candidate sources can produce either the required emittance, current, or duty factor, there exists no one source capable of meeting these three specifications. However, it is believed that with modest development, a suitable source can be obtained. A recent workshop [7] at Lawrence Berkeley Laboratory, under the auspices of a site-independent study, has further explored source development for this application.

The problem of chopping the beam (235 ns beam off, 436 ns beam on), to maintain a clean ($< 10^{-4}$ contamination) gap for extraction from the ring, seems more difficult [8]. The LAMPF chopper (a traveling-wave deflector) operates in a long low-energy transport line (LEBT) at 750 keV. Neutralization effects and other difficulties may preclude chopping in the proposed 100-keV LEBT; since the RFQ accelerates to 7 MeV and must be closely coupled to the first DTL, no convenient place exists for this form of chopping. Splitting up the RFQ into low- and high-energy sections with chopping between may succeed without undue emittance

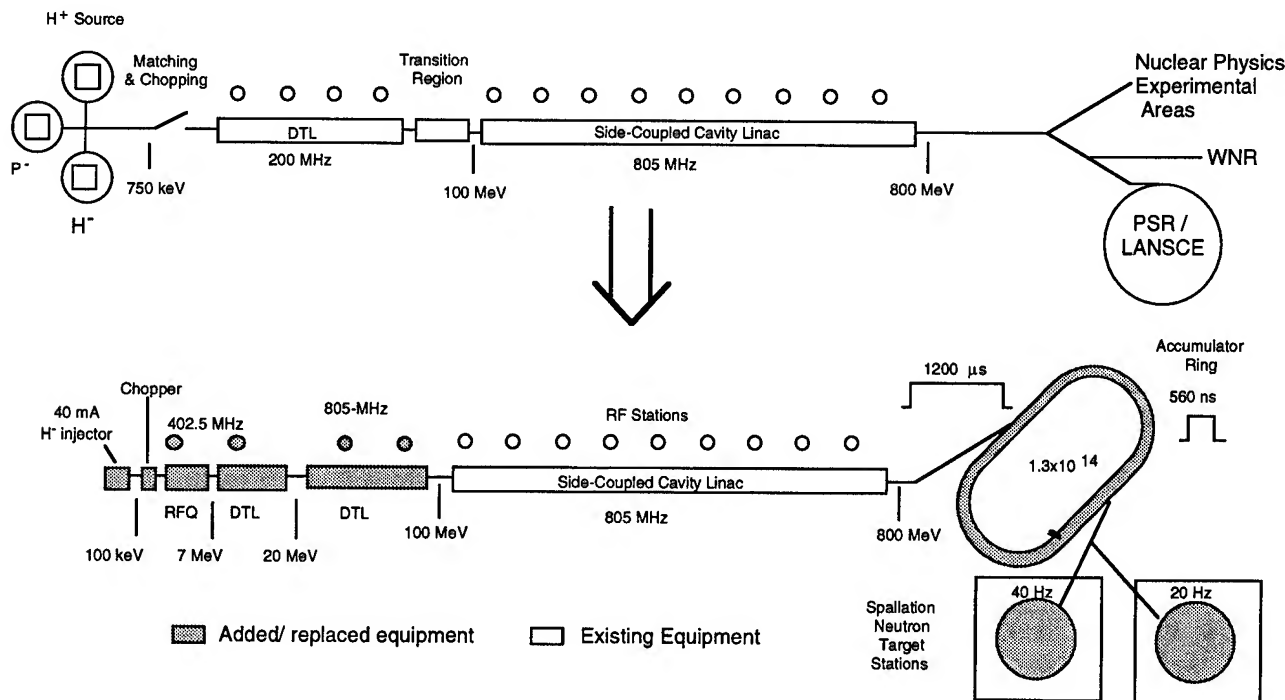


Figure 1. Schematic layout of the 1-MW upgrade. The present configuration of LAMPF is shown at the top.

growth. However, the longitudinal and transverse focusing arrangements needed become very elaborate. High-energy chopping requires undue pulsed power and high beam-power deposition to dump the unwanted portion of the beam.

Chopping in the source by some rapid-modulation method appears very attractive. Preliminary progress toward this end has been made by placing a toroidal collar near the extraction aperture of a Penning discharge source [9]. Pulsing the collar to 38 V and 100 A provides better than 90% chopping efficiency and 1- μ s rise time. These results are limited by equipment and more sophisticated experiments are planned. The technique may be useful in reducing dumped beam power at a second stage of chopping at higher energy even if desired efficiencies are not obtained.

The RFQ and DTL designs are based on extrapolation of experience with linac facilities constructed for projects such as the Ground Test Accelerator (GTA) [10] and other designs. By comparison, the currents and beam quality required here are relatively modest and the front end should perform adequately at substantially higher currents.

B. The Side-Coupled Linac

The SCL is required to operate at nearly twice the peak current (29.7 mA) routinely experienced during present operation (13 to 17 mA). However, the charge per rf bucket is actually less because the beam frequency is doubled, thus easing the beam-dynamics stress. Moreover, the peak-average current (19.3 mA averaged over the 1.2-ms macropulse) is only slightly increased.

It remains to show that the rapid current variation during the 1.49-MHz chopping cycle does not affect linac operation. We expect that the rf fields in the SCL tanks will experience cyclic variations of about 1% in amplitude and 0.3° in phase over each 671-ns chopping cycle, a phenomenon we call "drop." Simulations show that a 5% amplitude drop would not appreciably affect the output energy or beam quality. Because of the increased power flow along each linac module from average beam loading, the field at the tank ends decreases relative to that at the rf-feed point in the presence of beam. This "droop" should not be a concern because of the small current increase from proven operation.

To validate these calculations and to assess general linac robustness, beam experiments on the linac were performed with chopped and unchopped beam at peak-current levels of up to 27 mA at 201.25 MHz. A droop of less than 2% was measured at each end of a 211-MeV module. The separate and combined effects of drop and droop were inferred from ΔT measurements. In accord with the beam-dynamics simulations, inappreciable effects were seen at the experimental current levels.

The results of these experiments (which included testing of new adaptive feed-forward rf-control techniques developed for GTA) and other assessments show the linac to be very robust for the 1-MW scenario. Further work is necessary to elucidate the high loss rate noted for H^- beams and more sophisticated tuning algorithms are under study. At peak

currents above 100 mA, substantial modifications would be required to prevent deterioration of beam quality. These include dividing the tanks into smaller units in order to increase the number of rf feeds and decrease the focusing period.

C. Accumulator ring

The proposed accumulator ring [11] has a doublet lattice, is racetrack shaped and features dispersionless straight sections for extraction and a chicane region that places the injection point outside the ring body. The nominal tunes are 4.23 and 5.19 and the maximum beta functions are 16.62 m and 17.93 m for the x and y planes, respectively. Maximum dispersion in the achromatic arcs is 7.70 m with a momentum acceptance of $\pm 1\%$. The ring acceptance is maintained at 33π cm mrad for a nominal beam (laboratory) emittance of 15π cm mrad.

Particular attention was paid to loss mechanisms that have been predominant in causing activation in the PSR. Loss should be diminished by the nature of the lattice, improved injection matching, and larger apertures. Other loss mechanisms require special measures.

A particular loss mechanism that was first noted on the PSR, and must play a role in any foil-stripping injection scheme, involves the production, by the foil, of neutral hydrogen atoms in excited states [12]. These neutrals then move outside the ring acceptance due to subsequent relative deflection by the field of a downstream magnet; most are stripped by the magnet's field and are lost in downstream areas. For the PSR, about 0.25% of the injected beam is thus lost. A mechanism has been devised, involving placement of the stripper foil in a magnetic field, to decrease this loss by over two orders of magnitude and is described elsewhere [13].

Scattering of the injected and stored beam by the foil leads to inevitable losses. Nuclear scattering accounts for some 15 nA which is lost immediately downstream of the foil. Coulomb scattering and other unspecified sources are assumed to lead to 150 nA of loss. A series of collimators, directly downstream of the injection section and with magnetized tips, have been devised to localize this loss so that most of the ring can be maintained without remote handling. The ring momentum acceptance is also limited by a collimator in a dispersive arc. Performance of a first-order collimator scheme has been verified by simulations.

Further loss mechanisms are linked to the beam formation process and the detailed beam dynamics.

The longitudinal injection process is important in maintaining a clear gap (~ 100 ns) in the beam for rise of the extraction kicker and in achieving a maximum bunching factor (~ 0.6). A large bunching factor is important in minimizing the space-charge tune shift, hence affecting the number of particles that can be stored. A "barrier-bucket" rf-bunching waveform, consisting of the 1.49-MHz fundamental and four harmonics, is selected for this purpose. The bucket exerts a force on accumulated particles only near the bucket extremes. By sweeping the injected-beam energy through

four cycles by ± 4 MeV and using measured results for the beam-energy spread, adequate confinement of particles can be achieved, but with a resultant rf-power cost of over 1.5 MW in the 13 ferrite-loaded buncher cavities. With this arrangement, the gap remains particle free to the 10^{-4} level and a bunching factor of 0.55 is achieved.

The large rf-power requirement is inevitable under the assumptions for injected-beam momentum spread but is undesirable, and presents a large longitudinal impedance to the beam because of the large number of cavities needed. The rf power may be reducible by rf-compaction of the injected beam-energy spread; however, the beam longitudinal halo may be highly nonlinear and not amenable to such measures. It is also possible to reduce the rf power by decreasing the value of the ring transition gamma (γ_T), at the possible cost of beam stability. Substantial reduction of γ_T is only possible by abdicating the feature of the dispersionless straight section that contains the injection chicane. Thence, the injection-painting scheme, uncoupled between longitudinal and transverse planes, must be forsaken as well as the last vestige of ring symmetry in the second-order-achromat-configured arcs. Our initial studies conclude that high rf-power use may be necessary to maintain an acceptable loss budget.

Maintenance of a beam-free gap and a large bunching factor may also bear on the problem of beam stability. A rapidly rising instability has been observed in the PSR that presently limits PSR peak currents [14]. The effect has the signature of a two-stream instability and is attributed to the presence of protons in the extraction gap, from insufficient rf capture, with consequent trapping of electrons. Further exploration of this instability is essential to any new facility.

Transverse-beam formation is accomplished by separate vertical and horizontal bumps using four pulsed magnets in each plane. The achromatic injection-transport line maintains the injected beam at a constant location on the foil. The foil is assumed to have a free corner and, with bump sequencing to produce a uniform distribution, less than 10 encounters with the foil will be experienced on average by each injected particle. The bumps are maximum at the start of injection and relax to zero at the end. This particular injection scheme produces an octupolar distribution in the beam that is of consequence in the beam evolution. Other sequencing arrangements under consideration can grow an elliptical beam, but do not provide an immediate tune shift to the operating point. Foil heating is substantial, with peak temperatures approaching 2500 K; experiments are called for to determine foil durability.

The beam tune shift is about 0.11, to a region of tune space that is free of low-order resonances. However, the tune spread is sufficiently large to require ring-chromaticity correction. Resonance correction through fifth order is planned to provide ample margin in tune space. The lack of supersymmetry in the ring is not seen as a problem during the short storage time.

IV. A LINAC-DRIVEN LPSS

The Long-Pulse mode requires 1 MW of delivered beam power at 60 Hz with 1-ms macropulse length, implying a peak current of 21 mA. The peak-current and duty factor requirements of the LPSS are hence similar to those of the SPSS. However, we have considered an option that addresses near-term reliable low-beam-loss operation, with substantially lower cost but with little possibility of upgrading to provide higher duty factors or peak current.

The present LAMPF linac operates very reliably with low activation at peak H^+ currents of about 14 mA. Beam powers exceeding 1 MW have been routinely produced at 120 Hz operation. Hence the linac is currently suitable for LPSS operation at about 0.6 MW. However, beam loss increases very rapidly with peak current and beam loading in the 201.25-MHz DTL exceeds the capacity of the rf systems. A study [15] shows that transient loss occurs in the DTL at the start of the macropulse due to the effective speed of the rf-control loops. Most of the non-transient loss is due to the longitudinal beam tails injected into the DTL that are a consequence of initial bunching by single-frequency cavities in the low-energy transport line before the DTL. Additional loss occurs because of the lack of longitudinal matching in the transition region between the DTL and SCL.

The LPSS study has proposed the changes shown in Figure 2. The changes include features that preserve capabilities for providing beam to the present facilities, LANSCE (with possible upgrades to 60 Hz) and the Weapons Neutron Research (WNR). Both facilities utilize H^- beam and require chopping. The suggested changes are:

- 1) Replace the present injectors and DTL first tank with a 201.25-MHz Radio-Frequency Quadrupole (RFQ) linac to accelerate to an energy of 5.395 MeV. The H^+ and H^- beams are focused, chopped, and merged by a new transport line at 100 keV, before the RFQ. A two-buncher matching section is placed after the RFQ. This arrangement produces the appropriate transverse and longitudinal match to the second tank of the DTL.
- 2) Replace the 201.25 MHz rf system with a new-tube version that will produce adequate peak and average power.
- 3) Install an 805-MHz bucket-rotator cavity in the transition region that will provide a good longitudinal match to the SCL.
- 4) Upgrade the low-level rf-control system on the SCL for operational ease and removal of initial transient loss on the macropulse.
- 5) Provide an upgraded set of beam-diagnostic systems.
- 6) Provide transport to the LPSS target
- 7) Install a laser system that neutralizes H^- beam to provide chopping for WNR operation.
- 8) Provide a computer-control-system upgrade in support of the modifications.

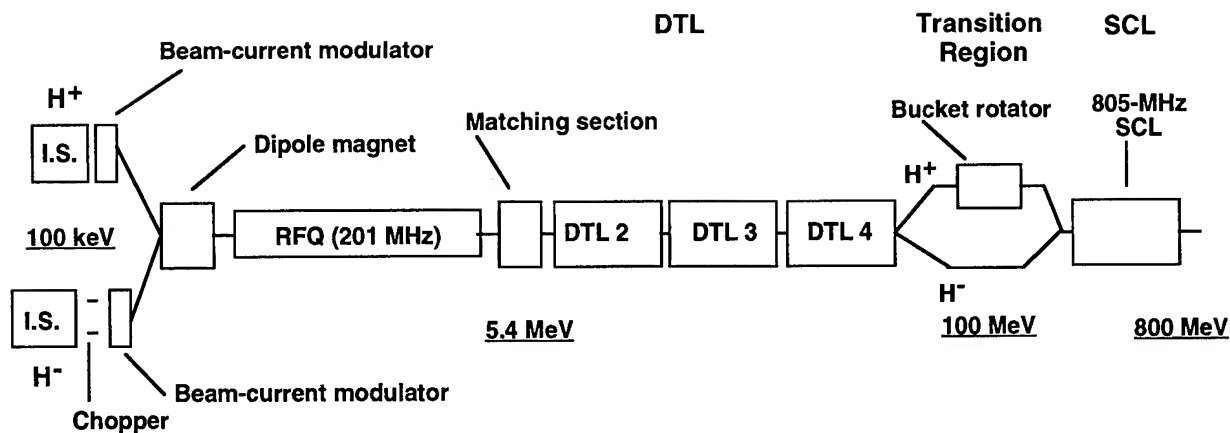


Figure 2 Schematic layout of the LAMPF linac after modification for the LPSS mode.

The inherent ability of the RFQ to produce cleanly bunched beams, along with excellent matching to the DTL eliminates the longitudinal loss while an adaptive feed-forward-control system installed on the 805-MHz SCL rf system controls the transient loss. A peak-current capability of over 28 mA is expected with these modifications, limited by the rf capacity of the SCL. Negligible beam losses are expected.

Requirements for LANSCE and WNR operation are met by two separate chopping operations of the H⁻ beam. The 2.8-MHz LANSCE chopper resides in the 100-keV transport line just after the source. Although, as previously noted, chopping is difficult in this region, the high line energy and low-peak current (15 mA) should allow successful operation. Developmental studies are under way. WNR requires chopping for individual micropulse selection at 5.6 MHz. Such chopping is incompatible with the RFQ and is to be done, on the basis of previous feasibility studies, at 800 MeV in a transport line by the neutralization of individual micropulses in the LANSCE macropulse.

The LPSS target is to be located in Area A, some 100 meters directly downstream of the linac. Area A currently contains several facilities and instruments used for nuclear-physics work. These will be removed and a target, surrounded by a monolith shield with remote-target-handling capabilities, installed. The proton beam strikes a 7-cm-diameter water-cooled tungsten target horizontally and neutrons are delivered to the experimental instrumentation through several horizontal beamlines that penetrate the shield.

Beam is transported to the target by much of the existing transport line with a 30-m-long final expansion region. A novel expander incorporates nonlinear elements to produce a hard-edged beam on the target with parabolic profiles from the initially gaussian-distributed beam.

VI. REFERENCES

- [1] I. S. K. Gardner, "ISIS Status Report," Proc. Fourth European Particle Accelerator Conference, London (1994), p3.
- [2] R. J. Macek, et al., "Status of the PSR Improvement Program," Proc. 1993 PAC, p 3739.
- [3] R. J. Macek, "Machine Studies at the Los Alamos Proton Storage Ring," Proc. Twelfth Meet. International Collaboration on Advanced Neutron Sources (ICANS XII), Abingdon, England (May 1993), Vol 2, p A-25.
- [4] G. Russell, LER, Los Alamos National Laboratory, private communication.
- [5] F. Mezei, "Comparison of Neutron Efficiency of Reactor and Pulsed Source Instruments," Proc. Twelfth Meet. International Collaboration on Advanced Neutron Sources, Abingdon, England (May 1993), Vol. 2, p I-377.
- [6] A. J. Jason, et al., "A Los Alamos Design Study for a High-Power Spallation-Neutron-Source Driver," in Proc. 1993 PAC, p. 3760.
- [7] In "Proceedings of the Workshop on Ion Source Issues Relevant to a Pulsed Spallation Neutron Source," ed. Lee Schroeder, et al., LBL-36347, Berkeley, October 24-26, 1994.
- [8] S. Nath, T. P. Wangler, and R. R. Stevens Jr., "Conceptual Design of Beam Choppers for RFQ Linacs," in these proceedings.
- [9] H.V. Smith, Jr., P. Allison, J. D. Schneider, and J. E. Stelzer, "Experimental Study of a Simple Method to Chop Penning SPS H⁻ Beams," Proc. Linear Acc. Conf., August 22, 1994, KEK, Japan.
- [10] K.F. Johnson, et al., "Commissioning of the First Drift Tube Linac Module in the Ground Test Accelerator," Proc. 1993 PAC, p 1669.
- [11] B. Blind, A. J. Jason, and F. Neri, "Lattice Design of the LANL Spallation-Source Compressor Ring," in Proc. 1993 PAC, p 56.
- [12] R. Hutson and R. Macek, "First-Turn Losses in the LAMPF Proton Storage Ring (PSR)," Proc. 1993 PAC, p 363.
- [13] A. J. Jason, et al., "Minimization of First-Turn Losses by Excited Neutrals in Charge-Changing Injection of Accumulator Rings," Proc. Fourth European Particle Accelerator Conference, London (1994), p 1219.
- [14] T. Wang, et al., "Recent Study of Beam Stability in the PSR," Proc. 1993 PAC, p. 3297.
- [15] R. W. Garnett, et al., "Simulation Studies of the LAMPF Proton Linac," in these proceedings.

High Average Power, High Current Pulsed Accelerator Technology

Eugene L. Neau

Sandia National Laboratories, Albuquerque, NM

I. ABSTRACT

High current pulsed accelerator technology was developed during the late 60's through the late 80's to satisfy the needs of various military related applications such as effects simulators, particle beam devices, free electron lasers, and as drivers for Inertial Confinement Fusion devices. The emphasis in these devices is to achieve very high peak power levels, with pulse lengths on the order of a few 10's of nanoseconds, peak currents of up to 10's of MA, and accelerating potentials of up to 10's of MV. New high average power systems, incorporating thermal management techniques, are enabling the potential use of high peak power technology in a number of diverse industrial application areas such as materials processing, food processing, stack gas cleanup, and the destruction of organic contaminants. These systems employ semiconductor and saturable magnetic switches to achieve short pulse durations that can then be added to efficiently give MV accelerating potentials while delivering average power levels of a few 100's of kilowatts to perhaps many megawatts. The Repetitive High Energy Pulsed Power project is developing short-pulse, high current accelerator technology capable of generating beams with kJ's of energy per pulse delivered to areas of 1000 cm² or more using ions, electrons, or x-rays. Modular technology is employed to meet the needs of a variety of applications requiring from 100's of kV to MV's and from 10's to 100's of kA. Modest repetition rates, up to a few 100's of pulses per second (PPS), allow these machines to deliver average currents on the order of a few 100's of mA. The design and operation of the second generation 300 kW RHEPP-II machine, now being brought on-line to operate at 2.5 MV, 25 kA, and 100 PPS will be described in detail as one example of the new high average power, high current pulsed accelerator technology.

II. TECHNOLOGY INTRODUCTION

The very high peak power, single-pulse accelerators developed during the early 60's through the present were designed to simulate weapons effects (HERMES-III⁽¹⁾, DECADE⁽²⁾) or as drivers for the Inertial Confinement Fusion program (PBFA-I⁽³⁾, PBFA-II⁽⁴⁾) or to power beam devices (ATA and ETA-I⁽⁵⁾). The development and commercial availability of METGLAS[®] alloys during the

early 80's allowed the development of a new class of high average power accelerator that is capable of efficient repetitive operation up to 10⁴ PPS⁽⁶⁾ using semiconductors, thyatrons, and saturable core magnetic switches. The saturable switches were employed in the ETA-II⁽⁷⁾ accelerator, were investigated for use on PBFA-II⁽⁸⁾, and are now employed in current high average power systems. The Physics International Company CLIA accelerator⁽⁹⁾ is capable of high power short burst mode output, to 120 kW. The short-pulse systems, by incorporating thermal management techniques⁽¹⁰⁾, can run continuously as demonstrated by the Science Research Laboratories SNOMAD-IV operating at 38 kW⁽¹¹⁾, the Sandia RHEPP-I operating at 120 kW⁽¹²⁾ and RHEPP-II at about 240 kW⁽¹³⁾. Application development can follow the availability of new tools, such as the high current pulsed accelerators, and these high-power systems are beginning to generate new fields of commercial interest. This paper discusses some of the application issues that are driving the development of short-pulse, high current machines and the modular technology approach taken in the development of the RHEPP systems.

III. IDENTIFICATION OF SHORT-PULSE APPLICATION REQUIREMENTS

Short-pulse, high peak power technology was developed to address specific military single-pulse threats and involves a number of stages of pulse compression to deliver the 10's of nanosecond wide output pulses. Short-pulse, high average power accelerators, with their unique capabilities, are, in general, more complex than other high voltage, high average power technologies such as the DC Dynamitron machines from Radiation Dynamics Inc.⁽¹⁴⁾, the North Star Research Corp. Nested High Voltage Generator (also having pulsed output capabilities)⁽¹⁵⁾, or the ELV series of accelerators from the Former Soviet Union (FSU)⁽¹⁶⁾. The new short-pulse machines, with kJ's of energy per pulse, also have capabilities that are distinct from those provided by high power RF machines such as the Atomic Energy Canada Ltd. IMPELA⁽¹⁷⁾ or the Ion Beam Applications Rhodotron⁽¹⁸⁾. These presently available technologies, including the pulsed SNOMAD-IV accelerator, rely on output beams, at 1000 A or less, that are a few

millimeters in diameter and are scanned across the product under treatment. The high current accelerators delivering 10's of kA per pulse, with kJ's of beam pulse energy, offer the possibility of treating 100's to 1000's of square centimeters per pulse, without beam scanning, depending on the energy per unit volume required by the target to achieve the desired internal effects. The required beam accelerating potential, for any of the above systems, is set by the desired energy penetration in the target material. The beam penetration sets the dose uniformity in the target. To offset the cost of the pulse compression stages in the short-pulse, high average power, high current machines, applications must be identified that require some combination of 1) high volume or mass throughput, 2) very high dose levels, 3) high dose rates, 4) large area uniform beams, 5) radiochemistry enhanced by short pulses, and 6) short pulses of energy to allow unique non-equilibrium material conditions. Short-pulse applications, in general, are non-thermal processes such that the temperature of the bulk treated material does go much above ambient conditions. A number of Ion Beam Surface Treatment (IBEST)⁽¹⁹⁾ applications are processes that offer increased surface hardness, surface smoothing, increased corrosion resistance, specifically because of the short energy deposition and melt times followed by rapid resolidification through thermal diffusion into the base material. Continuous commercial applications of IBEST technology to treat polymers and metals will require simple and reliable short-pulse repetitive driver systems operating at 100's of kW. Some organic chemical decomposition processes can be enhanced by using short pulses with high dose rates and large total dose⁽²⁰⁾. Current application development efforts are focusing on identifying and demonstrating basic processes that can be expected to improve when using the short-pulse beam technology.

IV. HIGH POWER, HIGH CURRENT SYSTEM CONSIDERATIONS

High peak power capabilities were achieved by combining very high voltages, to 20 million volts⁽²⁾, with very high current handling capabilities, to 30 million amperes⁽⁴⁾. High voltage operation was made possible by using the increase of dielectric strength of various materials and interfaces that occurs when using sub-microsecond pulses⁽²¹⁾. Pulses, with a FWHM of a few 10's of nanoseconds can be added together in transmission line structures, with or without magnetic blocking cores⁽²²⁾, to efficiently achieve higher voltages in more compact structures than are possible with directly switched compression schemes.

A. High average power switching techniques

The required pulse compression in the high peak power accelerators is achieved by employing switching techniques in the pulse compression stages based on plasma formation, or control, between metal electrodes either in a vacuum or immersed in a gas or liquid insulant. These switching techniques, while suitable for single pulse or low repetition rate systems are difficult to use in very high average power systems because the energy deposited in the insulant during the transition from high-to-low impedance results in electrode damage and erosion. Saturable core magnetic switches, first proposed for use in pulse compression lines by Melville⁽²²⁾, became an economically viable replacement for plasma switches with the development of the METGLAS[®] alloys by AlliedSignal in the early 80's. A prototype magnetic switch that operates at 500 kW in the RHEPP system is shown in Figure 1 with oil cooling manifolds.

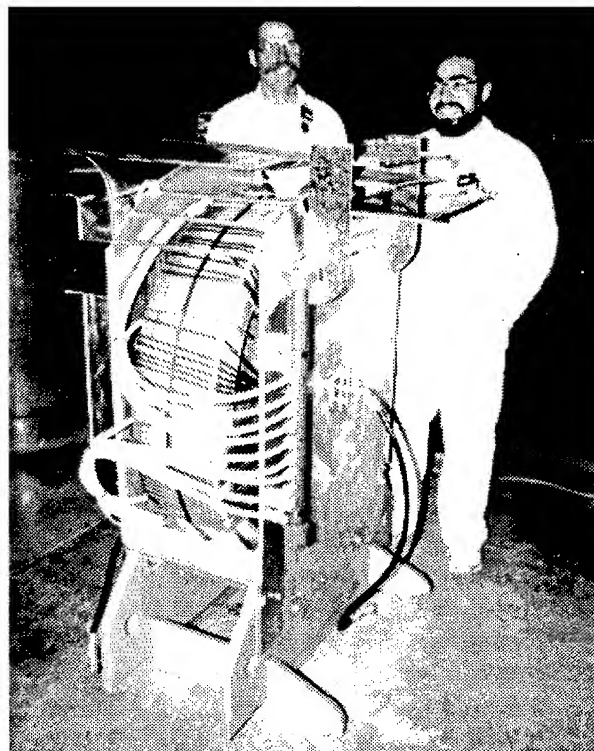


Figure 1. Fifth stage RHEPP 250 kV magnetic switch, with oil cooling manifold

The energy lost during each switching cycle, which requires the addition of cooling, is held to about 1% in the windings plus another 1% in the alloy core. While the switch of Figure 1 does compression on the microsecond time scale, similarly wound magnetic switch cores are employed in a coaxial geometry to produce the 60 ns FWHM pulse forming line output pulses at 250 kV, 130 kA, and 350 kW. The simplicity of the basic switch design combined with the low energy losses during

switching, allow such devices to pass currents greater than 1 MA⁽⁸⁾ without difficulty. Magnetic switch volume can be shown to be proportional to pulse energy, but practical considerations limit the operating voltage while operating currents and pulse risetimes are limited by circuit impedances.

B. High average power voltage multiplication

The high pulse current capabilities of magnetic switches can be combined with high-current linear induction voltage adder (LIVA) technology that has demonstrated operation up to 20 MV and 700 kA in HERMES-III⁽²⁾. The basic adder geometry has been described elsewhere. The central transmission line may be oil insulated as in the RHEPP-I accelerator, as a magnetically insulated transmission line (MITL) when fields are sufficient to cause electron emission, or as a vacuum insulated line when fields are at or below emission thresholds as in RHEPP-II.

V. RHEPP-II SYSTEM DESIGN AND OPERATION

A. Power compression to the microsecond time scale

The five stage magnetic compressor shown in Figure 2, previously employed on the RHEPP-I system, has been modified to use an SCR switcher between the compressor and a DC charged energy storage capacitor, rather than the fixed 120 Hz, 600 kW Westinghouse alternator used in the previous system⁽⁹⁾.

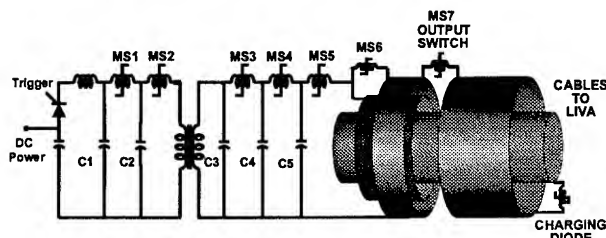


Figure 2. Basic RHEPP pulse compression circuit

This change was dictated by the desire to demonstrate applications on RHEPP-II at a specified pulse repetition rate, specified total number of pulses (burst-mode), and specified total dose. The variable pulse rate also improves the conditioning of the vacuum insulated LIVA transmission line and cathode holder. This 5 stage modulator has a measured energy transfer efficiency of approximately 85%, includes active cooling of all components, and has operated for several hours at full power. All switches are high power semiconductors or tape wound magnetic switches with oil cooling channels. Similarity of construction to capacitors should allow long-life reliable operation, however this has not yet been

quantified. The high overall system efficiency minimizes operating costs in commercial applications.

B. Fast Blumlein pulse forming line operation

The 5-stage microsecond compressor charges a magnetically inverted, water-filled coaxial Blumlein pulse forming line (PFL) also shown in Fig. 2. A magnetic switch, MS6 in Fig. 2, inverts the outer transmission line to causing 500 kV to be impressed on the final output switch. The magnetic switch, MS7 in Fig. 2, forms the 60 ns wide output pulse which is delivered by 50 coaxial cables to the 10 stage voltage adder shown in Figure 3.

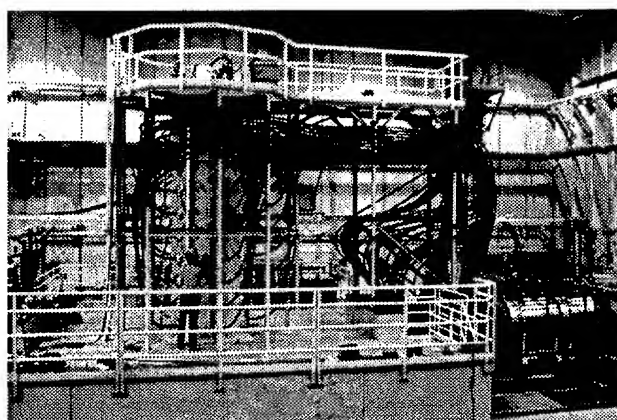


Figure 3. 2.5 MV RHEPP-II voltage adder

C. 10 stage linear induction voltage adder

Each of the 10 LIVA cavities are fed by five, 44 ohm Dielectric Sciences cables and each cavity delivers a 250 kV pulse through an oil-vacuum insulator to the center transmission line stalk. The center transmission line operates with fields below 300 kV/cm so that it is not expected to operate in the MITL regime, but rather as a vacuum insulated transmission line. Inner and outer wall B-dot measurements indicate that vacuum electron flow is absent after very few pulses. The output of the 10 stage, 80% efficient, voltage adder is approximately 2.3 MV and 25 kA in a 60 ns FWHM pulse at up to 100 PPS, as set by the primary SCR trigger.

D. Broad area e-beam cathode and beam measurements

The design and implementation of a long-life cathode structure capable of emitting 25 kA of current in a 60 ns pulse at repetition rates of up to 120 PPS could pose a difficult problem. Low current RF accelerators or Linear Induction Adders (LIA's) typically use dispenser cathodes, which require good vacuum conditions, to

create the very low emittance beams that propagate through the accelerating structure

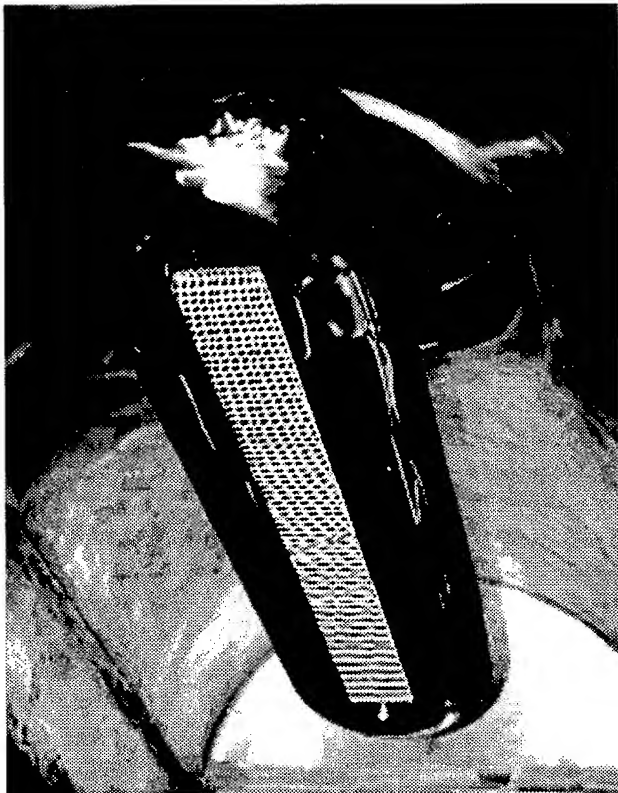


Figure 4. 10 cm by 100 cm flashover cathode assembly

With the single accelerating gap approach used in the RHEPP machines, field emission cathodes, with simple construction, have demonstrated lifetimes of about 10^8 shots at current densities of about 25 A/cm^2 at the Institute of High Current Electronics in Tomsk, Russia. The Rhepp-II accelerator uses a 10 cm by 100 cm cathode, shown in Fig. 4, that matches the accelerator impedance of 88 ohms with an anode-to-cathode gap of 20 cm.

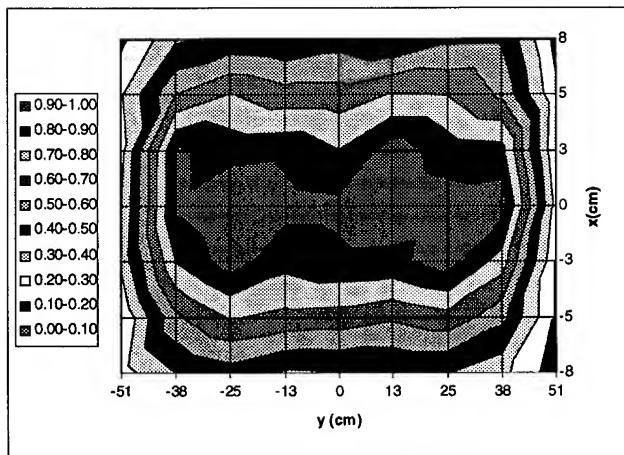


Figure 5. Measured electron beam uniformity 10 cm below the foil window (10% bands)

The preliminary beam uniformity (measured when oil was present in the adder and diode system) is shown in Fig. 5. The measurement were made by an array of 63, 1 cm^2 radiochromic film dosimeters that were located in a plane 10 cm below the 15 mil titanium beam exit window. The dosimeters were mounted in a rectangular beam confinement box, at atmospheric pressure. We are characterizing the operation of this system in both the electron beam and x-ray modes of operation.

E. Operational controls

The RHEPP systems are designed to allow the acquisition of experience necessary to design systems capable of operation in a full scale production plant. The required power operating costs are low due to high system efficiency (50% wall-plug-to-beam). To reduce manpower costs, we have simplified and integrated operational aspects around low cost Programmable Logic Controllers (PLC's) which use simple commands from a touch screen panel to set all accelerator operating parameters. This aspect of the accelerator implementation is still in the early stages of development but we are already experiencing the benefits provided by this approach.



Figure 6. Programmable Logic Controller operational center for the RHEPP-II system

VI. CONCLUSION

The high average power, high current pulsed accelerator technology development, as represented by the RHEPP machines, offers new opportunities in commercial applications. The short pulses can deposit energy in specific product volumes by using large area beams of ions, electrons, or x-rays without raising the temperature of the bulk material. This non-thermal deposition gives rise to high overall system efficiencies because only the desired effects are targeted by the beam. Ion beam

treatment of surfaces is one example where short pulses can cause rapid melting and re-solidification for increased hardness, corrosion etc. Recent demonstrations, at greater than 200 kW average power and 2.5 MV on the RHEPP-II accelerator, offer exciting possibilities for industrial application developments.

VII. ACKNOWLEDGMENTS

The author gratefully acknowledges the continued long term support of Donald Cook, Kenneth Prestwich, and J. Pace VanDevender and especially the entire RHEPP development team at Sandia. This work was supported by the United States Department of Energy under Contract DE-AC04-94AL85000.

VIII. REFERENCES

- [1] C. McDonald and P. Sincerny, "Electrical Modeling of a Fast Charge, Inductive Store Concept for DECADE", Proc. of the Eighth IEEE International Pulsed Power Conference, San Diego, CA, June 16-19, 1991, pp 675-679
- [2] J. J. Ramirez, et al, "The HERMES-III Program", Proc of the Sixth IEEE Pulsed Power Conf, Arlington, VA, June 29-July1, 1987, pp 294-299
- [3] T. H. Martin, et al, "Pulsed Power Accelerators for Particle Fusion", Conf. Record of the 1980 Fourteenth Pulse Power Modulator Symposium, June 3-5, 1980, pp 300-304
- [4] T. H. Martin, et al, "PBFA-II, The Pulsed Power Characterization Phase", Proc of the Sixth IEEE Pulsed Power Conf, Arlington, VA, June 29-July1, 1987, pp 225-232
- [5] L. L. Reginato and R. E. Hester, "Overview of the ETA/ATA Pulse Power", Conf. Record of the 1980 Fourteenth Pulse Power Modulator Symposium, June 3-5, 1980, pp 297-299
- [6] M. Greenwood, et al, "An Investigation Into Repetition-Rate Limitations in Amorphous Alloy Pulse-Compression Cores", Conf. Record of the 1992 Twentieth Power Modulator Symposium, Myrtle Beach, SC, June 23-25, 1992, pp 217-222
- [7] M. A. Newton, et al, "Design and Testing of the 5 kHz, 3 MW Thyatron Modulators for ETA-II", Conf Record of the 1988 Eighteenth Power Modulator Symposium, Hilton Head, SC, June 20-22, 1988, pp 71-74
- [8] E. L. Neau, T. L. Woolston, and K. J. Penn, "COMET-II, A Two-Stage Magnetically Switched Pulsed-Power Module", Conf Record of the 1984 Sixteenth Power Modulator Symposium, June 18-20, 1984, pp 292-294
- [9] S. Asby, et al, "CLIA - A Compact Linear Induction Accelerator System", Proc. of the Eighth IEEE Int'l

- Pulsed Power Conf., San Diego, CA, June 16-19, 1991, pp 940-942
- [10] R. W. Wavrik, et al, "Thermal Management in High Average Power Pulsed Compression Systems", Conf Record of the 1992 Twentieth Power Modulator Symposium, Myrtle Beach, SC, June 23-25, 1992, pp 223-226
- [11] D. L. Goodman, et al, "High Energy Linear Induction Accelerators for Material Processing Applications", Proc. of the Radiation Tech. Int'l. Conf., Boston, MA, 1992
- [12] D. L. Johnson, et al, "Results of Initial Testing of the Four Stage RHEPP Accelerator", Proc. of the Ninth Int'l Pulsed Power Conf., Albuquerque, NM, June 21-23, 1994, pp 437-440
- [13] E. L. Neau and K. R. Prestwich, "New Developments in High Average Power Short-Pulse Induction Accelerators for Industrial and Environmental Applications", to be published in the Proc. of the Thirteenth International Conf. on the Applic. of Accelerators in Research and Industry, Denton, Tx., Nov 7-10, 1994
- [14] C. C. Thompson and M. R. Cleland, "High-Power Dynamitron Accelerators for X-ray Processing", Nucl. Instr. and Meth. in Phy. Res., B40/41 (1989)
- [15] R. J. Adler, US Patent #5,124,658
- [16] M. E. Veis, et al, "High Voltage Electron Accelerators at a Power of Up to 90 KW", Radiat. Phys. Chem., Vol. 35, Nos 4-6, pp 658-661, 1990
- [17] D. R. Kerluke and J. McKeown, "The Commercial Launch of IMPELA", Radiat. Phys. Chem., Vol. 42, Nos 1-3, pp 511-514, 1993
- [18] A. Nguyen, et al, "RHODOTRON, First Operations", in Proc. European Particle Accelerators Conf., Vol. 2, Nice, Fr, pp 1840-1841
- [19] R. W. Stinnett, et al, "Thermal Surface Treatment Using Intense, Pulsed Ion Beams", Mat. Res. Soc. Symp. Proc., Vol. 316, 1994
- [20] E. L. Patterson, N. E. Brown, and G. E. Samlin, Sandia National Laboratories Report SAND92-1969 • UC-602
- [21] J. C. Martin, "Nanosecond Pulse Techniques", Proceeding of the IEEE, Vol. 80, No. 6, June 1992, pp 934-945
- [22] W. S. Melville, "The Use of Saturable Reactors as Discharge Devices for Pulse Generators", Vol 98, Part3, No. 53, p. 185, 1951
- [23] J. J. Ramirez, K. R. Prestwich, and I. D. Smith, "High-Power, Short-Pulse Generators Based on Induction Voltage Adders", Proceeding of the IEEE, Vol. 80, No. 6, June 1992, pp 946-957

STUDIES OF LOCALIZED SPACE-CHARGE WAVES IN SPACE-CHARGE DOMINATED BEAMS*

J. G. Wang and M. Reiser

Institute for Plasma Research, University of Maryland, College Park, MD 20742

The results of the experiments on localized space-charge waves are presented. This includes the generation and propagation of space-charge waves in coasting beams, the end effect on space-charge waves in bunched beams, and the application of localized space-charge waves to beam diagnostics.

I. INTRODUCTION

Space-charge waves are an important subject in the study of charged particle beams [1,2]. They have wide applications in microwave and free-electron laser generation, in particle accelerators, and in plasmas. The topic has been studied extensively. Experiments and analyses are usually carried out with sinusoidal signals. In many applications like in particle accelerators, space-charge waves are often generated in the form of localized perturbations due to short time-scale disturbances. For understanding of beam physics, controlled experiments with localized space-charge waves would be useful.

We have studied space-charge waves in the form of localized perturbations in space-charge dominated electron beams. Three topics have been investigated, including the generation of space-charge waves, the measurement of the geometry factor g , and the effect of bunch ends on space-charge waves. These studies have led us to develop a new beam diagnostic technique.

Our experiments are performed in an electron beam transport facility consisting of a short-pulse electron beam injector and a five meter long periodic solenoid focusing channel. The key device in the injector is a gridded electron gun which is able to produce the desired beam parameters with localized perturbations. The beam is matched with three solenoids into the transport channel consisting of 36 short solenoid lenses with a period of 13.6 cm. The beam pipe has a radius of 1.9 cm and the beam radius is less than 1 cm depending on the beam current, energy and focusing conditions. The diagnostic tools along the channel include five fast wall-current monitors for non-destructive beam current measurement, and three beam energy analyzers for the time-resolved beam energy measurement. At the end of the channel a diagnostic chamber houses a beam transverse image identifier and a beam energy spectrometer. Typical beam parameters in the experiments are: beam energy of 2.5 keV to 5 keV, beam current of 30 mA to 70 mA, transverse effective emittance ($4 \times \text{rms}$) of about 90 mm mrad, and pulse length of 30 to 70 ns. The beams are fully space-charge dominated.

II. GENERATION OF LOCALIZED SPACE-CHARGE WAVES

* Research supported by the US Department of Energy.

Conventionally, space-charge waves are generated in velocity modulation devices always in pairs, i.e. both slow wave and fast wave with almost the same amplitudes. We have demonstrated that with the introduction of a current modulation and strong enough space-charge effect, either a single slow wave or a single fast wave can be produced experimentally. Combinations of the two waves with different amplitude and polarity relations can also be generated. The experimental results are supported by a more complete time-domain analysis [3].

In our experiment the initial perturbation is introduced to the beam by modulating the rectangular cathode-grid pulse with a small bump. This corresponds to a positive velocity perturbation on the beam particles, which in turn produces the initial density, and current perturbations. The space-charge waves then propagate along the beam in the form of localized perturbations. The relative strength of the initial current, or density perturbation over the given velocity perturbation can vary over a wide range.

Figure 1 shows the beam current waveforms measured at two different locations along the transport channel. The slow and fast waves appearing in the beam current signals, are generated in almost equal amplitudes and opposite polarities. The two space-charge waves become more and more separate from each other with distance of propagation. This effect is what is usually discussed in the literature about generation and propagation of space-charge waves.

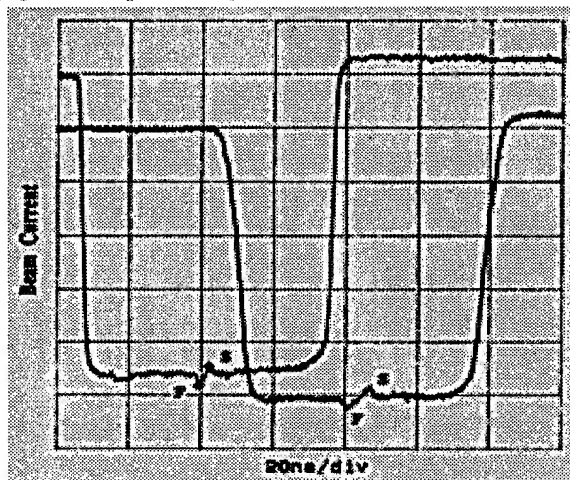


Fig. 1. Beam current waveforms with perturbations measured at the channel distances of $s=0.624$ m and $s=3.48$ m, respectively ($s=0$ is the cathode position), where F is for the fast wave and S is for the slow wave.

Figure 2 shows localized space-charge waves produced with initial perturbation conditions different from that in Fig. 1. Only one fast wave with a positive polarity has been generated on the electron beam current, which propagates toward the beam front. By contrast, Fig. 3 shows the beam

current waveforms with only one slow wave, which has a negative polarity and propagates toward the beam tail. Similar results are also obtained from the beam energy measurement. These new phenomena happen in a space-charge dominated beam and require specific, initial perturbation conditions on the beam parameters.

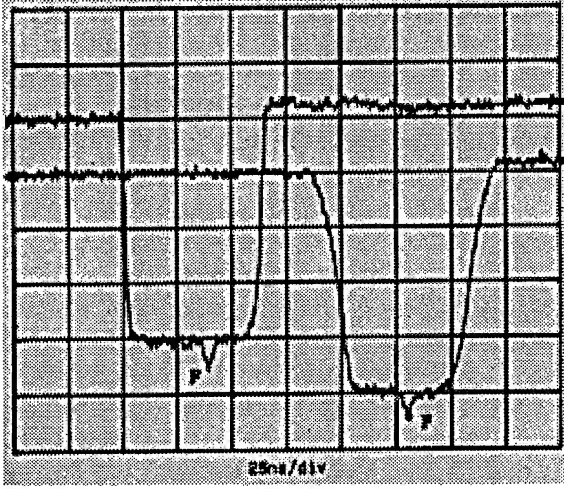


Fig. 2. Beam current waveforms with only one fast wave, taken at the same locations as that in Fig. 1.

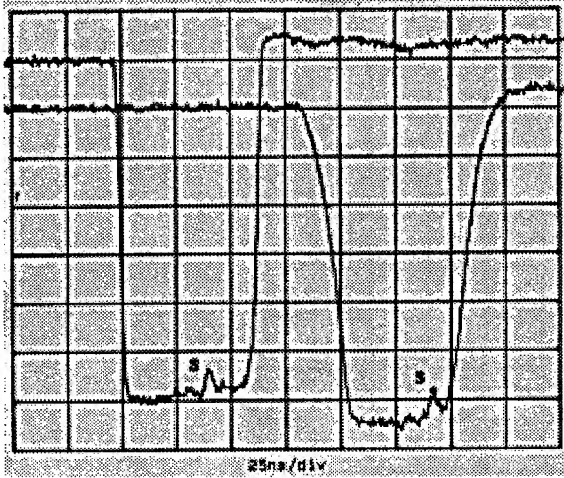


Fig. 3. Beam current waveforms with only one slow wave as measured at the same locations as that in Fig. 1.

An one-dimensional cold fluid model has been employed to investigate the generation of localized space-charge waves in time domain. The analysis shows that the perturbed beam line-charge density Λ_1 , velocity v_1 , and current i_1 are

$$\begin{aligned}\Lambda_1(z, t) = & -\frac{\Lambda_0}{2} \left(\frac{v_{1i}}{c_s} - \frac{\Lambda_{1i}}{\Lambda_0} \right) h \left(t - \frac{z}{v_0 - c_s} \right) + \\ & + \frac{\Lambda_0}{2} \left(\frac{v_{1i}}{c_s} + \frac{\Lambda_{1i}}{\Lambda_0} \right) h \left(t - \frac{z}{v_0 + c_s} \right), \\ v_1(z, t) = & + \frac{c_s}{2} \left(\frac{v_{1i}}{c_s} - \frac{\Lambda_{1i}}{\Lambda_0} \right) h \left(t - \frac{z}{v_0 - c_s} \right) + \\ & + \frac{c_s}{2} \left(\frac{v_{1i}}{c_s} + \frac{\Lambda_{1i}}{\Lambda_0} \right) h \left(t - \frac{z}{v_0 + c_s} \right),\end{aligned}$$

$$\begin{aligned}i_1(z, t) = & -\frac{i_0}{2} \left(1 - \frac{c_s}{v_0} \right) \left(\frac{v_{1i}}{c_s} - \frac{\Lambda_{1i}}{\Lambda_0} \right) h \left(t - \frac{z}{v_0 - c_s} \right) + \\ & + \frac{i_0}{2} \left(1 + \frac{c_s}{v_0} \right) \left(\frac{v_{1i}}{c_s} + \frac{\Lambda_{1i}}{\Lambda_0} \right) h \left(t - \frac{z}{v_0 + c_s} \right).\end{aligned}$$

Here $h(t)$ is the perturbation waveform with an amplitude of unity, the subscripts 0 and 1i are for the unperturbed and initial perturbation amplitudes, respectively, and

$$c_s = \sqrt{\frac{eg\Lambda_0}{4\pi m\epsilon_0\gamma^5}} \quad (1)$$

is the speed of the waves in the beam frame, with g being a geometry factor described in next section. The condition for generating only one fast wave is

$$\frac{v_{1i}}{c_s} = \frac{\Lambda_{1i}}{\Lambda_0}, \quad \text{or} \quad \frac{i_{1i}}{i_0} = \left(1 + \frac{v_0}{c_s} \right) \frac{v_{1i}}{v_0}, \quad (2)$$

while the condition for producing only one slow wave is

$$\frac{v_{1i}}{c_s} = -\frac{\Lambda_{1i}}{\Lambda_0}, \quad \text{or} \quad \frac{i_{1i}}{i_0} = \left(1 - \frac{v_0}{c_s} \right) \frac{v_{1i}}{v_0}. \quad (3)$$

The wave velocity c_s is a measure for the effects of space charge in a beam. A beam with a large c_s reduces the required value of the relative current perturbation for a given relative velocity perturbation in a practical device. Thus Eqs. (2) and (3) can be more easily satisfied in a space-charge dominated beam.

III. MEASUREMENT OF GEOMETRY FACTOR

The geometry factor g is an important parameter in longitudinal beam dynamics, which relates the longitudinal electric field associated with a perturbation in a beam with the line charge density variation as

$$E_z(z, t) \cong -\frac{g}{4\pi\epsilon_0\gamma^2} \frac{\partial\Lambda(z, t)}{\partial z} \quad (4)$$

For a cylindrical, unbunched beam of radius a in a pipe of radius b the g -factor can be represented by the general, long-wavelength formula

$$g = 2 \ln \frac{b}{a} + \alpha, \quad (5)$$

where α is a constant for which different values (1, 0.5, and 0) can be found in the literature. Neil and Sessler, in their original work [4], treated longitudinal instabilities of coasting beams in particle accelerators. They used a uniform-beam model with constant radius a , and derived the relation

$$\alpha = 1 - \left(\frac{r}{a} \right)^2, \quad (6)$$

with r being the radial position within the beam. This relation implies that the g -factor, as well as the field E_z , is a maximum with $\alpha=1$ on the axis, and reduces parabolically to a minimum with $\alpha=0$ on the beam surface with $r=a$. Averaging the field over the beam cross section yields $\alpha=0.5$. There is another model in unpublished papers which yielded $\alpha=0$ by assuming a constant volume charge density and perturbed beam radius. Hence, there is the question as to which value of α should be used. Further, the question also concerns some fundamental beam physics such as the correct model, the field distribution within the beams, surface wave or body wave, incompressibility of plasmas, etc.

We have developed a novel method to determine the parametric dependence of the g -factor associated with longitudinal perturbations in a beam [5]. In this technique, localized space-charge waves are launched on electron beams in a periodic solenoidal focusing channel and the propagation velocities of these waves are measured. At the same time, the beam radius a is independently measured by a phosphor screen plus CCD camera technique. This leads to an experimental determination of the parametric dependence of the geometry factor g on the radius a .

As shown in Fig. 1, the two localized space-charge waves move away from each other. The time interval between the two waves, which can be measured very accurately at different locations along the channel, is related to the traveling distance s by

$$\Delta t = \frac{2c_s}{v_0^2 - c_s^2} \cdot s \quad (7)$$

Figure 4 plots the time interval of the two space-charge waves at five channel locations for two different phase advances σ_0 . The beam energy is 5 keV and the beam current is 56 mA in this measurement. A least-square fitting of the experimental data yields $\Delta t/s$, and hence the wave velocity c_s according to Eq. (7); using this value of c_s one can determine the geometry factor g from Eq. (1).

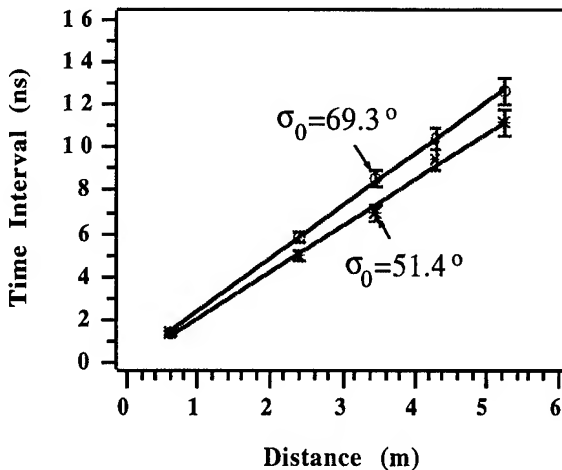


Fig. 4. Time interval between two space-charge waves vs. drifting distance for two different phase advances σ_0 , as measured by the five current monitors. The solid lines are least-square fitting of the experimental data.

The beam radius a is measured by the phosphor screen plus CCD camera technique. Using the two independent, experimental results for the g -factor and the beam radius a , we plotted the g -factor against the corresponding beam radius in the form of $\ln(b/a)$ for different experimental conditions as shown in Fig. 5. A least-square fitting of these data yields the relation of the g -factor as a function of the beam radius a , suggesting the correct formula for the g -factor is $g=2\ln(b/a)$, i.e. $\alpha=0$.

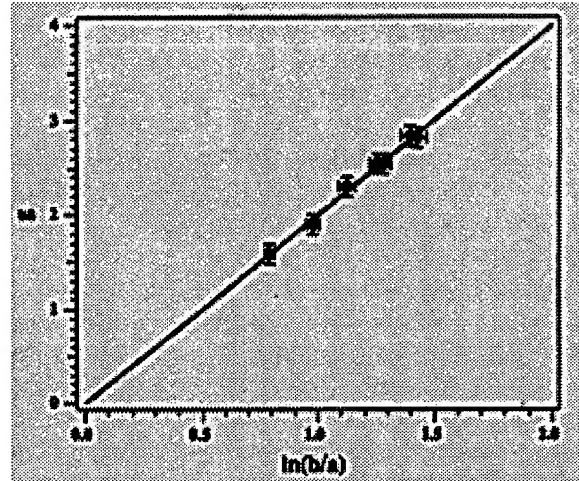


Fig. 5. The measured g -factor vs. $\ln(b/a)$. A least square fitting of the experimental data yields $g=2.01 \ln(b/a)-0.01$, suggesting the correct formula $g=2 \ln(b/a)$ as indicated by the solid line.

Our experimental result agrees with the model which assumes a constant volume density and perturbed beam radius. In space-charge dominated beams the perturbed electrical field within the beam is independent of the radial position. Though the volume charge density remains constant, the line charge density varies with perturbation due to the change of the beam radius. The perturbations do not compress the beam plasma density in this case. However, it is inappropriate to apply the surface wave concept since the perturbed field does penetrate through the whole medium.

IV. BUNCH END EFFECT ON SPACE-CHARGE WAVES

The effect of bunch ends on space-charge waves is important for the understanding and analysis of longitudinal instabilities in particle accelerators where perturbations often reach beam bunch ends. It is essential to know if the fast waves reflect off bunch front ends and become the slow waves, and vice versa. The previous studies on this subject included some theoretical work and computer simulations [6-9], showing the reflection off parabolic bunch ends, defined as the vanishing density points. We have conducted an experiment to study the end effect with an initially rectangular electron bunch [10]. The beam "end" here is referred to as the boundary between the flat region and the finite edge, quite different from the vanishing density point in previous work.

The experiment is performed in a similar way as in the generation of space-charge waves, and in the measurement of the geometry factor g . However, the initial perturbation is

placed very close to the bunch ends. The initial test is done with two waves launched close to the beam real end. The reflection of the slow waves is observed. In order to increase the signal to noise ratio, a single fast wave close to the beam front end is employed. Figures 6 (a-c) show the measured beam current signals from the first three fast wall-current monitors. Each figure contains three scope traces: the top one is the beam current waveform without perturbation, the middle one is the beam current at the same conditions except that the perturbation is added, the bottom one is the difference between those two signals and represents the net perturbation signal on the beam. The ordinate, which has a conversion factor of about 0.5 mA/mV (slightly different for each current monitor), is for the bottom traces only. The abscissa shows the relative time scale of the three wall-current monitor signals along the channel. In Fig. 6(a) the signals are from the first current monitor which is $s=0.624$ m from the electron gun. The beam energy is 5 keV, the average beam current is 52 mA, and the full width at half maximum (FWHM) of the pulse is 38.2 ns. The current perturbation signal has a total width of about 6 ns and an amplitude of 5.7 mA which is 11% of the beam current. The peak of the perturbation is about 3.5 ns away from the beam front "end", defined here as the turning point from the flat region to the rising edge, while the wave front of this wave packet is already very close to the beam front end. This is a single fast wave which would keep its shape as long as it stays in the flat region of the beam pulse. The second wall-current monitor at $s=2.39$ m sees two perturbation peaks separated by 6.2 ns, as shown in Fig. 6(b). This is caused by the splitting of the incident fast wave on the beam front end, which happens somewhere between the first and second current monitors. The peak on the left, i.e. the transmitted wave, has an amplitude of about 3.1 mA and has moved down the front edge, while the peak on the right, i.e. the reflected wave, has an amplitude of 2.3 mA and moves back towards the beam center. The sum of these two peaks is close to the single fast wave amplitude in Fig. 6(a). Figure 6(c) shows the signals from the third current monitor at $s=3.48$ m where the time interval between the two peaks has increased to 8.6 ns. The fourth and fifth current monitors see similar pictures with even larger separation times of the two peaks.

The propagation speed of space-charge waves can be measured with the beam current signals. For the reflected and transmitted waves in this experiment their speeds are measured with respect to the beam center which can be determined by the time-of-flight technique. The results are plotted in Fig. 7 where $t=0$ represents the beam center, the stars are for the reflected wave, and the dots are for the transmitted wave. For the reflected wave the least square fitting yields t (ns) = 13.0-1.46s (m), while for the transmitted wave t (ns) = 11.7+1.49s (m). The speed v of these two waves in the beam frame can be calculated from the relation

$$\left| \frac{dt}{ds} \right| = \frac{v}{(v_0 - v)v_0}, \quad (8)$$

where v_0 is the beam center velocity in the lab frame. In this measurement the speed of the reflected wave is about 2.38 mm/ns, the speed of the transmitted wave is about 2.43 mm/ns.

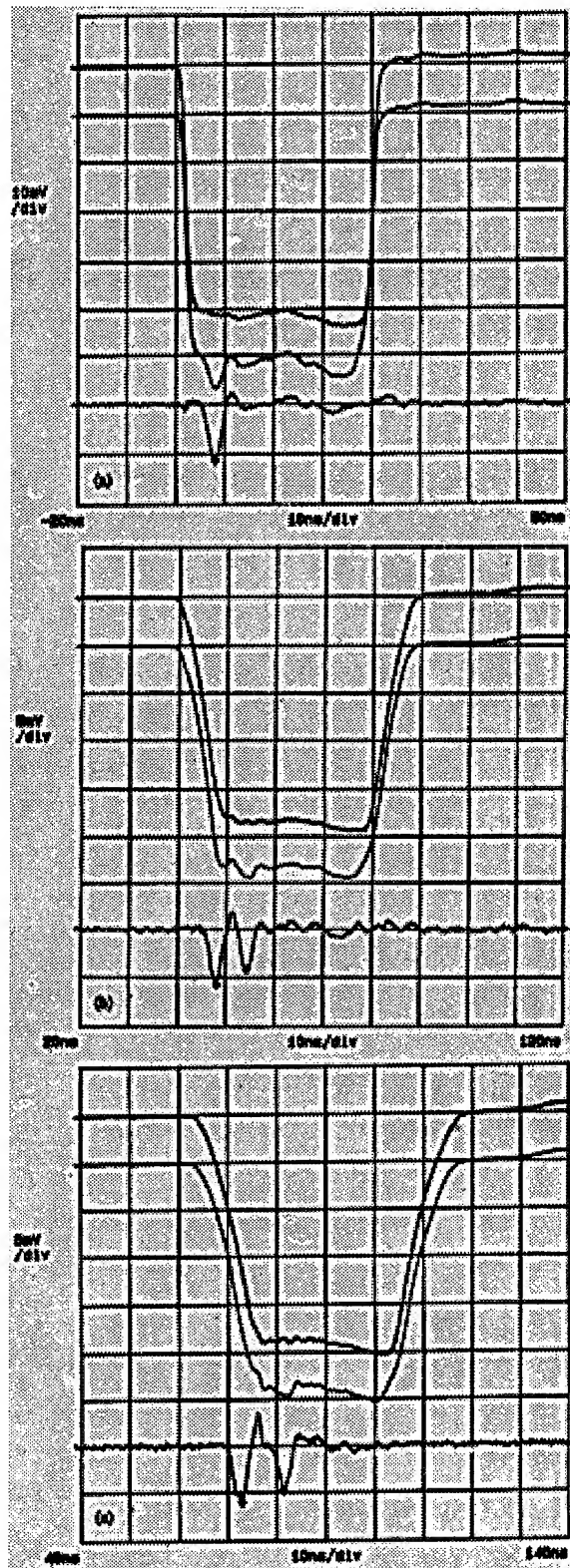


Fig. 6. Evolution of a fast wave around the beam front end:
(a) A single fast wave before reaching the beam front end, measured at $s=0.624$ m;
(b) Transmitted and reflected waves as measured at $s=2.39$ m;
(c) Transmitted and reflected waves as measured at $s=3.48$ m;

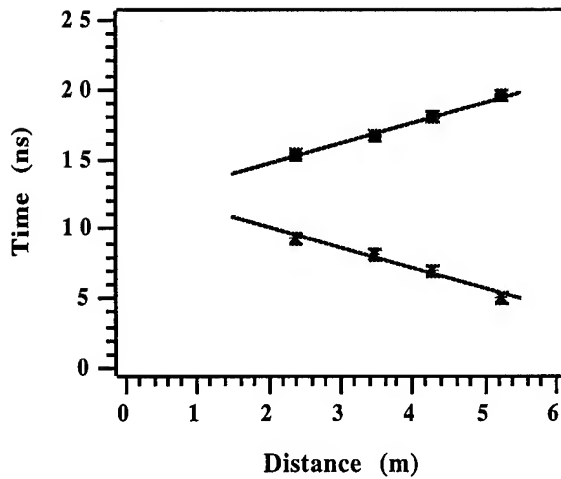


Fig. 7. Time interval between transmitted wave and beam center (dots), and between reflected wave and beam center (stars).

It is well known that an initially rectangular bunch suffers edge erosion due to the strong space-charge force at the beam edges [11, 12]. The top of both beam edges moves into the flat region with a speed c_s and the bottom of the edges moves outwards with a speed $2c_s$, where c_s is determined by Eq. (1). For space-charge dominated beams, c_s is a significant fraction of the beam center velocity v_0 , and the edge erosion is very rapid. The experimental parameters yield the speed c_s of 2.30 mm/ns. In the calculation we use for the geometry factor the value $g=2\ln(b/a)=2.6$, determined in Section III. Thus, the three speeds, namely, the speed of the transmitted wave, the speed of the reflected wave and the beam edge erosion speed c_s have approximately the same values from this measurement.

A dynamic model based on beam impedance matching has been developed [10] and the analysis shows that under the condition

$$k \gg \frac{2}{z_r}, \quad \text{i.e.} \quad z_r \gg \frac{\lambda}{\pi}, \quad (9)$$

where z_r is the beam edge length and λ is the perturbation wavelength, no reflection should occur. On the other hand, if the edge length z_r is negligibly smaller than λ/π , full reflection should occur. In the general situation between these two extremes, there should be partial reflection and partial transmission at the bunch end. The reflection coefficient can be calculated according to this model.

In the experiment the dependence of the reflected wave amplitude on the length of the front edge is qualitatively observed. When the initial perturbation is far away from the front end, the reflection is hardly seen in the experiment since the front edge is too long due to the edge erosion by the time the perturbation reaches the end. There is also experimental evidence showing that the amplitude of the reflected wave is significantly higher than the transmitted wave amplitude when the initial perturbation is very close to the front end so that the reflection happens with a short front edge.

V. BEAM DIAGNOSTICS WITH LOCALIZED SPACE-CHARGE WAVES

Through the study of the generation, propagation, and the bunch end effects of space-charge waves, a new beam diagnostic technique with localized perturbations has been developed [13]. Unlike the conventional approach with sinusoidal waves, a measurement of the propagation of localized space-charge waves in beam current or energy signals directly yields the propagation speed c_s of the perturbations according to Eq. (7). Thus, the geometry factor g can be calculated according to Eq. (1) after c_s is determined. For a space-charge dominated coasting beam the average beam radius can then be calculated by $g=2\ln(b/a)$. This provides a non-destructive method to diagnose beam size in high-current accelerators and transport channels. The measurement of the reflection of localized space-charge waves is demonstrated in Section IV. The other measurements with localized space-charge waves include the longitudinal space-charge wave impedance and longitudinal instability, etc. The details of this measurement is reported elsewhere [14].

Acknowledgment

The authors would like to acknowledge D. X. Wang and H. Suk for their contributions to this project.

VI. REFERENCES

- [1] J. D. Lawson, *The Physics of Charged-Particle Beams*, (Oxford University Press, New York, 1988), second edition, ch. 6.
- [2] M. Reiser, *Theory and Design of Charged Particle Beams*, (John Wiley & Sons, Inc., edited by Mel Month, New York, 1994), ch. 6.
- [3] J. G. Wang, D. X. Wang, and M. Reiser, *Phys. Rev. Lett.*, **71**(12), 1836 (1993).
- [4] V. K. Neil and A. M. Sessler, *Rev. Sci. Instr.* **36**(4), 429 (1965).
- [5] J. G. Wang, H. Suk, D. X. Wang, and M. Reiser, *Phys. Rev. Lett.*, **72**(13), 2029 (1994).
- [6] E. P. Lee, in the *Proceedings of the 1981 Linear Accelerator Conference*, p. 263, Edited by R. A. Jameson and L. S. Taylor, Santa Fe, NM, Oct. 19-23, 1981.
- [7] P. J. Channell, A. M. Sessler, and J. S. Wurtele, *Appl. Phys. Lett.*, **39**(4), 15 August 1981.
- [8] I. Hofmann, *Z. Naturforsch.*, **37a**, 939 (1982).
- [9] D. A. Callahan, A. B. Langdon, A. Friedman, and I. Haber, in the *Proceedings of the 1993 Particle Accelerator Conference*, Vol. 1, p. 730, Washington, D. C., May 17-20, 1993.
- [10] J. G. Wang, D. X. Wang, H. Suk, and M. Reiser, *Phys. Rev. Lett.*, **74**(16), pp. 3153-3156, April 17, 1995.
- [11] A. Faltens, E. P. Lee, and S. S. Rosenblum, *J. Appl. Phys.*, **61**(12), 5219 (1987).
- [12] D. X. Wang, J. G. Wang, and M. Reiser, *Phys. Rev. Lett.*, **73**(1), 66 (1994).
- [13] J. G. Wang and M. Reiser, *Rev. Sci. Instrum.*, **65**(11), 3444 (1994).
- [14] H. Suk, J. G. Wang, and M. Reiser, in this proceedings.

Design of the Jupiter Accelerator for Large X-ray Yields

Juan J. Ramirez, Ph.D.

Sandia National Laboratories

Albuquerque, New Mexico 87185-1178

ABSTRACT

Nanosecond Pulsed Power provides the unique capability to deliver high energy and high power at low cost and high efficiency. One important application of this technology is to the generation of intense, high-energy laboratory X-ray sources using magnetically driven implosions. Saturn generates ~500 kilojoules of x-rays using this process. This paper presents a detailed design concept for a ~15 MJ laboratory X-ray source and discusses the resultant capabilities for high energy density physics studies.

INTRODUCTION

The Particle Beam Fusion Accelerator-II (PBFA-II) was built at Sandia National Laboratories in 1985 as part of the national ICF program [1] and is the highest power accelerator in the world today. Saturn was built in 1987 [2] and is used as an intense source of ~1 MV bremsstrahlung radiation. It is also used as the power source for fast magnetically driven implosions and generates ~0.5 MJ of X-rays in this mode.

The generation of these intense X-ray pulses can be described in terms of the four stage process shown in Figure 1.

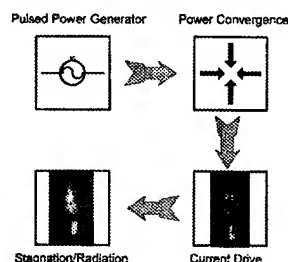


Fig 1. The four-stage process for magnetically driven implosions.

Individual high electrical pulses are first produced by a large number of pulsed power generator modules. The current pulses from these modules are added in the second stage and delivered to a cylindrical plasma load located at the center of a vacuum test chamber. During the third stage, the magnetic forces generated by the drive current cause the plasma to implode converting the electrical energy into particle

kinetic energy. The kinetic energy is finally converted into radiation energy in the final stage when the plasma stagnates near the axis of implosion. The magnetic energy stored near the load region continues to drive the collapsed plasma, producing additional radiation. The total X-ray energy produced can thus exceed the kinetic energy in the implosion. Since the implosion system represents an additional power compression stage, the prompt radiation pulse can be several times shorter than the driving current pulse. The entire power compression/energy conversion process can also be very efficient [3].

Progress in the field has been limited by problems associated with control of instabilities in the imploding plasma. However, the advent of fast pulsed power drivers in the 1980s has led to fundamental change and to rapid progress. An analysis of the scaling of MHD instabilities in imploding plasma lines by Hussey, et al. [4] shows that the Rayleigh-Taylor instability dominates in the worst, most unstable implosions. The result is that short high-temperature radiation pulses can be more readily obtained using shorter implosion times. The use of high-power, short-pulse generators to drive plasma implosions shifts the problem emphasis from control of plasma instabilities towards the design of reliable, high-efficiency, fast-pulsed power accelerator systems.

THE JUPITER FACILITY

Figure 2 shows a concept for the proposed ~15 MJ Jupiter laboratory X-ray facility.

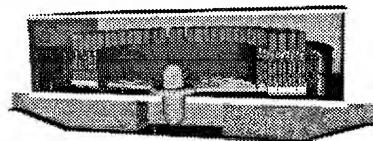


Fig 2. Concept for the proposed ~15 MJ Jupiter laboratory X-ray facility.

The driver consists of ~30 pulsed power generator modules based on the inductive voltage adder technology [5] that has proven to be robust and very reliable on the Hermes III facility [6] at Sandia National Laboratories. In this concept the outputs from the individual generator modules are added in parallel within a central vacuum chamber and the summed pulse is fed to a Z-pinch load located at the chamber axis.

The Jupiter pulsed power generator module is shown in Figure 3.

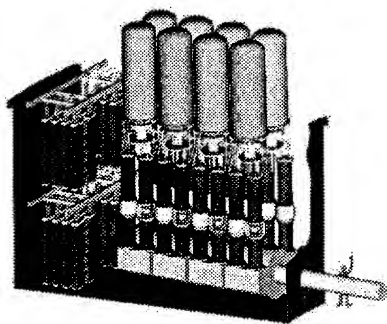


Fig 3. Drawing of the Jupiter pulsed power generator module.

It consists of a four-stage inductive voltage adder with four pulse forming lines (PFLs) feeding each of the stages (submodules). The generator module thus delivers four times the voltage and four times the current produced by an individual PFL. One of the Jupiter PFL modules delivers roughly the same voltage and half the power as one PBFA-II PFL module. The chosen architecture is highly modular and the design requires little extrapolation in peak performance over what has been achieved at the component level on existing pulsed power facilities. The principal challenge for the chosen generator concept is in our ability to execute a design that meets the high operational reliability, reproducibility, and the life cycle costs desired for Jupiter. Our plans are to complete construction of an advanced pulsed power module testbed by the end of FY96 and to develop the requisite integrated performance capability using this facility. This testbed will thus enable us to validate component design criteria, evaluate fault modes, establish the dynamic range for reliable system operation, and determine the service and maintenance requirements. Results will be integrated into a comprehensive system design study for Jupiter.

The major uncertainty in this effort pertains to our ability to scale the Z-pinch to the power and energy levels specified for Jupiter. Jupiter will provide implosion times ranging from ≤ 100 ns to ~ 500 ns to minimize concerns about Z-pinch plasma instabilities. The implosion time flexibility is provided by the pulse forming system. Each of the four submodules shown consists of a ~ 755 kilojoule Marx generator, a two-stage water-dielectric pulse forming system, and a high power induction cell. All of the pulse compression stages in this design use SF_6 insulated high voltage gas switches for increased efficiency and reliability. The submodules will each deliver 3.3-4.0 TW at ~ 2.5 MV depending on the ultimate performance that can be reliably achieved. The submodule is the basic pulse forming building block

and its output is synchronized to within a few ns by a laser triggering system. The generator module will deliver a 13-16 TW output pulse with a nominal FWHM of ~ 100 ns and a total energy of 1.2-1.5 MJ. Jupiter will consist of 30-36 of these modules arranged in parallel around a central target chamber. Longer implosion times are provided by shorting out the second stage of the water-dielectric pulse forming system. The induction cells are designed to contain sufficient core material to allow for the longer volt-seconds required in this mode.

The output from each of the generator modules will be delivered to the central target chamber via long self-magnetically insulated vacuum transmission lines (MITLs). Results of a study on the design of the inductive voltage adder and transport down these long MITLs is presented by M. G. Mazarakis in the proceedings of this conference [7]. A coaxial to double-triplet disk feed transition section at the periphery of the target chamber combine the individual current pulses [as shown in Figure 4]. Power flows down the triplate MITLs to post-hole convolutes located within a few centimeters of the chamber axis. These convolutes deliver the power to a single cylindrical Z-pinch load on axis.



Fig 4. Sectional view of power flow feeds within the central vacuum chamber.

PBFAII-Z

PBFA II-Z will provide a Z-pinch drive capability to PBFAII. It will enable 20-25 MA, ~ 100 ns, 1.5-2.0 MJ implosion experiments. This capability should be available by the Fall of 1996. The PBFAII-Z experiments will validate our understanding of vacuum power flow through convolutes and of Z-pinch implosion dynamics. It will represent a half-way step between Saturn and Jupiter and will provide the necessary confidence for scaling to Jupiter parameters.

SUMMARY AND CONCLUSIONS

Magnetically driven implosions using fast pulsed power generators form the basis for a growing international

collaboration on high-power, high-energy laboratory X-ray sources. Advances in nanosecond pulsed power technology in the past decade have enabled the development of intense pulsed X-ray sources with an overall capacitor to X-ray conversion efficiency of 15-20 percent. Experiments performed by a collaboration of U.S., U.K., and CIS scientists on Saturn at Sandia National Laboratories, and on Angara V at Trinity will be extended to PBFAII-Z which should provide radiation outputs of 1.5-2.0 MJ. The proposed Jupiter facility will extend that capability to ~15 MJ. Extrapolation of hohlraum results obtained to date show that temperatures ≥ 200 eV could eventually be achieved on Jupiter. It will provide an unparalleled capability for ICF, high energy density physics and radiation effects science experiments.

References

1. B. N. Turman, et al., "PBFA II - A 100 TW Pulsed Power Driver for the Inertial Confinement Fusion Program," Proc. 5th IEEE Pulsed Power Conf., Arlington, VA, June 10-12, 1985, pp. 155-161.
2. D. D. Bloomquist, et al., "Saturn, A Large Area X-ray Simulation Accelerator," Proc. 6th IEEE Pulsed Power Conf., Arlington, VA, June 29-July 1, 1987, pp. 310-317.
3. P. J. Turchi and W. L. Baker, J. Appl. Phys. 44, 4936 (1973).
4. T. W. Hussey et al., J. Appl. Phys. 51, 1452 (1980).
5. J. J. Ramirez, et al., "Very High Pulse-Energy Accelerators," Proc. 1989 Particle Accelerator Conf., Chicago, IL, March 20-23, 1989, 1446.
6. J. J. Ramirez, et al., "Hermes III - A 16 TW, Short Pulse, Gamma Ray Simulator," Proc. 7th International Conference on High Power Particle Beams, Karlsruhe, West Germany, July 4-8, 1988, pp. 148-157.
7. M. G. Mazarakis, et al., "Design and Power Flow Studies of a 500-TW Inductive Voltage Adder Accelerator", in Proceedings of this Conference.

DESIGN AND POWER FLOW STUDIES OF A 500-TW INDUCTIVE VOLTAGE ADDER (IVA) ACCELERATOR

M. G. Mazarakis, J. W. Poukey, J. P. Corley, D. L. Smith, L. Bennett and J. J. Ramirez, Sandia National Laboratories, Albuquerque, NM 87185-1193; P. Pankuch, EG&G, Albuquerque, NM; I. Smith, P. Corcoran, P. Spence, Pulse Sciences, Inc., San Leandro, CA 94557

ABSTRACT

We present a preconceptual design for a 500-TW pulsed power accelerator capable of delivering 15-MJ kinetic energy into an imploding plasma radiation source (PRS). The HERMES-III technology of linear inductive voltage addition in a self-magnetically insulated transmission line (MITL) is utilized to generate the 8-10 MV peak voltage required for an efficient plasma implosion. The 50- to 60-MA current is achieved by utilizing many accelerating modules in parallel. The modules are connected to a common circular convolute electrode system in the center of which is located an imploding foil plasma radiation source. This accelerator produces no electron beam since the total current from the voltage adders (IVAs) to the inductive load flows on the surface of metallic conductors or nearby in the form of electron sheath.

In this paper we outline the accelerator's conceptual design with emphasis on the power flow and coupling to the inductive load of the center section of the device.

INTRODUCTION

The proposed pulsed power accelerator (Fig. 1) is based on the successful HERMES-III [1] technology developed at Sandia during the last ten years in collaboration with Pulse Sciences Inc. Each of the 30 modules of Figure 1 are similar to HERMES III. This technology is fairly simple and couples the self-magnetically insulated transmission line (MITL) [2] principle with that of the induction linac [3] to generate a new family of linear induction accelerators, which we call linear inductive voltage adders. In these accelerators, the particle beam which drifts through the multiple cavities of conventional induction linacs is replaced by a metal conductor which extends along the entire length of the device and effectuates the voltage addition of the accelerating cavities. These devices can operate in either polarity to produce negative or positive voltage pulses. In a negative polarity voltage adder (Fig. 2), the center conductor is negatively charged relative to the outer conductor which is interrupted at regular intervals by the cavity gaps. The PRS accelerator voltage adder is negative polarity.

The selected number of modules, 30, is a trade-off between cost, manufacturing capabilities, and operations flexibility. An inductive voltage adder coupling more than ~ 2.5 -MA can be very large and cumbersome, requiring special and expensive manufacturing tools to machine the various components. In addition, the radial gaps of the self-magnetically insulated voltage adder become very small, which in turn increases the

probability for fast neutral atom closure [4], for the desired 100-ns FWHM pulses.

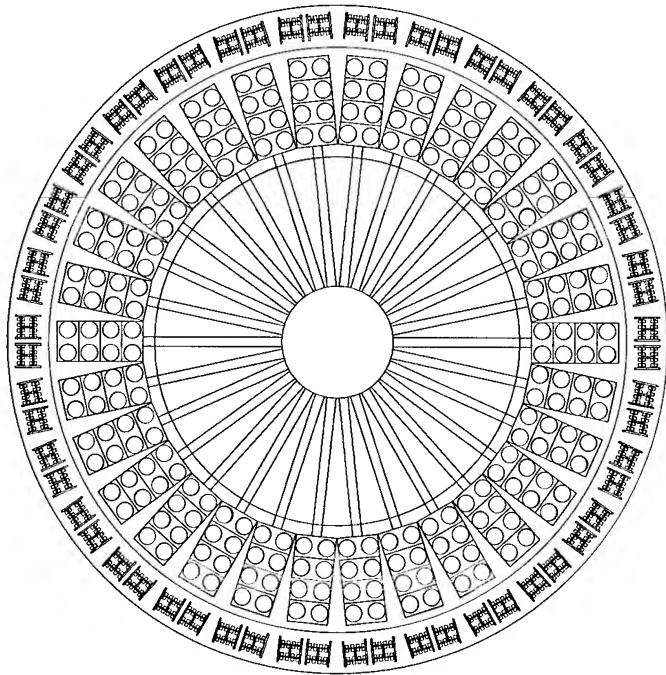


Figure 1. Top view of the PRS multimodular accelerator

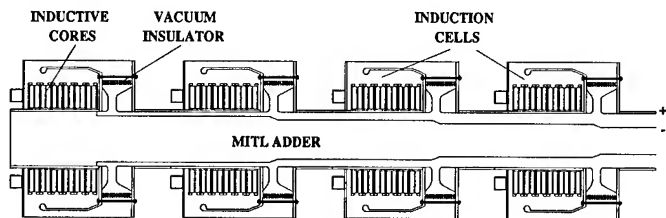


Figure 2. Schematic diagram of the PRS accelerator voltage adder. It is of negative polarity. There is a total of 30 voltage adders in the device.

*This work was supported by the U. S. Department of Energy under contract DE-AC04-94AL85000.

Table I

R anode = 38 cm

voltage adder segment i	distance from ground plate z [m]	segment voltage V _i [MV]	cathode radius r _i [cm]	operating impedance Z _i [Ω]	vacuum impedance Z _i [Ω]
1	0.30 - 1.98	2 - 2.5	37.0	1.11 - 1.16	1.6
2	1.98 - 3.65	4 - 5	36.1	2.22 - 2.28	3.08
3	3.65 - 5.33	6 - 7.5	35.3	3.33 - 3.41	4.42
4	5.33 - 7.00	8 - 10	34.6	4.44 - 4.54	5.62

ACCELERATOR DESIGN

All the 30 modules in the accelerator are identically composed of a four-stage voltage adder and an extension MITL. The voltage adder is 5.6-m long and contains 4 inductively isolated cavities. Each cavity can withstand ~ 2.5 MV for a 100-ns FWHM sine squared pulse shape. Table I summarizes the axial and radial dimensions of the voltage adder as well as the vacuum and operating impedances for two cavity operating points: 2 MV and 2.5 MV. Those correspond respectively to 430-TW and 660-TW total accelerator power. Each module delivers approximately the same power as HERMES III (16 TW); however, the voltage is half as large and the current more than double.

Due to their radial dimensions, the voltage adders cannot be brought close to the load; therefore, long extension self-magnetically insulated transmission lines (MITLs) are required to transfer and converge the power to the load. In the present design this length is 11.3 m. There are advantages and disadvantages to the utilization of long MITLs. It is our belief that the advantages outweigh the disadvantages. For instance, the erosion energy losses are compensated for by the flexibility of the voltage adder time isolation from the load. For most of the pulse duration, the load impedance seen by the voltage adder equals its self-limited operating impedance despite the fact that the actual load impedance can be up to ten times higher.

POWER FLOW STUDIES

Figure 3 shows one of the TWOQUICK [5] PIC code simulations used to validate the design, modeling one module with a six-meter long MITL. The accelerator center section (transition convolute and imploding plasma) is simulated by a coaxial cylindrical box whose inductance is 30 times larger than the actual inductance seen by the 30 parallel modules. The end plate of the coaxial line simulates the imploding cylindrical foil. The electron map is for 180 ns after the

beginning of the pulse, coincident with the 2.1-MA maximum current through the load. The energy coupled into the inductive load is $L I_{\max}^2/2 = 630$ kJ out of a total of 1,090 kJ energy input into the voltage adder, yielding a system efficiency of 58%. The simulation in Fig. 4 was performed to find the total energy loss in the 11.3 MITL. The voltage adder is not included; however, its voltage output (Fig. 5) was used as input. The output voltage pulse is shown in Fig. 6. The 60-ns erosion of the leading edge corresponds to 92-kJ lost. Besides the pulse shortening by ~ 60 ns, there is a small energy loss (20 kJ) in the main body of the pulse. Together this gives an average erosion rate of 10 kJ/m. Hence, if all the MITL length had been included in the simulation of Fig. 3, the energy efficiency would have been $\sim 50\%$.

Precise energy balance using TWOQUICK suggests the missing 50% of the input energy is distributed between reflections at the load (3%), erosion (10%), losses at the beginning of the inductor early in the pulse (10%), sheath electron losses at the load (20%), and field energy remaining inside the MITL (10%).

To calculate the overall accelerator efficiency driving an imploding plasma radiation source we used the SCREAMER [6] circuit code which gave an energy efficiency of 17%. That is, for a total of 90 MJ stored in the Marx generators of the 30 modules, 15 MJ is delivered to the imploding plasma.

CONCLUSION

The presented PRS accelerator design is based on the HERMES-III technology of inductively insulated voltage adders (IVA). It has 30 parallel modules and can deliver the required 15-MJ kinetic energy to an imploding plasma radiation load. The total energy erosion in the thirty 11-m long MITLs is of the order of 3.3 MJ and the overall energy efficiency of the accelerator is 17%. The modular configuration offers flexibility and risk mitigation by an anticipated staged construction. Components of the first test module are currently under construction.

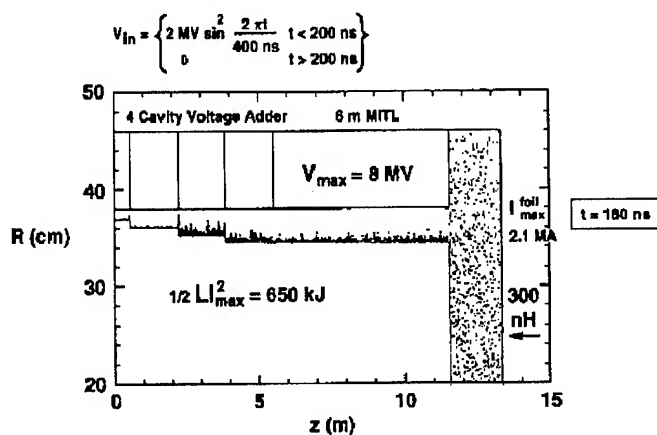


Figure 3. Numerical simulation of the voltage adder connected to a 300-nH inductive load via a 6-m long MITL. The electron map shown is simulated 180 ns later, following the injection of the voltage pulse (V_{in}) at the first cavity.

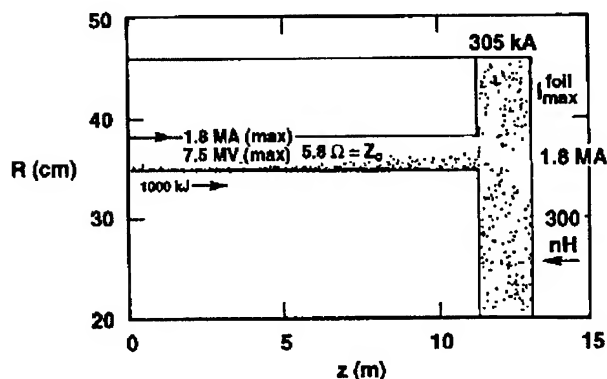


Figure 4. Simulation of the power flow in the 11.3-m long extension MITL of an accelerating module. The electron map is taken at 120 ns following injection.

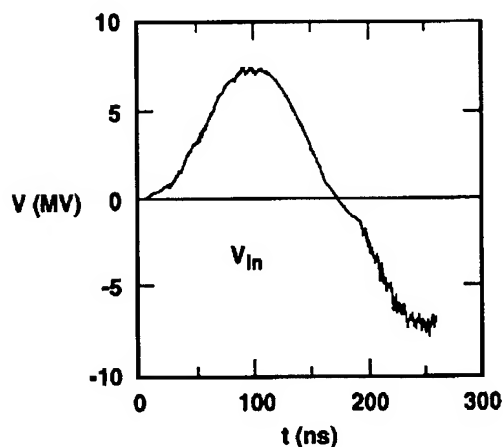


Figure 5. Simulated voltage output at the exit of the voltage adder (Fig. 3).

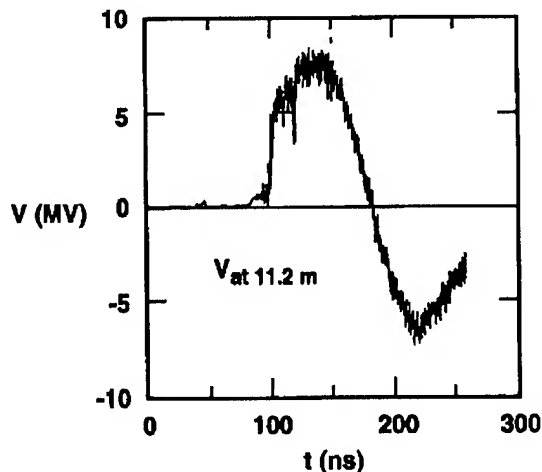


Figure 6. Voltage output pulse at the end of the 11.3-m long extension MITL of Fig. 4. The erosion at the leading edge of the pulse is apparent.

REFERENCES

- [1] J. J. Ramirez, et al., "HERMES-III—A 16-TW, Short Pulse Gamma Ray Simulator," *Proc. 7th International Conf. on High Power Particle Beams*, Karlsruhe, Germany, July 4-8, 1988, pp. 148-157.
- [2] J. H. Creedon, "Magnetic Cutoff in High-Current Diodes," *J. Appl. Phys.* **48**, No. 3, 1070 (1977).
- [3] N. Christophilos, et al., "High Current Linear Induction Accelerator for Electrons," *Rev. Scient. Instrum.* **35**, No. 7, 886 (1964).
- [4] Pace VanDevender, *Proc. 3rd IEEE International Pulsed Power Conference*, Albuquerque, NM, June 1-3, 1981, p. 248.
- [5] M. L. Kiefer, et al., "SCREAMER—A Pulsed Power Design Tool User's Guide," Sandia National Laboratories, June 26, 1991.
- [6] D. B. Seidel, et al., *Proc. CP90 Europhysics Conference on Computational Physics*, edited by A. Tenner (World Scientific, Singapore 1991), pp. 475-482.

COBRA Accelerator for Sandia ICF Diode Research at Cornell University

David L. Smith, Pete Ingwersen, Lawrence F. Bennett, and John D. Boyes
Sandia National Laboratories, Albuquerque, NM
David E. Anderson, John B. Greenly, and Ravi N. Sudan
Cornell University, Ithaca, NY

I. INTRODUCTION

The new COBRA accelerator is being built in phases at the Laboratory of Plasma Studies in Cornell University where its applications will include extraction diode and ion beam research in support of the light ion inertial confinement fusion (ICF) program at Sandia National Labs. The flexible 4-to 5-MV, 100-to 250-kA accelerator in Fig. 1 is based on a four-cavity inductive voltage adder (IVA) design. In combination with new ferromagnetically-isolated cavities and

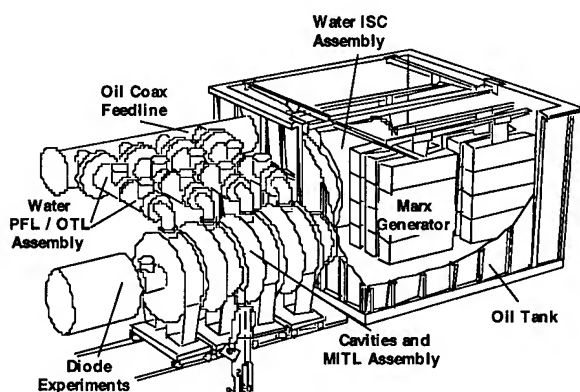


Fig. 1. The 1.3 TW COBRA accelerator at Cornell has a folded overhead pulsed-power geometry for compactness.

self-magnetically insulated transmission line (MITL) hardware, it includes components from existing Sandia and Cornell facilities. Those are the Marx generator capacitors, hardware, and power supply from the DEMON facility; water pulse forming lines (PFL) and gas switch from the Subsystem Test Facility (STF); a HERMES-III intermediate store capacitor (ISC); and a modified ion diode from Cornell's LION. The present accelerator consists of a single modified cavity similar to those of the Sandia SABRE accelerator and will be used to perform the first phase lower voltage tests. Four new cavities will be fabricated and delivered in the first half of FY96 to complete the COBRA accelerator. COBRA is unique in the sense that each cavity is driven by a single pulse forming line, and the IVA output polarity may be reversed by rotating the cavities 180° about their vertical axis. The site preparations, tank construction, and diode design and development are taking place at Cornell with growing enthusiasm as this machine becomes a reality. Preliminary results with the single cavity and short positive inner cylinder MITL configuration will soon be available.

II. RESEARCH PLANS

Ion diode experiments in support of the Sandia ICF program will be the first experimental activity on COBRA. The initial single-cavity COBRA is well matched to the extraction geometry, applied-B diode used on the previous Cornell accelerator, LION (1.2 MV, 4 Ohm, 40 ns), since 1992.[1] Figure 2 shows a sketch of the LION/COBRA diode. We will field this diode on COBRA to continue ion

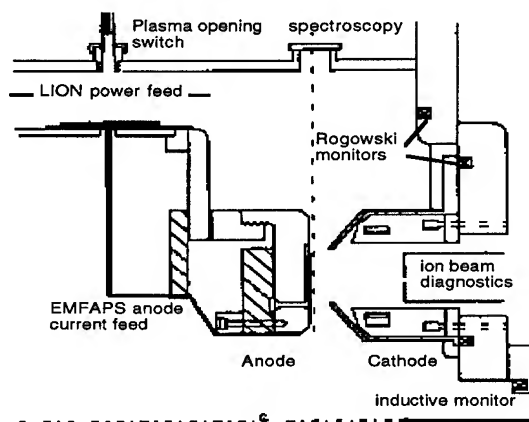


Fig. 2. The modified LION diode produces an ion beam of 10 cm mean radius. This diagram shows 25-cm axial extent.

source studies, particularly addressing the issues of ion species purity and parasitic load with lithium-bearing evaporating metal foil anode plasma source (EMFAPS) active anodes.[2] We will pursue innovations in foil fabrication and in-diode discharge cleaning techniques begun on LION.[3] Diagnostics will include: magnetically-insulated Faraday cups for beam current density; Rutherford-scattering shadowboxes for ion species-resolved beam divergence; Thompson parabola spectrometer and Rutherford-scattering magnetic spectrometer for ion species and energy composition; collimated bremsstrahlung detectors and in-anode collectors for diode voltage and current; and emission spectroscopy and visible light streak photography for in-gap light emission.

The substantial data base from the performance of this diode on LION will be compared to results on COBRA to illuminate issues of power coupling to the diode load on the new accelerator. In particular, the diode will first be mounted on COBRA with a very short (75 cm from cavity gap to diode gap) vacuum MITL. It is expected that with the single-point (azimuthal) power feed to the cavity, power flow in the MITL will be significantly azimuthally

asymmetric. We will diagnose effects of this asymmetry on diode performance. Our aim is to explore the tradeoff between diode performance degradation by power flow asymmetry for a short MITL and degradation by the delay between the vacuum-wave prepulse and the main power pulse at the diode with a long MITL.

After the full four-cavity COBRA is in place, the Cornell experimental program will make a transition from the long-standing emphasis on ion diode physics toward a more integrated development of the diode as part of a beam generation, transport, and focusing system. We will design a system using an extraction diode, a gas-filled transport region, and asolenoidal focusing lens to produce a small analog to a module of a large ICF driver such as the Laboratory Microfusion Facility (LMF).[4] Our aim is to diagnose and develop the accelerator, diode, beam transport, and lens as integrated, interacting components of the beam driver system to provide an overview of the issues involved and to investigate tradeoffs and optimization for LMF.

III. ACCELERATOR DESCRIPTION

The requirement for a 4-to 5-MV pulsed power driver led naturally to four 1.0-to 1.25-MV cavities that nearly duplicate the IVA technology presently used in the HERMES-III and SABRE machines at Sandia.[5] The cavity-to-cavity inductive isolation, performed by ribbon-wound annular cores of type 2605CO METGLAS[6] ferromagnetic material, and the vacuum MITL allow us the most compact machine design to maximize the available experimental area. As shown in Fig. 3, the inner cylinder of the MITL is tapered at each cavity output feed gap according to the impedance requirements to best couple to the diode load. Our choice for a single overhead water line to charge

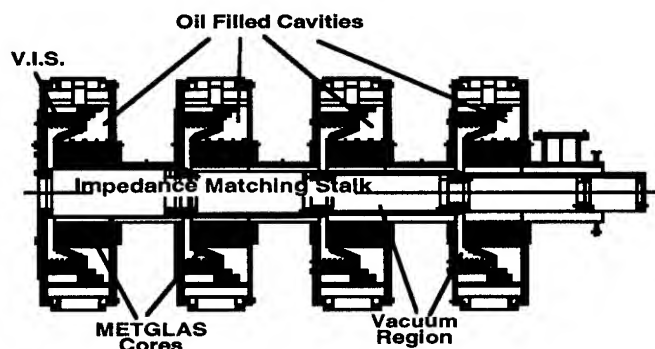


Fig. 3. The COBRA IVA consists of four radial cavities that deliver power to the coaxial vacuum MITL.

each cavity was influenced by cost and space limitations, but we did confirm that the MITL current flow (for negative polarity operation) was azimuthally symmetric within about 2 ns along the vacuum coaxial line from the cavity output gap. These tests were performed at the Sandia STF using the same water lines and cavity that are installed for the initial COBRA experimental series. Larger diameter cavities may

need two or more equally spaced feeds to optimize the flow symmetry.

The basic pulsed-power source for the IVA consists of one oil-insulated Marx generator, a water-dielectric ISC or transfer capacitor, a self-breaking multi-stage SF₆ gas switch, and water-dielectric coaxial PFLs with self-closing output water switches. The tools we used to iteratively design and model COBRA include the STF experiments, the SCREAMER circuit simulation code[7] and electrostatic field solvers like JASON[8] and ELECTRO[9] along with dielectric breakdown and flashover criteria like that originated by J.C. Martin.[10] The following Table I is a summary of the accelerator design parameters, peak values generated by the circuit models, and some of the hardware dimensions. Negative high voltage is assumed for the inner conductors of the coaxial lines. Note that the subscripts 'in' and 'out' typically refer to the inner and outer coaxial radii,

Table I. Cobra Accelerator Design Summary

Marx:	No.Caps = 24 ea V _{ch} = 90 kV V _{rated} = 100 kV V _{max} = 2.2 MV	C/Cap = 1350 nF E _{ch} = 131 kJ E _{ch} /E _{max} = 81% I _{Marx} = 111 kA
ISC: (HERMES-III)	R _{out} = 71.8 cm R _{in} = 53.3 cm Length = 130 cm V _{isc} = 2.7 MV E _{out} = 126kV/cm E _{in} = 170kV/cm	C _{isc} = 19.5 nF Z _{isc} = 1.98 Ohm T _{isc} = 38.6 ns T _{eff} = 200 ns E _o /F = 61% E _i /F = 36%
Gas Switch:	Length = 50.6cm Gap(x18)=16 cm V _{gas} = 2.7 MV I _{gas} = 405 kA (@ 900 ns) E _{diss} = 9.4 kJ	OD = 44.5 cm No.Channels<10 L _{sw} = 240 nH Q _{gas} > 83 mC E _{diss} /E _{out} = 12%
PFLs(4):	R _{out} = 17.8 cm R _{in} = 8.4 cm Length = 76.2 cm V _{off} = 2.3 MV E _{out} = 172 kV/cm E _{in} = 365 kV/cm	C _{off} = 4.6 nF Z _{off} = 5.0 Ohm T _{off} = 22.8 ns T _{eff} = 40 ns E _o /F = 47% E _i /F = 44%
H₂O Switches(4):	Gap = 4.2 cm V _{wat} = 2.3 MV I _{wat} = 248 kA (@ 1000 ns) E _{diss} = 2.4 kJ	Channels/Sw = 4 L _{sw} = 66 nH Q _{wat} > 17 mC E _{diss} /E _{out} = 16%
Cavities(4):	ID = 38.1 cm Length = 41.9 cm Cores/Cav = 4 V _{cav} = 1.31 MV (Matched Load) V _{load} = 1.28 MV I _{load} = 256 kA P _{load} = 328 GW (@ 1050 ns) E _{load} = 12.6 kJ	OD = 150 cm L _{cav} = 20 nH Wt/Core=51.1kg Volt-Sec = 0.077 T _r (10-90)=23.3ns FWHM = 49.2 ns E _{vis} = 87 kV/cm 4E _{load} /E _{ch} = 38%

and 'vis' is the oil/vacuum insulator stack. The E/F ratios correspond to the expected electric field stress divided by the calculated breakdown stress.

IV. PREDICTED PERFORMANCE

Our circuit simulation process involved a number of iterations as the COBRA accelerator design evolved and components were modified or better defined. All the feed line lengths, impedance variations, and major component values had to be accurately represented to allow confidence in the model predictions. We used transmission line models in the SCREAMER code to account for the proper physical separations and dimensions of the oil, water, vacuum, and plastic insulated components. These models provide a fixed propagation delay time and either a constant or a linearly tapered line impedance. The switch models are typically represented by a series combination of time-varying resistor and appropriate inductor with both elements shunted by a parallel stray capacitance. The switches are closed by reducing the initial high resistance exponentially to a final low resistance. The exponential time constants were determined from estimates of the resistive and inductive phase contributions to the switching action.[11] The choice for the final resistance is critical for determining the energy dissipated by the gas and water switches, which in turn affects the forward going pulse shape. Figure 4 shows the resulting voltage waveforms of one circuit simulation that corresponds to the parameters listed in Table I. This circuit

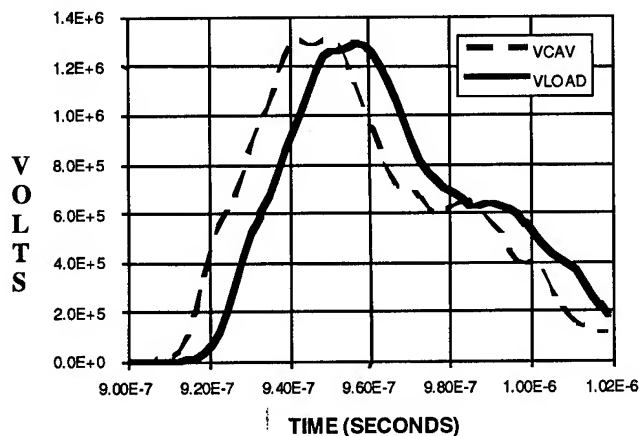


Fig. 4. SCREAMER generated these simulated voltage waveforms at the cavity input and output.

model did not include a "crowbar" switch in the output water transmission line (OTL) nor a saturable magnetic core model which could significantly affect the pulse shape depending on the core material loss properties. Since accurate ion diode models are still being developed for SCREAMER, the only load we have modeled is a constant matched resistance. The load voltage wave shape will definitely be sensitive to the impedance history of dynamic ion diodes.

V. CONCLUSIONS

With this paper we are announcing a new terawatt class accelerator intended to further the light ion ICF program with research and development of diodes, beam transport, and possibly beam focusing. COBRA is the result of a major cooperative effort between a university and a national laboratory (Cornell and Sandia) and, hopefully, may set a precedent for other similar endeavors. It represents technology currently being applied at Sandia and should be a robust, reliable research tool.

VI. ACKNOWLEDGMENTS

The authors wish to recognize the long term efforts of Don Cook, Doug Bloomquist, John Maenchen, and Juan Ramirez of Sandia Labs and Dave Hammer at Cornell University. Without their support this project would never have gone beyond a paper exercise. Special thanks are also due to Dan Jobe and Pat Ryan, Ktech contractors supporting Sandia, and Leo Brissette in Cornell whose enthusiastic support included the preparation, shipping, and assembly of the COBRA hardware at Cornell. This work was supported by the United States Department of Energy under Contract DE-AC04-94AL85000.

VII. REFERENCES

- [1] J.B. Greenly, et. al., "Extraction Ion Diode Studies for Optimized Performance: Divergence, Ion Species, and Parasitic Load," *Proc. 10th Intl. Conf. on High Power Particle Beams*, San Diego, CA, June 20-24, 1994, p. 398.
- [2] G.D. Rondeau, Ph.D. Thesis, Cornell University, 1988.
- [3] C.K. Struckman and B.R. Kusse, *J. Appl. Phys.* Vol. 74, No. 6, p. 3658, 1993.
- [4] J.J. Ramirez, et. al., "Design Issues for a Light Ion Beam LMF Driver," *Fusion Technol.*, Vol. 15, p. 350, 1989.
- [5] J.J. Ramirez, et. al., "The HERMES-III Program," *Proc. 6th IEEE Pulsed Power Conf.*, Arlington, VA, June 29-July 1, 1987, p. 294.
- [6] METGLAS is Allied Corporation's registered trademark for an amorphous alloy of metals.
- [7] M.M. Widner and M.L. Kiefer, "SCREAMER - A Pulsed Power Design Tool, User's Guide," Sandia Nat. Labs, Albuquerque, NM, Apr 25, 1985.
- [8] S.J. Sackett, "JASON - A Code for Solving General Electrostatics Problems, User's Manual," CID-17814, Lawrence Livermore Nat. Labs, Livermore, CA, 1978.
- [9] "ELECTRO Users and Technical Manual," Version 3.9, Integrated Engineering Software Inc., 46-1313 Border Pl., Winnipeg Manitoba, Canada, R3G 2X7.
- [10] J.C. Martin, "Nanosecond Pulse Techniques," Internal Report SSWA/JCM/704/49, AWRE, Aldermaston, Berkshire, England, April 1970.
- [11] J.P. VanDevender and T.H. Martin, *IEEE Trans. on Nucl. Sci.*, Vol. 22, No. 3, p. 979, 1975.

BEAM INJECTOR AND TRANSPORT CALCULATIONS FOR ITS

Thomas P. Hughes, Mission Research Corporation, Albuquerque, NM 87106
David C. Moir and Paul W. Allison, Los Alamos National Laboratory, Los Alamos, NM 87545

Abstract

The Integrated Test Stand at Los Alamos National Laboratory (LANL) is addressing issues in high-brightness electron beam generation, acceleration, and transport. The machine consists of a 3 kA, 3.5 MV injector, eight induction acceleration gaps, a drift section and a final-focus magnet which focuses the beam onto diagnostic targets. One of the goals of the program is to test and improve the predictive capability of numerical models. We have carried out detailed simulations of the diode and initial drift region with the particle-in-cell codes IVORY and SPROP, obtaining good agreement with experimental streak-camera data at several axial locations. Transport through the accelerating cells to the target 10 m from the cathode is modeled with the envelope codes LAMDA and XTR. The magnet settings for minimum spot-size are close to the experimental values. From the measured value of the minimum spot-size we infer a normalized Lapostolle emittance of about 0.2 cm-rad. We have characterized the sensitivity of the spot-size to variation in the machine parameters.

I. INJECTOR SIMULATIONS

The standard injector geometry in the ITS has a 18 cm AK gap and a flat 3" diameter velvet emitting surface (Fig. 1). This surface is indented by 2 mm from the surrounding flat electrode. The small scale of this indentation means that a fine mesh is needed to simulate the AK gap. We used the particle-in-cell simulation code IVORY and the iterative trajectory code PBGUNS [1] to model the injector. The codes agree well with each other and with the experimental beam current measurement (3 kA at 3.5 MV), as shown in Fig. 2. The effect of the indentation is to reduce the current density at the beam edge, and provide some radial focusing to the emitted beam. With a previous flush emitting surface, we were unable to get close agreement between experiment and simulation [2]. The measured emission current was about 15% higher than the calculation, and current was lost to the anode even when the extraction field was relatively high. We believe that this was due to poorly understood effects at the edge of the velvet emitter which produced low quality, divergent emission in this region.

The simulation in Fig. 1 had no intrinsic emittance at the cathode. Such emittance, inferred from spot-size measurements discussed below, can easily be added to the simulation as an effective transverse temperature of the emitted particles. For the large beam radii in Fig. 1, the transport is space-charge dominated.

II. RADIAL CURRENT PROFILE COMPARISONS IN PRE-ACCELERATOR DRIFT

A series of measurements of the beam radial current density profile was made by placing a quartz fiber across the beam diameter to generate Cherenkov light. The light was imaged with

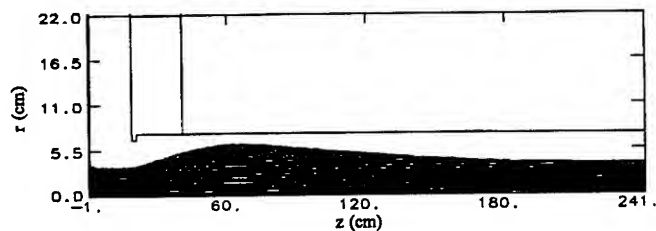


Figure 1. Beam particle positions for IVORY simulation of ITS indented cathode. Mesh is $\Delta z \times \Delta r = 0.1 \text{ cm} \times 0.1 \text{ cm}$ in AK gap, and $0.4 \text{ cm} \times 0.2 \text{ cm}$ for $z > 40 \text{ cm}$. ($I_b = 3 \text{ kA}$, $V_b = 3.48 \text{ MV}$, anode magnet current = 175 A).

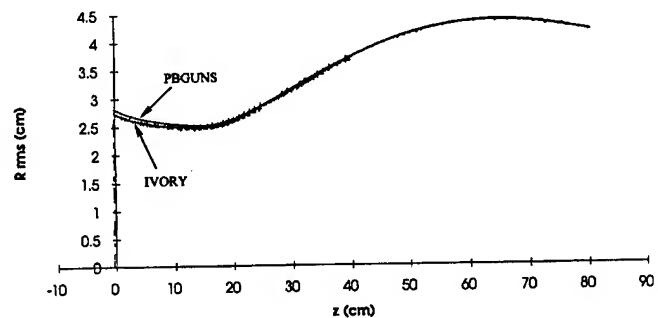


Figure 2. Comparison of r.m.s. beam radius from IVORY simulation and PBGUNS simulation of ITS cathode with 2 mm indentation. Emitted current for both simulations is 3 kA at 3.48 MV.

a streak camera to get a time-resolved measurement. To simulate beam transport from the diode to the location of these measurements (about 2 m from the cathode surface), we developed a beam slice code SPROP [3]. The field equations for this code are obtained from the full Maxwell equations by setting axial derivatives to zero and solving the resulting equations on a 1-D radial mesh using Fourier transforms in the azimuthal direction. The code is initialized with particles from an IVORY simulation at 101 cm from the cathode surface, which is in the downstream fringe-field of the anode magnet. Comparisons with the experiment were made at 170, 192 and 212 cm from the cathode electrode. The results at $z = 212 \text{ cm}$, shown in Fig. 3, are typical of the good agreement obtained. The result in Fig. 3(b) is about 60 cm downstream of where the beam focuses to a small ($\approx 0.5 \text{ cm}$ radius) spot.

III. BEAM RADIUS MEASUREMENTS AT FINAL FOCUS

The ITS injector is followed by eight ferrite induction accelerating cells which typically have voltages of 200–250 kV per gap. The beam then goes into a drift section which has an intermediate

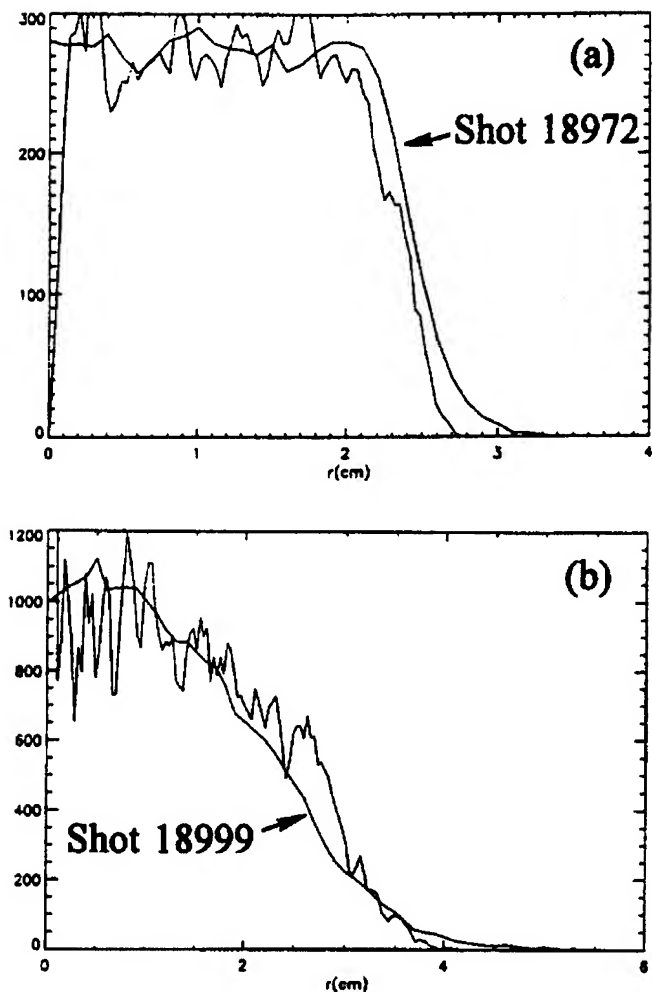


Figure 3. Comparison of experimental and numerical radial current density profiles at 212 cm from the cathode for anode magnet currents of (a) 185 A and (b) 210 A. Vertical scale is arbitrary.

focusing solenoid and a final focus solenoid (FFS). The purpose of the drift section is to prevent shrapnel from fragmented targets from damaging the acceleration cells. A rotating shutter is also used for this purpose.

Since the ITS is directed at radiographic applications requiring small beam spot-size, the principal diagnostic technique consists of measuring the radius of the focal spot as a function of FFS strength. We can model the entire transport using SPROP, but for speed we generally employ the envelope codes LAMDA [4] and XTR [5]. We have found that the effect of beam rotation in the focusing solenoids is non-negligible. Starting from exact laminar beam equilibria obtained by Reiser [6], a modified envelope equation was obtained to take account of this effect [3]. The envelope equation, which assumes constant emittance, closely matches SPROP, as shown in Fig. 4. The SPROP simulations show that in fact there is little emittance variation through the accelerator.

A comparison between the spot-size measurements at $z = 10$ m and LAMDA for a particular tune is shown in Fig. 5. The LAMDA beam envelope for the minimum spot-size is shown in

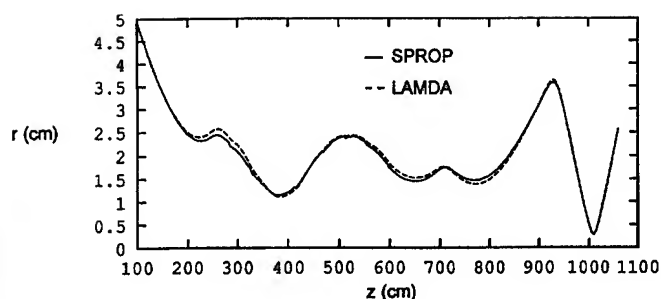


Figure 4. Comparison of envelope obtained from SPROP particle-in-cell simulation with LAMDA envelope simulation

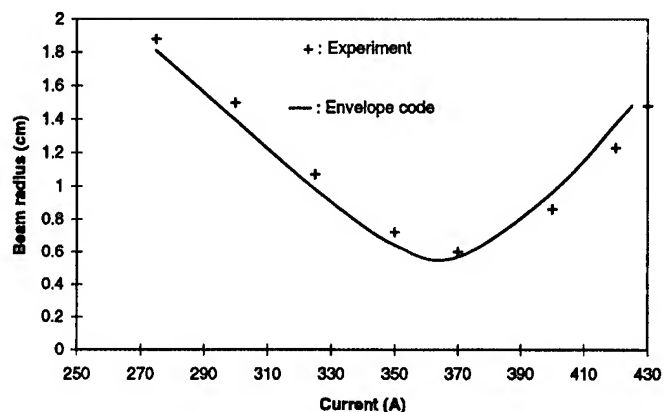


Figure 5. Beam radius at final focus as a function of final-focus solenoid current, comparing measurements with envelope code predictions. Experimental results are averaged over 60 ns flat-top.

Fig. 6. Based on this and other comparisons for different magnet tunes, we deduce a normalized Lapostolle emittance value of about 0.19 cm-rad. This value may be an overestimate because of the low energy threshold for light-production in quartz, which makes it difficult to make accurate spot-size measurements when the beam radius is small. To avoid this problem, a spot-size diagnostic using transition radiation in a Kapton target is currently being implemented. This will give a two-dimensional beam image with a 60 ns (the approximate pulse flat-top) gating on the camera.

Using the envelope code LAMDA, we have carried out a series of tests to measure the sensitivity of the minimum spot-size to various machine parameters. The results, shown in Table I, give an indication of the degree of control needed to obtain a small time-averaged spot-size for a particular beam pulse, and that needed for shot-to-shot spot-size reproducibility.

Experiments are currently being conducted on the REX machine to investigate a laser photocathode injector. This has the potential for significantly reducing the intrinsic emittance of the beam. A lower emittance, resulting in a smaller spot-size, would reduce the tolerances in Table I.

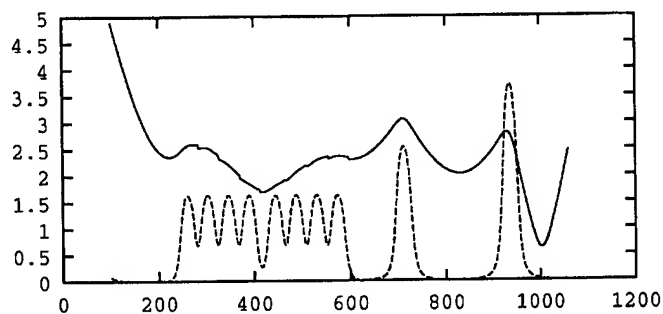


Figure 6. Beam edge radius (cm) vs. z (cm) for final focus magnet current of 370 A, obtained from LAMDA. Axial magnetic field, divided by 300 gauss, is superimposed.

Table I

Percent changes in accelerator parameters which result in 10% change in final-focus spot-size

AK voltage	+20%, -11%
Accelerating gap voltage	+30%, -16%
Cell magnet strength	+17%, -35%
Drift tube magnet	+4.7%, -10%
Final-focus magnet strength	+3.2%, -3.4%
Position of target	+3.5 cm, -8.9 cm

IV. ACKNOWLEDGMENT

This work was performed under the auspices of the U.S. Department of Energy by Los Alamos National Laboratory.

V. REFERENCES

1. J. Boers, Thunderbird Simulations Inc.
2. T. P. Hughes, R. L. Carlson and D. C. Moir, "Calculations for PIXY, ECTOR, REX, ITS and TGX," MRC/ABQ-R-1483, March, 1992.
3. T. P. Hughes, T. C. Genoni, P. W. Allison, R. L. Carlson and D. C. Moir, "Computational Support for ITS and REX," MRC/ABQ-R-1735, April, 1995.
4. T. P. Hughes, R. M. Clark, T. C. Genoni, and M. A. Mostrom, "LAMDA User's Manual and Documentation," MRC/ABQ-R-1428, April, 1993.
5. Paul Allison, "XTR, A New Beam Dynamics Code for DARHT," DARHT Technical Note #50, 13 July 1995.
6. M. Reiser, Phys. Fluids 20, 477 (1977).

STATUS OF THE AIRIX INDUCTION ACCELERATOR

Ph. EYHARTS, Ph. ANTHOUARD, J. BARDY, C. BONNAFOND, Ph. DELSART, A. DEVIN, P. EYL,
J. LABROUCHE, J. LAUNSPACH, J. DE MASCUREAU, E. MERLE, A. ROQUES,
P. LE TAILLANDIER, M. THEVENOT, D. VILLATE, L. VOISIN

Commissariat à l'Energie Atomique
Centre d'Etudes Scientifiques et Techniques d'Aquitaine
BP N°2 - 33114 LE BARP - FRANCE

Abstract

AIRIX Induction Accelerator (16-20 MeV, 3.5 kA, 60 ns) has been designed at CESTA for flash X-ray application. After two years of experimental studies on prototype cells and High Voltage Generators we started in 1994 the PIVAIR milestone which is a validation step at 8 MeV for AIRIX. The PIVAIR injector has been assembled and tested; it produces a 3.5 kA electron beam at 4 MeV with good voltage flatness ($\pm 0.35\%$) and low emittance. An accelerating module of eight induction cells has been constructed and four cells have been first connected with the injector. The other ones will be added this year and will use ferrite cores with high magnetic flux variation specially developed by CEA for this application. First results on beam characteristics will be given in this paper as well as progress achieved in diagnostic technologies, cell alignment and beam transport studies.

I - INTRODUCTION

Dedicated to flash X-ray radiography application AIRIX induction accelerator has been designed to produce a 16-20 MeV, 3.5 kA, 60 ns electron beam. Development of this machine started at CESTA in 1992 with the construction of two prototypes: an induction cell and a high voltage generator. After testing we decided to construct PIVAIR accelerator which is a validation step of AIRIX up to 8 MeV; it will permit to check the different technologies involved on AIRIX but also to study the beam transport and focusing.

PIVAIR installation will consist of a 4 MeV injector, sixteen 250 keV induction cells and a focusing solenoid. In march 1994 injector acceptance tests have been successfully performed at CESTA and by the end of the same year we tested four induction cells loaded with the 3.5 kA electron beam generated by this apparatus.

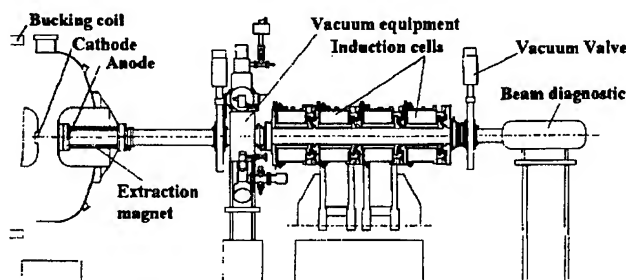


Figure 1 : PIVAIR setup

In the following sections we describe the existing PIVAIR equipments (fig.1) and we present the experimental results obtained.

II - INJECTOR

The injector used on PIVAIR was designed by PSI for the pulse generator and by LANL for the diode. It comprises a 1.5 MV glycol-insulated Blumlein which is pulse charged by a step-up transformer and switched out by four laser-triggered spark gaps. A series of increasing impedance transmission lines is used to transform the Blumlein output voltage to 4 MV at the diode.

The beam is generated by a 7.62 cm diameter rayon-velvet cathode surrounded by a non-emitting anodized aluminum field shaper; the distance between the re-entrant anode and cathode is 17.5 cm.

During acceptance tests beam characteristics were measured using diagnostics developed by CESTA [1][2]. A summary of the results are given in table 1. It appears that measured performances are in good agreement with AIRIX specifications except for emittance. We suspect that the value obtained for this parameter is higher than expected because data processing does not take into account diagnostic perturbations due to metallic mask focussing.

Table 1 . AIRIX injector characteristics

	Specifications	Measured
Diode voltage	≥ 4 MV	4029 kV \pm 4 kV
Voltage flatness	$< \pm 1\%$ in 60 ns	$< \pm 1\%$ in 60 ns $\pm 0.35\%$ in 50 ns
Voltage reproductibility	$\pm 1\%$	$\pm 0.60\%$ over 1000 shots
Beam current	≥ 3.5 kA	3.8 kA
Normalized rms emittance ($\pi \cdot \text{mm} \cdot \text{mrad}$)	≤ 1200	1600 at 3.77 kA
Jitter (1σ)	≤ 1.5 ns	≤ 0.5 ns

III- HIGH VOLTAGE GENERATORS

A high voltage pulse generator has been developed to drive two induction cells with 250 kV / 75 ns flat top pulses with voltage variation smaller than $\pm 1\%$.

A prototype described in a previous paper [3] was tested in 1993 and gave good results. On this base a series of four generators has been constructed last year to feed the first eight PIVAIR induction cells. They are now operating.

IV - INDUCTIONS CELLS

Each induction cells use 11 ferrite cores (250 mm I.D., 500 mm O.D. and 25 mm thick) housed in a non magnetic stainless steel body, a 4 layers bifilar-wound solenoid magnet and 2 printed circuit dipole trim coils. The 19 mm width accelerating gap has been shaped in order to minimize the beam coupling with the gap cavity and reduce the BBU instability (fig.2)

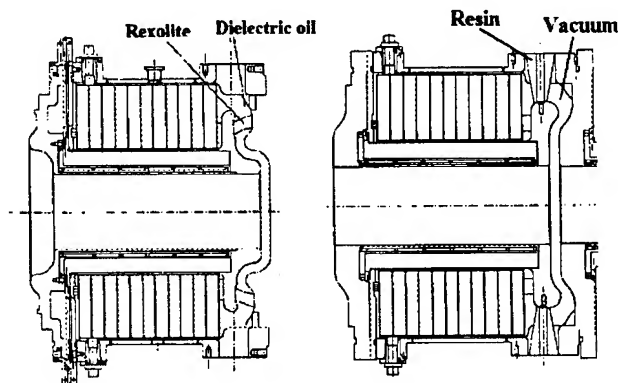


Figure 2 : PIVAIR induction cells

IV.a - High voltage testing

Three gap insulator technologies have been tested on the prototype cell. An alumina insulator brazed on cell body was first experienced. A good vacuum tightness was obtained (10^{-8} torr) but the cell exhibited numerous flashovers at voltage levels higher than 200 kV. Modifications of gap shape and alumina-field angle did not give best results. Consequently this technology was not chosen for AIRIX.

The second insulator tested was made of reticulated polystyrene (Rexolite) and used viton O-ring seals to ensure vacuum tightness. The gap geometry was chosen so that an angle of 40° was maintained between insulator surface and E-field. With this configuration the vacuum reached 10^{-6} torr in the cell and the high voltage strength was tested up to 300 kV without any flashovers. From these results we decided to construct four PIVAIR cells with Rexolite insulator.

In the third technology gap insulator is suppressed and dielectric oil surrounding the ferrite cores is replaced by vacuum. This technology is attractive for two reasons. First the vacuum interface and high voltage insulation are transferred on HV cable heads which is more convenient for accelerator maintenance in case of flashover. On the other hand BBU calculations show that transverse impedance is lower for such a cell.

Tested on prototype cell this configuration needed several months of experiment to be qualified for PIVAIR. At the beginning we observed a decrease in cell impedance for voltage pulse higher than 210 kV. We found that the default originated in current leakage along ferrite cores due to a too short distance between cores and metallic housing. Once this problem solved the cell was tested successfully with pulses up to 300 kV.

At present four induction cells without ring insulator are under construction and will be mounted on PIVAIR soon.

IV.b - Ferrite improvements

TDK PE11B ferrite used on the first cells are not sufficient to maintain 75 ns flat top with 250 kV pulses because cores saturation occurred too early. In order to increase the magnetic flux swing available on ferrite we decided to test two other compositions : TDK PE 16 and a CEA ferrite specially developed for AIRIX application. The best result was obtained with the last one which offers a 15 % increase in magnetic flux swing. So AIRIX and PIVAIR cells will be furnished with CEA ferrite cores.

V - DIAGNOSTIC DEVELOPMENT

Because electron beam characteristics are essential in providing high quality radiographic flashes, time resolved electron beam diagnostics have been developed at CESTA. They are described in details in a companion paper elsewhere in this conference [5]. A summary of their performances are given below.

Spectrometer: a magnetic spectrometer has been built to measure on a single shot, electron energy versus time ranging from 1 to 10 MeV. In this apparatus the beam is bended as it enters between poles of a semi-circular magnet. After deviation electrons are intercepted by a linear fiber optic array. The interaction between fibers and beam produces Cerenkov radiation which is analyzed with a streak camera. Time resolution of 1 ns and energy resolution $\Delta E/E$ of 0.1 % are currently obtained.

Emittance measurement: this diagnostic is based on the pepper-pot technique. It uses 3 mm thick tantalum plate with an array of 1 mm diam. holes. The beam first passes through the mask and is then intercepted by a plastic film scintillator. Image obtained is recorded on a gated CCD camera. With this equipment time resolved emittance can be measured in two transverse directions with 5 ns resolution.

Beam position and current monitors: to evaluate beam transport conditions (BBU perturbations and chromatic aberrations) beam position monitors have been developed. Each one comprises four pickup loops that measure the magnetic field associated with the beam. The resolution we need is $\pm 5\%$ for current and $\pm 100 \mu\text{m}$ for position in the 1 GHz bandwidth. To reach this objective we have improved the loop mechanical construction (accuracy, reproducibility) and the quality of data acquisition system (oscilloscopes, cables ...)

At present one monitor has been calibrated and is used on PIVAIR accelerator; its performances are under test.

VI - PIVAIR RESULTS

Alignment: by the end of 1994 four induction cells with Rexolite insulator were assembled in one block on a mounting stand using a laser beam for alignment. Then the cell block was aligned with a theodolite on a reference axis normal to the cathode. Accuracy obtained between cell and reference axis was $\pm 190 \mu\text{m}$ for offset and $\pm 210 \text{ mrad}$ for tilt angle [4].

Synchronization: high voltage generators spark gap triggering was controlled by a Stanford pulse delay generator

which offers a very high accuracy and a low jitter. Synchronization of HV generators was first tuned on a resistive load and then applied to the cells. This system was very satisfying.

Beam transport: to simulate beam transport conditions and determine axial magnetic field along accelerator we used the envelope code ENV developed at CESTA. This code was experimentally validated on LELIA accelerator [5] last year. On PIVAIR we first calibrated the guiding magnets by measuring, with a Hall probe, axial magnetic fields versus coil currents.

Then initial beam characteristics were obtained by evaluating the mean quadratic radius with an optical diagnostic placed just behind the extraction coil.

Beam acceleration: pulses up to 210 kV have been successfully applied to the cells loaded with 3.5 kA beam issued from the injector (fig.3). At this voltage level no flashovers were observed. For higher voltages, saturation of TDK PE 11 ferrite cores generates a peak of current which after reflection on HV cables produces an inverse voltage pulse on gap cell. This pulse appears 440 ns after the main pulse and induces flashover on the gap insulator. So with current ferrite cores accelerating pulses are limited to 210 kV

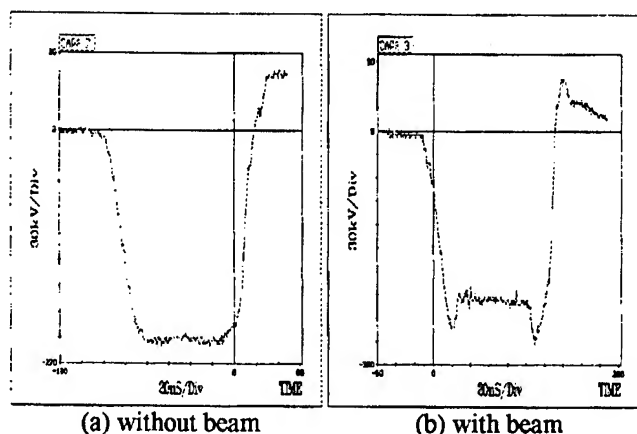


Figure 3 : PIVAIR cells response

Beam characteristics: an energy of 4.8 MeV has been measured with the spectrometer at the accelerator output (fig.4). This result confirms an energy gain of approximatively 210 kV by cell. Figure 4 -a and 4 -b show that energy spread obtained at injector output ($\pm 1\%$) is not affected by acceleration. Emittance measured at the accelerator end was about $1600 \pi \cdot \text{mm.mrad}$; this value agrees well with emittance predicted by ENV code. In order to complete code evaluation we must now perform beam radius measurements inside the accelerator tube.

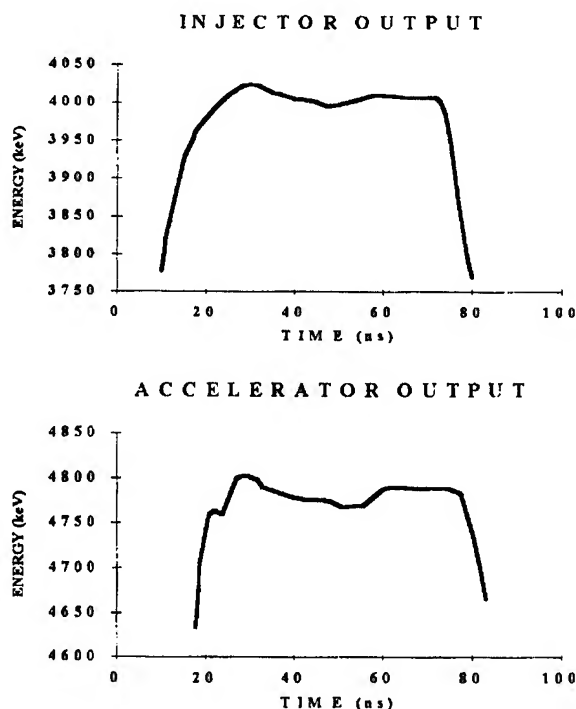


Figure 4 : Beam energy

VII - PIVAIR SCHEDULE

Eight inductions cells (4 vacuum cells and 4 Rexolite cells) are under construction and will be connected to the accelerator during summer 1995. After HV testing we plan to measure energy gain and start BBU experiment with 7 MeV / 3.5 kA beam.

VIII - REFERENCES

- [1] Recent Results on the DARHT and AIRIX 4MV \pm 1 3KA electron beam injectors
J.Launspach and al., CEA-CESTA, Le Barp, France
P. Allison and al., LANL, NM, USA
J.Fockler and al., PSI, San Leandro, CA, USA
Proceedings of BEAM's 94, San Diego, June 1994
- [2] Diagnostics development for high current electron beam at CESTA.
J.De Mascureau and al., CEA-CESTA, Le Barp, France
Proceedings of PAC 93, Washington, 17-20 May 1993
- [3] Design and Progress of the AIRIX induction Accelerator
P.Anthouard and al., CEA-CESTA, Le Barp, France
Proceedings of EPAC 94, London, June 1994
- [4] High current beam diagnostic development for AIRIX
D.Villate and al., CEA-CESTA, Le Barp, France
This conference
- [5] First Operation of the LELIA Induction Accelerator
P.Eyharts and al., CEA-CESTA, Le Barp, France
Proceedings of PAC 93, 17-20 May 1993

Pulse Modulators for Ion Recirculator Cells*

T.F. Godlove, L.K. Len, F.M. Mako, FM Technologies, Fairfax, VA 22032
and W.M. Black and K. Sloth, George Mason University, Fairfax, VA 22030

I. INTRODUCTION

Heavy-ion fusion (HIF) continues to be the choice method of inertial fusion energy for a combination of reasons --primarily driver efficiency, beam transport to target, and repetition rate. For more than a decade a group at the Lawrence Berkeley Laboratory (LBL) has explored the use of a multiple-beam induction linear accelerator for the driver. A review of technology development, particularly for a test accelerator called ILSE, has been given by Reginato [1]. Recently, the 5-MeV part of ILSE, dubbed ELISE, has been approved.

In 1989 studies began on the idea of recirculating the linac beams to reduce cost. While a recirculator introduces serious issues, the cost reduction incentive is real. A review of a two-year study, primarily at the Lawrence Livermore National Laboratory (LLNL), has been given by Barnard *et al* [2]. Also, initial technology development for a recirculator at LLNL has been reported by Newton and Kirbie [3].

We report here on a study of circuits for the accelerating modules in a recirculator. Future requirements are challenging: flat-top (or slightly rising) pulses with varying duration; beam currents as high as a kiloampere; a train of 50-100 pulses with instantaneous repetition rate as high as 50 kHz; and high efficiency. An accelerating module providing 200-400 kV to the beam might house 30-100 cores.

Our study uses cores of moderate size--we chose 20.3 cm diameter. The pulsers use tapered pulse-forming networks (PFNs) and provide core reset, 20- μ s recovery and variable duration. A novel addition is a separate, 150-kV, 200-A modulator used to simulate a constant-current ion beam, allowing a direct measurement of the cell dynamic impedance and the modulator-to-beam conversion efficiency.

The basic goal of the project is to explore the use of solid-state switches and low-voltage circuits with efficiency and low cost in mind. In this report we describe our circuits and salient results, then offer comments and conclusions.

II. CELL AND CIRCUIT

The cell design, shown in Fig. 1, is conventional. The housing provides for three coax inputs connected to the single-turn conducting wall and is designed for stacking by removing one end wall from each adjacent cell. The core is Metglas** 2605-SC, 10.2 cm ID, 20.3 cm OD, and 5.1 cm wide. It provides 1.94 kV- μ s per Tesla magnetic swing. We tried both annealed (before winding) and unannealed cores.

* Supported by DOE Small Business Innovation Research and in part by Virginia's Center for Innovative Technology.

** Registered trademark of Allied Signal Corporation.

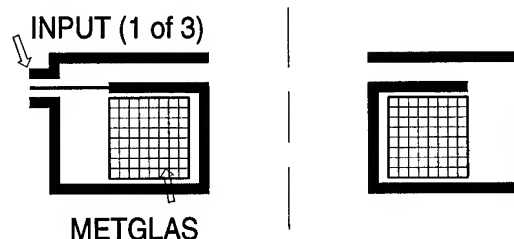


Fig. 1. Model cell. Core O.D. = 20 cm.

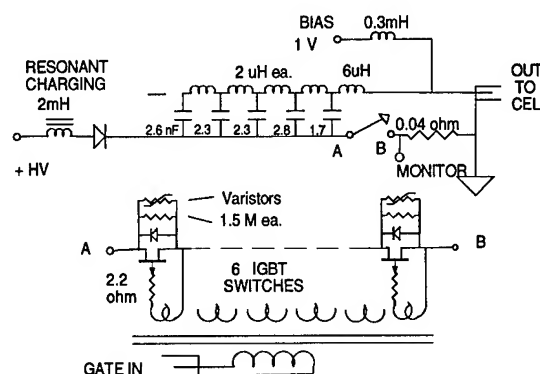


Fig. 2. Cell pulser, one of three for each cell.

Figure 2 shows our 0.4- μ s pulser circuit, one of three for each cell. We also built a 0.9- μ s, 8-section network. As shown, it uses a 3.5 kV power supply and diode-resonant charging. The charging current partially resets the core magnetization and is supplemented by a small dc current (<6 A) connected through a 0.3-mH isolating inductor. A non inductive, 40-m Ω resistor monitors the pulse current.

Transient suppression, not shown in Fig. 2, is included from A to B. For some tests, we connected the switch assembly between the network and the cell. In this case we lose the charging current reset. More dc bias current, up to about 12 A, is then required.

An important alternative circuit, command resonant charging, is discussed in the next section.

The PFN values are adjusted to give the best flat-top pulse taking into account the cell inductance, transient magnetization current, transient eddy current losses, core saturation, and the time-dependent switch resistance. While the well known design code PSPICE was extensively used and gave excellent agreement with a resistive load, final adjustment of the pulse shape was done empirically.

A principal motivation for the project was the advent of high power solid-state switches, MOSFET and IGBT (insulated-gate bipolar transistor). They provide turn-off capability and

can easily recover voltage hold-off in a few μ s. We decided early in the project to concentrate on IGBTs because of their higher power rating, in spite of their somewhat slower rise/fall time. Also, they were much lower in cost, although currently the MOSFETs are coming down in price. We used six in series, APT50GF100BN or Int'l Rectifier IRGPC50U or IRGPH50F, rated at 900-1200 V each and up to 200 A peak.

The switch gates are driven using a small pulse transformer with six single-turn secondaries and a six-turn primary driven by a single MOSFET. This method provides the necessary isolation, speed and peak current to the gates. Gate duration is adjusted to coincide with the natural fall of the PFN pulse, resulting in a faster fall time than the IGBT alone provides.

In general the switches only fail due to overvoltage. A varistor is connected in parallel with each switch for fault protection; more on this issue in the next section.

Simulation is accomplished using a separate high-impedance source as shown in Fig. 3. It is a thyatron-switched modulator driving a resistive load on the cell axis. A real beam is a constant-current source. Simulation requires that the voltage added by the cells be small compared to the modulator voltage. The rise time, 0.4 μ s, is longer than desired for rise-time simulation but adequate for impedance and efficiency measurements.

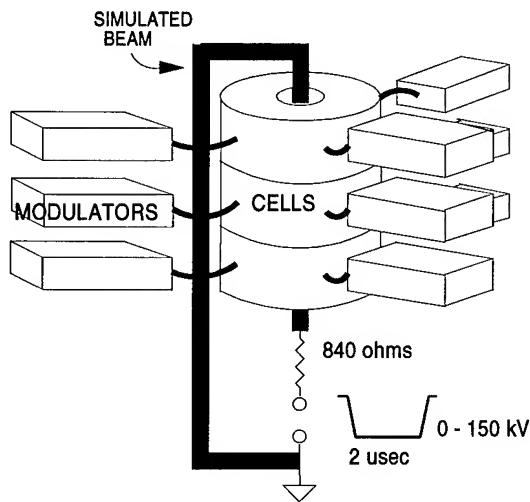


Fig. 3. Simulated beam setup with three cells, each driven by three modulators.

III. RESULTS AND COMMENTS

Figure 4 shows a set of typical waveforms for an annealed core with zero beam current, using the capacitor-grounded circuit and the longer pulse. The four traces show many aspects of circuit behavior. Trace 1 is the PFN voltage on a slow, 0.2 ms, sweep. It shows the 24- μ s recovery and voltage remaining after each of two pulses. We ignore the first pulse, since it is based on the supply voltage, 3.5 kV. The voltage then rises to 5 kV, which is the limit of our six switches, and the circuit is triggered again after a delay of 104 μ s (the delay

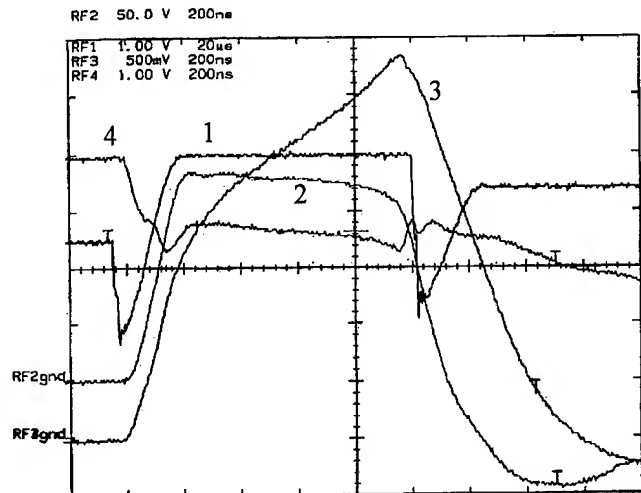


Fig. 4. Waveforms for one cell (1/27/95#1).

is arbitrary from 25 μ s to 1 ms, after which the PFN voltage droops).

Traces 2, 3 and 4 refer to the second pulse. They are the output gap voltage (3.7 kV), current from one pulser (67 A) and PFN voltage, respectively, with a 2- μ s sweep. The total current to the cell is $3 \times 67 = 201$ A peak. Trace 2 shows the droop and trace 3 the accelerated current rise during the last 200 ns of the pulse, both due to the onset of core saturation. (The gap voltage is flat at lower supply voltage.) Trace 4 shows, during the first 200 ns, effects of the transient switch resistance. (Note that the PFN is adjusted for trace 2 flatness, not trace 4.) Trace 4 also shows a small inductive transient just after the pulse.

After the second pulse, the PFN voltage rises to an intermediate value, 4.4 kV, a result of the resonant charging method combined with the fact that some energy remains in the PFN. This point is discussed below.

The general behavior shown in Fig. 4 is very similar for the 0.4- μ s pulse, and for the alternate circuit.

Variable Duration

The large negative overshoot seen in trace 2 of Fig. 4 is typical of these circuits and leads to an important conclusion. Early in the project we speculated that the pulse duration could be varied in two or three steps by setting the onset of one core pulse to coincide with the fall of another core pulse. In effect the beam would see a longer pulse. This method does not work, in part because of the overshoot, and also because of small transients where the two pulses overlap. However, the simpler alternative method works very well, as follows.

The pulse duration is varied by designing the PFN for the longest pulse and reducing the gate duration for shorter pulses. While this may be obvious given solid-state switches, we were concerned about switch burnout from the transient always present when large currents are turned off in inductive circuits.

We find that the transient is not serious. For long pulses, where the switch is opened at the end of the pulse, the current

and remaining energy is adequately small (trace 4 in Fig. 4). As the gate duration is shortened corresponding to higher required beam currents, loading by the beam dominates the circuit and the inductive "spike" is still small. Where efficiency is not an issue (e.g., for ILSE), the question is moot since the duration can be fixed.

Dynamic Impedance

As soon as the beam simulation circuit functioned, we demonstrated an important conclusion: the current supplied by the modulators automatically increases linearly as the simulated beam current is increased. For example, the total peak cell current increased from 114 A to 210 A as the beam current increased from zero to 125 A. At the same time the gap voltage decreased from 2.7 kV to 1.8 kV. We thus found the dynamic impedance, $-dV_{\text{gap}}/dI_b$, to be 7.3Ω for one cell with three PFNs. Three cells yielded 20Ω , in rough agreement with that expected.

Figure 5 illustrates a problem with our simulation: the rise time of the beam modulator is long ($\sim 0.4 \mu\text{s}$). The beam drives current into the strongly-coupled core pulsers before they are fully on. This results in the negative transient just before the main pulse and some distortion of the flat top. The distortion varies with the delay of the beam relative to the pulsers. The example shown, and the impedance values above, are for the $0.4\text{-}\mu\text{s}$ PFN, below saturation.

A lower dynamic impedance would reduce the above effect; it would also reduce the possibility of unstable behavior in a real recirculator. For this purpose additional core pulsers can be added. For example, six pulsers could be connected to each cell. The method pursued by the LLNL group, based on discharge of a large capacitor bank, provides a low source impedance but does not easily lend itself to pulse shaping and requires considerably more energy storage.

Efficiency

The efficiency of this cell/circuit combination is relatively good. To quantify this we use a simple, direct method to measure loss: compare the pulse energy delivered to the "beam" ($\tau V_{\text{gap}} I_b$, where τ is the duration), with the energy stored in the PFN ($CV_{\text{PFN}}^2/2$) minus any energy remaining in the PFN. For reasonable accuracy the method depends on the relatively rectangular pulse provided by the switches and the tapered PFN. At zero beam current the loss measured in this way is primarily core loss, including both magnetization and eddy loss. We found the switch loss is $\sim 8\%$ of the core loss.

Using this method we find the core loss for $0.9 \mu\text{s}$ fits the curve $W = 50(V_{\text{gap}})^{1.8}$ mJ, with V in kV, for the annealed cores up to our present limit, 3.6 kV. From these measurements we calculate a promising efficiency of 72% for a beam current, 250 A, roughly matched to the cell impedance. The unannealed core is considerably more lossy, e.g., at 3.2 kV it is 700 mJ vs. 405 mJ for the annealed cores. (At higher gap voltage the pulse shape for the unannealed core has substantial droop.)

For low beam current a significant amount of energy remains in the PFN after each pulse; for high beam current the core loss tends to be small compared to the energy delivered to

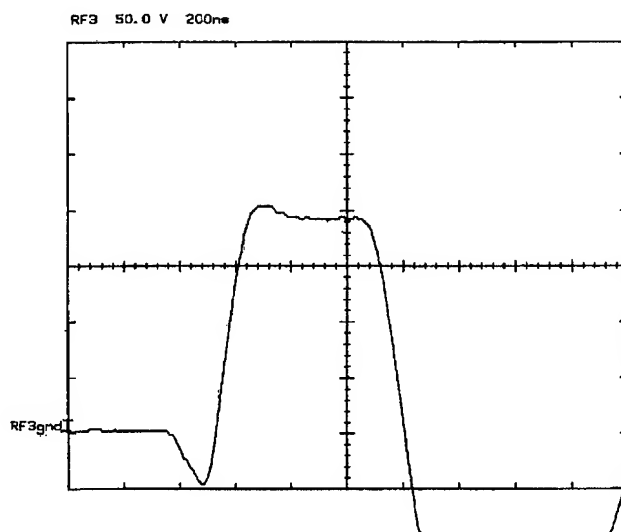


Fig. 5. $V_{\text{gap}} = 4\text{kV}$ (3 cores), with 96-A beam (11/7/94#1).

the beam. The core is basically viewed as a transformer, with little circuit loss other than the transformer itself.

Some dc bias reset current, in the 2-3 A range, was always necessary. Near saturation the required bias increased to 5 A for the circuit which provided reset and 10-15 A for the circuit which did not.

Command Charging

Command charging provides more precise control of the PFN voltage. We have used a single IGBT with a $20\text{-}\mu\text{s}$ gate to drive a 1:9 stepup transformer, yielding a secondary pulse of 5 kV. This pulse drives three PFNs directly with the normal 2-mH charging inductors removed. The leakage inductance of the pulse transformer is ideal for the resonance charging inductance. Command charging has an important bonus: the varistors used for fault protection can be chosen to use the most suitable regime of their nonlinear resistance, allowing optimum protection for the solid-state switches.

In summary, we have successfully developed core driving circuits which are relatively efficient, low in cost and whose pulse shape can be precisely tailored. We believe these methods can be extended to higher voltage.

We thank A. Fisher and many members of the LBL and LLNL HIF groups for discussions and assistance.

REFERENCES

- [1] L.L. Reginato, Proc. 1993 Part. Accel. Conf., IEEE Cat. 93CH3279-7, 656 (1993); also Proc. Int. Symp. on Heavy Ion Inertial Fusion, Nuovo Cimento **106A**, 1593 (1993).
- [2] J.J. Bernard, F. Deadrick, A. Friedman, D.P. Grote, L.V. Griffith, H.C. Kirbie, V.K. Neil, M.A. Newton, A.C. Paul, W.M. Sharp, H.D. Shay, R.O. Bangerter, A. Faltens, C.G. Fong, D.L. Judd, E.P. Lee, L.L. Reginato, S.S. Yu, and T.F. Godlove, Phys. Fluids **B5**, 2698 (1993); also J.J. Barnard *et al*, Nuovo Cimento **106A**, 1547 (1993).
- [3] M.A. Newton and H.C. Kirbie, Proc. Int. Symp. on Heavy Ion Inertial Fusion. Nuovo Cimento **106A**, 1575 (1993).

A High Charge State Heavy Ion Beam Source for HIF

S. Eylon, Duly Research Inc.*E. Henestroza, Lawrence Berkeley Laboratory.

Abstract

A high current low emittance high charge state heavy ion beam source is being developed. This is designed to deliver HIF (heavy ion Fusion) driver accelerator scale beam. Using high-charge-state beam in a driver accelerator for HIF may increase the acceleration efficiency, leading to a reduction in the driver accelerator size and cost. The proposed source system which consists of the gas beam electron stripper followed by a high charge state beam separator, can be added to existing single charge state, low emittance, high brightness ion sources and injectors. We shall report on the source physics design using 2D beam envelope simulations and experimental feasibility studies' results using a neutral gas stripper and a beam separator at the exit of the LBL 2 MV injector.

1. Introduction

The Heavy Ion Fusion Accelerator Research (HIFAR) program is looking into the possibility of using induction linacs as drivers in an inertial confinement fusion (ICF) power plant scenario [1]. An induction linac driver is envisioned now as a multiple beam accelerator [2] which after combining, acceleration, compression and final focusing hits the target in the energy plant reactor. Each accelerator's ion beam can be produced in a source injector system. A driver scale source system will deliver a 1 Amp beam with a line charge density of 0.25 micro C/m. The beam transverse emittance should be kept small (about 1 mm-mrad) to allow efficient final focusing and some growth when the beam pass through combining system. Heavy ion driver accelerator studies (1, 2) anticipate that the use of ion beams with a charge state q higher than 1 is desirable for lowering the accelerator length and cost. We propose a source system which consists of a neutral gas beam electron stripper followed by a high charge state beam separator. The system can be added to existing single charge state, low emittance, high brightness ion sources and injectors.

2. Source concept description

A schematic of the proposed source system is presented in Fig. 1. The source is placed at the exit of the matching section of the LBL 2 MV 0.8A K⁺ ion beam

injector. The injector output beam envelope is formed in Q1, an electrostatic quadrupole, to match geometrical requirements by the beam stripper design. The beam is emerging from Q1 having a sheet (rectangular) cross sections along a 60 to 70 cm path. The long path allows placing of the neutral gas beam stripping system and the electrostatic beam separator between Q1 and Q2.

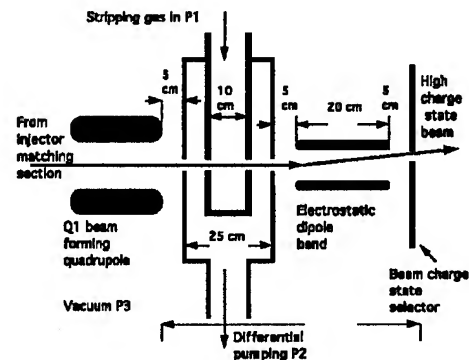


Fig. 1 High charge state source schematics

Preliminary 2D (MATCH code) beam envelope simulations to explore the physics design feasibility of the source system were performed. The simulations' results are shown in Fig. 2. One can see that the injector matching section output beam having a radius of 1.5 cm and 22 mr divergence, at the beam focus (waist), is formed into a beam having a 1.5 x 4 cm cross section at Q1 exit and about 1.5 x 6 cm at Q2 input. The beam propagates along a path of 70 cm allowing enough space for the beam stripping and separation systems while maintaining a narrow 1.5 cm beam between Q1 and Q2.

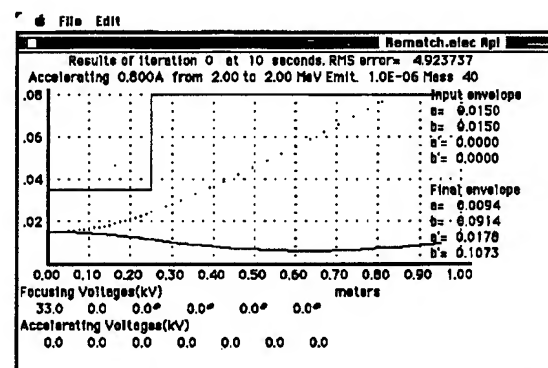


Fig. 2 Source beam envelope simulations using the 2D MATCH code.

Separating the various high-charge-state particles from the full (780 mA) beam could cause emittance growth in the separated beam components. This increase in emittance could originate from non linearities due to the space-charge fields from each component as well as the fringe fields from the separator. To quantify the emittance growth after separation, we have run computer calculation using the Particle-in-Cell codes WARP3D and ARGUS. Fig. 3 shows the K^{++} beam vertical and horizontal phase space profile at the exit of the separator. The calculation results show that the emittance of the K^{++} sources can be maintained to about 1 mm-mr.

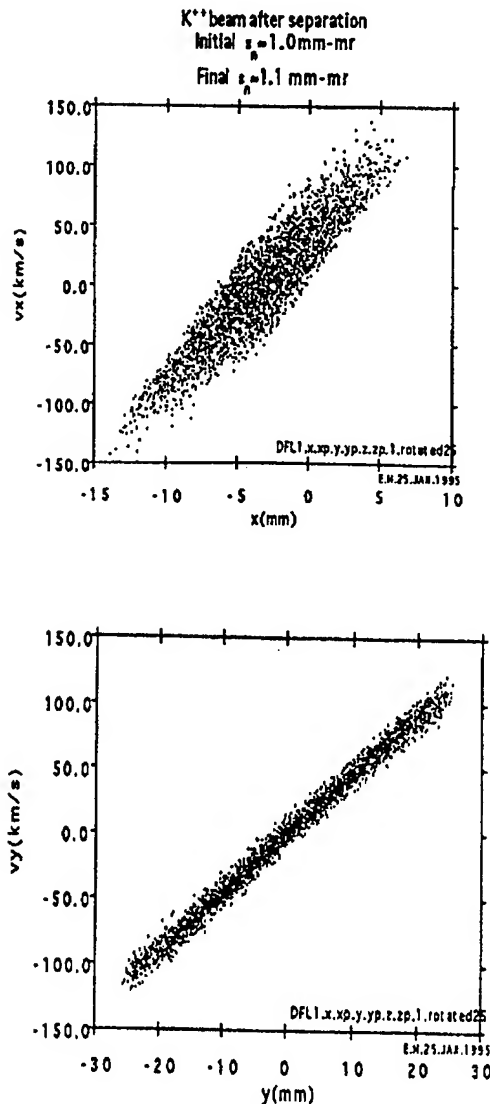


Fig. 3 Calculated K^{++} beam vertical (lower) and horizontal (upper) phase space at separator output. Initial normalized emittance is 1 mm-mr and final 1.1 mm-mr.

3. Source feasibility experiment

The stripping gas system was placed and tested at the exit of the LBL 2 MV K^+ ion beam injector within the injector existing "diagnostics box" tank. A 2 mm width beam aperture is used to limit the beam current, i.e., divergence, at the injector exit. The beam drifts along a distance of 12" within the diagnostics box into the beam stripping system. The stripping system consists of the stripping gas container (SGC) placed within the differential pumping compartment. The beam is apertured in the stripping system using four 0.5 by 20 mm slits at the inputs and exits of the SGC and differential pumping compartment. Using the apertures reduces the pumping system requirements and eliminates the need for high current beam containing (focusing) lenses (quadrupoles) by reducing the beam current. The beam stripping gas pressure can be controlled by a point sephire valve anywhere between a few mTorr up to above 1 Torr. The tilt of the SGC is fine aligned to coincide with the beam line using an adjusting system at the stripping gas inlet port. The beam out of the stripping system drifts toward the diagnostics tank exit where the following diagnostics options could be placed: A Faraday cup to measure the beam time resolved current, a slit-cup to measure the beam current density profile, i.e., beam width (angular distribution), or an energy analyzer which consists of a coaxial electro static beam 90 degrees bend. The measured beam width can lead to the evaluation of the beam transverse emittance assuming the slited beam (low current) is emittance dominated. The analyzer is used for separating the stripped beam into the various charge states and for each charge state it measures the time resolved beam longitudinal energy and current.

A simple and quick way for measuring the charge state integrated stripping efficiency is by measuring the total stripped beam current using the Faraday cup at the stripping system exit. The ratio of the stripped beam current (enhanced by the higher charge) I_p taken at a stripping gas pressure p to the vacuum current I_v , can be a measure of the charge state integrated stripping efficiency I_p/I_v or the mean charge state qm . Fig 4 presents a He stripped 1.1 MV beams pressure dependence of I_p/I_v and W_p/W_v where W_p is the beam width measured at a He pressure p W_v in vacuum. These results show that using the He gas beam stripping technique in the pressure range 50 to 100 mTorr can result a high charge state beam without degrading the beam emittance.

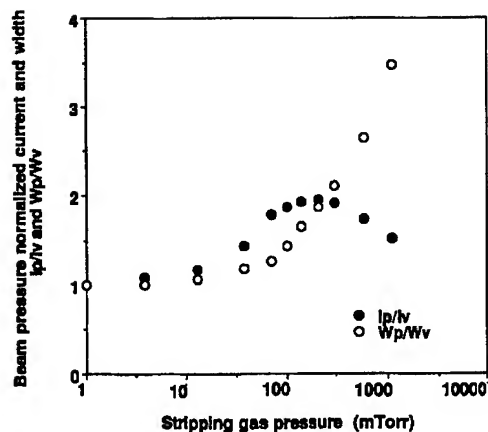


Fig. 4 Pressure normalized He stripped beam width W_p/W_v and current I_p/I_v vs. He pressure.

Fig 5 presents the measured q_m max vs beam energy U_b (up to 1.8 MV) in good agreement with calculations using Betz formula [3]. The measurements were repeated using heavier neutral stripping gas like N_2 and Ar showing a beginning of a growth in W_n , i.e., in the emittance in a lower stripping gas pressure.

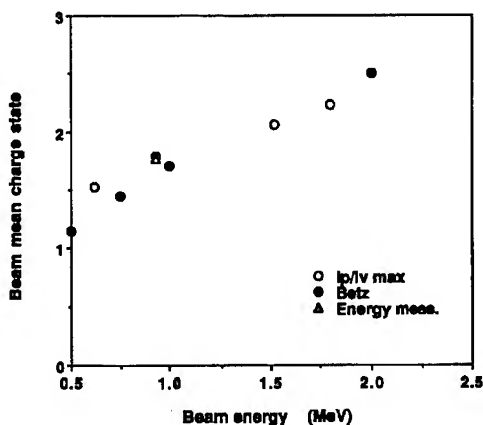


Fig. 5 Measured (Faraday cup, Energy analyzer) and calculated (Betz formula) mean charge state Q_m beam energy U_b .

Beam energy and current measurements for each beam charge state were taken on a 0.9 MV beam passing through 200m Torr of He gas using the beam energy analyzer. The measured beam time resolved longitudinal mean energy profiles in the separated beams indicated (within 0.1% analyzer resolution) small or no energy losses. Integrated beam current measurements in each charge state beam led to a beam particle distribution of 47%, 33%, 15%, 5% and current distribution

of 30%, 42%, 19%, 9% in charge states 1, 2, 3, 4 respectively.

4. Discussion

The above measurements in the He stripped beams were limited to beam energies of 1.8 MV. In anticipation of using the injector full energy beam (2 MV) we extrapolated the above measurements results to a 2 MV beam using Betz formula which was shown to be in agreement with our experimental results. Thus q_m of 2.3 measured in a 1.8 MV beam can be extrapolated to q_m of 2.5 in a 2 MV beam. The stripped beam charge states distribution width H is calculated using Betz [3] formula:

$$H = 0.271 (Z)^{1/2} = 1.18$$

Where $Z=19$ for a K ion. The increase in q_m to 2.5 with an H of 1.18 can lead to an increase, in the charge state two beam particles content, from 33% in a $U_b = 0.9$ MV beam to 42% in 2 MV. Further emittance reduction is anticipated in a stripped 2 MV beam when using emittance growth calculations (4) which accounts for beam scattering in the gas, and are consistent with our experiment for beam energies up to 1.5 MV. The above results demonstrate the feasibility of the natural gas stripping technique for achieving a source of high charge state, high current low emittance, heavy ion beam.

* Work supported in part by DOE SBIR grant no. DE-FG03-94ER81741.

References

- [1] D. S. Zuckerman et al. An Induction Linac Driven Heavy-Ion Fusion Systems Model. Fusion Technology Vol. 13, No. 2 Feb. 1988
- [2] J. Hovingh et al. Heavy-Ion Linear Induction Accelerators as Drivers for Inertial Fusion Power Plants. Fusion Technology Vol. 13, No. 2 Feb. 1988
- [3] H. D. Betz. "Heavy Ion Charge States". Applied Atomic Collision Physics, Vol. 4. Academic Press, Inc. 1983.
- [4] E. P. Lee et al. General Envelope Equation for Cylindrical Symmetric Charged-Particle Beams, Appendix A. Particle Accelerators Vol. 7, 83 95. 1976.

DESIGN AND OPERATION OF A 700kV, 700A MODULATOR *

J. D. Ivers, G. S. Kerslick, J. A. Nation and L. Schächter, Laboratory of Plasma Studies & School of Electrical Engineering, Cornell University, Ithaca, NY 14853, USA

Abstract

A 700kV, 700A pulse modulator capable of repetitive operation is under development for use in our high power microwave program. The output pulse is designed to give a flat top of about 200ns at the rated voltage. The transformer consists of two sets of ferrite cores with their primaries driven in parallel and their secondaries connected in series. The primary on each core consists of 24 windings of 2 turns each, distributing the flux evenly throughout the core. The secondary winding has 20 turns which links both cores, giving a 20:1 step-up transformer for a 1k Ω matched load. A novel pulser arrangement has been used to drive the transformer. Each core is driven by two 5 Ω pulse lines plus/minus charged to ~ 40 kV with a switch connecting the two lines. In matched conditions this gives a 40kV voltage across the load. This configuration produces a fast rising pulse eliminating the pulse rise time degradation associated with the transfer function of a discrete element pulseline. The transformer has been tested at 100kV with a variety of dummy loads at low repetition rate. Preliminary results are also reported at high voltage with the modulator under oil.

I. INTRODUCTION

We present in this paper a summary of results obtained in the development of a 700kV modulator capable of driving a high power microwave source suitable for a linear collider. The development is on going and a further version of the modulator will be required for the final device. We have to date bench tested two versions of the modulator and will report key results from each phase of the investigation [1]. In the first transformer tested each set of cores was powered by two 5 Ω artificial transmission lines and was expected to give an output voltage of up to 700kV at 350A. Low voltage tests were encouraging but both low and high voltage tests under oil (albeit in a rather small tank) indicated that parasitic capacitance loaded the secondary and that the rise time was degraded. We have since doubled the number of lines driving the primary and have carried out testing at low (~ 100 kV) output voltage. Initial tests at high voltage are also reported. The module rise time performance is degraded over that found with the two 5 Ω drivers, probably due to leakage inductance and/or non-uniform core excitation from the primary feed buss. Tests indicate that we should be able to produce a 200ns flat top pulse ($\pm 5\%$) into a 800 – 1700 Ω load in the current device, but that further modifications are required for optimal performance. In the following sections we detail the design of the transformer and present results on its performance. Indications of possible limitations in the performance of the present device are given and future modifications suggested.

*Work supported by US Dept. of Energy

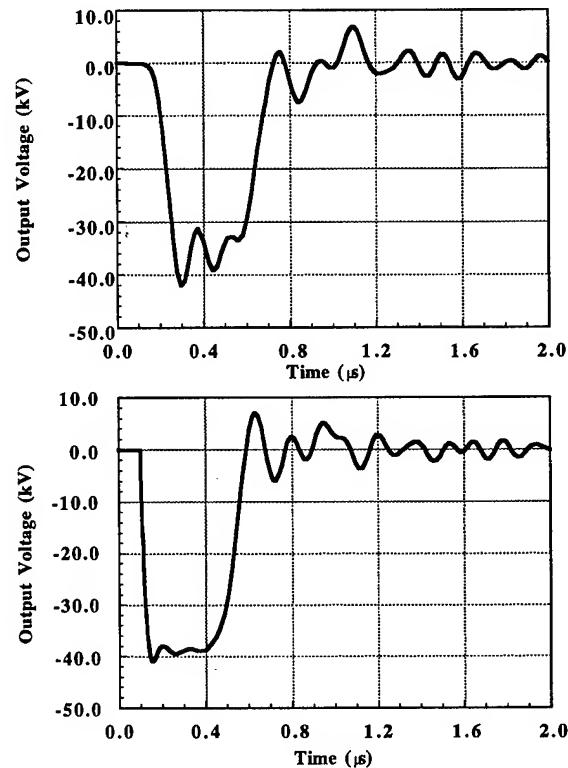


Figure 1. SPICE code results showing voltage into a matched load for a conventional Blumlein configuration (upper frame) and the plus/minus configuration (lower frame).

II. TRANSFORMER DESIGN.

Before discussing the transformer performance we illustrate the improvement in rise time of the driving pulse in the plus/minus charge configuration over that in the conventional Blumlein configuration. This result has been confirmed experimentally. Fig. 1 shows SPICE simulation results obtained for the output voltage pulse into a matched resistive load in both configurations. It is clear that the former configuration is better than that obtained with the Blumlein. A decrease in the rise time for a six section line into a matched load from about 100ns for the Blumlein to 50ns for the plus/minus charge arrangement is observed. The rise time in the plus/minus charge configuration is not degraded by the response of the artificial pulse line, nor are the fluctuations in the output, which are clear in the Blumlein configuration, apparent. We use this configuration in the transformer and obtain a rise time of the primary pulse of less than 100ns.

The pulse transformer is shown schematically in Fig. 2. It consists of two 10:1 step up transformers with their secondaries joined in series to give a 20:1 voltage gain for the transformer. Both of the transformer primaries are separately energized by

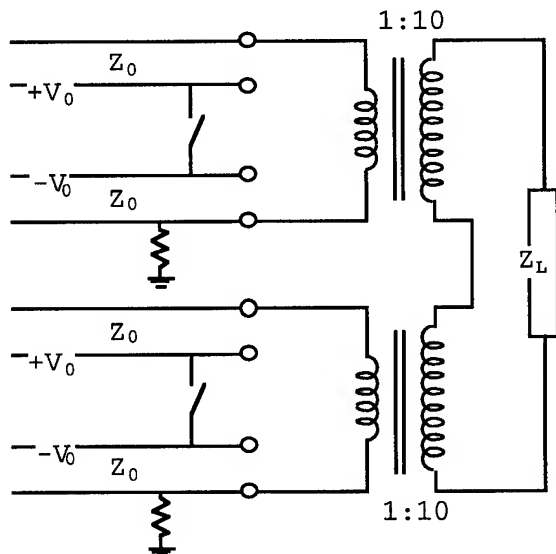


Figure 2. Schematic of pulse transformer

two 5Ω pulse lines plus/minus charged to 40 kV . The transformer cores consist of two sets of 3 TDK-PE14 Ferrite cores, each of which has a flux swing of 7 mVs . In order to distribute and maintain flux uniformity throughout the core material the primary winding consists of 24 equally spaced, two turn windings connected in parallel. The secondaries have two counterwound twenty turn windings to provide efficient coupling, and to separate the high voltage output from the low voltage terminal. The 20 turn secondaries encircle both sets of cores giving a voltage step up of 20:1. As discussed at the start of this section the transmission lines are switched by a low inductance triggered gas switch located between the two lines as shown in the figure. In this location the rise time of the system is decreased compared to that obtained from a Blumlein driver.

The 24 parallel two turn windings are wound tightly around the cores and are distributed uniformly around the circumference of the cores. The windings are separated from each other at the mid-plane of the cores by about 1.5 inches so that there is a substantial mutual inductance coupling tending to keep the currents in each path constant. The secondary windings are on a tapered former giving a variable spacing between the winding and the cores of 0.5 in. at the low voltage end up to 3 in. at the high voltage end. There are two sets of 20 turn windings counterwound on opposite halves of the cores so that the low and high voltage ends of the transformer are 180° apart. The transformer is immersed in an oil filled tank with internal dimensions $48\text{ in.} \times 27\text{ in.} \times 46\text{ in.}$. When used to drive an electron beam the output will be taken to an electron gun diode through a 20 in. diameter port. In most of the results reported in this paper the transformer is operated at low voltage ($\sim 100\text{--}140\text{ kV}$ output) and is not immersed in the oil. Two sets of data are presented, one with the transformer fed by two 5Ω lines and, in the second case with the number of driving elements doubled giving a matched input impedance of 5Ω and pulse line impedances of 2.5Ω . The total energy stored in the capacitors in the primary transmission lines is 270 Joules.

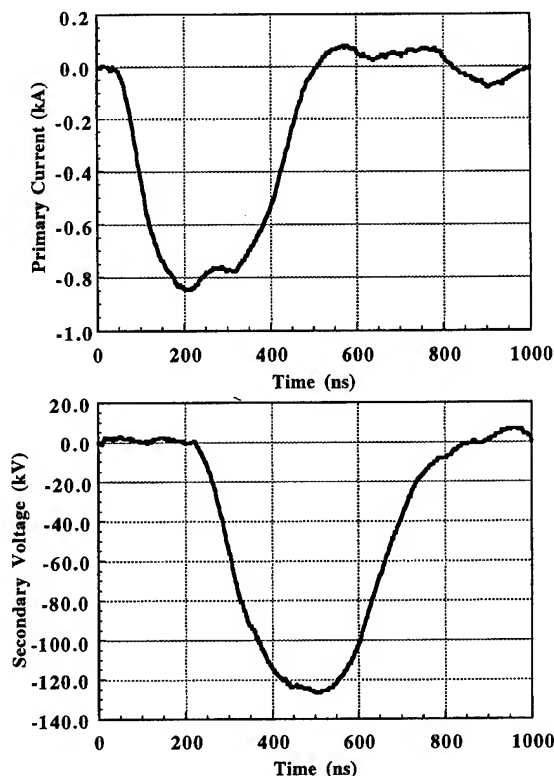


Figure 3. Primary current and the secondary voltage for the 5Ω line driven transformer.

III. EXPERIMENTAL DATA

In figure 3 we show waveforms for the first case (with the system fed by two 5Ω lines). The data show the primary current through a single section of the transformer and the secondary voltage with a resistive dummy load of $2\text{ k}\Omega$. The output voltage is about 125 kV and the current 60 A . The primary current is about 800 A , slightly higher than the factor of ten increase over the secondary current expected. The core magnetization current is about 50 A . The secondary voltage waveforms have a duration of 340 ns at half height and a duration of 190 ns above 90% of peak value.

When the transformer was immersed under oil the system was taken up to an output voltage of about 450 kV with an input voltage of approximately 23 kV . The output voltage waveform is shown in fig 4. The waveforms indicate adequate voltage insulation at the $400\text{--}500\text{ kV}$ level, but show the loading of the transformer, when it is immersed in oil. The loading is believed to be a result of the parasitic capacitance due to the proximity of the tank, and to the increase in the stray capacitance between the primary and the secondary due to the presence of the oil. A rate of change of voltage at the secondary of 10^{12} V/s (corresponding to low voltage operation at 100 kV) requires a capacitance of about 20 pF to account for the increase in the rise time of the output pulse. This is a 40% effect for the higher impedance drive line and 20% for the second case. In the latter case there is more current available than required and the effect is unimportant. Alternatively the use of a larger tank would alleviate the problem.

Similar data have been obtained for a variety of loads ranging from $700\text{--}1800\Omega$ with the input line impedance halved, but un-

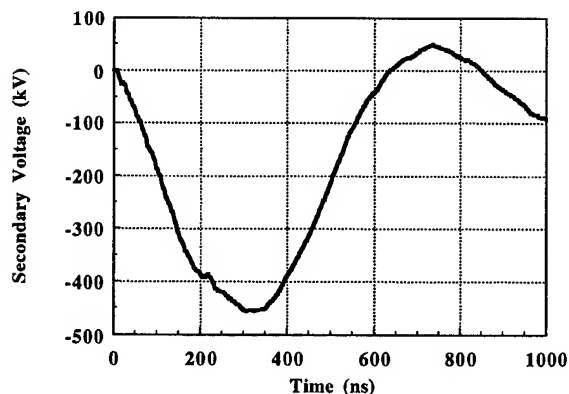


Figure 4. Secondary voltage with transformer under oil.

der otherwise comparable conditions. In this case we have confirmed that the gain is as expected and the system will hold voltage up to at least 450 kV , the highest voltage tested to date. The primary and secondary waveforms follow each other well but the rise time, again with the transformer under oil, is degraded compared to that expected.

IV. DISCUSSION OF RESULTS

In the experiments reported above we have investigated the performance of a pulse transformer under two sets of operating conditions. In the first configuration the transformer was effectively driven by a 5Ω transmission line with a 200 ns flat top. In this case the output voltage followed, in zero order, the input. However, when the transformer was immersed in oil the rise time was degraded to an unacceptable level. As a result the input drive impedance was halved by doubling the number of transmission lines feeding the transformer.

The rise time of the output pulse is controlled in part by the leakage inductance and the stray capacitance, and by the impedance of the driver pulse lines. In addition we have noted and measured a degradation in the rise time due to the time it takes the primary excitation wave to propagate around the cores. In the design used the primary turns are connected to a two wire buss which surrounds the cores. The buss is fed from both ends so that the propagation time is halved over that which would be obtained if the buss were fed from a single end. We have disconnected one of the two feeds and have observed an increase in the rise time of about 70 ns .

Unfortunately we cracked one of the cores in assembly and this caused breakdown in the low voltage tests in air. The crack became wider during the testing and the transformer performance deteriorated. The close coupling of the two sets of cores by the secondary winding causes the effect of the crack to affect both primaries and may be responsible in part for the slow rise time of the output signal.

V. CONCLUSIONS

The pulse transformer configuration tested has a number of novel features which lead to the realization of a compact high gain transformer with a short rise time. These include a novel switching arrangement and the series summation of the output of two 10:1 transformers in order to achieve a 20:1 voltage gain

device. The transformer is being disassembled to replace the cracked core and a number of improvements will be made in re-assembly. These will include splitting the primary feeds into at least 4 sections instead of the two used in the present work. The number of parallel turns in the primary will be reduced to 12 to reduce the stray primary to secondary capacitance. We also plan to slightly reduce the leakage inductance between the primary and secondary since the present gap is overly conservative. This change and the reduction in the capacitance work in opposite directions and careful modeling is required to quantify these effects. With these, and other less important modifications, we expect to obtain an output pulse with a better rise time, a higher energy transfer efficiency and a flat top output of at least 200 ns at the rated output conditions.

References

- [1] *Pulse Generators*, edited by G. N. Glasoe & J. V. Lebacqz (McGraw-Hill, New York, 1948).

THE 3 MEV, 200 KW HIGH VOLTAGE ELECTRON ACCELERATOR FOR INDUSTRIAL APPLICATION

N. G. Tolstun, V. S. Kuznetsov, A. S. Ivanov, V. P. Ovchinnikov, M. P. Svinjin
D.V.Efremov Research Institute of Electrophysical Apparatus, 189631, St Petersburg, Russia

Abstract

The high-voltage electron accelerator with an energy of 3 MeV and a beam power up to 200 kW comprising a high-voltage generator based on a single-phase transformer-rectifier without iron core is under development. The accelerator is meant for purification of wasted waters, sterilisation of medical products and ecologically safe treatment of logs before transportation with the aim of suppressing the viability of fungus and pests, etc. The main units and systems of the accelerator are described. Versions of the extracting device with output of the beam into the atmosphere or with conversion of its energy into bremsstrahlung are presented. The accelerator is equipped with the unique electron irradiation field shaping system with an elongated turning magnet allowing an irradiation field up to 6 m in width to be produced.

For many years DC high-voltage electron accelerators for the radiation technology based on a single-phase transformer-rectifier without iron core with a particle accelerating tube arranged on its axis in the energy range from 0.3 to 2.5 MeV and beam current power up to 150 kW have been designed and manufactured at the Efremov Research Institute [1]. We have gained much experience in their operation and the design of accelerators has been sufficiently improved during the last years [2].

The accelerator of this type is placed in a metal vessel, filled with a pressurised electric insulating gas. The conic primary winding provides an alternating magnetic field with a frequency of about 1 kHz and an induction of about 100 G. The sections of the secondary winding form the voltage-doubler scheme and are connected in series, rectified voltage is applied to the metal-ceramic accelerating tube modules made by the diffusion welding method. The production of such accelerating tubes with ceramic insulators 100, 130 and 200 mm in diameters has been organised. The electromagnetic screening of the tube aperture is used to exclude the effect of alternating magnetic field of the transformer-rectifier on the accelerating electron beam [3]. The electron source with a LaB_6 emitter has a lifetime of several thousand hours. The accelerated electron beam is additionally focused and is scanned over the outlet device in two mutually normal directions. These accelerators are powered by commercial thyristor frequency converters. The

total efficiency of conversion of electric power into electron beam power (η_E) exceeds 80%.

The schematic of the accelerator with an energy up to 2 MeV and a beam power up to 150 kW is shown in Fig.1. The high-voltage rectifying column is 0.72 m in diameter and 2.4 m in height. The accelerated electron beam is extracted into an atmosphere through the 220×10 cm outlet window, closed by a 50 mkm titanium foil. This accelerator is under testing now.

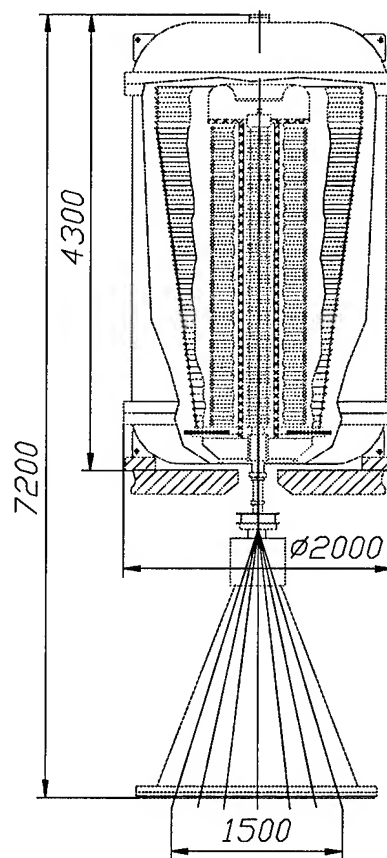


Figure 1. The schematic view of 2 MeV, 150 kW high-voltage electron accelerator based on the single-phased transformer-rectifier with the rectifying column 0.72 m in diameter.

Based on the rectifying modules with the above mentioned diameter the accelerator with an energy of 3 MeV and a beam power up to 200 kW is under development.

By increasing the diameter of the high-voltage rectifying column up to 1.2 m and using the two-period rectifying scheme it will be possible to increase the accelerator power up to 500 kW.

As all of the main components of accelerator are studied sufficiently, we do not foresee any serious technical or technological problems in designing such a machine. As seen from Fig.2, the dimensions of this accelerator are increased in comparison with the 2 MeV one, as they are determined in general by accelerating voltage, but they do not differ much from those of a 3 MeV, 200 kW machine.

The accelerators with these parameters can be used for the electron beam processing of materials and articles with a surface density up to 1 g/cm^2 (up to 2.5 g/cm^2 if double-sided irradiation is used), for example, in an installation for sewage purification.

Another possible application of such accelerators is the processing of materials and products by bremsstrahlung generated by the electron beam interacting with heavy metal targets (W, Ta).

Similar installations of a smaller capacity have been used to sterilise medical products, to treat food for increasing its preservation time and for another sterilisation processes. As the experience with the "Dynamitron" accelerators used for this purpose reveals, the cost of irradiation by bremsstrahlung at energies of 4 and 5 MeV does not exceed that of isotope sources [4,5].

The efficiency of the electron beam power conversion into bremsstrahlung (γ) at these energies is 0.15 and 0.18, respectively, the above mentioned accelerators have $\eta_e = 40 \pm 50\%$, thus the ratio of bremsstrahlung power (P_γ) to total electric consumed power (P_E) is 0.07 ± 0.08 .

The coefficient of electron energy conversion into bremsstrahlung for 3 MeV electrons is 0.12. With $\eta_e = 0.8$ the total efficiency $\eta_e \cdot \gamma = 0.096$ is possible. It allows the accelerators based on the single-phase transformer-rectifier to be considered as the effective source of bremsstrahlung.

Through the conversion of accelerated electrons energy into bremsstrahlung a certain portion of energy is carried away by reflected electrons (about 14% of beam power according to [5]). These losses are minimum when the angle between incident electrons and target surface is normal, and they increase with the angle deviating from the normal. If traditional scheme with beam scanning in the triangular vacuum chamber is chosen, the angles of incident electrons increase from the target centre and reach the maximum on its edges (see Fig.1). This causes also another problem, as the target effective thickness increases with a change in the angle.

These negative effects may be avoided by using the electron irradiation field shaping systems with extended bending magnets, which nowadays are used in our electron accelerators to extract the scanned electron beam through the outlet foil windows [1,3]. The projections of electron trajectories in such a system obtained by the numerical

simulation are presented in Fig.3. The angles between the target surface and incident electrons here differ from the normal along its length by not more than 7° .

In spite of directed character of bremsstrahlung, when calculating the production capacity of an irradiating installation, it should be taken into account that not more than 50% of bremsstrahlung is usually used effectively, i.e. $\eta_v = 0.5$. For obtaining a sufficiently homogenous dose

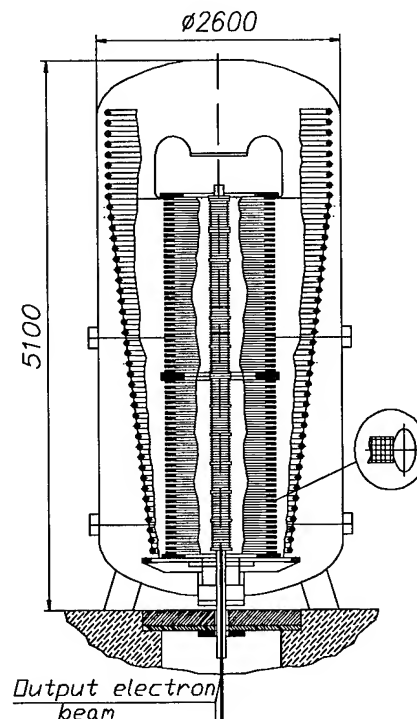


Figure 2. The schematic view of 3 MeV, 500 kW high-voltage electron accelerator based on the single-phased transformer-rectifier with the rectifying column 1.72 m in diameter.

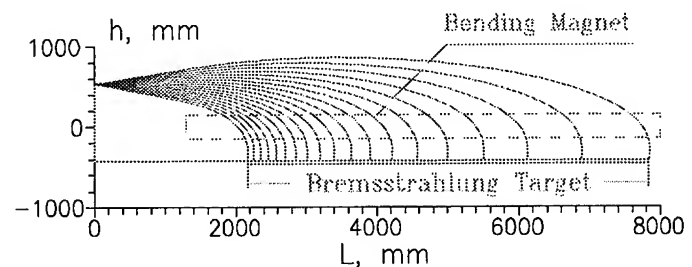


Figure 3. Electron trajectories projections in the irradiation field shaping system with an elongated bending magnet.

distribution in the whole volume of irradiated material it is important to determine its optimum thickness and to use double-sided irradiation or, if possible, to rotate the objects

during single-sided irradiation. The depth dose distribution under double-sided irradiation in material 0.6 m in thickness and 0.7 g / cm^3 in density is shown in Fig.4.

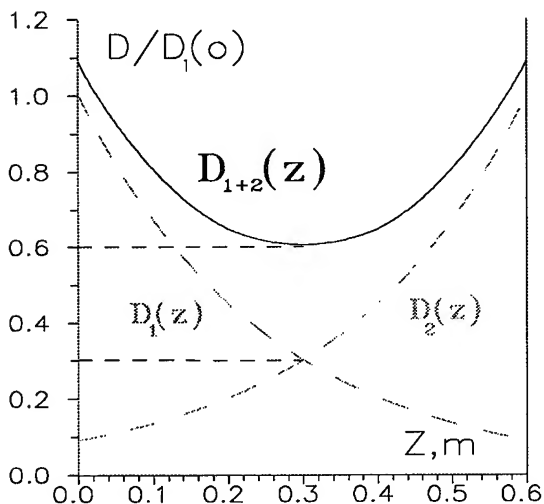


Figure 4. Doze distribution in material 0.7 g / cm^3 in density and 60 cm in thickness for single- and double-sided irradiation under 3 MeV electron bremsstrahlung.

The capacity of installation for bremsstrahlung treatment can be estimated as (considering the year as 7000 working hours of accelerator):

$$G = 25.4 \frac{P_E \eta_e \eta_v v}{\rho D_c} \cdot \frac{\mu a}{\exp(\mu a / 2)} \left[\frac{\text{T} \cdot \text{m}^3}{\text{year}} \right],$$

where:

P_E is electric power consumed by the accelerator, kW;

D_c is the central doze, kGy;

a is the material thickness, m;

μ is the average coefficient of irradiation flow reduction corresponding to an average energy of bremsstrahlung (1.5 MeV for electrons with energy of 3 MeV), m^{-1} ;

ρ is a density of treated material, g / cm^3 .

As an example of the installation with electron accelerators the process of timber sterilisation aiming at suppressing the vital functions of funguses and their spores on the wood surface and vermin and bacteria inside logs can be considered. The diameter of logs to be treated is $0.2+0.6$ m, the required dose in the log centre is 4 kGy and on the surface - not more than 10 kGy. The installation with double-sided irradiation including 2 electron accelerators 200 kW of beam power each (what equals to a total output of 48 kW of bremsstrahlung) will provide a capacity of about 160.000 m^3 per year with 7000 working hours pear year. As the calculations show, the cost of irradiation in this case will not

be more than \$10 per 1 m^3 , being approximately twice less than the cost of irradiation by isotope Co^{60} , whose irradiation penetrability is practically equal to 3 MeV electron bremsstrahlung. The sterilising installation with high-voltage electron accelerators is absolutely safe, when switched off, as there are no radioactivity in the installation components and in the treated material.

REFERENCES

- [1] A. S. Ivanov, V. P. Ovchinnikov, M. P. Svinjin, N. G. Tolstun, "Electromagnetic Electron Irradiation Field Shaping Systems for Industrial High Voltage Accelerators", Proceedings of the EPAC94, London, June 27 - July 1, 1994, World Scientific, V.3, pp.2655-2657.
- [2] B. I. Albertinsky, A. S. Ivanov, V. P. Ovchinnikov, Y. V. Sukharev, M. P. Svinjin, N. G. Tolstun, "Industrial High Voltage Accelerators", paper presented at the 13 Int. Conf. on the Appl. Accelerators in Res. & Industry, Denton, Texas, 10-17 of Nov., 1994.
- [3] A. S. Ivanov, V. P. Ovchinnikov, M. P. Svinjin, N. G. Tolstun, "New Irradiation Field Shaping Systems of High Voltage Accelerators for Industry", Proceedings of the PAC93, Washington, May 17-20, IEEE, 1993, V.1, pp.555-557
- [4] J. P. Farrell, S. M. Seltzer and J. Silverman "Bremsstrahlung Generators for Radiation Processing", Rad. Phys. & Chem., V 22, 1983, pp.469-478.
- [5] M. R. Cleland, C. C. Tompson, M. Strelczuk, D. P. Sloan "Advances in X-ray Processing Technology", Rad. Phys. & Chem., V 35, 1990, pp.632-637.

KLYSTRON MODULATOR FOR INDUSTRIAL LINAC

Yu.D.Tur, V.I.Beloglazov, E.A.Khomyakov, V.P.Krivchikov, V.B.Mufel, V.V.Zakutin, National Science Center-Kharkov Institute of Physics&Tchnology, 310108 Kharkov,

UKRAINE

Abstract

Date is given on research, development and testing of the HV-modulator with the following parameters: anode voltage up to 270kV, pulsed current up to 230 A, pulse width 5 μ s, repetition rate 300 Hz. Described are structural peculiarities aimed at enhancing the efficiency of pulse-forming, and results are presented of operational test on a working facility.

1.INTRODUCTION

In accordance with the program of upgrading the 2 GeV linear accelerator as injector for pulse-stretcher ring PSR-2000 [1], and, later, as warranted by the need of design and manufacture of industrial electron linacs with high average beam power and beam energy 10-15 MeV, we carry on research and development on rf-systems, in particular, modulators with pulsed power up to 70 MW and average power more 100 kW enough to drive the klystron tubes shown in Table 1.

Table 1: Main parameters of the high power klystron tubes.

Description	AURORA	ARKHAR
Operating Freq.(MHz)	2,797	2,797
Peak Power (MW)	20	18
Average Power(kW)	2.6	18
Pulse Length (μ s)	2.2	3.3
Rep. Rate (Hz)	50	300
Beam Voltage (kV)	270	240
Beam Current (A)	230	220
Gain (dB)	33	37
Efficiency (%)	30	35

As was shown early[2], upon optimization of heat load thermal emission by way of modification of beam guiding conditions at the klystron and outfitting them with an auxiliary cooling system, the industrial serial klystrons can become operable at high repetition rate and pulse width as regards the manufacturer's specifications. In addition, one considerably increase the average power output, in particular, this applies to the Russian 20 MW S-band klystron "AURORA" type, upon from 3 to 24 kW (see, curve 3 in Fig.1). It must be noted that these parameters may be achieved in the case forming HV-pulse with minimum head-sag lengths.

2. DESCRIPTION OF THE DESIGN AND PERFORMANCE CHARACTERISTICS

Basing ourselves on our experience over many years with the 2 GeV linac, SLAC accomplishments and other accelerators tech information, we chose to work in our R&D on the standard linear scheme with resonance charging of a single pulse forming network (PFN) and a subrefront discharging via a thyatron switch (5 kA, 50 kV). The ultimate goal of our work was to construct piecemeal and assemble a dependable, high-efficiency HV-modulator with the main specifications shown in Table 2.

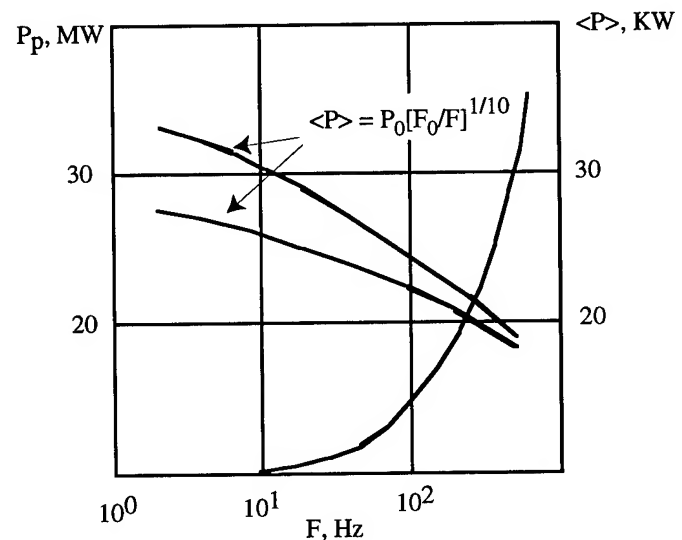


Figure 1: Experimental relationships of maximum pulsed-power operation output of klystrons of the types AURORA (curve 1) and ARKHAR (curve 2) vs. repetition rate. Curve 3 stands for average power relations of AURORA klystrons.

As is known, the most important elements that pre-determine the effectiveness of pulse shaping in a HV-modulator linear scheme are PFN and pulse transformer. In this connection, the mandatory conditions are wave resistance matching and enhanced componental undamageability at average power.

Table 2: Main specifications of the modulator.

Peak Power (MW)	62
Average Power (kW)	100
Output PFN Voltage (kV)	20
Output PFN Pulse Current(A)	3000
Pulse Repetition Rate (Hz)	300
Pulse Width (Flat Top) (μ s)	4.4
Pulse Flatness (%)	± 0.5
PFN Impedance (Ω)	6.5
Pulse Risetime (μ s)	0.4-0.5
Pulse Falltime (μ s)	1-1.1
Pulse Transformer Turn Ratio	1 : 13

In particular, experimental studies of self-inductance of industrial capacitors and its influence on the pulse-forming efficiency indicate (Fig.2) that with increasing of capacitor self-inductance (L_s) the pulse shape sustains a considerable distortion owing to an increased length of the downward curve and shortening of the flat-top. Capacitors of the IMK-45-0.027 type (manufacturer: Science Spon-Off Producer "Kondensator", Serpukhov, Russia; parameters: capacitance 0.027 μ F, operating voltage 45 kV, discharge current 4 kA) with self-inductance less than 0.1 μ H allow, together with employment of a strong, cell-to-cell inductive coupling[3], for pulse-forming with minimum head-sag lengths and pulse height deviation from flatness less than 0.5 %. Besides, additional dedicated R&D secured a vital decrease in heat losses in the above capacitors, in other words, a possibility of their utilization at high average power.

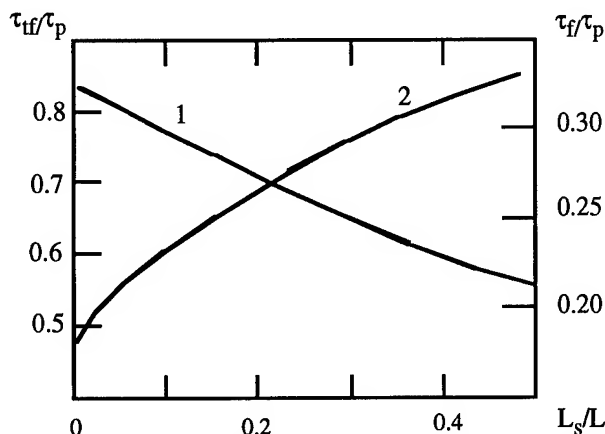


Figure 2: Relationships of duration variations of pulse flat-tops (curve 1) and downward declining (curve 2) during changes of the residual inductance of the capacitors.

Similarly, the pulse-forming efficiency is affected by an increased diffusion inductivity of the pulse transformer, in other words, a lessening of inductive coupling between windings. In our design version, we employ a ribbon-type conductor for the primary winding upon which is supliposed

the secondary in proportion 1 primary to 2 secondary turns. Such setup permits, as is the case with low-voltage transformers[4], the considerably decrease the diffusion inductivity which gives much room for diminishing the effect the pulse shape distortion.

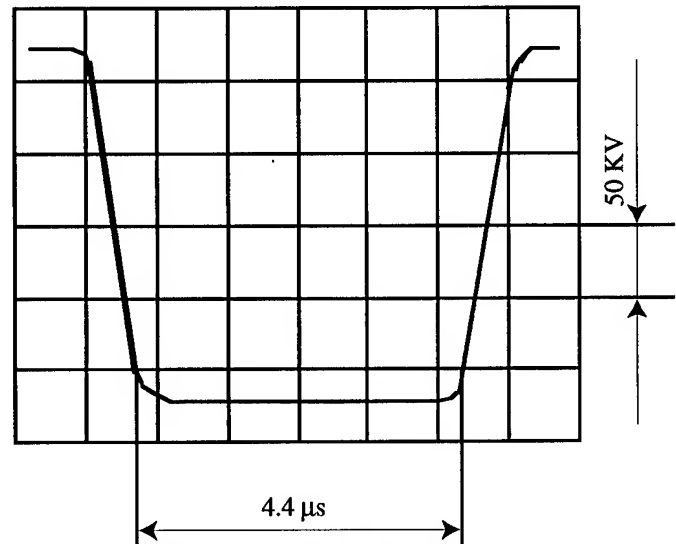


Figure 3: Oscillographic image of klystron HV- pulse in operation mode.

3. CONCLUSION

These results, as well as results from other research studies, laid the groundwork for blue-printed design work and building of prototypes.

The operating prototypes of HV-modulators, whose parameters are given in Table 2, have met all design specifications with pulse-forming efficiency > 85 % and total efficiency > 75 %. They have been operated with industrial accelerators for over 3000 h and displayed the necessary dependability and parametric stability.

4. REFERENCES

- [1] V. Boldyshev, P. Gladkih, V. Gonchar et al. Project of Circular Stretcher of the KPTI 2 GeV Electron Linac - Proc. All-Union Seminar "Electromagnetic Interaction of Nuclei at Low and Medium Energies", Moscow, 1987, p. 273.
- [2] V. Beloglazov, A. Dovbnya, V. Krivchikov et al. Parameters of Accelerator RF-Supply Sources for Non-Standard Operation Regimes - XIII Conf. on Charged Particle Accelerators, Dubna, 1992, p. 64.
- [3] M. Gladkih, A. Dolgov, V. Krivchikov et al. A High Precision Pulsed Modulator with an Artificial Bias on Vario-Couplers, PTE, 1985, vol.3, p.619.
- [4] A. Kulynich, A. Semenov. Pulsed Transformer, Patent USSR # 551712, 1977.

OPTIMIZATION OF HIGH-CURRENT ION BEAM ACCELERATION AND CHARGE COMPENSATION IN TWO CUSPS OF INDUCTION LINAC

Vyacheslav I. Karas'

National Scientific Center, "Kharkov Institute of Physics and Technology"
310108 Akademicheskaya St., 1, Kharkov-108, Ukraine

Nadya G. Belova

Institute of Physics and Technology, Russian Academy of Sciences
117218 Krasikov St., 25a, Moscow, Russia

Abstract

Results of the numerical simulation of the hollow high-current ion beam (HHCIB) dynamics in two magnet-isolated accelerating gaps separated by the drift gap are presented. The previous study has shown that the good charge and current compensations of the ion beam by the specially injected electron beam occur in the accelerating gaps of the induction linac. However in the drift gap the high positive electric potential due to the positive space charge of HHCIB was obtained because the essential difference between the electron and ion drift velocities exists under this compensation method. This disadvantage impairing the brightness of the ion beam can be considerably reduced by the additional injection of the thermal electrons into the drift region. In present report the some cases of the cold electron injection into drift gap are considered. The more optimal regime for the effective charge and current compensations of HHCIB without loss in the stability of ion beam was found.

I. INTRODUCTION

In the last ten years the production of charge compensation high-current beams by means of the linear high-current accelerator (linac) with magnet-isolated accelerating gaps are promising for controlled thermonuclear fusion research [1], [2]. The one of the many problems, which requires the particular attention, is the good charge compensation of the ion beam for suppressing the space-charge forces impairing the ion beam brightness. As shown our early numerical investigation [3]–[5] the ion beam is effectively neutralized only in the magnet-isolated accelerating gaps with the electron beam. The aim of the present work was the numerical optimization of the ion and electron beams propagation through the two magnet-isolated accelerating gaps separated by the drift gap.

II. EQUATIONS AND MODEL

To describe the collisionless plasma dynamics of beams the set of relativistic Vlasov's equations for the distribution functions of particles $f(\vec{p}, \vec{R}, t)$ in the axisymmetric ($\partial/\partial\theta = 0$) cylindrical geometry $\vec{R} = (r, z)$ has been used for the investigation of the transient and stationary processes in linac (here \vec{p} is momentum). The self-consistent electric $\vec{E}(r, z)$ and magnetic $\vec{B}(r, z)$ fields including in Vlasov's equations are determined by the Maxwell's equations, the right hands of which are defined as

the zeroth and first moments of the distribution functions.

From the set of Vlasov's equations can be obtained the set of the particles dynamic equations using the relations $\vec{u} = \gamma\vec{v}$, $\vec{v} = \{\dot{r}, r\dot{\theta}, \dot{z}\}$, $\psi = \gamma r^2 \dot{\theta} = P_\theta - \frac{q}{m} r A_\theta$, (P_θ is the dimensionless generalized particle momentum), $\gamma = [1 + u_r^2 + (\psi/r)^2 + u_z^2]^{1/2}$ is the relativistic factor. The Maxwell's equations using the Lorentz gauge ($\text{div}\vec{A} + \frac{1}{c} \frac{\partial\phi}{\partial t} = 0$) can be reduced to the wave equations for the scalar $\phi(r, z)$ and vector $\vec{A}(r, z)$ potentials.

The units of measurement using in the next treatment are defined by relations: $[v] = c$, $[r, z] = c/\omega_{pe}$, $[t] = \omega_{pe}^{-1}$, $[n] = n_{0e}$, $[q] = e$, $[m] = m_0$, $[\phi, A] = m_0 c^2 / e$, $[E, B] = (4\pi n_{0e} m_0 c^2)^{1/2}$, $[j] = en_{0e} c$, $[P_\theta] = [\psi] = c^2 / \omega_{pe}$, $[T_{ce}] = m_0 c^2$, where $\omega_{pe} = (4\pi n_{0e} e^2 / m_0)^{1/2}$ is the electron plasma frequency, n_{0e} , m_0 , e are the initial density, rest mass and charge of the electrons respectively, T_{ce} is the temperature of cold electrons.

The initial velocity of a given sort (s) of particles is defined by the boundary conditions for the distribution functions at $z = 0$: $f_s(m_s, \vec{u}, \vec{R}, t) = \delta(u_r)\delta(u_z - u_{0s})\delta(u_\theta)$ at $r_{min} \leq r \leq r_{max}$ and $v_z > 0$. Here r_{min} and r_{max} are the minimum and maximum beams radii respectively which define the initial r -coordinates of particles, $u_{0s} = V_s / (1 - V_s^2)^{1/2}$, V_s is a beams velocity. At $(r = 0, r = r_L)$ set the reflection regime. The particles exit free from the simulation region at $z = z_L$. At the initial time the particles are absent in modeling region.

The boundary conditions for the potentials are

$$\left. \begin{aligned} z = 0 : \\ z = z_L : \end{aligned} \right\} \begin{aligned} \frac{\partial A_z}{\partial z} &= -\frac{1}{r} \frac{\partial(r A_r)}{\partial r}, \\ \frac{\partial A_r}{\partial z} &= \frac{\partial A_\theta}{\partial z} = 0, \\ \phi|_{z=0} &= 0, \phi|_{z=z_L} = \phi_L; \end{aligned}$$

$$\begin{aligned} r = 0 : \quad & \partial\phi/\partial r = 0 \\ & \partial A_z/\partial r = A_r = \partial A_\theta/\partial r = 0, \\ r = r_L : \quad & \phi = \phi(z) \quad A_z = A_r = A_\theta = 0; \end{aligned}$$

where $\phi(z) = n\Delta_\phi$, $n = 0, \dots, \mathcal{K}$ in the drift gap, and $\phi(z) = (n-1)\Delta_\phi + \frac{\Delta_\phi}{\Delta_z}(z - (3n-2)\Delta_z)$, $n = 1, \dots, \mathcal{K}$ in the accelerating gaps, $\Delta_\phi = (\phi_L - \phi_0)/\mathcal{K}$, $\Delta_z = z_L/(3\mathcal{K})$ are the potential difference across the accelerating gap and the length of one, \mathcal{K} is the total number of cusps. The initial condi-

tions for the self-consistent fields are $\Delta\phi = A_z = A_r = A_\theta = 0$ (here Δ is Laplacian).

The configuration of the external magnetic field is defined by the expression $A_\theta = -\frac{B_0}{k} I_1(kr) \cos(kz)$ where $I_1(kr)$ is the first order modified Bessel function, B_0 is the amplitude of magnetic field, and $k = K\pi/z_L$.

The dynamics of particles is analyzed numerically using the modified discrete scheme of Belova, *et.al.* [3].

III. DISCUSSION OF RESULTS

Our previous investigations [3]–[5] of the interaction of a hollow magnetized electron beam with a hollow high-current unmagnetized ion beam injecting along z -axis into external magnetic field of both one- and two- cusps have shown that (i) charge and current compensations of the ion beam by the specially injected electron beam occur; (ii) the ion beam is stable for the time greater than the reciprocal Larmor and Langmuir ion frequencies; (iii) the brightness of the ion beam is impaired in the drift gap between two accelerating gaps of linac since the large positive space charge is generated by ions uncompensated by the retarded electrons of relativistic electron beam.

With the aim of optimization of the ion beam propagation through the drift gap of the two cusps linac we have studied the three ways of the ion beam compensation by the additional cold electrons injection. In all cases the beam current densities were equal to $q_e n_{0e} V_e = q_i n_{0i} V_i$. The mass ratio was $m_i/m_e = 100$, $m_e = 20m_0$, the number of particles in the cell was $N_e = 64$, $N_i = 180$. The electron and ion beam velocity were supposed $V_e = 0.85$, $V_i = 0.285$ respectively. The minimum and maximum beams radii were $r_{min} = 30$ and $r_{max} = 32.5$. The length and radius of the chamber were $z_L = 157.5$ and $r_L = 157.5$. The amplitude of the external field was $B_0 = 1.76$. The potential difference across one cusp was equal to $\Delta\phi = 0.8$. The velocities of cold electrons were defined by Maxwellian distribution function with the temperature $T_{ce} = 0.002$.

In first case the thermal electrons injection in drift gap has been started when the ion beam passed $2/3z_L$ of linac. By which time the ion beam was significantly spread and the cold electron cloud could not effectively compensate the ion beam. The maximum of the scalar potential has diminished moderately.

In second case the original injection of the thermal electrons was used. At first the cold electrons were injected into the ion beam which came out from the first cusp. Thereafter the injector of thermal electrons was localized at the center of the drift gap. And finally the thermal electrons were injected into ion beam coming out from the second cusp. That is the injection has been started when the ion beam passed $1/3z_L$, $1/2z_L$, $2/3z_L$ of linac. In this case the thermal electrons formed the negative bulk charge considerable compensating the charge and current of ion beam. This way of injection can be easily performed in a computational simulation and shown the encouraging results but it has not a perspective in real experiments. The results have shown that the thermal electron injection is ahead of the front of an ion beam.

Finally in third case the thermal electrons injection was started at the initial stage of injection of both the relativistic electron beam and the high-current ion beam to linac. The calculations were continued in during about ten reciprocal Larmor ion fre-

quency. The results of the simulation are demonstrated in fig.1,2. Fig.1 shows the distribution of $\rho(r, z)$, $\phi(r, z)$ and $j_z(r, z)$ for case without the thermal electrons injection (a), and with the additional injection of cold electron into the drift gap (b) once the ion beam has passed both of cusps. The maximum of the scalar potential in fig.1b is considerably low than in fig.1a. The distribution of the scalar potential shows that the system as a whole was charged negative. A great negative potential aid in additional focusing the ion beam. Fig.2 demonstrates the distribution functions of the electrons and ions at the stationary state for the case without thermal electron compensation (a) and for case with thermal electron compensation (b), and in fig.2c the time dependencies of the space-average ion beam velocity are compared. The maximum of the ion velocity were about 0.32 as shown in fig.2c. It is seen that the ion beam is effectively accelerated and has the high brightness in this simulation.

IV. CONCLUSIONS

The performed investigations of the beams propagation through the magnet-isolated accelerating gap of the induction linac has shown that the charge and current compensations of HHCIB by the accompanying relativistic electron beam and the thermal electron injection into drift gap are effectively. The aim of the following studies is to be a search of the optimal values of both accelerating field and electron beam energies.

The authors are grateful to Professor Ya.B. Fainberg for useful discussions.

References

- [1] A.I. Faltens and D. Keffe, "Review of Induction Linac," *Proc. of the 1981 Lin. Accel. Conf.*, Santa Fe, LA-9234c, pp. 205-208.
- [2] V.I. Karas', V.A. Kiyashko, E.A. Kornilov, Ya.B. Fainberg, *Nuclear Instruments and Methods in Physics Research*, A278, 245 (1989).
- [3] N.G. Belova, V.I. Karas', Yu.S. Sigov, *Fiz. Plazmy*, 16, 209 (1990) [*Sov. J. Plasma Phys.* 16, 115 (1990)].
- [4] N.G. Belova, V.I. Karas', *Part. Accel.*, 37-38, 225 (1992).
- [5] N.G. Belova, V.I. Karas', *Proc. of 1993 IEEE Part. Accel. Conf.*, Washington DC, Vol.1, pp. 664-666.

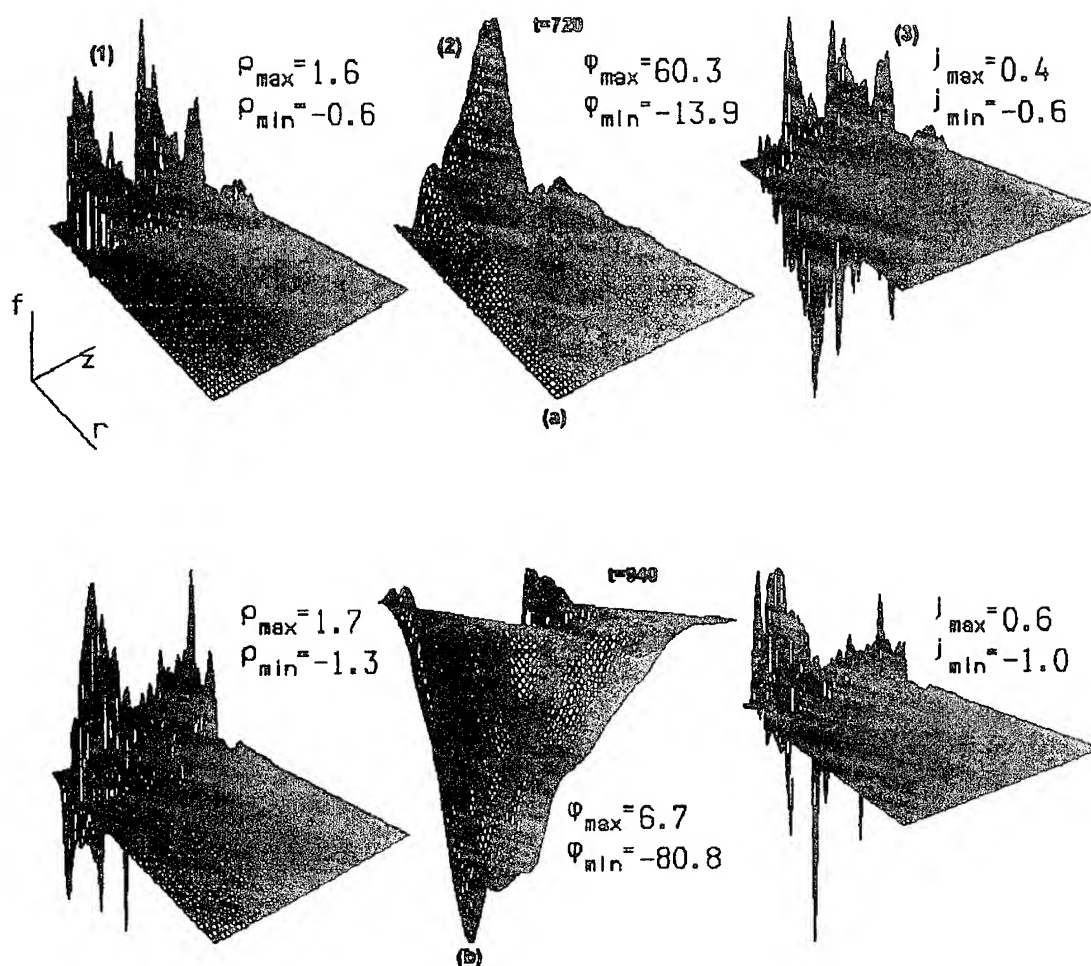


Figure 1. Distributions of the total charge density $\rho(r, z)$, scalar potential $\phi(r, z)$, axial current density $j_z(r, z)$ at $t = 640$ for the case without additional electron injection (a) and with one (b).

h

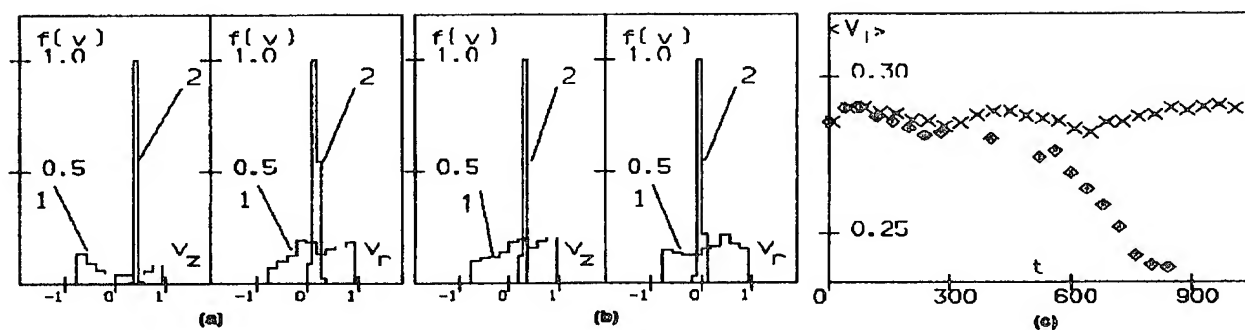


Figure 2. Distributions functions $f(V)$ of electron (1) and ion (2) beams versus the longitudinal (V_z) and transverse (V_r) velocities at the stationary state ohne the thermal electron injection (a) and with the thermal injection (b). Distributions of the averaged ion velocity $\langle V_i \rangle$ (c) versus the time ohne the thermal electron injection \diamond and with one \times .

2,5-DIMENSIONAL NUMERICAL SIMULATION OF PROPAGATION OF THE FINITE SEQUENCE OF RELATIVISTIC ELECTRON BUNCHES (REB) IN TENUOUS AND DENSE PLASMAS*

V.I. Karas', Ya.B. Fainberg,

Kharkov Institute of Physics and Technology, National Scientific Center, Kharkov, 310108 Ukraina,

V.D. Levchenko and Yu.S. Sigov,

M.V. Keldysh Institute of Applied Mathematics, Moscow, 125047 Russia

Abstract

Particle simulation results on the wake-field excitation with the programmed finite sequence of REB in tenuous and dense plasmas are presented. The REB/background plasma configuration is described by full set of 2D3V relativistic Vlasov equations for each plasma species and nonlinear Maxwell equations for self-consistent electromagnetic field. The physical parameters in runs carried out are close to those used in laboratory experiment at Kharkov IPT (Ya. Fainberg at all, 1994). The simulation points to the fact that the reached value of electric field depends on charge distribution and choice of intervals between bunches in programmed sequence.

I. INTRODUCTION

Charged particle acceleration by means of charge density waves both in plasmas and in noncompensated charge particle beams is the major trend in collective acceleration methods [1], [2]. The charge density variable part can be made very high (up to n_e); consequently, the accelerating field can reach values on the order of $10^7 - 10^9 \text{ V/cm}$. Chen et al. [3] suggested a modification of Fainberg's acceleration method [1] consisting of the use of wave trains. Katsouleas [4] considered this problem for different electron cluster profiles: a wedgelike one with a slow start growth and sharp terminal drop as well as a Gaussian-type distribution with different rise and fall rates. He presented proof [4] that the use of such inhomogeneous nonsymmetric clusters, instead of the homogeneous-density ones, might ensure particle accelerating field E_{ac} values many times (10-20) greater than the electric field stopping the cluster. The so-called transformation coefficient $T = E_{ac} E_{st}^{-1} = \gamma_{ac} \gamma_b$ is equal to $T = 2\pi N - \pi N$, where N represents the number of wave-lengths along the cluster length. Excitation of nonlinear stationary waves in plasma by a sequence of periodically spaced electron bunches was studied in [5], [6], where the electric field of the wave was shown to increase as γ rises in the case of plasma n_e and bunch n_b of comparable density. Nonlinear mode experiments on acceleration by means of wake fields emphasized the importance three-dimensional effects.

There are two distinct regimes where the plasma wake fields can provide large fields which may be of use in accelerator physics. If one utilizes an appropriate density plasma the short, wide beam can be used to drive large amplitude waves with

high-gradient electric fields useful for accelerating other particle bunches. On the other hand, the long, narrow beam can be strongly focused by its self-magnetic field which are left unbalanced when the plasma response neutralizes the beams space charge density.

The wake field excitation was studied using 2D3V axially symmetric electromagnetic code COMPASS [7]. Previously, this code was used to simulate an induction accelerator [8], modulated REB [9] and a single relativistic electron bunch or a sequence of such bunches in plasma [10]. Note that, as in experiments [6], the bunch initial transversal R_0 and longitudinal L_0 dimensions were smaller than c/ω_p at the REB density $n_b = \frac{1}{2}n_e$ (n_e is plasma density). The computer simulation [10] showed the transversal dimension of a bunch, propagating in plasma, to vary over a wide range.

This caused substantial changes in its density (more then order of magnitude) as well as a change in the excited wake field. It is shown too that the amplitudes of longitudinal and transversal fields increase upon additional bunch injection. However these amplitudes are not proportional to the number of injected bunches (as it should be in case of "rigid" bunches). For future experimental researches in the domain of intense microwave (wake) field excitation in plasmas and for use of these fields for charged particle acceleration it is expected to employ a new electron accelerator being constructed at KhIPT. Its parameters are as follows: energy $W = 200 \text{ MeV}$; number of electrons per bunch $N \sim 10^{10}$; number of bunches from 10 to 20; bunch repetition rate is 2797.16 MHz . The electron bunches will be injected into plasma of the following sizes: the length $L = 1 \text{ m}$ and the radius $R = 10 \text{ cm}$ (plasma density will be variable within $n_e = 10^{10} - 10^{14} \text{ cm}^{-3}$) with a minimum density longitudinal gradient. In our numerical simulation we shall keep in mind these parameters.

II. MATHEMATICAL MODEL

The REB dynamics is described by Vlasov relativistic equations (the Belyaev-Budker equations) for the distribution function of each plasma specie and by the Maxwell equation set for self-consistent electric \vec{E} and magnetic \vec{B} fields. The two-component main plasma ($m_e/m_i = 1840$, where m_i and m_e are the ion and electron mass respectively) is initially cold and fills completely the considered region $[0, L] \times [0, R]$. Usually, L and R are chosen to be 100 cm and 10 cm respectively. A finite sequence of cold REB is injected in the plane $z = 0$ in accordance with $n_b \theta(R_0 - r) \theta(V_b t - z + (n-1)\lambda_p) \theta(z - V_b t + Z_0 + (n-1)\lambda_p)$.

*The work is partly supported by the International Scientific Foundation, grant U27000 and Russian Foundation for Fundamental Research, project no. 94-02-06688.

Here n denotes the number of injected bunch. The beam velocity is $V_b = c\sqrt{1-1/\gamma^2}$; c is the velocity of light; the initial bunch sizes $L_0 \times R_0$ were equal to $0.4\text{cm} \times 0.5\text{cm}$; $\lambda_p = 2\pi c/\omega_p$, ω_p is the Langmuir plasma frequency; and n_b is the REB average density. The quantity $m_e\omega_p c/e$ served as a scale for electric and magnetic fields. Bunches and plasma components can leave the considered region through two boundary surfaces: $z = 0$ and $z = Z$. The plasma components can also reenter the region. On the inner boundary the following conditions exist: a metal surface at $r = R$ and open for electromagnetic wave radiation face and rear butt-end surfaces. Explicit scheme were used in calculations.

Four runs were considered to study the dependence of the excited fields: upon the number N of bunches injected into plasma; on the density ratio of bunch and plasma; on the bunch repetition rate; on the ratio of the bunch size R_0 and skin-depth c/ω_p . The parameters of these runs are listed in the table:

run id		Var1	Var2	Var3	Var4
bunch density	n_b cm^{-3}	2· 10^{10}	2· 10^{10}	4.86· 10^{10}	4.86· 10^{10}
plasma density	n_e cm^{-3}	4· 10^{10}	4· 10^{11}	9.72· 10^{10}	8.75· 10^{11}
plasma frequency	ω_p c^{-1}	1.13· 10^{10}	3.57· 10^{10}	1.76· 10^{10}	5.27· 10^{10}
skin-depth	c/ω_p cm	2.66	0.84	1.71	0.57
particles per bunch	N	6.28· 10^9	6.28· 10^9	1.53· 10^{10}	1.53· 10^{10}

The weight of model particles was assumed to be a function of their radial position. The plasma was assumed to have smaller numbers of particles in the less disturbed region distant from the axis. The total number of macro particles was about 10^6 . Note that all the calculations were carried out using a PC/Pentium-66 computer and a high-speed particle-in-cell technique.

III. RESULTS

The computer simulation showed the transversal dimension of the bunch, propagating in plasma, to vary over a wide range at the conditions $R_0 < c/\omega_p$ and $L_0 < c/\omega_p$. Contrary to popular consideration (with $L_0 \gg c/\omega_p > R_0$ or $R_0 \gg c/\omega_p > L_0$) we considered the conditions $L_0 \sim R_0 < c/\omega_p$ or $L_0 \sim R_0 \sim c/\omega_p$, which is corresponding to the experimental situation [11]. In these cases significant nonlinearities in both plasma and beam behavior have been observed. As we shall see subsequently in our simulation the ion motion plays significant role in the REB propagation in the plasmas. The dependence of the ion density n_i upon the radial coordinate r is presented in Fig.1 and Fig.2. One can see that ions form the plasma channel due to their transversal motion in self-consistent fields. The channel parameters are determined by density ratio of bunch and plasma, and by size ratio of bunch radial size R_0 and skin-depth c/ω_p .

The spatial distribution of the longitudinal E_z and radial E_r electric field is presented on Fig.3, 4, 5 and 6. One can see that amplitudes of E_z and E_r increase with injection of each additional bunch. However, these amplitudes are not proportional

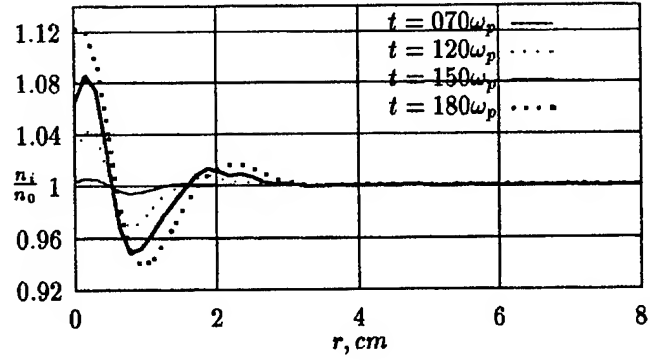


Figure 1. Var1: Dependence of the ion density n_i upon the radial coordinate r ($z = 10\text{cm}$)

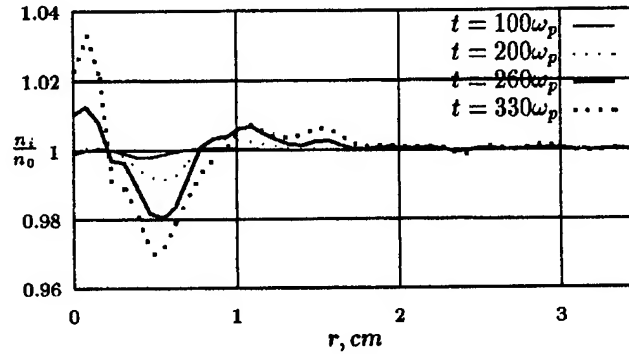


Figure 2. Var4: Dependence of the ion density n_i upon the radial coordinate r ($z = 10\text{cm}$)

to the number of injected bunch as this should be in the case of "rigid" bunches. This is due to transversal oscillations of bunch particles in self-consistent fields caused by the lack of charge and current compensation.

The shape of bunches are presented in Fig. 7. One can see that the envelope shape is not close to Bennet equilibrium case. However the REB expansion is appreciably retarded by the formation of the plasma channel with the ion radial motion. The conduct consideration of the three-dimensional nonlinear bunch-plasma behavior is useful for better understanding of fundamental physics of the plasma wake-field acceleration and focusing.

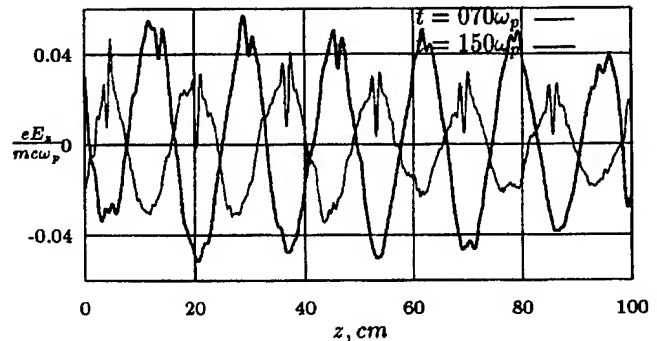


Figure 3. Var1: Dependence of the longitudinal electric field E_z on z ($r = R_0 = 0.5\text{cm}$)

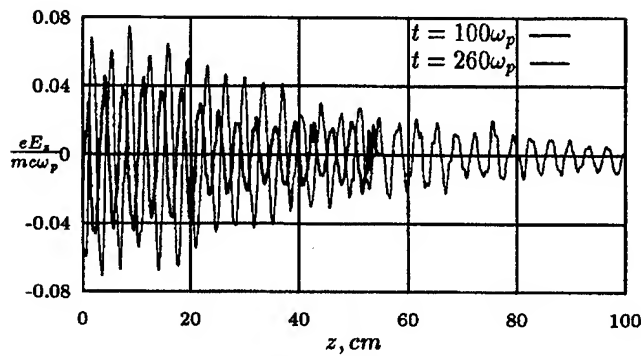


Figure 4. Var4: Dependence of the longitudinal electric field E_z on z ($r = R_0 = 0.5\text{cm}$)

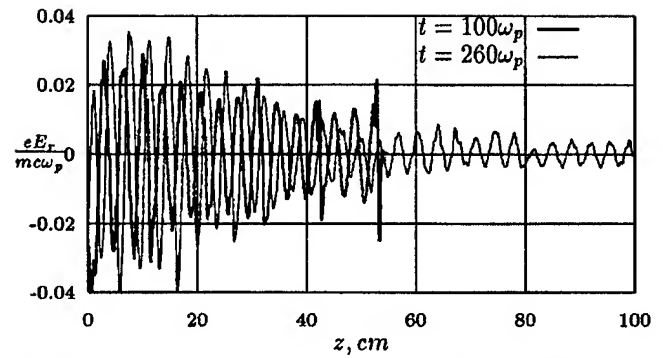


Figure 6. Var4: Dependence of the radial electric field E_r on z ($r = R_0 = 0.5\text{cm}$)

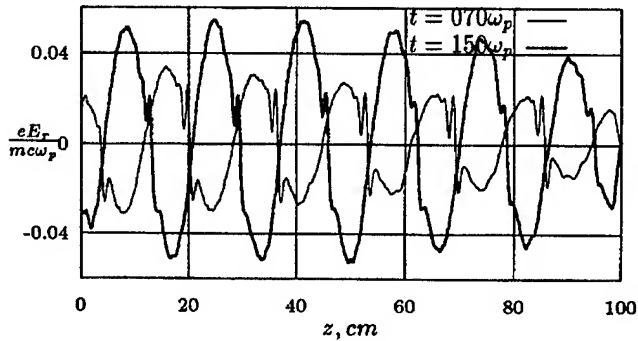


Figure 5. Var1: Dependence of the radial electric field E_r on z ($r = R_0 = 0.5\text{cm}$)

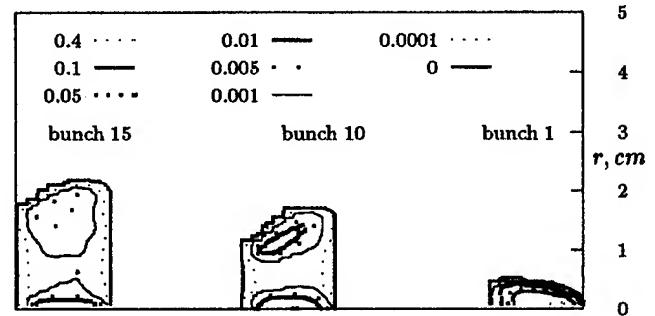


Figure 7. Var1: Density cross-section of bunches (number 1, 10 and 15) at moment of passing over $z = 60$.

References

- [1] Ya. B. Fainberg, The use of plasma waveguides as accelerating structures in linear accelerators. In *Proc. Symp. CERN*, volume 1, page 84, 1956.
- [2] Ya. B. Fainberg, Acceleration of charged particles by space-charge waves excited on plasmas by laser beams and relativistic electron beams. *Sov. J. Plasma Physics*, 13(5):350, 1987.
- [3] P. Chen, J. M. Dawson, R. W. Huff, and T. Katsouleas, Acceleration of electrons by the interaction of a bunched electron beam with a plasma. *Phys. Rev. Lett.*, 54:693, 1985.
- [4] T. Katsouleas, Physical mechanisms in the plasma wake-field accelerator. *Phys. Rev. A*, 33(3):2056–2064, March 1986.
- [5] A. Ts. Amatuni et al, Excitation of a high amplitude longitudinal waves in a plasma by electron bunches. *Sov. J. Plasma Physics*, 11:417, 1985.
- [6] J. B. Rosenzweig, Nonlinear plasma and beam physics in plasma wake-field. In *FERMILAB Conf. 90/40*, February 1990.
- [7] O.V. Batishchev, V.I. Karas', V.D. Levchenko, and Yu.S. Sigov, Kinetic simulation of open beam-plasma systems. *Plasma Physics Reports*, 20(7):587–595, 1994.
- [8] Karas' V.I. et al, *Journal of Particle Accelerators*, 37-38:281–288, 1992.
- [9] O. V. Batishchev et al, Self-focusing of a modulated ribbon reb in a dense plasmas. *Sov. J. Plasma Physics*, 19(6):738–747, 1993.
- [10] O.V. Batishchev, V.I. Karas', Yu.S. Sigov, and Ya.B. Fainberg, Kinetic simulation of open beam-plasma systems. *Plasma Physics Reports*, 20(7):583–586, 1994.
- [11] N.I. Aizatskii et al, *Plasma Physics Reports*, 20(7):603, 1994.

KINETIC SIMULATION OF FIELDS EXCITATION AND PARTICLE ACCELERATION BY LASER BEAT WAVE IN NON-HOMOGENEOUS PLASMAS*

V.I. Karas', Ya.B. Fainberg,

Kharkov Institute of Physics and Technology, National Scientific Center, Kharkov, 310108 Ukraina,

V.D. Levchenko and Yu.S. Sigov,

M.V. Keldysh Institute of Applied Mathematics, Moscow, 125047 Russia

Abstract

Resonance excitation of longitudinal plasma electrostatic wave by double-frequency laser radiation is investigated numerically to study in detail conditions of particle beat wave acceleration. The computer simulation is based on the highly specialized code SUR, using splitting technique. Both the space uniform and slightly non-uniform cases are investigated. Maintaining of phase synchronism between accelerated particles and excited longitudinal wave is provided by a choice of density plasma profile.

I. INTRODUCTION

The method of charged particle acceleration by charge density waves in plasmas and in non-compensated charged particles, which Ya.B. Fainberg proposed in 1956 [1], seems to be one of the promising methods of collective acceleration [2], [3]. The primary challenge in all plasma acceleration schemes is to produce a substantial plasma density perturbation with a phase velocity to be close to velocity of light c . At present the most promising concepts are plasma beat-wave acceleration and plasma wake field acceleration.

In the plasma beat-wave acceleration scheme [4], two copropagating laser beams with slightly different frequencies are injected into a plasma. C. Toshi et al (1993) obtained the electric field strengths of the charge-density wave of $0.7 \cdot 10^7 \frac{V}{cm}$, and detected the accelerated electrons with an energy of $9.1 MeV$ (injection energy was $2 MeV$). The resonant plasma density was $8.6 \cdot 10^{15} cm^{-3}$, but already in January 1994, the $1 cm$ length, the electrons acquired $28 MeV$.

Resonance excitation of longitudinal plasma electrostatic waves by electromagnetic waves is investigated numerically with help of the SUR code. The SUR code is based on solving the finite-difference analogs of the Maxwell and Vlasov-Fokker-Planck equations through the successive use of the splitting technique over physical processes and variables of phase space.

In order to economize our machine time, we do not yet pose the problem to be solved with its real parameters [5].

II. COMPUTATIONAL MODEL

Consider a linearly polarized electromagnetic wave propagating in the x direction with the electric vector \vec{E} directed along the

y -axis and the magnetic field vector \vec{B} oriented along the z -axis (p -polarization). The action of such a wave onto plasma particles can give rise only to the V_x and V_y velocity components. In the case where the distribution function does not depend initially on y and z , three phase space coordinates x, V_x, V_y are sufficient to describe subsequent plasma behavior; the relevant distribution function is $f(\vec{r}, \vec{p}) = f(x, V_x, V_y)\delta(V_z)$.

The plasma electron dynamics may be described by the Vlasov equation

$$\begin{aligned} \frac{\partial f_e}{\partial t} + V_x \frac{\partial f_e}{\partial x} - e(E_x + \frac{V_y}{c} B_z) \frac{\partial f_e}{\partial p_x} \\ - e(E_y - \frac{V_z}{c} B_x) \frac{\partial f_e}{\partial p_y} = 0. \end{aligned}$$

This equation is solved by a variant of the method of splitting over phase-space coordinates [6].

Effects due to charged-particle collisions in the plasma cannot significantly affect the time of electromagnetic wave propagation through the simulated system. Because of this, we do not take the Fokker-Planck collision term in the equation into account.

The similar equation might be written for the plasma ions; however, in these computations the ions, being heavy compared to electrons, were assumed to be motionless.

The longitudinal electric field E_x is determined from the Poisson equation, which, in one-dimensional case, can be written as

$$E_x = E_x|_L + 4\pi e \int_{x_L}^x (n_i(\xi) - n_e(\xi)) d\xi,$$

where $n_i(x)$ is the ion background; $n_e(x, t) = \int f d\vec{p}$ is the electron density; x_L and $E_x|_L$ represent the coordinate and field value on the system left boundary, respectively.

The transverse electromagnetic field must be satisfy the Maxwell equations:

$$\begin{aligned} \frac{1}{c} \frac{\partial B_z}{\partial t} &= -\frac{\partial E_y}{\partial x} \\ \frac{1}{c} \frac{\partial E_y}{\partial t} &= -\frac{\partial B_z}{\partial x} - \frac{4\pi}{c} j_y, \end{aligned}$$

where $j_y = -e \int f_e V_y d\vec{p}$ is the current density. The latter two equations can be written in a form more convenient for numerical computations:

*The work is partly supported by the International Scientific Foundation, grant U27000 and Russian Foundation for Fundamental Research, project no. 94-02-06688.

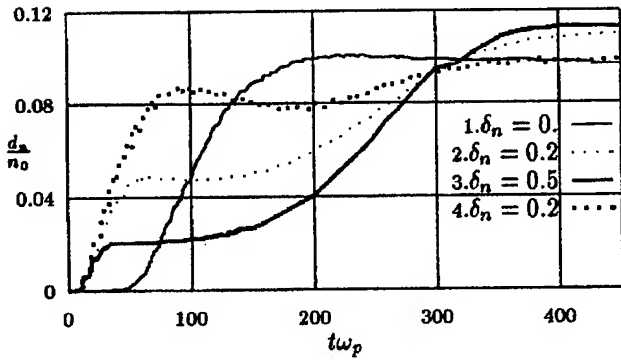


Figure 1. Temporal dependence of the maximum amplitude of the perturbed electron density d_n for different plasma density profiles along the x -axis: (1) $\delta_n = 0$; (2,3) rising profiles: $\delta_n = 0.2$ and 0.5 ; (4) descending profile: $\delta_n = 0.2$

$$\left(\frac{\partial}{\partial t} \pm c \frac{\partial}{\partial x}\right) F^{\pm} = -4\pi j_y,$$

where $F^{\pm} = E_y \pm B_z$. This enables one to employ the integration over characteristics technique.

The simulated system represent a "plasma in a box" with total particle reflection from the rated-region boundaries. At the same time, these boundaries are radiation-transparent, radiation entering through the left system boundary and emerging through the right one. This is provided by the assignment of boundary conditions:

$$\begin{aligned} F^+|_L &= F(t)[F_1 \sin(\omega_1 t + \phi_1) + F_2 \sin(\omega_2 t + \phi_2)]; \\ F^-|_R &= 0 \end{aligned}$$

where the subscripts $|_L$ and $|_R$ denote the values of quantities on left-hand and right-hand boundaries, respectively. As the charge is not build up on the "walls" and the plasma is neutral as a whole, we can assume $E_x|_L = E_x|_R = 0$.

At the initial time, the values of ion and electron density are defined as $n_i(x) = n_e(x, t = 0) = n_0$ for the uniform plasma profile and

$$n_i(x) = n_e(x, t = 0) = n_0 \pm \delta_n \left(\frac{1}{1 + e^{-\kappa(x-L/2)}} - \frac{1}{2} \right)$$

for a non-uniform one.

To describe the simulated system in dimensionless variables, let us rescale the time, length, velocity, electric field strength, and density by introducing the scale units ω_p^{-1} ; c/ω_p ; c ; $mc\omega_p/e$ and n_0 respectively. Here

$$\omega_p = \sqrt{\frac{4\pi n_0 e^2}{m}}$$

represents the electron plasma frequency. The initial parameters of the problem are the frequencies ω_1 and ω_2 of the two incident electromagnetic waves, their dimensionless amplitudes

$$\alpha_{1,2} = \frac{eE_{1,2}}{m\omega_p c} \frac{\omega_p}{\omega_{1,2}},$$

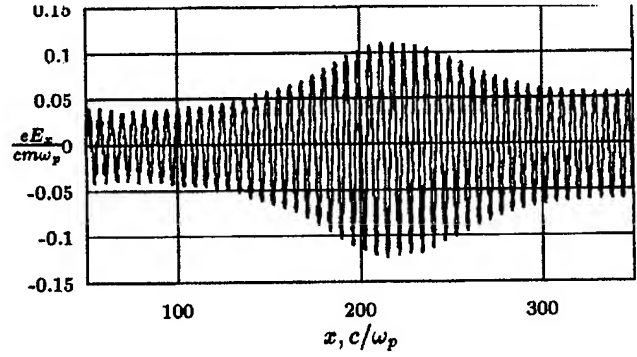


Figure 2. Spatial dependence of the longitudinal electric field E_x for the plasma density rising ($\delta_n = 0.2$) x -profile

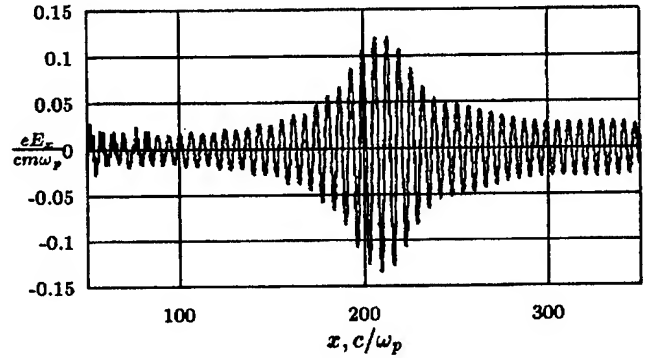


Figure 3. Spatial dependence of the longitudinal electric field E_x for the plasma density rising ($\delta_n = 0.5$) x -profile

the system length L , the electron thermal velocity V_{Te} , and the initial plasma density profile (fixed ion density profile). In a given run we considered the following parameters values:

$$\begin{aligned} \omega_1 &= 4; \omega_2 = 5; \\ \alpha_1 &= 0.1; \alpha_2 = 0.08; \\ L &= 400; V_{Te} = 0.1; \kappa = 0.2; \\ F(t) &= \frac{1}{1 + \exp(-0.5(t-10))}; \\ \phi_1 &= \phi_2 = 0. \end{aligned}$$

The difference between the runs consisted in the value and direction of the profile variation and in the se cases we took $\delta_n = 0; 0.2; 0.5$.

III. RESULTS

Figure 1 presents the perturbed electron density maximum amplitudes d_n as a function of time $t\omega_p$ for the uniform (curve 1), rising (curves 2 and 3) and descending (curve 4) plasma profile along x -axis. One can see that, at the early stage, a rise of d_n is in good agreement with theoretical results obtained in [7], [8], [9]

$$\frac{\partial d_n}{\partial t} = \frac{1}{4} \alpha_1 \alpha_2 \omega_p.$$

Then the amplitude d_n growth slows down and all the curves saturate at the level of about $0.1n_0$. The simulated saturation

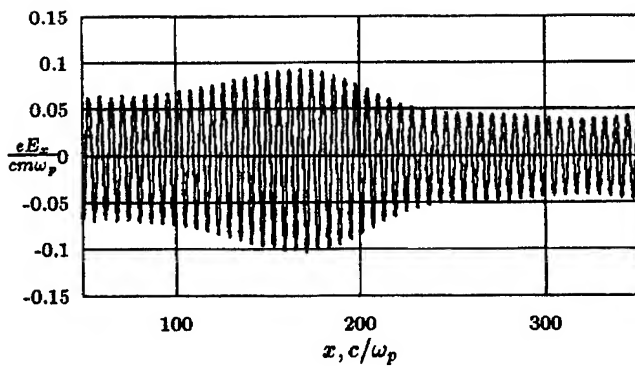


Figure 4. Spatial dependence of the longitudinal electric field E_x for the plasma density descending ($\delta_n = 0.2$) x -profile

level is considerably lower than the theoretically estimated one due to the relativistic shift of the Langmuir frequency obtained for cold plasma in [7], [8], [9]:

$$d_n^{sat} = \sqrt[3]{\frac{16}{3}\alpha_1\alpha_2} \sim 0.34$$

For nonuniform density profiles, the saturation level is higher than for the uniform one (curve 1). This is caused by the fact, for the case of uniform profile, the plasma density was chosen to ensure the exact equality of the Langmuir frequency to the beat frequency $\omega_s = \omega_1 - \omega_2$. During the transition to a steady state, the location of the perturbed electron density maximum is determined by the distance from the left boundary to some point, where the plasma density has such a value that the difference between the electron Langmuir frequency and the beat frequency is equal to a quantity $\delta\omega_{opt}$ (optimal frequency shift) proportional to $(\alpha_1\alpha_2)^{2/3}\omega_s$.

Figures 2-4 shows the steady-state spatial distributions of the longitudinal electric field E_z for the plasma density profile rising (Fig.2 and 3) and descending (Fig.4) along the x -axis. It is seen that the longitudinal electric field reaches its maximum at points where the local plasma frequency exceeds the beat frequency by a value of $\delta\omega_{opt}$ determined in its turn by the amplitudes and frequencies of electromagnetic waves. The plasma density $\pm 10\%$ variation within the rated region results in an acceptable spatial distribution of E_x . This allows one to hope (see Fig.4) that the descending plasma profile may be of practical use in this beat-wave acceleration method: an appropriate density gradient may help to prolong the accelerated particle synchronism with a longitudinal beat wave [10].

References

- [1] Ya. B. Fainberg. The use of plasma waveguides as accelerating structures in linear accelerators. In *Proc. Symp. CERN*, volume 1, page 84, 1956.
- [2] Ya. B. Fainberg. *Plasma Physics Reports*, 20(7):549, 1994.
- [3] J. S. Wurtele. *Physics Today*, (7):33, 1994.
- [4] T. Tajima and J. Dawson. *Phys. Rev. Lett.*, 43:267, 1979.
- [5] C. E. Clayton et al. In *Proc. 1993 IEEE Particle Accelerator Conference. IEEE*, volume 4., 1993.
- [6] Cheng and G. Knorr. *J. Comp. Physics*, 22:330, 1976.
- [7] M. Rosenbluth and C.S. Liu. *Phys. Rev. Lett.*, 29:701, 1972.

- [8] C.M. Tang et al. *Phys. Fluids*, 28:1374, 1985.
- [9] P. Chen, J. M. Dawson, R. W. Huff, and T. Katsouleas. Acceleration of electrons by the interaction of a bunched electron beam with a plasma. *Phys. Rev. Lett.*, 54:693, 1985.
- [10] Ya. B. Fainberg. Acceleration of charged particles by space-charge waves excited on plasmas by laser beams and relativistic electron beams. *Sov. J. Plasma Physics*, 13(5):350, 1987.

An Upgraded Proton Injection Kicker Magnet for the Fermilab MIR

J. Dinkel, R. Reilly

Fermi National Accelerator Laboratory*

P.O. Box 500, Batavia, Illinois 60510

I. INTRODUCTION

In order to maximize the efficiency of the injection process into the Main Injector Ring, the beam gap required for the extraction and injection kickers can be reduced. A switching magnet which will achieve full field within 1% on the order of 30 to 40 nSec is required to achieve efficient transfers of beam between Booster and the MIR with the removal of only one bunch from the Booster ring. The magnet designed to perform this task is a 25Ω traveling wave device which reaches its full field of 136 Gauss in 30 nSec. The field is developed across an aperture of 102 mm, 51 mm in width, by a pulse current of 1200 amps. To minimize reflections, the termination resistor has become an integral part of the magnet structure.

II. DESIGN PARAMETERS

6 batches of 8 GEV beam will be injected vertically into the MIR from the booster. The trajectory of this beam must be bent upward 1.05 mR to place it on the equilibrium orbit of the MIR. Rise and fall times are specified to insure that the circulating beam is not disturbed by the transition field at the beginning and end of the pulse. Relevant design parameters are listed in Table 1.

Beam aperture - 101.6 mm (H) x 50.8 mm (V)
Kick angle - 1.05 mR vertical
 $\int B \cdot dl$ - 340 g-m
Field rise time - <50 nSec
Field fall time - <150 nSec
Field flattop - 1.60 nSec
Field flatness ($\Delta B/B$) - $\pm 1\%$
Repetition rate - 15 Hz

Table 1

To meet these requirements, three independent kicker systems will be employed. On a practical basis, the operating voltage for the magnet is limited by the peak voltage to which the cable PFL may be reliably charged in order to achieve a reasonable PFL lifetime. We have found that operating the PFL at 60 kV provides longevity of the cables. If we choose a 25Ω system, then the peak current is 1200 amps. With a gap of 111.1 mm between pole tips, we

* Operated by the Universities Research Association, Inc. under contract with the U.S. Department of Energy.

can achieve a flux of 136 gauss in that gap. To develop the required kick, a magnetic length of 2.5 meters is required. To achieve a reasonable rise time, three 83.3 cm long kicker magnets are used. The inductance as calculated from aperture dimensions is 598 nH. The field propagation time through the magnet can be calculated from the inductance and the characteristic impedance as:

$$T_p = L_m / Z_o = 598 / 25 \text{ nSec} = 24 \text{ nSec}$$

In order to operate as a traveling wave magnet, capacitance must be present between the high voltage conductor and the ground plane. To achieve an impedance of 25Ω , the required capacitance is:

$$C_m = L_m / Z_o^2 = 598 / 25^2 \text{ nF} = .957 \text{ nF}$$

The magnet parameters are summarized in Table 2

Peak current - 1200 A
Field at peak current - 136 G
Impedance - 25Ω
Gap height - 111.1 mm
Gap width - 63.5 mm
Magnetic length - 75.8 cm
Field rise time - <30 nSec
Inductance - 598 nH
Capacitance - 957 pF
Field flatness on mid plane - $\pm 1\%$

Table 2

The magnet uses "C" shaped ferrite pole pieces to efficiently guide the flux into the gap. The material is CMD5005 which was chosen after extensive testing¹. The dimensions have been chosen to minimize the time dependent reluctance drop in the ferrite and to maximize the flux penetration into the ferrite material. The propagation velocity of the magnetic wave which penetrates the ferrite poles of the magnet can be calculated for CMD-5005 using:

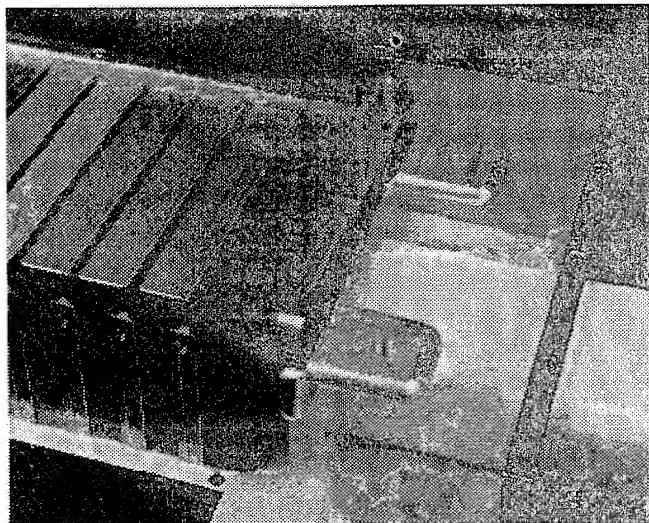
$$V_f = 3 \times 10^8 / \sqrt{\mu \epsilon} = 3 \times 10^8 \sqrt{1000 \times 12} = 2.74 \times 10^6 \text{ m/Sec}$$

Since the width of the pole piece is 0.75 inches (.0191m), the resonance would be 72 MHz which is above the magnet cutoff frequency. No shaping of the pole tips is necessary to obtain a field flatness of 1 % on the mid plane.

III. Magnet Design

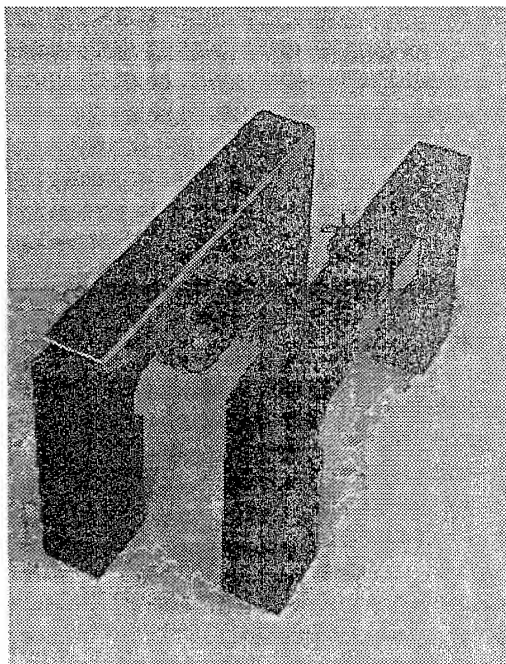
Each magnet is made up of 24 ferrite pole pieces 1 inch wide and spaced .250 inches apart. In order to distribute the required capacitance along the axis of the magnet, "Z"

plates are installed along the high voltage bus extending between consecutive pole pieces to form parallel plate capacitors with the ground plane. This is shown in Figure 1. Each of these capacitors in addition to the stray capacitance of the high voltage bus provides the required 40 pF per cell to achieve the 25Ω characteristic impedance..



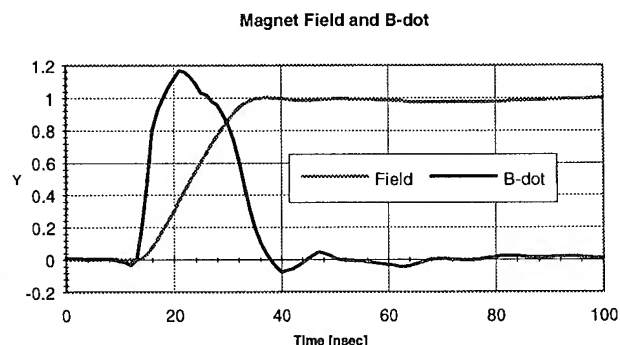
Ferrite pole pieces with "Z" plates installed
Figure 1

The displacement current which flows into the capacitors formed by the "Z" plates must pass between two adjacent ferrite pole pieces which greatly increase the series inductance of this capacitor. This inductance lowers the

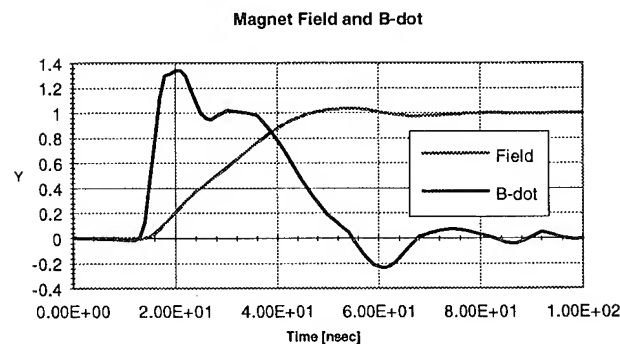


Pole pieces with cross-coupling and "Z" plates
Figure 2

natural resonant frequency of the individual cells which degrades the transient performance of the magnet. To negate this effect, cross coupling windings have been added between adjacent pole pieces to act as a shorted turn on this pseudo-inductor². A window is provided in each "Z" plate to accommodate these windings as pictured in Figure 2. The windings are .002 inch adhesive backed copper foils bonded to the ferrite pole pieces. Copper straps 0.125 inch in width are soldered to these foils to provide the interconnections. The effect of these windings is striking as seen by comparing Figures 3a and 3b. We have also found that nearly twice the calculated shunt capacitance is necessary to achieve the required impedance of 25Ω without the cross coupling windings.



Normalized $|Bdl|$ and field with cross coupling
Figure 3a

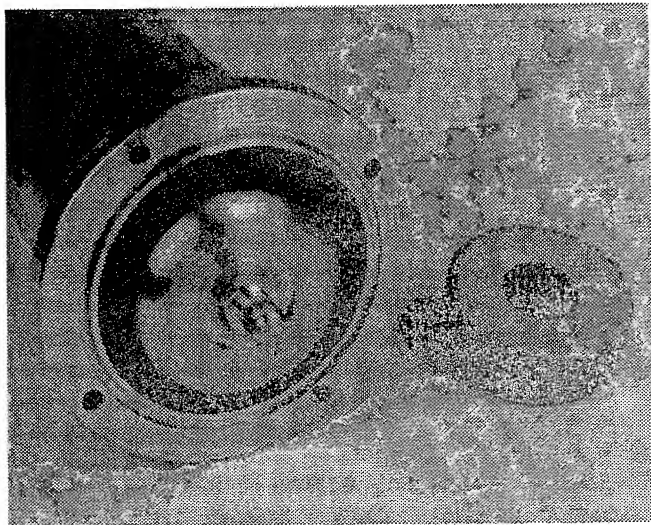


Normalized $|Bdl|$ and field without cross coupling
Figure 3b

The 25Ω load consists of two stacks of 10 - 5Ω resistive washers clamped in a coaxial housing. The clamping force of 1500 lbs. required to interface these washers is provided by a 1 inch diameter G-10 rod with 3/8-16 Keenserts installed with epoxy into each end. From a heat dissipation standpoint, the worst case operating scenario is a burst of 6 pulses once every 2.4 seconds. This requires that 175 watts be dissipated in the load. Although full power tests have not been performed on this magnet yet, preliminary heat transfer calculations indicate that we can expect a temperature rise of 9°C . The two stacks are connected to the high voltage bus using louvered contact bands as shown in

Figure 4. Wide band current viewing resistors are provided on each load resistor which have sensitivities of 5 mv/A.

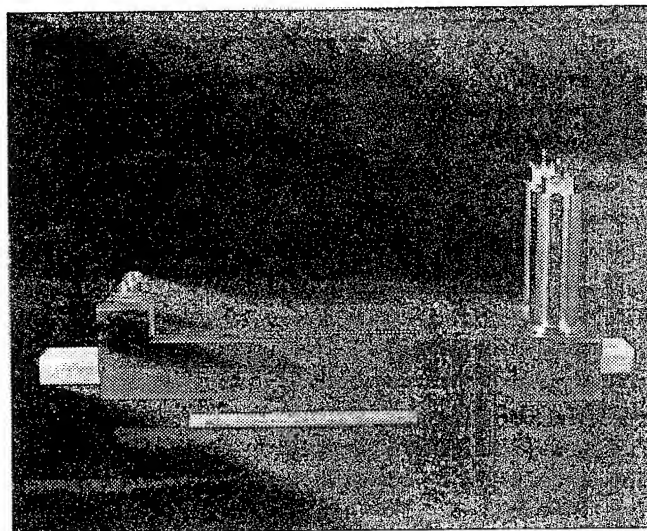
We had originally planned to use commercially available connectors to couple the RG/220 cables into the magnet, but tests on the first prototype indicate unacceptable reflections due to their high inductance. At this point, we are examining ways to modify these connectors into a low inductance device.



Load resistor and Resistive Washer
Figure 4

The magnet and load resistor assembly are potted with Sylgard 184 clear silicone rubber. This material has reasonable heat transfer properties, a dielectric strength of 450 volts/mil, and a relative dielectric constant of 2.7. Since the potting compound also serves as the "Z" plate capacitor dielectric, the required spacing between "Z" plate and the cover is 0.260 inches which puts a nominal voltage stress of 125 volts/mil in the potting material at full voltage.

The magnet which is shown in Figure 5 has a physical length of 40 inches. The 50 inch ceramic beam tube has been recycled from a previous kicker which has the same aperture.



Proton Injection Kicker magnet
Figure 5

IV. Acknowledgments

The authors would like to thank Clifford Foster, Jay Hoffman, and David Tinsley for their help in the fabrication of this magnet.

References

1. Jensen, C. et al., "Comparison of ferrite Materials for Pulse Applications", IEEE Transactions on Magnetics, Vol. 31, No. 1, January 1995
2. Dinkel, J. et al., "A Precise High Field Injection Kicker Magnet for the Fermilab Tevatron", Ninth IEEE International Pulsed Power Conference, June 1993

Fermilab Main Injector Abort Kicker System

C. C. Jensen, J. A. Dinkel, Fermi National Accelerator Lab, Batavia IL 60510

The Fermilab Main Injector will require an updated abort kicker system. A new modulator and modified magnet are required to meet the new requirements. Two Main Ring abort magnets will be modified to contain a $12.5\ \Omega$ load resistor in series with the existing magnet. A pulse transformer is used with a $3.1\ \Omega$, $10\ \mu\text{s}$ pulse forming network to reduce the capacitor voltage to 34 kV and allow operation in air. The pulse transformer primary is floated to allow grounded cathode operation of the thyatron and a grounded terminal on the pulse forming network capacitors.

I. INTRODUCTION

The Fermilab Main Injector is a new 150 GeV synchrotron now under construction. The Main Injector has been designed to replace the existing Main Ring but with an increased aperture. This increase, along with other accelerator upgrades, has been designed to support a luminosity in excess of $5 \times 10^{31}\ \text{cm}^{-2}\ \text{s}^{-1}$ in the Tevatron. While some components will be moved from the old Main Ring to the new Main Injector, the abort kicker modulator must be redesigned and the abort kicker magnet must be modified.

Siting constraints have forced the abort kicker modulator to be located $\sim 100\ \text{m}$ from the kicker magnet itself, much further than the existing distance of $\sim 12\ \text{m}$ in the Main Ring and $\sim 40\ \text{m}$ in the Tevatron. At the same time, the rise time of the field has been decreased from $1.8\ \mu\text{s}$ in the Main Ring to $1\ \mu\text{s}$ in the Main Injector. To meet specifications, a pulse forming network is required in place of the circuit used in the Main Ring [1] and Tevatron.

II. DESIGN TOPOLOGY

The circuit currently used for the Main Ring abort kicker is shown in simplified form in Fig. 1. That this circuit can not be used follows from the explanation of its operation. The initially charged capacitor, C, is switched through S to the cable, TLIN, and the inductance of the abort magnet, LMAG. If a simple lumped circuit model is used for the cable, the energy is resonantly transferred from the capacitor to the inductance of the magnet and cable. When the capacitor voltage begins to reverse, the current is allowed to free wheel through the anti-parallel diode, D, across this inductance. The result is a quarter sine rise and a long exponential tail due to diode forward drop and magnet and cable resistance. This is the fundamental operation of the circuit if the magnet current rise time is much less than the cable transit time, since then the cable may be treated as lumped inductance and

capacitance. But if the magnet current rise time is much greater than the cable transit time, a RC snubber should be added at the magnet. The circuit operates then as a low impedance source connected through a transmission line to a high impedance load. The cable RC termination reduces the reflections from the magnet and the effect of those reflections on the rise time.

The magnet is always initially driven by the characteristic impedance of the cable during the cable round trip transit time. For the Main Ring abort kicker, which has a required field rise time of $1.8\ \mu\text{s}$, the cable round trip transit time is 120 ns. The magnet voltage has several steps on it as the current builds up over several cable transit times. Conversely, the Main Injector abort kicker has both a required field rise time and a cable round trip transit time of $1\ \mu\text{s}$. If this magnet has a RC snubber, then almost as much energy will be used charging the RC snubber as charging the magnet. But, if the magnet has no snubber, neither the rise time nor the flat top specifications can be met. There are two circuits that can be used to meet specifications.

Both circuits require a source that is impedance matched to the transmission line. Therefore, a constant impedance pulse forming network (PFN) must be used to drive a cable with the same impedance. In one method, the magnet is terminated with a series resistance equal to the source impedance. In the other method, no magnet termination is used, but a matched impedance back termination is required at the PFN. All the pulse energy will go into the termination resistor, whether located at the magnet or at the end of the PFN. There are several tradeoffs for each method.

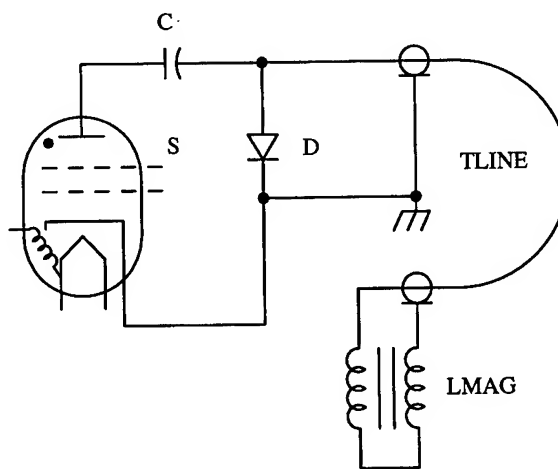


Figure 1

Typical Fermilab Abort Kicker Magnet System

Table I, Main Injector Abort Kicker Specifications

Field rise time (10 % - 70 %)	700 ns
(10 % - 90 %)	1 μ s
Field flat top	>9.8 μ s
Field flatness ($\Delta B/B$)	$\pm 10\%$
Field fall time	NA
$\int B dl$ (Total kick/ 2 Magnets)	0.37 kG m (8 GeV) to 2.51 kG m (150 GeV)
Repetition Rate	0.4 - 0.7 Hz
Magnet Inductance	5.05 μ H
Magnet Current	2700 A
Magnetic Gap	50.8 mm
Magnetic Length	1.89 m

For the back termination case, no cooling is required in the tunnel at the magnet. However, active cooling is required in the modulator cabinet to dissipate the 750 W of power. The back termination diode also conducts full current on each pulse. With the magnet termination case, cooling is now needed in the tunnel. While this is one more component actually in the tunnel enclosure, there is an ample supply of low conductivity water for cooling magnets in the tunnel. The series resistance termination at the magnet was therefore chosen for this application.

A source and load impedance of 6.25 Ω would be required to safely meet the specifications in Table I given the magnet inductance. Given the source impedance and the maximum peak current, 120 % of nominal, the PFN charge voltage is $2 I_{pk} Z_0$, ~ 40 kV. A PFN and switch can be made to operate with these parameters, however there is concern regarding the voltage across the magnet. There is currently an occasional breakdown problem in the Main Ring and Tevatron kicker magnets when operating at a peak voltage of 35 kV.

For a pulse forming network with a "fast" rise time, the magnet will have almost 100% overshoot, 40 kV, across it during the field rise time because it presents an open circuit to the leading edge of the pulse. The typical kicker magnet is made of many LC sections and the voltage overshoots very little as long as the rise time from the PFN is comparable to the rise time for one section of the magnet. This abort kicker magnet is simply a lumped L, so a PFN rise time not fast compared to $\tau_{mag} \equiv L/(2 R)$ [magnet inductance / (2 x source impedance)] is required to keep the overshoot small.

This last requirement changes the current rise time to the convolution of the input voltage with the magnet operational impedance. Assuming an exponential rising magnet voltage with time constant τ_V and assuming $\tau_V = \tau_{mag}$, the magnet time constant, the 10 % - 90 % current rise time will be approximately 3.45 τ_{mag} . While a 10 Ω system would nominally meet specifications, there would be little room left for jitter and variable delay in thyatron conduction with voltage. Therefore, a 12.5 Ω impedance is required. This then impacts back upon the magnet voltage. With a 12.5 Ω impedance, a 80 kV PFN charge voltage is required.

There is however some further gain that can be made by lowering the PFN charge voltage. The possibility of operating the PFN in air results in a much more maintainable modulator than one submersed in oil. The modulator can also be cheaper if the cost of a pulse transformer is less than the cost of the oil enclosure. That is the case for this modulator and a 1:2 step up transformer was chosen. This step up transformer maintains the peak voltage at the magnet to ~ 30 kV and reduces the PFN charge voltage to ~ 40 kV. In addition, the pulse transformer primary is floated at the PFN charge potential. This makes the thyatron auxiliary circuits much easier.

A simplified schematic of the new abort kicker power supply is shown in Figure 2.

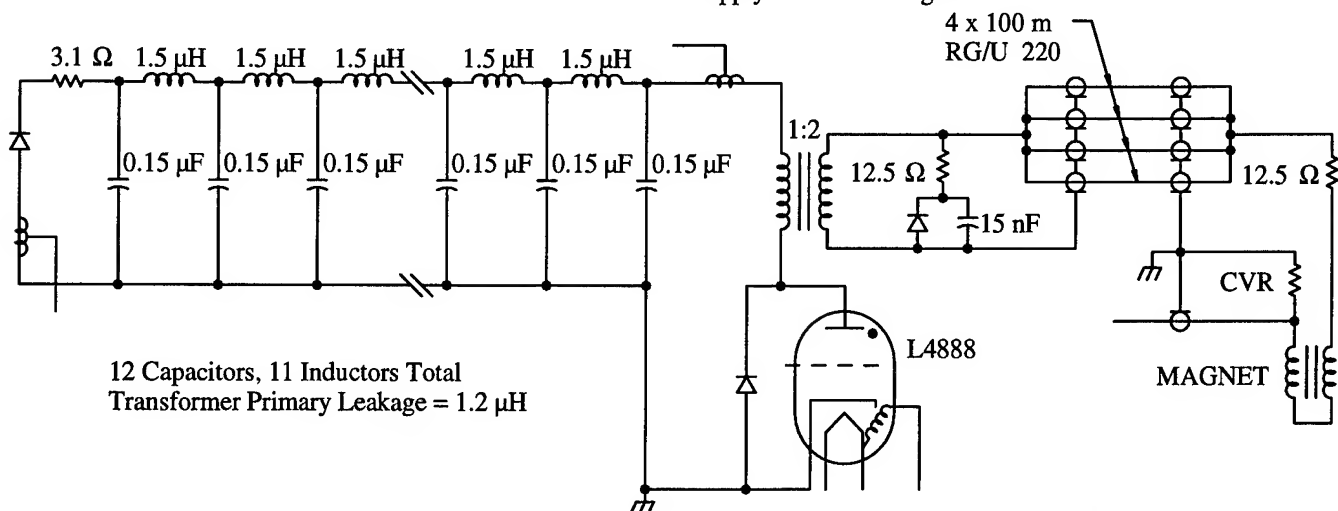


Figure 2

Main Injector Abort Kicker Schematic

III. EXPERIMENTAL RESULTS

There has been only one serious problem to date with the system. It was originally hoped that the system would fit into one 19" relay rack. There have been partial discharge problems with this configuration, especially near the transformer primary connections to the thyatron. The system has only been able to operate up to 85 %, 30 kV, of the nominal voltage. The system has been rearranged to fit into three 24" shielded relay racks. A new cabinet to house the modulator has been ordered and operation at 120% of nominal voltage should be achieved then.

The magnet current and voltage waveforms are shown in Fig. 3 for operation at 75% of nominal. Minimal tuning was performed to obtain these waveforms. The measured performance of the system is shown in Table II and meets or is better than specifications. While the raw rise time specification has been easily met, at least an additional 100 ns will be needed to account for jitter and the change in thyatron conduction delay with the wide range in operating voltage, from 4 kV to 40 kV. Delay and jitter will be minimal at the nominal voltage, and therefore the decrease in rise time over specification should reduce activation in the magnets downstream from the abort kicker.

The magnet voltage has also been kept to a minimum. At maximum operating voltage, 120 %, the magnet voltage will be below 30 kV, still below the current operating voltage of 35 kV. This should ensure reliable operation of the magnets for their new duty in the Main Injector.

Table II, Main Injector Abort Kicker Measured Performance

Field rise time (10-70%)	450 ± 20 ns
(10-90%)	720 ± 20 ns
Field flat top	10.4μ s
Field flatness ($\Delta B/B$)	$\pm 5\%$

IV. CONCLUSIONS

The Main Injector required an updated abort kicker system. This system has been operational at 85% voltage for several months now and to date has met performance specifications. Full voltage operation will happen within the next year and the system will be burned in for approximately a year before installation and commissioning in the Main Injector are required.

V. REFERENCES AND ACKNOWLEDGMENTS

This work is supported by the U.S. Department of Energy under contract No. DE-AC02-76CHO3000.

[1] Abort Kicker Power Supply Systems at Fermilab, G. Krafczyk, G. Dugan, M. Harrison, K. Koepke, E. Tilles, IEEE Trans. Nuc. Sci., Vol. NS-32, No. 5, October 1985, pp. 3581-3583

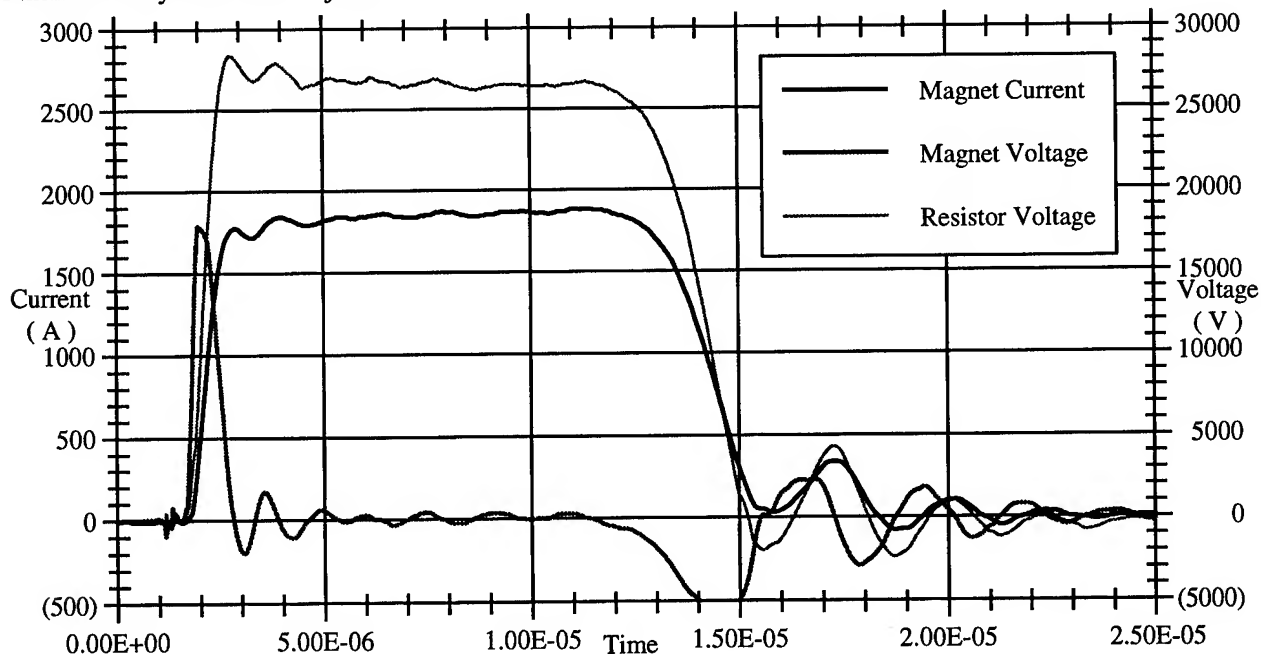


Figure 3

Measured Magnet Current at 75% Operating Level

Analysis of the Electrical Noise from the APS Kicker Magnet Power Supplies*

J.A. Carwardine and J. Wang

Advanced Photon Source, Argonne National Laboratory
9700 South Cass Avenue, Argonne, Illinois 60439 USA

Abstract

The APS kicker magnet power supplies deliver damped sinusoidal currents in excess of 2400A peak with a half-period of 300ns to the kicker magnets. Conducted and radiated electromagnetic interference (EMI) is created by this system in the low megahertz range. This interference affects a number of beam diagnostics in the APS injector. The sources and coupling mechanisms for the EMI generated by this system are described and solutions discussed.

I. INTRODUCTION

Systems producing high amplitude current pulses with fast risetimes generate significant levels of electromagnetic interference (EMI) [1]. These high levels mean that special care must be taken with the implementation and installation of the noise-producing system itself, and with 'hardening' of equipment operating in its vicinity.

Conducted EMI can be a problem because of the high current levels, thus special care must be taken to control the current paths and to prevent current flow into other parts of the facility. Radiated EMI is typically low impedance (i.e. magnetic), and can be difficult to shield, especially close to the source where fields are highest.

The kicker power supplies in the APS deliver fast high-current pulses to magnets which deflect a positron beam during its injection to, or extraction from, the APS rings. They operate in an environment where beam diagnostics are required to detect low-level analog signals, and interlock systems protect against events such as arcing in the rf cavities. The levels of EMI generated by the kicker magnets have limited the usability of some of these diagnostics.

Most kicker noise investigation work in the APS has been carried out on kickers in the positron accumulator ring (PAR) [2]. These operate at a repetition rate of 60Hz, have voltages on their pulse-forming networks (PFNs), and produce larger current pulses than the other APS kickers, therefore offering the worst case.

Measurements have been made of both conducted and radiated EMI, and while most of these were done at a PFN voltage of 5kV rather than the nominal level of 25kV, insight has been obtained into the EMI sources and their coupling mechanisms. Data was processed using the Self-Describing Data Sets (SDDS) toolkit [3].

II. KICKER OPERATION

The PAR kicker power supplies are designed to deliver a nominal 2400A peak, half-sinusoidal current with a rise time

of ~160ns to the kicker magnets [4]. A simplified schematic of the power supply is shown in Figure 1.

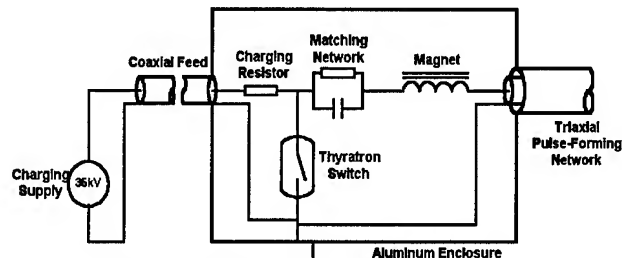


Figure 1: Simplified Schematic of PAR Kicker Power Supply

Prior to a current pulse, the open-ended PFN is charged to a nominal 25kV. When a current pulse is required, the thyatron switch is triggered, causing energy stored in the PFN to discharge through the magnet winding. The pulse duration is determined by the time constant of the PFN which forms a quarter-wave transmission line.

Physically, the PAR kicker system is comprised of three separate chassis: the magnet and PFN; the thyatron switch assembly; and the high voltage charging supply/control chassis. The magnet and thyatron assembly sit close together in the PAR enclosure, however the charging supply/control unit is located outside the PAR radiation shield and is connected to the thyatron assembly by several meters of cable. This arrangement differs from the other APS kickers where both the charging supply/control unit and thyatron assembly are located outside the radiation shield in the same cubicle.

The grounded aluminum enclosures for the magnet and thyatron assembly provide protection from high voltage hazards, are intended to provide some shielding against radiated EMI, and act as a ground plane for the system. The outer shield of the PFN and the shield of the high-voltage feed are connected to these enclosures.

A typical magnet current pulse is shown in Figure 2.

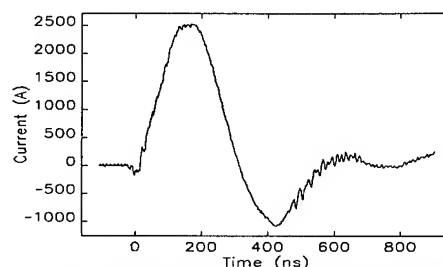


Figure 2: Kicker Magnet Current Pulse at 25kV

III. EMI CONSIDERATIONS

Figure 1 shows a near ideal situation where all components are contained within a Faraday enclosure. However, the concept is compromised in several ways (see Figure 3).

* Work supported by U.S. Department of Energy, Office of Basic Energy Sciences, under Contract No. W-31-109-ENG-38.

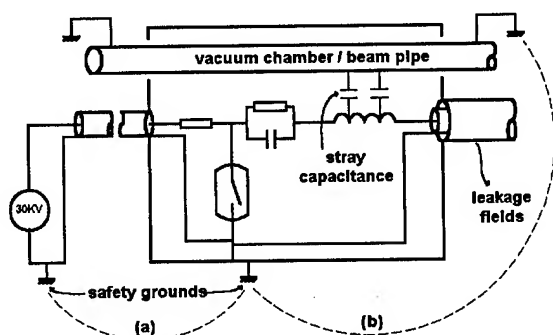


Figure 3: Modified Power Supply Schematic

First, since the high voltage supply is located some distance from the remainder of the system, it requires a local safety ground. This creates an additional return path ('ground loop') for the charging supply current since all of the local grounds are part of the overall facility ground system.

Second, while the magnet winding is completely contained within the enclosure, the vacuum chamber which it surrounds must pass through the enclosure. Since there is capacitive coupling between the magnet winding and the vacuum chamber, current can flow from the magnet to the vacuum chamber and hence to the outside world (forming another 'ground loop').

Third, the Faraday shield is not perfect, and possibilities exist for radiated fields to leak through the enclosure boundaries and through cable shields.

In many situations, the above-described weaknesses may be of little consequence. However, they contribute significantly to the EMI generated by the APS kickers because of the magnitude of the currents involved.

IV. CONDUCTED INTERFERENCE

Conducted EMI is a direct consequence of there being current loops outside of the kicker enclosures. The existence of loops (a) and (b), shown in Figure 3, means that part of the magnet current pulse flows through the facility ground system and hence through any equipment connected to it.

The magnitude of the current flowing in any given loop depends on its impedance relative to that of the primary current path. The fact that surprisingly large currents have been measured in apparently unrelated cables clearly means that the loop impedance is not high enough (based on the nominal magnet current, even a path isolated by 100dB from the main circuit would see a 12mA current pulse).

The conducted EMI problem is widespread because of the mesh of parallel paths formed by the mass of "ground" cables and busbars. Any equipment connected into the ground system experiences voltage and/or current transients (depending on how it is configured relative to the ground system). The closer the equipment is (electrically) to the kicker system, the larger the transient it will experience.

The net current in the charging supply cable is effectively the total current flowing through loop (a) (if the supply and return currents are equal, there is no net current flow).

The measured current is shown in Figure 4. As expected, the dominant frequency is the same as that of the current pulse.

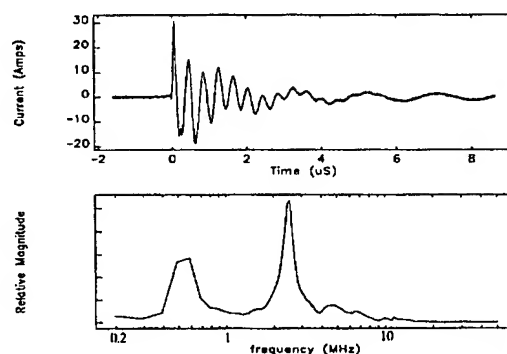


Figure 4: Current on the Charging Cable at 5kV

This current has been traced through various cables connected to the charging supply/control unit. Significant currents have been measured on the 480V power feed, the charging supply safety ground, and on cables to the APS control system.

Current flowing in loop (b) is believed to be the most disruptive to the beam diagnostics which connect directly to the vacuum chamber. It is difficult to measure the bulk current flowing in this loop, since the physical layout of the kicker system and the large number of ground connections to the vacuum chamber make it impossible to select a single conductor which carries all of the loop current.

In order for loop (b) to exist there must be capacitive coupling between the magnet winding and the vacuum chamber. The measured capacitance is 50-100pF, which offers an impedance of around 1k Ω to the main current flow. The main circuit impedance is 16 Ω which means that if this capacitance were to dominate the loop impedance, more than 1% of the current pulse could be coupled through the vacuum chamber.

Measurements were made during checkout of a synchrotron kicker in order to look at this coupling path using a dummy beam pipe. Figure 5 shows the current measured in the ground connection of the dummy beam pipe at a PFN voltage of 15kV. While a direct comparison cannot be made with the installed PAR kicker, the fact that such a large current was measured demonstrates the significance of this coupling path.

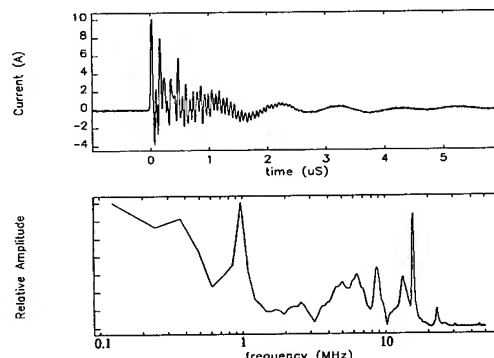


Figure 5: Beam-Pipe Current in Test Configuration

V. RADIATED INTERFERENCE

The single most significant source of radiated EMI has been found to be the PFN cables. This was not entirely surprising given the magnitude of the currents they carry, their length (12 meters), and the fact that braided shields were chosen to give some flexibility to the bulky cables. A triaxial cable was chosen for the APS kicker systems in order to provide additional shielding over a coaxial design.

Since the PFN shields are only grounded at one end, at a distance the cable would appear as if it were a simple E-field antenna. However, in the case of the kicker system, the near-field situation is of greater interest because of the close proximity of other equipment. In this case, the PFN cables appear to be a long wire and they behave like a magnetic source. The leakage field through the shield gives the impression of a net current flow along the cable. Measurements at 5kV, using a close-field probe, indicated leakage fields equivalent to a 1-2A current flow (~0.5% of the total current). Assuming a simple long wire model, this would produce a magnetic field of 50-100mA/m [5] which agrees well with measured radiated magnetic fields under the same conditions (shown in Figure 6).

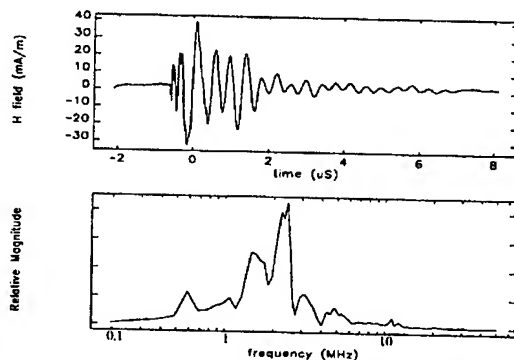


Figure 6: Magnetic Field, 3 meters from Source at 5kV

Similar measurements of the radiated electric field were also made. By taking the ratio of the E and H fields, the source impedance was determined to be around 12Ω indicating a strongly magnetic source.

VI. SOLUTIONS

Initially, EMI levels were high enough that the kicker supply itself would trip on noise well below its nominal operating level, and signals on the PAR beam current monitor were large enough to trip the safety interlock.

The current flowing around loop (a) in Figure 3 was reduced by installing EMI filters on the cables connecting the thyatron assembly and the charging unit. These increased the relative impedance of the loop and reduced the amplitude of the current by around 20dB. This alone was sufficient to allow the kicker systems to operate without tripping on noise.

The most promising approach to reducing the current in loop (b) is considered to be the addition of an electrostatic shield around the magnet winding. Tests have been carried out on a mock-up which indicate that reductions of 20dB or more could be achieved in the coupling to the beam pipe. However,

care is needed in providing a very low impedance path from the shield back to the energy source, since the degree of coupling can be increased by a wrong connection.

In order to reduce the radiated fields, additional shielding is required around the PFN cables. Since the radiated fields are magnetic and the shield material would be installed close to the field source, a material with good absorption loss is required. Thick-walled steel conduit is ideal for this type of application. In theory, a 2mm thickness of steel provides in excess of 200dB absorption loss at 2MHz, and the material is readily available. A low cost improvement in the radiated fields was obtained by wrapping the PFN cables in aluminum baking foil. The measured attenuation was 3dB, consistent with the theoretical absorption loss for 1mil of soft aluminum at 2MHz.

VII. SUSCEPTIBILITY

In parallel with the investigations of the EMI source, attempts have been made to reduce the susceptibility of diagnostics affected by the noise. Clearly any improvement in their susceptibility will complement reductions in the magnitude of the EMI sources.

An example is the PAR beam current monitor which consists of a current toroid encircling the PAR vacuum chamber. Considerable attention had been given to protecting the current monitor against radiated EMI, the sensor being housed in a multi-layer electromagnetic shield which is bonded to the vacuum chamber. Nevertheless, unacceptably large pulses appeared on the current monitor signal every time a kicker fired. Originally the toroid was electrically floating inside its electromagnetic shield with the low-level signal being transmitted over a coaxial cable. By bonding the shield of the coaxial cable to the electromagnetic shield of the toroid, the noise coupled to the current monitor was reduced by 20dB. Kicker currents flowing in the ground system develop voltages between different locations all deemed to be at ground potential. By bonding the toroid and its shield, the voltage between them is reduced. This effect is believed to be the cause of the improvement in the noise on the current monitor.

The fact that these mechanisms are not fully understood illustrates the difficulties in predicting EMI effects and emphasizes the need for experimentation.

VIII. REFERENCES

- [1] J. Carwardine, G. Pile, T. Zinnerman, "Management of High Current Transients in the CWDD Injector 200kV Power System," *Proceedings of the 1993 IEEE Particle Accelerator Conference*, p. 3210, 1993.
- [2] M. Borland, "Commissioning of the Argonne Positron Accumulator Ring," these proceedings.
- [3] M. Borland, "A Self-Describing File Protocol for Simulation Integration and Shared Postprocessors," these proceedings.
- [4] J. Wang, "Design and Test Results of Kicker Units for the Positron Accumulator Ring at APS," these proceedings.
- [5] D. White and M. Mardiguian, "EMI Control Methodology and Procedures," (Interference Control Technologies Inc., 1989).

Design and Test Results of Kicker Units for the Positron Accumulator Ring at the APS*

J. Wang

Argonne National Laboratory
9700 South Cass Avenue, Argonne, Illinois 60439

Abstract

Three fast kicker units have been designed, tested, and installed in the positron accumulator ring (PAR) at the Advanced Photon Source (APS) for beam injection and extraction. The performance of these kicker units has been satisfactory. This paper presents the design and test results.

I. INTRODUCTION

Three fast kicker units are required in the PAR at the APS. Two of them, named P1K and P2K, are used for both beam injection and extraction with injection as the main function. A third unit, named P4EK, is required for beam extraction only. Based on the ring size and the beam length, the time specifications for the kicker's magnetic field are listed in Table 1.

Table 1. Kicker Specification

Rise time	0 to 100%	< 190 ns
	20% to 100%	< 100 ns
Fall time	94% to 50%	< 70 ns
Flat top	3% flatness	> 35 ns
Ringing	% of peak	< 30%

The required kicker field strengths are 283 Gauss for injection and 435 Gauss for extraction.

In the original design, three kickers had identical circuit configurations in order to reduce the amount of design work and the number of spare parts. However, during initial test it was found that it was the best to tune the kickers differently based upon their main function, i.e., beam injection or beam extraction, to meet the different requirements.

II. KICKER CIRCUIT

Kicker Magnet

The kicker magnet has a window-frame structure with an 11 cm by 5.3 cm aperture to accommodate the coil and the vacuum chamber. The magnet is 35 cm long and constructed with ferrite CMD5005 by Ceramic Magnetics, Inc. The magnetic field inside the ferrites is kept well below the saturation point even under maximum current. The total inductance of the magnet, not including the inductance due to the connections, is about 844.8 nH. This inductance is too high for the fast rise-time and fall-time requirements. In

order to reduce the inductance, the magnet is divided into two half-turn magnets, each having a separate pulse forming network (PFN). The magnet is also divided longitudinally into multiple sections to make it a distributed magnet.

Pulse Forming Network

The pulse forming network consists of two parts. Part one is made of AA7949 triaxial cables by Times Microwave Systems, Inc. Each cable is made 12 meters long and then trimmed to the proper length during the test to give the desired rise time. The nominal characteristic impedance of the cables is 16.4 Ω , calculated from the nominal inductance and capacitance per unit length. However, the manufacturer specifies it as a 13- Ω cable. The test shows that its impedance is around 15 Ω . In the computer simulation 16.4 Ω is used. The propagation velocity of the cable is 0.16 m/ns. For each half-turn magnet, there are two cables connected in parallel to form an 8.2- Ω PFN.

Part two of the PFN is the magnet itself. Since each half-turn magnet has an inductance of 422.4 nH, it would have a time constant of 55.3 ns if terminated with an 8- Ω resistor. This time constant would be too large for the required rise times, especially for the rise time between 20% and 100%. To reduce the effect of the magnet inductance on the field rise time it was decided to make the magnet a distributed magnet instead of a lumped one. Each half-turn magnet is divided into multiple sections by lumped capacitors. Apparently, the more sections the magnet is divided into, the closer it is to a true transmission line. However, because of the limit of the physical size of the capacitors, the number of sections cannot be too big. In reality it has to be a compromise between the time requirement and the sizes of the magnet and the capacitors.

With a distributed magnet, the rise time of the field in the magnet gap is determined by the sum of the time that is required for the current in the load resistors to reach the peak and the time that is required for the current wave to travel through the magnet. The rise time of the current depends on the overall inductance in the connections between the magnet and the resistor load, in the resistor load assembly, and in the thyatron assembly. The speed at which the field wave travels through the magnet is given by

$$v = 1 / \sqrt{L_0 C_0}$$

where L_0 and C_0 are the inductance and the capacitance of

* Work supported by U.S. Department of Energy, Office of Basic Energy Sciences Under Contract No. W-31-109-ENG-38.

each section. Then for a magnet that has N sections the traveling time through the magnet is $T = N/v = N\sqrt{L_0 C_0}$.

In the design C_0 is chosen first because not many capacitors are available for this type of applications. The TDK UHV-12A high-voltage ceramic capacitor was chosen for its high voltage rating and relatively small physical size. It has a nominal capacitance of 1.72 nF and is rated at 50 kV. Using these values, N is determined to be 4 and T is equal to 53.9 ns. The characteristic impedance of the half-turn magnet, given by $Z_0 = \sqrt{L_0 / C_0}$, is then equal to 7.84 Ω which is close to the characteristic impedance of the cable portion of the PFN.

Since four sections are not enough to make the magnet behave like a true transmission line, there will be ringing between the sections if no damping is introduced. The SPICE computer simulation showed that adding a resistor with the same value as the PFN impedance to each capacitor eliminated the ringing without slowing the speed significantly.

HV Power Supply

The high-voltage power supplies used for the kicker units are rated at 50 kV and 6 kJ/s. This power supply operates in the constant-current-charging mode before the output voltage reaches the set point, then it switches into the constant-voltage-regulating mode. The output can be easily controlled by an HV ON/OFF TTL logic signal. The output voltage level can be controlled by the reference voltage within $\pm 0.5\%$ (though the HV power supply's specification is better) from shot to shot even for a load less than 30 nF. This is very important to our application since the injection kickers require different voltage levels at the beam injection and the beam extraction.

The HV power supply also has a built-in 100-200 μ s dead time after the load is suddenly discharged to give enough time for the thyatron to recover. This type of power

supply is ideal for capacitive loads that are charged and discharged repeatedly. It eliminates the need for an external high voltage regulator and makes the control simple.

A circuit diagram of a half-turn magnet and its PFN is shown in Fig. 1. This circuit is used in the computer simulation. The capacitor, C_T , is not included in the simulation and there is only one capacitor at the end of the half-turn magnet. The PFN cable length used in the simulation is 12 meters one way. The simulation showed this circuit would produce a waveform with 80-ns rise time and fall time and 80-ns flat top [1].

III. TEST RESULTS OF THE KICKER UNITS

A prototype kicker, shown in Fig. 2, was built according the circuit shown in Fig. 1. During the test a few problems were found with the original design.

First, the current and the magnetic field had a rise time close to 120 ns—much longer than what the simulation showed. The fall time was even longer, more than 200 ns. Second, looking at the currents or voltages at different sections of the magnet, the propagation of the field along the magnet was not clear. There was some time delay among the first three sections, but very little delay between the last two sections. The test showed that the inductance of all the connections, the thyatron assembly, and the resistor load was greater than the original estimate, 50 to 100 nH. Also, there was some magnetic coupling between adjacent magnet sections. In the design, there is a 1/8 inch gap between two sections. The test showed that this gap is not big enough to stop magnetic flux flowing from one section to another. The result is a magnetic coupling between two adjacent sections which makes the magnet act more like a lumped magnet. According to J. Dinkel, et al. [2], the space between adjacent sections can be up to 40% of the ferrite width without significant effect on the field. Some effort was spent on inserting copper plates between magnet sections to prevent

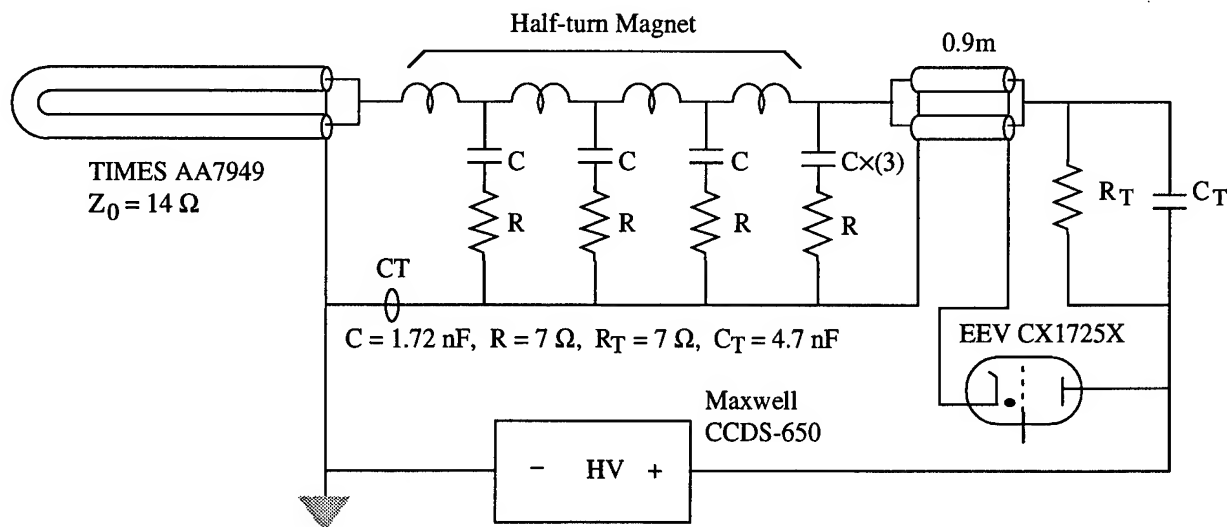


Figure 1. Circuit diagram of the kicker unit for the PAR

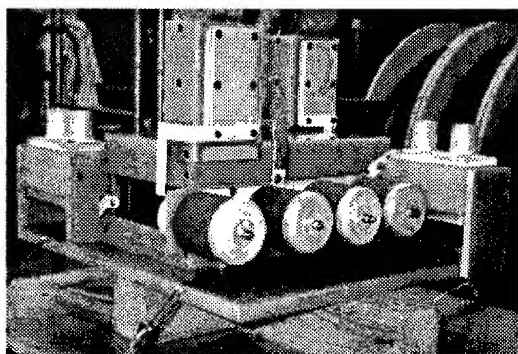


Figure 2. Prototype kicker magnet

the flux from crossing the gaps. However, because of size limitations, the copper plates could not stop the flux effectively.

Because of the schedule, it was not possible to redesign the magnet. Much effort was spent on making adjustments in the circuit to compensate for the slow magnet. For the injection kickers, the total rise time satisfied the requirement, but the rise time from 20% to 100% exceeded the limit. Its fall time also needed to be greatly reduced.

To reduce the rise time, a capacitor, C_T , was added to the load resistor. This capacitor not only reduced the rise time and the fall time, but also increased the ringing at the end of the pulse. Therefore, C_T could not be too big. A 4.7-nF capacitor was found to be the optimal choice, providing the needed time reduction without an excessive increase in the ringing.

To further reduce the fall time, the capacitor value at the output of the magnet was tripled. This greatly reduced the fall time, but the rise time increased as a side effect. To compensate, the PFN cables were shortened so the traveling wave from the PFN would come back early and the magnetic field would reach the peak early. The negative side of shortening the PFN was that greater PFN voltage would be needed to produce the required current. After extensive tests, the best configuration for the injection kickers was achieved. For the best configuration, the PFN cables were shortened to 8 meters and the third R-C branch from the input of the magnet was removed. Figure 3 shows the field waveform obtained.

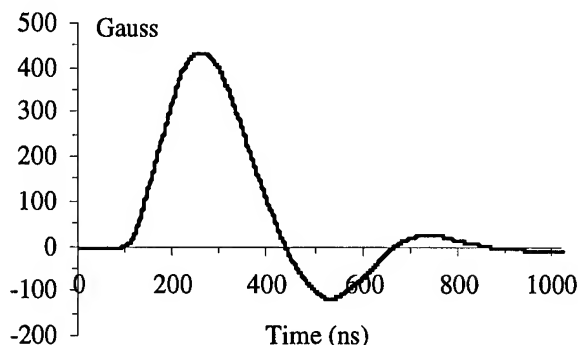


Figure 3. The magnetic field of the beam injection kicker

For the extraction kicker, the fall time and the ringing are not important since the PAR is empty after beam extraction. The flat top can be narrower because of a much smaller beam size, less than a nanosecond, at the extraction. The important parameter is the rise time. After some adjustment, the best configuration was found. Its cable PFN is 9 meters, and the half-turn magnet only needs the first and the last R-C branches (with only one C in the last branch). The 4.7-nF capacitor, C_T , is also required. Figure 4 shows the magnetic field of the extraction kicker, and Table 2 shows the achieved parameters of the injection and extraction kickers.

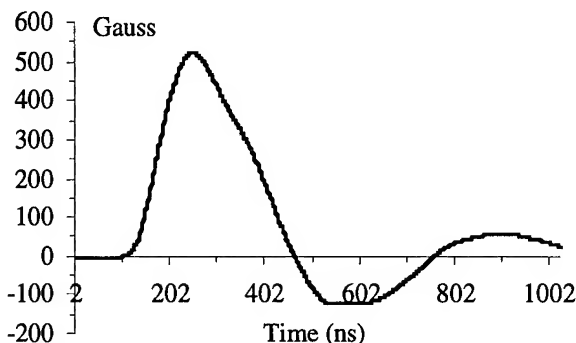


Figure 4. The magnetic field of the beam extraction kicker

Table 2. Achieved Kicker Parameters

	Injection	Extraction
Rise time 0 to 100%	160 ns	142 ns
20% to 100%	98 ns	88 ns
Fall time 94% to 50%	70 ns	
Flat top 3% flatness	60 ns	46 ns
Ringing % of peak	26%	

IV. CONCLUSION

Since the prototype, three kicker units have been built. Their PFNs and the magnet configurations were adjusted according to the test results from the prototype. These kicker units have been installed in the PAR for more than a year, with each injection kicker accumulating more than 25 million pulses. The performance of these kickers has been satisfactory—near 100% beam injection and extraction efficiency has been achieved.

V. REFERENCES

- [1] J. Wang and G. Volk, "Design and Simulation of Fast Pulsed Kicker/Bumper Units for the Positron Accumulator Ring at APS," *1991 IEEE Particle Accelerator Conference*, San Francisco, CA, May 6-9, 1991.
- [2] J. Dinkel, et al., "Development of a High Quality Kicker Magnet System," FERMILAB-TM-1843, Fermi National Accelerator Laboratory, May, 1993.

Development of a Modular and Upgradeable Fast Kicker Magnet System for the Duke Storage Ring*

R. J. Sachtschale, C. Dickey, P. Morcombe
Duke University, Free Electron Laser Laboratory
Box 90319 Durham, NC 27708-0319

Abstract

A cost effective injection kicker has been developed for the electron storage ring at Duke. Magnet components and driver circuitry are integrated in a modular format that has resulted in a low cost, highly maintainable and upgradeable development system. The driver and magnet can be easily reconfigured from a simple LRC circuit(parallel or series) that provides a pulse approximating a half sinusoid to one utilizing a pulse forming line to provide a more trapezoidal pulse shape. The modular development platform has permitted the kicker to evolve with the storage ring in a way that minimizes further expenditures of time and materials.

I. Introduction

The injection kicker for the Duke Storage Ring is a basic split frame magnet. The magnet is split along a longitudinal vertical plane, with respect to the electron beam path, essentially forming two C-core magnets. The core material is CMD10 from Ceramic Magnetics Inc., Fairfield, NJ. It is a Ni-Zn ferrite chosen for it's high saturation flux density and very high curie point. The magnet halves are joined with their open ends facing each other as shown in figure 1.

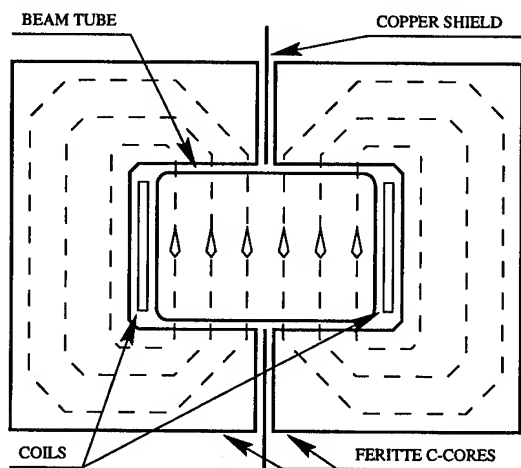


Figure 1. End View of a Split Frame Magnet

The current coils extend the length of the magnet and are driven with equal but opposite current pulses. This induces an equal but opposite magnetic flux to circulate in each of half of the magnet.

At the interface between the two halves, the opposing flux is forced up through the gap inside the beam tube. This produces a

vertical magnetic field in the chromium coated beam tube which is used to *kick* the electrons to the left. The required kick varies from 2.927 mrad for stacking to 5.853 mrad for single bunch injections. If the current pulses to the coils are not equal and opposite, a flux imbalance would allow an unopposed net flux to cross the interface and circulate between the two halves. To prevent the possibility of a net circulating flux, a copper shield is typically placed between the halves.

Although this is a common type of magnet geometry, budget constraints required the following features:

- Reliable and serviceable system that excludes the need for a complete spare backup magnet.
- Driver upgradeable to handle injections from 250 MeV to 1 GeV(integrated field range of 2.44 to 19.51 kGs * cm).
- Driver reconfigurable from a 150 ns half sinusoid pulse to a trapezoidal pulse with 350 ns flat-top and < 75 ns rise/fall-times.

A major benefit of a split frame magnet is that it can be removed from the beam tube without disturbing the vacuum system. This feature was exploited to make the most failure prone component serviceable at the beamline. Typically the most failure prone component is the insulation of the magnet coils.

II. Magnet Design

A common mode of failure in kicker magnets is the breakdown of the potting compound. A common potting compound is silicone. Kicker magnets employ one turn coils to minimized inductance resulting in large electrical stress. When combined with ionizing radiation and rf heating, silicones are more prone to damage than other materials like epoxy. However silicones are more easily removed than epoxies when a repair is required. We decided upon a hybrid approach. The magnet was potted in RTV Silicone from General Electric while the coils were potted as separate disposable assemblies in ceramic filled epoxy.

The potted copper strap that forms the coil is shown in figure 2. Connecting posts are attached to each end. Five layers of kapton film are wrapped around the strap in a spiral fashion between the two posts. It is then placed in a mold and vacuum potted with Stycast 2850ET Ceramic Filled Black Epoxy from Emerson Cumming Inc., Woburn, MA.

The connecting posts of the coils fit into a mating socket in the magnet body. The mating socket is molded into the silicone potting compound that surrounds the ferrite in the copper magnet case. Female bridge formed Louvretac bands from AMP Inc. Harrisburg, PA are used in the mating socket to make circumferential contact with the connecting posts. Final assembly of the magnet can be seen in figure 3.

The coil assembly and mating connections were tested with 1.6kA, 500ns pulses at a rep rate of 10 pps. This test was performed 8 hours per day for five days, resulting in over 1 million

*Supported by the U.S. Air Force Office of Scientific Research, contract F49620-93-1-0590 and the U.S. Army Space & Strategic Defense Command, contract DASG60-89-C-0028.

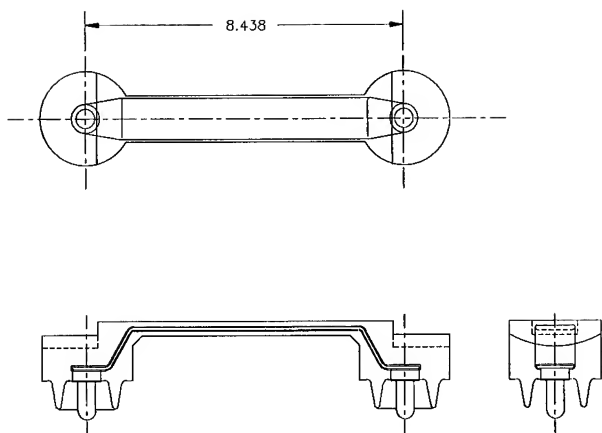


Figure 2. Magnet Coil Assembly

cycles without any sign of degradation. The same coil assemblies and connectors have been in use since storage ring commissioning began the first week of November '94.

External connections to the magnet are made with 1-5/8" 50Ω coaxial hardline. Flanges that mate to the hardline are built into the magnet case. Since the hardline is pressurized with SF_6 , O-rings, held in place by a nylon carrier, are used to keep the SF_6 from leaking out through the magnet.

The complex impedance of the magnet and connecting hardware was measured with a Hewlett-Packard 4194A Impedance Analyzer. The results of these measurements were used to build a simple circuit model. Computer simulations using this model helped to determine the appropriate capacitance and resistance values used in the driver circuit. The schematic of the final circuit is shown in figure 4.

III. Driver Assembly

The driver circuitry is housed in a cylindrical brass vessel. The circuit components are assembled on the bottom plate. The upper half of the vessel (the top plate welded to the 12 inch pipe) is lowered over the assembled components and bolted to the bottom plate. An O-ring in the bottom plate and a 12 hole bolt circle provide a seal that allows the interior volume to be pressurized with SF_6 . Figure 5 shows the layout of the principle components in the driver assembly. A Maxwell 40184 Spark Gap is used along with a Maxwell 40168 Trigger Generator (not shown). This combination was chosen for its low jitter specification. Omitted from the figure are the spark gap bias resistors, and the blocking capacitors that isolate the driver circuit from the spark gap trigger generator. Maxwell specified components were used.

The disk resistor is a 0.2Ω Carborundum current shunt. A 4.95kΩ resistor is connected from the node of the disk resistor and capacitor bank, to the center of a BNC bulkhead feed-through in the bottom plate. This provides a 100:1 divider into a 50Ω scope channel for monitoring the driver current in the control room. The Belleville washers provide the 25psi contact force recommended for the disk resistor. Although this circuit uses a parallel damping resistor, a series damping resistor could be

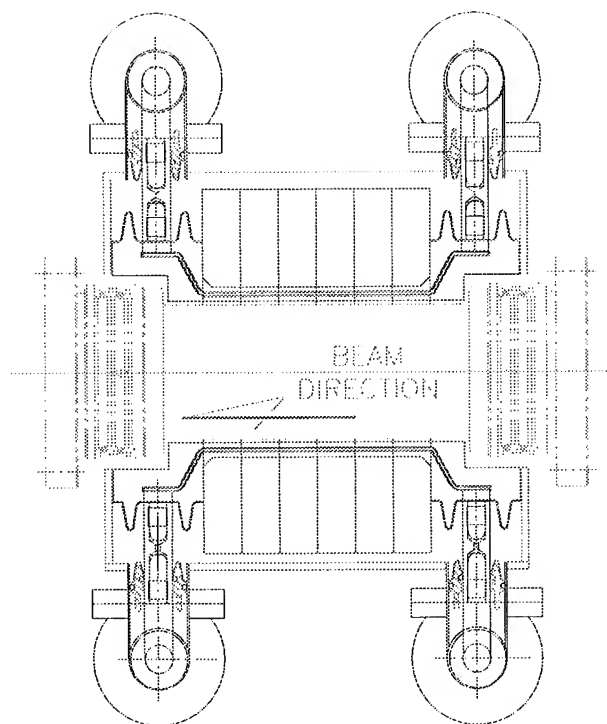


Figure 3. Top View of Kicker Magnet

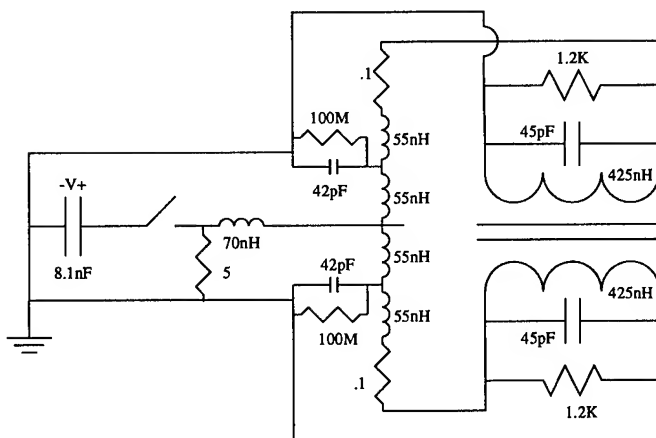


Figure 4. Schematic of Model Kicker Circuit

employed by increasing the value of the series disk resistor.

1-5/8" coaxial hardline flanges are welded to the top and bottom plates. By using a variety of these standard fittings and modifying them as needed for our applications, a very modular development system unfolded. For instance, original specifications for the kicker pulse required a long flat-top to be provided by a pulse forming line (pfl). The pfl was to be fashioned from four lengths of RG-213, with all eight ends attached to the spark gap switch in place of the capacitor bank. For this a 3-1/8" to 1-5/8" 50Ω taper was modified and attached to the 1-5/8" flange in the bottom plate. A 3-1/8" blind flange was made to mate to the large end of the taper. Holes and cable shears for nine RG-213

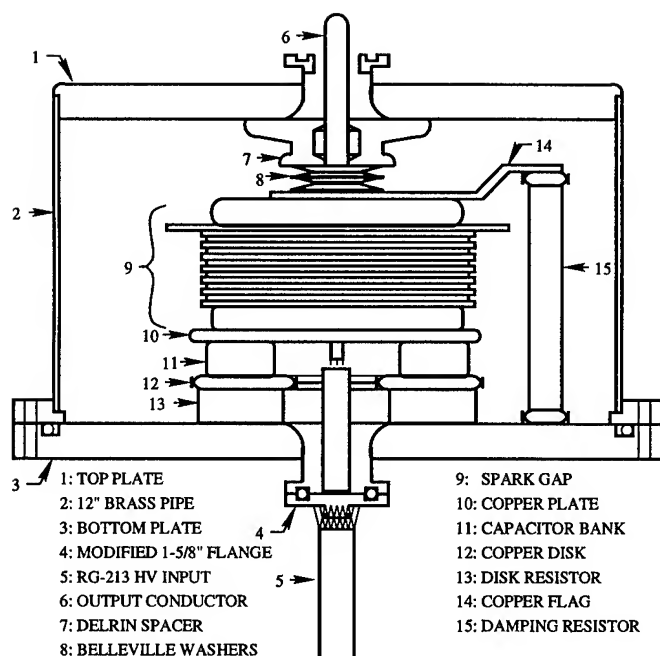


Figure 5. Driver Housing

cables(8 pfl ends and 1 HV lead) were added to the blind flange. Inside the taper the center conductors attached to a common post similar to the output post at the top of the driver housing. This sort of installation is depicted in figure 6.

To connect the driver to the magnet, the hardline was modified in-house to form an electrical Y connection with one input and two outputs. The input of the Y is connected to the driver circuit. The outputs of the Y are hooked up to opposite ends and opposite sides of the magnet so that the driver current is flowing in opposite directions in the two coils. The other end of each coil is shorted to the magnet case which provides the return path back to the outer conductor of the hardline.

IV. Conclusion

Our modular design approach has provided us with an extremely reliable fast kicker magnet. A variety of adapters have been made during the course of development to provide a system that can be readily reconfigured. The only failure as of the time of this writing has been of the current limiting resistors in the spark gap trigger circuit. These were quickly repaired and their failure was likely due to the kicker being operated without sufficient dielectric gas pressure between the spark gap electrodes. This caused runaway self-triggering of the spark gap and exceeded the average power rating of the current limiting resistors.

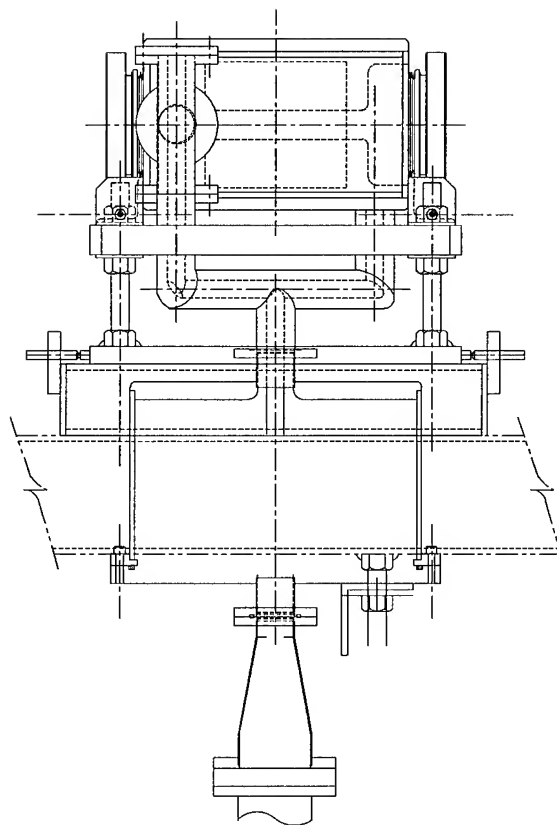


Figure 6. Installation Side View

HIGH CURRENT HIGH ACCURACY IGBT PULSE GENERATOR*

V. V. Nesterov and A. R. Donaldson

Stanford Linear Accelerator Center, Stanford, CA 94309 USA

A solid state pulse generator capable of delivering high current triangular or trapezoidal pulses into an inductive load has been developed at SLAC. Energy stored in a capacitor bank of the pulse generator is switched to the load through a pair of insulated gate bipolar transistors (IGBT). The circuit can then recover the remaining energy and transfer it back to the capacitor bank without reversing the capacitor voltage. A third IGBT device is employed to control the initial charge to the capacitor bank, a command charging technique, and to compensate for pulse to pulse power losses. The rack mounted pulse generator contains a 525 μF capacitor bank. It can deliver 500 A at 900V into inductive loads up to 3 mH. The current amplitude and discharge time are controlled to 0.02% accuracy by a precision controller through the SLAC central computer system. This pulse generator drives a series pair of extraction dipoles.

I. INTRODUCTION

A "flat top" pulse generator energizes a bending magnet to extract particle beams from the linear accelerator for the PEP II injector [1]. The IGBT Pulse Generator described in this article, and earlier ones based on Darlington transistors, are used at SLAC in applications where relatively low voltage, low current and slow extraction kickers are required [2]. Major features of these pulse generators are their simple topology, compactness and reliability.

II. BASIC CIRCUIT DESCRIPTION

Figure 1 shows a simplified schematic of the pulse generator. Initially the storage capacitor C is charged up to the power supply output voltage. To initiate the discharge of capacitor C into the magnet L, both transistors Q1 and Q2 are simultaneously turned on. The feedback loop current is constantly monitored and compared to the desired "flat top" reference value. When the current reaches the specified level, which could be up to 500 A, one of the IGBT switches, for example Q1, is turned off. The current still present in the magnet L will continue to flow through the magnet, but by using a different path: freewheeling through the diode D1 and conducting transistor Q2, thus creating a "flat top" on the current pulse.

This "flat top" current will decay exponentially until,

at the predetermined time, the second transistor Q2 is turned off and the remaining magnet current is redirected into the capacitor bank C through the diodes D1 and D2, so that the voltage across the capacitor C never changes in polarity. After the command charging transistor Q3 is turned on, the dc power source recharges the capacitor C back to its original voltage, making up for any energy losses that occur during the discharge cycle. To increase the flatness of the initial portion of the "flat top" the first IGBT Q1 is turned off slowly by using a rather high value resistor in series with the gate. The drive resistor also minimizes the switching transient voltage at turn-off. A consequence of this slow turn-off is higher power dissipation within the device, but since the unit operates at only 120 Hz this does not present a problem.

Figure 2 shows the waveforms for various parts of the circuit.

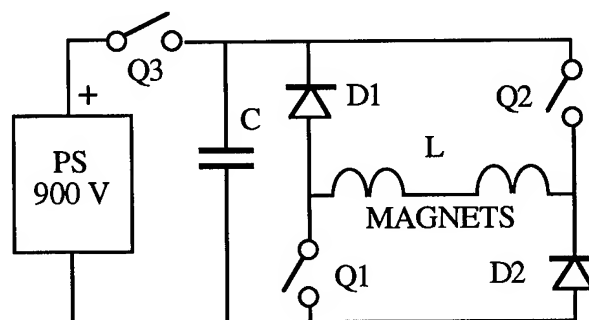


Figure 1. Block diagram of the pulse generator.

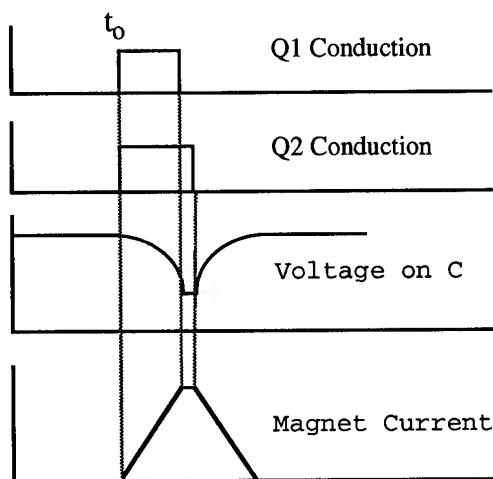


Figure 2. Waveforms for the pulse generator circuit.

*Work supported by DoE contract DE-AC03-76SF00515

III. CONTROL CIRCUIT

A block diagram of the control circuitry for the IGBT pulse generator is shown in Figure 3. A "NIM" input signal is converted to a CMOS pulse, that activates Timer 1. The output of this timer controls the beginning and the duration of the Q1 and Q2 conducting periods, and limits the maximum rise time of the pulse generator discharge current. As was mentioned above, IGBT Q1 is feedback coupled, and when the feedback signal at the input of the precision comparator reaches the reference level, the output of the "AND" gate will change state, and turn off Q1.

Timer 2 triggered by the input pulse, isolates the dc charging supply from the pulse generator for the load pulse duration. Timer 3 limits the trigger rate to a safe range of repetition rates and protects it from misfiring. The peak detector provides a dc voltage read back scaled to the load current pulse amplitude. It self-resets at the initiation of each current transducer pulse. If triggering pulses disappear for a period longer than the one second time out of Timer 4, this timer will reset the peak detector to zero.

This circuit is contained in a separate chassis that is mounted above the pulse power chassis.

IV. DESIGN CONSIDERATIONS

The components for the pulse generator are contained in a single rack mounted chassis with the following dimensions: 19" wide, 10.5" high and 20" deep. The 525 μ F capacitor bank is composed of 15, 35 μ F, 660 VAC

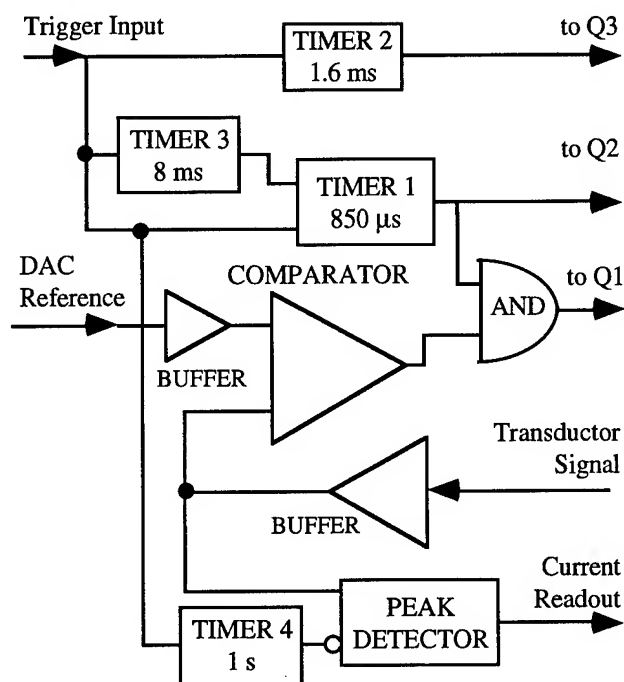


Figure 3. Block diagram of pulse generator controls.

parallel capacitors. These units are manufactured by GE.

Powerex 600 A, 1200 V IGBT's are used as the Q1 and Q2 switches in conjunction with Semikron drivers. Semikron drivers were selected because they have high voltage rating for input to output isolation, they need only one +15 V dc source at the grounded side of the control circuit, and their ability to drive IGBT's directly.

Two IGBT and two diode modules are mounted on a common water cooled heat sink. Particular attention has been given to the mechanical layout of the generator chassis to reduce the influence of all parasitic parameters and in effect minimize switching transients. Snubber networks are used across the IGBT's to protect them against transient over voltages. An SCR protection crowbar, as an option, can also be installed at the pulse generator output.

The photo below shows the top of the water cooled heat sink with one IGBT and one diode module visible. The other pair is mounted on the bottom of the heat sink along with the charge control IGBT Q3. The photo only displays three of the 15 capacitors in the bank.

The water hoses for the heat sink are terminated on the back panel of the chassis with quick disconnect fittings.

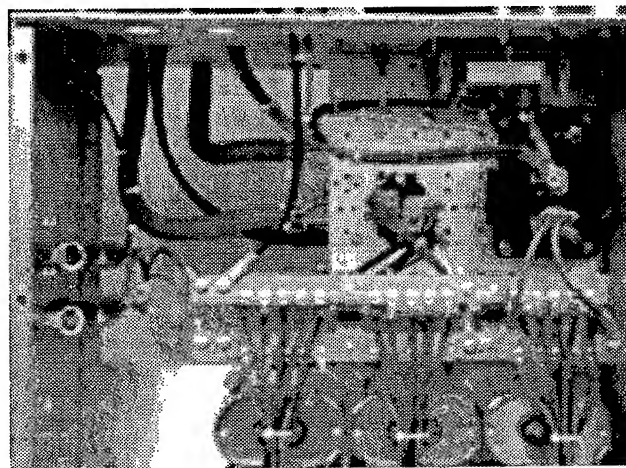


Figure 4: Mechanical layout of pulse power chassis.

A Danfysik 500 A dc transducer is used in the current feedback loop, as the pulse current sensor. The unit is an integrated zero flux transducer. The measuring head and the electronic circuit for control and feedback are enclosed one compact package. These units have been temperature cycled over 40°C ranges and exhibit stability and accuracy of better than 0.01%. The unit has a small signal band width of 100 kHz that is very adequate for this application.

The initial energy for the capacitor bank and the pulse to pulse make up energy are provided by a 900 V, 8 kJ/s capacitor charging supply. This power supply will operate up to a maximum voltage of 850 V. It is manufactured by Electronic Measurements, Inc.

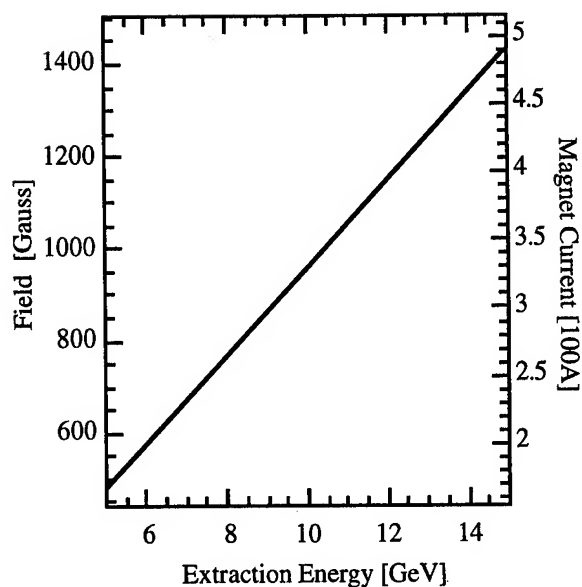


Figure 5. Magnet current vs. extraction energy.

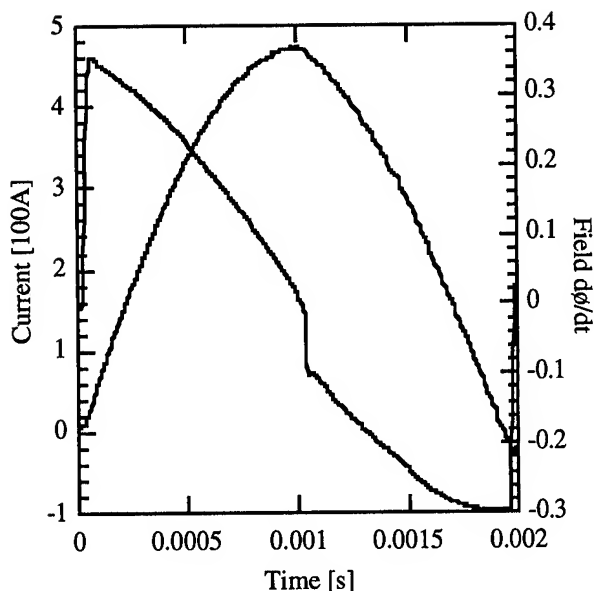


Figure 6. Magnet current and $d\phi/dt$ waveforms.

V. CONCLUSIONS

The generator has been tested into an inductive load of 1.6 mH (the actual magnet pair) and was delivering current pulses up to 470 A with a 100 μ s flat top. The pulse to pulse stability at the flat top is equal to or better than 0.02%.

The energy range for extracted beam will be from 8 to 10 GeV [2]. The generator has been tested with the intent to operate up to 12 GeV.

The operating range for extraction energy, magnet field and current is shown in Figure 4.

The actual magnet current waveform with a 100 μ s "flat top" at 470 A, somewhat in excess of that needed for 12 GeV, is shown in Figure 5.

The "flat top" was established at 100 μ s which minimizes any pulser turn-on jitter that would be deleterious to constant energy extraction. The generator can produce much wider "flat top" times, but at the consequence of some droop. We have developed techniques to eliminate the droop, but in this application only a 100 μ s "flat top" or less is needed for the very short beam pulses being extracted. The current pulse looks somewhat triangular as a result of the narrow "top," but it is very clean and does not exhibit any overshoot or ripple.

V. ACKNOWLEDGMENTS

The authors extend their appreciation and gratitude to Scott Hewitt for his design skills during prototype construction and testing, and then we salute Victor Popov for his excellent testing support, construction skills and devotion to the project.

VI. REFERENCES

- [1] T. Fieguth et al, "PEP II Injection Transport Construction Status and Commissioning Plans," contributed to this conference.
- [2] V. Nesterov and R. Cassel, "High Current Transistor Pulse Generator," proceedings of the 1991 IEEE Nuclear Science Symposium, pp. 1009-1011.
- [3] T. Fieguth et al., *ibid.*

ANALYSIS AND DESIGN MODIFICATIONS FOR UPGRADE OF STORAGE RING BUMP PULSE SYSTEM DRIVING THE INJECTION BUMP MAGNETS AT THE ALS*

G. D. Stover, Lawrence Berkeley Laboratory, University of California, Berkeley, CA 94720 USA

A fast (4.0 ms half period) resonant discharge pulse system, using SCRs, was designed and constructed to drive the injection bump magnet system at the Advanced Light Source (ALS)[1]. The commissioning process revealed a high frequency resonance ($T = 800$ NS) superimposed on the driver discharge wave form. In addition, the peak amplitude of the magnet load recovery current exceeded design specifications. A SPICE analysis confirmed the suspected mechanisms for the parasitic ringing and the excessive load current "undershoot." This paper will address the subsequent analysis, measurements, and modifications carried out during the maintenance shutdown in June 1993.

I. INTRODUCTION

This paper will a short review the pulser electrical system design, and continue with a more extensive discussion of the problems discovered during commiss-ioning, the subsequent SPICE analysis of the system, the subsequent modifications made to the electrical system and finally the discuss the new wave forms measured more complete description of the injection process, the magnet layout and specifications and electrical system of the magnet drivers can be found in a previous paper.

II. BASIC SYSTEM LAYOUT

The sinusoidal current wave form required to drive the injection magnets is generated by the resonant discharge of a capacitor bank through a distributed array (64 total) of high voltage Silicon Controlled Rectifiers (SCRs) switches through a very low inductance transmission line (4 groups or 8 parallel cables) to the predominantly inductive magnet load. The basic topology for the pulse system is shown in Figure 1. The four parallel bipolar SCR-capacitor discharge modules that are shown in Figure 2.

III. ORIGINAL MEASUREMENTS

The bottom trace in Figure 3 is the output current from one of the four SCR pulse units.

*Work supported by the Director, Office of Energy Research, Office of Basic Energy Sciences, Material Sciences Division, U.S. Department of Energy, under Contract No. DE-AC03-76SF00098.

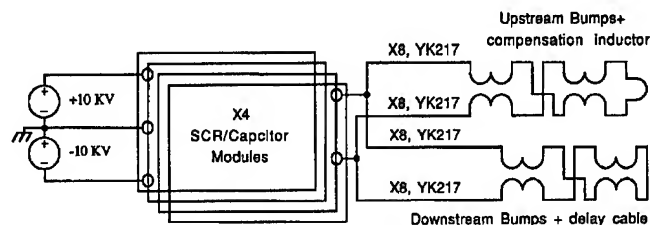


Figure 1. Bump pulse system

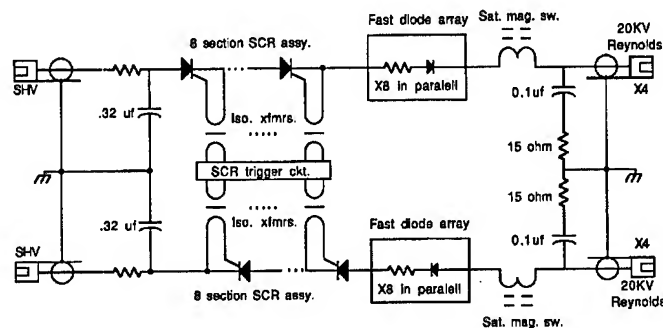


Figure 2: One of four bipolar SCR-capacitor discharge modules

The high frequency ringing superimposed on the discharge pulse has a nominal period of 800 ns. Due to this parasitic ringing the peak di/dt at the moment of turn-on has been measured as high as 3300 amps/ μ s over a period of 500 ns. This specification is more than twice the specified maximum listed for the SCR switches and was a potential source of damage. Additionally, as seen in figure 4, the current in the magnet load rings negative to about 20 % of the peak forward current. This value a 20 times larger than the 1.0% reverse ring specified for the injection bump magnets and could have adverse effects the smooth injection of stored beam. The distributed design of the pulse system prevented the iterative process of component substitution. A circuit analysis engine was adapted to solve the problem.

IV. A SPICE ANALYSIS

A simplified model of the pulse system was developed using an Integrated Circuit Emulator (IsSPICE)[2]. The basic SPICE circuit is shown in figure 5. This simple circuit is a distillation of the major circuit elements of the pulse system: the series/parallel combination of the 16 energy storage

Task Running: Waiting for Trigger

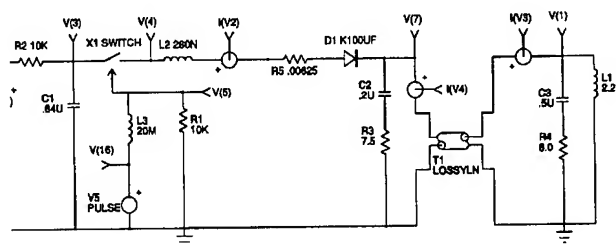
Ch3 100ms 1.00V

Ch4 1.84V

15.7V
2.50µs
15.8V

The lumped elements L2 and R5 represent the distributed inductance and resistance of the SCR switches. C2,3 and R3,4 represent the combined RC anti-ringing snubber circuits employed in the system. Circuit elements that have underlying complex sub circuit models include: LOSSYLN, T1 a distributed parameter lossy transmission line and voltage source PULSE, V5 which contains a switch control wave form that mimics the delay and nonlinear turn-on characteristics of the SCRs modeled by SWITCH, X1.

A reasonable solution to the resonance problem is shown in Figure 7. The parasitic ringing on the pulser current (top trace) is almost completely eliminated and the magnet load current reverse recovery amplitude is within the 1% specification. This effect was brought about by halving the number of coaxial cables from 16 to 32, thus lowering the cable input capacity and replacing the RC snubbers with resistors thereby considerably reducing the parasitic and bulk (undershoot) resonance effects. Further reducing the number of cables would decrease the ringing effects and the excessive di/dt but conversely increase the period of the magnet current pulse beyond its specified requirements. The magnitude of the di/dt at the beginning of the pulse current wave form was moderately reduced and its duration, in excess of 1500 amps/us specification, was halved.



1255

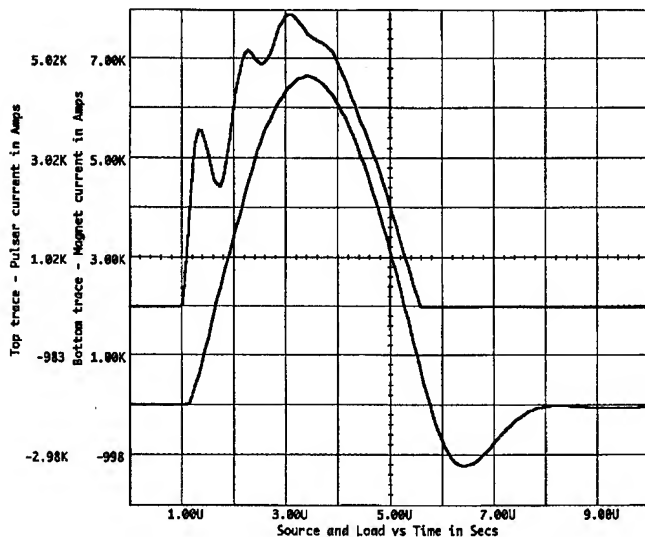


Figure 6: SPICE model output wave forms before modifications: Pulsar output current (upper trace, 1000 amps/div.) and magnet load current (lower trace, 1000 amps /div.).

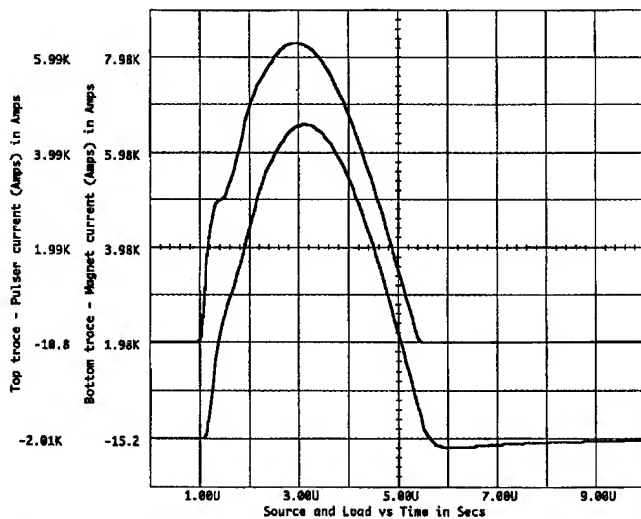


Figure 7: SPICE model output wave forms after modifications: Pulsar output current (upper trace, 1000 amps/div.) and magnet load current (lower trace, 1000 amps /div.).

V. ACTUAL MODIFICATIONS AND RESULTS

All the component values suggested by the SPICE models were applied to the Bump system. The number of coaxial cables was halved and the R-C snubbers were replaced by straight resistors. The resistor size was selected by power dissipation calculations obtained from the SPICE runs. As a protective measure, the core area of the saturating magnetic switches was doubled to further protect the SCR's from the remaining excessive di/dt . The correlation between the SPICE wave forms and the actual measured wave forms in Figures 8 and 9 is quite good.

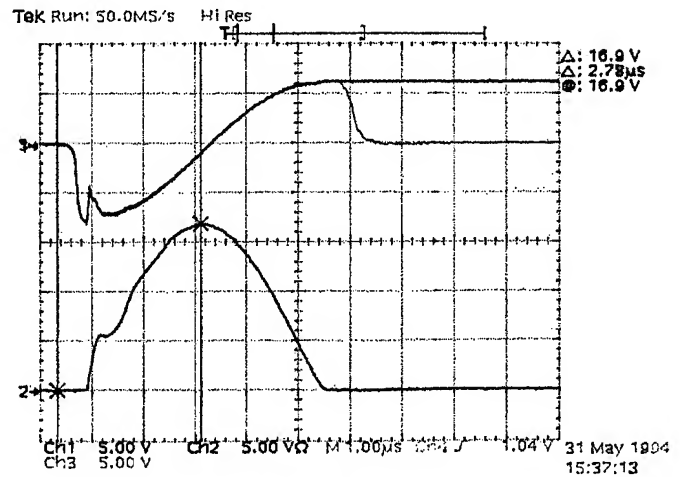


Figure 8: Actual pulse unit output current (lower trace 500 Amps/div.).

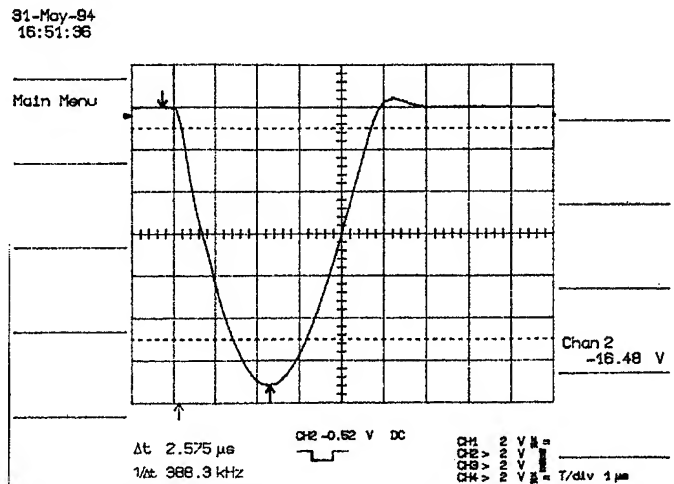


Figure 9: Actual magnet load current (1000 amps /div.).

VI. CONCLUSION

A condensed and simplified SPICE model was been created to understand the mechanism of excessive di/dt , and parasitic ringing observed in the current wave forms of the recently constructed resonant discharge pulse system at the ALS. The SPICE model identified significant circuit problems and the appropriate corrections were made.

VII. REFERENCES

- [1] G. Stover, L. Reginato, "Analysis and Design Modifications for Upgrade of Storage Ring Pump Pulse System Driving the Injection Bump Magnets at the ALS", Proceedings of 1993 IEEE Particle Accelerator Conference, Washington, D.C., vol. 2, p. 1351-1353.
- [2] Trademark of Intusoft, P.O. Box 710, San Pedro, CA 90733-0710, (310) 833-0710.

EDDY CURRENTS INDUCED IN A MUON STORAGE RING VACUUM CHAMBER DUE TO A FAST KICKER*

W.Q. Feng, Physics Department, Nanjing University, Nanjing, China

E.B. Forsyth, AGS Department, Brookhaven National Laboratory, Upton, New York 11973 USA

Abstract

The goal of AGS E821 is a precision measurement of the muon magnetic moment (g-2) value to 0.35 ppm. A problem with muon injection is the effect of the residual magnetic field during the measurement period due to the eddy currents in the vacuum chamber induced by the kicker pulse. The paper presents a mainly analytical look at the nature of the eddy currents as an equivalent RL circuit and describes a method to solve 2D Maxwell's operations under pulse excitation with some quantitative estimates of the decay time constants. Analysis of the results show that the field due to eddy currents is dependent on the chamber dimensions, type of material, and duration of pulse rise, flattop and fall. The field created by the rising edge of the waveform is largely cancelled by the falling edge, providing the pulse is short compared to the diffusion time of the eddy current. The simulation results agree with the theoretical analysis and confirm the residual integral field at the start of the measurement period is acceptable.

I. INTRODUCTION

A new experiment is being built at Brookhaven National Laboratory to measure the g-2 value of the muon to a precision of 0.35: an improvement of a factor of 20 over the best available data. The ultrahigh precision aimed for at BNL presents unusual challenges in physics and in technology. Muon injection plays an important role in achieving the precision of 0.35 ppm, because direct muon injection into the storage ring is more efficient in producing stored muons, and the hadronic background associated with many pions interacting with storage ring material is absent. Direct muon injection into the storage ring is accomplished by giving the muon beam a 10 milliradian kick at a quarter of a betatron wavelength from the inflector. The disadvantage of direct muon injection is that one has to deal with the effect of the residual magnetic field of the fast kicker due to eddy currents in the vacuum chamber.

The method of attack is to derive LR circuits for the eddy currents and to solve 2D Maxwell's equation with pulse excitation, thus obtaining a group of solutions of the eddy current magnetic field, eddy currents and decay time

*Work performed under the auspices of the U.S. Department of Energy.

constants [1]. Some computer simulations are given of eddy currents induced by a fast kicker. The simulation results agree with the theoretical analysis and confirm the residual integral field at the start of the measurement period is acceptable.

II. SOLUTION OF THE DIFFUSION EQUATION

In Fig. 1, if $l \gg w$ and $h \gg d$, then the two-dimensional kicker magnetic field in the chamber wall, parallel to the wall can be considered.

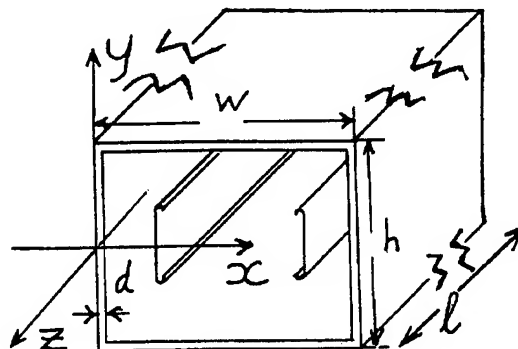


Fig. 1. Vacuum chamber with two-plate kicker.

In this situation, $\frac{\partial \vec{D}}{\partial t} \ll \sigma \vec{E}$ and Maxwell's equations are:

$$\nabla \times \vec{E} = -\mu \frac{\partial \vec{H}}{\partial t}, \quad \nabla \times \vec{H} = \sigma \vec{E} \quad (1a), (1b)$$

where $\mu = \mu_0 \mu_r$ is the magnetic permeability, and σ is the electrical conductivity. Applying boundary conditions we obtain the diffusion equations for the special situation:

$$\frac{\partial^2 E_z}{\partial x^2} = \sigma \mu \frac{\partial E_z}{\partial t}, \quad \frac{\partial^2 H_y}{\partial x^2} = \sigma \mu \frac{\partial H_y}{\partial t} \quad (2a), (2b)$$

An iterative form of solution has been examined [2], assuming the fast kicker produces an exponential step pulse. In the beginning of the iteration, the magnetic field $H_0(t)$ is uniform over the cross section of the chamber wall; this field is perturbed by the eddy currents. The decay times

Table 1
Time Constant L_n/R_n

$L_n(t)/R_n(t) \text{ } (\mu\text{S})$							
$\sigma[10^6(\Omega\cdot\text{m})^{-1}]$	d (mm)	n = 1	n = 2	n = 3	n = 4	n = 5	n = 6
38.2 (Al)	3	10.9	2.74	1.22	0.68	0.44	0.11
38.2 (Al)	5	30.4	7.60	3.38	1.90	1.22	0.30
38.2 (Al)	10	122	30.4	13.5	7.60	4.86	1.22
1.11 (S.S.)	3	0.32	0.08	0.035	0.02	0.013	0.0032
1.11 (S.S.)	5	0.88	0.22	0.098	0.055	0.035	0.0088
1.11 (S.S.)	10	3.53	0.88	0.39	0.22	0.14	0.035

have been calculated, represent in Fig. 2 by $L_n(t)/R_n(t)$, quantitative results are given in Table 1.

Typical time constant for the decay in aluminum is $\sim 500 \mu\text{s}$. In practice the excitation waveform of the kicker has both a rising and falling edge with a width that is much less than L_1/R_1 . The net effect due to the difference between positive and negative eddy currents will produce residual magnetic field which could affect the accuracy in determining the overall field integral around the storage ring. Calculation shows the next field decays much more quickly than for a unidirectional pulse due to the cancellation effect: a short pulse is required relative to the diffusion times. The rise and fall times can be optimized to keep the eddy current field to a minimum.

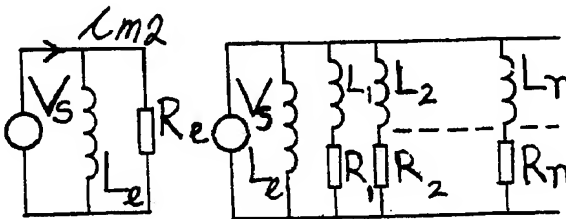


Fig. 2. Eddy current equivalent circuits.

III. COMPUTER SIMULATION

The required high precision implies the integrated residual field $R \int_0^{\theta_1} B_e d\theta$ should become less than 1 part in 10^7 of the integrated main dipole magnetic field $R \int_0^{2\pi} B_e d\theta$

on the mid-plane at the start of the measurement ($\sim 10 \mu\text{s}$), where B_e is the eddy current field, B_0 is main dipole field, θ is the angle subtended to the center of the ring, θ_1 is the angle occupied by the fast kicker, and R is the radius of the storage ring.

For the magnetic kicker, using an underdamped sine waveform the eddy current field/main field is $< 1 \times 10^{-7}$ if $t_r < 100 \text{ ns}$. The eddy current field at beam centerline using the program PE2D with a waveform assumed to have 60 ns. The vacuum chamber material is 2020 aluminum. Table 2 lists the eddy current contribution to $\int_0^{\theta_1} B_e d\theta$ as a function of time after injection for a stripline kicker (E & H field deflection). The time dependent diffusion of eddy currents is clearly seen: there is a rapid change immediately after the end of the kicker excitation pulse which slows as time increases.

IV. CONCLUSIONS

The analysis has served to emphasize the following important points:

- (1) The field due to eddy currents is dependent on the chamber dimensions, type of material and times of rise, flat-top and fall of the excitation pulse.
- (2) The eddy current field has a fast transient component and a steady state component.
- (3) The cancellation of the field produced by the rising edge of the excitation wave form is largely produced by the falling edge, providing the flat-top portion is brief.
- (4) Numerical computations indicate the residual integral field due eddy currents to eddy currents at the start of the measurement period will be < 1 part in 10^7 of the main bending force for a fast kicker with an optimized excitation waveform.

Table 2
Ratio of Kicker Field
Deflection to Main Field Deflection

Time, ns	Ratio, pts in 10^6	Comments
65	0.92×10^3	Half the total deflection of 11 mrad comes from the H field
165	1.3	End of kicker deflecting pulse
1020	0.43	-
5020	0.18	-
20,000	0.10	-

ACKNOWLEDGEMENT

The authors would like to thank W. Meng and S. Kahn for their support and helpful discussions.

REFERENCES

- [1] W. Feng and E. B. Forsyth, private communication.
- [2] Jiri Lammeraner and Miles Stafl, "Eddy Currents" CRC Press, 1966.

HIGH PULSE POWER MODULATOR UPGRADE FOR A S-BAND TRANSMITTER

J. DeCobert, B. Binns, R. Campbell, A. Hawkins, D. Wang, A. Zolfaghari
MIT-Bates Linear Accelerator Center
Middleton, MA 01949, USA

INTRODUCTION

This paper describes transmitter systems upgrade plans for the Bates Linear Accelerator. There are six modulator systems. They are dual output S-band systems with a peak operating power of 4.5 MW and 100 KW average. They are floating-deck hard-tube modulators operating a parallel pair of Litton L-5097 switchtubes in series with a Varian VA-938 klystron.

UPGRADE PHILOSOPHY

The major goal of the modulator deck upgrade is to increase system reliability. System downtime needs to be significantly reduced to improve the overall efficiency of beam delivery. This will be accomplished by identifying the failure prone components and circuitry, and applying modern circuit design methodologies. This will also permit the elimination of outdated circuit components which are becoming increasingly harder to find. In addition, time to repair must be significantly reduced to minimize downtime. This will be accomplished in two ways. First, by optimizing ease of repair. Presently, transmitter subsystems generally use bolt-in-place components, which are difficult and time consuming to replace. These will be replaced by chassis with quick disconnects and plug-in cards. Second, by improving our capability to analyze quickly fault conditions. This will be accomplished by adding more diagnostics, and by using technologies that were not available for the original design [Figs. 3 and 4].

PRESENT OPERATION

The six transmitters were designed in the late 1960's and were installed in the early 1970's. The basic transmitter consists of a 176 KV power supply which has its positive terminal connected to ground. The power supply negative terminal B- is connected directly to the cathode of four switchtubes. Each transmitter contains two klystrons. Each klystron's collector is connected to B+ and its cathode is connected to the anodes of two switchtubes. The modulating anodes of all four switch tubes receive their drive signals from a common switchtube driver circuit. The switch tube drive circuit, regulator, and other modulator circuits are mounted on a deck which floats at high voltage. This design has proven reliable and we do not wish to change it. The problem is trying to maintain beam delivery with

30 year old equipment, equipped with a 30 year old diagnostics system, interlock system, and monitoring system.

The present operation of the modulator deck is as follows [Fig. 3]. A pulsed signal is sent to the bootstrap chassis via a pulsed thyatron to a photomultiplier (PM) tube on the floating deck. The PM tube signal is amplified and sent to the bootstrap chassis, which initiates the leading edge of the pulse. When the pulse voltage reaches a set voltage, the Regulator chassis begins operation to keep the flattop portion of the pulse to within 0.1%. At the time of turn-off, a pulse is sent via a separate thyatron/PM link to the tailbiter chassis, which initiate the falling edge and returns the modulator to its original state [Fig. 1].

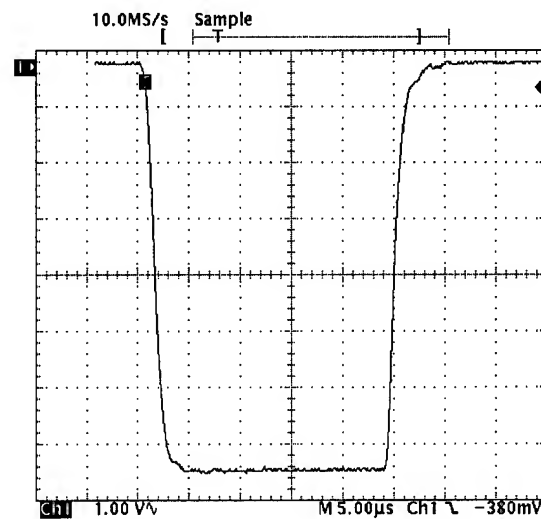


Fig. 1. Klystron cathode current pulse, 70 A peak.

START AND STOP SIGNALS

As mentioned earlier, the start and stop signals are transmitted to the floating deck electronics via a pulsed thyatron. The light output of the thyatron is directed down a Lucite rod to a photomultiplier tube on the floating electronics. This hardware will be replaced with fiber optics which will eliminate the need for high voltages for the thyatron and photomultiplier tubes. It will also eliminate problems in the alignment of the Lucite rods between the tubes, and extraneous signals being received by the photomultipliers.

BOOTSTRAP AND TAILBITER

The subsystems which are responsible for the switching of the floating deck, the bootstrap and tailbiter chassis, are two of the most failure prone of the modulator. To replace one failed unit requires a complete system shutdown. Typical turn around times of such an operation are in excess of 1 1/2 hours.

By mounting the circuits on plug-in cards, the need for total system shutdown and removal of the modulator deck should be eliminated. A rapid replacement of the circuits by putting the system into standby mode, or by shutting off only a few of the power supplies, should be possible. This would reduce the turnaround time by at least 75%. Card mounted circuits should allow us to bench test the operation of these circuits, obviating the need to install them into a working spare deck, as is done now.

An effort to include inherent circuit redundancy is being made. For the critical trigger circuits, we will include a standby parallel circuit that may be either manually or automatically switched. This will allow for effective repair of the system without the need of shutting the system down or spending considerable time in removing the faulty circuits. It may also be simple enough for the operating staff to operate, so that time is not spent in waiting for repair personnel to arrive.

REGULATOR

The shunt regulator subsystem of the modulator deck will also be updated. This subsystem is responsible for the exceptional pulse flatness of the modulator. It currently has a vacuum tube based error amplifier. This error amplifier is somewhat difficult to troubleshoot, and balance, requiring a day long service to adjust. When the error amplifier fails, its repair time is on the order of a least one day. In emergencies the entire modulator deck electronics package may be replaced. This subsystem could be greatly simplified by using present day high voltage solid state methods. This will eliminate the long tuning procedure, and allow for a rapid replacement of failed units. Such solid state methods are already in use in similar systems. [Ref. 1]

INTERLOCKS

The modulator deck interlock system will be updated. In the existing system, the presence of required voltages are sensed through incandescent light falling on a photoresistor in series with a sealed electromechanical relay. This system allows for wide variations in the required voltages, and has become difficult to maintain as original manufacturers no longer make many of the system elements, such as the electromechanical relays. In addition, no information from the interlock chain is transmitted to the ground level control, other than a SUM indication. By using modern opto-isolators, fiber optics and solid

state relays, positive interlock window control will be implemented. In addition, each interlock, or at least subsets, can be transmitted via fiber optics to the control system. This will allow operators to be provided with better information on the system status, as well as provide helpful information for troubleshooting and repair.

SYSTEM DIAGNOSTICS AND MONITORING

A major reason for the lack of diagnostic and monitoring information designed into the system was the difficulty of bringing signals floating at high voltage to ground. Today, transmitters are designed using fiber optic technology to isolate signals floating at high voltage from ground. Hewlett-Packard and others have developed low cost, very reliable fiber optic transmitters and receivers. Manufacturer test data indicates for 12 lots of 330 HFBR-2402 fiber optic receivers, tested for 2,370,000 hours at 85 degrees Celsius, resulted in one failure. [Ref. 2]

To better understand the operation and failure modes of the deck, new fiber optic technology will be used to transmit the modulator deck status, as well as critical voltage and current parameters. This will be implemented by using precision voltage-to-frequency and RMS-to-DC converters on the floating electronics, and transmitting via fiber optic to ground referenced circuitry. In this manner, critical voltage and current levels can be monitored while the modulator is in operation. Analog fiber optics will be used to send pulsed signals from the floating electronics to be monitored from the ground level. This technique has been used successfully in other systems [Ref. 3]. By adding this capability, it should be possible to rapidly analyze faults in the system [Fig.2]

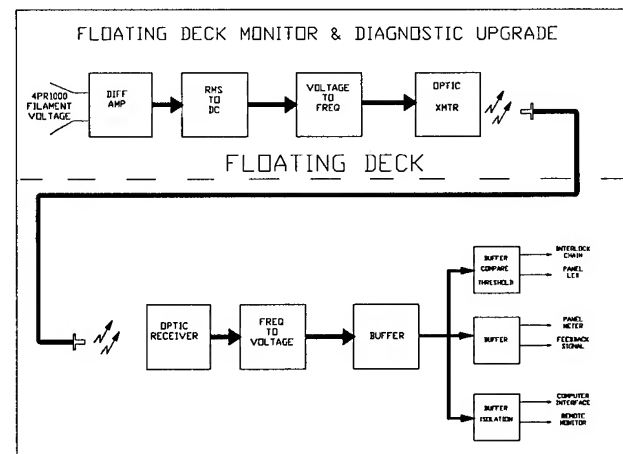
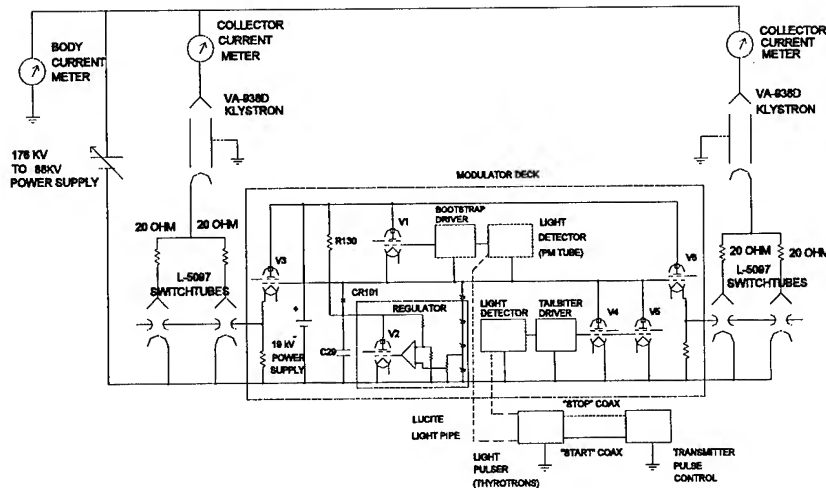
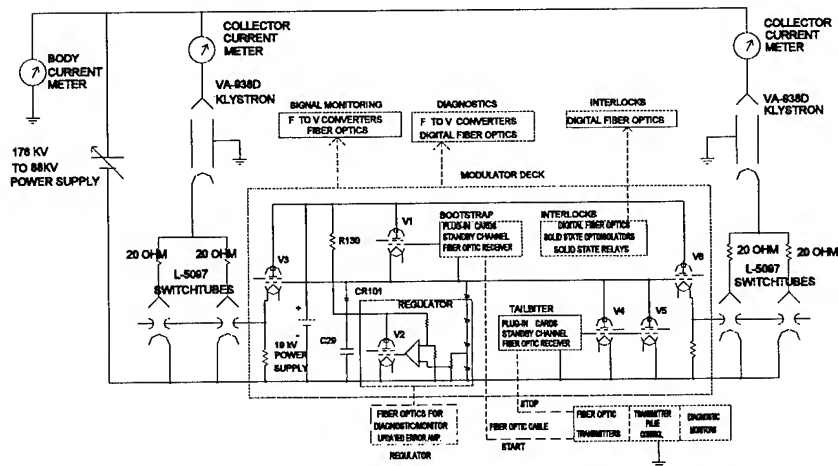


Fig. 2 Use of fiber optics in diagnostics and monitoring.



Simplified modulator schematic

Fig. 3



Simplified modulator schematic showing upgrades

Fig. 4

REFERENCES:

1. Bill North, GTE Government Systems, Bill Reass, Los Alamos National Laboratory, "Electrical Design and Operation of a Two-Klystron RF Station from the Los Alamos National Laboratory's Neutral Particle Beam Experiment" 1992 IEEE Twentieth Power Modulator Symposium, Conference Record, P.15
2. Hewlett-Packard, "Fiber Optic Transmitter and Receiver Reliability Data" Bulletin Number 5954-2221 (8/89).
3. R. Litte and R. Limpacher, Avco Research Laboratory, Inc. "Fiber Optic Transmission of High Speed Analog Data in High Voltage Pulsed Power Systems" 1986 IEEE Seventeenth Power Modulator Symposium, Conference Record, P.287

MODULATOR FOR KLYSTRON 5045

N. S. Dikansky, V. Akimov, B. Estrin, K. Gubin, I. Kazarezov, V. Kokoulin, N. Kot

A. Novokhatsky, V. Rashenko, Yu. Tokarev, S. Vasserman
Budker Institute of Nuclear Physics, Novosibirsk 630090, Russia

Abstract

The first modulator for a forinjetor klystron of VEPP – 5 is being tested now in BINP in Novosibirsk. The forinjetor of VEPP – 5 will involve a 510 MeV Linac consisting of four accelerating modules. The Klystron 5045 manufactured at SLAC [1] was chosen to drive the accelerating modules. This paper presents a design and some testing results of this modulator.

- facility are placed in two racks in front of the cabinet. The cabinet with a line-operated facility is also placed in front of the main cabinet between the two racks. To make the service convenient, the racks can be rotated as shown in Fig.4. The photo in Fig. 5 shows a view of the modulator.

The main characteristics are presented in Table 1.

Table 1. Modulator specification

Parameter	Required	Tested
Peak output power	150MW	150MW
Peak output voltage	23.5kV	5 to 22.5kV
Pulse width	5 μ S	5 μ S
Flat-top width (tol. \pm 0.5%)	4 μ S	3.5 μ S
Repetition rate	50pps	0 to 50pps
Peak klystron voltage	350kV	360kV
Peak RF power	67MW	60MW

I. INTRODUCTION

The modulator is a conventional line type modulator with some supplementary characteristics. A simplified electrical layout of this modulator is shown in Fig. 3. The voltage value in a filter capacitor C_F is determined by a phase-control system with six SCRs. The C_F charging current is limited by three 500 μ H inductors connected to the primary winding of the rectifier transformer. In addition, this system provides "soft-start" capability and fast protection. The PFN is resonantly charged through a charging high-voltage SCR-switch (HV-switch), a charging inductor, and de-spiking circuits. The resonant PFN charge goes only after starting the HV-switch. A de-Qing system provides precise setting of the PFN voltage by stopping the charge when a required voltage is reached. When the thyatron is fired, the PFN is discharged through a coaxial cable to the klystron pulse transformer or to the load resistor. The 1:15 pulse transformer delivers a 350 kV pulse to the cathode of the klystron. The thyatrons TGI-2500/50 are used in the modulator. Output pulse waveform at the Klystron 5045 shown in Fig. 1 was obtained in the process of modulator adjustment.

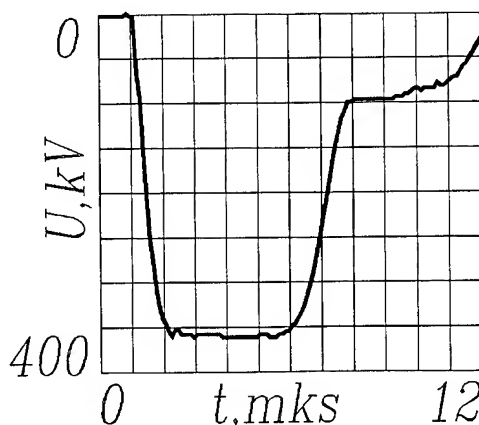


Figure 1. Output pulse waveform

The position of the main modulator components and the Klystron 5045 is shown in Fig. 4. The main elements shown in Fig. 3 are installed in a common cabinet. The control and measurement elements, low-power supply sources, and the CAMAC

A. Rectifier assembly

The rectifier assembly designed earlier [2] consists of 18 1.5 kV sections connected in series and placed on the common core. Each section is protected with fuses; that's why if one or two of them would fail, it would not be necessary to take off and repair the whole rectifier.

II. High voltage switch

A high-voltage charging commutator consisting of 64 thyristors connected in series makes possible to charge the PFN immediately before pulse generating. In addition, such commutator is a convenient and reliable protection element. It allows us also to change the repetition rate 0 to 50 pps. To turn on simultaneously 64 thyristors, the circuit shown in Fig.2 is used.

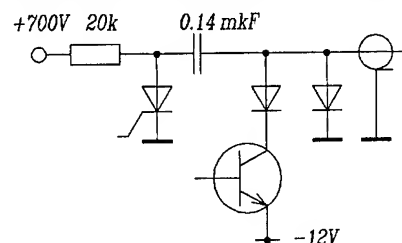


Figure 2. Control HV-SCR circuit

The capacitor and thyristor form a 2 μ S leading edge of the HV-switch control pulse, then a 1 mS flat-top is formed by the transistor switching-on. The control pulse current is more than 0.1 A. To suppress unwanted oscillation of the charging circuit, the special measures are undertaken. After the charging current

has stopped, the de-Qing thyristor is kept in the ON-state till the oscillation caused by the thyatron switching dies down.

III. Pulse Forming Network

The modulator comprises two PFNs in parallel. Each of them consists of 13 sections with a fixed capacitor and a tunable inductor. It is placed in an oil-filled tank. The total characteristic impedance of each PFN is 8Ω . The inductors may be regulated from the outside of the tank.

IV. EOLC system

EOLC system comprising a diode and a resistor is used to remove the excessive negative voltage swing and to protect the klystron in the case of a break-down. The EOLC diode is composed of 60 rectifying elements connected in series and alternating with washers used as radiators with forced air cooling. A small size of diode assembly (total length is 370 mm) provides low inductance of EOLC.

V. Dummy load

The dummy load with the characteristic impedance 4Ω is designed and installed to test the modulator without the klystron in a required range of output power. The dummy load is composed of 8 high-voltage resistors S5 – 41 connected in parallel. The introduction of water cooling allows us to raise the dissipated power of the load from 4 kW to 40 kW.

VI. Conclusion

Since the modulator is rigged with computer control and measurement, the protection system, the dummy load, and with a wide range of working voltage and repetition rate, it is possible to use it as the stand for testing and studying of both the modulator components and klystrons.

References

- [1] M.A. Allen et al. "Performance of the SLAC linear collider klystrons," Particle Acceleration Conference, 1987, v.3
- [2] B.A. Baklakov et al. "High-voltage modulator for power supply of atomic beam injectors," Thermonuclear synthesis series, 3, p. 55-58, 1985.
- [3] A.R. Donaldson, et al. "The second generation SLAC modulator," SLAC, 1986

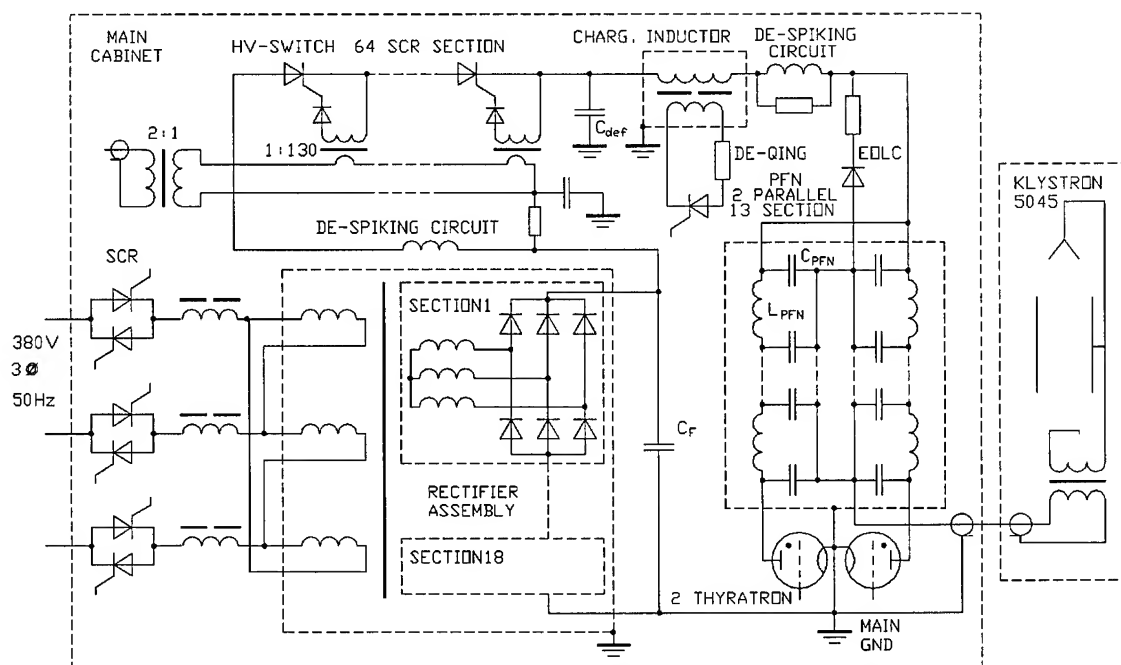


Figure 3. Simplified electrical layout of the modulator

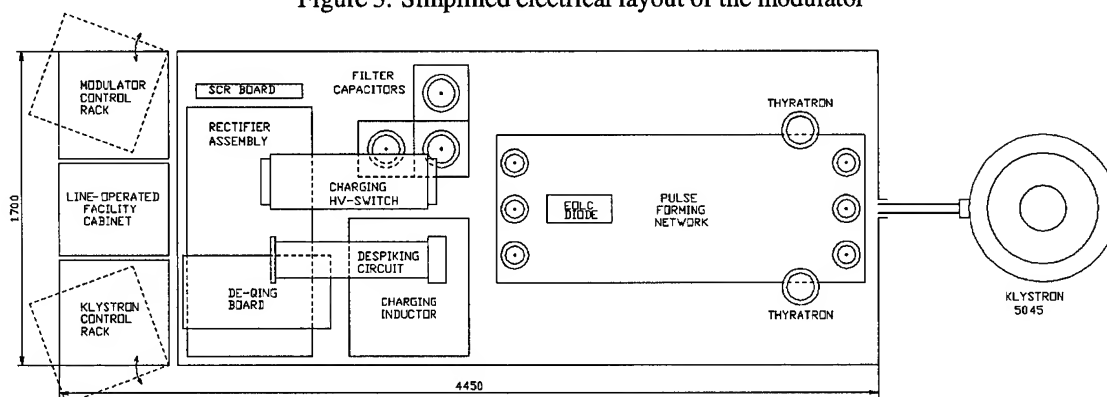


Figure 4. Position of the main components in the cabinet (sizes are in mm).

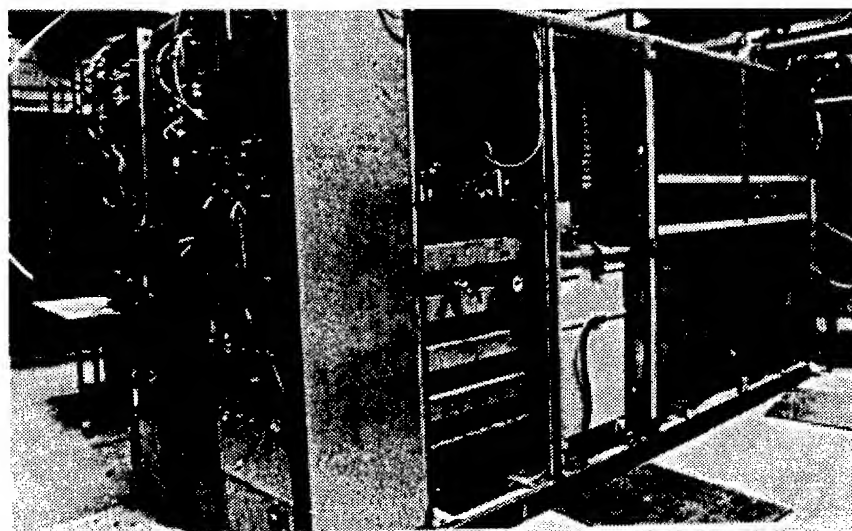


Figure 5. View of the modulator

High Voltage Nanosecond Generators For SIBERIA-2

A. Kadnikov, Kurchatov Institute, 123182 Moscow, Russia

V. Deviatilov, V. Korchuganov, Yu. Matveev and D. Shvedov, Budker Institute of Nuclear Physics, 630090 Novosibirsk, Russia

A single turn injection scheme with two kickers and one septum is used for injection into booster (SIBERIA-1 storage ring) and into main ring (SIBERIA-2). One kicker and one septum are used for extraction from SIBERIA-1 into transport line to main ring. The fast kickers generate electromagnetic pulses with rise and down time of 3 ns and flat top of 15 ns duration. The high voltage pulse generators with double coaxial forming lines and three electrode nitrogen filled spark gaps are intended for linac electron gun and fast kickers supply. The output pulses are up to 60 kV in amplitude. A root-mean-square time spread of the moments when the signal comes to the kicker plates is 0.7-0.8 ns. The experimental results of operation of the generators obtained while commissioning SIBERIA-2 are presented.

I. INTRODUCTION

The injection part of the SIBERIA-2 consists of 80 MeV electron linear accelerator, a 450 MeV booster storage ring SIBERIA-1 and two electron transfer lines - TL-1 and TL-2[1]. The single turn injection scheme uses fast kickers for injection into booster and from booster to main ring [2]. In November - December of 1992 the linac and SIBERIA-1 were commissioned and now the work is continued with the 450 MeV electron in SIBERIA-1. SIBERIA-1 operates in single bunch mode and the stored current is supposed to be 100 mA. The 450 MeV beam has the energy spread $\sigma_E/E = 3.9 \times 10^{-4}$, the bunch length is $\sigma_s = 30$ cm and its horizontal

emittance is $\epsilon = 8.6 \times 10^{-5}$ cm-rad. In July 1994 the 450 MeV electron bunch was extracted from SIBERIA-1 and conducted through transfer line TL-2. In December 1994 SIBERIA-2 were commissioned and we have got first turn of electron beam. February 1995 - there were about one thousand turns. And on April 17 there was first beam in storage ring with life time about 2 hours.

The injection scheme requires pulses for kickers with 7 -- 60 kV amplitude (Table 1). For efficiency of injection a time stability about 1--2 ns of the moment when the pulse comes to the kicker is needed.

II. HIGH VOLTAGE NANOSECOND GENERATORS

The kickers are fed by the bipolar high voltage nanosecond generators and operate in a traveling wave mode. Figure 1 presents a scheme of the bipolar generator. The generator operates on the basis of the fast discharge of double forming lines which are connected to the kicker plates by SF₆ filled coaxial cables. The discharge is realized by gaseous spark gap (the so-called 3-electrode discharger). The discharge is initiated by a thyatron connected to the central electrodes of the dischargers. The discharge moment is tuned by varying the pressure (5 - 17 atmospheres) of nitrogen inside discharger. The pulse duration is equal to double propagation time of electromagnetic wave traveling along the forming line.

Table 1

Parameters of the kickers and the generators

Device	Forming line voltage, kV	Gap width, mm	Kicker plates voltage, kV	Rms time spread, ns	Notes
Linac electron gun	53	0.6 1.2	-40	0.6 - 1.3	Operates since June 2, 1992, 6.5 million pulses
SIBERIA-1 kicker	37	0.4 0.8	±6	0.6 - 1.5	Attenuation 6×
SIBERIA-1 prekicker	31	0.31 0.62	+4.6	0.7 - 1.2	Attenuation 6×, monopolar
SIBERIA-1 extraction kicker	38	0.42 0.85	±31	0.6 0.8	
SIBERIA-2 prekicker	52	0.6 1.2	±45	??	Commissioning and first testing
SIBERIA-2 kicker	52	0.6 1.2	±45	0.5 - 0.9	

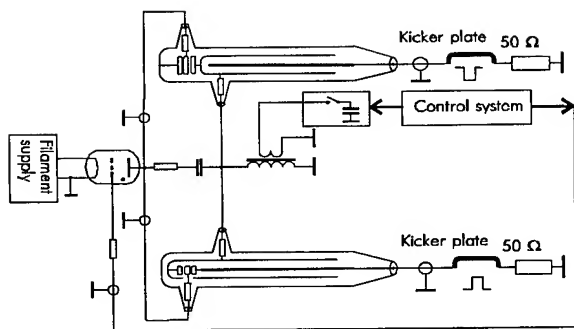


Figure 1: The simplified scheme of high voltage generator.

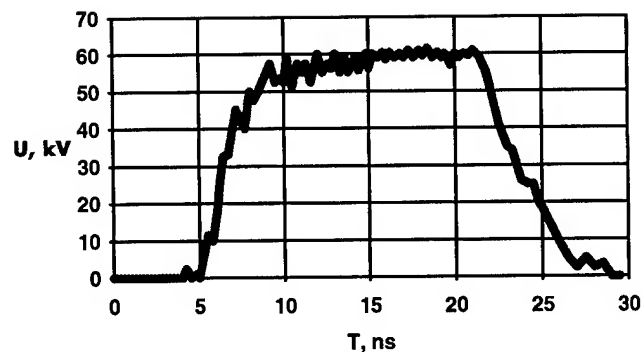


Figure 2: Oscillogram of output impulse 60 kV in amplitude.

In the case of high amplitude nanosecond pulse, the double forming line has a following advantages in comparison with the single forming line: it enables one to reduce twice the charging voltage and to simplify the scheme of the generator, because this makes it possible to give up invertors for producing pulses of opposite polarities. Polarity of output pulse depends on how gaps are connected up between forming lines.

The discharger's electrodes are made of duralumin, because this material provides appropriate training time of electrodes.

A pulsed hydrogen thyatron is used to start up spark gaps. All elements of generator, transport lines and kickers have wave impedance 50 Ohm. A pulsed transformer with epoxy isolation and transformation coefficient about 100 charges forming lines. Start up circuit is charged to one third of charging voltage due to capacity divider.

A low voltage (800 V) pulsed generator feeds a primary winding of the transformer. SF_6 gas fills cables and cable lead-ins at a pressure 5 atmospheres to increase electrical strength.

Resistance's and capacity's dividers (not shown in Figure 1) allow us measure voltage and monitor shape of pulses.

A control system uses electronics in CAMAC standard: microcomputer, ADC unit, etc. For time measurements we use time-digit converter unit with 0.6 ns per bit resolution. Software can measure average time delay, root-mean-square spread and changes of these values during long time.

III. EXPERIMENTAL RESULTS

An oscillogram of output positive pulse with amplitude 60 kV is shown in Figure 2. The spark gaps provide enough fast rise and down time of pulse. The rise time is about 3 ns, pulse's flat top is 13 ns, and down time is 5 ns.

A negative impulse has roughly the same characteristics. We have got 0.7--0.8 ns root-mean-square

time spread of the moment when the pulse comes to kicker plates after careful installation, tuning and 100,000 pulses training of the spark gaps. This is right when charging voltage is between 20 and 60 kV and spark gap width is in range 0.4 - 1.2 mm. In the case of lower voltages (for kicker and prekicker of SIBERIA-1) we should use 50 Ohm attenuators at the entrance of the forming lines. The results of examining of time stability of the generator during working shift are shown in figures 3, 4.

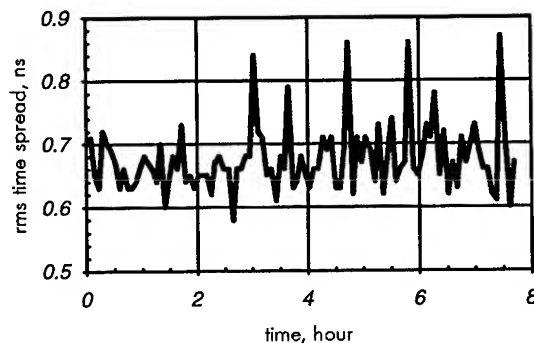


Figure 3: Rms time spread of the moment when pulse comes to kicker plates during working shift.

A stable thyatron operation needs stabilization of filament voltage not worse then 0.05% (decrease of 1% gives about 50 ns increase of output time).

With long operation time, erosion of electrodes occurs that leads to increase of gaps. First it results in increase time of gaps and then leads to decrease of operation's stability of generator. Figure 5 shows increasing of time delay of spark gaps due to wear and tear of electrodes.

Figure 6 shows the range of charging voltage with stable operation of extraction kicker generator. We use pressure of nitrogen in dischargers to obtain suitable time spread (rms not more than 1.5 ns) and number of electrical breakdowns in spark gaps (not more than 1%).

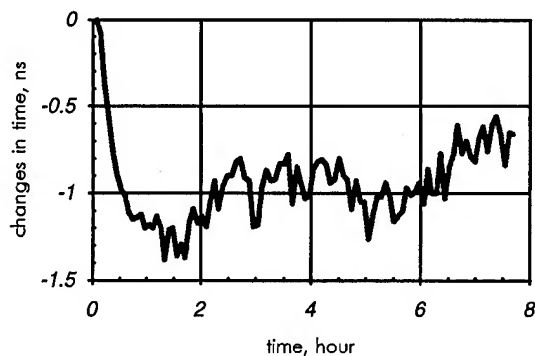


Figure 4: Changes of time when the pulse comes to kicker plates during working shift.

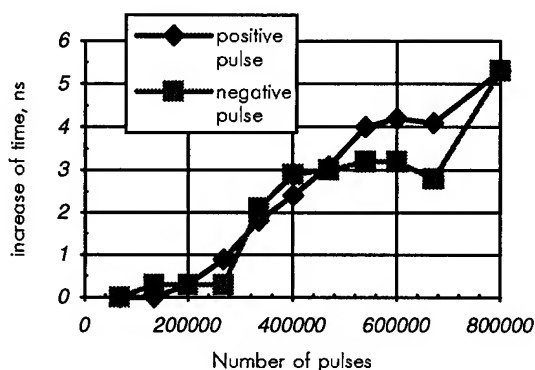


Figure 5: Time delay's increasing of spark gaps due to wear and tear of electrodes.

The generators have sufficient resources. The

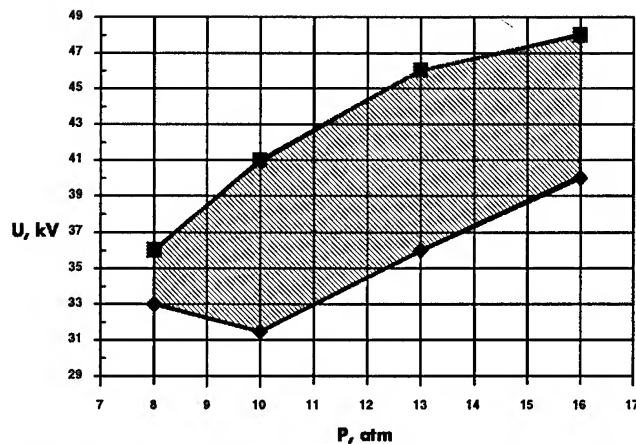


Figure 6: The range of the stable operation of the generator for extraction kicker of SIBERIA-1.

generator for linac electron gun operates during 250 working shifts (about 6.5 million pulses) without any repair.

The obtained results let us make a conclusion that these high voltage generators suit for reliable pulsed power supply of injection system for SIBERIA-2 storage ring.

For more detailed information on the subject, please contact us by the addresses given under the headline, or use e-mail: kadnikov@ksrs.msk.su.

IV. REFERENCES

- [1] V.V.Anashin et al, Nucl. Instr. and Meth. A282 (1989) 369 - 374
- [2] G.Erg et al. "Injection system for the SIBERIA-2 storage ring", Proceedings of the 1993 IEEE Particle Accelerator Conference, Washington, 1384 - 1386.

HIGH GRADIENT INSULATOR TECHNOLOGY FOR THE DIELECTRIC WALL ACCELERATOR*

S. Sampayan, G. Caporaso, B. Carder^{a)}, Y. Chen, C. Holmes, E. Lauer, and D. Trimble, Lawrence Livermore National Laboratory, Livermore, CA 94551 USA, J. Elizondo^{b)}, Tetra Corporation, 3701 Hawkins Street NE, Albuquerque NM, 87109 USA, M. Krogh, B. Rosenblum, Allied Signal Aerospace KCP, Kansas City, MO 64141 USA, C. Eichenberger and J. Fockler, Pulse Sciences Incorporated, 600 McCormick Avenue, San Leandro, CA, 94577 USA

Insulators composed of finely spaced alternating layers of dielectric and metal are thought to minimize secondary emission avalanche (SEA) growth. Most data to date was taken with small samples (order 10 cm² area) in the absence of an ion or electron beam. We have begun long pulse (>1 μ s) high voltage testing of small hard seal samples. Further, we have performed short pulse (20 ns) high voltage testing of moderate scale bonded samples (order 100 cm² area) in the presence of a 1 kA electron beam. Results thus far indicate a 1.0 to 4.0 increase in the breakdown electric field stress is possible with this technology.

I. INTRODUCTION

The dielectric wall accelerator (DWA) is a new accelerator concept particularly suited for short pulse (<50 ns) and high currents (>1 kA). As we previously presented, the pulsed acceleration field is developed by a series of asymmetric Blumleins (i.e., pulse forming lines) incorporated into the insulator structure (Fig. 1) [1,2].

The maximum gradient of this accelerator is defined by the dielectric strength of the wall dielectrics and the maximum surface flashover electric field capability of the interior vacuum interface in the acceleration region. Solid insulator materials can typically meet the 20-30 MV/m requirement; the interface at the vacuum wall typically cannot.

High electric fields are possible with properly angled insulators. These insulators, however, are generally unipolar and are not optimum in the simplest configuration of the DWA (i.e., Fig. 1, where the electric field in the dielectric is always applied to the insulators). Thus we select a straight wall insulator as optimum.

*Performed under the auspices of the US Department of Energy by Lawrence Livermore National Laboratory under contract No. W-7405-Eng-48.

a)Consultant.

b)Present affiliation: Voss Scientific, 416 Washington Street SE, Albuquerque, NM 87108.

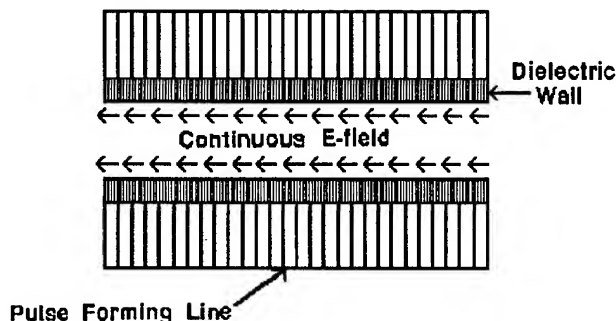


Figure 1. Dielectric Wall Accelerator (DWA).

Typical data for conventional straight wall vacuum insulators is shown in Figure 2. It is clear from this data, that to achieve the necessary gradients, alternate technologies should be investigated.

Improvements to existing technology can be made based on an understanding of the failure process. The most simplified vacuum surface breakdown model suggests that electrons originating from the cathode-insulator junction are responsible for initiating the failure [3]. When these electrons are intercepted by the insulator surface, additional electrons,

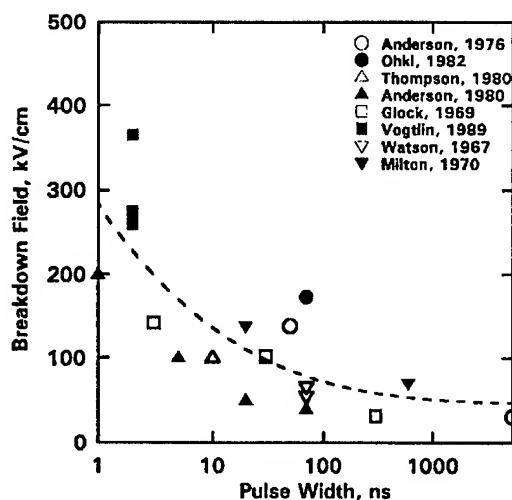


Figure 2. Breakdown thresholds for 0° vacuum insulators.

based on the secondary emission coefficient, are liberated. This effect leaves a net positive charge on the insulator surface, attracting more electrons and leading to escalation of the effect or the so-called secondary emission avalanche breakdown (SEA).

It has been shown that full evolution of the streamer discharge occurs within a fraction of a millimeter [4]. Placing slightly protruding metallic structures spaced at an equivalent interval is believed to interrupt the SEA process and allow the insulator to achieve higher gradients before failure [5,6]. This is the high gradient insulator concept being developed. When the DWA is combined with this high gradient vacuum insulator technology, short-pulse-high-gradients of greater than 20-30 MV/m may be possible.

II. APPARATUS

Several small sample (approximately 2.5 cm diameter by 0.5 cm thick) insulators were fabricated. The first was fabricated from interleaved layers of 0.064 mm stainless steel and 0.127 mm polycarbonate film. Two other small hard seal samples were fabricated from alumina and fused silica. The alumina sample was fabricated with 0.28 mm thick material and the fused silica sample was fabricated with 0.25 mm thick material. The interleaved metallic layers were formed by depositing gold on each planar insulator surface by a sputtering technique and then bonding the stacked layers by heating while applying pressure. Concentricity was ensured by performing a finish grinding operation.

Small sample testing was performed in a turbo-molecular pumped, stainless-steel chamber at approximately 10^{-6} T. High voltage was developed with a 10 J "mini-Marx". The Marx developed a pulsed voltage of approximately 1.3 μ s, FWHM (3 μ s, base-to-base) and up to 250 kV amplitude across the sample. Failure of the insulator was determined by a prompt increase in Marx current and a corresponding prompt collapse in the voltage across the sample.

Dimensions of the larger high gradient insulator were 14.5 cm I.D. by 22.1 cm O.D. by 2 cm length. The structure consisted of multiple kapton sheets layered and thermally bonded to form a single 45° stepped conic section on the interior of the stack between each stainless steel grading ring. Spacing between each grading ring was 1-2 mm. Supporting stainless steel flanges, bonded to each end of the insulator structure, provided mechanical attachment to the remaining structure.

Testing the larger, high gradient insulator structure in the presence of an electron beam was performed with a 1 MV, 20 ns, oil insulated Blumlein pulse generator. A 2 cm

diameter velvet emitter, bonded to an aluminum cathode support plate, was used to generate the electron beam. Unwanted emission in the area immediately next to the emitter was suppressed by applying a hard anodized coating.

Transport between the emitter and graphite collector was done by placing highly transparent (96%) tungsten meshes in the beamline. These meshes locally short out the radial component of the electric field. Convergence then results from the self-magnetic field of the beam. Optimized placement of the meshes was determined using GYMNOS [7] and full transport required three meshes; one at the anode plane and two spaced at 12 cm and 21 cm from the cathode.

II. EXPERIMENTAL RESULTS AND DISCUSSION

Small sample high voltage testing results are tabulated in Table I. To obtain a particular data set, the insulators were subjected to several low voltage conditioning pulses. The voltage was then increased a small amount incrementally until breakdown occurred. Voltage was then reduced for several shots and then incrementally increased again until a consistent value resulted.

From this method, we measured an ultimate flashover strength for the small samples of approximately 125 kV/cm for the alumina substrate, 175 kV/cm for the fused silica substrate and 200 kV/cm for the polycarbonate substrate for a

Table I. Small sample tests results

SUBSTRATE	BREAKDOWN FIELD
Polycarbonate	200 kV/cm
Fused Silica	175 ^{a)}
Alumina	125

a) Type III anodized coating on electrodes

pulse width of 1.3 μ s, FWHM. The trend in conventional technology (Fig. 2) for 0° insulators indicates a breakdown threshold of approximately 50 kV/cm. Thus, there was a net increase in the performance with these insulators over conventional technology of 2.5, 3.5, and 4.0, respectively.

A similar scenario was used to determine the flashover strength of the larger high gradient insulator with and without an electron emitter installed. A total of 125 pulses at different voltages without the emitter installed were taken; 35 additional shots with the 2 cm diameter velvet emitter in place were also taken. These two tests were performed to de-

termine the effects of an emitter and electron beam in the vicinity of the insulator.

A slightly different manifestation of failure was observed in these tests (Fig. 3). For fields above 190 kV/cm, we observed an increased collector current up to about 210 kV/cm when we observed late-time, fast transient currents and a decreased voltage pulse. The normal signature of an insulator failure, i.e., prompt and complete collapse of the voltage, was not observed until about 250 kV/cm. These observations lead us to believe that the primary failure mechanism was resulting from strong explosive emission occurring in the vacuum gap.

Further manifestations of this effect is shown in Figure 4. Below about 210 kV/cm, we observed currents consistent with the GYMNOS predictions. Above an electric field of 210 kV/cm, we began to observe a strong trend away from this predicted current; 1.6 kA compared with the predicted 1.1 kA at 250 kV/cm. We observed this ultimate threshold

to be consistent with breakdown data taken in the absence of an electron beam.

Further physical evidence of this failure mode was observed upon opening the structure; we observed explosive emission sites, i.e. pitting on the stainless steel cathode structure supporting the insulator.

Further testing of this structure is planned. In these upcoming experiments, we intend to test the effects of explosive emission suppression coatings on the entire cathode electrode surface and the metallic gradient rings within the high gradient insulator.

IV. SUMMARY

We began testing a new high gradient insulator technology. The insulator consists of finely spaced metal electrodes interleaved with the insulator substrate. The spacing of these metal electrodes is on the order of a streamer formation distance. For small samples, we observed significant improvement over conventional 0° insulators subjected to long pulse fields. For moderate size insulators in the presence of an electron beam, we observed slightly reduced improvement but begin to observe the effects of explosive emission from the cathode surface.

V. REFERENCES

- [1] G. Caporaso, presented at the 1994 Joint Topical Course "Frontiers of Accelerator Technology", Maui, Hawaii, 1994.
- [2] S. Sampayan, et. al., presented at the 1995 Particle Accelerator Conference on High Energy Accelerators, Dallas, Texas, 1995.
- [3] H. Miller, in Proceedings of 1992 15th International Symposium on Discharges and Electrical Insulation in Vacuum (Vde-Verlag Gmbh, Berlin, 1992), pp. 165-174.
- [4] W. Glock and S. Linke, Laboratory of Plasma Studies, Cornell University Report No. LPS 24, 1969.
- [5] E. Gray, Private Communication.
- [6] J. Elizondo and A. Rodriguez, in Proceedings of 1992 15th International Symposium on Discharges and Electrical Insulation in Vacuum (Vde-Verlag Gmbh, Berlin, 1992), pp. 198-202.
- [7] D. Hewett and J. Larson, Lawrence Livermore National Laboratory Report No. UCRL-ID-110499, 1992.

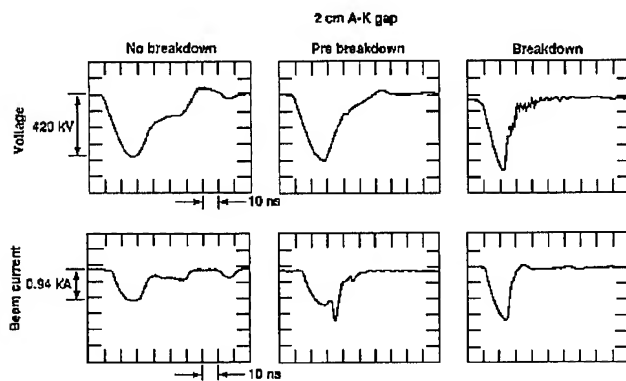


Figure 3. Typical pre-breakdown and closure pulses

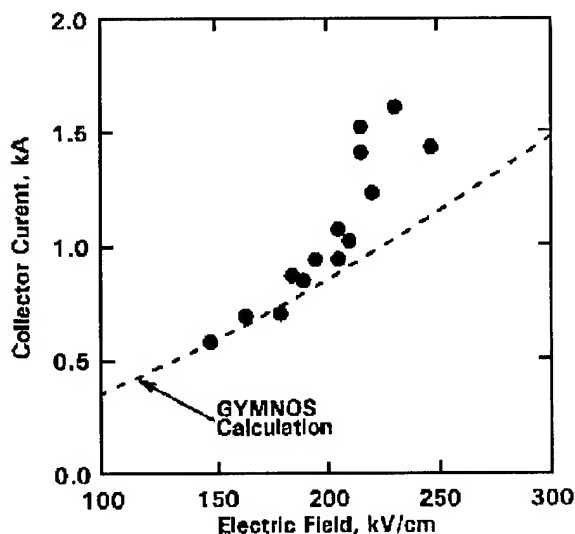


Figure 4. Comparison of predicted and measured currents.

STATUS OF THE FIRST STAGE OF LINEAR INDUCTION ACCELERATOR SILUND-21

A.A. Fateev, G.V. Dolbilov, I.I. Golubev, I.N. Ivanov, V.V. Kosukhin, N.I. Lebedev,
V.A. Petrov, V.N. Razuvaikin, V.S. Shvetsov, M.V. Yurkov
Joint Institute for Nuclear Research, 141980 Dubna, Moscow Region, Russia

In the present paper we report on status of the project of SILUND-21 LIA which is under development at JINR [1]. SILUND-21 will provide electron beams with the energy up to 10 MeV, peak current ~ 1 kA and pulse duration 50 – 70 ns. SILUND-21 will serve as a base of experimental facility to study microwave electronics, FEL technique and two-beam acceleration. It is assumed also to perform experiments to adopt the FEL bunching technique for generation of the CLIC driving beam.

I. Introduction

The SILUND-21 linear induction accelerator will serve as a base of experimental facility to study microwave electronics, FEL technique and two-beam acceleration. We plan also to perform experiments to adopt the FEL bunching technique for generation of the CLIC driving beam [2]. In this case the driving beam is produced in an FEL amplifier constructed on the base of linear induction accelerator (LIA). One of the main problems to realize such a way of the CLIC driving beam generation is that of LIA. To achieve the required parameters, LIA should provide electron beam with the energy about of 10 MeV and peak current about of 1 – 2 kA at a high repetition rate. We plan also to study the problems of the beam bunching preservation at further acceleration of the driving beam.

Linear induction accelerator SILUND-21 is constructed using the equipment of LUEK-20 accelerator developed for experimental investigations of the collective method of acceleration [3]. It is assumed to upgrade the main pieces of the LUEK-20 equipment using the experience of construction and operation of SILUND, SILUND-II, SILUND-20 and LUEK-20 linear induction accelerators developed at JINR [3] - [7].

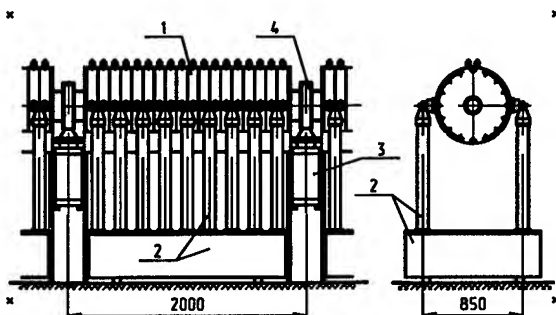


Figure 1. Accelerating module. Here: (1) – induction section; (2) – modulator; (3) – sputter-ion pump.

II. Accelerator design

A. Accelerating modules

SILUND-21 accelerator consists of seven accelerating modules. Each module provides 1.5 MV accelerating voltage at 1 kA beam load. The general layout of the accelerating module is presented in Fig.1. Induction section (1) consists of 36 permalloy cores. The core exciting windings are commutated in parallel and the input impedance of the section is equal to 0.5Ω at nominal beam load. Pulses of accelerating voltage with 42 kV amplitude and 50 – 70 ns duration are formed by modulator (2) with 0.5Ω internal resistance. TG11-2500/50 hydrogen thyatron (2500 A, 50 kV), which is used as a commutator, does not provide commutation of the required level of the peak power, so nonlinear power compression schemes are used to increase the peak power.

The modulator scheme (see Fig.2) is based on the application of the nonlinear power compression technique. Its key element is nonlinear double forming line (NDFL) which consists of 18 double forming lines evenly spaced along the accelerating module. Hydrogen thyatron T operates in a pulsed mode with 3 μ s pulse duration and provides the following parameters: $U = 30$ kV and $I = 10$ kA. Permalloy reactor L and transformer Tr fulfil the roles of ferromagnetic switches. Transformer Tr is composed of three transformers with the transfer factor equal to $2/3$ which are placed along the accelerating module. NDFL is charged within the time period 1 μ s and then produces high-voltage pulse ($U = 42$ kV, $I = 84$ kA, pulse duration 50 – 70 ns, rise time about of 5 ns).

The voltage of six inductors (4), commutated in a consecutive order, is fed to the accelerating gap (2) which is formed by cone diaphragm (1) (see Fig.3). The amplitude of accelerating voltage at each of six accelerating gaps of the accelerating section is equal to 250 kV.

Focusing of the electron beam is provided by guiding field of solenoid. The solenoid winding is sectional and the number of the sections is equal to the number of permalloy cores. Parameters

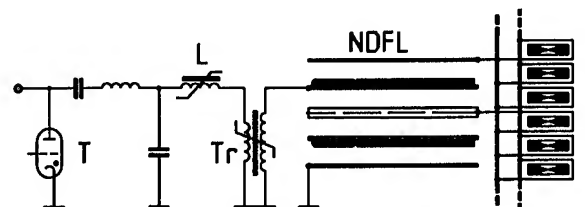


Figure 2. Modulator scheme. Here: T – hydrogen thyatron; L – peralloy reactor; Tr – peralloy transformer; nonlinear double forming line.

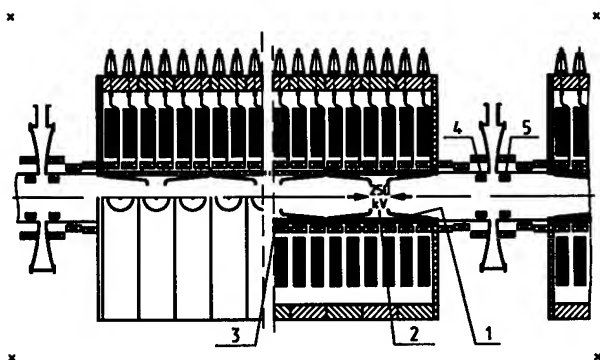


Figure 3. Accelerating section. Here: (1) – diaphragm; (2) – accelerating gap; (3) – magnetic lens; (4) – Rogowsky coil; (5) – beam position monitor.

of the solenoid power supply, developed for accelerator LUEK-20, allow one to provide the guiding magnetic field with the amplitude up to 1.4 T and pulse duration about of 0.8 ms.

B. Injection module

The first accelerating module differs from all the other modules and is combined with the electron source. Accelerating voltage of the electron source is equal to 500 kV – 1/3 of the total accelerating voltage of the module (see Fig.4) The choice of the electron source type depends on the mode of the accelerator operation. Our experience of work at the present accelerators has shown that at a low repetition rate (about of several cycles per second) it is more preferable to use the electron gun with graphite cathode (1) and gridded anode (2) [8](see Fig.4a). The value of magnetic field at the cathode is controlled by magnetic lens (3) to minimize the value of the electron beam emittance. At a high repetition rate (about of 50 cycles per second), we assume to use a plasma electron source without anode grid (see Fig.4b) [9], [?]. Ceramic tube (4) is destined to inject the plasma into the diode gap.

The both types of electron sources have demonstrated a high level of reliability and good output parameters during their operation at the accelerators SILUND, SILUND-II and SILUND-20.

III. Electron beam parameters

SILUND-21 will provide the electron beam with the following parameters: energy about of 10 MeV, peak current ~ 1 kA and pulse duration $\sim 50 - 70$ ns. Instant energy spread of electrons in the beam will be about of a fraction of per cent and the energy spread averaged over pulse duration will be $\sim 2 - 3$ %. At the accelerator exit we expect to obtain the values of the normalized emittance to be equal to 0.4π cm-rad, 0.15π cm-rad and 0.1π cm-rad at 90 %, 70 % and 50 % of the nominal value of the beam current.

IV. Present status

Three of the total number of seven accelerating modules are mounted in the site of the SILUND-21 accelerator. Now we

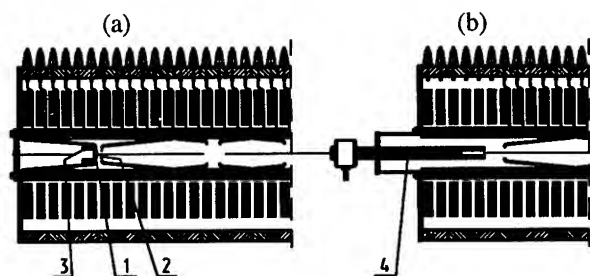


Figure 4. Injection section. Here: (1) – graphite cathode; (2) – gridded anode; (3) – magnetic lens; (4) – ceramic tube.

perform measurement of the electron beam parameters at the exit of the second accelerating module.

References

- [1] G.V. Dolbilov et al., Proceedings of the EPAC94 Conference (London, 1994), V.1, p. 748
- [2] B. Autin et al., preprint CERN/PS 94-16 (LP), CERN, Geneva, 1994
- [3] V.S. Aleksandrov et al., Proceedings of the XIII International Conference on High Energy Accelerators", Novosibirsk, August 1986, vol.1, pp. 241-243
- [4] G.V. Dolbilov et al., preprint JINR-9-83-307, Dubna, 1983
- [5] B.G. Gorinov et al., preprint JINR-9-12148, Dubna, 1979
- [6] L.S. Barabash et al., Proceedings IX International Conference on High Energy Accelerators. Stanford, USA, 1974, p. 318
- [7] G.V. Dolbilov, V.A. Petrov, A.A. Fateev, preprint JINR-P9-86-290, Dubna, 1986
- [8] G.V. Dolbilov et al., preprint JINR-9-89-154, Dubna, 1989
- [9] G.V. Dolbilov et al., preprint JINR-P9-82-70, Dubna, 1982
- [10] V.S. Aleksandrov et al., JINR publication P9-83-613, Dubna, 1983, p.54-60

EMIR-M INSTALLATION IN THE MODE OF OPERATION WITH PLASMA OPENING SWITCH

V.P. Kovalev, V.M. Korepanov, B.N. Lavrent'ev, R.N. Munasyrov and B.A. Filatov

Russian Federal Nuclear Center – Institute of Technical Physics
(RFNC – VNIITPh)

P.O. Box 245, Snizhinsk (Chelyabinsk-70), 456770, Russia

Abstract

The EMIR-M generator is modified to perform a series of experiments to explore the Plasma Opening Switch (POS). Results of the first experiments with POS are described. EMIR-M operates in two different modes: first one, with Marx generator voltage of 0.95 MV and current of 300 kA; second one, 1.42 MV and 460 kA, correspondently. Vacuum diode and inductance (short-circuit diode) was used as a load. PIN-diodes and TLD detectors are used for radiation parameters measurements. The results have been obtained:

- voltage gain of 2.6;
- maximum conduction time of 2.3 μ s;

Current rise rate up to $3 \cdot 10^{13}$ A/s with front duration of $10 \div 13$ ns has been measured.

I. INTRODUCTION

During the past 10 years nano- and microseconds POS has been investigated at VNIITPh. The investigations are the logical continuation of the works with inductive pulsed power accelerators based on fuse used as an opening switch. Using POS has a significant advantage over fuse because of the productivity increasing, size reduction, and ecological cleanliness.

POS investigations at VNIITPh showed real possibility of POS using in existing and developing installations.

The paper presents the first stage of POS investigations for power pulse forming on EMIR-M.

Figure 1 shows the geometry of experiments.

POS is located in the gap of the EMIR-M diode container. Experiments were conducted using central electrode (cathode) diameter of 40 and 60 mm. The cathode-anode flange of container distance D was taken in two cases: first one: short-circuit regime, and second one, in the range of 10-30 mm. In the first case the experiments with inductance load were conducted with the parameters: 0.26 μ H and correspondent cathode diameter of 60 mm; and 0.32 μ H and correspondent cathode diameter of 40 mm. Second case is suitable for vacuum diode regime. Plasma injection unit and plasma guns unit (PGU) is located on the steel ring (Figure 1). Up to 40 guns could be located at the ring. Ring design permits the radial shift of the guns and their hermetically sealed location. POS consists from PGU and cathode central electrode. From 10 to 15 plasma guns charged from individual high-voltage generator are the sources of plasma in the experiments. Usual coaxial cable-type guns are used.

Electrical circuit of the experiment is shown in Figure 2.

Plasma formed by plasma guns is injected from anode to the POS region. After fixed time of delay the Marx generator starts

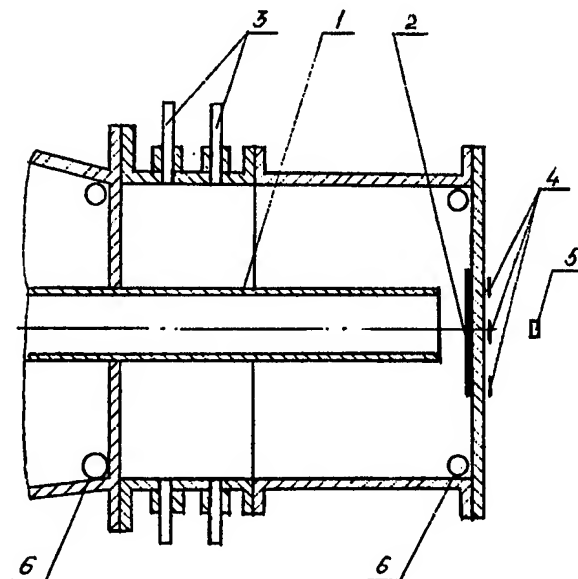


Figure 1. EMIR-M POS configuration in the switch region: 1 - cathode, 2 - anode, 3 - cable plasma guns, 4 - TLD dosimeters, 5 - PIN-diode, 6 - Rogovsky coil.

to discharge. Current flows through the plasma in anode-cathode gap.

The voltage and current has been diagnosed using standard techniques: capacity voltage divider and Rogovsky coils (see Figure 2). Rogovsky coils have shielding design and are located in the gaps of anode container. PIN-diodes are used for bremsstrahlung radiation measurement in diode regime. TLDs are used for radiation dose measurement. Seven dosimeters are located at 1 cm distance from the anode surface (Figure 1).

II. EXPERIMENTAL RESULTS

Experiments were performed in two different regimes of installation's work. First one, Marx voltage of 0.95 MV and current amplitude of 300 kA. Total impedance of circuit is 2.85 Ohm. Plasma is created by 10 guns with correspondent currents of $4 \div 11$ kA and period of 3.5 μ s in individual gun. Marx generator operates with delay of $3.5 \div 10 \mu$ s. Second one, Marx voltage of 1.42 MV and current amplitude of 460 kA; total impedance of circuit is 2.4 Ohm. Plasma guns are the same as using in the first regime.

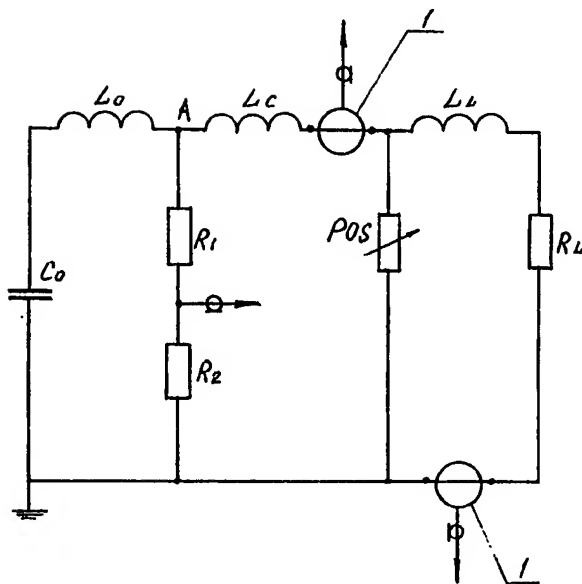


Figure 2. Discharge circuit: L_0 - Marx generator inductance, C_0 - Marx generator capacitance, L_c - cathode inductance, (R_1 - R_2) - voltage divider, L_d - load inductance, R_L - load resistance, 1 - Rogowski coil.

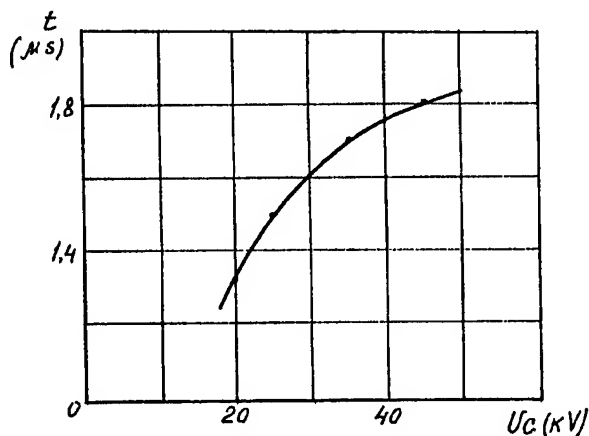


Figure 3. POS conduction time as function of plasma gun voltage.

The next problems were solved in the investigation:

- method search for conduction time increasing t_c ;
- maximum current rise rate obtaining;
- maximum voltage gain using POS obtaining.

Conduction time increasing allow to transmit the Marx generator energy into the load with increasing period of the generator discharge. Experimental results show the dependence t_c versus charged voltage of plasma guns generator. It could be shown that this allows to increase t_c up to $1.8\mu s$ (Figure 3). The dependence t_c versus delay t_d between the time of the guns generator operation and the time of Marx generator operation has been obtained. The unstable regime of work with the increasing of t_d has been observed. This unstable regime could be connected with the unstable processes in plasma (ion-acoustic instability development).

In regime 1 the maximum current rise rate in inductance load

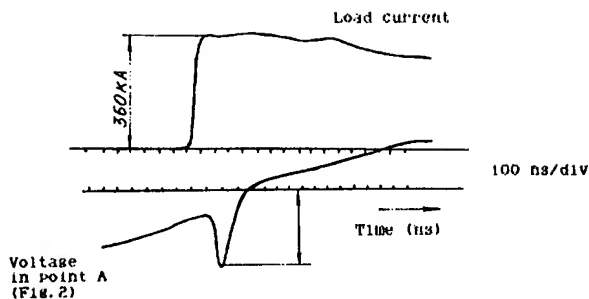


Figure 4. Load current and voltage waveforms measured at EMIR-M (Inductance Load).

of $\dot{I}_l \approx 10^{13}$ A/s was obtained for POS conduction time of $2\mu s$, guns generator voltage of 40 kV and $\tau_d = 3.5\mu s$. Current rise time in load (t_f) reaches 25 ns and current amplitude 270 kA (about 90% of maximum current amplitude). In the case of anode-cathode (A-C) distance of 30 mm the $\dot{I}_l \approx 7 \cdot 10^{12}$ A/s and $t_f = 25$ ns has been obtained. POS gap increasing up to 130 mm allows to obtain $t_f \approx 10$ ns for A-C distance of 30 mm and diode voltage of 3 MV.

In regime 2 the maximum current rise rate in inductance load of $\dot{I}_l \approx 2.8 \cdot 10^{13}$ A/s with $t_f \approx 13$ ns was obtained for POS gap of 50 mm and cathode diameter of 60 mm (Figure 4).

$\dot{I}_l \approx 1.8 \cdot 10^{13}$ A/s with $t_f \approx 13$ ns has been obtained in experiments with A-C distance of 30 mm. Cathode with diameter of 40 mm and 60 mm is used in the experiments. Greater voltage on POS $U_{POS} = 2.5$ MV has been obtained with cathode diameter $d_c = 40$ mm than with $d_c = 60$ mm (other parameters are identical). It is interesting to note that cathode was fused lengthwise of 70 cm on the distance of 55 cm from the plate of plasma guns location to the diode direction and 15 cm to the opposite direction. For the cathode diameter of 40 mm "fusing" was located on the distance of 65 cm from the guns plate to the load and during 25 cm in opposite direction. These differences could be explained by electrodynamic force action to the load. Average value of axial velocity reaches $30 \div 40$ cm/ μs . Radiational parameters are diagnosed by PIN-diodes and TLD detectors. Radiational dose achieved $8 \div 25$ kRads with the pulse width of $100 \div 150$ ns.

III. CONCLUSION

A considerable volume of research has been carried out that showed the principal possibility of EMIR-M operation using POS:

- voltage gain of 2.6 was reached;
- maximum conduction time $t_f = 2.3\mu s$ in regime 1 was obtained;
- current rise rate up to $3 \cdot 10^{13}$ A/s with front duration $10 \div 13$ ns was obtained.

With the goal of further improving of EMIR-M stable operation some experiments using POS are planned.

References

- [1] Diyankov, V.S., et al., "Device EMIR-M – generator of impulse electron beams, bremsstrahlung and electromagnetic fields," Proceedings of the 10th International Conference on High Power Particle Beams, San Diego, CA, 1994, p.371.

NEW DEVELOPMENTS IN NIOBIUM TITANIUM SUPERCONDUCTORS

D. C. Larbalestier and P. J. Lee

Applied Superconductivity Center, University Of Wisconsin-Madison, Madison, WI 53706 USA

After a very active period of Niobium Titanium superconductor strand development in the mid 1980s, progress slowed as the SSC scaled up for production and emphasis moved towards guaranteeing, rather than enhancing performance. However, this period also produced several advances in the understanding of flux pinning in Niobium Titanium alloys and in the fabrication of composites containing artificial pinning centers (APC). This paper reviews some of this progress and attempts to assess its implications for future accelerator conductors.

I. STATE OF THE ART

A. Overview of the development of properties with time

The High Energy Physics (HEP) accelerator community has been the most consistent and effective driving force behind the major advances that useful superconductors have achieved in the last 30 years. The principal material advanced is Niobium Titanium of composition Nb-47wt.%Ti. There are at least three major reasons why the HEP community has played such a large role in superconducting wire development: One is that the accelerator community knows that increased magnet performance is always driven by an ever increasing critical current density (J_c), two the broader HEP community has stuck with superconductor development, even when there was not an immediate big accelerator project and three that there has been a commitment from key figures in the community to encourage productive links between the basic science of flux pinning in superconductors, the accelerator magnet community and the superconducting industry. In a series of workshops sponsored by the US Department of Energy, Division of High Energy Physics, held at least annually from 1983 until the present day, a community of US researchers, users and manufacturers have catalyzed each other in a continued attempt to wrest more performance from Nb-Ti conductors. Figure 1 collects information on some of the advances in performance of representative strands of this material. This progress is impressive. Figure 1 contains information on present and future applications of Nb-Ti. The early large scale US procurements of conductors for Mirror Fusion Test Facility (MFTF) and for the Fermilab Tevatron in about 1980 developed the industry. Production of hundreds of billets generated genuine production statistics and also allowed researchers like ourselves to ask questions about which fabrication variables were really important in controlling the then rather variable, properties. The Fermilab J_c (5T, 4.2 K)

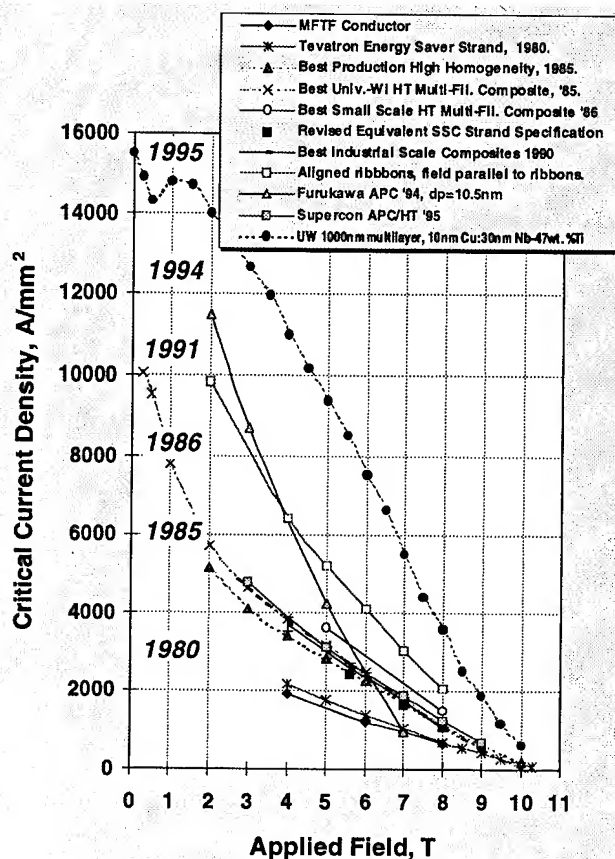


Figure 1 Advances in the Critical Current Density of Nb-Ti Based Superconductors. All data are at 4.2K. Key: MultiFil = Multifilamentary strand, HT = Precipitation Heat Treated, APC = Artificial Pinning Center (aligned ribbons ref. [1], Furukawa APC ref. [2], Supercon APC/HT ref.[3]).

specification of 1800 A/mm² was less a carefully thought out attempt to determine what the material was capable of than an attempt to challenge production to a consistent, deliverable level. Its realization required simultaneous work on the raw alloy, the copper, the extrusion process, large rod drawing and fine wire drawing and the heat treatment capabilities of a still small industry. Without a firm idea of what the empirical optimization processes employed by industry really were doing to the microstructure and thus to the flux pinning which controls J_c , it is not surprising that there was eventually a considerable extra margin of performance to be found in the material, the exploitation of which in the mid to late 1980s led to the SSC benchmark 50% larger of about 2750 A/mm², while at the same time diminishing the filament size from ~10 to 6 μ m.

Underpinning the big jump from 1980 to 1985 was the discovery of the large role played by uncontrolled microscale chemical inhomogeneities in the raw Nb-Ti alloy[4]. When, with a great deal of help from collaborations with R. M Scanlan (LBL) and W. K. McDonald at Teledyne Wah Chang Albany (TWCA) [5], the first high homogeneity Nb-Ti alloy was delivered, it became almost immediately possible to get the 50% increase in performance in an industrial scale billet. This improvement was based on a sound understanding of the factors controlling the microstructure [6,7,8]. Further exploitation of this understanding on a laboratory scale led to large filament conductors which could achieve $\sim 3700 \text{ A/mm}^2$, although with larger filaments[9]. Since 1985-1986, engineering the very best laboratory scale properties into very long length (several km), very fine filament ($6 \mu\text{m}$ or even lesser diameters) cabled conductors has been the principal emphasis of the industry. This was triumphantly done in the latter stages of the SSC-CDG R&D program in a collaboration in which groups from the principal US industrial suppliers (IGC, OST, Supercon and TWCA) worked together with teams at principally BNL, Fermilab, LBL and the University of Wisconsin to characterize, understand and to devise engineering solutions that stood in the way of realizing the scientific control of microstructure that underpinned the industrial fabrication process (these results are reviewed in greater detail elsewhere[10]).

Two recent benchmarks significantly lift the potential of Nb-Ti alloys. One was a proof-of principle experiment conducted in our group [1], aimed at answering the question of whether Nb-Ti had absolutely run out of its capacity to develop any higher J_c . In this case we took an already very

high J_c sample and rolled it to a high aspect ratio so that the pinning microstructure (Figure 2) was highly aligned for one axis of the wire. J_c (5T) was raised from about 3500 to 5300 A/mm^2 without any degradation at higher fields. This proved that there was a greater potential in the material. The second aspect studied after 1985 was the question of whether a better array of pinning centers could be incorporated into Nb-Ti than was supplied by nature, even in the highly optimized process that had evolved in the early 1980s. Artificial pinning center (APC) arrays were first introduced by Dorofeev et al. [14] at the 1985 Magnet Technology Conference, just as the conventional process was reaching its full understanding. The best realization of this concept is by Matsumoto et al. [2] from Furukawa Electric Co., as indicated by the 1994 plot in Figure 1. This composite was the first and is still the only round wire to have broken the 4000 A/mm^2 (5T) barrier. This result is all the more impressive in that the wire clearly lacks a competitive high field performance (it crosses over with standard wires at $\sim 6 \text{ T}$), as we discuss further later in this paper. In fact recent APC multilayers [11] and [12] have shown that highly aligned pinning layers can produce $>10,000 \text{ A/mm}^2$, first at a similar expense to the high field J_c [11] and now without any compromise for the high field properties [12].

In the rest of this paper we briefly review some of the implications of these recent advances for new accelerator conductor possibilities, first briefly defining the difference between conventional and APC conductors.

B. Conventionally Processed Material

Virtually all material made up until now has been conventionally processed, where the term conventional means that the starting point is a Nb-Ti alloy which is sheathed in Cu, and after various compaction, extrusion and drawing processes is then heat treated multiple times within the $\alpha + \beta$ two phase field so as to produce a fine dispersion of α -Ti precipitates. These α -Ti precipitates (Figure 2) are the dominant flux pinning centers in conventional wire and their optimization is the goal of the complex fabrication procedures through which Nb-Ti composites are manufactured. Advanced accelerator strands optimized using such a process can today be expected to have critical current densities of the order of 2750- 3000 A/mm^2 at 5T, 4.2K and 1100-1400 A/mm^2 at 8T, 4.2K and to consist of 1000-4000 2.5-10 μm filaments of Nb- 47wt.%Ti alloy, each clad in a thin Nb diffusion barrier and assembled within a Cu matrix for stability (Figure 3). Inherent limitations of the conventional process are that α -Ti is the pinning center and that the quantity of pinning center is limited to 20-25 vol. % for Nb-47Ti by the thermodynamic phase stability of the Nb-Ti system. The shape of the pins is constrained to the ribbon-shaped pin morphology of Figure 2 by the plane strain

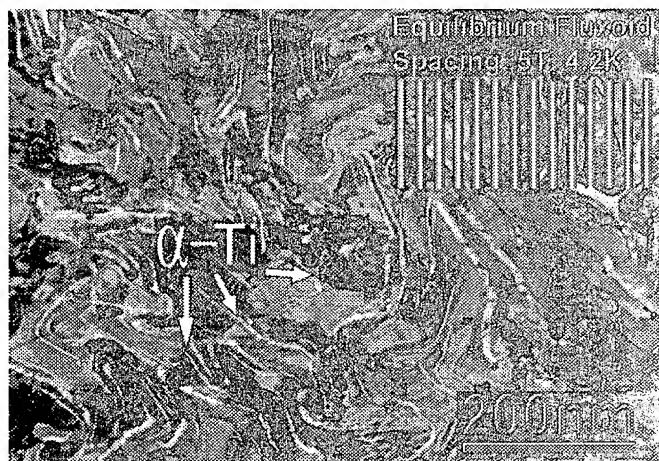


Figure 2 Typical Nb-47wt.%Ti high critical current microstructure (in transverse cross-section) showing the densely folded sheets of α -Ti pinning centers dispersed within the superconducting β -Nb-Ti matrix. Superimposed is a schematic illustration of the equilibrium fluxoid spacing and dimensions appropriate to Nb-47wt.%Ti at 5T, 4.2K.

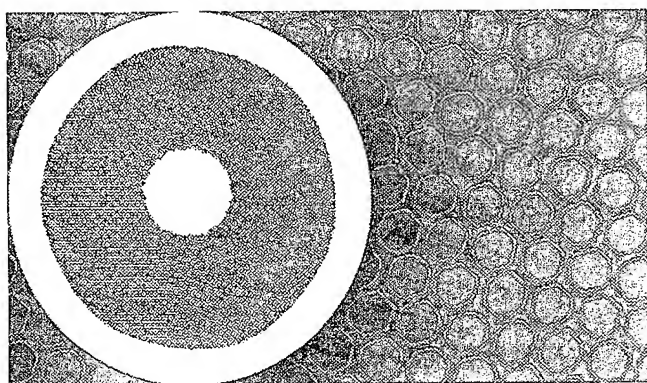


Figure 3 Cross-section of SSC-style multifilamentary superconducting strand at 26mm diameter superimposed on detail showing filaments and their diffusion barriers (fabricated by IGC as part of the SSC-CDG R&D program).

deformation dynamics of the body centered cubic β -Nb-Ti alloy. It is an amazing gift from nature that it is possible to produce two phase nanometer scale microstructures such as that seen in Figure 2 in complex many thousand filament composites such as that shown in Figure 3 and to have the piece length be several km. No wonder that competition with standard process Nb-Ti is so hard!

C. Artificial Pinning Centers (APC)

An alternative approach, first used by Dorofeev et al. [14], is to mechanically assemble the desired pinning structure in a composite at large size and then to reduce the structure to the dimensions of the fluxoid lattice by multiple extrusions and wire drawing. Such a process has great conceptual flexibility in the selection of pin, superconducting matrix, and pinning center geometry. One realization of such a composite is shown in Figure 4. The figure shows an important and common attribute of APC composites, namely that the final size nanostructure is not the idealized macrostructure that was assembled. In fact the final size nanostructure of APC composites is seldom explicitly studied and this is certainly one of the key drawbacks to much recent work on trying to understand why disappointing performance

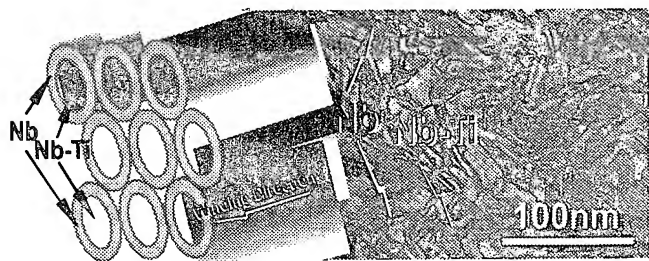


Figure 4 TEM image of original IGC APC at final size (in transverse cross-section) compared with the original "flux tube" design from the patent of Zeitlin et al. [13].

has so far been more common than outstanding performance. With these two concepts in mind we now turn to a wider discussion of the potential that the two processes offer for accelerator conductors.

II. OUTSTANDING ISSUES FOR FUTURE DEVELOPMENT

Three issues underlie the development of higher J_c : The first is that of understanding the flux pinning mechanism, the second is ensuring that the upper critical field H_{c2} is not degraded by the choice of pinning center and the third is making composites that are fabricable in useful lengths at appropriate cost. We shall aim our discussion towards these 3 points.

A. Flux-pinning.

The keys to our present understanding of flux-pinning came from careful correlation of superconducting property measurements to a quantitative microstructural description. This turns out to be particularly necessary for understanding the APC composites, many of which do not have well-understood nanostructures [15]. The Volume Flux Pinning Force, F_p ($F_p = J_c \times B$) is a particularly valuable optimization parameter. The microstructural and flux pinning basis of present optimization was described in the studies of Meingast, Lee and Larbalestier [16]. There are systematic changes in the shape of F_p as the wire and its precipitates are drawn to different sizes, as is shown in Figure 5. Two important issues of great practical relevance are that drawing the wire to its optimum size raises F_p at all fields and that the maximum in F_p occurs at about $0.5H_{c2}$. This behavior is unlike that of APC Nb-Ti and almost all other high field superconductors and is the reason why Nb-Ti magnets are effective so close to their upper critical field. Two other very important results [17] are that F_p and J_c are linearly dependent on the volume percentage of pinning material and that the H_{c2} of the optimized composite is the same as that of the homogeneous starting alloy. This result was extremely surprising when first obtained because the matrix of the superconductor is strongly depleted of Ti by the formation of about 20 vol.% of α -Ti. This occurs because the optimum size precipitates (Figure 2) are thinner than the superconducting coherence length, ξ . Thus there is a remixing of matrix and pin so far as T_c and H_{c2} are concerned. The enormously beneficial surprise of this result is that this remixing does not in any way lose the heterogeneous nanostructure required for optimum flux pinning. This principle has further important implications for the optimization of ternary Nb-Ti-Ta compositions and APC composites.

The question posed at the start of this section is whether flux pinning is well understood. At the conclusion of [16], the answer appeared to be a qualified yes. The microstructure and the flux pinning force had been directly correlated for the very highest J_c composite over more than an order of magnitude change in pin dimension and F_p . By correlating these two it was possible to deduce the thickness dependence of the elementary pinning force and to compare this to calculations of the vortex core interaction with the pin. These calculations correctly predicted the observed linear dependence of the elementary pinning force f_p on pin thickness up to a pin thickness of 2ξ , the vortex diameter. This was a considerable success. However, there was one flaw in the agreement.

The basis for flux pinning was long believed to be a core pinning interaction between the normal α -Ti precipitate and the normal vortex core. However, the α -Ti pins are so narrow that they are proximity coupled to the matrix, thus creating an important theoretical complication not treated in the simple models used to compute f_p . A second issue is that the thickness dependence of f_p was found to fit best in the limit of T tending to T_c , where the field dependence of F_p was not a good fit to the field dependence of the order parameter. This apparently small inconsistency was attacked by Cooley et al. [19] in the context of the shape of the $F_p(H)$ curves of APC conductors, virtually all of which exhibit a peak at low

fields, about $0.25H_{c2}$, rather than the $0.5 H_{c2}$ of the conventional materials (see Figure 1 and Figure 5). The proposal was made there without much justification that the pinning mechanism in the APC was a magnetic one, rather than a core pinning one. In fact it now seems that this may be the dominant mechanism in conventional Nb-Ti too [20,21]. A key prediction of the new model [21] is that optimum f_p occurs when the pin is decoupled from the matrix. The thickness of the pin and its electron mean free path determine this.

Within this model it is easy to rationalize the poor high field performance of most APC conductors: The reason is that their pins are pure Nb, which has a much longer coherence length than the alloyed α -Ti precipitate of the conventional process. The consequence of being optimized for thicker ($\sim 2-4 \xi$) pins is that their density is lower than for thinner pins, thus reducing the number density of vortex-pin interactions. Thus the low field pinning benefits strongly but the higher field suffers. The remedy is thus to dirty up the pin. Experimental tests of this hypothesis are now underway.

This is not quite the whole story since Figure 1 shows that the H_{c2} of the very good APC wire is $\sim 7.5T$, rather than the $10.5T$ of conventional wires. This is principally the consequence of the billet being experimental. Nb-47wt.%Ti was used for the matrix and Nb for the pins, meaning that the overall composition was very far from the optimum H_{c2} composition. As the correct choice of pinning center becomes better understood this aspect of the reduced high field performance will be designed out by making sure that the overall composition of matrix and pin is one with a high H_{c2} .

One final note about APC wires should be made. The most successful one practically has been the jellyroll design of Supercon that uses co-wound sheets of pure Nb and Ti. This technique produces a strand that is claimed to be cost competitive with conventionally made material. Both dipole and MRI magnets have been made with the design. The properties are very similar to conventional Nb-Ti but do not exceed the normal material. At this stage the nanostructure produced in the wires is not very clear.

B. Upper Critical Field.

A contour plot of H_{c2} at 2K for alloys in the ternary Nb-Ti-Ta system is shown in Figure 6. Ta and Nb are mutually soluble, similar chemically and mechanically and H_{c2} ($T < 4.2K$) is greater in the ternary than in the binary. As indicated by the figure, $H_{c2}(2 K)$ can be increased from a maximum of 14.25 to $15.5T$. These data indicate the prime reason for using Nb-Ti-Ta. In most other respects except one, the alloy processes well and can be used to replace the binary alloy when $1.8-2 K$ operation is required. So far at least 4

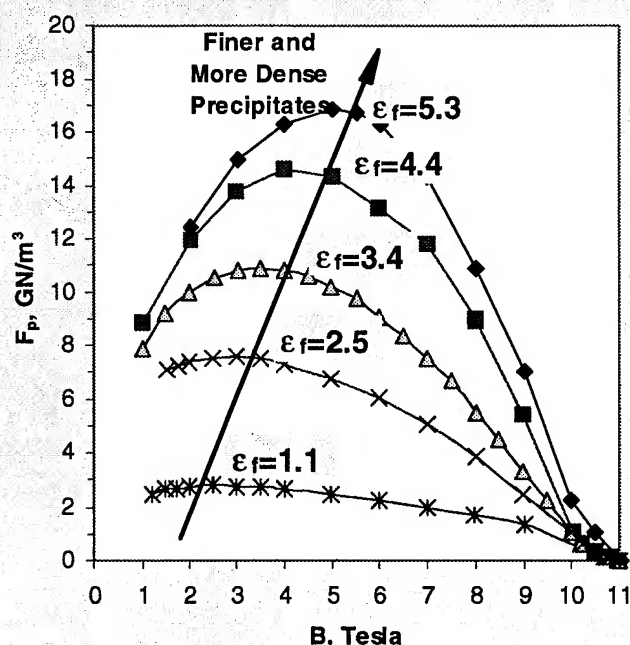


Figure 5 For conventionally processed Nb-Ti the bulk pinning force increases in magnitude with drawing strain after the last heat treatment. The increase occurs at all fields as the precipitate size and spacing are reduced to less than a coherence length in thickness (see Figure 2) (data from [18]).

fairly large billets have been made of different alloys in the system:

Nb- 43wt.% Ti-25wt.% Ta	1980 UW[22,23]
Nb- 41wt.% Ti-15wt.% Ta	1983 Fermi/UW[4]
Nb- 44wt.% Ti-15wt.% Ta	1987 Fermi/UW[24,25]
Nb- 37wt.% Ti-22wt.%Ta	1992 Kharkov[26]

None of these has had the maximum H_{c2} composition, principally because of the desire to minimize the more expensive Ta.

Any new alloy must strike a balance between ensuring that there is enough Ta to raise H_{c2} and enough Ti to get sufficient α -Ti for pinning. In fact the best Nb-Ti-Ta alloys made so far have had $J_c(4.2K)$ values which are a little lower than the binary but they do improve at 2 K. There have been few problems with Nb-Ti-Ta alloy, making it a rather simple retrofit if 2K use is being considered.

C. Fabricability

Conventional Nb-Ti and Nb-Ti-Ta fabricate extremely well, often producing piece lengths exceeding several km. Thus there is no concern about them. By contrast, APC conductors are sometimes quite hard to make. The problems are of several types. First is the fact that multiple extrusions

are required to make an APC, except in the special case of the Supercon design mentioned above. Since each extrusion has a yield of ~85% at maximum, it is easy to see that a design requiring 3 or 4 extrusions has an inevitably low yield. An additional problem is that the composite is two-phase from the very beginning of fabrication and this leads to early work hardening and sometimes to fracture. This does not have to lead to problems but it is probably true that wire breaks are more common than with the standard process. These issues will take a greater importance as more of them made in an industrial environment.

III. SUMMARY

Recent advances in Nb-Ti alloys have been reviewed. A better understanding of flux pinning in the system offers opportunities for new and better prototype designs, perhaps of multilayers and APC conductors. APC composites as presently made suffer from having the wrong overall composition and perhaps also from having pure metal pins. Ternary alloys should be capable of further optimization since too few having close to optimum compositions have yet been made. Near term designs of specialty magnets for low beta quadrupoles may provide a stringent test of the potential of these new concepts, since applications of this type are not too sensitive to conductor cost. It does appear that Nb-Ti conductors with better properties can still be developed. The challenge is to integrate the lessons of the much better flux pinning properties of multilayers into more conventional round wire designs.

We gratefully acknowledge discussions with many present and former UW colleagues, particularly Lance Cooley, Robert Heussner, Paul Jablonski, Erik Kadyrov and Alex Gurevich. We are also greatly indebted to continued collaboration and encouragement from Ron Scanlan and Al McInturff (LBL), Dave Sutter (DOE) and colleagues in the superconductor industry, particularly Eric Gregory (IGC), Seung Hong (OST), and William McDonald (TWC-Huntsville). Early help from Bruce Strauss, formerly of Fermilab, is also gratefully acknowledged.

IV. REFERENCES

- [1] L. D. Cooley, P. D. Jablonski, P. J. Lee and D. C. Larbalestier, "Strongly enhanced critical current density in Nb-47 wt.% Ti having a highly aligned microstructure," Appl. Phys. Lett. 58, pp. 2984-2986, 1991.
- [2] K. Matsumoto, H. Takewaki, Y. Tanaka O. Miura, K. Yamafuji, K. Funaki, M. Iwakuma, and T. Matsushita, "Enhanced J_c properties in superconducting NbTi composites by introducing Nb artificial pins with a layered structure," Appl. Phys. Lett, vol. 64(1), pp.115-117, 1994.
- [3] J. M. Seuntjens, M. Rudziak, C. Renaud, T. Wong

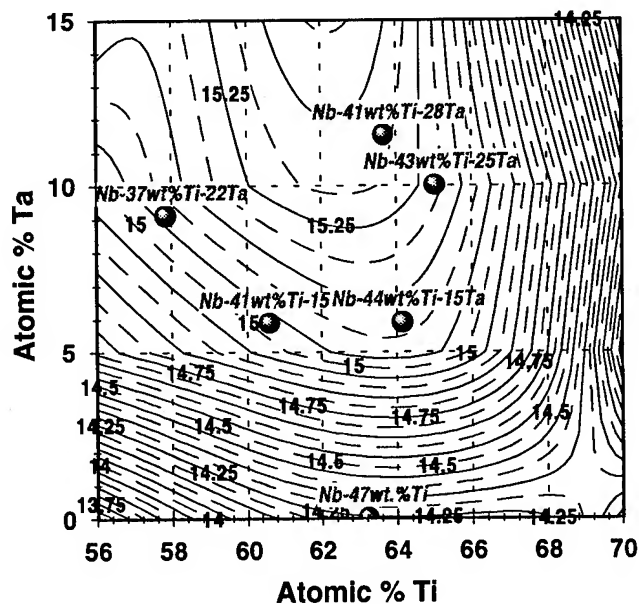


Figure 6 Contour plot of H_{c2} at 2K for Nb-Ti-Ta from the data of Hawksworth [22] and Muller [27]. The investigated alloy compositions are superimposed on this plot along with the standard binary Nb-47wt.%Ti. We use atomic composition here rather than the commonly used weight percentage because the all important volume % of α -Ti is more closely related to the atomic % Ti and the weight percentage values for the ternary are often misleading in this respect.

and J. Wong, "Development Progress of the Supercon APC Process," presentation to the 1995 Low Temperature Superconductor Workshop, Boulder CO, March 1995.

[4] A. W. West, W. H. Warnes, D. L. Moffat and D. C. Larbalestier, "Compositional inhomogeneities in Nb-Ti and its alloys," IEEE Trans. Mag., 19, pp.749-753, 1983.

[5] D. C. Larbalestier, A. W. West, W. Starch, W. Warnes, P. Lee, W. K. McDonald, P. O'Larey, K. Hemachalam, B. Zeitlin, R. Scanlan and C. Taylor, "High critical current densities in industrial scale composites made from high homogeneity Nb46.5Ti," IEEE Trans. Mag., 21, pp. 269-272, 1985.

[6] A. W. West and D. C. Larbalestier, "Microstructural Changes Produced in a Multifilamentary Nb-Ti Composite by Cold Work and Heat Treatment," Met. Trans. A, 15, pp. 843-852, 1984.

[7] D. C. Larbalestier and A. W. West, "New perspectives on flux pinning in Niobium-Titanium composite superconductors," Acta Metallurgica, 32, pp. 1871-1881, 1984.

[8] P. J. Lee and D. C. Larbalestier, "Development of nanometer scale structures in composites of Nb-Ti and their effect on the superconducting critical current density," Acta Met., 35, pp. 2526-2536, 1987.

[9] Li Chengren and D. C. Larbalestier, "Development of high critical current densities in Niobium 46.5wt% Titanium," Cryogenics, 27, pp. 171-177, 1987.

[10] P. J. Lee and D.C. Larbalestier, "An examination of the properties of SSC Phase II R&D strands," IEEE Transactions on Applied Superconductivity, 3, pp. 833-841, 1993.

[11] J. D. McCambridge, N. D. Rizzo, X. S. Ling, J. Q. Wang, D. E. Prober, L. R. Motowidlo and B. A. Zeitlin, "Flux pinning in NbTi/Nb multilayers," IEEE Trans. Appl. Superconductivity, pp. 1697-1699, 1995.

[12] E. Kadyrov, A. Gurevich and D. C. Larbalestier, "Very high critical current densities in Nb-47%Ti multilayers with a planar copper flux pinning microstructure," submitted for publication in Appl. Phys. Lett., September 1995

[13] B. A. Zeitlin, M. S. Walker and L. R. Motowidlo, "Superconductors having controlled laminar pinning centers, and method of manufacturing same," US Patent 4,803,310, 1989.

[14] G. L. Dorofeyev, E. Yu Klimenko, and S. V. Frolov, "Current carrying capacity of superconductors with artificial pinning centers," Proceedings of the 9th International Conference on Magnet Technology, Ed. by C. Marinucci and P. Weymuth (pub. Swiss Institute for Nuclear Research, Villigen, Switzerland), pp. 564-566, 1985.

[15] P. J. Lee, D. C. Larbalestier, and P. D. Jablonski, "Quantification of Pinning Center Thickness in Conventionally Processed and Powder Processed Artificial Pinning Center Microstructures," IEEE Trans. Appl. Superconductivity, 4, pp. 1701-1712, 1995.

[16] C. Meingast, P. J. Lee and D. C. Larbalestier, "Quantitative description of a high J_c Nb-Ti superconductor during its final optimization strain: I. Microstructure, T_c , H_{c2} and resistivity," J. Appl. Phys., 66, pp. 5962-5970, 1989.

[17] P. J. Lee, J. C. McKinnell, and D. C. Larbalestier, "Restricted Novel Heat Treatments for Obtaining High J_c in Nb-46.5wt%Ti," Adv. Cryo. Eng., 36, 287-294 (1990).

[18] C. Meingast and D. C. Larbalestier, "Quantitative description of a very high critical current density Nb-Ti superconductor during its final optimization strain: II. Flux pinning mechanisms," J. Appl. Phys., 66, pp.5971-5983, 1989.

[19] L. D. Cooley, P. J. Lee and D. C. Larbalestier, "Is Magnetic Pinning a Dominant Mechanism in Nb-Ti?," IEEE Trans. Mag., 27, 1096-1100, 1991.

[20] A. Gurevich and L.D. Cooley, "Anisotropic flux pinning in a network of planar defects," Phys. Rev. B, 50, pp. 13568-13576, 1994.

[21] L. D. Cooley, P. J. Lee and D. C. Larbalestier, "Evidence that magnetic pinning is the dominant pinning mechanism in Nb-Ti superconductors and the effect that proximity coupling of the pins to the matrix has on the pinning force," submitted for publication in Phys. Rev. B, August 1995.

[22] D.G. Hawksworth, and D.C. Larbalestier "Further investigations of the upper critical field and the high field critical current density in Nb-Ti and its alloys," IEEE Trans. Mag., 17, pp. 49-52, 1981.

[23] H.R. Segal, T.M. Hrycaj, Z.J.J. Stekly, Z.J.J., T.A. de Winter, and K. Hemachalam, "Nb-Ti based conductors for use in 12 Tesla toroidal field coils," in Proc. of 8th Symp. on Engineering Problems in Fusion Research, IEEE Pub. 79-CH-1441-5 NPS, pp.255-259, 1979.

[24] A. D. McInturff, Carson, D. C. Larbalestier, P. J. Lee, J. C. McKinnell, Kanithi, McDonald, O'Larey - "Ternary Superconductor "NbTiTa" for High Field Superfluid Magnets," IEEE Inter. Magnet Conf., Digest of Technical Papers, Brighton Polytechnic, Brighton, U.K., p: AP15, 1990.

[25] P. J. Lee, D. C. Larbalestier, J. C. McKinnell and A. D. McInturff, "Microstructure property relationships in Nb-Ti-Ta," IEEE Transactions on Applied Superconductivity, 3, pp. 1354-1357, 1993.

[26] B. G. Lazarev, O. V. Chernyj, G. E. Storozhilov, L. G. Udov, N. F. Andrievskaya, L. A. Kornienko, L. S. Lazareva, N. A. Chernyak, P. A. Kutsenko, B. K. Pryadkin, Y. A. D. Starodubov, M. B. Lazareva and V. M. Gorbatenko, "The Study of the Microstructure and J_c in Nb-37Ti-22Ta Superconductor Produced with Different Duration of Treatments," Proc. 7th Int. Workshop on Critical Currents in Superconductors, Alpbach, Austria, Ed. H. W. Weber, World Scientific Press, Singapore, 1994.

[27] H. Muller, "The upper critical field of niobium-titanium," Ph.D. Thesis, University of Wisconsin-Madison, 1988.

SUPERCONDUCTING MAGNETS

R. Perin, CERN, 1211 Geneva 23, Switzerland

Abstract

Superconducting magnets have become essential components of hadron accelerator/colliders and compact electron accelerators. Their technology has greatly progressed in recent years thanks to the Tevatron and HERA operation experience, the production of the RHIC magnets and the intense R&D programs for SSC, UNK and LHC. For the LHC, at present the most important and advanced project, dipoles, quadrupoles and corrector R&D magnets have been successfully built in industry and laboratories. Major milestones have been recently passed with test and measurement of several industry made, 10 m long, twin-aperture dipoles and the successful operation of a "string" test facility simulating the basic machine half-cell.

I. INTRODUCTION

High Energy Physics has been for almost three decades the prime promoter of applied superconductivity, magnets and r.f. cavities, identified as the means to reach higher energy saving cost and space occupancy. Superconducting magnets have be

come the key to higher energies in hadron accelerator/colliders, and are more and more applied in experiments for momentum analysis of secondary particles. In low energy machines superconducting magnets are used in industrially made compact electron accelerators as, e.g. "portable" synchrotron light sources and small cyclotrons for medical applications [1, 2].

This paper covers only a few aspects of the main magnets of the high energy colliders presently under construction and is mainly focussed on the dipoles because of their importance in the economy of the projects and of their technical difficulties.

The evolution in field and field gradient of superconducting main magnets for accelerators is recalled in Table I.

Improvement in performance of superconductors [3, 4], better insulation systems and force containment structures and refinements in manufacturing have permitted to raise field and gradient. A bold step is being made with the LHC using the superfluid helium technique, thus enhancing the performance of the traditional NbTi superconductor, and by the adoption of the two-in-one configuration leading to a considerable reduction of costs and space occupancy.

Table I
Design parameters of superconducting main magnets in accelerator/colliders

	Dipoles			Quadrupoles			Operation temperature (K)
	Central field (T)	Coil aperture (mm)	Eff. unit length (m)	Field gradient (T/m)	Coil aperture (mm)	Eff. length (m)	
TEVATRON	4.4	76.2	6.1	75.8	88.9	1.7	4.6
HERA	4.7	75	8.8	91.2	75	1.9/1.7	4.5
RHIC	3.5	80	9.5	71.8	80	1.1	4.6
UNK	5.0	80	5.7	96.1	80	3.0	4.6
SSC	6.6	50	15.2	206	40	5.2	4.35
LHC	8.4	56	14.2	220	56	3.0	1.9

II. SSC MAGNETS

The SSC magnet development programme, presently ended due to the unfortunate termination of the project, has been during a decade the main stimulation of accelerator magnet progress and has led to many advancements in understanding, design, materials and fabrication techniques [5]. Most of the prototype dipoles were built at BNL and FNAL. Their quench performance at the operation temperature of 4.35 K was excellent with little training. Their field quality was generally within requirements, only the drift of the skew quadrupole component at injection needed to be better controlled. Full length prototype quadrupoles were built at LBL. Typically they exhibited training from 6.6÷7.2 kA to 8 kA and some

retraining after thermal cycling. Their field quality was better than specified. Some 1 m long model quadrupoles were manufactured by a US/German consortium. They reached the conductor short sample limit, 8.4 kA, after a few quenches starting at about 7.5 kA.

The last important activity on the SSC magnets, after the decision to terminate the project, was the power test of a full cell of the machine, comprising ten dipoles, two quadrupoles and three spool pieces [6]. The very valuable experience gathered with this test will help any future accelerator project using superconducting magnets and in particular the LHC. Among the results of general interest the following should be mentioned:

- There was no evidence of quench propagation between adjacent quarter cells (the string was subdivided into quarter cells) by heat transported through helium. Propagation occurred instead because of a too fast down-ramp rate during the current decay through an external dump resistor, which caused quenching of dipole inner coils in other quarter cells.
- The finding of considerable over voltages to ground at quench in a string of magnets protected by the same bypass diode. It has been shown that this is mainly caused by differences in the normal resistance at low temperature of the outer coils (those fired by the strip heaters). The cure is a better matching of magnets in this respect and in diminishing as much as possible the quench start time in the different magnets by using more efficient heaters. These observations have already had important consequences in the evolution of the LHC magnet quench protection system. The idea of protecting the half cell magnets by a set of diodes grouped in the short straight section has been abandoned in favour of the initial scheme with a set of two diodes placed in superfluid helium and connected across the magnet terminals.
- A catastrophic failure of the insulating vacuum in a half-cell was simulated by opening a valve to air. The system did not suffer from this type of event, dispelling the fears raised by some computer simulation models and confirming the results obtained at CERN with a similar test performed on the TAP magnet by breaking the insulation vacuum with helium, thus simulating a failure of the helium tank [7]. Also in this test (which is considered more severe, since helium cannot freeze as air does on the thermal screens) no damage was produced.

III. UNK SUPERCONDUCTING MAGNETS

A number of dipoles had been successfully tested in the past years. The results were satisfactory regarding quench performance, losses at ramp, field quality and reproducibility. Because of the known difficulties the series production of these magnets could not be launched. Last year a string of four dipole magnets has been successfully tested [8] and the work is continuing as we will hear in this conference.

IV. MAGNETS OF THE RELATIVISTIC HEAVY ION COLLIDER (RHIC)

Construction and testing of the RHIC magnets will be presented in a next talk by P. Wanderer [9] and more details will be given at this conference.

The cross-section of the main dipole is shown in Fig. 1. The design is very clever in its simplicity with coils wound in only one layer of a 30 strand cable and coil clamping provided by the steel laminations of the yoke assembled in "collars" style and encased by a stainless steel shrinking cylinder. The design of the quadrupoles follows the same principles. After intense R&D at BNL the series manufacturing of dipoles and quadrupoles was entrusted to

a firm, to which the required technology was transferred. Complete dipoles in their cryostat are delivered to BNL by the industrial company. On the contrary, the quadrupole magnets (manufactured by the same firm), the sextupoles (manufactured by another company), the corrector coil assemblies (manufactured at BNL) and the beam position monitors are all combined into cold mass units and inserted into common cryostats at the Laboratory.

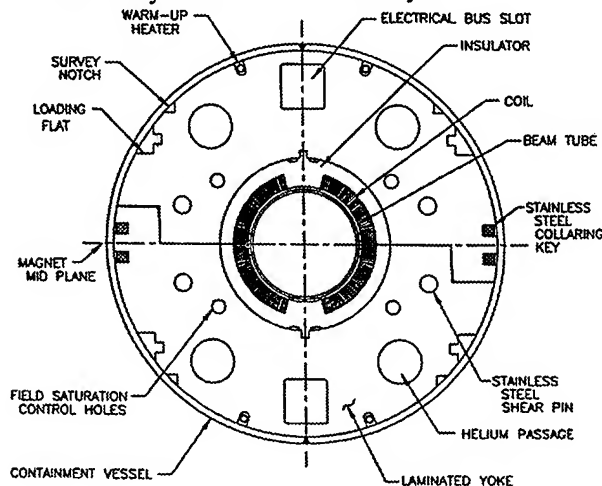


Figure 1: Cross-section of RHIC dipole cold mass.

The production of all these components is successfully proceeding according to schedule and the first important milestone of 30 produced dipoles was passed in September 1994. All these magnets and several others have been tested and measured and are now installed in the RHIC tunnel. The quench performance shows that these magnets have a good margin with respect to the specified operation field.

V. LARGE HADRON COLLIDER (LHC) MAGNETS

The up-to-date design of the Large Hadron Collider will be presented at this conference by L. Evans.

A re-optimization of the accelerator/collider with the aim of maximizing global dipole occupancy in the arcs led to a new lattice based on 23 cells per octant and three main dipole magnets per half-cell. The layout of the new standard half-cell is shown in Fig. 2. Considerations on beam stability, reliability and cost has led to some changes in the magnet characteristics. The coil aperture is increased from $\varnothing 50$ mm to $\varnothing 56$ mm and the magnetic length of the dipole units is extended to 14.2 m. The operational field of the dipoles is 8.4 T for a proton beam energy of 7.0 TeV [10, 11].

A. Dipoles

1. Main features

The main parameters of the dipole magnet are listed in Table II and the cross-section is shown in Fig. 3.

The basic design features of the first R&D dipoles which have been confirmed by the results of the R&D programme, i.e. cooling with superfluid helium at 1.9 K, two-in-one configuration, two-layer coils, aluminium alloy collars common to both apertures, vertically split yoke and stainless steel shrinking cylinder are maintained. With respect to the first generation R&D dipoles a number of changes have been introduced in the new design to match the larger aperture and the reduced field requirements and to make the construction simpler. The cable width is reduced from 17 mm to 15 mm.

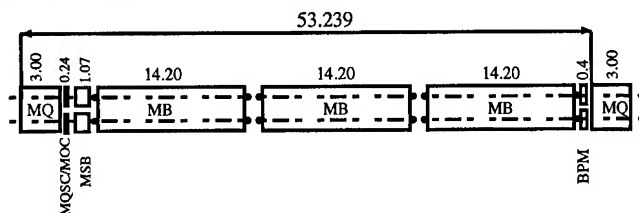


Figure 2: Schematic layout of the LHC half-cell.

MB: Dipole magnets. MQ: Lattice quadrupoles.
MQSC: Skew quadrupoles. MQC: Octupole
MSB: Combined sextupole and dipole corrector.
BPM: Beam position monitor.
- o -: Local Sextupole or decapole corrector.

Table II
Dipole Parameters

Operational field	8.4	T
Coil aperture	56	mm
Magnetic length	14.2	m
Operating current	11'500	A
Operating temperature	1.9	K
Coil turns per aperture	inner shell 30 outer shell 52	
Distance between aperture axes	180	mm
Outer diameter of cold mass	580	mm
Overall length of cold mass	~ 15	m
Overall mass of cryomagnet	31	t
Stored energy for both channels	7.4	MJ
Self-inductance for both channels	119	mH
Resultant of e-magnetic forces in the first coil quadrant	ΣF_x (1.70 MN/m)	24.0 MN
inner layer	ΣF_y (- 0.14 MN/m)	- 2.0 MN
outer layer	ΣF_y (- 0.60 MN/m)	- 8.5 MN
Axial e-magnetic force on magnet ends	0.52	MN

The number of yoke parts is reduced from 4 to 2 making the structure less sensitive to dimensional tolerances on stacked laminated assemblies. The wanted field distribution at all field levels is maintained by the insertion of magnetic steel pieces in the collars. These steel inserts, punched out of the 6 mm thick steel sheet of the yoke laminations, are at the same time used to firmly lock pairs of collars together.

Strands (ϕ 1.065 mm for inner layer and ϕ 0.825 mm for outer layer) and cables of the new design have already

been produced and delivered to CERN. One particular problem is that of current sharing among strands distorting the magnetic field during ramping. The effect at injection field would be acceptable with a contact resistance ranging between 6 and 10 $\mu\Omega$. An interstrand resistance of 10 $\mu\Omega$ has been set as the goal of a development programme. A number of coating materials for the cable strands, as well as resistive barriers are under investigation.

The expected field errors originated by the coil and yoke configuration are well within the requirements at all field levels. The computed persistent current sextupole and decapole components at injection field (~ 0.56 T) are

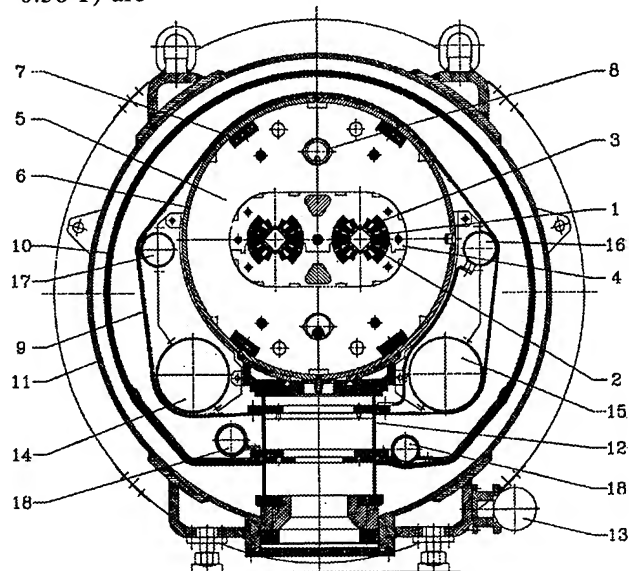


Figure 3: Cross-section of LHC dipole in its cryostat.

1. Beam screen, 2. Beam pipe, 3. Superconducting coils, 4. Non-magnetic collars, 5. Iron yoke, 6. Shrinking cylinder/HeII vessel, 7. Sc. bus-bars, 8. Heat exchanger pipe, 9. Radiative insulation, 10. Thermal shield (55 to 75 K), 11. Vacuum vessel, 12. Support post, 13. Alignment target, 14. 1.8 K GHe pipe, 15. 20 K GHe pipe, 16. 4.5 K GHe pipe, 17. 2.2 K GHe pipe, 18. 50-75 K GHe pipe.

- 3.58×10^{-4} and 0.18×10^{-4} respectively (in units of 10^{-4} of B_0 at $r = 1$ cm). These systematic error components are, however, corrected by small sextupole and decapole magnets located at each dipole end. More studies are necessary on some effect of persistent and eddy currents at injection, in particular concerning the skew quadrupole component. Great care must be applied in the interpretation of the magnetic measurements at this low field: e.g. in the presence of the above mentioned persistent current sextupole, a 1 mm misalignment of the measuring coil with respect to the dipole axis (which is quite possible) produces an apparent skew or normal quadrupole of 0.7 units, having a sign which depends on the direction of the probe coil eccentricity.

The quench protection system is based on the so-called "cold diode" concept [12]. The diodes will be installed in

the HeII cryostat of each dipole and quadrupole unit. In each twin dipole, a set of two series connected diodes is connected across the terminal. This solution provides safe blocking voltage at ramp and a welcome redundancy: in case of failure of one diode, the LHC can still run albeit at reduced ramp rate.

2. Status of R&D programme

a) Twelve 1.3 m long dipole models have been constructed and tested. Initially all models were built in industry, then a magnet building facility was set up at CERN about three years ago, because of the need for detailed investigations and rapid turnaround. One twin-aperture and two single-aperture models were built in Japan by KEK in collaboration with industrial companies [13]. Detailed results of several models have been reported elsewhere [14, 15]. No difference in quench performance was seen between single-aperture and twin-aperture models. All models have largely exceeded 9 T, with the best reaching 10.5 T. The last single aperture KEK magnet, tested in February 1995, attained the conductor short sample limit at 10.2 T at 1.95 K after twelve training quenches [16]. A twin-aperture model built at CERN with SSC cables presented a quench behaviour similar to that of the other models, reaching the conductor short sample limit at 9.65 T after training. In all these magnets as well as in the 10 m long prototypes the great majority of quenches started in the magnet ends or in the region of the splice between the coil inner and outer layer [17]. The short model programme at CERN is therefore now concentrated on improving these critical regions.

b) After the success of the first 10 m long magnet, named TAP, made with HERA-type coils mounted in a twin-aperture structure, seven 10 meter long prototypes have been ordered to industry and the first four have been delivered and tested at CERN. The first two, CERN-INFN1 (MTP1A1) and CERN-INFN2 (MTP1A2), were funded by the Italian "Istituto Nazionale di Fisica Nucleare" (INFN). The quench behaviour of the tested magnets is shown in Fig. 4. In the first three magnets all quenches occurred at "singular" places, the splice and the coil ends, as in short model magnets. The fourth one, MTP1N1, manufactured by a different company, had a different behaviour. Training was longer, and, contrary to the previous experience in short and long magnets, all quenches started in the regular straight part, almost all in the outer layer of the same pole of one aperture. As this indicates the existence of a weak point, it has been decided to disassemble this magnet and to reassemble it at CERN in order to find out the cause of the anomaly. On the other hand, this magnet had a different design of the splice region, probably a good one, since no quench occurred there. The field distribution and orientation were measured in the first three magnets in both apertures in 11 positions along the longitudinal axis, at three field levels, 0.58 T, 6 T and 8.65 T at 1.9 K and at room temperature. The multipole errors are close to the expected values in both

apertures. The orientation and parallelism of the B vector was also measured: the first magnet exhibits some torsion (~ 10 mrad), the second and the third a negligible amount, further in all three the parallelism of the B vectors is better

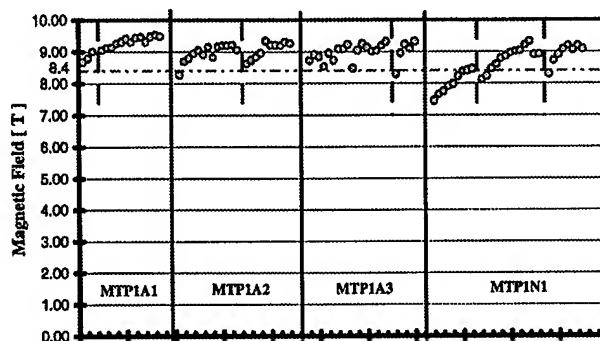


Figure 4: Quench history of the first four 10 m long prototype LHC dipoles.

than 0.2 mrad (Fig. 5). The correlation between measurements taken at room temperature and at 1.9 K was found to be very good, both concerning multipole errors and field orientation, in all three magnets. The quench protection system worked satisfactorily and the maximum temperatures and voltages were as expected.

The first two dipoles are now installed, together with a prototype short straight section, in a "string" test facility simulating the basic half-cell.

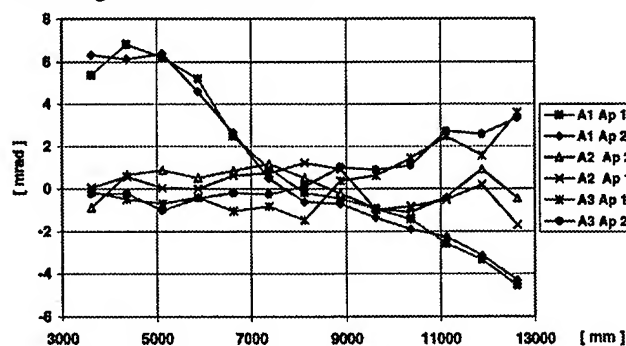


Figure 5: Field orientation in both apertures of MTP1A1, A2 and A3 prototypes.

B. Quadrupoles

The main parameters of the lattice quadrupoles are listed in Table III. Two full size quadrupoles of 56 mm aperture and 3 m length have been designed, constructed and tested at CEN, Saclay (F) in the frame of a CERN-CEA Collaboration [18]. The design gradient was reached for the two magnets after very few training quenches (Fig. 6).

In one of these quadrupoles an experience of field modulation has been successfully performed, as a preparation for the precise measurement of the LHC beam position with respect to the magnetic axis of the quadrupoles, the so-called k-modulation method [19]. This is particularly important for a superconducting machine, in

which the quadrupole magnet axis is difficult to report to the external fiducials.

Table IV
Main Parameters of LHC lattice quadrupole magnets

Operational field gradient	220	T/m
Coil aperture	56	mm
Magnetic length	3.00	m
Operating temperature	1.9	K
Distance between aperture axes	180	mm
Yoke outer diameter	~ 450	mm

C. Continuation of the R&D programme

The other three 10 m long magnets will be delivered to CERN in the coming months. Short models of the new design are being manufactured at CERN. Ten metre long collared coils and other components have been ordered to industry. Manufacturing of a final length ($L_m = 14.2$ m) prototype has started in the frame of a new collaboration agreement between INFN and CERN.

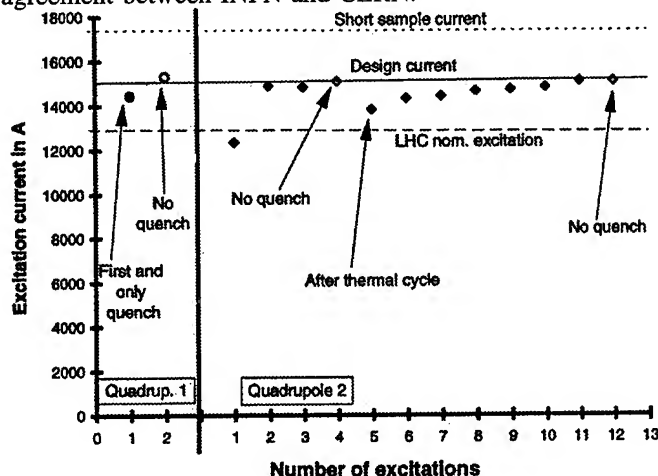


Figure 6: Quench history of the two prototype quadrupoles.

VI PERSPECTIVES FOR HIGHER FIELDS

The quest for higher fields continues to be motivated by economy in space, capital investment and operation cost, but the way is a very difficult uphill one [20].

A 11.5 T twin-aperture model using Nb_3Sn superconductor has been designed by a FOM-UT-NIKHEF-CERN collaboration [21]. A single-aperture version of this magnet is at the final assembly stage and results should come very soon. At LBL an experimental dipole, called D20, designed for a central field of 13 T and featuring a 4 layer coil wound with Nb_3Sn conductor is in an advanced assembly phase [22]. A dipole for the same design field had been studied at DESY. Thirteen tesla is probably the highest field which could be achieved in the classical cos ϕ coil configuration using Nb_3Sn superconductor. "Block-coil Dual Dipoles" or the so-called "Pipe Dipole", as proposed by LBL and TAC [23], may be the way in the

future to reach higher fields, perhaps using new HTS superconductors when they become available in technically usable form. If working models based on these concepts would be built, a lot of interesting ideas could be tested, e.g. the proposed porous inorganic insulation. In the author's opinion, such high field magnets may find applications for special use where a few units of exceptional characteristics are indispensable or produce large benefits. The first practical application could be in second generation low-beta quadrupoles for the LHC.

Large scale applications of the size of the LHC do not appear feasible in a near future. The use of NbTi superconductors has permitted a factor 5 gain in beam energy for the same accelerator size. To gain another factor five is impossible; a factor two, requiring about 17 T central field, may be thought of, but will require a tremendous R&D effort.

VII. REFERENCES

- [1] M.N. Wilson et al., "The Compact Superconducting Storage Ring X-ray Source Helios 1", IBM Journal of Research and Development, Vol. 37 No. 3 pp. 351-371, May 1993.
- [2] J. Gordon, M. Kruip, A. Reed, "Atom Smashers for Profit and Pleasure", Physics World, June 1994.
- [3] A. Green, "Recent Status of Superconductors for Accelerator Magnets", ICFA Workshop on AC Superconductivity, KEK Proc. 92-14, pp. 100-108, 1992.
- [4] D.C. Larbalestier, "New Developments in Superconductors for Accelerators", presented at this conference.
- [5] R.I. Schermer, "Status of Superconducting Magnets for the Superconducting Super Collider", IEEE Trans. on Magn., Vol. 30, No. 4, pp. 1587-1594, 1994.
- [6] P. Kraushaar et al., "The SSC Full Cell Prototype String Test", Proc. ASC, Boston, October 1994.
- [7] B. Szeless, L. Williams, Private Communication, 1994.
- [8] A. Alexandrov et al., "Investigation of the String of Four UNK Superconducting Magnets", Proc. IV EPAC Conference, EPAC-94, Vol. 3, p. 2313, 1994.
- [9] P.J. Wanderer "Superconducting Magnet Construction and Testing for the Relativistic Heavy Ion Collider (RHIC) at BNL", paper presented at this conference.
- [10] L.R. Evans, "Advanced Technology Issues in the LHC Project", presented at 1994 EPAC Conference, London, June 1994.
- [11] R. Perin for the LHC Magnet Team, "Status of LHC Programme and Magnet Development", Proc. ASC-94, Boston, Oct. 1994.
- [12] L. Coull, D. Hagedorn, V. Remondino, F. Rodriguez-Mateos, "LHC Magnet Quench Protection System", IEEE Trans. on Magn., Vol. 30, pp. 1742-1745, July 1994.
- [13] A. Yamamoto et al., "Development of Twin-aperture Dipole Magnets for the Large Hadron Collider", Proc. ASC-94, Boston, October 1994.
- [14] M. Bona, D. Leroy, R. Perin, P. Rohmig, B. Szeless, W. Thomi, "Design, Fabrication Variants and Results of LHC Twin-aperture Models", Proc. of MT12, Leningrad, 1991.
- [15] The LHC Magnet Team, reported by R. Perin, "Status of the Large Hadron Collider Magnet Development", IEEE Trans. on Magn., Vol. 30, pp. 1579-1586, July 1994.
- [16] A. Yamamoto, Private Communication, March 1995.
- [17] J. Billan, A. Siemko, L. Walckiers, R. Wolf, "Quench Localization in the Superconducting Model Magnets of the

LHC by Means of Pick-up Coils", Proc. ASC-94, Boston, October 1994.

- [18] P. Genevey et al., "Cryogenic Test of the First Two LHC Quadrupole Prototypes", *Proc. ASC-94, Boston, Oct. 1994*
- [19] K.N. Henrichsen, *Private Communication, April 1995.*
- [20] R. Perin, "State of the Art in High-field Superconducting Magnets for Particle Accelerators", *Proc. 14th Int. Conf. on Part. Accel., Tsukuba, Aug. 1989, Vol. III, pp. 625-638.*
- [21] A. den Ouden et al., "First Test Results of the 11.5 T Nb₃Sn Single Aperture Dipole Magnet", *Proc. ASC-94, Boston, Oct. 1994.*
- [22] R.M. Scanlan et al., "Fabrication and Preliminary Test Results for a Nb₃Sn Dipole Magnet", *Proc. ASC-94, Boston, Oct. 1994.*
- [23] P.M. McIntyre, R.M. Scanlan, W. Shen, "Ultra-High-Field Magnets for Future Hadron Colliders", *Proc. ASC-94, Boston, Oct. 1994.*

Assembly and Commissioning of the LHC Test String

P. Faugeras, for the LHC String Team, CERN, 1211-Geneva 23, Switzerland

I. INTRODUCTION

The LHC Project incorporates novel design features which are particularly challenging: twin aperture superconducting magnets with a stored energy higher than 5 MJ per magnet and working in a bath of superfluid helium. It was therefore decided in 1991 to order several full length prototype magnets, and install them in a test string, to demonstrate the feasibility of the LHC. This paper describes the String assembly in its first phase, which consists of a short straight section with its quadrupole and of two dipoles, together with the necessary cryogenics and powering. One will then give the first commissioning results as well as future plans.

II. THE STRING PHASE 1

It was originally foreseen to build a string made of one quadrupole and four dipole magnets, which corresponded to a full LHC half-cell at that time, [1]. In fact, as the delivery of the 10 m long dipole prototypes was delayed, it was decided to install the String with first the quadrupole and only two dipoles, which are sufficient for assessing the validity of the main design choices. Similarly, the correction elements such as sextupoles, tuning quadrupoles, closed orbit correctors which are normally in the short straight section, (SSS) of the LHC lattice, were replaced by dummies in the prototype SSS.

Fig. 1 shows a schematic of the overall installation. The String starts with the String Feed Box, (SFB), which is a large tank under vacuum, containing cryostat, helium heat

exchanger, all the valves and regulators which are necessary for feeding the superconducting magnets with the different cryogenic fluids. Several pairs of current leads are mounted on the large upper flange of the SFB, both for the dipole and quadrupole excitation (15 kA), and for powering later on the correction elements (500 and 1500 A).

The SSS is connected directly to the SFB and is followed on the other side by the dipole magnets. The String ends with the String Return Box (SRB), which closes the string cryostat vacuum and which contains the short circuits for the electrical busbars, as well as some cryogenic valves.

The SFB is also connected to the central cryogenic station as well as to an additional device, called Cooling and Warming-up Unit, (CWU), which provides gaseous helium at adjustable temperature and pressure, for both cooling and warming up of the String. An insulated reservoir installed behind the SFB is used for recuperating the gaseous helium which is ejected from the String during a magnet quench.

The power converter, (15 kA, 20 V), the two safety switches and the dump resistors are close to the SFB and interconnected with several water-cooled cables in parallel.

III. MECHANICAL ASSEMBLY

To reproduce the worst conditions one can find in the LEP tunnel, where LHC will be installed, the test String was built on a concrete beam, as wide as the LEP tunnel and with a slope of 1.4%. The support beam is 110 m long which allows future extension of the String to a full LHC lattice cell. As it was originally foreseen to install the LHC machine above the LEP collider, all the String elements are mounted on Γ shaped supports, which brings the cryostat axes at about 1.5 m above the floor level and leaves underneath sufficient free space for LEP components.

The SFB and the SRB, which are described in more details in [2], were assembled and fully tested at 1.8 K, in another hall before being installed in the String.

As compared to the original design, [3], the SSS cold mass prototype contains dummy steel masses of equivalent thermal capacity in place of the corrector magnets. Quench protection diodes for the main quadrupole and auxiliary diodes, for protecting the dipoles against overvoltages produced by quench heater delays, (see chapter 4), are also mounted inside the SSS cold mass. The SSS was built on a separate bench and tested for vacuum tightness but not cryogenically before installation, the main quadrupole having been tested before at Saclay on its own at 1.8 K.

The two dipole prototypes, [4], were produced by industry and fully tested at CERN, both cryogenically and magnetically, in the same hall as the String, and prepared there for their installation in the String which included the adjustment of the electrical busbars to the right shape and length, the welding of bellows and the cleaning of the two cold bores.

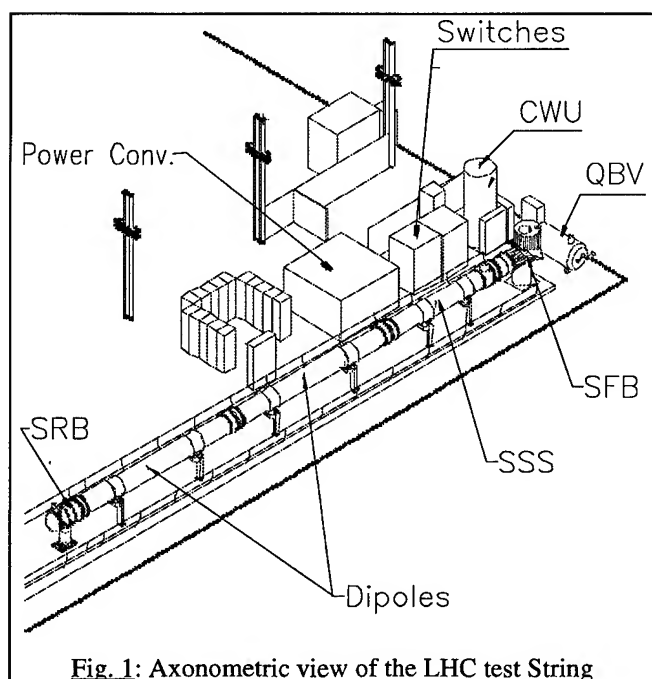


Fig. 1: Axonometric view of the LHC test String

Magnet Interconnections

The String forms in fact a single cryostat, containing all the cryogenic lines necessary for its operation: a cryo-magnet must then be connected at both extremities to another one and/or to the SFB or SRB before being cooled down and powered. The magnet interconnections are very critical for LHC, because the space needed to weld together the large number of pipes must be kept as short as possible, in order to maximize the active length of the final LHC. At the same time, the magnet interconnections must cope with the mechanical tolerances and alignment errors, be designed to absorb the 30 mm magnet contraction during cool-down, while being able to withstand the 20 bars pressure rise which may be produced during a magnet quench, [5].

In the present cryostat design, see fig. 2, the 14 pipes are interconnected in a space 440 mm long, for a cryostat inner diameter of 960 mm. It should be noted however that the magnets are not yet equipped with a beam screen in each cold bore, which simplifies somewhat the junction. An all-welded construction has been chosen, as this is the best long term reliable solution against helium leaks, [6].

The interconnection is started by brazing the main and auxiliary electrical busbars, and by insulating the resulting junctions. The pipes are then TIG-welded together with one of two special orbital machines which cover the whole range of diameters (50 to 180 mm). Another orbital machine allows the pipes to be cut, if necessary.

The tightness of the junctions is insured by monitoring the welding parameters and also by visual inspection. Whenever possible, local and global leak tests are performed, in some cases by inverting the direction of the pressure. The innermost pipes are welded first and one finishes by the installation of the quench relief valve, which is not welded but bolted to the magnet cold mass, so that it can be easily changed in case of blockage. The actuator of the valve is linked to the valve body via a long rod passing through the various screens and the vacuum tank.

The magnet interconnection is completed by installing the local radiation and thermal screens, with their layers of

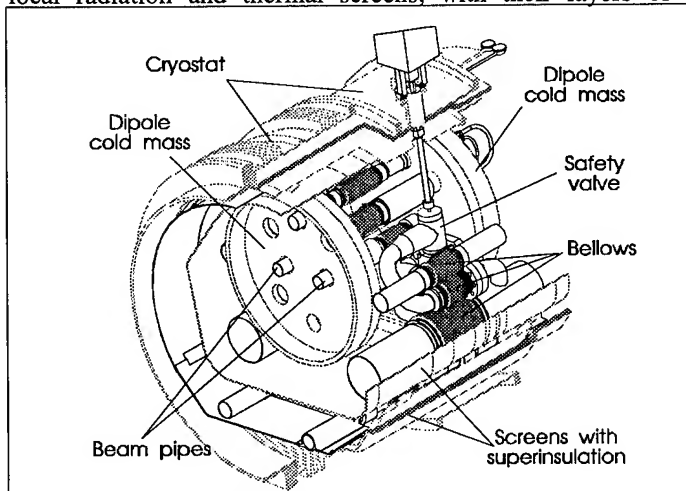


Fig. 2: Schematic view of magnet interconnection

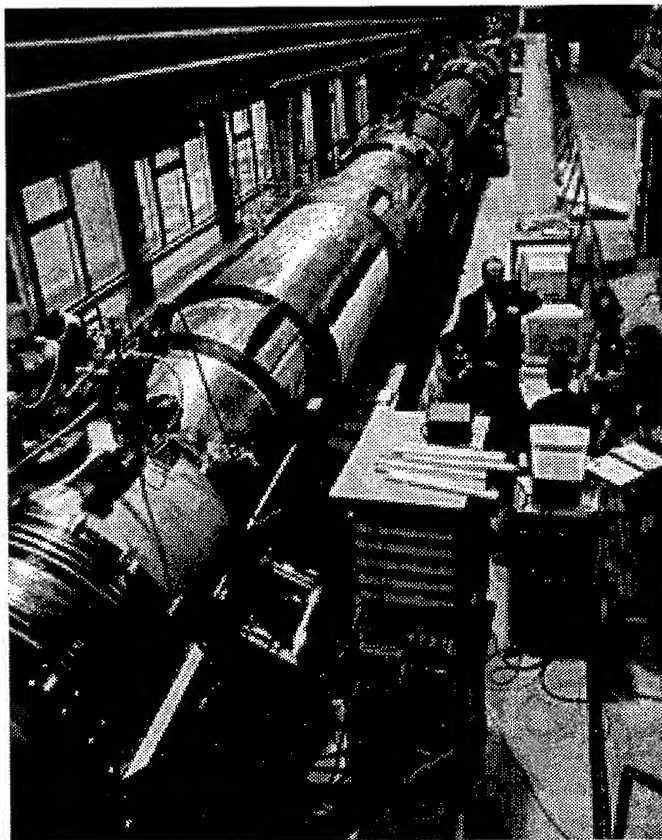


Fig. 3: Overall view of the LHC String in SM18

superinsulation, and by insuring the continuity with the neighboring screens. The outer tanks are closed by a sliding cylinder fitted with a large bellows for flexibility. Fig. 3 shows a picture of the String, seen from the top of the SFB.

Vacuum performance

The String is pumped with two large turbomolecular pumps, one attached to the SFB, the other in the middle of the String. A vacuum barrier, [3], installed at the front face of the SSS cold mass, allows separation of the SFB vacuum from the rest of the string. This has proven to be very useful when checking the whole String for helium tightness. In fact, only one leak was found between the SSS and the SFB. It was due to a corrosion problem and could be repaired in situ. Otherwise, all the welded junctions in the interconnections were perfectly leak tight.

Once the pressure of the insulation vacuum was below 10^{-2} Torr, a global leak test was performed by pressurizing all the cold masses and the internal cryogenic lines to 19 bars with gaseous helium. No leak was observed. This pressure test also served as a safety test to demonstrate the capability of the whole String to withstand the high pressures generated during a magnet quench.

When pumping down the String for the first time, it took about a week to reach a pressure in the 10^{-4} Torr range, because of the humidity accumulated in the superinsulation layers. When cooling the String to 80K, the 10^{-6} Torr range is obtained. The beam vacuum is separated from the insulation vacuum and is usually better than 10^{-9} Torr.

III. CRYOGENIC PERFORMANCE

Cooling the string can be started when the insulation vacuum is low enough, i.e. in the 10^{-2} - 10^{-3} Torr range. It is made in 3 phases, using the equipment and procedures as described in ref. [2].

The first phase implies the use of the Cooling and Warming-up Unit, (CWU), which produces gaseous cold helium at a pressure around 10 bars. This gas is injected in the pipes attached to the radiation shield and in the magnet cold masses through the SFB. Its temperature is controlled in the CWU with a liquid N_2 heat exchanger and is adjusted to 50 K below the highest temperature measured in the magnet cold masses. Fig. 4 shows the resulting magnet temperature variations. The temperature gradient limit of 50 K was chosen so as to avoid excessive mechanical stresses and possible magnet deformation during cool-down. This limit could in fact be applied to each magnet individually, as the temperature front is almost perpendicular to the string axis and propagates longitudinally. This would reduce somewhat the time required for this phase.

When the 80 K level is reached, the helium gas flow is stopped in the cold masses, but is maintained in the pipes attached to the radiation shield. The second cooling phase, from 80 K to 4.5 K, was done first by filling the large cryostat inside the SFB with liquid helium at 4.5 K and by letting this liquid vaporize at 1 bar in the magnet cold masses, until the 4.5 K level is reached and the cold masses filled with liquid. A more efficient and faster way was also used and is illustrated in the second graph of fig. 4: by suitably pressurizing the cold masses and the SFB internal cryostat, one can cool with supercritical helium, which allows 4.5 K to be reached in some 15 hours for the whole string. The internal pressure is brought back to 1 bar or less at the end of the phase, which fills all the magnet with liquid. Note that the temperature spikes at the end of this phase were due to an insufficient level of liquid helium in the large storage Dewar of the central cryogenic station and not to problems in the String. In total, about 700 l of liquid helium are needed for completely filling the String, including the SFB cryostat, which corresponds well with the calculated value of 25 l of liquid per metre of dipole.

The last cooling phase is quite fast: by lowering to 10-15 mbar the pressure in the technical service module located in front of the SSS, [3], the liquid helium inside it becomes superfluid and the HeII heat exchanger, which runs across the cold masses of the String starts to operate, [2]. The magnets are cooled down to the 1.8 K level simultaneously in 3 hours about, (see last curve of Fig. 4).

One has also verified the response of this HeII heat exchanger to an external heat load. When dissipating 9 W in each magnet, which simulates more than the heat which may be deposited by the proton beams, [1], the regulation system opens the Joule-Thomson valve which controls the primary helium flow of the heat exchanger and keeps the temperature changes in the String below 0.1 K. This clearly demonstrates the efficiency of this important system for LHC.

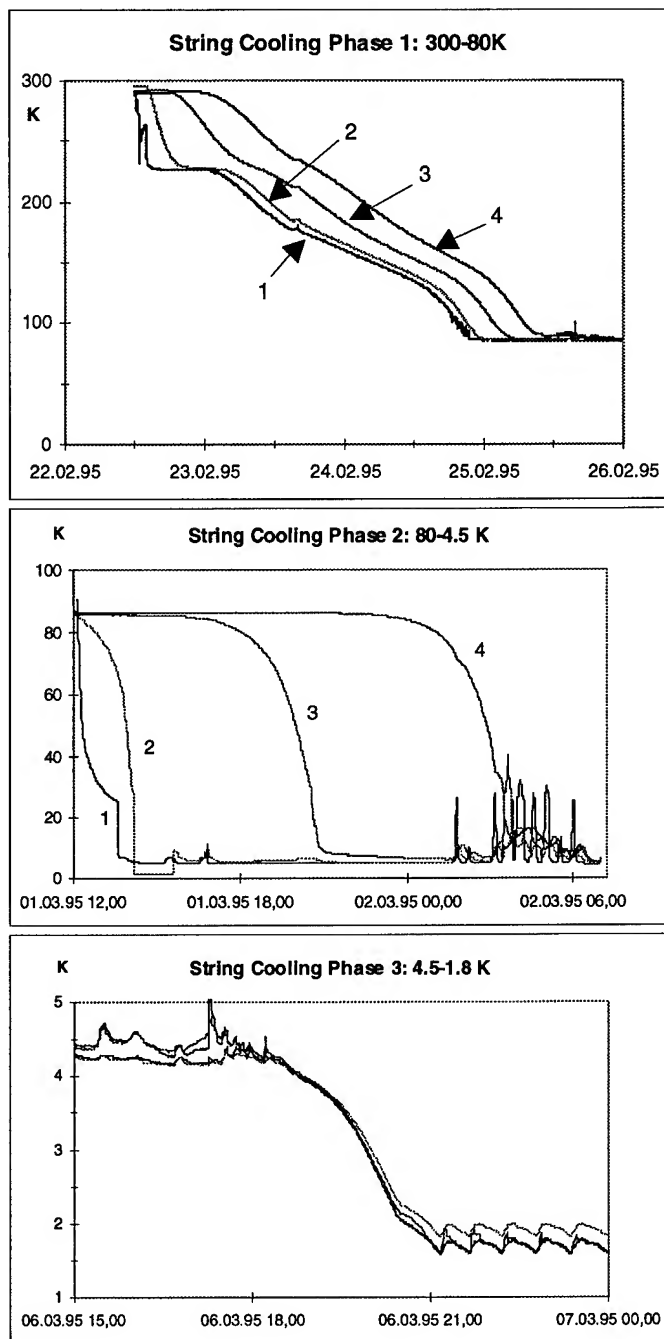


Fig. 4: LHC String Cooling Phases
Magnet Temperatures: 1- SSS entrance; 2- Dipole 1 entrance
3- Dipole 2 entrance; 4- Dipole 2 exit

In total, two complete String cooling sequences have been performed so far: with the present refrigeration capacity one needs about five days to cool down to 1.8 K from 300K, if there are no problems. The end-of-the-year shutdown was an opportunity to test also the warming-up sequence, which, with the same temperature gradient limit of 50 K, was found to take slightly less than five days. These results are important, as they allow reliable extrapolation to determine the time which will be required for cooling and warming-up a full octant of the final LHC machine, and to design accordingly the cryogenic plants.

IV. POWERING AND QUENCH PROTECTION

A simplified electrical circuit of the String is shown in Fig. 5. The power converter (20 V, 15 kA), is unipolar and has an internal current regulation loop, which allows adjustment of the current ramp rate within the voltage limits. It is paralleled by free-wheel diodes and grounded through a 1 Ω resistor. Two switches, between the power converter and the String can open the circuit, namely a fast thyristor switch and a slower mechanical circuit breaker. Each is paralleled by a resistor, which allows quick discharging the circuit in case of a quench. Water-cooled cables connect the power supply and switches to the main current leads on top of the SFB.

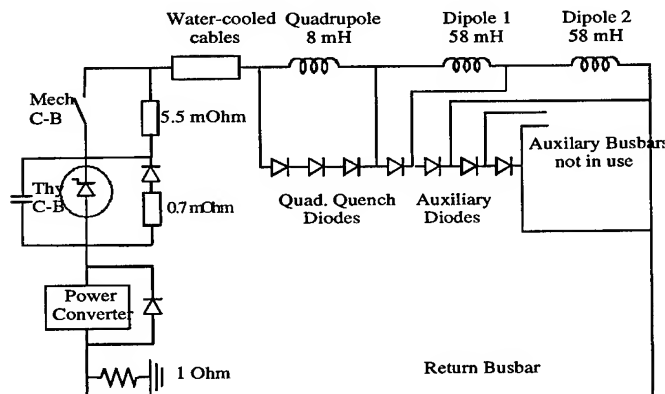


Fig. 5: Equivalent electrical circuit of the String

The principle of the quench protection system is described in ref. [7]. Voltage taps are used to constantly monitor the voltage across each magnet half coil. When a voltage difference exceeding a preset value appears between two half-coils or between two coils of the same magnet, or in between two magnets, the quench protection is triggered:

- capacitor banks are discharged in heaters inside all magnets, inducing a resistive transition in the whole String,
- the quench relief valves are opened,
- the two circuit-breakers are opened and the power supply is stopped.

As the whole String makes a resistive transition when the quench protection is fired, protection diodes across each magnet are not mandatory. They were nevertheless installed across the main quadrupole, to gain experience. In the case of the dipoles, it was realized lately that different delays in the resistive magnet transition when firing the quench heaters may induce excessive voltages across the magnet, [8]. The remedy was to install auxiliary diodes in the quadrupole cold mass and connect one diode across each dipole with some of the auxiliary busbars running along the String, (see fig. 5).

V. CONTROLS AND DATA ACQUISITION

The control system for the String is essentially based on industrial control technology, each subsystem having its own Programmable Logic Controller, (PLC), [9]. Whenever possible, the PLC was bought with the equipment it had to control, as for example for the CWU. Others, like the one for the SFB, which were more difficult to specify, have been

designed in-house. The supervision of the String PLCs makes use of a workstation running commercial software packages, such as FactoryLink, (TM). This type of controls has been found to be very efficient and has allowed the final String commissioning, that is the first rise to the nominal current as well as the 24 hour run, to be performed entirely remotely from the String control room.

It was also realized very early that a high performance data acquisition system was essential for running the String and analyzing the experimental data. This system was entirely built by industry, [10], and is made of two parts:

- the archiver, which can monitor continuously up to 450 channels at sampling rates ranging from seconds to hours,
- an externally triggered transient recorder, which can sample some of the above channels at rates of up to 100 Hz.

Both types of data are stored locally for some time, but are periodically transferred to a central Oracle (TM) data base, and can then be retrieved and analyzed on an EXCEL sheet for instance from any PC of the CERN network.

VI. GLOBAL TESTS AND EXPERIMENTS

Commissioning of the String was done in successive steps. The power converter and the two switches were tested first on a short circuit. After having checked the voltage insulation of the whole String against earth, the quench protection was fired with the String powered at 1 kA. This has allowed verification of the interlocks matrix logics and to eliminate transient voltage spikes induced by opening the thyristor switch. The same experiment was repeated at 5 kA, to verify that, when fired, the quench heaters indeed induce a resistive transition in each magnet (at this level, the dipoles are still self-protected). A global test of the system at 7 kA completed this phase.

The String was then ready to be powered up to the LHC nominal current, i.e. 12'350 A. The current was ramped at 5 A/s from 0 to 9 kA and at 2 A/s above. The first attempt was stopped by a quench in Dipole 2 at 12'200 A. Although somewhat frustrating, this clearly demonstrated the perfect functioning of the quench protection system. The String then reached the nominal LHC current on the second attempt. This was followed by a long run, (Fig. 6), in which the String was

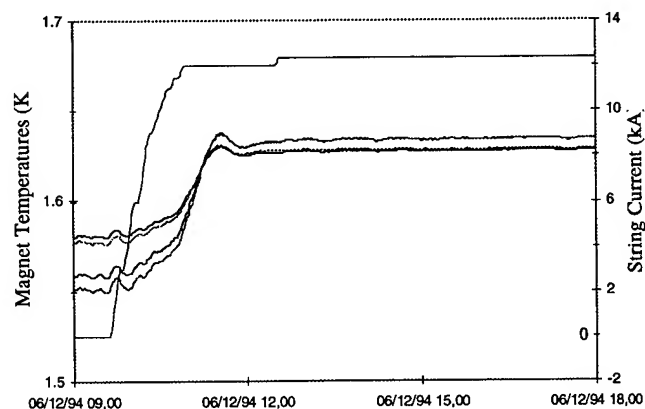


Fig. 6: First part of the 24 hour run of the String

powered for 24 hours at 12'350 A without problem. Fig. 6 shows that the magnet temperatures increase slightly when ramping the current but were stabilized quite rapidly, by the HeII heat exchanger described above. At that time, the thermometers had not yet been calibrated and in reality the magnet temperatures were in fact about 0.1-0.15 K higher than those shown in fig. 6.

After 24 hours at nominal current, the String current was again raised at 2 A/s until a quench occurred in Dipole 1 at 13'070 A, i.e. at about 9 T, which shows that there is some safety margin in the operating field of the LHC magnets. The evolution of the voltages across the different String elements during that quench can be seen in Fig. 7, while Fig. 8 shows the evolution of the corresponding magnet internal pressures. After calibration, the maximum value recorded does not exceed 12 bars, that is less than anticipated.

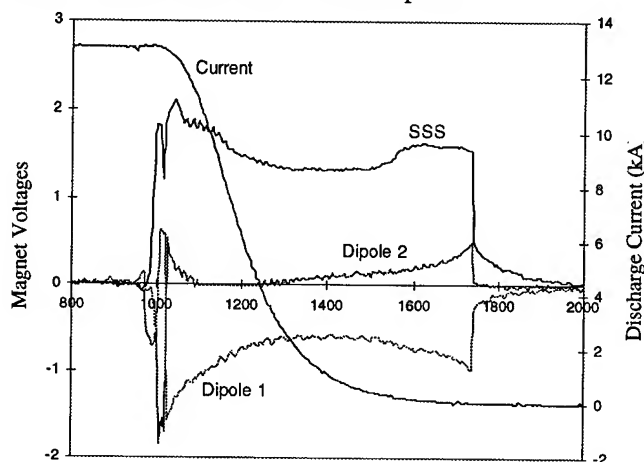


Fig. 7: Magnet voltages during the quench at 13'070 A

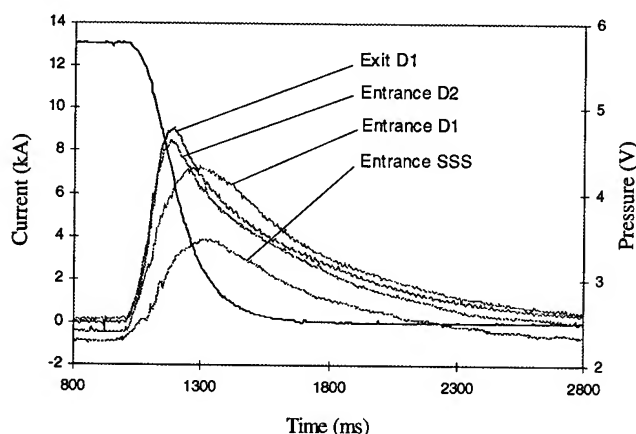


Fig. 8: Magnet pressure during the quench at 13'070 A

The LHC String can be considered as being operational. It will now be used to validate the technical choices made for LHC and to hopefully improve the machine design. Experiments are being conducted for measuring the performance of the cryogenic system, for studying quench propagation, vacuum behaviour, etc. To this end, the String will be completed with two more magnets, as soon as they become available.

On the longer term, the SSS will be reconstructed, to incorporate all correction elements and the dipole magnets will be replaced by 14.2 m long magnets in order to have the String as close as possible to the final LHC half-cell, [11].

VII. ACKNOWLEDGEMENTS

The LHC String project has benefited from the constant support of G. Brianti and L. Evans, the former and present LHC Project Leaders. This project was launched in 1991, but the final installation and commissioning were done in a very short time, from July to December 1994, thanks to the hard work and enthusiasm of a number of people in the Accelerator and Technical Sectors of CERN. It is not possible to mention them all here but their contribution to the success of the String is gratefully acknowledged.

VIII. REFERENCES

- [1] The LHC Study Group, Design Study of the Large Hadron Collider (LHC), CERN 91-03, May 1991.
- [2] A. Bezaguët, J. Casas-Cubillos, B. Gaillard-Grenadier, Th. Goiffon, H. Guinaudeau, L. Serio, A. Suraci, L. Taviani and R. van Weelderén, The superfluid helium cryogenic system for the LHC test string, to be presented at the Cryogenic Engineering Conf., July 1995.
- [3] W. Cameron, B. Jenny, G. Riddone, P. Rohmig, R. van Weelderén, Design and Construction of the Prototype cryostat for the Short Straight Sections of the CERN LHC, CERN MT/93-04 (ESH), Cryogenic Engineering. Conf., Albuquerque, July 1993.
- [4] R. Perin, for the LHC Magnet Team, Status of the LHC Programme and Magnet Development, Applied Superconductivity Conf., Boston, 1994, CERN AT/94-41(MA).
- [5] J.C. Brunet, J. Kerby, Ph. Lebrun, P. Rohmig, B. Szeless, L.R. Williams, Design of LHC Prototype Dipole Cryostats, CERN/AT-MA/92-19, Cryogenic Engineering. Conference, Kiev, July 1992.
- [6] J.C. Brunet, M. Genet, C. Reymermier, Ph. Trilhe, Interconnexion entre les composants magnétiques prototypes du LHC, CERN/MT/93-06 (ESH), May 1993.
- [7] L. Coull, D. Hagedorn, G. Krainz, K. Petersen, F. Rodriguez Mateos, L. Williams, Electrical Performance of a string of LHC magnets, to be presented at the 14th Magnet Technology Conf., Tampere, Finland, June 1995.
- [8] A. MacInturff, private communication, see also: W. Burgett et al., Power Tests of a String of Magnets of the Superconducting Super Collider, to be published, 1995.
- [9] P. Faugeras, R. Saban, Contrôle-Commande de la Cellule de Test LHC au SM18, CERN int. note, Jan. 1994, see also R. Saban, this conference.
- [10] Specifications ref CERN/AT/94-02(IC), CERN, May 1994, also INCAA Computers, Apeldoorn, Holland, private communication, September 1994.
- [11] The LHC Study Group, The Large Hadron Collider Accelerator Project, CERN/AC/93-03, Nov. 1993.

CONSTRUCTION AND TESTING OF ARC DIPOLES AND QUADRUPOLES FOR THE RELATIVISTIC HEAVY ION COLLIDER (RHIC) AT BNL*

P. Wanderer, J. Muratore, M. Anerella, G. Ganetis, A. Ghosh, A. Greene, R. Gupta, A. Jain, S. Kahn, E. Kelly, G. Morgan, A. Prodell, M. Rehak, W. Sampson, R. Thomas, P. Thompson, E. Willen
Brookhaven National Laboratory, Upton, New York 11973-5000 USA

The production run of superconducting magnets for the Relativistic Heavy Ion Collider (RHIC) project at Brookhaven National Laboratory (BNL) is well underway. Of the 288 arc dipoles needed for the collider, more than 120 have been delivered. More than 150 arc quadrupoles have been delivered. All of these magnets have been accepted for RHIC. This paper reports the construction and performance of these magnets. Novel features of design and test, introduced to enhance technical performance and control costs, are also discussed. Other papers submitted to this Conference summarize work on the sextupoles and tuning quads [1], arc correctors [2], and combined corrector-quadrupole-sextupole assemblies (CQS) [3].

I. ARC DIPOLES

A. Design and Construction

The arc dipole cold mass, shown in Figure 1, has a measured central field of 3.40 T at 5.0 kA operating current, an effective length of 9.44 m, and an 80 mm bore. The NbTi filaments have a diameter of 6 μm , with a minimum critical current density of 2600 A/mm² at 5 T, 4.2 K. The cable is made up of 30 wires with diameter 0.648 mm [4]. The 32-turn single-layer coil uses three wedges to achieve good field quality.

The magnet includes several novel features designed to reduce cost and improve quality. The turn-to-turn insulation of the cable is a double wrap of Kapton CI [5] polyimide with a polyimide adhesive on the outside of the outer wrap. This insulation offers numerous advantages, including better protection against punch-through and coils with better azimuthal size uniformity than previous wraps using fiberglass [6]. When the coils are molded, the high temperature necessary to set the adhesive is applied only briefly (225 C for 5 min. at minimum pressure) to avoid degradation of interstrand resistance. The high pressure used to size the coils is applied as a separate step at lower temperature (140 C for 30 min.). The azimuthal sizes of the coils selected for a magnet differ by at most 25 μm .

Another novel feature is the use, in three places, of injection-molded parts. An RX630 [7] phenolic spacer located between the coil and the yoke defines the pole angle, provides coil insulation to ground, and reduces saturation effects. The coil end saddles and spacers are made of high-temperature Ultem 6200 [8] able to tolerate deformation due to the high temperatures of the coil cure cycle. The three posts that support the cold mass in the cryostat are made of Ultem 2100.

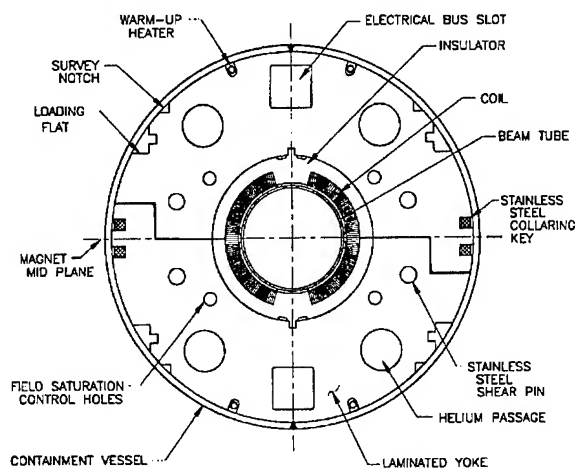


Fig. 1. Cross section of RHIC arc dipole cold mass.

Also novel is the use of the iron yoke as a collar for the coil, providing both prestress and flux return. The yoke laminations are 6.35 mm thick (to allow their use as collars), with dimensional precision of 25 μm maintained by the use of fine blanking. The cold mass sagitta is large, 46 mm. A more detailed description of the magnet is given elsewhere [9].

The dipoles are being manufactured by the Northrop Grumman Corporation (NGC) ready for tunnel installation, under a build-to-print contract. A total of 373 80 mm dipoles have been ordered: 298 9.44 m dipoles (including 10 spares) and 75 shorter dipoles with the same cross section for use in the insertion regions. The delivery rate is now one per day, with the entire order scheduled for completion in June 1996. A more detailed account of the manufacturing process is in preparation [10].

B. Test Procedures and Results

Tests performed on all dipoles at room temperature include hipot, optical survey, and field quality. The harmonics and field angle are measured at the vendor's site with a system containing a 1 m-long rotating coil and gravity sensors ("mole") supplied by BNL [11]. The integral field is measured with a stationary coil, by ramping the magnet. Field quality measurements are made at currents up to 30A.

The horizontal and vertical field components, B_x and B_y , throughout the magnet aperture are given in polar coordinates (r , θ) by

*Work supported by the U.S. Department of Energy under Contract No. DE-AC02-76CH00016.

$$B_y + iB_x = 10^{-4} B(R) \sum_{n=0}^{\infty} (b'_n + ia'_n) (\cos n\theta + i \sin n\theta) \left[\frac{r}{R} \right]^n$$

where i is the imaginary unit and $B(R)$ is the magnitude of the field due to the *fundamental* at the reference radius (R). In a normal dipole, $b_0 = 10^4$ and $B(R) = B_0$. In a normal quadrupole, $b_1 = 10^4$ and $B(R) = GR$ where G is the gradient $\partial B_y / \partial x$ at the magnet center.

Each of the initial 33 dipoles was quench-tested at BNL. Quench location data from an antenna system were taken for nearly all magnets. Field integrals were measured near injection (660 A), transition (1450 A), and store (5 kA). A number of magnets had additional tests to check the quench performance after thermal cycling and the AC and time-dependent properties of the superconductor. Fortunately, for RHIC operation, cable time-dependent characteristics are not significant.

Following careful review of the cold-test results from these dipoles and of the correlation between the field quality measured at room temperature ("warm") and cold, the RHIC Project implemented a plan to reduce the cost of cryogenic testing by cold-testing only 10% of the remaining magnets. Every tenth dipole is nominally scheduled for cold test. However, magnets with unusual construction histories are added to or substituted for the nominal magnets as the occasion arises.

Dipoles were cold-tested at 4.6 K, 5 atm He with a mass flow rate of 100 g/sec. Conductor-limited quenches were calculated from cable short-sample data to lie in the range 6.9 kA - 7.3 kA. The initial ramp to quench was made at 25 A/sec, with pauses of 0.5 minute each 500 A (to monitor bus and lead stability), except for a 1 hour wait at 5.5 kA (to check that the magnets would operate at the RHIC power supply limit without quenching). No magnet has quenched below 5 kA. Subsequent ramps to quench were at the design ramp rate of 83 A/sec. Typically magnets were quenched six times, with the last four quench currents lying in a narrow range ("on plateau"), at the expected conductor limit.

Dipoles quenching within a 100 A range above 6.5 kA (30% margin) are accepted automatically. Dipoles quenching in the range 6.3 kA - 6.5 kA are reviewed individually. All 41 cold-tested dipoles have been accepted; two have been reviewed individually. A summary of the plateau quench currents of all the magnets is given in Figure 2.

The integral transfer function, measured with the stationary coil at room temperature, is plotted against the dipole production sequence number in Figure 3. The accelerator requirement is that the rms fractional variation in the transfer function be less than 0.05%. For the 119 magnets in the figure, the fractional variation is 0.03%. Several features of the history catch the eye. First, the decrease at number 10, which occurred when NGC switched from BNL-supplied RX630 spacers to their own supplier. Second, the decrease at number 89, which investigation determined to be associated with the RX630 spacers, some of which had insufficient radial thickness. Beginning with number 108, each RX630 piece was inspected to insure sufficient radial thickness. RX630 pieces now being supplied have sufficient radial thickness. Magnets with low transfer function have been paired with magnets with high transfer function to reduce the load

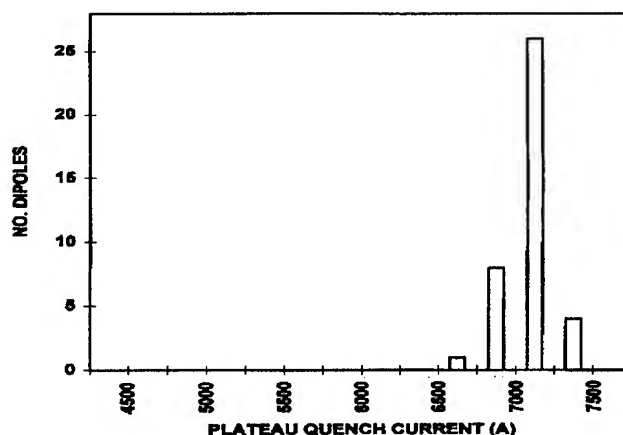


Fig. 2. Distribution of plateau quench currents of RHIC arc dipoles

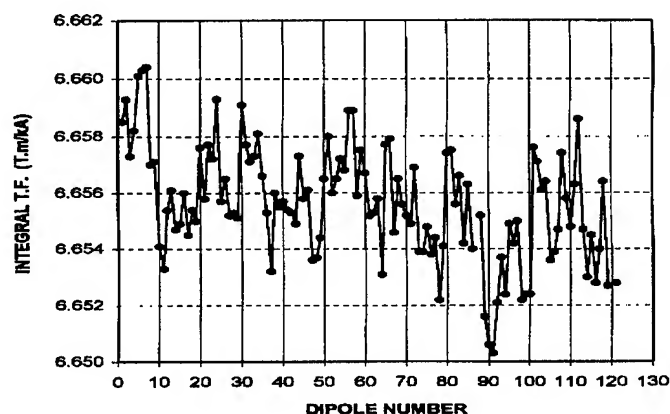


Fig. 3. Trend plot of arc dipole integral transfer function measured warm

on the trim dipoles, as described in another paper to this Conference [12]

The correlation between the warm and cold measurements of the integral transfer function is shown in Figure 4. The average ratio of the warm to the cold measurements of the transfer function is about 0.96. The magnet indicated by the solid symbol was excluded from the average. The rms variation of this ratio, 0.02%, characterizes the uncertainty in calculating the cold transfer function from warm measurements and is sufficiently small that the accelerator requirement, 0.05%, can be assured. The success of the stationary coil for warm, low-field measurements was essential, since NMR cannot be used at such low fields.

Integral values of the dipole angle have all been less than 3.2 mrad, averaging -0.4 mrad. Up to 5 mrad offset can be compensated during magnet installation into RHIC. The correlation between warm and cold measurements of the dipole angle is shown in Figure 5. Magnets with identical warm and cold measurements would lie on the line. The rms variation of the difference between warm and cold measurements is 0.15 mrad, much smaller than the accelerator tolerance of 1 mrad for installed magnets.

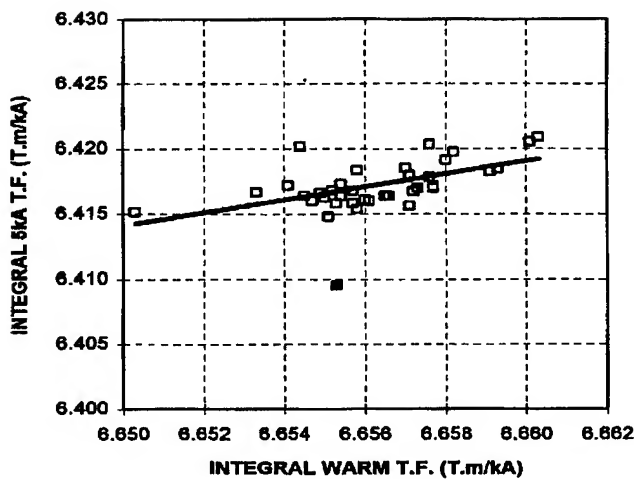


Fig. 4. Correlation of warm and 5 kA measurements of arc dipole integral transfer function

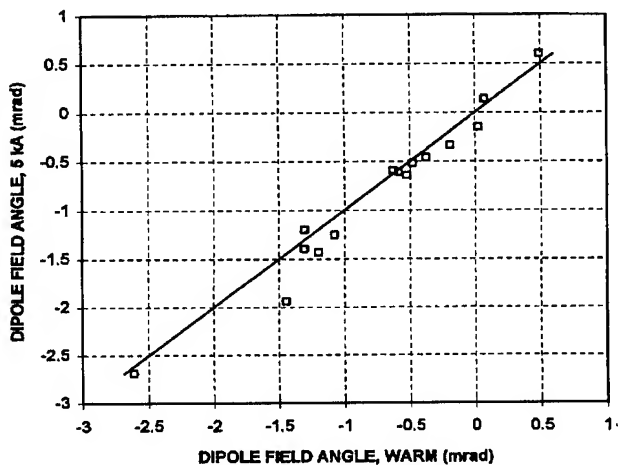


Fig. 5. Correlation of warm and 5 kA measurements of arc dipole integral field angles

The dipole twist is characterized by the rms variation of the eight measurements made with the mole in the straight section of the magnet during an axial scan. An increase can be noted for magnet numbers 83 through 90 (Figure 6). It appears to have been associated with a temporary change in the method used to obtain the proper sagitta. Discussions of the twist with NGC at this time resulted in an overall decrease. The allowed value of twist is 3 mrad.

The skew quadrupole term a_1 is an important indicator of the quality of magnet construction since it is produced by top-bottom asymmetries in the magnet. The most common of these is the difference in the azimuthal sizes of the upper and lower coils, for which the sensitivity is about 2 units of a_1 per 25 μm of difference. The skew quadrupole is plotted as a function of magnet sequence number in Figure 7. The mean a_1 is -0.02 units, with an rms variation of 1.4 units. These compare favorably to the values estimated for the series production, a mean of 1 unit or less, rms of 1.3 units. (The large value of a_1 in dipole number 105 is due to the use of coils which differed in size by about 75 μm . The pairing of these coils was forced by

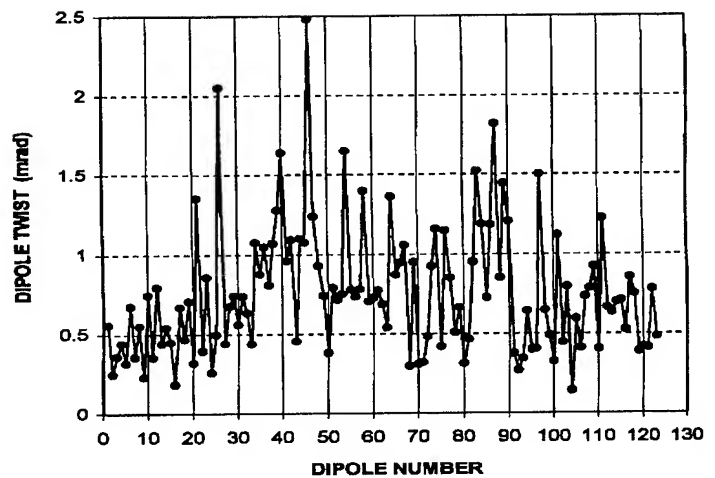


Fig. 6. Trend plot of the arc dipole twist

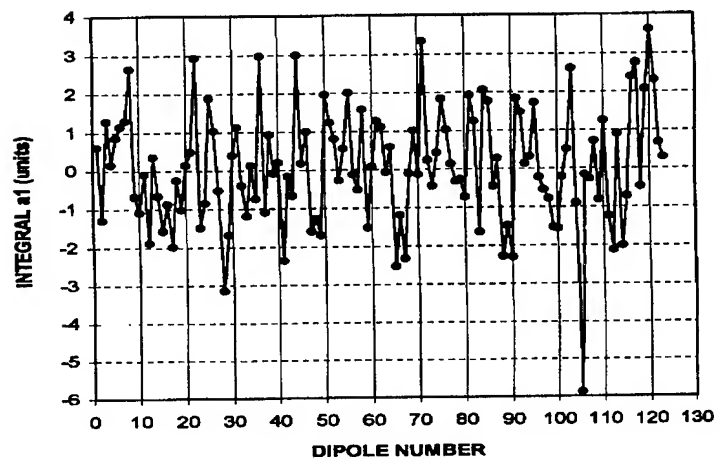


Fig. 7. Trend plot of arc dipole integral skew quadrupole

the change in coil cross section.)

The correlation of the warm and 5 kA values of the skew

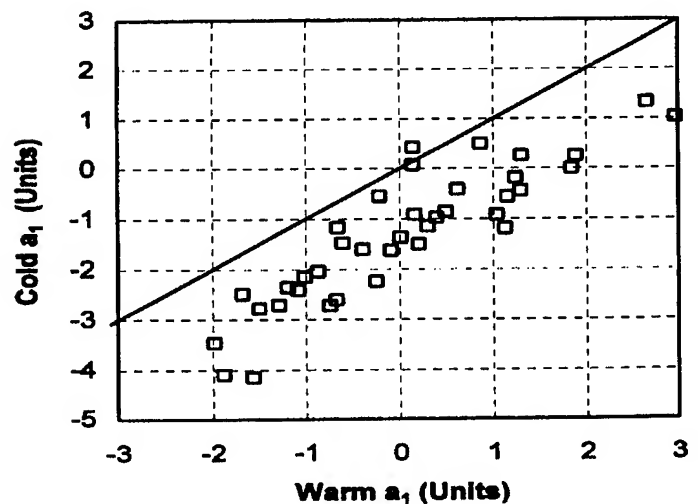


Fig. 8. Correlation of warm and 5 kA measurements of arc dipole integral skew quadrupole

quadrupole is shown in Figure 8. The rms variation of the warm - cold difference is 0.6 units. Magnets with identical warm and cold measurements would lie on the line. At 5 kA, a_1 is 1.6 units lower than at room temperature due to field leakage from the yoke and the asymmetric design of the position of the cold mass in the iron vacuum vessel. Efforts have been made during the production run to reduce a_1 at 5 kA by introducing a compensating asymmetry in the weight of the yoke blocks [13]. Small changes in the allowed harmonics, b_2 , b_4 , etc. have been made during the production run. These are discussed in detail in another paper submitted to this Conference [14].

II. ARC QUADRUPOLES

A. Design and Construction

A cross section of the quadrupole is shown in Figure 9. The arcs will contain 276 quadrupoles of 80 mm aperture, 1.11 m magnetic length, and a gradient of 75 T/m measured at the 5 kA operating current. The insertion regions will contain 144 additional 80 mm quadrupoles with lengths ranging from 0.93 m to 1.81 m. Including spares, NGC will produce 432 80 mm quadrupole cold masses. Production is scheduled to be completed at the end of 1995. (Incorporation of the quadrupoles into a CQS assembly is done at BNL [3].)

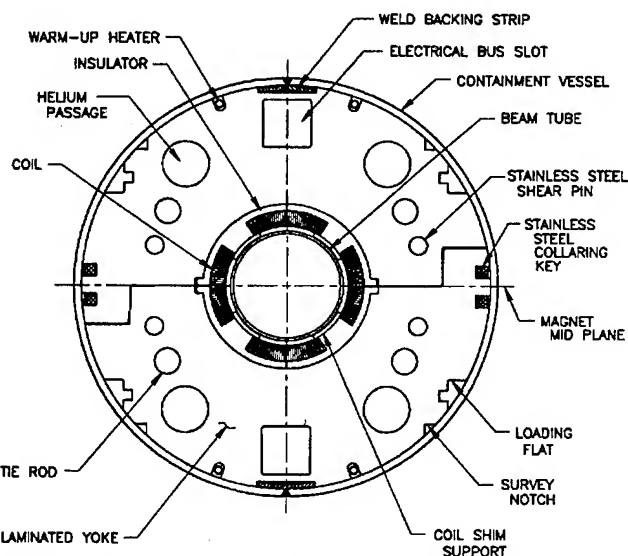


Fig. 9. Cross section of RHIC arc quadrupole cold mass

For reasons of economy, these magnets use many features of the dipole design, including the 30-strand cable with all-Kapton insulation, an injection-molded phenolic spacer between the coil and yoke, and a two-piece yoke with a tapered midplane and horizontal split. The yoke laminations are the same thickness as those used in the dipole. The single-layer coil has 16 turns and a symmetric copper wedge. Additional details of the magnet design are given elsewhere [15].

B. Test Procedures and Results

Cryogenic tests of the quadrupole cold masses were carried out in vertical dewars filled with liquid helium at 4.35 K and 1.12 atm. The magnets were ramped at 83 A/sec until they quenched. Magnets were quenched typically six times, to establish whether they were at the conductor limit. The quench performance was very good. All have quenched above 8 kA, with 90% reaching the conductor limit. All 58 tested so far have been accepted, with only one requiring individual review. Each of the initial 20 quads was cold-tested. Additional testing was done to confirm the effects of production changes. At present, 10% of the quads are being cold-tested.

The gradient and harmonics were measured with rotating coils long enough to obtain the integral with a single measurement, warm and cold. Warm measurements were carried out in a precision fixture built so that the axis of the quadrupole yoke and that of the measuring coil coincided within about 0.1 mm. It is expected that a well-built magnet, mounted in this fixture, will have a vertical field angle, with a small offset due to the leads. For these quadrupoles, the average field angle was -1.8 mrad, with an rms variation of 0.4 mrad. Similarly, it is expected that the axes of the field and the yoke will coincide. In the precise fixture the average horizontal offset was 0.03 mm, with an rms variation of 0.06 mm. The average vertical offset was 0.14 mm, also with 0.06 mm rms variation. The vertical offset could be due to the magnet leads. These measurements indicate that the quadrupoles are precisely made. (The measurements used for installation are made after construction of the CQS as a whole.)

The mean value of the quadrupole integral transfer function measured warm is 16.5 T/kA, with an rms variation of 0.05%, equal to the RHIC tolerance. The correlation between warm (10A) and cold values of the integral gradient is shown in Figure 10. The cold values are higher than the warm by 0.07% and the fractional rms variation of the cold - warm difference is 0.035%.

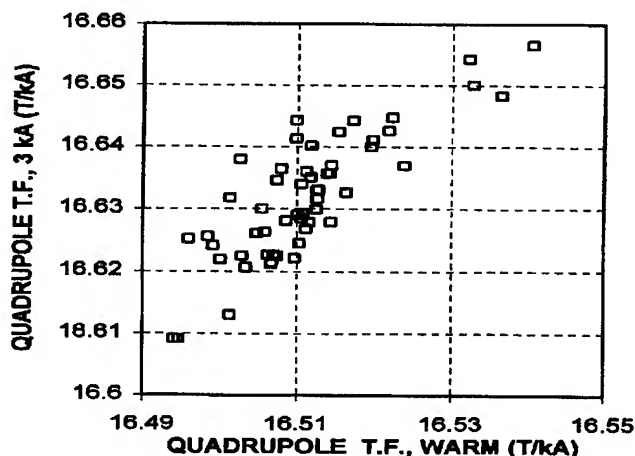


Fig. 10. Correlation of warm and 3 kA measurements of arc quadrupole integral gradient

The average value of the first allowed harmonic in quadrupoles, the dodecapole b_5 is 1.4 units (warm). Shifts at the level of 0.5 units have occurred during the production run. A finite

value is also expected for the octupole b_3 due to the dipole symmetry of the yoke. The average value of b_3 is -0.6 units (cold). However, five quadrupoles have b_3 in the range of 5 to 6 units due to misplacement of shims early in the production run. These magnets have been accommodated at special places in the lattice [12].

III. ACKNOWLEDGEMENTS

We acknowledge with pleasure the hard work and technical expertise of the Northrop Grumman staff.

IV. REFERENCES

[1] P. Thompson et al., "Superconducting Sextupoles and Tuning Quadrupoles for RHIC," Proc. 1995 International Particle Accelerator Conference (PAC'95), Dallas.

[2] A. Morgillo et al., "Superconducting 8 cm Corrector Magnets for the Relativistic Heavy Ion Collider (RHIC)," *ibid.*

[3] S. Mulhall et al., "Combined Element Magnet Production for the Relativistic Heavy Ion Collider (RHIC) at BNL," *ibid.*

[4] A. F. Greene et al., "Manufacture and Testing of the Superconducting Wire and Cable for the RHIC Dipoles and Quadrupoles," Proc. 1994 Applied Superconductivity Conf., Boston (to be published) and BNL Report No. BNL 60350.

[5] Kapton is a registered trademark of the DuPont Corporation.

[6] M. Anerella et al., "Improved Cable Insulation for Superconducting Magnets," Proc. 1993 Particle Accelerator Conference (Washington, D.C.), pp. 2790 - 2792.

[7] RX is a registered trademark of the Rogers Corporation.

[8] Ultem is a registered trademark of the General Electric Corporation.

[9] P. Wanderer et al., "Dipole Magnet Development for the RHIC Accelerator," pp. 175 -187, *New Techniques for Future Accelerators III*, ed. G. Torelli, Plenum Press, New York, 1990.

[10] M. Anerella et al., "Industrial Production of RHIC Magnets," to be submitted to 1995 Magnet Technology Conference (MT14), Tampere, Finland.

[11] R. Thomas et al., "Performance of Field Measuring Probes for SSC Magnets," pp. 715-718, *Supercollider 5*, ed. P. Hale, Plenum Press, New York, 1994.

[12] J. Wei et al., "Field Quality Evaluation of the Superconducting Magnets for the Relativistic Heavy Ion Collider," Proc. PAC'95.

[13] R. Gupta et al., "Skew Quadrupole in RHIC Dipole Magnets at High Fields," to be submitted to MT14, Tampere, Finland.

[14] R. Gupta et al., "Field Quality Control Through the Production Phase of the RHIC Arc Dipoles," Proc. PAC'95.

[15] P. Wanderer et al., "Test of Eight Superconducting Arc Quadrupoles for RHIC," IEEE Trans. Magnetics, Vol. 30, No. 4 (July 1994), p. 1734; P. Thompson et al., "B Series RHIC Arc Quadrupoles," Proc. 1993 Particle Accelerator Conference, p.2766.

PERMANENT MAGNET DESIGN FOR THE FERMILAB MAIN INJECTOR RECYCLER RING

G.W.Foster, K. Bertsche, J.-F Ostiguy, B.Brown, H. Glass, G. Jackson, M. May, D. Orris, Fermi National Accelerator Laboratory¹, MS 345, P.O.Box 500, Batavia, IL 60510 USA
Dick Gustafson, University of Michigan Physics Department, Ann Arbor, MI.

ABSTRACT

The design of permanent magnets for use in the Fermilab Main Injector "Recycler" ring is described. The magnets are a hybrid design with the field shape determined from accurately machined pole tips and the field driven by strontium ferrite blocks. The choice of magnetic material is discussed. A temperature compensation scheme has been demonstrated which uses a low Curie-temperature alloy to null out the intrinsic temperature coefficient to the ferrite. 1.2m prototype magnets have been constructed which achieve the design goal of $\Delta B/B < 10^{-4}$ over an aperture of 3.5"(h) x 2"(v).

I. INTRODUCTION

Raising the luminosity of the Tevatron requires collecting and stacking more antiprotons. A key element in this is the "Recycler" ring [2], an 8 GeV storage ring located in the 3.3km Main Injector tunnel under construction at Fermilab [3]. Permanent magnets are an attractive option because of the fixed energy and the 0.1T average guide field. Low cost and reliability are also important considerations in favor of permanent magnets. A workshop was held at LBL in November 1994. Since the successful outcome of that workshop, prototype work has begun with the goal of starting production in 1996 and commissioning the ring in 1998.

II. BASIC DIPOLE MAGNET DESIGN

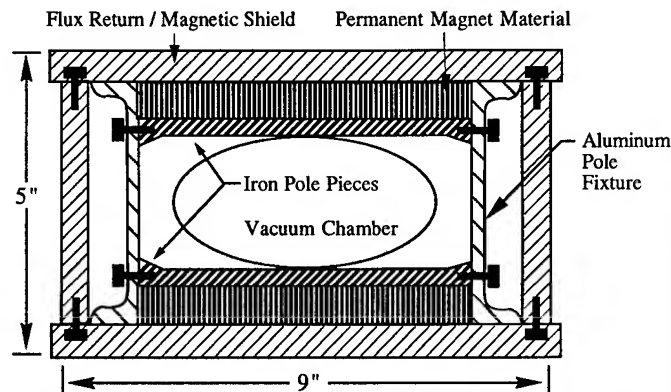


Figure 1: Cross-section of the 1 kG hybrid permanent magnet dipole. This design duplicates the Main Injector beam pipe dimensions and good field aperture ($\pm 1.75"$ at $\Delta B/B_0 = 10^{-4}$). The overall dimensions are 5"x9" and the weight of a 6 m section is approximately 2500 lbs. The field is driven by two permanent magnet blocks 3/4" thick by 6" wide.

In this "hybrid" design, the field quality is determined largely by the shape and placement of the iron pole tips located immediately above and below the beam pipe. The flux return is fabricated from 1/2" thick bar stock and provides a "box beam" structure which provides most of the mechanical rigidity. The peak field in the flux return is approximately 6 kG.

The assembly sequence used for the prototypes is to build the magnet from the inside out. First, the pole tip spacing is set by clamping them into position against a precisely machined 2.0000" thick bar of tool steel, then bolting or pinning them to side supports made from aluminum U-channel. This ensures the parallelism of the pole pieces which is essential to minimize gradient errors. Next, individual bricks are clamped or glued onto the pole tip/side support structure. Finally the entire assembly is slid into flux return and tested with a rotating coil harmonics probe.

The overall strength of the magnet can be controlled by any of the following: adjusting the amount of magnetic material included in each magnet, sorting the bricks by strength, using a commercially available fixture to perform a controlled demagnetization of the bricks to a standard level, or inserting small steel rods into the region alongside the bricks to help "steal" flux away from the pole tips and thereby trim the magnet strength. The gradient and sextupole can be controlled by means of wedge or parabolic end shims affixed to the ends of the pole tips. This procedure is straightforward because the shims need only function at one level of magnetic excitation. We plan to reserve one end of the magnet for production trims to ensure that all magnets have identical multipole content, and reserve the other end for "field modifications" to adjust e.g. the tune or chromaticity of the ring.

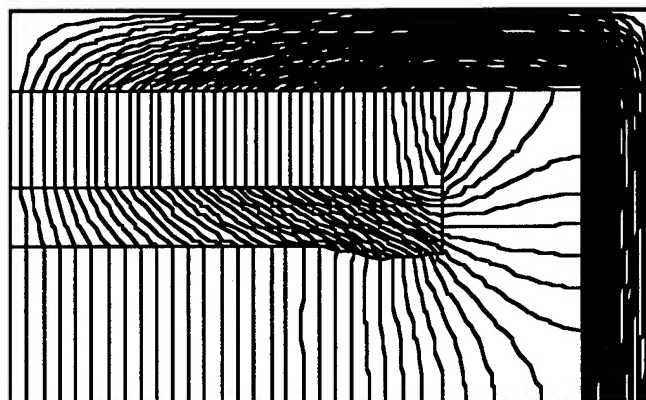


Figure 2: POISSON field map of the upper-right quadrant of the permanent magnet dipole shown in fig. 1.

III. CHOICE OF MAGNETIC MATERIAL

Several magnetic materials were considered for the Recycler magnets, including Samarium Cobalt, Alnico, Neodymium-Iron-Boron, and Strontium or Barium Ferrite. Strontium Ferrite was selected on the basis of cost, ease of fabrication, radiation hardness, and stability over temperature and time. Samarium cobalt was roughly 30 times more expensive and has suspect radiation resistance [4]. Alnico was approximately 10x more expensive and an optimized Alnico design results in a tall, bulky magnet. Barium Ferrite is a largely obsolete material with no advantages over Strontium Ferrite and was not seriously considered.

IV. SAMPLE-TO-SAMPLE UNIFORMITY

Strontium Ferrite is the most commonly used permanent magnet material in automotive applications and can be obtained in standard sizes and strengths from a number of manufacturers [5]. We chose the standard 4"x 6"x 1" high "bricks" made of Type 8 strontium ferrite for the magnets in our prototype program. Samples of ~100 bricks were obtained from a number of foundries, and a single-brick testing device was made at the Magnet Test Facility at Fermilab. The design of our hybrid magnet makes the field quality insensitive to the details of the magnetization of the material. Thus the magnetic strength of each brick could be adequately characterized by a test fixture which consisted of a magnetic circuit with approximately the same reluctance as the brick would see in the final magnet design. Individual bricks were inserted in the magnetic circuit and the resultant flux was recorded via a pickup coil and integrator. The distribution of brick strengths from samples one lot from one particular vendor is given in the figure below.

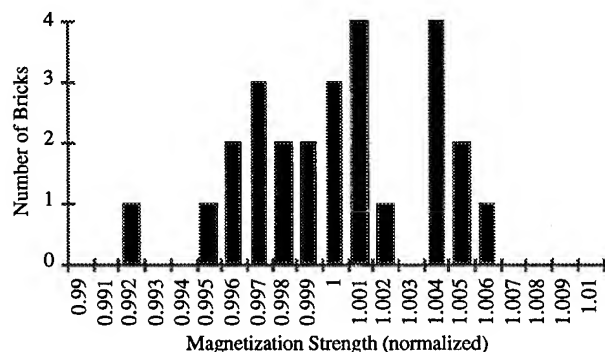


Figure 3: Histogram of the first 26 bricks tested with the MTF single brick field strength tester. The full spread of the bricks tested was 1.3% and the RMS spread was 0.3%. This measurement indicates that within a single lot of bricks we expect the variation to be less than the $\pm 10\%$ tolerance specified by the manufacturer.

V. TEMPERATURE COMPENSATION

One major drawback of strontium ferrite in accelerator applications is a reversible temperature coefficient of the residual field B_r of $-0.19\%/^{\circ}\text{C}$. A technique has been proposed and tested [6] which uses an Iron-Nickel alloy with a Curie Temperature of $\sim 55^{\circ}\text{C}$ to shunt flux away from the pole tip in a temperature-dependent manner and thereby null out the temperature coefficient of the magnet. See fig. 4

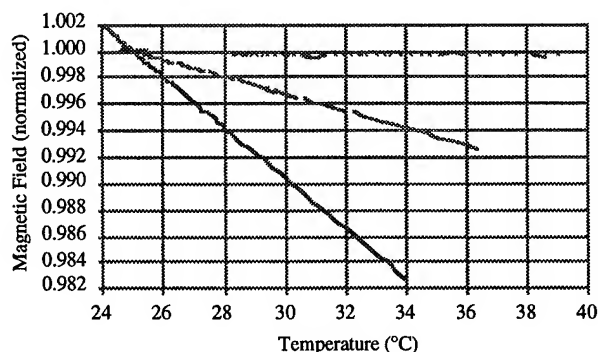


Figure 4 Cool-down curves showing variation of the magnetic field in a permanent magnet prototype with various size temperature compensation shunts. Bottom curve: uncompensated magnet showing the expected temperature coefficient of $-0.19\%/^{\circ}\text{C}$. Middle curve: first attempt at a temperature compensation shunt. Top curve: second attempt using a shunt of a larger size estimated from the performance of the first shunt. The temperature coefficient has been reduced by approximately two orders of magnitude, more than adequate for our application.

IV. LATTICE AND MAGNET OPTIONS

The lattice and permanent magnet design present a set of interrelated tradeoffs involving field strength vs. number of magnets, separated function vs. combined function magnets, laminated vs. "bar stock" construction, and sagitta'd magnets vs straight magnets with a larger horizontal aperture. The four main lattice options under consideration are shown in fig. 5.

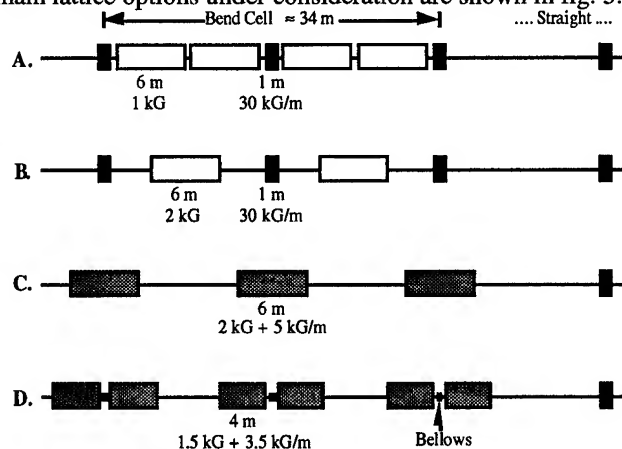


Figure 5: Sketch of the permanent magnet options under consideration in the magnet prototype program. Option A is a direct copy of the Main Injector lattice, while the 1.5 kG combined function option D is currently favored.

The "bar stock" magnet construction chosen argues in favor of straight magnets. Combined function magnets (fig. 6) reduce the number of quadrupoles from 208 to 36 at the cost of complicating the dipole pole tip machining and magnet measurements, and reducing the bend field by about 5%. A stronger field can be obtained by putting more bricks behind the pole tips, but one reaches a point of diminishing returns as the field asymptotically approaches the residual field B_r of the driving material. At the present stage in our prototype program we favor a 1.5kG combined-function, non-sagitta'd magnet driven by a single 1" thick brick behind each pole tip.

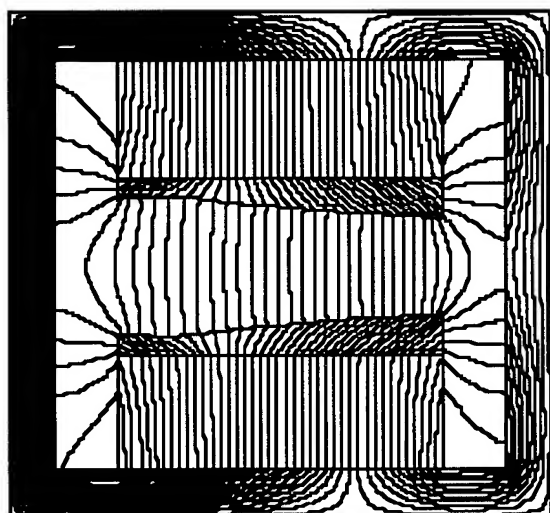


Figure 6: Cross section of a 2 kG gradient-sector magnet for lattice option C described in the text. The field is driven by two 1" high by 6" wide permanent magnet bricks at each pole tip. Overall dimensions are 8" x 12". The magnetic center of this dipole is 12" from the beam, so that its gradient is intermediate between that required for the arcs (17") and dispersion suppressor dipoles (8.6") needed for lattice option C.

VII QUADRUPOLE DESIGN

The quadrupole prototype currently under construction is shown in figure 7.

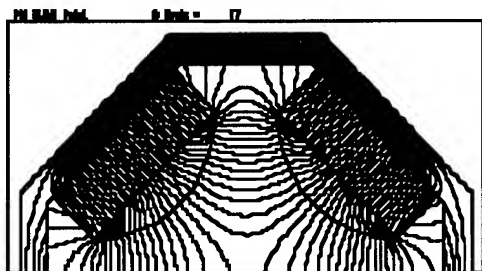


Figure 7: Magnetic field map for the upper half of the permanent magnet quadrupole magnet cross section used in all lattice options. Field shaping is provided by iron pole tips with circular inner surfaces. The field is driven by Ferrimag 8A material ($B_r=3.9$ kG) in blocks 1" x 3" in cross section. An iron flux return shell 1/2" thick surrounds the assembly.

The quadrupole magnet has the additional challenge that the strengths of the diagonally opposite poles must be matched in order to obtain a pure quadrupole field between the pole tips. Thus in production each pole tip must be individually trimmed to the specified strength, rather than trimming the overall strength as in the case of the dipole.

VIII. PROTOTYPE RESULTS AND STATUS

Following the temperature compensation test magnet, several 1.2m prototype magnets have been constructed. In general there have been no surprises in the construction of these magnets, with typical assembly times "from parts" of approximately an hour. The first prototype dipole had flat (non-shimmed) pole tips. The second had pole tips machined to the shape determined by POISSON. This 2nd prototype met the field quality specification ($dB/B < \pm 0.0001$ over a 3.5" horizontal good-field region) with the help of a angled shim at the end of the pole tip to remove a minor gradient error. The first 1.2m combined-function prototype awaits test and a quadrupole is under construction. We expect to begin construction of 4-5m full length prototypes soon.

III. ACKNOWLEDGMENTS

It is a pleasure to recognize the contributions of all of the participants of the "Workshop on Issues Surrounding the Construction of Permanent Magnet Synchrotrons" and especially Klaus Halbach for his guidance in this project.

IV. REFERENCES

- [1] Operated by Universities Research Association Inc., under contract with the U.S. Department of Energy.
- [2] "Storage Ring for Increased Antiproton Production at Fermilab", G.W. Foster and G.P. Jackson, these proceedings.
- [3] "The Fermilab Injector Complex", D. Bogert et al, these proceedings.
- [4] R. Holzinger, these proceedings.
- [5] "Permanent Magnet Materials" and "Permanent Magnet Guidelines", publications of the Magnetic Materials Producers Association, 11 S. LaSalle St. Chicago IL 60603 (312)201-0101.
- [6] "Temperature Considerations in the Design of a Permanent Magnet Storage Ring", K. Bertsche, G.W. Foster, and J-F. Ostiguy, these proceedings.

Recent Advances in Insertion Devices

E. Gluskin and E. R. Moog

Advanced Photon Source, Argonne National Laboratory, Argonne, IL 60439, USA

ABSTRACT

The demand for more and better insertion devices (IDs) at new third-generation synchrotron radiation facilities has prompted significant advances in ID technology. Since the advances are being made at different laboratories around the world, an overview is given here of this progress. The focus is on those results that apply to IDs in general rather than to those from one specific ID or laboratory. The advances fall into two general categories: those that reduce the net effect that the ID has on the particle beam, and those that enhance the quality of the emitted light spectrum. The need for these advances, the factors that are most important in achieving them, and the current state of the art are discussed.

I. INTRODUCTION

Significant progress has been made in the field of insertion devices, particularly during the past three or four years, because of the construction and initial operation of third generation synchrotron radiation sources. New developments have been reported at recent PAC/EPAC conferences, Synchrotron Radiation Instrumentation conferences, and in review articles. [1-5]

In the late 1970's, the first insertion devices (IDs) were installed on first-generation synchrotron radiation sources. Their radiation properties were studied, and it was shown that IDs can be compatible with storage rings. [6] Ten years later, a wide variety of IDs occupied straight sections on almost all existing storage rings. With the advent of third-generation synchrotron radiation sources in the early 1990's, there has been a dramatic increase in the number of insertion devices (IDs) installed or planned worldwide, as shown in Fig. 1. These new storage rings may be designed to have ten times as many IDs installed as was typical for older sources. ESRF has been running for the past two years with more than a dozen IDs installed; it is the first machine so far to operate with so many IDs.

Fig. 1 also shows that undulators are increasingly preferred over wigglers. This is because many experiments today require very high brilliance. This high brilliance can be achieved without unnecessary power loads from unneeded wavelengths of light by using undulators, because high-quality undulators have very sharply-peaked emitted-light spectra. Recent significant advances in the ability to build and tune high-quality undulators have encouraged this trend. The magnetic field of an undulator can now be tuned so that the spectrum of emitted light has sharp and strong harmonic peaks out to very high harmonic numbers.

The magnetic field tuning techniques that have been developed not only ensure a high-quality spectral output, but also minimize the net effect that an ID has on the stored particle beam. This has become increasingly important with the newer small-emittance storage rings that have many IDs

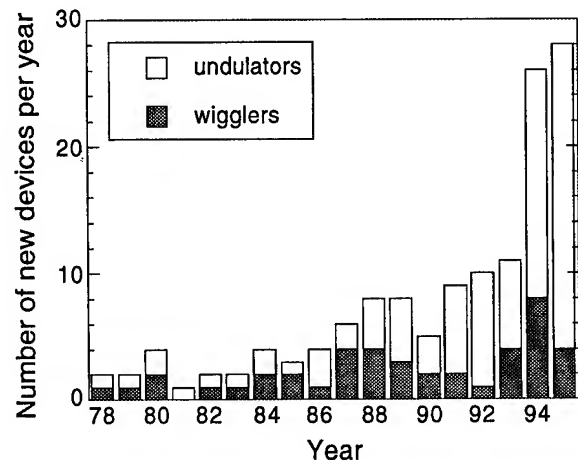


Figure 1. Number of new insertion devices constructed per year, worldwide, from 1978 to 1995. (This does not include free-electron lasers.)

installed, since the cumulative effect of all the installed IDs must be considered.

Of the many IDs [3] that have been built or proposed, some are optimized to produce specific radiation characteristics, such as variable polarization. Other IDs have particularly short or particularly long period lengths. Some of these special IDs have been installed on older synchrotron radiation sources, where they can produce useful light and also serve as prototypes for IDs for newer storage rings.

In what follows, we will discuss recent progress in both reducing the net effect that IDs have on the stored particle beam and in tuning IDs for high-quality spectral output.

II. ID-STORED BEAM INTERACTION

Insertion devices that are installed into storage rings can have undesirable net effects on the closed orbit in the ring. Such effects have been a major concern since the first insertion device was installed into a storage ring [7]. In addition, IDs can cause betatron tune shifts, decreased beam lifetime due to dynamic aperture changes, and vertical-horizontal coupling. In first and second generation sources, various local and global feedback schemes were used to correct closed-orbit distortions. [8, 9]

The requirements of new third-generation sources are more stringent, however. The emittance of the stored particle beam and the physical aperture of the beam are smaller, so that allowable ID-related orbit distortions are smaller. This smaller allowable effect is distributed among a much larger number of insertion devices, making the requirements for each individual ID more demanding.

Orbit distortions are also, in general, a strong function of the magnetic gap of the insertion device. An undulator needs to have its gap changed whenever its user wants a different photon energy. With an increase in the number of undulators on a storage ring, there is also an increase in the frequency of gap-change requests. Users of the synchrotron radiation facility rapidly lose patience with "orbit correction" interruptions or beam instabilities that are due to gap changes in someone else's ID. Third-generation storage rings therefore demand IDs that are "fully compensated", i.e., that have negligible effect on the stored beam at any magnetic gap.

Orbit perturbations can be limited by setting maximum values for the first and second integrals of the magnetic field through the insertion device, and by setting maximum values for the higher order integrated magnetic moments (i.e., how the first integral of the field varies as one moves away from a line through the exact center of the ID). The first field integral through the ID determines the angle between the pre- and post-ID trajectories of a particle, while the second field integral determines the displacement. The maximum allowed first and second integrals can be chosen using the following expressions so that the effect of the ID is much less than the beam emittance:

$$\frac{\int B_{x,y} dz}{B \cdot \rho} \ll \sqrt{\frac{\epsilon_{y,x}}{N \cdot \beta_{y,x}}}$$

$$\frac{\int \int B_{x,y} dz' dz}{B \cdot \rho} \ll \sqrt{\frac{\epsilon_{y,x} \cdot \beta_{y,x}}{N}}$$

where $B_{x,y}$ is the horizontal or vertical magnetic field, $B \cdot \rho$ is the rigidity parameter for the storage ring, $\epsilon_{y,x}$ is the vertical or horizontal emittance, $\beta_{y,x}$ is the vertical or horizontal beta function, and N is the number of IDs on the storage ring. Table 1 shows the first and second integral tolerances for the APS storage ring.

Table 1. APS Insertion Device Tolerances

Quantity	Normal	Skew
First integral (G-cm)	20	20
Second Integral (G-cm ²)	20 000	20 000
Quadrupole (G)	50	50
Sextupole (G/cm)	200	100
Octupole (G/cm ²)	300	50

These same requirements for beam size stability also determine the maximum allowed integrated quadrupole moments. Requirements for higher moments that affect the dynamic aperture can be determined by using storage ring tracking codes [10] to evaluate the effect of these moments. The integrated multipole tolerances for the APS storage ring are included in Table 1. In general, however, these numbers depend on the good field region required for the ID because the higher order moments are a description of how the field

integral varies as the line of integration is moved laterally within the good field region. Typical good field regions are less than a few centimeters horizontally and less than a centimeter vertically.

A number of different ID designs and fabrication techniques have been tried in order to meet these challenging magnetic field quality requirements. At some labs, the approach has been to demand very high mechanical and magnetic precision for everything that goes into an ID and to sort the magnets very carefully, with the goal of producing a device whose field is so good that it needs no post-assembly shimming. [11] At other labs, inexpensive components have been a greater priority. The magnets are carefully sorted, but large field errors remain after assembly. Much work then goes into magnetic shimming in order to achieve a high-quality field. [12, 13]

In order to be able to measure the properties of IDs sufficiently precisely, the accuracy and reliability of magnetic measurements has had to improve. New techniques and improved old techniques now make the necessary measurements possible [14]. For example, first field integrals through a 5-meter-long ID are now measured with a reproducibility of less than a Gauss-cm, as required for accurate higher-order multipole measurements.

There is now a better understanding of how to suppress magnetic moments, both by maintaining high tolerances during the selection of magnetic materials and during fabrication, and by using shimming techniques to correct the effects of imperfections in an assembled device. Impressively small ID magnetic moments have been achieved. In Table 2, experimental results for an ESRF and an APS planar ID are shown.

Table 2. Multipole moments achieved [15]

Moment	at ESRF	at APS
Dipole (G-cm)	<20	15
Quadrupole (G)	<10	20
Sextupole (G/cm)	<10	40
Octupole (G/cm ²)	<10	10

For non-planar IDs, such as sources of elliptically or circularly polarized radiation, magnetic tuning is even more challenging. Nevertheless, two such devices — the helical undulator Helios [16] and the Elliptical Multipole Wiggler (EMW), which has an AC electromagnet [17] — have been successfully operated at ESRF and NSLS, respectively. In Helios, the vertical positions of the upper and lower jaws can be moved independently (one jaw produces a vertical field, the other a horizontal field), and a relative longitudinal displacement is possible. The polarization and wavelength are altered by moving the magnetic arrays so as to change the 3-D magnetic field distribution. In the EMW, the horizontal field component from the electromagnet changes at frequencies of up to 100 Hz so that a dynamic compensation system is required. For both devices, however, the closed orbit displacements are negligibly small. For Helios, the closed orbit distortion was less than 6 μm , and for the EMW it was less than 1 μm .

The few examples above show the substantial progress that has been made in minimizing the effects that IDs

have on a storage ring. The next goals are to eliminate the need for a local feedback system and, once it has been demonstrated that a gap change will have no effect on other beamlines, to allow synchrotron radiation users to change their ID gaps freely.

III. ID SPECTRAL PERFORMANCE

Magnetic field errors also affect the spectral performance of an undulator. Errors can arise from such things as non-uniformities in the magnetic properties of the materials used and finite mechanical tolerances on the magnetic structure components. The effect of these errors on the spectrum of the undulator is to decrease the brilliance of the harmonic peaks. Higher harmonics suffer greater decreases than lower harmonics. Therefore, the spectral quality of an undulator can be defined by how close the brilliance of the emitted spectrum is to that of an ideal undulator.

The real test of spectral performance for an undulator is, of course, measurement of the absolute flux of radiation emitted as a function of frequency. Even before the device is installed in the storage ring, however, its performance can be predicted from magnetic field measurements. The magnetic field map is used to calculate particle trajectories through the undulator and, in turn, the brilliance of the light that will be emitted as a function of wavelength.

It has been shown that the best predictor of brilliance reduction is the rms value of the phase error [18]. Walker [19] showed the quantitative relationship between the two. Phase error arises from differences in the time intervals between

successive wiggles in the particle trajectory. The real trajectory is calculated from measurements of the magnetic field along the undulator. The phase in this real trajectory is then compared with the phase for an ideal undulator to obtain the rms phase error, which is in turn used as a figure of merit for optimizing the undulator magnetic field. Walker [19] found that the decrease in brilliance compared with the ideal case varies like $\exp(-(n\cdot\phi)^2)$, where n is the harmonic number and ϕ is the phase error.

In order to optimize the undulator magnetic field, the magnet blocks are carefully measured, then sorted into an arrangement that will give as perfectly periodic a field as possible. For a hybrid undulator that uses high-permeability pole pieces, the poles can be sorted by size as well. Once the undulator is assembled, it can be shimmed to correct the field integrals, the moments of the field integrals, and the trajectory as a function of undulator magnetic gap. Shimming is also used to minimize the phase errors. The typical result is an rms phase error of several degrees, leading to a reduction in the fifth harmonic brilliance of about 20%. Post-assembly shimming along the ID has not been used much during ID fabrication at ALS, nor is it planned to be used at BESSY II. Nevertheless, very impressive performance results have been achieved by careful selection and sorting of magnets and by maintaining extremely tight mechanical tolerances in the magnetic structure. Some of these results are shown in Fig. 2. [20] Fig. 2 shows the on-axis flux measured from the ALS U8.0 undulator at $K=5.24$, along with the flux calculated from the measured magnetic field. For comparison, the flux density calculated for an ideal ALS U8.0 magnetic field is also shown. The harmonics shown start at the 18th.

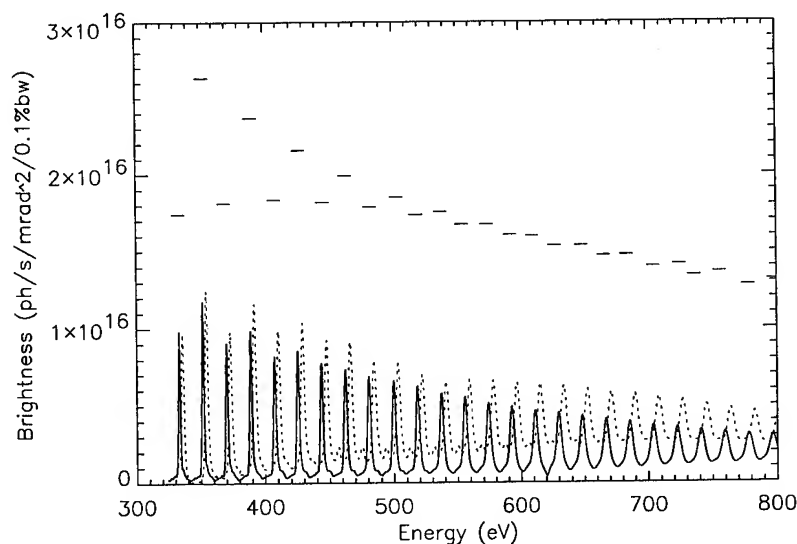


Figure 2. High-harmonic flux from the ALS U8.0 undulator at $K=5.24$. The dotted line shows the flux measured from the installed device. The solid line shows the flux calculated from the measured magnetic field. The calculated peak flux values from an ideal U8.0 magnetic field are also indicated by the dashed lines. The harmonics shown start at the 18th.

Recently, a phase-shimming technique was used to achieve rms phase errors of less than a degree. This small phase error leads to the 20% reduction in brilliance not occurring until about the 27th harmonic. [21] Similar results have been achieved at ESRF using their 'spectral shimming' technique. At ESRF, radiation from harmonics up to the eleventh will be used. These techniques have both been applied to pure permanent magnet IDs. At APS, a phase-shimming approach has been used to optimize the spectrum of a hybrid undulator. The phase errors were reduced to 4°, which corresponds to a seventh harmonic brilliance of about 80% of ideal.

With these advances, undulators are now being built whose spectral performance is very close to what is theoretically possible. Future effort will probably be directed towards the development of specialized IDs.

Many different types of advanced IDs have been described in recent papers. Third-generation storage rings still have many straight sections that are as yet unoccupied by IDs. Therefore, a wide and long (particularly at Spring-8, with its 30-meter-long straight sections) field is open for future developments that will also benefit the fourth-generation synchrotron radiation sources.

IV. ACKNOWLEDGMENTS

We thank the many contributors to the information gathered for Fig. 1, including M.-E. Couprie, P. Elleaume, M. Eriksson, M. Green, S. Krinsky, S. Marks, S. Sasaki, R. Walker, and H. Winick. We also thank R. Walker, P. Heimann, and D. Mossessian for sharing information before its publication, and R. Dejus for help in preparing Fig. 2.

This work was supported by the U.S. Department of Energy, BES-Materials Science, under Contract No. W-31-109-ENG-38.

V. REFERENCES

- [1] R.P. Walker, Advanced Insertion Devices, Proc. EPAC, London, June 1994, p.310.
- [2] P. Elleaume, ESRF Newsletter N21, June 1994, p.10 and ESRF Newsletter N23, March 1995, p.10.
- [3] Proceedings of the International Workshop on Insertion Devices for Circularly Polarized Light, BESSY, Berlin, November 1993.
- [4] R.D. Schlueter, Wiggler and Undulator Insertion Devices, LBL Report-35565, May 1994.
- [5] H. Kitamura, Rev. Sci. Instrum. 66, 2007 (1995).
- [6] H. Winick, et al., Physics Today 34, 50 (May 1981).
- [7] L. Smith, ESG Technical Note-24 (January 1986).
- [8] O. Singh, Proc. Particle Accelerator Conference, Washington D.C. (May 1993).
- [9] J.N. Galayda, Y. Chung and R.O. Hettel, "Synchrotron Radiation Sources, A Primer", Ed. H. Winick, World Scientific, 1995, p.344.
- [10] Y. Chung, these proceedings.
- [11] E. Hoyer, private communication.
- [12] D.C. Quimby, et al., Nucl. Instrum. Meth. A285, 281 (1989).
- [13] J. Chavanne, International Workshop on Magnetic Measurements of Insertion Devices, September 1993, ANL/APS/TM-13, p.79.
- [14] International Workshop on Magnetic Measurements of Insertion Devices, September 1993, ANL/APS/TM-13.
- [15] ESRF results are from ESRF Newsletter N23, March 1995, p.10. APS results are for a 3.3-cm period Undulator A at 15.5 mm gap.
- [16] P. Elleaume, J. Synchrotron Rad. 1, 19 (1994). The first double-helical undulator with a self-compensated magnetic configuration (chicane-type) was built and installed at the VEPP-2M storage ring in 1984 (preprint INP 84-111).
- [17] E. Gluskin, et al., these proceedings.
- [18] B.L. Bobbs, et al., Nucl. Instrum. Meth. A296, 574 (1990).
- [19] R.P. Walker, Nucl. Instrum. Meth. A335, 328 (1993).
- [20] P. Heimann and D. Mossessian, to be published in Nucl. Instrum. Meth.
- [21] R.P. Walker, et al., these proceedings.

PERMANENT MAGNET BEAM TRANSPORT

R. F. Holsinger, Aster Enterprises, Inc., N. Billerica, MA 01862 USA

Abstract

Permanent Magnet (PM) quadrupoles, dipoles and other multipoles have been developed and used in an increasing number of accelerator applications for transporting and manipulating charged particle beams. Research applications include Drift Tube Linear Accelerators, Storage Rings, and Recirculators. Industrial applications include various accelerators for Isotope Production and Neutron Generation Accelerators. The inherent advantages and disadvantages of permanent magnet technology as well as practical implementation will be discussed. The possibility of new innovative applications for both research and industrial accelerators will also be discussed.

I. INTRODUCTION

Approximately 15 years ago the first iron-free ring type rare earth PM Quadrupoles (PMQ's) were constructed and installed in linear accelerators [1], [2]. Since that time, this technology has been implemented in an increasing number of beam transport applications. The fundamental theory for ring type PM multipoles was described by K. Halbach [3], based on anisotropic samarium-cobalt PM materials that were developed in the early 1970's. These new materials and design ideas led to several important developments of PM devices for beam transport and manipulation.

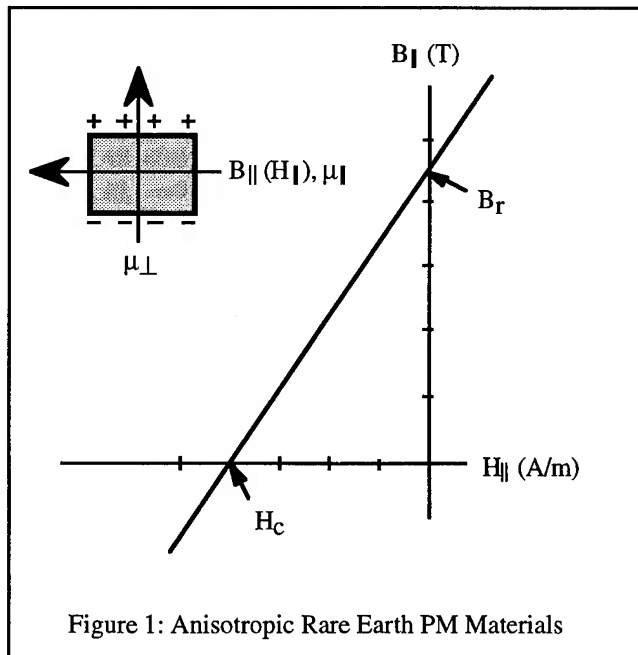


Figure 1: Anisotropic Rare Earth PM Materials

II. RARE EARTH PM MATERIALS

Subsequently, other important rare earth based materials have been developed, e.g. Neodymium-Boron-Iron. Figure 1 shows the idealized B(H) characteristics for these types of materials.

In these materials:

$$\mathbf{M} = \mathbf{B}/\mu_0 - \mathbf{H}$$

If we make the assumption that:

$$B_r/\mu_0 = H_c, \text{ then } |\mathbf{M}| = \text{constant},$$

and for $B_r = 1.0$ Tesla, $|\mathbf{M}| \approx 8,000$ Amp/cm.

Thus, the equivalent surface current flowing around the surface of blocks of these materials, as illustrated in Figure 1, is sizable, and it is no surprise that such blocks are difficult to position near each other or near other permeable materials.

Three different anisotropic PM materials may be considered for multipole design: Samarium-Cobalt, Neodymium-Boron-Iron, and Ceramic (Hard Ferrite). Table 1 below shows the range of magnetic properties which are available with these materials.

PM Material	B_r (kGuass)	H_c (kOe)	H_{ci} (kOe)	E_{max} MGoe
Sm_1Co_5	8.8 - 10.0	8.7 - 9.5	19.0 - 20.0	19 - 25
$\text{Sm}_2\text{Co}_{17}$	10.2 - 10.7	9.6 - 10.3	18.0 - 21.0	24 - 28
Nd-B-Fe	10.4 - 13.5	18.0 - 21.0	12.0 - 24.0	26 - 44
Sr-Fe-O	2.05 - 4.35	1.70 - 3.50	2.35 - 4.20	0.9-4.3

Table 1: PM Material Magnetic Properties

Several temperature characteristics of PM materials need to be considered in the design of PM devices. PM materials will undergo long term decay of their field strength, the decay amount and time constant being dependent on the specific material. This can be considered aging and may be avoided by "temperature stabilization" of the material. This consists of heating the magnetized PM material to a temperature greater than its highest operating temperature for several hours, which

essentially pre-ages the material. Other important temperature characteristics of these PM materials are the reversible temperature coefficients of B_r and H_c which are different from each other and vary depending on the material. The reversible temperature coefficients of B_r and H_c in units of (% Change / °C) are shown in Figure 2. The coefficient of H_c for ceramic is positive, which uniquely creates concern for low temperature environments.

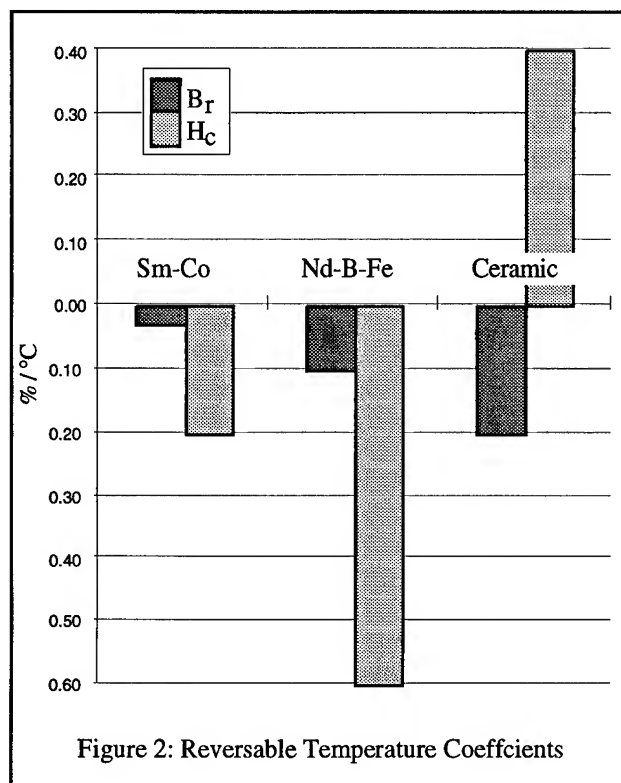


Figure 2: Reversible Temperature Coefficients

The radiation damage resistance of PM materials has been investigated by several researchers, e.g. [4], [5]. For Ba-Fe-O ceramic PM materials, no damaging effects on magnetic properties are observed up to a integrated flux of 10^{18} neutrons / cm^2 (fast Epicadium neutrons, $E > 0.5$ eV). Samarium Cobalt PM materials show a similar resistance to damage, with $\text{Sm}_2\text{Co}_{17}$ generally showing more resistance to damage than Sm_1Co_5 materials. Nd-B-Fe materials however show significantly less resistance to damage with noticeable effects observed at integrated flux levels of 10^7 neutrons / cm^2 . Results for rare earth based materials are, however, somewhat equivocal with the same alloy from different manufacturers showing quite different damage results.

The cost of PM materials varies greatly, depending on the specific material, the accuracy and amount of machining, and the quantity. The maximum energy product $(B \times H)_{\text{max}}$ is a reasonable measure of

effectiveness of the PM material in magnetic circuit design. Based on actual quotations that the author has received in the last year, Figure 3 shows the cost per unit volume ($\$/\text{cm}^3$) and the cost per unit volume- E_{max} ($\$/\text{cm}^3 \cdot E_{\text{max}}$). It can be observed from the figure that Ceramic and Nd-B-Fe overlap in their ($\$/\text{cm}^3 \cdot E_{\text{max}}$) values.

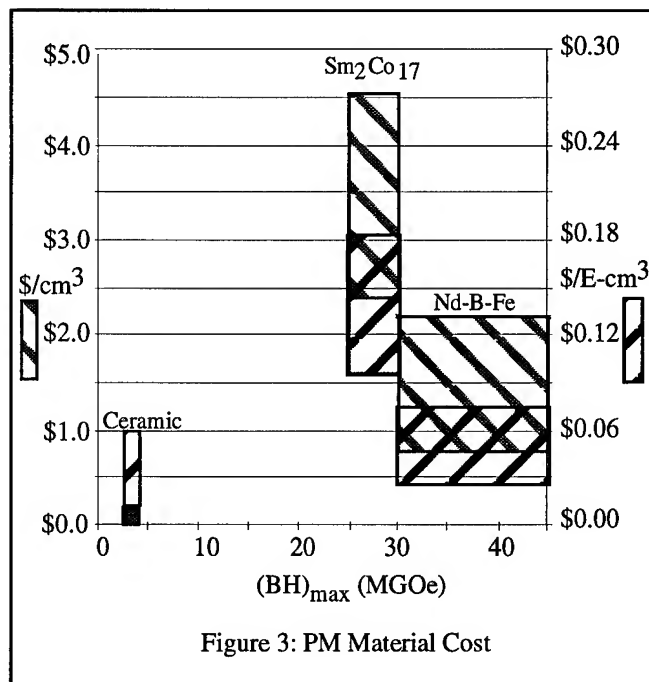
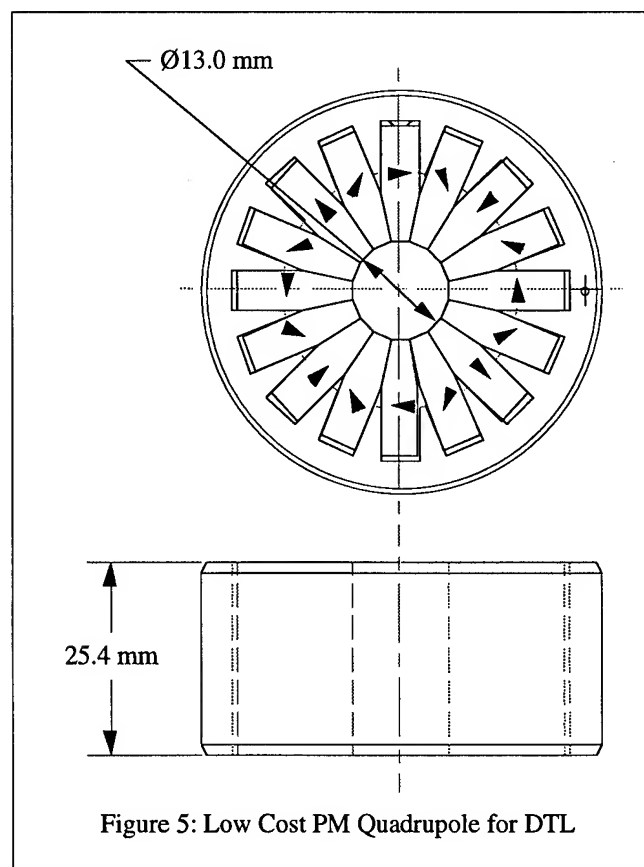
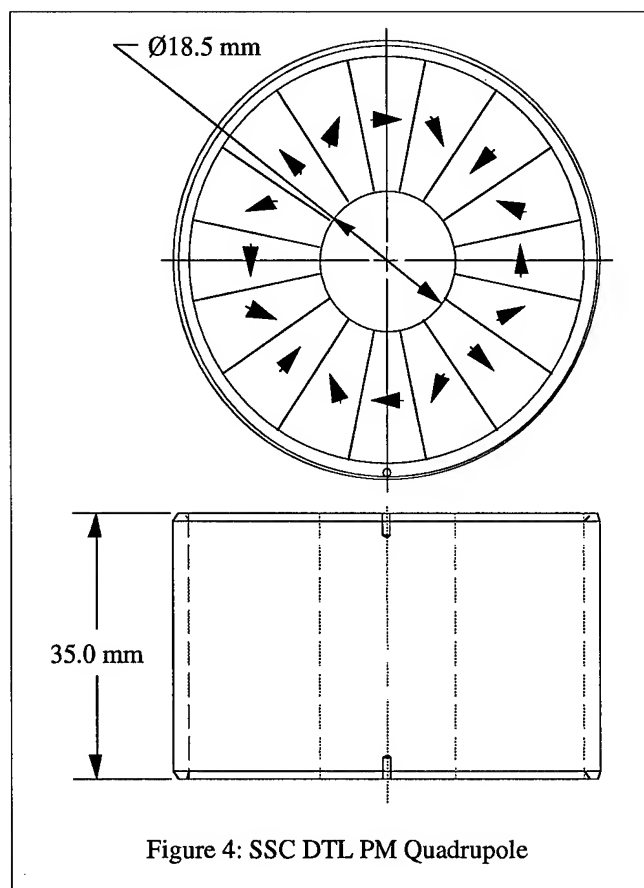


Figure 3: PM Material Cost

III. PM Multipole Applications

Although many applications of PM multipoles have been implemented, conventional electromagnetic multipole are still more widely used. The primary reason is the requirement for adjustable field strength. Although adjustability can be implemented in PM multipoles, in many other cases the reason that they are not used is unfamiliarity with and unavailability of the technology. The descriptions below show several easily and economically implemented examples of PM multipoles for beam transport.

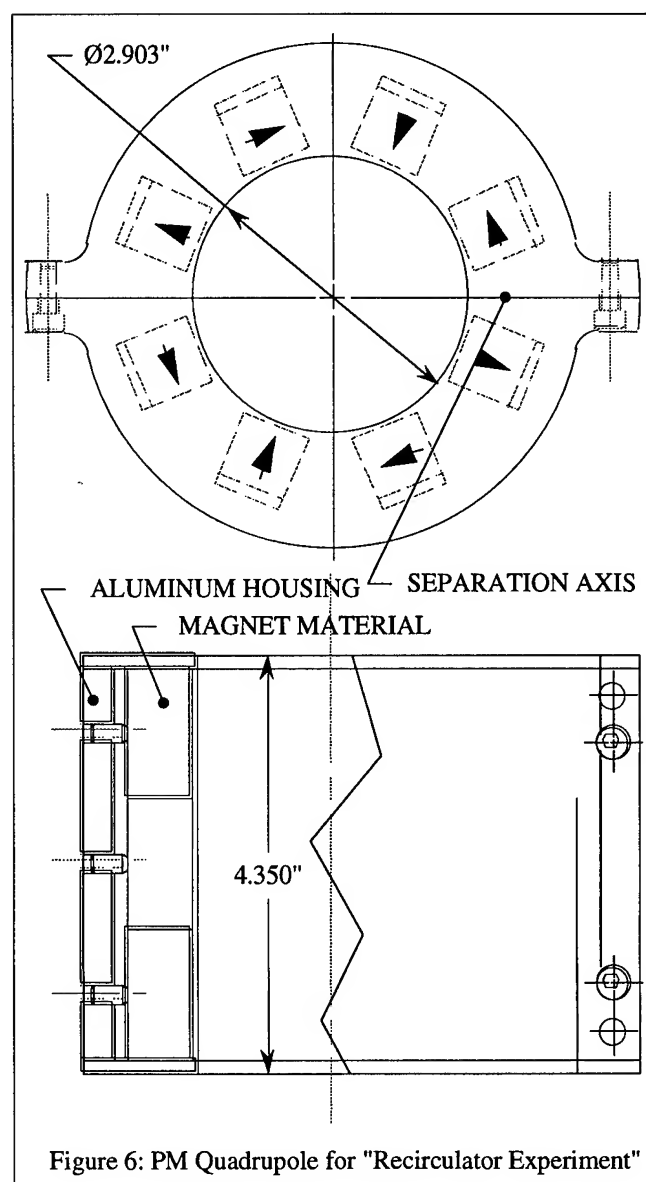
The most widely adopted example of PM quadrupole (PMQ) technology is for beam focusing in the drift tubes of ion linear accelerators. Figure 4 shows the design of the 156 identical PMQ's which were produced for the SSC drift tube linac (DTL). These PMQ's have a gradient of 133 T/m and integrated strength of 4.64 T. Their cost was relatively high due to their high strength requirement and low allowable error harmonics, coupled with the compact design. The PM blocks are positioned in a "zero clearance" assembly and the outer housing is a press fit aluminum ring. This design requires PM blocks with 5 different orientations manufactured with very high mechanical and magnetic precision. Tuning is



accomplished by machining the bore to reduce the error harmonics to the required values.

If the requirements for the DTL PMQ's are less stringent in terms of aperture, error harmonics and allowable physical size, a low cost design is possible. This approach is applicable for example in linear accelerators used for PET isotope production and neutron generation. Typical requirements for such PMQ's are a gradient of 157 T/m and integrated strength of 4.0 T. The design for such a PMQ is shown in Figure 5. The PM blocks are positioned in an aluminum spline and if tuning is required, adjustment may be accomplished by either machining or mechanical displacement of the PM blocks.

The "Small Recirculator" experiment presently underway at the Lawrence Livermore Laboratory [6], is designed incorporating PM quadrupoles. The requirements for these PMQ's leads to a design which is perhaps the lowest cost possible. The required integrated strength is 0.93 Tesla and the design utilizes 8 PM blocks with only



one orientation. The design for these PMQ's is shown in Figure 6. This design allows the quadrupole magnets to be split so that they may be easily be installed over the vacuum chamber.

The examples above describe iron-free ring quadrupole designs. A different approach is usually appropriate for the design of dipole magnets for charged particle beam bending. Figure 7 shows a bending magnet that was designed for the SRL Tandem Cascade Electrostatic Accelerator for target switching at the output of the accelerator. This magnet has a field strength of $B_0 = 3.6$ kGauss and an effective length of 100 mm. The design incorporates a resistive coil for adjusting the B_0 value by approximately $\pm 25\%$. The disadvantage of such a hybrid PM / electro-magnet design is that the coil sees an effective air gap which includes the thickness of the PM layer, thus requiring considerably more power to excite a given ΔB_0 than an electromagnet alone.

The entire magnet is designed so that it can be rotated about the beam axis, allowing beam switching between four different targets for the production of PET isotopes.

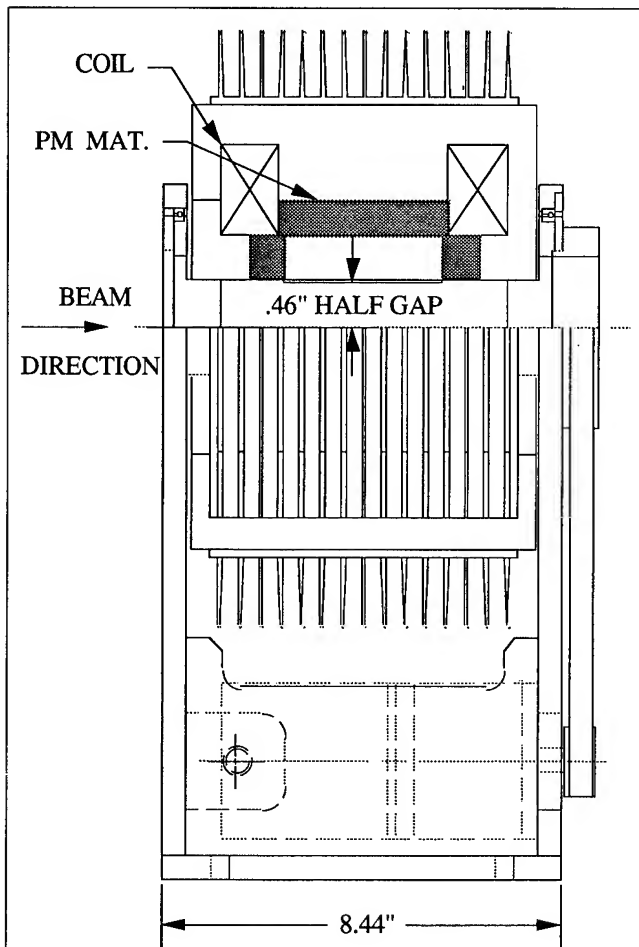


Figure 7: Hybrid PM / Electro-Magnet Dipole

IV. Planned PM Multipole Applications

Dr. S. Martin at the KFA, Jülich, Germany has designed a "Proton Pipe" which would be a low cost and efficient means of transporting a proton beam over a wide range of energies from 30 MeV to 200 MeV, [7]. The only adjustment required would be at the end for matching, and this could be accomplished with two triplets which could also be PMQ's, with the variables being the distance between elements. Figure 8 shows the beam radius and Beta X functions for a matched 70 MeV proton beam.

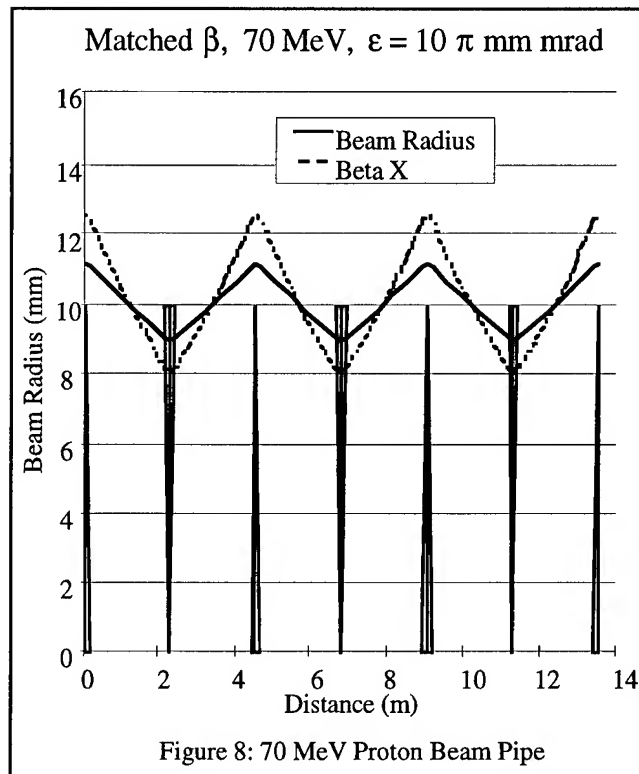


Figure 8: 70 MeV Proton Beam Pipe

The PMQ's for this Proton Pipe require a gradient of 1 Tesla/meter and a length of 25.4 mm. The distance between the F and D elements is 2 meters. A design for the PMQ's in this application is shown in Figure 9, which is based on Ceramic PM material. The cost of the quadrupoles in such a system is probably comparable with the cost of the vacuum pipe and vacuum system components.

As a another example of a planned new application, a very high frequency low current linac is being studied for proton radiation therapy. Quadrupole focusing would be provided by PMQ's located between multi-cell cavities in a 3 GHz RF structure. The problem for the PMQ design in this application is in the miniaturization of the magnet assemblies and the measuring system. Typical requirements for these PMQ's are a gradient of 200 Tesla/meter and a length of 40 mm. A diagram showing the proposed design and the scale is shown in Figure 10.

V. REFERENCES

- [1] R.F. Holsinger, "The Drift Tube and Beam Line Quadrupole Permanent Magnets for the NEN Proton Linac", Proceedings of the 1979 Proton Linac Conference, Montauk, New York, 1979.
- [2] N.V. Lazarev, V.S. Skachkov; "Tipless Permanent Magnet Quadrupole Lenses", Proceedings of the 1979 Proton Linac Conference, Montauk, New York, 1979.
- [3] K. Halbach; "Design of Permanent Multipole Magnets with Oriented Rare Earth Cobalt Material", NIM 169, pp.1-10, 1980.
- [4] R.S. Sery, et al; "Radiation Damage Thresholds for Permanent Magnets", NOLTR 61-45, U.S. Naval Ordinance Laboratory, 1961.
- [5] J. Cost, et al, "Effects of Neutron Radiation Damage on Nd-Fe-B Magnetic Properties", LA-UR-86-4245, Los Alamos National Laboratory, 1986.
- [6] A. Friedman, et al; "Progress toward a Prototype Recirculating Induction Accelerator for Heavy-Ion Fusion", these proceedings.
- [7] S.Martin, to be published

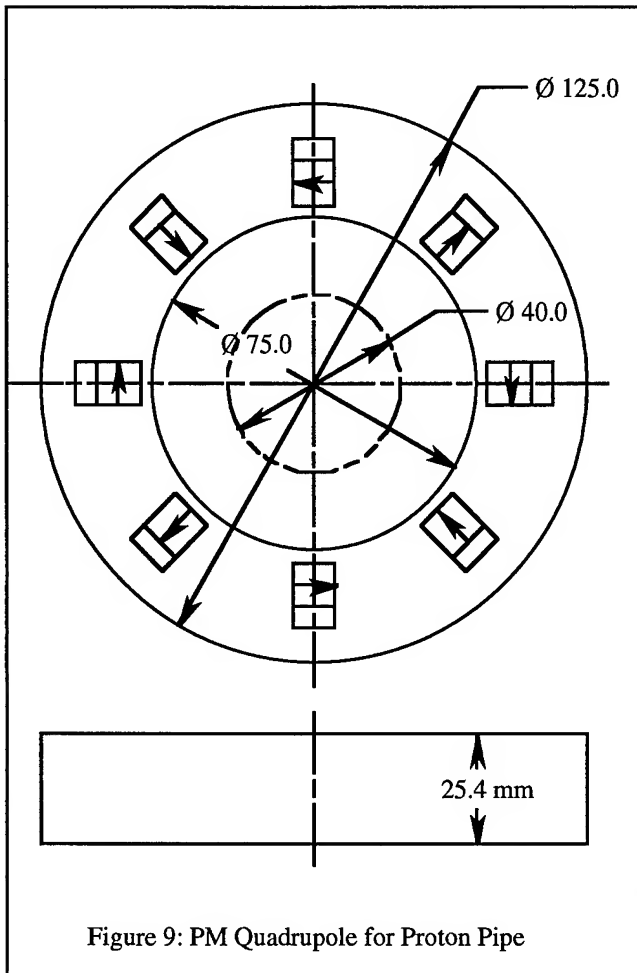


Figure 9: PM Quadrupole for Proton Pipe

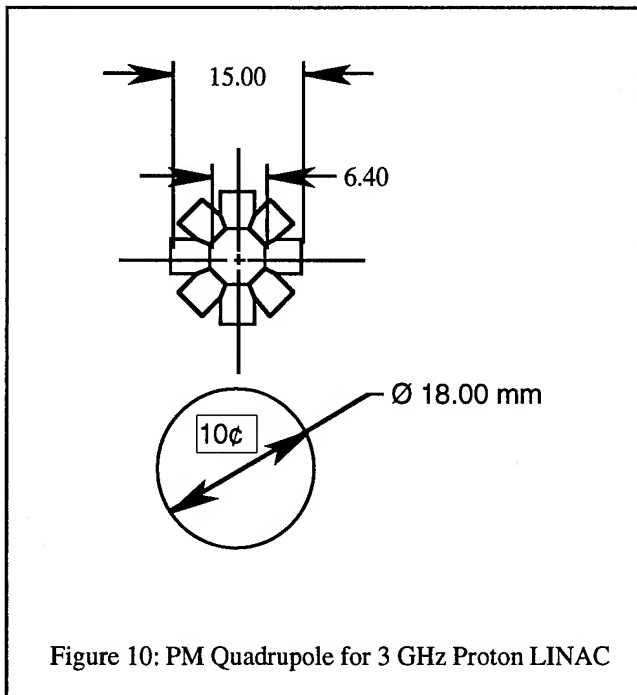


Figure 10: PM Quadrupole for 3 GHz Proton LINAC

Statistical Analyses of the Magnet Data for the Advanced Photon Source Storage Ring Magnets*

S. H. Kim, D. W. Carnegie, C. Doose, R. Hogrefe, K. Kim and R. Merl
Argonne National Laboratory, Argonne, IL 60439 USA

Abstract

The statistics of the measured magnetic data of 80 dipole, 400 quadrupole, and 280 sextupole magnets of conventional resistive designs for the APS storage ring is summarized. In order to accommodate the vacuum chamber, the curved dipole has a C-type cross section and the quadrupole and sextupole cross sections have 180° and 120° symmetries, respectively. The data statistics include the integrated main fields, multipole coefficients, magnetic and mechanical axes, and roll angles of the main fields. The average and rms values of the measured magnet data meet the storage ring requirements.

I. INTRODUCTION

The Advanced Photon Source (APS), now undergoing commissioning for operations at Argonne National Laboratory, is a national facility dedicated to providing highly-brilliant synchrotron radiation beams [1]. The APS accelerator system consists of a 7-GeV positron storage ring (SR), an injector synchrotron, a positron accumulator ring, and a linear accelerator. The 1104-m-circumference SR has 40 sectors of Chasman-Green lattice with two dipole, ten quadrupole (quad), seven sextupole (sext), and eight corrector magnets in each sector. The main parameters for the SR magnets are listed in Table 1. The five quad families have three different magnetic lengths with the same two-dimensional (2-D) geometry and a bore radius of 40.0 mm. The four sext families are the same design with a bore radius of 49.0 mm. The 80 dipole magnets are excited by a single power supply and the 400 quads and 280 sexts by individual power supplies. The required beam stay-clear aperture is $x = \pm 35$ mm and $y = \pm 25$ mm.

The integrated fields and field qualities for all SR magnets have been measured and evaluated to a few parts in 10^{-4} to verify the tolerance requirements. The magnetic and mechanical axes and roll angles with respect to the fiducials located on top of the magnets were measured within tolerances of 0.060 mm and 0.3 mrad, respectively. This paper summarizes the statistics of the measured magnet data for the SR magnets.

II. DESCRIPTION OF THE MAGNETS

In spite of the conventional nature of the magnets, the designs of the magnet cross sections are severely constrained to accommodate the vacuum chamber with its antechamber. Because of this requirement, rotation symmetries of 180° and 120° have been chosen for the quad and sext magnets, respectively, to minimize the undesired

multipole field components. The cores of the magnets use 1.52-mm-thick laminations of low-carbon steel, coated on both sides with "C5" or a 13- μ m-thick "B-stage" epoxy.

The C-type lamination core of the dipole magnet is stacked with a bending radius of 38.9611 m. The end-packs for both ends of the lamination core are assembled with 20 laminations. The pole-end bevels are designed so that the integrated and 2-D field shapes within ± 25 mm in the transverse direction are not significantly different. Before magnetic measurements, the production dipoles were installed on girders and corrected for any mechanical distortions of the magnets along their lengths.

In order to accommodate the vacuum chamber, the top and bottom halves of the quad are not connected with flux-return yokes; they are connected mechanically with aluminum spacers between the halves [2]. Each of the top and bottom halves consists of two welded quadrant stacks. The magnet has pole-end bevels and pole chamfers.

Table 1
Main parameters for the SR magnets.

The quads have five families and the sexts have four.
Quad aperture radius=40.0 mm, Sext aperture radius=49.0 mm

Dipoles	B (T)	l (m)	Bp (Tm)	I (A)	Pole Gap (mm)
80	0.5991	3.06	23.349	450	60.0
Quads	Q ₁	Q ₂	Q ₃	Q ₄	Q ₅
# Magnet	80	80	80	80	80
l (m)	0.50	0.80	0.50	0.50	0.60
B' (T/m)	-10.84	15.79	-10.59	-18.90	18.25
I (A)	215	312	210	386	370
Sexts	S ₁	S ₂	S _D	S _F	
# Magnet	80	80	80	40	
l (m)	0.2527	0.2527	0.2527	0.2527	
B'' (T/m ²)	185.07	-359.59	-415.0	192.62	
I (A)	64	135	160	67	

The cores of the sext magnet are assembled from three identical stacks of laminations, each with two poles and a flux-return path joining them [2]. The vacuum chamber extends into one of the 102-mm air gaps between neighboring stacks. At each end, 12.7-mm-thick stainless steel plates hold the core sections in position; they are pinned and bolted to the core sections with an assembly fixture. The assembly of the magnet using the stainless steel plates is designed so that the upper two poles of the magnet core can be moved for installation of the vacuum chamber.

*Work supported by the U.S. Department of Energy, Office of Basic Energy Sciences, under Contract No. W-31-109-ENG-38.

III. MEASURED MAGNETIC DATA STATISTICS

A. Dipole Data

The production dipoles were measured comparatively with respect to a reference dipole. Two sets of curved coils were connected in series, one fixed in the reference and one in the testing production magnet. The integrated field strengths were measured by ramping the excitation current of the dipole up and down while the field shapes were measured by moving the coil set in a transverse direction. A second reference dipole was used to check the effects of the large number of pulses of the first reference dipole during the production measurements. The probe coils are flat printed circuit coils connected in series according to the curvature of the magnet. A printed circuit coil is 0.5 m long with an average width of 6.8 mm, height of 3.3 mm, and 170 turns [3].

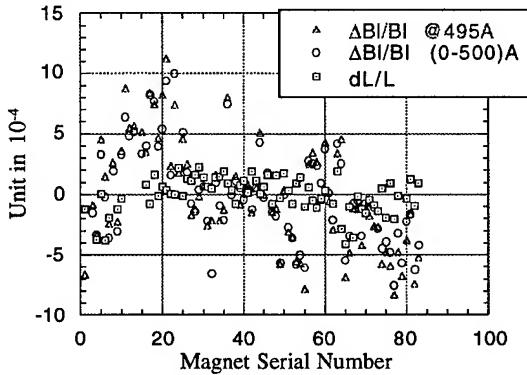


Fig. 1. Variations of the integrated fields and core lengths for the SR dipole magnets.

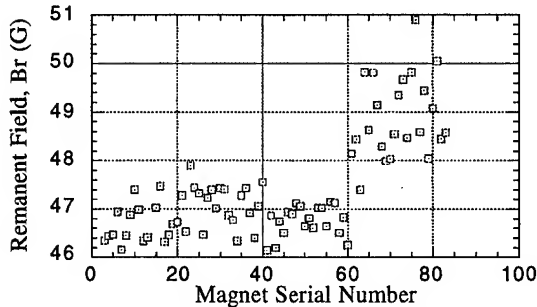


Fig. 2. Remanent fields of the SR dipoles.

Figures 1 and 2 show the relative variations of integrated fields at 495A, 0-500A, lamination core lengths, and remanent dipole fields for the dipole magnets. It is seen that, for magnets with serial numbers 61-83, the integrated fields are weaker by approximately 5×10^{-4} on average. At the same time, the remanent fields are higher by 2 Gauss. It is clear that these differences are due to different lamination properties. The root-mean-square (rms) values of the integrated fields are approximately 2.5 times that of the core lengths due to the tolerances of mechanical dimensions of the magnets. Because of these weaker dipoles with higher remanent fields, the histogram of the integrated fields for the dipoles in Fig. 3 is shifted toward the negative side. During compilation of the production

magnet measurements, conducted for over a year, the measurement repeatability for the reference magnet was $(2 \pm 1.5) \times 10^{-4}$.

The variations of the integrated fields within ± 25 mm of the transverse positions were less than 1.5×10^{-4} . The quad and sext coefficients obtained from a least square fit of the field variations in the midplane of the pole gap are shown in Fig. 4. Overall, the coefficients at the operating current of 450A are less than 1.5×10^{-4} .

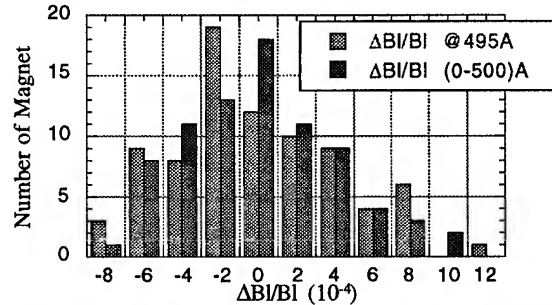


Fig. 3. Histogram of the integrated fields for the SR dipoles.

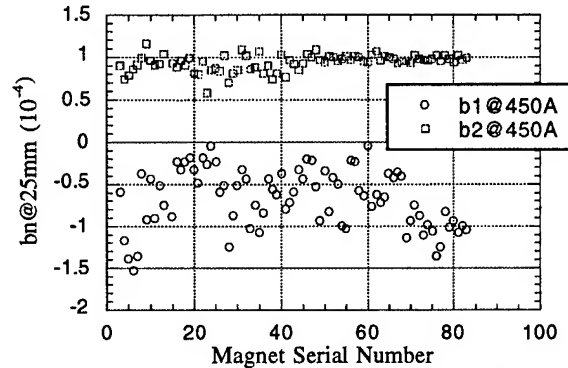


Fig. 4. Quad and sext coefficients within $x=\pm 25$ mm in the midplane of the SR dipoles.

B. Quadrupole Magnet Data

The integrated fields and multipole field coefficients were measured using a rotating coil technique. The probe coil consists of "radial" and "tangential" coils on one cylinder [3]. The integrated field quality of a 2-D magnetic field in Cartesian coordinates, $B = B_y + i B_x$, is expressed in terms of dimensionless normal and skew multipole field coefficients, b_n and a_n ,

$$B l = B_0 l \sum_{n=0}^{\infty} (b_n + i a_n) [(x + i y)/r_0]^n,$$

where l is the effective magnetic length for an integral measurement and B_0 is the design main field. ($B' = B_0 b_1/r_0$ and $B''/2 = B_0 b_2/r_0^2$ are the gradient and second-derivative fields of quad and sext magnets, respectively.) The multipole coefficients are defined as $b_1 = 1.0$ and $a_1 = 0$ for a quad, and $b_2 = 1.0$ and $a_2 = 0$ for a sext magnet at a reference radius $r_0 = 25$ mm.

Similar to the dipole data, the integrated quad fields at four excitation currents and the remanent fields are plotted in Figs. 5 and 6 for the SR 0.5-m quads. It has been identified that the steel laminations have three different

kinds of heat treatment, one for magnet numbers 1-200 and two for 201-250. The data replotted in Fig. 7 shows that those quads with Br_l higher than $0.064T$ have weaker $B'l$ by 2×10^{-3} on average and the rms is relatively larger. It is also seen that the rms is larger at higher currents for all quads and the spread is even larger for those with higher Br_l . The asymmetrical shape of the histogram for the quad fields plotted in Fig. 8 is due to those different lamination properties.

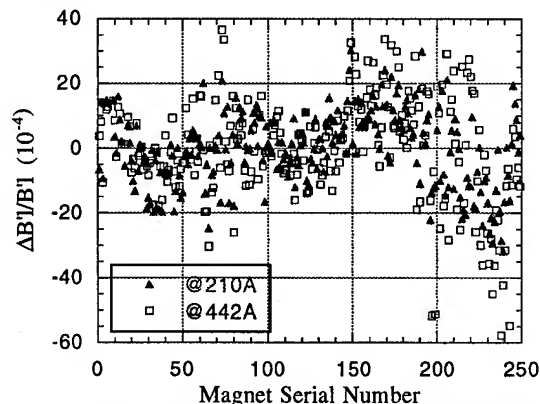


Fig. 5. Variations of the integrated quad fields for the SR 0.5-m quads.

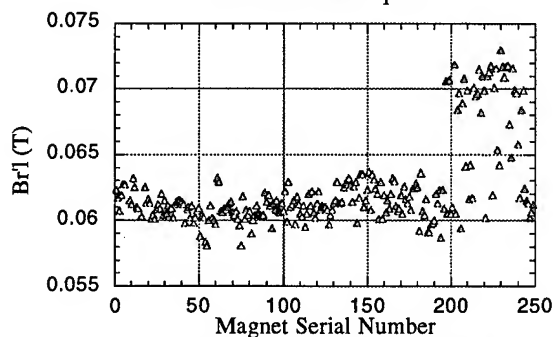


Fig. 6. Integrated remanent quad fields of the SR 0.5-m quads.

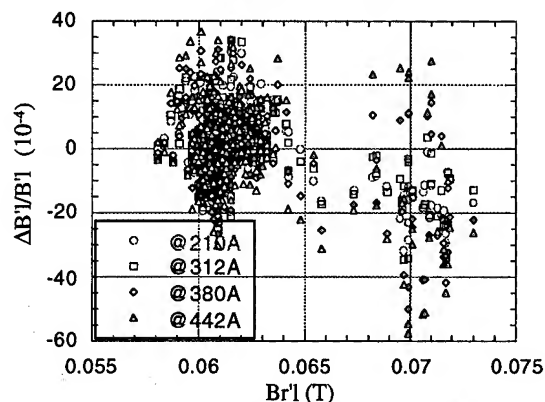


Fig. 7. Variations of the integrated quad fields at four excitation currents vs. remanences for the 0.5-m quads.

A few "forbidden" multipole coefficients for the 0.5-m quads are plotted in Fig. 9. Even if the quads were assembled from four quadrants, Fig. 9 shows that both the normal and skew sext coefficients (b_2 and a_2) remain consistent on average during the assembly period. On the other hand, b_3 gradually increases by 2×10^{-4} over the

period, which seems to be related to the increase of the $B'l$ shown in Fig. 5 except for those quads with higher Br_l . This suggests a decrease in the gap between the top and bottom halves of the quads as the quad numbers increased. The data spread of the "allowed coefficient" b_5 , shown in Fig. 10, is due to the dimensional tolerances of 20-mm-thick end-packs with end-bevels for the ends of the magnets. Other allowed higher coefficients hardly changed. During the whole period of the measurement, b_3 of the reference quad changed less than 0.2×10^{-4} .

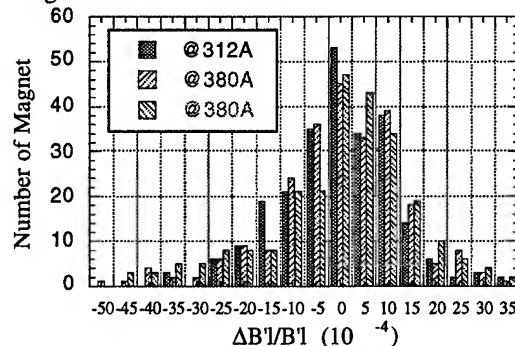


Fig. 8. Histogram of the integrated quad fields for the SR 0.5-m quads.

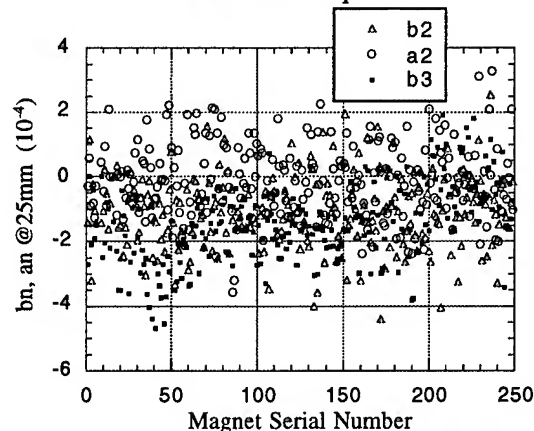


Fig. 9. "Forbidden" multipole coefficients for the SR 0.5-m quads.

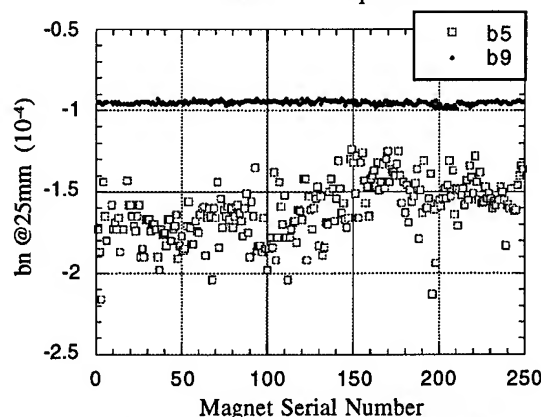


Fig. 10. "Allowed" multipole coefficients for the SR 0.5-m quads.

The axis of the rotating coil was aligned to the magnetic axis by adjusting the magnet position to where the dipole and quad field components of the quad and sext magnets, respectively, vanished. Prior to this procedure the

bore axis of the quad was aligned to the axis of the two air bearings defining the axis of the rotating coil using the following method. A laser beam unit was installed and aligned with the axis of the air bearing. A photo-quadrant detector was placed at the bore axis of the magnet aperture. After detecting the beam position along the bore axis, the magnet position was adjusted to align the bore axis to the laser beam. This procedure not only ensured parallelism between the bore and magnetic axes to at least ± 0.2 mrad, but it also enabled measurement of the offset of the two axes.

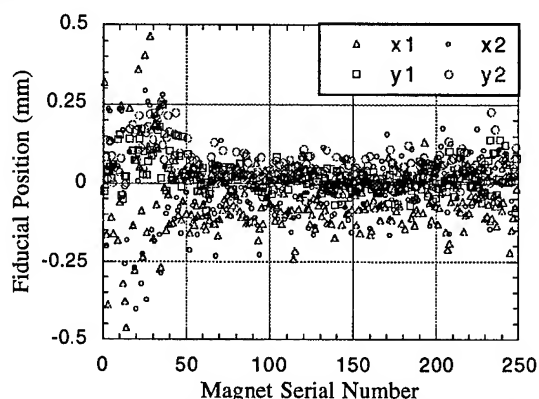


Fig. 11. Two fiducial positions relative to the magnetic axes. y_1 and y_2 have an offset of 384.629 mm.

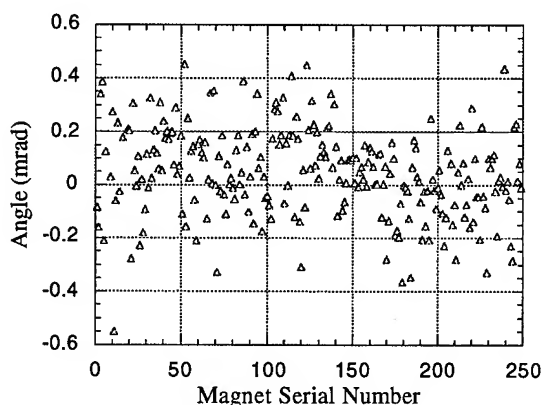


Fig. 12. The roll angles on top of the core surfaces when magnetically aligned for the 0.5-m quads.

Plotted in Fig. 11 are the two fiducial positions relative to the magnetic axis which were measured when the dipole components and the roll angles of the quad fields were zero. These fiducial ball bases were welded prior to the magnetic measurements. At the same time, the angle of the core surface on top of the magnet, shown in Fig. 12, was measured for the survey and alignment. The vertical positions have an offset of 384.629 mm. It is seen that the rms of the fiducial positions for the first 50 quads is relatively large, suggesting that it was a learning period of welding the fiducial bases to specified positions. It has been found that the horizontal positions and the angles have a relatively weak correlation; the average value of the horizontal positions, -0.058 mm, is due to a systematic error of the angle measurements by 0.15 mrad, assuming that

dimensional errors of the quads and the welded fiducial positions are random.

Shown in Fig. 13 is the offset of the magnetic and mechanical axes. During the magnetic alignment, a magnet was moved only in parallel from the mechanical axis. Therefore, only the average coordinate positions for the two fiducials are plotted. The average y -offset for all 0.5-m quads, -0.059 mm, is due to the fact that the diameter of a photo-quadrant detector used for the mechanical axis was 0.051 mm smaller than the quad aperture diameter.

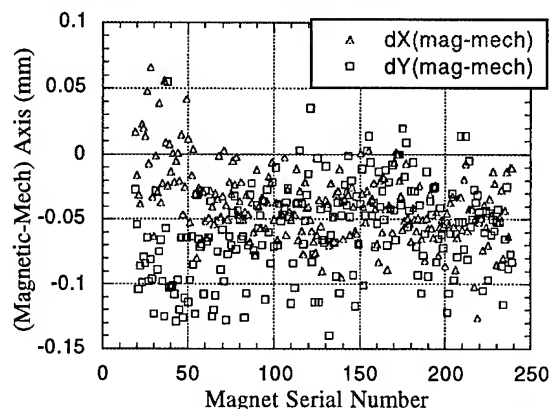


Fig. 13. The offsets between the magnetic and mechanical axes for the 0.5-m quads.

The measured data statistics for all 0.5-m, 0.6-m and 0.8-m quads are summarized in Table 2. The rms of the integrated field measurements of a 0.5-m reference quad for over a year was 1.1×10^{-4} , and those for the fiducial positions and the roll angle were 0.026 mm and 0.083 mrad, respectively.

Table 2

Measured data statistics for the SR quads.

$\Delta B^1/B^1$ in 10^{-4} unit, b_n and a_n at $r=25$ mm, and Δx and Δy are (magnetic-mechanical) axes.

	0.5-m Quad	.06-m Quad	0.8-m Quad
$\Delta B^1/B^1@312A$	± 11.17	± 12.14	± 6.92
$\Delta B^1/B^1@442A$	± 16.25	± 10.79	± 8.47
$b_2 (10^{-4})$	-1.11 ± 1.11	-1.0 ± 0.86	-0.72 ± 0.94
a_2	-0.08 ± 1.12	-0.01 ± 0.103	0.15 ± 0.85
b_3	-1.42 ± 1.22	-1.22 ± 1.19	-0.86 ± 1.10
b_5	-1.61 ± 0.18	-1.43 ± 0.15	-1.24 ± 0.15
b_9	-0.95 ± 0.012	-0.87 ± 0.045	-0.75 ± 0.010
$Br^1 (10^{-2} T)$	6.24 ± 0.33	7.36 ± 0.15	10.28 ± 0.16
θ (mrad)	0.046 ± 0.177	0.096 ± 0.175	0.108 ± 0.221
Δx (mm)	-0.037 ± 0.028	-0.034 ± 0.032	-0.044 ± 0.033
Δy (mm)	-0.059 ± 0.036	-0.062 ± 0.031	-0.048 ± 0.031

C. Sextupole Magnet Data

The integrated sext fields and those of the remanence are plotted in Figs. 14 and 15 for the 280 sexts. It is seen that there are at least three levels of remanences. The data is replotted in Fig. 16 to see the correlation between the sext strength and the remanence. For sexts with lower Br^1 than the average by 22%, the sext strengths are higher by 7×10^{-3} on average. It is seen also that the data spread is larger at higher current for all magnets and more severe for those with higher Br^1 . The dipole field components at 150A and 0A are plotted in Fig. 17. The total dipole field

for all the sexts at 150A is approximately 3×10^{-4} of the 80 dipole magnets. The multipole coefficients and alignment parameters for the sexts are much less stringent compared to those for the quads.

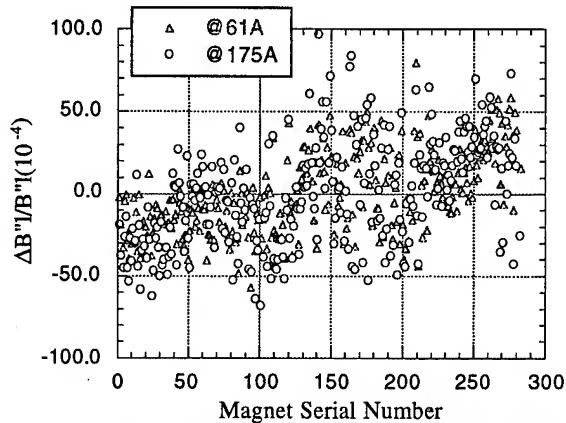


Fig. 14. Variations of the integrated sext fields for the SR sext magnets.

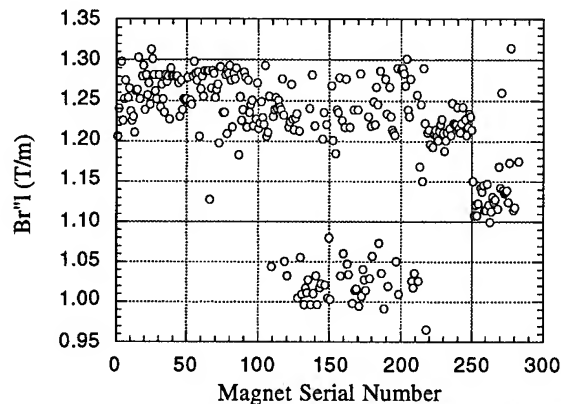


Fig. 15. Variations of the integrated remanent sext fields for the SR sexts.

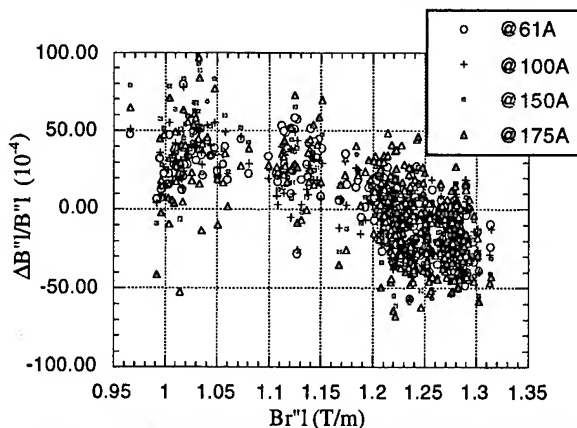


Fig. 16. Integrated sext fields vs. remanences for the sexts.

IV. SUMMARY

Measured data and allowed tolerances for the SR magnets are summarized in Table 3. For the dipoles, the use of laminations with different properties was a major factor for the data spread of dBI/BI . Within ± 25 mm of the transverse positions, the variation of dBI/BI was less than 1×10^{-4} . Similarly, the data spreads of the field strengths for

the quads and sexts were due to different lamination properties. Because of the use of individual power supplies for these magnets, the magnitude of the spread is not an issue. The consistency of the data for the multipole coefficients, the fiducial positions, the offsets of the magnetic and mechanical axes, and the roll angles indicate that the mechanical tolerances of the quad and sext magnets were well maintained during the entire magnet fabrication period. The rms of the fiducial position and roll angle for the reference 0.5-m quad data during the period of the production measurements were 0.025 mm and 0.12 mrad, respectively.

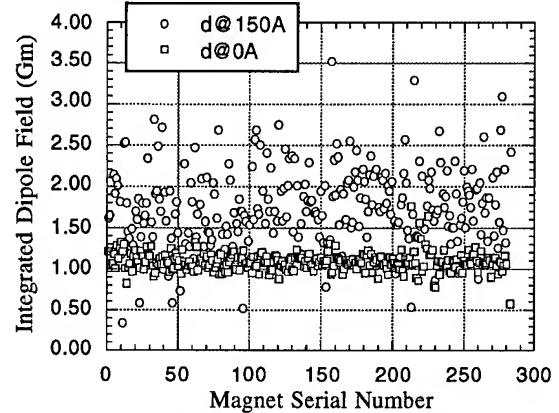


Fig. 17. Integrated dipole field components at 150A and remanences for the SR sexts.

Table 3

Data summary for the SR magnets. Relative field strengths and multipole coefficients are in 10^{-4} .

	measured average	measured rms	allowed tolerance
<u>Dipoles</u> $\Delta BI/BI$		4.37	5.0
b_1	-0.67	0.35	2.5
b_2	0.94	0.10	3.1
<u>Quads</u> $\Delta B'/B'$		11.3	5.0
b_2	-0.95	1.01	2.5
a_2	-0.02	1.08	2.5
b_3	-1.22	1.27	3.1
<u>Sexts</u> $\Delta B''/B''$		31.6	25.0
b_3	0.76	2.45	31.0
a_3	1.78	3.30	31.0
<u>Reference</u> x,y (mm)		0.026	0.060
<u>Quad</u> θ (mrad)		0.12	0.30

Measurement repeatabilities for dipole, quad, and sext were 1.5, 1.1, and 5 in 10^{-4} unit.

V. REFERENCES

- [1] "7-GeV Advanced Photon Source Conceptual Design Report," Argonne National Laboratory, ANL-87-15, 1987, and J. N. Galayda, "The Advanced Photon Source," these proceedings.

- [2] S. H. Kim, C. Doose, K. Kim and K. M. Thompson and L. R. Turner, "Performance of Quadrupole and Sextupole Magnets for the Advanced Photon Source," *IEEE Trans. on Magnetics*, Vol. 30, pp. 2612-2615, 1994.
- [3] S. H. Kim, C. Doose, R. Hogrefe, K. Kim and R. Merl, "The Magnet Measurement Facility for the Advanced Photon Source," *IEEE Trans. on Magnetics*, Vol. 30, pp. 2616-2619, 1994.

THE MAGNET SYSTEM FOR THE BESSY II INJECTOR SYNCHOTRON *

T. Knuth, D. Krämer, E. Weihreter

BESSY II, Rudower Chaussee 5, Geb. 15.1, 12489 Berlin, Germany

I. Chertok, S. Michailov, B. Sukhina

The Budker Institute of Nuclear Physics, SB RAS, Novosibirsk 6300090, Russia

Abstract

Injector for the 3rd generation synchrotron light source BESSY II [1] is a 1.9 GeV full energy 10 cps rapid cycling synchrotron. The 96 m circumference FODO lattice consists of 16 cells having one H-type dipole and the F and D quadrupole magnets on a common girder. A complete pre-series cell has been manufactured by the Budker Institute of Nuclear Physics (BINP), Novosibirsk. Detailed investigations of the field quality were performed at BINP as well as at BESSY.

I. INTRODUCTION

The lattice structure of the BESSY II booster synchrotron contains 16 bending magnets of 2.62 m length and 32 quadrupole lenses. The energy gain in the booster between injection at 50 MeV and extraction at 1.9 GeV is as large as 38. The dipole field varies according to

$$B(t) = \frac{1}{2} B_0 (1 - a \cos \omega t) \quad (1)$$

with $a = 0.95$, $\omega = 2\pi 10$ cps and $B_0 = 0.95$ T, thus the resulting field levels are $B_{inj} = 0.025$ T and $B_{ext} = 0.95$ T. The dynamical range for the quadrupole lenses is $g_{inj} = 0.29$ T/m to $g_{ext} = 11.2$ T/m.

BINP manufactured a complete booster cell, fig. 1. Field measurements were performed on the prototypes at Novosibirsk and at Berlin.

II. DESIGN AND MANUFACTURING OF THE SYNCHROTRON MAGNETS

A. Synchrotron Dipoles

The synchrotron bending magnets, fig. 2, are of H-type. The core is built from four individual blocks forming a polygon rather than having a curved core following the radius of curvature of 6.67 m. Low carbon 2% silicon steel grade GOST 2312 of 0.5 mm thickness is used for the laminations. The coercive force of this steel is within the limit of $H_c = (60 \pm 5)$ A/m. The individual blocks are stacked, pressed between epoxy impregnated end packs and finally welded to four steel bars to achieve a rigid assembly. The stacking factor is 97.5%. A Rogowski type of chamfer is applied to the ends of the core. The achieved flatness of the poles is 0.08 mm while the gap varied less than ± 0.03 mm for the prototype. The coils are made from rectangular OFHC copper conductor, 22×22 mm² in size with a 8 mm diameter cooling duct. Though the large size of the conductor gives eddy current losses of about 0.5 kW in the coil, the total voltage across

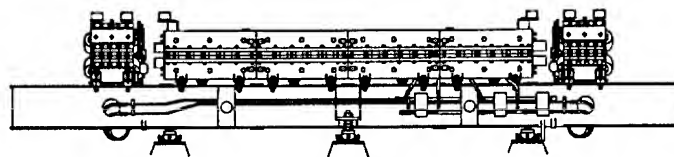


Figure 1. Unit cell (1/16 of the synchrotron) with one dipole and two quadrupole magnets on a common girder.

Magnet	H-type, parallel ends
Repetition frequency	10 cps
Max. field	1 T
Gap	36 mm
Core length	2602.5 mm
No of turns	12
Resistance	2.87 mΩ
Inductance	2.57 mH
Current	2400 A
Power loss	7.1 kW

Table I

the dipole circuit does not exceed 3 kV due to the small inductance. Table 1 gives a list of electrical and magnetic data for the bending magnets.

B. Synchrotron Quadrupoles

For the quadrupoles, the same steel quality and techniques are used as for the dipole. F and D quads are identical, both having a 300 mm long symmetrical core and an aperture radius of $r = 35$ mm, fig. 3. The race track coils are wound from a 12.5×12.5 mm² hollow copper profile giving a total voltage drop for each family of 650 V. The main magnetic and electrical parameters are summarized in table 2.

III. Field Measurements

Magnetic measurements were performed on the dipole and the quadrupole lenses at BINP using a hall probe array of 11 probes calibrated with NMR. Complete field maps of the dipoles and quadrupoles were measured with the array on a chariot passing on the magnet mid planes. For the harmonic analysis rotating coils were used, and flat coils for AC excitation of the bending magnet. AC measurements of the dipoles and harmonic analysis of quadrupoles were repeated after delivery of the magnets using a DANFYSIK Model 692 harmonic measurement system. Excellent agreement of the measurement results was achieved de-

*Funded by the Bundesministerium für Bildung, Wissenschaft, Forschung und Technologie and by the Land Berlin

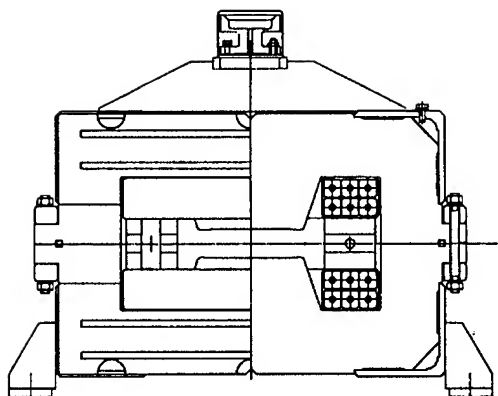


Figure 2. The synchrotron bending magnet

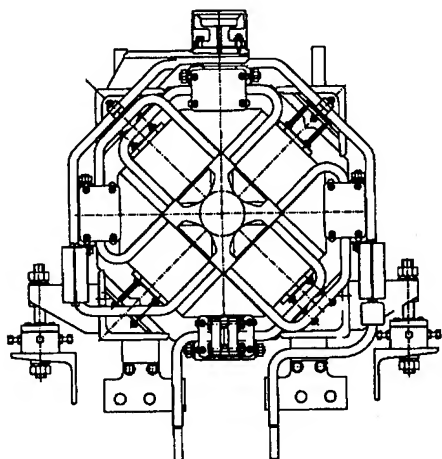


Figure 3. The synchrotron quadrupole magnet.

spite the 6000 km trip of the synchrotron magnets from the BINP works to Berlin.

A. Dipole Field Quality

The bending strength $\int B \cdot dl$ was determined as a function of the horizontal position at current settings from 60 A to 3000 A, corresponding to fields ranging from 0.025 to 1.25 T, fig. 4. Except for the lowest excitation level, the relative bending strength is constant within $\pm 3.5 \cdot 10^{-4}$ in the good field area of $52 \times 28 \text{ mm}^2$. Only at 250 G the influence of the 11 G remanent field leads to a nonhomogeneity of $\pm 6 \cdot 10^{-4}$.

Electrons were tracked through the mapped DC fields, assuming that the particle momentum corresponds to an exact 22.5° bend. The deviation of the trajectories from the ideally constant radius of curvature was calculated, fig. 5. A maximum deviation of 0.5 mm results from the effective magnetic length which is 11 mm more than the design value of 2619 mm. Therefore, the series magnets will be shortened by this amount, reducing the sagitta to less than 0.1 mm. The offset of the orbit at the magnet exit is due to asymmetries of the field distribution along the beam orbit, leading to amplitudes of 0.2 mm. Again, the remanent field leads to twice this distortion at injection.

Magnet type	symmetrical quad
Repetition frequency	10 cps
Max. gradient	14 T/m
Aperture radius	35 mm
Core length	300 mm
No of turns	11
Resistance	7 m Ω
Inductance	1.76 mH
Current	630 A
Power loss	1.1 kW

Table II

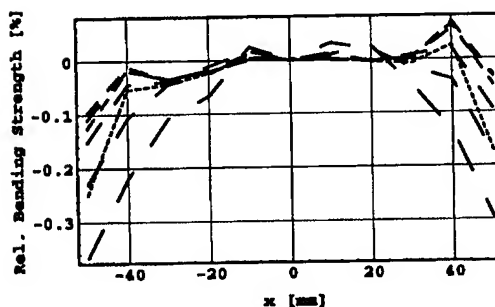


Figure 4. Relative bending strength in the mid plane for 7 different current settings corresponding to bending fields of 0.025 to 1.25 T.

Measurements at 10 cps AC showed a reduction of the effective magnetic length of up to $7 \cdot 10^{-4}$ during ramping. This effect is due to the eddy current field in the coil overhang. Using the POISSON code [2] the eddy currents were determined from the field at the location of the individual coil conductors. Thus, the eddy current induced magnetic field was calculated resulting in a time-dependent variation of the bending strength which is shown as a solid line in fig. 6. The agreement with the experimental data is excellent demonstrating that there are no saturation effects at the magnet ends.

B. Synchrotron Quadrupole

A harmonic analysis of the quadrupole lenses was performed at DC for various excitation levels. A typical example for the consistency of data taken at BINP and by BESSY is shown in fig. 7, where the relative integrated quadrupole strength $d(GL)/GL$ is plotted. The error bars were estimated from a detailed study of the 256 measured angular steps and the fitted harmonics allowing to determine the variance of the multipole coefficients.

The relative gradient distribution dG/G measured with a short coil at the center of the magnet is constant in the mid plane within $\pm 6 \cdot 10^{-4}$.

The integrated quadrupole strength $d(GL)/GL$, fig. 7, shows nevertheless significant contributions of multipoles $N = 6$ and $N = 10$ from the fringe field, resulting in non-homogeneity of $d(GL)/GL$ of up to 1.5% in the mid plane. A special chamfer was developed by cutting the outer edges of the poles sensitive

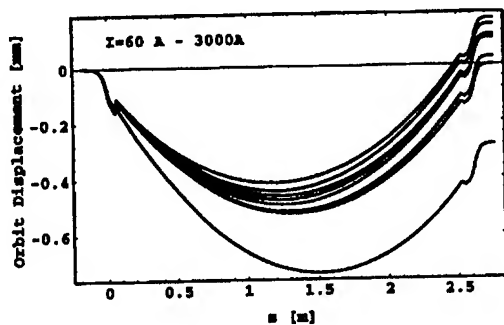


Figure 5. Difference orbits of tracked particles with respect to an ideal hard edge field distribution for 7 different measured field maps ranging from injection energy to the final energy.

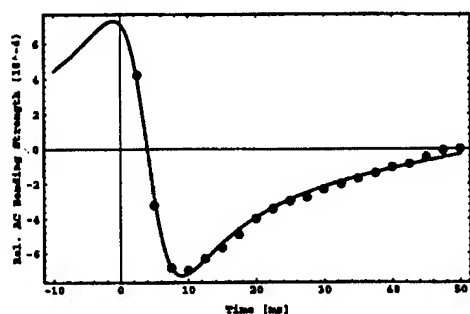


Figure 6. Calculation of the relative variation of bending strength during the ramp resulting from eddy current fields in the coil (solid curve) compared to experimental data.

to the $N = 6$ only. By varying the length L of this chamfer the radial homogeneity in the mid plane was considerably improved, fig. 8. At a chamfer length of $L = 31$ mm the dodecapole vanishes completely.

An iso-error curve at $d(GL)/GL < 3 \cdot 10^{-3}$ for the $L = 0$ and $L = 31$ mm chamfer length, fig. 9, demonstrates the significant increase of the physical good field area to 54 mm horizontally and 40 mm vertically for the chamfered magnet. The pattern of the contour clearly resembles the dominating contribution of the $N = 6$ for no chamfer and $N = 10$ for the 31 mm deep cut.

Acknowledgement

The authors would like to thank all staff members of the BINP workshop for the skillful work and their enthusiasm in arranging the prototypes in a time of just 6 month and supplying excellent magnets to the BESSY II project.

References

- [1] E. Jaeschke for the BESSY II team, this conference
- [2] Los Alamos Accelerator Code Group, LA-UR-87-115, LANL 1987

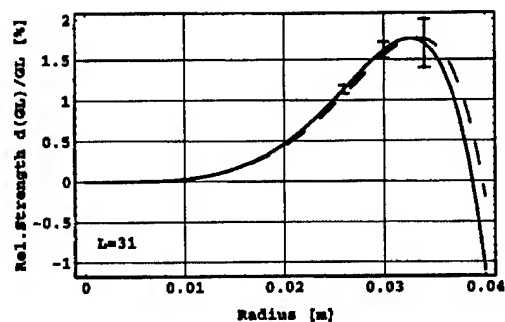


Figure 7. Relative focussing strength in the mid plane. Dashed curve BINP data, solid curve measurements performed after delivery at BESSY.

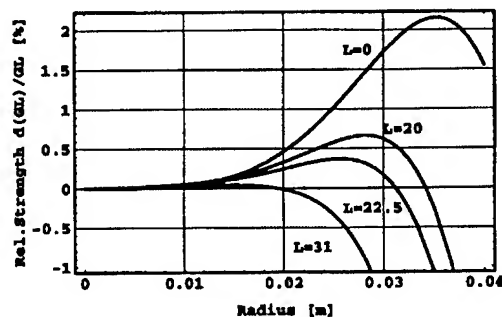


Figure 8. Relative gradient distributions at mid plane for different chamfer lengths.

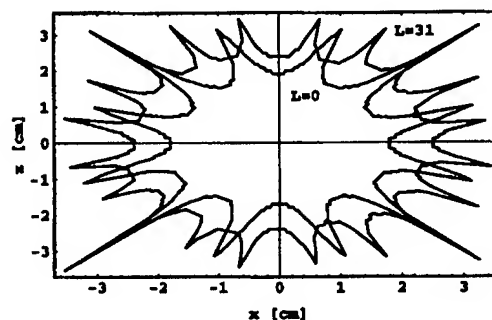


Figure 9. Iso-error curves for chamfer of $L = 0$ and $L = 31$ mm.

SEGMENTED HIGH QUALITY UNDULATORS

J. Chavanne, P. Elleaume, P. Van Vaerenbergh
European Synchrotron Radiation Facility, B.P. 220, F-38043 Grenoble Cedex, France

Several issues related to the engineering of permanent magnet undulators and wigglers are addressed. Shimming performs the correction of the integrated multipole components and provides a high brilliance on high harmonic numbers of the radiation spectrum. A design of termination is given which allows the removal of any electro-magnet correction on hybrid wigglers. Another design of termination is presented which allows the phasing of two pure permanent magnet undulators at any gap value. Finally, some magnetic designs are presented which allow a high magnetic field for a short or medium spatial period.

I. ESRF Insertion Devices

The European Synchrotron Radiation Facility (ESRF) is a third generation synchrotron source optimised to produce Hard X-rays in the 1 to 100 keV range. The commissioning of the source started in 1992 and it has been open to the user community since 1994. The majority of the beamlines use an insertion device (ID) as a source point which generates high fluxes and brilliance in the 2 to 40 keV range of photon energy. 26 IDs have been installed with fields ranging from 0.1 to 5 Tesla and spatial periods from 22 to 230 mm. All these IDs have been designed, built and measured in-house. They are nearly all made of permanent magnet material with magnet blocks placed in the air outside the vacuum chamber of the electron. The minimum magnetic gap is presently 20 mm and will be reduced to 16 mm in 1995 by changing the vacuum chambers. The source is optimised for a high brilliance which has recently reached the record $1.0 \cdot 10^{19}$ phot./sec/.1%/mm²/mrad² at a photon energy of 14 keV. A factor 10 improvement is envisaged in the near future.

II. Magnetic Field Shimming

A. Multipole Shimming

Special steel plates (shims) with typical dimensions of 5 x 20 x 0.2 mm are placed at specific places on the surface of the magnetic blocks to eliminate all multipoles. The following table shows the typical residual multipoles as measured on the 12 conventional undulators built so far.

Dipole	< 20 Gcm
Quadrupole	< 10 G
Sextupole	< 10 G/cm

Octupole	< 10 G/cm ²
Decapole	< 10 G/cm ³

These values apply for both normal and skew components of the multipoles at any value of the magnetic gap above 20 mm without any electro-magnet corrector. This shimming technique has been applied routinely to all IDs produced at the ESRF.

B. Spectrum Shimming

A refinement of this shimming has been implemented that allows the correction of the so-called phase errors allowing an enhancement of the brilliance on the high harmonic number. By using this technique it is now possible to routinely build undulators with a brilliance of more than 80% of that of a perfect one, up to harmonic #15. 95% has been reached on a few undulators. This technique is now routinely applied.

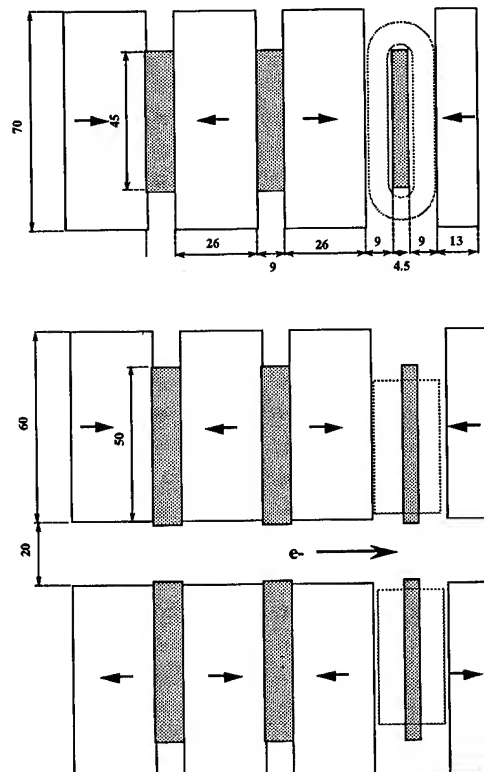


Fig:1 Terminaison of an Hybrid Wiggler generating extremely low field integral at any gap above 20 mm.

III. Undulator Termination

A. Hybrid Termination

One of the most delicate design works in a hybrid wiggler is the termination. Fig. 1 presents a termination of a wiggler that we have designed with our own 3D magnetostatic code [1]. It is optimised to produce negligible field integrals as a function of the magnetic gap. The field integral measured on the 1.6 m long device fluctuates in the range of ± 15 G-cm for both the horizontal and vertical components of the field at any gap value without any electro-magnet correction. The peak field of this wiggler is 0.85 T at a gap of 20 mm. Both terminations were in the most delicate symmetric configuration which prevents any residual field integral error from canceling as it is the case in the so-called antisymmetric configuration. Two of these wigglers are now installed on the ring and are routinely operated without any correction. For safety reasons we have left some space for inserting a coil (see Fig.1), however, this is not used.

B. Phasing Section

The straight sections of the ESRF are 5 m long. The undulators installed in these sections are segmented in three units each 1.65 m long. The segmentation allows the use of several different and/or identical IDs in the same straight section. If the field and period of the adjacent sections are identical, one needs to phase the segments with respect to

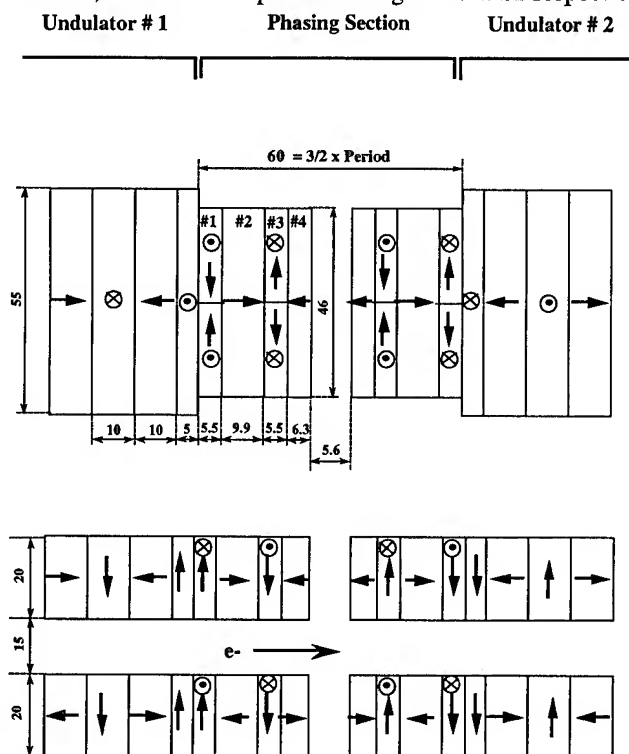


Figure 2: Termination of a pure permanent magnet undulator which allows nearly perfect phasing over harmonics 1 to 21 for any gap value between 15 and 50 mm.

each other to obtain the optimum brilliance.

Fig. 2 presents the magnetic design that we have produced which is capable of phasing two undulator segments with a period of 40 mm within the whole gap range of 15 to 50 mm.

Note that we have intentionally left a longitudinal gap between the magnets arrays of 5.6 mm in order to reduce any magnetic or mechanical interactions between each segment. Fig. 3 presents the peak angular flux computed on various odd harmonics of the radiation spectrum from the field of 2 such segments, each 12 periods compared to the one of a single undulator of 25 periods. One notices that the phasing section provides ideal performance up to harmonic 21 at a gap of 15 mm and it has a low dependence on the magnetic gap.

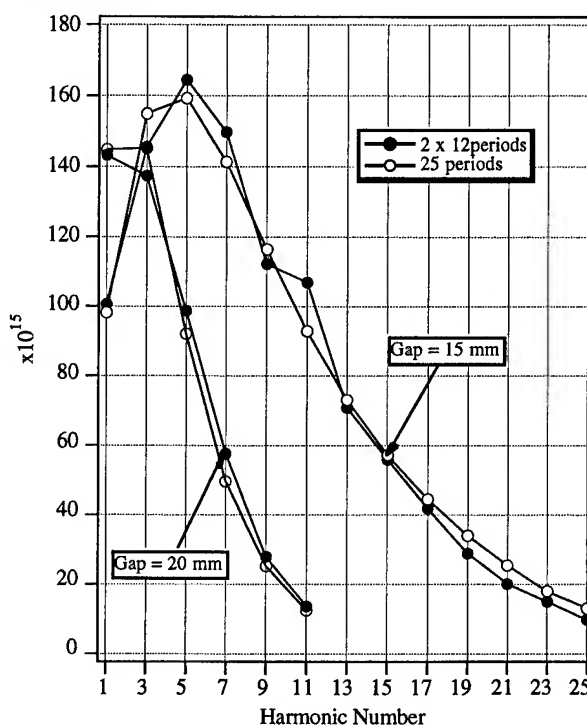


Figure 3: Peak angular flux computed as a function of the odd harmonic of the spectrum for a 25 period undulator and 2 segments of 12 periods phased according to Fig.2.

Note that such performance would not be reached if one removed the phasing section of Fig.2 except if one placed both undulator segments in close contact which would seriously complicate both installation and control. Another advantage with our phasing section is that both undulator segments are still fully independent, one can switch one, two or three segments remotely without any intervention in the ring tunnel. This feature is particularly attractive to match the ring's current condition to the maximum acceptable heat load in the beamline. 6 undulator segments of this type have been ordered and installation in the tunnel should start before the end of 1995.

IV New Magnetic Designs

For some applications it is essential to obtain the maximum field for a given spatial period. One way is to reduce the magnetic gap, another approach is to optimise the magnetic design. Figure 4 presents a magnetic design for a pure permanent magnet assembly which is easy to manufacture and achieves 11% higher field at the minimum gap of 15 mm. Two undulators of this type are currently being measured and will be installed before the end of 1995. The price to pay is a reduction of the transverse roll-off of the peak field.

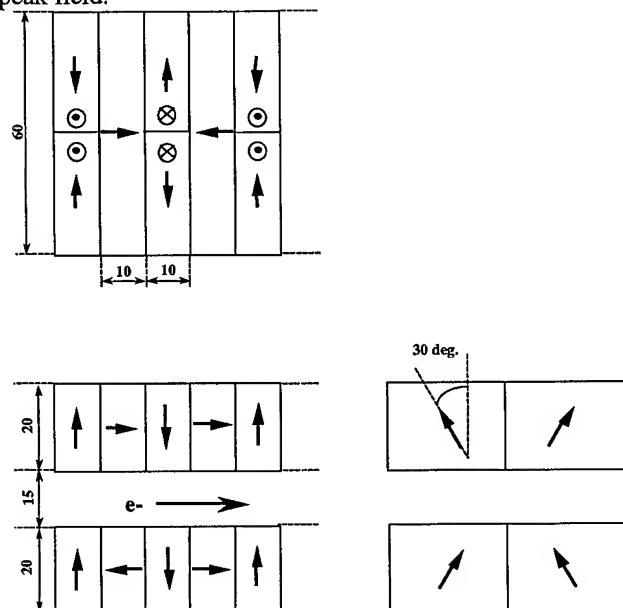


Figure 4: Pure permanent magnet design of an undulator which allows a 11% higher magnetic field than a conventional design of the same period (40 mm) and same gap (15 mm).

For some other applications the highest peak field is desirable together with a reasonably short period. In these cases hybrid technology which combines NdFeB magnets and poles made of cobalt steel with a high saturated field is the most effective. Fig. 5 presents a design of one period of such a wiggler. It presents a 150 mm period. For a magnetic gap of 20 mm a peak field of 1.9 T has been measured in good agreement with the modeling. With the new chambers of 16 mm, a field of 2.15 T is expected. Two of such wigglers have been built and installed on the ring. By reoptimising the design and operating with a 10 mm magnetic gap, we believe that a peak field of 3 T could be reached with a period around 200 mm.

A higher field would require the superconducting electro-magnet technology. A 5 T three pole device has been designed and built by Siemens for the ESRF. It has an effective period of 200 mm, a warm bore with a beam

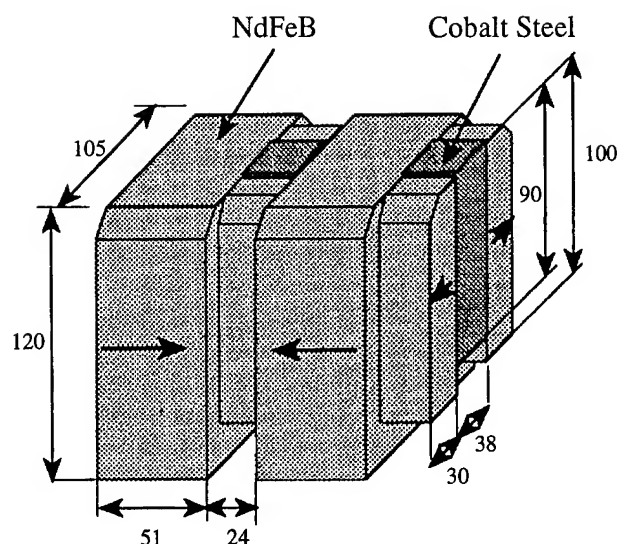


Figure 5: Magnetic design of a high field hybrid wiggler with 150 mm period and peak field of 1.9 T for a 20 mm gap.

stay clear of 16 mm. This wiggler is currently in operation. Its cryostat is equipped with a small refrigerator which cools two shields at 70 and 20 deg K respectively. A Joule Thomson loop pre-cooled by the refrigerator makes the necessary cooling capacity at 4 K to fully recondense the boiling Helium. Such a refrigerator significantly reduces the running costs.

Finally one should mention the installation of three variable polarisation linear/helical undulators with periods of 52 and 85 mm. The concept for this undulator has already been published[3]. Their most important feature is to allow the user to select independently the vertical and horizontal component of the magnetic field together with their phase. They cover the photon energy range from 0.5 to 20 keV with linear/circular polarisation rates in the 90 to 100 % level. Circularly polarised radiation of higher energy is obtained from two asymmetric wigglers[4] with respective peak fields of 1.1 and 1.9 Tesla and from the superconducting wiggler.

VI. REFERENCES

- [1] J. Chavanne, P. Elleaume, "Undulator and Wiggler Shimming", Synchrotron Radiation News, Vol.8 No1, p18 (1995).
- [2] b3d code, manuscript under preparation.
- [3] P. Elleaume, Nucl. Instr. and Meth. A291, p371-377 (1990). see also J. of Synchr. Radiation (1994), 1, 19-26.
- [4] J. Goulon, P. Elleaume, D. Raoux, Nucl. Instr. and Meth. A254, 192-201 (1987).

DESIGN OF THE PEP-II LOW-ENERGY RING ARC MAGNETS*

T. Henderson, N. Li, J. Osborn, J. Tanabe, D. Yee, and R. Yourd,
Lawrence Berkeley Laboratory, Berkeley, CA 94720 USA,
W. Du, Y. Jiang, and Y. Sun, Institute for High Energy Physics, P. R. China

We describe the PEP-II Low-Energy Ring (LER) arc quadrupole and dipole magnets, being designed and built by a Lawrence Berkeley Laboratory (LBL) and Institute of High Energy Physics (IHEP) collaboration. The LER requires 292 "standard" 43-cm long, 10-cm bore aperture laminated quadrupoles. A 2-piece construction was chosen to reduce the influence of assembly tolerances on field quality. Laminations with an optimized pole profile are punched from 1 m x 2 m x 0.5 mm steel sheet, a standard product in China. The chosen design is patterned after that of the Advanced Light Source (ALS) booster quadrupole. As some of the quadrupoles are run in long strings and others in short strings, two coil types (15-turn and 58-turn, each with several cooling-circuit topologies) are being fabricated. The majority of coils are aluminum but a few quadrupoles require copper coils due to their high excitation. Fabrication, assembly, magnetic measurements and fiducialization will be carried out at IHEP. Dipoles will be fabricated similarly. We require 192 dipoles, 45-cm long, with a magnetic radius of 13.75 m and a good-field aperture of 90 mm; the pole shape is optimized for field levels up to 3.5 GeV beam energy. Coils are an aluminum pancake configuration designed to keep power consumption moderate.

I. COLLABORATION

The construction of PEP-II is a joint collaboration of scientists, engineers, and technicians at three institutions in the U. S. (SLAC, LBL, and LLNL). An international collaboration has been established with IHEP in the P. R. of China to develop and produce some of the LER arc magnets (Fig. 1). Scientists and engineers from IHEP visited LBL in the summer of 1994 to review magnet requirements and to participate in the development of the designs for both the quadrupole and dipole magnets required for the PEP-II LER. Discussions extended to methods of magnetic measurements and fiducialization of the magnets. Arrangements for the construction of magnet prototypes, the production quantities, and measurement and fiducialization of the magnets were formalized in two agreements signed by representatives of IHEP, LBL, and SLAC in November, 1994 and March, 1995. The schedule calls for the completion of the quadrupole prototype by July, 1995, the dipole prototype by November, 1995 and fabrication of the production quantities of magnets through February, 1997.

*Work supported in part by the Director, Office of Energy Research, Office of High Energy and Nuclear Physics, High Energy Physics Division of the U. S. Department of Energy, under contract number DE-AC03-76SF00098.

II. MAGNET REQUIREMENTS

The LER is designed to operate for positron energies which range between 2.4 to 3.5 GeV. The multipole values listed below are normalized to the fundamental at the indicated radius.

A. Quadrupoles

No. Required:	292
Bore Radius:	50 mm
Effective Length:	430 mm
Excitation Range:	$0.67 \leq B' \leq 19.21$ T/m
String Magnet Excitation:	4.5 T/m @ 3.1 GeV
Magnet-to-Magnet Reproducibility:	$\leq 1 \times 10^{-3}$
Line-Integral Field Quality Systematic Multipoles:	$\leq 1 \times 10^{-3}$ at 50 mm radius
Random Multipoles:	$\leq 5 \times 10^{-4}$ at 50 mm radius

B. Dipoles

No. Required:	192 + 8 for Wiggler Chicanes
Magnet Gap:	63.5 mm
Effective Length:	450 mm
Central Field:	0.75 T @ 3.1 GeV
Magnet-to-Magnet Reproducibility:	$\leq 1 \times 10^{-3}$
Line-Integral Field Quality Uniformity:	$\leq 1 \times 10^{-3}$ for $-45 \leq x \leq 45$ mm
Sextupole Content:	$\leq 1 \times 10^{-4}$ at 30 mm radius

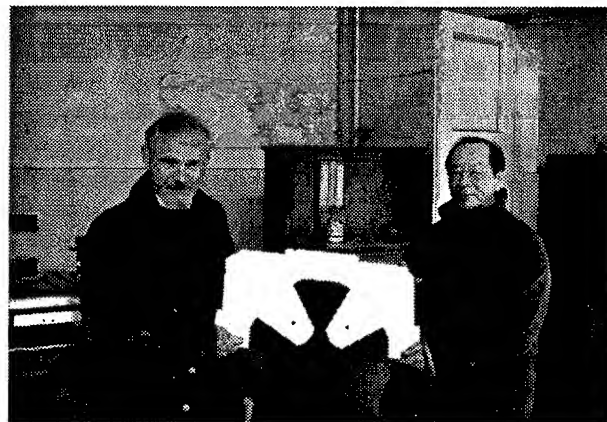


Figure 1: Tom Henderson (LBL) and Jiang Yan Ling (IHEP) with punch from quadrupole lamination die set.

III. QUADRUPOLE DESIGN

The majority of the quadrupoles are divided among two families which are connected in two long power supply strings. Other quadrupoles control the dispersion, the tune, and shape the beam in the wiggler and interaction regions of the lattice and are connected in short power supply strings. Because of these varied applications, and since the LER lattice is designed to operate over a range of energies (2.4 to 3.5 GeV) a common magnet design was needed to satisfy a wide range of excitation. Detailed design of the PEP-II LER quadrupoles, including a summary of two-dimensional magnetostatic calculations, electrical parameters and water flow and cooling calculations, is included in reference [1].

A. Yoke design

A yoke design (Fig. 2) was chosen and analyzed to satisfy the demanding field-quality requirements for the quadrupoles over a wide range of excitation. This same yoke design is shared among all the quadrupoles in the LER except for selected magnets in the interaction region.

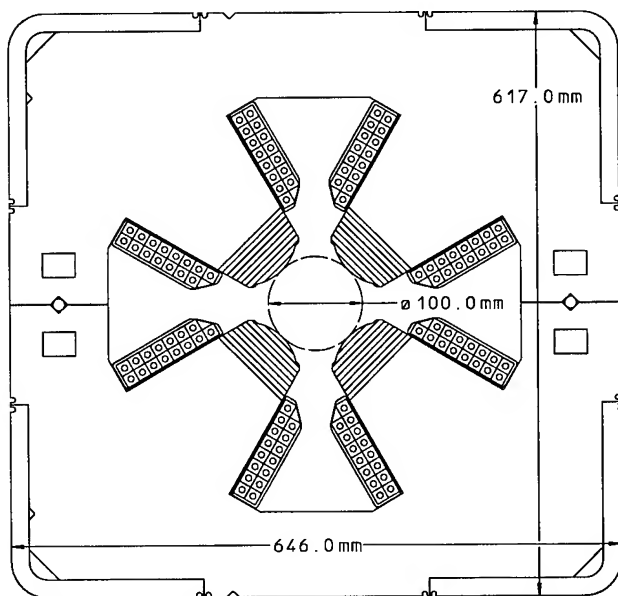


Figure 2: Quadrupole Layout with 15 turn per pole Coil.

The pole tip design is a scaled version of the optimized pole originally developed for the ALS (scaled from 32.5 mm to 50 mm pole radius). The original pole shape was shared among the ALS booster, storage ring, and beam transport quadrupoles and was developed with the goal of reducing the multipole errors allowed by the four-fold rotational symmetry ($n=6, 10, 14, 18, \dots$) to values $\leq 1 \times 10^{-4}$ of the fundamental when measured at the pole radius. With this high quality for the two-dimensional field, the chamfer developed to minimize the multipoles due to the three dimensional fringe fields can be used for any magnet,

independent of its magnetic length. This allowed us to scale both the chamfer and the pole shape for the PEP-II LER quadrupoles from the ALS design with full confidence that the field quality for the line integral of the magnet will meet the same good-field quality as achieved for the ALS.

The yoke is made in two pieces rather than four pieces to enhance its rigidity and simplify magnet assembly. This made it possible to reduce the potential assembly errors and the resulting random multipole errors. The advantages of this approach were first exploited during the fabrication of the PEP Insertion quadrupoles in 1979[2]. The ease of precisely shimming the halves of the two piece magnet with respect to each other allows the cancellation of selected multipole errors[3].

B. Coil design

The two piece yoke design constrained the coil geometry. To install the coil, its width could be no wider than the space between adjacent poles. Reduction of the quadrupole power required reducing the current density by increasing the coil height. This resulted in a rather tall and narrow coil cross section and limited, somewhat, the choice of conductors that could be used to satisfy power supply and power distribution constraints. Moreover, since many of the old PEP magnets with aluminum coils are used in the High Energy Ring (HER), a further requirement for the LER magnet coils was to use aluminum conductor so that the water-cooling system could be shared.

The arc quadrupoles connected in long strings have coils with 15 turns per pole wound with 0.5 inch hollow square aluminum conductor. Other quadrupoles connected in short strings have 58 turn per pole coils wound with 0.25-inch hollow square conductor. All but a few of the 58-turn coils are made using aluminum conductor. The few magnets which utilize copper conductor are located in the interaction region of the PEP-II ring. These require higher currents and take advantage of the local water system provided in that area for other copper and stainless steel accelerator components. The 58-turn coil magnet water cooling circuits are arranged in a variety of different configurations, depending on the power dissipation for the particular magnet application. Parameters for two of the coil configurations are listed below.

58 Turn per pole aluminum coil:	1 circuit
Resistance	279.2 m Ω
Maximum Current	46 A
Maximum Gradient	2.68 T/m
Water Flow @ 130 psi	0.075 gpm
58 Turn per pole aluminum coil:	4 circuits
Resistance	279.2 m Ω
Maximum Current	139 A
Maximum Gradient	8.10 T/m
Water Flow @ 130 psi	0.682 gpm

IV. DIPOLE DESIGN

The arc dipoles in the LER are connected in two series power supply strings. Thus, they share, with the majority of the quadrupoles connected in series strings, very stringent magnet to magnet reproducibility requirements. Therefore, the manufacturing plan, developed by LBL and IHEP, includes careful shuffling of the steel and laminations required for the large number of magnets to ensure the distribution of any variations in iron magnetic properties and any systematic variation in laminations due to die wear. Detailed design of the PEP-II LER dipole, including summary of two and three dimensional magnetostatic calculations, electrical parameters and water flow and cooling calculations are included in reference [4].

A. Yoke design

An "H-type" geometry (Fig. 3) was selected for the yoke so that a simple pancake coil can be utilized. The pole width was selected and the shape of the rectangular bumps at the edges of the pole was optimized in order to satisfy the field quality requirements for the magnet in the central two-dimensional region of the magnet. The pole edges were slightly tapered in order to minimize iron saturation at the pole root when operating at the high end of the required excitation range.

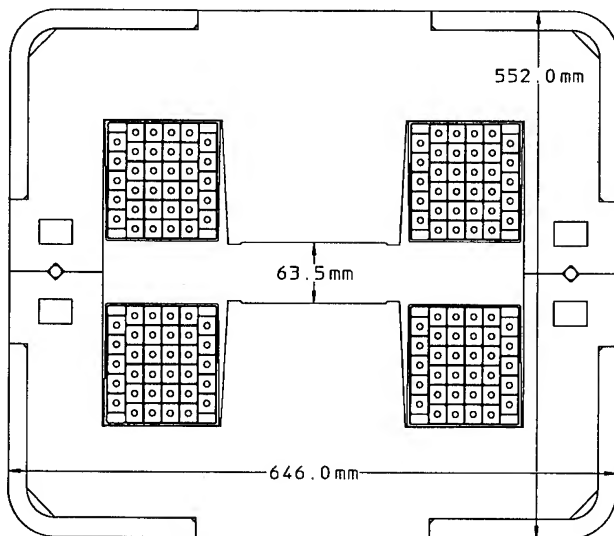


Figure 3: Dipole Layout.

Since the dipoles are relatively short, the variation of the fringe field at the end of the magnet is expected to dominate the line-integral field uniformity. Field distribution studies were made using Amperes[®] [5] (a three-dimensional magnetostatic code using the boundary element method) in order to estimate the shape of the chamfer (Fig. 4) which will satisfy the field-integral uniformity requirement for the dipole.

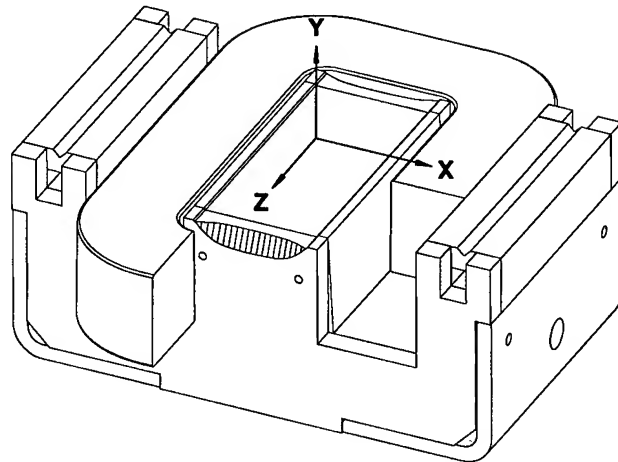


Figure 4: Dipole Chamfer.

B. Coil design

The dipole coil has thirty-four turns of 0.715 inch square hollow aluminum conductor in order to satisfy power supply and power distribution constraints. The 34 turns are enclosed in a cross section sized for 36 conductors. Two turns were lost due to "soft" crossovers which allowed easy transitions between coil rows and layers.

34 Turn per pole aluminum coil - 1 water circuit

Resistance	10.97 mΩ
Current @ 3.1 GeV	563 A
Field @ 3.1 GeV	0.75 T
Water Flow @ 130 psi	0.933 gpm

V. ACKNOWLEDGEMENTS

The authors would like to acknowledge the guidance provided by Mike Zisman and the drafting support provided by Mike Knolls.

VI. REFERENCES

- [1] J. Tanabe, J. Osborn, N. Li, D. Yee, "Standard 43 cm Quadrupole Engineering Design", LBL Mechanical Engineering Note M7498A, October, 1994.
- [2] R. T. Avery, T. Chan, K. Halbach, R. Main, J. T. Tanabe, "PEP Insertion Quadrupole Design Features", Proceedings of the IEEE Particle Accelerator Conference (PAC), San Francisco, CA, March, 1979, pp. 4033-4035.
- [3] J. T. Tanabe, "ALS Storage Ring Quadrupole, Shimming Procedures", LBL Engineering Note M7156, December, 1990.
- [4] J. Osborn, J. Tanabe, "Standard 45 cm Arc Dipole Engineering Design", LBL Mechanical Engineering Note M7512A, March, 1995.
- [5] Amperes[®], Integrated Engineering Software, 46-1313 Border Place, Winnipeg, Manitoba, Canada R3H0X4.

Prototype Development of the BESSY II Storage Ring Magnetic Elements*

T. Becker, D. Krämer, S. Küchler, U. Strönisch,
BESSY II, Rudower Chaussee 5, Geb. 15.1, 12489 Berlin, Germany,
and

V. Korchuganov, N. Kuznetsov, E. Levichev
The Budker Institute of Nuclear Physics, SB RAS, Novosibirsk, Russia

Abstract

The lattice magnets for the 3rd generation synchrotron light source BESSY II under construction were designed and storage ring dipole, quadrupole and sextupole preseries magnets are presently manufactured in industry. This paper reviews the design as well as the main magnet parameters and describes the features of the magnetic elements according to the specific constraints by the compact lattice structure.

I. Introduction

BESSY II presently under construction at Berlin, Germany, is a 240 m circumference 1.9 GeV low emittance high brilliance 3rd generation synchrotron light source [1]. The 16 double bend achromat structures are composed out of two dipole, four quadrupole and 3 sextupole magnets. A quadrupole triplet and doublet each of them on one side of the achromat with two sextupoles in the zero dispersion regions complete the structure, Fig.1. As experiments require full operation at energies ranging from 0.9 to 1.9 GeV all magnet yokes are made from 0.5 and 1.0 mm thick low carbon 2% Si transformer steel to ensure low hysteresis and high reproducibility for the magnet settings. The lamination thickness selected was based on a compromise of meeting the tight tolerances for the stamped lamination of typically 0.015 mm and economic considerations.

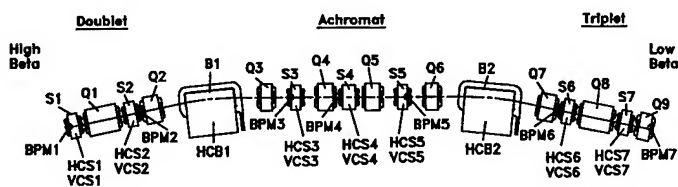


Figure 1. BESSY II DBA-cell.

All laminations will be shuffled in order to provide high reproducibility and identity within each magnet family. This implies flipping the lamination to compensate the barrel effect present in all laminations.

II. Storage Ring Magnet Designs

A. Dipole Magnet

As the storage ring is an isomagnetic lattice 32 C-shaped dipoles with parallel poles are used. Fig. 2 gives a view of the bending magnet. Though the bending radius is $\rho = 4.355$ m the core is a straight box type with parallel ends rather than a curved

yoke in order to facilitate meeting the mechanical tolerances of the magnet. The additional costs of iron due to the sagitta of 10.5 mm were considered advantageous for a straight core compared to smaller pole size implying a much stronger influence on mechanical tolerances of shims. To achieve a magnetic length of 855 mm the core of the 50 mm gap dipoles was set to a mechanical length of 810 mm deduced from the magnetic data of similar magnets [2]. The content of higher harmonics in the integrated field will be mainly of sextupole type when a chamfer of $45^\circ \times 8$ to 10 mm in length is applied. An integrated sextupole component of $m \cdot L < -0.5 \text{ m}^{-2}$ is expected.

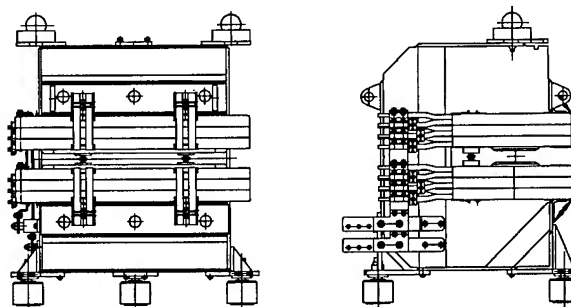


Figure 2. View of the storage ring dipole magnet.

The yoke will be made from 0.5 mm thick laminations which are insulated by back-lack. The stack is compressed by stiff baked endplates and plates are welded to the other sides of the core. A SURAHAMMA DK-70 steel grade is used for the inorganic insulated laminations. Coils are made from rectangular hollow OFHC conductors of $21 \times 12 \text{ mm}^2$ in size giving six pancakes of 84 windings altogether. To minimize coil overhang, to give more space for the crotch absorbers, the height of the coil cross-section is significantly larger than its width. Fig. 3 gives the expected excitation curve as was calculated by the 2D code POISSON [3]. To correct for finite length of the bending magnet the increase of flux density in the iron core due to the endfield was taken into account, resulting in a much steeper saturation at high field levels. At full beam energy corresponding to a field of 1.45 T, saturation is expected to be below 3%. Table 1 gives a list of magnetic and electric parameters.

B. Storage Ring Quadrupoles

There are 144 quadrupole lenses grouped into nine families. All magnets are made from laminations of same cross section but differ in core length L ($L=200, 250$ and 500 mm). The poles and shims were optimized in 2D approximation using the codes [3], [4]. For achieving gradients of up to 16.5 T/m the poles have

*Funded by the Bundesministerium für Bildung, Wissenschaft, Forschung und Technologie and by the Land Berlin.

SR Dipole Magnet	
Rectangular C shaped type	
Gap	50 mm
Field range	0.7 - 1.45 T
Good field area	60×35 mm ²
Homogeneity dB/B	5·10 ⁻⁴
Current	710 A
Resistance	16 mOhm
Inductance	38 mH

Table I

Design parameters for storage ring dipole magnets.

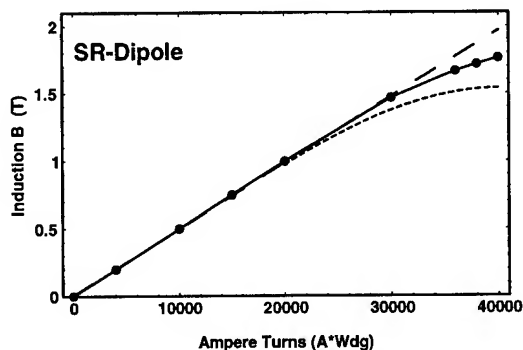


Figure 3. Calculation of the storage ring excitation curve. The solid dots were calculated by the 2D POISSON code. Correction of the data for the finite length results in saturation starting much earlier (dashed line). At design field of 1.45 T saturation of less than 3% is expected.

conical shape at the same time allowing for inserting simple and cost-efficient race-track coils.

The geometry of the lamination is mainly determined by the boundary that synchrotron radiation beamlines are penetrating the return yoke. Thus the magnets are figure of eight type using variable formed spacers at the mid plane in order to allow 22 mm vertical clearance. To retain the magnet symmetry the spacers are mirror symmetrical as they are made from soft magnetic steel. This was decided to be advantageous to shield the magnet center from external fields and shunt the iron regions to compensate the anisotropy in permeability.

A chamfer of 45° × 8.5 mm is considered to be sufficient to cancel the dominant systematic harmonics in the focussing strength (e.g. N=6 and N=10) to achieve homogeneous integrated gradient distribution $dGL/GL < 0.002$ within a radius of 30 mm. Fig.4 gives a view on the storage ring quadrupole, the main performance data are listed in table II. 2D calculations, corrected for the finite length of the lenses were performed, showing that the design gradient is achieved at a saturation level of 0.7% / 6.8% / 11.8% for the 500/250/200/ mm long elements, Fig. 5.

C. Storage ring sextupole magnets

Seven families of 16 magnets each are used as chromatic and harmonic sextupoles. As for the other multipoles the yokes are

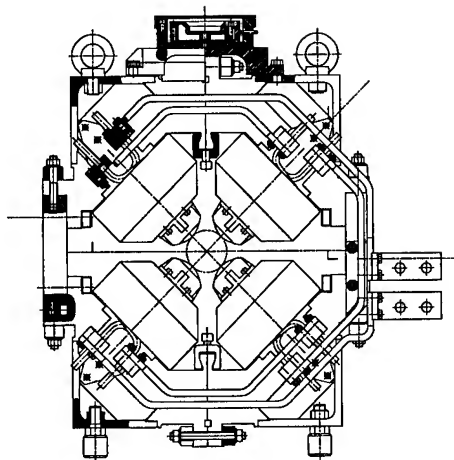


Figure 4. Storage ring quadrupole magnet.

SR Quadrupole Magnet	
Magnet type	Figure of eight
Apertur radius	35 mm
Core length	500/250/200 mm
Gradient	16.5 T/m
Good field radius	r=30 mm
Homogeneity	$dGL/GL \leq 2 \cdot 10^{-3}$
Current	365 A
Resistance	34/19/16 mOhm
Inductance	38/19/10 mH

Table II

Design parameters for storage ring quadrupole magnets.

stacked from identical laminations to two different types differing in length ($L = 160$ and 210 mm).

A sextupole strength of 600 T/m² is required to be able to combat resistive wall instability though in the standard optics the strength is considerable less. Furthermore the magnets will be used as horizontal and alternatively as vertical dipole correctors. These fields are generated by additional coil systems. The reason for the integrated function is the lack of space in the compact lattice which does not allow installation of lumped correctors. Fig. 6 gives a view of the sextupole which is build up from 3 segments to retain the odd symmetry rather than being of C shape type. Massive low carbon soft magnetic spacers from ARMCO iron modelled according to the crossing SR beamlines are used. Thus it is expected to minimize irregular harmonics during dipolar correction associated with significant flux density changes in the core, resulting in running at different hysteresis loops for neighbouring poles. In table III the magnetic and electric data are listed.

The excitation curve of the sextupoles was calculated in 2D approach and corrected for the finite element length by taking into account that the actual flux density in the core will be about 1.65 times larger than in the pure POISSON calculation. Correcting for this effect results in a saturation curve as shown in fig. 7. Saturation at max. sextupole strength is expected to be in the order of 5%, still tolerable.

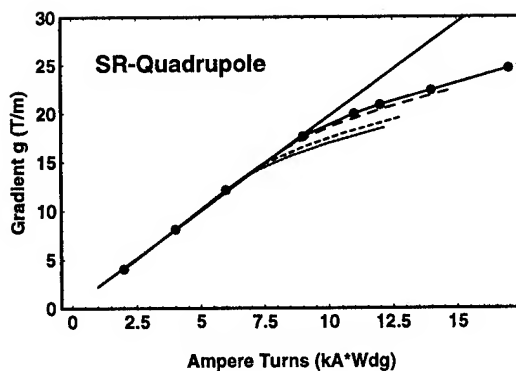


Figure 5. Dependence of gradient as function of excitation current. The solid line represents the POISSON 2D results. The expected excitation curves for the three lenses of 200/250/500 mm in length is given by the dashed lines.

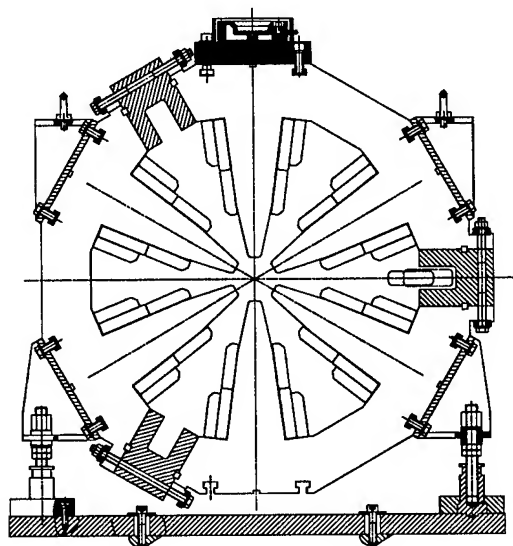


Figure 6. View of the storage ring combined sextupole and dipole corrector.

References

- [1] E. Jaeschke for the BESSY II design team, *Status of the High Brilliance Synchrotron Radiation Source BESSY II*, this conference
- [2] F. Brinker, *DELTA Int. Rep. 93-5, Dortmund, 1993*
- [3] POISSON, Los Alamos Accelerator Code Group, LA-UR-87-115, LANL 1987
- [4] MERMAID, BINP Novosibirsk, *unpublished*

SR Sextupole Magnet	
Aperture radius	38 mm
Core length	160/210 mm
Gradient	600 T/m ²
Good field radius	r=30 mm
Homogeneity	$dG'L/G'L \leq 2 \cdot 10^{-2}$
Current	250 A
Resistance	39/33 mOhm
Inductance	7/5 mH
Corrector strength	2 mrad

Table III

Electric and magnetic parameters of storage ring sextupole magnets.

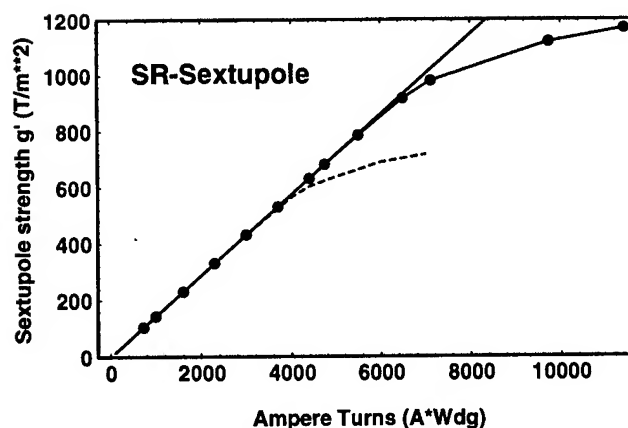


Figure 7. Calculated excitation curve for the storage ring sextupoles. The solid line is according to the POISSON 2D calculation, the dashed line represents the expected saturation behaviour after correction for the finite element length.

Design, Construction, and Procurement Methodology of Magnets for the 7-GeV Advanced Photon Source*

A. Gorski, J. Argyrakis, J. Biggs, E. Black, J. Humbert, J. Jagger[†], K. Thompson

Advanced Photon Source, Argonne National Laboratory,
9700 South Cass Avenue, Argonne, Illinois 60439 USA

Abstract

All major magnets of the Advanced Photon Source (APS) have now been measured and installed in the facility. This paper describes the mechanical design, construction, procurement philosophy and methodology, and lessons learned from the construction and procurement of more than 1500 magnets for the APS storage ring, injector synchrotron ring, and positron accumulator ring.

I. INTRODUCTION

The Advanced Photon Source (APS) is located in the southwest corner of the Argonne National Laboratory (ANL) approximately 35 miles southwest of Chicago, IL USA. Ground was broken for the 79-acre site on June 4, 1990. APS, the world's most brilliant x-ray source, is scheduled for operation in the fall of 1996. A plan view of the site is shown in Fig. 1. The storage ring has a circumference of 1104 m (3640 ft) and contains 1128 magnets which direct and focus 7.0-GeV positrons in their vacuum environment of 10^{-10} Torr. The injector synchrotron contains 302 magnets, and the positron accumulator ring (PAR), which produces a single circulating bunch for injection, contains 36 magnets. With the addition of the low and high energy transport (LET and HET) lines, the total number of magnets is 1514 (excluding the linac system). This paper will discuss the methodology used to design, construct, and procure these magnets.

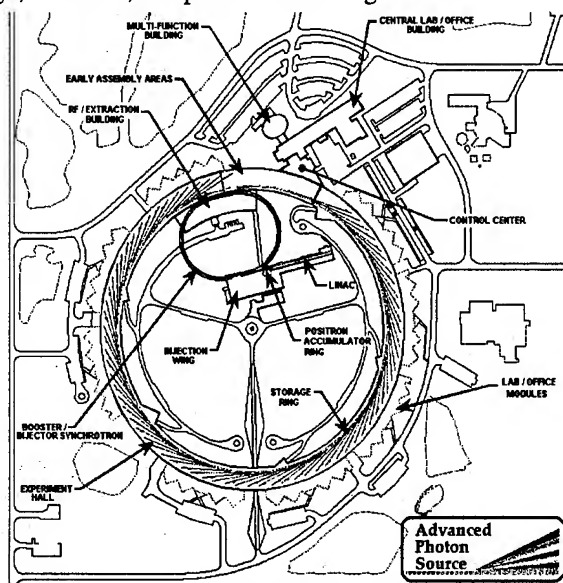


Fig. 1: APS Site Plan View

* Work supported by the U.S. Department of Energy, Office of Basic Energy Sciences, under Contract No. W-31-109-ENG-38.

[†] Magnet Group Leader during the course of this work.

II. MAGNET DESIGN AND CONSTRUCTION PROCEDURE

The task of fabricating 1514 APS magnets of 19 different types was accomplished by the following 7-step process:

1. Conceptual Phase - Title 1 Process
2. Prototype Phase - Title 2 Process
3. Prototype Phase
4. Construction Phase
5. Tooling Design and Fabrication
6. Travelers and Inspection Forms
7. Final Inspection/Shipment

In the Conceptual Phase, the physics design is reduced to a conceptual design in terms of magnet mechanical parameters, pole profiles, coil packaging, and construction materials. The resulting conceptual design is then reviewed by internal and external peer reviews. Only after acceptance by all reviewers is the design committed to Title 2.

In the Prototype Phase - Title 2 Process prototype drawings are prepared using computer-aided design (CAD) techniques. These drawings are again reviewed by internal and external peer reviews including the originating physics design team. After passing these reviews, the design is committed to prototype construction.

The prototype is built and tested in the Prototype Phase. In construction of the prototype, basic traveler documents are created outlining construction details and process measurements during fabrication. These travelers, which each magnet has during its construction and operational lifetimes, also use standard QA/QC methods. Again, the prototype and its performances are reviewed internally and externally. Only after passing these requirements are final construction drawings prepared.

In the Construction Phase, specifications, statements of work, and work packages are prepared to procure steel, copper, laminations, parts, and complete magnets from industry. At this point a strong relationship is essential between engineering staff and procurement specialists. Basically, four processes were used to fabricate the required magnets.

- Procure parts from industry and assemble magnets in-house at ANL and by industry. This method was used to fabricate storage ring quadrupoles, sextupoles, and corrector magnets.
- Procure parts from industry, fabricate some in-house, and assemble magnets at ANL. This method was used to fabricate synchrotron dipole, quadrupole, sextupole, and corrector magnets, and the PAR corrector magnets.
- Procure complete magnets from industry from specifications supplied by APS physics personnel. Several magnet

types were purchased complete: storage ring dipoles and correctors, PAR dipoles and PAR quadrupoles, LET dipoles and quadrupoles, and HET dipoles and quadrupoles. These complete magnets were manufactured both in the U.S. and abroad.

- Pulsed magnets, not considered in this paper, were built completely in-house and are primarily considered prototypes.

The tooling used in the construction phase was designed by APS and used to fabricate prototypes. Only then is it "certified" for construction use and sent to vendors. Travelers and inspection forms are created jointly by engineering and QA/QC personnel. When the magnet is completed, tested and inspected again, all paper work is reviewed before shipment to the APS site for installation.

III. PRODUCTION MAGNETS AND RESULTS

Magnet profiles for the synchrotron dipole, quadrupole, sextupole, and corrector magnets are shown in Fig. 2. Magnetic measurements have been reported [1] and [2] and show that, e.g., for the synchrotron dipole, the integrated field shape is flat to within 2.5×10^{-4} in the required field region. Multiple coefficients of the quadrupoles and sextupoles satisfy required field specifications. Magnet profiles for the storage ring are shown in Fig. 3. Results for the quadrupole magnets have been published [3] and [4] and meet or exceed tolerance requirements. Results for the other storage ring magnets will be reported in these proceedings. The major groups of magnets procured solely from outside vendors are the storage ring dipole and corrector magnets and the PAR dipole and quadrupole magnets. The latter two are shown in profile in Fig. 4. All magnets were measured in the APS Magnet Measurement Facility [5].

IV. PROCUREMENT STRATEGY

Three predominant strategies surface when one scrutinizes the acquisition process for the large number of magnets installed in the APS. The strategies which were strongly supported by APS management can be summarized as follows:

1. Establish and maintain throughout the course of the procurement cycle a strong partnership between the APS procurement specialist and the magnet design engineer. To this end, a procurement specialist was assigned to process all of the major and/or critical purchases emanating from the Magnet Group. Front-end involvement in tasks such as the preparation of statements of work, identification of potential bidders, and the assessment of vendor qualifications was a shared responsibility. Ownership for the success of the acquisition process further enhanced and strengthened the linkage and teamwork between procurement and engineering.
2. Maintain direct control over the procurement of the essential raw materials utilized by subcontractors in fabricating major magnet subassemblies such as coils and cores. The quality of the magnet steel, the copper conductor tubing

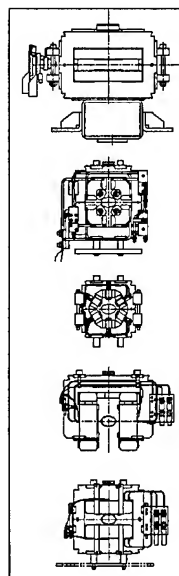


Fig. 2

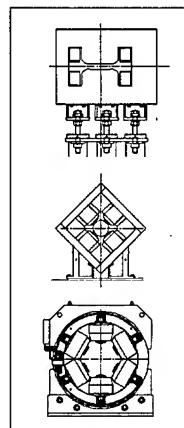


Fig. 4

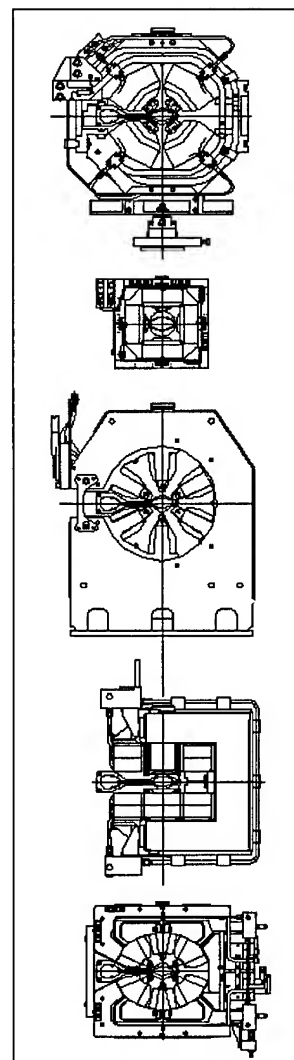


Fig. 3

and the laminations were designated at the outset as critical applications, requiring the Laboratory's direct control in specifying, purchasing, and inspecting. These items for all of the synchrotron and storage ring magnets became Laboratory-furnished material for subcontractors contracted to fabricate cores and coils.

3. Commit to providing APS resources, specifically technical expertise, to accelerate learning and diminish start-up anxieties for vendors fabricating key magnet components. This effort consisted of two basic elements. First was the supply of critical tooling and prototype units developed at the Laboratory. For example, Procurement coordinated the shipment of core stacking fixtures utilized in prototype development, for use by the vendor in setting up production. Also, sample cores fabricated by the Laboratory were sent to a number of vendors for their use in checking dimensional requirements as well as form and fit. Secondly, the Laboratory was adamant about dispatching skilled, senior-level magnet technicians to work with our vendors' production personnel at the outset of the contract term, to develop the assembly/fabricating skills learned at

the Laboratory during prototype development. This training was invaluable in assuring a successful first-article review.

V. PROCUREMENT METHODOLOGY

The typical major magnet procurement (\$500,000 and above) generally followed the sequence described below. The reasons for the successful completion of these procurements are (1) the clear-cut contract authority and responsibility assigned to the procurement specialist and magnet engineer and (2) the continuing communications between the engineer and specialist throughout the term of the contract.

The sequence of events from planning to contract close-out were as follows:

1. Advance Procurement Plan—Laboratory policy dictates that a procurement plan be written which addresses the critical issues concerning major procurements. Areas such as "make or buy"; potential sources of supply; the need for dual sourcing; risks associated with technical, cost, and delivery factors; schedule and budget constraints; and QA matters such as reliability and first-article requirements were all discussed and documented. The Plan became the first opportunity to bring the purchasing representative together with the engineer and acted as the first building block in cementing a strong interdepartmental relationship.
2. Bid List Formation—Cooperation was enhanced because of the dual responsibility for formation and approval of the bidders list. Although recognizing magnet engineering's expertise and pre-eminence in this area, Procurement was allowed to augment the bidders listing to assure compliance with socio-economic requirements mandated by DOE. An important point to make is that a significant number of prospective bidders were known entities as a result of pre-bid vendor visits and market surveys.
3. Contract Review—Prior to issuance of the completed contract, an internal review was conducted to insure that the cognizant engineer was knowledgeable concerning his/her duties and obligations. Sometimes if the value and complexity of the contract warranted it, the vendor was brought into the picture in a face-to-face meeting to make certain that all the parties understood those contracted obligations.
4. Contract Administration—It was clear and unequivocal that Procurement would act as the clearinghouse and focal point for data dissemination in order to assure contract compliance. It was also clear that direct dialog between the magnet engineer and the vendor concerning technical matters was encouraged. Having already formed a strong link with Procurement, it became very easy for the engineer to recognize when a problem warranted Procurement intervention and resolution.
5. Contract Closeout—As a shared responsibility the magnet engineer and procurement specialist assured that the vendor was diligent in supplying inspection data sheets, that there was proper disposition of rejected items, that pay-

ments would be made upon receipt of goods (signatures of both parties required on all invoices), and that surplus Laboratory-furnished material and all loaned tooling was properly returned.

In retrospect, the strategies and methodology employed to procure magnets for the APS proved to be quite reliable and served to bring two somewhat divergent groups (procurement and engineering) together as a team, focused solely on assuring the successful installation of the APS.

VI. CONCLUSION

Due to the efforts of many people, the APS facility is nearing completion. All major magnets have been fabricated, tested, and installed in the facility. Magnet performance has been reported in the literature, and facility commissioning is now proceeding.

VII. ACKNOWLEDGEMENTS

The authors wish to thank all members of the Accelerator Systems Division for their support in this work. An effort of this magnitude requires the best efforts of many people. We especially appreciate the efforts of the CAD personnel which included S. Hanuska, C. Pitts, G. Cherry, T. Crain, D. Haid, C. Ostermeyer, M. Harkins, K. Costello, D. Lee, and A. Oberfeld. The engineers, technicians, and riggers who built and transported these magnets accurately and safely are not to be forgotten. They include: S. Reeves, D. Warner, M. Vogt, R. Putnam, A. Kelly, K. Bult, E. Theres, R. Bechtold, J. Pace, E. Russell, and M. Bosek. And last but not least, the authors wish to acknowledge the outstanding secretarial efforts of Ms. B. Hall who never lost faith in the magnet effort.

VIII. REFERENCES

- [1] K. Kim, et al., "Design and Tests of the Injector Synchrotron Magnets for the 7-GeV Advanced Photon Source," *Proc. of the 1993 IEEE Particle Accelerator Conference*, pp. 2808-2810, 1993.
- [2] K. Kim, et al., "Magnetic Measurement Data of the Injector Synchrotron Dipole Magnets for the 7-GeV Advanced Photon Source," *Proc. of the 1993 IEEE Particle Accelerator Conference*, pp. 2799-2801, 1993.
- [3] S.H. Kim, et al., "Magnetic Measurements of the Storage Ring Quadrupole Magnets for the 7-GeV Advanced Photon Source," *Proc. of the 1993 IEEE Particle Accelerator Conference*, pp. 2805-2807, 1993.
- [4] S.H. Kim, et al., "Fabrication and Tests of Prototype Quadrupole Magnets for the Storage Ring of the Advanced Photon Source," *Proc. of the 1991 IEEE Particle Accelerator Conference*, pp. 2375-2377, 1991.
- [5] S.H. Kim, et al., "Magnetic Measurement Facility for the 7-GeV Advanced Photon Source," *Proc. of the 1993 IEEE Particle Accelerator Conference*, pp. 2802-2804, 1993.

THE MAIN INJECTOR TRIM DIPOLE MAGNETS

R. Baiod, D.J. Harding, D. E. Johnson, P.S. Martin, S. Mishra, Fermi National Accelerator Laboratory*,
P.O. Box 500, Batavia, IL 60510 USA

Abstract

To correct field and alignment errors, provide full aperture steering at injection, and control the horizontal orbit in the straight section, a 0.060 T-m and a 0.090 T-m correctors were designed. The two magnets were chosen to have identical lamination cross section and identical coil packages, however the normal low field corrector has no cooling while a water cooled plate is incorporated to the high field one. Diffusion of the heat through the copper conductor, insulations, and magnet steel, with and without plate cooling, was analyzed, and temperatures were estimated. We report in this presentation the calculations of the various magnet parameters, and in particular, the procedure to optimize the temperature of the steel and the temperature of the inner copper coil.

I. Design requirements and constraints

Tracking studies at 8.9 and 120 GeV/c [1] have established that correctors with rms value of $\pm 35 \mu\text{r}$ in strength, will provide adequate correction at all energies. With a strength of 0.060 T-m, our normal corrector will provide $120 \mu\text{r}$ of steering at 150 GeV, a factor of 3.4 standard deviation at the highest energy. This should allow for correction for unexpected field/alignment errors and/or future orbit control requirements at high field. To reduce unexpected dipole field variations, we will consider shuffling the main ring dipoles during installation, and realigning the quadrupoles during commissioning. Stronger correctors around the straight sections are required to provide position and angle control around the electrostatic septa and Lambertsons during injection and extraction. To minimize corrector strengths at these locations, the high field orbit is first determined by quadrupole alignment. Then a corrector strength of only 0.090 T-m will provide $180 \mu\text{r}$ at 150 GeV/c and still provides a safety factor of about 2 above the required strength.

In addition to the beam requirements, the design of the trim dipole correctors was strongly restricted by first, the available space, and second, the necessity to accommodate existing power supplies. The horizontal trim dipoles are to be located upstream in the proton direction of each quadrupole, occupying a space of no more than 17 inches. For the normal trim dipoles, the maximum current allowed is 10 amperes with a duty factor of 0.7. To provide the stronger dipoles for injection and extraction manipulations, we investigated the possibility of having an optional water cooled plate added to the coil to be able to reach higher currents.

These specifications and constraints were used as a basis of a top-down optimization procedure that is described below. The allowed currents, given the desired ampere turns, precluded us from using copper tubing, but rather required low gauge solid

*Operated by Universities Research Association under contract with the United States Department of Energy

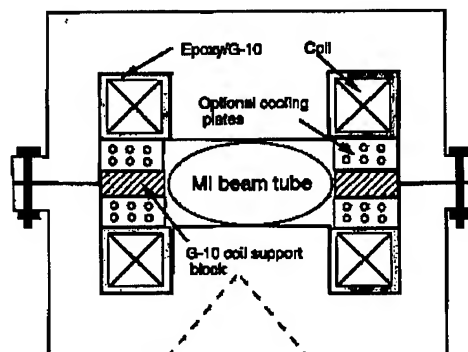


Figure 1. Horizontal magnet corrector cross-section. The dashed line shows an eventual way to increase the magnet area for better heat transfer.

copper wire. We therefore concentrated our efforts in modeling and evaluating the various mechanisms of heat transfer within the magnet components and convection at the outside surface. The main challenge in this optimization was to minimize the temperature of the inner copper to reduce the risk of insulation failure and the temperature of the steel surface for personnel safety consideration. We decided to limit the copper temperature to 95°C (epoxy rating). We also plan in using Dupont Pyre-ML wire coating which can withstand 220°C . The steel temperature is limited to 50°C . Based on failure data of past dipole correctors and other small magnets, we do not believe that extra cooling is necessary for the normal corrector.

We assume an H type of magnet, with pancake coils around the poles. The magnet aperture to accommodate the Main Injector beam pipe is 2 inches for the gap and 5 inches for the pole width, and these define the pole gap and pole width in our magnet. The magnet cross-section is shown in Figure 1

II. Thermal model

The heat starting from the copper wire, flows through the wire coating, the epoxy potting and G10 around the coil, the steel core, and finally is dissipated by convection in the ambient atmosphere at a 30° C temperature. Each one of this processes generates a temperature differential that will be estimated. A simple series configuration is assumed, and alternate paths with higher resistance to thermal flow have been neglected. We should mention that a more elaborate thermal model of existing Fermilab corrector magnets has been attempted. In this circuit-like model thermal resistances and capacitances (heat capacities) are fitted to measurements.[2]

To start with, we may assume that good thermal contact between the coil and the steel can be realized only at the bottom or top coil surfaces. Using an electrical parallel circuit analogy, the thermal impedance between the side of the copper coil to the steel pole is much larger than its counterpart at the top or bottom interface. Alternatively, we also consider the possibility where good thermal contact is easier to accomplish at the two coil sides. It should be added that a small air gap will add a significantly high series resistance to the heat flow. Therefore, we plan to use thermal grease in all interfaces with the coil, as well as maintaining good contact pressure.

The conductor coil made of copper wire and coating around each wire is modeled as a distributed heat source with an effective thermal conductivity that depends on the coating conductivity, coating thickness, and wire gauge. This effective thermal conductivity can be derived by considering a unidimensional heat flow through a layer of copper, in between two layers of insulation. The accumulated temperature gradient is then:

$$\Delta T = \frac{P}{S} \left(\frac{2t}{\lambda_i} + \frac{g}{\lambda_c} \right) \quad (1)$$

where $\frac{P}{S}$ is the heat flow per unit area, t is the coating thickness, and g is the wire thickness (gauge); λ_i and λ_c are the respective conductivities. Since the copper conductivity is much higher than the insulator conductivity, the effective conductivity of this medium is:

$$\lambda_e = \lambda_i \frac{g}{2t} \quad (2)$$

More detailed calculations for the case of cylindrical wires can be found in [3].

We assume a 4 mil thick Dupont Pyre-ML wire coating which can sustain higher temperature (higher glass transition at which mechanical properties change drastically). For this material the thermal conductivity is about 0.16 watt/m.°C. The coil will be dipped in epoxy to reduce air pockets.

The assumption of only one coil-steel contact simplifies the heat transfer within the copper source to an inhomogeneous 1-dimensional Poisson equation that can be solved easily:

$$\frac{d^2 T}{dx^2} = -\frac{p}{\lambda_e} \quad (3)$$

p being the heat production rate in a unit volume of copper. In the case of top/bottom contact, the temperature difference between

the hottest point ($\frac{dT}{dx} = 0$), on one side of the coil, and the opposite point closest to the steel interface at a distance h (the coil height) is:

$$\Delta T = \frac{p}{2\lambda_e} h^2 \quad (4)$$

In the alternate case of side coil-steel contact, the temperature depends on w (the coil width):

$$\Delta T = \frac{p}{2\lambda_e} \left(\frac{w}{2} \right)^2 \quad (5)$$

Next, the heat flow through the epoxy and G10, described by an equation similar to Equation 1, assumes a thermal conductivity of 0.65 watt/m.°C. The respective thicknesses are 30 mils and 1/16 inch.

Finally, the convection at the steel surface is described by:

$$\Delta T = \frac{P}{AH} \quad (6)$$

A is the external magnet area, and H is the heat transfer coefficient by natural convection. Vendor painted aluminum plates can reach about 14 watt/m².°C. Our magnet will be painted, and we will assume this optimum value.

III. Optimization of the copper and steel

The size of the copper cross-section, and the length of the steel core are dictated by the necessity to simultaneously

- reduce the power needed to energize the normal corrector.
- minimize the temperature of the hottest spot inside the copper,

The total length of the magnet, coil and steel being restricted to 16 inches, we loose steel length as the coil package increases in width. We are left with only the coil width w and coil height h as free parameters.

For a given magnet strength, the power and the inner coil temperature scales like:

$$power \sim \frac{1}{wh} \left(\frac{1}{L - 2w} \right)^2 \quad (7)$$

where $L = 16$ inches, and

$$\Delta T \sim \frac{1}{w^2(L - 2w)^2} \quad (8)$$

for a top/bottom contact, or

$$\Delta T \sim \frac{1}{4h^2(L - 2w)^2} \quad (9)$$

for a contact from both sides. These relations are plotted in Figure 2.

Figure 2. suggests that a square coil of size 2 inch is a good compromise that does not overdesign the magnet size. This is the value adopted in the present design. The backleg and yoke are fixed to a thickness of about 1 inch to have enough mechanical strength. No saturation is expected given the low value of the field in the gap.

The magnet core as well as the copper coil are sufficiently defined now to derive other parameters. In particular the amount of heat produced when the magnet is powered to the required

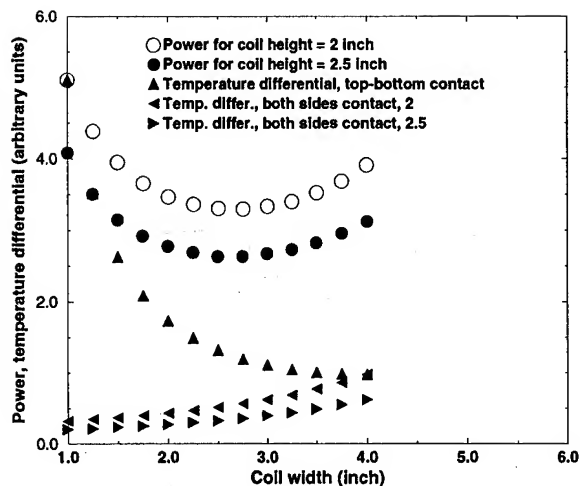


Figure 2. Effect of coil size on the amount of heat and on hot spot temperature

strength and duty factor allows us to estimate the temperature of the different components using the above model.

The steel temperature is found to be 58° C. This temperature will be decreased by increasing the magnet area. We are exploring two possibilities. The first one is to have wide endplates while the second one is to have a wedge on the top and bottom of the magnet. The latter reduces the weight of the magnet. The former may create a bottleneck for the heat flow, and increase temperature gradients. In any case, we assume that the temperature of the steel can be maintained below 50° C.

Next, the temperature of the epoxy at the copper coil interface is evaluated. The epoxy is a vulnerable component. If the contact between the steel, G10, and epoxy is tight (thermal grease is utilized), then this interface will be at temperature of about 57° C. An air gap of 5 mils with the same heat flow, will raise this temperature by 12° C.

Last, the inner coil temperature is found to be around 81° C. This is below the limit we specified. At this point we should say that some gradients are short-circuited if we put a water-cooled plate against the bottom or top of the epoxied coil winding. For this option, with a higher current of 15 ampere and the same duty factor we reach a temperature of about 91° C. This is to be compared to 120° C with no plate cooling.

IV. Summary

The modeling of the trim dipole has been dominated by the desire to minimize the temperature of sensitive components. It gave us the following directions in which to orient the engineering efforts:

- There must be as much contact as possible between the coil and the steel.
- The winding impregnation should get rid of the air pockets to maximize the effective thermal conductivity.

- The insulating materials are limiting components, and their thermal conductance and temperature resistance should be as high as possible.
- The lamination design should maximize the external magnet surface.
- The steel should preferably be painted in black.

In addition to the thermal calculations we are in the process of adding bumps in the poletip to maximize field uniformity. This design will have to take into account the sextupole captured at the ends since our magnet steel is rather short, 12 inches.

V. Acknowledgements

We are grateful to J. A. Hoffman, and N. S. Chester for their help with the properties and limitations of insulating materials. We also would like to thank G. E. Krafczyk and P. S. Prieto for communicating to us the results of their thermal modeling and measurements of Fermilab corrector magnets.

References

- [1] C.S. Mishra, *Study of the Alignment Tolerance and Corrector Strength in the FMI Lattice*, MI Note-0109 (1994).
- [2] G. E. Krafczyk, and P. S. Prieto, private communication.
- [3] D. J. Kroon, *Electromagnets*, Boston Technical Publishers, Cambridge (1968).

THE MAIN INJECTOR CHROMATICITY CORRECTION SEXTUPOLE MAGNETS: MEASUREMENTS AND OPERATING SCHEMES

C.M. Bhat, A.Bogacz, B.C. Brown, D.J. Harding, Si J. Fang, P.S. Martin, H.D. Glass and J.Sim
Fermi National Accelerator Laboratory*
P.O. Box 500, Batavia, IL 60510

Abstract

The Fermilab Main Injector (FMI) is a high intensity proton synchrotron which will be used to accelerate protons and antiprotons from 8.9 GeV to 150 GeV. The natural chromaticities of the machine for the horizontal and the vertical planes are -33.6 and -33.9 respectively. The $\Delta p/p$ of the beam at injection energy of 8.9 GeV is about 0.002. The chromaticity requirements of the FMI are primarily decided by the $\Delta p/p = 0.002$ of the beam at injection. This limits the final chromaticity of the FMI to be ± 5 units. To correct the chromaticity in the FMI, two families of sextupole magnets will be installed in the lattice, one for each plane. A sextupole magnet suitable for the FMI needs has been designed [1] and are being built. New chromaticity compensation schemes have been worked out in the light of recently proposed faster acceleration ramps. On a R/D sextupole magnet, the low current measurements have been carried out to determine the electrical properties. Also with a Morgan coil, measurements have been performed to determine the higher ordered multipole components up to 18-poles. An overview of these results are presented here.

I. CHROMATICITY COMPENSATION SCHEMES FOR THE FMI

Previously a scheme for chromaticity compensation in the FMI had been worked [2] out taking into account the effect of beam tube eddy current, saturation, and end-pack sextupole fields generated by the dipole magnets. The data were taken from measurements on R/D dipole magnets. Since then, several developments have taken place:

1. The measured [3] combined contribution of the saturation and static fields in the dipoles showed a slightly negative sextupole component (i.e., $b_2 = -0.05m^2$) at low fields (which is in contrast with the earlier scheme).
2. The material of the FMI beam tube is selected to be 316L stainless steel (resistivity of $74 \times 10^8 Ohm m$)[4].
3. A faster ramp [4] is selected to reduce the emittance dilution at transition. The \dot{p}_t at transition in the present FMI operating scheme is about 280 GeV/c-sec, which is nearly a factor of two larger than the previously proposed ramp.

Hence, a new chromaticity compensation scheme has been developed. Here we essentially adopt the method outlined in the Ref. 2.

The Figs. 1 and 2 show examples of operating schemes for the FMI for two different values of \dot{p} at transition. The selection of $\dot{p}_t = 280$ GeV/c-sec has resulted in a very large amount of

*Operated by the Universities Research Association, under contracts with the U.S. Department of Energy.

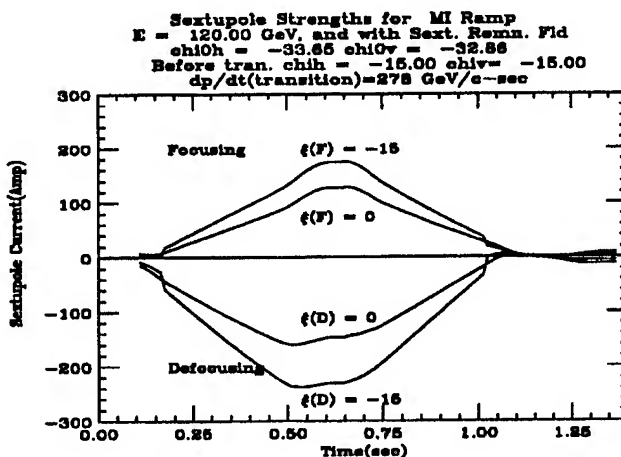


Figure 1. FMI Scheme for 120 GeV fast ramp

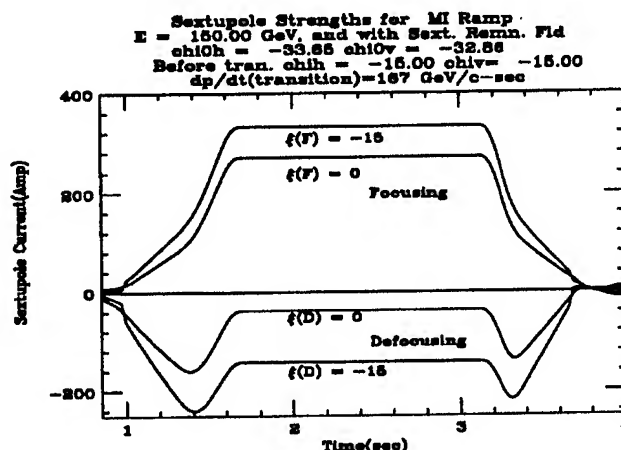


Figure 2. FMI scheme for 150 GeV slow ramp

eddy current contribution to the sextupole field at low B fields. For instance, the contribution to the sextupole component, that is arising from the eddy current reaches a maximum value of $0.8 m^2$ for the ramps with $\dot{p}_t = 280 \text{ GeV/c-sec}$. For the ramp with $\dot{p}_t = 167/\text{sec}$, the eddy current adds only about $0.5 m^2$ of sextupole strength. This suggested that with enough safety margin we might need a bipolar power supply for focusing family of sextupoles. For the de-focusing family however, the unipolar power supply should be sufficient.

II. ELECTRICAL MODEL

The sextupole magnet is a three-terminal device with two coil terminals and one magnet case ground. The electrical characteristics of the magnet can be described by a 3x3 impedance matrix

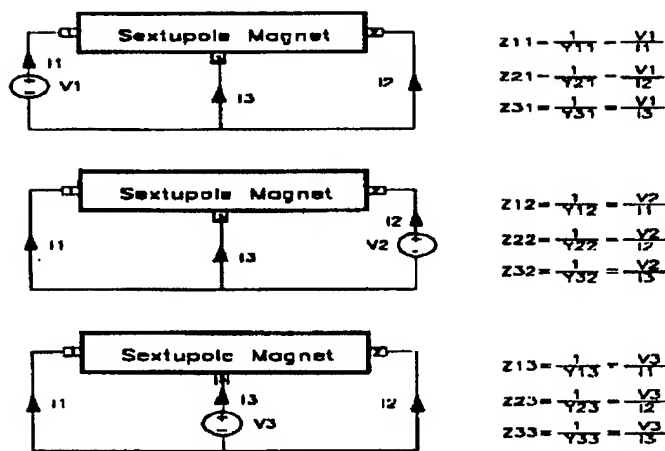


Figure 3. Impedance Matrix Measurement

at non-saturation. The equations for this three-terminal device network can be written as

$$\begin{bmatrix} I_1 \\ I_2 \\ I_3 \end{bmatrix} = \begin{bmatrix} Y_{11} & Y_{12} & Y_{13} \\ Y_{21} & Y_{22} & Y_{23} \\ Y_{31} & Y_{32} & Y_{33} \end{bmatrix} \begin{bmatrix} V_1 \\ V_2 \\ V_3 \end{bmatrix}$$

The elements in the matrix are frequency dependent variables. The magnet equivalent circuit can be determined by measuring the impedance matrix as shown in Fig. 3.

Terminal 1 and 2 are coil bus terminals and terminal 3 is the case ground. Z_{11} , Z_{22} , Z_{12} and Z_{22} measure the coil bus impedance. Total bus to ground capacitance is measured by Z_{33} , Z_{13} and Z_{31} measure the capacitance between terminal 1 and ground, while terminal 2 is shorted to ground. Similarly, Z_{23} and Z_{32} measure the capacitance between terminal 2 and ground, while terminal 1 is grounded. The Z_{13} , Z_{23} and Z_{33} are capacitance measurements since the slope of the measurements data is -20 dB/decade in Bode plot.

The circuit simulation program Spice is used to curve fitted the sextupole magnet electrical model into its impedance matrix as shown in Fig.4 for Z_{11} .

Figure 5 shows the sextupole magnet electrical model. T1 represents the copper loss and R2 is for the core loss. L1 and R3 are the air core inductance and skin depth effects respectively

III. MAGNET MEASUREMENTS

The magnets are measured at the Fermilab Magnet Test facility (MTF) using a rotating Morgan coil with the database-controlled MTF software [5]. The coil is rotated at the center of the magnet at a constant current. Activating different coil windings allows the measurements of the sextupole strength and the contributions to the field shape from other harmonic components up to 18 poles. In these measurements we have measured both normal as well as skew components. We find none of the components are of significant importance for FMI operation scheme except the remnant field. A remnant field of $-0.3(\text{Tm/m}^2)$ seen for the magnet that is ramped up to 350 Amp. Using the scheme outlined in Ref.6 we have extracted the non-linear part of the sextupole field. The result is shown in Fig. 6. In our chromaticity compensation scheme developed for FMI in section I,

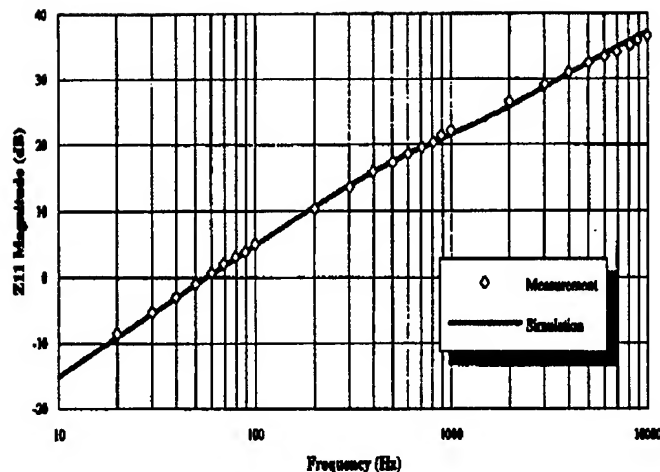


Figure 4. Z_{11} Magnitude Plot

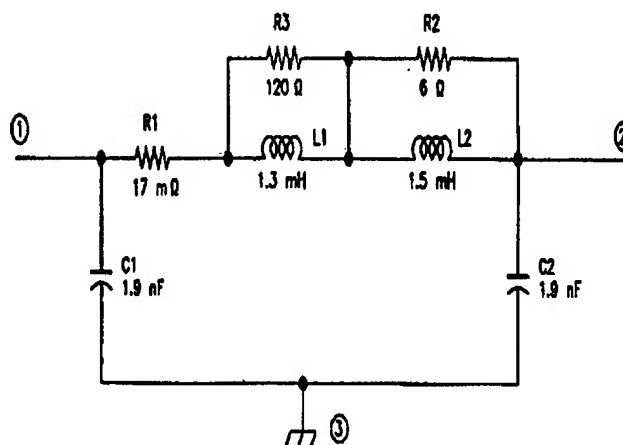


Figure 5. Main Injector Sextupole Electrical Model

we have included this non-linear part of the sextupole field. The sextupole field arising from the eddy current and the remnant field of the sextupole magnet counteract. Hence, the focusing sextupole magnet power supplies need not go much negative.

Authors would like to thank the MTF personnel for their help during the magnet measurements.

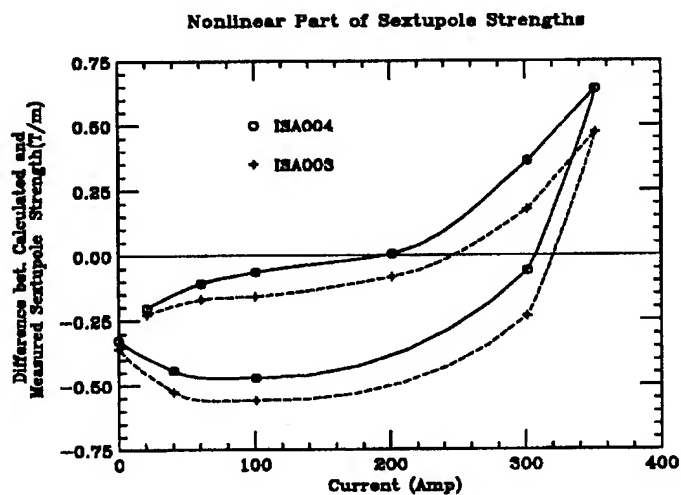


Figure 6. Impedance Matrix Measurement

References

- [1] D.J. Harding, N.Chester, and R. Baiod, Proc. of Part. Accel. Conf. (1993) 2826.
- [2] S.A. Bogacz, Proc. of Part. Accel. Conf. (1993) 77.
- [3] H. D. Glass, Private Communication.
- [4] The Main Injector Technical Design Handbook 1994.
- [5] J.W. Sim *et al.*, "Software for a Database-Controlled Measurements System at Fermilab Magnet Test Facility" (these proceedings).
- [6] B.C. Brown, "Analysis of Magnet Strengths from Steel B-H Curves and Geometry", Fermilab MTF-94-0078, (1994).

MAGNETIC FIELD MEASUREMENTS OF THE INITIAL FERMILAB MAIN INJECTOR PRODUCTION QUADRUPOLES*

D.J. Harding, R. Baiod, B.C. Brown, J.A. Carson, N.S. Chester, E. Desavouret, J. DiMarco, J.D. Garvey, H.D. Glass, P.J. Hall, P.S. Martin, P.O. Mazur, C.S. Mishra, A. Mokhtarani, J.M. Nogiec, D.F. Orris, J.E. Pachnik, A.D. Russell, S.A. Sharonov, J.W. Sim, J.C. Tompkins, K. Trombly-Freytag, D.G.C. Walbridge, and V.A. Yarba, Fermi National Accelerator Laboratory*, P.O. Box 500, Batavia, IL 60510 USA

Abstract

A large sample of the 2.54-meter quadrupoles for lattice matching in the Fermilab Main Injector have been fabricated and measured. The resulting properties are reported and compared to the accelerator requirements.

I. Magnet requirements

The Fermilab Main Injector is a new proton and antiproton accelerator currently under construction at Fermi National Accelerator Laboratory. It will replace the existing Main Ring in all functions. While many of the quadrupoles used in the Main Injector will be reused from the Main Ring, the lattice requires some new quadrupoles of the same design but different lengths (2.54 m and 2.96 m, compared to 2.13 m for the Main Ring quads) to run on the same busses. The performance requirements of the quadrupoles have been studied extensively [1] [2] [3]. The two significant areas of magnetic performance are the magnet-to-magnet variation in the integrated magnetic field ("strength") and the variation of the strength as a function of transverse position ("shape"). These are discussed here separately.

A. Strength

We define the strength to be $\int_{-\infty}^{\infty} (dB_y/dx) dz$. The integral is taken at the center of the aperture. When discussing relative strengths we quote fraction differences in "units" of parts in 10^4 .

Based on experience, we expected to be able to hold the variation in strength to 10 units (10×10^{-4}). The majority of our tracking studies have used the more generous assumption of a root mean square deviation of 24 units and have found that with that distribution we only need to select which magnet is placed on which bus (focussing or defocussing).

B. Shape

We define the shape to be the variation in the strength as a function of position. We characterize the field by its harmonic decomposition. The normal component of a quadrupole's field can be reconstructed as

$$B_y(x) = B_1(b_1 + 1(\frac{x}{r_0})^1 + b_3(\frac{x}{r_0})^2 + b_4(\frac{x}{r_0})^3 + \dots),$$

where B_1 is the quadrupole strength, b_n are the normal harmonic components. We quote the components at $r_0 = 25.4$ mm and in

"units" of parts in 10^4 . Properly centered, the dipole component b_1 is zero.

From the symmetry of the magnet design we expect the field to have significant quadrupole, octupole, and twelve-pole components. For our tracking studies we have assumed distributions of the forbidden components that are consistent with the measured spread in values. While these values are larger than the measurement errors and not yet understood, they have no significant impact on the beam dynamics. We concentrate here on the allowed components.

Given the known octupole component in the existing Main Ring quadrupoles, we could choose the octupole of the new quads to meet the beam dynamics needs. The octupole has two demands placed upon it. One need is that the dynamic aperture be large enough to meet the accelerator requirements. The beam should not fall out of the machine on its own. The other need is that the beam be close enough to the edge of stability so that the existing trim octupoles can bring the beam to the point of slow extraction. The beam should fall out of the machine given a little push in the right direction. Based on simulations, an average of 4 to 8 units appears to satisfy both requirements. Magnet-to-magnet variations are not significant dynamically.

The twelve-pole component is clearly measurable, but not large enough to pose a problem for the dynamic aperture of the accelerator. Reasonable variations in the twelve-pole are not significant.

II. Measurement systems

The equipment and software used in measuring the magnets is described with more detail in other papers at this conference and elsewhere [4]. The request from the Main Injector project is that every magnet be measured and that in production the strength and shape be determined by at least two independent methods.

To date only a rotating coil system, using a Morgan coil that extends through the length of the magnet, has been implemented. The probe has two orthogonal dipole coils, two orthogonal quadrupole coils, and one each sextupole, octupole, decapole, 12-pole, and 20-pole coils. One quadrupole coil is used to measure the strength of the magnet. The other coils measure the harmonic components while suppressing the signal from the quadrupole field. The rotating coil measurements are performed at multiple currents on every magnet.

A single wire stretched wire system is currently being commissioned. This will provide the redundant strength and shape information requested, as well as magnet center data.

*Work supported by the United States Department of Energy under contract No. DE-AC02-76CH0300

III. Measurement Data

A. Strength

We have averaged the strength at each current. Figure 1 shows the deviation of the average strength from a linear excitation calculated assuming infinite steel permeability.

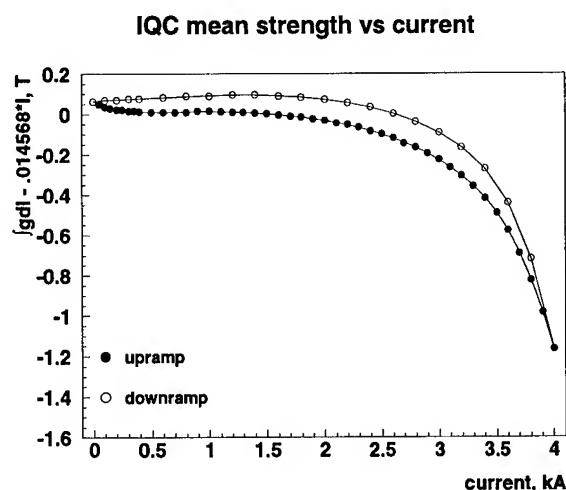


Figure 1. Deviation of average quadrupole strength from linear vs current

To present the magnet-to-magnet variation, we calculate the fractional deviation of individual magnets from the average. Figure 2 shows the strength at 500 A for all magnets in the sample, relative to the average of all magnets except the first seven. Those seven magnets are significantly different from the later magnets due to experimental modifications of the lamination. In the low current regime the strength is dominated by the geometry, with only a small contribution from the permeability of the steel. Note that the strengths are tightly clustered, indicating good control of the geometry. All magnets fall within the expected range. Similarly, even as the steel begins to saturate, the spread in strength is small, as shown in Figure 3.

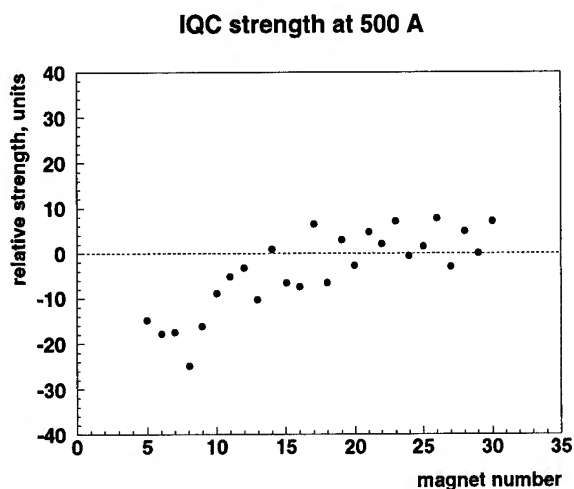


Figure 2. Relative strength of quadrupoles at 500 A

IQC strength at 3500 A

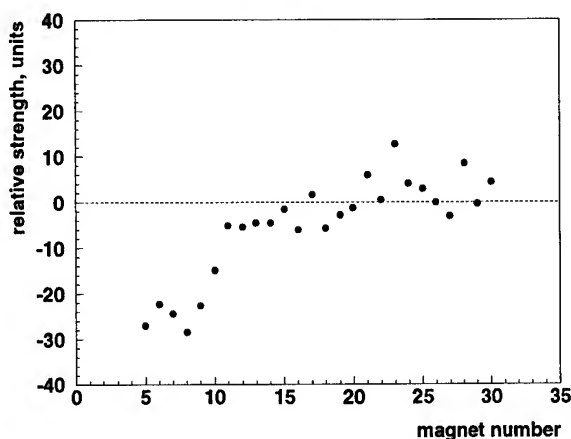


Figure 3. Relative strength of quadrupoles at 3500 A

B. Shape

Figure 4 shows the average octupole b_4 as a function of current. This meets both the need for stability and for slow extraction. The octupole strengths are histogrammed in Figure 5. All magnets fall near the target values, and the average is certainly acceptable. The distribution of the twelve-pole component at 1500 A is shown in Figure 6. It is also within the established limits.

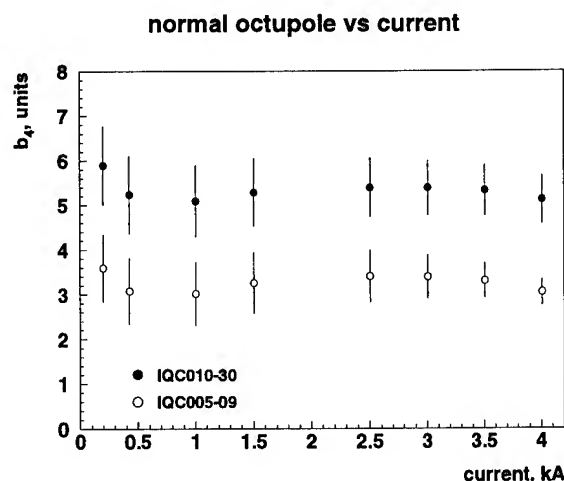


Figure 4. Average octupole component vs current

IV. Conclusions

The Fermilab Main Injector project is well into production of the new quadrupoles for the ring. By the end of March 1995 30 2.54 m quadrupoles, out of 32 required for the ring, had been completed and measured. Magnet performance is within the acceptable range established through tracking studies. Production had just begun on the 48 2.96 m quadrupoles that are required.

References

- [1] C.S. Mishra P.S. Martin D.J. Harding H.D. Glass and B.C.Brown. Fermilab Main Injector Magnet Acceptance

b_4 distribution at 1500 A

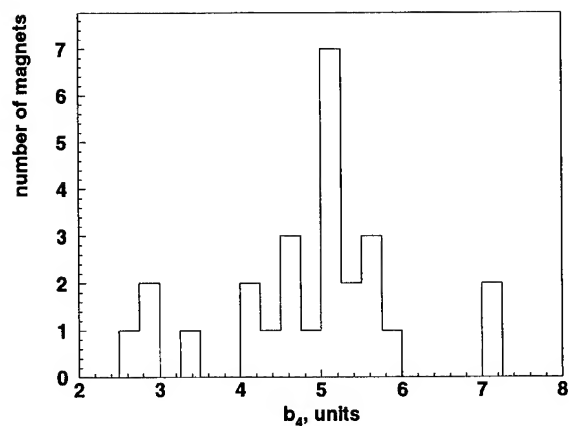


Figure. 5. Distribution of octupole strengths at 1500 A

b_6 distribution at 1500 A

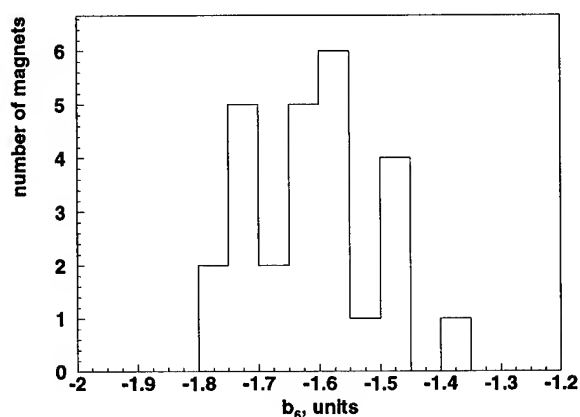


Figure. 6. Distribution of 12-pole strengths at 1500 A

Criteria. In *Proceedings this conference*, 1995.

- [2] C.S. Mishra. Requirement of the Fermilab Main Injector Quadrupole Strength Matching. In *Proceedings this conference*, 1995.
- [3] C.S. Mishra. Fermilab Main Injector Quadrupole Placement Scheme. In *Proceedings this conference*, 1995.
- [4] J.W. Sim et al. Software for a Database-Controlled Measurement System at the Fermilab Magnet Test Facility. In *Proceedings this conference*, 1995.

MAGNETIC FIELD MEASUREMENTS OF THE INITIAL FERMILAB MAIN INJECTOR PRODUCTION DIPOLES*

D.J. Harding, R. Baiod, B.C. Brown, J.A. Carson, N.S. Chester, E. Desavouret, J. DiMarco, J.D. Garvey, H.D. Glass, P.J. Hall, P.S. Martin, P.O. Mazur, C.S. Mishra, A. Mokhtarani, J.M. Nogiec, D.F. Orris, J.E. Pachnik, A.D. Russell, S.A. Sharonov, J.W. Sim, J.C. Tompkins, K. Trombly-Freytag, D.G.C. Walbridge, and V.A. Yarba, Fermi National Accelerator Laboratory*,
P.O. Box 500, Batavia, IL 60510 USA

Abstract

A large sample of the 6-meter dipoles for the Fermilab Main Injector have been fabricated and measured. The resulting properties are reported and compared to the accelerator requirements.

I. Magnet requirements

The Fermilab Main Injector is a new proton and antiproton accelerator currently under construction at Fermi National Accelerator Laboratory [1]. It will replace the existing Main Ring in all functions. While many of the Main Ring quadrupoles will be reused in the Main Injector, the dipoles are a new design. The performance requirements of the dipoles have been studied extensively [2]. The two significant areas of magnetic performance are the magnet-to-magnet variation in the integrated magnetic field ("strength") and the variation of the strength as a function of transverse position ("shape"). We discuss these topics separately here.

A. Strength

We define the strength to be $\int_{-\infty}^{\infty} B_y dz$. The integral is taken at the center of the aperture and follows the path of the central orbit, curving with the magnet. We quote relative strengths in "units" of parts in 10^4 .

Based on experience, we expected to be able to limit the variation in strength to 10 units (10×10^{-4}). The majority of our tracking studies have used the more generous assumption of a root mean square deviation of 10 units and have found that with that distribution no selection of magnets for placement in the ring is necessary. We have also tried a broader Gaussian distribution with $\sigma=15$ units and a bimodal distribution with two narrow peaks separated by 30 units [3]. In the former case, we can expect the planned trim dipoles to correct the closed orbit even with random assignment of the dipoles. In the latter case, a simple magnet placement plan is needed.

B. Shape

We define the shape to be the variation in the strength as a function of transverse position. We characterize the shape by the horizontal variation $\int_{-\infty}^{\infty} B_y(x) dz$ of the field integral and by the harmonic decomposition of the integral. We can link the two by writing

$$B_y(x) = B_0(1 + b_2(\frac{x}{r_0})^1 + b_3(\frac{x}{r_0})^2 + b_4(\frac{x}{r_0})^3 + \dots),$$

where $B_y(x)$ is the integral, B_0 is the strength, and b_n are the normal harmonic components. We quote the components at $r_0 = 25.4$ mm and in "units" of parts in 10^4 .

From the symmetry of the magnet design we expect the field to be both left-right and up-down symmetrical. For our tracking studies we have assumed distributions of the forbidden components that are consistent with the measured spread in values without questioning whether these values are real or primarily measurement error, either random or systematic. The measured values are small. We concentrate here on the allowed components.

The chromaticity sextupole system [4] is designed to compensate for the average size of the sextupole component of the dipoles. The accelerator is not very sensitive to variations in the sextupole around the ring. The decapole component is clearly measurable, but not large enough to pose a problem for the accelerator.

II. Measurement systems

The equipment and software used in measuring the magnets is described with more detail in other papers at this conference and elsewhere [5]. The request from the Main Injector project was that every magnet be measured and that in production the strength and shape be determined by at least two independent methods. A third strength measurement is used on a sample of magnets for further redundancy.

The flatcoil system uses a long, narrow, multi-turn coil that extends through the length of the magnet, performing the integral over z . The coil form is rigid and curved to match the central orbit of a particle through the curved magnet. The magnet strength, exclusive of the remanent field, is determined by measuring the change in flux through the coil as the magnet is excited with the probe held in the center of the magnet. The horizontal variation in the field is determined by measuring the change in flux as the probe is moved laterally with the current held fixed. A polynomial fit to the shape data yields coefficients proportional to the normal coefficients of a harmonic decomposition of the magnetic field. The flatcoil measurements are performed at multiple currents on every magnet.

The rotating coil system uses a tangential coil that extends through the length of the magnet. The G-10 coil form has a small enough diameter that it easily conforms to the curved central orbit of the magnet and flexes as it is rotated to maintain the curvature. A coil wound on one diameter of the probe provides a measurement of the absolute strength of the magnet. The tangential coil, bucked against the equal-area diameter coil, pro-

*Work supported by the United States Department of Energy under contract No. DE-AC02-76CH03000

vides flux measurements on a circle, from which the normal and skew harmonic components are extracted. The rotating coil measurements are performed at multiple currents on every magnet.

The pointscan system uses both a Hall probe and an NMR probe to scan the magnetic field along the magnet's length in 25.4 mm steps. Numerically integrating the field measurements gives the magnet strength. These time-consuming pointscan measurements are performed at two currents on a sample of magnets.

III. Measurement Data

A. Strength

For each measurement system we have averaged the strength at each current. Figure 1 shows the deviation of the average strength from a linear excitation calculated assuming infinite steel permeability.

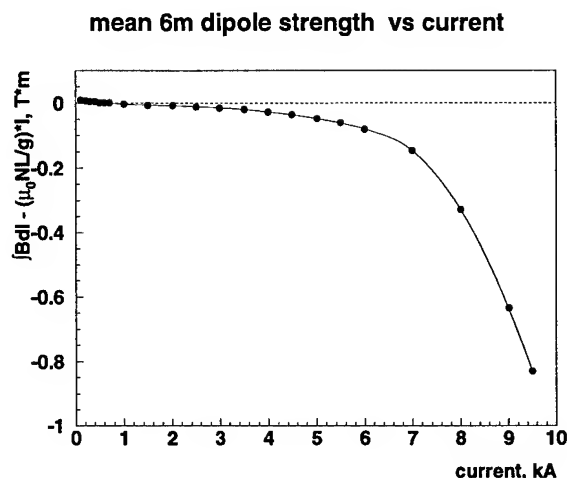


Figure 1. Deviation of average dipole strength from linear vs current

To present the magnet-to-magnet variation, we calculate the fractional deviation of individual magnets from the average. Figure 2 shows the strength at 1500 A for all magnets in the sample, relative to the average of all magnets except the first eight, whose measurements are significantly noisier than the later measurements. At this current the strength is dominated by the geometry, with only a small contribution from the permeability of the steel. Note that the strengths are tightly clustered, indicating good control of the geometry. All magnets fall within the expected range.

Figure 3 shows the strength at 9500 A (a little over full excitation) for all magnets in the sample relative to the average of all magnets except the first eight. Note that the local average of the strengths started to increase about half way into this group of magnets. Although no magnet falls outside the acceptable range, it is important to understand and control the process so that the variation does not increase further.

The nature of the increase can be better appreciated by looking at the relative strength as a function of current for a limited number of magnets, as shown in Figure 4. Here we see that the strength deviation depends on current, a strong indication that

we are seeing a magnetic property of the steel, as opposed to a geometrical effect.

Analyzing the composition of the magnets, we determined that the strength deviation of the magnet was closely correlated with the mix of laminations in the magnet stamped from different processing runs of steel. A detailed examination of the magnetic data on the sample strips from steel coils shows statistically significant differences among the runs of steel. Two-dimensional modeling of the magnetic field using the different B-H curves reproduces the differing magnet excitation curves.

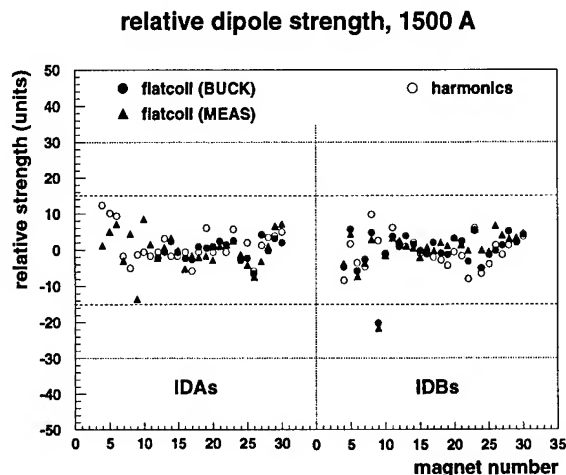


Figure 2. Relative strength of all dipoles at 1500 A

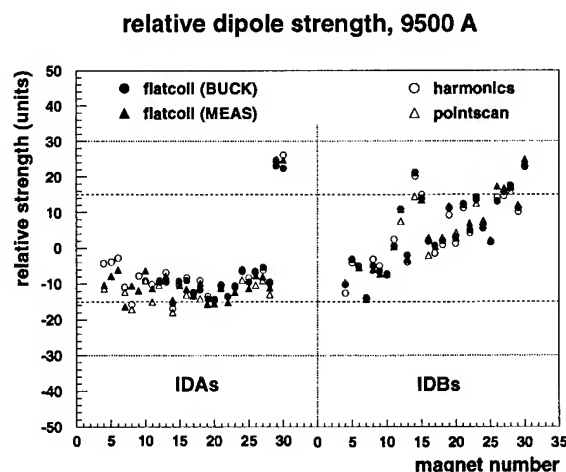


Figure 3. Relative strength of all dipoles at 9500 A

B. Shape

The complementary measurement techniques, flatcoil and harmonics, give consistent results. Figure 5 shows the average b_3 as a function of current. This is consistent with calculations and with the performance of the prototype dipoles, upon which the chromaticity sextupole design was based.

The sextupole components at 9500 A are histogrammed in Figure 6. All magnets fall well within the expected range of values. The distribution of the decapole component at 9500 A is shown in Figure 7. All magnets are within the established limits.

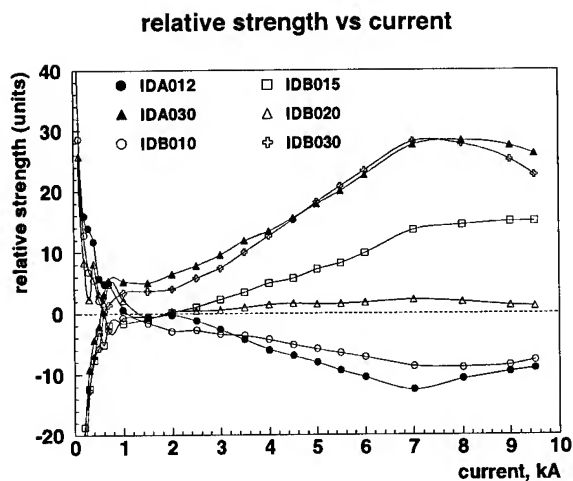


Figure 4. Relative strength of representative dipoles as a function of current

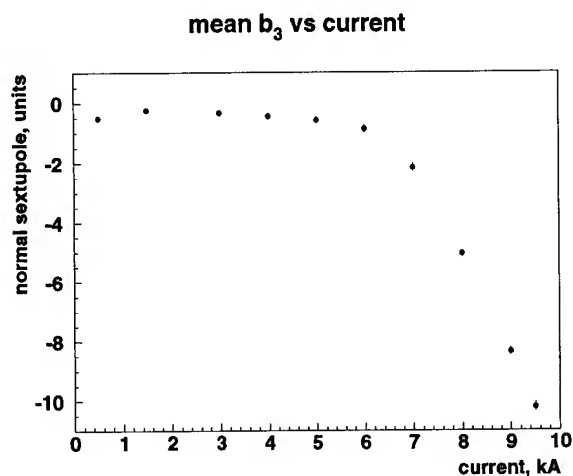


Figure 5. Average sextupole component vs current

IV. Conclusions

The Fermilab Main Injector project is well into production of dipoles for the ring. By the end of March 1995 54 6-m dipoles, out of 216 required for the ring, had been completed and measured. Magnet performance is within the acceptable range established through tracking studies.

References

- [1] D. Bogert. The Fermilab Injector Complex. In *Proceedings this conference*, 1995.
- [2] C.S. Mishra P.S. Martin D.J. Harding H.D. Glass and B.C.Brown. Fermilab Main Injector Magnet Acceptance Criteria. In *Proceedings this conference*, 1995.
- [3] C.S. Mishra. Simulation of the Fermilab Main Injector with Production Magnet Data. In *Proceedings this conference*, 1995.
- [4] C.M. Bhat et al. The Main Injector Chromaticity Correction Sextupole Magnets: Measurements and Operating Schemes. In *Proceedings this conference*, 1995.

b_3 distribution at 9500 A

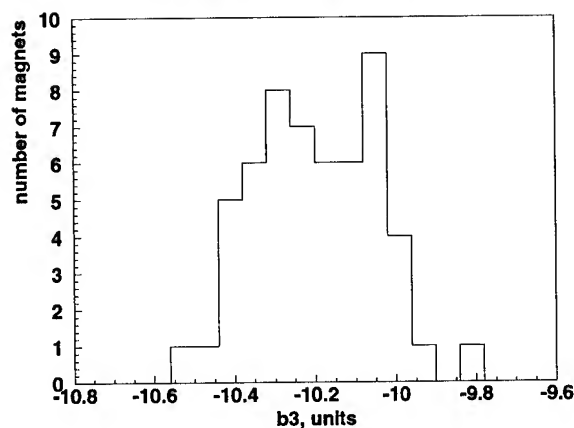


Figure 6. Distribution of sextupole strengths at 9500 A

b_5 distribution at 9500 A

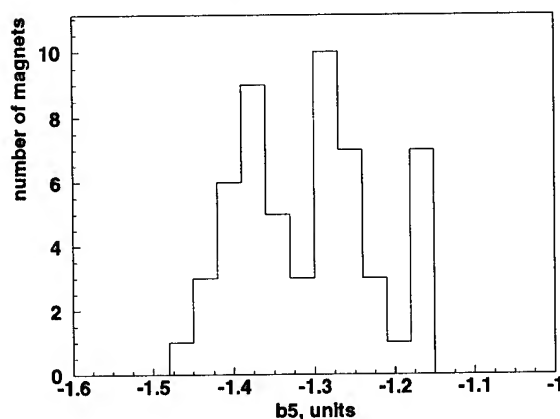


Figure 7. Distribution of decapole strengths at 9500 A

- [5] J.W. Sim et al. Software for a Database-Controlled Measurement System at the Fermilab Magnet Test Facility. In *Proceedings this conference*, 1995.

THE FERMILAB MAIN INJECTOR DIPOLE AND QUADRUPOLE COOLING DESIGN AND BUS CONNECTIONS

J. A. Satti

Fermi National Accelerator Laboratory*
P. O. Box 500, Batavia, IL 60510

ABSTRACT

The proposed system for connecting the low conductivity water (LCW) and the electrical power to the magnets is explained. This system requires minimum maintenance. Stainless steel headers supply LCW to local, secondary manifolds which regulate the flow to the dipole and to the copper bus which conduct both power and cooling water to the quadrupole. A combination of ceramic feedthroughs and thermoplastic hoses insulate the piping electrically from the copper bus system. The utilities for the Main Injector are grouped together at the outside wall of the tunnel leaving most of the enclosure space for servicing. Space above the headers is available for future accelerator expansion. The new dipoles have bolted electrical connections with flexible copper jumpers. Separate compression fittings are used for the water connections. Each dipole magnet has two water circuits in parallel designed to minimize thermal stresses and the number of insulators. Two electrical insulators are used in series because this design has been shown to minimize electrolyses problems and copper ion deposits inside the insulators. The design value of the temperature gradient of the LCW is 8°C.

I. INTRODUCTION

The Fermilab Main Injector (FMI) is a new 150 GeV synchrotron now under construction at the Fermi National Accelerator Laboratory.¹ The FMI will replace the existing Main Ring. New conventional dipole magnets, with water cooled conductors, will provide the primary bending for this accelerator. The proposed system for connecting the power and the water to the FMI is similar to the existing Main Ring. Where possible, the power bus is used to carry both power and water to the magnets.

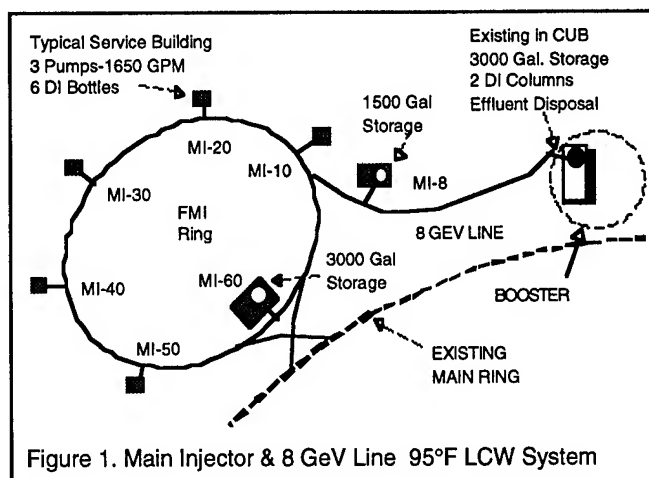
II. LOW CONDUCTIVITY WATER SYSTEM

Figure 1 shows the FMI and the 8 GeV Line LCW System. There will be six utility buildings uniformly spaced around the FMI ring. These are labeled MI-10, MI-20, MI-30, MI-40, MI-50, MI-60. Each utility building will supply power and cooling water to about 1,815 feet of circumference in the FMI. The closed loop system will receive makeup water from the Central Utility Building (CUB).

A total of 18 pumps will be installed around the ring

with 3 pumps per service building. Each pump has a 100 hp motor and delivers 550 GPM of LCW with a pressure head of 164 psi (380 TDH). Six inch stainless steel pipe headers will be installed above the magnets along the 10,891-foot circumference of the FMI. Eight inch headers will be used to connect the pumps from the service buildings to the manifolds in the accelerator enclosure.

All components are connected in parallel and, with the proper hydraulic resistance across each secondary manifold, the local water distribution will be balanced between service buildings. The centrifugal pumps, also connected in parallel with the magnets, will share the flow and will balance the pressure head to match the resistance across the LCW manifolds. A similar LCW system has worked well in the existing Main Ring where the hydronics have been operational for twenty-three (23) years.²



At the pipe penetrations leading to the enclosure, valves will be installed to isolate each sector of the ring. At each utility entrance, as well as at locations half-way in-between, the enclosure has a ceiling that is one foot higher than the standard tunnel. The purpose of this extra space is to provide space for the stainless steel expansion joints. At these locations, the enlarged enclosure allows the pipes to cross over the cable trays without obstructing the normal tunnel clearance for the magnet moving vehicle.

One heat exchanger per service building is required to transfer the LCW heat load to the pond water. The normal heat load removal capacity per building will be about 2.7 MW. Approximately 8,000 GPM of LCW will be required to cool the magnets, bus, and power supplies in the FMI enclosure and the service buildings. The centrifugal pumps are capable of delivering approximately 9,900 GPM at the designed head

*Operated by the Universities Research Association, Inc., under contract with the U.S. Department of Energy

of 164 psi. The temperature of the water is regulated to be 95°F by a 3 way control valve which diverts a portion of the water around the heat exchanger when less cooling is required. A constant flow of pond water is circulated in the tube side of the heat exchanger. The heat in the pond is removed by evaporation. In the FMI design, the size of the ponds is the limiting factor in cooling the electrical components.

In each service building around the ring, portable, mixed-bed deionizer bottles will be installed. A continuous polishing flow of about 40 GPM per service building will be required to maintain low conductivity in the water. The bottles are only used for polishing action. Their use will guarantee that an average of $9M\Omega$ -cm resistivity of the LCW will be maintained. LCW fills will be done from the CUB via the 8 GeV Line. The CUB has large industrial deionizer columns that meet the appropriate EPA guidelines for effluent discharge systems. The portable deionizer bottles will be regenerated in the CUB using its existing regeneration system. In service building MI-60, a 3,000 gallon combination storage and expansion tank is now being installed for emergency LCW make-up for the FMI. A 1,500 gallon tank will be in the MI-8 service building as additional storage. The FMI will require an estimated 37,000 gallons of LCW to fill the pipes, tanks, bus, and magnets. A net clockwise flow in the ring will be accomplished with restricting orifices at each of the entrances. In addition to the local water circulation around each service building, about 100 GPM of circular flow will allow good mixing and deionizer processing at the CUB.

III. ENCLOSURE UTILITIES

The FMI components and associated utilities are grouped together at the outside wall of the tunnel leaving most of the space for servicing, as shown in figure 2. As with all accelerators, radiation damage to materials and exposure time to personnel is of great concern. Plans for servicing the accelerator must be taken into account so that maintenance time in any radiation environment is kept to a minimum. The general practice will be to replace a component rather than to repair it in place. All connections to the magnets are designed to be accessible from the inner space of the enclosure. Space above the headers is available for future accelerator expansion. The utilities are wall mounted with brackets bolted on channel inserts embedded in the enclosure wall at pre-determined regular intervals.

Figure 3 shows a schematic representation of the cooling for a typical hydraulic cell in the FMI. A group of magnets, consisting of two dipoles, one quadrupole, and a sextupole, is cooled in parallel from a 2 inch water manifold. This manifold can be isolated from the main 6 inch header water pressure with one 1-1/2 inch ball valve and two check valves to prevent back-flow. The secondary manifold permits access to the magnet connections and minimizes the number of required electrical insulators. The smaller manifolds are electrically insulated from ground. With a second insulator at the magnets, each LCW connection to the bus has two insulators in series. In the existing Main Ring, this design has

reduced the copper ion deposits inside the insulators. One inch thermoplastic hose will be used for the insulators farthest away from the beam line. The flexibility of a hose is required where the thermal expansion of the main headers can be up to 3.5 inches after a shutdown. Ceramic insulators will be used at the magnets where radiation is more severe and where restrictions are required to regulate the water flow. Approximately two years ago thermoplastic hoses were installed in the Main Ring for testing the strength integrity in a radiation environment. So far, no signs of deterioration have been detected for about fifty (50) operational hoses. The water pressure differential around the FMI ring is about 120 psi. The hydraulic cell is designed to give the correct flow to allow an average temperature rise of 8°C across each individual magnet.

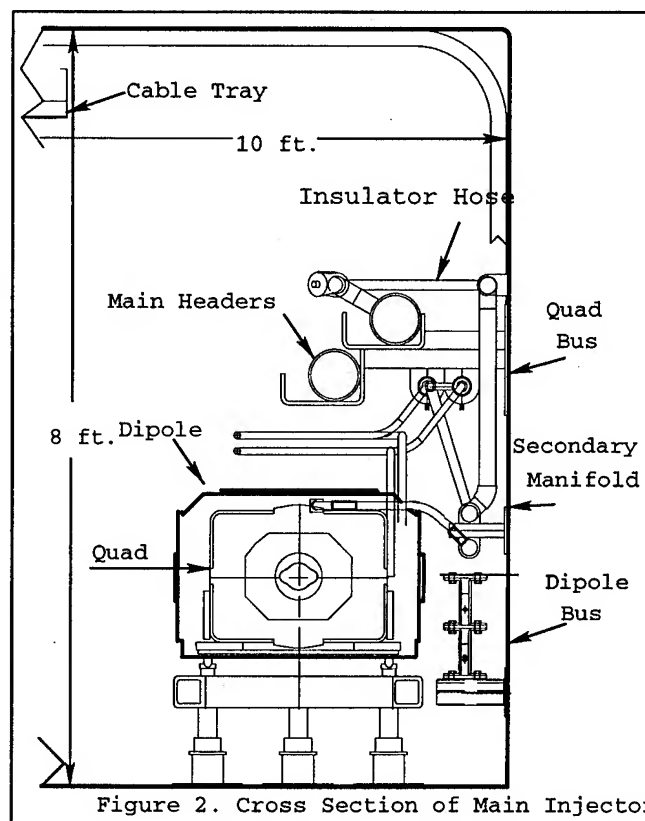


Figure 2. Cross Section of Main Injector

New, rectangular copper bus (1"x4") will be used for connecting the dipoles in the enclosure around the quadrupoles. The bus will be supported from the wall with insulating structural fiberglass material. The support will have adjustments for alignment with the magnets. The flexible jumpers, with bolted connections allow for thermal expansion of the coils and the bus. Pipe bus (4 square inches in cross section) will be used at the entrances going to the power supplies in the service buildings. The quadrupoles will have a pipe bus (2 square inches in cross section) with 2-1/8 inch outside diameter. This size will allow the use of standard channel supports will be used for all round bus.

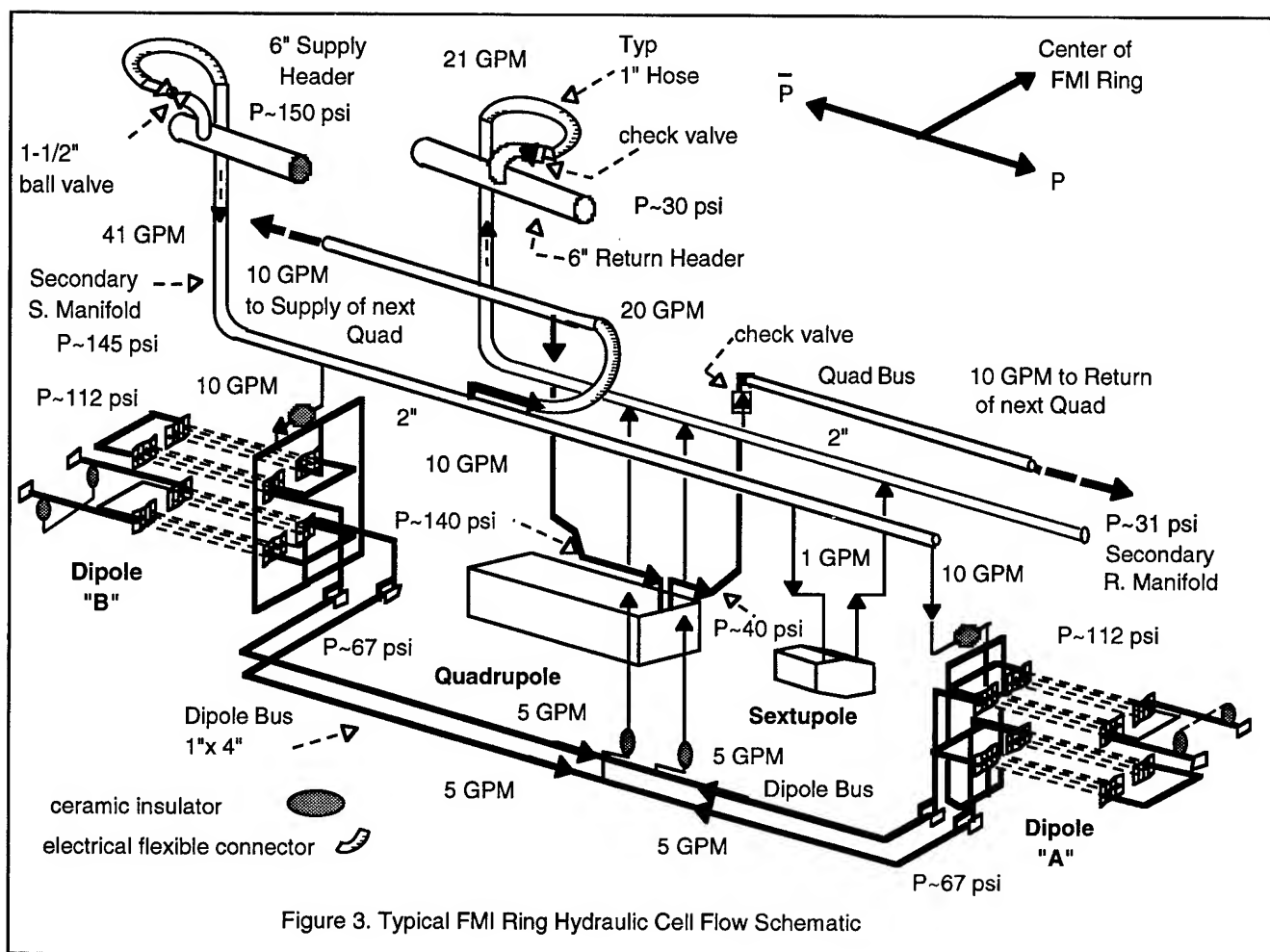


Figure 4 shows a prototype hydraulic cell installation in the normal enclosure next to the MI-60 area

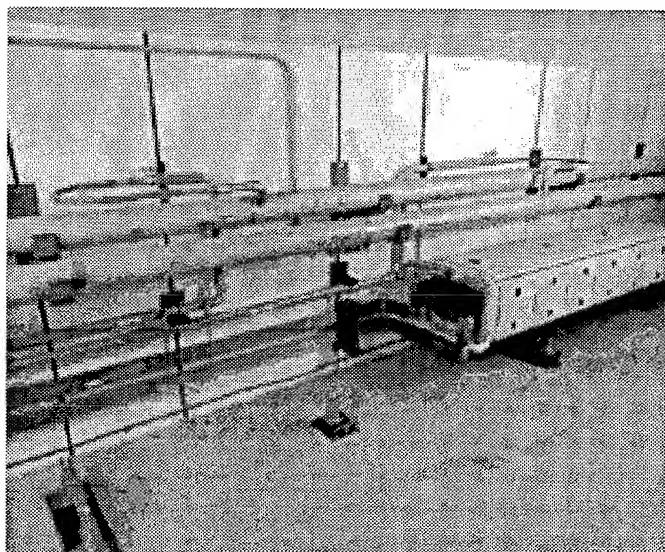


Figure 4. Prototype Q601 Hydraulic Cell Installation

V. ACKNOWLEDGMENTS

The design, procurement, and installation of the FMI Low Conductivity Water cooling and bus systems is the result of work of many people at Fermilab. I wish to acknowledge the contribution of M. Ball, J. Domanus, J. Fritz, P. Gentry, R. Gloor, T. Hamerla, B. Hoffman, R. Kellett, B. Krueger, T. Kuhar, C. Lee, J. Meisner, J. O'Malley, F. Rios, B. Rush and R. Schultz for the engineering, design and the technical assistance of the piping system. T. Larson contributed in the procurement of the components. I wish to thank R. Slazyk and K. Williams for the installation coordination. The author would like to acknowledge the helpful suggestions of P. Martin, FMI Deputy Head for Accelerator Systems.

VI. REFERENCES

- [1] The Fermilab Main Injector Technical Design Handbook, August 1994.
- [2] J. A. Satti, "The Power and Cooling Interconnection of The 200 GeV Synchrotron Magnets", IEEE Trans. Nucl. Sci., Vol. NS-16, p. 782, March 1969

DESIGN OF THE FERMILAB MAIN INJECTOR LAMBERTSON

D. E. Johnson , R. Baiod, D.J. Harding, P.S. Martin, M. May

*Fermi National Accelerator Laboratory**

P.O. Box 500

Batavia, Illinois 60510

Abstract

A common design has been adopted for a high field (1.1T) Lambertson magnet for use in the four injection/extraction channels of the Main Injector (MI) as well as the Tevatron injection channel [1]. To support the extraction/injection of 150 GeV/c protons and pbars, the field within the "field region" of the Lambertson should reach 1.1 Tesla with less than 0.3% variation in a 2 by 12 inch good field aperture. Utilization for the 8.9 GeV/c pbars and resonant extraction of 120 GeV/c protons place stringent aperture requirements on the magnet design. In addition, this magnet must simultaneously support circulating beam in the energy range of 8.9 GeV/c to 900 GeV/c, through its "field free" region. At maximum excitation, the leakage field in this region must be kept to a minimum to avoid any deleterious effects on the circulating beam. The magnet design parameters which meet the aperture, magnetic, and structural requirements as well as the selection criteria of the steel are discussed.

I. MAGNET REQUIREMENTS

The extraction channels in the Main Injector utilize three vertically bending Lambertsons, with an integrated strength of 9 T-m , and a vertically bending c-magnet with an integrated strength of 3.5 T-m to clear the downstream MI magnets. Four vertically bending Lambertsons, with an integrated strength of 12.1 T-m are required for injection into the Tevatron. Assuming a 1.1 T field for a symmetric Lambertson, imposed by tolerable leakage field, the magnetic length of the Lambertson was set at 2.8 meters. This, in conjunction with the available free space in the MI lattice, set the flange to flange length at 3.054 m.

The trajectory of 8.9 GeV/c pbars from the Antiproton Source through the de-energized set of Tevatron Lambertsons and into the MI define both the gap width (pole-to-pole dimension) and the minimum physical height of the gap (pole tip width). A minimum of 20% of the aperture is reserved for steering. The field free region must support circulating beam so the aperture defined by the height, width, and opening angle of this region should not be the limiting aperture. The maximum septa thickness is governed by the separation of the injected/extracted beam from the circulating beam. This separation is a function of the kicker or electrostatic septa strength. The physical aperture requirements for usage in both the MI and the Tevatron are listed in Table 1.

The good field height in the bend region, as listed in Table 2, is determined by the maximum excursions of the extracted beam through the Lambertsons in both the MI extraction and the Tevatron injection channels. The field uniformity in this region

should not contribute more than 1% to the emittance growth of the extracted beam.

Table I
Aperture Specifications

	MI	Tevatron	
Gap width	2	2	inches
Gap height	± 5	± 7	inches
Field free region height	≥ 2	≈ 3	inches
Field free region width	3.5	3.5	inches
Opening angle	≥ 90	≥ 90	degrees
Septum Thickness	.157	.157	inches
Straightness (both planes)	10	10	mils

Besides the magnitude of the field and field quality in the bending region, the body leakage field into the field free region and the end field contributions, which impact the circulating beam, are specified. The specifications listed here set limits for the sum of the body and end field. Without any compensation, the end field contribution can be an order of magnitude larger than that due to the body leakage field. With careful attention, this can be reduced to the same order of magnitude as the leakage field. The current end field compensation scheme is discussed in a companion paper. [2]

Table II
Magnetic Specifications

	MI	Tevatron	
Nominal field	1.072	1.072	Tesla
Good field height	± 4.6	± 6	inches
Field Uniformity	< 0.28	< 0.28	percent
Leakage Field	< 0.038	< 0.019	T-m
Leakage Gradient	$< .78$	$< .336$	Tesla-m/m

Due to the symmetry of the magnet, the predominant body leakage fields to contend with are the dipole, and skew quad. The magnitude of the allowed dipole field is specified to produce less than a 2 mm closed orbit distortion without downstream orbit compensation. From this the total allowed dipole field in the field free region is estimated and the results are listed in Table 2.

To set the upper limits on the skew quad field allowed in the field free region, the magnitude of the allowed tune shift (assuming a fully coupled ring) for the circulating beam in the field free region at maximum excitation has been specified to be less than 0.005 units. This criteria corresponds to

*Operated by the Universities Research Association under contract with the U. S. Department of Energy

$\int dB_x/dxdl < 4\pi\delta\nu(\beta\rho)/\beta$ in units of Tesla-m/m, again as a sum of the contributions from the body leakage field and the end field.

The project requires 16 Lambertsons plus spares, so a common design will reduce design effort, fabrication costs, and the quantity of required spares. Therefore, the design is based upon the requirements for usage in the Tevatron which automatically satisfies the Main Injector specifications.

II. PHYSICAL DESIGN

The requirement for a large aperture (both planes) in the bending region, led to the design of a Lamberton absent of an internal beam pipe. This is accomplished by using two sets of symmetric laminations, one set for the inner cores and one for the outer cores, as shown in Figure 1. The inner cores are assembled with a precision ground matched set of stainless steel space bars near each coil to define the gap width. The left/right symmetry of the inner cores assure an assembly which meets the straightness criteria in bend plane. This assembly is "skinned" with a 30 mil Type 321 stainless steel vacuum skin and terminated at each end by a single vacuum end plate. All vacuum welds are external. A set of 8 distributed 30 liter/sec ion pumps (4 on each side) are utilized to maintain a vacuum of $\approx 5 \times 10^{-9}$ torr for use in the Tevatron.

The coil is a 24-turn split saddle coil with the saddle extending laterally beyond the inner core to allow for the inner core end assembly to extend beyond the coil with out interference. The conductor dimensions and number of turns are determined by the desire to utilize an existing 200 Volt/2500 Amp power supply while maintaining adequate copper volume and cooling.

The coil and inner core assembly are captured by a pair of symmetrical outer cores designed to provide straightness in the non-bend plane. The assembly is held together by a set of tie plates which produce stiff boxed beam structure.

Construction of previous Lambertsons at FNAL have required laborious straightening techniques of welding stripes on the outer core to meet the straightness criteria. This design deviates from the construction of previous Lambertsons at FNAL in that it is designed to meet the straightness criteria without the previously required straightening techniques.

III. MAGNETIC DESIGN

A 2D magnetic model was constructed to allow adjustment of basic geometrical parameters such as the septum thickness, septum radius, septum angle, and geometries of the field free region, inner core, outer core, gap height and width, pole face contour, and tiebars to aid in magnet design choices. The model additionally included the stainless steel skin around the inner cores and air gaps around the skin and tiebars. These parameters were adjusted to optimize the field uniformity in the gap, minimize the leakage field in the field free region, and trim the back leg.

A. Field Region Design

The uniformity in the central region of the gap is governed predominately by the location of the field free region. Its symmetric location provides excellent uniformity in this central re-

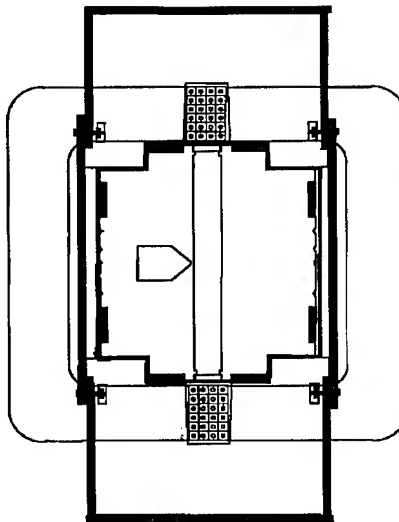


Figure 1. Cross section of Lamberton core showing inner and outer cores, tiebars, and coil configuration.

gion. The height of the "good field" region, defined by the uniformity specification, is governed by the coil and stainless steel spacer bar geometry and the shape of the pole tip near the coil. Without any pole tip shaping, the good field region extended to ± 5 inches, about a gap width less than the physical height. Adjusting the width of the stainless spacer bar (i.e. its penetration into the iron of the inner cores) and adding a ± 50 mil thick by 200 mil long pole tip shim increased the height of the good field region to ± 6 inches, meeting the specification, as seen in the lower plot of Figure 2. However, the field falls off rapidly and increasing the pole tip height from 7 to 8 inches linearly increases the height of the good field from 6 to 7 inches as shown in the upper plot of Figure 2.

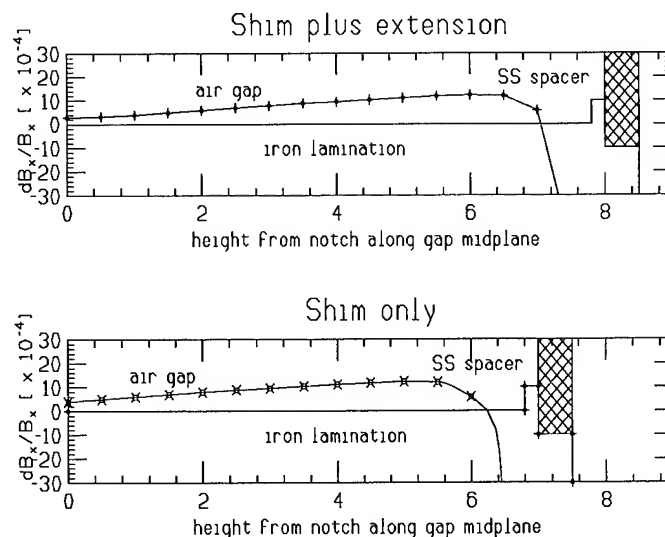


Figure 2. Calculated field uniformity in the bend region after shimming and extending the field region.

B. Field Free Region Design

The leakage field from the iron into the field free region is governed by the continuity condition that $H(\text{parallel})$ must be continuous across the iron/air interface. From this boundary condition, the flux density (in Gauss) in the field free region will just be $\mu_0 H_{\text{steel}}$. To maintain control over the leakage field, a steel with a high permeability at the expected values of H in the iron near the cavity should be chosen. The choice of steel is discussed in the next section.

The selection of septum thickness, septum radius and opening angle are not only based upon the aperture requirements discussed earlier, but were selected to minimize the saturation in the iron near the septa, the magnitude of skew quad in the cavity, and the magnitude of the leakage flux density, respectively.

Figure 3 shows the magnitude of the field, in Gauss, on axis in the field free region as predicted by OPERA-2D. The small skew quad component is realized by a combination of reducing the opening angle from the 90 degree specification to 78 degrees and increasing the septum radius to 0.2 inches maintaining the vertical aperture near the notch. The magnitude of the field in the gap is 1.1 Tesla.

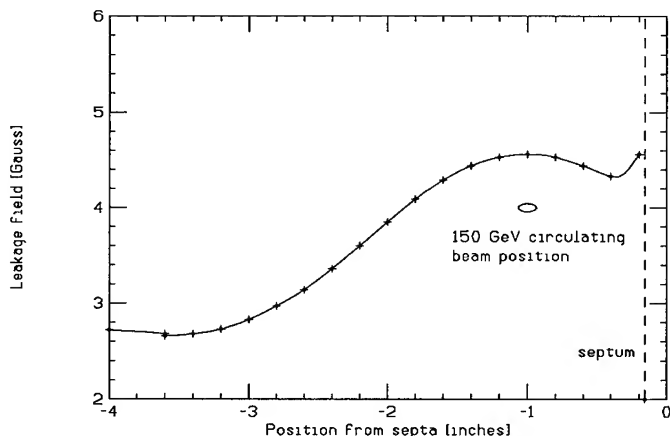


Figure 3. Leakage Field in the field free region at a bend field of 1.1T.

C. Steel Selection

The selection of steel is not only governed by technical specifications but by more realistic issues like market availability and cost. For example, cobalt/vanadium alloys such as supermendure offer a high permeability at the lower excitations, which would offer better shielding around the cavity or decrease the integrated magnet length. They are, however, cost prohibitive at $\approx \$30/\text{lb.}$ as compared to $\approx \$0.50/\text{lb.}$ for Si and low carbon steel. Therefore, we limited our selection of steel for the Lambertson magnet to either a silicon electrical steel or a low carbon steel. Figure 2 shows the measured hysteresis curves for 24 gauge Epstein strip samples of a fully processed low carbon (0.006 %) steel and a M-47 grade Si steel. This shows the Si steel clearly having a higher permeability and a lower coercive force than the low carbon steel in the sheared condition (dashed line). Shearing and lamination punching increase stress within the steel which lowers its permeability. Both sets of samples were stress relief

annealed at 750 degrees C for two hours. The permeability of both samples is shown as the solid lines. A more pronounced improvement from stress relief annealing is seen in the low carbon steel. For this project, the low carbon steel had acceptable parameters.

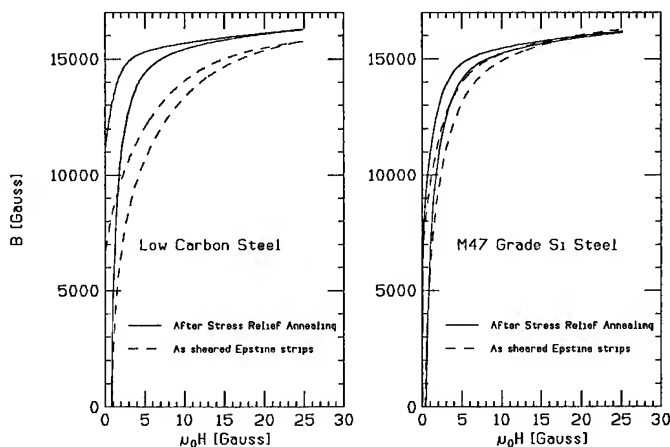


Figure 4. Hysteresis curves of low carbon and Si steel showing the improvement to each due to stress relief annealing.

D. End Design

A 30" prototype Lambertson has been constructed to aid in the design of the magnet end configuration. The ratio of magnetic length to physical (flange-flange) length must remain $\approx 92\%$ due to space constraints in the Main Injector. The geometry of the prototype includes a 2 by 13 inch gap without any shimming. The field free region geometry used is listed in Table 1.

IV. ACKNOWLEDGEMENTS

The authors would like to thank Linda Alsip, John Carson, Nelson Chester, Gerry Davis, Fritz Lange, Arie Lipski, Gale Pe-witt, Reid Rihel, Bill Robotham, Kay Weber, John Zweibohmer, for their contributions to this design.

References

- [1] The Fermilab Main Injector Technical Design Handbook, August 1994.
- [2] J.-F. Ostiguy and D.E. Johnson, "3D End Effects in Iron Septum Magnets", these proceedings.

THREE-DIMENSIONAL END EFFECTS IN IRON SEPTUM MAGNETS

J.-F. Ostiguy and D.E. Johnson

Fermi National Accelerator Laboratory *, P.O. Box 500, Batavia, IL 60510

Abstract

Among the technical difficulties encountered in designing an iron septum magnet, controlling the field quality at the longitudinal extremities of the field-free region is one of the most challenging. Without proper termination, flux jumping between the edge of the field-free region and the opposite pole piece results in a strong dipole kick and undesirable levels of higher order harmonics. The deleterious effects of the fringe field can be mitigated by reducing and channeling the leakage flux. We present 3D calculations and measurements performed on various end configurations for the Fermilab Main Injector iron septum magnets R&D program.

INTRODUCTION

In principle, an iron septum magnet, commonly referred to as a "Lambertson" is a simple device: a specially shaped hole is carved into one of the two pole pieces of a conventional dipole. Because of the high permeability of the iron, the flux circulates around the hole, establishing a so-called field-free region where the beam can drift freely. When a pulsed kicker is fired downstream of the septum magnet, the beam moves from the field-free region into the bending region where it is deflected and subsequently extracted into a beamline. The exact shape of the field-free region depends on many factors. For high-energy beams, the septum thickness is determined by the available kicker strength and is typically on the order of a few mm. The induction in the bending region is limited to 1.1-1.2 T since above that level, the septum region quickly saturates and the flux begins to penetrate into the field free-region. Using standard 2-D codes, it has become a relatively straightforward matter to design the cross section of an iron septum magnet. The field magnitude in the body of the magnet can easily be kept below a few Gauss; as a result, the bulk of the deleterious effect on the beam is due to the fringing flux at the longitudinal extremities of the magnet.

The end region must be analyzed as a fully three-dimensional problem; furthermore, saturation effects cannot always be neglected. Only five years ago, a typical run of a 3D finite-element code was limited to approximately 20000 nodes. The availability of faster processors and perhaps more importantly, of large amounts of physical memory has resulted in an order of magnitude increase in that number. Runs involving in excess of 10^5 nodes are now considered routine. Although 10^5 is a large number, one must keep in mind that linear resolution scales like the cube root of N . As a result, the mesh must be judiciously graded in order to obtain reliable results; this is an iterative process which tends to be time-consuming. Although 3D calculations are very useful for the magnet designer, they must be validated with measurements.

STRAIGHT END

As a starting point, it is instructive to understand and quantify what happens when no special precautions are taken to control

* Operated by the Universities Research Association, Inc., under contract with the U.S. Department of Energy.

the fringing flux. Consider the simple straight termination illustrated schematically in Figure 1. A plot of the vertical field along a line located 2.5 cm above the septum is shown in Figure 2. Note the sign inversion near the edge ($z = 0$), which is caused by the fact that some flux lines terminate inside the field-free region. Figure 2 and all the other results in this paper were obtained for a prototype of the magnet described in reference [1]. The coil is a symmetric saddle, the bending region is approximately 2 in \times 14 in, and the bending field at full excitation is approximately 1.2 T (corresponding to 12×2000 A-turn/pole). The septum is approximately 5 mm thick. The agreement between measurement and calculation is excellent, despite the fact that the geometry was modeled rather crudely. For each extremity, the net dipole kick experienced by a particle traveling 2.5 cm above the septum would be 0.032 T-m. For the sake of comparison, at the same excitation, the field within the body of the magnet is on the order of 8 Gauss. For a 3 m magnet, this represents a total body contribution of 0.0024 T-m, more than an order of magnitude smaller.

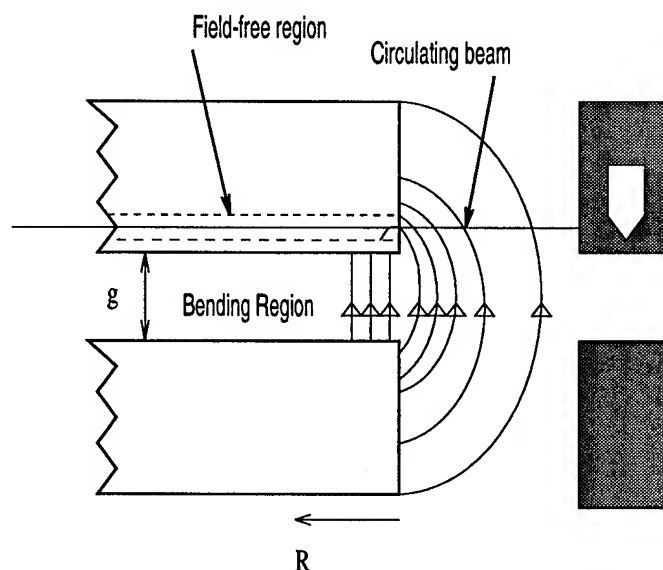


Figure 1. Longitudinal and transverse views of an iron septum magnet. The coils have been omitted to simplify the diagram. The circulating beam is shielded except in the end region where it traverses the fringe field. Some flux lines terminate inside the field free region, causing an inversion of the transverse field along the path of the beam.

EXTENDED END

To reduce the transverse field integral, the most obvious strategy consists in extending the pole containing the field-free region with respect to the other one. This method is effective, but only to a point. The relevant scaling here is the gap g ; to reduce the integral by a factor n , the recess distance R (as shown in Fig. 1) must be on the order of $(n - 1)g$. Extraction regions are often quite busy from a lattice point of view; as a result space is tightly constrained, and it is not possible to increase the overall

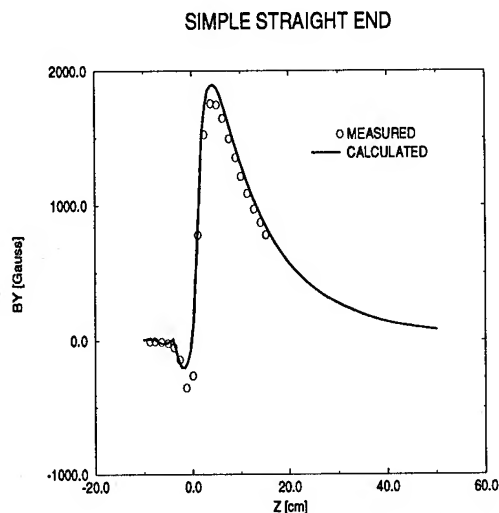


Figure 2. Field of a simple straight end, along a line 2.5 cm above the septum wall. The agreement between measurement and 3D calculation is excellent.

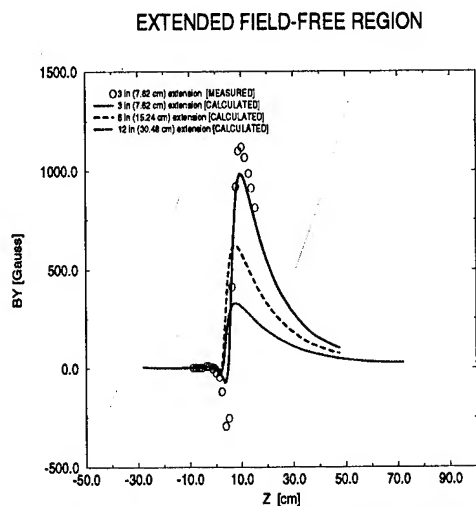


Figure 3. Fringe field of magnets with extended end region, along a line 2.5 cm above the septum wall. The dots corresponds to a measurement performed with $R = 7.62$ cm.

length of the magnet much beyond what is required to provide sufficient deflection to extract the beam. Unequal pole lengths also degrade the field quality in the bending region; although not as critical, this degradation eventually becomes significant. A plot of the field for three different distances between the upper and lower cores is presented in Figure 3. As expected, the field integral scales inversely with the average fringe path length $R + g$.

MIRROR PLATE

To minimize the overall length of the magnet while keeping the fringing field integral under control, one possible approach is to channel the leakage flux through a steel plate as illustrated in Figure 4. Instead of jumping to the opposite pole, the flux now travels longitudinally into the plate, is channelled around the field-free hole and returns into the opposite pole. Provided there is not too much saturation, the plate surface is approximately at constant magnetic potential and there should be no field beyond the outer edge of the plate. In the region between

the end of the field-free region and the plate, the flux has a transverse component, but the integrated effect cancels out due to symmetry. This explains why such a plate is sometimes referred to as a "mirror plate". Figure 5 is a plot of the measured and calculated field for the configuration illustrated in Figure 4. At low excitation, the plate has high permeability and the fringe field is completely quenched. At maximum excitation, the plate saturates considerably; the result is a drop in magnetic potential along the plate surface, hence the re-appearance of a long slowly decaying tail. To improve the situation, one needs to reduce the magnitude of the induction in the plate either by increasing the distance between the plate and the edge of the field-free region or by increasing the thickness of the plate. An important observation is that the magnetic potential drop in the plate is seriously affected by the width of the bending region aperture sides. This is illustrated in Figure 6 and 7. Note the dramatic increase in the field integral when this width is reduced to 2.5 cm.

CONCLUSION

We have demonstrated that 3D calculations of the fringe field at the extremities of an iron septum magnet are reliable. Such calculations have made it possible to understand and quantify the importance of saturation effects in a mirror plate.

ACKNOWLEDGMENTS

The authors would like to thank Dave Harding, Henry Glass, and the Fermilab Magnet Test Facility personnel.

References

- [1] D.E. Johnson et al., "Design of The Fermilab Main Injector Lambertson", These proceedings.
- [2] M. Harrison and F.N. Rad, "Symmetric and Non-Symmetric Lambertson Magnets", Nucl. Inst. Meth. 227, (1984) 401-410

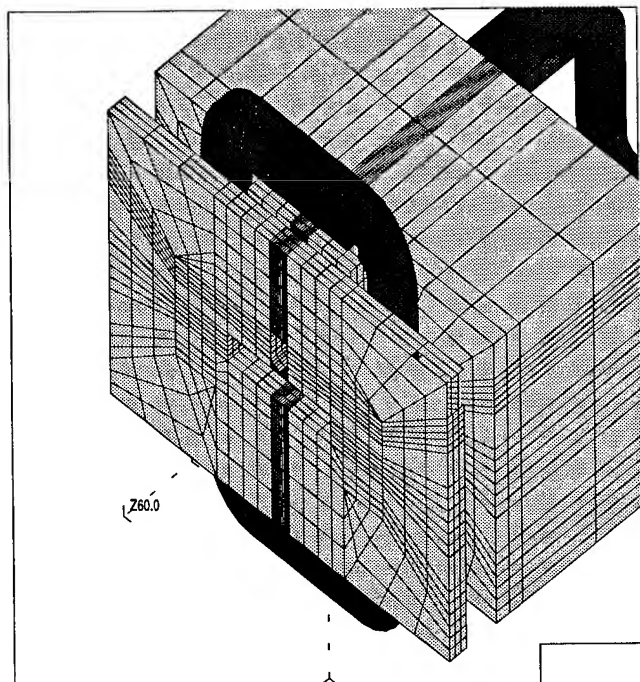


Figure 4. Mirror plate configuration. The field free-region has been extended 7.62 cm longitudinally. The plate is 2.54 cm thick and separated by 1.27 cm from the edge of the field-free region.

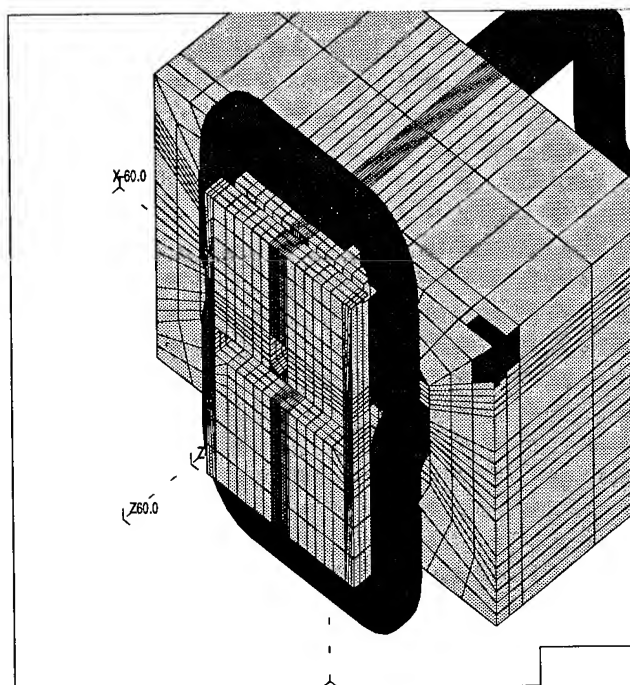


Figure 6. Mirror plate configuration. The geometry is the same as in Figure 4, but the plate width has been reduced. The sides of the bending region aperture are 2.54 cm wide.

EXTENDED FIELD FREE REGION + MIRROR PLATE

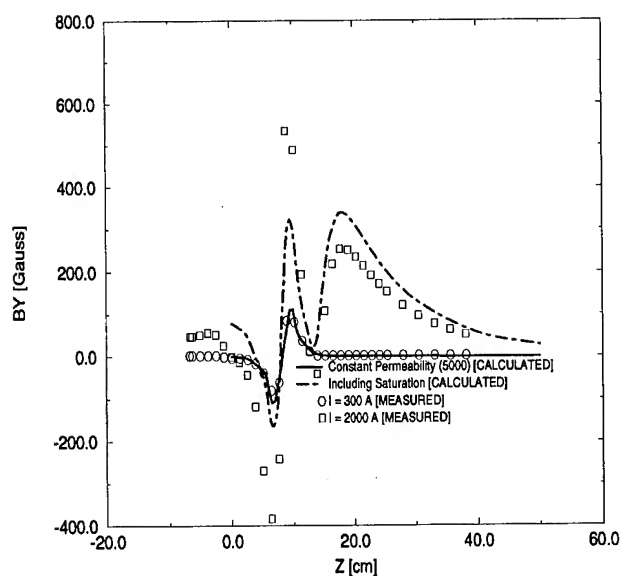


Figure 5. Calculated and measured fields for the configuration shown in Figure 4. The plot labeled "constant permeability" corresponds to $I = 300$ A. The field are plotted along a line located 2.54 cm above the septum wall.

EXTENDED FIELD-FREE REGION + MIRROR PLATE

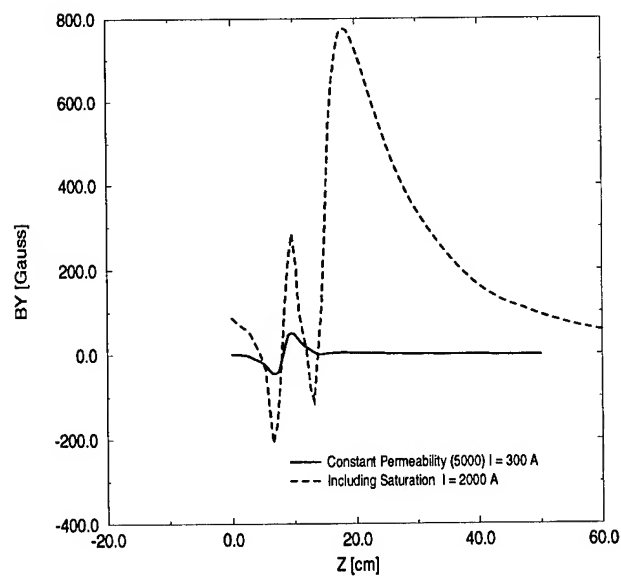


Figure 7. Calculated field for the configuration shown in Figure 6. The plot labeled "constant permeability" corresponds to $I = 300$ A. Note the increase in the size of the tail compared with Figure 5.

DESIGN AND B-FIELD MEASUREMENTS OF A LAMBERTSON INJECTION MAGNET FOR THE RHIC MACHINE*

N. Tsoupas, E. Rodger, J. Claus, H.W. Foelsche, and P. Wanderer

Brookhaven National Laboratory

Associated Universities, Inc.

Upton, New York 11973

Two Lambertson-type injection magnets have been designed, constructed and tested magnetically. One magnet is the mirror image of the other and each will serve as an injector in the rings of the Relativistic Heavy Ion Collider (RHIC) accelerators under construction at Brookhaven National Laboratory (BNL). To obtain the required field quality in the injected beam region and low stray fields in the circulating beam region of the magnet, an optimization study was performed using computer codes to provide solutions for a two and three dimensional model of the magnet. The calculations are compared to the magnetic field measurements taken in the injected and circulating beam regions mentioned above. Field inhomogeneities in the injected beam region were less than 6×10^{-4} for either measured or calculated B-fields. The magnetic-field strength in the circulating beam region was less than 0.1 Gauss (measured or calculated). A description of the mechanical design of the magnet as well as a detailed comparison of the measured magnetic fields to those calculated using the two and three dimensional computer codes is presented here.

I. INTRODUCTION

The Lambertson injection magnet which will be described in this paper is the last magnetic element of the beam transfer line between the Alternating Gradient Synchrotron (AGS) and RHIC accelerators at BNL. Two such magnets have been constructed, each of which will inject into the counter circulating beam-rings of the RHIC machine. Since each magnet is the mirror image of the other, we will only describe the magnet which injects into the counterclockwise circulating beam-ring of RHIC.

II. GEOMETRY and DESIGN PARAMETERS

The relative location of the magnet with respect to the straight section of the RHIC ring is shown in Fig. 1a (top view), 1b (side view), and 1c (view looking upstream).

Fig. 1a shows the injected beam at the entrance of the magnet which will bend by ~ 38 mrad and will then continue at the exit of the magnet on the same vertical plane as the RHIC circulating beam.

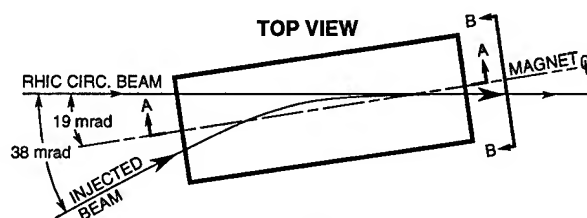


Figure 1a.

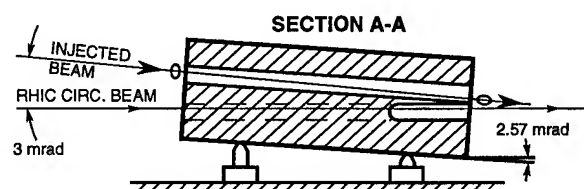


Figure 1b.

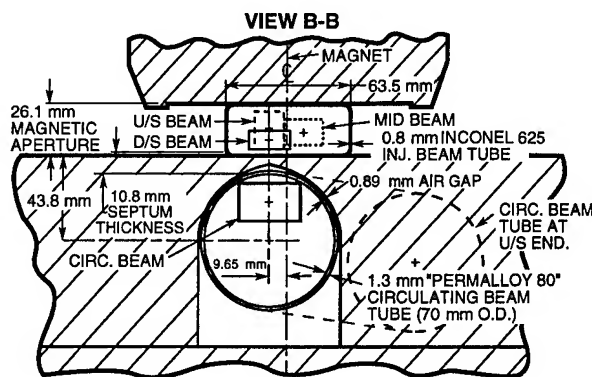


Figure 1c.

*Work performed under the auspices of the U.S. Department of Energy.

A cross section of the magnet by a vertical plane containing the symmetry axis (AA) of the magnet is shown in Fig. 1b. In this figure, the central ray of the injected beam makes an angle of ~ 3 mrad with the central ray of the RHIC circulating beam. Beam size considerations at the entrance and exit of the magnet for both the injected and circulating beams dictated that the surface of the bottom pole of the magnet make an angle of ~ 2.57 mrad with the central ray of the circulating beam, and ~ 2.24 mrad with the axis of the circulating beam pipe. This geometry helps minimize the septum thickness of the magnet, which is 10.8 mm as seen in Fig. 1c.

Fig. 1c, a view of the magnet looking upstream shows the injected and circulating tube sizes, wall thickness, and their relative locations. There is a ~ 0.89 mm air space between the circulating beam tube and the magnet iron. The locations of the beam at the upstream (U/S) and downstream (D/S) ends of the magnet is also shown.

The design parameters of the magnet, which appear below and in Figs. 1a through 1c were determined from optimization calculations, taking into account the geometry of the injection region the magnetic properties of the magnet steel and permalloy-80 pipe, and the maximum field at the beam injection gap, which in turn was determined by the field requirements in the injection and circulating beam regions.

Magnet design parameters

1. Length = 4 m
2. Bend angle = 38 mrad @ $B_p = 100$ T.m
3. Magnet gap = 26.1 mm
4. Inner diam. of circulating beam tube = 67 mm
Wall thickness = 1.3 mm

III. MECHANICAL DESIGN

Details of the mechanical design of the magnet as well as the magnetic properties of the steel and the high permeability of the circulating beam tube appear in Ref. 1.

IV. MAGNETIC FIELDS (CALCULATIONS and MEASUREMENTS)

The magnetic field calculations were performed using the computer code OPERA of VECTOR FIELDS Inc. (Ref. 2) and were separated into two parts: first in the calculations of the fields well inside the magnet where the 2-D version of the code was used, and second, the calculations of the fields at the entrance and exit of the magnet where the 3-D version of the code was used.

A) Two Dimensional Calculations.

The 2-D calculations were performed in order to determine the minimum septum thickness (minimum distance of the RHIC beam pipe from the lower magnetic

pole of the magnet) and the maximum radius of the circulating beam pipe, which will keep stray fields in the circulated beam region at values of less than 1 Gauss, and field uniformity in the injected beam region of $\Delta B/B \leq 6 \times 10^{-4}$. One of the cross sections of the magnet where 2-D calculations were performed is shown in Fig. 2 and corresponds to the middle of the magnet.

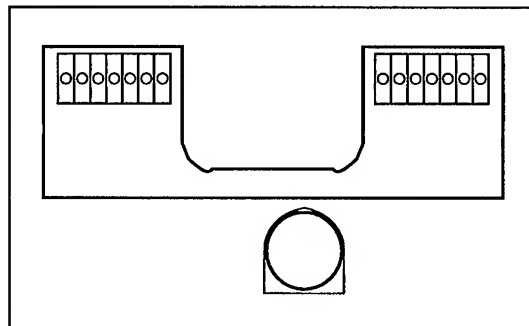


Figure 2.

Because of the ~ 3 mrad vertical slope of the magnet axis with respect to the horizontal plane (Fig. 1b), the septum thickness along the magnet varies and is at a minimum at the exit of the magnet. For this reason we performed the 2-D calculations on a cross-section at the exit of the magnet and subsequently verified that the optimum 2-D solution at the exit of the magnet also satisfies the B-field requirements mentioned above at any other cross-section of the magnet. The permeability of the magnet's iron and that of the permalloy-80 tube used in the calculations were equivalent to C1006 steel, and to μ -metal respectively.

The results of an optimized solution for a cross section at the middle of the magnet and at an excitation current corresponding to a 38 mrad bend of a 100 Tm rigid beam are as follows: In the injected beam region the calculated field uniformity is $\Delta B/B \leq 6 \times 10^{-4}$ and is computed over the area covered by 95% of the injected beam. The measured field uniformity is $\Delta B/B = (5.0 \pm 0.5) \times 10^{-4}$.

The measurements of the field uniformity in the injected beam region, were performed with a 30" long rotating coil of radius=1 cm. The axis of the measuring coil was parallel to the center axis (AA) (Fig. 1a) and at ~ 1.2 cm above the bottom surface of the magnet's gap and the coil was inserted well inside the magnet gap and away from the fringe field region. The measurements were performed at three locations inside the magnet with the axis of the coil placed (-1, 0 and +1 cm) away from the (AA) symmetry axis of the magnet.

The measurements of the B field (for the same excitation current as above) in the circulating beam region were made by placing the 30" long coil well inside the circulating beam tube with its axis parallel to, and 1.8 cm above, the circulating beam tube axis. The measured field value was (0.04 ± 0.01) Gauss. The corresponding calculated

value of the B-field was 0.055 Gauss.

In order to demonstrate the effect of the high permeability material of the circulating beam tube, the 2-D calculations above were repeated on the same cross section (at the middle of the magnet), except this time the circulating beam tube was made of the same material as the magnet and the air space between the tube and the magnet was filled with the same material as the magnet. The results of the calculated B field at the same location inside the circulating beam tube as above was 7.5 Gauss, which is two orders of magnitude higher as compared to the corresponding field of 0.055 Gauss when the permalloy-80 tube is in place.

B) Three Dimensional Calculations

The 3-D calculations were necessary to help us design the entrance and exit regions of the magnet in order to minimize the fringe fields in the circulating beam tube at the entrance and exit of the magnet. An isometric schematic plot of the entrance and exit regions of the magnet with the magnet coil and the field clamps is shown in Fig. 3.

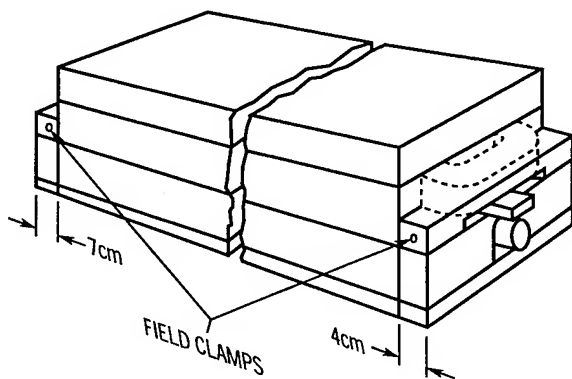


Figure 3.

The lower pole piece of the magnet was extended by 7 cm at the entrance and 4 cm at the exit beyond the edge of the top pole piece of the magnet (Fig. 3) to reduce the fringe field at the circulating beam region. The field clamps also shown in Fig. 3 were placed at the entrance and exit of the magnet to further reduce the fringe field inside the circulating beam pipe.

The calculated cumulative effect of the B_y (vertical) component of the fringe field inside the circulating beam region on a 100 Tm rigid beam is equivalent to 0.4 μ rad bend when the extensions of the lower magnetic poles and the field clamps are in place. The experimental measurements of the corresponding field integral inside the circulating beam pipe were done with a 4.946 m long coil which was placed inside the circulating beam pipe with end of the coil extending well beyond the

fringe field region of the magnet. From these measurements a beam bend of $(0.8 \pm 0.1) \mu$ rad was calculated. This value is in good agreement with the calculated value of 0.4 μ rad.

In order to demonstrate the effect of the extensions and field clamps mentioned above, we performed 3D calculations on the same magnet with the extensions and field clamps removed. The calculated fringe field integral of the B_y component of the field in the circulating beam pipe, with the extensions and the field clamps removed, yields a bending angle of 75 μ rad on a 100 Tm rigid beam.

A plot of the calculated B_y component of the field inside the circulating beam pipe at the exit of the magnet from -10 cm inside the magnet to 40 cm outside, (with the extensions and field clamps removed), is shown in Fig. 4. The high fields (~ 1000 Gauss) and high field gradients shown in Fig. 4 were reduced by a factor greater than 1000 with the use of extensions and field clamps. This reduction of the fringe field is shown in Fig. 5 of Ref. 1. This figure is a view of a 3-D plot of the B_y component of the fringe field in the region of the circulating beam pipe of the magnet, with extensions and field clamps in place.

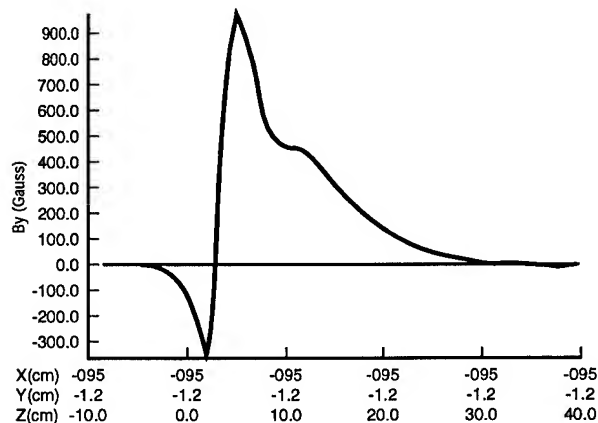


Figure 4

V. REFERENCES

- [1] Design of a Lambertson injection magnet for the RHIC machine. E. Rodger, N. Tsoupas, J. Claus, H.W. Foelsche. BNL PAC Washington DC May 17-20 1993.
- [2] Vector Fields Inc.

The APS Direct-Drive Pulsed Septum Magnets*

S. Sheynin, F. Lopez and S.V. Milton

Advanced Photon Source, Argonne National Laboratory
9700 South Cass Avenue, Argonne IL 60439, U.S.A.

Abstract

The Advanced Photon Source (APS) consists of four separate machines: linac, booster, positron accumulator ring (PAR) and storage ring (SR), plus three transfer lines interconnecting the machines. At least one thin, pulsed septum magnet is located at each splice joint [1]. The stray field tolerances for two of these septum magnets are very stringent. As an example, for clean operation during the proposed top-up mode in the storage ring, the stray fields from the septum magnet must not exceed 1 G-m. The septum wall thickness must also not exceed 2.4 mm. To meet these requirements, direct-drive septum magnets with magnetic shield pipe around the stored beam region were developed and built. These magnets have now been tested and installed, and are used in daily operation. We describe the magnet(s) design, the measurement results, the actual operation, and performance.

I. INTRODUCTION

There are six pulsed septum magnets interconnecting the four APS machines. Two of these, the PAR injection/extraction septum magnet and the SR injection septum magnet, have a septum thickness of 2.4 mm. The "field-free" region, i.e., the area where the circulating beam traverses, has strict maximum field requirements of 10 G-m for the PAR and 1 G-m for the SR. Both are of the direct-drive configuration. In this paper, we are concerned with these two magnets only.

Table 1 lists the specification for the PAR and the SR septum magnets.

Table 1: Septum Magnet Parameters

	PAR	SR
Thickness (mm)	2.4	2.4
Peak Field (T)	0.75	0.73
Pulse Width 1/2 Sine-Wave (μ sec)	250	500
Peak Current (kA)	13.2	13.6
Peak Power (kW)	58	143
Avg. Power (kW)	0.57	0.11
Leakage Field ^a (G-m)	10	1
Leakage Field ^b (G-m)	20	1
Repetition Rate	60	2

a. Maximum leakage field, defined as the field which makes it into the field-free region, allowed at the bumped beam location.

b. Maximum leakage field allowed on the closed orbit.

Although the two magnet designs, in concept, are similar to one another, in actuality they vary dramatically. The PAR magnet is used for both injection and extraction and must run continually at 60 Hz, its core is in vacuum, and water cooling is mandatory. On the other hand, the SR magnet is used only for injection. It runs at 2 Hz, its core is completely outside the vacuum, and it can be operated air-cooled.

II. DESIGN AND ANALYSIS

Electromagnetic simulations of the main field in the gap and the field-free region for the PAR and SR septum magnets were performed using the OPERA 2-D (PE2D) software [2]. Specifically, transient solutions for various geometries of laminated core, conductors, and the magnetic shields for the field free regions have been analyzed.

In pursuing the engineering design and fabrication of these magnets the following considerations and constraints were taken into account:

1. The steel core and conductors of the SR magnet must be kept out of the vacuum. This is possible because, unlike the PAR magnet, the SR septum magnet is used for injection only; therefore, there is adequate radial distance at the upstream end to allow a vacuum chamber in the gap region of the septum and utilize the magnetic shield in the field free region (i.e. closed orbit) as a separate vacuum channel. These two pipes converge to a common flange at each end of the magnet. A cross-section drawing of the magnet is shown in Figure 1.

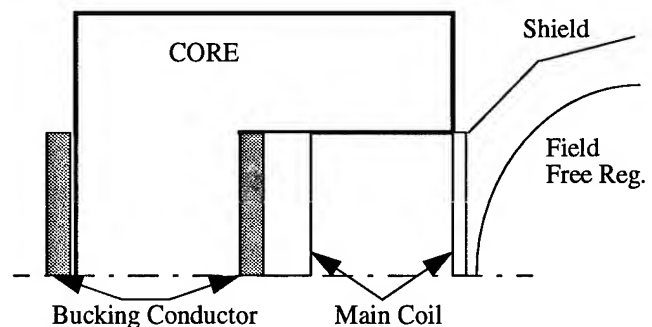


Figure 1: Bucking and main coils in the SR septum magnet

2. The SR septum magnet leakage field must be made < 1 G-m. Although our simulations indicated this to be possible with the basic design, as an added safety margin a backleg "bucking coil" was built into the magnet [3]. This additional winding produces a field in the gap which is in the same direction as the field produced by the main coil; however, outside the gap the field produced is opposite in sign to the leakage field from the main coil.
3. The PAR septum magnet is used for injection and extraction. There is not sufficient radial distance at either end to

* Work supported by U.S. Department of Energy, Office of Basic Sciences, under Contract No. W-31-109-ENG-38.

separate the vacuum chambers in the gap and in the field-free regions; therefore the entire PAR magnet is placed in a vacuum box. Also, because of the less stringent field-free region leakage field requirements (10 G-m) it does not require the additional bucking coil.

4. The PAR septum magnet is pulsed at a 60-Hz repetition rate; average power is 400 watts in the septum conductor and 170 watts in the backleg conductor. To provide adequate cooling, a special effort in design and fabrication of the septum conductor is required. Since the total septum thickness is only 2.4 mm and the vertical gap is 22 mm (limited by the peak field achievable with the peak current), there is no room to braze the cooling tubes to the septum conductor. Straight extension of the septum conductor outside the vertical gap will result in shunting current out of the gap which in turn will destroy the uniform field in the gap and significantly increase the field in the field free region. For this reason, the septum plate conductor was designed with slots and lugs, effectively open-circuiting this undesirable current path. This open circuit is ruined somewhat by the attachment of the cooling pipes; however, as was found in measurement, the resulting field quality was still within the specifications. The PAR septum plate conductor is shown in Fig. 2.

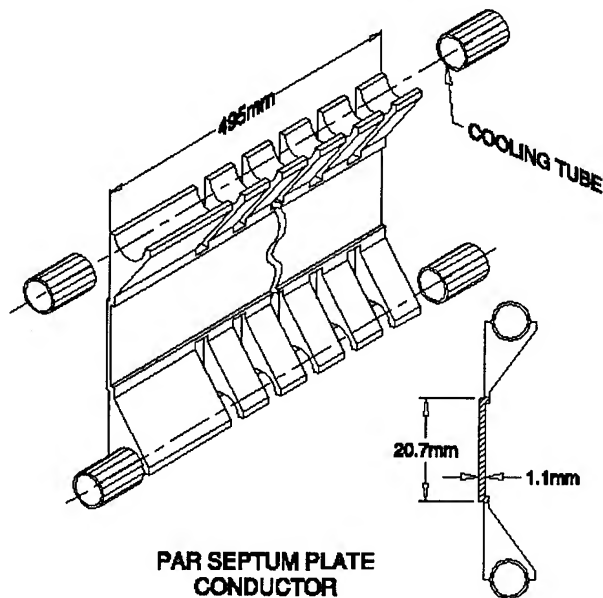


Figure 2

III. MEASUREMENTS AND PERFORMANCE

Measurements were made of the gap and field free regions under various operating conditions. The measurement setup consisted of both PC-board search coils and Hall probes mounted on computer-controlled translation stages. All data logging was automated making measurements very quick.

3.1 Storage Ring

Measurements of the SR septum magnet indicate very little leakage field. At peak current, the field in this region was

< 0.5 G-m, well within the specifications without use of the supplemental bucking coil.

The field in the gap was also measured to be within tolerance. Figure 3 shows the body field and the field integral in the gap normalized to the peak pulse current. The average effective length over the current range of interest was measured to be 1.07 m. Some saturation is seen at the higher currents; however, the measured peak integrated field was 0.826 T-m. This is 8% higher than what is required for 7-GeV injection into the storage ring.

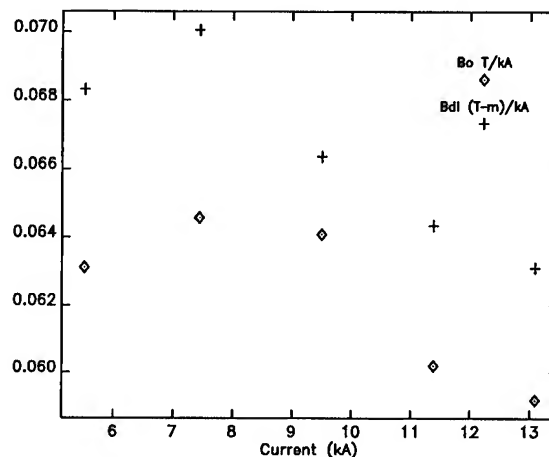


Figure 3: SR septum magnet main field measurements

The effectiveness of the air cooling was checked by operating the magnet at full field strength and repetition rate (2 Hz) for many hours. The maximum temperature change measured was 23°C.

This magnet is presently installed in the SR and its performance with beam has been measured. Preliminary measurements indicate that the leakage field at the position of the stored beam is indeed below 0.5 G-m. Our measurements indicate no influence of the septum field on the closed orbit of the beam.

3.2 PAR

The primary challenge of the PAR magnet is to build it durable enough to withstand the 60-Hz repetition rate at full field strength. An initial magnet was constructed and installed in the machine only to fail catastrophically after three weeks of operation. The failure was attributed to poor mechanical contact between the cooling tubes and the septum copper. Inadequate cooling was the result, and the septum copper literally blew itself apart.

The design was modified to provide much better mechanical/thermal contact between the stainless steel cooling tubes and the septum copper. First, however, we set about insuring that the mechanical fix did not spoil significantly the field properties.

A series of measurements were made on an early prototype of the PAR septum magnet. Cooling tubes, septum conductor, and shield pipe were assembled in various ways to

encompass all cases of electrically insulated or shorted components in the circuit. The impact of each case on the field quality at full strength (13.2 kA, 0.75T) was measured. Table 2 contains the results of these measurements. The best compromise of effective cooling and ideal electrical insulation of the septum conductor is Case 3 where the shield pipe is electrically insulated from the septum conductor and the stainless steel cooling tubes are brazed directly to the septum conductor lugs. The measured leakage field was 4.4 G-m, below the 10 G-m design goal, and the field distortion was still tolerable.

Table 2: Prototype PAR Measurements

Case	Main Field Bdl [T-m/kA]	Main Field Bdl rel. diff%	dB/B [%]	Leakage [G-m]
1	0.0255503	0.00	1.7	3.8
2	0.0254943	-0.22	1.2	38
3	0.0257437	0.76	2.5	4.4
4	0.0256601	0.43	2.5	31
5	0.0253744	-0.89	1.4	48

Case descriptions:

1. The reference case. The shield pipe is electrically insulated from the septum. There are no cooling tubes.
2. The shield pipe is shorted to the septum. There are no cooling tubes.
3. The shield pipe is electrically insulated from the septum. The cooling tubes are brazed to the septum.
4. The shield pipe is shorted to the septum. The cooling pipes are brazed to the septum
5. The septum conductor is spot welded to the shield pipe in 8 places. Thin wall cooling tubes are brazed to the septum.

Construction of the final version of this magnet is nearly complete. However, as a result of the testing performed on the prototype, we fully expect this magnet to perform within the design performance specifications.

IV. CONCLUSIONS

We have built both the SR and PAR thin septum magnets. The SR magnet meets the design performance specifications, and, in fact, the leakage fields of the SR magnet are better by at least a factor of 2 than the design goals. The PAR magnet has yet to see extended running time. It should easily meet the field free region design goals; however, the real test will be when we run it at 60 Hz for long periods of time at full field strength.

V. ACKNOWLEDGMENTS

We express great thanks to K. Halbach for motivating our switch to the direct-drive septum magnet. We also would like to thank C. Doose and S. Kim of the Magnet Measurement Group for their commitment to making the magnetic measurements for us.

VI. REFERENCES

- [1] F. Lopez, F. Mills, S. Milton, S. Reeves, S. Sheynin, K. Thompson and L. Turner, "The APS Thin Pulsed Septum Magnets," *Proc. of the 1994 EPAC*, 2406-2408 (1994)
- [2] VECTOR FIELDS Ltd, Oxford, England, "Software for Electromagnetics," 1992.
- [3] K. Halbach pointed out this possibility to us.

DEVELOPMENT OF THE PULSE MAGNETS FOR THE BOOSTER SYNCHROTRON OF SPRING-8

H.YONEHARA, H.SUZUKI, T.NAGAFUCHI*, M.KODAIRA*, T.AOKI, N.TANI,
S.HAYASHI, Y.UHEYAMA, T.KANEDA, Y.SASAKI, H.ABE and H.Yokomizo

JAERI-RIKEN Spring-8 Project Team, Kamigori, Ako-gun, Hyogo 678-12 JAPAN

*TOSHIBA co.,2-4, Suehiro-cyo, Tsurumi-ku, Yokohama 230, JAPAN

Abstract

Injection and extraction scheme of the SPring-8 synchrotron was designed. One kicker magnet, two septum magnets and one bump magnet which will be installed in the synchrotron to eject the electron beam of 8 GeV were tested and successfully completed.

I. INTRODUCTION

The SPring-8 synchrotron is required that the synchrotron accepts the electron beam of 1 GeV from the SPring-8 linac, accelerates the beam energy upto 8 GeV and ejects the electron beam to make stacking into the SPring-8 storage ring with the repetition period of 1s. In multi-bunch mode-operation of the ring, the long-pulse electron-beam which has macro-bunch length of $1\mu\text{s}$ from the linac is accepted in half-number, continus buckets of the synchrotron. The beam train of $1\mu\text{s}$ is handled as a continous beam in the synchrotron. In a single-bunch mode-operation, the synchrotron accepts the short-pulse beam which has macro-bunch length less than 1ns from the linac corresponding to one bucket length of the synchrotron. Moreover, the synchrotron is required to improve the beam current of the single-bunch mode-operation at the stacking of the ring. And 8 buckets of the synchrotron are occupied by the short-pulse beam from the linac and every spacings between the two buckets which are neighbor are the same length. And the electrons which occupy the 8 buckets are injected in a single bucket of the ring with controllling the time schedule of trigger signals for the electron gun of the linac and the pulse magnets of the injection and extraction systems of the synchrotron.

II. INJECTION AND EXTRACTION SCHEMES

A. Injection Scheme

Beam injection of the synchrotron was designed to be on-axis injection method. Injection system of the synchrotron is composed of two septum magnets and two kicker magnets. The injection scheme is shown in Fig. 1 and the aimed parameters of the magnets are shown in Table I. In this Table, the effective lengths of the magnetic fields along the beam orbit are defined with the core lengths. Leakage flux of the septum magnets on the injected beam is expected to enlarge the amplitude of the betatron oscillation. And allowance of the magnetic rigidity due to the leakage flux is estimated in order to suppress the betatron enlargement less than 1mm at Si2 where the physical aperture of the synchrotron is the minimum size. Apertures of the magnets are to be so large that the beam passes through the magnetic

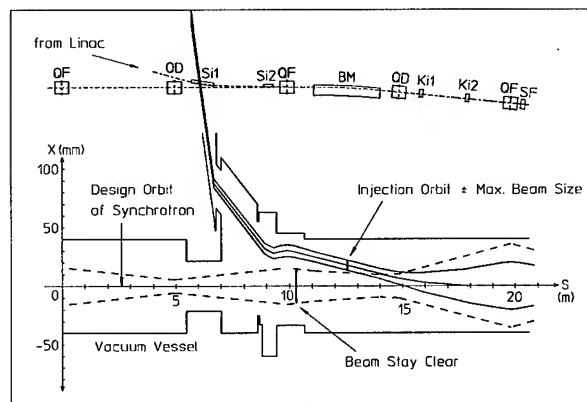


Figure 1. Beam Injection Scheme (Horizontal) — Solid line shows horizontal beam size on injection line from the linac and broken line shows beam-stay-clear of the injected beam.

Table I

Design Parameters of Pulse Magnets — Allowance of leakage shows field strengths on the designed orbit in the case of the injection magnets, and on the bump orbit in those of the extraction magnets.

Pulse Magnets	Mag. Field Strength(T)	Effective Length(m)	Allowance of Leakage(Tm)
Si1	0.789	0.987	3.3×10^{-4}
Si2	0.250	0.400	1.9×10^{-4}
Ki1	0.0264	0.200	—
Bp1	0.112	0.170	—
Bp2	0.159	0.170	—
Bp3	0.0966	0.170	—
Bp4	0.156	0.170	—
Ke	0.0395	0.400	—
Se1	0.263	0.200	1.2×10^{-3}
Se2	0.257	0.400	1.2×10^{-3}
Se3	0.970	1.110	2.1×10^{-3}
Se4	1.152	1.400	1.1×10^{-3}

field and the beam size is given in Table II with the positron-beam parameters of the linac. Beam size at the beam injection and the closed orbit distortion(COD) before COD correction are estimated by using "RACETRACK" with the electron-beam parameters of the linac and the beam-stay-clear shown in Table II.

B. Extraction Scheme

Extraction system of the synchrotron consists of three kicker magnets, four septum magnets and four bump magnets, which are used to extract the electron beam with 8 GeV from the synchrotron. The extraction scheme is shown in Fig. 2. The aimed parameters of the magnet are shown in Table I and the beam

Table II
Beam Size and BSC at Injection

	r_1	D	r_2	COD	BSC
1st Septum	3.8	88	2.7	6.6	9.3
2nd Septum	4.6	28	4.7	11	14.7

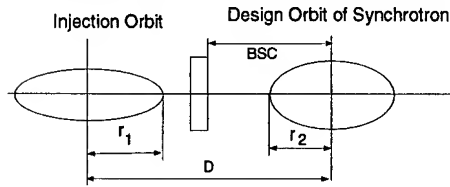
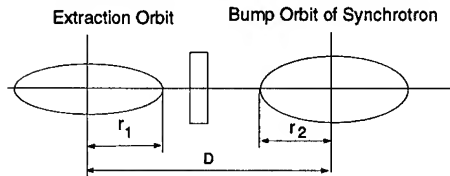


Table III
Beam Size at Extraction

	$r_1(2.5\sigma)$	D	$r_2(3\sigma)$
1st Septum	4.4	19	5.2
2nd Septum	4.5	22	5.0
3rd Septum	2.1	36	2.5
4th Septum	3.0	91	3.6



size is given in Table III with the parameters of the synchrotron. Leakage flux of the septum magnet on the bump orbit is expected to enlarge the amplitude of the betatron oscillation, and allowance of the magnetic rigidity due to the leakage flux is estimated to suppress the betatron enlargement less than 0.4mm at Se1 where the horizontal spacing between the bump orbit and the septum plates is the narrowest size. The performances of two septum, one kicker and one bump magnets, which will be installed in the extraction system, were tested and successfully completed.

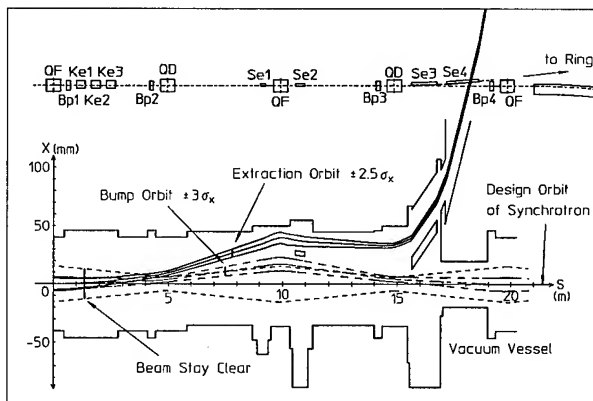


Figure 2. Beam Extraction Scheme (Horizontal) — Solid line shows horizontal beam size on extraction line from the synchrotron and broken line and dotted line show bump orbit and beam-stay-clear of the injected beam.

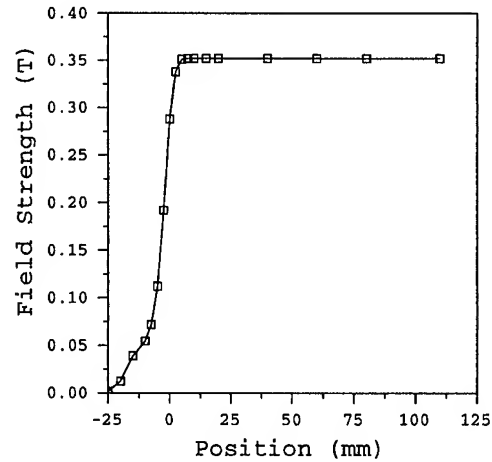


Figure 3. Magnetic-Field Distribution of Se2 at the Upstream End — The position of $s=0$ mm shows the core end of Se2.

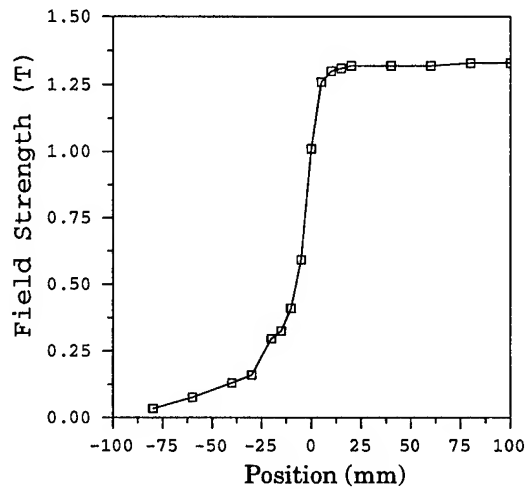


Figure 4. Magnetic-Field Distribution of Se3 at the Upstream End — The position of $s=0$ mm shows the core end of Se3.

III. PULSE MAGNETS

A. 2nd Septum Magnet of Extraction System

Magnetic-field strength of the 2nd septum magnet was measured. The field distribution on the extraction orbit at the magnet end is shown in Fig.3. The effective length of the field is 9 mm longer than the core length, and the magnetic rigidity of 3.4×10^{-5} Tm due to the leakage flux is smaller than the leakage allowance of 1.2×10^{-3} Tm.

B. 3rd Septum Magnet of Extraction System

Magnetic-field strength of the 3rd septum magnet was measured. The field distribution on the extraction orbit at the magnet end is shown in Fig. 4. The effective length of the field is 20 mm longer than the core length, and the magnetic rigidity of 1.1×10^{-3} Tm due to the leakage flux is smaller than the leakage allowance of 2.1×10^{-3} Tm.

C. Kicker Magnet of Extraction System

In order to achieve the single-bunch mode-operation of the storage ring, rise time and fall time of the magnetic field have

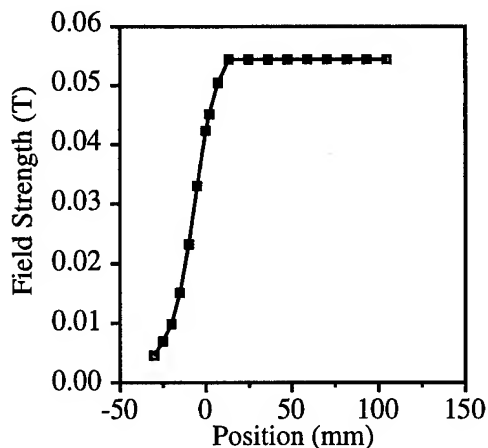


Figure 5. Magnetic-Field Distribution of Ke1 — The position of $s=0$ mm shows the pole end of Ke1.

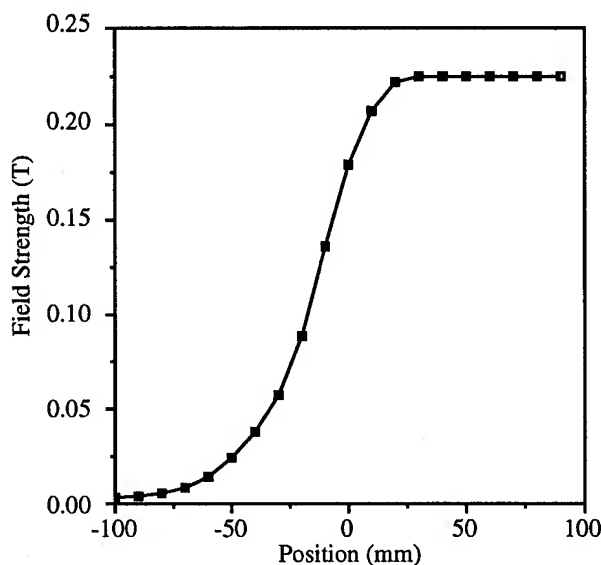


Figure 6. Magnetic-Field Distribution of Bp2 at the Downstream End — The position of $s=0$ mm shows the core end of Bp2.

to be shorter than 50 ns and 150 ns, respectively. The flat-top time is required to be longer than 60 ns. Trial manufacture of the kicker magnet was completed successfully.¹⁾ The field distribution of Ke1 along the design orbit is shown in Fig. 5. The effective length is 18 mm longer than the pole length, and the waveform of the magnetic field is gratified.

D. Bump Magnet of Extraction System

The waveform of the kicker magnet at the beam extraction must be very fast. It is difficult to get strong magnetic-flux density and make long pole length of the kicker. The bump orbit is formed with four bump magnets and the extraction orbit is achieved on the bump orbit because of the low magnetic-rigidity of the fast kicker. The field distribution of Bp2 along the design orbit is shown in Fig. 6 and the effective length is 36 mm longer than the core length of the magnet.

IV. CONCLUSION

In the synchrotron, fifteen pulse magnets are installed to inject and eject electron beam. Some magnets which had been considered to have some difficulties in manufacturing have been constructed in an early stage of the synchrotron-construction plan. These magnets and the power supplies were completed successfully. We have started to manufacture the remainders of the pulse magnets on schedule.

V. ACKNOWLEDGEMENT

The authors are thankful to computer control group of the SPring-8 injector team for their supporting DTP and CAD of this article.

VI. REFERENCE

- 1) Y. Sasaki, H. Yonehara, H. Suzuki and T. Aoki; Proceedings of the 9th Symposium on Accelerator Science and Technology, Tsukuba, Japan p.255, 1993.@

MAGNETIC DESIGN OF THE LNLS TRANSPORT LINE

R. H. A. Farias, Liu Lin and G. Tosin, LNLS, Campinas, SP 13081-970 BRAZIL

The transport line for the injection system of the LNLS UVX storage ring is described. The line connects an underground 100 MeV LINAC to the 1.15 GeV UVX electron storage ring. The designs for the magnets are reviewed and the measurements of the prototypes are presented.

I. INTRODUCTION

The magnetic lattice of the transport line consists of a quadrupole doublet just after the underground LINAC, an achromatic vertical translation which brings the beam to the ring level and a horizontal achromatic deflection, including the septa, which leads the beam to the injection point [1]. Although the injection energy is chosen to be 100 MeV, the line has been designed for 250 MeV electron energy, allowing for future upgrade of the injection system either by recirculating the beam in the LINAC or by using SLED.

The transport line is 20.031 m long, including the septa. A lay-out is shown in figure 1. The line presents some flexibility for optical function matching. Presently it can be operated either with the optical functions matched to the storage ring functions, or with the functions mismatched so that the injected beam ellipse occupies the maximum area in the available storage ring acceptance. The vacuum chamber will be cylindrical, with inner diameter $\varnothing=35$ mm. This limits the maximum beam energy deviation in the line to $\pm 1.6\%$ since the maximum dispersion function is 1.09 m. The dipole chambers will be squeezed to 24 mm (inner dimension) in the gap direction, which does not decrease the beam stay-clear.

The line is made up of 4 dipoles, 12 quadrupoles and 2 septa. Additional coils in the quadrupoles and trim coils in the dipoles will be used as built-in steering elements. This

choice makes alignment and supports easier. The dipoles can be used to correct the orbit in their respective bending planes, whereas the quadrupoles can be used to correct in both planes.

Simulations of orbit distortion and correction for the matched injection mode have shown that the beam path can be kept within ± 1.5 mm displacement for maximum steering strengths of ± 3 mrad (including a 50% safety margin). The steering coils are designed to provide this steering strength at the energy injection of 250 MeV.

All the transport line magnets have been designed with the 2D POISSON [2] package. The precision in the lamination dimensions as determined by the laser cutting process has been simulated in the design project of the magnets. Both the precision and the roughness of the cut are of the order of $\pm 25\mu\text{m}$.

II. SEPTA

The final deflection of the injected beam towards the storage ring will be carried out by two septa deflecting the beam in the plane of the stored beam orbit. The parameters for these magnets are shown in table 1 [3,4].

Both septa are conventional non-staggered laminated C-core d.c. magnets (figures 2-3). The yokes are composed of stacks of 1.5 mm thick low coercivity (1.0 Oe) low carbon steel laminations kept together by tie rods, without special end plates. The thick septum consists of two pieces aligned to each other by means of a precision dowel pin in a V groove and held together by means of aluminum clamps (figure 3). The magnetic field in these magnets is

Table 1 - Parameters for the transport line septa (@250 MeV).

	Thin septum	Thick septum
Deflection	3°	15°
ρ (m)	15.33	3.83
Magnetic length (m)	0.8027	1.0027
Physical length (m)	0.7744	0.9413
Gap (mm)	21	44
B (T)	0.054	0.218
Good field width (mm)	41	166
Septum thickness (mm)	5.0	50
Number of turns	4	264
Current (A)	227	30
Voltage (V)	3.3	21
Power (W)	750	630
Inductance (mH)	0.05	600

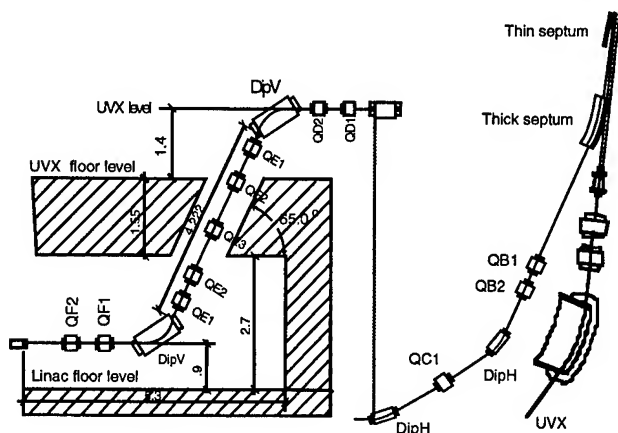


Figure 1 - LINAC-UVX transport line: magnetic lattice.

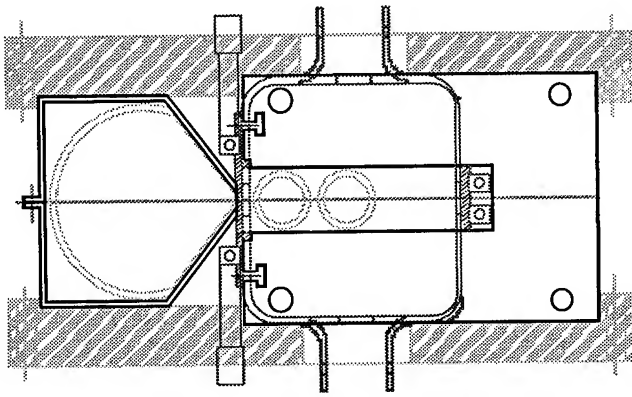


Figure 2 - Transverse cut of the thin septum. The core and the magnetic shield are inlaid in an aluminum box used for support and alignment.

low—even for the highest energy injection—and no ‘chamfering’ has been introduced in the longitudinal pole profile.

The coils are made of solid copper conductors with rectangular cross sections. For the thin septum coil an efficient cooling system is of paramount importance. For the injection energy of 250 MeV, the power dissipated in the septum wall is of the order of 270 W and the current density reaches 23 A/mm². The four turns of the coil are assembled on a water cooled brass support.

For the thick septum, the coil is a unique package of 264 turns of non-water cooled copper conductor encapsulated in insulation varnish. The maximum current

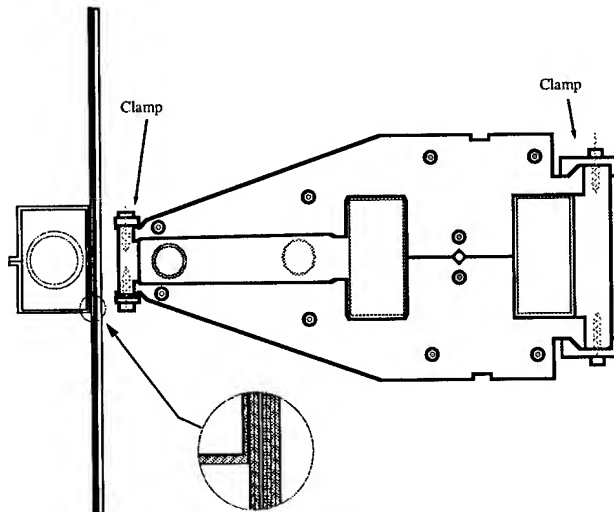


Figure 3 - Thick septum: transverse cut.

density in the most demanding conditions is 1.7 A/mm².

The thin septum has been assembled and measured. Measurements obtained using a Hall probe have shown good agreement with the numerical simulations (Figure 4). The screening of the magnetic field in the storage ring vacuum chamber region satisfies the design specifications. Measurements of the lateral fringing field have shown a

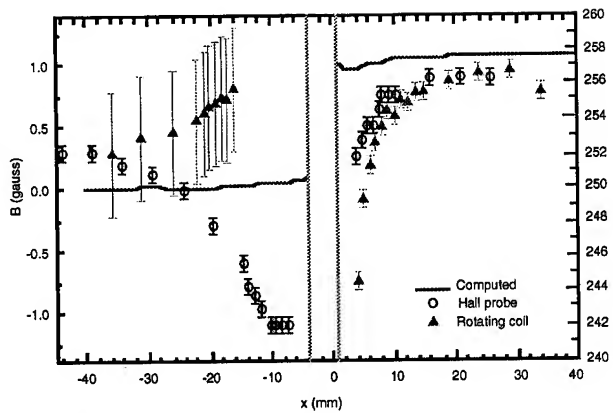


Figure 4 - Thin septum: measured and computed fields. At left, the field inside the stored beam region. At right the field inside the septum gap. The scales are different for the two regions. The measurements correspond to the injection energy of 120 MeV ($I=108.9$ A).

maximum remanent field of 1.1 gauss for 120 MeV injection energy. Measurements of the integrated longitudinal field using the rotating-coil technique show a difference of approximately 0.3% as compared to the hard-edge model. In this case the coil has shown excellent thermal behaviour. For 250 MeV injection energy, modifications will be required in the cooling system of the coil.

III. DIPOLES

The four bending magnets of the transport line are grouped into two families (Table 2)[5]. These dipoles are standard C-core magnets consisting of 1.5 mm thick laminations stacked and held together by tie rods. Special

Table 2 - Parameters for the transport line dipoles (@250 MeV).

	Vertical	Horizontal
# of elements	2	2
Deflection	65°	33°
ρ (m)	0.80	0.80
Magnetic length (m)	0.9076	0.4608
Physical length (m)	0.8997	0.4544
Gap (mm)	30.0	30.0
B (T)	1.04	1.04
Good field width (mm)	20.0	125.3
Number of turns	460	460
Current (A)	28.1	28.4
Voltage drop (V)	64.1	44.8
Power (kW)	1.8	1.27
Inductance (H)	3.9	2.6

20 mm thick laminations of non-ferromagnetic stainless steel are used as end plates.

The laminations for the vertical deflection dipoles are staggered due to the large deflection angle and to the geometrical constraints in the transport line. In order to prevent non-linear effects due to saturation of the magnetic field in the core corners, the ends of both dipoles have been rolled off. The longitudinal profile of the poles have a 30 mm radius circular chamfer.

The coils for the dipoles are constructed as flat pancakes with two layers of solid copper conductors amounting to 92 windings each pancake. Each pancake is wrapped with insulation polyester tape and impregnated with insulation varnish. Each dipole holds two coils, which in turn is composed of five pancakes. The built-in steering capabilities are attained by supplying additional trim coils wound along the backleg of the dipoles. Using 16 mm² cross section extra-flexible copper wire, the magnetic field required for the maximum deflection of 3.0 mrad can be reached with 8 windings for the vertical and 16 windings for the horizontal dipoles (for a current of ± 9.8 A).

According to numerical simulations, the transversal field homogeneity along the good field region is $4 \times 10^{-3}\%$ for the vertical dipole and $5 \times 10^{-2}\%$ for the horizontal one.

IV. QUADRUPOLES

There are 12 quadrupoles in the transport line [6]. They are composed of four identical parts, each one corresponding to a pole. This is particularly suitable for the shuffling of the laminations which provides better uniformity of the magnetic characteristics. The laminations are stacked without end plates and held together by tie rods.

Table 3 - Parameters for the transport line quadrupoles (@250 MeV).

# of elements	12
Maximum Gradient (T/m)	5.1
Magnetic aperture radius (mm)	20.0
Magnetic length (m)	0.2
Gap (mm)	30.0
B (T)	1.04
Good field width (mm)	20.0
Number of turns/coil (main coil)	72
Maximum Current (A)	12
Maximum Voltage drop (V)/mag.	3.7
Power (W)	44
Inductance (mH)	43

Each main coil is composed by 80 mechanical windings. Neither the main or the steering coils are water cooled.

The tolerance for the maximum relative deviation of the magnetic field profile from a pure quadrupole field is 5.0×10^{-3} at the internal wall of the vacuum chamber. Simulations show for the transport line quadrupoles an expected maximum relative deviation of the order of 5.0×10^{-4} .

V. CONCLUSIONS

We have presented the design project for the transport line from the LNLS LINAC to the UVX storage ring, including a brief description of the lattice and the magnetic design of all components. Among these, in our case, the thin septum was the most critical item. The results of its magnetic, mechanical and thermal characterization showed, however, that the constructed piece characteristics is within the required tolerances. Simulations have shown that besides the mechanical tolerances of the laminations, the septum coil positioning precision is as well a critical parameter for the field quality. This is probably the main reason for the small differences between the measured and the simulated fields near the septum wall.

The thick septum laminations are already cut as well as part of the quadrupoles. They will be assembled in the near future. The remaining transport line magnets will be constructed and characterized by August 1995.

VI. REFERENCES

- [1] Liu Lin, "Updated LINAC to UVX transport line", LNLS CT-01/95, 1995.
- [2] Reference Manual for the POISSON/SUPERFISH Group of Codes, Los Alamos Accelerator Code Group, LA-UR-87-126.
- [3] A. R. D. Rodrigues and R. H. A. Farias, "Projeto Magneto-mecânico de um Septum Fino D.C.", LNLS CT-15/94, 1994.
- [4] A. R. D. Rodrigues and R. H. A. Farias, "Projeto do Septum Grosso D.C.", LNLS CT-02/95, 1995.
- [5] A. R. D. Rodrigues and R. H. A. Farias, "Projeto dos Dipolos da Linha de Transporte", LNLS CT-12/95, 1995.
- [6] A. R. D. Rodrigues and R. H. A. Farias, "Projeto dos Quadrupolos da Linha de Transporte", LNLS CT-13/95, 1995.

CONSTRUCTION AND CHARACTERIZATION OF COMBINED FUNCTION QUADRUPOLES

G. Tosin, LNLS, C.P. 6192, 13081-970, Campinas, SP, Brazil

The magnetic lattice of the Brazilian Synchrotron Light Source uses combined function quadrupole magnets, i.e., special coils are included in the quadrupoles to produce a sextupolar field component. These combined quadrupoles are used in the dispersion free straight sections and the sextupolar component is employed in the minimization of geometrical aberrations produced by the chromatic correction sextupoles. The sextupolar component reaches 26 Tesla/m², superimposed on the main quadrupole component of 17 Tesla/m. The magnet core consists of laser cut steel laminations. In this report, we present results on mechanical and magnetic characterization of these magnets, including harmonic analysis and an investigation on the positioning repeatability of the magnetic axis with respect to the reference girder.

I. INTRODUCTION

This work describes the construction and magnetic characterization of combined quadrupoles which have additional coils to produce a sextupolar field. These quadrupoles are present in the dispersion-free straight sections of the LNLS UVX electron storage ring and their sextupolar components are used as a means to correct geometric aberrations produced by the chromatic correction sextupoles, thus improving the dynamic aperture.

II. CONSTRUCTION

Two air yoke coils are installed so as to produce a dipolar field with a high sextupolar content (figure 1). The dipolar component is then cancelled out by means of compensating coils.

The air yoke coils were designed to be included into already existing quadrupoles and to reach $d^2B/dx^2 = 26$ Tesla/m². Fourteen turns of polyester-coated copper wire are wound on a water-cooled brass yoke. The two coils are serially connected and the current density to produce the necessary field is 12.8 A/mm², dissipating 150 Watts. Under these conditions the coils reached a final temperature of 42 °C.

The core of the host quadrupole is fabricated with laser-cut steel lamination, of 1.5 mm thickness, with accuracy of ± 0.03 mm. It has a quadrupolar component of 17 Tesla/m with 225 Amps through the main coils. Additional coils are provided for compensating the dipolar field dipolar field originated in the sextupolar coils.

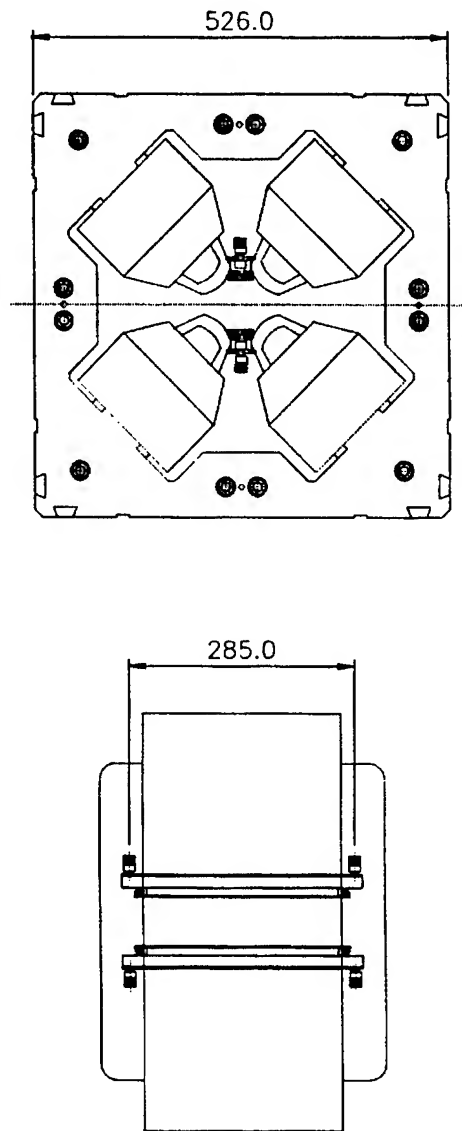


Figure 1: Front and side view of combined quadrupole prototype

III. MEASUREMENTS

The measurements of the first prototype were performed with the rotating coil technique. Excitation curves of the integrated sextupolar component with quadrupole currents of 10.5 A, 120A and 225 A are shown in Figure 2. These currents correspond to lowest quadrupolar field during injection and to lowest and highest quadrupolar field at full energy, respectively. Negative values come from mixing the sextupole

produced by air yoke coils and the sextupole components due to construction errors.

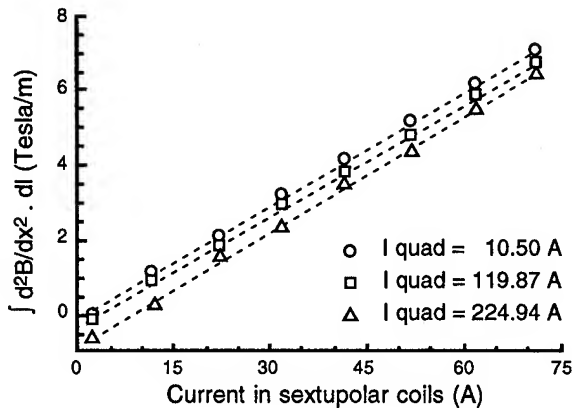


Figure 2: Excitation curve.

Figure 3 shows the harmonic analysis of a pure quadrupole at 10.5 A, a combined quadrupole also with 10.5 A, but with 72 A in sextupolar generating coils and the results of simulation with no quadrupolar current and 71.4 A in sextupolar coils. Note the increase of the undesired 10-pole, 14-pole and 18-pole components.

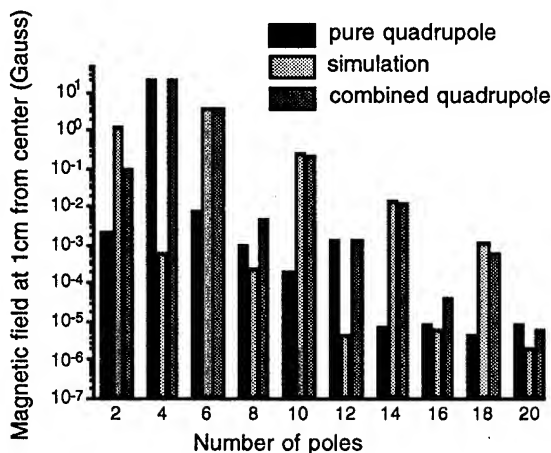


Figure 3: Harmonic analysis. The simulation results were obtained with the 2d code POISSON [1].

In parallel with these measurements, the possibility to align the magnets in straight sections using only one reference girder was tested. To achieve this purpose, high mechanical precision is needed in the construction of the magnet and the reference girder rails.

The procedure used to test this possibility consisted in putting a small girder, which simulates with high accuracy the real girder of a straight section, on top of an upside down quadrupole. This way, mechanical

deformations of the small girder are avoided. In this small girder, references were fixed to relate the theoretical central orbit position, called geometric center, with the magnetic center of quadrupole localized by rotating coil measurements. The accuracy of these measurements is .01 mm.

The results of placing and taking off the small girder several times on the same quadrupole showed a repeatability of the magnetic center positioning of ± 0.01 mm. The repeatability of the magnet center positioning among several quadrupoles is of ± 0.1 mm.

IV. CONCLUSIONS

A combined function quadrupole has been built and characterized and the results showed a significant increase in unwanted high multipole components. The alignment of the magnets in the straight sections will be done with the help of a reference girder, the production of which has been started.

V. REFERENCES

- [1] Reference Manual for the POISSON/SUPERFISH Group of Codes, Los Alamos Accelerator Code Group, LA-UR-87-126.

DIPOLE MAGNETS FOR THE SLAC 50 GeV A-LINE UPGRADE*

R. Erickson, S. DeBarger, C. M. Spencer, and Z. Wolf, Stanford Linear Accelerator Center, Stanford University, Stanford, CA 94309 USA

The SLAC A-Line is a transport system originally designed to deliver electron beams of up to 25 GeV to fixed target experiments in End Station A. To raise the beam energy capability of the A-Line to 52 GeV, the eight original bending magnets, plus four more of the same type, have been modified by reducing their gaps and adding trim windings to compensate for energy loss due to synchrotron radiation. In this paper we describe the modifications that have been completed, and we compare test and measurement results with predicted performance.

The original magnets were conservatively engineered and have run without failure to support a large number of high energy physics experiments over this long period of service.

Over the last decade, the linac has been upgraded as part of the SLC project, so that long-pulse beams can now be accelerated up to about 33 GeV, and short-pulse beams can be accelerated up to about 50 GeV. The purpose of the present project is to upgrade the A-Line so that these higher energy beams can be transported to End Station A for use in fixed target experiments.

I. HISTORY AND MOTIVATION

The A-Line is one of SLAC's two original beam transport systems and has been in use since 1966. The function of the A-Line is to guide and focus the electron beam from the linac through the Beam Switch Yard (BSY) to the experimental facilities in End Station A. From there, the beam drifts to a high-power beam dump in a heavily shielded chamber in the hillside east of End Station A. The A-Line consists of a series of magnets, collimators, diagnostic devices, vacuum chambers, and associated

II. MAGNET REQUIREMENTS

As originally designed, the A-Line used eight large dipole magnets to deflect the beam through a total bend angle of 24 degrees. These are conventional magnets, each nominally three meters long, consisting of water-cooled copper coils on solid iron cores. The design, fabrication, and measurement results for the original magnets are described in detail in Reference 1. To transport a beam with energy greater than 25 GeV requires that the total

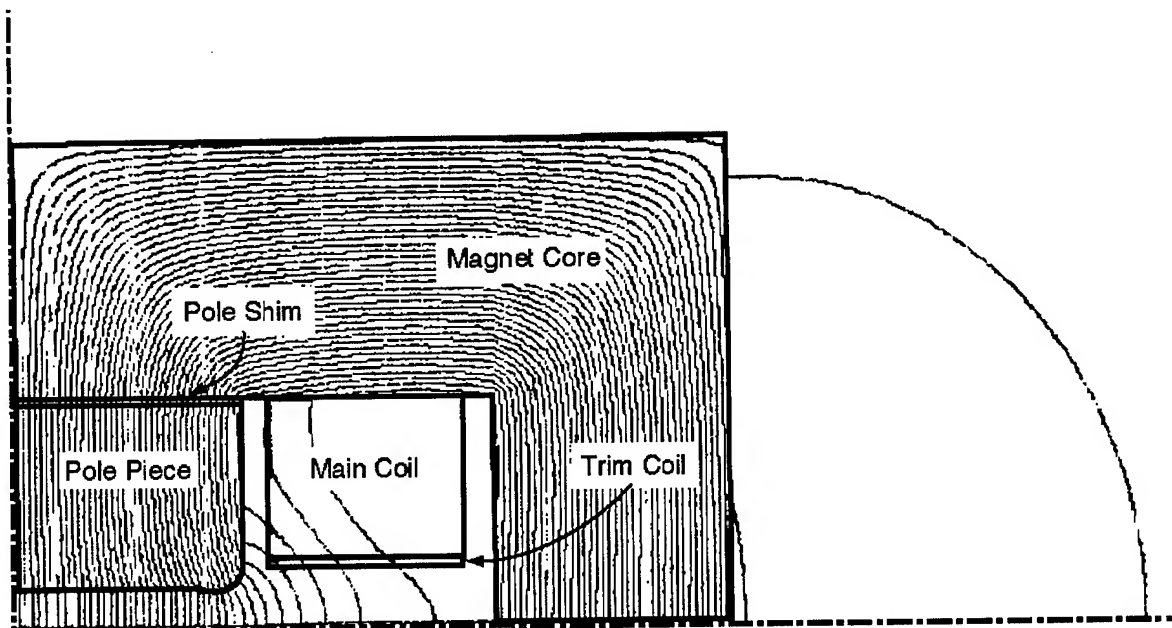


Figure 1. POISSON model of one quadrant of a modified dipole showing magnetic flux lines.

* Work supported by Department of Energy contract DE-AC03-76SF00515.

bending strength be increased. This will be done by installing four additional magnets, identical to the original eight, which will be powered in series with the original eight. All twelve magnets have been modified to increase their strengths by reducing their pole-to-pole gaps. This has been done by installing steel shim plates under each pole piece of each magnet. In addition, the LCW plumbing is being modified to increase the flow of cooling water to the magnets.

Each magnet originally had a 60 mm pole-tip gap and was designed for a maximum integrated strength of approximately 44 kG-m. To achieve the desired strength of about 61 kG-m, the gap has been reduced to 46 mm. This choice was based on a requirement that the beam stay-clear be at least 3 sigma for a 5 GeV beam. This was also a convenient choice because it was small enough to accommodate the required trim windings sandwiched between the existing main coils and the new vacuum chamber, yet was just large enough to stay clear of the beam aperture as defined by existing collimators. Figure 1 illustrates the cross section of one quadrant of a modified magnet. Superimposed on the magnet are magnetic flux lines as calculated with the POISSON program assuming a current of 1382 amps, which corresponds approximately to the field needed for a 52 GeV beam. At this current, the pole tip field was calculated to be 20.11 kG. The flux leakage outside the iron return yoke indicates substantial saturation at this field strength.

The original magnet coils were cooled with low conductivity water (LCW) from a system capable of supplying approximately 12 gallons/minute to each magnet. Calculations indicated that this would be inadequate for the higher beam energies, even with the reduced gap. To avoid coil damage due to high temperatures, the plumbing system is being modified to provide LCW from the pumping system used for the research area, which was designed to support numerous large spectrometer magnets. It has been estimated that the pressure drop across each magnet will be approximately 200 psi with this system, corresponding to a flow of about 20 gallons/minute in each magnet.

At energies above about 30 GeV, the emission of synchrotron radiation by the beam is significant as it passes through the bend magnets in the A-Line. The next two fixed target experiments planned at SLAC require a longitudinally polarized electron beam with an energy of about 48.6 GeV. This energy corresponds to a total spin precession of 15π rotations as the beam traverses the beam transport system from the linac to the experimental target. At this energy, the total loss due to synchrotron radiation is about 0.8 percent. To keep the beam properly steered through the A-Line, it will therefore be necessary to adjust the magnet strengths according to a "synchrotron taper" scheme. Although there are several ways to accomplish this, the most conceptually straight forward is to provide individual trim windings on each dipole. The main bend power supply can then be set to a value appropriate for the beam energy as it exits the last of the twelve bend magnets

and the trims can then be used to boost the strength of each of the other magnets to a level corresponding to the beam energy at each point. Computer simulations have shown that grouping the magnets in pairs for this purpose gives a smooth enough taper; i.e., the trim windings of pairs of consecutive magnets may be powered in series. Therefore, a total of six trim supplies will be sufficient if each supply powers the trims on two adjacent magnets.

The strength required of the trim windings is based on the calculated beam energy loss. The energies corresponding to 15π and 16π electron spin precessions in the A-Line are approximately 48.6 GeV and 51.8 GeV, respectively, in the absence of synchrotron radiation. With synchrotron radiation, the energy corresponding to 15π precession is achieved with 48.75 GeV at the end of the linac and 48.36 GeV in End Station A. For 16π rotations, the corresponding numbers are approximately 52.04 GeV and 51.54 GeV, respectively. The most demanding requirement for the trim windings is in boosting the first pair of magnets to 52.04 GeV when their main windings are powered to 51.54 GeV. This requires raising the strength of each magnet from 60.067 kG-m to 60.65 kG-m, an increase of about 1 percent.

III. DESIGN AND FABRICATION

The magnets, which are constructed of solid pieces of iron, were completely disassembled to permit the removal of the pole pieces from the rest of the magnet core. It was interesting to note that, after some 28 years of service, the magnet components were still in excellent condition. There was very little evidence of radiation damage to the epoxy insulation of the main coils. The ceramic insulators which carry LCW to the main coils were generally free of deposits and exhibited no defects.

The steel shims were fabricated out of AISI 1006 steel and precision ground to 7 mm (0.276 inch) thickness. Prior to release for fabrication, special attention was paid to the metallurgical certification of the shim material in an effort to obtain the optimum magnetic permeability. In an additional attempt to enhance permeability, the steel was heat treated by firing in air for a 9.5 hour cycle of controlled heating and cooling, with a peak temperature of 760°C (1400°F).

The trim coils were wound from 6.5 mm (0.255 inch) square copper with a 3.2 mm (0.125 inch) round internal passage. Prior to winding, the conductor was insulated using double dacron glass. Each nineteen turn coil was wound in a single layer and installed in the magnet with a layer of 0.23 mm (0.009 inch) dacron-mylar-dacron between the main and the trim coils. The position of the trim coil is indicated in Figure 1.

IV. MEASUREMENT RESULTS

Each completed magnet is being processed through an extensive series of measurements before installation in the BSY. The measurements are done using a long flip coil which has been calibrated against an NMR system. Measurements of the first complete magnet were used to develop a standardization procedure to be used whenever high accuracy is desired. The standardization procedure adopted involves ramping the magnet current from 25 amps to 1400 amps at a rate of 11 amps/sec for 90 percent of the way to the end point, followed by a ramp of 5.5 amps/sec for the remaining 10 percent. The magnet is then allowed to settle at 1400 amps for 60 seconds before ramping down in the same way to 25 amps. Again the magnet is allowed to settle for 60 seconds before proceeding. If this cycle is repeated three times before ramping up to the final desired set point, then the field accuracy is reproducible to a level of 5.3×10^{-4} . With the main coils powered to 1400 amps and the trim windings powered to 130 amps, the temperature rise in the main coil, as measured at the LCW outlet, is 35°C, and the rise in the trim winding is 32°C. These values are consistent with the expected temperature rise, and are acceptable for reliable long-term operation. The finished magnet properties are summarized in Table 1.

Pole to pole gap	46.0 mm
Effective length	3.0277 m @ 1400 A
Weight	30,000 lb. approx.
Main coil	2x (48 turns/pole)
I (main)	1400 amps max.
Terminal voltage	133 volts @ 1400 A
Trim coil	2x (19 turns/pole)
I (trim)	120 amps max.
LCW flow (main)	20 gal/min. @ 200 psi
Temp. rise	35°C @ 1400 A
$\int B \cdot dl$	62.008 kG-m @ 1400A

Table 1. Summary of bend magnet specifications.

Figure 2 shows the integrated magnetic strength vs. current for the first completed magnet. The round data points are measurements made with a 60 mm pole tip gap before the magnet was modified. The square data points are measurements of the finished magnet with a 46 mm gap. The smaller dots show design values calculated using the POISSON modeling program. Note that the measured performance matches the calculated field strength closely for currents up to about 600 amps, and is somewhat stronger than anticipated for higher excitation. This can be attributed to better magnetic properties of the steel yoke material and shims than was assumed in POISSON.

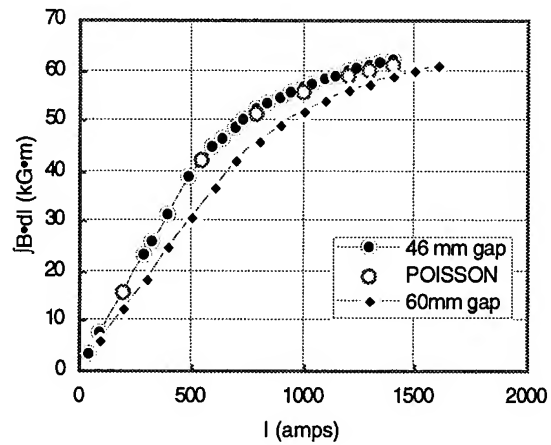


Figure 2. Integrated magnetic strength vs. current.

Figure 3 shows the measured properties of the trim windings on the first complete magnet. The increase in integrated magnet strength due to the trim coils is plotted against trim coil current for two values of the main coil current: 550 amps, where the magnet response is very linear, and again at 1000 amps, where the iron is significantly saturated. The hysteresis effect, which is clearly evident when the main coil is set to 550 amps, becomes negligible as the iron becomes saturated.

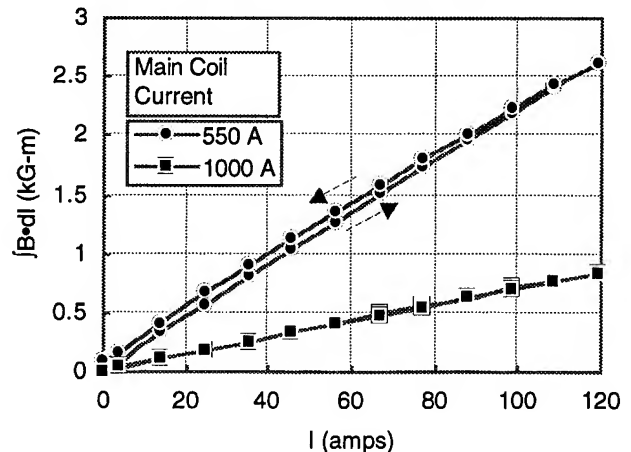


Figure 3. Trim coil strength vs. trim current for two values of the main coil current.

VI. REFERENCES

- [1] *The Stanford Two-Mile Accelerator*, R. B. Neal, Editor, 1968.

DESIGN AND TESTING OF THE MAGNETIC QUADRUPOLE FOR THE HEAVY ION FUSION PROGRAM

R. Benjegerdes, A. Faltens, W. Fawley, C. Peters, L. Reginato, M. Stuart
Lawrence Berkeley Laboratory, Berkeley, CA 94720

ABSTRACT

The Heavy Ion Fusion Program at the Lawrence Berkeley Laboratory is conducting experiments in the transport and acceleration of "driverlike" beams. The single beam coming from the four-to-one beam combiner will be transported in a lattice of pulsed magnetic quadrupoles. The present beam transport consists of high field, short aspect ratio magnetic quadrupoles to maximize the transportable current. This design could also be converted to be superconducting for future uses in a driver. The pulsed quadrupole will develop a maximum field of two Tesla and will be housed within the induction accelerator cells at the appropriate lattice period. Hardware implementation of the physics requirements and full parameter testing will be described.*

INTRODUCTION

The initial transport for the heavy ion beam from the 2 MeV injector to 5 MeV of acceleration is provided by electric quadrupole. At the 5 MeV level, it becomes more effective to use magnetic focusing. The detail of the physics design and requirements of the focusing field are covered in a separate paper at this conference. The electromechanical design of this quadrupole has been optimized for the Elise accelerator. Design codes for a real driver indicate that the optimum design will most likely consist of superconducting quadrupoles and a transition from electric focusing to magnetic focusing will occur at a higher energy level.

MECHANICAL DESIGN AND MANUFACTURING

The HIF program's magnetic quadrupole has a cylindrical geometry with an aperture radius of 1/3 the effective coil length. The physics design requires a peak field of 2 T over a 1 millisecond pulse delivered at a repetition rate of 1 Hz. The aperture radius has been set at 75 mm, and the effective magnetic length at 249 mm. In an effort to create a magnet that will meet the requirements of a heavy ion accelerator, one prototype has been created and tested and a second prototype is now in progress. In the first prototype we concentrated our design efforts on creating a magnet that would be electrically and mechanically reliable over the short- and long-term. In the second prototype, which we are currently building, we are

refining the design so as to improve the magnetic field quality of the magnet.

The magnetic quadrupole is made up of a coil form, the conductors, electrically insulating-heat conducting epoxy, cooling passages, and a flux return yoke. See figure 1. The coil form is a plastic cylinder in which elliptical ended "race-track" shaped grooves are numerically machined into so as to provide precise positioning of the conductor cables. The quadrupole has 24 turns per pole, arranged in two layers with identical azimuthal distributions so as to provide the 130 kA-turns per quadrant necessary for producing the required 2 Tesla. Rectangular litz wound cable is used as a conductor so as to minimize eddy current losses. Once the conductor has been wound into the coil form, the assembly is vacuum potted with thermally conductive epoxy. A 3 mm layer of epoxy radially distant from the conductors and coil form is left so as to provide electrical insulation between the conductors and the water used to cool them. A cooling jacket is made by stacking a number of PVC rings, which had a step cut into them and off set holes to provide a water passage, which are slid over the magnet. The I.D. of the PVC rings is such that there is an interference fit with the outside of the potted magnet. The whole assembly is then potted into a yoke constructed of steel laminations.

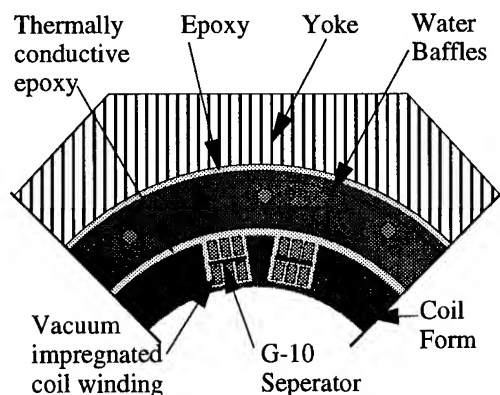


Fig. 1 Cross-sectional view of one quadrant of the Magnet

Making the first prototype electrically and mechanically reliable meant minimizing the voltage across the leads, providing enough insulation between the cables, and providing enough cooling and conductance of the heat generated by the cables. Electrical breakdown problems were dealt with by vacuum potting the magnet so as not to introduce any bubbles and then applying one atmosphere of pressure to the curing epoxy so as to make any bubbles that did exist as small as possible. That way

*This work was supported by the Director, Office of Energy Research, Office of Fusion Energy, U.S. Dept. of Energy, under Contract No. DE-AC03-76SF00098.

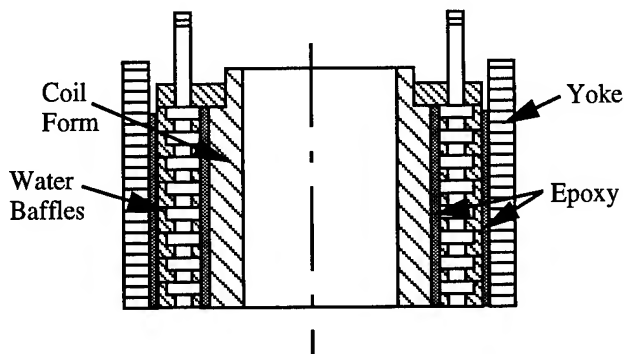


Fig. 2. The Magnetic Quadrupole Cooling Jacket

we would minimize the chance of plasma forming in pockets within the epoxy. Choosing the conductor cross sectional area also had an effect on the potential for break down as well as the chance of over heating the magnet. In choosing a conductor, the ease at which it could be wound and formed was also a consideration. The relationships of conductor size, power dissipation, lead voltages, and number of turns per quadrant of the magnet are shown in figure 2. Also shown in this figure is the fact that the total conductor area must be at least 55% of the cross section in order to obtain correct spacing for the required cos θ quadrupole current distribution.

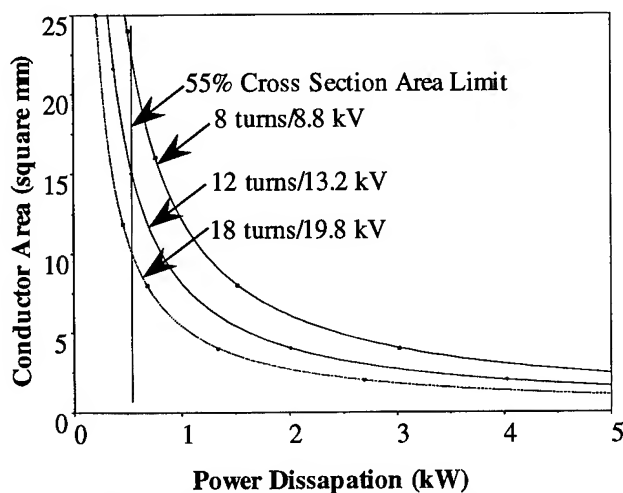


Fig. 3 Conductor size versus energy loss

A reasonable conductor to optimize the power, voltage, and windability equation would be a 3x5 mm stranded conductor. In the first prototype a 3.2 x 6.4 mm litz twisted cable constructed of 7, 14 gage, copper wires was chosen to be used with 24 turns per quadrant. The resulting current was 5400 A and a voltage across the leads of 10.8 kV. Thermal modeling (which assumed a 1.1 kW power loss in the conductors) showed a temperature gain from outside to inside of about 40°C and a maximum inner conductor temperature of 60°C. In the second prototype the stiffer conductor was exchanged for a more flexible conductor of the same overall cross sectional area, so as to meet the more stringent bending requirements necessary for improving the magnetic field quality. The "new" cable is a litz twisted cable constructed of 7 bundles of

13 strands of 26 gage wire. Although the overall cross sectional area of the second conductor remained the same as the first, the actual current carrying area of the cable was reduced by 20%, causing the temperature differential between the water and the inner cable to increase to 55°C. The inner conductor in the second prototype will operate at approximately 75°C.

The design of the second prototype magnetic quadrupole was directed towards manufacturing a magnet with the field quality that will eventually be necessary for focusing a beam of heavy ions in a linear accelerator from an energy of 5 MeV to 10 MeV. The two features of the previous magnet that needed improvement were the path that the conductors took when crossing from one "race-track" across to another, and removing the effective solenoid loop created by the connection of the cable leads at the end of the magnet. See figures 3 and 4. The "cross-overs" of the leads in the first prototype used long gentle curves such that the leads made a "V" shape between each of the race track grooves. Each "V" of the conductor can be represented as an equivalent dipole, which is an undesirable addition to the quadrupole field we are trying to achieve. In order to remove this feature we rerouted the cross over cables such that they make an "X" between the "race-tracks". Due to the geometry of the coil form, the triangle shaped areas formed by the top and the bottom of the "X", which represent effective dipoles, could not be made equal in area to each other. From magnetic calculations it was determined that up to a 40 square mm total difference in the areas between the top triangular shaped areas and the bottom triangular shaped areas, could be tolerated. By reducing the minimum bending radius of the cables to 6.4 mm, and by using a more flexible wire, we were able to meet this requirement.

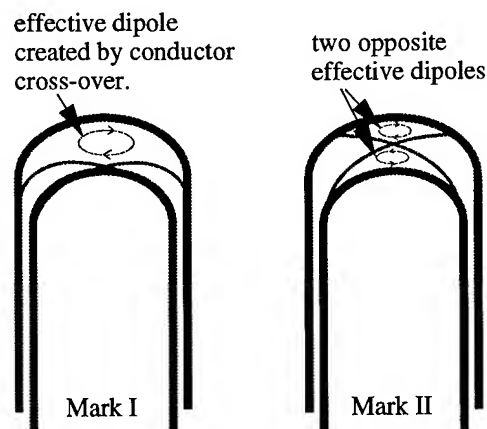


Fig. 4 Changing the coil winding geometry to improve magnetic field quality.

The removal of the solenoidal loop was accomplished by cutting a double helical groove into a piece of lucite rod, wrapping the cable in one groove all the way to one end, making a "u-turn" and wrapping the cable back down the second groove. The whole twisted pair was then heated up and wrapped around a mandrel so that it could then fit around the end of the magnet. The leads from each quadrant would then be spliced into the twisted pair loop.

The results of using a twisted pair loop for the magnet leads is that it will create two solenoids of opposite sign twisted around each other, which will look like a string of very small dipoles with alternating sign. Neighboring dipoles will cancel each others fields out in a very short distance, leaving the magnetic field region in the center of the quadrupole unaffected.

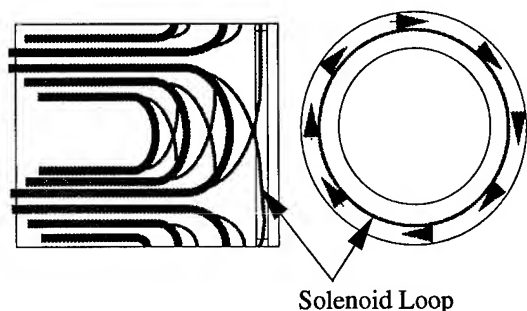


Fig. 5 Unwanted Solenoid Loop

ELECTRICAL DESIGN AND TESTING

The goal of the electrical engineer is to provide the drive for the magnet which achieves the desired physics parameters with the simplest, most reliable and least expensive power source. In this case, a current of 5,400 A is required to produce 2 Tesla. The Elise beam pulse duration is only a few microseconds at a repetition rate of one Hertz. Hence, the 5,400 A are required with an accuracy of 0.1% for the same beam duration and repetition rate. The optimum system is one which provides the required field with a minimum of power dissipated which dictates a pulsed magnet. The simplest pulser is one which provides a sinusoidal waveform. In order to maintain a constant field of better than 0.1% for 5 μ s, a maximum sinusoidal half period of 200 μ s is allowed. This requirement sets an upper bound on the driving frequency, but the actual optimum is determined by the combined magnet losses which consist of the coil losses, the yoke losses, and the induced losses in the beam pipe and flanges which are frequency dependent. Furthermore, the beam pipe eddy currents must not cause a significant reduction in magnetic flux since this reflects into higher current requirements to maintain the same 2 T field.

A number of tests were performed on the first magnetic quadrupole prototype. A broad minimum power requirement was found at a frequency of 1 kHz. Since the system costs are determined also by the cost of the power supply and associated equipment, it was decided that the period of 500 μ s would result in a more costly power supply due to the need of twice the quantity of the series silicon controlled rectifiers (SCR's) for witching the energy. Hence, a half sinusoidal period, $\tau = \pi\sqrt{LC}$, of 1 ms was chosen. This lower frequency yields an additional advantage of producing a lower voltage between coil windings resulting in higher reliability. This period produced an ample constant field during beam time and was well within the di/dt ratings of the SCR's.

The simplified block diagram is shown on fig. 6 The charging power supply consists of a six-stage three phase

multiplier circuit which is controlled by solid state switches. Once the desired voltage is reached, the switches are turned off by the comparator.

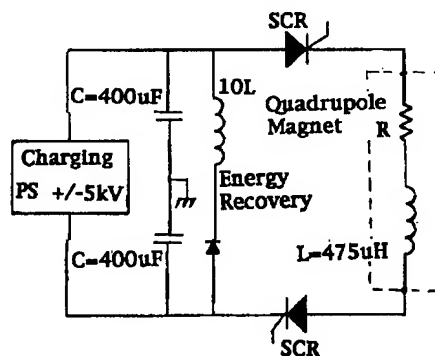


Fig. 6 Simplified block diagram of Pulsed Quadrupole Magnet System

Since the discharge period has been chosen and the quadrupole inductance is known, the power system can now be designed. The period $\tau = \pi\sqrt{LC}$ and the voltage $V = I\sqrt{L/C}$. By substitution we find that $C = 200 \mu F$ and $V = 8.1$ kV. Allowing for cable and SCR losses, we chose a power supply charging voltage of 8.5 kV. In order to achieve higher reliability we have chosen a bipolar power supply of ± 4.25 kV rather than a unipolar one of 8.5 kV. This reduces the voltage from the pulsed coil to ground insuring higher safety factors at a small increase in cost of the power supply. The total energy (E) required to establish the 5.4 kA is $E = CV^2/2 = 7.2$ kJ. At one hertz, this would require a 7.2 kW charging power supply. From fig. 7, we can see that at the time that the SCR current is cut-off, 28% of the initial energy has been dissipated in the magnet (including a 1 mm beam pipe and the yoke). The remaining energy returns to the capacitors but with the wrong polarity. It was cost-effective to include an energy recovery system which allowed us to construct a charging power supply 1/3 the size of the system without energy recovery. The inductor and diode shown on fig. 6 recharge the capacitor in the proper polarity recovering 66% of the original energy as shown on fig. 7. This magnet was pulsed for 45 minutes at one Hertz and at full current. The temperature rise was well within the calculated values.

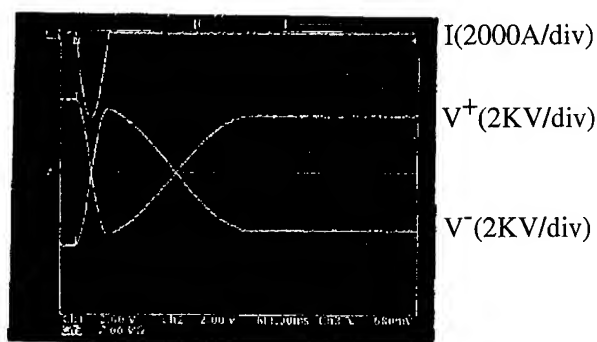


Fig 7 Output current and energy recovery waveforms

DESIGN AND CONSTRUCTION OF A LARGE APERTURE, QUADRUPOLE ELECTROMAGNET PROTOTYPE FOR ILSE*

M. Stuart, A. Faltens, W.M. Fawley, C. Peters, and M.C. Vella
Lawrence Berkeley Laboratory, University of California
Berkeley, CA 94720 USA

Abstract

We are currently constructing a prototype quadrupole electromagnet for the proposed Induction Linac Systems Experiment (ILSE) at LBL. ILSE will address many physics and engineering issues relevant to the design of a heavy-ion fusion driver accelerator. The pulsed electromagnet has two layers of current windings and will produce a field gradient exceeding 25 T/m at a repetition rate of 1 Hz steady-state. In this paper, we discuss how the interaction of various concerns such as maximum dynamic aperture, short lattice period, field quality, iron yoke weight, heat transfer, and voltage standoff have led to our particular design choices. We also present 2- and 3-D numerical calculations concerning field topography and the results of transport simulations of space-charge dominated ion beams with ILSE parameters.

I. INTRODUCTION

The great bulk of the beam transport in heavy ion fusion (HIF) drivers will be done with strong-focusing, magnetic quadrupoles. In many driver designs, electrostatic quadrupoles will provide focusing from the ~ 2 MV injector to approximately 50-100 MV at which the transition to magnetic transport is made. The actual transition energy depends critically upon the maximum transportable current by the magnetic quadrupole lattice which scales as $(a/L)^2 V^{3/2}$ where a is the useful dynamic aperture, L is the half-lattice period, and V is the beam energy. Thus, in the low energy portion of the magnetic transport section, there is a premium for maximizing the aperture ratio.

In the past few years, the LBL HIF group has developed a conceptual design for the 10-MV ILSE ("Induction Systems Linac Experiment") accelerator which, if and when fully funded by a presently parsimonious DOE, will allow examination of many physics and engineering issues common to HIF drivers. As part of this effort, we have designed and are currently building the latest iteration of a large aperture, short lattice period, pulsed electromagnet prototype to be used in the 5-10 MV magnetic transport section of ILSE. The magnet must operate dependably at a continuous, 1-Hz repetition rate and transport $\approx 1 - 1.5 \mu\text{C/m}$ of a space-charge dominated K^{+1} beam with minimal emittance degradation. In the remainder of this paper, we discuss the design philosophy and tradeoffs that have determined our particular choices for this magnet.

II. BASIC BEAM AND MAGNET PARAMETERS

As presently conceived, the ILSE injector will produce four individual beams of $\sim 0.2 \mu\text{C/m}$ line charge density which will be accelerated by induction cores, slowly compressed longitudinally to perhaps as much as $0.3 \mu\text{C/m}$, and transported via electrostatic quadrupoles up to ≈ 5 MV energy. At this point, the beams will be combined and merged into one single beam and then transported magnetically to the beam dump. The half-lattice period L increases in the electrostatic transport region from 0.25 m to 0.40 m and the present beam combiner/merger design has $L \approx 0.5$ m.

For a strongly space-charge dominated beam ($\sigma \ll \sigma_0$),

$$\left(\frac{a_b}{L}\right)^2 = \frac{2Q}{(1 - \cos \sigma_0)} = \frac{\lambda}{4\pi\epsilon_0 V} \quad (1)$$

where Q is the beam perveance, and σ and σ_0 are respectively the undepressed and space-charge depressed phase advance per full lattice period $2L$. If $\sigma_0 \approx 72^\circ$ at 5 MV and $\lambda = 1.5 \mu\text{C/m}$, the perveance is 2.7×10^{-3} and the required a_b/L is less than 0.1. Although this seems to be a comfortably small number, in fact due to longitudinal "packing factor" constraints induced by the space required for the accelerating gap, insulators, couplers, etc., the magnet windings in the latest ILSE prototype design occupy only about one-half of the half-lattice period. Hence, the ratio of the winding radius to the effective length exceeds 0.2 and one must be careful to minimize anharmonic fringe field and higher order multipole components.

The required field gradient may be roughly estimated from the relation

$$\sigma_0 = \frac{v_z B' L^2}{V 2\pi} \quad (2)$$

where B' is measured in T/m and we presume that the field is dominated by the fundamental longitudinal harmonic. For 5 MV K^{+1} , $L = 0.5$ m and $\sigma_0 = 72^\circ$, the required gradient is about 18 T/m.

A. Current Winding Geometry

To minimize anharmonic field components, we follow the philosophy of Laslett *et al.* [1] and make such components disappear in the z -integrated sense over a half-lattice period. Ignoring for the moment turn-to-turn crossovers, Our actual coil ends have elliptical projections in (θ, z) space (see Fig. 1 of ref. [2]), a geometry that avoids sharp bends for the individual wires. In order to limit the current per turn to 5 kA or less, the magnet has two layers of twelve turns each. Ideally, the end curve of each turn would be individually separated in z from its neighbors (this allows one to suppress the maximum number of unwanted harmonic overtones in θ) but in practice we found it necessary to

*This work was supported by the Director, Office of Energy Research, Office of Fusion Energy, U.S. Department of Energy, under Contract No. DE-AC03-76SF00098

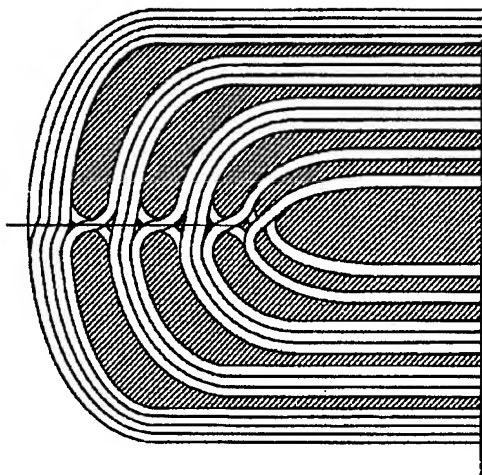


Figure 1. Artist's depiction of the projected coil turn geometry of the quadrupole magnet prototype.

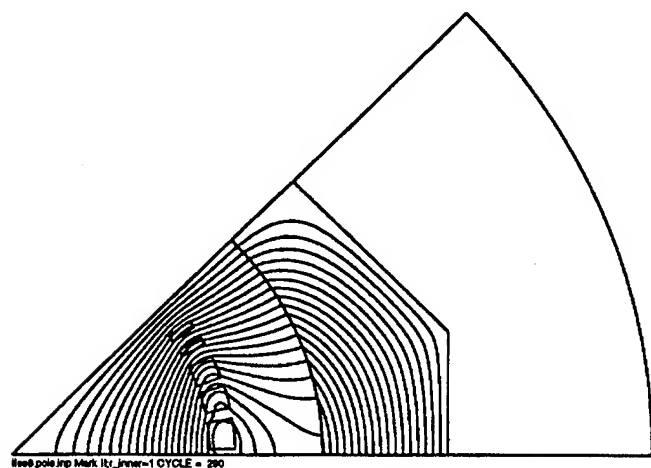


Figure 2. 2D POISSON results showing the field line topology in the $r - \theta$ plane of an octant of the quadrupole magnet plus iron yoke. The midplane field gradient at $r = 0$ was 26.5 T/m. The peak field in the iron yoke is 1.5 T/m.

distribute the 12 turns in each layer into 5 individual "blocks" in a 4-3-3-1-1 pattern (see Fig. 1) to obtain sufficient spacing for the cutting tool in θ between adjoining blocks (and adjacent quadrants).

From "engineering" constraints (see §IIB and IIC discussion), the iron yokes of adjoining magnets must be separated approximately 13 cm in z . We have also specified that each end of the yoke should extend approximately one wire radius (8.5 cm) in z beyond the outermost coil wire in order to confine the fringe fields in z . Hence, the maximum z -length of each coil is thus ≈ 30 cm for $l = 60$ cm. Setting the z -extent (2.0 cm) of the curve of each coil block end, the z -separation (1.0 cm) between adjoining blocks, and the wire diameter (0.32 cm for our particular braided copper choice), the total z length of each block and its individual wires is fully determined. The azimuthal positions of each block are then found numerically by forcing the z -integrated harmonic overtones to zero (see ref. [3] for details).

In our previous prototype which had been constructed primar-

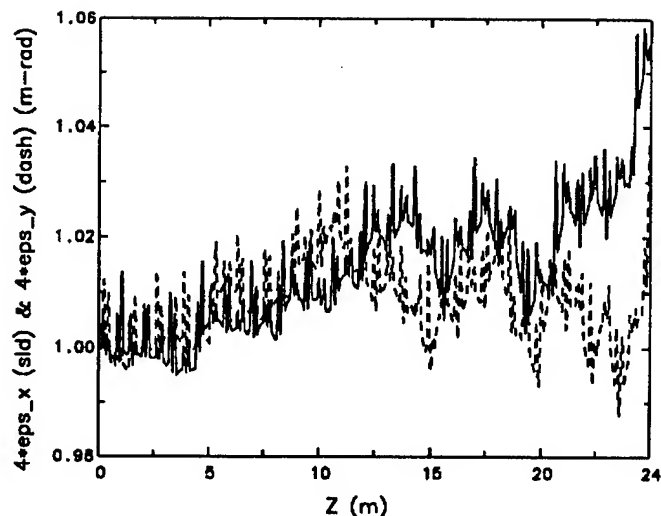


Figure 3. HIFI simulation code results for emittance growth, normalized to the initial value of $\varepsilon_N = 5\pi$ mm-mrad, over 24 m of magnetic transport of a $1.5 \mu\text{C/m K}^{+1}$ beam at $\sigma_o = 72^\circ$ and $\sigma = 7^\circ$. The solid curve refers to the $x - x'$ plane and the dashed curve to the $y - y'$ plane.

ily to investigate thermal heat dissipation, we had not paid careful attention to either the geometry of the wire crossovers from one block to another (which caused net dipole current loops) nor the presence of a solenoidal loop caused by the azimuthal advance of the wire leads leaving one quadrant and entering another. In our current design, we have carefully created "X"-shaped crossovers (see Fig. 1) when projected on the $\theta - z$ plane whose net dipole area is less than 0.5 cm^2 for each layer of each quadrant. We have also returned the exiting wire lead of the fourth quadrant back the "long way" azimuthally to the first quadrant in order to eliminate the solenoidal loop problem. Hence, we expect a much higher quality magnetic field when we make detailed measurements of this magnet over the next year.

We have done a series of POISSON and TOSCA calculations to examine the effects of the iron yoke upon the magnetic field. The 2D POISSON runs (Fig. 2 shows the output from one example) suggest that at field gradients ≤ 26.5 T/m the maximum B-field strength in the yoke remains below 1.5 T and saturation effects are minimal. We are particularly concerned with saturation (which will be due to the dominant quadrupole component) destroying the z -integrated cancellation of higher harmonics (in particular the dodecapole) within each half-lattice period. The 3D TOSCA runs indicate that field gradients of up to 28.6 T/m at the magnet center in z are possible with minimal field leakage (≤ 10 G) radially outside the iron yoke. When the 95% packing fraction of the iron laminations is included in the TOSCA runs, field gradients of up to 26 T/m appear to be safe. Both codes show that the yoke enhances the interior quadrupole field gradient by approximately 20%. The effective length of the quadrupole component is 0.24 m; without enhancement from the iron yoke, a field gradient of 19.5 T/m (corresponding to 4.2 kA wire current) is required for $\sigma_o = 72^\circ$ at 5 MV.

B. Iron Yoke Design

The iron yoke enclosing the current windings and the beam pipe serves a number of purposes. First, it minimizes magnetic fringe fields from extending greatly in z or r and interfering either with the beam transport or the induction core material (and vice versa). It also mechanically confines the windings and prevents their expansion and distortion under the magnetic stresses. Finally, it also provides a fiducial for mechanical alignment and adjustment.

In designing the yoke, the two major requirements were first to make sure that we had a sufficient amount of iron at a great enough distance from the conductors such that the iron will not saturate during pulsed operation, thus adversely affecting the quality of the magnetic field, and secondly to minimize the effective outer diameter of the yoke once the inner diameter had been fixed due to the magnetic saturation concerns.

Minimizing the effective outer diameter of the yoke reduces the weight, making support and articulation easier, but, more importantly, it also reduces the inner diameter of the induction cores which surround the magnet. The annular shaped induction cores have a fixed, required cross sectional area. Hence, choosing a larger I.D. for the cores leads to greater volume and cost. In order to minimize the effective diameter in our second prototype, we changed the material of the yoke to low carbon steel which has a higher saturation induction of 2.08 T as compared to 1.96 T for the 3% silicon steel used in a prototype previously constructed. We also changed the originally square cross section of the yoke to an irregular octagon by cutting off the "corners" of the square yoke and checking for saturation effects with the POISSON code. We chose an inner yoke radius of 12.13 cm which is large enough to allow the magnetic fields to fall off by more than a factor of two from their values at the current windings but not so large as to increase magnetic core costs significantly. Taken together, these modifications reduced the effective outer yoke radius by 3 cm which translates into a projected savings of $\approx 250\text{K\$}$ on the magnetic quadrupole focusing section for ILSE.

C. Mechanical Design Details

In order that the magnets be powered, have their heat dissipated safely, and the beam actually be accelerated, a number of elements must be placed between adjoining magnets. In particular, electrical insulators made of 98% alumina with field grading rings are necessary to prevent electrical breakdown in the accelerating fields produced by the induction cores. These insulators occupy $\approx 80\%$ of the required intermagnet gap. The gap also includes O-ringed flanges and bellows to support the insulators and magnets, water pipes for the required magnet cooling water ($\sim 3\text{ GPM}$), and insulated electrical leads (10 kV required for 5.4 kA current). Fortunately, many of the components can be made re-entrant with the iron yoke to reduce the required intermagnet separation.

III. PARTICLE SIMULATION CODE STUDIES

We have used the 2D particle simulation code "HIFI" [3] to model the transport dynamics of a $1.5\text{ }\mu\text{C/m}$ space-charge dominated 5-MV, K^{+1} beam through 24 m of magnetic trans-

port without acceleration gaps. The magnetic fields, comprised of the quadrupole, dodecapole, pseudo-octupole, and pseudo-dodecapole components, were taken from a 3D field solution which does not include the effects of the iron yoke. The peak field gradient at the center of each magnet was set to 19.5 T/m giving an undepressed phase advance σ_0 of 72 degrees per lattice period. The normalized edge emittance of the beam was set to $5\pi\text{ mm-mrad}$ which gave to a space-charge depressed tune σ of approximately 7 degrees. The beam was initialized with a KV distribution in transverse phase space which led to a maximum beam envelope extent of 69 mm as compared with a presumed beam pipe radius of 75 mm. Over the 20 lattice periods, no simulation particles were lost and the emittance growth was of order 5% or less. Consequently, we are confident that if the magnet performs according to design it will be able to transport the specified beam line charge without serious degradation.

References

- [1] Laslett, L.J., Caspi, S., and Helm, M., *Particle Accel.*, **22**, 1 (1987).
- [2] Fawley, W.M., Laslett, L.J., Celata, C.M., Faltens, A., and Haber, I., "Simulation Studies of Space-Charge-Dominated Beam Transport in Large Aperture Ratio Quadrupoles", *Proceedings of the 1993 IEEE Particle Accelerator Conference*, **93CH3279-7**, 724 (1993).
- [3] Fawley, W.M., "Space-dominated Beam Transport in Magnetic Quadrupoles with Large Aperture Ratios", **LBL-33608**, 1993.

A PERMANENT RACE-TRACK MICROTRON END MAGNET

A.I. Karev, P.N. Lebedev Physical Institute, Leninsky Pr. 53, Moscow 117924, Russia

V.N. Melekhin, P.L. Kapitza Institute for Physical Problems, Russia

V.I. Shvedunov, Moscow State University. Institute of Nuclear Physics, Russia

N.P. Sobenin, Moscow Engineering Physics Institute, Russia

W.P. Trower, Physics\Virginia Tech, Blacksburg VA 24061 USA

We present a design for a Rare-Earth Permanent Magnet end dipole magnet for our 70 MeV mobile Race-Track Microtron. We review the properties of these magnetic materials, describe the optimal magnetic circuit configuration and our choice of magnet parameters, and propose a method to form and tune the magnetic fringe field.

I. INTRODUCTION

A new class of rare-earth magnetic materials have opened a new chapter in permanent magnet technology. To date Rare-Earth Permanent Magnet accelerator applications have been confined to small aperture quadrupoles, ring dipoles, and undulators [1,2]. Encouraged, we have designed an electron recirculator dipole magnet for our 70 MeV mobile Race-Track Microtron [1].

Three rare-earth transition metal magnets are produced commercially, all of which have extremely large coercivity and maximum energy product $(BH)^{\max}$ as seen in Table I. The \mathbf{B} vs. \mathbf{H} hysteresis diagram of these materials shows that \mathbf{B} - \mathbf{H} coordinates are nearly linear in the second quadrant, $(BH)^{\max}$ lying at the center and the return path following the hysteresis profile. Thus, a REPM is demagnetized neither by external fields nor by disassembly/assembly, a useful practical property. REPM anisotropy is described by

$$\mathbf{B}_{\parallel} = \mathbf{B}_r + \mu_0 \mu_{\parallel} \mathbf{H}_{\parallel}$$

and

$$\mathbf{B}_{\perp} = \mu_0 \mu_{\perp} \mathbf{H}_{\perp},$$

where the directional indices are with respect to the preferred field orientation, the so-called ease axis. Since μ_{\parallel} and μ_{\perp} are unity a REPM does not concentrate external magnetic flux in its body.

Table I.
Some REPM material parameters.

	H_c (kOe)	$(BH)^{\max}$ (MGOe)
SmCo ₅	7.8 - 9.0	20 - 22
Sm ₂ Co ₁₇	8.2 - 10.0	25 - 27
Nd ₂ Fe ₁₄ B	9.2 - 11.4	35 - 40

II. MAGNETIC CIRCUIT CONFIGURATION

The three principal bending magnet magnetic circuits depend on the REPM placement as seen in Fig. 1. In the first, the REPM flux is transported to the gap by a steel yoke and pole ferrules. In the second, the REPMs are placed in center of the yoke, while in the third case the REPMs are placed adjacent to the gap. The magnetic flux in the gap, Φ_g , depends on the REPM location, no isolators being in the magnetic circuit, and the accompanying parasitic fringe flux. Therefore, the total REPM flux, Φ_t , is the sum of the useful flux, Φ_g , and the parasitic flux which is approximately the sum of the flux between the a magnetic circuit elements, Φ_a , between the b elements, Φ_b , and between the ends of element c , Φ_c . A REPM usage quality is defined by its disperse coefficient,

$$\sigma = \Phi_t / \Phi_g = 1 + (\Phi_a + \Phi_b + \Phi_c) / \Phi_g.$$

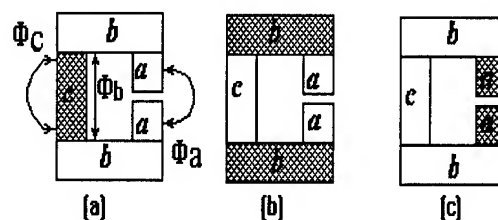


Fig. 1. Bending magnet configurations.

The flux coupling the magnetic circuit elements is proportional to the magnetic potential difference between these elements. For configuration [a] these differences are largest for elements a - a and b - b , so Φ_a and Φ_b are large. For configuration [c] the magnetic potential difference between elements a - a and b - b is zero, and so the REPM is better used here than in configuration [a] as only one the parasitic flux, Φ_a , is present in contrast to three - Φ_a , Φ_b , and Φ_c in [c]. Intermediate is configuration [b]. The calculated relative gap induction ratio, $[a]/[b]/[c]$, is 0.45/0.75/1.0. Thus, the optimum circuit configuration for our RTM end bending magnets is approximated by configuration [c].

III. OPTIMAL MAGNET PARAMETERS

The magnet working point is usually near $(BH)^{\max}$ so the total REPM thickness, h , of C-type magnet pole pieces is approximately equal to the gap height, g , which produces a gap magnetic field, B_g , of $\mu_0 H_c/2 \sim 0.5$ T, obtainable with minimal REPMs quantity. However, for our RTM bending magnets this result may be not optimal since B_g may require that the magnet dimensions and weight be as small as possible.

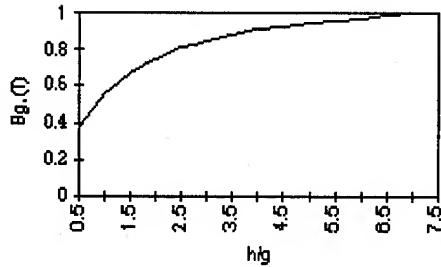


Fig. 2. B_g dependence on the REPM thickness-gap height ratio, h/g for $H_c = 10.8$ kOe and $(BH)^{\max} = 31.3$ MGOe.

Our simulated [3] RTM magnet gap field dependence on the total REPM thickness is shown in Fig. 2. The REPM volume is hA_p , where A_p is pole face area is defined by the radius of last microtron orbit, $\sim 1/B_g$. Thus, the $V(B_g)/V_0$ dependence on h/g , where V_0 is the REPM volume with $h = g$ can be calculated. Fixing the RTM output energy, the magnetic induction in the steel magnet parts, and $B_g = B_0$, if B_g is decreased then pole dimensions and the magnetic flux are increased by $1/B_g$ and end magnet weight also increases.

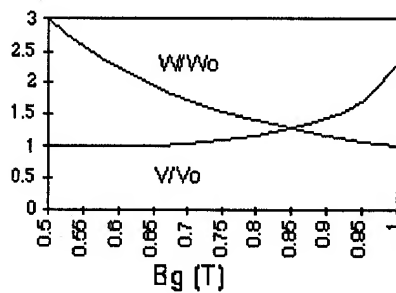


Fig. 3. Magnet weight and REPM volume dependence on B_g .

The REPM volume and end magnet weight dependence on B_g are shown in Fig. 3, where W_0 is weight of a magnet with $B_g = 1$ T. The choice of B_g is a compromise which defines the total magnet cost. A small RTM, energy 10-20 MeV, will be relatively light and cheap with an optimal B_g of 0.6-0.8 T. A 50-100 MeV RTM acceptable gap field

requires larger and heavier magnets. If B_g is increased the energy gain per turn will increase proportionally, while if B_g is decreased more RTM orbits will be required for the same output energy, thus complicating beam focusing and increasing the linac current load. So for our mobile 70 MeV RTM [4] we chose $B_g = 0.9$ T requiring a REPM volume of ~ 0.0145 m³, gap height of 20 mm, and pole face area of 60×32 cm².

IV. MAGNET FRINGE FIELD SHAPE

The RTM bending magnet fringe field is strongly defocusing requiring a special reverse direction fringe magnetic field to obtain stable vertical oscillations [5]. This in turn reduces the orbit diameter requiring a complicated reverse direction acceleration system to allow the beam to clear the linac. After the first linac passage the end magnet fringe field focuses the beam. Thus, the beam optics and trajectory geometry must be solved simultaneously requiring an appropriate fringe field configuration in the design stage and a careful accelerator tuning procedure in the operational stage. The effective orbit diameter depends on the distance between the main bending field region and the reverse direction field which in conventional RTM bending magnets is formed by adding steel poles and coils located a considerable distance from the main poles to avoid unacceptably distorting total fringe field.

We use the anisotropic REPM properties to construct a fringe field with reversed magnetization direction. Since each REPM element is magnetically independent an additional REPM element may be placed close to the main REPM segment thus reducing the reverse-main field distance while increasing the first orbit diameter. By using a narrow axially asymmetry linac [6] we obviate our original complicated first orbit loop geometry. Moreover, using REPMs decouples the problem of stable transverse motion from that of trajectory geometry allowing an optically better fringe field configuration to be found. Thus, our REPMs simplify accelerator tuning while improving the beam parameters.

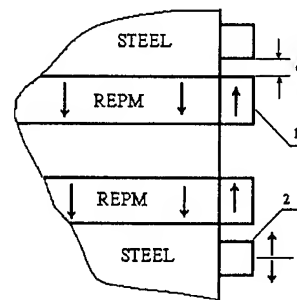


Fig. 4. Magnetic circuit end configuration: 1 - added REPM units and 2 - movable steel elements.

The additional reverse magnetization REPM elements, shown in Fig. 4, define the fringe magnetic field distribution. By varying the geometry of these elements we found a fringe field shape which allows the first orbit diameter in our mobile 70 MeV RTM to increase to 40 mm and still have sufficient focusing power. To shape the fringe field we place simple movable steel elements near the magnet end. These elements change the air gap dimensions, δ , and, thus, magnetic circuit parameters and the reverse field amplitude. An increase in δ from zero to 5 mm decreases the reverse field amplitude by 15%.

V. CONCLUSIONS

The large REPM magnetization energy and anisotropic properties allow us to obtain magnetic gap induction with which to shape better fringe fields than we achieved with conventional electromagnets. Furthermore, a RTM with REPM bending end magnets no longer requires magnet coils, (other than small correcting coils), their power supplies and cooling equipment. This results in reduced total accelerator power consumption, simplified construction and servicing, a streamlined control system, enhanced overall operational reliability, and reduced space requirements. Important additional advantages accrue to mobile RTMs, for example, serving as a light source to detect explosives in buried military munitions and land mines [7].

We express our appreciation to Klaus Halbach for pioneering REPM accelerator applications and for his generous help in initiating us to this field, and to V.S. Skachkov for general discussion of REPM implementation.

REFERENCES

- [1].K. Halbach, *J. Appl. Phys.* vol. 57, p. 3605 1985.
- [2].K. Halbach, LBL-8811-1 (1989).
- [3].J.L. Warren, M.T. Menzel, G. Boicourt, H. Stokes, and R.K. Cooper, LANL-LA-UR-87-126 (1987).
- [4].V.I. Shvedunov, A.I. Karev, V.N. Melekhin, N.P. Sobenin, and W.P. Trower, Improved Mobile 70 MeV Race-Track Microtron Design, in these Proceedings.
- [5].H. Babic and M. Sedlacek, *Nucl. Instr. and Meth.* vol. 56, p.170 1967.
- [6].N.P. Sobenin, V.N. Kandurin, A.I. Karev, V.N. Melekhin, V.I. Shvedunov and W.P. Trower, Rectangular Microtron Accelerating Structure, in these Proceedings.
- [7].W.P. Trower, *Nucl. Instr. and Meth.* vol. B79, p.589 1993.

Planar Permanent Magnet Multipoles: Measurements and Configurations*

T. Cremer, R. Tatchyn
Stanford Linear Accelerator Center, Stanford, CA 94305, USA

Abstract

Biplanar arrays of N rectangular permanent magnet (PM) blocks can be used to generate high quality N -pole fields in close proximity to the array axis. In applications featuring small-diameter charged particle beams, N -poles of adequate quality can be realized at relatively low cost using small volumes of PM material. In this paper we report on recent measurements performed on planar PM multipoles, and discuss techniques for improving the field quality of such devices at distances appreciably far away from the axis. Applications to hybrid/PM insertion device designs for linac-driven Free Electron Laser (FEL) operation in the x-ray range are described.

I. INTRODUCTION

In recent years, the development of a novel class of PM multipole (N -pole) field generators has been initiated [1,2]. The basic construction principle, illustrated in Fig. 1, is to arrange N rectangular PM pieces, magnetized with the easy axis perpendicular to two opposed faces, into a biplanar array with $N/2$ pieces per plane. In general, while the pieces in each quadrant of the x - y plane can have arbitrary dimensions, x -placements, and magnetizations, the overall structural and field geometries possess symmetry with respect to the y - z and x - z planes, and the normal convention is to have each of the two sets of magnet surfaces closest to the x - z plane be coplanar. If we postulate an ideal N -pole generator to be a structure with N -fold rotational symmetry [3], the essential concept of planar PM multipoles is seen to be based on the reduction from N -fold to 2-fold rotational symmetry. This reduction, while allowing the design and fabrication of N -poles with fully open horizontal apertures and configurations of utmost economy and simplicity, incurs the penalty that the field away from the axis develops a much higher multipole content than an "ideal" structure with N -fold ($N > 2$) rotational symmetry. In the following sections, selected theoretical and experimental aspects of planar PM multipole field distributions are reviewed and possible applications to FEL insertion device design are considered.

II. PLANAR PM MULTIPOLE FIELDS

The entire class of planar PM multipoles can be grouped into two families: 1) $N=4n$; and 2) $N=4n-2$; where $n \in \{1, 2, \dots\}$.

* Supported in part by DOE Offices of Basic Energy Sciences and High Energy and Nuclear Physics and Department of Energy Contract DE-AC03-76SF0015.

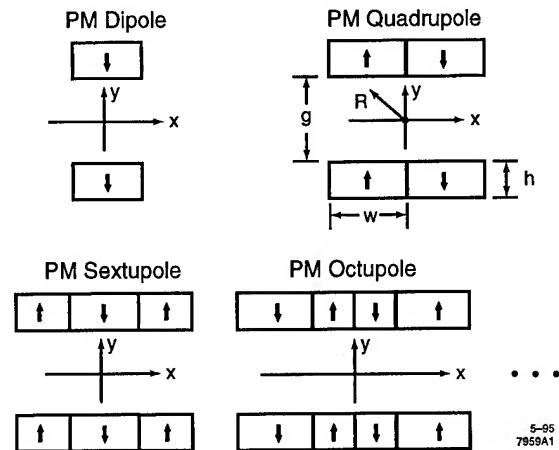


Figure 1. Planar PM multipoles composed of pieces of equal height (h), with no lateral spacing between pieces. Symmetry axis (z axis), along which all the PM pieces have equal length L , is perpendicular to the page.

Thus, the first family includes the quadrupole (quad), octupole, dodecapole, etc., and the second family includes the dipole, sextupole, decapole, etc. For each family, the corresponding magnetic scalar potential (for $L \gg g$) in the vicinity of the symmetry axis can be approximated by a real Taylor series expansion as follows:

$$\phi_{4n} \equiv C_{11}xy + E_{13}(xy^3 - x^3y) + G_{15}(3xy^5 - 10x^3y^3 + 3x^5y) + \dots; \quad (1)$$

and

$$\phi_{4n-2} \equiv B_{01}y + D_{21}(3x^2y - y^3) + F_{41}(5x^4y - 10x^2y^3 + y^5) + \dots; \quad (2)$$

where the subscripted capital coefficients are functions of the PM parameters. To configure a given N -pole, the dimensions, spacings, and magnetizations of the N pieces must be designed to eliminate all the multipole coefficients lower than the desired leading N -pole coefficient. As formulas (1) and (2) explicitly indicate, the field of each such N -pole will not only exhibit its leading N -pole coefficient, but will also contain an infinitude of higher-pole terms with strengths proportional to increasing integral powers of distance (R) from the z axis.

To illustrate, the configuration of a planar PM sextupole (leading coefficient D_{21}) demands the establishment of $B_{01}=0$, which in general can be used to help determine the relative dimensions and/or magnetizations of the PM pieces [2]. To illustrate an example of the higher multipole content associated with a general N -pole, a measured rotating-coil spectrum [4] of a SmCo quadrupole (see Fig. 1, top right) is shown in Fig. 2. The measured peaks agree to better than 0.5% with the corresponding amplitudes calculated with a computer code

PLANAR PM (SmCo) QUADRUPOLE SPECTRUM

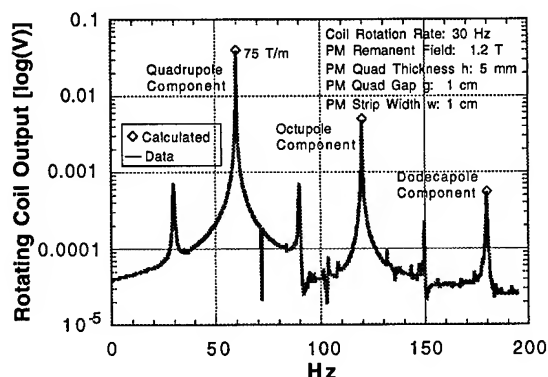


Figure 2. Rotating-coil planar PM quadrupole spectrum. Coil parameters: 50 turns; dimensions 1 cm x 2 mm. The peaks at odd multiples of 30 Hz stem from coil axis misalignments.

written to simulate both the planar multipole fields and the rotating coil apparatus.

III. APPROACHES TO PLANAR MULTIPOLE FIELD QUALITY IMPROVEMENT

Theoretically, it is well known that N-fold rotationally symmetric multipoles generating a single N-pole field component can be closely approximated. This is accomplished by shaping the (equipotential) pole surfaces to make the variable coefficient in the desired N-polar potential term equal to a constant along the pole contour. In general, this implies that the elimination of all but the N-polar term requires pole contours of infinite extent. With infinite contours, for example, the ideal quadrupole and sextupole potentials would be given, respectively, by $\phi_4 = C_{11}xy$ and $\phi_6 = D_{21}(3x^2y - y^3)$. In practice, of course, all pole contours must be finite, which results in a non-vanishing set of higher-pole field components in practical structures. Notwithstanding this, in a well-designed 4-fold rotationally symmetric quad the total field energy in the higher-pole field components can be made typically less than 10^{-6} of that in the leading component in regions proximate to the symmetry axis [5].

By contrast, the freedom of adjusting the parameters of planar PM multipoles to attain a comparable degree of field purity is seen to be severely limited. Specifically, the shapes of the PM pieces (all rectangular cross sections) cannot be modified, forcing all equipotential surfaces to be planar. Secondly, confinement to a plane prevents the rotation of the pieces as a means of approximating to a curved 2-dimensional equipotential contour. Under these constraints, the principal means of improving the field quality has to be associated with the adjustable degrees of freedom of the planar PM multipole, namely, the number, dimensions, x-placements, and magnetizations of the PM pieces. Approaching the problem from this perspective, eq's. (1) and (2) immediately suggest a systematic way of enhancing the field quality of a planar PM

N-pole; namely, by the successive removal of its higher-pole field components.

The basic principle behind this approach is illustrated in Fig. 3. For an optimized planar PM quad with the field spectrum shown on the top left side, the octupole component can be nulled by centering a planar PM octupole whose leading field component, O_Q , is equal and opposite to the quad's octupole component, O_Q , over the symmetry axis of the quad. We note that since the potential is given by the same canonical form for each structure (viz., by eq. (1)), making $O_Q = -O_Q$ will null the octupole component (E_{13} in our notation) for all values of R. Due to the operative principle of linear superposition, all the higher-pole components of the PM octupole will also tend to subtract from the corresponding higher-pole components of the quad.

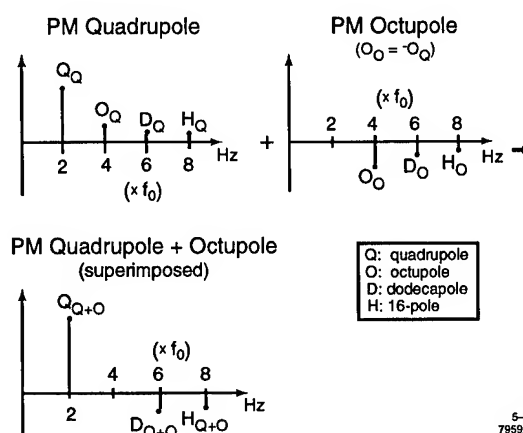


Figure 3. Linear superposition of planar PM octupole and quadrupole rotating-coil spectra as a means of nulling the octupole component in the combined structure. f_0 is the coil rotation frequency.

This procedure can be, of course, repeated to eliminate the next higher (dodecapole) component of the combined

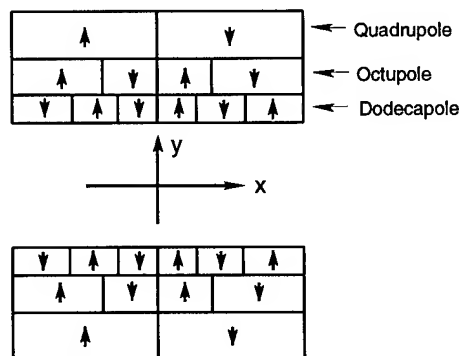


Figure 4. Planar PM quadrupole structure with nulled octupole and dodecapole field components.

quad+octupole structure (see Fig. 4). Further repetition can be used to successively remove as many of the higher multipole

components as desired. Clearly, the extirpated field components do not have to be adjacent to any other nulled component, but can be arbitrarily located. Consequently, the same method can be used to purify the field of any planar PM N-pole. Of course, practical considerations will limit the number of field components that can be nulled in this fashion, but the important result is that even with the planar PM N-pole's reduced symmetry, it is theoretically possible to make its field approximate - as closely as desired - that of an ideal (N-fold rotationally symmetric) structure. It is easy to show that if an individual PM multipole is used for each cancellation, the total number of PM pieces required for a quad with m successively nulled next-higher components would be $4+6m+2m^2$, and the corresponding number of pieces for a sextupole would be $6+8m+2m^2$.

IV. APPLICATIONS TO X-RAY FEL DESIGN

The original proposal for using planar PM quadrupoles was for applications in which the electron beam was small enough, and close enough to the axis, to make the higher-pole components negligible with respect to the leading field component [1]. Here we demonstrate calculated trajectories through a planar PM FODO lattice (Fig. 5) that support the soundness of this proposal. The computer code, developed originally for FEL simulations [6], employs a rigorously realistic model of fields generated by assemblies of PM pieces (i.e., the field experienced by the particles is everywhere divergence and curl free). The general parameters, typical of those that might be used for a 1.5 Å FEL [7], are: electron energy 12 GeV; electron emittance 4.2×10^{-11} r-m; FODO lattice period 40 cm; PM quad gap 3 mm; PM quad length 10 cm; PM piece remanent field 1.2 T; PM piece height 3.5 mm; PM piece width 1 cm; and FODO lattice betatron wavelength 8 m. For longer FEL structures the quad parameters (e.g., gap size) could be substantially relaxed. With the developments outlined above, field-improved planar PM elements can now

also be considered for use in much lower-energy FELs with substantially smaller emittances (i.e., bigger beams).

V. SUMMARY

More general discussions of the properties and various other applications of planar PM N-poles can be found in the cited prior literature. For FEL applications, rigorous modeling has been found to support the effectiveness of using planar PM N-poles. Application of the field-improvement techniques outlined above should enable improved planar PM N-poles (in particular the quad and sextupole) to find a broader range of applications than heretofore proposed. To this end, methods for further minimizing the number of PM pieces required for PM multipole field improvement are being investigated.

VI. ACKNOWLEDGMENTS

The authors would like to thank David Jensen and Zack Wolf of SLAC's Magnetic Measurements Laboratory for their invaluable assistance with the rotating-coil measurements.

VII. REFERENCES

- [1] R. Tatchyn, "Selected applications of planar permanent magnet multipoles in FEL insertion device design," Nucl. Instrum. Meth. A341, 449(1994).
- [2] R. Tatchyn, "Planar Permanent Magnet Multipoles for Particle Accelerator and Storage Ring Applications," IEEE Trans. Mag. 30(6), 5050(1994).
- [3] K. Halbach, "Design of Permanent Multipole Magnets with Oriented Rare Earth Cobalt Materials," Nucl. Instrum. Meth. 169, 1(1980).
- [4] J. Cobb and R. Tatchyn, "Tests of planar permanent magnet multipole focusing elements," Nucl. Instrum. Meth. A347, 562(1994).
- [5] D. C. Carey, "The Optics of Charged Particle Beams," Harwood, New York, 1987.
- [6] R. Tatchyn, T. Cremer, and P. Csonka, "Design considerations for a new weak-field soft x-ray undulator/FEL driver for PEP," Nucl. Instrum. Meth. A308, 152(1991).
- [7] R. Tatchyn, K. Bane, R. Boyce, G. Loew, R. Miller, H.-D. Nuhn, D. Palmer, J. Paterson, T. Raubenheimer, J. Seeman, H. Winick, D. Yermian, C. Pellegrini, J. Rosenzweig, G. Travish, D. Prosnitz, E. T. Scharlemann, S. Caspi, W. Fawley, K. Halbach, K.-J. Kim, R. Schlueter, M. Xie, R. Bonifacio, L. De Salvo, P. Pierini, "Prospects for High Power Linac Coherent Light Source Development in the 100nm-0.1nm Wavelength Range," presented at the 4th International X-Ray Laser Colloquium, Williamsburg, VA, May 16-20, 1994.

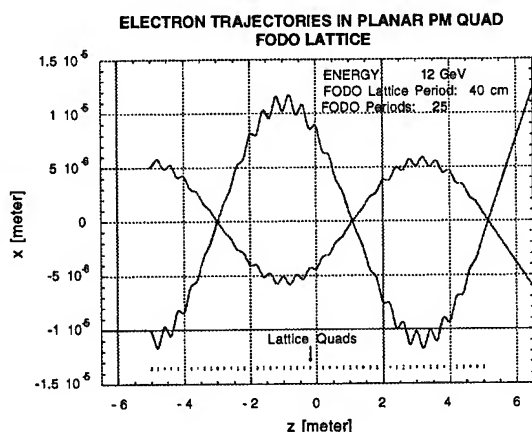


Figure 5. Electron trajectories for electrons entering FODO lattice (from the left) at 5μ and -10μ off axis in the x-z plane.

TEMPERATURE CONSIDERATIONS IN THE DESIGN OF A PERMANENT MAGNET STORAGE RING

K. Bertsche, J.-F. Ostiguy and W.B. Foster
Fermi National Accelerator Laboratory *, P.O. Box 500, Batavia, IL 60510

Abstract

To improve the luminosity of the Fermilab Tevatron proton-antiproton collider in the post Main-Injector era, the most straightforward approach is to increase the intensity of the antiproton beam. A number of schemes based on fixed energy storage rings have been suggested to accomplish this goal. A fixed energy ring can be used to accumulate freshly produced antiprotons and/or to recycle used antiprotons at the end a store. For reasons of cost and reliability, permanent magnets are strong contenders for the magnet assemblies, with ceramic ferrite the material of choice. Since ferrite magnetization has a relatively large temperature coefficient, temperature considerations are very important. In this paper, we investigate the expected temperature environment for a fixed energy ring at Fermilab, the required temperature stability and possible methods of compensating temperature dependent effects.

Introduction

To improve the antiproton intensity available in the Fermilab collider, a fixed energy storage ring is under serious consideration. Such a ring would be housed in the newly constructed main injector tunnel and would be used to accumulate freshly produced antiprotons and/or to recycle used antiprotons at the end of a store. The most attractive option appears to be a ring whose main bending magnets are low field (< 5 kG) based on permanent magnet technology. The modest field makes practical the utilization of inexpensive ferrite ceramic – of the same type used in large quantities by the automotive industry – rather than the considerably more costly rare earth samarium-cobalt or neodymium-boron magnets. At this point, a lattice based on combined function magnets of the hybrid “box” design [1] appears to be among the most interesting possibilities. Details are given in another paper presented at this conference [2]. Although ferrite is inexpensive the rather large dependence of its magnetization to temperature variations is a major source of concern.

Temperature Effects

Four classes of materials account for virtually all permanent magnets in use today.

- Alnico
- Hard Ferrites: $\text{BaO} \cdot 6\text{Fe}_2\text{O}_3$, $\text{SrO} \cdot 6\text{Fe}_2\text{O}_3$
- Rare Earth Cobalt (REC): SmCo_5 , $\text{Sm}_2\text{Co}_{17}$
- Neodymium-iron-Boron (NEO): $\text{Nd}_2\text{Fe}_{14}\text{B}$

Some relevant properties of these materials are summarized in Table 1. The bulk magnetization of a permanent magnet is the result of the collective alignment of the atomic spins via the quantum

	Alnico	Ferrite	REC		NEO
Composition	Fe-alloy	$\text{SrO} \cdot 6\text{Fe}_2\text{O}_3$	SmCo_5	$\text{Sm}_2\text{Co}_{17}$	$\text{Nd}_2\text{Fe}_{14}\text{B}$
B_r	1.3	0.4	0.9	0.9	1.1
$d \log(B_r)/dT$	-0.02	-0.2	-0.06	-0.04	-0.12
H_c	150	320	2400	2000	1400
Curie T	800	450	750	800	300
Density (g/cm ³)	7.2	5.0	8.2	8.4	7.4
Cost (rel)	10	1	80	80	70

Table I
Magnetic material properties.

exchange interaction. As temperature increases, thermal fluctuations induce more and more random variations in individual atomic spin orientations. Eventually, a phase transition occurs: all the spins are randomly oriented and the bulk magnetization abruptly disappears. The transition temperature is known as the Curie temperature, T_C and can be considered as a measure of the magnitude of the exchange forces. For a simple element like Fe, the temperature dependence of the magnetization is well predicted by the classical Brillouin function. For ferrites and other alloys, the situation is much more complex and depends on the determination of specific forms of orbital overlap for three dimensional arrays of atoms of different types. Nevertheless, one still expects the magnetization to be a roughly decreasing exponential function of the ratio (T/T_C), so that $d \log M/dT$ is approximately constant over a wide temperature range. The maximum sensitivity obviously occurs when $T/T_C \simeq 1$. Referring to Table 1, one can indeed see that materials with similar Curie temperatures have similar temperature coefficients. Furthermore, ferrite and neodymium-boron have the lowest T_C and the highest temperature coefficients, as expected.

Temperature Environment

The temperature environment in an accelerator is composed of two distinct components:

- variations of the average temperature
- random temperature variations at different locations around the ring

Average temperature variations correspond to variations in the reference energy of the ring. Since no external adjustment is possible, a permanent magnet ring would have to be accommodated by other rings in the complex. Seasonal variations in temperature can be quite large in the Main Injector tunnel, on the order of 20 C between summer and winter. For ferrite magnets, this corresponds to a 4 % variation in ring energy.

More serious is the problem of random temperature fluctuations around the ring. These fluctuations have a time scale of hours. Typically, magnet to magnet variations in relative integrated strength larger than 0.001 must be corrected. To the extent that both dipole and quadrupole elements would be based on permanent magnet technology, correction would be required for both functions. Measurements made over a period of a month

*Operated by the Universities Research Association, Inc., under contract with the U.S. Department of Energy.

in the Main Ring tunnel indicate that rms temperature fluctuations on the order of 1 C around the ring can be expected. For ferrite magnet structures this results in dipole and quadrupole relative integrated strength fluctuations on the order of 0.002.

Compensation Schemes

Because of these expected temperature variations, a reduction of the temperature sensitivity by an order of magnitude or more is needed. An obvious possibility would be to utilize a permanent magnet material with a higher Curie temperature. REC and Neodymium-Boron are prohibitively expensive. The cost of Al-nico may seem more reasonable but the active magnet volume needed to prevent the demagnetizing field from overcoming the coercivity would result in substantially larger overall dimensions.

Active correction of magnetic field, by adding windings to the permanent magnets or adding small outboard electromagnetic trim dipoles was discussed. This option was rejected because it would eliminate the possibility of keeping antiprotons in the ring during a short power outage without the added complexity of non interruptible power supplies. Quasi passive temperature control, by circulating water through the magnet structures and/or by coupling magnets through heat pipes was quickly dismissed because of added cost, complexity and potentially reduced reliability.

The scheme which we propose is purely passive. The field of each magnet structure is stabilized using one or more temperature sensitive flux shunts. These shunts are composed of alloys having permeability with high temperature coefficient. Binary alloys of Ni-Fe and Ni-Cu have been used for this purpose [3]. The alloy is placed in the magnet structure in such a position that it shunts some of the flux which would ordinarily appear across the magnet gap. As temperature increases, the ferrite supplies less flux to the magnet poles, but the flux shunt also shunts less flux. If the flux shunt has a higher temperature coefficient than that of the ferrite, it may be sized in such a way that the field in the gap is independent of temperature. A similar technique is routinely used in small structures, such as watt-hour meters and automobile speedometers. As far as we know, it has never been used for large scale accelerator magnets.

Temperature compensation alloys such as Fe-Ni have a Curie temperature close to the ambient temperature. Basically, the Curie temperature and the saturation magnetization of the Fe-Ni system change rapidly when the Ni fraction reaches 30%, due to a change in crystal structure. At the phase boundary, both T_C and the saturation magnetization vanish. By carefully controlling the composition and heat treatment of the material, the Curie temperature can be adjusted to be slightly above the ambient temperature, resulting in high temperature sensitivity of the saturation magnetization. By adjusting the thickness of a thin strip of compensating alloy, it is then possible to compensate the weaker temperature dependence of a larger volume of ferrite material.

A possible configuration for a box dipole magnet is shown in Figure 1. A strip of alloy is placed in the center of the magnet, between two ferrite blocks, in order to suppress odd multipoles. Fe-Ni has a temperature coefficient $d \log B_r / dT \simeq 2\%/C$. This is about an order magnitude higher than ferrite, so approximately 10% of the flux must be shunted. It should be noted that the temperature coefficient of compensating alloys generally depends on

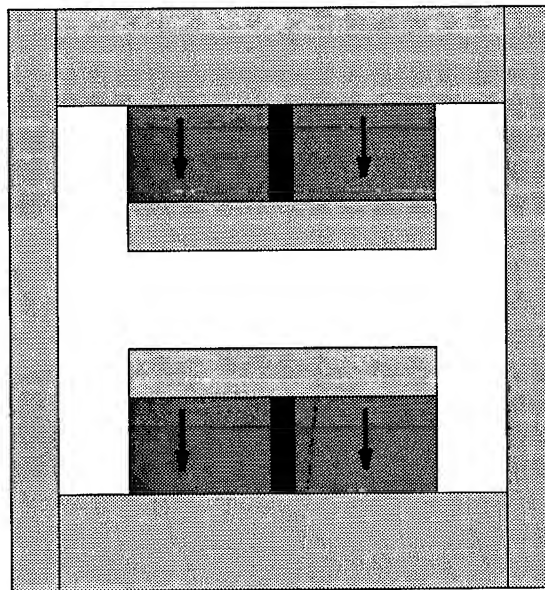


Figure 1. Cross section of a dipole magnet. Temperature compensating strips are placed symmetrically between blocks of ferrite material.

magnetic field as well as temperature. In applications where the field is very weak it is necessary to take this into account. In the present case, the regime of operation is such that the compensating material is completely saturated. The strip behaves like a thin bar magnet of strength M_S polarized in the direction opposite to the ferrite blocks and M_S is essentially independent of H in the strip. As a result, the compensation effect is expected to scale linearly with the strip thickness.

Results

A 2 kG prototype dipole magnet was constructed both to understand basic assembly problems and to study temperature compensation. For the sake of this experiment, the thin strip of compensating alloy was placed on one side of the gap, though in practice this would affect field quality (Figure 1 is the preferred configuration). The result shown in Figure 2 is spectacularly better than anticipated; Line A represents the field in the center of the magnetic gap without the compensating strip. Line B represents a first iteration based on a rough estimate of the thickness. Line C represents the result obtained by linearly scaling the thickness on the basis of result B. $\frac{d \log B_0}{dT}$ was reduced by more than 2 orders of magnitude from the original 2000 ppm/C to less than 100 ppm/C between 25 and 30 deg C and below 10 ppm between 30 and 40 deg C.

Conclusion

We have demonstrated that the strength of a magnet built with ferrite material can be passively temperature stabilized at a level more than sufficient to build a storage ring without the need for expensive correctors. Work is in progress to build a larger model and a full scale prototype.

FE-NI ALLOY COMPENSATION

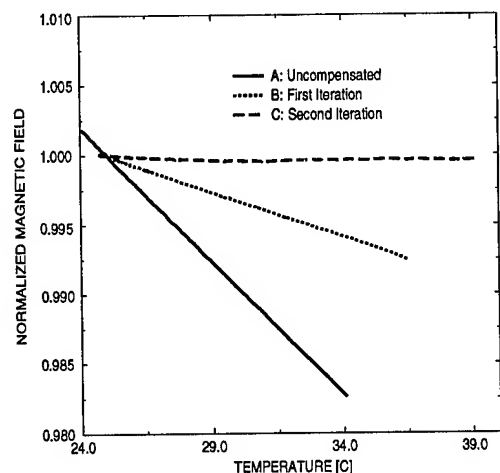


Figure. 2. Experimental results.

References

- [1] K. Halbach, "Speciality Magnets", in AIP Conference Proceedings No. 153 p. 1277. M. Month and M. Dienes Ed., New York 1987.
- [2] "Issues Surrounding the Construction of Permanent Magnet Storage Rings", G. P. Jackson et al., these proceedings.
- [3] Eric A. Brandes ed., *Smithells Metals Reference Book*, 6th ed., (London: Butterworths) p 20-20 ff.
- [4] F. N. Bradley *Materials for Magnetic Functions*, (New-York: Hayden, 1971)

3D NUMERICAL ANALYSIS OF MAGNETS AND THE EFFECT OF EDDY CURRENT ON FAST STEERING

T. Nagatsuka, T. Koseki, Y. Kamiya and Y. Terada^A
 Institute for Solid State Physics (ISSP), The University of Tokyo
 3-2-1, Midori-cho, Tanashi, Tokyo 188, Japan
^ATechnical Research Institute, Hitachi-Zosen Corporation
 2-2-11, Funa-machi, Taisho, Osaka 551, Japan

I. INTRODUCTION

Using the computer code of MAGNA, a product of Century Research Center in Japan, we made numerical analyses of magnets for a high-brilliant VUV and soft X-ray synchrotron radiation ring being designed at ISSP and Photon Factory ring of KEK. It is possible for MAGNA to calculate 2D and 3D magnetic fields and include the effects of eddy currents in the calculations.

II. 3D ANALYSIS OF PF BENDING MAGNET

First, in order to check the applicability of MAGNA to magnet design, we made the 3D analysis of the bending magnet used at Photon Factory of KEK. the calculated result fairly agreed with the measured one (Fig. 1). the s in the figure is the distance from the center of the magnet along the longitudinal direction. It has thus been demonstrated that MAGNA can calculate a 3D magnetic field with a sufficient accuracy.

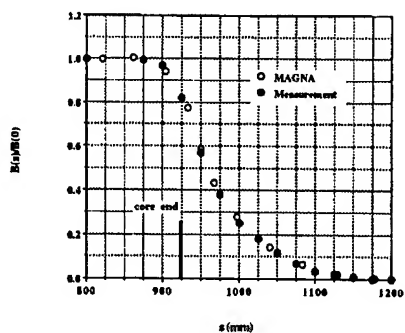


Figure 1: The field of PF bending magnet.

III. 3D ANALYSIS OF DC STEERING MAGNET

We then made the 3D analysis of DC steering magnet for the high-brilliant ring. Table 1 gives its parameters and Figure 2 shows a quadrant of its cross section. Figure 3 shows the horizontal field strength integrated by s . Figure 4 also shows the integrated vertical field strength. As shown in these figures, both fields have sufficient uniformity. Since the edges of the horizontal steering coils are closer to the iron core than those of the vertical steering coils, the vertical field is more like 2D and flatter than the horizontal field. We also made the same analysis for a fast steering. Because its shape is similar to the DC steering (see Fig. 5), the results are also similar to the above ones.

Table 1: Parameters of DC steering magnet.

	Vertical steering (2 coils)	Horizontal steering (2 coils)
Number of turns	1260/coil	720/coil
Current (A)	5	5
Magnetic field (G)	400	350
Effective length	0.15	0.115
Bend angle (mrad)	0.89	0.6
Inductance (H)	0.1	0.1

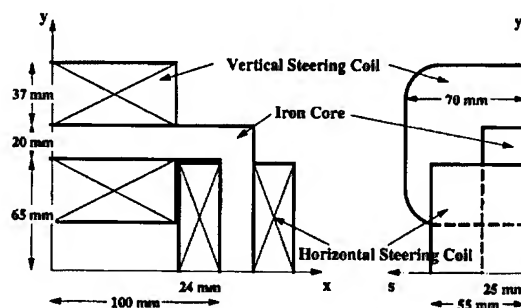


Figure 2: A quadrant of DC steering magnet.

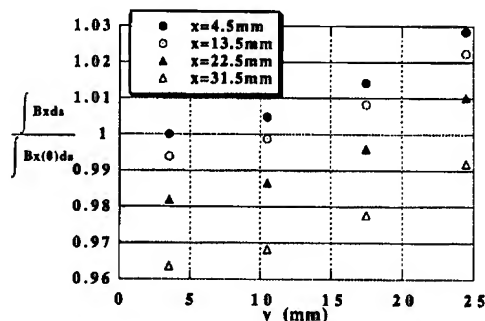


Figure 3: Integrated strength of horizontal field.

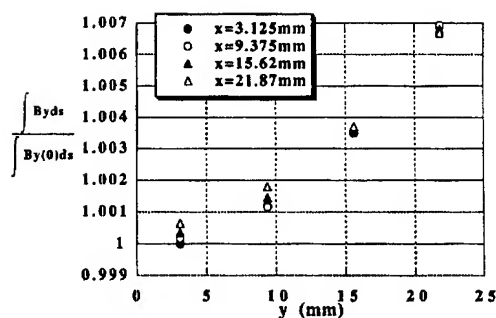


Figure 4: Integrated strength of vertical field.

IV. 2D ANALYSIS OF THE EFFECT OF EDDY CURRENT ON FAST STEERING

As the fast steerings are expected to operate in a frequency range up to 100 Hz, we have examined the effect of eddy current induced on the vacuum chamber. The analysis is two dimensional in this section. Table 2 gives its parameters and Figure 5 shows a quadrant of its cross section together with the chamber. The shape of the chamber was simplified to reduce the number of meshes. Figures 6 and 7 show the fields at the center of the magnet in the cases of aluminum and stainless steel chambers, respectively. As seen in Fig. 6, the vertical magnetic field is strongly attenuated for the aluminum chamber. Therefore, it may be difficult to control the horizontal closed orbit by fast feedback, though the effect of eddy current almost does not influence the field uniformity.

Table 2: Parameters of fast steering magnet.

	Vertical steering (2 coils)	Horizontal steering (2 coils)
Number of turns	140/coil	120/coil
Max. current (A)	5	5
Magnetic field (G)	55	110
Effective length (m)	0.11	0.065
Bend angle (mrad)	0.09	0.1
Inductance (mH)	1.2	2.7

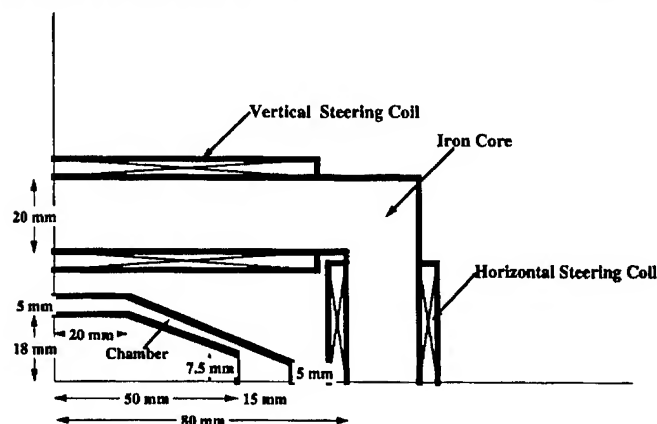


Figure 5: Fast steering and its chamber.

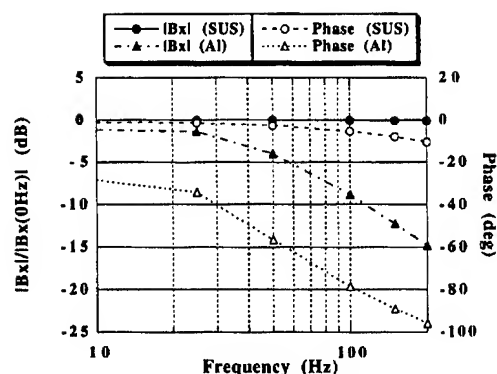


Figure 6: Bode diagram for vertical steering.

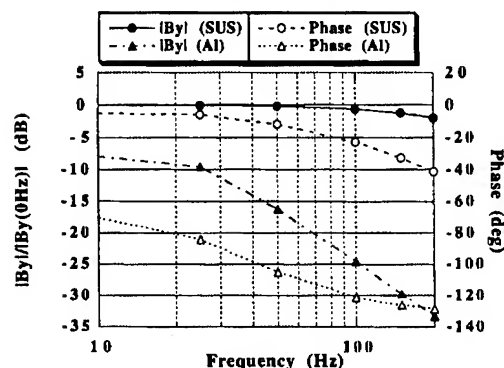


Figure 7: Bode diagram for horizontal steering.

In order to check the calculation, we measured the magnetic fields of a PF vertical steering with an aluminum chamber for quadrupole magnet and compared the result with the calculated one. Figure 8 is a quadrant of its cross section together with the chamber. to make a vertical field, we added horizontal steering coils to the PF steering. The chamber used was about 1 m long. figures 9 and 10 show the results. A close agreement between the measured and the calculated values was obtained for the horizontal magnetic field (Fig. 9). but they are somewhat different for the vertical field (Fig. 10). The reason why such differences occur is as follows. In spite of the short magnet length, the eddy current generated by horizontal field on the chamber behaves like 2D at least more than for vertical field since the height of the chamber is smaller than its width. As a result, both 2D calculation and measurement may agree each other for the frequency dependence of horizontal field, whereas it is not the case for vertical field.

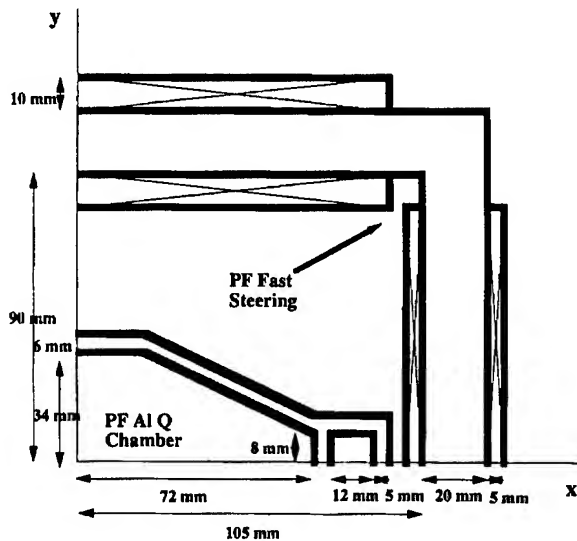


Figure 8: the PF steering magnet and AI Q chamber.

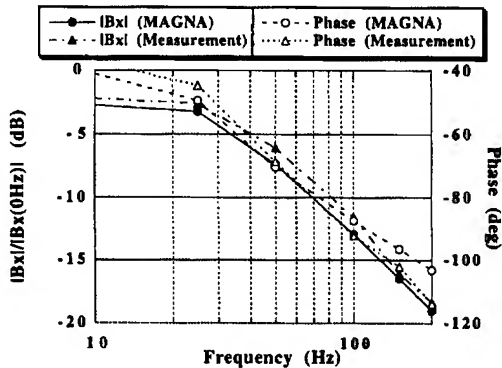


Figure 9: Bode diagram for PF vertical steering.

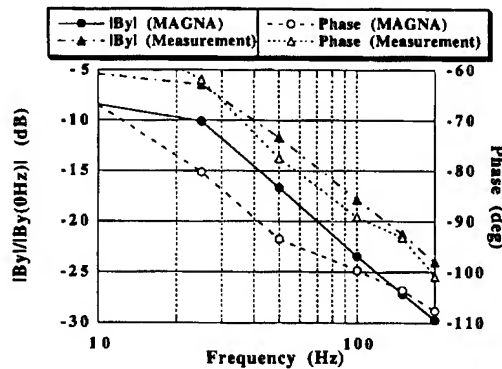


Figure 10: Bode diagram for PF horizontal steering.

V. 3D ANALYSIS OF THE EFFECT OF EDDY CURRENT ON FAST STEERING

Using 3D analysis we tried to study the effect of eddy current for the above PF steering with its chamber. Because we had to deal with a finite length of the chamber and our WS had not enough memory for 3D calculation, we covered the chamber with aluminum plates at its end to simulate a long chamber (Fig. 11). It was showed that 10 to 20 % of the central DC field strength remained at the plate. Nevertheless,

the 3D calculation showed that the normalized vertical fields in both cases of calculation and measurement well agrees with each other for the horizontal steering, as shown Fig. 12.

For the integrated field strength and for horizontal field, 3D calculation did not give satisfactory results, because we were short of computer power and probably took inaccurate data for a long search coil to measure the integrated field. In near future, we will improve the WS power and the field measurement of frequency dependence.

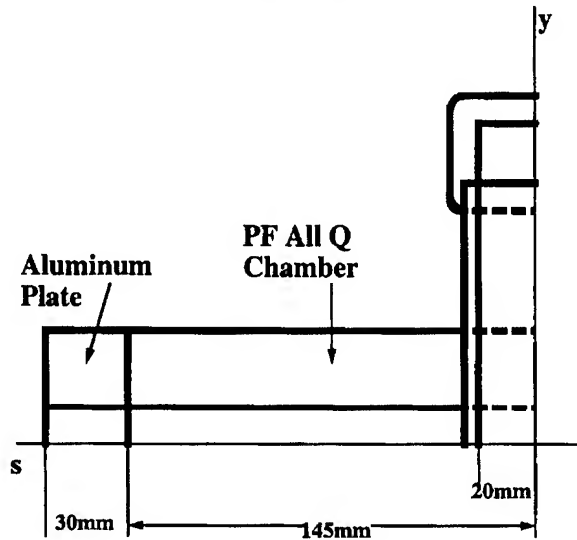


Figure 11: The steering magnet and covered chamber.

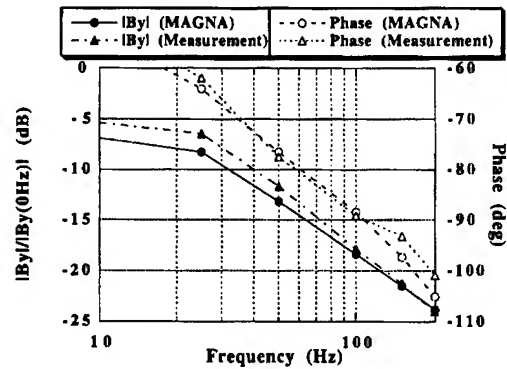


Figure 12: Bode diagram of PF horizontal steering.

MEB RESISTIVE MAGNETS PROTOTYPES MANUFACTURING

G. Batskikh, G. Mamaev, T. Latypov
I. Tenyakov, Y. Tereshkin
MRTI RAS, Moscow, Russia
W. Heilbrunn, SSCL, Texas, USA

This report presents the work, that was done under the agreement between the Moscow Radiotechnical Institute of Russian Academy of Science (MRTI RAS) and Superconducting Super Collider Laboratory of USA (SSCL), signed in May, 1992. According this agreement, 245 quadrupoles and 406 dipoles had to be done in Russia for Middle Energy Booster (MEB). The whole program was to be completed till 1996. Because of SSCL elimination in 1993 only two magnets (one dipole and one quadrupole prototypes) were done in 1994.

COOPERATION FOR MAGNET PRODUCTION

To fulfill the work properly and in time the following cooperation was organized in Russia:

Moscow Radiotechnical Institute (MRTI RAS),
The Central Research Institute for Ferrous Metallurgy (CRIFM),
Novolipetsky Integrated Iron and Steel Works (NIISW),
Joint Stock Company "SILA" (the former St. Petersburg's Electrical Engineering Pilot Production Works (SPEEPPW)),
Electrophysical Apparatus Pilot Production Works (EAPPW),
Research and Technology Center "TEMP" (RTC "TEMP"),
Institute for High Energy Physics (IHEP).

This cooperation was build to utilize the equipment and experience of participants which they had in a field of resistive magnets building for Accelerating-Storage Complex (UNK) that was being created in Russia (Protvino, IHEP).

MAIN REQUIREMENTS

The main requirements to magnets were quality, reliability, interchangeability and accuracy. That's why very stringent requirements were imposed on geometrical, mechanical, electrical and magnetic parameters. This requirement has resulted from a very high degree of accuracy of different parameters. For example:

- a) tolerance on working and base surfaces of magnets laminations - 25 μm ;
- b) tolerance on unflatness of base magnets surfaces - 50 μm .

c) tolerance on effective magnetic length, according to SSCL specification - 0.1 %.

Such a rigid tolerances can ensure the opportunity of interchangeability of main ring elements. However the cost of such a convenience may be rather hard.

There were several types of dipoles and quadrupoles to be done for using in MEB. Tables below presents main parameters of typical quadrupole and dipole which were put in the foundation of design work.

NOMINAL CHARACTERISTIC OF MEB DIPOLE

Effective length (m)	6.441
Injection current (A)	273
Extraction current (A)	4983
Max. mag. field (T)	1.7
Max. integrated field (T-m)	11.60
High field error at 25 mm	3.0×10^{-4}
Low field error at 25 mm	1.0×10^{-4}
Weight of magnet (kg)	21136
Power consumption (kW)	44
Core length (m)	6.450
Lamination height (mm)	600.0
Lamination width (mm)	15.4
Lamination thickness (mm)	1.5
Minimum pacing factor (%)	97
Minimum air gap (mm)	50.8×101.6
Sagitta (mm)	14.01
Copper weight/mag (kg)	2200
Number of turns / mag.	2x8
Conductor:	
Width (mm)	22
Height (mm)	55
Hole diameter (mm)	9
Number of water circuits/mag	2

NOMINAL CHARACTERISTICS OF MEB QUADRUPOLE

Effective length (m)	2.441
Injection current (A)	252
Extraction current (A)	4210
Extract. current dens. (A/mm ²)	6.8
Max. mag. field in core (T)	1.5
Max. gradient (T/m)	21.5

Max. integrated field (T)	52.237
High field error at 25 mm	3.4×10^{-4}
Low field error at 25 mm	4.8×10^{-4}
Weight of magnet (kg)	5500
Power consumption (kW)	49
RMS power consumption (kW)	20
Core length (m)	2.400
Lamination height (mm)	666
Lamination width (mm)	662
Minimum packing factor (%)	98
Core weight/mag (kg)	4932
Copper weight/mag (kg)	486
Number of turns / mag.	4x4
Conductor	
Width (mm)	26
Height (mm)	26
Hole diameter (mm)	8
Number of water circuits / mag	2

MAGNETS PRODUCTION

2082 and 2083 steel sorts for magnets production were developed by Novolipetsky Integrated Iron and Steel Works (NIISW). The technology of steel manufacturing included the following stages: continuous casting, decarburizing, hot reduction of 20 mm thickness steel sheets, pickling, cold reduction till 0.75 mm (for quadrupoles) or 1.5 mm (for dipoles) thickness, annealing, insulating coating formation, and sheet cutting into bands of needed width. Steel had the saturation induction 2.12 Tl, coercive force was less than 1.9 Oe for quadrupoles (2082 steel) and less than 1.0 Oe for dipoles (2083 steel). Carbon consumption was less than 0.01%. The resistance of insulation coating was tested after steel production using Franklin testing machine.

Laminations stamping was made by stamping line using 300 tons Japan press AIDA. Stamping die for quadrupole production was made with the use of Swiss-made electrical erosion machine AGIECUT-300. The die for dipole production was manufactured in USA. Stamped laminations were measured after experimental stamping with the use of three-directional measurement machine "OPTON UMESS". Measurement accuracy was detected to be not more than 5 μ m. The profile of working part of magnets pole corresponds to tolerance limits.

Quadrupole quadrants and dipole half-cores were manufactured by stacking of 50 laminations packs. Mixing procedure was developed to ensure identical magnetic properties of the packs, to ensure the quadrupole and dipole magnetic properties reproduction and to maximize the filling factor. Preliminary experiments showed us that it was necessary to enlarge the press pressure to achieve 97% core stacking factor up to 25 kg/cm². Needed press force for dipole appeared to be 40 T instead of former 25 T. Lateral force was increased up to 2 tons per meter.

Magnets cores assembling was conducted using 50 tons hydraulic press.

After the assembling was finished, the straightness of assembly were checked, and semiautomatic welding in neutral gas in accordance with welding process card was produced.

The control has shown the practical conformity of quadrupole core parameters to drawing requirements: the deviation from flatness when resting on flat surface, taking twist into account - not more than 1,4 mm (1 mm without taking twist into account). When loaded - less than 0,05 mm. The stacking factor for four quadrants was obtained to be inside (97.02% - 97.4%) interval.

The quality of dipole core was in turn good enough to satisfy the preliminary requirements.

The coils were produced using hollow conductor. The conductor was made from an oxygen-free copper. Bus splices were executed by silver brazing of copper sleeves.

After coil winding and before insulation, hydrostatic test was conducted with the use of water under pressure 17 kg/cm.

Insulation curing process was performed with the use of termo-pressing in a mould. We used b-stage insulation technology. Polyimide tape, fiberglass tape and mica paper were used as a main components of an insulation. They were glued and saturated with epoxy compound with latent hardener.

Coils were electrically tested before and after turn insulation curing and after ground wall insulation curing. Induced voltage test used 12 V/turn voltage to detect turn-to-turn insulation quality. Impulse test used standard voltage pulse to examine the ground wall insulation. High-voltage insulation tests were conducted by application of DC 5 kV voltage between the coil conductor and the grounded foil with gradient rings during one minute period.

The assembling of coil and magnet cores to get a quadrant or half dipole was made with the use of special fixture with individual coil adjustment with the use of screw press.

The quadrupole and dipole geometry was supervised by linear measuring rods and feelers gauges (interpole distance). This testing showed us that the quality of dipole mounting could be better, if the technology of mounting was more stringent.

MAGNET TESTING

To check the quadrupole and dipole quality, prototypes magnetic measurements program was developed. According to this program, prototypes magnetic measurements were done at the Institute for High Energy Physics (IHEP). Test stands were developed for dipole and quadrupole prototypes integrated strength, body and end field and gradient, magnetic axis position, and higher multipoles measurements.

For MEB dipole prototype investigation the next methods and apparatus were used:

1. NMR magnetometer was used for the calibration of Hall probes, and measuring of body fields (B vs I scan, longitudinal scan). Measuring range (0.1-1.9) Tl, number of probes - 5, absolute accuracy - 10^{-5} . The relative accuracy of magnetometer ($5 \cdot 10^{-6}$) was checked at 0.15 Tl in a C-type permanent magnet. The absolute accuracy is defined by hyromagnetic ratio of protons in a rubber sample.

2. Hall probes were used for the measuring of nonuniformity of body field and the end field mapping. Sizes of sensitive zone was (1.5 x 0.5) mm², nominal current-100 mA, offset voltage -(1-4) uV, sensitivity (70 -75) mV/Tl.

Temperature coefficients for Hall voltage - 10^{-3} %/K, for offset voltage - 30.0 nV/K, for nonlinearity - 0.6 % at 2 Tl.

3. Integrated field BL were measured by stretched wire moving in a magnet median plane. To achieve a good resolution the signal from a wind was gained by preamplifier and then was integrated by V - integrator. Both amplifier and integrator were carefully calibrated. The maximum integrated voltage measurement error is equal to $1.2 \cdot 10^{-4}$.

The difference between a stretched wire length and length of a magnet along centerline due a sagitta was took into account during the measurements. Summing all contributions the field integral is determined with an accuracy of $2.0 \cdot 10^{-4}$.

4. Integrated field harmonics were measured by a short pick-up rotating coil. To obtain the integrated field harmonics ten measurements of body field at various distances from magnet ends (5 from both ends of magnet) and two of fringe fields were produced. The integrated field harmonics were received as an average value of these measurements. The dispersion of measured harmonics amplitudes does not exceed $1 \cdot 10^{-5}$ for $k=1..6$ at radius 25.4 mm.

5. The magnet current was measured by Constant Current Transformer (CCT), calibrated by HOLEC. Measuring range of CCT - 10 kA, absolute accuracy 10^{-4} , linearity - 10^{-5} .

Methods and apparatus, used during quadrupole testing were similar to dipole.

Movable platform table with adjusted magnet support for quadrupole prototype measurements enable the lens's geometric axis to be aligned with the mechanical axis of the measurement system. Supports with air bearing brackets, stepping motor drive and angle-to-code transducer ensure precise rotation of measuring coils. The air bearing axis is adjusted with regard to the mechanical axis of the measuring system. Optical system was developed to provide necessary adjustment of the len's geometrical axis with the use of the Taylor-Hobson telescope. Adjustment accuracy is better than 20 microns.

Measurement tube with induction coils and stretched wires were used to provide axis position adjustment and harmonics content measurements. There were two types of pipes: 2 meter long and 0.8 meter long. Each pipe had carbon-plastic body. Precise pipe manufacturing enable us to ensure precise coil position inside a pipes.

Main results of the quadrupole prototype magnetic measurements meet all the requirements of preliminary design and confirm high quality of prototype manufacturing. Magnetic axis position is as can be seen from the table below stable sufficiently within full current operation interval.

I (kA)	0.252	0.425	2.0	4.146
Δx (μ m)	-8	-12	-37	-36
Δy (μ m)	90	80	52	86

Focal strength and effective length measured by means of 2.0 m rotating coil, coincide practically with design values. Current dependence of integrated efficiency GL/I is presented by the next table:

I (kA)	0.24	0.4	2.0	4.15
GL/I	13.045	12.932	12.92	12.608
(T/kA)				

MEB quadrupole prototype main integrated gradient normal and skew harmonics are inside the design goal.

Dipole magnetic measurements results show good results too. The production process for quadrupole prototype was very close to one for serial units. In turn this demanded less shop personal qualification factor and simplified the control and tests. As for dipole prototype, the time interval to organize dipole production was very narrow, and its quality was dependent on the personal qualification. Nevertheless it was sufficient to make the work properly. It must be said, that technology was prepared for dipole serial production too, but it was no sufficient time to make the tooling in needed grade to check it.

The experience of such kind of work gave us the confidence that cooperation of Russian works and institutes can be a reliable partner for various projects managers.

CONCLUSION

In conclusion we want to say our thanks to the main participants of the work: V.I. Barankevitch, A.D. Malakhov, V.I. Peregud, B.S. Tanaev, M.T. Fedotov, E.A. Podkamanev, Y.A. Konstantinov, M.N. Kosiakin, A.V. Bukiev, V.P. Nikitin, V.S. Smirnov, N.N. Dergunov, K.F. Gertsev, S.V. Trofimov, B.G. Zarucheisky.

Abe, H. FAP13, 1358
Abe, S. TAQ35, 1608
Abraham, W. WPA01, 902
Abramenko, N. RPR10, RPR15, 1143, 1155
Abramsky, P. WPP11, 1681
Adachi, Toshikazu TPR16, 3275
Adamski, J. FAA27, 248
Adamski, J.L. FAA28, 251
Adolphsen, C. WAG11, RPB03, RPB04, RPC01, RAE03, TPQ17, WAB07, WAC18, 646, 662, 665, 698, 2389, 2989, 3031, 3112
Adolphsen, Chris WAB08, 3034
Afanasiev, O. FAQ06, 1399
Agafonov, A.V. TPR13, TPR14, 3269, 3272
Ahrens, L.A. TAP11, TAP12, TAP13, WAB04, RAQ22, 378, 381, 383, 3022, 3334
Aizatsky, N.I. WPQ22, TPA14, 1773, 3229
Akai, K. FAE09, WPQ08, WPQ09, WPQ17, WPR05, WPR09, RPQ06, WAC08, 1503, 1735, 1738, 1759, 1797, 1806, 2675, 3085
Akasaka, N. RPA20, FAE09, WPQ09, WPQ17, WPR05, WPR09, TPC08, TPC29, TAG01, 1099, 1503, 1738, 1759, 1797, 1806, 2613, 2655, 2742
Akemoto, M. WPR02, WPR03, 1788, 1791
Akimov, V. WAA17, 1263
Akre, J. FAQ24, FAQ25, 1444, 1447
Akre, R. WPR15, WAB12, 1821, 3046
Alessi, J. WPC09, 1013
Alexahin, Y. RAA17, 560
Alexandrof, V.A. TAG01, 2742
Alimov, A. RPA19, 1096
Alimov, A.S. RAR04, 3361
Alinovsky, N.I. TAC06, 143
Allen, C.W. RPA24, 1111
Allen, Christopher K. MPC04, 2324
Allen, J. RAR23, 3406
Allen, L. WPA06, 917
Allen, M.A. WPQ06, 1729
Allen, Ray TPP13, 1645
Alley, R. MPE10, 887
Allison, Paul W. TAE08, 1207
Allison, S. RAE03, 2389
Alonso, Jose R. WPE01, 58
Alton, G.D. MPE05, WPC12, WAQ26, 871, 1022, 1897
Altuna, X. WAP12, WAP13, 464, 467
Amankath, H. RPA26, 1116
Amiranoff, F. WAG07, 634
Anderson, David E. TAE07, 1204
Anderson, K. WAQ22, WAR17, 1888, 1939
Ando, A. RPQ15, 2699
Andreev, V.G. WPP19, 1702
Andreev, V.V. FAC09, 2856
Andriishchin, A. FAQ06, 1399
Anerella, M. TPE04, FAQ04, 1293, 1396
Angerth, B. RPE02, 1999
Ankenbrandt, C. FAG06, 86
Anthouard, Ph. TAE09, 1210
Antonsen, T.M. WAG04, 621
Aoki, T. FAP13, 1358
Arai, S. RPG13, 351
Arbuzov, V. WPP11, 1681
Ardonceanu, J. WAG07, 634
Argyakis, J. FAP03, 1328
Arinaga, M. RAB13, 779
Arnold, N. RPA11, RPA14, MPQ08, 1073, 1082, 2467
Asano, K. TPP03, TPP16, 1620, 1652
Ashton, J.R. RPB05, 668
Assadi, S. TAG10, RAP03, WAB01, 2777, 2886, 3016
Asseev, A.A. WAR23, 1955
Assmann, R. RAA19, WAG11, RPB02, 567, 646, 659
Astapov, A.A. RPE13, 2029
Auble, R.L. WAQ26, 1897
Auch, S. RPR06, 1131
Aune, B. WPB22, 998
Ausset, P. WPQ26, 1781
Austin, R.H. FAA19, FAA31, 234, 260
Autin, B. RPC11, WAE09, 722, 2178
Averill, R. RPG05, RAA31, 327, 600
Azorsky, N.I. TAQ34, 1605
Baartman, R. RPG12, WAQ07, WAC20, 348, 1858, 3119
Baba, T. WAQ06, 1855
Babzien, M. MPE11, 890
Backmor, Rudolf TAQ13, 1550
Bailey, J.D. TAP07, TAP08, TAP09, 366, 369, 372
Bailey, R. WAP12, WAP13, RAA11, 464, 467, 548
Bainan, Ding FAA26, 246
Baiod, R. FAP04, FAP06, FAP07, FAP09, MPB06, 1331, 1337, 1340, 1346, 2285
Bak, J.S. RPA06, 1061
Baker, S. WAR19, 1945
Bakker, R. RPG06, 330
Baklakov, B. TAA01, RAR30, 2078, 3424
Balakin, V. TAG01, 2742
Balewski, K. FAR07, 275
Balhan, B. RAA15, 557
Ball, M. TPB24, RAP21, RAP22, WAC12, RAQ23, RAQ24, 2583, 2934, 2937, 3094, 3337, 3340
Ballauff, M. FAR06, 272
Bamblevski, V.P. RPE13, 2029
Bane, K. RPA04, WAC17, 1058, 3109
Bane, K.L.F. RPA20, TPQ16, TPQ17, WAB07, WAC16, WAC18, 1099, 2986, 2989, 3031, 3105, 3112
Bangerter, R.O. WAQ04, 1852
Baptiste, K. TAR03, 801
Baranov, V.I. MPG10, WAR21, 426, 1949
Baranova, L.A. TAP16, 389
Barber, D.P. WPG08, 511
Bardy, J. TAE09, 1210
Barker, D. MPR13, 2265
Barklow, T. RPB01, 656
Barletta, W. TAA28, 2135
Barlow, T.A. TPC13, 2628
Barnard, J. TAR17, 837
Barnard, J.J. TAR14, TPB14, TPR18, 828, 2557, 3278
Barnard, John J. TPR02, 3241
Barnes, P. FAE13, WPQ02, RAQ04, 1515, 1720, 3294
Barov, N. WAG06, WPB11, 631, 976
Barr, D. MPQ03, RPQ16, TPQ19, 2452, 2702, 2992
Barry, W. RAE13, RPQ08, 2423, 2681
Barts, T. MPB10, 2294
Batchelor, K. MPE11, WPB13, RAE09, WXE03, TPB01, 890, 982, 2411, 2432, 2530
Batskikh, G. FAP24, 1387

Batskikh, G.I. RPR07, 1134
 Batygin, Y. WPC01, 1001
 Batygin, Y.K. TPR06, 3251
 Batygin, Yuri K. TPR07, 3254
 Beadle, Edward R. TPB08, TPB09, 2545, 2548
 Beauvais, P.-Y. RAG07, 3173
 Becher, D. MPE05, 871
 Bechstedt, U. TPB20, 2574
 Bechtold, V. FAR06, 272
 Becker, T. FAP02, 1325
 Becker, U. TAQ06, WAE13, 1533, 2190
 Beebe, E. WPC09, 1013
 Behne, D. MPP12, MPP20, 2064, 2075
 Beisel, U. WPA04, 911
 Bekefi, G. TPG14, RPC15, 192, 734
 Belkovets, V. TAC16, 152
 Beloglazov, V.I. TAE14, 1225
 Belomestnykh, S. FAE13, WPP11, RAQ04, RAR18, RAR19, 1515, 1681, 3294, 3391, 3394
 Belov, W. RAQ14, 3315
 Belova, Nadya G. WAA01, 1227
 Belser, C. RAA04, 530
 Belser, F.C. WPC06, TAA22, 1729, 2129
 Belugin, V.M. RPR07, 1134
 Ben-Zvi, I. MPE11, WPB13, RAE09, WXE03, TPB01, 890, 982, 2411, 2432, 2530
 Benesch, J. FAE12, 1512
 Benjamin, J. TAP11, 378
 Benjegerdes, R. WPA01, FAP17, 902, 1369
 Bennett, L. TAE06, 1201
 Bennett, Lawrence F. TAE07, 1204
 Benson, S. FAG11, FAA25, WPA17, WPC24, 102, 243, 942, 1052
 Benvenuti, C. FAE11, TPP12, 1509, 1642
 Bercher, M. WAG07, 634
 Berenc, T. WPB06, 961
 Berezin, A.K. RAB15, 782
 Berg, J. TAA22, 2129
 Berg, J.S. FAB06, TPQ16, 2804, 2986
 Berg, J. Scott TPQ07, WAC05, 2962, 3076
 Berg, W. RPA11, MPQ10, 1073, 2473
 Berger, D.D. WPQ06, 1729
 Bergher, M. RAP19, 2928
 Berkelman, K. FAE13, 1515
 Bernal, Santiago TAA17, 2117
 Bernard, D. WAG07, 634
 Bernard, M. WPB01, WPB22, 945, 998
 Berridge, S. TAA28, 2135
 Bertagnolli, H. FAR06, 272
 Bertinelli, F. RPE02, 1999
 Bertolini, L. RAA03, 527
 Bertsche, K. TPE05, FAP21, WAQ09, MPQ21, TPB19, 1298, 1381, 1864, 2503, 2572
 Bertuzzi, J.-P. MPP15, 2069
 Berwald, D. RPR20, 1164
 Berz, Martin MPC09, 2336
 Bessonov, E.G. RAP06, 2895
 Beveridge, J.L. RPG12, 348
 Beyer, K.A. TPC13, 2628
 Bharadwaj, V. MPG02, WAP04, RPC20, RPC21, WPB08, TAG01, 396, 443, 749, 752, 967, 2742
 Bhat, C.M. FAP05, WAR02, TAA12, WAC06, 1334, 1903, 2105, 3079
 Bialowons, W. RPE08, 2017
 Bialy, J. FAR06, 272
 Bickley, M. MPA12, MPR19, 2220, 2276
 Bieniosek, F.M. WAR17, WAR18, 1939, 1942
 Biggs, J. FAP03, 1328
 Billen, J.H. RPR08, RPR09, 1137, 1140
 Billen, James H. MPB16, 2306
 Billing, M. FAE13, FAB12, TPA04, RAQ04, 1515, 2820, 3206, 3294
 Billing, M.G. RAE14, 2426
 Binns, B. WAA16, TPB04, 1260, 2536
 Birukov, I.N. RPR01, 1119
 Biryukov, V.M. MPG10, WAR20, WAR21, 426, 1948, 1949
 Biryukov, Valery WAR24, 1958
 Biscardi, R. TPP06, WPP03, 1626, 1660
 Bisognano, J. FAG11, FAA25, WPA17, 102, 243, 942
 Bisognano, J.J. RPQ11, 2690
 Bisognano, Joseph J. MPC25, RAG12, 2370, 3188
 Bizek, Hana M. RAR27, 3418
 Bjerklie, S. FAG06, 86
 Black, E. FAP03, 1328
 Black, W.M. TAE10, 1213
 Blanchard, R. WAP12, WAP13, 464, 467
 Blas, F. MPG09, 423
 Blaskiewicz, M. TAP11, TAP12, TAP13, WAC24, 378, 381, 383, 3131
 Blaskiewicz, M.M. RAQ22, 3334
 Blastos, J. TPG14, 192
 Blazhevich, S.V. FAG12, 105
 Bleser, E.J. TAP13, WAR13, 383, 1930
 Bloess, D. TPP12, 1642
 Blondel, A. RAA19, 567
 Bloom, E. WAQ15, 1876
 Blosser, H. RPG11, 345
 Bluem, H.P. TAA32, 2141
 Blum, E. FAR10, 284
 Blum, E.B. FAR01, MPQ01, 263, 2450
 Bocchetta, C. FAR06, 272
 Bocchetta, C.J. FAA13, FAR21, TAG05, 222, 309, 2762
 Boehnlein, D. FAG06, 86
 Boer-Rookhuizen, H. MPQ17, 2491
 Boers, Jack E. MPB18, 2312
 Bogacz, A. FAP05, WAR19, RAR17, 1334, 1945, 3388
 Bogacz, S.A. RAB20, TAR20, 790, 843
 Bogard, D. RAG07, 3173
 Bogaty, J.M. TPC12, 2625
 Bogdanovich, B. RPR10, RPR15, TAQ24, 1143, 1155, 1575
 Bogdanovich, B.Yu. TAB13, TAQ23, 125, 1572
 Böge, M. RAP08, 2901
 Bogert, D. MPG01, 391
 Bohl, T. WAP12, WAP13, RAA11, FAE10, 464, 467, 548, 1506
 Bohlen, H. FAE07, 1497
 Bohn, C.L. FAG11, 102
 Bojon, J.-P. RPE06, 2014
 Bolme, G.O. WPA08, RPR19, 923, 1161
 Bolotin, I. WPR19, 1833
 Bolser, C. MPC01, 2317
 Bonati, R. WAR11, 1924
 Bondarev, B.I. RPR07, 1134
 Bongardt, K. TPA01, TPA02,

TPA03, 3197, 3200, 3203
Boni, R. RPA26, 1116
Bonifacio, R. FAA12, 219
Bonin, B. TPP09, 1632
Bonnafond, C. TAE09, 1210
Bonnafond, Ch. TPC17, 2640
Bookwalter, V. MPR13, 2265
Borden, M. RAR23, 3406
Borland, M. FAR11, WAE11, MPQ10, 287, 2184, 2473
Borodich, A.I. TPA15, 3232
Bortnyansky, A. TAA18, 2120
Bosch, R.A. FAR20, 306
Bosotti, A. TAA07, 2093
Bossard, P. MPG09, 423
Bossart, R. RPC10, 719
Bosser, J. RAP23, RAP24, 2940, 2943
Bostic, D. MPP10, 2057
Bothe, W. FAR06, 272
Botman, J.I.M. WAQ19, WAQ20, RPP04, RPQ31, 1882, 1885, 1970, 2738
Bourdon, J.C. WPB22, 998
Boussard, D. FAE10, TPP12, 1506, 1642
Bowden, G.B. RPB04, RPA23, 665, 1108
Bowers, J. WAC17, 3109
Bowling, B. MPR13, 2265
Bowling, B.A. WAE10, 2181
Bowling, S. RPR19, 1161
Boyd, John K. MPC13, 2339
Boyes, John D. TAE07, 1204
Bozoki, Eva RPQ14, 2696
Brabson, B. RAP21, RAQ23, RAQ24, 2934, 3337, 3340
Bracco, R. FAQ19, 1432
Bradley, S. RPG05, 327
Brandt, D. RAA17, RAA20, FAC03, 560, 570, 2841
Brauer, S.O. RPE09, 2020
Braun, A. RPC21, 752
Braun, H. RPC09, RPC10, 716, 719
Brefeld, W. FAA02, FAR07, 195, 275
Brennan, J.M. TAP11, TAP13, FAE05, MPQ30, RPQ17, RPQ25, WAB04, RAQ22, 378, 383, 1489, 2518, 2705, 2723, 3022, 3334
Bricault, P.G. RPG12, RPR02, RPR03, 348, 1122, 1125
Bridges, J.F. WPP16, 1693
Brillson, L.J. FAG11, 102
Brinker, F. FAA02, 195
Brinkmann, R. MPG04, RPB07, RPE08, 406, 674, 2017
Brodowski, J. WPP07, WPQ19, RPQ17, 1669, 1765, 2705
Brogle, R. WAG09, WPC20, 640, 1039
Broome, W. TPP06, 1626
Brouet, M. MPP15, 2069
Brouzet, E. WAP13, 467
Browman, A. TAR12, TPB13, 822, 2554
Brown, B. TPE05, 1298
Brown, B.C. FAP05, FAP06, FAP07, MPB05, MPB06, 1334, 1337, 1340, 2282, 2285
Brown, D. TPB13, 2554
Brown, K. RPC06, MPR13, 707, 2265
Brown, K.A. TPA06, 3212
Brown, Nathan RPR23, 1170
Brown, R. WPC08, 1010
Brown, V.W. WPA08, 923
Bruhweiler, D. RPR20, TPR07, 1164, 3254
Bruhweiler, D.L. TPR08, 3257
Brunelle, P. FAR14, 293
Brunet, J.-C. RPE02, 1999
Brüning, O. TAG09, 2774
Brüning, O.S. MPG07, 420
Brunner, O. WPG09, 514
Bruns, Warner RPA15, RPA16, 1085, 1088
Bryant, P.J. RPG03, 322
Budilin, V. WPR19, 1833
Budnick, J. RAP21, RAQ23, RAQ24, 2934, 3337, 3340
Bugg, W. TAA28, 2135
Bugorsky, A.P. MPG10, 426
Buhler, S. WPB22, 998
Bula, C. TAA28, 2135
Bulfone, D. TPG11, FAR21, 186, 309
Bulos, F. WAQ15, TAG01, 1876, 2742
Bulyak, E. FAR17, TPA12, TPA13, 299, 3223, 3226
Buon, J. RPC20, TAG01, 749, 2742
Burke, D. RPC01, RPC20, TAA08, WXE07, TAG01, 698, 749, 2096, 2444, 2742
Burkhardt, H. WAP12, WAP13, RAA11, 464, 467, 548
Burlet, A. MPP15, 2069
Burnham, B. FAA08, RAA01, RAB22, MPA10, MPA11, MPQ06, FAC20, 213, 524, 796, 2214, 2217, 2461, 2877
Burnside, C. MPP15, 2069
Burov, A. WAB16, WAB17, 3055, 3058
Burrini, D. RAQ05, 3297
Burton, A. RAA15, 557
Bushuyev, A. WPP11, 1681
Bussa, M.P. WAP14, 470
Butteris, J. FAQ32, 1465
Buxton, W.E. MPA19, 2235
Byrd, J. RPC02, MPC01, RAE12, RAE13, RPQ08, TPQ16, 701, 2317, 2420, 2423, 2681, 2986
Byrd, J.M. WXE06, RPQ09, 2441, 2684
Byrne, M. WPR15, 1821
Cable, M.D. TAR14, 828
Cai, Y. RAA22, RAA25, RAA26, RAA27, 576, 585, 588, 591
Cain, T.D. FAG05, 83
Calabrese, R. RAE05, 2399
Calame, J. TAQ17, 1561
Calame, J.P. TAQ18, TAQ19, 1563, 1566
Calder, R. RPE02, 1999
Calish, S. TAR18, 840
Callahan, D.A. TAR14, TPR19, 828, 3282
Callahan, Debra A. TPR01, 3238
Callin, R.S. TAQ28, 1587
Camas, J. TPC21, 2649
Cameron, P. TAA09, 2099
Cameron, P.R. MPQ05, 2458
Campbell, R. WAA16, 1260
Capone, D. FAQ14, 1417
Caporaso, G. RPC16, MPE14, WPC16, WAA19, TAA20, 737, 899, 1027, 1269, 2123
Cappl, R. TAP14, MPG09, 386, 423
Carboni, G. WAP14, 470
Carder, B. WAA19, TAA20, 1269, 2123
Cardman, L. FAG11, WPA17, 102, 942
Cardman, L.S. WPC17, 1030
Cargnello, F. TPG11, 186
Carlier, E. RAA15, 557
Carlsten, Bruce E. WPB15, FAE06, 985, 1494
Carnegie, D.W. TPE08, 1310
Carrigan, D. WAR19, 1945
Carroll, Frank E. FAG04, 80
Carson, J.A. FAP06, FAP07,

1337, 1340
Carter, A. RPG05, 327
Carter, F. FAA08, RPA17, MPA11, 213, 1090, 2217
Caruette, A. TPP11, TPP14, 1639, 1648
Carwardine, J.A. WAA08, RPP03, RPQ18, 1242, 1967, 2708
Caryotakis, G. FAE07, 1497
Casella, R. RPP02, 1964
Caspers, F. RPE02, RAP24, 1999, 2943
Caspi, S. FAQ23, 1441
Cassel, R.L. WAR06, 1915
Castellano, M. TPG11, 186
Castillo, V. RPQ07, 2678
Castle, M. TAQ18, TAQ19, 1563, 1566
Castro, P. RAA20, FAC03, 570, 2841
Catras, P. TPG14, 192
Caussyn, D.D. RAP21, RAQ23, RAQ24, 2934, 3337, 3340
Cayla, J.N. WPB01, 945
Celata, C.M. TPA10, 3220
Cevenini, F. TPG11, 186
Chae, Y.-C. TAP05, FAB09, 363, 2811
Chae, Yong-Chul TPQ20, TPQ21, RAR24, RAR25, 2995, 2998, 3409, 3412
Chamouard, P.-A. RAG07, 3173
Chan, A. TAR18, 840
Chan, K.C.D. FAA16, TAR12, 228, 822
Chanel, M. RAP24, 2943
Chang, C.H. FAQ26, 1450
Chang, H.P. FAA07, RAA24, TPQ10, 210, 582, 2971
Chang, L.H. FAA04, RAA24, FAQ26, TPQ08, 201, 582, 1450, 2965
Chang, Peace TAR04, 804
Chang, Y.M. MPQ32, 2524
Channell, P. WAC29, 3146
Chao, A. MPC01, WAC17, 2317, 3109
Chao, A.W. WAB09, WAB11, RAQ02, 3037, 3043, 3288
Chao, Alex FAC02, WAB10, 2838, 3040
Charruau, G. WPQ26, 1781
Chattopadhyay, S. TPG07, RPC16, TAA28, 174, 737, 2135
Chautard, F. RPC10, 719
Chavanne, J. TPE10, 1319
Chehab, R. WPB22, 998
Chen, B. WAB20, 3064
Chen, Bo WAB10, 3040
Chen, C.-I. TPC15, 2634
Chen, D. WAR19, 1945
Chen, J.R. FAA07, 210
Chen, J.S. MPR10, TPB29, 2256, 2592
Chen, Jenny MPR10, MPQ16, TPB29, 2256, 2488, 2592
Chen, P. RPC01, TAA28, RAP15, 698, 2135, 2919
Chen, Pisin RAQ18, 3326
Chen, R.-C. TPC15, 2634
Chen, S.C. MPE12, WPB03, WPB04, 893, 951, 954
Chen, T. RAA26, TAG06, RAP09, RAP11, RAP12, WAC17, 588, 2765, 2904, 2910, 2913, 3109
Chen, Y. RPC16, WPC16, WAA19, 737, 1027, 1269
Chen, Yinbao FAA21, RAQ25, RAQ26, 237, 3343, 3346
Cheng, J. TAQ18, TAQ19, 1563, 1566
Cheng, Wen-Hao RAG09, TPR12, 3179, 3266
Cheng, Y. FAA04, FAA07, 201, 210
Chepurinov, A. RPA19, 1096
Chepurinov, A.S. FAG12, RAR04, 105, 3361
Cherenshchikov, S.A. WPA15, WPA16, 938, 939
Chernikov, V.I. WAR09, 1918
Chernogubovsky, M.A. WPP04, 1663
Chertok, I. TPE09, 1316
Chertok, I.L. TAC06, 143
Chesnokov, Yu.A. MPG10, WAR20, WAR21, 426, 1948, 1949
Chester, N.S. FAP06, FAP07, 1337, 1340
Chiang, R. RAQ04, 3294
Chiaveri, E. FAE11, 1509
Chin, A. TPG07, 174
Chin, Y.H. TPC08, WAC07, WAC08, 2613, 3082, 3085
Chiou, T.C. RAB02, RAB08, 761, 773
Chirkov, P.N. FAB02, 2792
Cho, M.H. TAR07, RPA06, TAQ15, 813, 1061, 1556
Cho, Y. TAP05, TPQ22, TPQ23, 363, 3001, 3004
Cho, Y.S. FAA10, 216
Cho, Yanglai RAR25, 3412
Choi, J. TAR07, RPA06, 813, 1061
Choi, Sewan RPP11, 1985
Chojnacki, E. WPB11, WPB12, WPQ02, RAQ04, 976, 979, 1720, 3294
Chou, P.J. MPQ13, WAC09, WAC10, 2479, 3088, 3091
Chou, W. WAP02, WAP03, MPB10, TPQ15, 437, 440, 2294, 2983
Chowdhary, M. MPR14, RAE11, 2268, 2417
Chu, C.C. MPQ26, RAR05, 2515, 3364
Chu, C.-C. TPC15, 2634
Chu, W.T. RAE04, 2394
Chubar, O.V. RAE06, WXE08, 2402, 2447
Chubarov, O. RPA19, 1096
Chubarov, O.V. RAR04, 3361
Chumakov, S.N. TAC06, RPP08, 143, 1979
Chung, K.H. FAA10, 216
Chung, S.C. RAR05, 3364
Chung, Y. MPQ03, MPQ08, TPC03, RPQ15, RPQ16, 2452, 2467, 2598, 2699, 2702
Chupp, W. TPA10, 3220
Church, M. TAR16, 834
Church, Mike RPG07, 333
Ciardullo, D.J. MPQ30, 2518
Cieslik, W. MPQ11, 2476
Ciocci, F. TPG11, 186
Clark, D.C. WPA08, 923
Clark, G.S. RPG12, 348
Clarke, J.A. TPG09, WAC23, 180, 3128
Claus, J. FAP11, 1352
Claus, R. RAE12, RPQ01, RPQ05, 2420, 2660, 2672
Clayton, C. TPB18, 2569
Clayton, C.E. WAG08, RAB01, RAB02, RAB04, RAB05, 637, 758, 761, 767, 770
Clendenin, J. MPE10, WPC21, 887, 1043
Clendenin, J.E. MPE08, WPC18, 877, 1033
Cleveland, E.K. FAG05, 83
Clifft, B.E. TPC12, 2625
Cline, D. TAA28, 2135
Cline, D.B. TAB06, WPG11, RAB20, TAR21, 119, 520, 790,

846

Codutti, A. FAQ19, 1432

Colby, E. WPB05, WPB08, 957, 967

Colestock, P. WPP01, RAP21, WAB01, RAQ24, 1655, 2934, 3016, 3340

Colestock, P.L. TAG04, WAC01, 2757, 3067

Colestock, Patrick L. WAC02, 3070

Collier, P. WAP12, WAP13, RAA10, RAA11, RAA12, RAA13, 464, 467, 545, 548, 551, 554

Collins, J. TPB24, 2583

Colton, E. WAC29, 3146

Coluzza, C. FAR06, 272

Comunian, M. RPC10, 719

Conde, M. WAG06, WPB08, WPB11, 631, 967, 976

Conkling, C.R. MPA16, 2226

Connolly, R. RPR19, WPP07, 1161, 1669

Connolly, R.C. RPR22, TPC06, 1167, 2607

Cooper, R. WAC29, 3146

Cooper, Ronald WPB15, 985

Corbett, J. RPQ21, RPQ22, RAQ17, 2714, 2717, 3323

Corcoran, P. TAE06, 1201

Corlett, J. RPC02, WPR14, MPC01, RAE12, RAE13, RPQ08, TPQ16, 701, 1818, 2317, 2420, 2423, 2681, 2986

Corlett, J.N. WXE06, 2441

Corley, J.P. TAE06, 1201

Cornacchia, M. FAA25, RAA18, RAQ17, 243, 564, 3323

Cornelis, K. WAP12, WAP13, RAA11, RAA17, RAA20, FAC03, 464, 467, 548, 560, 570, 2841

Corredoura, P. RPQ02, RPQ03, RPQ05, 2663, 2666, 2672

Corsini, R. RPC09, RPC11, 716, 722

Corvin, C. TAA16, 2114

Cosso, R. FAE11, 1509

Couillaud, C. RAG06, 3170

Cours, A. RPA11, 1073

Cours, Alexander TAQ16, 1559

Coverdale, C.A. RAB01, 758

Cox, G. WAG06, WPB11, 631, 976

Craddock, M.K. FAB14, 2823

Craddock, W. TAA28, 2135

Crandall, K.R. RPG10, 342

Crane, G. TAR18, 840

Crawford, J. WAP04, 443

Crawford, K. RPQ29, 2732

Cremer, T. FAP20, 1378

Crofford, M. WXE01, 2429

Cromer, K.D. RAP01, 2880

Cros, B. WAG07, 634

Crosbie, E. TAP05, RAA29, RAG05, 363, 597, 3167

Crosbie, E.A. RAR26, 3415

Crowe, T. TPC04, 2601

Cruikshank, P. RPE02, 1999

Cutolo, A. TPG11, 186

Cyvot, G. MPG09, 423

d'Amico, E.T. RPC12, 725

D'Auria, G. TPG11, FAA13, FAR21, 186, 222, 309

D'Ottavio, T. MPR20, 2279

D'Yachkov, M. WAC20, 3119

Daclon, F. TPG11, FAR21, 186, 309

Dalin, J.-M. RPE02, 1999

Daly, E. TAA22, MPC01, 2129, 2317

Daly, E.F. MPP08, MPP10, MPP12, MPP20, 2051, 2057, 2064, 2075

Dangor, A.E. WAG08, 637

Danilewsky, A.N. FAR06, 272

Danilov, O. TAQ21, 1569

Danly, B.G. MPE12, 893

Darrow, C.B. WAG08, RAB01, 637, 758

Datskov, V.I. MPP01, 2034

Dattoli, G. TPG11, TPC03, 186, 2598

Davies-White, W. RAA04, 530

Davis, P. WPC20, RPA21, RPA22, 1039, 1102, 1105

Dawson, J. WAG09, TPC16, 640, 2637

De Angelis, A. TPG11, 186

De Brion, J.P. RAG06, 3170

de Groen, P. TAQ12, 1547

de Jager, C. RPG06, 330

de Leeuw, R.W. WAQ19, WAQ20, RPP04, RPQ31, 1882, 1885, 1970, 2738

De Martinis, C. TPC10, 2619

De Mascureau, J. TAE09, 1210

De Rijk, G. RAA11, 548

de Rijk, G. WAP12, WAP13, 464, 467

de Wijs, M.C.J. WAQ19, 1882

Deadrick, F. RPC18, TAR17, WPA02, TAE01, 743, 837, 905, 1178

Deadrick, F.J. TAR14, TPB14, 828, 2557

DeBarger, S. FAP16, 1366

Debraine, A. WAG07, 634

Decker, C.D. RAB01, RAB02, 758, 761

Decker, F.J. WAG11, RPB04, WAC17, 646, 665, 3109

Decker, F.-J. RPB02, WPR15, TPC20, RAP15, RAP16, RAP17, WAB05, WAB07, RAQ03, 659, 1821, 2646, 2919, 2922, 2925, 3025, 3031, 3291

Decker, G. FAR13, FAR19, MPQ03, MPQ08, MPQ10, RPQ16, 290, 303, 2452, 2467, 2473, 2702

Decker, Glenn RAR24, 3409

Decking, W. FAA02, FAB01, FAC19, 195, 2789, 2874

DeCobert, J. WAA16, 1260

Degen, C.M. TPB12, 2551

Dehnel, M. WAQ07, 1858

Dehning, B. WAP14, RAA19, 470, 567

Deltinghoff, H. WPA04, RPR06, RPR18, 911, 1131, 1158

Dejus, R. TPC03, 2598

Delahaye, J.P. RPC10, 719

Delahaye, J.-P. RPC09, 716

delaRama, F. TAE01, 1178

Dell, G.F. MPC05, FAB20, 2327, 2829

Dellwo, J. MPE05, WPC12, 871, 1022

Delsart, Ph. TAE09, 1210

Deluen, J.-P. RAA15, 557

Demko, J.A. MPP01, 2034

Den Hartog, P. MPP16, 2072

Deng, D. WAC24, 3131

Deng, D.P. WPP07, WPQ19, 1669, 1765

Deng, D.-P. MPB08, RAQ22, RAR29, 2288, 3334, 3421

Deppe, G. TPP11, 1639

Derenchuk, V. WPC08, RAP22, RAQ24, 1010, 2937, 3340

Desavouret, E. FAP06, FAP07, MPB06, 1337, 1340, 2285

Desmons, M. WPB22, 998

Despe, O. FAQ18, 1429

Deviatilov, V. WAA18, 1266

Devin, A. TAE09, TPC17,

1210, 2640
Dewa, H. FAR08, RPA13, WAQ01, 278, 1079, 1843
Dey, J. WPP08, WPP09, WPP23, RAQ13, 1672, 1675, 1714, 3312
Di Bona, A. WPC23, 1049
Di Crescenzo, J. RAG06, 3170
Dickey, C. FAA08, RPA17, WAA10, MPA11, 213, 1090, 1248, 2217
Dieperink, J. RAA15, 557
Dieulot, J.M. WAG07, 634
Dikansky, N. WPG06, TAR11, 500, 819
Dikansky, N.S. TAC06, WAA17, 143, 1263
DiMarco, J. FAP06, FAP07, 1337, 1340
Dinehart, M.R. WAQ26, 1897
Dinkel, J. WAA05, WAR01, 1236, 1900
Dinkel, J.A. WAA07, 1239
Dipace, A. TPG11, 186
Diviacco, B. FAQ19, 1432
Dobbe, N. MPQ17, 2491
Dobbins, J.A. RAE14, 2426
Dobeck, N. RPP06, 1973
Dobrovodsky, J. TAA18, 2120
Dodson, G. RPG05, 327
Dohlus, M. RPB15, RPB16, TAQ06, WPP05, WAE13, MPC16, 692, 695, 1533, 1666, 2190, 2345
Doinikov, N. MPC21, 2359
Dolbilov, G.V. WAA20, TAQ34, 1272, 1605
Dolique, J.-M. TPR04, TPR05, 3245, 3248
Donald, M. RAA22, 576
Donald, M.H.R. RAA27, 591
Donaldson, A.R. RPB05, WAA11, WAR06, RPP07, 668, 1251, 1915, 1976
Donaldson, T. WAQ15, 1876
Dooling, J.C. RAQ16, 3320
Doolittle, L. MPR13, MPR14, 2265, 2268
Doornbos, J. RPG12, 348
Doose, C. TPE08, 1310
Doria, A. TPG11, 186
Douglas, D. FAA25, WAQ14, 243, 1873
Douglas, D.R. WXE01, 2429
Dovbnya, A.N. WPA15, WPA16, WPB16, 938, 939, 988
Dow, K. RPG05, 327
Dowell, D.H. FAA27, FAA28, WPB20, 248, 251, 992
Dowling, D.T. TAP07, WAQ26, 366, 1897
Doyle, E. FAE07, 1497
Drago, A. RAE12, RPQ01, 2420, 2660
Drees, A. RAA19, 567
Dressler, J. RAA03, 527
Drevlak, M. RPB14, 689
Drury, M. FAE12, 1512
Du, W. FAP01, 1322
Dugardin, F. TAB04, 116
Dunbar, A. WAB04, 3022
Dunham, B. MPR15, TPC07, 2271, 2610
Dunham, B.M. WPC17, 1030
Dunnam, C.R. RAE14, 2426
Dunning, F.B. WPC21, 1043
Durand, R. TPP04, WPQ02, 1623, 1720
Durfee III, C.G. WAG04, 621
Durieu, L. TAP14, 386
Durkin, A.P. RPR07, 1134
Dutto, G. RPG12, MPE03, WAQ07, 348, 864, 1858
Dykes, D.M. WPQ18, WAC22, 1762, 3125
Dylla, F. WPA17, 942
Dylla, H.F. FAG11, FAA25, 102, 243
Early, R. RPC02, 701
East, G. RAP21, RAP22, RAQ23, RAQ24, 2934, 2937, 3337, 3340
Ecklund, S. RPB01, RPC01, 656, 698
Ecklund, S.D. WPC18, 1033
Edighoffer, J. RPA26, 1116
Efimov, S. FAR17, RAA08, 299, 542
Egawa, K. RAA33, 603
Ehrlich, R. FAE13, 1515
Ehrlichmann, H. RPE08, 2017
Eichenberger, C. WAA19, 1269
Eichhorn, K.D. FAR06, 272
Eigenmann, B. FAR06, 272
Einfeld, D. TPG08, FAR06, WPQ24, 177, 272, 1776
Ekelöf, Tord TPC11, 2622
Elias, L.R. FAA29, 254
Elizondo, J. WAA19, TAA20, 1269, 2123
Elleauume, P. TPE10, 1319
Ellison, M. WPP20, WPP21, RAP21, RAP22, WAC12, RAG10, RAQ23, RAQ24, 1705, 1708, 2934, 2937, 3094, 3182, 3337, 3340
Ellison, T. TPB24, RAP22, 2583, 2937
Elsener, K. WAP14, 470
Emamian, M. FAA08, TAA02, 213, 2081
Emery, L. MPR01, MPB17, MPQ10, 2238, 2309, 2473
Emma, P. WAG11, RPB01, RPC03, RPC06, WAB07, 646, 656, 704, 707, 3031
Emma, Paul WAG01, 606
Emoto, T. TAQ08, 1539
Enchevich, I.B. WPP18, 1699
Engels, O. WPA04, WPA05, 911, 914
Engwall, D. FAG11, WPA17, 102, 942
Enjeti, Prasad N. RPP11, 1985
Enomoto, A. TAQ08, TAQ25, TAA04, 1539, 1578, 2087
Erdman, K. WAQ07, 1858
Eremeev, I.P. FAG10, TAC11, 98, 146
Erg, G.I. FAQ17, 1426
Erickson, R. RPA24, FAP16, 1111, 1366
Ermakov, D. RPA19, 1096
Ermakov, D.I. RAR04, 3361
Erochin, A. FAQ06, 1399
Escallier, J. FAQ03, 1393
Esin, S.K. RPR24, RPR25, RAE08, 1173, 1175, 2408
Estrin, B. WAA17, 1263
Etzkorn, F.J. WPQ26, 1781
Evans Jr., K. MPQ03, 2452
Evans, L.R. FPD04, 40
Everett, M. RAB05, 770
Everett, M.J. RAB04, 767
Evtushenko, Yu.A. FAQ17, 1426
Eyharts, Ph. TAE09, 1210
Eyl, P. TAE09, 1210
Eylon, S. TAR14, WPA02, WPA09, TAE01, TAE11, WAQ04, 828, 905, 926, 1178, 1216, 1852
Ezura, E. FAE09, TPP16, WPQ08, WPQ17, WPR05, WPR09, RPQ06, 1503, 1652, 1735, 1759, 1797, 1806, 2675
Fabris, A. FAR21, WPQ04,

TAG05, 309, 1723, 2762
Fabris, R. FAR21, 309
Fackler, O. RAA03, 527
Fahmie, M. RPQ08, 2681
Fainberg, Ya.B. RAB15, WAA02, WAA03, 782, 1230, 1233
Fallis, M.C. WPR20, 1835
Faltens, A. FAP17, FAP18, TPA10, 1369, 1372, 3220
Fan, T.C. FAQ26, 1450
Fang, C.S. MPQ32, 2524
Fang, S. MPR16, 2273
Fang, S.X. WAB20, 3064
Fang, Si J. FAP05, 1334
Fang, Ye TAR22, 850
Fant, K. WPR08, 1803
Farias, R.H.A. FAP14, 1361
Farkas, Z.D. WPR15, 1821
Farkhondeh, M. RPG05, 327
Farvacque, L. TPG05, 167
Farvid, A. MPP09, 2054
Fateev, A.A. WAA20, TAQ34, 1272, 1605
Fathizadeh, M. TAP05, 363
Faugeras, P. TPE03, 1288
Faugier, A. WAP12, WAP13, RAA11, 464, 467, 548
Faure, J. FAR14, 293
Fawley, W. FAP17, 1369
Fawley, W.M. FAA12, RAB03, FAP18, TPA10, 219, 764, 1372, 3220
Fazio, Michael V. FAE06, 1494
Fedin, O.L. MPG10, 426
Fedotov, A.P. RPR07, 1134
Fedotov, Alexei V. TPR12, 3266
Fedotov, Yu. MPR11, 2259
Feerick, B. WAQ15, 1876
Feldl, E. TPC04, 2601
Feldman, Donald W. WPB15, 985
Fellenz, B. MPQ13, 2479
Feng, W. WAR12, 1927
Feng, W.Q. WAA15, 1257
Ferdinand, R. RPR11, RAG07, 1146, 3173
Ferguson, M. RPP12, 1988
Ferianis, M. TPG11, FAR21, 186, 309
Feriolli, F. WAP13, 467
Fernow, Richard MXG03, 53
Ferrario, M. WAC13, 3097
Feschenko, A.V. RAE08, 2408
Fessenden, R.W. TAB17, 131
Fessenden, T. TAR17, 837
Fessenden, T.J. TAR13, TAR14, TPB14, 825, 828, 2557
Fidecaro, G. WAP14, 470
Fieguth, T. WAQ15, 1876
Field, R. TAG01, 2742
Field, R.C. WXE07, 2444
Fietier, N. FAG09, 95
Filatov, B.A. WAA21, 1274
Filtz, M. MPC28, 2373
Fink, C.L. FAG14, 110
Fiorentini, G. WPB10, 973
Firjahn-Andersch, A. WPA03, 908
Fischer, C. RPC14, TPC21, 731, 2649
Fischer, Henk WAB06, 3028
Fischer, W. TAG07, 2768
Fisher, A. TPG14, RAA04, 192, 530
Fitzgerald, D. WPC10, WAC29, RAR23, 1016, 3146, 3406
Fitzgerald, J.B. TPG09, RAE10, 180, 2414
Flanz, J.B. RPE03, 2004
Flechtner, D. WPC19, 1036
Fleckner, K. RPA26, 1116
Fliflet, A.W. TAQ37, 1611
Flood, R. RPP13, 1991
Flora, R. WAE07, 2172
Flöttmann, K. TAA08, TAG01, 2096, 2742
Flynn, G. FAE13, RAR18, 1515, 3391
Fockler, J. WAA19, 1269
Foelsche, H. FAQ15, 1420
Foelsche, H.W. FAP11, 1352
Foley, M. FAG06, WPP01, 86, 1655
Fomin, M. WPP11, 1681
Fong, K. MPR16, 2273
Forest, E. RAA22, RAA25, FAB06, 576, 585, 2804
Forsyth, E.B. WAA15, WAR10, WAR12, 1257, 1921, 1927
Foster, G.W. MPG11, WAP16, TPE05, 428, 473, 1298
Foster, J. WPB06, 961
Foster, W.B. FAP21, 1381
Foualdy, M. TPP09, TPP11, TPP14, 1632, 1639, 1648
Fougeron, C. WPQ26, 1781
Fowkes, W.R. FAE07, TAQ28, 1497, 1587
Fowler, W. MPG01, 391
Fox, J. RAA04, RAE12, RAE13, RPQ01, RPQ08, 530, 2420, 2423, 2660, 2681
Fox, T. MPR13, 2265
Frachon, D. FAQ17, FAQ18, 1426, 1429
Franks, R.M. WPQ06, 1729
Franzke, B. MPC15, 2342
Freund, A. WAP14, 470
Fricks, R. MPA11, 2217
Friedman, A. TAR14, TAR15, TAR17, FAQ17, TPR19, 828, 831, 837, 1426, 3282
Friedman, Aharon RPQ14, 2696
Friedrich, L. FAR06, 272
Friedsam, H. TAP05, TAA03, 363, 2084
Friesel, D. WPP20, WPP21, RAQ24, 1705, 1708, 3340
Friesel, D.L. RPG08, TAP03, WAQ08, 336, 357, 1861
Frisch, J. WAG11, MPE10, 646, 887
Fu, Shinian FAA21, RAQ25, RAQ26, 237, 3343, 3346
Fugitt, J. FAG11, FAA25, WPA17, RPQ30, 102, 243, 942, 2735
Fuja, R. RPA10, RPA11, MPQ08, MPQ10, 1070, 1073, 2467, 2473
Fuja, R.E. TPC01, 2595
Fujino, T. TPP07, 1629
Fujita, H. FAR08, RPA13, WAQ01, 278, 1079, 1843
Fukuma, H. RAA33, 603
Fukutomi, M. TPP16, 1652
Fullett, K. WAR17, WAR18, 1939, 1942
Funahashi, Y. TPP07, 1629
Funakoshi, Y. MPQ31, WAC08, 2521, 3085
Furman, M. RPC02, TPQ16, 701, 2986
Furman, Miguel A. RAP14, 2916
Furuya, T. TPP03, 1620
Fusellier, J. WAG07, WPB22, 634, 998
Gai, W. WAG06, WPB11, MPQ11, 631, 976, 2476
Galayda, J. RPQ16, 2702
Galayda, John N. MAD02, 4
Gallardo, Juan C. MXG03, WPB21, 53, 995
Gallerano, G.P. TPG11, 186
Gamo, N. TPP03, 1620
Ganetis, G. TPE04, FAQ02,

FAQ03, FAQ04, FAQ15, 1293,
 1390, 1393, 1396, 1420
Ganetis, G.L. TAA09, 2099
Gangeluk, M. WPR13, 1815
Gao, J. RPA03, 1055
Gao, Jie WPQ01, 1717
Garcla, R.C. TPC06, 2607
Gardner, C.J. TAP11, TAP13,
 378, 383
Garnett, R.W. RAG11, 3185
Garoby, R. MPG09, 423
Garosi, F. TPG11, 186
Garrel, N. WAP12, RAA15,
 464, 557
Garren, A. WPG11, 520
Garren, A.A. TAB06, 119
Garvey, J.D. FAP06, FAP07,
 1337, 1340
Garvey, T. WPA14, WPB22,
 935, 998
Gavaggio, R. MPP15, 2069
Gavrillov, N.G. FAQ17, 1426
Gay, T. WPC21, 1043
Gayet, Ph. MPP02, 2037
Geisik, C. WPC10, 1016
Gelato, G. MPG09, 423
Gelfand, N.M. RAB19, 787
Gelfand, Norman M. WAP07,
 452
Geller, J. WAR11, RPP02,
 1924, 1964
Geng, X. MPA01, 2193
Genova, L. RAA04, 530
Georges, J.P. TAB04, 116
Georges, P. WPB01, 945
Geschonke, G. TPP12, 1642
Gevchuk, A. FAR17, 299
Ghiorso, W. TPA10, 3220
Ghosh, A. TPE04, FAQ03,
 FAQ04, 1293, 1393, 1396
Giacuzzo, F. MPP04, 2042
Giannessi, L. TPG11, 186
Giannini, M. TPG11, FAR21,
 186, 309
Gilgenbach, R.M. TAQ32,
 1599
Gillespie, G.H. RPR20, 1164
Gillespie, George H. FAG13,
 MPB14, 107, 2300
Gilpatrick, J.D. RPR19,
 RPR22, TPB16, TPB22, 1161,
 1167, 2563, 2580
Giordano, G. RPC17, 740
Giovannozzi, M. FAC06, 2847
Glove, D. TAA07, TPC10,
 2093, 2619
Giovenale, E. TPG11, 186

Gladkikh, P. FAR17, 299
Glass, H. TPE05, 1298
Glass, H.D. FAP05, FAP06,
 FAP07, MPB05, MPB06, 1334,
 1337, 1340, 2282, 2285
Glazov, A. WPC13, WPR19,
 1025, 1833
Glenn, J.W. TAP13, WAR13,
 383, 1930
Glock, H.-W. RPB15, RPB16,
 692, 695
Glover, E. TPG07, 174
Gluckstern, R. RPA04, 1058
Gluckstern, R.L. TPQ14, 2980
Gluckstern, Robert L.
 RAG09, TPR11, TPR12, RAR12,
 3179, 3263, 3266, 3376
Gluskin, E. TPE06, FAQ17,
 MPP16, 1301, 1426, 2072
Goddard, B. RAA15, 557
Goderre, G. WAP08, 455
Goderre, G.P. WAP05, 446
Godfrey, G. WAQ15, 1876
Godlove, T.F. TAE10, 1213
Godlove, Terry F. TAA17,
 2117
Godot, J.C. RPC10, 719
Goffeney, N. RPC17, 740
Gold, C. RPA10, 1070
Gold, S.H. TAQ37, 1611
Goldberg, D.A. WPQ13, 1747
Goldman, M.A. TAA09, 2099
Goldstein, J.C. FAA16, 228
Golkowski, Cz. TAQ01, 1518
Golubev, I.I. WAA20, 1272
Golubev, V. WPC03, 1004
Goncharov, A.D. TAC06,
 RPP08, 143, 1979
Gonichon, J. MPE12, 893
Gonin, I.V. RPR01, 1119
Goral, J. RPA11, 1073
Gordeeva, M.A. MPG10, 426
Gordon, D. RAB04, RAB05,
 767, 770
Gorelov, D.V. RPR01, 1119
Gorev, V.V. MPE06, 874
Gorin, M.Yu. WAR23, 1955
Gorniker, E. WPP11, 1681
Gorski, A. FAP03, 1328
Goto, A. WPC01, 1001
Gougnaud, F. WPB22, 998
Gournay, J.F. WPB22, 998
Govil, R. TPG07, RAB10, 174,
 776
Gower, E. RPA26, 1116
Graber, J. FAE03, 1478
Gracila, J. RAA04, 530

Granatstein, V.L. TAQ17,
 TAQ18, TAQ19, 1561, 1563,
 1566
Gras, J.J. TPC21, 2649
Grassi, R. FAC06, 2847
Grau, M.C. MPQ05, 2458
Graves, W.S. FAQ13, 1414
Gray, E.R. RAG11, 3185
Green, M. WPG11, 520
Green, M.A. TAB06, 119
Greene, A. TPE04, FAQ03,
 FAQ04, FAQ15, 1293, 1393,
 1396, 1420
Greenly, John B. TAE07,
 1204
Greenwald, Z. FAE13, TPA04,
 1515, 3206
Grelick, A. RPA11, 1073
Grelick, A.E. RPA10, RPA14,
 RPE09, 1070, 1082, 2020
Greth, V.N. WAR20, 1948
Gridasov, V. FAQ06, 1399
Grieser, M. RPR06, 1131
Grigor'ev, Yu.N. RAA07,
 RAQ28, 539, 3349
Grimm, T. RPG11, 345
Grimmer, J. RPE09, 2020
Grishin, V.K. FAG12, FAA14,
 105, 225
Gröbner, O. RPE02, 1999
Gromme, T. RAE03, 2389
Gross, G. WAR06, 1915
Grossberg, P. RAE03, 2389
Grosse-Wiesmann, P. RAA19,
 567
Grote, D. TAR17, TAE01, 837,
 1178
Grote, D.P. TAR13, TAR14,
 TAR15, WPA09, TPR19, 825,
 828, 831, 926, 3282
Grote, H. RAA19, 567
Grudlev, A. MPB09, 2291
Grunder, Hermann A. MAD01,
 1
Gubin, K. WAA17, 1263
Guckel, H. WPE02, 63
Gudkov, K. RPA19, 1096
Gudkov, K.A. FAG12, 105
Guharay, Samar K. MPC04,
 2324
Guidi, V. RAE05, 2399
Guignard, G. RPC09, RPC12,
 RPC13, 716, 725, 728
Guinand, R. RAA15, 557
Guo, H. TAQ17, 1561
Guo, Z. TPQ03, 2955
Gupta, R. TPE04, FAQ04,

FAQ16, TAA09, 1293, 1396,
 1423, 2099
Gupta, R.C. WAP10, 461
Gur'yev, M.P. MPG10, 426
Gurov, G. MPG06, 416
Güsewell, D. MPP02, 2037
Gusinskii, G.M. TAP16, 389
Gustafson, Dick TPE05, 1298
Gustavsson, J. FAA08, 213
Guy, F.W. RPG10, 342
Gyr, M. WAP14, WAQ24, 470,
 1891
Haber, I. TAR15, TPR19, 831,
 3282
Haberichter, W. TPC16, 2637
Habib, Salman RAG01, 3149
Habs, D. RPR06, 1131
Haddock, C. FAQ14, 1417
Haebel, E. TPP12, 1642
Haffmans, A.F. RAG14,
 RAQ20, 3194, 3329
Hafizi, B. TAQ37, 1611
Haga, K. RPQ23, 2720
Hagedoorn, H.L. WAQ19,
 WAQ20, RPP04, RPQ31, 1882,
 1885, 1970, 2738
Hahn, H. TPQ02, 2952
Hahn, K.D. TPA10, 3220
Hahn, U. FAR07, 275
Haimson, J. RPC22, TAQ03,
 755, 1524
Hairapetian, G. WPC20,
 RPA21, RPA22, 1039, 1102,
 1105
Hakota, M. TAQ35, 1608
Hall, P.J. FAP06, FAP07,
 MPB06, 1337, 1340, 2285
Haller, M. FAR06, 272
Halling, M. RPC20, RPC21,
 TAG01, 749, 752, 2742
Hamilton, B. TPB24, RAP21,
 RAP22, RAQ24, 2583, 2934,
 2937, 3340
Hammel, E. TPB07, 2542
Han, Bumsoo TAB09, FAR03,
 122, 269
Han, D.H. WPR11, 1812
Hanna, B. WAR01, 1900
Hanna, S.M. RPA23, 1108
Hanne, G.F. WPC21, 1043
Haouat, G. RAG06, RAG07,
 3170, 3173
Hardek, T. WAC29, 3146
Hardek, T.W. TAQ31, 1596
Harding, D.J. FAP04, FAP05,
 FAP06, FAP07, FAP09, MPB05,
 MPB06, 1331, 1334, 1337,
 1340, 1346, 2282, 2285
Harkay, K. TAP05, TPQ22,
 TPQ23, 363, 3001, 3004
Harrison, M. MPG03, TAA09,
 401, 2099
Harrison, M.A. MPG12, 431
Hartill, D.L. RAE14, 2426
Hartley, R. FAA19, 234
Hartley, R.A. FAA31, 260
Hartman, S. RPB02, RPC20,
 WXE07, TAG01, 659, 749,
 2444, 2742
Hartman, S.C. RPB04, TPC29
 665, 2655
Hartnagel, H.L. MPC15, 2342
Hartung, W. FAE13, TPA04,
 RAQ04, RAR18, RAR19, 1515,
 3206, 3294, 3391, 3394
Harwood, S.L. WXE01, 2429
Hasegawa, K. RPG09, 339
Haseroth, H. MPG09, 423
Haseroth, H.D. MPG05, 411
Hashimoto, S. FAQ21, 1438
Hathaway, D. MPP12, MPP20,
 2064, 2075
Hawkins, A. WAA16, 1260
Hayakawa, A. WXE07, 2444
Hayano, H. RPA20, WPR03,
 TPC05, TAG01, 1099, 1791,
 2604, 2742
Hayashi, E.K.C.S. MPQ33,
 2527
Hayashi, S. FAP13, 1358
Haynes, D.L. WAQ26, TPC18,
 1897, 2643
Haynes, W. Brian FAE06,
 1494
Hays, S. WAE07, 2172
Hays, T. FAE13, TPP02,
 WPQ02, 1515, 1617, 1720
Hayward, T.D. FAA27, FAA28,
 WPB20, 248, 251, 992
Hedblom, K. WPP20, WPP21,
 WAQ08, RAP21, 1705, 1708,
 1861, 2934
Heese, R. FAR10, 284
Heifets, S. MPC01, MPC08,
 TPQ16, 2317, 2333, 2986
Heifets, S.A. TAA22, MPC02,
 MPC03, MPC18, 2129, 2319,
 2321, 2351
Heim, J. RAA03, 527
Heimlinger, G. TAG01, 2742
Heine, E. TAQ12, MPQ17,
 1547, 2491
Heinrichs, G. TPB20, 2574
Helm, R. RAA22, RPC06,
 RPC07, RPC20, TAA08, TAG01,
 576, 707, 710, 749, 2096,
 2742
Helvajian, H. FAG11, 102
Hemelhoet, G.H. WAE09, 2178
Hémery, J.-Y. TAP14, 386
Hemmer, M.F. TAA09, 2099
Henderson, S. FAE13, 1515
Henderson, T. FAP01, 1322
Hendrickson, L. RAE03, 2389
Hendrickson, L.J. WAG11,
 RPB03, 646, 662
Henestroza, E. RPC16, RPC17,
 RPC19, WPA02, WPA09, TAE01,
 TAE11, MPC01, MPC08, TPA10,
 737, 740, 746, 905, 926,
 1178, 1216, 2317, 2333, 3220
Henke, H. TAQ30, WPQ14,
 WAB11, 1593, 1750, 3043
Henkel, D.P. FAG11, 102
Hentges, M. MPP01, 2034
Herold, W. WPA12, 929
Herr, W. WAP14, WPG09, 470,
 514
Herrup, D.A. TPQ25, TPQ26,
 3007, 3010
Hershcovitch, A. WPC09,
 1013
Herz, P. TPB07, 2542
Hettel, R. MPQ22, RPQ21,
 RPQ22, 2506, 2714, 2717
Heutenik, B. TAQ12, 1547
Heydari, Huschang WAP09,
 458
Higashi, Y. WPQ15, 1753
Higgins, D.S.G. WPQ18, 1762
Higgins, S. MPR13, 2265
Higo, T. FAQ08, WPQ15,
 WPR02, WPR03, 1405, 1753,
 1788, 1791
Higo, Toshiyasu FAE02, 1474
Higuchi, A. RAQ06, 3300
Higuchi, T. TPP07, 1629
Hilaire, A. WAP12, WAP13,
 464, 467
Hill, B.W. RPR20, 1164
Hill, Barrey W. MPB14, 2300
Hill, S.F. WAC21, 3122
Hilleret, N. TPP12, 1642
Himel, T. RAE03, 2389
Hindi, H. RAE12, 2420
Hinode, F. WPQ16, WPR02,
 WPR03, TPC05, 1756, 1788,
 1791, 2604
Hipple, R. WPA01, TAE01,
 902, 1178
Hiramoto, K. TAB03, WPQ21,

113, 1770
Hirano, K. TAQ08, 1539
Hirata, K. RAP02, 2883
Hirata, Y. WPR02, 1788
Hirota, J.I. TAB03, WPQ21, 113, 1770
Hizanidis, K. RAQ01, 3285
Ho, C. WPB11, 976
Ho, C.H. WPB07, 964
Hoag, H. RPA04, WPQ05, 1058, 1726
Hoag, H.A. RPA23, 1108
Hobson, B. RAA03, 527
Hodges, T. RPG12, 348
Hodgkins, D. MPE04, WPA08, 867, 923
Hodgson, J. WPR08, 1803
Hoeflich, J. RAE12, 2420
Hoffstätter, G.H. FAB07, 2807
Hofler, A. MPR13, 2265
Hofmann, A. RAA17, RAA18, RAA20, FAC03, 560, 564, 570, 2841
Hogan, B. TAQ18, TAQ19, 1563, 1566
Hogan, M. FAA23, RPA21, RPA22, 240, 1102, 1105
Hogrefe, R. TPE08, 1310
Hohbach, R. TAQ33, 1602
Holdener, F.R. MPP12, MPP20, TAA22, 2064, 2075, 2129
Holmes, C. WAA19, 1269
Holmes, S. MPG01, 391
Holmes, S.D. WAP01, 434
Holmquist, T. RAE14, 2426
Holsinger, R.F. TPE07, 1305
Holt, J. RPC20, 749
Holt, J.A. WAP01, WAP08, RPC21, TAG01, WAC01, 434, 455, 752, 2742, 3067
Holtkamp, N. FAR06, RPB12, RPB13, RPB15, RPB16, WPA12, WPP05, MPC16, 272, 683, 686, 692, 695, 929, 1666, 2345
Holtzapple, R.L. WXE05, WAB05, WAC04, WAC17, 2438, 3025, 3073, 3109
Honda, T. RPQ23, 2720
Honecker, V. FAR06, 272
Hopster, H. WPC21, 1043
Horan, D. TAP05, RPP12, 363, 1988
Hori, T. WPC22, MPA07, 1046, 2208
Houck, T. RPC16, RPC17, WPC16, 737, 740, 1027
Houck, T.L. TAQ03, 1524
Hovater, C. FAE12, TPC26, RPQ29, 1512, 2652, 2732
Howell, J. TAR08, 816
Hower, N. FAA08, RPA17, TAA02, MPQ06, 213, 1090, 2081, 2461
Hower, Nelson WPA13, 932
Hoyer, E. FAQ24, FAQ25, 1444, 1447
Hoyt, E. MPP09, MPP12, MPP20, 2054, 2064, 2075
Hoyt, M. MPP09, MPP12, MPP20, 2054, 2064, 2075
Hseuh, H.C. TAP11, TAP12, MPP11, 378, 381, 2060
Hsieh, H. RAA05, RPA26, 533, 1116
Hsiung, G.-Y. TPC15, 2634
Hsu, I. TAA28, 2135
Hsu, Ian MPQ26, TPC15, RAR05, 2515, 2634, 3364
Hsu, K.T. FAA04, FAA07, RAA23, RAA24, MPR10, MPQ16, MPQ19, MPQ32, TPB29, TPQ08, TPQ09, TPQ10, 201, 210, 579, 582, 2256, 2488, 2497, 2524, 2592, 2965, 2968, 2971
Hsu, R.-C. TPC15, 2634
Hsu, S.Y. WPB07, 964
Hsue, C.S. RAA24, TAR04, TPQ09, TPQ10, 582, 804, 2968, 2971
Huang, Gloria MPR10, 2256
Huang, H. TPA06, 3212
Huang, J.Y. TPG06, 171
Huang, N. RAA21, WAC27, 573, 3140
Huang, Zhibin FAA21, RAQ25, RAQ26, 237, 3343, 3346
Huang, Zhirong RAQ18, 3326
Huffman, G. FAE07, 1497
Hughes, Thomas P. TAE08, 1207
Hülsmann, P. RPB15, RPB16, 692, 695
Humbert, J. FAP03, 1328
Hümmer, K. FAR06, 272
Humphries, D. FAQ24, FAQ25, 1444, 1447
Hunt, D. MPP13, 2067
Hustache, R. WAP14, 470
Hutson, R. WAC29, 3146
Hutson, R.L. TAR12, 822
Huttel, E. FAR06, 272
Hutton, A. TPC26, 2652
Hwang, J.I. WPB07, 964
Hwang, O.H. TAQ14, 1553
Hwu, K.H. MPQ19, 2497
Iazzourene, F. FAR21, TAG05, 309, 2762
Ieiri, Takao TPB17, 2566
Igarashi, Y. TAQ25, 1578
Igarashi, Z. WPC07, 1007
Ignatyev, A. TAB13, TAQ23, TAQ24, 125, 1572, 1575
Ihloff, E. RPG05, 327
Iida, S. TPP03, 1620
Ikegami, K. WPC07, 1007
Ikegami, M. FAR08, RPA13, WAQ01, 278, 1079, 1843
Ilijinov, A.N. RPR01, 1119
Imai, Y. FAQ08, 1405
Imanishi, A. RPG13, 351
Imel, G.R. TAC12, 149
Inagaki, S. TPP16, 1652
Inaguchi, T. FAQ08, 1405
Ingalls, W. WPC10, 1016
Ingwersen, Pete TAE07, 1204
Inman, T.K. RPA24, 1111
Ino, H. RPG09, 339
Inoue, H. TPP07, 1629
Inoue, M. FAR08, RPA13, RPA18, WPQ21, WAQ01, 278, 1079, 1093, 1770, 1843
Irwin, J. RAA22, RAA25, RAA26, RAA27, RPC01, RPC06, RPC07, RPC08, RPC20, TAA08, TAG01, TAG06, FAC18, RAP09, RAP11, RAP12, 576, 585, 588, 591, 698, 707, 710, 713, 749, 2096, 2742, 2765, 2871, 2904, 2910, 2913
Irwin, John MPC31, 2376
Irwin, M. WPQ13, 1747
Isagawa, S. TPP16, 1652
Ishi, Y. TAP04, TPP03, 360, 1620
Ishida, T. MPQ18, 2494
Ishihara, N. TAG01, 2742
Ishii, H. MPQ31, 2521
Ishkhanov, B. RPA19, 1096
Ishkhanov, B.S. FAG12, FAA14, 105, 225
Issinsky, I.B. WAR09, FAC12, 1918, 2863
Ito, I. TAQ35, 1608
Ito, N. RPG09, 339
Itoh, Y. MPA07, 2208
Ivanov, A. TAC16, 152
Ivanov, A.A. WAR20, 1948
Ivanov, A.S. TAE13, 1222

Ivanov, I.N. WAA20, 1272
 Ivanov, P. RAA31, 600
 Ivanov, P.M. FAQ17, FAQ18, 1426, 1429
 Ivanov, S. WPP05, MPC16, TPQ01, TPQ04, 1666, 2345, 2949, 2958
 Ivanov, Yu.D. RPR07, 1134
 Ivers, J.D. WPC19, TAE12, 1036, 1219
 Iverson, R. RPC20, TAA28, WXE07, TAG01, 749, 2135, 2444, 2742
 Iwashita, Y. FAR08, RPA13, RPA18, WPQ21, WAQ01, 278, 1079, 1093, 1770, 1843
 Izawa, M. TPP03, WPQ07, WPR04, 1620, 1732, 1794
 Jablonka, M. WPA14, WPB22, 935, 998
 Jackson, A. FAA03, FAA05, RPC02, 198, 204, 701
 Jackson, G. MPG11, WAP16, TPE05, WAR19, MPQ13, RAP20, WAC09, WAC10, 428, 473, 1298, 1945, 2479, 2931, 3088, 3091
 Jackson, L.T. RPP01, RPP07, 1961, 1976
 Jackson, T. RAA04, FAQ24, 530, 1444
 Jacob, J. TPG05, FAR06, 167, 272
 Jacobs, K. RPG05, RAA31, 327, 600
 Jacquemard, B. WPB22, 998
 Jacquet, F. WAG07, 634
 Jaeschke, E. RPR06, FAQ12, 1131, 1411
 Jaffery, T.S. FAQ32, 1465
 Jagger, J. FAP03, 1328
 Jain, A. WAP10, TPE04, FAQ03, FAQ04, FAQ16, TAA09, 461, 1293, 1393, 1396, 1423, 2099
 Jamison, R.A. RPR20, 1164
 Jan, G.J. MPR10, MPQ16, TPB29, 2256, 2488, 2592
 Jang, J.S. TPG06, 171
 Jarvis, H. WPR15, 1821
 Jason, A. WAC29, 3146
 Jason, Andrew J. TAE02, 1183
 Jayamanna, K. MPE03, WAQ07, 864, 1858
 Jean, Benedikt FAG03, 75
 Jeanjean, J. RPC20, TAG01, 749, 2742
 Jeanneret, B. FAC04, 2844
 Jenner, D. WPP20, WPP21, 1705, 1708
 Jensen, C. WAR01, 1900
 Jensen, C.C. WAA07, 1239
 Jensen, D. FAQ08, 1405
 Jensen, E. MPG09, 423
 Jiang, D.M. RPE10, 2023
 Jiang, Shicheng TPR11, 3263
 Jiang, W.S. MPP11, 2060
 Jiang, Y. FAP01, 1322
 Jianjun, Deng FAA26, 246
 Jin, K. WPP05, 1666
 Jin, L. RAA21, WAC27, 573, 3140
 Jinsul, Shi FAA26, 246
 Jobe, K. WPR15, 1821
 Jobe, R.K. WAB05, 3025
 Joffe, D. RPR02, 1122
 Joh, Kihun TAB09, FAR03, 122, 269
 Johnson, B. WPC21, 1043
 Johnson, C. RPC09, 716
 Johnson, D. RPG11, 345
 Johnson, D.E. TAB06, FAP04, FAP09, FAP10, 119, 1331, 1346, 1349
 Johnson, J. WPR14, RAE13, RPQ08, 1818, 2423, 2681
 Johnson, J.W. WAQ26, 1897
 Johnson, K.F. RPR19, RPR22, TPC06, 1161, 1167, 2607
 Johnston, M. WPC21, 1043
 Johnstone, C. FAG06, 86
 Johnstone, J. WAP01, 434
 Joho, W. FAB14, 2823
 Joly, J.M. WAG07, WPA14, WPB22, 634, 935, 998
 Joly, S. RAG06, 3170
 Jones, C.M. TPC18, 2643
 Jones, G.S. RPP06, 1973
 Jones, R.M. TAA33, MPC03, 2144, 2321
 Jones, W.P. TPB24, RAQ24, 2583, 3340
 Jongewaard, E. FAE07, 1497
 Jonker, M. WAP12, WAP13, RAA11, 464, 467, 548
 Jordan, K. FAG11, FAA25, WPA17, 102, 243, 942
 Joshi, C. WAG08, WAG09, RAB01, RAB02, RAB03, RAB04, RAB05, WPC20, RPA21, RPA22, TPB18, 637, 640, 758, 761, 764, 767, 770, 1039, 1102, 1105, 2569
 Judd, D.L. TAR14, 828
 Judkins, J. WPQ10, WPR08, 1741, 1803
 Juillard, M. WAG07, WPB22, 634, 998
 Junck, K. TPQ28, WAB01, 3013, 3016
 Jung, R. TPC21, 2649
 Junquera, T. WPB22, TPP09, TPP11, TPP14, 998, 1632, 1639, 1648
 Juras, R.C. WAQ26, MPA05, 1897, 2202
 Juras, S. TPP12, 1642
 Jurgens, T.G. MPB15, 2303
 Kachtanov, E. FAQ06, 1399
 Kadnikov, A. WAA18, WPR13, MPA04, 1266, 1815, 2199
 Kadokura, E. MPQ18, 2494
 Kageyama, T. FAE09, WPQ09, WPQ17, WPR05, WPR09, 1503, 1738, 1759, 1797, 1806
 Kahana, E. MPQ03, MPQ10, RPQ15, 2452, 2473, 2699
 Kahn, S. TPE04, FAQ16, 1293, 1423
 Kakigi, S. FAR08, RPA13, WAQ01, 278, 1079, 1843
 Kako, E. TPP07, 1629
 Kalashnikov, V.V. TPB25, 2586
 Kalbreier, W. RAA15, 557
 Kalfas, C. RAQ01, 3285
 Kaltchev, D. FAB14, 2823
 Kamber, I. RPC10, 719
 Kaminsky, A. TAC16, 152
 Kamiya, Y. FAR09, FAP22, WPQ07, WPR04, 281, 1384, 1732, 1794
 Kando, M. FAR08, RPA13, WAQ01, 278, 1079, 1843
 Kandrunin, V.N. WPR17, 1827
 Kaneda, T. FAP13, 1358
 Kang, Kyungwoo TAB09, FAR03, 122, 269
 Kang, Wongu TAB09, FAR03, 122, 269
 Kang, X. TAP03, WPP20, WPP21, RAP21, WAC12, RAG10, RAQ23, RAQ24, 357, 1705, 1708, 2934, 3094, 3182, 3337, 3340
 Kang, Y.G. FAR19, FAQ18, 303, 1429
 Kang, Y.W. WAG10, WPP16, RPE09, 643, 1693, 2020
 Kang, Yoon WPP12, 1684

Kaplan, R. FAE13, WPQ02, 1515, 1720
 Karantzoulis, E. FAR21, TAG05, 309, 2762
 Karantzoulis, Emanuel MPR12, 2262
 Karas', V.I. WAA02, WAA03, 1230, 1233
 Karas', Vyacheslav I. WAA01, 1227
 Karetnikov, M. RPR10, RPR15, 1143, 1155
 Karev, A.I. TAR05, FAP19, WPR17, 807, 1375, 1827
 Karl, F.X. TAA09, 2099
 Karn, J. MPR15, 2271
 Karnaukhov, I. FAR16, FAR17, RAA08, 296, 299, 542
 Karpenko, V. TAR17, 837
 Karshev, Yu. MPR11, 2259
 Kashikin, V. FAR06, 272
 Kasuga, T. RPQ23, RPQ26, RAQ06, 2720, 2726, 3300
 Katoh, M. RPQ23, 2720
 Katoh, T. MPA06, 2205
 Katsouleas, T. WAG09, RAB02, RAB08, TAA28, TPB18, 640, 761, 773, 2135, 2569
 Kaul, O. FAA02, FAC19, 195, 2874
 Kawai, M. RPG09, 339
 Kawakubo, T. RAB13, WAR04, MPQ18, 779, 1909, 2494
 Kawakubo, Tadamichi TPR16, 3275
 Kazarezov, I. WAA17, 1263
 Kazimi, R. WXE01, TPC07, 2429, 2610
 Keane, J. FAR10, TPP06, 284, 1626
 Keeley, D. RPQ21, RPQ22, 2714, 2717
 Keffeler, D. TAQ02, 1521
 Keffeler, D.R. WPA08, 923
 Kehne, D. FAG11, FAA25, WPA17, 102, 243, 942
 Keil, E. WPG09, 514
 Keith-Monnia, E. WAB04, 3022
 Keizer, R. WAP12, 464
 Kelley, M.J. FAG11, 102
 Kelly, D.R.C. RPE08, 2017
 Kelly, E. TPE04, FAQ03, FAQ04, FAQ15, 1293, 1393, 1396, 1420
 Kelly, K.W. TAA32, 2141
 Kemper, A.H. RPP04, 1970
 Kendall, M. RAA03, 527
 Kennedy, K. MPP13, 2067
 Kerner, T.M. MPA18, 2232
 Kerns, C. WPR21, 1838
 Kerns, J.A. TAA22, 2129
 Kerns, Q. WPR21, 1838
 Kerslick, G.S. WPC19, TAE12, TAQ01, 1036, 1219, 1518
 Kewisch, J. MPR20, 2279
 Khabiboulline, T. WPP05, 1666
 Khan, S. FAQ12, WAQ17, WAB03, 1411, 1879, 3019
 Kheifets, S.A. MPC18, 2351
 Khomyakov, E.A. TAE14, 1225
 Khrutchinsky, A.A. TPA15, 3232
 Kihara, Motohiro TPR16, 3275
 Kijima, Y. TPP03, 1620
 Kikuchi, M. RAA33, 603
 Kikutani, E. RPQ26, 2726
 Kikuzawa, N. TPG02, 159
 Kim, Byungmun TAB09, FAR03, 122, 269
 Kim, C. FAA03, FAA06, 198, 207
 Kim, C.H. FAA05, 204
 Kim, G.N. TAR07, 813
 Kim, J. TAA11, 2102
 Kim, J.W. RPR05, FAQ09, RAR21, 1128, 1408, 3400
 Kim, Jinsoo TAB09, FAR03, 122, 269
 Kim, K. TPE08, 1310
 Kim, K.-J. TPG07, TAG13, RAR02, 174, 2786, 3358
 Kim, Keeman TAB09, FAR03, 122, 269
 Kim, Kwang-Je RAP06, 2895
 Kim, S. FAR19, TAP05, FAB09, 303, 363, 2811
 Kim, S.H. FAA10, TPE08, 216, 1310
 Kim, Sungmyun TAB09, FAR03, 122, 269
 Kim, T.H. FAQ08, 1405
 Kim, T.Y. FAA10, 216
 Kim, Y.S. WPR11, 1812
 Kim, Younghee TAB09, FAR03, 122, 269
 Kim, Yuri TAB09, FAR03, 122, 269
 Kimura, W.D. WAG05, 626
 Kindermann, H.P. TPP12, 1642
 Kinkead, A.K. TAQ37, 1611
 Kinross-Wright, John M. WPB15, 985
 Kinsho, M. WPC07, WAQ06, 1007, 1855
 Kinter, R. RAB02, 761
 Kirbie, H.C. TAR14, 828
 Kirby, R. MPE10, MPP09, 887, 2054
 Kircher, J. FAR06, 272
 Kirchgessner, J. FAE01, FAE13, WPQ02, RAQ04, RAR18, RAR19, 1469, 1515, 1720, 3294, 3391, 3394
 Kirchman, J. RPQ15, RPQ16, 2699, 2702
 Kirk, Harold G. WPB21, 995
 Kiseljov, V.A. RAB15, 782
 Kishek, R. TAQ32, 1599
 Kishiyama, K. MPP12, MPP20, 2064, 2075
 Kiver, A. MPP03, 2040
 Kleffner, C.-M. RPR06, 1131
 Klein, H. RPB15, RPB16, 692, 695
 Klein, W.B. WAE08, 2175
 Klem, J. WAP14, 470
 Kleman, K.J. WPR01, 1785
 Klewe-Nebenius, H. FAR06, 272
 Klippert, T. MPP16, 2072
 Klopenkov, M. TAA18, 2120
 Kneisel, Peter TPP13, 1645
 Knobloch, J. FAE13, TPP04, 1515, 1623
 Knöchel, A. FAR06, 272
 Knuth, T. TPE09, 1316
 Ko, I.S. TAR07, RPA06, MPA02, 813, 1061, 2196
 Ko, K. RPA04, RPA11, RPA14, TAQ06, WPQ05, WPQ12, WPR07, MPC01, 1058, 1073, 1082, 1533, 1726, 1744, 1800, 2317
 Kobayashi, A. FAA30, 257
 Kobayashi, T. RAB13, WPQ17, 779, 1759
 Kobayashi, Y. FAR09, RPQ23, 281, 2720
 Kodaira, M. FAP13, 1358
 Koga, A. FAA30, 257
 Kogan, M. TPB04, 2536
 Kohaupt, Rolf-Dieter RPQ32, 2741
 Koike, S. WPQ15, 1753
 Koiso, H. TAG11, 2780
 Kokoulin, V. WAA17, 1263

Kokura, S. TPP03, 1620
Kolomiets, A.A. TPA05, 3209
Kolonko, J. WPG11, 520
Kolonko, J.J. TAB06, 119
Komarov, V. MPP03, MPR11, 2040, 2259
Komori, K. TPP16, 1652
Konecny, R. WAG06, WPB11, WPB12, 631, 976, 979
Kononenko, S. FAR16, FAR17, RAA08, 296, 299, 542
Konovalov, V.A. RPR07, 1134
Koontz, R. WPR15, 1821
Koopman, J. TPC21, 2649
Korchuganov, V. WAA18, FAP02, 1266, 1325
Korepanov, V.M. WAA21, 1274
Korolev, A.P. TPA05, 3209
Kos, N. RPE02, 1999
Koscielniak, S. RPG12, RAQ15, 348, 3317
Koscielniak, S.R. WAC19, 3115
Koseki, T. FAP22, WPQ07, WPR04, 1384, 1732, 1794
Köbler, V. RPR06, 1131
Kosterin, S.A. FAG12, 105
Kostin, D.V. WPR18, 1830
Kosukhin, V.V. WAA20, 1272
Kot, N. WAA17, 1263
Kotaki, H. WPC22, 1046
Kotov, V.I. MPG10, WAR20, WAR21, 426, 1948, 1949
Kouptsidis, J. RPE08, 2017
Kourbanis, I. WPP08, WPP23, RAQ13, 1672, 1714, 3312
Koutchouk, J.P. RAA17, 560
Koutchouk, J.-P. FAC04, 2844
Kovach, P. TAA18, 2120
Kovachev, V. FAQ14, 1417
Kovalev, V.P. WAA21, 1274
Kowalski, S. RPG05, RAA31, 327, 600
Kozawa, T. RAB13, 779
Kozin, V. FAR17, 299
Kozlov, O.S. WAR09, 1918
Kponou, A. WPC09, 1013
Krafft, G.A. WAQ14, RAE11, WXE01, TPC04, TPC07, 1873, 2417, 2429, 2601, 2610
Krämer, D. TPE09, FAP02, FAQ12, WAQ17, 1316, 1325, 1411, 1879
Kramer, S.L. MPQ23, 2509
Krasnopolsky, V. WPC13, WPR19, 1025, 1833
Krasnykh, A. TAC01, TAC16, 134, 152
Krauter, K. RAE03, 2389
Kravchuk, L.V. RPR24, RPR25, 1173, 1175
Krawczyk, Frank L. MPB16, MPC22, 2306, 2361
Krebs, G. FAB01, 2789
Krejcik, P. WAG11, RPB02, RPC02, WAB07, WAB12, WAC17, 646, 659, 701, 3031, 3046, 3109
Kreps, G. WPP05, 1666
Kriens, W. WPA12, 929
Krienstein, B. RPB16, TAQ06, 695, 1533
Krinsky, S. FAR10, FAQ17, WXE04, TPQ14, 284, 1426, 2435, 2980
Krishnaswamy, J. FAA19, FAA31, 234, 260
Krivchikov, V.P. TAE14, 1225
Kroc, T. FAG06, 86
Kroes, F. RPG06, TAQ12, MPQ17, 330, 1547, 2491
Krogh, M. WAA19, 1269
Kroll, N. RPA04, 1058
Kroll, N.M. WPQ10, TAA33, 1741, 2144
Kroll, Norman M. WPR10, 1809
Kruijjer, A. TAQ12, 1547
Krüssel, A. FAR06, 272
Krutikhin, S. WPP10, 1678
Krycuk, A. RPQ29, 2732
Krylov, Y. MPA04, 2199
Krylov, Yu. WPR13, 1815
Kuba, A. MPA07, 2208
Kubo, K. WAG12, RPC02, RPA20, WPR03, TPQ16, TPQ17, WAC18, 649, 701, 1099, 1791, 2986, 2989, 3112
Kubo, T. MPQ18, 2494
Kuchar, J. TAP08, 369
Küchler, S. FAP02, 1325
Kudo, M. TPP03, 1620
Kuljt, J. MPQ17, 2491
Kukhtin, V. MPC21, 2359
Kulevoy, T. TAC05, 140
Kulikov, A. RPE14, TAA22, 2032, 2129
Kulikov, A.V. WPC18, 1033
Kulipanov, G.N. FAQ17, 1426
Kumada, M. RPP09, 1982
Kumagai, S. TPP16, 1652
Kumpe, G. FAR06, 272
Kunkel, W.B. TPB07, 2542
Kuo, C. RAA24, 582
Kuo, C.C. FAA04, FAA07, RAA23, TPQ08, TPQ10, 201, 210, 579, 2965, 2971
Kuo, C.H. MPR10, MPQ16, TPB29, 2256, 2488, 2592
Kuo, T. WAQ07, 1858
Kuptsov, I. WPP10, WPP11, 1678, 1681
Kurakin, V.G. WAB14, 3049
Kurennoy, Sergey S. RAR11, RAR12, RAR13, 3373, 3376, 3379
Kurita, N. MPP07, MPP08, TAA22, MPC01, MPQ15, MPQ25, 2048, 2051, 2129, 2317, 2485, 2512
Kurkin, G. WPP11, 1681
Kurkin, Grigori WPR22, 1841
Kurokawa, S.-I. MPA06, 2205
Kurokawa, Shin-ichi WPG04, 491
Kurz, M. RPB15, RPB16, 692, 695
Kusano, J. RPG09, 339
Kushin, V. TAC05, 140
Kushnir, V.A. WPB16, 988
Kustom, R. TAP05, WPP13, WPP14, RPP12, 363, 1687, 1690, 1988
Kustom, R.L. WAG10, 643
Kustom, Robert WPP12, 1684
Kuznetsov, M.I. WPP18, 1699
Kuznetsov, N. FAP02, 1325
Kuznetsov, S. WPR13, MPA04, 1815, 2199
Kuznetsov, V.S. TAE13, 1222
Kvasha, A.I. RPR24, RPR25, 1173, 1175
Kwiatkowski, S. WPP07, WPQ19, 1669, 1765
Kwok, P. TAA28, 2135
Kwon, M. TPG06, WPR11, 171, 1812
Kwon, Y.S. WAQ26, 1897
Labrousche, J. TAE09, 1210
Lacarrere, D. FAE11, 1509
Lackey, J. FAG06, 86
Laclare, J.L. TPG05, 167
Laffin, M. RAA15, 557
Lagniel, J.-M. RPR11, RAG07, 1146, 3173
Lagniel, Jean-Michel TPA17, 3235
Lahti, G. MPR13, MPR14, 2265, 2268

Lai, A.-T. TPC15, 2634
 Lai, C.H. WAG09, 640
 Lai, P. RAB02, TAA28, 761, 2135
 Lal, A. RAB04, RAB05, 767, 770
 Lam, R. TPC16, 2637
 Lambertson, G. MPC01, RAE13, RPQ08, 2317, 2423, 2681
 Lamont, M. WAP12, WAP13, WPG09, RAA11, RAA15, 464, 467, 514, 548, 557
 Lampel, M. RAB03, RPA21, RPA22, 764, 1102, 1105
 Lamzin, E. MPC21, 2359
 Lancaster, C. FAA27, 248
 Lane, S.N. TAP07, 366
 Langdon, A.B. TPR19, 3282
 Langdon, A. Bruce TPR01, 3238
 Langton, J. MPP08, 2051
 Lara, P. MPE04, 867
 Lara, P.D. WPA08, 923
 Larbalestier, D.C. TPE01, 1276
 Lasutin, E.V. FAG12, 105
 Latypov, T. FAP24, 1387
 Lau, W.C. FAA04, 201
 Lau, W.K. RAA23, RAA24, WPB07, TPQ08, TPQ10, 579, 582, 964, 2965, 2971
 Lau, Y.Y. TAQ32, 1599
 Lauer, E. WAA19, 1269
 Launspach, J. TAE09, 1210
 Lauritzen, T. RPE12, 2026
 Laverty, M. MPR16, 2273
 Lavrent'ev, B.M. WAA21, 1274
 Lawrence, G.P. FPD03, 35
 Lawson, W. TAQ17, TAQ18, TAQ19, 1561, 1563, 1566
 Lawton, D. RPG11, 345
 Laxadal, R. WAQ07, 1858
 Laxdal, R.E. WAR15, 1936
 Le Diberder, F. RPC20, 749
 Le Goff, A. TPP09, 1632
 Le Taillandier, P. TAE09, 1210
 Lebedev, A.N. TPR13, 3269
 Lebedev, N.I. WAA20, TAQ34, 1272, 1605
 Lebedev, O.P. WPP02, 1658
 Lebedev, P. TAA01, RAR30, 2078, 3424
 Leblond, B. WPB01, 945
 LeCroy, C.T. TPC18, 2643
 LeDiberder, F. TAG01, 2742
 Lee, Edward P. FAC01, 2835
 Lee, H.S. RPA06, TAQ14, 1061, 1553
 Lee, J.C. FAA07, RAA24, TAR04, TAR06, TPQ09, TPQ10, 210, 582, 804, 810, 2968, 2971
 Lee, P.J. TPE01, 1276
 Lee, S.Y. RPG08, TAP03, WPP20, WPP21, RAP21, WAC12, RAG10, RAQ23, RAQ24, 336, 357, 1705, 1708, 2934, 3094, 3182, 3337, 3340
 Lee, Sangil TAB09, FAR03, 122, 269
 Lee, T. TPG06, TAQ06, WPQ05, 171, 1533, 1726
 Lee, Terry G. TAQ27, 1584
 Lee, Y. TPB07, 2542
 Lee, Y.Y. MXG03, TAP11, WAR13, 53, 378, 1930
 Leemans, W. TPG07, RAB10, WAQ04, TAA28, 174, 776, 1852, 2135
 Legg, R. WAQ14, WXE01, TPC07, 1873, 2429, 2610
 Lehrman, I.S. FAA19, FAA31, 234, 260
 Lemaire, J.-L. RAG07, 3173
 Len, L.K. TAE10, 1213
 Lenci, S. FAE07, 1497
 Lenisa, P. RAE05, 2399
 Lenkszus, F. MPQ07, RPQ16, 2464, 2702
 Lennox, A. FAG06, 86
 Lenz, J.W. RPG10, 342
 Lepeltier, V. RPC20, TAG01, 749, 2742
 Lessner, E. TAP05, FAB09, TPQ22, 363, 2811, 3001
 Letoumelin, R. TAB04, 116
 Letta, P. MPR13, 2265
 Leung, E.M. TAB06, 119
 Leung, K.N. TPB07, 2542
 Levashov, Y. TAA02, 2081
 Levchenko, V.D. WAA02, WAA03, 1230, 1233
 Level, M.-P. FAR14, 293
 Leveling, A. FAG06, 86
 Levichev, E. FAP02, 1325
 Levy, C.D.P. MPE03, 864
 Ley, R. RAP24, 2943
 Leyh, G. WAQ15, 1876
 Leyh, G.E. RPP07, 1976
 Li, D. TAP03, WPA04, WPP20, WPP21, RAP21, WAC12, RAG10, RAQ23, RAQ24, 357, 911, 1705, 1708, 2934, 3094, 3182, 3337, 3340
 Li, H. RPC16, RPC17, RPC19, 737, 740, 746
 Li, N. FAP01, 1322
 Li, Rui WAQ12, MPB11, 1870, 2297
 Li, W.M. RPE10, 2023
 Li, Xiao-Ping RAP25, 2946
 Li, Z. FAG11, FAA25, 102, 243
 Li, Zenghai MPC25, RAG12, 2370, 3188
 Liang, C. TPC07, 2610
 Libault, David TPA17, 3235
 Lien, E. FAE07, 1497
 Limberg, T. RAP08, WAC17, 2901, 3109
 Lin, C.L. MPE12, 893
 Lin, G. TPQ09, 2968
 Lin, Glory MPQ16, 2488
 Lin, K.K. FAA07, MPQ19, MPQ32, 210, 2497, 2524
 Lin, Leon C.-L. WPB03, WPB04, 951, 954
 Lin, Liu FAP14, 1361
 Lin, T.F. TAA14, MPQ16, 2108, 2488
 Lin, X. MPC01, 2317
 Lin, X.E. WPQ12, 1744
 Lin, X.T. RPA04, 1058
 Lin, Xintian E. WPR10, 1809
 Lindner, M. FAQ04, 1396
 Linebarger, W. RPA24, 1111
 Linnecar, T. WAP12, WAP13, FAE10, 464, 467, 1506
 Linnik, A.F. RAB15, 782
 Linscott, I. RAE12, RPQ01, RPQ22, 2420, 2660, 2717
 Liou, R. WAG09, TAA28, 640, 2135
 Lisin, A. MPP10, WAC17, 2057, 3109
 Littlejohn, R.G. RAR02, 3358
 Littmann, B. TAQ30, 1593
 Littmann, Bengt WPP22, 1711
 Litvinenko, V. MPA11, 2217
 Litvinenko, V.N. FAA08, RAA01, RAB22, RPA17, MPA10, MPQ06, FAC20, 213, 524, 796, 1090, 2214, 2461, 2877
 Liu, H. FAG11, WPA17, WAQ11, 102, 942, 1867
 Liu, H.-X. FAA25, 243
 Liu, J. TPP16, WPP20, WPP21, WAC12, 1652, 1705, 1708,

3094
Liu, J.Y. TAP03, RAP21, RAG10, RAQ23, RAQ24, 357, 2934, 3182, 3337, 3340
Liu, W. MPA01, 2193
Liu, Y.C. FAA04, FAA07, RAA24, WPB07, 201, 210, 582, 964
Liu, Y.-C. TPC15, 2634
Liu, Zuping FAQ29, FAQ30, 1456, 1459
Lo, C.C. TAR03, 801
Lobov, I. MPR11, 2259
Loew, G. RPC01, 698
Loew, G.A. WAG13, 653
Loewen, R. RPA23, 1108
Loewen, R.J. WAG13, 653
Lofnes, T. TPC31, 2658
Long, H. WPA14, 935
Longinotti, D. TAR17, 837
Longinotti, D.B. TAR14, 828
Lopez, F. FAP12, 1355
Lorenz, R. TPC14, 2631
Lou, W. FAB12, 2820
Lou, W.R. TPA04, 3206
Lou, Weiran TAA29, 2138
Louie, W. TAA09, 2099
Loulergue, A. RAG06, 3170
Lovato, Richard WPB15, 985
Lu, J.J. TAQ33, 1602
Lucas, Peter W. WAP06, 449
Luccio, A. FAQ28, 1453
Ludmirsky, E. RAB21, 793
Luger, G. WAE08, 2175
Luijckx, G. RPG06, 330
Lumpkin, A. MPQ08, MPQ09, MPQ10, MPQ11, TPC03, RPQ15, RPQ16, 2467, 2470, 2473, 2476, 2598, 2699, 2702
Lund, S. TAR17, 837
Lund, S.M. TAR14, TPR18, 828, 3278
Luo, G.H. FAA07, RAA24, RAR05, 210, 582, 3364
Luo, Gwo-Huei FAA04, 201
Luo, H. MPA01, 2193
Luo, X. FAC04, 2844
Luong, M. TPP09, 1632
Lussignol, Y. WPB22, 998
Lüttgert, S. WAE13, 2190
Lykke, Keith R. WPC11, 1019
Lyons, S. TAB17, RPA26, 131, 1116
Lysenko, W.P. RPR19, RPR22, 1161, 1167
Maas, R. RPG06, TPB03, 330, 2533
Maccaferri, R. RAP24, 2943
Macek, R. TPB13, WAC29, RAR23, 2554, 3146, 3406
Macek, R.J. TAR12, 822
MacGregor, I. TAR18, 840
Machida, S. TAP04, WPC07, WAR05, 360, 1007, 1912
MacKay, W.W. WAC24, RAQ22, 3131, 3334
MacKenzie, R. RAE03, 2389
MacLachlan, J.A. WAC06, 3079
Madert, M. RPR06, 1131
Madey, J.M.J. FAA08, RAB22, RPA17, FAC20, 213, 796, 1090, 2877
Madlung, J. WPA03, 908
Madsen, J. RPC09, 716
Madsen, J.H.B. RPC10, 719
Madura, D. WPG11, 520
Madura, D.D. TAB06, 119
Magugumela, M. WPC21, 1043
Mahoney, K. TPC26, 2652
Maier, R. TPB20, 2574
Maines, J. FAQ17, 1426
Mair, R. MPE10, 887
Maissa, S. TPP09, 1632
Maj, J. WPP13, 1687
Makarov, A. RAQ14, 3315
Mako, F.M. TAE10, 1213
Malakhov, N. TAC16, 152
Maletic, D. RAG14, RAQ20, 3194, 3329
Malka, V. WAG08, 637
Malone, R. MPE11, 890
Malygin, A.N. RPP08, 1979
Mamaev, G. FAP24, 1387
Mammosser, J. FAE12, TPC07, 1512, 2610
Manca, J.J. WPR20, 1835
Manca, J.P.J. WPR20, 1835
Mandrillon, P. FAG09, 95
Mane, V. WAC24, WAC25, WAC26, 3131, 3134, 3137
Mangili, P. TPC10, 2619
Manglunki, D. MPG09, 423
Mangra, D. FAR19, 303
Mao, N. WAQ09, 1864
Mapes, M. MPP11, 2060
Margaritondo, G. TPG11, 186
Marhauser, F. WPA05, 914
Mariotti, E. RAE05, 2399
Markiewicz, T. RPC01, 698
Markov, V. FAR17, 299
Marks, S. FAQ24, FAQ25, 1444, 1447
Marneris, I. WAR11, RPP02, 1924, 1964
Marone, A. FAQ03, 1393
Marriner, J. WAP01, TPQ28, WAB01, 434, 3013, 3016
Marsh, K.A. WAG08, RAB01, 637, 758
Martens, M. WAP01, 434
Martens, M.A. WAP05, WAP08, 446, 455
Marti, F. RPG11, TAP08, TAP10, 345, 369, 375
Martin, D. MPQ15, MPQ25, 2485, 2512
Martin, E.J. RPP06, RPP13, 1973, 1991
Martin, K. WAE07, 2172
Martin, P. MPG01, 391
Martin, P.S. FAP04, FAP05, FAP06, FAP07, FAP09, WAR02, TAA12, 1331, 1334, 1337, 1340, 1346, 1903, 2105
Martini, M. TAP14, WAE09, 386, 2178
Martlew, B.G. RAE10, 2414
Maruyama, T. MPE10, 887
Marx, M. RPB15, 692
Masalov, V. WPC13, 1025
Mashiko, K. FAR08, RPA13, 278, 1079
Massarotti, A. TPG11, FAR21, WPQ04, 186, 309, 1723
Massoletti, D. FAA05, 204
Mastovsky, I. TPG14, RPC15, 192, 734
Masunov, E.S. RPR12, 1149
Matheson, R. MPQ22, 2506
Mathewson, A. RPE02, 1999
Matricon, P. WAG07, 634
Matsuda, K. FAR09, 281
Matsumoto, H. WAG12, RPA20, WPR03, 649, 1099, 1791
Matsumoto, S. RPB04, RPA20, 665, 1099
Matsuoka, M. TPP07, 1629
Mattel, P. RPR11, 1146
Matthews, P.J. WAG10, 643
Matthews, Paul WPP12, 1684
Matthieussent, G. WAG07, 634
Mattison, T. RPC02, 701
Mattison, T.S. WAR06, 1915
Matveev, Yu. WAA18, 1266
Matyukov, A.V. TAP16, 389
Mau, R. WAP04, 443
Maury, S. RAP23, RAP24, 2940, 2943

Maury, Stephan RPG07, 333
May, Lisa M. FAE06, 1494
May, M. TPE05, FAP09, 1298, 1346
Mazaheri, G. RPB04, 665
Mazarakis, M.G. TAE06, 1201
Mazur, P.O. FAP06, FAP07, 1337, 1340
McAllister, B. RPG05, 327
McCormick, D. RPB01, RPB04, 656, 665
McCrory, E. FAG06, 86
McCrory, Elliot S. WAP06, 449
McCune, E. FAE07, 1497
McDaniel, B.D. RAE14, 2426
McDaniel, M.R. TAA22, 2129
McDonald, K.T. TAA28, 2135
McDonald, M. MPE03, 864
McDowell, W. TAP05, 363
McGhee, D. FAR19, TAP05, 303, 363
McGhee, D.G. RPP03, 1967
McGinnis, D. WAP01, TPQ26, TPQ28, 434, 3010, 3013
McIntosh, P.A. MPC19, WAC22, 2353, 3125
McInturff, A.D. FAQ07, 1402
McIntyre, Peter M. FAQ31, 1462
McKee, B. WAC17, 3109
McManus, A. WAR19, 1945
McMichael, G.E. TAC12, 149
McMichael, Gerald E. FAG13, 107
Mead, J. TPB12, 2551
Mecklenburg, B. RPC22, TAQ03, 755, 1524
Meddahi, M. WPG09, RAA17, 514, 560
Medvedko, A.S. FAQ17, 1426
Medvedko, E.A. FAQ17, FAQ18, 1426, 1429
Meigs, M.J. WAQ26, MPA05, TPC18, 1897, 2202, 2643
Melekhin, V.N. TAR05, FAP19, WPR17, 807, 1375, 1827
Mencick, M. WPB22, 998
Mendelsohn, S.L. RPR20, 1164
Menshikov, L. TAC16, 152
Méot, F. FAC04, 2844
Meredith, J. TAR17, 837
Meredith, J.W. TPB14, 2557
Merl, R. FAR19, TPE08, 303, 1310
Merle, E. TAE09, TPC17, 1210, 2640
Merminga, L. FAG11, FAA25, RPQ11, RPQ30, 102, 243, 2690, 2735
Mertens, V. RAA15, 557
Merz, W. RPP13, 1991
Meshcherov, R. WPC13, 1025
Meshkov, I. RAP23, RAP24, 2940, 2943
Metz, H. TAQ19, 1566
Metzmacher, K. MPG09, 423
Meuth, H. WPQ26, 1781
Meyer, J. RPQ15, 2699
Meyer, S. TAR18, 840
Meyerer, Thomas WPB21, 995
Meyerhofer, D.D. TAA28, 2135
Meyers, T. RPR20, 1164
Mezi, L. TPG11, 186
Michailov, S. TPE09, 1316
Michelato, P. WPC23, 1049
Michelotti, L. WAP08, 455
Michelotti, Leo FAB15, 2826
Michine, A.V. TAB15, 128
Michnoff, R. MPA17, 2229
Micklich, B.J. FAG14, 110
Miertusova, J. MPP04, MPP05, 2042, 2045
Mikhailichenko, A. TAG01, 2742
Mikhailichenko, A.A. RAB18, 784
Mikhailov, V.A. WAR09, FAC12, 1918, 2863
Milchberg, H.M. WAG04, 621
Milder, M.L. WPA08, 923
Milder, Martin L. WPB15, 985
Miller, H. TAQ11, 1544
Miller, J.M. TPR18, 3278
Miller, R. TAB17, RPB02, RPC01, MPE10, RPA04, RPA26, 131, 659, 698, 887, 1058, 1116
Miller, R.A. WPC18, 1033
Miller, R.H. WPB13, WXE03, 982, 2432
Millich, A. WPQ25, 1779
Milliman, L. FAA27, 248
Millo, D. FAQ19, 1432
Mills, F. TAP05, 363
Mills, G.D. MPE05, WAQ26, 871, 1897
Milton, B. WAQ07, 1858
Milton, B.F. FAG07, 89
Milton, S. MPQ10, 2473
Milton, S.V. RAA28, FAP12, RPP03, RPQ18, 594, 1355, 1967, 2708
Mimashi, T. MPA06, 2205
Minagawa, Y. RPQ26, 2726
Minamihara, Y. FAQ24, FAQ25, 1444, 1447
Minato, T. FAQ08, 1405
Miné, Ph. WAG07, 634
Minehara, E.J. TPG02, 159
Mingalev, B. MPC21, 2359
Minty, M. WAG11, RPC02, RAE03, TPQ16, 646, 701, 2389, 2986
Minty, M.G. RAA06, RPB03, RAP10, WAB09, WAB12, WAC17, TPA09, 536, 662, 2907, 3037, 3046, 3109, 3217
Miram, G. FAE07, 1497
Mirzoev, K. MPP03, 2040
Mishin, A.V. RPA25, 1114
Mishra, C.S. FAP06, MPB05, MPB06, TAG10, RAP03, 1337, 2282, 2285, 2777, 2886
Mishra, S. FAP04, FAP07, 1331, 1340
Mitchell, M. WPR15, 1821
Mitra, A.K. TAQ33, 1602
Mitrochenko, V.V. WPB16, 988
Mitsuhashi, T. RAQ06, 3300
Mitsunobu, S. TPP03, 1620
Miura, T. WPR02, 1788
Miya, K. RAB13, 779
Miyahara, Y. FAQ20, FAQ21, RAQ30, 1435, 1438, 3355
Miyai, Y. TAQ35, 1608
Miyauchi, Y. FAA30, 257
Mizumoto, M. RPG09, 339
Mizuno, A. WPC22, MPA07, 1046, 2208
Mizuno, H. FAQ08, TAQ29, 1405, 1590
Mocheshnikov, N. FAR17, 299
Modena, A. WAG08, 637
Moe, H. TAP05, 363
Moe, H.J. RPA07, 1064
Moffat, D. FAE13, RAQ04, RAR19, 1515, 3294, 3394
Möhl, D. RAP23, 2940
Mohr, J. FAR06, 272
Moi, L. RAE05, 2399
Moibenko, A. WAE07, 2172
Moir, David C. TAE08, 1207
Moiseev, V.A. RPR01, 1119
Moisseev, V. WPR13, 1815
Moisseev, V.I. TPB25, 2586
Mokhov, N.V. RAB19, 787

Mokhtarani, A. FAP06, FAP07, 1337, 1340
 Molinari, G. RAP24, 2943
 Möller, K.D. FAR06, 272
 Møller, S.P. WAP14, 470
 Möller, W-D. TPP11, 1639
 Molodkin, V. FAR16, FAR17, 296, 299
 Montag, C. TAA01, TAA06, RAR30, 2078, 2090, 3424
 Montès, B. WAG07, 634
 Montjar, B. MPR13, 2265
 Moog, E.R. TPE06, 1301
 Mora, P. WAG04, WAG07, 621, 634
 Morano, R. WAG07, 634
 Morcombe, P. FAA08, WAA10, MPA11, MPQ06, 213, 1248, 2217, 2461
 Morcombe, Peter WPR22, 1841
 Moretti, A. WPA07, 920
 Morgan, G. TPE04, FAQ03, FAQ04, FAQ16, 1293, 1393, 1396, 1423
 Morgan, J. TAR16, 834
 Morgillo, A. FAQ03, 1393
 Mori, W.B. WAG09, RAB01, RAB02, RAB08, TPB18, 640, 758, 761, 773, 2569
 Mori, Y. TAP04, MPE03, WPC07, WAQ06, WAR05, 360, 864, 1007, 1855, 1912
 Morii, Y. TAQ35, 1608
 Morillo, J. WAG07, 634
 Morpurgo, G. RAA20, FAC03, 570, 2841
 Morris, J.T. WAB04, 3022
 Mortazavi, P. TPP06, WPQ20, 1626, 1768
 Morvillo, M. MPQ05, 2458
 Moser, H.O. FAR06, 272
 Moshhammer, W. RPC02, 701
 Mosko, S.W. TAP07, WAQ26, 366, 1897
 Mosnier, A. WPB22, WAC13, 998, 3097
 Mostowfi, D. RPQ21, RPQ22, 2714, 2717
 Moulin, F. WAG07, 634
 Mouton, B. WPB22, 998
 Mufel, V.B. TAE14, 1225
 Mugge, M. MPP12, MPP20, 2064, 2075
 Muggli, P. WAG09, WPC20, 640, 1039
 Mulhall, S. FAQ15, TAA09, 1420, 2099
 Mulhollan, G. MPE10, WPC21, 887, 1043
 Muller, H. FAE13, TPP04, RAR19, 1515, 1623, 3394
 Müller, W.F.O. RPB15, 692
 Munasyrov, R.N. WAA21, 1274
 Munneke, B. TAQ12, 1547
 Murata, H. RPG09, 339
 Muratore, J. TPE04, FAQ02, FAQ03, FAQ04, 1293, 1390, 1393, 1396
 Murin, B.P. RPR07, 1134
 Murphy, C.T. WAR19, 1945
 Murphy, J.B. FAR10, TPQ14, 284, 2980
 Murray, S.N. MPE05, 871
 Mustafin, E. RAP23, 2940
 Myakishev, D. RPA12, 1076
 Myakishev, D.G. MPC17, 2348
 Myers, S. WPG01, 476
 Mytsykov, A. FAR17, 299
 Myznikov, K. FAQ06, 1399
 Nadji, A. FAR14, 293
 Nagaenko, M. FAR06, 272
 Nagafuchi, T. FAP13, 1358
 Nagai, A. FAA30, 257
 Nagai, R. TPG02, 159
 Nagaitsev, S. RAP22, 2937
 Nagaoka, R. FAR21, TAG05, 309, 2762
 Nagatsuka, T. FAP22, WPQ07, 1384, 1732
 Nagchaudhuri, A. MPA11, 2217
 Naidenov, V.O. TAP16, 389
 Naito, F. FAE09, WPQ17, WPR05, WPR09, 1503, 1759, 1797, 1806
 Najmudin, Z. WAG08, 637
 Nakajima, K. RAB13, TAA28, 779, 2135
 Nakamura, N. RPQ23, 2720
 Nakamura, T. WAC14, 3100
 Nakamura, T.T. MPA06, 2205
 Nakanishi, H. RAB13, TPP16, TAA28, 779, 1652, 2135
 Nakata, K. TAQ35, 1608
 Nakayama, H. WAR03, TAG01, 1906, 2742
 Nam, S.H. TPG06, 171
 Namkung, W. TAR07, RPA06, TAQ14, TAQ15, MPA02, 813, 1061, 1553, 1556, 2196
 Naqvi, S. TAQ01, 1518
 Nasonov, N.N. FAG12, 105
 Nassiri, A. WPB06, RPA10, WPP16, 961, 1070, 1693
 Nath, S. RPR08, RPR09, 1137, 1140
 Nath, Subrata WAQ02, 1846
 Nation, J.A. WPC19, TAE12, TAQ01, 1036, 1219, 1518
 Natrass, L. TAR17, 837
 Natrass, L.A. TAR14, 828
 Nawrocki, G. MPQ08, 2467
 Nawrocky, R.J. MPQ23, 2509
 Neu, Eugene L. TAE03, 1188
 Neil, G. FAA25, WPA17, RPQ30, 243, 942, 2735
 Neil, G.R. FAG11, 102
 Neil, George R. TAC03, 137
 Nelson, D. WAQ15, 1876
 Nelson, M. TAR17, 837
 Nelson, M.B. TAR14, 828
 Nemoshkalenko, V. FAR16, FAR17, 296, 299
 Nesemann, H. FAA02, FAC19, 195, 2874
 Nesterov, N. TAC05, 140
 Nesterov, V.V. WAA11, 1251
 Nesterovich, A. RPR10, RPR15, 1143, 1155
 Nett, D. TAB17, RPA26, 131, 1116
 Neubauer, M. WPQ10, WPR07, WPR08, 1741, 1800, 1803
 Neuffer, D. FAG11, WPA17, WAQ11, 102, 942, 1867
 Neuffer, D.V. FAA25, 243
 Neuffer, David MXG03, 53
 Newton, M.A. TAR14, 828
 Nezhevenko, O. RPA12, TAQ21, 1076, 1569
 Ng, C. WPR07, MPC01, MPQ25, 1800, 2317, 2512
 Ng, C.K. TAA28, 2135
 Ng, C.-K. WPQ10, WPQ12, MPP07, MPQ15, WAB18, WAC17, 1741, 1744, 2048, 2485, 3061, 3109
 Ng, K.Y. RAP21, TPQ12, RAQ23, RAQ24, RAR17, 2934, 2977, 3337, 3340, 3388
 Ng, K.-Y. TAR20, 843
 Nghiem, P. FAR14, 293
 Nguyen, D.C. FAA16, 228
 Nicol, T. WPB08, 967
 Nielsen, R. TAP05, 363
 Nieuwenkamp, H. MPQ17, 2491
 Niki, K. RPG13, 351
 Nikiforov, S. WPC03, 1004

Niquille, C. WAP13, 467
Nishi, M. TAB03, WPQ21, 113, 1770
Nishida, Y. RAB13, TAA28, 779, 2135
Nishihara, S. FAA30, 257
Nishimura, H. MPR03, MPR04, 2244, 2247
Nishimura, Hiroshi WAE04, 2162
Nobel, R.J. WPA07, 920
Noda, A. FAR08, RPA13, RPA18, WPQ21, WAQ01, 278, 1079, 1093, 1770, 1843
Noda, K. TAB03, 113
Nogiec, J.M. FAP06, FAP07, MPB06, 1337, 1340, 2285
Noguchi, S. TPP07, 1629
Nolen, J.A. RPG14, FAQ09, TPC13, RAQ16, 354, 1408, 2628, 3320
Noomen, J. RPG06, 330
Noomen, J.G. MPQ17, 2491
Noonan, J. RPE09, 2020
Nordberg, E. FAE13, 1515
Nordby, M. MPP08, MPP12, MPP20, TAA22, MPC01, MPQ25, 2051, 2064, 2075, 2129, 2317, 2512
Nordby, M.E. MPP07, 2048
Norek, G. TAP05, 363
Norem, J. RAA29, TAA28, TPC16, 597, 2135, 2637
Norris, B.L. WAE02, 2152
Norton, M. TAA20, 2123
Norum, B.E. RAP01, 2880
Norum, Blaine E. RAE07, 2405
Nosochkov, Y. RAA22, RAA25, RAA27, 576, 585, 591
Nosyrev, S. WPP10, WPP11, 1678, 1681
Novikov, A. WPP10, 1678
Novikov, S.A. WAR09, 1918
Novikova, T.A. FAA14, 225
Novokhatsky, A. WAA17, 1263
Nuhn, H.-D. FAA12, FAA17, 219, 231
Nusinovich, G.S. TAQ17, 1561
Nyman, M. RPQ08, 2681
O'Connor, T. RAA03, 527
O'Day, S. WAQ22, 1888
O'Shea, P. FAA08, MPA11, 213, 2217
O'Shea, P.G. RPA17, TAQ07, 1090, 1536
O'Shea, Patrick G. WPA13, WPB09, TAG12, 932, 970, 2783
O'Sullivan, M. RPP13, 1991
O'Sullivan, M.K. RPP06, 1973
Obina, T. TPC08, RPQ26, 2613, 2726
Oerter, B. MPA16, 2226
Ogata, A. RAB13, TAA28, 779, 2135
Ogawa, Y. TAA04, 2087
Ogitsu, T. FAQ02, FAQ08, 1390, 1405
Oguri, H. RPG09, 339
Oh, J.S. TAQ15, 1556
Ohgaki, H. MPR04, 2247
Ohmi, K. RAP02, 2883
Ohmori, Chihiro TPR16, 3275
Ohshita, E. TAQ35, 1608
Oide, K. RPC20, RPA20, TAA08, WXE07, TAG01, TAG11, WAB20, WAC08, WAC16, 749, 1099, 2096, 2444, 2742, 2780, 3064, 3085, 3105
Oide, Katsunobu WAB10, 3040
Okada, M. RPG13, 351
Okamoto, H. FAR08, RPA13, RPA18, WAQ01, 278, 1079, 1093, 1843
Okamoto, Hiromi TPR11, 3263
Okuma, S. FAA30, TAQ35, 257, 1608
Okumura, Y. RPG09, 339
Okun, L. FPD05, 45
Olivieri, D.N. TAR16, 834
Olsen, D.K. RPG01, TAP07, WAQ26, 312, 366, 1897
Olsen, J. RAE12, 2420
Omeich, M. WPA14, WPB22, 935, 998
Onillon, E. RPQ17, RPQ25, 2705, 2723
Onishchenko, I.N. RAB15, 782
Onken, R. WPQ24, 1776
Ono, M. TPP07, 1629
Opanasenko, A.N. WPA15, WPA16, 938, 939
Oren, W. WXE01, 2429
Oreshnikov, A. TAC05, 140
Orris, D. TPE05, 1298
Orris, D.F. FAP06, FAP07, 1337, 1340
Ortiz, R. MPQ22, 2506
Osborn, J. FAP01, 1322
Oshita, E. FAA30, 257
Ostanin, V.P. RPP08, 1979
Ostiguy, F. TAG04, 2757
Ostiguy, Francois WAC02, 3070
Ostiguy, J.F. WPB08, 967
Ostiguy, J.-F. TAR20, TPE05, FAP10, FAP21, MPC07, 843, 1298, 1349, 1381, 2330
Ostojic, R. FAC04, 2844
Ostroumov, P.N. RPR01, RPR24, RAE08, 1119, 1173, 2408
Otake, Y. TAQ29, 1590
Otock, R. TAA11, 2102
Otock, R.D. RPE09, 2020
Ottarson, J. TAP08, 369
Ottaviani, P.L. TPG11, 186
Oude Velthuis, R.G.J. RPP04, 1970
Ovchinnikov, V.P. TAE13, 1222
Owen, H.L. TPG09, 180
Oxoby, G. RAE12, RPQ01, 2420, 2660
Ozaki, Y. WXE07, 2444
Pabst, M. TPA01, TPA02, TPA03, 3197, 3200, 3203
Pachnik, J.E. FAP06, FAP07, MPB06, 1337, 1340, 2285
Padamsee, H. FAE13, TPP02, TPP04, WPQ02, RAQ04, RAR18, RAR19, 1515, 1617, 1623, 1720, 3294, 3391, 3394
Pagani, C. WPB10, WPC23, TAA07, RAQ05, 973, 1049, 2093, 3297
Pai, C. MPP11, 2060
Palkovic, J. TPB19, 2572
Palmer, D. RPA26, 1116
Palmer, D.T. WPB13, WXE03, 982, 2432
Palmer, Robert B. MXG03, 53
Palrang, M. MPP10, 2057
Pan, K.T. MPQ16, 2488
Pang, A.W. WPC21, 1043
Pangos, N. FAR21, MPP05, 309, 2045
Pankuch, P. TAE06, 1201
Pantazis, R. MPA11, 2217
Pantenburg, F.J. FAR06, 272
Pappas, G.C. WAR10, WAR12, 1921, 1927
Papureanu, S. RPR06, WPQ26, TPB20, 1131, 1781, 2574
Paramonov, V.V. WPP17, WPP18, WPP19, 1696, 1699, 1702
Parazzoli, C. FAA27, 248
Parazzoli, C.G. FAA28, 251
Pardo, R.C. WAQ03, 1849
Park, H.J. WPR11, 1812

Park, Heunggyu TAB09, FAR03, 122, 269
Park, Jongpil TAB09, FAR03, 122, 269
Park, S. RPA21, RPA22, 1102, 1105
Park, S.H. FAA08, RAB22, TAQ14, 213, 796, 1553
Park, S.S. TAQ15, 1556
Park, Sanghyun WPB02, 948
Parkhomchuk, V. TAR11, 819
Parzen, G. FAB03, FAB04, FAB05, 2795, 2798, 2801
Pasotti, C. WPQ04, TAG05, 1723, 2762
Pasquinelli, Ralph J. RAE01, 2379
Patavalis, N. MPR13, 2265
Paterson, E. RPC01, 698
Patteri, P. TPG11, 186
Patterson, D. MPQ10, 2473
Paulson, C.C. RPR20, 1164
Pavlovets, M. TAA18, 2120
Pawlak, T. MPG01, 391
Payet, J. FAR14, 293
Peacock, M.A. RPR20, 1164
Pearson, C. FAE07, 1497
Pearson, Pauline MPR07, 2250
Peck, S. FAE13, 1515
Pedersen, F. MPG09, 423
Peggs, S. MPG12, TAA09, MPC05, FAB20, FAB22, WAC24, WAC25, WAC26, RAQ21, RAQ22, RAR29, 431, 2099, 2327, 2829, 2832, 3131, 3134, 3137, 3331, 3334, 3421
Peggs, S.G. WAP10, 461
Pei, A. TAP03, WPP20, WPP21, RAP21, WAC12, RAG10, RAQ23, RAQ24, 357, 1705, 1708, 2934, 3094, 3182, 3337, 3340
Pei, Yuan Ji RPE10, 2023
Pekeler, M. TPP11, 1639
Pelaia, T.A. RAE14, 2426
Pellegrini, C. FAA23, RAB03, RPA21, RPA22, RAQ17, 240, 764, 1102, 1105, 3323
Pendleton, R. WPR07, WPR16, 1800, 1824
Penicka, M. TAA03, 2084
Pennacchi, R. WPR15, 1821
Perin, R. TPE02, 1282
Perkins, C. RAA04, MPP09, MPP10, MPP12, MPP20, TAA22, MPC01, MPQ25, 530, 2054, 2057, 2064, 2075, 2129, 2317, 2512
Perkins, L. TPB07, 2542
Peschke, C. RPB16, 695
Peters, C. RPC16, RPC18, WPA01, TAE01, FAP17, FAP18, TPA10, 737, 743, 902, 1178, 1369, 1372, 3220
Peters, F. TAG01, 2742
Peterson, K.J. TAP05, 363
Petracca, S. WAE12, 2187
Petrenko, I.I. FAB02, 2792
Petrenko, V. WPR13, 1815
Petrenko, V.V. TPB25, 2586
Petri, H. WPC08, 1010
Petrov, S.P. FAQ17, 1426
Petrov, V. WPP11, 1681
Petrov, V.A. WAA20, TAQ34, 1272, 1605
Petty, L. MPP15, 2069
Pfeffer, H. WAE07, 2172
Pflüger, J. FAR07, 275
Phillips, R. FAE07, 1497
Phinney, N. WAG11, RPB01, RPC01, 646, 656, 698
Phung, B. WPB22, 998
Piaszczyk, C. RPR20, 1164
Piataev, V. TAC16, 152
Pichoff, N. RAG06, RAG07, 3170, 3173
Pickard, D. TPB07, 2542
Pietryka, M. RAA04, WAC17, 530, 3109
Pilat, F. FAQ28, FAB22, 1453, 2832
Pilyar, N. TAC16, 152
Pinto, I.M. WAE12, 2187
Pipersky, P. FAQ24, FAQ25, 1444, 1447
Pirkl, W. WPP07, WPQ19, 1669, 1765
Pirovano, R. TAQ12, 1547
Pisharody, M. FAE13, WPQ02, RAE14, TPA04, RAQ04, RAR18, 1515, 1720, 2426, 3206, 3294, 3391
Piskarev, I. RPA19, 1096
Pitel, Ira J. RPP11, 1985
Placidi, M. RAA19, RPB01, 567, 656
Plass, G. FAG08, 92
Plate, D. FAQ24, FAQ25, 1444, 1447
Plate, S. FAQ15, 1420
Plato, John G. WPB15, 985
Platonov, Yu.P. MPG10, 426
Plesko, M. TPG08, FAA13, FAR06, 177, 222, 272
Plesko, Mark MPR12, 2262
Plotnikov, S. TAC05, 140
Plouviez, E. TPG05, RPQ15, 167, 2699
Plum, M. TPB13, WAC29, RAR22, RAR23, 2554, 3146, 3403, 3406
Podebrad, O. RPB16, 695
Podobedov, B. WAC17, 3109
Poelman, A. MPQ17, 2491
Pogorelsky, I. MPE11, 890
Poilleux, P. WAG07, 634
Poirier, R.L. TAQ33, WPP18, 1602, 1699
Polyakov, V. RAP24, 2943
Poncet, A. RPE02, MPP15, 1999, 2069
Ponds, M. TAQ07, 1536
Poole, J. WPG09, RAA15, WAE03, 514, 557, 2157
Poole, M.W. TPG09, 180
Popik, V.M. FAQ17, 1426
Popov, Yu. TAC16, 152
Popovic, M. FAG06, WPA06, WPA07, WPR21, 86, 917, 920, 1838
Porterfield, D. TPC04, 2601
Portmann, G. FAQ24, RPQ13, FAB01, 1444, 2693, 2789
Potter, James M. FAE06, 1494
Poukey, J.W. TAE06, 1201
Pourre, J.L. TAB04, 116
Power, J. WAG06, WPB11, WPB12, RPR19, 631, 976, 979, 1161
Power, J.F. TPB22, 2580
Powers, T. FAE12, 1512
Powers, Tom TPP13, 1645
Pozdeev, M. TPQ04, 2958
Prabhakar, S. RAE12, 2420
Preble, J. FAE12, 1512
Prelec, K. WPC09, 1013
Prescott, C. MPE10, 887
Price, E. TPC04, 2601
Prieto, P. WAE07, 2172
Primdahl, K. WPP13, WPP14, 1687, 1690
Proch, D. FAE08, TPP11, WPQ24, 1500, 1639, 1776
Prodell, A. TPE04, 1293
Pruyn, J. WPA01, 902
Ptitsin, V.I. RAQ21, 3331
Puchkov, A. RPR10, 1143
Pullia, M. TPC10, 2619
Puntus, V. WPP05, 1666
Puzo, P. RPC20, TAG01, 749,

2742
Qian, Y.L. RPA08, RPA11, 1067, 1073
Qian, Zubao TPP01, 1614
Qin, Q. TPQ03, 2955
Qing, Li FAA26, 246
Qiu, X. MPE11, 890
Qiu, X.Z. RAE09, TPB01, 2411, 2530
Queralt, X. TPG09, 180
Quinn, P.D. RAE10, 2414
Qunell, D. WAR01, 1900
Rackelmann, A. WAC17, 3109
Radloff, W. TPC09, 2616
Radusewicz, P. FAQ08, 1405
Rafael, F.S. MPQ33, 2527
Rago, C. WAC17, 3109
Raimondi, P. WAG11, RPB01, RPC20, TAA08, TAG01, RAP15, RAP16, 646, 656, 749, 2096, 2742, 2919, 2922
Rakowsky, G. FAQ17, WXE04, 1426, 2435
Ramachandran, S. WAR19, 1945
Ramamoorthy, S. MPA15, 2223
Ramamoorthy, Susila MPR07, RPQ14, 2250, 2696
Ramirez, G. WPP03, 1660
Ramirez, J.J. TAE05, TAE06, 1198, 1201
Raparia, D. RAR16, 3385
Rasmussen, J.O. WAQ04, 1852
Rasmussen, N. MPG09, 423
Ratti, A. WPP07, WPQ19, RPQ17, WAC24, 1669, 1765, 2705, 3131
Raubenheimer, T. RPB02, RPC01, RPC03, TPQ16, TPQ17, WAC17, 659, 698, 704, 2986, 2989, 3109
Raubenheimer, T.O. RPC02, TAG03, WAC15, WAC18, RAQ03, 701, 2752, 3102, 3112, 3291
Rauchas, A. TAP05, 363
Ravn, Helge L. MPE02, 858
Razuvakin, V.N. WAA20, 1272
Reece, C. FAE12, 1512
Reece, R.K. TAP11, TAP13, 378, 383
Reed, L. TPC16, 2637
Rees, D. WPA08, TAQ02, TAQ31, 923, 1521, 1596
Reginato, L. RPC16, RPC18, WPA01, TAE01, FAP17, WAQ04, 737, 743, 902, 1178, 1369, 1852
Rehak, M. TPE04, 1293
Reid, J. TAQ11, 1544
Reilly, J. FAE13, WPQ02, 1515, 1720
Reilly, R. WAA05, WAR01, 1236, 1900
Reiser, M. TAE04, TAQ17, TAQ18, TAQ19, TPQ11, 1193, 1561, 1563, 1566, 2974
Reiser, Martin RPR23, TAA17, MPC04, 1170, 2117, 2324
Renieri, A. TPG11, 186
Renken, D. TPP11, 1639
Renner, T. WXE06, 2441
Repnaw, R. RPR06, 1131
Repond, J. RAA29, 597
Repose, G. TAR17, 837
Reusch, M.F. RPR20, TPR08, 1164, 3257
Reuter, E. RAA04, TAA22, 530, 2129
Revol, J.L. TPG05, 167
Reyermier, C. RPE02, 1999
Rhoades, J. WAR19, 1945
Riabko, A. TAP03, WPP20, WPP21, RAP21, WAC12, RAG10, RAQ23, RAQ24, 357, 1705, 1708, 2934, 3094, 3182, 3337, 3340
Rice, D. FAE13, FAB12, 1515, 2820
Rich, D. RAQ23, 3337
Richard, Frank FAC07, 2850
Riche, A.J. MPC24, 2367
Richter, R. FAR21, 309
Rimmer, R. WPR07, WPR14, 1800, 1818
Rimmer, R.A. WPQ06, WPQ13, WPR08, 1729, 1747, 1803
Rindi, A. TPG11, 186
Ringwall, A.D. RPG10, 342
Rinolfi, L. RPC10, 719
Rintamaki, J. TPB14, 2557
Risselada, T. FAC04, 2844
Ritson, D. RAA26, 588
Ritson, D.M. RAA22, RAA27, 576, 591
Riunaud, J.-P. TAP14, 386
Rizawa, T. WPR16, 1824
Robin, D. FAA06, RPC02, RPQ13, FAB01, 207, 701, 2693, 2789
Rode, Claus H. RPE01, 1994
Rodger, E. FAP11, 1352
Rodier, J. WPB22, 998
Rogers, J. FAE13, TPA04, 1515, 3206
Rogers, J.T. RAE14, WAB15, 2426, 3052
Rojak, M. MPB09, 2291
Rokni, S. TAG01, 2742
Romanov, G. MPC16, 2345
Romasko, V.P. WPA15, 938
Rookhuizen, H. Boer RPG06, 330
Root, L. RPG12, WAQ07, 348, 1858
Ropert, A. TPG05, 167
Roques, A. TAE09, 1210
Rose, J. WPP07, WPQ19, RPQ17, WAC24, 1669, 1765, 2705, 3131
Rosei, R. TPG11, 186
Rosenblum, B. WAA19, 1269
Rosenzweig, J. FAA23, WPB05, WPB08, RPA21, RPA22, TAA28, 240, 957, 967, 1102, 1105, 2135
Rosenzweig, J.B. WAG06, MPE13, 631, 896
Roser, T. TAP11, TAP12, TAP13, RPQ07, RAG02, 378, 381, 383, 2678, 3154
Rosing, M. WPB11, 976
Ross, M. RPB01, RPB04, RPC01, WPR15, WAQ15, TAA28, 656, 665, 698, 1821, 1876, 2135
Ross, M.C. WAG11, WAC17, 646, 3109
Ross, W. RAE12, RPQ01, 2420, 2660
Roßbach, J. FAC19, 2874
Rosbach, J. TPG12, WAG02, TAA01, TAA06, RAR30, 189, 611, 2078, 2090, 3424
Rossi, C. FAA13, FAR21, 222, 309
Rossmannith, R. FAR07, 275
Rossmannith, Robert RAE07, 2405
Roster, William WAB06, 3028
Rotela, E. MPQ07, 2464
Rotela, R. TAR08, 816
Rothman, J.L. MPQ01, 2450
Roudier, P. WPB22, 998
Roy, G. WAP12, WAP13, RAA11, RAA17, TAG01, 464, 467, 548, 560, 2742
Roybal, W. TAQ02, 1521

Rubbia, C. FAG09, TPG11, 95, 186
Rubin, D. FAE13, RAQ04, 1515, 3294
Rubin, David L. WPG02, 481
Rudenko, V. TAC16, 152
Ruemmler, J. WAR14, 1933
Rufer, C. FAC04, 2844
Ruggiero, A.G. RAG14, RAQ20, 3194, 3329
Ruggiero, F. RPE02, WAE12, 1999, 2187
Ruiz, C. RAG06, RAG07, 3170, 3173
Ruland, Robert E. RPE04, 2009
Rusnak, Brian TPP10, 1636
Russell, A. MPB06, 2285
Russell, A.D. FAP06, FAP07, WAR02, MPB05, 1337, 1340, 1903, 2282
Russell, S.J. TPB22, 2580
Russell, Steven WPB15, 985
Russell, T. RPA11, RPE09, 1073, 2020
Russell, Thomas J. TAQ16, 1559
Rusthoi, D.P. RPR22, TPC06, 1167, 2607
Ruth, R. RPC01, RPA04, 698, 1058
Ruth, R.D. WAG13, TPQ17, 653, 2989
Ruth, Ronald D. WAG03, TAQ26, TAQ27, WAC05, RAQ18, 616, 1581, 1584, 3076, 3326
Ruth, Thomas J. WPE03, 67
Ryan, W.A. MPQ04, 2455
Rybarcyk, L.J. RAG11, 3185
Ryne, Robert D. MPB16, RAG01, 2306, 3149
Ryu, C.M. TAQ14, 1553
Saab, A.H. RPP01, 1961
Saadatmand, K. FAG05, 83
Saba, J. WPQ06, 1729
Saban, R. WAE01, 2147
Sabbi, G.L. RAA20, FAC03, 570, 2841
Sabia, E. TPG11, 186
Sachtschale, R. RPA17, TAQ07, MPA11, 1090, 1536, 2217
Sachtschale, R.J. WAA10, 1248
Sachtshale, R. FAA08, 213
Sackett, J. FAE07, 1497
Saeki, K. FAA30, 257
Saewert, G.W. MPB15, 2303
Sáez, P. MPE10, WPC21, 887, 1043
Safa, H. TPP09, 1632
Safranek, J. FAR02, RPQ19, FAB11, 266, 2711, 2817
Sagan, D. FAE13, TPA04, RAR15, 1515, 3206, 3382
Sagan, David RAP04, 2889
Sah, R. FAG05, 83
Saile, V. TAA32, 2141
Saito, K. TPP07, 1629
Sakae, T. MPE03, 864
Sakai, H. WPQ15, 1753
Sakai, I. WAR05, 1912
Sakaki, H. WPC22, MPA07, 1046, 2208
Sakanaka, S. WPQ16, WPR02, WPR03, RAQ06, 1756, 1788, 1791, 3300
Salah, W. TPR04, 3245
Saltmarsh, C. MPR20, 2279
Sampayan, S. MPE14, WPC16, WAA19, TAA20, 899, 1027, 1269, 2123
Sampson, W. TPE04, FAQ03, FAQ04, 1293, 1393, 1396
Sandberg, J.N. WAR11, RPP02, 1924, 1964
Sander, O.R. RPR19, RPR22, TPC06, 1161, 1167, 2607
Sanders, D.A. RAB20, 790
Sandler, P.H. RAB20, 790
Sandoval, D.P. TPC06, 2607
Sangster, C. TAR17, 837
Sangster, T.C. TAR14, 828
Sannibale, F. RPA26, 1116
Sapozhnikov, L. RAE12, RPQ01, RPQ05, 2420, 2660, 2672
Sapp, W. RPG05, 327
Sarantsev, V.P. TAQ34, 1605
Saraph, G. TAQ19, 1566
Sarau, B. FAA02, 195
Sarstedt, M. TPB07, 2542
Sasaki, S. FAQ21, RPQ15, 1438, 2699
Sasaki, Y. FAP13, 1358
Sass, R. RPB03, RAE03, 662, 2389
Sathe, S. MPR20, 2279
Sato, H. WAR04, WAR05, 1909, 1912
Sato, I. TAQ08, TAQ25, TAA04, 1539, 1578, 2087
Satogata, T. MPR20, TPB21, RAQ22, 2279, 2577, 3334
Satoh, K. WPR02, WAC07, WAC08, 1788, 3082, 3085
Satoh, Kotaro MPQ14, 2482
Satti, J.A. FAP08, 1343
Saulter, Q. WAQ14, 1873
Saury, J.L. WPB22, 998
Sawamura, M. TPG02, 159
Scandale, W. WAP14, FAC04, FAC06, 470, 2844, 2847
Scanlan, R.M. FAQ07, 1402
Schachinger, L. MPR04, RPQ13, 2247, 2693
Schachinger, L.C. TAB06, 119
Schächter, L. WPC19, TAE12, TAQ01, 1036, 1219, 1518
Schaffner, S. MPR13, 2265
Schafstall, P.J. WPA08, 923
Schank, C.V. TPG07, 174
Schaper, J. TPG08, FAR06, 177, 272
Scharlemann, E.T. FAA12, FAA17, 219, 231
Scheidt, K. TPG05, RPQ15, 167, 2699
Schempp, A. WPA03, WPA04, WPA05, RPR06, 908, 911, 914, 1131
Schiffer, John P. RAG04, 3164
Schindl, K. MPG09, 423
Schirm, K.M. FAE11, 1509
Schirmer, D. FAQ12, WAQ17, 1411, 1879
Schlösser, K. FAR06, 272
Schlueter, R. FAQ23, FAQ24, FAQ25, 1441, 1444, 1447
Schlüter, R. FAA17, 231
Schmenk, E.G. TAA32, 2141
Schmickler, H. WAP12, WAP13, RAA10, RAA11, RAA13, 464, 467, 545, 548, 554
Schmidt, C. FAG06, 86
Schmidt, C.W. WPA06, 917
Schmidt, F. TAG07, 2768
Schmidt, R. WPG09, RAA19, 514, 567
Schmieder, R. WPC09, 1013
Schmitz, M. WPA12, 929
Schmor, P. WAQ07, 1858
Schmor, P.W. RPG12, MPE01, MPE03, 348, 853, 864
Schnase, A. WPQ26, TPB20, 1781, 2574
Schneider, G.C. MPG09, 423
Schneider, H.R. RPG12, RPR02, RPR03, 348, 1122,

1125
Schneider, J.D. MPE04,
 WPA08, 867, 923
Schnell, W. RPC09, 716
Schoenlein, R. TPG07, 174
Schoessow, P. WAG06,
 WPB11, 631, 976
Scholl, E.H. TPB21, 2577
Scholz, T. RPE02, 1999
Schönauer, H. MPG09, WAQ25,
 423, 1894
Schönfeld, Frank WPP22,
 1711
Schreiber, S. RPC10, 719
Schreuder, H.W. RPG02, 317
Schulte, Elmar TPC11, 2622
Schultheis, R. MPC15, 2342
Schultz, D. WPC21, WAQ15,
 1043, 1876
Schulz, G. FAR06, 272
Schulze, M.E. FAG05, 83
Schumburg, N. RPP02, 1964
Schuppler, S. FAR06, 272
Schwalm, D. RPR06, 1131
Schwandt, P. RAP22, 2937
Schwarz, H. RAA04, WPQ06,
 WPR07, WPR08, RPQ05, 530,
 1729, 1800, 1803, 2672
Schweickert, H. FAR06, 272
Scott, B. RPC02, TPQ16, 701,
 2986
Sears, J. FAE13, WPQ02,
 1515, 1720
Sebek, J. MPQ22, RPQ22,
 2506, 2717
Sedlyarov, I. WPP10, WPP11,
 1678, 1681
Seeman, J. RAA27, RPE14,
 MPP12, MPP20, MPC01,
 MPC02, 591, 2032, 2064,
 2075, 2317, 2319
Seeman, J.T. WPG10, RAA04,
 TAA22, RAQ03, 517, 530,
 2129, 3291
Seeman, John T. WPG03,
 WAB06, 486, 3028
Segreto, A. TPG11, 186
Seguin, S. RAG06, 3170
Seidel, I. FAR06, 272
Seidl, P. TPA10, 3220
Seidl, Peter RAG03, 3159
Selesnev, V.S. WAR20, 1948
Seleznev, D. TAC05, 140
Sellyey, W. MPQ10, TPQ19,
 2473, 2992
Sen, T. TAG09, 2774
Senichev, Yu.V. WPP18, 1699

Sennyu, K. TPP03, 1620
Senyukov, V. TAB13, TAQ23,
 TAQ24, 125, 1572, 1575
Serafini, L. MPE13, WPB10,
 WAC13, RAQ05, 896, 973,
 3097, 3297
Sereno, N. RPA14, 1082
Sereno, N.S. RPA10, RPA11,
 1070, 1073
Serio, M. RAE12, RPQ01,
 2420, 2660
Sermeus, L. MPG09, 423
Serov, V.L. RPR24, RPR25,
 1173, 1175
Sertore, D. WPC23, 1049
Servranckx, R.V. FAB14,
 2823
Sessler, A. FAA06, RPC16,
 RPC17, TAA28, 207, 737, 740,
 2135
Sessler, Andrew RAP25,
 2946
Sessler, Andrew M. FPD02,
 30
Settles, R. TAG01, 2742
Severgin, Y. FAR06, 272
Severgin, Yu. MPC21, RAQ14,
 2359, 3315
Sgobba, S. RPE02, 1999
Shalnov, A. TAB13, RPR10,
 RPR15, TAQ23, TAQ24, 125,
 1143, 1155, 1572, 1575
Shapiro, Alan WPB15, TPP10,
 985, 1636
Sharma, S. FAR19, TAR08,
 303, 816
Sharonov, S.A. FAP06,
 FAP07, 1337, 1340
Sharp, W. TAR17, 837
Sharp, W.M. TAR13, TAR14,
 TPR09, 825, 828, 3260
Shatilov, D.N. RAP05, 2892
Shatunov, Yu. RAA31, RAR31,
 600, 3427
Shatunov, Yu.M. RAQ21, 3331
Shchedrin, I.S. RPA25, 1114
Shchepunov, V.A. FAC12,
 2863
Shcherbakov, A. FAR16,
 FAR17, RAA08, 296, 299, 542
Shea, D. MPR20, 2279
Shea, T.J. MPQ04, MPQ05,
 TPB12, WAC24, 2455, 2458,
 2551, 3131
Sheehan, J. MPE11, MPA15,
 890, 2223
Sheffield, Richard L. MPE09,

882
Shen, Weijun FAQ31, 1462
Sheng, I.C. TAR08, 816
Shenzong, Hu FAA26, 246
Shepard, K.W. RPR05, FAQ09,
 RAR21, 1128, 1408, 3400
Sheppard, J. RPC01, WAQ15,
 698, 1876
Sheppard, R. RPA26, 1116
Sherman, J. MPE04, 867
Sherman, J.D. WPA08, 923
Sherwood, Boyd WPB15, 985
Sheu, R.J. TPQ09, 2968
Sheynin, S. FAP12, 1355
Shibata, H. RAB13, 779
Shiltsev, V. TAA01, TAA21,
 RAR30, 2078, 2126, 3424
Shimer, D. RAA04, 530
Shimer, D.W. RPP01, 1961
Shinas, M.A. TPC06, 2607
Shinn, M. FAG11, FAA25,
 WPC24, 102, 243, 1052
Shintake, T. WAG12, RPC20,
 RPA20, FAE09, WPQ09, WPQ17,
 WPR05, WPR09, TAA28,
 WXE07, TPC08, TPC29, RPQ04,
 TAG01, 649, 749, 1099, 1503,
 1738, 1759, 1797, 1806,
 2135, 2444, 2613, 2655,
 2669, 2742
Shinto, K. WPC07, WAQ06,
 1007, 1855
Shirai, T. FAR08, RPA13,
 RPA18, WAQ01, 278, 1079,
 1093, 1843
Shirakata, M. WAR05, 1912
Shishido, T. TPP07, 1629
Shoae, H. WAE10, RAE03,
 RAE11, 2181, 2389, 2417
Shoji, Y. TAP12, WAR04,
 WAR05, 381, 1909, 1912
Shpak, A. FAR16, FAR17, 296,
 299
Shu, D. MPQ08, 2467
Shu, Q.S. TPP11, TPP14,
 1639, 1648
Shukeilo, I. FAR06, 272
Shumakov, A. RPA19, 1096
Shumakov, I.V. RPR07, 1134
Shurina, E. MPB09, 2291
Shurter, R.B. TPB22, 2580
Shvedov, D. WAA18, 1266
Shvedunov, V. RPA19, 1096
Shvedunov, V.I. FAA14,
 TAR05, FAP19, WPR17, RAQ01,
 RAR04, 225, 807, 1375, 1827,
 3285, 3361

Shvets, G. RAB08, 773
 Shvetsov, V.S. WAA20, TAQ34, 1272, 1605
 Sibley, C. RPG05, 327
 Siemann, R.H. WXE05, RAP10, RAP11, RAP12, WAB12, WAC17, TPA09, 2438, 2907, 2910, 2913, 3046, 3109, 3217
 Sigov, Yu.S. WAA02, WAA03, 1230, 1233
 Sikora, J. TPA04, 3206
 Sikora, J.P. RAE14, 2426
 Sikora, R.E. MPQ05, 2458
 Sim, J. FAP05, 1334
 Sim, J.W. FAP06, FAP07, MPB05, MPB06, 1337, 1340, 2282, 2285
 Simopoulos, C. WXE05, WAB05, WAC04, WAC17, 2438, 3025, 3073, 3109
 Simpson, J. WAG06, WPB11, WPB12, 631, 976, 979
 Simrock, S. RPQ29, RPQ30, 2732, 2735
 Simrock, S.N. MPR14, RAE11, 2268, 2417
 Simrock, Stefan MPB11, 2297
 Sinclair, C. FAG11, FAA25, WPA17, TPC07, TPC26, 102, 243, 942, 2610, 2652
 Sinclair, C.K. WPC17, 1030
 Singh, A. TAQ17, 1561
 Singh, O. FAQ17, MPA15, RPQ19, 1426, 2223, 2711
 Singh, Om V. RPQ27, 2729
 Singleterry Jr., R.C. TAC12, 149
 Sisson, D. TPG14, 192
 Skaritka, J. MPE11, 890
 Skarpaas, K. MPP10, 2057
 Skrinsky, A. MAD04, TAR11, 14, 819
 Skuratov, V. WPR19, 1833
 Slaton, T. WAG11, RPB01, RPB03, 646, 656, 662
 Slaton, Tim WAB08, 3034
 Sloan, T. RAQ23, RAQ24, 3337, 3340
 Sloth, K. TAE10, 1213
 Sluijk, T. TAQ12, MPQ17, 1547, 2491
 Smirnov, A. RAP24, 2943
 Smirnov, A.I. MPG10, 426
 Smirnov, A.V. RPR13, 1152
 Smith, D. FAA27, 248
 Smith, D.L. TAE06, 1201
 Smith, David L. TAE07, 1204
 Smith, G.A. RPQ07, 2678
 Smith, H. WPR15, TPC20, 1821, 2646
 Smith, I. TAE06, 1201
 Smith, J. MPA15, 2223
 Smith, J.D. MPR08, 2253
 Smith, John MPR07, 2250
 Smith, M. RPR22, TPC06, 1167, 2607
 Smith, P. WAQ15, 1876
 Smith, R. WAQ03, 1849
 Smith, S. MPQ15, MPQ25, 2485, 2512
 Smith, S.L. TPG09, RAE10, 180, 2414
 Smith, T.L. WPP16, 1693
 Smithe, D.N. WPC12, 1022
 Snyder, S.L. TAP10, 375
 Snyderstrup, L. MPP11, 2060
 Sobczynski, S. RPG05, 327
 Sobenin, N.P. TAR05, FAP19, WPR17, WPR18, 807, 1375, 1827, 1830
 Solnyshkov, D. WPC03, 1004
 Solomon, L. FAQ13, WXE04, RPQ19, 1414, 2435, 2711
 Soloveichik, Yu. MPB09, 2291
 Somersalo, E. FAE08, 1500
 Sommer, M. FAR14, 293
 Somov, L. TAC16, 152
 Song, J.J. RPA10, WPP16, TAA11, 1070, 1693, 2102
 Sotnikov, G.V. RAB15, 782
 Soukas, A. TAP11, WAR11, WAR13, RPP02, 378, 1924, 1930, 1964
 Specka, A. WAG07, 634
 Spence, David WPC11, 1019
 Spence, P. TAE06, 1201
 Spence, W. WAG11, RPC20, TAG01, WAC17, 646, 749, 2742, 3109
 Spence, W.L. RAA06, WAB09, 536, 3037
 Spencer, C. WAQ15, 1876
 Spencer, C.M. FAP16, 1366
 Spencer, J. RPC02, RPC08, TAA28, TPC16, WAC17, 701, 713, 2135, 2637, 3109
 Spencer, J.E. RPB06, 671
 Spentzouris, L.K. TAG04, 2757
 Spentzouris, Linda Klamp WAC02, 3070
 Sprehn, D. WAE13, 2190
 Spyropoulos, B. TAA15, 2111
 Srinivasan-Rao, T. MPE11, 890
 Stanek, M. RPA24, TPC20, 1111, 2646
 Stefan, P.M. WXE04, 2435
 Stege, R. WAG11, RPB04, WAC17, 646, 665, 3109
 Steimel, J. TPQ26, 3010
 Steimel Jr., James M. RAE02, 2384
 Stein, P. TPP11, 1639
 Steinbach, Ch. TAP14, 386
 Steinbock, L. FAR06, 272
 Steinhäuser, N. WPQ24, 1776
 Steininger, R. FAR06, 272
 Stelzer, J.E. WPC10, 1016
 Stenz, C. WAG07, 634
 Stepashkin, O. RAP24, 2943
 Stephenson, E. WPC08, 1010
 Stepin, D.L. WPB16, 988
 Stepp, J. MPQ08, 2467
 Stevens Jr., R. MPE04, 867
 Stevens Jr., R.R. WPC10, 1016
 Stevens Jr, Ralph R. WAQ02, 1846
 Stevens, R.R. WPA08, 923
 Stevens, T. MPP13, 2067
 Stevenson, G.R. WAQ24, 1891
 Stevenson, N.R. FAG07, 89
 Stierlin, U. TAG01, 2742
 Still, D. RPC21, 752
 Stillman, A. TPB15, 2560
 Stillman, Arnold MPA09, 2211
 Stirbet, M. TPP12, 1642
 Stockhorst, H. TPB20, 2574
 Stoeffl, W. WPG10, RAA03, MPP12, MPP20, TAA22, MPC01, MPC02, 517, 527, 2064, 2075, 2129, 2317, 2319
 Stoker, J. WPA01, 902
 Stoker, J.D. TAE01, 1178
 Stolyarsky, V.I. TPA15, 3232
 Stolzenburg, C. TPP11, 1639
 Stoner, R. TPG14, 192
 Stovall, J.E. RPR08, RPR09, MPC23, 1137, 1140, 2364
 Stover, G. RAE12, 2420
 Stover, G.D. WAA14, 1254
 Straub, D. FAA08, 213
 Striby, S. RAG06, 3170
 Strohmman, C.R. RAE14, 2426
 Strönisch, U. FAP02, 1325
 Strubin, P.M. RPE06, 2014
 Struckmeier, Jürgen FAC10, 2860
 Stuart, M. FAP17, FAP18,

1369, 1372
Studebaker, Jan WPB15, 985
Stupakov, G. MPC01, WAC15, 2317, 3102
Stupakov, G.V. RAQ02, RAQ09, RAQ10, 3288, 3303, 3306
Stupakov, Gennady V. RAR11, RAR12, 3373, 3376
Sturges, Ronald WPB15, 985
Su, J.J. TAA28, 2135
Suberlucq, G. RPC10, 719
Sudan, Ravi N. TAE07, 1204
Sugimoto, M. TPG02, 159
Suk, H. TPQ11, 2974
Sukhina, B. TPE09, 1316
Sukhina, B.N. TAC06, RPP08, 143, 1979
Suller, V.P. TPG09, 180
Sullivan, M. RAA25, 585
Sumbaev, A. TAC16, 152
Sun, D. WPP01, 1655
Sun, Y. FAP01, 1322
Surma, I.V. RAQ01, 3285
Sutter, S. RPA26, 1116
Suzuki, H. FAP13, 1358
Suzuki, S. WPC22, 1046
Suzuki, T. FAA30, TPP07, 257, 1629
Svandrlík, M. FAR06, FAR21, WPQ04, TAG05, 272, 309, 1723, 2762
Svinin, M. WPC03, TAA18, 1004, 2120
Svinjin, M.P. TAE13, 1222
Swan, T. RAA03, 527
Swenson, D.A. RPG10, 342
Swenson, D.R. WPC10, 1016
Swift, G. FAA08, RPA17, TAQ07, 213, 1090, 1536
Symon, K. TAP05, RAG05, 363, 3167
Sypfers, M. RAP21, RAQ23, RAQ24, 2934, 3337, 3340
Sypfers, M.J. TAP13, MPG12, WAB04, 383, 431, 3022
Syresin, E. RAP23, RAP24, 2940, 2943
Sytchev, V. FAQ06, 1399
Sytchevsky, S. MPC21, 2359
Tachibana, S. TPP03, 1620
Tadano, M. RPQ23, 2720
Tadokoro, M. TAB03, 113
Tajima, T. TPP03, 1620
Takagi, A. WPC07, WAQ06, WAR05, 1007, 1855, 1912
Takahashi, T. TPP03, 1620
Takaki, H. FAR09, 281
Takao, M. FAQ20, FAQ21, 1435, 1438
Takashima, T. RPQ06, 2675
Takashina, H. TPP03, 1620
Takatomi, T. WPQ15, 1753
Takeda, H. FAA16, RPR08, RPR09, MPC23, 228, 1137, 1140, 2364
Takeda, Harunori MPB16, 2306
Takeda, O. WAG12, 649
Takeda, Y. RPG13, 351
Taketani, A. RPQ15, 2699
Takeuchi, Y. FAE09, WPQ17, WPR05, WPR09, TAG01, 1503, 1759, 1797, 1806, 2742
Tallerico, P.J. TAR12, TAQ02, 822, 1521
Talman, R. RAP03, 2886
Tambini, U. RAE05, 2399
Tan, J. TPP09, 1632
Tanabe, J. FAP01, 1322
Tanaka, M. WAR13, 1930
Tang, Cha-Mei WPE05, 70
Tang, H. WAG11, RPC01, MPE10, WPC18, WPC21, 646, 698, 887, 1033, 1043
Tang, J. MPR13, 2265
Tang, Y.N. MPR08, 2253
Tani, N. FAP13, 1358
Taniuchi, T. WPC22, 1046
Taniyama, N. TPP03, 1620
Tantawi, S. WPQ05, 1726
Tantawi, S.G. TAQ28, 1587
Tantawi, Sami G. TAQ26, TAQ27, TAA27, 1581, 1584, 2132
Tarabrin, V. TAC16, 152
Tarakanov, M.V. MPG10, WAR20, WAR21, 426, 1948, 1949
Tarasenko, A. RAA08, 542
Tarnetsky, V. RPA12, TAQ21, 1076, 1569
Tarovik, M. RAQ14, 3315
Tatchyn, R. FAP20, FAQ23, 1378, 1441
Tatum, B.A. TAP07, WAQ26, MPA05, 366, 1897, 2202
Taufer, M. FAE11, 1509
Taurel, E. RPQ15, 2699
Taurigna-Quere, M. WPB22, 998
Tauschwitz, A. WAQ04, 1852
Tavares, Pedro F. RAQ29, 3352
Taylor, B. TAR03, 801
Taylor, T. RAA04, FAC04, 530, 2844
Tazzari, S. TPG11, 186
Tazzioli, F. TPG11, WAC13, 186, 3097
Tecimer, M. FAA29, 254
Tecker, F. RAA19, 567
Tejima, M. RAA33, MPQ31, TPC05, 603, 2521, 2604
Tejima, Masaki MPQ14, 2482
Telegin, Yu. FAR17, 299
Temkin, R.J. MPE12, 893
Temnykh, Alexander B. TAG08, 2771
Tenenbaum, P. RPC06, RPC20, TAA08, WXE07, TAG01, 707, 749, 2096, 2444, 2742
Teng, L. RAA29, 597
Teng, L.C. RAR26, 3415
Teng, Lee C. FAB10, 2814
Tenyakov, I. FAP24, 1387
Tepikian, S. TAA09, MPR20, FAB22, 2099, 2279, 2832
Terada, Y. FAP22, WPQ07, 1384, 1732
Terashima, A. FAQ02, 1390
Terekhov, V. MPP03, 2040
Terekhov, V.I. MPG10, WAR20, 426, 1948
Tereshkin, Y. FAP24, 1387
Terrell, R. MPR14, 2268
Terunuma, N. WAR03, TPC05, 1906, 2604
Tessier, J.-M. WAC13, 3097
Teytelman, D. RAE12, RPQ01, RPQ08, 2420, 2660, 2681
Thern, R. TPA06, 3212
Theuws, W. RPQ31, 2738
Theuws, W.H.C. WAQ19, RPP04, 1882, 1970
Thevenot, M. TAE09, 1210
Thieberger, P. TAP11, 378
Thielheim, K.O. RAR09, 3370
Thiery, Y. WPB22, 998
Thivent, M. MPG09, 423
Thomas, M. TPP06, WPQ20, 1626, 1768
Thomas, M.D. TAB17, 131
Thomas, P. WPB01, 945
Thomas, R. TPE04, TAA09, 1293, 2099
Thompson, K. TAP05, RPC01, RPC02, RPA04, FAP03, 363, 698, 701, 1058, 1328
Thompson, K.A. TPQ16, TPQ17, WAC18, 2986, 2989,

- 3112
Thompson, P. TPE04, FAQ03, FAQ04, FAQ16, 1293, 1393, 1396, 1423
Thorndahl, L. RPC09, 716
Thur, W. RPE12, 2026
Tian, F. WAG11, RPB01, TPC20, WAC17, 646, 656, 2646, 3109
Tiefenback, M. MPR15, 2271
Tiefenback, M.G. WAQ12, 1870
Tieger, D. RPG05, 327
Tigelis, J. RAQ01, 3285
Tighe, R. RPQ03, RPQ05, 2666, 2672
Tigner, M. FAE13, RAQ04, 1515, 3294
Timmer, Carl WPB15, 985
Timmermans, C.J. WAQ19, WAQ20, RPP04, RPQ31, 1882, 1885, 1970, 2738
Timossi, C. MPR03, 2244
Tinsley, D. WAR01, 1900
Titcomb, Ch. MPP02, 2037
Tiunov, A.V. RPR01, RAQ01, RAR04, 1119, 3285, 3361
Tiunov, M. MPB09, 2291
Tkachev, P.L. RAR04, 3361
Tkatchenko, A. FAR14, 293
Tobiyama, M. RPQ26, RAQ06, 2726, 3300
Todd, A.M.M. RPR20, 1164
Todesco, E. FAC06, 2847
Toge, N. RPB01, RAP02, 656, 2883
Tojyo, E. RPG13, 351
Tokarev, Yu. WAA17, 1263
Tokuda, N. RPG13, TAP04, 351, 360
Tokumoto, S. TAQ29, WPR02, WPR03, 1590, 1788, 1791
Tölle, R. TPB20, 2574
Tolstun, N.G. TAE13, 1222
Tomimasu, T. FAA30, TAQ35, 257, 1608
Tomlin, R. TPQ26, 3010
Tompkins, J.C. FAP06, FAP07, 1337, 1340
Tongu, E. FAA30, 257
Torre, A. TPG11, 186
Torun, Yagmur MXG03, 53
Tosa, M. TPP16, 1652
Tosello, F. WAP14, 470
Tosi, L. FAA13, FAR21, TAG05, 222, 309, 2762
Tosin, G. FAP14, FAP15, 1361, 1364
Touchi, Y. RPG09, 339
Toyama, T. WAR05, 1912
Trahern, C.G. WAP10, MPR20, 461, 2279
Trakhtenberg, E. FAQ17, MPP16, 1426, 2072
Tran, H.J. RAQ15, 3317
Tran, P. RAQ17, 3323
Tranquille, G. RAP24, 2943
Trantham, K. WPC21, 1043
Travier, C. WPB01, 945
Travish, G. FAA23, RPA21, RPA22, 240, 1102, 1105
Trbojevic, D. WAP10, TAA09, FAB22, WAC25, RAQ22, 461, 2099, 2832, 3134, 3334
Treas, P. TAB17, RPA26, 131, 1116
Tremblay, K. WXE01, 2429
Trenkler, T. FAC04, 2844
Trikalinos, C. RAQ01, 3285
Trimble, D. MPE14, WAA19, TAA20, 899, 1269, 2123
Trombly-Freytag, K. FAP06, FAP07, MPB05, MPB06, 1337, 1340, 2282, 2285
Tronc, D. TAB04, 116
Trotz, S.R. MPE12, 893
Trower, W.P. TAR05, FAP19, WPR17, 807, 1375, 1827
Trzeciak, W.S. FAR20, 306
Tsai, H.J. TPQ10, 2971
Tsang, K.L. FAA07, RAR05, 210, 3364
Tsarik, S.V. MPG10, WAR20, WAR21, 426, 1948, 1949
Tschalaer, C. RPG05, 327
Tseng, P.K. FAA04, 201
Tseng, P.-K. TPC15, 2634
Tsentalovich, E. RPG05, 327
Tsoupas, N. FAP11, 1352
Tsuchiya, K. FAQ02, 1390
Tubaev, M. RPR15, 1155
Tückmantel, J. TPP12, 1642
Tuozzolo, J.E. WAR10, 1921
Tupikov, V.S. RPP08, 1979
Tur, Yu. WPB17, 990
Tur, Yu.D. WPB16, TAE14, 988, 1225
Turchinets, W. RPG05, RAA31, 327, 600
Turner, J. WAG11, RPB01, WAC17, 646, 656, 3109
Turner, J.L. RPB04, 665
Turner, L.R. FAQ17, 1426
Tzeng, K.-C. RAB01, RAB02, 758, 761
Ueda, T. RAB13, 779
Uemura, T. FAQ08, 1405
Ueng, T.S. MPQ19, MPQ32, 2497, 2524
Uesaka, M. RAB13, 779
Ueyama, Y. FAP13, 1358
Uggerhoj, E. WAP14, 470
Uhm, Han S. TAQ04, TAQ05, 1527, 1530
Umezawa, H. TPP07, 1629
Urakawa, J. WPR02, WPR03, WAR03, TPC05, 1788, 1791, 1906, 2604
Ursic, R. TPC26, 2652
Ushkov, V. WPR13, 1815
Uskov, V.V. RAB15, 782
Uythoven, J. TPP12, 1642
v. Blanckenhagen, P. FAR06, 272
v. Es, J. MPQ17, 2491
v. Hartrott, M. WAQ17, 1879
v. Rienen, U. RPB16, 695
Vacca, J.H. RPA07, 1064
Valdez, M. MPR03, 2244
Valentinov, A. MPA04, 2199
Valeri, S. WPC23, 1049
Van Asselt, W. RPQ07, 2678
van Asselt, W.K. WAB04, RAQ22, 3022, 3334
van Bibber, K. MPP12, MPP20, 2064, 2075
v.d. Laan, J. MPQ17, 2491
van der Laan, J. RPG06, 330
van Greevenbroek, H.R.M. WAQ20, 1885
van Oers, W.T.H. MPE03, 864
van Oort, J.M. FAQ07, 1402
van Rooij, M. MPG09, MPP15, 423, 2069
Van Vaerenbergh, P. TPE10, 1319
van Zeijts, J. WAE10, 2181
van Zeijts, Johannes MPR02, MPC20, 2241, 2356
VanAsselt, W. TAP13, 383
Vanecek, D. RPC18, WPA01, TAE01, 743, 902, 1178
Varenne, F. RAP23, RAP24, 2940, 2943
Varfolomeev, A. FAA23, 240
Varisco, G. TAA07, 2093
Vasilevsky, A. MPP03, 2040
Vasiljev, A.A. RPR07, 1134
Vasserman, I. FAQ17, FAQ18, 1426, 1429
Vasserman, S. WAA17, 1263

Vassiliev, L. FAQ06, 1399
Vaziri, K. FAG06, 86
Vella, M.C. FAP18, 1372
Veluri, V.R. RPA07, 1064
Verdier, A. WPG09, RAA17, FAC03, 514, 560, 2841
Verdier, André FAC07, FAC08, 2850, 2853
Verhagen, H. RAA15, 557
Verkooyen, J. TAQ12, 1547
Vescovi, M. RPA26, 1116
Veselov, O. FAQ06, 1399
Veshcherevich, V. WPP10, WPP11, RAR19, 1678, 1681, 3394
Vetter, A.M. FAA27, FAA28, WPB20, 248, 251, 992
Vignola, G. WPG05, RPA26, 495, 1116
Villate, D. TAE09, TPC17, 1210, 2640
Vincent, J. RPG11, 345
Vinokurov, N.A. FAQ17, 1426
Virchenko, Yu.P. RAQ28, 3349
Virostek, S. RPB04, 665
Visintini, R. TPG11, FAR21, 186, 309
Vlieks, A.E. WAG13, RPA23, TAQ26, TAQ27, TAA27, 653, 1108, 1581, 1584, 2132
Vobly, P. MPB09, 2291
Vodopianov, F.A. TAR02, TAQ10, 799, 1542
Voisin, L. TAE09, 1210
Volfbeyn, P. TPG07, RPC15, RAB10, 174, 734, 776
Völker, F. MPG09, 423
von Hahn, R. RPR06, 1131
von Holtey, G. WPG09, 514
Vormann, H. WPA04, 911
Vorogushin, M.F. WPP04, 1663
Voronin, G. WPC03, 1004
Voronin, V.S. TPR13, 3269
Vos, L. RAR07, 3367
Voss, G.-A. TAG01, 2742
Voss, Gustav-Adolf FPD01, 27
Votaw, A. MPQ08, MPQ10, 2467, 2473
Votaw, A.J. RPQ16, 2702
Voykov, G. TPC03, 2598
Vuagnin, G. WAP14, 470
Wachter, J. MPQ22, 2506
Wadlinger, E.A. RPR19, 1161
Wagner, S.R. TAG01, 2742
Wake, M. FAQ32, TPP07, 1465, 1629
Wakisaka, K. FAA30, 257
Wakita, K. FAA30, TAQ35, 257, 1608
Walbridge, D.G.C. FAP06, FAP07, MPB05, MPB06, 1337, 1340, 2282, 2285
Waldschmidt, G. WPB06, 961
Walker, N. RPB01, 656
Walker, R.P. TPG11, FAA13, FAR21, FAQ19, TAG05, 186, 222, 309, 1432, 2762
Wallén, E. RPE02, 1999
Walling, L.S. RPG10, 342
Walters, G.K. WPC21, 1043
Walther, R. WPA12, 929
Walton, J. WAR01, 1900
Walz, D. RPC08, WXE07, TAG01, 713, 2444, 2742
Wan, Weishi MPC09, 2336
Wanderer, P. WAP10, TPE04, FAP11, FAQ02, FAQ04, FAQ16, TAA09, 461, 1293, 1352, 1390, 1396, 1423, 2099
Wanderer, P.J. FAQ03, 1393
Wang, B. MPA01, 2193
Wang, C. MPA01, 2193
Wang, C.J. MPR10, TPB29, 2256, 2592
Wang, C.-P. TPC15, 2634
Wang, Ch. FAA04, RAA24, FAQ26, TPQ08, 201, 582, 1450, 2965
Wang, Chun-xi MPC31, 2376
Wang, Chunxi FAC02, 2838
Wang, D. WAA16, WXE01, TPB04, TPC04, WAC27, 1260, 2429, 2536, 2601, 3140
Wang, D.X. MXG02, 48
Wang, J. RPA04, WAA08, WAA09, 1058, 1242, 1245
Wang, J.G. TAE04, TPQ11, 1193, 2974
Wang, J.M. TPP06, 1626
Wang, J.P. TAA14, 2108
Wang, J.Q. WAB20, 3064
Wang, J.W. WAG13, RPA23, 653, 1108
Wang, L. TAP03, WPP20, WPP21, RAP21, WAC12, WAC27, RAG10, RAQ23, RAQ24, 357, 1705, 1708, 2934, 3094, 3140, 3182, 3337, 3340
Wang, M.H. RAA24, TAR06, TPQ08, TPQ09, TPQ10, 582, 810, 2965, 2968, 2971
Wang, P. FAA08, RPA17, 213, 1090
Wang, Ping WPA13, WPR22, 932, 1841
Wang, Shu-Hong WPG07, 506
Wang, T. WAC29, 3146
Wang, T.S. RAR23, 3406
Wang, Tai-Sen F. WAC28, 3143
Wang, X. MPQ07, MPQ08, MPQ10, 2464, 2467, 2473
Wang, X.J. MPE11, WPB13, RAE09, WXE03, TPB01, 890, 982, 2411, 2432, 2530
Wang, X.-J. TPG14, 192
Wang, X.Q. RPE10, 2023
Wang, Y. TAB17, MPA01, RAP21, 131, 2193, 2934
Wang, Y.L. TAQ08, 1539
Wangler, T.P. RAG11, 3185
Wangler, Thomas P. WAQ02, RAG01, 1846, 3149
Wanzenberg, R. RPB14, 689
Ward, C. TAR17, 837
Warkentien, R. MPA18, 2232
Warner, A. RAQ22, 3334
Warner, D. TAP05, 363
Warnock, R.L. FAB06, 2804
Warnock, Robert L. TPQ07, 2962
Warren, David WPB15, 985
Warwick, A. FAA03, 198
Watson III, William A. WAE05, 2167
Watson, W. WAE10, MPR13, MPR19, 2181, 2265, 2276
Watson, W.A. RAE11, 2417
Webber, Robert C. RPQ10, 2687
Weber, M. TPB07, 2542
Webers, G.A. WAQ19, WAQ20, RPQ31, 1882, 1885, 2738
Wedekind, M. WPC08, 1010
Wehrle, U. FAE10, 1506
Wei, F. FAR21, 309
Wei, J. WAP10, FAB22, WAC24, RAQ22, 461, 2832, 3131, 3334
Wei, Jie RAP25, 2946
Weidemann, A.W. TAA28, 2135
Weihreter, E. TPE09, WAQ17, 1316, 1879
Weiland, T. RPB16, TAQ06, WAE13, MPC01, MPQ15, WAB18, 695, 1533, 2190, 2317, 2485, 3061

Weinberg, J. WAQ15, WAC17, 1876, 3109
Weingarten, W. FAE11, 1509
Weinstein, A. TAR18, 840
Weise, H. RPB08, 677
Weisend, J.G. MPP01, 2034
Weiss, R. RPR22, 1167
Weisse, E. WAP14, WAQ24, 470, 1891
Weisz, S. WAP14, FAC04, 470, 2844
Welch, J. FAE13, 1515
Welch, James J. TAA29, TAG08, FAC14, RAG13, 2138, 2771, 2866, 3191
Welton, R.F. MPE05, WPC12, 871, 1022
Welz, J. MPE03, 864
Wendt, M. TPC09, 2616
Weng, W.T. FAA07, RAA23, RAA24, RAG08, RAR05, 210, 579, 582, 3176, 3364
Wenjun, Zhu FAA26, 246
Wenninger, J. WAP12, RAA11, RAA19, RAA20, 464, 548, 567, 570
Werkema, Steven J. RAR20, 3397
Wermelskirchen, C. RPQ22, 2717
Wesolowski, W. RPA11, 1073
West, C. MPR13, 2265
Westenskow, G. RPC16, RPC17, MPE14, WPC16, TAA28, 737, 740, 899, 1027, 2135
Westenskow, G.A. TAQ03, 1524
Westervelt, R.T. WAE08, 2175
Wetherholt, D. MPR13, 2265
Wharton, K. RAB04, 767
White, K. MPA12, MPR13, 2220, 2265
White, M. TAP05, RPA07, RPA08, RPA10, RPA11, RPA14, TPC01, 363, 1064, 1067, 1070, 1073, 1082, 2595
Whitham, K. TAB17, RPA26, 131, 1116
Whittum, D. RAB13, TAA28, WAC17, 779, 2135, 3109
Widgren, J. FAA08, 213
Wiemerslage, G. MPP16, 2072
Wienands, H.-U. RAA27, 591
Wienands, U. RAA04, TAA22, MPC01, 530, 2129, 2317
Wight, G.W. MPE03, 864
Wildman, D. WPP08, WPP09, WPP23, RAQ13, 1672, 1675, 1714, 3312
Wildner, E. MPG09, WAE09, 423, 2178
Wilkinson, C. WAC29, 3146
Wilkinson, C.A. TAR12, 822
Willeke, F. MPG07, TAG02, TAG09, 420, 2747, 2774
Willen, E. TPE04, FAQ03, FAQ04, FAQ15, FAQ16, 1293, 1393, 1396, 1420, 1423
Williams, C.E. WAQ26, 1897
Williams, G. FAR06, 272
Williams, M.D. TPB07, 2542
Williams, Mel WPB15, 985
Williams, R. TAA28, 2135
Williams, S. TAG01, 2742
Wilson, I. WAG13, RPC09, RPC10, RPC15, 653, 716, 719, 734
Wilson, K. FAR06, 272
Wilson, P. RPC01, RPC02, RPC06, 698, 701, 707
Wilson, P.B. FAE04, TAA33, TPQ16, 1483, 2144, 2986
Winick, H. WPB13, WXE03, 982, 2432
Winje, R.A. FAG05, 83
Winkler, G. MPP02, 2037
Winn, David MXG03, 53
Wise, M. MPR13, 2265
Wiseman, M. FAG11, FAA25, WPA17, 102, 243, 942
Witherspoon, S. WAE10, MPR13, 2181, 2265
Witkover, R. RPQ07, 2678
Witkover, R.L. TPB26, 2589
Witte, K. MPE10, 887
Wolf, Z. FAP16, FAQ08, 1366, 1405
Wolff, D. WAE07, 2172
Wolff, S. RPB09, 680
Wollnik, H. WAQ26, 1897
Wong, J. TAR18, 840
Wong, V. RPQ07, 2678
Woo, B. MPC18, 2351
Wood, P. TPC04, 2601
Wood, R.L. RPR08, RPR09, 1137, 1140
Woodle, M. WPB13, WXE03, 982, 2432
Woodley, M. WAG11, RPB01, RPB03, RPB04, RAE03, 646, 656, 662, 665, 2389
Woods, M. RPC08, 713
Woody, K.A. TPC13, 2628
Wright, D. MPP09, MPP12, MPP20, MPC01, WAC17, 2054, 2064, 2075, 2317, 3109
Wright, E. FAE07, 1497
Wright, E.L. TAQ28, 1587
Wrulich, A. TPG11, FAA13, FAR21, TAG05, 186, 222, 309, 2762
Wu, X. RPG11, 345
Wu, Y. FAA08, RPG06, RAA01, RAA21, RAB22, RPA17, MPA10, MPA11, MPQ06, FAC20, 213, 330, 524, 573, 796, 1090, 2214, 2217, 2461, 2877
Wu, Y.Y. TPB03, 2533
Wu, Ying WPR22, 1841
Wuensch, W. WAG13, RPC09, RPC10, RPC15, 653, 716, 719, 734
Wurtele, J. TAA28, 2135
Wurtele, J.S. RAB08, MPE12, WPB03, WPB04, 773, 893, 951, 954
Wüstefeld, Godehard FAC16, 2868
Wyss, C. TPP12, 1642
Xi, Boling RPP04, 1970
Xiao, A. WAC27, 3140
Xie, Jialin TPG04, 162
Xie, Ming TPG10, 183
Xu, G. RAA21, TPQ03, WAC27, 573, 2955, 3140
Xu, J. MPA01, 2193
Xu, S. MPP16, 2072
Yakimenko, V. TAR11, RAR31, 819, 3427
Yakovlev, V. RPA12, TAQ21, 1076, 1569
Yakovlev, V.P. MPC17, 2348
Yamada, R. MPC07, 2330
Yamada, S. MAD03, 9
Yamaguchi, H. MPQ18, 2494
Yamaguchi, S. TAQ25, 1578
Yamamoto, N. RPC20, MPA06, WXE07, TAG01, 749, 2205, 2444, 2742
Yamane, Isao TPR16, 3275
Yamazaki, Y. FAE09, WPQ08, WPQ09, WPQ17, WPR05, WPR09, 1503, 1735, 1738, 1759, 1797, 1806
Yan, Y. RAA22, 576
Yan, Y.T. RAA26, RAA27, TAG06, 588, 591, 2765
Yanagida, K. WPC22, 1046
Yang, B. MPQ09, MPQ10,

MPQ11, TPC03, 2470, 2473,
2476, 2598
Yang, J. RAQ17, 3323
Yang, Ming-Jen MPQ20, 2500
Yang, X.-F. TPC16, 2637
Yano, Y. WPC01, 1001
Yaramishev, S.G. TPA05,
3209
Yarba, V.A. FAP06, FAP07,
1337, 1340
Yarygin, N. FAQ06, 1399
Yarygin, S.N. WPR18, 1830
Yasumoto, M. FAA30, 257
Yavor, S.Ya. TAP16, 389
Yazynin, I. WAR22, 1952
Yee, D. FAP01, 1322
Yeremian, A.D. WPC18, 1033
Yi, He FAA26, 246
Yifang, Wang TAR22, 850
Yin, Yan TPC11, 2622
Ylä-Oljala, P. FAE08, 1500
Yokomizo, H. WPC22, FAP13,
MPA07, 1046, 1358, 2208
Yokoya, K. RPA20, WAB20,
1099, 3064
Yokoyama, M. RPQ23, 2720
Yokoyama, S. FAQ08, 1405
Yonehara, H. FAP13, 1358
Yoon, M. TPG06, WPR11, 171,
1812
York, R.C. RPG11, 345
York, R.L. WPC10, 1016
Yoshida, Y. RAB13, 779
Yoshihara, K. TPP16, 1652
Yoshii, J. TPB18, 2569
Yoshii, M. TAP04, WPC07,
WAR05, 360, 1007, 1912
Yoshikawa, H. WPC22,
MPA07, 1046, 2208
Yoshimoto, S. RPQ06, 2675
Young, E. RAP07, 2898
Young, L.M. RPR08, RPR09,
1137, 1140
Young, Lloyd M. MPB16, 2306
Yourd, R. FAP01, 1322
Yourd, R.B. RAA05, 533
Yu, C.I. MPQ26, RAR05, 2515,
3364
Yu, C.-I. TPC15, 2634
Yu, I.H. WPR11, 1812
Yu, S. RPC16, RPC17, RPC18,
WPA01, TAE01, 737, 740, 743,
902, 1178
Yu, S.S. RPC19, TAR14,
WPA09, WAQ04, 746, 828,
926, 1852
Yu, Y. MPA01, 2193

Yuan, D. WAQ07, 1858
Yuan, V. RPR19, 1161
Yuan, V.W. RPR22, TPC06,
1167, 2607
Yudin, I.P. MPB19, FAC09,
2314, 2856
Yugami, N. RAB13, 779
Yuldashev, O.I. MPB19, 2314
Yuldasheva, M.B. MPB19,
2314
Yule, T.J. FAG14, 110
Yunn, B. WPA17, 942
Yunn, Byung C. MPB11,
RAQ11, 2297, 3309
Yupinov, Y. MPA04, 2199
Yupinov, Yu. WPR13, 1815
Yurkov, M.V. WAA20, TAQ34,
1272, 1605
Zako, A. FAA30, 257
Zakutin, V.V. WPA15, TAE14,
938, 1225
Zangrando, D. TPG11, FAQ19,
186, 1432
Zante, A. TAB17, RPA26, 131,
1116
Zaugg, T. WPA08, 923
Zavadtsev, A.A. WPR18, 1830
Zazula, J.M. WAQ24, 1891
Zegenhagen, J. FAR06, 272
Zelenski, A.N. MPE03, 864
Zelinsky, A. FAR17, RAA08,
299, 542
Zelinsky, A.Yu. RAA07, 539
Zeller, A.F. RPG11, 345
Zenkevich, P. RAP23, 2940
Zenkevich, P.R. TPA05, 3209
Zeno, K. TAP12, 381
Zhan, M. MPA01, 2193
Zhang, C. WPG09, TPQ03, 514,
2955
Zhang, R. RAB03, RPA21,
RPA22, 764, 1102, 1105
Zhang, S.Y. TAP13, RAG08,
TPA08, 383, 3176, 3214
Zhang, W. WAR10, WAC25,
1921, 3134
Zhang, Zhenhai RAQ25, 3343
Zhao, Aihua FAQ29, FAQ30,
1456, 1459
Zhao, J. MPA01, 2193
Zhao, S. TAA03, 2084
Zhidkov, E.P. MPB19, 2314
Zhiglo, V.F. WPA15, 938
Zholents, A. RAA03, RAA22,
FAB01, 527, 576, 2789
Zholents, A.A. RAP05, 2892
Zhou, J. WPB06, TAA11, 961,

2102
Zhou, Ping TPB05, 2539
Zimmermann, F. WPG10,
WAG11, RPB01, RPC03, RPC06,
RPC07, TPQ16, TPQ17, WAB07,
WAC15, WAC17, 517, 646,
656, 704, 707, 710, 2986,
2989, 3031, 3102, 3109
Ziomek, C. TAQ31, RPQ02,
RPQ05, 1596, 2663, 2672
Zisman, M. MPC01, 2317
Zisman, M.S. RAA03, RAA05,
527, 533
Zolfaghari, A. RPG05, WAA16,
TPB04, 327, 1260, 2536
Zolotorev, M. WPG10, RPE14,
MPC01, MPC08, 517, 2032,
2317, 2333
Zolotorev, Max TAQ27, 1584
Zotter, B. RAA20, RPC09,
570, 716
Zubovskiy, V. TAC05, 140
Zwart, T. RPG05, RAA31, 327,
600
Zyngier, H. TPG01, FAR14,
155, 293

